EuroSun 2016

PROCEEDINGS

11th ISES EuroSun Conference

Palma (Mallorca), Spain
from 11 to 14 October 2016

Edited by:
Dr. Víctor Martínez
Dr. José González

UIB Universitat de les Illes Balears
UIBCongres
ASOCIACIÓN ESPAÑOLA DE ENERGÍA SOLAR
AEDES
INTERNATIONAL SOLAR ENERGY SOCIETY
ISES International Solar Energy Society

Proceedings of the ISES EuroSun 2016 Conference

Edited by
Dr. Víctor Martínez
EuroSun 2016, Co-Chair of the Scientific Committee

and

Dr. José González
EuroSun 2016, Co-Chair of the Scientific Committee

International Solar Energy Society
Wiesentalstr 50
79115 Freiburg
Germany

Tel: + 49 761 45906 – 0
Fax: + 49 761 45906 – 99
Email: hq@ises.org
Web: http://www.ises.org

ISBN: 978-3-9814659-6-9

Produced by:
International Solar Energy Society

Notice
The International Solar Energy Society, University of the Balearic Islands, Asociación Española de Energía Solar (AEDES) nor any one of the supporters or sponsors of the EuroSun 2016 makes any warranty, express or implied, or accepts legal liability or responsibility for the accuracy, completeness or usefulness of any information, apparatus, product or process disclosed, or represents that its use would not infringe privately on rights of others. The contents of articles express the opinion of the authors and are not necessarily endorsed by the International Solar Energy Society, University of the Balearic Islands, AEDES or by any of the supporters or sponsors of the EuroSun 2016. The International Solar Energy Society, University of the Balearic Islands and AEDES do not necessarily condone the politics, political affiliation and opinions of the authors or their sponsors.

Organizers

UIB Universitat de les Illes Balears

UIBCongres

ASOCIACIÓN ESPAÑOLA DE ENERGÍA SOLAR

AEDES

INTERNATIONAL SOLAR ENERGY SOCIETY

ISES International Solar Energy Society

Collaborators

Ajuntament de Palma

Consell de Mallorca

Sponsors

ITW

Testing and Development of:

- Solar Collectors
  - Hot Water Stores
  - Solar Thermal Systems
  - Solar Cooling Systems
  - Combined Solar Thermal and Heat Pump Systems
  - Multifunctional Building Components
  - Advanced Thermal
- Energy Stores
  - Solar Active Houses
  - Seasonal District Heating Systems with Seasonal Heat Storage
- Other Services
  - Simulation and Monitoring of Solar District Heating Systems
  - Simulation Studies
  - Energy Concepts
  - Eco-Assessment
  - Elaboration of Long-Term Technology Strategies
  - Development and Production of Solar Test Facilities
  - Consulting, Training, Seminar, Conferences

Institute of Thermodynamics and Thermal Engineering (ITW) - University of Stuttgart
Pfaffenwaldring 6
70550 Stuttgart, Germany
Phone: +49 (0)711 685-63611
Email: haaf@itw.uni-stuttgart.de

www.itw.uni-stuttgart.de

TISUN

Space-saving design, simple installation, modern design and high efficiency make the TiSUN products to the ideal solution for sustainable energy saving. A tight distribution and service network ensures that TiSUN professionals are always close at hand. TiSUN will advise you which solar solution is best for your private house, company or project. Our specialists will endeavour to design and produce an energy optimisation solution which is right for you.
For more than 25 years TiSUN has been working to convince the world that using the inexhaustible source of solar energy is cost-effective. In addition to our quality and innovation, our customer service has made us one of the top European suppliers in the area of solar heating.

TiSUN GmbH
Stockach 100
6306 Söll • Austria
Phone: +43 (0) 5333 201-0
E-mail: office@tisun.com

www.tisun.com

MENERGA

We supply air conditioning systems individually designed for your require-ments. Our philosophy, “Creating a good indoor climate – through Minimal ENERGy Application“, is something we have succeeded in every single day, since the company was founded over 35 years ago. We are proud to be part of the international successful Systemair group since 2013. Our systems are first-class, intelligent works of engineering and handcraft. They remain reliable in operation for many, many years, significantly reducing operating costs. How is this possible? In the basic design stages we already integrate all the components for air conditioning, such as the ventilation, heating and refrigeration systems, and equip everything with an intelligent control and regulation system. Every system is fully tested before delivery within the framework of a test run. The compact units are always delivered “ready for connection“. At the building site, they are connected up and made operational in just a few work stages. With over 40,000 systems installed worldwide, we cover almost every area of application. We do not only sell the units, but also offer you our many years of experience. When looking for the best solution, we jointly analyse the specific conditions at the location together with you. For the optimal solution we ask a lot of questions. Might it also be possible to use an alternative source of energy in order to reduce the operating costs even further? In this manner, we and our partners have jointly implemented countless projects which have received many awards for being energy efficient. We are proud of this. But what we really like about this is the know- how from jointly developed solutions, which allows operators and investors to save hard earned money- day after day, month after month, and year after year. The investment costs are amortised within a short period. We will be happy to produce reference lists for the building types in which you are interested in. And in the event that you surprise us with a totally new project: We are convinced to find the right solution for you. With our eyes sharpened by countless special projects, e.g. the “ALMA” telescope facility in the Atacama Desert or the “Princess Elisabeth Station” at the South Pole, we will be happy to accept the challenge.

Menerga GmbH
Alexanderstraße 69
45472 Mülheim an der Ruhr – Germany
Phone: +49 208 9981-0
Email: info@menerga.com
www.menerga. com

HIPPOKRATES

Hippokrates GmbH
Gottlieb-Dunkel-Straße 47 / 48
12099 Berlin – Germany
Phone: +49 30 3030 7969

www.hippokrates-clima.com

VELA SOLARIS

The company Vela Solaris develops and distributes the simulation software Polysun. Polysun software offers valuable support with the design, analysis and calculation of installations in the field of renewable energies.
We offer the right solution for every need. Our offer contains:
Polysun Simulation Software - the sales and design tool
Polysun Online - the online version for a first approach to simulations
Individual company solutions
Most important facts and figures
1992: The first version of Polysun is released by the SPF Institut für Solartechnik
2007: Vela Solaris is founded as a spin-off company of SPF Institut für Solartechnik
Head office of Vela Solaris in Winterthur (Switzerland)
Vela Solaris employs about 10 people
Key attributes: Innovation - Because of the origins of our company, we work closely with universities and the industry. We are constantly developing Polysun software. That way, you are always up-to-date, and can advise your customers in a professional and reliable way.
Mission: We feel responsible for making our contribution to a cleaner future. Polysun software supports the transition of the global energy supply to renewable energies.
Corporate culture – Also in our daily work, we rely on sustainable energy, covering our energy demand exclusively with certified solar electricity. Brochures and business cards are printed without water, chemicals or VOC.

Vela Solaris AG
Stadthausstrasse 125
8400 Winterthur - Switzerland
Phone: +41 55 220 71 00
Email: info@velasolaris.com
http://www.velasolaris.com/

ISES International Solar Energy Society

Conference Proceedings

EuroSun 2016

Palma de Mallorca (Spain), 11 – 14 October 2016

Foreword to the EuroSun 2016 International Conference on Solar Energy for Buildings and Industry

Andreu Moià[1], Wolfgang Streicher[2], José González[3] and Víctor Martínez[3]

[1] Chair of the Organizing Committee

[2] Chair of the International Committee

[3] Chairs of the Scientific Committee

It is a pleasure for us to introduce the Proceedings of the ISES EuroSun 2016 conference. Since its first edition in 1996, the ISES European solar energy conferences gather the research community on solar energy in Europe and nowadays it has become an international must-attend event in this field. For the first time, Spain hosted the ISES EuroSun conference in its 11th edition, an event jointly organized by the University of the Balearic Islands (UIB), the Spanish Association on Solar Energy (AEDES) and the International Solar Energy Society (ISES). EuroSun 2016 has been a unique platform to discuss the latest developments with leading solar energy specialists as well as policy makers and industry representatives. Topic sessions, keynote speakers, plenary sessions and open discussion forums, as well as social events, have offered an exceptional opportunity to network, to meet old friends and to make new contacts.

Thermal demands on buildings and industrial processes account for one of the largest amounts of energy consumption worldwide. As the energy supply chain shifts to a more sustainable model, a number of issues arise, such as “What would be the future energy mix for those sectors?”, “Would in-situ energy production take a significant share of that mix?” or “How will the variability of the renewable sources be managed?”

In any case, solar energy, in any of its forms, is called to play a key role in the future supply of such demands. In a fast-evolving market, options that just ten years ago were regarded as non-feasible, such as the use of PV for thermal applications, the construction of net zero energy buildings, the operation of solar district heating networks or the generalized use of solar energy for industrial processes, are now regarded as promising options under different phases of development.

This context creates new opportunities (for example, the Concentrated Solar Power industry may now find new markets in process heat or the PV market goes thermal via heat pumps), but it also creates new challenges like the requirement to develop safe-and-cost effective storage solutions at different temperature ranges and to establish standards, testing procedures, and application guidelines that cover the novel as well as more consolidated technologies. This ever-changing panorama provides a continuous source of challenges for the scientists and engineers as well as to the academic

community involved in solar energy.

Several conclusions of the ISES EuroSun 2016 conference can be highlighted:

• A 100% Renewable Energy Society is possible and affordable by means of combination of energy efficiency measures and an intelligent mix of all renewable energy technologies

• Transition towards an energy system scenario using 100% renewable energy can be achieved within 20 to 30 years from a technical point of view, although important transformations have to be initiated now, especially regarding market and policy aspects.

EuroSun 2016 has accomplished all the initial expectations. 310 participants from 53 nations around the world attended the event. Attendees from Africa, Asia, Australia and North and South America joined their European colleagues making the EuroSun 2016 truly international.

357 extended abstracts were submitted to the 2016 EuroSun conference, resulting in 140 oral presentations, 150 poster presentations and 187 submitted and accepted full papers, which are now published in these proceedings. The proceedings of the ISES EuroSun 2016 conference, which collect those manuscripts carefully reviewed by the Scientific Committee, are published by ISES with a Digital Object Identifier for each paper.

Last but not least, we would like to say a special thank you to all members of the scientific and organizing committees for their valuable support, strong effort and commitment, which has made it possible to achieve this successful conference.

Scientific Program

01. Solar Architecture and Net Zero Energy Buildings

02. Solar Heat for Industrial Processes

03. Thermal Storage

04. Solar Thermal Systems: Domestic Hot Water, Space Heating and Cooling

05. Solar Assisted District Heating and Cooling and Large Scale Applications

06. Testing & Certification

07. Solar Thermal Collectors and Solar Loop Components

08. PV and PVT Systems for Buildings and Industry

09. Solar Resources and Energy Metereology

10. Solar Education

11. Renewable Energy Strategies and Policies

01. Solar Architecture and Net Zero Energy Buildings

Conference Proceedings

EuroSun 2016
Palma de Mallorca (Spain), 11 - 14 October 2016

Energy strategies to nZEB sports hall

Alessia Accili, Joana Ortiz[1] and Jaume Salom[1]

[1] Catalonia Institute for Energy research (IREC), Barcelona (Spain)

Abstract

The Energy Performance of Buildings Directive recasts that by 2020 all new buildings constructed within the EU after 2020 and public buildings after 2018 should reach nearly zero energy (nZEB) levels. The present work aims to test, through the dynamic simulation tool TRNSYS, different energy strategies to design nearly zero energy sports halls in Mediterranean climates. The study is complemented with short period measurements of thermal comfort parameters and air quality indicators in a selected sports hall. The nZEB concept is achieved implementing passive strategies in combination with renewable energy systems. The impact of the identified energy solutions on the indoor thermal comfort and environmental indoor quality is also evaluated.

Key words: nZEB; sports hall; energy efficiency; TRNSYS simulation; IEQ; thermal comfort

1. Introduction

As reported in the article 2 of the European Union Directive 2010/31, a "nearly zero energy building" (nZEB), due to its very high efficiency, is characterized by very low energy requirements, satisfied by significant extent trough renewable sources available on-site or nearby. More than half of the member states (MS) are managing sport facilities as a precise nZEB subcategory (D'Agostino 2015). The Catalan region of Spain alone accounts for 2417 public buildings identified as sport facilities, responsible for 14% of the total primary energy consumption of the public building stock (Radulov 2014). Specifically, a standard sports pavilion uses 238 kWh/m^2 of primary energy every year. More than half of the current energy consumption of Catalan sports halls are relate to lightning (56%), a relevant energy use is due to domestic hot water (DHW) (28%), while heating and ventilation demand accounts for 4% (other electric consumptions accounts for 12% of the total) (ICAEN 2012). Those figures suggest that the energy performance improvement of sport facilities has a key role in the fulfilment of the article 9 of the Energy Performance of Buildings Directive. It states that MS shall ensure that all new public buildings must be nZEBs by December 31, 2018. The energy demand profile of a sports hall is closely related to the performed sport activity, the timetable of the sports centre, the public attendance during the matches and the climate conditions (Arutso and Santangeli, 2008). Sport halls in the continental European zone require the double amount of energy than the Mediterranean ones (Trianti-Stourna et al. 1998). In the German sports halls of Dresden-Weixdorf, through the installation of renewable energy technologies, storage systems and high efficiency devices, passive house standards have been achieved and the energy use optimized (Felsmann et al. 2015). Similarly, the study conducted by Flourentzou et al. (2015) assesses natural ventilation as strategy for energy consumption and costs reduction in a Swiss gym designed as a typical passive building. However, few researches investigated the energy use and generation patterns in relation to the comfort level perceived by the users of sports facilities. Summer overheating in passive sports structure is a studied phenomenon. It is possible to find in literature evaluations of effective and low energy demanding methods for thermal discomfort mitigation, as direct evaporative cooling, shading strategies, night ventilation, and openings optimization (Kisilewicz and Dudzińska 2015) (Tsoka 2015). The approach proposed in this paper supports the design of a nearly zero energy sports hall in Mediterranean climate through the implementation of different energy strategies and the evaluation of the

doi:10.18086/eurosun.2016.01.17 Available at http://proceedings.ises.org

thermal comfort condition in the different scenarios, aiming to guarantee a comfortable environment to the building users.

2. Methodology

Firstly, the indoor air quality and thermal behaviour of an existing sports facility are evaluated trough a field measurements campaign. The collected data are used to perform a comfort analysis according to the adaptive comfort methodology and the procedures described in the ASHRAE 55 (ASHRAE 55, 2004) and UNE-EN 15251 (AENOR 2008) standards. Consequently, a typical Spanish sports hall is identified as base case study and nZEB strategies are introduced. When the base case sport hall 3D geometry is defined in Google Sketch Up, energy efficiency measures are tested using the dynamic simulation tool TRNSYS, in order to estimate their impact on thermal comfort, air quality and energy needs. The implementation of renewable energy systems, specifically the potential contribution of the installation of a photovoltaic system, is estimated trough the Google Sketch Up plug-in Skelion.

2.1 Measurements campaign

The data regarding occupation patterns and environmental indoor quality are collected through field measurements in an existing facility. The main goal is to evaluate the indoor environment quality (IEQ) and the thermal condition of the sports hall. The field measurement campaign is realized in the "Poliesportiu Pla Del Bon Aire" located in Terrassa (Barcelona) and currently not equipped with a ventilation system neither a heating system. The measurements are performed along two days during the second weekend of March 2016. The thermal parameters as indoor air temperature at different heights, radiant temperature, air velocity, relative humidity and air quality indicators, as CO_2 concentration, are measured under different usage conditions. The instrumentation is installed compromising between quality of measurements, equipment safety and reduction of the interaction with building users. All data are recorded with 3 minutes intervals. The appropriate clothing insulation and metabolic activity profiles are estimated (tab.1). At the same time of the measurements campaign, the subjective perception of the users has been investigated through a questionnaire survey. Following the procedures described in ASHRAE 55 standard, the adaptive thermal comfort model is applied to evaluate the indoor comfort conditions, for spectators and for players. The exterior CO_2 concentration is considered equal to 450 ppm.

Tab. 1: **Metabolic activity (expressed in met; 1 met = 58.2 W/m^2 body surface) and clothing parameters (expressed in clo; 1 clo = 0.155 m^2 °C/W) (ASHRAE 55, 2004)**

	Activity	Metabolic activity [met]	Garments	Clothing insulation [clo]
Players	Basketball	6.3	Walking shorts, short sleeve shirt	0.36
Audience	Seated, heavy limb movement	2.2	Trousers, long-sleeve shirt plus long-sleeve sweater	1.01

2.2 Energy strategies to nearly zero energy sports halls

As mentioned, sports halls are characterized by very specific consumption profile. With the goal of fulfil the energy requirements of this particular kind of installation satisfying the users comfort needs and achieving a significant reduction of the primary energy use, appropriate nZEB strategies have been identified. The selection has been made in the light of the climatic conditions and of the type of use that characterize the investigated sports facility. Consequently, a suitable set of passive approaches, energy efficiency measures and renewable energy systems have been applied to the analysed base case building (table 2).

Tab. 2: Proposed nZEB strategies

	Measures	Implementation	Objective
Passive strategies and control	Thermal behaviour	• Selection of building materials to ensure low thermal transmittance of the envelope • Optimization of the ratio opaque components/ windows of the façade according to the building orientation • Installation of shading device in the South-east façade	✓ ensure good thermal insulation ✓ take advantage of the solar gains ✓ avoid risk of overheating
	Natural light	• Design of the South-east façade to maximize the contribution of natural light • Installation of diffuses light sources • Installation of skylight devices	✓ ensure visual comfort ✓ avoid glare
	Natural ventilation	• Definition of control system • Nigh ventilation • Design independently from the natural light system	✓ ensure thermal comfort of the users ✓ ensure good air quality
Renewable energy system	PV installation	• Design of the façades and the roof to allow the installation of PV panels • Study of the optimal roof slope and orientation to maximize the energy production	✓ reduce energy costs ✓ reduce CO_2 emissions
Active system	Artificial light	• Installation of LED lamps • Regulation with control system	✓ reduction of energy costs

2.3 Building simulation

The base case sports hall is defined following the technical indications provided by the Catalan sports council (Consell Català de l'Esport 2005, *CCE*) concerning a triple sports hall. A triple sports hall is a sports installation equipped with a playing field that can be divided in three transversal spaces, increasing its versatility. It results that 133 on 564 Catalan sports halls fall in this category; therefore, it is a representative building typology. The studied sports installation is located in Barcelona. The building geometry is modelled in Google Sketchup (fig.1) and then is introduced in the simulation by a 3D model, using the plugin Trnsys3D. The sports halls energy consumption is closely related to the number of users of the installation. For this reason, with the contribution of the data collected during the measurements campaign, realistic profiles of the sports hall occupancy have been defined. Two main occupancy patterns are identified, corresponding to weekdays and weekend. The information regarding the occupancy schedule is reported in table 4. The air tightness of the building is assumed equal to n_{50} = 2.6/h. According to UNE-EN 15242 (AENOR 2007), the considered value corresponds to a level of airtightness medium. Only the behaviour of the playing arena of the sports hall is simulated. Thermal performance and energy consumption of other environments, as lockers rooms, that typically form part of this type of buildings, are not taken into account in this research. Moreover, it is specified that, being based on a real sports hall project, this work has to comply with some limitations and does not involve the study of default parameters, as the building orientation.

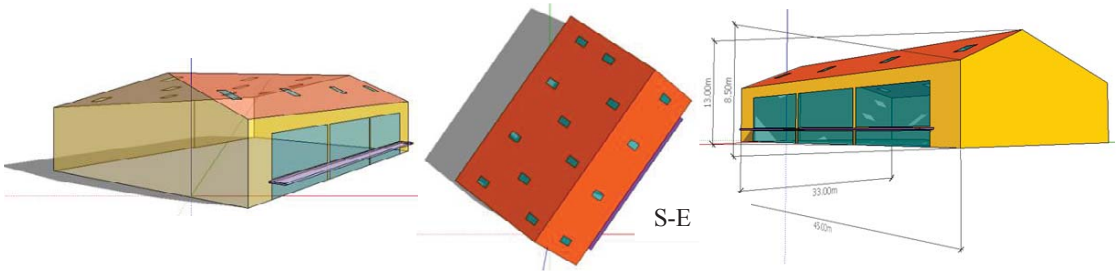

Fig. 1: Sports Hall 3D model

Tab. 3: Sports Hall dimension

	Volume [m³]	Area [m²]
Sports hall	13618	1485

Tab. 4: Sports Hall occupation pattern. (1°= Saturday; 2°= Sunday)

	occupation														
	Weekdays	Weekends													
schedule	17-22	7-9		9-11		11-14		14-16		16-19		19-20		20-22	
		1°	2°	1°	2°	1°	2°	1°	2°	1°	2°	1°	2°	1°	2°
players	45	0	0	40	40	40	40	0	0	35	35	35	35	35	35
audience	20	8	10	40	50	48	60	8	10	40	50	64	80	200	300
Total	65	8	10	80	90	88	100	8	10	75	85	99	115	235	335

2.3.1 Thermal behaviour

The thermal characteristics of the selected opaque components of the envelope are reported in table 6, while the thermal performance of the windows in table 5. The façades and the windows are in contact to the exterior environment. There is only an interior wall located in the North West direction and assumed in contact to the lockers room. The boundary temperature for this partition wall is considered of 23 °C or 18 °C, respectively during the summer and winter occupied periods. While, the unoccupied periods are characterized by a boundary parameter evaluated as average of the previous values and the exterior registered temperature. The thermal behaviour of the building is affected by the installation of a fix horizontal overhang that aims to prevent excessive temperature increase during the warm season.

Tab. 5: Thermal performance of the windows

	Window 1_lower level		Window 2_higher level		Window 3_skylight	
	Frame	Glazing	Frame	Glazing	Frame	Glazing
Composition	Aluminium with thermal break	Clear double glazing 6/16/6	Aluminium with thermal break	OKAPANE with glass fibre tissue, 16 mm, air 40 mm	Aluminium with thermal break	Double glazing with prismatic lens
U – value (W/m²K)	2.27	1.26	2.27	1.24	2.27	1.4
g – value (-)		0.368		0.335		0.589
Area frame glazing (%)	15	85	5	95	5	95

Tab. 6: Thermal performance of the construction elements

	U – value (W/m²K)
Façade NE and SW	0.284
Façade SE and NW	0.296
Interior wall	0.304
Roof	0.284
Floor	1.366

2.3.2 Natural ventilation

Natural ventilation has been investigated in detail. It is chosen as the main strategy to ensure optimal indoor air quality and thermal comfort, avoiding the energy consumption due to mechanical system. The thermal comfort is evaluated applying the adaptive comfort model. The comfort conditions are set according to the limits defined in the standard UNE-EN 15251 and observing the requirements reported in the document redacted by the Catalan sports council. The indoor optimal operative temperature (Top_{opt}) is calculated following the procedure proposed by the standard. The CO_2 concentration is the parameter used to evaluate the indoor air quality (table 7). Cross-natural ventilation is modelled through TRNFLOW (Weber et al., 2003), the extension for the integration of the airflow and pollutant transport model COMIS into the building thermal model of TRNSYS. Two identical openings are introduced in opposite façades of the building, taking into account the prevalent wind direction of the site. The characteristic of the openings are reported in table 8. The wind pressure coefficients, the discharge coefficients and the wind velocity profile are introduced according to the parameters reported in literature and in the TRNFLOW manual. The flow coefficient is calculated taking into account the desired infiltration in the building. $CO_{2\ is}$ the only examined pollutant inside the zone. The outside concentration is set to 450 ppm and assumed constant for all the external nodes and directions. The occupants of the sports halls are considered as CO_2 sources in proportion to their metabolic activity. Therefore, the contaminant exhalations from the audience accounts for 21.5 l/s per person while players are responsible for 62.5 l/h per person (Demianiuk et al. 2010). The air velocity in the building is assumed equal to 0.25 m/s when the natural ventilation is not operating and of 0.5 m/s when the openings are open. The selected values are in the range of acceptability considering that the recommended upper limit for indoor air movement is usually 0.8 m/s (Allard 2002). The control of the simulated natural ventilation system depends on the occupancy, the interior operative temperature and the CO_2 concentration. Natural ventilation is activated only when the building is occupied. Natural ventilation activation implies that the openings are opened if the operative temperature exceeds the upper limit of the selected thermal category or if the indoor CO_2 concentration is outside the air quality range. Specifically, the interval of indoor tolerable concentration is restricted respect to the recommendations of the standard.

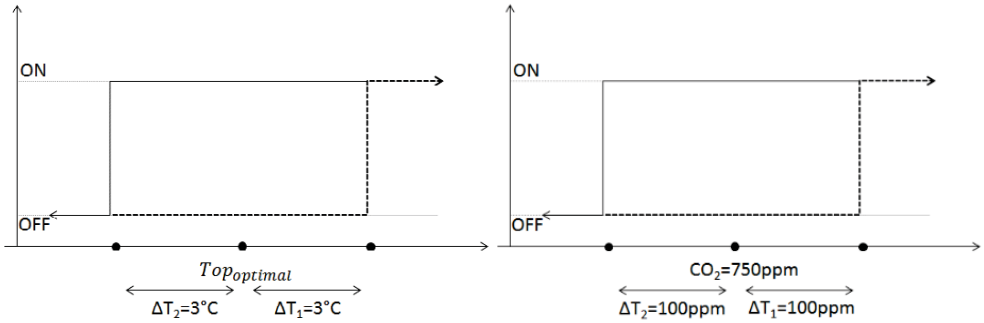

Fig. 2: Natural ventilation control. Simple line: openings behaviour if the actual state of the natural ventilation system is ON. Dashed line: openings behaviour if the actual state of the natural ventilation system is OFF

This configuration is introduced to give stability to the system, to avoid frequent on / off cycles and to allow the removal of the excess CO_2 while there is continuous emission from the occupants. The operation of the

control system is schematized in figure 2. Additionally, the opening factor is adjusted to reduce the risk of overcooling and air draft. At this scope, the openings are more or less opened depending on the difference between the interior and exterior temperature during the cold season and on the wind velocity during the warm one, as table 9 shows. Moreover, during the weekend, when the CO_2 production is significant, the system is forced to work with an opening factor equal to 1, unless the wind velocity is greater than 6 m/s. Again, this condition is suggested to maintain the stability of the system, namely to avoid that a substantial flow of air can rapidly reduce the pollutant concentration causing the closure of the openings. Indeed, it is desirable that the natural ventilation system works constantly during the period of high occupancy. To verify the effect on overheating risk reduction, night ventilation is also tested. In summer, natural ventilation is activated after that the users leave the sports hall if the exterior air temperature is lower than the interior one. In general terms, set this conditions, natural ventilation stays on until the morning hours.

Tab. 7: Comfort parameters

	Lower limit	Upper limit	Source
Operative temperature (°C)	$Top_{opt} - 3$	$Top_{opt} + 3$	UNE-EN 15251
Indoor temperature (°C)	14°C	-	*CCE*
CO_2 concentration (ppm)	-	1200	UNE-EN 15251

Tab. 8: Natural ventilation system components

Opening	Description	Dimension [m^2]	Position: height [m]
North-West façade	Horizontal sliding	9	6.3
South-East façade	Horizontal sliding	9	0.4

Tab. 9: Natural ventilation control strategy. Opening factor

Opening factor	Summer Wind velocity (m/s)	Winter $T_{interior} - T_{exterior}$ (°C)
0.2	>15	> 9
0.4	15 – 11.25	9 – 7.5
0.6	11.25 – 7.5	7.5 - 5
0.8	7.5 -3.75	5 - 4
1	< 3.75	< 4
1	if Occ=max and wind velocity < 6m/s	

2.3.3 Internal gains

The internal gains of a building are formed by the release of sensible and latent heat from indoor heat sources. This study considers the contribution of the building occupants and of the lights appliances. The sensible heat produced by the occupants depends on their metabolic activity and on the indoor air temperature, as reported in Michaelsen and Eiden (2009). The total sensible heat produced by the users of the sports hall is considered 30% convective and 70% radiative (ASHRAE 1993). The artificial lights system is mounted at 13 meters high. It is composed of 30 led lamps consuming 276 W each, with luminous efficiency of 80% (Ortiz et al., 2015). The installed systems is designed to ensure 300 lux of indoor illuminance, following the recommendation of ICAEN (2012) for basket arenas. Therefore, the contribution of the lights equipment to the internal heat load is calculated in function on the natural light availability. Artificial lights are assumed to be on when the sports hall is occupied and the natural light provided by the 14 skylights placed on the roof and by the windows on the façade is lower than the required illuminance level (according to Consell Català project). The data, regarding the hourly average daylight availability are provided by an external collaborator for a typical day of each month and introduced as input in TRNSYS.

2.3.4 PV system

PV Building Integration (BIPV) is a practice that refers to the use of PV modules as architectural elements, being a collaborative part of the design of the building envelope and having an architectural function in symbiosis with functional properties and economic regenerative energy conversion (Achenza and Desogus, 2013). Part of this research has dealt with the test of different PV system configurations designed to contribute to the energy needs of the investigated sports facility. The analysis is performed through the Google Sketchup plug Skelion and the relative findings are shown in the results section 3.3.

3. Results and discussion

3.1 Measurements campaign

After the data acquisition phase, the measured indoor conditions of the reference sports building have been analyzed in combination with the weather variable, the results of the survey and the assumed parameters. According to the survey answers (54), 84% of the audience was experiencing a thermal discomfort, mainly due to overheating: 33% affirmed that the environment was slightly warm, 28% that it was warm and 17% that it was very warm (only 3 people considered it slightly cold). Regarding the humidity variable, the majority of the audience (65%) considered the environment neutral, while the air movement was perceived mainly as inadequate (slightly low for 33% and very low for 37%). However, results of the comfort analysis show that the adaptive comfort requirements reported in the ASHRAE 55 standard are complied, as well as the design criteria established by the standard UNE-EN 15251 (fig.3) in relation to the acceptable indoor relative humidity. Conversely, looking at the level reached by the interior CO_2 concentration, it results that the comfort condition recommended by the UNE-EN 15251 standard are not always met (fig.4).

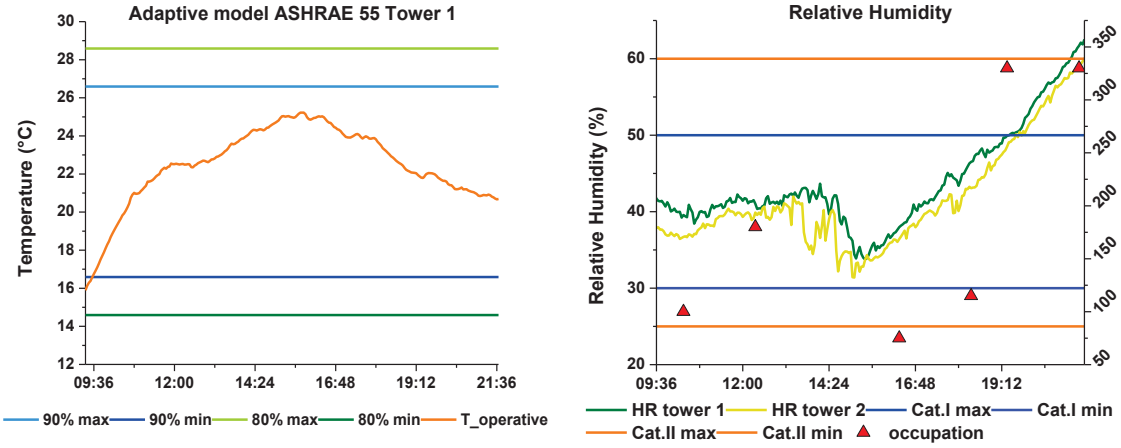

Fig. 3: Left: Adaptive thermal comfort evaluation; Right: relative humidity measurements and comfort categories

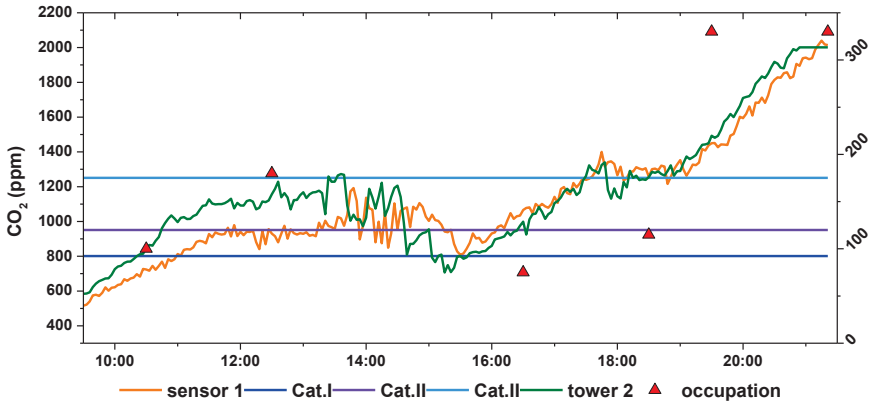

Fig. 4: CO_2 concentration measurements and comfort categories

Therefore, taking also into account that the mentioned standards are not specifically elaborated for sports facilities and for the consequent high level of metabolic activity of the users, the sharp increase of the indoor relative humidity and the excessive CO_2 concentration during the hours of maximum occupation appear as the main cause of perceived discomfort.

3.2 Building simulation

The objective of the building simulation is to verify to which extend the selected nZEB strategies are able to reduce the primary energy consumption of the studied sports hall without causing discomfort to the users. The TRNSYS results are organized in table 10 and reported in function of the natural ventilation state, being the only variable parameter. Observing figure 5, that shows the TRNSYS simulation outputs for a selected winter week, it results that the designed control system works correctly. The thermal discomfort and the air quality are assessed only during the occupied hours. It is assumed that the overheating phenomenon occurs if $Top_{int} > Top_{opt} + 3$, as the technical indications provided by the Catalan sports council do not set a maximum indoor temperature requirement. The building is overcooled if the condition $Tair_{int} < 14°C$ is verified. The maximum registered ACH is 9.97h^{-1}. The average ACH with natural ventilation on is 1.57h^{-1}, while the infiltration on average equals to 0.05h^{-1}. The presented results are achieved without the introduction night natural ventilation. As shown in table 10, the discomfort due to overheating is very low thank you to the contribution of the infiltration and the high thermal insulation of the building. The effect of additional night ventilation further reduces the overheating phenomenon to 0.1% of the occupied time. Therefore, the implementation of night ventilation technique results to have a limited impact on the thermal comfort improvements of this study case building situated in a moderate climate. However, night cooling can be considerably beneficial in extreme climate conditions and if heat wave phenomenon occurs in moderate climate. Closely analysing the discomfort events, it results that for 2 days overcooling occurs during 2.75 hours, the maximum consecutive period of overcooling thermal discomfort. The maximum consecutive period of discomfort due to excessive CO_2 concentration is 3 hours and it occurs only one day along the annual simulation. Overall, considering thermal and air quality parameters, annually the sports hall users experience 16 days of discomfort with the distribution shown in figure 6. The results deviates from the limit values for maximum 329 ppm, 4.61°C in case of overcooling and 0.48°C in case of overheating.

Tab. 10: Building simulation results

	% of the occupied time	
	winter	summer
natural ventilation ON	54.76	50.09
Overcooling	1.69	-
Overheating	-	0.36
CO_2 > 1200 ppm	1.20	0.71

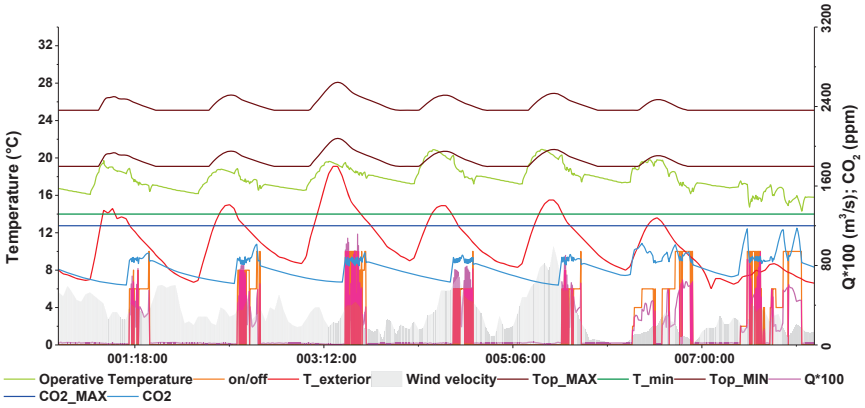

Fig. 5: System behaviour during a selected winter control week

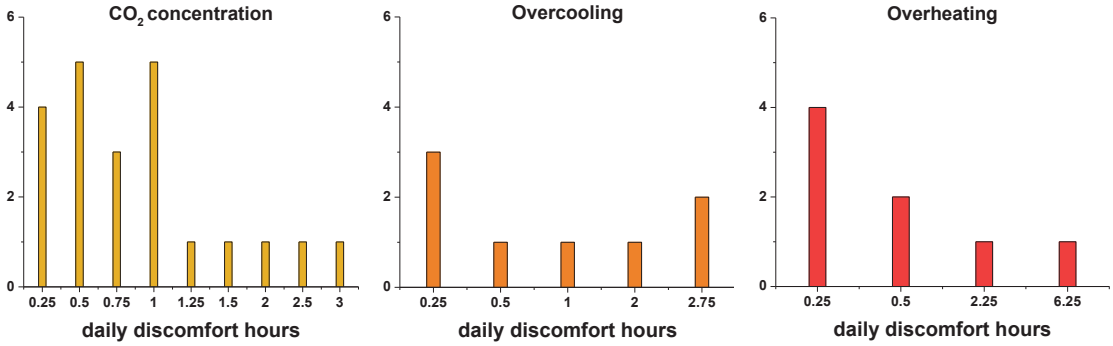

Fig. 6: x-axis= discomfort hours; y-axis=number of day

3.3 PV system

Table 11 summarizes the results of the PV designs analysis. The economic data are extrapolated from Hulb el al. (2014). The comparison of the different PV system configuration suggests that, considering the available surface for PV modules integration and the weather condition of the site, the most advantageous solution is the one tested in case 10. In a range of acceptability of 5%, case 2 and case 6 have similar performance. The mentioned cases are characterized by the installation of the panels with a slope of 38° and an orientation toward the south direction (182°). The integration of the PV panels in the façade and on the shading device of the building results less convenient.

Tab. 11: PV system configurations

		Azimuth	Slope	Panels	kWp	Specific generation (kWh/kWp)	Total generation (kWh)	Specific cost (€/kWh)
1	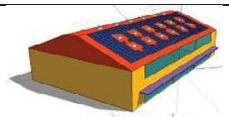	135	20	367	42	1255	52985	1.11
2	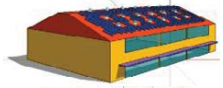	182	38	190	22	1364	29807	1.02
3	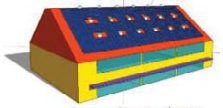	135	38	568	365	1267	82746	1.10
4	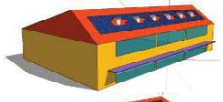	135	37	162	19	1266	23589	1.10
5	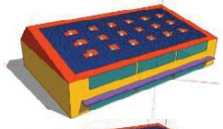	135	14	719	83	1230	101718	1.13
6	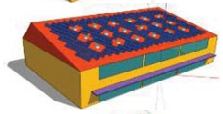	182	38	302	35	1371	47623	1.02
7	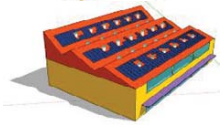	135	17 23 37	441	51	1245 1256 1265	63583	1.11
8	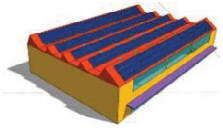	135	37	600	69	1263 1256 1254 1268 1213	86494	1.11

9	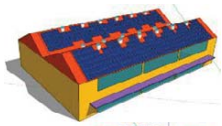	135	34	470	54	1269 1258	68374	1.10
10	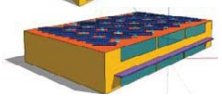	182	38	294	34	1381	46680	1.01
11	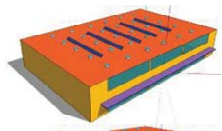	225	38	60	7	1297	8352	1.15
12	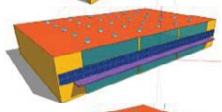	135	90	68	12	876	10606	1.59
13	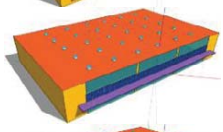	135	90	56	10	876	8734	1.59
14	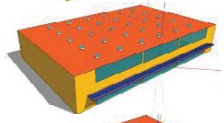	180	0	51	6	975	5718	1.43
15	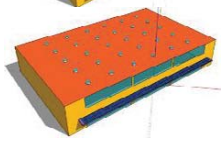	180	0	70	8	979	7882	1.42
16	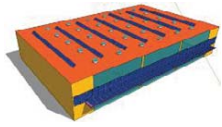	180 225 134.66	0 37.6 0	265	35	979 1297 876	37442	1.29

Within the 16 tested PV system configurations, case 2 has been selected and simulated in TRNSYS through type 94. The obtained results allow evaluating, for every time step along the yearly simulation, the energy balance between electricity demand and electricity production. According to the TRNSYS calculation, the total annual generation of case 2 is 35'426 kWh. This value differs from the output obtained through Skelion. In this regard, it must be taken into account that weather data and the PV module technical features used by the two software are also different. The PV system is able to cover 10% of the electricity building energy demand, including artificial lighting and ventilation.

3.3.2 Energy balance

From the analysis of the building energy needs, it results that the thermal load necessary to comply with the minimum temperature requirements equals to 213 kWh/y (0.14 kWh/m^{2}y) while the light consumption accounts for 13'968 kWh/y. The electricity demand due to the automation of the natural ventilation systems is estimated at 509 kWh/y. Elaborating the data made available by ICAEN (2012), the obtained results are compared to the heating, lighting and ventilation performance of a standard triple sports hall and of an efficient one, concerning which energy efficacy measured are applied. Additionally, the respective not renewable primary energy requirements are compared in figure 7. It is assumed that the thermal demand of the simulated sports hall is covered by the installation of a condensing boiler (η=1.09) combined with an emission and distribution system consisting of radiant panels (η=0.9). The considered not renewable primary energy conversion factor are 1.954 kWhPE/kWhFE and 1.190 kWhPE/kWhFE, used respectively for electricity and natural gas consumption (RITE 2014). It is evident that the selected energy strategies substantially contribute to the objective of energy consumption reduction set for the simulated building. Overall, it consumes 87.5% less energy than a standard sports hall and 70% less than an efficient one.

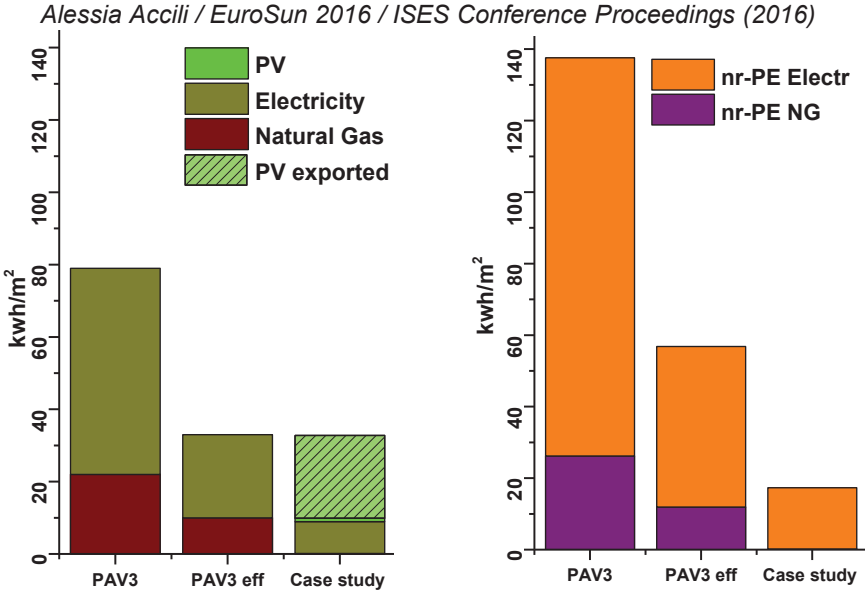

Fig. 7: Left: final energy; right: not renewable primary energy

4. Conclusion

Under a holistic approach, different energy measures to design nearly zero energy Sports halls have been tested. A novel aspect of the study is the focus on the peculiarity of the Mediterranean climate context. The first step of the research involves a field measurement campaign in an existing facility. The obtained data suggest that in a standard sports hall comfort issues are closely linked to indoor air quality. Excess of CO_2 concentration causes discomfort perception, even though the registered thermal parameters fall within the acceptability range. Secondly, TRNSYS simulation confirms that the combination of reduction of thermal transmittance of the envelope, optimization of the window surface, correct façades orientations, introduction of shading devices, installation of energy efficiency systems, and use of natural and night ventilation, is advantageous for the reduction of heating, cooling and artificial lightning demand. The described strategies minimize the period of overcooling and overheating, and provide good air quality conditions for most of the occupied time along one-year simulation. The design of the natural ventilation system and of the relative control play a relevant role. It is estimated that a natural ventilated sports hall, not equipped with a heating system, will be overcooled for 1.69% of the winter occupied time, while CO_2 concentration will exceed normative limits only during 0.95% of the year. It is verified as well that PV system integration positively affects the sports hall performance toward nZEB standards. Future development of the study can involve the evaluation of the sports hall DHW needs and investigate the potential contribution of a thermal solar system. Furthermore, it is important to report that the accuracy of this investigation is compromised by the absence of comfort and thermal standards specifically elaborated for the sports building category.

Acknowledgment

The authors would like to thank the Poliesportiu Pla Del Bon Aire of Terrassa and Consell Català d'Esport for their collaboration in the development this research.

5. References

Achenza, M., Desogus, G., 2013, Guidelines on building integration of photovoltaic in the Mediterranean area, ENPI CBC Mediterranean Sea Basin Programme

AENOR, 2008, Parámetros del ambiente interior a considerar para el diseño y evaluación de la eficiencia energética de edificios incluyedo la calidad del aire, condiciones térmicas, iluminación y ruido. UNE-EN 15251. Madrid: AENOR

AENOR, 2007, Ventilación de los edificios. Métodos de cálculo para la determinación de las tasas de los caudales de aire en edificios, incluyendo la infiltración. UNE-EN 15242. Madrid: AENOR, 2007

Allard F., 2002, Natural ventilation in buildings: a design handbook. 2nd ed. James & James Ltd

Artuso, P., Santiangeli, A., 2008, Energy solutions for sport facilities, International Journal for Hydrogen Energy, 33, pp.3182-3187

ASHRAE 55, ANSI/ASHRAE Standard 55-2004, 2004, Thermal environmental conditions for human occupancy, American Society of Heating Refrigerating and Air-Conditioning Engineers Inc., Atlanta

ASHRAE fundamentals handbook (SI), 1994, Atlanta: American Society of Heating, Refrigeration and Air-conditioning Engineers (ASHRAE)

Consell Català de l'Esport, Generatlitat de Catalunya, 2005, Fitxes tècniques d'equipaments esportius, Pavello triple poliesportiu

D'Agostino, D., 2015, Assessment of the progress towards the establishment of definitions of Nearly Zero Energy Buildings (nZEBs) in European Member States, Journal of Building Engineering, 1, pp. 20–32

Demianiuka, A., Gładyszewska-Fiedoruka K., Gajewskia A., Ołówb A., 2010, The changes of carbon dioxide concentration in a cinema auditorium, Civil and Enviromental Engineering 1, ISSN: 2081-3279

Felsmann, C., Schmidt, J., Kalz, D., Vietor, Kalz, 2015, Schlsussbericht, ENOB-MIDELLPROJEKT ZWEIFELDSPORTHALLE IN PASSIVHAUSBAUWEISE. Monitoring, Evaluierung und Systemanalyse,

Flourentzou, F., Pantet, S., Ritz, K., 2015, Automatic natural ventilation in large spaces: a passive ventilation technology for passive buildings, 36th AIVC Conference "Effective ventilation in high performance buildings", Madrid

Google, Google SketchUp 8.0.11752, 2010 d, Spain, 23-24 September 2015

ICAEN, 2012, L'Energia a les instal·lacions esportives 2a ed: Col·lecció Quadern pràctic 6 Versió rev.i actualitzada de l'ed. de 1998

Kisilewicz, T., Dudzińska, A., 2015, Summer overheating of a passive sports hall building, Archives of civil and mechanical engineering, 15, pp.1193-1201

Michaelsen, B., Eiden, J., 2009, HumanComfort Modelica-Library Thermal Comfort in Buildings and Mobile Applications, Proceedings 7th Modelica Conference, Como, Italy, Sep. 20-22, 2009

Ortiz J., Fonseca, A., Salom, J., Russo, V., Garrido, N., Fonseca, P., 2015, Optimization of energy renovation of residential sector in Catalonia based on comfort, energy and costs, Proceedings of BS2015: 14th Conference of International Building Performance Simulation Association, Hyderabad, India, Dec. 7-9, 2015

Radulov, L., Kaloyanov, N., Petran, H., 2014, RePublic_Zeb. Report on the preliminary assessment of public building stock

RITE, 2014, Reglamento de Instalaciones Térmicas en los Edificios, Factores de emisión de CO_2 y coeficientes de paso a energía primaria de diferentes fuentes de energía final consumidas en el sector de edificios en España

Solar Energy Laboratory (SEL), 2012, University of Wisconsin, TRNSYS 17.1

Huld T., Jäger Waldau, A., Ossenbrink, H., Szabo, S., Dunlop, E., Taylo,r N., 2014, Cost Maps for Unsubsidised Photovoltaic Electricity, Scientific and Policy Report by the Joint Research Centre of the European Commission

Trianti-Stourna, E., Spiropoulou, K., Theofilaktos, C., Droutsa, K., Balaras, C.A., Santamouris, M., 1998, Energy conservation strategies for sports centers. Part A sports halls, Energy and Buildings, 27, pp. 108–121

Tsoka, S., 2015, Optimizing indoor climate conditions in a sports building located in Continental Europe, 6th International Building Physics Conference, IBPC 2015, Energy Procedia, 78, pp. 2802 – 2807

Weber, A., Koschenz, M., Dorer, V., Hiller, M., Holst, S., 2003, TRNFLOW, a new tool for modelling of heat, air and pollutant transport in buildings within TRNSYS, Eighth International IBPSA Conference Eindhoven, Netherlands August 11-14, 2003

Conference Proceedings

EuroSun 2016
Palma de Mallorca (Spain), 11 - 14 October 2016

Optimization of time-of-use tariffs demand side management coupled with cold Thermal Energy Storage (TES) and solar PV to reduce on-peak demand

Mohammad Saffari[1], Alvaro de Gracia[2], Cesar Fernández[3], Martin Belusko[4], Dieter Boer[2], Luisa F. Cabeza[1]

[1]GREA Innovació Concurrent, Universitat de Lleida, Lleida (Spain)

[2]Department of Mechanical Engineering, Universitat Rovira i Virgili, Tarragona (Spain)

[3]Computer Sciences Department, Universitat de Lleida, Lleida (Spain)

[4] Barbara Hardy Institute, School of Advanced Manufacturing & Mechanical Engineering, University of South Australia, Adelaide (Australia)

Abstract

Industries are responsible of emitting 40% of total energy-related CO_2 emissions and about one third of total final energy consumption. Introducing energy management systems allow companies to manage and control their energy use, enabling them to lower energy costs, and enhance productivity and competitiveness. Demand side management using thermal energy storage and off-grid solar photovoltaic technologies could enhance the performance of energy systems and reduce on-peak demand for industries. In the present paper, the feasibility of reducing the annual electricity bill mainly by peak shifting will be studied by applying cold TES and off-grid solar PV along with a proper time-of-use tariff structure. Simulations results have shown that adopting a proper time-of-use tariff structure in combination with cold TES coupled with off-grid solar PV can considerably increase annual energy savings mainly by shifting electricity demand to nighttime off-peak period. Additionally, it was estimated that for the analyzed case study (450 kW of electrical demand 9 hours/day for cooling processes) 5000 € to 75000 € of annual energy bills can be saved by applying TES and solar PV with different capacities. Moreover, it was found that the combination of TES and solar PV technologies based on time-of-use tariff structure can improve the economic savings by 3% to 9% in comparison to using the two mentioned technologies separately.

Keywords: *cold storage, thermal energy storage, solar PV, demand side management, optimization.*

1. Introduction

Industry accounts for about one third of total final energy consumption and almost 40% of total energy-related CO_2 emissions which are expected to rise by 46% by 2040 (Makridou et al., 2016). The European Union´s (EU) Energy Roadmap 2050 explores solutions towards decarbonisation by 2050 by over 80% while at the same time guaranteeing security of energy supply and competitiveness (European Commission, 2011). On this basis, the European commission (European Commission, 2011) is placing increasing priority on energy savings in all decarbonisation scenarios and furthermore, supporting the significant increase of renewable energy sources. Electricity storage in a large scale is not feasible; therefore electricity has to be consumed in real time covering the demand. On the other hand, since generation plants with different supply sources such as thermal, solar photovoltaic (PV), hydro, wind and other renewables of variable efficiency are used to meet demand, the cost of electricity varies hour to hour, day to day, and month to month (Faruqui et

Selection and/or peer review under responsibility of Scientific Committee
doi:10.18086/eurosun.2016.03.07 Available at http://proceedings.ises.org

al., 2010). Additionally, variability in both demand profiles and renewable energy sources makes the energy management of the grid more difficult and increases the cost of electric power generation (Batalla-Bejerano and Trujillo-Baute, 2016).

Peak electricity demand is a global policy concern which causes transmission constraints and congestion, and increases the cost of electricity for all end-users. Further on, a huge investment is needed to upgrade electricity distribution and transmission infrastructure, and build generation plants to provide power during peak demand periods (Strengers, 2012). Furthermore, commonly service suppliers charge a higher price for peak-time services than for off-peak services in order to compensate for the costly electricity generation at peak hours (Kim et al., 2016). So that, cutting off some of this peak demand would benefit the whole energy system since, on one hand, it would eliminate the need to install expensive extra generation capacity such as combustion turbines for peak hours which are less than a hundred hours a year (Faruqui et al., 2007) and on the other hand, consumers can eliminate penalties due to exceeding power demands in their electricity bill. In addition, due to infrequent use of peak plants, making them more efficient is not fair. So that, normally it is cheaper to feed peak electricity generators by oil which results in more CO_2 emissions (Faruqui et al., 2010). Accordingly, even a small percentage of peak demand reduction can promise substantial savings in generation, transmission, and distribution costs (Faruqui and Sergici, 2010). Using flexible resources in the power system such as renewable generation, storage, and demand management could be a solution to increase the security and satiability of the whole energy system, to save energy and to reduce the hazardous emissions (European Commission, 2011).

Demand side management (DSM) is a proactive way to make customers energy-efficient in the long-term (Barbato and Capone, 2014). The most prominent DSM methods include reducing peak loads, shifting load from on-peak to off-peak , increasing the flexibility of the load and reducing energy consumption in general (Müller et al., 2015) where load shifting has been found as the most effective load management technique (Esther and Kumar, 2016). DSM can reduce both the electricity peak power (kW) and the electricity consumption (kWh) (Warren, 2014; Zhou and Yang, 2015). Further on, some countries have adopted or are investigating time-of-use distribution network tariffs such as Spain (Real Decreto 1164/2001, 2016), which aim at shifting consumption to off-peak hours to avoid grid constraints (European Commission, 2015). Time-of-use tariffs can encourage customers to take advantage of price variations in different periods of time to regulate their electricity use. In such schemes, a group of prices are determined in advance and they apply to different periods of time, where the electricity prices are discriminated by patterns and rates (Li et al., 2016). Thus, based on the information provided by suppliers, high energy consumers can decide how to distribute their loads according to variable electricity tariffs using different technologies (Buryk et al., 2015; Yalcintas et al., 2015). They will be able to shift their electricity consumption away from times of high prices (peak hours) to times of low prices (off-peak hours) and by that reduce their energy bill.

Energy storage technologies can have a valuable role to play in any energy system, including those with high and low proportions of renewable generation (e.g. solar PV) with variable nature due to weather conditions (Kousksou et al., 2014). Thermal energy storage (TES) has been the center of attention of many researchers during the past decades (Zalba et al., 2003). In particular, the application of cold storage systems has been broadly developed in the power generation sector, the building sector, and the industrial sector because of their high potential to temporally shift the increasing cooling demand, reducing the stress on the energy system (International Energy Agency, 2011) and on the other hand, reduce the greenhouse gas emissions (Cabeza et al., 2015; Yau and Rismanchi, 2012). Refrigeration systems producing artificial cold with electrical or heat driven chillers, infrequently operate at full capacity. They usually operate during day to meet the cooling demand and are designed to satisfy the maximum cooling demand, which occurs only a few days each year. A wide range of economic, technical and energetic advantages are attainable by integration of a cold storage in such a system to supply cold such as: energy cost reduction, investment cost reduction by selecting a smaller chiller, possibility of using off-peak cheap electricity tariffs, increasing the flexibility of the system, reduction of peak electricity loads on the grid (if compression chiller is used), improving energetic efficiency (COP) of chiller, etc. (Mehling and Cabeza, 2008; Oró et al., 2014). However, further research and advancement are required for electric load management (Arteconi et al., 2012) to address the potential energy savings and peak load shaving regarding the new time-of-use tariff structure and elevated

electricity prices, high surplus demand charges, and variable solar PV share and its uncertainties in the energy system. On this ground, numerous studies have focused on DSM applying optimization techniques (Ikeda and Ooka, 2016; Muralitharan et al., 2016). The present study is an attempt to address the potential for implementation of incentive time-of-use tariffs (according to the Spanish electricity tariff structure) by an industrial consumer to reduce the electricity bill. However, it should be noted that, this method could be implemented in other countries with incentive time-of-use tariff structure. Particularly of interest are, on one hand, to reduce contracted power demands and to shift electrical chiller peak loads from high price times (peak hours) to low price times (off-peak hours), by taking advantage of cold TES (sensible systems, ice or phase change materials) and off-grid solar PV; and on the other hand, to find out the optimum combinations of power demand contracts with TES and solar PV technologies to reduce final electricity bill and comparing that with a conventional energy system.

2. Methodology

To have a better understanding of the methodology an overview is presented in this section. In section 2.1 the case study is described; section 2.2. is dedicated to the solar PV simulation; in section 2.3. the cold TES model is explained; section 2.4. focuses on the time-of-use tariff structure; and eventually section 2.5 defines the optimization procedure. Figure 1 shows a schematic of the implemneted approach.

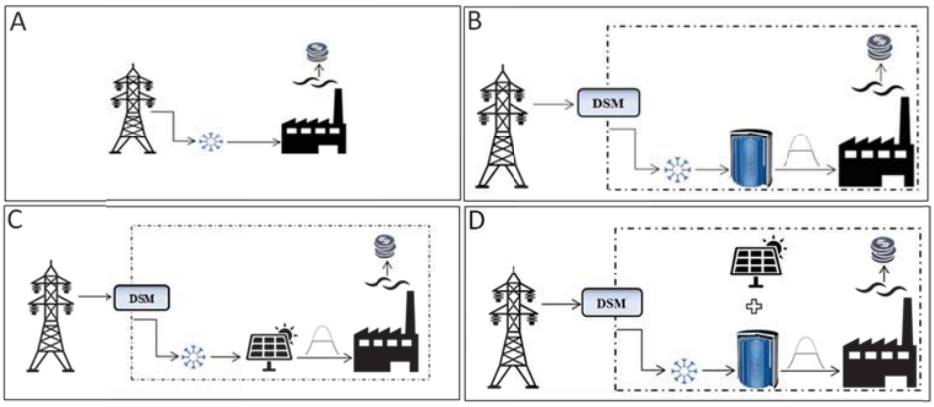

Figure 1. Schematic view of the methodology.

2.1. Case study

To give an estimate of the annual energy bill for an industrial consumer it has been assumed that for running the industrial processes of this industrial unit, a conventional energy system with no demand management facilities and with a conventional tariff structure has been used. So that, the industrial consumer directly uses the electricity network to provide electricity for its processes whenever it is required without considering the on-peak demand and off-peak demand periods (Figure 1.A). The industrial processes take place from 8:00 to 17:00 all days except Saturdays and Sundays requiring 450 kW of electrical demand for cooling processes. On this basis, the monthly electricity bill was calculated according to the Spanish electricity tariff structure (6.1A plan) which is divided into six different tariff periods (according to month and hourly basis) and is explained in detail in section 2.4.1.The annual electricity bill can be calculated using eq.1. Moreover, it is assumed that for all tariff periods the industrial consumer contracts 450 kW power demand with 100% of load factor during operational hours.

$$Elec_{tot} = (E_p + E_e) + [(E_d + E_e) \times \text{VAT}] \qquad \text{(eq. 1)}$$

$$E_p = \sum_{i=1}^{i=6}(P_i \times CP_{pi})$$

$$E_e = \sum_{i=1}^{i=6}(P_i \times CEp_i \times h)$$

Where $Elec_{tot}$ is annual electricity bill, E_p is power demand cost, E_e is energy consumption, VAT stands for

value added taxes; P stands for different tariff periods; CP and CE are cost of power [kW] and energy [kWh] for different periods according to Table 2, respectively. Investigation will be made into the possibility of shifting peak loads from daytime to nighttime by integrating a tariff-based DSM system with three different energy system designs. 1. tariff-based design coupled with a cold TES system (Figure 1.B), 2.tariff –based design coupled with an off-grid solar PV (Figure 1.C), and 3.tariff-based design coupled with both cold TES and off-grid solar PV systems (Figure 1.D). In case 1 (Figure 1.B), the cold TES tank has to be charged at nighttime during the cheapest tariff period and later on, it has to be discharged during day especially at expensive hours of electricity rates. In case 2 (Figure 1.C), the feasibility of applying only off-grid solar PV to reduce the energy bill will be assessed. Eventually, in case 3 (Figure 1.D) the possible energy benefits due to coupling both cold TES and solar PV and their mutual impacts on each other will be investigated.

2.2. Simulation of PV module

In order to analyze the solar PV electrictiy generation in the desired climate, TRNSYS 17 (transient system simulation tool) (Klein, 2010) was used. This software has an extensive library of components in which appropriate models (called types) could be selected for simulating thermal and electrical energy systems. In the present study, Type 15.3 (weather file reader), Type 16a (radiation processor), Type 94a (crystalline solar PV module), Type 25c (printer), and Type 65d (online printer) were selected and appropriately interconnected to carry out the solar PV simulation.

The potential solar-generated electricity can be calculated using Type 94a which models the electrical performance of a photovoltaic array and could be used in simulations involving electrical storage batteries, direct load coupling, and utility grid connections. It applies equations for an empirical equivalent circuit model to predict the current-voltage characteristics of a single module. This circuit consists of a DC current source, diode, and either one or two resistors. The strength of the current source is dependent on solar radiation and the IV characteristics of the diode are temperature-dependent (TRNSYS 17, 2016). Sunrise SR-M762315-B solar PV (Figure 2) (Sunrise, 2016) technical data as shown in Table 1 was introduced to Type 94a and four different nominal installation power of 25, 50, 80, and 100 kWp were considered. Further on, all the solar PV modules were considered to have 40º of array slope and 0º of azimuth.

Figure 2. Sunrise SR-M672315 module (Sunrise, 2016).

Table 1. Sunrise SR-M672315 module specifications (Sunrise, 2016).

Maximum power [W]	315
Module area [m^2]	1.94
Tolerance [%]	0~+3
Open circuit voltage (Voc) [V]	45.42
Short circuit current (Isc) [A]	9.24
Maximum power voltage (Vm) [V]	36.69
Maximum power current (Im) [A]	8.59
Module efficiency [%]	16.20
Solar cell efficiency [%]	18.85
Cell type [mm]	156x156(Mono-Crystalline Silicon)
Number of cells [Pcs]	72(6x12)
Maximum system voltage [V]	DC1000
Temperature coefficient of Voc [%/ºC]	-0.35
Temperature coefficient of Ise [%/ºC]	0.05

Temperature coefficient of Pm [%/ºC]	-0.45
Operating temperature [ºC]	-40 to 85
Nominal operating cell temperature (NOCT) [ºC]	45±2
Maximum series fuse [A]	15
Wind bearing [Pa]	2400
Pressure bearing [Pa]	5400
Standard Test Conditions (STC):1000W/m^2 AM=1.5 25 ºC	

Simulations were performed using time steps of 15 minutes for fifteen consecutive years (1991-2005) using historical solar radiation data of Denver international airport, Colorado, US (Köppen-Geiger classification: BSk) which was derived from NREL data base (National Renewable Energy Laboratory, 2007). This climate was selected because of two reasons, first, because we did not have historical weather data of the desired climate and second, the climate classification of the desired city which is in Lleida provice, Spain presents the same climate classification as Colorado.

2.3. Cold TES model

Cold TES system was included into the design to shift both the electric demand (kW) and the energy consumption (kWh) from higher cost (on-peak) and middle cost (partial-peak) periods to the lower cost (off peak) period. This design was based on an operating schedule with two modes: mode (1) charging the cold TES during the nocturnal period (the cheapest period); and mode (2) discharging the cold TES tank during the diurnal period (avoiding or reducing compressor operation), with assumed peak capacities ranging from 2 to 250 kW. The cold TES was sized to hold different storage capacities (25 to 3000 kWh) in order to evaluate the effect of the storage capacity in the economic benefits. Commonly, standby heat gains occur in storage tanks due to the heat conduction, convection and infiltration. These losses are very dependent on the indoor and outdoor boundary conditions, insulation level of storage tanks etc. On this basis, in order to take into account these heat losses, some heat loss values corresponded to cold storage tanks were derived from experimental results available in literature (Stovall, 1993; Therese K. Stovall, 1991; Therese K.Stovall, 1991a, 1991b). Afterwards, standby heat losses values of 0, 0.50, 1, 1.5 kW were considered to be implemented into a model with 50 kWp solar PV to see the impact of heat losses on the final energy cost.

2.4. Time-of-use tariff structure

2.4.1. Electricity tariffs

The electricity tariffs used in this case study are based on the Spanish current prices. Spain has several major electricity companies, of which Endesa S.A. (“Endesa S.A.,” 2016) is the holding company for the active players in the electricity market. These players include generation, transmission, and customer relations. Transmission includes the network which delivers electricity from generators to customers. They are responsible for constructing and servicing this grid. This service is charged via a network charge priced in €/kW. These charges are regulated by government legislation and therefore transparent. Generators are large conventional power stations which generate power and either sells it to the electricity market or through contract with customer relations. The electricity spot market involves bids and purchases by generators and customer relations, and prices are cleared every period. Customer relations are the principle agent by which households and businesses interact with the electricity grid. They pass on transmission charges at cost, and an energy price charged per kWh usage. The energy price is negotiated but there are standard prices publicly available. Many large customers have their own transformer and make Endesa transmission manage it. Alternatively, Endesa transmission pays for the transformer and manages it, and this is negotiated.

2.4.2. The electricity bill

The electricity bill consists of an energy charge, peak demand charge, and taxes. Taxes are significant and include an electricity tax of 5.1% and a value-added tax (VAT) of 21%. The charges depend on your demand category as followings: 2.0 A: demand less than 10 kW; 2.1 A: 10 < demand < 15 kW; 3.0 A: demand > 15 kW; 3.1 A: demand < 450 kW; and 6.1 A: demand > 450 kW. Depending on which demand category the

consumer fits in, it determines how many charge categories are applied to the contract. The residential sector has P1 and P2 charge categories, where the 6.1A demand categories vary from P1 to P6. In each charge category a peak and energy charge is applied. For category 6.1, the one contracted by the case study of the present paper and by most of the industrial applications, the applied incentive time-of-use tariffs are shown in Figure 3.

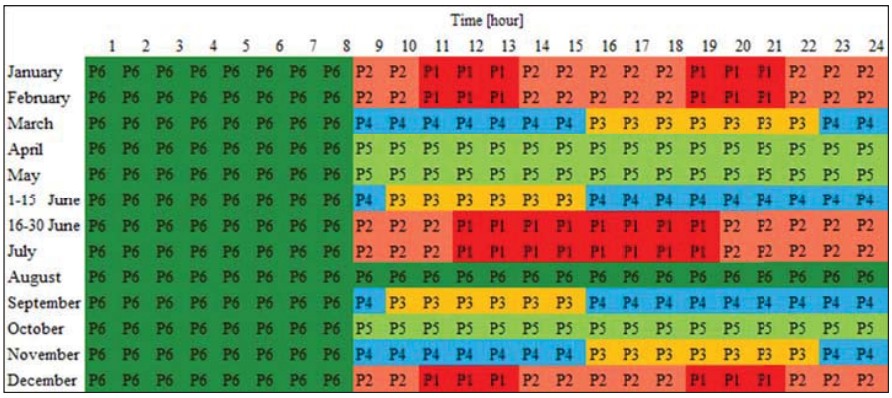

Figure 3. Hourly distribution of electricity rates.

Figure 4 shows the hourly and monthly periods during which each tariff structure is applied. PX refers to the tariff price profile consisting of a peak, off peak and middle peak price. P6 refers to all prices at off peak rates. The tariff consists of both an energy price and a demand price per period (see Table 2).

Table 2.Incentive time-of-use electricity prices ("Endesa S.A.," 2016).

	P1	P2	P3	P4	P5	P6		
Power	39.139	19.586	14.334	14.334	14.334	6.540	€/kW/ year	Regulated price
Energy	0.120	0.096	0.092	0.074	0.0708	0.065	€/kWh	Standard free price

2.4.3. Charges due to power excess

In case that an industrial consumer requires more demand that it is contracted in each determined time interval (for some minutes or even hours), a penalization due to power excess is charged to the bill. This penalization is calculated according to the power contracted in each tariff period and, if applied, depending on each tariff period, the actual demanded power rates are metered using electricity metering equipment. The billing of the excesses of power for the 6.1 tariffs is calculated according to the formula established in Royal Decree 1164/2001 (Real Decreto 1164/2001, 2016) (see (eq.2) and (eq.3)), and it is measured every 15 minutes.

$$F_{ep} = \sum_{i=1}^{i=6} K_i \text{ x } 1.4064 \text{ x } A_{ei} \qquad \text{(eq. 2)}$$

Where F_{ep} stands for charges in Euros and A_{ei} is a factor that weights excess of demand depending on the period (Real Decreto 1164/2001, 2016), K_i is the coefficient that takes the values depending on the tariff period i as shown in Table 2, A_{ei} is calculated according to the following formula:

If Pdj <= Pci

$A_{ei} = 0$

Else if

Pdj > Pci

$$A_{ei} = \sqrt{\sum_{j=1}^{j=6} (Pdj - Pci)^2} \qquad \text{(eq. 3)}$$

Where Pdj is demanded power in each quarter of hour which is excessed (higher than Pci), Pci is contracted power in each period and in the considered period.

Table 2. Ki coefficients according to the tariff periods.

Period	1	2	3	4	5	6
K_i	1	0.5	0.37	0.37	0.37	0.17

These powers are expressed in kW and the excesses of power are billed monthly. For tariffs 6.1 at every breach is charged a penalty i.e. every 15 minute breach. Thus, it means that if the user overpasses the contracted power during one hour, the penalty is charged four times.

2.5. Optimization

A large and growing body of literature has been published on optimization techniques for DSM based on TES and solar PV to reduce energy-related costs of residential buildings and industrial processes (Barbato and Capone, 2014; Lee et al., 2009; Muralitharan et al., 2016). Some of these optimization methods are namely, mixed integer linear programming (MILP) and dynamic programming for a global optimal solution. Further on, metaheuristic methods such as particle swarm optimization and evolutionary algorithms have been implemented by many researchers (Müller et al., 2015). It could be understood that for given electricity consumption requirements, an optimization problem can be derived based on the power contracting plan, i.e. how much power is contracted for each one of the 6 period tariffs. The optimization problem results deterministic when no PV production is considered. Otherwise, PV uncertainty will lead to stochastic optimization. On both cases, Constraint Integer Programming (CIP) has been used as a novel paradigm that integrates constraint programming (CP), mixed integer programming (MIP), and satisfiability (SAT) modeling and solving techniques in order to model and solve our problem (Achterberg, 2009, 2008; Achterberg et al., 2008). Without PV production, the system may be described as sets, parameters and functions as follows:

$P = \{P_1 .. P_6\}$, is the set of tariff periods; $CE_i, i \in \{1..6\}$ is the cost of energy consumption during period P_i according to Table 1 in €/kWh; $K_i, i \in \{1..6\}$ is the coefficient as defined in Table 2; *SL* is the cold TES storage limit capacity in kWh; *H, D* and *M* are the set of hours, days and months respectively; *T=H*D*M* is the set of hour periods in a year; $Period: T \rightarrow P$, is a function that maps an hour period to its corresponding tariff as corresponding to Figure 4; $C_i, i \in H$, is the required energy during an hour. However, in our particular case:

$$C_i = \begin{cases} 450kW \cdot h, & i \in 8..17 \\ 0, & Otherwise \end{cases}$$

It should be noted that for a constant energy demand, $C_i = 4 \cdot P_{dj}$, being P_{dj} the demanded power in each quarter of hour as stated in eq.3.

$$f(x) = \begin{cases} x, & x > 0 \\ 0, & x \leq 0 \end{cases}$$

$PC_i \in \mathbb{R}, i \in 1..6$, is the contracted power for tariff P_i; $S_t \in \mathbb{R}, t \in T$, is the supplied energy from the grid in time *t.* When suitable, one can also denote S_t as $S_{h,d,m}$. Therefore, the cost of contracting power (*CP*) can be expressed as:

$$CP = \sum_{i=1..6} CP_i \cdot PC_i \qquad \text{(eq. 4)}$$

and the cost of the consumed energy is:

$$CE = \sum_{t \in T} S_t \cdot CE_{Period(t)} + K_{Period(t)} \cdot 1.4064 \cdot f\left(S_t - PC_{Period(t)}\right) \quad \text{(eq. 5)}$$

Finally, the following assumptions have been made: 1. PCM storage period ranges from hour 00:00 to 07:00. This is an obvious optimal assumption because those are the cheapest periods and no demand exists. 2. The stored energy can only be consumed during the same day. The objective is to find an optimum assignment of $PC_i \in \mathbb{R}, i \in 1..6$, that minimizes CP+CE, which could be written as:

$$\min_{PC_i}(CP + CE) \quad \text{(eq. 6)}$$

subject to the following constraint:

$$SL > \sum_{h=0}^{7} S_{h,d,m} > \sum_{h=8}^{17} C_h - S_{h,d,m}, \forall (d,m) \in D * M \quad \text{(eq. 7)}$$

For example, for each day, the stored energy must not surpass the storage limit and must supply the eventual lack of obtained energy from the grid. In order to reduce the number of variables, symmetries may be considered. As energy requirements are invariant from day to day (C_i), the number of variables can be drastically reduced. More specifically, S_i can be indexed in *H*M* instead of *T*. We encoded and solved eq.6 and eq. 7 with SCIP version 3.2.0 ("SCIP Optimization Suite," 2015) in a 1.9 GHz processor. The problem results in 581 variables and 484 constraints, being solved in less than 2 seconds. When solar PV production is considered, it can be taken into account as a multivariate random variable $PV_y = \left(pv_{1,y}..pv_{|T|,y}\right)$, being $pv_{i,y}$ the PV production at hour $i \in T$ in year *y*. Then, for a given year *y*, eq.7 becomes:

$$SL > \sum_{h=0}^{7} S_{h,d,m} > \sum_{h=8}^{17} C_h - S_{h,d,m} - pv_{h,d,m,y}, \forall (d,m) \in D * M \quad \text{(eq. 8)}$$

When PV production is available over a set *Y* of years, we compute the expected optimization as:

$$E\left[\min_{PC_i}(CP + CE)\right] = \frac{1}{|Y|} \sum \min_{PC_i} (CP + CE)$$

subject to constraint as in eq.8. Under this scenario, symmetry reduction as previously stated is no longer feasible and each year optimization problem results in 16469 variables and 16846 constraints, with a resolution time from 5 to 25 minutes depending on SL value.

3. Results

3.1. DSM economic benefits

3.1.1. Influence of time-of-use DSM with cold TES capacity

Optimization results due to the use of only cold TES with different capacities are shown in Figure 4. Note that the y-axis is logarithmic base 10 scale; otherwise the correlation between energy savings and storage capacity will be misinterpreted as a linear trend. It can be seen that energy savings sharply increase by adding storage of about 200 kWh and this trend continues gradually up to approximately 500 kWh. After this point, the increase of storage capacity has a very little impact on energy bill savings, despite being upward.

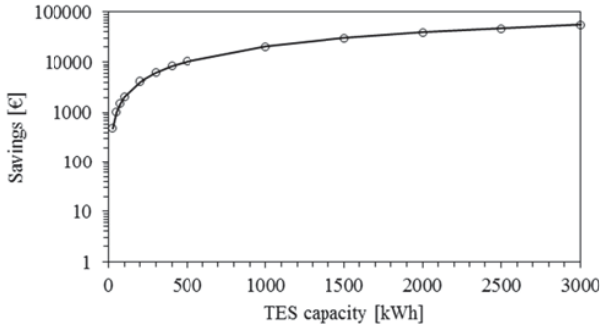

Figure 4. Energy savings by using DSM and cold TES.

3.1.2. Influence of time-of-use DSM with solar PV

The energy impact of tariff-based DSM coupled with off-grid solar PV system has been compared with a conventional energy system and the results are shown in Figure 5. It could be seen that energy savings vary from approximately 2% to 10% (4300 to 17000 euros) depending on the nominal installation capacity. However, it should be taken into account that the saving trend line is sharper from 25 to 80 kW of solar PV capacity and by increasing the solar PV to 100 kW this trend increases slightly. It should be considered that in previous results the impact of heat losses was not considered, on this basis calculations have been carried out taking into account three different levels of heat losses (0.50, 1, 1.50 kW/h) of the storage tank. It was found that 0.2 to 1% of the final energy bill could be increase due to heat losses of storage tank.

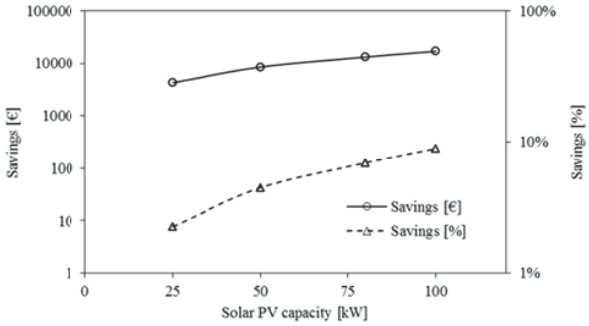

Figure 5. Energy savings by using only solar PV.

3.1.3. Influence of time-of-use DSM with cold TES coupled with solar PV

An important issue that should be discussed herein is how the combination of solar PV and short-time cold TES technologies coupled to a proper time-of-use DSM can shift peak demands and eventually improve the energy system and save final energy bill. To determine benefits due to interconnection of these two systems, savings due to integration of only cold TES and only solar PV should be summed and then subtracted from savings due to coupling cold TES with solar PV. For example in case of integrating PV 50 kW and TES with storage capacity of 1000 kWh, the benefits will lead to savings of about 8500 euros due to PV (see Figure 5) and 20600 euros due to storage (see Figure 4), however, the coupling of these two technologies achieved savings of 30400 euros.

Figures 6 and 7 show energy improvements ratios and energy savings (logarithmic base 10 scale), respectively, due to interconnection of solar PV and cold TES. It could be seen that the energy improvement is not linear and it is highly depends on the storage size and the solar PV power. For example, by looking at the trend line of solar PV with 25 kW power in Figure 6 it can be seen that the peak energy improvement occurred when storage with less than 200 kWh was coupled to the system and the increase of storage capacity decreased the performance of the whole system. Actually, when the solar PV share of the system is smaller, lower storage capacity is needed to provide the smoothness in the system. On the other hand, when higher shares of solar PV considered, higher short-term TES storage was required which is consistent with

findings of Bussar et al. (Bussar et al., 2016). This could be also seen in Figure 8, in case of 25 kW PV savings sharply increase by coupling TES in the range of 50-200 kWh; after this point by the increase of TES capacity further savings could be achieved, however, it would not be as beneficial as the efficient range of 25-200 kWh. In other words, the higher the dependency of energy system on the solar PV, the higher the storage is needed to ensure the security of electricity supply of the system without intermittency. Further on, it can be derived from Figure 7 that adding energy storage has the potential to further improve the performance of the whole system by reducing demand charges during periods when the solar PV system is not producing enough power due to weather conditions. Also, it can be derived that higher demand shifting is feasible by integration of cold TES, whereas, off-grid solar PV can reduce the energy consumption when solar radiation is available.

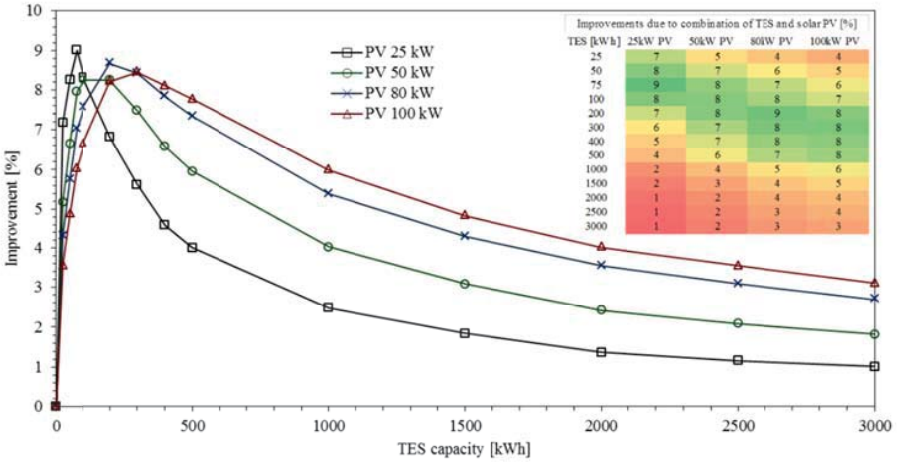

Figure 6. Improvements due to combination of solar PV & TES.

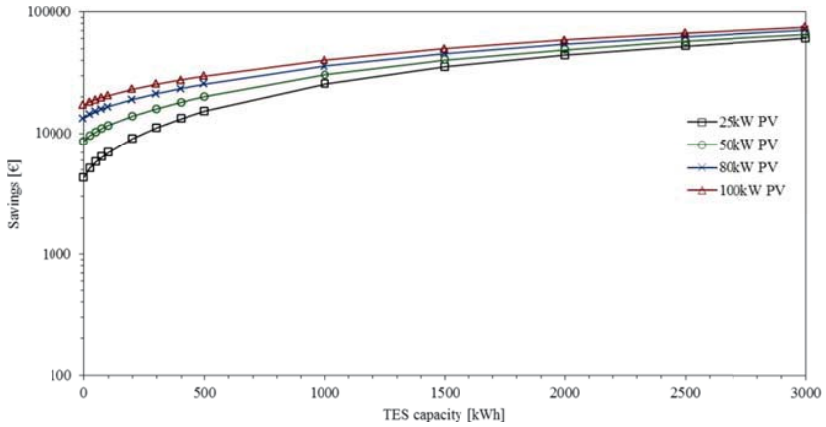

Figure 7. Energy savings due to combination of solar PV & TES.

4. Conclusions

The present paper is a simulation-based optimization study which investigates the implementation of time-of-use DSM combined with short-term TES and off-grid solar PV technologies to shift on-peak demand of an industrial electricity consumer under a certain climate zone. Through numerical optimization and simulation it has been found that both the cold TES and the off-grid solar PV coupled to an appropriate tariff structure can yield savings in final energy bills. Analyzing the results, it could be derived that savings attributed to the integration of TES are generally higher than those achieved by only off-grid solar PV. This is basically because of variability of solar radiation intensity and climate condition since when the expected solar power is not achieved; excess power is demanded from the consumer by cost of considerable charges. In addition, solar PV without storage can reduce the energy term and not significantly the power term of the

energy bill. However, it should be highlighted that when an interconnected TES and solar PV energy system was analyzed, it was found that further energy improvements are attainable due to combination of these two systems. By this, it could be explained that the implementation of TES not only can shift the on-peak load but also can improve the performance of the off-grid solar PV system.

5. Acknowledgments

The work partially funded by the Spanish government (ENE2015-64117-C5-1-R (MINECO/FEDER), ENE2015-64117-C5-3-R (MINECO/FEDER), TIN2015-71799-C2-2-P and ULLE10-4E-1305). The authors would like to thank the Catalan Government for the quality accreditation given to their research group (2014 SGR 123) and the city hall of Puigverd de Lleida. This project has received funding from the European Commission Seventh Framework Programme (FP/2007-2013) under Grant agreement NºPIRSES-GA-2013-610692 (INNOSTORAGE) and from the European Union's Horizon 2020 research and innovation programme under grant agreement No 657466 (INPATH-TES). Alvaro de Gracia would like to thank Ministerio de Economia y Competitividad de España for Grant Juan de la Cierva, FJCI-2014-19940.

6. References

Achterberg, T., 2009. SCIP: Solving constraint integer programs. Math. Program. Comput. 1, 1–41.

Achterberg, T., 2008. PhD thesis - Constraint Integer Programming. Universität Berlin.

Achterberg, T., Berthold, T., Koch, T., Wolter, K., 2008. Constraint Integer Programming: A New Approach to Integrate CP and MIP, in: CPAIOR 2008. pp. 6–20.

Arteconi, A., Hewitt, N.J., Polonara, F., 2012. State of the art of thermal storage for demand-side management. Appl. Energy 93, 371–389.

Barbato, A., Capone, A., 2014. Optimization Models and Methods for Demand-Side Management of Residential Users: A Survey. Energies 7, 5787–5824.

Batalla-Bejerano, J., Trujillo-Baute, E., 2016. Impacts of intermittent renewable generation on electricity system costs. Energy Policy 94, 411–420.

Buryk, S., Mead, D., Mourato, S., Torriti, J., 2015. Investigating preferences for dynamic electricity tariffs: The effect of environmental and system benefit disclosure, Energy Policy.

Bussar, C., Stöcker, P., Cai, Z., Moraes, L., Magnor, D., Wiernes, P., Bracht, N. van, Moser, A., Sauer, D.U., 2016. Large-scale integration of renewable energies and impact on storage demand in a European renewable power system of 2050-Sensitivity study. J. Energy Storage 6, 1–10.

Cabeza, L.F., Miró, L., Oró, E., de Gracia, A., Martin, V., Krönauer, A., Rathgeber, C., Farid, M.M., Paksoy, H.O., Martínez, M., Fernández, A.I., 2015. CO_2 mitigation accounting for Thermal Energy Storage (TES) case studies. Appl. Energy 155, 365–377.

Endesa S.A. [WWW Document], 2016. URL http://www.endesaonline.com/ES/Hogares/ (accessed 7.19.16).

Esther, B.P., Kumar, K.S., 2016. A survey on residential Demand Side Management architecture, approaches, optimization models and methods. Renew. Sustain. Energy Rev. 59, 342–351.

European Commission, 2015. Study on tariff design for distribution systems.

European Commission, 2011. Energy Roadmap 2050, (COM (2011) 885 final. Brussels.

Faruqui, A., Harris, D., Hledik, R., 2010. Unlocking the €53 billion savings from smart meters in the EU: How increasing the adoption of dynamic tariffs could make or break the EU's smart grid investment. Energy Policy 38, 6222–6231.

Faruqui, A., Hledik, R., Newell, S., Pfeifenberger, H., 2007. The Power of 5 Percent. Electr. J. 20, 68–77.

Faruqui, A., Sergici, S., 2010. Household response to dynamic pricing of electricity: a survey of 15 experiments. J. Regul. Econ. 38, 193–225.

Ikeda, S., Ooka, R., 2016. A new optimization strategy for the operating schedule of energy systems under uncertainty of renewable energy sources and demand changes. Energy Build. 125, 75–85.

International Energy Agency, 2015. Energy Policies of IEA Countries - Spain 178.

International Energy Agency, 2014. Energy Technology Perspectives 2014 Harnessing Electricity's Potential Explore the data behind ETP.

International Energy Agency, 2011. Technology Roadmap- Energy Storage.

Kim, J.-Y., Lee, M.H., Berg, N., 2016. Peak-load pricing in duopoly. Econ. Model. 57, 47–54.

Klein, S.A., 2010. TRNSYS 17: A Transient System Simulation Program, Solar Energy Laboratory, University of Wisconsin, Madison, USA.

Kousksou, T., Bruel, P., Jamil, A., El Rhafiki, T., Zeraouli, Y., 2014. Energy storage: Applications and challenges. Sol. Energy Mater. Sol. Cells 120, 59–80.

Lee, W.-S., Chen, Y. –Ting, Wu, T.-H., 2009. Optimization for ice-storage air-conditioning system using

particle swarm algorithm. Appl. Energy 86, 1589–1595.
Li, R., Wang, Z., Gu, C., Li, F., Wu, H., 2016. A novel time-of-use tariff design based on Gaussian Mixture Model. Appl. Energy 162, 1530–1536.
Makridou, G., Andriosopoulos, K., Doumpos, M., Zopounidis, C., 2016. Measuring the efficiency of energy-intensive industries across european countries. Energy Policy 88, 573–583.
Mehling, H., Cabeza, L.F., 2008. Heat and cold storage with PCM: an up to date introduction into basics and applications, 1st ed. ed. Springer, New York.
Müller, D., Monti, A., Stinner, S., Schlösser, T., Schütz, T., Matthes, P., Wolisz, H., Molitor, C., Harb, H., Streblow, R., 2015. Demand side management for city districts. Build. Environ. 91, 283–293.
Muralitharan, K., Sakthivel, R., Shi, Y., 2016. Multiobjective optimization technique for demand side management with load balancing approach in smart grid. Neurocomputing 177, 110–119.
National Renewable Energy Laboratory, 2007. National Solar Radiation Database 1991 – 2005 Update : User's Manual. Task No. PVA7.6102 472.
Oró, E., Miró, L., Farid, M.M., Martin, V., Cabeza, L.F., 2014. Energy management and CO_2 mitigation using phase change materials (PCM) for thermal energy storage (TES) in cold storage and transport. Int. J. Refrig. 42, 26–35.
Real Decreto 1164/2001, 2016. Real Decreto 1164/2001, de 26 de octubre, por el que se establecen tarifas de acceso a las redes de transporte y distribución de energía eléctrica. [WWW Document]. URL https://www.boe.es/diario_boe/txt.php?id=BOE-A-2001-20850 (accessed 7.24.16).
SCIP Optimization Suite [WWW Document], 2015. URL http://scip.zib.de (accessed 7.24.16).
Stovall, T.K., 1993. FAFCO Ice Storage Test Report. Oak Ridge.
Strengers, Y., 2012. Peak electricity demand and social practice theories: Reframing the role of change agents in the energy sector. Energy Policy 44, 226–234.
Sunrise, 2016. Monocrystalline Modules-Sunrise SOLARTECH (Solar Panel, Solar Module) [WWW Document]. URL http://www.srsolartech.cn/html/Monocrystalline_Modules/32.html (accessed 7.13.16).
Therese K. Stovall, 1991. Calmac Ice Storage Test Report. Oak Ridge.
Therese K.Stovall, 1991a. Turbo Refrigerating Company Ice Storage Test Report. Oak Ridge.
Therese K.Stovall, 1991b. Baltimore Aircoil Company (BAC) Ice Storage Test Report. Oak Ridge.
TRNSYS 17, 2016. TRNSYS 17–Standard Component Library Overview, Volume 3 [WWW Document]. URL www.trnsys.com/assets/docs/03-ComponentLibraryOverview.pdf (accessed 7.14.16).
Warren, P., 2014. A review of demand-side management policy in the UK. Renew. Sustain. Energy Rev. 29, 941–951.
Yalcintas, M., Hagen, W.T., Kaya, A., 2015. Time-based electricity pricing for large-volume customers: A comparison of two buildings under tariff alternatives. Util. Policy 37, 58–68.
Yau, Y.H., Rismanchi, B., 2012. A review on cool thermal storage technologies and operating strategies. Renew. Sustain. Energy Rev. 16, 787–797.
Zalba, B., Marín, J.M., Cabeza, L.F., Mehling, H., 2003. Review on thermal energy storage with phase change: materials, heat transfer analysis and applications. Appl. Therm. Eng. 23, 251–283.
Zhou, K., Yang, S., 2015. Demand side management in China: The context of China's power industry reform. Renew. Sustain. Energy Rev. 47, 954–965.

Conference Proceedings

EuroSun 2016

Palma de Mallorca (Spain), 11 – 14 October 2016

Research of Application of Renewable Energy Sources and Energy Saving Technologies in Residence Houses Construction in the Central Part of Russia

Sergey M. Karabanov [1], Valeriy V. Kirakovskiy [2], Pavel P. Bezrukikh [3] and Pavel P. Bezrukikh (Jr.) [4]

[1] Ryazan State Radio Engineering University, Ryazan (Russia)

[2] Promgrazhdanproject Ltd., Ryazan (Russia)

[3] G.M. Krzhizhanovsky Power Engineering Institute JSC, Moscow (Russia)

[4] LUCOIL JSC, Moscow (Russia)

Abstract

Application of energy saving technologies and renewable energy sources is one of the main directions in residential building. The central part of Russia has moderate continental climate with the average temperature of -10.6 °C in January and in July - + 19.7°C, the heating season lasts for about 200 days. Therefore the solution of energy saving problem is important. The paper presents the research results on determining optimum conditions of renewable energy sources choice, on definition of architectural solutions for construction of a power efficient house, the monitoring results of power supply system operation of the house and its operation costs.

Keywords: *architecture, energy saving, renewable energy*

1. Introduction

Energy saving is the most important goal in residential building. Now, when the prices for electricity, public services constantly grow, it is necessary to look for new approaches for the problem solution of the energy operation costs reduction.

The central part of Russia, in particular, Ryazan region, has moderate continental climate. The average temperature in January is -10.6 °C, in July - + 19.7°C, the heating season lasts for approximately 200 days. This data determines to a large extent the design and technological approaches to the energy saving problem solution in residential building.

The paper presents the research results for the choice of renewable energy sources for energy and heat supply of a residential house: photovoltaics, wind power, solar collectors and heat pumps; approaches to the energy-efficient house design, the monitoring results of the house energy system and maintenance costs.

2. Approaches to house design

A multifamily residential house located in Russia, Ryazan region, Rybnoe town (latitude 54 north, longitude 39 east) was chosen as the object for the project engineering design (Fig. 1) [1].

The basic house features:

- number of floors – 2,
- number of sections – 2,
- architectural volume – 3902 m^3,
- total house area – 713.5 m^2,
- common corridors and common areas – 52.2 m^2,

doi:10.18086/eurosun.2016.01.15 Available at http://proceedings.ises.org

- total apartments area – 622.6 m^2,
- living space – 322.4 m^2,
- number of apartments – 13, including:
  - one-room – 1,
  - two-room – 9,
  - three-room – 3.

Fig. 1: Multifamily residential house with hybrid power supply

As a whole, the measures implemented at the house design can be divided in the following groups (Table 1): Group 1 – heat loss reduction; Group 2 – reasonable consumption of energy resources; Group 3 – independent power generation for reduction of operating costs on living space maintenance by the house tenants; Group 4 – introduction of automated CONTROL SYSTEMS of the house, in particular, control of consumed energy resources.

Tab. 1: The complex of power-efficient solutions used in the house

Group 1	Group 2	Group 3
- heating-up of the building: basement, basement area, walls, attic floor, roof; - installation of glass units with low-emissivity glass; - equipping of entrances with lobbies; - application of door closers for front doors; - installation of supply-extract ventilation system with heat recuperation.	- installation of motion sensors in common areas; - LED equipment for courtyard lighting; - application of energy-saving lamps in apartments; - one button electric power switching off; - meridian orientation of the house; - horizontal distribution of the house heat supply system; - apartments decoration using light colours.	- installation of bivalent heating system using low-potential heat of lower layer of the Earth (heat pump); - installation of PV modules generating emergency power, and for courtyard area lighting; - installation of water heating vacuum solar collectors.
Group 4		
- installation of **consumed resources meters** in each apartment; - installation of meters registering the consumption of the house energy resources; - installation of independent meters registering power resources generated and consumed by the equipment using renewable energy sources.		

The applied design and technological concepts allow to cut expenses for the house operation, to make direct observations, measurements of quantitative and qualitative changes of maintenance by the tenants of the multiafamily residential house having a high class of power efficiency.

Due to space-planning solution of the house the biggest area of windows is located in the south. The outside walls of the house are made of ceramsite concrete with external heat insulation. To minimize the heat loss through walls,

base, attic floor and roof the modern heat insulating materials have been used. The windows consist of three chamber glass units with low-emissivity glass. The staircases are equipped with lobbies with automatically closing doors and reliable pressurization system. The heating of the house is made as a bivalent plant: geothermal heat pumps and a block boiler room with condensation boilers, having a heat meter in each apartment.

3. The analysis of renewable energy sources operation for energy and heat supply of the house

In order to choose a renewable energy source for power and neat supply it is necessary to take into account the following factors:

- geographic location of the house and climate pattern of the place;
- the building characteristics (area, architectural volume, building location);
- power consumption of the building (energy consumption and heat flow rate) during a year.

The use of combined power sources (wind-solar power stations, solar collectors, heat pumps) for heat and energy supply is optimal. The present paper studies the application of power from a PV power station and wind generator for electrical power generation. A heat pump was used for heat supply and solar collectors – for hot water supply.

3.1. The use of wind-solar power

When analyzing the wind-solar power station operation the scheme for monitoring the power generation was used (Fig. 2) [3]. The monitoring data was used for working out recommendations for the house engineering and building. Figure 3 shows simulation and the average value of solar and wind power generated during the investigated period. The calculation was carried out by standard methods on the basis of total month irradiation data and the most apparent wind speeds [3].

For calculation the simple models of the components were used.

- Power generated by a PV generator is directly proportional to irradiation (when using PV modules with good fill factor, 36 cells in series).
- Current of the wind generator is proportional to the cube of wind speed of up to 14m/sec (stronger wind was not taken into account due to its small probability).
- The storage battery charge efficiency was considered to be constant, the depth of discharge (DOD) was equal to70 % (in order to exclude overdischarge losses), the battery operating range was 20 … 28 V. The battery overcharge losses were not taken into account.

We observed coincidence of the calculated and monitoring data. The deviation does not exceed 20%. The largest deviation is observed in winter. It is connected with more cloudy weather during last years. This period is considered to be more critical and is characterized by shortage of power, especially as far as photovoltaics is concerned: it does not exceed 20 kWh/kW that is 5 times less than that of wind energy – up to 100 kWh/kW. In summer solar energy dominates (up to 140 kWh/kW) while wind energy is not more than 25 kWh/kW. Such different potential of wind and solar energy results in irregular power supply of consumers.

Below the most optimal proportions of nominal capacity of the wind and PV generators ($P_{nomwind}/P_{nomPV}$) are analyzed. The optimization was conducted by minimum irregularity of average monthly power production according to the formula:

$$\frac{\sum_{n} |\,(P_{average} - P_n)\,|}{P_{average}} = min \qquad (1)$$

where $P_{average}$ - simple average of power production for the investigated period (one year or one season), P_n- monthly power production (n=1 … 12).

Figure 4 shows the obtained curve shapes for different proportions of nominal capacities of wind and PV generators.

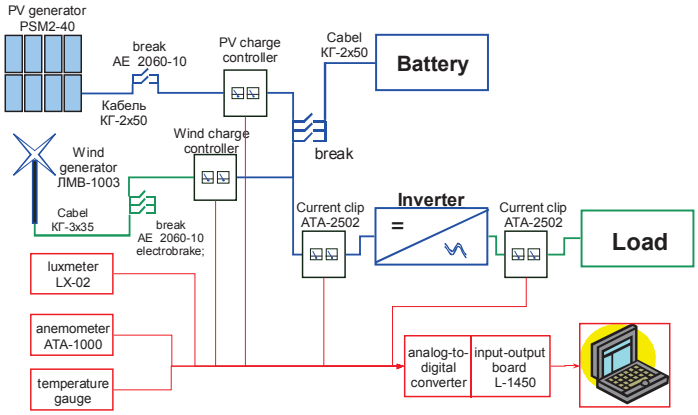

Fig. 2: Monitoring scheme

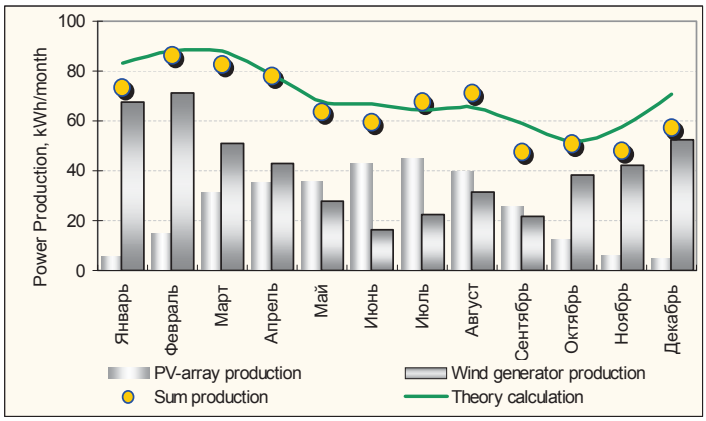

Fig. 3: Monitoring data

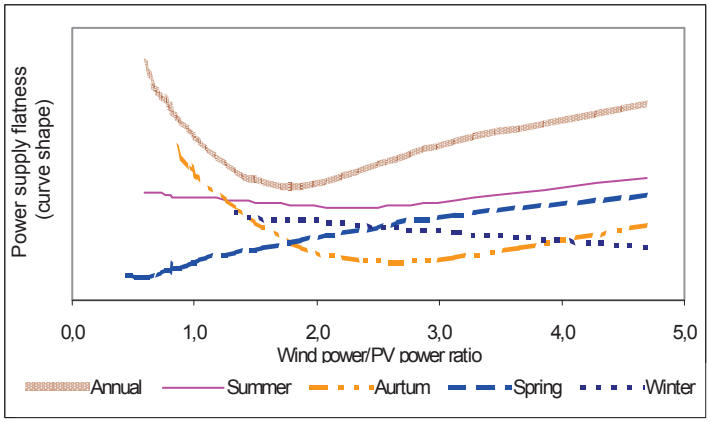

Fig. 4: The curve shapes for different proportions of nominal capacities of wind and PV generators. X-axis is the wind and PV generator ratio; y-axis is the change of the output power in dimensionless units (the figure shows only the curve form).

The flat trend of curves in winter and summer indicates the absence of influence of PV generator power increase on the character of power supply in winter and increase of the wind generator power in summer.

In spring, and especially in autumn, the variation of the power ratio is usually extreme. The optimal ratio for spring is 0.6, for autumn – 2.5-3. The optimal proportion for the whole year is 1.9.

The choice of proportions depends on the character of load consumption, its criticality to power supply irregularity in different seasons or in a year, and also on the proportion of the prices per watt of wind and solar energy. In the station under consideration the proportion of 2.35 is realized.

When designing the house only a PV power station was used as it was difficult to locate a wind generator in the apartment complex. A PV power station had to provide power supply of the house communal facilities (stairs, corridors), a courtyard territory and a heat pump. The calculated peak power of the PV station was 7.5 kW. For the calculation the procedure developed in [2] was used.

Monthly electrical energy generation E_{pv} for a PV generator is determined by the following equation:

$$E_{pv} = G_m(\beta) \cdot S \cdot \eta_{pv} \cdot (1 - \eta_{cable}) \cdot \eta_{mp} \quad (2),$$

where S is the PV generator area, η_{pv} - conversion average efficiency of a PV module, η_{cable} - cable losses (value 0.03), η_{mp} – losses identified by absence of mpp tracking (value 0.8).

The coefficient η_{mp} allows for losses appearing when mpp tracking system is absent. The application of MPP tracking device in the system results in necessity to calculate hourly amounts of solar irradiation and also to have the data of monthly average temperature.

For a battery the stored energy was calculated by:

$$E_{bat} = E_{pv} \cdot \eta_{bat} \quad (3),$$

where ηbat - conversion mean efficiency of battery. The battery capacitance was calculated by

$$C_{bat} = \frac{E_{bat}}{DOD} \cdot (N + 1) \quad (7),$$

where N – quantity of sunless days, DOD – depth of discharge.

Input data for the calculation is the monthly amount of global solar irradiation for the given region, geographic latitude, modules slope (season optimisation is provided). The programme allows to calculate the required quantity of PV modules to provide load power supply during specific period of time and to calculate storage battery minimum capacity taking into account sunless days. The calculation data was taken from [3].

PV power plant structure:

Peak power – 7.5 kW

PV modules – RZMP-235-T, 32 pcs.

Inverter – TripleLinx 8k, 1 pc.

Storage battery – 200A2/12Bx32

3.2. Heat pump choice

In order to use heat pumps the information about the source of low potential heat, power consumed by the pump, necessary volume of the released heat was analyzed. The heat pump scheme and its structure was chosen taking into account this data.

Corsa-30 (Russia) geothermal heat pump with the rated heat power of 24 kW was used for the house heat supply. This heat pump can operate at high temperature modes (to warm a heat carrier up to +80°C) maintaining a high operation factor of renewable natural heat. To provide pump operation the electric energy of 6.4 kW is necessary. The power is supplied from a PV station. Copeland scroll compressor was used in a heat pump. The compressor has a high transformation ratio of 3.14: the ratio of obtained heat power to consumed energy.

3.3. Solar collector choice

For solar collector use optimal operation time when the collectors work effectively, providing the house with hot water, was chosen.

On the basis of design works the system of vacuum solar collectors, EE-SHS/250 (12 collectors) and EE-SHS/100 (6 collectors), was chosen and installed. The system used Cordivari boilers. The system provides 210 liters of hot water (55°C) during 6 months per year (May-September). The designer and installer of the hot water supply system is EnergEco (Moscow, Russia).

Fig. 5: Solar collectors for seasonal (summer) water heating

4. Architectural and other solutions

Ventilation in the apartments is made as supply-extract system of recuperation, returning the heat of removing air at venting.

The system of natural and controlled forced ventilation provides energy saving and prevents mould growth on the house enclosing structures.

Flat solar collectors for seasonal (summer) water heating in a hot water supply system and a PV power plant accumulating electric power from PV modules were installed (Fig. 5).

Illumination of the courtyard area and common areas is carried out from the combined power supply system with the application of a PV station. Motion sensors providing electric light switching off have been installed at each entrance. For street lighting LED lamps are used.

Energy-efficient electrical equipment is installed in apartments and common areas. In each apartment the light is switched off with one button.

The whole building and each apartment is equipped with an automated power consumption measurement system.

5. Economic aspects of the project

During the development of the project the comparison of different options of its realization has been made (Table 2).

Tab. 2: Comparative characteristics of variants of power and material saving in a 13-apartment house in Ryazan region

Variant	Total cost, mln. Rub	Cost of 1 m^2	Saving
Traditional	17.7	27 500	-
With effective heat insulation of enclosure structures and use of effective insulating glass units	25.7	40 000	50%
With application of heat pumps and PV modules	34.1	53 000	90%

Table 3 shows the technical-and-economic indexes of the project.

Tab. 3: Technical-and-economic indexes

Indexes	Energy efficient house	Standard house
Apartment area, m^2	644	644
Estimated costs, kRub.	30 036	19 964
Cost of 1 m^2, Rub.	46 640	31 000
Building heat losses, kW	19	27
Savings due to architectural solutions, kWh/m^2	20	-
Power from renewables, kWh/m^2	46.1	-

The value of the building energy efficiency according to the calculations is 98 kWh/m^2 per year whereas the target energy efficiency is 66.4 kWh/m^2.

The monitoring of the house economic efficiency within 3 years has shown that total operational costs decrease twice.

6. Research results

1. It is established that for uninterruptible power supply of the house in this territory, taking into account meteorological data and use of the previously developed calculation program, the optimum ratio of capacities of the PV and wind generator is 2:1. The 7.5 kW PV generator was developed and installed.

2. It is defined that for the chosen region the optimum time for solar collector use is May - September. For providing the house with hot water a solar collector with the capacity of 2100 liters per days is used.

3. A 24 kW heat pump providing year-round heat supply was installed on the ground.

4. The following design solutions have been developed:

- the requirements for thermal insulating materials were established and the materials were chosen;
- energy efficient ventilation system was chosen;
- lighting system was chosen;
- automated accounting and control systems of energy carrier for each flat and the house was chosen;
- power and heat supply system monitoring during 3 years demonstrating stability of all systems operation was carried out;
- the house operating costs monitoring was done. It was established that the costs were two times lower.

6. Conclusion

The paper shows the possibility of efficient application of renewable energy sources for power and heat supply of a residential house in the central part of Russia. The multipurpose use of renewable energy and energy efficient architectural and design solutions allowed to decrease considerably (two times) the house operation costs.

7. References

[1] Karabanov, S.M., Evseenkov, O.V., Kirakovskiy, V.V., Hybrid power supply of a residential house in Central Russia using a PV station, pp. 4426-4427, ISBN: 3-936338-33-7, DOI: 10.4229/28thEUPVSEC2013-5CV.7.32.

[2] Karabanov, S.M., Kukhmistrov, Y.V., Calculation of ground photovoltaic systems by meteorological data, Technical Digest of 3rd World Conference on Photovoltaic Solar Energy Conversion, Osaka, Japan,

May 11-18, 2003, pp. 521-522.

[3] Karabanov, S.M., Kukhmistrov, Sazhin, B.N., Shushkanova, T.A., Environmental tests of a wind-solar power station, Full Proceedings of World Renewable Energy Congress-VII, 29 June – 5 July, 2002, Cologne, Germany.

Conference Proceedings

EuroSun 2016

Palma de Mallorca (Spain), 11 – 14 October 2016

ISES EuroSun 2016

MONITORING AND PROCESS OPTIMIZATION- THE WILLIBALD-GLUCK-GYMNASIUM IN NEUMARKT (i.d.OPF)

Christian Kley, Franziska Bockelmann and M. Norbert Fisch

Technische Universität Braunschweig – Institut für Gebäude- und Solartechnik (IGS),
Mühlenpfordtstraße 23, 38106 Braunschweig, Tel:0531-391 3557, Fax: 0531-391 8125,

Abstract

The newly constructed building of the Willibald-Gluck-Gymnasium in Neumarkt i.d. OPf. is a great example for integral planning of school buildings and enables the study of future-oriented technical and energy concepts.

Within the scope of this Federal Ministry for Economic Affairs and Energy-funded research project and the participation in the accompanying research "Energieeffiziente Schulen" (EnEff:Schule), the building's performance is being monitored and optimized to obtain and document verified insights about the system's performance. Innovative operation strategies for educational buildings are developed and evaluated with respect to high energy efficiency and increasing consumption of self-produced electricity. Accordingly geothermics as a low temperature heat source combined with heat pumps are used for heating the school building and gym.

The integral building concept unifies architectural ideas of alignment and shape of the building, a high quality and air-tight building shell with small heat transfer coefficients, and energy efficient building technology for heat and electric supply. Furthermore the available space is used optimally as an area collector is installed below the sports ground.

Keywords: School, energy concept, heat pump, low temperature heat source, monitoring, optimization

---

doi:10.18086/eurosun.2016.01.06 Available at http://proceedings.ises.org

1. Introduction

In the town of Neumarkt i.d. OPf. the Landkreis Neumarkt erected the new building of the Willibald-Gluck-Gymnasium (WGG) for approximately 1400 students including a gym. The four-story-building with inner atria and a net floor area (NFA) of about 11500 m² started operation in the winter term of 2015/2016. The sports hall with three fields and a NFA of 2900 m² was built at the same time (Fig. 1).

Fig. 1: Site plan of the school and gym

Prospective to the EU directive regarding the overall energy efficiency of buildings, the complex was to be realised as an "EnergyPLUS-School". It thereby implements the standard of "nearly zero energy buildings" as a demonstration project. The integral and innovative energy concept is based on energy optimised, sustainable, functional, comfortable, and architecturally valuable design. The necessary technology has been implemented and evaluated. The project demonstrates these conceptual aspects visibly and takes a role model function for public educational buildings.

The realised, innovative technologies are taken into operation using the new method of the "Performance Test Bench (PTB)" and monitored throughout their operation. The built-in measurement and monitoring infrastructure allows the sophisticated analysis of operation variables, building performance and air quality in the rooms.

A learning platform for teachers and students benefits the transparency and acceptance of this future-oriented project. To this purpose, the "Active Functional Specification (AFS)" is implemented in the PTB, a web-based platform for specifying building services' functions, validating their implementation, and detecting errors. It was developed by the IGS and Synavision. Energy performance and comfort in school buildings are to be visualised for the students and teachers. The treatment and analysis of the processes will take place during an energy laboratory lesson in the school's schedule.

2. Architecture

Light, transparency, open communication, and clear alignments are just some of the self-stated quality factors for interior architecture and the architecture of the new school. The main goal is creating an optimal learning and teaching climate for both students and teachers. Coloured windows, weather protection for wings of the windows, create cheerful atmosphere. Noise reducers are integrated as formative elements (Fig. 3).

Students and teachers experience open and bright rooms in the entire building, e.g. through apertures in the rooms' walls. Light and visibility are enhancing an open and communicative school. Two great atria are sending daylight into the building's core. Lucid corridors connect all areas. Dark hallways are nowhere to be found. The halls are more like open streets with open spaces for free communication and calm alcoves for resting (Fig. 2 and Fig. 3).

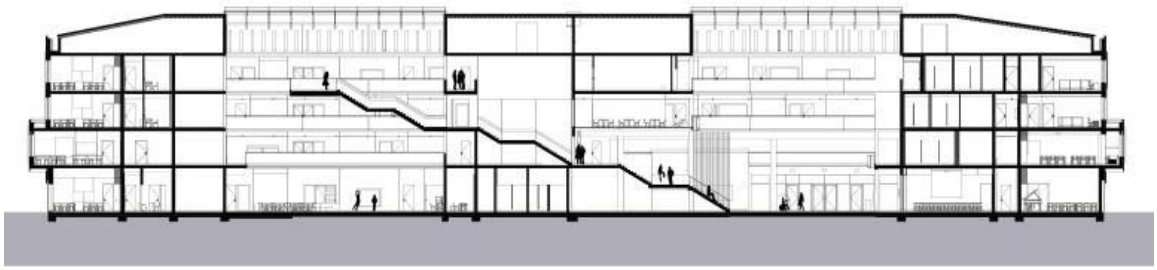

Fig. 2: Longitudinal section of the school

Entrance area

Class room

Inner courtyard

Gym

Fig. 3: Photographs of the WGG's new building and the gym
(© office Berschneider + Berschneider and Photographing Petra Kellner)

3. Energy concept

As a lighthouse project for the new building type EnergyPLUS-School, the WGG utilises photovoltaics, heat pump and the new vanadium redox battery (VR-battery). With these components the building works as a decentralised energy producer. The concept's main medium is electricity, causing an economic and energetic interest to use the photovoltaic power in the building.

Geothermal energy is used as both source and sink. It works as a thermal storage with its more than 99 foundation piles (piles) and its area collector (ground-heat exchanger "Agrothermiefeld") below the sports ground. The geothermal heat pumps cover the heat demand of the floor heating system, the concrete core activation, and the ventilation system.

All class rooms are ventilated manually to ensure the room air quality (CO_2-concentration lower than 1500 ppm) that is essential for educational buildings (Fig. 4). The ventilation system has an integrated heat recovery to reduce heat losses and an adiabatic air humidification for cooling in summer. The supply air reaching corridors, halls, and resting areas is taken in through the class rooms. The exhaust ventilation is accomplished by a central suction system stored in the roof area in each of the two atria. A night time ventilation assists the school's cooling. For rapid heating of the class rooms during the heating period, the rooms are preheated before the beginning of the classes in the morning. The ventilation system can deliver variable amounts of supply air based on demand signalled by the CO_2-concentration ($\leq$ 1.500 ppm). The maximum flow rate is limited to 4.4 1/h.

The cooling of the class rooms and the IT/electrical installation rooms is realised passively (recirculation) in connection with the foundation piles and the area collector. The heat generation is adapted to the heat sources and provides heat with low temperature. This improves the integration and usage of renewable energy and serves as a foundation for energy efficient operation of the building and especially the heat pumps. The renewably generated electricity from the photovoltaics is primarily used in the building. Surplus power is fed into the electricity grid. The energy concept estimates that approximately 70 % of the heat demand will be covered by the heat pumps. Peak load (30 %) will be covered by a gas condensing boiler.

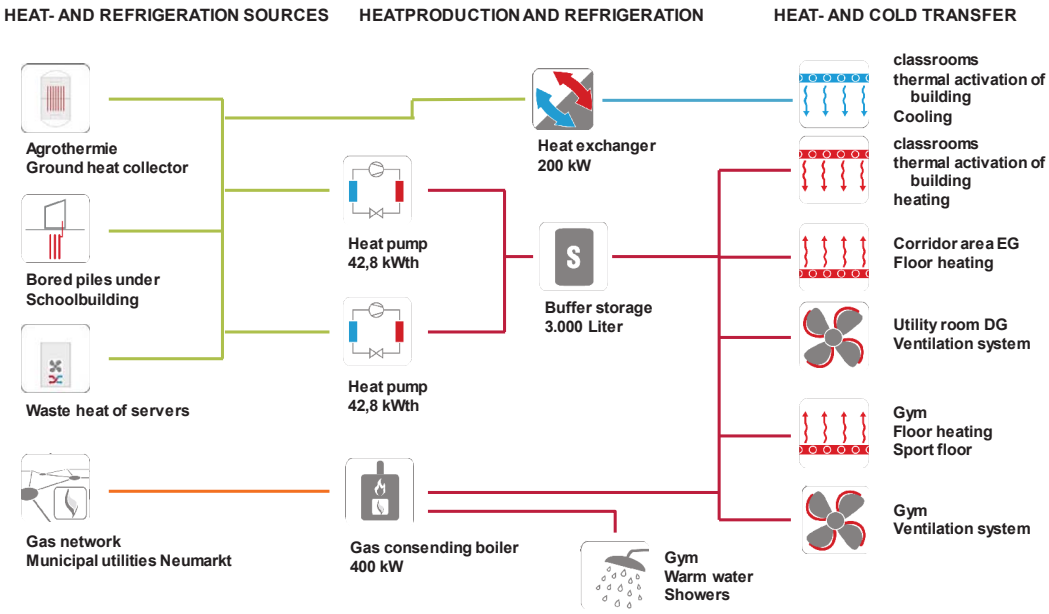

Fig. 4: Energy concept- heating and cooling

With a power capacity of approximately 290 kW_p the rooftop mounted PV-installation on the school building and the gym (Fig. 5) produces the greater part of the electrical power demand in the year's theoretical balance. For reaching the state of the EnergyPLUS building and later a negative primary energy consumption, the power capacity would need to be increased to approximately 500 kW_p. An enlargement of

the system up to 600 kW_p has already been taken into consideration during the planning of the building and the structure is suitable. The enlargement of the installation will be implemented at a later time by the building owner.

The concept includes a usable fraction of the electric energy of 65 % by including a VR-battery. The other 35 % will be fed to the electrical grid. The combination of the PV-system and the VR-battery facilitates a solar coverage of 40 % according to the design (Fig. 6).

Fig. 5: Aerial photos of the PV-installation on the school building (left) and the gym (right)

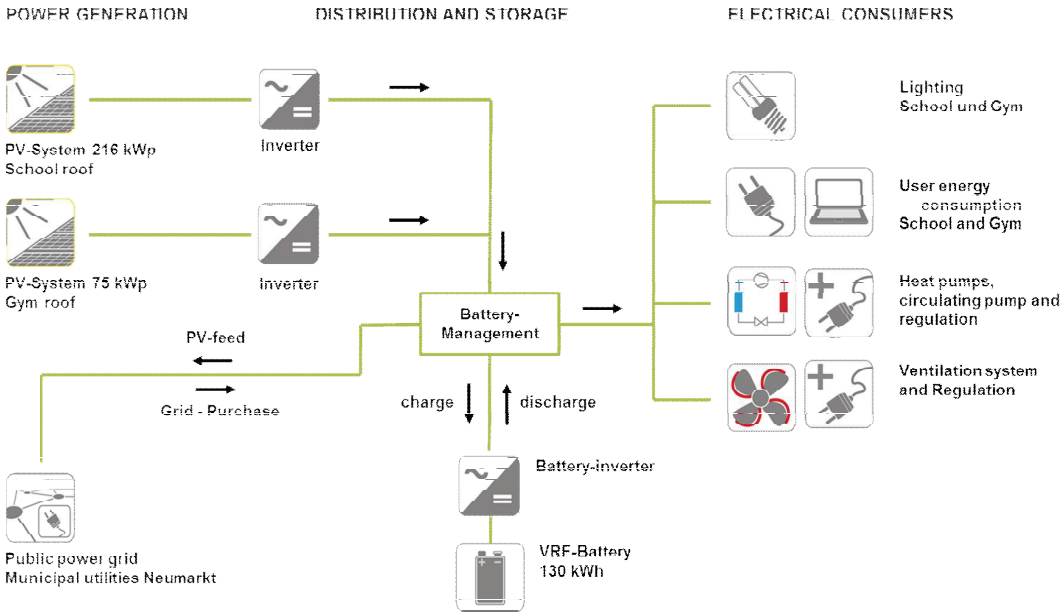

Fig. 6: Energy concept- electricity

3.1 Ground-heat exchanger "Agrothermiefeld"

Below the sports grounds next to the school an "Agrothermiefeld" has been realised. The field, an area collector, has been installed using an innovative technique in the field of geothermics. The piping system is brought two meters into the ground by specially designed plough. An active area of up to 4400 m² has been installed in total (Tab. 1). The installation process has been completed in August, 2015, without any major complications (Fig. 7).

Tab. 1: Information „Agrothermiefeld"

Number of pipes	47 pipes à 93,5 m
Dimensions of pipes	D_a 40 x 3,7
Installation depth	ca. 2,26 m (ploughing)
Collector area	ca. 4.400 m²

Fig. 7: Ploughing with pipe installation and completed sports field including the pipes

3.2 VR-battery

The installation and start-up of the vanadium redox battery manufactured by Gildemeister took place between September and October, 2015. In December the battery took up full operation. In January and February, 2016, minor changes in the internal control system were implemented. Since March 2016 the battery is being charged, discharged, and controlled as designed. Already in August, 2016, an optimisation of the internal controlling parameters has been executed. The overview information about the battery is listed in Tab. 2. Photos of delivery and installation are shown in Fig. 8.

Tab. 2: Overview vanadium redox battery

Manufacturer	Gildemeister
Type	CellCube FB 30-130
Electrical storage capacity	130 kWh
Utilisable capacity	100 %
Max. charge power	30 kW_p
Max. discharge power	30 kW_p
Weight of the filled system	14.000 kg

Fig. 8: Delivery and installed VR-battery

3.3 Energy balance

The energy consumption has been certificated based on the current "Energieeinsparverordnung" (EnEV 2009 / DIN V 18599-1:2007-02). Furthermore, the user electricity consumption is to be supplied sustainably. The heating power consumption takes less than one third of the annual energy demand. Two thirds belong to electricity consumption for ventilation, lighting, and other purposes (Fig. 9).

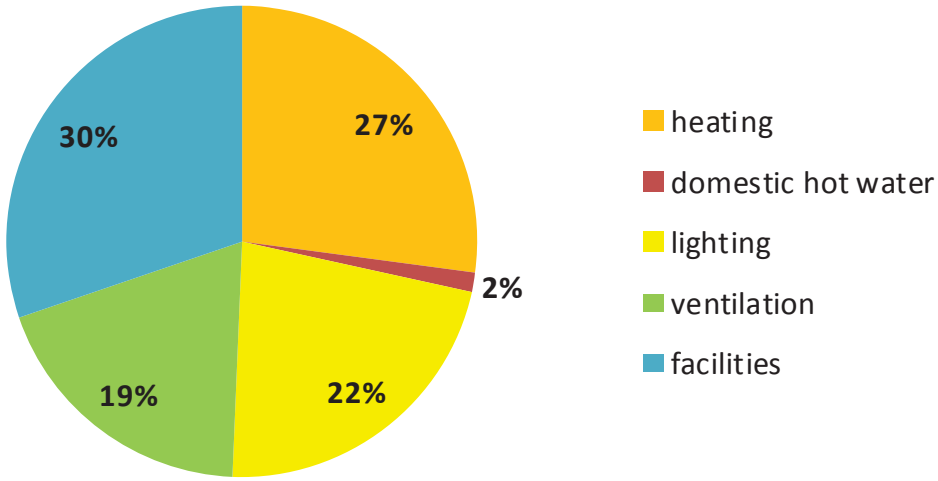

Fig. 9: Overall energy distribution

The quality of the implemented edificial standard and building technology undercuts the legally defined specifications of the EnEV 2009 (EnEV 2014) to the primary energy consumption by approximately 50 %. The characteristics for the EnEV-calculation are summed up in Tab. 3. In addition to the values contained in the balance of the EnEV, the equipment's power consumption is being included. The school complex is supposed produce a net surplus in primary and overall energy. The demand values are calculated based on DIN V 18599 (Fig. 10).

Tab. 3 Characteristics of the WGG-building

	School	Gym
Year of construction	2015	2015
Net floor area (NFA based on DIN V 18599)	12.732 m²	2.855 m²
Heated edifice volume V_e	63.056 m³	17.264 m³
Annual heating energy demand	25 kWh/(m^2_{NFA}a)	
Annual cooling energy demand	10 kWh/(m^2_{NFA}a)	
Overall electricity demand incl. equipments	40 kWh/(m^2_{NFA}a)	

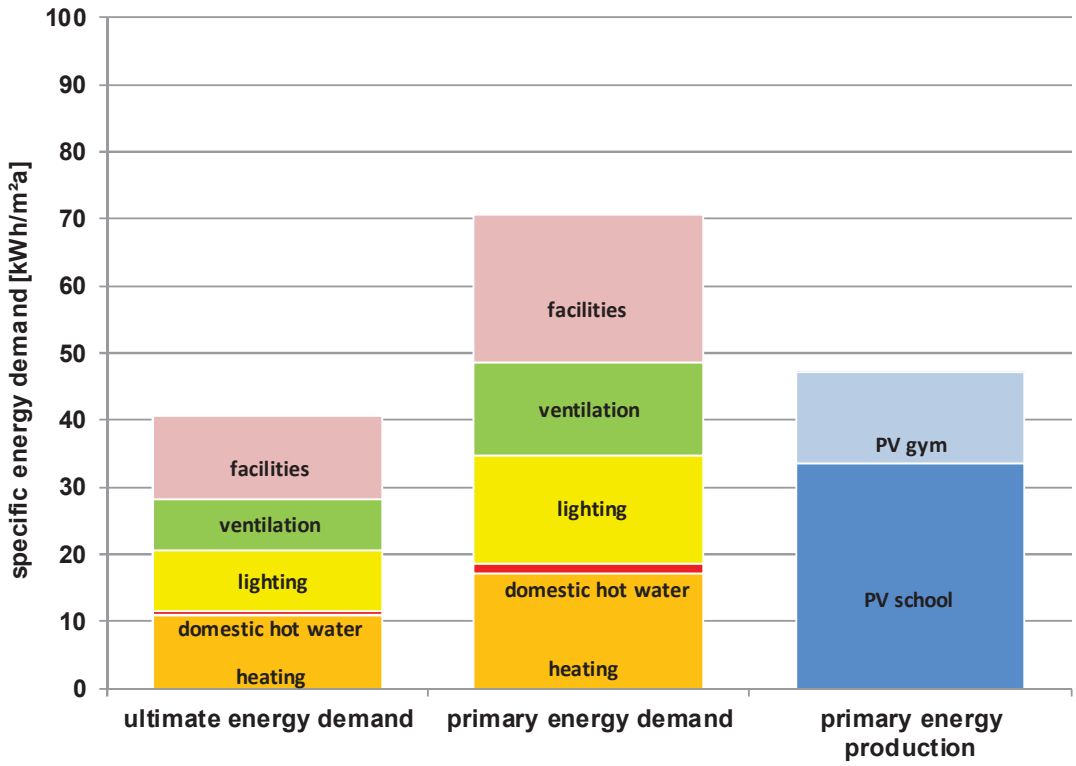

Fig. 10: Energy balance demand vs. production (DIN V 18599)

4. Monitoring

A concept containing a set of indicators for the system and building performance has been developed. It enables the analysis and assessment of the energy efficiency and different modes of operation. Based on the definition of aims, a measuring and monitoring concept has been realised. Respective specification for process measuring and control technology / building automation have been formulated.

Due to delay in construction and the installation of the process measuring and control technology, the recording of data started in May / June 2015.

4.1 Comfort monitoring

Fig. 11 shows the results of the comfort monitoring in the rooms 115, 216, and 230 in July 2016. The results show that the room air quality is mostly held within an acceptable or good state. Room 230 temporarily reaches temperatures >26 °C. The room is an IT room in the inside of the building causing greater thermal loads. By tendency, the room temperatures lie within the warmer comfort zone. The night time ventilation (01:00 to 06:00) achieves a temperature drop of 1 or 2 Kelvin. The average room temperature of the three rooms lies between 24 and 25 °C.

Fig. 11: Room temperatures in July 2016 between 07:00 and 18:00

The maximum CO_2-concentration of 1500 ppm is satisfied on most occasions in all of the three rooms (Fig. 12). Temporarily the limit is succeeded. On average, the concentration during the classes (07:00 – 18:00) moves between 515 and 730 ppm. This corresponds with good comfort.

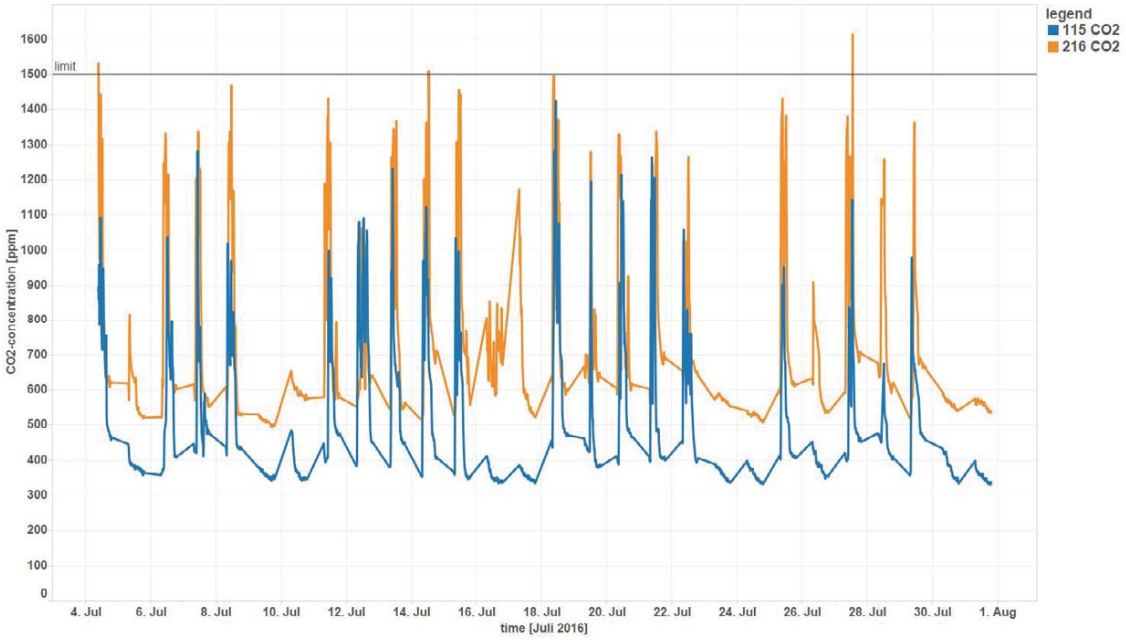

Fig. 12: CO_2-concentration in the rooms R115 und R216 July 2016 between 07:00 and 18:00

4.2 PV-production

Fig. 13 shows the electricity production of the PV-plant, the overall electricity consumption, and the resulting amount of coverage in the week of 11.-17.07.2016. Depending on the PV-power, the electricity demand of school and sports hall can temporarily be covered entirely by the plant (coverage = 100 %). The weekly average is approximately 40 %.

The photovoltaic electricity production in the time between 01.01. and 31.07.2016 amounts to 116,3 MWh (400 kWh/kW_p). Of this amount, 60,6 MWh are being consumed in the school and sports hall, corresponding to an ad-hoc-consumption of about 52 %.

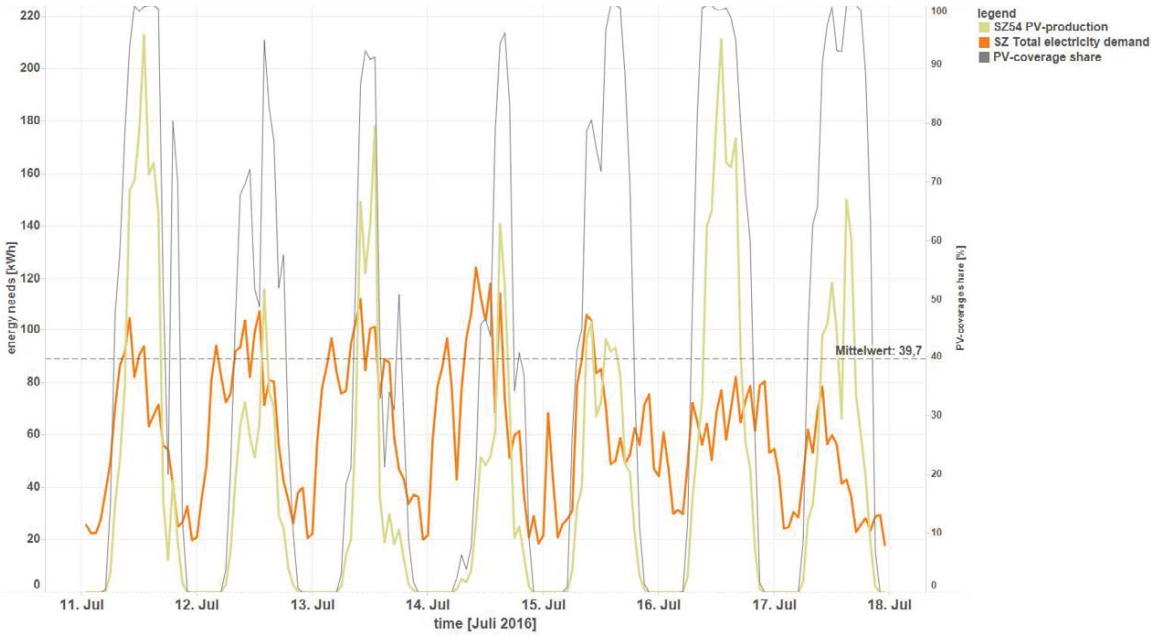

Fig. 13: PV-production, electricity consumption and amount of coverage (11.-17.07.2016)

4.3 VR-battery

After initial difficulties with the control system, the VR-battery is in orderly operation since 18.08.2016. During the day, the battery is being charged (up to battery level 100 %). During the night time, the battery is discharged down to a level of 5 %. Fig. 14 shows the battery level in the time 19.-26.08.2016.

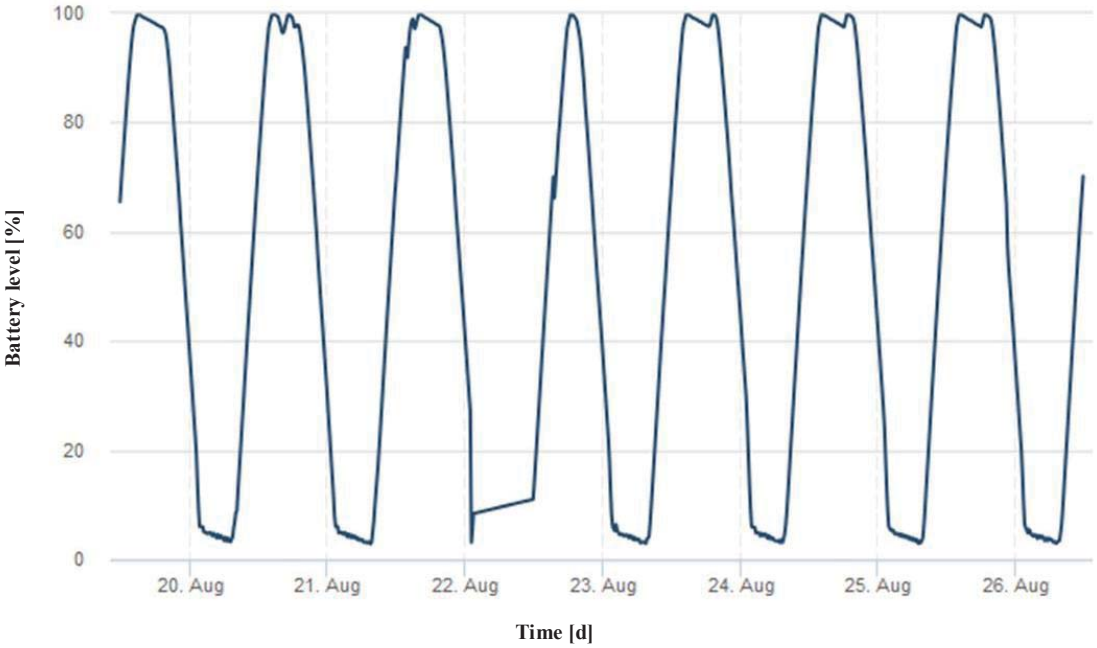

Fig. 14: Battery level in the time 19.-26.08.2016

5. Conclusion

The pilot project gives a great example of future building standards. It reveals the frame for the development and evaluation of necessary methods and tools for educational building and public edifices.

The scheduled completion of the technical system at the beginning of the school year in August 2015 was tenable. The school's operation started in the winter term 2015/16, though with limited and unplanned operation of heating and ventilation. The heat pumps were activated in February 2016. From August 2015 to February 2016 the school and sports hall were solely heated by the condensation boiler which was intended as a peak-load unit. The concrete core activation was started up in January 2016. Before that, the heat was transferred solely by ventilation air and floor heating.

The notable optimisation potential of the building system became visible in the course of the first months of operation. The results and insights uncovered in this research project help avoiding these problems and optimising operation in future construction projects. The new buildings serve as role models and are, due to their typical use and characteristics, suitable to be multiplied.

Only in practical application, singular technologies can be observed in their effective behaviour and integrated into the construction process. The operator's and user's ability to work and maintain the systems in a suitable manner can also only be assessed after the installation and start-up of the actual machinery. The necessity of early planning, documentation, and intensive surveillance for the successful implementation of an energy concept containing low-ex-heat sources has been proven within this project. The final realisation of the project is only possible in interdisciplinary cooperation of all parties involved.

6. Expression of thanks

The research project „EnOB: Monitoring und Betriebsoptimierung des Willibald-Gluck-Gymnasiums in Neumarkt (i.d.OPf.)“ is funded by the Federal Ministry for Econimic Affairs and Energy under the reference number 03ET1308B.

Conference Proceedings

EuroSun 2016
Palma de Mallorca (Spain), 11 - 14 October 2016

Study of Passive Solar House SOLAR-SB

Pavel A. Kazantsev [1], Valeriy V. Knyazhev[2] and Vladimir V. Loschenkov[2]

[1] Engineering school of Far Eastern Federal University, Vladivostok (Russia)

[2] Institute of Marine Technology Problems FEB RAS, Vladivostok (Russia)

Abstract

One of the first specially designed passive solar house on Russian Far East monitoring in winter 2015-16 has confirmed a high efficiency of a traditional architectural model of solar heating in the natural climatic conditions of the south part of region. Continuous examination of the passive system for the all cold season in the house without additional heating sources was held in the region for the first time. The revealed causes of system's high inertia in the morning hours, as well as a positive effect of additional solar warming of the house in the evening time, will allow developing measures in perfecting the passive solar systems of residential buildings in the region.

Keywords: *solar heating, solar house, solar architecture, ecological architecture, passive solar system.*

1. Introduction

Passive solar heated houses design in the Russian Far East was a design in drawings to the present. For this reason it was impossible to confirm the effectiveness of passive solar systems here, which also stopped their development in the mass construction. For example, in 2005, a designer company Argus-Art developed an experimental project design of a single-family eco-house Solar-5 (authored by Pavel Kazantsev, an architect) [5]. The active solar system of the eco-house was designed by Laboratory 07 of FEB RAS IMTP (Fig.1).

Fig. 1: Eco house Solar-5. Project views

doi:10.18086/eurosun.2016.01.10 Available at http://proceedings.ises.org

According to the lab calculations, the passive solar system accounted for up to 57% of the house heating during the cold season. (Fig.2). This result was mainly achieved via a non-standard architectural solution patented as invention of an energy-efficient architectural form RU2342507 and awarded at international and Russian exhibitions.

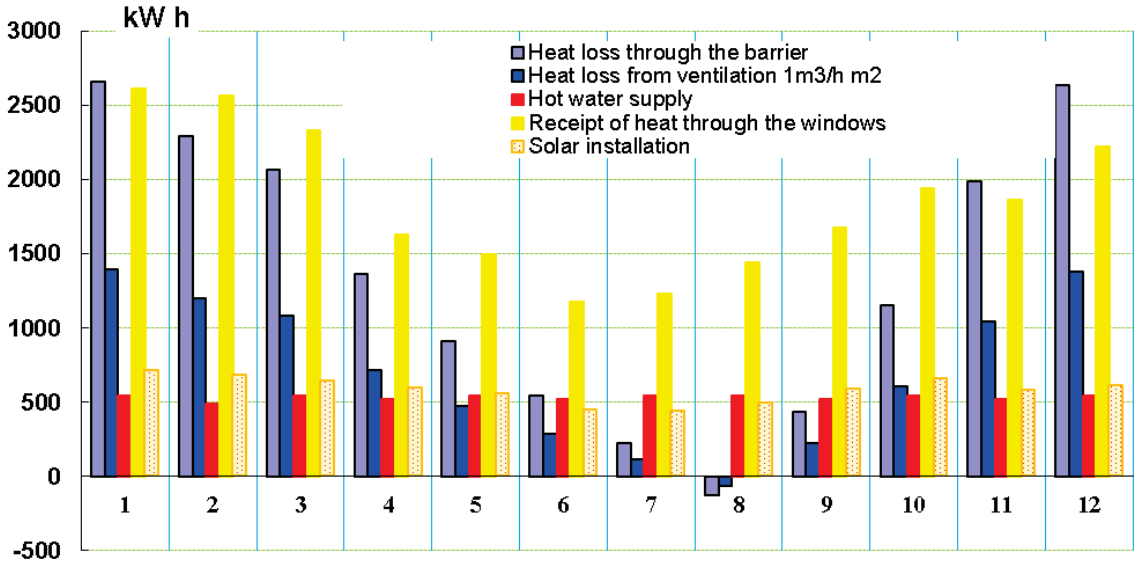

Fig. 2: Estimation of the heat balance of eco house Solar-5 throughout the year. According to the calculation, the contribution of passive and active solar heating system should reach 81%

In 2011, the FESPI/FEFU Technopark implemented a one-floor sample of the eco-house – a training-experimental eco-module Solar-5m (Fig.3); however, there was no opportunity to confirm the high expected properties of the passive solar heating in practical terms [3].

Fig. 3: Training-experimental eco-module Solar-5m

Therefore, in order to define the properties of the passive solar system in the conditions of south part of Far East, research was conducted in the winter of 2015-16 at the constructed single-family house with passive solar heating. The research was conducted jointly with the Training studio of resource-saving architecture within the Department of Architecture and Urban Planning in FEFU and Laboratory 07 of the FEB RAS IMTP – Energetics of the Underwater Robotic Complexes. Absence of the heating sources other than direct solar radiation during the observation period was the primary criteria for choosing the object. It is for this reason that measurements have been allowed in an uninhabited house with an incomplete interior finish, but practically closed external warm contour.

2. Specific features of the eco-house architectural solution

A single-family house with passive solar heating has become an object of this research. The house shell is made of pressed straw panels. The project design was developed in 2012-2013; the house has been under construction since June, 2014 in Primorsky Krai, Nadezhdinsky district, Novyi settlement. The design project was authored by architects Pavel Kazantsev (FEFU, Vladivostok) and Anna Lyashko (M-ARC, Vladivostok). The structural design and straw panel technology were developed by Domantas Surkys, Audris Krucius, Marius Tarvidas (Ecococon company, Vilnius, Lithuania). Customer: Vladimir Kazantsev (Fig.4, 5).

Fig. 4: General view of the house from the south-east in the winter of 2015-2016

Fig. 5: The design of the house at the end of construction

An architectural model traditional for temperate latitudes of the Northern Hemisphere was taken as a basis for structuring the passive solar system of the pilot straw eco-house Solar-Sb. A double-height atrium with a south-facing stained-glass window and dormer windows in the roof is a building core of the house. The atrium was to have included

massive inner walls providing for the thermal inertia of the house, but in the process of construction they were replaced with a frame (Fig.6). Living room spaces open into the atrium. In depth the house is divided in 2/3 proportion of living space in the south and 1/3 of the buffer space from the north, with the account for the depth of solar ray penetration in winter. A sleeping area on the second floor also takes into account the effect of "heat sack" and reduces the heating expenses for the first floor area at night. The width of the house is increased providing for its exposure to the sun. The northern windward façade is blind; the roof pitch is lowered to the wearing floor of the second floor. Balconies in the shorter side of the house form intermediate half-open spaces providing for additional protection in bad weather conditions. They are supposed to reduce the façade overheating in summer (in combination with a vertical green screen) and cover the eastern façade from slanting rains.

Fig. 6: The interiors of the house during the observation period in the winter 2015-2016.

The works are not completed

The attic on the third level is a part of living space; however, it will be separated from the warm core of the house with heat-insulated dividers to ensure its seasonal use. In the first half of the summer, the windows in the opposite walls of the attic contribute to additional airing of the atrium through the divider opening by air draft under the roof ridge. A connected structure of the roof is the only innovation in the shape of the straw house: its angles are optimized for installing the solar collector of water heating system (the Sun in the late January) and the photoelectric system (the equinox solar altitude in Vladivostok latitude).

The major technical and economic features of the project are as follows: construction area 117 m^2., living space 133.7 m^2., total area 187.8 m^2. The type of passive solar system: Direct gain (Haggard, Bainbridge, et al., 2009). The windows are triple-pane selective Low-e Ro = 0.7-0.76 m^2 KW^{-1} (according to the design project), the area of southward stained-glass windows – 25.0 m^2, thermal area at the moment of observation – 24.0 m^2 light-grey concrete floor with 0.15 m insulation, without matte black coating. External walls are made of 3.0x0.8x0.4m straw panels with 120 kgm^{-3} density and 15% humidity level of the straw; the heat conductance in the panel center is U = 0.23 W $m^{-2}K^{-1}$.

3. Research provisions

Two types of measurements have been made. The first one involved operator's recording of internal air temperature with alcohol thermometers in three points: first, second floor and attic, and external air temperatures – near the northern façade at 9 a.m., 1 p.m., and 7 p.m. in order to reveal the general dynamics of internal (by levels of the indoor living space) and external air temperatures between December 14, 2015 and February 19, 2016 (the coldest period in southern Primorsky Krai, 68 days), (Fig.7).

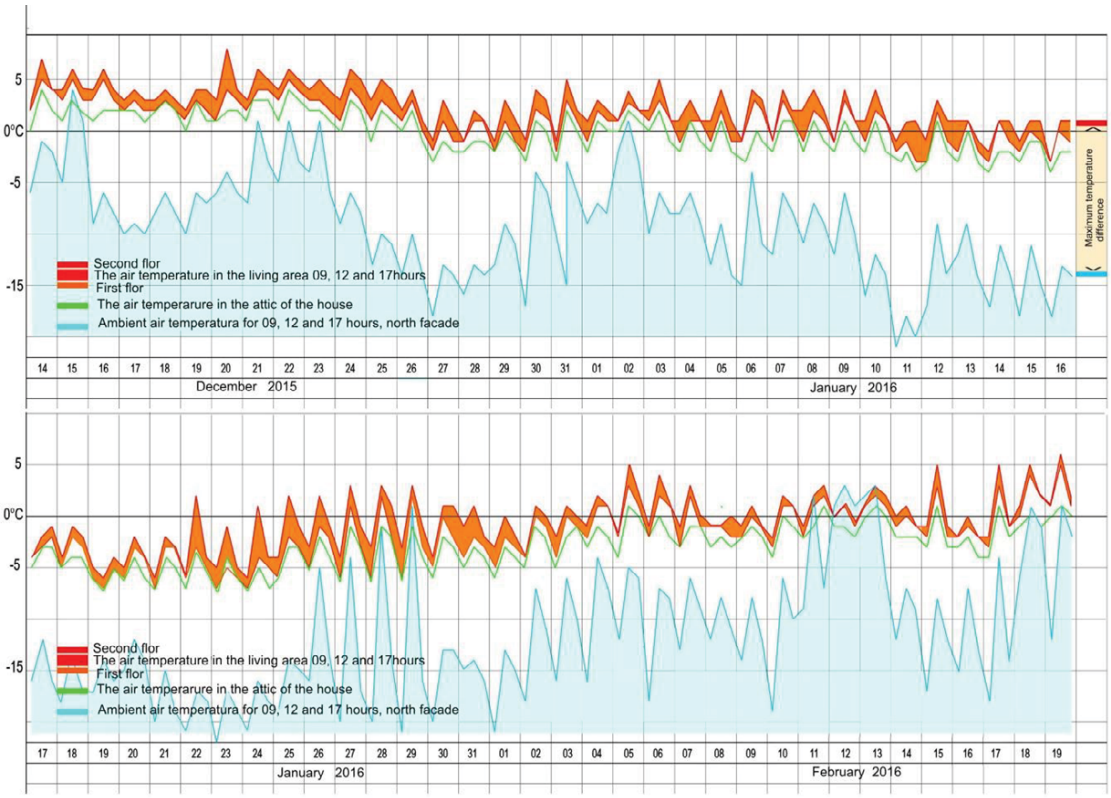

Fig. 7: Operator record results from December 14, 2015 to February 19, 2016

The second type of measurements involved a non-stop recording of external meteorological parameters at automated meteorological stations HOBO Weather Station between February 8 and March 14, 2016 (the complete observation period until March 31, 2016) including the speed and direction of winds, humidity, temperatures, and rate of solar radiation on horizontal surface tilted southward by 450, on southward vertical surface of the vertical stained-glass windows of the house as well as a non-stop recording of the 24-hour dynamics of temperature, air humidity indoors and the rate of solar radiation entering the house through the southward stained-glass window (Fig.8.).

The software developed by HOBOware Pro Onset Computer Corporation was used to assess the observation results at automated meteorological station HOBO Weather Station. Comparison of the data obtained from both types of measurements of the indoor air temperature at the level of 1st and 2nd floors between February 8 and February 19 has shown a high degree of similarity between the results of operator's recordings and observation results at the automated station.

4. Observation of passive solar system properties

Winter temperatures in Primorsky Krai. are much low than those in the same latitudes of the European part of Russia. However, substantial solar resources of the territory can compensate for its low temperatures. Thanks to its south latitude and monsoon climate, Primorsky Krai. has a high potential for developing the generation of thermal solar energy. Radiation balance in the north of the region is 1885 MJm^{-2}, in the south – 2010.2 MJm^{-2}, the length of the sunshine is 1900-2500 hours per year [1]. The majority of sunny days are observed in the cold season (Fig.9).

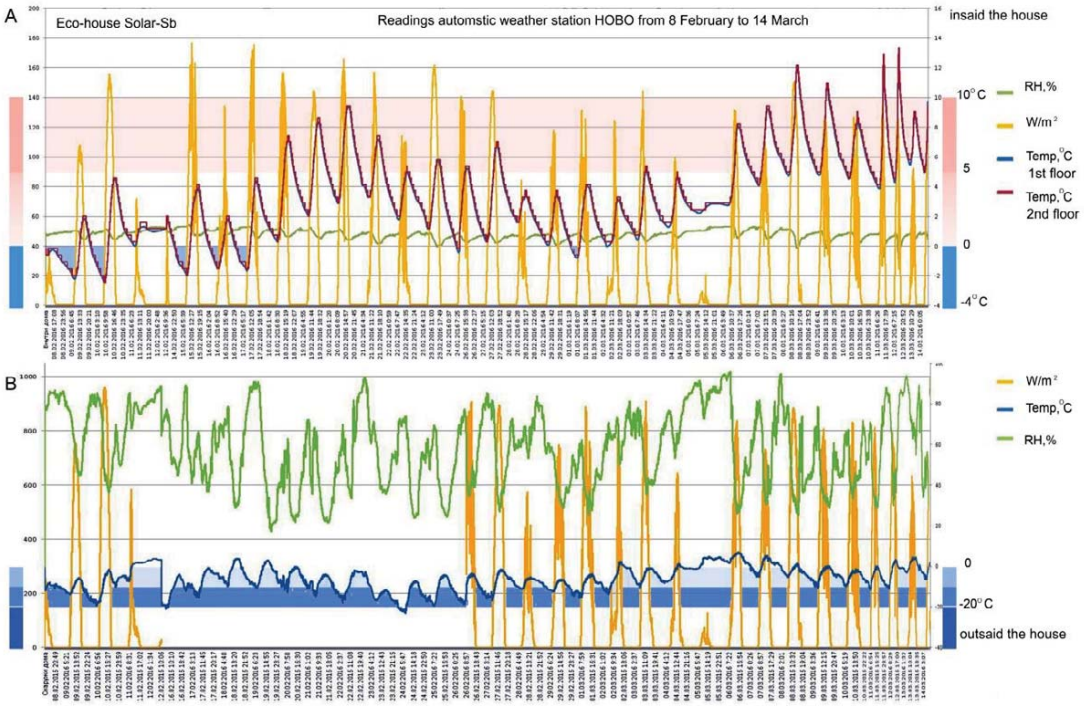

Fig. 8: General view of the readings of the automatic weather station from 8 February to 14 March

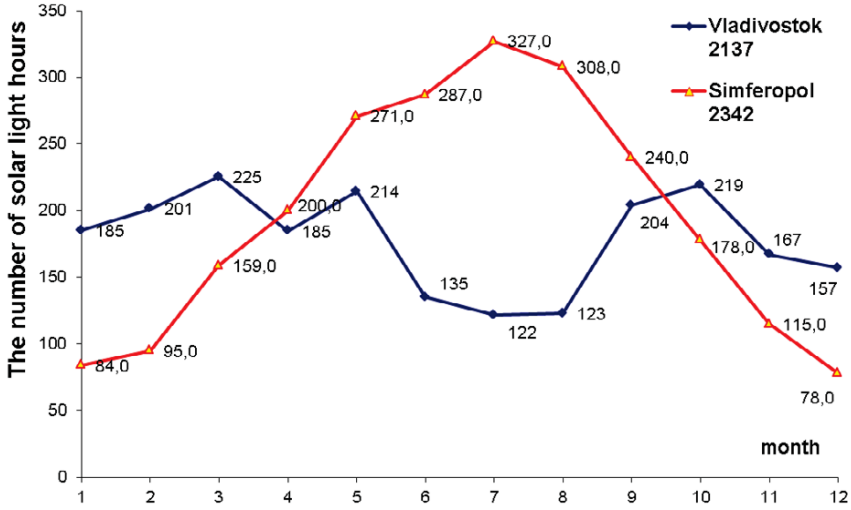

Fig. 9: Duration of solar glowing. Vladivostok and Simferopol

In general, during the observation period between December 14 and March 14, the air temperature in the living spaces of the house (1 and 2 floor) was around 0ºC. The temperature was slowly going down from positive numbers in December (+9ºC on December 20) until the mid-January, reaching the minimum numbers on January 9 after a two-day snowstorm (-7ºC at 13.00 and -4ºC at 17.00). The indoor air temperature started growing with the growing sunshine exposure comprising +7ºC at 1 p.m. on February 19 (Fig.10,11). Out of 92 observation days, the daytime air temperatures below 0ºC were recorded inside the living section of the house only during 6 days – January 17-21 and January 23. The temperature about -5ºC inside the house at night was registered only for 4 days. At the same time, the daylight air temperature -10ºC and below in the basin of the horticultural cooperative Serebryanka (Novyi settlement) was observed for 26 days, below -15ºC at night – for 34 days.

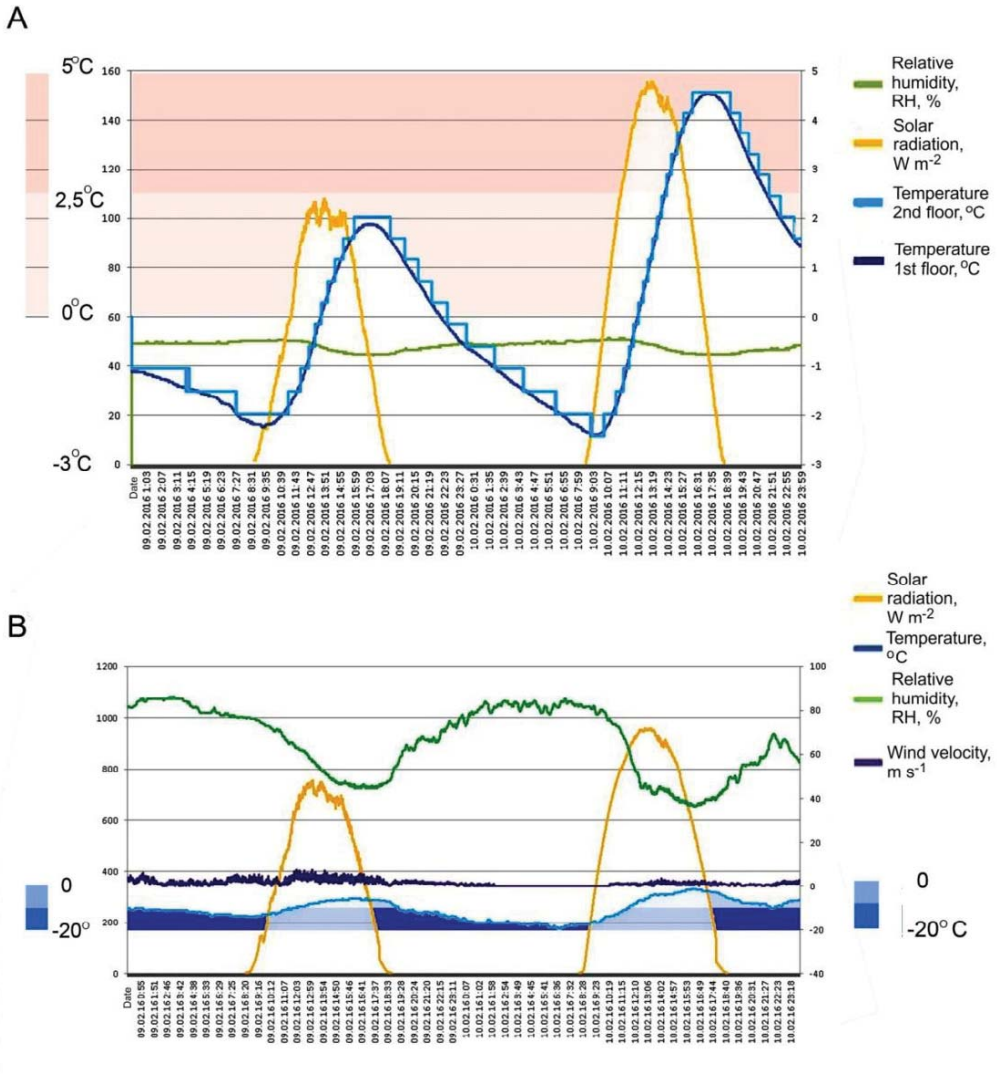

Fig. 10: General view of the readings of an automatic weather station on 9-10 February.

A - in the house, B - outside the house.

Maximal numbers of integral flow of solar radiation through the vertical southward stained-glass window of the atrium were 150 – 179 Wm^{-2} around noon – much lower than the numbers observed on the vertical outside surface of the house – 775 – 1039 Wm^{-2}. All figures and tables should be cited in the text, numbered in order of appearance and followed by a centered title. All table columns should have a brief explanatory heading.

Maximal difference between external and internal air temperatures in the coldest days with minimal cloud cover have reached 12 – 20ºC (for example, 11.01, 23.01., 9-10.02., 16.02). During the days with clear sky, the lowest temperatures inside the house were registered about 9 a.m., the temperature minimum held until 11 a.m. despite the incoming solar heat through the southwards stained-glass windows approximately from 9 a.m. Starting from 11 a.m., the air temperature in the house grew substantially reaching the maximal numbers by 5-6 p.m. when incoming solar heat through the southward window was already dramatically low. The observed maximum of internal temperatures lay behind the maximum by 3 hours approximately. (Fig.10,11; Tab.1,2)(days with clear sky and minimal outdoor temperature in February).

Good inertia properties of the house were also shown by the obvious consistency of indoor air temperatures regardless of dramatic changes in the outdoor air temperatures; for example, from -6ºC down to -21ºC in three days in January (9-11.01, Fig.7). High circadian dynamics of external temperatures can probably be attributed to the effect of the night air drainage and accumulation of cold air in the basin of the horticultural cooperative Serebryanka (Novyi settlement).

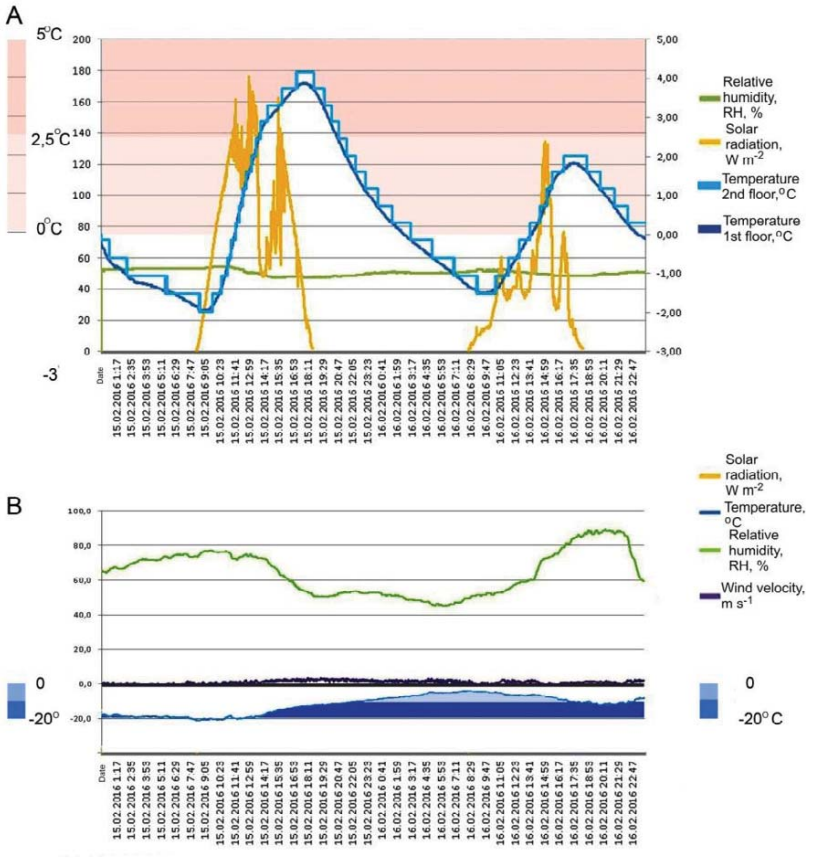

Fig. 11: General view of the readings of an automatic weather station on 15-16 February.

A - in the house, B - outside the house

Tab. 1: Sample readings automatic weather station on 9-10 February

Local time	09:00	10:00	13:00	14:00	17:00	18:00	21:00	24:00	03:00	06:00	09:00
Temperature, 1st floor, TºC	-2,18	-2,18	-0,59	+0,41	+1,89	+1,75	+0,49	-0,62	-1,27	-1,84	-2,39
Temperature, 2nd floor, TºC	-1,97	-1,97	-0,6	+0,29	+2,03	+2,03	+0,73	-0,15	-1,05	-1,51	-1,97
Temperature outdoor, TºC	-13,8	-13,1	-8,63	-7,38	-6,19	-6,73	-12,4	-14,6	-16,3	-18,2	-16,8
Solar radiation	4.4	23,1	104,4	104,4	44,4	10,6	0,6	-	-	0,6	14,4

W m^{-2}, inside											
Solar radiation W m^{-2}, outside	29,4	179,4	738,1	775,6	334,4	90,6	0,6	-	-	0,6	1 58,1
Humidity in the house, %	50,25	50,25	49,25	47,25	44,75	44,75	47,25	49,25	48,75	49,75	50,25
Humidity outside, %	76,25	73,25	58,25	52,75	45,25	45,25	67,75	76,25	84,25	79,25	81,75
Wind velocity, NW, m s^{-1}	3,53	2,23	6,31	4,45	2,97	3,71	2.01	0,93	0,0	0,0	0,0

Tab. 2: Sample readings automatic weather station on 15-16 February

Local time	**18:00**	**21:00**	**24:00**	**03:00**	**06:00**	**09:00**	**13:00**	**14:00**	**18:00**	**21:00**	**24:00**
Temperature, 1st floor, TºC	+3,88	+2,37	+0,88	-0,7	-0,78	-1,41	-0,39	+0,05	+1,80	+0,79	-1,12
Temperature, 2nd floor, TºC	+4,15	+2,46	+1,17	+0,29	-0,6	-1,05	-0,15	+0,29	+2,03	+1,17	+0,29
Temperature outdoor, TºC	-15,8	-16,1	-17,6	-17,8	-20.2	-17.2	-9.7	-8,26	-5,05	-10,3	-8,38
Solar radiation W m-², inside	21.9	0,6	-	-	0.6	09,4	41.9	63.1	06,9	0,6	-
Humidity in the house, %	47,25	47,75	50,25	50,75	50,25	51,25	50,75	50.4	48,25	49,75	50,75
Humidity outside, %	56,25	58,25	65,25	66,25	73,25	71,75	52,25	50,75	51.25	80,75	59,25
Wind velocity, SE, , m s-1	0,3	0,3	0,56	0,0	0,74	1,86	2,41	1,3	0,16	0,56	2,41

5. Observation results

Disadvantages of the traditional scheme: Observation results have shown the need in adding a convectional solar system to work mostly in the morning to the passive system of solar heating of the house. They also seem to confirm a positive effect of additional solar heating of the house in the evening in February through the westward stained-glass windows (the total area of stained-glass windows is 12.5 m²; the amount of incoming solar radiation was not estimated).

Evaluation of the passive system contribution: As a result of unfinished interior works, the volume of space heated by the passive solar system was a third bigger than designed in the winter of 2015-2016. Thus, there were no dividers between the living and the buffer zones, there was no warm floor between the second level and the attic, and the attic was not insulated completely; the wind porches had not been built yet for the front and back doors. Also the interior straw panels were not covered with clay plaster. This partially explains a high inertia of the system in the morning hours of solar exposure as well as a substantial circadian dynamics of temperatures inside the house during the

observation period (in some days 6-7°C decrease from the day maximum to the minimum at 9 a.m.).
Nevertheless, to confirm the effectiveness of passive solar heating in the southern Far East, the data obtained can be taken into account. First of all the data of the passive system should be expected to improve after the warm contour of the attic is completed. Also, a passive solar system with direct gain was not designed as the main heating system, but the data obtained showed its high potential for contributing to the overall house heating system. It also took into account the fact that continuous monitoring of the passive solar system during the all cold period was carried out in the region for the first time.

6. Additional heating the house from renewable energy sources.

Taking into account the obtained data, we can propose that the traditional architectural solution can provide relatively comfortable conditions on a sunny winter day, replenishing up to 50% of the required heating. Since the number of sunny days per winter is about 80% it is possible to consider the autonomous system of generating heat from renewable energy sources for single-family houses in region.
In accordance with the project design, the passive solar system works together with the active solar system of heating and hot-water supply based on vacuum trickle collectors SUNRAIN TZ58-1800-25R1 (was not installed yet during the observation period). Photoelectric panels were supposed to support the autonomous functioning of the solar system of heating and water supply. But the system improvement may be proposed.
In the conditions of cold monsoon climate of Russian Far East, this design of a house needs a combined system of heating and cooling with a solar-geothermal heat pump (GSHP) [6, 7]. A hybrid system and seasonal accumulation of heat surpluses from the solar system and cold from the winter night air will provide for 90% of the annual heating and cooling. The remaining 10% will be used as electricity for devices, automatic equipment, a reverse-running heat pump and will be provided by the photoelectric panel. The exploitation results obtained for the hot-water supply and heating solar panels created by the Laboratory 07 of FEB RAS IMTP (Fig.12), [8], confirm the efficiency of using solar power in south part of Far East in a single-family house construction, which is of great importance in terms of preserving natural resources and establishing a prospective sustainable model of natural resource exploitation in the region.

Fig. 12: Experimental solar installation of hot water and heating.

7. Conclusion.

The research conducted in the constructed passive solar house in the winter of 2015-16 with no additional heating sources is relevant since it has confirmed a high efficiency of passive solar architectural solutions, even within a traditional architectural model of the solar house. High efficiency of a passive solar system and simultaneous use of a seasonal active solar system make it possible to consider dwelling houses autonomous from the heating utility networks in the region.

8. References

[1] *Derkacheva L.N., Rusanov V.I.,* 1990. The climate of the Primorsky Territory and its impact on human activity. Vladivostok, Pacific Institute of Geography FEB RAS.

[2] *Haggard K., Bainbridge D., Aljifant R*.., 2009 Passive solar architecture pocket reference book. ISES, Germany.

[3] *Kazantsev P.A.,* 2012. Ekomodul Solar-5M/S for educational and research purposes. Journal of the School of Engineering FEFU, №2 (11), 21-25.

[4] *Kazantsev P.A.*, 2015 Passive solar homes: 2012-2014 projects and construction. II All-Russia Scientific Conference "Energy and resource efficiency of low-rise buildings" (Novosibirsk, March 25, 2015)- Novosibirsk Institute of Thermal Physics SB RAS, 17-28.

[5] *Kovalev O.P., Volkov A.V., Loschenkov V.V., Kazantsev P.A.*, 2007. Sunny house in coastal areas of the Primorsky Territory. Technical problems of the world's oceans, conference materials October 2-5, 2007, Vladivostok, Dal'nauka, 489-493.

[6] *Molotkov V.E., Loschenkov V.V.,* 2013. The combined system of power supply in water treatment and heating of industrial facilities mariculture. Proceedings of the Fifth All-Russian Scientific and Technical Conference "technical problems of development of the world's oceans" Vladivostok, Dalnauka, 358-362.

[7] *Slesarenko V.V., KopylovV.V., Knyazhev V.V.,* 2010. Evaluating the effectiveness of solar power plants in district heating systems. Bulletin of the Far East Branch. Russian Academy of Sciences. 3, 125-130/

[8] *Slesarenko V.V., Kopylov V.V., Knyazhev V.V.,* 2010. Application of combined solar systems with heat pump on Far East of Russia. Proceedings of conference RENEWABLE ENERGY 2010, 27 June – 2 July, Pacifico Yokogama, Yokogama, Japan, O-Th-8-2.

Conference Proceedings
EuroSun 2016
Palma de Mallorca (Spain), 11 – 14 October 2016

BIPVT System Integrated with GSHP for Net Zero Energy Buildings

E. J. LEE[1,2*†], E. C. KANG[1], K.S. LEE2, M. Ghorab[3], L. YANG[3], E. ENTCHEV[3]

[1] Korea Institute of Energy Research, Deajeon, Republic of Korea

[2] University of Science and technology, Deajeon, Republic of Korea

[3] Natural Resources Canada, CanmetENERGY, Ottawa, Canada

Abstract

One way to improve the efficiency of renewable energy system is by integrating two or more devices or so called the hybrid system. In this study, the change of the Ground Source Heat Pump (GSHP) seasonal performance factor will be observed when it is integrated with Photovoltaic-Thermal (PVT) to meet the multiple loads of house and office. Basically, the strategy to get this efficiency improvement is by combining the water outlet of GSHP which firstly heated by desuperheater and the output of PVT in one (preheat) tank. In the solar preheat tank, the heat from PVT will be added through heat exchanger as the supplementary to the hot water which is previously from city water passing desuperheater of GSHP. The final output of GSHP with the heat addition from PVT and the efficiency of stand-alone GSHP will be compared. GSHP-PVT hybrid system has the lowest energy consumption followed by GSHP stand-alone and reference case (simple sum of house and office) with 31.8kWh/m2-yr, 78.7kWh/m2-yr and 107

Keywords: *Ground Source Heat Pump (GSHP), Photovoltaic-Themal (PVT), Multi-Load, Energy*

1. INTRODUCTION

The requirement for alternative low-cost and efficient energy sources has triggered people to the development of Ground Source Heat Pump (GSHP) system for residential and commercial heating and cooling applications. Earth temperature always sTab. throughout the year and this is also the reason why GSHP is very attractive. The heat pump on GSHP system operates using the same cycle as a vapor compression refrigeration cycle. Both systems absorb heat at a low temperature level and reject it to a higher temperature level. The difference between these two systems is that a refrigeration application is only concerned with the lower temperature effect produced at the evaporator, while a heat pump may be concerned with both cooling effect produced at the evaporator as well as the heating effect produced at the condenser in GSHP system. A reversing valve system is used to switch between heating and cooling modes by changing the refrigerant flow direction. GSHP system can be seen in Fig.1

A photovoltaic-thermal or PVT module is a combination of photovoltaic cells with a solar thermal collector, forming one device that converts solar radiation into electricity and heat simultaneously. The excess heat that is generated in the PV cells is removed and converted into useful thermal energy. The PVT system can produced efficiency up to 75% and as the efficiency of PVT increases, the cell temperature is decreased. PVT can be distinguished into two types based on the manufacturing process: PVT collectors and PVT panels. PVT collectors are very similar in appearance to a regular solar thermal collector, consisting of a PV-covered absorber in an insulated collector box with a glass cover. PVT panes on the other hands are similar in appearance to regular PV panels. Due to lack of extra insulation and a glass cover, PVT panes have a lower thermal efficiency but higher electrical yield. Fig.2 shows the PVT panels. In this study, two cases will be compared which are GSHP system and GSHP coupled by PVT system in order to perform the annual performance analysis.

doi:10.18086/eurosun.2016.01.12 Available at http://proceedings.ises.org

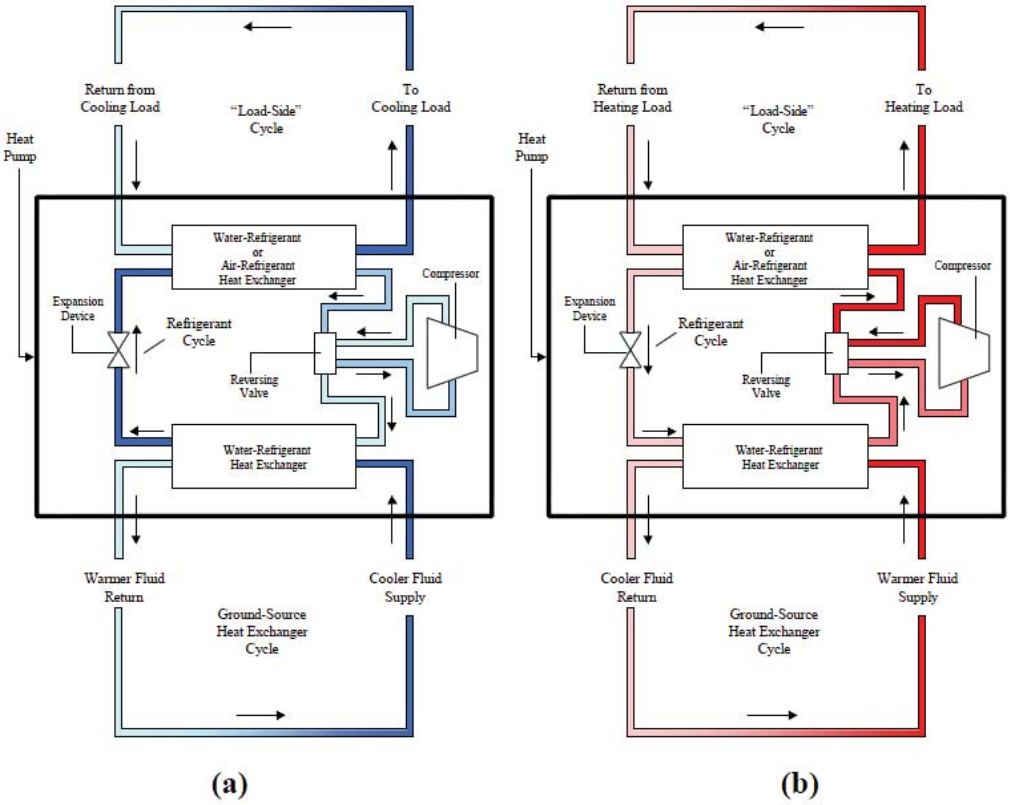

Fig.1. Ground Source Heat Pump (GSHP) Cycle in (a) Cooling mode and (b) Heating Mode

Fig.2. PVT Module

2. MICRO-GENERATION SYSTEM MODELING FOR EACH CASE STUDIES

In this study, three systems will be introduced for applications in residential and commercial buildings. Case one is simple sum of residential and commercial buildings (house and office) heating/cooling demand. Both thermal loads of residential and commercial buildings are provided by boiler and chiller system also fan coil unit as presented in Fig.3. The fan coil unit is located inside the building and a duct system is used to distribute the cooling/heating air inside the building. Domestic hot water (DHW) tank in installed inside the house and connected with the boiler via pipelines. This case will be the reference case for this simulation study.

Case two is a load sharing system with Ground Source Heat Pump (GSHP) to meet the combined load of houses and offices. Case two is load sharing hybrid system of GSHP integrated with PVT module. Load sharing in this case means houses and offices will use one system to provide heating and cooling demand instead of using separate system for each house and office. In case one, as presented in Fig.4, uses GSHP system to provide the heating/cooling demand instead of boiler/chiller system (conventional system). The desuperheater of GSHP is used to preheat the city water for DHW usage. A hot water storage tank is equipped to provide space heating and DHW heating. A gas burner is located at the bottom of the tank to provide supplementary heat in cases where GSHP alone cannot provide sufficient heat in very cold days or to heat the DHW water in summer. Water from the hot water tank is supplied to the two buildings through pipelines for DHW demand loads. In this case, the city water has enough pressure to flow the water in the system without using a pump. A cold water storage tank is used in the cooling season to provide chilled water for the cooling coils. Three way valves are used to switch between GSHP heating and cooling loops in winter and summer cooling seasons.

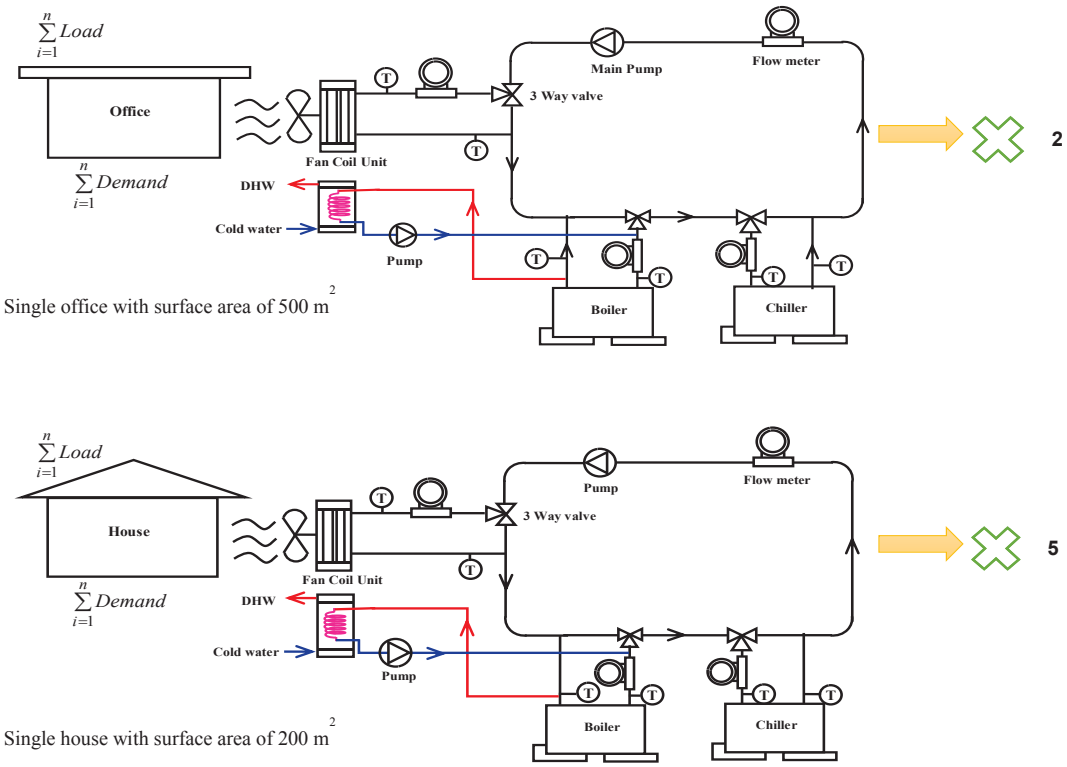

Fig.3. Simple Sum of Residential and Commercial Buildings System

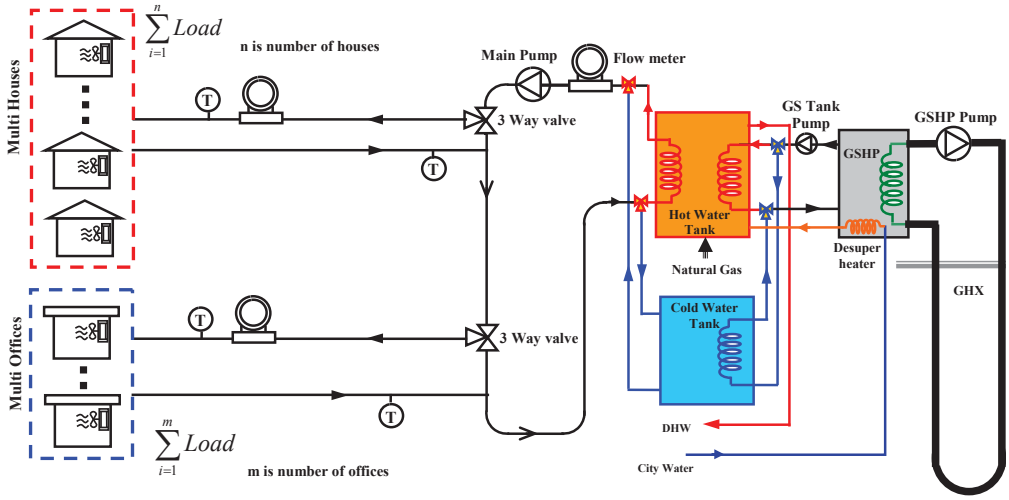

Fig.4. Load Sharing (Houses & Offices) Using GSHP System

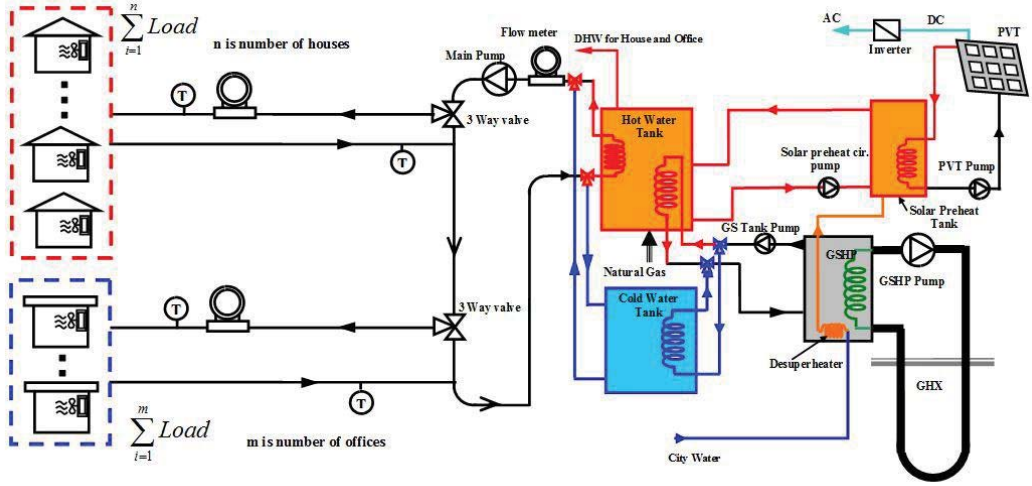

Fig.5. Load Sharing (Houses & Offices) Using Hybrid Micro-Generation System (GSHP-PV/T)

Tab. 1. Summary of Modelling Cases

Cases	Heating/Cooling Systems			Remarks
	Cooling	Heating	DHW	
Case 1	Chiller + Fan-Coil	Boiler + Fan-Coil	Boiler + DHW Storage Tanks	Simple Sum Loads (House + Office)
Case 2	GSHP - Fan-Coil	GSHP - Fan-Coil	GSHP (DSH) + Storage Tanks	Load Sharing
Case 3	GSHP - Fan-Coil	PV/T- GSHP- Fan-Coil	PV/T-GSHP (DSH) + Storage Tanks	Load Sharing

Case three is a hybrid micro-generation system integrating a photovoltaic thermal system to a GSHP system. PVT panels can generate both electric and thermal energy. The generated energy can be used to reduce the electrical power import from the grid to houses and offices and also used for space and water heating. There are many possible ways to integrate the PVT's thermal system to the GSHP system. In this study, system configuration with solar preheat-tank as shown in Fig.5 was chosen for the present study. The collected solar thermal energy is stored in a preheat-tank for two purposes: preheat the DHW and transfer the heat to the hot water storage tank in condition where the preheat-tank bottom temperature is few degree Celsius higher than the top of hot water storage tank. The remaining part of the system is same as that in case one.

Tab. 1 presents a summary of different modeling case studies and the corresponding technologies used for space heating, space cooling and DHW heating

3. SIMULATION AND ANALYSIS METHODOLOGIES

In the present study, all hybrid system models analysis from previous chapter are done by TRaNsient SYStems (TRNSYS-17) which a popular software platform for advanced dynamic building energy simulation. TRNSYS library includes a large database of component models related to buildings, thermal and electrical energy system, input and output data management and other dependent functions. All components models in this study were selected from TRNSYS libraries and enhanced with latest manufactures' system performance data. Additional models were developed for some components that are not present in the TRNSYS libraries such as PV module, GSHP desuperheater and etc.

Based on that approach, detailed simulation models were developed and applied for all three cases. In order to evaluate the load sharing system performance, multi-building block consists of five identical houses (with floor area 200m2 each) and two identical houses (with floor area of 500m2 each) were introduced. The building specifications meet the building envelope requirements for climate zone 4 recommended by ASHRAE Standard 90.1-2007.

For systems serving multiple buildings, it will typically have a lower thermal peak than the sum of thermal peaks of each homogeneous house and office. This is mainly due to the fact that individual buildings reach their respective thermal peaks at different times during the day. A load diversification factor is commonly used to take this phenomenon into consideration in load estimation and equipment sizing for systems that serve a number of mixed buildings. This factor is commonly in the range of 0.90 and tends to be lower when the central system serves a mix of office and residential buildings with peak demand occurring at different times.

The simulation models were run with Incheon, South Korea weather data over a year to simulate and analyze the energy systems' performance. The energy consumption results from the TRNSYS simulations were then used for energy and cost analyses to evaluate and compare the performance of various systems (cases)

4. ENERGY ANALYSIS RESULTS AND DISCUSSION

In this section, simulation results of the case one, case two and case three systems that serving multiple buildings (five houses and two offices) will be presented and discussed. While the houses are identical to the house studied in the previous section with a floor area of 200 m2 per house, the office is enlarged and each has a floor area of 500m2. The total combined floor area with five houses and two offices is 2000 m2.

Both thermal and non-HVAC electric loads of the simulated houses and offices were analysed through appropriate time series methodology prior to the system simulation models development. The houses and offices were assumed to be separated from each other with no thermal interaction between them. Both type of buildings are square shaped and are assumed with a single interior zone in the simulations. The domestic

hot water volume assumption was according to ASHRAE-124 recommendations for residential and small office buildings. Non-HVAC electric loads were developed based on "average" consumption of a detached house and a small office in Canada which is 43.9 kWh/m2-yr. Those are presented in Tab. 2:

Tab. 2. Annual Thermal Load and Non-Electric Load Intensities

Load Intensity (kWh/m^2-yr)	Building Blocks Five Houses + Two Offices ($5x200\ m^2 + 2x500\ m^2 = 2000\ m^2$) Incheon	
DHW	8.6	6.6%
Space Heating	47.2	36.1%
Space Cooling	31.2	23.8%
Non-HVAC Electricity	43.9	33.5%
Total	*130.9*	*100%*

Initial simulation study found out that if a GSHP system integrates with PVT panels only, the PVTs thermal and electrical energy generations are restricted by the volume and temperature of the solar pre-heat tank directly and building thermal demand indirectly. Therefore, it may be more efficient to design a GSHP-PV/T system with combination of both PVT and PV panels rather than installing PVTs only. In this way, the electricity generation will not be restricted or reduced by the thermal demand compare to systems with all PVT panels. In addition, it is anticipated that the initial capital cost could be reduced as PV panels are usually cost less than PVTs. For this reason, 5 GSHP-PVT systems (Case 3) with various combinations of PVT and PV panels were simulated, as shown in Tab. 3:

Tab. 1. GSHP-PVT Systems for Simulation Study

Number of PV Panels	Number of PVT panels	
	0	60
0	GSHP	GSHP-PVT60-PV0
120	GSHP-PVT0-PV120	GSHP-PVT60-PV120
240	GSHP-PVT0-PV240	GSHP-PVT60-PV240

Tab. 2. Energy Analysis of Multiple-Building for Each Case Study

Incheon (Multiple Buildings)		Five Houses + Two Offices ($5x200\ m^2 + 2x500\ m^2 = 2000\ m^2$)						
Energy Intensity (kWh/m^2-yr)		Case 1	Case 2	Case 3				
		SIMPLE SUM (REFERENCE)	GSHP	PVT=60 PV=0	PVT=0 PV=120	PVT=60 PV=120	PVT=0 PV=240	PVT=60 PV=240
Space + DHW Heating	N. Gas	55.9	3.6	0.7	3.6	0.7	3.6	0.7
	Electricity	-	13.5	11.8	13.5	11.8	13.5	11.8
Space cooling	Electricity	16.2	8.6	7.9	8.6	7.9	8.6	7.9
Fans		4.2	5.3	6.0	5.3	6.0	5.3	6.0
Pumps		0.8	3.8	3.1	3.8	3.1	3.8	3.1
Non HVAC (lighting, equip.)		43.9	43.9	43.9	43.9	43.9	43.9	43.9
Electricity Production		0	0.0	-3.8	-19.0	-22.8	-38.0	-41.8

Total (Net) Energy Use	*107.6*	*78.7*	*69.8*	*59.7*	*50.8*	*40.7*	*31.8*
Energy Savings	-	*28.9*	*37.8*	*47.9*	*56.8*	*66.9*	*75.8*
Energy Savings (%)	-	*26.9%*	*35.1%*	*44.5%*	*52.8%*	*62.1%*	*70.4%*

The result shows that the reference case (Case 1) has the highest total energy consumption at 107.6 kWh/m2-yr followed by GSHP system at 78.7 kWh/m2-yr and GSHP-PVT systems are showing better energy consumption compared to others ranged from 31.8 kWh/m2-yr until 69.8 kWh/m2-yr. The main reason why GSHP-PVT has better energy consumption is because this system only use small amount of natural gas for auxiliary burner inside the hot water burner and also GSHP-PVT system produced electricity so that reduced the net amount of energy consumption. Those results are shown in Tab. 4 and Fig. 6

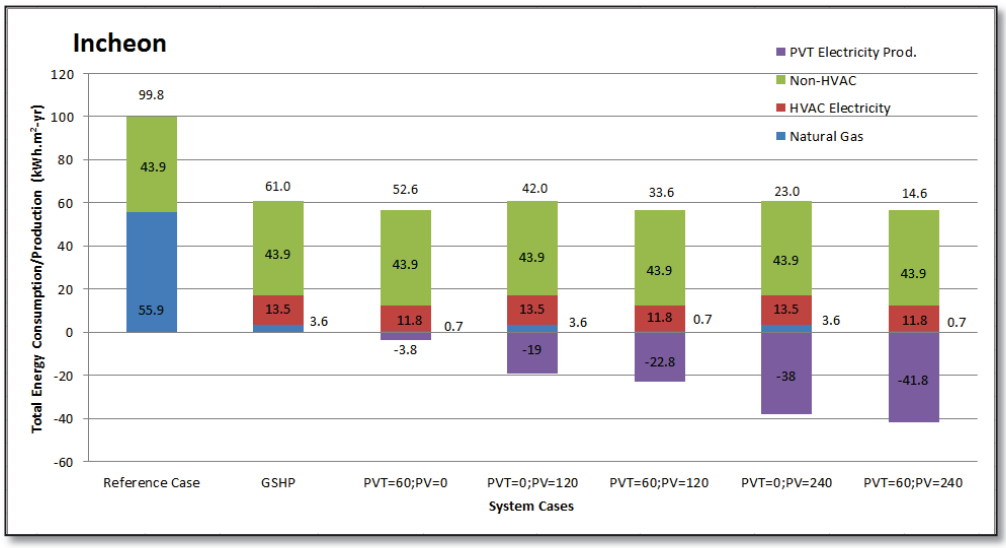

Fig. 6. Energy Analysis Results for Each Study Case

Based on those Tab. and graph, the system performance is evaluated and presented in COP values for the three studied cases. The COP is the ratio of the total energy delivered to the buildings (which includes space heating, space cooling, and DHW energy as well as electricity production if any) to the total consumed energy (natural gas and electricity) in the respective period as shown in Tab. 6

Tab. 3. System Performance (COP) For Multi-Building Cases In Incheon

Incheon	COP		
	Heating Period	Cooling Period	Overall/Annual
Reference System	0.92	1.47	1.08
GSHP	2.87	2.09	2.50
GSHP-PVT60-PV0	3.09	2.56	2.85
GSHP-PVT0-PV120	3.42	2.64	3.05
GSHP-PVT60-PV120	3.70	3.24	3.49
GSHP-PVT0-PV240	3.97	3.19	3.59
GSHP-PVT60-PV240	4.30	3.92	4.13

The result in Tab. 5 shows that Case 3 which is GSHP-PVT system has the highest COP ranged from 2.56 to 4.30 followed by GSHP system (Case 2) and simple sum of residential and commercial buildings (case 1).

This result indicates that hybrid system has a better performance compared to conventional system and GSHP-PVT is the best combination. One of the reasons is the additional contribution from solar energy to produce electricity so that electricity that consumed from the grid can be reduced as shown in Tab. 6

Tab. 4 Annual Electricity Generation and Supply of Various GSHP-PVT system

Incheon	PV/T Electricity Generation		System Electricity Supply	
	Used by System	Exported to Grid	Supplied by PV/T	Supplied by Grid
Reference System	-	-	-	100%
GSHP	-	-	-	100%
GSHP-PVT60-PV0	100.0%	0.0%	5.2%	94.8%
GSHP-PVT0-PV120	83.4%	16.6%	21.1%	78.9%
GSHP-PVT60-PV120	80.5%	19.5%	25.2%	74.8%
GSHP-PVT0-PV240	62.3%	37.7%	31.5%	68.5%
GSHP-PVT60-PV240	60.0%	40.0%	34.4%	65.6%

The results in Tab. 6 indicate that the PV/T panels, depending on its capacity, meets 5.2% to 34.4% of the total electrical loads in Incheon. The remaining 65.6% to 94.8% required electricity is imported from the grid. Increase of the PV/T capacity certainly reduces the hybrid MG system's dependency on the electric grid, on the other hand this will result high initial capital costs

5. CONCLUSION AND FURTHER WORK

In this study, three different renewable and hybrid micro-generation cases were analyzed for application in combination of residential and commercial buildings. Five houses and Two Offices were selected in this study to perform the annual energy performance for each technology. Based on the result in previous chapter, we can conclude that:

• The total energy consumption of all the studied GSHP-PV/T systems (Case 3) is lower than that of the GSHP system (Case 2), and also the reference case (case 1) due to the use of geothermal and solar renewable energies. The overall system performance (COP) increases with the increase of the PV/T panels.

•The simulation results show that it is more efficient to design a GSHP-PVT system with combination of both PVT and PV panels. The PVT panels (operated with thermal-load control strategy) are primary used for covering part of the building heating loads and the PV panels (operated when there is solar radiation available) are mainly used for generating electricity for building usage. In this way, the electricity generation will not be restricted or reduced by the thermal demand compared to systems with all PVT panels. Any excessive electricity could be sold to the grid for additional income or stored in batteries for later use.

• Due to the PV/T electricity production is intermittent and not synchronized with the building demand, the GSHP-PV/T systems not only require electricity from the grid, but also have excessive electricity to be exported to the grid. The amount of electricity imported and exported to the grid is dependent on the number of the PV/T panels integrated to the systems.

• The GSHP-PV/T systems are able to meet 5.2%-34.4% of the building total electric load in Incheon. The remaining electric load is met by the grid. Increase the number of PV/T panels certainly reduces the system

dependency on the electric grid.

• For the simulated GSHP-PV/T systems, between 60% and 100% of the PV/T generated electricity is used by the buildings themselves and the remaining 0% to 40% excessive electricity is exported to the grid. The percentage of exported electricity increases with the increase of the PV/T panel numbers.

For Further work, an artificial intelligence (AI) control strategy to be embedded in a gateway wireless platform for optimal control of the hybrid system will be developed. The strategy will be simulated and investigated for variety of system sizes and applications. The hybrid systems will be optimized and the optimal component and system configurations will be simulated and assessed for maximum utilization. Variety of simulations will be conducted using system integration optimization technique to approach real life situations where a group of multi-type buildings will be served by the hybrid energy system in load sharing applications. Further, and more in depth, economic analyses will be performed to investigate the viability of the hybrid energy systems in selected scenarios and their impact on the overall installation and operation costs.

6. ACKNOWLEDGEMENT

This research was supported by a grant(code# 16CTAP-C096424-02) from Technology Advancement Research Program (TARP) funded by Ministry of Land, Infrastructure and Transport of Korean government

7. REFERENCES

E. Saloux, A. Teyssedou, M. Sorin 2013. “Analysis of photovoltaic (PV) and photovoltaic/thermal (PV/T) systems using the exergy method” Energy and Buildings Journal, Vol.67, pp.276

Entchev, E. Yang, L. Ghorab, M. 2013. “Photovoltaic Thermal-Ground Source Heat Pump Simulation Study, Second year report”. CanmetERNERGY-Ottawa, Natural Resources Canada.

Lee, E.J. Kang, E.C. Cho, S.Y. Entchev, E. Yang, L. Ghorab, M. Performance Assessment and Integral Effect Test of Fuel Cell – Ground Source Heat Pump and Photovoltaic Thermal – Ground Source Heat Pump. Annex54-KIER- subtask B report. Available from: http://www.annex-54.sharepoint-live.de

Lee, E.J. Kang, E.C. Cho, S.Y. Entchev, E. Yang, L. Ghorab, M. Performance Assessment and Integral Effect Test of Fuel Cell – Ground Source Heat Pump and Photovoltaic Thermal – Ground Source Heat Pump. Annex54-KIER- subtask C report. Available from: http://www.annex-54.sharepoint-live.de

Dott, R., M. Haller, H, J. Ruschenburg, F. Ochs and J. Bony, 2012, IEA-SHC Task 44 Subtask C technical report: The Reference Framework for System Simulation of IEA SHC task 44 / HPP Annex 38: Part B: Buildings and Space Heat Load, IEA-SHC, Paris, www.iea.org/task44

Stegman M., Bertram E., Rockendorf G. & Janben S., 2011. Model of an Unglazed photovoltaic thermal collector – based on standard test procedures. Proc. Of ISES Solar World Congress 2011, Solar Heating and Cooling, International Solar Energy Society (ISES), p.252-260, Kassel, Germany

Clean Energy Project Analysis: RETScreen Engineering & Cases Textbook Ground-Source Heat Pump Project Analysis Chapter, Minister of Natural Resources Canada

Conference Proceedings
EuroSun 2016
Palma de Mallorca (Spain), 11 – 14 October 2016

Block of Flats from 1958, Solar Rejuvenated with Wood 2012/14

Florian Lichtblau, DI Univ. Architect
Kaufmann.Lichtblau.Architekten BDA
Soeltlstraße 14, D- 81545 Munich, Germany
florian.lichtblau@lichtblau-architekten.de

Abstract, Dates and Facts

A rundown 1958 post-war housing estate in the west of Munich was first an object of study, then a planning model and finally a showcase project for holistic wood renovation. For an ideal lifecycle balance and overall economy, the following is vital: maintain the carrier substance, rebuild, recompress, passive-building envelope pre-fabricated in wood, timeless design and regenerative energy supply.

Keywords: Solar architecture, renew stock, recompress, set of objectives, lifecycle balance, grey energy, wooden construction, pre-fabrication, passive house, solar thermal and photovoltaic energy.

Fig. 1: Renewal post-war housing estate Munich, arcade view to the East, phase 1

doi:10.18086/eurosun.2016.01.11 Available at http://proceedings.ises.org

Location	Munich-Sendling, Badgasteiner-/ Fernpaßstraße
Building owner	GWG Städt. Wohnungsgesellschaft München mbH
Planning+construction management	KLA Kaufmann.Lichtblau.Architekten, München/ Schwarzach
Struct./Systems planning	MKP Merz.Kley.Partner/ EST Energie.System.Technik
Funding/ Research	KFW, dena, LH München, E2ReBuild
Construction Dates	Original 1958/ Constr. Phase 1 2010-12, Phase 2 2012-14
Net Dwelling Area	1: 3.323 m2 (origin. 2.012, + 65 %), 2: 2.027 m2 (origin. 792, + 155 %)
Residential Units	1: 46 flats/ district office (origin. 36 flats), 2: 35 flats (origin. 16)
Envelope Qual. Ht'	1: 0.26 W/m2K (origin. 1.56 W/m2K), 2: 0,24 W/m2K (origin. 1,64)
End Energy	1: 22 kWh/m2a (origin. 280), 2: 21 kWh/m2a (origin. 296), measured
Primary Energy	1: 22 kWh/m2a (origin. 340), 2: 18 kWh/m2a (origin. 362), calculated
Building Costs	1: 950 €/ m2 GFA, 2: 1.075 €/m2 GFA (gross, cost groups 300/400 minus funding ca. 20 %)
Active Climate Protection	1.100 m3 Constr. Timber, CO2 Reservoir 1.100 to, plus Substitution ..

The prototypical GWG project received important awards and it attracts visitor groups from Europe and many other countries. But may be the most important research result is: The tenants feel notably very happy in their new wooden houses ..

1. How is our 'big house' doing?

'Holistic' solutions for building restoration – is that just a new name for an age-old problem? We don't think so. I would like to try to briefly explain why, an idea and a concrete project example. The question here is what does sustainable mean? The answer is to get started with the holistics .. let me start with a very personal story. My children, Leoni, 19, and Lucia, 16, grew up in the south of Munich. Their ecological footprint on the world is still small – and it should stay that way. But if we listen to serious forward thinkers – which we definitely should – by the time they reach our age, their world should be a completely different one than today...

Should we be afraid of that? Well, we probably don't need to be and fear is never a good starting point when trying to find sustainable solutions. The term 'respect' fits better here – faced with the boundless complexity of global events as a result of a burn out of our knocking off economy. The more we think we know, the less we manage to maintain a natural balance. Prof. Radermacher, for example, calls it the boomerang effect. No wonder that there are children who say: we cannot leave the shaping of our future up to the adults anymore. What more can you say to that?

How to handle this 'seven-headed Hydra'? I have found a suitable approach for myself: it is the daily effort to constantly contribute to a solution instead of the problem. Only by living out that idea can a temporary state of calm be reached. Planning and construction offer a rewarding area of work in this respect. The key functions of energy, material and capital circulation are each approximately half directly or indirectly linked to our building construction and present the highest potential by far for sustainable collaboration with their owners and users. Success solely depends on us, the social skills towards high priorities, strength of character and communication.

2. Challenge and objective

Buildings are and will remain our most costly and longest lasting commodity. We are faced with the simple fact that with the turn of the millennium, we entered an era in which we need to reflect on those unique key energies and materials, which have always made living even possible: our sun, its light. High-tech on the roof, smart-tech in the house and/ or religious beliefs of divine salvation is not enough. But what does 'solar construction and restoration' mean? Integral planning concepts are aimed at a rational, sustainable overall context of:
- Induced energy and land consumption in urban building or landscape preserving credibility,
- energy consumption due to production and transport and the minimisation of synthetic materials in construction,

- of operational energy consumption when using the building and installations, linked to optimised quality of use,
- energy input and problem waste on ‘re-use/ down-cycling/ disposal’ after restoration or demolition,
- and the easing or reshaping of our social, cultural and economic network of relationships.

Energy, anything material and also our culture are not reproducible. Solar architecture is about the complex equilibrium of energy and material balance of our earth. Above all, it is pleasing and works simply, is flexible and long-lasting – three barely perceived, but ultimately decisive multiplier properties for the ecologically rational lifecycle balance. This suggests a decisive turnaround against our political and economic behaviour, our smart and responsible contribution towards an open solution process – as an essential contribution towards peace and the well-being of generations.

The building owners may ask: Who should pay for that? The counter question is: what is the future worth to us? Stay calm, thinking helps. Independent expertise and creative reflection are by far the most cost efficient resources for real sustainable construction. A macroeconomic observation – compiled under ecological cost transparency – leads to extensive different decisions than in today’s building industry. Relevant research results have expressly proven this several times. The simple, comprehensive dynamic CO2 taxation would be a highly effective motor.

Long-term ecology will become long-term economy by the time the overdue internalisation of external costs at the latest. ‘Holistic and sustainable’ will become the only form of building construction we will be able to afford in the future. Good architecture has so much more to offer than low energy demand values, but only when architects and engineers take on this system-changing planning attitude in design realisation and render a backward-looking, knotted sustainability certification redundant, will a substantial economy, new ‘archi-culture’ and genuine quality of life synergistically arise – wouldn’t that be a legacy worth striving for?

3. The example: From object of study to prototype

A large part of the overall housing stock in Germany is functionally outdated, has high operational costs, is inadequate in terms of energy consumption and does not comply with society’s living standards of today, let alone of the future. That means, that our central construction tasks lie in the renewal of our existing building stock. This necessity poses many dangers, however, when thought through it poses unique opportunities: it calls for a fundamental approach and new interpretation of old housing. Structural sins of the past can be alleviated or even eliminated and the demand for a more sensitive recompression and redesign presents the possibility of sustainable urban corrections linked with high overall economic efficiency and an attractive future orientation.

As an example we present a Munich GWG housing estate in Sendling: Mass commodity in the 1950s, masonry bolts with unit floor plans and individual room heating, after two generations it is still in its original condition for the most part. The heating requirement is approximately at factor 5 above the new construction value according to EnEV2009/13. It was only the excellent location, that kept the building from permanent vacancy. In 2006/7 we had focused on a study design about sustainable development goals by the chair of wooden constructions at the TU Munich – with remarkable results. A research project ‘TES Energy Facade’ subsequently followed, then the contract for the planning and implementation by the public housing association to our ArGe Kaufmann.Lichtblau.Architects – in short: it got serious!

Fig. 2: Renewal post-war housing estate Munich, paths of the sun 21 March / Sept.

So the modern engineer's wooden construction was to become the renovation method of building stock?! Until now, a lot was theory as in architecture. The design, it is said, shows the talent; the art begins with the implementation and realisation. The building owner and our planning team – after detailed preliminary discussions – agreed on a set of objectives. This corresponds entirely with the requirements and, among other things, the widest possible preservation of existing primary structures to the prevention of grey energy and waste from demolition and reconstruction. An upgrade-free economic life expectancy of at least 40 years for complete renovation – 46 flats and new regional administration in the lowest energy standard – essentially covers three areas, our set of objectives:

A / The use: Quantity, quality and environment
- Compress rentable living areas of the 1b site by above 100 % - use building ground, ensure revenue,
- Create market-conform mix of flats with light, attractive layout – offer new living quality,
- Interlock disabled, elderly and child friendly functional residential use – include demography,
- Make the new living environment spacious, social, close to nature and robust – design urbanity,
- Studies of the yearly suncycles show daylight quality in each residential area in the quarter.

B / The energy concept: Standard, maintenance, economy
- Lower the energy demand, heating, air and light to under 50 % of a new construction – achieve maintenance security,
- As much as possible, provide regenerative residual energy from heating and electricity – achieve zero emissions,
- 'triple win' – ease the burden of the owner/ tenant/ environment – produce overall profitability,
- Offer simple, safe, long-lasting technology for ease and cosiness – promote health and comfort.

C / The structure: Ecology, process and design
- Perfectly ecological assembly system of high quality and precision – optimise life cycle balance,
- Constructive integration of sound insulation and fire protection, as well as statics, hvac and solar active components – understand flexibility,
- Digital on-site measurement and a maximum pre-fabrication, low weight and short construction period – track process efficiency,
- Low maintenance surfaces and many selectable design variations – enable time-less, attractive architecture.

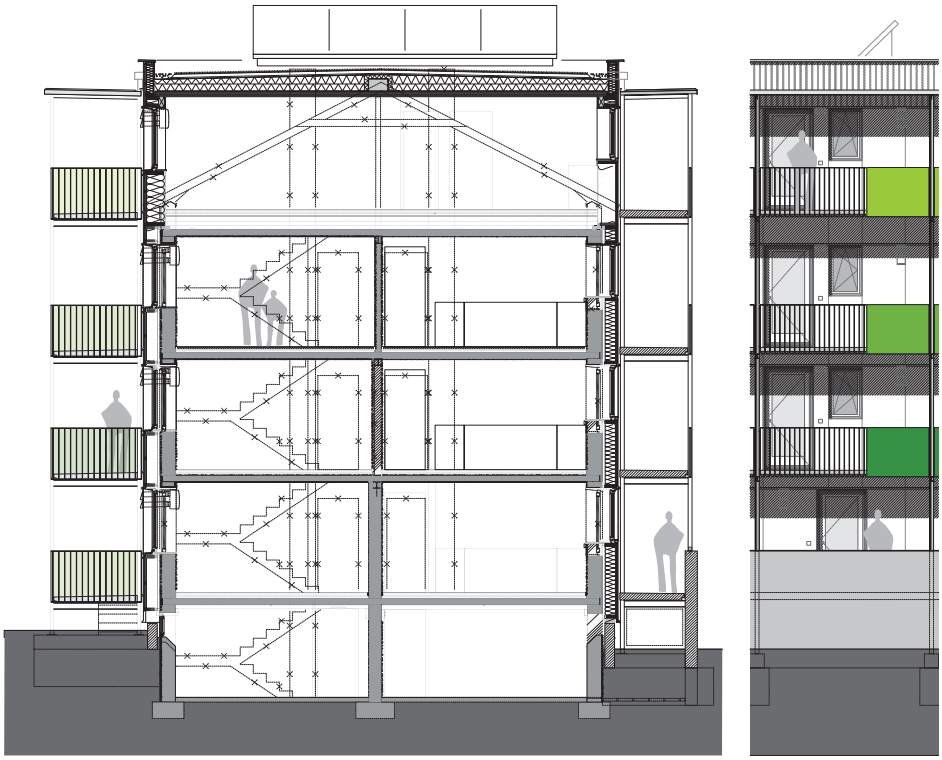

Fig. 3: Renewal post-war housing estate Munich, layout construction in wood, phase 1

The provocative demand of the building owners to the planners: all aforementioned objectives should be reached cost-neutrally within public housing subsidies. The unavoidable extra costs for prototypes with 'sustainable attributes' must be financed in full by appropriate subsidies for energy renovations and 1 € / m2 rent exclusive of service charges as a user contribution for minimal energy costs. That should occur through the holistic added value as described, and furthermore a new 'league of efficiency' will be reached. Despite obstacles and risks we accepted the challenge.

The planning team led by Kaufmann.Lichtblau.Architekten developed a higher-density 'Rejuvenation' model, 100 % additional living area where realised. Construction Phase 1: By incorporating a new building for the district office of GWG, the load-bearing structure of the original buildings could be retained but the access was changed, and the flats were transformed into individual modern residential units, barrier-free and with attractive outdoor areas. The new building envelope, including that for an added storey, consists of pre-fabricated wooden elements meeting passive-building standards, with maintenance-free wall cladding and green roofs.

Exemplary solutions were developed for life-cycle and energy balances, building science and structural aspects, fire safety, sound insulation and an efficient construction process. Construction Phase 2: The existing structures prooved to be quite unflexible, the necessary quantity and quality of flats, including an underground garage, could not be found in a reasonable way. So the client decided to break the old structure down and design and optimised new building in wood construction as in phase 1. The minimal energy demand is primarily covered by regenerative sources.

The first building phase was completed in 2012, phase 2 in 2014. An extensive monitoring for result validation was carried out and prooved: holistic value enhancement, energy efficiency which is fit for the future and a wooden construction offering active climate protection, combined with optimal usage quality, promise the highest total economic viability for generations. With a widely successful completion of the comprehensive mutual set of objectives, K.L.A. has consciously entered new territory for GWG and in doing so has also reached unforeseeable limits to the affordable input of working time. We owe that to our cause, our building owners and their (happy) tenants.

Provisional conclusion: The obtained result is an example of the simple fact that the renewal of existing buildings with the title 'real sustainability' – on today's conditions – is achievable, of course not by means of standard planning, standard processes with standard partners and at standard costs. We also had to deal with obstacles and risks, as well as priority struggles and completely new solutions. Follow-up work shows plenty of valuable experience and learning success, which we will hopefully be able to consistently develop. We cannot go back. The reward for all our efforts lies in durable high use and structural quality with unbeatable overall profitability, but with reference to the life cycle – just like in sustainable forestry.

4. The second chance: Future perspectives ..

At this point a discussion about the new planning and construction techniques 'wooden pre-fabrication' would be appropriate. What systematic wooden construction is really capable of achieving for climate change was first shown at the 'Building with wood – ways into the future' exhibition at the architecture museum in Munich, then in Vienna, actually in Berlin. It aroused an interest which never existed before in modern wooden construction, our GWG project was chosen as the restoration example. We urgently demand a policy be issued to duly support planners and building owners on the development of this enormous CO2 reduction, active climate protection potential.

The focus is on attaining industrial cost-saving production and in doing efficiently increase building stocks' slowing restoration rate, using the most natural, healthy and environmentally friendly materials and processes as possible. Only through competently optimised planning under equal observation of effective land use, ecological structural engineering, zero-emission building operation as well as first class use and design quality is macroeconomic, affordable and real sustainability achieved. 'Solar construction and restoration' as we know it does not harm anybody, it presents the basis for personal freedom and in doing so embodies true modernism.

Therefore it should be up to us construction masters to change the attitude from the bottom up, to learn something new, to present results and to tell happy customers: it really works! Wooden construction marks the most sensible way of using raw material, whose abundance and innocence will finally pass. Every well-

made, energy autonomous and nice looking wooden architecture can become a clear sign of change. Let's protect our riches of timber against foreign desires and wrong usage. With wood as a construction material, warmth returns as a life metaphor, haptic trust creates a new confidence that there are solutions for our problem of the century: sustainability. They grow in the forest and demand nothing more than our sensitivity, fantasy and unity. That is why it is important to endlessly discover new things, rediscover and develop further.

I would like to finish the illustrated boardsheet with this: let me quote what occurred to me when I woke up in the night and luckily found a pencil and paper. I will take the liberty of including our partners and building owners: 'We have not dedicated our lives to architecture to later on have to say: we failed on the most important dimension of construction: a universal sustainability. It may appear quite emotional to some people – nevertheless and now more than ever: we will not stop being nonconformist and controversial until we hand over to our children and grandchildren'. That is what we can do - and what you can do with us. Thank you all the best !

Fig. 2: Renewal post-war housing estate Munich, garden view to the West, phase 2

Kaufmann.Lichtblau.*Architekten*, 05'2016 before ..

Conference Proceedings

EuroSun 2016
Palma de Mallorca (Spain), 11 - 14 October 2016

Cold-Climate Supermarket attached Greenhouse: A Case Study

Anders MacGregor[1] and Caroline Hachem-Vermette[1]

[1]University of Calgary, Calgary (Canada)

Abstract

Supermarkets are responsible for large amounts of energy consumption, for building operations (HVAC and refrigeration) as well as for transportation of produce and other goods. This study is based on an on-going research to reduce the energy consumption of this type of buildings by attaching a greenhouse to an energy efficient supermarket for locally grown organic produce. Using a parametric approach, a design model for a supermarket attached greenhouse for improved energy performance is proposed. The analyzed parameters pertain to passive design (building envelope, shape, day-lighting, PCMs, aerogels) and active design (photovoltaic, semi-transparent photovoltaics, supermarket waste heat harnessing), to develop a model for year-round production in Calgary, Canada (51ºN). The results indicate that energy consumption can be reduced by up to 85% as compared to the base case.

Keywords: *Supermarket, Energy efficiency, Parametric study, optimization, building envelope, phase change material, photovoltaics*

1. Introduction

The population of Canada and the world is increasing with higher concentrations of people living in dense urban areas (Ackerman, et al. 2014). With the global risk of climate change, it is pertinent to centralize commodities, mainly food, to restrict GHG emissions and energy consumption associated with rural agriculture (Sanyé-Mengual, et al. 2015). Supermarkets are already a centralization of commercial products, however, energy required to transport these products to the consumer site of purchase, and the associated GHG emissions, can be significant. Coupling energy efficient greenhouse to supermarkets for locally grown organic produce has the potential to achieve two goals: utilization of waste heat from the supermarket in the greenhouse, and reducing the negative impact of food transportation. The supermarket can generate significant amount of heat (MacGregor and Hachem, 2016) that can be used to supply some of the heating requirement of the greenhouse.

Designing a greenhouse to operate year-round is presented with some obvious challenges when the target location is Calgary, Canada (51ºN). The most apparent challenge is harsh winters that embrace the city for nearly half of the year with temperatures often dropping to sub-zero levels. The second is the high-latitude location of this city resulting in low angled sun in the winter and limited day length, increasing thus dependencies on artificial lighting and heating. The summer season can also be relatively warm with higher incident solar radiation and temperatures reaching 30-35ºC (EnergyPlus, Weather Data Sources) for several weeks leading to potential overheating especially when designing an all-glass greenhouse.

This paper investigates the feasibility of implementing an on-site greenhouse, attached to a supermarket, for the year round growth of organic produce in Calgary, Alberta, Canada (51ºN). This in-depth study aims at examining the potential of coupling these two structures (greenhouse and supermarket) in view of exploring methods of energy sharing between these buildings, and consequently the mitigation of the negative environmental impact, of both types of buildings.

2. Methods

doi:10.18086/eurosun.2016.01.01 Available at http://proceedings.ises.org

The study employs a model of supermarket that has been previously optimized (MacGregor and Hachem, 2016). and an attached glass greenhouse, built according to standards (see below). This paper presents, in addition to an outline of the optimized supermarket design, the optimization process of the greenhouse, and the potential of energy sharing between the two buildings.

A number of parameters are explored to increase the energy efficiency of the greenhouse including the insulation values in the opaque wall assemblies (Fokaides, et al. 2014), the window assemblies (Carmody and Haglund, 2012) and advanced building materials such as aerogels (Buratti, 2012) and phase change materials (PCM) to passively regulate heat (Tabares-Valasco et al., 2012). The parametric study also focuses on designing building envelope components which maximize the buildings ability to generate on-site electricity through the use of building integrated photovoltaics (BIPV) and semi-transparent photovoltaics (STPV) while still maintaining energy efficiency.

2.1 Supermarket Design

The design of the supermarket is optimized for increased energy performance and to achieve a near net zero energy status (MacGregor and Hachem, 2016). This is reached by using high efficiency LED lighting and a thermally optimized building envelope as well as the use of on-site generation of electricity. The characteristics of this energy efficient supermarket design are summarized in Table 1. The supermarket model accounts for essential electrical and thermal loads associated with this building type, such as refrigeration units, cooking appliances, lighting, occupancy and miscellaneous electrical equipment. This supermarket design consumes 25% less energy (234 kWh/m^2) than a base model (319 kWh/m^2) designed to be representative to those found in the location of study.

The rooftop of the supermarket is designed to maximize the solar capture at Calgary's latitude. A saw-tooth roof configuration is adopted (Fig.1) with 50 ° tilt angle, towards the south. This tilt angle is optimal for year-round solar collection in Calgary (Hachem. *et al* 2011). The south facing surfaces of the saw-tooth structures are covered with BIPV panels of 18% electrical efficiency. Taking into account the BIPV electricity generation, the net energy consumption is about 94 kWh/m^2, representing 70% less than the base model, described above (Macgregor and Hachem, 2016).

Role of the supermarket

The supermarket can benefit the attached greenhouse in two ways. The rooftop space of the supermarket can be utilized for photovoltaic generation to subsidize some of the energy costs of the building complex (i.e. supermarket + greenhouse). The other method of utilization of the supermarket is the use of refrigerator waste heat to reduce the heating load for the entire building complex. These refrigerator compressors are constantly running to maintain safe temperatures for food preservation, releasing thus large amounts of heat. This heat is partially vented to the exterior and partially transferred into the supermarket interior space increasing thus the cooling load of the building. Theoretically, a thermal storage tank and heat pump can be used to capture the heat and utilize it in the adjacent thermal zone- namely the greenhouse. This paper presents an estimation of the amount of waste heat is needed to fully subsidize the complex total heating load.

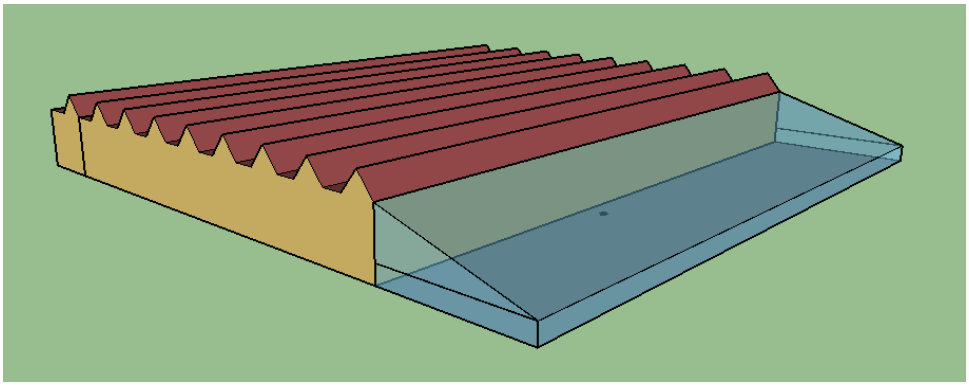

Figure 1: SketchUp model of attached greenhouse on supermarket. Saw-tooth structures on supermarket are sloped at 50° for photovoltaic generation.

Table 1: Supermarket Design Considerations (MacGregor and Hachem, 2016)

Design Parameters and Conditions	Value
Insulation	Wall: 3.3 m^2K/W; Roof: 5 m^2K/W
Windows	No Windows
Lighting	High efficiency LED; 8w/m^2
Phase Change Material	In ceiling and in walls
Building Integrated Photovoltaics	18% efficiency, on south facing side of saw-tooth roofing design
Dimensions	45 m x 35 m x 4.3 m
Annual Electrical Load	474 MWh (includes refrigerators, lighting, electrical HVAC and miscellaneous equipment)
Annual Electricity Generative Capabilities	258 MWh

2.2 Base case design

The base model is used as a reference case for the simulations presented hereafter. This base model is defined as the base level greenhouse attached to the optimized supermarket. Loads analyzed below are those associated with the entire complex.

EnergyPlus (Version 8.4.0, 2016) is employed to carry out the simulations within this parametric study. This energy simulation tool allows control over individual processes and designs within the reference building as well as an extensive array of output options. Assumptions and initial inputs adopted for simulations are shown in Table 2. The heating, cooling and lighting loads are studied to analyze the effect of various parameters on the energy performance of the complex.

Table 2: EnergyPlus initial assumptions or inputs for base model

Assumption/Input	Value
Run Period	1 Year, simulated at 10 m intervals
Weather File and Location	Calgary, Alberta, Canada
Heat Balance Algorithm	Conduction Finite Difference
Base Window Assembly	Single Pane
Ventilation Rate	0.5 ACH, only day-time. Only available above 0°C (1)
Infiltration Rate	0.03 ACH
HVAC System	COP 1. (EnergyPlus' Ideal Loads System)
Thermostat Range	20 – 26°C (2)
Humidity Range	50-90% (2)
Lighting Requirements	25 W/m^2 (3)
Daylighting Set-Point	7000 lux, on dimmer control (3)

[1](Vadiee, 2013), [2](von Zabeltitz, C. 2010), [3](Jahns, T.R, 2009)

2.3 Parametric investigation

This section presents the studied parameters, in view of optimizing the overall energy performance of the complex of buildings.

Greenhouse Design. The designs used in this study are based on the standard, all-glass greenhouses. Three different shapes of greenhouses are investigated to identify the impact on heating, cooling and lighting loads. All three of the cases are attached to the south facade of the supermarket with the roof sloping downwards until it intersects with the south façade of the greenhouse. This façade is the aspect of the design which is modified to determine the impact on the various loads, while other parameters remain constant (as for the base case design, see above). The south façade is 1.7 m, 2.7 m and 3.7 m high for the cases 1, 2, and 3, respectively (Figure 2). 1.7 m is chosen for the shortest south façade height such that a person can attend easily to the plants

against the wall. The north façade, as it is attached to the supermarket at this side, is of an opaque wall assembly.

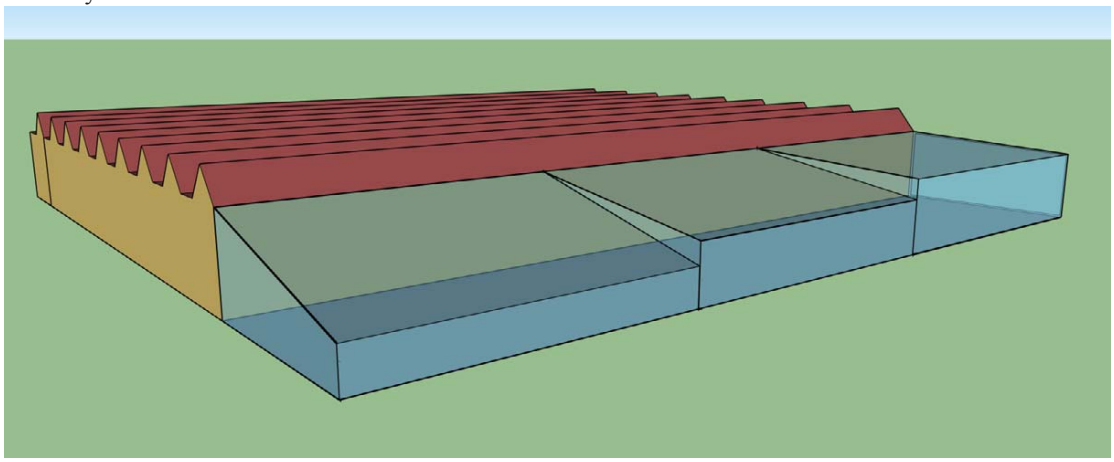

Figure 2: SketchUp design of the three different designs. In the image they have been presented beside each other to better showcase the differences. In the simulations, the designs span the entire length of the supermarket.

Boundary Insulation. The insulation level of the barrier between the two thermal zones (i.e. greenhouse and the supermarket) is systematically changed to determine the insulation level that reduces the HVAC loads of the entire complex. The optimal thermal resistance value for the supermarket's walls are found to be 3.3m^{2}K/W (MacGregor and Hachem, 2016) and the values chosen for the boundary wall's insulation are iterated between 25 – 400 % of this value.

Window Assemblies. The envelope construction of the greenhouse consists of transparent fenestration in nearly 100% of the surfaces. Determining the optimal window assembly to reduce the greenhouse loads is essential to the goal of designing a high energy performing supermarket with attached growing area. Clear, single paned windows are used as the base model to simulate commonly used fenestration surfaces in greenhouses. The different assemblies are as shown in Table 3. The building's heating, cooling and lighting loads are used to determine which assembly is optimal for this design.

Table 3: Window assemblies and corresponding characteristics used in simulations. (Carmody and Haglund, 2012)

Assembly	Frame	U-Value (W/m^{2}K)	SHGC	VT
Single, Clear	Aluminum	5.778	0.82	0.88
Double, Clear	Aluminum	4.71	0.65	0.63
Double, low-e, High SHGC, Argon Filled	Aluminum	3.63	0.38	0.61
Triple, low-e, High SHGC, Argon Filled	Improved non-metal	1.14	0.41	0.5
Triple, low-e, Low SHGC, Argon Filled	Improved non-metal	1.08	0.18	0.37
Double, low-e, Low-SHGC, Argon Filled	Aluminum	3.57	0.26	0.49
Quadruple, low-e, High, SHGC, Krypton Filled	Improved Nonmetal	0.77	0.41	0.36

Infiltration. Airtightness has an important impact on the thermal loads of a building. For the greenhouse the effect of this parameter is studied over a range of 0.03 - 10 air change per hour (ACH) under normal atmospheric pressure. The results are compared to the base model's performance with an infiltration rate of 0.03 ACH. This minimal infiltration rate is selected to control the CO_2 levels for healthy agricultural production. A ventilation rate of 0.5 ACH is adopted during day-light hours which replenishes the carbon dioxide for photosynthesis (Vadiee and Martin, 2013). The effect of increasing the infiltration rate is investigated.

Aerogels. Aerogels are transparent or semi-transparent building materials which offer much higher thermal resistance than the traditional window assemblies. Two different aerogel products are used in the simulations and the characteristics of both are shown in Table 4. Aerogels are employed in two different scenarios: 1) to replace all the glazed areas, 2) to replace all glazed areas except for the roof. The roof in the latter scenario is assumed to take the configuration of the optimal window assembly, determined above.

Table 4: Aerogel characteristics used in simulations (Buratti, 2012)

AeroGel	U-Value (W/m^{2}K)	SHGC	Visible Transmittance
Monolithic	0.65	0.74	0.8
Granular	0.44	0.31	0.8

Shades and Moveable Insulation. Due to the nature and design of greenhouses, the interior can overheat due to high solar radiation. Two types of moveable fenestration covers are introduced in this study. The first being an inflatable thermal barrier that expands and covers the greenhouse. This thermal barrier is an inflating polyethylene cover which sheathes the greenhouse portion of the building at sunset and then is deflated at sunrise. When inflated, the cover has a thermal resistance value of 1.79 m^{2}K W-1 (Arinze, et al, 1988). A rollout shading device on the roof of the greenhouse is explored in this study to reduce overheating. The shades are assumed to have no effective thermal resistance but block out a portion of the incoming radiation. Three different transmittance values are investigated; 75%, 50% and 25%. These solar screens are activated when the solar radiation is high during the summer months.

Semi-Transparent Photovoltaics. Semi-transparent photovoltaics is investigated as means to subsidize the electrical loads while providing some shade to the interior due to the inherent design of these panels. The semi-transparent photovoltaics simulated in this study are termed STPVXX, where XX is the percentage of the photovoltaics per area of surface. The remaining surface area is comprised of double paned glass window assemblies. The characteristics of each of the cases and their corresponding thermal and transmittance qualities are shown in Table 5. STPVs are assumed to replace all transparent surfaces. This is to determine the maximum on-site electricity generation that can be produced.

Table 5: Semi-transparent photovoltaics characteristics used in simulations (Kapsis, 2015)

Assembly	U-Value (W/m^{2}K)	SHGC	Visible Transmittance
STPV90	1.634	0.146	0.061
STPV80	1.634	0.219	0.122
STPV70	1.634	0.292	0.183
STPV60	1.634	0.364	0.244
STPV50	1.634	0.437	0.305

Phase Change Material. Phase change materials can regulate internal climate due to their ability to store thermal energy within the material as they undergo phase transition. When the material then reverts back to its prior state, this thermal energy is released back into the room. This cycle can help reduce cooling loads as the PCM is melting and also reduces heating loads as the PCM freezes. This type of material is shown to be effective in controlling the heat gain within the attached supermarket associated with the refrigeration and lighting (MacGregor and Hachem, 2016). An example of this material exists in the EnergyPlus and has been added to the boundary wall between the supermarket and greenhouse in this study.

3. Analysis of Results

This section presents the results of the optimization of the energy performance of the complex coupling the greenhouse and the supermarket. The supermarket performance is analyzed, both as isolated structure and as a part of the complex. In addition, this section analyses the impact of the building envelope design parameters, and outlines the aspects of the supermarket which can be utilized in developing a more unified and efficient complex.

3.1 Base Case Building Loads

The two components constituting the complex investigated in this study are the supermarket and the greenhouse. Figure 3 compares the building loads of the isolated supermarket, and then as attached to the greenhouse in addition to the entire base case complex's energy consumption, on per unit are basis. The base case-complex combines the optimized supermarket and the standard greenhouse. Coupling the greenhouse to

the supermarket, the building loads of the supermarket decreases due to thermal transfer with the inefficient greenhouse as well as the slightly reduced size of the supermarket. The southernmost 10 m of the supermarket is replaced by the greenhouse for this study in order to maintain the same size of complex. In the parametric analysis below, the entire complex will be the object of optimization.

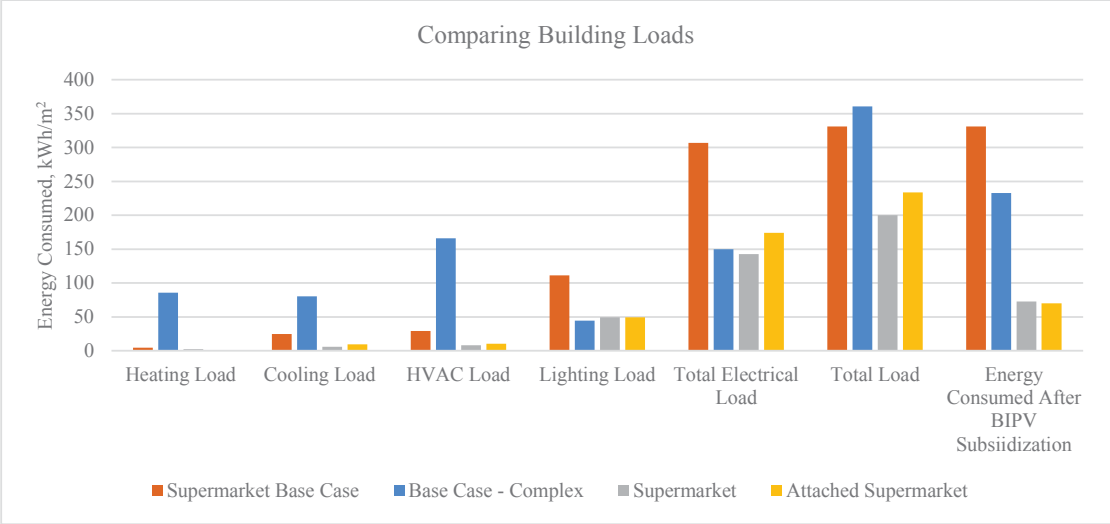

Figure 3: Comparison of the building loads of the supermarket by itself, attached to the greenhouse and then as the entire complex. The base case-complex loads are the target of optimization in this study.

3.2 Effect of greenhouse design parameters

Greenhouse shape. The three different geometrical designs of the greenhouse, perform very similarly. Each design has approximately the same total energy consumption, with case 3 (largest south façade and lowest sloping roof) having marginally more energy consumed annually. The increase in height with the front façade, and the resulting decrease in slope angle for the roof, the heating load increases as cooling load decreases. The lighting load is not affected. The front façade height of 1.7 m is adopted for all following models.

Boundary Insulation. The thermal resistance in the boundary wall between the supermarket and greenhouse does not have significant effect on energy consumption. Since the impact is less than 1%, the optimal insulation of the supermarket is maintained as it is the larger energy consumer of the two zones.

Window Assemblies. Triple paned, low-e, low shgc and argon filled assembly reduces the energy consumed in the design significantly as compared to other assemblies. For instance, this assembly reduces the heating and cooling energy consumption by 80% as compared to the base case. Limiting the solar heat gain in the greenhouse the cooling load is substantially reduced, as displayed in Fig. 4.

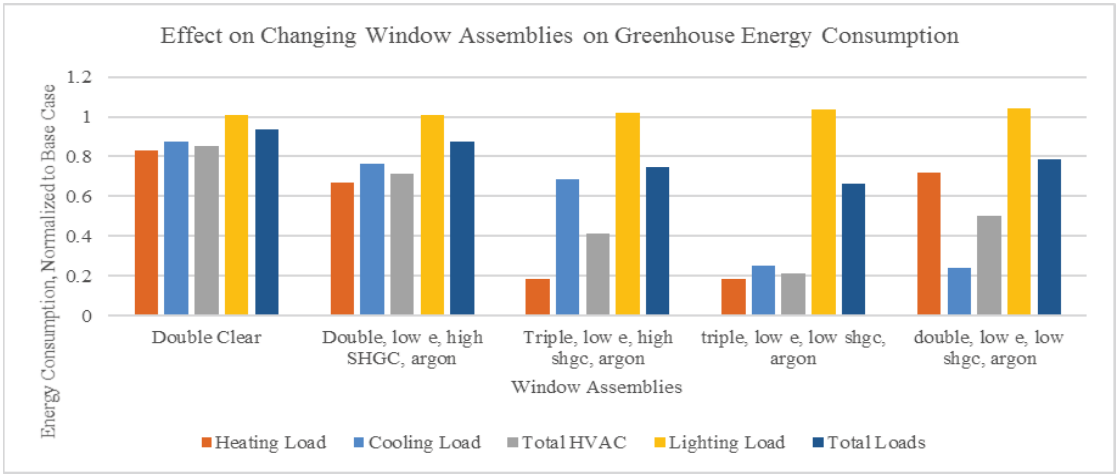

Figure 4: Best case window assemblies are triple, low-e, low shgc and argon filled. Reduces combined heating and cooling load by 80%

Infiltration. These simulations are completed using the optimal window assembly found above as these assemblies allow significant improvements to the interior environment. The results of analyzing the impact of increased infiltration rate indicate that the lowest rate is the most favorable for reducing heating and cooling loads.

Aerogels. Aerogels show promise in reducing HVAC energy loads while allowing light to penetrate the envelope. The insulating qualities of these materials leads to an increase in cooling loads, when used in place of all window (see Figure 5). Replacing all fenestrations but the roof (which maintains the optimal window assembly; triple, low-e, low shgc, argon filled) with aerogel leads to a total reduction in heating and cooling loads of 70%. However, even though these reductions are significant, the scenarios which contain the triple, low-e, low-shgc and argon filled assemblies in all fenestrations perform marginally better (2% difference in total load reduction).

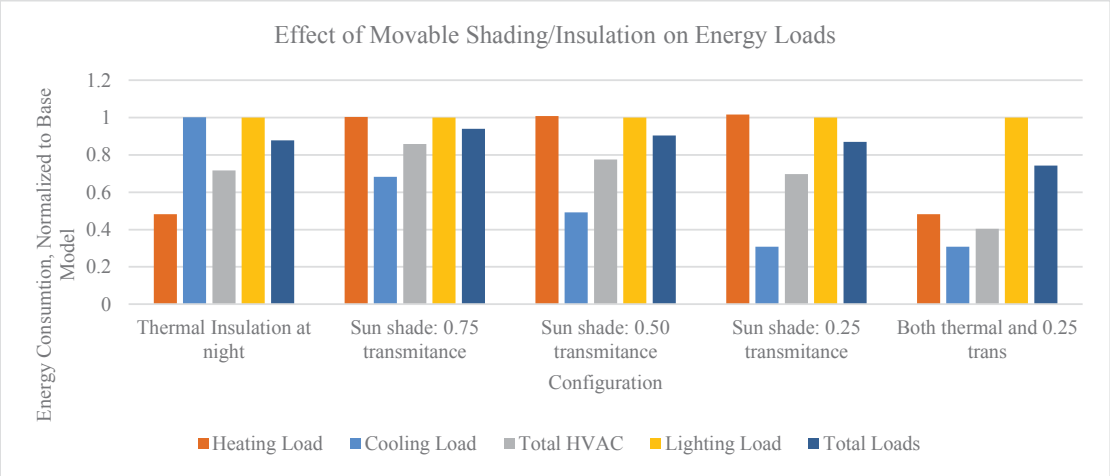

Figure 5: Granular aerogel in all fenestration but the greenhouse roof shows reduction in total energy consumption of 25%

Shades and Movable Insulation. The polyethylene inflatable cover which activates at sunset, reduces the heating load by 52% as compared to the base case, while it does not impact the other loads. The rolling shade with 75% transmittance qualities shows a reduction in the cooling load by 32%. Rolling shade with 25% solar transmittance shows even greater results with a reduction in cooling loads by 70% as compared to the base model. The best case of all these scenarios is the addition of the night time insulation to the 25% transmittance shade with a simulated reduction in heating and cooling loads by 60% (See Fig 6) and an overall reduction in energy consumed by 26%.

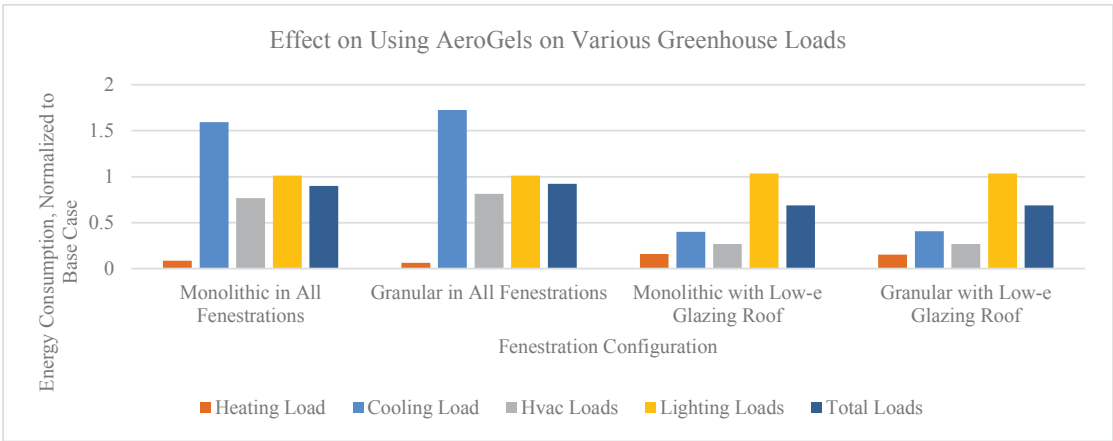

Figure 6: Using night-time thermal covers and 25% transmittance roll-out shade shows reduction in combined heating and cooling loads by 60%.

Semi-Transparent Photovoltaics. The STPV are useful in two aspects. The first is the reduction of the heating and cooling loads by the thermal and optical properties of these assemblies. The STPV assemblies are in part

opaque which blocks solar radiation from entering the greenhouse, thus reducing cooling loads. This cooling load increases linearly with the decrease in opaque areas of the different assembly configurations. The thermal properties of the assembly (Low –e, argon fill gap) reduce the heating loads by 70% as compared to the base case across the different configurations (Fig. 7).

The electrical loads are high in the supermarket-greenhouse complex and using semi-transparent photovoltaics help in the reduction of energy consumed from non-renewable sources. There is an obvious increase in the lighting load as the STPV assemblies block incoming radiation, however, this assists in minimizing the cooling loads. The potential electricity generation can reduce the total energy consumption by approximately 20%, in the case of STPV 90. This potential decreases to 10% in the case of STPV 50.

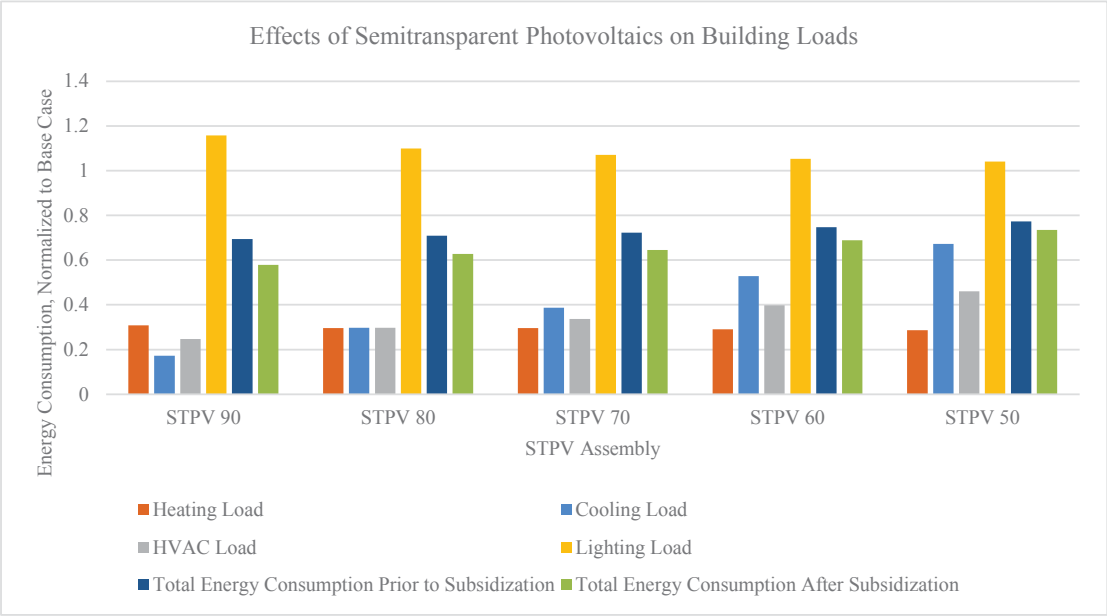

Figure 7: STPV can reduce the total energy consumption by 42% by blocking incoming solar radiation and generating electricity.

Phase Change Materials. Using PCMs in the greenhouse boundary wall shows that some of the heating and cooling loads can be controlled. The simulations are carried out for the base case as well as the optimal window assembly case. In both cases, the combined heating and cooling load reduction is about 10% and 5% for the base case and the low-e glazing case, respectively.

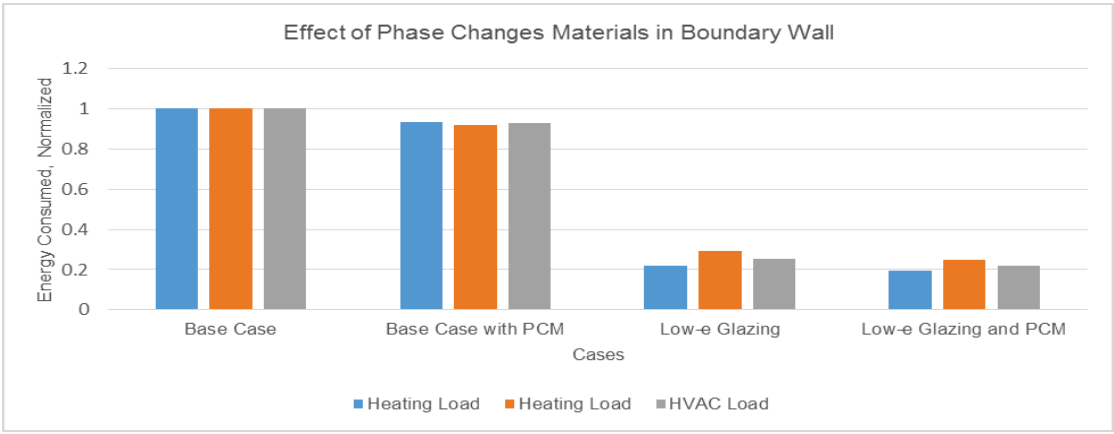

Figure 8: Phase change materials can reduce some of the heating and cooling loads by adding them to the boundary wall construction.

3.2 Utilization of Supermarket

BIPV electricity generation. A BIPV is assumed to cover the south surfaces of the saw-tooth roof structures

This BIPV system generate about 258 MWh annually. This amounts to 35% of the total energy requirements of the base model (base model consumes 360 kWh/m^2 annually) and 53% of the total energy consumption of the optimized model (241 kWh/m^2, annually). If combined with the energy generated from the semi-transparent photovoltaic assemblies, 80% of the energy requirements of the entire complex can be met with on-site generative means.

Heat recovery potential. The supermarket has two sets of refrigerator units with their corresponding compressor racks; the self-contained refrigerators with built in compressors as well as the medium (4°C) and low (-15°C) temperature refrigerators and their back-room standalone compressor rack. The supermarket back-room refrigerator compressor racks generate about 521 MWh of heat. Much of this heat is ejected into the outdoor environment as to have a minimal impact on the building's HVAC system. The heating requirements of the base model is 153 MWh annually, and the case with optimal window assemblies is 34 MWh, annually. Both of these loads are a fraction of the available heat of the compressor racks (30% and 6%, respectively). Especially in the case of the high efficiency windows, it can be assumed that the entirety of the heating load can be accounted for by a mechanism which captures the necessary amount of waste heat from this ejected source. On the other hand, the self-contained refrigerator/compressor units are responsible for a large portion of the internal heat gain, in the supermarket. Implementing a mechanism to capture all or part of this available heat has the potential to significantly reduce the cooling load. For instance, assuming that all heat gain generated by the self-contained refrigerator/compressor is captured, the cooling loads of the whole complex can be reduced by approximately 40%. When 50% of the available heat is captured, reduction of about 25% can be achieved.

3.3 Proposed Models

Table 6 shows the most influential parameters, selected based on the above analyses, to represent an optimized model. Heating and cooling loads are reduced by up to 95% as compared to the base model. The lighting loads are slightly higher than the original base model due to the shading devices and to the properties of the window assemblies. The overall electrical energy consumption, without accounting for the BIPV electricity generation, is reduced by 39% (241 kWh/m^2). With the utilization of the supermarket BIPV system, an overall energy consumption reduction to 62% of the original values is realized. Including STPV assemblies in only the roof portion of the greenhouse, a reduction of 82% in energy consumption is achieved. Finally, when the supermarket is fully utilized with the use of the refrigerator compressor racks to supply the heating requirements, 86% of the base model's energy consumption are reduced to a final value of 54 kWh/m^2.

Table 6: Parameters Chosen for Optimized Model

Parameter	Value
Greenhouse Design	Case 1; 1.7 m south façade
Boundary Insulation	3.3 m^{2}K/W
Window Assembly	Triple, low-e, low shgc, argon filled. On roof only
Aerogels	Granular. All fenestrations but roof
Infiltration	0.03 ACH
Movable shades and insulation	25% transmittance shade and night-time thermal insulation
STPV	STPV90 in roof only (In specified case in Figure 9)
PCM	Located in boundary wall

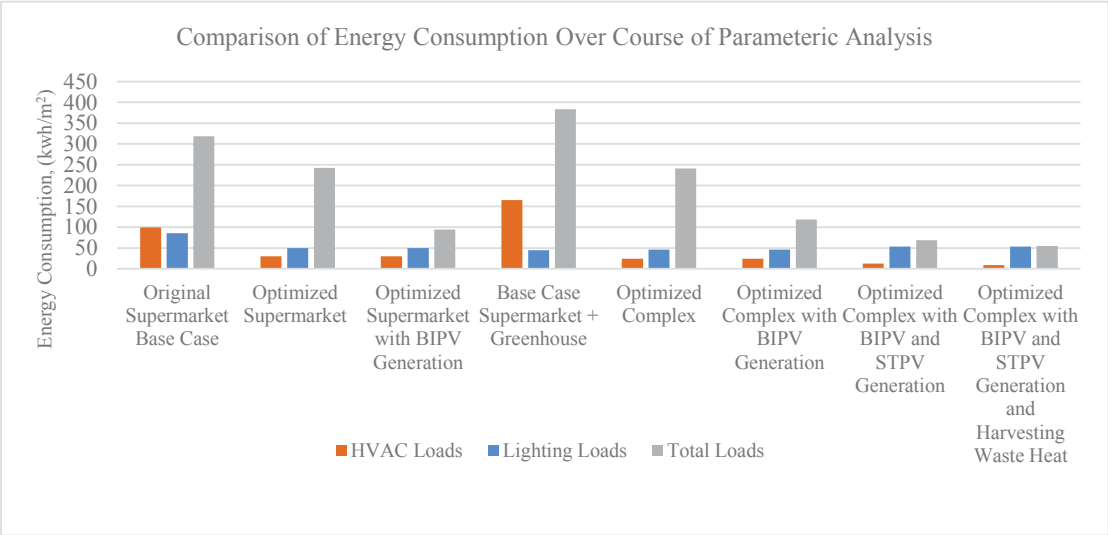

Figure 9: Total energy can be reduced by 86% as compared to the base model with a yearly electrical consumption of 54 kWh/m2. Final model performs 50% more efficiently than optimized supermarket design.

Discussion and Concluding Remarks

This study examines the potential of coupling greenhouse and supermarket in view of reducing energy consumption of the two buildings and exploring methods of energy sharing between them. An 86% reduction in energy requirements is reached through an optimized building envelope and increased potential of on-site electricity generation and heat recovery. However, despite this reduction, the building's energy intensity is 54 kWh/m^2, largely due to the use of inefficient refrigeration/compressor systems. This reduction is the topic of future research as followed:

- *Mechanical Optimization of Refrigeration.* The supermarket still relies on a number of refrigeration units to keep food at safe temperatures. However, these refrigerators often do not utilize the exterior temperatures for the source of the cooling, rather a reliance on compressor racks. Utilizing exterior temperatures in Calgary's cold winters may prove worthwhile in electrical load reduction.
- *Investigating Minimally Glazed Greenhouse Design.* The design adopted in this report adheres to greenhouse standards. A transparent greenhouse, as compared to an opaque building design, requires much less artificial lighting and allows for a higher degree of solar heating. However, an opaque building construction for the greenhouse could perform better in an environment whose temperatures fluctuate so rapidly over the course of the year as is shown in another study where limiting transparent fenestration to only 30% of the south façade and implementing, rooftop photovoltaics, day-lighting devices and increased insulation values produced a net-positive energy scenario of a stand-alone growing facility (Hachem and MacGregor, 2016). Investigation of this opaque design applied to the supermarket-greenhouse complex is an important next step.

This study is a step towards a more sustainable future by increasing the resiliency of communities. Providing the means for communities to centralize their source of food in a low energy consuming manner will further reduce the dependencies of these communities on fossil fuels and associated GHG emissions.

References

Ackerman, K, Conard, M, Culligan, P. Plunz, P. Sutto, M, Whittinghill, L. 2014. Sustainable Food Systems for Future Cities: The Potential of Urban Agriculture. The Economic and Social Review 45 (2):189-206.

Arinze, E., Schoenau, G., Besant, R., 1988. Computer simulation of heating requirement and evaluation of the effects of permanent and movable external thermal insulations on energy conservation in greenhouses, Computers and Electronics in Agriculture, Volume 2, Issue 3, Pages 209-231, ISSN 0168-1699, http://dx.doi.org/10.1016/0168-1699(88)90025-7.

Buratti, C., Moretti, E., 2012, Glazing systems with silica aerogel for energy savings in buildings, Applied Energy, Volume 98, Pages 396-403, ISSN 0306-2619, http://dx.doi.org/10.1016/j.apenergy.2012.03.062.

Carmody, J. Haglund, K. 2012. Measure Guidline: Energy-Efficient Window Performance and Selection Building Technologies Program. Edited by: Energy Efficiency and Renewable Energy, United Stated Department of Energy

EnergyPlus. Version 8.4.0. 2016. Retrieved from: https://energyplus.net/downloads

Fokaides, P. Papadopoulos, A. 2014. Cost-optimal insulation thickness in dry and mesothermal climates: Existing models and their improvement. Energy and Buildings 68, Part A:203-212.

Hachem C., Athienitis, A., Fazio, P., 2011, Parametric investigation of geometric form effects on solar potential of housing units. Journal of Solar Energy, Volume 85, Issue 9, Pages 1864-1877.

Hachem, C., MacGregor, A., 2016. A Report on the Growing Center's Optimized Building Envelope Design. University of Calgary. NSERC Engage Grant Technical Report. Pages: 1-28.

Jahns, T.R., Smeenk, J. and University of Alaska Fairbanks. Cooperative Extension Service. 2009. Controlling the Greenhouse Environment: University of Alaska Fairbanks, Cooperative Extension Service.

Kapsis, K. Athienitis, A. May 2015. A study of the potential benefits of semi-transparent photovoltaics in commercial buildings, Solar Energy, Volume 115, Pages 120-132, ISSN 0038-092X, http://dx.doi.org/10.1016/j.solener.2015.02.016.

MacGregor A., Hachem C. 2016. Investigation of Design Strategies for Improved Energy Performance in Supermarkets: A Case Study. E-Sim (IBSA Canada) Conference, Hamilton, Canada.

Mpusia, P. 2006. Comparison of water consumption between greenhouse and outdoor cultivation. ITC, Enschede.

Sanyé-Mengual, E, Jordi Oliver-Solà, J. Ignacio, M., Rieradevall, J. 2015. An environmental and economic life cycle assessment of rooftop greenhouse (RTG) implementation in Barcelona, Spain. Assessing new forms of urban agriculture from the greenhouse structure to the final product level. The International Journal of Life Cycle Assessment 20 (3):350-366. doi: 10.1007/s11367-014-0836-9.

Tabares-Velasco, Paulo Cesar, Craig Christensen, Marcus Bianchi, and Chuck Booten. 2012. Verification and Validation of EnergyPlus Conduction Finite Difference and Phase Change Material Models for Opaque Wall Assemblies. Building and Environment, Volume 54, Pages 186-196, ISSN 0360-1323, http://dx.doi.org/10.1016/j.buildenv.2012.02.019.

Vadiee, A., Martin, V., 2013. Thermal energy storage strategies for effective closed greenhouse design, Applied Energy, Volume 109, Pages 337-343, ISSN 0306-2619, http://dx.doi.org/10.1016/j.apenergy.2012.12.065.

von Zabeltitz, C. 2010. Integrated Greenhouse Systems for Mild Climates: Climate Conditions, Design, Construction, Maintenance, Climate Control: Springer Berlin Heidelberg.

Conference Proceedings

EuroSun 2016
Palma de Mallorca (Spain), 11 - 14 October 2016

Energy savings through solar reflectance and thermal insulation on roofs of residential and non-residential buildings in Mexico.

Jorge Lucero-Álvarez[1], Ignacio R. Martín-Domínguez[2]

[1] Centro de Investigación en Materiales Avanzados, S.C., Chihuahua, Chih. (México)

[2] Centro de Investigación en Materiales Avanzados, S.C. - Unidad Durango, Durango, Dgo. (México)

Abstract

Thermal building simulations were carried out for the climate conditions of 20 cities in Mexico. We analyze the effects on thermal loads of variations in both solar reflectance and thermal insulation of a roof's exterior surface. The results are quantitative estimates of the reductions in annual (cooling + heating) loads reachable through adequate solar reflectance and thermal insulation of buildings in each city. Additionally, the adequate range of solar reflectance values is defined for each climate zone.

Keywords: *Solar Reflectance, Thermal Insulation, Cool Roofs, Energy Savings, Buildings*.

1. Introduction

According to the 2014 National Energy Balance, 17.97% of the total energy consumption in Mexico (including liquefied petroleum gas, firewood, electricity, natural gas, and thermal solar energy) occurs in buildings—residential, commercial, and public. Of the total energy consumption, 14.71% goes to residential buildings and 3.26% goes towards commercial and public buildings combined. It is estimated that, of the total energy used in residential buildings, 18.7% is used for heating and air conditioning (Fernández, 2011), but this percentage varies with the local climate conditions. In extremely hot climates, up to 50% of the electricity consumed can be dedicated to air conditioning.

The number of households with air conditioning in Mexico has increased since 1996, with an average annual growth rate of 7.5%, while the total number of households in the country has increased 2.7% over the same period (Oropeza and Østergaard, 2014). Rosas-Flores *et al.* (2011) published data on the increase in the fraction of Mexican households with air conditioning, which reached 24% in 2006. Due to the distribution of building types around the country, the greatest consumption of electricity comes from residential buildings, followed by schools and then restaurants/hotels (CMM, 2010).

This indicates that an important and growing part of the total energy consumption in Mexico is dedicated to air conditioning. The energy consumption needed for cooling a building depends to a large extent on the materials used in the building envelope, since some physical properties of these materials affect the heat flux that occurs between the building interior and the environment.

In Mexico, and generally in any location with tropical and arid regions, the roof is the part of a building's envelope that presents the greatest heat fluxes. One of the most effective measures for reducing energy consumption is to select an adequate value of solar reflectance (SR) for the roof. In warm climates, a combination of high SR values and high infrared emissivity (IE) is most energy-efficient. High SR reduces the amount of heat absorbed (rather than reflected) by the roof, which contributes to the heat flow to the building interior. A high IE, meanwhile, allows for more building heat to be emitted from the building and into the atmosphere.

doi:10.18086/eurosun.2016.01.18 Available at http://proceedings.ises.org

The annual savings associated with high SR in buildings have been estimated to reach 51 USD per 1000 ft^2 (about 0.55 USD per m^2) in residential buildings (Akbari *et al.*, 1999), and up to 1.14 USD per m^2 in commercial buildings (Levinson and Akbari, 2010); other studies have calculated the reductions in CO_2 emission (Akbari *et al.*, 2009), and the mitigating effects on urban heat islands in the USA (Rosenfeld *et al.*, 1995; Taha, 2008; Santamouris, 2014). Many other effects of cool roofs have been studied and reported for various other regions of the world; these effects include energy savings, improvements in thermal comfort, reduction of greenhouse gas emissions, and compliance with national and international standards (Boixo *et al.*, 2012; Bozonet *et al.*, 2011; Zinzi and Agnoli, 2012; Dias, *et al.*, 2014; Hamdana *et al.*, 2012, Hernández-Pérez *et al.* 2014). Some countries have even implemented cool roof regulations that specify minimum values of SR and IE—or indexes that include both properties—for the exposed surfaces of building roofs (Akbari and Levinson, 2008; Akbari and Matthews, 2012).

However, there are also downsides to cool roofs. In cities with temperate climate, where there are both heating and cooling needs, high values of SR and IE create a benefit during the summer but an added energy cost during the winter (Syneffa *et al.*, 2007). If applied to sloping roofs, furthermore, high-albedo coatings can be uncomfortably bright for people on the ground or in nearby buildings. Similarly, radiation reflected from a roof can impact neighboring high-rise buildings and affect their own energy balance.

Thermal insulation greatly increases the resistance of building envelopes to conductive heat transfer. However, the benefits of insulation in roofs depend greatly on the SR of the roof surface. Certain combinations of low thermal insulation but high SR can yield overall cooling costs similar to those of high thermal insulation and low SR (Simpson and McPherson, 1997).

Gentle *et al.* (2011) studied the combined effect of three factors—SR, IE, and conductive heat transfer resistivity (R)—on the heat gains and losses through the roof, using simulation in EnergyPlus. These authors used a simple building model with no windows, high R in walls and roof, and the arid climate conditions of Sydney, Australia. One of their main conclusions was that the highest benefits of reflective roofs (high SR) appear when R is small. In fact, high SR and low R result in lower energy use overall than high R alone, due to the contribution of low R to desirable nocturnal heat dissipation. A cost-benefit analysis of thermal insulation in walls and roofs of 6 Mexican cities with different energy needs showed that thermal insulation is not effective in reflective roofs for the tropical city of Acapulco (Lucero-Álvarez-García *et al.*, 2016).

Mexico has implemented some standards related to the thermal energy efficiency of buildings, including NOM-008-ENER-2001 and NOM-020-ENER-2011, which limit heat gains through the envelope of non-residential and residential buildings, respectively. The recommended measures for reducing heat transfer during the summer include insulation of walls and roof, as well as the shading of windows. Studies have measured the energy savings from both these passive methods, and those studies were used to develop the standards mentioned above (Halverson *et al.*, 1994; Álvarez-García *et al.*, 2014), but both these cases considered only the energy costs from cooling. A new non-mandatory standard for evaluating the solar reflective performance of roof coatings (PROY-NMX-U-125-SCFI-2015) is currently also under development (Mendez-Florián *et al.*, 2016).

For the purpose of building thermal analysis, Mexico has been divided into four climate zones based on the Degree-Day method (NMX-C460-ONNCCE-2009). Climate zones 1 and 2 have high cooling needs, with refrigeration degree-days (RDD) above 5,000 and above 3,000, respectively. Climate zone 3 has high energy requirements for both refrigeration (2,500 to 3,500 RDD) and heating (<3,000 heating degree days, HDD), which climate zone 4 has higher heating (>2,000 HDD) than refrigeration needs (Table 1).

Tab. 1: Criteria for defining climate zones in Mexico

Climate Zone	Refrigeration Degree-Day (RDD10)	Heating Degree Day (HDD18)	Type of Region
1	> 5,000		Low elevation, tropical and arid-warm
2	3,500 - 5,000		Sub-tropical and arid-dry
3*	2,500 - 3,500	< 3,000	Mexican Plateau, semi-arid and temperate
4*	< 2,500	> 2,000	Semi-arid and temperate, cold winters

*Climate Zones 3 and 4 are subdivided into three categories (A, B and C), according to the average annual precipitation.

A detailed dynamic simulation study evaluated the impact of cool roofs on 7 Mexican cities (Alvarez *et al.*, 2014). The analysis consisted of varying the roof SR of non-residential and residential buildings meeting Standard NOM-008-ENER-2001 and NOM-020-ENER-2011, to determine the effect of SR on the cooling loads of these buildings. The greatest savings were observed for hot and dry climates, with no significant savings in temperate climates. Due to its extensive urban area, in Mexico City there were significant savings for non-residential buildings.

Another previous work evaluated the effect of roof SR, IE, and R on the annual energy load of buildings, including cooling as well as heating (Lucero-Álvarez *et al.*, 2014). This work included a parametric analysis in which the optical properties were changed between 0.1 and 0.9, at 0.1 intervals, for low income single-family houses with two levels of insulation and one case of no insulation. The authors used climate data from 20 Mexican cities, and found that the greatest energy savings occur in cities from climate zones 1 and 2. Both zones require high levels of SR, and insulation (R) has a significant effect only if the SR values are inadequate.

In this work, we analyze the combined effect of SR and R on two building models. Both models (one residential and one non-residential building) are comparable to those used to develop the Mexican regulations. This study considers both cooling and heating, in order to determine the specific values of solar reflectance most appropriate for various cities and when it is most useful to use thermal insulation.

2. Methodology

TRNSYS simulations were used to estimate energy needs, considering both SR and R. 20 cities in Mexico were selected to represent the 4 climate zones defined by Mexican regulations for energy efficiency in buildings. These 20 cities are listed in Table 2 and are ordered according to their climate zones as they appear on the Mexican Standard NMX-C460-ONNCCE-2009.

Tab. 2: Representative cities in the thermal zones

Zone 1	Zone 2	Zone 3A	Zones 3B and 3C	Zone 4
1. Acapulco	5. Cuernavaca	9. Mexico City	13. Chihuahua (3B)	17. Tlaxcala (4A)
2. Campeche	6. Guadalajara	10. Morelia	14. Coahuila (3B)	18. Toluca (4A)
3. Culiacán	7. Hermosillo	11. Puebla	15. San Luis Potosí (3B)	19. Pachuca (4B)
4. Veracruz	8. Monterrey	12. Queretaro	16. Orizaba (3C)	20. Zacatecas (4C)

Figure 1 presents a map of the climate zones in Mexico and the cities studied in this work.

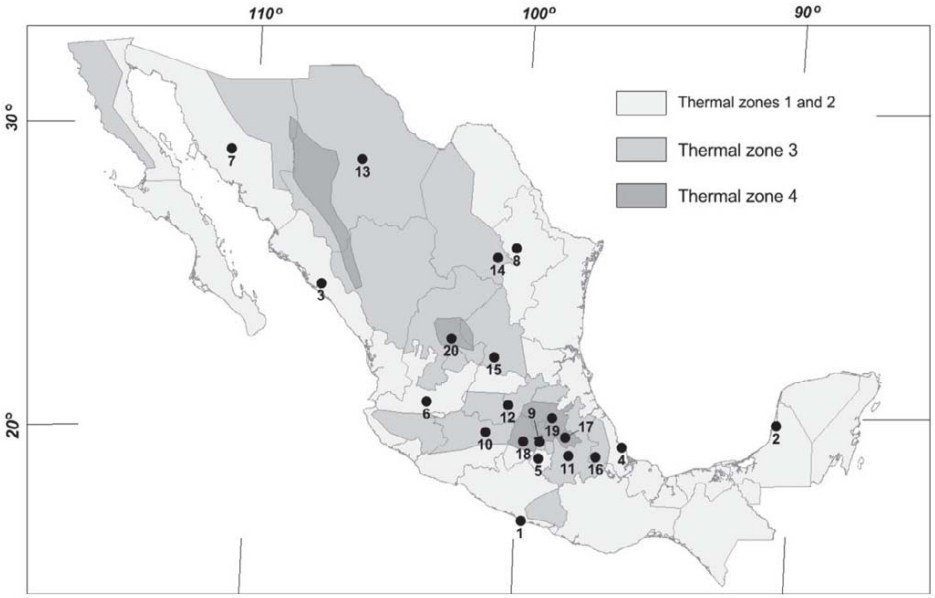

Fig. 1: Location of cities considered in this analysis. The borders of the thermal zones are illustrative and based on the standard NMX-C-460-ONNCCE-2009. Numbers correspond to the list of cities in Table 2

The roof coatings most commonly used in Mexico include asphalt-based waterproofing (SR of about 0.1) and acrylic paint that vary from red (SR ~ 0.3) to white (SR ~0.8). The values of SR in our simulation were varied between 0.1 and 0.9, in increments of 0.1. In addition to the base cases (zero insulation), we considered two common thicknesses of building insulation, 1 and 2 inches of extruded polystyrene, which we approximated as 25 and 50 mm. The prices of different coatings vary over a small range, compared to the typical cost of thermal insulation.

The main parameter evaluated in this study was the annual thermal load, which corresponds to the sum of the thermal loads of cooling and heating. We considered a set point temperature of 25ºC for cooling calculations, in agreement with previous studies, and a set point temperature of 20ºC for heating.

2.1. Climate data

In order to perform thermal simulations of buildings, it is necessary to have climate data representative of the city where the building is located. These data include ambient temperature, relative humidity, wind speed, and solar radiation, all available at relatively short time intervals (1 hour). In this work, that climate data was generated in TRNSYS from mean monthly measurements of the same variables. The mean monthly values of solar radiation were obtained from the Solar Radiation Data Service (SoDA, 2012), while the mean values for temperature, relative humidity, and wind speed were obtained from the Mexican National Meteorological System (SMN, 2010).

2.2. Building characteristics

The relevant parameters for residential and non-residential buildings were obtained from a report prepared for WinBuild Inc (Álvarez-García *et al.* 2014). These buildings models correspond to those used to develop the Mexican Standards NOM-008-ENER-2001 and NOM-020-ENER-2011 (Halverson *et al.* 1994; Álvarez-García *et al.* 2014), which makes it possible to compare these results with those from previous works. Both kinds of buildings are built with brick walls and single-pane windows, and have roofs made of a 10 cm concrete slab with plaster finish on the inside and waterproofing on the outside.

Residential building

The residential building is a typical Mexican 2-story house, with a total construction area of 100 m², a roof area of 54 m², and a north-facing façade. The geometry of the house was an important determinant of the shading of walls and windows. The walls were simulated with an SR of 0.1. The building is inhabited by 4 people, who are present in the building from 0:00 to 8:00 hours and 15:00 to 24:00 hours every

weekday, and 24 hours on Saturday and Sunday. The heat gains from the inhabitants were calculated in TRNSYS according to the parameters established in Standard 7730, and added to heat gains from electrical appliances and lighting. The infiltration for the building is 2 air change per hour (ACH), not considering the ventilation.

The windows were modeled as single-pane glass with the thermo-physical properties given by the TRNSYS library (thermal transmittance or U-value of 5.68 W/m²•K and solar transmittance of 85.5%). The windows cover a surface of 5.20 m² in the walls that face north, 5.60 m² that face south, 0.8 m² that face east, and 2.0 m² that face west.

Non-residential building

The non-residential building model has three stories, each with 625 m² of surface area and a square floor plan (25 m on the side). The walls each contain 40% window space, and have an albedo (SR) of 0.25. This work's simulation considered internal heat gains from electrical equipment, lighting, and people that were present Monday through Friday, between 8:00 AM and 10:00 PM. The ventilation requirements during work hours correspond to ASHRAE Standard 62, which states an air exchange value of 0.043 m³/min•m² (Halverson *et al.* 1994). The properties of the building materials and their distribution throughout the building envelope (of both building models) are shown in Table 3.

Tab. 3: Construction materials and their thermal-physical properties

Building section	Material	Thickness l [m]	Thermal conductivity λ [kJ/h·m·K]	Specific heat Cp [kJ/kg·K]	Density ρ [kg/m³]
Ground floor	Tile	0.01	4.0896	0.795	2600
	Concrete	0.1	6.264	0.84	2300
Upper floors	Tile	0.01	4.0896	0.795	2600
	Concrete	0.1	6.264	0.84	2300
	Plaster	0.015	1.3392	1	800
Wall	Plaster	0.015	1.3392	1	800
	Brick	0.14	2.916	0.8	1600
	Mortar	0.015	2.592	0.837	1890
Roof	Plaster	0.015	1.3392	1	800
	Concrete	0.1	6.264	0.84	2300
	Waterproofing	0.02	0.612	0.8	1127

3. Results

3.1. Comparison with previous studies

Figure 2 compares the cooling loads from this study with those obtained by Álvarez-García *et al.* (2014). The annual loads agree for some cities, such as residential buildings in Monterrey and Hermosillo. Other city results disagree, such as non-residential buildings in Guadalajara. The greatest reduction in cooling load attributable to SR (the difference between the highest and lowest cooling loads for a given building and location) varied the most between these two studies for residential buildings in Hermosillo.

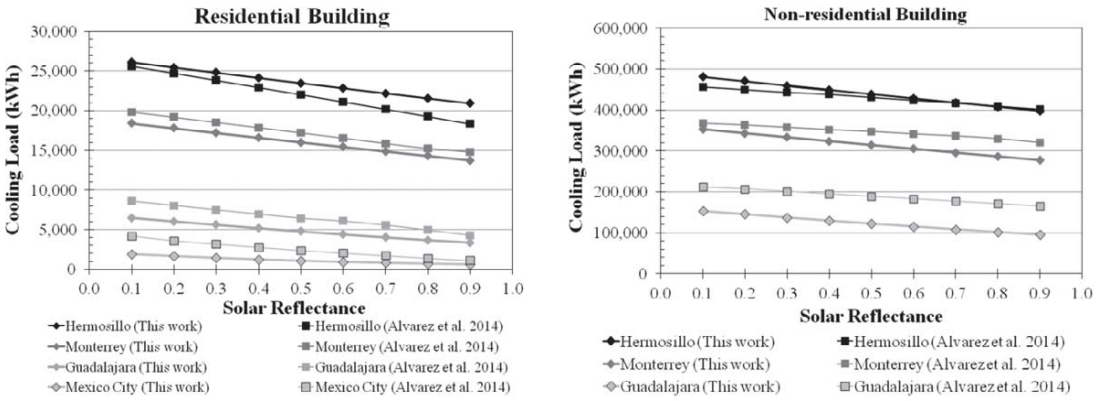

Fig. 2: Comparisons between this work and Alvarez-Garcia *et al.* (2014)

3.2. Effect of SR on a roof with no thermal insulation.

Figures 3 to 7 show the effect that different values of SR can have on the annual cooling load of the two types of modeled buildings. Climate zones 1 and 2 correspond to the hottest climates (and to Figures 3 and 4, respectively), where cooling needs dominate over heating needs. These zones show an inverse linear relationship between thermal load and SR; moreover, the annual loads were consistently higher per m^2 for the non-residential building. This thermal load varies between 230 and 370 kWh/m^2 in the non-residential building, and between 150 and 230 kWh/m^2 in the residential building. Despite this difference in magnitudes between the two buildings, the effect of SR (given by the slope of the lines) was very similar. These are the climate zones with the greatest energy savings achievable through changes in SR.

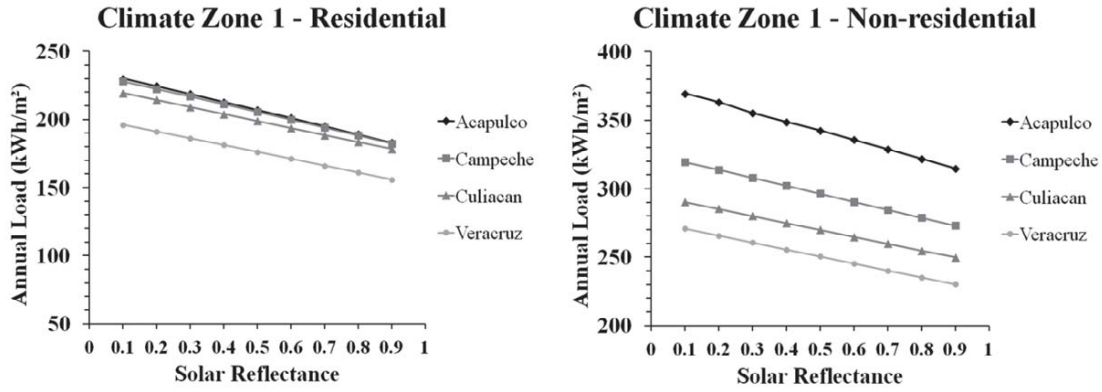

Fig. 3: Annual thermal load as a function of solar reflectance for cities in climate zone 1

The annual load can vary significantly among cities in Thermal Zone 2. Hermosillo and Monterrey, for example, show annual loads comparable to those of cities in Thermal Zone 1. Figure 4 compares the annual loads for these two cities against those of Cuernavaca and Guadalajara, which are also located in Thermal Zone 2 but have very different local climate.

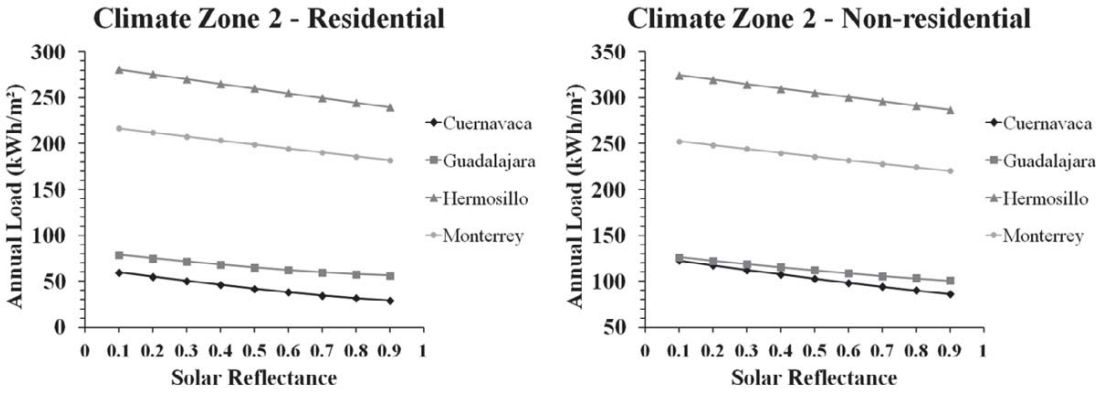

Fig. 4: Annual thermal load as a function of solar reflectance for cities in climate zone 2

Figures 5 and 6 show the results for climate zone 3. This zone has lower cooling needs than climate zones 1 and 2, but higher need of heating. Some of the cities in climate zone 3 present a linear relationship between annual energy load and SR, as had been observed in climate zones 1 and 2. The optimal reflectance for these cities is 0.9, similar to that of climate zones 1 and 2. However, in zone 3 there potential for energy savings is lower than in the hotter zones. The graphs for cities like Mexico and Puebla contain local maxima, marking optimal SR values different than 0.9, and also have smaller differences between the minimum and maximum values of the annual load (Figure 5).

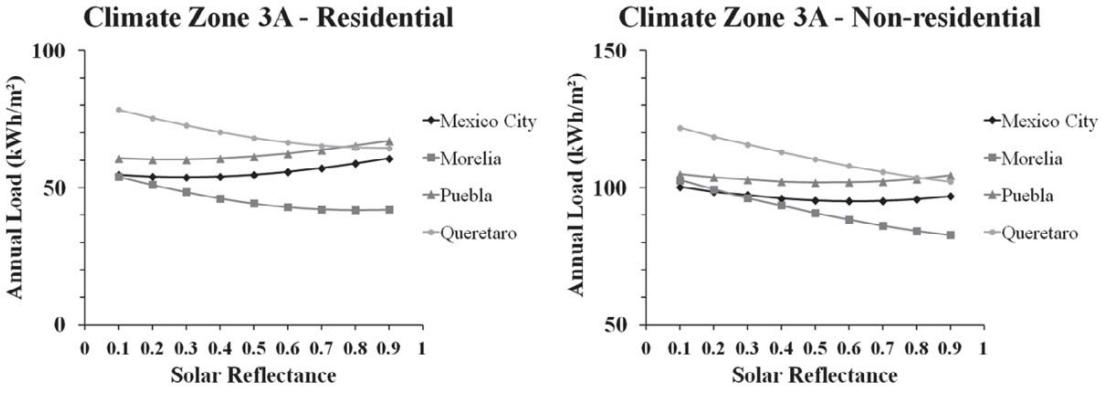

Fig. 5: Annual thermal load as a function of solar reflectance for cities in climate zone 3A

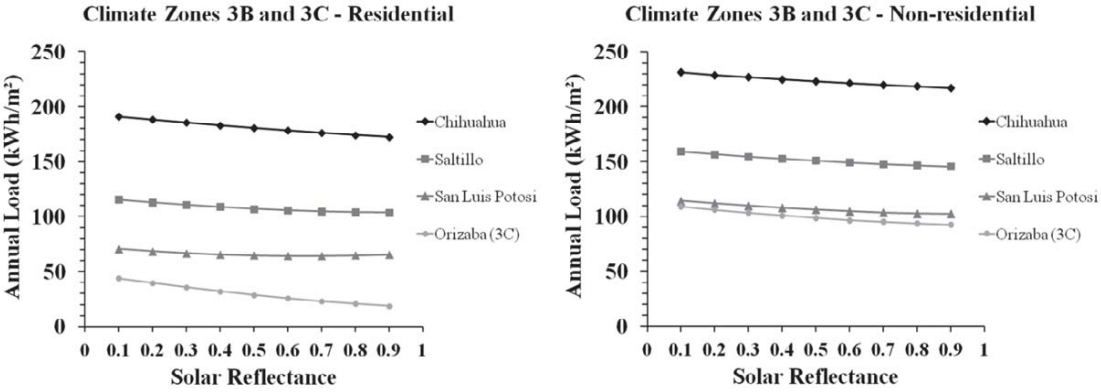

Fig. 6: Annual thermal load as a function of solar reflectance for cities in climate zones 3B and 3C

Climate zone 4 has drastically higher heating needs and lower cooling needs compared to the other zones. This results in relatively horizontal curves; SR has little effect on the annual load. In Toluca, heating needs actually dominate cooling needs and the normal relationship between SR and thermal load is inverted. Thus, the optimal value of SR for this city is very low (Figure 7).

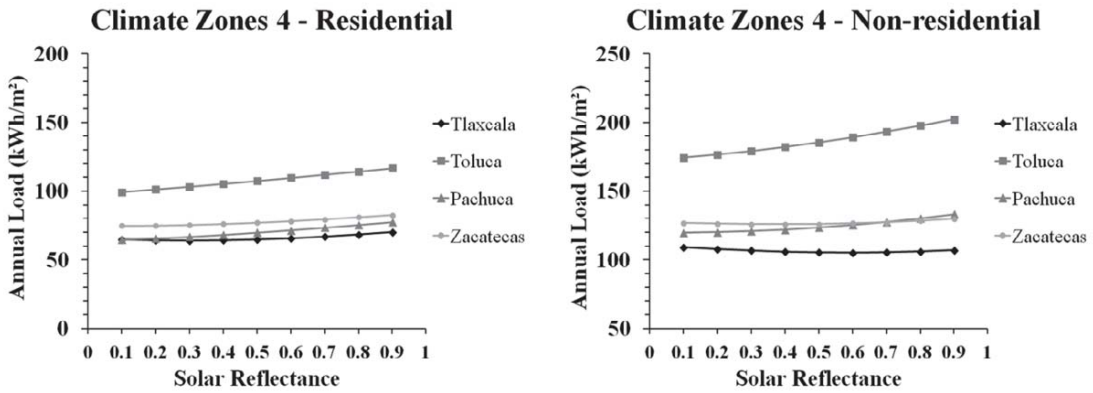

Fig. 7: Annual thermal load as a function of solar reflectance for cities in climate zone 4

3.3. Combined effect of thermal insulation and solar reflectance

The effect of insulation depends to a great extent on the use of an adequate value of SR in the roof. Figure 8 shows the annual energy load for three levels of insulation in the residential building, using climate data for Acapulco and Chihuahua. In Acapulco, insulation can have a very important effect only for low values of SR. If, on the other hand, roofs have a proper value of SR such as 0.9, then the added savings from insulation are negligible. In some cities with a significant cost of heating, such as Chihuahua, insulation has a significant effect even for optimal values of SR (Figure 8).

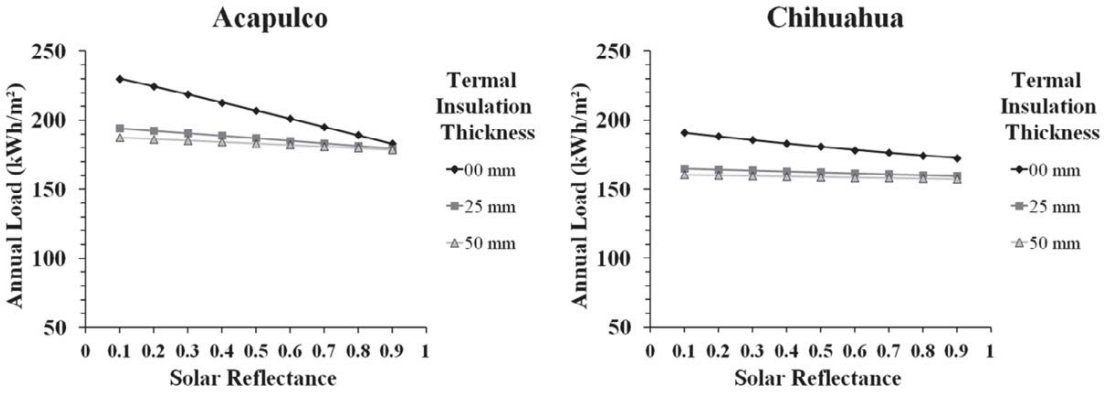

Fig. 8: Annual thermal load as a function of both solar reflectance and thermal insulation of roofs in Acapulco and Chihuahua

Although some improved coatings have SR values as high as 0.9, it is important to consider that this value tends to diminish over time. That is why we consider 0.8 to be the highest realistic value of SR. The value of SR has a strong effect on the benefits of insulation on the cost of energy needed to maintain the inside of buildings within comfortable ranges. Figure 9 shows the annual energy savings from 25 mm of insulation for 3 values of SR that correspond to coatings commonly used in Mexico (0.1 for black asphalt, 0.3 for red acrylic, and 0.8 for white acrylic). This figure shows how the savings from insulation vary greatly between different values of SR, especially in cities from climate zones 1 and 2. In a few cities such as Mexico City, Puebla, and Tlaxcala, the savings from insulation are almost the same for all three values of SR.

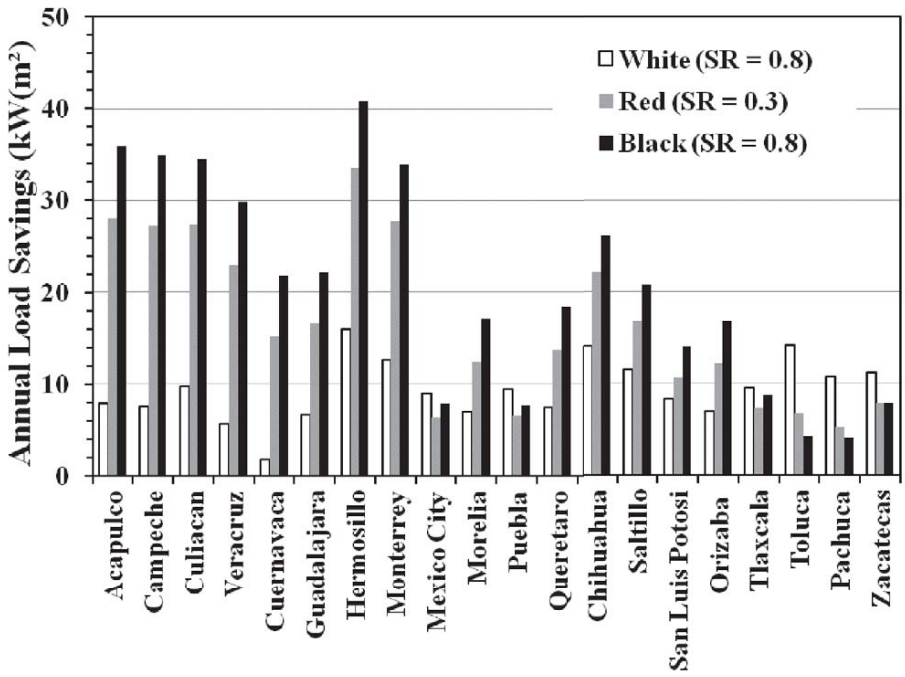

Fig. 9: The annual load savings from 25 mm of thermal insulation for three common values of solar reflectance of roof coatings used in Mexico

Insulation is a very costly investment, compared to the difference in cost between coatings with very different SR values. Figures 10 and 11 show the difference in energy costs between buildings with the best and worst coatings (black bars). The additional savings from insulation are shown in gray bars; these additional savings are calculated considering an optimal choice of coating.

In both building models it is apparent that for climate zones 1 and 2 the selection of a high SR value is a key factor in reducing the annual thermal load. Only in some cities from climate zone 2 (semi-arid climate, such as Monterrey and Hermosillo) can insulation be an important measure for increasing energy savings; this occurs at an SR value of 0.8.

Climate zone 3 (where optimal SR values vary between 0.3 and 0.9) and climate zone 4 (0.1 to 0.5) present a lower effect of SR on thermal load than climate zones 1 and 2. This is due to the penalty associated with using extreme SR values during the wrong period, such as a high SR when trying to heat the building or a low SR when trying to cool it. For some cities from climate zones 3 and 4, which have relatively high heating needs, the use of insulation is more important than the choice of SR—especially for non-residential buildings.

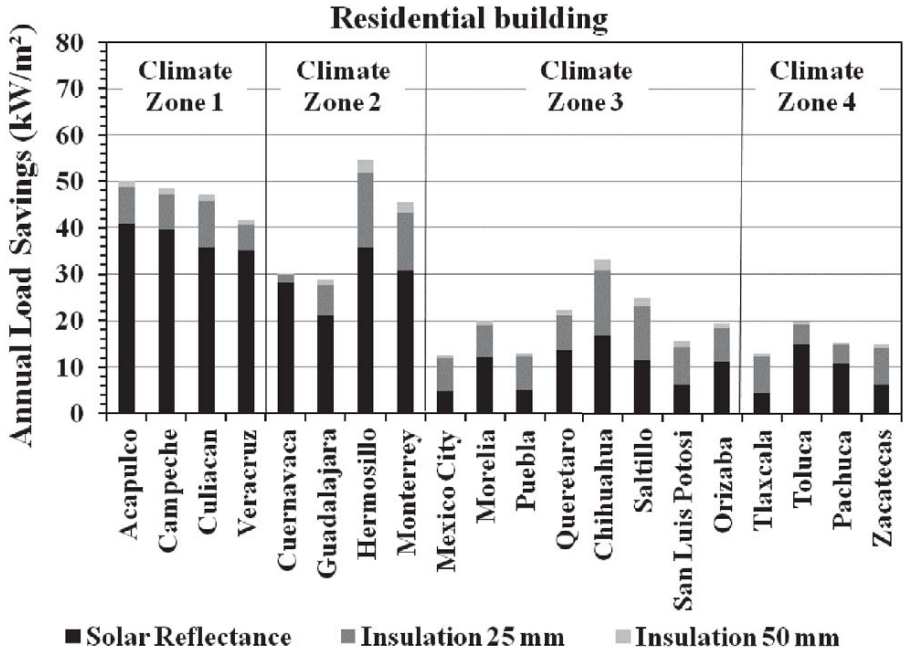

Fig. 10: Annual load savings achievable through solar reflectance optimization, followed by 25mm and 50mm of thermal insulation, in residential buildings

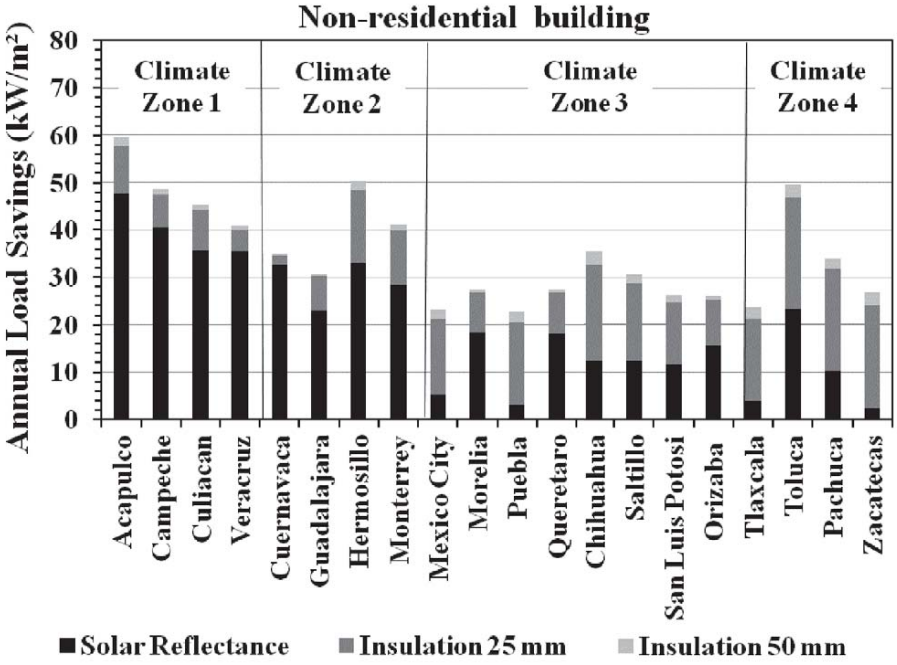

Fig. 11: Annual load savings achievable through solar reflectance optimization, followed by 25mm and 50mm of thermal insulation, in non-residential buildings

4. Conclusions

In warm climates with minimal heating needs, it is best to reduce energy consumption through adequately

high values of solar reflectance. In Mexico, cool roof regulations that maximize the values of SR are justified in climate zones 1 and 2. The use of insulation can be suggested in cities with semi-arid climate that have heating needs during the winter, or required to replace the effect of a high SR in cases where buildings choose to have lower reflectances. This may be the case for buildings with heavily sloped rooftops, which can reflect a significant amount of radiation to neighboring buildings, but also for short buildings next to taller ones or for homeowners that simply want non-reflective roofs for aesthetic purposes.

The use of insulation is appropriate for climate zones 3 and 4, where heating is an important component of the thermal load. The effect of SR is very modest in some of these cities, which is why a deeper analysis is needed on whether it is useful to regulate a range of acceptable SR values. Insulation may be suggested—or even required for non-residential buildings—since it does create an important extra reduction in the energy load than can be obtained from proper choice of SR.

5. Acknowledgement

The authors would like to thank the support given by the ***Centro Mexicano de Innovación en Energía Solar*** (**CEMIE-Sol**), Convocatoria 2013-02, Fondo Sectorial Conacyt - Sener - Sustentabilidad Energética, for the development of this work

6. References

Akbari, H., Konopacki, S., Pomerantz, M. 1999. Cooling energy savings potential of reflective roofs for residential and commercial buildings in the United States. Energy 21, 391-407.

Akbari, H., Levinson, R. 2008. Evolution of Cool-Roof Standards in the US. Advances in Building Energy Research 2, 1-32.

Akbari, H., Menon, S., Rosenfeld, A. 2009. Global cooling: increasing worldwide urban albedos to offset CO2. Climatic Change 94, 275-286.

Akbari, H., Matthews, H.D. 2012. Global cooling updates: Reflective roofs and pavements. Energy and Buildings 55, 2-6.

Álvarez-García, G. S., Shah, B., Rubin, F., Gilbert, H., Martin-Dominguez, I.R., Shickman, K.. 2014. Assesing energy saving form "Cool Roofs" on residential and non-residential buildings in Mexico. Comisión Nacional de Uso Eficiente de Energía.

Boixo, S., Diaz-Vicente, M., Colmenar, A., Castro, M. 2012. Potential energy savings from cool roofs in Spain and Andalusia. Energy 38, 425-438.

Bozonnet, E., Doya, M., Allard F. 2011. Cool roofs impact on building thermal response: A French case study. Energy and Buildings 43, 3006-3012

CMM (Centro Mario Molina). 2010. Edificaciones Sustentables Estrategia Sectorial para Lograr un Desarrollo Sustentable y de Baja Intensidad de Carbono en México, pp. 11-16. Avalaible via: http://centromariomolina.org/wp-content/uploads/2012/05/11.-RESUMEN-EJECUTIVO-Edificaciones-Sustentables-PRIMERA-ETAPA-2011.pdf

Dias, D., Machado, J., Leal, V., Mendes, A. 2014. Impact of using cool paints on energy demand and thermal comfort of a residential building. Applied Thermal Engineering 65, 273-281.

Fernández, X. 2011. Indicadores de eficiencia energética en el sector residencial. Taller de Indicadores de Eficiencia Energética en México. Secretaría de Energía.

Gentle, A.R., Aguilar, J.L.C., Smith, G.B. 2011. Optimized cool roofs: Integrating albedo and thermal emittance with R-value. Solar Energy Materials & Solar Cells 95, 3207-3215.

Halverson, M.A., Stucky, D.J., Fredrich, M., Godoy-Kain, P., Keller, J.M., Somasundaran, S. 1994.

Energy effective and cost effective building energy conversation measure from Mexico. Pacific NW Laboratory, Richland, Washington

Hamdana, M. A., Yamina, J., Abdelhafezb, E. A. 2012. Passive cooling roof design under Jordanian climate. Sustainable Cities and Society 5, 26-29.

Hernández-Pérez, I., Álvarez, G., Xamán, J., Zavala-Guillén, I., Arce, J., Simá E. 2014. Thermal performance of reflective materials applied to exterior building components—A review. Energy and Buildings 80, 81-105.

Levinson, R., Akbari, H. 2010. Potential benefits of cool roofs on commercial buildings: conserving energy, saving money, and reducing emission of greenhouse gases and air pollutants. Energy Efficiency 3, 53-109.

Lucero-Álvarez, J., Alarcón-Herrera, M. T., Martín-Domínguez, I. R. 2014. The effect of solar reflectance, infrared emissivity, and thermal insulation of roofs on the annual thermal load of single-family households in México. Conference proceedings Eurosun 2014, Aix-Les-Bains, France.

Lucero-Álvarez, J., Rodríguez-Muñoz, N. A., Martín-Domínguez I. R. 2016. The Effects of Roof and Wall Insulation on the Energy Costs of Low Income Housing in Mexico. Sutainability 8, 1-19.

Méndez-Florián, F.; Velasco-Sodi, P.; Gabilondo, A.I.; Galindo, R.; López-Silva, M. Estrategia Nacional para la vivienda sustentable. Available online: http://fundacionidea.org.mx/assets/files/F.IDEA_Estrategia%20vivienda%20sustentable%20_130311_FINAL.pdf (accessed on 19 May 2016). (In Spanish).

Oropeza-Pérez, I., Ostergaard, P. A. 2014. Global Energy saving potential of utilizing natural ventilation under warm conditions – A case study of Mexico. Applied Energy 130, 20-32.

Rosas-Flores, J. A., Rosas-Flores, D., Morillón Gálvez, D. 2011. Saturation, energy consumption, CO2 emission and energy efficiency from urban and rural household's appliances in Mexico. Energy and Buildings 43, 10-18.

Rosenfeld, A. H., Akbari, H., Bretz, S., Fishman B. L., Kurn, D. M., Sailor, D., Taha, H. 1995. Mitigation of urban heat islands: materials, utility programs, updates. Energy and Buildings 22, 255-265.

Santamouris, M. 2014. Cooling the cities – A review of reflective and green roof mitigation technologies to fight heat island and improve comfort in urban environments. Solar Energy 103, 682-703.

Simpson, J. R., McPherson, E. G. 1997. The effects of roof albedo modification on cooling loads if scale model residences in Tucson, Arizona. Energy and Buildings 25, 127-137.

SMN (Sistema Meteorológico Nacional). 2010. Resúmenes Históricos (Normales Climatológicas, Periodo 1981-200), http://smn.cna.gob.mx/index.php?option=com_content&view=article&id=29&Itemid=93 (accessed on 2 Jun 2012). (In Spanish).

SoDA (Solar Energy Service for Profesionals). 2012, http://www.soda-is.com. (accessed on 10 Jan 2014).

Synnefa, A., Santamouris, M., Akbari, H. 2007. Estimating the effect of using cool coatings on energy loads and thermal comfort in residential building in various climatic conditions. Energy and Buildings 39, 1167-1174.

Taha, H. 2008. Meso-urban meteorological and photochemical modeling of heat island mitigation. Atmospheric Environment 42, 8795-8809.

Zinzi, M., Agnoli, S. 2012. Cool and green roofs. An energy and comfort comparison between passive cooling and mitigation urban heat island techniques for residential buildings in the Mediterranean region. Energy and Buildings 55, 66-76.

Conference Proceedings

EuroSun 2016
Palma de Mallorca (Spain), 11 - 14 October 2016

Energetic analysis of the implementation of renewable energies in a Canary Island Hotel

Ana I. Palmero-Marrero[1], João Costa[1], Isabel Martín[2] and Armando C. Oliveira[1]

[1] Faculty of Engineering of University of Porto, Porto (Portugal)

[2] Department of Industrial Engineering, Universidad de La Laguna (ULL), La Laguna (Spain)

Abstract

The European Directive on Energy Performance of Buildings has established a target of Nearly Zero-Energy Buildings (nZEB) for a sustainable future. For this target, hotels take a special interest, as shown in the neZEH project (Nearly Zero Energy Hotels project) (neZEH, 2016), (Tsoutsos et al., 2013). In this work, a hotel located in Tenerife (Canary Island, Spain) is analyzed. With the objective of reaching the nZEB label, an exhaustive energetic analysis of the hotel was performed and the implementation of different renewable energy systems was proposed. The utilization of solar thermal collectors, photovoltaic collectors and heat pumps are analyzed in this work. Also, the passive solar characteristics, namely related to internal shading, were considered.

Keywords: *hotel, renewable energies, island, energy performance, TRNSYS*

1. Introduction

Buildings consume 40% of the total energy and emit 36% of greenhouse gases in Europe, therefore representing a high potential for energy savings. Specific measures to reduce energy consumption in the building sector have been introduced by the European Union with the European Directive on Energy Performance of Buildings in 2002 (EU Directive, 2002) and its recast in 2010 (EU Directive, 2010). These directives have established a target of Nearly Zero-Energy Buildings (nZEBs) for a sustainable future. The implementation of nZEB as the building target from 2018 onwards represents one of the biggest challenges to increase energy savings and minimize greenhouse gas emissions (Delia, 2015). An nZEB is a building that "has a very high energy performance with a low amount of energy required covered to a very significant extent by energy from renewable sources, including energy from renewable sources produced on-site or nearby" (EU Directive, 2010). However, the concept of nZEB is still not well developed in most EU countries. Large scale renovations of existing buildings towards Zero Energy are in the forefront of the European Union and national policies. For this goal, longstanding hotels located in places with high solar exposition take a special interest for the implementation of renewable technologies.

To know the energy performance of a hotel, and if it should be a nZEB, it is necessary to analyze the amount of energy consumed by the hotel from conventional sources and renewable sources (if any renewable systems are installed). In this work, for a given hotel and after this analysis, the possibility of using alternative renewable sources to replace conventional ones is proposed.

2. Building description

In this work, a hotel located in Tenerife (Canary Island, Spain) was analyzed. The location and a hotel view are shown in figure 1. The hotel is located 99 m above the sea level and 1.4 km from the coast. The hotel main façades are 29ºNW oriented. It is surrounded by gardens, with very high solar exposition (no significant shading from the surroundings). The latitude and longitude of the place are 28.4ºN and 16.2ºW, with sub-tropical climate. Using the METEONORM software, the meteorological data of the local were obtained. At the hotel location, the annual horizontal incident solar radiation is 1640 kWh/m^2 and the annual average temperature is 21ºC.

doi:10.18086/eurosun.2016.01.02 Available at http://proceedings.ises.org

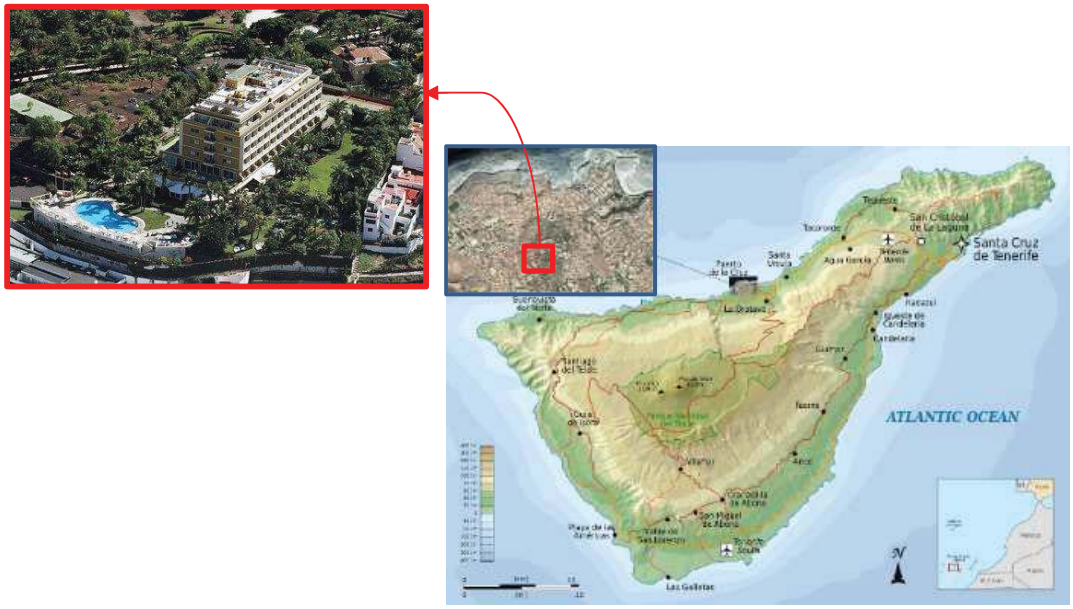

Fig. 1: Hotel location in Tenerife Island and hotel view.

The hotel was opened in 1959 and renovated by July 2015. This is a medium size hotel with high standards regarding the environment. The hotel management has been certified several times and received different awards from 1995 until today, always with the motivation to have a sustainable hotel. The hotel category is 4 stars, with 83 rooms distributed in 4 floors, ground floor and cave, with 5940 m^2 of net floor area. The east and west façades are characterized by extensive glazed areas and balconies with high solar exposition. The characteristics of each floor, such as floor areas, façade areas and percentage of glazed area per façade area, are shown in Table 1. The façade areas are detailed for each orientation (N: North, S: South, E: East and W: West).

Tab. 1: Characteristics of the different floors of the hotel.

Floors	Floor area (m^2)	Façade area (m^2)				Glazed area / Façade area (%)			
		N	S	E	W	N	S	E	W
Cave	1482	106	28	247	247	85	0	13	39
Ground floor	1278	75	75	171	165	63	56	50	52
Floor 1	840	53	53	144	144	16	0	38	50
Floor 2	840	53	53	144	144	16	0	38	50
Floor 3	840	53	53	144	144	16	0	38	50
Floor 4	660	45	45	132	132	36	48	0	71

The external walls of the hotel are massive and constituted by plaster, two concrete layers and insulation between the concrete layers, with a total thickness between 37 cm and 47 cm, depending on the floor, and U-value of 0.70 W/m^2K approximately. The other U-values are: 0.49 W/m^2K for the ground and 0.35 W/m^2K for the roof. All windows have double glazing with a U-value equal to 3.21 W/m^2K and a g-value equal to 0.72.

The hotel has unglazed solar thermal collectors to heat the water of the external swimming pool, and flat plate collectors (FPC) to heat the water consumed in the hotel, as can be seen in figure 2. The thermal collectors installed on the roof have a useful area of 117 m^2 and an annual heating useful energy of 107 MWh/year. The average occupancy of the hotel is 138 guests per day during the year.

Fig. 2: Top view of the hotel with the solar thermal collectors on the roof (GoogleEarth).

For the air-conditioning, a new Water-Sourced Liquid Chiller/Heat Pump (Carrier 61W) was installed in 2014, with 99 kW of heating capacity ($COP_{heating}$ = 3.1) and 67 kW of cooling capacity ($COP_{cooling}$ = 2.1), in the most unfavorable case (condition in heating mode: condenser water entering/leaving temp.=55ºC/65ºC).
For both water and air heating applications, the strategy at the hotel is to use the solar thermal collectors (FPC), the heat pump and only after the diesel boiler (as backup). When solar radiation is not enough to heat the swimming pool, the diesel boiler is also used. In the kitchen only propane is used.

3. Modelling system

The hotel and its components were modelled with the TRNSYS 17 simulation program. The climatic data were obtained through METEONORM, provided by TRNSYS and distributed under license from Meteotest.

For the building simulation in TRNSYS, the floors were divided in different sub-zones with similar characteristics of utilization. In total, 14 sub-zones were considered for the numerical simulation. For example, as can be seen in Figure 3, the ground floor (GF) was divided in 3 sub-zones: lounge (zone GF.1), rooms (zone GF.2) and reception (zone GF.3). The cave was divided in 3 sub-zones and each floor was divided in 2 sub-zones, corresponding to the east and west façades.

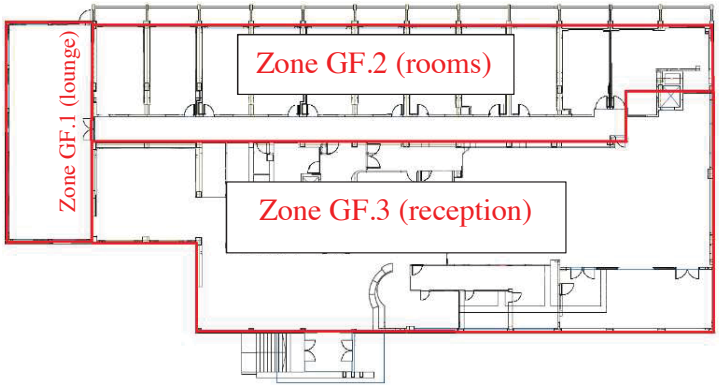

Fig. 3: Ground floor and sub-zones.

The building cooling and heating load, for an indoor air temperature thermostatic control of 25ºC and 20ºC, were calculated for the cooling and heating seasons, under climatic conditions of Tenerife. These temperatures were considered to maintain operative temperatures in the range proposed in ISO 7730 (between 20ºC and 26ºC for 1.2 met), within thermal comfort requirements. The study was extended throughout a whole year. Also, indoor temperatures were calculated through numerical simulations.

A multi-zone building model (TRNSYS type 56) was used. Besides the definition of geometry and materials, other input data considered were: infiltration rate of 1.2 air changes per hour, room internal gains corresponding to two persons per day in each room, artificial lighting of 5 W/m^2, TV, computers in the reception, different equipment in the kitchen, etc. The metabolic rate (heat production depending on action level) was assumed as

1.2 met (1 met = 58.2 W/m^2). This corresponds to seated and light activity at home, office, hotels, etc. (ISO 7730:2005).

Also, the installation of the photovoltaic collectors (PV) and thermal solar collectors (FPC) were analyzed through numerical simulation. Table 2 shows the FPC and PV modules characteristics used in the numerical simulation.

Tab. 2: Characteristics and technical data of the FPC and PV collectors.

FPC		**Constante Solar-Cu-1208-P**
Collector efficiency parameters related to aperture area:	η_0	0.79
	a_1	3.64 W/m^{2}K
	a_2	0.02 W/m^{2}K^2
Gross Area		2.63 m^2
PV panels		**TSM-300**
Nominal peak power*		300 Wp
Nominal voltage (Vmp)*		36.9 V
Nominal current (Imp)*		8.13 A
Nominal efficiency		15.5 %
Open-circuit voltage (Voc)*		41.3 V
Short-circuit current (Isc)*		2.02 A
Module area (A_{PV})		1.94 m^2
Cells		Multicrystalline

*STC: 1000W/m^2, AM 1.5, 25ºC.

4. Results

4.1. Analysis of hotel energy demand

For estimating the hotel energy demand, space heating and cooling requirements were determined for all sub-zones, according to the operating conditions presented in Section 3. Monthly incident solar radiation (total) on horizontal and vertical façades is shown in Fig. 4. The annual horizontal incident solar radiation is 1640 kWh/m^2.

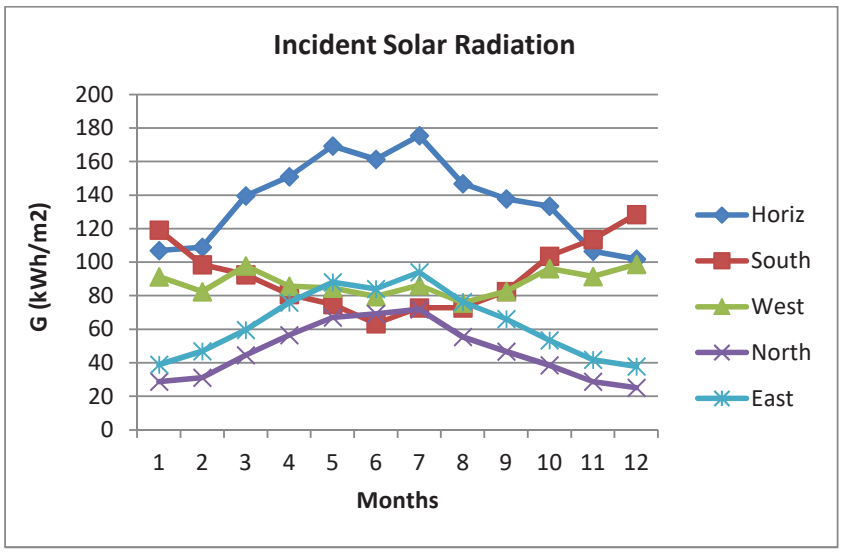

Fig. 4: Monthly incident solar radiation for horizontal and vertical façades.

Figure 5 and Figure 6 show the hourly simulated indoor air temperature without cooling or heating system, and the outdoor ambient temperature for 2 sub-zones (Ground Floor-reception and East sub-zone in Floor 3), during the 21st of July (when the incident solar radiation and the ambient temperature are very high) and 21st of December (when the incident solar radiation and the ambient temperature are lower). In these figures, no use of internal or external shading, such as blackout curtains or blinds, was considered.

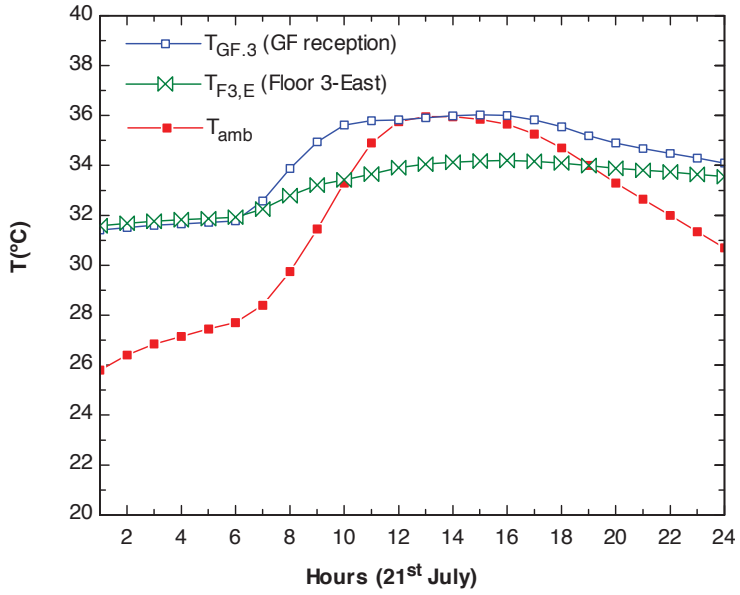

Fig. 5: Hourly indoor air temperature without cooling, and outdoor ambient temperature during 21st July.

Note that the indoor air temperature is higher than 25ºC during the July day, when the cooling system (Chiller/Heat Pump) is not used. Also, during the cooling season higher indoor air temperatures could be achieved in the different floors if solar passive strategies were not used; then, comfort conditions could almost never be reached in the hotel during this period.

A solar passive strategy adopted by the hotel employees is to close the interior blackout curtains during the day in the cooling season, after cleaning the rooms. This possibility was also studied in this work. When the interior curtains are closed during the day, the internal average temperature in the rooms decreases between 0.2 to 0.9ºC, depending on the floor.

When comparing the indoor air temperatures of the East and West sub-zones in each floor, it was possible to verify that the West sub-zones have a higher temperature than the East sub-zones (about 0.2ºC difference). It can be justified by the higher glazed area/façade area in the West façade, as seen in Table 1.

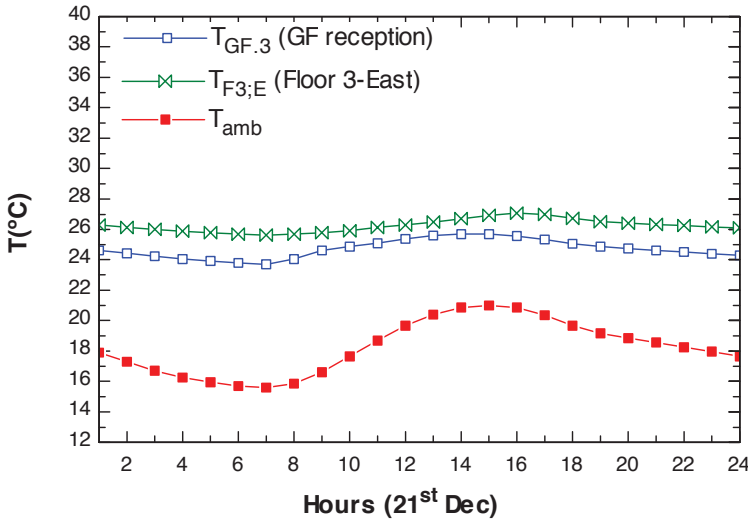

Fig. 6: Hourly indoor air temperature without cooling or heating, and outdoor ambient temperature during 21st December.

As can be seen in Figure 6, in a cold day in winter the outdoor temperature range is between 16 and 21ºC. If the indoor air temperature thermostatic control for the heating season is set for 20ºC, the heating system will be

connected only a few hours during the year in the hotel. The usual guests of this hotel are foreign elderly persons in the winter time. For that, usually the air-conditioning with a thermostatic control of 24ºC is used in the rooms.

Table 3 shows the monthly and annual energy demand for heating and cooling with different thermostatic control set points. In the last row, the annual energy demand is divided by the net floor area of the hotel (5940 m^2).

Tab. 3: Monthly and annual energy demand for heating and cooling.

Month	Heating (MWh) ($T_{control}$=20ºC)	Heating (MWh) ($T_{control}$=24ºC)	Cooling (MWh) ($T_{control}$=25ºC)
January	0.08	10.33	2.31
February	0.08	6.03	3.97
March	0.01	2.88	10.81
April	0.00	0.87	14.67
May	0.00	0.27	26.41
June	0.00	0.00	38.67
July	0.00	0.00	63.79
August	0.00	0.00	62.13
September	0.00	0.00	52.90
October	0.00	0.00	45.48
November	0.00	0.37	19.69
December	0.00	2.19	9.58
Annual (MWh)	**0.18**	**22.95**	**350.42**
Annual (kWh/m^2)	**0.03 kWh/m^2**	**3.86 kWh/m^2**	**58.99 kWh/m^2**

Note that the energy demand for cooling is considerably higher than the energy demand for heating. These values are similar at hotels with similar climates as shown in the literature (Polanco and Yousif, 2015).
Using the Chiller/Heat Pump installed in the hotel ($COP_{heating}$ = 3.1 and $COP_{cooling}$ = 2.1), the annual electricity consumption in the hotel for air-conditioning is 7.4 MWh/year for heating and 167 MWh/year for cooling. Considering the energy consumed in 2015, see Figure 7, the air-conditioning represents about 30% of the electricity consumption of the hotel.

4.2. Actual hotel energy consumption

- Domestic Hot Water (DHW)

Considering the occupancy 138 guests per day during the year, and a water heating consumption of 60 l/guest, the annual energy consumed for hot water (HW) is about 160 MWh/year. Knowing that the useful energy from the solar thermal collectors (FPC) for water heating is 151 MWh/year, the utilization of the heat pump is also necessary for HW.
On the other hand, the useful energy from the other solar collectors used for swimming-pool heating, may not be enough for the whole year. For that, the utilization of the boiler should be considered.

- Energy consumption (electricity, propane and diesel)

The energy consumed in the hotel from non-renewable energy sources is shown in Figure 7. These values were obtained from the invoices delivered by the hotel staff.

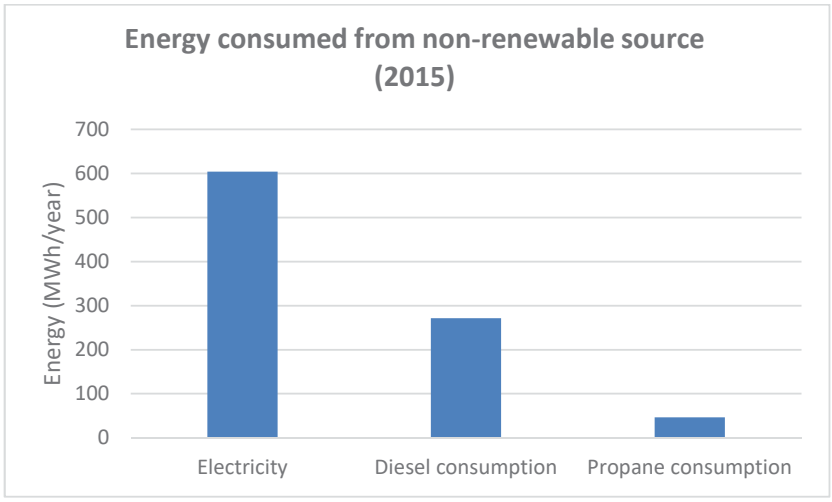

Fig. 7: Main hotel consumptions from non-renewable sources during the year 2015.

Figure 7 shows the energy consumed in the hotel without considering the contribution from the FPC installed on the roof. In this distribution, electricity represents 66%, diesel 29% and propane 5% of the total consumption. Note that diesel is used in the boiler and propane is only used for the kitchen equipment. When the contribution of FPC is considered (151 MWh/year) these percentages change, as can be seen in Figure 8. The annual energy consumption from non-renewable sources was 1073 MWh/year for the year 2015.

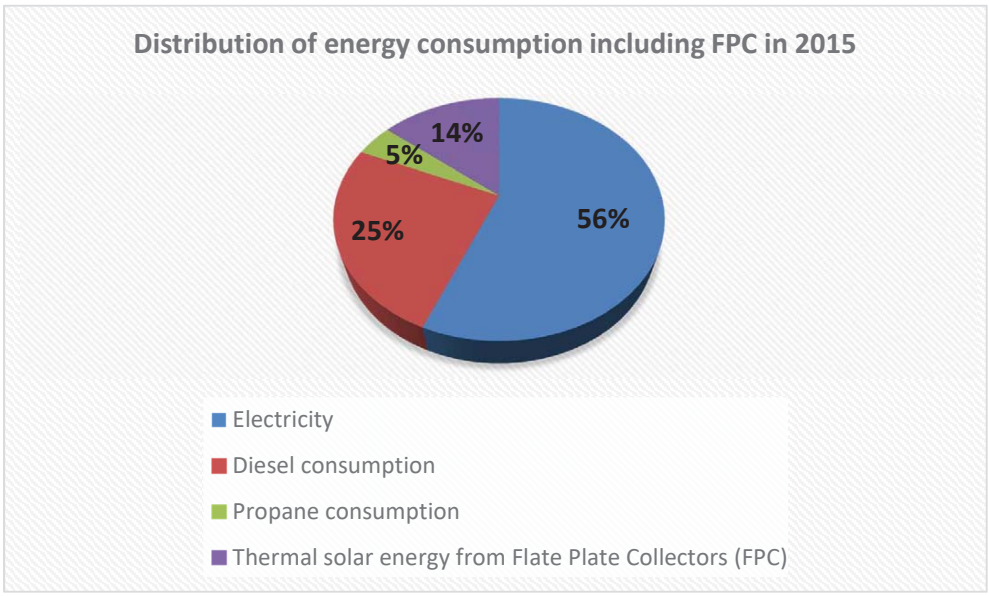

Fig. 8: Main hotel consumption from non-renewable and renewable sources during the year 2015.

After analyzing the annual energy consumption of the hotel, different options using renewable energy should be considered. The next section analysis the different options proposed in this work to achieve the nZEB for the hotel.

4.3. Energy consumption using renewable sources

Figure 8 demonstrates that electricity represents the most important energy consumption in the hotel. For that, the utilization of photovoltaic collectors (PV) is proposed. After analyzing the available space in the hotel to place photovoltaic collectors, two places were chosen: the car park and a nearby parking area. The number of panels to install will be 355 modules with a total aperture area of 689 m^2, and the electricity production was obtained

At the same time, it is possible to increase the number of solar thermal collectors on the roof of the hotel. Thus, using the same type of collectors, the useful area will increase 30 m^2 (from 117 m^2 to 147 m^2) and the annual heating useful energy will increase from 151 MWh/year to 189 MWh/year.

Table 4 shows the hotel energy consumption in 2015 and the expected energy consumption with the referred PV and FPC collectors' implementation in the hotel.

Tab. 4: Annual energy consumption using PV and FPC collectors.

		Energy consumed in 2015 (MWh)	Energy consumed improved with Renewable Sources (MWh)
Non-renewable sources	Electricity from grid	604	426
	Diesel consumption	271	233
	Propane consumption	47	47
Renewable sources	Thermal energy from FPC	151	189
	Electricity from PV	0	178
Total energy consumption		1073	1073

Figure 9 shows the annual distribution of the energy consumption considering the data of 2015, using FPC and PV. As can be seen, it is possible to achieve a total of 34% of the consumed energy with renewable energies (18% from FPC and 16% from PV).

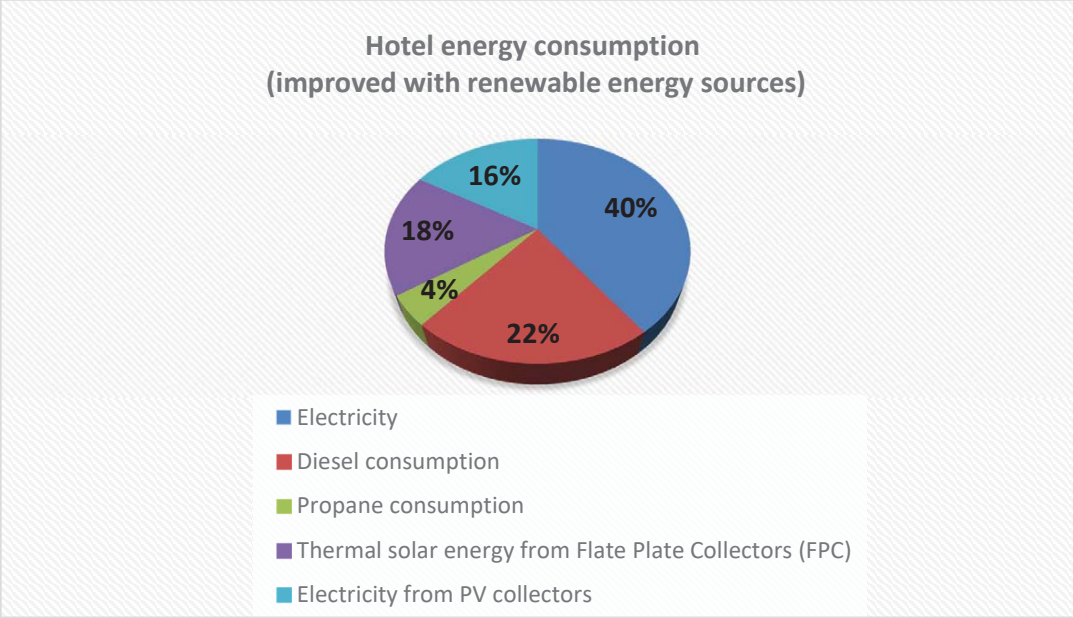

Fig. 9: Annual energy consumption distribution using renewable systems.

Using the definition of nZEB explained in the Introduction (Section 1), with the results obtained through the utilization of solar collectors, the target of nZEB for this hotel is still not achieved.

On the other hand, the diesel consumption used in the hotel is very high due to the utilization of the boiler during a long period. This boiler is used especially for water heating in HW and swimming-pool. We can propose to replace the actual diesel boiler by a biomass boiler. Biomass is considered a renewable source and it could be a good solution to reduce fossil fuel consumption. In Canary Island, the utilization of biomass boilers in hotels is starting and it has shown a promising future (Arlangton comp., 2016).

If a biomass boiler is used in this hotel for water heating, the diesel consumption will be null. In this case, it is possible to achieve 56% of the energy consumption with renewable energies (18% from FPC, 16% from PV and 22% from biomass).

5. Conclusions

In this work, the energetic analysis of a hotel located in Tenerife was performed and the implementation of different renewable energy systems was proposed.

During the cooling season it was demonstrated that higher indoor air temperatures could be achieved in the different floors, if the chiller or solar passive strategies were not used. The annual energy demand for cooling, to maintain the indoor air temperature below 25ºC, is about 350 MWh/year (58.99 kWh/m^2). When shading devices are considered, the indoor air temperature decreases between 0.2 to 0.9ºC, depending on the floor. Using the Chiller/Heat Pump installed in the hotel, the annual electricity consumption for air-conditioning is 7.4 MWh/year for heating and 167 MWh/year for cooling. Then, air-conditioning represents about 30% of the hotel electricity consumption.

After analyzing the annual energy consumption, different options using renewable energy (FPC and PV) were considered. It was demonstrated that it is possible to achieve 34% of the consumed energy with renewable energies (18% from FPC and 16% from PV). On the other hand, the diesel consumption is high because of the use of the boiler for water heating. If the actual diesel boiler is replaced by a biomass boiler, it is possible to achieve 56% of the consumed energy with renewable energies (18% from FPC, 16% from PV and 22% from biomass).

With the results obtained through the utilization of solar collectors and biomass, the target of nZEB is still not achieved for this hotel. Anyway, with the proposed improvements, the energy consumption using renewable sources would increase 4 times, from 14% to 56%.

Acknowledgments

The authors gratefully acknowledge the assistance provided by Mr. Enrique Talg, Director of Tigaiga Hotel, to access all information about the hotel (plans, energy consumption, etc.).

References

Arlangton Company. http://www.arlangton.com/ahorro-y-eficiencia-energetica/energias-renovables/biomasa-en-canarias/; accessed August 2016.

Delia D'Agostino, 2015. Assessment of the progress towards the establishment of definitions of Nearly Zero Energy Buildings (nZEBs) in European Member States, J. of Building Engineering 1, 20-32.

EU Directive 2002/91/EC, 2003. Directive of the European Parliament and of the Council of 16 December 2002 on the Energy Performance of Building, Official Journal of the European Communities, 65-71.

EU Directive 2010/31/EU, 2010. Directive of European Parliament and of the Council of 19 May 2010 on the Energy Performance of Building (recast), Official Journal of the European Union, 15-35.

Nearly Zero Energy Hotels (neZEH), 2016. Available from: http://www.nezeh.eu/home/index.html

Polanco, J. and Yousif, C., 2015. Prioritising energy efficiency measures to achieve a zero net-energy hotel on the island of Gozo in the central Mediterranean, Energy Procedia 83, 50-59.

Tsoutsos, T., Tournaki, S., Avellaner Santos, C., Vercellotti, R., 2013. Nearly Zero Energy Buildings Application in Mediterranean hotels, Energy Procedia 42, 230-238.

ISES International Solar Energy Society

Conference Proceedings

EuroSun 2016

Palma de Mallorca (Spain), 11 – 14 October 2016

Microclimate Mitigation for Reducing Summer Overheating in Historic District

Anna Laura Pisello[1,2], Veronica Lucia Castaldo[1], Cristina Piselli[1], Ilaria Pigliautile[1] and Franco Cotana[1,2]

[1] CIRIAF - Interuniversity Research Center, University of Perugia, Perugia (Italy)

[2] Department of Engineering, University of Perugia, Perugia (Italy)

Abstract

In the context of dense cities, which typically suffer from the Urban Heat Island (UHI) phenomenon, environmental quality is strongly affected by urban design choices and can significantly vary depending on the local boundary conditions and local climate phenomena. In this scenario, the present work analyzes the complex relation between the urban built environment and its local microclimate at neighborhood-urban scale, by means of both experimental field monitoring and numerical analysis. To this aim, an historic urban district in the city center of Perugia (central Italy) was continuously monitored during summer 2015 and the UHI intensity was assessed. Therefore, the validated numerical analysis of the area was carried out through ENVI-met simulation engine in order to quantify the thermal benefits achievable by applying specific tailored mitigations strategies, i.e. green façade, cool roof, and cool pavement, in both summer and winter conditions. The monitoring campaign confirmed that buildings' density and greenery percentage are able to considerably affect outdoor microclimate even in historical districts where the design choices are relatively limited compared to the new urban developments. The numerical analysis highlighted the major role of green façade in generating the most important air temperature drops in a summer day. Moreover, the effectiveness of the proposed mitigation technique is demonstrated also in winter conditions.

Keywords: *Outdoor microclimate, Urban Heat Island, Experimental monitoring, Numerical analysis, Local boundary conditions*

1. Introduction

Nowadays, more than half of the world's population lives in urban districts and it was assessed that in 2050 the 66% of the world's population will be an urban population (United Nations, 2015). This represents a great growth compared to the 30% registered in 1950. For this reason, the necessity to design healthy, efficient, and sustainable built environments is becoming a crucial issue for both designer and urban planners.

As underlined in various studies (Chen and Ng, 2012; Nikolopoulou and Lykoudis, 2006), human outdoor comfort depends on both physiological factors and the thermal conditions of the environment, which have a considerable role in influencing people's usage of urban spaces. Therefore, human thermal comfort has been detected to be one of the most important factors determining the quality of outdoor environments (Lai et al., 2014). One of the main threaten to the quality of urban microclimate is represented by the Urban Heat Island (UHI) phenomenon, which consists in higher air temperatures inside urban areas compared to those of the surrounding rural environment (Mirzaei and Haghighat, 2010). A huge research effort about this local climate phenomenon is carried out with the aim of understating and defining it from both a qualitative and a quantitative point of view. In this view, different approaches have been developed by means of both experimental analyses through in-field measurements and numerical analysis (Mirzaei and Haghighat, 2010). For instance, Papanastasou and Kittas (2012) detected a maximum temperature difference of 3.4 K and 3.1 K

doi:10.18086/eurosun.2016.01.16 Available at http://proceedings.ises.org

in winter and summer, respectively, between the city center and a suburban area of Volos (i.e. a medium-size coastal city in Greece) by comparing data collected from two fixed meteorological stations. Similarly, Mhosin and Gough (2012) assessed the great UHI variability in Toronto, by detecting an increase of about 0.02 K per decade between 1970-2000. On the other hand, mobile surveys were implemented in Padua (Busato et al., 2014) to experimentally characterize the UHI phenomenon. Such approach was able to reveal an UHI up to 6 K inside the city.

UHI is able to influence the weather conditions of a built environment at several scales (Oke, 1976), and the consequences at the urban canopy layer can significantly affect the well-being and health of citizens. Moreover, the global climate change and the increase in frequency and intensity of extreme heat events (Luber and McGeehin, 2008) may contribute in threatening human society even at a local scale, in terms for instance of outdoor visual and thermal comfort for pedestrians (Rosso et al., 2015), human health (McMichael et al., 2006), building energy consumption (Santamouris, 2014b), and also from an economy point of view (Stern and Treasury, 2007). Therefore, the investigation of the complex relationship existing between local variations of urban/suburban microclimate and the built environment could help to (i) reduce the negative effects of the UHI, (ii) find suitable mitigation strategies for each specific urban contest, and (iii) support a sustainable and energy efficient urban planning. In this scenario, Santamouris et al. (2015) showed how a deep knowledge of the microclimate conditions of a city could help to develop specific policy issue and the most appropriate resilience plan to fight the UHI. By using numerical analysis i.e., Teleghani et al. (2014) studied the relationship between the environment configuration and its microclimate by implementing in ENVI-met the model of five simple ideal urban forms. The aim was to provide basic suggestions for urban planners to be easily adapted to realistic situations.

On the contrary, Coronel and Álvarez (2001) found that the ancient neighborhood of Santa Cruz (Seville, Spain) during summer presents better thermal behavior compared to the new areas of the city due to peculiar characteristics of the urban environment, such as diffuse presence of trees and water fountains, high thermal mass of the external walls, mostly white-colored, and aspect ratio and orientation of the narrow streets. In fact, the alteration of local microclimate parameters in built environment is mainly due to a modification of the energy balance inside urban areas which depends on the above mentioned factors, and the presence of anthropogenic heat sources (Giridharan et al., 2007). Over the years different mitigation strategies were demonstrated to be able to improve such energy balance, i.e. the implementation of greenery (Bowler et al., 2010) and high-albedo materials inside built areas (Santamouris, 2014a). Such UHI mitigation techniques have been studied and tested through both experimental and numerical analysis to evaluate their effectiveness (Bruse and Fleer, 1998; Ridder et al., 2004). In the specific context of dense historical cities, Pisello et al. (2015b) tested a combination of these two strategies, since other invasive mitigation techniques cannot be applied due to architectural constraints. Furthermore, in order to overcome such constraints, innovative cool colored coatings were developed to ensure the same esthetic properties of the traditional coatings, but a more selective absorption band in the infrared part of the spectrum. Synnefa et al. (2007) found a maximum temperature difference of 10.2 K between a cool and standard colored coating, and almost the same values were obtained by Pisello et al. (2013) for a clay tile coatings suitable for applications in historic constructions.

2. Motivation

During summer 2015, a monitoring campaign of the outdoor environmental parameters was conducted in four different districts inside the historical city of Perugia, in central Italy. Data collected underlined the presence of higher air temperatures inside the area of the historical city center, which is characterized by dense urban design and lack of green areas. Building upon these finding and previous studies, the purpose of the present work is to investigate the effectiveness of studied suitable strategies to reduce the summer overheating in this context. Therefore, through numerical analysis, green facades, cool roofs, and cool pavements were implemented inside a realistic validated model of the area of interest to assess the benefits achievable in terms of local microclimate parameters and pedestrians' comfort.

Although the main aim is to mitigate summer overheating, microclimate variations were studied also in

winter conditions so as to evaluate possible consequences or benefits of the proposed mitigation techniques on outdoor thermal parameters during the cold season.

3. Materials and Methods

In order to pursue the outlined targets, a numerical model of the monitored area within the historical center of Perugia during summer 2015 (Fig. 1a) was developed. To ensure the reliability of simulation results, a (i) preliminary phase of validation was conducted. Once reached an acceptable correspondence between measured and simulated data, (ii) alternative scenarios to the real one (with well-acknowledged mitigation strategies), were simulated during a summer and a winter day. More in detail, the daily weather profiles were selected from the typical July (July, 15th) and typical January (January, 15th) provided by IGDG TMY (Typical Meteorological Year) for the city of Perugia, built on 1951-1970 period of record (U.S. Department of Energy, 2014). Therefore, (iii) the microclimate output obtained from the simulation were analyzed in terms of the outdoor thermal comfort index PET (Physiological Equivalent Temperature) (Chirag and Ramachandraiah, 2010) to assess how these mitigation strategies could affect pedestrian perception of the surrounding environment (Fig. 1).

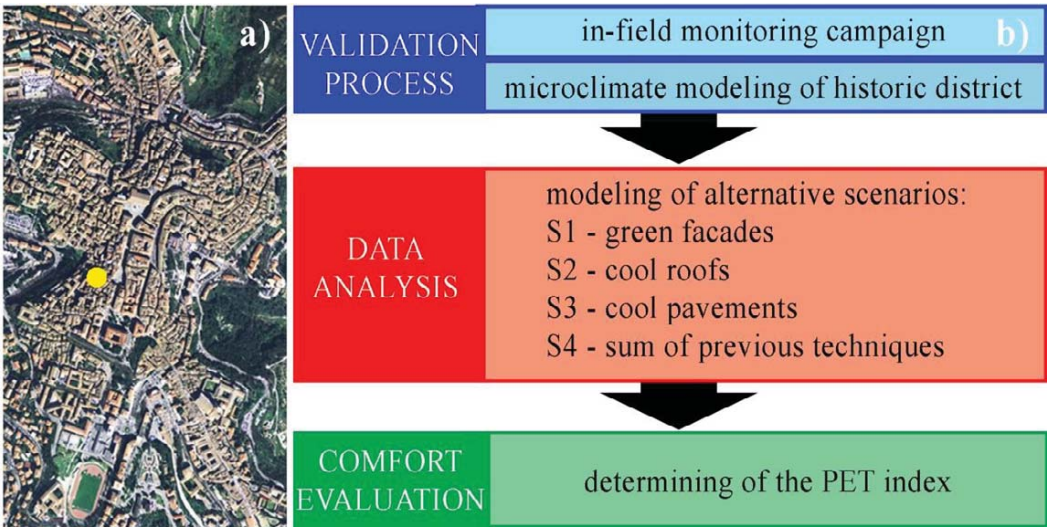

Fig. 1: (a) Position of the modeled area within the historic center of Perugia and (b) scheme of the adopted methodology

3.1. Modeling and validation process

The studied area is an East-West oriented street, 40 m long with a width varying from 3 to 12 m along its length (Fig. 2). Moreover, between the eastern and western side there is a height difference of 5 m. As the area is located in the historical center of the city, buildings surrounding the street are characterized by thick stone walls and the outdoor pavements are covered by bricks and plates made of *pietra serena* (except for the final western side which was recently asphalted) (Fig. 2c).

A three-dimensional microclimate modeling system, i.e. within ENVI-met V4 environment, designed to simulate the surface-plant-air interactions with a resolution from 0.5 to 10 m in space and from 1 to 5 sec in time, was used for the numerical analysis (Huttner and Bruse, 2009). The choice of the software was related to the high accuracy in space provided, which is optimal to study urban microclimate at a low scale, i.e. within the Urban Canopy Layer, where this work is focused. A realistic model of the area was developed and calibrated by using experimental data collected during the summer 2015 monitoring campaign. The calibration was performed following the suggestions of the ASHRAE GUIDELINE 14-2002 (ASHRAE, 2005), through both a statistical and graphical approach. The geometrical base of the model is a 3D grid of dimensions 30x60x35 having 1m side cube as unit. The materials used to characterize walls, roofs, and pavements were selected from the software database and their thermo-physical properties are summarized in Tables 1 and 2.

In order to have the necessary data for the calibration, during the monitoring campaign a portable weather

station placed at 15 m height (Pisello et al., 2014) and two Tinytag temperature and relative humidity probes and data-loggers (Pisello et al., 2015a) located at 2 m above the ground (Fig. 2d) were installed. As weather input the following data were used:

- Initial wind speed: value collected from the weather station at 6 a.m., start time of the simulation;
- Wind direction: value prevailing during the three days of the monitoring campaign;
- 24h air temperature and relative humidity forcing: data collected by the probe located on the South-oriented side (Fig. 2d, point B).

The simulation has been running for 24h and the data comparison for the calibration corresponded to those collected from the North-oriented probe (Fig. 2d, point A) and those extracted from its representative point within the model.

Fig. 2: View of the street from the (a) western and (b) eastern sides, (c) view of the street crossing the studied one on the East, and (d) localization in the plant of the monitoring probes

Tab. 1: Characteristics of the walls and roofs composing the reference scenario

Element	Albedo [-]	Emittance [-]	Specific heat [J/kg·K]	Thermal conductivity [W/m·K]	Density [kg/m^3]
Walls	0.30	0.90	840	0.86	930
Roofs	0.50	0.90	800	0.84	1900

Tab. 2: Characteristics of the different pavement profiles composing the reference scenario

Pavement profile	Albedo [-]	Emittance [-]	Volumetric Heat Capacity (upper layer) [J/m^3·K]	Heat Conductivity (upper layer) [W/m·K]
Brick Road	0.30	0.90	$2.00 \cdot 10^6$	1.00
Basalt Brick Road	0.80	0.90	$2.39 \cdot 10^6$	1.73
Asphalt Road	0.20	0.90	$2.25 \cdot 10^6$	0.90

3.2. Modeling of alternative scenarios

Alternative scenarios to the reference one, named S0, were developed by modeling the application at urban level of the following strategies for Urban Heat Island mitigation:

- Increase of urban greenery: introduction of vertical green systems on the buildings' facades, i.e. scenario S1;

- Replacement of traditional materials with high-reflectance ones: highly reflective roofs, i.e. scenario S2, and pavements, i.e. scenario S3, developed by using cool solutions for the coating material;
- Combination of the three mitigation strategies, i.e. scenario S4.

All the strategies, as summarized in Table 3, were selected to be realistically implemented in the case study area, which presents architectural constrains since it is located inside the historical center of the city. In particular, cool materials characterized by the same spectral response of traditional ones in the only visible region were considered in order to preserve buildings' heritage value, while providing higher reflectance values in the other ranges of the solar spectrum (Pisello et al., 2013). Moreover, pavement's thermal properties were optimized based on the real necessity to substitute the current asphalt area. The last technique, i.e. green façade, can be well integrated with the existing context as it is already installed in a building facing the crossing street (Figure 2c).

Tab. 3: Characteristics of the components modified in each mitigation scenario

Scenario	Element	Mitigation technique	Properties
S1	Walls' Façade	Greenery	Leaf Area Density: 2 m^2/m^3 Foliage albedo: 0.60
S2	Roofs	Cool material	Albedo: 0.75
S3	Pavement	Cool material	Albedo: 0.85
S4	Combination of all the above mentioned techniques		

The five scenarios were simulated during a representative summer and winter day in the climate context of Perugia, Italy, by using as weather input the TMY weather files for the months of July and January, respectively.

3.3. Outdoor thermal comfort analysis of mitigation scenarios

In order to evaluate the benefits achieved through the implementation of the mitigation strategies, the weather data obtained as output in the numerical simulation were analyzed in terms of thermal comfort improvements inducted in the surrounding outdoor area. A comparison between data obtained in the reference and alternative scenarios was performed by analyzing (i) the spatial distribution of the environmental parameters through describing maps and (ii) their variation in time during the day. Maps were generated when air temperature reaches its maximum value (i.e. 3:00 p.m.) and just after the sunset (i.e. 9:00 p.m.). Time series were extracted at 1.5 m, i.e. pedestrian level, from the ground in two different points selected because of their different characteristics (Fig. 3).

Furthermore, the Physiological Equivalent Temperature (PET) was chosen as the parameter representative of the outdoor comfort of pedestrians. The index was evaluated through RayMan data post-process software (Matzarakis et al., 2007).

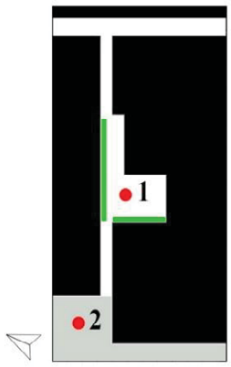

	Location	SVF	Time range when reached by direct solar radiation
Point 1 [x=12, y=28, z=5]	3 and 4 m distant from the east-west and the north-south oriented green walls, respectively	0.15	12:00-2:00 p.m.
Point 2 [x=5, y=8, z=1]	above the area originally presenting pavement made by asphalt	0.51	3:00-8:00 p.m.

location of green facades

asphalted area

Fig. 3: Location in the model of the two points selected to extract simulation data (at 1.5 m height)

4. Results and Discussion

4.1. Model calibration

The graphical and statistical approach followed for the model calibration was carried out as suggested by the ASHRAE GUIDELINE 14 (ASHRAE, 2005). The results depicted in Fig.4 show that the difference in terms of air temperature, between the measured and simulated values, is always lower than 3 K and mostly lower than 1 K. The maximum gap is reached during the hottest hours of the day, when the software tends to overestimate this parameter. Moreover, the difference in terms of air relative humidity is always lower than 10 %.

In addition to the graphical analysis presented in Fig. 4, two statistical indexes, i.e. *Mean Bias Error* (MBE) and *Root Mean Square Error* (RMSE) (ASHRAE, 2005), were evaluated, as reported in Table 4. According to the obtained results, the model can be considered representative of the real area with good approximation. Therefore, it can be used to simulate which could be the improvements in the outdoor microclimate of the zone due to the application of the selected mitigation strategies.

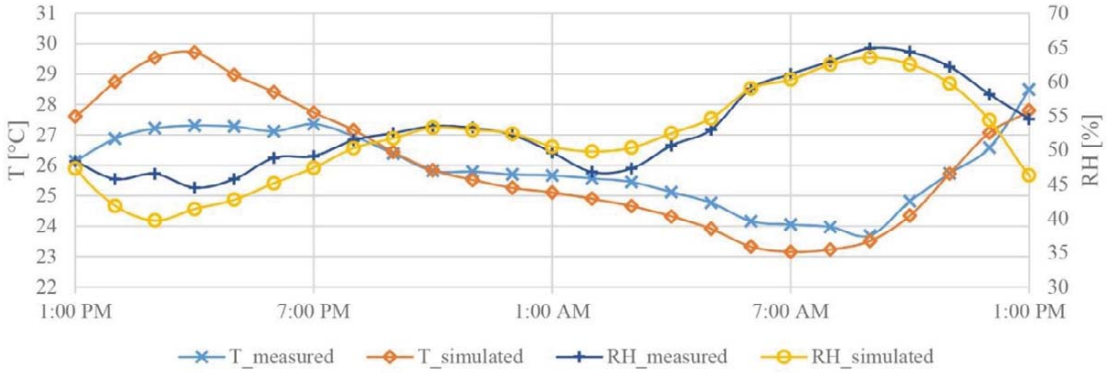

Fig. 4: Comparison of measured and simulated air temperature and relative humidity values trend for model validation

Tab. 4: Calibration parameters results

Parameter	MBE	RMSE
Air Temperature	0.82 K	1.05 K
Relative Humidity	2.21 %	2.96 %

4.2. Summer analysis

The analysis of the alternative simulated scenarios shows that, as expected, scenario S4, combining all the mitigation solutions, is the most advantageous one in summer (July, 15th) in terms of air temperature reduction, especially at pedestrian level (Fig. 5). In fact, by examining the air temperature values in the two analyzed positions, a decreasing trend is detected in the daytime. The best improvement is achieved at point 2, the one located in the previously asphalted area, where an air temperature decrease is registered during all the daytime, varying from -0.5 K (at 8:00 a.m.) to -0.85 K (at 3:00 p.m.).

By analyzing each strategy contribution, the implementation of greenery (S1) seems to be the most effective solution. Moreover, this strategy is the only one leading to benefits in both the points selected. However, in the point closest to the green façade (point 1) the maximum cooling, equal to -0.36 K, is obtained at around 3:00 p.m., i.e. in the peak temperature hours. Whereas, in point 2 the cooling benefit is not perceived during the daytime and the maximum cooling (about 0.4 K) is reached during the coolest hours, i.e. at around midnight, given the different exposition to direct solar radiation of the two points and the reduced heat emission from the walls due to the presence of greenery.

Opposite results, but similar behavior, are detected in S2, where high reflectance tiles are applied on the building roof. In both the points the air temperature increases during the daytime if compared to the reference scenario, especially in point 2. However, these worst values registered in presence of solar radiation (the

maximum increment of air temperature, equal to +0.21 K, is found at 7:00 p.m.) are balanced by improvements obtained during the night, leading to a difference up to -0.26 K at 6:00 a.m. This effect is due to the lower surface temperatures of the built surfaces and, therefore, to their lower contribution in the thermal balance during the nighttime.

Unlike previous results, a different behavior can be noticed in scenario S3, where the pavement reflectance is increased. In particular, in point 2 a drop in temperature is registered during the whole day leading to a mean daily reduction equal to -0.29 K, compared to the reference scenario, i.e. S0. On the other hand, at point 1 the temperature values are slightly increased from 12:00 to 7:00 p.m., with negligible differences up to +0.04 K (at 2:00 p.m.). In fact, point 2 is located above the ground surface covered by asphalt in the reference configuration and, therefore, the thermal properties improvement of the proposed materials are mostly perceived. On the contrary, point 1 seems to suffer from the presence of solar radiation, both direct and diffuse, since it is reached by higher mutual reflections of short wave radiation from the surrounding structures.

The relative humidity trend is strictly connected to the air temperature. However, relevant differences can be noticed just in scenarios S1 and S4 where greenery acts like a vapor source due to plants transpiration. The ratio between the ΔT and ΔRH is detected to be around -0.32 in the scenarios without greenery, but gets lower (-0.19 at point 1, the closer to the green facades, and -0.25 at point 2) after the introduction of vegetation.

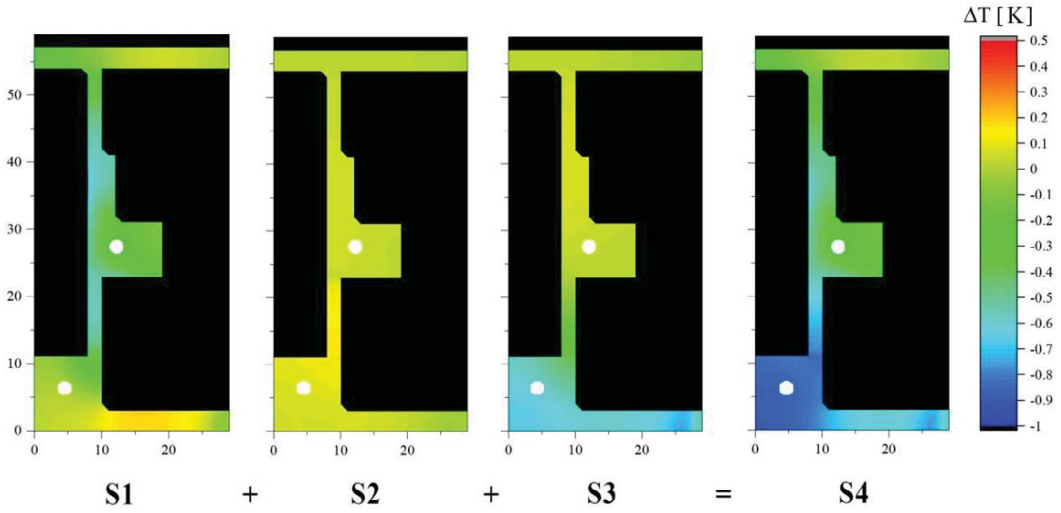

Fig. 5: Air temperature difference between reference (S0) and different mitigation scenarios in the summer day at 3:00 p.m.

Furthermore, the mean radiant temperature (MRT) values were analyzed (Fig. 6). The trend of the MRT shows one peak at point 1, while two peaks at point 2, since direct solar radiation occurs at different times in the two selected locations. At point 1, the peak coincides with the maximum values of reflected solar radiation (at around 1:00 p.m.). At point 2, a first relative peak is detected due to the maximum value of reflected radiation and an additional one is achieved at 3:00 p.m., when the point is reached for the first time by direct solar radiation. Additionally, unlike the previous results in terms of air temperature, the scenario S4 shows worst MRT values with respect to S0, and the solution which mostly influences this effect is the cool paving, i.e. scenario S3. In fact, the pavement reflectance, where high-albedo materials are applied, is able to significantly affect this parameter. Therefore, in the new comprehensive solution S4, a higher mean radiant temperature is observed during the daytime with respect to S0. Although this behavior is registered in both points, a wider range of values is detected in point 2, where MRT achieves its worst value (i.e. +7.62 K at 1:00 p.m.). However, it maintains lower values during the night (mean nighttime increase of +0.1 K) if compared to point 1 (mean nighttime increase of +1.5 K), where the SVF is lower. This is also the reason why in S4 an enhancement of the MRT, i.e. up to -0.11 K, is registered after sunset only in point 2.

An opposite behavior, but with relatively minor impact on the final results, is detected for S2, where

modification of buildings' roof reflectance properties are implemented by increasing the albedo of a 50% (i.e. from 0.5 to 0.75). In this scenario, the wider temperature variation is registered in point 1, from a minimum of -0.9 K at 8:00 a.m. up to a maximum of +0.8 K at 8:00 p.m., while in point 2 the range is between -0.55 K and +0.42 K.

Finally, benefits are registered also in terms of MRT by comparing the scenario characterized by the presence of greenery, i.e. S1, and S0. In detail, at point 1, which is closer to the green façade, lower values of MRT are detected, compared to S0, for almost all the daytime reaching a maximum of -2.84 K at 2:00 p.m. Therefore, an average daily reduction of MRT equal to -0.28 K is detected. Similar but lower effect is registered at point 2, where the achieved mean daily drop of MRT is equal to -0.21 K.

In order to assess the effect of the proposed strategies on the outdoor thermal comfort conditions, the PET index was calculated for the different scenarios (Fig. 7). The PET is strictly related to the trend of the mean radiant temperature, and it was obtained by imposing a clo (static clothing insulation) equal to 0.5. Results show how the midday MRT increase due to the implementation of the high reflective paving causes the increase of the PET in scenario S3 and S4 when the two points are reached by the direct solar radiation and when the peak of reflected solar radiation occurs. Whereas, the pedestrian comfort is improved in particular in point 1 due to the positive effect of the green facades.

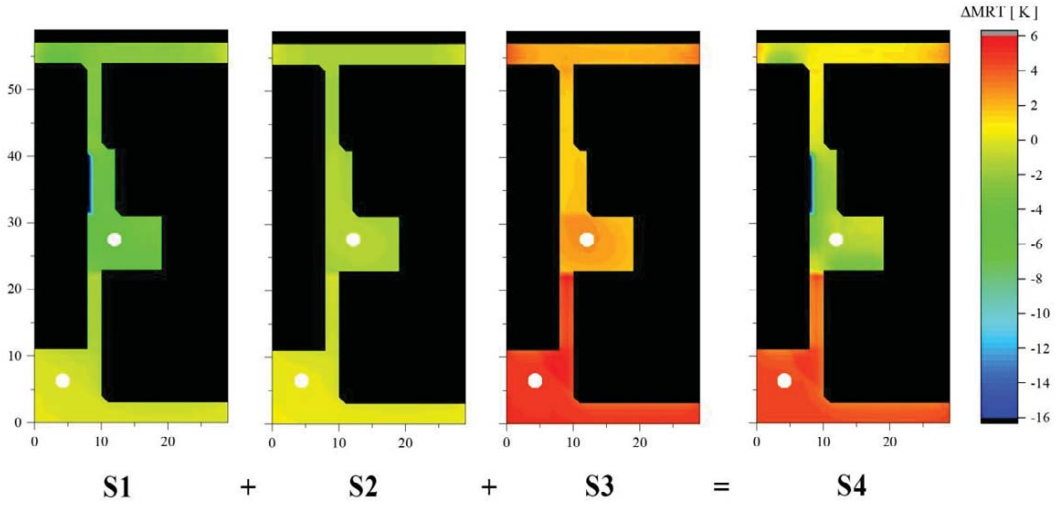

Fig. 6: Mean radiant temperature difference between reference (S0) and different mitigation scenarios in the summer day at 3:00 p.m.

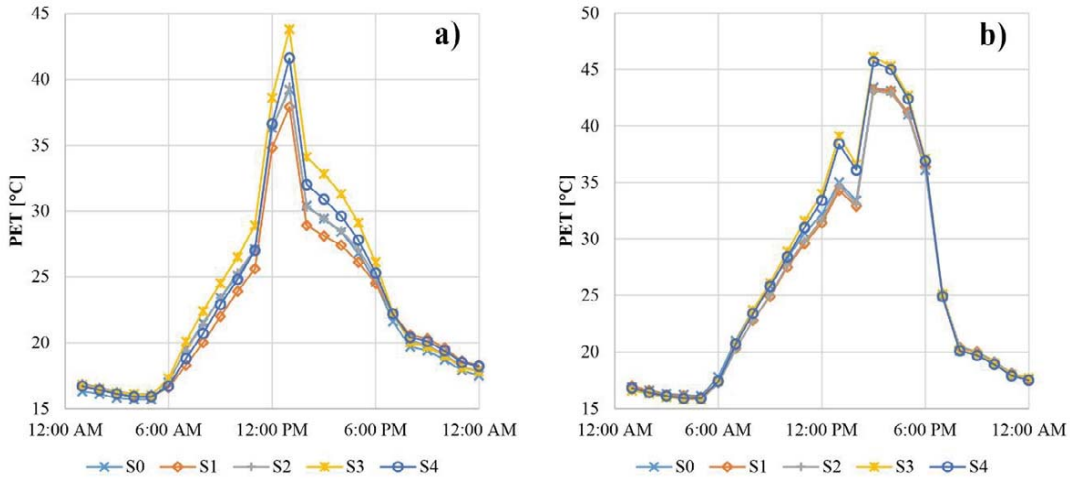

Fig. 7: PET daily trend in all simulated scenarios at (a) point 1 and (b) point 2 in the summer day

4.3. Winter analysis

Even if the proposed mitigation techniques are specifically designed to improve the outdoor thermal comfort conditions of the case study area during the hottest season (when the worst conditions in terms of outdoor thermal comfort are experienced at these latitudes), this section describes the results of the analysis of their effects during winter (January, 15th). The aim is to evaluate if the thermal comfort could be enhanced also in the cold season, or at least not reduced, and to quantify the potential benefits of the applied strategies, which are expected to be lower, compared to the summer ones.

In terms of air temperature, low improvements were detected in almost all the scenarios (Fig. 8). The only exception is registered in S3, i.e. in presence of high reflectance pavements, at point 2 from 12:00 to 4:00 p.m. However, a maximum decreasing of air temperature of only -0.06 K is detected at 2:00 p.m., meaning that paving surfaces are reaching lower surface temperatures even if subjected to the same direct radiation (as expected for cool materials). Nevertheless, S3 is globally the scenario where the higher air temperature increase is detected, with a mean daily variation, of +0.10 K at point 2 with respect to the reference scenario (S0). Instead, at point 1 the maximum mean daily variation, equal to +0.08 K, is registered in S1, i.e. where green facades are implemented. Moreover, higher air temperature improvements occur during the nighttime, when the lowest values of the parameter are reached.

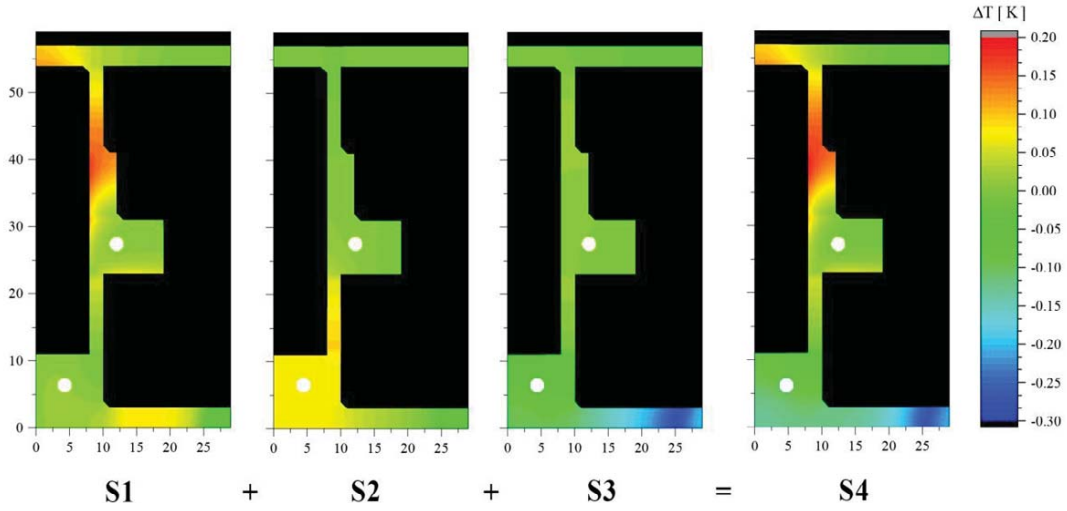

Fig. 8: Air temperature difference between reference (S0) and different mitigation scenarios in the winter day at 3:00 p.m.

Greater variations were found in terms of mean radiant temperature (Fig. 9), in particular at point 1, the one presenting the lower value of SVF (i.e 0.15). In fact, during winter both the selected points are never reached by direct solar radiation, due to the lower height of sun in this season. Therefore, in the absence of direct solar radiation, the effect of mutual reflectance between built surfaces has a stronger impact on the MRT. The highest values of the MRT occur in S3 (characterized by cool pavements) where a maximum difference of +3.41 K, compared to the reference scenario, is detected at 2:00 p.m., i.e. when the reflected radiation reaches its maximum. On the other hand, the introduction of greenery, i.e. S1, causes a drop in the MRT equal to -2.12 K in point 1, where the presence of the green vertical system is more perceived. After the sunset (i.e. at 5:00 p.m.) the effect of all mitigation strategies is almost the same and vary from +2.93 K (i.e. in S1) to +4.00 K (i.e. in S3) at point 1, and from +1.54 K (i.e. S1) to +2.32 K (i.e. S3) at point 2.

As regards the outdoor comfort assessment, the PET (Fig.10) was evaluated also in winter conditions by imposing a cloth resistance of 1.2 clo. In general, although the improvements are detected to be low, apart for S3, it is interesting to notice that the PET gap between the improved scenarios and the reference one is more significant in the nighttime rather than during the day. It means that the applied strategies induce an increment in terms of PET especially in the coldest hours. Therefore, even if the proposed solutions were specifically designed to fight discomfort conditions during the hot season, their effect is non-negligible also during winter, even if less significant.

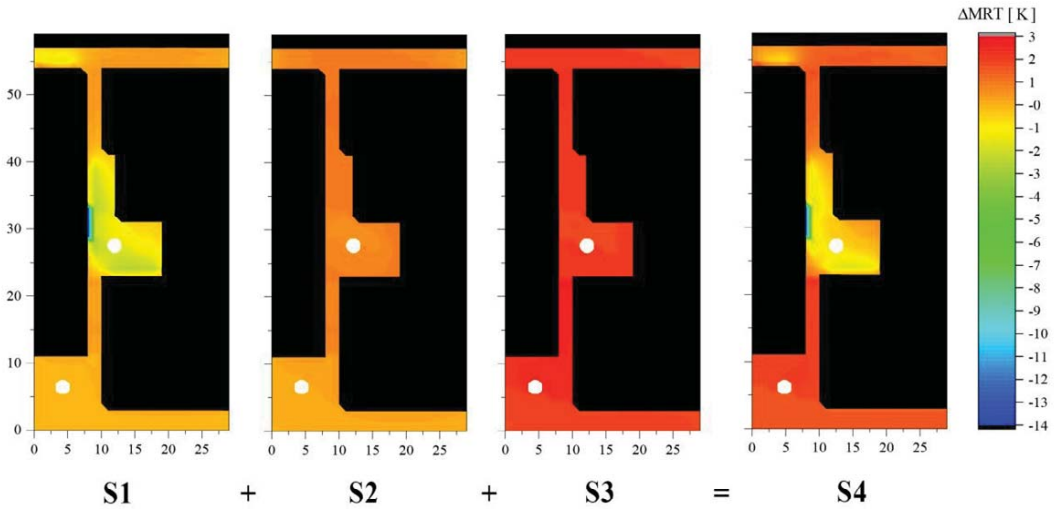

Fig. 9: Mean radiant temperature difference between reference (S0) and different mitigation scenarios in the winter day at 3:00 p.m.

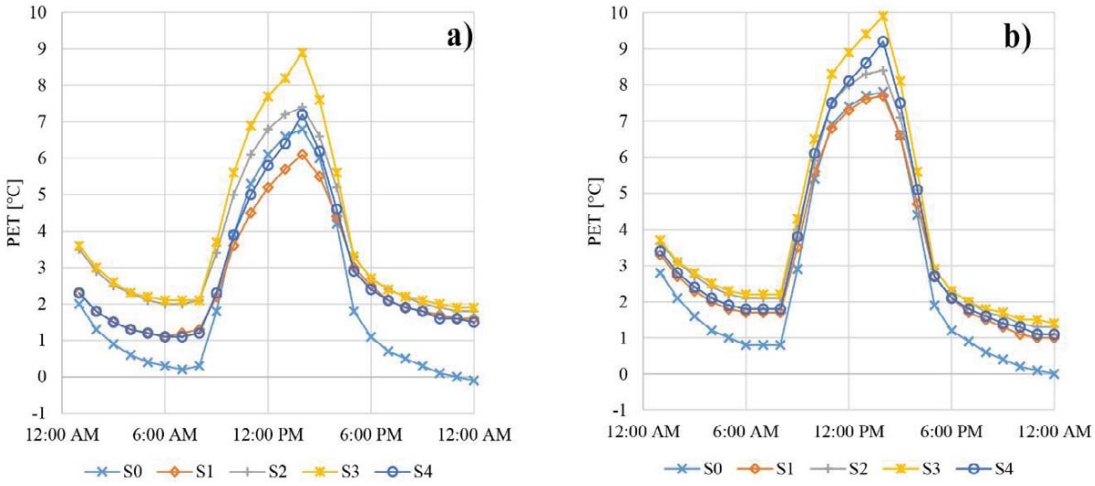

Fig. 10: PET daily trend in all simulated scenarios at (a) point 1 and (b) point 2 in the winter day

5. Conclusions

Urban microclimate has a strong influence on many aspects of human life in the cities. In dense urban environments, the Urban Heat Island phenomenon is a threat to the quality and the livability of the outdoor built environment. In this work, the impact of different UHI mitigation strategies implemented within a real historical precinct was assessed through calibrated numerical analysis, i.e. by using ENVI-met V4. Four possible mitigation scenarios were evaluated under both summer and winter conditions, i.e. the implementation of (i) greenery on building facades, (ii) cool roofs, (iii) cool pavements, and (iv) the combination of these three strategies. The possible thermal benefits deriving from their application were quantified in terms of microclimate parameters and outdoor comfort index, i.e. PET.

Generally, results showed improvements in terms of air temperature for all the solutions both during a summer and a winter day. The implementation of greenery led to the greater temperature gaps in summer, with respect to the reference scenario, i.e. an average daily difference (calculated for the whole analyzed area) of -0.25 K (at 1 m height) compared to the -0.05 K and -0.18 K obtained by implementing cool roofs and cool pavements, respectively. Whereas in winter, when lower effects were registered, no strong differences were noticed among the different scenarios. Furthermore, greenery was the only solution that improved the radiative balance of the outdoor environment in summer. On the contrary, the implementation

of cool materials, and in particular of cool pavements, caused a huge increase of the mean radiant temperature, which negatively affected the human thermal perception of the outdoor space in summer.

Future developments of this work will analyze the effects of such mitigation strategies applied diffusely within the city, enlarging the area of study. The final aim will be to provide reliable information to support both designers and urban planners in the design and development of policies to improve dwellers and pedestrians' quality of life.

References

ASHRAE, 2005. ASHRAE's Guideline 14-2002 for Measurement of Energy and Demand Savings: How to Determine What was Really Saved by the Retrofit. American Society of Heating, Refrigerating and Air-Conditioning Engineers, Atlanta, GA.

Bowler, D.E., Buyung-Ali, L., Knight, T.M., Pullin, A.S., 2010. Urban greening to cool towns and cities: A systematic review of the empirical evidence. Landsc. Urban Plan. 97, 147-155.

Bruse, M., Fleer, H., 1998. Simulating surface–plant–air interactions inside urban environments with a three dimensional numerical model. Environ. Model. Softw. 13, 373-384.

Busato, F., Lazzarin, R.M., Noro, M., 2014. Three years of study of the Urban Heat Island in Padua: Experimental results. Sustain. Cities Soc. 10, 251-258.

Chen, L., Ng, E., 2012. Outdoor thermal comfort and outdoor activities: A review of research in the past decade. Cities 29, 118-125.

Chirag, D., Ramachandraiah, A., 2010. The significance of Physiological Equivalent Temperature (PET) in outdoor thermal comfort studies. Int. J. of Eng. Sci. Te. 2 (7), 2825-2828.

Coronel, J.F., Álvarez, S., 2001. Experimental work and analysis of confined urban spaces. Sol. Energy 70 (3), 263-273.

De Ridder, K., Adamec, V., Bañuelos, A., Bruse, M., Bürger, M., Damsgaard, O., Dufekb, J., Hirschf, J., Lefebrea, F., Pérez-Lacorzanac, J.M., Thierrye, A., Weberf, C., 2004. An integrated methodology to assess the benefits of urban green space. Sci. Total Environ. 334-335, 489-497.

Giridharan, R., Lau, S.S.Y., Ganesan, S., Givoni, B., 2007. Urban design factors influencing heat island intensity in high-rise high-density environments of Hong Kong. Build. Environ. 42 (10), 3669-3684.

Huttner, S., Bruse, M., 2009. Numerical modeling of the urban climate – A preview on ENVI-MET 4.0. The seventh International Conference on Urban Climate, 29 June-3 July 2009, Yokohama, Japan. <http://www.envi-met.com/documents/papers/ICUC7_ModellingV4.pdf>.

Lai, D., Zhou, C., Huang, J., Jiang, Y., Long, Z., Chen, Q., 2014. Outdoor space quality: A field study in an urban residential community in central China. Energ. Buildings 68, 713-720.

Luber, G. McGeehin, M., 2008. Climate Change and Extreme Heat Events. Am. J. Prev. Med. 35, 429-435.

Matzarakis, A., Rutz, F., Mayer, H., 2007. Modelling radiation fluxes in simple and complex environments-application of the RayMan model. Int. J. Biometeorol. 51, 323-334.

McMichael, A.J., Woodruff, R.E., Hales, S., 2006. Climate change and human health: present and future risks. Lancet. 367, 859-869.

Mirzaei, P.A., Haghighat, F., 2010. Approaches to study Urban Heat Island – Abilities and limitations, Build. Environ. 45, 2192-2201.

Mohsin, T., Gough, W.A., 2012. Characterization and estimation of urban heat island at Toronto: Impact of the choice of rural sites. Theor. Appl. Climatol. 108, 105-117.

Nikolopoulou, M., Lykoudis, S., 2006. Thermal comfort in outdoor urban spaces: Analysis across different European countries. Build. Environ. 41, 1455-1470.

Oke, T.R., 1976. The distinction between canopy and boundary layer urban heat islands. Atmosphere 14, 268-277.

Papanastasiou, D.K., Kittas, C., 2012. Maximum urban heat island intensity in a medium/sized coastal Mediterranean city. Theor. Appl. Climatol. 107, 407-416.

Pisello, A.L., Cotana, F., Nicolini, A., Brinchi, L., 2013. Development of clay tile coatings for steep-sloped cool roofs. Energies 6, 3637-3653.

Pisello, A.L., Cotana, F., Nicolini, A., Buratti, C., 2014. Effect of dynamic characteristics of building envelope on thermal-energy performance in winter conditions: In field experiment. Energ. Buildings 80, 218-230.

Pisello, A.L., Pignatta, G., Castaldo, V.L., Cotana, F., 2015a. The impact of local microclimate boundary conditions on building energy performance. Sustainability 7 (7), 9207-9230.

Pisello, A.L., Piselli, C., Cotana, F., 2015b. Thermal-physics and energy performance of an innovative green roof system: The Cool-Green Roof. Sol. Energy 116, 337-356.

Rosso, F., Pisello, A.L., Pignatta, G., Castaldo, V.L., Piselli, C., Cotana, F., Ferrero, M., 2015. Outdoor Thermal and Visual Perception of Natural Cool Materials for Roof and Urban Paving. Procedia Eng. 118, 1325-1332.

Santamouris, M., 2014a. Cooling the cities – A review of reflective and green roof mitigation technologies to fight heat island and improve comfort in urban environments. Sol. Energy 103, 682-703.

Santamouris, M., 2014b. On the energy impact of urban heat island and global warming on buildings. Energ. Buildings 82, 100-113.

Santamouris, M., Cartalis, C., Synnefa, A., 2015. Local urban warming, possible impacts and a resilience plan to climate change for the historical center of Athens, Greece. Sustain. Cities Soc. 19, 281-291.

Synnefa, A., Santamouris, M., Apostolakis, K., 2007. On the development, optical properties and thermal performance of cool colored coatings for the urban environment. Sol. Energy 81, 488-497.

Stern, N.H., Treasury, G.B., 2007. The economics of climate change: the Stern review, Cambridge University Press.

Taleghani, M., Kleerekoper, L., Tenpierik, M., van den Dobbelsteen, A., 2014. Outdoor thermal comfort within five different urban forms in the Netherlands. Build. Environ. 83, 65-78.

United Nations, Department of Economic and Social Affairs, Population Division, 2015. World Urbanization Prospects: The 2014 Revision. <https://esa.un.org/unpd/wup/Publications/Files/WUP2014-Report.pdf>.

U.S. Department of Energy, Energy Efficiency and Renewable Energy, 2014. <http://apps1.eere.energy.gov/buildings/energyplus/cfm/weather_data3.cfm/region=6_europe_wmo_region_6/country=ITA/cname=Italy>, WMO Station Region 6: Italy, Perugia 161810 (IGDG).

Conference Proceedings

EuroSun 2016
Palma de Mallorca (Spain), 11 - 14 October 2016

Mathematical modelling of the electric load profile of a low energy laboratory building in Spain

Y. I. Alamin[1], M. Castilla[2], J.D. Alvarez[1], A.E. Ruano[3], and M. Perez[1]

[1] University of Almería, Agrifood Campus of International Excellence (ceiA3)
CIESOL Joint Centre University of Almería -CIEMAT, Almería (Spain)

[2] Department of System Engineering and Automation, School of Engineering, University of Seville, 41092 Seville, (Spain)

[3] Faculty of Science and Technology, University of Algarve, Faro, Portugal and, IDMEC, Instituto Superior Técnico, Universidade de Lisboa, Lisboa, (Portugal)

Abstract

Energy saving and the integration of renewable energies are critical issues in Net Zero Energy Buildings (NZEB). In this context, the availability of methods for the prediction of the Electrical Load Demand (ELD) is extremely important mainly due to its relevance for an appropriate energy management, sizing of NZEB energy systems, and, especially, for the implementation of suitable energy control strategies, such as energy storage. This paper describes the development and assessment of an electricity demand short-term predictive Artificial Neural Network (ANN) model for a characteristic laboratory within an NZEB located at Almería (Southeastern Spain). As the model is aimed to be used as part of advanced building energy control schemes, some specific requirements, as a tradeoff between accuracy and simplicity, have been considered. The work presented in this paper contains both a description of the algorithms and reference data for an appropriate development of this kind of models. Moreover, a detailed discussion of the obtained ANN model which has been validated using real data obtained from the NZEB used as case-study has been included.

Keywords: *Net Zero Energy Buildings, Electrical Load Demand, Artificial Neural Network, Radial Basis Functions.*

1. Introduction

Nowadays, the concept of NZEB and energy efficiency measurement applied to buildings are receiving an extensive attention all around the world mainly due to their huge contribution to reduce climate change (Kolokotsa et al., 2001). Therefore, the prediction of ELD within the scope of NZEB is presently being widely studied since the optimization of the use of renewable energy sources by means of specific control systems requires an accurate knowledge of building energy consumption patterns, both for the peak and average loads and for the short and medium-term building rooms use dynamics (Castilla et al., 2014).

In this work, a bioclimatic building has been considered as a case of study. More specifically, this building is located at Almería (Spain) and it has been built to take advantage of the benefits provided by solar energy and natural ventilation for passive heating and cooling. In addition, it has a Heating, Ventilating and Air Conditioning (HVAC) system which uses solar thermal energy for active cooling of the rooms. Furthermore, a grid connected photovoltaic (PV) installation completes the building energy infrastructure to cope with the building electricity demands.

In literature, there are many studies that take into account the consumption of the whole building (Khosravani et al., 2016; Mena et al., 2014), several buildings or even the whole city (Ferreira et al., 2010), others are related to the power demand, wind speed, power forecasting and solar irradiance forecasting with different

doi:10.18086/eurosun.2016.01.20 Available at http://proceedings.ises.org

range of parameters (Ren et al., 2015). The approach presented in this paper takes into account one room (a laboratory) which can be observed in Fig.1, as a representative environment of the building. In this case, there are several factors that influence energy consumption such as weather variables, building's construction, building's occupants and their behavior, the use of artificial lighting, the use of the HVAC system, etc.

Artificial Neural Networks (ANNs) have been used to obtain predictive models for the power consumption. In addition, the modeling capabilities of Radial Basis Functions (RBFs) are influenced by the shape of basis functions, the number and placement of the centers, and the width (spread) of the basis function (Ferreira et al., 2012). The using of ANNs for forecasting has led to a tremendous increment in research activities in this field in the past years. As the interesting reader can check in the following works (Zhang el at, 1997; Mena et al, 2014).

In this work, an ANN for the prediction of the energy consumption of the laboratory has been considered. More specifically, it takes into account the energy consumption of artificial lighting, computers, and other equipment in the laboratory.

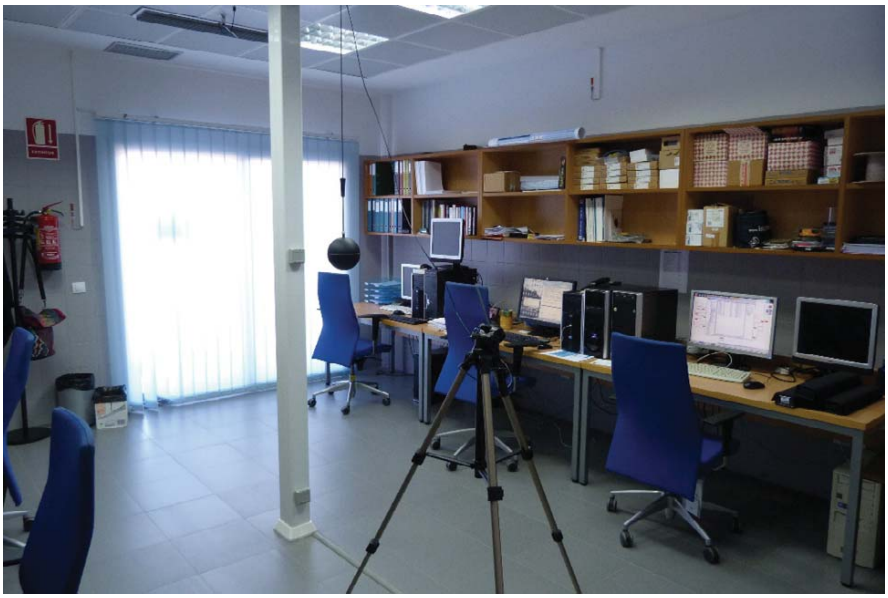

Fig. 1: Representative environment of the CIESOL building

The paper is organized as follows: Section 2 describes the scope of the work. The methodology used to obtain the ANN is presented in Section 3. In Section 4 the obtained results are briefly discussed. Finally, Section 5 includes the main conclusions and future works.

2. Scope of the work

The CIESOL building (http://www.ciesol.es) is a solar energy research center, see Fig. 2, which is located inside the Campus of the University of Almería in the southeast of Spain. This geographic location is characterized by having a typical desert Mediterranean climate, with an annual average number of 2965 hours of sunshine (climate values registered at the meteorological station of the Almería airport, located 3.5 kilometers far from CIESOL). This building is distributed into two different floors with a total surface of 1071.92 m^2. In addition, it was built following several bioclimatic criteria that affect to its architecture, as the use of photovoltaic panels to produce electricity and an HVAC system based on solar cooling.

This HVAC system makes use of a solar collector field, a hot water storage system, a boiler and an absorption machine with its refrigeration tower in order to produce heat or cold air as a function of the demanded necessities. Moreover, it has a wide network of sensors and actuators, and an appropriate data acquisition and measurement system. The availability of these data will allow to understand the behavior of each one of the

bioclimatic strategies which are implemented in this building, the energy saving and CO_2 emissions reduction which can be obtained with them, and also, to perform energy scheduling tasks to optimize the use of renewable energies against conventional energy sources.

Fig. 2: CIESOL building

3. Methodology and experiments

ANNs can be seen as weighted directed graphs where the neurons are nodes and the directed edges (with weights in each) are connections between input and output neurons. They are used for non-linear mapping between the input data $\boldsymbol{X}$ and the output vector $\boldsymbol{Y}$ in order to model relations or detect patterns among them. ANNs are black-box models and, thus, their parameters and structure have to be determined from data.

3.1 Architecture and structure selection: RBF Neural Network

The ANN is an artificial intelligence technique that mimics the human brain's biological neural network in the problem solving processes. As humans solve a new problem based on the past experience, a neural network takes previously solved examples, looks for patterns in these examples, learns these patterns and develops the ability to correctly classify new patterns. In addition, the neural network has the ability to resemble human characteristics in problem solving that is difficult to simulate using the logical, analytical techniques of expert system and standard software technologies (Daosud et al., 2005). In this work an RBF neural network is used. As it can be observed in Fig. 3, an RBF ANN has three layers. The first layer represents the inputs to the network from the outside environment. The second layer, also denominated hidden layer, applies a non-linear transformation on the input set. This layer usually has a large number of neurons to achieve better results. Finally, the third layer, which usually has a single neuron, performs a linear combination over the outputs of the neurons from the previous layer, that is, the hidden layer. Hence, the output of this layer is the result provided by the neural network.

Therefore, the output of an RBF ANN can be expressed as:

$$y = \sum_{i=1}^{n} w_i f_i \cdot (\|c_i - x\|_2) \qquad \text{(eq. 1)}$$

where w_i is the weight associated with the i^{th} hidden layer node, f_i is the radial function, c_i is the center location and x is the input point. The modeling capabilities of this network are determined by the shape of the radial function, the number and placement of the centers, and the width (spread) of the function. Moreover, different

options can be selected as radial function, such as radial linear function, radial cubic function, Gaussian function, thin plate spline function, multi-quadratic function, inverse multi-quadratic function or shifted logarithm function. However, the most used radial function is the Gaussian, see (eq. 2):

$$f_i(x) = e^{\left(-\frac{\|c_i - x\|_2^2}{2\sigma_i^2}\right)} \qquad \text{(eq. 2)}$$

where σ is the standard deviation, c_i is the center of the distribution, and x is the input point.

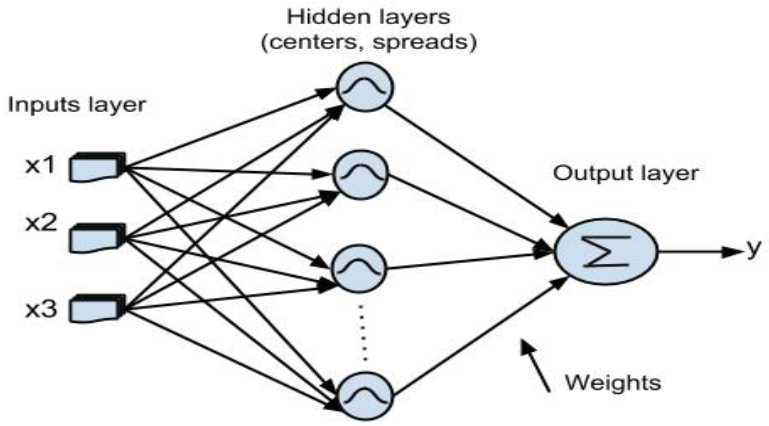

Fig. 3: RBF ANN simple diagram

In general, during the training process, the training error decreases. However, generalization error, that is, the accuracy of the used algorithm to predict the output for previously unseen input values, evolves as it is shown in Fig. 4. This problem is known as overfitting. Typically, the generalization error is estimated as the difference between the expected and the empirical error over a generalization data-set, which is a fixed set of data samples not from the training data-set. Therefore, the initial data-set should be partitioned into a training data-set and a testing data-set. Afterwards, the training data-set is split into two different data-sets: one to estimate the model, and the other to its validation. Hence, three different data-sets are used: training, generalization, and testing (Haykin 2005).

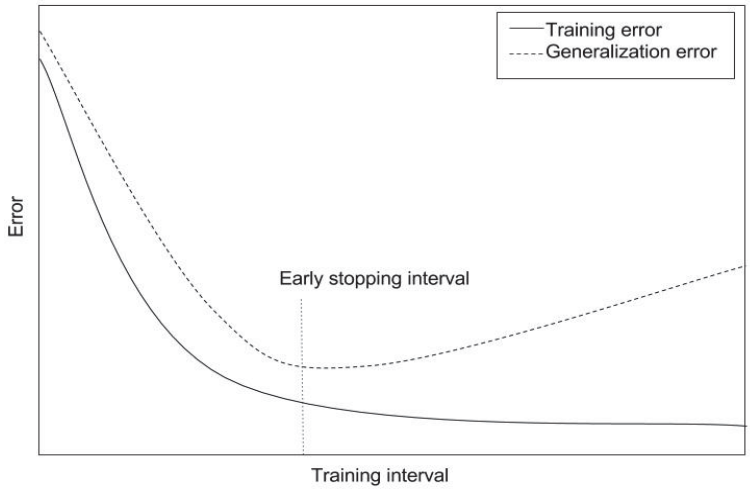

Fig. 4: Training error versus generalization error: early stopping interval (Haykin 2005)

3.2 Data-sets construction

To obtain the RBF ANN proposed in this paper, a set of historical data from the CIESOL building has been used. Concretely, the historic data-set comprises since the 11th of December 2013 to the 11th of February 2014, so it has a total length of 63 days, with a sample time of 1 minute, that is, 90720 points. These points were obtained from different measurement systems. Hence, to synchronize both of them, 60 points (1 hour) were removed from the historic data-set. Therefore, the final number of points was 90660 points.

Due to the sample time of the historic data, the power consumption signal had a random noise in it. Therefore, to remove this noise a smooth filter has been used. More specifically, the MATLAB *smooth* function has been applied to the data. This function smooths data using a 5-point moving average, that is, the

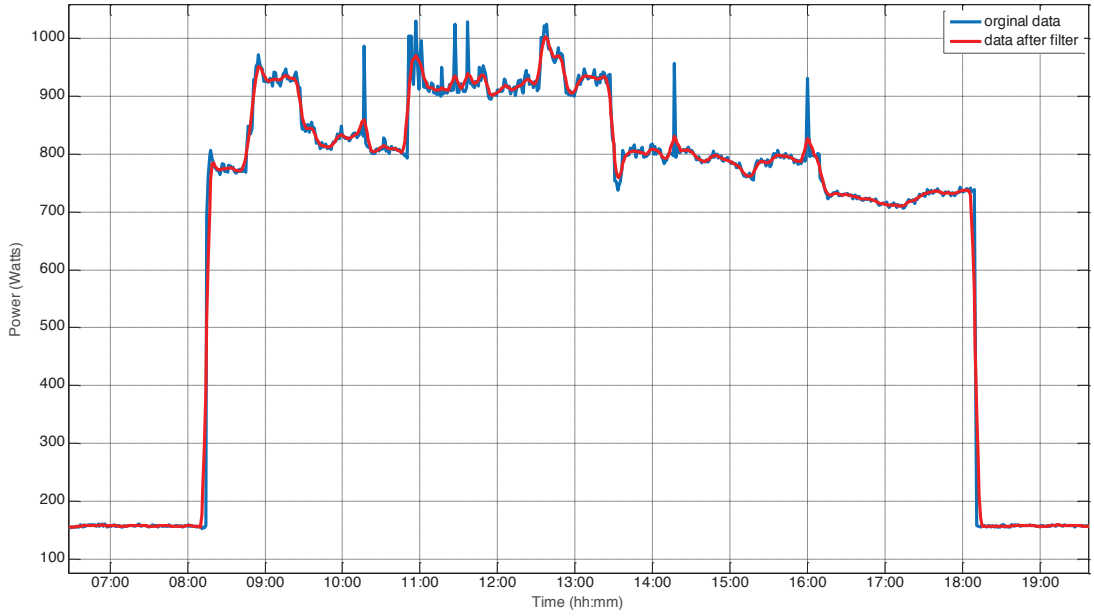

Fig. 5: Results provided by the smooth filter over the power demand signal

moving average filter smooths data by replacing each data point with the average of the neighboring data points defined within the span. This process is equivalent to a low pass filter. Hence, the response of the smooth function is given by the following difference equation:

$$y_s(i) = \frac{1}{2N+1}\left(y(i+N) + y(i+N-1) + \ldots + y(i-N)\right) \quad \text{(eq. 3)}$$

where $y_s(i)$ is the smoothed value for the ith data point, N is the number of neighboring data points on either side of $y_s(i)$, and $2N+1$ is the span (MathWorks Website, 2016). Fig. 5 shows a fraction of the data before and after the filter process has been applied.

3.3 ANN inputs and size

As has been pointed out within the Introduction Section, the output of the ANN model presented in this paper is the prediction of the power demand (excluding the HVAC system) of a representative laboratory of the CIESOL building, see Fig. 1. The original data-set has a total length of 63 days but, after removing the mistaken, unavailable, and unwanted data the size is reduced to 40 acceptable days that can be useful for modeling purposes, see Fig. 6. Figure. 7 shows the power demand of these 40 days in cyan color, and the average power demand in blue color. Finally, from this subdata-set only 23 days have been selected to be used for design the ANN.

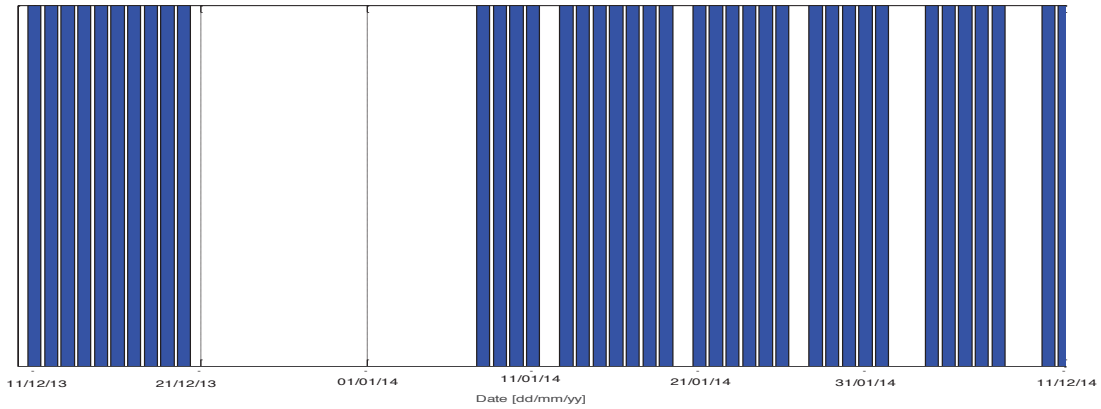

Fig. 6: Data used from the period

This subdata-set of 23 days has been divided into three different data-sets: training, generalization, and testing data-sets which contains the 12%, 8%, and 80% of total points respectively. These points have been selected randomly from the subdata-set of 23 days and, thus, the final size of training, generalization and testing data-set are 3974, 2650 and 26496 points respectively.

The ANNs proposed in this paper uses as inputs 2 lags of the power demand [W] of the laboratory, the CO_2 concentration inside the laboratory [ppm], the outside direct irradiance [W/m^2] and the number of people inside the modeled room [-]. The behavior of occupants have a major effect on the power consumption in the building (Virote and Neves-Silva, 2012). More specifically, they have a direct effect from their physical presence in the space, and an indirect effect derived from their social behavior and awareness of the power saving aspect (Oikonomou et al., 2009).

Moreover, the output of the ANNs is the prediction of the power demand in the laboratory. In Fig. 8 the three exogenous inputs data and the power demand of the period considered in this study are shown. The structure of the proposed ANN can be observed in Fig. 9.

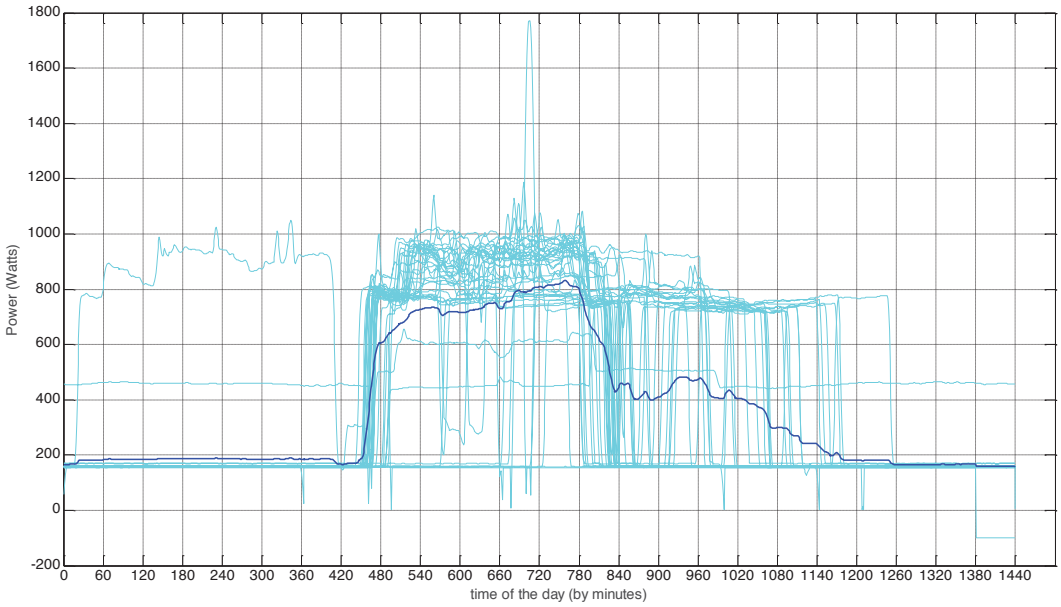

Fig. 7: Daily power of Laboratory with average of the period

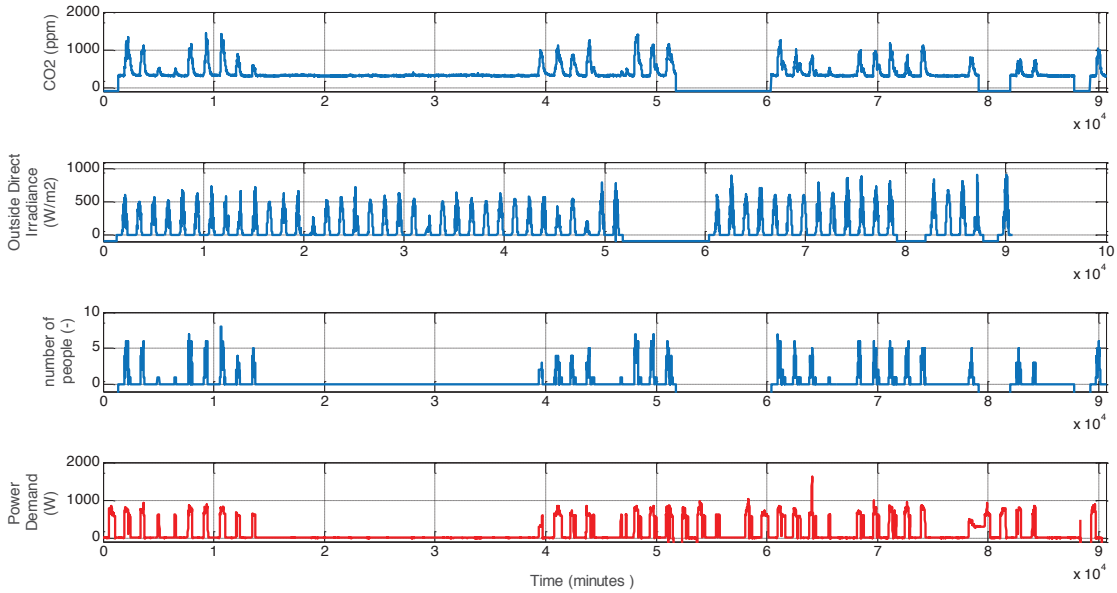

Fig. 8 The inputs and the output data

As different ANNs to predict the power demand of a representative laboratory have been obtained, each of them with different configurations, it is necessary to determine which of the proposed ANNs is the best one. For this aim, the Normalized Root Mean Square Error (NRMSE) has been used. This index is the percentage of the Root Mean Square Error (RMSE). In addition, this index has also been used to validate the proposed ANNs as a function of the prediction horizon (from 1st step and 16th step), see eq. 4, where λ is a weighting factor for each NRMSE:

$$rmseF = \frac{\lambda * NRMSE_{v-1st} + (1-\lambda) * NRMSE_{v-16th}}{2} \quad \text{(eq. 4)}$$

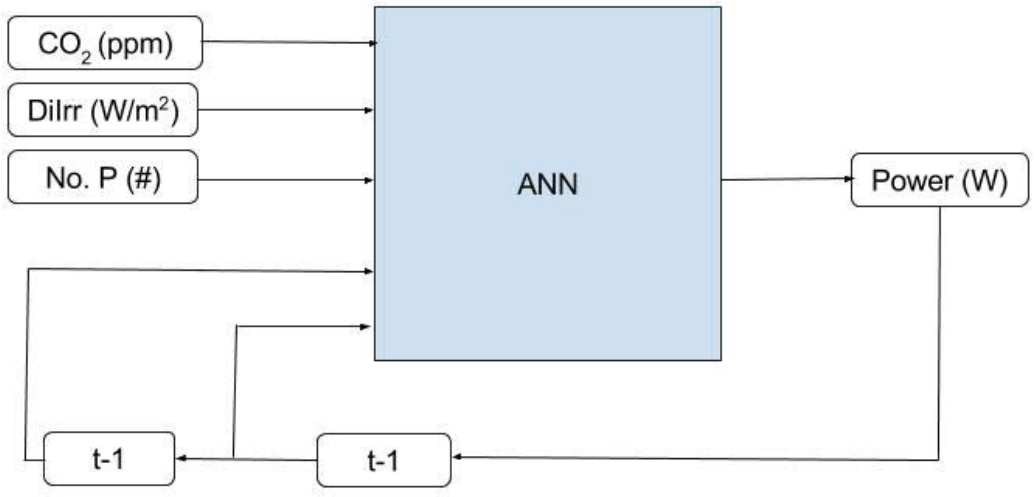

Fig. 9: Structure of the ANN proposed in this paper to predict the power demand in a laboratory of the CIESOL building

In the previous equation $NRMSE_{v-1st}$ and $NRMSE_{v-16th}$ are the NRMSE of the validation data-set for 1st step and 16th step prediction horizons respectively, and λ, in this case, has been fixed to 0.5.

The experiments had been run for all the combinations of these parameters:

- The number of the centers can be 3, 6, 9, 12 and 15.
- The τ parameter with values of 0.05, 0.01, 0.005 and 0.001, which is the termination criterion with early stopping, since an early stopping method with generalization data-set has been used.

In this work, the RBF ANN used to predict the power consumption of the laboratory has been trained using the Levenberg–Marquardt (LM) algorithm (T. Olofsson, 1998; D.W. Marquardt, 1963) which minimizes a modified training criterion (A. Ruano, et al, 1991; P.M. Ferreira and A.E. Ruano, 2000). This method has been successfully used in (P.M. Ferreira, 2012).

4. Results and discussion

In Table 1 a summary of the different models which have been obtained from training the ANN with real data from the bioclimatic building are shown. More specifically, the NRMSE index has been used to assess the performance on the different models. Moreover, validation results for one step ahead (using 1 minute interval) show an appropriate performance with a NRMSE less than 5% in the worst case. However, it does not happen with the worst case for 16 step ahead, which is higher. Thus, a final RMSE, which is the mean of the previous ones (1 and 16 steps ahead), has been calculated to select the most suitable model in both cases.

Finally, the results of the power demand for these 5 models in Table 1 are shown in Fig. 10, and the prediction of the 16 steps of the first model are shown in Fig. 11. In addition, the validation results of the 1st and 16th step prediction ahead for model number 1 can be observed in Fig 12.

The number of neurons that compose the hidden layer of the ANN, the small size of the data window and the parameters of the training algorithm for the experimental works carried out in this paper suggest that these values should be carefully studied, but anyway, many neurons were not needed to get satisfactory results.

Tab. 1: Results of the best five obtained models

Model number	Number of centres	NRMSE training	NRMSE generalization	NRMSE testing for 1 step ahead	NRMSE testing for 16 step ahead	Final RMSE
1	3	0.0099	0.0095	0.0097	0.2124	0.0555
2	3	0.0102	0.0105	0.0104	0.2125	0.0557
3	3	0.0103	0.0099	0.0103	0.2131	0.0558
4	3	0.0099	0.0095	0.0097	0.2172	0.0567
5	3	0.0102	0.0104	0.0103	0.2174	0.0569

Tab. 2: Statistical analysis of the best five obtained models

Model number		Mean Absolute Error (MAE)	Mean Relative Error (MRE)	Maximum Absolute Error (MaxAE)	Standard Deviation Error (SN)	Normalized Mean Absolute Error (NMAE)
1	1st step	1.1898	0.0855	58.4	3.8921	1.0298
	16th step	45.6813	6.1393	1041.6	84.8871	2.4538
2	1st step	1.2927	0.1060	94.0	4.1700	0.6938
	16th step	48.0858	8.1748	777.5	84.3525	3.1858
3	1st step	1.3399	0.1262	81.7	4.1145	1.0006
	16th step	49.2480	8.3953	1316.6	84.4973	2.5201

Model number		Mean Absolute Error (MAE)	Mean Relative Error (MRE)	Maximum Absolute Error (MaxAE)	Standard Deviation Error (SN)	Normalized Mean Absolute Error (NMAE)
4	1st step	1.1754	0.0838	57.8	3.8782	1.0333
	16th step	46.0759	6.3502	1060.8	86.7969	2.3949
5	1st step	1.1957	0.0953	105.1	4.1120	0.5983
	16th step	47.2486	10.4861	1077.7	84.7124	2.4327

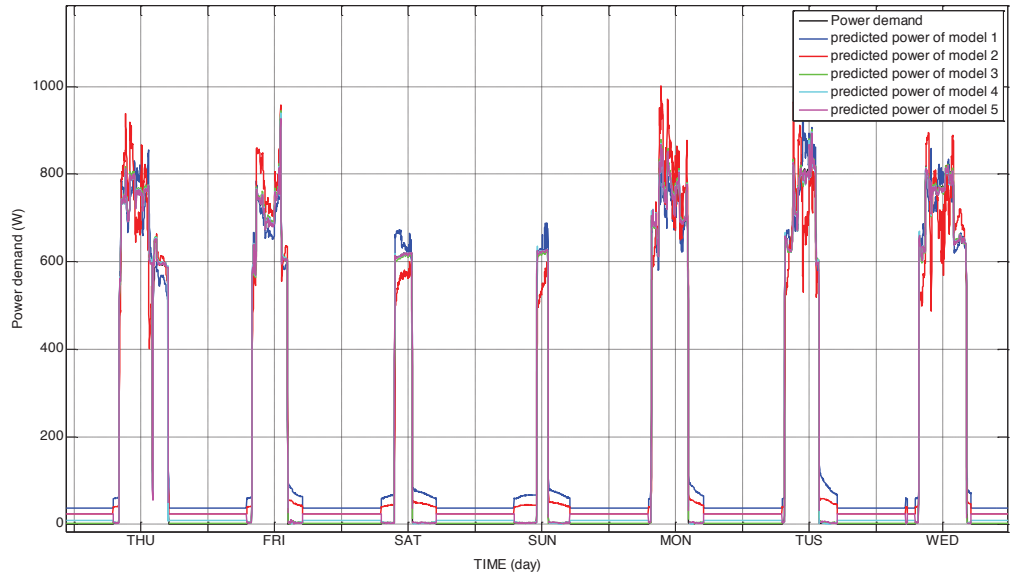

Fig. 10: Power demand prediction for one step ahead of the 5 obtained models

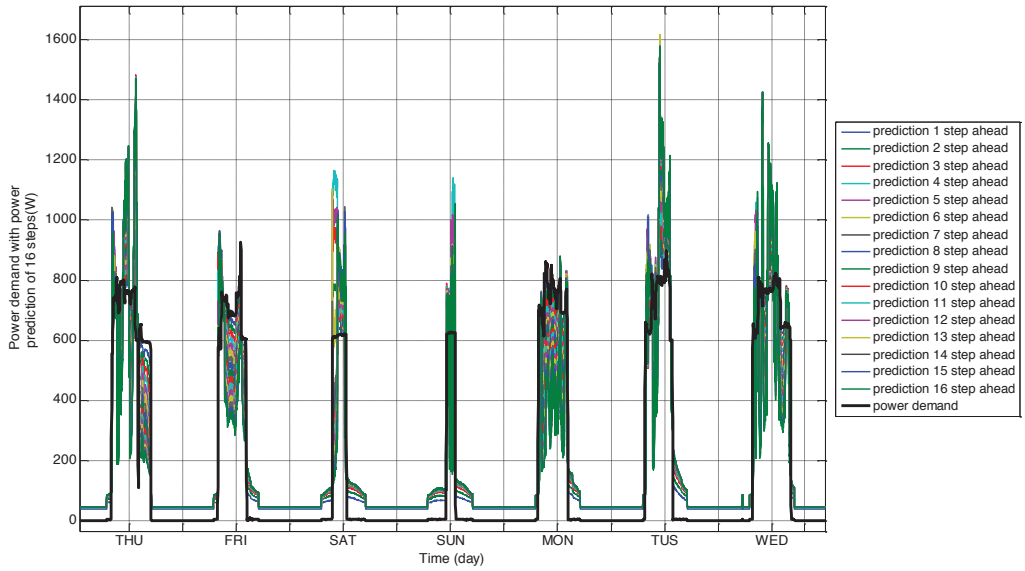

Fig. 11: Model 1 16 steps ahead power demand prediction

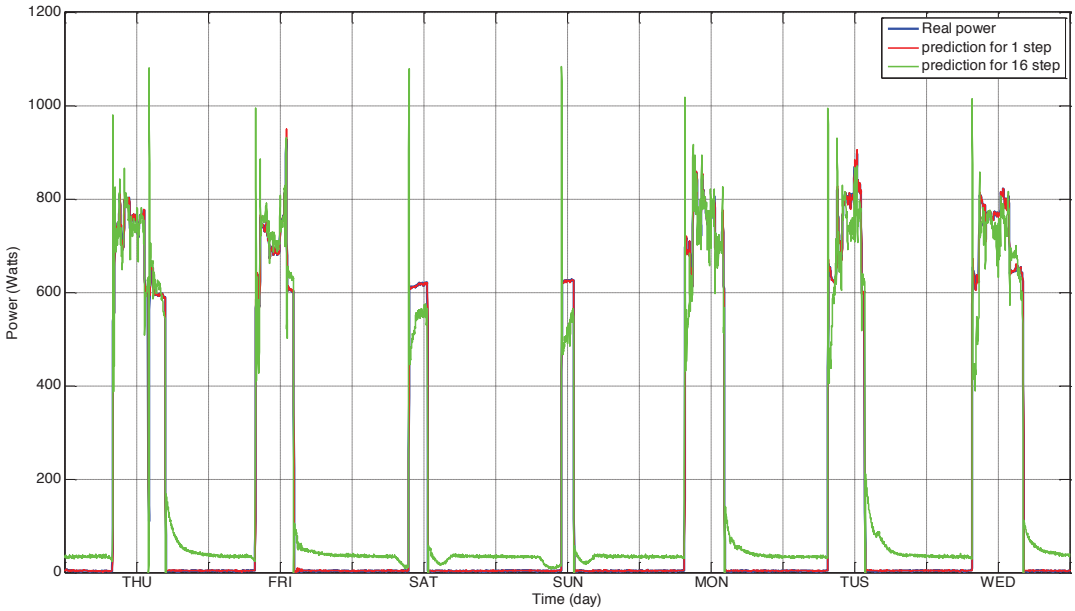

Fig. 12: Model 1 validation results

5. Conclusions and future work

The obtained RBF ANN shows optimistic results with a simple structure as a method for the prediction of electric load in one room. The main virtue of this ANN model is its simplicity, which is based on the fact that the developed tool is very simple and the resources for its application are tiny and available at modern automation systems. In particular, in order to apply it to a control system, only data from simple sensors and electric power measurements are required.

As a future work, another ANN will be developed in order to predict the HVAC power consumption used for cooling/heating the laboratory. Moreover, other future research line is the use of the ANN as the basis of a control system which, through the ANN model, will be able to maintain the thermal comfort of the users of building whereas the energy consumption necessary to reach this thermal comfort situation is minimized.

6. Acknowledgement

This work has been partially funded by the following project: DPI2014-56364-C2-1-R (financed by the Spanish Ministry of Science and Innovation and EU-ERDF funds) and Competitiveness and ERDF funds, and by the Fundación Iberdrola España, through its Call for Research on Energy and Environment Grants "ENERGY FOR RESEARCH". Y. I. Alamin is a fellow of the MARHABA, an Erasmus Mundus Lot 3 project. M. Castilla is a fellow of the Spanish Juan de la Cierva – Formación contract program. J.D. Álvarez is a fellow of the Spanish Ramon y Cajal contract program.

7. References

Castilla, M., Álvarez, J.D., Rodríguez, F., Berenguel, M., 2014. Comfort control in buildings. Springer-Verlag.

Daosud, W., Thitiyasook, P., Arpornwichanop, A., Kittisupakorn, P. Hussain, M.A., 2005. Neural network inverse model-based controller for the control of a steel pickling process. Computers & Chemical Engineering, 29(10), 2110–2119.

Ferreira, P.M., Ruano, A.E., 2000. Exploiting the separability of linear and non-linear parameters in radial basis function neural networks, in: IEEE Symposium 2000: Adaptive Systems for Signal Processing, Communications and Control, Canada, pp. 321–326.

Ferreira, P.M., Ruano, A.E., Pestana, R., 2010. Improving the identification of RBF predictive models to forecast the Portuguese electricity consumption. In Control Methodologies and Technology for Energy Efficiency 1(1), 208-213.

Ferreira, P.M., Ruano, A.E., Silva S., Conceicao, E.Z.E., 2012. Neural networks based predictive control for thermal comfort and energy savings in public buildings, Energy and Buildings, 55, 238–251.

Haykin, S., 2005. Neural Networks A comprehensive Foundation, Second ed., PEARSON Prentice Hall, Ontario, Canada.

Khosravani, H.R., Castilla, M., Berenguel, M., Ruano, A.E., Ferreira, P.M., 2016. A comparison of energy consumption prediction models based on Neural Networks of a bioclimatic building. Energies, 9(1), 57.

Kolokotsa, D., Tsiavos, D., Stavrakakis, G.S., Kalaitzakis, K., Antonidakis, E., 2001. Advanced fuzzy logic controllers design and evaluation for buildings' occupants thermal–visual comfort and indoor air quality satisfaction. Energy and buildings, 33(6), 531-543.

Marquardt, D.W., 1963. An algorithm for least-squares estimation of nonlinear parameters. Journal of the Society for Industrial and Applied Mathematics 11 (2) 431–441.

MathWorks Website, 2016, http://es.mathworks.com/help/curvefit/smoothing-data.html. Accessed: 15th September 2016.

Mena, R., Rodríguez, F., Castilla, M., Arahal, M.R., 2014. A prediction model based on neural networks for the energy consumption of a bioclimatic building. Energy and Buildings, 82, 142-155.

Oikonomou, V., Becchis, F., Steg, L., Russolillo, D., 2009. Energy saving and energy efficiency concepts for policy making. Energy Policy, 37, 4787-4796.

Olofsson, T., Andersson, S., Ostin, R., 1998. A method for predicting the annual building heating demand based on limited performance data. Energy and Building, 28, 101-108.

Ren, Y., Suganthan, P.N., Srikanth, N., 2015. Ensemble methods for wind and solar power forecasting—A state-of-the-art review. Renewable and Sustainable Energy Reviews, 50, 82-91.

Ruano, A., Jones, D., Fleming, P., 1991. A new formulation of the learning problem of a neural network controller, in: Proceedings of the 30th IEEE Conference on Decision and Control, vol. 1, pp. 865–866.

Virote, J., Neves-Silva, R., 2012. Stochastic models for building energy prediction based on occupant behavior assessment. Energy and Building, 53, 183-193.

Zhang, G., Patuwo, B.E., Hu, M.Y., 1998. Forecasting with artificial neural networks: The state of the art. International Journal of Forecasting, 14(1), 35-62.

Conference Proceedings

EuroSun 2016
Palma de Mallorca (Spain), 11 - 14 October 2016

OPTIMAL SIZING OF ACTIVE SOLAR ENERGY AND STORAGE SYSTEMS FOR ENERGY PLUS HOUSES

Luis Ramirez Camargo[1,2], Raphaela Pagany[1] and Wolfgang Dorner[1]

[1] Applied Energy Research Group, Technologie Campus Freyung, Technische Hochschule Deggendorf, Freyung (Germany)

[2] Institute of Spatial Planning and Rural Development, University of Natural Resources and Life Sciences, Vienna (Austria)

Abstract

Buildings generating more energy than they require are a promising possibility to increase the share of renewable energies in the energy matrix. The German Federal Ministry for the Environment, Nature Conservation, Building and Nuclear Safety funded projects that provide a proof of concept of residential buildings producing energy beyond their own requirements, the so called "Efficiency Houses Plus" (EHP). The present work builds up on data of one of these buildings to propose an optimization model that minimizes the energy provision costs for a building while achieving the EHP standard. The model considers solar energy systems, a heat pump as well as electric and thermal storage systems. The model is used to determinate system configurations able to achieve the EHP standard under seven different scenarios. The results serve to discuss the relevance of each of the considered technologies for EHPs in the near future.

Keywords: *photovoltaics, solar thermal, heat and electric storage systems, energy plus house, net zero energy building, monitoring, MILP*

1. Introduction

The European Union (EU) has set the goals of a 20% share of renewable energy sources (RES) in the gross final energy consumption and a reduction of 20% of greenhouse gas emissions in comparison to the levels of 1990 by 2020 (Commission of the European communities, 2007). The EU long term aspirations include a decrease in greenhouse gas emissions of at least 80%, which would imply a share of RES of 75% by 2050 in the gross final energy consumption and 97% in electricity consumption (European Commission, 2011). The building sector has one of the highest potentials to contribute to this goals due to the fact that energy requirements for buildings account for 40% of the total energy consumption in the EU (European Commission, 2010, 2003). The largest share of this energy requirements (66%) can be attributed to energy demand for heating and cooling (Institute of Communication and Computer Systems of the National Technical University of Athens, 2008). Retrofitting measures for the existent building stock and high energy standards for new buildings can contribute to reduce these energy requirements considerably. However the strategy of the EU goes beyond that and the directive 2010/31/EU of the European parliament sets the 31st of December 2020 as the deadline when all new buildings shall be Net Zero Energy Buildings (NZEB).

The general idea behind the NZEB is a highly efficient building that produces as much energy as it would require from the grid or fossil sources to cover its demand over a certain period of time (Good et al., 2015). This is, however, a definition that can be interpreted in several ways and therefore, there is no consensus on the NZEB concept. Sources of discrepancy are, among others, the system boundaries and the weighting factors for the different used energy sources. Extensive discussions on this issue can be found in Marszal et al. (2011) and Sartori et al. (2012). One step ahead NZEBs are the so called "Energy plus houses" or "Positive Energy

doi:10.18086/eurosun.2016.01.08 Available at http://proceedings.ises.org

Buildings" (Ionescu et al., 2015). The German Federal Ministry for the Environment, Nature Conservation, Building and Nuclear Safety describes the "Efficiency House Plus" (EHP) as a building, which produces energy from renewable sources beyond its final and primary energy needs in a balance period of a calendar year (Bundesministeriums für Umwelt, Naturschutz, Bau und Reaktorsicherheit, 2012). The balance includes the energy need for space conditioning, building operation and equipment (Bockelmann et al., 2015). This definition has been used to fund several projects across Germany. These projects serve to show that technologies are already available, which allow the construction of EHPs. In the present paper hourly data from one of these EHPs are used to calibrate an optimization model that aims at conceiving energy generation systems, which allow buildings to achieve the EHP standard at the minimum possible cost. The model is applied to generate system configurations in scenarios where the system boundaries and assumptions are changed compared to the reference building. These scenarios serve to discuss the relevance of every one of the considered technologies for energy plus houses in the near future.

The paper is structured as follows: In the next section the main characteristics of the studied EHP are presented. Section 3 describes the optimization model and section 4 the case studies. Section 5 is devoted to results. Finally, in the last section of the paper conclusions are drawn.

2. The Schlagmann-BayWa EHP, monitoring concept and data

The investigated building is a family house located in Burghausen, Upper Bavaria, Germany. The building was inhabited by a three-person household during the entire study period. They were allowed to use the house for residential purposes without any restrictions. The house has two storeys, 176 m² of heated living area, a cellar and an external garage. It was built with massive single-shell brick filled with heat-insulating perlite. The energy certificate estimates that the energy demand for heating corresponds to the German Energy Savings Regulation (EnEV) 40 standard. The EHP is equipped with 10.76 kWp of photovoltaics (PV) (4.28 kWp on the main building's roof that is oriented towards south and has a 44° inclination as well as 6.48 kWp on the roof of the garage oriented towards east and west with half of the capacity in each direction and a 30° inclination). A 10.8 kWh electric storage system, a 51 m² solar thermal system, an electric car and an automatic steering system are also part of the concept. One additional feature of this EHP is a seasonal warm water storage able to store up to 4000 kWh with a volume of 48,000 L. It is dimensioned to cover the energy need for heating and warm water of the house during winter with solar energy harvested during summer.

The EHP was equipped with monitoring and optimal operation systems. All nodes of the energy system were monitored considering also environmental data inside and outside of the building. Data of more than 120 measuring nodes were stored continuously over two operation years (February 1st 2014 to January 31st 2016). The energy production and consumption of PV, solar thermal systems, heat pump, input and output of the storage systems as well as the energy demand for lighting and appliances, room conditioning, warm water, house operation equipment and the electric car were logged. Afterwards data processing, analysis and visualizing were carried out. Monthly amounts of the measured yields and consumptions (see Fig. 1) as well as the hourly averages and sums of the days per month (see Fig. 2) were investigated.

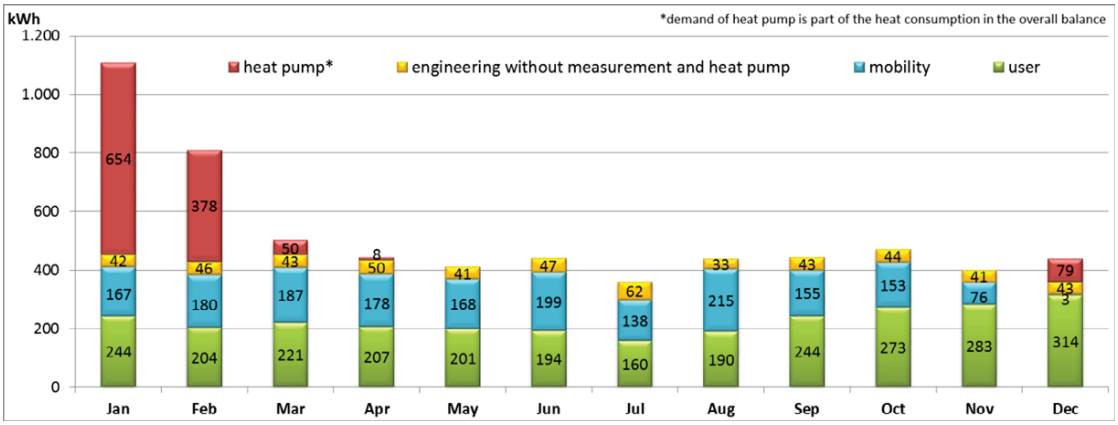

Fig. 1. Electric demand and mobility per month, measured in 2015

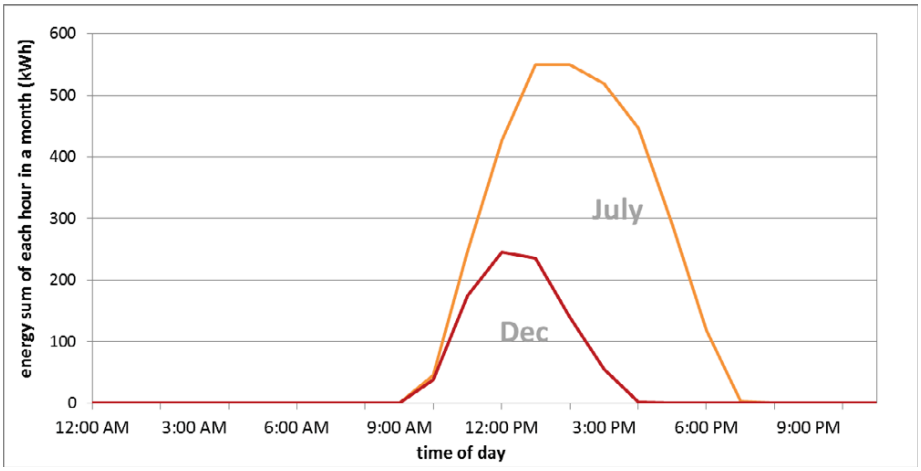

Fig. 2. Energy input into the warm water storage from the solar thermal system. Sum per hour of all days in a month for July and December 2015

The monitoring enables an evaluation of the energy standard and efficiency of technologies, the comparison with the predicted values and the analysis of the temporal development of energy production and consumption. Hourly data of 2015 from the monitoring are the reference for the proposed optimization model, which is described in the next section.

The evaluation of these data provided the evidence that the house of Schlagmann and BayWa fulfill the EHP – standard. On the one hand, the building required in 2015 13,084 kWh for room and hot water heating (incl. heat pump) and 6,464 kWh of electrical energy for the household itself (lighting, cooking and electrical equipment), installation engineering, other heating techniques, battery, other losses and also for the electric car (Fig. 3). On the other hand, the solar system had a yield of 20,675 kWh (solar thermal) and the PV installation generated 10,562 kWh of electric energy (Fig. 3). In total, the energy production exceeded the energy requirements by 11,689 kWh and the balance of primary energy was -14,060 kWh in 2015.

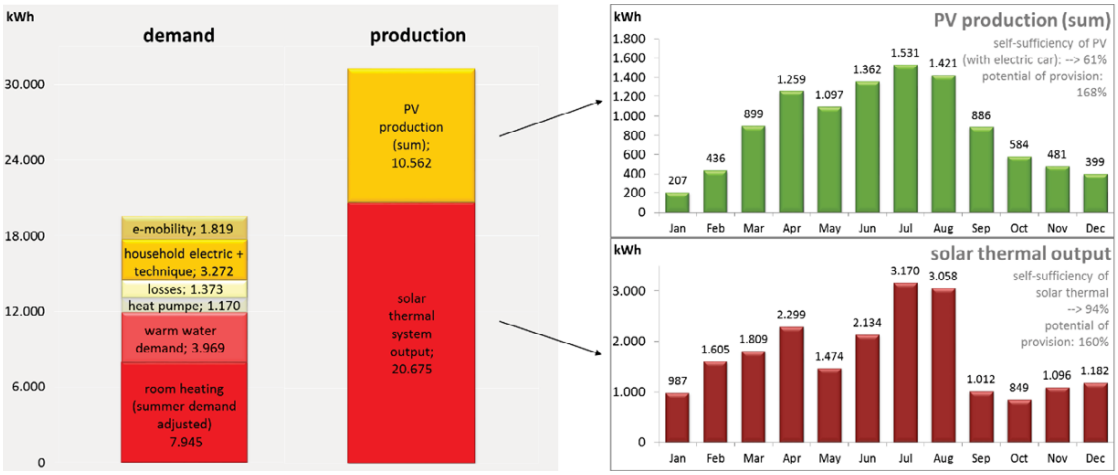

Fig. 3. Overall balance of the monitoring of the EHP of Schlagmann for the year 2015

The data confirm the functional interaction between the warm water system, the heat pump and the input from the solar thermal system. Fig. 4 presents the hourly progress of the heating system over the year 2015. The state of charge (SOC) was accounted on the basis of temperature variations in the warm water storage (sum of the average temperature of the low and the high temperature tanks; every tank has 10 measurement points distributed evenly). Higher solar thermal yields in summer raised the SOC of the warm water storage to a maximum in September and October. Afterwards, the SOC decreased in the winter days until the heat pump was necessary to produce additional heat. The different SOCs at the beginning and end of the year correspond to manual adjustments in the steering system.

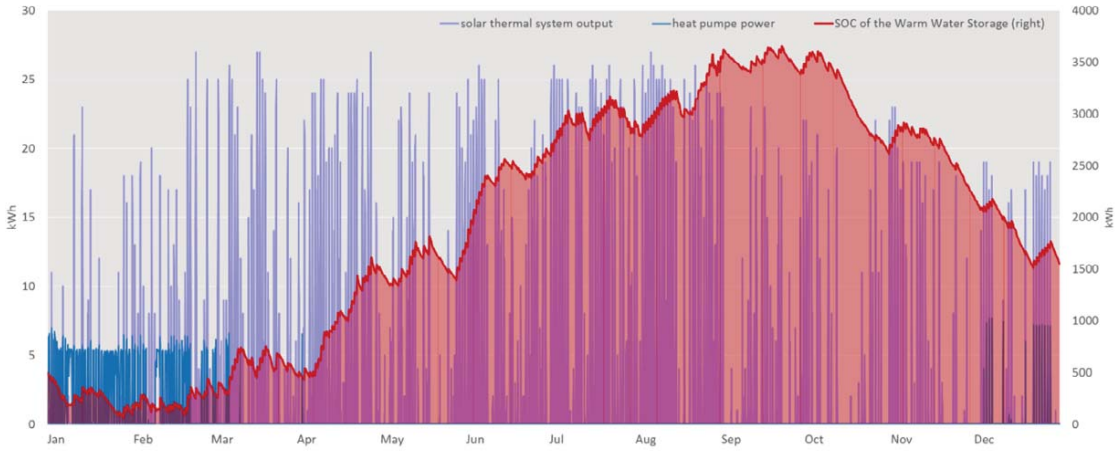

Fig. 4. Results of the monitoring for every hour in 2015 for the State of charge (SOC) of the warm water storage, the usable solar thermal system output and the heat pump output

3. A mixed integer-linear program for minimizing energy provision costs of EHPs

Design optimization of hybrid renewable energy systems for buildings is a research field that has gained significant attention in the last years (Lu et al., 2015a). A multitude of approaches and tools have been developed and some of them, such as the Hybrid Optimization Model for Electric Renewables (HOMER), have been used in dozens of projects all around the world (Erdinc and Uzunoglu, 2012). One of the most common approaches is mathematical programming, where the optimal sizing of hybrid renewable energy systems is reduced to linear, MILP or non-linear optimization problems (Evins, 2013). A MILP is for example the basis of the RED-CAM tool, which has been under development since 2000 and serves to optimize system configurations from a wide range of technologies based on minimum costs or minimum CO_2 emissions (Stadler et al., 2014). The model presented in this paper is also a MILP, but is a tailor-made model since widely used tools such as HOMER or RED-CAM and further tools, reviewed by Lu et al. (2015a), do not address at the same time three characteristics that are important when sizing a system for an EHP: 1) Space constraints for active solar energy generation technologies: The optimal use of space is a critical issue when deciding between technologies that could deliver the same type of energy. Furthermore, the energy input profile of active solar systems depends on geometric and location related characteristics that should be considered (Lang et al., 2015). In an optimal system configuration the right technologies should be installed in the right parts of the building's roof; 2) Use of the full length of data: in order to decrease the computational requirements for finding optimal solutions most of the existent tools rely on typical days or weeks per month to describe energy demand and energy generation yearly profiles. This strategy does not allow to account e.g. for entire weeks of snow coverage of PV systems, which are decisive when dimensioning storage systems. The proposed model uses as input time series of at least one entire year in the highest available temporal resolution. 3) Interdependences in the energy demand of energy generation systems: This is one of the most well-known limitation of HOMER. The tool is unable to account for the electric energy demand of a heat-pump unless this is known apriori and is entered in the model as an input (Lu et al., 2015b). The proposed model accounts for the energy demand profile of every system component that is part of the solution set.

The energy provision costs of the EHP are defined as the sum of the total installation costs, the operation and maintenance costs of the system and the costs of the energy requirements from the grid discounting the earnings of the energy surplus feed into the grid. The objective is to minimize the following problem:

$$\text{Min}((pvCost * \sum_a pvSize_a) + (stCost * \sum_a stSize_a) + (esSize * esCost * esReplace) + (hsSize * hsCost) + (hpSize * hpCost) + (opCost * lt) + (lt * eB * \sum_t eGrid_t) - (lt * eS * \sum_t pvSurplus_t)) \quad \text{(eq. 1)}$$

where $pvSize_a$ is the amount of kWp installed in every roof part and $pvCost$ its corresponding cost per kWp. $stSize_a$ is the size in square meters of the solar thermal system to be installed in every roof part. $stCost$ is the

cost per square meter of installed solar thermal system. $esSize, esCost$ and $hsSize, hsCost$ are the size and related cost per unit of the electric storage and heat storage systems. Both $esSize$ and $hsSize$ are given in kWh. For the electric energy storage an additional replacement factor, $esReplace$, is added to account for the short system life expectancy of current storage systems compared with the life time expectancy of components as PV installations. This factor depends on the expected life time of the storage system and lt, which is the expected operation time of the whole system. $hpSize$ is the maximum electrical input of the heat pump in kW and $hpCost$ is the corresponding cost per kW installed capacity. $opCost$ are the yearly maintenance costs of the system. $eGrid_t$ is the amount of electricity that must be consumed from the grid in every period of time in kWh and eB the electricity tariff per kWh. The surplus energy from the PV systems that cannot be used or stored in a certain time step, $pvSurplus_t$, is sold to the grid at a rate eS per kWh.

Several balancing conditions applied. First, the total PV generation per time step is to be divided in three possible uses; PV electricity can be directly used ($ePVUse_t$), it can be stored ($ePVStore_t$) or it can be sold to the grid ($pvSurplus_t$):

$$\sum_a pvSize_a * pvOutput_{t,a} = ePVUse_t + ePVStore_t + pvSurplus_t, \forall t \quad \text{(eq. 2)}$$

where $pvOutput_{t,a}$ is the output of one kWp PV in t. This depends on weather conditions and the geometric and shadowing conditions of every PV system. The calculation of $pvSurplus_t$ relies on the assumption that all electricity generation surplus can be sold to the grid and no curtailment is required.

Second, the solar thermal systems are assumed to work analogically to the PV systems but the surplus ($stSurplus_t$) cannot be sold to a grid and the energy output cannot be directly used but works depending on the warm water storage system and the heat pump i.e. for energy from the solar thermal systems there are not three but two possible uses:

$$\sum_a stSize_a * stOutput_{t,a} = hSTStore_t + stSurplus_t, \forall t \quad \text{(eq. 3)}$$

Third, the electric energy supply has to meet the demand, which includes the electricity demand of all appliances in the house ($eDemand_t$), the heat pump ($hpeDemand_t$) and the amount of energy required to operate the heat distribution system ($peDemand_t$):

$$eDemand_t + hpeDemand_t + peDemand_t = ePVUse_t + eStorDischarge_t * eStorDischargeEff + eGrid_t, \forall t \quad \text{(eq. 4)}$$

The electricity supply includes not only the part of the PV output for direct use and the amount of electricity that must be consumed from the grid but also the output of an electric storage system ($eStorDischarge_t$) decreased by the discharge efficiency of the storage system ($eStorDischargeEff$), which is assumed to be linear.

Fourth, in a similar way the energy demand for heating and warm water ($hDemand_t$) has to be met by the supply. The latest is assumed to be completely delivered by the heat storage system, which also has a discharge efficiency ($hStorDischargeEff$) that is assumed to be linear:

$$hDemand_t = hStorDischarge_t * hStorDischargeEff, \forall t \quad \text{(eq. 5)}$$

The variables $eStorDischarge_t$ and $hStorDischarge_t$ are bounded by the state of charge of the corresponding storage systems in $t-1$.

Fifth, the state of charge of the electric storage system $eSOC_t$ is calculated with the following equation, taking into account linear charging efficiency $eStorChargeEff$ and energy storing efficiency $eStoringEff$:

$$eSOC_{t+1} = eStoringEff * eSOC_t + eStorChargeEff * ePVStore_{t+1} - eStorDischarge_{t+1}, \forall t \quad \text{(eq. 6)}$$

The $eSOC_t$ is never negative and the first and last time steps in a year are assumed to be equal. The latest condition ensures the continuous operation of the system during winter days from one year to the next.

Sixth, the state of charge of the heat storage system ($hSOC_t$) is calculated in the same way as $eSOC_t$ with the corresponding storing and charge efficiencies ($hStoringEff$, $hStorChargeEff$), the part of the solar thermal output to be stored, the heat pump output to be stored $hHPStore_t$ and the discharge of the heat storage system $hStorDischarge_t$:

$$hSOC_{t+1} = hStoringEff * hSOC_t + hStorChargeEff * hSTStore_{t+1} + hHPStore_{t+1} - hStorDischarge_{t+1}, \forall t \quad \text{(eq. 7)}$$

Seventh, $hpeDemand_t$ is determined by the coefficient of performance of the heat pump $hpEff$ and the part of $hStorable_t$ that is not directly covered by the energy generation of the solar thermal system $hHPStore_t$:

$$hpeDemand_t * hpEff = hHPStore_t, \forall t \quad \text{(eq. 8)}$$

$$hStorable_t = hHPStore_t + hSTStore_t, \forall t \quad \text{(eq. 9)}$$

The highest $hHPStore_t$ serves to determine the size of the heat pump:

$$hHPStore_t \leq hpEff * hpSize, \forall t \quad \text{(eq. 10)}$$

The storage sizes are defined by the highest state of charge of each system:

$$eSOC_t \leq esSize, \forall t \quad \text{(eq. 11)}$$

$$hSOC_t \leq hsSize, \forall t \quad \text{(eq. 12)}$$

Additional constraints for $ePVStore_t$, $eStorDischarge_t$, $hSTStore_t$ and $hStorDischarge_t$to the capacities of the corresponding storage systems $eCapLimit$ and $hCapLimit$ are also necessary:

$$ePVStore_t \leq eCapLimit, \forall t \quad \text{(eq. 13)}$$

$$eStorDischarge_t \leq eCapLimit, \forall t \quad \text{(eq. 14)}$$

$$hSTStore_t \leq hCapLimit, \forall t \quad \text{(eq. 15)}$$

$$hStorDischarge_t \leq hCapLimit, \forall t \quad \text{(eq. 16)}$$

The size of the PV system in m² is calculated multiplying the required installed capacity in kWp by the amount of square meters necessary to fit one kWp ($AreaPV$) and the solar thermal and PV total systems size is constrained by the available area of every roof part ($roofArea_a$):

$$pvSize_a * AreaPV + stSize_a \leq roofArea_a, \forall a \quad \text{(eq. 17)}$$

Finally, the system configuration should be able to generate sufficient energy to allow the building to achieve the EHP standards. To comply with this, two balance equations are included. One for the final energy balance and one for the primary energy balance of the house, which correspond to the calculation method described in the DIN 18599-1 (Europäisches Komitee für Normung, 2011):

$$\sum_t (eDemand_t + hpeDemand_t + peDemand_t + eGrid_t) \leq \sum_t \sum_a pvSize_a * pvOutput_{t,a} \quad \text{(eq. 18)}$$

$$eGridFactor * \sum_t (eDemand_t + hpeDemand_t + peDemand_t + eGrid_t) \leq eDisplacementFactor * \sum_t \sum_a pvSize_a * pvOutput_{t,a} \quad \text{(eq. 19)}$$

These equations include the assumption that the only external energy input for the EHP comes from the grid. The last equation corresponds to the primary energy balance where $eGridFactor$ accounts for the energy sources mix of electricity delivered by the grid and $eDisplacementFactor$ is the displacement factor of PV electricity when replacing other energy sources.

4. Scenarios

Seven scenarios with different system restrictions are studied. These scenarios range from the case of a building that represents the current state of the EHP described in Section 2 to the case of a building, which is able to achieve the EHP standard while assuming that there is no energy input from the grid and no feed-in tariff (full auto-sufficient building). These serve to calibrate the model, calculate the limits of auto-sufficiency of domestic buildings and discuss the relevance of every one of the considered technologies for EHPs in the near future. The description of the scenarios is presented in Tab. 1.

Tab. 1. Scenario description

Scenario	Description
Scenario 1 - Current state of the Schlagmann-BayWa EHP	The lower and upper boundaries of the PV, solar thermal, heat pump, and storage systems sizes variables are set to the values of the currently installed systems. The parameter roof area is equal to the real available area of every roof part where a PV or a solar thermal system is installed.
Scenario 2 - minimum system size that would achieve the EHP status under current constraints	Differently to the scenario 1, the lower boundaries of the PV, solar thermal, heat pump, and storage systems sizes are not defined apriori. The objective of this case study is to determine the minimum system sizes that would be necessary to achieve the EHP standard assuming that the maximum installation size of a certain system is the current system size.
Scenario 3 - minimum system size that would achieve the EHP status with flexible sizes	Differently to the scenario 2, the upper boundaries of the PV, solar thermal, heat pump, and storage systems sizes are not defined apriori. The only system size boundary for the PV and solar thermal systems are the roof part sizes.
Scenario 4 - minimum system size that would achieve the EHP status under current constrains without feed-in tariff	This Scenario is equal to scenario 2 except that the feed-in tariff value is set to 0 EUR.
Scenario 5 - minimum system size that would achieve the EHP status with flexible sizes without feed-in tariff	This scenario is equal to scenario 3 except that the feed-in tariff value is set to 0 EUR.
Scenario 6 - EHP standard without electric energy input from the grid	The starting point of this scenario is scenario 3. It is additionally assumed that no electricity energy input from the grid is allowed and that the size of the roofs is three times the current one of the Schlagmann-BayWa EHP. The first additional constraint is equivalent to the assumption that the EHP standard is achieved at every time step.
Scenario 7 – EHP standard without electric energy input from the grid and without feed-in tariff.	In this scenario the impact of no feed-in tariff is studied for the system with the boundaries assumed in scenario 6.

The common parameters for all scenarios include the energy demand for heating, warm water and electricity that have been measured in the house during 2015. The electricity demand includes the residential use and the electric car. The energy generation profiles of the PV and solar thermal systems per unit of installed capacity (kWp and m² respectively) correspond to the hourly time series of measurements from the installations in 2015. $peDemand_t$ ranges from 0.04 kWh when there is no energy demand for heating or warm water to 0.18 when the pumps for the heating system must be activated (This values are based on the measurements of the electricity demand of the corresponding pumps). $hpeDemand_t$ depends on the size of the system to install, the profile of the energy demand for heating and warm water and the output of the solar thermal system. $hpEff$ has been defined as 300% based on the average of the measurements when the only input for the heating system was coming from the heat pump. The efficiency of the storage systems is defined as a round trip efficiency (Solomon et al., 2012), where the charging efficiency is equal to average efficiency of storage systems (75%

for the electric and 85% for the warm water storage systems) and the discharging efficiency is 100%. The hourly self-discharge ratios of the storage systems are set to 0.01%. The final price per kWh of electric energy from the grid is assumed to be 0.28 EUR and the feed-in tariff (in case it is considered in the scenario) is 0.12 EUR. The assumed lifetime of the system is 20 years and $esReplace$ is equal to 2. The installation prices per unit are rounded average prices from multiple vendors presented in Tab. 2. $eGridFactor$ and $eDisplacementFactor$ are taken from the DIN 18559 in its official version of 2012, in that year (when the house EHP was planned) these values where 2.4 and 2.8 respectively.

Tab. 2. System prices per unit (Average from multiple vendors)

System	Price in EUR
PV (kWp)	2100
Solar thermal (m^2)	350
Heat pump (kW)	5000
Warm water storage (kWh)	10
Electric energy storage (kWh)	1000

5. Results

A summary of the results for the seven case studies and the monitoring data of the EHP for 2015 for comparison is presented in Tab. 3. It includes the resulting system sizes, the sum of the results for one year of seven further variables and the minimum energy provision costs for the 20 years lifetime of the system.

The results of scenario 1 show differences to the measured data that have an explanation in the optimal operation under perfect forecast that takes place in the optimization model. While the steering system in the actual EHP operates demand driven and based on current data, the optimization model generates a solution relying on data for the whole year. In the optimization model operation decisions are taken knowing exactly which will be the demand of the building and which is going to be the resources availability for every single time step. As a consequence, the final total output of the PV and solar thermal installations remains equal to the reference building but the internal use of the energy changes. The direct use of PV electric energy is higher while the requirements for energy from the grid and the energy surplus sold to the grid are lower. These differences between the actual EHP and the optimization model show that there is place for improvement in the operation of the energy generation and storage system of the building. Furthermore, despite of its simplicity, the model is able to reproduce the behavior of the warm water storage and the heat pump during the year. As it is presented in Fig. 5, in the scenario 1 the warm water storage stores energy from the solar thermal system in summer in order to meet the energy demand for heating and warm water during the beginning of winter. Consistently, the heat pump is in operation only during the winter months and the first half of spring. The major differences between the model and the actual system are presented at the end of the year (see Fig. 4). These can be explained by the (perfect forecast) information available for the optimization model and the restriction that obligates the model to finish the year at the same level that it starts with.

Scenario 2 shows that less installed capacity would also have been sufficient to achieve the EHP standard. The same PV installed capacity, a heat pump with a third less capacity, considerably smaller solar thermal and warm water storage systems would have been sufficient to produce energy beyond the final and primary energy requirements. Moreover, the electric storage system is not part of the system configuration even though the energy input from the grid is considerably larger than in scenario 1. Due to the considerable system size reduction in scenario 2, the energy provision costs are less than half of the costs of the reference scenario.

When the roof parts can be used without restrictions for every technology (Scenario 3), the solar thermal system is considerably smaller, the available area is covered by a larger PV system and no PV system is required on the roof of the garage. These changes mean an increment in the total energy yield of the PV system, in the PV electric energy direct use, the amount of energy injected into the grid, the energy demand of the heat pump and the energy requirements from the grid. Nonetheless, this system configuration presents lower energy provision costs than the resulting configuration of scenario 2.

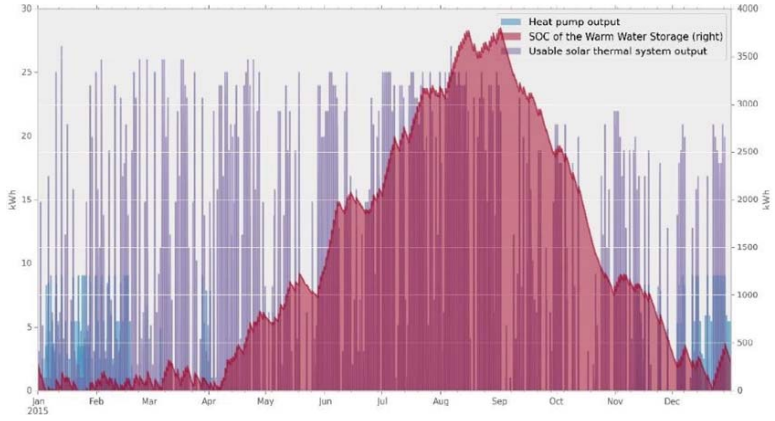

Fig. 5. Results of the scenario 1 for the State of charge (SOC) of the warm water storage, the usable solar thermal system output and the heat pump output for every hour in 2015.

In absence of feed-in tariffs (scenarios 4 and 5) solar thermal systems play an important role covering part of the energy demand for heating and warm water and therefore reducing the electric energy demand of the heat pump. Since surplus electric energy from the PV systems does not generate any income, it is more cost effective to install cheap solar thermal systems to cover part of the energy demand for heating and warm water than to install relatively expensive PV systems to supply the heat pump. This shows that mechanisms for promoting the adoption of renewable energies should be designed while taking into account interactions between technologies. If the interactions are not considered, the final system configurations would not only be more expensive for the system owner but also for the public treasury. It is important to note that even in the absence of feed-in tariffs, the electric energy storage does not appear as part of the solution system configuration.

A totally self-sufficient EHP is unfeasible under the actual system constraints. It would be necessary to have a building with at least three times as much roof space for accommodating active solar energy generation systems (scenarios 6 and 7) to conceive a 100% self-sufficient EHP. Only with PV installations several times larger than in the actual EHP and with an electric energy storage almost eight times larger than the currently installed ones, it would be possible to cover the energy demands of the building during the whole year. The most relevant factor for the large electric storage requirements is a series of consecutive days in winter when there is only little or no PV energy yield (due to snow covering the panels). An example for most part of January is presented in Fig. 6. If the PV yield between 24th and 28th January would be similar to the one of the previous weeks only half of the electric energy storage would be necessary to cover the system's requirements. This situation cannot be observed in optimization tools that rely on average or typical data to represent a whole year of data. Concerning the solar thermal system, this would be only slightly smaller in scenario 6 and a fifth larger in scenario 7 than the one that is currently installed. The warm water storage could be a third of the actual size. Finally, in the absence of feed-in tariffs (scenario 7) the PV system is smaller, the electric energy storage is used more intensely and the solar thermal system is larger than in scenario 6.

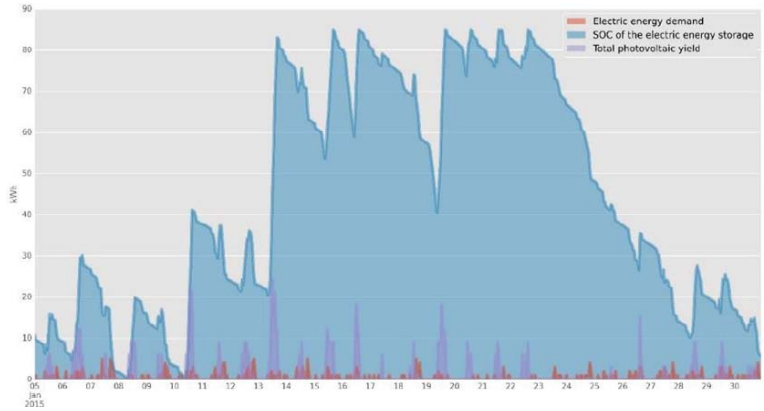

Fig. 6. Results of the scenario 6 for the state of charge (SOC) of the electric energy storage, the total PV yield and the electric energy demand for every hour of the period 05/01/2015-30/01/2015

Tab. 3. Scenario results summary

Variable	Actual EHP	Scenario 1	Scenario 2	Scenario 3	Scenario 4	Scenario 5	Scenario 6	Scenario 7
Electric energy storage (kWh)	10.8	10.8	0	0	0	0	84	86
PV1 (kWp)	4.28	4.28	4.28	10.35	4.28	6.22	26.9	19.02
PV2 (kWp)	6.48	6.48	3.82	0	2.45	0	19.74	19.74
Heat pump size (kW)	3	3	1	1	1	1	1	1
Solar thermal (m2)	51	51	12.32	5.32	26.91	13.9	47.58	62.89
Warm water storage (kWh)	4000	4000	95	95	107	95	1279	1326
Total PV generation (kWh)	10562.22	10562.22	8631.12	14162.3	7641.54	8505.88	51119.4	40355.34
PV direct use (kWh)	1364	2739	3185.95	3706.04	2714.7	3024.02	3177.4	3513.93
Electric energy to the grid (kWh)	6144	5594.01	5445.17	10455.63	4926.82	5481.86	43125.19	30349.65
Battery output (kWh)	1993	1655.87	0	0	0	0	3546.59	4737.91
Electric energy demand household (kWh)	4590	4590	4590	4590	4590	4590	4590	4590
Electric demand heat pump (kWh)	1176	779.35	3233.04	3881.97	2238.2	3111.64	1328.63	2856.48
Electricity demand heating system (kWh)	809	805.4	805.4	805.4	805.4	805.4	805.4	805.4
Electric energy from Grid (kWh)	3218	1778.85	5442.45	5571.38	4918.98	5482.86	0	0
MILP Solution (EUR)	n.a.	120306	50688.6	41683.07	63158.75	60581.37	205678.06	302528.73

6. Conclusions

State of the art technology can transform a residential building into a power plant. The data of the Schlagman-BayWa EHP show that a single family house can produce energy beyond its own final and primary energy requirements. In fact, to reach the EHP standard considering a yearly balance it would have been sufficient to install a significantly lower capacity, regarding not only the solar thermal, but also the electric and warm water storage systems. In contrast to the first five scenarios, the sixth and seventh scenario, which describe a building without energy input from the grid (equivalent to a building achieving the EHP standard in every time step), are unfeasible considering the available roof areas for installation of PV and solar thermal systems. The proposed MILP can only find a solution for these scenarios when the roof areas are assumed to be three times larger than the current size. The realization of such complete self-sufficiency scenarios would require not only larger energy generation systems, but also electric storage capacities several times higher than the one currently installed in the Schlagmann-BayWa EHP. Self-sufficiency seems to be hardly realizable even for the small demand of a single family house.

The use of the full length of data serves to identify that the main reason for the high electric storage requirements in these scenarios are series of consecutive days where only very little energy can be generated by the PV installations. Furthermore, the modelling showed that even in absence of feed-in tariffs for the PV energy surplus sold to the grid, electric storage systems are only part of the optimal solution when no input from the grid is allowed. It is also only in absence of a feed-in tariff for the surplus PV energy production that the solar thermal systems gain relevancy in the solution system configurations.

Finally, the EHP standard can be achieved in numerous ways, but the economic viability of such buildings requires the selection of the appropriate system configuration, which can be determined using the proposed MILP. It is also important that the design of economic mechanisms to promote certain renewable energy technology takes into account the interactions between technologies, otherwise energy generation systems installed by house owners would be more expensive not only for the owner but also for the public that is paying for these promotion mechanisms.

7. Acknowledgement

The authors would like to thank the consortium of the Schlagmann-BayWa EHP project for providing the monitoring data used in this study.

8. References

Bockelmann, F., Kley, C., Fisch, M.N., 2015. Smart Building as Power Plant – EnergyPLUS House with Energy Charge Management, in: Conference Proceedings EuroSun 2014. Presented at the International Conference on Solar Energy and Buildings, International Solar Energy Society, Aix-les-Bains, France. doi:10.18086/eurosun.2014.20.02

Bundesministeriums für Umwelt, Naturschutz, Bau und Reaktorsicherheit, 2012. Richtlinie über die Vergabe von Zuwendungen für Modellprojekte im Effizienzhaus Plus-Standard, Anlage 1.

Commission of the European communities, 2007. Communication from the commission to the European council and the European parliament: An Energy Policy for Europe.

Erdinc, O., Uzunoglu, M., 2012. Optimum design of hybrid renewable energy systems: Overview of different approaches. Renew. Sustain. Energy Rev. 16, 1412–1425. doi:10.1016/j.rser.2011.11.011

Europäisches Komitee für Normung, 2011. Energetische Bewertung von Gebäuden - Berechnung des Nutz-, End- und Primärenergiebedarfs für Heizung, Kühlung, Lüftung, Trinkwarmwasser und Beleuchtung - Teil 1: Allgemeine Bilanzierungsverfahren, Begriffe, Zonierung und Bewertung der Energieträger.

European Commission, 2011. Communication from the commission to the European parliament, the council, the European economic and social committee and the committee of the regions: Energy Roadmap 2050.

European Commission, 2010. Directive 2010/31/EU of the European Parliament and of the Council on the

energy performance of buildings (recast).

European Commission, 2003. DIRECTIVE 2002/91/EC OF THE EUROPEAN PARLIAMENT AND OF THE COUNCIL of 16 December 2002 on the energy performance of buildings.

Evins, R., 2013. A review of computational optimisation methods applied to sustainable building design. Renew. Sustain. Energy Rev. 22, 230–245. doi:10.1016/j.rser.2013.02.004

Good, C., Andresen, I., Hestnes, A.G., 2015. Solar energy for net zero energy buildings – A comparison between solar thermal, PV and photovoltaic–thermal (PV/T) systems. Sol. Energy 122, 986–996. doi:10.1016/j.solener.2015.10.013

Institute of Communication and Computer Systems of the National Technical University of Athens, 2008. European Energy and transport: trends to 2030-update 2007. European Commission: Directorate-General for energy and transport, Belgium.

Ionescu, C., Baracu, T., Vlad, G.-E., Necula, H., Badea, A., 2015. The historical evolution of the energy efficient buildings. Renew. Sustain. Energy Rev. 49, 243–253. doi:10.1016/j.rser.2015.04.062

Lang, T., Gloerfeld, E., Girod, B., 2015. Don't just follow the sun – A global assessment of economic performance for residential building photovoltaics. Renew. Sustain. Energy Rev. 42, 932–951. doi:10.1016/j.rser.2014.10.077

Lu, Y., Wang, S., Shan, K., 2015a. Design optimization and optimal control of grid-connected and standalone nearly/net zero energy buildings. Appl. Energy 155, 463–477. doi:10.1016/j.apenergy.2015.06.007

Lu, Y., Wang, S., Zhao, Y., Yan, C., 2015b. Renewable energy system optimization of low/zero energy buildings using single-objective and multi-objective optimization methods. Energy Build. 89, 61–75. doi:10.1016/j.enbuild.2014.12.032

Marszal, A.J., Heiselberg, P., Bourrelle, J.S., Musall, E., Voss, K., Sartori, I., Napolitano, A., 2011. Zero Energy Building – A review of definitions and calculation methodologies. Energy Build. 43, 971–979. doi:10.1016/j.enbuild.2010.12.022

Sartori, I., Napolitano, A., Voss, K., 2012. Net zero energy buildings: A consistent definition framework. Energy Build. 48, 220–232. doi:10.1016/j.enbuild.2012.01.032

Solomon, A.A., Faiman, D., Meron, G., 2012. Appropriate storage for high-penetration grid-connected photovoltaic plants. Energy Policy, Strategic Choices for Renewable Energy Investment 40, 335–344. doi:10.1016/j.enpol.2011.10.019

Stadler, M., Groissböck, M., Cardoso, G., Marnay, C., 2014. Optimizing Distributed Energy Resources and building retrofits with the strategic DER-CAModel. Appl. Energy 132, 557–567.

Conference Proceedings

EuroSun 2016
Palma de Mallorca (Spain), 11 - 14 October 2016

Control strategies and user acceptance of innovative daylighting and shading concepts

Michaela Reim[1], Werner Körner[1], Daniel Gerstenlauer[1], Stephan Weismann[1], Detlev Kranl[1], Helmut Weinläder[1]

[1] Bavarian Center for Applied Energy Research (ZAE Bayern), Wuerzburg (Germany)

Abstract

At the last Eurosun in Aix-les-Bains 2014 the daylighting and shading concept of the Energy Efficiency Center was presented (*Reim et al. 2014*) – a translucent membrane roof with subjacent translucent aerogel modules improves the daylighting especially in the room depth, highly innovative solar blinds guide the visual spectrum of the sunlight only into the rooms while blocking the infrared parts. Roller blinds for glare protection with special low-e-coatings improve thermal comfort in the offices. A high-level building automation system controls the different systems. After these measurements surveys were performed to determine the effect of the different daylighting and shading systems on the users in the different offices. The results of the conducted surveys with the users of the EEC in the offices will be assessed and the consequences for the optimization of the control strategy will be discussed. Finally, the influence of the aerogel glazing on the energy consumption will be discussed.

Keywords: *daylighting, shading, artificial lighting, user acceptance, aerogel glazing, control strategies,*

1. The Energy Efficiency Center

The Energy Efficiency Center (EEC) is a combined office (1st floor) and laboratory (ground floor) building with a function room attached to the north side, shown in Fig. 1. It is located in Würzburg, Germany, and was finished in June 2013. The overall aim of the project was to create a reference building which implements innovative techniques, serves demonstrational purposes, and sets new standards (*Weismann et al. 2016* and *Römer et al. 2016*).

Fig.1: Energy Efficiency Center viewed from north-east, the north-orientated rooms on the first floor and the roof of the technical center. Clearly visible is the textile roof with translucent PTFE-glass membranes and partially transparent ETFE films in the ridge of the roof.

doi:10.18086/eurosun.2016.01.13 Available at http://proceedings.ises.org

2. Lighting and shading concept

The goal of the lighting and shading concept is to minimize the energy consumption of the artificial lighting system by maximizing the daylight input into the rooms while, at the same time, reducing the heating/cooling loads by maximizing/minimizing the solar energy input into the offices as applicable. Depending on the heating or cooling demand of the office the solar energy input can be varied by using either the outside (low solar energy input) or inside (high solar energy input) shading device.

The roof of the main building consists of translucent PTFE-glass-membranes and partially of transparent ETFE films. The membrane acts as a climate interlayer above the thermal insulation level, the ceiling of the 1st floor which is partly transparent or translucent. Some ceiling areas of the office rooms away from the façade consist of translucent double skin sheets filled with Lumira-aerogel thus enabling a high room illumination in the depth. The roof of the function room to the north consists of translucent, double-layered, air filled PVC-membrane cushions.

The sun protection system on the south façade consists of outside blinds from WAREMA Renkhoff SE with spectrally selective lamellae. The solar reflectance of the lamellae in the visible spectral range is significantly higher than the reflectance in the solar spectral range. The result is a total solar energy transmittance which is lower than that of non-selective lamellae with the same visual transmittance. Additionally, all rooms are equipped with an inside glare protection system, a roller blind with a low-emissivity coating on the inner surface to improve thermal comfort of the inhabitants. The luminaries are switched and dimmed automatically based on combined occupancy and illuminance sensors in each room. Depending on the heating or cooling demand of the room, the solar energy input through the facade can be varied by using either the outside (low solar energy input) or inside (high solar energy input) shading device. The operation of the lighting and sun protection system was tested for all weather conditions. When the correct operation of the control system was verified the interaction of the users with the control system was investigated by surveying the user interventions with the building control system during winter conditions (*Reim, M.,* et al., 2014). Other surveys to optimize control strategies will follow.

2.1. Control of lighting and sun protection system

Each room is equipped with a ceiling-mounted combined occupancy and illuminance sensor. The occupancy sensor selects a low-power mode for the room when nobody is present. This includes switching off the light and operating the external sun protection system depending on whether there is heating or cooling demand (completely open or completely close the sun protection system) for the room.

When occupied, a default illuminance level of 500 lx (*EN 12464-1, 2011* for office rooms) at the work places is maintained using dimmable artificial lighting if necessary. The position of the shading system (open or closed) depends on the outside illuminance on the respective façade:

- It is closed at an outside illuminance higher than 45 klx. The lamellae angle is set depending on the position of the sun and the heating or cooling demand of the room. When heating demand is present the lamellae are closed just a few degrees more than the cut-off-angle, which ensures that no direct irradiation passes the sun protection system. The cut-off-angle is the angle to which the lamellae have to be closed in order to completely prevent direct radiation to pass through the sun protection system depending on the solar height. When cooling is needed the lamellae angle is set 10° higher than the cut-off-angle or a minimum of about 20°, further reducing the solar energy input to the room.
- It is opened when the outside illuminance is lower than 20 klx for some time.
- When the outside illuminance is higher than 30 klx the sun protection system is closed with a lamellae angle of 0° (horizontal). The same state is reached when the system is closed and the outside illuminance is lower than 30 klx.

All automatic settings for lighting and outside sun protection system can be overruled by the user; the control system is reset to automatic mode after 30 minutes without occupancy. The roller blinds used as inside glare protection are controlled manually.

Following a survey from spring 2015 the control strategy for the building was optimized as follows:

- The starting time for the room heating on Mondays after the weekend setback was changed from 6 am to 4 am to increase the room temperatures in the morning, especially in the corner offices.
- The maximal closing angle of the sun protection system of 50° was too big. Most of the users felt uncomfortable with the nearly fully closed shading system and artificial lighting switched on, so we set the maximum closing angle to 45°.
- At outside temperatures above 8°C, heating demand for the room and illuminance at the south façade above 45 klx the sun protection system was fully closed so far. In the rooms with room-high glazing we changed the control so that the sun protection system stops at a façade height of 40 % for the case of heating demand in the room. This improves the user acceptance, allows better visual contact to the outside and additionally increases the solar gains during the heating period.

After these changes, we performed new surveys to check if the changes really improved the situation in the offices. These results were presented in *Reim et al. 2015*. In nearly every room the number of the interventions by the users was reduced after the optimization of the control strategy of the sun protection system. Even in the rooms, where the users often intervene with the building control, the number of interventions was reduced after the optimization.

2.2 Daylight input through aerogel glazing

The ceilings in the back of the offices are equipped with aerogel glazing, shown in Fig.2. The aerogel glazing should improve the illumination in the room depth by daylight that is transmitted through the translucent textile roof. This should reduce the electric consumption needed for artificial lighting. To quantify this effect, measurements were made in two comparable rooms, one with and one without aerogel glazing (the aerogel glazing was covered for the measurements in this room) and the power signal for the artificial lighting was detected and analyzed.

Fig.2: Aerogel glazing in the back of the offices

3. Results

3.1 User surveys

After the control strategy of the sun protection system was changed as discussed in section 2.1, the efficiency of the changes was investigated. Assuming that the more comfortable the user feels the less he is intervening with building control, we compared the user interventions before and after the optimization, see Fig.3. The number of user interventions decreased, especially the cases when the sun protection system was manually opened fully (case "open") or partially (case "middle").

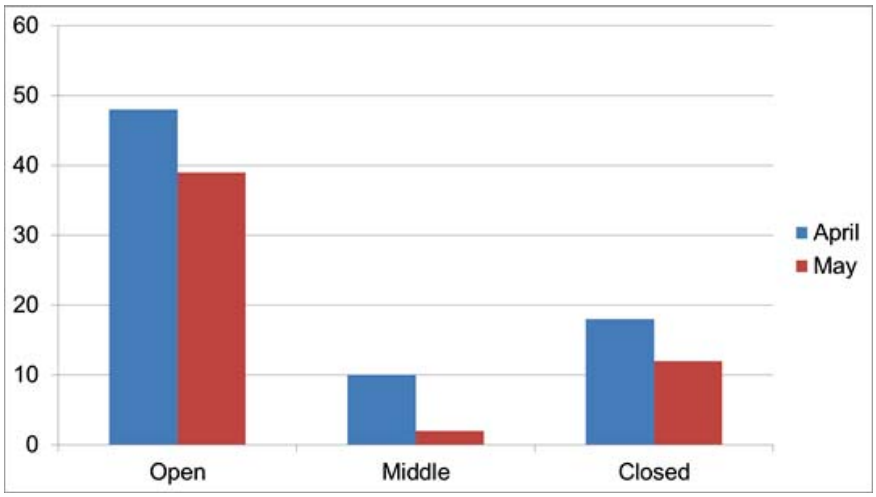

Fig.3: Number and sort of user interventions with the shading system before (april) and after (may) optimization of the control strategy.

After these changes, we checked the number of user interventions (see table 1) and additionally performed new surveys to check if the changes really improved the situation in the offices.

Table 1: Number of user interventions with the building control for different rooms before (april) and after (may) optimization of the control strategy.

Room Intervention	1	2	3	4	5	6	7	8	9	10	Total	Mean per workday
april	12	11	-	2	3	2	4	4	14	6	58	2.9
may	6	9	-	3	3	-	1	2	8	5	37	2.1

In a ‚pop-up' survey we asked users about their satisfaction with their working environment (happy/unhappy). After this window a second pop-up window opened asking for reasons for satisfaction/dissatisfaction (temperature/ light/ other reasons). In order to keep the user from choosing the shorter version of answering the survey, the number of windows and the number of clicks had to be similar. This was discussed with a psychologist in advance. In the course of the survey a problem became obvious: one can easily determine whether the office is too warm, cold, dark or bright, but it is difficult to decide if the office is just as warm or cold as one would like it to be. Many users got put off by the number of clicks needed (3 - 6). Hence the survey was reduced to one window with 2 clicks,Fig 4.

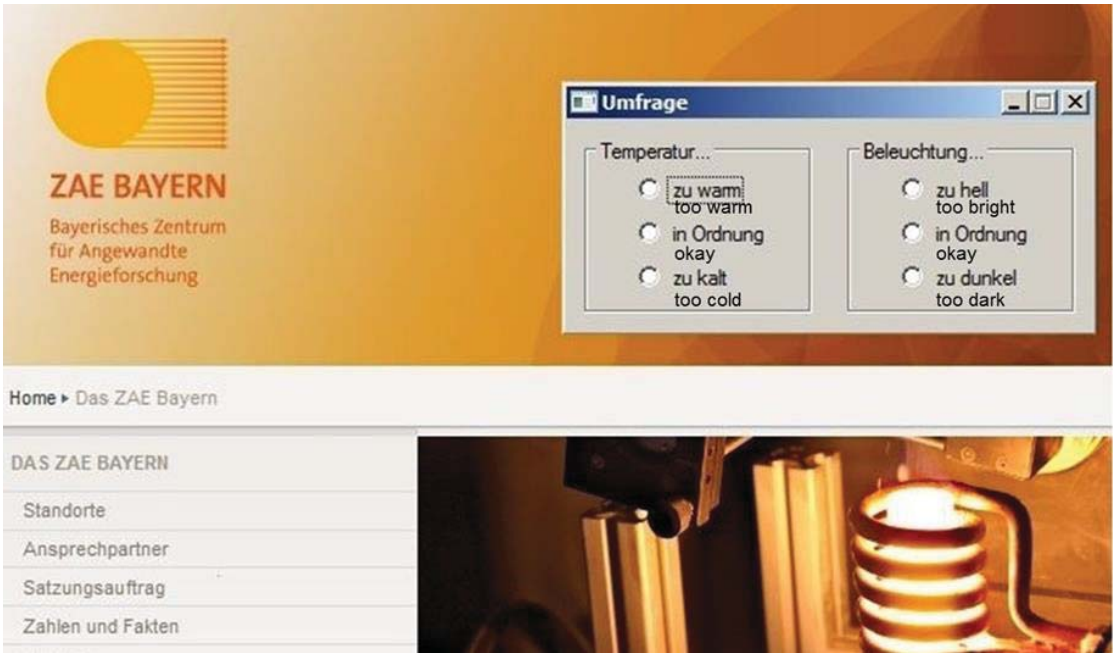

Fig.4: Optimized Pop-up window.

Evaluation of the survey between 16/08/2016 and 16/09/2016 is depicted in table 2 and table 3. In this timeframe the weather was very warm and sunny. In table 2 the user satisfaction in south- and north-facing as well as corner offices is depicted.

Table 2: Comparison of user satisfaction in south- and north-oriented as well as corner rooms

	South orientated	North orientated	Corner
too warm	1.6 %	3.8 %	8.1 %
okay	90.3 %	90.9 %	90.4 %
too cold	8.1 %	5.3 %	1.5 %
too bright	0.9 %	3.4 %	5.6 %
okay	95.3 %	90.0 %	92.1 %
too dark	3.8 %	6.6 %	2.3 %

With an overall satisfaction over 90 % we conclude, that for all offices – independent of their direction – the sun-protection and artificial light regulation is working very well at least for summer conditions.

In table 3 the user satisfaction as a function of daytime is depicted.

Table 3: Comparison of user satisfaction depending on daytime

	too cold	too warm	too dark	too bright
before 10 am	10.0 %	1.5 %	4.9 %	3.8 %
10 am – 2 pm	7.3 %	2.6 %	3.3 %	2.5 %
after 2 pm	2.0 %	5.5 %	5.2 %	2.0 %

There is neither a correlation between daytime and sensitivity of light, nor for perception 'too dark' (average 4.5 %) or too bright (average 2.8 %).

However, there seems to be a tendency in perception of temperature. During morning hours it is often too cold, in the afternoon often too warm.

One important change to the control was the last point mentioned in section 2.1, where the sun protection system was not closed completely any longer at outside temperatures above 8°C and heating demand as well as illuminance levels at the south façade of more than 45 klx but instead stopped at a façade height of 40 % thus shading only 60 % of the façade area instead of 100 %. This should lead to a reduced heating demand due to increased solar gains. In order to estimate this effect, we investigated the control log of the sun protection system and looked how long the sun protection system was in this optimized mode from September 1st 2015 to September 1st 2016. During the whole year, twelve office rooms stayed in this optimized mode for a total of 1891 hours in which the solar energy input was increased by 40 %, which equals a mean value of 158 hours per year and room.

In case of high irradiance on the south façade, which causes the mode of maximal shading angle this adds up to 2271 hours per year, which equals a mean value of 189 hours per year and room, in which most users switched on electric light, since it was too dark for them. Therefore, some energy savings should be achieved in this mode, however it is difficult to estimate how much.

3.2 Energy savings potential of aerogel glazing

Finally, we compared the illuminance and the lamp control signal for two similar rooms – one with and one without aerogel ceiling panel, see Fig. 5.

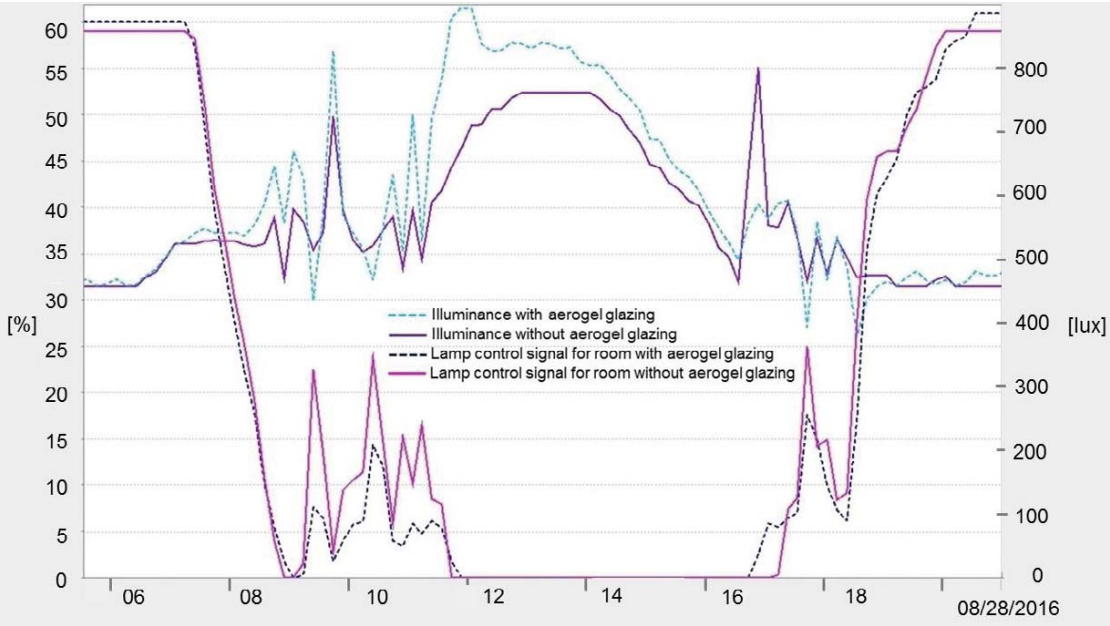

Fig.5: Comparison of illuminance in a room with (dotted line) and without (single line) aerogel glazing as well as the signal for lamp control; illuminance right axis [lx], lamp control signal left axis [%].

On the August 28th depicted in Fig. 5 the amount of daylight between 11:30 am and 4:30 pm is sufficient to illuminate the offices with 500 lx without any artificial lighting (lamp control is off). Here the illuminance during midday hours of a room with aerogel glazing exceeds that of a room without aerogel glazing by 100 lx. During morning (8:30 – 11:30 am) and evening hours (4:30- 6 pm) artificial lighting is added by the control strategy to guarantee a working place illuminance of 500 lx. In order to conduct measurements with defined boundary conditions, the control of the sun protection system was identical for both rooms and the presence was turned on all day without any user influence.

An overview of the measured electrical energy consumption in the two rooms with and without aerogel glazing is depicted in Fig. 6 for some days in May and August 2016. If we ignore the first measurement day on May 14th because of the very low consumption values with a corresponding high measurement error, typical energy savings of 10 % – 50 % can be achieved with the aerogel glazing as headlight. The mean value for all five measurement days yields energy savings of 30 %.

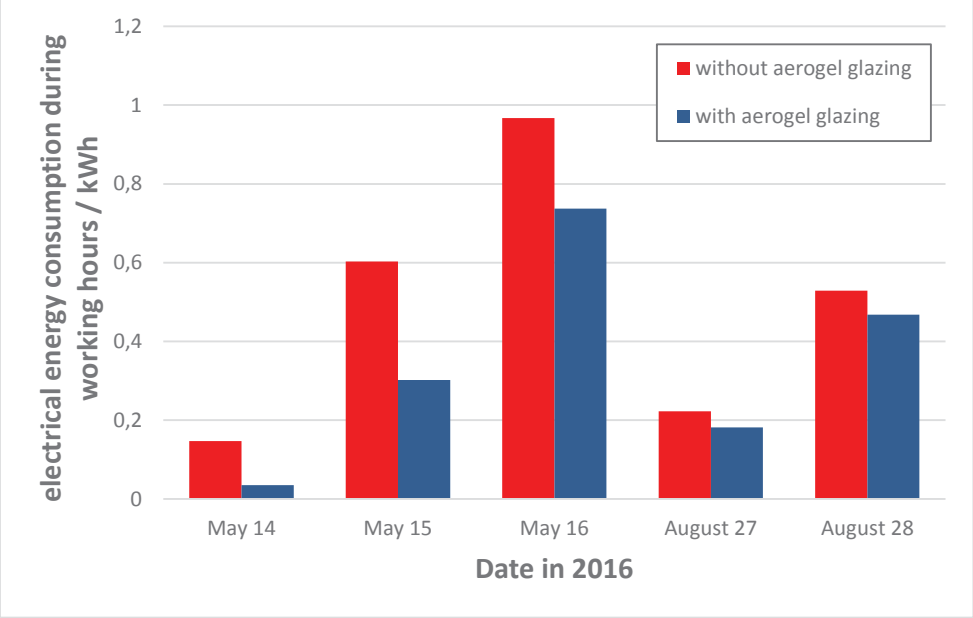

Fig. 6: Electrical energy consumption for artificial lighting in two rooms with and without aerogel glazing as headlight.

4. Summary and Outlook

During recent work, the building control of the Energy Efficiency Center with its innovative daylighting and sun protection concept was investigated and optimized. The various optimization measures were controlled and confirmed by user surveys. In addition, we started to evaluate the electrical energy savings potential of aerogel glazing as headlight in the offices to reduce artificial lighting. First measurement results are presented here that show an electrical energy savings potential of about 30 %.

Further surveys will be made to continuously check the quality of the building control. Measurements of the electrical energy consumption due to artificial lighting in the two offices with and without aerogel glazing will also continue.

5. Acknowledgement

This research was carried out as part of the project “DEENIF” and was funded by the German Federal Ministry of Economics and Technology by resolution of the German Federal Parliament as well as by the Federal state of Bavaria. We thank Cabot Corporation, Energy Glas GmbH, Hightex GmbH, Okalux GmbH, Siteco Beleuchtungstechnik GmbH, Verseidag-Indutex GmbH, Warema Renkhoff SE for their support.

6. References

EN 12464-1, 2011. Light and lighting - Lighting of work places - Part 1: Indoor work places; German version EN 12464-1:2011.

Reim, M., et al., 2014. Daylighting and Shading of the Energy Efficiency Center, Eurosun proceedings.

Reim, M., et al., 2015. Control strategies and user acceptance of innovative daylighting and shading concepts, ABS Bern proceedings.

Römer, C., et al., 2016. Switchable thermal insulation for increasing energy efficiency of building façades, Eurosun proceedings.

Weismann, S., et. al., 2016. Energy Efficient Building Cooling by Combining a Regenerative Cooling System, a large TES and a Phase Change Material Cooling Ceiling, Eurosun proceedings.

Conference Proceedings

EuroSun 2016

Palma de Mallorca (Spain), 11 – 14 October 2016

Passive systems for energy savings of buildings in tropical climate

Lídia Rincón[1], Leônidas Albano[2], Sergi Vall[1], Marc Medrano[1]

[1] Department of Computer Science and Engineering, University of Lleida. Carrer Jaume II, 69. 25001 Lleida (Spain). Phone: +34-973003551, e-mail: lrincon@diei.udl.cat

[2] Department of Arts and Architecture, Pontifícia Universidade Católica de Goiás. Avenida Universitária 1069, Goiânia 74605-010, Goiás (Brazil). e-mail: la@leonidasalbano.com

Abstract

Passive systems and bioclimatic architecture principles applied to modern architecture are able to reduce the energy demand of the building sector, and to meet the Nearly Zero-Energy Building goals. The aim of this research is to reduce the discomfort time of buildings located in tropical climate, by using passive systems taken from vernacular architecture and bioclimatic modern buildings. For this purpose, a model building has been designed, meeting the tropical climate requirements. Energy simulation has been done to compare the thermal behavior and thermal comfort conditions of the model building, under different passive systems cases: thermal mass, solar protections, crossed ventilation, and dehumidification. The results reveal that a combination between high thermal inertia with nocturnal ventilation, the use of solar protections on the north facade, dehumidification, and the use of thermal insulation in the roof is fundamental for achieving the thermal comfort in buildings located in tropical weather.

Keywords: *Energy simulation, bioclimatic strategy, passive design, thermal comfort, office building.*

1. Introduction

Building sector consumes 40% of the final energy consumption (Economidou 2011). Half of this energy consumption is due to the use of active systems for heating and cooling (Meijer et al. 2009). For these reasons, the greatest energy savings potential is associated to the building sector, and to the reduction of the energy demand from heating and cooling systems (Economidou 2011). To reduce buildings energy consumption, it is created the concept Nearly Zero-Energy Building (NZEB). This concept has become part of the energy policies of many countries, to make possible the reduction of emissions of CO_2 generated by the building sector (COM 2011; Crawley et al. 2009). Passive systems and bioclimatic architecture principles applied to modern architecture are able to reduce the energy demand of the building sector, and to significantly contribute to the NZEB goals. These strategies were broadly used in vernacular architecture (Manzano-Agugliaro et al. 2015). However, the major part of contemporary architecture does not use them. Most of modern buildings are not designed in adaptation to their climatic conditions and, therefore, they require active systems for achieving the indoor thermal comfort.

The aim of this paper is to reduce the number of hours not meeting thermal comfort criteria of buildings located in tropical climate. This is done by using passive systems taken from vernacular architecture and bioclimatic modern buildings. For this purpose, this paper analyses the thermal behavior of a model building that incorporates different cooling passive systems, by using energy simulation. The building is located in Goiânia, a city of the interior of Brazil, with tropical climate (Aw according to Köppen). This research is part of an initiative that aims to build a prototype with the NZEB concept, named Model House, to realize experimental researches about thermal comfort and energy efficiency.

Selection and/or peer review under responsibility of Scientific Committee
doi:10.18086/eurosun.2016.01.14 Available at http://proceedings.ises.org

2. Passive systems for tropical climate

2.1 The climatic conditions of the location

The analyzed building in the simulation is hypothetically located in Goiânia, the capital of the State of Goiás, Brazil (Latitude -16.7º, Longitude -49.3, Elevation 741 m). The region of Goiás is within the Tropical savanna climate area (Aw), according to Köppen climate classification (Kottek et al. 2006). This climate is characterized by two main seasons: wet -from October to April- and dry -May to September- (Tab. 1). In Goiânia, the predominant winds are; north (16% of the time), south east (16% of the time), east (14% of the time), and north west (13% of the time).

Tab. 1: Climatic conditions of Goiânia, Brazil (World Climates 2016).

Month	Average Air temperature*	Relative humidity*	Daily solar radiation		
			Roof	South Facade	North Facade
	ºC	%	kWh/m^2·d	kWh/m^2·d	kWh/m^2·d
January	23.8	75	5.13	1.03	-
February	23.8	76	4.67	0,14	0,27
March	23.9	74	4.69	-	1,10
April	23.6	71	5.50	-	3,00
May	22.1	65	4.66	-	3,77
June	20.7	60	4.47	-	4,36
July	22.9	53	4.67	-	4,25
August	24.6	47	5.04	-	3,29
September	24.6	53	5.68	-	1,96
October	24.6	65	4.74	0,14	0,35
November	24.0	73	5.58	0,88	-
December	23.5	76	4.58	1,18	-

**Climatological average (1961-1990)*

In this latitude, the North facade is exposed to winter insolation. For this reason, it should be well protected from solar radiation and should have a reduced glass surface (Fernandes 2006). The south facade can have a wider glass surface, but still requires solar protections in summer period, when solar radiation can reach it. Along all the year, the roof is the part of the building which receives the highest solar radiation (Tab.1).

2.2 Bioclimatic strategies

According to this climate conditions, the thermal comfort is achieved during 27.4% of the year (Fig. 1). The rest of the year, the recommended bioclimatic strategies are:

- Solar heating (15% of the year).
- Thermal inertia for heating (13.4% of the year).
- Ventilation (13.8% of the year).
- Night ventilation (10.1% of the year).
- Thermal inertia for cooling (10.1% of the year).
- Evaporative cooling (10.1% of the year).

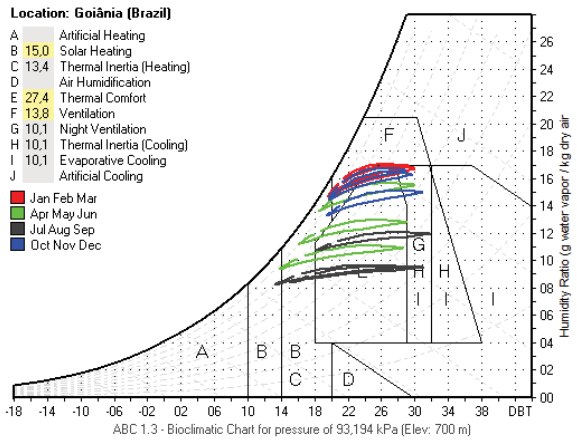

Fig. 1: Architectural bioclimatic classification according to psychometric abacus. Source: Roriz (1992).

The bioclimatic strategies for tropical climate are identified, selected, and applied to the building model. They are presented in Tab. 2.

Tab. 2: Bioclimatic strategies for tropical climate, based on Manzano-Agugliaro et al. (2015).

Bioclimatic strategy	Temperature	Relative Humidity	Operation	Architectural implementation
1. Solar protection	>20ºC	-	Avoiding heat gains through solar radiation. Avoiding temperature increases to remain in the comfort zone. Protection is focused on all building openings but can also be generally applied to the building envelope.	• Pergolas with deciduous vegetation • Porches • Awnings • Interior store • Exterior (sunblind) blinds • Exterior brise soleils.
2. Cooling through a high thermal mass	20-35 °C	-	The thermal mass of the building envelope that receives and subsequently transmits radiation to the interior with a phase difference to achieve climate uniformity throughout the day.	• Capacitive materials help to create a phase difference in the daily energy transmission and temper the intensity. Nocturnal dissipation by the facade and roof is necessary. • It is ideal to place a mobile daytime protection device to avoid gains and promote nocturnal dissipation
	From 24 ° C	80–50%		
	Up to 35 °C	30%		
3. Cooling by high thermal mass with nocturnal renovation	20 °C- 44 °C	-	Creating a phase difference between the effect of the daytime and night time outside temperatures to conduct a nocturnal renovation It is effective when the climate exhibits significant thermal differences between the day and night periods.	• The building envelope should comprise capacitive materials that transmit energy with the largest phase difference possible (approximately 12 h) with some damping. • At night, dissipation and renovation should be conducted through openings, patios and roofs.
	44 °C	5%		
	31.5 °C	32%		
	24 °C	80%		
4. Cooling through natural ventilation	20 °C - 31.5 °C	95% - 20%	A greater thermal sensation is achieved while the indoor air is simultaneously cleaned.	• Cross-ventilation from north to south facades or dominant winds • The chimney effect • A solar chamber • Subterranean ventilation • Wind towers • Evaporative towers • Vertical spaces within a building • Patios
	From 31.5 °C	50%		
	Up to 26.5 °C	95%		
5. Conventional dehumidification	> 25 °C	> 80%	The objective is to incorporate strategies to absorb water from the environment in order to achieve the comfort zone.	By using absorbent salts and saline cells and requires complementation with other strategies.
6. Thermal insulation in the roof	-	-	Avoid heat gains from solar radiation (perpendicular to the roof in tropical latitude)	Incorporation of thermal insulation in the roof.

3. Building design

This research is part of an initiative that aims to build a prototype with the NZEB concept, named Model House. This building will be used to realize experimental researches about thermal comfort and energy efficiency. In this paper energy simulations will be carried out to quantify and compare the benefits of the proposed bioclimatic strategies and to improve the building design. Once built, the building will be monitored to validate experimentally the simulation results.

The Model House is designed according to bioclimatic criteria, based on the tropical climate conditions and latitude. These criteria take into consideration the optimum shape factor in plan and volume, window size, surface façade and roof color, solar protection, and indoor natural daylighting (Fig. 2).

Moreover, the building is designed for meeting both requirements; experimental research and office use. For this reason, the building has two identical office rooms; the first one will be the reference case, and the second one the case of study. Both rooms share a common patio. This patio has local vegetation ("Cerrado") and a fountain to generate shadow and evaporative cooling. The mobile facades allow the connection of the offices to the patio, depending on the experiment.

According to Olgyay (1963), the optimum shape in plan of a building in tropical climate is 1:1.7, with a range to 1:3. Therefore, the shape plan 1:2 of the designed office space is between this range.

The net floor area of each office is 32.80 m^2 (8.20 m x 4.00 m). The interior height is 2.70 m. The building facilities (toilette, kitchen and storage) are located separately, in the east and west part of the building.

The roof is designed for projecting shadow over the building. This double roof protects the building from temperature variations due to solar radiation.

The east and west facades are highly insulated. The north and south facades are removable to make possible the change of experiments. Prefabricated construction systems are used to make possible the removal of materials.

Windows are the 30% of the total facade, according to Rizki et al. (2016), who determined three optimum solutions of window size, orientation and wall reflectance with regard to various daylight metrics and lighting energy demand in simple buildings placed in the tropical climate. They determined that the most optimum solution is the combination of window-to-wall ratio 30%, wall reflectance of 0.8, and south orientation (in the North hemisphere).

Fig. 2: General view of the Model House, a building designed with bioclimatic principles for experimental purposes in tropical climate.

The building also meets the Brazilian habitability and construction regulations (NBR 9050/2004, NBR 15220/2003, NBR 15575/2013). According to these regulations (ABNT NBR 15220-3), the maximum overall heat transfer coefficient (or U-value) for facades is 2.2 $W/m^2 \cdot K$, for the roof is 2.0 $W/m^2 \cdot K$. The physical characteristics of the materials used are shown in Tab. 3. The U-values are calculated for each construction system, according to their construction materials.

Tab. 3: Physical characteristics of the materials used in the building envelope.

Part of the building	Construction system	U-value [W m^{-2} K^{-1}]	Material	Thickness [cm]
Roof	Insulated roof	0.441<2.0	Gravel	6
			XPS	6
			Asphalt membrane	1
			Cement mortar	2
			Concrete slap & beams	30
			Plaster coating	1.5
	Non-insulated roof	1.980<2.0	Gravel	6
			Asphalt membrane	1
			Cement mortar	2
			Concrete slab & beams	30
			Plaster coating	1.5
	Highly insulated roof	0.248<2.0	Gravel	6
			XPS	12
			Asphalt membrane	1
			Cement mortar	2
			Concrete slab & beams	30
			Plaster coating	1.5
South & North Facade	Concrete panel*	2.777>2.2	Mortar coating	2
			Precast concrete panel	10
			Plasterboard	1.5
	Ceramic brick	2.175<2.2	Mortar coating	2
			Ceramic Brick	11.5
			Plasterboard	1.5
East & West Facade	Timbered facade	0.172<2.2	Plywood	2
			Mineral wool	10
			Glass wool	12
			Plasterboard	1.5
Windows	Window	5.689	Wooden frame, simple glass	-
Doors	Door	3.280	Wood	4.5
Floor	Non-insulated floor	4.351	Reinforced concrete	10
			Cement mortar	2
			Ceramic tile	1

**Used in the four facades in experiment #3.*

The space type for both offices is defined by regulation EN 16798, as well as the occupancy schedule. This means that it is stablished 17 m^2/person, or 2 people in each office space. The occupancy will be distributed from 8-12 AM and 1-7 PM.

No heating or cooling device is simulated, only free floating temperatures, because bioclimatic strategies are evaluated.

4. Energy simulation experiments

The thermal behavior of the Model House is simulated before its construction. This simulation is done with Energyplus software, by using Opens Studio (Fig. 3). The simulation results will be validated with the monitoring of temperature, humidity, and air flow in the constructed building. The experiments will take place under hot and humid, and hot and dry weather conditions for the tropical climate. The experiments held in the building model are:

- **Solar protection:** Comparison of a window with solar protection (horizontal brise soleils) versus a window with no solar protection (Fig. 3).
- **Cooling through a high thermal mass:** Comparison of two different materials in the facade; high thermal mass (concrete panel) versus low thermal mass material (ceramic brick), and different wall resistance (Tab. 3).
- **Cooling through a high thermal mass with nocturnal renovation**: Comparison of the use of night ventilation and no ventilation, with concrete panel in the four facades (Tab. 3).
- **Cooling through natural ventilation:** The effect of ventilation in the thermal comfort, comparing a ventilated office by using infiltrations through the window area (4 renovations per hour) and a no ventilated office.
- **Conventional dehumidification:** The use of absorbent salts for decreasing the humidity of the air of the test office (simulated by using a HVAC Dehumidifier) compared to a non-dehumidified office.
- **Thermal insulation in the roof** (Fig. 3): Comparison of the effect of thermal insulation in the roof without solar protection, comparing a roof with and without insulation (Tab. 3).

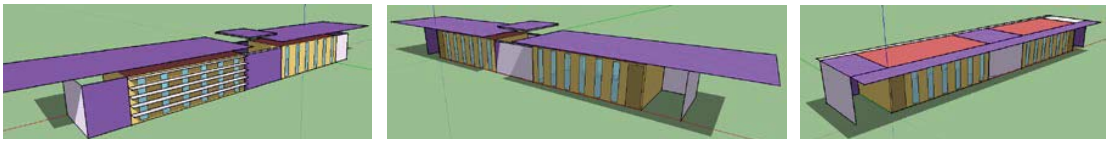

Fig. 3: Views of the office building (Model House) energy simulation done with SketchUp and Open Studio. From left to right: Solar protections, Cooling through natural ventilation, Thermal insulation in the roof.

Because of the latitude, the North facade receives solar radiation mainly in the winter season (Tab. 1). For this reason, the experiment #1 “Solar protections” will be done during solstice of June.

June is the month with wider thermal lag, reaching the coolest temperatures of the year during the night (Tab. 1). For this reason, winter solstice (the week around June 21st) is the selected period for the experiment #2 “Cooling by high thermal”.

The same experiment will be done with and without nocturnal renovation #3 “Cooling through a high thermal mass with nocturnal renovation”. Previous simulation with AnalisisBio (Albano 2013), points out this month as the optimum to reach the Nearly Zero Energy consumption.

The experiment #4 “Cooling through natural ventilation” will be done in both, dry and wet season. For this reason, the driest month, September, and the more humid month, December, are selected (Tab. 1).

December is the month with higher requirements of thermal comfort, due to the high relative humidity combined with the high air temperature (Tab. 1). This discomfort can be corrected by using natural ventilation (Albano 2016). It is in December, during the wet season, when will be done the experiment #5 “Conventional dehumidification”.

Finally, the experiment #6 “Thermal insulation in the roof” will be done during both solstices and the equinox in September, to test the differences in solar radiation along the key moments of the year (Tab. 4).

Tab. 4: Experimentation cases and timing.

Bioclimatic strategy to be tested	Reference Case A	Evaluated Case B	Period of time of the experiment
1. Solar protection in the north facade	No solar protection	Brise-soleils	14th – 28th June
2. Cooling through a high thermal mass	Ceramic brick	Concrete facade	14th – 28th June
3. Cooling by high thermal mass with nocturnal renovation	No nocturnal ventilation	Nocturnal ventilation	14th – 28th June
4. Cooling through natural ventilation 4.1. Dry season 4.2. Wet season	No Ventilation	All day ventilation	• Dry season: 1st-15th September. • Wet season: 14th – 28th December
5. Conventional dehumidification	No dehumidification	HVAC Dehumidifier	14th – 28th December
6. Thermal insulation in the roof 6.1. Solstice in June 6.2. Solstice in December 6.3. Equinox in September	No insulation	Insulation	14th – 28th June 14th – 28th December 14th – 28th September

5. Results

The thermal behavior of each office is evaluated by using the number of hours of discomfort in the office per the period of the experiment. Fig. 4 shows the "Time Not Comfortable" based on the ASHRAE Standard 55 Adaptive Comfort model, within the 80% acceptability limits. The ASHRAE Standard 55 Adaptive model is especially suited for naturally ventilated buildings with no mechanical cooling systems, and occupants have better control over their thermal comfort. More details about the requirements and features of the method are explained elsewhere (ASHRAE 2010). For the dehumidification case 5, the Fanger's Comfort model has been used instead, to be able to consider the effect of humidity on human comfort. The results are presented for the period of 2 weeks, during the time of occupation.

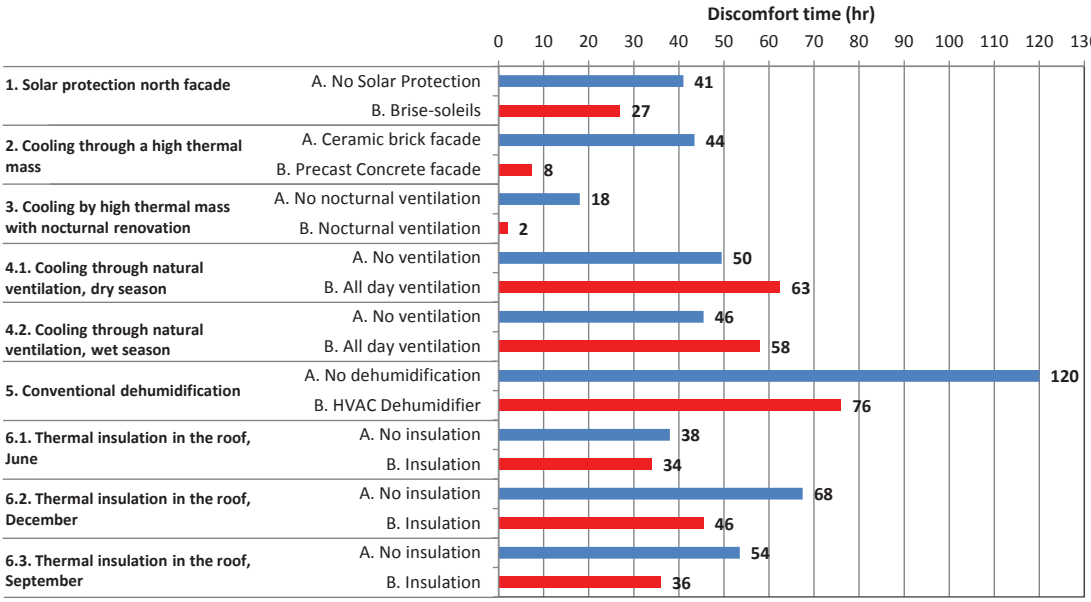

Fig. 4: Time Not Meeting the ASHRAE55 Adaptive Comfort Model with 80% Acceptability Limits during Occupied Hours. Units: hr.

The graphics of temperature, humidity, occupation, and air change rate for the selected period and each experiment are presented in Fig. 5: Outdoor temperature (black), indoor temperature in reference office (dark blue), test office (light blue), and occupation or ACH (pink dotted lines).

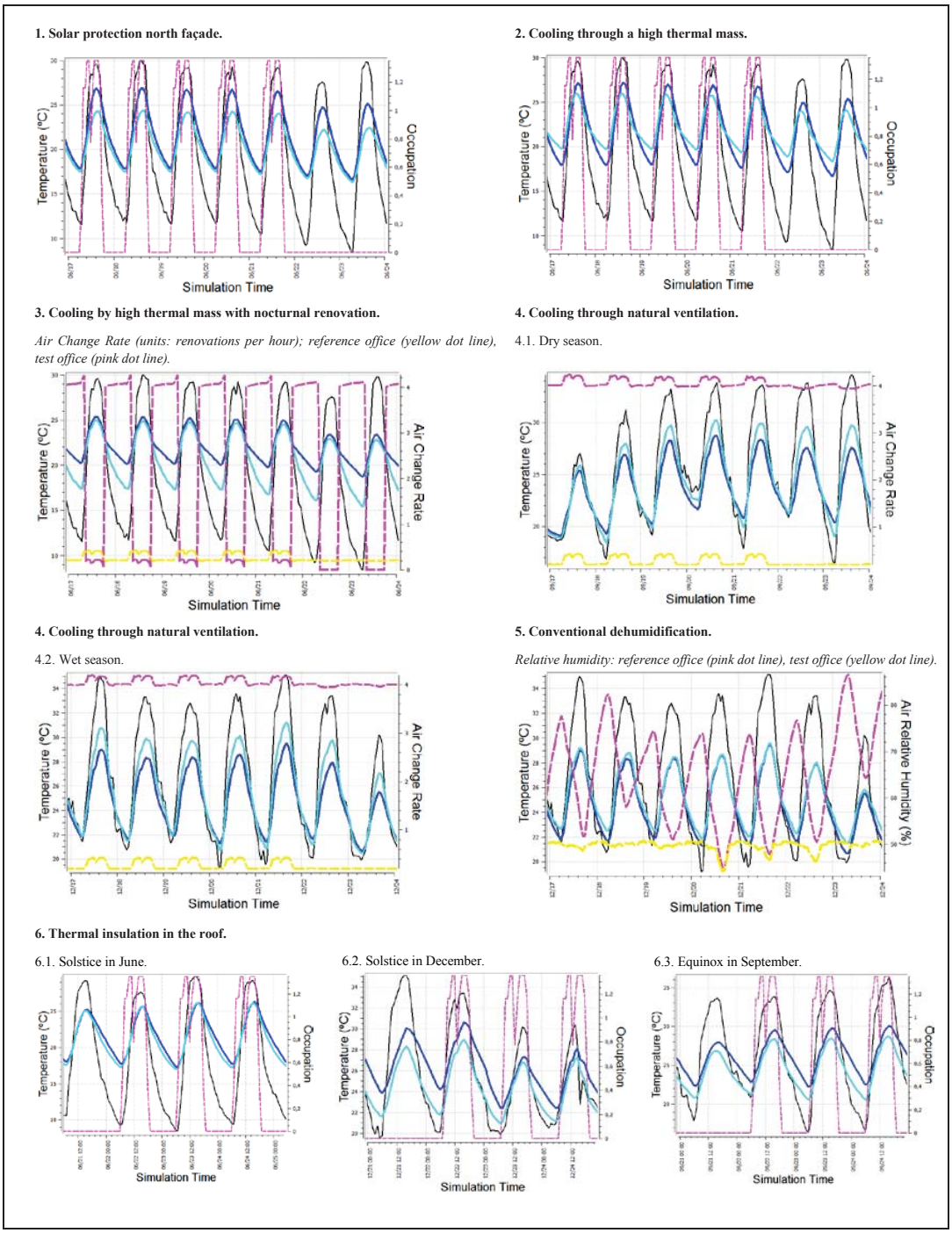

Fig. 5: Results for each experiment in the selected period: outdoor temperature (black line), reference office (dark blue line), test office (light blue line), occupation or Air Changes Rate (pink dot line).

6. Discussion

The more significant improvement performances were found in the following strategies:

- 1st: Cooling by high thermal mass with nocturnal renovation: 89% improvement.
- 2nd: Cooling through a high thermal mass: 83% improvement.
- 3rd: Solar protection on the north facade: 34% improvement (and even better, 52%, if we take the

90% acceptability limits.

- 4th: Thermal insulation in the roof during the Solstice of December and the Equinox of September: 33% improvement.

The implementation of materials with high thermal mass on the facade, such as the precast concrete panel, provided a more stable inner temperature in the office compared to the brick facade, despite the lower thermal transmittance of the concrete panel (Tab. 3). In the 2nd experiment, the thermal amplitude in the test office was 3 ºC lower than the reference office, reaching a maximum indoor air temperature between 1 ºC and 1.5 º lower than the reference office (Fig. 5). This temperature, together with the radiant mean temperature, yielded comfort conditions in most of the hours of occupation.

Night ventilation can help to decrease the day maximum air temperatures as long as there is high thermal mass in the building. In the 3rd experiment, a higher thermal mass was incorporated in the building by constructing the 4 facades with precast concrete panel. In this case, night ventilation was added. As a result, the maximum temperature was 1 ºC lower in the test office compared to the reference office. The minimum air temperature in the ventilated office decreased substantially during the night, a period with no occupation.

All day ventilation provided more hours of discomfort to the test office because it allowed the inlet of warm air from the hottest moment of the day. In both cases, dry hot and wet hot weather, the discomfort time in the ventilated office was around 26% higher than in the not ventilated office (Fig. 4). The maximum temperature in the ventilated office was around 2 ºC higher than in the non-ventilated office (experiments #4.1 and #4.2 in Fig. 5).

The use of horizontal brise soleils on the north facade was found to be an effective solar protection. The solar protection improved the temperature comfort during the afternoon, period with the maximum occupation. The maximum temperatures in the test office were 3 ºC lower than in the reference office (experiment #1, Fig. 5).

The incorporation of 12 cm of XPS in the roof, provided a significant improvement in the thermal comfort during the Solstice of December and the Equinox of September, when the solar radiation is more perpendicular to the roof, in tropical latitude (Tab. 1). In December, the maximum day temperature was around 2 ºC lower in the insulated roof office than in the non-insulated roof one.

The presence of a dehumidifier in the building simulation, maintaining the relative humidity below 50%, increases slightly the night minimum air temperatures (0.5 ºC), but helps achieving a 37% increase in thermal comfort hours, according to the Fanger's Comfort model, which takes into account, among others, the effect of the relative humidity in human comfort.

7. Conclusions

The use of passive systems in tropical climate contributes to reduce the discomfort time of buildings, in both wet and dry hot climate conditions. A combination between high thermal inertia with nocturnal ventilation, the use of solar protections on the north facade, dehumidification, and the use of thermal insulation in the roof is fundamental for achieving the thermal comfort in buildings located in tropical weather. However, the use of natural ventilation in the office has to be limited to the night, when it is effective due to the outdoor lower temperatures, but not to all the day. Daily crossed ventilation produce the increase of the maximum day temperatures in the office. For this reason, crossed ventilation can be only recommended when outdoor temperatures are below the maximum comfort temperature.

The implementation of these passive systems depends on the early stages of the design building process. This requires the knowledge of the architect and designers on bioclimatic strategies and passive systems. Technicians and designers need firstly to do a deep analysis of the climate and micro-climate conditions of the building site. Therefore, Nearly Zero Energy Buildings would require the implementation of passive systems in the design phase of new and renovated buildings and the spread of passive systems knowledge among technicians.

Acknowledgements

Lídia Rincón would like to thank Banco Santander Universidades for her research mobility fellowship "*Programa Becas Iberoamérica, Jóvenes Profesores e Investigadores y Alumnos de Doctorado. Santander Universidades. España, 2015*" and University of Lleida for her research mobility fellowship "*Ajuts per a estades en altres centres per desenvolupar tasques de recerca. Anys 2015-2016*". Sergi Vall would like to thank the *Secretaria d'Universitats i Recerca del Departament d'Economia i Coneixement de la Generalitat de Catalunya* for his research fellowship. The authors would like to thank the collaboration of Ana Carolina Costa Roriz de Araújo from Studio Accra in the design of the House Model (*Casa Modelo)*.

References

ABNT NBR 9050, 2004. Norma Brasileira. Acessibility to buildings, equipment and the urban environment.

ABNT NBR 15220, 2003. Norma Brasileira. Thermal performance of buildings.

ABNT NBR 15575, 2013. Norma Brasileira. Performance of buildings.

Albano, L., Romero, M., Neto, A., 2013. Designing "Sustainable Houses" before the establishment of this concept. Central Europe towards Sustainable Building 2013. Integrated building system.

Albano, L., 2016. Ambiente y crítica. Invariantes que trascienden del clima y del lugar. Universitat Politècnica de Catalunya.

ASHRAE, ANSI., 2010. ASHRAE/IES standard 55-2010, thermal environmental conditions for human occupancy. American Society of Heating, Air-Conditioning and Refrigeration Engineers, Inc, Atlanta.

COM, 2011. 112 final. A Roadmap for moving to a competitive low carbon economy in 2050.

Crawley, D., Pless, S., Torcellini, P., 2009. Getting to net zero. ASHRAE J 51, 18-25.

Economidou, M., 2011. Europe's buildings under the microscope. A country-by-country review of the energy performance of buildings. Buildings Performance Institute Europe (BPIE).

Fernandes, A. M. C. P., 2006. Clima, homem e arquitetura. Goiânia: Trilhas Urbanas.

Kottek, M., Grieser, J., Beck, C., Rudolf, B., Rubel, F., 2006. World Map of the Köppen-Geiger Climate Classification Updated. Meteorol Z. 15, 259-63.

Meijer, F., Itard, L., Sunikka-Blank, M., 2009. Comparing european residential building stocks: performance, renovation and policy opportunities. Build Res Inf. 37, 533-551.

Manzano-Agugliaro, F., Montoya, F.G., Sabio-Ortega, A., García-Cruz, A., 2015. Review of Bioclimatic Architecture Strategies for Achieving Thermal Comfort. Renew Sust Energ Rev. 49, 736-55.

Olgyay, V., 1963. Design with Climate: bioclimatic approach to architectural regionalism. Princeton, New Yersey: Princeton University Pres.

Rizki, M.A., Rohmah, M., Asri, A.D., 2016. Design Optimisation for Window Size, Orientation, and Wall Reflectance with Regard to Various Daylight Metrics and Lighting Energy Demand: A Case Study of Buildings in the Tropics. Appl Energ. 164, 2.

Roriz bioclimatica. Free software based on bioclimatic charts proposed by Baruch Givoni (Comfort, Climate Analysis and Building Design Guidelines. Energy and Building, vol 18. July/1992, pp. 11-23). http://www.roriz.eng.br/download_6.html Accessed April 2016.

World Climates 2016. http://www.world-climates.com/city-climate-goiania-brazil-south-america/ Accesed on May 2016.

Conference Proceedings

EuroSun 2016
Palma de Mallorca (Spain), 11 - 14 October 2016

ISES EuroSun 2016

Quality management as a key for efficient building performance

Oliver Rosebrock, Franziska Bockelmann and Univ. Prof. Dr.-Ing. M. Norbert Fisch

Institut für Gebäude- und Solartechnik, TU Braunschweig, Mühlenpfordtstraße 23, 38106 Braunschweig, Germany

Abstract

The use of complex building services opens up many possibilities to gain an increase of energy efficiency in buildings. On the other hand there are also threats that ecologically and economically planned energy concepts for buildings do not work as proposed. To reduce this risk a procedure was developed, based on so-called "active functional specifications". It covers the time span from planning phase up to building operation and allows, by running a digital test to verify whether the building services work as planned and whether the building's owner received what he has ordered.

In this paper the procedure is explained and results for an energy plus multi-family home are shown. The building's energy supply is based on electricity only. A heat pump using an ice storage and solar thermal collectors as heat source provides the energy for heating and domestic hot water.

Keywords: *quality management, building services, test stand, monitoring, energy efficiency*

1. Introduction

The application of complex building services with integrated measurement technology holds the prospect of grand increase in energy efficiency. Securing the actual utilization of these potentials in the building's operation is therefore becoming a significant challenge. Discrepancies between energy demand and consumption can turn economical concepts originating from the planning phase into cost-pushers in operation.

Past research projects and experiences from building service operation show the importance of quality management for reaching the desired efficiency and complying with energetic specifications, stipulated in the planning, in practical application. One of the principal problems is based on the non-standardized specification of the systems' functionalities.

"Active functional specifications" (AFS) present an innovative technique for effective and economical quality management. The definition and review of system functions is executed in the form of so called operating rules, e.g. for mass flows or powers, on a digital test bench. These rules must be fulfilled during operation. They therefore can be used as setpoint states for the construction and are being monitored during operation.

Within the frame of the research project "Effizienzhaus Plus, FFM Riedberg – EnergiePLUS im Geschosswohnungsbau" the ordinary energetic monitoring is supplemented by the newly developed method for assuring quality – the "active functional specifications". The research project is part of the research initiative "Zukunft Bau" funded by the BBSR.

doi:10.18086/eurosun.2016.01.07 Available at http://proceedings.ises.org

2. Multi-family house Riedberg

A multi-family house (MFH) with 17 accommodation units from two to five rooms is located in Frankfurt am Main in the district of Riedberg. It has four full stories and an attic floor (Fig. 1). The building is in use since August 2015. The standard of "Effizienzhaus Plus" is to be achieved with the help of a high-quality thermal building shell and optimal utilization of renewable energies.

The "Effizienzhaus Plus" standard demands that both the building's primary and end energy production exceed the consumption in the annual balance. In contradiction to the EnEV certificate the users' electricity consumption is also included into the balance.

The essential building characteristics are summed up in Tab. 1.

Fig. 1: Front view multi-family house Riedberg (source: egs-plan)

Tab. 1: Characteristics of the building in Riedberg

Year of construction	2015
Living area	1.600 m²
Number of accommodation units	17
Heated building volume	8.517 m³
Heated usable floor area A_N	2.407 m²
Annual heating energy demand	19 kWh/(m²$_{A_N}$a)
End energy demand electricity incl. household	25 kWh/(m²$_{A_N}$a)
Electricity production through photovoltaics	36 kWh/(m²$_{A_N}$a)
Electricity surplus (annual balance)	ca. 25.000 kWh/a

3. Energy concept

The MFH in Riedberg is an "electricity only building", meaning all energetic processes are driven by electricity.

The heat demand is supplied solely by an electrical brine/water heat pump with a thermal power of 50 kW. The building contains two distribution grids – a low-temperature grid of approximately 35 °C and a high-temperature grid of about 55 °C. The low-temperature grid serves the floor heating. The high-temperature grid is connected to the heating unit of the ventilation system, the bathroom radiators, and the preheating of the hot water in the fresh water stations of each flat. The additional heating of the hot water within the flats is realized electrically, too.

The building is ventilated mechanically. A heat recovery to reduce ventilation losses is implemented. Additional natural ventilation by opening of the windows is also possible.

The heat pump has two different heat sources, an earth-bound ice storage and solar thermal absorbers.

The solar thermal absorbers (11 modules, ca. 85 m²), which are located on the roof underneath PV panels, are used primarily to provide low-temperature environmental heat for the heat pump.

Additionally, an earth-bound ice storage of 98 m³ serves as an innovative heat source for the heat pump. The ice-storage uses the melting enthalpy (latent heat) of the phase change von liquid (water) to solid (ice). The latent heat per kg is nearly the same as the sensible heat provided by a temperature change of 80 K of a kg of water. When the amount of heat by the solar thermal absorbers is not sufficient, the heat source for the heat pump changes to the ice storage. The water in the storage cools down to 0°C and starts to freeze due to the heat extraction.

To maintain the functionality of the system the ice storage has to be regenerated, i.e. melting and heating up the water. The regeneration is done with natural heat from the surrounding soil and with the solar thermal absorbers when no heat is needed in the building and the temperature provided by the absorbers is higher than the temperature in the ice storage. The third option for regeneration of the ice storage is cooling of the building in summer.

The building is equipped with a cooling system. The floor heating system can be used for cooling in summer. The system works with free cooling and the ice storage is the heat sink, i.e. it provides the cooling energy.

PV modules on the roof (ca. 84 kW_p) and in the façade (ca. 15 kW_p) are planned to achieve a surplus of energy in the annual balance. The annual production of electricity exceeds the total electricity demand by approximately 40 % (ca. 25.000 kWh/a). The surplus is to be used for e-mobility. In addition to the electrical cars, a lithium-iron-phosphate battery (60 kWh) is used to increase the self-consumption of the produced electricity (Fig. 2).

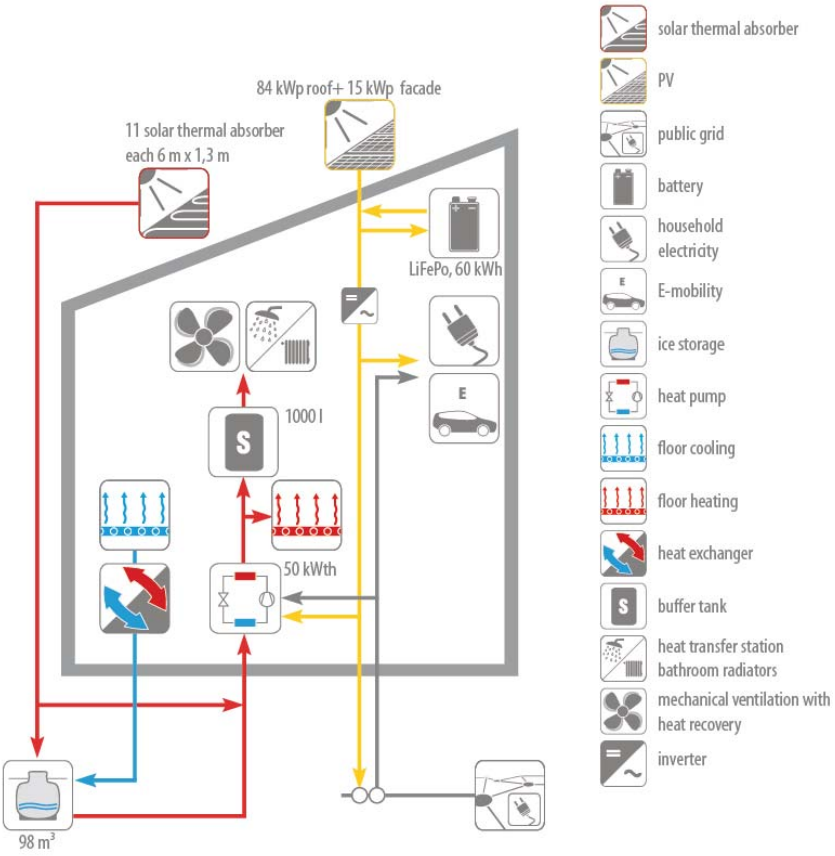

Fig. 2: energy concept multi-family house Riedberg

4. Active functional specifications

Within the scope of the active functional specifications operating modes and corresponding functions are already defined during the planning. These specifications, so called operation rules e.g. temperatures or valve positions, need to be fulfilled in the respecting operating mode.

Based on a simplified scheme the operating modes are being defined. Examples for different operating modes, rules, and definitions are presented in this paper. They are excerpts from the complex monitoring process.

The operating modes and rules are:

Operating mode BZ0 – OFF

All circulation pumps and the heat pump are inactive. All mass flows in the heat meters are equal to zero. The electrical power does not exceed standby needs.

Operating mode BZ1 – heating with heat pump - source ice storage

The heat pump (WP) is active due to a demand signal from the high- or low-temperature grid. The ice storage (ESp) serves the heat. The solar thermal absorber is inactive. The heat pump must be active for the correct operating mode 1. Heat meters WMZ3 and WMZ4 need to register mass flows, while the mass flows in WMZ1 and WMZ2 must be zero (Fig. 3, active circuits are coloured).

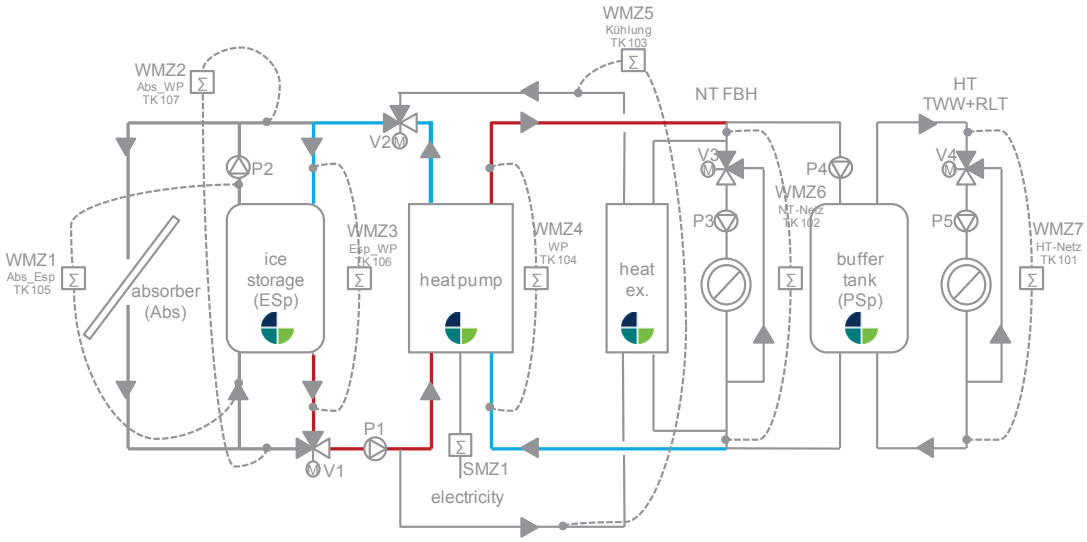

Fig. 3: operating mode BZ1 - source ice storage

Operating mode BZ2 – heating with heat pump - source absorber

In operating mode 2 the solar thermal absorber serves as the heat source. The ice storage is neither being charged nor discharged. For the correct execution operating mode 2 the mass flows at WMZ2 und WMZ4 are greater than zero and the heat pump is active (Fig. 4, active circuits are coloured).

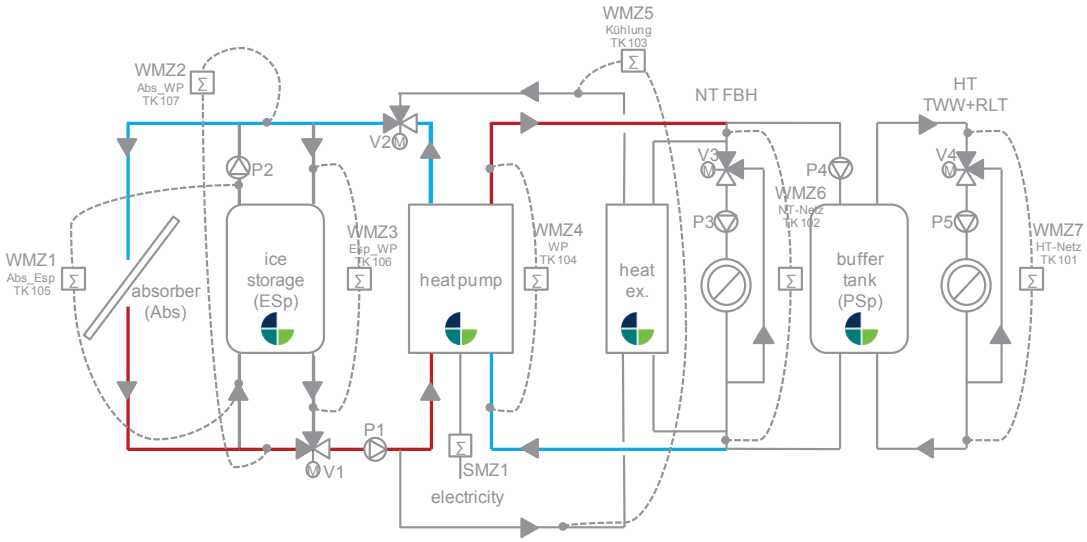

Fig. 4: operating mode BZ2 - source absorber

Operating mode BZ3 – regeneration of the ice storage

While the solar thermal absorber regenerates the ice storage, the WMZ1 must register a mass flow. The activity state of the heat pump can be either one, as it can operate during the ice storage regeneration, but does not need to (Fig. 5, active circuits are coloured).

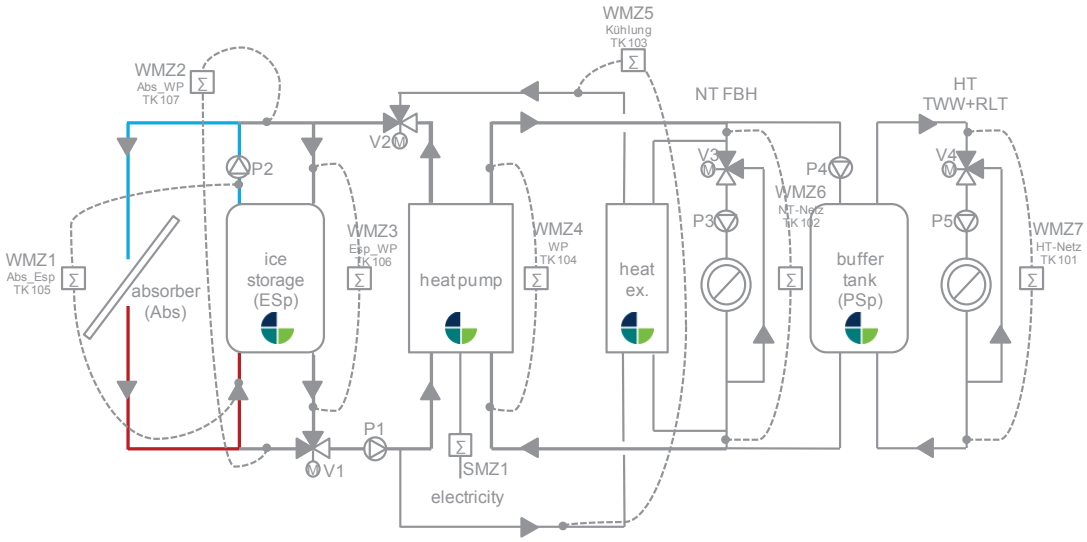

Fig. 5: Operating mode BZ3 – absorber to ice storage

Fig. 6 gives an overview about the operating rules that need to be fulfilled during the four operating modes. With all operating modes and rules defined, the monitoring and evaluation can be executed both during start-up and ordinary operation.

operating rule	BZ0 Off	BZ1 ice storage heat source	BZ2 absorber heat source	BZ3 absorber to ice storage
$\dot{m}_{WMZ1}$	0 kg/h	0 kg/h	0 kg/h	> 0 kg/h
$\dot{m}_{WMZ2}$	0 kg/h	0 kg/h	> 0 kg/h	0 kg/h
$\dot{m}_{WMZ3}$	0 kg/h	> 0 kg/h	0 kg/h	0 kg/h
$\dot{m}_{WMZ4}$	0 kg/h	> 0 kg/h	> 0 kg/h	0 kg/h
E_{SMZ1}	≤ 1,5 kWh	> 1,5 kWh	> 1,5 kWh	-

Fig. 6: overview operating rules

5. Operation and quality control

Only if all operating rules are satisfied, an operating mode (OPM) is being executed correctly. If not all rules are complied with, the operating mode is not active or incorrectly executed. Regulations like a set-point temperature comparison for the ice storage can be implemented to determine, whether an operating mode is supposed to be active.

The rate of correctly working OPM is transformed into the operating quality of the system. The operating quality describes the degree of conformity of the planned and the realised system. The automatic import of operating data from the building management system can be implemented to enable an automated control of the operating modes.

Fig. 7 displays the procedure for evaluating the operating quality. The monitoring data is assessed for every time step in the course of the year. The result of the analysis is stored as Boolean value (true/false, upper part of Fig. 7). The numbers of true and false values are compared to the overall number of assessment steps and form the operating quality (lower part of Fig. 7).

On the basis of a minimum ratio of true values the necessary conformity between planned and real operation can be defined.

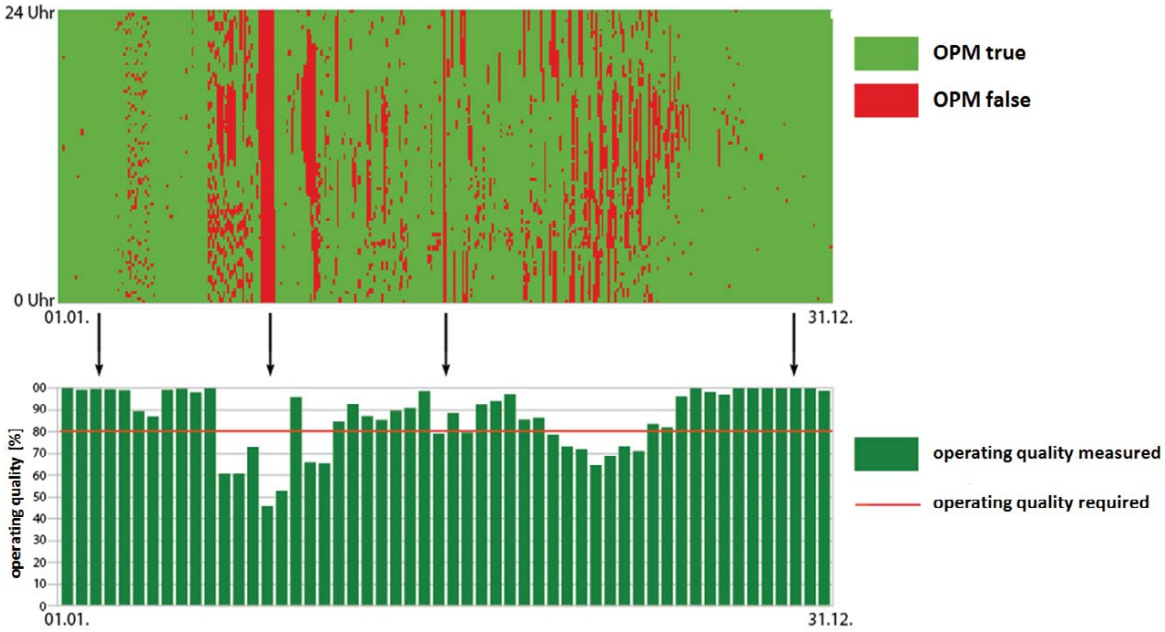

Fig. 7: Operating quality of the system (dummy values)

6. First monitoring results from MFH Riedberg

Measured data from the installed heat meters are available from November 2015 on. The analysis of the active functional specification (Fig. 8) shows that the system has been in OPM 1 (heating from ice storage) for most of the time. It is further visible that planning-conform operation has taken place in the beginning of the monitoring (green dots). From the middle of December on, the planned operation of the heat pump was not met (red dots). Where there is no point, the respective OPM was not active.

The problems in operation related to the heat source are easily visible in the operating quality (Fig. 9).

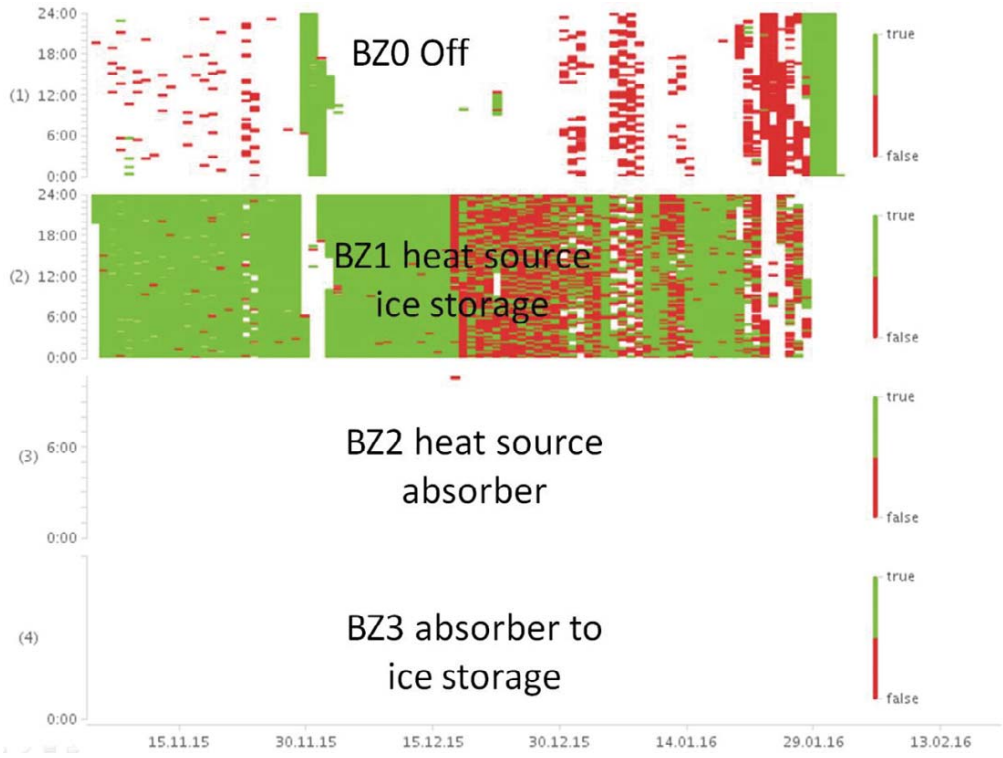

Fig. 8: Evaluation active functional specification - operating modes MFH Riedberg, November 2015 to January 2016

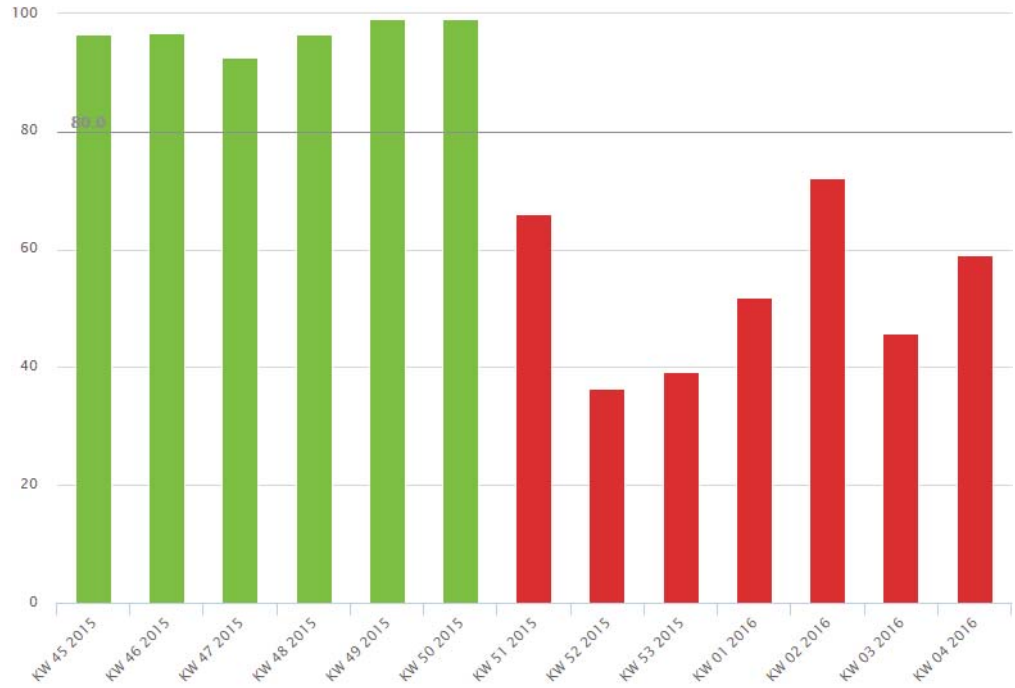

Fig. 9: Evaluation weekly operating quality MFH Riedberg, November 2015 to January 2016

Within the frame of the monitoring the inability of the absorber to deliver thermal power and the optimization need for the hydraulic system, especially regarding the control system, have been detected.

From February 2016 on, the system has been adjusted and altered to solve the problems of the hydraulic system. Among the solutions a buffer storage has been integrated into the low-temperature grid and the controls have been changed accordingly.

In the middle of June 2016 the last changes in the control system have been executed. The assessment of the operating quality shows planning-conformity since then (Fig. 10).

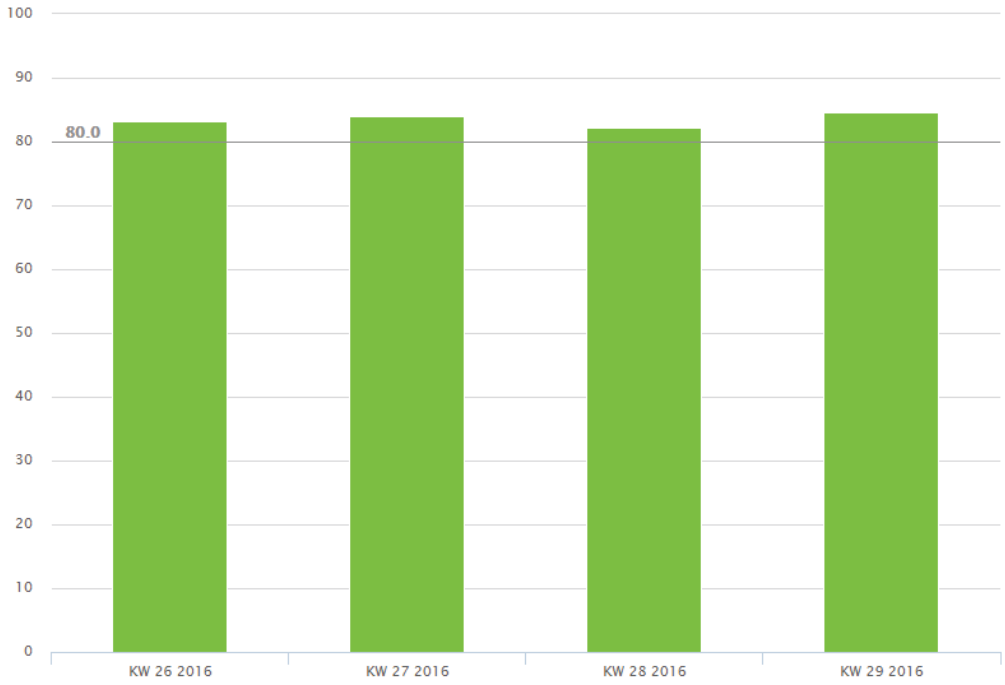

Fig. 10: Evaluation weekly operating quality MFH Riedberg, end of June 2016 end of July 2016

7. Conclusions and outlook

The assessment of the operating quality has made the early and easy detection of operating deviations from the planned design of the system possible. The active functional specification enables the efficient identification of errors. The scope of the detection goes from the broad view to the detail. In the first step the operating quality (Fig. 9) serves as an overview over the accordance to the planning. In case of deviations the operating modes are analyzed in detail. The singular operating rules are being evaluated and the source of trouble identified.

The combination of monitoring and the active functional specification have successfully detected the faulty operation of the heating system (absorber - ice storage - heat pump) and initiated the correction of the system.

First assessments after the reconstruction work show that the system has been in orderly operation since the beginning of the summer 2016. In the further course of the monitoring, the system functions are constantly being scrutinised and optimized.

A full evaluation of the system's performance is not yet possible because system was in irregular operation during the heating period 2015/16.

8. Acknowledgements

The monitoring of the MFH Riedberg is being funded with resources from the research initiative ZukunftBau of the Bundesinstitut für Bau-, Stadt- und Raumforschung (file reference PEH – A3-12 10 01/12.19).

The MFH Riedberg has additionally been included into a field test for the active functional specification (research project GA Spec&Check). This project is funded by the research initiative ZukunftBau of the Bundesinstitut für Bau-, Stadt- und Raumforschung (file reference SWD-10.08.18.7-14.37) as well.

Interested builders can receive further information and the possibility of participation under: https://www.tu-braunschweig.de/igs/forschung/specundchec

ISES International Solar Energy Society

Conference Proceedings

EuroSun 2016

Palma de Mallorca (Spain), 11 - 14 October 2016

Towards a nearly zero-emissions dwelling in Mallorca

Beatriz Rosselló-Batle[1] and Andreu Moià-Pol[1]

1 University of Balearic Islands, Physics department, Mechanical Engineering Area (ME)

Palma de Mallorca (Spain)

Abstract

Concern about climate change and its impact on the environment has become a problem of vital importance nowadays. New regulations have been approved and nearly zero-energy buildings have been defined as a target for the State Members in the European Union (EU). In this study the assessment of a nearly zero-emissions dwelling was shown in the Balearic Islands. The use of a system composed by different renewable energies in the building allowed getting a negative indicator both for primary energy consumption as well as for the CO_2 emissions per year.

Keywords: *Nearly zero-energy buildings, nearly zero-emissions buildings, dwelling, energy consumption, renewable energy.*

1. Introduction

More than 40% of European Union (EU) energy consumption and about 36% of CO_2 emissions comes from the construction sector and services, mainly composed of buildings (Nuij, 2013). New regulations have been approved in order to achieve the Kyoto Protocol compliance. The Energy Performance of Buildings Directive (EPBD) had as final objective the increase of the energy efficiency of buildings in the EU as well as the establishment by Member States of minimum requirements for energy efficiency, periodical inspection of energy systems and the creation of a methodology for the energy certification (The European Parliament and the Council of the European Union, 2002). The EPBD recast included the concept of a nearly zero-energy building (NZEB) as a building with a very high energy performance, in which the low amount of energy required should be covered mainly by energy from renewable sources with a very high level of energy efficiency (The European Parliament and the Council of the European Union, 2010). The Directive established all new buildings to be nearly zero-energy buildings before 2021, and two years earlier in the case of public buildings.

Ferrante and Cascella (2011) presented a study based on the design of a prototype dwelling in Italy. The authors highlighted the fact that zero balance both for energy and CO_2 emissions could be easily obtained in the Mediterranean area. Attia et al. (2012) presented a simulation tool as a support in the design phase of a NZEB in the residential sector in warmer climates. Zeiler and Boxem (2013) assessed the first school designed according to the principles of NZEB in the Netherlands and compared the results obtained with traditional schools. The present study arises from the current need to obtain effective reduction of CO_2 emissions and lower energy consumption patterns. The main objective is to assess the conversion of a conventional dwelling to a nearly zero-emissions dwelling in the Balearic Islands.

2. Methodology

In this study, an assessment to convert a single-family detached house to a nearly zero-emissions dwelling was proposed. For the energy demand assessment the "Unified Tool LIDER-CALENER" (Ministry of Development, 2013) was used. It is one of the official energy certification tools in Spain, and it comes from the unification of the tools LIDER and CALENER (already used in Spain previously) in the same platform. This tool includes a graphical interface for a 3D representation of the building and performs an hourly simulation

Selection and/or peer review under responsibility of Scientific Committee
doi:10.18086/eurosun.2016.01.05 Available at http://proceedings.ises.org

considering a transitional regime, taking into account thermal coupling between adjacent zones and thermal inertia (Instituto para la Diversificación y Ahorro de la Energía (IDAE) y Asociación de Investigación y Cooperación Industrial de Andalucía (AICIA), 2009). The validation of LIDER tool was made through Building Energy Simulation Tests (BESTEST) by the International Energy Agency (IEA) (Instituto para la Diversificación y Ahorro de la Energía (IDAE) y Asociación de Investigación y Cooperación Industrial de Andalucía (AICIA), 2009), where a great number of cases were evaluated under specific conditions and the results were compared with those obtained by other internationally known tools, such as TRNSYS or DOE2. Results were presented in per kWh/m^{2}year (1 kWh=3,6 MJ).

2.1. Case study building

In this study a single-family detached house located in Mallorca with two floors and sloping roofs was used for the assessment. Facades composition is shown in Tab. 1. An image of the building represented in the HU-tool is shown in Fig. 1. The system in the original building was composed by a heat pump air to water (10 kW) for hot water, a heat pump air to water (16 kW) for a multizone water heating system and a direct expansion air conditioning (3 kW) for cooling the living room. As it will be seen in the Results section a new system composed by renewable energies was proposed and evaluated in the building.

Tab. 1: Facades composition in the case study building

Facades composition	U-value (W/(m^{2}K))	Thickness (m)
Cement mortar (1.5 cm)/polyurethane panels (PUR panels) (12 cm)/concrete blocks (24 cm)/plaster(1.5 cm)	0.19	0.39

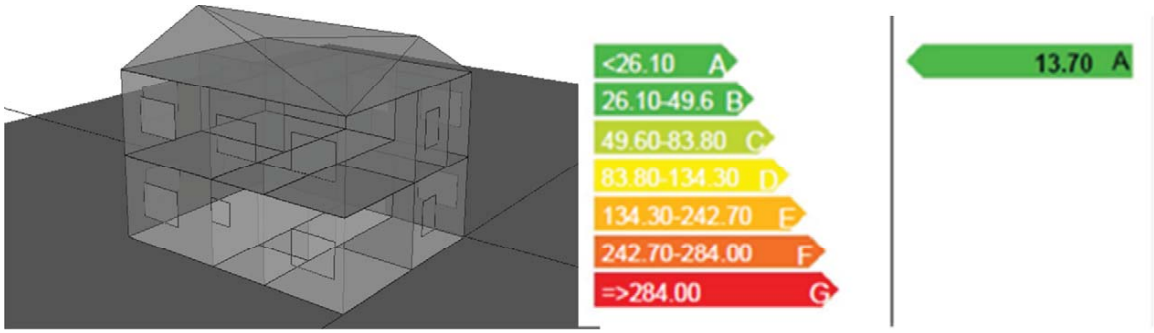

Fig. 1: Case study building represented in the HU-tool

3. Results

In this study a single-family detached house insulated with 12 cm of polyurethane panels and sloping roofs was used as a base case. Final thermal energy demand values obtained for the building were -12,97 kWh/m^{2}year for heating and 14,31 kWh/m^{2}year for cooling, under the limit established by the Spanish Building Technical Code for the Balearic Islands (15 kWh/m^{2}year). Heating and cooling energy demands per month are shown in Fig. 2. Heat losses and gains were evaluated per building component and results are shown in Fig. 3 and Fig. 4.

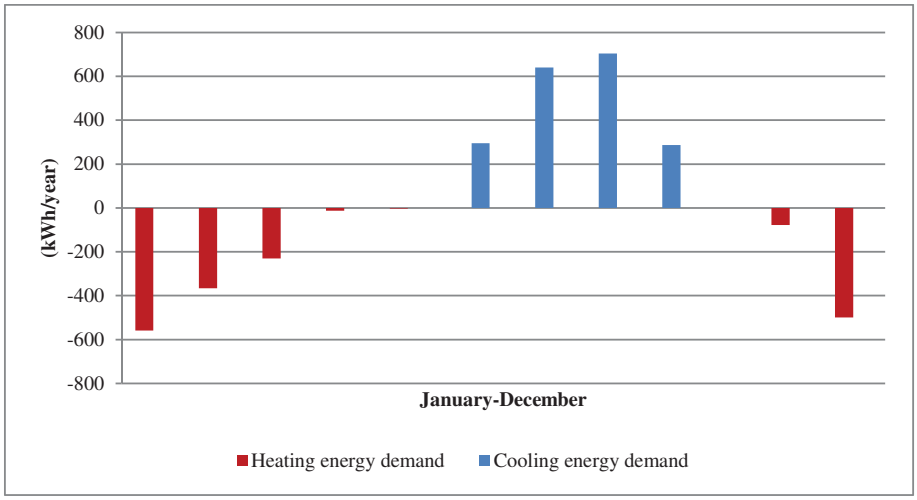

Fig. 2: Heating and cooling energy demands per month

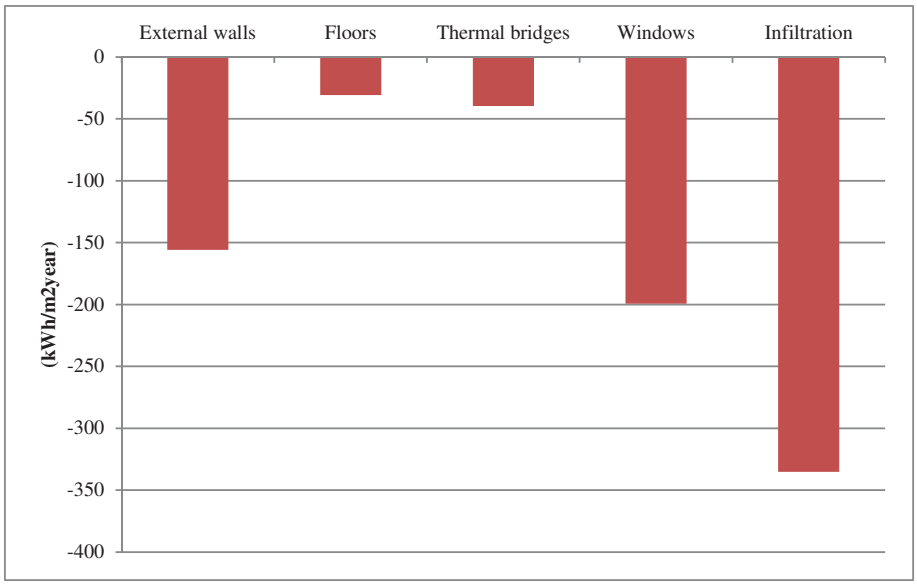

Fig. 3: Heat losses per building component

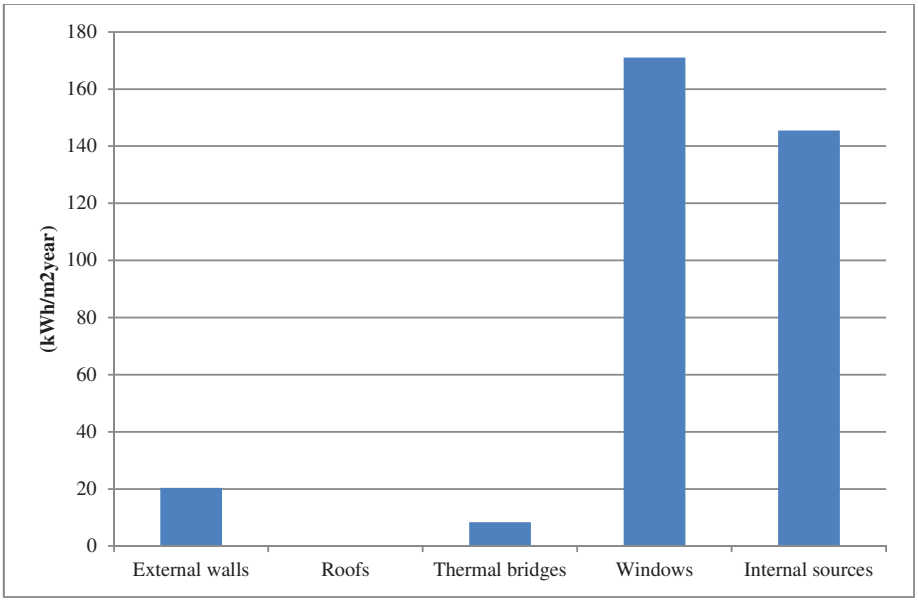

Fig. 2: Heat gains per building component

The results obtained for the base case taking into account the initial energy system of the building were 13,7 $kgCO_2/m^2year$ for the CO_2 emitted and a value of 46,8 kWh/m^2year for the non-renewable primary energy consumption. Specific primary energy consumptions for heating, cooling and hot water and specific CO_2 emissions are shown in Fig. 6.

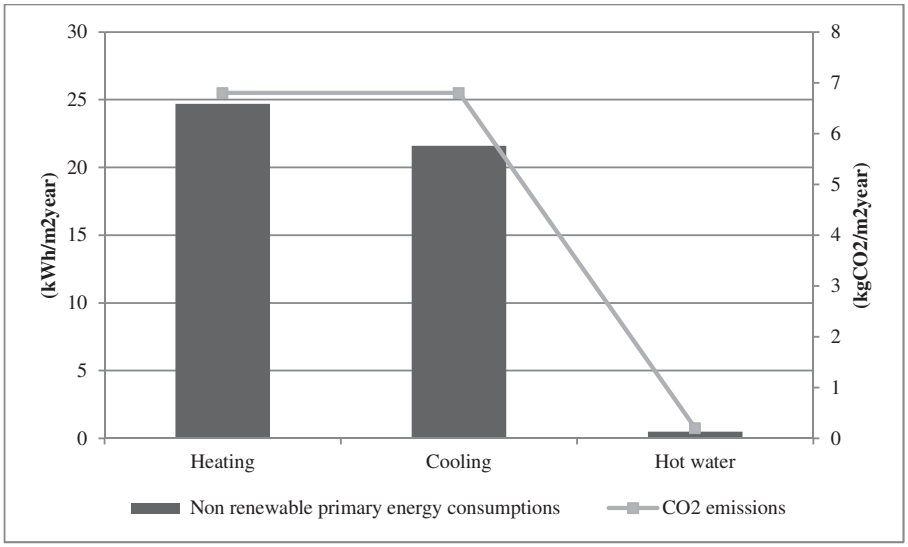

Fig. 6: Non renewable primary energy consumptions and CO_2 emissions for heating, cooling and hot water with the initial energy system

The alternative system proposed for the building was composed by a condensing biomass boiler (10 kW) and a solar water heating (SWH) covering the 95% of demand for hot water, a condensing biomass boiler (20 kW) for heating, a direct expansion air conditioning (3 kW) for cooling a single zone and a photovoltaic installation (1500 kWh/year). An indicator of -1,42 $kgCO_2/m^2year$ for the CO_2 emitted and a value of -1,12 kWh/m^2year for the primary energy consumption were obtained using the Unified Tool LIDER-CALENER. Specific primary energy consumptions for heating, cooling and hot water and specific CO_2 emissions are shown in Fig. 7. Self-consumed power is deducted from the global indicator and it is not shown for specific consumptions.

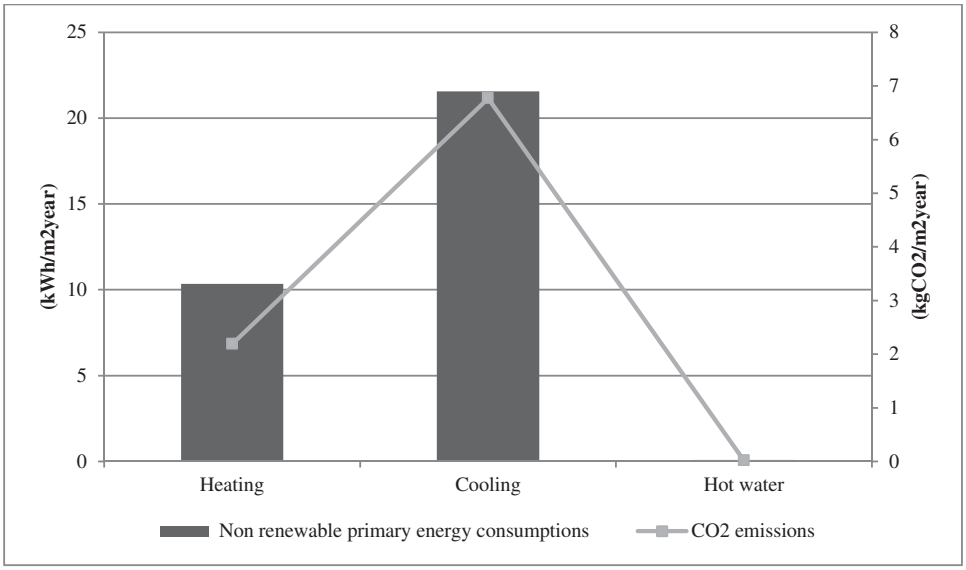

Fig. 7: Non renewable primary energy consumptions and CO_2 emissions for heating, cooling and hot water with the proposed alternative energy system

The label of the house will be A, with a few over cost of the solar thermal system and the PV system, only adding 2 m^2 more to the house and 1 kWp we can have almost zero energy buildings. In Spain the new buildings will be almost zero emissions in 2020, according to the EU law.

4. Conclusions

In this study, the conversion of a single-family detached house to a nearly zero-emissions dwelling was assessed in the Balearic Islands. Final thermal energy demand values obtained for the building were -12,97 kWh/m^2year for heating and 14,31 kWh/m^2year for cooling. It was observed that the greatest heat losses per building component were due to infiltration, windows and external walls. Whereas the greatest heat gains came from windows and internal sources.

The initial energy system for the building was composed by two heat pump air to water and a direct expansion air conditioning for cooling. The results obtained were 13,7 kgCO_2/m^2year for the CO_2 emitted and 46,8 kWh/m^2year for the non-renewable primary energy consumption. An alternative system composed by two biomass boilers, a solar water heating, a direct expansion air conditioning for cooling and a photovoltaic installation was proposed for the building. The results obtained were -1,42 kgCO_2/m^2year for the CO_2 emitted and -1,12 kWh/m^2year for the primary energy consumption.

4. References

Attia, S., Gratia, E., De Herde, A., & Hensen, J. L. M. (2012). Simulation-based decision support tool for early stages of zero-energy building design. *Energy and Buildings*, *49*, 2–15. http://doi.org/10.1016/j.enbuild.2012.01.028

Ferrante, A., & Cascella, M. T. (2011). Zero energy balance and zero on-site CO2 emission housing development in the Mediterranean climate. *Energy and Buildings*, *43*(8), 2002–2010. http://doi.org/10.1016/j.enbuild.2011.04.008

Gustavsson, L., & Joelsson, A. (2010). Life cycle primary energy analysis of residential buildings. *Energy and Buildings*, *42*(2), 210–220. http://doi.org/10.1016/j.enbuild.2009.08.017

Institute of Construction Technology of Catalonia (ITeC). (2015). BEDEC Database. Retrieved from http://itec.cat/nouBedec.c/bedec.aspx

Instituto para la Diversificación y Ahorro de la Energía (IDAE) y Asociación de Investigación y Cooperación Industrial de Andalucía (AICIA). (2009). Condiciones de aceptación de procedimientos alternativos a LIDER y CALENER. Retrieved from http://www.minetur.gob.es/energia/desarrollo/EficienciaEnergetica/CertificacionEnergetica/DocumentosReconocidos/OtrosDocumentos/Calificaci%C3%B3n energ%C3%A9tica. Viviendas/Guia-8_Condiciones_Alternativos.pdf

Ministry of Development. (2013). Unified Tool LIDER-CALENER (HU-Tool). Retrieved from http://www.codigotecnico.org/web/recursos/aplicaciones/contenido/texto_0004.html

Nuij, R. (2013). Intelligent Energy Europe. Retrieved from http://ec.europa.eu/energy/intelligent/files/events/doc/infoday13/parallel/buildings/1-nuij-energy-in-buildings-policy-overview.pdf

The European Parliament and the Council of the European Union. (2002). Directive 2002/91/EC of the European Parliament and of the Council of 16 December 2002 on the energy performance of buildings. Retrieved from http://eur-lex.europa.eu/legal-content/EN/TXT/PDF/?uri=CELEX:32002L0091&from=EN

The European Parliament and the Council of the European Union. (2010). DIRECTIVE 2010/31/EU OF THE EUROPEAN PARLIAMENT AND OF THE COUNCIL of 19 May 2010 on the energy performance of buildings (recast). Retrieved from http://eur-lex.europa.eu/LexUriServ/LexUriServ.do?uri=OJ:L:2010:153:0013:0035:EN:PDF

Zabalza Bribián, I., Aranda Usón, A., & Scarpellini, S. (2009). Life cycle assessment in buildings: State-of-the-art and simplified LCA methodology as a complement for building certification. *Building and Environment*, *44*(12), 2510–2520. http://doi.org/10.1016/j.buildenv.2009.05.001

Zeiler, W., & Boxem, G. (2013). Net-zero energy building schools. *Renewable Energy*, *49*, 282–286. http://doi.org/10.1016/j.renene.2012.01.013

Conference Proceedings

EuroSun 2016
Palma de Mallorca (Spain), 11 - 14 October 2016

Switchable Thermal Insulation for increasing energy efficiency of building façades

Constantin Römer[1], Helmut Weinläder[1], Stephan Weismann[1], Stephan Vidi[1] and Johannes Wachtel[1]

[1] Bavarian Center for Applied Energy Research (ZAE Bayern), Würzburg (Germany)

Abstract

A Switchable Thermal Insulation (STI) for using solar energy in winter was developed and evaluated at a test façade. As opposite to STI developed in previous research which was sealed by expensive and thermally inefficient stainless steel sheets, the new device with a switching function based on hydrogen and getter materials was sealed by high barrier foils. The results show a high energy input of about 67 kWh m^{-2} by using solar energy at the façade during one heating period. With a combination of STI and a massive wall the captured solar heat is transported through the façade with a time offset. Thus, nightly inside wall heating is possible.

Keywords: *building façade, switchable thermal insulation, vacuum insulation panel, hydrogen getters, high barrier foil, wall heating*

1. Introduction

Switchable thermal insulations (STI) based on hydrogen and getter materials were researched at ZAE Bayern in the end of the 90s (Horn et al., 2000; Meister et al., 1997). In the context of this research a demonstrator was built, which showed an excellent performance in using solar energy at building façades. During a heating period (October to April) a building energy input of 88 kWh m^{-2} through the demonstrator was reached by using solar energy (Horn, 2001). The demonstrator shell was realized by stainless steel sheets to avoid gas exchange with the environment. The research was continued in the funded project "Enotec" (Ebert et al., 2014). In this context a demonstrator shell was developed based on high barrier foils to reduce the thermal bridge at the demonstrator edges and to lower the costs of the element in contrast to a stainless steel STI.

2. Functional principle

The developed STI affords the opportunity to switch its thermal conductivity between a highly conductive and an insulating state on demand. Therefor a highly heat-insulated function block consisting of a getter material and an electric heater is placed in an evacuated porous insulation layer which is surrounded by a gas barrier such as a metallic shell. In case of the heat-insulating state of the STI the (cold) getter and hydrogen are ligated chemically. Due to the evacuated state of the porous insulation layer the gaseous thermal conductivity is compensated and the thermal conductivity of the insulation layer material dominates the effective thermal conductivity. In this state the thermal insulation is similar to the thermal insulation of a standard vacuum insulation panel (VIP). To get in a highly conductive state the function block is heated to a fixed temperature by low electric power. Thus, hydrogen is released by the getter and distributes in the porous insulation layer. Hydrogen has a high thermal conductivity about $186 \cdot 10^{-3}$ W m^{-1} K^{-1} and causes a significant rise of the effective thermal conductivity (see Figure 1). As shown in Figure 1 the thermal conductivity in the high-conducting state ($\approx 170 \cdot 10^{-3}$ W m^{-1} K^{-1}) is about 40 times higher than that in the insulating state ($\approx 4 \cdot 10^{-3}$ W m^{-1} K^{-1}) due to the increased hydrogen pressure.

doi:10.18086/eurosun.2016.01.04 Available at http://proceedings.ises.org

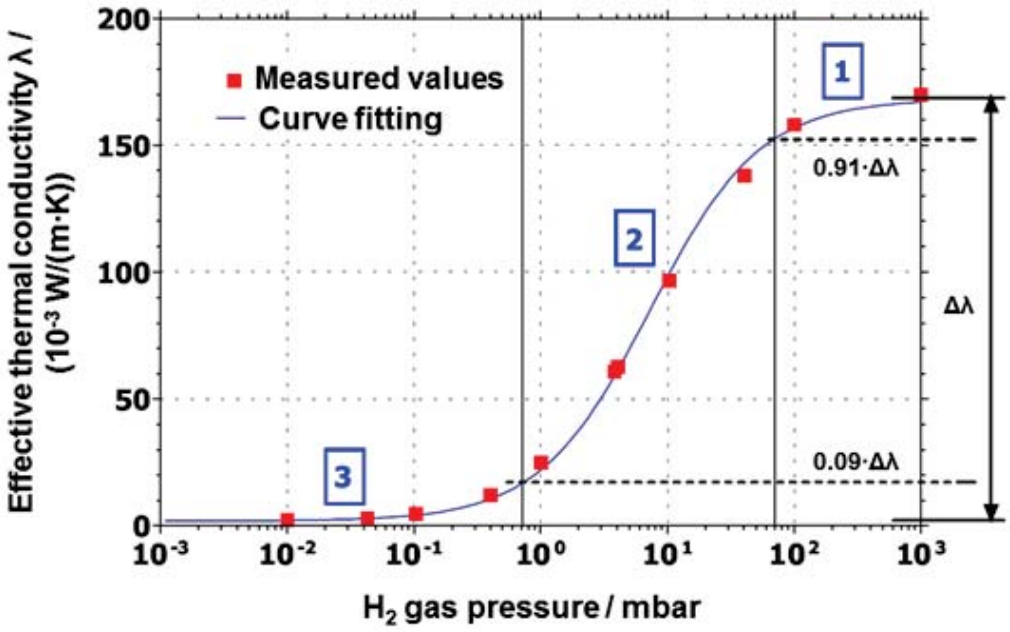

Figure 1: Thermal conductivity for a porous glass fiber system as a function of hydrogen gas pressure (Horn, 2001).

3. Use of solar energy

The STI setup shown in Figure 2 is used for capturing solar energy at the façade during a heating period. For the integrated STI a switching factor of 24.5 between high-conducting and high-insulating state was measured. The sand-lime brick wall behind the STI with a thickness of 0.24 m provides a good thermal storage so that heat is released indoors even during the night or during overcast sky. On the STI a metal sheet was installed to absorb solar radiation on the one hand and to press the STI on the sand-lime brick wall with a metal frame on the other hand. In order to prevent the heated absorber from cooling by outside air convection in winter, a glass panel was installed at a distance of about 40 mm from the absorber and was sealed at the edges. For the heating period 2014/2015 a monitoring of heat flux (inner surface), temperatures and switching states in the STI was initialized.

Figure 2: STI demonstrator with dimensions 80 cm x 50 cm, installed at a massive test façade. Left figure: Real STI demonstrator setup without surrounding insulation and plaster. Right figure: Real STI demonstrator setup after thermal insulating (black coloured) and plastering (white coloured).

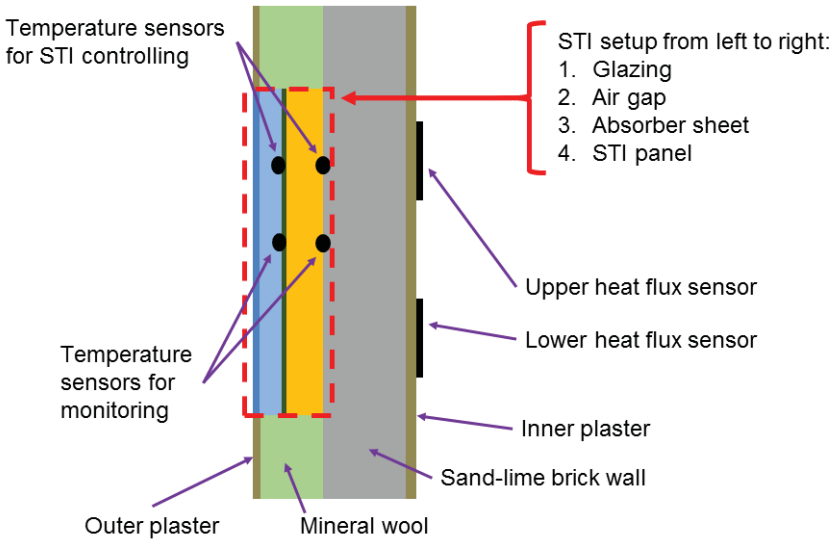

Figure 3: Sketched cross-section of the real STI setup with massive wall and surrounding thermal insulation and plaster.

4. Results

While conventionally insulated façades without STI show a negative energy input (heat losses), the measured heat flux on the test façade resulted in a (positive) energy input of about 67 kWh m^{-2} during the heating period 2014/2015. It should be noted, that the heat flux meters did not sense lateral heat fluxes to the sides, the top and the bottom of the sand-lime brick wall (see figure 3). Thus, the actual energy input probably will be significantly higher. Figure 4 shows this behavior. The one-dimensionally simulated heat flux values represent an ideal behavior of the STI test façade without lateral heat fluxes. For these calculations, a self-developed validated one-dimensional numerical simulation model for heat transfer was applied. The heat equation is therein solved by means of the finite volume method considering the switchability of the STI's thermal conductivity, convection and thermal radiation in the air gap as well as heat conduction (not in air gap), of course.

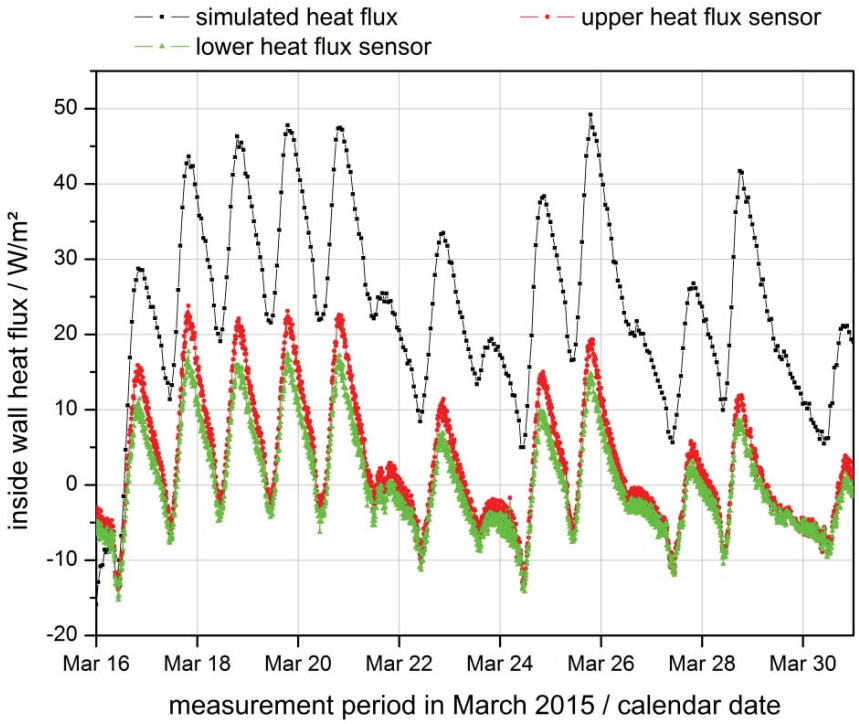

Figure 4: Measured and simulated heat flux of the STI test façade.

Meteorological data such as solar irradiance and air temperature recorded during measurements of the heat flow meters was used as boundary conditions for the simulations. While the simulation data show a very good agreement, regarding the curve progression the measured heat flux is significantly lower. The difference between measured and simulated heat flux mainly is due to already mentioned lateral heat fluxes in the sand-lime brick wall. However, in the one-dimensional simulation model the considered system boundaries are at the edges of the STI setup. Thus, heat is only possible to flow through the area behind the STI setup – in contrast to the real demonstrator setup.

The high thermal capacity of the sand-lime brick wall behind the STI causes a time offset to the heat input into the room. The time offset between absorber temperature peaks and inside wall heat flux peaks in Figure 5 is about 5 to 6 hours and shifts the heat gains into the room to the night hours. The higher the density, specific heat capacity or wall thickness the higher the time offset will be.

For comparison the heat transfer of a conventional façade with the same heat transfer coefficient as the STI setup in heat-insulating state (U = 0.22 W m^{-2} K^{-1}) was numerically simulated in WUFI (Künzel, 1994) for one heating period. Initial and boundary conditions as well as climate data were adapted to measured monitoring data. The simulation revealed an energy input of about -18 kWh m^{-2}. Taking the measured energy input of the STI of about 67 kWh m^{-2} into account the energetic benefit of the STI yields 85 kWh m^{-2}. During the heating period, a small maximum electrical power consumption of 1.5 kWh m^{-2} is necessary to switch the STI.

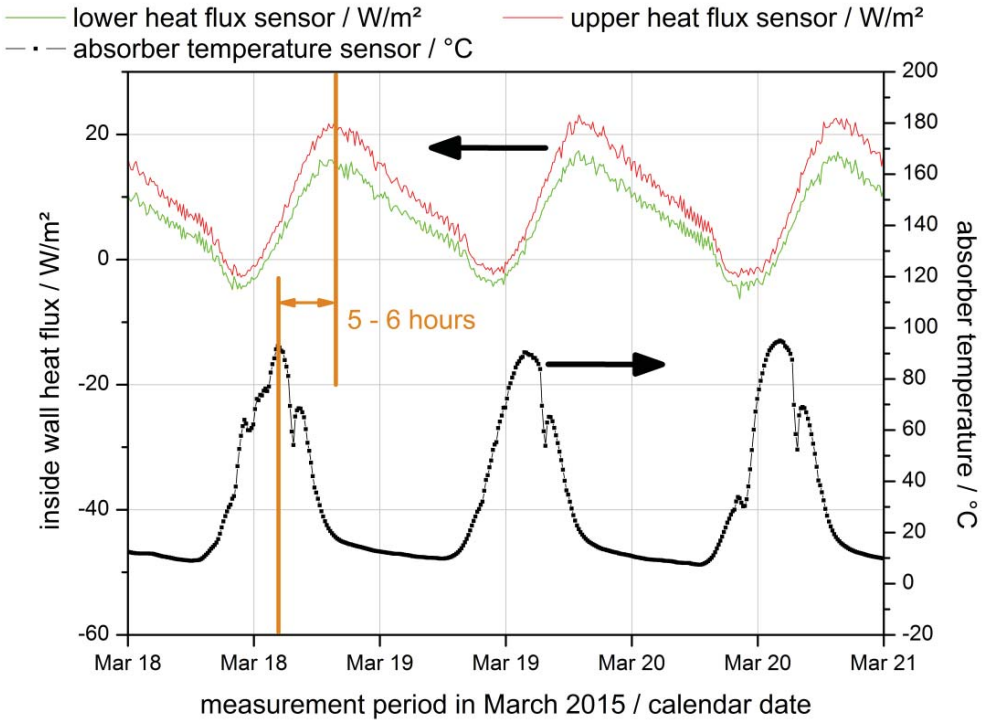

Figure 5: Time offset between absorber temperature peaks and inside wall heat flux peaks due to the thermal capacity of the sand-lime brick wall behind the STI.

5. Outlook

To raise the energy input of the STI during a heating period the thermal conductivity in the high-conducting state – respectively the switching factor – has to be increased by optimizing the function block. The getter material amount in the STI needs to be adapted to an ideal hydrogen filling so that costs for the expensive getter material are minimized while a high thermal conductivity is assured in the high-conducting state. Moreover, the STI can be used as a nightly summer cooling device by using low outdoor temperatures in combination with the high-conducting state.

6. Acknowledgement

This research was carried out as part of the project “Enotec” and was funded by the German Federal Ministry for Economic Affairs and Energy by resolution of the German Federal Parliament. We thank Saint Gobain ISOVER G+H and va-Q-tec AG for their support.

7. References

Ebert, H.-P., et al., 2014. Materialien und Komponenten zur energetischen Optimierung von Feuchte, Licht und Wärme in Gebäuden, EnOB-Symposium proceedings.

Horn, R., et al., 2000. Switchable thermal insulation: results of computer simulations for optimization in building applications, High Temperatures - High Pressures 32, 669-675.

Horn, R., 2001. Entwicklung und Untersuchung einer schaltbaren Wärmedämmung zur Solarenergienutzung, Diss., Würzburg.

Künzel, H., 1994. Verfahren zur ein- und zweidimensionalen Berechnung des gekoppelten Wärme- und Feuchtetransports in Bauteilen mit einfachen Kennwerten, Diss., Stuttgart.

Meister, M., et al., 1997. Switchable Thermal Insulation for Solar Heating, 24th International Thermal Conductivity Conference proceedings.

Conference Proceedings

EuroSun 2016
Palma de Mallorca (Spain), 11 - 14 October 2016

Environmental and Economical Assessment for Net Zero Energy Data Centres

Jaume Salom[1], Eduard Oró[1], Albert Garcia[1], Verena Rudolf[2], Nirendra Lal Shrestha[2], Thorsten Urbaneck[2], Mieke Timmerman[3], Óscar Camara[4], Angel Càrrera[4]

[1] IREC – Catalonia Institute for Energy Research, Sant Adrià de Besòs – Barcelona (Spain)

[2] Technische Universität Chemnitz, Chemnitz (Germany)

[3] Deerns, Rijswijk (The Netherlands)

[4] AIGUASOL, Barcelona (Spain)

Abstract

During the last years, the rapid increase of cloud computing, high-powered computing and the vast growth in internet use have aroused the interest in energy consumption and carbon footprint of data centres. The paper presents the results of an environmental and economic analysis to explore the path towards Net Zero Energy data centres. The economic and environmental assessment is presented for different data centre sizes (120 and 400 kW_{IT} of design IT power) and climate locations (Barcelona and Stockholm). It is the result of detailed TRNSYS simulations which have been developed in the framework of the European project RenewIT. Total cost of ownership and non-renewable primary energy consumption are used as main metrics to evaluate the performance of different energy concepts, energy efficiency strategies and the implementation of renewables, in particular PV and wind energy. Parametric analyses are presented to evaluate the influence of some of the main sizing variables for each concept.

Keywords: *Net Zero Energy Data Centres, renewable energy, energy efficiency, cost-benefit analysis*

1. Introduction

Data centres are unique buildings or dedicated spaces in other buildings which houses information technology (IT) rooms. The IT room is an environmentally controlled space that houses equipment and cabling directly related to computing and telecommunication systems which generate a considerable amount of heat in a small area. In the last years, the total energy demand of data centres has experienced a dramatic increase. This is why data centre industry and researchers are undertaking efforts to implement energy efficiency measures and to integrate renewable energy into its portfolio to overcome energy dependence and to reduce operational costs and CO_2 emissions (Salom, 2016). Oró et al. (2014) presented a comprehensive overview of the current data centre infrastructure and summarized a number of currently available energy efficiency strategies and renewable energy integration into the data centre industry together with the recent efforts for its characterization using numerical models. Shuja et al. (2016) presented a survey of case studies and enabling technologies to make cloud data centres more sustainable. In the framework of the European funded RenewIT project (Salom, 2016) holistic and dynamic energy models have been developed in TRNSYS (TRNSYS, 2012) to characterize the overall energy performance and the life-cycle economic impact of data centres after the implementation of energy efficiency strategies and renewables. This paper presents the economic and environmental results for different energy concepts as function of the data centre size (120 and 400 kW_{IT} of design IT power, being IT power the electrical power that must be supplied to the IT devices to work) and climate location in Europe (Barcelona and Stockholm).

doi:10.18086/eurosun.2016.01.19 Available at http://proceedings.ises.org

2. Methodology

Selected energy concepts which implement cooling and power supply of data centres with renewable energy systems are evaluated using detailed TRNSYS simulation. A set of TRNSYS projects to model the energy behaviour and compute the investment and running costs of different data centre concepts have been built in the framework of the RenewIT project. The different models are based on the combination of subsystems of a data centre facility using TRNSYS' macros capabilities and they have been run with a 15-min time step to derive the results presented in the current paper. Due to limited space, only a brief description of the modelled concepts (Shrestha et al., 2015; Rudolf et al., 2016) is presented in section 3 which have been validated with real life case studies (Salom et al., 2015; Oró et al, 2015) and lead to the development of the RenewIT tool (2016) (Garcia et al., 2016).

To evaluate the economic and the environmental impact of the use of advanced energy solutions in data centre portfolio different metrics have been evaluated. The total cost of ownership (TCO) is the main metric to evaluate the economic benefits of an applied solution. The TCO is the addition of the initial investment costs (CAPEX), the operational expenditures (OPEX) and the replacement cost minus the residual value of components, based on the methodology proposed by CEN (2008). The TCO is used to assess the true total costs of building, owning, and operating a data centre energy facility during a certain amount of years. In the present study, the assessment period is equal to the components life time span which is 15 years; therefore the cost of replacement of the components is neglected in the economics calculations and the residual value is zero. The OPEX is the net present value of the costs for running a data centre facility. It includes the energy costs ($OPEX_{EC}$), both electricity and/or other energy carrier costs as well as the costs derived from the data centre water consumption, the maintenance costs ($OPEX_{MC}$) and the environmental costs ($OPEX_{CO2}$), i.e. the cost of the CO_2 emissions. The energy costs are calculated for each energy carrier and prices are temporary dependent.

$$TCO = CAPEX + OPEX \quad \text{(eq. 1)}$$

$$OPEX = OPEX_{EC} + OPEX_{MC} + OPEX_{CO2} \quad \text{(eq. 2)}$$

The annual non-renewable primary energy consumption of the data centre (PE_{nren}) is used as main metric to evaluate the environmental performance although other metrics are widely used in the industry to evaluate the energy efficiency measures such as the well-known power usage effectiveness (PUE) or the data centre water consumption and CO_2 emissions. The non-renewable primary energy means energy from non-renewable sources which has not undergone any conversion or transformation process. The calculation of PE_{nren} is based on equations 3 and 4 (being equation 4 the evaluation of Pe_{nren} at each time step) and the energy fluxes through the data centre boundary depicted in Fig. 1, where both delivered and exported energy carriers are weighted using the non-renewable primary energy weighting factors.

$$PE_{nren} = \int_{year} Pe_{nren}(t) \cdot \mathrm{dt} \quad \text{(eq. 3)}$$

$$Pe_{nren} = \left[(e_{del,el} \cdot w_{del,nren,el}) + (e_{del,fuel} \cdot w_{del,nren.fuel}) + (e_{del,Dheat} \cdot w_{del,nren,Dheat}) + (e_{del,DCool} \cdot w_{del,nren,DCool}) \right] - \left[(e_{exp,el} \cdot w_{exp,nren,el}) + (e_{exp,heat} \cdot w_{exp,nren,heat}) \right] \quad \text{(eq. 4)}$$

where $e_{del,i}$ and $e_{exp,i}$ are the energy entering to and exported from the data centre boundary respectively for energy carrier i; $w_{del,nren,i}$ and $w_{exp,nren,i}$ are the non-renewable weighting (or conversion factor) for each energy carrier delivered or exported. About energy carriers, *el* means electricity; *fuel* can be natural gas, biogas or biomass; *Dheat* and *DCool* means thermal energy coming for a district heating and cooling infrastructure and *heat* means exported heat to a district heating or surrounding buildings. The renewable energy ratio (RER_{EP}), equation 5, is the metric that allows calculating the share of renewable energy use in a data centre. The renewable energy ratio is calculated relative to the total primary energy used in the data centre facility.

$$RER_{EP} = \frac{\sum_i e_{ren,i} + \sum_i [(w_{del,tot,i} - w_{del,nren,i}) \cdot e_{del,i}]}{\sum_i e_{ren,i} + \sum_i (w_{del,tot,i} \cdot e_{del,i}) - \sum_i [(w_{exp,tot,i} \cdot e_{exp,i})} \quad \text{(eq. 5)}$$

Notice that in order to compare the results between data centres of different size, both, PE_{nren} and TCO are normalized by the design IT power capacity of the facility [kW_{IT}]. Therefore, normalized PE_{nren} is expressed in [$kW \cdot h_{PE,nren}/kW_{IT} \cdot year$] while normalized TCO is expressed in [€/kW_{IT}]

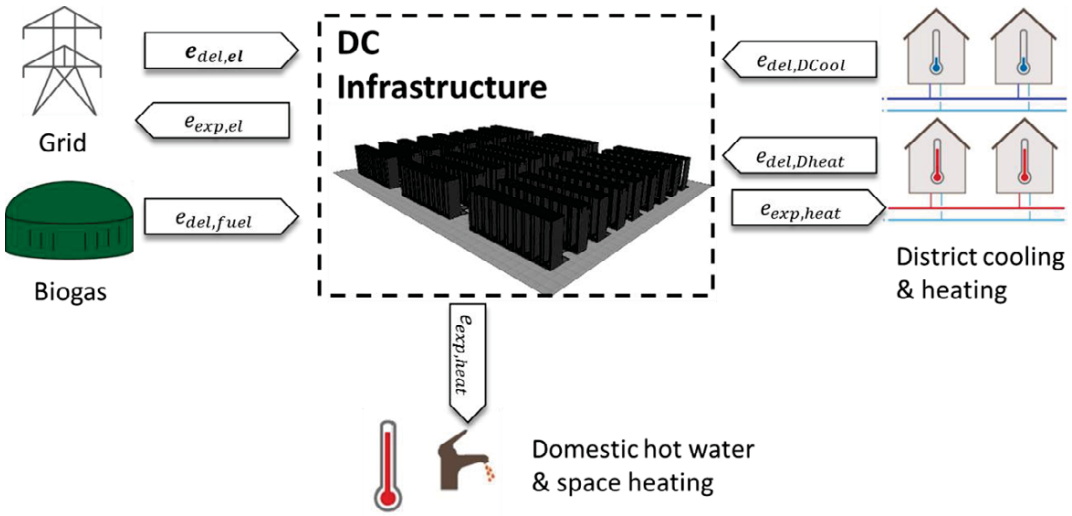

Fig. 1: Delivered and exported energy fluxes in a data centre facility

3. Concepts and scenarios

The present section describes briefly the different energy concepts, which have been simulated as well as the main characteristics of the four scenarios analysed: two sizes in two locations.

The concept 1, shown schematically in Fig. 2, is based on a conventional system where vapour-compression chillers along with dry coolers are used to produce cooling energy when it is required. Fig. 2 depicts the thermal and electric scheme of this concept. The electrical power required to drive the chiller and to run the IT hardware can be generated by a photovoltaic system and/or wind turbines installed in the building footprint; additional power is purchased from the grid. In winter, indirect air free cooling can be activated for efficient cooling supply to the data centre.

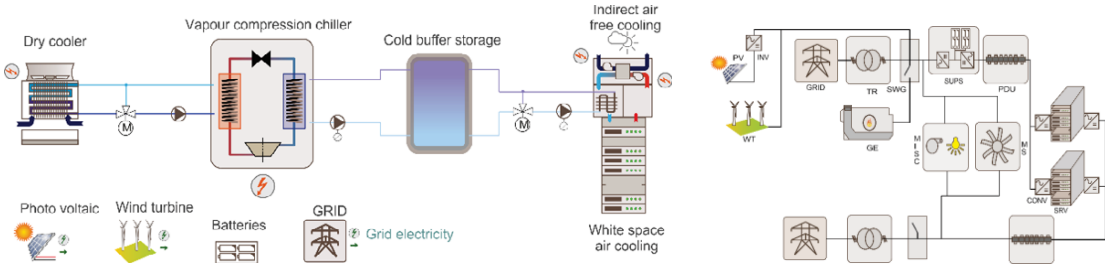

Fig. 2: Thermal scheme (left) and electric scheme (right) of concept 1 (conventional data centre concept with on-site PV and/or wind power systems)

Concept 2 is aimed for those data centres with liquid cooled servers. Depending on the technology used and implemented, part of the infrastructure will demand air cooling while other liquid cooling. Therefore, in this solution, chilled water for air-cooling is supplied by a district cooling system while heat from direct liquid cooling is reused for space heating and domestic hot water by means of a heat pump. A dry cooler could be used if there is no heat demand. Fig. 3 shows the thermal and electric scheme of this concept. Notice that during summer, chilled water from the district cooling system is used to cool the air flowing into the data centre but during winter, mostly indirect air free cooling can be conducted. With the objective to increase the use of renewables in the facility, this concept makes sense if the district heating and cooling system is fed by renewables at least to some extent. This is represented by the value used in the simulations of $w_{del,nren,DCool}$, which is 0.6, with the hypothesis of a district cooling system based on a biogas CHP system with absorption chillers.

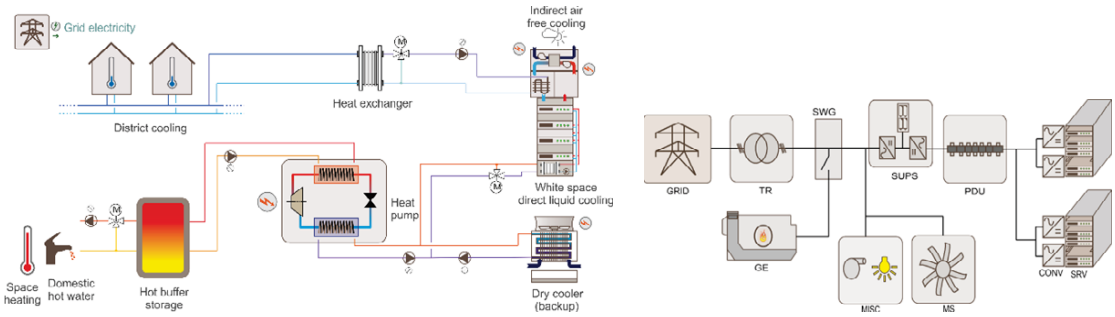

Fig.3: Thermal scheme (left) and electric scheme (right) of concept 2 (District cooling and heat reuse)

In concept 3, wet cooling towers (without the use of mechanical chillers) are used to produce cooling energy. Fig. 4 depicts the thermal and electric scheme of this concept. In winter, direct air free cooling is performed for efficient cooling supply to the data centre. When the evaporative free cooling is not possible, backup vapour-compression chillers along with the cooling towers are used. The electrical power required to drive the cooling towers and the backup chillers are purchased from the national grid.

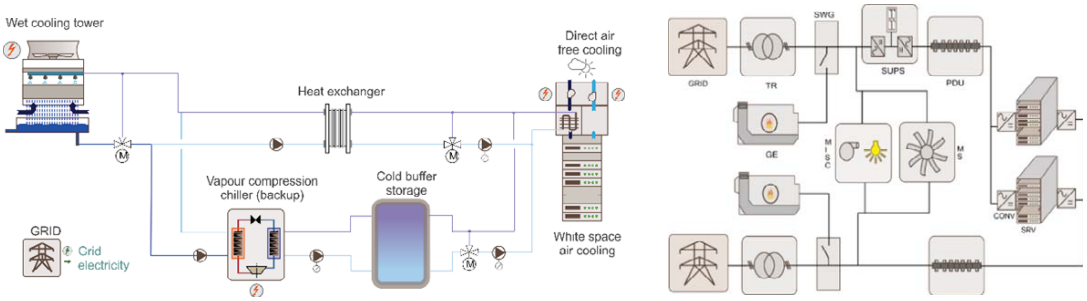

Fig. 4: Thermal scheme (left) and electric scheme (right) of concept 3 (Grid-fed wet cooling tower without chiller)

In concept 4, a biogas-fed fuel cell is applied for generating both power and heat, which is used for driving an absorption chiller during summer which produces cool (Fig. 5). In winter, indirect air free cooling avoids the operation of the chillers if it is activated. Then, the waste heat from the fuel cell can be recovered for space heating or might also be dissipated by a wet cooling tower. Because of the high temperature and pressure of the hot water, shell and tube heat exchanger are used for transferring the heat between the cooling tower and the fuel cell hot water circuit.

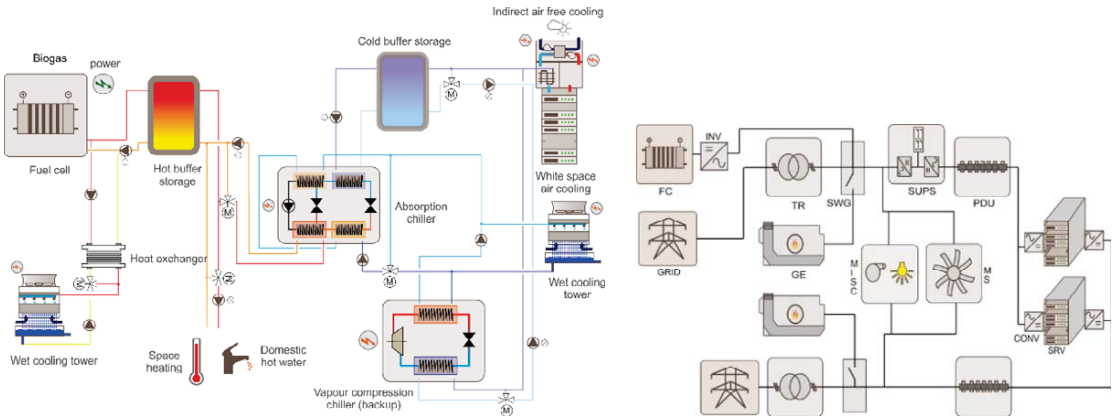

Fig. 5: Thermal scheme (left) and electric scheme (right) of concept 4 (Biogas fuel cell with absorption chiller)

The concept 5 shown schematically in Fig. 6 is based on biogas-fed tri-generation by means of a reciprocating engine combined heat and power (CHP) plant. The heat from this plant is used for driving a single-effect absorption chiller during summer and supplying space heating for offices or buildings close to the data centre during winter. Additionally, indirect air free cooling is implemented for efficient cooling

supply to the data centre especially during winter. Then, the heat from the CHP plant is used for space heating and producing domestic hot water if required.

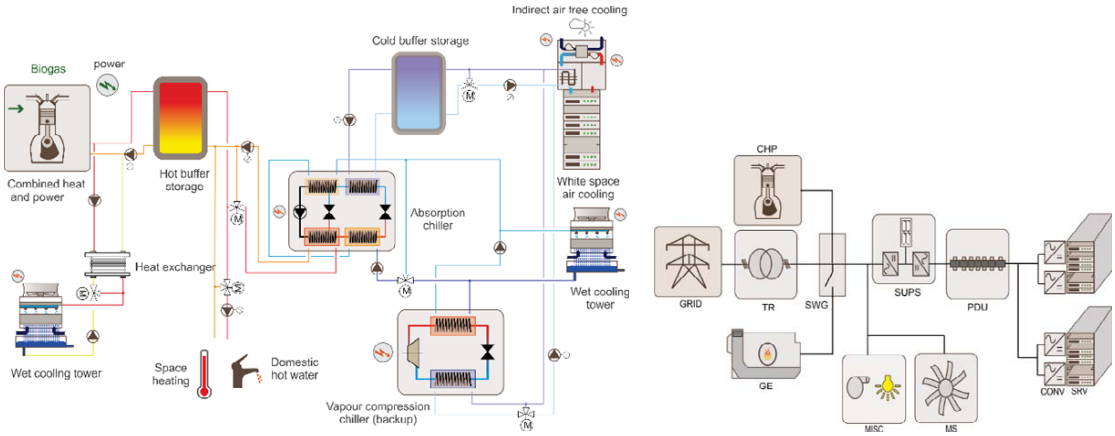

Fig. 6: Thermal scheme (left) and electric scheme (right) of concept 5 (Reciprocating engine CHP with absorption chiller)

Two different IT power capacities (120 kW and 400 kW) are analysed for each of the locations (Barcelona and Stockholm). In each of the scenarios, the main other parameters such as the rack density, the occupancy ratio (1.0 meaning fully occupied), the safety margin factor (1.0 meaning no safety margin), and the load profile are fixed as shown in Table 1. Safety margin factor indicates how much the data centre facility is oversized referred to the expected maximum IT Power, meaning 0.8 that the facility is 25% oversized. The white space area depends of the nominal IT Power capacity and the rack density and it was estimated using average ratios in the industry to determine the amount of floor occupied by a rack. In the present study the IT load profile used is a combination of the most standard/homogeneous IT workload profiles: Web, HPC and Data. In particular, the workload profile used is composed of 35% HPC, 30% Data and 35% Web based on Carbó et al. (2016). Table 2 shows some of the basic parameters used to define the sizing of the main elements in the different energy concepts. These parameters are used in the base cases scenarios for each of the concepts.

Table 1: Data Centre Scenarios

		Name of the scenarios			
Parameter	**Unit**	**BCN-120**	**BCN-400**	**STO-120**	**STO-400**
Location	[-]	Barcelona	Barcelona	Stockholm	Stockholm
IT power capacity	[kW]	120	400	120	400
Rack density	[kW/rack]	4	4	4	4
Occupancy ratio	[-]	1	1	1	1
Safety margin factor	[-]	0.8	0.8	0.8	0.8
White space area	[m^2]	90	300	90	300
IT Load profile	[-]	Mixed	Mixed	Mixed	Mixed
Average electricity price	[€/kW·h_{el}]	0.10	0.10	0.11	0.11
Biogas price	[€/kW·h_{biogas}]	0.08	0.08	0.08	0.08
District cooling price	[€/kW·h_{DCool}]	0.035	0.035	0.035	0.035
Exported heat price	[€/kW·h_{heat}]	0.025	0.025	0.025	0.025
CO_2 price	[€/tCO_2]	8.99	8.99	8.99	8.99
$w_{del,nren,el}$ (average)	[kW·h_{PE}/kW·h_{el}]	1.83	1.83	1.30	1.30
$w_{del,nren.biogas}$	[kW·h_{PE}/kW·h_{biogas}]	0.5	0.5	0.5	0.5
$w_{del,nren,DCool}$	[kW·h_{PE}/kW·h_{DCool}]	0.6	0.6	0.6	0.6
$w_{exp,nren,heat}$	[kW·h_{PE}/kW·h_{heat}]	0.7	0.7	0.7	0.7

Table 2: Specific assumptions for the investigated concepts. Base case scenarios

#	Description	Basic parameters
1	Vapour compression chillers with dry cooler. Additional on-site PV/Wind power system can be added	VCCH Nominal power • 180 kW (120 kW_{IT}) • 600 kW (400 kW_{IT})
2	District cooling and heat reuse	Heat reuse ratio = 1.0; Efficiency of liquid cooling = 0.65; Ratio of heat pump cooling power and max. liquid cooling demand = 0.50
3	Wet cooling tower	Wet cooling tower nominal power: • 225 kW (120 kW_{IT}) • 750 kW (400 kW_{IT})
4	Biogas fuel cell and absorption chiller	Heat reuse ratio = 1.0; Ratio of absorption chiller size related to the total cooling power of data centre = 0.3; Ratio of fuel cell size related to absorption chiller size = 1
5	Reciprocating engine CHP with biogas	Heat reuse ratio = 1.0; Ratio of absorption chiller size related to the total cooling power of data centre = 0.3; Ratio of biogas engine size related to absorption chiller size = 1

The simulation models developed allow the introduction of a set of energy efficiency measures individually or combined. The energy efficiency strategies are technical solutions that can be applied in almost all the data centres and combined with any system to supply cooling and power with or without renewable energy sources (RES). Therefore, first the strategies that allow to reduce the load demand as much as possible have been analysed before studying the use of the renewable resources available in the data centre's location. Further details about the energy efficiency measures can be found in Shrestha et al. (2015) which can be grouped in several categories:

- Advanced measures for building design. The building design may affect the cooling demand of the data centre.
- Advanced measures for electrical supply. Some well-known strategies are modular UPS and bypassed UPS which achieve a reduction of electrical losses in the power distribution lines. In the results presented in this paper, modular UPS have been applied when energy efficiency measures are mentioned.
- Advanced measures for cooling supply. These measures include the use of free cooling, hot/cold aisle containment for a better air management, variable air flow and the increase of allowable IT working temperatures. Using highly energy efficient components, in particular vapour compression chillers, can also lead to a significant reduction of the total energy demand.
- Advanced measures for IT management. Consolidation aims to concentrate IT workloads in a minimum number of servers to maintain the inactive servers in idle state. Then also those servers in idle state can be turned off. Finally, IT scheduling aims to move IT jobs according to the availability if RES when it is possible.

4. Results and discussion

4.1. Concepts comparison and impact of energy efficiency measures

Figure 6 presents the results of the different concepts proposed for the four scenarios analysed. In the same graph the results for each of the concepts applying the complete set of energy efficiency measures are presented and compared with the results of the base case where none of these energy efficiency measures are applied. Normalized TCO and normalized PE_{nren} are presented in Fig.6-left for Barcelona and in Fig. 6-right for Stockholm.

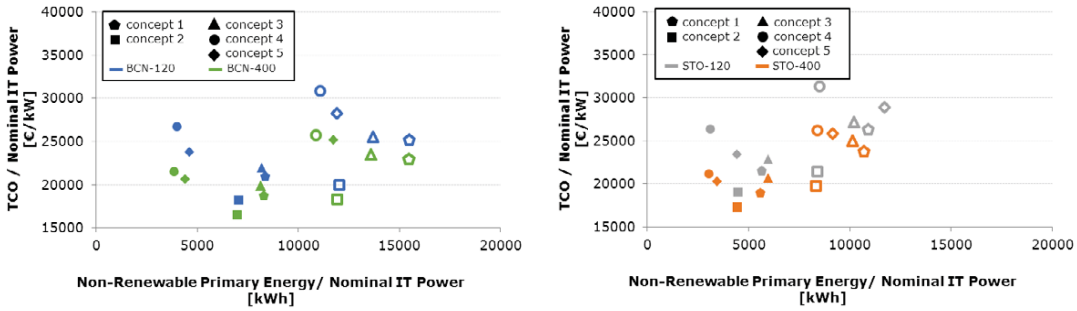

Fig. 6: Normalized TCO vs. normalized PE_{nren} for the location of Barcelona (left graph) and Stockholm (right graph). Results of no applying energy efficiency measures (unfilled shapes) and applying energy efficiency measures (filled shapes) are shown for all the concepts.

Analysing the influence of different sizes of the data centre for each of the concepts, the results show that the normalized PE_{nren} is similar for each concept independently of the size but there exists significant differences on the data centre cost. On average building and operating a data centre of 400 kW compared to one of 120 kW costs 13% less when energy efficiency measures are applied and 11% less for the base cases.

Talking about costs, one can observe that for the same concepts and the same sizes there are no significant differences between operating a data centre in Barcelona or in Stockholm under the hypothesis used in this study. TCO costs are mainly driven by the sizes of the main elements and labour costs of building a data centre to determine the CAPEX (which is not influenced by the location since average European prices have been used) and for the energy prices that influence the OPEX (which differences come from the differences in the electricity prices). The average difference of TCO between having a data centre in Stockholm or in Barcelona is 3%. However, the two locations present significant differences in the absolute values of PE_{nren} between the locations. As PE_{nren} considers the amount of non-renewable primary energy in the electricity network through the appropriate weighting factors there is a difference between the locations as well as in the influence of other climatic conditions: for example there are more hours of free cooling available in Stockholm than in Barcelona. Table 3 shows the results for concept 1 and concept 4, where differences between locations in normalized PE_{nren} are reduced because concept 4 is mainly based on biogas which has the same conversion factor for the two locations.

Table 3: Normalized PE_{nren} consumption [$kW \cdot h_{PE,nren}/kW_{IT} \cdot year$]

	BCN-400	STO-400
Concept 1- Conventional system: VCCH with dry coolers		
Without energy efficiency measures	15 314	10 711
With energy efficiency measures	8 194	5 541
Concept 4 - Biogas fuel cell with absorption chiller		
Without energy efficiency measures	10 884	8 415
With energy efficiency measures	3 846	3 033

For all the concepts and the locations, there is a significant benefit of applying as much energy efficiency measures as possible which will produce savings in the total costs and in the primary energy consumption. IT management strategies are the most beneficial ones, together with some measures which allow increasing the number of free-cooling hours or improving the efficiency in the electrical distribution. For the case studies presented here the impact of applying energy efficiency measures are 50% (in Barcelona) and 52% (in Stockholm) of reduction on PE_{nren} as well as 15% (Barcelona) and 17% (Stockholm) of TCO savings.

According to the results of the current study operating a conventional data centre (concept 1) without renewables can cost around 24450 €/kW_{IT} (± 7%) and consuming about 15383 $kW \cdot h_{PE,nren}/kW_{IT} \cdot year$ (± 0.5%) in Barcelona and 10750 $kW \cdot h_{PE,nren}/kW_{IT}$ (± 0.4%) in Stockholm. Although, it was commented that a significant reduction of TCO and PE_{nren} is possible applying different energy efficiency strategies, a reduction of primary energy resources is possible with different concepts to run a data centre. Among the ones presented in section 3, the concept 4 based on biogas fuel-cells gives the best results in terms of PE_{nren} reduction although it is an expensive concept compared with a conventional data centre. Having a CHP with

a biogas engine, concept 5, gives also promising PE_{nren} savings but is less expensive than concept 4 although still having TCO higher than a conventional data centre. Both concepts 4 and 5 rely also on the availability of biogas as local and/or imported resource. The most cost effective concept, i.e. the one that combines more PE_{nren} and TCO savings, is concept 2 which connects the data centre to a district cooling system and heat from the data centre can be used for heating purposes. The reduction of TCO can reach up to 21% and the PE savings up to 22% when no energy efficiency measures are applied. Concepts 2, 4 and 5 rely on a 100% reuse of the heat produced by the facility. Finally, the implementation of concept 3 based on wet cooling towers show slightly higher economic figures than the conventional case and moderate PE savings compared to other concepts which also dependent on the location and if free-cooling strategies have been applied.

4.2. Analysis of concept 1 adding on-site renewable energy systems

Fig. 7 depicts graphically the results of applying on-site renewable power systems to a conventional data centre: PV and wind turbines systems. On one hand, different sizes of on-site PV systems, which are characterized by their PV peak power, have been simulated. For the scenarios of 120 kW_{IT} and 400 kW_{IT}, PV systems are varied from 0 to 50 kW_p and from 0 to 100 kW_p, respectively (see Table 4). PV simulation which is integrated as part of the overall TRNSYS data centre models neglects the shadows effects of surrounding buildings and the own shadows of a large flat roof mounted PV field. The PV field is considered oriented south with an inclination slope of 32.2º for Barcelona and 44.6º for Stockholm. On the other hand, the use of small wind power systems has also been studied. For the 120 kW_{IT} data centre a unique 50 kW rated power wind turbine (Aeolos, 2015) is considered; while, for the 400 kW_{IT} data centre, the impact of having one and two identical wind turbines has been calculated.

Table 4: Specific assumptions of on-site PV and wind power systems for the investigated concept 1

Parameter	Unit	BCN-120 / STO-120	BCN-400 / STO-400
Total PV peak power	[kWp]	0, 10, 20, 30, 40, 50	50, 60, 70, 80, 90, 100
Total Wind rated power	[kW]	0, 50	0, 50, 100

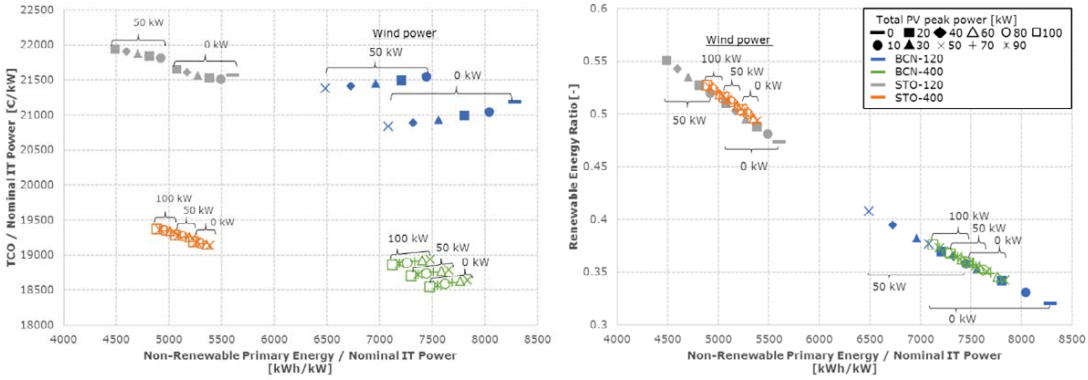

Fig. 7: Normalized TCO (left) and RER (right) vs. normalized PE_{nren} for different scenarios when adding on-site renewable power systems to concept 1

As expected, adding on-site PV and wind power systems implies an increase of the RER, as well as a decrease of the PE_{nren}. However, when analysing the economic and the energetic impact, it is shown that on-site PV systems are cost-effective when they are implemented in data centres located in Barcelona (south Europe) under the hypothesis of this study. PV systems in Stockholm are not cost-effective due to investment and the electricity prices considered and the low solar radiation over the year. Renewable electricity produced by on-site wind power systems in Barcelona and in Stockholm, which is based on wind availability in Meteonorm data files, is not enough to compensate the investment needed for such a systems. Using on-site wind power systems needs to be installed in locations where wind resource is available, which strongly depends on local conditions.

Table 5 shows the required roof space for a 50 kW_p and 100 kW_p PV field under the hypothesis that the PV field is mounted in a flat roof by tilted modules with a distance between rows based on rules which optimally minimize the occupancy of the roof and maximizes the PV production (RenewIT tool, 2016). The required

roof space depends on the size of the PV system and on the location. Although different types of data centre buildings exists and whitespace rooms can be part of large corporate buildings, available roof space (A_{roof}) is estimated in relation with the whitespace area ($A_{DC,room}$) as shown in equation 6 and based on information available from the industry. The required roof space for the PV field exceeds the available space. Results of the load cover factor, which represents the ratio between the power produced by PV and the overall electrical data centre consumption, are also presented in Table 5. Load cover factor is very low (less or equal to 10% in most of the cases) even with PV systems that go beyond the available roof space in all the cases analysed. This means, that under grid parity conditions having an on-site PV system is a good solution to reduce the environmental impact of a data centre. Although this will be very dependent on the case, conventional roof mounted PV fields are limited by the available roof space covering a small portion of the electricity consumption of a data centre. Using PV to have larger load cover factors would require to use additional space available in the data centre footprint or explore BIPV (Building Integrated PV) solutions.

$$A_{roof} = f_{roof\text{-}ws} \cdot A_{DC,room} \quad \text{where} \quad f_{roof\text{-}ws} \cdot = 2.2\ m^2_{roof}/m^2_{DC,room} \qquad \text{(eq. 6)}$$

Table 5: Required roof space, available roof space and load cover factor for different scenarios with on-site PV power system for the investigated concept 1

		Name of the scenarios			
Parameter	**Unit**	**BCN-120**	**BCN-400**	**STO-120**	**STO-400**
Required roof space – 50 kWp	[m^2]	796		1570	
Required roof space– 100 kWp	[m^2]	1593		3140	
Available roof space	[m^2]	198	660	198	660
Load cover factor – 50 KWp	[%]	16	5	10	3
Load cover factor – 100 KWp	[%]	-	9	-	6

4.3. Analysis of concept 2 for different liquid cooling solutions and amount of heat reuse

Fig. 8 presents the results of the parametric analysis for concept 2 (data centre connected to a district cooling and heating system with reuse of heat from direct liquid cooled servers) for data centres of 400 kW_{IT} in both locations (BCN-400 and STO-400). Only results for 400 kW_{IT} are presented to contribute to readability of the graphs. Maintaining the hypothesis that 100% of the heat extracted from the data centre can be reused, the sensitivity analysis for two parameters has been performed. On one hand, there is the type of liquid cooling system which is characterized by its efficiency: 0.65 for on-chip liquid cooling and 1.0≃0.99 for immersed liquid cooling system. This parameter means that for on-chip liquid cooling, 65% of the heat is extracted by water while the other 35% by air, while for immersed liquid cooling system, 100% of the heat is extracted by water. On the other hand, the size of the heat pump is varied which is characterized by the ratio between the heat pump cooling power and the maximum liquid cooling demand of the data centre. This ratio is varied from 0.1 to 0.5. The results shows that as the type of liquid cooling system allows extracting higher amount of heat from the servers, PEnren decreases as well as RER increases. As the ratio determining the size of the heat pump increases there is a reduction of the PE_{nren}, too. Having an immersed liquid cooling system with the capability to extract more heat is a bit more expensive, but with optimum sizes of the heat pump differences between different liquid cooling technologies are minimized both in terms of TCO and PE_{nren}. As it is shown in Fig. 8, the size of the heat pump has an important effect on the indicators having an optimal value between 0.4 and 0.5, while the differences between these two values of the parameter are negligible.

4.4. Analysis of concept 3 adding on-site PV power systems

Fig. 9 shows the results of applying on-site PV power sytems to concept 3 for the different scenarios. Results are in coherence with the findings of adding PV to concept 1 already explained in section 4.2. PE_{nren} decreases and RER increases as the size of the PV system increases, being cost-effective in Barcelona and not economically feasible for Stockholm in terms of TCO.

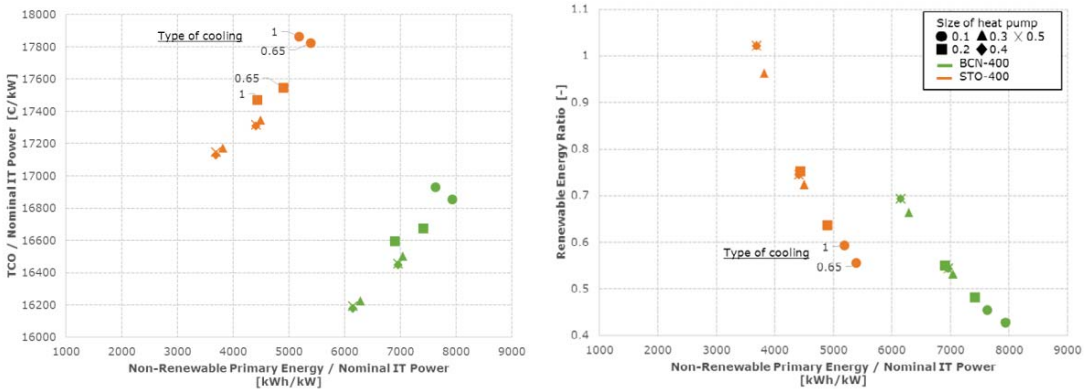

Fig. 8: Normalized TCO (left) and RER (right) vs. normalized PE_{nren} for different scenarios, types of cooling (On-chip/ Immersed) and sizes of the absorption chiller for concept 2

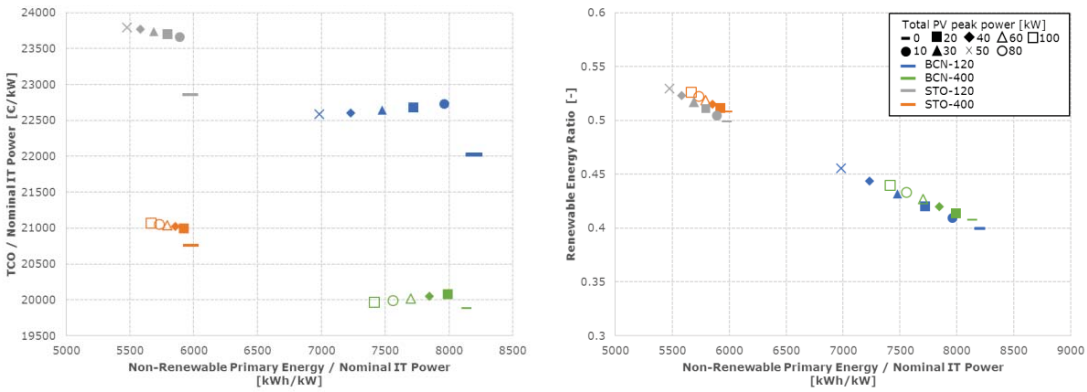

Fig. 9: Normalized TCO (left) and RER (right) vs. normalized PE_{nren} for different scenarios when adding on-site PV power systems to concept 3

4.5. Analysis of concept 4 with different sizes of absorption chiller and amount of heat reuse

Fig. 10 presents the results of a parametric analysis for concept 4 (data centre based on biogas fuel-cell driving an absorption chiller) for all the scenarios. Figure 10-right only shows results for 400 kW_{IT} data centre to improve the readability. The variation of two parameters has been analysed. One is the amount of heat produced by the facility which can be reused for other purposes outside the data centre: this is characterized by a ratio between 0.2 and 1.0, meaning 1.0 that 100% of the heat can be reused outside the data centre. The other parameters is the size of the absorption chiller which is characterized by a parameter from 0.2 to 0.5 which is the ratio between absorption cooling capacity and the total cooling power of the data centre. The results in Fig. 10 show that an increase of the absorption chiller size is not a cost-effective measure although it has an important effect on the reduction of the PE_{nren} and the increase of RER. For a ratio of the absorption chiller greater than 0.3, RER values are close to or great than 1.0 which indicates that the data centre facility is becoming a positive producer of primary energy even with low ratios of heat reuse. When the potential heat reuse is being reduced, the TCO increases as well as the PE_{nren} as consequence of the reduction of the exported heat.

4.5. Analysis of concept 5 with different sizes of absorption chiller and amount of heat reuse

Fig. 11 presents the results of a parametric analysis for concept 5 (data centre based on CHP – biogas engine driving an absorption chiller) for all the concepts. As in concept 4, the variation of two parameters has been analysed. One is the amount of heat produced by the facility which can be reused for other purposes outside the data centre; the other parameter is the size of the absorption chiller. The results in Fig. 11 show the same tendency than the ones for concept 4. An increase of the absorption chiller size is not a cost-effective measure although it has an important effect on the reduction of the PE_{nren} and the increase of RER. As well, as the amount of heat that can be reused is reduced (lower values of heat reuse ratio) the facility becomes more expensive to operate and PE_{nren} increases.

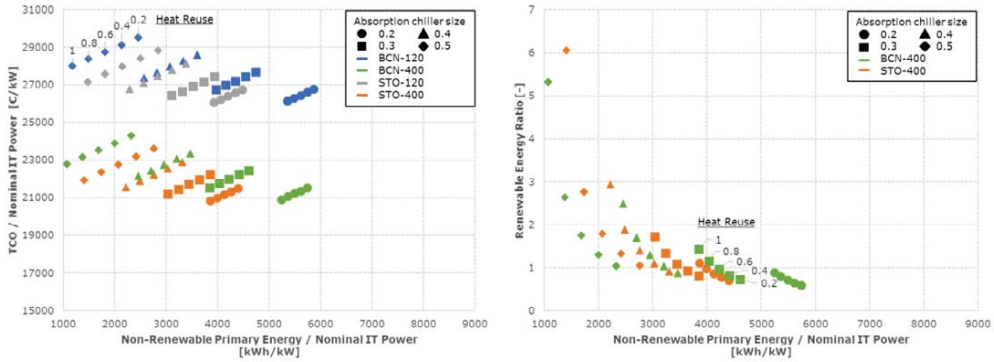

Fig. 10: Normalized TCO (left) and RER (right) vs. normalized PE_{nren} for different scenarios, relative absorption chiller sizes and amount of heat reuse ratio for concept 4

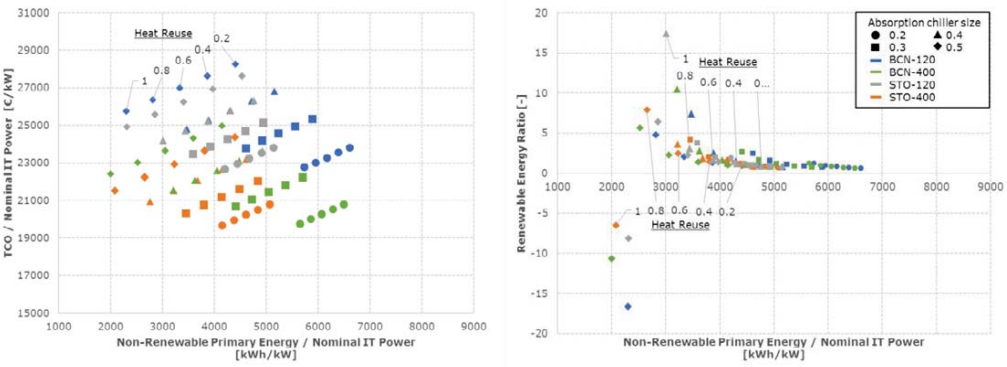

Fig. 11: Normalized TCO (left) and RER (right) vs. normalized PE_{nren} for different scenarios, absorption chiller sizes and amount of heat reuse ratio for concept 5

5. Conclusions

The extensive use of internet and cloud computing has increased the energy used for data centre industry. Thus, this paper studies the economic and environmental performance of different energy efficiency and renewable energy concepts in these unique facilities. Detailed TRNSYS simulation models developed in the European project RenewIT have been used to analyse the impact of those strategies in different data centre sizes and locations. In particular, the analysis has been performed for 120 and 400 kW_{IT} data centres in two climate locations: Barcelona and Stockholm. The aim of the different energy concepts analysed is to reduce the non-renewable primary energy consumption (PE_{nren}) as well as to explore how cost-effective each solution in terms of total cost of ownership (TCO) can be. Applying the most well-known energy efficiency measures such as free cooling, hot and cold aisle containment, the use of modular UPS, etc. lead to important reductions in PE_{nren} (about 50%) and in TCO (about 17%) and it should always be a must to explore energy efficiency measures alongside applying renewables. The concepts have also been compared to each other and the results show that the location has an influence on the absolute values of PE_{nren} due to climatic conditions and the differences between the shares of renewable in the national power grid, but there is not a lot of differences in TCO between the locations regarding the hypothesis about energy carrier prices considered in this study.

Data centres are very complex energy facilities and detailed optimization using the developed energy models is recommended together with information of local constraints, as energy prices or available space for renewables, to seek for a cost effective option. Together with the overview of the different energy concepts, basic parametric analysis have been performed in this paper varying some of the main parameters which characterizes the behaviour of each of the energy concepts. Concepts based on biogas CHP systems (with fuel cells or reciprocating engine) present promising numbers of PE_{nren} reduction but are not cost effective. These concepts rely on the availability of biogas as fuel resource as well as on reusing the heat which is not used by the absorption chiller outside the data centre whitespace. Small relative sizes of absorption chillers

give better values of TCO but PE_{nren} increases. The connection of a data centre to a district cooling and heating grid and reusing the heat from liquid cooled servers is a very promising solution and cost effective. Parametric analysis have been presented considering different heat pump sizes and different liquid cooling technologies and the reduction of PE_{nren} can be up to 22% compared to a conventional data centre. Using on-site PV or wind power production can be an interesting option towards Net Zero Energy data centres, but is dependent on the location: the local availability of wind resource for wind production and the availability of free space to integrate PV panels. In locations with grid parity situation PV is a feasible solution and load cover factor is limited by the availability of space for the PV panels.

6. Acknowledgment

The research leading to these results has received funding from the European Union's through FP7/2007-2013 under agreement no.608679—RenewIT project. "Advanced concepts and tools for renewable energy supply of IT Data Centres"

7. References

AEOLOS , 2015. AEOLOS-H50kW, http://www.nexosonline.com/web/categorias/Energia%20Renovable/Aeolos%20-%20Wind%20Turbine/Aeolos-H-50kw-Brochure.pdf [Accessed August 2016]

Carbó, A., Oró, E., Salom, J., Canuto, M., Macías, M., Guitart, J., 2016. Experimental and numerical analysis for potential heat reuse in liquid cooled data centres, Energy Conversion and Management, Volume 112, 135–145, http://dx.doi.org/10.1016/j.enconman.2016.01.003.

CEN, 2008, Energy performance of buildings – Economic evaluation procedure for energy systems in buildings, EN 15459:2008, European Committee for Standardization

Garcia, A., Oró, E., Salom, J., Manca, M., Isidori, D.. Cámara, O., Carrera, A., Timmerman, M., Donoghue, A., Rudolf, V., Pflugradt, N., Shrestha, N.L., Urbaneck, T., 2016. Online Tool to Evaluate the Implementation of Energy Efficiency Strategies and Renewable Energy into Data Centre Portfolio, CLIMA 2016 Conference.

Oró, E., Vergara, A., Salom, J., 2015, Dynamic Energy Modelling for Data Centres: Experimental and Numerical Analysis, J. Fundam Renewable Energy Appl 6:197. doi:10.4172/20904541.1000197

Oró, E., Depoorter, V., Garcia, A., Salom, J., 2015. Energy efficiency and renewable energy integration in data centres. Strategies and modelling review, Renewable and Sustainable Energy Reviews, Volume 42, pp. 429-445, http://dx.doi.org/10.1016/j.rser.2014.10.035.

RenewIT tool, 2016. http://www.renewit-tool.eu/ [Accessed September 2016]

RenewIT tool, 2016. Hypothesis for modelling: Solar PV power generation. http://www.renewit-tool.eu/Content/File/9-Photovoltaic%20energy%20production.pdf [Accessed September 2016]

Salom, J., 2016. RenewIT project. Available online in http://www.renewit-project.eu [Accessed April 2016]

Salom, J., Oró, E., Garcia, A., 2015. Dynamic modelling of Data centre Whitespace. Validation with collected measurements, 14th Conference of IBPSA, Hyderabad, India, Dec. 7-9, 2015, pp. 2841-2848

Shrestha, N.L., Pflugradt, N., Urbaneck, T., Carrera, A., Oró, E., Garcia, A., Trapman, H., De Nijis, G.,Van Dorp, J., Macías, M, 2015, Catalogue of advanced technical concepts for Net Zero Energy Data Centres, RenewIT project, Available online in http://www.renewit-project.eu/wp-content/files_mf/1449047911CatalogueofadvancedtechnicalconceptsforNZDC_low.pdf [Accessed September 2016]

Rudolf, V., Shrestha, N.L., Urbaneck, T., Pflugradt, N., Platzer, B., Salom, J., Oró, E., Garcia, A., Cámara, O., Carrera, A., Timmerman, M., Trapman, H., 2016. Simulation of on-site generation CHP systems for large-scale data centre, CLIMA 2016 Conference.

Shuja, J., Gani,, A., Shamshirband, S., Ahmad, R.W., Bilal, K., 2016.Sustainable Cloud Data Centers: A survey of enabling techniques and technologies, Renewable and Sustainable Energy Reviews, Volume 62, pages 195-214, http://dx.doi.org/10.1016/j.rser.2016.04.034.

University of Madison-Winsconsin, TRNSYS v17.1, 2012., http://sel.me.wisc.edu/trnsys/

ISES International Solar Energy Society

Conference Proceedings

EuroSun 2016

Palma de Mallorca (Spain), 11 – 14 October 2016

ENERGYbase office building:

A reality check by seven years of monitored energy system performance

Tim Selke[1], Werner Wiedermann[2]

[1]AIT Austrian Institute of Technology GmbH, Donau-City-Str. 1, 1220 Vienna, Austria

[2] Siemens Gebäudemanagement &-Services G.m.b.H.

Abstract

The architectural design and the energy system concept of the ENERGYbase office building in Vienna / Austria fulfils the requirements of the *'Passivhaus'* standard. The use of ecological construction materials, high insulation and air-tightness of building envelope, advanced and energy efficient technologies - like solar-assisted air-conditioning, heat pump technology, photovoltaics - as well as innovative systems in terms of high quality of indoor comfort reduces the energy consumption. Since August 2008 the ENERGYbase office building is in operation and a monitoring campaign was carried out. This publication reports on seven years energy building performance based on measurement data from 2009 till 2015. Key findings are drawn and finally the ENERGYbase office building exceeds its ambitious targets related to energy and high indoor comfort in reality.

Keywords: *Nearly zero energy office building, local renewable energy use, energy monitoring, reality check*

1. Introduction

According the recast of the EU-Directive [1], future buildings are 'Nearly Zero Energy Buildings' and technically a bright variety of future building concepts exists. Two essential measures lead to such high energy performing buildings: high energy efficiency for both a) the building envelope and the energy systems and b) the use of renewable energy sources on-site. In Europe 'Nearly Zero Energy Buildings' have to be built in 2021, thus there is a need of successful pilot-projects demonstrating the feasibility of such future building concepts. The ENERGYbase [2] office building, owned by the Vienna Business Agency and located in the 21st district of Vienna, was built to show up cutting-edge office designs, energy efficient technologies and the use of renewable energy gained from on-site resources with the goal of stimulating further use and development of these techniques. The contracted planning team achieved these ambitious energy targets by complying the energy requirements of the '*Passivhaus*' standard [3]. For designing the ENERGYbase technical solution further measures had high priority; the use of a) environmentally friendly materials, b) high quality insulation, c) a well-sealed building envelope and d) innovative energy technologies (e.g., photovoltaics, solar-assisted air-conditioning, and advanced heat pump technology) as well as e) the development of an innovative control strategy to provide a high quality indoor air and comfort. The architectural design and the applied technology mix lead to a significantly reduction of the energy demand for heating, cooling and artificial lighting in comparison to the existing building standard. The ENERGYbase building and its energy features where already presented on the EUROSUN 2008 -1st International Conference on Solar Heating and Cooling in Buildings eight years ago [4].

Building facts are listed in Table 1. Figure 1 shows two photos of the ENERGYbase, one shows the south and west façade and the other one north and east façade. The geographical position of the ENERGYbase

Selection and/or peer review under responsibility of Scientific Committee
doi:10.18086/eurosun.2016.01.03 Available at http://proceedings.ises.org

location and some selected weather parameter are presented in Table 2.

2006 during the planning phase of the ENERGYbase building project the energy demand values were calculated by applying the method of the Austrian energy performance certificate. Based on this data and simulation results experts indicated a total electricity demand for heating, cooling, air treatment and artificial lighting of one year ENERGYbase operation of 25 kWh_{el} per useful area and year. With the current Austrian conversion factors [5] for primary energy (PE, nonrenewable part) and CO_2-Emissions the ENERGYbase consumes 33 $kWh_{PE,nr}$ primary energy per useful area and year and emits 69 kg_{CO2} per useful area and year.

Figure 1: Photo of ENERGYbase showing left) south and west facade and right) north and east façade (Source: Hurnaus)

Table 1: Building facts of ENERGYbase

Type of building	Office
Location	1210 Vienna / Austria
In operation since	2008
System operated by	Siemens Facility Management
Area (Gross/ Useful/ Air-conditioned)	9,430 m²/ 7,544 m² / 5,000 m²
Use of solar energy	Photovoltaics 48.2 kW_p (peak) power
Use of shallow geothermal energy	Ground water coupled heat pump
Other innovation	Green ventilation (i.e., biological supply air treatment in wintertime for pre-humidification and filtering)
	Costume-made south façade oriented to the South and 7° to West
	Thermal mass activation for sensible heating & cooling

Table 2: Climate

Located	48°12’ N/ 16°22’ E
Tmean (Tmax / Tmin hourly)	9.5°C (28.9 / -14.6°C)
Global radiation on horizontal	1,122 kWh/m² year
Global diffuse on horizontal	627 kWh/m² year
Global direct on horizontal	495 kWh/m² year

2. Heating, Cooling and Ventilation System

The ENERGYbase office building is fulfils the requirements of the ‘Passivhaus’ standard. The heating, cooling and ventilation system is designed to use both a) water and b) an air based energy distribution systems. The air temperature of the office rooms in the ENERGYbase is controlled by thermally activated building construction elements. The concrete core activation (CCA) covers the sensible load for heating and cooling; due to the controlling of the water inlet temperature into CCA and the different air temperature levels in the office rooms heat is extracted from or delivered to the building construction mass. For controlling the indoor air humidity and for supplying fresh air, a solar heat driven Desiccant Evaporative Cooling (DEC) system is put into operation, which is an air-conditioning system without using conventional vapor compression chiller for cooling and dehumidification purposes. The assessment of the energy performance of the solar heat driven DEC system is already published [6].

Geothermal energy is exploited by means of ground water in the ENERGYbase building. Two heat pumps coupled to the ground water temperature levels raises the water temperature up to 45 degree Celsius in winter and the hot water is supplied on one hand to the CCA and on the other the hand to several heating coils of the air treatment system. In summer the ENERGYbase is cooled by extracting heat from CCA with the help of water circulated through the building construction. Finally a water to water heat exchanger transfers the extracted heat to the ground water. The ground water temperature in summer time is approx. 14 degree Celsius and is raised by around 4 Kelvin. In summer high ambient air temperature and humidity values are treated by the DEC system using solar heat. The collector area is around 285 m² and mounted on the upper part of the south façade – see scheme in Table 8. First of all the solar heat is used for the regeneration process of the loaded sorption material used in the DEC system and additionally for covering partly the heating demand of the CCA and the heating coils. Table 3, Table 4 and Table 5 list technical design data of the heating, cooling and air treatment system of ENERGYbase.

Table 3: Ventilation and air treatment system

Technology	Desiccant and evaporative cooling
N° of DEC systems	2 DEC system (twins)
Nominal volumetric flow rate	2 x 8,240 m³ per hr
Nominal capacity	~ 40 kW_{th} per DEC system
Brand of cooling units	robatherm
Cooling load subsystem	Central AHU
Dehumidification	Sorption wheel (Klingenburg SECO 1770)
Regeneration power	80 kW_{th} per DEC system

Technology	Air treatment system
N° systems / components	1 system, 1 heating & 1 cooling coil, 2 speed controlled fans, 1 heat recovery wheel
Nominal volumetric flow rate	6,000 m³ per hr
Set supply temperature	22°C (Winter & Summer)
Heat recovery efficiency	~ 0,66
Brand of cooling units	robatherm
Nominal motor el power for fan	4 kW_{el}
Dehumidification/ Humidification	No humidity treatment

Table 4: Heat generation

Heat pump system

Technology	Heat pump
Brand / Type	Climaveneta
Nominal heating capacity	2 x 160 kWth
Evaporator circuit temperatures	10/6°C
Evaporator circuit volume flow	36 m³ per hr
Condenser circuit temperatures	40/35°C
Condenser circuit volume flow	27.4 m³ per hr
Nominal electric power	38.1 kW_{el}

Solar collector system

Collector type	Flat-plate collectors
Brand of collector	Sonnenkraft /MEA DESIGN
Collector area	285 m² aperture area
Tilt angle/ orientation	32° / South and 7° to West
Collector fluid	Water/propylene-glycol (70/30)
Typical operation temperature	80°C
Mass flow operation mode	Low flow
Integration	Roof top mounted
Storage technology	Solar hot water tank
Storage volume	15,000 l

Table 5: Ground water / water heat exchanger design data

Nominal heat transfer capacity	270 kW_{th}
Primary circuit - Ground water	
Delta T	6 Kelvin
Nominal mass flow	38,700 kg per hr
Secondary circuit	
Delta T	4 Kelvin
Nominal mass flow	68,500 kg per hr
Ground water data	
Ground water temperature (min/max)	9°C / 14°C
Max volume flow	20 l per sec
Limited temperatures of fed in water (min/ max)	5°C / 18°C

3. Energy Performance Assessment

3.1 Annual Overall Energy System Performance

Since August 2008 the ENERGYbase office building is in operation and a monitoring campaign was permanently carried out. This publication reports on seven years energy building performance based on measurement data from 2009 till 2015. Table 6 lists selected annual amounts of energy of consumed and delivered electricity and heat generated and extracted from the building. Line I of Table 6 displays the percentage of rented office areas in the observation period. The displayed data are essentially registered by the facility management and cross checked by Austrian Institute of Technology. Monthly accumulated energy fluxes are regularly taken from different kinds of sources; a) building automation system, b) energy meters implemented in systems devices like inverters, heat meters etc., and c) energy data registered by meters of the energy supplying company. In most cases the figured monthly energy data are adjusted in consequence of different time intervals. The annual total electricity consumption indicated in Table 6 – see line A - represents annual consumed electricity for operating all technical devices for heating, cooling, ventilation, artificial lighting of general areas and all other building equipment, like permanent emergency lighting. The electricity consumed by the office usage of tenants is not included.

Table 6: Annual energy performance data from 2009 till 2015 (Source: FM Siemens)

			2009	2010	2011	2012	2013	2014	2015
	Consumed electricity								
A	**Total electricity**	**kWh**	158,259	164,959	151,566	141,086	166,734	147,092	160,068
B	**Electricity from grid**	**kWh**	131,621	135,520	118,160	108,699	136,382	116,940	128,904
C	**Air handling unit**	**kWh**	43,547	44,631	40,174	34,871	44,149	51,265	62,026
D	**Heat pump**	**kWh**	40,467	40,106	33,028	33,274	45,730	27,949	31,529
E	**Ground water pumps**	**kWh**	13,763	12,056	8,560	6,905	6,838	4,570	5,071
F	**Artificial lighting**	**kWh**	6,799	3,503	6,149	4,122	4,754	4,501	3,592
G	**Others**	**kWh**	53,683	64,663	63,655	61,914	65,263	58,808	57,849
	Selected key performance indicators								
H	**Spec. total electricity**	**kWh/m²**	21.0	21.9	20.1	18.7	22.1	19.5	21.5
I	**Ratio of rented area**	**%**	32%	48%	72%	87%	87%	87%	90%
J	**Ratio C/A**	**%**	28%	27%	27%	25%	26%	35%	39%
K	**Ratio D/A**	**%**	26%	24%	22%	24%	27%	19%	20%
L	**Ratio E/A**	**%**	9%	7%	6%	5%	4%	3%	3%
M	**Ratio F/A**	**%**	4%	2%	4%	3%	3%	3%	2%
N	**Ratio G/A**	**%**	34%	39%	42%	44%	39%	40%	36%
	Photovoltaics (PV) electricity								
O	**PV_{el} delivered**	**kWh**	36,038	38,015	47,430	45,859	44,208	40,544	42,878
P	**PV_{el} self-consumed**	**kWh**	26,638	29,439	33,406	32,387	30,352	30,152	32,982
Q	**PV_{el} fed into the grid**	**kWh**	9,400	8,576	14,024	13,472	13,856	10,392	9,896
R	**PV_{el} Yield**	**kWh/kWp**	748	789	984	951	917	841	890
S	**Ratio O/A**	**-**	0.23	0.23	0.31	0.33	0.27	0.28	0.26
T	**Ratio P/A**	**-**	0.17	0.18	0.22	0.23	0.18	0.20	0.20

U	**Ratio P/O**	**-**	0.74	0.77	0.70	0.71	0.69	0.74	0.77
	Heating (heat pump HP, solar collector)								
V	**Heat delivered by HP**	**kWh**	124,049	148,840	119,960	121,534	168,684	102,299	121,438
W	**$SEER_{HP}$ L/C**	**-**	3.07	3.71	3.63	3.65	3.69	3.66	3.77
X	**Solar heat delivered**	**kWh**	58,335	55,964	61,023	54,247	29,983	50,844	73,980
	Cooling								
Y	**Heat from CCA**	**kWh**	100,105	107,916	143,620	146,527	147,865	165,793	177,935
Z	**El. cold water pumps**	**kWh**	9,263	7,049	6,167	5,570	5,037	4,866	6,093
AA	**Ratio Y/Z**	**-**	10.81	15.31	23.29	26.31	29.35	34.07	29.21
	Weather[1]								
AB	**Glob. radiation, hor**	**kWh/m² y**	1,199	1,144	1,248	1,226	1,174	1,133	1,227
AC	**Mean $T_{Ambient}$**	**°C**	11.0	9.9	11.0	11.3	10.9	12.0	12.1

Due to the fact the ENERGYbase is only externally powered by the electric grid, i.e. there is no connection to district heat or gas network, the assessment of the consumed electricity is key. In the observation period of seven years the ENERGYbase was operated by electricity in a range from 141 MWh_{el} till 166.7 MWh_{el} per year, this corresponds to specific values from 18.7 kWh_{el} till 22.1 kWh_{el} per useful area and year. High ratio of the electricity consumption are achieved by the operation of the air handling unit, heat pump system and all other electric driven devices - see line J till N of Table 6. The south façade attached photovoltaic system delivers 23% up to 33% of the total consumed electricity for operating the heating, cooling, ventilation systems and all other general building service devices.

3.2 Monthly Energy System Performance in 2015

Figure 2 shows an energy flow chart displaying annual heat and electricity fluxes of the ENERGYbase without users' electricity consumption in 2015. The annual heat delivered to both the CCA and as well to the numerous heating coils (excl. the heat transferred to the regeneration coils of the air treatment system) is calculated to value of 19.7 kWh_{th} per useful area and year. In cooling mode the heat is extracted from CCA and transferred to the ground water, here the specific heat extracted from the building is 23.6 kWh_{th} per useful area and year. In 2015 the heat pump system delivered around 121.4 MWh heat per year with an electricity input of 32.2 MWh_{el} per year including the consumers a) control system, b) compressors and c) the pumps of the water circuits of condenser and evaporator part. This quantified energy fluxes result into a seasonal energy efficiency ratio $SEER_{HP}$ of the heat pump system of 3.77, which is calculated according to the formula expressed in Equation 1. The ratio of the used solar heat generated by the collector in relation to the cumulated heat transferred to the CCA, heating and regeneration coils of the air treatment system is around 38% und the formula of the solar fraction is expressed in Equation 2.

[1] Data source; Zentralanstalt für Meteorologie und Geodynamik, weather station ‚Hohe Warte' in Vienna

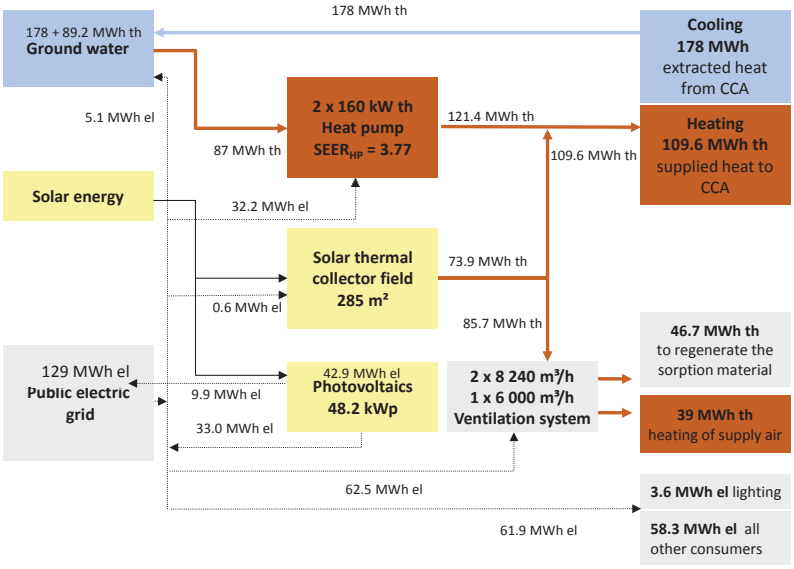

Figure 2: Annual energy fluxes (heat and electricity) of ENERGYbase in 2015 (Source: AIT)

Table 7 contains monthly values of electricity consumed by different energy systems. Furthermore the monthly values of heat transferred by circulated water to a) the CCA, b) the heating coils of the air treatment system and c) regeneration heating coil of the DEC system – see lines g, i and h of Table 7. As mentioned above the ENERGYbase is equipped with two heat pumps and one solar thermal collector field delivering hot water to heat distribution system described above. In 2015 the monthly calculated energy efficiency ratio $SEER_{HP}$ of the heat pump system operation is in range from 2.67 up to 3.87 – see line k of Table 7. The share of the solar heat used in the ENERGYbase can be calculated according to Equation 1. From May till September 2015 the solar heat covers fully the demand for the regeneration process of the sorption material in the DEC system, i.e. the solar fraction is accounted to 100%. Due to the lower availability of solar radiation in winter monthly values of the solar fraction decrease dramatically – see line m in Table 7.

$$SEER_{HP} = \frac{Q_{HP,\,Heat}}{E_{el,\,HP}} \left[\frac{kWh_{th}}{kWh_{el}} \right] \qquad \textbf{(eq. 1)}$$

Where:

$SEER_{HP}$	Seasonal energy efficiency ratio of the heat pump system [kWh_{th}/kWh_{el}]
$Q_{HP,\,Heat}$	Heat generated by the heat pump condenser, water cycle [kWh_{th}] – see line j in Table 7
$E_{el,\,HP}$	Electricity consumed by the heat pump components, i.e. motor for compressor and pumps of both circuits and the control unit [kWh_{el}] – see line j in Table 7

$$SF_{solar\,heat} = 1 - \frac{Q_{Heat\,Pump}}{Q_{CCA} + Q_{Heating\,Coil} + Q_{Reg.,Coil}} \left[\frac{kWh_{th}}{kWh_{th}} \right] \qquad \textbf{(eq. 2)}$$

Where:

$SF_{solar\,heat}$	solar heat fraction [-]
$Q_{Heat\,Pump}$	heat delivered by heat pump [kWh_{th}] – see line j in Table 7
Q_{CCA}	heat delivered to concrete core activation for heating purposes [kWh_{th}]
$Q_{Heating\,Coils}$	heat delivered to heating coils of the air treatment system [kWh_{th}]
$Q_{Reg.,\,Coil}$	heat delivered to heat coil of DEC system for regeneration purposes [kWh_{th}]

In 2015 the cooling season of the ENERGYbase started from April and ended in September. Monthly amounts of heat that has been extracted from the CCA are in the range from 14.92 MWh_{th} up to 43.64 MWh_{th} per month. The seasonal energy efficiency ratio $SEER_{Cool,\,Sys}$ of the water based cooling system can be expressed by eq. 3. According to line p in Table 7 the ENERGYbase ground water cooling system operates energy efficient and $SEER_{Cool,\,Sys}$ values are higher than 30.

$$SEER_{Cool,\,Sys} = \frac{Q_{Heat\ extr\ by\ CCA}}{E_{el,\,cold\ water\ pumps}} \left[\frac{kWh_{th}}{kWh_{el}} \right] \qquad \textbf{(eq. 3)}$$

Where:

$SEER_{Cool,\,Sys}$	Seasonal energy efficiency ratio for the cooling system [kWh_{th}/kWh_{el}]
$Q_{Heat\ extr\ by\ CCA}$	Heat extracted by the water cycle of CCA [kWh_{th}] – see line j in Table 7
$E_{el,\,cold\ water\ pumps}$	Electricity consumed by all cold water pumps [kWh_{el}] see line o in Table 7

Table 7: Monthly energy fluxes and key performance indicators for operating the air treatment system, heating and cooling system of ENERGYbase in 2015 (Source: FM Siemens)

	2015		Jan	Feb	Mar	Apr	May	Jun	Jul	Aug	Sep	Oct	Nov	Dec
	Consumed electricity by the energy system													
a	**Total**	**MWh**	18.34	15.11	16.20	10.31	11.51	10.27	10.35	10.85	12.38	13.32	17.07	16.17
b	**AHU**	**MWh**	4.52	3.79	6.52	4.95	5.88	5.92	3.59	6.17	7.22	5.03	4.98	4.01
c	**HP**	**MWh**	7.58	5.35	3.61	0.70	0.01	0.08	0.01	0.01	0.06	2.36	6.30	6.14
d	**GWP**	**MWh**	0.24	0.22	0.29	0.34	0.51	0.58	0.90	0.87	0.51	0.17	0.27	0.25
e	**AL**	**MWh**	0.31	0.25	0.24	0.32	0.27	0.29	0.38	0.39	0.34	0.31	0.29	0.23
f	**Others**	**MWh**	5.70	5.50	5.55	4.00	4.84	3.40	5.47	3.41	4.27	5.44	5.23	5.55
	Heat transferred to													
g	**Heat to SDEC**	**MWh**	-	0.00	0.04	0.10	4.11	6.48	8.16	19.05	8.00	0.81	-	-
h	**Heat to HC**	**MWh**	8.75	7.12	8.10	1.30	0.47	0.29	-	0.02	0.12	0.51	7.39	4.94
i	**Heat to CCA**	**MWh**	21.21	17.69	13.23	5.04	0.74	0.23	-	-	0.66	11.49	19.72	19.62
	Heat delivered													
j	**Heat from HP**	**MWh**	29.28	20.29	13.38	1.99	-	0.22	-	-	-	8.49	24.36	23.42
k	**SEER $_{HP}$ j/c**	**kWh/kWh**	3.86	3.80	3.71	2.85	-	2.67	-	-	-	3.60	3.87	3.82
l	**SH**	**MWh**	0.69	4.52	8.00	4.45	5.31	6.79	8.16	19.07	8.79	4.32	2.74	1.15
m	**SF = 1–j/(g+h+i)**	**%**	2%	18%	37%	69%	100%	97%	100%	100%	100%	34%	10%	5%
	Heat extracted from building (cooling)													
n	**Heat from CCA**	**MWh**	0.09	0.18	0.63	14.92	21.64	32.05	43.64	40.30	17.73	3.07	1.98	1.71
o	**El. CWP**	**MWh**	0.01	0.04	0.19	0.43	0.71	0.92	1.41	1.35	0.81	0.10	0.06	0.05
p	**$SEER_{Cool,Sys}$ n/o**	**kWh/kWh**	10.33	4.03	3.39	34.39	30.56	34.65	30.94	29.86	21.87	29.85	31.88	33.69
	Specific heat transferred per useful area													
q	**Sp. heat to sys**	**kWh/m²**	3.97	3.29	2.83	0.85	0.70	0.93	1.08	2.53	1.16	1.70	3.59	3.26
r	**Sp. heat extr.**	**kWh/m²**	0.01	0.02	0.08	1.98	2.87	4.25	5.78	5.34	2.35	0.41	0.26	0.23

Where:

a – Total: Overall electricity consumed by the technical equipment of the heating, cooling, ventilation system, lighting and other services

b - AHU: Electricity consumed by the fans, control unit and other devices of the Air Handling Units

c - HP: Electricity consumed by the heat pump by means of the a) control system, b) compressors and c) the pumps of the water circuits of condenser and evaporator part.

d - GWP: Electricity consumed by a) motors for ground water and cold water distribution pumps

e - AL: Electricity consumed by artificial lighting for general area

f – Others: All other electricity consuming devices

g – Heat to SDEC: Heat transferred to the two regeneration heating coils implement in the return air stream of the DEC system in dehumidification mode

h – Heat to HC: Heat transferred to all heating coils implemented in the air treatment system

i – Heat to CCA: Heat transferred to concrete core activation in order to lift the indoor air temperature

j – Heat from HP: Heat delivered by the heat pump systems, i.e. condenser water circuit

k – $SEER_{HP}$: Seasonal energy efficiency ratio of the heat pump according to eq. 1

l – SH: Used solar heat taken from the hot water storage

m – SF: Solar fraction expressed according eq. 2

n - Heat from CCA: Heat extracted from concrete core activation for lowering the indoor air temperature

o - El. CWP: Electricity consumed by motors of all required cold water pumps

p - $SEER_{Cool,Sys}$: Seasonal energy efficiency ratio of the cooling system according to eq. 3

q – Sp. heat to sys: Heat transferred to the energy system divided by useful office area (7.544 m²)

r – Sp. heat extr.: Heat extracted from concrete core activation divided by useful office area (7.544 m²)

3.3 Energy Performance of the Photovoltaics (PV)

The photovoltaic system with a nominal capacity of 48.2 kW_p is attached to a custom-made stepped south façade. Six module lines with three different kinds of cell and module technologies are attached to the façade. In order to maximize the solar electricity yield the modules are naturally ventilated by ambient air and tilted with an angle of 31.5 degree – see scheme in Table 8.

In addition the façade added photovoltaic systems was designed and planned as well for research purposes and a scientific monitoring system is implemented beside other measurement equipment of the inverter. The upper two PV module lines are designed and installed for research activities and three different kinds of cell technologies are integrated; namely a) monocrystalline, b) polycrystalline and c) polycrystalline with back contacts. These different modules can be investigated with regard to their different long-term performance. The other four modules strings configured only with modules using polycrystalline cells and investigation of the inverter performances are foreseen. The technical data of the photovoltaic system are listed in Table 8. Since February 2009 the PV system is in operation. Annual energy performance indicators like a) delivered electricity from the all 366 PV modules, b) self-consumed electricity from PV system and c) PV electricity fed to the public grid are quantified in Table 9.

Table 8: Technical data of the PV system (Source: ATB-Becker 2008)

Type of	Attached to façade/ natural
Orientation / tilt	South and 7° to West / 30°
Total nominal	48.2 kW_p
Total PV module	400 m²
Module type 1	Solarwatt M135-55 GEG LK
Cell type	monocrystalline
number of pieces	286
Nominal power	134 W_p
Module type 2	Solarwatt P 125-55 GEG
Cell type	polycrystalline
number of pieces	40
Nominal power	122 W_p
Module type 3	Solarwatt M135-55 GEG
Cell type	polycrystalline
number of pieces	40
Nominal power	127 W_p
Inverter	10 x Sunways, 2 x SMA

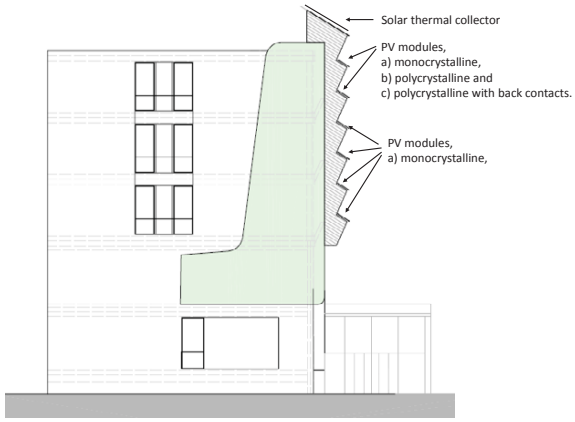

During the observation period from January 2009 till December 2015 the annual electricity delivered by the PV system is in the range from 36,038 kWh per year (2009) to 47,430 kWh per year (2011), this corresponds to specific solar electricity yields from 748 and 984 kWh per kW installed peak capacity. In the beginning of the building operation some outages of the inverters occurred. The ratio of the PV electricity used in house and the total annual electricity consumed by the operation of the ENERGYbase energy systems is in range from 0.17 up to 0.22. In 2011 the PV system fed 14,024 kWh into the public grid and 33,406 kWh were directly used to operate the office building, this corresponds to approx. 70% of direct used solar electricity on site.

Table 9 lists monthly energy fluxes and key performance indicators from January till December 2015. Due to the specific shape of the solar façade the PV system achieved maximal yields in March with 112 kWh per kW installed peak capacity and in July with 126.4 kWh per kW installed peak capacity. Based on this measured data the predicted high yields for May, June and July cannot be confirmed. Demonstrably there is shading effect from the upper cell string on at least one of the lower module line occurring in June. Figure 3 illustrates monthly solar electricity a) delivered by the PV system, b) used in house and c) fed to the public grid from January till December 2015.

Table 9: Monthly energy fluxes and key performance indicators of the PV system in 2015 (Source: FM Siemens)

			Jan	Feb	Mar	Apr	May	Jun	Jul	Aug	Sep	Oct	Nov	Dec
	Consumed electricity by the energy system													
A	**Total**	**MWh**	18,34	15,11	16,20	10,31	11,51	10,27	10,34	10,85	12,38	13,31	17,07	16,16
	Delivered electricity													
B	**PV el delivered**	**kWh**	745	3,410	5,399	4,639	4,691	2,768	6,092	3,828	4,058	3,924	1,657	1,668
C	**PV el self**	**kWh**	505	2,386	4,135	3,487	3,707	2,408	4,460	3,164	3,314	2,780	1,321	1,316
D	**PV el fed to grid**	**kWh**	240	1,024	1,264	1,152	984	360	1,632	664	744	1,144	336	352
	Key performance indicators													
	Ratio B/A	-	0.04	0.23	0.33	0.45	0.41	0.27	0.59	0.35	0.33	0.29	0.10	0.10
	Ratio C/A	-	0.03	0.16	0.26	0.34	0.32	0.23	0.43	0.29	0.27	0.21	0.08	0.08
	Ratio C/B	-	0.68	0.70	0.77	0.75	0.79	0.87	0.73	0.83	0.82	0.71	0.80	0.79
	Specific yield	**kWh/kWp**	15.5	70.7	112.0	96.2	97.3	57.4	126.4	79.4	84.2	81.4	34.4	34.6
	Specific yield	**kWh/m²**	1.9	8.5	13.5	11.6	11.7	6.9	15.2	9.6	10.1	9.8	4.1	4.2

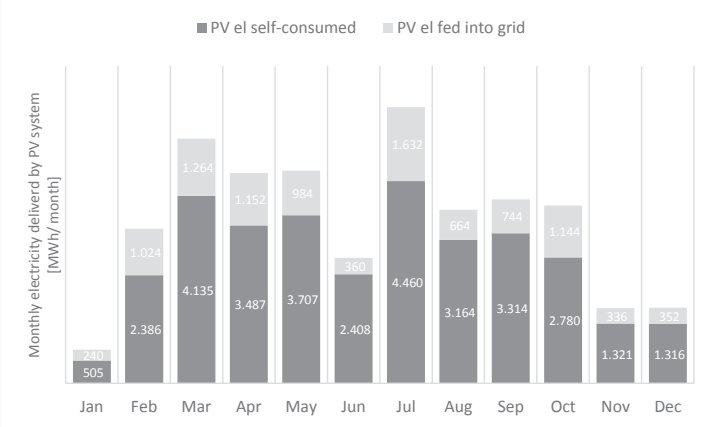

Figure 3: PV system energy performance in 2015

4. Key findings

Since August 2008 the ENERGYbase office building is in operation and a monitoring campaign was carried out. With this paper numerous annual energy fluxes and key performance indicators are presented from 2009 till 2015. Monthly energy system performance data are presented for 2015. The long-term observation allows an energy system performance assessment over seven years of the ENERGYbase office building operation. The electricity consumed by the office usage of the tenants, like using computers etc., is not part of this investigation. By analyzing the energy and key performance indicators following key findings are drawn:

- The ambitious energy targets stated in the initial ENERGYbase project phase were exceeded by the acquired energy data of seven years. From 2009 till 2015 the total electricity consumption for heating, cooling, air treatment, artificial lighting and other devices of the ENERGYbase is quantified from 141.1 MWh_{el} (2012) up to 166.7 MWh_{el} (2013), this corresponds to a range of specific values from 18.7 kWh_{el} up to 22.1 kWh_{el} per useful area and year. The allows the conclusion that the architectural design, the applied 'Passivhaus' standard and the implemented technology mix with a significant use of local renewable energy sources lead to a robust, reliable and predictable building energy performance.
- The convincing energy efficient performance is a result of a fruitful cooperation between the facility management and researchers on-site. The facility manager has carried out and investigated numerous measures achieving improvements in terms of energy efficiency, for instance permanently running pumps and fans have been operated in part load when motors are driven by frequency converters. AIT researcher performed several research projects focusing the optimization of subsystems of the ENERGYbase energy system. These activities are always a tradeoff between lowering the energy input and keeping the required high indoor comfort.

- The façade attached photovoltaic system delivered solar electricity in the range from 36 MWh_{el} up to 47.4 MWh_{el} per year. 69% up to 77% of the delivered solar electricity was self-consumed by the building operation and 17% up to 23% of the total electricity consumed was provided by PV system. Unfortunately self-shading effects of the shaped south façade result into relevant losses of solar electricity generation of the PV system when the solar altitude angle of the sun is near to its local maximum of $\alpha S \approx 65°$.

5. References

[1] EU-Directive 2010/31: The Energy Performance of Buildings Directive (2010/31/EU) recast Oct 2010

[2] https://viennabusinessagency.at/property/project-development/energybase/ Access: October 1st, 2016

[3] Wolfgang Feist, Passivhaus Institut (Hrsg.): PHPP 2007: Passivhaus Projektierungs-Paket 2007. 7. Auflage. Darmstadt 2007

[4] ENERGYbase - Sunny Office Future"; oral presentation: EUROSUN 2008 - 1st International Conference on Solar Heating, Cooling and Buildings, Lisbon, Portugal; 07.10.2008 - 11.10.2008; in: "EUROSUN 2008 - 1st International Conference on Solar Heating, Cooling and Buildings", SPES - Sociedade Portuguesa de Energia Solar, (2008), ISBN: 978-972-95854-7-0; Paper-N°. 357.

[5] http://www.oib.or.at/sites/default/files/richtlinie_6_26.03.15.pdf Access: October 1st, 2016

[6] T. Selke, A. Frein, M. Muscherà, S. Sethuvenkatraman, S. Handls, S. White: "SHC Task 48 B2 - Three GOOD Practice examples of solar heat driven desiccant evaporative cooling systems"; oral presentation: SHC 2015, International Conference on Solar Heating and Cooling for Buildings and Industry, Istanbul, Turkey; 01.12.2015 - 04.12.2015. SHC 2015, published in Energy Procedia, Volume 91, June 2016, Pages 832–843

Conference Proceedings
EuroSun 2016
Palma de Mallorca (Spain), 11 – 14 October 2016

Solar Decathlon Europe and the Energy Endeavour Initiative

Karsten Voss [1], Susanne Hendel [1], Peter Russel [2]

1 University Wuppertal (Germany) 2 Technical University Delft (Netherlands)

Abstract

The Solar Decathlon is a prominent student competition on the topic of net zero energy and energy plus buildings. This competition has already taken place 12 times worldwide, three times in Europe and is under preparation for its next European edition. The unique feature is the triple of "design, build and operate" in an educational showcase addressing building designers, the industry and the general public. Over the course of the European editions, the participating teams have expressed the need for a platform to assist future competition organizers to further develop the format to confront renovation and dense urban living issues. This paper summarizes the ongoing process to establish such a platform: it is called the Energy Endeavour. It's aim is to further the continuation of the event and its evolution aimed to increased impact related to education, communication, energy policy and building science. One major element is a publicly accessible knowledge platform for the documentation and analysis of past events. The paper describes the structure and capabilities of this platform together with some analysis examples.

Keywords: *Student Competition, Zero Energy Building, Building Grid Interaction, Knowledge Platform, IEA*

1. Introduction

The Solar Decathlon (SD) is an international competition based on the initial idea of founder Richard King from the U.S. Department of Energy (DOE) in 2000. In this competition, universities from all over the world are challenged to design, build and operate solar powered houses. It is the only student competition worldwide addressing the performance assessment of realized buildings. During the competition's final phase, each team assembles its house in a common Solar Village. The final phase includes exhibition, monitoring and 10 contests, the reason why the competition was named a "Decathlon". Twelve competitions have been conducted up to 2016 (link 1,2), three of these took place in Europe (Solar Decathlon Europe, SDE), the last one being in Versailles, France, 2014. The European interest in the competition was stimulated by the award winners in the US from the universities in Darmstadt (2007, 2009) and Vienna (2013). With the background of the 2012 restructuring of the European Energy Performance of Buildings directive and the ongoing national efforts to improve national building codes for new buildings towards "nearly zero energy buildings", the Solar Decathlon Europe's importance as part of the European energy policy is raised as is its public visibility.

Tab. 1: Past and currently planned Solar Decathlons worldwide. Status October 2016

Region	Country	City	Past Events	Planned
North America	USA	Washington DC (5), Irvine (2)	2002/5/7/9/11/13/15	2017
Europe	Spain, France	Madrid (2), Versailles (1)	2010/12/14	?
Asia	China	Datong	2013	2017
Latin America	Colombia	Cali	2015	2017
Middle East	UAE	Dubai	-	2018

Selection and/or peer review under responsibility of Scientific Committee
doi:10.18086/eurosun.2016.01.09 Available at http://proceedings.ises.org

2. Analysis & Evolution Examples

Due to its concept, the competitions all address so called "all-electric-buildings" only. Heating and cooling are - partly assisted by ambient and solar heat - supplied by heat pumps, electricity is generated by the photovoltaic systems. The houses thereby demonstrate the ongoing European trend of the decarbonisation of the heat supply by using heat pumps instead of gas or oil boilers and a power grid based on a high saturation with renewables. Due to the small size of the houses and thereby the high surface to volume ratio (above 1 m^2/m^3) they offer much more roof space per floor area than conventional, detached, terrace and in particular apartment houses. The installed PV power per floor area for the houses in the three European competitions is in the range of 150 W_p/m^2 compared to 69 W_p/m^2 on average for detached homes in the German demonstration program for energy plus buildings (BMUB 2014) and even 45 W_p/m^2 on average for net zero energy buildings investigated within the framework of the IEA research on net zero energy buildings (Voss 2012). Due to these large installations the visual impact is high. It is much higher than in usual net zero energy building practice. The 2014 competition rules limit the PV installation to 5 kW_p per house (2010: 15 kW_p, 2012: 10 kW_p) and illustrate the development from building sizes like small cottages to more usual layouts: the rules allow for up to 70 m² floor area, and up to 110 m² for 2-storey buildings respectively (resulting in max. installed power of 70 or 45 W_p/m^2), see Fig. 1. On the one hand this increases the practical relevance of the prototypes, and on the other hand the realization process with the students is becoming more complex due to the construction efforts. Innovations for smart living on less space are becoming less important. Due to the limited roof space available it is of major importance in the early design phase of multi-story net zero energy buildings to decide upon the integration of solar thermal systems as well as a combined PV/thermal approach (hybrid installations). Solar fades are another option but are hardly brought into practice due to increased system costs, strong design implications and shading losses in dense urban environments. Fig. 3 illustrates the distribution of the active solar systems within the three European competitions. Hybrid systems are an example for the link of the Solar Decathlon to solar system research.

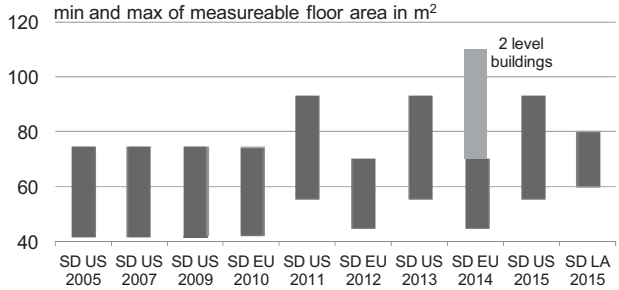

Fig. 1: Evolution of the allowable net floor area in the Solar Decathlon competition between 2005 and 2015, Source: University Wuppertal

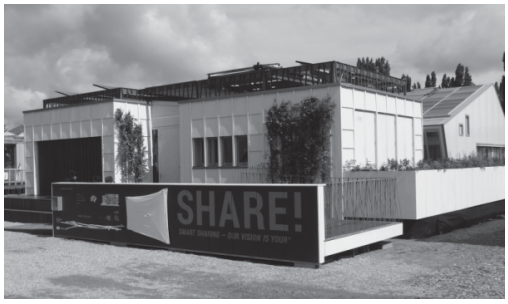

Fig. 2: The team Luzern contribution in Versailles 2014 addresses shared spaces to decrease the individual space needs per person. Source: University Wuppertal

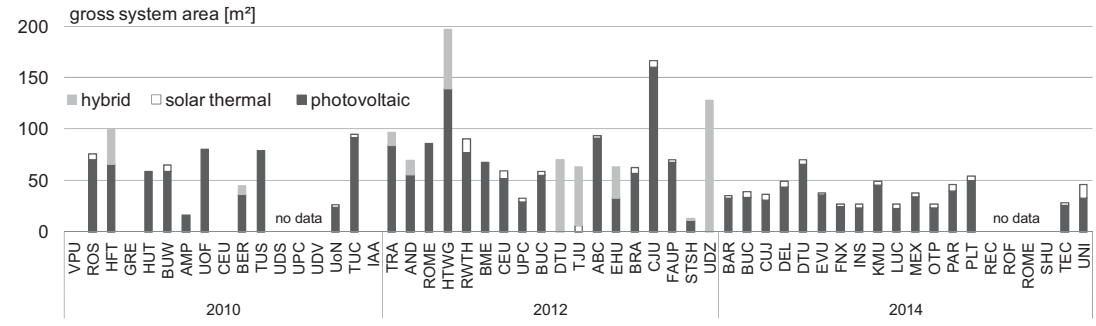

Fig 3: Distribution of the solar system gross area between solar thermal, photovoltaic and hybrid systems within the three European competitions. Source: University Wuppertal

The planned occupation of the buildings in the competitions is denser (30 m² per person) compared to real buildings in Europe (45 m² per person, Germany 2015). This addresses the enormous increase of today's life style in many countries: 3 times increased living area per person since 1950 (example Germany) is only partly compensated by the energy savings of more energy efficient buildings. Keeping this in mind, teams in the latest competitions addressed the topic of shared spaces as part of a more general shared-economy approach (Fig 2.).

Within the competition, the increased occupancy combined with energy efficient buildings resulted in an important role of appliances in the overall energy figure, Fig 4. The temporal correlation of demand and generation becomes an issue together with advanced energy storage and controls (Fig. 5 and section 3.).

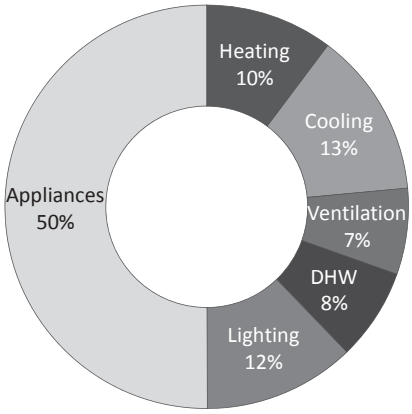

Fig. 4: Typical Distribution of the electricity demand of the solar houses presented at the Madrid competition 2012,
Source: University Wuppertal

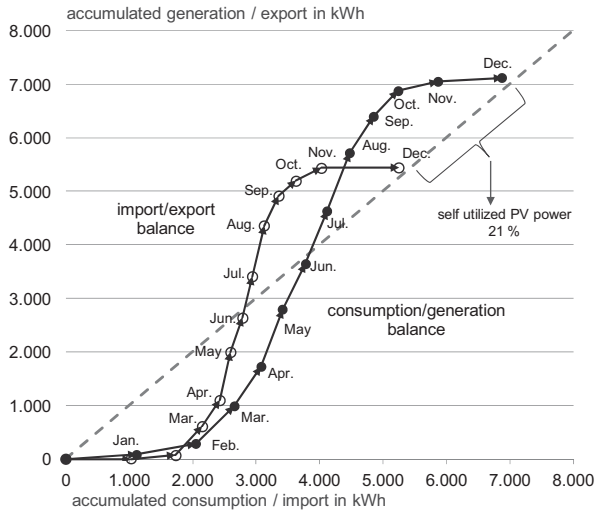

Fig. 5: The annual development of the electricity balance of the Team Wuppertal solar house during full year monitoring. The house was continuously occupied by a 2-person household (Arbach 2014).
Source: University Wuppertal

The competition is made up of 10 contests and generally: five are addressed by measurements and five judged by juries, Fig. 6. As the competition constellation varies between the events, the contest evolution is illustrated by the grouping of topics to 7 main ambitions. Fig. 7 illustrates the evolution of the weighting of these ambitions over the years. Starting with a relevance of 46%, the energy contest has lost half of its importance. This is mainly affected by introducing new contests, such as "affordability" and "sustainability". Whereas in the US the organizers tried to simplify und condense the competition rules (2002: 177 pages → 2015: 62 pages), the European edition of the rules has consistently contained about 150 pages.

The latest events in Europe and China already deal with renovation of existing buildings, mainly on the level of small homes, Fig. 8. This was not the effect of changes in the rules but individual decisions of the participating teams. Some teams work on dense urban structures although building small units in the competition by adding roof top apartments on existing apartment buildings, Fig. 9. A deeper relevance of building renovation and transformation is to be increased in future competition concepts within the new Energy Endeavour initiative (section 5).

The experiences with the large efforts to set up the infrastructure for the solar village together with the request for more intensive events, communication activities and research have stimulated the organizers of the upcoming competitions in China and Dubai to extend the operation of the solar village from two weeks to about three months and connect it to a series of further events.

Usual practice after the competition is the disassembly of the houses and the transport to the home countries of the participating teams. Many of the houses are exhibited on the home university campus and used for research or as office space extensions. This is already well documented for the US competitions, Fig. 10 (link

1). The post competition activities allow to extent the impact of the efforts at the home university in interdisciplinary research and education as well as communication. The joint project "10 Action" within the EU Intelligent Europe program, the summary books edited by the organizers of the two Spanish events (Vega 2011, 2013) or the German language book publication "SolarArchitektur [4]" following the SDE 2010 serve as successful examples of a coordinated after competition publicity in Europe (BUW 2011). The post competition activities at each participating university mean further work and a local budget allocated to it. Experiences from the German teams underline the big challenge in keeping the student teams alive and securing further financial support (Voss 2014). A convincing example from SDE 2010 is the utilization of the house of the Applied University Rosenheim: After two times presentation on large public fairs it was finally placed as part of a hotel development within a zero energy district development (link 3). The house can be regularly booked and experiences with the innovative building concept can be shared. A monitoring is running. A further convincing example is placing the award winner house of the US competition 2013 from the Team Austria in a commercial exhibition site for prefabricated houses near Vienna (link 4).

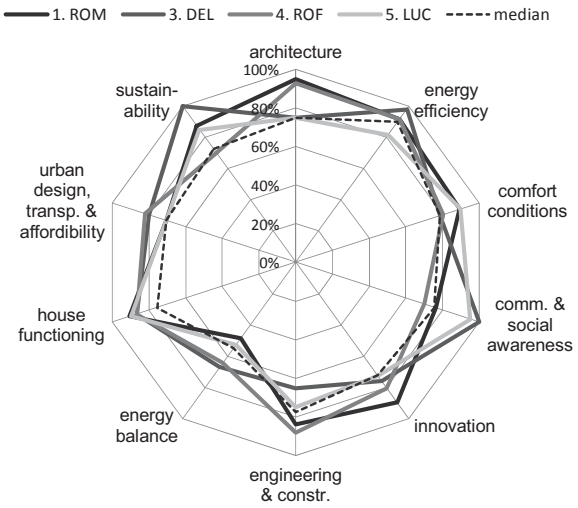

Fig. 6: Example for the contest rating in the SDE Versailles 2014 for the Delft (DEL), Lucern (LUC) and Berlin (ROF) houses in relation to the winner team from Rome (ROM) and the median of all 19 teams participating, Source: University Wuppertal

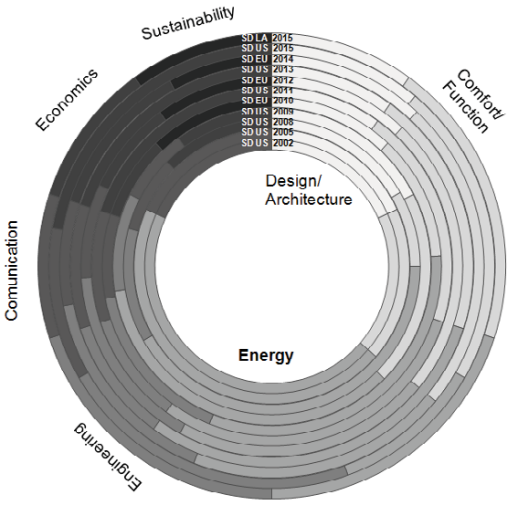

Fig. 7: Evolution of the contest weighting within the competitions worldwide between 2002 and 2015, Source: University Wuppertal

Fig. 8: The TU Delft entry to the competition in Versailles was the retrofit of a typical Dutch terrace home. Source: University Wuppertal

Fig. 9: The Berlin entry for Versailles addresses an apartment addition on top of a typical multifamily house. Source: University Wuppertal

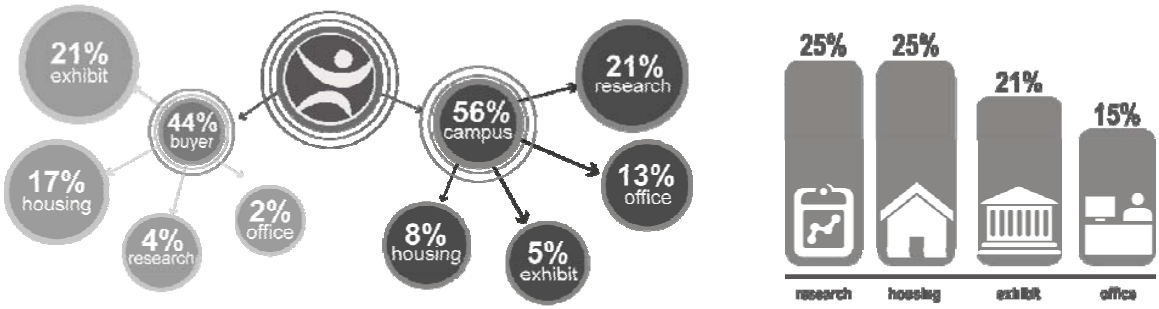

Fig. 10: Analysis of the post competition utilization of the Solar Decathlon US entries from 2005 to 2013.
Source: University Wuppertal

3. Scientific Liaison

Past Solar Decathlons focused on communicating innovative energy saving solutions and solar energy utilization in buildings to the general public. A special issue of the Energy & Buildings Journal 2014 was the first set of SD publications addressing the scientific value of the event (Vega 2014). A consequent analysis of the monitoring data from the competition week was not in the focus up to now. Some teams addressed building science questions by operating the solar houses as living labs back at home, Fig. 5 (Arbach 2014).

Within the competition, each building is designed for extremely low energy use according to the competition rules. All buildings together form a temporary solar village of all-electric-homes partly linked with electric vehicles, e.g. in Irvine, USA, 2015. Beside low energy consumption and solar energy generation, the correlation of demand and supply becomes a major issue in future energy systems, Fig. 11,12. Based on former research on net zero energy buildings within the framework of the International Energy Agency (IEA Task 40 SHCP / Annex 52 EBC) a new activity was started focusing on "energy flexible buildings" (Annex 67 EBC, link 5). The solar village of the next Solar Decathlon Europe is dedicated as a case study. The energy systems will be designed under consideration of performance indicators for energy flexibility. Heat and power storage together with advanced building automation systems will play a major role. An intelligent link between buildings and electric mobility has to considered. The measurements of the solar village´s smart grid will allow the comparison with the predictions as the basis for a scientific analysis.

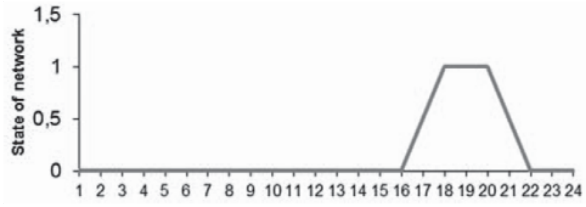

Fig. 11: Example of the energy contest rules in SDE 2014: To assess a house's energy consumption management ability at a certain time of day, the network maximum load period is simplified to a single consumption peak from 5 to 9 pm. If energy is sent to the network between 4 and 10 pm, points are won, proportionally to the amount sent. If energy is taken from the network between 4 and 10 PM, points are lost in proportion to the amount called.
Source: www.solardecathlon2014.fr

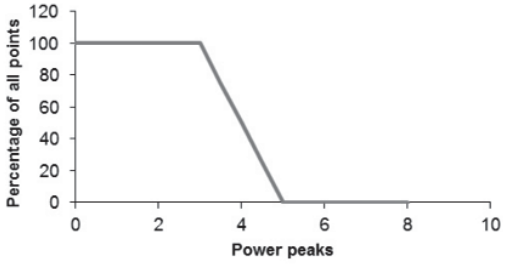

Fig. 12: The percentage of maximum points obtained by a team will depend on the average of the three highest positive peaks (electrical energy sent to the network) and three highest negative peaks (electrical energy used).
Source: www.solardecathlon2014.fr

4. Documentation & Analysis - The Knowledge Platform

Currently it is an extensive effort to gain precise information from past Solar Decathlons outside the US. As the competition concept spreads worldwide and has various national organizers, the information is presented on different web portals, in different forms, with different intensities and often disappears shortly after the competition. The SD knowledge platform is a major task to secure the information, experiences and data from past events as well as to feed in the information of new competitions in one place, Fig. 13,14. The web-based platform is currently under preparation at Wuppertal University and is planned for public accessibility in early 2017.

The audience for the information stored is made up of mainly the organizers as well as the participating teams of new events. The available information may stimulate scientific work and the utilization for education. The knowledge platform also will allow the user to do efficient research by using extensive filter possibilities and the full text document search. An interactive map will show all team origins and competition sites. The language of the knowledge platform is English. There will be also the possibility to use a browser built-in translator and filter documents for the language they are written in. After a test phase the teams of the Solar Decathlon China in 2017 and Solar Decathlon Middle East in 2018 will deliver their project manuals, project drawings, pictures and other media data as well as detailed information about their house directly to the knowledge platform.

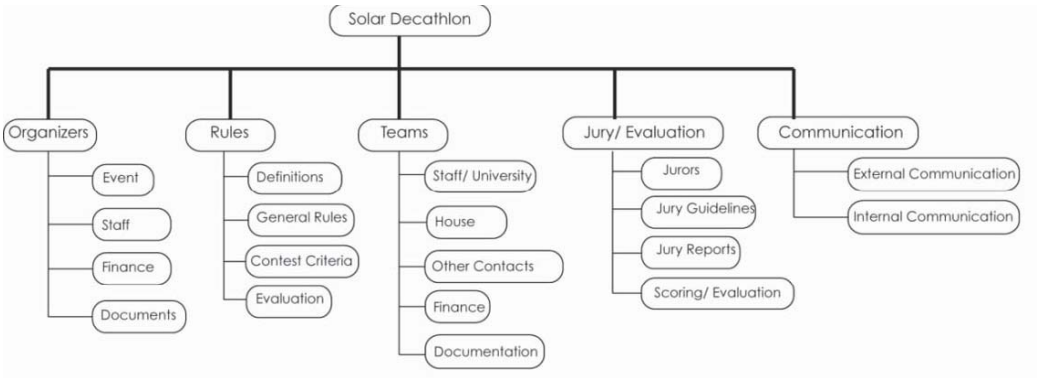

Fig. 13: Basic structure of the SD knowledge platform. Source: University Wuppertal

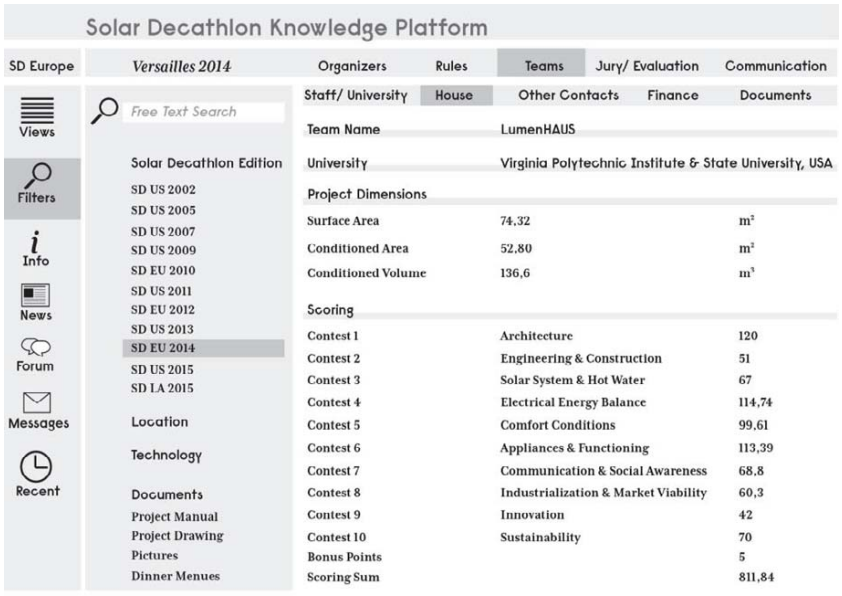

Fig. 14: Initial image of the frontend for the knowledge platform. Source: University Wuppertal

5. The "Energy Endeavour" Evolution

Contrary to the US competition, which is centrally managed by the Federal Department of Energy (DOE), the Solar Decathlon in Europe is an independent organization for each location. The hosting organization individually works on a memorandum of understanding (MOU) with the DOE. Starting already in 2010 with the "Proclamation of Madrid" (SDE 2010) the participating teams of the Solar Decathlon Europe called for a European profile of the competition and an evolution with regard to form and content. A small team of former SDE organizers and participants was establish to develop an improved European platform for the competition with a link to the DOE (Rollet 2014). This was followed by a series of meetings with European Commission representatives to ask for political and financial support. The European Commission included a small budget for communication of the SDE in the Horizon 2020 2016/2017 budget (EC 2016, link 6). In early 2015 an organizational and financial structure was proposed including the creation of a nonprofit organization (Russell 2015). A central web portal was also created in 2016 to link all SDE events and connecting them to the worldwide movement, Fig 15.

The participating teams formulated in the proclamation of Madrid the need for an evolution of the competition to also address existing buildings and dense urban living (SDE 2010). This was readdressed in a symposium in Madrid 2012 and in the Versailles Declaration of 2014 (SDE 2014). As starting point of a discussion process, an analysis of the strengths, weaknesses, opportunities and threats of the past SDE events was compiled (Tab. 2). The analysis indicates strong potentials in the evolution of the competition itself but also in the link to other events and competitions. Not every need can be covered by the SD format itself but a wider set of competitions including the SD as its currently prime event may improve the impact of all of the events considerably. The name for this framework of sustainability competitions was coined the "Energy Endeavour" by Louise Holloway. The Energy Endeavour is being assisted by the non-profit foundation. The foundation is also negotiating the MOU with the U.S. DOE as their partner in Europe to steward the values, message and content of the Solar Decathlon in Europe.

Fig. 15: The new home page of the Solar Decathlon Europe describes the Energy Endeavour initiative and links to the worldwide events, Source: www.solardecathlon.eu

Tab.2: SWOT analysis focusing on the three European competition editions.
Source: University Wuppertal

Strengths	Weaknesses
• topic of high relevance in society, policy, economy & building science • innovative show cases for communication of ZEB to the general public • unique "design-build-operate" approach for educating students • interdisciplinary work stimulates cross boarder education at the universities	• „insider event“, lack of links • no strong & harmonized communication outside the event weeks • limited market relevance by focus on new and small buildings • lack of links to building energy policy • missing scientific approach & relevance
Opportunities	**Threats**
• collaboration of all actors in the building sector • link to e-mobility • linking craftsmen and academic education • increased impact in research and energy policy • focus on existing buildings and dense urban structures • continuous evolution of topics, rules and form • continuous, harmonized communication and networking	• lack of interest of the general public, depending on location • decreasing degree of innovation (copy & paste) and interest • loss of organizational know-how from one event to the next • non secured financial foundation • risk of sufficient industry support

All past Solar Decathlon events underline the professional approach needed for the success of such an event. If the organizer cannot benefit from previous experience, even minor details can jeopardize success. The essential infrastructure for the competition phase demands considerable effort, from shuttle bus services to measurement technology. This in turn requires an adequate budget (in Europe about 10 million €). In many ways, in form, content and financially as well, new competitions profit from a certain continuity of know how. The Energy Endeavour network will serve as a know-how platform linking the experiences worldwide. This requires a certain financial foundation itself. On the other hand, the network service reduces the budget needed per event.

6. Outlook

An IEA annex addressing the Energy Endeavour initiative will be formally proposed within the program on Energy in Buildings and Communities (EBC) and discussed at its board meeting until the end of 2016. It will depend on the international support with regard to the content and shared funding, whether this new network can start work in 2017. The discussion on a follow up Solar Decathlon in Europe is still ongoing. In the case of successful installation of the Energy Endeavour network, it is intended that the location will be selected by a call for cities in 2017.

Acknowledgements

The work on the competition documentation and analysis as well as the knowledge platform is supported by the German Federal Ministry of Economy and Energy within its funding initiative for Energy Optimized Building (EnOB). The Energy Endeavour Foundation and its initial funding for setup, outreach and communication has been supported by the Faculty of Architecture and the Built Environment, TU Delft.

7. References

Literature

Arbach, S., Otto, J., Voss, K.: Nullenergiehaus im Praxistest, Sonne, Wind und Wärme, 10/2014

BMUB: What makes an Efficiency House Plus? Federal Ministry for the Environment, Nature Conservation, Building and Nuclear Safety, brochure, 2014

BUW 2011: SolarArchitektur 4, Detail, ISBN 978-3-920034-48-5, 2011

Rollet, P., Russell, P., Voss, K.: Solar Decathlon Europe - Beyond 2014, A position paper, 2014

Russell, P.: Solar Decathlon Europe Secretariat - Project Description, Structure and Finances, 2015

SDE 2010: Solar Decathlon Europe Proclamation, signet by the faculty advisors, 27 June 2010

SDE 2014: Versailles Declaration, signet by the faculty advisors, 12 July 2014

Vega, S., Serra, J.: Solar Decathlon Europe 2010 - Improving Energy Efficient Buildings, download: http://www.sdeurope.org/wp-content/uploads/downloads/2011/10/SOLAR-DECATHLON-EUROPE-2010.pdf

Vega, S., Serra, J.: Solar Decathlon Europe 2012 - Improving Energy Efficient Buildings, ISBN 978-84-695-8845-1, 2013

Vega, S., Rodriguez-Ubinas, E. (ed.): Science behind and beyond the Solar Decathlon Europe 2012, Energy and Buildings, Special Issue, vol. 83, 2014

Voss, K. et. al.: Solar Decathlon Europe - Dabei sein ist nicht alles, proceedings of the EnOB Symposium, Essen, Germany, 2014

Voss, K., Musall, E.: Net Zero Energy Buildings - International projects of carbon neutrality in buildings, Detail, 2nd edition, ISBN 978-3-920034-80-5, 2012

Web links

link 1: http://www.solardecathlon.gov/, last visited 21.9.2016

link 2: http://www.solardecathlon.eu, last visited 21.9.2016

link 3: http://www.solar-decathlon.fh-rosenheim.de/nachnutzung, last visited 21.9.2016

link 4: http://www.blauelagune.at/r/lisi-haus, last visited 21.9.2016

link 5: IEA EBC Annex 67: www.iea-ebc.org/projects/ongoing-projects/ebc-annex-67/, last visited 21.9.2016

link 6: ec.europa.eu/research/participants/data/ref/h2020/wp/2016_2017/main/h2020-wp1617-energy_en.pdf, last visited 21.9.2016

02. Solar Heat for Industrial Processes

Conference Proceedings

EuroSun 2016
Palma de Mallorca (Spain), 11 - 14 October 2016

Solar thermal energy use in lead acid batteries recycling industry: A preliminary assessment of the potential in Spain and Chile.

Elisa Alonso[1,3], Alessandro Gallo[1] and Héctor Galleguillos[2,3]

[1] University of Antofagasta. Antofagasta Center of Energetic Development. Antofagasta (Chile)

[2] University of Antofagasta. Chemical Engineering and Mineral Processes Department. Antofagasta (Chile)

[3] Solar Energy Research Center (SERC Chile). Santiago de Chile

Abstract

Lead acid batteries recycling industry has a significant heat demand, including processes at around 500 and 1000 ºC. Due to it, this work faces a preliminary approach to the integration of CSP technology with such an industry. A general description of the recycling process is presented as well as the thermal requirements of the different stages. Smelting and refining are retained among them and they are proposed to be provided with concentrated solar energy as source of heat. Two different locations are evaluated: Murcia, in Spain and Calama, in Chile. Combining the two processes and two locations, four cases are presented. Heliostat field and central receiver dimensions are estimated for each case and the percentage of annual solar fraction is obtained according to the energy demand. A solar multiple is considered in order to include thermal storage and to provide a constant heat demand. While in Spain the proposed solar plants are able to supply 68 and 76 % of the smelting and refining respective annual demands, in Chile the solar fraction achieves 90 and 94 %.

Keywords: *Lead-acid batteries recycling, Solar process heat, Central receiver, Spain, Chile*

1. Introduction

Industrial sector accounts a significant fraction of the global heat demand. For instance in the European Union the total useful heat demand in industry overpasses 4000 PJ/year and covers about 28% of the total primary energy consumption for final uses (Pardo et al., 2012). According to IEA and SolarPACES this consumption can be separated into three temperatures intervals: below 100 ºC, 100-400 º C and above 400 ºC (SHC IEA and SolarPACES, 2008) and concerning European countries, 30 percent of industrial processing requires heat below 100 ºC, 27 percent of industrial heating needs can be met with heat between 100-400 ºC, and 43 percent requires heat over 400 ºC.

The use of solar energy to supply thermal requirements in industrial processes is an environmental friendly alternative applicable to different industrial sectors. However, there is still much room for innovation which has been largely unexploited. In several countries, chemical, petrochemical, textile, food and beverage industries have been considered to assess the substitution of conventional fuels by solar energy, although such a development is still in research stage (Baniassadi et al., 2015). Other promising sectors considered in literature include paper, mineral products, wood, tobacco and machinery among others (Lauterbach et al., 2012). Most studies aimed to integrate thermal solar energy as industrial heat process have been done on below 100 ºC and 100-400 ºC temperature ranges (Calderoni et al., 2012; Frein et al., 2014). Nevertheless, the feasibility of using solar industrial process heat at high and extremely high temperatures has been studied only for small scale processes such as synthesis of chemicals and materials treatment (Steinfeld et al., 2001). (Calderoni et al., 2012). The latest developments in concentrating solar energy technologies tend to increase

doi:10.18086/eurosun.2016.02.17 Available at http://proceedings.ises.org

the operation temperature in order to improve thermal conversion efficiency. If temperatures higher than 1000 ºC are reached in large scale systems, other industrial processes such as some metallurgical reactions can be considered to be addressed with solar thermal energy.

The general challenge in the field is a proper integration of state of art solar thermal technologies according to the heat, temperature and transfer medium requirements. Economic arguments must be also taken into account: due to relatively low energy prices for industrial customers in several countries worldwide, solar thermal systems do often have pay-back times higher than their lifetime. In general, the heat is transferred through a heat transfer medium (water, steam, air, etc.). For those processes that need constant loads, thermal storage and/or fossil hybridization have to be considered.

The lead–acid battery (LAB) is one of the most recycled products throughout the world with a recycling rate in most countries exceeding 95%. Because LAB dominates consumption of the element, around 80% of world lead output, secondary lead sourced from batteries is the major contributor to the world's annual lead production of around 8.4 million tons (Stevenson, 2009). Recycling contributes to the minimization of environment pollution and the conservation of natural lead resource. Moreover, it is considered a profitable business because of the value of lead as a commodity ("Lead Recycling Sustainability in action," 2014) and currently is cleaner and safer thanks to the lasts regulations.

Although the traditional high pollution associated to LAB recycling plants is being decreased with the more recent developments, their high energy consumption is still environmentally harmful. Frías et al. (year not available) presented an innovative process to reduce global pollution in LAB recycling (Frias et al., year not available.). Although their proposal is cleaner than more conventional technology, it still consumes 1 MWh/t Pb. As with other industrial processes, thermal solar energy could be employed to provide heat to several stages of the recycling plant. Thus, the objective of this work is to carry out a preliminary assessment of the potential to integrate central receiver solar thermal technology as heat source for the recycling process, considering two different scenarios: Spain and Chile. More than 350000 tons of LAB are processed in Spain annually what means more than $1.40 \cdot 10^{11}$ kJ of heat consumption in the form of natural gas. On the contrary, the industry in Chile is much smaller, with around 25000 tons of batteries annually recycled. The availability of solar resource is also quite different in both countries, as shown in the corresponding section below.

2. Methodology for the potential assessment

In order to assess the potential use of thermal solar energy in the LAB recycling industry, a general description of the process is presented based on different sources of bibliography and several visits to the plants of Exide Technologies (San Esteban de Gormaz, Soria) and Recobat-Lyrsa (Albate del Arzobispo, Teruel) in Spain, as well as personal communications from the qualified staff of these companies.

A simplified scheme of the operations retained for the study is presented. Typical operation temperatures and distribution of heat demand per ton of produced lead are stablished. The medium through which the heat is supplied is also informed. Those processes that occur at high temperature are selected and solutions are proposed based on the integration of solar central receiver technology. Different thermal storage technologies are also taken into account for the analysis.

An overview of the LAB recycling industry situation in Spain and Chile is also presented. Because the volume of processed LAB is very different in the two countries, two different plant sizes are selected for the study according to both scenarios. Situation of the plants in Chile and Spain are selected among the locations of existing plants, taken into account the isolation conditions.

Assuming that the industries have a portion of available land in their neighborhood, where a solar plant could be installed, a solar field is dimensioned to supply heat to the recycling process. To do that, DNI data of Spain are taken from Meteonorm. Because such a database does not include some areas of Chile, DNI data of Chile are taken from measurements published by the Energy Ministry of Chile. Once the heliostat field and the receiver are dimensioned for the established cases, including a certain solar multiple and a storage capacity, the energy production is monthly calculated. Then, the annual solar fraction is also given.

3. Description of the industrial process

Recycling of spent LAB to obtain secondary lead involves several stages of a global process from the reception of the batteries to the final production of the lead. In general, recovery of the lead and other components is not difficult because the batteries are easily broken and divided into their various fractions. Thus, the recycling of LAB is well established practice throughout the world (Stevenson, 2009).

Although there is not a unique scheme but a combination of different alternatives, many countries have implemented similar recycling technologies able to maintain recycling rates greater than 90%. Stevenson (2009) offers an overview of the most common procedures. Once received at the recycling plant, a LAB undergoes several breaking operations. Free sulfuric acid is drained and pumped to a neutralization plant. The battery itself is dismantled through a hammer mill or roller crusher. The plastic fractions are usually separated by floatation. Other processes exit to separate the components of a LAB, such as using a saw to remove the plastic top and a trommel to extract the internal metallic fractions. The internal parts of a LAB are composed of small fractions of metals and other materials and mainly of the so-called paste, which is formed by the positive (lead oxide, 30-35 %) and negative (lead sulfate 55-60 %) active materials of the battery. The plastic fraction is composed of polypropylene and polyethylene and, to be recycled, it is required their melting at temperatures that varies between 150 and 200 ºC, depending on the fraction composition. Hot air is usually employed as heat transfer medium. Some batteries recycling plant do not include this process but they send the plastic to be recycled elsewhere. Two methods exist for the recovery of lead from battery paste, grid and other lead components; pyrometallurgical and hydrometallurgical. Pyrometallurgical are the dominant methods for both recovery and refining and they are particularly taken into account in this analysis because of their high demand of heat. Main pyrometallurgical operation is the smelting of the grids and active materials, which usually takes places in rotary kilns that are also loaded with iron, coke and other compounds as silica and sodium carbonate (Zabaniotou et al., 1999). The exact composition of kilns load depends on the desired composition of the final product. In general terms, two types of finished lead can be differentiated: one of higher purity (99.98%) that will be further employed to produce lead oxides for cathodes and another one, of lower purity, called hard lead (~97%) that will give rise to grids and the production of lead sulfates for anodes (Zhang et al., 2016). Furnaces temperature can vary in a range of 950-1100 ºC depending on the load. Exhaust gases are employed to preheated air that enters in the kiln at 400-500 ºC. Then, internal temperature of the kiln is increased through natural gas driven burners. After the smelting, lead is separated from the slag and conducted to refining stage. A kettle is operated at maximum temperature of 650 ºC although its temperature varies depending on the consulted source and the finished product composition. Different substances are also added in this stage, such as NaOH, NaCl or NH_3NO_3. The result from the refining operation is the commercial pure or hard lead. A general flowsheet of the recycling processes is shown in Figure 1. Although the plants usually operate 24 hours a day, the process is not always continuous. Thus several intermediate storages can be found between one stage and the next.

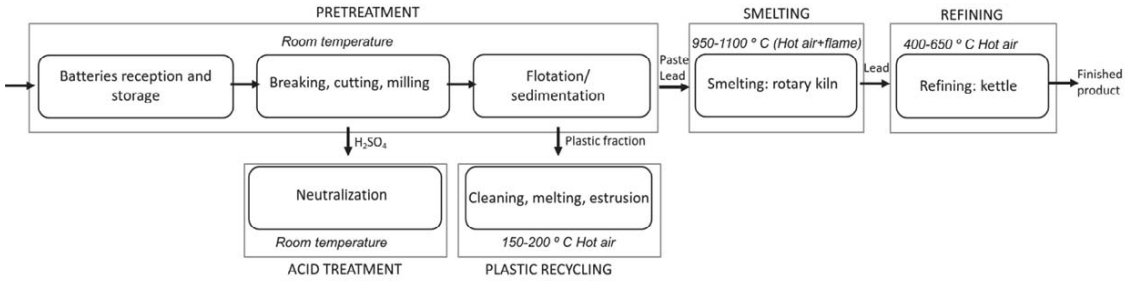

Fig. 1: Flowsheet of a typical lead-acid batteries recycling plant including the most common operations and working conditions.

4. Definition of the study

4.1. Heat demand

Because plastic fraction is usually send elsewhere for its recycling, it is not considered in this analysis. Then, the operations retained for this assessment work at temperature ranges characteristic of solar tower CSP systems.

Smelting temperature can vary between 950-1100 ºC and it is assumed as the average in this case: 1025 ºC. Rotary kilns employ natural gas burners and the heat consumption can be estimated in 43 m^3 per ton of finished product. Refining temperature can be also variable in a significant range but it is considered of 525 ºC for this preliminary analysis. Gas natural consumption of a typical kettle can be estimated in 18 m^3 per ton of finished product. Considered net lower calorific value of natural gas is 10.83 kWh/Nm^3. Note that the furnaces, both rotary and kettle, usually perform in batch mode, what implies the need of storing the material before each operation. Nevertheless, the furnaces are expected to operate also during nights, so for a preliminary analysis it can be considered a constant heat demand 24 hours a day all year round. Thus, thermal storage must be included in the analysis. These definitions are particularly stablished to carry out this work. Although they do not correspond with realistic data of any particular plant, they are based on the information provided by Exide Technologies and Recobat-Lyrsa.

4.2. Location, plant size and solar resource

LAB recycling is an extended practice in Spain with more than 350000 tons of batteries annually processed. (Gallardo Gómez, 2014). This represents a recycling rate over 95% but involves more than $1.40 \cdot 10^{11}$ kJ of heat consumption in the form of natural gas. It is important to note that primary lead production is null in Spain. Four important recycling plants are distributed in different locations of the country and they are indicated in Figure 2 together with their capacity in tons of lead annually produced. Other plants of less capacity are located around the country. The present study is based on a plant located in Murcia which capacity is defined in 30000 tons of lead per year. Murcia is one of the locations of higher DNI as it can be observed in Figure 2 (Geomodel, 2014, 2015).

The LAB recycling industry in Chile is much smaller, with around 25000 tons of batteries annually recycled. Many of the Chilean spent LAB are exported to other countries, mainly to Peru. For instance, 14000 ton of spent batteries were exported in 2008 to several countries. Moreover, there are a significant number of non-authorized recyclers that process batteries outside the law (Gobierno de Chile and GTZ, 2009). Figure 2 shows the location of the only authorized plant that currently operates in Chile whose capacity is about 8000 tons of end lead per year. It is placed in Calama, in the middle of the Atacama Desert where the insolation is the highest measured in the world. This plant is the reference for the definition of the Chilean cases.

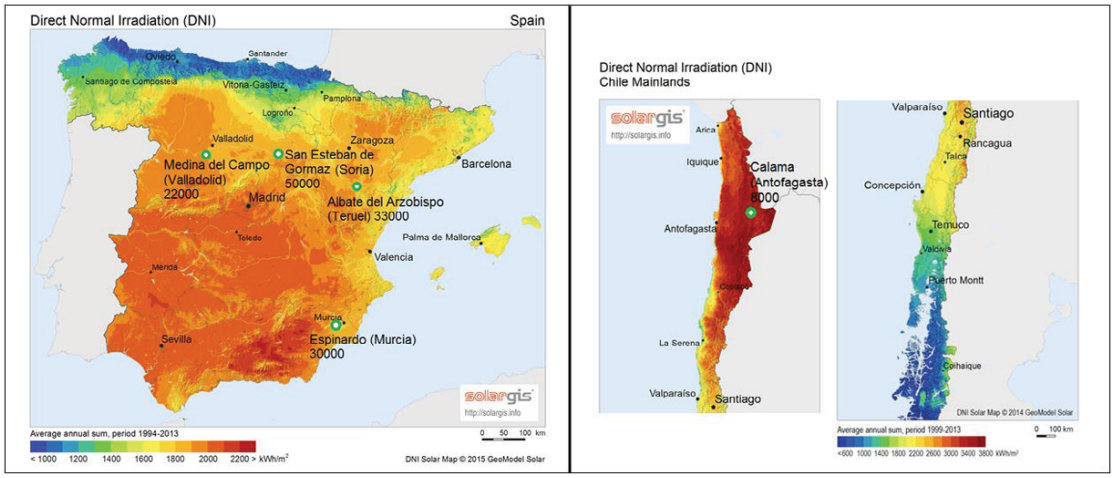

Fig. 2: DNI maps of Spain and Chile provided by SolarGis. Location of the main plants of lead-acid batteries recycling in Spain and Chile (indicated with a green circle) and their approximate capacities in produced tons of end lead per year.

4.3. Cases of study

Smelting and refining operation in both countries, Spain and Chile, have been selected as cases of study. Central receiver technology could be coupled with the processes according to the temperature values. Refining operation could be also coupled with a parabolic through plant but it is not analyzed in this work. Table 1 compiles the specific problems that are approached in this study. Combinations of different plant size, location and point of application in the industrial process leads to four cases of study. Heat demands are estimated for each case taken into account the selected plant capacity and the consumption previously defined for each operation.

Table 1. Definition of starting conditions for the present study. Four cases have been selected by combining different applications, location and plant size.

Case	Location	Operation	Heat demand (GWh/y)	Temperature (ºC)
1	Murcia (Spain)	Smelting	14	1025
2	Murcia (Spain)	Refining	5.8	525
3	Calama (Chile)	Smelting	3.7	1025
4	Calama (Chile)	Refining	1.6	525

5. Analysis of proposed cases

5.1. Case 1

A field of heliostats with an air central receiver can be considered for this case. Since the heat demand is 14 GWh/y and a constant demand is assumed, the required net thermal power is 1.6 MW. A high solar multiple has to be considered in order to overproduce a considerable amount of energy to supply such constant demand. A 3.5 is the selected value for this case and the following for comparative purposes. A storage capacity of 18 h is considered for calculations. Note that the storage capacity will be decreased according to the thermal storage system efficiency, which will depend on the TES system, but it is neglected for this analysis. This solar multiple lead to a receiver useful power of 5.6 MW and this value defines the plant size. For this power, one side oriented heliostats field coupled with a volumetric receiver could be used. In volumetric receivers airs flows through a porous structure and it is heated to high temperature. Ceramic volumetric are suitable to achieve up to 1200 ºC. The system may require a CPC when the peak concentrated solar flux is not sufficient to reach the process temperature. A typical efficiency of a ceramic volumetric receiver is taken from the average of the examples published by (Ávila-Marín, 2011) and it is 64%. Considering an efficiency of the heliostat field of 70 % (Falcone, 1986) for a conservative estimation, the required area of collection would be 12537 m^2. For this calculation, the maximum annual DNI of Murcia (997 W/m^2) was used. Advanced TES systems should be taken into account to be coupled with this type of solar plant. High temperature thermochemical storage (TCS), which is still in development stage, would be suitable to storage and release heat at temperatures ranges of 800-1200 ºC, depending on the employed material. Many works on such a topic can be found on literature (Agrafiotis et al., 2015; Alonso et al., 2015; Pardo et al., 2014)

5.2. Case 2

For this case, a one side oriented heliostat field combined with a central receiver is also selected. Because of the temperature range, this application can be easily coupled with more developed technologies: a cavity with a tubular receiver and the so called Solar Salt (60 % $NaNO_3$, 40% KNO_3) as thermal fluid. The heat demand is 5.8 GWh/y and for a constant demand, the required net thermal power is 0.74 MW. The efficiency of the receiver belonging to PS10 plant (Spain) is taken as a reference, which is close to 90% (Siva Reddy et al., 2013). Although this plant works with water as thermal fluid, the type of receiver can be coupled with the here exposed case. The considered heliostat field efficiency is 70%. A solar multiple of 3.5 is also included in this case as well as 18 hours of thermal storage, using for that a two tanks molten salts storage system, which is the most commercially developed currently. Thus, receiver power is set in 2.6 MW. The required collection area, calculated with the maximum DNI in Murcia results of 4139 m^2.

5.3. Case 3

Case 3 can be analyzed in a homologous form than Case 1. A one side oriented field of heliostat and a volumetric air central receiver are the technologies suitable to be integrated with the smelting operation. Constant heat demand is 3.7 GWh/y, that is, a power requirement of 0.4 MW. Assuming the same criterion to select the solar multiple, the receiver size would be 1.5 MW. The system may require a CPC when the peak concentrated solar flux is not sufficient to reach the process temperature. In comparison with the plant proposed in Case 1, better efficiencies of the heliostat field and volumetric receiver could be assumed due to the favorable climatic conditions of the plant location. A deeper analysis on the design parameters would be required to achieve a relevant evaluation. However, for this preliminary assessment, 70% and 64% are considered as heliostat field and receiver efficiencies respectively. The resulting collection area, for the maximum annual DNI in Calama (1132 W/m^2) is 2958 m^2.

5.4. Case 4

Case 4 would be equivalent to Case 2 in the employed technology and to Case 3 in the location and therefore, the climatic conditions. Proposed technology is a cavity with a tubular receiver coupled with a one side oriented field of heliostats. Thermal fluid would be molten salts (Solar Salt) as shown in Case 2 and it would be included a two-tanks thermal storage system able to take profit of the sensible heat of such molten salts. Constant heat demand is 1.6 GWh/y, that is, a power requirement of 0.18 MW. With a solar multiple of 3.5, the receiver power would be 0.63 MW. Receiver and heliostats field efficiencies taken for this case are 90% and 70% respectively. Then, the required collection area, calculated with the maximum DNI in Calama results of 918 m^2.

6. Annual energy supply

In this section, the annual energy supply estimated to each one of the previously analysed cases is presented. Figure 4 depicts the energy monthly produced according to the designs proposed in section 5. In Case 1, 68 % of the annual energy demand could be supplied by the solar plant, while 32 % should be provided by means of a fossil fuel source of energy. Thus, a hybrid installation will be required despite the use of thermal storage. A re-dimensioning of the plant could be interesting taking into account the cost of both the thermal storage and the fossil fuel back-up. Similar analysis can be done for Case 2 where 76 % of the annual demand could be covered by the solar plant. On the contrary, because of the favourable climatic conditions, those plants located in Calama would have a production close to the annual heat demand of the proposed industrial process. Calculations for Case 3 indicated the plant produce 90 % of the annual required energy, while result for Case 4 is 94 %. The production of a solar plant in Calama is more constant than in Murcia, which is favourable to be combined with a constant demand industrial process.

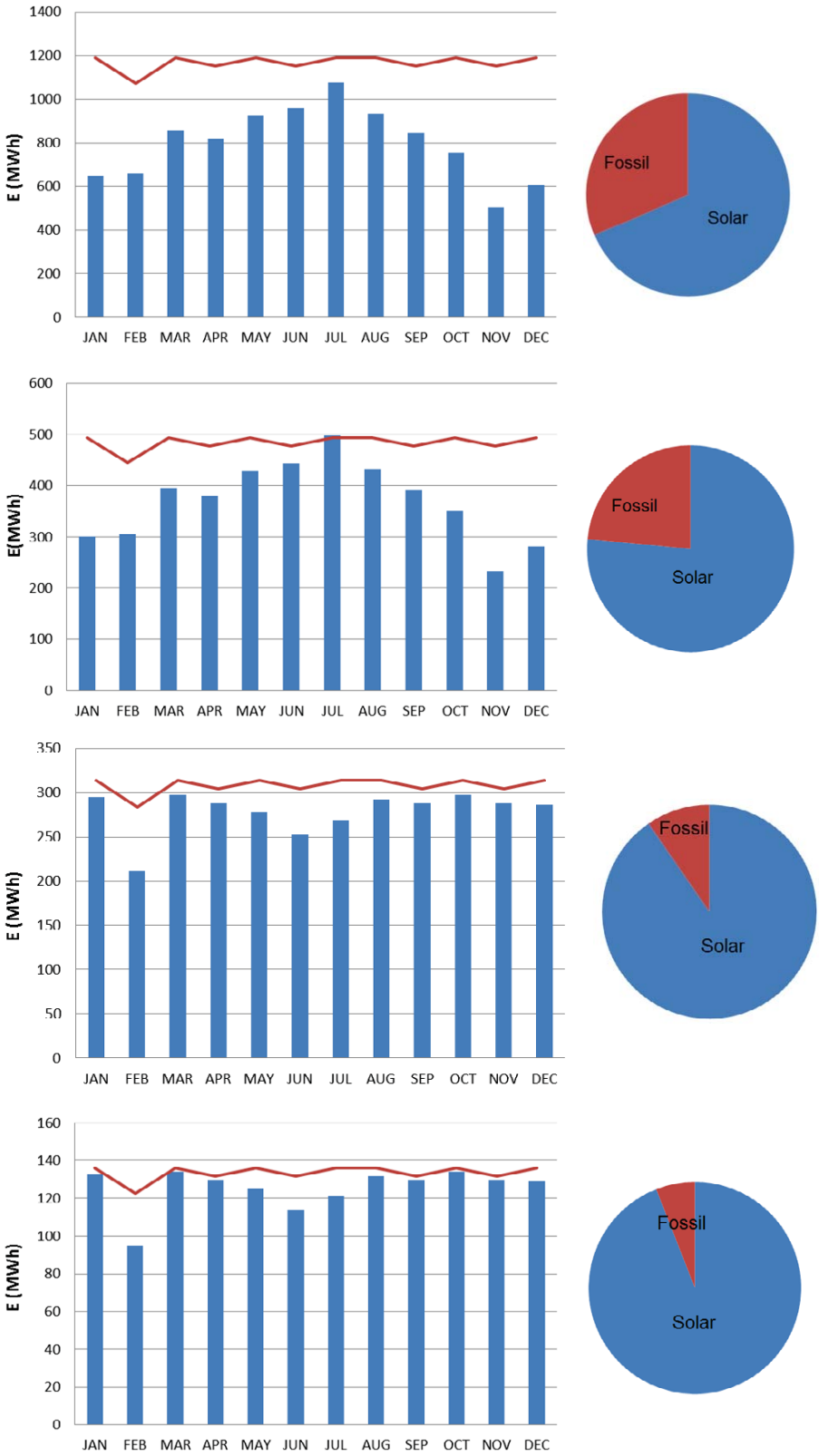

Fig.3. Energy production by the plants dimensioned to the cases described in section 5 per month during a typical year (case 1, 2, 3 and 4 respectively). Red line indicates the monthly heat demand. Fraction of the heat demand that should be provided by conventional fuels, according to the proposed designs.

7. Conclusions

Lead acid batteries (LAB) recycling industry is a strong sector all over the world and the associated heat demand is very significant. A preliminary analysis of the opportunities to integrate CSP technologies in the LAB recycling industry is presented in this work. Two operations, smelting and refining are retained for a concrete analysis and they are couple with central receiver technology. Two different locations are studied: Murcia (Spain) and Calama (Chile), with different climatic conditions. Thermal storage is considered by giving a solar multiple and a storage capacity. Using typical data of literature for plant dimensions estimation, the annual solar fraction of energy demand is obtained for the four proposed cases. While in Spain the proposed solar plants are able to supply 68 and 76% of the smelting and refining respective annual demands, in Chile the solar fraction achieves 90 and 94 %. The production of a solar plant in Calama is more constant than in Murcia, which is favourable to be combined with a constant demand industrial process. Economic aspects as well as daily energy supply management must be taken into account in a further stage for a more complete analysis.

Acknowledgments

The authors acknowledge the financial support provided by the FONDECYT project number 3150026 of CONICYT (Chile), the Education Ministry of Chile Grant PMI ANT 1201, as well as CONICYT/ FONDAP/ 15110019 "Solar Energy Research Center" SERC-Chile. Also, the second author wish to thank the University of Almeria for the assistance devoted to the development of his Ph.D research.

References

Agrafiotis, C., Roeb, M., Sattler, C., 2015. Hybrid sensible / thermochemical solar energy storage concepts based on porous ceramic structures and redox pair oxides chemistry. Energy Procedia 706–715.

Alonso, E., Pérez-Rábago, C., Licurgo, J., Fuentealba, E., Estrada, C.A., 2015. First experimental studies of solar redox reactions of copper oxides for thermochemical energy storage. Sol. Energy 115, 297–305. doi:10.1016/j.solener.2015.03.005

Ávila-Marín, A.L., 2011. Volumetric receivers in Solar Thermal Power Plants with Central Receiver System technology: A review. Sol. Energy 85, 891–910. doi:10.1016/j.solener.2011.02.002

Baniassadi, A., Momen, M., Amidpour, M., 2015. A new method for optimization of Solar Heat Integration and solar fraction targeting in low temperature process industries. Energy 90, 1674–1681. doi:10.1016/j.energy.2015.06.128

Calderoni, M., Aprile, M., Moretta, S., Aidonis, A., Motta, M., 2012. Solar thermal plants for industrial process heat in Tunisia : Economic feasibility analysis and ideas for a new policy 30, 1390–1400. doi:10.1016/j.egypro.2012.11.153

Falcone, P.K., 1986. A handbook for Solar Central Receiver Design 1–275. doi:10.2172/6545992

Frein, A., Calderoni, M., Motta, M., 2014. Solar thermal plant integration into an industrial process. Energy Procedia 48, 1152–1163. doi:10.1016/j.egypro.2014.02.130

Frias, C., Ocaña, N., Diaz, G., Piper, T., Bulkowski, B., Chmielarz, A., Claisse, P., Hemmings, S., Abrantes, L., Jansen, H., Erkel, J. Van, Franken, T., Kunicky, Z., Velea, T., n.d. A clean-lead factory is available for lead-acid batteries recycling by mens of the "cleanled process."

Gallardo Gómez, G., 2014. Analisis de viabilidad económica de una planta de reciclado de baterías plomo acido.

Gobierno de Chile, GTZ, 2009. Diagnostico de importación y distribución de baterías de plomo ácido usadas.

Lauterbach, C., Schmitt, B., Jordan, U., Vajen, K., 2012. The potential of solar heat for industrial processes in Germany. Renew. Sustain. Energy Rev. 16, 5121–5130. doi:10.1016/j.rser.2012.04.032

Lead Recycling Sustainability in action, 2014.

Pardo, N., Vatopoulos, K., Krook-Riekkola, A., Moya, J.A., Perez, A., 2012. Heat and cooling demand and market perspective. doi:10.2790/56532

Pardo, P., Deydier, A., Anxionnaz-Minvielle, Z., Rougé, S., Cabassud, M., Cognet, P., 2014. A review on high temperature thermochemical heat energy storage. Renew. Sustain. Energy Rev. 32, 591–610. doi:10.1016/j.rser.2013.12.014

SHC, I., SolarPACES, 2008. Potential for sola heat industrial processes. IEA SHC Task 33 and SolarPACES Task IV: Solar heat for industrial processes.Department of Mechanisc and Aeronautics, University of Romer "La Sapienza", Italy.

Siva Reddy, V., Kaushik, S.C., Ranjan, K.R., Tyagi, S.K., 2013. State-of-the-art of solar thermal power

plants - A review. Renew. Sustain. Energy Rev. 27, 258–273. doi:10.1016/j.rser.2013.06.037
Steinfeld, A., Zurich, C.-, Palumbo, R., 2001. Solar Thermochemical Process Technology. Encycl. Phys. Sci. Technol. 15, 237–256. doi:10.1016/B0-12-227410-5/00698-0
Stevenson, M., 2009. RECYCLING | Lead–Acid Batteries: Overview, in: Encyclopedia of Electrochemical Power Sources. pp. 165–178. doi:10.1016/B978-044452745-5.00402-0
Zabaniotou, A., Kouskoumvekaki, E., Sanopoulos, D., 1999. Recycling of spent lead/acid batteries: The case of Greece. Resour. Conserv. Recycl. 25, 301–317. doi:10.1016/S0921-3449(98)00071-8
Zhang, W., Yang, J., Wu, X., Hu, Y., Yu, W., Wang, J., Dong, J., Li, M., Liang, S., Hu, J., Kumar, R.V., 2016. A critical review on secondary lead recycling technology and its prospect. Renew. Sustain. Energy Rev. 61, 108–122. doi:10.1016/j.rser.2016.03.046

Conference Proceedings

EuroSun 2016
Palma de Mallorca (Spain), 11 - 14 October 2016

Yield Analysis of a Power Plant with Parabolic-Trough Collectors and Direct Steam Generation (DSG) using a Quasi-Dynamic Simulation Model in TRNSYS

Mario Biencinto[1], Lourdes González[1] and Loreto Valenzuela[2]

[1] Plataforma Solar de Almería (PSA-CIEMAT), Madrid (Spain)

[2] Plataforma Solar de Almería (PSA-CIEMAT), Tabernas (Spain)

Abstract

After the construction of the first commercial solar power plant with direct steam generation in Thailand, a new horizon will be open for this technology. In this industrial application for electricity generation, financing directly depends on the expected electricity production and corresponding financial revenues. The development of a simulation model for this technology will help reduce costs and hence increase plant output. The simulation model applied in this study reproduces the thermal and hydraulic behaviour of the solar field, including parabolic-trough collectors and connecting pipes. This quasi-dynamic model is able to address transient conditions with low computational resources. In addition, a power block suitable for a 35 MW_e solar plant is defined and analysed, allowing its implementation into the whole solar plant model. An economic optimization of the solar field size has been performed considering standard economic parameters. The main results of thermal and electrical energy obtained from the annual simulation of the optimized plant are presented in this paper.

Keywords: *direct steam generation, parabolic-trough collector, yield analysis, simulation model*

1. Introduction

At this moment, electricity generation is the most extended application of solar heat in industrial processes. Parabolic-trough systems, central towers and Fresnel linear collectors are the main technologies used in industrial applications. Solar thermal power plants based on parabolic-trough collectors are nowadays a successful technology with more than 4,000 MW_e installed and in operation around the world. Most of them operate with synthetic oil as heat transfer medium in receiver tubes, but recently other working fluids, such as water, are being investigated in order to improve the performance of parabolic-trough technology and avoid the environmental issues of synthetic oils. In direct steam generation (DSG), water is heated and evaporated through the solar field to feed a steam Rankine cycle or an industrial process, such as cleaning, heating or distillation in the food and beverage sector (Fernández-García et al., 2010), avoiding the need for heat exchangers and hence increasing the efficiency of the whole system (Eck et al., 2003).

A 5 MW_e solar power plant (Krüger et al., 2012) built in Kanchanaburi (Thailand) and connected to the grid in 2012 is the only commercial plant with parabolic-trough collectors and DSG in the world. This is a first step in the commercialization of this technology. At this point, a flexible simulation model of this technical concept can help calculate the energy production and perform viability studies of solar power plants with DSG in different places, with different collectors and solar field configurations.

This work addresses the simulation of a hypothetical 35 MW_e solar thermal power plant using DSG in parabolic-trough collectors, including the definition of a suitable power block. The simulation applies a quasi-dynamic model able to calculate annual results of thermal and electrical energy with low computational resources. In addition, a brief economic analysis is performed to optimize the size of the solar

doi:10.18086/eurosun.2016.02.05 Available at http://proceedings.ises.org

field considering expected electricity costs.

2. Plant model

The simulation model reproduces the thermal and hydraulic behaviour of each component of the plant including the main elements of the solar field and the performance of the power block. The model has been developed with the TRNSYS software tool (Klein et al., 2007), a graphically-based environment used to simulate transient systems. Models are created by connecting different components, providing a flexible tool that allows different configurations and sizes of the plant and an easy modification of details such as collector type, location, etc.

The solar plant is composed of two main systems: the solar field with collectors' loops of 1,000 m of effective length (20 collectors of 50 m length per loop) with North-South orientation and the power block with a steam turbine of 35 MW_e. Each loop of the solar field works as a preheater, evaporator and super-heater of the feed water, using the solar energy as primary source of energy. In nominal conditions the feed water enters at 206 ºC and 70 bar in each loop to be preheated, evaporated and super-heated in once-through operation mode. The super-heated steam generated in the solar field (450 ºC) is led to the turbine to complete the Rankine cycle, which can operate either in nominal or part-load conditions.

The following sections describe the model of collectors' loop developed to simulate the solar field, the definition and modelling approach of the power block and, finally, the integration of these subsystems in the whole solar plant model.

2.2. Model of collectors' loop

The model of each loop is developed by joining components such as solar collectors, connecting pipes and accessories to compose a whole arrangement. The TRNSYS model of the proposed collectors' loop for the solar plant is shown in Fig. 1, including components for parabolic troughs (type218), connecting pipes (type214) and injector (type228) which have been implemented in the Fortran programming language.

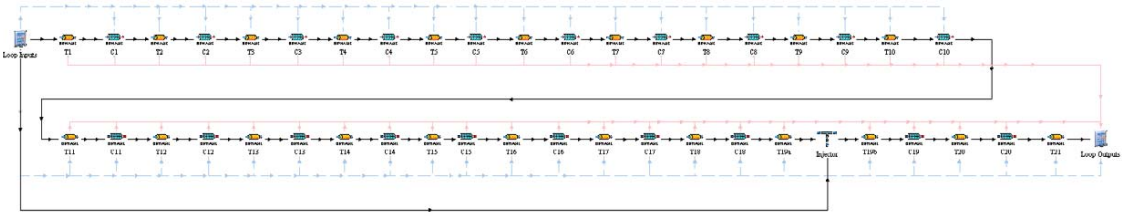

Fig. 1. Screenshot of the TRNSYS model for the collectors' loop

In general terms, the thermal model of parabolic-trough collectors is performed by evaluating the useful power gained by the fluid, $\dot{Q}_u$, with an energy balance between solar power absorbed by the system and thermal losses to the environment:

$$\dot{Q}_u = \eta_{opt,0^\circ}\, \eta_{clean}\, \eta_{sh}\, K(\theta)\, G_b\, cos(\theta)\, A_c - \dot{Q}_{loss} \qquad \text{(eq. 1)}$$

In this equation, G_b is the direct normal irradiance, A_c the net collector aperture area, θ the incidence angle, $K(\theta)$ the incidence angle modifier, $\eta_{opt,0^\circ}$ the peak optical efficiency, η_{clean} the cleanliness factor and η_{sh} the shadowing factor.

In this case, the expression applied to calculate the incidence angle modifier is based on the equation estimated for SkyFuel® concentrators (McMahan et al., 2010) from experimental data. However, SkyFuel® concentrators have 115 m length instead of the length of the foreseen collectors, 50 m. Hence, a correction with the ratio of end-losses factor for 115 m to end-losses factor for 50 m is applied. The resulting expression for incidence angle modifier is given by eq. 2, where θ is given in degrees.

$$K(\theta) = (1 - 2 \cdot 10^{-4} \cdot \theta + 3 \cdot 10^{-5} \cdot \theta^2) \cdot \frac{\eta_{end\ loss\ (50\ m)}}{\eta_{end\ loss\ (115\ m)}} \quad \text{(eq. 2)}$$

Regarding thermal losses in collectors, standard receiver tubes SCHOTT PTR®70 will be considered. The expression for thermal losses has been obtained (Valenzuela et al. 2014) from outdoor tests at PSA:

$$\dot{Q}_L = 0.342 \cdot \Delta T + 1.163 \cdot 10^{-8} \cdot \Delta T^4 \quad \text{(eq. 3)}$$

Where $\dot{Q}_L$ represents thermal power losses per unit length [W/m] and ΔT is the difference between average fluid temperature and ambient temperature [K]. Besides, the main parameters of the collectors and receiver tubes considered for the simulation are summarized in Table 1.

Tab. 1: Main parameters considered for solar collectors

Parameter	Value
Aperture length, m	6
Net collection area, m^2	272.7
Focal length, m	1.5
Peak optical efficiency, %	76.58
Cleanliness factor, %	97
Absorber tube length, m	48
Outer diameter of steel absorber tube, m	0.07
Inner diameter of steel absorber tube, m	0.0588
Inner roughness of absorber tube, m	$4 \cdot 10^{-5}$

During transient conditions, the model performs an energy balance taking into account the effect of thermal inertia due to the mass of fluid, m_{fluid}, and pipe, m_{pipe}, in a time step Δt. The useful energy absorbed by the fluid, $\dot{Q}_u \Delta t$, can be expressed as a sum of energy interchanged in each component. The specific enthalpy of the fluid at the collector's outlet, h_{out}, can be thus obtained knowing the rest of the elements in the following equation, where $\dot{m}$ is the mass flow rate, $\Delta \bar{T}_{pipe}$ and $\Delta \bar{h}$ the increase in average temperature of the pipe and average enthalpy of the fluid, respectively, since the previous time step, c_p the specific heat capacity of the pipe and h_{in} the specific enthalpy of the fluid at collector's inlet:

$$\dot{Q}_u \Delta t = m_{fluid} \Delta \bar{h} + m_{pipe}\, c_p \Delta \bar{T}_{pipe} + \dot{m}(h_{out} - h_{in}) \Delta t \quad \text{(eq. 4)}$$

In steady-state conditions, the two first terms of this equation are neglected ($\Delta \bar{h} = 0$ and $\Delta \bar{T}_{pipe} = 0$) and hence this expression is simplified.

The calculation of the temperature difference between fluid and absorber tube requires the estimation of the heat transfer coefficient by convection, which depends on the fluid phase. For one-phase flow, either liquid water or steam, the heat transfer coefficient is calculated by means of the Dittus-Boelter equation; for two-phase flow the heat transfer coefficient is obtained by means of the Kandlikar (1990) correlation.

On the other hand, thermal losses in connecting pipes are calculated by means of a model of thermal nodes composed of metal pipe and thermal insulation whose properties are known. Then, an energy balance is applied to calculate thermal losses to the atmosphere due to convection and to the sky due to radiation.

The hydraulic model is basically the same for both receiver pipes and connecting pipes between collectors and is based on the calculation of pressure drop through each component of the circuit. If the contribution of pressure losses due to change in kinetic energy is neglected, the calculation can be expressed in terms of pressure losses due to differences in height and friction in straight pipes and accessories. The pressure drop of a two-phase flow of water through a straight section of pipe is estimated from the pressure drop of liquid water by applying the Friedel (1975) proportionality factor; and the pressure loss of liquid water flowing through this pipe is calculated using the Darcy-Weisbach equation.

A detailed description of the TRNSYS model of collectors' loop developed for direct steam generation, together with its validation using the configuration and real data of the DISS loop at PSA, can be found in a previous work (Biencinto et al., 2016).

2.2. Description and model of the power block

A 35 MW_e power block suitable for the proposed DSG solar plant has been defined. This section describes and analyses the behaviour of this power block both at nominal and part-load conditions.

The power block proposed is based on a non-reheat Rankine cycle and includes a steam turbine with three extractions, a wet-cooling condenser, a deaerator, two surface heat exchangers for feed-water preheating and two water pumps. In nominal conditions, the steam produced by the solar field is driven to the turbine inlet at 450 ^{o}C of temperature and $6{\cdot}10^{6}$ Pa. The condenser pressure will be $6.6{\cdot}10^{3}$ Pa. Besides, standard values have been selected for the rest of parameters of the power block.

The analysis of the behaviour of the power block at nominal conditions has been performed with the IPSEpro (2016) software. Fig. 2 shows the basic diagram of the system obtained from this software tool including fluid conditions in relevant points of the system.

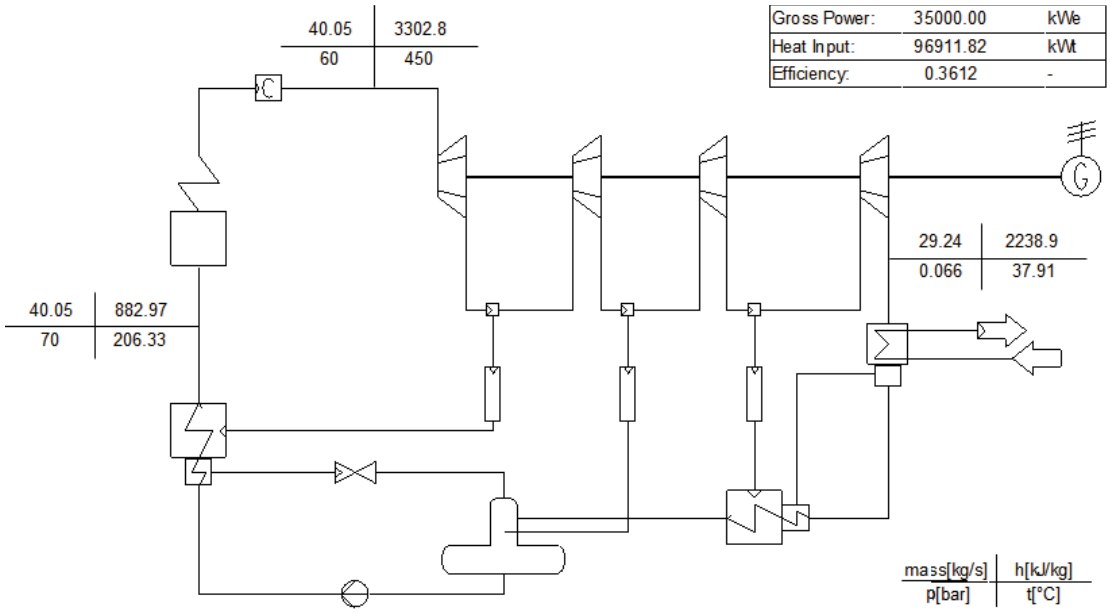

Fig. 2. Diagram of the power block design at nominal conditions in IPSEpro

Equal-enthalpy steps have been assumed for the selection of extraction pressures because this strategy is supposed to lead to an optimum efficiency (Kostyuk and Frolov, 1988). The analysis at nominal conditions in IPSEpro has been applied to determine the most relevant results of the power block that will be useful for the modelling, summarized in Table 2.

Tab. 2: Main results of the power block analysis at nominal conditions

Parameter	Value
Inlet water temperature for the solar field, °C	206.3

Inlet water pressure for the solar field, MPa	7
Steam quality at turbine outlet, %	86.3
Gross efficiency of the power block, %	36.12
Mass flow rate required from solar field, kg/s	40.05
Thermal power required from solar field, MWth	97
Parasitic consumption for water pumping, kWe	416.9

The methodology applied for part-load analysis is based on similar studies for typical Rankine cycles used in solar thermal plants (Montes et al., 2009). However, given the uncertainties associated to the regulation of the working pressure of the solar field in DSG, the control strategy will be based on fixed pressure instead of sliding pressure. Nevertheless, the regulation of part-load behaviour with fixed inlet steam pressure of the turbine by nozzle section control implies an efficiency reduction related to valves throttling and aerodynamic losses. In this way, an additional efficiency losses factor, taken from previous studies (Eck et al., 2008), has been applied for part-load regulation. The resulting isentropic efficiencies at part-load conditions including both conventional reduction and fixed-pressure regulation is shown in Fig. 3 for each turbine stage.

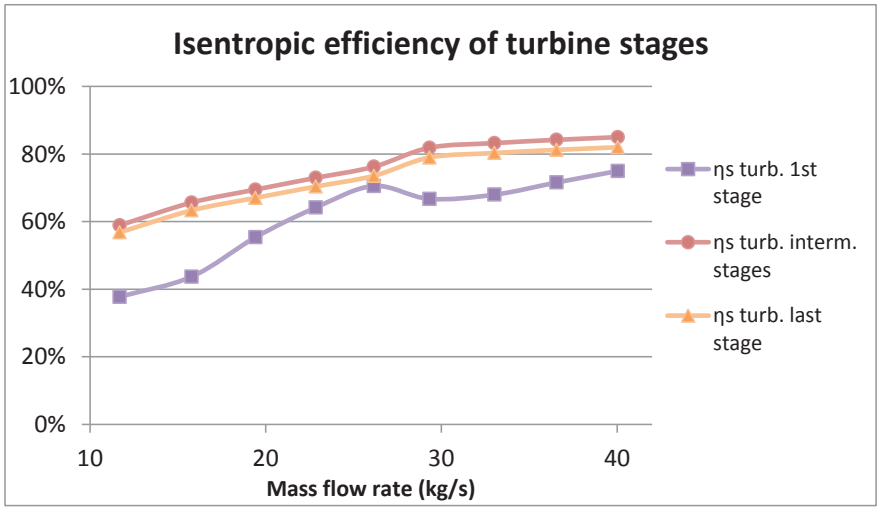

Fig. 3. Isentropic efficiencies for each stage of the turbine obtained at part-load behaviour

An efficiency-load curve has been obtained taking into account the above-mentioned assumptions and methodology. As a result, the evolution of gross efficiency of the power block at part load is shown in Fig. 4.

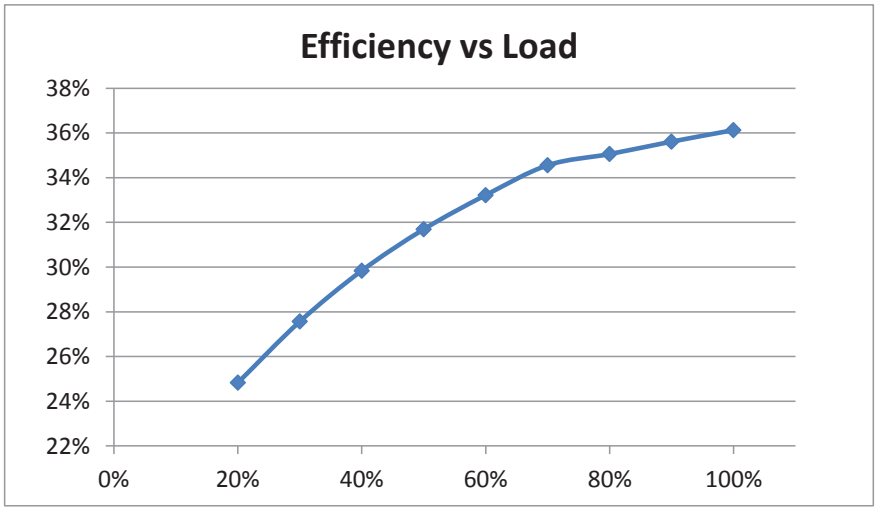

Fig. 4. Gross efficiency vs load curve obtained for the power block

Based on previous works (Eck et al., 2008), 10% overload will be allowed for the power block, leading to a maximum power of 38.5 MW_e. In this case, the nominal gross efficiency will be also applied.

Analogous curves have been obtained for inlet water temperature of the solar field and pumping consumptions. As a result, polynomic expressions relating gross efficiency, inlet temperature of the solar field and electrical losses with mass flow rate have been inferred. In addition, a quadratic curve has been included to simulate the start-up & preheating process of the turbine taking into account metal temperatures.

Finally, the approach explained in this section has been applied to implement a suitable model for the power block at part-load behaviour to be integrated with the proposed DSG solar field.

2.2. Solar plant model in TRNSYS

The general layout of the TRNSYS model for the whole solar plant is shown in Fig. 5, including equation editors, components from the TRNSYS standard library to read input data (Type9a) and determine solar angles (Type16g) and components specifically developed to retain values from the previous time step (type293) and to obtain thermo-physical properties of water/steam (type221). This overall model also includes macro-components that represent several subsystems of the plant: 'Collectors Loop', 'Distribution Pipes' and 'Solar Field Control'.

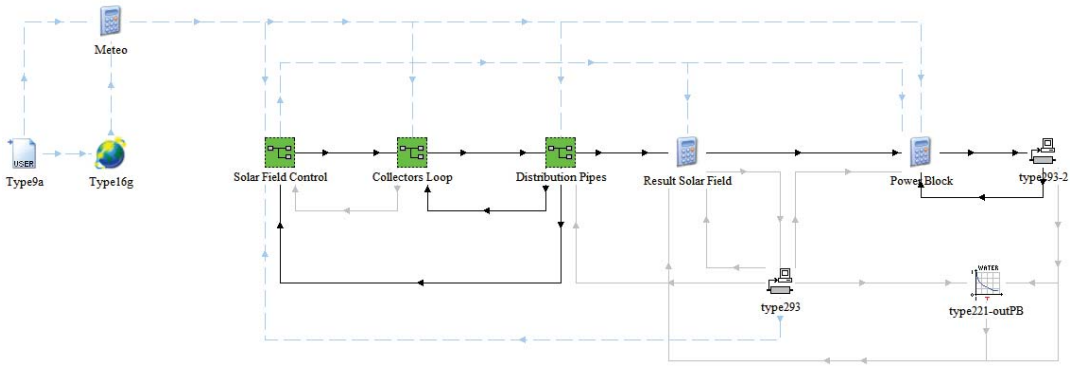

Fig. 5: Screenshot of the TRNSYS model for the solar power plant

The 'Collectors Loop' subsystem (seen in Fig. 1) simulates the behaviour of one loop with 20 collectors. Since all loops in the solar field are equal and they receive the same solar irradiance, the values of mass flow rate and thermal power of one loop are multiplied by the total number of loops to obtain the total results of the solar field.

Besides, the 'Solar Field Control' subsystem implements the corresponding control strategies to determine mass flow rates (loop and injection) and pressure, based on ideal schemes for once-through mode (Valenzuela et al., 2005). This subsystem also handles strategies for plant operation, such as mass flow rate assignment during start-up process, shutdown mechanisms, etc.

The 'Distribution Pipes' subsystem simulates the behaviour of the piping circuit (both hot and cold) between collectors' loop and power block for a solar field composed of two subfields with East-West orientation by means of the pipe component. Since the geometry of distribution pipes may strongly vary throughout the solar field, average diameters for pipe and insulation are applied to allow a simplified approach.

Finally, an equation editor is used to implement the power block model described in section 2.2, both at nominal and part-load conditions, giving as outputs the gross and net electric power generated, pumping consumptions and parasitic losses.

3. Solar field optimization and annual yield analysis

The solar plant model described in section 2 has been applied to perform annual simulations aimed at both optimizing the number of loops in the solar field and obtaining the electricity production of the optimized plant. The location selected for the plant is Plataforma Solar de Almería, Spain (37º05'30" N, 2º21'19" W),

and the input data used for the simulation is a typical meteorological year (TMY). This TMY file contains the record of direct normal irradiation (DNI) and ambient temperature every five minutes from the same site, yielding a yearly DNI balance of 2,071.46 kWh/m^2 and 3,658 hours of sunlight. The time step of every simulation is the same as the time step of input data, 5 min.

3.1. Economic optimization of solar field size

The solar field size needed to match the nominal thermal power required by the power block (97 MWth) will be given by the thermal power gained by the fluid in a collectors' loop at the design point, which is expected to be around 3.3 MWth. The resulting calculation leads to 30 loops in the solar field.

Besides, an important figure to assess the solar field size is the Solar Multiple (SM) of the plant, which is the ratio of thermal power gained by the fluid in the solar field at nominal conditions to nominal thermal power required by the power block. Hence, a number of loops of 30 will represent a SM = 1. However, a Solar Multiple of 1 may involve a limited production, mainly in winter, because low solar irradiances imply that the power block works at part-load condition and therefore at reduced efficiency. In this way, it is recommended to oversize the solar field to avoid part-load operation as much as possible. Nevertheless, the oversizing of the solar field will imply that in certain conditions with high solar radiation the thermal power that is able to produce the solar field will be higher than the maximum thermal power allowed by the power block. These situations will require a partial defocusing of the solar field, thus causing energy dumping.

To assess the effect of solar field oversizing, annual simulations for several solar multiples have been performed using the DSG solar plant model described in section 2. Fig. 6 shows the annual results of net electricity production and thermal energy dumped for the proposed plant, using solar multiples from 1 to 1.47. This range of solar multiples represents 30 to 44 collectors' loops in the solar field, respectively.

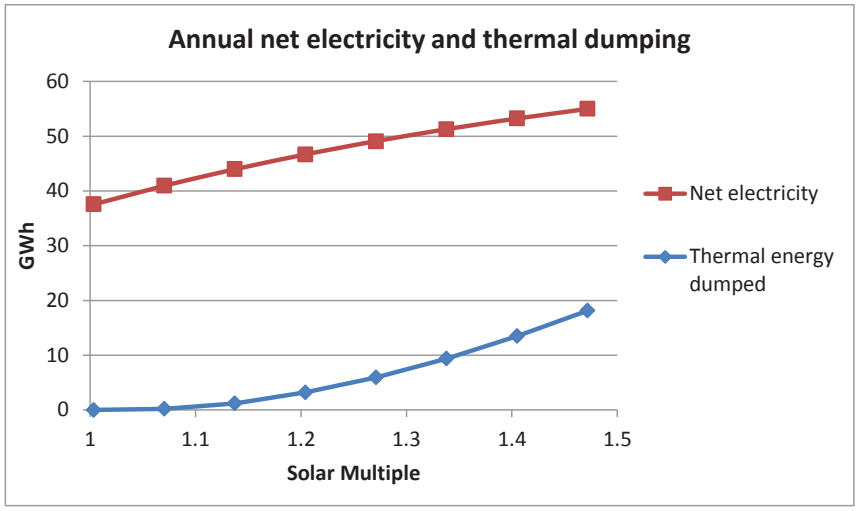

Fig. 6. Annual results of net electricity production and thermal energy dumped as function of the solar multiple for the DSG solar plant considered

In order to obtain the optimum value of the solar multiple (and therefore the number of loops in the solar field), a basic economic analysis has been performed taking into account a rough estimation of electricity costs. According to current definitions (AENOR, 2013), levelized electricity cost is given by the following expression:

$$LEC = \frac{CRF \cdot K_{invest} + K_{O\&M} + K_{fuel}}{W_{net}} \qquad \text{(eq. 5)}$$

Where K_{invest} is the total investment cost of the plant, $K_{O\&M}$ the annual cost of operation and maintenance, K_{fuel} the annual cost of fuel, W_{net} the annual net electricity production and CRF the capital recovery factor.

The economic parameters and specific costs considered for the *LEC* calculation are summarized in Table 3.

Tab. 3: Economic parameters and specific costs considered for the LEC analysis

Parameter	Value
Specific cost of solar field, €/m^2	190
Specific cost of power block, €/kW	350
Land specific cost, €/m^2	2
Engineering & building, % of K_{invest}	20
Annual O&M specific cost, €/(kW·SM)	56
CRF (Capital Recovery Factor), %	10.37

Fig. 7 represents the *LEC* values calculated for the above-mentioned range of solar multiples, together with the dumping factor. For this analysis, we define dumping factor F_{dump} as the ratio of thermal energy dumped to useful thermal energy to the power block.

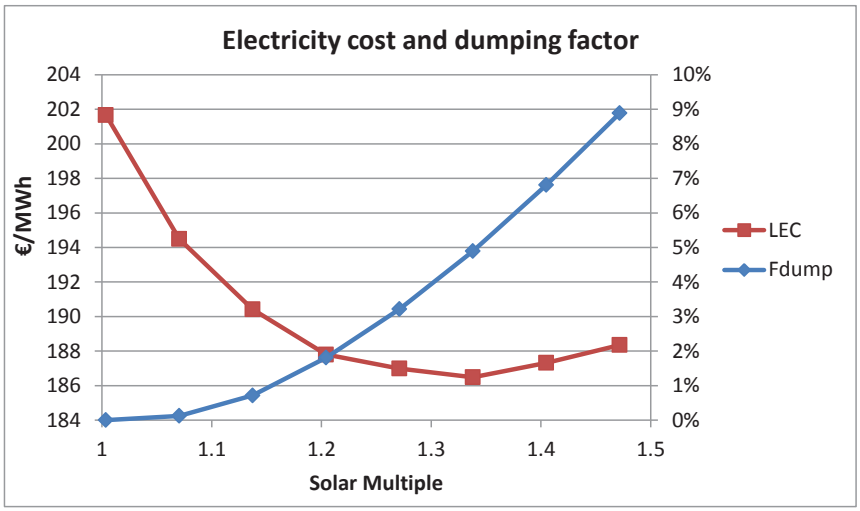

Fig. 7. Results of levelized electricity cost (*LEC*) and dumping factor (F_{dump}) as function of the solar multiple for the DSG solar plant considered

As seen in Fig. 7, the solar multiple that provides a lowest electricity cost is 1.338, which corresponds to a solar field with 40 loops of collectors, leading to a net collection area of 217,760 m^2. The resulting solar field lay-out proposed for this plant is shown in Fig. 8, with the power block in central location and 40 collector loops distributed in two subfields, West and East. Considering an extra space for access and maintenance purposes, the land area required for this arrangement would be around 1,100,000 m^2.

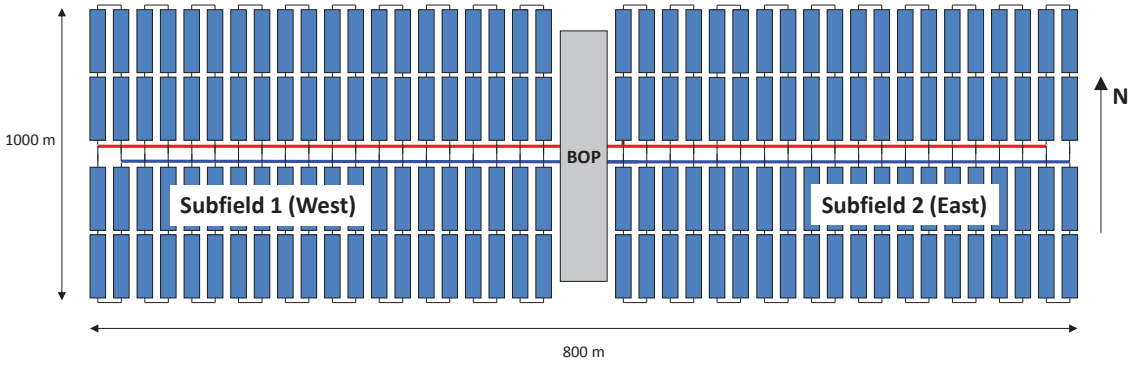

Fig. 8. Solar field lay-out proposed for the DSG solar plant

3.2 Annual yield results

Once defined the optimum solar field size and plant lay-out, an annual simulation has been performed to obtain either the thermal or electrical energy involved through each subsystem. As a result, Fig. 9 shows the monthly values of thermal energy gained by the fluid in the solar field and thermal energy useful to the power block.

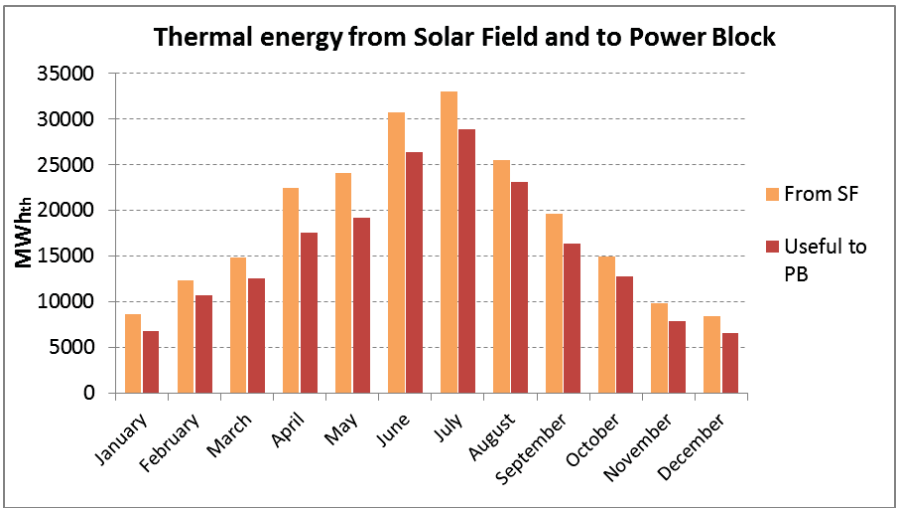

Fig. 9. Monthly results of thermal energy obtained from the solar field and useful to the power block for the DSG solar plant considered

As seen in Fig. 9, thermal energy results show a strong variation between summer and winter months, both from solar field and to the power block. The thermal energy obtained from the solar field in the worst month, December, is 25.6% of the result for the best month, July. In terms of thermal energy useful to the power block, this ratio is 22.6%.

The differences between both magnitudes are related to two main effects. On the one hand, some of the thermal energy obtained from the solar field cannot be used by the power block because the steam has not the required conditions of temperature, pressure or mass flow to feed the turbine. On the other hand, when thermal power produced by the solar field exceeds the maximum thermal power allowed by the power block, the remaining thermal energy is discarded as energy dumping. The monthly breakdown of these two effects is represented in Fig. 10. From this figure, we can point out that energy dumping becomes relevant from April to July.

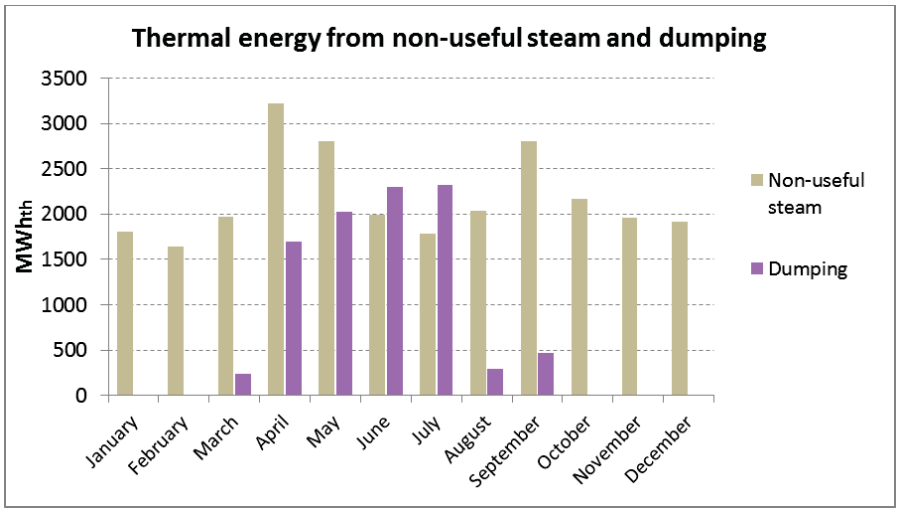

Fig. 10. Monthly results of thermal energy from non-useful steam and thermal energy dumping for the DSG solar plant considered

Fig. 11 shows the monthly results of gross and net electricity produced by the plant.

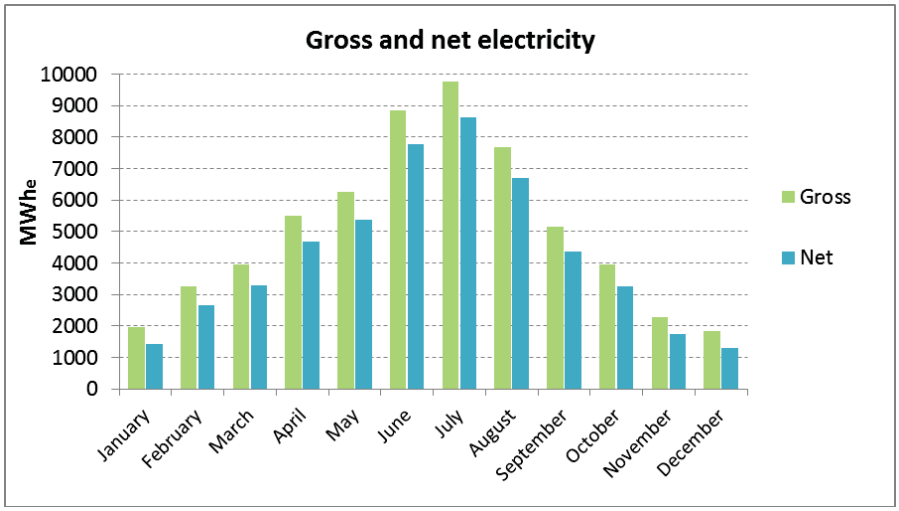

Fig. 11. Monthly results of gross and net electricity production for the DSG solar plant considered

In the same way as for thermal energy, a strong variation can be observed between summer and winter months. The ratio of worst month (December) to best month (July) production is 18.8% in the case of gross electricity and 15% in the case of net electricity. As inferred from these figures, this ratio decreases with each subsystem due to either thermal or electrical losses. In order to illustrate the evolution of energy losses, including optical losses in the solar field, the monthly results of available and useful radiant solar energy, thermal energy from solar field and useful to power block, gross and net electricity production is depicted in Fig. 12.

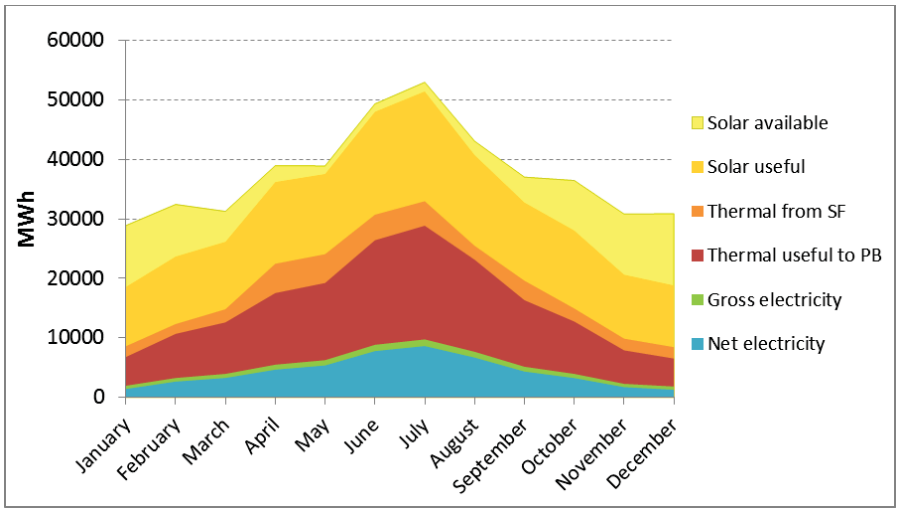

Fig. 12. Monthly results of available and useful radiant solar energy, thermal energy from solar field and useful to power block, gross and net electricity production for the DSG solar plant considered

Finally, Table 4 summarizes the main results obtained from the annual simulation of the plant. The efficiency values included in this table are obtained by dividing thermal or electrical energy results by available radiant solar energy (for plant and solar field efficiencies) or thermal energy useful to power block (for power block efficiencies). Besides, the equivalent operating hours are obtained as the ratio of net electricity production to nominal power (35 MW_e); and the annual capacity factor is the equivalent operating hours divided by the annual total hours (8,760 h).

Tab. 4: Main annual results obtained from the simulation of the DSG solar thermal power plant

Result	Value
Available radiant solar energy, MWh	451,081.56
Useful radiant solar energy, MWh	382,811.24
Thermal energy from solar field, MWh_{th}	224,330.91
Thermal energy dumped, MWh_{th}	9,357.30
Thermal energy in non-useful steam, MWh_{th}	26,107.33
Thermal energy useful to power block, MWh_{th}	188,866.28
Gross electricity production, MWh_e	60,469.84
Net electricity production, MWh_e	51,172.67
Solar field efficiency, %	49.73
Gross power block efficiency, %	32.02
Net power block efficiency, %	27.09
Gross plant efficiency, %	13.41
Net plant efficiency, %	11.34
Dumping factor, %	4.95
Equivalent operating hours, h	1,462.08
Annual plant capacity factor, %	16.69
LEC (Levelized Electricity Cost), €/MWh	186.5

4. Conclusions

Direct steam generation in parabolic-trough collectors may be an interesting solar technology both for industrial applications and electricity production. In this way, this work describes and analyses a 35 MW_e solar thermal power plant with DSG in parabolic troughs using a quasi-dynamic simulation model developed in TRNSYS. A solar field with North-South oriented loops of 1,000 m with 20 collectors of 50 m length, together with a suitable power block based on a steam Rankine cycle, has been defined for this plant. An economic optimization of the solar field size leads to a solar multiple of 1.338, which represent 40 collector loops. The annual simulation of this plant yields a net electricity production of 51,173 MWh_e and a capacity factor of 16.7%. Additionally, a brief economic analysis for this plant gives a levelized electricity cost of 186.5 €/MWh.

5. Acknowledgements

This work has been supported by the European Commission through the STAGE-STE project (work package #11, contract number: 609837) and by the Spanish government in the framework of the DETECSOL project (Ref. ENE2014-56079-R) with ERDF funds.

6. References

AENOR, 2013. Solar thermal electric plants. Terminology. Spanish Norm UNE 206009:2013. AENOR, Madrid, Spain.

Biencinto, M., González, L., Valenzuela, L., 2016. A quasi-dynamic simulation model for direct steam generation in parabolic troughs using TRNSYS. Applied Energy 161, 133-142.

Eck, M., Benz, N., Feldhoff, F., Gilon, Y., Hacker, Z., Müller, T., Riffelmann, K..J., Silmy, K., Tislaric, D., 2008. The potential of Direct Steam Generation in Parabolic Troughs – Results of the German Project DIVA. Proceedings of the 14th SolarPACES International Conference. Las Vegas, USA.

Eck, M., Zarza, E., Eickhoff, M., Rheinländer, J., Valenzuela, L., 2003. Applied research concerning the

direct steam generation in parabolic troughs. Solar Energy 74(4), 341–351.

Fernández-García, A., Zarza, E., Valenzuela, L., Pérez, M., 2010. Parabolic-trough solar collectors and their applications. Renewable and Sustainable Energy Reviews 14(7), 1695-1721.

Friedel, L., 1975. Modellgesetz fur den Reibungsdruckverlust in der Zweiphasenstromung. VDI-Forschungsheft 572.

IPSEpro, 2016. IPSEpro - SimTech Simulation Technology. Available from: <www.simtechnology.com/CMS/index.php/ipsepro>. SimTech GmbH. Graz, Austria (accessed 31.08.2016).

Kandlikar, S.G., 1990. A General Correlation for Saturated Two-Phase Flow Boiling Heat Transfer Inside Horizontal and Vertical Tubes. Journal of Heat Transfer 112, 219-228.

Klein, S.A., et al., 2007. TRNSYS 16: a transient system simulation program. Available from: <http://sel.me.wisc.edu/trnsys> Solar Energy Laboratory, University of Wisconsin. Madison, USA (accessed 31.08.2016).

Kostyuk, A., Frolov, V., 1988. Steam and gas turbines. Mir Editorial. Moscow, Russia. ISBN 5-03-000032-1.

Krüger, D., Krüger, J., Pandian, Y., O'Connell, B., Feldhoff, J.F., Karthikeyan, R. et al., 2012. Experiences with Direct Steam Generation at the Kanchanaburi Solar Thermal Power Plant. Proceedings of the 18th SolarPACES International Conference. Marrakech, Morocco.

McMahan, A., White, D., Gee, R., Viljoen, N., 2010. Field Performance Validation of an Advanced Utility-Scale Parabolic Trough Concentrator. Proceedings of the 16th SolarPACES International Conference, Perpignan, France.

Montes, M.J., Abánades, A., Martínez-Val, J.M., Valdés, M., 2009. Solar multiple optimization for a solar-only thermal power plant, using oil as heat transfer fluid in the parabolic trough collectors. Solar Energy 83, 2165-2176.

Valenzuela, L., López-Martín, R., Zarza, E., 2014. Optical and thermal performance of large-size parabolic-trough solar collectors from outdoor experiments: A test method and a case study. Energy 70, 456−464.

Valenzuela, L., Zarza, E., Berenguel, M., Camacho, E.F., 2005. Control concepts for direct steam generation in parabolic troughs. Solar Energy 78, 301–311.

Conference Proceedings

EuroSun 2016
Palma de Mallorca (Spain), 11 - 14 October 2016

ISES EuroSun 2016

Analysis of a Solar Thermal Installation for Medium Temperature Industrial Applications

Mircea Bunea, Catherine Hildbrand, Sara Eicher, Alexis Duret, Stéphane Citherlet

HEIG-VD, LESBAT, Solar Energy and Building Physics Laboratory

Avenue des Sports 20, CH-1400 Yverdon-les-Bains, Switzerland

Abstract

The analysis and optimisation of a medium temperature solar thermal installation for bitumen storage is presented in this article. Coupled with a gas boiler, a solar thermal installation was designed to provide heat to an onsite building, a bitumen tank and two bitumen emulsions tanks The behaviour and performance of this medium–temperature solar system for industrial process have been investigated based on measurements and simulations for subsequent optimisation of the process. A number of anomalies of the system have been identified, corrected and the impact on its performance evaluated. Results show that, on an annual basis, solar energy is mainly delivered to the water storage tanks. Simulations show that there is room for improvement and that the solar production could be roughly doubled if the system operates as designed. The life cycle impact assessment of the solar installation showed that the infrastructure impacts predominate over the entire life cycle. Environmental return on investment periods were found quite interesting in the case of an optimised solar bitumen storage system.

Keywords: *industrial application, solar thermal collectors, thermal storage, bitumen, simulation, measurements, LCA*

1. Introduction

In Europe, the industrial sector is responsible for 26% of the final energy consumption (Eurostat, 2013) which makes it an important player in the energy consumption and greenhouse gas emissions debate. Moreover, (Krummenacher and Muster, 2015) showed that 26% of the industrial process heat demand is lower than 100°C and 19% is between 100 and 400°C. A huge potential exists for these low to medium temperature heat demands to be delivered using existing conventional and advanced collector technologies. It is, therefore, very important to capitalise on this potential as today less than 0.1% of the heat demand in industry is supplied by solar energy (Mauthner and Weiss, 2015). The purpose of this study is to investigate the use of solar energy for bitumen and emulsion (mixture of water and bitumen) storage applications for a subsequent optimisation of the process.

Low temperature processes up to 100 °C are very suitable for using well-established conventional solar thermal systems. For processes in the medium temperature range up to 250 °C, several new types of collectors have been developed recently. Recently, within the framework of the International Energy Agency (IEA) Solar Heating and Cooling (SHC) Task 49 (IEA-SHC, 2014) 134 solar thermal installations supplying process heat were reported worldwide, with a total capacity of about 100 MW_{th} representing a very small fraction (less than 0.1%) of the total solar thermal capacity installed. Those figures demonstrate that there is a considerable untapped potential for solar thermal energy in the industrial sector.

doi:10.18086/eurosun.2016.02.18 Available at http://proceedings.ises.org

Bitumen and emulsions are used in road construction, an industry based on fossil energy with medium temperature heat demands. The operating temperature for bitumen emulsion ranges from 60 to 75°C while for bitumen it ranges from 160 to 200°C. These hot products must be stored, transported and used hot to maintain their workability. Conscious of the important potential of solar heating in the industrial context, but also of the economic and environmental issues related to fossil energy use, COLAS Switzerland, has implemented a medium temperature solar thermal system to maintain its bituminous products tanks at the required temperature.

A first pilot project was launched on an asphalt production site in Geneva in 2011. The solar thermal installation was designed to reduce energy consumption related to bitumen heating and implicitly, reduce emissions of greenhouse gases (Maranzana and Bornet, 2011). This first experience has shown the significant potential to cover the useful heat demand of bitumen heating. On the other side, simulations showed that the annual performance of the solar thermal system could be significantly improved with a better orientation and tilt, lower operating temperature or shorter distance between solar collectors and bitumen tanks. Based on this experience, COLAS Switzerland has integrated an improved and more flexible solar thermal system in its bitumen storage site in Yverdon-les-Bains (Switzerland). In both installations, the solar thermal heat was delivered using ultra high vacuum flat plate collectors.

This paper reports the findings of the R&D project funded by the Swiss Federal Office of Energy aimed to analyse and optimise the thermo-economic and environmental performance of this medium temperature solar thermal installation. (Bunea et al., 2013).

1.1 Description of the facility

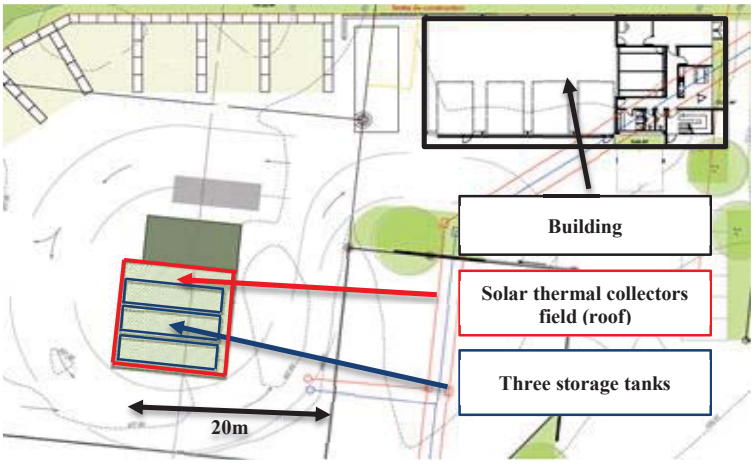

Fig. 1 : Bitumen storage site at Yverdon-les-Bains

In Yverdon-les-Bains, COLAS stores bitumen and its emulsions to be used in road construction. The products are delivered hot from the production plants and stored in three thermal insulated tanks. An ultra-high vacuum flat plate solar collector field backup by a gas boiler are used to heat the bituminous products to temperatures between 160 and 200°C for bitumen and between 60 and 75°C for emulsions. In addition, the heating system delivers energy for space heat and domestic hot water (DHW) for a building located next to the facility. Fig. 1 shows the location of the various components on the site.

There are two operating seasons:

- April to September: “Summer season” - bitumen and emulsions have to be permanently available at operating temperatures. Furthermore, DHW has to be provided to the office and workshop buildings on the site.
- October to March: “Winter season” - Bitumen or emulsions generally not stored, with an exception for dry winters where storage could be extended a few months. In the general case, only heat for space heating and DHW has to be provided.

1.2 Solar collectors

The solar thermal collectors are manufactured by SRB Energy and were developed at the European Centre for Nuclear Research (CERN). The SRB Ultra High Vacuum (UHV) collector (Benvenuti, 2013) uses a technology based on evacuated flat plate collectors. This collector can be combined with cylindrical mirrors, which are a cost-effective way to increase the aperture area and to improve performance at high temperatures.

These collectors are characterised by excellent thermal insulation provided by the ultra-high vacuum (10-8 mbar at ambient temperature) achieved and maintained using a Getter pump. This pump is activated by solar energy and it has the ability to remove air or any other gas molecules inside the collector through chemical reaction. This insulation combined with solar concentration allows the solar collector to reach a stagnation temperature of 400°C, significantly greater than conventional solar thermal collectors. Moreover, compared to the "classic" concentration collectors that only use direct solar radiation, these collectors take also advantage of the diffuse solar radiation, due to a larger absorber area. In Switzerland, the diffuse radiation is an important part of global solar radiation, accounting for more than 50% in Yverdon-les-Bains (Bunea et al, 2013).

The solar thermal field in Yverdon-les-Bains consists of 35 SRB UHV Type C2 solar collectors spread over 7 rows of 5 collectors in series for a theoretical peak power of 96.1 kW with a solar irradiation of 1000W/m^2. They are placed on a specially designed metal frame above the storage tanks, with an orientation of 50° West and 20° tilt. The heat transfer fluid (HTF) used in the system is a Shell mineral oil of type Thermia B supporting over 300°C, without chemical or physical degradation.

1.3 Storage tanks

The bitumen storage site contains four insulated storage tanks, see Fig. 2. Two of the tanks are used for emulsion storage, one for bitumen storage while the fourth is filled with water and serves as heat storage to meet the energy demand of the building but also for emulsion operating needs. The water, emulsion and bitumen storage tanks have a capacity of 23, 50 and 70 m^3, respectively.

The water and bitumen storage heat demand is provided by solar energy and a backup gas boiler whenever solar energy is no available. Emulsion storages heat provision is either through the water storage by means of a heat exchanger or with electric heaters for night operation.

Fig. 2 : Storage tanks of the installation

The bitumen storage site was designed to store solar heat at two temperature levels:

- Water tank: between 60 °C and 90 °C depending on the weather conditions, but also on the building and emulsion heat demand.
- Bitumen tank: between 160 °C (for viscosity reasons) and 200 °C (thermochemical decomposition of bitumen beyond this temperature).

1.4 Building

The building was built in 2012 and comprises a mechanical workshop with a heated volume of about 1500 m^3 and offices over two floors with a total volume of ~1200 m^3.

The building annual heating demand was measured to be 42'370 kWh and includes space heating during winter and DHW for office employees and mechanics who take daily showers.

1.5 Gas Boiler

When solar energy is insufficient, heat provision for the building or to compensate the bitumen tanks losses is supplied by a 350 kW gas boiler. This backup system was installed in 2013 and replaces an old 1000 kW oil boiler.

The boiler contains an important thermal oil storage (~2000 l) which gives a large thermal inertia to the boiler. Although this energy stock generates heat losses, the burner operates mostly at reduced power and provides better overall performance compared to the old oil boiler. In addition, the natural gas operation will reduce the system emissions of greenhouse gases.

1.6 System integration and regulation

The solar pump is switched on when the solar irradiation is larger than 300 $W \cdot m^{-2}$. It circulates the HTF through the solar collectors until the field temperature is above the storage tank temperature, see Fig. 3. In order to improve the solar collector's efficiency, solar heat is delivered priority to the water tank - at lower temperature range. If the water storage tank has reached the set point temperature, then the extra solar energy is delivered to the bitumen tank. Inflow and outflow pipes of the bitumen tank must always be kept at a temperature of 200°C by the gas boiler, to ensure a good consistent flow through loading and unloading periods.

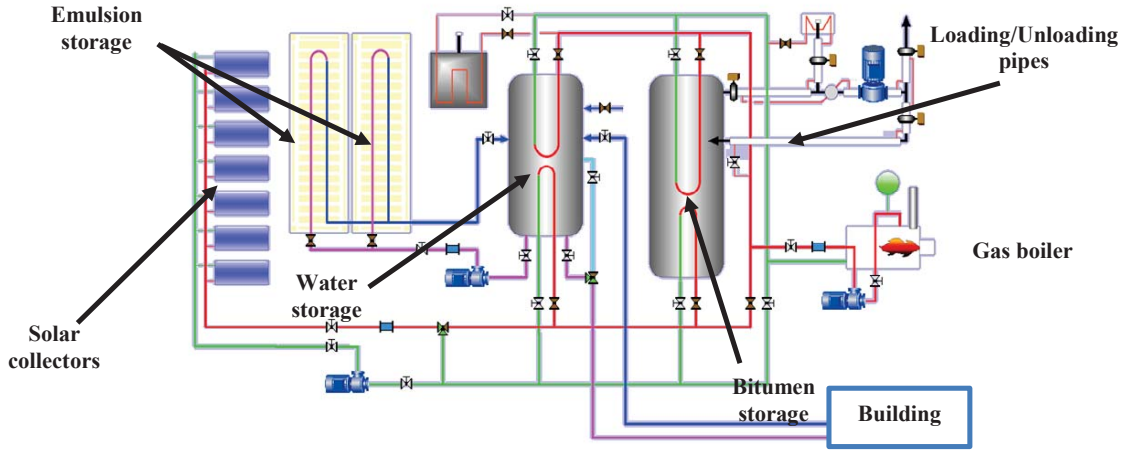

Fig. 3 : Schematic representation of the bitumen storage system.

2. Anomalies and failure analysis

In order to investigate the facility real behaviour and possible anomalies and failures to the expected operation, the facility was instrumented with sensors in the system lines to measure fluid temperatures and flow rates. Troubleshooting of this particular solar thermal system has revealed the following problems:

- The internal heat exchangers of the storage tanks are improperly sized, with a value 3 times lower when compared to the general rule of thumb (e.g. Jobin et al., 1994) for conventional solar collector applications. This causes performance of the system to be reduced.

- Estimation of the heat loss from tanks have shown that the insulation around the bitumen tank is probably improperly installed. For simulation purposes, the measured thermal insulation had to be reduced 10 times in order to have the same thermal loss as the measurements.

- Measurement of the collectors' efficiency have shown an important discrepancy between the accredited test values and the measured ones, see Fig. 4. Differences observed for the optical efficiency (15%) can be partly explained by eventual dust or bituminous particles deposits on the collector glasses and mirrors. A thermographic analysis of the solar collectors' field has further suggested that the thermal insulation of the UHV is also not fully ensured for some of the collectors. Consequently, global efficiency of the collector field is compromised, see Fig. 4. For high operating temperatures, the difference with the theoretical efficiency of the collector exceeds 50%. This highlights the fact that extrapolation of certified tests results beyond 100°C is not appropriate for evaluating these solar thermal collectors.

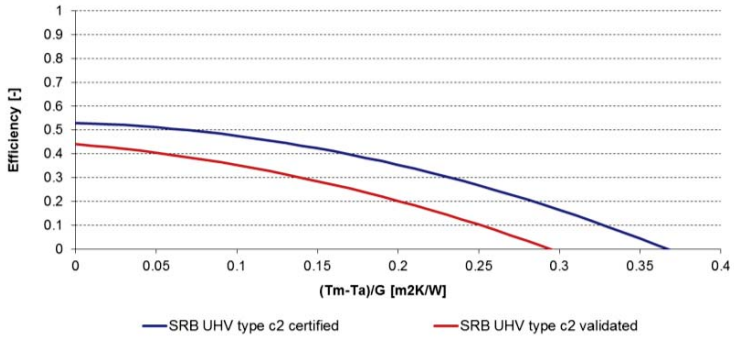

Fig. 4 : SRB UHV type C2 collector efficiency curve

3. Measurement campaign

The described system has been monitored continuously since 2014. This article presents the measurements performed between April 2015 and March 2016 following the modifications implemented from the preliminary study (Bunea et al., 2015). This period includes all improvements made to the system and a full year of measurements showing summer and winter periods.

Fig. 5 shows the weather conditions measured on the site during the investigated period (monthly values):

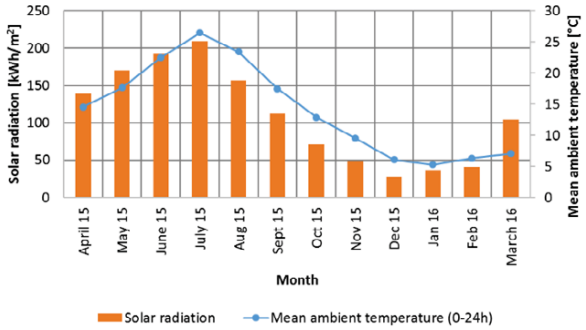

Fig. 5 : Monthly average solar radiation and ambient temperature for Yverdon-les.Bains from April 2015 to March 2016

Results for the period considered show an uncommon evolution during the year, see Fig. 6.

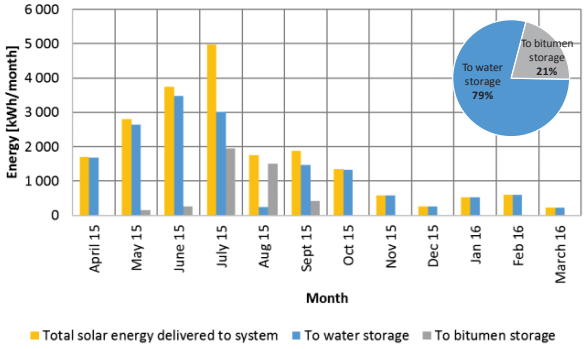

Fig. 6 : Monthly solar energy delivered to the system, 2015

From April to July, an increase almost linear of the solar energy production was observed, with a peak of about 5000 kWh in July. From August onwards, the total solar energy delivered to the system decreased substantially due to a hydraulic problem found in the water storage tank that was taken out of service for two months. Under this configuration, solar collectors delivered energy mainly to the bitumen storage, operating at higher temperatures, which greatly reduced the efficiency of the solar thermal system. The breakdown of solar energy

delivered to the bitumen and the water storage tanks on an annual basis was found to be 21 and 79%, respectively.

During the winter season, it can also be seen that solar energy is only delivered to the water storage tank for space heating and DHW purposes. This amount of solar energy is, nevertheless, low because the combination of shorter days and more diffuse radiation (Yverdon-les-Bains tends to be often overcast) means less solar radiation than in the summer season.

Switzerland's 2015-2016 winter season was an exceptionally dry and warm winter. For this reason, road construction activities kept going beyond de normal summer season and storage of bitumen carried forward until December. The required energy for the bitumen storage site, in this exceptional period, was supplied by the backup gas boiler. Fig. 7 shows the breakdown of the thermal energy delivered to the water tank, bitumen tank and the bitumen loading/unloading circuit, this latter heated exclusively with the gas boiler.

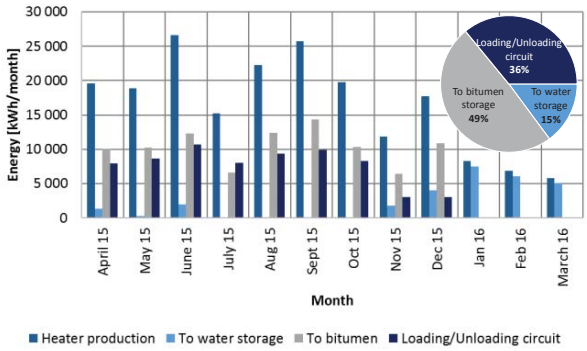

Fig. 7 : Breakdown of the energy delivered by the gas boiler

It can be seen that the gas boiler supplies energy to the water tank primarily during periods where bitumen is not stored. The maximum monthly energy from the gas boiler is found to be over 25000 kWh but the average monthly value for the summer season is about 20000 kWh. This value falls to about 10000 kWh in the winter period. The breakdown of energy delivered by the gas boiler shows that a significant part, 36%, is used to heat the bitumen loading/unloading circuit to enable sufficient fluidity and proper workability of the bitumen. Heating of the emulsion tanks were found to be 98% supplied by electricity and only 2% by the water tank.

Based on this information, it is possible to calculate the solar fraction of the installation, a key factor to evaluate the performance of the solar thermal system. The solar fraction is the ratio between the solar energy supplied to the water and bitumen tanks and the total energy required by the system, including gas and electricity energy consumptions.

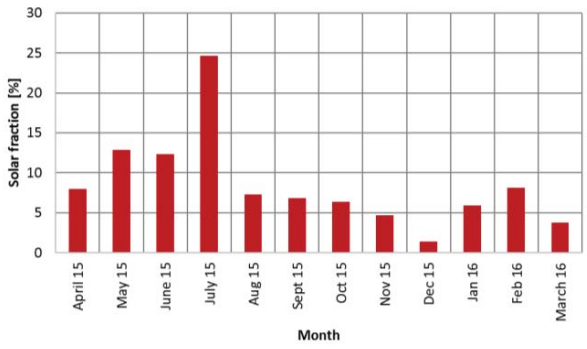

Fig. 8 : Average monthly solar fraction of the system

Fig. 8 presents the solar fraction of the installation on a monthly basis. It can be observed that for the entire year, solar fractions are generally quite low, with a majority less than 10%. The high value of ~25% solar fraction observed in July is due to the good climatic conditions, see Fig. 5, but also because of a low activity in the road surface construction sector and implicitly on the industrial site for this specific month.

The low values mean that for this particular application under current operating conditions, solar energy is not fully maximised. The operational problems encountered with the water tank in August have significantly contributed to this poor performance. However, an overall analyse of the system operation revealed a poorly use of the solar energy in the bitumen storage site to meet their specific energy saving goal. This is the case of the emulsion tanks that are mainly heated with electricity even when the water tank is able to provide the required energy. Furthermore, the real efficiency of the solar collectors was found to differ considerably from the theoretical values. Differences between these values are probably due to dirt accumulation on the glass cover and a potential vacuum loss, factors that were investigated in the simulation, see 4.2.

As the solar collectors supply energy to the water tank, their performance changes from that when energy is delivered to the bitumen tank due to their different operating temperature. To illustrate this Fig. 9 shows a comparison of the performances under these two supply configurations against the daily radiation.

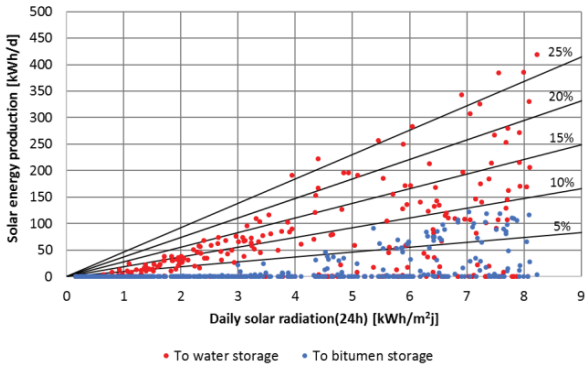

Fig. 9 : Performance distribution of solar collectors

Overall, the performance is low under all operating modes. The distributions indicate that the collectors' performance decrease when charging the bitumen tank (blue dots) with values below 10%. However, when delivering energy to the water tank (red dots) the performance is better and could reach 25%. In this case, scattering of the data is more pronounced because of the different utilisation modes of the water tank. Data points at 0% performance correspond to days where the collectors' pump was operating but no heat was delivered to any of the two tanks. This happens because the operating temperature is not higher than the storage tanks temperature. Consequently, 35% of the total energy used by the solar pump was spent for circulation only, clearly revealing a controller malfunction.

4. Numerical simulation

A simplified numerical model of the heating system was designed using the Polysun software, version 9.0.9. The complexity of the installation does not allow the use of Polysun current implemented models. Hence, a specific model was designed to reproduce the behaviour of the installation in Yverdon-les-Bains and to simulate its annual performance. This model will be further used in this project to optimise the solar thermal control system. Fig. 10 gives an overview of the simulation model and its different components.

4.1 Assumptions and simplifications

The gas boiler and its hydraulic system were modelled as integrated gas boilers placed within the storage tanks (see Fig. 10). This means that the pump and piping components connecting the gas boiler to the storage tanks were not taken into account. However, thermal losses due to fluid transport and the gas boiler oil storage were considered.

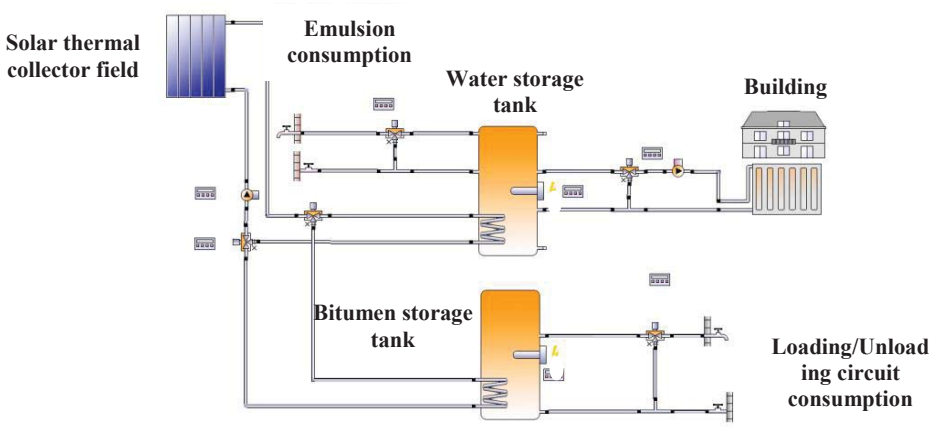

Fig. 10 : Schematic diagram of the simulation model of the bitumen storage installation in Yverdon-les-Bains.

Polysun is not designed to deal with tanks that are partially filled. Consequently, the energy consumed by the loading and unloading of emulsion and bitumen was taken similar to a DHW loading profile. A constant inlet temperature was fixed while the outlet storage tank temperature was set to 155°C for bitumen and 55°C for emulsion. The daily quantity of extracted fluid from the tanks was adapted in order to have the same amount of monthly energy consumption as measured for the given period. The electric heating elements for emulsion tanks were not included here, because in an ideal system, the emulsion should only be heated by the water tank.

Both storage tanks numerical models were validated against measurements taken when the tanks were turned off for several hours. This prevented any energy going in and out of the tanks, leaving heat loss from the tanks as the only driver. The collector model was provided by SRB Energy as it is not available in the Polysun database. The performance coefficients were estimated considering the certification test results.

4.2 Simulation results

To validate the overall operation of the system, measured monthly consumptions of the building, bitumen and emulsion tanks were introduced in Polysun. Fig. 11 compares the predictions of the annual energy consumption with the measurements and acceptable agreement is obtained. For the analysed period, heat supplied to the emulsion tanks was mainly by electricity. This working procedure leads to reduced energy consumption from the water storage in summer season and implicitly less solar energy production at lower temperatures.

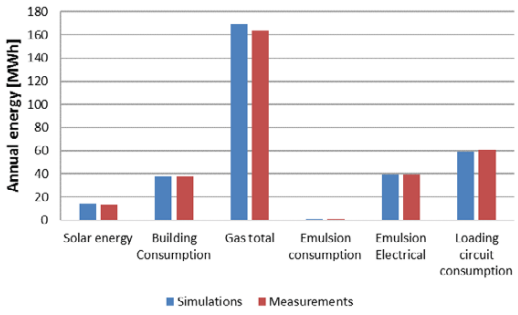

Fig. 11 : Simulated and measured annual energy flows

Based on the observed failures and improper operating practices, several simulations were performed to estimate the potential of this system operating under ideal conditions, namely: solar collector field performance as certified, well-insulated bitumen tank and improve control system operation. The latter allowing heat for emulsions to be supplied either by solar energy or by the gas boiler through the water storage.

Fig. 12 shows an increase of over 75% of the annual solar energy production when the collector performance is based on the certified values.

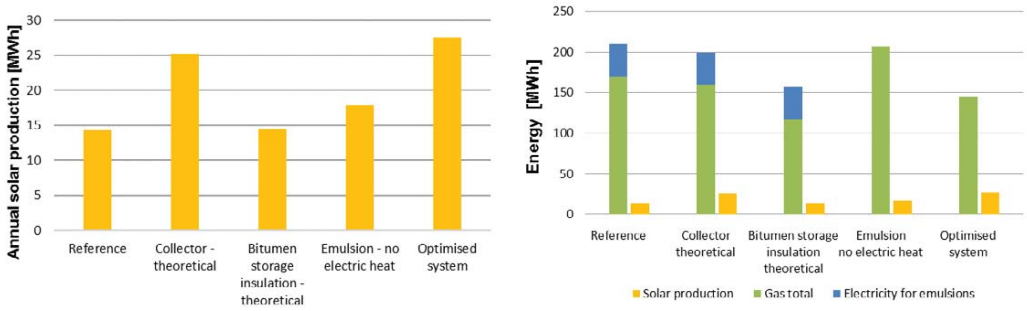

Fig. 12 : Predicted annual solar energy production and heat consumption for different system configurations

Improved insulation of the bitumen storage is found to have a significant impact on the gas consumption of the system (31%), but not on the solar production. The optimised system taking into considerations all enhancements presented above, while keeping the original heat demand, shows very promising results with an increase of over 90% for the solar energy production, no electric heating consumption and 15% less gas consumption when compared to the actual measured system. Nevertheless, in all cases, the overall share of solar energy contribution remains low (e.g. 19% for the optimised case).

The effect of different operating conditions on the performance of the optimised system was further investigated as a measure of the overall solar thermal efficiency. The effects of changing dimensions of the internal heat exchanger, collector field surface area as well as the collectors' orientation and tilt were studied, see Fig. 13.

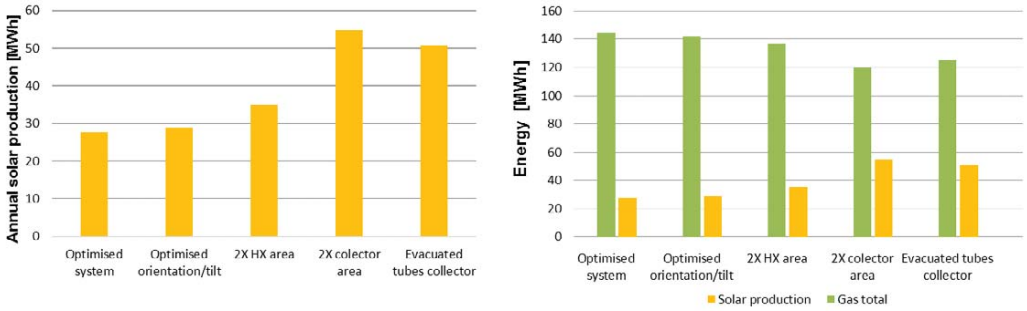

Fig. 13 : Predicted annual solar energy production and heat consumption for different operating conditions – optimised system

Collectors tilted 35°and south-oriented seem not to significantly increase solar production. In contrast, with larger heat transfer surface areas, high solar production is achieved due to a higher thermal performance of the heat exchangers and consequently lower inlet collector temperatures. Large solar thermal collector fields will certainly improve the annual solar energy production, but, because heat in summer is also supplied to the high temperature bitumen tank, collectors will present a low degree of efficiency.

As observed in Fig. 6, the large energy demand of the water storage results in a low solar energy supplied to the bitumen tank even with larger collector fields. The effect of replacing the SRB UVH C2 collectors by evacuated tube collectors for heating the water storage while bitumen was heated with gas revealed that it is possible to double the solar energy production while decreasing the gas consumption.

5. Life cycle analysis

An environmental assessment was conducted taking into account the environmental impacts of the installation materials as well as the energy consumed by the solar installation. The methodology applied in this study is conforming to standards ISO 14'040 series (ISO, 2006). The functional unit considered the impacts generated by the solar installation including the energy and materials consumption over an operational period of 20 years. The system boundaries include manufacturing and disposal of the materials used in the solar installation and the energy consumption throughout the use phase. Transport between the assembly site and the installation site is excluded from the analysis. All impact values were taken from KBOB database (KBOB, 2014) or Ecoinvent database v2.2 (Frischknecht et al., 2004). The indicators considered in this study are:

- *Cumulative Energy Demand NRE (CED_{NRE})* in MJ-eq considers non-renewable energy only. This indicator includes fossil, nuclear and biomass from primary forests (i.e. biomass consumption that contributes to deforestation or forest/woodland degradation)
- *Global Warming Potential (GWP)* in kg CO_2-eq

The analysis aims to estimate the environmental impact of the solar installation (solar collectors, pipework components and supporting structure) to compare to the potential energy savings it could possibly bring. Energy consumption of the installation was defined based on monthly simulations. The analyse considers the solar installation as operated between August 2015 and July 2016 (reference case) and the optimised system.

5.1 Impact of the solar installation

Data on material constituents of the solar installation, including the supporting structure of the solar collectors, was determined by the industrial partner or based on experience. Fig. 14 shows the environmental impacts of the main components of the solar installation. It can be seen that impacts due to the supporting structure predominate and are responsible for over 60% of the total CED_{NRE} impact because of the large number of components. Impact of solar collectors represent nearly 30% while pipework circuits 9%. A similar distribution is found for GWP indicator.

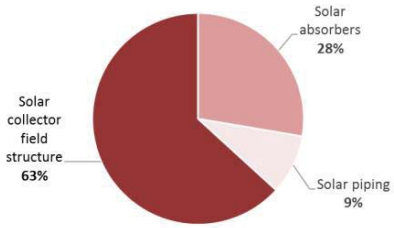

Fig. 14 : CED_{NRE} impact of main components of the solar installation

5.2 Assessment of the solar installation

The measurements and predictions have clearly demonstrated that the use of solar energy in bitumen storage can lead to energy savings. Thus, the solar energy used was converted into gas and electricity savings. Two cases were considered:

- Case 1: reference case where all supplied solar energy corresponds to gas savings as the emulsions were essentially electricity heated.
- Case 2: optimised installation according to simulations where all supplied solar energy corresponds to gas and electricity savings as the emulsions are only heated by the water storage.

In both cases, energy from the different pumps in the system (solar, boiler and emulsions) was taken into consideration.

The measured useful energy was converted into final energy by considering a thermal efficiency of 80% for the gas boiler (value from practice) and a 100% efficiency for conversion into electrical energy. The annual solar energy production for case 1 was predicted to be over 14000 kWh while for case 2 was above 27500 kWh. Fig. 15 shows the impacts of the solar installation due to infrastructure components and pump electricity

consumption and the gas and electricity savings that could be made over the entire life cycle span.

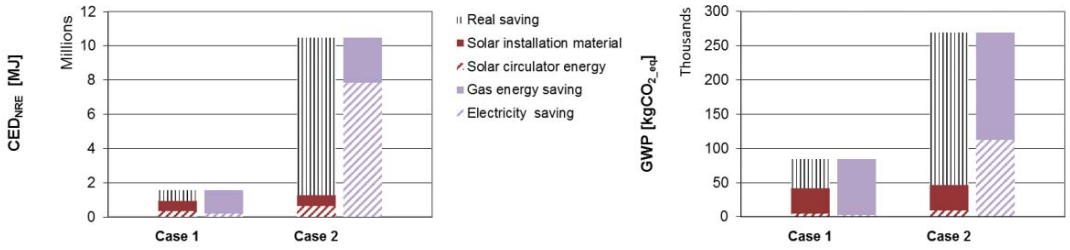

Fig. 15 : CED_{NRE} and GWP impacts of the solar installation and derived real savings

In both cases and for both indicators, the solar installation related impacts are lower than the derived savings of primary energy or emissions of greenhouse gases. This means that the use of solar thermal for this particular application is still interesting in terms of energy savings despite the strong impacts of the supporting structure.

An important difference of impacts is also observed between case 1 and case 2. Indeed, the operating problems observed during the investigated period strongly penalise case 1. In the optimise configuration (case 2), replacing emulsions electric heating by the water heating, contributes to significantly increase energy savings and consequently, decrease impacts.

The evolution of these impacts and potential savings over time has allowed defining the return on the investment this solar installation offers, see Fig. 16.

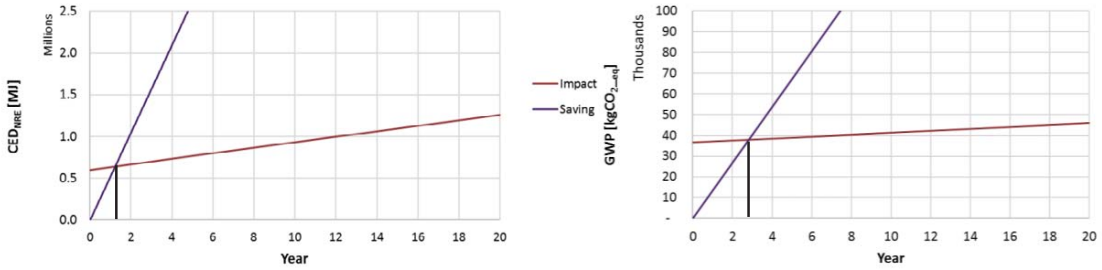

Fig. 16 : Return on investment for case 2

It can be seen that for case 2, the solar installation offers 1 and 3 years return on investment for CED_{NRE} and GWP, respectively. Longer return on investment times, approximately 10 years, were found for case 1. Thus, improving the bitumen storage system and in particular replacing emulsions electricity heating by gas and solar is not only environmental but economically interesting.

6. Conclusion

The behaviour and performance of a medium–temperature solar industrial process for bitumen storage have been investigated based on measurements and simulations for subsequent optimisation of the process. Important differences, up to 50% at 220°C, between the certified performances of the solar thermal collectors and measured were observed during this project. The low solar fractions (~10%) observed for this installation are a result of combining low and medium temperature applications with a variety of operating modes into a single solar installation.

Simulations show that there is room for improvement and that the solar production could be roughly doubled if the system operates as designed. Furthermore, simulations prove that the heat exchangers designed for both thermal storages are undersized. Increasing solar collector area results in higher solar productivity, but still relatively low annual collector field efficiency.

Supplying water storage with solar energy from evacuated tubes collectors for emulsions and building heating

needs, proved to be a cost-effective configuration for this industrial site.

The life cycle impact assessment of the solar installation showed that the infrastructure impacts predominate over the entire life cycle, accounting for over 60% of the total CED_{NRE}. Energy savings brought along by the solar installation more than compensate the additional material and energy related impact of integrating such a system. Less than 3 years environmental return on investment periods were found in the case of an optimised solar bitumen storage system.

7. References

Benvenuti, C., 2013. The SRB solar thermal panel. Europhys. News 44, 16–18. doi:10.1051/epn/2013301

Bunea, M., Duret, A., Péclat, L., Bornet, P., Maranza, M., Wendling, J.-B., Pauletta, S., 2013. Projet COLAS: Campagne de mesures : Installation solaire thermique à haute température de COLAS SA.

Bunea, M., Hildbrand, C., Duret, A., Eicher, S., Péclat, L., Citherlet, S., 2015. Analysis of a medium temperature solar thermal installation with heat storage for industrial applications, in: SHC 2015.

Eurostat, 2013. Energy, transport and environment indicators. Luxembourg.

Frischknecht, R., Jungbluth, N., Althaus, U.H.-J., Doka, G., Dones, R., 2004. ECOINVENT- Overview and Methodology Data v1.1 (Report). Swiss Center for Life Cycle Inventories, Dübendorf.

ISO, 2006. ISO EN 14040 - Management environnemental, analyse du cycle de vie, principes et cadres.

Jobin, C. (Agena S., Blum, B. (Fritz K.& C.A., Flück, P. (Flück H.A., Wiest, M. (Ernst S.A., 1994. Production d'eau chaude solaire Dimensionnement, montage, mise en service, entretien.

KBOB, 2014. eco-bau and IPB (2014) ecoinvent Datenbestand v2.2+; Grundlage für die KBOB-Empfehlung 2009/1:2014: Ökobilanzdaten im Baubereich, Stand April 2014. Koordinationskonferenz der Bau- und Liegenschaftsorgane der öffentlichen Bauherren c/o BBL Bundesamt für Ba [WWW Document]. URL www.lc-inventories.ch

Krummenacher, P., Muster, B., 2015. Methodologies and Software Tools for Integrating Solar Heat into Industrial Processes. IEA SHC Task 49.

Maranzana, M., Bornet, P., 2011. Projet pilote de maintien en chauffe d'un stockage de 80'000 litres de bitume à 160 °C par des panneaux solaires haute énergie. Rapp. OFEN 1–22.

Mauthner, F., Weiss, W., 2015. Solar Heat Worldwide - Markets and Contribution to Energy Supply 2013.

Conference Proceedings

EuroSun 2016
Palma de Mallorca (Spain), 11 - 14 October 2016

AGRICULTURAL GREENHOUSE SOLAR-ASSISTED CLIMATIZATION SYSTEMS DESIGN AND OPTIMIZATION, FOR THE SEMI-ARID REGION OF NORTHERN MEXICO

Jorge Escobedo-Bretado, Mario Nájera-Trejo, Ignacio R. Martín-Domínguez

Centro de Investigación en Materiales Avanzados, S.C. - Unidad Durango (CIMAV-Dgo)

Calle CIMAV 110, Ejido Arroyo Seco, 34147 Durango, Dgo. México. +52 614 439 4898

Abstract

An agricultural greenhouse is thermally analyzed using the simulation program TRNSYS 17. The thermal loads resulting from the heating and cooling are calculated to maintain the greenhouse temperature within the range of crop development. Construction materials, geographical location and the optimal development characteristics of the Saladette tomato and its different growing stages are also reported. The thermal performance inside and outside the greenhouse with and without air conditioning is also described. The heating and cooling loads are shown for an idealized air conditioning system considering the number of heat exchangers, temperatures required by the crop and the hot/cold water temperature available in the system. The results of a thermal analysis for a three day in June is described in detail. The temperatures inside and outside of the greenhouse, including the thermal load for the most critical day of the year are shown. Simulation results show that 4,231,966 GJ and 39,324,140 GJ are being demanded for heating and cooling respectively along a typical meteorological year. A case of study is presented in order to analyze the greenhouse in which energetic requirement is partially provided using solar energy. The simulation shows that in order to achieve a solar fraction of 72% for heating and 30% for absorption cooling, 300 solar collectors are needed.

Keywords*: Agricultural greenhouse, Solar heating and cooling, Trnsys simulation, Solar heat for industrial processes.*

1. Introduction

In Mexico tomato production in greenhouses with controlled environments is taking great importance. The use of highly automated greenhouses allows to control the necessary variables for tomato growing and thus significantly increase the volume of annual production in continuous operation (Kolokotsa et al., 2010). The main variables for a greenhouse are temperature, humidity, CO2 and the plagues (Attar et al., 2013), (Chargui and Sammouda, 2014), (Kamel and Fung, 2014). It is necessary to have a closed greenhouse in order to control the variables as proposed by Vadiee and Martin (2013 a). However, in extreme climates with low relative humidity, cold but sunny winters and hot summers, it is possible to get temperature variations up to 25 °C in a day. For a greenhouse under these conditions and continuous operation throughout a year, requires a high power supply so huge that become unaffordable for commercial operation. Currently, for a greenhouse optimum design it is necessary to calculate the heat transfer rates to and from the envelope, required to maintain the optimum temperature for the crop. Quantification of a greenhouse energy demand is a challenging task, due to the continuous variation of atmospheric variables. Therefore it is also uncertain to

Selection and/or peer review under responsibility of Scientific Committee
doi:10.18086/eurosun.2016.02.15 Available at http://proceedings.ises.org

develop a reliable economic analysis that allows to determine whether the obtained production profit justifies the initial investment and operating costs (Souliotis et al., 2009). Nowadays, there is specialized software such as TRNSYS that analyze different design scenarios, in order to compare the thermal performance of different configurations, sizes and types of technology used, delivering results with less than 6% of uncertainty (Almeida et al., 2014) (Attar and Farhat, 2015). TRNSYS has been used to model and analyze greenhouses, in places like Zimbabwe (Mashonjowa et al., 2013), Nepal (Seona et al., 2012) and Australia (Lu Aye et al., 2010), nevertheless studies for the northern part of Mexico has not yet been developed.

No papers were found for the energy performance and the economic analysis of greenhouses. Developed in this paper, is the analysis of the interaction of an agricultural greenhouse with the climatic conditions of the semi-arid region of northern Mexico, specifically in the proximity of 28° N latitude. An air conditioning system is proposed, based on the circulation of hot/cold water through heat exchangers located inside the greenhouse. The aim of this paper is to demonstrate that the amount of energy, and thus the air conditioning equipment required for a greenhouse throughout a year are enormous on its original architecture, resulting in low profitability. It is therefore proposed, a detailed analysis of technical alternatives to reduce the thermal loads of a greenhouse. Thermal insulation and shading are mainly considered to reduce as much as possible the investment needed for air conditioning operation. These will lead to an optimal design of the air conditioning system, including construction materials, shading system and a combination of heating and cooling equipment assisted with solar energy, that together aim to reduce the project cost and thus maximize production profit.

1.1. Crop Information

1.1.1. Tomato Variety

The greenhouse used as a case of study produces organic Saladette tomato in a variety called “Moctezuma and Cuauhtémoc” (Figure 1).

Fig. 1: Saladette tomato inside the greenhouse of this case of study

1.1.2. Requirements for temperature, humidity and CO_2

The requirements of temperature, relative humidity and CO_2 concentration of Saladette tomato are found in the following table.

Tab. 1: Required environmental specifications for the crop (Castellanos, 2004)(León, 2006).

Requirement	Values
Temperature for all production stages (°C)	15 – 30
Humidity (%)	70 – 85
CO_2 concentration (ppm)	700 - 800

1.2. Greenhouse information

1.2.1. Geographical location

The greenhouse analyzed in this work is located within the Agroindustrial Park Naica, Saucillo Municipality, Chih., Mexico. Its geographical coordinates are 28.062543 N, 105.534867 W.

1.2.2. Design and type of technology

The greenhouse is a multi-chapel type (greenhouse technology developed in Canada), designed for medium and highly automated operations. It has 9 chapels spread over a surface area of 1.6 hectares and an approximate volume of 100,000 m^3. The double-walled polyethylene cover is supported by metallic structures represented by dots in Figure 2.

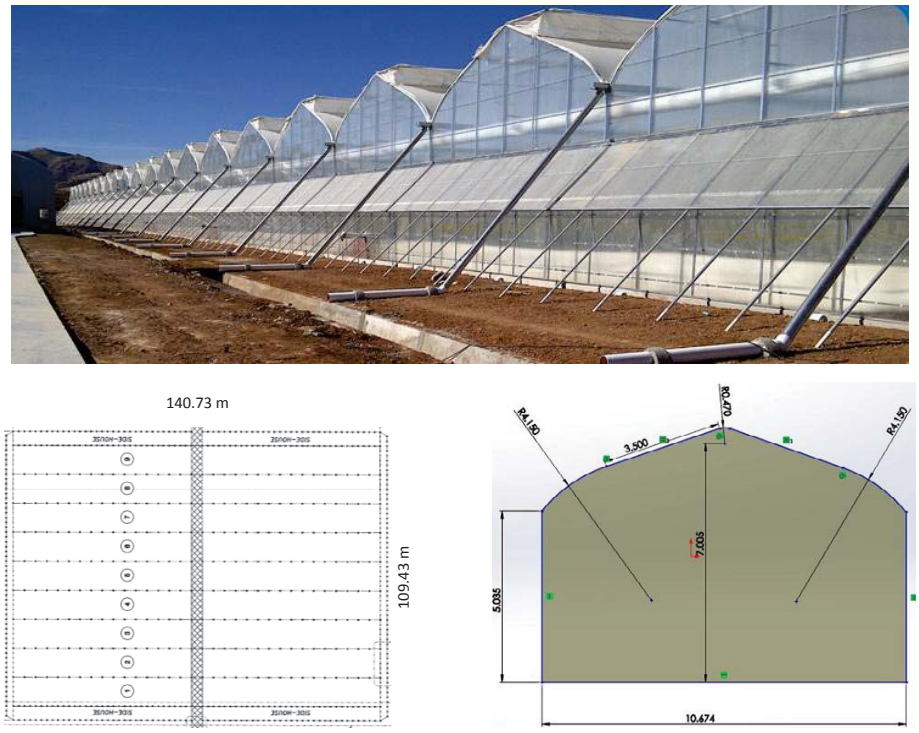

Fig. 2: Multi-chapel Greenhouse type

1.2.3. Current Climate Control

Currently the greenhouse has no air conditioning system. Instead, it has a double walled cover, and a natural ventilation induced by a vent system with a mechanized aperture, located at the top of the structure.

2. Proposed air conditioning system

The greenhouse air conditioning system proposed and its main components are shown in Figure 3. The system use a heat exchanger (water-air) network distributed in the greenhouse to cool or heat the air inside, without introducing external air that contaminates and dilute the CO^2 concentration. The heating system is mainly composed by a field of solar thermal collectors, a storage tank and an auxiliary heating system based on LPG. It also has a refrigeration equipment to produce cold water during summer.

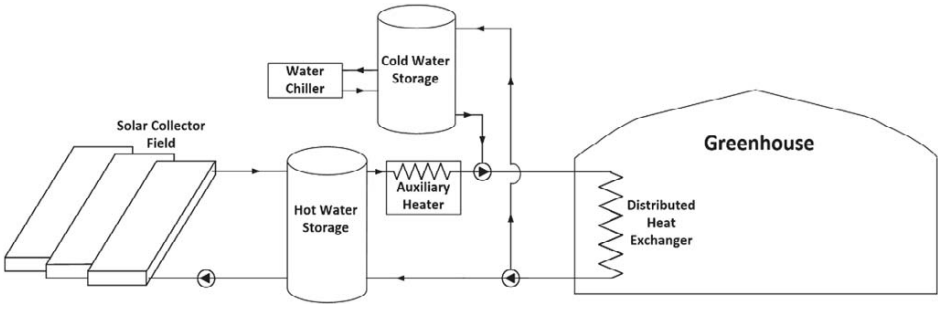

Fig. 3: Greenhouse air conditioning system proposed.

3. Simulation

3.1. Simulation tools

The software packages required for the proposed analysis, were among others, SketchUp Pro, Simulation Studio, TRNBuild, TRNEdit, Meteonorm, Berkeley Lab Window 7.2, MS Excel and TRNSYS 17. The greenhouse geometry was first modeled, then the materials physical properties of the envelope and the translucent cover were incorporated, after that, the thermo-mechanical components were simulated. In Figure 4, the type of greenhouse technology and its implementation in the SketchUp Pro software is displayed.

Fig. 4: Greenhouse technology type and SketchUp schematization.

The main components of the air conditioning system and its interaction is shown schematically by means of TRNSYS 17 Icons as shown in Figure 5.

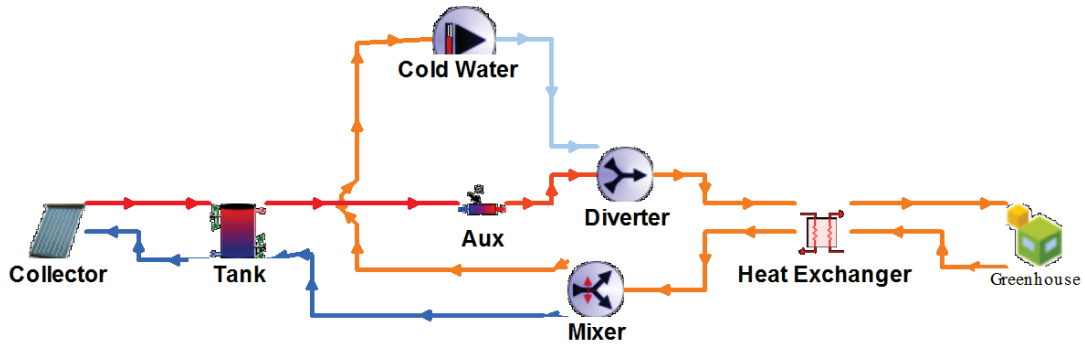

Fig. 5: TRNSYS system setup.

3.2. Simulation remarks

System operation was simulated throughout a typical year, in a 15 minute (step) based calculation. Parametric variation was performed using the climatic information (TMY) of the city of Delicias, Chihuahua. Instantaneous flow rates were integrated over periods of a day and a year to get the daily and annual cumulative.

4. Results

4.1. Thermal Performance

In Figure 6 the environment temperature behavior is shown for a typical meteorological year (TMY) in the specified greenhouse location. The temperature range recommended for a good development of a tomato crop at all stages is also displayed.

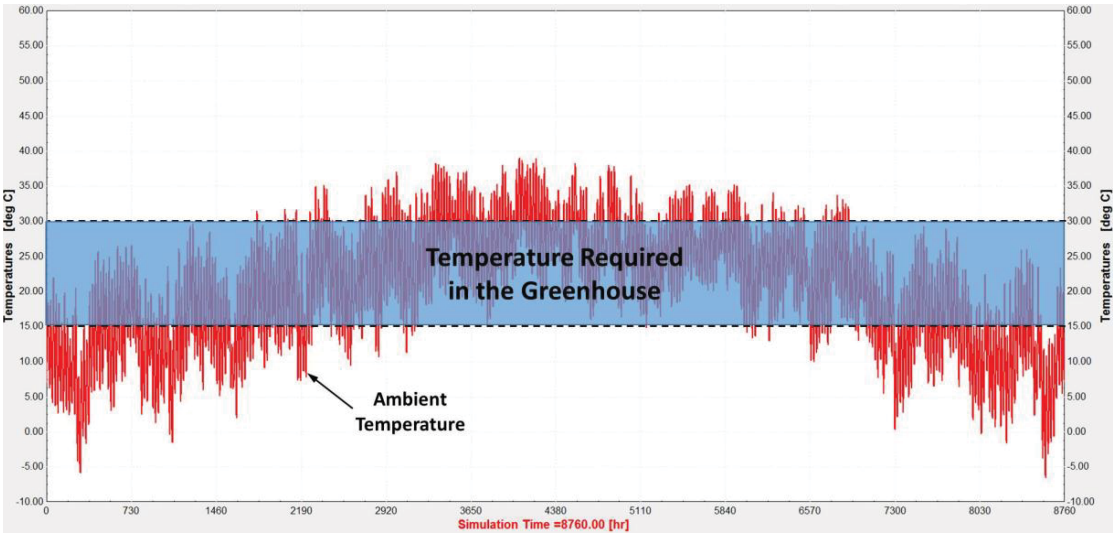

Fig. 6: Environment temperature and range required inside the greenhouse.

The air temperature performance inside the greenhouse is shown in figure 7, when operating closed and without air conditioning. The temperature range required for the crop development is also shown. In this case the greenhouse is performing closed in order to maintain relative humidity and CO2 concentration under control, however, the temperature remains within the comfort zone for only a few weeks a year.

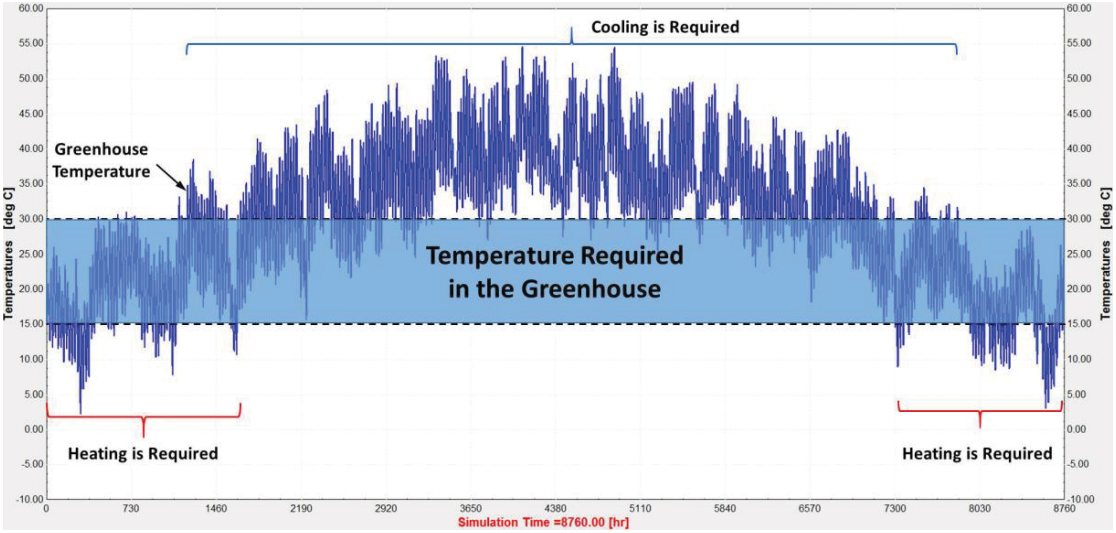

Fig. 7: Air temperature behavior inside the greenhouse without air conditioning, and the crop thermal comfort zone.

The time periods when heating or cooling is required are shown in figure 7. It is noted that for this climate conditions, cooling requirements during the summer season are significantly higher than those of heating in winter, due to the natural greenhouse effect. It can be observed that without air conditioning, the vast majority of time throughout the year, the air temperature inside the greenhouse is above the comfort zone, reaching lethal to plants temperature values, this makes not only impossible to harvest in summer, but necessary to replace dead plants at the end of the hot season.

4.2. Theoretical thermal loads for Heating and Cooling

To achieve a perfectly controlled climate within the greenhouse, it is required to supply heating and cooling to counteract the external thermal loads, at the same rate as they occur. In the simulation this is achieved assuming that there is an unlimited hot or cold water supply, and energy is transferred to or from the air instantly. This indoor ideal temperature control is obtained and the instant energy consumption is

determined. The greenhouse thermal simulation for the previously described is shown in Figure 8. The graph shows that for the coldest day, heat must be supplied at a rate of 1,370 kW to the greenhouse and for the warmest day heat needs to be extracted at a rate of 2,490 kW from the greenhouse.

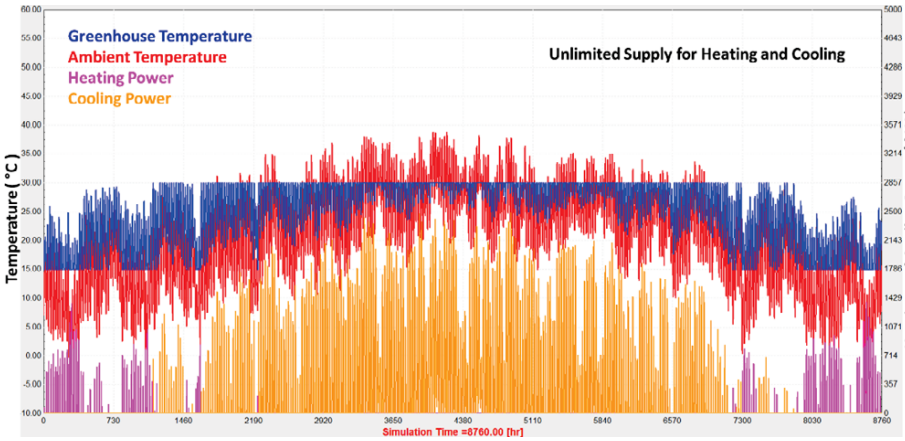

Fig. 8: Greenhouse inside and outside temperatures and the heating/cooling power.

However, by introducing the physical performance of the required equipment, the type and number of devices used for air conditioning are obtained, additionally an estimate of the cost is also obtained. Physical and economic data of real devices, available in the local market were used in this work to obtain an initial estimate of the economic impact of the greenhouse air conditioning.

4.3. Heat transfer equipment

To maintain the previously mentioned comfort zone inside the greenhouse, the effect on the use of different number of heat exchangers was analyzed. Figure 9 shows the behavior of the air temperature within the greenhouse based on the number of heat exchangers used for air conditioning. Commercially available fan and coil heat exchangers of an overall heat transfer coefficient of 400 W / ° C were simulated. The greenhouse performance using 0, 85, 145 and 180 exchangers is shown.

It is noted that in order to control the indoor temperature in winter using 85 heat exchangers is easily achieved, however cooling in summer requires more equipment. It is also noted that even when using 145 heat exchangers, there are periods at temperatures above the desired maximum level. Increasing the number to 185 it improves only marginally. This illustrates that the problem is no longer technical but economical and it is compulsory to determine how far it is appropriate to add equipment for an overall economic feasibility.

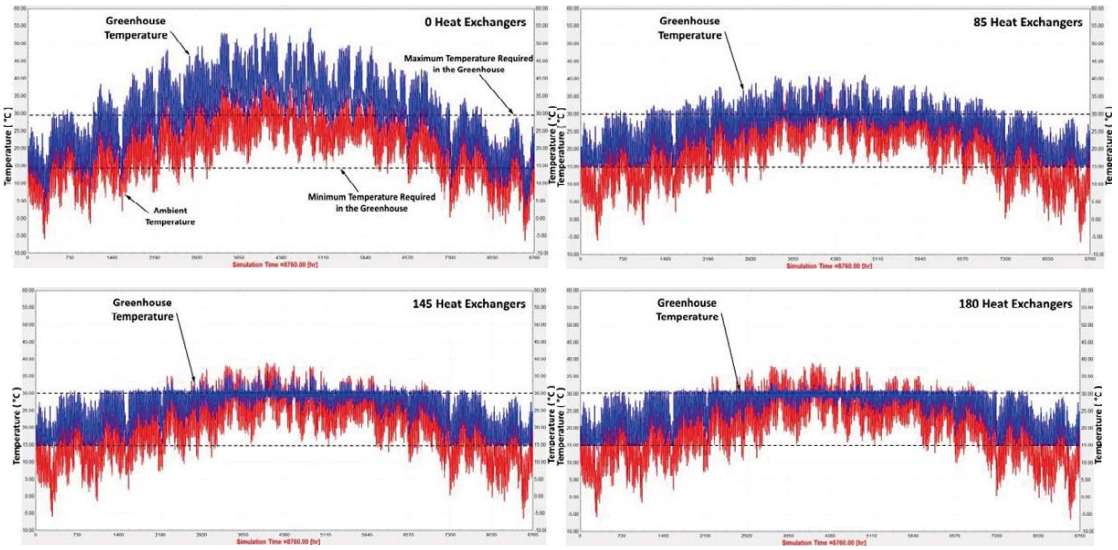

Fig. 9: Thermal performance in the greenhouse using 85, 145 and 180 heat exchangers.

From the technical point of view in the previous graphs, it can be concluded that the required number of heat exchangers for the air conditioning of the greenhouse should be 180 in order to ensure that the internal temperature will partially not exceed the maximum level in the year.

4.4. Actual thermal heating and cooling loads

To analyze the greenhouse thermal loads using the locally available heat transfer equipment, considerations shown in Table 2 were made.

Tab. 2: Considerations for the analysis of thermal heating and cooling loads.

Parameter	Value
Heat exchangers amount	180
Available hot water temperature (°C)	60
Minimum allowed temperature inside the greenhouse (°C)	15
Available cold water temperature (°C)	2
Maximum allowed temperature inside the greenhouse (°C)	30

Based on the limitations imposed in the table above, simulation shows that to maintain the greenhouse interior temperature within the comfort zone it is necessary to insert and remove the heat rate amount shown in Figure 10. The heating and cooling power values are of around 3,700 kW and 1,800 kW respectively.

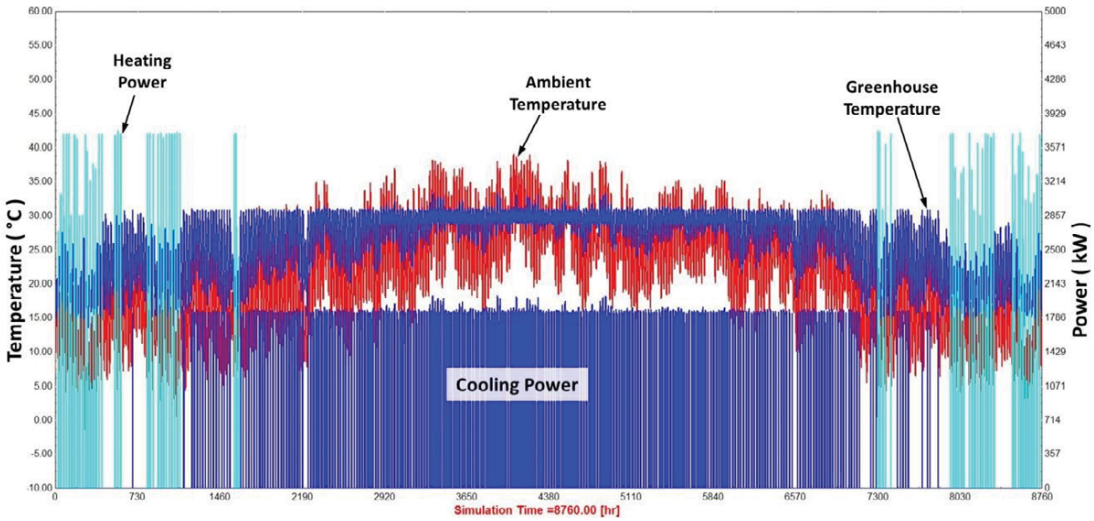

Fig. 10: Necessary heat transfer rate.

4.5. Greenhouse daily thermal performance

To analyze in detail the thermal performance outside and inside the greenhouse without air conditioning, simulation results on June 19th, 20th and 21st are shown in Figure 11. This figure shows that the temperature inside the greenhouse is above the maximum allowed temperature. Even the exterior temperature is generally above that temperature.

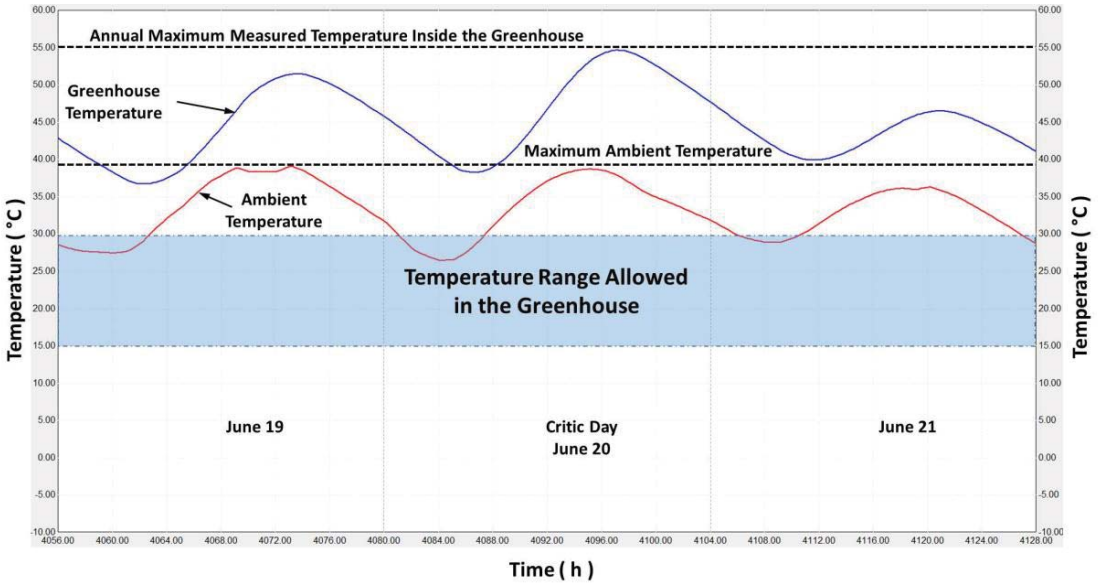

Fig. 11: Temperatures reached inside and outside the greenhouse on June 19th, 20th and 21st.

Figure 12 presents the thermal performance inside and outside the greenhouse when the air conditioning system is used. The power required for the three day cooling is also displayed, additionally the energy required on June 20th is included. The simulation showed that the highest cooling demand of the year is on that day.

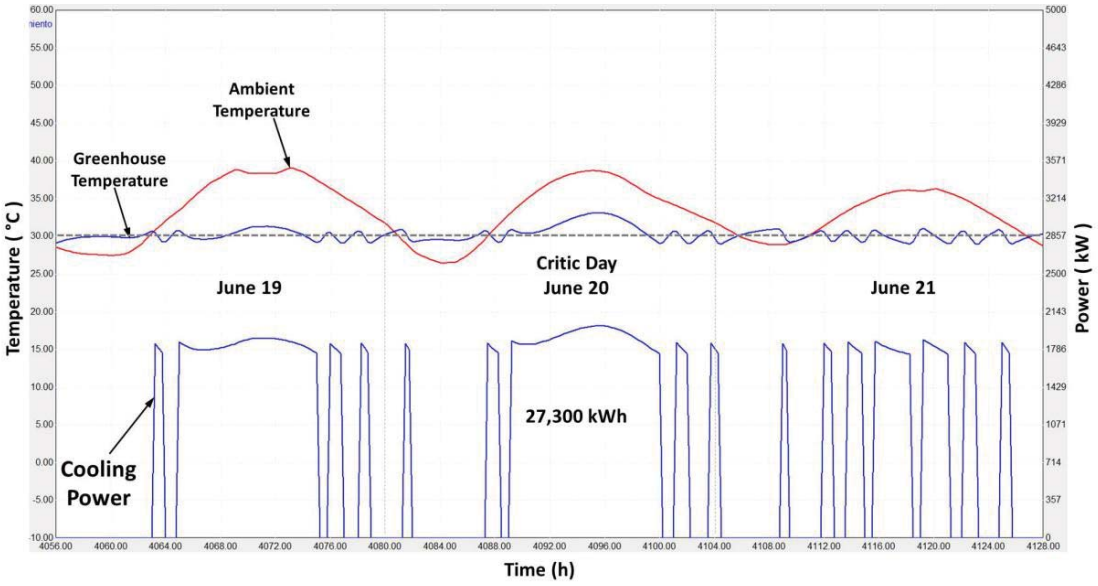

Fig. 12: Thermal performance inside and outside the greenhouse using air conditioning on June 19th, 20th and 21st.

Figure 13 shows the thermal performance inside and outside the greenhouse using air conditioning along with the power and energy inputs to achieve this. However, the necessary energy to extract heat from the greenhouse is 27,300 kWh and it can be supplied by a device with an output of 325 tons of refrigeration.

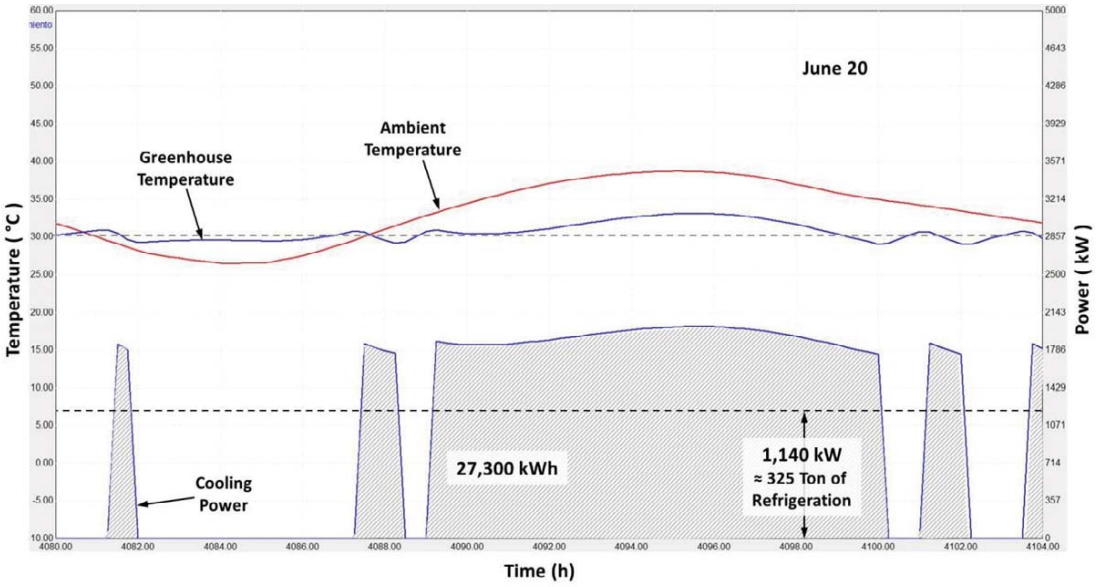

Fig. 13: Power, energy and thermal performance of the air conditioned greenhouse on June 20th.

4.6. General results

The simulation results allows to observe that the energy required for the greenhouse heating and cooling to keep the temperature within the optimum thermal zone for the crop development throughout the year is 4,231,966 and 39,324,140 GJ GJ respectively.

Once the number of heat exchangers is determined and the temperature considerations are set, the power calculated for heating and cooling results in 3,700 kW and 1,800 kW respectively.

This huge energy consumption can be supplied by several sources such as oil, LP gas, natural gas, electricity, biomass, and solar (Vadiee and Martin, 2013 b), (Vadiee and Martin, 2014).

The following case of study allows to analyze the system performance when part of the energy is met by a solar source. The simulation results show that in order to achieve a solar fraction of 72% for heating and 30% for absorption cooling, the equipment required is shown in Table 3.

Tab. 3: Required equipment to supply a specific solar fraction.

Equipment	Amount	Unit Price ($USD)	Total Price ($USD)
Evacuated tube solar collector (heat pipe)	300	500	150,000
Thermal storage @ 60 L/m^2	75 m^3	5,000 / 25 m^3	15,000
heat exchanger overall heat transfer coefficient (400 W/°C)	180	2,433	437,940
Auxiliary heater (1,000 kW)	1	53,552	53,552
Absorption refrigeration system (1,140 kW)	1	325,000	325,000

5. Conclusions

Energy requirements have been studied in order to maintain the greenhouse air temperature in an optimal range for the crop development, as well as the heat exchange equipment required for the air conditioning throughout the year.

It was found that the thermal loads for both heating and cooling are very high, thus making the technology implementation unfeasible either for conventional or solar energy supply in the crop production throughout a year.

Consequently, all of the above encourage to propose a detailed analysis of the technical alternatives applied to reduce the thermal loads in the greenhouse, mainly by means of the analysis of thermal insulation and shading and thereby predicting lower operation costs by heating and cooling.

After an energy efficiency analysis it is possible to propose the use of solar energy for the heating and the cooling of the greenhouse.

6. Acknowledgements

A profound recognition by the funding support received from: Centro Mexicano de Innovación en Energía Solar (CeMIE-Sol), through the project: P13 “Laboratorios de pruebas para baja y media temperatura, laboratorio para el diseño e integración de sistemas termo solares asistido por computadora” belonging to the call 2013-02: Fondo SECTORIAL CONACYT - SENER - SUSTENTABILIDAD ENERGÉTICA.

7. References

Almeida P., Carvalho M.J., Amorim R., Mendes J.F., Lopes V. (2014). Dynamic testing of systems – Use of TRNSYS as an approach for parameter identification. Solar Energy 104, 60–70.

Amir Vadiee, Viktoria Martin. (2013a). Energy analysis and thermoeconomic assessment of the closed greenhouse – The largest commercial solar building. Applied Energy 102, 1256–1266.

Amir Vadiee, Viktoria Martin. (2013b). Thermal energy storage strategies for effective closed greenhouse design. Applied Energy 109, 337–343.

Amir Vadiee, Viktoria Martin. (2014). Energy management strategies for commercial greenhouses. Applied Energy 114, 880–888.

Attar, I., Naili, N., Khalifa, N., Hazami, M., Farhat, A. (2013). Parametric and numerical study of a solar system for heating a greenhouse equipped with a buried exchanger. Ener gy Conversion and Man agement. 70, 163–173.

Attar, I., Farhat, A. (2015). Efficiency evaluation of a solar water heating system applied to the greenhouse climate. Solar Energy. 119, 212-224.

Aye Lu, Fuller R.J., Canal A. (2010). Evaluation of a heat pump system for greenhouse heating. International Journal of Thermal Sciences 49, 202–208.

Candy Seona, Moore Graham, Freere Peter. (2012). Design and modeling of a greenhouse for a remote region in Nepal. Procedia Engineering 49, 152 – 160.

Chargui R., Sammouda H. (2014). Modeling of a residential house coupled with a dual source heat pump using TRNSYS software. Energy Conversion and Management 81, 384–399.

Castellanos, Javier Z. (2004). Manual de producción hortícola en invernadero. 2da Edición. INTAGRI.

Kamel Raghad S., Fung Alan S. (2014). Modeling, simulation and feasibility analysis of residentialBIPV/T+ASHP system in cold climate—Canada. Energy and Buildings 82, 758–770.

Kolokotsa D., Saridakis G., Dalamagkidis K., Dolianitis S., Kaliakatsos I. (2010). Development of an intelligent indoor environment and energy management system for greenhouses. Energy Conversion and Management 51, 155–168.

León Gallegos, (2006). Guía para el cultivo de tomate en invernadero. 2da Edición.

Mashonjowa, E., Ronsse, F., Milford, J.R., Pieters, J. G. (2013) Modelling the thermal performance of a naturally ventilated greenhouse in Zimbabwe using a dynamic greenhouse climate model. Solar Energy 91, 381–393.

Souliotis M., Kalogirou S., Tripanagnostopoulos Y. (2009). Modelling of an ICS solar water heater using artificial neural networks and TRNSYS. Renewable Energy 34, 1333–1339.

ISES International Solar Energy Society

Conference Proceedings

EuroSun 2016

Palma de Mallorca (Spain), 11 – 14 October 2016

Evaluation of innovative integration concepts of combined solar thermal and heat pump systems for efficient thermal supply of industrial processes – based on case studies and the results of the project EnPro

J. Fluch[1], V. Wilk[2], D. Lange[3], D. Wertz[3], C. Brunner[1], A. Grubbauer[1], P. Königshofer[1], F. Veynandt[1], T. Fleckl[2], K. Ponweiser[3],

[1] AEE – Institute for Sustainable Technologies, Feldgasse 19, A-8200 Gleisdorf

[2] AIT Austrian Institute of Technology GmbH, Giefinggasse 2, A-1210 Wien

[3] TU Wien - Institute for Energy Systems and Thermodynamics, Getreidemarkt 9/E302, 1060 Wien

Abstract

Solar thermal energy and heat pumps are key technologies to increase the share of renewable energy in industry. In order to spread these technologies, integration barriers should be reduced, such as high investment costs, lack of experience, missing integration schemes and planning guidelines or lack of knowledge about technological developments. Within the Austrian research project EnPro appropriate guidelines for manufacturers, users and planners are being developed. Therefore, in total 12 case studies in food, paper, metal production and processing, laundries and insulation industry have been performed, three of them selected and presented in this paper. Based on a detailed assessment of the processes, their process parameters and energy demand as well as the energy supply of the industry, integration concepts of solar thermal and heat pump systems and their combinations have been developed. Possible integration concepts include the parallel use and three different variations of serial integration of solar thermal and heat pumps. As variation I solar thermal is integrated first in the supply cascade (heating demand of a process or the supply system), followed by the heat pump. Variation II is the reversal of the order while as variation III solar thermal is used as source for the heat pump. Integration points for all possible combinations have been detected in the assessed companies. The concepts will be economically evaluated. The focus is set on generalized integration schemes for solar thermal and heat pump systems and the combination of both followed by the identification of upcoming R&D topics to push the implementation of identified solutions.

Keywords: *solar thermal, heat pumps, combined integration, industry, energy efficiency, process heat, renewable energies*

1. Introduction

In order to address the challenge of climate change and global warming the European Union agreed on the ambitious targets to reduce greenhouse gas emission by 40 % and to increase energy efficiency and renewable energy by 27 % by 2030. Special emphasis is placed on energy efficiency and renewable energy in industrial processes as industry accounts for 30 % of the final energy demand in Austria (Statistics Austria, 2014). Solar thermal energy and heat pumps are considered as important measures to reach these targets. Therefore they play an important role in European guidelines as well as in national regulations (European Parliament, 2009).

Solar thermal systems and heat pumps are state of the art for covering heating and hot water demand in the building sector. Combined systems including solar thermal and heat pumps also play a considerable role

Selection and/or peer review under responsibility of Scientific Committee
doi:10.18086/eurosun.2016.02.02 Available at http://proceedings.ises.org

within this sector. However, these technologies are not yet wide spread in industry, as there are still significant barriers although the potential is high. The main reasons for these barriers are high investment costs, lack of experience or skepticism regarding the reliability of these technologies, lack of planning guidelines and integration concepts, as well as lack of users' knowledge of ongoing technological developments, such as high-temperature heat pumps or advanced solar collectors. Several studies and projects have proven that the required temperature range of industrial processes with a heating demand is suitable for the integration of solar thermal systems, heat pumps and the combination of both technologies. These industry sectors include for instance food and beverage, insulation, paper, metal processing and laundry (Hummel et al. 2013; IEA Heat Pump Centre, 2014; Wolf et al. 2014). The Austrian research project EnPro[1] aims to reduce these barriers, hence appropriate guidelines for manufacturers, users and planners are being developed. The bases for the guidelines are twelve case studies that are carried out in the project in different industrial sectors.

The choice of sectors ensures high potential for application of solar thermal energy and heat pumps and guarantees a high degree of replicability. In the companies, the current situation of energy supply and consumption is analyzed based on the European standard EN 16247. The aim is to identify and classify processes, that are suitable for the integration of solar thermal energy and heat pumps and their combination and to detect available waste heat streams and other suitable heat sources for heat pumps. Based on the energy demand of the respective process, integration concepts for solar thermal energy and/or heat pumps are developed to reach more energy efficiency and to increase the amount of renewable process energy. Special focus is set on efficient and cost effective integration concepts for solar thermal energy, heat pumps and the combination of both technologies. Within the framework of the project four different integration concepts for the combination of solar thermal energy and heat pumps are considered as basis for specific adaptions. The EnPro guidelines will consist of generalized concepts for the studied industrial sectors and a calculation tool that allows for basic planning of solar thermal and heat pumps for industrial use.

1.1 Solar thermal systems

Solar thermal systems use solar radiation for the supply of process heat, mainly hot water, but also process steam. Process heat collectors and their application can be divided into three temperature ranges: low temperature (<100 °C), medium temperature (100-250 °C) and high temperature (>250 °C) (Frank et al. 2012). The available technologies can be subdivided into concentrating and non-concentrating collectors, which show differences in design and in optimal operating temperatures. With increasing collector temperature, the efficiency of concentrating systems does not decrease as strongly, compared to non-concentrating collectors. Therefore flat plate collectors and vacuum tube collectors with reflectors are used to provide low temperature levels, vacuum tube collectors and low concentration systems are used for medium temperature levels, while stronger concentrating systems are used for high temperature levels.

1.2 Heat pumps

Heat pumps use low temperature streams to provide heat at a higher temperature level. In the building sector ambient air, ground water or the ground are commonly used as heat source for heat pumps, they usually supply hot water for domestic heating.
In industrial processes, waste heat streams often cannot be reintegrated into the production process or the energy supply of the process because of the inadequate low temperature levels. Therefore low temperature waste heat is released to the environment in many cases. This often goes along with additional cooling demand. Heat pumps allow for re-integration of waste heat streams into the production processes at a higher, useful temperature level and thereby increase energy efficiency. Currently heat pumps that provide temperatures from 90 to 125 °C are available on the market (IEA Heat Pump Centre, 2014; Wolf et al. 2014). Heat pumps that provide temperatures up to 160 °C have been in scope of research since several years. The mentioned temperatures can already be reached in experimental heat pumps and it can be assumed that heat pumps providing temperatures up to 160 °C reach market maturity in the next few years (Fukuda et al. 2014; Fleckl et al. 2014).

[1] The project EnPro (project number 848818) is an R&D service on behalf of the Austrian Climate and Energy Fund, financed by the Energy Research Programme 2014.

2. Problem statement, methodology and project introduction

2.1 Problem statement

There are different integration barriers for solar thermal energy, heat pumps and the combination of both technologies to increase market penetration. The most important barriers are high investment costs, lack of experience, missing best practice examples, missing integration schemes and planning guidelines and lack of knowledge about technological developments. When evaluating the technical integration of the technologies in an industry, several challenges related to the process and energy supply system can be identified such as:

- Heat supply of production sites are often grown structures (based on steam or hot water…) that do not allow a standardized integration
- Due to different used technologies the heat demand varies significantly:
    - Batch or continuous processes
    - Different load profiles and operating hours
    - Different requirements in process parameters (e.g. temperature…)

Another challenge is the choice of the suitable integration point and the development of an integration concept, defining how renewable energy is integrated in the production site. There are different levels for the integration of solar thermal and heat pump systems, on process level (direct supply of one selected process) or on supply level (integration in existing system). Requirements concerning storage and heat exchanger systems result from the defined integration concept. It has to be emphasized that not only the integration concept is important. With regard to the selection of the type of solar collector and the hydraulic connection (charging and discharging strategies of the solar storage), the needed temperature in the collector loop is essential aside from the chosen integration concept and the control strategy. Furthermore, the location of the production site (solar irradiation), its available areas (ground or roof), and static requirements to carry collector weight, orientation or shading are important to gain a maximum solar yield. (Muster et al. 2015) Regarding the integration of heat pumps also the required temperature of the process is an important parameter, as it relates to the refrigerant agent of the heat pump, the temperature of the heat sources, as it has a strong influence on the efficiency of the heat supply, the simultaneity of heat source and demand, as it decides whether storage is necessary. The available space to erect the heat pump and the distances to available heat sources also have to be considered.

Based on the results of IEA Task 49/IV, the main challenges for solar process heating systems are the achievement of a high solar cover ratio and the close alignment with process demands up to the development of "solar process technologies". Also the best possible combination of solar thermal systems with other technologies gets more and more important. This is precisely where the potential of combined solar thermal and heat pump systems can be seen: for example, the achievable temperature of the solar thermal system could be increased with a heat pump to meet process demands.

2.2 Methodology and project introduction

In order to identify and evaluate possible integration concepts in industrial sectors, a total of twelve production sites from different industrial sectors were chosen within the project EnPro. For the selection of the sectors, branches identified in a preceding project were considered and ranked based on high replicability (Hummel et al. 2013) Especially branches with a high number of companies and a high energy demand were selected. The chosen sites were analysed based on the European standard EN 16247. The current situation of energy supply and consumption of the industrial sites were evaluated and the thermally relevant unit operations were identified. The unit operations were classified to ensure high replicability of the integration concepts. The mentioned classification provides information concerning process technology, process and supply temperatures, process medium, load profiles and operating hours.

Also optimization potentials on process and system level were evaluated as basis for the integration of renewable energy. Pinch analysis was used as methodology to identify heat recovery potentials.

This was followed by the identification of processes that are suitable for the integration of solar thermal energy, heat pumps and their combinations to reach more energy efficiency and to increase the amount of renewable process energy in the industry. The basis was the classification of the unit operations and the evaluated parameters. Within this step, concepts and different schemes for the combined usage of the technologies were created, accompanied by site-specific simulations. Considering the classified processes and the integration concepts the achieved information are generalized resulting in general applicable integration

points for the different branches and general combination schemes. A main focus of the project EnPro is the development of guidelines and a basic planning and calculation tool.

The final guideline and tool will be designed as a basic planning instrument consisting of a decision tree that compares the different possible combinations for a specific case study. By the combined use of tool and planning guideline recommendation on the implementation of solar thermal energy and or heat pump technologies can be made. The tool includes the following features:

- stop/go criteria – pre-assessment of the integration potential
- definition and evaluation of the energy related status quo
- branch specific process definition possibilities and process optimization suggestions
- systems optimization including pinch analysis for the deduction a heat exchanger network
- generic integration concepts and
- assessment of solar thermal energy, heat pumps and the combination of both technologies

As a final step, based on the assessments and the developed integration concepts the project EnPro is defining upcoming R&D advices, taking also existing international R&D advices and roadmaps into account (e.g. "renewable heating and cooling technology platform" roadmap or results from IEA networks).

3. Case studies

In this paper, three of the twelve performed case studies are presented. A special focus is set on integration concepts for solar thermal and heat pump systems and the combination of both technologies.

3.1. Bakery

The audited production site is a large scale bakery. The main products are typical Central European bakery goods (i.e. bread, rolls, fine pastry…). Typical process steps for all products are shown in Fig. 1. First, the ingredients are processed followed by the fermentation step. There are different operation modes for the fermentation step in a bakery. For direct fermentation the step is finished before baking. The other way is to cool the piece of dough and process it later on. In this case a controlled heating step is necessary before the fermentation step. Rack ovens (batch-mode) or continuous baking machines (conveyer) are used for the baking process. Depending on the type of product the baking step is finished, the product gets packaged, stored (cooled) and distributed or it is pre-baked, deep frozen and distributed.

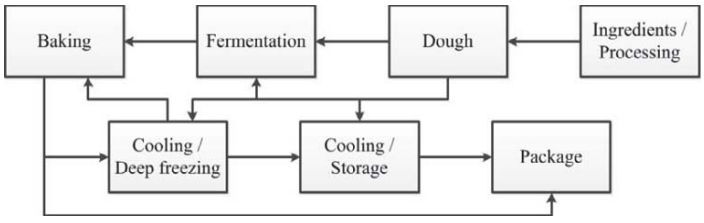

Fig. 1: Process steps with high energy demand in bakery

3.1.1 Energy supply and energy demand

The energy supply of the company is based on fuel oil, natural gas and electricity. Electricity is used by the cooling devices (approx. 40 %) and the bakery ovens (26 %). The rest is consumed by small consumers, pressurized air and the ventilation system. Natural gas is consumed by four boilers supplying the baking ovens as well as for supplying steam (process steam and heating system). The fuel oil is partly consumed by a thermal oil boiler and a steam boiler and partly distributed to directly fired baking ovens in the production hall. A detailed analysis of the last years shows a significant shift from fuel oil to natural gas.
Process steam is needed beside the demand of process heat (160 – 270 °C) during the baking process depending on the product type. Humidification of the baking goods ensures good heating transfer within the baking step. Simultaneously quality and taste of the product are influenced. The steam, provided by the steam boilers is also used for covering the space heating demand.

The cooling demand is a large part of the total energy demand of a bakery. Firstly the unbaked pieces are deep frozen (-4 to -23 °C) to stop the fermentation process. Secondly the ingredients (before the dough-

making-process) and the finished products have to be stored (deep) frozen. Hot water for cleaning is needed at a temperature level between 40 and 60 °C. Hot water storages support the heat distribution.

3.1.2 Optimization potentials and integration of solar thermal systems and/or heat pumps

Within the energy audit short term optimization measures have been identified. Partly due to the age of the baking ovens and due to the high energy demand high potential for process optimization has been identified. The primary direct fired baking ovens (including internal heat recovery) will be substituted by more efficient and central supplied (thermal oil) baking ovens step by step in the next years. High losses (mainly space heating and cooling) caused by high flow temperatures could be reduced by the integration of a central distribution system. The biggest potential was identified within heat recovery of cooling devices. The fuel oil boilers could be substituted step by step by optimizing the existing heat distribution network and integrating thermal energy in existing storages for the preparation of hot water for cleaning.

The baking process is suitable for the integration of solar thermal energy only to a limited extent due to the demand of high temperatures. Nevertheless two potential integration points have been identified. Firstly, the supply of hot water for cleaning in combination with the heat recovery from the cooling devices shows potential. The needed temperature of 60 °C is optimal for supplying the demand via flat plate collectors with a high efficiency. The existing storage infrastructure also supports the integration of a solar thermal system. Secondly, solar thermal energy could be integrated on system level for pre-heating of boiler feed water and for pre-heating of thermal oil.

There are two possibilities for the integration of heat pumps. The first possibility is to use the waste heat from the cooling devices as a heat source and to heat the cleaning water instead or in parallel to solar thermal system. The second possibility is a combination of solar thermal and heat pump system. Within this combination the solar thermal energy is used first for heating the cleaning water and a heat pump is used for increasing the temperature level provided by the solar thermal system using waste heat from the cooling devices as the heat source.

3.2. Metal surface treatment

The metal company analysed in the project produces hardware for windows and doors. The audit focuses on the thermal energy demand and was mainly done for the production area of metal surface treatment which consists of a barrel plant and a rack plant (rotating barrels or racks are used for the transportation of work pieces between different process baths). The process temperatures are in a range between 40 and 80 °C. This offers a potential for the integration of solar thermal and heat pump systems.

The surface treatment process steps can be divided into pre-treatment, main treatment and post-treatment as shown in Fig. 2.

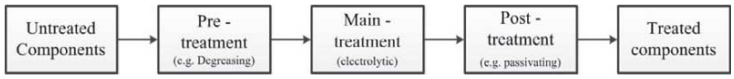

Fig. 2: Main process steps in metal surface treatment

The work pieces are pretreated to be clean from dust, grease and oil and to ensure uniform application and permanent adhesion of the surface treatment. Furthermore oxides are removed to ensure a chemically active surface. Pretreatment processes applied in the assessed company are degreasing, electrolytic degreasing, pickling and descaling. Rinsing is carried out between the processes steps with varying temperatures. For degreasing temperatures of 70 °C are necessary. The other pre-treatment steps do not have any heating demand. After pretreatment the core activities follow. In the audited company zinc coatings are used for the electrolytic surface treatment. During the exothermal electrochemical reaction, heat is released. It is necessary to cool the solution in order to keep the process baths within the required temperature range (23 to 26 °C) to ensure high quality of the products and minimize the breakdown of chemicals in the process bath. Afterwards the work pieces are post treated by brightening, passivation and sealing. Finally the work pieces are dried in order to avoid staining and corrosion. In the barrel plant centrifugal drying is used, whereas in the rack plant the dryer operates with circulatory air. The temperatures of the post-treatment are in a range from 40 to 80 °C. For centrifugal drying a temperature of 130 °C is provided by electric heating.

3.2.1 Energy supply and energy demand

The energy supply of surface treatment is based on natural gas (53 %) and electricity (47 %). Natural gas is consumed by a thermal gas boiler supplying heating process baths (25 %) and dryers (28 %), heating of production halls (46 %) and domestic hot water (1 %). During summer less natural gas is consumed as a result

of increasing ambient temperatures. The process baths have to be heated up before the process starts and a constant process temperature (cover also heat losses) has to be kept to ensure the product quality. Two chillers are operated in the area of surface treatment to provide cooling water for the zinc baths.

3.2.2 Optimization potentials and integration of solar thermal systems and/or heat pumps

Within this energy audit process optimization measures have been identified mainly in the field of the heating of production halls. There air curtains are an effective way to prevent the intrusion of cold outdoor air. In order to reduce energy losses of the process tanks, insulation can be applied at the tanks. Furthermore the surface of the process baths can be covered with a blanket of plastic floating spheres which reduce evaporation without restricting the access of work pieces, jigs or barrels.

For integration of solar thermal energy and heat pumps potential processes have been identified. First of all, solar thermal energy can be used on process level to heat up the process baths at temperatures between 40 and 80 °C. Flat plate collectors and vacuum tube collectors reach high efficiency in this temperature range. Secondly, solar thermal energy could supply the heating demand of domestic hot water.

For integration of heat pumps especially the process baths have been identified as appropriate integration points on process level. The return flow of the cooling water from the process baths could be used as a heat source for heat pumps. The upgraded energy can heat up other process baths. The advantage arising from this integration point is that heat sink and source occur at the same time, so far not used heat streams are utilized and the processes operate constantly over the whole year.

A combination of solar thermal and heat pump systems can be implemented on the one hand in a parallel integration in one storage tank supplying the above mentioned processes 24 hours a day. Furthermore, the decreasing solar thermal energy yield in winter months could be compensated by the heat pump. On the other hand, a possibility is rising up the temperature level provided by the solar thermal energy system with a heat pump using the waste heat from cooling the process baths as a heat source.

3.3. Laundry

This laundry is specialized on the cleaning of work wear. Fig. 3 shows the most important process steps concerning energy demand. The dirty laundry is delivered, sorted, manually loaded into washer extractor machines and washed. Depending on the type of fabric the clothing gets pre-dried via gas- or steam heated driers. Afterwards the clothing is straightened in a gas heated tunnel dryer (finisher) or pressed and dried. The dried clothes are sorted, packaged and delivered to the customers.

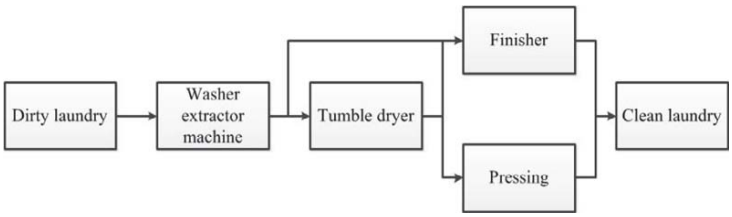

Fig. 3: Process steps in the laundry

3.3.1 Energy supply and energy demand

The energy supply of the company is mostly based on natural gas (83 %) that is used for steam generation. A total of 17 % of the energy demand is covered by electricity. The gas supplied steam generator provides up to 2 t/h of steam with 11 bar (saturated steam, 185 °C).

The most important consumers of thermal energy are the washer extractor machines, the driers and the finisher. The fresh water is preheated via heat recovery from waste water. Steam is injected directly to increase rapidly the temperature of the fresh water to the required washing temperature. The temperature range of the prewashing (30-70 °C) and the main washing step (40-70 °C) depends on the material and the degree of soiling. Two steam heated drum dryers and a gas heated drum dryer are used for the pre-drying step. Concerning the steam heated drum dryers steam increases the temperature of the air via heat exchanger up to 160 °C and is drained as condensate. The dryer operates with circulatory air. The drying air absorbs the moisture of the clothing and leaves the dryer as waste air with a temperature of around 70 °C. Concerning the gas heated dryer the hot exhaust gas of the burner is used for the drying process. The finisher is a continuous tunnel dryer. First, the clothing is sprinkled with steam. The following drying zones are heated with three gas burners to ensure an air temperature of around 130 to150 °C. Circulating fans ensure the circulation of air for

straightening the clothes. The saturated air passes an exhaust air system and is replaced by fresh air. The exhaust air has a temperature level of about 80 °C and is not used any further.

3.3.2 Optimization potentials and integration of solar thermal systems and/or heat pumps

The exhaust gas of the boilers has a temperature level of 140 °C. A further exhaust gas heat exchanger could be integrated to lower the exhaust gas temperature. In order to maintain the induced draft effect the described measure has to be coordinated with the boiler manufacturer. About 40 % of steam in the washer extractor machines and the finisher are used directly are replaced by fresh water. Preheating of the boiler feed water also increases the efficiency of the steam boiler

An integration potential of solar thermal energy could be the preheating of the boiler feed water or the process water for the washing machines. Integration for space heating is not possible in this laundry due to the existing heating system.

For the integration of heat pumps several waste heat streams were identified as possible heat sources that are currently released unused. Exhaust air streams of the dryers and the finisher are relevant streams for this concept. Possible heat sinks are preheating of the dryer air or preheating of the boiler feed water. The advantage of preheating the dryer air is that waste heat and heat demand occur at the same machine at the same time. The steam boiler is also an interesting heat sink as it has the longest operation time per day compared to the other processes. However, the distances between source and sink are significantly higher.

4. Integration concepts of combined solar thermal systems and heat pumps

Based on the case studies the following simplified integration schemes have been developed. Although ambient heat is a potential source for heat pumps supplying industrial processes on low temperature level, the focus was set on available waste heat streams from processes or utilities supplying heat pumps. The chosen combination possibilities and integration schemes are inspired by the IEA SHC Tasks 44 (system combinations of solar thermal systems and heat pumps for residential buildings) and IEA SHC Task 49 (different integration schemes and systems for solar thermal in industry). Within this paper only schemes for integration of combined solar thermal systems and heat pumps systems are presented. For the combination of the technologies, it is crucial to have a significant process heat demand that can be supplied with available solar irradiation and a suitable waste heat source.

The following four combination concepts have been identified within the project:

- Parallel combination - heat pump and solar thermal system supply in parallel
- Serial combination
    - Serial variation I - the process stream is heated first by the solar thermal system and then by the heat pump
    - Serial variation II - the process stream is heated first by the heat pump and then by the solar thermal system
    - Serial variation III – the solar thermal system is used as heat source for the heat pump supplying the process stream

4.1 Parallel combination

Solar collector and heat pump provide heat independently from each other as shown in Fig. 4. The combination can be operated with storages or the heat can be transferred directly to the process. Available waste heat (from processes or energy supply devices) is used as heat source for the heat pump. This combination is able to balance the lower yield of a solar system in winter and vice versa the operating time of the heat pump is reduced in summer because of the high solar yield. By an optimized system design the efficiency of both technologies van be optimized having also positive effects on the lifetime of the systems. (Hadorn, 2015a, 2016b)

Examples for possible integration points have been identified in the three case studies. Generally, the solar thermal and heat pumps systems supply the processes via an optional storage. The source for the heat pump is defined:

The parallel combination of both technologies offers the individual optimization of each system without any influence on the other. One option is that the heat pump provides heat when the collector does not deliver

due to seasonal or time of day. The other option is that the heat pump valorizes a waste heat stream that is available all the time and the solar collector adds more heat and by this fossil fuel consumption is further reduced. Which option is the most suitable has to be determined by a technical and economical evaluation for the specific industrial site. A disadvantage of this combination is that the provided maximum process temperature is limited by the technologies itself. This integration might be seen comparably easy concept and the R&D demand has to focus on maximum achievable temperatures of both technologies.

An example for this integration concept can be found in the bakery evaluated. A solar thermal collector and a heat pump supply heat via a storage for space heating and cleaning water demand. The source for the heat pump is the waste heat from a chiller.

Further examples - the source for the heat pump is defined:

- Metal surface treatment – heat pump source: return flow of cooling water
  - Heating of process baths
- Laundry – heat pump source: exhaust air streams
  - Space heating
  - Fresh water for washing machine

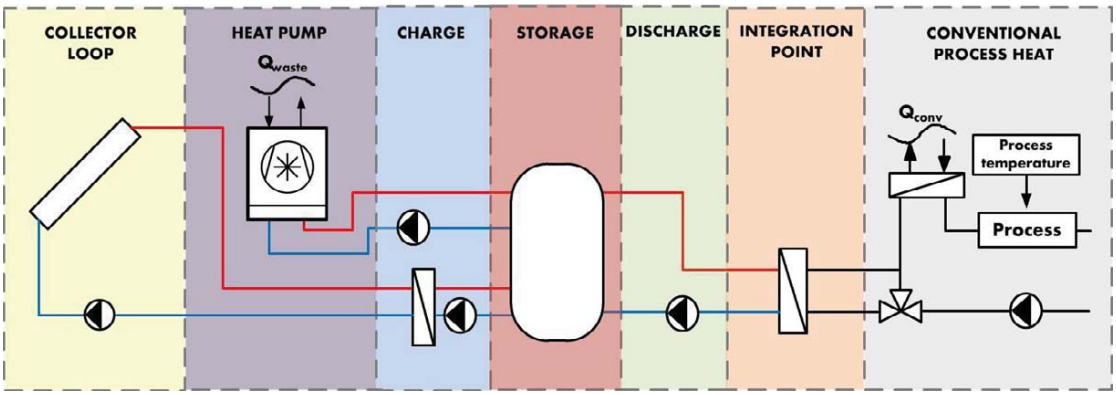

Fig. 4 Parallel combination of solar thermal systems and heat pump

4.2 Serial combinations

4.2.1 Serial variation I

In this combination first the process stream is heated by a solar system followed by the heat pump to reach higher temperatures (shown in Fig. 5). Available waste heat is used as heat source for the heat pump. Storages can be integrated to balance temporary deviations between heat supply and heat demand. If the solar thermal system supplies the total heat demand at necessary temperature, the heat pump is bypassed and the process is supplied only by the solar thermal system.

A clear advantage of this integration concept is the significant higher temperatures provided by the serial combination of the technologies. The solar thermal collector is operated in a suitable temperature range for flat plate and vacuum tube collectors offering high efficiencies. Heat pumps are able to provide temperatures up to 120 °C. To achieve high efficiency, a comparable warm heat source exceeding 40 °C is preferable. This waste heat has to be mentioned as a challenge. The upcoming R&D demand has to focus on the further development of heat pumps providing heat up to a temperature of 160 °C.

An example for this concept can be found in the metal surface treatment company. There the solar thermal collector could preheat the process baths or the air needed for heating the dryer up to a temperature of 70 °C. The heat pump, using the waste heat from the cooling system can further increase the temperature of this process stream up to a level of 100 – 120 °C.

Further examples - the source for the heat pump is defined:

- Bakery - heat pump source: waste heat chiller
  - Hot water for cleaning
  - Heating of thermal oil
- Laundry – heat pump source: exhaust air streams
  - Preheating of the dryer air

- Preheating of the boiler feed water
- Potentially space heating in case of hot water based heating system

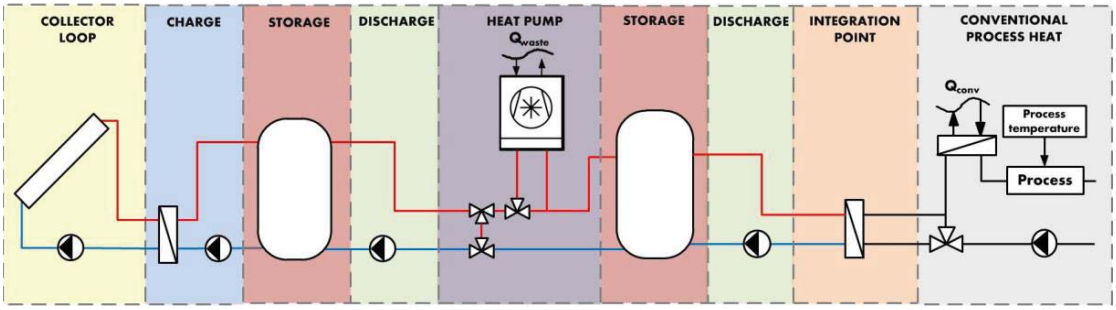

Fig. 5 Serial variation I of solar thermal system and heat pump

4.2.2 Serial variation II

First the process stream is heated by the heat pump followed by the solar system to reach higher temperatures (shown in Fig. 6). The heat pump uses available waste heat as heat source. If a process stream, that has to be cooled, can be used as heat source, a double benefit of the system occurs. Storages can be integrated to balance temporally deviations between heat supply and heat demand.

This serial integration concept is more suitable for low temperature heat sources from process waste streams or if available ambient air or ground water. A disadvantage is the demanded supply temperature (> 100 °C) of the solar thermal system and following low efficiencies of the flat plate and vacuum tube collectors. Furthermore, especially in Central European regions the direct solar irradiation is not sufficient to supply concentrating collectors and the limited maximum temperature is by this a challenge for this concept that has to be part of upcoming R&D activities.

An example for this combination concept can be found in the assessed laundry. There, the spent and cooled water from a washer can be used as heat source for the heat pump. An advantage is that the waste water is further cooled before charged into the sewage system. The process supplied is the fresh water for the steam boiler, which is preheated first by the heat pump followed by a suitable solar thermal system up to 80 – 110 °C to further decrease the fossil fuel demand of the boiler.

Further examples - the source for the heat pump is defined:

- Bakery - heat pump source: waste heat chiller
  - Heating of thermal oil
- Metal surface treatment – heat pump source: return flow of cooling water or chiller
  - Hot water for cleaning

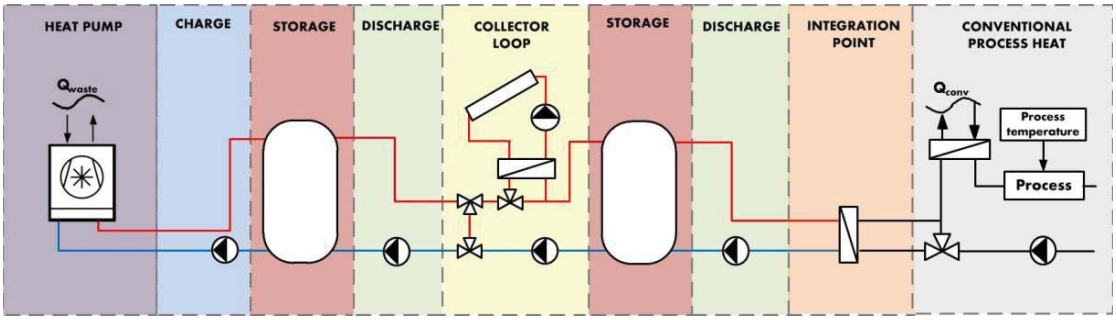

Fig. 6 Serial variation II of solar thermal system and heat pump

4.2.3 Serial variation III

In this integration concept the heat pump uses solar heat as heat source (shown in Fig. 7). Solar heat can be used directly by the heat pump or via storage. As the solar thermal system is used to provide temperatures up to 50 – 80 °C, flat plate and vacuum tube collectors operate at high efficiencies.

An advantage of this concept is that the solar thermal system provides heat for the heat pump at a higher temperature than ambient sources in case that no waste heat streams are available. Additionally available waste heat streams above 50 °C in the assessed industry were limited and this concept could overcome this challenge. By this the demanded temperature lift of the heat pump is reduced and the efficiency (also for higher temperatures) increases. In this concept a storage can be seen as mandatory. An upcoming R&D focus should be set on the further development of heat pumps providing heat above 120 °C.

An example for this concept can be found in the bakery. Available waste heat streams are already well integrated in the heat recovery system with only limited access for a heat pump concept. The integration of this stream as source for the heat pump is competing with this solution (a disadvantage in serial variation I). The solar thermal source for the heat pump addresses this challenge- A possible integration of the concept would be in the existing thermal oil based supply system. The solar thermal system supplying the heat pump that is providing heat above 100 °C.

Further examples:

- Metal surface treatment
  - Heating of process baths
- Laundry
  - Preheating of the dryer air
  - Preheating of the boiler feed water
  - Potentially space heating in case of hot water based heating system

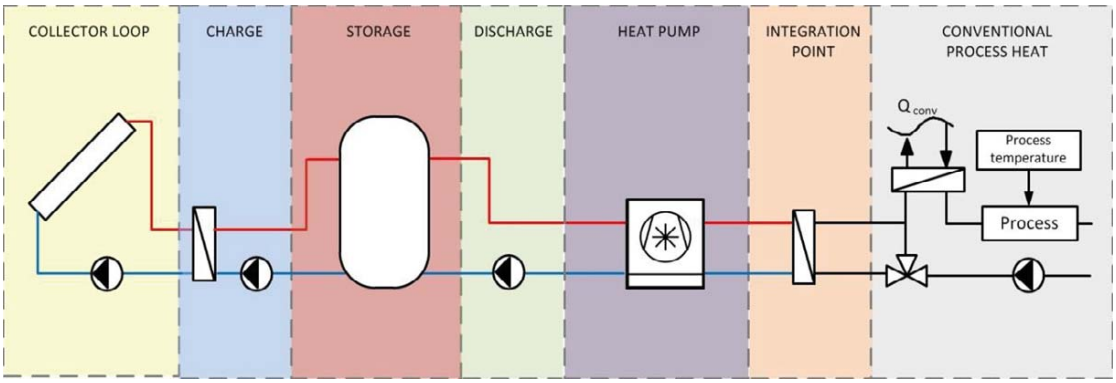

Fig. 7: Serial variation III of solar thermal system and heat pump

5. Conclusion

For assessing the energy supplies of an industrial company the energy demand on process level and its specific parameters (load profiles, temperature levels, etc.) as well as the type of supply system (media) have to be considered. Considering identified integration criteria different integration possibilities on process and supply level for solar thermal system and/or heat pumps were evaluated from a technical point of view. Examples for integration criteria are load profiles, temperature levels, temporal correlation between demand and supply, efficiency factors, solar yields, quality grades, payback periods or needed storages.

In the assessed industry examples for the single integration of solar thermal or heat pump systems have been identified. In bakeries for example hot water for cleaning is needed on process level, typical for the food and beverage sector with a significant cleaning demand. Hot water is also needed in laundries for the washing

process. This demand can be easily supplied by solar thermal system or heat pumps. Especially flat plate collectors are suitable for covering hot water demand with a temperature level of 60 °C (typical for cleaning processes), because of the high efficiency of flat plate collectors in this temperature range. Heat pumps are also suitable for supplying this hot water demand. Available waste heat streams as source are the waste heat of cooling machines (bakery and metal surface treatment) and humid exhaust air streams (laundry). The advantage of integration on process level is that heat sink and source occur at the same time, so far not used heat streams are utilized and the heat source is available at the same time the demand occurs.

An example for an integration of solar thermal system and heat pumps on system level is the integration in steam boiler systems as identified in the case studies bakery and laundry. The usage of direct steam leads to a fresh water demand. Both, solar thermal system and heat pumps could be used for pre-heating the fresh water/boiler feed water. Another option could be the production of steam but only with limited potential due to existing technical constraints further supported by regional difficulties (limited solar irradiation in Central Europe needed for concentrating solar thermal system providing steam). In many cases the needed integration concept for the integration on system level is easier compared to a direct integration on process level, which comes along with several research questions.

Besides the single integration of solar thermal system and heat pump systems, the combination of these offers a huge potential for an optimized system and a further boost of the technologies. The first technical assessment highlights four options as mentioned above parallel operation of solar thermal and heat pump system and three different serial connections.

Parallel combinations could be used for balancing seasonal differences in the solar yield as e.g. for heating of process baths in the metal surface treatment site. This concept offers the individual optimization of each system. One option is that the heat pump provides heat when the collector does not deliver due to seasonal or time of day. The other option is that the heat pump valorizes a waste heat stream that is available all the time and the solar collector adds more heat and by this fossil fuel consumption is further reduced.

Within the serial combination (variation I) first the solar thermal system is used supplying the demand (e.g. for heating the boiler feed water or other streams) and the heat pump technology is used for further increasing the temperature level. Depending on the used collector types and needed temperature level a possibility is also first going through the heat pumps followed by the solar thermal system (variation II). Finally as variation III the solar thermal system can operate as source for the heat pump. In all variations the provided temperature is higher compared to the parallel combination.

In variation I the solar thermal collector is operated in a suitable temperature range for flat plate and vacuum tube collectors offering high efficiencies. Heat pumps use waste heat streams as source in a temperature range between 50 – 70 °C and the system is by this able to provide temperatures up to 120 °C. The demand of a suitable waste heat stream (temperature range > 50 °C) has to be mentioned as a challenge. The serial variation II concept is more suitable for low temperature heat sources from process waste streams or in some cases ambient air or ground water. A challenge is the demanded supply temperature (> 100 °C) of the solar thermal system and following low efficiencies of the flat plate and vacuum tube collectors. In variation III the solar thermal system provides heat for the heat pump at a higher temperature than ambient sources in the case no waste heat streams are available. By this the demanded temperature lift of the heat pump is reduced and the efficiency, also for higher temperatures, increased.

6. Outlook

The case studies show the high potential for the integration of solar thermal system, heat pumps and the combination of both in industrial companies. Due to the fact that the considered process steps and supply structures are typical for each sector the possibilities for the integration can be multiplied and are supposed to be applicable for other companies. Based on the results of the case studies, generalized integration schemes were developed and will be further evaluated. By this, clear recommendations considering technical, ecological and economic evaluations of identified integration concepts will be available.

Further steps will be the definition of selection criteria for the different combinations and based on that the creation of a decision tree. The decision tree will lead the user to the most suitable technology or combination for a certain integration point. For the definition of selection criteria the detailed simulations of the case studies are the basis to identify efficiency ratios, performance numbers, solar yields and quality grades as

well as gained energy form heat pumps. Based on that, optimized integration concepts on process- and supply level for the case studies and derived conclusions for the industry sectors will be developed.

Furthermore the derived results will be integrated in an optimized version of a planning and calculation tool. Moreover the sectors and branch specific processes of the tool will be extended and linked to a planning guideline.

One of the main barriers for a market penetration of the technologies is the lack of best practice examples. Based on the selected case studies and developed concepts and a positive economic evaluation this obstacle is targeted to be addressed. Implemented integrations have to act as best-practice examples for other industrial companies. Hence the applicability of solar thermal system, heat pumps and the combination of both technologies is demonstrated.

In correlation with the described actions the need for research and development will be defined. One key aspect is the technological optimization of solar thermal and heat pump technologies. The optimization as well as the development of new refrigerating agents and compressors to increase the maximum condenser temperature of heat pumps is currently part of R&D. For solar thermal systems and components further development is necessary in order to simultaneously increase the efficiency and reduce the costs. Several studies show the need for technologies that supply energy demand at higher temperatures or even supply steam. The efficiency of concentrating solar systems for the supply of steam strongly depends on the regional solar radiation. Heat pumps that supply steam at typically required steam parameters of 5-10 bars are not available on the market yet. A strong need for research has to be seen in this field. The definition of research demand will be carried out after the detailed simulation of the case studies.

7. Acknowledgement

The project EnPro is a R&D service on behalf of the Austrian Climate and Energy Fund, financed by the Energy Research Programme 2014. The authors gratefully acknowledge the input and the commitment of the participants for the case studies Albin Sorger “Zum Weinrebenbäcker” GmbH & Co KG, Bichlbäck, Der Bäcker Ruetz Tiroler Backhaus GmbH, Norske Skog Bruck GmbH, SCA Hygiene Products GmbH, Roto Frank Austria GmbH, A&R Carton Graz GmbH, MKE Metall- und Kunststoffwarenerzeugungs-ges.m.b.H, Salesianer Miettex GmbH, Otto Wirl GmbH und Austrotherm GmbH.

8. References

European Parliament, 2009. Richtlinie 2009/28/EG des Europäischen Parlaments und des Rates vom 23. April 2009 zur Förderung der Nutzung von Energie aus erneuerbaren Quellen und zur Änderung und anschließenden Aufhebung der Richtlinien 2001/77/EG und 2003/30/EG.

Fleckl, T., Hartl, M., Helminger, F., Kontomaris, K., Pfaffl, J., 2014. Performance testing of a lab-scale high temperature heat pump with HFO-1336mzz-Z as the working fluid, in: European Heat Pump Summit 2015, Nürnberg, Germany, 20.-21. Oktober.

Frank, E., Hess, S., Zahler, C., 2012. General requirements and relevant parameters for process heat collectors and specific collector loop components. SHC IEA Task 49/IV.

Hadorn, J.C., 2015. The combination of heat pumps and solar components has great potential for improving the energy efficiency of house and hot water heating systems. SHC IEA Task 44

Hadorn, J.C., 2016. Solar and Heat Pump Systems for Residential Buildings, Wilhelm Ernst & Sohn, Darmstadt.

Hummel, M., Kranzl, L., Fluch, J., Brunner, C., Herzo,g U., Schnitzer, H., Titz, M., Bochmann, G., Drosg, B., Rothermann, F., Schanner, R., Gahbauer, H., 2013. In Richtung einer CO2-neutralen Wärmebereitstellung in der Lebensmittelherstellung - Erkenntnisse und Handlungsempfehlungen, Bericht im Rahmen des "Neue Energien 2020" Projekts "SolarFoods".

IEA Heat Pump Centre, 2014. Application of Industrial Heat Pumps. IEA Industrial Energy-related Systems and Technologies Annex 13 IEA Heat Pump Programme Annex 35 HPP-AN35, Final Report.

Fukuda, S., Kondou, C., Takata, N., Koyama, S., 2014. Low GWP refrigerants R1234ze(E) and R1234ze(Z) for high temperature heat pumps. International Journal of Refrigeration 40. 161–173.

Muster-Slawitsch, B.; Hassine, B. I., Helmke, A.; Heß, S.; Krummenacher, B.; Schmitt, B.; Schnitzer, H.; 2015. Integration Guideline, B. Muster-Slawitsch, Editor, IEA Task 49/IV.

Statistics Austria, 2014. Gesamtenergiebilanz Österreich 1970 bis 2014 (Detailinformation), www.statistik.at retrieved on 26.11.2015.

Wolf, S., Fahl, U., Blesl, M., Voß, A., Jakobs, R., 2014. Analyse des Potenzials von Industriewärmepumpen in Deutschland, Forschungsbericht, Institut für Energiewirtschaft und Rationelle Energieanwendung, Universität Stuttgart.

Conference Proceedings

EuroSun 2016
Palma de Mallorca (Spain), 11 - 14 October 2016

Considerations for using a rotary kiln for high temperature industrial processes with and without thermal storage

Alessandro Gallo[1,2], María Isabel Roldán[3], Elisa Alonso[1] and Edward Fuentealba[1]

[1] University of Antofagasta. Centro de Desarrollo Energético de Antofagasta (Chile)

[2] Doctorado en "Ciencias Aplicadas al Medio Ambiente" (RD99/11). University of Almeria (Spain).

[3] Plataforma Solar de Almería, Centro de Investigaciones Tecnológicas, Energéticas y Medioambientales (Almería, Spain)

Abstract

In this work, technical considerations and a comprehensive discussion on solar rotary kilns are reported. Rotary kilns permit to obtain well-mixed particles in a broad range of temperatures (up to 2000°C), and, for this reason, they are widely used for treating solid particles in several industrial sectors. In solar research field, they have been employed for processing materials in solar furnaces and, in some cases, they have also been proposed as receivers in solar tower plants. The aim of this work is to investigate the potential of solar rotary kilns as thermal receivers in solar tower plants, taking into account the constraints that limit their use. In particular, because of the shape of these reactors, circular heliostat fields are not allowed and the maximum power of the receiver is limited to less than 100 MWth. Thus, the reference case of a 50-MW_{th} central tower plant for the heating of sand as heat transfer medium is reported. Residence time and receiver thermal efficiency are evaluated using an analytical method. In addition, two possible heliostat fields with different size of mirrors are also proposed.

Keywords:*Concentrating solar heat, rotary kilns, industrial applications, scaling-up, thermal storage*

1. Introduction

Fossil fuels are currently the main energy source for heat-demanding industrial processes. However, solar thermal technologies can replace them offering an environmentally friendly and widely available solution. Different solar thermal technologies operate at low, medium and high temperature and can be considered to provide heat for industrial processes of variable requirements (Calderoni et al., 2012; Fuller, 2011; Lauterbach et al., 2012). Concentrating systems employ reflectors in order to collect the solar beams on a small area where the power levels are intensified (Liu et al., 2016). With concentration ratios of around 1000, systems efficiencies are maximized at high temperatures (700-1500 ºC). This represents a relevant advantage concerning the use of concentrating solar heat to drive high-temperature industrial processes (Romero and Steinfeld, 2012). Some of the most studied applications of concentrating solar energy, apart from electricity generation, focus on the production of solar fuels, including hydrogen, which is based on H_2O/CO_2 splitting and decarbonization processes (cracking, reforming, and gasification of carbonaceous feedstock) (Steinfeld, 2005). Other industrial applications are extractive metallurgy, ceramic material processing and calcination (Halmann et al., 2012; Meier et al., 2004; Nikulshina et al., 2009).

Concentrating solar energy can be coupled with thermal energy storage (TES) systems, representing an important advantage with respect to other renewable energy technologies as photovoltaics and wind. In the last years, efforts have been focused on developing more efficient TES with higher storage capacity in order to make concentrating solar energy more cost effective. Molten salts able to storage sensible heat are currently the more commercially exploited TES system but many other solutions are also under development (Kousksou et al., 2014; Mahlia et al., 2014; Pardo et al., 2014). Concerning the present work, the solar heating of solid materials, normally in form of particles, has been previously used to storage the energy as sensible heat (Gallo et al., 2015; Jemmal et al., 2016; Zhang et al., 2016) or as a combination of sensible and thermochemical heat (Alonso et al., 2015; Aydin et al.,

doi:10.18086/eurosun.2016.02.04 Available at http://proceedings.ises.org

2015; Block and Schmücker, 2016).

Receptors/reactors design plays an important role for increasing the efficiency of high temperature processes driven by concentrated solar energy. In direct absorption devices, there is not opaque barrier between the radiation and the absorber material. This material is usually the one that have to be heated as the final purpose of the tested process, such as an industrial reactant or a storage material. Direct absorption particles in solar receivers or reactors are commonly employed where the objective is to increase the temperature of such particulate material. Different types of particles can be found in literature according its configuration and performance (Alonso and Romero, 2015). Some authors have tried to innovate and to design novel engineering concepts. Many others have readapted classical technologies to integrate the direct solar radiation.

Rotary kilns have a long history of use in metallurgical and chemical industries, their performance is well known and they are able to operate at a very wide range of high temperatures (up to 2000 ºC) with greater thermal efficiencies than other reactor types. Since it is a well-known technology, several authors have developed prototypes of solarized rotary kilns that have been successfully demonstrated for different applications (Alonso et al., 2015). This work tries to analyze some relevant aspects of applying such a technology for industrial processes. A preliminary design of a 50-MW_{th} plant coupled with a rotary receiver is presented. Particles of sand are considered to be heated up until 750 ºC. With this assumption, an estimation of the kiln dimensions, residence time and particles flow-mass is given. A heliostat field design is optimized in order to reduce optical losses on the receiver aperture. The possibilities for integrating thermal storage within the solar plant are also discussed in this work.

2. Methodology for the preliminary design

The proposed methodology for the scale up of a solar tower plant based on a rotary kiln as central receiver consists of three main parts. In the first part, a simplified sizing of the kiln was carried out. Calculations were based on kilns working in a continuous mass-flow mode. In the second part, in order to calculate the receiver efficiency and to predict the thermal load, a thermal model was developed. This model was applied to a rotary kiln for the heating of sand without a quartz window at the aperture. Finally, in the last part, two heliostat fields based on different heliostat sizes were designed for such a receiver.

2.1. Receiver sizing

2.1.1. Industrial rotary kiln

Rotary kilns are widely utilized for several industrial processes because they supply well-mixed particles. In this way, uniform temperatures are obtained in the products. These reactors can be considered as a sort of cylindrical heat exchanger in which a gas phase transfers the heat to a solid phase. Generally, rotary kilns operate in continuous mode. In this system, particles are introduced at one of the ends and are extracted at the other one. The kiln usually presents a slight slop s to favor the particles axial movement. In the radial directions, particles movement depends mainly on both the rotational speed N and the Fill Ratio FR (percentage of reactor volume occupied by the particles). Different “bed-motions”, which depend on the kind of particles (size, shape, density) and wall-particle friction coefficient, can be achieved. Usually, rolling and cascading modes are the most used behaviors for industrial applications. The residence time τ is a measure of the particle permanence inside the reactor and it depends only on geometrical and operation parameters. Differently, a solar rotary reactor presents an aperture at one end of the kiln. In this way, the solar radiation can enter inside the device and impinges directly on solid particles. In some cases, a transparent quartz window is needed to work in established environments.

2.1.2. Residence time analysis

In the last decades, several models have been carried out to predict the residence time of particles in classical rotary kilns. Most of the authors proposed correlations based on few parameters. Usually those parameters were geometrical characteristics of the reactor or particles and a combination of some of them was normally used. Main parameters were the angle of repose of the particles, mass flow, reactor size, reactor slope, rotational speed, diameter, length, height of the dam, among others.

Normally, those correlations were based on laboratory rotary kilns whose dimensions were considerably smaller than industrial ones. Renaud et al. (2000) realized a comparative of some of these correlations with the experimental results obtained from an industrial rotary kiln. They observed most of the equations, when applied to larger reactors, underestimated the residence time from four to eight times, which means that most of the

correlations proposed were not applicable for the scale up of such devices. Hence, they suggested some improvements to the quite complex model developed by Cholette and Cloutier (1959) to predict the residence time, obtaining a good approximation with experimental results (lower than 9%). Nevertheless, one of the simplest correlation was the Sai's one which underestimated the experimental residence time less than 1.2 times. Hence, for the sake of simplicity this equation was used in the present work to estimate the residence time of a scaled up solar reactor. Sai's correlation is the following (Sai et al., 1990):

$$\tau = 60 \cdot \frac{1315.2 \cdot {h_{dam}}^{0.24}}{s^{1.02} \cdot N^{0.88} \cdot F^{0.072}} \quad (1)$$

where s is the slope of the reactor in degree, N is the reactor rotational speed in rpm, F is the mass flow in kg/h, and h_{dam} is the height of the dam in m. The dam allows maintaining the particle bed inside the reactor with an almost constant height along the axial directions to favor particle mixing and to increase the residence time.

2.1.3 Mass flow

In order to calculate the proper height of the reactor dam, a design mass flow has to be defined. Because of the characteristics of rotary kilns, the mass flow is estimated from the fill ratio (FR). As mentioned above, the fill ratio corresponds to the percentage of the reactor volume occupied by the particles. If the reactor cross section A_{RR} is assumed constant, it is possible to evaluate the area (A_p) and the height of the bed (h_{bed}) for a specific fill ratio. For a determined design conditions, the dam of the reactor has to be lower or close to the predicted bed height. In following equations, bed height was employed because it was considered the maximum limit for dam height ($h_{dam} \approx h_{bed}$). Equations 2, 3 and 4 show the formulae to evaluate the fill ratio, particle area and bed height:

$$FR = \frac{\dot{m} \cdot \tau}{V_{RR} \cdot \rho_b} \quad (2)$$

$$A_p = A_{RR} \cdot FR = \frac{1}{2} \cdot R^2 \cdot (\alpha - \sin\alpha) \quad (3)$$

$$h_{bed} = R \cdot (1 - \cos\frac{\alpha}{2}) \quad (4)$$

where $\dot{m}$ is the mass flow in kg/s, V_{RR} is the volume of the reactor, ρ_b is the bulk density of the particles, R is the radius of the reactor cross section, and α is the central angle determined by the particle bed.

Typical values for the fill ratio are limited in a range from 10 to 25% to achieve a good mixing of particles and they generally correspond to rolling and cascading subtypes of bed-motion in Mellmann classification (Mellmann, 2001). In the rolling mode, the solid material lines the bottom of the inner wall of the reactor up to a certain height and then the particles roll down on the upper surface of the bed. Thus, the particles that roll down constitute the active layer, while the particles that rotate as rigid body with the wall of the cylinder form the passive layer. From a certain fill ratio, a core of static particles appears in the central region of the bed, where mixing is not achieved. Analogously, when particles with different size or density are introduced inside the reactor, smaller and more dense particles segregate and form a static core (Boateng and Barr, 1996).

Moreover, the equation that links the absorbed power with the inlet and outlet temperatures was added to the previous ones (see equation 5). In this way, the proper residence time, the mass flow, the fill ratio and the height of the bed were calculated.

$$Q_p = \dot{m} \cdot (c_p^{T_{out}} \cdot T_{out} - c_p^{T_{in}} \cdot T_{in}) \quad (5)$$

where c_P is the specific heat of the treated material at the inlet (T_{in}) and outlet temperature (T_{out}).

2.2. Thermal Model

Heat transfer mechanisms are different in solar rotary reactor from traditional industrial kilns. In solar reactor, radiation is the main mechanism, while in classic kilns, particles heating is due to a combination of convection and radiation from the hot gas. Hence, in order to calculate the efficiency of the rotary kiln, a thermal model based on a particular cavity receiver was carried out. In the model, each kind of thermal losses was estimated following correlations found in literature. The gross power required (Q_{RR}) by the rotary receiver was calculated as the sum of the power absorbed by the particles (Q_p) and the total thermal losses (Q_l), see equation 6. In addition, kiln efficiency (η_{RR}) was obtained from equation 7.

$$Q_{RR} = Q_l + Q_p \quad (6)$$

$$\eta_{RR} = \mathrm{Q_p}/\mathrm{Q_{RR}} \quad (7)$$

Thermal losses were divided in radiative, convective, conductive, and reflection losses (see equation 8). Since conductive losses in solar receivers are more than one order of magnitude lower than other contributions, they were neglected in this work.

$$Q_l = Q_{l_{rad}} + Q_{l_{cv}} + Q_{l_{cd}} + Q_{l_{refl}} \quad (8)$$

2.2.1. Radiative losses

Radiative losses ($Q_{l_{rad}}$) were calculated with Stefan-Boltzmann law (see eq. 9) considering the effective emissivity ε_{eff} of a cylindrical cavity. In equation 9, $\sigma = 5.67 \cdot 10^{-8}$ W m^{-2} K^{-1} is the constant of Stefan-Boltzmann, A_{ap} is the aperture area of the rotary kiln, T_{amb} is the environment temperature, T_{cav} is the average temperature inside the reactor calculated with equation 10 and A_{cav} is the total area of internal surfaces of the reactor. T_i represents the average temperature of each surface that composes the cavity. In this case, the average bed temperature and the average wall temperature (T_w) were used. T_w was considered equal to stagnation temperature obtained from the average heat flux (q'') received by the internal cavity surfaces, see equation 11.

$$Q_{l_{rad}} = \varepsilon_{eff} \cdot \sigma \cdot \mathrm{A_{ap}} \cdot (T_{cav}^4 - T_{amb}^4) \quad (9)$$

$$T_{cav} = \frac{\sum_i T_i \cdot A_i}{\sum_i A_i} = \frac{\sum_i T_i \cdot A_i}{A_{cav}} \quad (10)$$

$$T_w = \sqrt[4]{\frac{q''}{\sigma \cdot \varepsilon_w}} = \sqrt[4]{\frac{Q_p}{A_{cav} \cdot \sigma \cdot \varepsilon_w}} \quad (11)$$

ε_{eff} was calculated following the methodology indicated in Bergman et al., (2011) applied to a cylindrical cavity with an aperture in one base (see equation 12). ε_{cav} corresponds to the average internal cavity emissivity, and the view factor ($F_{cav \to ap}$) was defined with equation 13. The radius of the aperture was assumed equal to the difference between the internal radius of the reactor and the dam height (see equation 15).

$$\varepsilon_{eff} = \frac{1}{F_{cav \to ap} \cdot \frac{1-\varepsilon_{cav}}{\varepsilon_{cav}} + 1} \quad (12)$$

$$F_{cav \to ap} = \frac{R_{ap}^2}{2 \cdot \mathrm{R}^2 - \mathrm{R_{ap}^2} + 2 \cdot \mathrm{R} \cdot \mathrm{L}} \quad (13)$$

$$A_{ap} = \pi \cdot \mathrm{D_{ap}^2}/4 \quad (14)$$

$$D_{ap} = 2 \cdot \mathrm{R_{ap}} = 2 \cdot (R - \mathrm{h_{dam}}) \quad (15)$$

2.2.2. Convective losses

In case of an open cavity rotary kiln, convective losses $Q_{l_{cv}}$ were expected similar to the losses of a static solar cavity receiver. Because rotational speed were not high and it was supposed the reactor/receiver was protected by a well-insulated static case, losses from the external walls of the reactor were neglected. Otherwise, convective losses in the interior of the cavity are not easy to calculate and a specific study has to be done on a case by case basis. However, several correlations have been proposed and used by many authors (Li et al., 2010; Ma, 1993; Mcdonald, 1995; Siebers and Kraabel, 1984). In this work, the methodology proposed by Siebers and Kraabel (1984) was followed. Convection losses were separated in forced $Q_{l_{cv}}^f$ and natural $Q_{l_{cv}}^n$ contributions as indicated in equation 16 and 17. Where *Nu* is the number of Nusselt, *K* the conductivity of the air and *D* the diameter of the reactor.

$$Q_{l_{cv}} = Q_{l_{cv}}^f + Q_{l_{cv}}^n = h_{conv} \cdot (T_{cav} - T_{amb}) \cdot A_{cav} \quad (16)$$

$$h_{conv} = h_{nc} + h_{fc} = \frac{Nu_{nc} \cdot K}{D} + \frac{Nu_{fc} \cdot K}{D} \quad (17)$$

Stine and Mcdonald indicated *Nu* for natural convection can be calculated by equations 18, 19 and 20, where *Gr* is the number of Grashof ($10^5 < \mathrm{Gr} < 10^{12}$); β, the coefficient of volumetric expansion; ν, the cinematic viscosity of the air at the ambient temperature, and *g* is the gravity acceleration (Mcdonald, 1995).

$$Nu_{nc} = 0.088 \cdot Gr^{\frac{1}{3}} \cdot \left(\frac{T_{cav}}{T_{amb}}\right)^{0.18} \cdot (\cos s)^{2.47} \cdot \left(\frac{Dap}{D}\right)^{S} \quad (18)$$

$$Gr = \frac{g \cdot \beta \cdot (T_{cav} - T_{amb}) \cdot D^3}{\nu^2} \quad (19)$$

$$S = 1.12 - 0.982 \cdot \left(\frac{D_{ap}}{D}\right) \quad (20)$$

To calculate *Nu* for forced convection, the following correlation from Ma (1993) was used:

$$h_{fc} = 0.1967 \cdot v_{wind}^{1.849} \quad (21)$$

where v_{wind} is the wind speed.

For the treatment of reactive particles or direct treatment of materials, a controlled atmosphere inside the reactor is required. Therefore, a window at the kiln aperture must be employed. In these cases, similar to industrial rotary kilns, convective heat losses are mainly due to the forced fluid flow inside the reactor. Nevertheless, gases in solar kilns are at relatively low temperatures and the heat passes from the wall and particles to the gas. On the contrary, in industrial devices, the heat passes from the hot gas to the particles and to the kiln walls. For this configuration, no specific equations have been developed so far, neither for solar rotary kilns nor for industrial rotary kilns. For instance, Brimacombe and Watkinson correlation underestimated convective heat losses for their classical rotary kiln (Brimacombe and Watkinson, 1978; Watkinson and Brimacombe, 1978). Yang and Farouk correlation was also discarded for the same reason (Yang and Farouk, 1997).

2.2.3. Reflection losses

In solar plants, part of the radiation impinging on the receiver is reflected by the receiver surface towards the environment. Cavity receivers reduce these losses, which can be calculated with equation 22. ρ_{cav} is the reflectivity of the internal surfaces of the cavity and it is calculated through equation 23 as the weight average reflectivity for the different constituent materials.

$$Q_{l_{refl}} = F_{cav \to ap} \cdot \rho_{cav} \cdot Q_{RR} \quad (22)$$

$$\rho_{cav} = \frac{(1-\varepsilon_w) \cdot A_w + (1-\varepsilon_p) \cdot A_{bed}}{A_{cav}} \quad (23)$$

2.3. Heliostats fields design

Solar tower plants consist of a receiver mounted on the top of a tower and a heliostat field. The distribution of the heliostat field can be either circular (around the tower), or at one side of the tower (north or south field, depending on the hemisphere where the plant is located). Because solar rotary kiln shape is similar to cavity receiver, only one-side configuration is suitable for these thermal processes. For this reason, the power range of such a solar tower plant is limited to 1-100 MWth, approximately.

In order to define the heliostat field for the plant, the software WinDelsol was used. WinDelsol is based on the original Delsol3 code from SANDIA National Labs. The software can design and optimize heliostat fields and determine the radiative flux on cavity, external or flat receivers. In this case, a tilted flat receiver was employed in order to reproduce the flux that reaches the aperture of the reactor. The location of the plant was supposed in the Tabernas Desert, Almeria (Spain) for which atmospheric attenuation parameters were known. Detailed characteristics of heliostats, aiming strategies and the required power on the receiver were introduced in the software as inputs for the calculation. With this information, WinDelsol could estimate the flux distribution on the selected receiver and at the same time, it delivered the optimized heliostat field, considering thermal losses due to cosine factor, shadowing, blocking, spillage and atmospheric attenuation. WinDelsol delivered also the number of heliostats (N_{HS}), the efficiency (η_{HS}), the total area ($N_{HS} \cdot A_{HS}$) and the reflected power (Q_{HS}) by the heliostat field. Alternatively, knowing the number of heliostats and the reference direct normal irradiation (DNI_{ref}), the power reflected by the heliostat field could be obtained with equation 24 and the efficiency with 25. A_{HS} is the reflecting surface of one heliostat. In this study, a minimum efficiency of 70% for the heliostat field was considered acceptable.

$$\mathrm{Q_{HS}} = N_{HS} \cdot A_{HS} \cdot DNI_{ref} \quad (24)$$

$$\eta_{HS} = \mathrm{Q_{RR}}/\mathrm{Q_{HS}} \quad (25)$$

Finally, the total efficiency of the plant can be calculated with equation 26.

$$\eta_{tot} = \mathrm{Q_p}/\mathrm{Q_{HS}} = \eta_{HS} \cdot \eta_{RR} \quad (26)$$

2.4. Storage system considerations

In this work, the kiln was treated as a thermal rotary receiver for sand or particles. Depending on the requirements, the system can store or not the absorbed solar energy. As previously explained, the shape of the reactor limits the maximum power available and, when the thermal demand is high, a plant without storage could result more advantageous to produce hot air, water or steam in a heat exchanger with the integration of an auxiliary heater. In other cases, when the heat demand of the process is considerably lower than the maximum power of the solar plant, a storage system should be considered. Thus, a specific solar multiple has to be defined for the plant, taking into account the requirements of each case. Finally, in plants working with direct treatment of material, a batch reactor could be more appropriate than a continuous one.

As mentioned, the plant can operate with or without thermal storage. If the plant is provided with an insulated hot tank, when the heat demand decreases or is null, the sand can be stored in it. In this way, the control of sand energy could be easier. However, residence time could not be sufficient to heat up the sand because of the intermittency and variations of solar energy. Although residence time can be varied by changing the rotational speed of the reactor, recirculation of sand in the reactor or an auxiliary heating system inside the hot storage should be implemented in order to achieve the desired particle temperature when weather conditions are not ideal. A schematic representation of a plant with thermal storage and with direct treatment of material is shown in figure 1.

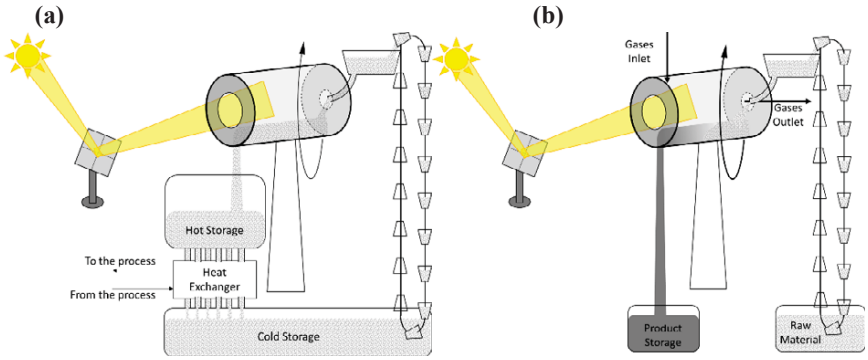

Fig. 1: Configurations of a plant a) with thermal storage and b) for direct treatment of material in the receiver.

3. Results

3.1. Receiver sizing, residence time and mass flow

A reference case based on PS10 solar tower plant is presented for which a thermal power (Q_p) of 50 MW was considered. Kiln size was determined in order to be similar to PS10 receiver. Furthermore, a rotational speed of 5 rpm and a receiver slope of 5° were assumed. Those values are within the typical range for industrial rotary kilns and they assure a bed motion in rolling or cascading mode. As mentioned, sand was the material designated for the study with a design outlet temperature of 750 °C. The considered sand properties were bulk density (1560 kg/m^3) and the specific heat, which was calculated at the entrance and at the outlet of the reactor according to equations 27 and 28 (Perry, 1997). In the case of a plant without storage, in which the particles are directly irradiated, the specific heat of sand has to be changed with the treated material's one (this case is not reported here). Sand properties used in the calculation are resumed in table 1.

$$C_{p_{SiO2,\alpha}} = \frac{4.187}{0.06} \cdot \left(10.87 + 0.008712 \cdot T - \frac{241200}{T^2}\right) \quad \text{for } 273 < T < 848 \text{ K} \quad (27)$$

$$C_{p_{SiO2,\beta}} = \frac{4.187}{0.06} \cdot (10.95 + 0.0055 \cdot T) \quad \text{for } 848 < T < 1873 \text{ K} \quad (28)$$

Table 1: Main physical properties of sand used for calculations.

Property	bulk density	Specific heat at 20 °C	Specific heat at 750 °C
Unit	kg/m^3	$J\ kg^{-1}\ K^{-1}$	$J\ kg^{-1}\ K^{-1}$
Sand	1560	740.9	1156.8

An iterative process was adopted in order to determine the proper size of the receiver. According to Mellmann classification, a fill ratio higher than 10% assures the achievement of a rolling bed motion inside the kiln. Nevertheless, increasing the fill ratio, segregation can arise inside the core of the particle bed. Another constraint is related to kiln aperture. As indicated above, aperture diameter depends on the height of the particle bed that defines the height of the kiln dam. A small aperture can reduce receiver heat losses; however, if it is too small, part of the flux reflected by the heliostat field could not enter and, as a consequence, spillage losses increase. Taking into account this consideration, an internal diameter of 9 m and an axial length of 8.7 m were selected for the receiver.

Table 2: Rotary kiln geometrical and operational characteristics.

Parameter	Internal Diameter	Length	Dam Height	Aperture Diameter	Fill Ratio	Residence Time	Mass Flow	Central Angle α
Unit	m	m	m	m	%	min	kg/s	degree
Value	9	8.7	1.4	6.2	10	28	51.7	93.3

3.2. Thermal model results

For the calculations, it was assumed that the rotary kiln had been heated before the addition of the particles. Once the size of the receiver was fixed and mass flow and temperature range were known, thermal losses were calculated. Air parameters used in the equations are shown in table 3. To evaluate radiative losses, a wall and a particle emissivity of 0.8 (Zhou et al., 2006) and 0.76 ("Engineering Toolbox," 2016) respectively, were assumed.

Table 3: Main physical properties of air used for calculations.

Property	Cinematic viscosity	Volumetric expansion	Conductivity	Wind speed
Symbol	ν	β	K	v
Unit	m^2/s	1/K	$W\ m^{-1}\ K^{-1}$	m/s
Air	$15.11 \cdot 10^{-6}$	$3.43 \cdot 10^{-3}$	0.0515	10

With these values, the results shown in table 4 were obtained. In case 1, convective losses were calculated considering an open cavity receiver, following the methodology proposed by Siebers and Kraabal with the correlation of Stine and Mcdonald for the natural convection and Ma´s correlation for the forced convection.

Table 4: Thermal results for the rotary kiln without transparent windows at the aperture.

	Inlet temp.	Outlet temp.	Absorbed Power	Radiative Losses	Convective Losses	Reflection Losses	Efficiency
Unit	°C	°C	MW	MW	MW	MW	%
Value	750	20	50	3.42	5.45	1.12	83

3.3. Heliostat field results

Two heliostat fields were calculated, assuming Tabernas Desert conditions, a tower height of 110 m and a minimum efficiency of 70%. The first field was based on PS10 heliostats. Those mirrors had a large size and a reflecting surface of 121 m^2 each one. Field with larger heliostats had the advantage to be cheaper, mainly because a minor number of elements is needed. With 713 heliostats, it was possible to concentrate 60 MW of solar radiation inside a circular area of 8 m in diameter placed at the receiver aperture plane. A maximum flux of 2320 kW/m^2 and an average flux of 994 kW/m^2 at the aperture were predicted. A secondary concentrator at the entrance of the kiln was needed because the calculated aperture of the kiln was smaller than the achieved flux distribution. Moreover, a second heliostat field was designed, considering a smaller heliostat size (13.5 m^2). In this case, it was predicted a heliostat field of 6622 elements, a maximum heat flux of 3620 kW/m^2 and an average one of

1656 kW/m^2. For this case, the flux fitted inside the kiln aperture of 6.2 m. In Fig. 2 both heliostat fields are shown.

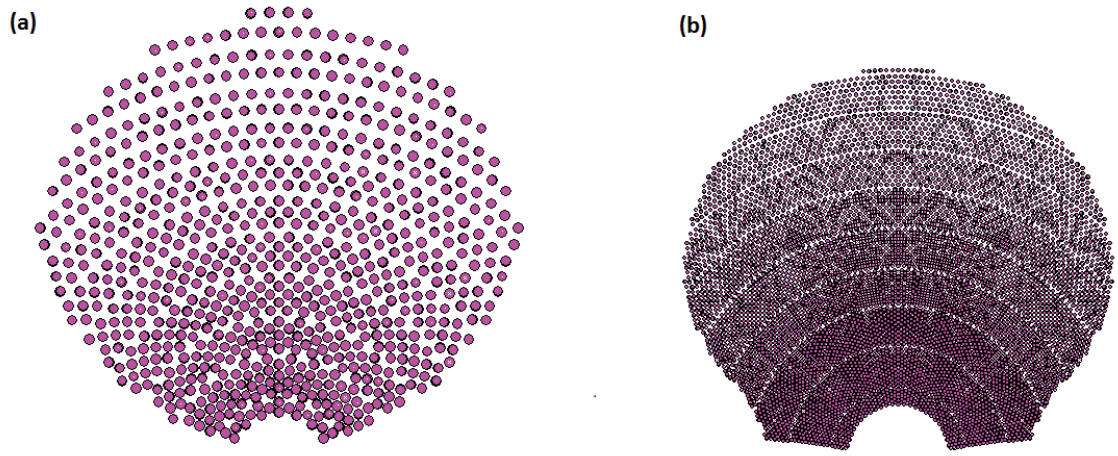

Fig. 2: Heliostat field a) with large heliostats and b) with small heliostats.

4. Discussion and further considerations

The design of the rotary receiver required the selection of several parameters. Geometrical parameter were based on the existing PS10 tower plant and solar rotary kilns proposed so far. In the analyzed example, the mass flow through the kiln was determined by the design power of the receiver and temperature conditions at the inlet and outlet. Working with solid particles at ambient temperature avoids freezing problems of conventional thermal fluids and reduces storage costs in comparison with other heat transfer fluids (i.e., molten salts). Moreover, because of the wider working temperature range, lower mass flows are needed to obtain an equal absorbed power. The outlet temperature of 750 °C was selected because it was higher than the limit of current commercial heat transfer fluid, but it was low enough to avoid a considerable increase of material cost, in particular, the cost of the transport system of the particles, heat exchanger and hot storage tank. Moreover, working with higher temperatures implies reducing the mass flow and as consequence the fill ratio or the kiln aperture. For the proposed example, those parameters were close to their lower limits.

Residence time estimation are quite complex for rotary kilns and in most cases, they are not applicable for scaling up from lab devices. Residence time presented in this work is a rough evaluation of the experimental residence time of an industrial rotary kiln. In the future, a detailed model for the rotary kiln will be developed with the aim to achieve more reliable results and to improve the scale up of such a device. Nevertheless, the estimation of the residence time presented in this work could be assumed as an initial information for the scale up of the plant. A calculated time of 28 min is a reasonable time for the operation in a solar device. An important issue for this solar systems is the control of particle temperature and because of variation in weather conditions, higher residence time could make it complex.

For the thermal model, the rotary kiln was considered similar to a cavity receiver and calculations were based on the existing models for this kind of elements. Therefore, calculated efficiency resulted close to typical efficiencies of these receivers. One of the greatest challenges for both, cavity receivers and rotary kilns, is a good prediction of convective losses. Moreover, an important difference consists in the heat transfer mechanisms for those technologies. In particular, for cavity receivers and solar rotary kilns, radiation is the principal mechanism, while for rotary kilns a combination of convection and radiation from the gas to the solid particles and the walls is the main one. In this work, a simplified model for convective losses was used for the case of a rotary receiver with an open aperture. The proposed thermal model indicates convective losses are the most relevant, corresponding to more than 5 MW. Radiative and reflective losses are 3.42 and 1.12 MW, respectively.

Heliostat fields obtained with the software WinDelsol present higher fluxes than those used in solar tower plants for electricity production. However, they are in an acceptable range for this kind of technology. For both heliostat fields the efficiency was 70% and, as it can be seen in figure 2, a more compact field can be obtained if smaller heliostats are used. Second field allows to fit the flux inside the reactor aperture without the need of a second concentrator. As a drawback, a considerable higher number of heliostats is needed and that could increase the

cost of the plant.

As future work, studies on a solar rotary kiln, which operates in batch mode, will be carried on. This operational mode could facilitate control of the temperature inside the receiver/reactor, but it needs time for charge and discharge phases. As a consequence, during these phases, part of the daily solar radiation cannot be used.

5. Conclusions

Considerations on central receiver plants with rotary kiln for production of process heat with or without storage have been analyzed and discussed in this work. In particular, the case of a 50 MW_{th} plant is presented. Because of the shape of rotary kilns, only one-side heliostat field can be suited in this kind of solar tower plant. A rotary kiln with sand particles is analyzed. A simplified thermal model was carried on and a receiver efficiency of 83% was calculated. A sand residence time of 28 minutes was also predicted. Finally, two heliostat fields are proposed. The first one consists of 713 large heliostats which focus solar energy on a secondary concentrator of 8 m in diameter. With the second one, it is possible to concentrate the required power by the receiver on the aperture of the kiln without the use of a secondary concentrator. As a drawback, more than 6600 small heliostats are needed. To conclude, a first analysis of central tower plants with rotary receiver was conducted. Initial results show the possibility to realize solar plants with these characteristics in future developments. However, more detailed models must be studied in order to more accurately predict the performance of such systems.

Acknowledgments

The authors acknowledge the financial support provided by the FONDECYT project number 3150026 of CONICYT (Chile), the Education Ministry of Chile Grant PMI ANT 1201, and the Solar Energy Research Center SERC Chile. The second author also wish to thank the University of Almeria and the Plataforma Solar de Almería for the assistance and collaboration devoted to the development of his Ph.D research.

6. References

Alonso, E., Pérez-Rábago, C.A., Licurgo, J., Fuentealba, E., Estrada, C.A., 2015. First experimental studies of solar redox reactions of copper oxides for thermochemical energy storage. Sol. Energy 115, 297–305. doi:10.1016/j.solener.2015.03.005

Alonso, E., Romero, M., 2015. Review of experimental investigation on directly irradiated particles solar reactors. Renew. Sustain. Energy Rev. 41, 53–67. doi:10.1016/j.rser.2014.08.027

Aydin, D., Casey, S.P., Riffat, S., 2015. The latest advancements on thermochemical heat storage systems. Renew. Sustain. Energy Rev. 41, 356–367. doi:10.1016/j.rser.2014.08.054

Bergman, T.L., Incropera, F.P., DeWitt, D.P., Lavine, A.S., 2011. Fundamentals of Heat and Mass Transfer.

Block, T., Schmücker, M., 2016. Metal oxides for thermochemical energy storage: A comparison of several metal oxide systems. Sol. Energy 126, 195–207. doi:10.1016/j.solener.2015.12.032

Boateng, A.A., Barr, P. V., 1996. Modelling of particle mixing and segregation in the transverse plane of a rotary kiln. Chem. Eng. Sci. 51, 4167–4181. doi:10.1016/0009-2509(96)00250-3

Brimacombe, J.K., Watkinson, A.P., 1978. Heat transfer in a direct-fired rotary kiln: I. Pilot plant and experimentation. Metall. Trans. B 9, 201–208. doi:10.1007/BF02653685

Calderoni, M., Aprile, M., Moretta, S., Aidonis, A., Motta, M., 2012. Solar thermal plants for industrial process heat in Tunisia : Economic feasibility analysis and ideas for a new policy 30, 1390–1400. doi:10.1016/j.egypro.2012.11.153

Cholette, A., Cloutier, L., 1959. Mixing efficiency determinations for continuous flow systems. Can. J. Chem. Eng. 37, 105–112. doi:10.1002/cjce.5450370305

Engineering Toolbox [WWW Document], 2016. URL http://www.engineeringtoolbox.com/emissivity-coefficients-d_447.html (accessed 10.6.16).

Fuller, R.J., 2011. Solar industrial process heating in Australia - Past and current status. Renew. Energy 36, 216–221. doi:10.1016/j.renene.2010.06.023

Gallo, A., Spelling, J., Romero, M., González-Aguilar, J., 2015. Preliminary Design and Performance Analysis of a Multi-Megawatt Scale Dense Particle Suspension Receiver. Energy Procedia 0, 388–397. doi:10.1016/j.egypro.2015.03.045

Halmann, M., Steinfeld, A., Epstein, M., Guglielmini, E., Vishnevetsky, I., 2012. Vacuum Carbothermic Reduction of Alumina, in: proceedings of ECOS 2012 - the 25th international conference on efficiency, cost, optimization, simulation and environmental impact of energy systems.

Jemmal, Y., Zari, N., Maaroufi, M., 2016. Thermophysical and chemical analysis of gneiss rock as low cost candidate material for thermal energy storage in concentrated solar power plants. Sol. Energy Mater. Sol. Cells 157, 377–382. doi:10.1016/j.solmat.2016.06.002

Kousksou, T., Bruel, P., Jamil, a., El Rhafiki, T., Zeraouli, Y., 2014. Energy storage: Applications and challenges. Sol. Energy Mater. Sol. Cells 120, 59–80. doi:10.1016/j.solmat.2013.08.015

Lauterbach, C., Schmitt, B., Jordan, U., Vajen, K., 2012. The potential of solar heat for industrial processes in Germany. Renew. Sustain. Energy Rev. 16, 5121–5130. doi:10.1016/j.rser.2012.04.032

Li, X., Kong, W., Wang, Z., Chang, C., Bai, F., 2010. Thermal model and thermodynamic performance of molten salt cavity receiver. Renew. Energy 35, 981–988. doi:10.1016/j.renene.2009.11.017

Liu, M., Steven Tay, N.H., Bell, S., Belusko, M., Jacob, R., Will, G., Saman, W., Bruno, F., 2016. Review on concentrating solar power plants and new developments in high temperature thermal energy storage technologies. Renew. Sustain. Energy Rev. 53, 1411–1432. doi:10.1016/j.rser.2015.09.026

Ma, R.Y., 1993. Wind Effects on Convective Heat Loss From a Cavity Receiver for a Parabolic Concentrating Solar Collector.

Mahlia, T.M.I., Saktisahdan, T.J., Jannifar, A., Hasan, M.H., Matseelar, H.S.C., 2014. A review of available methods and development on energy storage ; technology update. Renew. Sustain. Energy Rev. 33, 532–545. doi:10.1016/j.rser.2014.01.068

Mcdonald, C.G., 1995. Heat Loss from an Open Cavity.

Meier, A., Bonaldi, E., Cella, G.M., Lipinski, W., Wuillemin, D., Palumbo, R., 2004. Design and experimental investigation of a horizontal rotary reactor for the solar thermal production of lime. Energy 29, 811–821. doi:10.1016/S0360-5442(03)00187-7

Mellmann, J., 2001. The transverse motion of solids in rotating cylinders—forms of motion and transition behavior. Powder Technol. 118, 251–270. doi:10.1016/S0032-5910(00)00402-2

Nikulshina, V., Gebald, C., Steinfeld, a., 2009. CO2 capture from atmospheric air via consecutive CaO-carbonation and CaCO3-calcination cycles in a fluidized-bed solar reactor. Chem. Eng. J. 146, 244–248. doi:10.1016/j.cej.2008.06.005

Pardo, P., Deydier, A., Anxionnaz-Minvielle, Z., Rougé, S., Cabassud, M., Cognet, P., 2014. A review on high temperature thermochemical heat energy storage. Renew. Sustain. Energy Rev. 32, 591–610. doi:10.1016/j.rser.2013.12.014

Perry, R.H., 1997. Perry's Chemical Engineers' Handbook, 7th ed. McGraw-Hill, New York.

Renaud, M., Thibault, J., Trusiak, A., 2000. Solids Transportation Model of an Industrial Rotary Dryer. Dry. Technol. 18, 843–865. doi:10.1080/07373930008917741

Romero, M., Steinfeld, A., 2012. Concentrating solar thermal power and thermochemical fuels. Energy Environ. Sci. 5, 9234. doi:10.1039/c2ee21275g

Sai, P.S.T., Surender, G.D., Damodaran, A.D., Suresh, V., Philip, Z.G., Sankaran, K., 1990. Residence time distribution and material flow studies in a rotary kiln. Metall. Mater. 21, 1005–1011. doi:10.1007/BF02670271

Siebers, D.L., Kraabel, J.S., 1984. Estimating Convective Energy Losses From Solar Central Receivers. SANDIA Rep.

Steinfeld, A., 2005. Solar thermochemical production of hydrogen—a review. Sol. Energy 78, 603–615. doi:10.1016/j.solener.2003.12.012

Watkinson, A.P., Brimacombe, J.K., 1978. Heat transfer in a direct-fired rotary kiln: II. Heat flow results and their interpretation. Metall. Trans. B 9, 209–219. doi:10.1007/BF02653686

Yang, L., Farouk, B., 1997. Modeling of Solid Particle Flow and Heat Transfer in Rotary Kiln Calciners. J. Air Waste Manage. Assoc. 47, 1189–1196. doi:10.1080/10473289.1997.10464069

Zhang, H., Benoit, H., Gauthier, D., Degrève, J., Baeyens, J., López, I.P., Hemati, M., Flamant, G., 2016. Particle circulation loops in solar energy capture and storage: Gas–solid flow and heat transfer considerations. Appl. Energy 161, 206–224. doi:10.1016/j.apenergy.2015.10.005

Zhou, B., Yang, Y., Reuter, M.A., Boin, U.M.J., 2006. Modelling of aluminium scrap melting in a rotary furnace. Miner. Eng. 19, 299–308. doi:10.1016/j.mineng.2005.07.017

Conference Proceedings
EuroSun 2016
Palma de Mallorca (Spain), 11 – 14 October 2016

SOLAR HEAT FOR INDUSTRIAL PROCESSES (SHIP): MODELING AND OPTIMIZATION OF A PARABOLIC TROUGH PLANT WITH THERMOCLINE THERMAL STORAGE SYSTEM TO SUPPLY MEDIUM TEMPERATURE PROCESS HEAT

María V. Guisado[1], Fritz Zaversky[1], Irene Santana[1] and Ana Bernardos[1]

[1] National Renewable Energy Centre (CENER), Navarra (Spain)

Abstract

This paper presents the development of a simulation tool for a Solar Heat for Industrial Processes (SHIP) plants, based on Parabolic Though technology and equipped with direct thermocline Thermal Storage System (TES). The model developed is a one–dimensional model, based on the Modelica language, which allows the transient performance evaluation of the plant.

Key-words: Solar heat, Industrial process heat, Transient simulation, Modelica, Thermocline.

1. Introduction

This work have been carried out within the project ANTHOPHILA, a project of the Call RETOS-COLABORACIÓN 2014 of the R&D National Program of Research, Development and Innovation, funded by the Ministry of Industry, Energy and Tourism and with Ingeteam and CENER as partners. The main objective of this project is the research and development of new technologies that allows the procurement of a new concept of a hybrid solar thermal for industrial heat application.

Globally, industrial process heat accounts for more than two-thirds of total energy consumption in industry, and half of this demand is low-to-medium temperatures (<400ºC) (Kempener et al., 2016). This means that there is a big potential market for the application of solar thermal energy. Currently there are already installed 188 plants worldwide (AEE-INTEC, 2016) providing solar heat to industrial processes.

Due to the diversity of industrial processes and solar heat supply options, more detailed and accurate models for each of the plant components as well as transient simulation of the plant as a whole are required, in order to achieve efficient configurations.

This paper is focused on the application of a well-structured and flexible model, able to satisfy the requirements of the different industrial heat process plants. The model applies Modelica (Elmqvist and Mattsson, 1997) as modeling language and Dymola (Dassault-Systèmes, 2012) as simulation environment. The model has been applied in a small scale thermal plant for the hybridization of solar thermal and conventional combustion process for SHIP plants. The solar thermal process includes as TES a thermocline single-tank option, proposed by various authors in order to reduce costs, and which is hardly analyzable using the conventional quasi-steady state models.

2. Modelica Description and in-house model library

Modelica is a multi-purpose physical system modeling language which models the dynamic behavior of technical systems and it has been developed in an international effort in order to unify already existing

doi:10.18086/eurosun.2016.02.22 Available at http://proceedings.ises.org

similar modeling approaches and to enable developed models and model libraries to be easily exchanged. The concept is based on non-causal models featuring true ordinary differential and algebraic equations, i.e. differential-algebraic equation (DAE) systems (Elmqvist and Mattsson, 1997).

The object-oriented approach, the possibility of multiple inheritance and the re-declaration feature lead to a clear model structure, avoid multiple definitions of frequently used code and offer an incredible model flexibility. The code syntax and application guidelines are defined in the regularly updated Modelica Language Specification (Modelica-Association, 2012). Furthermore, the use of Modelica clearly decouples the modeler from the equation system solving. Instead of developing a specific solving algorithm for each modeling task, the Modelica tool reads the developed Modelica code, performs symbolic manipulations of equations and translates the Modelica model into numerical simulation code, using state-of-the-art algorithms developed for general application. Thus, developed models and model libraries are exchangeable, i.e. can be read and simulated using different Modelica environments. Today, commercial, as well as open-source Modelica environments are available (Dassault-Systèmes, 2012; Open-Source-Modelica-Consortium, 2013).

Based on the Modelica Standard Library (MLS), the Solar Thermal Energy Department of the Spanish National Renewable Energy Centre (CENER) has developed an in-house model library for the simulation of Concentrating Solar Thermal Plants (CSTLibrary).

The library is based on a one-dimensional fluid flow modeling approach, implemented according to the finite volume method (FVM) (Franke et al., 2009). The library includes a variety of components of thermal solar systems such as, solar collectors with different geometry and thermal loss models, several thermal energy storage solutions, including indirect and direct storage systems with two tanks and thermocline single-tank options, as well as heat exchangers and other thermo-hydraulic components: pipes, pumps, valves, etc., needed for a whole plant simulation. The transient models allow a detailed analysis of the components. Besides, any operation strategy can be integrated.

The modeling approach and the validation of single component models have been previously published in several works, e.g. (Zaversky et al., 2013; Zaversky, 2014; Hernández Arriaga et al., 2015).

3. Industrial Process Description and Model Implementation

The great flexibility of the models allows analyzing a wide variety of industrial heat processes. Concretely, in this work, the model has been applied to an industrial process consisting of a drying unit for the agricultural sector, whose heat is provided by a solar thermal system with parabolic trough technology working at medium temperature (100-250 °C), and an auxiliary fossil fuel boiler. The solar thermal plant also incorporates a storage system, whose size has been optimized considering the number of loops, with the objective to cover as much as possible the heat required by the process.

In order to demonstrate the flexibility of the model and at the same time, to analyze the technical feasibility of the industrial process, two types of thermal storage have been tested, the conventional two-tank storage system and a thermocline storage tank, which can provide a costs reduction but is hardly analyzable using the conventional quasi-steady state models. In addition, two absorber tubes of the same dimensions but different degrees of vacuum have been also analyzed in this work.

Fig.1 shows a basic scheme of the plant, which can be divided into three main systems: solar field, storage system and steam generator. The plant includes an auxiliary gas boiler in order to cover the thermal demand of the industrial process when the solar energy is not available.

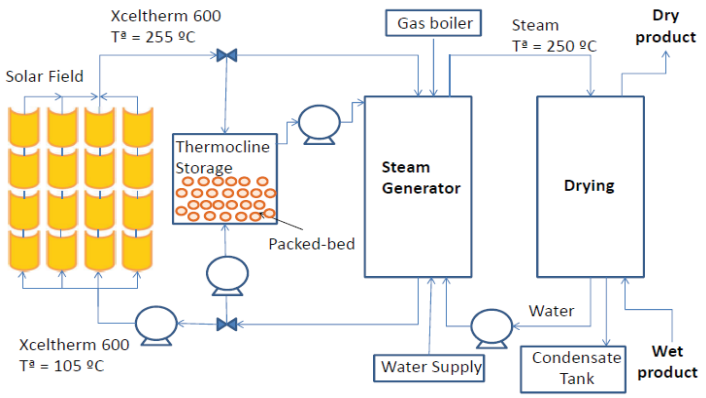

Fig. 1: Diagram of the reference plant with thermocline packed-bed storage

The following sub-sections show a brief description of the models used for each of the main systems mentioned above. They are described detailed in Zaversky (2014).

3.1. Solar Field

The solar field of a parabolic trough collector plant is composed of a number of solar collector loops of identical characteristics. A cold header pipe supplies the thermal fluid to the loops where the thermal fluid is heated by the solar energy and it drains into the hot header pipe. Each loop consists of solar collector assemblies (SCAs) connected in series and each solar collector assembly is composed of the basic solar collector components, as the parabolic mirrors and the solar absorber tubes, i.e. the heat collector elements (HCEs).

Fig. 2 shows a scheme of the solar field model used in this work. It consists of one representative solar collector loop, tow mass flow gains, and two additional dynamic pipe models that represent the cold and the hot header. Basically, the model is based on a 1-D approach according to Forristall (2003),and it discretizes the solar collector loop into a certain number of control volumes according the finite volume method. To correctly reproduce the dominant dynamics and the steady-state behavior, a certain minimum number of control volumes per loop are required.

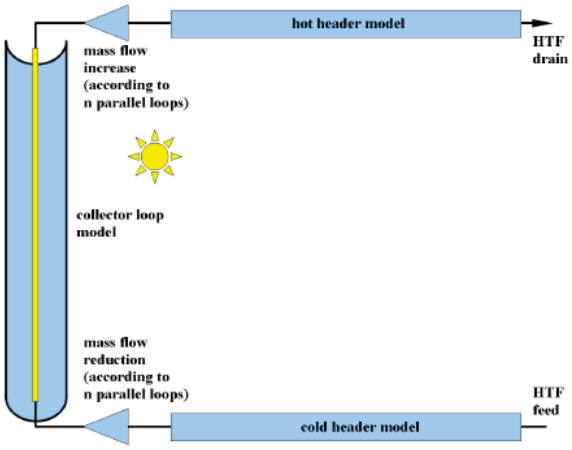

Fig. 2: The end-loop model of the parabolic trough collector field (Zaversky, 2014)

The total thermal power of the solar field is simply achieved via multiplying the mass flow of one loop by the number of total parallel loops.

The number of collectors per loop, and thus the final length of one loop, is defined by the plant´s operating conditions, such as the solar field´s nominal inlet and outlet temperature and the desired HTF mass flow rate for a given solar irradiance level.

Regarding the linear absorber of a parabolic trough collector, it is modeled as a straight steel pipe featuring a selective coating at the tube´s outer surface. It is discretized into a number of finite control volumes, and for each of them, the basic equations for mass and energy conservation are solved (see Fig. 3).

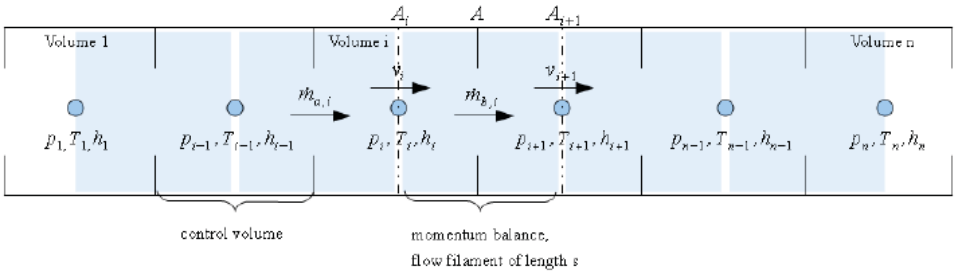

Fig. 3: Finite volume discretization scheme (Tummescheit, 2002)

In order to simplify the model, some assumptions are taken into account. Thus, the absorber tube as well as the glass envelope is assumed to have uniform circumferential temperatures and a uniform circumferential solar heat input. The glass envelope is considered opaque to infrared radiation (Forristall, 2003).

All solid material properties, thermal conductivity, density, and specific heat capacity are assumed to be constant and homogeneous. The heat conduction in longitudinal direction within the absorber tube and the glass envelope is neglected.

Finally, regarding the solar field sub-model, the thermal oil used is not yet available in open Modelica libraries, so these features have been newly implemented. It is modeled as incompressible fluid according to Radco-Industries-Inc. (2014).

Within the MSL, all specific media property functions are decoupled from the library components by defining a replaceable "medium package" in each of them. Basically, all fluid property function names and interfaces are defined within the base class "partial medium". In order to allow a full replaceability, each specific medium model extends from this base class the "partial medium" and defines the specific media related relationships by re-declaring each necessary medium property function. Thus, every single component of the library can easily be adapted for the use of different fluids, by simply replacing the default medium package when instantiating the final model.

3.2. Thermal Storage System

Regarding the thermal storage system, as it has been indicated previously, two types of systems have been analyzed, a conventional two-tank storage system and a single-tank thermocline with filler material. In both cases, the storage is a direct system in which the heat transfer fluid, thermal oil, is used as thermal storage fluid too.

Following sub-sections show a brief description of the main characteristics of each thermal storage system model.

3.2.1 Direct two-tank storage system

The active direct two-tank thermal energy storage system is composed of two tanks, physically separated such that the cold fluid is stored in one of them and the hot fluid in the other one. During charging, the thermal oil leaves the cold tank and it absorbs the energy provided by the solar field increasing its temperature and then it is stored in the hot tank. During discharging, the thermal oil from the hot tank provides heat to the steam generator when the energy from the solar field is not enough and the cold thermal oil is returned to the cold tank.

The basic components of a typical active direct two-tank system are the storage tanks (the hot tank and the cold tank).

The storage tank model is based on the assumption of having one representative thermal oil temperature. Hence, the thermal oil within the tank is modeled as a single control volume, defining an ideally mixed energy balance.

3.2.2 Direct thermocline storage system

Unlike the conventional two-tank storage system, in which the hot and cold fluid are stored in two different tanks, the thermocline storage system uses a single tank of slightly large dimensions in which the hot oil remains in the top of the tank and the cold fluid remains in the bottom, due to the thermocline effect.

The strongest temperature variation between these stratified layers occurs in a limited zone within the total thermal oil level height. For this reason, it is possible to provide almost constant thermal oil outlet temperatures, during a reasonable part of the discharging process. And vice versa, the cold thermal oil outlet temperature is almost constant during charging mode. About 69% of the total maximum thermal oil level height can be used for the actual storage capacity. Hence, about 31% of the thermal oil level height is required by the temperature gradient.

Furthermore, a packed bed is used in the thermocline tank as filler to increase the thermal capacity. The filler material avoids the convective mix and reduces the amount of fluid required for the storage system. The filler must have a high specific heat capacity, a minimal interstitial space, must be compatible with the storage fluid, and one should avoid toxic or hazardous materials.

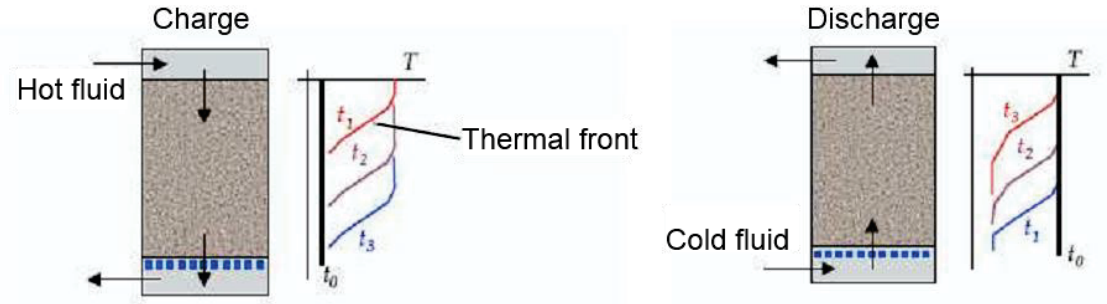

Fig. 4: Operation of a thermocline storage system with bed packed

The thermocline storage space can be divided into three zones. Starting from the bottom, the first zone is a rather constant low temperature zone (i) ranging from the bottom area of the tank up to the beginning of the pronounced temperature gradient zone. This temperature gradient zone (ii) is characterized by significant temperature changes of the storage fluid and the filler material. Finally, the temperature gradient zone is followed by the rather constant high temperature zone (iii) at the top of the tank (Yang and Garimella, 2010).

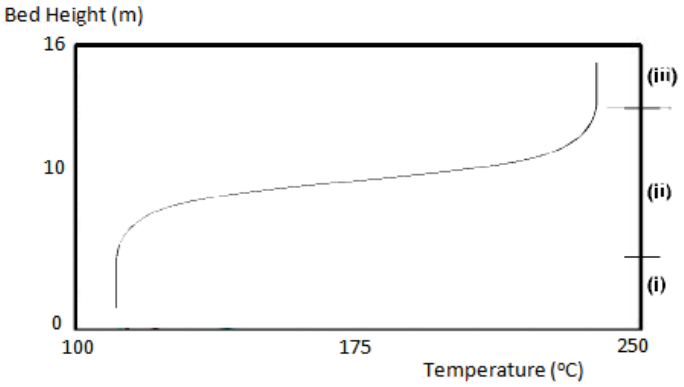

Fig. 5: Thermocline zones (i, ii, iii)

While discharging and charging, the temperature gradient zone moves towards the exit piping, leaving behind an expanding constant low temperature zone (discharging), or high temperature zone (charging), respectively.

In the constant temperature zones, the filler material is completely cooled or heated, providing a thermodynamic equilibrium between the thermal oil and the filler material. In the temperature gradient zone, the thermal energy is either transferred to the filler material (charging), or, in the case of discharging, to the thermal oil.

The thermocline problem can be described by the following set of coupled partial differential equations (PDEs), based on the pioneering work of Schumann (1929).This set of PDEs has to be discretized in order to obtain a set of ordinary differential equations (ODEs) suitable for the model formulation in Modelica. This has been done according to the finite volume method (FVM). In particular, the developed model is based on well-proven and freely available model structures and base classes, as provided by the Modelica Standard Library (MSL) (Modelica-Association, 2010). For a detailed model description, the interested reader is referred to Hernández Arriaga et al. (2015).

$$M_f c_f \frac{\partial T_f}{\partial t} + M_f c_f v \frac{\partial T_f}{\partial x} = h_{fs} P_{fs}\left(T_s - T_f\right) + k_{fe} A_c \frac{\partial^2 T_f}{\partial x^2} - U\, P_w\left(T_f - T_a\right) \quad \text{(eq. 1)}$$

$$M_s c_s \frac{\partial T_s}{\partial t} = h_{fs} P_{fs}\left(T_f - T_s\right) + k_{se} A_c \frac{\partial^2 T_s}{\partial x^2} \quad \text{(eq. 2)}$$

where

$$M_f = \epsilon\, A_c \rho_f \quad \text{(eq. 3)}$$

$$M_s = (1-\epsilon) A_c \rho_s \quad \text{(eq.4)}$$

$$v = \frac{\dot{m}_f}{\rho_f\, \epsilon\, A_c} \quad \text{(eq.5)}$$

3.3. Steam generator

The steam generator is modeled in quasi-steady manner, applying steady-state heat exchanger models implemented according to the logarithmic mean temperature difference method (Shah and Sekulic, 2003). The water medium model is implemented according to Wagner and Kruse (1998).

3.4. The transport system model, the control model and operation strategies

All sub-models for different systems of the plant are connected by the transport system model. The transport system model has the task to correctly distribute the mass and energy flows between the solar thermal plant's components. Further-more, the pumping power for the HTF circuit has to be estimated.

Basically, the transport system model consists of a steady-state pump model, an expansion vessel model, instances of a T-junction model and the corresponding connecting equations between the power plant components.

Next, the control of the plant model will be roughly outlined. Transient Modelica models of thermal processes where certain process variables need to be controlled, typically feature continuous feedback proportional-integral (PI) control. The solar field model´s mass flow control additionally features a feedforward term that uses a simple steady-state model of one representative loop, in order to predict a reasonable mass flow signal depending on the current direct normal irradiance.

Furthermore, besides the control loops for the nominal solar field outlet temperature, a defocusing control loop is implemented as well, in order to avoid overheating of the heat transfer fluid. In this work, this defocusing control is implemented using a simple PI feedback structure. Thus, whenever the HTF temperature exceeds a maximum value of 260°C, the loop is defocused in the model. Not that the set point for the solar field outlet temperature is 255ºC.

In a solar thermal system with thermal energy storage, the current solar field mass flow rate does not automatically define the thermal load of the steam generator, since a fraction of the solar field mass flow can either be used for storage system charging, or, in storage system discharging mode, a certain mass flow top-up can be supplied to the power block by the thermal energy storage system. Thus, for a solar thermal plant with storage, the desired thermal load of the steam generator is controlled via charging or discharging of the thermal energy storage system, of course, if the current state-of-charge of the storage system allows the desired operation. The solar field will be defocused if the storage system is full and the solar field provides more power than the steam generator is able to handle.

The top-level control block implements the operating strategy of the plant model, i.e. it acts as a virtual operator of the plant that defines allowed minimum and maximum mass flow rates, the solar field recirculation mass flow, the thermal load set point of the steam generator as well as the thermal energy storage system´s operation.

An important point of the operation strategy control block is that it features discrete time variables that change their values at certain events during simulation, so, any arbitrary operating strategy can be implemented that defines certain variable set points according to specific operating directives.

4. Results and Conclusions

4.1. Plant Description – Technical parameters

The solar field of parabolic trough collectors consists of loops of 300 m. Each loop is composed of 74 collectors of 4 m length each of them. The thermal oil used as heat transfer fluid and thermal storage fluid is XCeltherm 600, which is an adequate fluid for the working temperatures. The absorber tubes are tubes of 2 meters length and have an inner diameter of 37 mm. The number of loops of the plant is a parameter which is going to be optimized.

In the case of the thermocline single-tank, the storage system includes a filler material in order to improve the thermal efficiency. After analysis of several materials, Cofalit has been selected for this study. It is a post-industrial commercial ceramic obtained from industrial processing of asbestos and waste. It shows good properties for the storage of thermal energy in the form of sensible heat up to 1100 °C. It has a specific heat of 0.860 kJ / kg K and its cost is very low.

The storage size, analyzed in a range of 1-8 hours, has been technically optimized during the design process in order to cover the thermal demand of the drying process as long as possible. An initial objective is that at least in the months of June, July and August, the auxiliary boiler should not be necessary.

The auxiliary boiler with fossil fuel is used to provide heat to the drying process when the thermal power provided by the solar field and/or storage system is not enough to cover the thermal demand.

The operation strategy consists of an annual demand of 3170 MWh distributed hourly such as is shown in Table 1 knowing that 100% of the demand is 1.5 MWt. It has been stablished as an initial target that at least in the months of June, July and August it is not necessary to start-up the boiler.

Tab. 1:Hourly demand

Month / Day	0	1	2	3	4	5	6	7	8	9	10	11	12	13	14	15	16	17	18	19	20	21	22	23
Jan	0,58	0,61	0,63	0,66	0,68	0,69	0,79	0,81	0,81	0,60	0,45	0,31	0,22	0,18	0,15	0,13	0,11	0,13	0,22	0,30	0,38	0,46	0,51	0,54
Feb	0,57	0,60	0,62	0,64	0,66	0,66	0,76	0,77	0,75	0,53	0,39	0,29	0,25	0,21	0,18	0,16	0,15	0,16	0,19	0,27	0,35	0,43	0,50	0,53
Mar	0,48	0,53	0,57	0,60	0,61	0,63	0,76	0,78	0,67	0,38	0,22	0,12	0,06	0,02	0,00	0,00	0,00	0,00	0,02	0,12	0,20	0,30	0,40	0,45
Apr	0,19	0,24	0,29	0,32	0,34	0,37	0,48	0,50	0,47	0,23	0,07	0,02	0,00	0,00	0,00	0,00	0,00	0,00	0,00	0,00	0,00	0,03	0,09	0,13
May	0,07	0,12	0,17	0,21	0,25	0,28	0,40	0,42	0,39	0,10	0,00	0,00	0,00	0,00	0,00	0,00	0,00	0,00	0,00	0,00	0,00	0,00	0,00	0,03
Jun	0,02	0,07	0,10	0,13	0,16	0,18	0,29	0,31	0,26	0,03	0,00	0,00	0,00	0,00	0,00	0,00	0,00	0,00	0,00	0,00	0,00	0,00	0,00	0,00
Jul	0,04	0,07	0,10	0,12	0,14	0,16	0,27	0,28	0,25	0,04	0,00	0,00	0,00	0,00	0,00	0,00	0,00	0,00	0,00	0,00	0,00	0,00	0,00	0,01
Aug	0,07	0,12	0,17	0,21	0,23	0,25	0,36	0,37	0,36	0,10	0,00	0,00	0,00	0,00	0,00	0,00	0,00	0,00	0,00	0,00	0,00	0,00	0,00	0,01
Sep	0,09	0,13	0,16	0,18	0,21	0,23	0,33	0,35	0,35	0,14	0,00	0,00	0,00	0,00	0,00	0,00	0,00	0,00	0,00	0,00	0,00	0,00	0,02	0,06
Oct	0,37	0,42	0,47	0,51	0,54	0,58	0,69	0,71	0,71	0,45	0,16	0,00	0,00	0,00	0,00	0,00	0,00	0,00	0,00	0,00	0,03	0,14	0,24	0,31
Nov	0,56	0,60	0,63	0,67	0,70	0,72	0,83	0,85	0,75	0,41	0,19	0,05	0,00	0,00	0,00	0,00	0,00	0,00	0,06	0,17	0,30	0,39	0,46	0,52
Dec	0,69	0,73	0,78	0,83	0,85	0,88	0,98	1,00	0,94	0,62	0,37	0,16	0,05	0,02	0,00	0,00	0,00	0,00	0,13	0,23	0,37	0,50	0,57	0,62

The model has been run over a year at Valladolid in Spain (Latitude 41.65^{o}) with a specific weather input file.

4.2. Results

The detailed transient analysis carried out by this software allows extracting and analyzing a large number of variables for the different systems and connections of the plant. The output variables such as power, energy, temperature, enthalpy, pressure, mass flow or charge states of the storage systems can be obtained for any instant of simulated period.

Results from these detailed simulations allow an accurate evaluation of the annual performance of the different alternatives, thereby providing a powerful and reliable tool for heat process plant designers.

Fig. 6 shows some of these variables for a clear day.

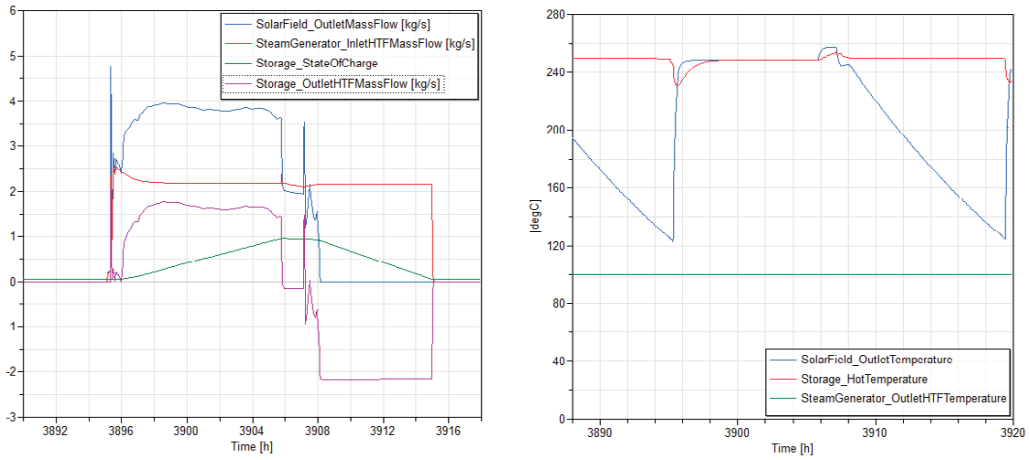

Fig. 6: Some variables provided by the software

During the optimization process, solar fields of 3-6 loops (1-1.5 MWt) and storage sizes of 1-8 hours have been analyzed, establishing as main aim to cover the demand of June, July and August. From this process, it can be concluded that, in order to cover that demand and due to that most of energy is required during the night, it is more profitable an increase of the storage size than an increase of the number of loops. So, among the options studied, a solar field with 3 - 4 loops and 8 hours of storage has been chosen as a technically optimal option. An increase in the number of loops would increase the defocusing and thus, would decrease the net plant performance but, it wouldn´t improve the coverage of the heat demand.

So, from the previous optimization process, several options have been analyzed including the different types of absorber tubes (Tube A and Tube B, which has a lower vacuum degree) and storage systems previously described.

The following tables show the main results for the options analyzed, from which can be observed that with a solar field of 4 loops, despite the annual energy generation decreases around 10-12% using the Tube B and a thermocline TES system, the power demand of June, July and August can be achieved.

So, in a next optimization stage, not included in the scope of this work, a detailed cost analysis for all components must be included in order to perform the techno-economic optimization of the complete plant and to confirm the potential feasibility of this TES system and the each type of tube for an industrial heat process.

Tab. 2:Results

	Two Tanks				Thermocline			
	Tube A	Tube B	Tube A	Tube B	Tube A	Tube B	Tube A	Tube B
Number of loops	3	3	4	4	3	3	4	4
Storage (h)	8	8	8	8	8	8	8	8
Energy Generation (MWh)	941	895	1072	1039	772	730	966	910
Annual Demand Coverage (%)	29.7	28.2	33.8	32.8	24.4	23.1	30.5	28.7
June, July and August Coverage (%)	100	96	100	100	89	87	98	98

Subsequently, in order to show the detailed analysis that the software can provide for each one of the

systems, several figures of the storage systems and the absorber tube behavior are included.

Fig. 7 shows the behavior of the thermocline storage system for two different days. For one of them, the storage is partially filled and for the other one, it can be completely filled. To carry out the simulations, the thermocline tank has been divided on 40 nodes and the full storage graph shows that, as described in the thermocline sub-model, about 69% (28 nodes) of the total maximum thermal oil level height is in the hot zone and can be used for the actual storage capacity.

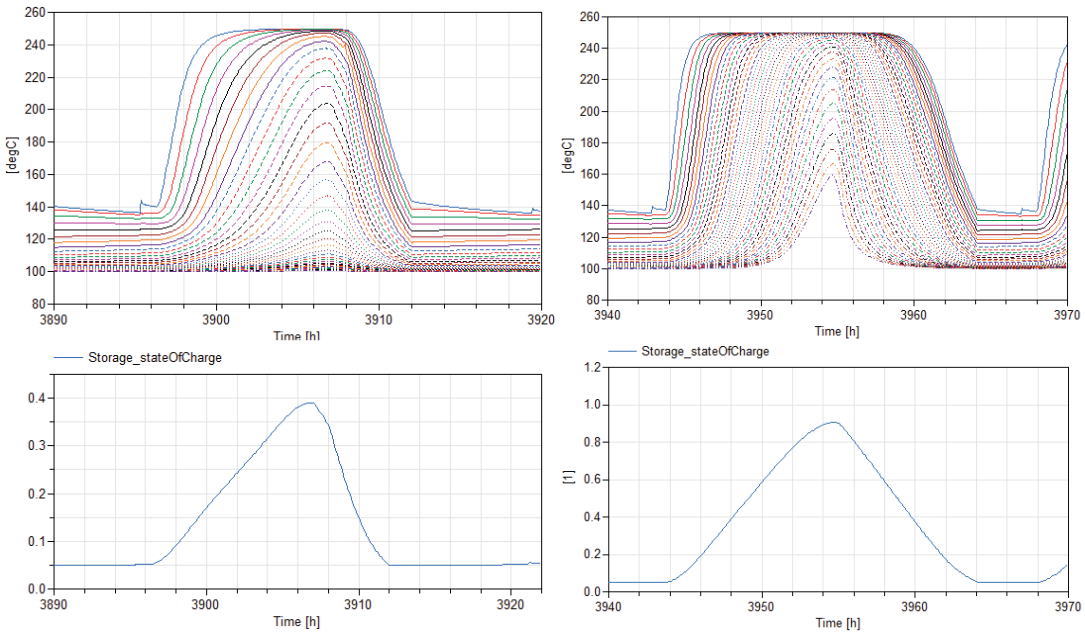

Fig. 7: Thermocline behavior

Finally, Fig. 8 shows the behavior of each type of absorber tube analyzed. It can be seen that the absorber tube B, which has higher thermal losses due to the lower vacuum degree, needs more time to achieve the output temperature (250ºC). Furthermore, nocturnal losses are bigger in this tube.

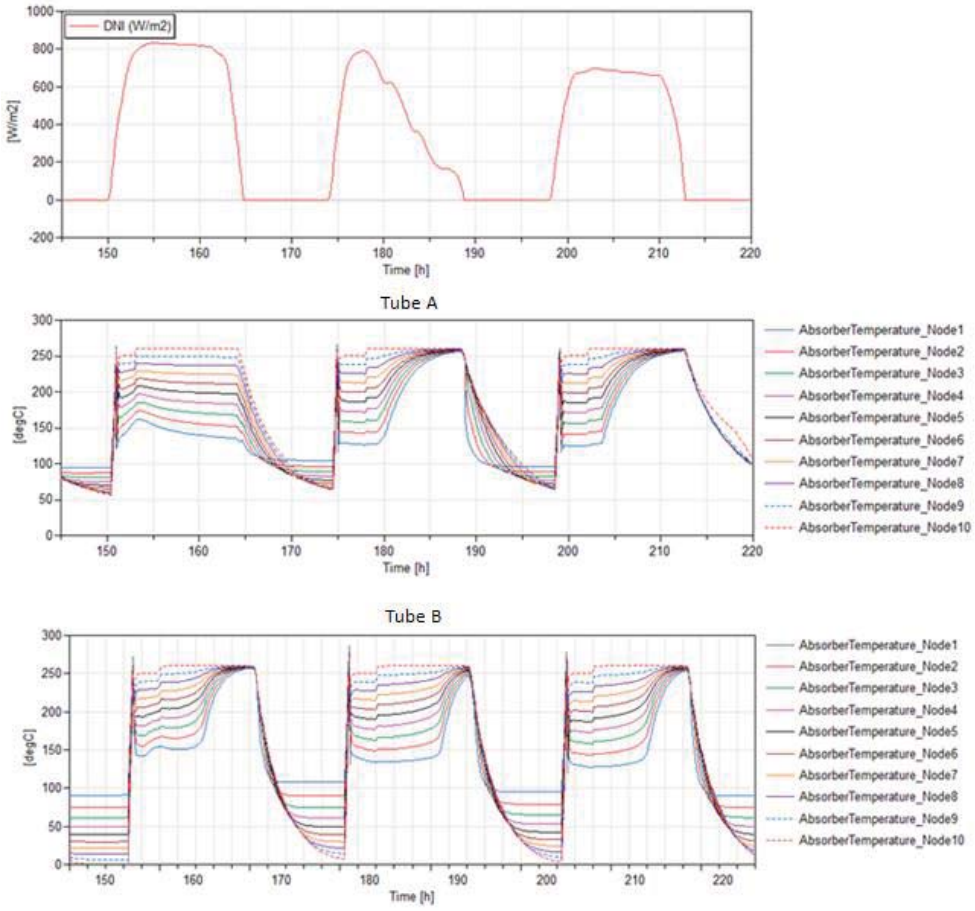

Fig. 8: Absorber tubes behavior

4.3. Conclusions

This work presents a well-structured and flexible model of a solar powered industrial process heat plant. In particular, the model has been applied on a small-scale hybridized SHIP plant, providing thermal power to a drying unit for the agricultural sector. The model applies Modelica as modeling language and Dymola as simulation environment. CENER's in-house model library (CSTLibrary) has been applied to model the system.

The transient analysis allows the evaluation of systems such as a thermocline single-tank storage, which has been proposed by various authors in order to reduce costs, and which is hardly analyzable using the conventional quasi-steady state models for process simulation.

Two types of thermal energy storage, the conventional two-tank concept, and the innovative single-tank thermocline option have been evaluated. Additionally, two types of solar collectors with different levels of vacuum have been analyzed.

The results of the simulations carried out show that with a solar field of 4 loops, despite the annual energy generation decreases around 10-12% using the Tube B and a thermocline TES system, the power demand of June, July and August can be achieved.

Future work will have to continue the optimization process also including costs to perform a techno-economic optimization.

5. References

AEE-INTEC (2016). Database for applications of solar heat integration in industrial processes. http://ship-plants.info/, AEE - Institut für Nachhaltige Technologien.

Dassault-Systèmes (2012). Dymola - Multi-Engineering Modeling and Simulation. http://www.3ds.com (accessed 14.11.2012), Dassault-Systèmes.

Elmqvist, H. and S. E. Mattsson (1997). Modelica - The next generation modeling language - An international design effort. Proceedings of the 1st World Congress on System Simulation. Singapore.

Forristall, R. (2003). Heat transfer analysis and modeling of a parabolic trough solar receiver implemented in Engineering Equation Solver, NREL/TP-550-169 Golden, Colorado, USA, NREL - National Renewable Energy Laboratory.

Franke, R., F. Casella, M. Sielemann, K. Proelss, M. Otter and M. Wetter (2009). Standardization of Thermo-Fluid Modeling in Modelica.Fluid Proceedings 7th Modelica Conference. Como, Italy.

Hernández Arriaga, I., F. Zaversky and D. Astrain (2015). "Object-oriented Modeling of Molten-salt-based Thermocline Thermal Energy Storage for the Transient Performance Simulation of Solar Thermal Power Plants." Energy Procedia **69**(0): 879-890.

Kempener, R., J. Burch, C. Brunner, C. Navntoft and D. Mugnier (2016). Solar heat for industrial processes - Technology brief. www.irena.org/Publications, IEA-ETSAP and IRENA.

Modelica-Association (2010). Modelica Standard Library 3.2 - Free library from the Modelica Association to model mechanical (1D/3D), electrical (analog, digital, machines), thermal, fluid, control systems and hierarchical state machines. http://www.modelica.org (accessed 14.11.2012), Modelica-Association.

Modelica-Association (2012). Modelica® - A Unified Object-Oriented Language for Systems Modeling - Language Specification - Version 3.3. https://www.modelica.org (accessed 14.11.2012), Modelica-Association.

Open-Source-Modelica-Consortium (2013). OpenModelica - An open-source Modelica-based modeling and simulation environment. http://www.openmodelica.org (accessed 8.1.2013), Open Source Modelica Consortium (OSMC).

Radco-Industries-Inc. (2014). XCELTHERM® 600 Engineering Properties. http://www.radcoind.com/industrial-energy/xceltherm-600-engineering/ (accessed 26.09.2016), Radco Industries, Inc.

Schumann, T. E. W. (1929). "Heat transfer: A liquid flowing through a porous prism." Journal of the Franklin Institute **208**: 405-416.

Shah, R. K. and D. P. Sekulic (2003). Fundamentals of Heat Exchanger Design. Hoboken, New Jersey, USA, John Wiley and Sons, Inc.

Tummescheit, H. (2002). Design and Implementation of Object-Oriented Model Libraries using Modelica, PhD Thesis Lund, Sweden, Department of Automatic Control - Lund Institute of Technology.

Wagner, W. and A. Kruse (1998). Properties of water and steam: the industrial standard IAPWS-IF97 for the thermodynamic properties and supplementary equations for other properties: tables based on these equations, Springer-Verlag.

Yang, Z. and S. V. Garimella (2010). "Thermal analysis of solar thermal energy storage in a molten-salt thermocline." Solar Energy **84**: 974-985.

Zaversky, F. (2014). Object-oriented modeling for the transient performance simulation of solar thermal power plants using parabolic trough collectors - A review and proposal of modeling approaches for thermal energy storage, PhD Thesis. Pamplona, Spain, Public University of Navarre.

Zaversky, F., R. Medina, J. García-Barberena, M. Sánchez and D. Astrain (2013). "Object-oriented modeling for the transient performance simulation of parabolic trough collectors using molten salt as heat transfer fluid." Solar Energy **95**: 192-215.

Solar Process Heat for South African Sugar Mills

Stefan Hess[1], Hendri T. Beukes[2], Gavin Smith[3] and Frank Dinter[1]

[1] Stellenbosch University, STERG, Stellenbosch (South Africa)

[2] MBB Consulting Engineers, Stellenbosch (South Africa)

[3] Sugar Milling Research Institute SMRI, Durban (South Africa)

Abstract

Solar thermal (ST) systems for the South African (SA) sugar industry could reduce coal consumption in the boilers and partly replace bagasse (pressed sugar cane fibres) as a heating fuel. Based on the heat and mass balance of a representative sugar mill, the most promising solar heat integration points were identified and pre-ranked according to their potential energetic and economic benefits.

The identified opportunities for solar process heat (SPH) are the generation of live steam and exhaust steam, the pre-heating of boiler feed water, the drying of bagasse and raw sugar, and the heating of clear juice. Without additional thermal storage, ST systems can supply between 12 and 27 % of the heat demand of these processes. The estimated levelized costs of heat (LCOH) for the SPH systems range from 2.57 Eurocent/kWh (0.42 ZAR/kWh) for solar drying of raw sugar during the crushing season (CS) to 4.57 Eurocent/kWh (0.75 ZAR/kWh) for all-year solar live steam generation.

This study assumes that SPH has to compete with coal, which is the cheapest energy source in SA, to replace bagasse. Using current coal prices and past price increase rates, the estimated achievable internal rate of return (IRR) for solar live steam generation is 4.6 % if the steam can be used during the whole year, e.g. for electricity export. The highest IRR of 9.1 % is expected for sugar drying during the crushing season.

Keywords: *solar process heat, energy efficiency, sugar production, electricity export, feasibility study*

1. Introduction

South Africa (SA) produces about two million tons of raw and refined sugar per year as well as a wide range of sugar by-products. Six milling companies operate 14 sugar mills. The vast majority of 12 mills are located in the KwaZulu-Natal province with the remaining two in Mpumalanga. The industry employs 79 000 people directly. SA is one of the leading exporters of sugar, competing with, among others, Brazil, Australia and India (DAFF, 2013). The crushing season usually stretches from March/April to November/December, depending on the amount of cane available in a particular year. On average, about 22 million metric tons of sugarcane are being processed per year (Wienese and Purchase, 2004, p. 41). The capacities of the SA sugar mills vary between 90 and 550 tons of cane per hour (t/h), with an average of about 300 t/h (Smithers, 2014, p. 917). The average length of the 2012/13 crushing season was 254 days and the overall time efficiency (OTE) was about 75.7 % (Smith et al., 2013, p. 30).

A decrease in coal consumption due to improved process management and energy efficiency directly reduces running costs. New income streams can be accessed if a share of the bagasse can be utilized for purposes other than energy generation for the sugar mills. This bagasse can be used to produce fertilizer, animal feed, or paper. It can also be used as feedstock for bio-ethanol production. Particularly interesting in the context of solar process heat (SPH) utilization is the use of steam from bagasse boilers to generate electricity for export to the SA national grid.

2. Sugar Production und Current Energy Supply

To provide a background for the SPH integration analysis to follow, this chapter gives a short introduction to the production of sugar from sugar cane, and on the energy supply to the different processes involved. The descriptions are all based on Rein (2007), unless otherwise stated.

doi:10.18086/eurosun.2016.02.14 Available at http://proceedings.ises.org

2.1 Sugar production process

A simplified representation of the main processes, the intermediate product streams, and the energy supply is given in Figure 1.

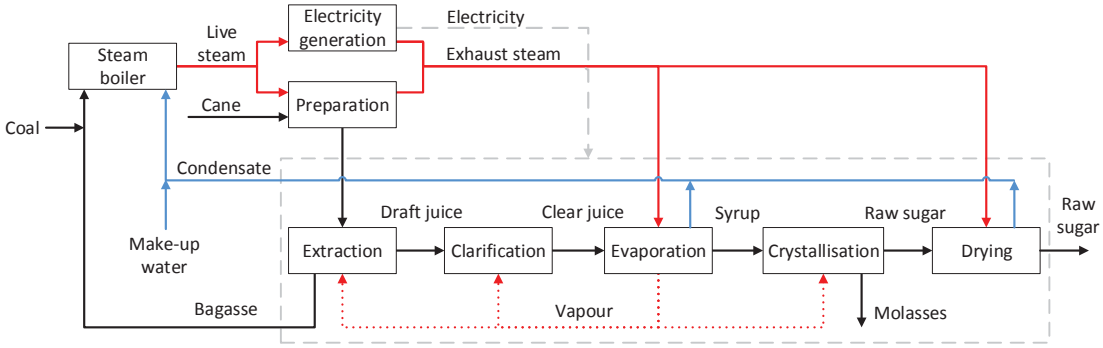

Figure 1: Processes and energy supply of a South African sugar mill

In SA, the cane is usually burned on the field to simplify manual harvesting even though this results in some of the biomass from the leaves being lost. The cane is cut, bundled and transported to the mills. It has to be processed as soon as possible to avoid a loss in sucrose.

Cane preparation refers to the removal of dirt and rocks, the cutting of the cane, and the fiberization of the cane by shredders. Modern sugar factories no longer mill the cane but use diffusers for the extraction of sucrose. In the diffuser, the sucrose is leached by repeatedly spraying heated juice onto a bed of cane fiber moving in counter-flow direction. The bagasse exiting the diffuser is pressed in roller mills to reduce the moisture content and to extract the maximum amount of sucrose. Cane knives, shredders and roller mills are referred to as 'prime movers'. They are usually run by live steam. In the clarification process, the impurities in the juice are removed. Therefore, the juice is pre-heated, flashed, and chemicals such as milk of lime are added.

By evaporation, the clear juice is concentrated to syrup by increasing its sucrose content. This is done in multiple effect evaporators, which have four or five heat exchangers that utilize low-pressure steam as a heating medium. The operating pressure is reduced in each consecutive effect to lower the saturation temperature of the vapor and the boiling point of the syrup. The first effect consumes exhaust steam, after which each successive effect consumes vapor bled from the preceding effect. Additionally, vapor is bled from the evaporators to serve as a heating medium for most of the other processes within the factory (cp. red dotted lines in Figure 1). To achieve crystallization, the syrup is boiled under vacuum in order to concentrate it to saturation. This is usually done by three different batch or continuous boiling pans, referred to as pans A to C. At the outlet of each pan, crystallizers cool the syrup and a centrifuge splits the mass in sugar and molasses. The molasses from the centrifuges of pans A and B is fed into the following pans, while the molasses from the pan C centrifuge is sold as a by-product, used for the production of ethanol, yeast, fertilizer or animal feed.

In the final drying process, the surface moisture content of the raw sugar is reduced by evaporation. For this, usually rotary cascade drums with counter flow hot air are used. After the sugar is dried, it is cooled with ambient air. Raw sugar can be sold directly, or be further refined at a refinery.

2.2 Current energy supply of SA sugar mills

For this study, the steady-state energy and mass balance of a theoretical South African sugar mill without energy efficiency measures is used. Temperatures, pressures and flow-rates are simulation results from the Biorefinery Techno-Economic Modelling project (BRTEM, Starzak and Zizhou, 2015). The BRTEM sugar mill represents the current practice in SA and assumes a throughput of 250 tons cane per hour.

Figure 2 shows besides a first SPH integration concept also the energy supply of the BRTEM sugar mill. The main energy source is bagasse from the roller mills after the extraction process. Live steam is used to perform mechanical work by driving the three prime movers, but it also drives a turbine, which runs a turbo alternator to generate the electricity needed in the production processes. The resulting exhaust steam is used to run the thermal processes of the plant with the highest exergy requirements.

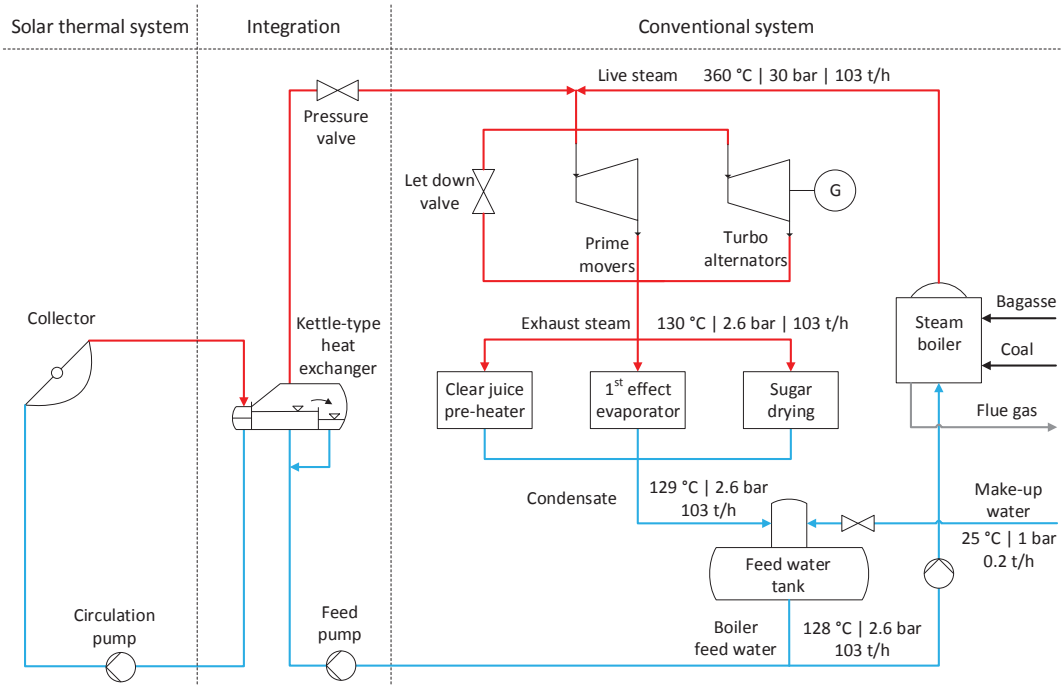

Figure 2: Integration scheme for indirect solar live steam generation (process values from Starzak and Zizhou, 2015)

Raw-sugar factories could be energy self-sufficient as the energy content of the bagasse is higher than their thermal and electrical energy demand. However, in SA, coal is used as an auxiliary fuel to supplement the bagasse. Factories without bagasse-export, electricity-export or a back-end refinery usually only need supplementary coal for abnormal occurrences. In the 2012/13 season, the SA mills had an average coal consumption of approximately 11 t per 1 000 t of cane. The industry consumes roughly 200 000 t of coal per season (Reid, 2006; Smith et al., 2013). The calorific value of 1 t coal equals that of 4 t of bagasse (Smith et al., 2013, p. 48).

3. Solar Heat Integration

3.1 Available solar resource

Figure 3 shows the annual variation of the mean daily global tilted irradiation (GTI) and direct normal irradiation (DNI) at characteristic sugar milling locations in KZN and Mpumalanga. The available irradiation in the KwaZulu-Natal (KZN) coastal region is about twice as high as in Central Europe and similar to other sugar milling locations in Brazil or India (Solar GIS, 2015).

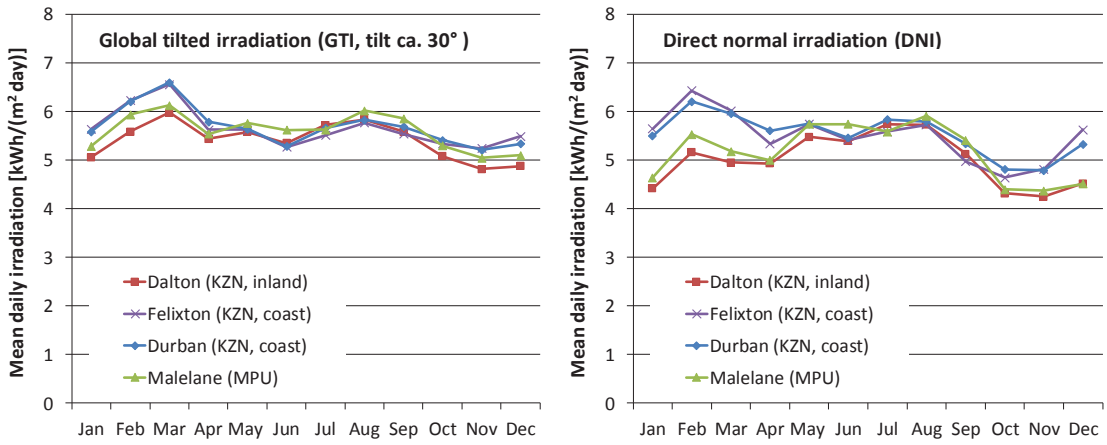

Figure 3: Mean daily GTI and DNI at sugar mill locations (values from PVGIS, 2015)

The GTI in Figure 3 is valid for a surface of 1 m^2 tilted approximately 30° towards the equator, i.e. orientated north. The DNI is the beam irradiance onto a surface of 1 m^2 tracking the sun. The annual sums of irradiance for the four locations in Figure 3 are shown in Table 1.

Table 1: Annual solar irradiation at sugar mill locations in South Africa (values from PVGIS, 2015)

Location	GHI [kWh/(m2 a)]	GTI [kWh/(m2 a)]	DNI [kWh/(m2 a)]	Optimal slope for GTI [°]	Fraction of diffuse [%]
Durban (KZN, coast)	1 825	2 077	2 018	32	34
Felixton (KZN, coast)	1 840	2 062	2 008	31	34
Malelane (MPU)	1 854	2 044	1 883	29	37
Dalton (KZN, inland)	1 737	1 975	1 825	33	37

Figure 3 and Table 1 show that the annual GTI varies by only 5 % between the SA milling locations; DNI varies by 10 %. The irradiance in Mpumalanga is very similar to KZN inland. For a first assessment, Durban can be used as a representative location for the SA sugar mills.

3.2 Integration point assessment

By analyzing the mass and energy flows of the BRTEM model (Starzak and Zizhou, 2015), 23 potential solar heat integration points (IPs) within the model sugar mill were identified. IPs are physical locations, e.g. heat exchangers, in the mill at which solar heat can replace conventional heating media. The potential SPH integrations points were evaluated considering the methodology discussed in the SPH Integration Guideline of Muster et al. (2015). The most relevant criterion was that the support of a heat sink with solar heat would result in direct savings of bagasse or coal. The next priority was saving live steam and then saving exhaust steam. In this first study, the potential integration points saving bleeding vapor were not considered further as the internal value of this steam is lower than that of live steam, and the reduction of bleeding vapor consumption would, without modification to the processes, not directly result in overall energy savings in the mill.

Other ranking criteria were a significant heat demand at the integration point, a sufficient temperature difference to transfer solar heat, and no interference of solar heating with present or future efficiency measures, e.g. the economizers of the boilers. This resulted in the selection of six integration points for further consideration. On supply level these are live steam generation, pre-heating of boiler feed water, exhaust steam generation, and the drying of bagasse. On process level, it is raw sugar drying and clear juice heating.

For each of these processes, integration schemes were developed following the scheme suggested by Helmke and Hess (2015). These schemes were published in Hess et al. (2016). The two most promising integration schemes are discussed in the following.

3.3 Solar live steam generation

Figure 2 above already showed a potential integration scheme for solar live steam generation. According to the BRETM model, the processing of 250 t cane per hour requires about 103 t/h of live steam, as indicated. The boiler in this reference sugar mill provides a power of 74.4 MW_{th}, calculated from the enthalpy difference between feed water and live steam. This is equivalent to the total power demand of the factory. Thus, solar generation of live steam parallel to the existing boiler is a way to utilize very high amounts of solar heat. From Smith et al. (2013) it can be calculated that every ton of solar generated live steam has the potential to offset approximately 0.5 t of bagasse or about 0.125 t of coal.

If we consider a value of 700 W_{th} peak power per square meter of solar collector area (Mauthner, 2015, p. 5), an area of 106 336 m^2 could at peak performance supply the whole power demand of the reference mill (neglecting the heat exchanger efficiency). However, since the SPH is normally only off-setting the fuel consumption of the existing bagasse boiler, the ability of this boiler for power modulation also has to be taken into account. In this paper, we assume that the boiler can only maintain its current efficiency if it produces 37 MW^{th} or more, i.e. more than 50 % of its BRTEM power. To maintain this condition, maximally 37 MW_{th} of solar steam power could be added without solar heat storage. This corresponds to a collector field of about

53 168 m^2. In Durban, high-temperature PTCs producing the required live steam parameters would yield approximately 1 110 $kWh_{th}/(m^2\,a)$, as shown in Table 2. If the collector field is only operated during the crushing season, the specific yield reduces to 768 $kWh_{th}/(m^2\,a)$. The field size mentioned above could substitute 12 % of the boilers' annual energy production if it operated throughout the crushing season, not considering OTE, and 17 % if operated all year. Collector field size and solar fraction can be further increased if a solar heat storage is installed.

By 2012, in India a total capacity of approximately 5 GW_{el} of bagasse-fueled power stations was installed (Tongaat Hulett, 2013). In Mauritius, 90 % of the sugar factories export electricity to the grid (Smithers, 2014). In Brazil, in 2013 a total amount of 15,067 GWh_{el} was produced by bagasse-fueled power plants for the national grid, and this shall be increased by a factor of 13 until the year 2022 (Burin et al. 2015).

Tongaat Hulett (2013, p. 12) estimates that the 14 SA sugar mills could generate about 800 MW_{el} to 1 000 MW_{el} for export to the SA grid. Tongaat Hulett's eight sugar mills in Mozambique, SA and Zimbabwe, in some instances, already feed electricity back to the grid. In the 2014/2015 season, Tongaat Hulett exported 32.65 GWh_{el} (Tongaat Hulett, 2015). Smithers (2014) estimated that the South African sugar industry could potentially produce a total of 600 MW of electricity by the end of 2016, accounting for approximately 1.5 % of the country's total generation capacity. In a financial viability and macro-economic impact analysis, Conningarth Economists (2013) strongly advocate for export of electricity by SA sugar mills. However, no large scale projects with electricity export are in place at SA sugar mills yet. The prices offered by the national SA power grid operator for electricity from sugar mills are all negotiated individually. The revenue being offered is apparently currently not making it viable to invest in equipment for increased export.

3.4 Solar drying of bagasse

An integration scheme for solar drying of bagasse is shown in Figure 4. The typical moisture content of bagasse after the dewatering mills in the juice extraction unit is approximately 50 % of weight. In the 2012/13 season, the average bagasse moisture content ranged between approximately 46 % and 52 % (Smith et al., 2013).

According to Rein (2007), the advantages of bagasse drying include improved boiler efficiency, reduced fuel consumption, higher flame temperature and reduced excess air requirements. Rein (2007) further states that the technical lower limit for the moisture content of bagasse is in the order of 30 %. According to Loubser (2015), however, the moisture content should not be reduced to below 40 % because of the risk of spontaneous combustion. It is expected that the gross calorific value of bagasse can be increased by approximately 20 % by reducing the moisture content from 50 % to 40 %.

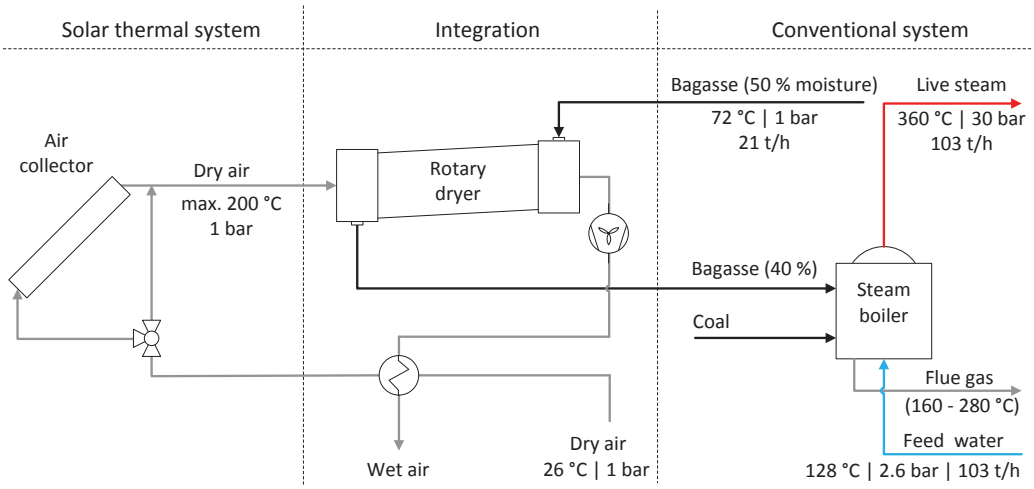

Figure 4: Integration scheme for solar drying of bagasse with air collectors (process values from Starzak and Zizhou, 2015)

Solar air collectors have already for long been applied for drying, e.g. of wood chips or fruit. Direct solar pre-heating of ambient air has the advantage of low collector absorber temperature to achieve high efficiencies. For bagasse drying, a fan would suck ambient air through an air collector field and into the rotary dryer. If a constant dryer inlet temperature is needed, or the dryer inlet temperature is controlled automatically depending

on output bagasse moisture, a mixing device can add some ambient air into the collector outlet stream. The drying air cannot be recirculated as the relative air humidity at the dryer inlet must be low. However, heat recovery can be implemented to pre-heat the collector air inlet from the dryer outlet air.

A first rough dimensioning of a rotary dryer for the task of evaporating a water amount of about 2 t/h resulted in an energy demand of approximately 6 GJ_{th}/h to achieve such an evaporation rate (based on Bruce and Sinclair, 1996). For heating of ambient air to a maximum dryer inlet temperature of 200 °C, the mean load of the dryer system without heat recovery would be 1.67 MW_{th}. The simulation results given in Table 2 indicate that the specific solar gains at the bagasse drying temperature level can reach 779 $kWh_{th}/(m^2\ a)$ during the crushing season. About 24 % of the overall bagasse drying heat demand during the crushing season could be supplied by a SPH system without storage. If the dryer could operate throughout the year, the solar gain would increase to 1 058 $kWh_{th}/(m^2\ a)$ and the solar fraction for drying the same amount of bagasse would increase to 33 %.

A pilot plant test for solar drying of bagasse in a sugar mill in the Dominican Republic showed a reduction in moisture from 50 % to between 36 % and 44 %, but it was noted that on a large scale the results could vary considerably (Rein 2007, p. 610). In his overview on bagasse drying technologies, Sosa-Arnao (2006) points out that a study on the trade-off between combustion air pre-heating, the economizer in the boiler and the drying of bagasse is still to be done. The option of solar drying could be included in such a study.

4. Solar Gains and Performance Indicators

Table 2 shows the heating power demand of each heat sink and the performance indicators that were estimated from literature (Live steam) or simulated (all other).

The heat demand is the maximum solar energy that could be fed in at this point. It is calculated from the mass flow at the integration point and the enthalpy difference between heat exchanger inlet temperature and pressure (process return), and heat exchanger outlet temperature and pressure (process feed). The maximum field size for all variants results from dividing the heating power demand by 700 W/m^2 peak power by 1 m^2 of collector area. This ensures that the solar heat generated is always below the demand (no storage). For live steam generation, the maximum area is additionally limited by the capability of the boiler for power modulation.

Table 2: Solar collector field dimensions with annual (A) and crushing season (CS) performance estimation in Durban without thermal storage

Heat sink	Heating power demand [MW_{th}]	Max. field size [m^2]	Process return temp. [°C]	Max. feed temp. [°C]	Collector type*	System efficiency on GHI [%]		Specific gains [kWh/m^2]		Solar fraction [%]	
						A	CS	A	CS	A	CS
Live steam	74.4	53 168	128	360	PTC-HT	61	61	1 110	768	17	12
Feed water	9.0	12 880	128	200	PTC-HT	61	61	1 110	768	34	24
					PTC-MT	31	32	567	402	18	12
Exhaust steam	62.5	89 238	128	130	PTC-MT	32	32	577	309	18	13
					ETC	38	40	688	510	21	16
Bagasse drying	1.7	2 381	26	200	FPC (water)	58	62	1 058	779	33	24
Sugar drying	0.6	899	26	80	FPC (water)	66	70	1 203	883	37	27
Clear juice	4.7	6 739	100	114	ETC	43	46	781	577	24	18

* parabolic trough collectors (PTC) for high temperature (HT) and medium temperature (MT) applications, evacuated tube collector (ETC), and flat-plate collector (FPC) with water as collector fluid

For the simulations, the software Polysun V8.011.21 (Vela Solaris 2014) was used. Since the objective was only to calculate realistic estimates of potential energy gains, very simple system hydraulics and control principles were used (cp. Figure 5). This was based on existing schemes in the Polysun library for the simulation of solar process heat systems.

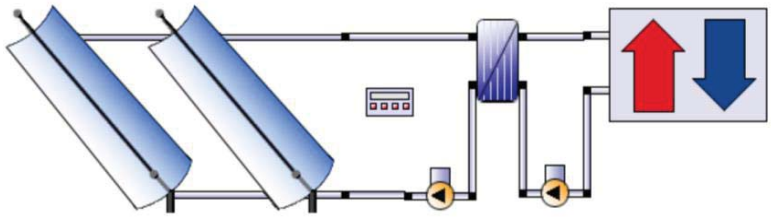

Figure 5: Simple hydraulic scheme in Polysun to estimate annual gains for solar feed water pre-heating with medium temperature parabolic troughs (PTC-MT)

On the right hand side of Figure 5 is a heat sink. In the simulations for the solar heating of feed water with PTC-MT collectors, the process return temperature was 128 °C, as given in Table 2. The mass flow of the process loop pump was constant and set to a value at which 200 °C is achieved if a power of 9 MW_{th} can be provided. The solar loop pump was speed controlled to ensure that a positive temperature gradient is always maintained between the solar loop and discharging loop of the heat exchanger. For a PTC-MT, for example, the parabolic trough of the company NEP (NEP, 2015) was used in Polysun. The receiver tube of this collector is not evacuated. It therefore has significant thermal losses at higher temperatures. For a highly efficient ETC, for example, the Ritter Aqua Plasma collector (Ritter, 2015) was used. The selected FPC is the Solid Gluatmugl HT (Solid, 2013). The solar drying processes should ideally be realised with air collectors. Since these collectors cannot be simulated in Polysun, the two drying processes were also simulated with the Gluatmugl HT flat-plate, ensuring that the air heating demand was correctly represented on the secondary side of the heat exchanger. However, for the case of applying air collectors (FPC-Air), the given gains have to be seen as a maximum value as this technology usually has higher heat losses than flat-plates with water as collector fluid, especially at higher working temperatures.
The annual gains of the high-performance parabolic trough collectors (PTC-HT) were also not simulated, but roughly assessed as follows: The average annual thermal solar field efficiency of concentrating solar power (CSP) PTC fields is in the range of 50 % to 60 % for DNI, according to Geyer et al. (2002, p. 6), Sargent and Lundy Consulting Group (2003, p. D 17), and Günther et al. (2012, p. 80). For this study, an efficiency of 55 % is used. The system efficiencies given in Table 2 all relate to GHI in Durban (GHI = 1 825 kWh/(m^2 a), DNI = 2 018 kWh/(m^2 a)). Thus, in Table 2 an annual system efficiency of 61 %, to allow for comparison to the other technologies, is given.

The *system efficiency* indicates which share of the global horizontal irradiance can be converted to useful solar heat for the process. The annual (A) efficiency considers the mean efficiency during the whole year; the efficiency during the crushing season (CS) considers only 1 March to 30 November. The efficiencies differ slightly due to varying irradiance and ambient temperatures. It is assumed that all solar heat can be used (no OTE influence on solar field operation). The *specific solar gains* per square metre of collector gross area give the useful heat produced per year (A) and during the crushing season (CS). Again, it is assumed that there is no OTE effect on the solar field operation. The *solar fraction* is the share of the annual heat demand of the heat sink, which can be covered by solar heat. It is valid for systems without heat storage. The solar fraction can be increased significantly when storage is installed, but this would also mean an increase in the solar thermal system costs. For this pre-condition, the *overall annual solar energy gains* can be calculated from Table 2. The PTC-HT field of 53 168 m^2 would yield 40 833 MWh_{th} during the crushing season, and about 59 016 MWh_{th} if it could be operated throughout the year. As explained above, the CS duration used is 254 days, with an OTE of 75.70 % (cp. season 2012/2013, Smith et al., 2013), so the boiler operates 4615 h/a. This results in an overall boiler steam energy generation of 343 356 MWh_{th}.
With these assumptions, the solar fraction would be 12 % if the solar field operates during the whole CS (not considering OTE), and 17 % if it operates the whole year. To roughly assess how the specific solar gain would be affected if the collector loop only operated at times of boiler operation, the specific gains during the crushing season can be multiplied by the OTE.

5. Economic Assessment

5.1 Solar heat as an alternative to coal

As outlined above, the heat demand of SA sugar mills is covered by steam from burning bagasse, in some cases supported by coal. Since bagasse is a by-product of sugar production, the costs of this steam are obviously very low. However, the true value of bagasse is determined by the opportunity costs. Integration of solar heat will only be considered if such an opportunity is pursued, i.e. if the heat demand of the mill increases e.g. from production of bio-ethanol, or export of electricity), or if bagasse is used for purposes other than heating e.g. the production of animal feed, fertiliser, or paper. In all scenarios, the cheapest alternative energy source in SA would be coal. Thus, this assessment of SPH for SA sugar mills compares solar heat to the heat from coal.

The price paid for coal by the different SA sugar mills varies as it includes the price for mining ('ex mine'-price) and the costs of transport to the respective mills. To estimate the costs of life steam from coal, a coal price of 1100 ZAR/t, an energy content of 27 GJ/t and a boiler efficiency of 75 % can be assumed (Peacock, 2016a). Thus, this work uses a current value of life steam from coal of 0.20 ZAR/kWh (1.2 EUR-ct/kWh) for comparison[1]. Since one ton of live steam can be let-down to approximately 1.2 tons of exhaust steam (Rein, 2007, p. 666), the current value of exhaust steam is considered to be 0.16 ZAR/kWh (1.0 EUR-ct/kWh). An analysis of annual coal prices for a large SA sugar producer provided by Peacock (2016b) revealed that the price after delivery increased on average by 12.3 % p.a. from 2004 to 2014.

5.2 Investment costs for SPH systems

In order to obtain reference values for the costs of SPH systems, the SHIP Plants (2015) database was analysed. By mid-April 2016 it included ca. 190 systems, but for many entries no cost data were given. However, it could be observed that the system costs per m^2 of collector gross area depend highly on the collector technology, the system size, and the country of installation.

The systems to consider for the SA sugar industry would be of several hundred or several thousand square metres (cp. Table 2), and for this first assessment have no thermal storage. Thus, to get a more realistic cost estimate, the database was filtered for systems above 200 m^2, and installation dates from the beginning of the year 2000 to end 2015. Since the number of systems without storage was too small, systems both with and without storage were included. For each technology, the median value of the investment costs per m^2 was determined. This resulted in 183 EUR/m^2 for installations with FPCs with air as collector fluid (based on data of only two plants), 188 EUR/m^2 for ETCs (10 plants), 388 EUR/m^2 for FPCs with water as collector fluid (16 plants), and 445 EUR/m^2 for PTCs-MT (nine plants).

The SPH plant database does not contain examples with CSP technology so for the PTC-HT troughs the costs had to be assessed from literature. According to Turchi et al. (2010, p. 6), the installed costs of a large PTC-HT field in the United States operating at 391 °C are expected to be 335 USD/m^2, including heat transfer fluid, in 2015. The authors give similar costs for a heliostat field with central receiver (HCR).

It must be noted that within each collector technology group, very high variances, even between similar installations, were found both in the SHIP Plants database and in the literature. Many of the SHIP plants have thermal storages included so that installed costs for the investigated systems in SA could be lower. To conclude, the costs used for this study are only a rough estimate. They cannot replace quotes for specific cases in future feasibility studies.

5.3 Levelized cost of heat (LCOH)

The levelized cost of energy LCOE is a common measure to assess and compare the financial feasibility of renewable energy projects. In this work, this measure is referred to as LCOH to stress that it reflects the levelized costs of heat, not of electricity. Note that the LCOH is the average heat price per unit of energy generated throughout the lifetime of a heating project; it is independent of the value of the energy replaced. Equation 1 gives the LCOH (NREL, 2014).

$$LCOH = \left. \sum_{n=0}^{N} \frac{C_n}{(1+d)^n} \right/ \sum_{n=1}^{N} \frac{Q_n}{(1+d)^n} \quad [\text{EUR/kWh}] \qquad \text{(eq. 1)}$$

[1] In this work, the exchange rates of 1.128 USD/EUR and 16.46 ZAR/EUR as of 13 April 2016 are used.

The LCOH compares the annual project costs (C_n) to the annual yield (Q_n) for each year n over the lifespan of the system in years (N). Costs and yields are discounted with the rate d to account for the time value of money. Figure 6 below shows the calculated LCOH from coal and solar thermal energy over 20 years.

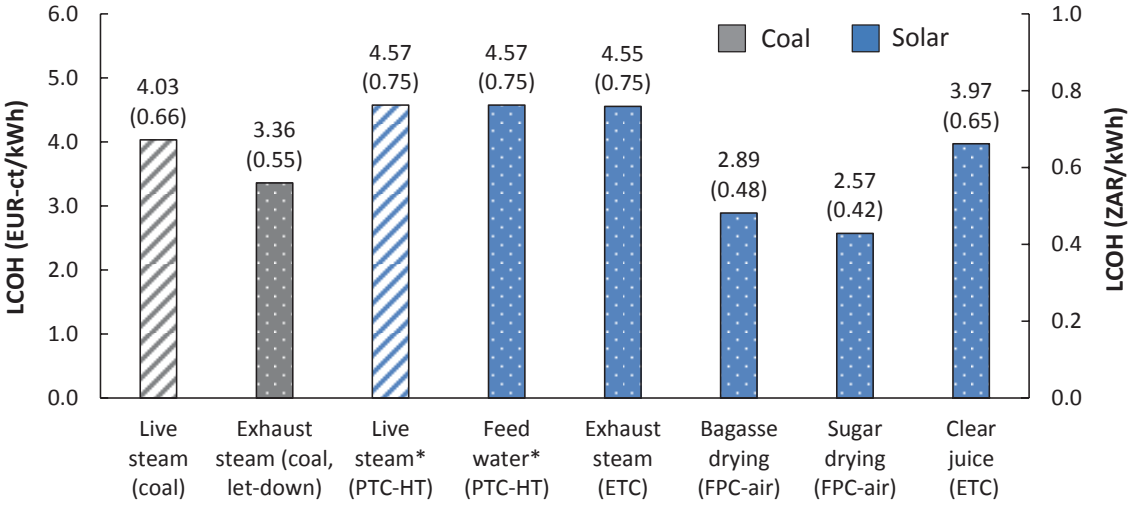

Figure 6: Estimated levelized costs of heat (LCOH) for SA sugar mills from coal and from solar thermal energy (*SPH systems for live steam and feed water operate for the whole year and the others only from March to November)

The PTC-LT variant, for both feed water and exhaust steam generation, had higher LCOHs than the technical alternative (cp. Table 3). In Figure 6, for each integration point only the variant with the lowest LCOH is indicated. In addition to the investment costs, annual operational costs were taken into account. These include maintenance and auxiliary energy consumption. For the annual maintenance, including replacement, of the large-scale non-tracking ST systems in this study, a value of 1 % of the capital expenditure was used (VDI, 2004, p. 65). For the annual auxiliary energy consumption of these systems, 2 % of the yearly energy yield was considered (VDI, 2004, p. 65), with a constant auxiliary energy tariff of 0.50 ZAR/kWh$_{el}$ (3.04 EUR-ct/kWh$_{el}$). The annual operational costs increase with the consumer price index (CPI) of South Africa of 6 % per annum (inflation). For the two parabolic trough systems, combined maintenance and auxiliary energy costs of 2 % of the capital costs are used, as is common for CSP power plants (Hernández-Moro and Martínez-Duart, 2012, p. 186). This was annually increased by the CPI as well.

To calculate the LCOH of the solar heating projects, a nominal discounted rate of 10 % has been used. This corresponds with the expected weighted average cost of capital (WACC) of the SA sugar industry (for 30 % equity with a return of 14 %, and 70 % debt with an interest rate of 8 % and a loan period of 10 years) (Foxon, 2015). A financial project life of 20 years was assumed, even though the service life of SPH systems may well exceed this. The LCOH for solar live steam and feed water generation was calculated from specific system yield Q_n of whole-year operation (cp. Table 2) as in this case an electricity export scenario independent from the sugar mill operation was assumed. The other four SPH systems operate during the crushing season only so the theoretical gains from November to January were not taken into account.

For comparison, the estimated LCOH from coal within the potential duration of a SPH project of 20 years is also given. For this, it is assumed that an existing boiler can burn variable amounts of coal without additional costs. Thus, for comparison with solar heat, only the fuel costs are considered. The levelized costs per kWh steam were calculated from current costs of 1.2 EUR-ct/kWh for live steam and 1.0 EUR-ct/kWh for exhaust steam, both increasing by 12.3 % annually. The LCOH was then calculated by using the CPI discount rate of 6 %.

Comparing the LCOH values of the six different SPH integration variants suggests that the solar drying of sugar and bagasse is possible at lower levelised costs than exhaust steam generation from coal. Note that for this first assessment equal gains of air flat-plates and water flat-plate collectors within the working temperature range were assumed (cp. comment above on flat-plate gains).

5.4 Internal rate of return (IRR)

Contrary to the LCOH, the internal rate of return (IRR) can be used as an indicator for the financial viability of a project because it takes the value of the conventional energy, which is replaced by SPH, into account. The IRR is an estimation of the discount rate that would result in a zero net present value (NPV). Table 3 summarises the results of the economic assessment of the most promising SPH variants. The estimated capital expenditure of the different collector fields is given under the premise that the maximum area possible without solar heat storage is installed.

Table 3: Estimated economic figures of the six SPH integration variants

Integration Point	Collector type	Heat demand [MW_{th}]	Max. field size [m^2]	System costs [EUR/m^2]	Capital expenditure [Mio. EUR]	LCOH [EUR-ct /kWh]	IRR [%]
Live steam*	PTC-HT	74.4	53 168	378	20.10	4.57	4.6
Feed water*	PTC-HT	9.0	12 880	378	8.46	4.57	2.6
Exhaust steam	ETC	62.5	89 238	188	16.78	4.55	3.3
Bagasse drying	FPC-Air	1.7	2 381	183	0.44	2.89	7.8
Sugar drying	FPC-Air	0.6	899	183	0.16	2.57	9.1
Clear juice	ETC	4.7	6 739	188	1.06	3.97	4.6

* Solar live steam generation and feed water heating for whole year operation (electricity export scenario), other SPH integration points operate during crushing season only (March to November)

The NPV is obtained by discounting all net cash flows (C_n) of each year (n) over the lifespan of the project (N) (NREL, 2014). Solving the NPV equation for the discount rate d gives the IRR. The income cash flows depend on the internal value of the energy, and thus the heating fuel, that is being substituted by SPH. In this first assessment it was assumed that only live steam from SPH replaces the actual internal live steam value from coal; all other integration variants replace the exhaust steam value (cp. hatched and dotted bars in Figure 6). The hurdle rate for projects or investments by the SA sugar milling industry is in the range of 10 % to 15 % (Foxon, 2015). A project is feasible if the IRR exceeds this hurdle rate.
The formula for the calculation of the NPV is provided in equation 2.

$$NPV = \sum_{n=0}^{N} \frac{C_n}{(1+d)^n} \quad \text{[EUR]} \qquad \text{(eq. 2)}$$

The results in Table 3 indicate that currently none of the prioritised six SPH integration schemes offers the expected return. The two solar drying applications are closest to financial viability and should be investigated in more detail. Their IRR would increase to 11.7 % for bagasse drying and 13.1 % for sugar drying if they could be operated the whole year.

6. Conclusions

For an electricity export scenario, *solar live steam generation* should be considered as an option if solar steam can also generate electricity independent of the mill operation, i.e. outside the crushing season. This SPH variant can cover a significant share of the heat demand of a mill. The feasibility here depends highly on the price received for export electricity.
Solar *drying of bagasse* is the only solar technology that has been demonstrated in sugar mills. To determine financial feasibility, the effect of dried bagasse on boiler efficiency must be studied in more detail, an energy balance of the solar drying process itself must be worked out, and the investment in a suitable dryer must be taken into account. LCOH and IRR of both drying applications have high uncertainties because the estimated system costs are based on data of two plants only, and the gains were simulated with FPCs with water as collector fluid. In addition, the drying processes seem well-suited for waste heat recovery.

With the framework conditions used for this first study, none of the six SPH integration variants achieved an IRR of the required 10 % to 15 %. The main reason for this is the very low coal price, even though a price increase of 12.3 % p.a. was taken into account. Another factor is the limited duration of the crushing season which limits the time of the year that solar heat can be used for processes within the mill. At more beneficial framework conditions, e.g. with government subsidies for SPH or a fixed minimum feed-in tariff for power export from cogeneration, including ST collectors, financial viability would be possible.

Further work on SPH for sugar mills must be based on the energy balance of a mill with all feasible heat recovery measures implemented. For such a mill, different scenarios like the implementation of high pressure boilers with condensing extraction steam turbine, or the production of bio-ethanol on site, have to be described so that more detailed SPH feasibility assessments can be performed.

Acknowledgements

This study was funded within the framework of the Sugarcane Technology Enabling Programme for Bio-Energy (STEP-Bio), which is co-funded by the SA Department of Science and Technology (DST) and the South African sugar industry under the DST Sector-specific Innovation Fund.
The authors are grateful to Steve Davis, Katherine Foxon, Paul Jensen, Richard Loubser, Matthew Starzak, all from the Southern African Sugar Milling Research Institute SMRI, and to Steve Peacock (Tongaat Hulett), for sharing expertise and data. The Centre for Renewable and Sustainable Energy Studies (CRSES) of Stellenbosch University supported this research with a bursary.

References

Bruce, D. and Sinclair M. 1996. *Thermal Drying of Wet Fuels: Opportunities and Technology*. EPRI Report (TR-107109 4269-01).

Burin E., Vogel, T., Multhaupt, S., Thelen, A., Oeljeklaus, G., Görner, K. And Bazzo, E. 2015. *Thermodynamic and economic evaluation of a solar aided sugarcane bagasse cogeneration power plant*. In Proceedings of ECOS 2015, Pau, France.

Conningarth Economists 2013. *Growing the Sugar Industry in South Africa*. Document 5: Investigation and Evaluation of Alternative Uses and Products from Sugarcane: A Cost Benefit and Macro-Economic Impact Analysis. Pretoria. Available: http://www.namc.co.za/upload/Document%205%20Alternative%20Uses.pdf. [14 April 2016].

DAFF 2013. *A Profile of the South African Sugar Market Value Chain*. Department of Agriculture, Forestry and Fisheries. Available from: http://www.nda.agric.za/doaDev/sideMenu/Marketing/Annual%20Publications/Commodity%20Profiles/INDUSTRIAL%20PRODUCTS/SUGAR%20MARKET%20VALUE%20CHAIN%20PROFILE%202014.pdf. [02 April 2016].

Foxon, K. 2015. Personal communication between Hendri Beukes (Stellenbosch University) and Katherine Foxon (SMRI) via email. [05 August 2015].

Geyer, M., Lüpfert, E., Osuna, R., Esteban, A., Schiel, W., Sweitzer, A., Zarza, E., Nava, P., et al. 2002. *EUROTROUGH - Parabolic Trough Collector Developed for Cost Efficient Solar Power Generation*. In 11th SolarPACES International Symposium on Concentrated Solar Power and Chemical Energy Technologies. Zurich. 1–7.

Günther, M., Joemann, M. and Csambor, S. 2012. Parabolic Trough Technology. In: *Advanced CSP Teaching Materials*. Deutsches Zentrum für Luft- und Raumfahrttechnik.

Helmke, A. and Hess, S. 2015, Classification of Solar Process Heat System Concepts in *Integration Guideline - Guideline for Solar Planners, Energy Consultants and Process Engineers*, ed B Muster. Available from: http://task49.iea-shc.org/. [03 April 2016].

Hess, S, Beukes, H, Smith, G and Dinter, F 2016, Initial Study on Solar Process Heat for South Afri-can Sugar Mills. *Proceedings of the South African Sugar Technologists' Association (2016) 89*: 324-349.

Hernández-Moro, J., Martínez-Duart, J.M., 2012. CSP electricity cost evolution and grid parities based on the IEA roadmaps. *Energy Policy* 41. 184-192.

Loubser, R. 2015. Personal communication between Hendri Beukes (Stellenbosch University) and Richard Loubser (SMRI) at SMRI in Durban, SA. [09 June 2015].

Mauthner, F., Weiss, W., Spörk-Dür, M. 2015. *Solar Heat Worldwide – Markets and Contribution to the Energy Supply 2013*. AEE INTEC. Available from: http://www.iea-shc.org/data/sites/1/publications/Solar-Heat-Worldwide-2015.pdf. [13 April 2016].

Muster, B. (ed.) et al. 2015. *Integration Guideline. Guideline for solar planners, energy consultants and process engineers*. IEA SHC Task 49. Available from: http://task49.iea-shc.org/. [8 April 2015].

NEP 2015. Technical Data of the PolyTrough 1800, v7. Available from: http://www.nep-solar.com/wp-content/uploads/2013/11/NEP-Solar-Polytrough1800_Datasheet.pdf. [8 April 2015].

NREL 2014. Levelized Cost of Energy. Available from: https://www.nrel.gov/analysis/sam/help/html-php/index.html?mtf_LCOH.htm. [2015, August 01].

Peacock, S. 2016a. Personal communication between Stefan Hess (Stellenbosch University) and Steve Peacock (Tongaat Hulett Ltd.) via email. [01 June 2016].

Peacock, S. 2016b. Personal communication between Stefan Hess (Stellenbosch University) and Steve Peacock (Tongaat Hulett Ltd.) via email. [03 June 2016].

PVGIS 2015. Photovoltaic Geographical Information System – Monthly global irradiation data. Available from: http://re.jrc.ec.europa.eu/pvgis/apps4/pvest.php?lang=enandmap=africa. [03 April 2016].

Reid, M.J. 2006. Why do we continue to burn so much coal. *Proceedings of the South African Sugar Technologists' Association*. 353–363. Available from: http://www.sasta.co.za/publications/congress-proceedings. [02 April 2016].

Rein, P.W. 2007. *Cane Sugar Engineering*. Berlin: Bartens. ISBN: 978-3-87040-110-8.

Ritter 2015. Data sheet of Aqua Plasma Collector. Annex to Solar Keymark Certificate. Available from: http://www.dincertco.de/logos/011-7S1889%20R.pdf. [9 Sept 2015].

Sargent and Lundy Consulting Group. 2003. Assessment of Parabolic Trough and Power Tower Solar Technology Cost and Performance Forecasts. Chicago.

SHIP Plants 2016. Database for applications of solar heat integration in industrial processes. Available from: http://www.ship-plants.info/. [12 April 2016].

Smith, G.T., Davis, S.B., Madho, S. and Achary, M. 2013. Eighty-Eighth Annual Review of the Milling Season in Southern Africa (2012-2013). *Proceedings of the South African Sugar Technologists' Association*. Durban. 24 – 54. Available from: http://www.sasta.co.za/publications/congress-proceedings. [02 April 2016].

Smithers, J. 2014. Review of sugarcane trash recovery systems for energy cogeneration in South Africa. *Renewable and Sustainable Energy Reviews*. 32:915–925. DOI: 10.1016/j.rser.2014.01.042.

SolarGIS 2015. Free solar radiation maps. Available from: http://solargis.info/doc/free-solar-radiation-maps. [02 April 2016].

Solid 2013. Data sheet of Gluatmugl HT collector. Annex to Solar Keymark Certificate. Available from: http://www.solid.at/images/pdf/Datasheet_oekoTech_HT.pdf. [9 Sept 2015].

Sosa-Arnao, J., Correa, L., Silva, M. and Nebra, S. 2006. *Sugar cane bagasse drying – a review*. Available from: https://www.researchgate.net/publication/239556788

Starzak, M. and Zizhou, N. 2015. *Biorefinery Techno-Economic Modelling*: Sugar Mill and Ethanol Distillery Process Model. Technical Report No. 2210, Sugar Milling Research Institute, Durban.

Tongaat Hulett 2015. *Integrated Annual Report 2015*. Available from: **Error! Hyperlink reference not valid.**. [11 April 2016].

Tongaat Hulett 2013. *Sugar Cane Potential*. Tongaat Hulett. Available: http://www.energy.gov.za/files/IEP/DurbanWorkshop/TH-Sugarcane-Potential-Food-Energy-30Oct2013.pdf. [02 April 2016].

Turchi, C., Mehos, M., Ho C.K., Kolb, G.J., 2010. *Current and Future Costs for Parabolic Trough and Power Tower Systems in the US Market*. Presented at SolarPACES 2010. Available from: http://www.nrel.gov/docs/fy11osti/49303.pdf. [13 April 2016].

Vela Solaris 2014. Polysun Version 5.10 User Manual. [21 August 2015].

VDI 2004. Solar heating for domestic water - General Principles, system technology and use in residential building. Verein Detuscher Ingenieure. Düsseldorf.

Wienese, A. and Purchase, B.S. 2004. Renewable Energy: An Opportunity for the South African Sugar Industry? *Proceedings of the South African Sugar Technology*

Conference Proceedings

EuroSun 2016
Palma de Mallorca (Spain), 11 - 14 October 2016

Solar Process Heat Potential in California, USA

Parthiv Kurup[1], Craig S. Turchi[1] and Guangdong Zhu[1]

[1] National Renewable Energy Laboratory (NREL), Golden, Colorado (USA)

Abstract

The cost for solar industrial process heat (SIPH) is quantified by defining the levelized cost of heat (LCOH). The state of California, in the United States offers a favorable environment for SIPH given its excellent insolation, industrial gas prices typically higher than the national average, and policies promoting solar-thermal deployment. Given historically low gas prices, competing with natural gas remains the primary challenge to deployment. However, this study finds that the solar LCOH from Concentrating Solar Power (CSP) collectors for many regions in California is expected to be lower than the LCOH from natural gas, using a representative installed solar hardware price and the average price for industrial natural gas in California. Lastly, modifications are in progress to the parabolic trough and Direct Steam Generation (DSG) trough and Linear Fresnel models within NREL's System Advisor Model (SAM) to allow users to more easily predict performance for these industrial heat and steam-generation applications.

Keywords: *solar industrial process heat, SIPH, IPH, parabolic trough, CSP, LCOH, California*

1. Introduction

In 1977 the International Energy Agency (IEA) established the Solar Heating and Cooling (SHC) program to create an environment for the development and progression of SHC (IEA, 2016). An EU-led collaborative project between the SHC program and the SolarPACES program known as Task 49/Task IV was created specifically to establish and help meet the potential of solar Industrial Process Heat (SIPH) (IEA, 2016; SolarPACES, 2016a). (Note that the IEA uses the acronym "SHIP" for solar heat for industrial processes. The term "industrial process heat" is recognized in the United States, and this paper will refer to these applications as solar IPH or "SIPH"). Much of the initial work in the IEA program dealt with the potential of nonconcentrating, flat-plate collectors. Flat-plate solar collectors are common in many countries, including the United States, where the overwhelming majority is applied to domestic home heating or water heating for swimming pools (SHIP, 2016). While these are excellent applications for low-temperature collectors, this paper deals with the growing interest in the deployment of concentrating parabolic trough collector technologies that can achieve temperatures needed within the industrial sector.

Thermal energy and steam are ubiquitous needs in industrial processes. From the extraction of raw materials to food processing, heat is a vital part of the processing and manufacturing sectors. In the 1970s and 1980s there was great interest in collection of solar-thermal energy for buildings and IPH applications (Kutscher et al., 1982). Despite significant effort, very few projects came to fruition, mainly due to high solar collector costs and an associated inability to effectively compete with natural gas (Carwile and Hewitt, 1994). In recent years, the improvement and proliferation of solar collectors for electricity generation and the development of sophisticated solar collector modeling tools has regenerated interest in solar process heat applications.

Despite great potential, the worldwide adoption of concentrating collectors for SIPH generation is modest. For example, as of Sept. 2016, of the 191 SIPH plants listed in the "IEA SHIP Plants" database, only 25 involve concentrating collectors of either parabolic trough or Linear Fresnel technologies (SHIP, 2016). The

doi:10.18086/eurosun.2016.02.07 Available at http://proceedings.ises.org

25 SIPH plants in operation are for industries such as food and dairy production (e.g., heat for sterilization of milk) (SHIP, 2016). Due to the excellent solar resource conditions in the United States (especially in the Southwest) and the ubiquitous need for IPH, the United States has a sizeable opportunity for greater deployment of concentrating solar-thermal collectors with the associated benefits of increased solar jobs and lower carbon emissions. For example, within the industrial sector in the United States the estimated consumption of energy for heat for applications such as washing, sterilization, and preheating was approximately 24,000 trillion Btu (TBtu, or 7,000 TWh_{th}) in 2014 (EPA, 2016). Depending on the specific industry in question, between 35% and 50% of the total energy consumption can be for IPH applications (EIA, 2013).

Linear-focus collectors, such as parabolic troughs and Linear Fresnel reflectors, can reach temperatures up to about 550°C (SolarPACES, 2016b). For solar hardware developers, expansion into IPH offers access to new markets for already well developed CSP collector technologies. For policy makers and businesses concerned about greenhouse gas emissions, solar-thermal energy is a potential valuable substitute for natural gas used for process heat in the industrial sector. This paper evaluates the installed cost of a modern parabolic trough collector and re-examines the potential for solar-thermal technologies to supply IPH in light of the demonstrated reductions in technology cost. The state of California is used as a prime example of where this application may grow in the United States.

2. Current Cost Of Parabolic trough Collectors

NREL recently completed a cost analysis of two different state-of-the-art parabolic trough solar collector assemblies (SCAs) (Kurup and Turchi, 2015a). The effort first developed a bill of materials (BOM) for the subject designs based on published literature and discussion with the system developers. A key tool in the analysis was a suite of software tools called Design for Manufacture and Assembly (DFMA). The DFMA software package is used industry-wide and has two parts: Design for Manufacture and Design for Assembly (Boothroyd Dewhurst, 2016). The DFMA tool has detailed databases and allows the user to calculate a primary manufacturing cost for each component and then assemble it within the overall product/assembly. Design for Manufacture was used for the majority of the components within the BOMs to model the SCA as if it were to be manufactured in commercial quantities. As such, the material, manufacturing processes, key dimensions, and machining steps were estimated.

A SCA is built of a string of trough modules controlled by a single drive and represents the smallest unit of a functional parabolic trough solar field. The DFMA methodology was applied to the trough structural assembly, i.e., frame, foundation and pylons. The cost of specialty components such as receiver tubes, drive systems, and glass mirror panels were based on quotes from representative suppliers.

Of the two trough modules examined—SkyFuel's SkyTrough and FLABEG's Ultimate Trough—the former is more amenable to deployment in small solar fields due to its smaller size and ability to be fabricated onsite without a specialized assembly jig or facility. These are important factors for SIPH, which is expected to use much smaller solar fields than systems for electric power generation. It is important to note, that the SkyFuel SkyTrough has already been used for solar heat addition to the overall process at the Stillwater hybrid solar-geothermal plant and is considered suitable for SIPH applications (NREL, 2016; Wendt et al., 2015).

The key subsystems for the SkyTrough module and SCA analysis were the receivers, receiver supports, mirror panels, parabolic ribs, space frame, torque plates, drives and control, drive pylon and regular pylons, and the foundations. The main subsystem categories for NREL's SkyTrough BOM and analysis are seen in Figure 1. The SkyTrough SCA consists of 8 modules and has a total length of 115 m and aperture width of 6 m. Details on the SkyTrough SCA can been viewed in the default *CSP Physical Trough* model within NREL's free System Advisor Model (SAM, https://sam.nrel.gov/), version 2016 release.

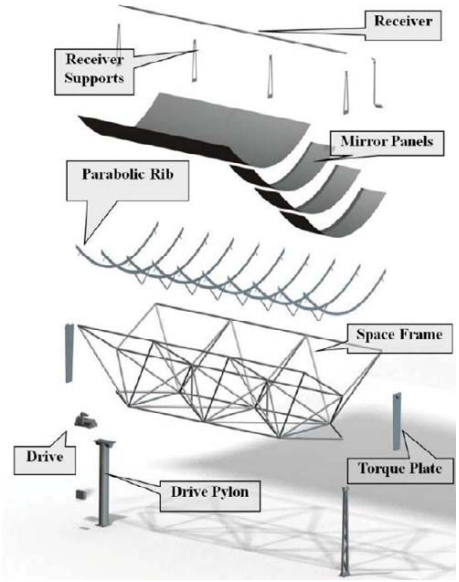

Fig. 1: Main components of the SkyTrough module and picture of regular pylon. (Illustration from SkyFuel)

Within each subsystem NREL estimated dimensions and costs using manufacturing analysis for the subsystems (including the manufacture of the drive and nondrive support pylons). Construction activities were estimated for the digging and placement of the foundations.

Each subsystem was broken down into the specific components that would make up a module and an individual SCA. From that point the BOM and the manufacturing, assembly, and installation analysis per SCA followed. Other troughs have been used for SIPH, e.g., Abengoa Solar's PT1 (California Energy Commission, 2010). Unlike the PT1 which uses silvered glass mirrors, the SkyTrough uses a polymer-film reflector. The vendor's quoted prices were used for capturing the cost of this component.

The NREL analysis on the manufacturing, assembly, installation equipment, and construction activities assumed a production volume of 1500 SCAs. The Installed Cost/m^2, as seen in Figure 2 for 1500 SCAs was found to be \$170/m^2. Hence, the assumption is made that a central manufacturing factory is making sufficient parts for 1500 SCAs per year, for combined SIPH or CSP applications, while the number of SCAs assembled on-site varies with project size. Given the thermal capacity of a SkyTrough SCA is about 2.2 SCAs/MW_{th}, and assuming a SIPH project size of 5 MW_{th}, 100 SCAs would represent about nine projects per year. For comparison, only two of the 25 concentrating solar projects in the SIPH database are ~5 MW_{th} (SHIP, 2016).

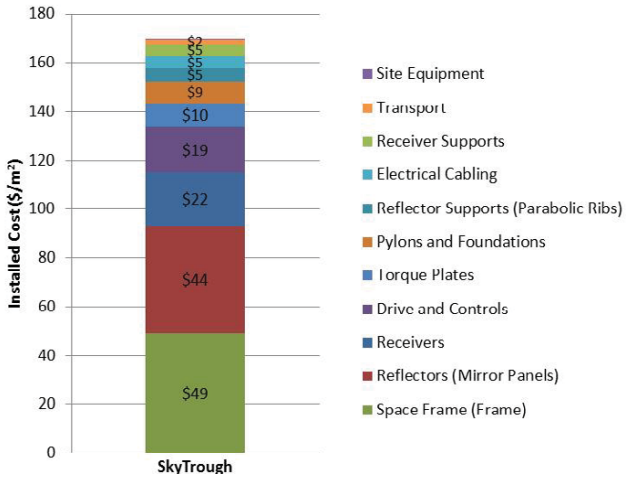

Fig. 2: Installed cost for the SkyTrough assuming 1500 SCAs. Total installed cost is estimated at \$170/m2. (Kurup and Turchi, 2015a)

3. Overall IPH Usage in the United States

In the present paper we have highlighted the results from a specific "top-down" methodology and analysis approach that first examined the regional solar resource potential and the thermal energy demand characteristics of potential user industries (Kurup and Turchi, 2015b). The work focused on specific industries that have the largest thermal energy requirements in the appropriate temperature range for concentrating solar collectors. This method provides an initial, high-level assessment of the SIPH potential (which was then focused on California). Full details of the methodology and its development are outside the scope of this paper. Understanding the conventional energy source (e.g., natural gas, waste heat, or electricity) is also examined to assess the economic potential.

The U.S. Manufacturing Energy Consumption Survey (MECS) is a national sample survey that collects information on the U.S. manufacturing establishment, their energy-related building characteristics, and their energy consumption and expenditures (EIA, 2010a). Based on MECS data, the U.S. manufacturing sector has three primary energy sources: fuel, steam generation, and electricity generation. Considering the direct and indirect (e.g., onsite steam production) use of all energy sources, process energy consumed approximately 10,000 TBtu (as in Figure 3). This represents approximately 42% of the total primary energy consumption in the U.S. manufacturing sector. (Note 1 TBtu ≈ 0.3 TWh_{th}.) From Figure 3, the importance of process heating within process energy as a whole is clear. For 2010, the MECS industries utilized 7,204 TBtu/yr (2,100 TWh_{th}/yr) for process heat—or approximately 29% of the total primary energy in the U.S. manufacturing sector.

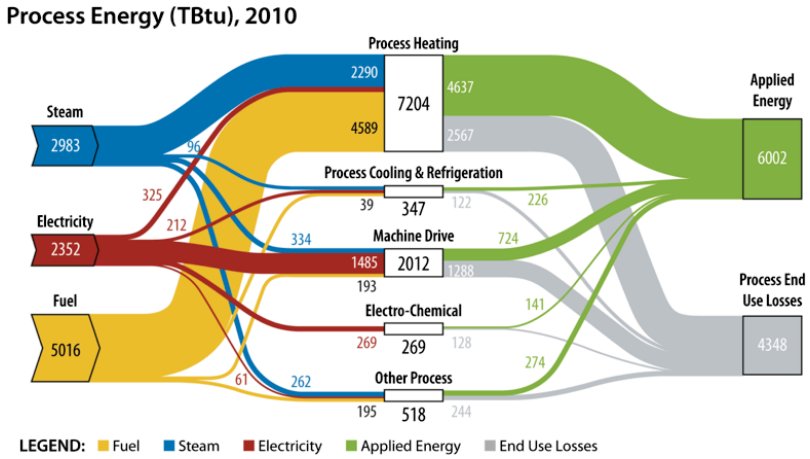

Fig 3: Sankey diagram of process energy flow in U.S. manufacturing sector in 2010 (EERE, 2016). Values are shown in trillion BTU

Figure 4 shows the fully compiled MECS 2010 end-use subcategories for natural gas, which is the fuel most often used for process heating, conventional boiler use, and combined heat and power (CHP) or cogeneration. In contrast, electricity is most commonly used for direct machine drive with some use in process heating. Data indicates that natural gas replacement is the biggest opportunity for SIPH. Situations where electricity can be offset will be rare although they may present favorable economics.

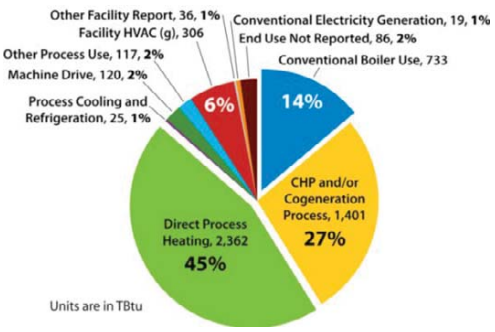

Fig. 4: 2010 United States MECS overall natural gas breakdown by end use (EIA, 2010b)

The U.S. industrial and manufacturing sectors are the largest consumers of natural gas and electricity for process heat either directly or indirectly through steam production via a conventional boiler (EIA, 2010b; Fox et al., 2011). A representation of the potential U.S. IPH market size for steam is provided in Figure 5, which depicts annual steam consumption for the manufacturing sectors of Food, Paper, Petroleum and Coal Products, Chemical and Primary Metal Manufacturing – the five sectors that have the greatest usage of natural gas. The total consumption in the range between 100ºC and 260°C amounts to about 1700 TWh_{th}/yr. To put this in perspective, the 64 MW_e Nevada Solar One CSP plant produces about 0.35 TWh_{th}/yr so the thermal energy potential depicted in Figure 5 represents the equivalent of about 4,800 such plants if all the sites were suitable for SIPH. All the sectors listed in Figure 5 utilize steam in temperature ranges suitable for solar generation; however, the food industry presents a particularly appealing target. As noted previously, the food sector has been the application of choice for many international SIPH plants.

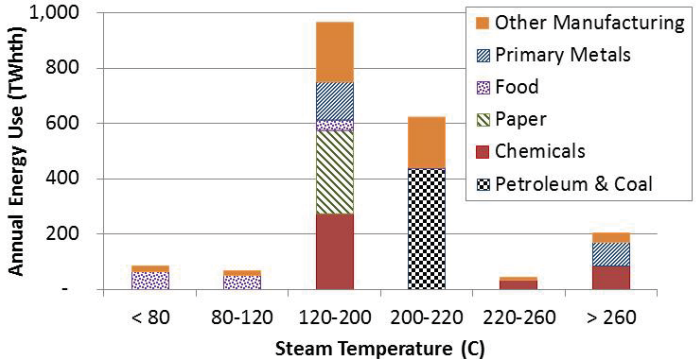

Fig. 5: IPH annual energy use for steam generation for the industries utilizing the greatest amount of natural gas (Fox et al., 2011)

4. Focus on California Industrial Natural Gas and Solar Potential

4.1 Industrial Natural Gas consumption in California

A 2014 California Energy Commission (CEC) study listed natural gas consumption for industries in California (Schrupp, 2013), and according to the MECS 2010 data, the food industry in the United States consumed approximately 59% of its total natural gas consumption for applications of direct process heating and conventional boiler use (EIA, 2010b). Assuming this percentage holds for the food industry in California, it can be estimated that about 10 TWh_{th}/yr were consumed for direct process heating and conventional boiler use in the state in 2014 (Schrupp, 2013), which is the thermal equivalent of about 30 solar fields as big as Nevada Solar One (NSO).

This methodology was continued across all MECS sectors listed in Table 1 below. Table 1 shows the GWh_{th} used by the MECS industries identified as the biggest consumers of steam at less than 260°C in California (i.e. for Food, Paper, Petroleum and Coal Products, Chemical and Primary Metal Manufacturing). The CEC concluded industries in California such as food processing, chemicals, petroleum, and primary metals manufacturing "represent prime areas of opportunity for reducing natural gas use" (Schrupp, 2013).

Tab. 1: Estimated natural gas consumption for direct process heating and boiler use in California for select MECS industries

MECS sector with North American Industry Classification System code	Natural Gas Consumption for Process Heating (GWh_{th}/year)
Food Manufacturing (311)	10,200
Paper Manufacturing (322)	1,244
Petroleum and Coal Products Manufacturing (324)	31,211
Chemical Manufacturing (325)	3,526
Primary Metal Manufacturing (331)	2,134
	48,100

4.2 Solar Industrial Process Heat Potential in California: A look at the Food Industry

In the present paper as mentioned, the results from a specific energy analysis are presented (Kurup and Turchi, 2015b). The full method and derivation of the results is outside the scope of this paper. When the Direct Normal Irradiance (DNI) resource and available land area at a 10-km by 10-km resolution are looked across California, the estimated Technical Thermal Energy Potential for California from using parabolic troughs was 23,000 TWh_{th}/year (Kurup and Turchi, 2015b). As can be seen, the Technical Thermal Energy Potential of California at ~23,000 TWh_{th}/year is orders of magnitude beyond the demand of 48 TWh_{th}/year shown in Table 1.

An objective for this paper is to highlight specific industries known for high use of natural gas or electricity for IPH to their local solar thermal energy potential. For this study, the Food industry and sample sub-industries in California were considered prime candidates. These include the MECS food sub-industries of animal-food manufacturing, breweries, dairy product manufacturing, and fruit and vegetable producers. To highlight that the thermal demand of these industries can be theoretically met with the SIPH potential found for California, maps have been created overlaying the location of the industries in California and the estimated Technical Thermal Energy Potential. Figure 6 shows the co-locations of known animal-food processing plants, breweries, and dairy products along with the Technical Thermal Energy Potential by county in California. These 3 sub-industries were selected as they were considered representative of the Food industry of California.

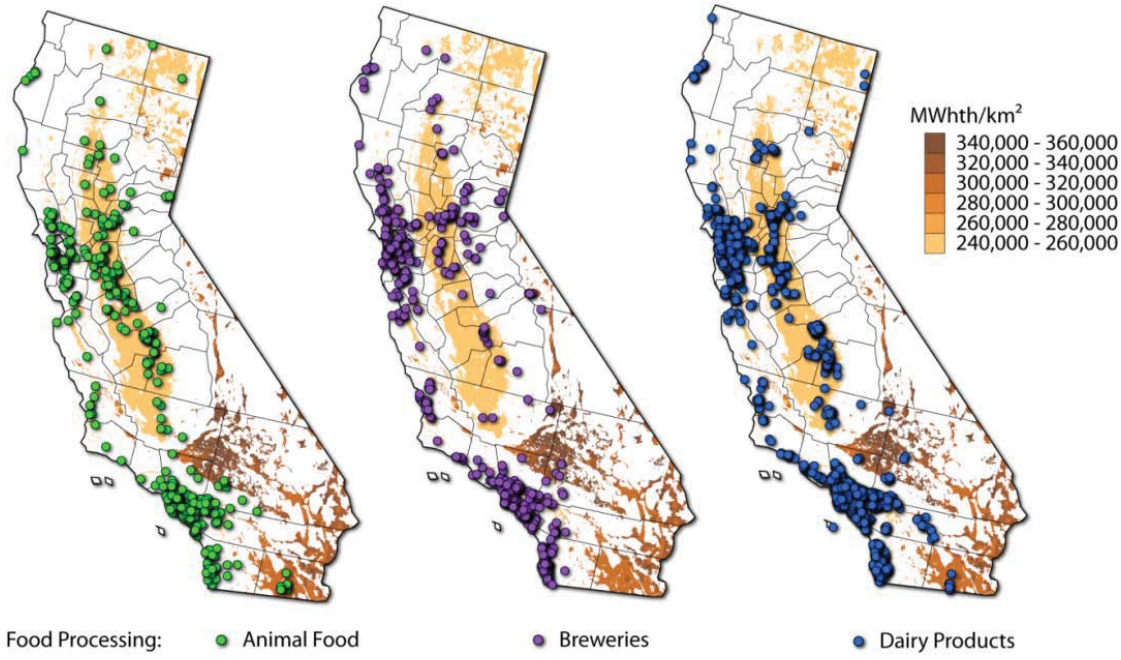

Fig. 6: Locations of animal-food manufacturing, breweries, and dairy products plants across California along with annual solar Technical Thermal Energy Potential (MWhth/km²/year) (Kurup and Turchi, 2015b)

Figure 7 zooms in on Fresno, California and shows the locations of the animal-food manufacturing, breweries, dairy product manufacturing, and fruit and vegetable producers overlaid with the solar thermal energy supply. Developed city areas and other exclusion zones are shown in white. While the majority of sites are within the Fresno city limits, there are clusters of specific industries that could potentially benefit from SIPH plants. As can be seen, clusters A, B, and C of fruit and vegetable manufacturing plants potentially have available land for solar developers to install SIPH facilities and provide heat to augment steam production processes. Clusters of multiple users near a potential SIPH plant site increase the likelihood of favorable economics.

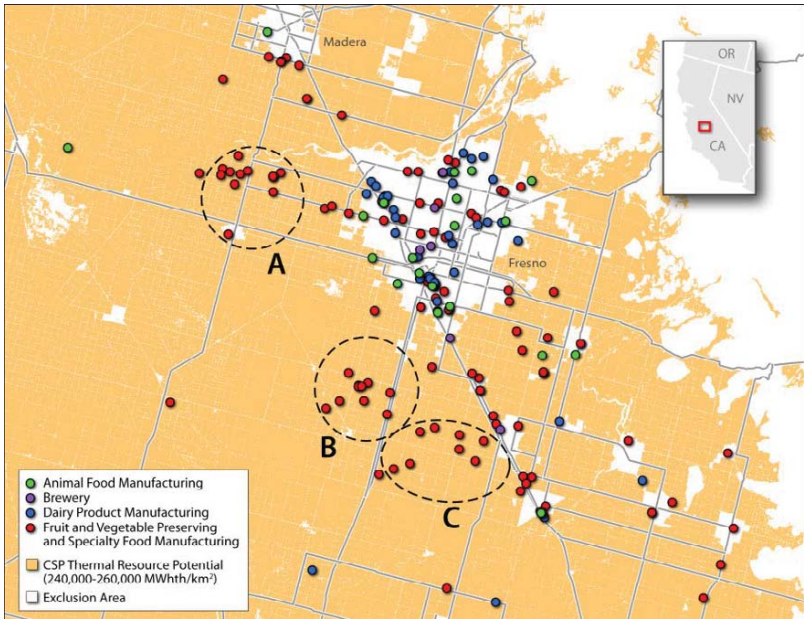

Fig. 7: Close-up of Fresno, CA showing the solar thermal generation potential and potential user industries. (Kurup and Turchi, 2015b)

4.3 Selection Of Heat Transfer Fluid (HTF) For SIPH

Different solar thermal collectors have different temperature capabilities (IRENA, 2012). Table 2 lists different temperature ranges and the likely solar collectors and HTFs to supply IPH at those conditions.

Tab. 2: Temperature regions and recommended HTFs for SIPH

Temperature Range	Solar Collector Type	HTF of Choice
< 80°C	Flat plate Non-tracking compound parabolic Solar pond	Water
80 to 200°C	Parabolic trough Linear Fresnel	Water/steam
200 to 300°C	Parabolic trough Linear Fresnel	Mineral oil or steam
300 to 400°C	Parabolic trough Linear Fresnel	Synthetic oil
400 to 550°C	Parabolic trough Linear Fresnel	Steam or Molten salt

Temperatures below about 80 °C can be achieved with non-tracking, non-concentrating devices such as solar ponds and flat-plate collectors to supply hot water, swimming pool heating, or space heating. While such applications are excellent matches for solar energy, the development and deployment of these systems are outside the scope of this study, which is dedicated to concentrating solar collectors.

At the other end of the spectrum, temperatures above about 550 °C exceed the limit of linear-concentrating systems and require the use of point-focus systems such as parabolic dishes and central receivers. These units most often deploy molten salt or high-pressure steam as the HTF, although some designs have been tested with air.

The region of interest for the present study is the realm of temperatures that can be achieved with tracking, linear-focus concentrating collectors. These collectors have a proven track record, utilize simple one-axis

tracking, and can be deployed in a modular fashion by adding additional collector length. The optics of linear-focus systems can achieve temperatures up to about 550°C. However, as one moves to higher temperatures, the requirements for the HTF and the receiver become more restrictive, which generally means more expensive hardware and fluids are required. Per Figure 5, it is anticipated that the majority of SIPH applications will target temperatures below about 220 °C.

4.4 Estimated Cost of Solar Thermal Heat

The levelized cost of heat (LCOH) is a convenient metric for estimating lifetime cost of a solar collector system for process heat applications. LCOH is defined analogously to LCOE, which conventionally refers to levelized cost of electric energy. In its simplest form, LCOH is defined as:

$$LCOH = \frac{(TIPC) * (FCR) + (Annual\ O\&M)}{Annual\ thermal\ generation} \qquad \text{(eq. 1)}$$

where TIPC is the Total installed project cost, FCR is the fixed charge rate, and annual O&M includes both fixed and variable operating costs. The FCR depends on a range of financial parameters that can have a significant influence on LCOH. NREL's SAM model includes various ways of estimating LCOE. The latest release includes a procedure for estimating and using the FCR method that is used in this study. Additional details on SAM's LCOE options can be found in the SAM Help Menu (NREL, 2015).

Figure 8 shows the LCOH for a range of installed solar costs and three different solar resource levels that are representative of California. For an installed solar field cost of about \$160/m^2, solar thermal energy is competitive with natural gas (i.e., has a lower LCOH) at its 2015 average California price of \$6.35/MMBtu (EIA, 2016) in California where DNI > 6 kWh/m^2/day. DNI > 6 kWh/m^2/day corresponds to all shaded regions shown in Figure 6. Note that Figure 8 shows the installed solar field cost and the assumed total project cost based on a multiplier for balance of plant and indirect costs. Total installed project cost includes solar field, site preparation, heat transfer fluid piping, heat exchanger, and other project costs. Added to these direct costs is a 7% contingency and 25% indirect costs. Like LCOE, the LCOH is sensitive to the financial assumptions. In this scenario the fixed charge rate is set at 0.101, which corresponds to a weighted average cost of capital of 6.2%.

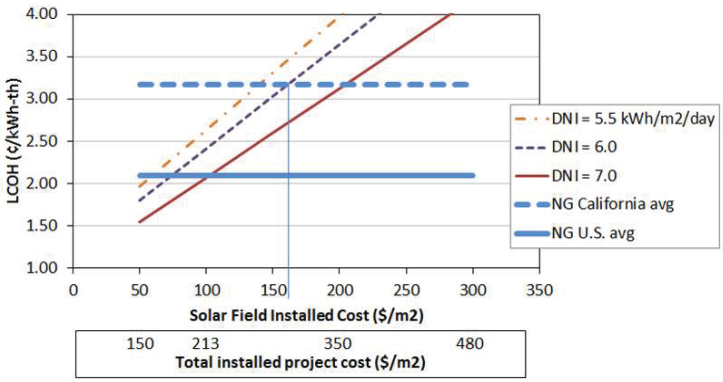

Fig. 8: Estimated LCOH for different solar resource and solar field costs compared with two natural gas (NG) prices from 2015. Total installed project cost includes solar field, site preparation, HTF piping, heat exchanger, and other project costs. No solar incentives are included. Gas costs include \$200/kW burner cost and 80% efficiency. Based on FCR = 0.101, WACC = 6.2% (updated from Kurup and Turchi, 2015b)

The data suggests that economic SIPH applications can be found in California at existing solar hardware costs and market gas prices, with incentives in the marketplace further expanding the range of feasible projects. For example, the California Solar Initiative–Thermal Incentive Program offers industrial sites up to \$800,000 to set up an SIPH plant for the displacement of natural gas (CPUC, 2016). Solar technology developers estimate that under this program, even with the relatively low gas prices of today, payback period on these projects could be less than three years. In summary, project viability will be strongly dependent on the specific solar project costs—including any incentives—and the specific gas pricing contract in place. The deployment of a few successful pilot projects would be expected to spur further utilization of SIPH with a concomitant decrease in project development costs.

5. Modifications to SAM to Facilitate SIPH

The solar-thermal models in SAM were developed to estimate the performance and cost of electric power generation. The first stage of the modeling is estimating the solar resource and the efficiency of the solar collectors. Operation of the system, however, is dependent on the demands of the integrated steam-Rankine power cycle. For users whose concern is thermal energy production, not electricity, there is no easy way to avoid interference from the power cycle constraints. In 2015 NREL showed that retention of the power cycle caused a 6% underestimation of performance from what should have transpired had the model been freed of the power cycle constraints (Turchi and Neises, 2015). This was after making changes to the SAM input values to minimize cycle impacts. In the absence of those changes, the underestimation was at least 14%.

NREL are currently modifying the SAM code to create a model set that does not require a power block and is suitable for SIPH modelling. The technologies chosen currently include: Parabolic trough with oil/water as the HTF; Direct Steam Generation (DSG) trough; and DSG Linear Fresnel. These changes are being applied exclusively to the *Physical Trough* and *Linear Fresnel* models within SAM, as these are the technologies expected to be most useful for SIPH applications. Initial validations of the new SAM code have been undertaken, with further testing and iteration expected.

6. Conclusions and next steps

Recent advances in parabolic trough design and manufacturing has led to reduced cost per square meter of aperture area. Analysis of the SkyTrough—a design that is suited for use in relatively small SIPH applications—predicts that the installed solar field cost can be as low as $\$170/m^2$. Collector designs that are tailored for efficient construction and deployment at small plant capacities are essential for viable SIPH systems. Inclusion of balance of system and indirect costs brings this total to about $\$350/m^2$ (Kurup and Turchi, 2015b).

An examination of solar resource and natural gas use for IPH in California indicates a Technical Thermal Energy Potential that far exceeds the appreciable demand in the state and highlights the food and dairy sectors as good candidates for early adoption of SIPH systems.

Three general application temperatures between 80°C and 400°C are defined for linear concentrating collectors based mainly on the preferred HTF. The low-temperature region of 80-200°C is best suited for use of water or steam, the intermediate region of 200-300°C can utilize DSG or mineral oils, and the high-temperature region of 300-400°C must use DSG or more costly synthetic oils. It is noted that the industrial demand for steam is dominated by temperatures in the range of 120 to 220°C; thus, the best SIPH market target is believed to be systems using pressurized water or steam in the range of 120 to 220°C.

California offers a favorable environment for SIPH given its good insolation, gas prices typically higher than the U.S. national average, and policies promoting solar-thermal deployment. Given historically low gas prices, competing with natural gas remains the primary challenge to deployment. However, this study finds that the solar LCOH for many regions in California is lower than the LCOH from natural gas, using a representative installed solar hardware price and the average price for industrial natural gas in California. The economic case for SIPH only improves as gas prices climb or if a price is leveed on carbon emissions.

Lastly, modifications underway to the *Physical Trough* and *Linear Fresnel* models within SAM which will allow users to more easily predict performance for these industrial heat and steam-generation applications. These changes will remove the requirement of having a steam-Rankine power cycle in the SAM model and allow users to design for steam as the final product. These modeling options are expected to debut in the parabolic trough and Linear Fresnel models in SAM 2017.

7. Acknowledgments

This work was supported by the U.S. Department of Energy under Contract No. DE-AC36-08-GO28308 w. Funding was provided by the Office of Energy Efficiency and Renewable Energy Solar Energy Technologies Program. The U.S. Government retains and the publisher, by accepting the article for publication,

8. References

Boothroyd Dewhurst Inc., 2016. DFA: Product Simplification and DFM: Concurrent Costing. http://www.dfma.com/software/dfma.htm , accessed September 19.

California Energy Commission, 2010. Industrial Process Steam Generation Using Parabolic trough Solar Collection. CEC-500-2011-040. California Energy Commission, Sacramento.

California Public Utilities Commission (CPUC), 2016. California Solar Initiative Thermal Program Handbook. California Public Utilities Commission, San Francisco. http://www.gosolarcalifornia.ca.gov/documents/CSI-Thermal_Handbook.pdf, accessed Sept. 19 2016.

Carwile, C., Hewitt, R., 1994. Barriers to Solar Process Heat Projects: Fifteen Highly Promising (But Cancelled) Projects. NREL/TP-472-7295. National Renewable Energy Laboratory, Golden, Colorado.

Environmental Protection Agency (EPA), 2016. Renewable Industrial Process Heat. https://www.epa.gov/rhc/renewable-industrial-process-heat, updated May 5 2016, accessed Sept. 19 2016.

Fox, D.B., Sutter, D., Tester, J.W., 2011. The thermal spectrum of low-temperature energy use in the United States. Energy Environ. Sci. 4, 3731–3740.

International Energy Association (IEA), 2016. Solar Heating and Cooling Programme. http://www.iea-shc.org/, accessed Sept. 19 2016.

International Renewable Energy Agency (IRENA), 2012. Concentrating Solar Power. Renewable Energy Technologies: Cost Analysis Series. International Renewable Energy Agency, Abu Dhabi.

Kurup, P., Turchi, C.S., 2015a. Parabolic trough Collector Cost Update for the System Advisor Model (SAM). NREL/TP-6A20-65228. National Renewable Energy Laboratory, Golden, Colorado.

Kurup, P., Turchi, C.S., 2015b. Initial Investigation into the Potential of CSP Industrial Process Heat for the Southwest United States. NREL/TP-6A20-64709. National Renewable Energy Laboratory, Golden, Colorado.

Kutscher, C.F., Davenport, R.L., Dougherty, D.A., Gee, R.C., Masterson, P.M., May, E.K., 1982. Design Approaches for Solar Industrial Process Heat Systems. SERI/TR-253-1356. Solar Energy Research Institute, Golden, Colorado.

NREL, 2015. System Advisor Model (SAM) release version 2015-06-30, LCOE calculator financial model. https://sam.nrel.gov/, accessed Sept. 19 2016.

NREL, 2016. Stillwater Geosolar Hybrid Plant. http://www.nrel.gov/csp/solarpaces/project_detail.cfm/projectID=4279, accessed September 19.

Schrupp, L., 2013. The Natural Gas Research, Development and Demonstration Program. CEC-500-2013-014. California Energy Commission, Sacramento.

Solar Heat for Industrial Processes (SHIP), 2016. SHIP Plants - Locations - United States. http://ship-plants.info/solar-thermal-plants, accessed September 19.

SolarPACES, 2016a. Task IV: Solar Heat in Industrial Processes. http://www.solarpaces.org/tasks/task-iv-solar-heat-integration-in-industrial-processes, accessed September 19.

SolarPACES, 2016b. CSP – How it Works. http://www.solarpaces.org/csp-technology, accessed September 19.

Turchi, C.S., Neises, T., 2015. Parabolic trough Solar-Thermal Output Model Decoupled from SAM Power Block Assumptions. National Renewable Energy Laboratory, Golden, Colorado.

U.S. DOE Office of Energy Efficiency & Renewable Energy (EERE), 2016. Sankey Diagram of Process Energy Flow in U.S. Manufacturing Sector. http://www.energy.gov/eere/amo/static-sankey-diagram-process-

energy-us-manufacturing-sector, accessed September 19.

U.S. Energy Information Administration (EIA), 2010a. 2010 MECS Survey Data. http://www.eia.gov/consumption/manufacturing/data/2010/, accessed Sept. 19 2016.

U.S. Energy Information Administration (EIA), 2010b. Table 5.4 End Uses of Fuel Consumption, 2010. http://www.eia.gov/consumption/manufacturing/data/2010/pdf/Table5_4.pdf, accessed Sept. 19 2016.

U.S. Energy Information Administration (EIA), 2013. Table 5.1 By Mfg. Industry with Net Electricity (physical units). http://www.eia.gov/consumption/manufacturing/data/2010/pdf/Table5_1.pdf, released March 2013, accessed Sept. 19 2016.

U.S. Energy Information Administration (EIA), 2016. Natural Gas Prices. http://www.eia.gov/dnav/ng/ng_pri_sum_dcu_SCA_a.htm, modified August 31 2016, accessed September 19.

Wendt et al., 2015. Stillwater Hybrid Geo-Solar Power Plant Optimization Analyses. Proceedings of the Geothermal Resources Council 2015 Annual Meeting, 20-23 September 2015, Reno, Nevada pp. 891-900.

Conference Proceedings

EuroSun 2016
Palma de Mallorca (Spain), 11 - 14 October 2016

Exergoeconomic and techno-economic analysis of a solar multi-generation plant with thermal energy storage

Roberto Leiva [1,2,a)] , Rodrigo Escobar [1] and Jose Cardemil [3]

[1]Escuela de Ingeniería, Pontificia Universidad Católica de Chile, Santiago, Chile

[2]Departamento de Mecánica, Universidad Técnica Federico Santa María, Viña del Mar, Chile.

[3]Departamento de Ingeniería Mecánica. Universidad de Chile. Santiago, Chile

[a)]Corresponding author: rleivaillanes@puc.cl , roberto.leiva@usm.cl

Abstract.

A exergoeconomic and techno-economic analysis of integrating multi-effect distillation, absorption refrigeration and process heat plants in a concentrated solar power plant is carried out. A solar multigeneration plant is modeled to simultaneously produce electricity, desalinated water, cooling, and process heat. The methodology considers modeling a multi-generation plant, applying exergoeconomic method and levelized cost method. The solar multi-generation plant is simulated in a typical meteorological year, with one hour time-step and a yearly total DNI of 3,389 kW h/m^2/year, considering the demand of a specific mining company located in northern Chile. The analysis of simulation shows that the levelized cost method overcharges electricity and undercharges water, cooling and process heat with respect to the exergoeconomic method. The exergoeconomic method is a robust method of cost allocation for applying in a solar multi-generation plant.

Keywords: *multi-generation, exergoeconomic, CSP, multi-effect desalination, absorption refrigeration.*

1. Introduction

The demand for electricity, water, cooling and process heat has been growing increasingly in Chile [1], especially due to the mining requirements. Consequently, electricity, water, and fuel prices have reached high levels, which negatively impact the competitiveness of companies. According to Chilean Energy Ministry [2], in 2014, 37% of electricity generated in Chile was consumed by the mining industry, other industries consumed 31%, the residential sector 17%, while the commercial and public sectors accounted for 14% of the electricity consumption. On the one hand, Chile has high availability of renewable energy resources, such as solar, wind, hydro, biomass and geothermal energy. Within these sources, solar energy is an important resource due to high rates of radiation existing in northern Chile, considered as the highest worldwide [3]. On the other hand, in the north of Chile there are several mining facilities, which demand a large amount of electricity, fresh water, heat process, and cooling [1], [4], utilities that are feasible to be delivered by multi-generation systems or stand-alone systems.

Multi-generation or polygeneration is defined as the concurrent production of two or more energy services and/or manufactured products that, benefiting from the energy integration of the processes, extracts the maximum thermodynamic potential of the resources consumed [5]. A multi-generation scheme has comparative advantages over stand-alone systems, since it allows reducing both primary energy consumption and emissions of greenhouse gasses displacing fossil fuels, as well as decreasing energy dependency at the country level, contributing to the diversification of energy sources. Multi-generation scheme is a process of

doi:10.18086/eurosun.2016.02.03 Available at http://proceedings.ises.org

integration of different technologies by which is possible to increase the thermodynamic efficiency and decrease the consumed resources [5]. This integrated process can be evaluated either by an levelized cost analysis or exergoeconomic analysis. Levelized cost analysis considers the first law of Thermodynamics and economic principles to determine the present value of the total cost of building and operating of a productive plant over its economic life, converted to equal annual payments. Costs are levelized in USD per unit of annual production. Key inputs to calculate levelized cost include capital expenditure, operational expenditure, fuel costs, and revenues from the sales of by-products, such as, carbon credits [6]. However, a conventional economic analysis, as levelized cost, does not provide criteria for apportioning the carrying charges, fuel costs, and operational expenses to the various products generated in the same system [7]. On the other hand, exergoeconomic or thermoeconomic analysis considers the second law of Thermodynamics and economic principles for determining the unit exergy costs and exergy cost rate of each product. According to Tsatsaronis [8], exergoeconomics is defined as the branch of engineering that appropriately combines, at the level of system components, thermodynamic evaluations based on an exergy analysis with economic principles, in order to provide the designer or operator of a system with information that is useful to the design and operation of a cost-effective system, but not obtainable either by regular energy, or exergy analysis, or economic analysis. Exergoeconomic assesses the cost of consumed resources, money and system irreversibilities in terms of the overall production process [5].

For the reasons mentioned above, a solar multi-generation system is configured and simulated in order to produce electricity, desalination water, industrial cooling and process heat required by the mining sector in northern Chile. The solar multi-generation plant proposed herein consists of a concentrated solar power (CSP) parabolic trough collector (PTC) field with thermal energy storage (TES) and backup system (BS), a multi-effect distillation (MED) plant, a single-effect absorption refrigeration system (Ref), and a countercurrent heat exchanger as process heat plant (PH), the last three plants use thermal energy to drive the processes.

CSP-PTC could be integrated into multi-generation system so as to deliver different products, such as electricity, fresh water, process heat and refrigeration [9], different studies have focused on cogeneration configurations [10]–[16] and trigeneration schemes [14], [17], [18]. However, there are studies which considered the levelized cost method and others the exergoeconomic one to evaluate the benefits of the integration, but both methods are unlike and produce different results. For this reason, the aim of the present work is to apply an exergoeconomic method and levelized cost method in a multi-generation plant to compare the unit costs of each product.

2. Materials and methods

The methodology considerers modeling a solar multi-generation plant and applying an exergoeconomic method and levelized cost method.

2.1. Multi-generation plant

The solar multi-generation plant is depicted in Figure 1, the CSP-PTC plant is configured and modeled considering a typical CSP plant as Andasol-1 power plant [19], [20]. The solar field (SF) consisting of EuroTrough collectors (ET-150), Schott PRT-70 absorber tubes, Dowtherm A as heat thermal fluid (HTF). The design temperature of SF is 393 ºC and the outlet temperature is 293 ºC. The irradiance and solar efficiency at design point are 1,010 W/m^2 and 0.72, respectively. The solar multiple (SM) is defined as 2.56 with 614,014 m^2 of aperture area. The solar multiple is a measure of the solar field aperture area as a function of the power block's nameplate capacity, and it is expressed as:

$$\mathrm{SM} = \frac{\dot{Q}_{\mathrm{th,solar\ field}}}{\dot{Q}_{\mathrm{th,power\ block}_{\mathrm{design\ point}}}} \qquad \text{(eq. 1)}$$

where $\dot{Q}_{\mathrm{th,solar\ field}}$ is the solar thermal energy produced by the solar field at the design point, $\dot{Q}_{\mathrm{th,power\ block}}$ is the solar thermal energy required by the power block at nominal conditions.

The power block (PB) consists of a regenerative Rankine cycle with reheat and six extractions, as suggested in Blanco-Marigorta et al. [21]. The TES is assumed as a two-tank indirect system using molten salts (60% $NaNO_3$, 40% KNO_3) as storage media, 95% of annual storage efficiency, and the design temperature in the hot tank is 386 ºC and 292 ºC for the cold tank. TES_{th} is the equivalent thermal capacity of the storage tanks, it is defined as:

$$TES_{th} = \frac{\dot{W}_{des.gross}}{\eta_{des}} t_{full\ load} \qquad \text{(eq. 2)}$$

where, $\dot{W}_{des.gross}$ is gross power, η_{des} is efficiency of Rankine cycle in design point, and $t_{full\ load}$ is the number of hours of thermal energy delivered at the power block's design thermal input level. It is assumed 12 hours of full load capacity.

The BS supplies thermal energy directly to the HTF in the PB. Other assumptions are made: SF outlet temperature has been kept constant [22]; startup and shutdown are not evaluated; the capacity factor is assumed as 96%; and CSP plant is a base load power station.

In the CSP plant, the point of coupling of MED, Ref and PH plants is selected according to the operating temperatures constraints imposed by each technology and to cause the minimum penalty for power production. Therefore, the MED plant replaces the CSP plant condenser, the Ref plant is coupled to the fifth turbine extraction, and the PH plant is coupled between feed water preheaters (FWP). It is not possible to regulate the amount of water produced because the MED plant is driven by the heat rejected from the power cycle. The production from Ref plant and PH plant can be regulated per the demand.

The desalination plant is modeled with 12 effects parallel-cross feed MED plant with 11 feed preheaters, as suggested in Zak et al. [23]. The fresh water production is 37,341 m^3/day and 9.1 of Gained Output Ratio (GOR).

The refrigeration plant is configured with a single-effect LiBr-H_2O absorption chiller, as suggested in Herold et al. [24] with 5 MW_{th} of cooling capacity and 0.7 of nominal coefficient of performance (COP).

Finally, a counter current heat exchanger is configured to produce process heat, with 7 MW_{th} heating.

The sizing chosen for each plant was selected according to the demand of a specific mining company located in northern Chile.

Each stand-alone system is modeled and validated. Then, the multi-generation plant is the combination of the validated stand-alone systems. The CSP-PTC stand-alone plant is validated from Blanco-Marigorta et.al [21] and SAM software [19]. The MED plant is validated from Zak et al. [23] and El-Dessouky et al.[25], and the cooling plant is validated from Herold et al. [24].

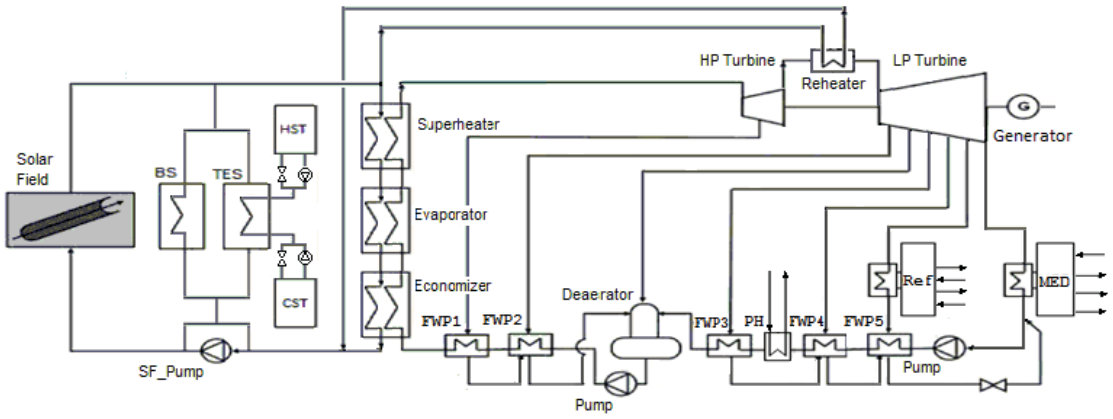

Fig. 1: Multi-generation plant configuration. CSP/TES + MED + Ref + PH.

Table 1 shows the main parameters of solar multi-generation plant.

Tab. 1: Main parameters of multi-generation plant at design point.

Property	Value Unit
TES	
Type / Storage fluid	2-tank / Molten Salt
Tank temperature (cold/hot) / Annual Storage Efficiency	(292 °C / 386 °C) / 95%
Full load hours of TES	12 h
Solar field (SF)	
Parabolic trough collector model	EuroTrough collector (Skal-et)
Solar Field inlet/outlet temperature	293.0 °C / 393.0 °C
Aperture area	614,014 m^2
Solar Multiple	2.56
Power block (PB)	
Gross power production	55.0 MW_e
HP turbine inlet pressure/temperature	103.57 bar / 373 °C
LP turbine back pressure/temperature	0.37 bar / 73.9 ºC
HP turbine / LP turbine isentropic efficiency	85.2% / 85.0%
Generator /motor / pumps efficiency	98.0 % / 98% / 70%
Multi-Effect Desalination (MED)	
Feed seawater intake temperature / salinity	25.0 °C / 0.042 kg/kg
Feed seawater after down condenser temperature	35.0 °C
Maximum salinity in each effect / Top Brine Temperature	0.072 kg/kg / 65.0 °C
GOR / Concentration factor	9.07 / 1.71
Single-effect absorption chiller (Ref)	
Cooling power	5.0 MW_{th}
Chilled water inlet / outlet temperature	10.0 °C / 6.0 °C
Cooling water inlet/outlet temperature	25.0 °C / 35.0 °C
Inlet temperature desorber / COP	108.5 °C / 0.70
Process Heat (PH)	
Process heat capacity	7.0 MW_{th}
Heat exchanger temperature inlet / outlet	63.0 °C / 90.0 °C

The software IPSEpro [26] was used for the modeling and simulations of the multi-generation plant and each stand-alone plant. IPSEpro can calculate mass and energy balances and simulate different kind of processes. IPSEpro solves the flowsheet of the process using Newton-Raphson method. IPSEpro provides only steady state solutions. In order to obtain the dynamic system behavior, IPSEpro has to be linked to Microsoft Excel by IPSEpro-PSExcel, where the solar multi-generation plant is simulated over a one-year period in time steps of one hour. Finally, MATLAB software is used for modeling and simulating TES behavior and for thermoeconomic and techno-economic assessment.

The multi-generation plant was evaluated to be installed in northern Chile, in Crucero, latitude -22.14°, longitude -69.3° and 3389 kW h/m^2/year of DNI [3].

In the model, variations of kinetic energy, potential energy, and pressure drops in the lines were disregarded.

2.2. Exergoeconomic method

A exergoeconomic evaluation is applied using Bejan et al. method [7]. Figure 2 depicts the delimitation of the boundaries analysis. The fuels and products are established, and mass, energy and exergy balances are applied. The exergy balance equation take the form:

$$\sum(\dot{Q}\left(1-\frac{T_0}{T}\right))-\dot{W}+\sum(\dot{m}_{in}e_{in})-\sum(\dot{m}_{out}e_{out})-\dot{E}_D=0 \quad \text{(eq. 3)}$$

where, $\dot{Q}$ is the heat power, T_0 is the temperature of reference, in K, $\dot{W}$ is exergy rates of work, $\dot{m}$ is the mass flow rate, e is the exergy specific, and $\dot{E}_D$ is the rate of exergy destruction.

The exergy rates from sun [27] is defined as:

$$\dot{E}_{sun}=A\cdot DNI\cdot(1+\frac{1}{3}\left(\frac{T_0}{T_{sun}}\right)^4-\frac{4}{3}\left(\frac{T_0}{T_{sun}}\right)) \quad \text{(eq. 4)}$$

where A is the solar field aperture area, and T_{sun} is the sun's surface temperature, taken as 6000 K.

For each system component is applied the economic balance in order to determine the unit exergy cost c_j and exergy cost rate $\dot{C}_j$ of each stream. The economic balance is expressed by:

$$\sum_{j=1}^{n}(c_j\dot{E}_j)_{k,in}+\dot{Z}_k^{CI}+\dot{Z}_k^{OM}=\sum_{j=1}^{m}(c_j\dot{E}_j)_{k,out} \quad \text{(eq. 5)}$$

where, c_j is the exergy unit cost, $\dot{E}$ is the exergy rate, $\dot{Z}_k^{CI}$ is the non-exergy-related cost rate associated with an investment cost (or capex), $\dot{Z}_k^{OM}$ is the non-exergy-related cost rate associated with an operation and maintenance cost (or opex).

The exergy cost rate is expressed as function of unit exergy cost by:

$$\dot{C}_j=c_j\dot{E}_j=c_j\left(\dot{E}_{ph}+\dot{E}_{ch}+\dot{E}_p+\dot{E}_k\right) \quad \text{(eq. 6)}$$

where the subscripts ph, ch, p, and k are physic, chemical, potential and kinetic, respectively.

The total cost rate of product $\dot{C}_p$ is the sum of total cost rate of fuel $\dot{C}_f$ and non-exergy-related cost rate $\dot{Z}$.

The exergy analysis considered a reference temperature of 25°C, a reference atmospheric pressure of 1.013 bar, a reference mass fraction of LiBr of 0.5542 kg/kg, and a reference mass fraction of water salinity of 0.042 kg/kg.

Investment cost in MUSD, and operating and maintenance cost in MUSD/year considered are: 397.3 and 17.8 in CSP [11], [19], [28], [29]; 59.5 and 1.8 in MED plant [25], [30]–[33]; 2.7 and 0.006 in Refrigeration plant [16], [34]; and finally 0.3 and 0.0006 in process heat plant [35], respectively. The fossil cost fuel is 0.0324 USD/kWh [36]. It has been considered a horizon of 25 years and a discount rate of 10%.

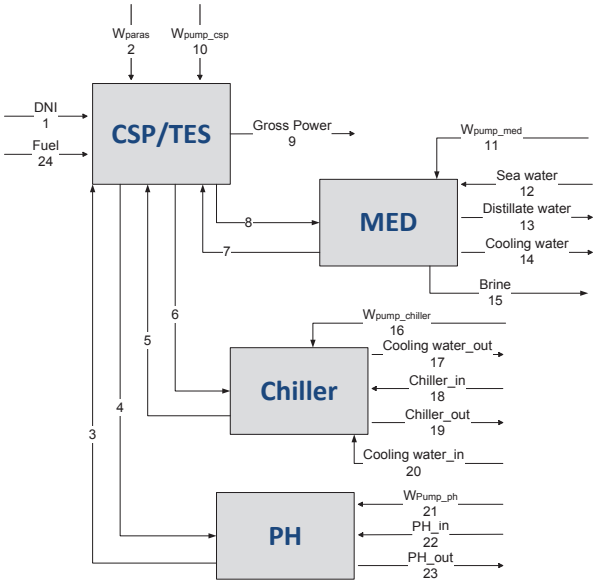

Fig. 2: Aggregation level for exergoeconomic assessment in multi-generation plant.

2.3. Levelized cost method

The levelized cost is the total cost of installing and operating expressed in USD per unit of product generated by the system over its life [11], [22], [37].

The levelized electricity cost (LEC), in USD/kWh, is defined by:

$$LEC = \sum_{j=0}^{n} \frac{capex_j crf + opex_j + C_{fuel\,j}}{(1+i)^j} / (E_{elect\_an\_j}) \quad \text{(eq. 7)}$$

where $capex$ is the capital expenditure, $opex$ is the operational expenditure, crf is the capital recovery factor, C_{fuel} is the annual fuel cost, i is the discount rate, n is the number of time periods, $E_{elect\_an\_j}$ is the annual production of electricity provided by the generator minus the parasitic loads of CSP plant. Fuel cost is calculated by:

$$C_{fuel} = c_{ff} \frac{Q_{\text{th,power block\_BS}}}{\eta_{\text{boiler}}} \quad \text{(eq. 8)}$$

where c_{ff} is the fossil fuel cost, in USD/kWh, $Q_{\text{th,power block\_BS}}$ is the thermal energy required by the power block from BS, in kWh/year, and η_{boiler} is the boiler efficiency, assumed as 0.9.

A similar procedure was used for the other levelized costs estimation. The levelized water cost (LWC), in USD/m^3, is defined by:

$$LWC = \sum_{j=0}^{n} \frac{capex_j crf + opex_j + C_{fuel\,j}}{(1+i)^j} / (V_{water\_an\_j}) \quad \text{(eq. 9)}$$

where $V_{water\_an\_j}$ is the annual production of water, in m^3/year, and C_{fuel} is the fuel cost, in USD/year. Fuel cost in the case of MED, refrigeration and process heat plants is the cost associated with electric consumptions, and it is calculated by:

$$C_{fuel} = LEC\ \text{En}_{\text{pumps}} \quad \text{(eq. 10)}$$

Where En_{pumps} is the annual energy consumption from pumps, in kWh/year.

The levelized cooling cost (LCC), in USD/kWh, is defined by:

$$LCC = \sum_{j=0}^{n} \frac{capex_j crf + opex_j + C_{fuel\,j}}{(1+i)^j} / (E_{cooling\_an\_j}) \quad \text{(eq. 11)}$$

where $E_{cooling\_an\_j}$ is the annual production of cooling, in kWh/year.

The levelized process heat cost (LHC), in USD/kWh, is defined by:

$$LHC = \sum_{j=0}^{n} \frac{capex_j crf + opex_j + C_{fuel\,j}}{(1+i)^j} / (E_{heat\_an\_j}) \quad \text{(eq. 12)}$$

where $E_{heat\_an\_j}$ is the annual production of process heat, in kWh/year.

3. Results and discussion.

3.1. Production and cost in the base case.

The monthly production of electricity, fresh water, cooling and process heat, in the solar multi-generation plant without BS, is presented in Figure 3. At the location, there is a seasonality of DNI, with shorter days and lower values of DNI in the winter season. Hence, the solar multi-generation plant shows a seasonal variation, presenting a lower production of electricity, fresh water, cooling and process heat during the winter (June and July). However, in February, the production decreases by the Altiplanic Winter which moistens the air coming from the east (where Bolivia is located) bringing unsettled weather and clouds.

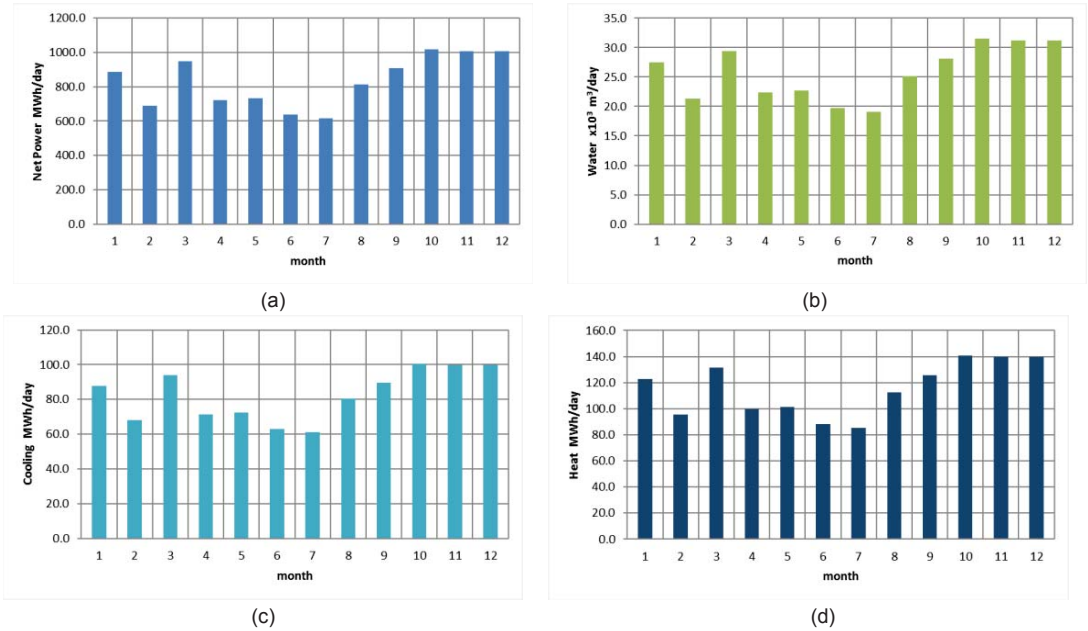

Fig. 3: Monthly productions from the solar: a) Net power. b and water. c) Cooling. d) Heat.

Figure 4a depicts the monthly capacity factor without BS, which is largest in the summer due to the seasonal variation in DNI available for collection. Figure 4b shows the monthly exergy destruction, which is greater in the CSP plant with an 89.4%. In the CSP plant, the SF is the most critical component in terms of exergy destruction. It is important to point out that exergy input of SF is derived solely from the sun which does not affect the consumption of fossil fuel. The second largest exergy destruction is in the MED plant with 9.6% of the total exergy input. In the case of cooling and process heat plants, the exergy destruction is less than 1%.

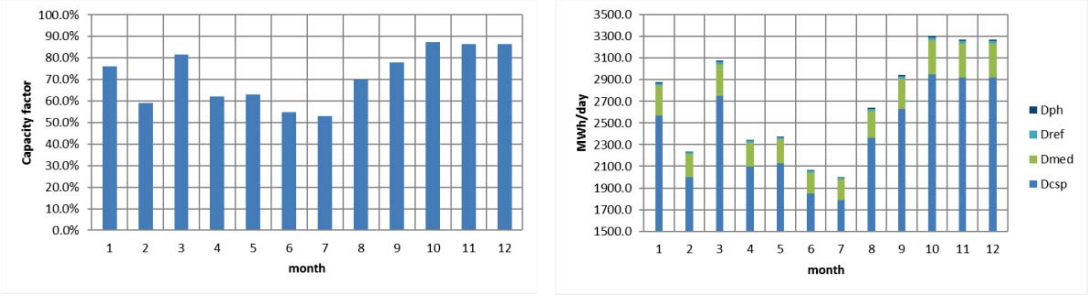

(a) (b)

Fig. 4: a) Monthly capacity factor without BS. b) Monthly exergy destruction without BS.

The annual productions in base case are: 463.1 GWh/year of gross power, 408.2 GWh/year of net power, 13.2 Mm^3/year of fresh water, 42.0 GWh/year of cooling, and 58.9 GWh/year of process heat.

The unit exergy costs (UEC) and levelized costs (LC) are presented in Figure 5. Two cases are considered in the case of water cost, without and with the cost of pumping the seawater to the plant location (about 70 km). The difference in value between UEC and LC is due to the form of cost allocation. Exergoeconomics uses the exergy as criterion to allocate the costs, and it is considered as a rational cost allocation. The levelized cost method overcharges electricity and undercharges water, cooling and process heat.

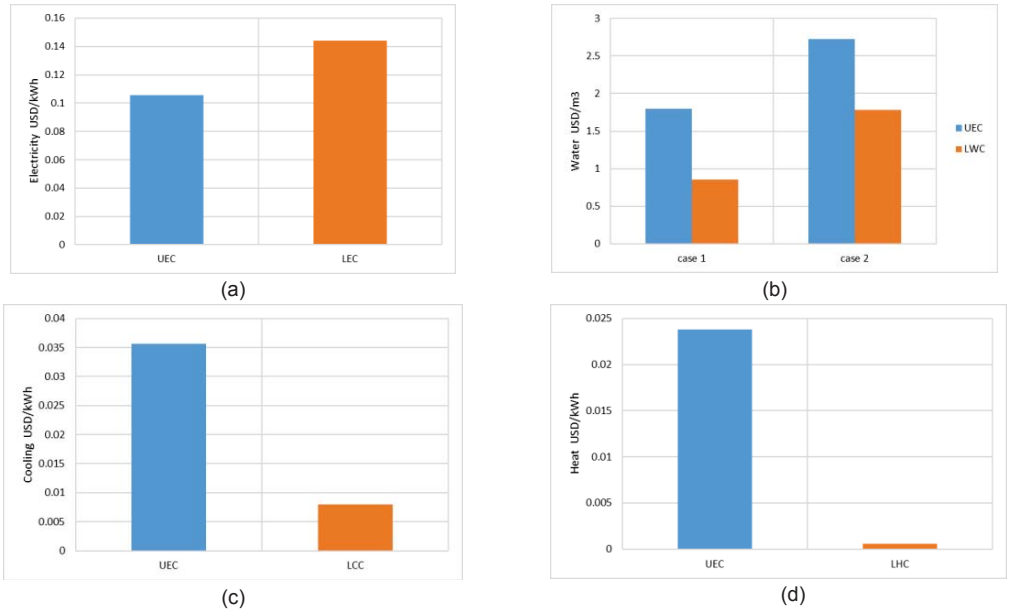

Fig. 5: Comparison between the levelized cost method and exergoeconomic method. Specific cost (UEC and LC) of: a) electricity, b) water, c) cooling, d) process heat.

If a system produces only one product, there are no problems to calculate the levelized cost because it is not necessary to use an allocation criterion of costs. However, if a system produces more than one product as in a multi-generation system, then, it is needed to establish an allocation criterion of costs in order to calculate the products cost. Conventional economic analysis does not provide criteria for apportioning the carrying charges, fuel costs, and opex to the various products generated in the same system [7]. Exergoeconomics provides criteria for apportioning the costs, therefore, exergy is the appropriate variable to use in this case.

On the other hand, the total exergy cost rate of products is 8,988.4 USD/h, which is distributed in 64.7% in electricity, 31.3% in fresh water, 2.2% in cooling, and 1.8% in process heat. In a process of optimization, the variable to be minimized is the total exergy cost of products.

3.2. Production and cost as functions of sizing SM and TES.

The solar multi-generation plant was hybridized with fossil fuel in order to fix the capacity factor in a 96%. Chile does not have restrictions to use fossil fuel in CSP plants. In contrast, Spain limits the use of fossil fuel in CSP plants. A solar multi-generation plant will be more dispatchable by coupling the solar multi-generation plant with BS. This also allows a more flexible generation strategy to maximize the value of the products generated. Figure 6 shows the capacity factor in the multi-generation plant without BS in which the capacity factor is increased with the SM and the hours of TES. This latter one allows storing excess energy collected by the SF when it is not used in the PB, and discharges that energy later when the DNI is lower, such as in cloudy days or at night. Consequently, the annual production of each product is increased too, as seen in Figure 7.

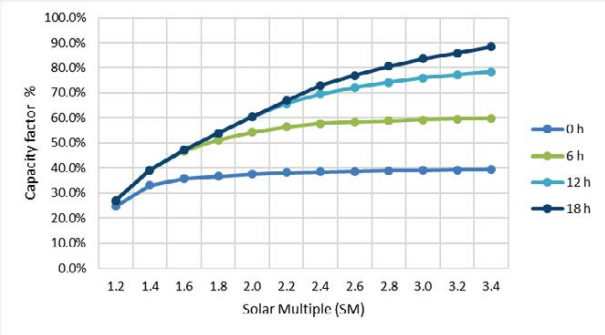

Fig. 6: Capacity factor in the multi-generation plant without BS.

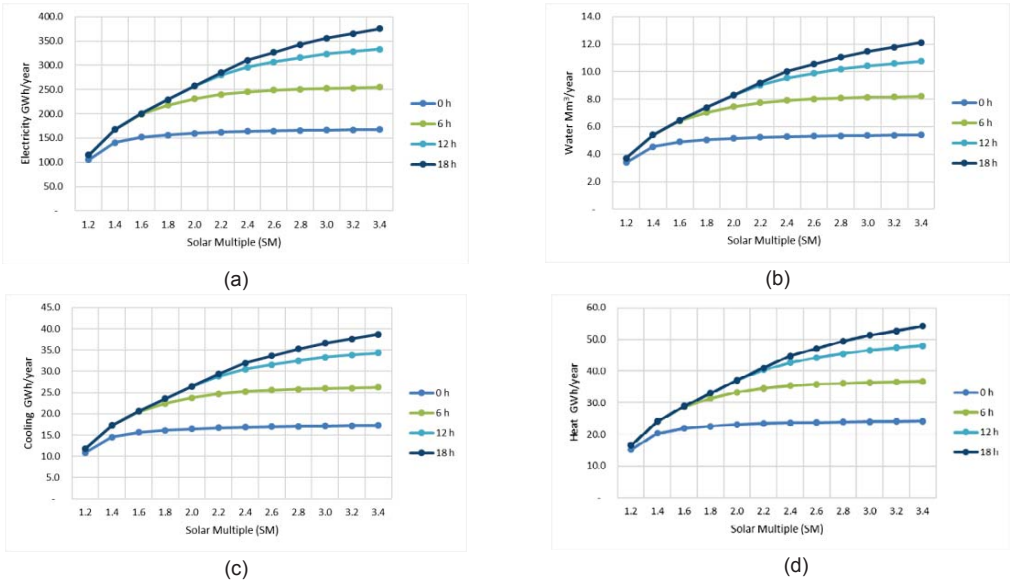

Fig. 7: Annual production of: a) electricity, b) water, c) cooling, d) process heat.

Figure 8 presents the unit exergy cost (UEC) and levelized cost (LC) of each product (electricity, fresh water, cooling, and process heat) as a function of SM, and with a TES of 12 hours. It is observed that UEC and LC are different, but the minimums UEC and LC are produced at the same SM, with an SM of 2.2. In a multi-generation plant, there are common costs associated with the products concerned, and it is necessary to determine the share of costs attributable to one or another product. So, the allocation cost needs an additional rational analysis to prevent allocation from being arbitrary. Regarding the levelized cost method, the fuel cost for MED, refrigeration and process heat plants only corresponds to the cost associated with electric consumptions and does not consider the steam cost because this latter one is assumed as an internal cost. On the other hand, allocation of costs based on exergoeconomic method equitably charges each product with the appropriate share of capex and opex that are involved in operating such component according to its exergy rate. Hence, the exergoeconomic method is more appropriate to multi-generation plant than levelized cost method.

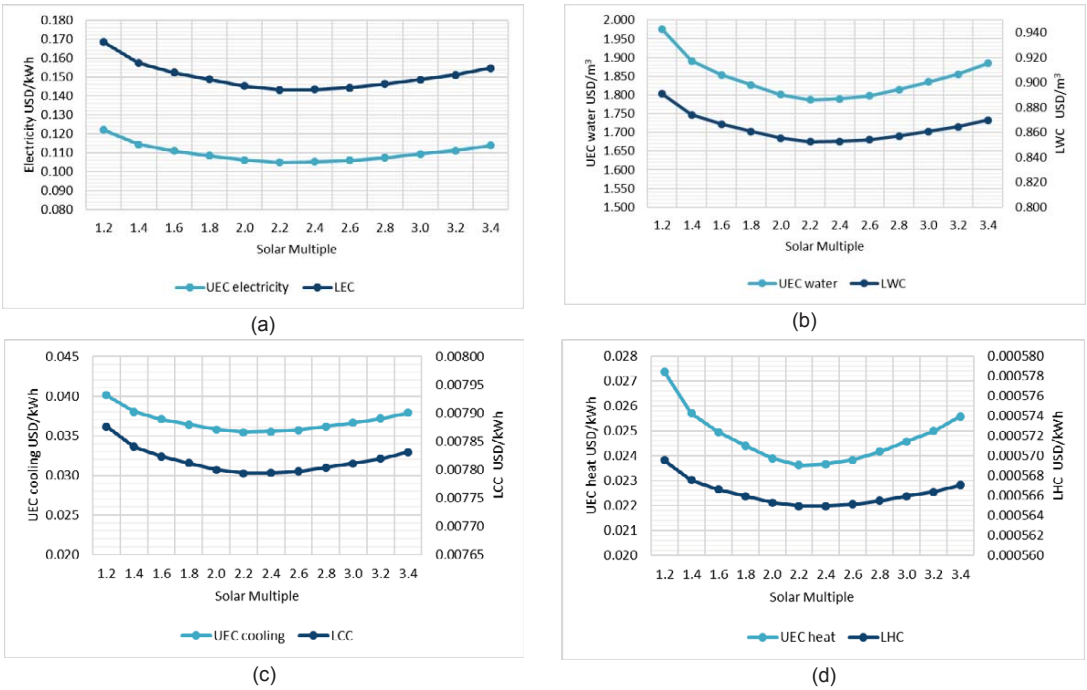

Fig. 8: Specific cost (UEC and LC) as a function of SM. a) electricity, b) water, c) cooling, d) process heat.

An optimal sizing of SF and TES should minimize installation and operating costs, and maximize the amount of time in a year to drive the power cycle at its nominal capacity. This point is reached with the minimum levelized cost and unit exergy cost. The unit cost in the solar multi-generation plant is dominated by the investment cost of CSP plant. The unit cost varies significantly, depending on the capacity factor, which in turn depends on the DNI, hybridization (BS) levels, and sizing of SF and TES.

4. Conclusions

The levelized cost method and the exergoeconomic method were applied to a solar multi-generation plant to compare the unit costs of each product. The solar multi-generation plant was made up of concentrated solar power plant, multi-effect distillation, absorption refrigeration, and process heat plants. The solar multi-generation plant was simulated hourly during a typical meteorological year.

The levelized cost method overvalues the electricity cost and undervalues the water, cooling, and process heat costs because the allocation cost does not charge all internal cost to MED, Ref and PH plants.

The exergoeconomic method is more appropriate than levelized cost method since the allocation cost is based on the second law of Thermodynamics and economic principles. Then, there is an equitable distribution of the appropriate share of non-exergy-related cost rate and exergy cost rate in each product.

The minimums UEC and LC happened at the same sizing of SM and TES, however, the unit costs have different values. Hence, independently of the method used, in a process of optimization of sizing of SM and TES, it is obtained the same sizing.

In terms of exergy destruction, the highest exergy destruction of the CSP plant is produced in SF and PB. The second highest is produced in the MED plant, but in the case of Ref and PH plant, the exergy destruction is about 1%.

In future studies, it is recommended that an exergoeconomic analysis and life cycle analysis be done in the solar multi-generation plant in order to use the cost accounting in the environmental evaluation. Likewise, another research line could be to evaluate different schemes of solar multi-generation plant coupled with other technologies, such as reverse osmosis desalination and vapor compression refrigeration systems.

Finally, an exergoeconomic evaluation with low aggregation level in CSP plant should be done at the level of individual components, such as the turbine, pump, solar field, and so on.

Acknowledgments

This research work was funded by CONICYT-PCHA/Doctorado_Nacional/año2013-folio21130634 and Fondecyt 1130621.

References

[1] COCHILCO, "Proyecciones del consumo de electricidad en la minería del cobre 2015-2016.," *COCHILCO, Comisión Chilena del Cobre.*, 2015. [Online]. Available: https://www.cochilco.cl/Listado Temtico/Proyeccion_del_consumo_de_electricidad_en_la_mineria_del_cobre_2015_-_2026_VF.pdf. [Accessed: 21-Sep-2016].

[2] CNE, "Balances Energeticos," 2014. [Online]. Available: http://datos.energiaabierta.cl/datastreams/111597/bne-2014-balance-energia-global/.

[3] R. A. Escobar, C. Cortés, A. Pino, M. Salgado, E. B. Pereira, F. R. Martins, J. Boland, and J. M. Cardemil, "Estimating the potential for solar energy utilization in Chile by satellite-derived data and ground station measurements," *Sol. Energy*, vol. 121, pp. 139–151, Nov. 2015.

[4] COCHILCO, "Proyecciones del consumo de agua en la minería del cobre al 2026.," *COCHILCO, Comisión Chilena del Cobre*, 2015. [Online]. Available: https://www.cochilco.cl/Listado Temtico/Proyeccion_de_consumo_de_agua_2015_al_2026.pdf#search=precio del agua en el norte. [Accessed: 21-Sep-2016].

[5] L. M. Serra, M.-A. Lozano, J. Ramos, A. V. Ensinas, and S. a. Nebra, "Polygeneration and efficient use of natural resources," *Energy*, vol. 34, no. 5, pp. 575–586, May 2009.

[6] IEA-NEA, "Projected costs of generating electricity 2015," p. 16, 2015.

[7] A. Bejan, G. Tsatsaronis, and M. Moran, *Thermal Design and Optimization*, 1 edition. John Wiley & Sons, 1996.

[8] G. Tsatsaronis, "Definitions and nomenclature in exergy analysis and exergoeconomics," *Energy*, vol. 32, no. 4, pp. 249–253, Apr. 2007.

[9] A. Fernández-García, E. Zarza, L. Valenzuela, and M. Pérez, "Parabolic-trough solar collectors and their applications," *Renew. Sustain. Energy Rev.*, vol. 14, no. 7, pp. 1695–1721, 2010.

[10] F. Trieb, H. Müller-Steinhagen, J. Kern, J. Scharfe, M. Kabariti, and A. Al Taher, "Technologies for large scale seawater desalination using concentrated solar radiation," *Desalination*, vol. 235, no. 1, pp. 33–43, 2009.

[11] P. Palenzuela, D.-C. Alarcón-Padilla, and G. Zaragoza, "Large-scale solar desalination by combination with CSP: Techno-economic analysis of different options for the Mediterranean Sea and the Arabian Gulf," *Desalination*, vol. 366, pp. 130–138, 2015.

[12] P. Palenzuela, G. Zaragoza, D. Alarcón, and J. Blanco, "Simulation and evaluation of the coupling of desalination units to parabolic-trough solar power plants in the Mediterranean region," *Desalination*, vol. 281, pp. 379–387, Oct. 2011.

[13] B. Ortega-Delgado, L. García-Rodríguez, and D.-C. Alarcón-Padilla, "Thermoeconomic comparison of integrating seawater desalination processes in a concentrating solar power plant of 5 MWe," *Desalination*, vol. 392, pp. 102–117, 2016.

[14] F. A. Al-Sulaiman, I. Dincer, and F. Hamdullahpur, "Thermoeconomic optimization of three trigeneration systems using organic Rankine cycles: Part I – Formulations," *Energy Convers. Manag.*, vol. 69, pp. 199–208, May 2013.

[15] F. Calise, M. Dentice d'Accadia, and A. Piacentino, "Exergetic and exergoeconomic analysis of a renewable polygeneration system and viability study for small isolated communities," *Energy*, Apr. 2015.

[16] C. Infante Ferreira and D.-S. S. Kim, "Techno-economic review of solar cooling technologies based on location-specific data," *Int. J. Refrig.*, vol. 39, pp. 23–37, Mar. 2014.

[17] R. Buck and S. Friedmann, "Solar-Assisted Small Solar Tower Trigeneration Systems," *J. Sol. Energy Eng.*, vol. 129, pp. 85–90, 2007.

[18] U. Sahoo, R. Kumar, P. C. Pant, and R. Chaudhury, "Scope and sustainability of hybrid solar–biomass power plant with cooling, desalination in polygeneration process in India," *Renew. Sustain. Energy Rev.*, vol. 51, pp. 304–316, Nov. 2015.

[19] NREL, "System Advisor Model (SAM) Case Study: Andasol-1," pp. 1–10, 2013.

[20] M. J. Wagner and P. Gilman, "Technical manual for the SAM physical trough model," *Contract*, vol. 303, no. June, pp. 275–3000, 2011.
[21] A. M. Blanco-Marigorta, M. Victoria Sanchez-Henríquez, and J. A. Peña-Quintana, "Exergetic comparison of two different cooling technologies for the power cycle of a thermal power plant," *Energy*, vol. 36, no. 4, pp. 1966–1972, Apr. 2011.
[22] M. J. Montes, A. Abánades, J. M. Martínez-Val, and M. Valdés, "Solar multiple optimization for a solar-only thermal power plant, using oil as heat transfer fluid in the parabolic trough collectors," *Sol. Energy*, vol. 83, no. 12, pp. 2165–2176, Dec. 2009.
[23] G. Zak, A. Mitsos, and D. Hardt, "Master Thesis. Thermal Desalination : Structural Optimization and Integration in Clean Power and Water," Massachusetts Institute of Technology, 2012.
[24] K. Herold, R. Radermacher, and S. Klein, *Absorption Chillers and Heat Pumps*, 1st editio. CRC Press; 1 edition (January 18, 1996), 1996.
[25] E. H. M. El-Dessouky H.T, *Fundamentals of Salt Water Desalination*. Elsevier, 2002.
[26] SimTech GmbH, *IPSEpro Process Simulation Environment*, Rev 5.0. SimTech Simulation Technology, 2011.
[27] R. Petela, *Engineering Thermodynamics of Thermal Radiation for solar Power Utilization*, 1 edition. McGraw-Hill Education; 1 edition (February 2, 2010), 2010.
[28] IRENA, "Concentrating Solar Power," 2012.
[29] IRENA, "Renewable Power Generation Costs in 2014 : An Overview," 2015.
[30] F. Verdier, "MENA Regional Water Outlook Part II Desalination Using Renewable Energy FINAL REPORT Task 1 -Desalination Potential Task 2 -Energy Requirement Task 3 -Concentrate Management," 2011.
[31] A. Cipollina, G. Micale, and L. Rizzuti, *Seawater Desalination: Conventional and Renewable Energy Processes*, 2009 editi. Springer Science & Business Media, 2009.
[32] IEA-ETSAP and IRENA, "Water Desalination Using Renewable Energy," 2012.
[33] N. Ghaffour, T. M. Missimer, and G. L. Amy, "Technical review and evaluation of the economics of water desalination: Current and future challenges for better water supply sustainability," *Desalination*, vol. 309, pp. 197–207, 2013.
[34] M. Noro and R. M. Lazzarin, "Solar cooling between thermal and photovoltaic: An energy and economic comparative study in the Mediterranean conditions," *Energy*, vol. 73, pp. 453–464, Aug. 2014.
[35] R. Turton, R. Bailie, W. Whiting, J. Shaeiwitz, and D. Bhattacharyya, *Analysis, Synthesis, and Design of Chemical Processes*, 4th editio. Prentice Hall; 4 edition (July 2, 2012), 2012.
[36] CNE, "Informe de Proyección de precios de combustibles 2015-2030," *CNE, Comisión Nacional de Energía, Chile.*, 2015. [Online]. Available: https://www.cne.cl/wp-content/uploads/2015/11/ResEx541_2015_Comb-informe-final-Informe-Proyecciones-Precios-Combustibles.pdf. [Accessed: 21-Sep-2016].
[37] W. Short, D. Packey, and T. Holt, "A manual for the economic evaluation of energy efficiency and renewable energy technologies," *Univ. Press Pacific*, vol. 2, no. March, p. 120, 2005.

Nomenclatures

A : aperture area, m^2
BS: backup system
Capex : capital expenditure, USD
Cf_j : fuel cost, USD/year
$\dot{C}_j$: exergy cost rate, USD/h
$\dot{C}_{D,k}$: exergy destruction cost rate, USD/h
$\dot{C}_{F,k}$: exergy fuel cost rate, USD/h
$\dot{C}_{P,k}$: exergy product cost rate, USD/h
c_j : unit exergy cost, USD/kWh
cfr: capital recovery factor, %
CSP: concentrated solar power
CST: cold storage tank
COP: Coefficient of performance, -
D: exergy destruction, kWh
DNI: direct normal irradiance, W/m^2
e : exergy specified, kJ/kg
$\dot{E}$: time rate of exergy or exergy rate, kJ/s
$\dot{E}_{heat}$: time rate of exergy heat process, kJ/s
$\dot{E}_{sun}$: time rate of exergy from sun, kJ/s
$\dot{E}_{ph}$: time rate of physical exergy, kJ/s
$\dot{E}_{ch}$: time rate of chemical exergy, kJ/s
$\dot{E}_D$: time rate of exergy destruction rate, kJ/s
$\dot{E}_{F,k}$: time rate of exergy fuel rate, kJ/s
$\dot{E}_{P,k}$: time rate of exergy product rate, kJ/s
i: discount rate, %
FWP: feed water preheater
GOR: gained output ratio, -
HTF: heat thermal fluid
HST: hot storage tank
HP: high pressure
LC: levelized cost
LCC : levelized cooling cost, USD/kWh

LEC : levelized energy cost, USD/kWh
LHC : levelized heat cost, USD/kWh
LWC : levelized water cost, USD/m^3
LP: low pressure
$\dot{m}$: flow rate, kg/s
MED: multi-effect distillation
n: number of time periods, years
Opex : operational expenditure or operation and maintenance cost, USD/year
$\dot{Q}_{th,power\ block}$: thermal power demanded by the power block, kW
$\dot{Q}_{th,solar\ field}$: thermal power produced in the solar field, kW
SM : solar multiple, -
Ref: refrigeration
PB: power block
PH: process heat
T_0 : ambient temperature, °C
TBT: top brine temperature, °C
TES: thermal energy storage
$t_{full\ load}$: hours of full-load hours of TES, h
UEC: unit exergy cost
$w_{des,gross}$: power cycle thermal in design-point , kW
$\dot{Z}$: Non-exergy-related cost rate, USD/s
$\dot{Z}_k^{CI}$: capital investment cost rates, USD/h
$\dot{Z}_k^{OM}$: operating and maintenance cost rates, USD/h

Conference Proceedings

EuroSun 2016
Palma de Mallorca (Spain), 11 - 14 October 2016

Competitive Assessment between Solar Thermal and Photovoltaics for Industrial Process Heat Generation

Steven Meyers, Bastian Schmitt, and Klaus Vajen

[1] Institute of Thermal Engineering, University of Kassel, Kassel, Germany

Abstract

The interest in photovoltaic heating has grown in recent years due to falling technology costs and ease of installation, though mainly in the residential sector. A study was conducted to determine under which conditions photovoltaic heating may become less expensive than solar thermal in low temperature industry (e.g. food and beverage). A broad parametric simulation study was conducted in TRNSYS which determined specific energetic yields for solar thermal and photovoltaic heating systems. A comparative analysis followed suit, conducted in a way to generate an assessment tool which functions for nearly every industrial, climatic, or economic setting. Results indicated that for lower temperature applications, solar thermal will remain a preferred choice in most climates. For higher temperature industrial process heat requirements, photovoltaic heating may already provide a lower cost solution in low and medium solar irradiation climates.

Keywords: *renewable heat, solar thermal, photovoltaic, process heat*

1. Introduction

In the wake of COP 21, nations across the world agreed to begin reducing their carbon emissions, namely through renewable electricity and lower carbon transport. While important, it overlooks an equally relevant carbon emitting sector, industrial manufacturing, which consumes mainly thermal energy. Lower carbon heat can be achieved through a few mechanisms, but solar offers the nearest term and most complete solution for the quickest reduction. Solar thermal (ST) collectors are an obvious choice for obtaining thermal energy, but in some niche markets photovoltaic (PV) heating systems are now being offered. While their focus is primarily on the domestic hot water sector, it provides an example where PV electrical resistance heating may be more cost effective than solar thermal.

The choice for PV resistance heating is easy to understand. The costs continue to drop year after year, installation is nearly fail proof, and its thermal energy generation capability is nearly independent of the process temperature level. Until now, minimal research (Fanney and Dougherty, 1997; Le Berre et al., 2014) has been done to compare the thermal energy generation costs of ST and PV at various temperature levels. Therefore, an assessment was conducted to determine their specific energy generation capabilities, paying close attention to their cost competitiveness for various climates, industrial process temperatures, load profiles and storage tank sizes.

2. Methodology

Two simulation decks were constructed in TRNSYS 17 to obtain the energetic yield potential of solar thermal and solar photovoltaic heating systems under various boundary conditions. Specific energy yields (per m^2 for ST and per W_p for PV) were then used to calculate the Levelized Cost of Heat (LCOH),

doi:10.18086/eurosun.2016.02.01 Available at http://proceedings.ises.org

subsequently used to determine the Cost Ratio (CR), an inflection point which indicated a preferred heating technology.

2.1. Solar Thermal Heating Model

The TRNSYS thermodynamic model was constructed around the popularly used collector model Type 832 (v5.01), developed by Haller et al. (2013), shown in Fig. 1. A constant speed pump in the solar loop operated between an upper and lower deadband of 7 K and 3 K between the collector (T_{coll}) and the bottom storage tank temperature ($T_{0.1}$), respectively. Connected pipes, insulation, charging/discharging heat exchangers and pump flow rates in the loops were sized in accordance to VDI 6002 (VDI, 2014). A storage tank was included (Type 534) to allow for flexibility in heat storage and delivery. For the charging loop, the storage tank had two inlet valves, located at a relative height of 0.9 and 0.6 from the bottom, allowing for stratification, as well as an outlet at 0.1. A constant speed pump in the charging loop was activated using the same deadband as the solar loop, though comparing temperatures between the heat exchanger ($T_{solarHX}$) and the bottom storage tank temperature ($T_{0.1}$). The process discharge loop was activated when the temperature difference between storage tank ($T_{0.9}$) and process return ($T_{process\ return}$) was greater than 10 K and deactivated at 5K. Temperature controls were put into place for the collector and storage tank, protecting both from stagnation and overheating. The discharge flowrate ($\dot{m}_{discharge}$) was regulated by a Type 805 heat exchanger (Heimrath and Haller, 2007), controlling the process flow temperature ($T_{process\ flow}$) to its set temperature when possible. If not achievable due to insufficient stored energy, the pump was operated at its maximum flow rate, which was set at 90% of the maximum flow rate of the process. The process was defined in section 2.3.

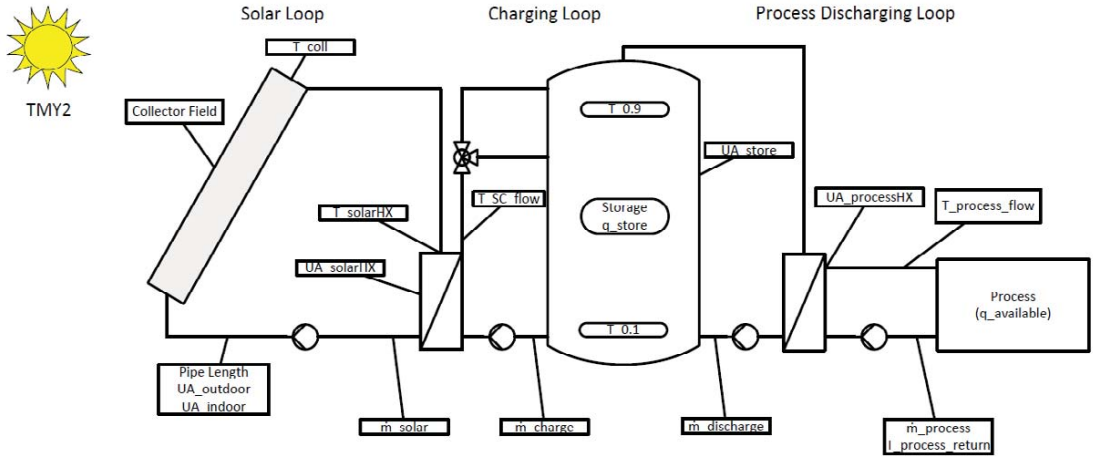

Fig. 1: The design of the solar thermal heating model in TRNSYS

2.2. Photovoltaic Heating Model

The solar loop for the PV heating model was built using Type 562, with inputs modelled after a high efficiency mono-silicon module, shown in Fig. 2. Two resistance heaters were implemented to directly heat the process fluid or water in the storage tank with an assumed efficiency of 98%. If the process load heating requirement ($q_{available}$) was greater than the available energy produced by the PV solar loop (q_{pv}), all electrical energy was directed to the process resistance heater. If excess energy was available, it was sent to the charging loop (storage) resistance heater. The charging loop variable speed pump adjusted the flow rate ($\dot{m}_{charge}$) to store the heat (Type 534) with high stratification. The discharge mass flow rate ($\dot{m}_{discharge}$) of the storage tank was controlled by determining the difference between $q_{available}$ and q_{pv}. If there was a deficit, the mass flow rate was calculated to heat the difference. This only occurred when there was a 10 K or greater difference between the upper storage tank temperature ($T_{0.9}$) and the process return temperature ($T_{process\ return}$). If the storage tank ever became full while the process load was completely heated by the PV system, any excess energy produced was considered wasted or sent to the local grid.

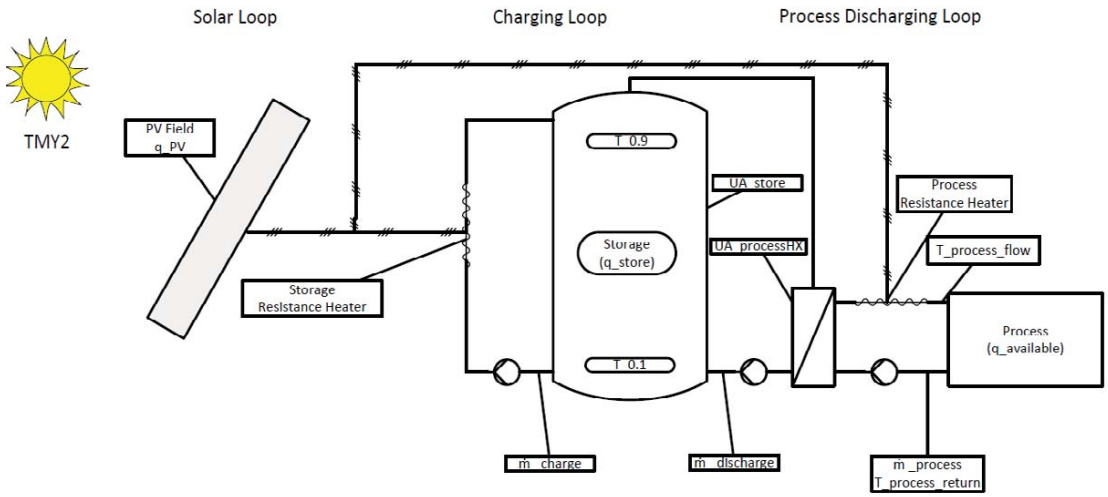

Fig. 2: The design of the solar PV heating model in TRNSYS

2.3. Simulation Parameters and Cases

A large parametric study was conducted to include geographical and industrial manufacturing conditions found all over the world. Quantities have been normalized to allow for easily scalability for specific conditions. For each parametric case, both a ST and PV simulation was conducted and subsequently compared.

Process Load and Profile

The process load quantity and temporal (daily, weekly) profile are two key parameters which have a significant influence on the overall performance of the industrial solar heating system. The load was defined as the daily energetic demand of the process divided by the gross area (A_g) of installed solar collector area (eq. 1). For instance, if the process has a daily flow of 30 m^3 from 45..75 °C with 125 m^2 of installed collectors, the specific daily load was calculated at 8.2 kWh/m^2d. Three various load quantities were simulated for this study, at 4, 6, and 10 kWh/m^2d, which represent a low, medium and high load demand. A load of 20 kWh/m^2d was also simulated to determine an ideal case which all thermal energy was immediately transferred to the load, thus eliminating the need for a storage tank.

$$q_{available} = \dot{V}_{process} \cdot \rho \cdot c_p \cdot \Delta T / A_g = 8.2 \ \frac{kWh}{m^2 d} \qquad \text{(eq. 1)}$$

Multiple daily and weekly load profiles have been recommended by Lauterbach (2014) for various cases found in industry. The best case scenario (highest efficiency) for a solar plant was a constant daily load profile which operates seven days a week (minimal heat losses). The mentioned load profile was partitioned into hourly sections, shown in Fig. 3. The hourly energy load, used in the TRNSYS simulations, was then determined by multiplying the hourly share of daily demand (Fig. 3) by specific daily load ($q_{available}$).

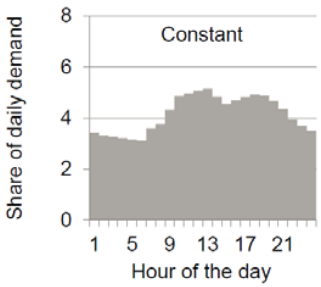

Fig. 3: Simulated daily load profile (Lauterbach, 2014)

Storage Tank Size

The available specific storage tank capacity (q_{store}) was defined by the stored thermal energy between the maximum rated storage tank temperature and the process load return temperature divided by the gross area of the ST system. Lauterbach (2014) recommended a specific storage tank capacity between 3 and 9 kWh/m^2 for low temperature solar thermal systems in central European climates. Due to higher process temperatures

and simulations conducted in higher solar resource regions, the specific storage tank sizes were 3, 5, 7, 9, and 11 kWh/m^2. The storage tank specific volume (v_{store}) was subsequently calculated (eq. 2), which determined the storage tank size capacity, in l/m^2. A typical non-pressurized storage tank had a $T_{0.9max}$ of 95 °C. If the $T_{process\ return}$ was 25 °C and a large q_{store} was desired (9 kWh/m^2), the calculated storage tank specific volume was 112.6 l/m^2.

$$v_{store} = q_{store}/c_p \cdot \rho \cdot \left(T_{0.9max} - T_{process_{return}}\right) = 112.6\ \frac{l}{m^2} \quad \text{(eq. 2)}$$

At higher temperatures, less energy was stored due to the storage tank thermal limitations. As a reference, the maximum storage tank temperatures were as followed (Tab. 1), based upon the process flow temperature.

Tab. 1: The relationship between process flow temperature and maximal allowed storage tank temperature

$T_{process\ flow}$ (°C)	$T_{0.9max}$ (°C)
< 90	95
< 120 and >90	130
>120	$T_{process\ flow}$ + 30

Collectors and Process Temperatures

Four solar thermal collectors (Flat Plate [FPC], Evacuated Tube [ETC], Compound Parabolic Concentrator [CPC], Parabolic Trough [PTC]) and one photovoltaic collector were selected for simulation. Each thermal collector was simulated at three temperature ranges, fitting for their potential applications in industry while the single PV collector covered all noted temperature ranges, as is the nature of electric heating. The ST collector model (Type 832V5.01) implemented the quasi-dynamic testing method (EN 12975-2 and ISO 9806:2013) for the parameters used by TRNSYS (Tab. 2). The PV model parameters (Type 562) were provided by the manufacturer (Tab. 3). All parameters are in terms of gross area, A_g. Incident Angle Modifiers (IAM, transverse, longitudinal, and diffuse) were also implemented.

Tab. 2: Solar thermal collector simulation parameters and load temperatures

		FPC	ETC	CPC	PTC
η_o (-)		0.77	0.48	0.56	0.59
c_1 (W/m^{2}K)		3.25	1.21	0.78	0.21
c_2 (W/m^{2}K^2)		0.0150	0.0038	0.0009	0.0013
c_5 (J/m^{2}K)		4425	12870	7379	1906
Process 1 (°C)	Return	30	45	60	75
	Flow	60	75	90	105
Process 2 (°C)	Return	45	60	75	90
	Flow	75	90	105	120
Process 3 (°C)	Return	60	75	90	110
	Flow	90	105	120	140

Tab. 3: Solar PV collector simulation parameters, G_T is defined as the incident irradiation on the tilted collector surface

	PV (Mono-silicon)
Reference Efficiency (%) at 25 °C and G_T:1000 W/m^2	19
Temperature Efficiency Modifier (1/C)	-0.0038
Radiation Efficiency Modifier (%)	$0.0502 \cdot \ln(G_T)+0.6833$

Locations

It was critical to select simulation sites whose results can provide analysis for nearly every location in the world. The two main factors which affected the performance of ST and PV systems were the daytime ambient temperature ($T_{amb,day}$) and diffuse ratio ($DR=H_d/H_t$). Given three levels (low, medium, and high) of both, nine sites were selected from the extended weather database in TRNSYS to conduct the parametric study, shown in Tab. 4. Fig. 4 included these nine sites, plotted in a line by similar diffuse ratios (indicated in Tab. 4), along with 1079 other sites within the TRNSYS database, which indicated how these nine sites provided representation for nearly all global climate conditions.

Tab. 4: The selected sites for simulation analysis, detailing their solar irradiation, average daytime ambient temperature, diffuse ratio, and latitude

Site	GHI (kWh/m²a)	DNI (kWh/m²a)	$T_{amb,day}$ (°C)	DR	Latitude (°)
Dongola, Sudan	2476	2843	29.8	0.22 (low)	19.17
Jerusalem	2093	2404	18.3	0.26 (low)	31.78
Eagle, Colorado, USA	1715	2031	9.6	0.33 (low)	39.65
Abu Dhabi, UAE	1957	1605	29.2	0.45 (mid)	24.43
Sydney, Australia	1608	1450	19.5	0.46 (mid)	-33.87
Kursk, Russia	1222	1334	9.1	0.46 (mid)	51.77
Copenhagen, Denmark	988	899	10.6	0.56 (high)	55.67
Bologna, Italy	1201	894	16.8	0.57 (high)	44.53
Kuching, Malaysia	1603	907	27.4	0.60 (high)	1.15

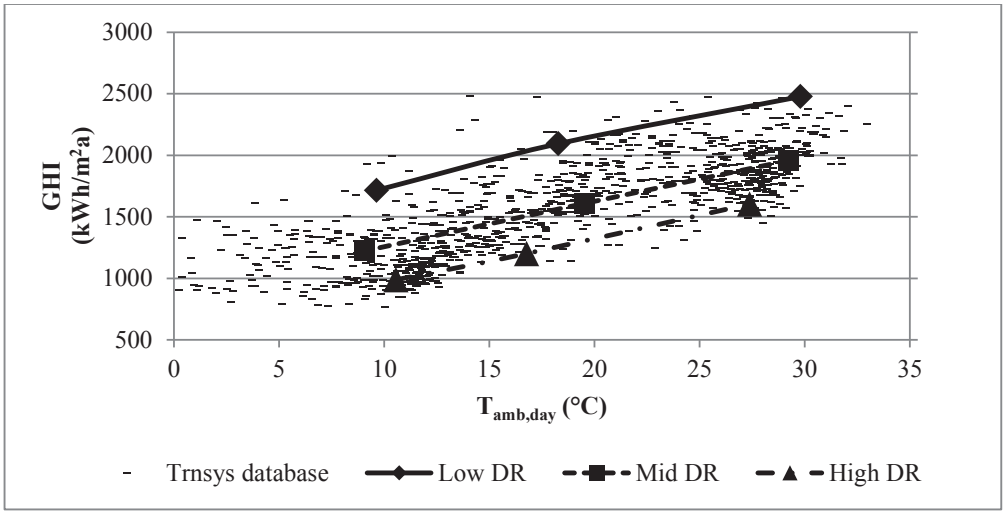

Fig. 4: Illustration of the nine selected sites for simulation, plotted in three lines respective of their DR levels, along with other sites found in the TRNSYS database

Simulation Setup and Key Results

The ST model was validated by comparing results to a similar model created by Lauterbach (2014) (validated on a solar process heat plant at a brewery in Germany), which yielded a system utilization ratio difference of less than -2%. The PV model used the same main components (pipes, storage tank, insulation, heat exchangers), only replacing the solar heating source. While not directly validated, it serves as a good approximation as what may be installed in the future, as no PV process heat plant is currently in operation.

The ST and PV parametric simulations were conducted using TRNEdit, once the TRNSYS simulation deck was finalized. Completed annual simulations recorded key variables such as the specific annual system yield (eq. 3), the annual system utilization ratio (eq. 4), and the solar fraction (eq. 5). The specific annual system yield was defined by the total energy delivered to the process load from the ST or PV system, taking into

account thermal losses of the hydraulics and storage tank. The annual utilization ratio was determined by dividing the specific annual system yield by the quantity of useable solar irradiation on the collector surface during the year (total or beam). The solar fraction was calculated by the dividing the specific annual system yield by the annual specific load.

$$Q_{yield}^{ST,PV} = \sum_{0}^{8760} \Delta Q_{process} \quad \text{(eq. 3)}$$

$$\eta_{system}^{ST,PV} = Q_{yield}^{ST,PV} / H_{t,b} \quad \text{(eq. 4)}$$

$$f_{sol}^{ST,PV} = Q_{yield}^{ST,PV} / \sum_{0}^{8760} q_{available} \quad \text{(eq. 5)}$$

There was an inherent mismatch between the standard units of ST and PV systems, as ST specific performance and costs are commonly per square meter and PV per watt peak (W_p). While these respective units are used in subsequent comparative analysis, a conversion was made between the two to ensure that both thermal systems have the same parameters (i.e. $q_{available}$, q_{store}) while being simulated. The peak specific energy yield by the ST system was estimated using the simulated collector parameters and expected mean collector temperature (Tab. 2). A similarly sized (by energy) PV system was then determined by dividing the ST peak specific energy yield by the nominal PV efficiency. For example, if a ST system generated 0.6 kW/m^2 for a given process temperature while assuming a 19% nominal efficiency of the PV system (0.19 kW/m^2), the simulated PV system must have gross surface area 3.15 times lager to yield the same peak thermal energy (input into TRNSYS). Through this, the previously mentioned specific simulation parameters can be used by both the ST and PV models, allowing for an equal comparison.

2.4. Energetic and Cost Comparisons

The Levelized Cost of Heat (LCOH) is a standard metric used when comparing two or more technology types to determine which has the lowest heat generation cost over a certain time period. Absolute LCOH values are important to determine when building solar systems, but for a comparison study relative costs are more insightful and allow for flexibility for multiple cost conditions.

The LCOH for both the ST and PV systems is shown in (eq. 6) with key parameters listed in Tab. 5.

$$LCOH = \frac{CapEx_{ST,PV} + \sum_{n=1}^{20} \frac{OM_{ST,PV}}{(1+DR)^n}}{\sum_{n=1}^{20} \frac{Q_{yield}^{ST,PV} * (1-SD)^n}{(1+DR)^n}} \quad \text{(eq. 6)}$$

Tab. 5: The input parameters to calculate the Levelized Cost of Heat

Parameter	Definition	ST Value	PV Value
$CapEx_{ST,PV}$	Capital Expenditure (€/m^2 or €/W_p)	Variable	Variable
$OM_{ST,PV}$	Operation and Maintenance (€/m^2 or €/W_p)	2% of CapEx	1% of CapEx
DR	Discount Rate	3.50%	3.50%
SD	Degradation Rate	1.0%	0.5%
n	Years of Operation	20	20

The LCOH Ratio was defined by the division of the LCOH of the ST system by that of the PV system for the same simulation case (eq. 7). This value was required to help calculate the Cost Ratio and also serves as an indicator to the lower cost solar heat system. When this value is greater than one, the heat generated from the PV system is less expensive, and when less than one, the heat from the ST system is.

$$LCOH_{ratio}(LHR) = \frac{LCOH_{ST}}{LCOH_{PV}} \quad \text{(eq. 7)}$$

If the $LCOH_{ratio}$ is set to one, it can be rearranged ($LCOH_{ST} = LCOE_{PV}$) and reformulated to determine the Cost Ratio (CR) (eq. 8), which is the $CapEx_{ST}$ divided by $CapEx_{PV}$. To do this, an assumed $CapEx_{PV}$ was input into the equation, along with the known annual ST and PV system yields. An iterative loop was written

in Matlab to determine the $CapEx_{ST}$ which makes $LCOH_{ST}$ = $LCOE_{PV}$ true, providing both inputs to determine the Cost Ratio, which was calculated for every parametric run.

$$CR = \frac{CapEx_{ST}}{CapEx_{PV}} \left(\frac{W_p}{m^2}\right), when\ LHR = 1 \quad \text{(eq. 8)}$$

For example, in a particular simulation the specific ST yield was 452 kWh/m^2 and the PV 1001 kWh/kWp. Using (eq. 6) with parameters from Tab. 5 and an assumed $CapEx_{PV}$ of 1.5 €/W_p (Shah and Booream-Phelps, 2015), the iterated $CapEx_{ST}$ was 576 €/m^2, leading to a CR of 384 W_p/m^2. When doing the same iteration under various $CapEx_{PV}$, the same CR was calculated.

The advantage of the CR is that it allows the comparative analysis in any currency to be flexible for the ever changing $CapEx_{ST,PV}$, whether it is from technology/system improvements or changes in local subsidies. It is used in two ways: either one CapEx is known and the other is determined using the simulated CR; or both $CapEx_{ST,PV}$ are known and are compared against the simulated CR. For the first case, the $CapEx_{PV}$ tends to be less variable than that of ST, due to the commoditization of PV panels and is for example purposes, set at 1.3 €/W_p. Assuming a simulated CR of 384 W_p/m^2, these two values are multiplied together to determine the maximum cost of a comparable ST system (eq. 9) for it to be financially competitive with the PV system. For the second case, if both CapExs are known (450 €/m^2 and 1.6 €/W_p), the CR is calculated to be 281 W_p/m^2 (eq. 10) and when less than simulated CR, ST produced heat at a lower cost.

$$1.3 \frac{€}{W_p} \cdot 384 \frac{W_p}{m^2} = 499 \frac{€}{m^2} \quad \text{(eq. 9)}$$

$$450 \frac{€}{m^2} / 1.6 \frac{€}{W_p} = 281 \frac{W_p}{m^2} \quad \text{(eq. 10)}$$

Graphical representation of the CR as a function of solar irradiation and ambient temperature were constructed per simulation case to serve as an easy to use guide to determine which industrial solar heating system has the lowest cost.

3. Simulation Results

3.1. Energy Yields and Cost Ratios

Three simulation sites are shown to illustrate the type of results obtained from the parametric study with indicated process temperatures and selected ST technology. The first site was Copenhagen (FPC), the second Sydney (CPC), and the final Abu Dhabi (PTC) (Fig.5). For this example, the process load ($q_{available}$) was 6 kWh/m^{2}d and storage tank size (q_{store}) 9 kWh/m^2, indicating a medium load and large store. The process temperatures for each case are noted on the x-axis. The primary y-axis shows the system utilization ratio (η_{system}) and the secondary the associated Cost Ratio (CR).

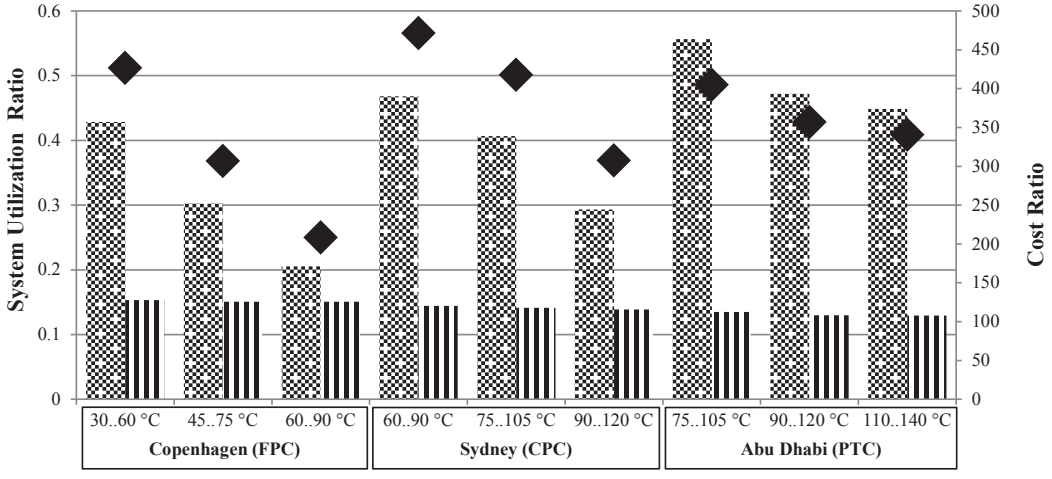

Fig. 5: Three exemplary sites showcasing the ST and PV system utilization ratios and Cost Ratio for three temperature levels and ST technologies

3.2. Comparison Graphs

To graphically compare ST and PV heating systems, new plots were constructed with the CR on the x-axis and the respective available solar irradiation on the y-axis for the nine sites during one parametric simulation (one collector, process temperature, load, and storage tank size). Sites with similar ambient daytime temperatures (Low~10°C, Medium~18°C, High~28°C) were connected with lines, which represent LHR lines. The CR and GHI cases above this line represents situations when the LHR<1, indicating that heat generated by a ST system is less expensive, and the contrary below said line. Fig. 6 shows a lower temperature case with FPC while Fig. 7 was for a higher temperature case with PTC. The previously mentioned sites are circled in each figure as a reference.

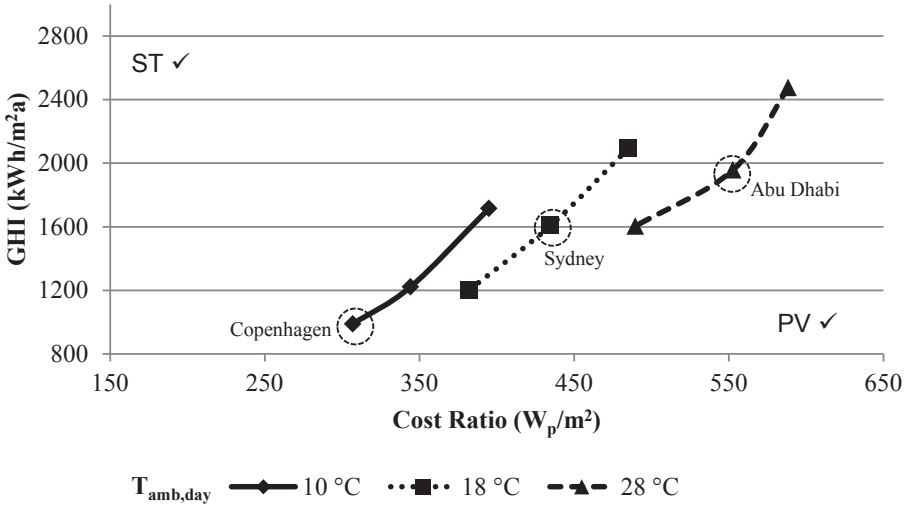

Fig. 6: Solar Thermal and PV comparison graph for a FPC with a process of 45..75 °C, specific load of 6 kWh/m²d, and specific store of 9 kWh/m²

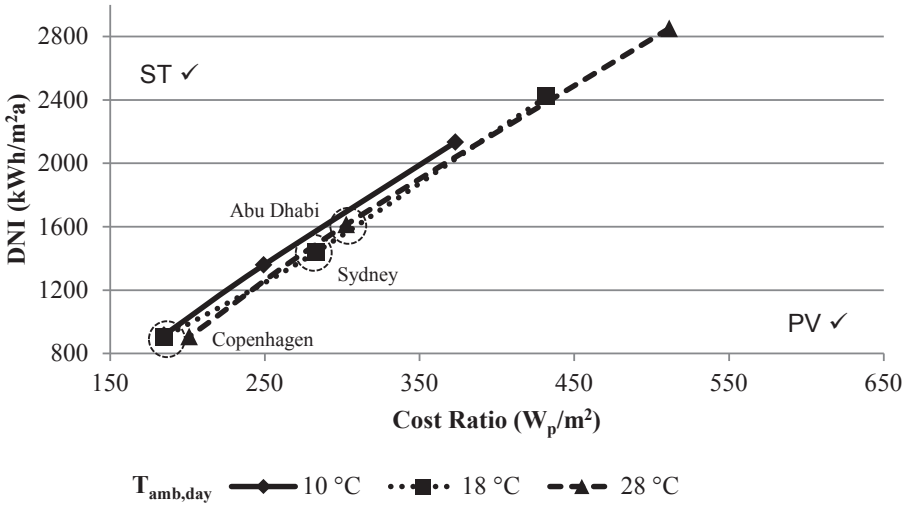

Fig. 7: Solar Thermal and PV comparison graph for a PTC with a process of 110..140 °C, specific load of 10 kWh/m²d, and specific store of 9 kWh/m²

3.3. Example Application of Comparison Graphs

The use of the comparison graphs provided a powerful yet easy to understand tool to determine which industrial solar heating technology can provide a lower cost of heat. As an example case, Fig. 8 detailed two ST collectors (FPC, CPC) for one case (process temperatures 60..90 °C, load 6 kWh/m²d, store 7 kWh/m²);

something which may happen in reality when deciding between different collectors for a system. Tab. 6 highlighted four technology comparisons for two different locations along with the determined CR by using Fig. 8. This was done per site by drawing a horizontal line from the y-axis at the corresponding GHI to the fitting temperature line (or interpreted between two lines) of the desired ST technology. From this point, a vertical line was drawn to the x-axis, which determined the CR for that case. The CR was then used, as in (eq. 9), to determine the competitive maximum cost of a ST system by simply multiplying the known PV cost (€/W_p) by the Cost Ratio (W_p/m^2) (Tab. 6). If a Cost Ratio was already known through local ST and PV costs, the comparison can be done in reverse. A vertical line could be drawn up from the x-axis and a horizontal line right from the y-axis (given the local solar irradiation). The intersection point of these two lines was compared to the local temperature line (the LHR line). If this point was above the line, ST was a better choice (indicated by the ST check mark in the upper left hand corner). If below the curve, PV was selected (PV check mark in the lower right hand corner).

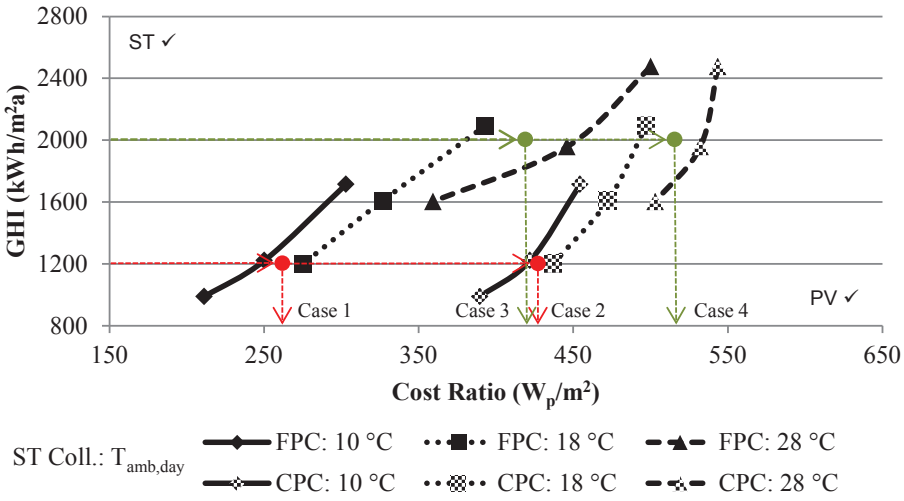

Fig. 8: An example of how to use the comparison graphs to determine the Cost Ratio for specific locations and system cases. These plots are valid for process temperatures 60..90 °C, load 6 kWh/m²d, and store 7 kWh/m²

Tab. 6: Input parameters and results for use in the comparison graph example in Fig. 8

Case	Site	GHI (kWh/m²a)	$T_{amb,day}$ (°C)	ST Technology	CR (W_p/m^2)	PV Cost (€/W_p)	ST Max. Cost (€/m²)
1	1	1200	14	FPC	265	1.2	318
2	1	1200	14	CPC	430	1.2	516
3	2	2000	23	FPC	420	1.5	630
4	2	2000	23	CPC	515	1.5	773

4. Discussion

The resulting energetic simulations in TRNSYS revealed the expected results for the both the ST and PV heating systems. For all three presented cases (Fig. 5), the ST system utilization ratio decreased as a function of process temperature, due to increased collector thermal losses. While three different technologies were used for Copenhagen, Sydney, and Abu Dhabi, it was clearly shown that ambient temperature plays a large role in the effectiveness of such collectors, as Abu Dhabi's showed the highest average system utilization factor and Copenhagen the lowest. The opposite was true for the PV systems, where a lower system utilization ratio occurred in the higher irradiation regions, namely due to greater ambient temperatures and the technology's negative temperature efficiency modifier. The higher process temperature PV systems showed a small decrease in performance due to larger thermal losses in the storage tank. Combining these two trends together, it was understandable that the Cost Ratio for all ST technologies decreased as a function of process temperature. The rate of decrease was less for the PTC and CPC, as both technologies had smaller thermal losses (c_1, c_2) and are more immune to reduced performance at higher process temperatures.

The results shown in Fig.6 and Fig.7 demonstrated the goals of this research, to create an easily understood graph which helps determine the preferred renewable solar heating technology; no matter where it is geographically located, when it may be built, and which currency is used. Analysis of this graph determined clear trends which are supported by other simulations not detailed in this paper. The best conditions for ST systems are exhibited in Fig. 6, for a lower temperature heating process load met using relatively inexpensive FPC. In higher temperature regions with high solar irradiation like Abu Dhabi, given present and future PV costs, it does not seem likely that PV would ever overtake ST. In lower temperature and solar regions like Copenhagen, PV heating may pose a near term threat. This was mainly due the location's numerous cold and cloudy days in which no energy was produced by ST while PV still could, actually benefiting from the colder temperatures and having a lower minimum solar irradiance requirement for energy production. The contrary was shown in Fig. 7, the situation where PV may soon, if not already, overtake ST as the preferred industrial solar heating choice. For higher temperature processes requiring a concentrating collector, all three temperature lines are shifted left towards the y-axis, indicating a decreased Cost Ratio and thus more competitive PV system. This can be a challenge, as concentrating collectors tend to be more expensive than other solar thermal technologies. If PV costs were assumed to be 1 €/W_p, then even in regions with a DNI resource of greater than 2000 kWh/m^2a, the installed cost of a PTC system must be less 400..500 €/m^2, difficult given their current estimated costs (Frank et al., 2013).

5. Conclusion and Future Work

This study was conducted in order to provide insight into the future of industrial process heating by solar energy. Traditionally, this has been done with solar thermal collectors. However, with the continued development of lower cost PV systems and their inherent ease of installation, this technology may prove to provide a lower cost source of low carbon heat. Through energetic simulations and comparative financial analysis, it was shown that for lower temperature process heat cases, solar thermal systems will most likely remain the preferred technology choice. The contrary was true for higher temperature applications, especially in colder, lower solar resource locations, where PV is already a competitive choice for heat generation. The exhibited results were crafted in such a way that they can be used for nearly any industrial process heat condition, global location, and present or future technology cost. The opportunity cost of not using PV energy for offsetting local electricity consumption was not considered. This is one avenue of future work, along with the assessment of industrial heat pumps working together with ST and PV to provide the lowest carbon emission heat source for industrial applications.

6. Acknowledgements

The authors wish to acknowledge the European Union for funds received through the People Programme (Marie Curie Actions) of the Seventh Framework Programme FP7/2007-2013/ under REA grant agreement n° 317085 (PITN-GA-2012-317085), commonly known at the SHINE (Solar Heat INtegration Network) Program (https://www.uni-kassel.de/projekte/solnet-shine/home.html).

7. References

Fanney, A. H. and Dougherty, B. P., 1997. A Photovoltaic Solar Water Heating System, J. Sol. Energy Eng, 119, 126–133, doi:10.1115/1.2887891

Frank, E., Feuerstein, M., Minder, S., and & AG, N. S.: Parabolrinnenkollektoren für Prozesswärme in Schweizer Molkereien, 2013.

Haller, M., Peres, B., Bales, C., Paavilainen, J., Dalibard, A., Fischer, S., Bertram, E., 2013. TRNSYS Type 832 v5.01 "Dynamic Collector Model by Bengt Perers" Updated Input-Output Reference

Heimrath, R. and Haller, M., 2007. The Reference Heating System, the Template Solar System. A technical report of Subtask A. A Report of IEA-SHC Task 32. Institute of Thermal Engineering, Division Solar Energy and Thermal Building Simulation, Graz University of Technology, Graz, Austria

ISO, E. (2013). 9806: 2013. Solar energy–Solar thermal collectors–Test methods.

Lauterbach, Christoph, 2014. Potential, system analysis and preliminary design of low-temperature solar process heat systems. PhD Dissertation, University of Kassel

Le Berre, R., Dupeyrat, P., Plotton, A., Doucet, J.-F., and Lindsay, A., 2014. PV Domestic Hot Water System, EuroSun Proceedings, Aix-les-Bains, France

Shah, V. and Booream-Phelps, J.,2015. Crossing the Chasm: Solar Grid Parity in a Low Oil Price Era, Deutsche Bank

Standard, B. S., & EN, B. (2006). EN 12975-2: 2006, Thermal solar systems and components. Solar collectors. Test methods

Verein Deutscher Ingenieure (VDI), 2014. 6002 - Solar heating of potable water, Basic principles

Conference Proceedings

EuroSun 2016
Palma de Mallorca (Spain), 11 - 14 October 2016

Modelling of a Solar Dryer for Food Preservation in Developing Countries

Joakim Olsson[1] and Henrik Davidsson[1]

[1] Lund University (Sweden)

Abstract

Food insecurity has proven to be a significant problem in many developing countries, which in some cases occurs due to the lack of adequate methods of preserving foods for longer periods of time. Solar drying of foods could be a feasible method for preserving foods in developing countries. To maintain a good product quality, the design of the solar dryer used needs to be considered. A faulty design will result in the foods being exposed to either excessive heat, which will degrade nutrients such as Vitamin C, or exposed to insufficient heat which could result in growth of mold or bacteria.

In this study a base scenario for a solar dryer design has been set up and mathematically analyzed to find ways of improving the design and identifying the most important parameters to consider. The study will serve as a part of an ongoing project at Lund University in Sweden, which will be implemented in Mozambique. The results of the study imply that the collector performance can be improved significantly if the most important parameters are optimized. For future work, more practical measurements would be required to verify the results, particularly regarding the evaporation rate of the drying products.

Keywords: *Solar drying, food preservation.*

1. Introduction

The malnutrition in developing countries has proven to be a persistent problem over the decades and appears to remain unsolved despite the economic growth that has occurred in some of the countries. Among these developing countries is Mozambique, which had a Human Development Index (HDI) positioned at rank 180 out of 188 countries and territories in 2014 by the United Nations Developing Programme, despite the HDI value being 75 % higher than in 1980 (UNDP, 2015). Almost one-third of Mozambicans, most of them living in the south and centre regions, suffer from chronic food insecurity and the country is prone and sensitive to natural disasters such as drought and flooding (World Food Programme, 2016).

Even if a major number of Mozambicans are suffering from malnutrition, it is not due to insufficient harvests. Previous studies have found that Mozambique suffer 25 % to 40 % post-harvest losses of crops, mainly due to inadequate preservation methods and infrastructure (Phinney et al., 2015). Since Mozambique currently is lacking the economical means and infrastructure to support conventional preservation methods of non-developing countries, improvement of the current drying methods is limited in terms of complexity. Having this problem in mind, an ongoing project at Lund University aims to find a simple and economical method for food preservation that can be implemented in Mozambique.

One method for preserving the fruit is using an indirect solar dryer consisting of a solar collector connected to a drying tower according to Fig. 1, which will be the main focus of this study. An indirect solar dryer uses a solar collector to heat air which is then transported to a drying unit which is protected from direct sunlight (Kumar et al., 2015). Since the sunlight doesn't directly irradiate the surface of the drying products, the risk of crust formation on the drying products, which tends to reduce the drying rate, is greatly reduced (Mills-Gray, 1994). Another benefit of an indirect solar dryer is the hygiene of the products as they are more protected from

doi:10.18086/eurosun.2016.02.19 Available at http://proceedings.ises.org

the environment. To further improve the hygiene, Solar Assisted Pervaporation technology (SAP) can be used in combination with indirect solar dryers. The SAP-technology involves a textile semi-permeable to water, being impermeable to liquid water while water vapor can pass freely through the textile. Using this textile, pouches can be made to hold various fruit juices for drying, which will be referred to as SAP-pouches. The liquid fruit juice will be kept inside the pouch, protecting it from contamination, while the evaporated water can still escape the pouch. The textile is also designed to prohibit any microorganisms from entering the pouches. This means that if the fruit juice becomes pasteurized inside the pouch, it will remain sterile and thus preserve the foods for longer (Phinney et al., 2015). The drying process of indirect solar dryers mainly depends on the drying conditions inside the drying chamber, being the air mass flow rate, airflow temperature and relative humidity (Blanco-Cano et al., 2016). In other words, if these three key parameters can be improved, the dryer performance will also be improved.

The aim of the study is to set up a mathematical model for an indirect solar thermal dryer that can be used to dry SAP-pouches containing fruit juices in developing countries such as Mozambique. Furthermore, the model was used to generate simulations to identify ways of improving the dryer performance. To perform the simulations, the model was implemented in a calculation tool which could also assist the project in Mozambique in the future. The calculation tool was programmed in Maple 2015, a software used analyse, visualise and solve mathematical problems (Maplesoft, 2016).

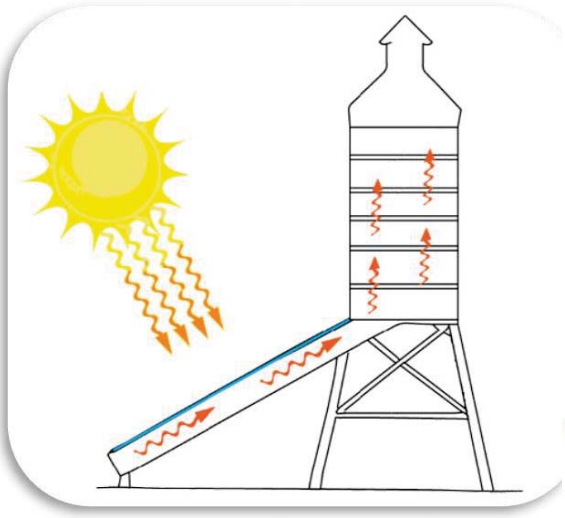

Fig. 1: Schematic figure of a solar dryer. The orange arrows inside the dryer are representing the air flow *(PAEGC & TH Cologne, 2016)*.

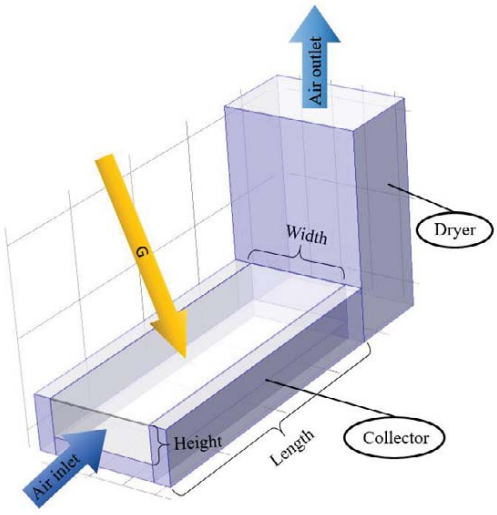

Fig. 2: Schematic figure of the model. The solar dryer is consisting of two parts: the collector and the dryer. The collector consists of a glass layer on the top, insulation on the sides and the bottom and an absorber plate on top of the bottom insulation layer. The dryer is insulated on the sides and contains shelves with SAP-pouches.

2. Method

To set up the model for the solar dryer, the solar dryer was divided into two sections according to Fig. 2; the collector and the dryer. This was essential since collector and the dryer are containing different conditions for setting up energy balances. The output air temperature of the collector will be used as an input temperature for the dryer air flow. The main idea for the model is to identify all flows of energy going in and out of the collector and the dryer in order to set up energy balances. The energy balances made for each surface of the collector and dryer respectively, i.e. the absorber plate, glazing and walls, will serve as equations that can be used in equation systems for the collector and the dryer. The equation systems are solved for relevant surface temperatures and the drying rate of the SAP-pouches is estimated from the drying conditions. To simplify the model, the following assumptions were made:

2.1. Assumptions

- The collector and dryer are in steady state for a constant solar irradiation. In reality the solar radiation will vary with time and weather conditions.
- No air leakages.
- The collector inner sides are assumed to have the mean temperature of the absorber and the glazing of the collector.
- The temperatures of the SAP-pouches are equal to the surrounding air temperature and the bags are not dried out. In practise the evaporation rate from the SAP-pouches will differ when the dryer is warming up since the pouch temperature will increase, absorbing heat.
- The parameters ρ (density), C_P (specific heat), μ (dynamic viscosity), λ_{air} (heat conductivity for air) and Pr (Prandtl number for air) have been assumed to be constant for 300 K and 1 atm.
- The inner sides of the collector will not reflect any radiation. Instead, all heat radiation is reflected between the absorber and the glass. Furthermore, the heat radiation from the absorber to the glass is also assumed to be normal to the absorber. In practise the heat will radiate in several directions from the absorber and the glass.
- Fully developed laminar air flow for Re (Reynold number) < 3000 and fully developed turbulent air flow for $3000 \leq Re \leq 5 \cdot 10^5$. For the turbulent interval, the characteristic length of the collector/dryer must be at least 10 times greater than the hydraulic diameter.
- No heat transfer between SAP-pouches.
- The ambient temperature is within the interval 0 °C < T_{amb} < 100 °C, the valid interval for using Antoine's equation for saturation pressure.
- The glass does not absorb any sunlight ($\alpha_{glass} = 0$).
- The collector sides and bottom and the dryer do not absorb any sunlight on the outside. Additional heat gains of the dryer will be added independently of the solar irradiation G.
- The convective heat transfer coefficient for all exterior walls $h_{con,\ out}$ is assumed to be a constant value of 20 W/(m²·K) (Sekhar et al., 2009) (Kumar Moningi, 2016).
- The outward heat radiation of the side areas of the collector and the dryer walls are assumed to radiate 50 % towards the sky temperature (T_{sky}) and 50 % towards the ground (T_{amb}).

2.2. The collector

For the collector, four different surfaces are identified: the glazing, the air flow, the absorber plate and the exterior walls of the sides and bottom. Each surface will have a certain temperature according to Fig. 3, dependant on the ambient conditions and the design of the collector. Energy balances for each of the four surfaces can be put together as an equation system for the entire collector and solved in Maple 2015. The energy balances will be set up with regards to the three possible ways of heat transfer; convection, conduction and radiation according to Fig. 3. Note that Fig. 3 displays the cross section of the collector and that the absorber will have absorbed some of the solar irradiation G, referred to as G_e. For explanation of all parameters used in the study, see the Nomenclature section of the appendix.

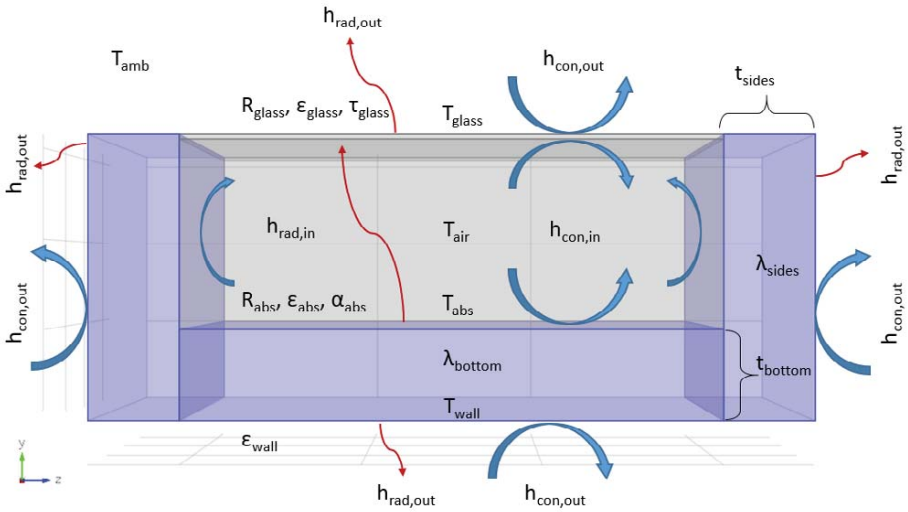

Fig. 3 : Schematic figure for all energy flows and temperatures that are included in the model for the collector. Energy balances for the glass, air flow, absorber and outer wall of the collector will be set up according to this figure. Blue arrows are representing convective heat transfer, red arrows are representing radiative heat transfer and lambdas are representing conductive heat transfer.

2.2.1 The glazing

The energy balance for the glazing consists of four energy flows according to Fig. 3. The warm absorber plate will radiate heat towards the glazing and the heated air flow will transfer heat to the glass by convection, which can be considered as the heat gains of the glazing. The heat losses of the glazing occur by radiation towards the sky and convection to the ambient air. Having identified the heat gains and losses of the glazing, the energy balance can be set up according to eq. 1.

$$h_{con,in} \cdot A_{abs} \cdot \left(\frac{T_{in}+T_{out}}{2} - T_{glass}\right) + h_{rad,in} \cdot A_{abs} \cdot \left(T_{abs} - T_{glass}\right) - h_{con,out} \cdot A_{abs} \cdot \left(T_{glass} - T_{amb}\right) - h_{rad,out} \cdot A_{abs} \cdot \left(T_{glass} - T_{sky}\right) = 0 \quad \text{(eq. 1)}$$

The external convective heat transfer coefficient $h_{con,out}$ is assumed to be a constant value of 20 W/(m²·K), but $h_{con,in}$, $h_{rad,in}$ and $h_{rad,out}$ needs to be calculated using relevant equations. Radiative heat transfer can be calculated according to eq. 2 for the heat radiating from the absorber and eq. 3 can be used to calculate the heat radiating from the glazing to the atmosphere (Incropera & Dewitt, 2002).

$$h_{rad,in} = \frac{\frac{1}{\frac{1}{\varepsilon_{abs}} + \frac{1}{\varepsilon_{glass}} - 1} \cdot \sigma \cdot \left(T_{abs}^4 - T_{glass}^4\right)}{T_{abs} - T_{glass}} \quad \text{(eq. 2)}$$

$$h_{rad,out} = \frac{\varepsilon_{glass} \cdot \sigma \cdot \left(T_{glass}^4 - T_{sky}^4\right)}{T_{glass} - T_{sky}} \quad \text{(eq. 3)}$$

The internal convective heat transfer coefficient for turbulent flows can be calculated using the definition of the Nusselt number according to eq. 4, where the definition of the hydraulic diameter of the collector can be found in eq. 5. For laminar air flows, $Re_{air} < 3000$, the Nusselt number is set to a constant value depending on the ratio between the height and the width of the collector (Incropera & Dewitt, 2002).

$$Nu = \frac{h_{con,in} \cdot D_h}{\lambda_{air}} \quad \text{(eq. 4)}$$

$$D_h = \frac{2 \cdot Height \cdot Width}{Height + Width} \quad \text{(eq. 5)}$$

To calculate the Nusselt number, eq. 6 can be used where the friction factor *f* is defined according to eq. 7. The Reynold number Re_{air} is calculated using the hydraulic diameter of the collector (Incropera & Dewitt, 2002).

$$\mathrm{Nu} = \frac{\left(\frac{\mathrm{f}}{8}\right) \cdot (\mathrm{Re_{air}} - 1000) \cdot \mathrm{Pr_{air}}}{1 + 12{,}7 \cdot \left(\frac{\mathrm{f}}{8}\right)^{\frac{1}{2}} \cdot (\mathrm{Pr_{air}}^{\frac{2}{3}} - 1)} \quad \text{(eq. 6)}$$

$$\mathrm{f} = (0{,}790 \cdot \ln(\mathrm{Re_{air}}) - 1{,}64)^{-2} \quad \text{(eq. 7)}$$

Using eq. 4 and eq. 6, the internal convective heat transfer coefficient can be calculated, resulting in all heat transfer coefficients of eq. 1 being identified as functions of various collector temperatures. Eq. 1 can now be used as one out of four equations of the equation system for the collector.

2.2.2 The air flow

Unlike the glazing, the air flowing through the collector will not absorb or emit any considerable amounts of heat radiation. The heat gains and losses of the air flow will thus only be convective heat transfer as well as the energy required to raise the temperature of the air. Since the air will contain moisture, especially in a sub-tropical country such as Mozambique, the water vapour passing through the collector should also be considered. Taking the water vapour into consideration will also be important for determining the drying rate.

The absorber and the inner sides of the collector will transfer heat to the air through convection, resulting in the first two terms of eq. 8, the energy balance of the air flow. At the same time, convective heat losses are likely to occur towards the glazing, resulting in the third term of eq. 8. Note that the absorber area and the glazing area are equally large. The fourth and fifth term of eq. 8 are representing the heat that is absorbed by the air flow, where the fourth term is dry air and the fifth term is water vapour.

$$\mathrm{h_{con,in}} \cdot \mathrm{A_{abs}} \cdot \left(\mathrm{T_{abs}} - \frac{\mathrm{T_{in}}+\mathrm{T_{out}}}{2}\right) + \mathrm{h_{con,in}} \cdot \mathrm{A_{sides}} \cdot \left(\frac{\mathrm{T_{abs}}+\mathrm{T_{glass}}}{2} - \frac{\mathrm{T_{in}}+\mathrm{T_{out}}}{2}\right) - \mathrm{h_{con,in}} \cdot \mathrm{A_{abs}} \cdot \left(\frac{\mathrm{T_{in}}+\mathrm{T_{out}}}{2} - \mathrm{T_{glass}}\right) - (\mathrm{T_{out}} - \mathrm{T_{in}}) \cdot \rho_{\mathrm{air}} \cdot \mathrm{C_{P,air}} \cdot \mathrm{u_{air}} \cdot \mathrm{A_{inlet}} - (\mathrm{T_{out}} - \mathrm{T_{in}}) \cdot \mathrm{C_{P,H2O}} \cdot \mathrm{m_h} = 0 \quad \text{(eq. 8)}$$

Using eq. 4-7, $h_{con,in}$ can be identified in eq. 8, resulting in the water mass flow m_h, being the only unknown parameter of eq. 8. The air velocity u_{air} is not considered as being temperature-dependent in the model and is set to a constant value. To determine the mass of water that passes through the collector each second, the relative humidity of the ambient air can be used. The relative humidity is defined as the ratio between the vapour pressure of the water and the saturation pressure of pure water at the same temperature (Alvarez H., 2006). This is shown in eq. 9.

$$\mathrm{RH} = 100 \cdot \frac{\mathrm{P_w}}{\mathrm{P_{ws}}} \quad \text{(eq. 9)}$$

To find the partial pressure of the water vapour, the saturation pressure needs to be calculated for a specific temperature. Using Antoine's equation, found below as eq. 10, the saturation pressure can be calculated where *A*, *B* and *C* are constants valid for a certain interval of temperatures (R.K.Sinnot, 2005).

$$\log(P_{ws}) = A - \frac{B}{T+C} \quad \text{(eq. 10)}$$

Combining eq. 9 and eq. 10 results in the partial pressure P_w being identified as a function of the air temperature. The water vapour in the air flowing through the collector can be assumed to be an ideal gas, meaning that the mass flow of water through the collector can be calculated according to eq. 11 (Atkins P. & de Paula J., 2002), resulting in all parameters of eq. 8 being identified as functions of various collector temperatures.

$$\mathrm{m_h} = \frac{\mathrm{P_w}}{\mathrm{R_V} \cdot \mathrm{T_{amb}}} \cdot \mathrm{A_{inlet}} \cdot \mathrm{u_{air}} \quad \text{(eq. 11)}$$

2.2.3 The absorber

The absorber plate contains one unique parameter, being the effective solar irradiation G_e. To calculate G_e, the optical properties of the glazing and the absorbers ability to absorb sunlight needs to be considered in terms of reflection, transmission and absorption. The resulting equation can be found in eq. 12. Note that expression contains no absorbance coefficient for the glazing, since the glazing is assumed to not absorb any sunlight.

$$G_e = \frac{G \cdot \tau_{glass} \cdot \alpha_{abs}}{1 - R_{abs} \cdot R_{glass}} \quad \text{(eq. 12)}$$

Having identified G_e, the full equation for the energy balance for the absorber is set up according to eq. 13. Note that the energy losses from the interior walls to the exterior walls of the collector have been included in the energy balance, where the interior walls are assumed to have the mean temperature of the absorber and the glazing.

$$\mathrm{G} - \mathrm{h_{con,in}} \cdot \left(\mathrm{T_{abs}} - \frac{\mathrm{T_{in}}+\mathrm{T_{out}}}{2}\right) - \mathrm{h_{rad,in}} \cdot \left(\mathrm{T_{abs}} - \mathrm{T_{glass}}\right) - \frac{\lambda_{\mathrm{bottom}}}{\mathrm{t_{bottom}}} \cdot \left(\mathrm{T_{abs}} - \mathrm{T_{wall}}\right) - \frac{\lambda_{\mathrm{side}}}{\mathrm{t_{side}}} \cdot \frac{\mathrm{A_{sides}}}{\mathrm{A_{abs}}} \cdot \left(\frac{\mathrm{T_{abs}}+\mathrm{T_{glass}}}{2} - \mathrm{T_{wall}}\right) - \mathrm{h_{con,in}} \cdot \frac{\mathrm{A_{sides}}}{\mathrm{A_{abs}}} \cdot \left(\frac{\mathrm{T_{abs}}+\mathrm{T_{glass}}}{2} - \frac{\mathrm{T_{in}}+\mathrm{T_{out}}}{2}\right) = 0 \quad \text{(eq. 13)}$$

The parameter $h_{con,in}$ is calculated using the same method as for the glazing and the parameter $h_{rad,in}$ is calculated using eq. 2.

2.2.4 The external walls of the collector

The external walls of the collector include the bottom and the sides of the collector. The amount of heat being transferred from the external walls to the ambience are important to acknowledge, since these will correspond to the amount of heat that is lost through the insulation. All heat gains to the exterior walls will be heat being conducted from the interior or the collector through the insulation layer, as shown in first two terms of eq. 14.

$$\frac{\lambda_{\mathrm{bottom}}}{\mathrm{t_{bottom}}} \cdot \left(\mathrm{T_{abs}} - \mathrm{T_{wall}}\right) + \frac{\lambda_{\mathrm{side}}}{\mathrm{t_{side}}} \cdot \frac{\mathrm{A_{sides}}}{\mathrm{A_{abs}}} \cdot \left(\frac{\mathrm{T_{abs}}+\mathrm{T_{glass}}}{2} - \mathrm{T_{wall}}\right) - \mathrm{h_{con,out}} \cdot \frac{(\mathrm{A_{abs}}+\mathrm{A_{sides}})}{\mathrm{A_{abs}}} \cdot \left(\mathrm{T_{wall}} - \mathrm{T_{amb}}\right) - \mathrm{h_{rad,out1}} \cdot \left(\mathrm{T_{wall}} - \mathrm{T_{amb}}\right) - \mathrm{h_{rad,out1}} \cdot \frac{\mathrm{A_{sides}}}{2 \cdot \mathrm{A_{abs}}} \cdot \left(\mathrm{T_{wall}} - \mathrm{T_{amb}}\right) - \mathrm{h_{rad,out2}} \cdot \frac{\mathrm{A_{sides}}}{2 \cdot \mathrm{A_{abs}}} \cdot \left(\mathrm{T_{wall}} - \mathrm{T_{sky}}\right) = 0 \quad \text{(eq. 14)}$$

The heat losses of the external walls will occur by convection affecting the sides and the bottom, but also by radiation. The sides have been assumed to radiate 50 % towards the atmosphere and 50 % to the ground and the bottom of the collector will radiate towards the ground. This can be seen in eq. 14 as the last three terms, where $h_{rad,out1}$ and $h_{rad,out2}$ are calculated according to eq. 15 and eq. 16 respectively. The ground is assumed to have the same temperature as the ambient air, T_{amb}.

$$\mathrm{h_{rad,out1}} = \varepsilon_{\mathrm{wall}} \cdot \sigma \cdot \frac{\mathrm{T_{wall}^4} - \mathrm{T_{amb}^4}}{\mathrm{T_{wall}} - \mathrm{T_{amb}}} \quad \text{(eq. 15)}$$

$$\mathrm{h_{rad,out2}} = \varepsilon_{\mathrm{wall}} \cdot \sigma \cdot \frac{\mathrm{T_{wall}^4} - \mathrm{T_{sky}^4}}{\mathrm{T_{wall}} - \mathrm{T_{sky}}} \quad \text{(eq. 16)}$$

After identifying equations for energy balances for the glazing, the air flow, the absorber and the external walls of the collector, an equation system for eq. 1, eq. 8, eq. 13 and eq. 14 can be set up and solved for T_{out}, T_{abs}, T_{glass} and T_{wall}. To create more accurate results, the equation system can be solved multiple times after dividing the collector into segments, also known as the finite element method. The segments are distributed over the length of the collector and the equation system is solved individually for each segment. The calculated outlet air temperature of the first segment can then be used as the input temperature for the air flow of the next segment. As an example, if a 1 m long collector is divided into two segments the first segment will include the first 0,5 m of the collector and show the mean temperatures for that length. The reason why more segments enhance the accuracy of the simulation is because the radiative heat transfer

coefficient will vary from segment to segment in a non-linear manner.
The number of segments that can be used are unlimited using Maple 2015, but a higher number of segments (a higher resolution) will result in a slower simulation speed. The resolution used to generate the results of the study was set to 250, which can be regarded as more than sufficient for solar collectors since they are generally rather short.

2.3 The dryer

Once the air has been heated up in the solar collector, it will enter the dryer containing the SAP-pouches. The dryer is modelled according to Fig. 4, where three surfaces can be identified; the dryer air flow, the internal- and the external walls of the dryer. Unlike the collector, the dryer will be split up in segments according to the number of shelves within the dryer, where each shelf will hold a certain number of SAP-pouches from which water will evaporate. Note that Fig. 4 is an example of a dryer section for a dryer holding one SAP-pouch per shelf. The released water from the shelves will accumulate from shelf to shelf, which will increase the resistance for evaporation of the bags further up in the dryer.

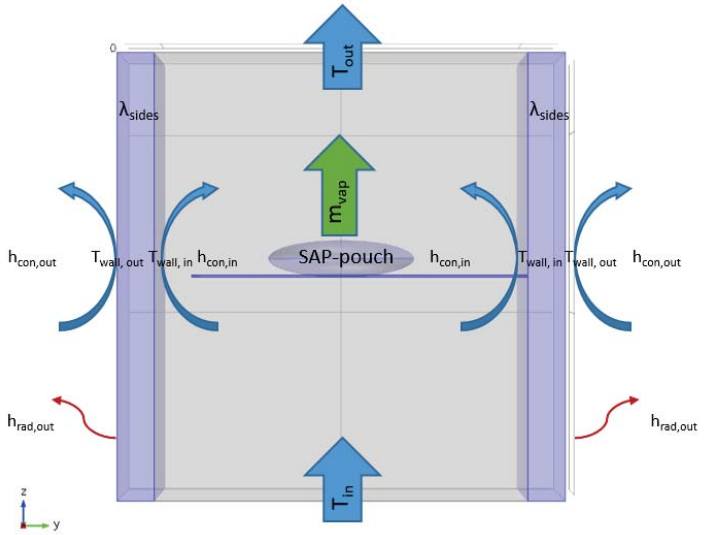

Fig. 4 : Schematic figure for all energy flows and temperatures that are included in the model for the dryer. Energy balances for the air flow, inner and outer wall of the collector will be set up according to this figure.

2.3.1 The internal walls of the dryer

The energy balance for the internal walls of the dryer include convective heat transfer from the dryer air flow as well as conductive heat transfer through the dryer insulation layer, shown in eq. 17.

$$h'_{con,in} \cdot \left(\frac{T_{in}+T_{out}}{2} - T_{wall,in}\right) - \frac{\lambda_{dryer}}{t_{side}} \cdot \left(T_{wall,in} - T_{wall,out}\right) = 0 \qquad \text{(eq. 17)}$$

Note that $h'_{con,in}$ is calculated using the same method as for the collector, but the air velocity in the dryer could differ from the collector. If the cross section area of the dryer is larger than the cross section area of the collector, the air velocity will be lower in the dryer than in the collector. A different air velocity and a different cross section will result in a new Reynold's number, meaning that the flow characteristics of the collector and the dryer could be different. For this reason, the Reynold's number for the dryer needs to be calculated.

2.3.2 The external walls of the dryer

The energy balance for the external sides of the dryer is set up according to the same method used for the collector sides in section 2.2.4, meaning that half of the heat radiation will radiate towards the ground and half will radiate towards the sky. The resulting equation can be found in eq. 18, in accordance with Fig. 4. One parameter that has been added to the energy balance for the external walls of the dryer is the additional heat gain z. The additional heat gain represents the average solar irradiation of all four outer walls of the dryer. The additional heat gains will increase the outer wall temperature of the dryer, which will reduce the heat losses through the walls or, if the outer walls are warmer than the inner walls, add heat to the air.

$$\frac{\lambda_{dryer}}{t_{side}} \cdot \left(T_{wall,in} - T_{wall,out}\right) - h_{con,out} \cdot \left(T_{wall,out} - T_{amb}\right) - \frac{1}{2} \cdot h_{rad,out1} \cdot \left(T_{wall,out} - T_{amb}\right) - \frac{1}{2} \cdot h_{rad,out2} \cdot \left(T_{wall,out} - T_{sky}\right) + z = 0 \quad \text{(eq. 18)}$$

2.3.3 The dryer air flow

For the dryer air flow, the same method used in section 2.2.2 for the collector air flow is used with the addition of a mass flux of water vapor from the SAP-pouches. This means that the calculations need to include an accumulation of the water molecules from shelf to shelf. For the first shelf, the inlet mass flux of water will be according to the absolute humidity which was calculated in the collector, m_h, while the outlet mass flux will also have gained water vapour from the SAP-pouches of the first shelf. The outlet mass flux of water from the first shelf will then be used as input for the inlet mass flux of water for the second shelf. Also note that the shelf is placed in the center of the dryer section, meaning that the SAP-pouch will have the section mean air temperature at steady state. The full expression used for the dryer air flow can be found in eq. 19, where E_{vap} corresponds to the amount of energy absorbed by the SAP-pouches, see eq. 20.

$$\left(T_{in} - T_{out}\right) \cdot \rho_{air} \cdot C_{P,air} \cdot u_{air} \cdot A_{inlet,dryer} - h'_{con,in} \cdot A_{sides} \cdot \left(\frac{T_{in}+T_{out}}{2} - T_{wall,in}\right) + \left(T_{in} - T_{out}\right) \cdot Cp_{H2O} \cdot m_h + \left(\frac{T_{in}+T_{out}}{2} - T_{out}\right) \cdot Cp_{H2O} \cdot m_{vap} - E_{vap} = 0 \quad \text{(eq. 19)}$$

$$E_{vap} = m_{vap} \cdot \Delta h_{vap,H2O} \quad \text{(eq. 20)}$$

Combining eq. 19 and eq. 20, the only unknown parameter is m_{vap}, which can be regarded as the drying rate of the SAP-pouches. For this reason, finding a good way to calculate m_{vap} is essential to evaluate the solar dryer performance. Since SAP-pouches can consist of various materials, the drying rate will differ depending on the pouch material (Phinney et al., 2015). For this study, measurements were provided from a separate study[1] where the drying rate of a specific type of SAP-pouch was measured for different temperatures, air flow rates and relative humidity. The data provided from the measurements were used to create a mathematical expression for the drying rate as a function of relative humidity and air velocity, shown in eq. 21.

$$m_{vap} = \frac{A_{bags}}{3600} \cdot \left(-1{,}0015 \cdot u_{bags} - 0{,}9565\right) \cdot RH + 0{,}3088 \cdot u_{bags} + 0{,}6297 \quad \text{(eq. 21)}$$

Note that the SAP-pouches will obstruct the air flow, reducing the effective cross section area of the dryer. To take this into consideration, the air velocity used to calculate the drying rate u_{bags} is calculated for the effective cross section area of the dryer. In other words, placing more SAP-pouches per shelf results in a higher u_{bags}.
The relative humidity *RH* of eq. 21 is calculated for the conditions around the SAP-pouches, i.e. the absolute humidity and the dryer air temperature.

3. Results

The main aim of the study was to create a calculation tool in Maple 2015 which can be used to generate approximate values for the drying rate and various temperatures for a user defined design of a solar dryer. Using the method described a calculation tool was built capable of simulating temperatures for the absorber, the glazing, the air flow and the external walls of the collector as well as the drying rate and temperatures of the air flow, internal- and external walls of the dryer. However, it was also decided to include a parametric study to find ways of improving the solar dryer performance. Several parameters were examined, where the most important ones will be presented in this paper with regards to temperature increase, drying rate how and suitable the solution would be to a developing country.

[1] Phinney, R. Unpublished data. Department of Food Technology, Engineering and Nutrition. Lund University

3.1 Adding fins to the absorber plate

To simulate fins being added to the absorber plate, a factor was added to the second term of eq. 13, being the convective heat transfer from the absorber plate to the air flow. As an example, a convective heat transfer factor of 2 means that fins with a total area equal to the absorber plate have been installed. A factor of 3 means that the area of the fins is twice as large as the collector plate and so on. The outlet air temperature of the collector, i.e. the inlet air temperature for the dryer, for various convective heat transfer factors can be found in Fig. 5. A schematic example of a collector with fins can be found in Fig. 7.

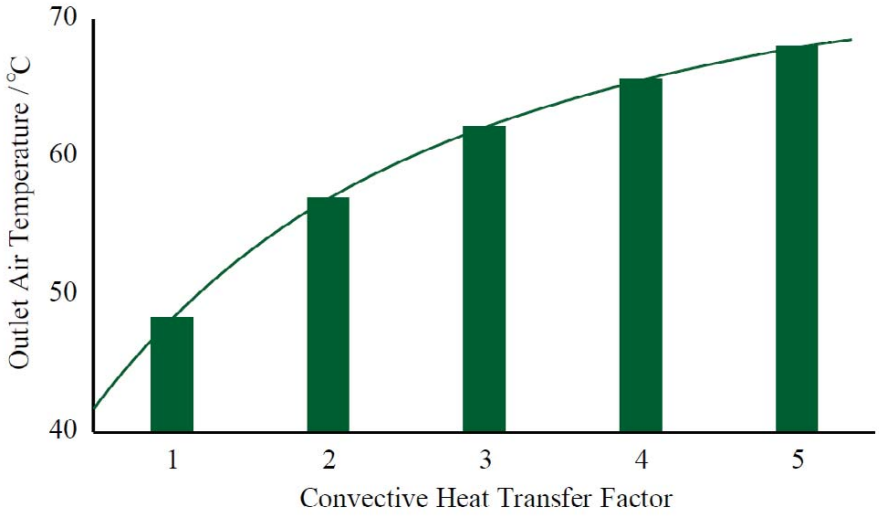

Fig. 5 : Calculated outlet temperatures of the collector for the base scenario for different convective heat transfer coefficient factors of the absorber.

3.2 Varying the number of SAP-pouches in the dryer

The number of SAP-pouches placed in the dryer is likely to affect the drying rate, since more bags per shelf will cause greater accumulation of water vapour from shelf to shelf. Varying the number of pouches placed per shelf is also a way of simulating the effects of uncertainties of the equation used for the drying rate, eq. 21. For the results of the study, simulations were made for 1, 2 and 3 pouches per shelf for a dryer with 8 shelves. The results for the drying rate per shelf can be found in Fig. 6.

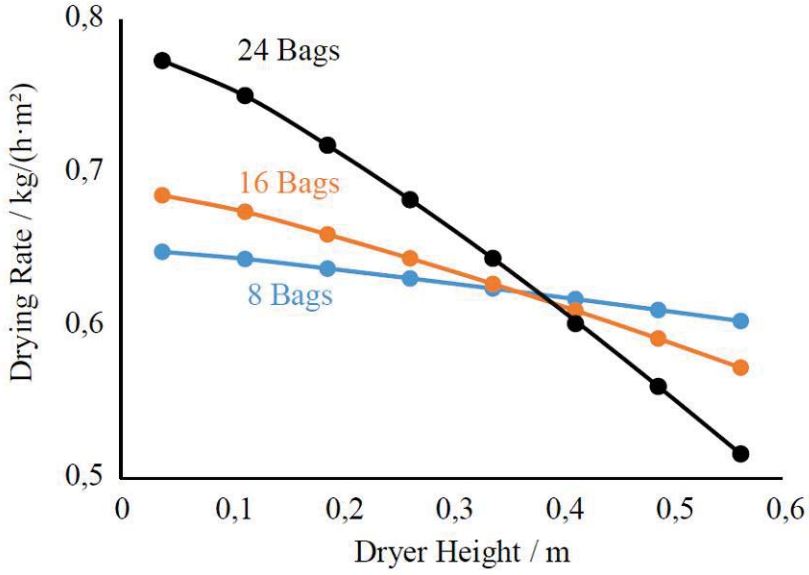

Fig. 6 : Simulated values for the drying rate for one (blue), two (orange) and three (back) SAP-pouches per shelf. Each dot represents one of the eight shelves inside the 0,6 m high dryer.

4. Discussion

4.1 Adding fins to the absorber

Increasing the outlet air temperature of the collector is a good method for increasing the drying rate. For the model used in this study, a higher air temperature results in a lower relative humidity inside the dryer, which increases the drying rate in eq. 21. Several different methods can be used to increase the air temperature of the collector, but it's important to consider which methods that are applicable in a developing country.

To avoid potential problems with complex materials unsuitable for developing countries, fins can be built using cheap materials with sufficient heat conductivity, see Fig. 7. The fins will conduct heat from the absorber, practically resulting in the contact area between the air flow and the absorber to be increased. As shown in Fig. 5, adding fins has good potential of increasing the collector air temperature and thus the drying rate. The air temperature gains from adding fins appears to decrease exponentially with increased convective heat transfer coefficients. This indicates that fins are most efficient for low convective heat transfer coefficients, as the temperature gains from adding excessive amounts of fins may not justify the material costs.

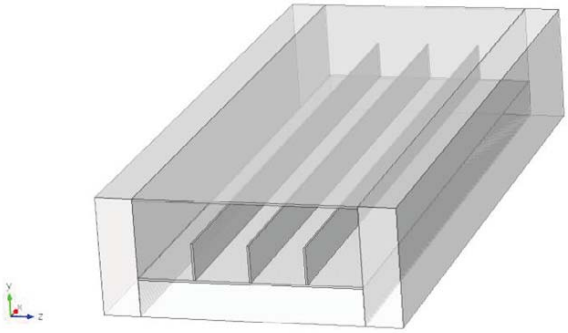

Fig. 7 : Schematic picture of a solar collector with fins attached to the absorber.

4.2 Potential problems with overloading the dryer

As shown in Fig. 6, the drying rate of the SAP-pouches will differ from the entrance to the outlet of the dryer. The pouches placed on the first shelf, closest to the entrance, will be exposed to a lower relative humidity than the pouches placed further up in the dryer. This occurs due the absolute humidity being higher further up in the dryer as well as the temperature being lower, since heat will be absorbed by the pouches and lost through the walls. Both the lower air temperature and the higher absolute humidity will result in a higher relative humidity, which reduces the drying rate. Also, if the SAP-pouches are obstructing a large portion of the dryer cross section area the air velocity surrounding the pouches will be higher, which according to the model will result in a higher drying rate. This can be seen in Fig. 6, where the drying rate for the first shelf is considerably higher when placing three pouches per shelf compared to placing one pouch per shelf.
Bearing the variations of the drying rate this in mind, it's important to acknowledge that every pouch placed in the dryer is required to have a sufficient drying rate. If the drying rate variation is too great, it could result in only the pouches placed on the first shelf to dry out completely. The lower drying rate of the remaining shelves could also cause the drying process to become too slow, resulting in the contents of the pouches becoming spoiled.

To avoid the problem described, there are two parameters worth considering; the volumetric air flow of the dryer and the number of SAP-pouches placed in the dryer. Increasing the volumetric air flow in the dryer results in better ventilation of the vapour generated by the pouches. To increase the volumetric air flow, the air velocity in the dryer could be increased. This will have two positive effects according to eq. 21, as the air velocity is increased and the relative humidity is decreased.
But increasing the volumetric air flow also has negative effects on the drying rate. Since the dryer is connected to the collector, the volumetric air flow will also be increased inside the collector. This will result in lower air temperatures in the collector and thus in the dryer.
Furthermore, increasing the air flow could require installations of fans. While fans are very likely to improve the solar dryer performance, they may not be a suitable solution in a developing country since a source of electricity is required. As a conclusion, finding a good balance between the collector outlet temperature, the dryer air velocity and the number of pouches placed in the dryer is the key to designing a good solar dryer.

5. References

Alvarez H. (2006). *Energiteknik.* Lund: Studentlitteratur AB.

Atkins P. & de Paula J. (2002). *Atkins' Physical Chemistry.* Oxford: Oxford University Press.

Blanco-Cano et al. (2016). Modeling the thin-layer drying process of Granny Smith apples: Application in an indirect solar dryer. *Applied Thermal Engineering Volume 108*, 1086–1094.

Department of Chemical Engineering of Lund University. (2013). *Handbook.* Lund: MediaTryck.

Incropera, F. P., & Dewitt, D. P. (2002). *Fundamentals of Heat and Mass Transfer.* New York: John Wiley & Sons, Inc.

Kumar et al. (2015). *Progress in solar dryers for drying various commodities.* Hisar, India: Guru Jambheshwar University of Science & Technology.

Kumar Moningi, M. (2016, March 29). *Conduction Convection Radiation processes of a solar collector using FEA*. Retrieved from unix.ecs.umass.edu: http://www-unix.ecs.umass.edu/mie/labs/mda/fea/fealib/moningi/moningiReport.pdf

Maplesoft. (2016, August 29). *New Maple 2016 offers advanced problem-solving for math, science, engineering*. Retrieved from Maplesoft: http://www.maplesoft.com/company/publications/articles/view.aspx?SID=154030

Mills-Gray, S. (1994, May 15). *Quality for Keeps: Drying Foods*. Retrieved from University of Missouri Extension: http://extension.missouri.edu/p/GH1562

PAEGC & TH Cologne. (2016). *Renewable Energy Resources and Technology Overview (Chapter B1)), Massive Open Online Course (MOOC).* Retrieved from Powering Agriculture - Sustainable Energy for Food: https://gc21.giz.de/ibt/var/app/wp385P/2624/wp-content/uploads/2015/03/PAEGC_MOOC_COMPILED_READER.pdf

Phinney et al. (2015). *Solar assisted pervaporation (SAP) for preserving and utilizing fruits in developing countries.* Kruger National Park, South Africa: Third Southern African Solar Energy Conference.

R.K.Sinnot. (2005). *Chemical Engineering Design: Chemical Engineering Volume 6.* Swansea: Butterworth-Heinemann.

Sekhar et al. (2009). Evaluation of Heat Loss Coefficients in Solar Flat Plate Collectors. *ARPN Journal of Engineering and Applied Sciences*, 15-19.

UNDP. (2015). *Briefing note for countries on the 2015 Human Development Report, Mozambique.* New York: UNDP.

World Food Programme. (2016, February 20). *Mozambique*. Retrieved from World Food Programme: http://www.wfp.org/countries/mozambique

6. Appendix

6.1. Nomenclature

A_{abs}	Collector absorber area (= glass area)	m²
A_{bag}	The effective area for evaporation of a SAP-pouch	m²
A_{bags}	Total effective evaporation area of SAP-pouches per shelf	m²
A_{eff}	Effective cross section area for the dryer airflow	m²
A_{inlet}	Collector inlet area	m²
A_{sides}	Collector side area	m²
a_w	Water activity	1
$C_{P,\ air}$	Specific heat capacity for air	J/(kg·K)
$C_{P,\ H2O}$	Specific heat capacity for steam	J/(kg·K)
D_H	Hydraulic diameter of the collector	m
E_{vap}	Total power required for evaporation for all SAP-pouches placed on a shelf in the dryer	W
G	Total solar irradiation	W/m²
G_e	Effective solar irradiation (heat absorbed by the absorber)	W/m²
$h_{con,\ in}$	Heat transfer coefficient for internal convection	W/(m²·K)
$h_{con,\ out}$	Heat transfer coefficient for external convection	W/(m²·K)
$h_{rad,\ in}$	Heat transfer coefficient for internal radiation	W/(m²·K)

$h_{rad,\ out}$	Heat transfer coefficient for external radiation	W/(m²·K)
m_h	Water mass flow	kg/s
m_{vap}	Water mass flow from SAP-pouch	kg/s
n	Number of bags per shelf in the dryer	1
Nu	Nusselt number for uniform surface heat flux	1
Pr_{air}	Prandtl number for air	1
P_w	Vapour pressure for water	Pa
P_{ws}	Water saturation pressure	Pa
R_{abs}	Absorber reflectance	1
Re_{air}	Reynolds number for air	1
R_{glass}	Glass reflectance	1
RH	Relative humidity	1
R_V	Specific gas constant for water vapour	J/(kg·K)
S	Number of shelves in the dryer	1
T_{abs}	Absorber temperature in the collector	K
T_{air}	Mean temperature of T_{in} and T_{out}	K
T_{amb}	Ambient temperature (= 25 °C for the simulations)	K
t_{bottom}	Bottom insulation thickness	m
T_{glass}	Glass temperature in collector	K
T_{in}	Inlet temperature for a section	K
T_{out}	Outlet temperature for a section	K
t_{side}	Side insulation thickness	m
T_{sky}	Sky temperature (= 5 °C for the simulations)	K
T_{wall}	Wall temperature of dryer	K
T_{wall}	Outer wall temperature in the collector	K
$T_{wall,\ in}$	Inner wall temperature in the dryer	K
$T_{wall,\ out}$	Outer wall temperature in the dryer	K
u_{air}	Collector inlet air velocity	m/s
u_{bags}	The air velocity surrounding the SAP-pouches	m/s
z	Additional heat gains for the outer walls of the dryer	W/m²
α_{abs}	Absorber absorbance	1
$\Delta h_{vap,\ H2O}$	Enthalpy of vaporization for water	J/kg
ε_{abs}	Absorber emissivity	1
ε_{glass}	Glass emissivity	1
ε_{wall}	Collector outer wall emissivity	1
$\varepsilon_{wall,\ dryer}$	Dryer outer wall emissivity	1
λ_{air}	Air thermal conductivity	W/(m·K)
λ_{bottom}	Collector bottom insulation thermal conductivity	W/(m·K)
λ_{side}	Collector side insulation thermal conductivity	W/(m·K)
λ_{wall}	Dryer wall thermal conductivity	W/(m·K)
μ_{air}	Air dynamic viscosity	kg/(m·s)
ρ_{air}	Air density	kg/m³
σ	Stefan-Boltzmann constant	W/ (m²·K⁴)
τ_{glass}	Glass transmissivity	1

Conference Proceedings

EuroSun 2016
Palma de Mallorca (Spain), 11 - 14 October 2016

POTENTIAL APPLICATION OF SOLAR PROCESS HEAT IN THE MEAT SECTOR CONSIDERING HEAT RECOVERY AND INDUSTRIAL HEAT PUMPS AS COMPETING TECHNOLOGIES

Felix Pag[1], Bastian Schmitt[1] and Klaus Vajen[1]

[1] Institute of Thermal Engineering, Kassel University, Kassel (Germany)

Abstract

Food industry, specifically the slaughter and meat processing industry, is a promising field for solar process heat. Several processes, such as scalding or hot water generation for washing and cleaning, offer feasible integration points due to the low temperature level and conventional heating equipment. For the German meat sector, a technical potential of one million square meters of collector area was estimated. However, heat recovery systems can reduce this potential significantly, especially if they are installed in combination with industrial heat pumps. Thus, the questions arise how heat recovery systems can be operated most economically with respect to the condensation temperature of compression chillers and which influences have to be expected for the integration of solar heat and industrial heat pumps.

Keywords: Solar process heat, Slaughter and meat processing industry, Heat recovery, Industrial heat pumps

1. Introduction

Based on the temperature level and constant high heat loads, the food and beverage industry hast the highest potential for solar heat in industrial processes (Schmitt et al., 2015). However, the market penetration of solar process heat failed to meet the expectations in this field of application based on several reasons. One crucial point is the identification of a feasible integration point which can be very complex. Due to a high hot water demand for washing and cleaning purposes, the German slaughter and meat processing industry has been analyzed regarding that fact. Based on the high cooling demand for preserving the meat products, low temperature waste heat from compression chillers plays a particularly important role for the evaluation of solar heat integration. Additionally, the waste heat offers the opportunity to install industrial heat pumps using it as heat source ending up in an improved efficiency.

2. Suitable applications and technical potential of solar process heat in the German slaughter and meat processing industry

In contrast to other branches of the food industry the diversity of heat consuming processes in the slaughter and meat processing industry is rather limited as a literature research has proven. Additionally, the heat demand is mostly limited to process temperatures below 100 °C. This demand is dominated by the preparation for hot water which is especially used for washing and cleaning processes. To reduce the bacteria load, the carcasses as well as any utility that have been in contact with the carcasses has to be cleaned regularly. Especially the cleaning of animal transporters, which is done after unloading on site, guarantees a constant warm water demand. At least once a day, all production rooms have to be lathered and cleaned.

The slaughter processes of pigs and poultry are very comparable. After several prewashing steps with warm and cold water, the carcasses have to be scalded at temperatures between 50..65 °C, making the subsequent step of bristle removing and de-feathering much easier. Therefore, the carcasses are moved through one or

doi:10.18086/eurosun.2016.02.20 Available at http://proceedings.ises.org

several warm water baths. These baths have to be kept at temperature during all time which is ensured by external heat exchangers or steam injections. However, due to the high bacteria load and the carryover by the carcasses, fresh water has to be fed constantly. But, the bacteria load can only be reduced to a certain extent by feeding fresh water. Consequently, the whole bath capacity has to be changed at least once a day. In alternative to these baths, the carcasses can also be sprayed with warm water which ensures a reduced water and energy demand in addition to a reduced bacteria load on the carcasses. The bristles and feathers are removed by scrapers and rollers, partially supported by valves which spray warm water on the carcasses. Pigs have to be processed in a gas oven additionally, where any remaining bristle is burned at temperatures above 200 °C. The carcasses of cattle don't have to be scalded, because the skin is peeled off. In summary, there are several integration points for the use of solar process heat in the slaughter industry: The integration on the supply level using the hot water network is just as feasible as the integration on the process level, for example maintaining the bath temperature in scalding processes in the set temperature range.

Beside the supply of hot water for cleaning, it is more complicated to integrate solar heat in processes in the meat processing industry. The filling of kettles and other machineries in cooking and pasteurizing processes at the beginning of every day or batch can be done with solar heated water. In contrast, the use of solar heat for the continuous heat demand to maintain or increase the process temperature is very often restricted by technical reasons and the conventional heating equipment.

Other processes such as smoking and maturing are conventionally heated by steam, gas burners, or electrical heaters. Although the products are processed at relatively low temperatures, the integration of solar heat is difficult due to the conventional heating equipment. Depending on the product, the temperature range of smoking can vary between 10 to 100 °C while the process time is inversely proportional to the temperature. Often steam is used directly to generate smoke, which makes it almost impossible to replace it by solar heat. In these cases, the limited space does not allow the retrofit for a water based heating system which is necessary for the utilization of solar heat. However, in case of a significant amount of direct steam consumption, the required make-up water can be supplied with solar heat easily.

Whereas in smoking chambers it is not possible to integrate solar heat, maturing halls, for example for sausages, is more promising instead. The maturing process can take up to several days or even weeks. During this time, the products are placed in big halls which are temperature- and humidity-controlled. Steam injections for heating and humidification on the one hand and cooling machines for cooling and dehumidification on the other hand try to control temperature and humidity in a very small range, which is necessary for an optimal maturing result. If the control is not balanced here, there is a relevant potential for energy savings. Since maturing halls typically have a lot of available space and a relative continuous load profile, it can be possible to replace the conventional heating by steam injections to water heating surfaces here. Such modification would allow the efficient use of solar heat at a low temperature level here.

There are several processes, especially for a dry heat treatment as baking or roasting, where the use of solar heat is impeded– on the hand due to the temperature level and on the other hand due to the fact that the conventional heating is based on direct electrical heating.

To sum up, there are several promising integration points in heat consuming processes within the slaughter and meat processing industries as shown in Tab. 1. In both industries the majority of the heat demand is used for hot water preparation, which makes it generally easy to identify a suitable integration point for solar heat on supply level. The use of solar process heat in maturing halls is a very promising application on process level due to the very low temperature level and the constant heat demand due to dehumidification.

Tab. 1: Heat consuming processes in the slaughter and meat processing industries regarding the potential for the use of solar process heat; The solar potential is evaluated with respect to the climate in Central Europe

Process	Temperature level	Annotations	ST Feasibility
Both sectors			
Cleaning and Washing Processes	50..60 °C	High and constant hot water demand, simple integration at supply level	+
Make-up water	15..95 °C	Material use of steam requires constant replacement of feed-water	+
Slaughter Industries			
Scalding	50..65 °C	Bath filling and refilling with solar heated water and continuous bath heating	+
Singeing	> 200 °C	No potential due to conventional heating equipment	-
Meat Processing Industries			
Scalding and Cooking	60..100 °C	Bath filling with solar heated water. Continuous heating not feasible	0
Pasteurizing	80..100 °C	Possible use of solar heat depends on heating equipment	0
Sterilizing	> 100 °C	Temperature level and heating equipment impede the use of solar heat	-
Smoking	10..100 °C	No potential due to conventional heating equipment	-
Maturing	15..25 °C	Promising application, needs modification of heating equipment	0
Baking, Frying, Roasting	> 200 °C	No potential due to conventional heat supply and heat transfer	-

Based on the process analysis, a technical potential for use of solar process heat in the German meat sector has been calculated. The overall energy demand in the German slaughter and meat processing industry was 7.3 GWh in 2011 (BMEL, 2013), whereby 58 % of the energy was consumed for heat generation by fossil fuels[1] (excluding heat generated by electricity). Almost 60 % of the heat demand is eased by the meat processing industry, whereas 40 % are consumed in slaughter houses. The heat supply is dominated by the central combustion of natural gas feeding steam or hot water networks distributing the process heat.

In slaughter houses for cattle and poultry, all heat demand, as shown before, is needed at a temperature level below 100 °C which makes it very feasible for solar heat. During the slaughter process of pigs, there is also a heat demand at a higher temperature level for the bristle burning which accounts for 30 % of the heat demand in the pig slaughter process (Rosenwinkel, 2014). Taking into account the average heat demand per carcasse (weight) (VDI, 2009) and the absolute slaughter figures (Maennel, 2014), the heat demand can be distributed to heat which is needed below 100 °C (78.4 %) and above (21.6 %). Using the methodology of Lauterbach et al. (2012), taking into account a potential for efficiency measures, competing technologies and a limited solar fraction as well as suitable roof areas, there is a technical potential for solar heat of 172.4 GWh_{th} (383,000 m^2[2]) in slaughterhouses.

For the meat processing industry, it has to be relied on cross-sectoral data for the food industry presented by Nast et al. (2010), whereas 43 % of the heat demand is needed below 100 °C, 41 % between 100..150 °C and 16 % above. This results in a technical potential of 239.5 GWh_{th} (532,000 m²) with respect to a feasible

[1] Electricity which is used for heat generation, for example in baking processes, is not included here.
[2] Assuming a solar yield of 450 kWh/m²a.

temperature level up to 150 °C.

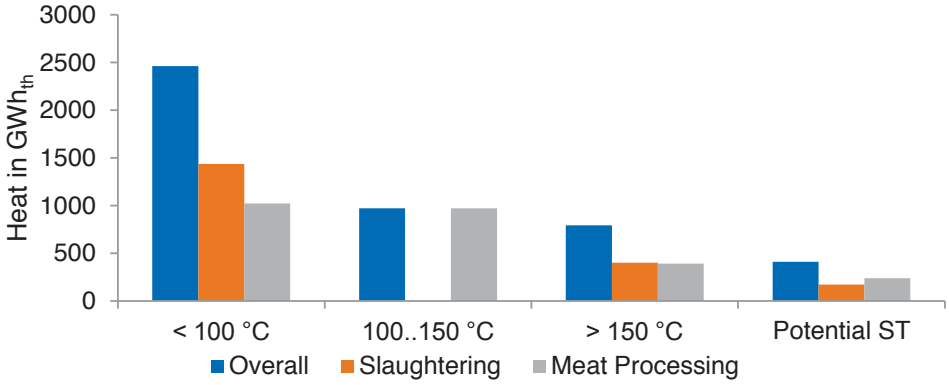

Fig. 1: Distribution of the heat demand and technical potential for solar process heat in the German slaughter and meat processing industry

In total, referring to Fig.1, there is a technical potential for solar process heat of almost 412 GWh$_{th}$ (< 150 °C) in the German slaughter and meat processing industry which is corresponding to a collector potential of almost 1,000,000 m².

However, this potential has to be seen in relation to the massive potential for low temperature waste heat due to the widespread application of compression chillers. Here, it is estimated that more than 114,000 cooling systems are operated up to a cooling capacity in the megawatt range (Steimle et al., 2002). Following Preuss (2011) this potential can be calculated assuming an average COP (Coefficient of Performance) depending on the cooling temperature[3], operational time and installed cooling capacity with respect to the size of the company. Using eq. 1, a theoretical potential for heat recovery (hr) from compression chillers can be calculated.

$$\dot{Q}_{hr} = P_{el} \cdot (COP + 1) \qquad \text{(eq. 1)}$$

Theoretically, there is a potential for low temperature waste heat from compression chillers of 5.2 TWh$_{th}$ in the German meat sector, whereby this potential exceeds twice heat demand below 100 °C in this sector and the technical potential for solar process heat by the factor 10. Still, only a share of this heat recovery potential can be exploited due to the low temperature level (20..40 °C), the lack of storage possibilities and other technical limitations. Still, this comparison shows that waste heat can massively reduce that potential of solar heat using it for example for water preheating.

3. Heat generation costs of industrial heat pumps

Industrial heat pumps have a great potential to cover the low temperature process heat demand in industrial applications, especially if waste heat with a temperature about 30 to 40 °C can be used as heat source in the evaporator. Still, there are only a few industrial heat pumps (approx..80 in 2011) installed in Germany so far (Preuss, 2011) but the market development is positive. In the meantime heat pumps with a thermal capacity up to a double-digit MW$_{th}$ range are available. Supply temperatures with single-stage heat pumps can reach up to 75 °C. Beyond that, the heat pump has to be operated two-staged. There, even supply temperatures above 100 °C can be provided. In general, heat pumps and solar thermal systems have in common that they can work most efficiently if they produce heat at a low temperature level. Thus, even if they can be installed in combination with solar thermal systems they are a concurrent technology to solar process heat.

To evaluate the competitive situation, the heat generation costs of single-stage industrial heat pump systems are calculated with fixed parameters in a reference scenario for the design data. Part-load performance or a

[3] For this calculation, it is assumed that normal refrigeration accounts for 40 % and deep freezing accounts for 60 %.

certain load profile have not been respected. The parameters of this scenario are given in Tab. 2.

The heat generation costs are calculated over a period of 20 years with the annuity method. The investment and installations cost are taken from Lambauer et al. (2008). As it can be seen in fig. 2, the specific costs per installed capacity are heavily decreasing with the thermal capacity of the heat pump system until a capacity of 500 kW_{th}. Beyond that, the specific investment costs are more or less the same. Regarding the investment costs, the conditions of German subsidies are taken in to account[4] for the calculation of the heat generation costs. The supply temperature, the heat pump has to provide, is 65 °C (hot water generation) whereas the source temperature is 30 °C. This source temperature can easily be provided by the compression chillers' waste heat referring to a condensation temperature of 35 °C considering a temperature difference of 5 K for the heat exchanger.

Tab 2: Parameters of the reference case for the calculation of the heat generation costs of an industrial heat pump

Parameter	Value
κ_{el}	0.15 ct/kWh_{el}
$T_{E,HP}$	30 °C
$T_{C,HP}$	65 °C
$\dot{Q}_{HP}$	300 kW_{th}
Full Load Hours	1530 h/a
j_{el}[5]	1 %/a
Refrigerant	R134a

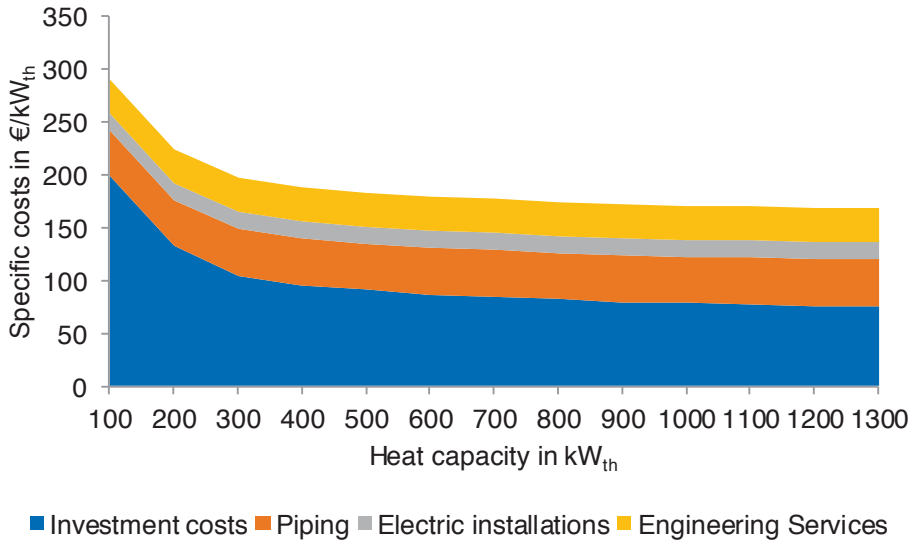

Fig. 2: Investment and additional cost for the installation of an industrial heat pump from Lambauer et al. (2008)

With the given parameters, the heat generation costs are 3.9 €-ct/kWh_{th}.

Subsequently, the sensitivity of these parameters is analyzed to quantify their effects on the heat generation costs. The results of the sensitivity analysis with a variation of the parameters by 50 % are given in Fig. 3

[4] Heat pumps with a heating capacity of > 100 kW_{th}, 30 % of the total investment cost can be funded.
[5] Increase of electric costs in %/a

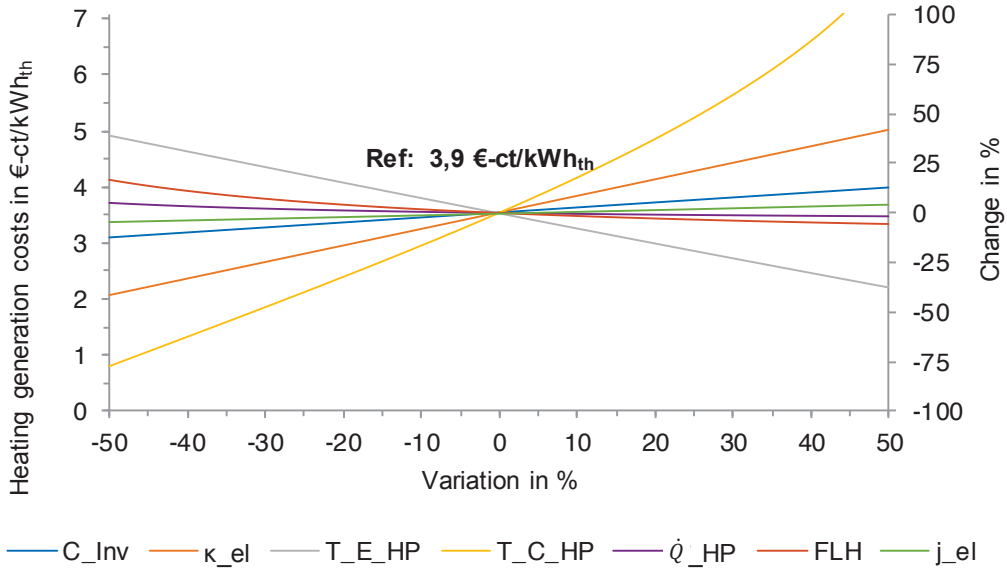

Fig. 3: Results of the sensitivity analysis with the absolute heat generation costs (left axis) and the change in percentages (right axis)

The sensitivity analysis underlines that the main determining parameters for the heat generation costs are on the one hand the temperatures of the low temperature heat source (TE,HP) and the heat sink (TC,HP) and on the other hand the price for electric energy (κel). The influence of the total investment costs (CInv), in contrast, are less relevant. Here, an increase of the investment costs by 50 % only results in an increase of the heat generation costs of 12 %. Such an increase of the price for electric energy would lead to heat generation costs of about 5 €-ct/kWh$_{th}$ (+ 41,7 %). The operational time and the amount of delivered heat does also only play a minor role due to the fact that the investment costs are less relevant. Decreasing the operation time does only result in higher investment costs per delivered heat. But this change in the heat generation costs secondarily in relation to the operation costs for electricity.

As the price of electricity and the operation temperatures of the heat pump has been determined as the key factors for the heat generation costs of an industrial heat pump, several simulations has been carried out with varying parameters. The results are given in fig. 4. There, the heat generation costs are given in dependence of the temperature lift of the heat pump (x-axis) and the price of electricity (y-axis) for a process temperature of 60 °C (e.g. hot water preparation). The temperature loss which has to be taken into account due to the use of heat exchangers is already respected. Thus, if the waste heat temperature, which is used as heat source for the heat pump, is about 30 °C and the process temperature 60 °C, a temperature lift of 30 K has to be used in the diagram. The efficiency of the heat pump is calculated with additional 10 K, resulting in a temperature lift of 40 K. As it can be seen, quite low heat generation costs can be achieved by a heat pump if waste heat at a suitable temperature is constantly available. With the given example (ΔT_{HP}=30 K), the heat generation costs would be in the range of less than 3 ct/kWh$_{th}$ up to 5 ct/kWh$_{th}$ depending in the price of electricity. These costs can be very different, even in industries, especially if there is a high electricity demand. Obviously other waste heat sources apart from compression chillers might be used as well.

$\dot{Q}$

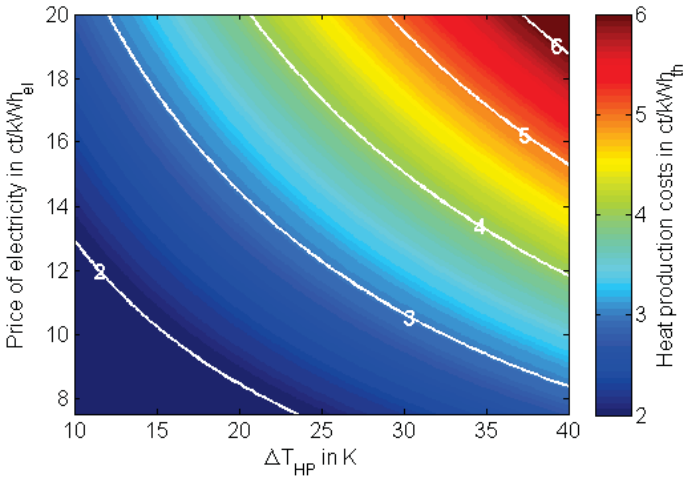

Fig. 4: Heat generation costs in €-ct/kWh$_{th}$ of industrial heat pumps in dependence of the temperature lift the heat pump has to provide (x-axis) and the price of electricity (y-axis) for a process temperature of $T_{Process}$=60 °C

4. Optimized operational mode of compression chillers with respect to the condensation temperature

As shown in Section 2, there is a huge theoretical potential for the use of waste heat from compression chillers. The subsequent technical potential is mainly dependent on the temperature level in the condenser (T_C) which can be varied according to the system and the temperature in the evaporator (T_E). Generally, this condensing temperature has to be chosen as low as possible, operating the compression chiller as efficient as possible (high COP) according to Eq. 2, whereas the evaporating temperature (T_E) is typically limited by the transfer and distribution of the cooling energy in the cooling room. Calculating the COP via the temperatures T_C and T_E, only gives the theoretical optimum. In practice, the COP is much lower due to technical reasons.

$$COP = \frac{\dot{Q}_c}{P_{el}} = \frac{T_C}{T_C - T_E} \qquad \text{(eq. 2)}$$

However, there is also a minimum for the condensation temperature, which is given by the installations for recooling and the ambient conditions. It has to be guaranteed, that the waste heat from the compressor can always be dissipated by air or water cooling. For air cooling, the condensation pressure has to be chosen to result in a condensation temperature which is about 10 K above the ambient air. So, the chiller works with a floating condensation temperature over the year in dependence of the air temperature resulting in a changing efficiency (COP), too. In case of water cooling, the wet-bulb temperature, which is always below the ambient air temperature, determines the condensation temperature. Very often, especially with outdated chillers constant condensation levels over the year can be found in industry, resulting in inefficient operation during the majority of the year.

As shown before, a low condensation level results in an efficient cooling system. In contrast, a higher condensation temperature might result in a higher amount of heat that can be used. Thus, the operator ends up in a target conflict between an efficient cooling system and an increased waste heat potential. To find the optimal solution, simple considerations were made with respect to the design values. As before, regarding the consideration of the heat pump, neither a part-load behavior of the compressor or the whole chiller nor any specific cooling load were considered. On the one hand, the additional amount of waste heat energy (ΔQ_{hr}), that can be used for water preheating by increase of the condensation temperature by 1 K can be determined with Eq. 3 if the daily hot water demand ($V_{HW,d}$) is known.

$$\Delta Q_{HR} = V_{HW,d} \cdot c_{p,HW} \cdot 1K \qquad \text{(eq. 3)}$$

On the other hand, you have to take into account the additional amount of electric energy per day, you have to use for the less efficient cooling system (Eq.4). Here, the factor f is used to approximate the decline of efficiency.

$$W_{el,d,new} = f \cdot W_{el,d,old} \qquad \text{(eq. 4)}$$

Afterwards, the relation of saved costs by the surplus of recovered heat to the extra costs for electricity has to be considered with the specific costs for heat (κ_{th}) and electricity (κ_{el}). K_{hr} represents the saved costs by increasing the condensation temperature. Subsequently conventional energy needed for heating the water can be saved. K_{el}, however, represents the additional cost for electricity which have to be paid due to the less efficient cooling system.

$$\frac{K_{hr}}{K_{el}} = \frac{V_{WW,d}}{W_{el,d,old}} \cdot \frac{\kappa_{th}}{\kappa_{el}} \cdot \frac{c_{p,W} \cdot 1K}{f} \qquad \text{(eq. 5)}$$

As shown in Eq. 5, there are two ratios which determine the most cost efficient mode of operation. At first, this is the ratio between the amount of water that can be preheated by the heat recovery system. The more water can be heated, the more interesting it can be to use the chiller as a heat pump, whereas this is less attractive if there is a lot of electric energy demand for cooling. The second ratio is the relation between the costs for heat and electricity which play an important role. In case of a company that has to pay high prices for electricity in relation to the costs for heat generation, it is energetic and economical more efficient to operate the chiller with the lowest condensation possible. This should be the case in most companies. But in turn an institution has to pay relatively low prices for electricity and a relevant amount of the waste could be used, for example for water preheating, it might be profitable to increase the set temperature of the condensation.

Finally, the factor f has to be determined. Therefore, a model has been built in Matlab (MATLAB, 2010) using the database CoolProp (Bell et al., 2014), which offers the possibility to calculate compressor load and the amount of waste heat from the condenser in dependence of the cooling load and the ambient temperature. The parameters of the model are given in Tab. 3.

Tab. 3: Models Parameter

Parameter	Value
Refrigerant	R134a, R404A, R407C, NH_3
Cooling load	200 kW_{th}, constant
T_E	-20..0 °C
T_C	35..45 °C
$\Delta T_{overheating}$	5
$\Delta T_{subcooling}$	3
$\eta_{isentropic,comp}$	0.7
$\eta_{el,comp}$	0.9

As shown in Fig. 5, the factor f is dependent from the temperature level in the evaporator as well as from the refrigerant. In deep freezing applications the effect in the decrease of the COP is less relevant (approx. 2.2 %/K) than for normal refrigeration (approx. 3 %/K). Additionally, there are differences in the performance dependent on which refrigerant is used. Cooling systems which are filled with Ammonia (NH_3) are more attractive to use as heat pump, generally. In contrast, if R404A is used, the decrease of the efficiency of the cooling system is stronger.

Having determined the factor f, the target conflict can be solved with respect to the ratio of energy costs and the demand supply ratio which can be calculated easily. The range of the realistic ratio of energy costs is from 0.2 to 0.55 (ct/kWh_{th})/(ct/kWk_{el}). Fig. 6 shows the ratio of cost savings for a factor f of 2.2 % (left) and 3 % (right). The white line is marking the inflection line, where a change of the condensation temperature would have no cost saving effect. Below this line, the company should decrease the condensation temperature as far as possible to benefit from savings. Since, the saved conventional heat generation costs cannot be amortized by the heat recovery system. Here, the costs for electricity outweigh the savings. Otherwise, if the demand-supply-ratio and the ratio of energy cost result in an intersection point above the white line, the operator of the cooling system can save costs by increasing the condensation temperature and use the chiller as a heat pump.

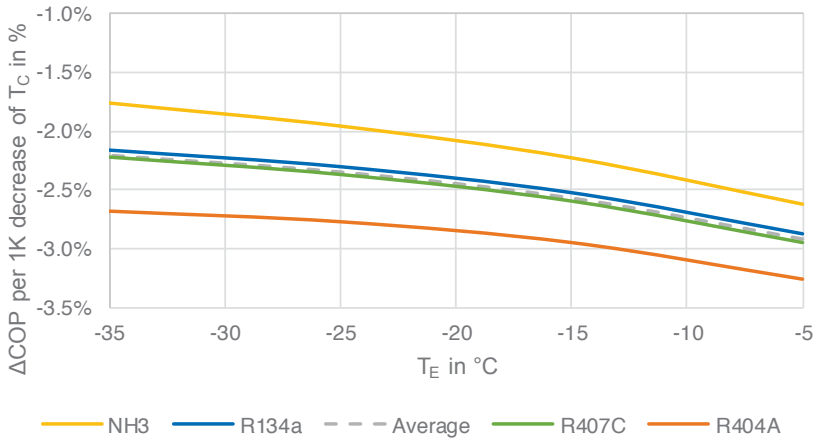

Fig. 5: Change of COP (factor f) per 1 K decrease of T_C in dependence of the evaporation temperature and common refrigerants

As an example, a company of the meat processing industry is considered. The daily hot water demand is approx. 45 m³/d, whereas 375 kWh_{el}/d are consumed for normal refrigeration and the same amount for deep freezing. Assuming that for each cooling application, there is an own heat recovery system, 22.5 m³/d can be preheated by each system. This results in a demand-supply-ration of 0.06 (m³/d)/(kWh_{el}/d).

Here it is assumed, that ratio of the meat processing factory has a value of 0.4. As it can be seen in Fig. 3 in case of normal refrigeration and a factor f of 2.2 %, the cooling system can be used as a form of heat pump since an increase of the condensation temperature is interesting from an economical point of view. Here, the savings in heat generation account for up to 30 % in relation to the additional costs for the electric energy demand for cooling. In contrast, with a view to the deep freezing system on the right, the cooling system should be operated as efficient as possible with the deepest condensation temperature possible.

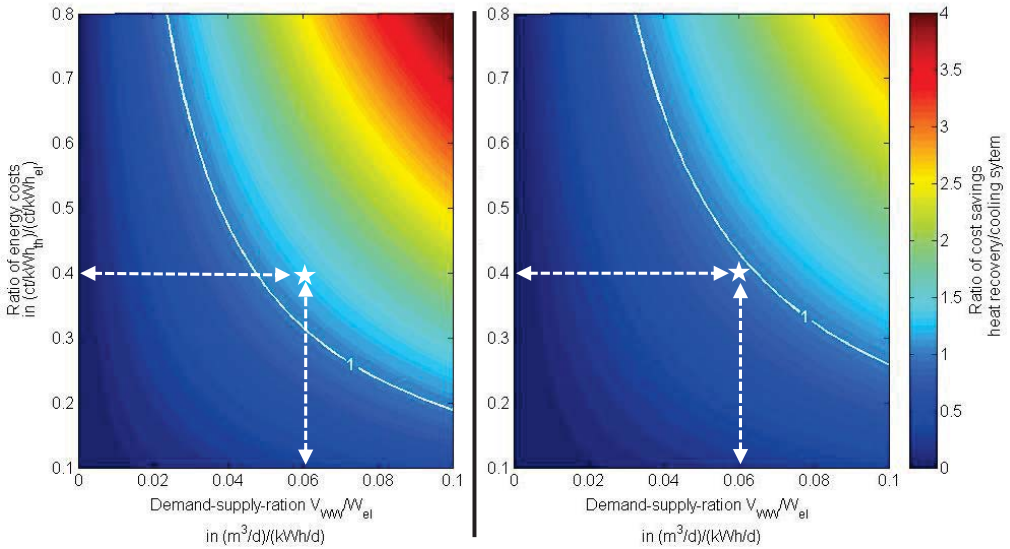

Fig. 6: Ratio of cost savings operating the cooling system most efficiently in dependence of the defined ratios, left: factor f=2.2 %, right: factor f=2.9 %

This calculation does only take the preheating of hot water into account. If there is another heat consuming process on a low temperature level (25..35°C) which can be fed by the heat recovery system, the savings due to an increase of condensation temperature can be even more relevant. Additionally, the costs for recooling the waste if not needed are not considered. This could make a use of the chiller as heat pump even more attractive, because the heat can be used and does not have to be recooled for which additional electricity for fans and pumps, as well as water in case of evaporative recooling, is needed.

Finally, it has to be discussed how to operate a cooling system if a heat pump system is installed downstream, using the chiller's condenser waste as heat source for its evaporator. Therefore, several simulations have been carried out. These simulations aimed at the increase of required electric energy demand for cooling by increasing the condensation temperature of the cooling system in relation to the decrease of the electric energy demand of a heat pump system by increasing the evaporator's temperature level. The results are given in Fig. 7. The change of electric energy is given in dependence of the temperature level of the condenser of the chiller (first x-axis) and of the evaporator of the heat pump (second x-axis). As before, it is assumed, that if the heat pump uses the chiller as heat source, there is a temperature difference between the two temperature levels of 10 K due to the two required heat exchangers. With the given figure and in knowledge of the electric energy demand for the cooling system as well as for the heat pump, it is possible to decide if is more profitable to decrease the condensation temperature of the cooling system and let the heat pump take this additional temperature lift or vice versa. As it can be seen, especially for normal cooling, for a lower condensation temperature level of the cooling system, the percentage reduction of the energy demand for cooling is higher than the percentage increase of the energy demand for the heat pump. In deep-freezing applications with lower evaporation temperatures, the temperature difference between evaporator and condenser in the compression chiller is already that big, that an additional increase does not affect the total energy demand significantly. The same effect can be seen for the heat pumps with the higher set target temperature, even though for higher evaporation temperatures the efficiency is increasing faster. For a better understanding, in the following, an example is given

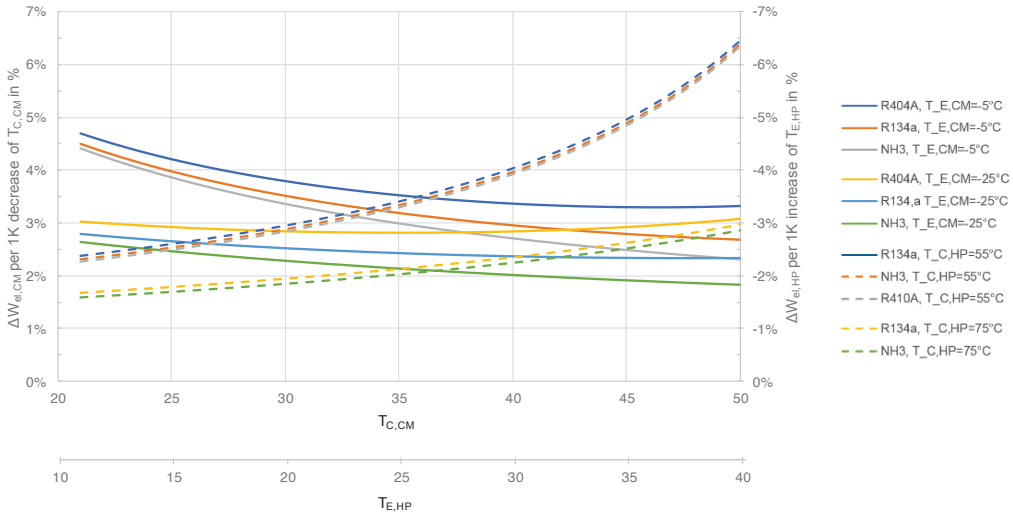

Fig. 7: Comparison between the increase of the electric energy demand per 1 K increase of the condensation temperature of the chiller (left axis, continuous line) and the decrease of the electric energy demand per 1 K increase of the evaporation temperature of a heat pump (right axis, dashed line). Valid for customary refrigerants and evaporation temperatures (chiller) and condensation temperatures (heat pump)

5. Conclusion

The process and energetic analysis has shown that there is a significant potential for solar process heat in the German meat sector. The technical potential is 1,000,000 m². The big amount of hot water simplifies the identification of a suitable integration points. Especially the maturing process is promising regarding the further use of solar heat. It has to be weighed if the retrofit to water heating is beneficial.

Due to the massive use of compression chillers for cooling the products, industrial heat pumps can reach low heat generation costs. The solar heat industry should focus on creating complementary systems of solar collectors and heat pump. If there is only a small temperature lift to provide. Heat pumps are going to be the favourable solution. As is could be shown, in general, cooling systems should be operation as efficient as

possible, resulting in a very low condensation temperature. If there is a significant demand for hot water in relation to the used electric energy for cooling, it can be beneficial to use the compression chiller as heat pump, enabling an intensified use of heat out of the condenser. The combination of heat pumps and compression chillers is very promising. But, finding the optimal combination heavily depends on the system. If all of the waste can be used in a heat pump it can be profitable to increase the condensation temperature of the cooling system making the heat pump even more efficient.

References:

Bell, I. H., Wronski, J., Quoilin, S., Lemort, V. 2014. Pure and Pseudo-pure Fluid Thermophysical Property Evaluation and the Open-Source Thermophysical Property Library CoolProp. Industrial and Engineering Chemistry Research. Volume 53. Issue 6. 2498-2508,

Lambauer, J., Fahl, U., Ohl, M., Blesl, M., Voß, A. 2008. Industrial heat pumps – potential, barriers und best-practise. IER. Stuttgart. Germany. in German

Lauterbach, C., Schmitt, B., Vajen, K. 2012, The potential of solar heat for industrial processes in Germany. Renewable and Sustainable Energy Reviews. Volume 16. Issue 1. pp. 5121 - 5130

Maennel, A.. Fleischatlas 2014. Data and facts about animals as food. in German

MATLAB and Statistics Toolbox Release 2010b. The MathWorks, Inc. Natick, Massachusetts. United States.

Nast, M., Pehnt, M., Frisch, P. 2010. Process heat in MAP, ifeu Institut für Energie- und Umweltforschung, Heidelberg, Deutsches Zentrum für Luft- und Raumfahrt. Stuttgart. Germany. in German

Preuss, G. 2011. Energy demand for cooling systems. Forschungsrat Kältetechnik e.V. Frankfurt. Germany. in German

Rosenwinkel, K.H. 2004. Analysis about the state of the art of the environment protection in the food industry. Final report. Hannover. Germany. in German

Steimle, F., Kruse, H., Wobst, E., Jahn, J. 2002. Energy demand for cooling in Germany. Forschungsrat Kältetechnik e.V. Frankfurt. Germany. in German

VDI Richtlinie 2596. 2009. Reduction of emissions – sluaghter houses,.Verein Deutscher Ingenieure. Düsseldorf. Germany. in German

6.

Conference Proceedings

EuroSun 2016
Palma de Mallorca (Spain), 11 - 14 October 2016

Optimizing design of a Linear Fresnel Reflector for process heat supply

Diego Pulido Iparraguirre[1, 2], Juan J. Serrano-Aguilera[1], Loreto Valenzuela[1] and Aránzazu Fernández-García[1]

[1] Plataforma Solar de Almería (CIEMAT-PSA), Spain

[2] Centro de Desarrollo Energético Antofagasta (CDEA), Universidad de Antofagasta (UA), Chile

Abstract

Lineal Fresnel Reflectors (LFR) is a promising technology in the field of concentrating solar thermal collectors which presents several advantages in comparison with the widely used parabolic-trough collectors (PTC). A methodology to properly design a LFR is presented as well as several issues arisen out the study of a particular case. As first step, a brief review was performed to select the proper receiver configuration, resulting in a trapezoidal cavity with multitube absorber receiver. Secondly, several stages of the optimized process were followed using an in-house ray tracer computer code to simulate the optical behavior of the system. Different characteristics, as width of the mirrors, number of rows, mirror geometry profile, height, length and configuration of the receiver, were optimized setting the power impinging in the absorber tube surface as the objective function. According to the results obtained, the shape of the mirrors was stablished based on the optical advantages that parabolic mirrors have over flatted ones. The point strategy was focused on achieving a homogeneous flux in the receiver tubes surface. The height of the receiver over the mirrors plane was selected as the one that maximizes the impinging power. A practical analysis related with the facilities characteristics was carried out to set the number and width of mirrors. In addition, a thermal balance between the impinging power and the thermal energy gained by the heat transfer fluid (HTF) was performed to calculate the length of the receiver tubes. Finally, the results of the analytical model were cross checked with a ray tracer software (Tonatiuh), with satisfactory results.

Keywords: *Lineal Fresnel Reflector, ray tracer, multitube absorber, point strategy.*

1. Introduction

LFR is a promising technology in the field of concentrating solar thermal collectors (Singh et al. 1999). The operating principle relays on a set of long and narrow mirrors that might be flat or slightly curved, which reflect direct solar radiation by tracking the sun along the day. The reflected solar beams are absorbed by a fixed receiver, which is the key component of the system. The energy absorbed by the receiver is transferred to the HTF circulating inside it, which increases its enthalpy. Several designs of receivers are found in the literature (Zhu et al. 2014), including receiver tubes arranged individually or in group protected from the ambient by a cover in order to minimize heat loses.

PTC are the main technology in terms of number of plants installed and currently in operation (Fernandez-Garcia et al. 2010), mostly because of the optimum results of SEGS plants in Mojave Desert, California, which are being producing electricity since the 80's until now. It has been found that LFR technology presents some significant advantages compared with PTC (Sahoo et al. 2012; Sait et al. 2015). On one hand, the costs of the optical components is lower in LFR, according to the nearly flat shape of the mirrors (Boito & Grena 2016) and also the absence of metal-glass welds in the receiver tubes, because in most of the designs the receiver tubes are not directly exposed to the ambient and no vacuum is needed. On the other hand, as the receiver is fixed, they do not use ball joints, as PTC does, at the points where the distribution pipe meets the start and end of the collector. As a consequence of this, lower maintenance and operation costs for LFR plants is achieved (Haeberle et al. 2002).

doi:10.18086/eurosun.2016.02.21 Available at http://proceedings.ises.org

On the contrary, the main disadvantage of LFR compared with PTC, is the lower optical efficiency, explained by the longitudinal component of the radiation impinging the receiver's tubes, which increases when sun is far away from the zenithal position. Also, significant optical errors due to the large distance between the mirrors and the focal point contribute to decrease the optical performance (Boito & Grena 2016).

The receiver of a LFR may be considered as the most relevant component of the system because it is the place where the energy conversion process occurs. Its geometrical and optical configuration has changed, depending mainly on the application. Previously, the most common design was based on a single tube with a secondary reflector (see Fig. 1 left). This design could be conceived with a second glass tube surrounding the metal one and vacuum between both, or just a single steel tube with a glass flat cover sealing the receiver from outside climate conditions (Montes et al. 2016). Recent designs agree in using a trapezoidal cavity with a multitube absorber (see Fig. 2 right). The main advantages of trapezoidal cavity with multitube absorber are a higher efficiency in the transfer process and a more flexible design leading to simpler control of the flow through the tubes (Abbas et al. 2012).

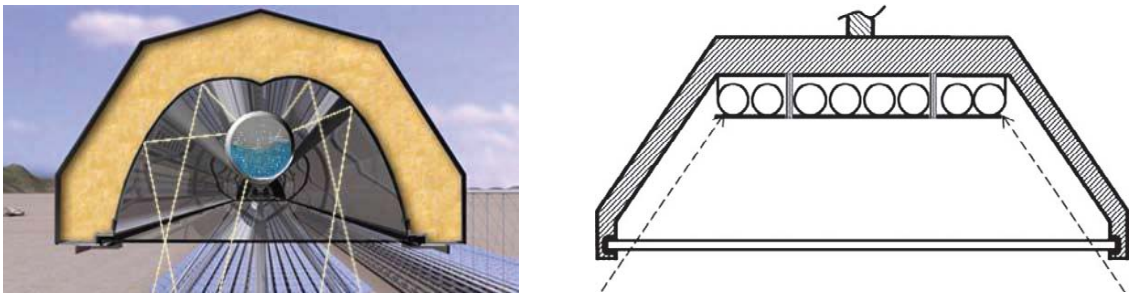

Fig. 1: Left: Single tube receiver configuration (source: Novatec Solar). Right: Trapezoidal cavity with multitube absorber receiver (source: Abbas et al. 2012).

Although the thermal energy consumption in industrial processes is significantly high (Kalogirou 2003) and LFR represents an economically feasible and clean solution, this technology is not as mature as expected. This paper presents a methodology to optimize the design of a LFR oriented to production of thermal energy for industrial process heat (IPH) applications at temperatures up to 200 ºC.

2. Methodology

This section includes the methodology followed in the design process of a LFR prototype for IPH applications. Different characteristics, as width of the mirrors, number of rows, mirror geometry profile, height, length and configuration of the receiver, were optimized, setting the power impinging in the absorber tube surface as the objective function.

2.1. Ray tracer

An in-house ray tracer computer code based on a Monte Carlo stochastic method developed in Matlab® was created (see the algorithm steps in Fig. 2), in order to study different configurations and geometries of the LFR prototype. This code gives the possibility to choose the Sunshape distribution from Buie, Neumann or Pillbox (Buie et al. 2003; Neumann et al. 2002). As a second step, an accumulated distribution function was obtained.

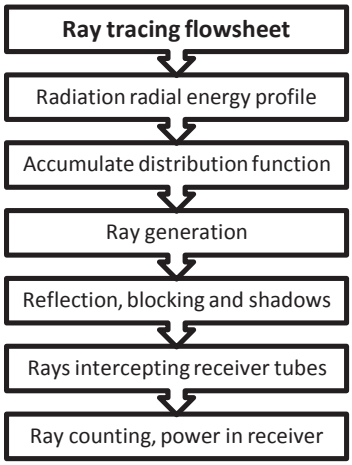

Fig. 2: Ray tracer flowsheet scheme.

A two-dimensional design was considered, in order to minimize the computing time of the simulations, folding the longitudinal coordinates into transversal plane and using a proper variable change. With this approach, the number of equations and variables was considerably reduced. This method does not disregard the longitudinal component of the impinging radiation, though. It involves a significant advantage because in case only the transversal component of the rays were considered, the path of the rays reflected from the mirror to the receiver would be considerably shorter than the path of those rays with longitudinal component.

In the rays path, reflection, blocking and shading are considered before the rays reach (or miss) the receiver surface. The rays that intercept the receiver tubes are then counted, given a power value assigned of each ray. Then, the concentrated flux profile on the receiver ($f(\theta)$) is calculated. The whole power impinging on the receiver is simply the sum of all of them, as indicated in equation (1).

$$q_t = \sum_{i=1}^{n} \int_{-\pi}^{\pi} r_{abs,i} \cdot f_i(\theta) \cdot d\theta \qquad \text{(eq. 1)}$$

where q_t [Wm^{-1}] is the sum of the power impinging in the n receiver tubes, $r_{abs,i}$ [m] is the radius of the tubes, and $f_i(\theta)$ [Wm^{-2}] is a function of the power received in every differential of the angular direction of the tube, θ.

Several simulations were done to develop an optimized design of a LFR. As base case, the code was run by using the meteorological data and the sun position of the *Plataforma Solar de Almería* (southern Spain). Five hours before and after noon were utilized for the simulations of one day from every month of the year. The power impinging in the receiver was maximized, and the geometry of the LFR that achieves this maximum was accepted as the optimal design.

2.2. Receiver configuration

The first step followed to select the receiver configuration for the LFR under design was to perform a literature revision, taking into consideration the operating conditions of the industrial process where the LFR designed will be used. The trapezoidal cavity with a multi-tube receiver was selected as the proper configuration (see section 3.1) and the number of tubes was set.

2.3. Shape of mirrors

Once the receiver configuration was chosen, the next step was to select the shape of the concentrating mirrors. The possibilities were restricted to flat shape or parabolic shape due to practical and economic issues. The analysis was made by simulating the power impinging in the receiver for both alternative shapes.

As shown in Fig. 3a, the image reflected by flat mirrors on the receiver, w_r, is approximately equivalent to the width of the mirrors, w_1 ($w_1 \approx w_r$). That is, the distance traveled by the reflected rays from the mirror to the receiver will not considerably increase the final width of the image at the receiver surface. For this reason, the optimal width for flat shaped mirrors should be close to the width of the receiver, w_R ($w_r \approx w_R$). If this condition was not stablished and wider mirrors were used (with a width of w_2, being $w_2 > w_1$ as displayed in Fig. 3b), the reflected image would certainly be wider than the receiver ($w_r > w_R$) and several rays will miss the target.

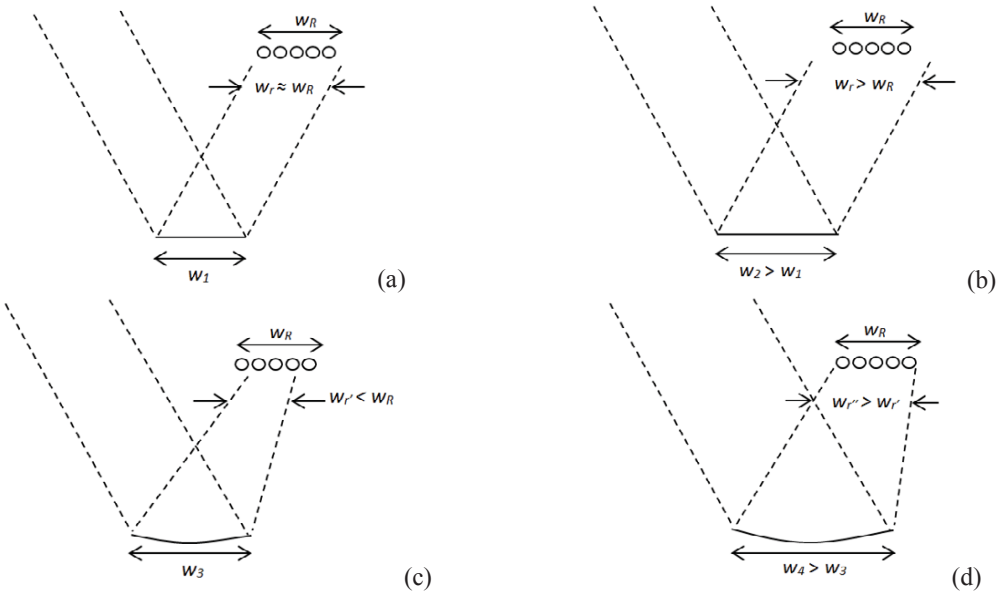

Fig. 3: Schemes representing the influence of the width in flat and parabolic shaped mirrors in the image reflected over the receiver.

In case of using parabolic mirrors (with a certain width, w_3), the image reflected by the mirrors will tend to converge to the focal point of the parabola, reflecting a beam of rays whose width ($w_{r'}$) is lower than the receiver width, $w_{r'} < w_R$ (Fig. 3c). In order to increase the power impinging into the receiver, wider mirrors ($w_4 > w_3$) could be considered without the limitation found in flat shaped mirrors. Wider mirrors imply more radiation in the reflector aperture ($w_{r''} > w_{r'}$), which leads to raise the concentration factor of the LFR (Fig. 3d). In addition, the height of the receiver over the lines of mirrors must be adjusted in order to fit the image reflected to the target.

2.4. Point strategy

The point strategy, i.e. the image that reflected rays form in the receiver transversal surface, has a significant relevance in the overall performance of LFR. Due to the fact that the receiver is not a singular aiming point, but a group of tubes, every tube should be lightened homogeneously. In other words, a homogeneous flux should be maintained so that hot spot which could lead to thermal stress in the tube material can be avoided. Several point strategies were analyzed with the in-house ray-tracing simulation code in order to address this issue along with the concentration ratio.

2.5. Height of the receiver

The distance from the mirrors plane to the receiver was established by maximizing the power delivered to the receiver. A set of calculations for different heights, fixing the rest of parameters, was carried out to study the relationship among the different geometrical parameters and to find the combination that yields an optimum height.

2.6. Number and width of mirrors

Having on goal the collection of maximum power, the selection of the number and width of mirrors is not a trivial issue. More and wider mirrors imply a larger reflecting surface which leads to more solar radiation collected in the aperture of the LFR. As a consequence, the power maximization cannot be the only design criterion to find the optimum number and width of mirrors. An economical approach combined with practical and technical aspects of the industrial facilities, where this system will be installed, is the best strategy to follow.

2.7. Length of receiver tubes

When the rest of the parameters explained in the previous sections were selected and the power in the receiver was obtained by the software developed, the next step was to simulate the thermal behavior of the receiver to calculate the tubes length required to achieve a certain increase of HTF temperature. In LFR technology,

thermal losses from tubes to ambient are mostly governed by radiation effect, having the convection mechanism a lower influence, and the conduction phenomena a negligible contribution (Pye et al. 2003; Singh et al. 2010). Different authors (Kumar et al. 2012; Reynolds et al. 2002; Sahoo et al. 2012) have developed experimental correlations for the same receiver configuration selected in this work. They consider the Nusselt number (see eq. 2) as the principal parameter to study the thermal losses due to both radiation and convection from the tubes to the glass cover window. The correlations given by these three studies mentioned were analyzed and compared among them.

$$Nu_{\sigma+h} = \frac{q_{\sigma+h} \cdot D}{k_f \cdot (T_{abs} - T_{cov})} \qquad \text{(eq. 2)}$$

where $Nu_{\sigma+h}$ [-] is the overall Nusselt number that regards radiation and convection effect, $q_{\sigma+h}$ [Wm^{-2}] is the overall heat flux, D [m] is the distance from the tubes to the glass cover window, k_f [$Wm^{-1}K^{-1}$] is the thermal conductivity of the fluid, T_{abs} [K] is the temperature of the tubes and T_{cov} [K] is the temperature of the glass cover window.

Additionally, a fourth correlation, in which a theoretical approach is made, was included in the study. This theoretical approach considers two flat parallel plates (Incropera, 2007). The hot one (simulating the tubes) is located above and facing down and the cold one (simulating the glass cover) is situated below. The equations ruling this condition respond to external free convection flows over horizontal plates.

3. Results

The results obtained in the LFR design process by using the in-house software developed in this work are presented in this section. This results belong to particular requirement stablished, however the process could be followed by any other set of conditions.

3.1. Receiver configuration

The final receiver configuration selected was based on the information collected from the literature along with the operating conditions of the industrial process to be supplied, i.e. thermal energy demand, fluid temperature and mass flow rate. A trapezoidal cavity with a multitube absorber design presents the best operation condition in terms of flow control alongside the simplicity of the receiver assembly. After considering several configurations (ranging from 2 to 8 tubes), the design option chosen incorporates 6 parallels tubes. This design is flexible and allows restricting the flow to central tubes, if radiation is lower than a certain value, in order to maintain a stable operation temperature.

3.2. Shape of mirrors

A comparison of the power impinging in the receiver was made between parabolic and flat shaped mirrors (see section 2.3). An increase in the width of the mirrors delivered similar results for both options until mirrors reach the same width of the receiver, w_R (see Fig. 4). For mirror widths higher than w_R, the increase of this parameter leads to directly enhance the power for the parabolic shape. However, the flat shape does not respond in the same way because of the overflow effect previously explained. According to these results, the parabolic shaped mirrors are preferred instead of flat shaped mirrors.

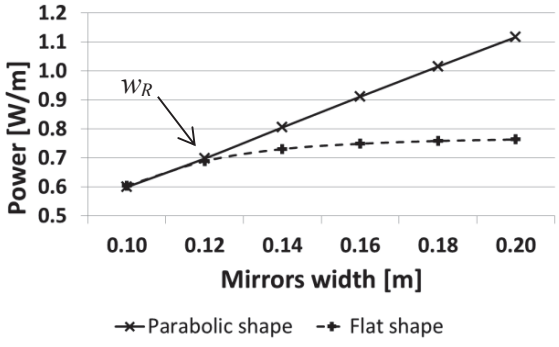

Fig. 4: Normalized power ($Power_{reference}$ = 1 Wm^{-2}) in the receiver according to the width of flat and parabolic shaped mirrors. For a configuration of 12 rows of mirrors.

Cylindrical shaped mirrors, which present quite similar optical behavior compared with parabolic shaped mirrors, are a suitable alternative solution from a practical and financial perspective because they involve an easier and cheaper manufacturing process. The main characteristic of cylindrical mirrors is the radius of curvature, which is twice the focal length of parabolic shaped mirrors for the same receiver height (Abbas et al. 2012). A higher radius of curvature implies a smoother geometrical profile, which entails a significant advantage for the manufacturing of the concentrator because it may be accomplished with thin glass mirrors glued over a cylindrical preformed pattern, which is easy to achieve.

In LFR systems, every mirror has a singular focal distance to the receiver, which leads to a different radius of curvature for each mirror. Manufacturing different preformed pattern with every radius of curvature certainly increases the cost of the LFR. An iteration process was performed with the goal of maximizing the power impinging in the receiver while using one single radius of curvature for all mirrors. At each iteration, a specific radius of curvature was employed for all mirrors, which was changing from the focal distance of the farthest mirrors from the receiver to the focal distance of the nearest mirror. It was established that the radius of curvature of the farthest mirror delivers the best results. In addition, it was concluded that the impinging power in the receiver for this particular configuration (i.e. the radius used for all the mirrors is the one corresponding to the farthest one) is similar to the power achieved when every mirror has its own specific radius.

3.3. Point strategy

Fig. 5 shows the image form by the rays if every mirror would point to the central position in the receiver. In this approach, the rays are concentrated in the central tubes, leaving the external tubes with no rays at all. As it was explained in section 2.4, this point strategy leads to generate hot spots that are prejudicial to the overall performance of LFR.

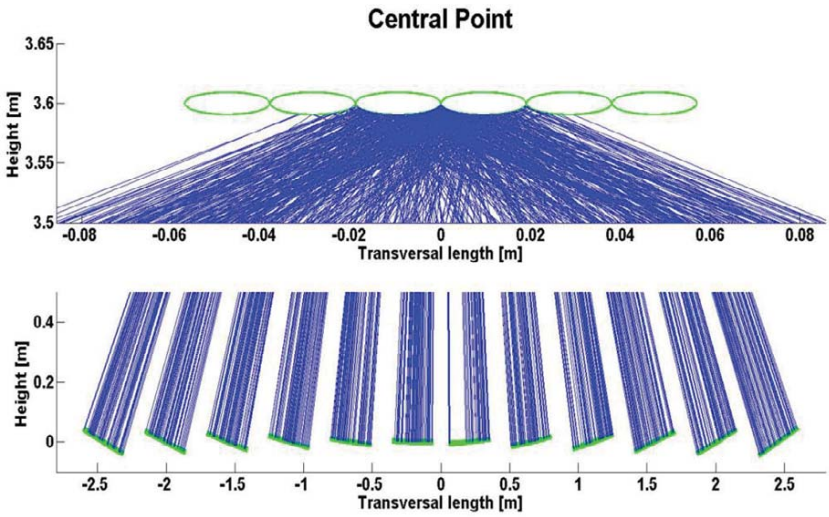

Fig. 5. Rays impinging in receiver following a central point strategy.

On the contrary, if an individual point strategy is taken into account, in which a group of mirrors aims exclusively at a specific tube, the image formed by the rays is much more homogeneously distributed, as expected. As it can be seen in Fig. 6, the power flux in the receiver is more uniform when this strategy is applied. In this figure, the red lines represent those rays missing the receiver.

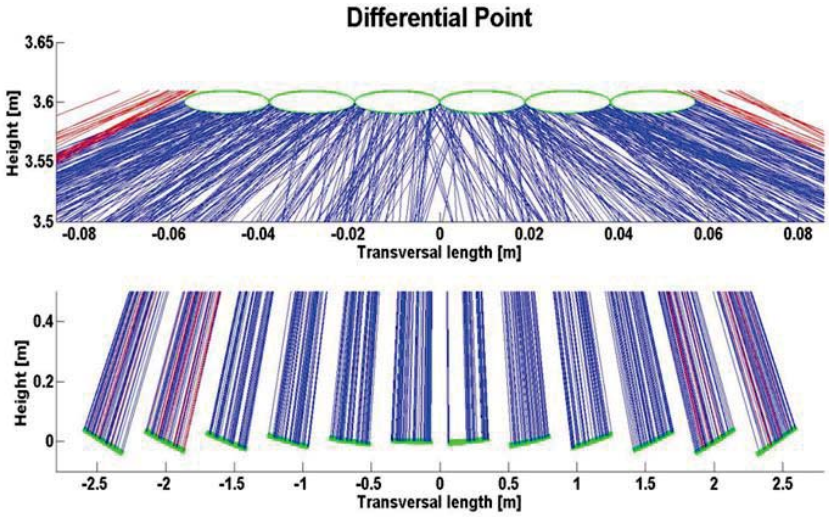

Fig. 6. Rays impinging in receiver following a differential point strategy.

The point strategy assumed in this case is based on a compromise between the concentration ratio and flux distribution.

3.4. Optimized height of receiver

Fig. 7 shows the power obtained when the height of the receiver is varied, for different number of mirror rows. Every number of rows presents one specific receiver height in which the power is maximized (indicated by the red circles in the graph). If the receiver is placed below the optimum height, blocking and shadows become predominant and consequently fewer rays reach the receiver, and therefore reducing the impinging power. On the contrary, in case of locating the receiver above the optimal position, it implies a higher rate of rays missing the target because the effect of sunshape becomes noticeable when the distance traveled by reflected rays increases. Additionally, a stochastic approach to model the deviation of rays caused by mirrors aberrations was included in the model. The longer distance traveled by the rays, the more noticeable this phenomenon is. If the receiver height is not increased after adding mirrors, the furthest one will present a pronounced tilt, which will lead to increase shadings on the neighbor mirrors and consequently a reduction in the power with respect to the corresponding optimum height for that number of mirrors. For this reason, the optimized receiver height is larger for a higher number of rows of mirrors. Finally, for the selected configuration with 12 rows of mirrors the optimal height of the receiver is 3.4 m.

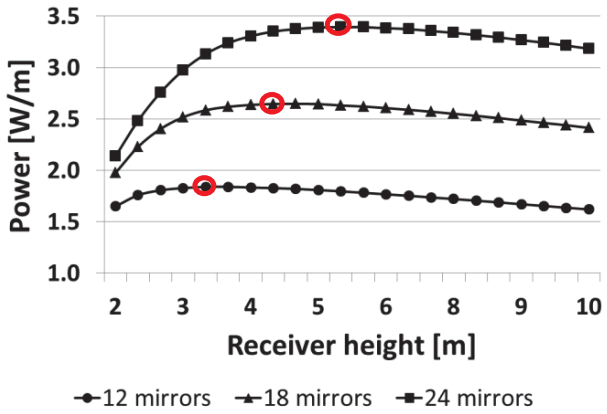

Fig. 7. Normalized power ($Power_{reference}$ = 1 Wm^{-2}) in receiver related with its height for different number of mirrors.

3.5. Number and width of mirrors

According to the methodology explained in section 2.6, the number and width of mirrors could be selected with the in-house code presented in this work, for every specific facility, by considering both the expected power and several technical, economical and practical aspects. For example, as shown in the previous section, every

mirror configuration involves an optimum receiver height, which must be suitable for the facility characteristics as well. The selected configuration is made up of 12 rows of mirrors of 0.28 m width.

3.6. Length of receiver tubes

The thermal energy model described in section 2.7 was applied. An increase of 20 ºC in the HTF temperature was set as the criterion to determine the absorber length. Such a high thermal gain was imposed in order to minimize the temperature relative errors when carrying out the experimental test campaign. The accuracy of the measurement instruments was also considered at the time of setting the temperature difference in the LFR. The length of the receiver that satisfied this condition is in the range of 10 to 12 meters.

The four heat loss correlations explained in section 2.7 were not in agreement among them. It was found a difference of up to 30% in the calculated length of the receiver. All the correlations regarded use different criterion for the definition of ΔT This disagreement could be the reason of such an inconsistent results.

3.7. Benchmarking of ray-tracing code

The optical model presented in this work was cross checked with a free ray tracer software, called Tonatiuh (Blanco et al. 2009). This software allows simulating a LFR with its geometrical and optical characteristic. The results of the comparison are showed in Fig. 8. Six charts can be seen in this figure, one for each tube in the receiver. In every chart, the normalized power impinging in the receiver is presented versus the angular coordinate around the tube perimeter (expressed in radians).

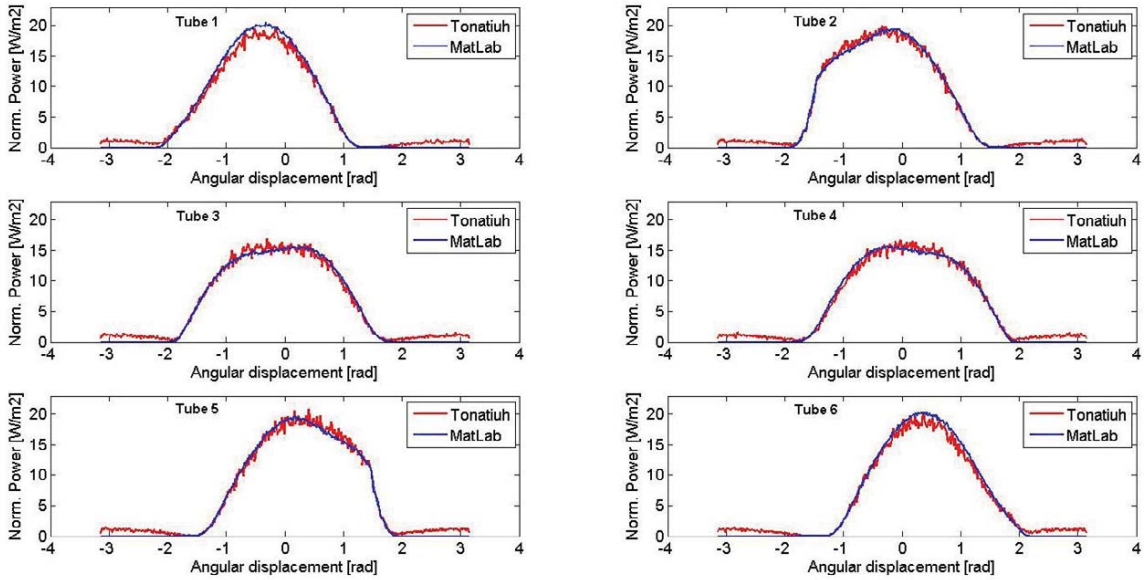

Fig. 8.Simulated normalized power impinging in receiver tubes from Tonatiuh software (red) and in-house Matlab code (blue). ($Power_{reference}$ = 1 Wm^{-2}, Location: Plataforma Solar de Almería, Spain).

For every single tube of the receiver, it was found that the curves profile and values of normalized impinging power match satisfactorily in both simulations.

4. Conclusions

A detailed design procedure for a Linear Fresnel solar collector was described. The collector was designed to provide thermal energy in IPH applications. The reflector configuration was determined by means of an in-house ray tracing code. The mirrors follow a cylindrical shape, the number of rows selected for the prototype to be built is 12 and the width chosen for each one is 0.28 m. The receiver configuration is a multitube cavity receiver composed of 6 parallel tubes and a trapezoidal cavity around 11 m long located 3.4 m over the mirrors plane. For mirrors tracking, a differential point strategy was analyzed with the objective of achieving a more homogeneous flux distribution on the multitube receiver panel. The next steps in the design process are optimizing the final design and building a prototype at the *Plataforma Solar de Almería*. Further work, can be

done from the current model, including the optimization of the mirrors shift value according to economical and technical restrictions.

5. References

Abbas, R., Montes, M.J., et al., 2012. Solar radiation concentration features in Linear Fresnel Reflector arrays. Energy Conversion and Management. 54(1), 133–144.

Abbas, R., Muñoz, J. & Martínez-Val, J.M., 2012. Steady-state thermal analysis of an innovative receiver for linear Fresnel reflectors. Applied Energy. 92, 503–515.

Blanco, M.J. et al., 2009. Preliminary validation of Tonatiuh. SolarPaces Conference.

Boito, P. & Grena, R., 2016. Optimization of the geometry of Fresnel linear collectors. Solar Energy. 135, 479-486.

Buie, D., Monger, A.G. & Dey, C.J., 2003. Sunshape distributions for terrestrial solar simulations. Solar Energy. 74(2), 113–122.

Fernandez-Garcia, A. et al., 2010. Parabolic-trough solar collectors and their applications. Renewable and Sustainable Energy Reviews. 14(7), 1695–1721.

Haeberle, A. et al., 2002. The Solarmundo line focussing Fresnel collector. Optical and thermal performance and cost calculations. Proceedings of SolarPACES, 1–11.

Incropera, F.P., 2007. Fundamentals of Heat and Mass Transfer 6th ed.

Kalogirou, S., 2003. The potential of solar industrial process heat applications. 76, 337–361.

Kumar, S., Independent, N. & Madras, T., 2012. Heat loss characteristics of trapezoidal cavity receiver for solar linear concentrating system. Aplplied Energy. 93, 523–531.

Montes, M.J. et al., 2016. Performance model and thermal comparison of different alternatives for the Fresnel single-tube receiver. 104, 162–175.

Neumann, A. et al., 2002. Representative Terrestrial Solar Brightness Profiles. Journal of Solar Energy Engineering. 124(2), 198.

Pye, J.D., Morrison, G.L. & Behnia, M., 2003. Modelling of Cavity Receiver Heat Transfer for the Compact Linear Fresnel Reflector. Manufacturing Engineering, 1–9.

Reynolds, D.J., Behnia, M. & Morrison, G.L., 2002. A Hydrodynamic Model for a Line-Focus Direct Steam Generation Solar Collector. Solar 2002, 1–6.

Sahoo, S.S., Singh, S. & Banerjee, R., 2012. Analysis of heat losses from a trapezoidal cavity used for Linear Fresnel Reflector system. 86, 1313–1322.

Sait, H.H. et al., 2015. Fresnel-based modular solar fields for performance/cost optimization in solar thermal power plants: A comparison with parabolic trough collectors. Applied Energy. 141, 175–189.

Singh, P.L., Ganesan, S. & Yàdav, G.C., 1999. Performance study of a linear Fresnel concentrating solar device. Renewable Energy. 18(3), 409–416.

Singh, P.L., Sarviya, R.M. & Bhagoria, J.L., 2010. Heat loss study of trapezoidal cavity absorbers for linear solar concentrating collector. Energy Conversion and Management. 51(2), 329–337.

Zhu, G. et al., 2014. History, current state, and future of linear Fresnel concentrating solar collectors. Solar Energy. 103, 639–652.

Conference Proceedings

EuroSun 2016
Palma de Mallorca (Spain), 11 - 14 October 2016

Industrial Integration of Mid-Temperature Solar Heat – First Experiences and Measurement Results

Alois Resch[1], Rudolf Kraft[1]

[1] Fachhochschule Oberösterreich Forschungs & Entwicklungs GmbH, A-4600 Wels

Abstract

The integration of solar thermal energy at mid-temperature level (up to 200 °C) in industrial applications has an enormous potential. Developing a flexible simulation environment within the software MATLAB/Simulink for various kinds of industrial processes is therefore one of the main goals of the present project work. Furthermore, a modular hydraulic system has been developed and installed at the University of Applied Sciences Upper Austria, which provides the possibility to recreate processes on a laboratory scale in order to gain measurement data for verifying and adjusting the simulation environment. A centerpiece of the hydraulic system is a concentrating solar collector (Fresnel system) driven by thermal oil, which is currently being operated within a long-term measurement to achieve a comprehensive characterization at the location of Wels, Austria.

By the end of this project work a simulation environment with unique reliability will be available, which will highly support the integration of mid-temperature solar energy in industrial processes.

Keywords: *Fresnel, mid-temperature, solar thermal, industrial processes*

1. Introduction

Solar thermal energy is worldwide already well established for applications like domestic hot water generation, where temperatures of up to 100 °C are required. For temperatures beyond this limit there is still a huge potential for the substitution of fossil fuels by solar energy. Therefore, the present project was started to investigate the integration of mid-temperature solar thermal energy (up to 200 °C) for various applications in the industrial sector.

The centerpiece of this project is a modular hydraulic system consisting of several heat sources and heat sinks that can be combined in a very flexible way by a loop to be able to emulate different cases of application, like solar cooling, solar district heating or industrial process heat. One hydraulic loop works with water and can handle configurations up to 95 °C, whereas the second loop is driven by thermal oil for applications up to 200 °C. The central mid-temperature heat source is a Fresnel collector with an aperture area of 22 m², which provides the heat to the thermal oil loop by a plate heat exchanger. One of the heat sinks is an absorption chiller with a cooling power of 19 kW, driven by the water loop with temperatures up to 95 °C.

doi:10.18086/eurosun.2016.02.11 Available at http://proceedings.ises.org

In parallel to the hydraulic investigation of these applications another main task of this project is to develop a dynamic simulation of the entire hydraulic system using the software MATLAB/Simulink. After a deep verification of the simulation environment by matching the simulation results with the measurement results, it will be extended to a "hardware-in-the-loop" system, so that single hydraulic components can be characterized with a simulated environment.

By the end of this project work a verified and well tested simulation environment will be available to analyze and optimize the integration of solar thermal energy in industrial processes. Applications with a thermal power of up to 50 kW can also be demonstrated and measured on the modular hydraulic testing center.

2. Functional requirements

The designing phase of this system started with a definition of the functional requirements. The three main limitations in functionality are the following:

- Heat transfer medium only in liquid phase (steam or gas applications are not considered)
- Maximum application temperature: 200 °C
- Maximum thermal power: 50 kW

The required operation modes of this test stand were summarized in flow charts like the one that is displayed in Fig. 1.

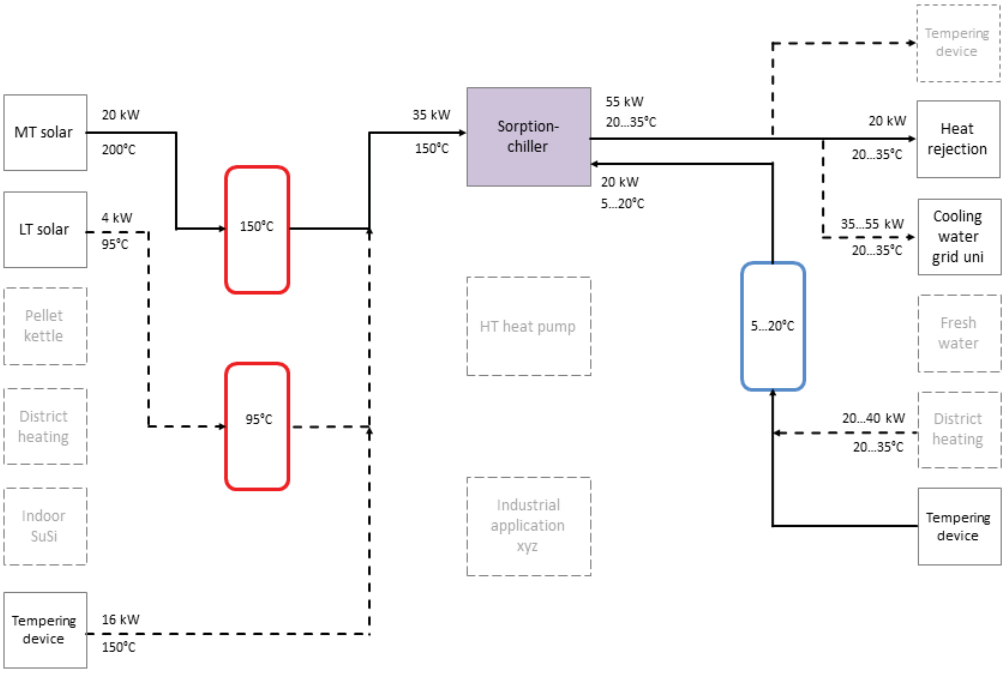

Fig. 1. Flow chart of operation mode "sorption chiller"

Using this kind of flow charts for describing the various configurations within the hydraulic system (heat sinks and heat sources) provides an appropriate overview of the thermal energy flow and shows the activated parts for each operation mode. The implemented components are the following:

- MT Solar: Mid-Temperature solar thermal collectors; 11 m² vacuum tube collectors + 22 m² Fresnel collector
- LT Solar: Low-Temperature solar thermal collector; optional flat plate collectors (up to 8 m²)

- Pellet boiler: 15 kW
- District heating: interface to the local district heating supplier (optional)
- Indoor SuSi: Connection to the available indoor sun simulator (optional)
- Tempering device: provides heating and cooling power at a precise temperature
- Heat rejection: optional connection of heat rejection for sorption chiller
- Cooling water grid uni: university´s internal cooling water for all kinds of heat rejection; constant temperature of 15 °C is provided
- Fresh water connection
- Thermal oil storage: two tanks with a volume of 1,300 liters
- Cold water storage: tank with a content of 1,000 liters; used as cooling load
- Hot water storage: tank with a content of 1,000 liters; used as storage for the low-temperature solar thermal collectors resp. as heat source for all water applications
- Sorption chiller: Cooling power of 19 kW

3. Hydraulic concept, simulation and engineering

The basic hydraulic concept of connecting the mentioned high number of heat sources and heat sinks by a loop is illustrated in Fig. 2. Depending on the required operation mode each branch of the loop (collector, district heating…) can be either activated or by-passed, providing the possibility to realize various combinations of the hydraulic components. This first loop is driven with silicon oil, so that all applications with temperatures between 100 °C and 200 °C can be operated without exceeding the boiling point of the fluid.

The second loop driven with water for low temperature applications is realized in a similar way, including a tempering device, water storage, the district heating interface and the absorption chiller.

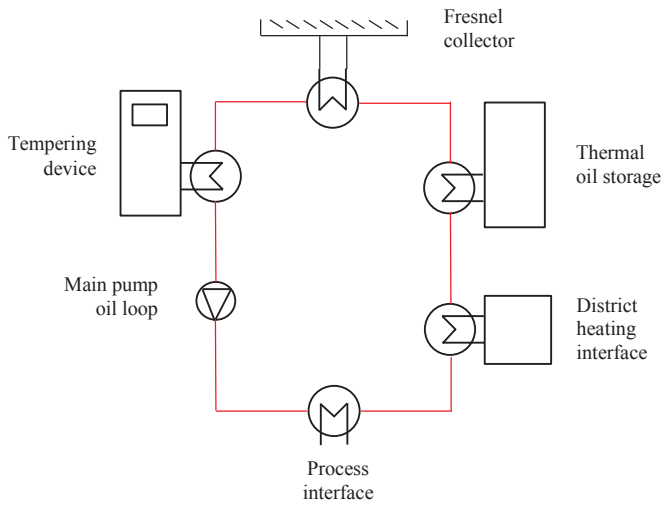

Fig. 2. Hydraulic concept of the thermal oil loop

All heat exchangers are equipped with temperature sensors on the inlet and outlet. In combination with a precise mass flow measurement in each separate hydraulic circuit all heat transfers (positive and negative) can be measured very exactly.

Basing on the hydraulic concept, first calculations of the system have been performed to quantify the main parameters like pipe dimensions, pressure losses, pump dimensions, mass flows etc. These first designing results have been used as initial information to set up the hydraulic circuits within the simulation software MATLAB/Simulink. The following Fig. 3 displays a segment of the simulation of the water loop with the collector circuit and its interface to the hydraulic ring (heat exchanger in red). With this detailed simulation the hydraulic engineering of the entire system could be finalized in a much more precise way. Furthermore, the simulation of different control strategies for all possible combinations of heat sinks and sources provided valuable information for a reliable and safe operation of the system.

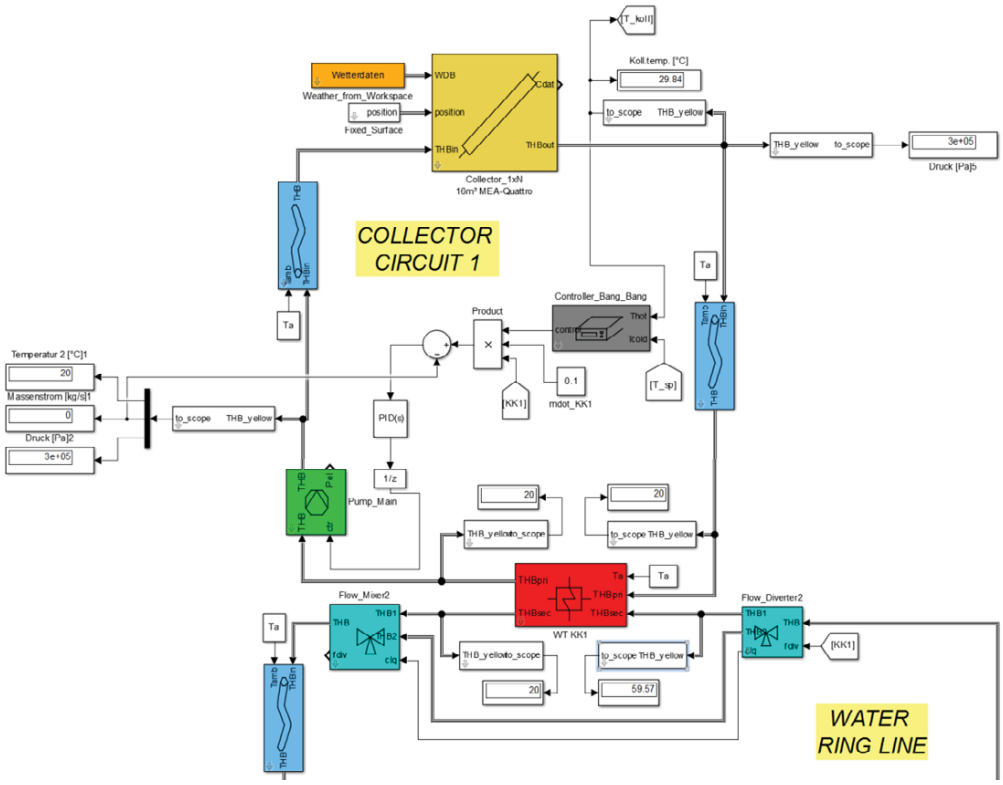

Fig. 3. Simulation segment of the water loop in MATLAB/Simulink

The basis for the final engineering of this test bench was the detailed hydraulic schematic, which cannot be illustrated within this paper due to its complexity and dimension. Nevertheless, the following numbers of implemented appliances and fittings shall demonstrate the scale of this hydraulic system:

- 14 pumps: speed-controlled
- 27 valves: 3-way, mainly motor driven
- 14 plate heat exchangers
- 300 m of pipes
- 10 mass flow meters
- 69 temperature sensors

4. Selected components in detail

4.1. Concentrating collector

The main solar heat source of this test stand is a Fresnel collector shown in Fig. 4. It works with 110 planar mirrors (dimension 70 mm x 2860 mm) reflecting the sunlight to the linear absorber, which consists of a steel pipe with selective coating, a glass cover and a secondary reflector. The collector has a total dimension of 5.8 m x 4.6 m (gross area 26.68 m², mirror area 21.68 m²) and a weight of 740 kg.

Fig. 4. Installed Fresnel collector [Fresnex, 2015]

4.2. Thermal oil storage

Two tanks with a volume of 1,300 liters each are used as mid-temperature storages. Mineral heat transfer oil serves as storage medium, whereas the oil is not stored stationary in the tanks. During each charging or discharging cycle the thermal oil is pumped from one tank into the other one, ensuring that the temperature at the heat exchanger to the loop is always constant for the cycle time. The empty volumes of the tanks are filled with Nitrogen to achieve a passivation of the oil surfaces.

As the implemented pump is not able to turn its direction of rotation, an external hydraulic solution had to be found to be able to change the flow direction between the two tanks. Therefore, two motor driven 3-way-valves (V901 and V902) were installed, see Fig. 5.

Temperature sensors and filling level sensors are also implemented in the construction of the tanks in order to guarantee a safe and well monitored operation of the mid-temperature storages.

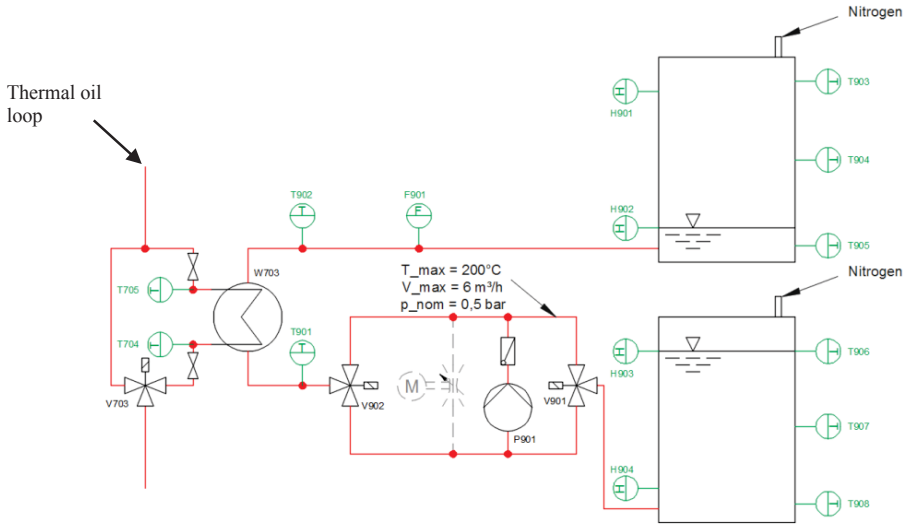

Fig. 5. Hydraulic implementation of thermal oil storages

4.3. Control and measurement equipment

The main goal of this test stand is to quantify the transfer of thermal power as precise as possible. The necessary information of mass flow and temperature difference is gained by using the following measurement equipment:

- Magnetic inductive flow meters for all water circuits: accuracy < 0.2 % of measured value
- Coriolis flow meters for all thermal oil circuits: accuracy < 0.1 % of measured value
- Temperature sensors PT100 1/10 DIN

The data of all sensors in the system are centralized by a programmable logic controller (PLC), which operates and controls all appliances and components of the test stand by applying appropriate control algorithms.

As the testing center will be used for research tasks as well as for demonstration and teaching purposes, operation and measurement of this complex system must be possible in a simple way. Therefore, the creation of full system visualization was mandatory. The visualized low temperature part can be seen in the following Fig. 6.

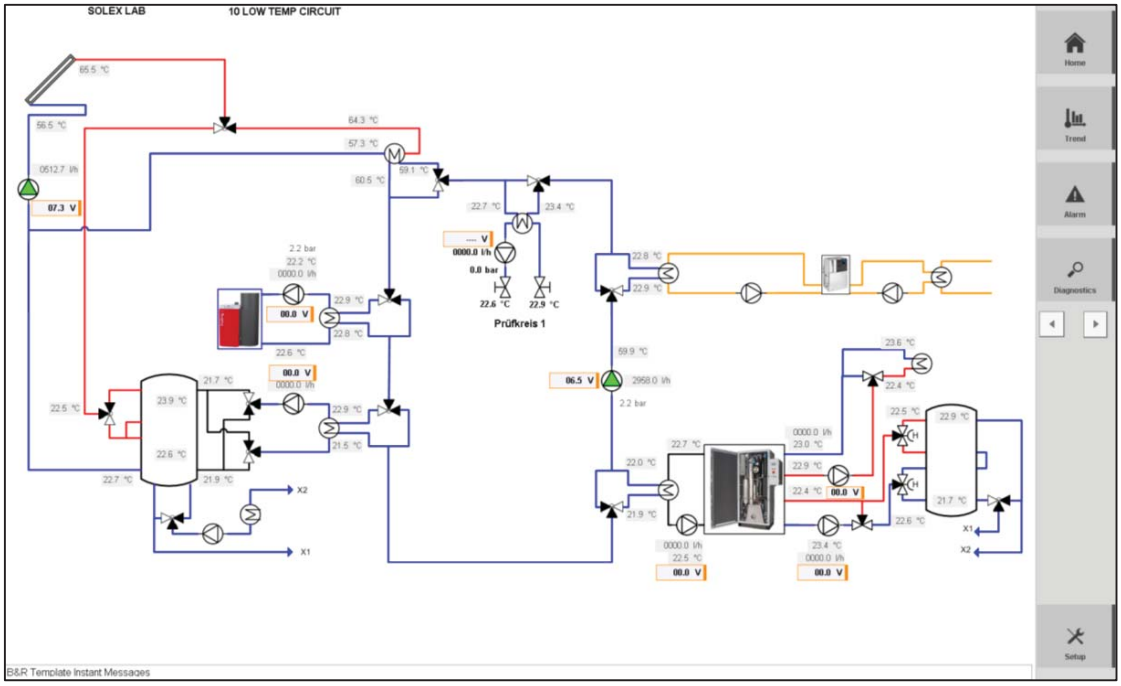

Fig. 6. Visualization of the low temperature part of the testing center

5. Start-up phase and first measurement results

During the start-up phase of the entire hydraulic system each branch and each hydraulic combination was tested thoroughly. Algorithms for the mass flow control had to be implemented, as well as various safety strategies to ensure reliable operation within the specified limits of the test stand.

Exemplary among all performed start-up measurements, Fig.7 illustrates the hydraulic configuration for the operation mode “pellet boiler characterization”. Only the components drawn in solid line are activated in this setup, whereas all other parts of the low temperature system are by-passed or inactive (dotted line). The pellet boiler provides its heat via the plate heat exchanger to the water loop, where the energy is transferred to the heat exchanger of the hot water storage by the main pump. Furthermore, the pump of the hot water storage circuit feeds the transferred thermal energy into the tank.

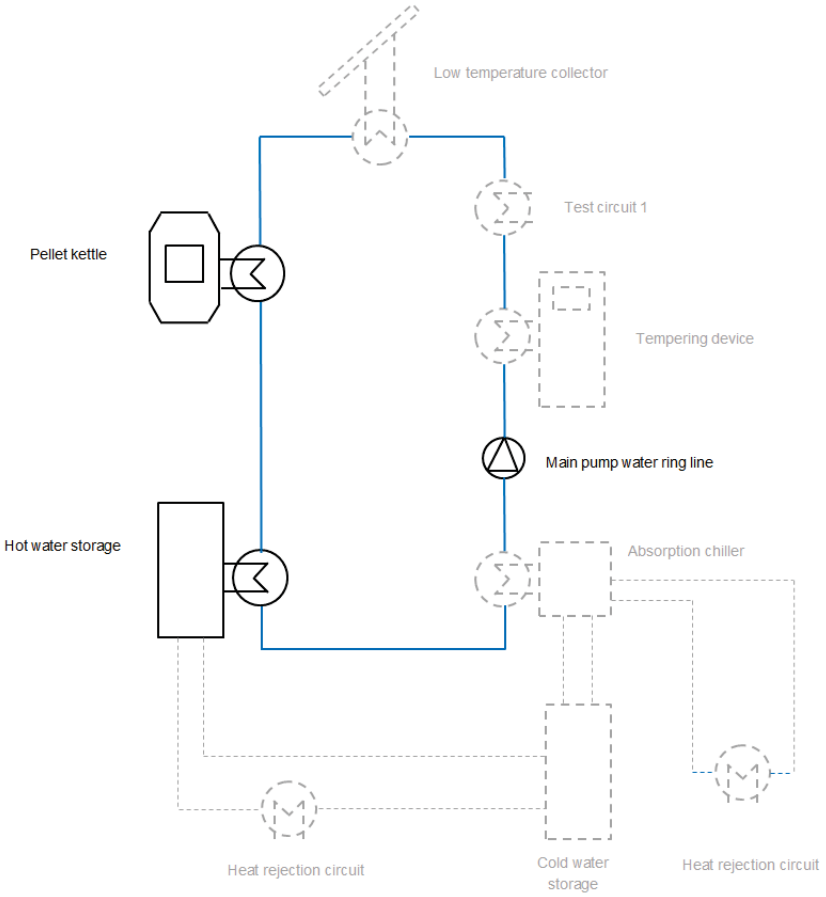

Fig. 7. Hydraulic setup for the characterization of a pellet boiler

Due to the mentioned speed-controlled pumps and the available tempering device, the pellet boiler can be driven with all possible thermal loads between 1 and 20 kW as well as a wide range of return flow temperatures between 10 °C and 95 °C.

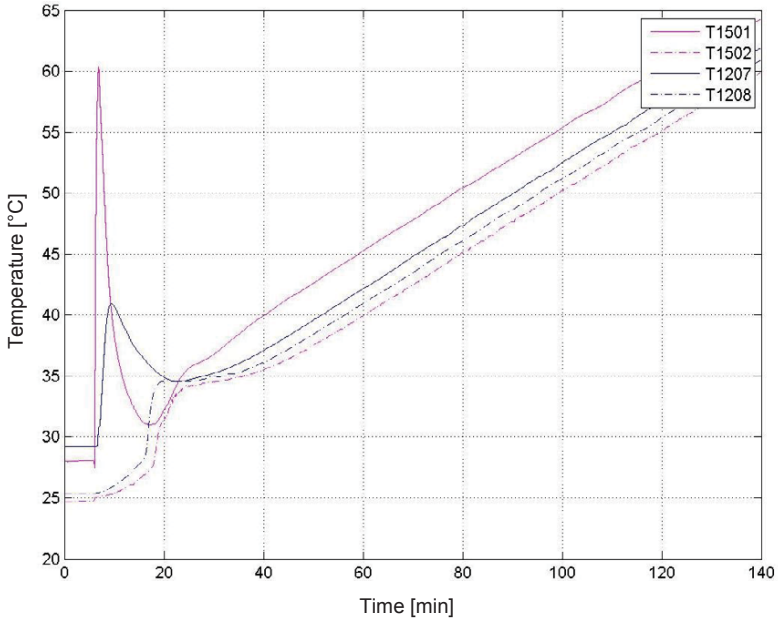

Fig. 8. Temperature rise during the characterization of a pellet boiler

For this described start-up measurement the hot water storage tank had an average temperature of 27 °C. The pellet boiler was pre-heated to an internal temperature of 67 °C. After starting the heat transfer from the boiler to the storage tank, the temperature rise displayed in Fig. 8 could be observed. After a stabilizing phase in the first 20 minutes of the measurement the temperatures rise constantly.

The temperature sensor T1207 is located in the storage tank at the height of the outlet connector. During the measurement period between “minute 30” and “minute 110” this sensor shows a temperature increase from 35 °C to 55 °C. Assuming that around 800 liters of the content of the storage is circulated in this configuration, the required thermal power can be calculated as follows:

$$P = \frac{m * c_p * \Delta T}{t} = \frac{800\ kg * 4.187\ \frac{kJ}{kg*K} * 20\ K}{80 * 60\ s} = 13{,}96\ kW \qquad \text{(eq. 1)}$$

The pellet boiler has a nominal power of 15 kW, meaning that the start-up measurement shows reasonable results.

6. Outlook and further work

The long-term aim of this entire project is to increase the use of mid-temperature solar energy to substitute fossil fuels in various industrial processes by providing a flexible and dynamic simulation environment. The basis for this simulation environment was already created during the engineering process for the hydraulic test stand, but further refining and extension has to be done. Moreover, new simulation models have to be created within the used CARNOT-blockset of MATLAB/Simulink to be able to apply the simulation environment for a large number of industrial processes.

In parallel to this simulation work all possible operation modes of the test stand have to be measured and characterized in a more detailed way and in long-term operation in order to gain statistical relevant amount of data. This experimental information will afterwards be used to verify and adjust parameters in the simulation environment, which provides the opportunity to realize a high precision and dynamic simulation tool for a substantial number of different industrial processes in the mid-temperature range.

7. Acknowledgements

The described work is carried out within the project “SOLEX – Solare Exergiebereitstellung”, which is partially funded by the program “COIN-Aufbau”, supported by the Austrian FFG (Forschungsförderungsgesellschaft).

8. References

Fresnex GmbH, Brown-Boveri-Straße 1, 2351 Wiener Neudorf, Austria, 2015

Conference Proceedings
EuroSun 2016
Palma de Mallorca (Spain), 11 – 14 October 2016

RECOMMENDATIONS FOR THE REDUCTION OF FAILURESDURING THE PLANNING AND INSTALLATION PHASES OF SOLAR THERMAL PROCESS HEAT SYSTEMS

Dominik Ritter, Lennart Paape, Bastian Schmitt, Klaus Vajen
Institute of Thermal Engineering, University of Kassel, Kassel (Germany)

Abstract

Although several studies investigated failures in large solar thermal systems (STS) in the past, some of these failures still occur in recently built systems for solar process heat applications. Besides technical issues according to the long term reliability of components, which have to be addressed by the manufacturers, many problems lead back to insufficient planning or failures during installation. Such failures in STS can reduce the performance perceptibly and will continually impair the image and acceptance for solar thermal process heat systems. To support the market development of large individualized STS the "human caused failures" should be reduced significantly. Therefore, wide spread problems, especially those with a high impact on the performance, will be collected, analyzed and disseminated to the target groups to provide applicable failure prevention recommendations.
Keywords: *failure prevention, large solar thermal systems, individualized systems, solar process heat*

1. Introduction

Even if there is a large potential of 50 TWh/a for industrial and commercial applications up to a temperature of 250°C[1] for STS in Germany, the market uptake is rather slow. In fact the growth of market for solar process heat, that could be detected between August 2012 and the beginning of 2015, is declining at the moment. Besides the major influence of the dropped oil prices in the middle of 2014, some other barriers have to be addressed for a lasting increase of the number of newly installed solar process heat systems in Germany and other countries.

At first the relation between the high installation costs and the low operating costs of STS seem to be a barrier for many entrepreneurs. To address this barrier 50 % of the overall investment costs for solar process heat systems is subsidized in Germany, enabling investors to achieve an amortization time of seven to ten years in most cases. But these amortization times are still too long for many companies, although STS have a long operating life of 20 to 25 years.

The second problem is the missing knowledge of most entrepreneurs that solar thermal can be used to provide heat for processes. In addition, some of those who are aware of this fact fear a bad influence on the operational reliability, although there should be no risk if planned and installed correctly. Also, as solar thermal process heat systems should be realized after the implementation of obvious energy efficiency measures, there is an extra effort to realize such projects. In addition the systems have to face the competition to combined heat and power (CHP) and industrial heat pumps (HP). Perhaps in future even direct PV-heating could compete with solar thermal in industry, depending on the development of prices for PV and STS.

[1] including space heating and domestic hot water

doi:10.18086/eurosun.2016.02.06 Available at http://proceedings.ises.org

Another important factor that is slowing down the market is that only few companies deal with solar thermal process heat systems professionally and even fewer companies are offering the full projecting of planning, installation, start-up and if necessary also the operation of STS as a package. Besides, there are installers at the market with no trust and no will to deal with solar thermal process heat systems, as conventional oil and gas boilers as well as CHP and HP are normally less complex in planning and installation.

This complexity leads to the last point, the higher efforts for a precise planning and faultless installation of solar process heat systems, which are mostly individualized systems in contrast to the standardized systems for domestic applications. Especially in such a small market where new companies are trying to sell projects, the required high precision during planning and installation unveils a large potential for human caused failures that can be done.

Although there has been intense research on the performance of and failures in large scale solar heating systems, the resulting knowledge has not been condensed into applicable guidelines or tools as it was done e.g. for process heat specific knowledge on the pre-dimensioning and the definition of integration points [Schmitt et al. 2015, Muster et al. 2015]. This was one reason for the German Federal Ministry for Economic Affairs and Energy to fund the research project "Analysis and Development of the German Market for Solar Process Heat in Germany" (Ident. No. 03MAP286). This project has three work packages: The first one is the economic and technical analysis of planning documents that have to be handed in to apply for the 50 % investment grant. The second work package is the assessment of the solar yield of STS with a collector area larger than 100 m^2_{gross} and the detailed monitoring of three selected systems newly built within the funding program. The third work package is the preparation of gained knowledge out of the project as well as existing knowledge and the dissemination into the market by organization and conduction of regional roadshows and workshops for planners and installers. A very important part of the work package is the preparation and dissemination of specific knowledge as guides for planners and installers to reduce failures in large scale STS with the focus on solar process heat. The input for these guides are mainly failures detected within the technical analysis of the planning documents done in work package one and the identified problems in the three monitored systems. These failures are extended with the documented problems in literature. At the end the guides should cover common failures especially those with a large impact on the performance. They have to be provided in a compact but comprehensive way to both target groups – planners and installers. These guides for planning and installation will probably become a standard whose abidance planers and installers have to confirm as an indication on following the state of the art. The guides will be provided as additional information material together with the application form for requesting the subsidies.

2. Failures in Large Scale Solar Thermal Systems

Although several studies investigated failures in large scale STS in the past, a lot these failures still occur in recently built systems for solar process heat applications. Besides technical issues according to the long term reliability of components, which have to be addressed by the manufacturers, many problems lead back to insufficient planning or failures during installation. Such failures in STS can reduce the performance of the particular system perceptibly and will additionally lead to a continually impair of the image and acceptance for solar thermal process heat systems. To support the market development of individualized solar process heat systems, the "human caused failures" should be reduced significantly. Therefore, wide spread problems, especially those with a potentially high impact on the solar yield, were collected and analyzed to provide applicable failure prevention recommendations.

For the preparation of these recommendations, the failures detected in the three monitoring systems within the before mentioned research project as well as within over 260 planning documents and those out of literature were collected. The main used literature sources on failures in large scale STS are Peuser et al. (2009), Croy and Wirth (2006), Fink et al. (2006), Wiese (2006), Lanz et al. (2013), Remmers et al. (2001), Peuser et al. (2001), Lauterbach et al. (2012). Finally, a list of nearly 80 different failures could be prepared.

Out of these failures those that are not relevant anymore were deleted like the discoloration of the absorber or torn inner collector covers (material problems with the used foil) as well as leak absorber pipes. Afterwards failures that are not caused by inaccurate planning or installation but by quality problems according the long

term reliability of the components were identified, as they are disregarded for the recommendations for the planning and installation phases. These problems concerning material defects or production failures have to be addressed by the manufacturers. In addition, as such failures according the long term reliability can never entirely be prevented, the University of Kassel is starting a research project on the automated system evaluation and failure detection together with several partners out of solar industry. Applying the FSC method (fractional solar consumption) developed in IEA Task 32, which is used to compare the actual fractional energy savings of a system with the theoretical maximum of the actual systems configuration, manual analysis of measurement data will be redundant. Moreover, an algorithm-based fault detection method can be applied, which is able to determine in which subsystem or component a fault has probably occurred.

Having deleted the failures not relevant anymore and disregarded those occurring during several years of operation, a list of failures that can be caused by insufficient planning or poor installation remains. These failures can be referred to different parts of the solar system, as it can be seen in Figure 1 [in German language].

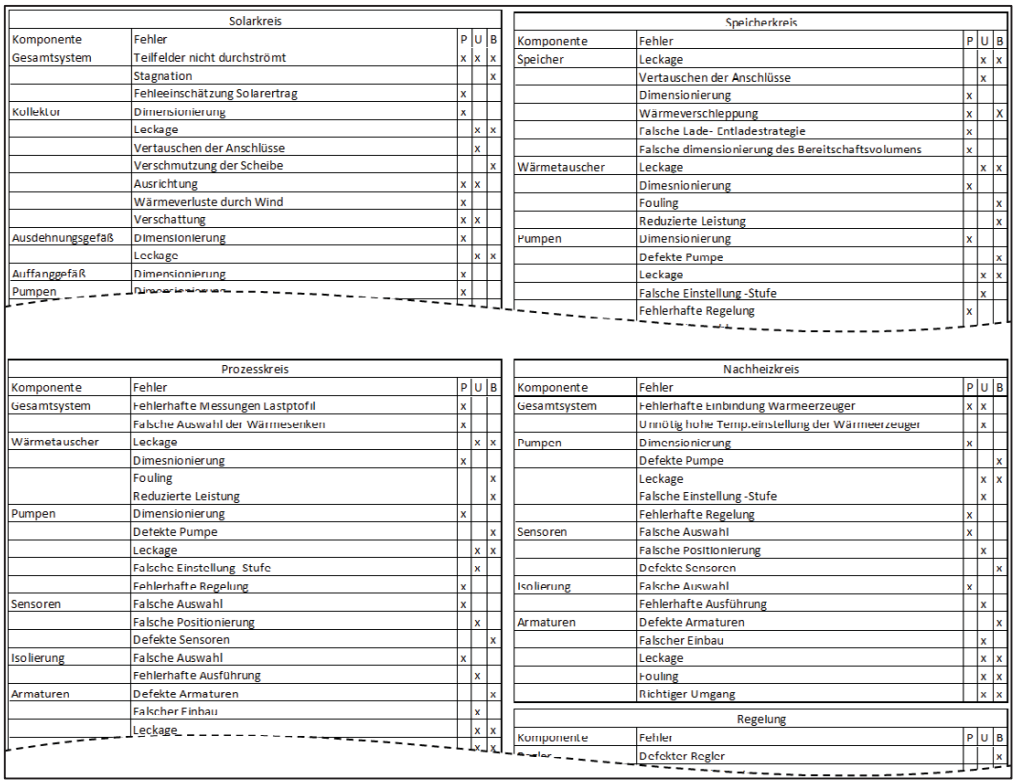

Solarkreis

Komponente	Fehler	P	U	B
Gesamtsystem	Teilfelder nicht durchströmt	x	x	x
	Stagnation			x
	Fehleeinschätzung Solarertrag	x		
Kollektor	Dimensionierung	x		
	Leckage		x	x
	Vertauschen der Anschlüsse		x	
	Verschmutzung der Scheibe			x
	Ausrichtung	x	x	
	Wärmeverluste durch Wind	x		
	Verschattung	x	x	
Ausdehnungsgefaß	Dimensionierung	x		
	Leckage		x	x
Auffanggefäß	Dimensionierung	x		
Pumpen	Dimensionierung	x		

Speicherkreis

Komponente	Fehler	P	U	B
Speicher	Leckage		x	x
	Vertauschen der Anschlüsse		x	
	Dimensionierung	x		
	Wärmeverschleppung	x		X
	Falsche Lade- Entladestrategie	x		
	Falsche dimensionierung des Bereitschaftsvolumens	x		
Wärmetauscher	Leckage		x	x
	Dimesnionierung	x		
	Fouling			x
	Reduzierte Leistung			x
Pumpen	Dimensionierung	x		
	Defekte Pumpe			x
	Leckage		x	x
	Falsche Einstellung -Stufe		x	
	Fehlerhafte Regelung	x		

Prozesskreis

Komponente	Fehler	P	U	B
Gesamtsystem	Fehlerhafte Messungen Lastptofil	x		
	Falsche Auswahl der Wärmesenken	x		
Wärmetauscher	Leckage		x	x
	Dimesnionierung	x		
	Fouling			x
	Reduzierte Leistung			x
Pumpen	Dimensionierung	x		
	Defekte Pumpe			x
	Leckage		x	x
	Falsche Einstellung -Stufe		x	
	Fehlerhafte Regelung	x		
Sensoren	Falsche Auswahl	x		
	Falsche Positionierung		x	
	Defekte Sensoren			x
Isolierung	Falsche Auswahl	x		
	Fehlerhafte Ausführung		x	
Armaturen	Defekte Armaturen			x
	Falscher Einbau		x	
	Leckage		x	x

Nachheizkreis

Komponente	Fehler	P	U	B
Gesamtsystem	Fehlerhafte Einbindung Warmeerzeuger	x	x	
	Unnötig hohe Temp.einstellung der Wärmeerzeuger		x	
Pumpen	Dimensionierung	x		
	Defekte Pumpe			x
	Leckage		x	x
	Falsche Einstellung -Stufe		x	
	Fehlerhafte Regelung	x		
Sensoren	Falsche Auswahl	x		
	Falsche Positionierung		x	
	Defekte Sensoren			x
Isolierung	Falsche Auswahl	x		
	Fehlerhafte Ausführung		x	
Armaturen	Defekte Armaturen			x
	Falscher Einbau		x	
	Leckage		x	x
	Fouling		x	x
	Richtiger Umgang		x	x

Regelung

Komponente	Fehler	P	U	B
	Defekter Regler			x

Figure 1: Example for the allocation of the detected failures to the different parts of the solar system

The first part of the system failures can occur in is the solar loop. Main source for potential failures are related to the collector field like an uneven flow distribution in the different collector rows. Also the dimensioning and installation of the expansion vessel and the pump seems to be a problem in some cases. The second part is the storage loop, here including the heat exchanger for charging the storage. Most problems emerge due to incorrect connections causing natural circulations. The dimensioning of the storage volume and the heat exchanger is also a common source for failures. Following, the process loop was defined, starting with the heat exchanger for the discharge of the storage. An example of failures for this loop is the underestimation of the peak load of the heat sink, leading to an undersized heat exchanger. Completing this classification failures were also allocated to the secondary heating loop (e.g. oil or gas burner) and the controller loop. Examples are fouling in the heat exchanger due to the wrong choice of the type or simply a wrong control strategy that could for example use the conventional boiler as primary heat source instead of the solar thermal process system.

In the following section some examples for failures made during planning or installation of recently built systems are named as well as a short description of the effect on the system.

3. Examples for Failures found in Solar Process Heat Systems

The analysis of planning documents and the detailed monitoring of three selected STS in industry and commerce within the project "Analysis and Development of the German Market for Solar Process Heat" (Ident. No. 03MAP286) showed that several failures were made during planning and installation. In addition, the University of Kassel had the opportunity to discuss with several planners and installers as well as with companies that invested into a solar process heat system, which could be used as an additional source of information. Following some examples of the failures that were found are given. Some of these failures appeared several times in different STS.

It was assessed that some planers do not choose the collector type according to the application with its necessary temperature levels. They typically use one specific collector type independent from the intended application (domestic hot water or process heat). Using this approach, systems were built with evacuated tube collectors heating up cold water to a desired flow temperature of only 40 °C. For this temperature level a single glazed flat plate collector would have been a more efficient choice compared to evacuated tubes additionally with lower costs at higher specific solar yields. Even unglazed collectors would reach a higher efficiency over a long period of the year. Such a poor choice of the collector type leads to unnecessarily high solar heat generation costs due to higher cost for the component and the lower solar yield.

Another failure that often occurs is the realization of the desired storage volume by connecting several small storages, often in parallel. The highest number of interconnected storages was 14, each with a volume of only 1 m³, realized as two storage batteries each with seven storages connected in parallel. Compared with a one single large storage, the interconnection of multiple storages leads to significantly increased costs for hardware and installation as well as increased heat losses due to the higher storage surface and multiple connections between the storages. In addition measurements in STS showed that storages connected in parallel always start interacting over the time, even if they were installed correctly hydraulically balanced. This leads to uncontrollable charge and discharge of the storages and therefore to a mixing of different temperature levels, reducing the useful solar yield. In general, the monitoring of several systems showed, that it is always preferable to use one single storage but never more than two in parallel or three in series (Peuser er al., 2001).

According to the realization of the storage, some systems were planned to be built with vacuum-insulated storages. As they are very expensive – prices between 3,000 and 3,500 €/m³ were found in the planning documents – it can only be reasonable to use them as mid or long term storages for systems with excess energy gains in summer or autumn. As the systems were designed to achieve a solar fraction of less than 50 % in the summer months, there is no need for such storage. The only effect is an increase of the solar heat costs. An exception for using a vacuum storage in such cases could be very little space at the installation site.

One point that came up during discussions with owners/operators and planners of solar thermal process heat systems was that the installing company used tap water instead of demineralized water for the storage. This resulted in a rapidly decrease of heat transfer from the primary to the secondary solar loop as the plates of the heat exchangers were calcified. This finally led to a lower utilization ratio as the heat produced by the collectors cannot sufficiently be transferred into the storage leading to higher temperatures in the solar loop and therefore to higher heat losses and lower collector efficiencies.

Another failure caused during the planning phase was the selection of incorrect pump combinations, leading to unbalanced capacity flows in the primary and secondary solar loop. Systems were found in which the capacity flows of the primary loop always exceeded the capacity flow of the secondary loop. In this case, the temperature of the storage was charged with heat very close to the solar flow temperature. As the solar loop fluid cannot be cooled down to the return flow temperature of the storage charging loop, the heat losses increase and the collector efficiency drops as its mean plate temperature is unnecessarily high. Once again, this failure leads to a lower system utilization ratio and higher solar heat generation costs.

It could be also found that single speed pump designed for medium irradiations on the collectors were selected for the primary solar loop. The utilization of these kinds of pumps causes inefficient operating conditions at low radiation as well as at times with high radiation. At low radiation, the volume flow is very high for heating up the solar loop fluid and only very low temperature differences between flow and return flow can be achieved. The result is a comparably long time until the storage can be charged with the desired minimum or set temperature. In contrast, at times with high solar radiation, the average temperature in the solar loop is very high as the produced heat cannot sufficiently be dissipated. Summed up, in the morning, evening and on days with a low radiation, there are unnecessarily high electricity costs for the pump and unfavorable operating conditions for the solar thermal system. On days with a high radiation the temperature in the solar loop is higher than required, causing higher heat losses, a lower collector efficiency and probably even unnecessary additional stagnation times.

An additional problem, planners have to take care of, is the determination of the daily load and the peak load of the chosen heat sink. As this data is usually not available in companies, it should be measured on a typical production day and not only be estimated. But as the measurement takes a little time and financial effort, the system dimensioning is often done using a rough estimation. The estimation of a higher daily load leads to lower solar yields compared to the simulation, as less heat is needed than expected. If the peak loads are estimated too low, it is very likely that an undersized heat exchanger will be installed, not able to heat up the process medium or fluid stream to the designed temperature, even if the storage is fully charged. This leads to a higher conventional heat demand than necessary and higher heat losses of the storage as the discharge is lower than expected. Both mistakes – overestimation of the daily load and underestimation of the peak load – were found within the project.

It also happened that the chosen gaskets in the solar loop were sufficiently temperature resistant for regular operation conditions but not for stagnation. The results were leakages at the connections of the solar loop making it necessary to drain the loop, dismount all connections close to the collector that could be affected during stagnation, and to renew the gaskets. At the end the solar yield that could have been gained between the time the leakages emerged and the resumption of operation were given away and additional costs for the reparation were caused.

Another failure that could be found is missing valves to reliably close different loops being used at different times at different temperatures providing several heat sinks. This is necessary to avoid fault forced circulation between the loops. The effect of missing valves is a mixing of flows and / or return flows with different temperatures making it nearly impossible to achieve the desired temperature in the different heating loops.

The last detected problem that will be mentioned here, is the inaccurate installation of the temperature sensors in the last collector of each collector row. In two systems the sensor was not correctly plugged in the collector causing an offset between the measured and real temperature. In addition the offset increased with higher temperatures. If this measured temperature is used as the solar flow temperature for the controller to control the pump, the result is again an unnecessary high temperature in the solar loop, causing additional heat losses and a lower collector efficiencies.

4. Concept for Failure Prevention Recommendations

To prospectively prevent the failures found within the analyzed systems as well as those found in literature, they have to be prepared in such way planners and installers are willing to consider within their daily routine. Therefore it had to be evaluated, which information at which extend is suitable for these two target groups. As these groups have different needs and duties, two varied designs of the failure prevention recommendations with diverging information are the result of this evaluation.

For both groups it has to be as short as possible without being inaccurate and the recommendations should only cover the most important points to reduce the paperwork that should be used by the target groups. As it cannot cover the whole planning and installation steps of a solar thermal system, it can only be used as an addition to the existing knowledge and tools to prevent the most common failures.

First draft of the recommendations for planners

The main steps the planner is responsible for, is collecting the necessary data to make a feasibility study and to submit an offer to the particular company. Afterwards a detailed system design and hydraulic scheme has to be prepared including all dimensions and specifications for the required components. In addition, a suitable control strategy has to be designed. After the realization of the solar process heat system an appropriate documentation of the system should be handed over to the operator.

As the planner should be used to deal with paperwork and formulas to design a whole system, it seems reasonable to provide recommendations of two to three pages for the components failures often occur including descriptions in continuous text or bullets together with schemes and formulas for the correct dimensioning. Figure 2 gives an example on the recommendations, in this case for the collector field [in German language].

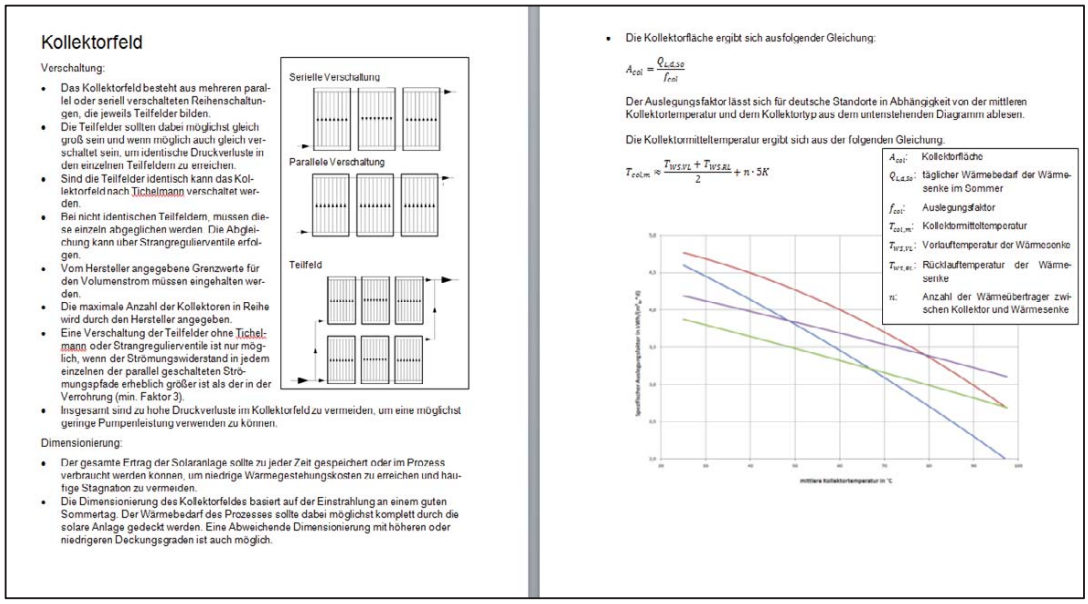

Figure 2: Example for the failure prevention recommendations for planners

The recommendations for the planners are not as standardized as the hints for installers, as the aspects are varying. They include short descriptions of the general requirements, advices on which aspects have to be considered for a suitable selection of the particular part of the system as well as formulas and graphs to support the correct dimensioning. If the failures found in literature and within the project indicated the necessity, there are also hints on how to integrate the particular part correctly into the whole system.

First draft of the recommendations for installers

The installers' job is to install the system according to the planners' specification and with respect to the state of the art. In addition he is responsible (sometimes together with the planner) for the start-up of the system, giving the owner of the system an introduction.

As installers are always dealing with one component or connection after another, they need specific hints regarding single components, not the whole system. In addition, during installation there is normally no time to deal with extensive paperwork. Therefore, very short but precise hints on how to prevent common failures are necessary, always dealing with one single installation step. To support a quick grasp of the information included in the recommendations, schemes are given. Figure 3 is an example of the first draft of the hints that should be considered to reduce failures made during installation [in German language]. The format of each hint is a half DIN A4 page.

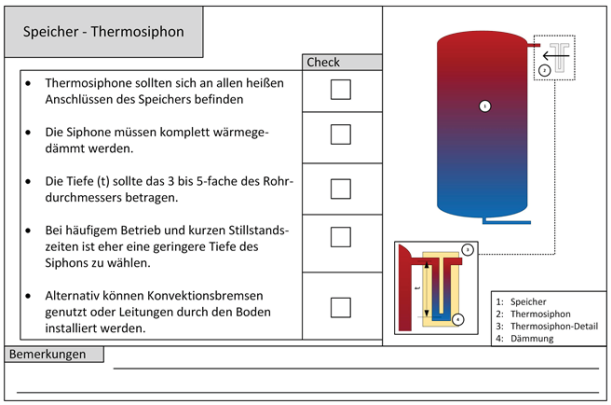

Figure 3: Example for the failure prevention recommendations for installers

The figure shows a few bullet points – here for the installation of thermos syphons at the hot connections of storages - with the information needed to prevent natural convection losses. Beside these bullet points are check boxes that can be used to confirm the observance of the given information. On the right hand side of the recommendations is a scheme with a short legend naming the parts visualized in the scheme. If necessary or helpful selected parts of the scheme are zoomed to capture more details. At the bottom of the hints an empty space is left where special circumstances, problems occurred or alternate solutions can be written down.

5. Outlook

As failures during the planning and installation phases were done in the past and will occur in the future there is a need to reduce them by giving guides like it is described in the previous sections.

The developed concept was discussed with a company mainly offering the planning, installation and if requested also the operation of solar process heat systems or other large scale STS, to confirm if the key aspects are covered in the recommendations and if they are short but still precise enough to be used by the target groups. As the feedback was positive and some additional input could be added, the recommendations seem to be suitable for the failure prevention.

Although the gathered recommendations can never cover every possible failure, a solid basis of identified failures occurring during planning and installation as well as hints to their prevention could be developed. In addition, the list of recommendations can easily be extended or revised if it is necessary.

The next steps are the final editing and dissemination of the hints and a definition on how to ensure, that planners and installers are aware of the content. To ensure that, one way of publishing the recommendations will be the download together with the application forms for the 50 % investment grant.

After publishing, the recommendations will become a defined document for the state of the art for realizing solar process heat systems. It is even possible that these recommendations will become a standard that have to be used if the planners and installers want to apply for the investment grant. This could be ensured by the need of signature that the system will be realized with respect to these failure prevention recommendations. With this approach a lot of failures could be prevented, supporting a market development on basis of systems delivering good performances.

A further module for supporting solar process heat systems to achieve constantly high yields even after several years of operation is the project on the automated evaluation of the fractional energy savings mentioned before.

6. Acknowledgement

The authors gratefully acknowledge the financial support provided by the German Federal Ministry for Economic Affairs and Energy (contract no. 03MAP286) and the cooperative work with the Federal Office for Economic Affairs and Export Control and the KfW Group.

References:

Croy, R., Wirth, H. P., 2006: Analysis and evaluation of large combisystems for domestic hot water and space heating (in German language). Final Report, Ident. No. 0329268B.

Fink, C. Riva, R., Pertl, M., Wagner, W., 2006: OPTISOL Monitoring of demonstration projects for optimized and standardized solar systems for multi-family-housing (in German language). Reports "Energie- und Umweltforschung 50/2006". Ministry for Transport, Innovation and Technology.

Muster, B., Hassine, I. B., Helmke, A., Heß, S., Krummenacher, P., Schmitt, B., Schnitzer, H., 2015: Integration Guideline. Guideline for solar planners, energy consultants and process engineers giving a general procedure to integrate solar heat into industrial processes by identifying and ranking suitable integration points and solar thermal system concepts. IEA SHC Task 49. Deliverable B 2.

Lanz, M., Schramm, S., Wirth, H.-P., Adam, M., Anthrakidis, A., Faber, C., 2013: Solar-Process Heat-Standards. Short title: Sol-Pro-St, (in German language). Final report, Ident. No. 0329609G & 0329609F.

Lauterbach, C., Schmitt, B., Vajen, K., 2012: Pilot plant for solar thermal process heat at the Hütt brewery (in German language). Proc. Gleisdorf Solar 2012, Gleisdorf, Austria, 12.-14.09.2012.

Peuser, F. A., Remmers, K., Schnauss, M., 2001: Long-term experience with solar thermal. Guide for the successful planning and installation of solar thermal systems (in German language), Berlin: Solarpraxis

Peuser, F. A., Croy, R., Mies, M., Rehrmann, U., Wirth, H. P., 2009: Solarthermie-2000, program part 2 and Solarthermie2000plus. Scientific and technical supervision and monitoring (phase 3) (in German language). Final report, Ident. No. 0329601L.

Remmers, K., Antony, F., Fischbach, M., Luchterhand, J., 2001: Large scale solar thermal systems. Getting started in planning and practice (in German language), 2nd revised edition, Berlin: Solarpraxis

Schmitt, B., Lauterbach, C., Vajen, K., 2015: Guideline for the pre-dimensioning of solar process heat. Feasibility assessment and pre-dimensioning of solar thermal process heat systems (in German language). http://www.solfood.de/uploads/1/9/8/3/19830089/solfood_leitfaden_vorplanung.pdf

Wiese, F., 2006: Long term monitoring of large solar integrated heat supply systems (in German language). Dissertation (Dr. Ing). Department for Mechanical Engineering. Kassel University. kassel university press.

Conference Proceedings

EuroSun 2016
Palma de Mallorca (Spain), 11 - 14 October 2016

Direct Radiation Measurements for the Evaluation of Process Heat Systems with Concentrating Solar Thermal Collectors

Mercedes H. Rittmann-Frank, Mattia Bataglia, Jana Möllenkamp, Matthias Rommel, Andreas Häberle

SPF Institute for Solar technology, Rapperswil (Switzerland)

Abstract

For the evaluation of the performance of thermal and photovoltaic concentrating solar systems a detailed determination and measurement of the Direct Normal Irradiance (DNI) is essential. The most accurate way of measuring this is with a bi-axial tracking pyrheliometer. However due to its high investment cost and need of maintenance, cost-efficient alternatives are of interest, especially for monitoring projects. This work presents an investigation of the performance and reliability of different alternative devices for the determination of the DNI, which are a sunshine pyranometer SPN1 device and a Rotating Shadowband Irradiometer (RSI). While the pyrheliometer directly measures the DNI via 2-axis tracking, the SPN1 and RSI determine the DNI through the measurement of the global and the diffuse irradiation and the information of the location and solar time. In order to investigate the suitability and reliability of these alternative instruments we have recorded data of about two years in 10 s resolution for the pyranometer SPN1 and pyrheliometer and of about 1 year in 1-minute resolution for the RSI and analyzed the data up to an irradiance of 950W/m^2.

Keywords: *Direct Normal Irradiance measurements, Pyrheliometer, Sunshine Pyranometer SPN1, Rotating Shadowband Irradiometer RSI*

1. Introduction

Accurate and reliable solar irradiance measurements of the global horizontal irradiance (GHI) and its fractions, such as the direct normal irradiance (DNI) and the diffuse horizontal irradiance (DHI), play an important role for solar resource assessments, either for short–term forecasting or for monitoring of solar plants. For solar power plants with concentrating systems, which can be photovoltaic or thermal collectors, the determination of the DNI is essential to evaluate their performance. Also solar thermal plants, which cover a lower temperature range (<300°C) compared to solar thermal power plants have been gaining a lot of attention for applications in industry and are becoming a promising source for process heat.

With the increasing awareness for the need of a more environmentally friendly and energy efficient industry, in the past few years several plants with solar thermal collectors have been installed in Swiss companies and are being monitored and evaluated by the SPF Institute for Solar Technology. For process temperatures between 100°C and 300°C concentrating collectors (parabolic trough and linear Fresnel collectors) are the most suitable technology and are used in three dairies in Switzerland. In order to evaluate the performance of these fields an accurate measurement of the DNI is essential. The most accurate way to do this is by a bi-axially tracking pyrheliometer. Collector developers and research institutes therefore use this instrument. However, a tracking pyrheliometer requires some maintenance and the costs are relatively high (approximately 15'000 Euros). For monitoring projects with field measurements of systems providing solar process heat such costs are in most cases too high.

In this study, we present our evaluation of two less expensive alternative instruments for the measurement of direct normal irradiation DNI: (1) the "Sunshine Pyranometer" SPN1 and (2) the "Rotating Shadow band

doi:10.18086/eurosun.2016.02.13 Available at http://proceedings.ises.org

Irradiometer" RSI in comparison to the bi-axial pyrheliometer for DNI and pyranometers for GHI and DHI measurements. For this, all devices are setup and evaluated at the test facilities at the SPF Institute of Solar technology in Rapperswil. In the case of the above-mentioned solar process heat plants, SPN1 devices are used for the measurement of the DNI. The here presented results are the basis for further studies on how to consider the deviation of the SPN1 or RSI devices to the pyrheliometer in the evaluation of solar plants when using these alternative instruments.

2. Materials and Methods

The evaluation of the radiation meters is carried out using the instruments and test stands at the SPF Institute for Solar Technology in Rapperswil, Switzerland. A bi-axially tracking pyrheliometer is used as the reference instrument for the DNI measurements (figure 1c). In Fig. 1 a (left) the pyranometer and a pyranometer with a shadow-ring are shown, which are used for the reference instrument for the GHI and DHI respectively. All instruments are cleaned daily.

While the pyrheliometer directly measures the DNI via 2-axis tracking and a view-limiting aperture of 5°, the SPN1 and RSI compute the DNI through the measurement of the global and the diffuse irradiation and the information of the location and solar time. In the SPN1 (Fig. 1a (center)) six sensors are placed on a hexagonal shape and one sensor in the center on a horizontal plane behind a complex shading mask. The shape of the shading mask ensures that at least one of the sensors is completely shaded and at least one is fully exposed to the solar irradiation, which allows measuring simultaneously GHI and DHI. The big advantage of the SPN1 is that no moving parts in need of continual accurate alignment are required, decreasing the maintenance cost. In the RSI instrument (Fig. 1b) two Silicon-based semiconductors sensor measure the GHI. Every 30s the shadow band rotates 360° around the sensors, which leads to a momentary shading. During the rotation phase of about 1s duration, data is collected in a frequency of 1kHz from which an internal algorithm computes the DHI after two cycles (about one minute).

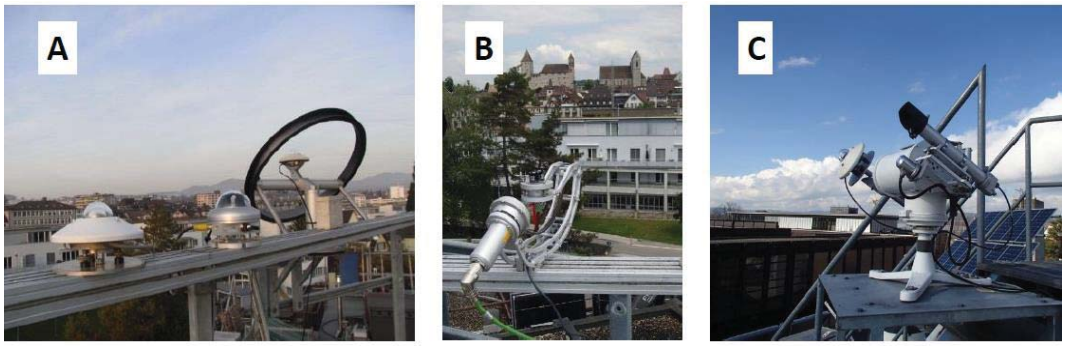

Fig. 1: (A) Pyranometer for the measurement of the horizontal global radiation (left), "Sunshine Prynometer SPN1" (center), pyranometer with shadow-ring for measurement of the horizontal diffuse radiation (right). (B) "Rotating Shadow band Irradiometer RSI". (C) Tracking pyrheliometer for DNI measurements used as reference. All instruments are installed at the SPF Institute for Solar Technology in Rapperswil, Switzerland

We have recorded data of about one year (8.8.2015-7.8.2016) in 10 s resolution for the SPN1, the pyranometer and pyrheliometer and in 1-minute resolution for the RSI and analyzed the data up to an irradiance of 950W/m^2. Data that showed obvious discrepancy due to operation failure was removed from the study. All data was evaluated using the recommended quality control test (Roesch et al., 2011)

The DNI value is calculated via

$$DNI = \frac{GHI - DHI}{\sin(\gamma_s)} \qquad \text{(eq. 1)}$$

where γ_s represents the elevation angle of the sun.

The evaluation of the measurements relative to the reference instruments and the quantitative criteria to describe the absolute and relative dispersion was done based on the publication of Badossa (2014). The slope

of the data was determined by a linear regression forced to zero. The standard deviation around the fitting line was calculated as follows:

$$STDE = \sqrt{\frac{\sum_{t=1}^{N}(I_{SPN1/RSI} - I_{ref} \cdot slope)^2}{N}} \qquad \text{(eq. 2)}$$

I stands for DHI, GHI or DNI. The index indicates the measuring device SPN1, RSI or by any of the reference instruments. N is the total number of values. The regression coefficient R^2 is calculated via:

$$R^2 = 1 - \frac{\sum_{t=1}^{N}(I_{SPN1/RSI} - I_{ref} \cdot slope)^2}{\sum_{t=1}^{N}(I_{SPN1/RSI} - \bar{I}_{SPN1/RSI})^2} \qquad \text{(eq. 3)}$$

$\bar{I}_{SPN1/RSI}$ Indicates the average value. Coefficient values larger than 0.99 indicate a high correlation.

3. Results for RSI and SPN1 vs Pyrheliometer and Pyranometer

In the following figures the deviation between the measurement values for DNI, GHI and DHI for the reference methods (pyrheliometer, pyranometer) and the alternative detectors SPN1 and RSI are shown.
An overview of all irradiance measurements during a day with clear sky conditions for all measuring methods is shown in **Error! Reference source not found.**. It can be seen, that the RSI measures lower values for DHI and DNI, while the SPN1 overlaps well with the reference measurements. The DNI line for the SPN1 shows a step around noon. This was observed for several days. One possible explanation is a mismatch of the different detectors with the SPN1 device or to dome lensing (Badossa (2014)). Further investigations are planned in order to resolve this issue.

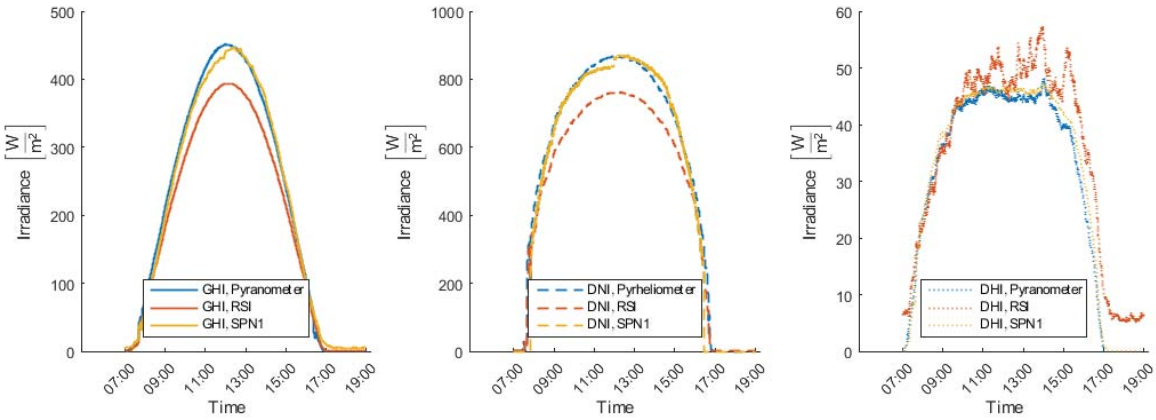

Fig. 2 Overview of GHI, DHI and DNI measurements with SPN1 and RSI and reference devices for one day with clear sky conditions at Rapperswil, Switzerland

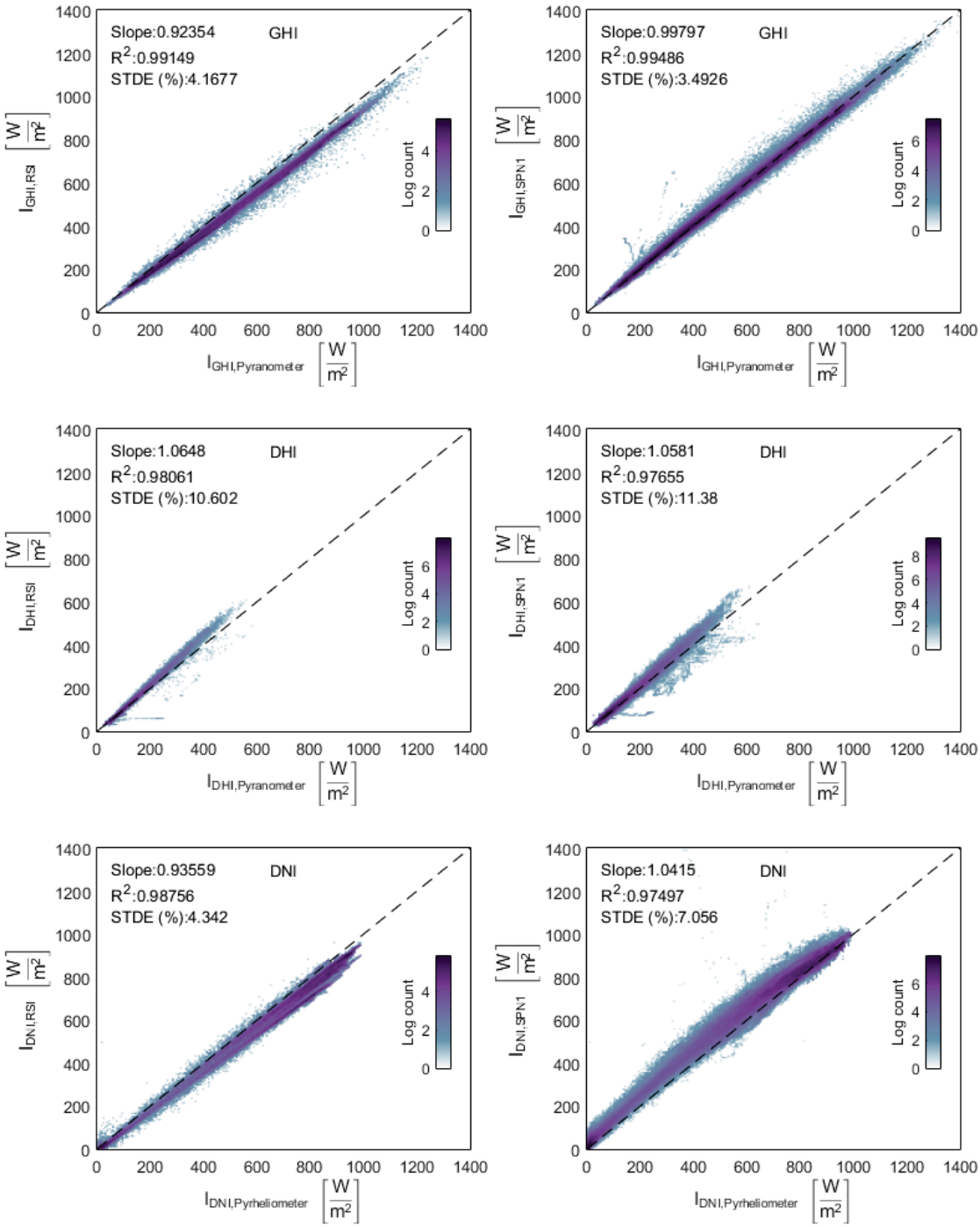

Fig. 3: Scatter plots of GHI, DHI and DNI for SPN1 and RSI in comparison to the pyranometer, pyranometer with shadow-ring and bi-axial tracking pyrheliometer, respectively. Measurements were performed at Rapperswil, Switzerland.

The scatter plots in Fig. 3 show the comparison between SPN1 or RSI vs the reference instruments, the pyrheliometer for the DNI and the pyranometers with and without shadow ring for the DHI and GHI measurements. The slope values indicated in each graph are obtained via a linear regression. The scatter plots show for both, SPN1 and RSI, the smallest spread of data points for the GHI and the largest spread (STDE 4.2% and 3.5%) for the DHI (STDE 10.6% and 11.4%). Furthermore, we see that the data spread becomes narrower for values above 800W/m^2. The slope values reflect well the previous observation done for **Error! Reference source not found.**. The slope value of 0.92 for the RSI measurement indicate an underestimation for GHI. While the slope of 0.998 confirms the good agreement between the GHI measured by the SPN1 and

the pyranometer. For the DHI comparison, both devices overestimate the values as indicated by the slope of 1.06. The SPN1 overestimates the DNI value, as indicated with the slope of 1.04. The RSI instrument underestimates the DNI value with a slope of 0.93. Furthermore, we observe for the RSI DNI several lines. Since those lines are not visible in the DHI and GHI measurements, we assume that they are an artifact caused by the internal algorithm that is used to determine the DNI.

In the following, we will focus on the relative deviation for the DNI between the values of the reference pyrheliometer and the SPN1 and RSI devices, since these values are the most important for the evaluation of the performance of concentrating collectors.

DNI : RSI vs Pyrheliometer

Fig. 4 shows the relative deviation for the RSI from the values measured by the pyrheliometer. The data shows a broad spread of data points for low irradiance values, due to the division by values near to zero at low sun elevation angles (eq. 1). For the evaluation of concentrating collectors the more interesting range of irradiance is above 600W/m^2, where the spread is also narrower and the maximal deviation is around 15%. For a better visualization, the histograms in Fig. 5 show the distribution for different irradiance values: (400 ±25)W/m^2, (600 ±25)W/m^2 and (800 ±25)W/m^2. For all three graphs we observe a negative deviation, which shows the underestimation of the DNI. Furthermore, two clusters at -5% and -12% are clearly visible. In Fig. 6 the relative deviation for the RSI from the values measured by the pyrheliometer for a restricted irradiance range between 700 W/m^2 to 900W/m^2 is shown. In addition, the data points are associated with the seasons. From this representation we discover clear lines for each season. Based on this, we can assign the two clusters observed in the histograms to the seasons. The lower deviation corresponds to summer and spring, while the higher deviation value can be attributed to winter and autumn. This is an indication of the dependency of the measurements and the solar altitude.

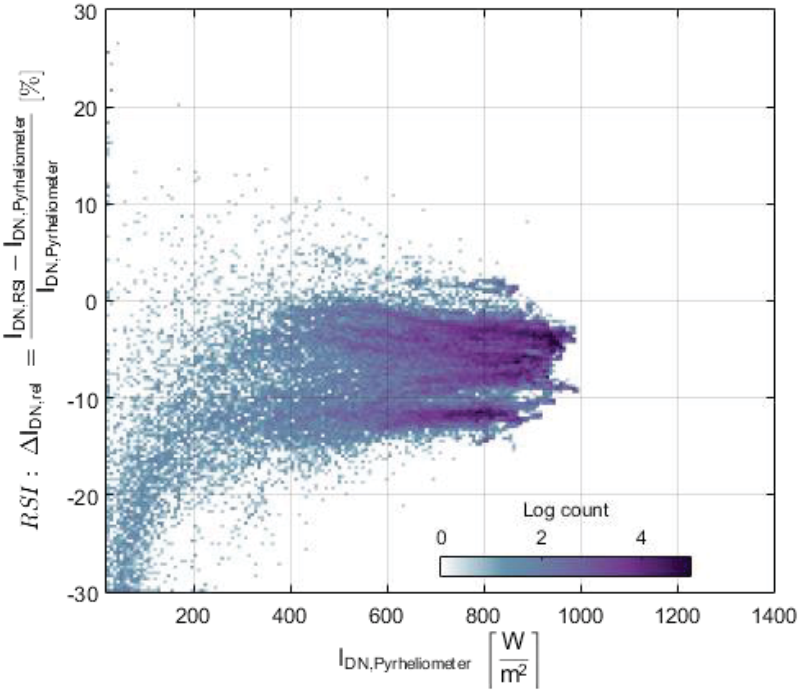

Fig. 4: Relative deviation of the calculated DNI for the RSI vs the values measured by the pyrheliometer.

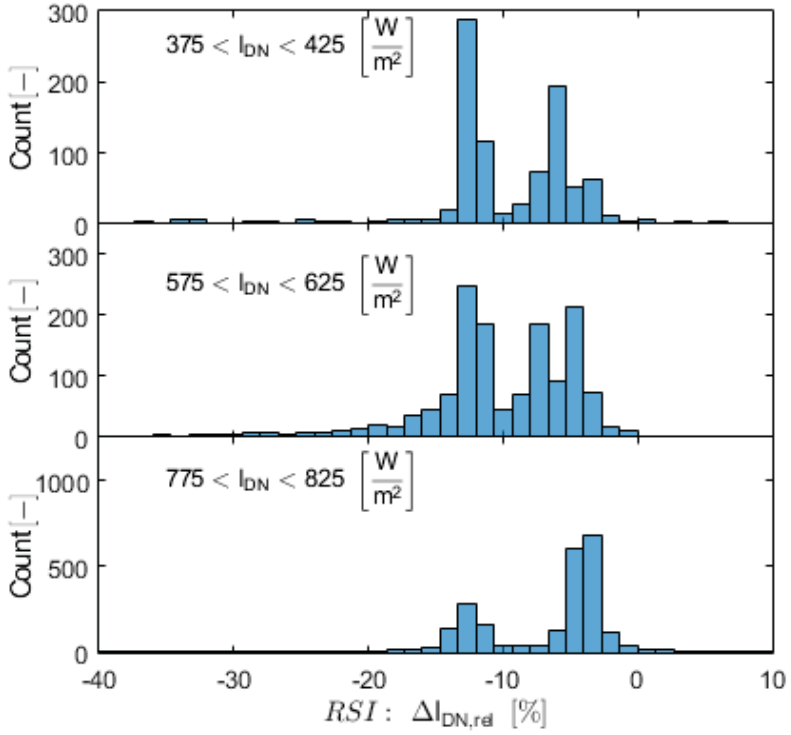

Fig. 5 Histogram indicates the distribution for the relative deviation of the calculated DNI for the RSI vs the values measured by the pyrheliometer at different irradiance values measured (400 ±25)W/m², (600 ±25)W/m² and (800 ±25)W/m².

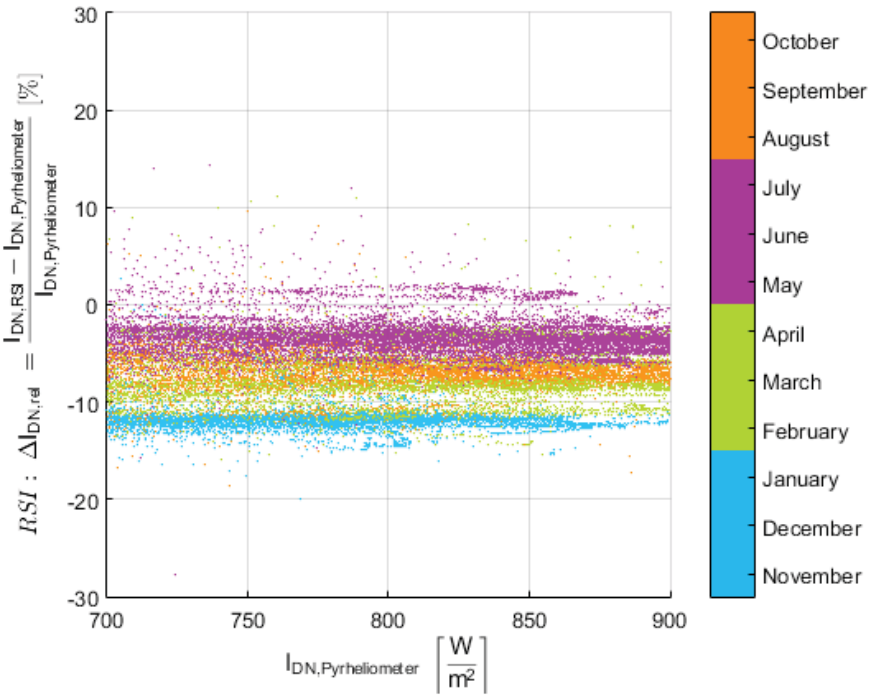

Fig. 6: Zoom of figure 4. Relative deviation of the calculated DNI for the RSI vs the values measured by the pyrheliometer. Color code indicates the seasonal correspondence of each data point.

DNI : SPN1 vs Pyrheliometer

Fig. 7 shows the relative deviation for the SPN1 from the values measured by the pyrheliometer. Similar to the data for the RSI in figure 4, the data shows a broad spread of data points for low irradiance values, due to the division by values near to zero at low sun elevation angles (eq.1). The positive deviation indicates an overestimation of the SPN1 in comparison to the pyrheliometer. The histograms in Fig. 8 show the spread of the data points at different irradiance values: (400 ±25)W/m^2, (600 ±25)W/m^2 and (800 ±25)W/m^2. In contrast to the RSI data, the data for the SPN1 show a more symmetric Gaussian shaped distribution around one center value, which moves closer to zero with increasing irradiance value. For (400 ±25)W/m^2 the mean value is at 16% , at (600 ±25)W/m^2 it is about 9% and for (800 ±25)W/m^2 it is around 3%. The variance μ and the STDE of the distribution also decreases with increasing irradiance values. The representation of the deviation in correspondence of the seasons (Fig. 6) shows no striking seasonal dependency, as could be observed for the RSI measurements in Fig. 9. Only for values lower than 800W/m^2 there is a slight difference visible between summer and winter months.

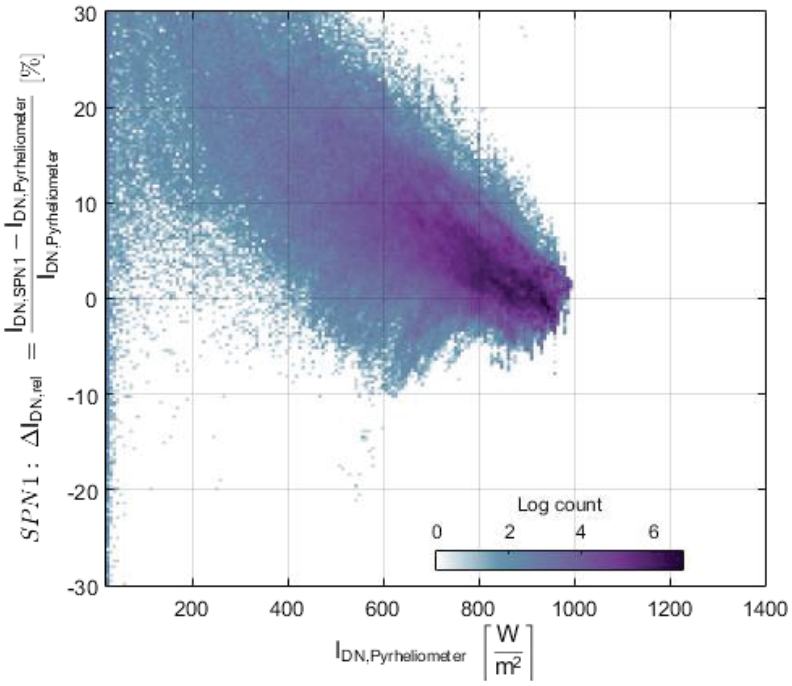

Fig. 7: Relative deviation of the calculated DNI for the SPN1 vs the values measured by the pyrheliometer.

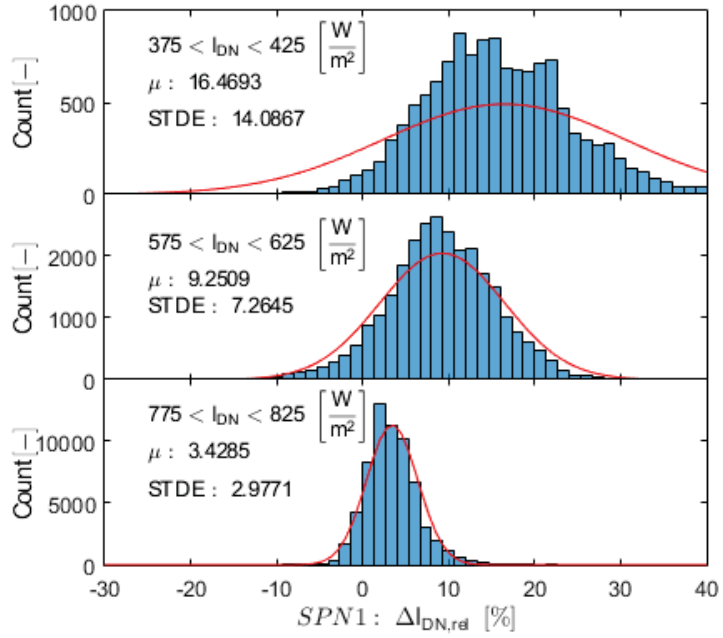

Fig. 8 The histograms indicate the distribution for the relative deviation of the calculated DNI for the SPN1 vs the values measur by the pyrheliometer at different irradiance values measured (400 ±25)W/m², (600 ±25)W/m² and (800 ±25)W/m².

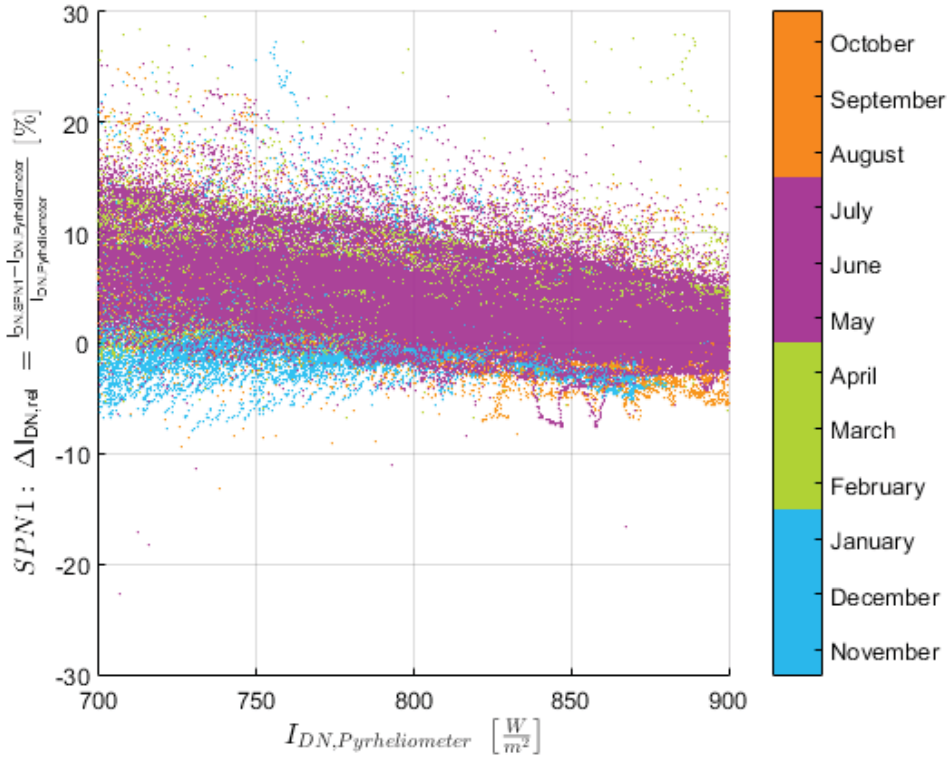

Fig. 9: Zoom of figure 7. Relative deviation of the calculated DNI for the SPN1 vs the values measured by the pyrheliometer. Color code indicates the seasonal correspondence of each data point.

4. Conclusion and Discussion

When comparing the RSI and the SPN1 it can be stated that the data for the RSI is less spread and shows the tendency to underestimate the DNI. The measurement for the SPN1 show a wider spread and indicate a slight overestimation of the DNI. The slope value for the SPN1 is in agreement with values obtained by Badosa et al. (2014), who determined a slope of 1.05 for Payerne, a location with similar conditions as Rapperswil. Both, the SPN1 and RSI device show a broad data spread for lower irradiance values below 400 W/m^2. The data shows a strong increase of the deviation for data points with very low irradiance values, due to the division by values near to zero at low sun elevation angles (eq.1). However, for the range above 600W/m^2, which is more relevant for concentrating collectors, the spread becomes narrower. The overestimation of the DNI by the SPN1 can be explained by the inclusion of a larger part of the circumsolar aureole at certain solar angles in comparison to the pyrheliometer, which has a limiting opening aperture (Badosa (2014)). For the SPN1 the results indicate a mean deviation of about 9% from the Pyrheliometer at 600W/m^2, which is in good agreement with previous studies (Badossa et al. (2014), D.R. Myers(2010), Rommel and Larcher (2015) and Rommel et al. (2016)). In addition, it only shows a deviation of 3.4% at an irradiance of 800W/m^2. For the RSI the deviation varies depending on the season, for summer 5% and 15% for winter season depending on the altitude of the sun.

We conclude that both alternative devices, SPN1 and RSI, show reliable measurements of the DNI at ranges above 600W/m^2 and are suitable for field monitoring of solar plants with concentrating collectors. These results are the basis for further investigations and detailed analysis of the accuracy and handling characteristics of these alternative devices with the aim to propose how to incorporate our findings into the evaluation of the performance of solar fields with concentrating collectors.

References

J. Badosa et al., 2014, Solar irradiances measured using SPN1 radiometers: uncertainties and cues for development, Atmos. Meas. Tech., 7, 4267-4283

D. Myers, 2010, Comparison of direct irradiance derived from silicon and thermopile global hemispherical radiation detectors, Conference Paper, NREL/CP-550-48698

M. Rommel *et al.,* 2016. Direktstrahlungsmessung zur Bewertung von konzentrierenden Kollektorfelder in Prozesswärmeanlagen*,* Conference Paper Gleisdorf Solar 12. Internationale Konferenz für solares Heizen und Kühlen

M. Rommel *et al* , 2015. Experimental Investigation on the Accuracy of Alternative Devices to Measure DNI in Comparison to Tracking Pyrheliometers, SolarPACES 2015, AIP Conf. Proc. 1734

Conference Proceedings
EuroSun 2016
Palma de Mallorca (Spain), 11 – 14 October 2016

Direct steam generation for process heat applications in compound parabolic collector (CPC)

Madhavi V. Sardeshpande[1], Vishal R. Sardeshpande[2]

[1] Industrial Flow Modeling Group, Chemical Engineering Division, National Chemical Laboratory, Pune – 411 008 India

[2] Centre for Technology Alternatives for Rural Areas, Indian Institute of Technology, Bombay, Powai, Mumbai-400 076 India

Abstract

In recent years, CPC (Compound Parabolic Collector) is gaining its acceptance for temperature range higher than non-concentrating stationery solar collectors like flat plate collectors but lower end of temperature range of concentrating solar collectors like PTC (parabolic trough concentrators). Generally, pressurized hot water or thermal oil is used as a working fluid in the CPC. The elimination of solar tracking in CPC provides flexibility for installation and lower price point compared to other concentrating technologies with tracking.

Steam is one of the universally accepted working fluid for process heat applications due to availability, non-toxic and high heat carrying capacity. Many industrial sectors such as food and beverages, textile, chemical processes etc utilize steam as a working fluid for process heat applications. Direct steam generation as a working fluid through a CPC has various operational, integration and cost advantages. The use of CPC for direct steam generation at saturation steam temperature range 105-145 °C (equivalent saturation pressure 0.5-3 bar (g)) can cater for low temperature process heat demand. Solar radiation intensity changes with the time of the day leading to change in heat flux for steam generation. There are challenges for handling two phase flow (steam generation) in 'U' shaped metal tubes due to pressure drop, flow instabilities and control of steam dryness fraction under varying solar heat flux.

The focus of the present research work is to analyze a CPC system for direct steam generation. This paper discusses an experimental setup and challenges for direct steam generation. The experimental measurements will be focused on behavior of the thermal flow pattern inside the inclined metal tube at various heat flux conditions throughout the day, measurement of local heat transfer coefficients and corresponding vapor quality. Experimental data analysis and understanding will be useful to develop direct steam generation engineering schemes and its integration approach with various end-use applications.

Keywords: *CPC, process heat, process steam, two phase flow*

1. Introduction

The fossil fuel is used for electricity generation and process heat applications. Considering adverse effects of fossil fuels such as air pollution and global warming, it is important to promote renewable energy technologies especially in industries (Garud and Purohit 2013). The process heat requirement in an industry typically varies from 80 ºC to 250 ºC. Steam is widely accepted working fluid to cater the temperature range of 80-180 ºC, thermal oil is a preferred choice above 180 °C.

Solar thermal technologies are of concentrating and non-concentrating type. Traditionally, the non-concentrating technologies are used for end-use temperatures less than 80 ºC, and the concentrating technologies are used for medium end-use temperature applications. The concentrating technologies track the Sun and reflect its radiation to the focal point of a concentrator. Medium temperature concentrating

doi:10.18086/eurosun.2016.02.09 Available at http://proceedings.ises.org

technologies provide temperatures in the range 80–400°C and are used mainly for process heat applications (Sukhatme & Nayak, 2008).

The major considerations for adoption of solar thermal technologies for process heat applications are existing working fluid, end-use temperature requirement, shadow free space available for solar installation and cost of solar thermal technology. The solar thermal technology providers are innovating to brake the conventional barriers for working fluid limitation, maximize system efficiency (reduce area and improve ability to cater higher temperature) and minimize cost of solar thermal system.

The CPC (Compound Parabolic Concentrator) technology is in the market from more than 25 years, it is combination of a stationery (evacuated tube) and a concentrating technology (reflector) with no tracking requirement, this also known as a non-imaging technology. The elimination of solar tracking provides ample flexibility for choice of installation areas and simple operation. Generally, single phase working fluids like pressurized hot water or thermal oil is used in the CPC for the temperature range of 80-130 °C. The use of CPC operating with single phase working fluid in steam system requires additional heat exchange devices and higher solar system operating temperature leading to increased capital cost and reduced thermal performance (due to high operating temperature).

This paper discusses the considerations and approach for the direct steam generation from the CPC. An experimental setup and measurement protocol for proposed for direct steam generation is also discussed in the paper.

2. Industrial process heat and solar thermal technologies

2.1 Industrial process heat

Process heating is an essential component in the manufacture of most of the industrial products, typically, the energy used for process heating accounts for 2% to 15% of the total production cost (U.S. Department of Energy 2001).

Share of industrial heat demand for different temperature ranges based on data from 32 countries is shown in figure 1. About 30% of the total industrial heat demand is required at temperatures below 100°C and 27% at temperatures below 400°C (IEA SHC Task 33 2008).

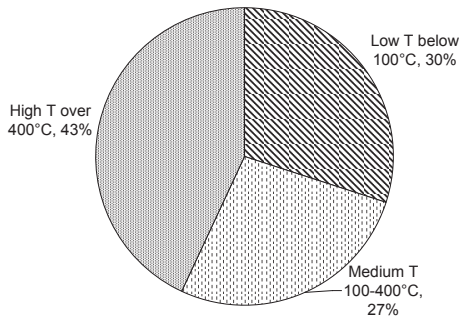

Figure 1: Share of industrial heat demand by temperature level. (IEA SHC Task 33 2008)

The majority of heat demand in industrial sectors, is at low and medium temperature. Saturated steam is generally a preferred working fluid for process heat demand below 180 °C. Steam system of a process plant has three major sections namely, generation, distribution and utilization. The steam generation is performed in a boiler (fired pressure vessel) and it is distributed using insulated steel pipes in the plant. Saturated steam has fixed pressure and temperature relationship; the desired temperature is achieved by adjusting the steam

pressure. A typical steam generation, distribution and utilization system is presented in figure 2. Steam is generated at a pressure close to the boiler design pressure, even if this is higher than is needed in the plant. The steam pressure is adjusted to desired end-use temperature using pressure reducing station.

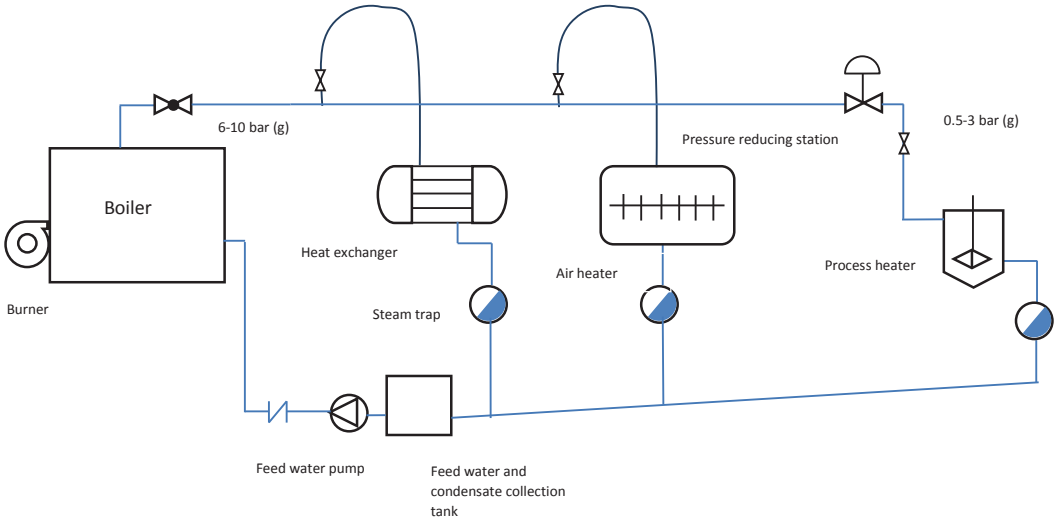

Figure 2 Typical steam system in a process plant

The key sectors utilizing industrial process heat are food (including wine and beverage), textile, metal, plastic, paper, dairy and chemical. The areas of application with the most suitable industrial processes, include cleaning, drying, evaporation and distillation, blanching, pasteurization, sterilization, cooking, curing, painting, and surface treatment. The typical temperature range for various applications is presented in table 1.

2.2 Solar thermal technologies

The popular concentrating and non-concentrating technologies for the process heat application is presented in figure 3. The temperature range for these technologies is presented in figure 4. There are different concentrating technologies suitable for different temperature ranges. There are two major types of concentrating technologies non-imaging (no tracking) and imaging (with tracking). The typical concentration ratio for non-imaging technologies is in the range of 1-10 and above this concentration ratio imaging technologies i.e. technologies with tracking are practiced (Rabl 1985).

Non-imaging concentrators have the capability of reflecting to the absorber all of the incident radiation within wide limits. The absence of tracking makes the CPC to accept incoming radiation over a relatively wide range of angles.

Imaging concentrators use tracking reflector systems to focus radiation onto a receivers (absorber) that is located at the focal point. Parabolic trough concentrators use parabolic trough reflectors to produce a linear focus on a receiver that moves with the trough as it tracks the Sun. Linear Fresnel systems use an array of smaller parallel reflectors that track individually onto a fixed linear receiver. Paraboloidal dish concentrators focus to a point focus receiver located at the focal point.

Table 1: Industrial sectors and processes with the greatest potential for solar thermal uses (Intelligent Energy, Europe 2006)

Industry	Process	Temperature ^{0}C
Dairy	Pasteurization Sterilization Drying Concentrators Boiler feed water	60-80 100-120 120-180 60-80 60-90
Tinned food	Sterilization Cooking Bleaching	110-120 60-90 60-90
Textile	Bleaching, dyeing Drying, degreasing dyeing Fixing Pressing	60-90 100-130 70-90 160-180 80-100
Paper	Cooking, drying Boiler feed water Bleaching	60-80 60-90 130-150
Chemical	Soaps Synthetic rubber Processing heat Preheating water	200-260 150-200 120-180 60-90
Meat	Washing, sterilization Cooking	60-80 90-100
Beverages	Washing, sterilization Pasteurization	60–80 60–70
Flours and by-products	Sterilization	60–80
Timber by-products	Thermo diffusion beams Drying Pre-heating water Preparation pulp	80–100 60–100 60–90 120–170
Bricks and blocks	Curing	60–140
Plastics	Preparation Distillation Separation Extension Drying Blending	120–140 140–150 200–220 140–160 180–200 120–140

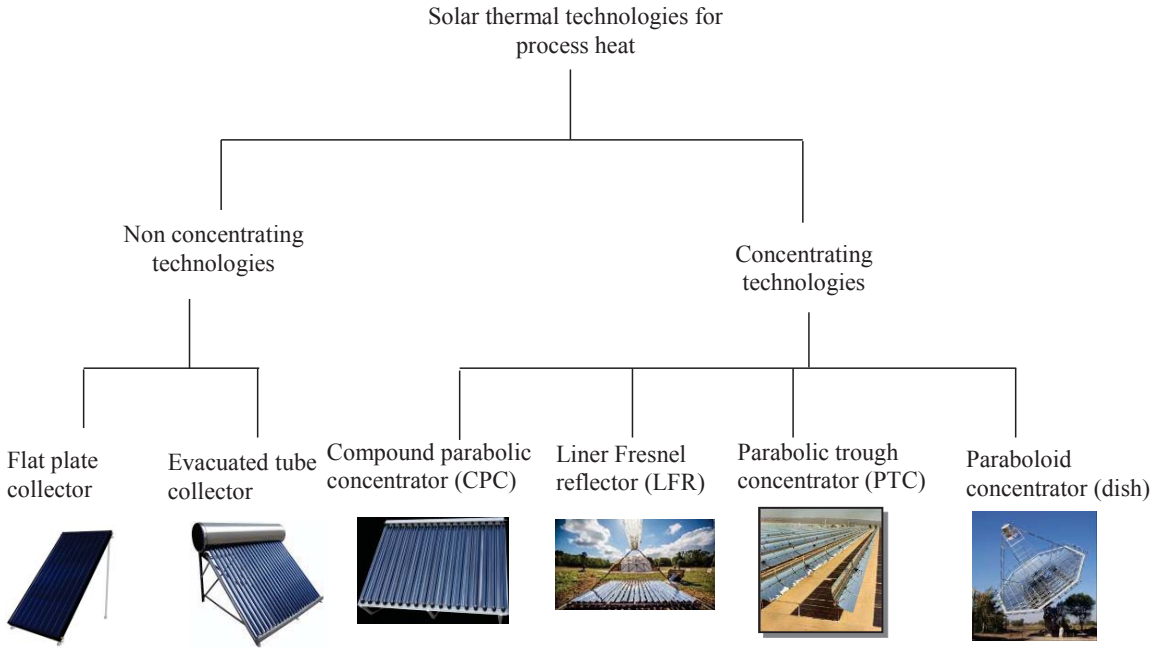

Figure 3 Popular solar thermal technologies for process heat applications

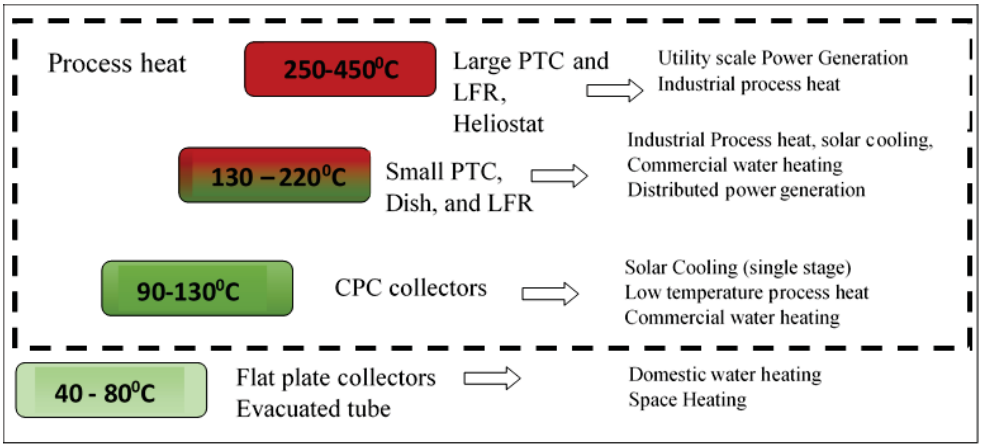

Figure 4 Solar thermal technologies and generation temperature range (ccilaportugal 2016)

It should be noted that quite often industrial processes utilize medium temperature heat in the form of steam even though for actual process lower working temperatures (below steam temperate in the range of 80-130 °C) would be sufficient. Performance of solar thermal system is better at lower operating temperature. Therefore, in order to assess correctly the feasibility of the solar thermal in an industrial process, one should look at the actual temperature needed by the process itself and not get driven by the utilization temperature of the heat carrier being used. Such an approach should be adopted to maximize overall performance of the solar thermal systems in process heat application.

Apart from temperature requirement, the other major consideration for solar thermal technology adoption is a system cost and suitability of an installation area. The CPC is non-imaging technology suitable to deliver heat at 90-130 °C temperature range at 20-40% lower system cost compared to imaging type technologies. The lower cost is mainly on account of no tracking requirement, no moving parts and simple installation structure. In addition to the system cost advantage, the CPC is flexible to install on a slanting roofs and has weight 18-22 kg/ m^2 aperture area compared to other concentrating technologies which have limitation for installation on the slanting roofs and the weight of such systems is in the range of 40- 80 kg/ m^2 aperture area

There are variety of applications like steam tracing, evaporation, boiling processes in cooking, essential oil extraction, pasteurization, sterilization etc. requires heat at 90-130 °C temperature range in the form of steam. In the process plants steam for such applications is supplied after PRS (pressure reducing station) in the pressure range of 0.5-3 bar (g) (shown in figure 2).

Generally, liner receiver systems use sensible heating working fluid either thermal oil or pressurized hot water for extracting heat from the solar thermal system. The sensible working fluid can be used for indirect steam generation using external heat exchanger and accessories. Indirect steam generation as process heat working fluid from concentrating solar system has various operational limitations and cost disadvantages captured as follows:

- Indirect steam generation requires additional steam generating system increase system cost, not very economical for small systems (below 100 m^2 aperture area)
- Lower solar thermal system performance as the sensible working fluid temperature needs to be 10 to15 °C higher than the steam generating temperature
- Continuous operation of sensible working fluid circulation pump leads extra energy cost for pumping
- Design of steam generating heat exchanger for varying sensible working fluid flow (30% -100%) on account of variation in the solar radiation during the day

3. CPC technology

3.1 Basics of CPC

Compound Parabolic Concentrator (CPC) is a special type of solar collector fabricated in the shape of two meeting parabolas. It is a hybrid, non-imaging solar thermal system with high aperture area. The concentration ratio up to 10 can be achieved in the non-tracking mode easily (Rabl 1985). The geometry of a CPC is as shown in figure 5. It has two parabola sections AB and CD of parabola 1 and 2 respectively. AD is the aperture area with width ‘w’, while BC is the absorber area with width ‘b’. The axis is oriented in such a way that C is the focus of parabola 1 and B is the focus of parabola 2. Also the height of the collector is so chosen that tangents at A and D are parallel to the axis of the collector.

The acceptance angle of the CPC is the angle AED. It is obtained by joining the focus to the opposite aperture edge. In the CPC, reflector segments are oriented such that the focus of one segment lies at the base of the other segment which is in contact with the receiver. With this type of arrangement, the rays which falls in the central region reaches the absorber directly whereas those falling near the edges undergo certain reflections. The optical efficiency for a CPC is around 65%, which is 8% more as compared to a parabolic trough collector (Sukhatme & Nayak, 2008). The concentration ratio (CR) is given by w/b. For a

concentrating collector the amount of diffused radiation that can be collected is given by 1 /CR. Thus the advantage of a CPC is that it can collect diffuse radiation delivers partial heat output during cloudy atmosphere.

CPC are generally oriented in the East – West direction with south facing aperture area (for northern hemisphere), so that the maximum sunlight is utilized. However, for application where the concentration ratio is high or the acceptance angle is less, than tracking is to be provided to ensure that sunlight falls continuously on the CPC.

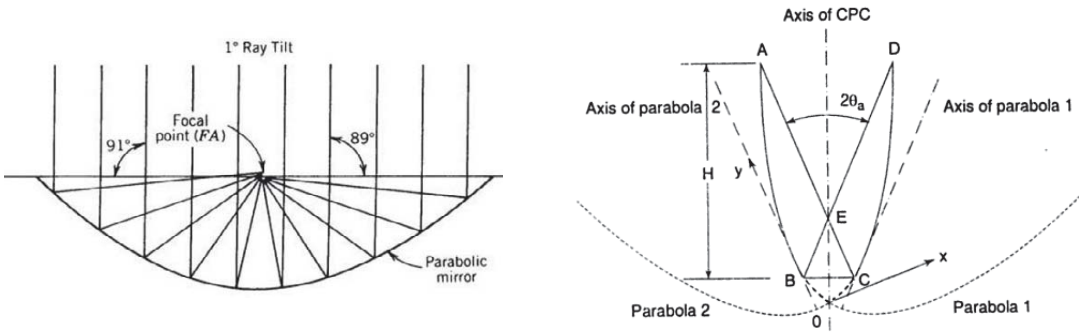

(a) (b)

Figure 5: Construction of Compound Parabolic Concentrator (a) single parabolic mirror (b) two intersecting parabolas (Sukhatme & Nayak, 2008)

3.2 Construction of CPC

The main components of CPC technology are an evacuated tube, a compound parabolic reflector and a metal tubes (enclosed in the evacuated tubes) for transporting working fluid. The evacuated tube is a double sided selective surface coated glass tube receiver with vacuum envelop in the two glass surfaces. The evacuated tube is mounted inside the compound parabolic reflector. An 'U' shaped metal tube is enclosed in the evacuated tube, the metal tube is connected to the common headers for supply and return of working fluid. Pictorial view of CPC is as shown in figure 6.

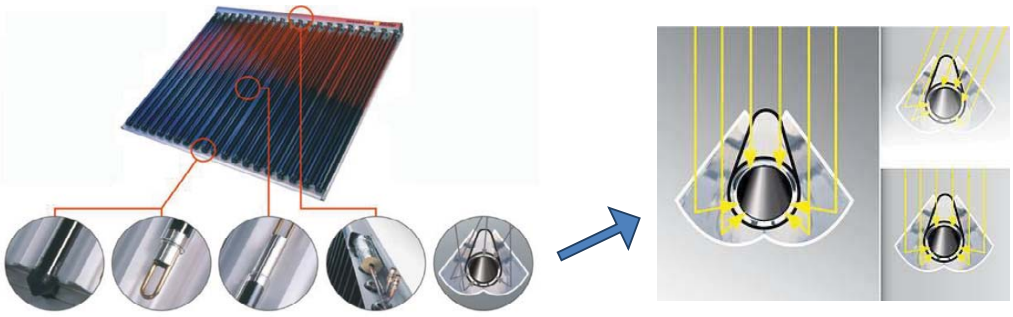

(a)

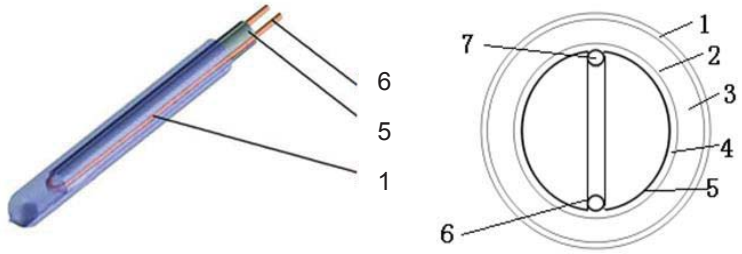

(b)

1: Outer tube 2: Selective absorption coating 3: Vacuum gap 4: Inner tube 5: Transfer plate 6: U metal pipe 7: Working fluid

Figure 6: (a) Pictorial view of Compound Parabolic Concentrator (b) Internal 'U'tube (Linuo Ritter International 2014)

The evacuated tube receives direct solar radiation from upper surface (surface facing the sun) and receives reflected solar radiation from the bottom surface (surface facing reflector). The radiation received on the upper surface utilize both beam and diffuse component of solar radiation (global radiation) and the bottom surface utilizes only reflected beam component of solar radiation. Direct, diffuse and reflected solar radiation is received on the outer layer of a glass tube (evacuated tube); it is then passed through the vacuum, and is then absorbed upon a specialized coating on the inner layer of the glass tube. Heat is then radiated and conducted from the inner layer of the glass tube to a metal tube. Heat absorbed by the metal tube is transferred to a working fluid flowing inside the metal tube. Pressurized hot water or thermal oil is used as the working fluid to extract heat captured in the evacuated tube. The general arrangement for the sensible heating of working fluid using the CPC array is presented in figure 7. The major components of the system are CPC modules, a circulation pump, an expansion tank, a heat exchanger and piping accessories.

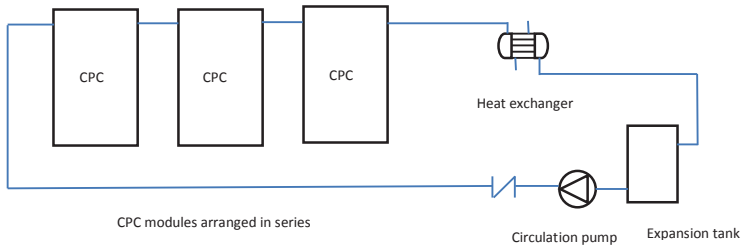

Figure 7: The general arrangement for the sensible heating of working fluid using CPC system

4. Steam generation from CPC system

Use of steam as a process working fluid for process heat has number of advantages like high heat carrying capacity, high heat transfer coefficient, constant temperature boundary condition during end-use heating, non-toxic, inexpensive, easily available etc.

There is limited literature about direct steam generation in a CPC in the recent past. Heinzel and Holzinger (1987) reported direct steam generation for process heat steam production from flat plate tubular collector. The steam generation from tubular collectors suffers from flow instabilities like steam blockage and flow pattern changes leading to vibration and unsteady release of steam (Heinzel and Holzinger 1987). The experimental setup of Heinzel and Holzinger (1987) was a natural circulating loop with heated riser glass tubes, release of the two phase flow in a steam drum and down comers to feed water back to the riser glass tubes. The experimental setup was operated with two modifications 1) use of orifice at the outlet of steam drum and 2) use of enlarge header for steam water separation at riser glass tube exist, both the modifications helped in curtailing flow instabilities.

El-Assy (1987) discussed the effect of a CPC thermal performance on steam exist condition (direct steam generation) using analytical equations. The effect of various parameters like concentration ratio, solar radiation, and mass flux on steam exit condition were predicted.

The challenges for direct steam generation in the CPC are as follows:

- Uniform water flow distribution in array of 'U' metal tubes enclosed in evacuated tube
- Steam lockout and flow instabilities in an array of the steam generating 'U' tubes
- High pressure drops for low pressure (low temperature) steam generation process
- Variation in solar radiation intensity leading to dry-out condition (100% steam dryness fraction) in individual tubes during operation

The challenges need detail investigations though experimentation for direct steam generation in the CPC system. The experimental measurements are expected to throw light on following aspects of direct steam generation from the CPC:

- Effect of variation in solar radiation on the different flow patterns in a tube boiling
- CPC solar collectors are generally mounted in an inclined position to maximize the intercept of solar radiation; the effect of inclination influences the transport processes in the bubbly and the intermittent flow regimes in two phase flow boiling.
- Two phase flow pressure drop, flow instabilities, wall temperature variations, control of dryness fraction under varying solar heat flux
- Source of two phase flow induced vibrations in the CPC system will be investigated
- The norms for acceptable water quality and steam exist dryness fraction will be studied to eliminate possibility of clogging of tubes

A suitable configuration for direct steam from the CPC will be developed considering various aspects investigated in experimental measurements

4.1 Experimental setup

CPC module mounted on the platform and integrated with supply line of water for direct steam generation will be the primary experimental setup. Schematic representation of experimental set up is as shown in Figure 8. The water at ambient temperature entering the CPC module will be heated from solar radiations. In order to study the steam generation in the CPC, there are two levels of measurement a) overall measurement of CPC module and b) local measurement of single tube

The overall measurement system consists of measurement of an inlet / outlet temperature to CPC modules, flow rate of water to CPC modules, heat flux incident on the CPC modules and dryness measurement of the

outlet steam. The flowrate of water is measured with the amount of condensate collected in the tank. The heat flux incident on the CPC module is estimated based on global and diffuse radiation measured with pyranometer. The measurement of dryness fraction is discussed by Sardeshpande et al (2011). The analytical equations for experimental measurements are given in Appendix-A.

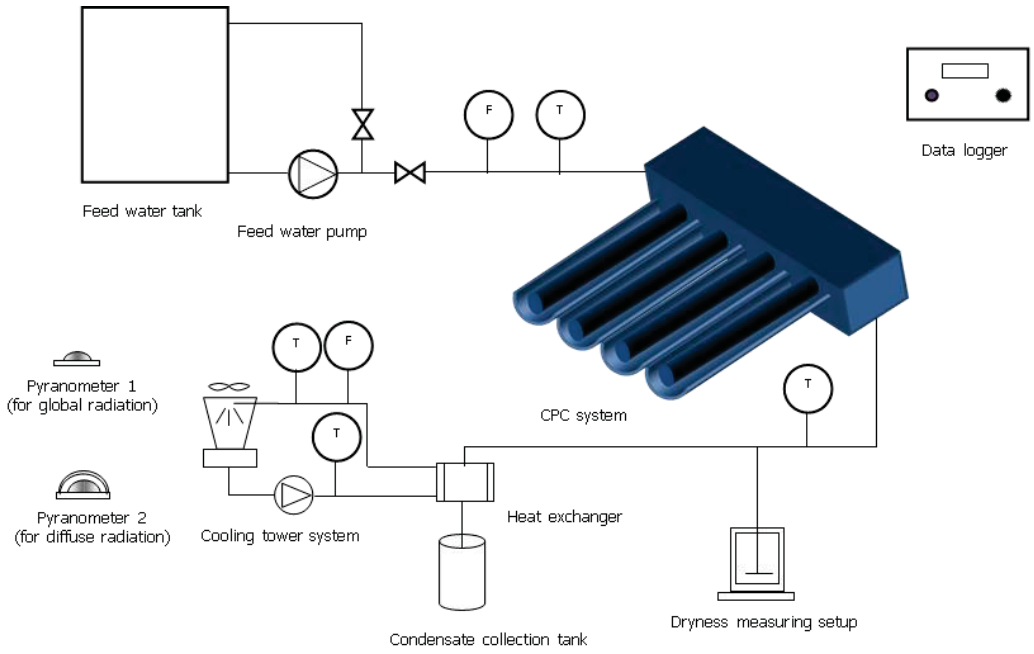

Figure 8: Schematic representation of proposed experimental set up

The local measurement consists of 10 temperature sensors installed along the length of a metal tube at an interval of 0.2 m distance. Along with this, two pressure sensors will be installed at the inlet and outlet of the tube to check the pressure fluctuations and overall pressure drop. The tube wall temperature as recorded by the temperature sensor will be the influenced by the heat transfer across the walls and formation of flow regimes inside the tube. The data generated by the temperature and pressure sensors will be recorded in data logger at suitable capturing frequency. The effects of solar radiation variations on steam dryness fraction and flow regimes in the tube will be investigated in this setup. The variation in tube wall temperature with solar radiation for constant mass flow rate indicates presence of different flow regimes. Schematic representation of local experimental plan is as shown in figure 9.

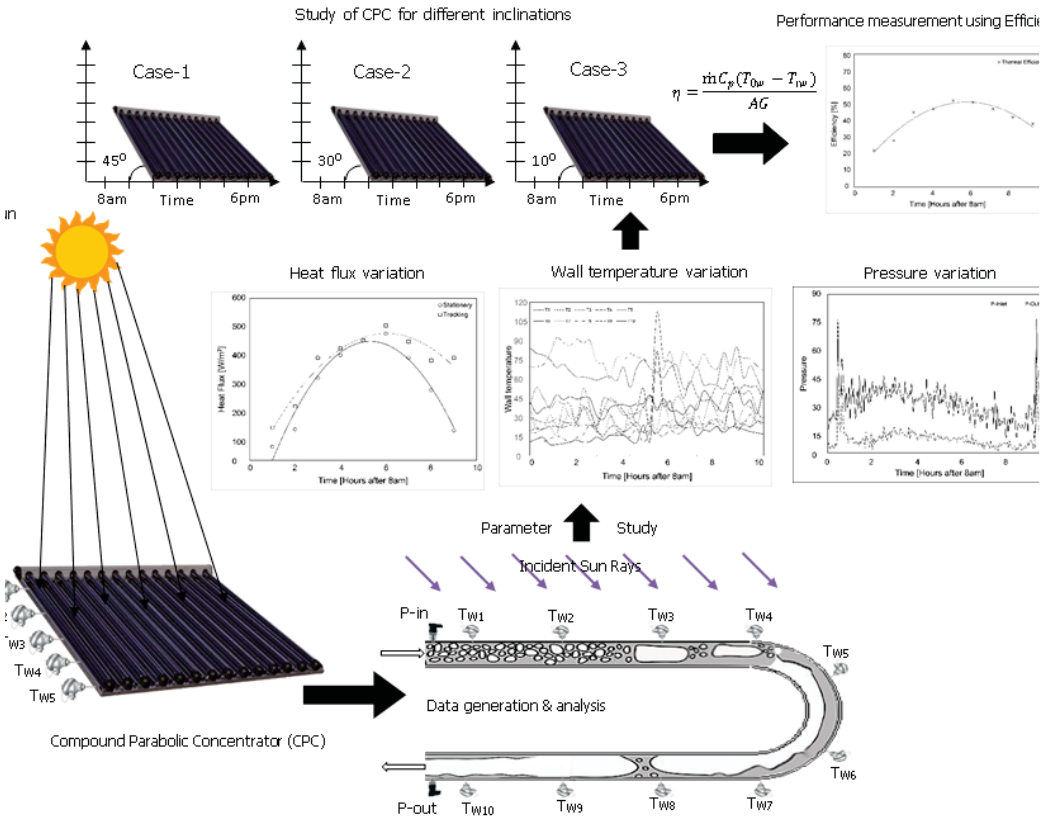

Figure 9: Schematic representation of Solar CPC and overall experimental plan

5. Conclusion

The direct steam generation from the CPC system has cost and operational advantages. However, it has many challenges on account of two phase flow in the metal tube enclosed in the evacuated glass tube. The two phase flow boiling patterns introduce flow instabilities and higher pressure drop. The present research work is focused on understanding and quantification of the direct steam generation in the CPC system.

The experimental setup proposed will undertake a) overall measurement of the CPC module and b) local measurement of single tube inside the CPC module. The overall measurement will be focused on the study of flow balances in various tubes, dryness fraction at the outlet of the CPC module for different solar radiation conditions and overall performance (thermal efficiency) of the CPC module. The local measurement of single tube will be focused on the wall temperature measurement along with mass flow rate of water and heat flux of solar radiation. The wall temperature will be used for the estimation of the boiling heat transfer coefficient. Experimental data analysis and understanding will be useful to develop direct steam generation engineering schemes and its integration approach with various process heat end-use applications.

6. References

Garud S. and Purohit I., 2007, Making solar thermal power generation in India a reality, Overview of technologies, Opportunities and Challenges, Proceedings of All India seminar on 'India's energy independence strategies & strides, 26-27 October, Institute of Engineers, Hydrabad, India

Sukhatme S.P. & Nayak J.K., 2008, Solar Energy: Principles of Thermal Collection and Storage, Third Edition, The McGrawHill Company

LRI-Product Catalogue 0001/V.1.3/03/2014 EN, Linuo Ritter International Co., Ltd., 2014

http://www.linuo-ritter-international.com/fileadmin/user_upload/documents/Download/Product_catalogue_EN_2014_final.pdf__last visited in January 2016

http://www.ccilaportugal.com/fileadmin/ahk_portugal/site_upload/pdf_diverses/PDFs_energiasRenovaveis/pdf_apresentacoes_simposio2010/Mirrox_Unternehmenspraesentation.pdf last visited in January 2016

U.S. Department of Energy Office of Industrial Technologies, Roadmap for Process Heating Technology Priority Research & Development Goals and Near-Term Non-Research Goals To Improve Industrial Process Heating, Industrial Heating Equipment Association, Capital Surini Group International, Inc., Energetics, Incorporated, March 16, 2001

Intelligent Energy, Europe, Solar Industrial Process Heat – State of the Art, Report, *European Solar Thermal Industry Federation*, 2006, available online, http://www.erec.org/fileadmin/erec_docs/Projcet_Documents/K4_RES-H/D23-solar-industrial-process-heat.pdf

IEA SHC Task 33 and SolarPACES Task IV: Solar Heat for Industrial Processes, "Potential Solar Heat for Industrial Processes" Edited by C. Vannoni, R. Battisti and S. Drigo, Italy, 2008 Solar Heating and Cooling Executive Committee of the International Energy Agency (IEA) http://www.iea-shc.org/publications/downloads/task33-

Heinel V., Holzinger J., 1987. Direct evaporating flat plate and tubular collectors for process steam production, in: Bloss W. H., and Pfisterer F. (Eds.), Advances in solar energy technology. Pergamon Press, Hamburg, pp.1436-1440

El-Assy A.Y., 1987. Thermal analysis and operational limits of compound parabolic concentrators in two phase flows with saturated exit state, in: Bloss W. H., and Pfisterer F. (Eds.), Advances in solar energy technology. Pergamon Press, Hamburg, pp.1339-1350

Rabl, A., 1985. Active Solar Collectors and their Applications, Oxford University Press, New York.

Sardeshpande V.R, Chandak A.G., Pillai I.R., 2011. Procedure for thermal performance evaluation of steam generating point-focus solar concentrator, Solar Energy, 85, pp. 1390–1398

Appendix -A: **EXPERIMENTAL MEASUREMENT ANALYTICAL EQUATIONS**

The experiments on CPC will be conducted for different combination of inclinations, flow rates and solar heat requirement and according to the results obtained it will be put to optimum use. The plot of efficiency of the CPC collector against time will reveal the optimum time for the use of CPC. The theoretical energy calculations about the quantity of steam or hot water required, the capacity of the CPC to handle this load will be investigated on daily basis as per the following.

$$Q_u = \dot{m}_w \times \left(h_{g,out} - h_{f,in}\right) \quad (1)$$

$$h_{g,out} = (1 - x) \times h_{f,out} + x \times h_{fg,out} \quad (2)$$

where Q_u = heat gain during the steam generation (kJ)
m_w = mass flow rate of water (kg/s)
x = dryness fraction of steam generated
$h_{g,in}$ = Enthalpy of steam at saturation outlet temperature (kJ/kg)
$h_{f,in}$ = Enthalpy of water at saturation inlet temperature (kJ/kg)
$h_{f,out}$ = Enthalpy of water at saturation outlet temperature (kJ/kg)
$h_{fg,out}$ = latent heat of evaporation corresponding to saturation outlet temperature (kJ/kg)
The total energy received by the CPC depends upon the average solar radiation normal to aperture and the aperture area. The total solar energy received by the reflecting surface of the concentrator is presented in equation 3.

$$Q_r = A_{ap} \times I_g \times t \quad (3)$$

where Q_r = solar energy received (kJ)
I_g = normal beam radiation (kW/m^2)
A_{ap} = aperture area of concentrator (m^2)
t = duration of test (s)
The thermal efficiency of CPC is ratio of useful heat recovered to the total heat received on the aperture area as presented in equation 6.

$$\eta_{th} = \frac{Q_u}{Q_r} \quad (4)$$

η_{th} = Thermal efficiency of CPC

$$Q_{u,st} = \frac{Q_u}{N} \quad (5)$$

Where, $Q_{u,st}$ = heat gain during the steam generation for single tube (kJ)
N= Number of tubes

$$Q_{u,st} = \varphi_{avg} \times A_{sa,st} \times \left(T_{w,avg} - T_{f,avg}\right) \quad (6)$$

φ_{avg} = Average heat transfer coefficient for single tube (W/m^{2}K)
A_{sa} = Surface area of metal tube (m^2)
$T_{w,avg}$ = Average wall temperature of sensors (°C)
$T_{f,avg}$ = Average fluid temperature (°C)

The instruments used for testing are listed in table 3. The test setup also includes a steam dryness fraction measuring setup where a small amount of steam is introduced into an insulated container. This setup is adapted from the method proposed for measuring steam quality[25]. The change in the temperature is measured along with increase in weight of the water in the container. The mass balance of the sample taken for steam moisture measurement is given in equation 7.

$$m_s = m_{w,f} - m_{w,i} \quad (7)$$

where m_s = mass of steam in the sample for dryness measurement (kg)
$m_{w,f}$ = final mass of water after steam is bled in the container (kg)
$m_{w,i}$ = initial mass of water before sample of steam is introduced (kg)
After the estimation of mass of steam introduced in the container of the moisture measurement setup, the moisture fraction in the steam sample is estimated using the equation 8.

$$x = \frac{\left[m_{w,f} \times C_{p,w} \times \left(T_f - T_i\right) - m_s \times C_{p,w} \times \left(T_{sat} - T_i\right) + m_c \times C_{p,c} \times \left(T_f - T_i\right)\right]}{\left(m_s \times h_{fg}\right)} \quad (8)$$

where x = dryness fraction of steam
$C_{p,w}$ = Specific heat of water (kJ/kgK)
T_f = Final temperature of water in container (°C)
T_i = Initial temperature of water in container (°C)
T_{sat} = Saturation temperature of water at the saturation pressure when test is conducted (°C)
m_c = mass of the container (kg)
$C_{p,c}$ = Specific heat of material of container (kJ/kgK)

Conference Proceedings

EuroSun 2016
Palma de Mallorca (Spain), 11 - 14 October 2016

Solar assisted production of expanded polystyrene with high efficiency flat plate collectors

Elisabeth Schneider, Jan Steinweg, Lukas Machelett, Federico Giovannetti

Institut für Solarenergieforschung Hameln, Emmerthal (Germany)

Abstract

The use of solar thermal energy for process heating in industry is a young field which has a high theoretical potential to reduce the consumption of fossil fuel, but also represents a high technical and economical challenge. In the framework of a running project we investigate the integration of a solar heating system into an existing production process of expanded polystyrene (EPS), through utilization of recently developed high efficiency flat plate collectors. For this purpose a detailed process analysis based on an extensive measuring campaign and a simulation study with different solar integration and efficiency strategies are conducted. The results should provide a basis for the development of a suitable integration concept. This paper features the results of the analysis and of the simulation study, showing different solutions for solar integration with reductions of fossil fuel consumption up to 11 %.

Keywords: *Process heat, high efficiency flat plate collector, industry, expanded polystyrene, EPS, efficiency*

1. Introduction

The use of solar thermal energy to support industrial processes is a young field which has a high theoretical potential to reduce the consumption of fossil fuel, but also represents a high technical and economical challenge.

In the context of a R&D project, which is supported by the Deutsche Bundesstiftung Umwelt (DBU) and in cooperation with the industrial partners Solvis GmbH and Kluth Dachbaustoffe GmbH we analyse the use of solar heat for the production of expanded polystyrene (EPS).

According to a first estimation based on market data (Sprengard et al., 2013) and extrapolated consumption data the current annual heat demand of the entire EPS-plants in Germany is around 150 – 200 GWh/a and will increase due to a rising market. This energy is required as process heat at temperature levels between 40 °C and 110 °C. The annual course of production, which depends on the typically seasonal intensity of activities at the building sites, shows a minimum in the winter months. These two aspects represent good prerequisites for the use of low-temperature solar heat.

The aim of the project is to develop suitable solar integration concepts for EPS-plants with new high efficiency flat plate collectors. These spectrally selective, double glazed collectors were developed in the context of a completed research project (Föste et al., 2013). In order to improve their cost effectiveness the size is increased (from 2 m² to 8 m²) and design modifications are implemented.

The article focuses on the integration of solar heat into the EPS-production process and on energy efficiency measures based on the existing plant configuration of the Kluth Dachbaustoffe company. After a detailed analyses of the production process, the plant is modeled with the simulation software TRNSYS and a simulation study with various kinds of system optimization and sizes of the solar system as well as different control strategies is carried out. The results provide a decision basis for the solar integration concept and for the system dimensioning.

doi:10.18086/eurosun.2016.02.10 Available at http://proceedings.ises.org

2. Analysis of the production process

In this section the foaming process of EPS is explained. Figure 1 shows the simplified process scheme of the production line.

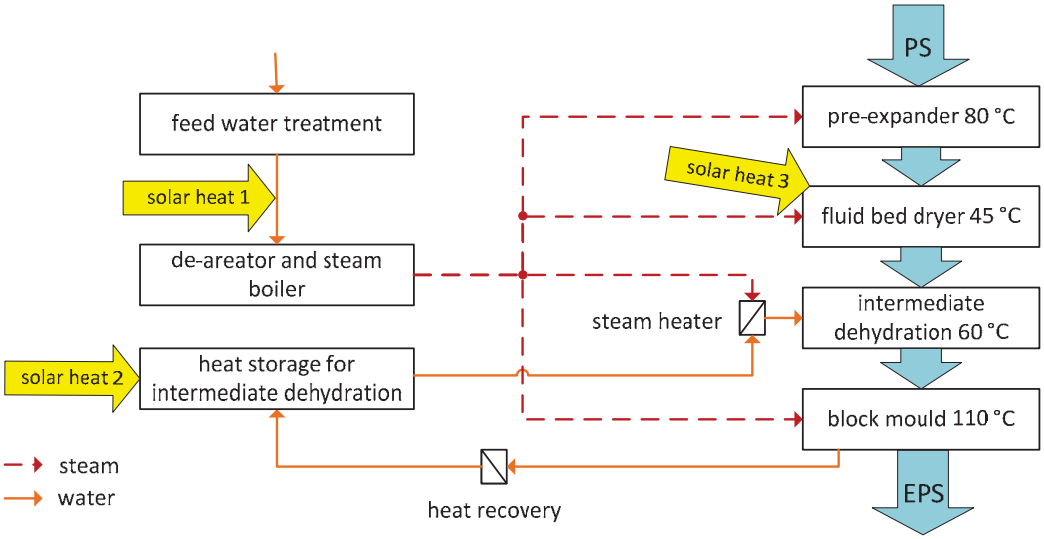

Figure 1: Simplified scheme of the foaming process and suggested integration points for solar heat.

The initial material is polystyrene granulate (PS), which contains of the main component polystyrene and the foaming agent pentane (Demacsek, 2016). This granulate first gets expanded in the pre-expander by steam at a temperature of around 80 °C, where it experiences a volume increase by about 5000 %. In the next step the pre-expanded and still in loose form existing polystyrene particles are pre-dried in the fluid bed dryer, which operates with steam heated air. Afterwards the EPS is stored in the intermediate dehydration. During the dehydration process the humidity, which has entered with the steam, is evaporated out to stabilise the EPS. Furthermore for the following processes the content of pentane has to be decreased to a defined percentage. The intermediate dehydration takes place in large silos and operates with an airflow heated by warm water from a heat storage tank (volume: 6 m³)[1]. This water gets thermal energy from a heat recovery of the block mould and, if necessary, receives an additional re-heating from a steam heater before it supplies the dehydration-process. In the current plant configuration the re-heating is conducted without a control strategy and the temperature in the silos ranges between 25 °C and 85 °C. According to the statement of the plant operator a provided dehydration temperature of around 60 °C would be optimal for a high quality product. When the material is ready for the next process, it is foamed in the block mould to blocks of 6 m³. The block mould operates with steam at a temperature of 110 °C. The EPS-blocks are then stored in a warehouse for further drying before they get cut and finished.

The production process runs during the day from Monday to Friday. The daily production time depends upon the seasonal demand, featuring a minimum during wintertime and a maximum in the late summer and in autumn. At night and on weekends there is no production. The yearly operation time amounts to approximatly 1000 hours. Currently the whole process plant of the company is supplied with heat from steam, generated by a natural gas-fired boiler. The annual energy demand of the boiler is about 1.6 GWh/a, the production volume is around 110.000 m³ EPS per year.

Following a pre-analysis of the production plant, an extensive measurement campaign has been started in July 2015, focusing on analysing the detail of heat flows and temperature levels at single plant sections. Through the data analysis three potential integration points for solar heat have been identified: the preheating of feed water before entering the boiler (solar heat 1), the intermediate dehydration (solar heat 2) and the fluid bed dryer (solar heat 3). These integration points are chosen because of their temperature levels (below 100 °C) and the fact, that steam is not directly needed as a process component.

To verify the potential for energy efficiency measures, additional measurements have been carried out. The waste

[1] The heating of the intermediate dehydration process is a specific feature of the considered EPS-plant.

heat flow of the pre-expander, the occurring condensate, waste heat from vacuum pumps and process-related radiant waste heat have been investigated. With the exception of the vacuum pumps, all analysed heat sources have a relatively low heat amount and/or a quite low temperature level making an useful and effective integration into the production process hardly possible. The cooling water of the heat pumps, which has an average temperature level around 50 °C at a flow rate about 7.2 m³/h and operates parallel to the block mould (circa 1000 h/a), is therefore taken into further consideration as heat recovery source. Additionally, the hydraulic interconnections of the single components were analysed with the aim of improving the process efficiency by considering the temperature levels of the available heat. This approach applies particularly to the heat recovery of the block mould and the intermediate dehydration.

3. Modelling the production plant

In order to evaluate the potential and possibilities of the considered efficiency measures and the implementation of the solar integration points in more detail, the relevant processes are modelled with the simulation software TRNSYS and a simulation study is carried out. Figure 2 shows the modelled components as well as their hydraulic interconnection schematically.

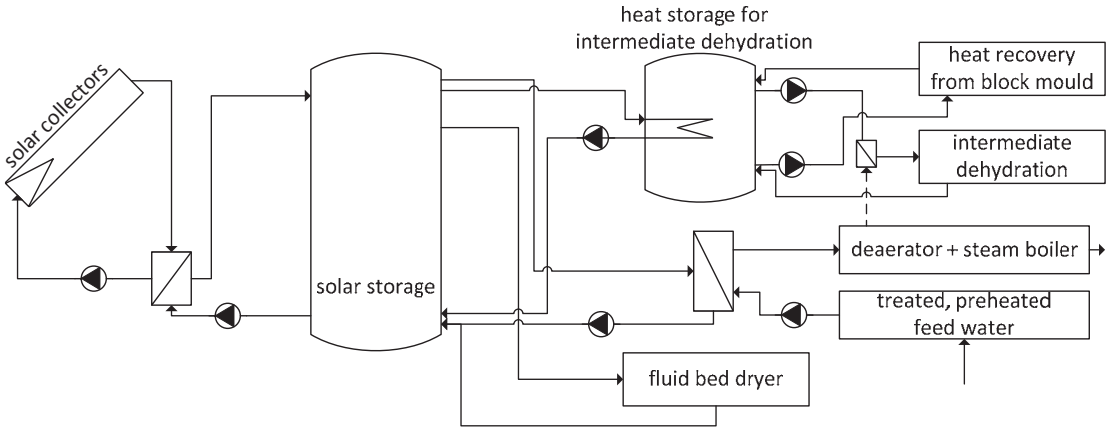

Figure 2: Schematic representation of the basic TRNSYS model for the current plant configuration supported by a solar thermal system.

The following components of the plant are modelled:

- Feed water supply (treated and pre-preheated by further heat recovery)
- Steam boiler
- Intermediate dehydration + associated steam heater
- Hot water tank for supplying the intermediate dehydration
- Heat recovery from the block mould (including the operation mode of the block mould)
- Fluid bed dryer

The single components are modelled considering the annual load profiles based on the measurement analysis.

The model for the solar thermal system includes the highly efficient solar collectors, a solar heat storage with an external heat exchanger for solar charging, a heat exchanger for pre-heating the feed water and a hydraulic connection between the solar storage and the heat storage for the intermediate dehydration.

Based on this model different simulation variations are calculated. Following parameters are varied:

- Solar system specific parameters:
  - Collector field area (given consideration of the available roof area)
  - Slope of the collectors
  - Construction of the collectors with its characteristic performance values
  - Volume of solar heat storage
  - Arrangement of the hydraulic connections at the heat storage
- Production plant specific parameters:
  - Hydraulic integration of the solar process heat

- Control strategy of the intermediate dehydration and its steam heater
- Hydraulic arrangement of system components (intermediate dehydration, heat recovery from the block mould)

4. Simulation results

The discussion is limited to the most significant findings of the simulation study. For the solar integration points, the following results are considered:

- Control strategies for the intermediate dehydration
- Integration of solar heat
  - Impacts of the hydraulic arrangement of intermediate dehydration and heat recovery: parallel connection vs. series connection
  - Integration of an additional heat recovery

All of the configurations are examined with different sizes of the solar thermal system. The collector parameters represent a highly efficient flat plate collector with spectrally selective air-filled double glazing (eta0 = 0.799, a1 = 2.45 W/m²/K, a2 = 0.101 W/m²/K², slope of the roof: 10 °).

4.1 Control strategies for the intermediate dehydration

As previously mentioned, in the current plant configuration the steam heater, which is responsible for the inlet temperature of the intermediate dehydration, runs uncontrolled. In order to ensure a high product quality, the ideal inlet temperature for the dehydration process is approximately 60 °C. Under this assumption, different control strategies are modeled and evaluated. Two exemplar configurations are considered here: System 1 - required temperature of 55 °C with continuous operation; System 2 - required temperature of 60 °C operating parallel to the plant operation.

The most significant differences of these two control strategies are shown in Figure 3.

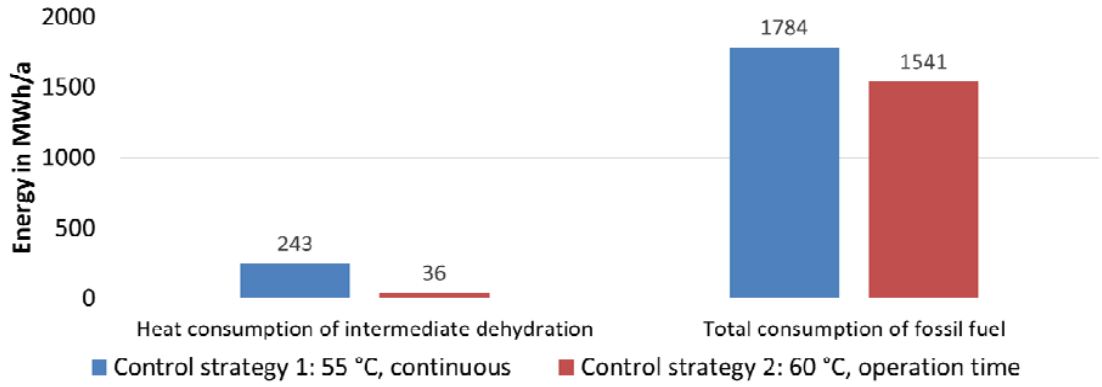

Figure 3: Calculated energy consumptions of the intermediate dehydration and in total for the considered control strategies without solar heat supply.

The energy consumption of the intermediate dehydration of system 1 is about 6 times higher than in system 2, mainly due to the different operation times. System 1 runs all over the year (except during the winter break), system 2 runs just about 1000 h/a, so nearly one-eighth of system 1. Because of the steam heater efficiency, the difference of 243 MWh/a between the total energy consumptions is a little higher than between the dehydration consumptions of 207 MWh/a.

To which extend the quality improvement of the product can compensate the significant increase of the energy demand, can only be evaluated by the plant operator on the basis of a comprehensive economic assessment.

In the following investigations both control strategies are considered. Since control strategy 2 has a lower heat demand for the intermediate dehydration, the control takes in case of available solar heat an additional heating for the dehydration beyond the operating periods into account.

4.2 Integration of solar heat

As previously mentioned, three solar integration points are considered. Based on the measured data of the current plant configuration, first estimations concerning the range of solar heat integration potential are done.

The theoretical potential for the feed water pre-heating (integration point 1) is defined by the temperature limitation in the solar storage tank, which amounts to 90 °C. On the assumption that the feed water can be pre-heated over the course of the year to 90 °C, the fossil energy savings are around 7 %. With the assumption that solar heat substitutes the complete supply of the steam heater, the theoretical solar heat integration potential of the intermediate dehydration (integration point 2) for the uncontrolled operation in the current plant configuration is about 8 %.

The estimated heat demand of the fluid bed dryer, therefore its maximum potential for the usage of solar heat is about 4 %. The current configuration features a heat exchange with steam supply. To ensure a sufficient heat supply by warm water laborious modifications of the existing supply system are necessary. Thus a solar heat supply for the fluid bed dryer is not taken into consideration for our simulations.

4.2.1 Impacts of the hydraulic arrangement of intermediate dehydration and heat recovery

In the current plant configuration the intermediate dehydration and the heat recovery from the block mould are parallel connected to the heat storage. To figure out if a series connection is more efficient than the existing one, both configurations are simulated, as shown in Figure 4.

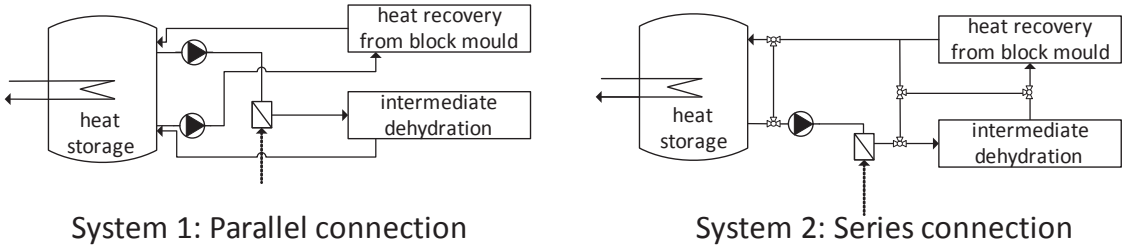

Figure 4: Sketch of the two different system configurations.

The simulation results for control strategy 1 and 2 are shown in Figure 5. The graph illustrates the reductions of fossil fuel as well as the additional heat supply of the intermediate dehydration for control strategy 2. The energy amounts are calculated in reference to the existing parallel plant configuration without the use of solar heat.

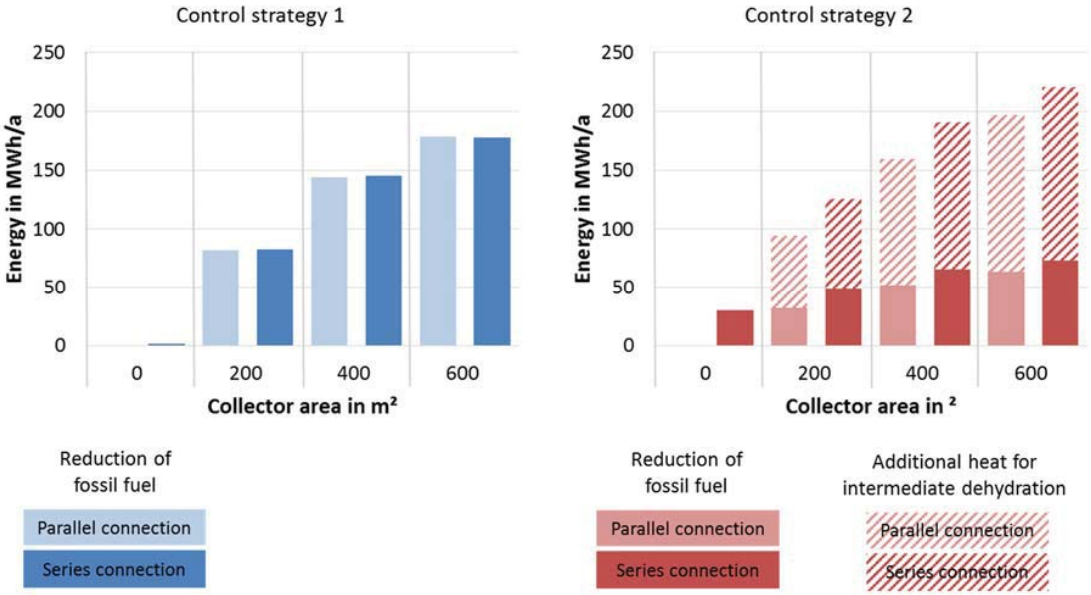

Figure 5: Calculated reduction of fossil fuel by changing the parallel connection into a series connection depending on the size of the solar thermal system.

As Figure 5 shows, for control strategy 1 the kind of interconnection has an insignificant impact on the consumption of fossil fuel. The main reason is that the system can take advantage of the series connection only when the two components are operating simultaneously. This occurs during approximately 12 % of the dehydration time, since the heat recovery only runs 1000 h/a. As a result most of the time the intermediate dehydration operates directly from and into the heat storage. Consequently there are no useful advantages with the change of this interconnection for control strategy 1.

On the contrary, for control strategy 2 a series connection leads to significant savings of fossil energy, due to a more efficient use of temperature levels of the available heat: The fluid, cooled down by the intermediate dehydration moves directly into the heat recovery where it can absorb more thermal energy at a lower temperature. Through a bypass these energy gains can be used directly for the intermediate dehydration. Compared to the parallel interconnection where the intermediate dehydration is supplied by a lower temperature from the heat storage, this series connection needs less steam for re-heating. This results in a significant reduction of fossil fuel. The difference of energy savings decreases by increasing the amount of solar energy production (size of the solar energy system). With a higher amount of solar energy the temperature of the heat storage in both systems rises. Therefore the advantage of using the heat recovery output directly for the dehydration decreases. Solar energy and heat recovery are partially in competition with each other.

The change from a parallel to a series hydraulic interconnection represents an energetically reasonable approach for control strategy 2 and is assumed for both strategies in the further simulation study.

In the next step, the theoretical maxima of fossil energy savings by the use of solar heat are calculated. For the feed water pre-heating fossil energy savings for both control strategies about 7 % of total energy demand were calculated, the same result as mentioned in the previous section. The fossil savings potential by heating the intermediate dehydration depends significantly on the control strategy. For control strategy 1 that results in a fossil energy reduction of 16 %, for strategy 2 in a reduction of 2 %. The theoretical total energy savings potential is about 23 % for control strategy 1 and about 9 % for control strategy 2.

The following figures present the achieved reductions of fossil fuel and the solar heat gains with collector fields up to 600 m² and as a function of the solar storage volume. Figure 6 shows the results for control strategy 1, Figure 7 for strategy 2.

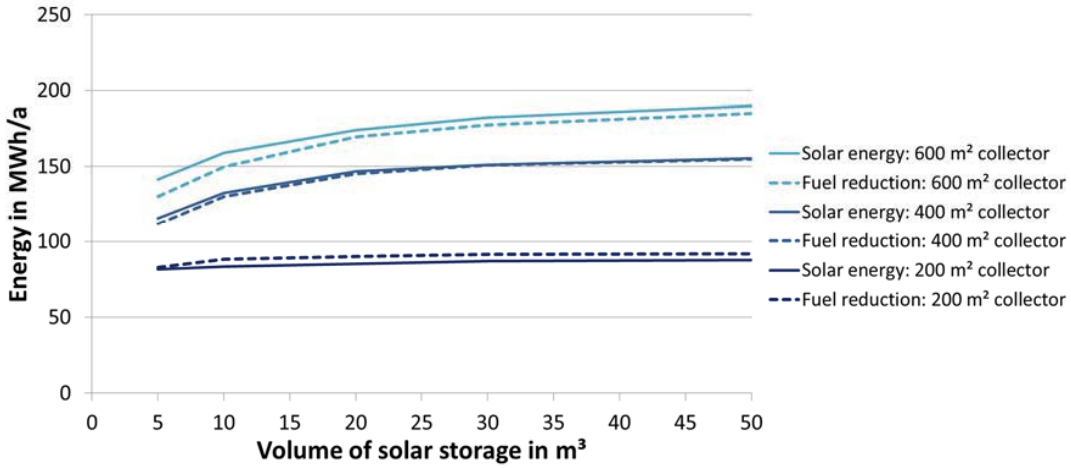

Figure 6: Control strategy 1: Calculated solar energy gains and fossil fuel reductions depending on collector area and storage volume.

Depending on the dimensions of the solar thermal system, control strategy 1 achieves solar gains up to 190 MWh/a. This corresponds to savings of fossil fuel up to 11 %. The amounts of solar heat gains and reductions of fossil fuel are approximately equal. The small deviations result from the boiler efficiency and heat losses of the solar thermal system. On the contrary, the results for control strategy 2 show significant differences between solar gains and fossil fuel savings. While the total solar gains are up to 200 MWh/a, the reductions of fossil fuel consumption reaches just 75 MWh/a, which correspondents to about 5 % of the total energy demand. The remaining solar heat gains up to 125 MWh/a are used to increase the process temperature for the intermediate dehydration, beyond the operation times, which is supposed to improve the quality of the EPS.

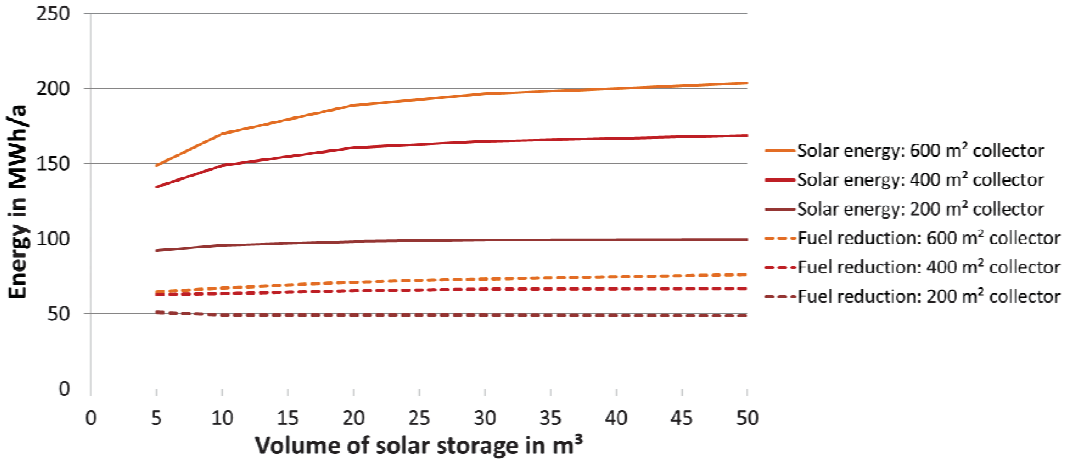

Figure 7: Control strategy 2: Calculated solar energy gains and fossil fuel reductions depending on collector area and storage volume.

Compared to the calculated theoretical fossil fuel savings potentials by the use of solar heat, control strategy 1 reaches 48 % with a collector field area of 600 m² and control strategy 2 reaches, at the same collector field size, 55 % of the potential energy savings.

4.2.2 Integration of waste heat from the vacuum pumps

As already noted, the cooling water of the block mould vacuum pumps could be used as a source for heat recovery. To analyse if this energy can be integrated usefully into the process, we carry out additional simulations. In the simulation model we assume that the heat from the recovery moves directly into the solar storage. Therefore, the potential heat sinks are the pre-heating of the feed water and the intermediate dehydration.

Figure 8 shows the savings of fossil fuel by heat recovery from the vacuum pumps for both control strategies and with different sizes of a solar thermal system with refer to the configuration without heat recovery and without solar heating supply.

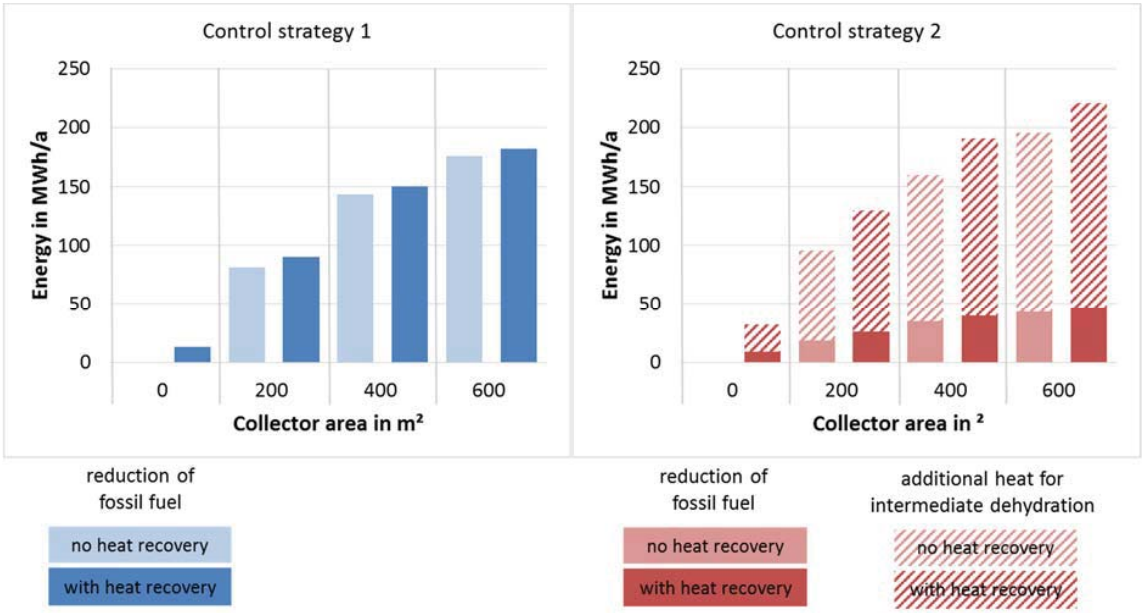

Figure 8: Calculated reductions of fossil fuel by using the heat recovery from the vacuum pumps depending on the control strategy and the solar thermal system.

The use of the heat recovery without a solar supply leads to fossil fuel reductions of 13 MWh/a and 9 MWh/a. The reason for the higher fuel reductions within system 1 is the higher energy demand for the dehydration and, thus, for pre-heating the feed water. In control strategy 2 additional heat for dehydration is available. In the

dehydration downtimes, when the steam heater is not operating, recovered heat even at relatively low temperatures can be used for the dehydration process. The amount of recovered heat decreases by an increasing solar heat supply. Consequently the use of solar energy and the recovered heat are partially in competition with each other.

To assess the reasonableness of this measure economic aspects should also be taken into consideration.

The final decision of which plant configuration is more appropriate to save fuel and to optimize the product quality has to be made by the EPS plant operator. For this purpose and also for dimensioning the solar plant an economical assessment and an analysis of the product properties should be carried out.

5. Conclusion and Outlook

We carried out a simulation study based on experimental data from a real plant to analyse the potential of solar heating for assisting the production of EPS. According to our simulation results, combining energy efficiency measures with the use of solar energy at the investigated EPS plant provide a potential for fossil fuel reduction up to 11 % are possible. The pre-heating of the feed water and the intermediate dehydration are identified as suitable heat sinks. The fluid bed dryer operates at a low temperature and could be qualified for solar assistance as well. The practical implementation requires a laborious modification of the existing supply system and was not taken into consideration for our analysis.

In the next step, both the solar system integration as well as the heat recovery measures should be evaluated under economic aspects.

The results should provide a basis for developing a solar integration concept for EPS-plants. The final aim of the research is not only to evaluate the suitability of solar process heating within this specific production facility but also to assess the transferability of the results to the broad EPS-industry.

6. Acknowledgements

The project underlying this publication "Solar supported production of expanded polystyrene with high efficiency flat plate collectors" is funded by the Deutsche Bundesstiftung Umwelt (reference number 32455/01) and carried out in cooperation with the industrial partners Solvis GmbH, Kluth Dachbaustoffe GmbH and Teklenburg Proconsult & Engineering. The authors are grateful for the support. The responsibility for the content of this publication lies with the authors.

7. References

Demacsek, C., 2016 Herstellung von Styropor, Homepage Güteschutzgemeinschaft Polystyrol-Hartschaum: http://www.styropor.at/in-dex.php/produkt/was-ist-styropor (07.03.16)

Föste S. et al., 2013 Hocheffiziente Flachkollektoren mit selektiv beschichteten Zweischeibenverglasungen Abschlussbericht zum BMU-Forschungsvorhaben, FKZ 0325873 A-D

Sprengard, C. et al., 2013 Technologien und Techniken zur Verbesserung der Energieeffizienz von Gebäuden durch Wärmedämmstoffe – Metastudie Wärmedämmstoffe – Produkte – Anwendung – Innovationen FIW München, p. 74

Conference Proceedings

EuroSun 2016
Palma de Mallorca (Spain), 11 - 14 October 2016

Technical assessment of a concentrating solar thermal system for industrial process steam

Panagiotis Tsekouras, Rosie Christodoulaki and Vassiliki Drosou

CRES- Centre for Renewable Energy Sources and Saving, 19th km Marathonos Ave. Pikermi, 19009 Greece

Abstract

The aim of this study is to present a techno-economic assessment of a concentrating solar thermal system for steam production for a food industry located in Kalamata, Greece. The solar system mainly consists of the parabolic trough collectors, the steam generator and the thermal oil storage.

Initially, the potential hydraulic configurations of the system were demonstrated and evaluated. Following a thorough evaluation of a series of parameters, the most appropriate one was selected for analytical energy simulation. Energy simulation was performed with the Greenius software; the outcome of the simulations leads to measurable indicators of the overall system performance. The energy results of the selected system were presented in details followed by a parametric analysis modifying important system variables. The last section of this study provides technical conclusions accompanied with recent economic figures.

Present study aims to further assist the penetration of such systems to a market which is still under development in Greece.

Keywords: Concentrating solar thermal system, parabolic trough collectors, industrial process heat, solar steam

1. Introduction

Worldwide, 66% of heat is generated by fossil fuels and 45% of that is used in industry as process heat (European Union, 2013). At European level, 27% of total energy concerns heat consumed by industries. 30% regards temperatures below 100 ^{o}C, 27% temperatures in the range of 100 - 400 ^{o}C and the remaining 43% at higher temperatures (European Commission, 2009).

The efficacy of solar thermal systems in applications other than hot water production i.e. process heat and solar cooling has already been presented in former studies (Tsekouras et al., 2014; Tsoutsos et al., 2009; Drosou et al., 2009). However solar heat for industrial processes still presents a quite modest share of about 88 MWth installed capacity (0.3% of total installed solar thermal capacity, at European level) (Ecoheatcool, 2006). Solar thermal systems are considered to be cost effective mainly in low temperature applications. Moreover, at a European level there is intense research activity to broaden the applications of solar thermal systems beyond their established domains and to foster their participation in the energy maps of the EU-Member States.

The Concentrating Solar Thermal (CST) systems are expected to play a key role in this effort, especially for medium temperatures needed for industrial applications. The CST systems use a combination of mirrors or lenses to concentrate the direct irradiation radiation to produce heat. The most mature CST technologies are the parabolic trough collectors, the central receivers and the linear Fresnel collectors.

Greece is identified as one of the world-leading countries in the use of solar systems for hot water production presenting one of the highest ratios in the installed solar thermal collector area per capita. The main solar thermal product was, and still is, the thermosiphon water heater, comprising of flat plate collectors and

doi:10.18086/eurosun.2016.02.12 Available at http://proceedings.ises.org

storage tank. From the early 1990s to the present, several successful solar thermal systems for industrial process heating applications have been in operation in Greek industries; however, they are limited to flat plate solar systems, mainly due to the low level temperatures for hot water production. Among the industrial applications in Greece food industry, textiles, chemical industry and beverage industry are identified as presenting significant amounts of heat needs at a medium temperature level. As the industrial heat in Greece is produced by costly and polluting use of fuels (heavy oil, natural gas, fuel oil) this sector is ideal for solar thermal systems in terms of technical, environmental and economic feasibility. Apart from that, the climate change and the rising trend in energy costs require sustainable solutions that may use the domestic high solar potential.

2. Description of industrial user

For the purpose of the study, an existing industry was chosen, whereas the CST system will support the production steam needs. The industry is a food process industry situated in Kalamata, Greece. The production schedule requires energy throughout the year, seven days per week from 07:00 to 18:00, as depicted in Fig 1.

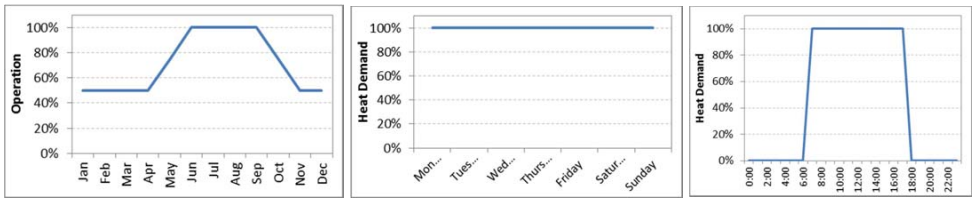

Fig 1: Time profile for year, week and day operation

Currently, the thermal energy requirements are covered by a conventional steam oil boiler with the technical characteristics summarised in Table 1.

Table 1 : Technical characteristics of the existent energy system

Description	Value
Steam temperature	170 °C
Steam pressure	7 bar
Steam supply	700 kg/hr
Annual energy consumption	1.554 MWh p.a.
Oil boiler efficiency	75 %
Annual oil consumption	207 tn p.a.

The meteorological data for the Kalamata site is extracted from the Meteonorm software, having a reference period from 1986 to 2005. The concenetrating solar collectors use only the Direct Normal Irradiation (DNI) which accounts for the specific site to 1,923 kWh/m^2 per year.

The DNI monthly distribution shows high mean daily values of approximately 8.7 kWh/m^2 during the summer period and low values of 3.1kWh/m^2. Fig 2 shows the distribution of DNI during a summer day.

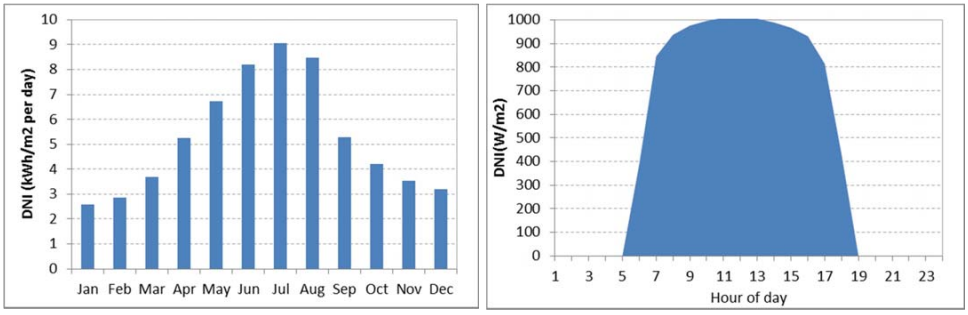

Fig 2: DNI distribution per month (left) and per hour of a summer day (right)

Fig 3 shows the number of hours during a calendar year when the irradiation exceeds a specific level. As such it can be noticed that, out of the annual 8760 hours the 1957 hours have DNI level higher than 500 W/m^2. This duration is a quite important factor for the annual system performance of a concentrating solar system considering that high radiation levels are provided during a significant part of the year. DNI of 500W/m^2 can be deemed as general threshold for CST plants operation. In this sense the optimum regions for CST plants are those with high levels of DNI occurred in long time in daily and yearly basis.

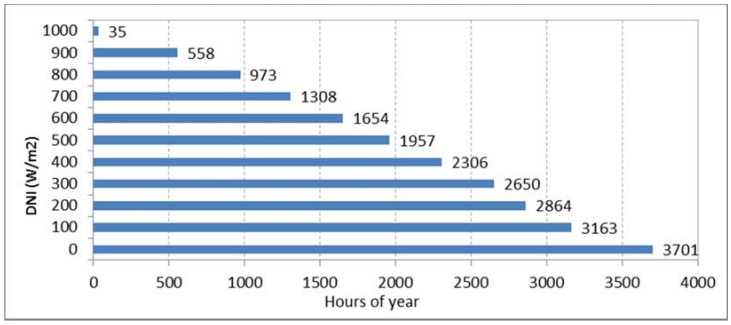

Fig 3: Annual distribution of hours for specific DNI irradiation levels.

3. Solar system configurations for industrial applications

In the following section, three suitable solar configurations for steam production using the solar system in parallel with the conventional one are examined. The parabolic trough collectors can operate either with thermal fluid (indirect steam production) or with two phase water (direct steam production).

3.1 Configuration C1: Indirect steam production via parabolic trough collectors with liquid thermal fluid and no storage

Starting from the concentrating solar collectors, the parabolic mirrors track the sun in one axis in order to concentrate the solar irradiation into the linear receiver located at the focal line. The receiver converts the concentrated irradiation to useful heat raising the temperature of the liquid thermal fluid which is circulated inside the receiver pipe. The thermal fluid, in higher temperature now, transfers its solar heat to the water in the steam boiler. When the produced steam reaches the required conditions, the steam is supplied to the thermal processes. If the solar system supplies less steam than the required amount, the conventional steam boiler covers the remaining requirements.

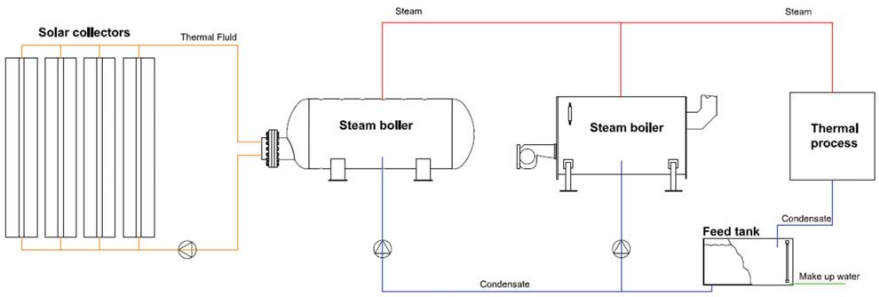

Fig 4: Configuration C1 -Indirect steam production via parabolic trough collectors with liquid thermal fluid and no storage

3.2 Configuration C2: Indirect steam production via parabolic trough collectors with liquid thermal fluid and thermal storage

This configuration is similar to C1, with only difference the integration of a thermal energy storage to the system which aims to exploit better the solar heat especially in cases when the solar heat flows are higher than the required. In this way, when appropriate sun conditions exist the thermal fluid is circulated at the parabolic trough collectors absorbing heat. Then the heated up thermal oil is stored at the thermal energy

storage. In case of steam demand, the thermal fluid from the storage drives the steam boiler. In this way the energy supply and demand are decoupled to some extent.

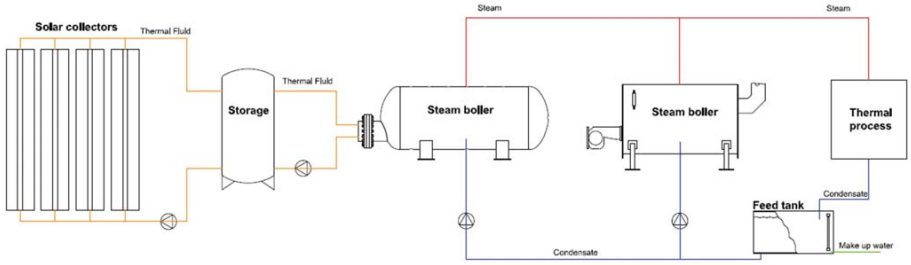

Fig 5: Configuration C2 - Indirect steam production via parabolic trough collectors with liquid thermal fluid with storage

3.3 Configuration C3: Direct steam production via parabolic trough collectors

This is the simplest configuration since it does not have additional steam boiler and storage system. Instead of a liquid thermal fluid, the two phase water is circulated inside the receiver pipes. In brief, the water passes through the first part of the solar collectors and it is heated up to the saturated liquid point. When it passes through the second part, the heated up liquid water starts boiling and being converted to steam and then to superheated steam. The produced steam enters directly the steam network and heads to the consumption.

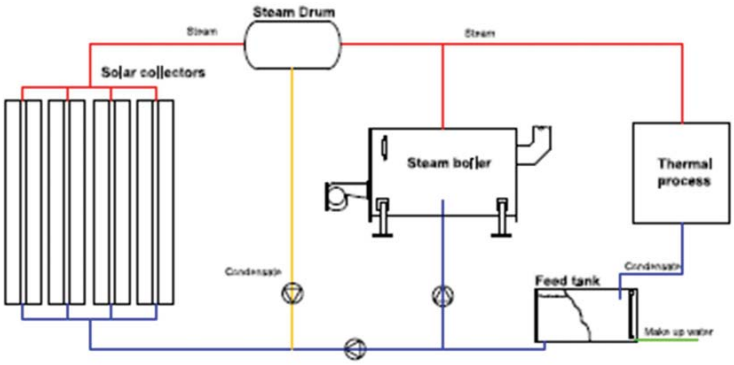

Fig 6: Configuration C3 - Direct steam production via parabolic trough collectors

4. Methodology

The initial scope of this study is present a proposal for implementation of a CST system in the industrial sector. Specifically, an integrated CST using parabolic trough solar collectors is discussed, used to support the steam production for a food industry located in Kalamata, Greece.

The Configuration C2 was selected for the purpose of this study as it combines the following advantages: good heat transfer characteristics, modest cost of heat transfer medium, lower operational pressure of solar system and commercial maturity. This section presents the technical characteristics of the major system components. In the present study, the below system case is used as the base scenario for the parametric analysis.

The technical characteristics and efficiency curves of the parabolic trough collector are summarized in Table 2 and Fig 7. The solar field consists of 80 solar collectors with reflective area of 1,056 m^2. The solar collectors are aligned in 8 parallel series with North – South orientation and 10 collectors in series. The optical losses due to dust in the mirrors are assumed to be 3% all year long, taking into consideration a regular cleaning and maintenance schedule.

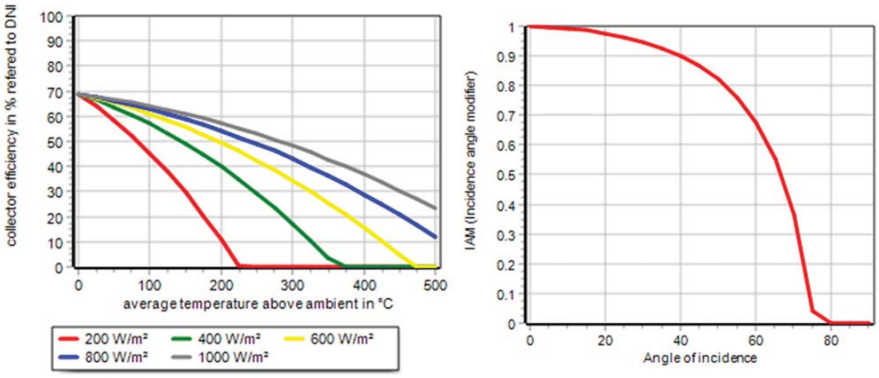

Fig 7: Efficiency curves of the parabolic trough collectors

Table 2 : Technical characteristics of the parabolic trough collector

Description	Value
Aperture width	2.3 m
Collector length	5.75 m
Effective mirror area	13.2 m^2
Receiver diameter	0.0508 m
n_o	0.689
a_1	0.36 W/(m^2K)
a_2	0.0011 W/(m^2K^2)
Number of collectors / rows / collectors per row	80 / 8 / 10
Orientation	North - South
Total effective mirror area	1056 m^2
Total absorber length	460 m

For the selected configuration, a specific type of thermal oil has been selected for the solar field that meets the following prerequisites: liquid state in the operational temperature range, low freezing point, good heat transfer, thermal stability, non-corrosive, low initial cost. As the parametric analysis included operation of the solar field in temperature up to 350°C the selected thermal oil has the following characteristics. In the base scenario the thermal oil supply temperature from the solar collectors is 250°C with returning temperature of 200°C.

Table 3 : Properties of the thermal oil

Temperature (oC)	Density (kg/m^3)	Heat capacity (Wh/kg.K)
65 / 255 / 355	1023.7 / 854 / 734	0.4725 / 0.6197 / 0.712

The thermal storage is a single tank with volume of 10 m^3 corresponding to thermal storage capacity of 250kWh in the range of 200-250°C.

Table 4 : Technical characteristics of the thermal storage

Description	Value
Thermal energy capacity	250 kWh
Operational temperature range	200 - 250 °C
Storage volume	10 m^3

Tank material	Stainless steel
Insulation material	Mineral wool 100kg/m^3
Insulation thickness	50 cm

5. Results and Discussion

5.1 Methodology

The energy study is conducted with the software Greenius (Greenius, 2016), considering the simulation algorithm as shown in Fig 8. . In brief, the simulation starts by reading the climate data (i.e. DNI, ambient air temperature, sun position) of the specific location. The climate data along with the characteristics of the parabolic trough collectors (i.e. solar module characteristics, efficiency coefficients, incidence angle modifier), the solar field (i.e. number of modules, orientation, series distance, operating temperature, piping characteristics) and the thermal storage result in the potential solar heat gains from the solar collectors. This heat is divided in the heat losses and the useful solar field heat. The later can be exploited by the end user (useful solar heat) in order to cover the energy requirements. Still, there is a small portion of the solar field heat that owing to time and load restrictions cannot be utilized (dump solar heat). The heat load is calculated based on the energy profile of the end user. When the solar system cannot meet the full energy demand, the auxiliary boiler is activated supplying the extra heat required.

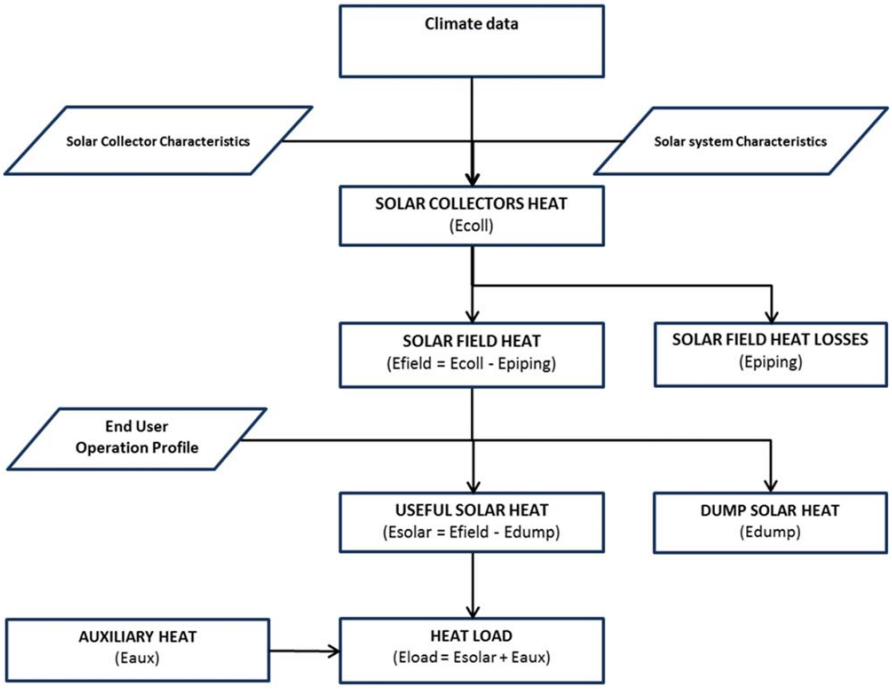

Fig 8: Algorithm for energy simulation of the system

5.2 Energy results

For the specific dimensioning and configuration that analyzed in the previous sections, the simulation energy results are presented below. The graphical representation of the direct normal irradiation (DNI) annual variation, the heat produced by the solar collectors (Ecoll), the solar collectors efficiency ($\eta_{\_coll}$), the solar heat produced by the solar field (Efield), the dump energy (Edump), the useful solar heat of the solar plant (Esolar = Efield – Edump), the solar field efficiency (η_field), the overall solar fraction (RF) and the heat load (Eload) variation are shown in Table 5, 6, 7 and Figure 9 & 10.

Table 5: Summary of energy simulation results

Parameter	Value
Direct Normal Irradiation (DNI)	2 031 MWh
Solar collector heat (Ecoll)	739 MWh
Solar collectors efficiency (n_coll)	36 %
Useful solar heat (Esolar)	655 MWh
Solar Fraction (SF)	42 %
Oil saving	87 333 lt
Reduction of CO_2 emmissions	213 960 kg

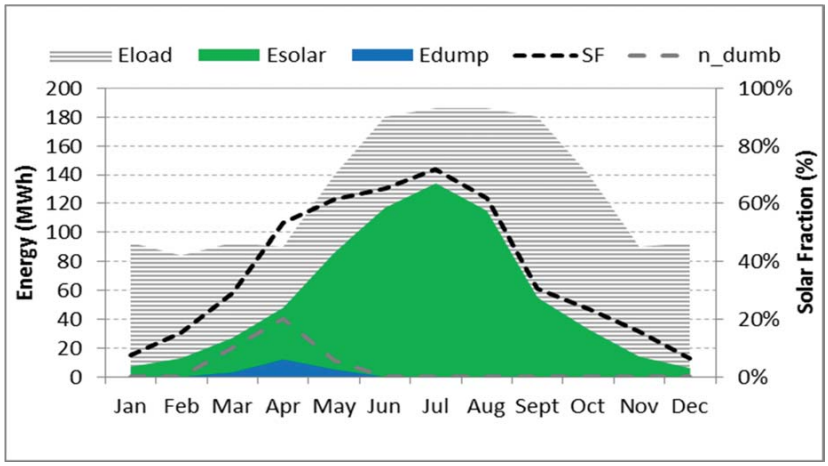

Fig 9: Overall system energy performance

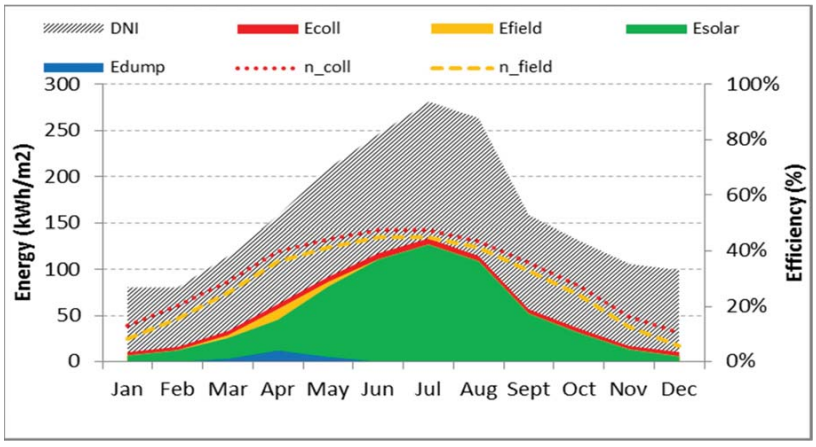

Fig 10: Solar field energy performance

The annual solar irradiation is 2,031 MWh (or 1,923 kWh/m^2), with the solar collectors being able to produce at maximum 739 MWh (700 kWh/m^2) of heat operating with an annual efficiency of 36%. Given the heat losses and the thermal inertia of the solar system, the available solar field heat (Efield) is at maximum 675 MWh (639 kWh/m^2). Moreover, owing to the mismatching of the supply and demand, a small portion of the solar heat cannot be exploited (Edump) and therefore the final heat supplied to the end user (Esolar) equals to 655 (620 kWh/m^2). The solar system achieves solar fraction (SF) of 42%, with the energy savings corresponding to oil savings of 87 tn per year and CO_2 emissions of 213tn.

Table 6 summarizes the energy results in monthly base.

Table 6: Energy simulation results in monthly basis (part I)

	Direct Normal Irradiation	Solar collector heat	Solar field heat	Dump solar heat	Useful solar heat	Auxiliary heat	Heat load	Solar fraction
	DNI	Ecoll	Efield	Edump	Esolar	Eaux	Eload	SF
	MWh	MWh	MWh	MWh	MWh	MWh	MWh	-
Jan	85	11	7	0	7	86	93	8%
Feb	84	17	13	0	13	71	84	15%
Mar	121	35	30	3	27	66	93	29%
Apr	166	66	60	12	48	42	90	53%
May	220	97	91	5	86	54	140	61%
Jun	260	124	117	0	117	63	180	65%
Jul	297	141	134	0	134	52	186	72%
Aug	278	121	115	0	115	71	186	62%
Sep	167	60	55	0	55	125	180	31%
Oct	138	38	33	0	33	106	140	24%
Nov	111	18	14	0	14	76	90	16%
Dec	104	11	6	0	6	87	93	6%
Year	2031	739	675	20	655	899	1555	42%

Table 7: Energy simulation results in monthly basis (part II)

	Direct Normal Irradiation	Solar collector heat	Solar field heat	Dump solar heat	Useful solar heat	Solar Collectors efficiency	Solar Field efficiency	Solar System efficiency	Percentage of dump solar heat
	DNI	Ecoll	Efield	Edump	Esolar	n_coll	n_field	n_solar	n_dump
	kWh/m^2	kWh/m^2	kWh/m^2	kWh/m^2	kWh/m^2	-	-	-	-
Jan	80	10	7	0	7	13%	8%	8%	0%
Feb	80	16	12	0	12	20%	15%	15%	0%
Mar	115	33	28	3	26	29%	25%	22%	10%
Apr	157	63	57	11	45	40%	36%	29%	20%
May	208	92	86	5	81	44%	41%	39%	5%
Jun	246	117	111	0	111	48%	45%	45%	0%
Jul	281	134	127	0	127	47%	45%	45%	0%
Aug	263	115	109	0	109	44%	41%	41%	0%
Sep	158	57	52	0	52	36%	33%	33%	0%
Oct	131	36	31	0	31	28%	24%	24%	0%
Nov	105	17	13	0	13	16%	13%	13%	0%
Dec	98	10	6	0	6	11%	6%	6%	0%
Year	1923	700	639	19	620	36%	33%	32%	3%

5.3 Parametric analysis

The solar system of the previous paragraphs has been used as the base scenario for each parametric analysis as a result of the 35 cases that were examined and analyzed in

Table 8.

Table 8: Variables of parametric simulations

Variable	Minimum	Maximum	Step	Number of simulations	Value of base scenario
Orientation of the parabolic trough collectors	0°	90°	10°	10	0°
Outlet temperature from the solar collectors with constant DT =50K	225 °C	350 °C	25°C	6	250°C
Outlet temperature from the solar collectors with constant inlet temperature of 200°C	225 °C	350°C	25 °C	6	250°C
Solar aperture area	500	2,000	250	7	1056 m^2
Series distance expressed in multiples of the collector aperture width	1	4	0,5/1	6	2.5

5.3.1 Variable 1 - Orientation of the parabolic trough collectors

In this parametric set, the effect of the orientation of the parabolic trough collectors at the system energy performance was investigated. In total 10 cases were simulated from the North-South orientation to the East - West with a step of 10° field rotation.

The optimum orientation is the North – South with annual solar field heat accounts for 639 kWh/m^2 and solar system efficiency of 33%. Deviations up to 20° in the orientation result in small reduction in the system efficiency up to 3%. The reduction is evident in cases with deviation from 30° up to 90° (East-West) in which there is 27% less heat production.

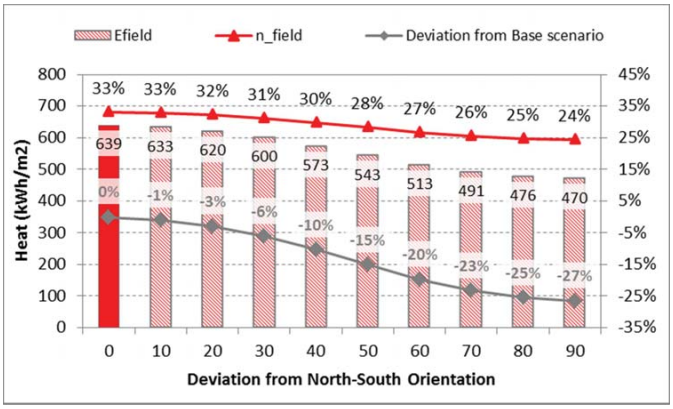

Fig 10: Effect of the orientation at the system energy solar field heat (Efield) production and the solar field efficiency (n_field)

5.3.2 Variable 2 - Outlet temperature from the solar collectors with constant temperature difference

In this parametric set, the effect of the outlet temperature from the solar collectors at the system energy performance was investigated, keeping constant the temperature difference (outlet and inlet in the solar field) DT =50K. In total 6 cases were simulated from outlet temperature of 225 to 350°C with a step of 25°C.

The outlet temperature of 225°C results in 8% increase in the energy production compared to the base scenario, whereas the outlet temperature of 275, 300 and 350°C results in less energy production by 8, 16 and 31% respectively. The significant decrease in the efficiency was expected as the specific parabolic trough model is optimized for operation at around 250°C and in higher operational temperature presents significant reduction in the solar heat production. In system level, the increase of the operational temperature leads to use of hydraulic equipment, pumps and thermal oil of higher temperature and this leads to increased system

cost. On the other hand, the increase of the operational temperature reduces the heat exchanger of the steam boiler and therefore its initial cost. Balancing the above reasons the outlet temperature of 250°C was selected as base scenario.

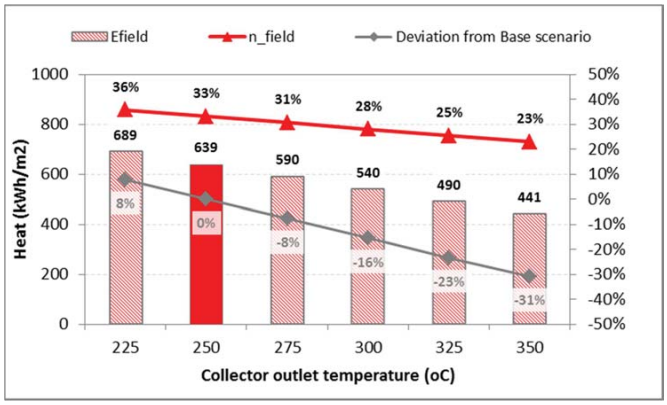

Fig 11: Effect of the Outlet temperature from the solar collectors with constant DT =50K at the system energy solar field heat (Efield) production and the solar field efficiency (n_field)

5.3.3 Variable 3 - Outlet temperature from the solar collectors with constant inlet temperature

In this parametric set, the effect of the outlet temperature from the solar collectors with constant inlet temperature of 200°C at the system energy performance was investigated. In total 6 cases were simulated from outlet temperature of 225 to 350°C with a step of 25°C.

On the contrary to the previous parametric set, the increase in the outlet temperature has limited effect on the system energy performance up to 5%. This is explained by the fact that the mean temperature is kept in lower levels owing to the constant inlet temperature.

Even though, there is limited effect in the energy yield, this case may have crucial effect on the systems economics especially in cases where high thermal storage volume is required in order to smooth high difference between supply and demand. The higher thermal oil operation temperature reduces the storage volume and consequently the system cost. Though, special care is required in the dimensioning of the solar field as the minimum required flow rate should be ensured. On the other hand, the gain from the thermal storage cost should counterbalance the extra cost of the more expensive equipment in the solar field including the thermal oil owing to the higher operation temperature.

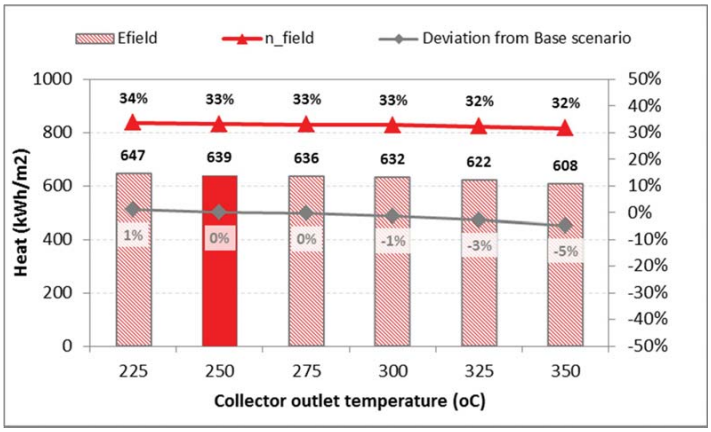

Fig 12: Effect of the Outlet temperature from the solar collectors with constant inlet temperature of 200oC at the system energy solar field heat (Efield) production and the solar field efficiency (n_field)

5.3.4 Variable 4 - Solar aperture area

In this parametric set, the effect of the solar aperture area at the system energy performance was investigated. In total 7 cases were simulated from area of 528 m^2 to 2,112 m^2 with a step of approximately 250 m^2.

Starting from the base scenario of 1,056 m^2, the decrease of the aperture area leads to almost equivalent reduction. For example area of 528m2 which is 50% less than the base scenario (1056m^2) leads to solar fraction of 22% which is reduced by 49%.

On the other hand, the increase of the solar aperture area offers limited increase of the solar fraction. For example the increase of the solar area by 40% (1,478m^2) leads to increase of solar fraction only by 21% (from 42 %to 51%).

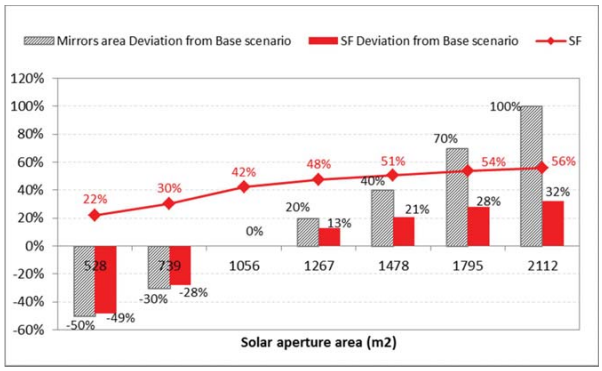

Fig 13: Effect of the solar aperture area at the system solar fraction (SF)

5.3.5 Variable 5 - Series distance expressed in multiples of the collector aperture width

In this parametric set, the effect of the series distance expressed in multiples of the collector aperture width (2.3m) at the system energy performance was investigated. In total 6 cases were simulated from series distance of 1 to 4 multiples with a step of approximately 0.5.

The series distance of 1 multiply (2.3m) leads to ground coverage of 100% but the energy production is reduced by 34% compared to the base scenario of 2.5 (5.75m). Series distances of 2 to 3 multiples have limited effect at the energy production (-4% to 2%) and the ground coverage lays between 33% and 50%. Respectively, the series distance of 4 multiples lead to increase of energy production only by 5% but the ground coverage is 25%.

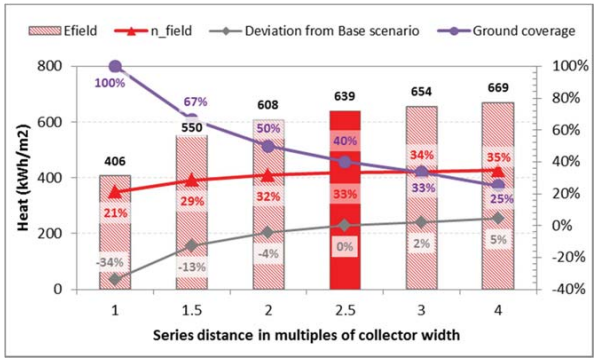

Fig 14: Effect of the series distance expressed in multiples of the collector aperture width at the system energy solar field heat (Efield) production and the solar field efficiency (n_field)

6. Economic assessment

The overall system budget accounts for 573 k€, with the solar collectors absorbing the highest percentage. The figures of the major system components are based on recent quotations while the rest are based on estimations from previous projects.

The main analysis assumptions are the following: 1% / year efficiency system reduction, 4% operation and Maintenance cost,75% conventional system efficiency, 1 €/lt oil cost and 10% increase rate of energy cost.

Based on the above considerations, the simple payback period time is calculated at 7 years.

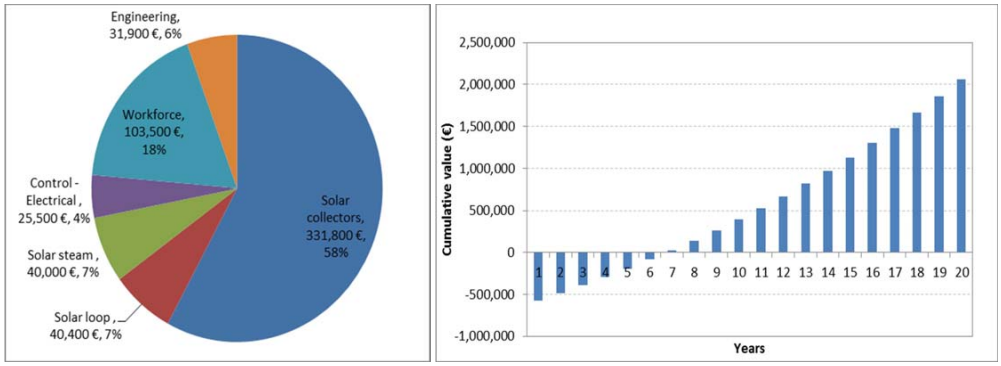

Fig 15: System economic figures

7. Conclusions

Present study attempted to present a techno-economic evaluation of a concentrating solar system for steam production at a food industry in Kalamata. The solar system consisted of the parabolic trough collectors (1 056m^2), the thermal storage (4.7tn of thermal oil) and the solar steam boiler (530kW). The field orientation was North – South, the series distance of the parabolic trough collectors was 5.75m and the thermal oil operation temperature was in the field is 200 - 250^{o}C. A parametric analysis of the above parameters was performed in order to investigate their effect in the system performance.

According to the energy simulation for the base scenario, the solar fraction (SF) was 42%, saving energy of 655MWh per year which corresponds to oil savings of 87.3 tn and 213tn CO_2 emissions. Of the 700kWh/m^2 heat production of the parabolic trough collectors 89% (620kWh/m^2) were actually delivered to the system. Regarding the economic potential of the system, the initial cost was 573 k€, the annual Operation and Maintenance cost was 4%, and the oil cost was 1 €/l, resulting to a simple payback of the system, without any subsidy, of 7 years. Considering the cumulative value at the end of the system lifetime (20 years) the present study indicates that the concentrating solar systems can play an important role at the energy saving in the sector of process heat in Greece.

8. References

Drosou, V., Tsekouras, P., Oikonomou, T., Kosmopoulos, P., Karytsas, C., 2014, The HIGH-COMBI project: High Solar Fraction Heating and Cooling Systems with Combination of Innovative Components and Methods, Journal of Renewable & Sustainable Energy Reviews 29, 463-472

Drosou, V., Karagiorgas, M., Travasaros, C., 2011, The Greek Solar Thermal Market and Industrial Applications, Proceedings of World Sustainable Energy Days, Conference Solar Process Heat, Austria

ECOHEATCOOL Intelligent Energy for Europe Program, 2006, Solar heating for industrial processes.

European Commission, 2009 Market Observatory For Energy, Europe's energy position markets and supply, ISBN: 978-92-79-14175-1

European Union, 2013, Eurostat Pocketbooks, Energy, transport and environment indicators, ISBN 978-92-79- 33105-3

Greenius software, 2016, Version 4.3.1 http://freegreenius.dlr.de

Tsekouras, P., Christodoulaki R., Tsekouras, G., Lamaris,V., Lamaris,P., 2014, Techno-economic assessment of a concentrating linear Fresnel system for steam production, IHT – 10th Conference on Renewable Energy Sources, Greece

Tsoutsos, T., Karagiorgas, M., Zidianakis, G., Drosou, V., Aidonis, A., Gouskos, Z., Moese, C., 2009, Development of the applications of solar thermal cooling systems in Greece and Cyprus. Fresenius Environmental Bulletin, 18(7b), 1367-1380

Conference Proceedings

EuroSun 2016

Palma de Mallorca (Spain), 11 – 14 October 2016

PARA-RUBBER SHEET DRYING WITH THE COMBINED SOURCES OF SOLAR ENERGY AND SOLAR POND

Sura Tundee * and Kanchit Rongchai

Department of Mechanical Engineering, Faculty of Engineering, Rajamangala University of Technology Isan Khon Kaen Campus,Thailand.40000 Tel. +66-43-336371 Fax. +66-43-237483

*Corresponding Email:suratundee@hotmail.com

Abstract

The objectives of this research was to study the efficiency of two para - rubber sheet drying methods; solar drying and solar drying combine solar pond. The solar energy house of 1.8 x 2 x 3 m^3 with the capacity of 100 sheets was constructed in Amphoe Mueang Khon Kaen district,Khon Kaen province Thailand, in conjunction with the solar pond which was 8 meters in diameter and 2.5 meters in depth. In order to evaluate energy using aspect, the energy using studies were divided to 2 systems. System I was only solar drying. System II was using solar drying at day time and solar pond at night time. The initial humidity of para-rubber sheet was about 29 - 33% respectively. The experimental results showed that the temperature distribution in the solar energy house was uniform. The night time average inside temperature solar energy house was higher than that outside 3°C, 10°C for system I, II respectively. The solar energy house was that system I required the longest time 120 hours while system II required the shortest time 84 hours. Moreover, it was found that, the humidity of para-rubber sheet range was about 0.5 – 1.25% after drying.

Keywords:*solar energy; parabolic dish; Thermoelectric,*

1. Introduction

Thailand is currently the largest natural rubber (NR) producing and exporting country in the world. Natural rubber is commercially produced in four forms: ribbed smoked sheet (RSS), block rubber, rubber concentrated latex, and miscellaneous other forms. The factors affecting the drying of rubber sheets are temperature, velocity and humidity of the drying air. The drying time can be reduced and the quality of the rubber sheets can be improved. (Prasertsan et al., 1991;Wattana et al., 2005)

Rubber sheet drying, which is one of the most important parts of the natural rubber industry, can be divided into two types according to the processes of drying (Office of Industrial Economics ., 2013) According to the survey of rubber sheet smoking factories, (Prasertsan et al., 1991;Wattana et al., 2005) in the southern part of Thailand, the quantity of rubber tree fire-wood used to smoke rubber sheets each year is approximately 229,994 m^3 (1 m^3 of firewood = 600 kg). In other words, such vast amount of firewood can generate heat to dry rubber sheets at 226.8 GJ. Therefore, it follows that costs associated with drying can be saved if energy consumption can be reduced. (Beymayer et al., 1993) introduced the solar air heater to the rubber sheet smoking system. It was found that the drying rate was faster; the normal smoking took process took 12 days, but only 5-6 days with the solar air heater. (Nilchuewong et al., 2012) studied rubber sheet drying with hot air and a conservatory. Their results showed that the drying rate of the hot air drying was better. However, the

doi:10.18086/eurosun.2016.02.16 Available at http://proceedings.ises.org

energy consumption of the hot air drying ranged from 8–20 MJ/kg of water evaporated. The quality of the rubber sheets from both experiment conditions passed the local market criteria (Grade 1–3) and the yellowness of dried rubber sheets proportionally varied with drying temperatures.

Many previous studies have used solar energy to dry raw rubber sheets during daytime but there has been no reports of harnessing solar energy for night time drying. This research has investigated a novel method of using solar energy to dry rubber sheets both day and night. The rubber drying plant is designed to combine heat from solar energy and a solar pond in order to reduce the amount of time required in the production process for rubber sheet drying. The drying plant has additionally provided good quality rubber sheets with low moisture contents and desirable appearance. The current paper presents the design and testing of the new system. Results are then discussed and interesting conclusions are made.

1.1 Solar pond

A solar pond is a device that collects and stores solar energy. It can operate continuously throughout the year. Solar ponds collect energy from solar radiation. The radiant heat is collected at the bottom part of the pond and this amount of heat can be used later. The temperature difference between the top and the bottom of the solar ponds can be as high as 50–60 °C. Thermal energy stored in the solar pond can be utilized for heating of buildings (hydrophonic), power production and desalination purposes (Akbarzadeh et al., 2005).

The structure of a solar pond is shown in Fig. 1**.** It is noted that the size of the pond depends on the aim of energy use such as water heating, crop drying, desalination and electrical power generation. There is an amount of saline inside the pond. Generally, the saline solution is sodium chloride or magnesium chloride solution. The pond can be divided into three regions namely the upper convective zone (UCZ),the middle non-convective zone (NCZ) and the lower convective (LCZ).

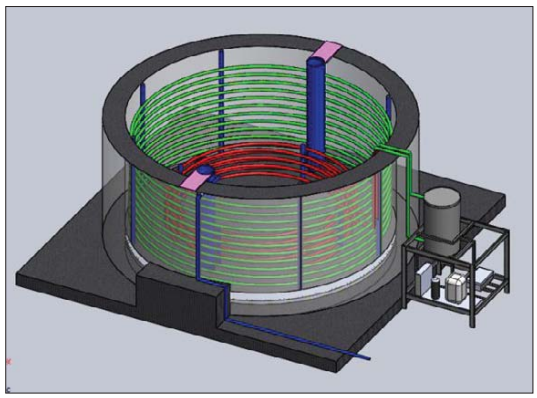

Fig. 1: Schematic of the solar pond

The upper convective zone is located at the top of the pond. The temperature of this zone is close to ambient temperature. The salt concentration is also near that of clean water. Due to the contact between the top layer of the UCZ and the ambient air, there is inevitable energy loss from convection and evaporation.

The middle zone, the NCZ, is sandwiched by the UCZ and the LCZ. In this zone, the salt concentration changes with depth measured from the interface of the upper convective zone and non-convection zone. An increase of depth from this interface results in an increase in salt concentration. The function of this zone is to inhibit heat convection away from the LCZ. However, there is an optimal thickness such that heat can be

transferred from the UCZ downwards without significant heat loss, yielding the high efficiency of energy storage inside the pond (Andrew et al., 2005).

The bottom zone, the LCZ, has the highest salt concentration which is also uniform. When the pond receives heat from solar radiation, the heat penetrates through the upper and non-convection zones to be stored at the LCZ. Thus, it is clear that heat energy is extracted from this zone for useful applications.. Two methods have been used to extract energy from solar ponds. Firstly, fresh water or glycol is circulated through a submerged heat exchanger in the pond. This method is limited by heat transfer by natural convection within the lower convective zone, and the surface area of the submerged heat exchanger can be determined accordingly. Secondly, brine from the lower convective zone is circulated through an external heat exchanger installed outside the pond. This brine-withdrawal method requires less heat exchanging surface, but the flow-distribution system must be carefully designed to avoid erosion of the non convective zone. In the present research it is shown that by combining thermosyphons and thermoelectric cells, it would be possible to utilize the temperature difference existing between the top and the bottom of a solar pond and produce electric power in a fully passive way, i.e. no moving parts. In such a scheme, the heat is transferred by the thermosyphon from the lower region of the pond to the 'hot' side of thermoelectric cells which maintains a good thermal contact with the top of the thermosyphon tube. The 'cold' sides of the cells are in contact with the cold environment of the top layer of the solar pond (Tundee et al., 2010; Randeep et al., 2011).

2. Experimental setup

The experimental setup was composed of a solar pond and a rubber drying plant as schematically illustrated in Fig.2. The solar pond, made of concrete, was a cylinder with a diameter of 800 cm, height of 250 cm and the pond's wall's thickness of 25 cm. Within the solar pond, two sets of heat exchangers (dubbed Set 1 and Set 2) were installed. Set 1was installed within the lower convective zone and Set 2 was installed at the inner wall of the solar pond 50 mm away from the wall. the temperature output had reached a steady state, K-type thermocouples ($\pm$0.5 °C accuracy) were also installed in the solar pond at an interval of 0.1 m from the bottom floor to the upper convection layer in order to measure the heat accumulated within the solar pond. Data is collected every 1 minute using a temperature recorder Yokogawa, DA100$\pm$0.1°C with 24 channels and subsequently stored in a data acquisition device for further analysis. 100 sheets of rubber were stored in the rubber drying plant which was 1.8 × 2 × 3 m in size. The tests were carried out three times by using three flow rates of water from the solar pond to the heat exchanger, which were 3, 2.5 and 2 litters per minute respectively.

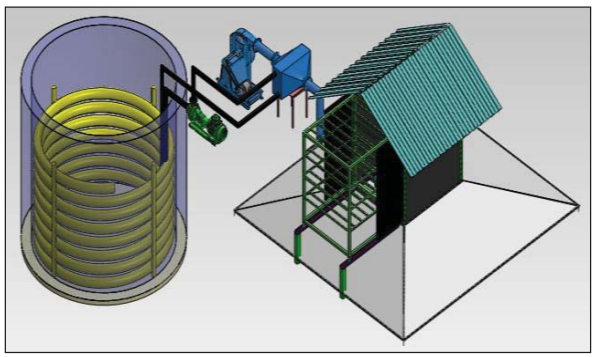

Fig. 2 : Schematic view of the solar pond and the heat extraction system.

3. Results and discussions

3.1 The effect of solar radiation

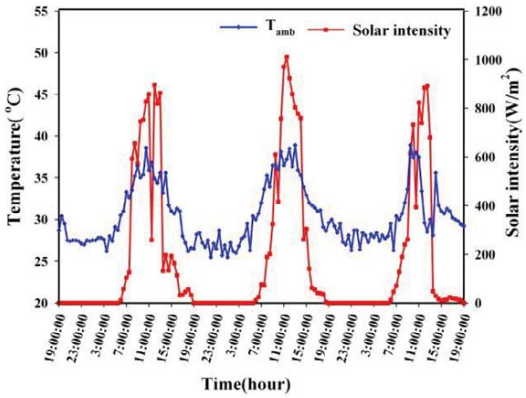

Fig. 3: Time variation of solar radiation on the test site over the three days of test duration.

Fig. 3 shows the time-varied solar radiation during the experiment using a pyranometer measuring the solar radiation in experiment area. The data logger was used to record radiation values every two minutes and average values were calculated every 30 minutes, as shown in Fig. 3 by collecting data over three days during the drying period . It can be seen that the thermal radiation values changed due to changeable day-to-day weather factors including cloudiness, sunlight or rain. Having many clouds in the sky on the third day of the experiment, the radiation value was noticeably reduced.

3.2 The density of solution in the solar pond

Fig. 4 shows the density of the solution in the solar pond, after salt had been added for 2, 30 and 60 days. The density value of the solution remained constant throughout the two-month period. The density profile shows is divided into three layers. The top layer, the UCZ has a thickness of 20 cm and the density of the solution is similar to water. It is followed by the NCZ. The density value of the solution increases steadily downwards and becomes constant at the onset of the LCZ. The thickness of the NCZ was 150 cm. The final layer, the LCZ, has a thickness of 80 cm. Its density is constant throughout the layer, similar to the saturation value of saline solution.

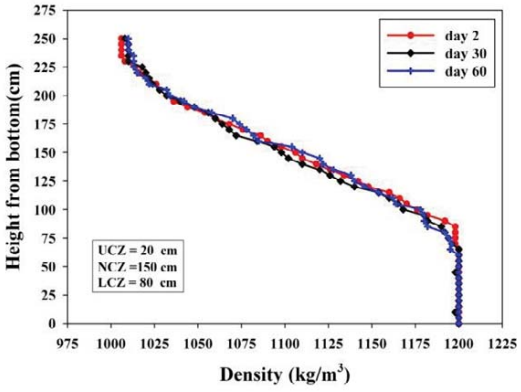

Fig. 4 : Density profile of the salinity gradient solar pond located at RMUTI Isan in Summer.

3.3 Internal temperature in the solar pond

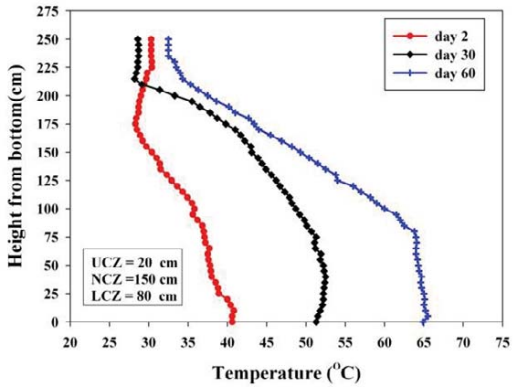

Fig. 5: Temperature profile of the salinity gradient solar pond located at RMUTI Isan in summer.

Fig. 5 shows the internal temperature of the solar pond, measured on the same day as the density profile in Fig.4. The temperature of the solar pond was measured at every 5 cm from the LCZ at the bottom of the solar pond to the NCZ and the UPZ. The figure shows that when the solution had been added to the pond for two days, the internal temperature of the solar pond in the layer of LCZ was approximately 41 °C, and the value decreases with the height from the solar pond's floor. The temperature in the UPZ was approximately 29 °C, close to ambient temperature and uniform through the entire layer. When the test duration of 2 months days had elapsed, the temperature in the layer of LCZ reached approximately 65 °C, which gradually reduced with height above 80 cm from the floor to the bottom boundary of the UPZ.

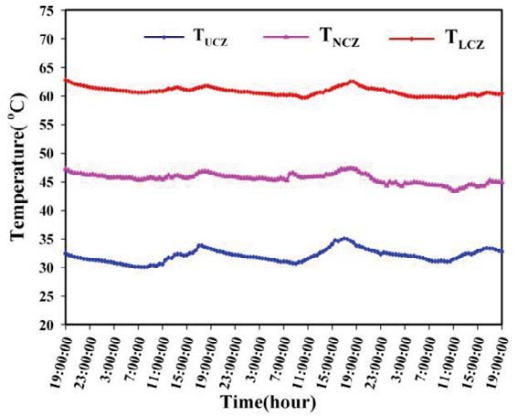

Fig. 6: Average temperature in the solar pond at the UCZ, NCZ and LCZ.

Fig. 6 shows average temperature in the solar pond at the UCZ, NCZ and LCZ. Thermocouples were installed in the solar pond with a distance of 5 cm from the bottom of the solar pond up to the upper layer. The average values were calculated from five measure points in the 20-cm-thick UCZ. . The temperature in the UCZ was similar to the ambient value. It can be seen that during daytime, when the temperature of the atmosphere was high, the three average temperatures increased accordingly. At night, when the atmospheric temperature dropped, the temperature in the UCZ dropped as a result. By contrast, the average temperature of the NCZ exhibited small reduction or increase during the night and daytime respectively. In the rubber drying experiments, during the period from 6:00 AM to 18:00 PM, thermal energy came from the sun directly. From 18:00 PM to 6:00 PM, stored energy in the solar pond is extracted for drying, hence a steady night time

temperature drop of the solar pond in Fig. 6. The temperature in the solar pond increased again upon receiving daytime solar energy.

3.4 The features of rubber sheet in the rubber drying plant

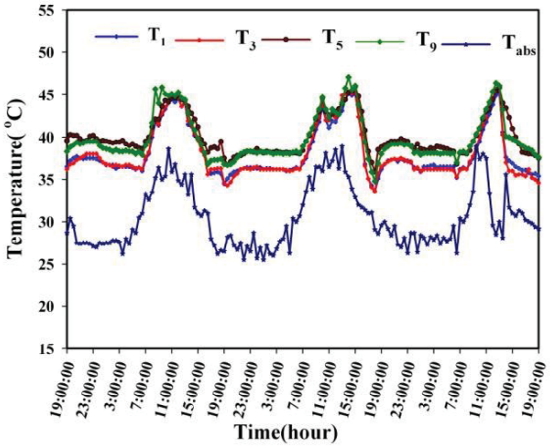

Fig. 7: Time-varied ambient temperature and temperature in the rubber drying plant measured at 4 locations T1, T3, T5 and T9.

Fig. 7 shows the temperature in the rubber drying plant at four points in the rubber drying plant. There were four measurement locations in the drying plant: T1 and T3 were installed at the top of the plant whereas T5 and T9 at the bottom. Ambient temperature was also recorded. The figure shows similar values amongst all the four locations, which changed in accordance with ambient temperature. Under sunlight, the temperature rise in the rubber drying plant above the atmosphere varied around 15-20 °C during the day, and around 10 °C during the night when the rubber drying plant was heated by the solar pond.

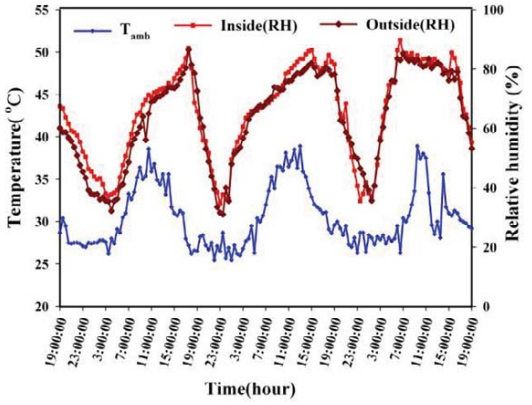

Fig. 8: The humidity values in the rubber drying plant.

Figure 8 shows humidity values in the rubber drying plant, It can be seen that humidity in the rubber drying plant follows the temperature outside. When the outdoor temperature increased, the indoor humidity increased. It can be observed from 15.30 PM, the humidity in the rubber drying plant was about 25-38 percent. During the day, the humidity outside the plant was about 23-35 percent. During the night, the humidity in the rubber drying plant increased because the temperature outside the plant decreased, thereby lowering the saturation level and consequently increasing relative humidity. Humidity in the drying plant at 04:30 AM was about 87-82 percent, but 80-84 percent outside.

Fig. 9: Features of the rubber sheets (a) before and (b) after 2 days of drying.

Fig. 9 shows the features of the rubber sheets before drying and after drying for 2 days. The rubber sheets were installed on the racks in the drying plant. The rubber sheets before drying were raw rubber sheets. They were pre-dried in the air to drain before loading into the drying plant. 100 rubber sheets (maximum capacity of the plant) were loaded in the experiment where they were placed on nine panels. Eight panel had 12 rubber sheets, but the ninth panel had four. The weight of a rubber sheet before drying was about 1 kg.

After drying for two days, the rubber sheets appear pale yellow, clear but with some white partially-wet patches.

Fig. 10: The features of rubber after drying for three days in solar drying chamber

Fig. 10 shows the features of rubber sheets after drying for three days in the drying chamber, the rubber sheets appeared clear, pale yellow and evenly-coloured which would have been difficult to achieve by smoking method. When subjected to further drying, the moisture contents of the rubber sheets were unchanged, rendering them suitable for discharge after only 3 days of drying.

4. Conclusions

The solar drying chamber for para rubber sheets that works in conjunction with the solar pond was investigated. During daytime, the drying plant uses solar energy for drying and then thermal energy extracted from the solar pond at night. The system has been shown to elevate the temperature of the rubber drying plant from ambient by 10 °C at night, and shorten the length of drying time by two days compared with drying without a solar pond, and faster by up to 6 days compared with typical sun drying in the open air. The rubber sheets that passed through the current drying process appeared light yellow, evenly-coloured and without any black dots or air bubbles which are desirable characteristics of high-grade rubber sheets.

5. Acknowledgments

The authors would like to express their appreciation to the Rajamangala University of Technology Isan and Research & Development Institute, Faculty of engineering Rajamangala Rajamangala University of Technology Isan Khon Kaen Campus for providing financial support for attending International Conference on Solar Energy for Building and Industry.

6. References

Akbarzadeh, A, Andrews, J, and Golding, P., 2005. Solar Pond Technologies: A Review and Future Directions, Chapter 7, Advances in Solar Energy, EARTHSCAN.

Andrew, j., Akbarzadeh, A., 2005. Enhancing the thermal efficiency of solar pond by extracting heat from the gradient layer, Solar Energy, Vol.85, 371 – 378.

Breymayer, M., 1993. Solar-assisted smokehouses for the drying of natural rubber onsmall-scale Indonesian farms, Renew. Energy 3, 831–839.

Ninchuewong, T, A. Ekphon, S. Tirawanichakul, Y. Tirawanichakul., 2012. Drying ofair dried sheet rubber using hot air dryer and solar dryer for smallentrepreneurs and small rubber cooperatives, Burapha Sci. J. 17, 50–59.

Office of Industrial Economics., 2013.Introduction to rubber industry and rubberproducts. Wongsawang publishing and printing Ltd.

Prasertsan,S, G. Prateepchaikul, N. Coovattanachai, P. Kirirat, S. Nakgul, P.Honghirunrung, P. Ngamsritragul., 1991. Wood utilization in the smoked rubberindustry: Southern Thailand case study, RERIC, Int. Energy J. 13 (1) 19 – 28.

Randeep Singh, Sura Tundee, Aliakbar Akbarzadeh., 2011. Electric power generation from solar pond using combined thermosyphon and thermoelectric modules, Solar Energy, Vol.78, 704 – 716.

Tundee, S., Terdtoon, P., Sakulchangsatjatai, P., Singh, R., Akbarzadeh, A., 2010. Heat extraction from salinity-gradient solar ponds using heat pipe heat exchangers. Solar Energy 84 (9), 1706–1716.

Wattana, T, W. Chaison, Smoked rubber sheet technology and designingsmoking chamber save energy, Technique 224 (2005) 161–172.

Conference Proceedings

EuroSun 2016
Palma de Mallorca (Spain), 11 - 14 October 2016

Analysis of results of a parabolic concentrator's pipe receiver to heat air for drying process of black tea in Cusco, Peru

Sandra Vergara[1], Miguel Hadzich[1]

[1] Sección Ingeniería Mecánica, Pontificia Universidad Católica del Perú, Lima (Perú)

Abstract

The objective of the design is to solve the problem of shortage of fuel for drying process in a black tea conditioning factory, through the use of solar thermal concentration with the adaptation of the receiver tube of a linear parabolic concentrator for heating air. This is part of a pilot project to develop and implement in tea enterprise AGROINKA SAC a prototype cogeneration system with solar thermal energy, made of 6 lines of 10 concentrators (60 linear concentrators). The company AGROINKA is in a rural area of the region of Cusco. It has little access to other possibilities of thermal energy resources and technologies for different processes of his production chain of black tea. It is an area dedicated to the processing of tea to supply 80% of the market in the country and 750 families depend on tea production. This paper describes the behavior of hot air in the receiver pipe along a line of 10 concentrators. The results of this paper correspond the winning project of the National Fund for Research and Development Competition for Competitiveness – FIDECOM (for its acronym in Spanish); entitled "Development and integration of a cogeneration system with solar thermal energy for processing of black tea in the Cusco region" 210-FINCyT-FIDECOM -PIPEI-2012.

Keywords: thermal solar energy, drying, tea, Cusco, rural sector, productive use

1. Introduction

The Support Group for the Rural Sector (GRUPO PUCP) is an operating unit of the Department of Engineering at the Pontificia Universidad Católica del Perú (PUCP) founded in 1992. We work to develop appropriate technologies using renewable energy for the rural sector. The project "Development and integration of a cogeneration system with solar thermal energy for the processing of black tea in the Cusco region" was developed in partnership with the company AGROINKA of Cusco.

The processes for obtaining black tea from the Camellia sinensis's leaves are: withering, by leaving the leaves rest for a day in a dry and dark place; cutting, where the leaves are crushed to initiate the oxidation process; fermentation, which gives the black color to the black tea; drying, to remove the moisture and to stop fermentation; and classification.

For the drying process the enterprise uses industrial furnaces, which are fed with wood, in low energy efficiency, resulting the low productivity and high consumption of fuelwood. Then hot air is injected at a temperature between 80 °C and 90 °C to the drying chambers. It has been developed and implemented linear parabolic concentrators to replace a percentage of wood used in the drying process. This paper describes the behavior of hot air in the receiver pipe with 5" diameter along a line 10 concentrators.

2. Project

As mentioned, the project was developed in partnership between GRUPO PUCP and the company AGROINKA. Tea or Camellia Sinensis is originally from Asia but today it can be found in tropical and subtropical regions around the world. Depending on the processing of Carmellia Sinensis' leaves, many

doi:10.18086/eurosun.2016.02.08 Available at http://proceedings.ises.org

types of tea can be obtained with different scents and flavors.

The area has a diverse agriculture by the various ecological floors and microclimates. They can be found in a 2.5 hours' journey from the mountain "Veronica" (4316 m) up to the low jungle in the district of Quillabamba (1050 m). The town of Huyro, where the project took place, is located in the district of Huayopata in the province of La Convención. To reach the town you need to make a 3.5 hours trip from the city of Cusco. According to coordinates, the location is on the south latitude 12 ° 0'23 " S (-13.01), West Longitude: 72 ° 33 '. 25.8 "W (-72.56) and is located at an altitude of 1562 meters above sea level. This area has been identified with an excellent tropical climate for tea production, as well as other products like coffee, cinnamon, fruits, etc.

The company uses 400 truckloads of firewood per year, equivalent to 4000 m3 of wood at a cost of 5.00 soles (approximately $1.5) per kg. For the drying process they use 2 furnaces, which are fed with firewood for heating the air. Then this air is injected at temperatures between 80° C and 90° C to the drying chambers (one fluidized bed and one orthodox). This process reduces the moisture of the tea leaves and stops the fermentation process which gives the characteristic color to the black tea.

The company doesn't have access to other fuel for thermal energy. But they are also aware that its high consumption generates environmental impacts like pollution and deforestation, affecting the landscape, the biodiversity, soil fertility and by increasing the likelihood of landslides.

The design was implemented using a clean and sustainable technology that serves as an alternative to firewood. This prototype system consists of a solar thermal power cogeneration composed by 3 modules of 20 linear concentrators (60 linear concentrators in total). The system is integrated to one of the furnaces which permits the use of hybrid system. Unlike other solar thermal energy, this design does not use a heat exchanger and the air is injected directly into the oven. There's no need to storage the hot air, as the company works up to 3 shifts during the year.

Fig. 1: The solar concentrator's installation in Yanayaco, Cusco, Perú

Fig. 2: Panoramic view of the solar concentrator's installation in Yanayaco, Cusco, Perú

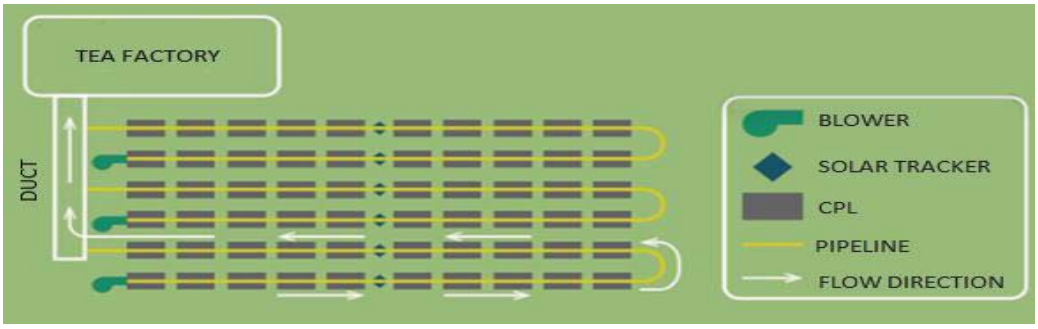

Fig. 3: The solar concentrator's diagram in Yanayaco, Cusco, Perú

Each linear concentrator used anodized aluminum for reflected material and has made with a specific geometry presented in showed in the next table. The 5" pipe was made of carbon steel with a matt black paint coating.

Tab. 1: Concentrator Geometry (Vergara Dávila & Hadzich Marín, 2014)

Description		Units
Semi straight side length	0.530	m
Concentrator Height	0.201	m
Diameter of the pipe	0.127	m
Concentrator length	2.4	m
Concentrator aperture size	2.544	m
Concentrator aperture angle	3.0639	rad
Semi-apparent angle of the sun equal to 16'	0.00465	rad
Pipe Height (different than focus line height)	0.2216	m

3. Methodology

To cover the demand of thermal energy, linear parabolic concentrators were used to generate hot air with the air flowing through the receiver tube making possible working without a heat exchanger. The innovative part of the system is that the air functions as the fluid that flows through the pipeline. However, this carries some difficulties, such as the size of the receiver pipe used which as being too big, it cannot work with a glass tube as insulation. The different air behaviors due to speed flow of the air is also a complication dealt with in this project.

We tested a line of 10 concentrators that reaches the approximate distance of 26 meters. We took data from the inside of the receiver pipe to obtain the temperature curve for the air at different speeds and these tests were repeated with and without insulation on the top of the pipeline.

To obtain information from the behavior of air in the receiver pipe without and with insulation, 11 holes were made along a line of 10 concentrators, where a bimetallic thermometer was introduced.

Additionally, during the test stage, 2 more holes were made in a second line or returned line from the receiver pipe (10 concentrators). The first one at the start point of second line's receiver pipe and the second one at the end of the second line receiver pipe or entry point to the duct to tea factory.

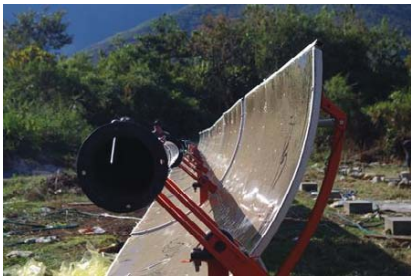

Fig. 4: Section view of the receiver pipe

The Weisz's bimetal thermometer was used. It has a temperature range of 10 ° C to 150 ° C.

Fig. 5: Weisz's bimetal thermometer

On parallel to the temperature's measurement, the beam irradiance was measured. This measurement was made using an irradiance measurer by the brand R & S Renewable Energy Systems. First, we measured global irradiance and subsequently diffuse irradiance. The difference between the two irradiances gives us as a result the beam irradiance.

Fig. 6: R&S Renewable Energy Systems's irradiance measurer

Kestrel brand equipment was used for measuring the air velocity inside the receiver pipe. This was placed at the end of the pipeline.

Fig. 7: Kestrel's air speed measurer

4. Results

Through data collection, temperature curves could be obtained and also the delta of temperature between each sampling point of the receiver pipe with and without insulating varying the air velocity.

Initially air measurement was performed with a speed of 3 m s-1 inside receiver pipe without insulation.

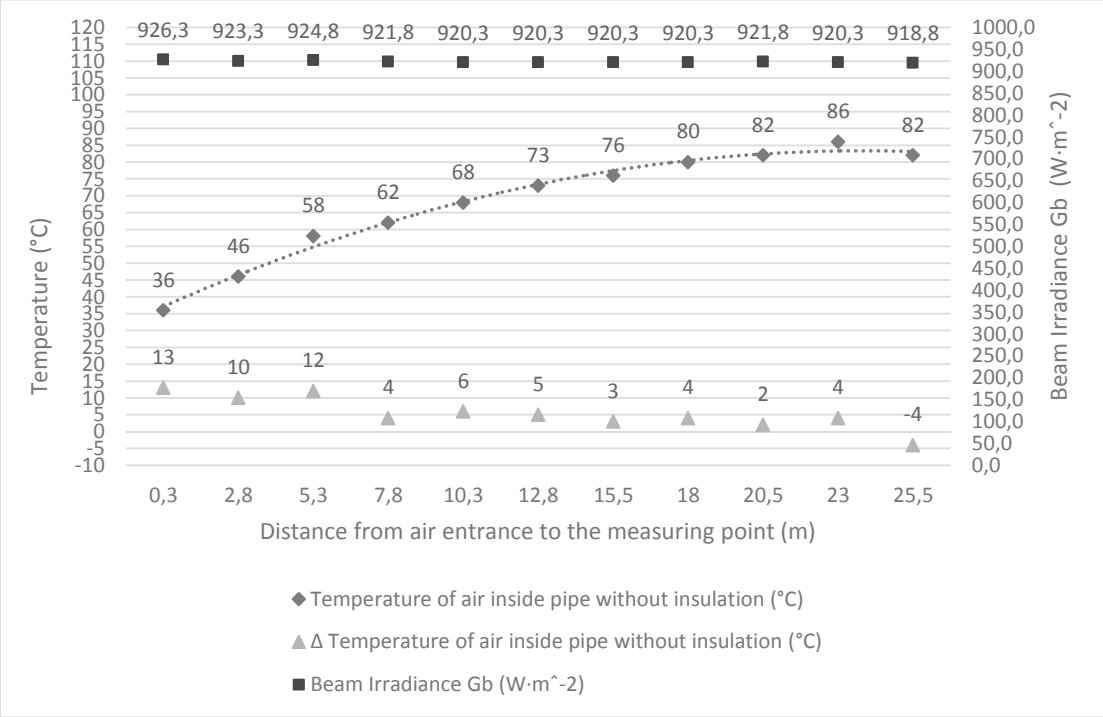

Fig. 8: Behavior of air into the receiver pipe without insulation to 3 m s^{-1}

It can be seen in Fig. 8, that in the first meters the delta of air temperature is higher subsequently it decreases. At 23 m in the receiver pipe the air temperature drops from 86 ° C to 82 ° C. The maximum temperature that air could reach was 86 ° C into the pipe.

Making use of a thermal imaging camera, images of the receiver pipe were taken. As shown in Fig. 9 the temperature is higher in the area where the receiver tube receives sunlight reflected by the concentrators, however, the temperature at the top reached around 60 ° C.

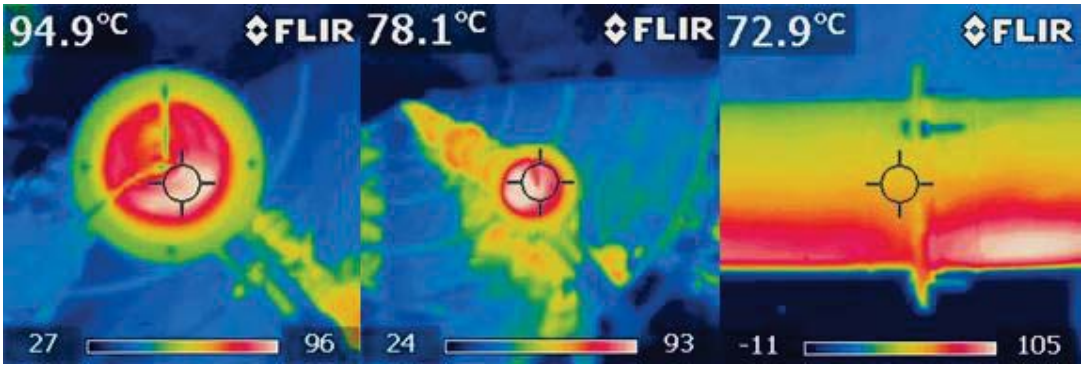

Fig. 9: a) sectional view of the receiver pipe without insulation; b) view of receiver pipe without insulation ; c) side view of receiver pipe without insulation

Afterward it was considered to place on the top of the receiver pipe of 5" diameter, a fiber insulation glass with a top cover in case of rain. The tests were repeated with a speed of 3 m s-1.

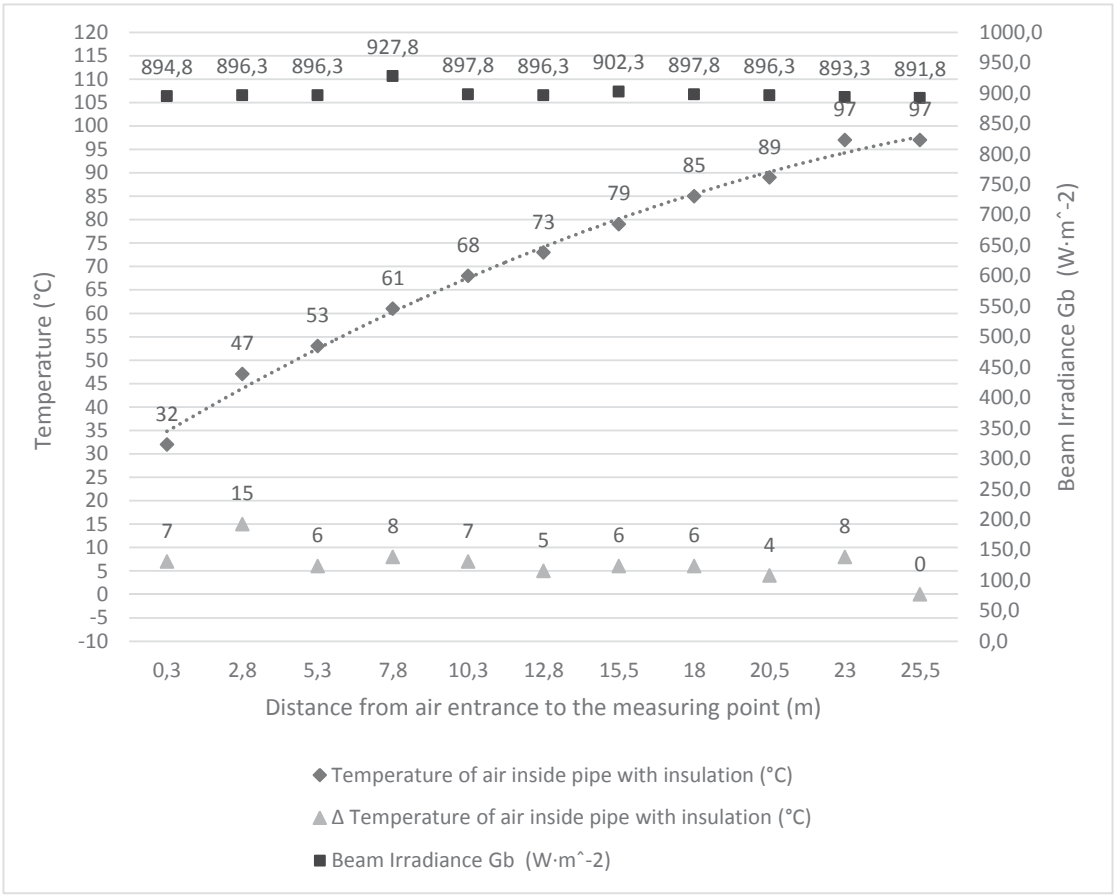

Fig. 10: Behavior of air into the receiver pipe with insulation to 3 m s^{-1}

Can be seen in Fig. 10 in the first meters, the delta of air temperature is higher. However delta of air temperature remains constant along the receiver pipe. As in the previous case, from 23 m of the receiver pipe, air temperature decreases. The maximum temperature that air reached was 97 ° C into the pipe.

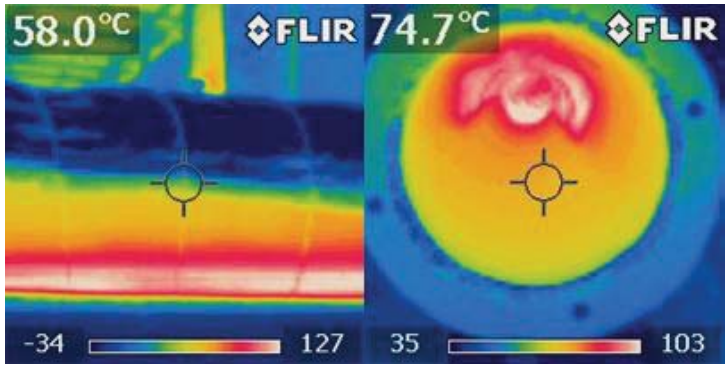

Fig. 11: a) lateral view of the pipe with insulation; b) sectional view of the receiver pipe with insulation

It can be seen in Fig. 11 the thermographic image of lateral and sectional view of the receiver pipe after fitting with insulation.

For better comparison of the behavior of air temperature, both insulated and non insulated receiver pipe were integrated in Fig. 12.

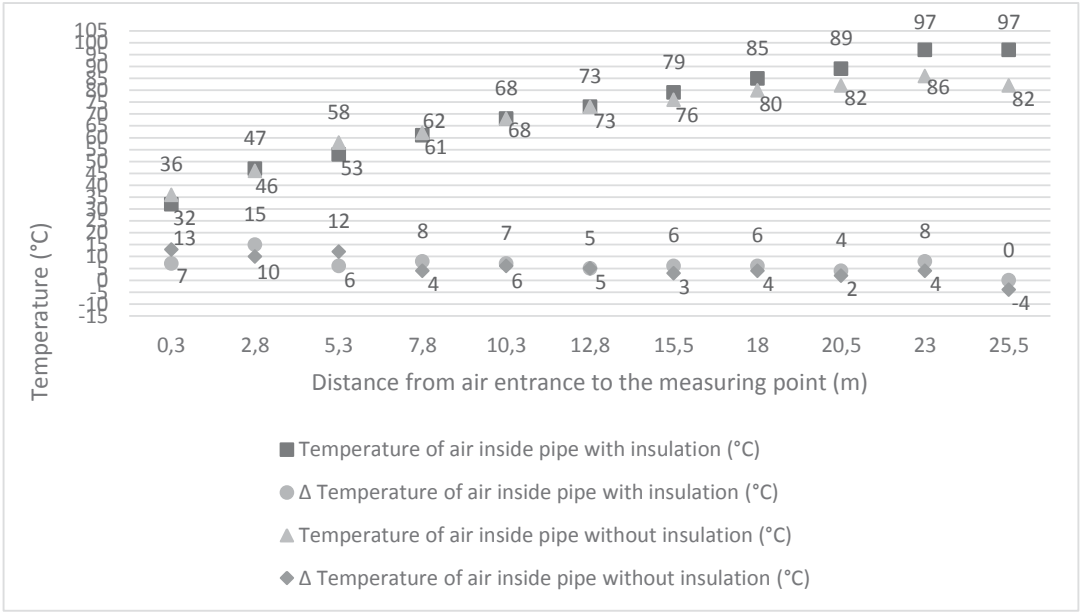

Fig. 12: Behavior of air into the receiver pipe receiver with and without insulation to 3 m s^{-1} air velocity

As shown in Fig. 12 from the 15.5 m of the receiver tube, the air in the insulation system reaches higher temperatures.

It's important to mention that in the second line, for a velocity of 3 m/s with insulation, we obtained in the start point of the second line's receiver pipe (first hole) a temperature of 88°C. This is because, the pipe curve that connect first line with second line has a heat loss of 10 ° C. Meanwhile, in the end of the second line receiver pipe (second hole) or entry point to the duct, we archived a temperature of 108°C.

This showed us, that total delta temperature of air on the first line with 3 m/s and insulation is around 65°C, meantime that total delta temperature of air on the second line with 3 m/s and insulation is around 20°C. In consequence, due to economic and financial viability the rest of testing stage was focused on the first line.

The same procedure was repeated with the receiver pipe insulated by varying the air velocity to 8.5m s^{-1}. This variation was conducted by opening the gate of the blower air flow.

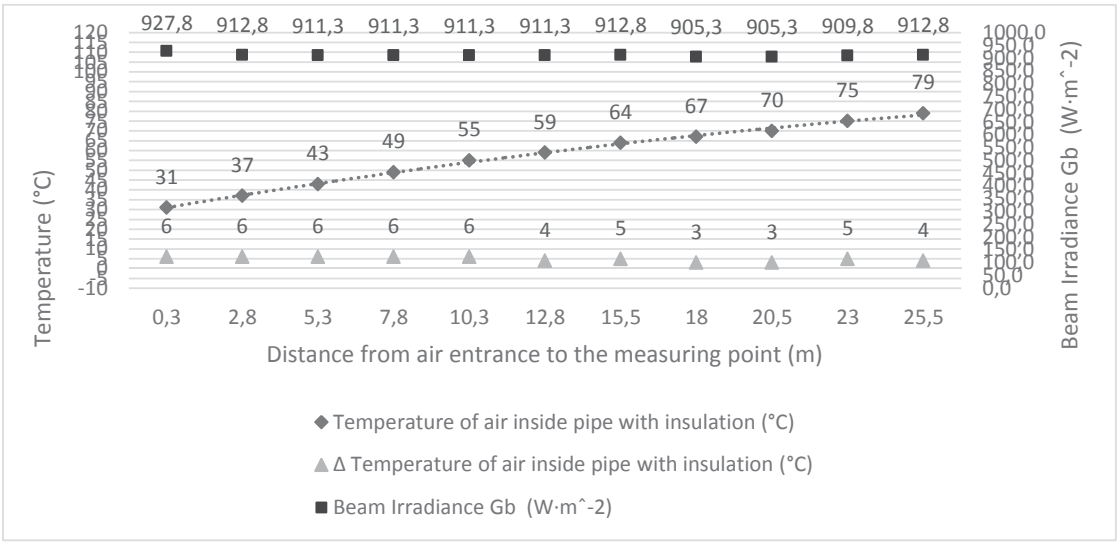

Fig. 13: Behavior of air into the receiver pipe with insulation to 8.5 m s^{-1}

It can be seen in Fig. 13 that the delta air temperature is constant from the start, along the receiver pipe. It could reach 79 °C of air temperature inside the pipe with a speed of 8.5 m s^{-1}.

Finally, the same procedure was repeated with the receiver pipe insulated varying the air speed to 14m s^{-1}. This variation was conducted by opening the gate of the blower air flow.

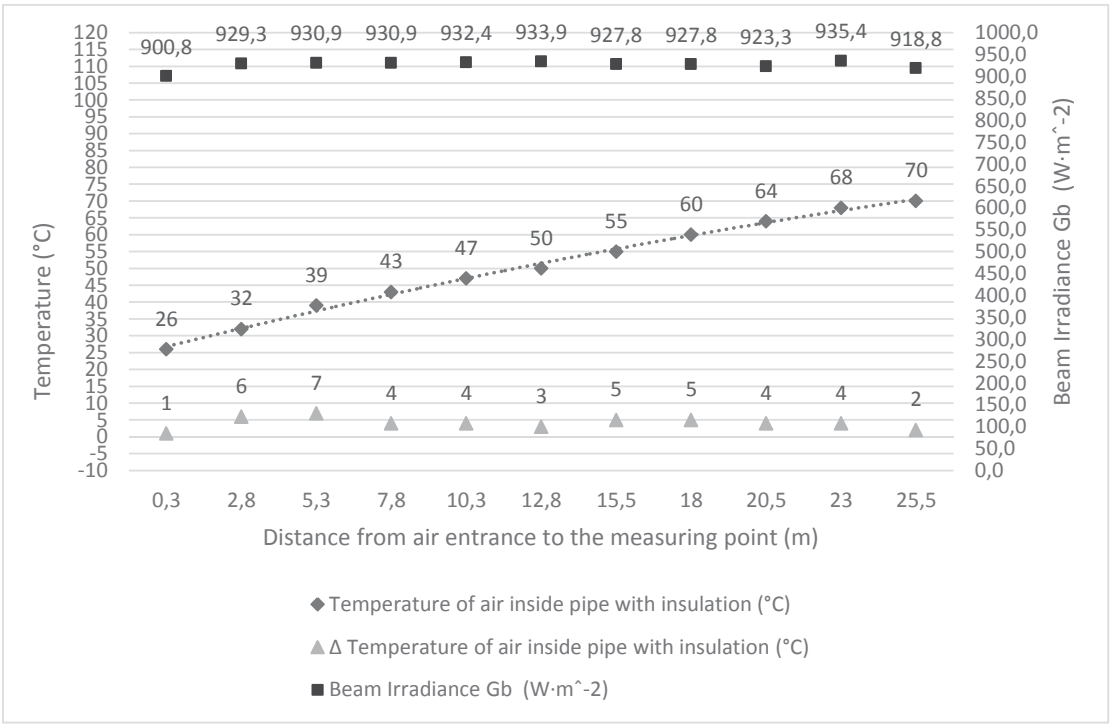

Fig. 14: Behavior of air into the receiver pipe with insulation to 14 m s^{-1}

It can reach 70 °C of air temperature inside the receiver pipe with a maximum speed of 14 m s^{-1}.

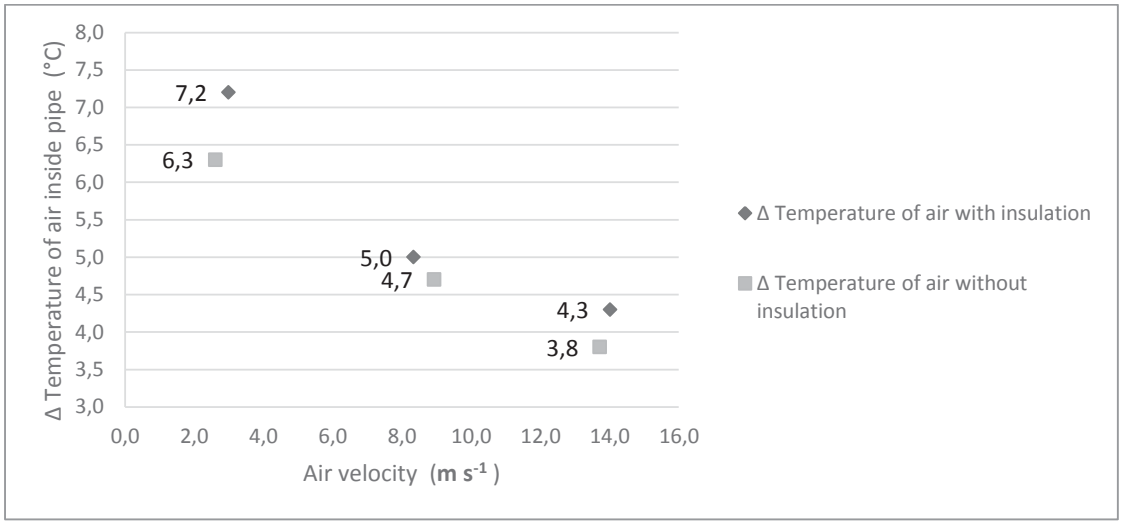

Fig. 15: Δ Temperature of the air in the pipe with and without insulation depending on the speed

It can be observed that the higher the air's velocity gets, the lower delta of temperature of air is obtained, and the delta of temperature of air in the receiver pipe with insulation is greater than without insulation.

5. Conclusions

It can be concluded that a large difference in temperatures can be reached when comparing receiver pipe with and without insulation. For example, in Fig. 12 we observe that at the last meters the receiver pipe with insulation has a difference of 15°C compared to the receiver pipe without insulation. In addition, the receiver pipe with insulation is better to reach higher temperatures spite of different speeds how we observe in Fig. 15

Likewise, depending on the speed with which the air is transported, a variation in the temperature delta is obtained, mainly because of heat losses depending on the flow characteristics.

It can also be concluded that using air as the carrier fluid with 3 m/s of air velocity, we can achieve a temperature of 97 °C at 25.5 meters inside the receiver pipe with 5 inches of diameter and insulation in Fig. 10.

6. References

C. Palaniappan, V. S., 1998. Economics of solar air pre-heating in south Indian tea factories: a case study. Solar Energy, 31-37.

Creus, A., 2010. Energía Termosolar. Cataluña: Ceys

Vergara Dávila, S. G., & Hadzich Marín, M. Á. (2014). Diseño de un tubo receptor de un concentrador parabólico lineal para calentar el aire para proceso de secado de té negro en Cusco, Perú. *XI CONGRESO IBEROAMERICANO DE ENERGÍAS RENOVABLES Y XXXVIII SEMANA NACIONAL DE ENERGÍA SOLAR*. Querétaro. Obtenido de http://www.isdmex.com/PubSemNal/data/6/3/O/DISEC391O%20DE%20UN%20TUBO%20RECEPTOR%20DE%20UN%20CONCENTRADOR%20PARABOLICO%20.pdf?

Zanabria Pacheco P., 2012. Radiación Solar en el Cusco. Lima: Guzlop.

03. Thermal Storage

Conference Proceedings

EuroSun 2016
Palma de Mallorca (Spain), 11 - 14 October 2016

THERMAL ENERGY STORAGE WITH CONCENTRATED SOLAR POWER FOR A MORE RELIABLE AND AFFORDABLE ELECTRICITY TO INDUSTRIAL APPLICATIONS

El Ghali Bennouna[1,2] and Abdelaziz Mimet[2]

[1] Institut de Recherche en Energie Solaire et en Energies Nouvelles, Benguerir (Morocco)

[2] Ecole Normale Superieure – Université Abdelmalek Essaâdi, Martil (Morocco)

Abstract

The implementation of Concentrated Solar Power for industrial applications has become a topic of high interest both for CSP plants developers and potential client industries. The integration of CSP for industrial processes can be done follow various needs ranging from power generation to steam generation, drying, heating and even cooling applications. Although the interest for the latter "less common" applications has gained more importance for researchers over power generation, this options has still a lot of interest for industrials especially when this power generation can be more flexible and cheaper thanks to a good Thermal Storage System integration and to encouraging market conditions and availability of the solar resource.

In this paper we studied the possibility for large industrial facilities to exploit small scale CSP plants as fossil fuel and grid saving mechanism considering the variable grid pricing and an appropriate TES integration.

Keywords: *Concentrated Solar Power (CSP), Thermal Energy Storage (TES), industrial application…*

1. Context

Since its creation, IRESEN has placed small scale CSP-ORC systems among the main priorities. Such systems are considered as possible solutions for small power consumers (below 5MW). In this regard a first demonstration and research pilot CSP-ORC plant of 1MW capacity is being commissioned at the green energy park in Benguerir, Morocco.

During the project planning period, the development of an appropriate thermal storage add-on to increase the dispatchability of the plant, and help demonstrate the benefits of storage for this package and the potential clients.

Fig. 1: Picture of the 1MW CSP-ORC plant under commissioning in Benguerir, Morocco

Industry is out of doubt one of the most energy intensive sectors, standard energy needs for industry cover electricity for machines supplying, electrolyze processes, cooling, lightning and others. On the other hand, various needs for heat at various grades and on various ways (hot air for drying, high pressure steam, furnaces, processes preheating…), this heat is mostly obtained via the combustion of fossil fuels but can also be produced by electricity at higher cost while many industrial processes based on fossil fuel are being supported by others based on electricity such as for steel industry.

doi:10.18086/eurosun.2016.03.17 Available at http://proceedings.ises.org

The costs of fossil fuel have decreased significantly during the last few years, this has put CSP for heating applications in a less comfortable position, although this can be regarded as a temporary situation which can change following geopolitical conjuncture.

On the other side, electricity prices are more or less constant in many countries regardless of fossil fuel prices. The price of electricity from the grid are generally linked to the power demand or load either at a national or regional level. In Morocco for example, electricity from the national grid (ONEE) follows a time dependent pricing approach for industrial consumers (middle and high voltages), the highest prices correspond to the hours of higher power demand (peak hours and also super peak hours for high voltage consumers).

Tab. 1: ONEE power pricing in Morocco for middle and high voltage consumers (ONEE, 2016)

Pricing options 60kV	Yearly capacity price per	kWh price (MAD/€)			
	kW/year (MAD/€)	SHP	HP	HPL	HC
Very long use	1 933,23 / 172.45	0,8482 / 0.075	0,7725 / 0.069	0,6284 / 0.056	0,5733 / 0.051
Long use	773,96 / 69.04	1,6692 / 0.148	1,0457 / 0.093	0,7561 / 0.067	0,5733 / 0.051
Short use	386,97 / 34.52	2,2166 / 0.197	1,2280 / 0.011	0,8793 / 0.078	0,5989 / 0.053
Emergency use	343,30 / 30.62	2,5715 / 0.229	1,4246 / 0.127	0,9077 / 0.081	0,6029 / 0.054
Capacity Reduction Factor		1	0,8	0,6	0,4
Pricing options 150kV & 225kV	Yearly capacity price per	kWh price (MAD/€)			
	kW/year (MAD/€)	SHP	HP	HPL	HC
Very long use	2 160,77 / 192.75	0,8652 / 0.077	0,7881 / 0.071	0,6419 / 0.057	0,5908 / 0.053
Long use	865,31 / 77.19	1,7696 / 0.158	1,1087 / 0.099	0,7871 / 0.070	0,5908 / 0.053
Short use	431,82 / 38.52	2,4909 / 0.222	1,3800 / 0.123	0,9251 / 0.082	0,6195 / 0.055
Emergency use	383,09 / 34.17	2,8897 / 0.258	1,6010 / 0.142	0,9550 / 0.085	0,6236 / 0.056
Capacity Reduction Factor		1	0,8	0,6	0,4

In this configuration, the price of electricity during super peak hours can raise to more than three times the base price at off load hours. Peak and super peak hours are generally between 6:00 and 10:00 in the evening. This opens a large opportunity for large industries which have large power needs and whose processes are working continuously to integrate CSP with storage in order to use less electricity from the grid especially during the evenings.

By offering the possibility to extend a CSP plant production to the evening, thermal energy storage has then a double benefit if we consider a “grid saving” approach:

- Benefit of higher grid prices during the evenings allowing the operator to profit from a better competitiveness versus grid power;
- Benefit of generally lower ambient temperatures which contribute to a higher power cycle efficiency, hence a higher production and a better economic efficiency;

2. Methodology

The Noor-Ouarzazate 1 plant is seen as a breakthrough in terms of CSP competitiveness with a kWh price around 15 cents, nevertheless, this price might seem very high for basic Moroccan consumers which do not pay electricity on a time based pricing. For middle voltage and high voltage clients the variability of electricity price between peak and off peak hours offers a high potential for the integration of CSP with storage.

The aim of this paper is to study the impact of integrating a small CSP unit with thermal storage to supply an industrial installation. This can be achieved by simulating the CSP plant production with a home developed model at IRESEN based on the 1MW CSP-ORC plant of Benguerir. Although this model is very simple, it was successfully compared in many occasions with more proven tools such as GREENIUS (J. Dersch). The simulations will be integrated on an economical balance taking into account all consumers specifications and electricity pricing (V. Quaschning et al., 2011).

2.1. Plant simulation input

The simulations for production are based on three calculation modules:

- The solar field performance: the total heat production of the solar field is based on the weather conditions, mainly, the Direct Normal Irradiation or DNI, the ambient temperature and the solar angles (Azimuth and Elevation) combined with the solar collector performances (A. Soteris Kalogirou, 2004).
- Storage and heat dispatch: this module defines the amount of heat to be stored and the share to be dispatched, it also calculates the charging level of the storage system based on the solar field output and the dispatched heat (J. Pacheco, 2002).
- ORC module: the ORC performance is calculated using the supplier's correction curve, the ambient temperature and the amount of heat dispatched by the solar field and storage.

Among the available weather data sets, actual measurements data were preferred over satellite data, the data set used for the simulations contains a measurement value for each 10 second and was obtained with a high precision tracker based weather-station.

Concerning the solar field, the adopted configuration consists of 16 loops with 4 linear Fresnel collectors on each, the total surface area of the mirrors is 26500m^2, and the nominal solar field capacity is 11.3MW_{th} at a reference DNI of 750kWh/m^2 (A. Haberle et al., 2002). The heat transfer fluid enters each solar field loop at 185°C and exits at 315°C.

The storage technology is thermocline with Quartzite rocks bed, the heat capacity is 27MWh equivalent to 5 storage hours. Charging of the storage system is given priority over ORC operation, which is similar to a partial production shifting mode.

Discharging is oriented to the peak hours while the charging rates are based on the season and the average solar irradiation for the few hours preceding the calculated time slot, this means that during winter for example, a full production shifting occurs to the peak hours while in summer there is only a partial charging of the storage during the first hours of operation and depending on the amount of heat produced by the solar field.

The ORC set used on the simulations has a nominal net capacity of 1MW at an ambient temperature of 20°C and heat input of 4.8MW. The efficiency of the power cycle varies proportionally to the heat input and inversely to ambient temperature.

2.2. Economic configuration

The selected potential client for the simulated plant is an industrial unit connected to the national grid at high voltage with a medium/long consumption contract (3500 to 6000 hours per year). In this case the price of electricity will follow 4 different time slots as presented on figure.

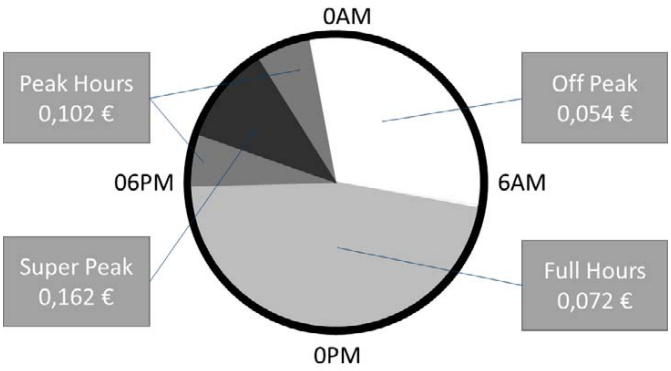

Fig. 2: Power pricing for middle/long consumption at high voltage connection (150 & 225kV)

For the following calculations we assume that the industrial client can sustain the full investment, meaning an equity ratio of 100% (this might be likely with small CSP units requiring relatively reduced investments). In addition, it is also assumed that the required land surface is owned by the client, hence land costs are not considered in calculations.

Tab. 2: Plant main properties and components cost

Plant main properties			Main components specific costs		
Solar field total mirrors area	26500	m²	Solar Field specific cost	240	€/m²
ORC nominal capacity	1000	kWe	ORC specific cost	1600	€/kWe
Thermal storage capacity	27000	kWh	Thermal Storage specific cost	35	€/kWh
Total required surface area	2.5	ha	Operation & Maintenance costs	0.01	€/kWh

The total investment is 9.15M€ based on the information in table 2. The economic assessment is done over a period of 20 years, followed by another 5 years with higher maintenance costs (+50%).

Operation and maintenance costs are generally close to 0.015$/kWh (IRENA, 2012), in the CSP-ORC plant case, a specific configuration and particular design requirements were set to allow for maximal automation and minimum operation leading to much lower O&M requirements.

3. Simulation results and conclusions

The simulations were done for one complete year using hourly data (average values from 10 seconds values). However, two representative days were selected to show the impact of an operation strategy specifically oriented to the peak hours.

4.1 Results for representative days

When observing figures 3 and 4 a slight difference can be noticed in terms of power production, although the sum of the daily production is comparable with both approaches.

Regarding the cash flow curve, a strong difference between the two figures can be noticed despite being representative of the same day. This is mainly due to the production being shifted with the peak oriented operation strategy, while the second strategy only focuses on smoothing the production. Hence, a large share of the power is produced during the day, which means out of peak hours, and does not occur during hours with the highest pricing.

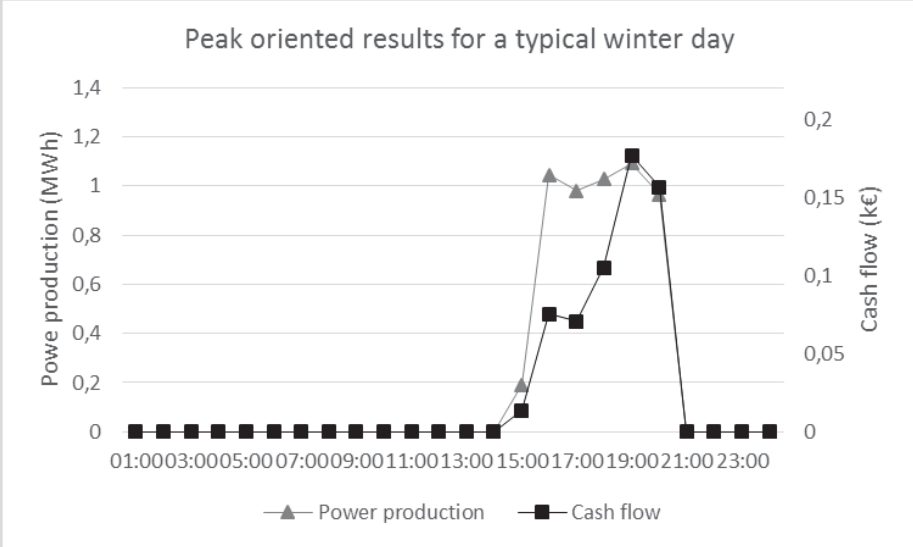

Fig. 3: Power production and cash flow results for a typical winter day with peak oriented operation

It is important to notice that the ORC efficiency increases with lower ambient temperatures until a certain limit, this is a reason not to shift the production beyond 11PM, as temperatures can go easily below 10°C which is a threshold for ORC operation. Moreover, the stored heat has to be completely discharged before 11PM as the pricing moves directly to off peak period leading to an intense drop of electricity pricing.

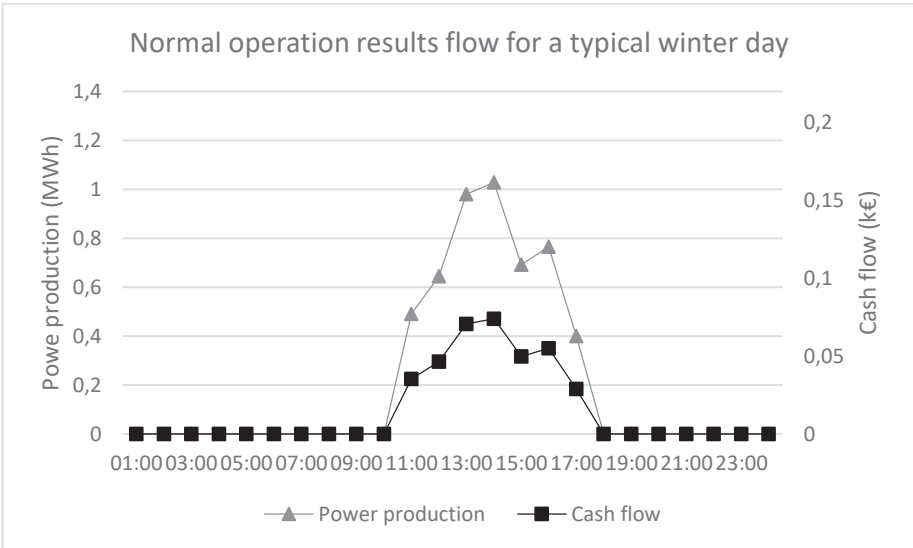

Fig. 4: Power production and cash flow results for a typical winter day with normal operation

During summer, the situation is quite different, when comparing figures 5 and figure 6, the overall shape of the power production curves of both figures is more or less the same. There is only a slight difference on the top of the curve (plateau shape), as the production is limited to 1MW before discharge and around 1.2MW after discharge for the peak oriented operation strategy, while the opposite happens with normal operation.

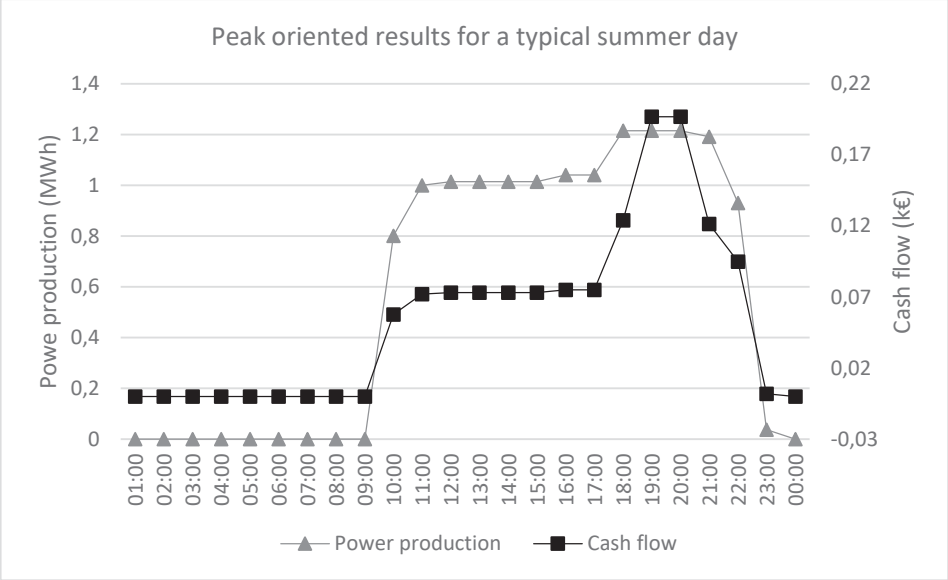

Fig. 5: Power production and cash flow results for a typical summer day with peak oriented operation

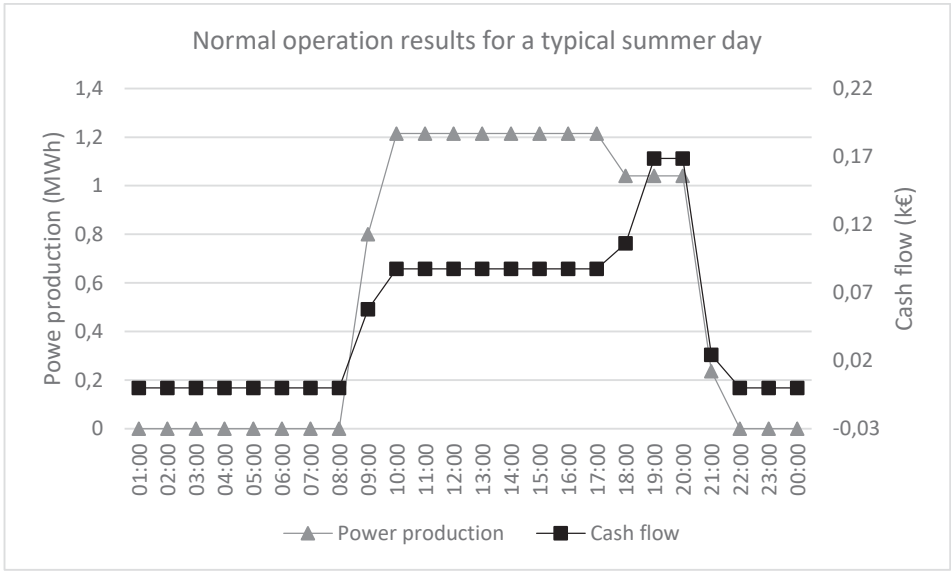

Fig. 6: Power production and cash flow results for a typical summer day with normal operation

In terms of cash flow, there is a certain difference between the two operation approaches, and this is due to the higher amount dispatched during the evening with the peak oriented operation. Nevertheless, this difference is not as important as for the winter example, simply because in this case both strategies tend to extend the production to the evening with different intensities.

4.2 Yearly results

Concerning the yearly simulations, there is slightly equivalent overall production. But when analyzing average values for the summer and winter period, it appears that there a larger increase of production in winter when applying the peak oriented strategy over the normal approach. This is due to the higher efficiency of the ORC with a controlled discharge at high ORC input over spread production with generally low heat input.

Tab. 3: Summary of the main simulation results

Simulated operation strategies	Yearly production		Average Summer day production		Average winter day production	
	Power generation (MWh)	Cash flow (k€)	Power generation (MWh)	Cash flow (k€)	Power generation (MWh)	Cash flow (k€)
Scenario with focus on peak hours	3637	356	15.09	1.34	5.3	0.59
Scenario with normal operation	3611	312	15.01	1.22	4.6	0.37

The cash flow results show an increase for both periods with respectively 10% for summer and 60% for winter, for an entire year the total cash flow gain is 14%.

The initial investment of the plant is set at 9,460,000€, over a period of 20 year, the total incremental costs are 10,020,000€, by extending the operation to 25 years, these costs reach 10,270,000€. In the studied case no debt financing was considered, otherwise, the total incremental costs would have largely exceeded the latter value.

After 20 years of operation, the plant should have produced 72GWh. With a normal operation, this production can generate 6,200,000€, while a peak oriented strategy can generate up to 7,100,000€ which represents 71% of the total incremental costs.

By extending the operation for further 5 years and increasing operation and maintenance costs by 50%, the figures can reach 8,900,000€ and 87%. A 10 years extension of the operation can drive the total revenues up to 10,680,000€ which exceeds the total costs (10,600,000€) including doubled operation costs for the last 5 years.

Such a plant operated with a classical approach would need 5 additional years for amortization, which tends to be difficult with the increasing O&M costs.

The objective of this work is not only to display applicability of small CSP units for industrial consumers, but also to demonstrate that the integration of thermal storage to such plants can help achieve better economic results. It is common to compare CSP projects LCOE with the base power pricing, however, in the case of systems with storage, the comparison is not as simple and must include some other parameters.

A plant with an LCOE of 0.18€ or 0.22€ (which is the average of small scale CSP units) might seem totally unfeasible with an average electricity price of 0.1€/kWh, it appears that such a plant when equipped with an appropriate storage system, can be amortized with a reasonably extended operation lifetime.

Although the approach followed in this study does not consider debt financing, no land cost and relatively long operation in comparison to average plants lifetime simulations, it is still sufficiently reliable to demonstrate the advantage of a peak oriented operation over normal production extension.

It also demonstrate the ability of CSP to supply reliable electricity during the peak periods and compensate for other energy sources especially with a high penetration of renewables on the grid (J. Jorgenson et al., 2014).

In any case, the obtained results show that a slight increase in electricity pricing in Morocco and the mastering of CSP technologies combined with economies of scale (when applicable) and with reasonably high fossil fuel prices can make small CSP applications able to enter the market within the coming few years.

4. References

IRENA, (2012). IRENA working paper, Renewable Energy Technologies: Cost Analysis Series, Volume1-Power Sector Issue 2/5 – Concentrating Solar Power June 2012.

J. Dersch, GREENIUS – Green Energy Systems Analysis, Manual Version 3.7, Deutsches Zentrum für Luft- und Raumfahrt e.V. Solarforschung, http://freegreenius.dlr.de/.

A. Soteris Kalogirou, Solar thermal collectors and applications (Progress in Energy and Combustion Science 30 (2004) 231–295).

A. Haberle, C. Zahler, H. Lerchenmüller, M. Mertins, C. Wittwer, F. Trieb, J. Dersch, 2002, The Solarmundo line focusing Fresnel collector. Optical and thermal performance and cost calculations, SolarPACES International Symposium, pp. 5-8.

J. Pacheco, Final Test and Evaluation Results from the Solar Two Project, Sandia National Laboratories, Albuquerque, 2002, p. 55-63.

V. Quaschning, W. Ortmanns, R. Kistner, M. Geyer, GREENIUS - A New Simulation Environment for Technical and Economical Analysis of Renewable Independent Power Projects, Solar Forum 2011 – Solar energy : The power to choose, April 21-25, Washington DC.

J. Jorgenson, P. Denholm, M. Mehos, (2014). Estimating the Value of Utility-Scale Solar Technologies in California under a 40% Renewable Portfolio Standard. NREL/TP-6A20-61685. www.nrel.gov/.

Office National de l'Electricite et de l'Eau Potable – ONEE, 2016, http://www.one.org.ma/.

Conference Proceedings

EuroSun 2016

Palma de Mallorca (Spain), 11 – 14 October 2016

Importance of thermal energy storage pilot plant facilities for solar energy applications

Gerard Peiró[1], Jaume Gasia[1], Laia Miró[1], Cristina Prieto[2] and Luisa F. Cabeza[1]

[1] GREA Innovació Concurrent, Universitat de Lleida, edifici CREA, Pere de Cabrera s/n, 25001 Lleida (Spain)

[2] Abengoa Research, C/ Energía Solar 1, 41012 Seville (Spain)

Abstract

A pilot plant facility focused on testing thermal energy storage (TES) systems both at pilot and commercial scale was designed and built at the University of Lleida in 2008. This facility was designed and equipped with the measuring devices needed to measure and analyse the thermal behaviour of all the systems tested as a previous step to commercial development. The versatility of this facility has allowed simulating real working conditions and therefore testing different TES systems, mainly for solar thermal applications such as domestic hot water, solar cooling or solar power generation, but also for other applications such as industrial waste heat recovery or combined heat and power (CHP). In this paper the main characteristics of components of the pilot plant of University of Lleida as well as the main results of the tests performed with both sensible and latent TES are shown.

Keywords: *thermal energy storage; solar thermal applications; phase change material; sensible heat; pilot plant scale*

1. Introduction

In recent years, research on renewable energies has become an important issue to achieve the main goals established by the most important international agencies and governments in order to fight against global climate change and to ensure a sustainable development for the future generations (International Energy Agency, 2014).

The most promising renewable technologies are based on solar energy. However these technologies are extremely dependent on the climate, causing temporal differences between the energy supply and the energy demand. In recent years thermal energy storage (TES) has been widely studied and represents one of the possible solutions to overcome this mismatch. Chidambaram et al. (2011) reviewed the TES systems coupled to solar cooling technologies and stated that TES integrated in solar cooling systems increases the cooling availability and improves the overall performance of the solar field. Considering solar power generation, Gil et al. (2010) showed a classification of current storage systems for solar power generation. They divided these systems depending on the materials used and the different storage concepts. They highlighted that TES systems allow a better dispatchability of power plants and enhance their power capacity.

TES systems can be classified in sensible thermal energy storage (STES), latent thermal energy storage (LTES), sorption energy storage, and thermochemical energy storage (TCES) and they can be applied in a wide range of applications at different temperatures, such as domestic hot water (DWH), solar cooling, combined heat and power (CHP), industrial waste heat (IWH) recovery, and concentrated solar power (CSP) plants. TES materials are a key factor in the solar technology field to improve the techno-economic performance. Most of the current literature evaluates the performance of the TES materials at laboratory scale (Fernandez et al. (2010); Pereira and Eames (2016)). However, it is known that the behaviour of those materials could be size-dependant (Rathgeber 2014). Moreover, there are several aspects such as operation, instrumentation, compatibility of materials (dynamic and static corrosion), and the behaviour of the TES material under the real operation conditions which need to be improved before the commercial development of the TES system. This previous research allows providing solutions to technical problems and to reduce the

Selection and/or peer review under responsibility of Scientific Committee
doi:10.18086/eurosun.2016.03.18 Available at http://proceedings.ises.org

cost of commercial plant (Rodríguez et al. (2014); Prieto et al. (2016)).

With this purpose, a pilot plant facility was designed and built at University of Lleida in 2008 (Peiró et al (2016a)). Its design simulates a real CSP plant and allows testing different sizes and configurations of TES storage tanks. Moreover, it is equipped with many measurement devices which record the different parameters to analyse the thermal behaviour of the pilot plant and their components. Up to now, this facility has been used to analyse both STES and LTES systems with configurations such as shell-and-tube tanks and two-tank system. Thus, the objective of this article is to summarize and discuss the experimentation performed using this facility.

2. Description of the pilot plant facility

The pilot plant facility presented in this paper is mainly integrated by three systems:

- The heating system, which consists of a 24 kWe electrical boiler that heats up the heat transfer fluid (HTF) simulating the solar energy source in a real application. In this facility, two different fluids have been used as HTF, thermal oil Therminol VP-1 (T-VP1) and silicone fluid Syltherm 800 (S-800). Their flow rate is measured with a differential pressure transmitter and controlled by a proportional-integral-derivative controller.
- The cooling system, which consists of an air-HTF heat exchanger of 20 kWth to cool down the HTF. It simulates the energy consumption of the real application.
- The TES system, which consists of different storage tanks that store the thermal energy during the charging process and releases it during the discharging process. These tanks are equipped with several Pt-100 temperature sensors located strategically in order to obtain a proper map of temperatures of both the TES material and HTF.

Moreover, this facility has several auxiliary systems in order to ensure a proper operation, such as pumps, piping, valves, electrical system, and control and recording data system. All these components are suitably insulated to minimise the heat losses to the surroundings. Rockwool is used for the surfaces in contact with the ambient and Foamglass and refractory concrete for the surfaces in contact with the ground. Fig. 1 shows an overview of the different components of the previously described pilot plant facility.

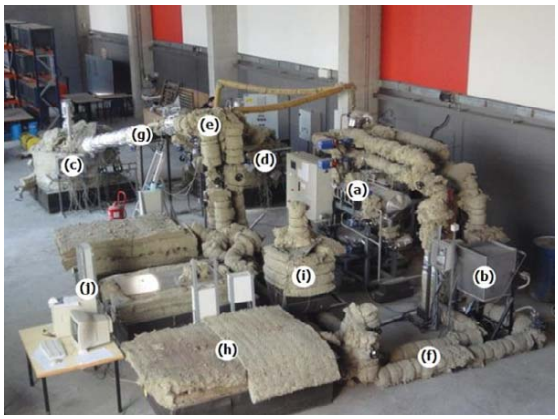

Fig. 1: Overview of the pilot plant facility available at the University of Lleida. (a) Electrical heater, (b) air-HTF heat exchanger, (c) molten salts hot tank, (d) molten salts cold tank, (e) HTF-molten salts heat exchanger, (f) HTF loop, (g) molten salts loop, (h) LTES system, (i) solid STES system, and (j) acquisition and recording system (Peiró et al. (2016a)).

3. Description of thermal energy storage systems

Different TES tanks and materials for both STES and LTES have been tested in this facility. The main characteristics of these systems are shown in this section.

3.1. Sensible thermal energy storage (STES) systems

Two different STES configurations were constructed and tested: a shell-and-tube STES tank and a two-tank TES system.

The shell-and-tube STES tank design consists of a vertical tube bundle with four tubes through which the HTF is circulated and a housing surrounding the tubes serves as storage material container. Fig. 2 shows a 3D view of the STES tank and Table 1 its design characteristics.

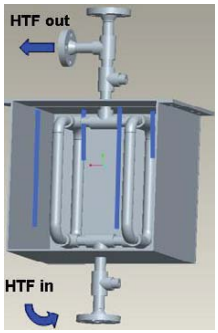

Fig. 2: Shell and tube STES tank: 3D view.

Table 1. Design characteristics of STES tank.

Dimensions of the tank	
width x height x depth	0.35 x 0.42 x 0.35 m
Packing factor	0.54
Walls of the tank	
Material	Stainless steel 304L
Thickness	0.005 m
Tubes	
Material	Stainless steel 304L
Outer diameter (OD)	0.025 m
Total length	1.74 m

The two-tank STES system is composed of two identical storage tanks (called hot and cold tanks due to their thermal level). Both tanks are designed with the same aspect ratio (L/D) than commercial storage tanks. The design of the tank consists of a cylinder-shaped vessel, where the TES material is housed, which is closed with a Klöpper cover welded on the top. Fig. 3 shows a view of the storage tank of the two-tank molten salts TES system and Table 2 its main design characteristics. The walls and cover of the tank are manufactured with some openings in order to place the electrical heaters used to heat up the TES material, to place the different measuring devices, and to place the molten salts pumps. These pumps are responsible to move the molten salts from one tank to the other tank through a multiple pass plate heat exchanger. The heat exchanger is the component responsible to carry out the heat exchange between the molten salts and the HTF (Fig. 4 and Table 3).

Fig. 3: Two-tank molten TES system.

Table 2. Design characteristics of storage tank of the two-tank molten salts TES system.

Dimensions of the tank	
Internal diameter	1.2 m
Cylinder height	0.5 m
Klöpper cover height	0.267 m
Aspect ratio	0.41
Walls of the tank	
Material	Stainless steel 316L
Thickness	0.004 m

Fig. 4: HTF-molten salts plate heat exchanger.

Table 3. Design characteristics of the HTF-molten salts plate heat exchanger.

Plate Heat exchanger	
Length x width x height	0.208 x 0.191 x 0.618 m
Plate material	Stainless steel 316

3.2. Latent thermal energy storage (LTES) systems

Two storage tanks were designed and built in order to test the LTES concept with different phase change materials (PCM). The design of the tanks was based on the shell-and-tube heat exchanger concept. It consists of a rectangular-shaped vessel with a tubes bundle inside. The PCM was located in the housing of the shell part. The HTF circulated inside the bundle of tubes, which was integrated by 49 tubes bended in U-shape and distributed in square pitch (Fig. 5). One of these tanks was built with a 196 transversal squared fins assembled along of the tube bundle in order to enhance the heat transfer between HTF and PCM (Fig. 6). Table 4 shows the main design characteristics of the LTES tanks.

Fig. 5: Shell-and-tube LTES tank without fins.

Fig. 6: Shell-and-tube LTES tank with fins.

Table 4. Design characteristics of LTES tank with and without fins.

Dimensions of the tank	
width x height x depth	0.527 x 0.273 x 1.273 m
Packing factor	0.80-0.84
Walls of the tank	
Material	Stainless steel 304L
Thickness	0.004 m
Tubes	
Material	Stainless steel 304L
OD	0.017 m
Average length	2.485 m
Tank with Fins	
Packing factor	0.80
Material	Stainless steel 304L
Number of fins	196
Dimensions	0.25 x 0.25 m
Thickness	0.0005 m

4. Description of the storage materials

A total of six different TES materials have been studied at pilot plant scale for both STES and LTES systems. Regarding the STES, two different TES materials were tested: on one hand, granulated NaCl, a by-product from the potash industry, which was used in the STES tank; on the other hand, molten salts, which were used in the two-tank system. Regarding the LTES tanks, four PCMs have been used: RT58 (a paraffin), bischofite (a by-product from the mining industry), d-mannitol (a sugar alcohol), and hydroquinone (an aromatic compound). Table 5 shows the main characteristics of these PCMs, such as specific heat for materials used in STES and melting temperature and enthalpy for materials used in LTES tank. These characteristics were obtained with differential scanning calorimeter (DSC) tests.

Table 5. Main characteristics of the STES and LTES materials used for testing.

TES Material	Type of energy storage	Specific heat [kJ/kg·K]	Melting temperature [ºC]	Melting enthalpy [kJ/kg]
NaCl	Sensible	0.738 (solid)	-	-
Molten salts	Sensible	1.51 (liquid)	-	-
RT-58	Latent	-	53-59	120.0
Bischofite	Latent	-	100-110	115.0
d-mannitol	Latent	-	162-170	246.8
Hydroquinone	Latent	-	168-173	205.8

5. Experimental procedure

Based on the operation performance of TES material, the experimentation carried out at the pilot plant facility consisted of several charging and discharging processes. Different HTF flow rates and arrangements, and different temperature ranges were considered in order to simulate real application operation conditions. In the LTES and the STES tanks the experimentation procedure is the following: before starting the charging process a warming period is done in order to achieve the initial required conditions. Once the TES material reached the initial required temperature, the HTF is heated up outside the tank until charging temperature is reached. After that, the charging process is able to start. During the charging process, the inlet temperature of HTF is kept at desired temperature. The charging process is stopped when the average temperature of the main temperature probes of the TES material tanks reaches the same temperature than the inlet HTF temperature. Then, the HTF is cooled down outside the tank with cooling system until the discharging temperature is reached. After that, the discharging process starts and it is considered finished following the same criteria than in the charging process. In the two-tank molten salts system, the charging and discharging processes are carried out with a different procedure simulating the operation in a solar power plant. During the charging process, the molten salts are pumped from the cold tank to the hot tank through the heat exchanger system. In this system, the molten salts are heated up with the HTF, which has been previously heated with the heating system. The process is considered to be finished when the level of the molten salts at the cold tank reaches the minimum level for a proper performance of the molten salts pump. On the contrary, during the discharging process, the molten salts are pumped from the hot tank to the cold tank through heat exchange system. In this system, the HTF is heated up with the molten salts to be further cooled down at the cooling system, simulating the power block. The discharging process is considered to be finished when the level of the molten salts at the hot tank reaches the lowest level.

Table 6 shows a summary of the main working conditions of the different experiments carried out at the pilot plant facility. The temperature range was selected according to the materials characteristics and to the final application, while the flow rate was selected to study its influence on the charging and discharging processes.

Table 6. Summary of the characteristics of experimentation carried out at pilot plant facility.

System	TES material	Mass tested [kg]	HTF	HTF flow rate [l/h]	Temperature range [ºC]	Ref.
STES tank	NaCl NaCl + water	59	T-VP1	1000- 3000	100-200	Miró et al. (2014)
Two-tanks	Molten salts	1600	T-VP1	435	298-343 303-372	Peiró et al. (2016b)
LTES Tank without fins	RT58	107.5	S-800	550- 2750	48-68	Gasia et al. (2016)
	Bischofite	204	S-800	1650	80-120	Gasia et al. (2015)
	Hydroquinone	170	T-VP1	500-3000	145-187 130-200	Gil et al. (2013a)
	d-mannitol	165	T-VP1	500-3000	145-187 130-200	Gil et al. (2013a)
LTES Tank with fins	RT58	106	S-800	550- 2750	48-68	Gasia et al. (2016)
	Hydroquinone	155	T-VP1	500-3000	145-187 130-200	Gil et al. (2013b) Gil et al. (2014)
Multiple PCM	Hydroquinone + d-mannitol	170 + 165	T-VP1	3000	145-187	Peiro et al. (2015)

6. Results

6.1. Sensible thermal energy storage systems

The experimental work with STES tank presented in Miró et al. (2014) was focused on comparing the thermal behaviour of granulated NaCl and NaCl compacted with water. Four thermal cycles (charge and discharge) were performed with temperature range of 100-200 ºC. The main differences between the thermal cycles were the HTF flow rate (1000 l/h and 3000 l/h) and the duration of the processes (4 h and 8 h).

Fig. 7a and Fig. 7b show the temperature profile of the HTF and average temperature of both granulated NaCl (salt A) and NaCl compacted with water (salt B). In the four thermal cycles performed, both salt A and salt B do not reach the fixed temperature set-point for charging (200 ºC) because the two proposed intervals of time were not sufficient to ensure a full charge. However, it can be observed that the temperature profile of the salt A and salt B are significantly different. Notice that at the end of the 4 h charging process (Fig. 7a) the salt B temperature is around 25 ºC higher than the temperature of salt B. The reason lies on the fact that the thermal conductivity of salt B (2.84 W/m·K) is 8.6 times higher than the salt A (0.33 W/m·K). From Fig. 7a, it also can be observed that there are not significant differences between the temperature profiles of the salts when the HTF flow rate was increased. Moreover, during this experimentation the energy accumulated or delivered by the salts was analyzed. During the charging process, salt A average accumulated energy was 0.63 kWh, while it was 0.75 kWh for salt B (the wetted compacted salt). This fact represented an increase of 19% in energy accumulated when using salt B. During the discharging process the average energy delivered by salt A was 0.40 kWh and 0.66 kWh for salt B. That represented an increase of 68%. The reason is because in the same period of time, the conductivity had a big impact. The average thermal efficiency was 63% for salt A and 88% for salt B, which represented an increase of 40%. It was also observed that there was no influence in the energy accumulated with an increase of the HTF flow rate. As expected, when the duration of experiments was doubled, an average increase of 27.8% (salt A) and 16.3% (salt B) of the energy accumulated during the charging process, and an increase of 30.6% (salt A) and 22.3% (salt B) of the energy delivered during the discharging process. With these results, the main conclusion reported in the study performed by Miró et al. (2014) is that NaCl compacted with water represents a better and cheaper option than other STES materials for TES due to the reduction of air gaps inside the solid.

The two-tank molten salts TES system experimentation presented in Peiró et al (2016) represents the first study in the literature at pilot plant scale with molten salts as TES material and thermal oil (Therminol VP-1) as HTF operating in a plate heat exchanger. The main objective of this work was to study the effects of varying the flow arrangement (parallel and counter flow) in the plate heat exchanger and the effects of modifying the temperature gradient between the HTF and the molten salts (46 ºC ± 3 ºC and 68 ºC ± 1 ºC).

From the results of the experiments carried out, it was observed that for the same temperature gradient, counter flow arrangement performed better than parallel flow. Higher values of power were obtained with counter flow arrangement in both charging and discharging processes (from 65.5% to 78.8% higher). The reason of this behavior lies on the fact that in counter flow arrangement a more constant thermal gradient between the hot and the cold fluid at the heat exchanger is obtained during the whole process. On the other hand, it was observed that with the same flow, the experiments carried out with a higher thermal gradient provided values of power from 12.9% to 35.5% higher in both charging and discharging processes as a result of an increase in the driving force for the heat transfer.

Fig. 7c and Fig. 7d show the temperature evolution of both HTF and molten salts during the charging and discharging processes at inlet and outlet of the heat exchanger of two-tank system for the best working conditions (counter flow arrangement with a temperature gradient between 305 ºC and 370 ºC). The shaded areas represent the periods used to achieve the operational conditions required for the experimentation. The HTF temperature is represented in dotted lines while the molten salts are represented in straight lines. Moreover, in both charging and discharging processes, the hot fluids are plotted in red while the cold fluids are plotted in blue. During the charging process (Fig. 7c), the energy released by the HTF (7.8 kWh with an average thermal power of 13.0 kW) is higher than the energy absorbed by the molten salts (6.8 kWh with an average thermal power of 11.6 kW), which gives a process efficiency of 89%. On the contrary, during the discharging process (Fig. 7d), the energy released by the molten salts (7.5 kWh with an average thermal

power of 11.75 kW) is higher than the energy absorbed by the HTF (7.09 kWh with an average thermal power of 11.12 kW), which gives a process efficiency of 94.53%. The differences between the energy of HTF and salts are due to the heat losses of heat exchanger. Notice that the energy released by the salts during the discharge is higher than the energy absorbed in the charge process, due to the salts temperature difference between the inlet and outlet, which is slightly higher in discharge than in charge as a result of the electrical resistances placed inside the hot storage tank.

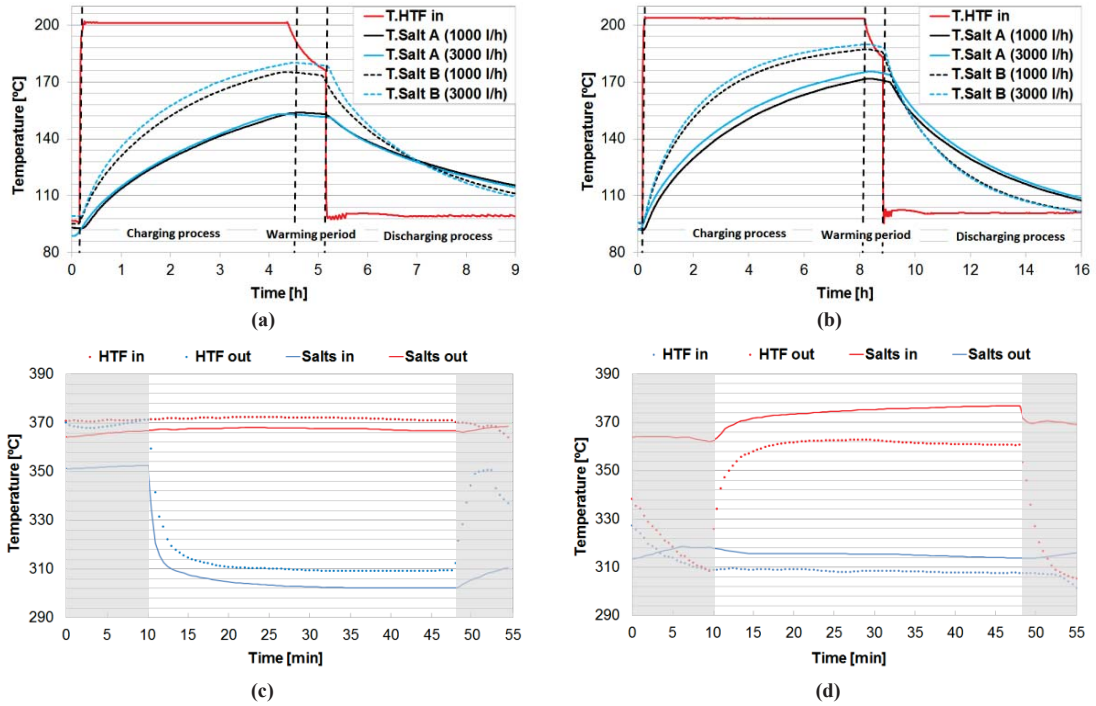

Fig. 7: STES systems temperature profiles. STES system: (a) thermal cycle of 4h and (b) thermal cycle of 8h. Two-tank molten salts TES system: (c) charging process and (d) discharging process.

6.2. Latent Thermal Energy Storage systems

The LTES systems, with the four above-mentioned PCMs, were analyzed under different HTF flow rates and working temperatures in order to test different operational conditions. Moreover, the effect of adding extended surfaces and the arrangement in series of different PCM's with different melting temperature and melting enthalpies were also studied.

The first PCM presented in this paper is RT58. This material was selected for DWH taking into account its melting temperature range (Table 5). The experimental work with RT58 presented in Gasia et al. (2016) was carried out with the objective of characterizing this material as PCM. Several charging and discharging processes were performed with a temperature range of 48-68 ºC for three different flow rates: 550 l/h, 1650 l/h and 2750 l/h. Fig. 8a shows the HTF and average temperature of RT58 charge and discharge temperature profiles for the different HTF flow rates. Notice that the higher the flow rates, the faster the PCM was charged or discharged. Taking into account the properties of Sylthem 800, only laminar flow regime could be achieved. Hence, the heat transfer coefficient was constant for the different flow rates evaluated, and therefore the temperature difference between HTF and PCM determined the value of heat transfer rate. With a higher flow rate, the temperature difference was higher and, as a consequence, the heat transfer was higher, which caused the PCM to heat up or cool down faster. The energy accumulated and delivered by the HTF and RT58 was also analysed. For instance, during the charging process with an HTF flow rate of 1650 l/h, the energy stored by the PCM was 5.74 kWh and the energy released by the HTF was 6.33 kWh, giving an efficiency of 90.68%. During the discharging process, the energy recovered by the HTF was 5.03 kWh, which was obtained from the PCM and the metallic parts of the TES system, which gives an efficiency of 89.15 %.

Regarding the evaluation of bischofite, Gasia et al. (2015) studied the suitability of bischofite as TES material in both sensible storage and latent storage. This material was selected for IWH and CHP purposes taking into account its melting range of temperatures (100-110 ºC). Several charging and discharging processes with a flow rate of 1650 l/h were performed, going from from 50 ºC to 80 ºC to evaluate the TEs material under the sensible form, and from 80 ºC to 120 ºC to test the latent form (Fig. 8b). Notice that the first two hours corresponded to the charge in sensible form, and from the 3rd hour until 7.64 h corresponded to the latent form. Discharging took place between 9.69 h and 14.12 h. During the experimentation, the subcooling effect at pilot plant scale was observed to be lower than the results obtained at laboratory scale. Regarding in energy stored/released during the first charging process, it was observed that the energy released by the HTF was 4.02 kWh and the energy stored by the bischofite was 3.07 kWh, giving an efficiency of 76.4%. During the second charging process, the energy given by the HTF was 13.5 kWh and the energy stored by the bischofite was 11.97 kWh, giving an efficiency of 88.7%. The reason for this difference between the two charging processes lies on the fact that while in the first charging process the bischofite increased 30 ºC in the sensible form, in the second charging process the bischofite increased 40 ºC in both the sensible and latent form. Moreover, results showed a good behavior of the 204 kg of bischofite evaluated at pilot plant but further research is needed because of the bischofite nature and the impurities embedded in it.

As shown in Table 6 two more PCMs have been studied, tested and compared at the pilot plant of University of Lleida in order to find the best PCM candidate for a real solar cooling plant available at University of Seville (Spain)(Gil et al. (2013a)). Several charging and discharging processes were performed with two different temperature ranges, 130-200 ºC and 145-187 ºC, and with three different flow rates: 1400 l/h, 2200 l/h and 3000 l/h (Fig. 8 c and Fig. 8d). As for the results obtained with RT58, the higher the flow rates, the faster the PCMs were charged or discharged. However, due to the thermophysical properties of the Therminol VP-1, the three representative flow regimes could be obtained for the three studied flow rates: laminar, transition and turbulent. The subcooling effect at pilot plant scale of hydroquinone was also lower than the results obtained at laboratory scale. However, d-mannitol showed high subcooling and polymorphism at pilot plant scale. Furthermore, for the same boundary conditions, the energy stored and released by d-mannitol was higher than hydroquinone. For instance, during the charging process with d-mannitol as PCM, with a temperature range of 145-187 ºC and an HTF flow rate of 1400 l/h, the energy released by the HTF was 22.35 kWh and the energy stored by the d-mannitol was 19.89 kWh, giving an efficiency of 88.9%. On the other hand, with hydroquinone, the energy released by HTF was 17.55 kWh and the energy stored by hydroquinone was 14.82 kWh, giving an efficiency of 84.4%. During the discharging process with d-mannitol, the energy recovered by the HTF was 18.11 kWh and energy released by d-mannitol was 18.46 kWh, giving an efficiency of 88.6 %. With hydroquinone, the energy recovered by the HTF was 13.30 kWh and the energy released by hydroquinone was 14 kWh, giving an efficiency of 92%. Results showed that d-mannitol and hydroquinone were good candidates as PCM for solar cooling applications. However, the subcooling effect is a parameter which should be addressed if these materials are selected.

In all the PCMs evaluated, it was found that that one of the most important drawbacks were their low values of thermal conductivity in both solid and liquid, which causes a limitation in the heat transfer ratios between the HTF and the PCM. In order to overcome such drawback, different heat transfer enhancement techniques were tested at the pilot plant facility. Two studies were carried out with the aim of evaluating the influence of adding fins: hydroquinone (Gil et al. 2013b) and RT58 (Gasia et al 2016). Another project was carried out with the objective of testing the multiple PCM concept, or cascaded, with hydroquinone and d-mannitol (Peiró et al 2015). Results showed that the addition of fins increased up to 28% the time of the charging/discharging process under the same working conditions. Moreover, results also showed that the multiple PCM configuration introduced a higher uniformity on the HTF temperature, and introduced an effectiveness enhancement of around 20%.

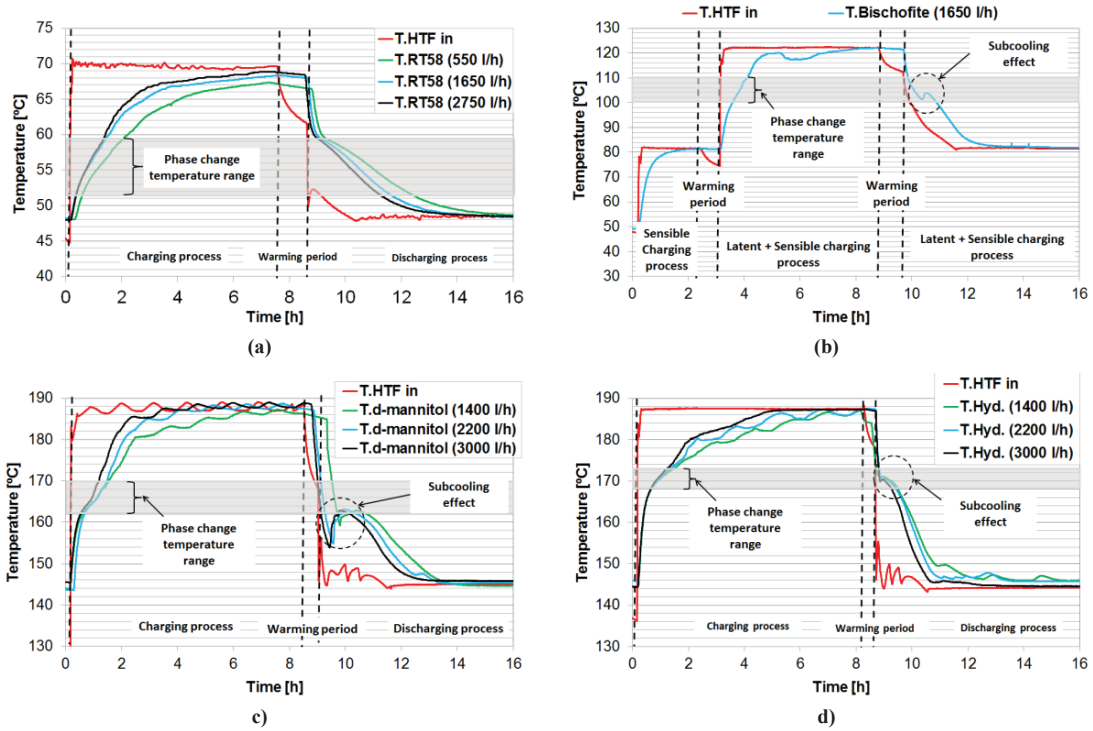

Fig. 8: Charge and discharge LTES tank temperature profiles of HTF and PCM. a) RT58 b) bischofite. c) d-mannitol and d) hydroquinone.

7. Conclusions

In the literature, most of the TES materials thermal behaviour analyses are performed at laboratory scale. Taking into account that some thermophysical properties are present size-dependant behaviour, analyses at higher scales are needed.

In the present paper, some results of all the experimentation performed at the pilot plant facility designed and built at University of Lleida with different TES materials (in both sensible and latent forms) are presented. In the experimentation carried out to test STES materials, a TES tank based on shell-and-tube heat exchanger concept and a two-tank molten salts system were used. In the experimentation performed to test LTES materials, a different storage tank based on shell-and-tube heat exchanger concept. The effects of the TES materials thermophysical properties, HTF flow rates, the addition of fins, and the multiple PCM concept was tested and analysed. Moreover, six different materials were used in the experimentation: NaCl and molten salts as STES materials, and RT-58, Bischofite, d-mannitol and hydroquinone as PCM.

The experimentation carried out at the pilot plant facility of the University of Lleida, has shown the relevance of testing at a relevant scale in order to face important progress in the roadmap to reach commercial development. A proper design of a pilot plant has allowed the evaluation of various materials, different designs of TES tanks, instrumentation, auxiliary equipment, and different operational strategies such as the effect of adding fins or the flow arrangement, using the same installation. Moreover, this experimentation has shown that the thermophysical behaviour of the TES materials is different at different scales such as subcooling effect.

Acknowledgements

The research leading to these results has received funding from Spanish goverment (Fondo tecnológico IDI-20090393, ConSOLida CENIT 2008-1005) and from Abengoa Solar NT. The work is partially funded by the Spanish government (ENE2008-06687-C02-01/CON, ENE2011-22722, ENE2015-64117-C5-1-R (MINECO/FEDER) and ULLE10-4E-1305). The authors would like to thank the Catalan Government for the quality accreditation given to their research group GREA (2014 SGR 123). This project has also received

funding from the European Commission Seventh Framework Programme (FP/2007-2013) under Grant agreement NºPIRSES-GA-2013-610692 (INNOSTORAGE) and from the European Union's Horizon 2020 research and innovation programme under grant agreement No 657466 (INPATH-TES). Laia Miró would like to thank the Spanish Government for her research fellowship (BES-2012-051861). Jaume Gasia would like to thank the Departament d'Universitats, Recerca i Societat de la Informació de la Generalitat de Catalunya for his research fellowship (2016FI_B 00047).The authors would like to thank Dr. Eduard Oró from Catalonia Institute for Energy Research (Spain) and Dr. Antoni Gil from Massachusetts Institute of Technology (USA) for their help during the initial stages of the experimentation.

References

Chidambaram, L.A., Ramana, A.S., Kamaraj, G., Velraj, R., 2011. Review of solar cooling methods and thermal storage options. Renew. Sust. Energ. Rev 15, 3220-3228.

Fernandez, A.I., Martinez, M., Segarra, M., Martorell, I., Cabeza, L.F., 2010. Selection of materials with potential in sensible thermal energy storage. Solar Energy Materials & Solar Cells 94, 1723-1729).

Gasia, J., Gutierrez, A., Peiró, G., Miró, L., Grageda, M., Ushak, S., Cabeza, L.F., 2015. Thermal performance evaluation of bischofite at pilot plant scale. Appl.Energ. 155, 826-833.

Gasia, J., Miró, L., de Gracia, A., Barreneche, C., Cabeza, L.F., 2016. Experimental evaluation of a paraffin as phase change material for thermal energy storage in laboratory equipment and in a shell-and-tube heat exchanger. Appl. Sci. 6(4), 112.

Gil, A., Medrano, M., Martorell, I., Lázaro, A., Dolado, P., Zalba, B., Cabeza, L.F., 2010. State of the art on high temperature thermal energy storage for power generation. Part 1—Concepts, materials and modellization. Renew. Sust. Energ. Rev. 14, 31–55.

Gil, A., Oró E., Peiró, G., Álvarez, S., Cabeza, L.F. 2013a. Material selection and testing for thermal energy storage system in solar cooling. Renew. Energ. 57, 3661-371.

Gil, A., Oró, E., Castell, A., Cabeza, L.F., 2013b. Experimental analysis of the effectiveness of a high temperature thermal storage tank for solar cooling application. Applied Thermal Engineering 54, 521-527.

International Energy Agency https://www.iea.org/ [accessed: 29/08/2016].

Miró, L., Navarro, M.E., Suresh, P., Gil, A., Fernández, A.I., Cabeza, L.F., 2014. Experimental characterization for a solid industrial by-product as material for high temperature sensible thermal energy storage (TES). Appl.Energ. 113, 1261-1268.

Peiró, G., Gasia, J., Miró, L:, Cabeza, L.F., 2015. Experimental evaluation at pilot plant scale of multiple PCMs (cascaded) vs. single PCM configuration for thermal energy storage, Renew. Energy 83, 729-736

Peiró, G., Prieto, C., Gasia, J., Miró, L., Cabeza, L.F., 2016 a. Two-tank molten salts thermal energy storage system for solar power plants at pilot plant scale: lessons learnt and recommendations for its design, start-up and operation. Submitted to Sol Energy.

Peiró, G., Gasia, J., Miró, L., Prieto, C., Cabeza, L.F., 2016b. Experimental analysis of charging and discharging processes, with parallel and counter flow arrangements, in a molten salts high temperature pilot plant scale setup. Appl. Energy 178, 394-403.

Pereira da Cunha, J., Eames, P., 2016. Thermal energy storage for low and medium temperature applications using phase change materials – A review. Appl. Energy 177, 227-238.

Prieto, C., Osuna, R., Fernández, A.I., Cabeza, L.F., 2016. Molten salt facilities, lessons learnt at pilot plant scale to guarantee commercial plants; Heat losses evaluation and correction. Renew. Energ. 94, 175-185.

Rathgeber, C., Miro, L., Cabeza, L.F., Hieber, S. 2014. Measurement of enthalpy curves of phase change materials via DSC and T-History. When both methods needed to estimate the behaviour of the bulk materials in applications. Thermochim. Acta. 596, 79–88

Rodríguez-García, M.M., Herrador-Moreno, M., Zarza-Moya, E., 2014. Lessons learnt during the design, construction and start-up phase of a molten salt testing facility. App. Therm. Eng. 62, 520–528.

ISES International Solar Energy Society

Conference Proceedings

EuroSun 2016
Palma de Mallorca (Spain), 11 - 14 October 2016

EXPERIMENTAL INVESTIGATIONS OF HEAT EXCHANGERS IN ICE STORAGES FOR COMBINED SOLAR AND HEAT PUMP SYSTEMS.

Daniel Carbonell , Martin Granzotto, Mattia Battaglia, Daniel Philippen and Michel Y. Haller.

SPF, Institut für Solartechnik , HSR, Hochschule für Technik ,
CH-8640 Rapperswil, Switzerland

Abstract

In the present paper different heat exchangers designed to be installed into an ice storage for solar and heat pump heating applications are experimentally investigated. Analyzed heat exchangers are capillary mats and flat plate types. For each heat exchanger, different designs, materials and number of heat exchanger units are evaluated using two different mass flows. This paper aims at i) characterizing different heat exchanger designs by means of measurements in a laboratory-size ice storage of 2 m^3, ii) determine specific advantages and disadvantages of different heat exchanger concepts for ice storages used in combination with solar collectors and a heat pump and iii) provide a source of experimental data for model validation.

Keywords: ice storage, heat exchangers, solar-ice.

Nomenclature

A_{ext}	external area of one hx [m^2]	Q	energy delivered to the storage [kWh]
A_{hx}	total hx area in the storage [m^2]	$T_{w,avg}$	averaged storage temperature [^oC]
d_i	inside diameter of CM tubes [m]	$T_{f,in}$	heat transfer fluid temperature at the inlet of the hx [^oC]
d_o	outside diameter of CM tubes [m]	$T_{f,out}$	heat transfer fluid temperature at the outlet of the hx [^oC]
H_{hx}	height of FP hx [m]	U	heat transfer coefficient of the hx [$W/(m^2K)$]
L_{tube}	length of U-shape tubes [m]	$\dot{V}_n$	nominal volume flow of the experiments [l/h]
L_{hx}	length of FP hx [m]	V_r	ice fraction [kg_{ice}/kg_{water}]
$\dot{m}$	mass flow rate of the brine [kg/s]	V_r^*	ice fraction calculated from energy exchanged [kg_{ice}/kg_{water}]
n_{hx}	number of hx in the storage	x_{tubes}	distance between tubes in one CM [mm]
n_{tubes}	number of tubes in one CM	x_{hx}	distance between hxs [mm]

CM	capillar mats	Nu	Nusselt number
FP	flat plate	PP	polypropylene
G-type	commercial name of a CM	Re	Reynolds number
heating	energy provided to the storage	SS	stainless steel
hx	heat exchanger	S-type	commercial name of a CM

doi:10.18086/eurosun.2016.03.01 Available at http://proceedings.ises.org

1. Introduction

Ice storages are a well proven technology for cooling applications where their main role consists in peak shaving of cooling loads at noon or in providing high cooling power for industrial processes (ASHRAE, 2007). On the other hand, ice storages can also be used for solar heating applications where less extraction power is needed because they serve as heat source for a heat pump and not to cover peak demands. Therefore, ice storages used in solar heating applications, in so-called solar-ice systems, can be designed with less heat exchanger area per storage unit volume compared to cooling applications (Carbonell et al., 2016b). However, this is not often the case when companies that have been traditionally working for the cooling sector are trying to enter the solar heating market designing the ice storage with the experience gained from cooling applications only.

In solar-ice applications, it is important to provide ice storages at low cost in order to be competitive with respect to alternative solutions such as boreholes for ground source heat pump systems. Furthermore, ice storages have to be reliable to keep maintenance costs as low as possible. In order to reduce installation costs, a de-icing concept can be used to avoid installing heat exchangers in the whole ice storage volume (Philippen et al. (2012),Carbonell et al. (2015)). However, for small ice storages, e.g. below 10 m^3, the ice fraction that can be achieved using a de-icing concept is significantly smaller than using a non de-icing concept. For single family houses, a solar-ice system with a large ice storage, e.g. higher than 10 m^3, will most likely not be cost competitive compared to a ground source heat pump system. Therefore, for single-family houses, ice storages based on a non de-icing concept seem to be a more attractive solution. Moreover, market available ice storages are based on a non de-icing concept, not only for small, but also for large ice storages. Most of ice storages installed in Europe are based on ice-on-coil heat exchangers, and although other heat exchanger concepts exist on the market, their specific advantages and disadvantages remain unclear.

This paper is focused on the experimental analyses of several heat exchangers for ice storage concepts that do not use a de-icing concept. The aim is to compare different heat exchanger concepts in terms of efficiency and cost with the final goal to define the cost effective heat exchanger area needed for solar heating applications. In order to achieve the final goal, it is necessary to simulate the complete solar-ice system with a well validated ice storage model that is able to consider all heat exchanger designs. Therefore, the experimental data presented in this paper will be used to validate an ice storage model in a second step. Examples of complete solar-ice system simulations can be found in recent publications, e.g. Trinkl et al. (2009), Tamasauskas et al. (2012), Winteler et al. (2014) and Carbonell et al. (2016a). Moreover, the experiments presented in the paper are also helpful to understand the physics behind the solidification and melting of ice on the different heat exchangers.

2. Experiments

2.1. Experimental set-up

The scheme of the experimental set-up is shown in Fig. 1. The inner dimensions of the ice storage are 2 m x 1 m x 1.3 m and it is insulated with 5 cm of Armaflex® (λ = 0.041 $W/(m \cdot K)$). The storage is filled with 2 m^3 of water. The heating and cooling is provided by a chiller with approximately 6 kW heating and cooling power. Five Pt100 sensors are installed inside the storage for measuring the temperature at different heights. Three Pt100 sensors are installed at the inlet/outlet of the heat exchangers, considering two possibilities for loading/unloading. An ultrasonic sensor is used to measure the height of the water level and to derive the total fraction of ice inside the storage. A volume flow sensor is installed and the volume flow is regulated by a PID control. A LabVIEW interface has been developed to run all testing sequences automatically.

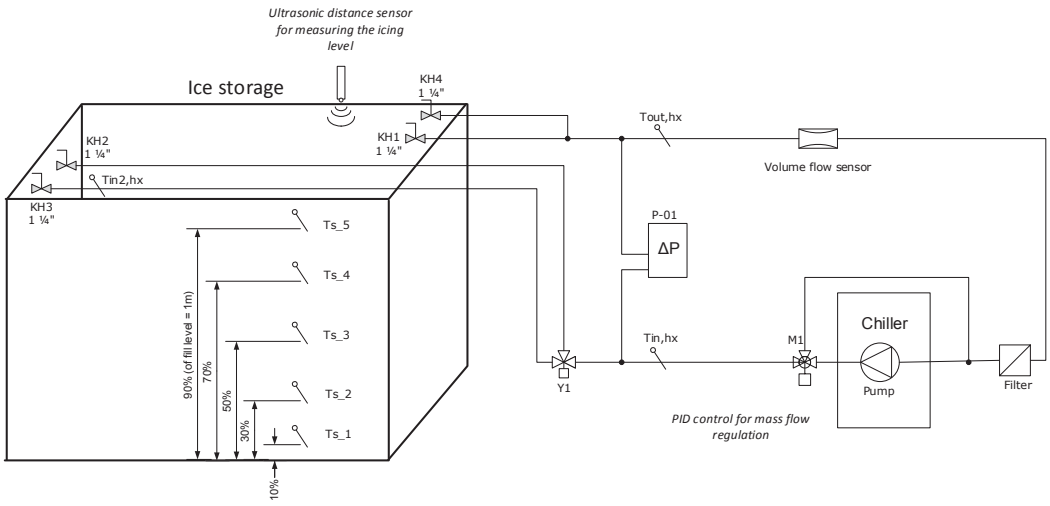

Fig. 1: Hydraulic scheme of the experimental set-up with sensor locations.

2.2. Measurement uncertainties

The temperature sensors have been calibrated in a Fluke Dry-Block Calibrator for the temperature range of the test cycles ($(-10)-40°C$). Based on the calibration, the output values of each temperature sensor were corrected according to a 1^{st} order polynomial. The remaining uncertainty of the Pt100 sensors after calibration was in the order of 0.03-0.04 K. The mass flow rate measurement was done using a magnetic flow meter, that has been calibrated for flows between 500 and 1400 l/h. The relative uncertainty of the volume flow rate measurement after the calibration of the flow sensor was determined to be 0.6% . For the glycol concentration, an acceptable range of 31.92%-34.66% has been defined. The maximal relative uncertainty of the mixture density is then estimated to be 1.0%. The relative uncertainty of the specific heat capacity is smaller than 1.3%. All these uncertainty values are used to calculate the total uncertainty of the derived values such as power or heat transfer coefficient. The relative uncertainty of the extracted power is in the order of 2%. The calculated heat transfer coefficient is affected by an uncertainty that ranges from 2.5% up to 14%. High uncertainty values are caused by small temperature differences when the ice storage temperature approaches the chiller set point temperature. Thus, system operating points with significant energy transfer are not affected by this large uncertainty values. The ice fraction calculation was done based on the changing water level in the storage tank when ice is formed or melted. The ultrasonic sensor has a precision of 0.5 mm which results in an uncertainty of the icing fraction in the order of 0.5%-1%.

2.3. Heat exchangers tested

Two capillary mats (CM) from the manufacturer Clina have been experimentally evaluated: G and S-type. All CM are made with the same kind of tubes and materials but have a slightly different design (see Fig. 2). In the S-type, the U-shape of the tube observed in the G-type is modified and the down-flow and up-flow on each tube are on the same plane. Therefore, S-types are plane and G-types are U-shaped. The G-type has 22% more heat exchanger area than S-type, but the S-type can be installed with half the time approximately.

In both designs, the mats have been connected in parallel to the distribution pipes and are tested with two different number of heat exchangers, 16 and 8. In total, four capillary mats combinations have been tested as shown in Table 1.

Two different flat plate heat exchangers have been tested, one made of stainless steel (SS) from the manufacturer Energie Solaire and the other made of polypropylene (PP) from the manufacturer MEFA. The physical

Tab. 1: Heat exchanger data for capillary mats.

Type	n_{hx} [-]	n_{tubes} [-]	L_{tube} [m]	d_i [mm]	d_o [mm]	A_{hx} [m^2]	x_{tubes} [mm]	x_{hx} [mm]
G-16	16	64	1.96	2.75	4.25	30.75	30	30
S-16	16	96	0.98	2.75	4.25	24.06	20	60
G-8	8	64	1.96	2.75	4.25	15.38	30	60
S-8	8	96	0.98	2.75	4.25	12.03	20	120

Tab. 2: Heat exchanger data for flat plates.

Type	n_{hx} [m]	L_{hx} [m]	H_{hx} [-]	A_{hx} [m^2]	x_{hx} [mm]
SS-10	10	1.854	0.834	30.93	100
SS-8	8	1.854	0.834	24.73	125
SS-6	6	1.854	0.834	18.55	167
PP-10	10	1.875	0.860	32.25	100
PP-8	8	1.875	0.860	25.80	125

data of the heat exchangers is given in Table 2.

(a) (b) (c)

Fig. 2: Examples of heat exchangers (a) 16 S-type capillary mats (b) 8 G-type capillary mats and (c) 8 polypropylene flat plates.

3. Methodology

In order to test the heat exchangers an experimental sequence has been defined and programmed in LabView. The testing sequence is summarized in Table 3. The nominal mass flow rate defined as $\dot{V}_n$ has been set to 2000 l/h. The parameter n is a factor used to reduce the mass flow when desired. All heat exchangers have been tested with n = 1 and with n = 0.5 where the volume flow is regulated with a PID control. Each test lasted around one week for each mass flow and a total of 9 heat exchanger set-ups have been evaluated. This means a total of 18 weeks of testing time are shown in this paper.

3.1. Performance indicators

For each test sequence several indicators are calculated. The heat exchanger power $\dot{Q}$ is calculated as:

$$\dot{Q} = \dot{m} c_p (T_{f,out} - T_{f,in}) \tag{1}$$

Tab. 3: Testing sequences considered for each heat exchanger.

Test phase	Name	Mass Flow	T_{set} of the chiller	Begin of sequence	End of sequence
Sensible heating	T1	$n \cdot \dot{V}_n = 1000$ l/h	20 °C	Storage at 10 °C or end of T8	steady state
	T2	$n \cdot \dot{V}_n = 2000$ l/h	40 °C	End of T1	steady state
Sensible cooling	T3	$n \cdot \dot{V}_n = 1000$ l/h	-10 °C	End of T1	$T_{s,av} \approx 0$ °C
	T4	$n \cdot \dot{V}_n = 2000$ l/h	-10 °C	End of T2	$T_{s,av} \approx 0$ °C
Solidification	T6	$n \cdot \dot{V}_n$ [a]	-10 °C	End of T3 or T4	$V_r \approx 95\%$ (or 3 days)
Cycling : Ice/melt	T8	$n \cdot \dot{V}_n$ [a]	-10 °C (40 min)		
			10 °C (20 min)	End of T6	10 cycles
Melting	T9	$n \cdot \dot{V}_n$ [a]	10 °C	End of T8	steady state

[a] with n=0.5 and n=1

where $\dot{m}$ is the mass flow, c_p the specific heat capacity and T_f the heat transfer fluid temperature. The cumulated energy for the whole test sequence until the time t is calculated as:

$$Q = \int_{t=0}^{t} \dot{Q} \cdot dt \tag{2}$$

where the time step dt is set to 10 seconds. The ice fraction is calculated as the ratio between the mass of ice and the total amount of water of the storage.

$$V_r = \frac{M_{ice}}{M_{water}} \tag{3}$$

The ice fraction is experimentally evaluated measuring the change of height of water due to the volume change between water and ice. For some processes, e.g. melting cases where the initial ice fraction is very large and the ice is above water level, the mass of ice can not be accurately obtained from experiments and therefore it is calculated from the energy exchanged with the storage, neglecting heat gains from ambient trough the storage walls. Ice fraction results that are calculated from the exchanged energy are labeled as V_r^*.

The global heat transfer rate of the heat exchanger UA is obtained from:

$$UA = \frac{\dot{Q}}{LMTD} \tag{4}$$

where the logarithmic mean temperature difference LMTD is calculated as:

$$LMTD = \frac{(T_{f,out} - T_{w,av}) - (T_{f,in} - T_{w,av})}{ln\left(\frac{T_{f,out} - T_{w,av}}{T_{f,in} - T_{w,av}}\right)} \tag{5}$$

where $T_{w,av}$ is the averaged water temperature in the storage.

The heat transfer coefficient of the heat exchanger is calculated as:

$$U = \frac{UA}{A_{ext}} \tag{6}$$

where A_{ext} is the external surface area of each heat exchanger

4. Results

The experimental results are split into sensible heating , sensible cooling, icing, melting and cycling of icing/deicing. Results for flat plates made of polypropylene with a volume flow of 1000 l/h are not shown in the following sections because we have detected problems in the flow distribution.

4.1. Sensible heating (T1 and T2)

Measured overall heat transfer coefficients for sensible heating process with capillary mats and flat plates are shown in Fig. 3 . Circle marks are for 2000 l/h and for T2, i.e. the storage is heated from 20 °C to 40 °C. Filled triangles are for 1000 l/h and for T1, i.e the storage is heated from 10 °C to 20 °C.

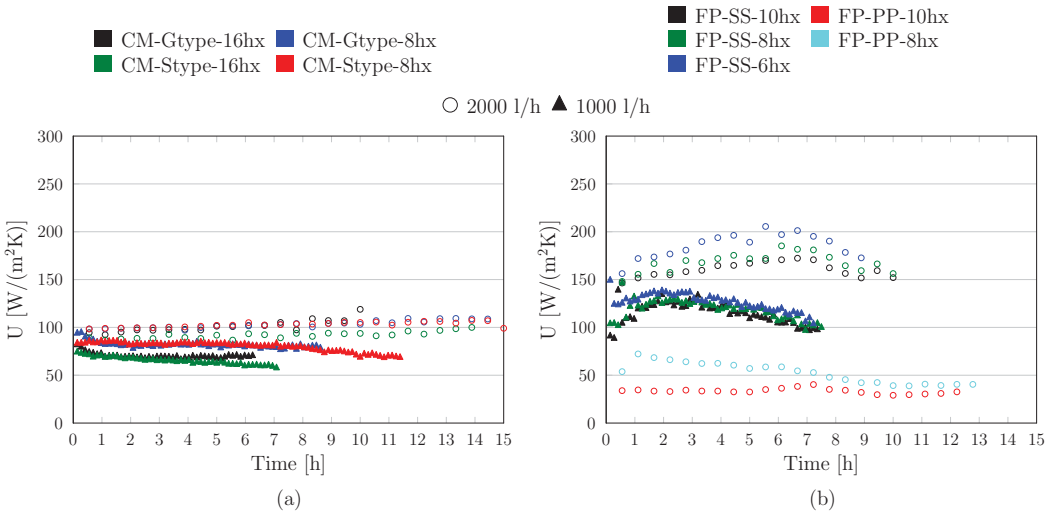

Fig. 3: Overall heat transfer coefficient results for sensible heating sequences T1 and T2 for (a) CM and (b) FP. Circle marks are for 2000 l/h and T2 (heating from 20 °C to 40 °C) and filled triangles are for 1000 l/h and T1 (heating from 10 °C to 20 °C)

The overall heat transfer coefficient U is shown in Fig.3. FP-SS show higher capacities for providing energy to the storage by means of sensible heat. For a flow rate of 2000 l/h, U is in the range of 90-110 W/(m^{2}K) for CM and between 150-200 W/(m^{2}K) for FP with SS. For 1000 l/h U values are decreased to values between 70 and 90 W/(m^{2}K) for CM and to 100-140 W/(m^{2}K) for FP-SS approximately. The main difference between the two different designs of capillary mats, G and S types, is the heat exchanger area as U values are very similar. FP-PP show a much lower performance compared to FP-SS and the performance of CM is better than the one of FP-PP but worse than the one of FF-SS. The performance of CM and FP-PP remains relatively constant for all the sequence even that the Reynolds number (Re) increases due to the lower viscosity of the fluid when it is heated. During the whole test sequence the Re number remains below 400 for 2000 l/h and below 150 for 1000 l/h and therefore is always in a theoretical laminar regime. In a laminar flow regime the Nussel number is relatively constant and therefore the performance of the capillary mats are not affected by the increase of Re during the heating process and only slightly due the change of mass flow. However, FP-SS are significantly affected by the mass flow because they have a special design that enhances turbulence. For these type of heat exchangers the Re number where the flow is turbulent is much lower than that for smooth pipes. The flow regime found in these experiments for FP-SS are most of the time in the transition regime between laminar and turbulent and therefore, the Nu numbers, and thus the U values, are affected by the Re number.

4.2. Sensible cooling (T3 and T4)

Overall heat transfer coefficients U for capillary mats and flat plates for sensible cooling process are shown in Fig. 4 . Circle marks represent $\dot{V}_n$ of 2000 l/h and a test sequence in which the storage temperature is cooled from 40 °C to 0 °C. Triangle marks represent $\dot{V}_n$ of 1000 l/h and a test sequence in which the storage temperature is cooled from 20 °C to 0 °C.

The overall heat transfer coefficient shows a very different behavior for CM and FP-SS. For FP-SS, the U values decrease significantly with time. For CM the U values remain approximately constant for a large time period. The reason for that is the same given in section 4.1, i.e. capillary mats are always in a laminar regime while

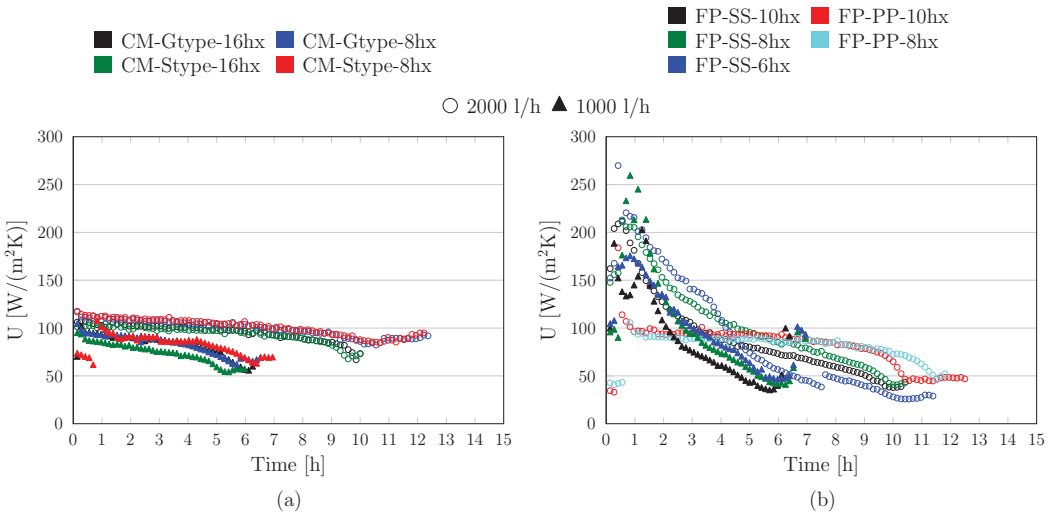

Fig. 4: Overall heat transfer coefficient results for sensible cooling sequences T4 for (a) CM and (b) FP. Solid lines are for 2000 l/h and the cycle starts at T_s of 40 °C; dashed lines are for 1000 l/h and the cycle starts at T_s 20 °C

FP-SS are in the turbulent and transition regime. In this case, the Re number decreases along the sequence because the fluid's viscosity is increased when cooled down to 0 °C. At the beginning of the test sequence, FPs perform significantly better than the CMs, and the opposite is true at the end of the test sequence. The U values range from 120 to 75 W/(m^{2}K) for 2000 l/h and from 100 to 60 W/(m^{2}K) for 1000 l/h when CMs are used; and they range from 220 W/(m^{2}K) to 40 W/(m^{2}K) using 2000 l/h and from 175 W/(m^{2}K) to 40 using 1000 l/h when FP-SS are used. The evolution of U along time for FP-PP is similar to the one observed with CM when 2000 l/h are used. The U values are relatively constant and in the range of 100 W/(m^{2}K) for a large period. The efficiency of the heat exchangers is reduced when the storage water temperature is close to 0 °C, when ice starts to grow, the U value increases.

4.3. Solidification (T5)

The amount of ice produced for capillary mats and for flat plates are shown in Fig. 5. From these results it seems clear that capillary mats are faster compared to flat plates in the process of water solidification. Ice fractions above 95 % were achieved with CM without damaging the casing. Due to the specific height of the

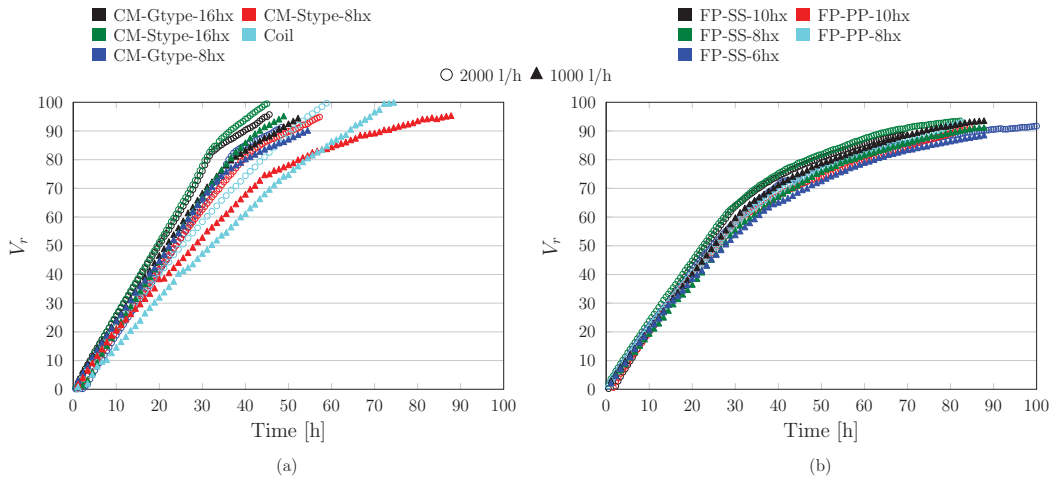

Fig. 5: Evolution of the ice fraction over time for the icing sequence T5 for (a) CM and (b) FP.

FP, only 85% of the storage height was covered by the heat exchangers, limiting its capacity to ice the whole storage. Mass ice fractions higher than 85% with FP are possible but with very low power since ice has to grow on the surface of a compact ice cube that includes all plates with a long path between the heat transfer fluid in the heat exchanger and liquid storage water. For FP, ice fractions above 90% where achieved and the casing of the storage did not show any problem.

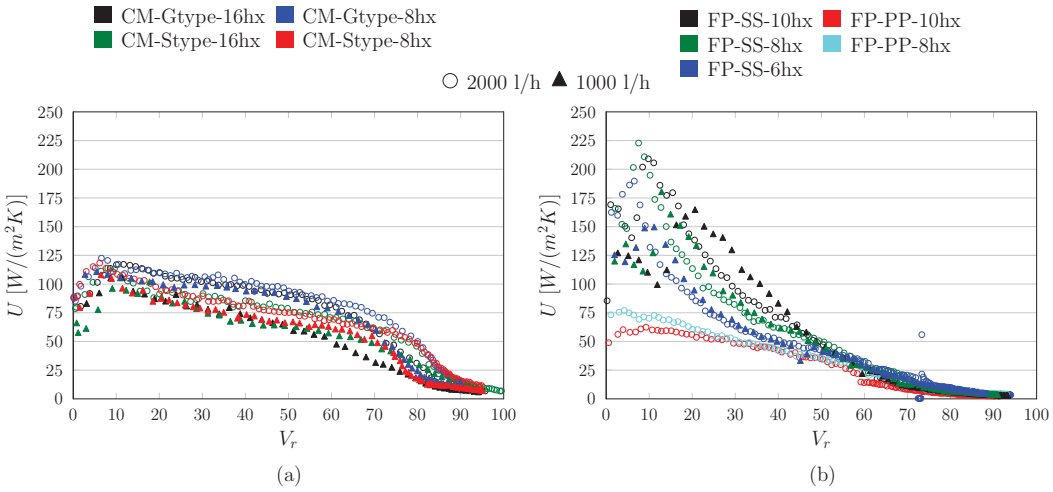

Fig. 6: Overall heat transfer coefficient as a function of the ice fraction for the icing sequence T5 for (a) CM and (b) FP.

The overall heat transfer coefficient is shown in Fig. 6 as a function of the ice fraction. From this graph it can be observed that the decrease of U for CM is much smaller compared to FP. Considering the ideal case of ice growing on a single tube, the higher thermal resistivity of the ice layer when ice grows is partially compensated by the higher contact area on the outside of the tube. Therefore, the heat transfer rate UA value remains relatively constant when ice grows on a cylinder (Carbonell et al., 2015). However, CM, are composed of many tubes very close to each other and the ideal unidimensional ice growing on a single tube is only valid until ice growing from neighboring tubes contact with each other. For example, for the S-type, the distance between tubes in one heat exchanger is 20 mm. Assuming that ice grows homogeneously on all pipes and along the whole pipe length, ice layers start to touch to each other within one heat exchanger when V_r is approximately 27% and 14% for 16 hx and 8 hx respectively. For G-type, the distance between pipes is 30 mm, this means that ice layers between pipes touch when the ice fraction is approximately 80% and 40% for 16 hx and 8 hx, respectively. The phenomenon of physical contact between ice layers is usually called constrained ice growing (Jekel et al., 1993). For all CM, the heat exchangers suffer of a two step constrained ice growing, the first one when the ice is constrained within one heat exchanger (ice between adjacent tubes touch each other) and the second when ice is constrained between neighboring heat exchangers. When ice growing is constrained the overall heat transfer coefficient decreases compared to the unconstrained case because the contact area between the growing ice and storage water decreases. However, in the experimental results it is not possible to observe a sharp decrease of the U value when ice constrainment occurs because ice grows unequally along the length of each tube and thus the ice growing is constrained slowly over a long period. For FP ice starts to be constrained when the ice thickness is half the distance between heat exchangers. This corresponds always to an ice fraction of approximately 83%. At these conditions all water between heat exchangers is frozen and ice can only grown on the surface of a solid cube of ice with very low U values. Comparing CM with FP one can observe that for low ice fractions the U values of FP-SS are higher. However, the decrease of the U value when ice grows is much more pronounced for FP-SS compared to CM. As said before, the contact area between ice and water increases when ice grows in CMs. Instead, for FPs the ice surface area remains approximately constant and the U value decreases rapidly. For FP with PP, the decrease of efficiency is much less pronounced in comparison to SS because the heat transfer resistance of the polypropylene is the limiting factor, in comparison to the FP-SS

where the ice thickness is the limiting factor.

4.4. Melting (T9)

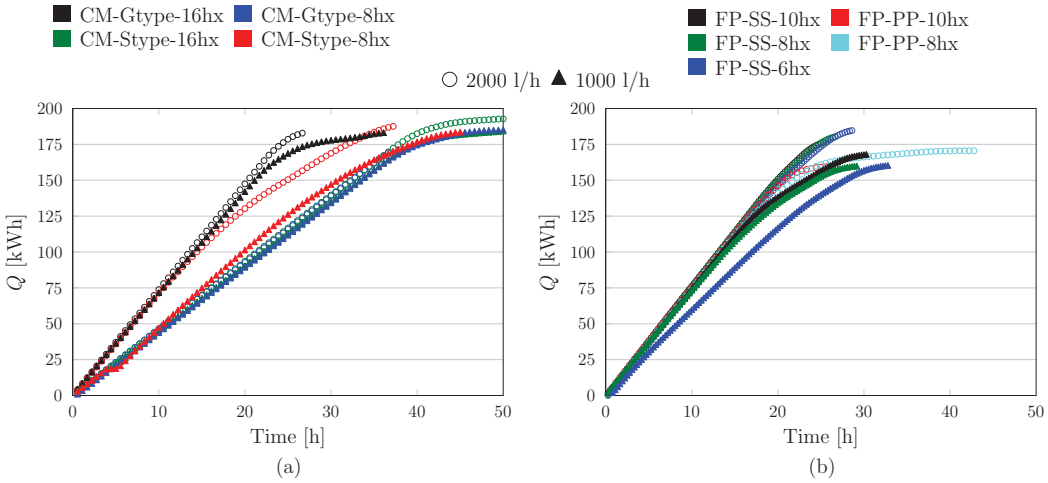

Fig. 7: Energy delivered to the storage by the heat exchangers for the melting sequence T9 for (a) CM and (b) FP.

The energy delivered for melting the ice is shown in Fig. 7. Melting 2 m^3 of water needs about 185 kWh. On top of that, the energy needed to heat the subcooled ice to 0 ^oC and the sensible heat to raise the temperature from 0 ^oC to 10 ^oC needs to be considered. Comparing CM with FP one can observe that FP-SS are usually able to melt completely the ice in less time. The measure for the ice fraction for capillary mats was not accurate with the method used in these experiments. A water layer above the ice block was not always present at high ice fraction (> 95%) and the measure of solid ice was disturbing the accuracy. Because the flat plates had a layer of 17 cm of water above them, the measurement of the melted ice were much more accurate. However, even in this case, with the method used, it is not possible to measure the ice fraction until the melted ice connects to the water of the storage. Before this cavity of ice is melted, the change of density when the ice is melted creates an underpressure around the hx that would either expand the heat exchanger or evaporate part of the water until the change of volume is filled.

Overall heat transfer coefficients are shown in Fig. 8. FP-SS have the highest melting capacity at high ice fractions with values above 250 W/(m^2K). For ice fractions below 60% the U values reduce to 50-60 W/(m^2K) for FP with SS. For CM, the U values are more stable over the whole melting process with values between 50-80 W/(m^2K).

4.5. Cycling (T8)

The cycling experiment consist of 10 sequences of heating and cooling which are used for melting and icing. This test sequence is performed at a very high ice fraction after the icing sequence T5. Each cycle is performed with a constant time of 20 min for heating and 40 min for cooling. All experiments with CM were tested with cycles always on the subcooled zone and therefore melting was not achieved. For this reason the test control was changed such that it heats up the storage until the outlet of the heat exchanger is close to zero before cycling starts. In this way it is ensured that ice is melted and solidified during each cycle. As an example, results for cycling sequence are presented in Fig. 9 for FP with 10 hx. For all the cycles the inlet temperature of the heat exchangers increases above 0 ^oC, which means that it is always possible to melt ice, at least the entrance of the heat exchangers. For the first four cycles, the outlet temperature remains at 0 ^oC, which means

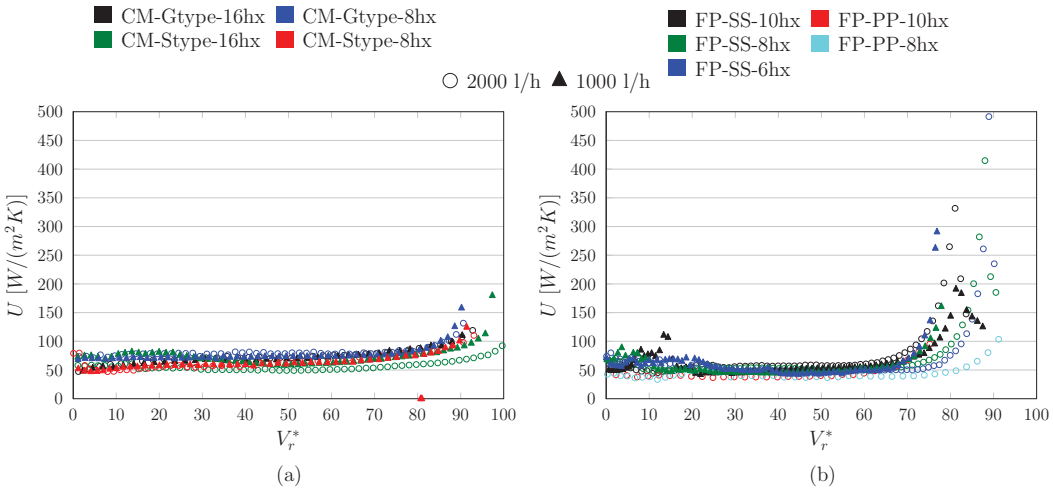

Fig. 8: Overall heat transfer coefficient for melting sequence T9 for (left) CM and (right) FPs.

that ice is never subcooled at the end of the heat exchanger. After the first cycles, the outlet temperature starts to drop below 0 °C which means that ice is subcooled, and the UA values are reduced because the heat of fusion is not released along the whole length of the hx.

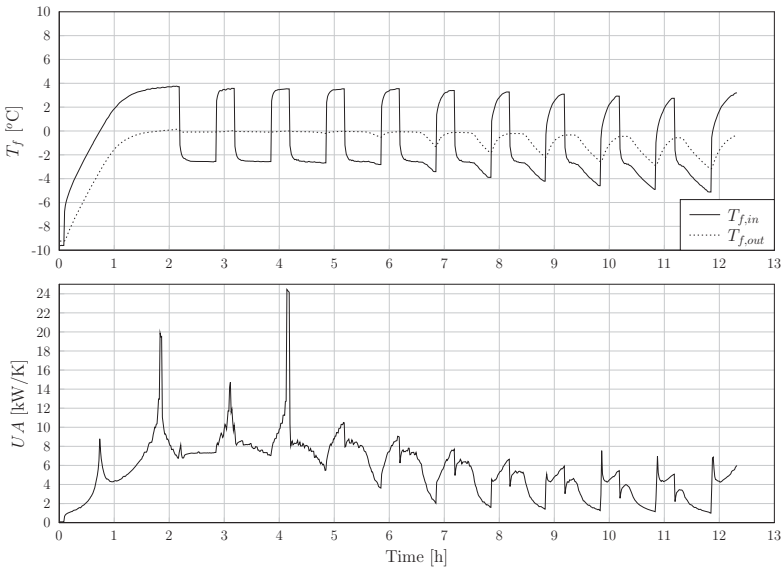

Fig. 9: (a) Heat exchanger temperatures and (b) overall heat transfer coefficient for cycling sequence T8 and FP.

The danger of breaking the casing of the storage is potentially higher when cycles of melting and icing exist at high ice fractions. In normal icing conditions without any cycles, the solid ice will always push the liquid water to the surface. Therefore, as long as there is an escape way for the water, there is no risk for the casing. The problem may occur when a volume of water in contact with the casing is trapped within an ice block. If then this water is iced, the volume expansion will produce a strong force to the wall of the casing with the danger of breaking it. This situation may occur when the dynamics of the system are on a specific state, which was never the case in the lab.

In this test several cycles of melting and icing have been performed at very high ice fractions in order to test the robustness of the heat exchangers under these dynamic conditions. The mechanical stress that was caused

by the dynamics of icing and melting was neither found to be a problem for the heat exchangers nor for the storage casing. However, long term tests should be performed to investigate the robustness and stability.

The cycling sequence will also be very useful for the validation of the ice storage model (not provided in this paper), since in each cycle different physical phenomena take place. Fig. 10 shows one cycle of melting and icing for FP-SS with 10 hx (zoom into Fig. 9). The sequence has been split into five zones, from I to V as shown in Fig. 10. Zones I to II correspond to heating/melting and zones III to V correspond to cooling/icing.

- Zone I : switch from cooling to heating.
- Zone II: the ice is heated from the subcooled state to 0 ^{o}C and melted starting from the entrance of the heat exchangers. Most likely, melting does not occur over the whole length since the outlet temperature remains below 0 ^{o}C.
- Zone III: cooling of the water until freezing conditions.
- Zone IV: icing of the water.
- Zone V: subcooling of ice.

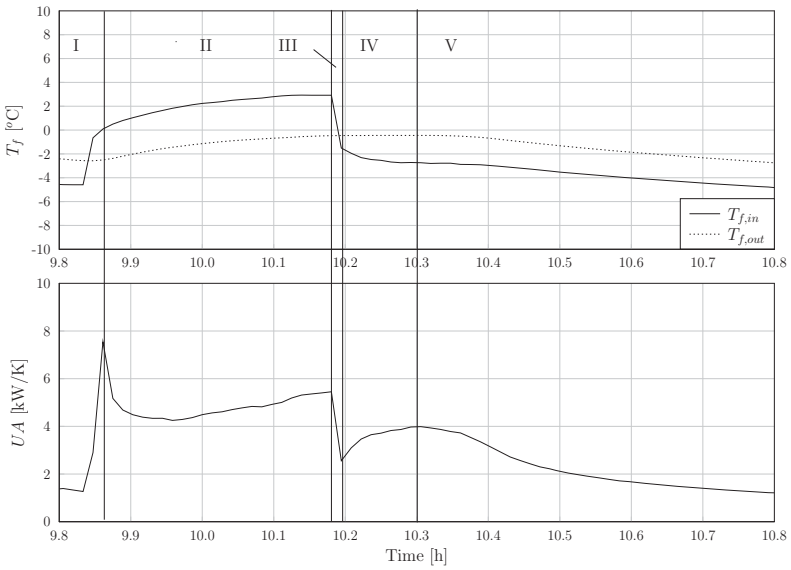

Fig. 10: (a) Heat exchanger temperatures and (b) heat transfer rate for cycling sequence T8 and FP.

5. Conclusions and future actions

In the present work several heat exchangers have been analyzed, including capillary mats with different designs made of polypropylene and flat plates made of stainless steel and polypropylene. The area analyzed has been modified for each heat exchanger and all test have been performed using two different mass flow rates. In total, nine possibilities have been experimentally evaluated for several test sequences including sensible heating and cooling, icing, melting and cycling. The main conclusions of the study can be summarized as:

- Very high ice fraction can be reached with all heat exchangers and mass flows.
- The casing did not show any damage under high ice fraction conditions. This means that designing an ice storages able to reach 95% ice fraction or higher should be safe.

- All heat exchangers showed to be reliable and robust under the test conditions. Long term tests were not carried out.
- Flat plates made of stainless steel are better suited compared to capillary mats for sensible heating and cooling and for melting processes.
- Capillary mats are better suited compared to flat plates for the icing process due to the strong decrease of performance that flat plates suffer when ice grows.
- Flat plates made of polypropylene have shown the worst thermal performance of all tested hxs.
- The poor flow distribution for 1000 l/h in the case of flat plates made of polypropylene needs to be further investigated.

An ice storage model able to consider all these heat exchanger designs has been developed and it is being validated with the experiments presented here. As a next step, system simulations with TRNSYS will be carried out with the validated ice storage model. With these simulations, it will be possible to find an optimum between the energetic system efficiency and the cost of the ice storage as a function of the heat exchanger area.

Acknowledgments

The authors would like to thank the Swiss Federal Office of Energy (SFOE) for the financing support received under the project Ice-Ex.

References

ASHRAE, 2007. Handbook : HVAC Applications. American Society of Heating, Refrigerating and Air-Conditioning Engineers, Inc.

Carbonell, D., Philippen, D., Granzotto, M., Haller, M.Y., 2016a. Simulation of a solar-ice system for heating applications. system validation with one-year of monitoring data. Energy and Buildings 127, 846 – 858.

Carbonell, D., Philippen, D., Haller, M.Y., 2016b. Modeling of an ice storage buried in the ground for solar heating applications. Validations with one year of monitored data from a pilot plant. Solar Energy 125, 398–414.

Carbonell, D., Philippen, D., Haller, M.Y., Frank, E., 2015. Modeling of an ice storage based on a de-icing concept for solar heating applications. Solar Energy 121, 2–16.

Jekel, T.B., Mitchell, J.W., Klein, S.A., 1993. Modeling of ice storage tanks. ASHRAE Transactions 99, 1016–1024.

Philippen, D., Haller, M.Y., Logie, W., Thalmann, M., Brunold, S., Frank, E., 2012. Development of a heat exchanger that can be de-iced for the use in ice stores in solar thermal heat pump systems, in: Proceedings of EuroSun, International Solar Energy Society (ISES), Rijeka and Opatija, Croatia.

Tamasauskas, J., Poirier, M., Zmeureanu, R., Sunyé, R., 2012. Modeling and optimization for a solar assisted heat pump using ice slurry as a latent storage material. Solar Energy 86, 3316–3325.

Trinkl, C., Zörner, W., Hanby, V., 2009. Simulation study on a domestic Solar/Heat pump heating system incorporating latent and stratified thermal storage. Journal of Solar Energy Engineering 131, 041008.

Winteler, C., Dott, R., Afjei, T., Hafner, B., 2014. Seasonal performance of a combined solar, heat pump and latent heat storage system. Energy Procedia 48, 689–700. Proceedings of the 2nd International Conference on Solar Heating and Cooling for Buildings and Industry (SHC 2013).

Conference Proceedings

EuroSun 2016
Palma de Mallorca (Spain), 11 - 14 October 2016

A novel heat battery to save energy & reduce CO_2 emission

Ruud Cuypers, Anca Anastasopol, Ard-Jan de Jong, Henk Oversloot, Laurens van Vliet, Pavol Bodis, Christophe Hoegaerts

TNO Process & Instrument Development, Leeghwaterstraat 44, 2628 CA Delft, The Netherlands,
T: +31-88 866 24 72; E: ruud.cuypers@tno.nl

Abstract

In our labs and pilot sites, a novel heat battery for dwellings and offices is being developed. Based on a thermochemical sorption reaction, space heating, cooling and generation of domestic hot water will eventually be demonstrated in an existing dwelling by using solar or waste heat in the CREATE project. Developments of the active materials, of the reactor and components, and of the system were mainly performed in the MERITS project, and results are briefly described. Upon wide-spread use, the technology of compact thermal storage can be the game changer in the transformation of our existing building stock towards near-zero energy buildings.

Keywords: *thermal storage, energy storage, sorption storage, thermochemical storage, seasonal storage*

1. Introduction

For the transition to a 100% renewable energy economy, the application of solar energy (including electricity and thermal energy) is essential. As solar energy strongly fluctuates not only during the day but also during a year, it will be necessary to store large amounts of energy during at least half a year. Diurnal thermal storage can be arranged by mature boiler technology (sensible storage), but seasonal storage requires considerably lower heat losses. Besides, seasonal heat storage for domestic applications requires compact systems. Thermochemical storage provides a favorable solution, theoretically being loss-free during storage, and very compact. In this paper, we show (Fig. 1) that for the first time thermochemical energy storage has been demonstrated on a large and relevant scale.

Fig. 1: MERITS Field Test Demonstrator 3D systems model (left) and Field Test Demonstration container during pre-testing in Lleida, Spain (right)

doi:10.18086/eurosun.2016.03.08 Available at http://proceedings.ises.org

In practice, energy storage densities can be reached that are in the order of boiler technology storage densities, but with much reduced thermal energy losses during storage periods. The current paper describes results obtained from the MERITS project (www.merits.eu), which was aimed at designing, building and evaluating prototypes of a compact seasonal solar-thermal energy storage system based on thermochemical storage materials, i.e. a thermal battery. The team worked with a novel thermochemical material reaction having high energy density that can supply required heating, cooling and domestic hot water (DHW) for a dwelling with up to 100% renewable energy sources throughout the year. Furthermore, an outlook of future improvements to be performed in the CREATE project (www.createproject.eu) will be given. The CREATE project has as main aim to develop and demonstrate a heat battery, i.e. an advanced thermal storage system based on Thermo-Chemical Materials, that enables economically affordable, compact and almost loss-free storage of heat in existing buildings. To this end, demonstration will eventually take place in a dwelling.

2. Improvement over available thermal energy storage techniques

Loss-free compact affordable thermal energy storage would greatly enhance the use of sustainable heat from solar or waste sources. Different forms of thermal energy storage exist today: sensible storage, latent storage (through phase-change materials) and thermochemical storage.

Sensible storage makes use of the thermal capacity of a liquid or solid. Through heating, a certain quantity of heat can be sensibly stored in said materials, e.g. in hot water systems. Roughly 50 m^3 of water would be needed for storing 10 GJ (2778 kWh) of heat in a temperature range between 40 and 90 °C. Even when this volume would indeed be available in domestic applications, it will have insufficient storage capacity because of the thermal losses.

Latent thermal energy storage makes clever use of melting/solidification of certain classes of materials (phase change materials, PCMs). Examples are ice/water, different kinds of salts, or paraffins, having storage densities roughly between 0.2 – 0.4 GJ/m^3 (roughly 56 – 111 kWh/m^3) on a materials level and for temperature ranges for domestic applications. Although slightly more compact than sensible energy storage, losses play a large role here as well.

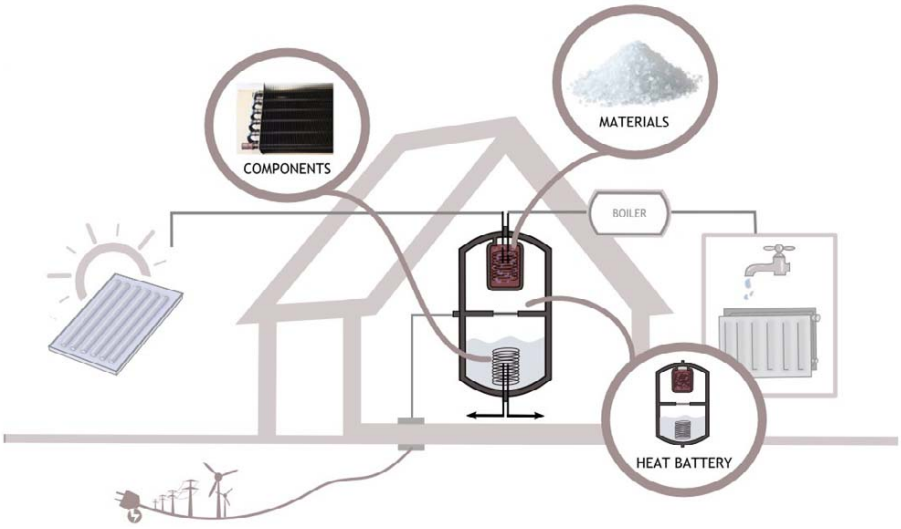

Fig. 2: Schematic of the project concept for heat battery development for dwellings application (Low-temperature heat source not shown)

Thermochemical storage is the process of using heat of reaction (enthalpy) of reversible chemical reactions for thermal storage applications. In theory, very high thermal storage densities can be reached (as high as 1-3 GJ/m^3 or 278 – 833 kWh/m^3 at the level of storage material for typical sorption reactions of salt hydrates around temperatures of 60-140°C). In addition, no thermal losses occur during storage. For this reason, the MERITS project ultimately targeted demonstration of thermochemical storage solutions for dwelling applications. Further key development issues are delivery of heat on different dedicated temperature levels

for heating, cooling and DHW, design and development of a dedicated solar collector, integrated design for the components and enhanced thermochemical materials, including the control system, and development of business models and market strategies to foster swift market take-up. Many of these developments have been described already elsewhere (see e.g. de Jong et al., 2014; Solé et al., 2015; Volmer et al., 2015)). The follow-up project CREATE aims to deal with 3 key aspects:

- Economical affordability: For the existing building stock our project will target at least a reduction of 15% of the net energy consumption on building level with a potential simple payback time shorter than 10 years;
- Compactness: Novel high-density materials will be used in order to limit the use of the available space to a maximum of 2.5 m^3 thermochemical material;
- No heat losses during storage: This is an intrinsic material/system property of thermochemical storage technology, thereby enabling long-term storage.

As sub-objectives of these aspects, stable and efficient materials for thermochemical storage, a long life-time, affordable technology, efficient and high power discharge, and safe and reliable operation are specifically addressed. In addition, the future value-chain is mobilized, having all the required key players in the supply and value chain from the material level up to the system level and the energy grid in the current consortium. The project concept is based on advanced compact thermal storage for existing dwellings using thermochemical storage materials (Fig. 2). The heart of the system is a modular setup consisting of vessels that contain the salt. In the time between dehydration and hydration the energy is stored in the salt. We envision two applications for the heat battery:

- Decentral thermal energy storage bridging supply and demand of renewable thermal energy;
- Decentral grid-connected storage for increasing energy efficiency and introducing flexibility in the electricity grid, e.g. using a heat pump.

A more efficient system design will enable demonstration of the concept in the real conditions: the system will be installed into a single family house in Warsaw, Poland, where a continental climate delivers both cold winters and warm summers.

3. Thermochemical storage – principle

Several possible examples of reversible thermochemical reactions taking place in the relevant temperature range are given below:

$K_2CO_3 + 1½H_2O \rightarrow K_2CO_3.1½H_2O$ (eq. 1)

$Na_2S.½H_2O + 4½H_2O \rightarrow Na_2S.5H_2O$ (eq. 2)

$MgCl_2.2H_2O + 4\ H_2O \rightarrow MgCl_2.6H_2O$ (eq. 3)

$CaCl_2 + 2H_2O \rightarrow CaCl_2.2H_2O$ (eq. 4)

The same hydration states occur in the reverse reactions.

When heating the hydrated salt to 80°C and condensing the water at a temperature below 20°C, both dehydration steps can theoretically be used and a very high theoretical storage density (up to 2.9 GJ/m^3 hydrate or 806 kWh/m^3 hydrate, at the level of the storage material) can be achieved forming the dried salt and water. On hydrating the salt by evaporating the water again at a temperature of >10°C, heat is released at temperature levels that can be used for heating and DHW purposes (>60°C). Keeping the compounds separate ensures storage of the reaction enthalpy, i.e. the heat. Typically, a low-temperature heat resource, e.g. a nearby lake, canal, or ground-source, takes care of the heat necessary for evaporation and of

condensation upon drying. Unlike in the sensible and latent thermal storage techniques, thermochemical storage takes place at ambient rather than at elevated temperatures because technically chemical potential is stored. In turn, it makes efficient thermal storage independent of storage times. Only when the products are brought together the enthalpy of reaction is released again, thereby generating heat. Uniquely, this ultimately enables long-term low-loss heat storage with very high thermal energy storage densities. The MERITS technology has been previously shown to enable theoretical storage densities around 1000 MJ/m^3 (278 kWh/m^3; de Jong et al., 2016). Further requirements playing a role are of course cycleability, safety, and toxicity, alongside cost.

4. Field test demonstration

The current system, the demonstration system of the MERITS project containing various subsystems such as solar collectors, short term storage vessel, long term thermochemical storage modules, underfloor heating, ceiling cooling, and a DHW system, was designed in July 2014. All compartments, i.e. the heating & cooling systems, the technical space and the single family dwelling compartment complete with windows, ventilation and door, are integrated in a 45 ft. sea container and fully equipped with measuring and control equipment (Fig. 1).

The performance of the MERITS Field Test Demonstrator (FTD) (Fig. 3) has been tested successfully at different levels: subsystem testing, where each component (i.e. Short Term Storage Vessel (STSV), High Temperature Solar Collectors (HCS), Space Heating Distribution System (HDS), Adsorption Cooling Distribution System (CDS), Domestic Hot Water Distribution System (WDS), Long Term Storage System with Thermochemical Storage Modules (LTS), Power supply, and data acquisition and control system) is tested under specific initial and boundary conditions; scenario testing, where each component is tested according to its standard operation; and 'MERITS mode' testing, where all subsystems are tested altogether according to the standard operation of the whole field test demonstrator.

The long term storage system, the main innovation in the FTD, is connected to the short term storage vessel and in periods with surplus of solar heat, used to sequentially charge the long term storage modules. During periods wherein the solar collectors do not provide sufficient heat, the modules are discharged into the short term storage vessel to provide sufficient temperature in the storage vessel, to provide DHW and heating of the dwelling at all times. All relevant volume flows and temperatures and additionally also the pressures inside the TCM modules are measured and recorded using the data acquisition and control software.

Until now, the actual application of thermochemical storage in the built environment has not been demonstrated. The main reason for this is that the thermochemical storage system is currently still complex, and as yet still too large and costly. Laboratory tests have been performed with thermochemical storage modules in an emulated environment, using the parameters below for loading and unloading the thermochemical material.

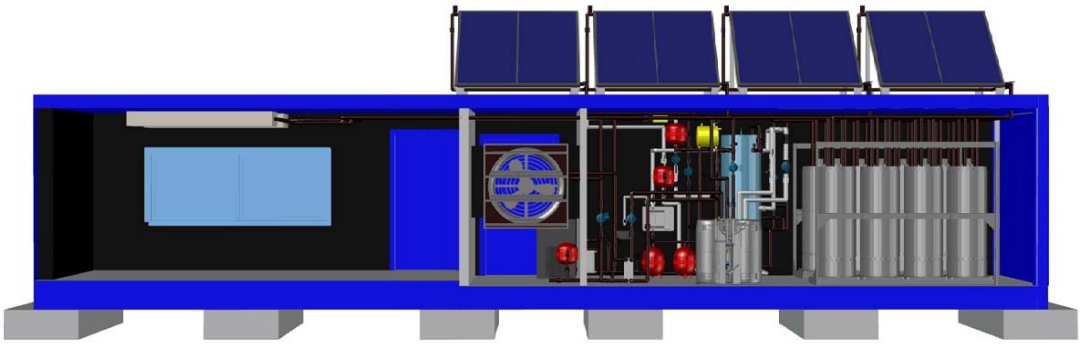

Fig. 3: 3D Visualization of the FTD

The goal of field test demonstration of a heating system with thermochemical storage modules is to enable scientists and application engineers to assess characteristics of the full system including all interactions

outside of laboratory circumstances. Not only is the tested system more complex and more voluminous than any tested laboratory setup, variations in conditions deliver 'real' and ever changing use-case conditions. Whereas in the laboratory the external conditions can be fully specified and controlled, in a real environment these conditions vary widely with time (day/night, seasons) and this will have a great impact on the system performance; especially the influence of condenser heat sink and evaporator heat source temperature fluctuations on system performance should be properly assessed. The system behavior with these varying circumstances offers a wealth of data for analysis and improvement. Moreover, the field test container is mobile, and therefore enables testing in different climate zones.

The long term thermochemical storage system (heat battery) in the MERITS project consists of 8 modules providing a low-loss design thermal energy storage capacity of 482MJ delivered from the water and salt working-pair. The 8 modules are placed into two racks (Fig. 4). Each rack is equipped with header piping, actuator valves and electronics to control the water flow through the TCS module and control the internal valve of TCS module. In order to limit the thermal energy losses during the start-up processes before the actual charge or discharge of a module can be executed, the choice has been made to build 4 smaller modules per rack rather than one big one. In addition, modularity helps to tune the system to the local needs without the need to make dedicated designs for every particular case.

Fig. 4: Rack with 4 thermochemical storage modules inside the Field Test Demonstrator

5. Active materials cycling – results

For the FTD's, 7 batches of ~90kg salt hydrate powder have been produced after which the modules were filled. After finishing of the modules, they have been tested in the lab before integration into the FTD container. Constant and well-defined testing conditions have been applied to evaluate both the potential storage density as well as the dynamics of charging and discharging. Additional tests with closed internal valve have been performed to evaluate the thermal losses. In addition, after integration of the modules into the FTD container, more charging and discharging tests have been performed before the system was actually run with the automated system control.

Fig. 5 shows a typical example of the measured powers on evaporator/condenser side and on absorber/desorber side for a discharge/charge/discharge cycle with a desorber inlet temperature of 80°C during charging reaching 52°C during discharge at a constant evaporator/condenser inlet temperature of 10°C both for charge and discharge. During discharge a power >500W with a plateau between 600 and 700W is delivered for about 12h (Fig. 5 red line, first half cycle). In sum, more than 30 MJ of energy is released in this module under these conditions. After recharging for 30 hours (Fig. 5, second half cycle),

another discharge took place with similar characteristics (Fig. 5 red line, third half cycle). Taking into account the losses (especially internal losses between reactor and evaporator) and the thermal mass of the reactor (heat exchanger, active material), an amount of about 9 kg of water is cycled under these conditions. This is roughly half of what would theoretically be possible from material equilibrium data.

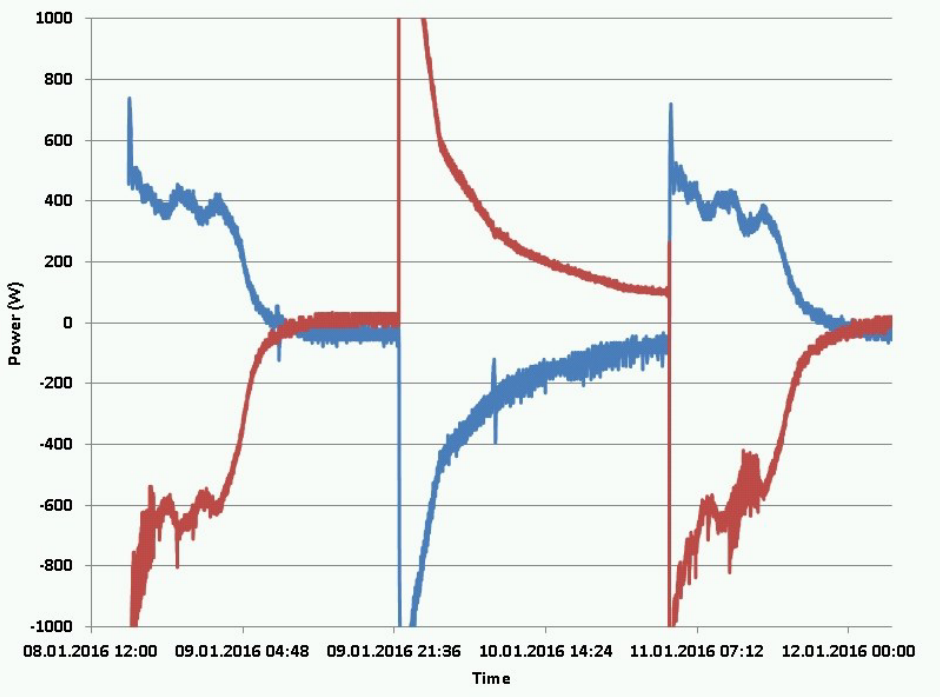

Fig. 5: Power of a typical module during 3 consecutive half-cycles (discharge/charge/discharge) of 30 hours each, showing reversible behavior during loading and unloading of the thermochemical material under relevant operating conditions, with power exerted in the absorber/desorber in red, and power exerted in the evaporator/condenser in blue; + is heat delivered to heat exchanger; - is heat delivered by heat exchanger.

During operation of the FTD, it became clear that several operational issues still have to be resolved. For example, the low amount of water cycling inside the field test demonstrator might be due to the fact that the charging power drops to very low values due to an additionally observed gas pressure in the charging phase that reversibly disappears during discharge. Furthermore, additional losses in the external hydraulic circuit and specific behavior of the discharge control are thought to be to blame for this.

6. Conclusions & outlook

For the first time, a thermochemical storage system has been demonstrated on a relevant scale for domestic application (heating & DHW), with thermochemical energy storage densities in the order of sensible storage density on a module level, but without thermal energy losses during storage periods. Initial results demonstrate the applicability of the compact long-term storage system for seasonal solar energy storage. In the present studies, our initial results show a storage density of around 100 MJ/m^3 (28 kWh/m^3) on a module level, i.e. in the same order of magnitude of some existing sensible thermal storages but with the benefit of unlimited storage times. In the CREATE project, salt selection is still under investigation. In future application in the CREATE project, a theoretical thermal energy storage density of up to 600 MJ/m^3 (168 kWh/m^3) should be achievable on a module level, i.e. well beyond existing thermal storages on the market today.

The system heat storage density depends on much more than just the active material reaction storage density, because additional components such as vapor and heat conducting structures (e.g. tubing, vessel, heat exchangers, etc.) are present. The main challenge of designing the FTD was to dimension all components

properly. Another challenge was the scale-up of the material production from lab-scale to full size prototype-scale.

Future research is directed towards further clarifying the cyclic behavior of the thermochemical storage modules, amongst others by clarifying cycling behavior of the active materials alone or as composites. In addition, the major points of attention are to increase thermal storage density in the modules significantly, and to increase the storage capacity on a system level. Also an in-depth life-cycle analysis will be performed after the first major improvements have been made.

In short, during operation of the FTD, it became clear that several operational issues still have to be resolved. Implementation of the CREATE project concept taking into account many of these issues is foreseen in typical European dwellings. To demonstrate applicability of the thermochemical storage solution and its operation in real life conditions and to receive early user feedback, a full scale solar TCS system will be installed in a single-family house in Warsaw, Poland, where a continental climate delivers both cold winters and warm summers. Optimizing the current compact storage technology to its full extent will lead to reduction of CO_2 emission and energy savings due to better use of available renewable energy sources instead of fossil energy.

7. Acknowledgements

The research leading to these results has received funding from the European Commission Seventh Framework Program (FP/2007-2013) under grant agreement No ENER/FP7/295983 (MERITS) and from the H2020 research programme under grant agreement No 680450 (CREATE). All MERITS and CREATE partners of TNO (De Beijer RTB, Fraunhofer ISE, Glen Dimplex, Mostostal Warszawa, Tecnalia, Ulster University, Universitat de Lleida, and VITO, and AEE INTEC, Caldic, D'Appolonia, DOW, EDF, Fenix, Luvata, Mostostal Warszawa, Tessenderlo Chemie, TU Eindhoven and Vaillant, respectively) are gratefully acknowledged for their invaluable contributions. In particular we thank Mostostal for Fig. 1 (left) and Fig. 3, UDL for Fig. 1 (right) and RTB for Figs. 4 and 5.

8. References

de Jong, A.J.,Finck, C., Oversloot, H., van 't Spijker, H., Cuypers, R., 2014. Thermochemical heat storage (TCS) - system design issues. Energy Procedia, 48, 309 – 319.

de Jong, A.J., van Vliet, L., Hoegaerts, C., Roelands, M., Cuypers, R., 2016. Thermochemical heat storage – from reaction storage density to system storage density. Energy Procedia, 91, 128-137.

Solé, A., Miró, L., Barreneche, C., Martorell, I., Cabeza, L.F., 2015. Corrosion of metals and salt hydrates used for thermochemical energy storage. Renewable Energy, 75, 519-523.

Volmer, R., Eckert, J., Schnabel, L., 2015. Analyse geometrischer Einflussfaktoren auf die Niederdruckverdampfung von Wasser an Lamellenwärmeübertragern. DKV Tagung, November 2015.

http://www.createproject.eu/ *(accessed October 7, 2016)*

http://www.merits.eu/ *(accessed October 7, 2016)*

Conference Proceedings

EuroSun 2016
Palma de Mallorca (Spain), 11 - 14 October 2016

Experimental Investigation of Water Evaporation for Closed Adsorption Storage Systems

Bao Nam Dang[1], Wim van Helden[1], Michael Olbricht[2] and Andrea Luke[2]

[1] AEE - Institute for Sustainable Technologies, Gleisdorf (Austria)

[2] University of Kassel, Kassel (Germany)

Abstract

Closed adsorption for thermal energy storage is a promising technology, which was recently proven on real scale. Nevertheless further improvements of its material and components are necessary to enhance the system performance and to make it economically viable. One of the issues is the evaporation of water at low pressure during discharging ("adsorption") of the storage. The current lack of accurate experimental data and correlations for the heat transfer coefficient makes the design of the evaporator difficult. Therefore the goal of the work is to gather deeper knowledge in order to design the evaporator more properly and thus improve the sorption storage efficiency. In this work a test rig was designed and constructed for the experimental investigations of water evaporation at sub-atmospheric pressure. For the commissioning, first experiments with falling film evaporation were conducted on a copper tube bundle (3 x 8 tubes) to determine the relation of the outer heat transfer coefficient to different parameters. In all experiments the observed flow patterns between the tubes consist of columns. Varying the saturation pressure from 20 to 23 mbar or the range of the $Re_{\dot{I}}$ 29 to 109 shows no effects. Apart from that, the measured results were compared to values from two correlations. It is concluded that the Nu numbers from the measurements were in good agreement with those from the Lorenz and Yung model.

Keywords: closed adsorption thermal storage, falling film evaporation, water

1. Introduction

Efficient seasonal thermal energy storages are necessary to cover all the domestic heat demand with solar thermal energy over the whole year. An innovative and proven concept in real scale - the solid sorption heat storage - uses the reversible adsorption/desorption process of water vapor in zeolite 13XBF. This material pair provides a significantly higher energy density S (theoretically: 250 kWh/m³) compared to water. In general a sorption storage system consists of one or more vessels with the sorption material, a condenser/evaporator and a water reservoir. For loading the storage ("desorption") the moist zeolite is dried by the heat from solar collector and the emerging vapor is condensed and stored separately in a water tank (Fig. 1a).

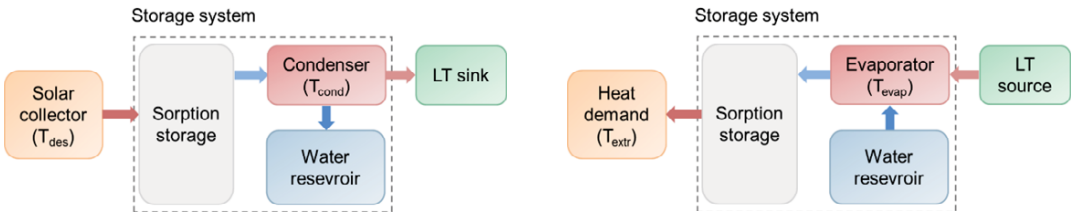

Fig. 1: Scheme of the sorption storage system during desorption (a) and adsorption (b)

doi:10.18086/eurosun.2016.03.09 Available at http://proceedings.ises.org

Regardless of the sensible heat, the thermal sorption energy can be stored over months virtually without losses. To discharge the sorption storage, the distilled water is evaporated at low temperature using the heat of the low temperature source. The vapor will be adsorbed by the zeolite and the resulting heat from the adsorption can be used for domestic hot water, space heating or other purposes (Fig. 1b). In reality the storage is limited by the operation conditions and cannot be fully charged or discharged. Because the storage system is evacuated, the pressure difference drives the vapor transport between the sorption storage and the heat exchanger for evaporation/condensation, and depends on the temperature in the single components. In order to achieve a high material energy density, a maximal desorption (T_{des}) and a minimal condensation temperature (T_{cond}) is required during the desorption as well as a maximal evaporation (T_{evap}) and a minimal extraction temperature (T_{extr}) during the adsorption process. This means an efficient evaporator with high heat transfer leads to smaller temperature overheating and thus a higher evaporation temperature, which as a result enhances the energy density and the storage efficiency (Tab. 1). This coherence was also verified by our closed adsorption storage system for a single-family house from the "COMTES"-project, which was operated successfully during the last heating period from October 2015 to January 2016. Further improvement of the evaporator is only possible with a thorough knowledge of the evaporation process of water at low pressures. (Engel, 2016) (Köll, 2016)

Tab. 1: Material energy density (*S*) of zeolite 13XBF. (In all cases: T_{des} = 180 °C and T_{extr} = 25 °C) (Köll, 2016)

T_{evap}	*S* (T_{cond} = 17°C)	*S* (T_{cond} = 25 °C)	*S* (T_{cond} = 35 °C)
10 °C	126 kWh/m³	115 kWh/m³	106 kWh/m³
15 °C	146 kWh/m³	135 kWh/m³	126 kWh/m³
20 °C	150 kWh/m³	139 kWh/m³	130 kWh/m³

In recent years the experimental studies on water evaporation with different concepts and at temperatures from 5 to 20 °C has been intensified. Still, there is a lack of accurate experimental data. Furthermore there are many known and unknown factors, which influence each other and have a different impact depending on the prevailing conditions. These are the heat flux density, the fluid properties, the saturation pressure, the roughness and the material of the heating surface, the dimension of the apparatus and operation-specific parameters. In sum, the proper design and the improvement of the evaporation of water at low temperatures is currently imprecise and troublesome. One of the main issues for water as refrigerant is the local saturation pressure with p_{evap} = 8.7 to 23.4 mbar, which also depends on the liquid level above the heating surface. Due to the hydrostatic pressure of the water, the pressure increases around 0.98 mbar per cm ($\Delta p = \rho \cdot g \cdot \Delta h$). For example, a flooded evaporator operates at 10 °C with a corresponding pressure of 12.3 mbar. Its heating surface lays 3 cm deep under the water level, which causes a hydrostatic pressure of 2.9 mbar. Hence the local saturation pressure is 15.2 mbar and the temperature 13 °C. This temperature increase can immensely diminish the evaporation power. Because of this concepts with evaporating thin liquid films are preferred to minimize the hydrostatic pressure effect, like the falling film and the capillary assisted evaporation.

Recently the capillary assisted evaporation is increasingly investigated. Its working principle is using capillary structured or coated heating surfaces, which are partly immersed into the refrigerant pool. Due to the capillary forces a thin liquid film covers the surface passively, so no further active components like pumps are necessary. However, the heat transfer coefficient still depends heavily on the liquid level. In addition the long-term functionality is not clear, because fouling can easily accumulate in the capillaries and limit the capillary forces. Overall these evaporators are less complex and have lower weight. But they are probably more suitable for systems with low volume of the refrigerant capacity. (Bahrami, 2016) (Xia, 2007) Falling film-type evaporators with horizontal tubes have been used in different applications like desalination, refrigeration and air conditioning. Furthermore their functionality is also proven for absorption cooling systems. In contrast to the large falling film evaporators like in the food or pharmaceutical industry, the evaporating liquid film will be sprayed or dropped on to the top of a horizontal tube bundle. So the film falls gravitational from tube to tube redistributing itself on each tube again. Therefore a good alignment of the tubes and the proper liquid distribution are required in order to maintain the wetting of the heating surfaces area and thus an efficient evaporation. Especially for deep bundles it is difficult to have a consistent flow and prevent local dry outs. Although it is more complex, this type of evaporator works with much less refrigerant and has higher performances than flooded evaporators. Due to the thin liquid layer with inner turbulences,

the evaporation occurs by natural convection with low surface overheating. Therefore the falling film evaporation seems to be suitable for the application of the seasonal sorption storage and will be experimentally investigated in this work. (Ribatski and Jacobi, 2005) (Thome, 2009)

2. Experimental design and procedure

The goal of this work is to experimentally determine the heat performance $\dot{Q}_{evap}$ and the heat transfer coefficient h_o of a falling film evaporator at certain conditions. Therefore a test rig was designed and built that is similar to the apparatus of Li (2010a, 2010b) or Olbricht (2013, 2016). As shown in Fig. 2, it consists of a cylindrical evacuated vessel, containing the test tube bundle. The vessel contains also temperature sensors and a pressure sensor for measuring the conditions inside. On top of the bundle is the feeding system, which is fed from a water reservoir (in Fig. 2: Reservoir 1). This reservoir collects all the surplus water that is not evaporated at the bundle. To minimize the liquid pool at the bottom of the vessel, tilted plates below the tube bundle channel the water to the drain. Meanwhile the vapor from the evaporator will be drawn off into a plate heat exchanger, where it condenses and falls into a second reservoir. Both reservoirs are hydraulically connected to each other, so shifting the amount of water between the both reservoirs is possible. As seen in the Fig. 2, each of them consists of two differently sized tanks, where the smaller contains a liquid level sensor. Depending on the valve control between the two tanks, the liquid level in the smaller tank and in the vertical tube, which parallel to the tank, is measured with or without the level in the bigger tank. Overall there are three liquid circuits in the test rig: the water used for the evaporation (refrigerant), the water circuit for heating the tube bundle from the inside and the cooling water circuit for the condensation. The last two of these are connected via heat exchangers to our laboratory's hot water and cold water circuit. They are also equipped with sensors for measuring the inner flow's inlet and outlet temperature and the volumetric flow rate.

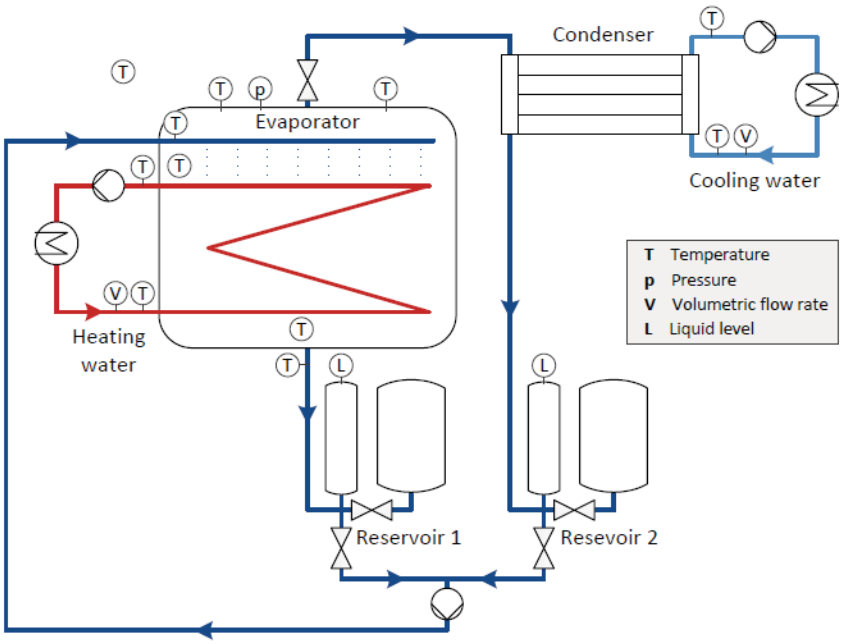

Fig. 2: Scheme of the test rig

The tested tube bundle is similar to the bundle of Olbricht (2013, 2016). It consists of three parallel tube rows, whose outer and inner diameters are 12.70 mm and 12.04 mm (Fig. 3). Both sides of the tube surfaces are plain and not processed. Each single tube row is eight columns high with a center to center tube spacing of 31.75 mm and the inlet and outlet are all connected to the bigger header tube. The liquid feeder is shown in Fig. 4. It consists of three parallel tubes, perforated at the bottom, where the sub cooled refrigerant drops out into a closed box. The box's floor consists of 3 x 39 small pipes, which are all vertically positioned and arranged directly over each tube row of the bundle. The pipe diameter is 1 mm and the spacing is 10 mm. In

addition, all the pipes jut out around 3 mm at both floor's side, so water drains out gravitationally of the box, when there is a small liquid pool in it.

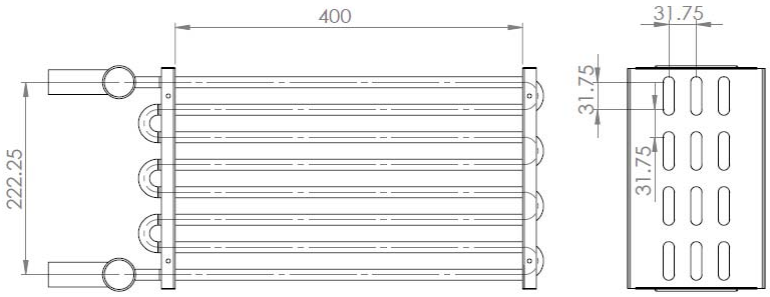

Fig. 3: Sketch of the tube bundle

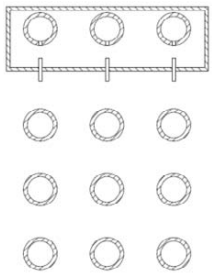

Fig. 4:Sectional view of the liquid feeder

Before the experiment starts, the refrigerant will be conditioned below the saturation pressure, such that when it leaves the feeder it will not evaporate directly until it gets heated by the tube bundle. This will be checked with one temperature sensor inside the feeding tubes and two sensors at the drain of the vessel. During the experiments the inlet temperature of the heating ($T_{hw,in}$) and cooling water ($T_{cw,in}$) are maintained constant. The volumetric flow rate for the refrigerant and the heating water is also set. For controlling the pressure inside the vessel, a PD controller changes the flow rate of the cooling water in the condenser. Tab. 2 shows the setting temperatures, which were set at the examined saturation pressures.

Tab. 2: Setting temperature for each pressure condition

p_{evap}	$T_{\mathrm{H_2O,liq}}$	$T_{hw,in}$	$T_{cw,in}$
20 mbar	17 °C	23 °C	9 °C
23 mbar	19 °C	25 °C	9 °C

Furthermore in each pressure condition, the irrigation density for the refrigerant has been also varied over a range of 0.007 to 0029 kg/(ms), which correspond to a $Re_{\dot{\Gamma}}$ from 29 to 107.

3. Measurement evaluation

There are two different options to measure the performance of the evaporator at stationary conditions. The first option is by measuring the temperatures and the volumetric flow rate of the heating and cooling water. With these values the heat flow at each component can be calculated.

$$\dot{Q}_{hw} = \dot{m}_{hw} \cdot c_{p_{hw}} \cdot \left(T_{hw,in} - T_{hw,out}\right) \quad \text{(eq. 1)}$$

$$\dot{Q}_{cw} = \dot{m}_{cw} \cdot c_{p_{cw}} \cdot \left(T_{cw,in} - T_{cw,out}\right) \quad \text{(eq. 2)}$$

Another method is using the liquid level of the reservoirs. During the measurements, all the valves at Reservoir 2 are closed. So the liquid levels in the vertical tube from the condenser and in the smaller tank rise. The heat flow can then be determined with the change of the liquid volume per time, the liquid density and the vapor enthalpy of water.

$$\dot{Q}_{rv2} = \Delta \mathrm{H}_{\mathrm{H_2O},vap} \cdot \rho_{\mathrm{H_2O,liq}} \cdot \dot{\mathrm{V}}_{\mathrm{H_2O,liq}} \quad \text{(eq. 3)}$$

Ideally, the three measured heat flows should be equal. But because the ambient of the test rig cannot be conditioned, heat gains or losses need to be considered when calculating the evaporation performance. For this, the thermal heat transfer coefficient of the vessel and the condenser was identified. Overall the experiments show that the results of all three measurement methods for the evaporation performance $\dot{Q}_{evap}$. With the temperature difference between the mean temperature of heating water flow and the saturation

temperature of the refrigerant, the overall heat transfer coefficient UA can be calculated. Taking it into account, the results of all three measurement methods for the evaporation power $\dot{Q}_{evap}$were in good agreement.

$$UA = \frac{\dot{Q}}{\Delta T} \qquad \text{(eq. 4)}$$

In all measurement the Reynolds number of heating water inside the tubes was in the range of 5600 to 5900. So for calculating the convection heat transfer coefficient h_i, the relations of Gnielinski (2010) for the transition region between laminar and turbulent flow are used:

$$Nu_i = (1-\gamma)\cdot Nu_{lam,2300} + \gamma \cdot Nu_{tur,10^4} \qquad with \qquad \gamma = \frac{Re - 2300}{7700} \qquad \text{(eq. 5)}$$

The mean outer heat transfer coefficient h_o, which is the heat transfer coefficient of the falling film evaporation, can be calculated by using the tube's thermal resistance formula.

$$h_o = \frac{1}{d_o \cdot \left(\frac{\pi \cdot l_{tube}}{UA} - \frac{1}{h_i \cdot d_i} - \frac{1}{2 \cdot k_{tube}} \cdot \ln\left(\frac{d_o}{d_i}\right)\right)} \qquad \text{(eq. 6)}$$

For the complete measurement evaluation, the irrigation density $\dot{\Gamma}$and the associated Reynolds number $Re_{\dot{\Gamma}}$ are also calculated with the following equations. In this case $\dot{m}_{H_2O,liq}$ is the total mass flow which is used for wetting the total tube length of the bundle l_{tube}.

$$\dot{\Gamma} = \frac{\dot{m}_{H_2O,liq}}{2 \cdot l_{tube}} \qquad \text{(eq. 7)}$$

$$Re_{\dot{\Gamma}} = \frac{4 \cdot \dot{\Gamma}}{\mu_l} \qquad \text{(eq. 8)}$$

4. Experimental results

At constant saturation pressure condition and with a fixed flow rate for the heating water inside the tubes, the irrigation density or the Reynolds number for the falling film was gradually reduced. As seen in Fig. 5a, the flow pattern between the tubes with low irrigation density consists of droplets and very thin columns. These columns remain only for a few seconds, then they shortly break up and subsequently form again mostly at the same place. With increasing irrigation density more columns occur, which are also thicker (Fig. 5b). However, they exist only for a few seconds, too. Apart from that, few liquid droplets or jets do not fall vertically on the next below tubes. Because of the high flow velocity at the radial edge of the tubes, they will be deflected and fall diagonally. This happens at every experimental setting and mainly at the first three top tube rows, when the liquid falls with too high momentum. Furthermore, very few local dried out spots can be identified at every condition. Mostly they are at the lowest tube rows or at the longitudinal ends of the tubes. A change of number and size of the dried out spots was not visible with different parameter settings.

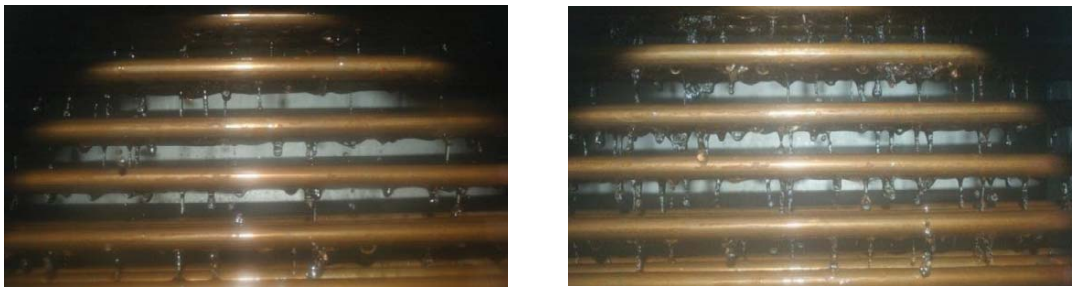

Fig. 5: Flow pattern during measurements with low (a) and high irrigation (b)

Fig. 6 depicts the measured outer heat coefficient in dependency of the saturation pressure and the Reynolds Film number. In our investigated range for $Re_{\dot{\Gamma}}$, the outer heat coefficient at the tubes maintains nearly constant. Similar measurement results can be also found from Li (2010a, 2010b). Furthermore reducing the saturation pressure does not have any effect on the heat coefficient in our experiments, because all deviations are within the accuracy of the measurements. This can be expected as a small difference in pressure, which is equivalent to small temperature changes, leads to very small alteration of the water's properties.

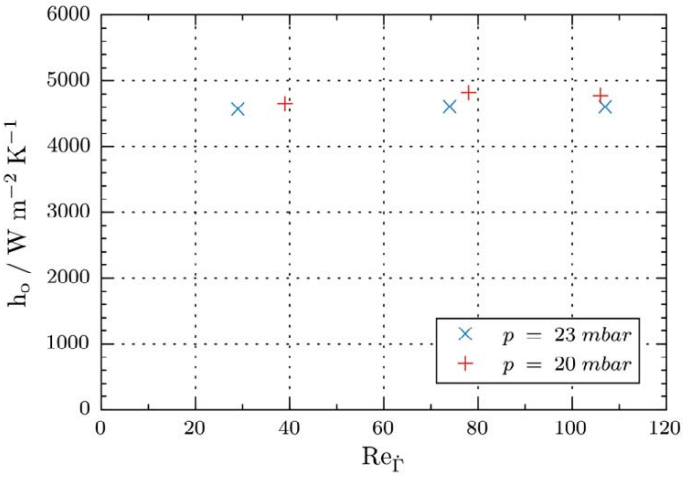

Fig. 6: Results of the measurements at 23 mbar and 20 mbar.

For comparing the measurement results, two correlations were used. The first one is from Hu and Jacobi (1996), where the different types of flow patterns are considered and can be identify by $Re_{\dot{\Gamma}}$. In our case with a Re_{Γ} between 29 and 107, the droplet flow model can be used. The Nusselt Number for this flow pattern can be calculated with the following formulas. Here, D is the outer diameter of the tubes and S is the center to center spacing between two of them.

$$Ar = \frac{D^3 \cdot g}{\nu^2} \qquad \text{(eq. 9)}$$

$$Nu_{\dot{\Gamma},droplet} = 0{,}113 \cdot Re_{\dot{\Gamma}}{}^{0{,}85} \cdot Pr^{0{,}85} \cdot Ar^{-0{,}27} \cdot \left(\frac{S-D}{D}\right)^{0{,}04} \qquad \text{(eq. 10)}$$

The other empirical model is from Lorenz and Yung and is described by Thome (2009). Instead of using several empirical equations for each flow pattern, the heat transfer coefficient is described by a combined model for the evaporation of a subcooled $h_{\dot{\Gamma},dev}$ and of a saturated film $h_{\dot{\Gamma}}$ and the nucleate boiling h_{nb}:

$$h_o = h_{\dot{\Gamma},dev} \cdot \frac{L_{dev}}{L} + h_{\dot{\Gamma}} \cdot \left(1 - \frac{L_{dev}}{L}\right) + h_{nb} \qquad \text{(eq. 11)}$$

where L is the circumference of a single horizontal plain tube and L_{dev} is the developing length of the film, which is calculated by the Nusselt theory for liquid films. The ratio of both lengths is calculated by this equation:

$$\frac{L_{dev}}{L} = \frac{\frac{\dot{\Gamma}^{\frac{4}{3}}}{4 \cdot \pi \cdot \rho \cdot a} \cdot \sqrt{\frac{3 \cdot \mu}{g \cdot \rho^2}}}{\pi \cdot D} \quad . \qquad \text{(eq. 12)}$$

The falling saturated film is calculated by the model of Chun and Seban, which consists of two empirical equations for determining the laminar and the turbulent heat transfer in the evaporating film. For predicting the type of the film flow the Weber Number (We) can be used. In all measurements We was lesser than 1, so the liquid film is laminar and will be calculated with the following equation:

$$h_{\dot{\Gamma},lam} = 0{,}821 \cdot \left(\frac{\mu_l^2}{g \cdot \rho_l^2 \cdot k_l^3}\right)^{-0{,}33} \cdot Re_{\dot{\Gamma}}{}^{-0{,}22} \quad . \qquad \text{(eq. 13)}$$

The heat transfer coefficient of the film's developing region $h_{\dot{\Gamma},dev}$ can be determined with this equation.

$$h_{\dot{\Gamma},dev} = 0{,}375 \cdot c_p \cdot \frac{\dot{\Gamma}}{L_{dev}}. \qquad \text{(eq. 14)}$$

In our experiments, nucleate boiling did not appear and its heat transfer coefficient h_{nb} can be ignored. Therefore only the heat coefficients of the film evaporation are used for calculating with (eq. 12). With the resulting overall heat transfer coefficient of the evaporation film, the associated Nu will be determined.

$$Nu = \frac{h_O}{k} \cdot \left(\frac{\nu^2}{g}\right)^{\left(\frac{1}{3}\right)} \quad . \qquad \text{(eq. 15)}$$

As shown in the diagram of Fig. 6a, there are huge discrepancies between the measurements results and the correlation of Hu and Jacobi, especially at low irrigation density. However at $Re_{\Gamma} > 100$ the values match well. Another point to note is the deviation with the flow pattern. As already mention we observed a column flow patterns between the tubes, which did not change with varying the irrigation density. But according to this model and with a $Re_{\dot{\Gamma}}$ ranging from 29 to 107 it should be droplet flow. A possible reason for this is the different liquid feeder, which was used in Hu and Jacobi's experiments. They used a feeder tube, which has a row of small holes along the bottom, and placed a second tube directly underneath it to help distribute the flow. It has to be assumed that with this configuration the water falls with lower momentum on to the tubes than with the feeding system in this work. However, the empirical results from Lorenz and Yung's correlation are in good agreement with our measurements (see Fig. 6b). Still further detailed investigations are needed to justify the results.

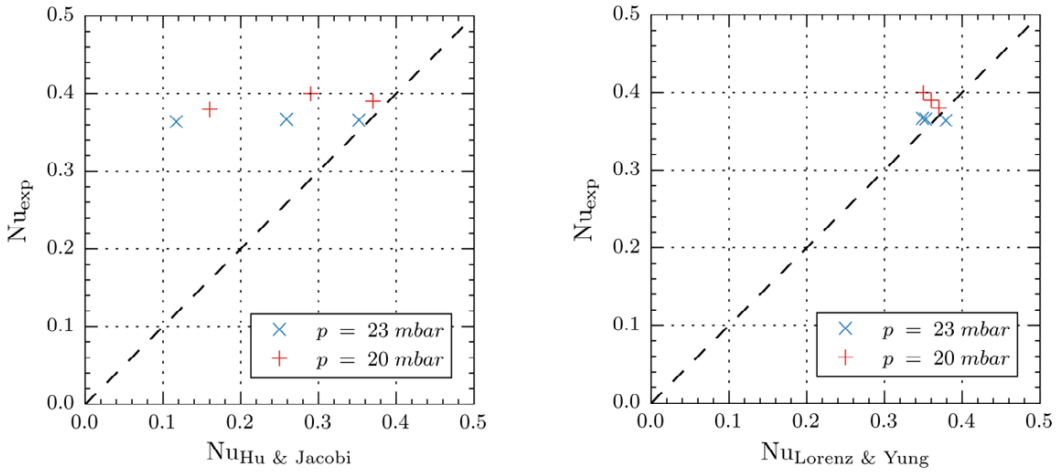

Fig. 7: Comparing measurements results with the correlation of Hu and Jacobi (a) and of Lorenz and Yung (b)

Apart from that, it has to be point out that the determination of the outer heat coefficient depends heavily of the identification of the heating water's inner heat coefficient h_i and of the corresponding temperature difference for calculating the overall heat transfer coefficients UA. Because every other experimental work use different correlations or assumptions, so it can be troublesome to compare with other results and correlations. So for future precise measurements, it will be of interest to heat the irrigated tubes electrically and to measure simultaneous their temperatures.

5. Conclusion

A test rig for experimental investigation of the falling film evaporation was designed and built. For the commissioning, first measurements on a plain copper tube bundle were conducted and evaluated at saturation pressure of 20 and 23 mbar. Varying the falling film Reynolds number in a range from 29 to 109 changes the flow pattern from droplets-columns to columns. However, the heat transfer coefficient for the film evaporation remains nearly constant. This was also observed, when the saturation pressure was differed with unchanged other settings. The experimental data were also compared with values from two empirical models. The comparison shows discrepancies with the correlation of Hu and Jacobi, especially at smaller irrigation density. However, the measurement results were in good agreement with the correlation of Lorenz and Yung. Still, further precise measurements are necessary to justify the results.

In future, further experiments need to be carried out with larger parameter density and range, like the irrigation density. Moreover, experiments at lower saturation pressure can be conducted. Another point is to test with a similar feeder system like from Hu and Jacobi, to check the reason of the discrepancy in this work. Finally, a critical point is the heating water flow, which has large influence on the determination of the evaporation film heat coefficient. Theoretically the flow mode is in the transition region, but it could be also more turbulent due to the elbows in the bundle. So for precise measurement results, experiments with electrical heating tubes and temperature sensors at the tubes should be considered. To sum up, this and all upcoming works are necessary for designing and operating efficient evaporators, which then will be beneficial for sorption storage systems and also other sorption applications, like cooling and heat pumps.

6. Acknowledgements

This research was funded by the project “Solar Heat Integration Network” (SHINE), which is part of the Marie Curie program of the European Union. We thank all our colleagues from AEE - Institute for Sustainable Technologies and the Institute of Technical Thermodynamics at the University of Kassel. Furthermore we want to thank the company Luvata UK Ltd. for manufacturing the tube bundle.

7. Reference

Bahrami, M., 2016. Effects of capillary-assisted tubes with different fin geometries on the performance of a low-operating pressure evaporator for adsorption cooling system applications. Journal Applied Energy, Volume 171, 2016, pp. 256–265.

Engel. G. et al., 2016. Demonstration of a Real-scale Hardware-in-the-loop Seasonal Solar Sorption Storage System. Proceeding: 10th International Renewable Energy Storage Conference, Düsseldorf.

Gnielinski, V., 2010. Heat transfer in pipe flow, in: VDI heat atlas. Book., Düsseldorf, pp. 693-699.

Hu, X. and Jacobi, A.M., 1996. The intertube falling film: Part 2 – Mode effects on sensible heat transfer to a falling liquid film. Journal of Heat Transfer, Vol. 118, pp. 626-633.

Köll, R. et al., 2016. Demonstration of a seasonal sorption storage system in real scale. Proceeding: Otti Conference of Thermal energy storage, Neumarkt, pp. 37-39.

Li, W. et al., 2010a. Falling film evaporation of water on horizontal configured tube bundles. Proceeding: International Heat Transfer Conference, Washington DC.

Li, W. et al., 2010b Falling water film evaporation on newly-designed enhanced tube bundles. International Journal of Heat and Mass Transfer 54 (2011), pp. 2990-2997

Olbricht, M. et al., 2013. Design and commissioning of an absorption chiller. Proceeding: German Society of Refrigeration and Air Conditioning Conference, Hannover.

Olbricht, M. et al. 2016 Heat and Mass Transfer in a Falling Film Evaporator with Aqueous Lithium Bromide Solution. Proceeding: 7th European Thermal-Sciences Conference, Krakau.

Ribatski, G. and Jacobi, A.M., 2005. Falling-film evaporation on horizontal tubes - a critical review. International Journal of Refrigeration, Vol. 28(5), pp. 635-653.

Thome J.R., 2009. Falling film evaporation, in Engineering data book III. Book., pp. 14/1-14/39.

Xia Z.Z. et al. 2007. Experimental investigation of capillary-assisted evaporation on the outside surface of horizontal tubes. International Journal of Heat Mass Transfer 51 (2008), pp. 4047-4054.

Conference Proceedings

EuroSun 2016
Palma de Mallorca (Spain), 11 - 14 October 2016

Advantages using inlet stratification devices in solar domestic hot water storage tanks

Janne Dragsted, Simon Furbo, Federico Bava

DTU Civil Engineering, Technical University of Denmark, Kgs. Lyngby (Denmark)

Abstract

The thermal performance of a domestic hot water system is strongly affected by whether the storage tank is stratified or not. Thermal stratification can be built up in a solar storage tank if the heated water from the solar collectors enters the tank through an inlet stratifier.

Measured thermal performances of two solar domestic hot water systems are presented. One system is a traditional high flow system with a heat exchanger spiral in the tank. The other system is a low flow system with an external heat exchanger and a newly developed inlet stratifier from EyeCular Technologies ApS installed in the tank. The two systems are otherwise identical which makes it possible to compare the thermal performance and the thermal stratification built up in each tank.

Based on a measuring period of 140 days in the period from April 26, 2016 to September 25, 2016, the investigation shows, that the system with the stratification device has a higher thermal performance compared to the system with the heat exchanger spiral inside the tank.

The relative performance (defined as the ratio between the net utilized solar energy of the low flow system and the net utilized solar energy of the high flow system), is a function of the solar fraction. The lower the solar fraction is, the higher the relative performance will be. Weekly relative performances up to about 1.10 are measured. That is, weekly extra thermal performances of up to 10% are measured for the system with the inlet stratifier.

Keywords: Solar domestic hot water system, thermal performance, thermal stratification, measurements.

1. Introduction

1.1. Background

The heat from solar collectors is, in most marketed solar domestic hot water (SDHW) systems, transferred to the hot water tank in such a way, that the entire tank is heated to a uniform temperature since hot water tanks with built in heat exchanger spirals are typically used as solar tanks. The lack of thermal stratification in the hot water tank can result in up to a 25 % reduction in the thermal performance of a solar domestic hot water system. Thermal stratification in hot water tanks is therefore important in order to obtain a high thermal performance of the solar domestic hot water systems (Furbo et al 2004, Furbo et al 2005, Andersen et al 2006).

Thermal stratification in a storage tank can be established with a stratification device used to transfer solar heat to the hot water tank (Andersen et al, 2007). Stratification devices can be designed in different ways, for instance rigid pipes with holes, with or without flaps preventing back flow and flexible stratifiers made of fabric or polymer films, with one or more layers (Andersen et al, 2007).

doi:10.18086/eurosun.2016.03.11 Available at http://proceedings.ises.org

In this paper investigations of an inlet stratifier from Eyecular Technologies ApS are presented. In 2013 EyeCular Technologies ApS invented a new flexible stratifier with good results both in terms of performance and durability in accelerated long term tests. The stratifier makes use of the pressure difference between the water in the storage tank and the incoming water in the stratifier.

1.2. Side-by-side laboratory tests of small SDHW systems

Two small solar domestic hot water systems are installed side by side in the solar heating test facilities at the Technical University of Denmark (DTU), Lyngby, Denmark. The systems are identical, with the exceptions of the stratification device and the heat exchanger methods, see Fig. 1.

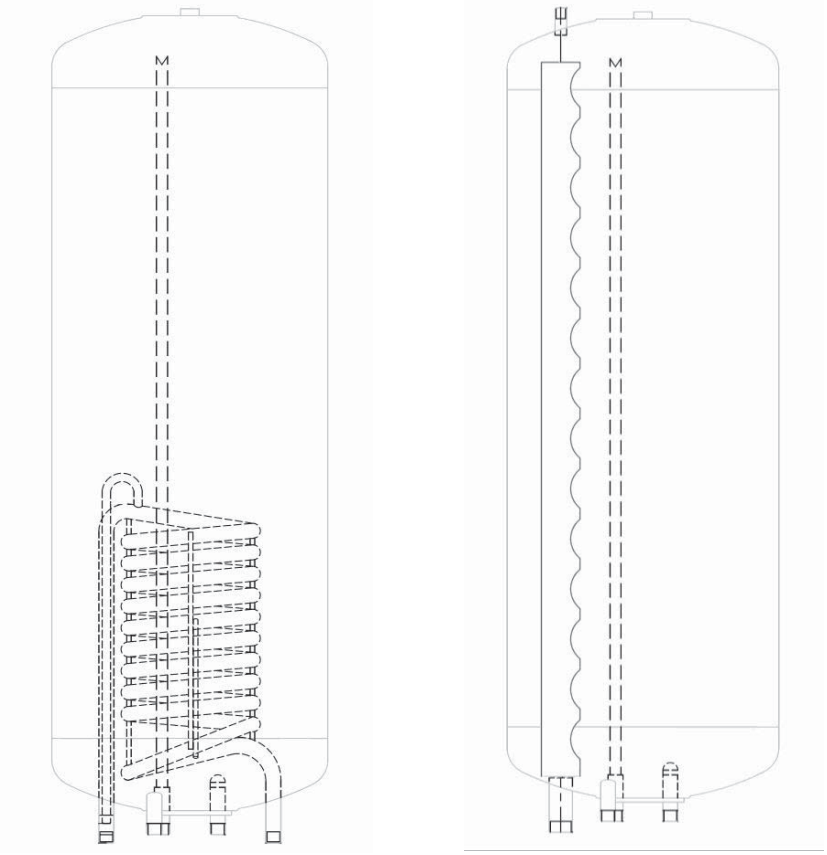

Fig. 1: Sketches of the two tanks in the SDHW systems.

The solar collectors for each system have an aperture area of 2.36 m², see Fig. 2. The solar collectors are facing south with a tilt of 45°. The data of the collectors are given in table 1.

Tab. 1: Data for solar collectors used in the two SDHW systems

Collector type	TLP ACR 2600, Hewalex, Poland
Maximum efficiency	0.827
First order heat loss coefficient	3.247 W/m²K
Second order heat loss coefficient	0.020 W/m²K²
Incidence angle modifier for an incidence angle of 50°	0.94

The daily hot water consumptions for each system is 135 liter heated from 20 °C to 50°C, corresponding to approximately 4.5 kWh. The daily hot water consumption is tapped at 7 am, at noon and at 7 pm in three

equal volumes. The tanks, which are produced by METRO THERM A/S, Denmark, have volumes of 255 l, see figure 2.

One of the systems is a typical marketed small solar domestic hot water system with a built in heat exchanger spiral in the hot water tank.

The other system has an identical tank but without the spiral heat exchanger. This tank is equipped with a polymer film inlet stratifier developed by EyeCular Technologies ApS.

The specific stratifier model applied in the present test is developed for low flow solar combi systems with flows rates from 2 - 4 l/min. If operated at lower flow rates than 2 l/min, the efficiency of this specific stratifier model will, according to the company, decrease due to heat loss from the stratifier. Unfortunately, the company has not yet developed a stratifier for flow rates below 2 l/min, let alone a flow rate of 0.5 l/min.

An optimized low flow system operates at a flow rate of 0.15 – 0.20 l/min/m² solar collector. In the present test, the low flow system should therefore ideally be operating at a flow rate of approx. 0.5 l/min. Higher flow rates than 0.5 l/min will reduce the thermal performance of the system somewhat. Together with the company, a compromising flow rate of 1.0 l/min was decided upon, still knowing, that this flow rate is not ideal for the stratifier nor the system.

The solar heat is transferred from the solar collector fluid to the DHW water through an external flat plate heat exchanger. The heat exchanger has a heat exchange capacity rate of about 150 W/K. The propylene glycol/water mixture used as solar collector fluid in the solar collector loops is a 40% mixture.

Fig. 2 Pictures of the storage tanks and solar collectors in the two SDHW systems.

The high flow system with the heat exchanger spiral has a volume flow rate of 2.5 – 3.0 l/min in the solar collector loop. The low flow system with the stratifier has a volume flow rate of 1.0 l/min, both in the solar collector loop and in the DHW water loop transferring the solar heat to the tank. The upper 95 l of the tanks have the option of being heated to 50.5 °C by means of 3 kW heating elements.

Copper pipes with a total length of 34 m for each system are used in the solar collector loops.

The solar collector loop in the high flow system with the heat exchanger spiral is equipped with a circulation pump having a power consumption of 50 W in order to ensure a flow of about 2.5 – 3.0 l/min throughout the entire test duration. The two circulation pumps on either side of the external heat exchanger in the low flow system with the stratification device, has a power of 36 W and 50 W to ensure a flow rate of 1.0 l/min in both loops.

In both systems the circulation pumps are controlled by differential thermostats based on temperature sensors measuring temperature differences between the outlet from the solar collectors and the bottom of the tanks.

2. Measurements and calculation of performance

The data collected from both systems consist of temperature levels, flow rates and energy readings. Temperatures are measured at the in- and outlet of the solar collectors along with the in- and outlet

temperatures from the heat exchanger and from the tank. Also temperatures are measured inside the tank in different levels in order to evaluate the level of thermal stratification build up in each tank.

The thermal performances of the two systems are compared by the net utilized solar energies and the solar fractions. The net utilized solar energy is determined as the energy drawn from the system subtracted the auxiliary energy supply to the tank. The solar fraction is the ratio between the net utilized solar energy and the energy drawn from the system. By subtracting the net utilized solar energy from the solar heat transferred to the hot water tank the heat losses from the tank are given.

Tab. 2: Measured energy quantities for the two SDHW systems in the period 18/4-2016 – 26/9.2016 (Excluding the period 27/6 2016 - 17/7 2016 due to malfunction of measurement system).

Energy quantity	SDHW system with stratification device	SDHW system with heat exchanger spiral
Hot water consumption (kWh)	596	598
Auxiliary energy supply (kWh)	95	109
Net utilized solar energy (kWh)	501	490
Solar fraction (-)	0.84	0.82

The measured quantities for both systems are shown in Tab. 2 for the period from 18/4-2016 to 27/6-2016 and from 17/7-2016 to 25/9-2016. The period from 27/6-2016 to 17/7-2016 is excluded due to measurement malfunction. Measurements are available for 140 days during the summer 2016. In Tab. 2 it is seen that the total hot water consumption from each system is 596-598 kWh, which is approximately 4.3 kWh a day. Also as expected the consumption of auxiliary energy is higher for the high flow system with the heat exchanger spiral compared to the low flow system with the stratification device. This results in a higher net utilized solar energy for the low flow system with the stratification device.

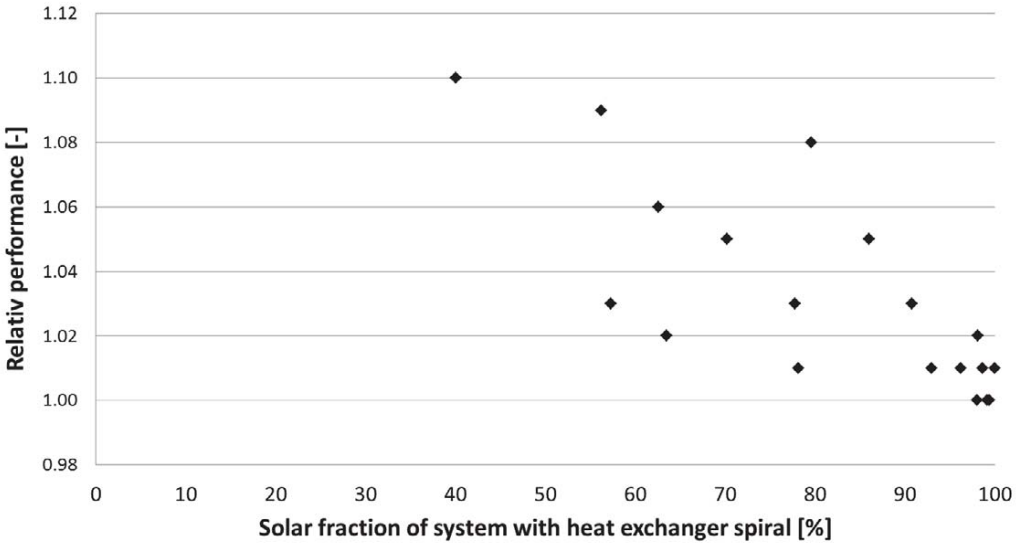

Fig. 3: Weekly relative performance of system with stratification device as function of the weekly solar fraction of the spiral tank system

The 140 days of measurements are divided into 20 periods of 7 days. Weekly relative performances as a function of the solar fraction of the system with the heat exchanger spiral tank are shown in Fig. 3. The relative performance is defined as the ratio between the net utilized solar energy of the system with the stratification device and the net utilized solar energy of the system with the heat exchanger spiral.

Fig. 3 shows as expected that the relative performance increases with a decreasing solar fraction. The measurements show that the thermal performance of the system with the stratification device is up to 10 % higher than the thermal performance of the spiral tank system at solar fractions between 40-50 %.

3. Conclusions

Measurements of thermal performances of two small SDHW systems tested side-by-side under realistic conditions in a laboratory test facility are carried out. One system is a traditional high flow system with a heat exchanger spiral in the tank. The other system is a low flow system with an external heat exchanger and a newly developed inlet stratifier from EyeCular Technologies ApS installed in the tank. The two systems are otherwise identical.

The relative performance defined as the ratio between the net utilized solar energy of the low flow system with the inlet stratifier and the net utilized solar energy of the high flow system with the spiral tank is a function of the solar fraction. The lower the solar fraction is, the higher the relative performance will be. Weekly relative performances up to about 1.10 are measured for solar fractions around 50%. That is, the extra thermal performance is about 10% if the solar fraction is about 50%.

The measurements will be continued during the autumn and winter 2016-2017. It is expected that the extra thermal performance of the system with the stratification device will increase in the winter period with low solar fractions, and that the extra yearly thermal performance will be about 12% if the yearly solar fraction is about 30%.

4. References

Furbo S, Mikkelsen S E. Is Low Flow Operation an Advantage for Solar Heating Systems? ISES Congress Proceedings, Hamburg, September 1987.

Furbo S, Vejen N K, Shah L J. 2005. Thermal performance of a large low flow solar heating system with a highly thermally stratified tank. Journal of Solar Energy Engineering, Vol 127.

Andersen E., Furbo S. 2006. Fabric inlet stratifiers for solar tanks with different volume flow rates. Proceedings EuroSun 2006 Congress, Glasgow, Scotland.

Andersen E., Furbo S., Fan J. 2007. Multilayer fabric stratification pipes for solar tanks. Solar Energy, Vol. 1, p. 1219-1226.

Andersen E., Furbo S., Hampel M., Heidemann W., Müller-Steinhagen H. 2007. Investigations on stratification devices for hot water stores. International Journal of energy research, Volume 32, issue 3, pp. 255-263.

Conference Proceedings

EuroSun 2016
Palma de Mallorca (Spain), 11 - 14 October 2016

Seasonal Thermal Energy Storage with Aqueous Sodium Hydroxide – Experimental Methods for Increasing the Heat and Mass Transfer by Improving Surface Wetting

Mihaela Dudita[1], Xavier Daguenet-Frick[1] and Gantenbein Paul[1]

[1]Institute for Solar Technology SPF, HSR University of Applied Sciences, Rapperswil (Switzerland)

Abstract

Using thermochemical storage based on water absorption/desorption in a fluid with high volumetric energy density like sodium hydroxide solution (NaOH-H_2O) is an effective method for developing seasonal thermal energy storage. For the desorption process step which takes place in summer, a high renewable energy fraction can be reached by using solar thermal collectors. The system efficiency is influenced by the residence time of concentrated NaOH in the water vapor and the surface wetting behavior of the heat and mass transfer unit. This strongly depends on the solid surface characteristics and on the thermo-physical properties of sodium hydroxide, especially the high surface tension of the concentrated NaOH solution from the absorption process. An improved wetting of the concentrated NaOH was achieved by modifying liquid's properties (e.g. surface tension) or by changing the solid surface structure and chemistry.

Keywords: *seasonal thermal energy storage, sodium hydroxide, surface wetting, surfactant, surface texturing*

1. Introduction

Almost half of the final energy demand in Europe is needed for heating and cooling applications. An important percentage can be supplied from sustainable heat sources like waste heat or renewables. However, the energy production is most of the times not synchronized with the energy demand. Seasonal heat storage/long-term storage of heat makes the energy available when it is needed. Moreover, these "heat batteries" are very advantageous when stand-alone systems are involved and when the security of supply is required.

Current research is focused on compact thermal energy storage (TES) technologies with high energy density like phase change materials (PCM) and thermochemical materials (TCM) or sorption processes. These concepts were investigated by researchers in different projects like the IEA joint Task/Annex 42/29 or the European financed COMTES project (Cabeza, 2015; Daguenet-Frick et al., 2015a; Navarro et al., 2016). Although considerable efforts were made to find and improve thermal energy storage materials, the seasonal/long term heat storage systems are still at lower technology readiness levels.

Water absorption/desorption in a high volumetric energy density sorbent as aqueous solutions like LiCl, LiBr, KOH or NaOH were successfully reported (Cabeza, 2015; Daguenet-Frick et al., 2015b; Navarro et al., 2016). Sodium hydroxide has the advantage of having high-energy density as well as low cost. Nevertheless, the challenges are related to process engineering and transferring the materials thermo-physical properties to a running system with the expected performance (Daguenet-Frick et al., 2015a; Fumey et al., 2014; Olsson et al., 1997).

Previous experiments made in the EU funded COMTES project have indicated a lower power compared with the theoretical value during the absorption (storage discharging) phase. This can be explained by the poor wetting of the concentrated sodium hydroxide over the tube bundle from the absorber/desorber unit

doi:10.18086/eurosun.2016.03.13 Available at http://proceedings.ises.org

(Daguenet-Frick et al., 2014; Fumey et al., 2014). The tube bundle made from stainless steel (AISI 316L) was not efficiently wetted with the sorbent fluid. The sorption process of water in sodium hydroxide is influenced by the residence time, while the heat transfer is strongly influenced by the fluid surface wetting.

The focus of our work is to develop a 1 kW absorption/desorption demonstrator unit using the falling film working principle. One of the first steps is to optimize the heat and mass transfer at the tube bundle surface by improving wetting of the NaOH-H_2O (sorbent-sorbate) pair (see Fig. 1). In this paper, we present several experimental methods used for increasing the surface wetting of the stainless steel tubes with the concentrated sorbent. As wettability is depending on the surface roughness, surface oxygen content and the polar components, different surface modifications (structuring, annealing) and fluid properties tuning (use of surfactants) were investigated.

2. Working principle of a thermochemical storage using sodium hydroxide

The aim of the work is to develop a seasonal heat storage based on water absorption/desorption in sodium hydroxide solution. The main objective of our lab-scale system (1kW, Fig. 1) is to develop and improve the power unit. There are two main processes in such a system: charging and discharging. The charging process occurs in the desorber unit under reduced pressure. The thermal energy produced by the solar collectors in summer is used to partially vaporize the water contained in a diluted sodium hydroxide solution. The water vapors are condensed in the condenser unit, which is connected to a heat sink, e.g. a borehole. Water and sodium hydroxide are stored at room temperature in separate tank. The storing tank is giving the storage capacity, while the heat and mass exchangers are the power unit. This closed sorption heat storage system has the advantage of power and storage capacity separation.

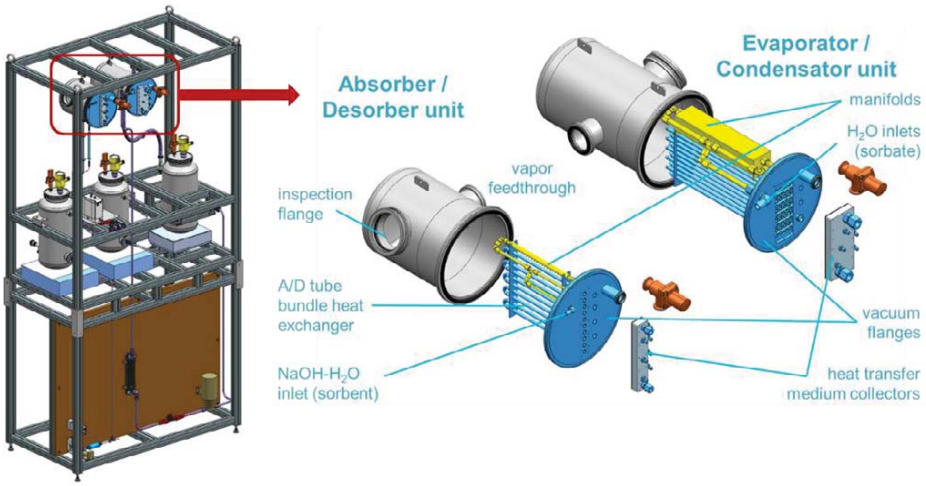

Fig. 1: Experimental 1kW thermochemical storage using sodium hydroxide - experimental facility (left) and construction details of the heat and mass exchangers: absorber/desorber unit (A/D) and evaporator/condenser unit(E/C), right

During the discharging process, the ground heat is used as a heat source to evaporate the stored water under reduced (sub-atmospheric) pressure in the evaporator. In the other chamber, the sorbent, concentrated NaOH solution (50 wt.%) is flowing as a falling film over the tube bundle of the A/D unit. Heat is gained from the water vapor absorption. Dissolution of the sodium hydroxide in water is a highly exothermic process (heat of solution at infinite dilution of NaOH is -44.51 kJ/mol at 25°C) (Parker, 1965). The heat is transferred to a working fluid (floor heating). Sodium hydroxide has a high water affinity; nevertheless, the fluid wetting on the tube bundle influences the efficiency when a fixed transfer area is involved.

3. Theoretical methods to improve the wetting

Wetting (Fig. 2) can be improved by modifying the liquid's properties (e.g. surface tension) or by changing the solid surface structure and chemistry.

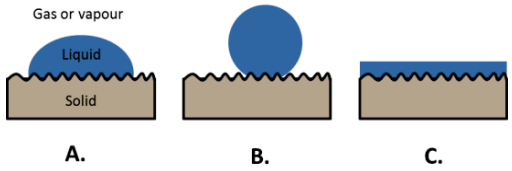

Fig. 2: Surface wetting : A - partial wetting, B - complete non-wetting, C - complete wetting

Surface tension of liquids at constant temperature and pressure and in equilibrium is physically equivalent to the specific surface free energy. The surface tension for liquids is depending on the London dispersion forces and hydrogen or metallic bonds, if they are present. According to Zisman (Tadros, 2006), total wetting is dictated by a single parameter called the critical surface tension, which is independent of the liquid. This model applies when only dispersion forces are considered. In other cases, the value obtained is not equal to the free energy of the surface, but it is a good practical measure of its liquid repellency. Stainless steel AISI 316L, the typical material used for tube bundle construction when NaOH is involved, has the critical surface tension between 20 to 33 mN/m. The value depends on the surface treatment: mechanically, electropolished or plasma treatment (Trigwell and Selvaduray, 2006). The surface tension is decreasing with temperature increasing, thus the highest value is expected to be at the minimum temperature from the system (room temperature in the 1kW system). In addition, the surface tension is decreasing for lower concentration, thus the worst case is for the concentrated solutions at low temperatures.

Sodium hydroxide has a surface tension of 116.72 mN/m for a 50 wt.% aqueous solution at 20°C (Feldkamp, 1969). To decrease it, surface active agents (or surfactants) in very low concentration can be used. The surfactant ability to reduce the surface tension is due to both hydrophilic and hydrophobic components (Tracton, 2006). The surfactant efficiency depends on the chemical structure and concentration, pH-value, temperature, and solid surface properties (e.g. composition, pore structure, surface roughness). Surfactants have a point of critical concentration called CMC – critical micelle concentration (Fig. 3). For higher solution concentrations than CMC, the surface tension does not decrease any more (reaches a rather constant value at constant temperature).

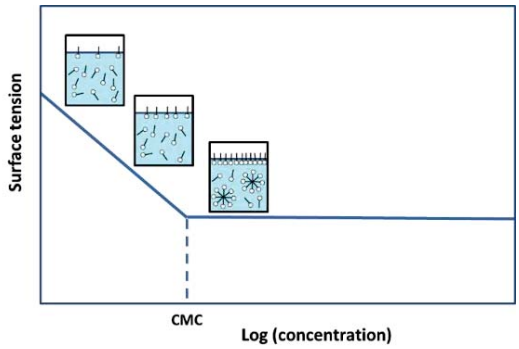

Fig. 3: Evolution of the surface tension depending on the critical micelle concentration

Based on their stability in hot alkaline solutions, two surface active agents (surfactants) were chosen for our study: 1,4-bis(1,3-dimethylbutyl) sulphonatosuccinate sodium salt (S1) and Triton™ QS-15 (S2). Sulfosuccinate surfactants are used in a wide range of industries from paints, adhesives, agrochemicals, plastics to cosmetics. Previous studies were performed on the wetting properties and stability of di-alkyl sulfosuccinate salts under alkaline solutions at different temperatures. It was shown that these anionic surfactants are stable in solutions with high pH and high temperature up to 80°C (Majmudar, 2014), which is at the desorption temperature level in a sodium hydroxide sorption heat storage. Triton™ QS-15 is also an anionic surfactant based on polyether sulfate (C12–14-tert-alkyl-ethoxylated sodium sulfate). It is soluble and stable in hot alkaline solutions, biodegradable and it will not persist in the environment. It is used for highly alkaline metal cleaners, bottle washing, zinc plating brightener, gas well cleaning, steam cleaners, etc.

The second category of methods for wetting improving is related to solid surfaces modifications. There are

three mechanisms: mechanical, physical and chemical. Better wetting is promoted when a large surface area is in contact with the liquid. Higher surface area is obtained by varying the surface roughness and mechanical texturing. According to Wenzel's equation, increased roughness will decrease the contact angle on hydrophilic surfaces, but it will increase the contact angle on hydrophobic surfaces. Thus, roughness amplifies both hydrophilicity and hydrophobicity, but not necessarily linearly (Brutin, 2015). In order to modify the surface chemistry, more techniques can be applied, e.g. changing the surface functional groups (Trigwell and Selvaduray, 2006). Studies have shown that a heat treatment is increasing the chromium oxide content in the surface (Williams, 2011). This would promote a better wetting due to the formation of physical bonding with the polar groups from the aqueous sodium hydroxide solution. It is favorable to have chromium and nickel oxide on the surface due to corrosion issues. However, different surface treatments have different effects. For example, the Cr concentration decreases, while the Fe concentration increases in the case of mechanically polishing process. In addition, the surface nickel content is reduced to about 3%. After mechanically polishing, Cr is mainly bounded in the oxide form (Cr_2O_3). The oxygen bonding in the oxide form is reduced by electropolishing, simultaneous to a considerably increase in oxygen bonding as hydroxide. This is because the process is done in an aqueous environment. An enrichment of chromium on the surface oxide layer normally occurs when stainless steel is electropolished. After plasma treatment, the proportion of Cr as Cr_2O_3 and Fe as Fe_2O_3 is increasing, to the detriment of metallic Cr and Fe and their hydroxides. In addition, the divalent Fe is oxidized. A chromium depleting effect takes place in the case of plasma treatment (Trigwell and Selvaduray, 2006).

Surface modifications by texturing or annealing and fluid properties tuning by using surfactants were experimentally investigated.

4. Experimental part for surface wetting improvement

Different tubes with a flat surface or structured (with horizontal, perpendicular or cross grooves) made from stainless steel AISI 316L were used. Moreover, a heat treatment in air at 300°C was applied for the optimum surface textured tube and for a plane tube.

Prior to the surface wetting experiments the samples were first washed with demineralized water and then with ethanol. To avoid carbonization of the sodium hydroxide with CO_2 from the air, experiments were performed into a glove bag (ca. 94x94x64 cm) filled with N_2. The N_2 4.5 (purity ≥99.995%) functions as the inert gas.

The following chemicals were used for performing the wetting experiments: sorbent to be used in the heat and mass exchanger - sodium hydroxide, 50 wt.% in H_2O (Sigma Aldrich), wetting agents: 1,4-bis(1,3-dimethylbutyl) sulphonatosuccinate sodium salt (S1, Sigma Aldrich) and Triton™ QS-1 (S2, DOW), demineralized water and ethanol (technical).

A computer-controlled multipurpose tension-meter (Sigma 700, Biolin Scientific, with OneAttension v. 1.6) from Transilvania University of Brasov was used to determine the surface tension of the sodium hydroxide solution with surfactant.

In order to avoid the influence of gravity, small volumes (100 μL) were used for the wetting experiments. When the radius of the droplet is much smaller than the capillary length, the effects due to gravity are negligible and the drop deposited on the solid substrate maintains a spherical shape.

5. The influence of surfactants and mechanical texturing on the surface wetting

5.1 The surfactant influence on the surface tension of the aqueous sodium hydroxide solution

Wetting and spreading of sodium hydroxide is mainly depending on the following physical properties of fluid: the dynamic viscosity of the liquid and the surface tension (Fig. 4 and Fig. 5, Feldkamp, 1969; Olsson et al., 1997). The values corresponding to aqueous sodium hydroxide solution are considerably higher compared with water, which is the low cost fluid for the classical sensible storage method. In order to have a good heat and mass exchange, the fluid properties must be tailored together with the surface properties of the

solid surface.

Thus, the influence of surfactants (e.g. S1) on the surface tension of concentrated sodium hydroxide solution was assessed. Previous research studies recommend the use of di-alkyl sulfosuccinate salts under alkaline solutions in concentration from 0.1 to 0.5 wt.%, under the critical micelle concentration (Majmudar, 2014).

The surface tension of different surfactant solutions (0.1 wt.%, 0.3 wt.%, 0.5 wt.%) was determined (at room temperature) and compared with the one corresponding to aqueous NaOH solutions and to NaOH-surfactant system (Fig. 6). The addition of small amounts of surfactant solution reduces the surface tension of the sodium hydroxide with approx. 39% in the case of concentrated sodium hydroxide (30 wt.%). Therefore, the wetting of the NaOH-H_2O over the tube bundle surface from the absorption unit can be improved. Further tests are under development for assessing the stability of the sodium hydroxide solution with surfactant in different system configuration.

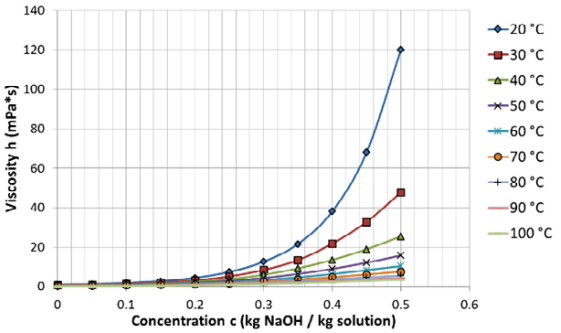

Fig. 4: Viscosity in function of temperature and concentration for aqueous solutions of sodium hydroxide

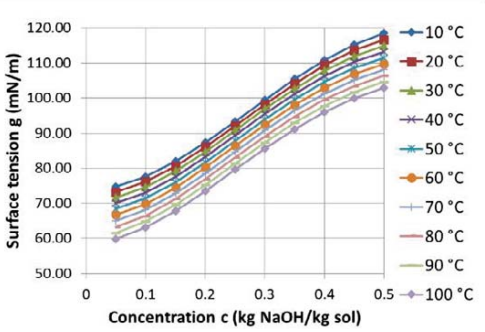

Fig. 5: Surface tension in function of temperature and concentration for aqueous solutions of sodium hydroxide

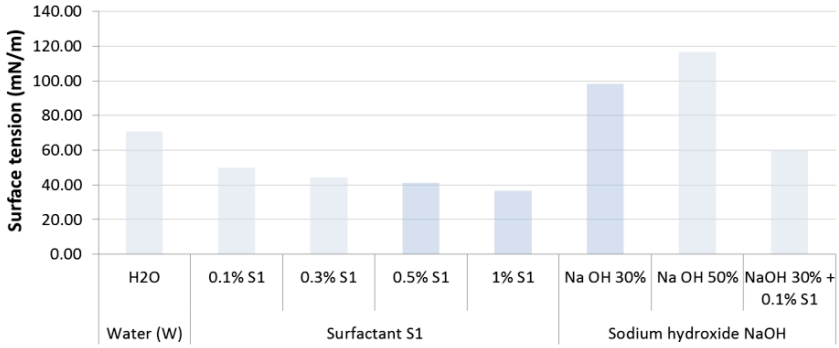

Fig. 6: Influence of the surfactant 1,4-bis(1,3-dimethylbutyl) sulphonatosuccinate sodium salt (S1) on the surface tension values

5.2 Surfactant impact on wetting stainless steel plane tubes

The influence of the two selected surfactants and concentration NaOH solutions on wetting the as received plane tubes was performed. The reference was a solution of NaOH 45 wt.%. The surfactants had the same concentration (1000 ppm). In order to quantify the wetting of the fluid over the tube, wetting time was used (Stache, 1995). This is defined as the shortest time until the drop (100 µL) wets and falls over the tube. Both surfactants lead to good wetting, compared to only sodium lye case (Fig. 7). In the reference case, the droplet was stable for minutes.

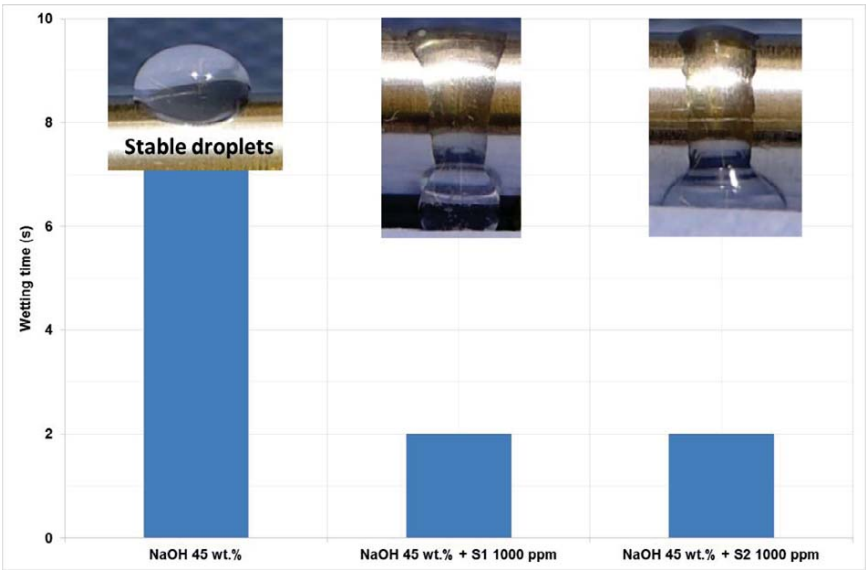

Fig. 7: Influence of the surfactants: 1,4-bis(1,3-dimethylbutyl) sulphonatosuccinate sodium salt (S1, 1000 ppm) and Triton™ QS-15 (S2, 1000 ppm) (S2, 1000 ppm) on the wetting time

5.3 Surface texturing and surfactant influence on the tubes wetting with concentrated sodium hydroxide solutions

The influence of different surface texturing on the wetting with concentrated sodium hydroxide, without/or with surfactant addition (S1 100 ppm) was assessed. Compared to the reference case (T0), where the aqueous concentrated sodium hydroxide solution forms stable droplets, all the textured tubes present better wetting. The surfactant addition leads to a better wetting, decreasing the wetting time. The best results were obtained in the case of sample T4. This pattern is also used in sodium heat pipes to improve the wetting (Bacanu, 1991). It was proven to have good stability in time in highly corrosion environments. Sample T1, with very small fines in the axial direction is a promising solution that can have good residence time. Sample T3 has lower wetting compared to the others due to the hill like structures. In the case of T5 and T6, good wetting can be achieved, but the vertical fins limit the fluid spreading.

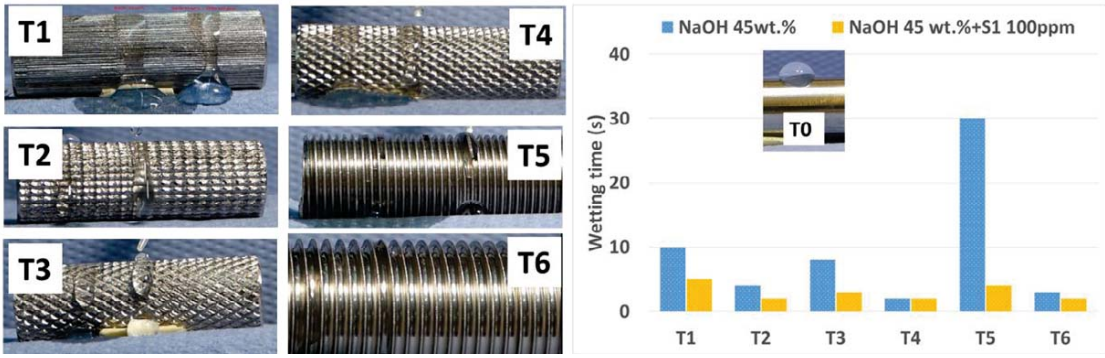

Fig. 8: Influence of surface texturing and surfactant addition (S1 100 ppm) on the surface wetting

5.4 The influence of thermal treatment on the wetting time

Annealing in air increases the surface metal oxide content. A plane tube (as received) and the optimum textured tube were thermally treated in air for 1h, 2h and 3h at 300°C. Wetting experiments were performed by placing a 100µL droplet of concentrated sodium hydroxide solution (45 wt.%), without surfactant or with the addition of Triton™ QS-15 (S2, 1000 ppm). A better wetting was obtained for all the annealed samples (see Fig. 9). The good wetting time values can be explained by physical bonding formation between active

groups from the testing fluid and from the metal surface. In the case of sample A1, very small droplets were added. This has led to a rather stable droplet, with higher wetting time.

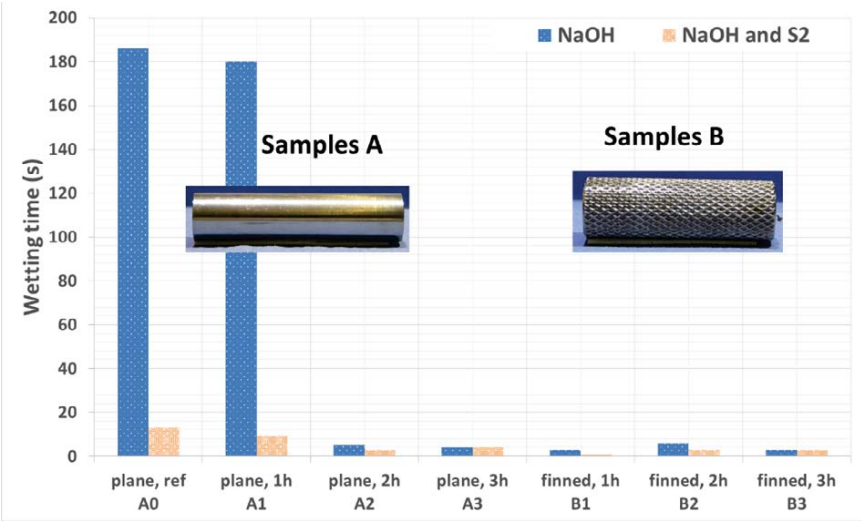

Fig. 9: Influence of thermal treatment on the wetting time for two types of surfaces and for sodium hydroxide with and without the surfactant S2 (Triton™ QS-15)

Moreover, in the heat and mass exchanger from the 1kW prototype, a manifold nozzle will be used. This was simulated by placing three large droplets (1000 µl of testing fluid, see inset image from Fig. 10) compared to the standard experiments where small droplets were used (100 µL). The pipet diameter was similar with the nozzle diameter from the prototype system (Fig. 1). A better spreading was observed in the case of the textured tube compared to the plane tube (see Fig. 10, bottom).

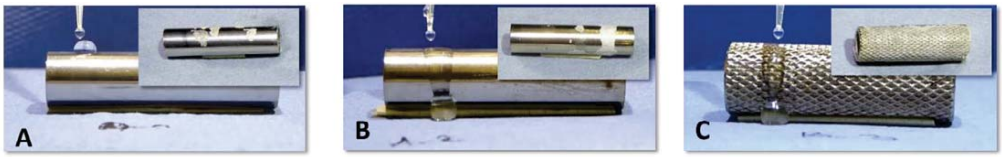

Fig. 10: Comparison between wetting of sodium hydroxide 45 wt.% and different tube surfaces – plane tube as received (A), plane tube, thermally treated for 2 hours at 300°C (B) and optimized textured tube, thermally treated for 3 hours at 300°C (C). The photos are taken 5s after adding 100 µL of sodium lye, while in the inset, a higher volume was used (3x1000 µL) and the photos were taken after the tubes were completely dried.

6. Conclusions

Water absorption/desorption in a high volumetric energy density fluid, as aqueous sodium hydroxide solution, is an efficient method to develop compact seasonal thermal energy storage. Previous experiments made in the EU funded COMTES project have indicated a lower power during the absorption (storage discharging) phase. This can be explained by the poor wetting of the concentrated sodium hydroxide over the tube bundle from the absorber/desorber unit.

The focus of our work is to develop a 1 kW absorption/desorption demonstrator unit using the falling film working principle with improved wetting of the NaOH-H_2O as sorbent-sorbate pair. One of the first steps is to optimize the heat and mass transfer at the tube bundle surface from the absorption process. This can be done by tailoring the surface wetting.

Different experimental methods were investigated for increasing the surface wetting of stainless steel tubes: surface modifications (structuring, annealing) and fluid properties tuning (use of surfactants). Higher surface area was obtained by mechanical texturing. The development of the structured surfaces not only enhances the heat transfer, but it also reduces the size of absorber unit. Annealing in air increases the surface metal oxide

content. A better wetting in terms of low wetting times was obtained for all the annealed samples. This can be explained by physical bonding between polar groups from the testing fluid and the surface metal oxide. The influence of different surface texturing on the wetting with concentrated sodium hydroxide, without/or with surfactant addition was assessed. Compared to the reference case, the surfactant addition leads to a better wetting, decreasing the wetting time.

Further work is related to the investigation of the fluid residence time in the water vapor. This can be improved by the number of tubes on each other or by a concept of inclined surface (from the vertical) over which the fluid is flowing. In addition, the use of ceramic foams is currently investigated. The improved tube bundles will be tested by integrating them in the 1 kW prototype.

7. Acknowledgments

This research was supported by the Swiss Federal Office of Energy in the frame of the Abstorex project and by Commission of Technology and Innovation CTI in the frame of SCCER Heat and Electricity Storage as well as by the University of Applied Sciences of Rapperswil.

8. References

Bacanu, G., 1991. The optimum design of heat pipe heat recovery exchanger. Transilvania University of Brasov, Brasov, Romania.

Brutin, D., 2015. Droplet Wetting and Evaporation: From Pure to Complex Fluids. Academic Press, Marseille, France.

Cabeza, L.F., 2015. Advances in Thermal Energy Storage Systems, Woodhead Publishing Series in Energy. Woodhead Publishing.

Daguenet-Frick, X., Gantenbein, P., Frank, E., Fumey, B., Weber, R., 2015a. Development of a numerical model for the reaction zone design of an aqueous sodium hydroxide seasonal thermal energy storage. Sol. Energy 121, 17–30. doi:10.1016/j.solener.2015.06.009

Daguenet-Frick, X., Gantenbein, P., Frank, E., Fumey, B., Weber, R., Goonesekera, K., 2015b. Seasonal thermal energy storage with aqueous sodium hydroxide - experimental assessments of the heat and mass exchanger unit. Presented at the International Conference on Solar Heating and Cooling for Buildings and Industry, Istanbul, Turkey.

Daguenet-Frick, X., Gantenbein, P., Frank, E., Fumey, B., Weber, R., Williamson, T., 2014. Seasonal Thermal Energy Storage with Aqueous Sodium Hydroxide – Reaction Zone Development, Manufacturing and First Experimental Assessments, in: EuroSun 2014. Aix-les-bains, France.

Feldkamp, K., 1969. Die Oberflächenspannung wäßriger NaOH- und KOH-Lösungen. Chem. Ing. Tech. 41, 1181–1183. doi:10.1002/cite.330412107

Fumey, B., Weber, R., Gantenbein, P., Daguenet-Frick, X., Williamson, T., Dorer, V., 2014. Development of a Closed Sorption Heat Storage Prototype. Energy Procedia, 8th International Renewable Energy Storage Conference and Exhibition (IRES 2013) 46, 134–141. doi:10.1016/j.egypro.2014.01.166

Majmudar, S., 2014. Investigation into the effects of pH, temperature & salinity on the stability and wetting performance of sulfosuccinate surfactants (Technical report, Cytec Industries).

Navarro, L., de Gracia, A., Colclough, S., Browne, M., McCormack, S.J., Griffiths, P., Cabeza, L.F., 2016. Thermal energy storage in building integrated thermal systems: A review. Part 1. active storage systems. Renew. Energy 88, 526–547. doi:10.1016/j.renene.2015.11.040

Olsson, J., Jernqvist, Å., Aly, G., 1997. Thermophysical properties of aqueous NaOH−H_2O solutions at high concentrations. Int. J. Thermophys. 18, 779–793. doi:10.1007/BF02575133

Parker, V.B., 1965. Thermal Properties of Uni-Univalent Electrolytes. Natl Stand Ref Data Ser. 2.

Stache, H.W., 1995. Anionic Surfactants: Organic Chemistry. CRC Press, Marl, Germany.

Tadros, T.F., 2006. Applied Surfactants: Principles and Applications. John Wiley & Sons.

Tracton, A.A., 2006. Coatings Materials and Surface Coatings. CRC Press.

Trigwell, S., Selvaduray, G., 2006. Effect of surface treatment on the surface characteristics of AISI 316L stainless steel. Med. Device Mater. III Venugopalan R Wu M Eds ASM Int. Mater. Park OH 208–213.

Williams, M.C., 2011. Fuel Cell Seminar 2010. The Electrochemical Society.

Conference Proceedings
EuroSun 2016
Palma de Mallorca (Spain), 11 – 14 October 2016

CORROSION EVALUATION ADVANCES FOR PROMISING TES MATERIALS IN ALUMINA FORMING ALLOYS

A.G. Fernández*, M. Henriquez, E. Fuentealba

Energy Development Center, University of Antofagasta, Avenue Universidad de Antofagasta 02800, Antofagasta, Chile

* Mail address: angel.fernandez@uantof.cl

Abstract

In the present study, new molten-salts are being proposed for Thermal Energy Storage (TES) materials at high temperature, but their corrosion characteristics are not available in the literature. The corrosion issues have to be resolved completely before commercial application of the molten-salts as the HTF in CSP plants.

To mitigate corrosion, different alumina forming alloys have been exposed to the most promising molten salts to be proposed for the new storage trends in CSP plants. This paper includes an extended corrosion study for these new developments, including nitrate, carbonate and chloride molten salts.

Ni base steels showed a better behavior in the corrosive environments and electrochemical impedance tests showed the formation of a protective layer in the first 24 hours.

The gravimetric results and SEM analyses that were performed, confirm the excellent behavior of the steels tested in nitrates and carbonates salts reducing the corrosion ability in these promising novel molten salts compared with the solar salt currently used in solar technology.

On the other hand chloride molten salt presents a very aggressive environment and the steels proposed are not recommended for its use as container materials in CSP plants.

Keywords: *Thermal Energy Storage, Molten Salt, Corrosion, Electrochemical Impedance Spectroscopy*

1. Introduction

High temperature corrosion is one of the most important issues for materials selection, structure design and service life prediction of engineering parts which are exposed to high-temperature enviroments. The prevention of high temperature corrosive attacks on materials play a critical role in aspects such as reliability, quality, safety and profitability of any industrial sector associated with high temperature process and in the study case, solar energy storage market, using inorganic molten salt (Vignarooban, Xu et al.).

Solar power tower technology is the current and future trend for CSP installation, because of its potential to achieve very high temperatures which leads to enhanced efficiency of converting heat into electricity.

The operating temperature range in the currently available solar power tower plants is between 300 and 565 C. In the future, even higher operating temperature up to 800^0C are anticipated (Kruizenga 2012). In this context, only molten-salts with extremely high boiling points can be used in the forthcoming solar power tower plants. Other possibility is reduce melting point in current molten nitrate salts in order to increase the work temperature range (Wang, Mantha et al.; Fernandez, Ushak et al. 2014). In this direction, LiNO3 is the most promising candidate and it´s eutectic formulation will be study in this paper.

doi:10.18086/eurosun.2016.03.16 Available at http://proceedings.ises.org

It is known that Electrochemical Impedance Spectroscopy (EIS) is a powerful technique that has been used to determine corrosion mechanisms in aqueous corrosion of alloys and metals for decades. The method has gained popularity since it can be performed in-situ, and also because it usually doesn't require any artificial acceleration of the corrosion process (Vidal 2014). The greatest advantage of this technique is the low intensity of excitation signal used which causes minimal disruption in the electrochemical system state, constituting a non-destructive technique and reducing the error associated with the measurement process. Impedance spectra obtained by this method are adjusted to an electrical circuit of a combination of resistors and capacitors (equivalent circuits), in order to interpret the corrosion processes.

This research is focus on corrosion ability of different thermal storage materials due to is one of the critical components for transferring thermal energy in concentrating solar power systems. Various types of thermal storage materials including nitrates, carbonates and chlorides have been selected in order to discuss the better materials for avoid corrosion issues in future developments.

The selected salts were the most promising candidates to be use in the new generation of CSP plants:

- 30wt% $LiNO_3$ + 57wt% KNO_3 + 13wt% $NaNO_3$
- 32wt% Li_2CO_3 + 33wt% Na_2CO_3 + 35wt% K_2CO_3
- 45wt% LiCl + 55wt% KCl

The corrosion tests were carried out at 550°C (nitrates), 650°C (carbonates) and 750°C (chlorides) during 1000 hours.

Regarding the materials selected, in the last years Oak Ridge National Laboratories (ORNL) have explored the effects of alloying additions on oxidation and creep behavior with an emphasis on the variation of Nb content as a function of Ni and Al levels. Niobium additions is an important factor in oxidation resistance because increase niobium and nickel levels may reduce alloy oxygen solubility, which favors external protective Al_2O_3 scale formation (Brady, Yamamoto et al. 2007) with a superior degree of protection that Cr_2O_3.

The AFA alloys show a promising combination of oxidation resistance, creep resistance, tensile properties and potential for good welding behavior. The optimal alloy composition appears in the range of (20-25%)Ni-(12-15%)Cr-(3-4%)Al-(1-3%)Nb wt% base, with a temperature limit from an oxidation standpoint approaching 9000C for alloy compositions at the higher aluminum, niobium and nickel contents of the range. The steels selected for this research are shown in table 1.

Tab. 1: Chemical composition of the steels tested in molten salts

Steels	Weight (%)							
	Al	Mn	Ni	Cr	Mo	Ti	Nb	Fe
AISI 304	-	1.7	8.04	18,28	0.27	0.01	0.008	Balance
OC-4	3.5	2	25	14	2	0.1	2.5	Balance
OC-T	3	-	35	14	-	2	3	Balance
In 702	2.7-3.7	-	75	14-17	-	-	-	2
HR224	3.2	-	47	21	-	-	-	27.5

2. Procedures

The saline nitrates that were used in the research were $NaNO_3$, KNO_3 and $LiNO_3$ (Merck 98%).
The dimensions of the analyzed samples in the gravimetric corrosion tests are 20 mm × 10 mm × 2 mm; the dimensions of each sample were measured using an electronic caliber, and each sample was weighed using an analytical balance with a 0.00001 g responsiveness. Subsequently, the samples were placed in alumina crucibles with the saline mixture and then were heated in a resistance oven at 550°C-650°C-

750°C. Gravimetric measurements were performed at 170, 335, 500, 675, 850, 1000h of the analysis for the isothermal immersion test. After the samples were removed from the oven, they were slowly cooled in warm distilled water to eliminate the salt in which they were immersed. Next, they were dried and weighed, with the average value of the weight obtained from five weight values. The formula (Eq. [1]) to calculate the mass gain over time is:

$$\frac{\Delta m}{S_0} = \frac{m_f - m_i}{S_0} \qquad \text{(Eq 1)}$$

where m_i is the initial mass of the specimen, m_f is the mass of the same at time t and S_0 is the initial area of the specimen.

The same procedure was following for carbonate salts Li_2CO_3, Na_2CO_3 and K_2CO_3 (Merk 98%) but in this case the samples was cleaned after immersion using a clark solution 10% H_2SO_4 in order to remove the salt remaining. This procedure was also used in chloride molten salt: LiCl, KCl (Merk 98%).

PPS and OCP were used to determine the Tafel slopes and corrosion rates of steels tested after immersion in molten 45wt% LiCl + 55wt% KCl at 750°C. EIS was employed to determine the corrosion mechanisms. Down selection of the best conditions per alloy was performed based on corrosion rates obtained from PPS tests. Nyquist plots obtained with time were employed to determine the corrosion mechanism change.

A two-electrode arrangement was used with the working electrode (WE) as the sample, the reference electrode (RE) and the counter electrode (CE) were connected in the same sample. The electrochemical tests were performed using a potentiostat (AUTOLAB–PGSTAT302N).

For the PPS experiments, the WE' potential (E) was continuously recorded starting immediately after its salt' immersion until dE/dt ≤ 100 µV/s was obtained and thus OCP was stablished. PPS test was conducted immediately after by applying cathodic (–) and anodic (+) external potentials from –0.35 V to +0.6 V around the OCP or corrosion potential at 0.001 V steps and 0.001 V/s. More than five coupons per test were performed under the same conditions to evaluate the reproducibility of the results. Some results were discarded based on PPS curve behavior. The corrosion current density, jcorr, was calculated from the intersection of the extrapolated straight sections of the cathodic and anodic Tafel slopes within an interval of 120 mV with respect to Ecorr.

3. Results

The steels tested in lithium nitrate salt at 550ºC were stainless steels, Inconel and AFA alloys (OC-4 and OC-T) with compositions presented in table 1; the steels were immersed in the molten salt for 1000 hours. The gravimetric gain that occurred in these steels is shown in figure 1.

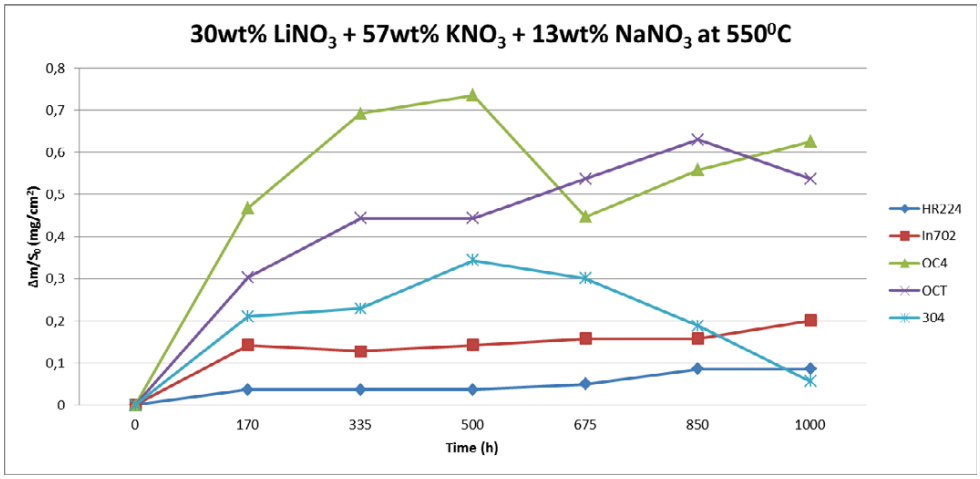

Figure 1: Gravimetric corrosion curve in saline 30%$LiNO_3$ +57%KNO_3 + 13%$NaNO_3$ at 550C for 1000 hours of test

The OC steels (with Al content) show higher mass gain after 1000 hours of saline exposition, resulting in an irregular growth of mass, with different weight gains and losses. In contrast, In702 and HR224 show the best behavior in this environment with a reduced mass gain.
It is important to point out the weight gain in 304SS with a linear corrosion rate until 500h of exposure and a change on this trend at the end of the experiment.
To explain this behavior, a micro-structural (superficial) study of the 304 stainless steel was performed using Scanning Electron Microscopy (SEM). Figure 2 shows the superficial appearance of the sample after 500 and 1000 hours of exposure as well as the EDX analysis performed.

Spectrum	O	Mg	Cr	Mn	Fe
Spectrum 1	32.46	4.08	3.02	2.04	58.39
Spectrum 2	22.39	7.99	2.55	2.63	64.44

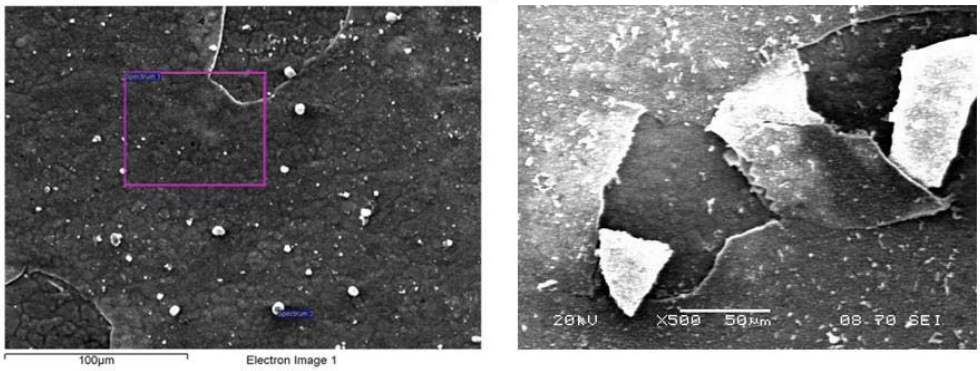

Figure 2: Superficial image of 304SS at left) 500 h and right) 1000h of test

The formed oxidation layer is very fragile, with several releasing zones, which explains the continuous fluctuations in the mass gain and the weight reduction at the end of the test.
HR224 (figure 3 left) and In702 (figure 3 right) showed the best behavior against corrosion due to the formation of a protective alumina scale.

Spectrum	O	Mg	Al	Cr	Fe	Ni
Spectrum 1	29.93	4.63	4.92	12.12	28.91	18.69
Spectrum 2	31.37	5.92	2.60	7.06	41.29	11.52
Spectrum 3	40.29	46.60	0.74	0.82	9.00	2.43

Spectrum	C	O	Mg	Al	Cr	Ni
Spectrum 1	9.00	28.64	8.89	2.13	5.80	45.53

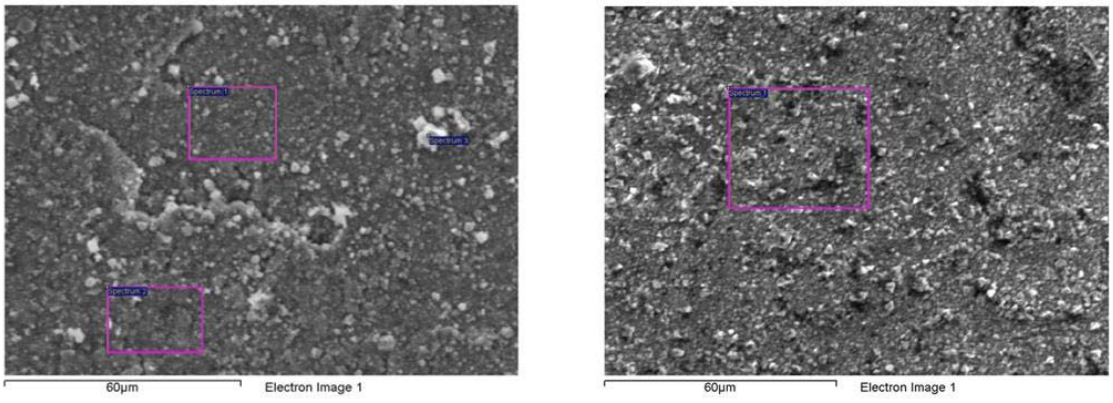

Figure 3: Superficial image of left) HR224 and right) In702 at 1000h of test

HR224 showed a higher Al and Cr content compared with In702 explaining the best behavior in the corrosive environment.
The steels tested in lithium carbonate salt at 650ºC were, the same alloys, 304SS, Inconels and AFA alloys (OC-4 and OC-T) with compositions presented in table 1; the steels were also immersed in the molten salt for 1000 hours. The gravimetric gain that occurred in these steels is shown in figure 4.

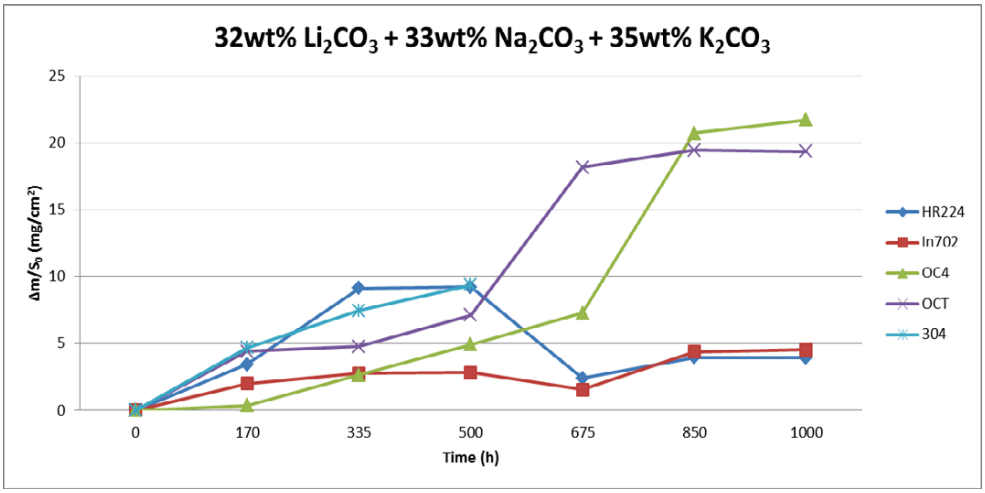

Figure 4: Gravimetric corrosion curve in saline 32%Li2CO_3 +35%K2CO_3 + 33%Na2CO_3 at 650C for 1000 hours of test

Corrosion rate showed a higher increase compared with nitrate molten salts. 304SS test only could be carried out until 500 hours of immersion, showing a severe and catastrophic corrosion spallation (fig 5).

Figure 5: Corrosion observed in 304SS immersed in saline 32%Li_2CO_3 +35%K_2CO_3 + 33%Na_2CO_3 at 650C during 500 hours of test

AFA alloys, OC4 (figure 6 left) and OCT (figure 6 right) showed the higher mass gain in contact with carbonate molten salt studied. The superficial study revealed small Al_2O_3 particles on OC4 surface that not offer a complete protection in the steel. Superficial study on OCT steel revealed an unprotective $MgFe_2O_4$ scale.

Spectrum	O	Al	Mn	Fe
Spectrum 1	56.74	37.06	3.69	
Spectrum 2	36.07			60.40
Spectrum 3	31.66			68.34

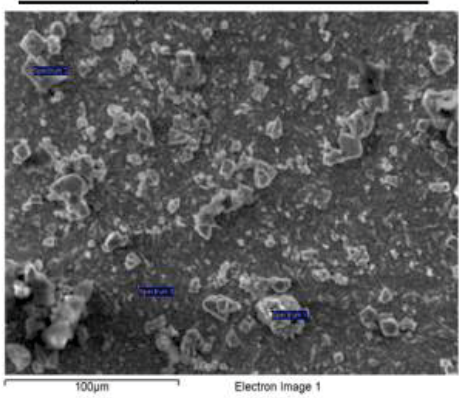

Spectrum	O	Mg	Fe
Spectrum 1	33.00	2.06	61.65
Spectrum 2	32.01	2.67	62.15

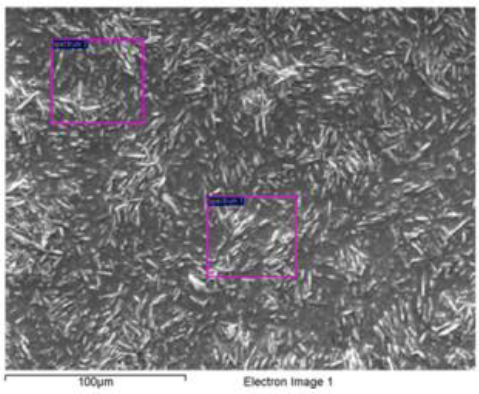

Figure 6 Superficial image of left) OC4 and right) OCT immersed in saline 32%$Li2CO_3$ +35%$K2CO_3$ + 33%$Na2CO_3$ at 650C during 1000 hours of test

HR224 and In702 shoed the best behavior against carbonate corrosion and, in this case, are forming a protective Al-O-Ni scale in the steel surface (Fig 7)

Spectrum	O	Al	Fe	Ni
Spectrum 1	23.80		2.26	73.95
Spectrum 2	21.41	1.59	2.51	72.98

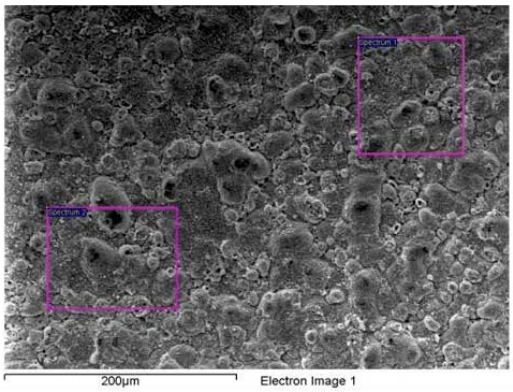

Figure 7: Superficial image of In702 immersed in saline 32%Li_2CO_3 +35%K_2CO_3 + 33%Na_2CO_3 at 650C during 1000 hours of test

According with results obtained, the corrosion study on chloride molten salt at 750^{0}C was only performed on HR224 and In702. The gravimetric results obtained are shown in figure 8.

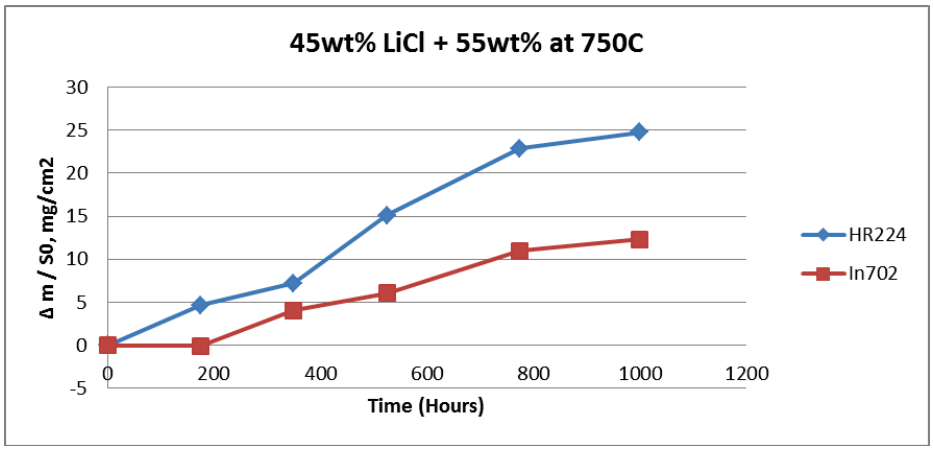

Figure 8: Gravimetric corrosion curve in saline 45%LiCl + 55%KCl at 750C for 1000 hours of test

In this case, In702 showed a lower mass gain compared with HR224 and this molten salt was the most corrosive tested in this study. Some EIS test has been developed in chloride molten salt in order to obtain corrosion rates and mechanism.
PPS and OCP were used to determine the Tafel slopes and corrosion rates of steels. Results are shown in table 2.

Tab. 2: PPS and OCP results obtained in EIS test

Alloy	Area immersed	CR, mm/y	Polarization Resistance	Test Temperature	OCP (LSV)	E corr
HR224	2,32412	0,93039	124,05	750	-0,348	-0,426
In 702	1,95158	0,61475	297,07	750	-0,414	-0,54

This technique was also used for monitorize the corrosion and Nyquist diagrams were obtained for In702 at 24 and 100h.

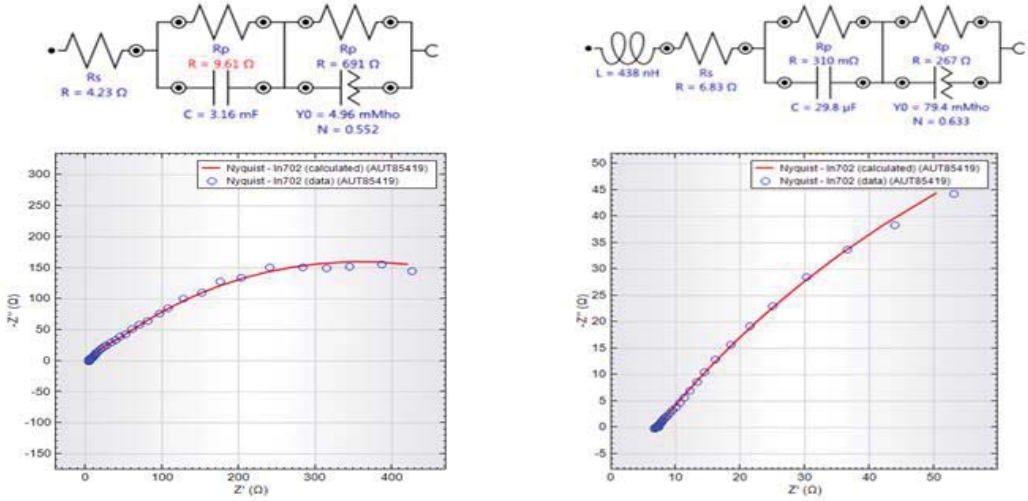

Figure 9: Nyquist diagrams for EIS study performed in saline 45%LiCl + 55%KCl at 750C for left) 24 h and right) 100 h of test

To fit the data, corrosion models in molten salts must be used. In this case, the Nyquist plots and their respective equivalent circuits are matching for a protective layer (fig 9 left) and localized corrosion model (fig 9 right).
Two semicircles are typical of protective layers and the latter type is produced by the rupture of protective layers which initiates pits creating a localized corrosion.

4. Conclusion:

Molten salts act as the electrolyte in a corrosive system that attacks the metal containers. High operating temperature is necessary to improve efficiency in the CSP system and molten-salts are the most promising TES materials at high temperatures. Different Alumina Forming Austenitic (AFA) steels have been proposed as container and pipping materials, HR224 and In702 showed the best corrosion resistance in the molten salt tested. On the other hand, their use it is not recommended for container material in storage tanks involving chloride molten salt.

Acknowledgements

The authors would like to acknowledge the financial support provided by CONICYT / FONDAP 15110019 "Solar Energy Research Center" SERC-Chile, Fondecyt Postdoctoral grant nº3140014, FIC-R Antofagasta Regional Government BIP: 30413089-0 and the Education Ministry of Chile Grant PMI ANT 1201."

5. References

Brady, M. P., Y. Yamamoto, et al. (2007). "Effects of minor alloy additions and oxidation temperature on protective alumina scale formation in creep-resistant austenitic stainless steels." Scripta Materialia 57(12): 1117-1120.

Fernandez, A. G., S. Ushak, et al. (2014). "Development of new molten salts with LiNO3 and Ca(NO3)2 for energy storage in CSP plants." Applied Energy 119(0): 131-140.

Kruizenga, A. M. (2012). "Corrosion Mechanisms in Chloride and Carbonate Salts." Sandia Report SAND2012-7594.

Vidal, J. C. G. R. T. E. (2014). "Hot Corrosion Studies using Electrochemical Techniques of Alloys in a Chloride Molten Salt (NaCl-LiCl) at 650°C " Proceedings of the ASME 2014 8th International Conference on Energy Sustainability.

Vignarooban, K., X. Xu, et al. "Heat transfer fluids for concentrating solar power systems " A review." Applied Energy 146: 383-396.

Wang, T., D. Mantha, et al. "Thermal stability of the eutectic composition in LiNO3-NaNO3-KNO3 ternary system used for thermal energy storage." Solar Energy Materials and Solar Cells 100(0): 162-168.

Conference Proceedings
EuroSun 2016
Palma de Mallorca (Spain), 11 – 14 October 2016

Design and testing of a latent heat storage for solar cooling applications

Andrea Frazzica[1], Valeria Palomba[1,2] and Vincenza Brancato[1]

[1] CNR - Istituto di Tecnologie Avanzate per l'Energia "Nicola Giordano", Via Salita S. Lucia sopra Contesse 5, 98126 Messina, Italy.

[2] Department of Engineering, University of Messina, C.da di Dio 98166 Messina

Abstract

The present paper reports the design, realization and testing of a lab-scale latent heat storage, specifically realized for solar cooling applications. The latent heat storage is based on a fin-and-tubes heat exchanger configuration employing a commercial paraffin as PCM. The paper mainly focuses on the experimental characterization, carried out by means of a test rig, available at the laboratory of the CNR ITAE, able to simulate working boundaries of a solar cooling plant. The experimental outcomes confirmed the increased heat storage density obtained by such a new component, compared to standard sensible heat storage. Nevertheless, still some limitations in the achievable heat transfer rate is highlighted, due to improper realization of the component.

Keywords: *heat storage, solar cooling, PCM*

1. Introduction

During last years, an innovative technology, known as solar cooling, has gained more and more interest (Henning, 2007). Such a technology exploits the fact that cooling demand of buildings is in phase with the highest availability of solar irradiation during the year. Accordingly, it is possible to couple solar thermal collectors to thermally driven chillers for air conditioning applications (Henning et al., 2013). Usually, a closed cycle solar cooling plant is based on three main components, namely, the solar collectors field, the high temperature thermal energy storage and the thermally driven chiller (Henning et al., 2013). In the past, a lot of efforts have been paid to the identification of the optimal plant layout, in terms of surface of solar collectors, high temperature thermal energy storage size, backup system and thermally driven heat pump nominal power (Iranmanesh and Mehrabian, 2014; Hang et al., 2013). For solar cooling systems employing non-concentrating solar collector technologies (i.e. flat plane and evacuated tubes solar collectors), the high temperature heat storage relies on the sensible heat storage technique, mostly employing water as heat storage medium. Nevertheless, it is quite known that there are other opportunities to efficiently store heat. Among them, latent heat storage, based on the employment of phase change materials (PCMs) could be an interesting alternative (Mehling and Cabeza, 2008). Indeed, since they store and release heat in a narrow temperature range, they allow to feed the thermally driven chillers with an almost-constant temperature for long time, which can be beneficial for the performance of the chiller itself, increasing, at the same time, the heat storage density. Since in a solar cooling plant, the temperature difference between inlet and outlet on the heat storage side is limited to the temperature difference across the regenerator of the thermally driven chiller, which, from experimental outcomes, is usually around 10°C (Monnè et al., 2011), the employment of PCMs as heat storage medium seems quite reasonable.

Accordingly, in the present paper, the design, realization and testing of a lab-scale compact latent heat storage based on a fin-and-tube heat exchanger and a commercial paraffin is presented. Particularly, thanks

doi:10.18086/eurosun.2016.03.10 Available at http://proceedings.ises.org

to a properly designed test rig, it was possible to verify the achievable performance under working conditions typical of a heat storage for solar cooling applications, both during charging and discharging phase.

2. Thermal storage system

2.1. Employed PCM

In the present paper, the studied PCM is the organic Plus-Ice A82 manufactured by PCM Products®, whose nominal melting temperature, 82°C, perfectly suits the typical working range of solar cooling plants driven by non-concentrating solar thermal collectors. It consists in blend of linear and branched hydrocarbons. Its calorimetric features have been evaluated by means of a DSC-1 Mettler – Toledo. Ten milligrams of the material were tested cycling five times between 30°C and 110°C, with rate of 5°C/min, in static air and in a closed stainless steel pan sealed by means of a Viton® O-ring. The results reveal that the Plus-Ice A82 present good stability, with replicable latent heat and limited supercooling phenomenon. The measured melting enthalpy was 140 J/g, peak temperature during melting process was 85.7°C and peak temperature during solidification process was 80.8°C, thus showing slight supercooling. In order to take into account both sensible and latent heat, the integral heat curve between 40°C and 100°C was drawn, as reported in Figure 1. It is a useful tool to evaluate achievable heat storage density under different working boundary conditions. In the same figure, the mathematical fitting for the integral heat curve is represented, through which the theoretical energy for charge/discharge has been calculated.

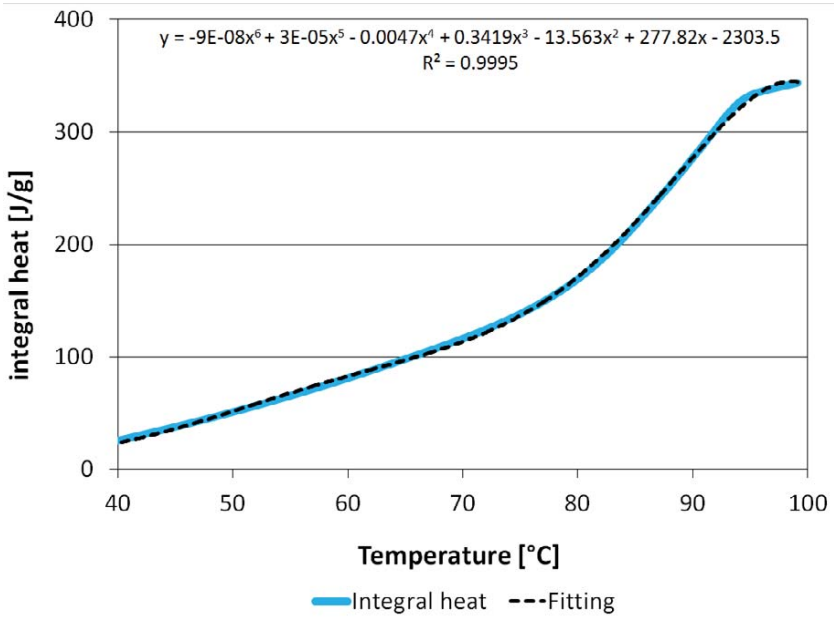

Figure 1: Integral curve of PCM PlusIce A82 and the numerical fitting.

2.2. Designed and realized prototype

In order to overcome the well-known limitations of low thermal conductivity of PCMs, in the present work, a fin-and-tube heat storage configuration has been designed through the aid of a detailed mathematical model.

In Figure 2, a 3D rendering of the storage and two picture of the realised system are presented, before and after the thermal insulation. The insulation has been realized with a 3 cm thick polymeric foam and by applying a layer of reflective aluminum foil.

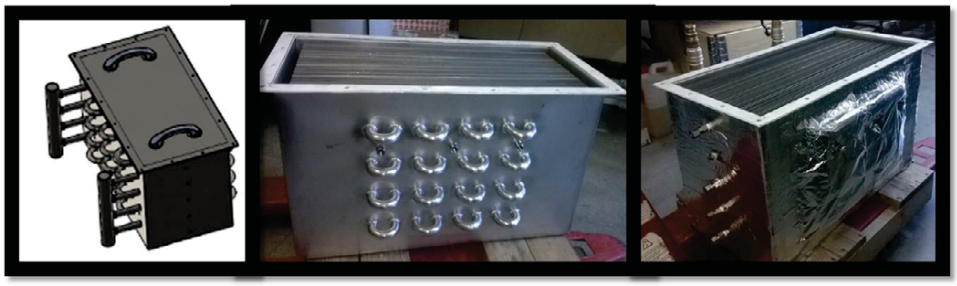

Figure 2: the fin-and-tube heat exchanger for the latent storage, 3D rendering and pictures of the system before and after thermal insulation.

The main features of the storage are summarized in Table 1. It consists of 48 fins and 4 parallel hydraulic circuits, each one made up of 8 pipes, connected to the external sources via a manifold. Fin distance chosen is 5 mm, which allows to partially compensate for the low thermal conductivity of the chosen material. All the components are realized in AISI 416L.

Table 1: Main features of the fin-and-tube heat storage.

Material	AISI 416
Technology	Fin-and-tube heat exchanger with welded fins
Number of pipes	32
Diameter pipes	½ ”
Ranks	4
Number fins	48
Fin dimensions	400 x 650 x 2 mm
Fin space	5 mm
Overall dimensions	400 x 650 x 350 mm
Overall weight	240 kg

8 thermocouples have been inserted inside the storage, their position chosen to highlight possible transversal and longitudinal temperature gradients, by distributing them along two different ranks and at different distances from the sides of the exchanger. The arrangement of the temperature sensors inside the storage is reported in Figure 3.

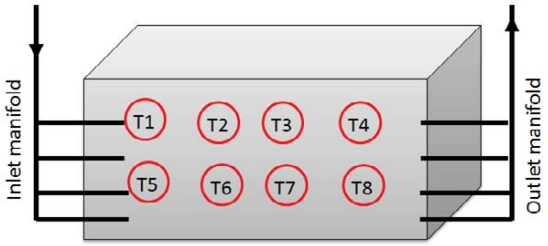

Figure 3: Schematic of the thermocouples position inside the compact heat storage.

3. Experimental testing

3.1. The testing rig

The tests of the prototype have been carried in a testing rig in the laboratory of CNR-ITAE, specifically designed for the characterization of latent heat thermal storages. The layout of the rig is shown in Figure 4, while Figure 5 shows a detail of the hydraulic circuit of the testing bench and the storage connected to it.

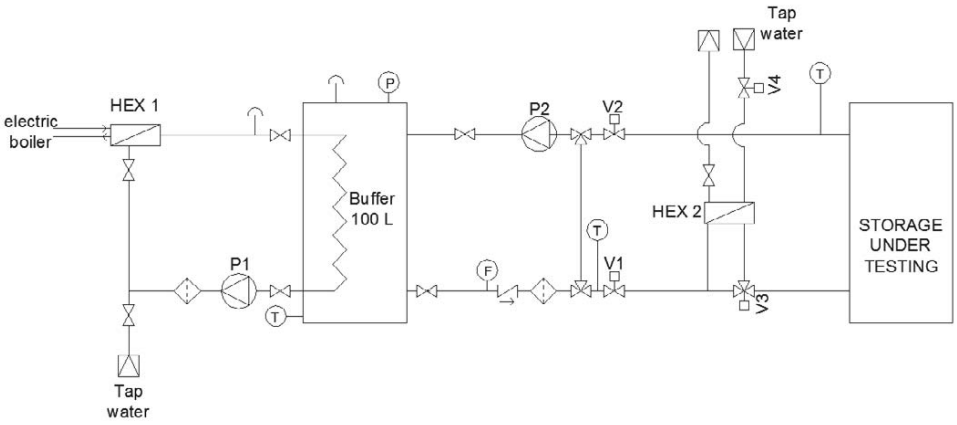

Figure 4: Layout of the test rig for latent heat storage.

Figure 5: detail of the storage during tests.

The main heat source of the testing bench is a 24 kW electric boiler that has been connected to a service buffer, with the aim of providing a constant temperature inlet. A plate heat exchanger is connected, through a mixing valve, to tap water and to the service buffer, thus allowing setting any desired temperature in the range 20°C-85°C for discharge. The management of the testing bench and the acquisition of all the main parameters are made through a software specifically compiled in LabVIEW® environment. For the measure of temperatures, class A thermocouples are used, while a magnetic flow meter with ±1% FS is used for the determination of mass flow rate of the heat transfer fluid (i.e. water). Uncertainty analysis has been carried out for the performed tests, the output showing that uncertainties of 5-8% for all the measured quantities are achieved.

3.2. Methodology

Following Figure 6 schematically represents the steps followed to perform both charging and discharging phase.

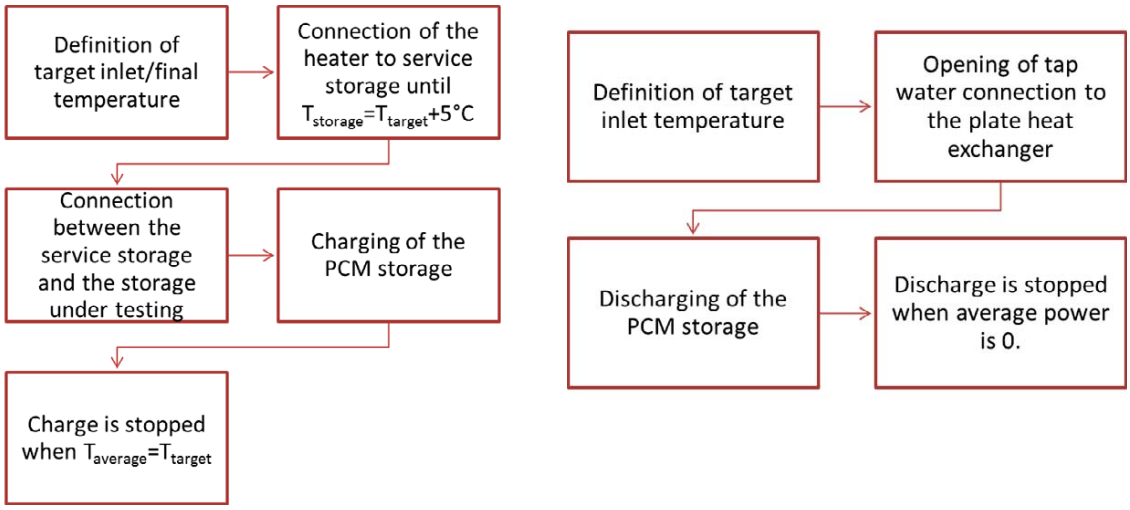

Figure 6: methodology followed for charge and discharge of the storage.

3.3. Calculated figures

The following figures have been calculated for characterization and comparison purposes:

- Charge/discharge energy, calculated as the integral of the instantaneous power for the whole duration of the charge/discharge process.

$$E = \int_0^{\tau_{fin}} \dot{m} c_p (T_{in} - T_{out}) \cdot d\tau \qquad \text{(eq.1)}$$

- Average power, calculated as the average of the instantaneous powers for the whole duration of the process.

$$P_{ave} = \frac{\sum_{i=0}^{t_{fin}} \dot{m}_i c_p (T_{in,i} - T_{out,i})}{t_{fin}} \qquad \text{(eq. 2)}$$

- Charge efficiency, calculated as the theoretical energy given to the system for the phase change over the total one.

$$\varepsilon_{ch} = \frac{E_{th,ch}}{E} \qquad \text{(eq. 3)}$$

- Discharge efficiency, calculated as the total amount of energy recovered from the system over the theoretical one.

$$\varepsilon_{disch} = \frac{E}{E_{th,disch}} \qquad \text{(eq. 4)}$$

4. Experimental results

4.1. Charging phase

Figure 7 shows the temperature evolutions of different thermocouples for various tests, differing for the applied flow rate. The same behaviour is shown by all of the sensor: there is an initial rapid increase up to about 75°C, representing the onset temperature of melting, followed by a slower increase, with an almost constant rate until the target temperature is reached and the test is stopped. The curves for T2 and T6 that are placed at two different heights (corresponding to 2 different ranks) show no significant temperature gradients along the height of the system. Instead, marked differences are visible by comparing, for example, the trend for T2 and T4, the

former one in the central part of the heat exchanger while the latter one is near the side wall. Along all the duration of the test a temperature difference of almost 15°C exists between them, mainly due to the poor heat transfer inside the material, which has a low thermal conductivity. It is clear that the material in the central part of the exchanger, which is closer to the fins and especially the tubes, exhibits the highest melting rate, whereas the material on the side of the exchanger even after 5 hours has not completed the phase change. It is interesting to notice that, as already reported in (Cho and Choi, 2000; Torregrosa-Jaime et al., 2013), the melting range is not easily identifiable, since the phase change occurs in a wide range of temperatures. The effect of flow rate is also recognisable: higher flow rates correspond to faster melting dynamics.

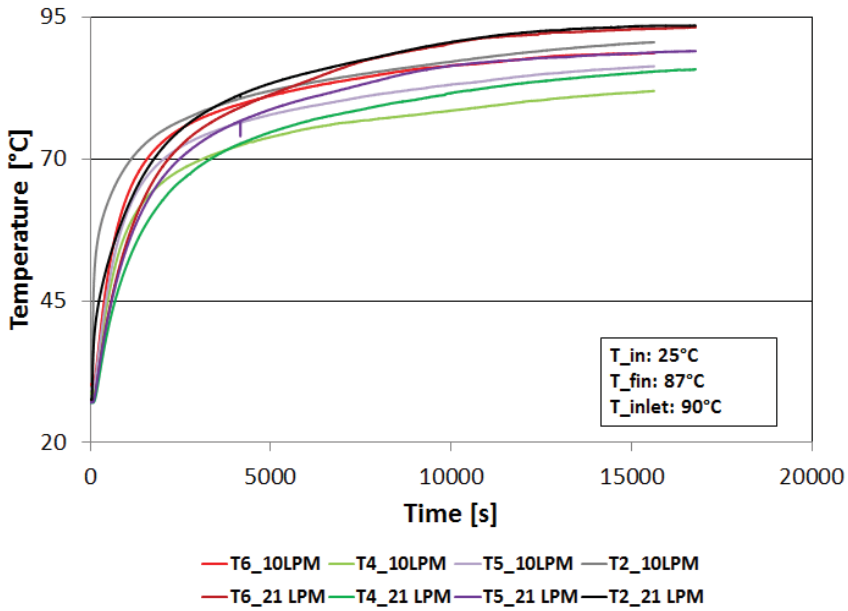

Figure 7: Temperature evolutions of four thermocouples for charging tests at different flow rates.

In Figure 8, efficiency of the storage for charging phase, defined according to eq. 3, is plotted against the temperature difference between the initial and final average temperatures in the storage. Temperature differences from 32°C to 63°C are considered, for two cases, differing in the final temperature reached. From the picture, it is clear that efficiency increases with the temperature difference inside the material, even though in a non-linear manner. The gap in the efficiency for the two series of test, in each condition, lies in the range of 2-4% and therefore is negligible in most conditions. Such a behaviour could be explained considering that, for higher temperature differences, the energy stored includes both the latent heat and a relevant amount of sensible heat, whereas, for lower temperature differences, the highest share in the energy stored is that of latent heat. Indeed, considering that the phase change is a slower process than the sensible heating up, the effect of thermal losses is more relevant when the temperature interval is smaller.

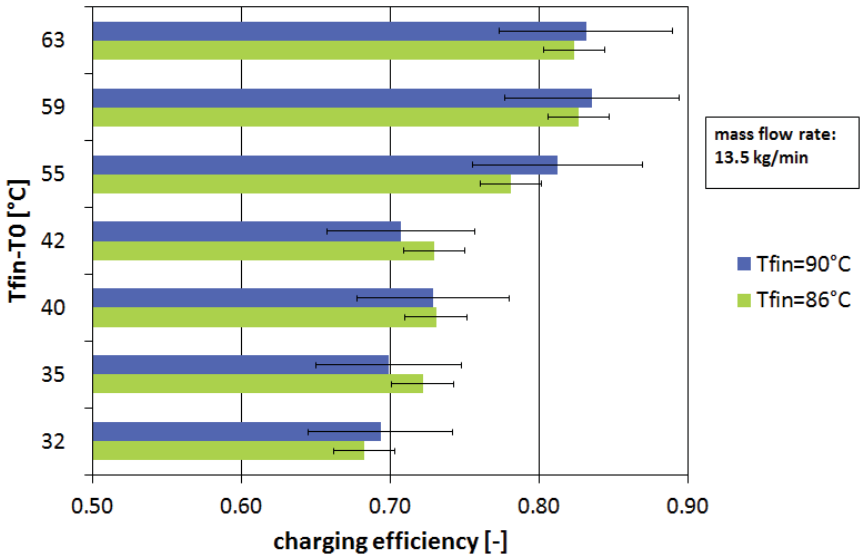

Figure 8: Efficiency vs temperature difference at the beginning and ending of charging tests.

Finally, Figure 9 shows the effect of the mass flow rate of the heat transfer fluid on both the efficiency and the average power supplied. As expected, increasing the average flow rate increases the power input to the storage. At the same time, this has a beneficial effect on the efficiency of the system: since the fluid is in laminar regime, increasing the average flow rate allows enhancing heat transfer from the heat transfer fluid to the material.

4.2. Discharging phase

The melting range of the chosen paraffin is suitable for the collection and storage of low-grade waste heat or solar energy, that are typical heat sources of thermally driven chillers. Considering the typical temperatures for the driving circuit of such chillers, discharging tests with temperatures of 65°C and 70°C were considered.

In Figure 10, the temperature evolutions of two thermocouples at variable flow rates are shown. In particular, the presented sensors are placed in the central part (T3) and in the side of the exchanger (T2). As for the charging phase, a typical behaviour can be identified for T3: at first, the temperature decreases rapidly, until a value of about 85°C is reached. At this temperature, as shown from DSC experiments, solidification starts, and is highlighted in the picture by a decrease of the temperature with a constant slope. Instead, the thermocouple indicated as T4, at the beginning of the examined tests, is around the onset value for solidification and therefore it undergoes a slow constant reduction in temperature for the whole duration of the test. Flow rate has a clear effect on the discharging process of the system, since higher flow rates lead to higher heat transfer dynamics, and therefore a more rapid completion of the phase change process.

In Figure 11, the efficiency of the storage is presented as a function of the initial temperature of the storage. The melting range is highlighted as well, in order to better clarify the results obtained. Indeed, a peculiar trend has been observed: when the initial temperatures are in the range 81°C to 86°C, the efficiency decreases with an increasing of initial temperature, while the efficiency tends to increase when the initial temperature falls below 81°C and when the initial temperature is above than 86°C. This indicates that the efficiency is lower when only the latent heat is released during the tests and increases when part of the sensible heat can be recovered.

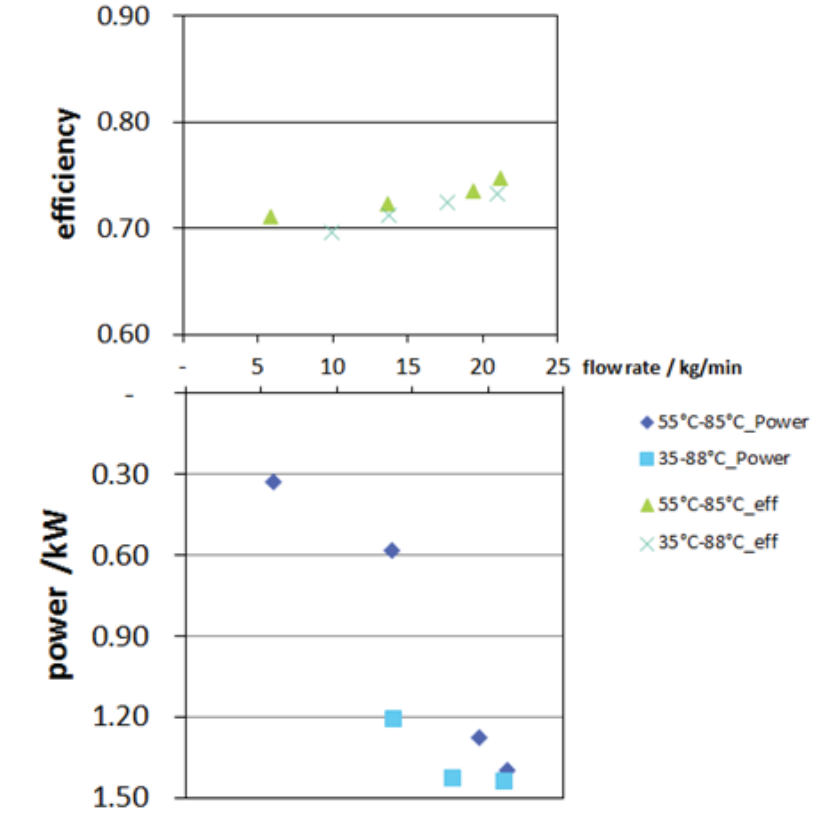

Figure 9: Effect of the flow rate of the heat transfer fluid on the charge of the storage.

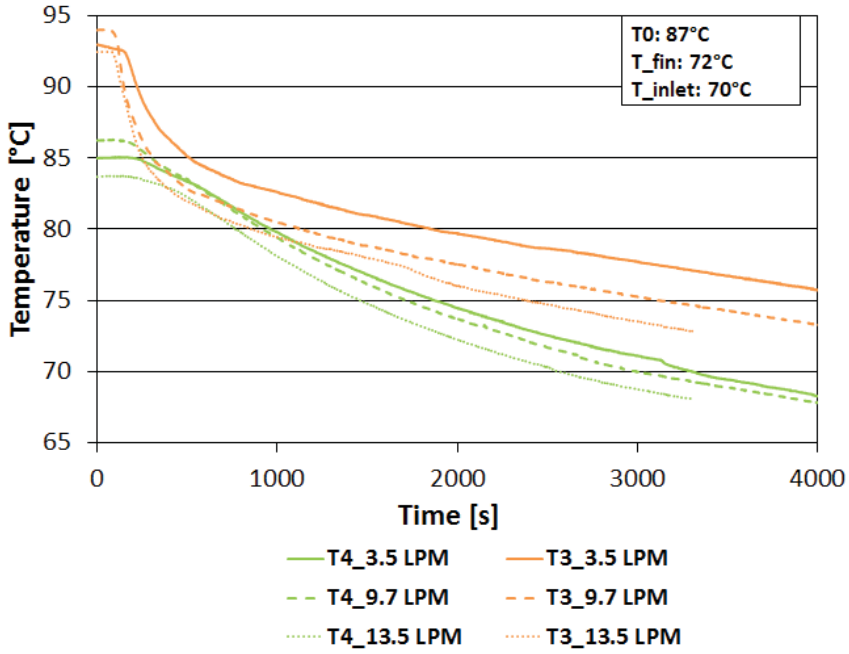

Figure 10: Temperature evolutions inside the storage for three discharging tests at different flow rates.

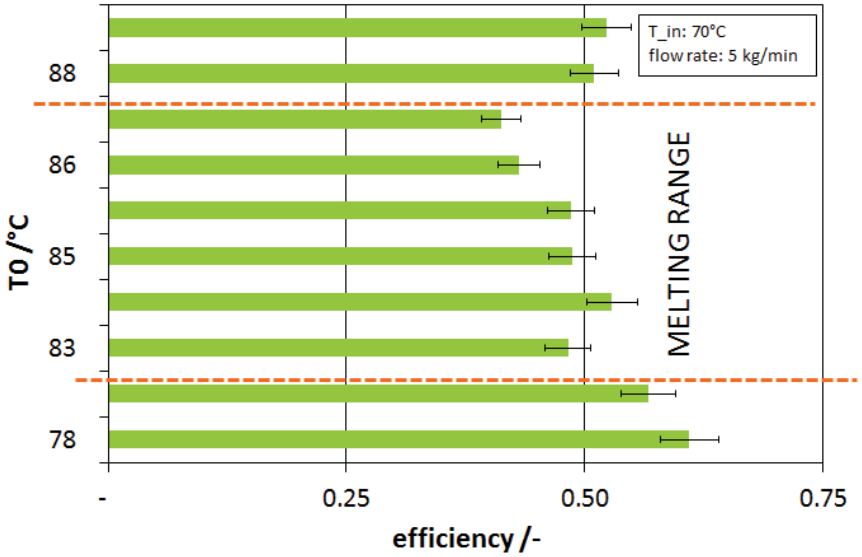

Figure 11: efficiency of the storage for different initial temperature of the storage.

Finally, average discharging power is shown in Figure 12 as a function of flow rate of the heat transfer fluid and average inlet temperature for discharging. The results obtained can be explained by considering that, for the phase change process, the main driving forces are the temperature difference between the storage and the heat transfer fluid, and its flow rate, which affects the rate at which heat is transferred from the fluid to the material on the external side of the pipes. Consequently, the tests with higher temperature of the storage and the lower inlet temperature of the heat transfer fluid correspond to higher power, up to 1.20 kW. The lowest measured powers, for discharging temperature interval of 85°C-70°C and flow rates of 3.5 kg/min or 5 kg/min are of 0.7 kW.

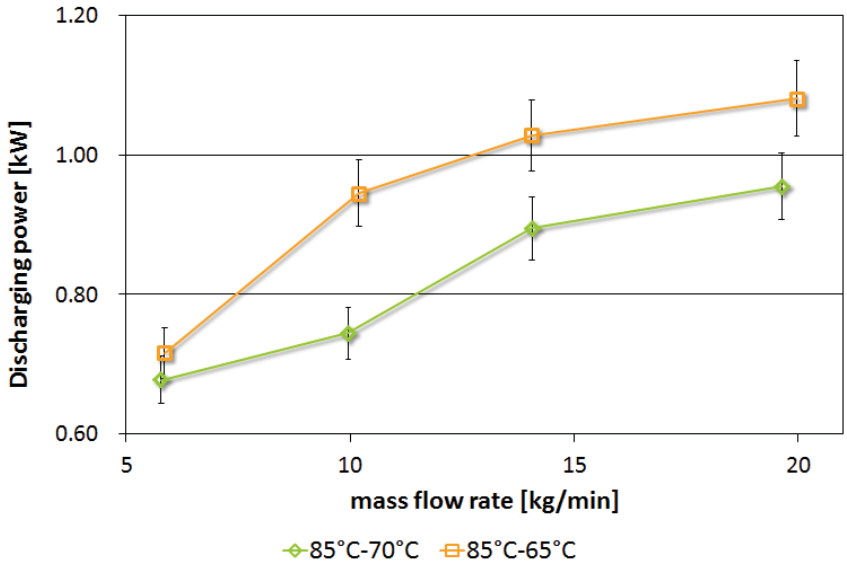

Figure 12: Average discharging power under different boundary conditions.

5. Conclusions

In the present paper, the experimental characterization of a lab-scale latent heat storage for solar cooling application is presented. It is based on the fin-and-tube configuration, employing an organic commercial PCM, PlusIce A82. The experimental outcomes confirmed that the system is characterized by good performance, both in terms of charging/discharging efficiency as well as achievable heat storage density. Indeed, efficiencies ranging between 0.7 and 0.9 during charging and between 0.45 and 0.6 during discharging have been measured.

Furthermore, the energy discharged under typical working conditions corresponds to an energy storage density of about 135 MJ/m^3, which is about 30% higher than a typical sensible heat storage working under the same conditions.

On the contrary, looking at the dynamic performance, in terms of charging and discharging power, it is evident that still the heat transfer efficiency of the system is not optimized. This is due to the intrinsic low thermal conductivity of the PCM as well as to the improper manufacturing of the heat exchangers. Indeed, the fins were not perfectly welded to the tubes, thus adding a high heat transfer resistance, which strongly limits the achievable dynamic performance.

Further investigations are still ongoing to simulate other working boundary conditions typical of a solar cooling plant.

6. Acknowledgements

The present work was founded by “Fondo per la Ricerca per il Sistema Elettrico – Adp MiSE-CNR”.

7. References

Cho, K., Choi, S.H., 2000. Thermal characteristics of paraffin in a spherical capsule during freezing and melting processes, Int. J. Heat Mass Tran. 43, 3183-3196.

Hang, Y., Du, L., Qu, M., Peeta, S., 2013. Multi-objective optimization of integrated solar absorption cooling and heating systems for medium-sized office buildings, Renew. Energ. 52, 67-78.

Henning, H-M., 2007. Solar assisted air conditioning of buildings – an overview. Appl. Therm. Eng. 27, 1734-1749.

Henning, H-M., Motta, M., Mugnier D., 2013. Solar cooling handbook – A guide to solar assisted cooling and dehumidification processes, 3rd Revised & enlarged edition.

Iranmanesh, A., Mehrabian, M.A., 2014. Optimization of a lithium bromide–water solar absorption cooling system with evacuated tube collectors using the genetic algorithm, Energ. Buildings. 85, 427-435.

Mehling, H., Cabeza, L.F., 2008. Heat and cold storage with PCM, Ed. Springer.

Monné, C., Alonso, S., Palacín, F., Serra, L., 2011. Monitoring and simulation of an existing solar powered absorption cooling system in Zaragoza (Spain). Appl. Therm. Eng. 31, 28-35.

Talmatsky, E., Kribus, A., 2008. PCM storage for solar DHW: An unfulfilled promise?, Sol. Energy. 82, 861-869.

Torregrosa-Jaime, B., Lopez-Navarro, A., Corberan, J.M., Esteban-Matias, J.C., Klinkner, L., Payà, J., 2013. Experimental analysis of a paraffin-based cold storage tank, Int. J. Ref. 36, 1632-1640

World Business Council for Sustainable Development (WBCSD), Energy Efficiency in Buildings Facts and Trends, Full Report, 2008.

NOMENCLATURE

Quantity	Symbol	Unit
Energy	E	J
Mass flow rate	$\dot{m}$	kg/min
Power	P	kW
Specific heat	c_p	J kg^{-1} K^{-1}
Temperature	T	K
Time steps	t	-
Efficiency	ε	
Time	τ	s
Subscripts		
charging	ch	
discharging	disch	
final	fin	
initial	0	

inlet	in
outlet	out
theoretical	th

Conference Proceedings

EuroSun 2016

Palma de Mallorca (Spain), 11 – 14 October 2016

CFD modeling of a small case Solar Pond

M. C. Giestas[a], J. P. Milhazes[b], P. J. Coelho[b], A. M. Joyce[a] and D. Loureiro[a]

[a]*LNEG, Estrada do Paço do Lumiar, 1649-038 Lisboa, Portugal*
[b]*IDMEC/IST, Avenida Rovisco Pais, 1049-001 Lisboa, Portugal*

Abstract

A Salt Gradient Solar Pond (SGSP) is a basin of water where solar energy is trapped due to an artificially imposed salinity gradient. Three main zones can be identified: the surface and bottom zones that are both convective and an intermediate zone in between intended to be non-convective. This zone acts as a transparent insulation allowing the storage of thermal energy at the bottom, where it is available for later use.
A numerical model where the SGSP dynamics is described in terms of velocity, pressure, temperature and salt concentration is presented. This model is based on the Navier-Stokes equations for an incompressible fluid, coupled to two advection-diffusion equations: one for temperature and another one for salt concentration. The fluid density ρ depends on temperature and salinity and the Boussinesq hypothesis is adopted. The variation of the daily solar radiation and its attenuation along the depth of the pond are also considered.
The objective of this work is to reproduce existing experimental data with a model robust enough to describe the physical phenomena involved for a long period of time. A transient computation with the finite element *deal.II* library and a finite volume model in *ANSYS Fluent* account for the dynamic behavior of the pond. This way it will be possible to contribute to the correct design and operation of these long thermal storage energy devices.

Keywords: Solar ponds, thermal storage, numerical modeling, finite elements, double advection-diffusion.

doi:10.18086/eurosun.2016.03.02 Available at http://proceedings.ises.org

1. Introduction

Tab. 1: Nomenclature

A	Thermal diffusivity (m^2/s)	α	Thermal expansion coefficient (K^{-1})
B	Salt diffusivity (m^2/s)	β	Salt contraction coefficient
b	Buoyancy		Kinematic viscosity (m^2/s)
$\mathbf{C_p}$	Specific heat of the fluid (J/kg ^oC)		Angle of declination (º)
g	Gravity acceleration (m/s^2)	ρ	Fluid density (kg/m^3)
h	Convection coefficient (W/m^2 K)		Incident and refracted angle (º)
I, I_R	Incident solar radiation (W/m^2)		Hour angle
L_1, L_2	Domain length and height (m)		Salt concentration (%)
n	Unit normal vector	**Ω**, ∂**Ω**	Domain, boundary
p	Pressure (Pa)		
k	Transparency coefficient	*Operators*	
T	Temperature (K)	∇	Gradient
t	Time (s)	∇.	Divergence
u	Velocity field (m/s)	Δ	Laplacian
x	Space coordinates (m)		
R	Reflection coefficient		
Subscripts		*Superscripts*	
0, *f*	Initial, final	ż	Time derivative
r	Reference values	*n*	Time instants
a	Ambient values		
1, 2, 3, 4	Left, right, bottom, top		

A Salt Gradient Solar Pond (SGSP) is a basin of water that collects and stores solar thermal energy. A temperature gradient is established in a natural way induced by solar radiation absorption at the pond surface. Three distinct zones are present in the SGSP: A upper convective zone (UCZ), a lower convective zone (LCZ) and an intermediate zone intended to be non-convective (NCZ). A salt concentration gradient (denser at the bottom and lighter at the top) is established to prevent convective motions. These motions would promote the return of the stored energy to the outside ambient destroying the SGSP very purpose. Thus a double advection-diffusion process occurs in the SGPS with the temperature and salinity fields making opposite contributions to the fluid density.

Studies of Solar Ponds have been performed since 1902, Kalecsinsky (1902). The experimental, analytical and numerical studies of SGSP pursued with Stommel et al. (1956), Weinberger (1964), Turner (1974), Tabor (1969) and Veronis (1968). A significant number of Solar Ponds were constructed with different characteristics: coupled to desalination units; as low cost seasonal thermal energy storage reservoirs for solar thermal energy production agricultural applications as greenhouse heating Joyce et al (2001) or heating aquaculture ponds especially if constructed near coastal zones.

Concerning modeling, Weinberger (1964) was the first to give a mathematical formulation of a SGSP behavior. The numerical solution of the governing equations that describes a SGSP was firstly reported by Hull (1980), and Hawlader and Brinkworth (1981). Rubin et al. (1988) applied a finite difference method to discretize the governing equations, while Jayadev and Henderson (1979) used a finite element method (FEM). Meyer et al. (1982) developed a numerical model to predict the time dependent behavior of the interface between the convective and the non-convective regions. Panahi et al. (1983) used a one-dimensional model. A SGSP year control operation was successful obtained with a one-dimensional model by Ouni et al (2003).

One of the critical factors in SGPS performance is the stability of the non-convective zone. Stability has been studied by researchers like Da Costa et al. (1981), Schechter et al. (1981), Dake et al. (1969), Akbarzadeh et al. (1980), Cha al. (1982), Meyer et al. (1982) and Giestas et al. (1996, 1997). They resorted in most cases to a linear perturbation theory. The results obtained provided important information regarding the onset of the instabilities, as well as the existence of several possible stable or unstable states that may arise (see Jin et al. (1996) and Mambole et al. (2004)). In Pina et al. (2005), a 2D numerical model that considers the viscosity dependent on both temperature and salt concentration was presented.

Mansour et al. (2006) solved numerically the problem of transient heat and mass transfer through a two-dimensional finite volume method. Angeli and Leonardi (2004, 2005) analyzed the evolution of salt concentration profiles in a SGSP.

Ould Dah et al. (2010) studied experimentally the transient evolution of profiles in a small Solar Pond in Tunisia. Boudhiaf and Baccar (2014) payed special attention to the hydrodynamic behavior of a two dimensional SGSP model in transient regime. Results have shown that the buoyancy ratio and the aspect ratio have an important effect in the thermal performance of the SGSP. Boudhiaf (2015) analyzed those effects using a finite volume technique in transient regime with a fixed salt concentration profile. Those authors used *ANSYS Fluent* to better understand ponds performance. With the development of this kind of finite volume analysis, a new way of visualization of SP behavior was possible.

This work presents a 2D CFD model for the described mathematical problem. Density is assumed to vary acording to the Boussinesq hypothesis, heat conduction is treated according to Fourier´s law and salt diffusion obeys Fick´s law. Initial and boundary condition are given in Section 2.2 and Section 2.4. To validate this model, comparisons with available experimental data, namely with the results of Ould Dah et al. (2010) are presented. These authors studied experimentally the time evolution of profiles in a small Solar Pond in Tunisia and presented results for temperature profiles. The cylindrical tank considered was insulated, the area of the surface is 0.64 m^2 and the depth is 0.90 m. In that small tank the temperature and salinity profiles were measured through a set of 27 thermocouples each of 6mm diameter. The obtained results give a special contribution to the validation of the model proposed here.

The solution of the time-dependent coupled system of equations of a SGSP is a difficult numerical task. To perform equally well the solution with respect to the several physical phenomena, a sequence of simpler sub-problems in correspondence with the underlying physics was performed. The study involves the splitting of the temperature, salinity and Navier-Stokes equations the later employing a pressure correction approach leading itself also to a decoupling of velocity and pressure. A general introduction to operator splitting techniques can be seen in Farago and Havasiy (2009). A computer code was developed using the finite element (FE) library *deal.II* (Bangerth et al. 2007) with some parallelization achieved in the assembling of element matrices and vectors and the solver of the linear system.

A 2D pressure based ANSYS Fluent simulation was also performed based on the same model hypothesis.

2. Physical and Mathematical Formulation

2.1 Physical model and simplifying assumptions

A numerical model for the SGSP dynamics of the fluid flow and heat and mass transfer was developed. The SGSP prototype is modeled as a rectangular cavity of height

We present below the governing partial differential equations as well as the boundary conditions adopted for the studied case. These governing equations are the standard conservation laws for continuum media.

Heat equation:

Therefore the domain in study is

Where

A bounded second order implicit scheme was chosen for the time marching solution. The time step was constant and equal to 0.8 seconds.

4. Results and discussion

Tab. 3: Constants values used to obtain the results

Symbol	Value	Unit
A	10.52×10^{-7}	$m^2 s^{-1}$
B	1.72×10^{-9}	$m^2 s^{-1}$
	110.0	$W m^{-2} K^{-1}$
	930.0	$W m^{-2}$
L_1	0.9	m
L_2	0.86	m
	1.068×10^{3}	$kg m^{-3}$
	3.8×10^{-4}	K^{-1}
	6.3×10^{-4}	$m^3 kg^{-1}$
	36.42	
	21.95	ºC
	0.0	$g kg^{-1}$
	0.99×10^{-6}	$m^2 s^{-1}$
	$8.2505\, x_2 + 25.6418$	ºC
	0.8	S

We present the results for computations in a transient regime in order to better describe and understand the inherent dynamics of a SGSP. A particular interest of this work is the long term simulation of the physical SGSP phenomena with heating of the fluid due to the absorption of solar radiation.

An important issue one should answer at this time is whether the model simplifications and the numerical methods for solving this problem are robust enough for a long term simulation (in order of days or even months) or not. The comparison of the numerical data with the available experimental data should provide some insight on this question and verify the respective limitations. Prior to this, it could in theory, be refined to model larger times and larger or different geometries.

The incident solar radiation

Fig. 4 also shows a good accordance with ED. Although, comparing Fig 3 with Fig.4, it can be observed that the F-ND differs mainly in the UCZ and NCZ. On the F-ND it can be observed a larger temperature gradient on the NCZ and a less sharp transition from the NCZ to the UCZ.

One important feature that is implemented in the present model is the time evolution of the LCZ, NCN and UCZ's. The dynamics of these zones are very important to the stability of the SGSP, thus it should not be neglected. Fig. 5 represents the salt concentration profiles, where the three zones can be identified. As expected, both UCZ, LCZ and salt concentration gradient increase with time.

Fig. 6 shows a visual representation of temperature and velocity taken for day 5 with *Ansys Fluent* post processing software. It is patent in this figure the two convective zones that separate the NCZ. Fig. 7 is a Schlieren representation, taken from *deal.II* data for the same day as the case of Fig. 6. Comparing Figs. 6 and 7, becomes clear that the UCZ is greater in Fig. 6 which corresponds to the F-ND.

6. Conclusions

The results presented here comprise a subset which is considered representative of the results available. Although, the validation of the results are for a small scale prototype, it is believed that the information gathered can be useful for the full scale SGPS dynamics.

The developed model seems to be able to predict the main features of the physics involved in a SGSP. Particularly, it was possible to get a good prediction for temperature in the three main zones of the SGSP with either the *deal.II FEM* code or with the *Ansys Fluent* software.

It is intended in future work to include the wall shading effect, heat extraction and long term SGSP simulation.

Fig. 3: Temperature profiles for experimental (ED) and *deal.II* numerical data (D-ND)

Fig. 4: Temperature profiles for experimental (ED) and *Ansys Fluent* numerical data (F-ND)

Fig. 5: Salt concentration profiles for experimental (ED) and *deal.II* numerical data (D-ND)

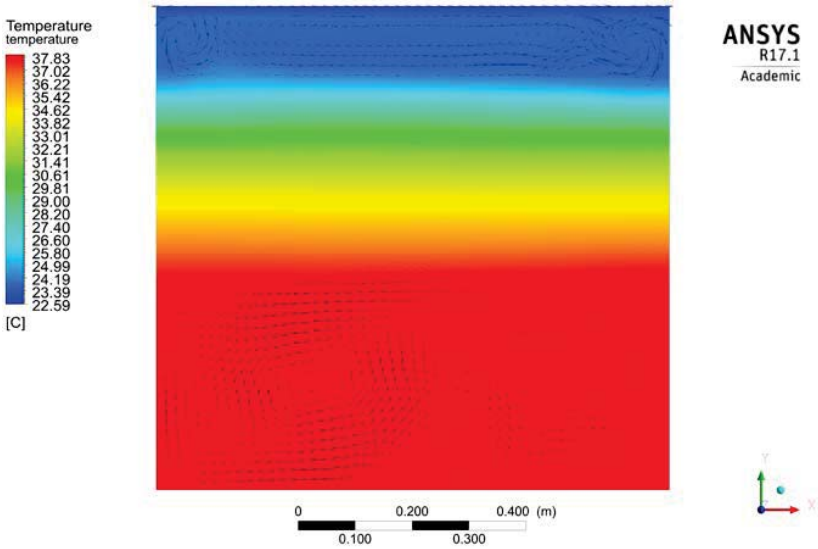

Fig. 6: *Ansys Fluent* visual representation of temperature and velocity taken for day 5.

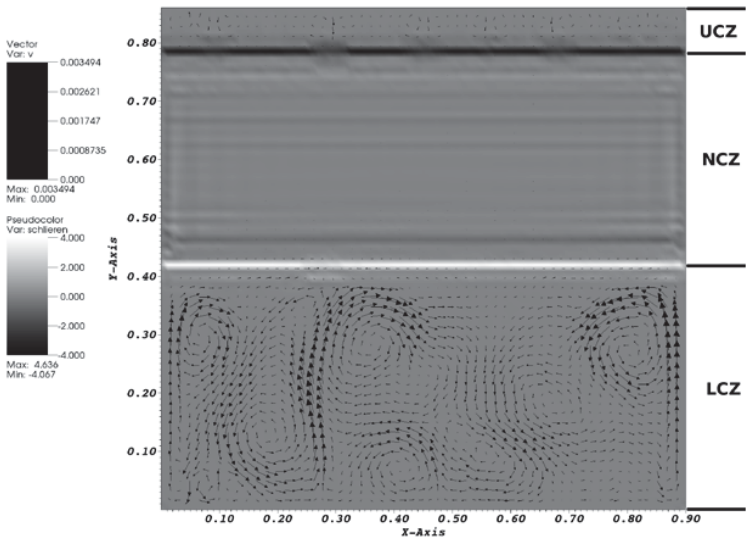

Fig. 7: Schlieren representation taken from *deal.II* data for day 5.

Acknowledgments

The present work was possible due to the help of Professor Dah, who kindly provided the experimental data for the solar pond prototype.

References

Angeli C. and Leonardi E. 2004. A one-dimensional numerical study of the salt diffusion in a salinity gradient solar pond. Int. J. Heat Mass Transfer.47, 1–10.

Angeli C. and Leonardi E. 2005. The effect of thermo-diffusion on the stability of a salinity gradient solar pond. Int. J. Heat Mass Transfer. 48, 21-22.

Akbarzadeh A. and Ahmadi G. 1980. Computer simulation of the performance of a solar pond in the southern part of Iran. Solar Energy. 24.

Bangerth W., Hartmann R. and Kanschat G. 2007 deal.II — a general-purpose object-oriented finite element library. ACM Trans. Math. Softw. 33, 4.

Boudhiaf R. 2003. Numerical Temperature and Concentration distributions in an insulated salinity gradient solar pond. Renewables: Wind, Water and Solar. 2, 10

Boudhiaf R. and Baccar. 2014. Transient hydrodynamic heat and mass transfer in a gradient solar pond study. Energy Conversion and Management. 79, 568-580.

Da Costa L. N.., Knobloch E. and Weiss N. O. 1981. Oscillations in double-diffusive convection. J. Fluid Mech. 109, 257, 25–43.

Dake J. M. K. and. Harleman D. R. F. 1969. Thermal stratification in lakes: analytical and laboratory studies. Water Resources Res. 5.

Duffie J. A., Beckman, 1980 Solar Engineering of Thermal Processes. John Wiley and Sons.

Farago I. and Havasiy A. 2009. Operator Splitting and their Applications. Nova Science Publishers.

Giestas M., Joyce A, and Pina H. 1996. The influence of radiation absorption on solar ponds stability. J. Heat Mass Transfer. 39, 18.3873–3885.

Giestas M., Joyce A., and Pina H.1997. The influence of non-constant diffusivities on solar ponds stability. J. Heat Mass Transfer. 40, 18.4379–4391.

Giestas M.C, Milhazes M. P., and Pina H.L.2014. Numerical Modeling of Solar Ponds. Energy Procedia. 57, 2416-2425.

Guermond J.L., Minev P., and Jie Shen. 2006. An overview of projection methods for incompressible flow. Comput. Methods Appl. Mech. Eng.195, 6011–6045.

Hairer E. and Wanner G. 1991. Solving Ordinary Differential Equations II – Stiff and Differential-Algebraic Problems. Springer-Verlag.

Hawlader M.N.A .and Brinkworth B. J.1981. An analysis of the non-convecting solar pond. Solar Energy. 27, 195–204.

Hull. J. R.1980. Computer simulation of solar pond thermal behavior. Solar Energy. 25, 33–40, 1.

Hundsdorfer W.and Verwer J. G. 2003. Numerical Solution of Time-Dependent Advection-Diffusion-Reaction Equation*s*. Springer - Verlag.

Jayadev T. S.and J. Henderson. S. 1979. Salt concentration gradient solar ponds. Modeling and optimization.

Jaefarzadeh M.R.2004.Solar Energy. Thermal behavior of a small salinity gradient solar pond with wall shading effect.77.281-290.

Joyce, A., Giestas, M., Loureiro, D., Tavares, C. 2001. The Portuguese Experience on Salt Gradient Solar Ponds. Workshop on Solar Ponds. Tunis.

Kalecsinsky A. V. 1902. Ueber die ungarischen warmen und heissen kochsalzseen als natuerlich waermeaccumulatoren. Ann. Physik IV, 7, 408. Cited by Nielsen C. 1979 in Dickinson W.C. and Cheremisinoff P.N. (Eds.) Solar Energy Handbook.

Knopp,T G. Lube G., and Rapin.G 2002. Stabilized finite element methods with shock capturing for advection–diffusion problems, Comput. Methods Appl. Mech. Engen. 191, 2997–3013.

Kurt H. F, Halicir, and Binark A. 2000. Solar pond conception - experimental and theoretical studies. Energy Conv. Manag. 41, 9.

Mansour R., Nguyen C., and Galanis N.2006. Transient heat and mass transfer and long-term stability of a salt-gradient solar pond. Mech. Research Communications. 33, 233–249.

Meyer K. A., Grimmer D. P., and Jones G. F.1982. An experimental and theoretical study of salt-gradient pond interface behavior. Progress in Solar Energy.

Ould Dah M. M, Ouni. M, Guizani, A. and Belghith A. 2010. Study of temperature and salinity profiles development of Solar Pond in laboratory. Dessalination.183, 179-185.
Panahi Z., Batty J. C. and Riley J. P.1983. Numerical simulation of the performance of a salt gradient solar pond. Trans. of ASME. J. of Solar Energy Eng.. 105, 361–374.
Pina H., Giestas M., Joyce A. 2005.Modelação tridimensional de Lagos Solares Congresso de Métodos Numéricos en Ingenieria. Granada, Espanha.
Rabl, A. Nielson, C.E 1975. Solar ponds for space heating Solar Energy.17, 1-12
Rubin H., Benedict B. A. and Bachu S. 1988 Modeling the performance of a solar pond as a source of thermal energy. Solar Energy. 32, 771–778.
Schechter R.S., Velarde M. G. and Platten J. K. 1981.The two-component Bénard problem. Wiley.
Stommel H., Arons B. and Blanchard D. 1956. An oceanographical curiosity: the perpetual salt fountain. Deep Sea Res. 3, 152–153.
Tabor H. 1969. Solar Ponds. Solar Energy. 12, 549–552.
Turner J. S. 1974. Double-diffusive phenomena. Ann. Rev. Fluid Mech.6, 37–56.
Wang Y.F. and Akbarzadeh, A.A 1983. Solar Energy. A parametric study on solar ponds.30, 555-562.
Washburn, E. W 1929 ed. McGraw Hill Book Co., Ina; NY 10036 Vol V.
Weinberger H. 1964. The Physics of the solar pond. Solar Energy. 8, 2.
Veronis G. 1968. Effect of a stabilizing gradient of solute on thermal convection. J Fluid Mech.34, 315–336.

Conference Proceedings

EuroSun 2016
Palma de Mallorca (Spain), 11 - 14 October 2016

Corrosion Behavior of Stainless Steel Alloys in Molten Solar Salt

A. Gomes[1], T. Paiva Luís[1], I. Figueira[1] and T.C. Diamantino[1]

[1] Laboratório Nacional de Energia e Geologia, Lisboa (Portugal)

Abstract

Molten nitrate salts ($NaNO_3$–KNO_3) have been widely used as heat transfer fluids (HTF) and energy storage media in concentrated solar power (CSP) plants. In the present work, the corrosion resistance of two austenitic stainless steels 316SS and 321SS was assessed during long term isothermal immersion in binary nitrate salt mixture, Solar Salt. The experiments were carried out at 550 °C under static conditions. The corrosion rates were determined by weight loss methodology, recording the weight changes of the coupons at different time intervals up to 3000 h. The corrosion scale products were characterized by scanning electron microscopy (SEM), energy-dispersive X-ray spectroscopy (EDS) and X-ray diffraction (XRD). The formation of multiple oxides was verified, being Fe_2O_3 and Fe_3O_4 the main products as confirmed by XRD. A stable $FeCr_2O_4$ inner layer was formed on the 316SS surface. At t>1000 h, a partial spallation occurred in the corrosion layers at 321SS. The corrosion rates were found to be 7.3 and 9.0 μm per year for 316SS and 321SS, respectively.

Keywords: *Molten nitrate salt, Heat transfer fluid, Thermal energy storage, Metallic corrosion*

1. Introduction

Thermal energy storage is a key performance parameter for improving the viability of the CSP plants. The accomplishment of this target allows the solar heat storage from solar radiation, to generate electricity at night or on overcast days with significant economic advantages of the solar plants. (Kuravi et al., 2013; Liu et al., 2016).

Nowadays, molten nitrate salts (MS) have been extensively used in CSP to transfer and store heat given their unique thermal properties (Vignarooban et al., 2015; Weinsten et al., 2015). In two-tank systems, based on MS as storage solution, the cold tank operates at 290 °C and the hot tank at temperatures greater than 550 °C. Due to the high operating temperature, the construction of the hot tank requires the use of stainless steel materials, being the austenitic stainless steels considered as prime candidates (Dorcheh et al., 2016).

At elevated temperatures, it was demonstrated that nitrate ions decompose giving rise to nitrite ions and oxygen (Nissen and Meeker, 1983). These strong oxidizing species combined with operating temperatures plus salt impurities generate propitious conditions for corrosion acceleration of stainless steels. In this context, it is crucial to evaluate the corrosion resistance and lifetime of stainless steels to optimize the material selection since their failure could lead to severe damage of the CSP plants operation.

In the present work, a comparative study of the corrosion resistance of two austenitic stainless steels, 316SS and 321SS, was assessed. The main objective was to evaluate the aging impact of the MS contact on the stability and corrosion properties of these container and piping materials, generally used in CSP, at the high-temperature at which the binary nitrate mixture (Solar Salt) is handled. To achieve this, static immersion tests have been performed, simulating the operative conditions in hot storage tanks at CSP plants.

The corrosion rates were determined by weight loss methodology, recording the weight changes of the coupons for long term isothermal immersion in Solar Salt (60% $NaNO_3$ and 40% KNO_3), for up to 3000 h at

doi:10.18086/eurosun.2016.03.12 Available at http://proceedings.ises.org

550 °C. The corrosion scale products were characterized by scanning electron microscopy, energy-dispersive X-ray spectroscopy and X-ray diffraction.

2. Experimental

Rectangular coupons measuring approximately 50 mm × 60 mm × 4 mm in thickness were cut from 316SS and 321SS stainless steel from Acerinox Europa and ACCIAITERNI (Italy), respectively. Table 1 shows the elemental composition of the studied stainless steels. Before corrosion tests, the coupons were ground with 320-grit SiC abrasive paper and then degreased by ethanol followed by rinsed with distillated water. After that the coupons were measured and weighted. Initial mass average values of (97.45±0.48) g for 316SS and (89.27±0.65) g for 321SS were recorded.

Tab. 1: Elemental composition of the studied stainless steels (wt.%)

Stainless steel	C	Mn	Si	P	Cr	Ni	Mo	Ti	Cu	Fe
316SS	0.020	1.346	0.361	0.036	16.635	10.025	2.011	–	–	Balanced
321SS	0.030	0.960	0.640	0.027	17.260	9.100	0.490	0.280	0.320	Balanced

The stainless steel coupons were mounted on sample hangers and fully immersed in binary nitrate molten salt mixture (60% $NaNO_3$ and 40% KNO_3). The nitrate salts were provided by SQM and COBRA and were used without further purification. The corrosion tests were performed at 550 °C with long-term duration up to 3000 h in presence of atmospheric air under static conditions. A vertical tubular furnace was used during this process. Four metallic samples were collected at different immersion intervals, namely 120, 1440 and 3000 h. After cooling at room temperature, the coupons were rinsed with distillated water and weighed after having been dried. Besides mass gain, descaling method was applied according to International Standard ISO 17245:2015 to evaluate the weight loss. From the descaled data, the corrosion rate (CR) was evaluated using equation 1 (Kruizenga and Gill, 2014)

$$CR\ (\mu m/yr) = \frac{87600\ \Delta m}{\rho\ t} \qquad \text{(eq. 1)}$$

where Δm is descaled mass loss per unit area (mg/cm^2), ρ is stainless steel density (g/cm^3) and t immersion time (hours).

To complement the stainless steel samples characterization, morphological and structural analysis were done before and after the corrosion process.

X-ray diffraction analysis of stainless steel coupons were carried out using a Rigaku Geigerflex D/MAX-III C diffractometer operating with a monochromatic Cu Kα radiation. XRD patterns were recorded in the 2θ range from 10 to 90°, using a 1.2º/min acquisition rate.

The elemental composition, surface and cross-sectional morphologies of the corrosion scale were investigated using a Phillips Scanning Electron Microscope, Model XL 30 FEG, coupled to an Energy Dispersive Spectrometer.

3. Results and discussion

The long-term corrosion process was evaluated through weight loss measurements as shown in Fig 1. Relatively low values of average weight loss were obtained. They increase with time, varying between 0.7 and 2.5 mg cm^{-2}. These results are acceptable for austenitic stainless steels under these experimental conditions and are similar to others reported by Kruizenga et al. (2013). After 3000 h of immersion, the corrosion rates were found to be 7.3 and 9.0 μm per year, at 550 °C, for 316SS and 321SS, respectively. The values obtained point to corrosion rate of 316SS is lower by 20% in comparison to 321SS. This suggests that

the corrosion scales formed in 316SS are slightly more protective than the ones formed in 321SS.

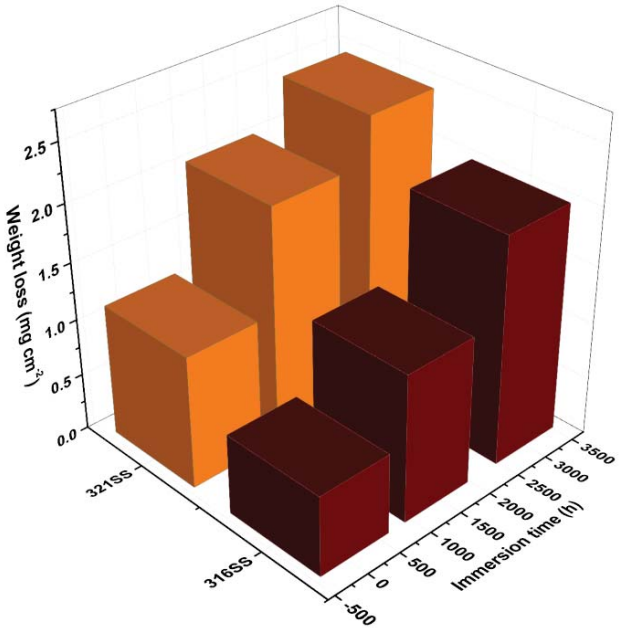

Fig. 1: Descaled weight loss data for 316SS and 321SS exposed to Solar Salt at 550 °C

After exposure to Solar Salt at 550 °C, corrosion products have been formed and the visual inspection of steel coupons shows that they lost their silver shiny aspect, acquiring a black colour for shorter times and a mixed black and rust-red coloration for longer times of immersion. By XRD analysis, it was depicted that the corrosion scale is composed of multiple crystalline oxide (Fe_2O_3, $FeCr_2O_4$, Fe_3O_4) compounds for both steel substrates, Fig 2. According to published studies, it could be assumed that Fe_2O_3 forms the external layer in contact with the molten salt, whereas Fe_3O_4 is located more internally near the metallic substrate (Fernández et al., 2012). Comparing the data recorded after 3000 h of exposure, it can be observed that the intensity ratio $I_{oxide\ scale}/I_{substrate}$ is higher for 316SS than for 321SS. This suggests that spallation phenomenon has occurred at the surface of 321SS for the longest immersion time. In addition, the XRD results pointed out that the relative abundance of iron oxides is different for the two stainless steels studied. Based on relative intensity of the diffraction peaks, it seems that the amount of spinel phases ($FeCr_2O_4$, Fe_3O_4) is more elevated at the 316SS surface. This may indicate that for 321SS, the surface protective Cr_2O_3 phase necessary to the formation of $FeCr_2O_4$ (see eq. 2) may be destroyed, promoting and accelerating the Fe corrosion due to the permeation of corrosion agents to the chromium depleted surface.

$$2\,Fe + 2\,Cr_2O_3 + O_2 \rightarrow 2\,FeCr_2O_4 \qquad \text{(eq. 2)}$$

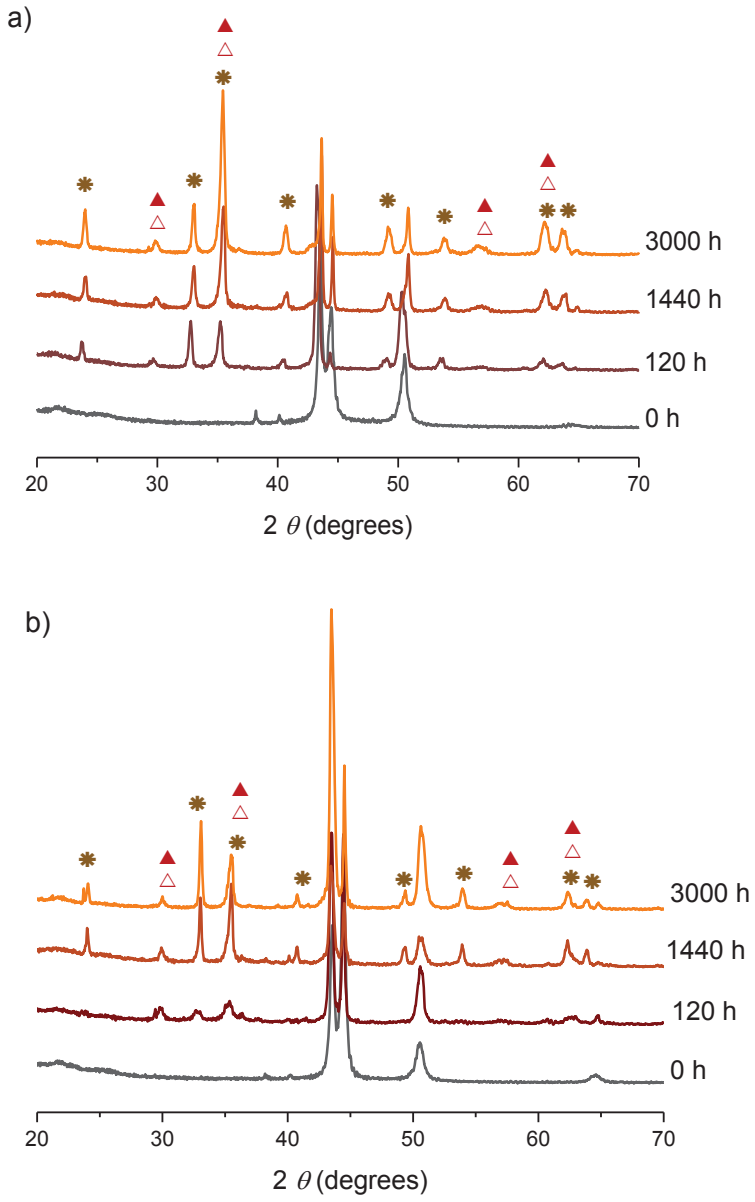

Fig. 2: XRD patterns of 316SS (a) and 321SS (b) immersed in Solar Salt for different time intervals (✱ - Fe_2O_3, △ - $FeCr_2O_4$, ▲ - Fe_3O_4)

Figures 3 and 4 show the morphological images of the surface of the oxide layers formed over time at the 316SS and 321SS, respectively. For comparison purposes, it is also shown the SEM image of the bare substrates where the abrasion marks can be easily observed. As it can be seen, after the oxidation process the surface of both steels became rougher and homogenously covered by an oxide layer. This is formed by polyhedral grains whose size increases with immersion time. At lower times, no cracks are observed at the oxide surface layer. However, partial surface spallation is observed on 321SS for exposure times equal or greater than 1440 h. This trend is not verified for the oxide scale formed at the 316SS, indicating that the scale corrosion is more adherent in this case. Spallation of oxide scales on stainless steel surfaces was previously reported (Trent et al., 2016), and explained due to stresses arising from the coefficient of thermal

expansion mismatch of the steel substrate and corrosion scale during cooling. In addition, the detachment of the oxide scales may also occur in –situ, leading to iron oxides re-growth (Scott and Wei, 1989).

From the cross-sectional images recorded after 3000 h of immersion, it is shown that the corrosion scales were multi-layered. For 316SS, a uniform and continuous inner layer was observed, and a less continuous and more irregular outer layer. According to this result, it seems plausible to assume that oxidation layers have been formed through uniform corrosion mode. For 321SS, it is evident that the oxide scale is detached from the substrate which is in agreement to other observations aforementioned. Furthermore, in this case it is more difficult to observe the irregular outer layer which could be related to mechanical failure during sample handling or metallographic preparation. Besides, in this sample, oxide features can also be seen just below the oxide-metal interface suggesting that oxide scale growth proceed via intergranular corrosion mode. More research is undertaken to better clarify the corrosion mechanism on both stainless steels.

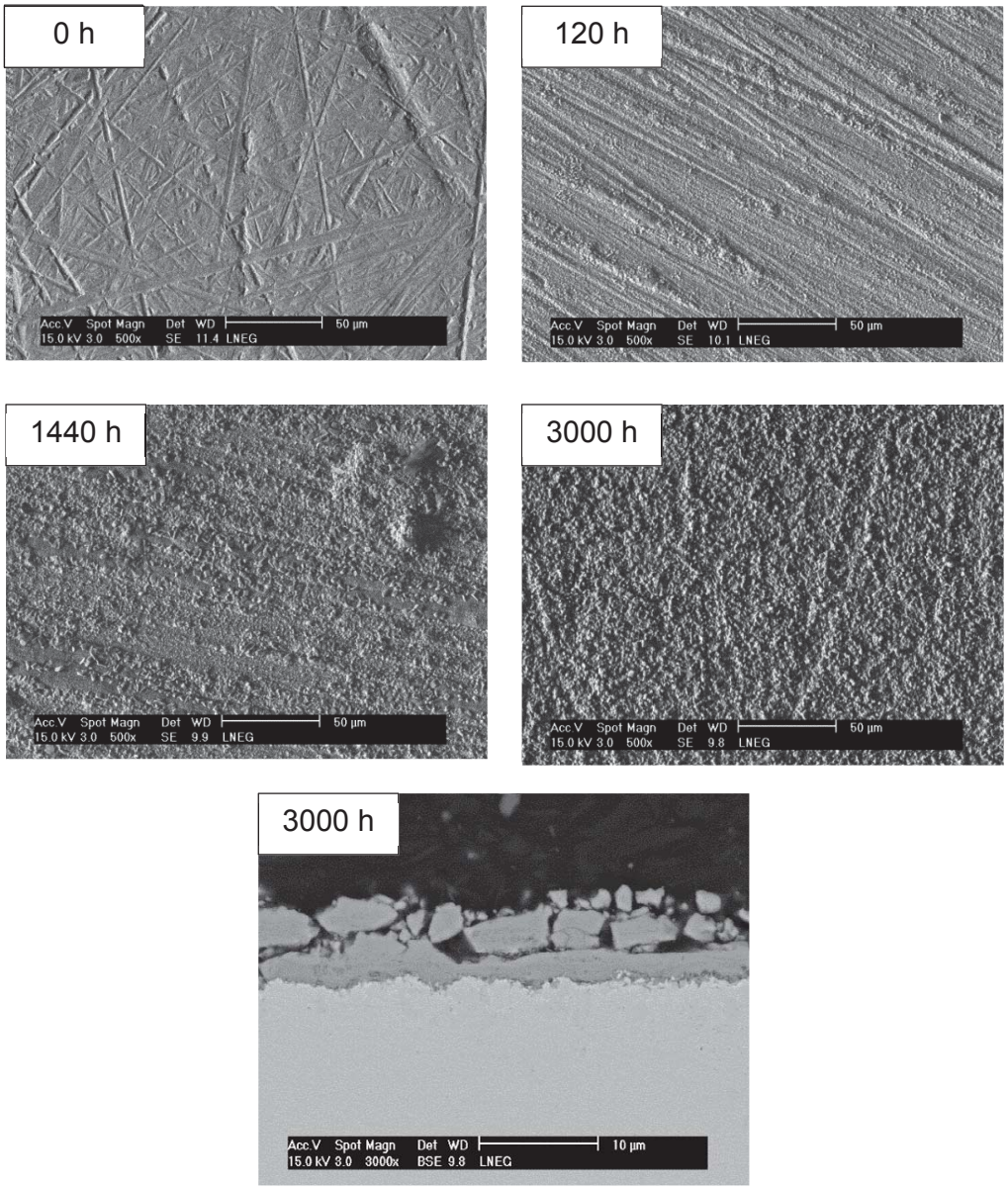

Fig. 3: Top view and cross-section SEM images of the oxide scales formed on 316SS after different immersion times in Solar Salt

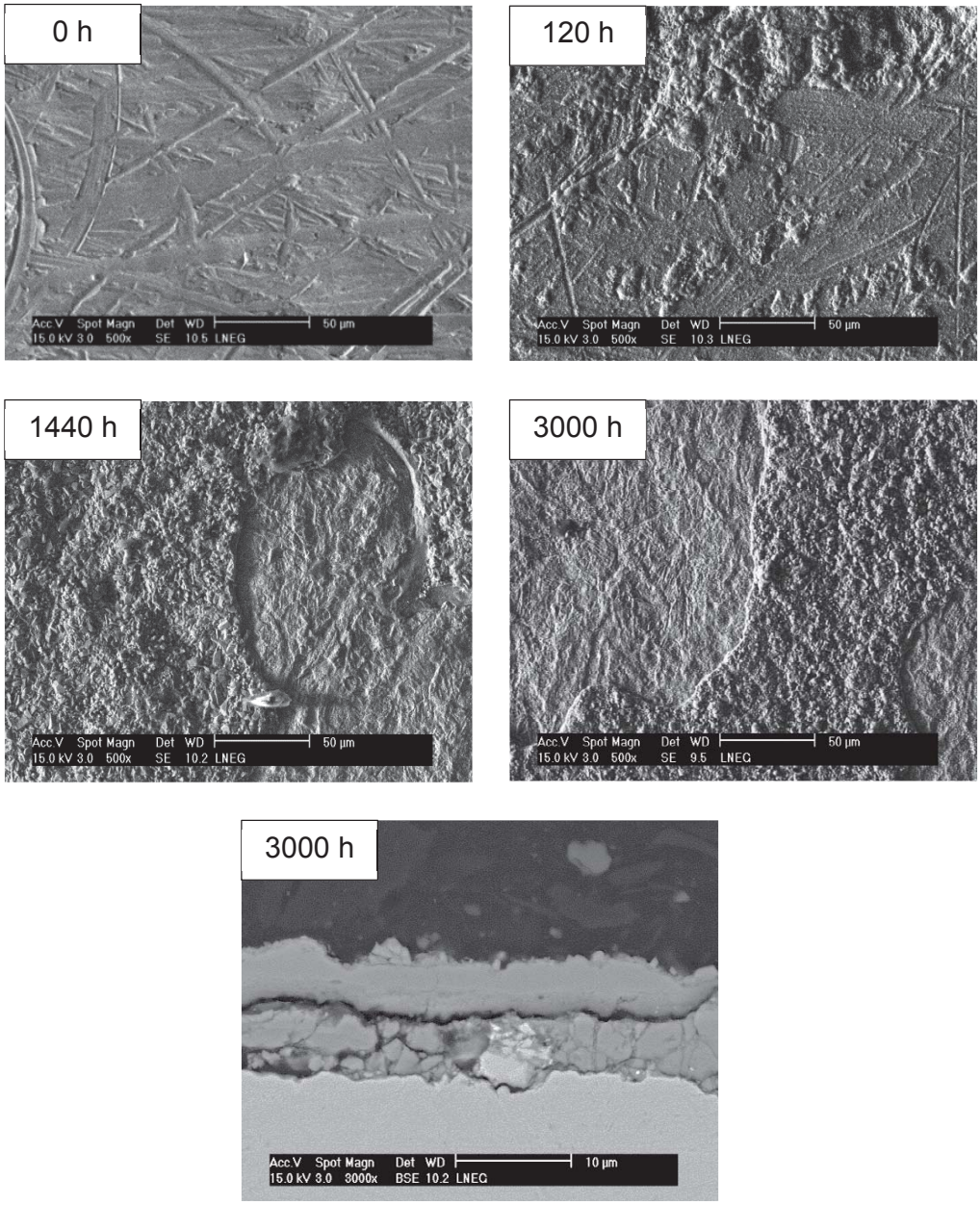

Fig. 4: Top view and cross-section SEM images of the oxide scales formed on 321SS after different immersion times in Solar Salt

Figure 5 show the elemental mapping of Cr, Ni, Fe and O for the corrosion scale developed after 3000 h of exposure for 316SS and 321SS, respectively. According to this figure, for both stainless steels, the outer layer of the corrosion scale is mainly composed by iron oxides. In the inner layer, an enrichment of chromium is verified. These results are in agreement with the XRD results. At the interface corrosion scale|steel substrate, nickel enrichment occurs, that is assumed to be the result of the depletion of chromium from the bulk (Kruizenga and Gill, 2014).

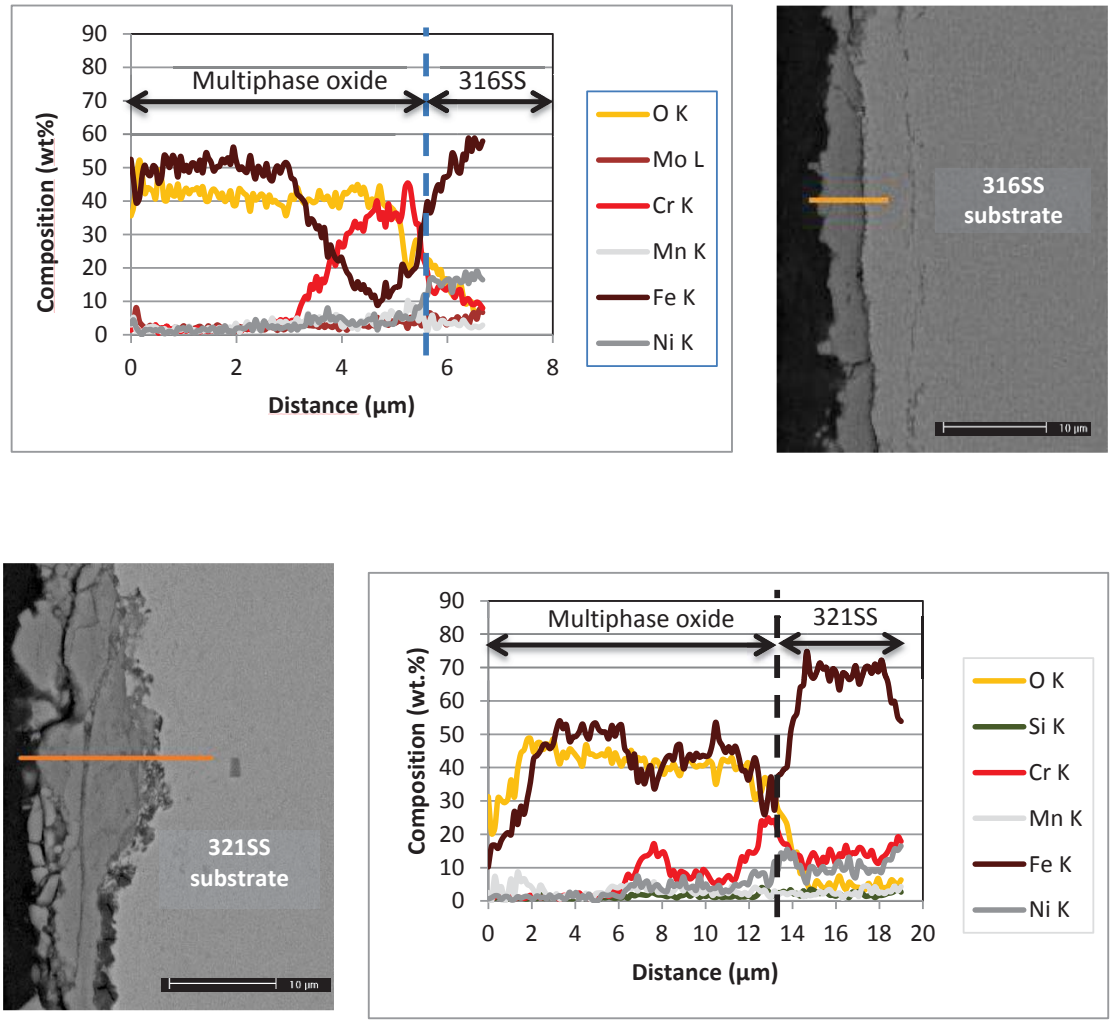

Fig. 5: Quantitative line scans and corresponding back scattered image of 316SS (a) and 321SS (b) after 3000 h immersed in MS

4. Conclusions

This study allows the following conclusions to be drawn:

- The formation of multiple oxides was verified, where Fe_2O_3 and Fe_3O_4 are the main corrosion products in both austenitic stainless steels.
- The scale morphology was similar for the two tested steel alloys.
- A stable $FeCr_2O_4$ inner layer was formed on 316SS surface.
- At t>1000 h, a partial spallation of the corrosion layers was observed at 321SS.
- After 3000 h of immersion, the corrosion rates were found to be 7.3 and 9.0 µm per year, at 550 °C, for 316SS and 321SS, respectively.

Further studies are underway to accurately determine the key factor that justifies the differences found on the corrosion behavior of these two austenitic materials.

Acknowledgments

The authors greatly appreciated the financial support from project STAGE-STE (http://www.stage-ste.eu/) Scientific and Technological Alliance for Guaranteeing the European Excellence in Concentrating Solar Thermal Energy, FP7 Grant Agreement 609837.

5. References

Dorcheh, A.S., Durham, R.N., Galetz, M.C., 2016. Corrosion behavior of stainless and low-chromium steels and IN625 in molten nitrate salts at 600 °C. Sol. Energ. Mat. Sol. C. 144, 109–116.

Fernández, A.G., Lasanta, M.I., Pérez, F.J., 2012. Molten salt corrosion of stainless steels and low-Cr steel in CSP plants. Oxid. Met. 78, 329–348.

ISO 17245: 2015 Corrosion of metals and alloys -- Test method for high temperature corrosion testing of metallic materials by immersing in molten salt or other liquids under static conditions.

Kruizenga, A., Gill, D., 2014. Corrosion of iron stainless steels in molten nitrate salt. Energy Procedia 49, 878 – 887.

Kruizenga, A.M., Gill, D.D., LaFord, M., McConohy, G., 2013. Corrosion of high temperature alloys in solar salt at 400, 500 and 680 °C. Albuquerque: Sandia National Laboratories. SAND2013-2526.

Kuravi, S., Trahan, J., Goswami, D.Y., Rahman, M.M., Stefanakos, E.K., 2013. Thermal energy storage technologies and systems for concentrating solar power plants. Prog. Energ. Combust. 39, 285-319.

Liu, M., Tay, N.H.S., Bell, S., Belusko, M., Jacob, R., Will, G., Saman, W., Bruno, F., 2016. Review on concentrating solar power plants and new developments in high temperature thermal energy storage technologies. Renew. Sust. Energ. Rev. 53, 1411–1432.

Nissen, D.A., Meeker, D.E., 1983. Nitrate/nitrite chemistry in $NaNO_3$-KNO_3 Melts. Inorg. Chem. 22, 716–721.

Scott, F.H., Wei, F.I., 1989. High temperature oxidation of commercial austenitic stainless steels. Mater. Sci. Tech. 5, 1140-1147.

Trent, M.C., Goods, S.H., Bradshaw, R.W., 2016. Comparison of corrosion performance of grade 316 and grade 347H stainless steels in molten nitrate salt. AIP Conf. Proc. 1734, 160017-1–160017-12.

Vignarooban, K., Xu, X., Arvay, A., Hsu, K., Kannan, A.M., 2015. Heat transfer fluids for concentrating solar power systems – A review. Appl. Energ. 146, 383–396.

Weinstein, L.A., Loomis, J., Bhatia, B., Bierman, D.M., Wang, E.N., Chen, G., 2015. Concentrating solar power. Chem. Rev. 115, 12797−12838.

Conference Proceedings
EuroSun 2016
Palma de Mallorca (Spain), 11 – 14 October 2016

Design and Simulation of a new Concrete Storage Unit

Luis Guerreiro[1], Doerte Laing-Nepustil[2], Daniel Lopes[1], Rameesh Sivabalan[2], Ulrich Nepustil[2] and Manuel Collares Pereira[1]

[1] Renewable Energy Chair, University of Evora, Palacio do Vimioso, P - 7002 Evora

[2] Hochschule Esslingen, University of Applied Sciences, D - 73037 Göppingen

Abstract

Solar Thermal Electricity (STE) is an important alternative to PV electricity production, due to the cost competitiveness in locations with high DNI as well as for the intrinsic value of having thermal storage which can give an important contribution to the energy mix in countries like Spain where STE has more than 2500MW installed capacity. In recent years, research has been performed, on alternative storage systems, to which features like modularity and validation of new thermal storage materials are important with the goal of achieving lower investment cost. Concrete storage has been studied in the past up to an operating temperature of 500ºC [1] [2], and several prototypes were built and tested without reaching commercial plants. Nowadays, new design and new concrete mixes are under research in order to validate its usage up to 550ºC [3]. Simulation results leading to this new design are presented.

Keywords: *Energy Storage, High Temperature, Concrete mix, Solid material*

1. Introduction

Decreasing the cost of an overall CSP plant is a fundamental goal in order to make this technology more cost competitive. Current commercial solutions include, a 2-tank molten salt indirect system (e.g. Andasol plant in Spain, 7.5h of storage capacity), a 2-tank molten salt direct system (e.g. Gemasolar plant in Spain, 15h of storage capacity) or steam accumulators (e.g. Khi plant in South Africa, 2h storage capacity). Alternative storage systems with concrete have been analyzed in the projects WANDA, ITES and WESPE (Fig.1), with thermal cycles performed between 315ºC and 390ºC and a thermal capacity of 350kWh. A specific heat capacity of 916 J/kgK [2] was measured for temperatures in the range 300-390°C. However, the concrete module design was optimized for a full scale 1010MWh storage for Andasol type CSP plants.

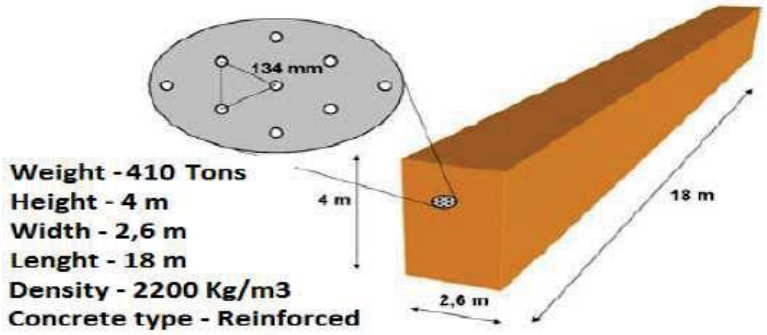

Fig. 1: Concrete Module designed in Project WANDA

doi:10.18086/eurosun.2016.03.14 Available at http://proceedings.ises.org

2. Methodology

In order to obtain a model that could be evaluated against previous work, a module with similar outer dimensions was used as a starting point, a cross section of the storage module is shown in Fig. 2. The tube register consists of 609 stainless steel tubes with an outer diameter of 18 mm. The tubes embedded in the storage module were arranged in a triangular pitch to obtain a better temperature distribution in the solid storage module. The entire storage consists in several storage units with regular hexagonal cross sections.

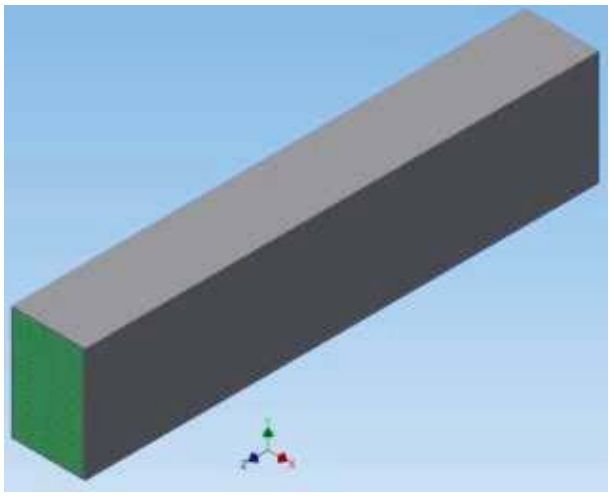

Fig. 2: Concrete Module with dimensions 2,6*18*4m [W*L*H]

The analysis of the storage unit was then simplified by substituting cylindrical storage unit geometry for the regular hexagonal shapes (Fig.3) with the same cross sectional area. The geometries were related by:

(eq. 1)

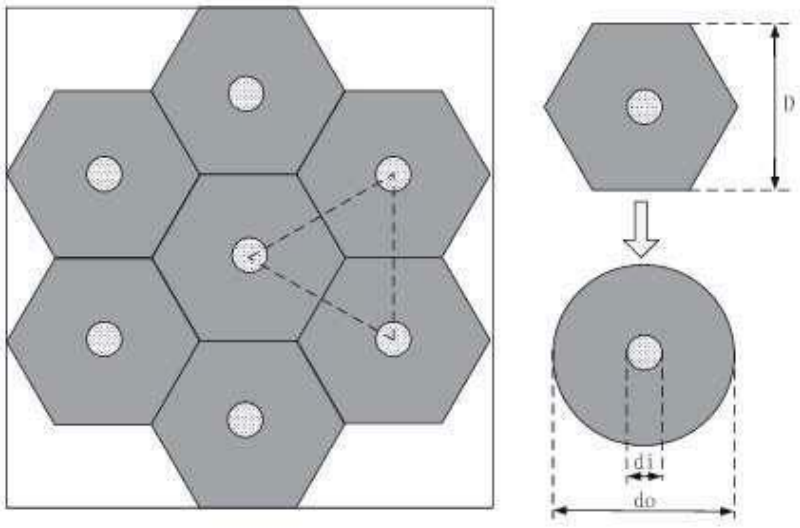

Fig. 3: Cross section of the solid storage module

The model is based on the following assumptions:

- the storage module has the same thermal behavior as the cylindrical storage unit shown in Fig. 4;
- thermal conduction in the axial direction in the fluid is negligible;
- the HTF directly contacts the solid;
- tube thickness can be assumed to be zero;
- there are no heat losses from the storage unit to the surroundings;

The finite element method is applicable to the thermal conduction in the solid media in the radial direction; thus:

(eq. 2)

The 3D model can be simplified to a 2D mesh of nodes.

Assuming that the mass flow rate, , is constant over the length of the tube, the thermal energy balance for the fluid in the differential control volume, *dz*, in Fig. 4 is:

— (eq. 3)

Where:

is the effective heat transfer coefficient in the tube;

P is the heat transfer surface perimeter

is the cross section of the tube

Substituting the average fluid velocity in the cylindrical heat storage unit , and rearranging Eq.(3), the fluid energy balance equation becomes:

— — —— (eq. 4)

For the solid storage material, a mesh of nodes was used in the same control volume *dz* as shown in Figs. 4 and 5. The same *dz* was used for the spacing in the nodes in the radial direction.

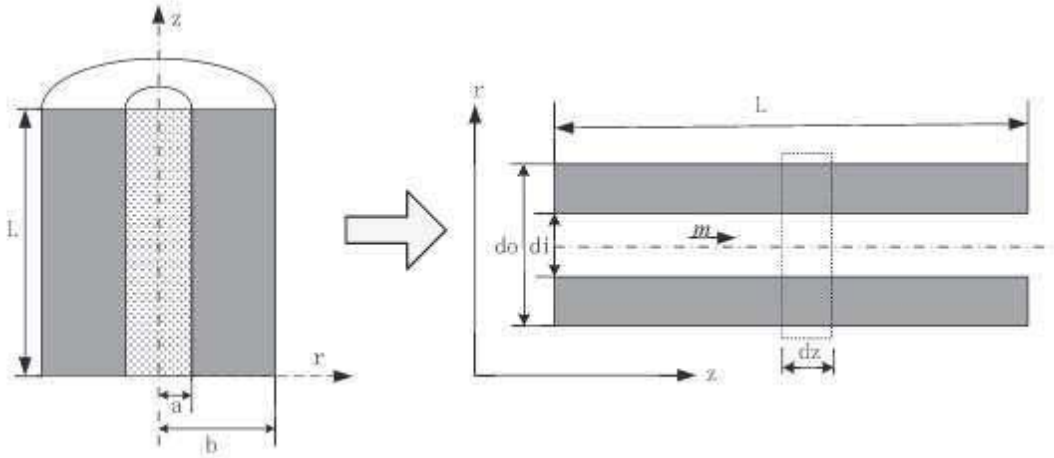

Fig. 4: Cylindrical heat storage unit model

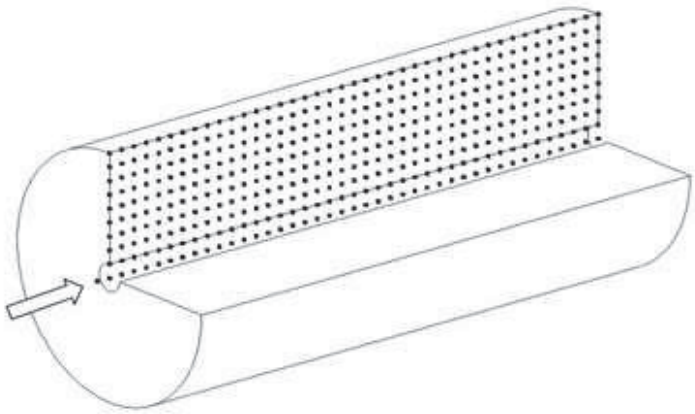

Fig. 5: Grid scheme of nodes in the cylindrical heat storage unit model

For the two-dimensional system of fig. 5, under transient conditions with constant properties and no internal heat generation, the appropriate form for the heat equation is:

— — — (eq. 5)

Concrete was used as the storage material and *Solar Salt* (a mixture of sodium and potassium nitrates) the Heat Transfer Fluid (HTF). The thermos-physical properties of the concrete mix considered are listed in table 1:

Tab. 1 - Thermal physical properties of concrete

Material	Density (kg/m^3)	Specific heat (J/kg K)	Thermal conductivity (W/m K)	Viscosity (Pa s)
Concrete (400 °C)	2250	1050	1.20	–

The temperature dependent equations used to obtain the thermo-physical properties of the fluid are listed below. Since the changes in the overall heat transfer coefficient are so low when we change the thermo-physical properties with temperature, a fixed temperature of 823 K was assumed in the calculation of the properties. The conductivity is not temperature dependent and it is assumed to be 0.45.

- For density: (eq. 6)
- For viscosity:

(eq. 7)

- For heat capacity: (eq. 8)

3. Results and Discussion

A Matlab simulation was performed using the methodology and equations described. To simulate real conditions of a solar power plant, an 8 hour charging cycle was assumed. Constant concrete properties during the cycle were considered. It is assumed that the fluid leaves the collector field at 550 ºC and enters the solid storage at that same temperature.

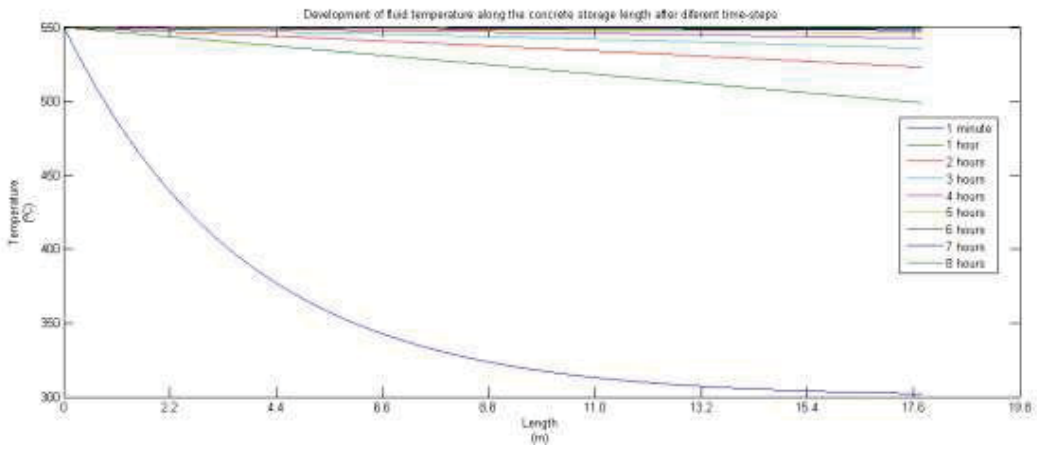

Fig. 6 - Development of fluid temperature along the concrete length with 1 hour intervals

In fig.6 it is represented the development of fluid temperature (solar salt) over the length of the module after different time steps varying from 1min up to 8hours.

In fig.7 it is represented the development of concrete temperature for radial nodes in an 8 hour charging cycle in the entrance and exit region of the module.

In fig.8 it is represented the development of temperature for different radial layers in the concrete over the module length. In these cases the considered was 250 ºC (initial temperature of 300ºC and final temperature of 550ºC for the concrete), the concrete thermal conductivity and the flow rate corresponding to the velocity of in the cross section of a single tube.

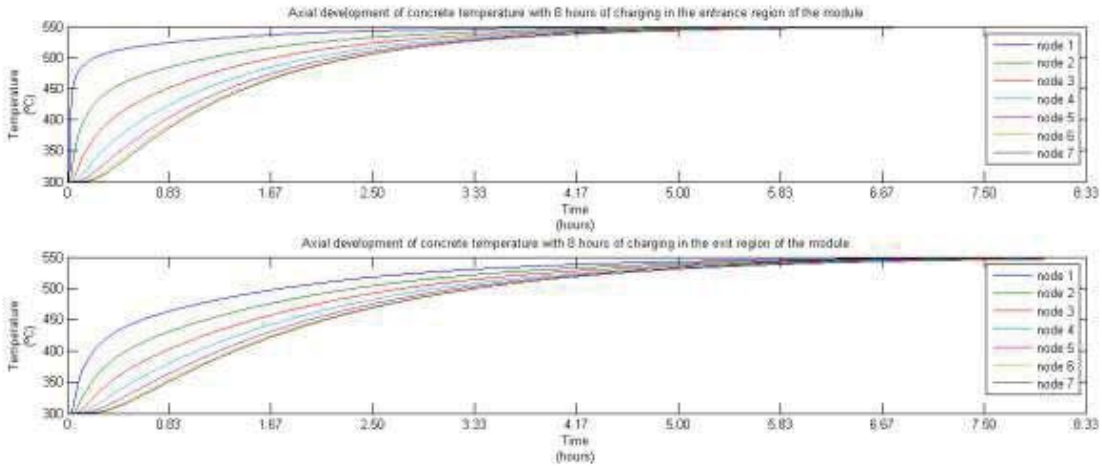

Fig. 7 – Development of concrete temperature in a 8 hour cycle in the entrance and exit region of the cylindrical module from node 1 (after fluid) to node 8 (concrete border)

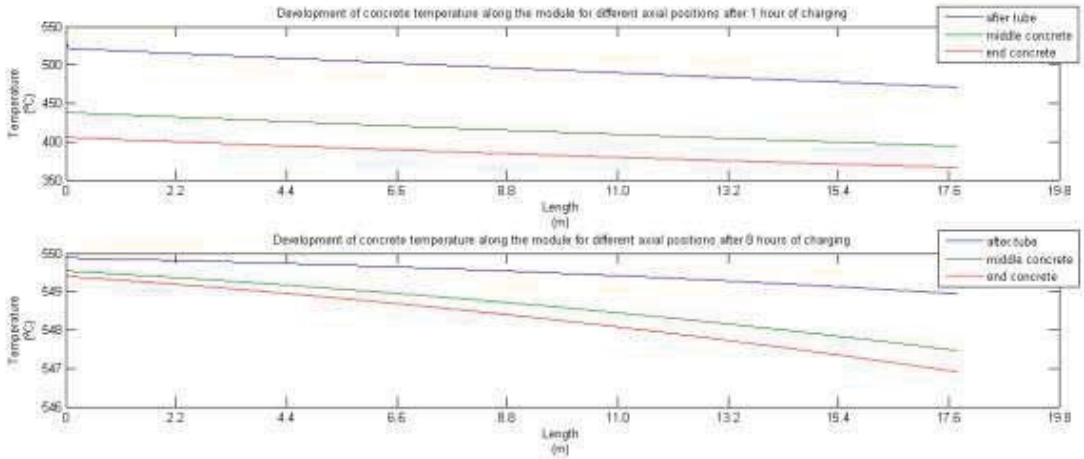

Fig. 8 - Development of concrete temperature along the length for different radial positions after 1h, 8h time steps

As it's shown in Fig. 6 the initial fluid temperature drop is very high, due to the high between the fluid inlet temperature and the concrete. This tends to change over time as the module reaches thermal balance.

In Fig. 7 is visible the radial development of temperature over time. In the entrance region the rise in temperature is faster than in the exit region as it is expected, especially the node nearest to the tube. After 5 hours one can observe that the module is fully charged, as the temperature in all the nodes reaches steady-state.

Finally in Fig. 8 it is visibly that temperature slightly drops along the concrete module length in every case as it is expected, with the nodes after the tube being always the ones with higher temperatures.

Knowing that concrete mix development is one of the current research topics, where interesting results have been obtained by several researchers, it was simulated an increase in the concrete thermal conductivity in order to evaluate changes in heat transfer and temperature development in the concrete storage unit.

The parameter thermal conductivity was simulated to have an enhancement to , behavior along the time, up to 8h is shown in the following figures.

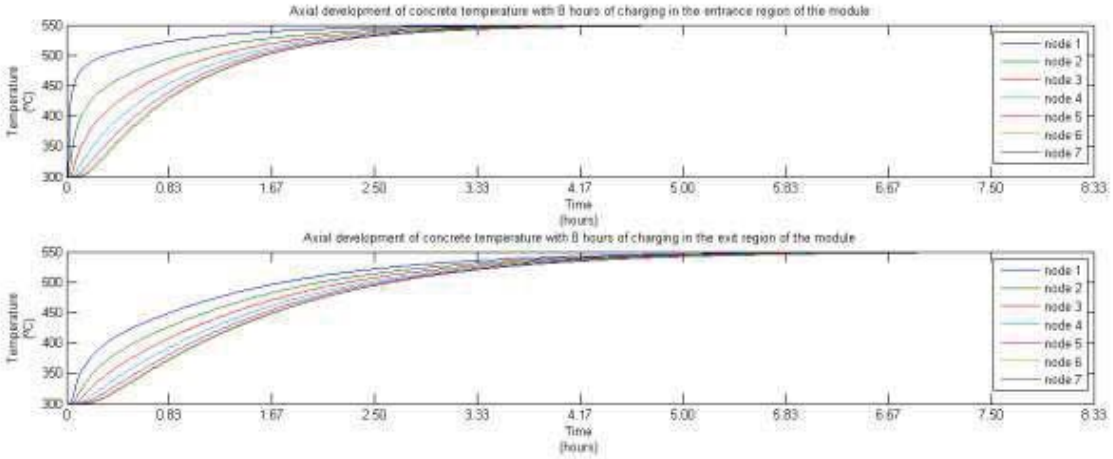

Fig. 9 - Development of concrete temperature in a 8 hour cycle in the entrance and exit region of the cylindrical module from node 1 (after fluid) to node 8 (concrete border), for radial development.

The main difference is observed in the radial development, where the development of temperature in different radial nodes is much more similar, seen in the less spaced curves of the different nodes.

In Fig.9 an increase in charging behavior can be observed when compared with Fig.7, that is, instead of 5h for full charge it takes less than 4h. However, in order to achieve further improvement in overall heat transfer, not only the material properties are important, but also the design needs to be optimized. For that reason, following the results obtained, a new design is proposed as shown in Fig.10 and Fig.11.

This new design section considers a new concrete mix developed with a thermal conductivity of about 2 W/m*K. The number of pipping is reduced significantly (when compared with steam as a HTF) since the heat transfer fluid are molten salts and not steam, meaning that the thickness of the pipes can be reduced, and heat exchange between fluid and concrete improved by means of fins welded to the pipping.

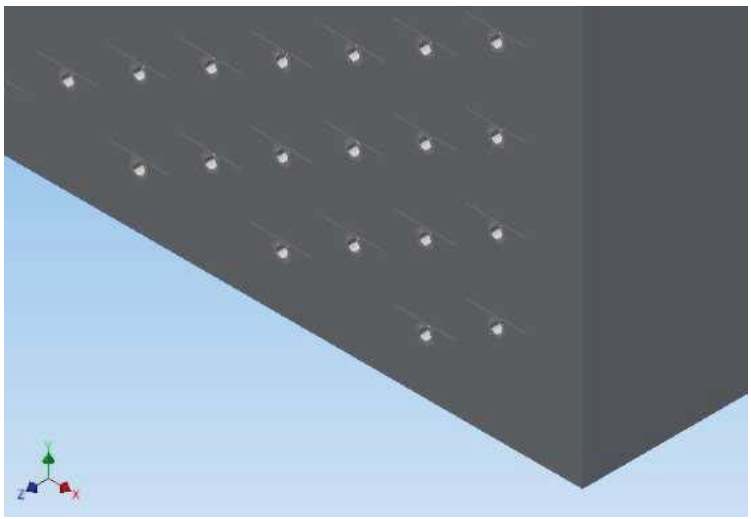

Fig. 10: Concrete Module new section design, isometric perspective

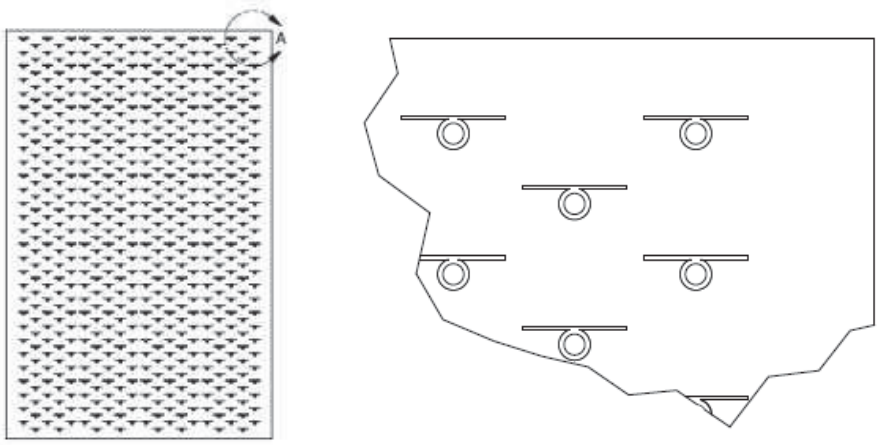

Fig. 11: Concrete Module new section design, (left side: section, right side: detail)

4. Conclusions

Simulation using Matlab is an appropriate tool for simulating thermal behavior of a concrete heat storage unit. Different cases have been simulated to demonstrate the methodology and the impact of improving some of its features. Enhancing properties like thermal conductivity is possible to be evaluated through the method applied. The improvement in the thermal conductivity of concrete allows a faster increase in temperature in the concrete as well as less difference in the temperature along the radial nodes, showing that the heat transfer inside the concrete is faster between the nodes.

Using the same method other parameters (like the flow rate) can be varied in order to simulate its behavior. Nevertheless, in order to increase significantly the charging and discharging performance, new section designs need to be fully evaluated and simulated. A new design has been proposed to improve the overall concrete storage unit behavior.

A concrete module is a concept that has several advantages: can be planned with a certain number of units, easily scalable, can be built in phases, the investment can be diluted for a longer period of time, can operate partly depending on the radiation among other advantages. If all technological aspects are taken into consideration, a significate improvement can be achieved, making concrete storage an interesting alternative to mainstream molten salts tank storage.

5. References

[1] Laing, D. *et al.* "High-Temperature Solid-Media Thermal Energy Storage for Solar Thermal Power Plants" *Proc. IEEE* **100,** 516–524 (2012).

[2] Laing, D., Lehmann, D., Fiß, M. & Bahl, C. "Test Results of Concrete Thermal Energy Storage for Parabolic Trough Power Plants". *J. Sol. Energy Eng.* **131,** (2009).

[3] Alonso, M., Guerreiro, L. "Calcium aluminate based cement for concrete to be used as thermal energy storage in solar thermal electricity plants", *Cement and Concrete Research* **82,** 74–86 (2016)

ISES International Solar Energy Society

Conference Proceedings

EuroSun 2016
Palma de Mallorca (Spain), 11 – 14 October 2016

Constrained Multi-Objective Optimization of Thermocline Packed-Bed Thermal Energy Storage Systems

Jan Marti[1], Lukas Geissbühler[1], Viola Becattini[1], Andreas Haselbacher[1], Aldo Steinfeld[1]

[1] Department of Mechanical and Process Engineering, ETH Zurich, 8092 Zurich, Switzerland

Abstract

A constrained multi-objective optimization approach is used to optimize the exergy efficiency and material costs of thermocline packed-bed thermal energy storage systems. The storage height, top and bottom radii, insulation-layer thickness, and particle diameter were chosen as design variables. The competing objectives of maximizing the exergy efficiency and minimizing the material costs are dealt with by forming a Pareto front. The Pareto front allows the identification of the most efficient design for a given cost and is an important tool in the design of thermal energy storage systems. Constraints are imposed to obtain storage systems with a specified capacity. The optimization approach is applied to identify the influence of various design variables on the exergy efficiency and the material costs. The results show that a storage shaped like a truncated cone with the smallest cross-section on top has a higher exergy efficiency than common designs with a cylindrical shape or a truncated cone with the largest cross-section on top. The basic thermodynamic mechanisms leading to this superior performance are identified with detailed information about the axial temperature distribution in the packed bed and thermal losses through the structure and insulation materials.

Keywords: *thermal energy storage, thermocline energy storage, packed bed, exergy efficiency, multi-objective optimization, Pareto optimality, Pareto front*

1. Introduction

Thermal energy storage (TES) systems are required when there is a time difference between the availability and demand of thermal energy. Examples are concentrated solar power (CSP) [1] and advanced adiabatic compressed air energy storage (AA-CAES) plants [2]. CSP plants have an irregular power input due to the time-dependent nature of solar radiation and require TES to control the electricity output by partially decoupling electricity production from solar radiation. AA-CAES plants store the thermal energy produced during compression in a TES and use the stored energy later to reheat the air before expansion in a gas turbine. For both CSP and AA-CAES plants, the integration of a TES improves the system efficiency and the competitiveness on the electricity market [2, 3]. Especially thermocline TES systems using a packed bed of rocks as sensible storage material are suitable because they require only low-cost storage materials and have been shown to have high thermal efficiencies [4, 5].

The design of TES systems requires an accurate and efficient numerical model. A TES system is characterized by a large number of design variables and may need to satisfy several constraints and objectives. Tab. 1 lists the operational, geometrical, thermophysical, and performance parameters of a general TES system. The operational parameters are in general defined by the application in CSP or AA-CAES plants, the values of the geometrical parameters are usually arbitrary but need to satisfy structural constraints, the thermophysical parameters depend usually on the temperature and pressure (and therefore the operational parameters), and the performance parameters are used to compare and characterize TES systems. The large number of geometric parameters can lead to very large number of design combinations. For example, considering ten values each of the storage height, the top and bottom radii, the two insulation layers, and the particle diameter would lead to 10^6 designs, each of which would need to be simulated long enough to reach quasi-steady-state conditions. If, in addition, a combination of three storage materials is

doi:10.18086/eurosun.2016.03.03 Available at http://proceedings.ises.org

considered, the number of simulations would increase to 10^8. Even with efficient one-dimensional numerical models, the computational cost of evaluating this many designs is prohibitive. To reduce the computational cost of finding the optimal design, a numerical optimization procedure is essential. By *optimal design*, we mean a TES design that combines high efficiency with low costs. It is important to note that it is in general not possible to identify any single design as optimal because high efficiency and low cost are usually contradictory requirements. Instead, the optimization procedure should provide a series of designs depending on the relative importance of high efficiency compared to low costs.

Tab. 1: Operational, geometrical, thermophysical, and performance parameters of general TES systems. The subscript *i* indicates that several instances of a particular parameter exist, such as multiple structural and insulation layers.

Operational parameters	Geometrical parameters	Thermophysical parameters	Performance parameters
Mass flow: $\dot{m}_c$, $\dot{m}_d$ Charge/discharge time: t_c, t_d Inflow temp.: $T_{f,\mathrm{in},c}$, $T_{f,\mathrm{in},d}$ Charge/discharge pressure: p_c, p_d	TES (packed-bed) height: H_{PB} Top/bottom radius: $r_{\mathrm{PB},t}$, $r_{\mathrm{PB},b}$ Structural thickness: $l_{\mathrm{struc},i}$ Insulation thicknesses: $l_{\mathrm{ins},i}$ Particle diameter: d_p Packed-bed porosity: ε	Thermal cond.: k_f, k_s, $k_{\mathrm{ins},i}$ Density: ρ_f, ρ_s, $\rho_{\mathrm{ins},i}$ Heat capacity: $c_{p,f}$, c_s, $c_{\mathrm{ins},i}$ Viscosity: μ_f	Charged capacity: E_c Net discharged energy: $E_{d,\mathrm{net}}$ Supplied energy: $E_{c,\mathrm{in}}$ Efficiency: η_{en}, η_{ex} Cost: C_{TES}

Several TES optimization studies were published that optimize only the thermal performance of TES systems without considering the TES costs [6, 7] or consider a multi-objective optimization approach where the TES efficiency and the costs are optimized simultaneously [8-10]. The above-mentioned publications use models with strong simplifications to predict the TES performance, such as algebraic equations to calculate the one-dimensional temperature distribution in packed-bed TES systems, together with basic optimization methods such as the direct search method to find optimal operating and design parameters. The restrictive model simplifications and basic optimization methods can be used for a rough evaluation of packed-bed TES systems. To advance the scope and improve the accuracy of TES optimization, the model must be more sophisticated to simulate realistic charging and discharging cycles. Therefore, the TES model in this work is capable of handling variable charging, discharging, and idle periods, multiple structural and insulation layers with different thicknesses, non-cylindrical TES geometries, and temperature-dependent thermophysical properties. In addition, an efficient optimization method is required to reduce the computational costs. In this work, the objective function is formed from the exergy efficiency at the quasi-steady state and the material costs. We expect the objective function to be continuous and to have a single maximum. Because reaching the quasi-steady state often requires a large number of charge-discharge cycles to be simulated, the objective function can be relatively expensive to compute. To decrease the computational cost, the number of evaluations of the objective function should be small. Therefore, the gradient-based sequential quadratic programming (SQP) algorithm is used for the optimization in this work.

The objective of the present study is to use multi-objective optimization to design packed-bed TES systems with rocks as heat-storage medium and air as heat-transfer fluid (HTF). The objective function is formed from the exergy efficiency and the material costs. The design variables include the packed-bed height, top and bottom radii, insulation-layer thicknesses, and particle diameter while the net discharged energy and the packed-bed volume are used as nonlinear constraints. The trade-off between increasing the exergy efficiency and reducing the TES material costs is demonstrated through the concept of Pareto optimality to identify optimal designs that combine a high efficiency with low costs.

2. Model and numerical method

The optimization tool is a combination of a previously developed heat-transfer model [4] and the optimization package NPSOL [11, 12]. The coupling of the heat-transfer model with the optimization package is described in [13].

2.1. TES model

The heat-transfer model can accurately predict the one-dimensional temperature distribution of packed-bed thermocline TES systems and is described in [4]. The model was verified with the exact solutions for the simplified cases of no axial conduction and wall losses during the first charging of the TES [14] and during the steady charging-discharging behavior in the limit of fast switching times [15]. Several experimental

studies were used to validate the model, including storages with rocks [5] and ceramic particles [16] using air as HTF and a storage with a combination of quartzite and sand using molten salt as HTF [17].

2.2. Optimization package

The optimization package NPSOL uses the SQP method to minimize an objective function that depends on design variables and linear and non-linear constraints [18]. The optimization problem can be formulated as

$$\text{minimize} \quad f(\vec{x}) \quad \text{subject to} \quad \vec{l} \leq r(\vec{x}) \leq \vec{u} \quad \text{with} \quad r(\vec{x}) = \begin{cases} \vec{x} \\ \bar{\bar{A}}\vec{x} \\ \vec{c}(\vec{x}) \end{cases} \tag{1}$$

where $\vec{x}$ is a vector of n design variables, $f(\vec{x})$ is the objective function, $\vec{l}$ and $\vec{u}$ are vectors with the lower and upper bounds of each design variable, $\bar{\bar{A}}$ is a $m_L \times n$ matrix describing the m_L linear constraints, and $\vec{c}(\vec{x})$ is a vector with m_N nonlinear constraint functions. The values of $\vec{l}$, $\vec{u}$, $\bar{\bar{A}}$, and the initial values of $\vec{x}$ are required as input parameters to NPSOL. The functions $f(\vec{x})$ and $\vec{c}(\vec{x})$ are calculated by the TES code described above and provided to NPSOL. Besides the function values of $f(\vec{x})$ and $\vec{c}(\vec{x})$, the SQP method requires also the gradients of $f(\vec{x})$ and $\vec{c}(\vec{x})$ with respect to each design variable.

2.2.1. Complex-step derivative approximation

To avoid the "step-size dilemma" of finite-difference methods, the complex-step derivative approximation is used [19-21]. This method uses complex calculus to calculate the derivative without subtraction and hence is unaffected by cancellation errors. This allows a very small step size to be used to reduce the truncation error and therefore the accuracy of the complex-step derivative approximation can exceed the accuracy of finite difference by several orders of magnitudes [19, 21].

To apply the complex-step derivative approximation, the floating-point variables and constants used in the TES code are converted into complex variables and constants and the intrinsic Fortran functions and operators are overloaded to handle complex arguments. The conversion process is automated by a code that adjusts all Fortran files and the overloaded intrinsic functions and operators are defined in an additional Fortran module similar to [21]. By introducing a complex step size to a specific design variable, e.g. x_1, while setting the complex part of the other design variables to zero, the complex part of the objective function $f(\vec{x})$ can be used to approximate the derivative of the objective function with respect to this particular design variable using

$$\frac{\partial f}{\partial x_1} \approx \frac{\mathrm{Im}[f(x_1 + ih, x_2, \ldots, x_n)]}{h} \tag{2}$$

where $x_{1,2,\ldots,n}$ are the design variables and h is the complex step size (typically chosen to be 10^{-12}). The same procedure can be applied to any function calculated by the converted TES code.

2.2.2. Multi-objective optimization

The objectives in multi-objective optimization are in general competing, so one objective can only be improved when at least another objective is worsened [22]. This trade-off can be visualized with the Pareto front that describes the best possible combinations of the competing objectives within the objective function space [23]. Several approaches exist to combine the competing objectives to calculate the Pareto front [24]. One of the simplest methods is the weighted-sum method in which a single objective function is calculated by combining the competing objectives according to

$$f(\vec{x}) = \sum_{i=1}^{N_o} w_i \hat{f}_i(\vec{x}) \tag{3}$$

where N_o is the total number of objectives and w_i is the relative weight of objective $\hat{f}_i(\vec{x})$. The sum of all weights is equal to unity. For competing objectives, the Pareto front can be computed by varying the weights gradually and computing for each set of weights the optimum of the weighted sum [25].

Two objective functions are considered in the present study: the exergy efficiency of one charge-discharge cycle at the quasi-steady state and the material costs of the TES. The weighted sum of these two

objective functions is given by

$$f(\vec{x}) = w(1-\eta_{\mathrm{ex}}) + (1-w)\frac{C_{\mathrm{TES}}}{C_{\mathrm{TES,ref}}} \quad (4)$$

where η_{ex} is the exergy efficiency, C_{TES} is the total material cost of the TES, and $C_{\mathrm{TES,ref}}$ is an estimation of the material cost. The normalization is used to avoid one objective function dominating the other. The exergy efficiency is defined in [4] and the material cost of the TES is computed from

$$C_{\mathrm{TES}} = \sum_{i=1}^{N_m} c_i V_i \quad (5)$$

where N_m is the total number of materials, c_i is the volumetric cost of material i, and V_i is the volume of material i. The material cost includes the storage material, the structural materials, and the insulation materials. The volumetric costs of the various materials are given in [4].

2.2.3. Non-linear optimization constraints

In the present study, two non-linear constraints are considered: the net discharged energy $E_{d,\mathrm{net}}$ and the packed-bed volume V_{PB}. The net discharged energy describes the net thermal energy extracted from the TES during discharging and is given by

$$E_{d,\mathrm{net}} = E_{d,\mathrm{out}} - E_{d,\mathrm{in}} = \int_0^{\Delta t_d} \dot{m}\left\{h_f\left(T_{d,\mathrm{out}}\right) - h_f\left(T_{d,\mathrm{in}}\right)\right\} dt \quad (6)$$

where $\dot{m}$ is the mass flow rate and h_f is the temperature-dependent enthalpy of the HTF. The volume of the packed bed is calculated with the well-known expression for a conical frustum.

3. Results

The results will be presented in two parts. In the first part, the optimization procedure is illustrated by using a simple TES configuration characterized by two design variables. This allows the objective and constraint functions to be visualized. In the second part, a pilot-scale TES, similar to that shown in [5], is optimized for several combinations of design variables. For the second part, each multi-objective optimization considers the exergy efficiency and the material costs as objective functions and uses the weighted-sum method as shown in Eq. (4) to find Pareto-optimal solutions. Each multi-objective optimization uses 9 values of the weight ($w = \{1.0, 0.99, 0.95, 0.8, 0.5, 0.2, 0.05, 0.01, 0.0\}$) to form the Pareto front. For all configurations, the TES geometry is a truncated cone with variable top and bottom radii. The structure of the TES is given by two concrete layers consisting of ultra-high performance concrete (UHPC) and low-density concrete (LDC) together with two layers of insulation material consisting of Microtherm® (MT) and Foamglas® (FG) as explained in [5]. To calculate the thermal losses through the structure and insulation layers, the outer wall of the TES is assumed to be at ambient temperature. The thermophysical properties of all structure, insulation, and thermal storage materials and the HTF are temperature-dependent as specified in [26]. Each TES simulation is run until a quasi-steady state is reached.

3.1. Visualization of optimization procedure

A simple method to visualize and examine the optimization procedure is to use one or two design variables and plot the objective and constraint functions as a function of the design variables. The visualization of the optimization procedure is done for the pilot-scale TES with a fixed packed-bed height of $H_{\mathrm{PB}} = 8$ m and the top and bottom packed-bed radii of the TES as design variables. The used model parameters are listed in Tab. 2. Fig. 1 shows contour lines of the exergy efficiency, the material costs, the net discharged energy, and the packed-bed volume, as a function of the top and bottom packed-bed radii. The visualization depicted in Fig. 1 is based on 400 quasi-steady-state TES simulations for discrete values of the design variables together with a linear interpolation routine to smooth the contour lines.

Fig. 2 shows on the left-hand side the exergy efficiency as a function of the top and bottom packed-bed radii together with the optimization iterations for different initial conditions and on the right-hand side a close-up of the computed optima together with the predicted optimum. Depending on the initial condition,

the optimizer requires between 12 and 35 iterations to reach the optimum. The computed optima differ by less than 0.01% from the optimum predicted from the interpolated results of the 400 quasi-steady-state simulations. Compared to a systematic approach with twenty discrete values for both design variables and the simulation of all design combinations, the gradient-based optimization reduces the computational cost by about 91 and 97%. This reduction will be even more significant when the number of design variables is increased.

Tab. 2: Operational and geometrical parameters of the pilot-scale TES model.

Operational parameters	charging duration, t_c	8.0 h	Geometrical parameters	void fraction, ε	0.342
	discharging duration, t_d	8.0 h		particle diameter, d_p	0.03 m
	mass flow rate, $\dot{m}_{\mathrm{air}}$	0.75 kg/s		1st concrete layer, l_{UHPC}	0.05 m
	charging temperature, T_c	823.15 K		2nd concrete layer, l_{LDC}	0.3 m
	discharging temperature, T_d	293.15 K		1st insulation layer, l_{MT}	0.1 m
	ambient temperature, T_0	293.15 K		2nd insulation layer, l_{FG}	0.1 m

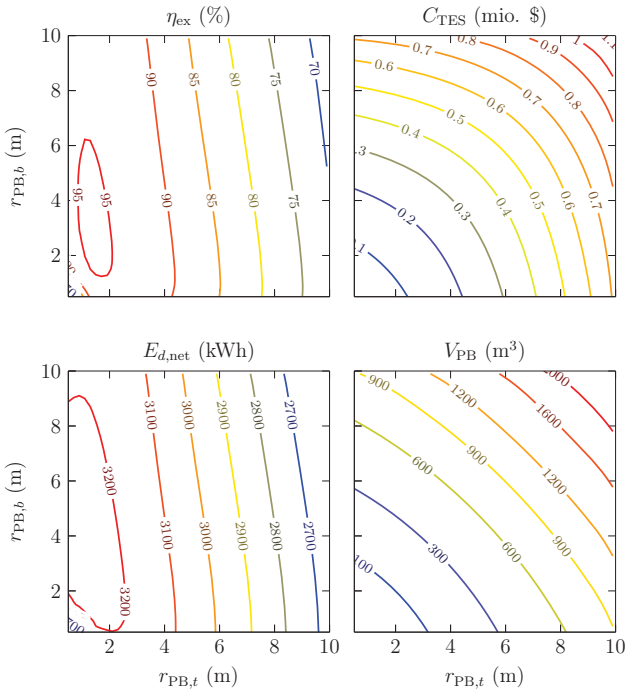

Fig. 1: Exergy efficiency, material cost, net discharged energy, and packed-bed volume as a function of the top and bottom packed-bed radii of the TES for a fixed packed-bed height of $H_{\mathrm{PB}} = 8$ m and TES model parameters according to Tab. 2.

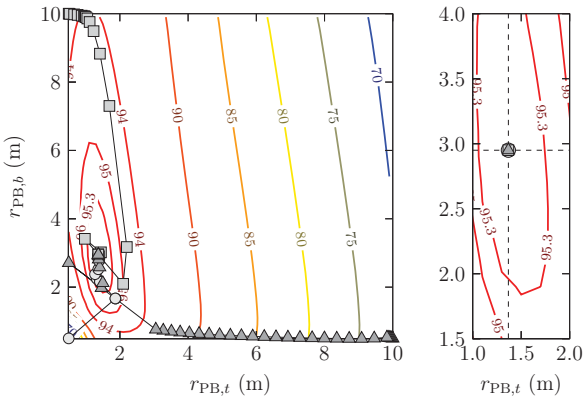

Fig. 2: Left-hand side: exergy efficiency as a function of the top and bottom packed-bed radii of the TES together with optimization iterations for different initial conditions. Right-hand side: close-up of the computed optima for all initial conditions (symbols) and the predicted optimum (dashed lines).

3.2. Pilot-scale TES

To simplify the interpretation of the multi-objective optimization results, the TES configurations have the same operating conditions but different numbers of design variables and constraints. With this approach, the influence of individual design variables on the optimization results can be pointed out. The optimization uses two nonlinear constraints and five design variables as shown in Tab. 3. The nonlinear constraints are the net discharged energy and the packed-bed volume and the design variables are the height, top and bottom radii of the packed bed, the outer insulation-layer thickness, and the particle diameter. For simplicity, the considered structure and insulation materials have on the top, bottom, and side walls of the TES the same thicknesses. Depending on the optimization configuration, the packed-bed volume and some of the design variables are fixed or variable as indicated in Tab. 3. To have a benchmark for the designs, the net discharged energy is used as constraint and must be $\mathrm{E}_{d,\mathrm{net}} \geq 3$ MWh. (For all configurations, $\mathrm{E}_{d,\mathrm{net}}$ does not exceed 3.3 MWh.)

Tab. 3: Nonlinear constraints and design variables of the pilot-scale TES optimization configurations.

Configuration		1	2	3
Nonlinear constraints	net discharged energy, $E_{d,\mathrm{net}}$	≥ 3 MWh	≥ 3 MWh	≥ 3 MWh
	packed-bed volume, V_{PB}	300 m^3	–	–
Design variables	packed-bed height, H_{PB}	8.0 m	0.5–10.0 m	0.5–10.0 m
	top radius, $r_{\mathrm{PB},t}$	0.5–10.0 m	0.5–10.0 m	0.5–10.0 m
	bottom radius, $r_{\mathrm{PB},b}$	0.5–10.0 m	0.5–10.0 m	0.5–10.0 m
	outer insulation, $t_{\mathrm{ins,out}}$	0.1 m	0.1 m	0.01–1.0 m
	particle diameter, d_p	0.03 m	0.03 m	0.001–0.1 m

3.2.1. Configuration 1

The first configuration uses $E_{d,\mathrm{net}} \geq 3$ MWh and $\mathrm{V_{PB}} = 300$ m^3 as nonlinear constraints and the top and bottom packed-bed radii as design variables. With a fixed packed-bed volume, all Pareto-optimal solutions must lie on the contour indicating a packed-bed volume of 300 m^3 in Fig. 1.

Fig. 3 depicts the TES geometries for the two extreme cases $w = 1.0$ and $w = 0.0$ together with the intermediate case $w = 0.5$ according to Eq. (4). (During charging, the HTF enters the TES from the top and exits from the bottom; during discharging, the flow direction is reversed.) The inflow and outflow ports are not indicated in Fig. 3 because they are not considered in the simulations.

For the Pareto optimal designs, a comparison of the TES material costs are presented in Fig. 4. Since the packed-bed volume is constant, the cost of the storage material is constant and the cost reduction is caused by the reduction of the required structure and insulation material. The cost of the storage material is negligible compared to the structure and insulation material. The cheapest design has a cylindrical shape because this minimizes the surface area per volume and accordingly requires the smallest amount of structure and insulation materials.

The Pareto front of the two objective functions is presented on the left-hand side of Fig. 5. The exergy efficiency can only be increased when the TES material costs is increased, which reflects the trade-off between maximizing the exergy efficiency and minimizing the material costs of a TES system. From the Pareto front, it is possible to identify the most efficient TES for a given cost and vice versa. The right-hand side of Fig. 5 shows the exergy efficiency as a function of the top and bottom radii of the packed bed. The difference between the top and bottom radii decreases with decreasing exergy efficiency while the top radius is smaller than the bottom radius until a cylindrical shape is reached. Next to the exergy efficiency, the left-hand side of Fig. 5 also presents the exergy-loss breakdown that indicates how the pumping work, thermal loss, and internal heat transfer decrease the exergy efficiency. The main decrease of the exergy efficiency results from an increase of the thermal loss while the exergy loss due to internal heat transfer stays for all designs almost constant and the required pumping power is negligible.

Fig. 6 shows on the left-hand side the net charged and net discharged exergy for each design. The net charged exergy stays constant and with a negligible exergy loss due to the required pumping power, the exergy efficiency depends mainly on the net discharged exergy. The net discharged exergy increases when the air outflow temperature during discharging increases. The comparison of the HTF outflow temperature during discharging for designs 1 and 9 is shown on the right-hand side of Fig. 6. As expected, for both designs the outflow temperature decreases during discharging while for design 1 the mean outflow

temperature is about 11 K higher than for design 9.

The mean outflow temperature during discharging is strongly influenced by the energy losses through the TES walls, particularly the top wall. Fig. 7 compares for all designs of Configuration 1 and for one charge-discharge cycle the energy losses from the storage material to the structure and insulation material through the top and side walls. When comparing the cheapest with the most efficient design, the losses increase by about 800 and 140%, respectively. This increase depends mainly on the increase of the top radius and accordingly an increase of the surface areas on the top wall and the upper part of the side wall where the temperatures and the temperature gradients to the outside are higher than in the lower section of the TES. The loss through the bottom wall is negligible compared to the top and side wall losses because the bottom wall temperature is close to the ambient temperature.

Fig. 8 shows the thermocline of the fully charged and fully discharged states for designs 1 and 9. The thermoclines of the two designs differ mainly in the upper section where the hot air enters the TES during charging. Compared to design 9, design 1 has a smaller cross-section in the upper part that leads to a higher flow velocity of the HTF and accordingly the temperature front moves further down during charging. An additional effect of the higher flow velocity is a higher Nusselt number that leads to a better interphase heat transfer.

The efficient designs in this study have, as depicted in Fig. 3, a shape like a truncated cone with the smaller cross-section on top and accordingly a negative cone angle. This shape is in contrast to existing designs that are either cylindrical [17] or have a positive cone angle [27, 28]. The trend of negative cone angles having smaller losses is consistent with the results shown in Fig. 13 of [27]. In prior works, negative cone angles appear to have not been considered because of possible drawbacks related to thermal ratcheting. Thermal ratcheting is a well-known problem of packed-bed TES systems caused by different thermal-expansion rates of the storage and structural materials. The different expansion rates can cause the storage material to settle and pack with cycling and eventually cause the storage structure to fail [29, 30]. To prevent material failure, positive cone angles have been suggested as a way to guide the expanding storage material upwards along the inclined wall and hence reduce the stresses on the storage and structural materials [27, 28]. This study does not consider mechanical stresses for simplicity. The practical implementation of a packed-bed thermocline storage with negative cone angle may require structured storage materials [31, 32] or additional material layers between the storage material and the structure to absorb the mechanical stresses [33].

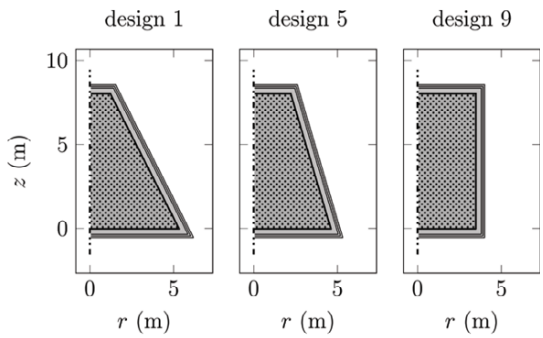

Fig. 3: Visualization of Pareto-optimal designs with w = 1.0, 0.5, and 0.0 of Configuration 1.

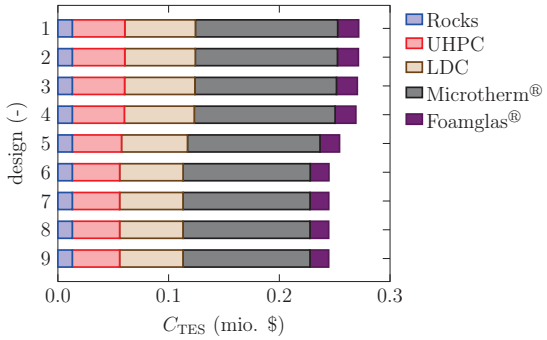

Fig. 4: Breakdown of the TES material costs for the Pareto-optimal designs of Configuration 1.

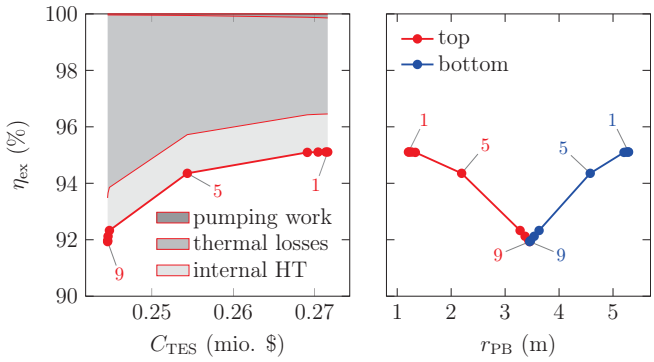

Fig. 5: Left-hand side: exergy efficiency and the exergy-loss breakdown as a function of the TES material costs. Right-hand side: exergy efficiency as a function of the top and bottom packed-bed radii of Configuration 1.

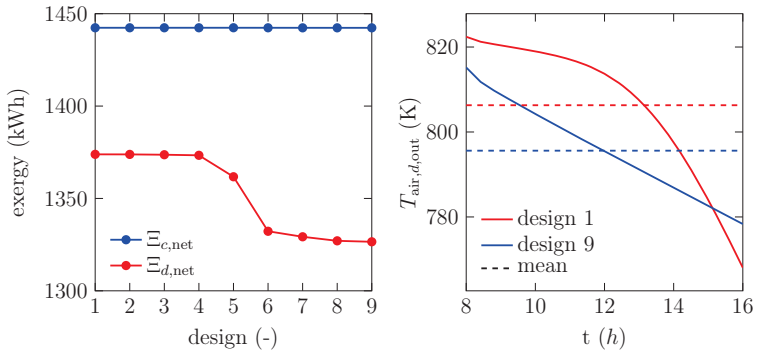

Fig. 6: Left-hand side: net charged and discharged exergies during one charge-discharge cycle for the Pareto-optimal designs. Right-hand side: HTF outflow and mean temperature during discharging for two designs of Configuration 1.

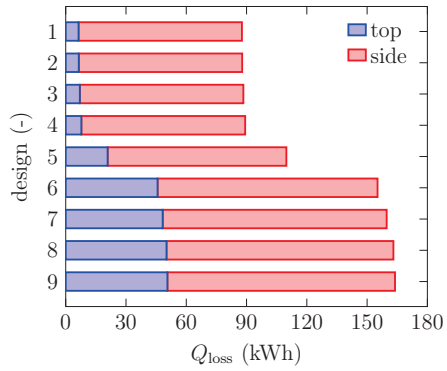

Fig. 7: Energy losses over the top and side walls from the storage material to the structure and insulation material during one charge-discharge cycle for the Pareto-optimal designs of Configuration 1.

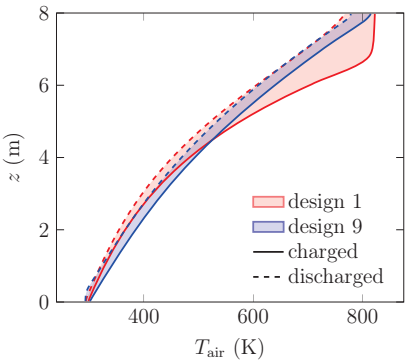

Fig. 8: Air temperature along the axial direction at fully charged and fully discharged state for two designs of Configuration 1.

3.2.2. Configuration 2

The second configuration of the multi-objective TES optimization uses $E_{d,\mathrm{net}} \geq 3$ MWh as a nonlinear constraint and the height and the top and bottom radii of the packed bed as design variables. Compared to Configuration 1, the packed-bed volume is variable. The storage geometries are depicted in Fig. 9 for the two extreme cases $w = 1.0$ and $w = 0.0$ and the intermediate case $w = 0.5$.

Fig. 10 shows the exergy efficiency as a function of the packed-bed height (left), the packed-bed volume (middle), and the material costs (right). When increasing the height, the volume and therefore the material costs increase considerably. An increased height has a favorable influence on the exergy efficiency by expanding the thermocline and reducing thereby the possibility of overcharging and overdischarging the

TES, which leads to an undesirable increase and decrease of the outflow temperatures during charging and discharging, respectively. This trend can be seen in Fig. 11 where the fully charged and discharged thermoclines of the most efficient and cheapest designs are presented. The most efficient design has temperature difference between the fully charged and discharged states of about 10 K at the top and bottom of the storage whereas the temperature differences of the cheapest design are about 200 K. Depending on the application of the TES, the minimum and maximum outflow temperatures during the charge-discharge cycle are important operational parameters that need to be considered during the design phase of the TES. For brevity, the breakdown of the TES material costs is not shown.

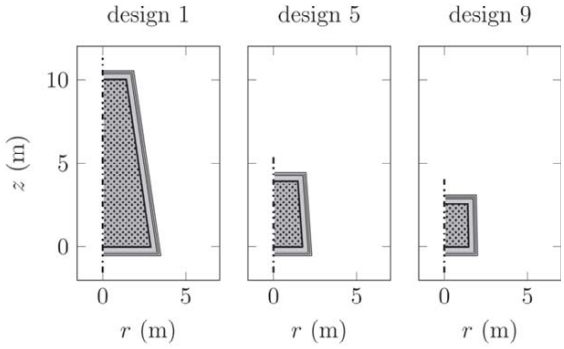

Fig. 9: Visualization of TES geometries for Pareto-optimal designs with w = 1.0, 0.5, and 0.0 of Configuration 2.

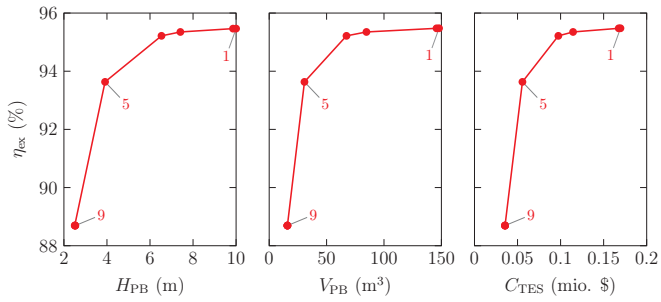

Fig. 10: Exergy efficiency as a function of the packed-bed height, pack-bed volume, and TES material costs for the Pareto-optimal designs of Configuration 2.

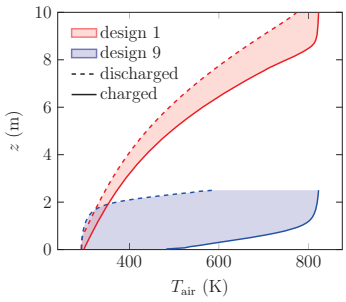

Fig. 11: Air temperature along the axial direction of the fully charged and fully discharged TES for two designs of Configuration 2.

3.2.3. Configuration 3

The third configuration of the multi-objective TES optimization uses $E_{d,\mathrm{net}} \geq 3$ MWh as a nonlinear constraint and the height, the top and bottom radii of the packed bed, the thickness of the outer insulation layer, and the particle diameter as design variables. The TES geometries for the two extreme cases $w = 1.0$ and $w = 0.0$ and the intermediate case $w = 0.5$ are depicted in Fig. 12. Compared to Configuration 2, the main difference of the TES geometries is the increased outer insulation-layer thickness of design 1.

Fig. 13 shows on the left-hand side the exergy efficiency as a function of the outer insulation-layer thickness consisting of Foamglas®. As expected, the more efficient designs have a larger insulation-layer thickness, which reaches the upper limit of 1.0 m and the lower limit of 0.01 m for the most efficient and for the cheapest designs, respectively. Increasing the insulation-layer thickness reduces the thermal losses through the top, bottom, and lateral walls but also increases the material costs as indicated on the right-hand side of Fig. 12. A breakdown of the material costs is shown in Fig. 14. For all designs, the cost for the insulation materials is the major contributor to the total TES material costs while the cost for the storage material is negligible. The four most efficient designs have an outer insulation-layer thickness between 0.66 and 1.0 m that contributes to about half of the total costs. Reducing the required amount of the insulation material is therefore essential to reduce the material costs.

Fig. 15 presents the exergy efficiency and the exergy-loss breakdown as a function of the particle

diameter. The exergy efficiency increases with increasing particle diameter. The least efficient design has a particle diameter that is equal to the lower limit of 1.0 mm while the most efficient design has a particle diameter that is 21.5 mm and therefore below the upper limit of 100.0 mm. A decreasing particle diameter influences the TES performance in two ways: it increases the heat transfer between the solid and fluid phase and it increases the pressure drop over the packed bed. An increasing heat transfer reduces thermal irreversibility and therefore increases the exergy efficiency while an increasing pressure drop increases the exergy loss due to the required pumping power and therefore decreases the exergy efficiency. The strong increase of the required pumping power for very small particles can be seen from the exergy-loss breakdown in Fig. 15. For design 9, the required pumping power is about 140 times bigger than for design 1. The increase of the heat transfer between the solid and fluid phase for a decreasing particle diameter results mainly from an increase of the specific surface area. The optimal particle diameter is therefore a trade-off between increasing the pressure drop and increasing the interphase heat transfer.

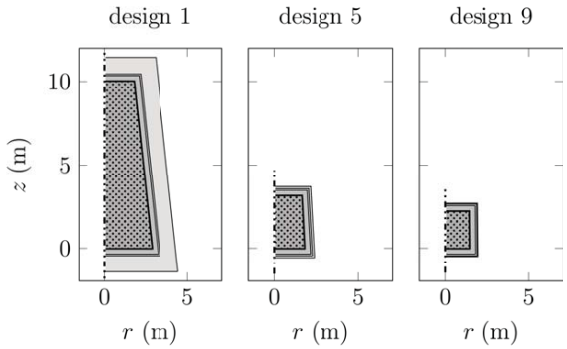

Fig. 12: Visualization of TES geometries for Pareto-optimal designs with w = 1.0, 0.5, and 0.0 of Configuration 3.

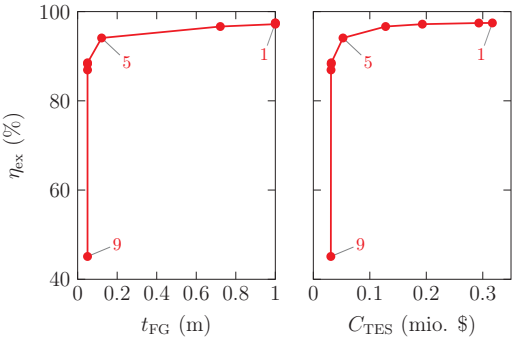

Fig. 13: Exergy efficiency as a function of the outer insulation-layer thickness (left) and the TES material costs (right) for the Pareto-optimal designs of Configuration 3

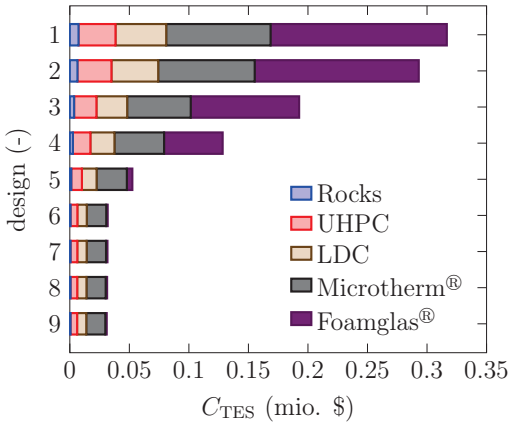

Fig. 14: TES material costs for the Pareto-optimal designs of Configuration 3.

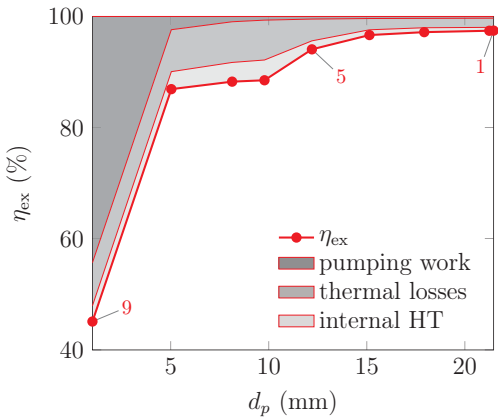

Fig. 15: Exergy efficiency and exergy-loss breakdown as a function of the particle diameter for the Pareto-optimal designs of Configuration 3.

4. Summary and Conclusions

A gradient-based multi-objective optimization method was used to optimize the exergy efficiency and the material costs of packed-bed TES systems based on their height, top and bottom radii, insulation-layer thickness, and particle diameter. Competing objectives like maximizing exergy efficiency and minimizing material costs are treated using Pareto fronts. The Pareto front shows the best possible TES designs and enables the most efficient TES for a given cost to be determined.

A systematic optimization of three pilot-scale TES configurations was used to point out the

influence of individual design variables on the exergy efficiency and material costs. In general, increasing the TES height increases the exergy efficiency but also increases the material costs. The optimization of the top and bottom radii showed that a TES design with a negative cone angle has a higher exergy efficiency than commonly used cylindrical shaped TES or designs with a positive cone angle. This results mainly from a reduced surface area in the hot upper section of the TES and therefore decreased thermal losses to the environment. The basic thermodynamic mechanisms leading to the superior performance of a TES with a negative cone angle were identified with detailed information about the axial temperature distribution in the packed bed and thermal losses through the structure and insulation materials. The potential mechanical drawbacks of a negative cone angle related to thermal ratcheting are not considered in this work but could perhaps be solved by using structured storage materials without loose particles or material layers that absorb the thermomechanical stress during charge-discharge cycles. Detailed material-cost breakdowns showed that for low-cost storage materials like rocks, a reduction of the required insulation material is essential to further reduce the TES material costs. In addition, the optimization revealed the trade-off between reducing the pressure drop and improving the interphase heat transfer when optimizing the particle diameter.

Acknowledgement

The authors gratefully acknowledge funding from the European Union's Horizon 2020 research and innovation programme under grant agreements No. 654387 (RICAS2020, www.ricas2020.eu) and 642067 (RESLAG, www.reslag.eu), from the Swiss Commission for Technology and Innovation through the Swiss Competence Center for Energy Research on Heat and Electricity Storage, from the Swiss National Science Foundation under NRP 70 grant No. 407040_153776, and from the European Union under the 7th Framework Program (grant No. 609837, STAGE-STE). The authors also acknowledge helpful discussions with Prof. R. T. Haftka from the University of Florida.

References

[1] M. Romero, A. Steinfeld, 2012. Concentrating solar thermal power and thermochemical fuels. Energy & Environmental Science. 5, 9234-9245.
[2] C. Bullough, C. Gatzen, C. Jakiel, M. Koller, A. Nowi, S. Zunft, 2004. Advanced adiabatic compressed air energy storage for the integration of wind energy, in: Proceedings of the European Wind Energy Conference, pp. 25.
[3] H.L. Zhang, J. Baeyens, J. Degrève, G. Cacères, 2013. Concentrated solar power plants: Review and design methodology. Renewable and Sustainable Energy Reviews. 22, 466-481.
[4] L. Geissbühler, M. Kolman, G. Zanganeh, A. Haselbacher, A. Steinfeld, 2016. Analysis of industrial-scale high-temperature combined sensible/latent thermal energy storage. Applied Thermal Engineering. 101, 657-668.
[5] G. Zanganeh, A. Pedretti, S. Zavattoni, M. Barbato, A. Steinfeld, 2012. Packed-bed thermal storage for concentrated solar power – Pilot-scale demonstration and industrial-scale design. Solar Energy. 86, 3084-3098.
[6] H. Torab, D.E. Beasley, 1987. Optimization of a packed bed thermal energy storage unit. Journal of Solar Energy Engineering. 109, 170-175.
[7] A.S.A. Ammar, A.A. Ghoneim, 1991. Optimization of a sensible heat storage unit packed with spheres of a local material. Renewable Energy. 1, 91-95.
[8] O. Maaliou, B.J. McCoy, 1985. Optimization of thermal energy storage in packed columns. Solar Energy. 34, 35-41.
[9] C. Choudhury, P.M. Chauhan, H.P. Garg, 1995. Economic design of a rock bed storage device for storing solar thermal energy. Solar Energy. 55, 29-37.
[10] R. Domański, G. Fellah, 1998. Thermoeconomic analysis of sensible heat, thermal energy storage systems. Applied Thermal Engineering. 18, 693-704.
[11] P.E. Gill, W. Murray, M.A. Saunders, M.H. Wright, 1986. User's Guide for NPSOL: A Fortran Package for Nonlinear Programming, in: Report SOL 86-2, Stanford University, Stanford, CA, Department of Operations Research.
[12] Stanford Business Software Inc., Stanford University, California, USA.
[13] J. Marti, L. Geissbühler, V. Becattini, A. Haselbacher, A. Steinfeld, 2016. Constrained Multi-Objective Optimization of Thermocline Packed-Bed Thermal Energy Storage Systems. in preparation.

[14] A. Anzelius, 1926. Über Erwärmung vermittels durchströmender Medien. Journal of Applied Mathematics and Mechanics/Zeitschrift für Angewandte Mathematik und Mechanik. 6, 291-294.
[15] H. Klein, G. Eigenberger, 2001. Approximate solutions for metallic regenerative heat exchangers. International Journal of Heat and Mass Transfer. 44, 3553-3563.
[16] A. Meier, C. Winkler, D. Wuillemin, 1991. Experiment for modelling high temperature rock bed storage. Solar Energy Materials. 24, 255-264.
[17] J.E. Pacheco, S.K. Showalter, W.J. Kolb, 2002. Development of a Molten-Salt Thermocline Thermal Storage System for Parabolic Trough Plants. Journal of Solar Energy Engineering. 124, 153-159.
[18] P.E. Gill, W. Murray, M.H. Wright, 1981. Practical optimization. Academic Press, London.
[19] J.N. Lyness, C.B. Moler, 1967. Numerical differentiation of analytic functions. Journal on Numerical Analysis. 4, 202-210.
[20] J.C. Newman, K.W. Anderson, D.L. Whitfield, 1998. Multidisciplinary sensitivity derivatives using complex variables. Mississippi State University Publication, MSSU-EIRS-ERC-98-08.
[21] J.R.R.A. Martins, P. Sturdza, J.J. Alonso, 2003. The complex-step derivative approximation. Transactions on Mathematical Software. 29, 245-262.
[22] A. Toffolo, A. Lazzaretto, 2002. Evolutionary algorithms for multi-objective energetic and economic optimization in thermal system design. Energy. 27, 549-567.
[23] Y. Censor, 1977. Pareto Optimality in Multiobjective Problems. Applied Mathematics and Optimization. 4, 41-59.
[24] R.T. Marler, J.S. Arora, 2004. Survey of multi-objective optimization methods for engineering. Structural and Multidisciplinary Optimization. 26, 369-395.
[25] D.W. Zingg, M. Nemec, T.H. Pulliam, 2008. A comparative evaluation of genetic and gradient-based algorithms applied to aerodynamic optimization. European Journal of Computational Mechanics/Revue Européenne de Mécanique Numérique. 17, 103-126.
[26] G. Zanganeh, 2014. High-Temperature Thermal Energy Storage for Concentrated Solar Power with Air as Heat Transfer Fluid, in, Diss. Eidgenössische Technische Hochschule ETH Zürich, Nr. 21802.
[27] G. Zanganeh, A. Pedretti, A. Haselbacher, A. Steinfeld, 2015. Design of packed bed thermal energy storage systems for high-temperature industrial process heat. Applied Energy. 137, 812-822.
[28] K.Y. Wang, R.E. West, F. Kreith, P. Lynn, 1985. High-temperature sensible-heat storage options. Energy. 10, 1165-1175.
[29] S. Flueckiger, Z. Yang, S.V. Garimella, 2011. An integrated thermal and mechanical investigation of molten-salt thermocline energy storage. Applied Energy. 88, 2098-2105.
[30] A. Dogangun, Z. Karaca, A. Durmus, H. Sezen, 2009. Cause of Damage and Failures in Silo Structures. Journal of Performance of Constructed Facilities. 23, 65-71.
[31] J.E. Skinner, M.N. Strasser, B.M. Brown, R. Panneer Selvam, 2013. Testing of High-Performance Concrete as a Thermal Energy Storage Medium at High Temperatures. Journal of Solar Energy Engineering. 136, 021004.
[32] S. Zunft, M. Hänel, M. Krüger, V. Dreißigacker, 2014. A Design Study for Regenerator-type Heat Storage in Solar Tower Plants–Results and Conclusions of the HOTSPOT Project. Energy Procedia. 49, 1088-1096.
[33] Z. Chang, X. Li, C. Xu, C. Chang, Z. Wang, Q. Zhang, Z. Liao, Q. Li, 2016. The effect of the physical boundary conditions on the thermal performance of molten salt thermocline tank. Renewable Energy. 96, 190-202.

ISES International Solar Energy Society

Conference Proceedings

EuroSun 2016

Palma de Mallorca (Spain), 11 – 14 October 2016

EXPERIMENTAL AND SIMULATIVE CHARACTERIZATION OF A FIN AND TUBES HEAT EXCHANGER WITH PCM FOR PROCESS HEAT APPLICATIONS

Hannah Neumann[1], Dominik Seiler[1], Peter Schossig[1] and Stefan Gschwander[1]

[1] Fraunhofer Institute for Solar Energy Systems ISE, Freiburg (Germany)

Abstract

Thermal storage is one option to make solar or conventional process heat applications more efficient. Phase change material (PCM) storages offer the potential to keep constant temperatures for different time periods. In this paper a fin and tubes heat exchanger filled with the sugar alcohol D-mannitol was characterized regarding its usability as PCM storage in the temperature range between 100 and 250 °C. D-mannitol melts at ca. 166 °C. Different heating and cooling experiments were carried out. The specific heat capacity of the PCM as well as the latent heat was determined. The heat flow into the storage was determined at different mass flow rates for heating and cooling processes. During the measurements thermal losses to the ambient were very high leading to high uncertainties. Due to the viscosity of D-mannitol natural convection between the fins seems to have no significant influence on heat transfer during melting of the PCM. Some results led to the assumption that the heat distribution in the heat exchanger was not even. A simulation model was created and a first validation was carried out. Geometry improvement with the aim of more even heat distribution and higher charge and discharge power will be carried out by using the simulation model and further measurements.

Keywords: *Phase Change Material, D-mannitol, fin and tubes heat exchanger*

1. Introduction

Thermal storage offers the potential to increase energy efficiency of solar or conventional process heat applications. Thermal storage based on phase change materials (PCM) is advantageous for applications having to ensure small temperature differences during several hours. PCM can store high energy densities in small temperature ranges due to the phase change from solid to liquid. When storing above 100 °C PCM storages can be run unpressurised compared to water storages. In the temperature range between 100 and 250 °C sugar alcohols are potential candidates. They have higher storage densities than other materials in this temperature range.

In order to charge and discharge a PCM storage with sufficient power a suitable heat exchanger type has to be chosen. In a recent project a heat exchanger concept based on plates will be developed. As a reference for comparison an optimized fin and tubes heat exchanger with PCM will be used.

In this paper the characterization of the fin and tubes heat exchanger in combination with a sugar alcohol will be described. It was experimentally characterized in a testing facility. From the results first information about the behavior of the heat exchanger as well as about the PCM in application scale could be derived.

2. Experimental setup

Fig. 1, top left, shows a picture of the empty fin and tubes heat exchanger. Its inner dimensions are 270 x 259 x 81 mm. The distance between the fins is 4.5 mm with a fin thickness of 0.3 mm. The heat exchanger is made of stainless steel. Fig. 1, bottom left, shows the dimensions in cross section. The height of the fins is 28 mm. Under the fins is a gap of 26.5 mm. Thus when filling the heat exchanger with PCM, a 26.5 mm PCM layer will be under the fins. The temperature of the PCM is measured at the same height as the tubes, at three different locations in the heat exchanger (indicated in Fig.1, right). Additionally the temperature at the inner and outer surfaces of the insulation surrounding the heat exchanger is measured (the insulation is not visible in Fig. 1).

doi:10.18086/eurosun.2016.03.06 Available at http://proceedings.ises.org

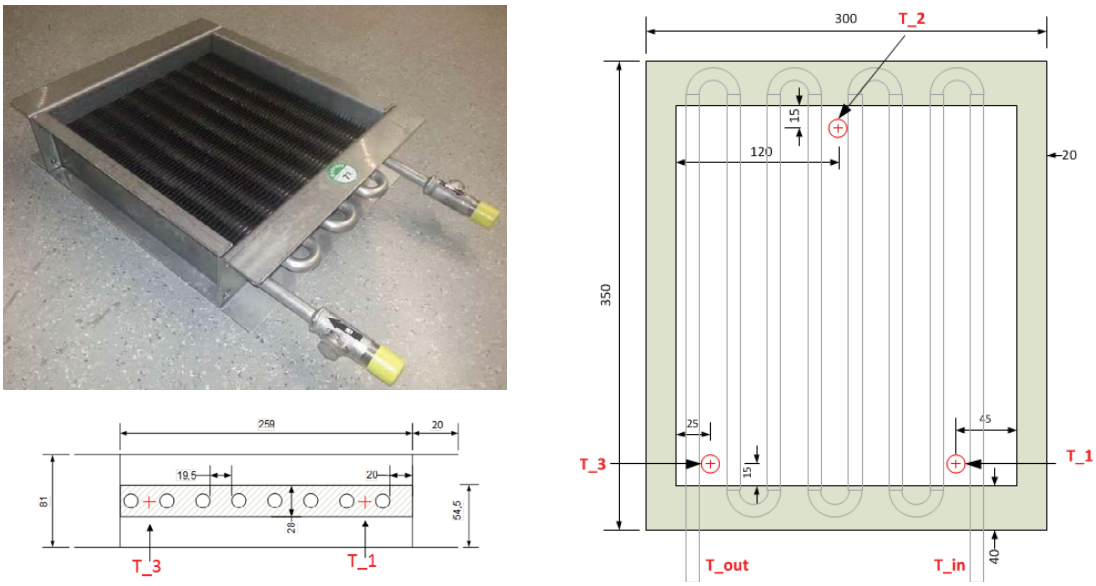

Fig. 1: Top left: fin and tubes heat exchanger used as PCM storage, bottom left: cross section of the heat exchanger with position of temperature sensors, right: position of temperature sensors from top view

In the testing facility thermal oil is used as heat transfer fluid (THERMINOL® 66 from FRAGOL GmbH+Co. KG). Mass flow is measured using a Coriolis mass flow meter. At the inlet and outlet of the heat exchanger the temperature of the oil is measured (Fig. 1, right).

The heat exchanger was filled with the sugar alcohol D-mannitol having a melting temperature of ca. 166 °C. Thermal properties of D-mannitol are presented in Tab. 1. The measurements not given a source were measured at Fraunhofer ISE.

Tab. 1: Thermal properties of D-mannitol

Property	Value solid	Value liquid	Material	Source
c_p (kJ kg^{-1} K^{-1})	1.79 (at 120 °C)	2.75 (at 180 °C)	Batch 1	
ρ (kg m^{-3})	1390 (at 150 °C)	1267 (at 170 °C)		(Godin, 2015)
k (W m^{-1} K^{-1})	0.88 (at 130 °C)	0.43 (at 190 °C)	Batch 2	
η (Pa s)	-	0.046 (at 170 °C)	Batch 2	
β (1 K^{-1})		1.3 * 10^{-3}		Based on (Godin, 2015)
Δh_m (kJ kg^{-1})	258.3 / 233.8		Batch 1 / Batch 2	
T_{onset} (°C)	160.9 / 150.4		Batch 1 / Batch 2	

3. Theory

To characterize the heat exchanger several properties were calculated.

The packing factor of the storage was calculated according to (Castell et al., 2011):

$$PF = \frac{V_{PCM}}{V_{storage}} \quad \text{(eq. 1)}$$

Heat flow of the heat transfer fluid was calculated as:

$$\dot{Q}_{HTF} = \dot{m}_{HTF} * c_{p\_HTF} * (T_{in} - T_{out}) \quad \text{(eq. 2)}$$

The energy balance equation is written as:

$$\int_0^t \dot{Q}_{HTF}\, dt = \int_0^t \dot{Q}_{loss}\, dt + Q_{HX} + Q_{PCM} \quad \text{(eq. 3)}$$

The energy of the insulation material was neglected.

With

$$Q_{HX} = m_{HX} * c_{p_{HX}} * dT \quad \text{(eq. 4)}$$

$$Q_{PCM} = m_{PCM} * c_{p_s} * \left(T_{pc} - T_{start}\right) + m_{PCM} * \Delta h_{PCM} + m_{PCM} * c_{p_l} * \left(T_{end} - T_{pc}\right) \quad \text{(eq. 5)}$$

The UA-value was calculated as:

$$U * A = \frac{\dot{Q}_{HTF}}{\Delta T_{lm}} \quad \text{(eq. 6)}$$

with the logarithmic mean temperature difference for a PCM storage according to (Mehling and Cabeza, 2008):

$$\Delta T_{lm} = \frac{\left(T_{pc} - T_{in}\right) - \left(T_{pc} - T_{out}\right)}{ln\frac{T_{pc} - T_{in}}{T_{pc} - T_{out}}} \quad \text{(eq. 7)}$$

The effectiveness was calculated according to (Castell et al., 2011) as follows:

$$\varepsilon = \frac{T_{in} - T_{out}}{T_{in} - T_{pc}} \quad \text{(eq. 8)}$$

The PCM temperature was assumed to be a mean value of the three measured temperatures in the PCM:

$$T_{pc} = \frac{(T_1 + T_2 + T_3)}{3} \quad \text{(eq. 9)}$$

4. Experiments

In the beginning measurements with the empty heat exchanger were carried out. Thermal losses to the ambient were determined at different temperatures and mass flow rates. Before starting the measurements the temperature was kept constant until steady state was reached. During the measurements a constant inlet temperature T_{in} was supplied for half an hour. $\dot{Q}_{loss}$ was calculated using (eq. 2). Afterwards the specific heat capacity of the empty heat exchanger was determined. Therefor a step function was implemented to the inlet temperature T_{in}. Calculation was done with (eq. 3) and (eq. 4). In (eq. 3) Q_{loss} was calculated from the determined losses in the measurement before and $Q_{PCM}$was zero. The results of these experiments were needed to calculate further values of the heat exchanger filled with PCM.

Afterwards the heat exchanger was filled with D-mannitol. The material was filled until the upper end of the fins. Thus a gap of air was left to tolerate the volume change of the PCM. D-mannitol was filled into the heat exchanger in fresh form, thus as a powder. Once the powder was filled until the upper end of the fins, it was heated over the phase change and cooled down again. Thus it melted and crystallized once. After crystallizing, the D-mannitol was a solid mass. Since the density of D-mannitol in this state is much higher than the one of the powder, five of these filling, melting and crystallization processes were necessary. During these processes coloration to brown started which is a hint for degradation (Solé et al., 2014).

After finishing most experiments a second filling process was done, because some experiments (heating and cooling through the phase change) were repeated using fresh material. For this filling process the D-mannitol was melted in an oven and afterwards poured into the heat exchanger in liquid state. Thus only one melting cycle was necessary leading to less degradation during the filling process.

In all experiments with D-mannitol a step function was implemented to the fluid inlet temperature T_{in} at constant mass flow. Before starting an experiment the oil inlet temperature was kept constant for several hours to reach steady state. First, experiments in sensible state of the PCM were carried out (in solid and in liquid state) in order to determine the specific heat capacity of the PCM in solid and liquid state. The calculation of the specific heat capacity was done using (eq. 3) and (eq. 4). Afterwards measurements including the phase change were carried out. Several step functions for heating and cooling at different mass flow rates were performed and analyzed. The latent heat, the UA-value, the effectiveness and the heat flow were calculated for this case using (eq. 2) to (eq. 9).

5. Results and discussion of experiments

5.1 Packing factor

In total 4.29 kg of D-mannitol were implemented into the heat exchanger during the first filling. As described, some experiments were repeated using fresh material and a different filling procedure. Using this procedure the heat exchanger was filled with 5.1 kg of D-mannitol. The filling level after the second procedure was a bit higher than after the first one. The PCM contents lead to packing factors according to (eq. 1) of 0.55 after the first filling and 0.61 after the second filling taking into account the inner dimensions of the heat exchanger (and thus the air gap). The packing factor of this heat exchanger mainly depends on the dimensioning of the air gap on top of the fins and the PCM layer under the fins.

5.2 Thermal losses

Fig. 2 shows the results of the thermal losses to the ambient measured in empty state of the heat exchanger. They increase with increasing oil inlet temperature T_{in}. The relative standard uncertainty of the thermal losses is quite high (up to 25 %). The reason for that is the small temperature difference between oil inlet and outlet temperature.

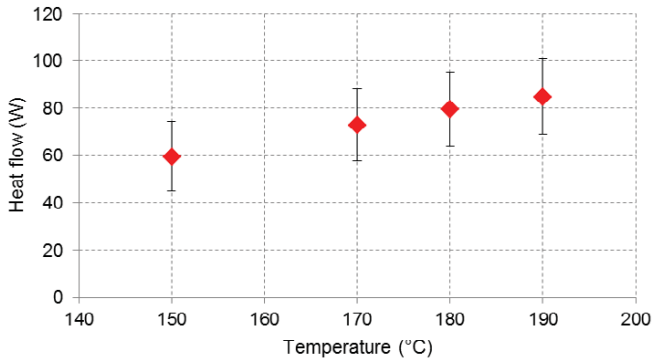

Fig. 2: Thermal losses of the heat exchanger through the insulation material at a mass flow rate of 5.5 kg/min and different oil inlet temperatures T_{in}

5.3 Natural convection

In liquid state of the PCM natural convection can occur. This heat exchanger has two different regions of PCM: the region between the fins and the PCM layer under the fins (see Fig. 1). The Rayleigh number for the region between the fins was calculated according to (Deborah A. Kaminski, Michael K. Jensen, 2011) (natural convection in vertical enclosures). The exact value of the Rayleigh number depends on the material property data. The expansion coefficient β was calculated based on density literature data and its uncertainty is not clear until now. A lower expansion coefficient would lead to a lower Rayleigh number. According to (Deborah A. Kaminski, Michael K. Jensen, 2011) viscous forces are much larger than buoyancy forces and no fluid motion occurs if the Rayleigh number is lower than 2000. Fig. 3 shows the calculated Rayleigh numbers depending on the fin distance and for three temperature differences between liquid PCM and wall. Assuming a temperature difference of 5 K, the Rayleigh number reaches 2000 at a fin distance higher than 5 mm. For a temperature difference of 10 K the value is reached slightly above 4 mm. Taking into account a temperature difference of 15 K, it is reached at approximately 3.6 mm.

It is assumed that natural convection will start developing slowly at Rayleigh numbers higher than 2000. In completely liquid state natural convection between the fins might occur very weakly in the present heat exchanger at temperature differences between PCM and fin higher than 10 K. During the melting process it is assumed that natural convection between the fins has no significant influence on the heat transfer of the heat exchanger. During melting the gap between the melted and the still solid PCM will grow. Until a liquid layer of 3.6 to 4 mm is reached, no natural convection will occur. After that, it might occur very weakly, but as the gap is only 4.5 mm width, most of the melting process has already happened without natural convection.

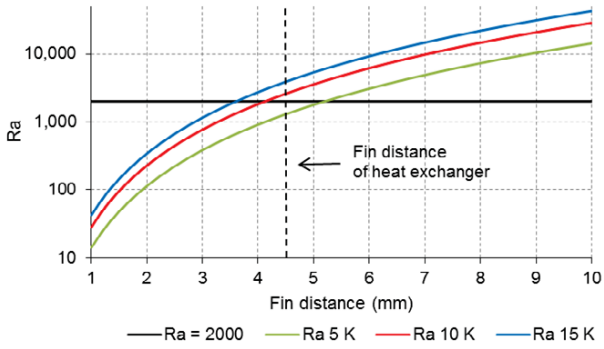

Fig. 3: Raleigh number of D-mannitol in a vertical enclosure according to (Deborah A. Kaminski, Michael K. Jensen, 2011)

In the PCM layer under the fins natural convection should occur when the PCM is completely in liquid state. Heating and cooling of the PCM layer takes place from the top. So during cooling convection in this region should be developed more intense than during heating.

5.4 Temperature profiles and temperature distribution in the PCM

Fig. 4 shows two examples of the step functions carried out in the sensible state of the PCM, the left one in solid and the right one in liquid state. Oil inlet and outlet temperature as well as the three PCM temperatures are shown. At the time the measurements were stopped the PCM had not reached the oil temperature. In solid state the PCM temperatures come closer to the oil temperature after 60 min than in liquid state. This is due to the higher heat conductivity of the solid PCM compared to the liquid PCM. As the PCM temperatures are measured between the fins and the temperature difference between the oil and the PCM is lower than 5 K after 60 min no natural convection occurs. Thus heat conductivity is the dominant factor for heat transfer in this case.

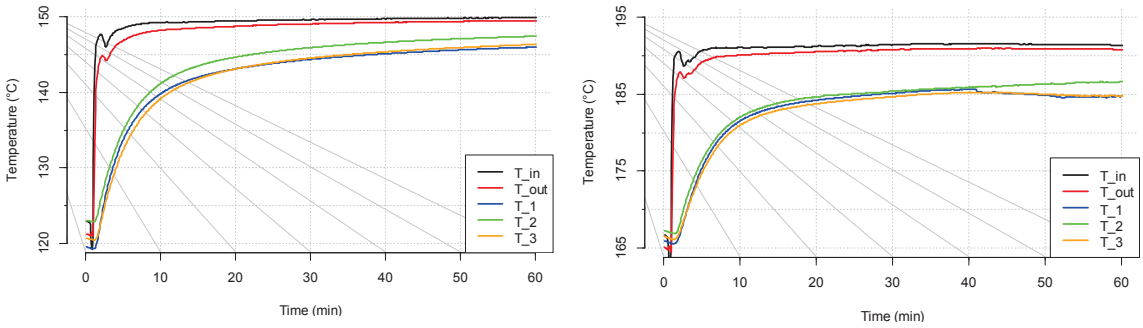

Fig. 4: Left: step function in solid state of the PCM (mass flow = 5.8 kg min^{-1})
right: step function in liquid state of the PCM (mass flow = 6 kg min^{-1})

Fig. 5 shows one melting (left) and one crystallization cycle (right) of the PCM in the heat exchanger. The inlet and outlet temperature of the oil as well as the PCM temperature is shown. Melting takes place at ca. 165 °C whereas the crystallization plateau is visible at 162.5 °C, thus a hysteresis of 2.5 K is visible. Additionally supercooling takes place during crystallization. DSC-measurements of D-mannitol showed hysteresis of up to 40 K (Solé et al., 2014). The much lower hysteresis in the heat exchanger can have several reasons: I) it could be due to the higher sample mass. II) If not all the PCM was melted in the heating cycle before, the still solid PCM could have acted as nucleus. III) The surface of the heat exchanger could also have acted as nucleus. This will be examined in future work.

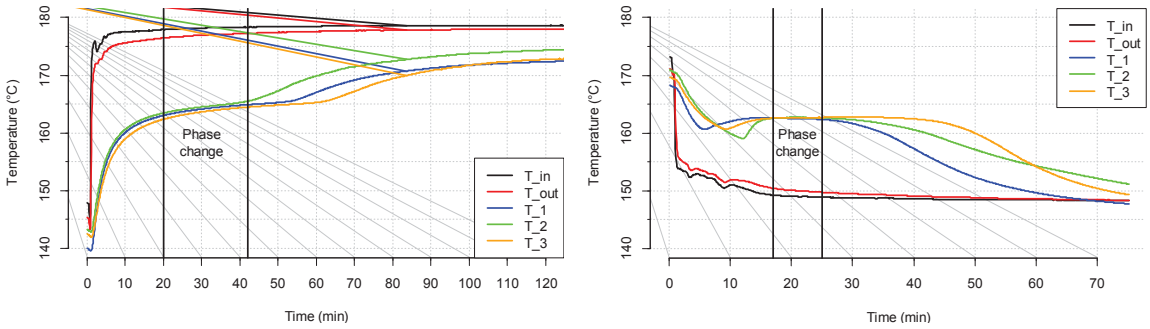

Fig. 5: Left: melting of the PCM; right: crystallization of the PCM both at a mass flow rate of 5.5 kg min^{-1}

Fig. 6 shows one measurement during the phase change. In this case the temperature sensors in the PCM were put deeper into the PCM close to the bottom plate of the heat exchanger. At the end of the measurement the PCM temperatures reach 170 °C, which is slightly above the melting temperature or could still be at the upper end of the melting range. Nevertheless the PCM temperature does not show a visible melting plateau.So it cannot be assured that the PCM at all locations of the heat exchanger was melted completely. The other measurements during the phase change were stopped after 180 min. Thus in these measurements it cannot be assured that all the PCM in the heat exchanger was melted, especially in the ones with lower temperature differences between oil inlet temperature and PCM temperature.

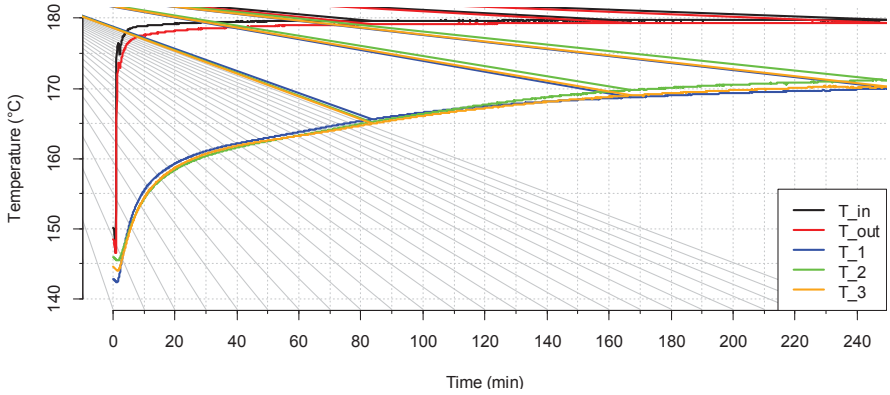

Fig. 6: Melting of the PCM with temperature sensors close to the bottom plate at 8 kg min^{-1}

At the right margin of the heat exchanger the distance between tube and margin is higher than the distance between the tubes in the other parts of the heat exchanger (see Fig. 1, right). After having finished all measurements and opened the heat exchanger, it was visible that the PCM in this part was less brown than the rest of the PCM surface, which might be an indication for less degradation. This effect might have been caused by lower temperatures occurring in this part or by melting this PCM less often than the PCM in the other locations. The darkest brown parts visible in Fig. 7 are on top of the tubes. It could be an indication that the PCM above the tubes was exposed to the highest temperatures.

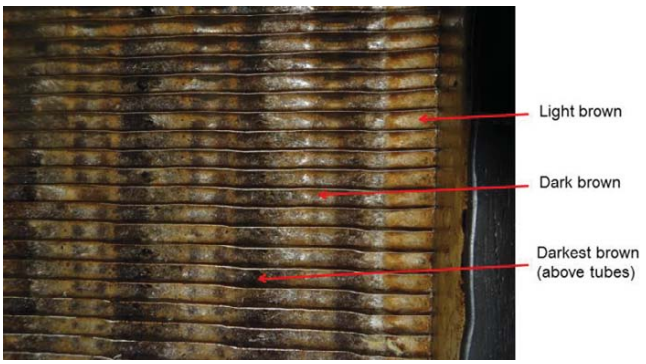

Fig. 7: Surface of the D-mannitol in the heat exchanger after having finished the experiments. The surface close to the right margin is lighter brown than the rest of the surface. The material above to the tubes shows the darkest brown coloration.

5.5 Determination of specific heat capacity and latent heat

Tab. 2 shows a summary of the calculated specific heat capacity and latent heat. Given values are mean values of several measurements. A comparison of the obtained cp-value for the empty heat exchanger with literature data shows good accuracy.

Tab. 2: Summary of determination of specific heat capacity and latent heat

Measurement	Result (mean value)	Comparative DSC-measurement respectively literature value
c_p HX (empty) (kJ kg^{-1} K^{-1})	0.55 +/- 11.3 % (at 152.6 °C)	0.518 (at 150°C) (Richter)
c_p D-mannitol solid (kJ kg^{-1} K^{-1})	1.65 +/- 33.3 % (at 134.2 °C)	1.79 +/- 5 % (at 120 °C)
c_p D-mannitol liquid (kJ kg^{-1} K^{-1})	2.86 +/- 28.5 % (at 175.9 °C)	2.75 +/- 5 % (at 180 °C)
Δh_m (kJ kg^{-1})		
1st filling	142.8	Fresh material: 258.3 After measurements in HX: 200.0
2nd filling	179.5	Fresh material: 233.8 After measurements in HX: 219.3

Comparing the specific heat capacity of D-mannitol in solid and liquid state to DSC-measurements, it is visible that the value of the solid state is lower than DSC and the one of liquid state is higher than the DSC measurement. Both heat exchanger measurements were stopped after 1 h (see Fig. 5). It is assumed that no homogeneous temperature distribution in the PCM was reached as the lower PCM layer is not well thermally coupled to the rest of the heat exchanger. This leads to an underestimation of the specific heat capacity. In liquid state heat transfer in the PCM layer under the fins might take place faster due to convection in this part. The high standard uncertainty of the thermal losses (see Fig. 2), that are taken into account in the calculation of the specific heat capacity, additionally lead to a deviation between the measurements in the heat exchanger and in the DSC.

The standard uncertainty of the specific heat capacity of the empty heat exchanger is lower than the one of the specific heat capacity of the PCM in solid and liquid state. The reason is the shorter measurements time of ten minutes in case of the measurement of the empty heat exchanger compared to 1 h in the other two cases. When considering energy balances, the uncertainty increases with increasing measurement time due to the uncertainty of the losses to the ambient (see Fig. 2).

The comparison of the latent heat with DSC-measurements shows differences. DSC-measurements of the PCM were carried out before filling the heat exchanger and after finishing all measurements. A decrease from 258.3 to 200.0 kJ kg^{-1} takes place. This is due to the degradation of D-mannitol under oxygen atmosphere (Solé et al., 2014). The calculation of the latent heat based on the heat exchanger measurements gives a value of 142.8 kJ kg^{-1} and thus almost 60 kJ kg^{-1} lower than the DSC-measurement after the treatment in the heat exchanger. Due to the geometry of the heat exchanger it could not be ensured that the PCM below the fins was melted completely (see Fig. 6). In the calculations the mass of the whole PCM is taken into account instead of only the molten part, which leads to an underestimation of the latent heat. A further reason for the difference between the measurements in the DSC and in the heat exchanger is the standard uncertainty of the heat losses to the ambient of the heat exchanger of up to +/- 16 W (see Fig. 2). Due to the long measurement time to determine latent heat of up to 3 h, the high standard uncertainty of the heat losses lead to an even higher standard uncertainty of latent heat. When calculating the latent heat with heat losses that are 16 W lower, a latent heat of approximately 180 kJ kg^{-1} is calculated. After the second filling the difference is a bit lower. In this case the temperature difference between inlet temperature and melting temperature was higher. So it might be possible that more PCM was melted.

5.6 Characterization of the phase change period

To be able to compare the performance of the investigated heat exchanger to the performance of other heat exchangers, some characteristic parameters were calculated. As the heat exchanger is used to melt or crystallize the PCM inside the storage, the parameters were calculated for these phase transitions (marked in Fig. 5). Afterwards a mean value over the phase change period was calculated to compare different measurements to each other.

Fig. 8 (left) shows the mean value of the heat flow of the heat transfer fluid during the phase change (absolute value). The logarithmic mean temperature difference between PCM and heat transfer fluid (see Fig. 8, right) was almost the same in all measurements, but in the case of crystallization with the mass flow of 1.8 kg min^{-1} it was lower than during melting.

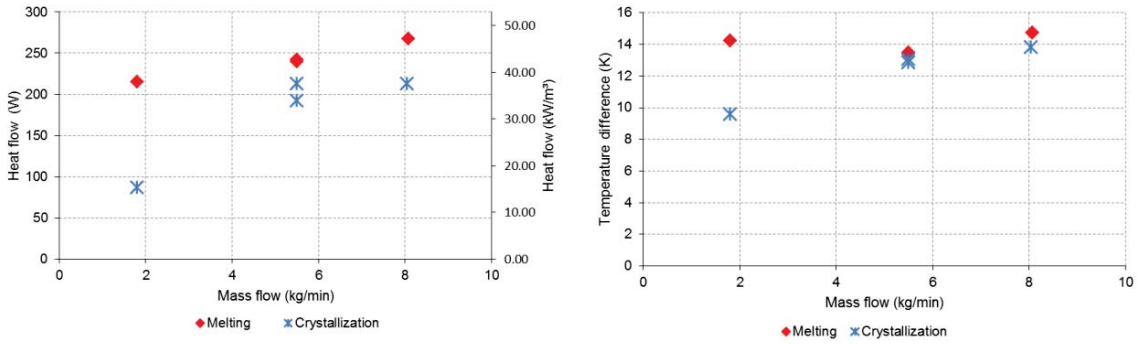

Fig. 8: Left: mean value of the heat flow ($\dot{Q}_{HTF}$) during the phase change (absolute value), right: mean value of the logarithmic mean temperature difference between PCM and heat transfer fluid during the phase change

To make the obtained heat flows comparable to each other, the UA-value of the heat exchanger was calculated taking the heat flow and the logarithmic mean temperature difference of Fig. 8 into account. Fig. 9 shows the results.

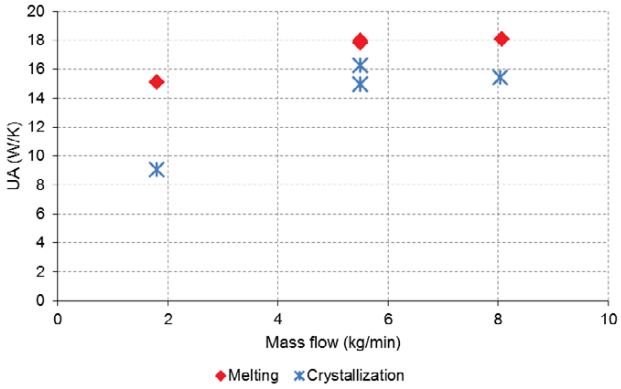

Fig. 9: UA-value at different mass flow rates

According to the results the UA-value is higher during melting than during crystallization. This result has to be interpreted carefully, because many uncertainties due to the way of calculating the UA-value appear. For calculating the UA-value of the heat exchanger properly, it would be necessary to consider only the heat flow between the heat transfer fluid and the PCM. The calculation for Fig. 9 was done using the heat flow of the heat transfer fluid ($\dot{Q}_{HTF}$) according to (eq. 2). This heat is not completely transferred to the PCM. During charging part of it goes to the storage enclosure and from there to the ambient and to the colder PCM. Thus the UA-value is overestimated. During discharging, not only the heat of the PCM is transferred to the heat transfer fluid, but also heat from the storage envelope. Part of the heat from the envelope and most likely from the PCM also goes to the ambient. Thus for discharging it cannot be judged if the UA-value is under- or overestimated without further investigation. In order to evaluate the UA-value properly further measurements and calculations have to be carried out to determine only the heat transfer between the heat transfer fluid and the PCM.

A further uncertainty is the calculation of the logarithmic mean temperature difference. The phase change temperature T_{pc} was calculated as a mean value of the three temperature sensors inside the PCM. As all of them are installed between the fins, the temperature regarded as PCM temperature might not be representative for the whole PCM. The phase change might take place at different times in different parts of the PCM.

Fig. 10 shows the effectiveness of the heat exchanger. It increases with decreasing mass flow. In case of the mass flow rate of 1.8 kg min^{-1} the effectiveness during crystallization is lower than during melting. The reason is the smaller logarithmic mean temperature difference during crystallization compared to melting (see Fig. 8, right). The effectiveness of this heat exchanger is low compared to other PCM-storages. (Castell et al., 2011) reach more than 50 % in a tube in PCM tank. One reason could be that the PCM layer under the fins is not

activated properly. Additionally the mass flow could be further reduced to increase the effectiveness.

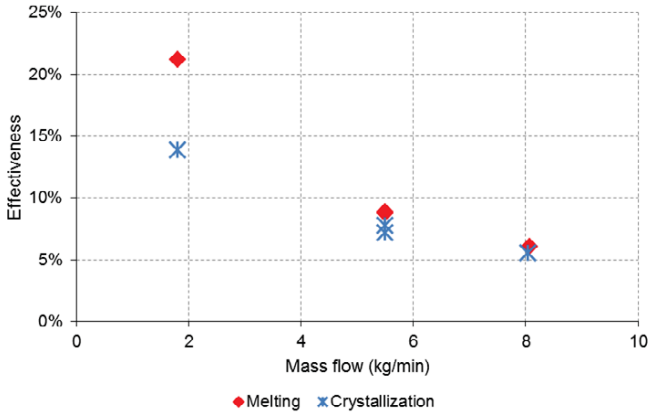

Fig. 10: Mean value of the effectiveness during the phase change

6. Model validation and simulation

A simulation model for the fin and tubes heat exchanger was created in COMSOL Multiphysics. A first model validation was carried out for one heating and one cooling cycle. Material properties of D-mannitol were chosen according to Tab. 1. Latent heat of the PCM was introduced to the model based on measured data from the DSC. Natural convection in liquid part of the PCM was not taken into account (neither between the fins nor in the PCM layer under the fins). The envelope and the insulation of the heat exchanger were not taken into account. Losses to the ambient were introduced as constant heat flow with values taken from the measurements according to Fig. 2. A comparison of the oil as well as PCM temperatures for the heating and the cooling case are shown in Fig. 11.

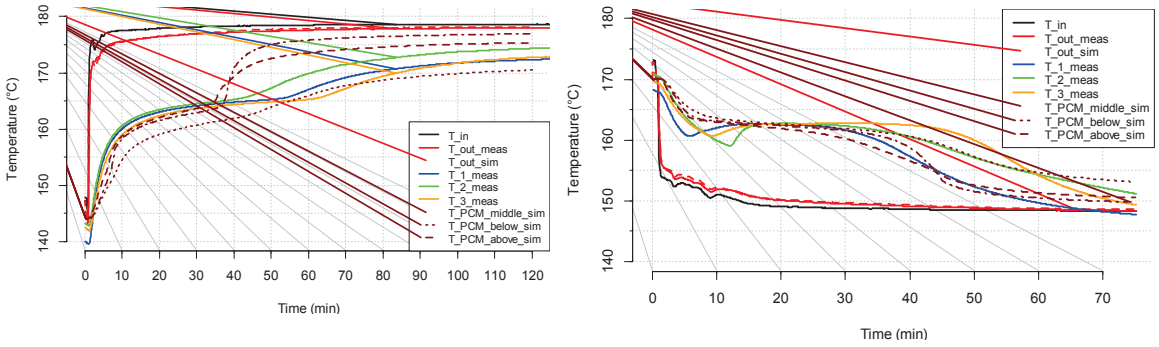

Fig. 11: Validation of the simulation model at a mass flow rate of 5.5 kg min^{-1}: comparison of simulated and measured temperatures for heating (left) and cooling (right)

The highest differences are visible in the PCM temperatures. One uncertainty is the latent heat of the D-mannitol due to its degradation. Measurements of the latent heat were carried out with the fresh material and after having finished all experiments. This experiment taking for validation was done at some time in between the two DSC measurements. Thus the value for the latent heat of the fresh material will be too high and the one of the degraded PCM will be too low. The DSC data taken is the one of the fresh material, thus latent heat in this simulation might be overestimated. The simulation shows that the height of the locations where temperature is measured is important. In the measurements it cannot be assured if the PCM temperature was measured exactly at a height in the middle of the tubes. The simulation shows that moving the temperature sensor 1 cm up or down can lead to temperature differences of up to 5 K.

In the cooling case the melting temperature of the PCM was shifted downwards 2.5 K. The nucleation is not modeled. Still the PCM temperatures seem to fit better to the measurement during cooling than during heating.

Although there are still uncertainties in model validation, the model reproduces the main characteristic of the fin and tubes heat exchanger with D-mannitol. That is why the model was already used to compare the heating and cooling process under similar circumstances to each other.

The same model used for validation was used in a simulation, but this time no losses to the ambient were introduced. Thus all the heat from the heat transfer fluid was transferred via the heat exchanger to the PCM. The envelope was not taken into account in this simulation. Fig. 12 shows the results of the UA-value. Here the result during crystallization is higher than during melting. As natural convection was not taken into account, thermal conductivity is crucial for the heat transfer. During melting it is the thermal conductivity in liquid PCM, during crystallization it is the one in solid state. Thermal conductivity in solid state is two times higher than the one in liquid state. This characteristic could not be shown in the measurements until now due to the above described reasons. Thus, the model helps to analyze the heat transfer processes in the heat exchanger in more detail and will be used for further analysis and optimization.

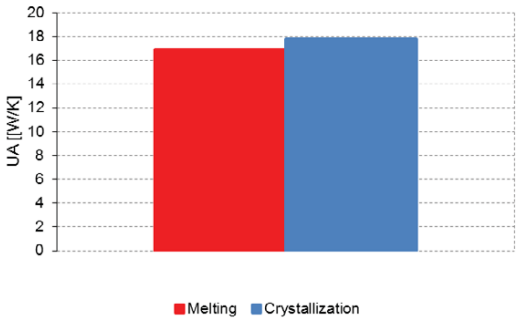

Fig. 12: Comparison of UA-value during melting and crystallization from a simulation without thermal losses to the ambient

7. Conclusion and outlook

A fin and tubes heat exchanger with D-mannitol was experimentally characterized. A simulation model was created and a first validation was carried out.

During experimental characterization the thermal losses to the ambient were very high in relation to the heat transfer of the heat exchanger itself. To reduce the losses and make the boundary conditions of different measurements more comparable a heating device will be installed around the heat exchanger in future. Thus ambient temperature will be raised and thermal losses reduced.

More temperature sensors will be installed in future experiments to determine the heat transfer more exactly. Inside the PCM more sensors are needed to determine temperature differences in the PCM as seen in the simulation. Especially differences in the height of the PCM are expected.

The strong degradation of D-mannitol in oxygen atmosphere leads to uncertainties during evaluation of the experiments and model validation. To reduce the degradation of D-mannitol the experiments should be carried out under controlled atmosphere. Alternatively a different PCM with a melting temperature between 100 and 250 °C that does not show degradation should be used.

When using D-mannitol as PCM a larger fin distance than 5 mm seems to be reasonable to increase charging power by the influence of natural convection. How much natural convection influences charging power at higher fin distance shall be examined by further tests and simulation. In general, the effect of different fin distances for charging and discharging process shall be tested by using the simulation model and further measurements.

The simulation model has to be improved. The envelope and the insulation will be taken into account to reduce deviations to the measurements. Additionally natural convection will be implemented in order to determine its effect also with the help of the simulation model. By improving the measurements with the means stated above, it will be possible to carry out the model validation with more accuracy.

To increase the thermal power of the PCM heat exchanger it might be reasonable to fabricate it out of a material with higher heat conductivity than stainless steel, e.g. aluminum. To ensure that the whole PCM will be melted or crystallized in convenient time, the layer of PCM below the fins should be reduced, thus the fins should reach the bottom plate of the heat exchanger. Further geometry parameters as fin thickness, piping and outer dimensions will be optimized by the help of the simulation model.

8. Acknowledgment

The authors are grateful to the German Federal Ministry for Economic Affairs and Energy for funding the work of this project (0325549A) and the Project Management Jülich for the administrative support.

9. References

Castell, A., Belusko, M., Bruno, F., Cabeza, L.F., 2011. Maximisation of heat transfer in a coil in tank PCM cold storage system. Applied Energy 88 (11), 4120–4127.

Deborah A. Kaminski, Michael K. Jensen, 2011. Convection Heat Transfer. Chapter 12, in: Deborah A. Kaminski, Michael K. Jensen (Ed.), Introduction to Thermal and Fluids Engineering, Updated Edition.

Godin, A., 2015. Sugar alcohols properties and performances. FP7 project - SAM.SSA, Workshop and Onsite Demonstration, 03/2015, Bilbao.
http://samssa.eu/fileadmin/samssa/downloads/workshop/presentations/Session-1_Alexandre-Godin_Sugar_alcohols_properties_and_performances.pdf. Accessed 26 September 2016.

Mehling, H., Cabeza, L.F., 2008. Heat and cold storage with PCM. An up to date introduction into basics and applications. Springer, Berlin Heidelberg.

Richter, F. Die physikalischen Eigenschaften der Stähle "Das 100-Stähle-Programm". Teil I: Tafeln und Bilder, Mülheim a. d. Ruhr.
https://www.tugraz.at/fileadmin/user_upload/Institute/IEP/Thermophysics_Group/Files/Staehle-Richter.pdf. Accessed 20.7.16.

Solé, A., Neumann, H., Niedermaier, S., Martorell, I., Schossig, P., Cabeza, L.F., 2014. Stability of sugar alcohols as PCM for thermal energy storage. Solar Energy Materials and Solar Cells 126, 125–134.

Conference Proceedings

EuroSun 2016

Palma de Mallorca (Spain), 11 – 14 October 2016

Microclimate Mitigation by means of Thermal-energy Storage: A case study in Central Italy

Anna Laura Pisello[1,2], Veronica Lucia Castaldo[1], Cristina Piselli[1], Ilaria Pigliautile[1], Luisa F. Cabeza[3], Gabriel Pérez[3] and Franco Cotana[1,2]

[1] CIRIAF - Interuniversity Research Center, University of Perugia, Perugia (Italy)

[2] Department of Engineering, University of Perugia, Perugia (Italy)

[3] GREA Innovació Concurrent, Universitat de Lleida, Lleida (Spain)

Abstract

Urban design and local boundary conditions have been detected to significantly affect the local microclimate and, therefore, the environmental quality of urban areas. In this view, the purpose of the present work is to investigate the local microclimate variation in historic districts with respect to the surrounding areas situated in the same temperate climate zone. To this aim, four areas around a historical city center in Italy were monitored during summer 2015 and investigated through microclimate simulation in summer and winter conditions. After the experimental monitoring, that allowed to characterize the main microclimate parameters of each case study area, a calibrated numerical analysis was performed in order to assess the Urban Heat Island (UHI) intensity of the historical district and the implementation passive mitigation techniques. Therefore, the effectiveness of thermal storage solutions as innovative UHI mitigation technique was studied by simulating the implementation of Phase Change Materials (PCMs) within (i) the buildings' walls and (ii) the outdoor pavement of the historic neighborhood. Thermal benefits due to the application of phase change materials were detected both in summer and winter. In summer, the high-capacity PCMs integrated pavement is able to reduce the outdoor air temperature by a maximum of about -0.3 K. On the other hand, in winter, the increased thermal storage potential seems to mitigate the nighttime cooling.

Keywords: *Urban Heat Island, Experimental monitoring, Numerical analysis, Microclimate simulation, Phase Change Materials*

1. Introduction and Motivation

Local microclimate can be significantly altered due to the complex interaction between microclimate parameters and the thermal-optical properties of urban and buildings' surfaces. Urban Heat Island (UHI) represents one of the main microclimate phenomenon able to generate discomfort in urban areas due to the high building density, lack of vegetation, reduced surfaces sky view factor, and convective mixing (Santamouris et al., 2015). Moreover, more than half of the world's population is living in urban settlements. Therefore, the necessity to design efficient, sustainable, and healthy built environments is becoming a crucial issue for both designer and urban planners (Nikolopoulou et al. 2001).

Many UHI mitigation strategies have been proposed over the course of the years, such as green and cool materials (Akbari et al., 2016; Galli et al., 2013; Santamouris, 2014) and tested through experimental and numerical analysis (Allegrini et al., 2015). On the contrary, the use of thermal storage technologies for such purpose (Navarro et al., 2016) as a further outdoor microclimate mitigation strategy is still not very well investigated. However, PCM doped infrared reflective coatings were proved to present lower surface temperatures than common and cool coatings of the same color (Kolokotsa et al., 2013). In particular, peak temperature differences occurred between PCM and common or cool coatings from 7:00 and 10:00 a.m. In this view, some works studied the performance of roofs with PCMs and cool materials to mitigate UHI

doi:10.18086/eurosun.2016.03.05 Available at http://proceedings.ises.org

effect. For instance, Roman et al. (2016) performed different thermal energy simulations of cool roof and PCM based roof with varying climatic zones within the United States. In general, increased albedo led to better performance in terms of UHI effect reduction. However, PCM roof showed a heat flux from roof surface to the surrounding environment of 40 % lower than the cool roof technology. By using experimental tests, Chung and Park (2016) analyzed PCM doped cool tiles for roof applications in an artificial environment and showed a decrease of surface temperature and air temperature in the chamber in summer conditions, while an increase of air temperature in winter conditions. Therefore, PCM doped roof reduced the heating penalty of the cool paint in winter. Similarly, Lu et al. (2016) measured the surface temperature and heat flux of a coupled PCM and cool roof in Tianjin of China, which showed a significant effect in decreasing temperature and heat flux peaks. Also heat-harvesting pavements were proposed to mitigate UHI phenomenon in urban environments (Qin, 2015). They seemed to be capable to stay cool and to harness renewable energy. However, such prototypes require further tests on the power output, durability, and lifetime. Moreover, the performance of cool and heat storage pavements was simulated by Qin and Hiller (2014). Increasing pavements albedo was demonstrated effective to suppress the sensible heat and mitigate the UHI effect, while raising the pavement thermal inertia decreased the sensible heat during the daytime but increased this factor at nighttime. On the other hand, no significant results have been found in the assessment of PCMs doped walls for the Urban Heat Island phenomenon mitigation.

Building upon the above mentioned considerations, in this work the local microclimate differences between four areas with different urban configuration and development located in the same climate zone were taken into account. In particular, the historical district of the city of Perugia (Italy) was found to be characterized by a non-negligible Urban Heat Island intensity. Therefore, the capability of innovative thermal storage solutions, i.e. phase change materials, to mitigate UHI phenomenon in the historic district when integrated in different buildings' elements and urban outdoor materials, i.e. external building walls and pavement, was evaluated by means of microclimate calibrated simulation.

2. Materials and Methods

The research methodology included two main steps. Firstly, the experimental monitoring campaign of four case study areas with different building density, configuration, and vegetation level, i.e. an historical urban district, a more recent urban neighborhood, and two suburban-rural areas, was carried out in the same city, i.e. Perugia (central Italy) during summer 2015. The local microclimate of each area was assessed by means of outdoor microclimate stations. Therefore, the numerical modeling of the historic district (Fig. 1a) was performed to evaluate the benefits achievable in terms of local microclimate by applying innovative passive cooling strategies in order to mitigate the UHI phenomenon.

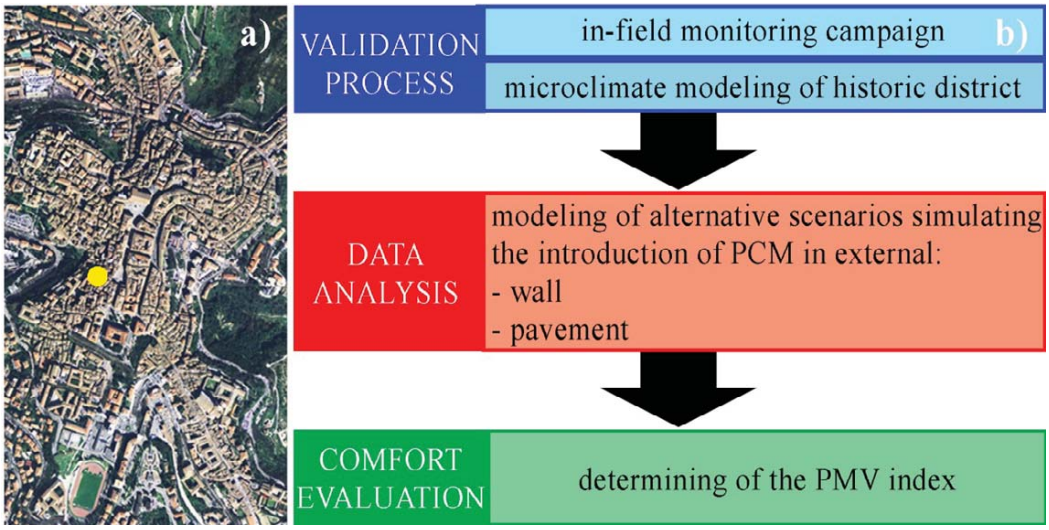

Fig. 1: (a) Position of the modeled area within the historic center of Perugia and (b) scheme of the adopted methodology

The microclimate simulation was carried out by using ENVI-met V4 in order to assess the effectiveness of thermal storage solutions for mitigating the Urban Heat Island phenomenon by preserving the environmental quality of the urban area and the thermal-visual comfort of the pedestrians. More in detail, the integration of Phase Change Materials in (i) the walls of the monitored building and (ii) in the outdoor paving was simulated in order to evaluate the impact of increased thermal capacity of the materials on the local microclimate, both in summer and winter conditions. To ensure the reliability of simulation results, a preliminary phase of validation was conducted. The daily weather profiles were selected from the typical July (July, 15th) and typical January (January, 15th) provided by IGDG TMY (Typical Meteorological Year) for the city of Perugia, built on 1951-1970 period of record (U.S. Department of Energy, 2014). Finally, the simulation results were analyzed in terms of the thermal comfort index PMV (Predicted Mean Vote) (ENVI-met 4, 2015; Fanger, 1972) to assess how the integration of PCMs could affect pedestrian perception of the local urban environment (Fig. 1).

2.1. Modeling and validation process

The simulated area in the historic district is an East-West oriented street, 40 m long with a width varying from 3 to 12 m along its length (Fig. 2). Moreover, between the eastern and western side there is a height difference of 5 m. Buildings in the street are characterized by thick stone walls and outdoor pavements are manly covered by bricks and plates made of *pietra serena* (except for the eastern side recently asphalted) (Fig. 2b), since it is located in the historical center of the city.

ENVI-met V4 was used for the numerical analysis, which is three-dimensional microclimate modeling system designed to simulate the surface-plant-air interactions with a resolution from 0.5 m to 10 m in space and from 1 s to 5 s in time (Huttner and Bruse, 2009). A realistic model of the area was developed and calibrated by using experimentally monitored data, according to the ASHRAE GUIDELINE 14-2002 (ASHRAE, 2005). In order to be representative of the real configuration, the 3D model has a square unit of 1x1 m and a geometrical rotation of 111° North out of the grid. Therefore, it is based on a 30x60x35 grid. The materials used to characterize walls, roofs, and pavements in the reference scenario were selected from the software database and their thermo-physical properties are summarized in Tables 1 and 2.

Fig. 2: (a) View of the street from the western side, (b) different kinds of pavement present in the area, and (d) localization in the plant of the monitoring probes

Tab. 1: Characteristics of the walls and roofs composing the reference scenario

Element	Albedo [-]	Emittance [-]	Specific heat [J/kg·K]	Thermal conductivity [W/m·K]	Density [kg/m^3]
Walls	0.30	0.90	840	0.86	930
Roofs	0.50	0.90	800	0.84	1900

Tab. 2: Characteristics of the different pavement profiles composing the reference scenario

Pavement profile	Albedo [-]	Emittance [-]	Volumetric Heat Capacity (upper layer) [J/m^3·K]	Heat Conductivity (upper layer) [W/m·K]
Brick Road	0.30	0.90	$2.00 \cdot 10^6$	1.00
Basalt Brick Road	0.80	0.90	$2.39 \cdot 10^6$	1.73
Asphalt Road	0.20	0.90	$2.25 \cdot 10^6$	0.90

The data for the calibration were collected through the monitoring campaign during summer 2015. A portable weather station was placed at 15 m height (Pisello et al., 2014) and two Tinytag temperature and relative humidity probes and data-loggers (Pisello et al., 2015) were installed at 2 m above the ground (Fig. 2c). As weather input for the model the following data were used:

- Initial wind speed: value collected from the weather station at 6 a.m., start time of the simulation;
- Wind direction: value prevailing during the three days of the monitoring campaign;
- 24 h air temperature and relative humidity forcing: data collected by the probe located on the South-oriented side (Fig. 2c, point B).

The simulation run for 24 h and the data compared for the calibration were those collected from the North-oriented probe (Fig. 2c, point A) and those extracted from its representative point within the model.

2.2. Modeling of alternative scenarios

Once calibrated the model, alternative scenarios to the reference one, named S0, were developed by analyzing the effectiveness of the application of PCMs at urban level for Urban Heat Island mitigation. Therefore, traditional materials were replaced with high-thermal capacity ones as follows:

- High-thermal capacity walls, i.e. scenario "wall";
- High-thermal capacity pavements, i.e. scenario "pavement".

The innovative materials, were selected to be realistically implemented in the case study area, which presents architectural constrains since it is located inside the historical center of the city. In particular, the thermal-storage capability of buildings' envelope was improved through the application of PCM wallboards. Moreover, pavement's thermal properties were implemented based on the real necessity to substitute the current asphalted area. Since PCMs dynamic characteristics and behavior cannot be modeled in ENVI-met V4, their modeling was simplified by increasing the materials heat capacity, as summarized in Table 3. Therefore, no specific PCMs' melting temperature was defined in this analysis. Nevertheless, in the investigated climate, PCMs with melting temperature from 20°C to 25°C are recommended in summer applications for this increase in heat capacity to happen.

Tab. 3: Characteristics of the components modified in each mitigation scenario

Scenario	Element	Mitigation technique	Properties
wall	Walls	Introduction of PCMs	Specific Heat: 1620 J/kg·K
pavement	Pavement	Introduction of PCMs	Volumetric heat capacity: $3.6 \cdot 10^6$ J/m^3·K

The three scenarios, i.e. S0 and the alternative scenarios, were simulated during a representative summer and winter day in the climate context of Perugia, Italy, by using as weather input the TMY weather files for the months of July and January, respectively.

2.3. Outdoor thermal comfort analysis of mitigation scenarios

In order to evaluate the effectiveness of the proposed mitigation strategies, the data obtained as output in the numerical simulation were analyzed in terms of microclimate improvements in the surrounding outdoor area.

The following parameters were considered: air temperature, relative humidity, reflected solar radiation, mean radiant temperature, and the PMV at the pedestrian level (Fanger, 1972), for the outdoor comfort of pedestrians. PMV was analyzed through the PMV Model implemented in ENVI-met (ENVI-met 4, 2015), which is the human thermal comfort model mostly used for indoor applications. In fact, it was originally developed for steady-state indoor situations, but it can also be applied, with limits, to outdoor situations by extending the energy flux related parts of the model with solar and long-wave radiation and allowing wind speeds above an indoor room situation. A comparison between data obtained in the reference and alternative scenarios was performed by analyzing the variation in time during the day of the above mentioned environmental parameters. Time series were extracted at 1.5 m from the ground in two different points selected because of their different characteristics (Fig. 3).

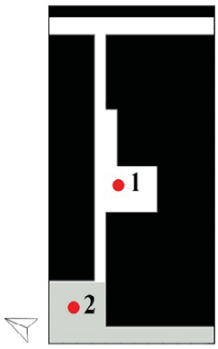

	Location	SVF	Time range when reached by direct solar radiation
Point 1 [x=12, y=28, z=5]	within the urban canyon, above the historical pavement	0.15	12:00-2:00 p.m. in summer, never in winter
Point 2 [x=5, y=8, z=1]	on the western part of the street, above the area originally asphalted	0.51	3:00-8:00 p.m. in summer, never in winter

originally asphalted area

Fig. 3: Positions of the points selected to extract data at pedestrian level

3. Results and Discussion

3.1. Model calibration

The statistical and graphical approach was carried out for the model calibration according to the ASHRAE GUIDELINE 14 (ASHRAE, 2005). The calibration accuracy was evaluated in terms of two statistical indexes, i.e. *Mean Bias Error* (MBE) and *Root Mean Square Error* (RMSE) (ASHRAE, 2005), as reported in Table 4. The maximum gap in terms of both air temperature and relative humidity is reached during the hottest hours of the day, when the software tends to overestimate the outdoor microclimate parameters. According to the obtained results, the model can be considered representative of the real area with good approximation. Therefore, it can be used to simulate which could be the improvements in the outdoor microclimate of the zone due to the application of the selected mitigation strategies.

Tab. 4: Calibration parameters results

Parameter	MBE	RMSE
Air Temperature	0.82 K	1.05 K
Relative Humidity	2.21 %	2.96 %

3.2. Summer analysis

Observations on the experimental monitoring carried out during summer 2015 in the different locations revealed a significant nighttime UHI phenomenon in the two monitored urban areas, with peaks of 2 K and 5 K temperature difference in the recent urban neighborhood and the historical district, respectively, compared to the suburban green area.

Therefore, the alternative scenarios were simulated to assess the possible benefits achievable from the implementation of phase change materials in the built surfaces, i.e. walls and paving, as mitigation technique. Summer results showed the major contribution of the high-thermal capacity pavement, i.e. scenario "pavement". In detail, the high-capacity PCMs integrated concrete pavement is able to reduce the outdoor air temperature by a maximum of -0.31 K in the summer day in point 2 (Fig. 4b). However, in point 1 the high thermal capacity soil effect is negligible in terms of air temperature reduction (Fig. 4a). In fact, at the point

with higher Sky View Factor (SVF) the peak air temperature is higher than in point 1 and it is detected two hours before the other one (at 1:00 p.m. instead of 3:00 p.m.). The reason is the different relation between these points and the built environment and the different time-period when they are exposed to direct solar radiation: just two hours for point 1 (from 12:00 p.m. to 3:00 p.m.) and five hours for point 2 (from 3:00 p.m. to 8:00 p.m.). Moreover, point 2 is located above the ground surface covered by asphalt in the reference configuration and, therefore, the effect of the materials' thermal properties improvement is higher. On the contrary, point 1 seems to suffer from the presence of solar radiation, both direct and diffuse, since it is subjected to higher mutual reflections of short way radiations from the surrounding structures. On the other hand, the scenario where increase of specific heat in walls is applied, i.e. scenario "wall", negligible effect is found in both point 1 and 2 during the daytime (Fig. 4). However, slightly better values are reached during the night in both points and in both scenarios, leading to differences up to -0.13 K and -0.26 K (6.00 p.m.), compared to S0, for "wall" scenario in point 1 and 2, respectively. These night-time lower temperature values are due to the less contribution of the built surfaces in the thermal balance determined by lower surfaces' temperatures. As regards the relative humidity trend, it is strictly connected to the one of the air temperature and no significant differences.

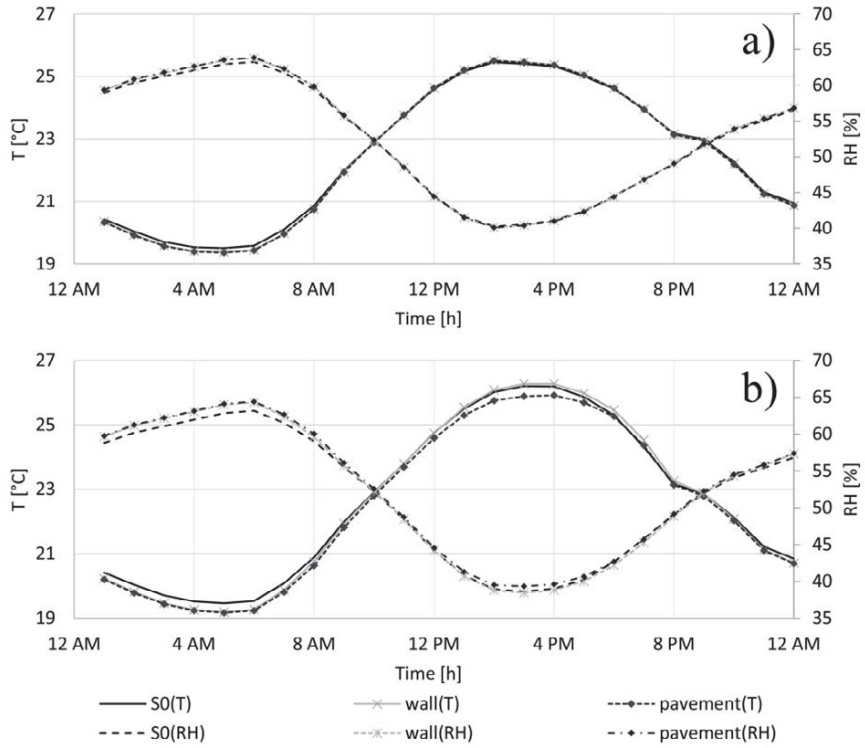

Fig. 4: Simulated air temperature and relative humidity hourly profiles in (a) point 1 and (b) point 2 in the different scenarios during the summer day

The reflected solar radiation and the mean radiant temperature were also analyzed (Fig. 5). It is interesting to notice that the trend of the MRT assumed in point 2 shows two peaks (Fig. 5b), differently from point 1 showing just one peak (Fig. 5a). This is due to the presence of direct solar radiation that occurs at different times in the two selected locations. In point 1, the peak coincides with the maximum values of reflected solar radiation (around 1:00 p.m.), while in point 2, a first relative peak is detected due to the maximum value of the reflected radiation and an additional one is achieved at 3:00 p.m., when the point is reached for the first time from the direct radiation. Conversely from the previous results, negligible differences between the mitigation scenarios and S0 are found in terms reflected solar radiation in point 2, while a significant increase is found in "pavement". Moreover, an increase of MRT is found in "pavement" with a maximum of +2.18 K at 3:00 p.m. and +2.28 K at 2:00 p.m. in point 1 and 2, respectively.

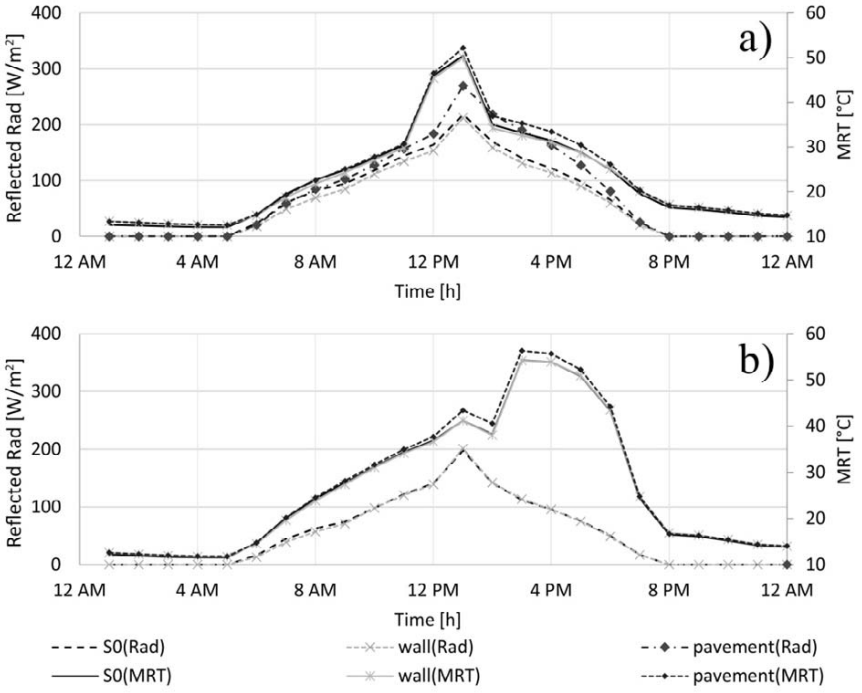

Fig. 5: Simulated mean radiant temperature and reflected solar radiation hourly profiles in (a) point 1 and (b) point 2 in the different scenarios during the summer day

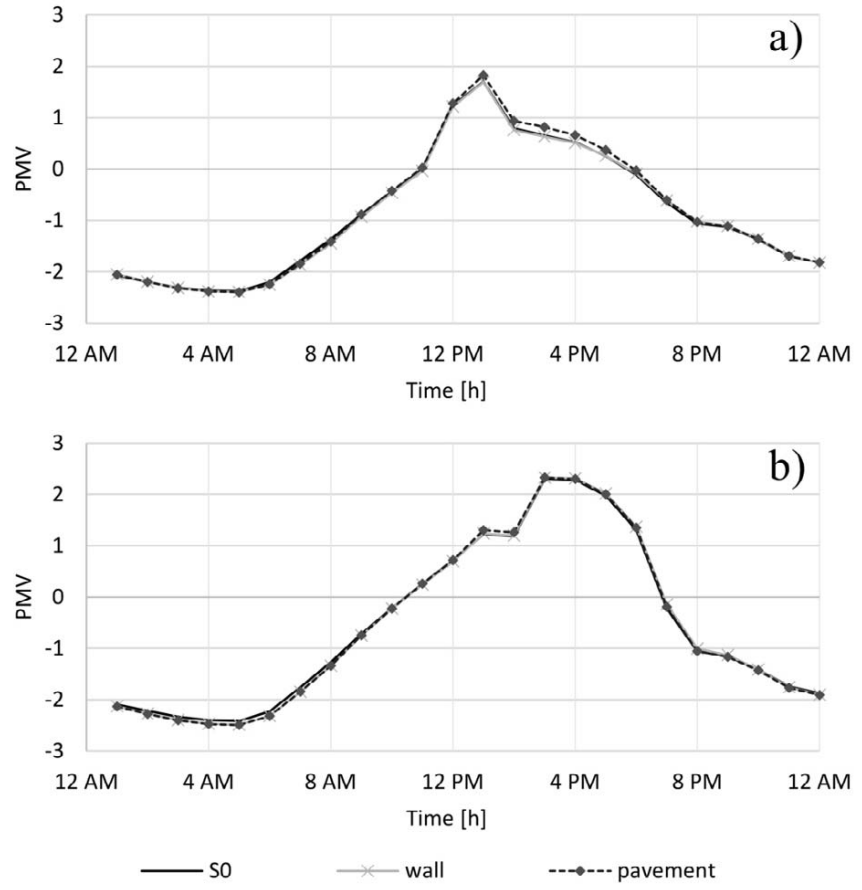

Fig. 6: Comparison between all the simulated scenarios in terms of PMV daily trend at pedestrian level in (a) point 1 and (b) point 2 during the summer day

As regards the pedestrians' comfort analysis (Fig. 6), the PMV was evaluated by imposing a clo (static clothing insulation) equal to 0.5. The resulting PMV values vary from a minimum of about –2.4, achieved before the sunrise, and a maximum of +1.8 and +2.3 (scenario "pavement") for point 1 and point 2, respectively. However, negligible variations in terms of PMV are found between the different scenarios, due to the small temperature difference.

3.3. Winter analysis

Although the proposed mitigation techniques were proposed to improve the outdoor microclimate conditions of the selected area during the hottest season (in order to mitigate the Urban Heat Island phenomenon), their effect during winter was also analyzed. The aim is to evaluate if the thermal comfort could be enhanced also in the cold season.

During the winter day, the increased thermal storage potential of the built surfaces leads to the mitigation of the night cooling (Fig. 7). Air temperature data extracted in point 2 (i.e. SVF = 0.51) are subjected to greater variations compared to the ones in point 1 (i.e. SVF = 0.15). In fact, the outdoor air temperature in point 2 increases up to +0.23 K and +0.32 K in scenario "wall" and "pavement", respectively, compared to S0 (Fig. 7b). On the other hand, lower improvements are detected in terms of air temperature from 11.00 a.m. to 4.00 p.m. All in all, scenario "pavement" seems to be the most effective strategy in winter conditions, when increasing the outdoor air temperature and, therefore, reducing the relative humidity.

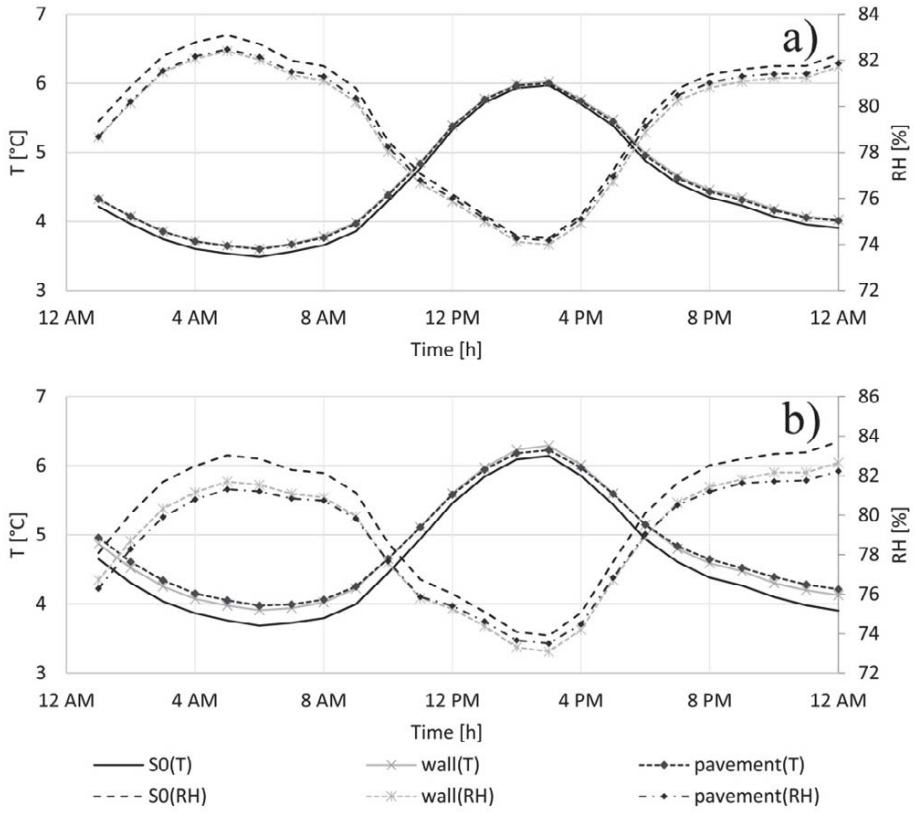

Fig. 7: Simulated air temperature and relative humidity hourly profiles in (a) point 1 and (b) point 2 in the different scenarios during the winter day

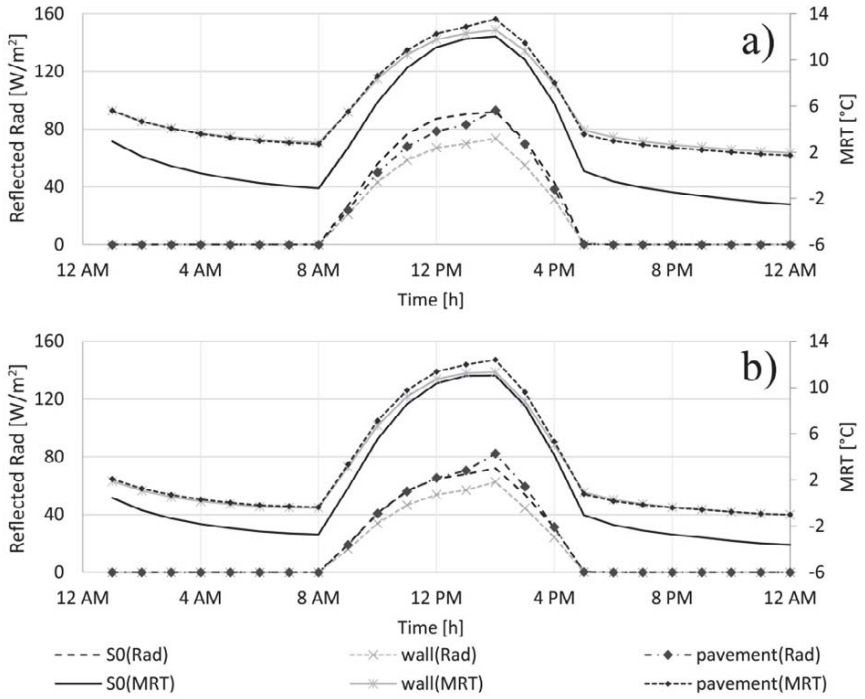

Fig. 8: Simulated mean radiant temperature and reflected solar radiation hourly profiles in (a) point 1 and (b) point 2 in the different scenarios during the winter day

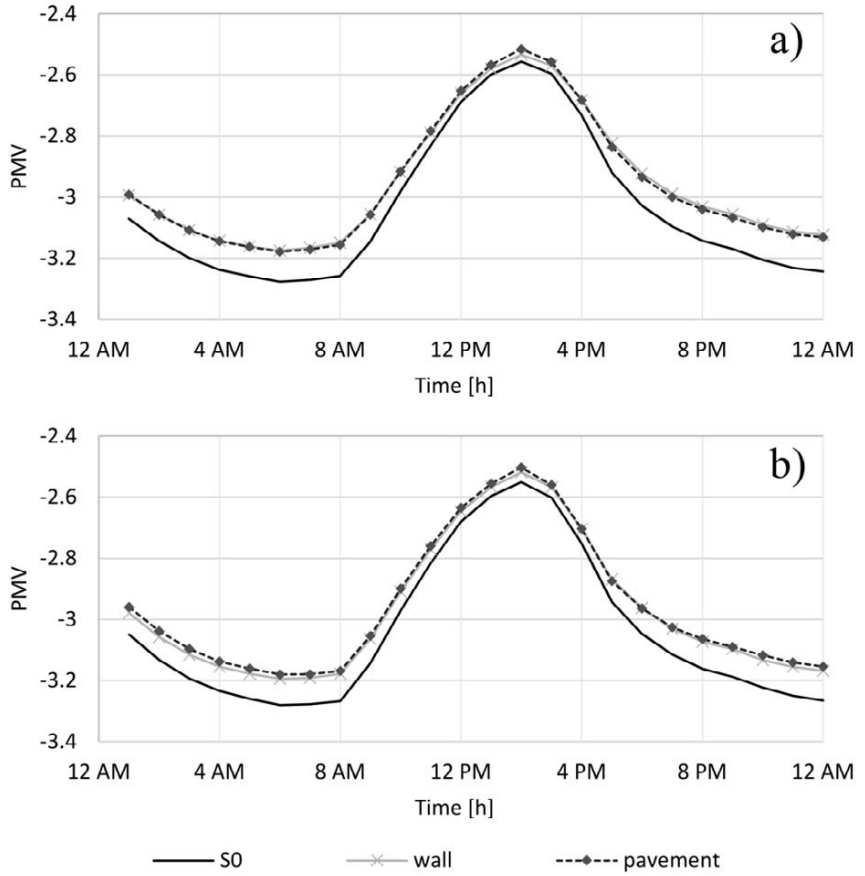

Fig. 9: Comparison between all the simulated scenarios in terms of PMV daily trend at pedestrian level in (a) point 1 and (b) point 2 during the winter day

Opposite behavior was detected in terms of mean radiant temperature, since greater modifications were obtained in point 1, the one presenting the lower value of SVF (Fig. 8). In fact, during the day both the points are not reached by direct solar radiation, due to the lower height of the winter sun, and, therefore, the effect of mutual reflectance between built surfaces has a stronger impact on the MRT. In general, the increased surfaces' heat capacity is able to significantly increase the MRT in the two analyzed points, with a slightly greater performance of pavement's included PMCs. In particular, after the sunset (i.e. from 5:00 p.m.) the effect of the applied mitigation actions provides a MRT increase up to +4.47 K and +2.60 K for "wall" and +4.25 K and +2.56 K for "pavement" at midnight, in point 1 and 2, respectively.

The PMV was evaluated also for winter conditions, by imposing a cloth resistance of 1.2 clo (Fig. 9). In general, improvements in terms of PMV are detected to be very low. However, it is interesting to notice that the PMV in the two mitigation scenarios is higher during the coldest hours of the day with respect to the reference scenario, showing a mitigation effect of the proposed strategies.

4. Conclusions

Microclimate variations due to local phenomena such as Urban Heat Island are nowadays very well acknowledged. This paper investigated the UHI in different areas belonging to the same climate zone with particular attention to the its intensity in a historic district. Therefore, the analysis of the impact of different boundary conditions on the local microclimate at neighborhood level was performed through coupled experimental and numerical analysis. The numerical analysis of the historical urban scenario, presenting the worst microclimate conditions, was performed in order to assess the effectiveness of thermal storage solutions, i.e. PCMs integration within building walls and outdoor pavements, as UHI mitigation measures in improving the thermal quality of the environment at neighborhood-urban scale.

The experimental campaign showed a significant nightly Urban Heat Island in the dense urban historic area compared to the other suburban areas. Therefore, the numerical analysis showed the non-negligible role of thermal storage strategies in mitigating outdoor air temperature both in summer and winter at local scale. In summer, the high-capacity PCMs integrated pavement appears to reduce the peak outdoor air temperature, while in winter PCMs are able to mitigate the nighttime cooling. Moreover, the MRT is improved under winter conditions when high thermal capacity materials are used.

The work demonstrated the importance of the relation between the built environment's characteristics and its microclimate. It was proved that the accurate analysis of the local boundaries conditions produces non-negligible findings supporting the realistic simulation of the urban environments.

References

Akbari, H., Cartalis, C., Kolokotsa, D., Muscio, A., Pisello A.L., Rossi, F., Santamouris, M., Synnefa, A., Wong, N.H., Zinzi, M., 2016. Local climate change and urban heat island mitigation techniques - The state of the art. J. Civ. Eng. Manag. 22 (1), 1-16.

Allegrini, J., Orehounig, K., Mavromatidis, G., Ruesch, F., Dorer, V., Evins, R., 2015. A review of modelling approaches and tools for the simulation of district-scale energy systems. Renew. Sust. Energ. Rev. 52, 1391-1404.

ASHRAE, 2005. ASHRAE's Guideline 14-2002 for Measurement of Energy and Demand Savings: How to Determine What was Really Saved by the Retrofit. American Society of Heating, Refrigerating and Air-Conditioning Engineers, Atlanta, GA.

Chung, M.H., Park, J.C., 2016. Development of PCM cool roof system to control urban heat island considering temperate climatic conditions. Energ. Buildings 116, 341-348.

ENVI-met 4. A holistic microclimate model, 2015. PMV/PPD. <http://www.model.envi-met.com/hg2e/doku.php?id=apps:biomet_pmv> (Last access: 2016/09/19).

Fanger, P.O., 1972. Thermal Comfort. Analysis and Application in Environment Engineering, ed. McGraw

Hill Book Company, New York.

Galli, G., Vallati, A., Recchiuti, C., De Lieto Vollaro, R., Botta, F., 2013. Passive cooling design options to improve thermal comfort in an Urban District of Rome, under hot summer conditions. Int. J. Eng. Technol. 5 (5), 4495-4500.

Huttner, S., Bruse, M., 2009. Numerical modeling of the urban climate – A preview on ENVI-MET 4.0. The seventh International Conference on Urban Climate, 29 June-3 July 2009, Yokohama, Japan. <http://www.envi-met.com/documents/papers/ICUC7_ModellingV4.pdf>.

Kolokotsa, D., Santamouris, M., Akbari, H., 2013. Advances in the development of cool materials for the built environment, ed. Bentham Science Publishers, Sharjah, U.A.E.

Lu, S., Chen, Y., Liu, S., Kong, X., 2016. Experimental research on a novel energy efficiency roof coupled with PCM and cool materials. Energ. Buildings 127, 159-169.

Navarro, L., de Gracia, A., Colclough, S., Browne, M., McCormack, S.J., Griffiths, P., Cabeza, L.F., 2016. Thermal energy storage in building integrated thermal systems: A review. Part 1. active storage systems. Renew. Energ. 88, 526-547.

Nikolopoulou, M., Baker, N., Steemers, K., 2001. Thermal comfort in outdoor urban spaces: understanding the human parameter. Sol. Energy. 70, 227-235.

Pisello, A.L., Cotana, F., Nicolini, A., Buratti, C., 2014. Effect of dynamic characteristics of building envelope on thermal-energy performance in winter conditions: In field experiment. Energ. Buildings 80, 218-230.

Pisello, A.L., Pignatta, G., Castaldo, V.L., Cotana, F., 2015. The impact of local microclimate boundary conditions on building energy performance. Sustainability 7 (7), 9207-9230.

Qin, Y., 2015. A review on the development of cool pavements to mitigate urban heat island effect. Renew. Sust. Energ. Rev. 52, 445-459.

Qin, Y., Hiller, J.E., 2014. Understanding pavement-surface energy balance and its implications on cool pavement development. Energ. Buildings 85, 389-399.

Roman, K.K., O'Brien, T., Alvey, J.B., Woo, O., 2016. Simulating the effects of cool roof and PCM (phase change materials) based roof to mitigate UHI (urban heat island) in prominent US cities. Energy 96, 103-117.

Santamouris, M., 2014. Cooling the cities – A review of reflective and green roof mitigation technologies to fight heat island and improve comfort in urban environments. Sol. Energy 103, 682-703.

Santamouris, M., Cartalis, C., Synnefa, A., Kolokotsa, D., 2015. On the impact of urban heat island and global warming on the power demand and electricity consumption of buildings - A review. Energ. Buildings 98, 119-124.

U.S. Department of Energy, Energy Efficiency and Renewable Energy, 2014. <http://apps1.eere.energy.gov/buildings/energyplus/cfm/weather_data3.cfm/region=6_europe_wmo_region_6/country=ITA/cname=Italy>, WMO Station Region 6: Italy, Perugia 161810 (IGDG).

Conference Proceedings

EuroSun 2016
Palma de Mallorca (Spain), 11 - 14 October 2016

Testing a new design of latent storage

Margarita M. Rodríguez-García[1] and Esther Rojas Bravo[2]

[1] Ciemat-Plataforma Solar de Almería, Almería (Spain)

[2] Ciemat-Plataforma Solar de Almería, Madrid (Spain)

Abstract

A modified spiral plate heat exchanger used as latent storage module for direct steam generation was proposed in the REELCOOP project. Under the failure of eight other phase change materials claimed in the literature as potential latent storage media, the phase change material used to meet the temperature range needed is the Hitec® salt. This paper presents the melting/ freezing tests performed with the Hitec® salt previous to its use in the storage module, the general scheme of the experimental facility constructed at the Plataforma Solar de Almeria, as well as the acquired know-how during the filling of the TES module and the commissioning of the facility.

Keywords: *Latent storage, phase change material, Hitec® salt.*

1. Introduction

One of the objectives in Prototype #3 of the REELCOOP project (7th Framework program of the European Union Ref N. 608466, www.reelcoop.com) is to drive an organic ranking cycle (ORC) using parabolic trough solar collectors with direct steam generation combined with a biogas boiler. In order to cover the gap between the full operation of the biogas boiler and the absence of solar radiation, a latent thermal energy storage was planned.

At Ciemat-Plataforma Solar de Almería, a modified spiral plate heat exchanger for its use as thermal energy storage (TES) has been selected for its test using Hitec® salt as storage medium. This salt has been tested both in nitrogen and argon atmospheres in order to demonstrate the feasibility of this material as phase change material (PCM).

The TES has been installed at the Plataforma Solar de Almería where some issues had to be solved previous to performing the tests. During the commissioning some problems had to be addressed: mainly the filling of the spiral thermal energy storage module and the presence of water remaining from a previous pressure test.

The present paper is organized as follows. The phase change material selected is presented in the next section and the tests performed with Hitec® salt are presented; section 3 presents the concept of the storage module. Section 4 describes the facility operation modes, while section 5 outlines the main issues solved during the commissioning. Finally, section 6 summarizes the main conclusions.

2. Phase change material selection

The working temperatures of the ORC machine in the REELCOOP Prototype#3 are in the range of 130 °C – 170 °C, and hence the material storing the thermal energy has to change phase in the same range of temperature.

From the several compounds suggested in the literature (Sharma and Sagara, 2005; Waschull et al., 2009) as good candidates for latent storage, D-mannitol, hydroquinone and salicylic acid were previously tested by Bayón (2015). Hydroquinone and salicylic acid presented a strong vapor emission upon melting, and D-

doi:10.18086/eurosun.2016.03.15 Available at http://proceedings.ises.org

mannitol displays supercooling during freezing, a decrease of the melting temperature and enthalpy together with a strong degradation under just few freezing/melting cycles. This degradation process of the D-mannitol can also be observed after melting/freezing cycling in both nitrogen and argon atmospheres (Rodríguez-García, 2016). Another four materials were also considered (X165, Galactitol, $CaCl_2 \cdot 2H_2O$, KNO_3-$Ca(NO_3)_2$ and $LiNO_3$-KCl) and all disregarded, either for being available at only specific shapes, or changing phase at a temperature a bit higher –around 190 ºC-, or having a thermochemical reaction more than a phase change, or becoming hydrated or for promoting pit corrosion)

The finally selected PCM was the Hitec® salt ($NaNO_3$-KNO_3-$NaNO_2$; 7/53/40 % w). The freezing point of this salt is 142 °C, presenting stability up to 535 °C. Other properties reported by Serrano-López et al. (2013) and Vignarooban et al. (2015) are stated in Tab. 1. This salt has been selected despite the relatively low enthalpy of fusion because its melting temperature fits in the selected temperature range, and because of its chemical stability when melting/freezing cycled.

Tab. 1: Thermal and physical properties of Hitec® salt.

Density, ρ, [kg/m^3] (T expressed in Kelvin)	Thermal conductivity λ, [W/mK]	Heat capacity Cp, [J/kgK]	Enthalpy of fusion ΔH, [kJ/kg]	Cost [$/kg]
ρ=2279.799- 0.7324·T	0.48	1560	83.6	0.93

Sohar, M.S. et al. (2013) describes that Hitec® salt is somewhat hygroscopic, containing absorbed moisture. Nitrite salt present in the Hitec® mixture can change to nitrate in O_2 presence, as shown in eq.1, increasing the fusion temperature of the mixture.

$$2NaNO_2 + O_2 \rightarrow 2NaNO_3 \qquad \text{(eq. 1)}$$

At the same time, the presence of water sustains the electrochemical corrosion mechanisms usually associated with aqueous systems, including galvanic corrosion. In order to avoid this, nitrogen has to be circulated through the TES module in the Hitec® channel.

The thermal behavior of Hitec® as phase change material, and its degradation after 50 melting/freezing cycling between 120 °C and 165 °C under inert atmosphere has been tested. Although nitrogen is cheaper than argon, it could somehow react with the molten salt, changing its chemical composition. According to this, both argon and nitrogen atmospheres have been considered for the tests.

The testing device is the one described by Rodríguez-García, M.M. et al. (2016). The melting/freezing cycles reproduce the "standard" daily operation conditions in a commercial plant. Understanding "standard" as a sunny day where the salt is melted sometime during the day (charging process), storing the energy for some hours and then giving up its latent energy to the water, i.e. the salt freezes, at a certain point of the day, e.g., the sunset (discharging process). In the tests, the salt is melted, keeping it liquid for 12 hours. After this period the salt provides its latent energy while it freezes, remaining frozen until the 24 hours are completed and a new cycle starts.

The fig. 2 (left) displays temperature/time curves of a 20 g Hitec® sample for the 1st and the 50th melting/freezing cycles under N_2 atmosphere. As can be seen the melting temperature interval for the first cycle has a well-defined plateau at 142 °C – 144 °C corresponding to the Hitec® salt melting that lasts around 10 minutes. The curve corresponding to the 50 cycles overlaps with the first cycle curve, and the melting temperature interval fits very well to the first cycle. The same can be said for the melting/freezing cycles under Ar atmosphere, as can be seen fig. 2 (right). As a result of these tests we can say that no degradation after melting/freezing cycling has been observed.

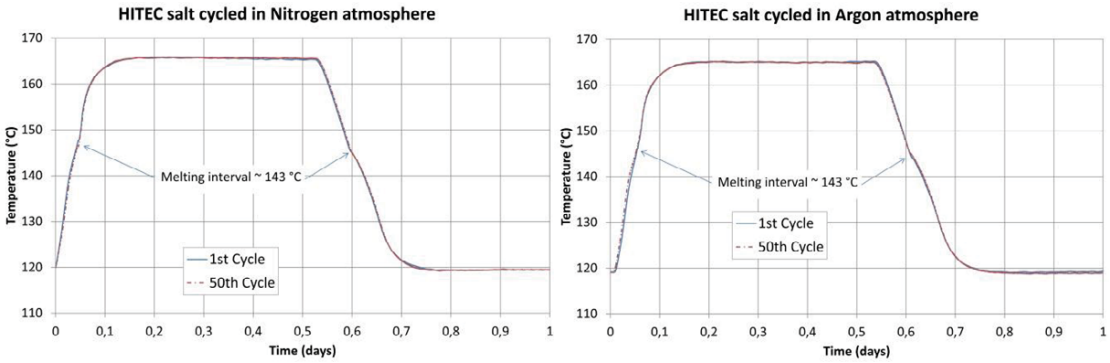

Fig. 1: Melting/freezing cycles of Hitec® in N_2 (left) and Ar (right) atmosphere.

3. Storage module

The proposed thermal energy storage design concept has a double spiral plate geometry, where one of the channels is filled up with the phase change material, remaining still along the time. Through the other channel runs the water in vapor or liquid state depending on the operation mode (charge of discharge). As stated by Rivas et al. (2012), this geometry presents a large energy exchange surface by unit volume providing an effective heat transfer, in spite of using storage medium with low thermal conductivity as most inorganic PCM have and that follows solid to liquid transitions to store the energy.

Patented by Rivas et al. (2011), the module tested in the REELCOOP project is an adaptation of a commercial spiral plate heat exchanger, due to limitations in budget and project time frame.

With 825 mm diameter and 1000 mm height, the spiral heat exchanger used as TES module has volume at the water/steam channel of 205 liters, and 230 liters at the molten salt channel. The effective heat transfer area is 29.3 m^2. The expected thermal capacity is 6 kWh, assuming a latent enthalpy of 50 kJ/kg, which is the figure we have obtained in the DSC tests we have previously performed (in previous literature a figure of around 84 kJ/kg can be found).

The TES module has been provided with thermocouples to follow the temperature evolution during the charging and discharging processes. Thermocouples were inserted through the four connecting flanges as represented in fig. 2a. Due to the internal structure of the TES module, with double spiral plates separated by separators, no additional thermocouples could be inserted at intermediate plates. Nitrogen injection lines were installed at the connecting flanges of the PCM channel (B1 and B2 in fig. 2a).

Once the instrumentation was settled at the TES module, this latter was installed adapting an already existing thermal storage testing facility, initially connected to the PSA Direct Steam Generation facility (DISS) but that was adapted, becoming independent of such a solar dependent facility. See Fig. 2b.

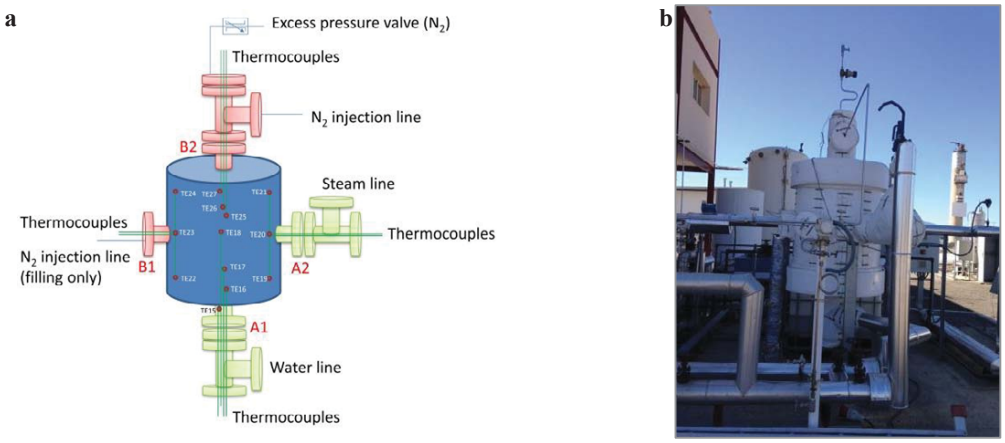

Fig. 2: a.- TES Temperature sensors and N_2 line. b.- Installation of the TES module at the PSA facilities.

4. Facility operation description

The used testing facility is designed to operate in both charging and discharging modes. Fig. 3a displays the charge mode, while the discharge mode is represented in fig. 3b. For the charging (discharging) mode a steam generator (water heater) provides saturated steam (warm water) to the storage module where energy is transferred to (from) the PCM. The storage module provides a mixture of steam and liquid water in an undetermined ratio or steam quality. This water-steam flow is later mixed with liquid water at known temperature and flow. The resulted water-liquid flow and its temperature is measured and the cycle is closed.

During the charge operation saturated steam at 150 °C enters the TES through the A2 conduction (see fig. 2a.) and, once the heat is transferred to the molten salt, saturated water at 140 °C exits the TES module through the A1 pipeline. During the discharge, the operation takes place in the contrary flow direction: saturated water at 130 °C enters the TES through the A1 conduction and, after evaporating in the TES, saturated steam at 130 °C. Tab. 2 summarizes the nominal operation conditions. Here it has been assumed that the pressure drop at the TES is 0.01 MPa.

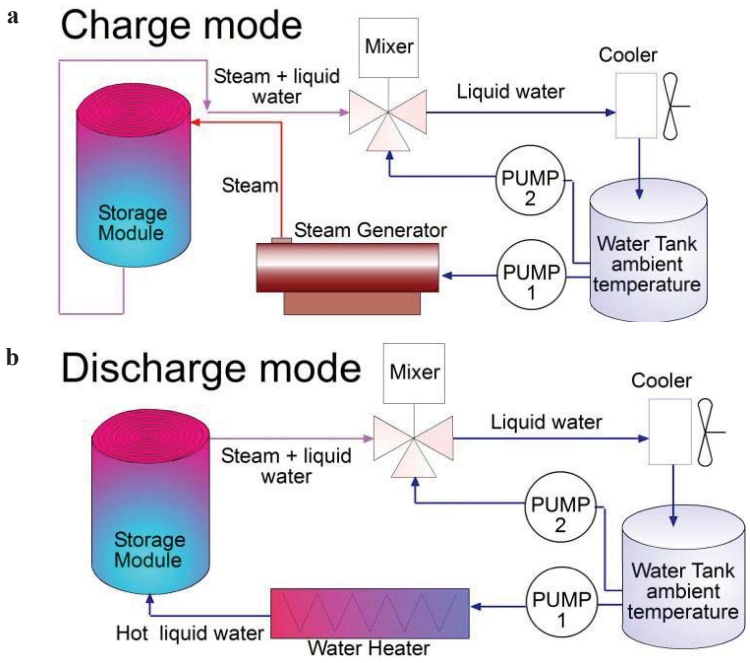

Fig. 3: Charge (a) and discharge (b) operation mode schemas of the test facility at Plataforma Solar de Almería

Tab. 2: Nominal operation conditions for the charge and discharge modes at TES module.

Charge mode				
	Temperature [°C]	Pressure [MPa]	Flow [kg/s]	Water phase
Inlet (A2)	150	0.47	0.04	Saturated steam
Outlet (A1)	140	0.36	0.04	Saturated water
Discharge mode				
	Temperature [°C]	Pressure [MPa]	Flow [kg/s]	Water phase
Inlet (A1)	130	0.27	0.05	Saturated water
Outlet (A2)	130	0.26	0.05	Saturated steam

5. Commissioning of the facility

During the filling of the TES module and the commissioning of the facility significant know-how has been acquired. The most remarkable aspects regarding commissioning of this experimental facility are explained in this section.

5.1. Water from the pressure test.

As stated in section 2, the presence of water and oxygen when using Hitec® as PCM should be avoided by blanketing the storage module with nitrogen. Blanketing should occur previous to the filling of the storage module with molten salt.

Nitrogen is injected on the top of the module (B2 in fig. 2a), exhausting it through the exit at the B1 connection. Since nitrogen is denser than air, the TES module will remain full of nitrogen when the B1 connection is closed by a screw cap and the upper flange in B2 is removed for the filling of the system.

The TES module should be preheated with steam at 150 °C in order to avoid any plug formation when the molten salt enters the system. During the preheating of the TES module unexpected water steam exhausted through the nitrogen venting system. This water was the remaining of the pressure test performed by the commercial company which sells the module previous to the delivery of the module to PSA and in accordance with the safety procedures any standard equipment that may work under certain pressure should follow. Nitrogen was injected via the B2 inlet (see fig. 2) passing through the complete spiral channel, and forcing the steam to move to the central upper exit B1 (see fig. 4a).

5.2. Filling the TES module with molten salt.

The spiral plate internal structure of the TES module makes necessary an external melting of the Hitec® salt previous to the filling of the module. Hitec® was melted in a separate furnace, provided with electrical resistances and a control that allows a safe melting of any salt and its release in the TES module. For this purpose, the flange at the top of the TES module was dismounted once the TES module had been innerted with nitrogen, allowing the molten salt charge

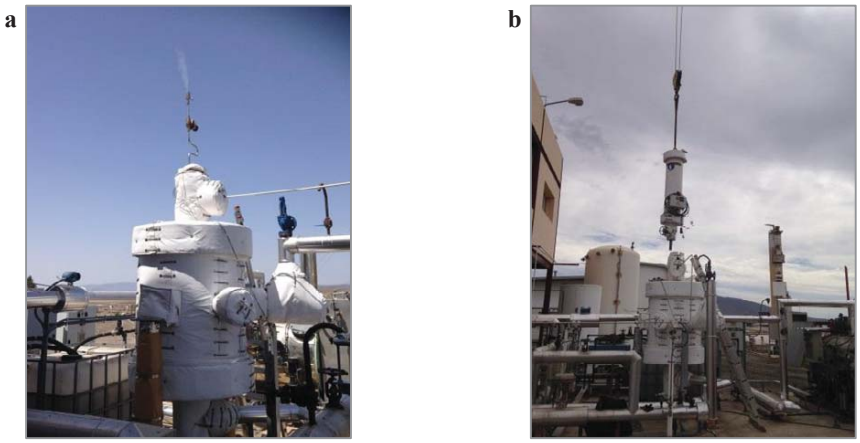

Fig. 4: a. Water steam exhausted through the nitrogen venting system. b. Filling of the TES with the external salt furnace.

6. Conclusions and future works

Candidate PCMs in the range of 130 °C to 170 °C have been studied. From the most promising ones proposed in the literature, hydroquinone and salicylic acid presented a strong vapor emission upon melting; and D-mannitol displays not only supercooling during freezing, but also a strong degradation after just 50 melting/freezing cycles. The commercial Hitec® salt has been selected because of its chemical stability and despite its relatively low enthalpy of fusion.

This salt is very hygroscopic, which can produce a change in the melting temperature, and forces to a previous drying of the TES module and a N_2 blanketing.

Due to the delay caused by the unexpected problems occurred during the commissioning, the expected testing procedure refinement and the evaluation of the thermal behavior are close future activities. The testing procedure to be followed is the one proposed at the SFERA project and named SFERA15T2#1 ('*HTF power curve in discharge/charge*'), case III (Rojas et al., 2011). This procedure allows establishing both discharging and charging curves working at different temperature/pressure pairs. From these curves it is possible to find out experimentally the real Biot number of the storage module, which may be important to validate the simulated behavior of the new design here implemented.

7. Acknowledgements

The authors would like to acknowledge the E. U. through the 7th Framework Program for the financial support of this work under the REELCOOP (Renewable Electricity cooperation) project with contract number: 608466, the DETECSOL project (Ref. ENE2014-56079-R) with ERDF funds, and the operation, instrumentation and maintenance departments at the PSA for their collaboration during the development of this work.

8. References

Bayón, R., Rojas, E., 2015. Characterization of organic PCMs for medium temperature storage. The Energy and Materials Research Conference, Madrid, February 2015.

Rivas, E., Rojas, E., Bayón, R., inventor, Ciemat, assignee. 2011 Aug. 11. Módulo de almacenamiento térmico basado en calor latente con altas tasas de transferencia de calor. Spanish patent P201131378.

Rivas, E., Rojas, E., Bayón, R., 2012. Innovative storage with PCM: Progress in the design of a new prototype. Proceedings of the SolarPaces Congress 2012, Morocco, September 2012.

Rodríguez-García, M.M., Bayón, R., Rojas, E., 2016. Stability of D-mannitol upon melting/freezing cycles under controlled inert atmosphere. Energy Procedia, Volume 91, 2016, Pages 218-225.

Rojas et al., 2011, Definition of standardized procedures for testing thermal storage prototypes for concentrating solar thermal plants. SFERA project. Last accessed: 09.2016. Available at http://sfera.sollab.eu/downloads/JRA/WP15/Deliverable15.2_StandardisedTestingProcedures.pdf

Serrano-López, R., Fradera, J., Cuesta-López, S., 2013. Molten salts database for energy applications. Chemical engineering and processing: Process intensification, Volume 73, 2013, Pages 87-102.

Sharma, S. D., Sagara, K., 2005. Latent heat storage materials and systems: a review. International Journal of Green Energy,vol. 2, pp. 1-56.

Sohal, M.S., Ebner, M.A., Sabharwall, P., Sharpe, P., 2013. Engineering database of liquid salt thermophysical and thermochemical properties. Idaho National Laboratory, INL/EXT-10-18297. Rev. 1.

Vignarooban, K., Xinhai Xu, Arvay, A., Hsu, K., Kannan, A.M., 2015. Heat transfer fluids for concentrating solar power systems – A review. Applied Energy, Volume 146, 2015, Pages 383-396.

Waschull, J., Müller, R., Römer, S., 2009. Investigation of phase change materials for elevated temperatures. Effstock09, Stockholm.

Conference Proceedings

EuroSun 2016
Palma de Mallorca (Spain), 11 - 14 October 2016

Energy efficient building cooling by combining a regenerative cooling system, a large TES and a phase change material cooling ceiling

Stephan Weismann[1], Felix Klinker[1], Helmut Weinläder[1], Dietrich Büttner[1]

[1] Bavarian Center for Applied Energy Research (ZAE Bayern), Würzburg (Germany)

Abstract

The Würzburg division of the Bavarian Center for Applied Energy Research (ZAE Bayern) moved into its newly-built research building, the Energy Efficiency Center, upon its completion in 2013. It is a highly innovative building and was designed as a living lab. The cooling system is highly efficient, incorporating a combination of Passive Infrared Night Cooling (PINC), thermal energy storage (TES) and newly-developed ceiling cooling elements with integrated phase change materials (PCM). The PINC system can achieve high energy efficiency ratios (EER) of approx. 10-20. The PCM in the cooling ceiling provides passive cooling during the daytime in the transition period. Active cooling is only required in summer. In practice, the large-scale thermal energy storage tank has provided cooling for periods even up to ten weeks. This paper presents the first results of the combined system (PINC, TES, and cooling ceiling) as well as some of the measures undertaken to optimize it, and ideas for further improvement.

Keywords: *passive infrared night cooling (PINC), phase change material (PCM), cooling ceiling, High-Level-Controller, thermal energy storage, energy efficiency ratio, monitoring*

1. Introduction

In 2010, a project was launched by the Energy Efficiency division of ZAE Bayern in Würzburg to design, finance and build a new headquarters for the expanding institute. This new building, the "Energy Efficiency Center" (EEC), incorporates the cutting-edge and energy-efficient building technologies, mainly developed by ZAE Bayern itself, and present information about their relevance and impact in an information center open to the public. This is described in details in Weismann et al. (2014). Not only are the current new technologies and systems used in the building monitored and improved, but the modular design of the structure enables experimental components and systems to be integrated into the building for testing and further development.

ZAE Bayern moved into the building in June 2013. The building automation system was gradually put into operation, initial improvements being made in the areas of heating, ventilation, cooling and, according to Reim (2016) in lighting as well.. The Energy Efficiency Center is being extensively monitoring within the framework of a project (MoniResearch).

doi:10.18086/eurosun.2016.03.04 Available at http://proceedings.ises.org

Fig. 1: South-west view of the Energy Efficiency Center in Würzburg. © ZAE Bayern, photo by Petra Höglmeier.

2. Cooling Concept

2.1 Passive Infrared Night Cooling

Building directives stipulated that the EEC needed two underground fire protection water tanks with a volume of 100 m^3 each. It was decided to additionally utilize them for cold water thermal energy storage. They are both connected to the building's water cooling circuits by means of heat exchangers.

Fig. 2: Underground fire protection water tank.

One tank is cooled by a conventional compression cooler (and used as a backup for PINC), the other is connected to the passive infrared night cooling system developed by ZAE Bayern. A schematic diagram of this system can be found in Fig. 3, more details are described in Rampp et al. (2013).

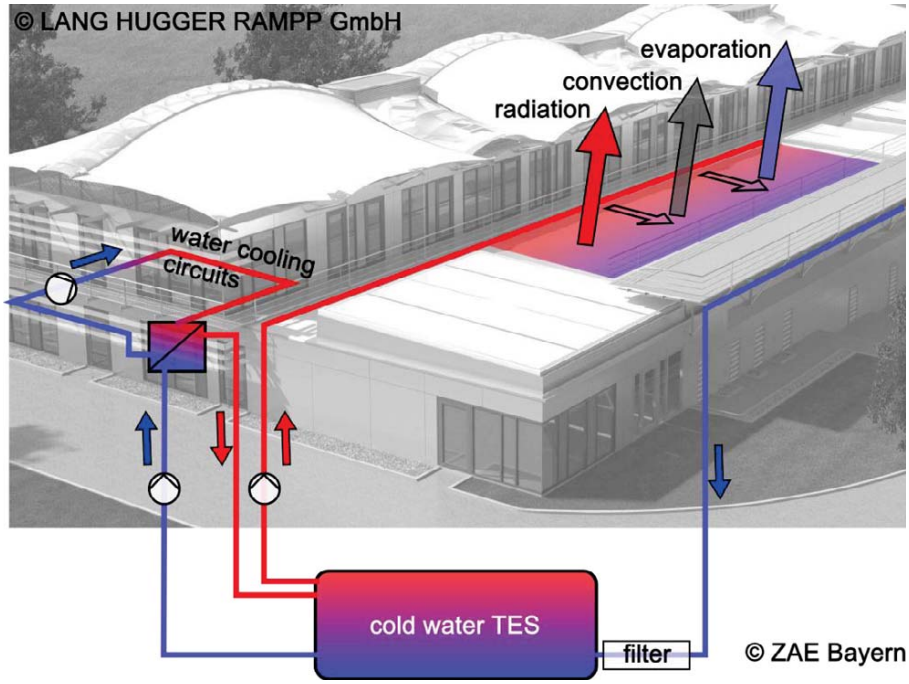

Fig. 3: The cooling load is connected to the TES by means of a heat exchanger. The water in the open circuit is re-cooled via infrared radiation, convection and evaporation when distributed over the surface of the roof when the temperature is sufficiently low (mainly at night).

Heat from cooling appliances in the laboratories and the PCM cooling ceilings in the offices is transferred into the TES by means of a heat exchanger. In order to re-cool the TES, the water is pumped onto the metal-sheeted area of the roof. Since it is a hydraulically open system, the water runs freely over the slightly sloped rooftop surface and ideally cools down to just under dew-point temperature. Heat is released via radiation exchange with the cold night sky, convection, as well as evaporation. The cooling power density is:

$$\dot{q} = \dot{q}_{rad} + \dot{q}_{conv} + \dot{q}_{ev}, \qquad \text{(eq. 1)}$$

The main part of the cooling power density is apportioned to the radiation exchange with the night sky which is given by

$$\dot{q}_{rad} = \varepsilon_w \cdot (\sigma \cdot T_w^4 - G), \qquad \text{(eq. 2)}$$

where ε_w is the emissivity of water, σ the Boltzmann constant, T_w the water temperature and G the radiation density of the long-wave radiation from the sky given by

$$G = \sigma \cdot T_{sky}^4, \qquad \text{(eq. 3)}$$

with the effective sky temperature T_{sky}.

It is recognizable in eq. 2 that there is a strong dependence between the cooling power density and the water temperature. Thus higher water temperatures lead to a higher cooling power density. Assuming typical water temperatures of about 18°C and the climate conditions in Würzburg, a cooling power density of around 60 to 120 W/m^2 roof area can be achieved at night even in summer.

The cooled water flows through rain pipes, a filter, and collects back in the cold water TES. Electricity is only needed to pump the water, so a high energy efficiency ratio (EER) can be achieved. As PINC is an open system, water evaporates and the loss is balanced out by rain water.

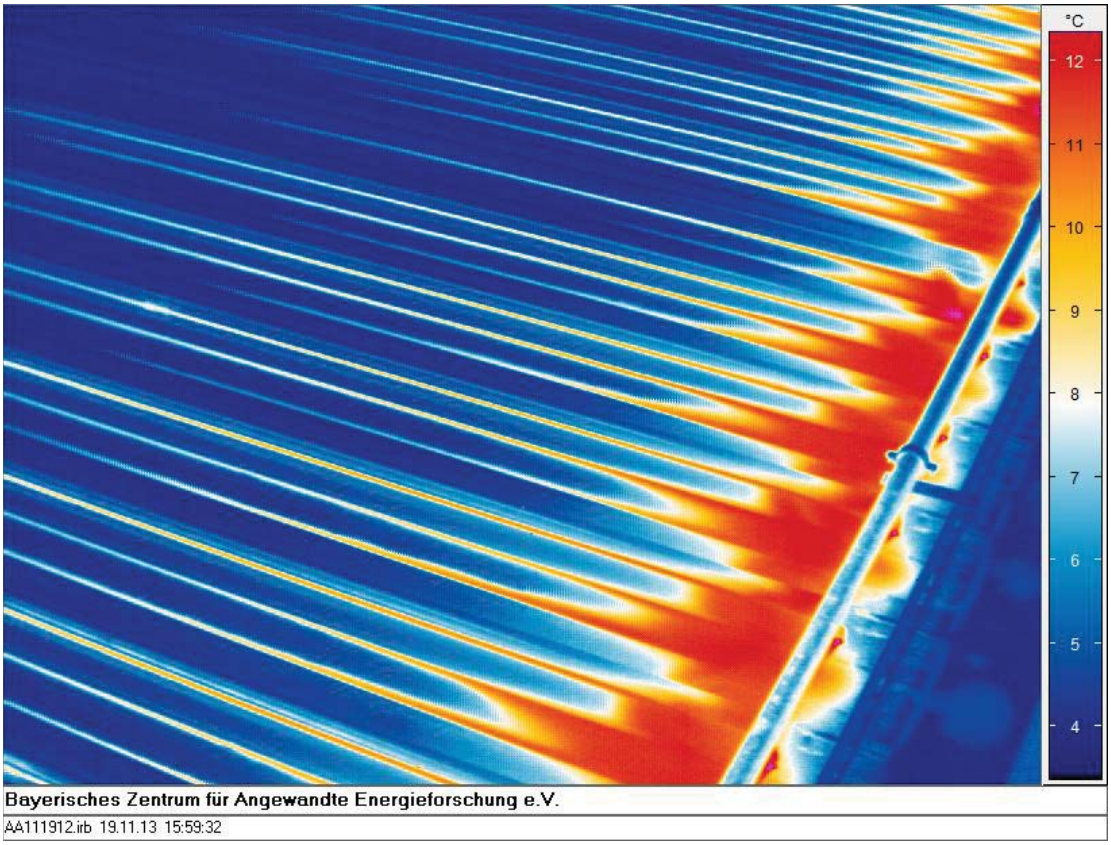

Fig. 3: Infrared image of the roof area used in the PINC system. On the right is the pipe which distributes the approx. 12 °C warm water over the roof surface. The water cools down over the roof to approx. 4 °C.

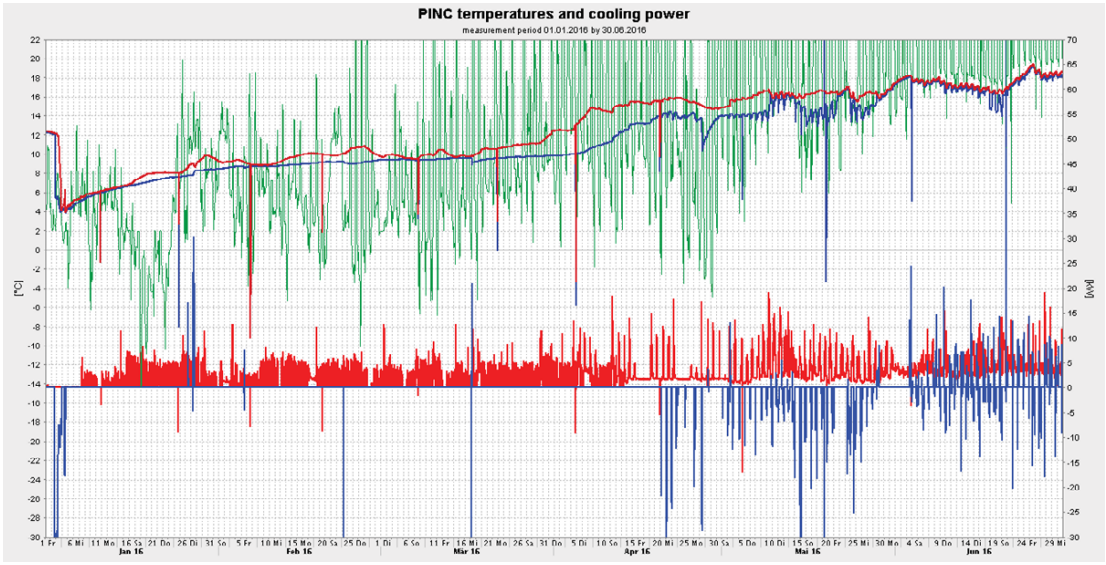

Fig. 4: PINC data from the first half of 2016. The red and blue plot lines in the top half show the temperatures in the TES, and the green represents the temperature on the metal roof. The bottom plot lines represent the cooling power (red = cooling required, blue = TES being cooled, right y-axis).

Fig. 4 shows the PINC data from the first half of 2016. Of particular note is the fact that right at the beginning of the year, on 03.01.2016, the PINC control system malfunctioned, causing the water in the TES

to be cooled down from approx. 12°C to approx. 4°C within a couple of days. The frost failsafe mechanism then kicked in and turned the PINC off. The temperature unintentionally reached in the TES was so low that the PINC system was not needed to provide cooling until the middle of April 2016. When the TES is used to provide cooling, the temperature of the water in the tank increases. When it reaches 14°C, the PINC system is activated. The PINC's cooling power is typically between 8 kW and 16 kW for the 300 m² roof area, on clear, cold nights even higher.

An almost complete set of data was collected for 2015. The PINC system is compared here to a conventional compression cooling system that serves as a backup in the EEC (a DYNACIAT LG/LGP 240V R410A manufactured by Ciat with a net cooling capability of 69.2 kW). Recent (2017) investigations have shown that the backup system supports the PINC system at 29 % of the measured time steps in 2015 and in approx. 30 % of the time steps in 2016, which is more support than designed and estimated. Therefore the control of the PINC and the backup system actually is redesigned.

Nonetheless, from the measured data the EER of the PINC and the backup system can be determined. Tab. 1 shows an evaluation of the collected data.

Tab. 1: Data collected for PINC in 2015 shown in comparison to a conventional cooling system, with data also given separately for winter and summer.

	Whole year conventional	Whole year PINC	Winter conventional	Winter PINC	Summer conventional	Summer PINC
Generated cool / kWh·a^{-1}	58570	21740	6080	6450	52490	15290
Electrical energy consumption / kWh·a^{-1}	16545	1102	975	157	15570	945
EER /	3,54	19,73	6,24	41,08	3,37	16,18

If the cooling generated for the whole year by the conventional system and PINC are compared (each measured directly at the cooling unit, not taking the heat exchanger and pumps into consideration), it can be seen that the conventional system produced considerably more cooling. The PINC's EER, however, is more than 5 times higher than that of the conventional system. The difference is even greater when comparing the data for winter: the PINC's EER of 41.08 is even 6 times higher than that of the conventional system. Winter is defined here as the period from November to March. During the remaining period (summer), the PINC's EER of 16.18 is still considerably higher than that of the conventional system (3.37).

If the additional energy consumption caused by pumps, valves and heat exchanger connecting the cooling systems to the TES are taken into consideration when calculating the EER, the conventional system has an EER of 1.95 and PINC has an EER of 10.66 (whole year each). The pump regulation system for the heat exchanger is, however, still a little bit faulty and requires optimization.

2.2 Cooling ceiling with integrated phase change material

Heating/cooling ceilings were installed in the upstairs offices of the EEC to utilize the cold generated by the PINC for energy-efficient building temperature control. These cooling ceilings were built by Lindner AG based on their cooling ceiling Plafotherm-E 200, and specially modified to incorporate PCM. 20 offices have cooling ceilings with macroencapsulated PCM modules on top of the water pipes (PCM on top), and 3 offices have cooling ceilings with the PCM modules attached underneath the water pipes (PCM at the bottom). Figure 5 shows the two different cooling ceilings. A graphite layer is used to improve the thermal

contact between PCM, water pipes and the cooling ceiling surface.

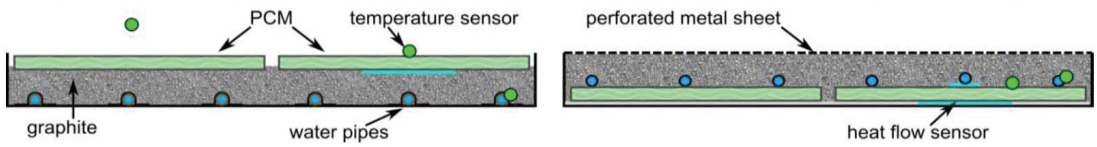

Fig. 5: Schematic diagram of the two PCM cooling ceiling systems "PCM on top" (ceiling type 1 on the left) and "PCM at the bottom" (ceiling type 2 on the right). The additional sensors are also indicated.

The PCM modules in both ceiling types are produced by Rubitherm Technologies GmbH. The metal cases contain a salt-hydrate-based PCM with a melting range between 22 °C and 24 °C. Five PCM modules are attached to one ceiling panel as shown in Figure 6.

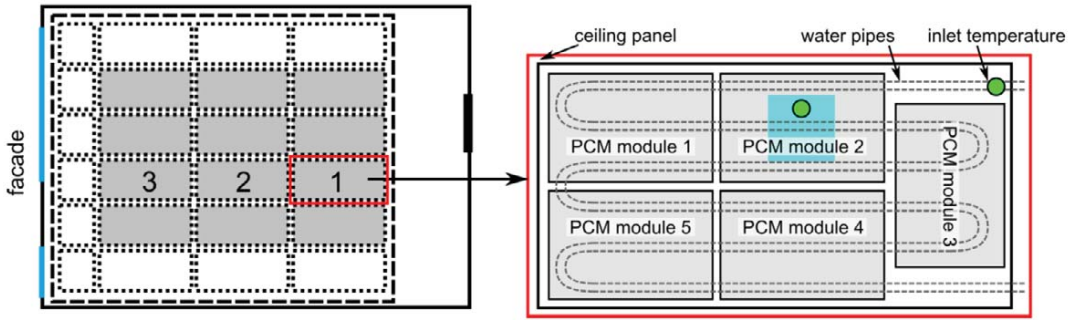

Fig. 6: Schematic diagram of the cooling ceiling panel arrangement in the offices (left) and the placement of the PCM modules on a single ceiling panel (right). The blue square indicates the position of the heat flow sensor.

The two different ceiling constructions were designed to enhance different operation modes of the ceiling. The operation modes are defined as follows:

- Passive cooling mode (PC mode):

  PC mode (no water flowing through the ceiling) occurs, if the system is not in one of the other operation modes mentioned below, and if the PCM temperature is below the operative room temperature.

- Active cooling mode (AC mode):

  AC mode occurs during the daytime, if the room temperature exceeds the set cooling temperature and the passive cooling power of the PCM is not sufficient. In AC mode, cold water flows through the ceiling.

- Active regeneration mode (AR mode):

  AR mode does the same as AC mode, but at night, thereby ensuring PCM regeneration.

The cooling circuit is connected to the PINC's TES by means of a heat exchanger. The standard room temperature is set at 24 °C, but this can be adjusted by the user by ±3 °C. Ceiling type 1 (PCM on top) was designed for balanced performance in every operation mode. This system performs well in AC mode as the water pipes have direct thermal contact to the ceiling panel, but also in AR and PC modes as the PCM has good thermal contact with the pipes and the ceiling surface via the graphite layer.

The design of ceiling type 2 (PCM at the bottom) is targeted towards PC mode. In PC mode, the system benefits from the direct contact of the PCM modules with the cooling ceiling surface. In AR mode, the system also shows decent results as the cold water in the pipes is not heated up by the room temperature while the PCM is regenerating. However, in ceiling type 2, the PCM acts as thermal resistance, meaning the

room temperature cannot be regulated as well in AC mode.

Data on the cooling ceilings' performance was collected at the weekend when the building was not occupied. To minimize the influence of factors which are hard to quantify (such as solar gains), the outside blinds were closed during the whole measurements. The internal heat gains in the rooms were replicated using electrical heating devices designed to emit the heat equally via radiation and convection. The heating devices could produce heating powers between 350 W and 1000 W which correspond to specific heat loads between 16 and 46 W/m² floor area. During typical measurement days the heating devices were turned on between 7 am and 8 pm. Weinläder et al. (2016) has found that the passive cooling power $P_{t,PCM}$ of the two PCM ceiling types was a function of the specific heat load as well as the room globe temperature . For a globe temperature of 26 °C typical passive cooling powers range from 10 to 15 W/m² (Figure 7). For these measurements the cooling set point of the room temperature was increased from 24 °C to 26 °C. This allowed globe temperatures of up to 27 °C before the active cooling mode started.

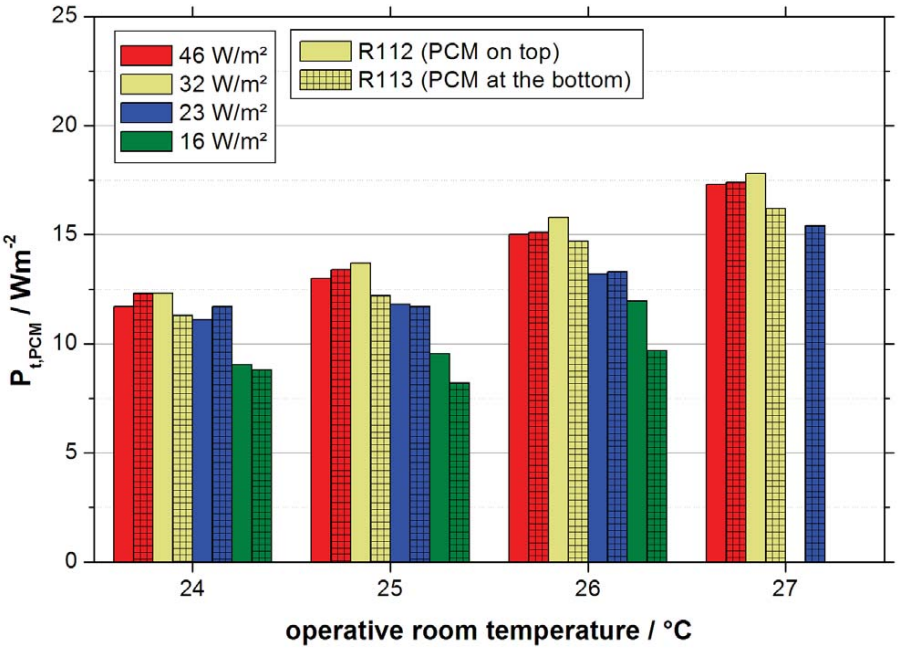

Fig. 7: Mean total passive cooling power $P_{t,PCM}$ of the PCM cooling ceilings as a function of operative room temperature for the different specific heat loads. No data are available in some cases for operative room temperatures of 27°C and for low specific heat loads.

The energy needed for active cooling was also measured during these weekends. The measurements took place in four office rooms with different systems as shown in Table 1. In addition to the PCM cooling ceilings all of the rooms except the reference room are equipped with PCM wallboards. For the sake of completeness further research results of passive PCM systems can be found at Kalnaes and Jelle (2015), Pomianowski (2012) and at Zhou et al. (2016).

Tab. 1: Overview of the different setups in the four measurement rooms.

room number and description	setup
R110: reference room	conventional cooling ceiling + conventional wallboards
R111: PCM on top + Energainboard	PCM cooling ceiling (PCM on top) + DuPont PCM wallboards (Energain)
R112: PCM on top + Comfortboard	PCM cooling ceiling (PCM on top) + Knauf PCM wallboards

	(Comfortboard)
R113: PCM at the bottom + Comfortboard	PCM cooling ceiling (PCM at the bottom) + Knauf PCM wallboards (Comfortboard)

The control during the day was the same for all four rooms, which means that the cooling set point for active cooling was 26 °C. During the night between 10 pm and 6 am the active regeneration mode was on in all the PCM rooms (R111-R113) but not the reference room. The cooling energy for active cooling was measured with a cold flow meter that detects the volume flow as well as the inlet and outlet temperature. The cooling energy is depicted in Figure 8 for the two periods during working hours (between 8 am and 6 pm) and outside working hours (from 0 to 8 am and 6 to 12 pm). The PCM passive cooling power was measured with heat flux sensors. The signal of the heat flux sensors was taken only during the working hours and only when the active cooling was turned off. The results for two measurement weekends (four days) during the summer with specific heat loads of 46 W/m² are depicted in Figure 8.

While the reference room has high cooling energy consumption during the daily working hours, the PCM systems reduce the active cooling energy during the day by 40 % to 80 %. This is achieved by their passive cooling potential (green bars in Figure 8). During the night, the rooms with the PCM systems require more cooling energy due to the regeneration process of the PCM (blue bars in Figure 8). This yields to a higher total amount of active cooling energy (sum of red and blue bars in Figure 8) in R111 and R112 compared to the reference room R110 while the total active cooling energy in R113 is slightly lower than that of R110.

It must be noted, that the PCM systems in R111 and R112 which had a higher total energy consumption could achieve mean globe temperatures during the working hours of about 1 °C lower than the reference room (temperature values in white areas in Figure 8). Even the PCM system in R113 which needed less cooling energy than the reference room achieved mean globe temperatures that were about 0.5 °C lower than that in R110.

The measurement results can be summarized as follows:

- PCM systems can shift a big portion of the daily cooling loads to the night
- PCM systems need a lot of energy for cooling down due to the nightly PCM-regeneration; this could lead to higher total cooling energy consumption than for a conventional cooling ceiling, depending on PCM system
- the PCM system in room R113 (PCM cooling ceiling with PCM at the bottom + Knauf PCM wallboards) is slightly advantageous compared to a conventional cooling ceiling with respect to the total energy consumption
- the efficiency of the cold production during the night is highly important for the investigated PCM systems
- since cold usually can be produced more efficiently during the night due to lower ambient temperatures, even the PCM systems in R111 and R112 with a higher total cooling energy consumption might be advantageous compared to a conventional cooling ceiling
- the PCM systems improve thermal comfort (lower mean globe temperatures) compared to the reference room at the same control parameters. Due to the time shift to the night, even with a much smaller TES the cooling energy in this case can be produced more efficient.

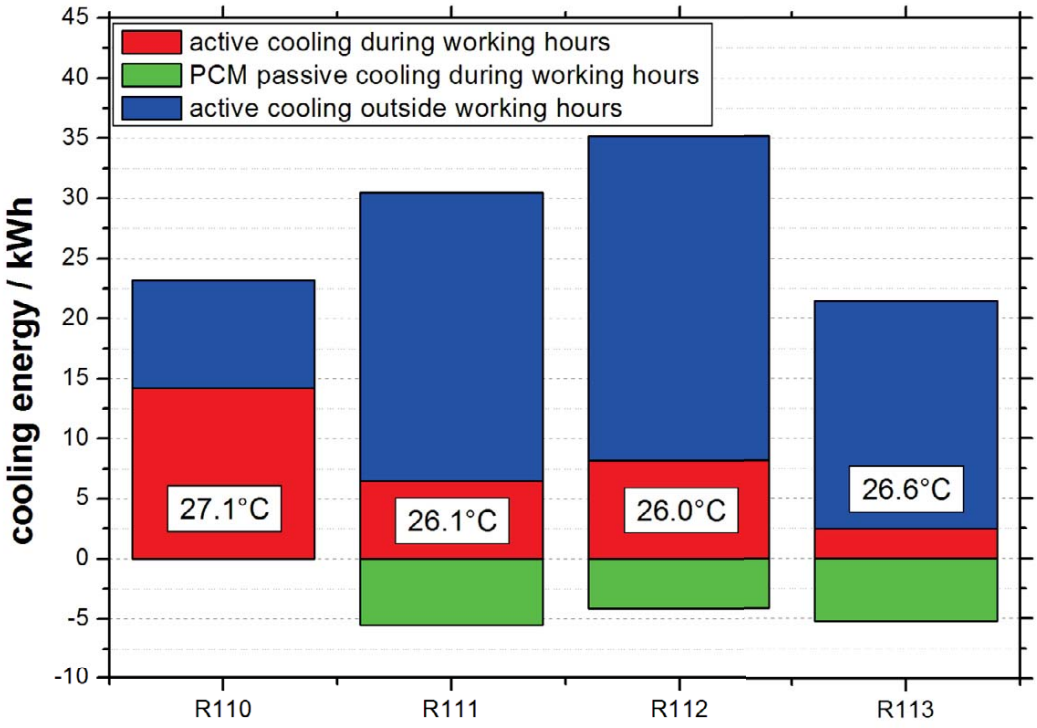

Fig. 8: Active and passive cooling energy of the cooling ceilings in four office rooms with specific heat loads of 46 W/m² between 7 am and 8 pm. The values in the white areas depict the mean globe temperature during the working hours.

3. Improvements and Outlook

A new water distribution method was introduced to increase the efficiency of the PINC system. The water is now distributed over the roof through a pipe with slits instead of nozzles, with hardly any loss in pressure.

The cooling circuits in the EEC are going to be restructured so that the PINC system can also be used in winter.

Furthermore, work is being carried out on developing the PINC's control system. Instead of using fixed trigger criteria, a high-level controller which factors in the weather forecast as well as cooling load prognoses calculated by means of building simulation enabling optimum control could improve the performance of the PINC. Simulations of the improved control system have shown an increase in efficiency of approx. 30% of the EER.

The conventional compression cooling unit (for backup purpose) is connected to ab big TES as well. For higher efficiency it is planned, to operate this cooling unit only at night time. At daytime, the TES should have sufficient cold stored for the cooling load of the EEC as shown at Gwerder and Illi (2016).

The PCM systems as well as two cold production systems (PINC + conventional compression chiller) will be implemented into a TRNSYS model that will be validated with the monitoring data. The models then will be used to investigate the performance of the PCM systems including cold production.

4. References

Weismann, S., Büttner, D., Ebert, H.-P., Kastner, R., Klinker, F., Körner, F., Lävemann, E., Rampp, T., Voland, P., Weinläder, H., 2014. Abschlussbericht zum Forschungsvorhaben Demonstration von Energieeffizienz und des Einsatzes erneuerbarer Energieträger am Neubau eines innovativen Forschungsgebäudes -DEENIF-. Würzburg. Published at TIB Hannover, DOI: 10.2314/GBV:834628120

Reim, M., 2016. Control strategies and user acceptance of innovative daylighting and shading concepts. Eurosun 2016 Conference proceedings

Rampp, T., Klinker, F., Ebert, H.-P., Körner, W., Weismann, S., Büttner, D., Weinläder, H., Mehling, H., 2013. The Energy Efficiency Center: Lightweight Construction With Smart Technology, Implementing Sustainability - Barriers and Chance. Sustainable Building Conference Graz 2013 Fullpapers. ISBN: 978-3-85125-301-6. Public access at http://castor.tugraz.at/doku/SB13_Graz/SB13_Graz_Fullpaper.pdf, last visited 26.09.2016

Weinläder, H., Klinker, F., Yasin, M., 2016. PCM cooling ceilings in the Energy Efficiency Center - passive cooling potential of two different system designs. Energy and Buildings 119 (2016) 93–100, DOI: 10.1016/j.enbuild.2016.03.031

Kalnaes, S.E., Jelle, B.P., 2015. Phase change materials and products for building applications: A state-of-the-art review and future research opportunities. Energy and Buildings 94 (2015) 150-176.

Pomianowski M., 2012. Dynamic heat storage and cooling capacity of a concrete deck with PCM and thermally activated building system. Energy and Buildings 53 (2012) 96-107.

Zhou, Y. et el., 2016. Thermal performance and optimized thickness of active shape-stabilized PCM boards for side-wall cooling and under-floor heating system. Indoor and Built Environment 25 (2016) 1279–1295, DOI: 10.1177/1420326X16671983.

Gwerder, M., Illi, B., 2016. Application of Model Predictive Cold Storage Management in a Demonstrator Building. CLIMA 2016 12th REHVA World Congress

5. Acknowledgments

The results in this paper are a part of the research project MoniResearch (FKZ: 03ET1245), which is funded by the German Federal Ministry for Economic Affairs and Energy on the basis of a resolution by the German Bundestag.

We also thank our sponsors and partners involved in the construction of the EEC:

Assmann Büromöbel GmbH & Co. KG, BSH Bosch und Siemens Hausgeräte GmbH, Bürgerstiftung Würzburg und Umgebung, Cabot Aerogel, Doerken GmbH & Co. KG, DuPont de Nemours, EEV GmbH, Ehrenfels Isoliertüren GmbH, Energy Glas GmbH, Hightex, Knauf Gips KG, Lindner AG, Maincor AG, Okalux GmbH, Porextherm Dämmstoffe GmbH, Roto Frank Bauelemente GmbH, Rubitherm Technologies GmbH, Saint Gobain PPL Cologne GmbH, SGL Carbon SE, Siemens Schweiz AG, Siemens AG Building Technologies Division, Siteco Beleuchtungstechnik GmbH, , Team Weber GmbH, Uhlmann & Zacher GmbH, uponor GmbH, va-q-tec AG, Versaidag-Indutex GmbH, Walter Stickling GmbH, Waldner Holding GmbH & Co. KG, Warema Renkhoff SE.

04. Solar Thermal Systems: Domestic Hot Water, Space Heating and Cooling

Conference Proceedings

EuroSun 2016
Palma de Mallorca (Spain), 11 – 14 October 2016

11th ISES EuroSun2016 – Design and Dynamic Simulation of a Small Multipurpose Solar Thermal System for Rural Necessities

Simone Amicabile[1], Christophe Hick[2], Surendranath Yagnamurthy[3], Mattia Roccabruna[1], Ankit Dev[4], Luigi Crema[1]

[1] ARES Unit, Fondazione Bruno Kessler, 38123 Povo, Trento (Italy)

[2] University of Liège, Campus du Sart Tilman - Bat: B49 - P33 4000 Liège (Belgium)

[3] Indian Institute of Technology, Hauz Khas, New Delhi, Delhi 110016 (India)

[4] Indian Institute of Technology Roorkee, Haridwar Highway, Roorkee, Uttarakhand 247667 (India)

Abstract

The proposed paper explains in detail the sizing process and dynamic simulation of a solar powered system designed to satisfy the energy demand of a school in the rural area of Haridwar district, India. The system is able to satisfy heterogeneous power demands for typical rural applications: hay pasteurization process, refrigerated storage for vegetables (explained in a second publication) and steam cooking. The considered layout is first described and evaluated under steady state assumption to identify the rough size of the main components. The specific configuration is then implemented and simulated using a Modelica-based layout, specifically developed for the case study. The dynamic behaviour of the system for different power requirements is simulated and analyzed over a typical day of usage. The goal to properly size and study the solar field, Phase Change Material (PCM) thermal storage and overall Balance Of Plant (BOP) is achieved.
Simulations results show that an optimal sizing can be achieved despite the large area of solar collectors required to ensure the power requirements of the facility. A better trade off between economic investment and system effectiveness can be accomplished slightly shifting the daily cooking activities.
The final designed system is going be implemented and commissioned in the proposed rural area. Future work will consist in comparing experimental data with the dynamic model predictions.

Keywords: CSP, Solar cooking, Solar cooling, Solar hay processing, Dynamic modeling, Dymola.

doi:10.18086/eurosun.2016.04.08 Available at http://proceedings.ises.org

Nomenclature

P&I	Pipe and Instruments
CSP	Concentrated Solar Power
PCM	Phase Change Material
BOP	Balance Of Plant
GDP	Gross Domestic Product
INR	Indian Rupees
ITPAR	India Trento Program for Advanced Research
Δh_{EVAP}	Delta enthalpy of vaporization
η_{POT}	Efficiency of the cooking pot system
CPC	Compound Parabolic Collectors
PTC	Parabolic Through Collectors
DNI	Direct normal Irradiation
θincid	Solar Incident angle
Tamb	Ambient temperature
Vwind	Wind speed
$\dot{q}_{tot,t}$	Total thermal energy transfer
$\dot{q}_{tot,g}$	Thermal energy transfer to the glass
$\dot{q}_{rad,air}$	Energy transfer to the ambient ait
η_{opt}	Optical efficiency
A_{ref}	Solar reference area
$A_{ext,g}$	External glass collector area
ϵ_g	Glass emissivity
σ	Boltzman's constant
$T_{ext,g}$	Glass external temperature
T_{sky}	Sky temperature
M_W	Wall mass
N	Discretization number
c_W	Heat capacity of the wall
T_W	Wall temperature
$\dot{q}$	Thermal heat transfer
A_{int}	Internal surface
U_l	Liquid heat transfer coefficient
U_{tp}	Two-phases heat transfer coefficient
U_v	Vapour heat transfer coefficient
$\varepsilon_{is,P}$	Pump isentropic efficiency
c_0, c_1, c_2, c_n	Non-dimensional constants
$\mathbf{f}_{\mathbf{P}}^{*}$	Pump frequency
$\mathbf{r}_{\mathbf{p,P}}^{*}$	Pressure ration
Δp	Pressure loss
k	Friction factor
ρ	Fluid density
A	Cross sectional area
$\dot{V}$	Volumetric flow rate

1. Introduction

India is the second most populated country in the world, almost 1.3 billion of people (Worldmeter, 2016) with more than 50% below the age of 25 and more than 65% below the age of 35 (BBC report, 2007). The astonishing population growth over the past 20 years can be mainly attributed to a remarkable economic growth, which placed the country among the 10 largest economies in the world by nominal Gross Domestic Product (GDP) (IMF, 2014). Economic progress made significant changes all around this vast nation, both in cities and minor villages, with a remarkable effect on the life style and habits of millions of people.

This rapid change eventually created strong disparities between rural and metropolitan areas. The signs of this important gap can be easily found in many aspects of people's daily life.

While most part of the Indian cities and central villages can base their daily activities on a reliable and stable electric power distribution grid, this is not liable for smaller communities. Rural areas are in fact non-uniformly electrified, depending on the financial resources of each single state. Due to this aspect, 400 million Indians are without electricity in rural India, 40% of the whole world's population without access to electricity (University of Washington, 2013). Lack of internal resources, economic poverty, and poor planning are some of the most relevant causes which has contributed to leave rural villages in India without electricity, while urban areas have experienced in the last few decades' growth in electricity capacity and consumption. In these circumstances, diesel generators fulfill the basic electric demand, which is normally used to guarantee food preservation (through refrigerators) or essential illumination. Cooking and heating necessities need also to be taken into account. In rural communities most part of the cooking activities are still accomplished through the use of traditional wood fired stoves or fossil fuels such petrol and kerosene. The dependence of rural households on traditional fuel is mainly due to the poor purchasing capacity of the people to buy commercial fuel and the easy accessibility to traditional sources like cow-dung and agricultural wastes (Kumar et al., 2010). As it is easy to expect, the thermal efficiency of these traditional sources is very low, approximately 15% (energy efficiency). The use of these traditional fuels is estimated to cause around 400,000 premature annual deaths due to various respiratory problems (NISTADS, 2008). Furthermore, the vast availability of unemployed and cheap manpower for fuel collection worsens this situation.

The government is increasingly trying to improve these harsh conditions by funding projects and initiatives related to biogas, solar and wind energy applications. Since the slow process of total electrification will perhaps take many years to provide an extended and reliable grid, alternatives, based on clean and abundant renewable energies, need to be evaluated as viable solution for small and middle size rural applications for India villages. Among the bigger programs, the Jawaharlal Nehru National (JNN) Solar Mission has the ambitious goal of implementing 20,000 MW of solar power by 2022 reducing the cost of solar power generation in the country (Ministry of new and renewable energy, 2013). The Indian government is also tying to sensitize people to clean energies. In a five-year plan, 30,000 million INR (approx. $500 million USD) are budgeted for clean cooking education in more than 500,000 schools (Wikia, 2016).

In this context, the India Trento Program for Advanced Research (ITPAR) is running the "Sustainable Technologies for distributed level Applications and energy support to Rural development" (STAR) project. ITPAR is bilateral collaboration supported by the Department of Science and Technology of the Indian Government (DST) and by the Province of Trento with the supervision of the Italian Ministry for Foreign Affairs. It involves some of the main university teams and research institutes of the Province of Trento and India. The STAR project is participated by the research institute Fondazione Bruno Kessler (FBK) from Trento, the Indian Institute of Technology (IIT) Roorkee, IIT Delhi and University South Campus Delhi. The project aims at the integration of a novel energy system in the district of Hardwar, composed of a combined solar thermal plant able to satisfy part of the daily thermal requirements of the Chudiyala Mohanpur village's high school. At the same time, the system is able to store thermal energy and run a hay processer prototype used by the village's farmers to improve the nutritional properties and quality of hay for animal feedstock.

The thermal system integrates two different technologies of solar collectors and a high capacity PCM thermal storage to decouple solar energy and thermal necessities. It is designed as demo system but it will be able to satisfy part of the energy-related necessities of the school.

The hay-processing device will be also implemented at a demonstrative size to prove the concept. In parallel, the school will be also supplied with an innovative solar cooler machine to store vegetables for short to mid

term periods. Since the analysis of this second system is beyond the scope of the paper, the description will not be included.

A preliminary system evaluation identifies energy requirements and components considering the steam requirements for the community's daily activities. After this first stage of design, the main components of the system are selected and a dynamic simulation in Modelica environment is chased with the objective of meeting collector's area and the thermal storage dimension. Figure 1 conceptually summarizes the paper structures and how the different chapters are structured and linked each other.

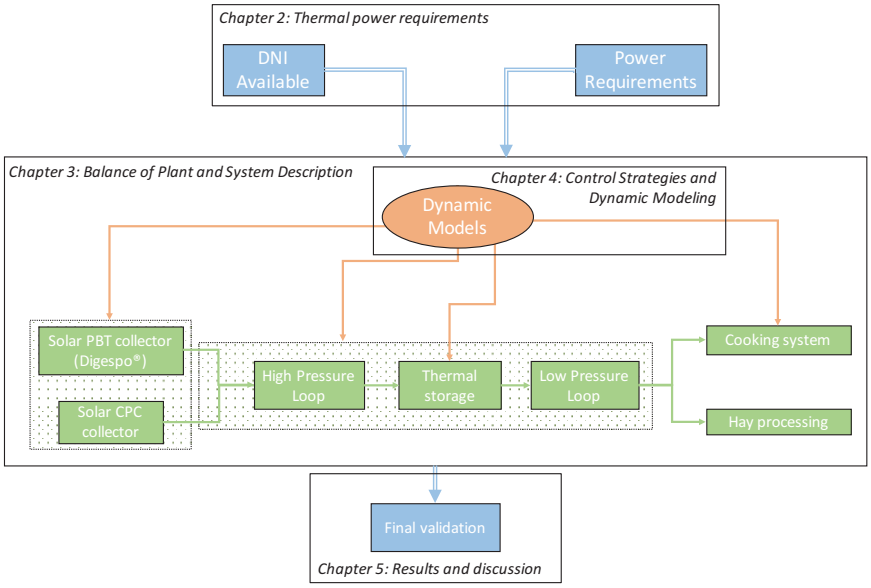

Fig. 1: Flow chart of the design development process. Inputs and outputs are highlighted in light blue. Dynamic model and P&I blocks are highlighted in orange and light greens, respectively.

2. Thermal power requirements

Within the framework of renewable energy system integrations for medium and small-size rural villages, a multi-purpose concentrated solar power (CSP) application is designed and presented. The proposed layout implements a thermal solution able to supply a reliable and clean source of thermal power. The system will be employed in a high school of an Indian rural village with a total number of about 600 people, including students and teachers.

The solar system has the initial target to demonstrate the application of the concept and further increase the size of the prototype. The researchers of the Indian Institute of Technology of Roorkee have assumed reference values for the quantity of food the system has to guarantee daily.

Assuming rice as the most common food prepared for the students, comprehensive analyses on the energy for cooking consumptions are available in literature. The studies help to estimate the energy required to cook rice, under specific assumptions such as type of cooking process, time needed and pre-treatment of the rice (Tribeni et al., 2006). Controlled energy input, cooking under pressure and soaking of rice before cooking are the three approaches that can be directly traduced into energy saving. (Dilip Kumar De et al., 2014) also chased a detail study related to the energy required for rice cooking process. According to this study, the energy consumption for fired open cooking of 1 kg of non-soaked rice requires 1.6 kg of water. Furthermore, the majority of the households in rural countries use firewood to prepare their daily meals. This process approximately needs 1.64 MJ of heat delivered to the pot. Energy cooking consumption easily varies depending on the process but values for fired open pots are reasonably similar to the ones for the discussed system (steam injected kettle). Hypotheses therefore are necessary to quantify the steam consumption on the working fluid side. Assuming that only the latent heat of vaporization/condensation of steam is transferred to the product, the delta enthalpy of vaporization for steam Δh_{EVAP} is 2326 kJ/kg. The specific heat of water is

assumed constant and equal to 4.186 kJ/kgK. Assuming a reference efficiency of the cooking system of η_{POT}: 75%, the amount of steam required to cook 10kg of rice can be estimated. Table 1 lists the constants introduced for this evaluation.

Tab. 1: Summary of the ingredients properties and total energy required for the cooking process.

Primary sources	Quantities (kg)	Heat capacities (kJ/kgK)	Total energy required (kJ)	Efficiency of the cooking pot	Total steam required for cooking (kg)
Rice	10	2.5	16400	75%	9.4
Water	1.6	4.186			

Once the energy demand of the main cooking process is identified, the power system is designed in order to fulfill the demand. The system will be opportunely oversized due to the uncertainty of some variables and assumptions such thermal losses due to poor insulation. Furthermore, the system has also to be able to provide the right amount of energy required to process the hay for the village's farmers.

3. Balance of Plant and System Description

Scheme of Figure 2 shows how the designed layout can be divided into two different main blocks. The plant has two separated loops: high pressure loop, circled within the blue line segment, and low pressure loop, highlighted in green. In the first circuit, high-pressure water is heated up close to the saturation temperature through a combination of Compound Parabolic Collectors (CPC) and an innovative Parabolic Through Collectors (PTC) technology. The proposed solution includes high efficiency CPC coupled with novel coaxial PTC, developed in the framework of the EU funded DIGESPO project (FP7-DIGESPO, grant agreement n° *241267*). Due to the high working temperature of the system, these two different technologies linked together ensure respectable values of nominal efficiency even with temperatures close to the upper limit set point. Because of this specific solution, high temperatures can be reached at the solar field outlet, ensuring good efficiency with acceptable investment costs. At the same time, high temperature energy can be stored inside the thermal storage, reducing for instance the risk of sub-cooled vapor at the low-pressure side. High-pressure loop works at nominal pressure of 10 bar (with possible maximum pressure of 12 bar). At this stage, water changes phase at approximately 179 °C, guaranteeing high temperature in the storage. The control of the solar system is implemented in order to work with a safe sub-cooling temperature of 10 °C. If outlet temperature T4 of Figure 1 overpasses the maximum temperature, a safety control defocuses the DIGESPO solar field, before emergency relief valves empty the system.
Temperature and pressure and mass flow sensors (according to the legend) are located in the most significant parts of the system.
The choice of using pressurized water instead of thermal oil is an advantage in terms of BOP simplicity and reliability. Avoiding oil allows the use of inexpensive working fluid and components, such pumps or expansion vessels. Solar collectors do not require any changes to work with pressurized water and both typologies of collectors can handle the nominal design pressure. Additionally, the maintenance cost is considerably reduced and spare components are expected to be easier to find for water or steam rather than for oil, especially in rural areas. This choice globally helps to decrease the initial investment cost as well as the maintenance of the storage system.
The final system, designed to exploit the solar thermal power for different rural applications widespread in most part of the Indian rural communities (Kuldeep Ojha, 2010), is expected to be flexible and easily scalable to increase its potential.

3.1 High-pressure loop

The high-pressure loop is composed by CPC solar collectors connected in series with PTC DIGESPO collectors. CPC field pre-heats the fluid before entering the DIGESPO collectors. In this part the fluid will reach the maximum target temperature with relatively low thermal losses. The fluid flow is regulated through variable speed pump of Figure 1, which can be tuned in order to reduce and eventually stop the flow. The pressurized loop discharges the liquid water directly inside the thermal storage. For this reason, the tank does

not have internal coil but is itself working at the same nominal pressure of the collectors. Two parallel loops are added in case the thermal storage requires maintenance or direct steam generation tests want to be carried out (see Figure 2).

3.2 Low-pressure loop

The low-pressure loop is in charge of delivering high temperature thermal energy using water at steam phase as thermal vector. In order to provide a low-pressure steam circuit, the thermal storage is built up with a finned internal coil to allow improved heat exchange between the hot pressurized water and the non-pressurized water. The expected temperature difference between the two loops (pressurized water inlet and non-pressurized water inlet) is around 100 °C. The thermal storage is filled with PCM balls in order to keep the temperature controlled inside the tank and to reduce its total dimensions.

The low-pressure distribution system, highlighted in green in Figure 2, connects this first part of circuit with all the final devices. A three-way valve allows to manually choosing whether to divert the steam flow to the hay processer or to the cooking kettle. If the steam produced is exploited through the hay processor, a reintegration of fresh water is necessary. In case the steam is used for the cooking system, no reintegration is needed since the loop is close. Despite this, a small condenser with steam trap is built-in directly in the kettle's loop to guarantee liquid phase before the feeding pump.

The feeding pump is chosen as variable speed, driving the mass flow rate in this loop. This choice is because a variable flow is able to guarantee a constant inlet temperature at the exchanger, guaranteeing the right amount and quality of steam.

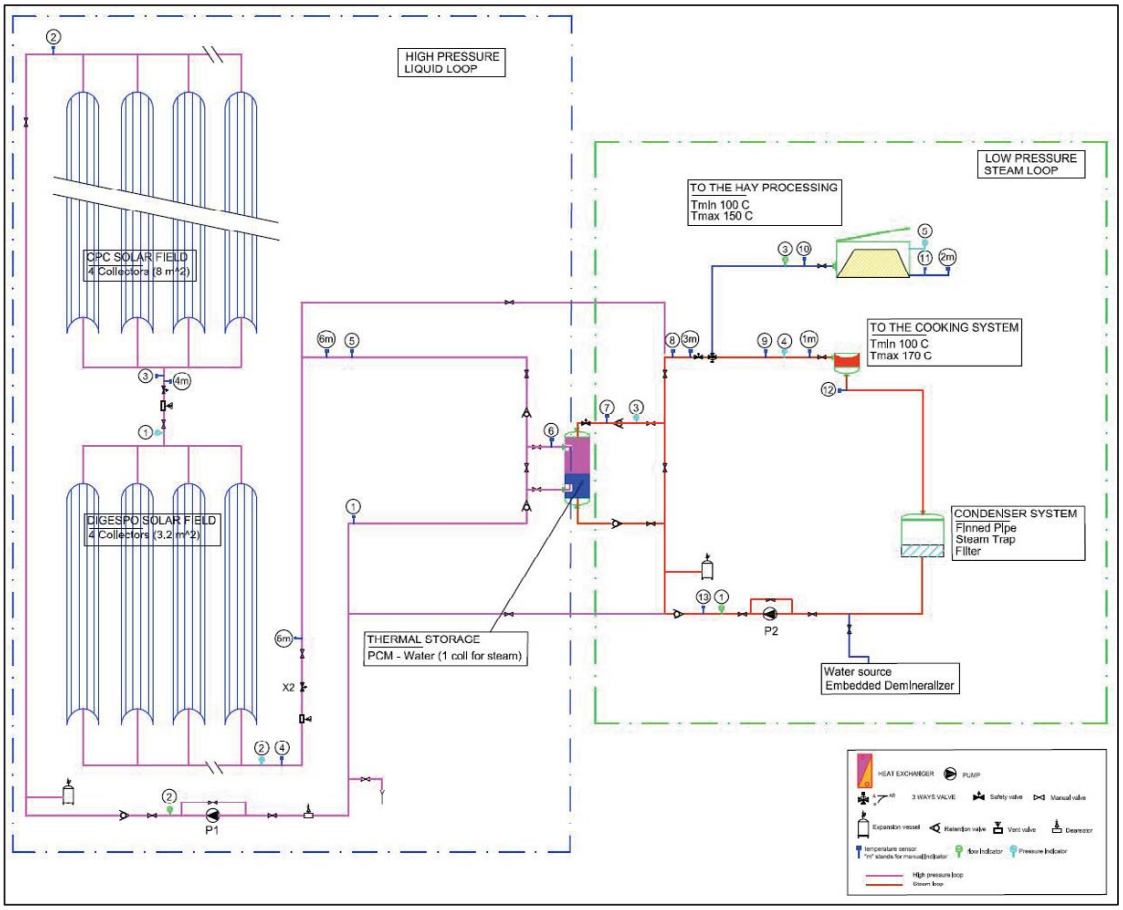

Fig. 2: BoP for the system proposed. High and Low pressure loops are highlighted in blue and green, respectively.

3.3 Thermal storage

The chart of figure 3 shows the typical DNI trend along the different seasons in the Uttarakhand sate. During the sunniest period of the year (summer season), the maximum value of DNI available in the demo site area hardly reaches 520 W/m^2. This is mainly due to the though typical weather of the region. Despite the high temperatures reached during summer season, clouds often cover sky, directly affecting the power available. Furthermore, the chart shows the irradiation distribution all along the day. The peak of power is expected around midday, when the sun is higher in the sky. This is a considerable issue for cooking applications, since they are expected to work at full load during this period of the day. The cooking system will be mainly used between 11AM and 1PM to prepare the daily meals for the school. Less problematic is the use of the hay process because it doesn't require activation during specific periods of the day. For these reasons, a thermal storage is necessary to partially decouple solar power and thermal demand. The thermal storage requires being capable to storage at least the amount of energy necessary to cook the preselected amount of food.
Since the power required for the cooking process is much higher than the power delivered through the sun, the storage will be rapidly discharged when the cooking process is active. Because of that, the dimension of the storage has to be enough large to avoid this problem. On the other hand a bigger storage could affect the maximum temperature reached.

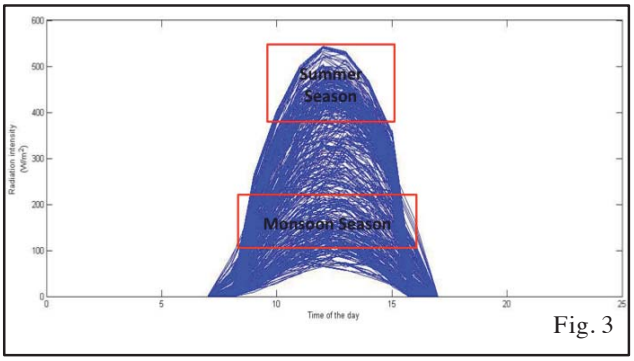

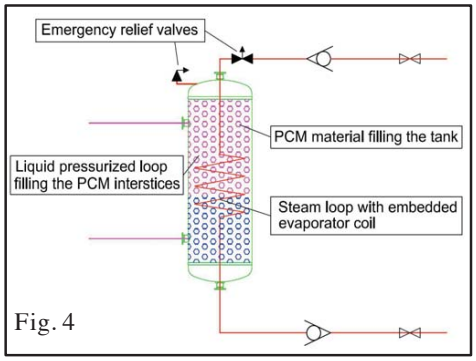

Fig. 3: Distribution of Direct Normal Irradiation (DNI) along the days of a typical year.
Fig. 4: Schematic of the pressurized thermal storage with PCM balls.

If the power available is not sufficient to charge the storage, the temperature reached could be too low to produce steam when necessary. This concern could be even more amplified with the use of PCM material inside the tank. If is true that PCM materials help reducing the total volume occupied by the storage, on the other hand the material has to reach the saturation temperature in order to change phase and to store sensible heat. If this doesn't occur, the PCM material is un-useful since only latent heat without a controlled temperature is stored. For these reasons the storage requires a careful sizing and a simplified approach to implement and study the dynamic behavior of the whole system is pursued. Figure 4 briefly describes how the storage is designed. The phase change material fill the pressurized vessel and the water coming from the solar field will fill the interstices among each ball. In this way the heat power will be directly exchanged between fluid and metal balls containing the PCM. The pressurized tank has a built-in coil connected to the low-pressure steam loop to provide the power only when necessary through the use of a variable speed pump.

3.4 Solar collectors

The designed system is characterized by two different kinds of collectors: CPC and PTC DIGESPO tubes. Parabolic through collectors with evacuated tubular absorber are renown as the most reliable technology in the Concentrated Solar Power (CSP) field (Cabello et al., 2011). In the proposed system, the CPC solar field works as a pre-heater for the CSP collectors, reducing the global investment cost of the solar field. CPC collectors have high reliability ensuring a good compromise between efficiency and capital cost.
CPC collector field is connected in series to the higher temperature DIGESPO technology collectors. This

second stage has the fundamental role to increase the temperature up to the maximum temperature before going directly to the thermal storage to heat up the PCM material. An external glass tube and an internal metallic support compose the evacuated solar tube developed within the DIGESPO project. The metallic support is tubular while an absorber pipe made from stainless steel had been specifically realized with a molybdenum protection layer and coated with CerMet. The potential problem arising from thermal stress dilation and glass cracks has been solved with the use of a coaxial tube. A spiral wire is present between the two coaxial pipes solving the thermal gradient problems and reducing thermal deformations. The full-evacuated solar tube has an inner diameter of 12 mm and a total length of 2 meters for an active surface of 0.8 m^2. The solar technology has been fully proven on a demonstration site. The solar plant prototype was installed in Malta, supplying thermal energy for industrial heat processes. The solar collector's efficiency reached 55% with DNI of 900 W/m^2 and working temperature of 300°C. Due to the noticeable efficiency that the collectors are able to show at high temperature, is reasonable to expect that the thermal losses related to the last stage of the solar field will be considerably low compare to a solution made by CPC collectors only.

3.5 Cooking system and hay processing

The low-pressure system delivers the steam directly to the steam-cooking kettle, a device specifically designed to use steam as thermal vector. The typical steam kettles are large container with a round or spherical bottom. Kettles have a double wall or "jacket" covering the bottom and at least half of the height of the sides, to provide space for steam to circulate thereby heating the cooking surface. In principle, the steam kettle operates like the classic kitchen double boiler. The kettle operates within a specific pressure range at which the steam can be injected into the kettle. This range is typically between 0,07 Bar and 3,5 Bar with nominal temperature up to 150°C. The kettle used for this application is 100-liter capacity SS304 kettle. The outlet part of the kettle is provided with steam safety valve and condenser system, including air vent, Y type strainer and steam trap.

Through a three-way valve, the steam coming from the PCM tank can be diverted to the hay processer when cooking demand is absent. The process for which the steam is involved is to pasteurize wheat straw without complete sterilize the cereal. Unlike sterilization, pasteurization is simply the process by which amounts of microscopic competitors in a substrate are reduced (IDFA, 2016). Sterilization in fact, would remove all living organisms, leaving the straw without beneficial bacteria and therefore susceptible to contaminants. As consequence, having beneficial microorganisms allows inoculating the straw without using special sterile procedures. Pasteurization generally occurs between 70-75° C but it is strongly dependent by the thermal death point of fungus or spores. Due to the scientific aspect of the system will be implemented, a maximum temperature up to 150°C is required for the hay processer. Steam temperature and exposure time are crucial components of this process.

4. Control Strategies and Dynamic Modeling

The control strategies for the system is developed and simulated using thermal daily requirements of the elementary school coupled with yearly weather data of the specific geographical area. Weather data are available at (Weather Data Reference, 2012).

The typical trend of thermal requirements for food cooking and hay processing is represented in the chart of Figure 5. Here, the simulated power requirements used for the dynamic simulation are depicted with time dependency.

At the very beginning of a typical day, thermal demand is absent since neither cooking stoves or hay system is activated. This is considered as small advantage for the system, which is therefore able to cumulate the solar energy available the early hours of the morning before cooking activities begin. At 11AM the school kitchen starts to warm up the circuits with high temperature steam. At this stage the power requirement is much higher then what instantly available from the solar field. For this reason, the lack of power is fulfilled through the thermal storage system.

The cooking energy requirement of 7 kWh can be reasonably approximated constant for one hour, between 11.30AM and 12.30AM when the school activities are still on going. This is approximately happening the

whole year, with exception for the monsoon season, which lasts from June to early September. During this period in fact, thermal cooking requirements are absent and the system will be completely dedicated to produce steam for hay processing or different sporadic activities requiring steam, such sterilization or cleaning. Outside the monsoon season, the hay process thermal requirements are satisfied during the afternoon period. Since this action does not need to respect strict schedule as the school lunchtime, hay processing activities are simulated as two sessions requiring 2, 5 kWh energy (including extra energy due to thermal inertia) for one hour each. This choice allows the system having enough time to store energy inside the thermal tank after the cooking period. This strategy has been developed and selected among different proposals and it will be implemented at the first stage of the on-field tests.

In order to forecast and study the transient behavior of the whole layout during the proposed typical day, a Modelica based system has been simulated with Dymola environment using the thermodynamic library ThermoCycle. ThermoCycle is an open-source Modelica Library (Modelica Website, 2016). This is a powerful tool able to describe in details the dynamic behavior of complex thermodynamic systems thanks to a user-friendly and widely tunable interface. (Desideri et al., 2015).

The model is first used to complete the design of the layout and to properly size the embedded thermal storage indispensable to decouple solar energy from power demand.

In Figure 6, the Dymola layout describing the implemented system is presented.

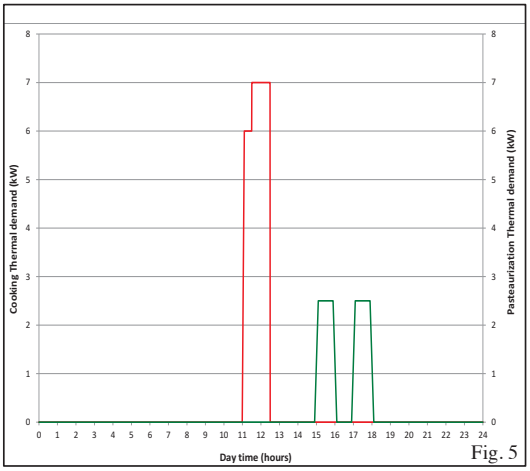

Fig. 5

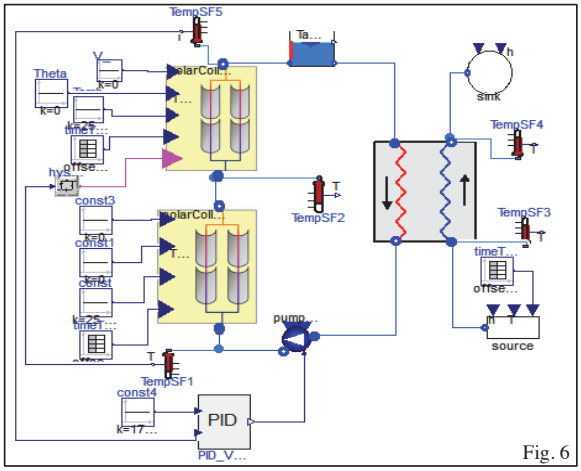

Fig. 6

Fig. 5: Scheduled thermal requirements of the system for both hay processing and cooking.
Fig. 6: Overview of the system layout implemented with Dymola.

High-pressure, liquid phase water is simulated inside the solar system while the evaporation process is modeled on the heat distribution part, right side of Figure 6. The water going to the storage tank warms up the phase change material to produce superheated steam through a dedicated boiling system. The steam loop is designed as open loop that delivers the power provided by the solar plant directly to the final users.

The dynamic modelling is necessary to define the size of the main components of the system as well as the reactiveness of the layout to rapid changes of working conditions. In addition, the dynamic model tests if safe working conditions in terms of maximum pressure and temperatures are guaranteed.

4.1. Dymola modeling: Solar collectors

Assuming homogeneous pressure drop and equal ambient input data, the solar field can be modeled as a single CPC collector in series with four PTC DIGESPO type collectors arranged in parallel. For this particular connection, the mass flow inside each single PTC collector is one fourth of the total mass flow. Parabolic through collector model of *ThermoCycle* library is used. Given the ratio between the diameter and the length of the parabolic through unit, the modeling approach is based on a finite volume one-dimensional discretization along the collector axial axis. The model is the result of two subcomponents. *Flow1Dim* component models the fluid flow through the Heat Collector Element (HCE) accounting for energy and mass transfer. At the same time, thermal inertia in the HCE is accounted by the *MetalWall* and *SolAbs* models as

depicted in Figure 7. Moreover, the model implements the relations between the environmental parameters (DNI, θ_{incid} , T_{amb} , V_{wind}) and the axial temperature distribution along the absorber. The equations defining the thermal energy transfer from the sun energy concentrated on the heat collector element to the heat transfer fluid are listed below. The first equation describes the thermal energy transfer from the sun to the metal wall of the absorber (refer to nomenclature table):

$$\dot{q}_{tot,t} = \frac{DNI \cdot \eta_{opt,t} \cdot A_{ref}}{A_{ext,t}} \quad \text{(eq. 1)}$$

Thermal energy transfer from the sun to the glass envelope:

$$\dot{q}_{tot,g} = \frac{DNI \cdot \eta_{opt,g} \cdot A_{ref}}{A_{ext,g}} \quad \text{(eq. 2)}$$

Radiation to the ambient air:

$$\dot{q}_{rad,air} = \epsilon_g \cdot \sigma \cdot (T^4_{ext,g} - T^4_{sky}) \quad \text{(eq. 3)}$$

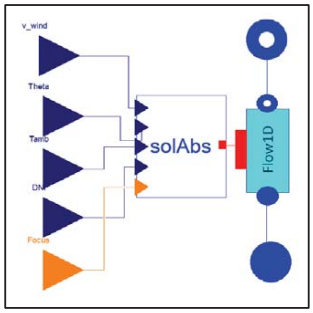

Fig. 7: Solar collector model available on ThermoCycle library.

4.2 Dymola modeling: PCM storage

A PCM tank is a major component for most part of the solar power plants due to its capacity to storage thermal energy for short and medium periods of time (Casati et al., 2013). The PCM storage of this study is modeled using three discretized one-dimensional subcomponents of the *ThermoCycle* library. Two *Flow1Dim* components accounting for mass and energy exchange in the two separated coils are merged with the PCM*Wall* component, which accounts for the overall energy accumulated in metal coils, metal balls containing the PCM and in the water filling tank. *PCMWall* component derives from the basic *MetalWall* component available on Modelica. *MetalWall* generally accounts for thermal energy accumulation in the metal wall. In this study this component has been modified in order to describe the typical thermodynamic behavior of PCM materials. The models are discretized based on the finite volume approach as depicted in Figure 8. No pressure losses are considered in the two *Flow1Dim* models and the temperature in the storage is supposed to be homogenous for each layer. Thermal energy accumulation is expressed as:

$$\frac{M_w}{N \cdot c_w} \cdot \frac{dT_w}{dt} = \Lambda_{ext} \cdot \dot{q}_{ext} + \Lambda_{int} \cdot \dot{q}_{int} \quad \text{(eq. 4)}$$

where M_w is the total mass of the wall, N is the number of cells and c_W is the heat capacity. The secondary fluid is modelled as an incompressible fluid whose density and specific heat capacity are assumed constant throughout the exchanger length. The component has been modified in order to consider the latent heat during the transition phase of the PCM at the specific temperature of 150°C. The computation of the heat transfer coefficient for the PCM storage and more generally for all the heat exchangers of the dynamic system, is based on a structure taking advantage of the object-oriented Modelica language. The basic interface, define an ideal heat transfer element with no thermal resistance. The object takes as an input the

bulk state of the fluid and computes the thermal energy flow per area.

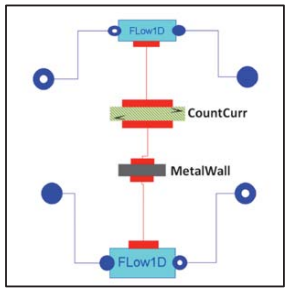

Fig. 8: Representation of the finite volume heat transfer basic block.

Based on these considerations, equation 4 is used to model convective heat transfer coefficient accounting for mass flow variation (refer to nomenclature table):

$$U = \frac{(U_l + U_{tp} + U_v)}{3} \left(\frac{\dot{m}}{\dot{m}_{nom}}\right)^n \quad \text{(eq. 5)}$$

where the exponent n varies depending on the flow regime between 0.65 and 0.8.

4.3 Dymola modeling: Cooking system

Three different models from ThermoCycle library compose the cooking pot model. *Flow1Dim* describes the steam flow through the cooking pot while *MetalWall* model is used to consider the thermal inertia of the device's metal wall. The last component takes into account the heat transfer between the steam and the food. Inputs for the final component are the food quantity and the cooking time to assess the power extraction considering constant convective and radiative ambient losses.

4.4 Dymola modeling: Pump, pressure drop, bypass valve and PID

The *Pump* model of *ThermoCycle* library is used to simulate the pump units installed on the system. It is a lumped fictitious model simulating the compression of a fluid in a turbo or volumetric machine, where given the flow fraction or the pump frequency, a constant volumetric and isentropic efficiency, the mass flow and the consumed power are computed (Desideri et al., 2015). The isentropic efficiency is simulated in Eq. 6 with a second order polynomial with cross terms as a function of the non-dimensional pressure ratio ($r^*_{p,P}$), and the non-dimensional pump frequency (f^*_P).

$$\varepsilon_{is,P} = c_0 + c_1 \cdot f_P^* + c_2 \cdot (f_P^*)^2 + c_3 \cdot r_{p,P}^* + c_4 \cdot (r_{p,P}^*)^2 + c_5 \cdot f_P^* \cdot r_{p,P}^* \quad \text{(eq. 6)}$$

$$\Delta p = \Delta p_{linear} + \Delta p_{quadratic}; \quad \Delta p_{linear} = k \cdot \dot{V}; \quad \Delta p_{quadratic} = \frac{1}{A^2} \cdot \frac{\dot{m}^2}{2 \cdot \rho} \quad \text{(eq. 7)}$$

A linear and quadratic pressure drop terms are used to compute the total pressure drop, as depicted in equation 7. *Valve* model from the *ThermoCycle* library is also a lumped model where no dynamic and thermal energy losses to the ambient are considered.

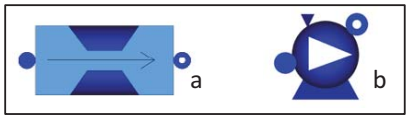

Fig. 9: (a) Pressure losses modelica block. (b) Ideal pump modelica block.

5. Results and Discussion

Four different configurations are simulated over the period of 24 hours and presented with the intention of properly address the solar field and energy storage sizing. A typical averaged day of the summer season has been identified to exploit the simulations. Phase change transitions directly affect the complexity of the simulations. For this reason only daily simulations can be performed at this stage of the study. During the worse season of the year, which is identified in as the monsoon season, the system will be totally deactivated; therefore there is no real necessity to perform simulations with the lowest irradiation values.
Each of the following charts presented includes the selected DNI used for the Dymola simulations. The solar system is composed of two different parts. Four DIGESPO parabolic through collectors for a total constant area of 3.2 m^2 and a CPC assembly, with a variable total collector area. An extensive study can become interesting if considering a future potential cost reduction of the DIGESPO collectors involving local manufacturing or large-scale production.
To summarize, the four scenarios describe the behaviour of the system changing the PCM total mass and the CPC collector area. The PCM change phase temperature equal to 150°C allows choosing among a wide range of phase change materials available on the market (Haillot et al., 2010).
Each simulation is described through two charts. Charts a) of each figure describes the trend of energy storage in the PCM tank as function of time and power demand (blue trend line). The systems starts in the morning at the storage tank lowest temperature set point of 140°C. In order to correctly estimate the actual size of the energy reserve, the reference value of the energy stored is set at 0 kWh for the simulation starting point. Charts b) of the four tests show the trends of the working steam temperature available at the thermal storage outlet and the average storage temperature.

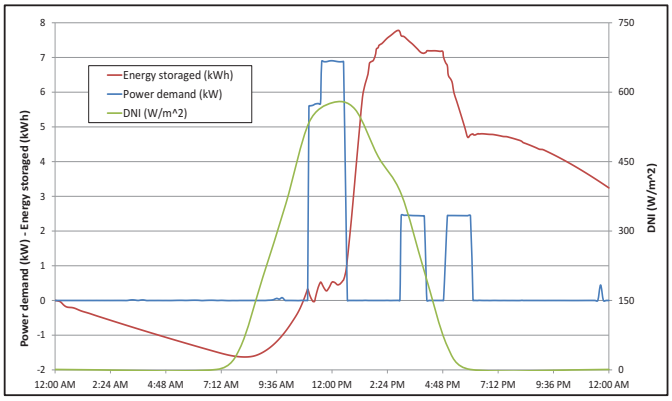

Fig. 10: Scenario 1_Power demand and energy available in the PCM storage

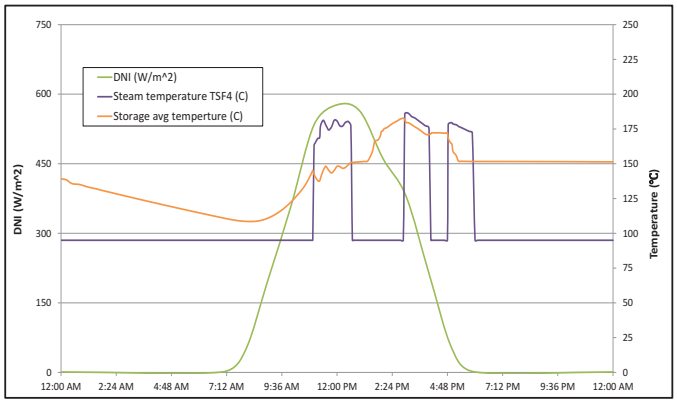

Fig. 11: Scenario 1_ Temperatures of supplied steam and tank average temperature over daily time.

Figure 10 describes the first scenario modelled shows interesting results regarding the potentiality of the thermal storage. This test is characterized by collector areas of 12 m^2 and 3.2 m^2 for CPC and PTC DIGESPO collectors, respectively.
The system depicts a natural drop in terms of energy at the beginning of the day. This is due to the thermal losses when sun is not shining (negative value is due to the reference starting point at 0 kWh). The storage temperature starts to increase when irradiation occurs (around 7.10 AM) together with the storage energy value. A small change of the energy storage slope is shows around 12.00AM when the cooking power requirements is at his top. Here, the power required can be higher than the power instantly available from the collector and the thermal storage working as backup is therefore strictly necessary. The large collector area allows a fast increase of the energy loaded through the PCM after lunch time, with a peak in energy available around 3 PM. At this stage the energy stored exceed the energy requirements of a typical day and Figure 11 shows a possible overheating of the PCM material. This suggests that a possible decrease of the thermal storage and collector area can be followed without affecting the thermal behaviour of the system.

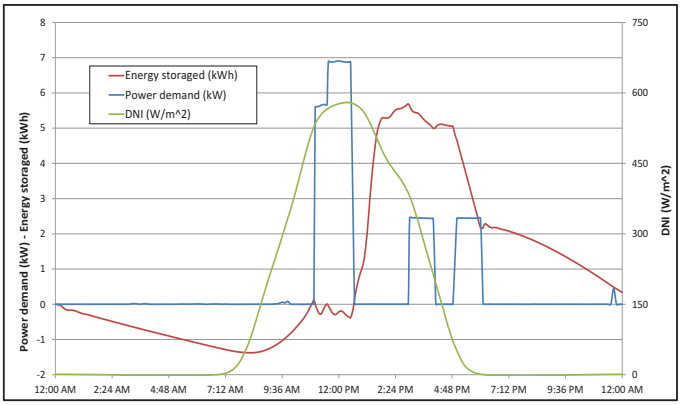

Fig. 12: Scenario 2_Power demand and energy available in the PCM storage

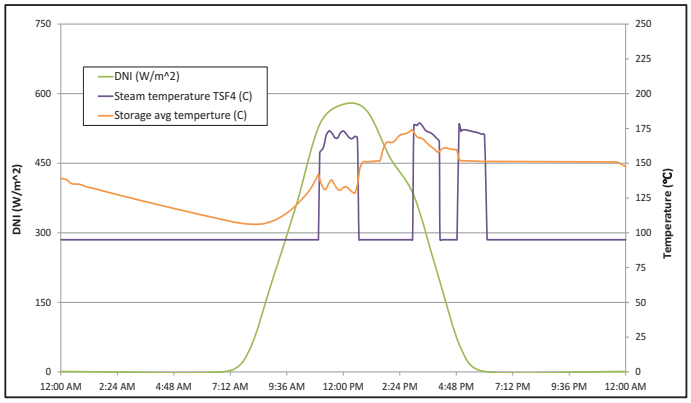

Fig. 13: Scenario 2_ Temperatures of supplied steam and tank average temperature over daily time.

Figure 12 describes the scenario modelled reducing the dimension of the CPC area to 10 m^2 and the storage tank total mass to 70 kg. This configuration seems to satisfy the power demand along a typical day. The maximum peak of energy saved is sufficient to cover the thermal power demand of the hay processing at the end of the day, but an overheating of the phase change material is still depicted in Figure 13.
Outlet steam temperature is strongly dependent by the instant solar irradiation (and therefore by the pressurized water) especially if the storage has not reached the target temperature yet. This behaviour is always true for the cooking power demand, and the highest influence is visible in Figure 13 observing the steam temperature trend. The power demand of the cooking process in fact is required along the morning when the solar radiation has not already refilled the PCM tank. On the other hand, the cooking demand

occurs when the sun is shining and for this reason the power collected is directly exploited by the cooking system and high temperature can be delivered to the cooking pot.
Test showed in chart Figure 13shows a total deployment of the energy stored despite an overheating is still visible in the simulation. Now the possible superheating of the thermal storage simulated does not overpass 190°C as in the previous case but still reaches almost 175°C, over a temperature transition phase of 150°C. This could be reasonably limited reducing the collector area of the power system.

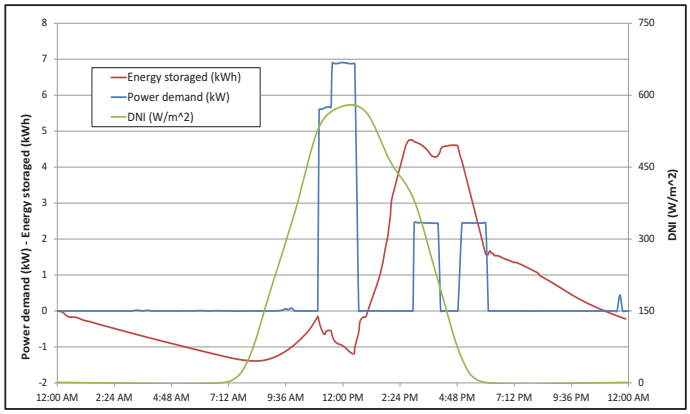

Fig. 14: Scenario 3_Power demand and energy available in the PCM storage

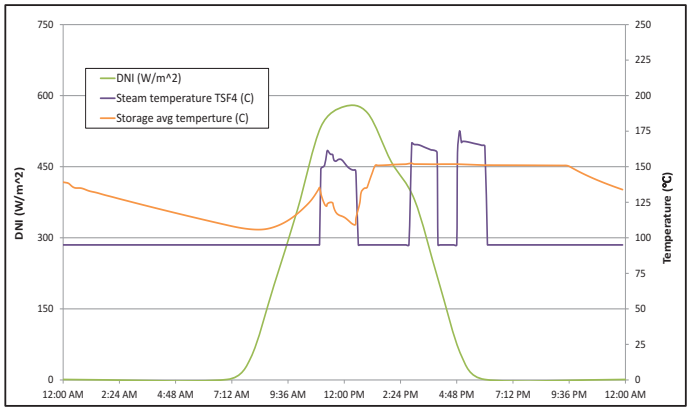

Fig. 15: Scenario 3_ Temperatures of supplied steam and tank average temperature over daily time.

Based on the previous considerations a third scenario is pursued and presented in Figure 14. Here, the total CPC collector area is further reduced. Thermal storage average temperature depicted in graph of Figure 15 does not overpass the PCM transition temperature of 150°C. Obviously, after the sunset a faster temperature drop is now visible. In this scenario the PCM storage works below the design temperature for almost all the typical morning, and a lower steam temperature is expected when lunchtime occurs. This is a second effect related to the CPC area reduction. The average temperature in the storage at 11AM is slightly above 125 °C and dramatically drops below 115°C at the end of the cooking process. This behaviour could affect the cooking effectiveness and reliability of the system, especially if thermal transmission losses on the real installation would be higher than what expected due to poor insulation during the commissioning phase. Moreover, an expected reduction of the optical performances of the solar collectors are normally expected during the lifetime and when used in dusty environments. This, would cause a dramatic decrease of the nominal power available from the collectors with an ulterior effect on the steam production. For these reasons, if the reduction of the collector area certainly reduces the overall economic impact of the system and eliminates PCM's overheating, criticalities regarding the maximum cooking temperature and minimum temperature of the storage are expected.

The last scenario described in Figure 16 further reduces the quantity of PCM material within the storage, keeping the same total collector area of Scenario 3. This reduction deeply affects the economic impact of the thermal storage. The direct consequence is showed in Figure 17. Here, a small peak of overheating is visible in the storage average temperature. Beside this, very low temperature is visible at the end of the day in the thermal tank, suggesting that the new match is not able to satisfy the power requirements. The minimum temperature of the storage tank reached at the end of the day here is much lower than in any other previous case. If this last scenario could show an expected reduction in terms of economic impact the thermal storage cannot be completely exploited, resulting in very low average temperature along the day.

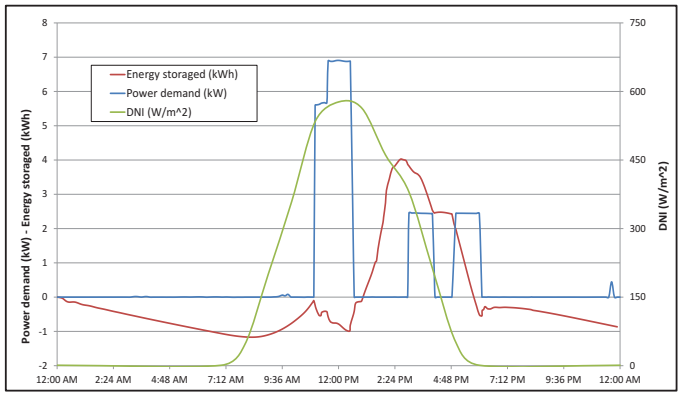

Fig. 16: Scenario 4_Power demand and energy available in the PCM storage

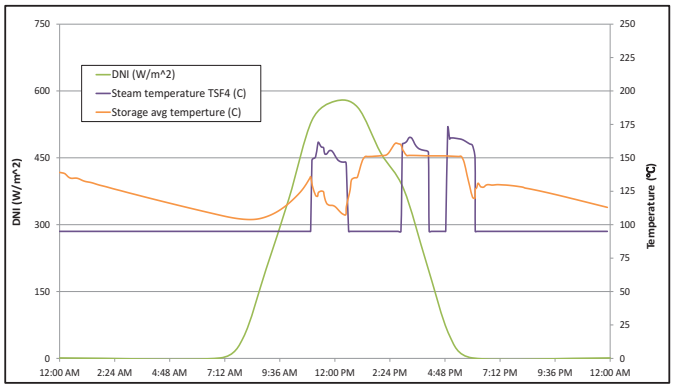

Fig. 17: Scenario 4_ Temperatures of supplied steam and tank average temperature over daily time.

5. Conclusions and Future Works

Dynamic simulations of four different scenarios have been studied in order to properly address the size of solar collectors and PCM thermal storage for a multifunctional rural energy system. The engineering of the system is looking to develop several forms of thermal energy supplied to the school. One of the priorities is a reliable and fossil fuel-free cooking system. Furthermore, the thermal energy accumulated is used during the afternoon to provide high temperature steam to a dedicated hay processing digester. Several technology scenarios have been modelled on a multi objective optimization. Results of the simulations are summarized in Table 2. Scenario 1 shows the best cooking temperature, with an average storage temperature close and stable at 150°C for the most part of the working daily time (a small overheating up to 180°C is visible in the simulation). Due to the large collector area this temperature is rapidly reached at the beginning of the day ensuring reliable temperatures even during the daily cooking activities. Scenario 3 also achieves interesting results. First, a reduction of collectors and PCM material definitely affects the total capital investment. In addition, no overheating is visible in the storage tank and the temperature is constant at 150°C. Despite this, the reduction of collectors' number deeply affects the temperature reached in the storage at the beginning of the cooking time, with dangerous effects on the cooking effectiveness. Scenarios 2 and 4 have been

discharged due to mismatching values between the storage availability and the steam generation temperatures.

Based on these considerations, Scenario 1 is identified and selected as the most reliable solution despite the initial investment cost. At the same time, Scenario 3 could be deeper investigated especially considering the possibility of shifting the cooking habits of the school by 30-45 minutes later in the morning. If agreed with the local community, solar power instantly available could be directly used to satisfy the thermal necessities of the school at lunchtime reducing the necessity of thermal backup. The system could be potentially resized in order to achieve a reduction of costs (reducing the PCM storage) without affecting the performances. This hypothesis may also help to reduce the required dimension of solar collectors, directly affecting the economic investment but maintaining the efficiency and reliability of the system.

Tab. 2: Technical specification of the simulations performed and summary results.

	CPC Area (m^2)	PTC Area (m^2)	PCM total mass (kg)	Max. Energy stored (kWh)	Max Storage avg. temp. (°C)	Min Storage avg. temp. (°C)	Max Steam temp. TSF4 (°C)
Scenario 1 (Fig. 4)	12	3.2	90	7,7	179	108	182
Scenario 2 (Fig. 5)	10	3.2	70	5,6	171	106	177
Scenario 3 (Fig. 6)	7	3.2	70	4,6	150	105	170
Scenario 4 (Fig. 7)	7	3.2	55	4	160	103	169

6. Acknowledgment

Authors acknowledge the support of several activities related to the activity of STAR project. In particular, the FP7-IRP-STAGE STE, grant agreement n° 609837 and the FP7-DIGESPO, grant agreement n° *241267*. The results of the study presented in this paper are part of the ITPAR III bilateral collaboration program between Indian Department of Science and Technology and the Autonomous Province of Trento.

References

1. (Accessed 20.05.2016) http://www.worldometers.info/world-population/india-population/
2. (Accessed 21.09.2016) http://news.bbc.co.uk/2/hi/south_asia/6911544.stm
3. World Economic Outlook. International Monetary Fund (IMF). Retrieved 2014-04-08
4. (Accessed 21.09.2016) University of Washington, Web article: https://artsci.washington.edu/news/2013-10
5. Ashwani Kumar, Kapil Kumar, Naresh Kaushik, Satyawati Sharma, Saroj Mishra. Renewable energy in India: Current status and future potentials. Renwable and Sustainable Energy Reviews, Volume 14, Issue 8, October 2010.
6. (Accessed 21.09.2016) http://www.nistads.res.in/indiasnt2008/t6rural/t6rur85.htm
7. (Accessed 21.09.2016) Ministry on new and renewable energy website: http://www.mnre.gov.in/solar-mission/jnnsm/introduction-2/.
8. (Accessed 21.09.2016) http://solarcooking.wikia.com/wiki/India
9. Tribeni Das, R. Subramanian, A. Chakkaravarthi, Vasudeva Singh, S.Z. Ali, P.K. Bordoloi. Energy conservation in domestic rice cooking. Journal of Food Engineering 75, July 2006.
10. Dilip Kumar De, Muwa Nathaniel, Narendra Nath De, Mathais Ajaeroh Ikechukwu. Cooking rice with minimum energy. Journal of Renewable and Sustainable Energy 6, January 2014.
11. (Accessed 5.04.2016) http://www.digespo.eu/default.aspx.
12. Kuldeep Ojha, Need of independent rural power producers in India – an overview. Journal of Clean Technologies and Environmental Policies, 12, November 2009.
13. J.M. Cabello, J.M. Cejudo, M. Luque, F. Ruiz, K. Deb, R. Tewari Optimization of the size of a solar thermal electricity plant by means of genetic algorithms. Journal of Renewable Energy 36, November 2011.
14. (Accessed 5.09.2016) http://www.paradigmaitalia.it/homepage
15. (Accessed 21.09.2016) http://www.idfa.org/news-views/media-kits/milk/pasteurization.
16. (Accessed 21.06.2016) Weather Data References: SEC, MNRE, Solar Energy Centre, Ministry of New and Renewable Energy, Government of India. http://mnre.gov.in/sec/solarassmnt.htm.

17. (Accessed 5.04.2016) https://www.modelica.org, last access April 2016.
18. Adriano Desideri, Simone Amicabile, Fabrizio Alberti, Silvio Vitali Nari, Sylvain Quoilin, Luigi Crema, Vincent Lemort. Dynamic modeling and control strategies analysis of a novel hybrid small CSP biomass plant for cogeneration applications in building, ISES Solar World Congress 2015, Conference proceeding.
19. Casati, E., Galli, A., Colonna. Thermal energy storage for solar-powered organic Rankine cycle engines. Solar energy 96, October 2013.
20. D. Haillot, T. Bauer∗, U. Kröner, R. Tamme. Thermal analysis of phase change materials in the temperature range 120–150 °C. Joiurnal of Thermochimica Acta 513, 2010.

Conference Proceedings

EuroSun 2016
Palma de Mallorca (Spain), 11 - 14 October 2016

Efficiency Analysis of Solar Assisted Heat Supply Systems in Multi-Family Houses

Oliver Arnold[1], Oliver Mercker[1], Jan Steinweg[1] and Gunter Rockendorf[1]

[1] Institut für Solarenergieforschung Hameln (ISFH), Am Ohrberg 1, 31860 Emmerthal (Germany)

Abstract

There are two major approaches to mitigate energy-related emissions of dwellings: Insulating the building's envelope on the one hand and modernizing its heat supply system on the other hand. Often the insulation of dwellings leads to lower energy savings than expected (Greller et al., 2010), which is assumed to be related to the heat losses of the heat distribution system itself. So attention needs to be drawn to the modernization of the heat supply system, which can lead to a significant reduction of the building's final energy demand (Jahnke et al., 2015). This paper is following this approach and focuses on the heat supply and distribution system of multi-family houses (MFH), representing a significant share of Germany's residential market. The present work compares different systems for multi-family houses by means of its primary energy demand, energy efficiency and economic aspects. Heat distribution losses are analyzed and their relevance for efficient systems is discussed. Based on this analysis, the work highlights effective integration routes of solar thermal supply systems which may lead to increased efficiency of the overall heat supply system.

Keywords: *Multi-family houses, heat supply, heat distribution, heat distribution losses, energy efficiency*

1. Introduction

Measured energy demands of insulated dwellings are often higher than theoretically expected, as shown by Majcen et al. (2013). One reason for this are so called 'rebound effects' caused by the dwelling's inhabitants, such as higher room temperatures or higher air exchange rates, which are difficult to model. Another, technical reason for the observed model/measurement divergences are commonly related to heat losses of the heat distribution system. A part of the distribution losses replaces normal operation of the room heating elements and thus may be credited to the energy demand. However, if there is no heat demand at a certain time and in an individual room, occurring distribution losses lead to overheating and as a result to increased transmission and ventilation losses of the building. In this case, the usability of the heat losses is very low. This effect is pronounced in well insulated buildings. In the present paper, this situation is analyzed by means of simulation studies.

A detailed model of a multi-family house has been established, using the TRNSYS software as appropriate modelling environment. The underlying building model refers to typical construction types and equipment which is representative for multi-family houses in Germany. The model allows the dynamic investigation of temperatures, mass flow rates and energy balances as well as the impact of heat distribution losses of individual rooms as well as the entire building. This allows a detailed investigation of the heat losses and their potential contribution to the space heating demand. As a matter of fact, such analysis must be based on simulations, because reproducible and highly analyzable field data are impossible to determine because of the enormous number of parameters, the inhabitant's behavior, the building and weather dynamics and distributed energy flows.

The modelling of the building's heat demand is based on an investigation of different systems that will be compared and rated in this paper. This investigation is initiated concerning the most common heating system in Germany. Based on this, different approaches are rationalized to reduce respective heat distribution losses, in order to improve their usability and – thereby – to decrease the system's energy demand.

doi:10.18086/eurosun.2016.04.21 Available at http://proceedings.ises.org

Eventually, a solar thermal system is suggested as effective approach to increase the energy efficiency of the building. The appropriate design of such solar thermal system is explained related to the analysis of building and energy system and economical aspects are reflected.

2. Simulation environment, building and meteorological model

The simulations are carried out employing the TRNSYS 17 modelling suite, a dynamic system simulation program. The temporal resolution is adjusted by a simulation time-step of one minute and the timescale of a typical simulation spans a one-year period. The building's heat distribution system is modelled quite detailed to correctly simulate the dynamic behavior of the heat distribution and especially the heat losses. It regards over 100 duct sections (using Type 604) for proper spatial resolution of the heat distribution system in the building, which are capable of dynamically calculating heat losses under local thermal and flux conditions.

The model of the considered multi-family house (MFH) was built employing the module TRNBUILD. The model is based on statistical data of MFH designs in Germany. The model comprises four floors, unheated basement and staircases and eight identical flats. Each flat contains five rooms and a corridor. The model assumes an occupation by two dwellers per flat. Every room of the building represents an individual thermal zone which is thermally interacting with adjacent rooms (zones) through walls, floors/ceilings and pipe ducts. In total, the model building consists of 52 thermal zones. The outer shell of the building is assumed to be insulated according to the corresponding German regulation EnEV (2014), always using the minimum values defined by here. For the internal room temperatures a set point of 20 °C is used. The climate model is based on Meteonorm data for the city of Zurich (Swiss), which is proven to be appropriate for central-European moderate climate situations, see Streicher et al. (2003). The resulting specific overall space heating demand of the model building is 35 kWh/(m² a) and a total heat demand is 56 kWh/(m² a). This includes load profiles for domestic hot water as described in Mercker et al. (2016a).

3. Investigated Systems

Four-line pipe network (4L)

A four-line heat distribution network with central heat generation, as shown in Figure 1, is a very common heat supply system for MFH in Germany, see Wolff et al. (2012). Heat for space heating (SH) and domestic hot water (DHW) is distributed via two separate pairs of pipes. The DHW is stored in a central storage at a minimal temperature of 60 °C for hygienic reasons. The heat generation system studied here represents a condensing gas boiler. The design temperatures of the space heating system are 50 °C (flow-line) / 35 °C (return-line) at an ambient temperature of -10 °C.

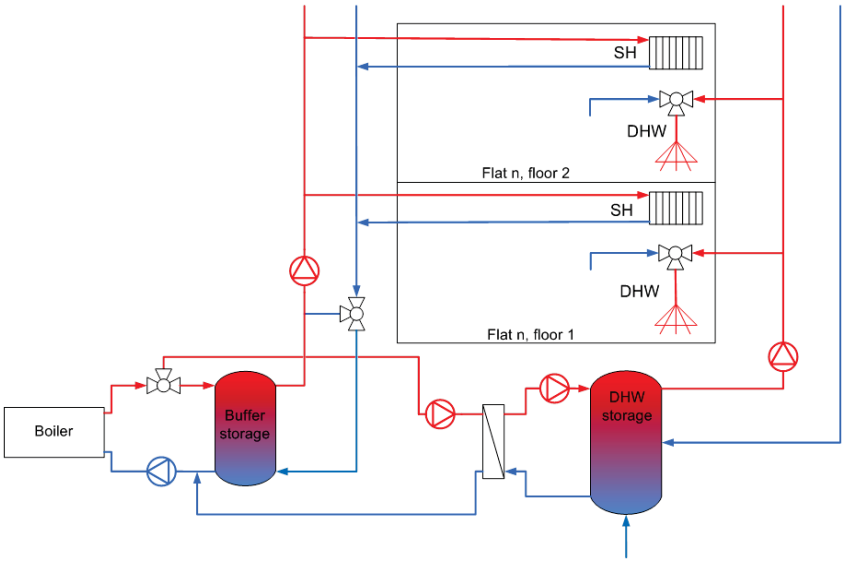

Fig. 1: Four-line pipe network with central heat generation

Dual-line pipe network (2L)

The second set-up considers a dual-line pipe network as shown in Figure 2. It comprises only one pair of pipes for both DHW and SH supply, which contains heating water. The DHW is then heated up on demand in decentralized heat transfer units, which are installed in every individual flat. Accordingly, the overall fluid temperature in the distribution pipes may be allowed to drop below 60 °C. The heat distribution network must meet a DHW comfort criterion of 45 °C draw temperature. To achieve this securely, the supply temperature is set to 50 °C in the simulation. The advantage of 2L over the 4L pipe network results from the lower forward line temperature, the absence of a central DHW-storage as well as the reduction of overall pipe length. Simplified integration of solar thermal heating technology is another advantage of 2L pipe networks in general. An optimized 2L system variant (2L-opt) allows a further reducing of the pipe network's temperature level by electric backup heaters in the local heat transfer modules of the individual flats. The backup heaters ensure the desired tap water temperature (of 45 °C - in this case). They are arranged after the DHW heat exchanger (compare Figure 2).

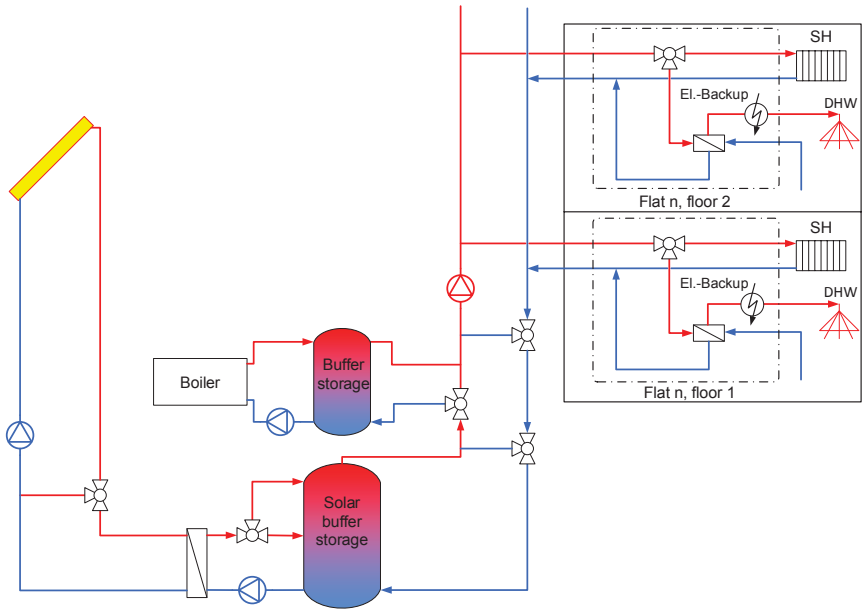

Fig. 2: Dual-line pipe network with central heat generation and integrated solar thermal system

Dual-line pipe network with decentralized storages

The design of this system is the same as standard 2L systems, but with decentralized buffer storages for DHW preparation. These buffers are assumed in each individual flat. The DHW is prepared on demand (when tapped) by near-by domestic hot water modules, which draw heat from the buffers for this purpose (compare Figure 3).

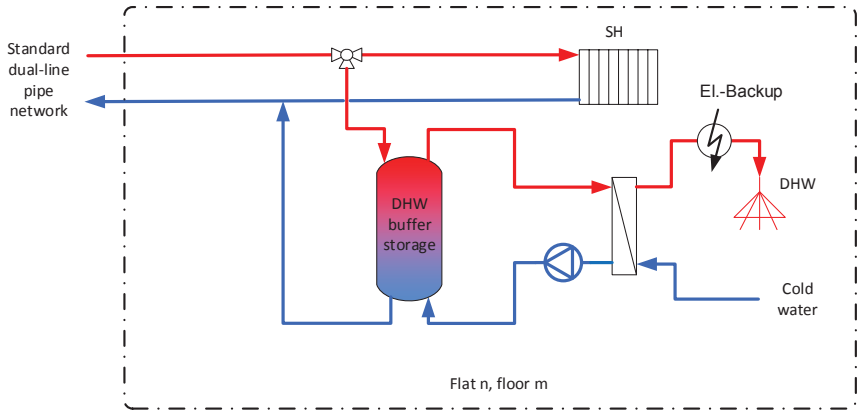

Fig. 3: Dual-line pipe network with decentralized storages in each individual flat

Dual-line pipe network with decentralized boilers

Another design approach to reduce distribution-related heat losses is the de-centralization of the heat generation using fossil fuels. In the present model this can be achieved by decentralized gas boilers installed in the individual flats (compare Figure 4). Because of the low-power level of the boilers, decentralized DHW storages (identical with those in the previous system) are necessary to grant for DHW-comfort. For this concept, the only heat distributed from the heat central to the flats is solar heat.

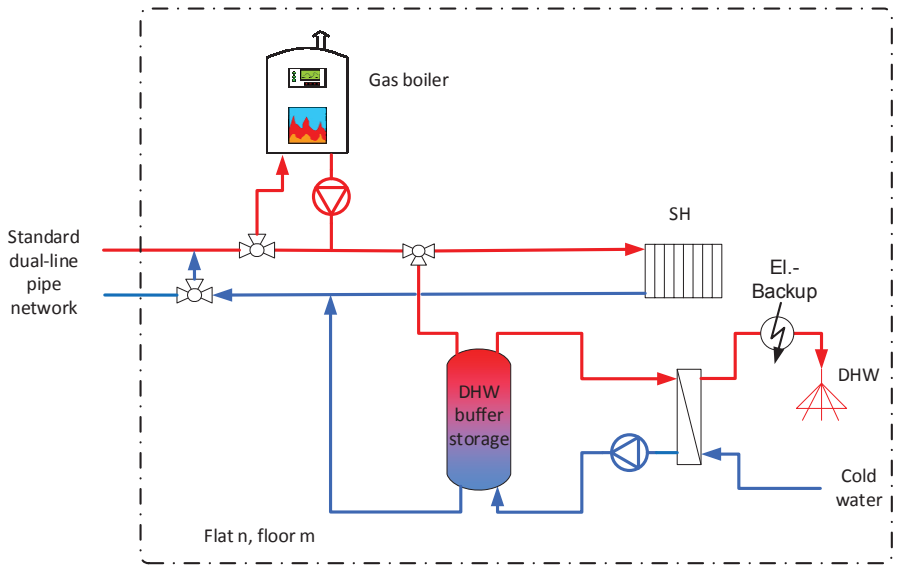

Fig. 4: Dual-line pipe network with decentralized boilers in each individual flat

Dual-line pipe network with decentralized heat pumps

Another design approach regards decentralized heat pumps for heat generation in the individual flats. The heat pumps are assumed to supply small, localized buffer storages. In contrast to the two previous model designs, the local storages, which contain heating circuit water, do supply heat for both SH and DHW, the latter via DHW modules (compare Figure 5). The model design assumes that the common heat source supplying the heat pumps is produced from geothermal resources through borehole heat exchangers. For this purpose, low-temperature geothermal heat is buffered in a central heat storage from which it is distributed to the individual heat pumps in the flats. In an alternative setting, the central heat supply may also be supported by a solar thermal system. In this case, the central storage keeps also the solar heat.

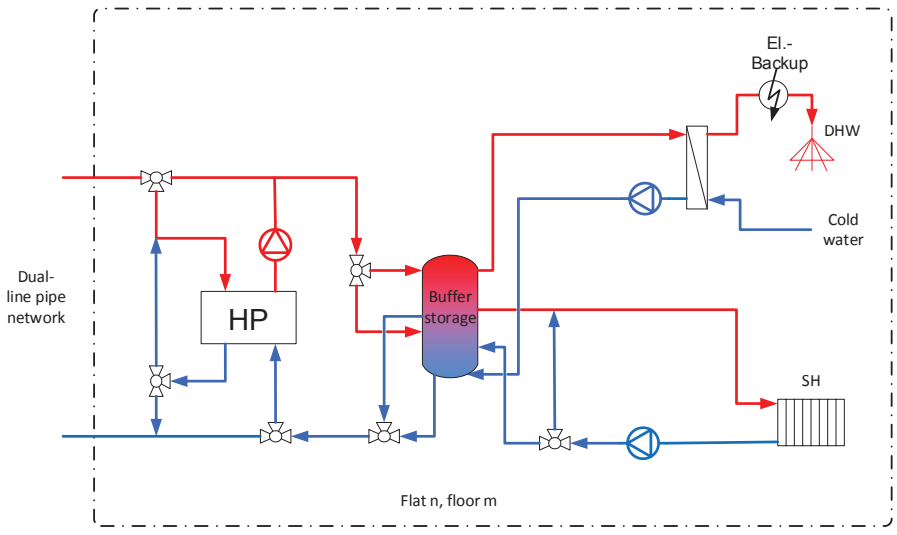

Fig. 5: Dual-line pipe network with decentralized heat pumps in each individual flat

4. Results

The results are presented in three separate sections: Firstly, regarding the optimization of the heat distribution network, secondly, regarding the utilization of solar heat and thirdly, regarding the alternative supply routes.

Optimization of the heat distribution network (2L-opt)

The optimization of the heat distribution network regards the transformation from the common four-line pipe network to the dual-line pipe network, keeping the conventional central gas boiler for heat generation in place. Figure 6 shows the impact of this configuration change on the building's overall heat demand, comparing four situations: (1) an idealized reference system without any heat distribution losses; (2) the four-line and (3) the dual-line systems as described above; (4) a further optimized dual-line pipe network, referred to "2L-opt" in Figure 6. The latter assumes electric backup heaters in the local heat transfer stations of the individual flats, which allows reducing the temperature level in the flow line pipe from 50 °C to 40 °C to further reduce the distribution losses without suffering in DHW comfort.

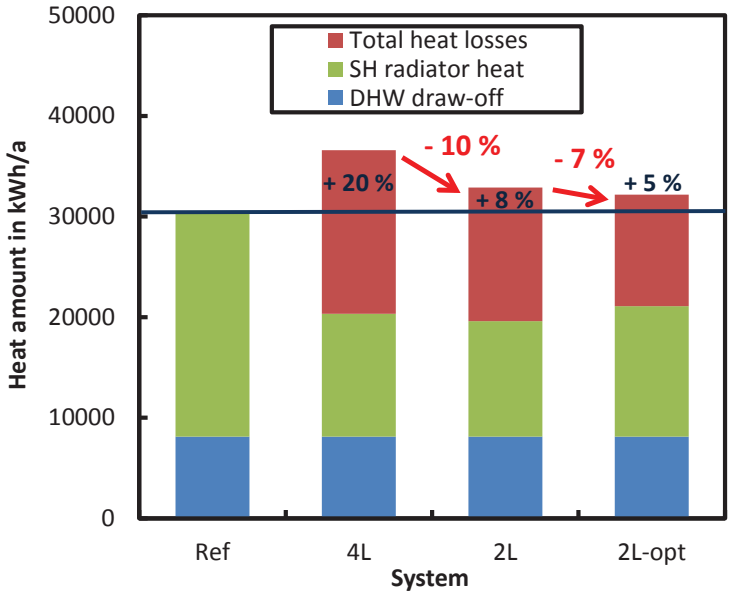

Fig. 6: Impact of distribution pipe network optimization on the buildings heat demand

The conventional 4L system exhibits 20% higher heat demand, than the idealized, loss-less reference system, thus indicating the total optimization potential of the supply design at given room comfort level. The configuration change from 4L to a basic 2L setting reduces the total energy demand by 10 % with respect to the conventional design, but the demand is still 8 % above the idealized reference system. The optimized 2L system allows further reduction by 7 %, resulting into an offset of 5 % above the ideal system. In other words, the reduction potential of the model building is already met to an extent of 75 % by a configuration change of the heat distribution network, without regarding advanced de-centralizing of the entire heat generation system (except for the electric DHW backup heaters). This reduction is the result of minimizing the heat exchanging surface area (from 4L to 2L) and the decreased pipe network temperatures (from 4L via 2L to 2L-opt). Figure 4 provides the details: Unusable heat distribution losses are reduced significantly by the described configuration change such that the distribution efficiency is increased. This efficiency may be judged from the usability of the heat losses, which is defined as the ratio of the usable heat losses of the system and the overall heat losses,

$$Usage\ factor\ of\ losses = \frac{Q_{loss,use}}{Q_{loss,total}} \qquad \text{(eq. 1)}$$

"Usable" are heat losses from the piping systems, if the heat leaks into the building so as to support the space heating. "Unusable" heat losses lead to higher room temperatures as designed and thus are finally dissipated

to the environment. As of Figure 7, the usability of the heat losses can be increased from 63 to 86 % by the design change from 4L to the 2L-opt setting.

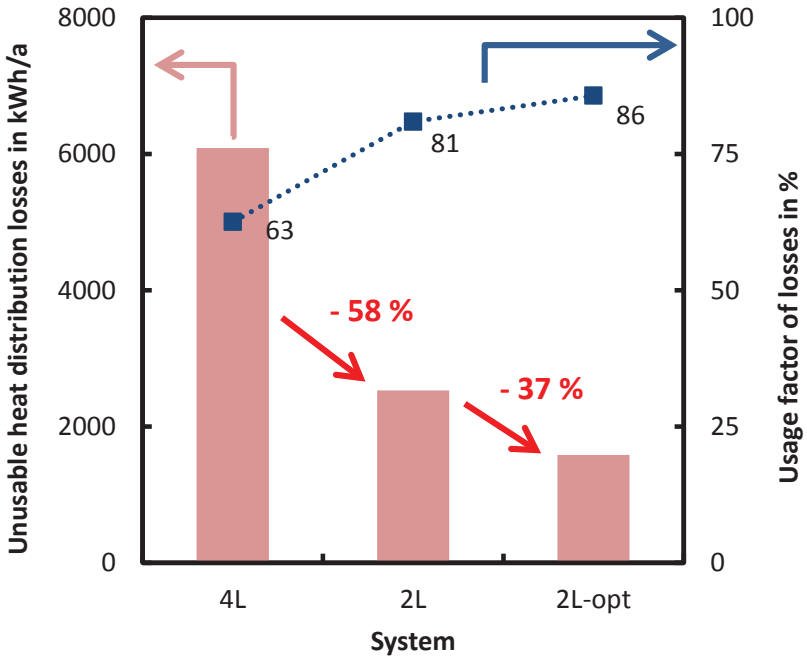

Fig. 7: Impact of the heat distribution network optimization on the usability of heat losses

The remaining unusable heat distribution losses, which mark the heat demand's reduction potential, amount to 1582 kWh or 5 % of the total energy demand according to Figure 6. These results are based on the strong assumption that all inhabitants share the same heating habits (single-zone temperature: 20 °C in all rooms). It may be noted that simulations performed with localized (multi-zone) room set temperatures exhibit even more reduced usability ratios, see Mercker et al. (2016b & 2016c). In non-homogeneously heated buildings the heat distribution losses are expected to be higher (doubling is possible) and their usability lower (even less than 50 %) – All despite this, the present study keeps the assumption of homogenous set temperatures of the rooms for the sake of simplicity (individual living behavior is difficult to predict) as well as comparability. Therefore, the discussed results mark the lower end of the expected spectrum.

Utilization of solar heat

The integration of a solar thermal system leads to both decreased fossil energy demand and significant reduction of heat distribution losses covered by fossil energy. Figure 8 indicates how solar radiation and unusable heat distribution losses coincide during the summer months. The coincidence can be used to increase the energy efficiency of heat supply systems.

The reason for the peak of unusable heat losses during summer lies in the fact of missing space heating demand during this period, which might profit from heat losses in a situation of still necessary DHW heat distribution demands. Therefore, 54 % of the total unusable heat losses occur during May to September. Because the solar thermal system has its production maximum during the same period, it is suitable to cover the summer heat demand from solar resources. The model predicts 54 % reduction of fossil energy consumption related to unusable heat distribution losses.

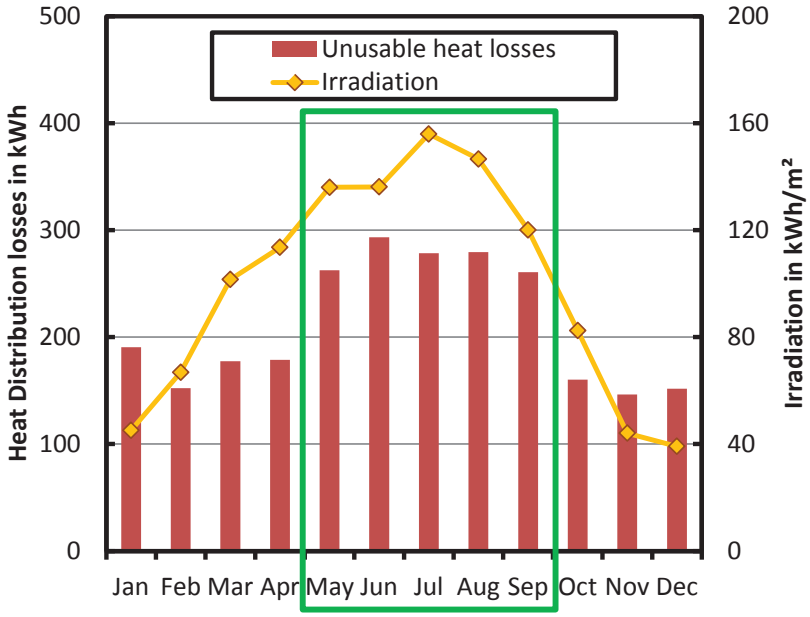

Fig. 8: Comparison of monthly solar irradiation and unusable heat distribution losses of a four-line pipe network

The collector aperture area is calculated with reference to the German guideline VDI 6002-1 (2004). The resulting field size is in the range from 5 to 8 m² or 0.3 to 0.5 m² per person. Additionally, collector areas of 16, 24 and 32 m² have been simulated to investigate the effect of larger solar thermal systems. The solar storage size is set to 50 l/m²coll. Table 1 shows the relation of different field sizes to the solar yield (as energy output of the solar storage) and the gained solar coverage of the total heat demand.

Tab. 1: Size comparison of the solar heat systems

Collector area in m²	Collector area in m²/person	Solar yield in kWh/m²	Solar coverage of total heat demand in %
8	0.5	474	12
16	1.0	411	20
24	1.5	350	26
32	2.0	306	30

We see that with a collector field size of 32 m², a solar coverage of the total heat demand of 30 % can be reached, comprising a collector yield of 306 kWh/m². Note that this field size is at least four times larger than the area recommended by the considered guideline VDI 6002-1 (2004).

Figure 9 shows both, the monthly heat demand, distinguished between SH, DHW and distribution losses, and the monthly solar yield for the four examined collector field sizes in one diagram. Both y-axis are limited to 2000 kWh, although the monthly heat demand (which is the sum of total heat losses, DHW-draw-off and radiator heat) exceeds 2000 kWh from November to March.

We conclude from this figure, that the total heat demand of the model building during May to September may be covered by a solar thermal system with a minimal collector area of 32 m². A 16 m² system still allows a (nearly) 100% solar fraction within July and August. The 8 m² system, designed according to the VDI 6002-1 (2004), however, only just covers the DHW demand, but nothing of the heat distribution losses.

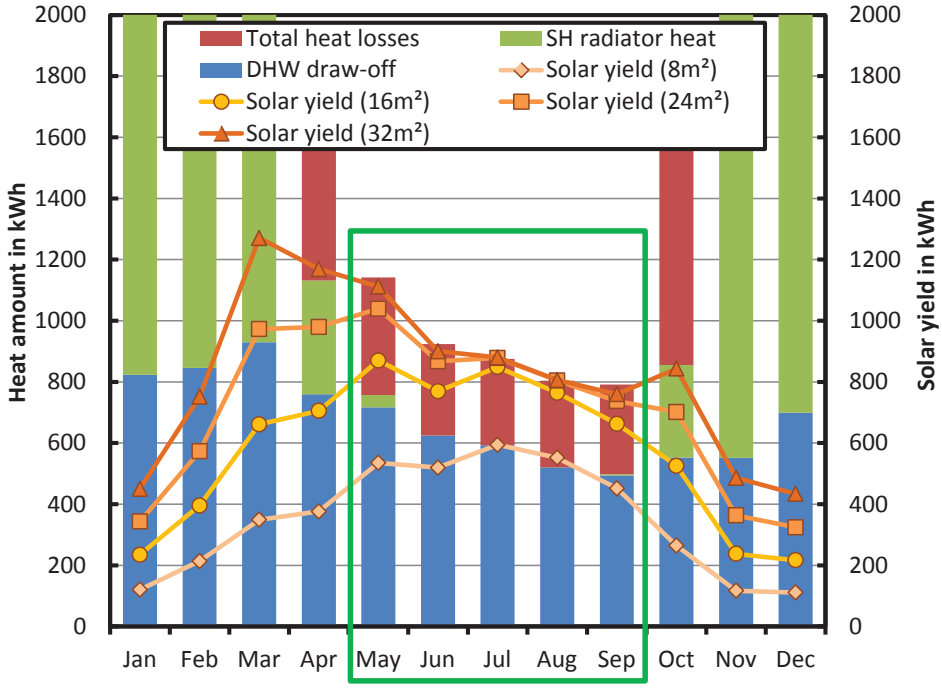

Fig. 9: Comparison of the monthly heat demand of an optimized dual-line pipe network and collector yield reached by different field sizes

Using a suitably scaled solar thermal system, the total heat demand – including distribution losses – may be completely supplied during May to September and the boiler may be turned off during this period. This saves ca. 54 % of the formerly fossil-fuel covered unusable heat losses, as well as the standby losses of the boiler and related inefficient part load operation during the summer season. In sum, this means that the remaining pipe network induced optimization potential for the building's heat demand of 5 % (or 1582 kWh/a according to concept 2L-opt) is reduced further to 2 % (or 728 kWh/a).

The alternative approach with the integration of electric backup heaters for DHW supply into the 2L system, installed in the local heat transfer stations of individual flats, allows the boiler to be turned off during the summer months without suffering a loss in DHW comfort (as with the design before), but the solar thermal systems may be designed smaller. The model predicts that in this case the solar thermal system may be down-sized to 8 m² collector area. Because a down-size of the solar thermal system also reduces the solar yield during spring, autumn and winter, this design approach incorporates less fossil-fuel savings, than the design without electricity supply, but larger solar yields than discussed before. Table 2 shows that with an enlarged solar collector from 8 to 16 m², the electric energy will be reduced by two thirds. With 32 m², electric heating is nearly negligible. Note, that the lower pipe network's temperature in summer leads to significantly higher collector yields at smaller collector areas.

Tab. 2: Heat generation and energy demands for different collector field sizes in the 2L-opt system

Collector area in m²	Solar yield in kWh/a	Electricity consumption in kWh/a	Gas consumption in kWh/a
8	4210	1156	31174
16	6891	399	29671
24	8586	147	28276
32	9869	65	27066

Alternative systems

The last studied design approach to minimize the unusable part of the heat distribution losses regards fully-decentralized heat generation. This situation is modelled concerning decentralized boilers or heat pumps in

individual flats with and without DHW storage tanks, see Section 3. Integration of local storages allows partial downtimes of the building-wide heat distribution network while still maintaining DHW comfort. The model regards nightly (11.00 pm to 5.30 am) downtimes of the central heat supply for this purpose. The results show that the respective distribution losses are avoided indeed. However, the decentralized storages incorporate increased heat leakage rates, thus counteracting the overall heat loss balance. In sum, losses of the storages exceed the savings of heat losses of the heat distribution network.

Figure 7 shows the total heat distribution losses of the examined systems and the respective usage factors. The diagram confirms the high loss-reduction potential of a 4L to 2L configuration change and the subsequent system optimization of Figure 6. Among the studied decentralized designs, the system with decentralized boilers exhibits lowest overall heat losses. The overall reduction potential of this design is comparable to the optimized 2L system, but the usage factors of the 2L-opt design is significantly higher: Heat leakage from commonly insulated DHW storages in the decentralized boiler system are significant but can be utilized for SH of the flats only during the heating season. The simulations show that the losses during summer are large enough to even counterbalance the annual usage factor below the level of the competing 2L-opt design.

The system design comprising decentralized heat pumps exhibits higher losses because the decentralized storage volumes for combined DHW and SH storage are two times larger than DHW-only storages. Larger storage volumes are necessary for the operation of the small heat pumps (2.5 kW condenser power in the present study).

To summarize, the simulation study suggests that decentralized storages should be avoided because of their significant heat loss rates, which may be utilized for space heating only partly during the course of the year. In specific design cases which allow avoiding decentralized storages, however, such de-centralized solutions are expected to be more efficient than centralized ones from the perspective of heat-loss reduction.

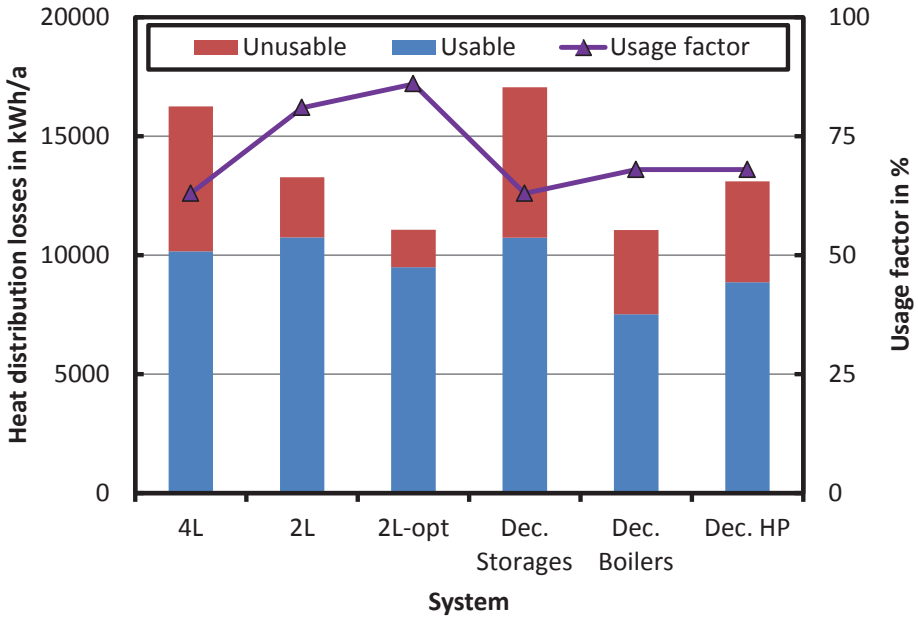

Fig. 10: Comparison of heat distribution losses and the respective usage factor for the studied systems.

The perspective of energy demand of the studied solar designs is provided in Figure 11, specifying both the final energy demand including losses (by columns) and the primary energy demand (by plot lines). The latter takes into account three different primary energy factors for the electricity part: 3.0 for fossil-based electric energy (EnEV 2002), 2.4 for the electric energy mix of Germany in 2015 (EnEV 2014) and 1.8 for the same mix as predicted for 2016 (EnEV 2016). All design cases regard a solar thermal system with 32 m² collector area.

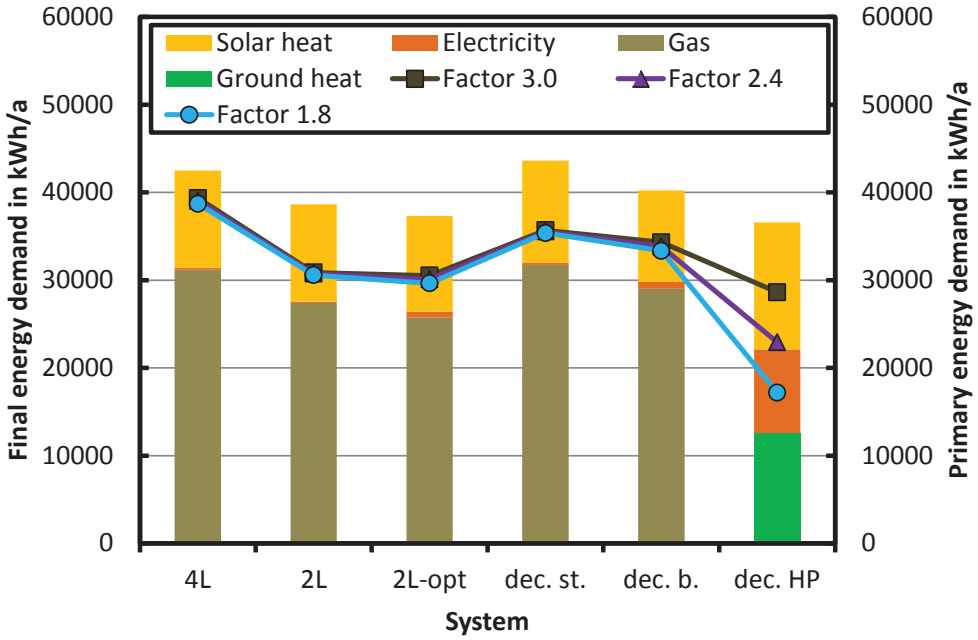

Fig. 11: Comparison of the final and primary energy demand of different systems

The solar thermal supply share is almost the same for all of studied model designs, except for the system with decentralized heat pumps. Here the solar share is significantly higher (ca. + 31 %), than for the other systems. The reason for this observation is that the solar heat can additionally be used indirectly – as a heat source for the heat pump (both, ground heat exchangers and solar collectors are supplying the same central heat storage). In fact, the direct use of the solar energy for DHW or SH is even lower than in other designs. The indirect integration route also incorporates the advantage of low-temperature solar energy production, which also allows using cheaper collector types (e.g. uncovered collectors).

Regarding the final energy demand of the studied systems the optimized dual-line pipe network shows the smallest demand among the fossil supplied designs. The system with decentralized storages has the highest demand owing to the heat losses of the storages. Designs with decentralized boilers have slightly higher final energy demands than the 2L system. The decentralized heat pump system has a lower final energy demand than the optimized dual-line pipe network. The reason for that is the further reduction of distribution heat losses, due to partial operation of the pipe network below indoor temperature even heat gains occur, because the ground heat exchangers deliver heat at an average temperature of 7 °C.

A comparison of the primary energy demands of the studied designs leads to the result that the design comprising decentralized heat pumps has the lowest demand, because it can benefit from the primary factor Germany's electric energy mix. Next to it is the design comprising the optimized 2L configuration.

5. Conclusion

Heat distribution losses have a significant impact on the heat demand of well insulated multi-family houses and must be regarded in situations of both, new constructions and system retrofits. Essential for decreasing the heat distribution losses is to minimize the length of pipe ducts and to lower the distribution net's temperature. Both can be realized by choosing a dual-line pipe network instead of a common four-line pipe network. When electric backup heaters are installed, the system's efficiency can be further increased by an additional reduction of the flow line temperatures.

A well-designed dual-line pipe network is even more effective regarding distribution heat losses as well as final and primary energy demand than systems with decentralized boilers, at least when they also have decentralized storages.

Solar thermal systems are of great advantage both to increase the system's effectiveness and to lower the system's final and primary energy demand. But it is of high importance to scale the system to the appropriate size. Common guidelines in Germany recommend field sizes that are quite small. This modelling study shows that such design is not able to cover the building's heat demand including distribution losses even in July and August. Thus, under energetic aspects, scaling the collector field to a bigger size is reasonable. This is because most of the system's unusable heat losses are occurring during the summer months because of their low usability in this period. With a large scaled solar thermal system of 2 m^2_{coll} per person, the heat demand can be covered completely by solar thermal energy from May to September and the boiler can be switched off during this time. By that, a total of 54 % of the overall unusable losses can be covered by solar heat. The same effect can be reached with smaller scales of the solar thermal system if electric backup heaters are installed in the heat transfer stations to compensate the lack of solar heat in case of a boiler that is switched off in summer.

Compared to a common four-line pipe network, an optimized dual-line pipe network with a sufficiently scaled solar thermal system (2 m^2_{coll} per person) reduces the unusable heat distribution losses by 87 %, which leaves a potential for further optimizations of only 2 % of the total heat demand. Doing that, the building´s heat demand is reduced by 12 %. The gas consumption is reduced by 39 % and the primary energy demand (factor 2.4 for electricity) by 36 %.

Using a heat pump for heat generation grants better use of solar energy and the lowest energy demand (regarding final and primary energy) of all investigated systems. Though not examined in this study, it can be assumed that an optimized dual-line pipe network in combination with a central heat pump and a suitable solar thermal system would be the most effective system in every aspect. Further research work is necessary to validate this.

6. Acknowledgement

The project MFH-re-Net (FKZ 03ET1194A) is funded by the German Federal Ministry for Economic Affairs and Energy based on a decision of the German Federal Parliament. Project partners of the ISFH are *Delta Systemtechnik GmbH*, situated in Celle, *ProKlima*, *Heimkehr Wohnungsgenossenschaft eG*, and *Gesellschaft für Bauen und Wohnen Hannover mbH (GBH)*, all situated in Hannover. The authors are grateful for the financial support. The content of this paper is in the responsibility of the authors. Moreover, the authors would like to express their appreciation to Prof. Dr.-Ing. Oliver Kastner for the detailed and valuable review of this paper.

7. References

Greller, M. et al., 2010. Universelle Energiekennzahlen für Deutschland. Bauphysik 32 (published in German)

EnEV, 2014. Verordnung über energiesparenden Wärmeschutz und energiesparende Anlagentechnik bei Gebäuden (Energieeinsparverordnung - EnEV), URL (abgerufen am 30.09.2016): http://www.enev-online.com/enev_2014_volltext/index.htm

Jahnke, K. et al., 2015. Wirksam sanieren: Chancen für den Klimaschutz. Co2online gemeinnützige GmbH, Berlin (published in German)

Majcen, D.; Itard, L.; Visscher, H., 2013. Actual and theoretical gas consumption in Dutch dwellings: What causes the difference? Energy Policy 61 460-471

Mercker, O. et al., 2016a. Ansätze zur Reduktion konventionell gedeckter Verteilverluste in solar unterstützten Mehrfamilienhäusern. Tagung Gleisdorf SOLAR 2016, Gleisdorf (published in German)

Mercker, O. et al., 2016b. Bestimmung, Bewertung und Reduktion von Wärmeverteilverlusten in Mehrfamilienhäusern. Tagung CESBP/BauSIM 2016, Dresden (published in German)

Mercker, O. et al., 2016c. Wie sind zentrale Wärmeversorgungssysteme in hochgedämmten Gebäuden zu gestalten? Ausführliches Skript zur OTTI Solarthermie Tagung 2016, Bad Staffelstein (published in German)

Streicher, W. et al., 2003 (revised February 2007): Analysis of System Reports of Task 26 for Sensitivity of Parameters - A Report of IEA SHC - Task 26: Solar Combisystems, Institute of Thermal Engineering, Graz University of Technology, Graz

Verein Deutscher Ingenieure, 2004. VDI 6002 Blatt 1 – Solar heating for domestic water. General principles, system technology and use in residential buildings. Düsseldorf

Wolff, D. et al., 2012: Einfluss der Verteilungsverluste bei der energetischen Modernisierung von Mehrfamilienhäusern – Analyse und Ableitung von Optimierungsmaßnahmen. Projekt im Auftrag des proKlima enercity-Fonds, Hannover/Braunschweig/Wolfenbüttel

Conference Proceedings

EuroSun 2016
Palma de Mallorca (Spain), 11 - 14 October 2016

Comparative experimental analysis of solar thermal energy counters

A. González Valero [1], J. Cadafalch [2]. R. Consul [2] y R. Ruiz [2].

[1] RDmes Technologies S.L., Terrassa (Spain).

[2] Universitat Politècnica de Catalunya BarcelonaTech, Barcelona (Spain).

Abstract

In order to monitor the energy yield of solar thermal systems, a thermal energy counter with connectivity must be installed. Multiple thermal energy counters and connectivity criteria are available. However, implementation and communication costs differ drastically from one to another. Taking into account market restrictions, in order to widely implement monitoring of energy yield of solar thermal systems these costs should be reduced as much as possible.

The paper presents an experimental comparison of the energy yield of a solar thermal system measured with different energy counters at communication time steps of one hour in order to reduce communication costs. These data are compared to those obtained from detailed measuring of the energy yield with time steps of 1 minute. The evaluated energy counters combine different technologies for the measuring of the flows and temperatures (ultrasound flow sensor, constant flow, single-jet flow meter, vortex flow sensors and RTDs).

Keywords: *solar thermal systems, energy counter, monitoring*

1. Introduction

Recently, there is an increased market demand of low cost monitoring equipment for solar thermal systems in order to evaluate their performance. Energy yield of the solar thermal system is the most basic parameter to be monitored. In the market there are multiple thermal energy counter solutions with different communication procedures.

The authors have recently been working on the measuring of solar thermal energy yield at the primary circuit using low cost commercial energy counters with energy integration time steps of one hour in order to minimize volume of data, and therefore, costs.

A number of three low-cost energy counters have been analysed. They have been installed in the primary circuit of a solar thermal system. The energy counters use different sensors technologies. Temperatures at the thermal fluid are measured by RTD sensors directly immersed in the flow or assembled in a sheath or using multivariable vortex flow meter. Volumetric flow is measured by a single jet meter, a vortex-flow meter, or set at a constant pre-calibrated value. Additionally, detailed measuring of the energy yield of the system primary loops is also performed in time steps of one minute with a none-intrusive meter based on ultrasound technology for the volumetric flow measurement and RTDs for the temperature measurements.

Main technical parameters of the analyzed energy counters are described in section 2 and 3. Results obtained are presented in section 4 comparing the instantaneous and daily energy yield measured with the different energy counters. Some conclusions are finally also presented.

2. Conceptual description of a thermal energy monitoring system

A thermal energy monitoring system is an instrument that reads the thermal energy produced in a plant and transfers the energy value through any kind of communication channel (Ethernet, sim…) to a computer that

Selection and/or peer review under responsibility of Scientific Committee
doi:10.18086/eurosun.2016.04.01 Available at http://proceedings.ises.org

collects the data and publishes it according to final user needs, where the user is any person that may be interested in the metered data.

Main components of the energy monitoring are the sensors, in-site device, communication and IT infrastructure. A conceptual scheme of the different parts of an energy monitoring system is shown in Figure 1.

The sensors are used to measure the temperature of the thermal fluid between the two points in which the thermal energy is to be measured, they will be here referred as Th (hot temperature) and Tc (cold temperature). Additionally, a sensor to measure the volumetric flow of the thermal fluid, V_{flow}, is also necessary. The in-site device reads the data from the sensors and calculates the thermal energy. The communication infrastructure reads the thermal energy in certain communication time steps, and transfers the data to the IT infrastructure. Finally, the IT infrastructure collects, processes and publishes the thermal energy data according to the user needs.

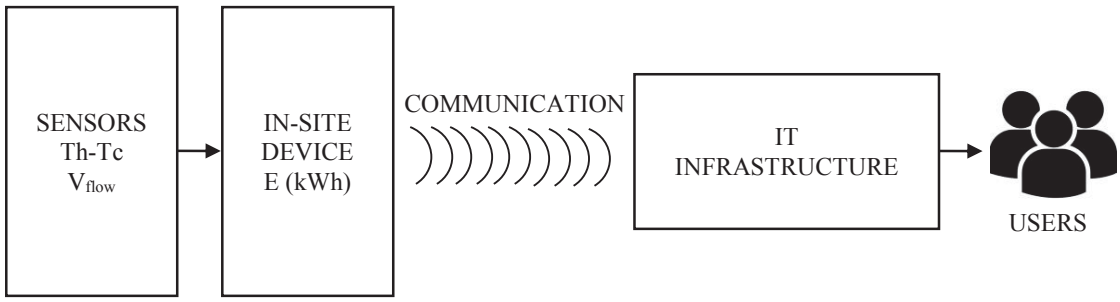

Fig. 1: Main parts of a thermal energy monitoring system. Conceptual scheme.

In order to develop a low-cost thermal energy monitoring system, attention has to be paid in the four components previously described. Commercial thermal energy counters, normally offers a compact solution of sensors and in-site device with internet connection interface. Additionally, a communication and IT Infrastructure is also needed.

The authors have developed an IT Infrastructure based on the free, simple and fast platform www.omnilus.com (2016). OmniluS reads the hourly thermal energy produced with a resolution of 1kWh. This drastically reduces the volume of data to be transferred from the in-site device to the cloud resulting into very low communication costs. More detailed explanation on how OmniluS works as intelligent energy meter can be found in González Valero et al. (2016).

3. Analysed energy counters

Three energy counters making use of the OmniluS platform have been analysed. Additionally, energy measurements have also been obtained with a none intrusive energy counter installed in-site with metering time step of one minute and finer communication energy counting resolution

Main technical parameters of the four energy counters are presented in Table 1.

The energy counters A, B and C, are connected the cloud platform OmniluS, and provide thermal energy data in intervals of Δt=1h with a resolution of 1kWh. The in-site devices use finer resolution to count the energy, however communicated energy resolution is set at 1kWh. This means that if during the previous communication interval (last hour), the energy produced was for example 14.6 kWh, a value of 14 is communicated, and the difference, 0.6 kWh, will be added to the energy to be communicated in the following time step.

The retail price of the components of the energy metering systems A, B, C ranges from 250 to 500 Euro, while the communication to cloud costs are below 4 Euro per month including data communication and cloud services.

Tab. 1: Main technical parameters of the analysed thermal energy metering systems

Name	Sensors			Communication		IT Infrastructure
	Th	Tc	Vflow	Resolution	Δt	
A	PT1000 immersed	PT1000 immersed	single jet	1kWh	1h	OmniluS
B	PT1000 sheath	PT1000 sheath	constant pre-calibration	1kWh	1h	OmniluS
C	PT1000 sheath	vortex flowmeter	vortex flowmeter	1kWh	1h	OmniluS
R	PT100	PT100	ultrasound	0.01kWh	1min	In-Site

4. Results and conclusions

The analysed metering systems A, B and C have been installed together with the reference system R at a solar thermal plant placed at the premises of the authors. The plant consists of a solar field of flat plat solar thermal collectors that collect energy from the sun which is accumulated in a storage tank with an internal serpentine by means of a single loop, so called primary loop.

The volumetric and temperature sensors have been placed at the inlet and outlet of the serpentine in order to measure the solar thermal energy yield of the primary loop. All of them have been carefully insulated. Additionally, silicone thermal cream has been used whenever necessary to assure thermal contact between the thermal fluid and the thermal RTD sensors.

The sensors have then been connected to the corresponding devices that calculate the instantaneous thermal power, count the energy yield and communicate the thermal energy yield. The devices of the metering systems A, B and C, transfer the thermal energy yield in intervals of one hour to the cloud were the OmniluS platform lives. On the other side, the thermal energy yield and the instantaneous power measured by the reference metering system R are recorded in-site (no connection to the cloud) in intervals of one minute.

No specific calibration of the sensors and devices has been performed, therefore data has directly been obtained with the instruments and sensors as delivered by the manufacturers with no additional post processing.

Data for seven different days is here presented in Figures 2 and 3 and Table 2. For each day, daily evolution of the energy yield and power measured with the four analysed metering systems A, B, C and R are shown in Figures 2 and 3.

Measured daily values of the energy yield are presented in Table 2. Additionally, absolute and relative differences of the daily energy yield are also shown by using the data measured by the system R as reference value.

As observed, although communication time steps and resolution in the systems A, B, C are large, the evolution of the cumulative daily energy yield measured with these systems pretty well reproduces the evolution of the cumulative daily energy yield measured with the detailed metering system R.

Of course the systems A, B and C cannot measure small time scale (minutes) phenomena and are therefore not appropriate for a detailed audit of the thermal system. However, they are able to predict the daily energy yield reasonably. As shown in Table 2, absolute differences of the daily energy yield measured with the systems A, B and C with respect with the data obtained with system R are below 2.5 kWh per day, which results into relative differences of the measured daily energy yield of 5%.

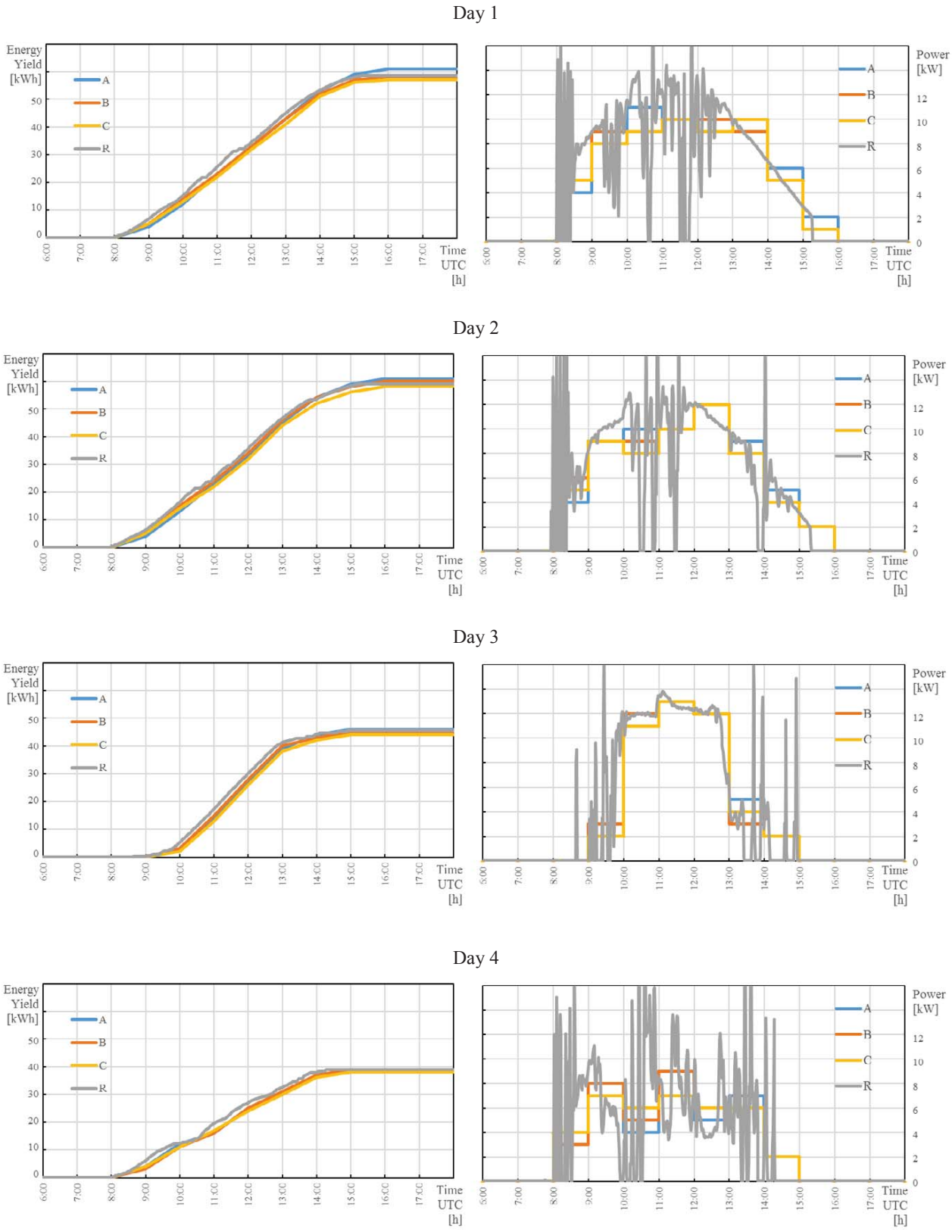

Fig. 2: Experimental results. Daily cumulative solar energy yield and instantaneous power obtained with the four analysed thermal energy metering systems: days 1, 2, 3 and 4.

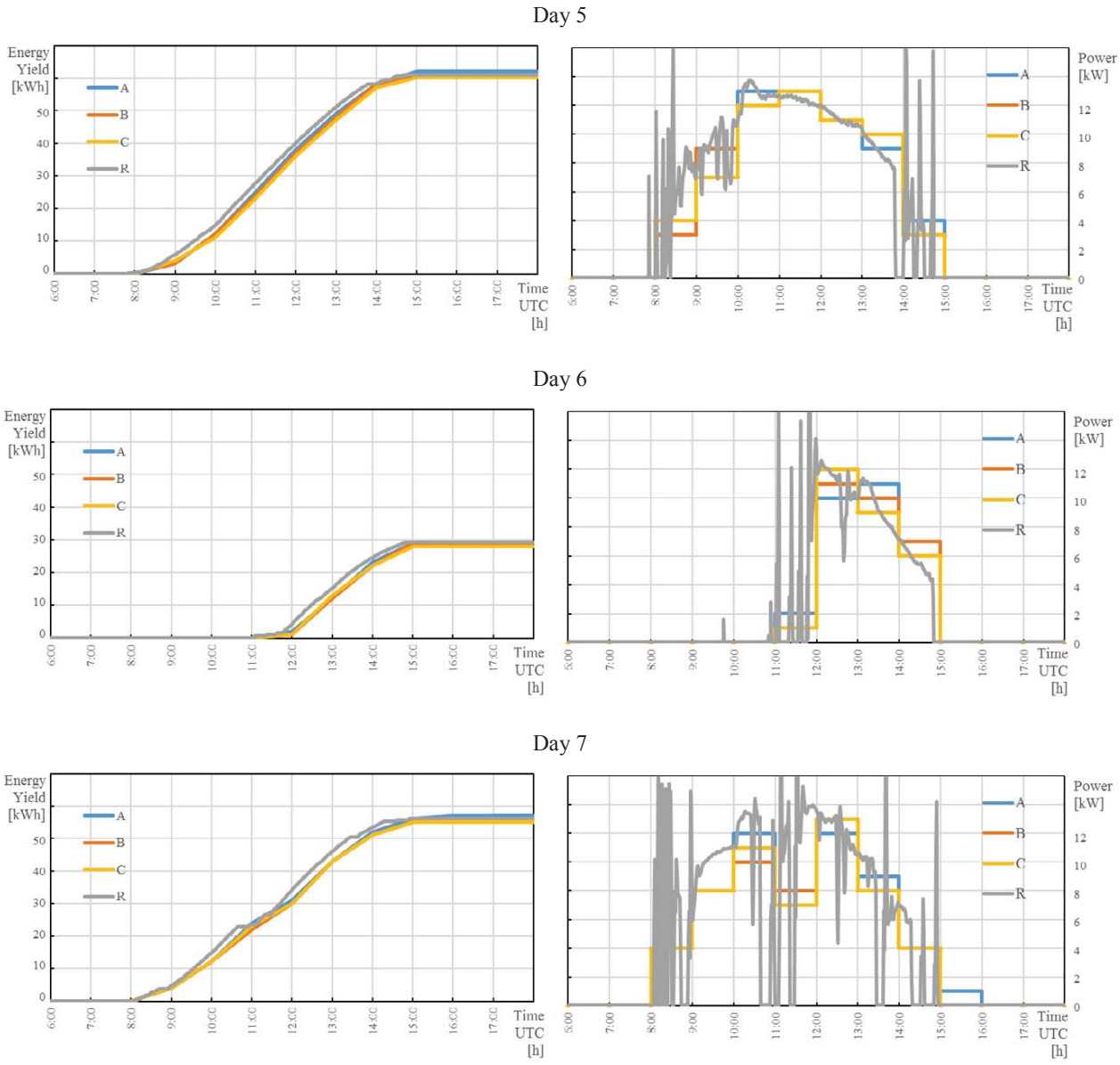

Fig. 3: Experimental results. Daily cumulative solar energy yield and instantaneous power obtained with the four analysed thermal energy metering systems: days 5, 6, and 7.

Tab. 2: Experimental results. Daily energy yield measured with the metering systems A, B, C and R. Analysis of absolute and relative differences of the daily energy yield of the systems A, B and C respect to the value measured with the system R.

	A			B			C			R
	Value	Difference		Value	Difference		Value	Difference		Value
Day	[kWh]	Abs [kWh]	Rel [%]	[kWh]	Abs [kWh]	Rel [%]	[kWh]	Abs [kWh]	Rel [%]	[kWh]
1	61	2,5	4,2	58	-0,5	-0,9	57	-1,5	-2,6	58,5
2	61	1,9	3,3	60	0,9	1,6	58	-1,1	-1,8	59,1
3	46	0,4	0,9	45	-0,6	-1,3	44	-1,6	-3,5	45,6
4	39	0,1	0,3	39	0,1	0,3	38	-0,9	-2,3	38,9
5	62	1,0	1,7	61	0,0	0,0	60	-1,0	-1,6	61,0
6	29	-0,2	-0,6	29	-0,2	-0,6	28	-1,2	-4,0	29,2
7	57	0,9	1,6	55	-1,1	-1,9	55	-1,1	-1,9	56,1

5. Acknowledgements

This work has partially been financially supported by the Agency for Management of University and Research Grants (AGAUR) of the Generalitat de Catalunya, under the Industrial Doctorates programme DI-2015.

6. References

González Valero, A., Cadafalch, J., Consul, R., Ruiz, R., 2016. “Equipo contador térmico telemático generador de alertas con un volumen bajo de datos de telecomunicación”. Spanish Patent P201630319.

González Valero, A., Cadafalch, J., Consul, R., Ruiz, R., 2016. Open data solar thermal meter for smart cities. Eurosun 2016, ISES Conference Proceedings.

http://www.omnilus.com, 2016, Cloud platform OmniluS.

Conference Proceedings

EuroSun 2016
Palma de Mallorca (Spain), 11 - 14 October 2016

Open data solar thermal meter for smart cities

A. González Valero [1], J. Cadafalch [2]. R. Consul [2] y R. Ruiz [2].

[1] RDmes Technologies S.L., Terrassa (Spain).

[2] Universitat Politècnica de Catalunya BarcelonaTech, Barcelona (Spain).

Abstract

In the near future, with the introduction of the Smart City concept, all systems and elements placed in a city will publish their performance data through open platforms. This paper presents an open data solar thermal meter component for the Smart City platform Sentilo. The solar meter includes four different sensors with instantaneous values of the solar energy yield, equivalent CO_2 emissions savings, economical savings and system status.

The paper describes the solar meter and how it is implemented within Sentilo, gives directions on how to create a solar meter using the data of any on-line connected solar thermal system, and gives examples on the data obtained from several solar thermal meters installed in different cities nearby Barcelona.

Keywords: *open data, solar thermal meter, Sentilo, smart cities*

1. Introduction

Solar thermal technology for domestic water heating (SDHW) is already a mature technology competitive to other conventional energy based systems. This has motivated some countries, regions or local authorities worldwide (Spain, Portugal, Italy, Chile...) to implement solar ordinances or regulations to obligate the use of solar thermal or other renewables in new and refurbished buildings. As a result, the number of residential apartment buildings (RA buildings) with SDHW systems has increased considerably during the last years. Only in Spain a total number of about 50.000 RA buildings with SDHW with a minimum collector area of about 15 m^2 are estimated, while more than 1 Million are estimated worldwide.

Practical experience, however, has shown as an important part of the SDHW in RA buildings are not performing appropriately resulting into reduced solar energy savings and bad reputation for the solar thermal technology.

Based on market experience, the authors have developed a low-cost smart solar thermal meter to support maintenance and operation of the SDHW systems. Research has been undergone in order to focus on costs (including devices and communications), standardization and best practices, effective and continuous metering and continuous communication with all involved bodies: users, O&M companies and public organizations as municipalities. Main technical results have already been patented, see González Valero et al. (2016).

With the increasing introduction of the Smart City concept, there is a need of further development of open data transversal platforms including standardized procedures to manage specific components data.

Cities in the area of Barcelona have been leading the implementation of Smart City solutions by making use of the horizontal, global and open platform called Sentilo, see www.sentilo.io (2016). Among others, the platforms sites for Barcelona and Terrassa are already available at http://connecta.bcn.cat and http://sentilo.terrassa.cat respectively.

doi:10.18086/eurosun.2016.04.06 Available at http://proceedings.ises.org

The number of instantaneous city data type uploaded to Sentilo is increasing constantly, ranging from sound sensors, trash-containers tracking, lighting, to electrical consumption.

Among the different systems in a city, solar thermal energy systems also play their role. There are many questions still to answer around the installed solar thermal systems related to their maintenance and real performance. The upload of instantaneous performance parameters of the solar thermal systems in an open Smart City platform will provide data that can be post-processed by anyone connected to the platform in order to obtain a response of these questions, and that will definitively contribute to improve the solar thermal technology reputation and dissemination.

The paper gives an overlook on the smart low-cost solar thermal meter developed by the authors, and how it is implemented as a component of the platform Sentilo. More than 30 SDHW plants in the area of Catalonia have already been equipped with this technology. Some examples on data obtained from these plants are also here presented.

2. The smart solar thermal meter

With the sensor technology available nowadays is of course possible and easy to monitor any data in a solar thermal system in small temporal intervals (in the range of seconds or even smaller) and send them to the cloud where the Sentilo platform lives through any kind of internet connection. However, the larger the number of sensors are installed and the smaller the temporal communication intervals the total implementation and communication costs increase.

In order to develop a solar thermal meter that would be accepted by the market, the costs of communication and devices (including sensors) to be installed must be reduced as much as possible.

The meter here described has been specifically designed for solar thermal plants with a maximum pick power of 70 kW. A scheme of the meter is shown in Figure 1. Metering is performed in two steps. The first step takes place in-site and the second step is done at the cloud by an instantaneous post processing of the data obtained in the first step.

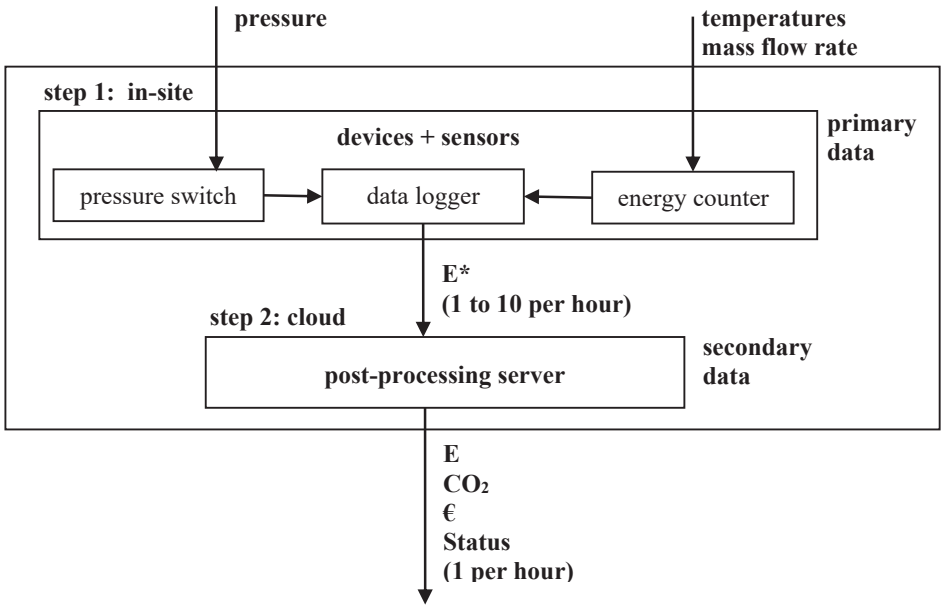

Fig. 1: Scheme of the smart solar thermal meter.

A data logger, a thermal energy counter and a pressure switch are installed in-site. The data logger must be connected to the internet. The value of the energy produced within the communication intervals is transmitted to the cloud. A frequency of communication of 2 to 10 transmissions per hour is suggested. This drastically reduces the communication data (and therefore costs) while, according to authors experience, having enough practical instantaneous data to monitor the plant status.

The pressure switch is installed at the primary loop (solar loop of the plant) and electrically connected to the electrical power input of the data logger. Therefore, in case the pressure at the loop decreases, which is one of the major failures in these plants, the data logger stops communication and no data is transmitted to the cloud.

Therefore, the only communication data used by the smart solar thermal meter is the energy produced in intervals of 1 to 10 transmissions per hour, whenever the pressure in the solar loop is enough to guarantee proper operations conditions. Otherwise, no value is sent. This energy production is called as smart energy yield, and is represented by the symbol E*.

At the cloud, a server instantaneously receives the value of the smart energy yield and calculates the instantaneous equivalent reduction of the CO_2 emissions, the economical savings and the Status de of plant. These three values, together with the value of the smart energy yield are then sent to Sentilo.

An important point to highlight is that the cost of the communication data from the step two (server at the could) and Sentilo is 0 because they both live in the cloud and are already connected to internet. However, the transmission data from the in-site infrastructure to the server at the cloud has a cost that may depend on type of communication used (e.g. Ethernet or SIM card).

The instantaneous value of the plant Status is to be calculated by software and in accordance to what is expected to be the theoretical production of the plant. Four status of the plant are considered:

- OK: the plant is working properly
- Overproduction
- Underproduction
- No reading: in case the instantaneous value of E* has not been transmitted to the cloud

A simple algorithm to determine the status when a value of E* is available, is to set the status at Overproduction in case E* is larger than the maximum energy production capacity of the plant during the communication interval, to underproduction in case E* is below 0 (this would mean a failure in the energy counting) and set the status to OK otherwise. This algorithm can of course be improved by providing intelligence to the server like statistical analysis of the instantaneous production of other equivalent solar plants.

The two steps could also take place in-site. However, this introduces two major additional difficulties. From one side, the amount of data to be transmitted from the in-site infrastructure to the cloud increases significantly resulting in larger communication costs. From another side, the data to be calculated in step two (CO_2 equivalent emissions, economical savings and plant status), require specific information of the plant that needs updating during all the meter life time. This introduces additional communication costs while when the second step takes place at the cloud this can be done automatically with no costs.

3. Coupling of the smart solar thermal meter with Sentilo

3.1. Sentilo configuration

All devices that send data to Sentilo have to be defined in an internal Sentilo data base. The smart solar thermal meter is defined as a new Sentilo component with four sensors as described in Table 1. The first sensor is the energy yield from the last communication step to the current communication step. As it is directly measured from in-site sensors it is labelled as a primary sensor. The other three sensors are secondary sensors calculated from the instantaneous value of the smart energy yield, and are the instantaneous plant status, and the economical savings and equivalent CO_2 emissions reduction corresponding the energy yield.

Extensive information on how to set-up a Sentilo server, define the data bases, sign up new sensors and download and upload data can be found in http://www.sentilo.io (2016).

Tab. 1: Sensors of the solar thermal meter component

Sensor	Type	Description
Energy Yield	Primary	Energy counter
Installation status	Secondary	Alerts generated from the energy yield
CO_2 equivalent emissions	Secondary	Post-processed value derived from the energy yield
Economical savings	Secondary	Post-processed value derived from the energy yield

3.1. Data flow

The smart solar thermal meter is designed to send cost-effective data of the solar thermal plants to those persons that may be interested. These persons will be identified as the data target. They can be classified in different groups depending of their role and connection to the solar thermal plants. Table 2 shows a simple classification in four groups, the plants owners, the O&M companies, public organizations and general public.

Tab. 2: Data target: classification in groups

Group Name	Description/role
Owner	Plant owner/s
O&M companies	Maintenance and operation performers
General public	Third parties
Public organization	City councils, energy agencies and policy makers

The data flow from the domestic hot water system to the target making use of the smart solar thermal meter and the platform Sentilo is represented in Figure 2. Sensors of temperature, mass flow and pressure (pressure switch) placed at the domestic hot water system, provide instantaneous data to the smart solar thermal meter. The meter, according to the procedure described in section 2, processes the input data and provides hourly values of the energy yield, the equivalent CO_2 emissions, economical savings and plant status to Sentilo. Finally, Sentilo publishes the data through its front-end platform and through its back-end.

The Sentilo front-end shows a map in which all monitored components are geolocated. With a simple click on a component it is possible to view real-time and some historical data of its sensors.

From another side, all data in Sentilo can be downloaded by external applications through its back-end using an API. For example, the authors have developed an application available through the free cloud platform www.omnilus.com (2016), called SeYe. This app is designed to automatize and simplify as much as possible the communication between the target groups and the monitored solar plant and provides three major functionalities: configuration of the solar system plant, edition of historical data and, automatic generation of emails to the different target groups informing about installation status and production.

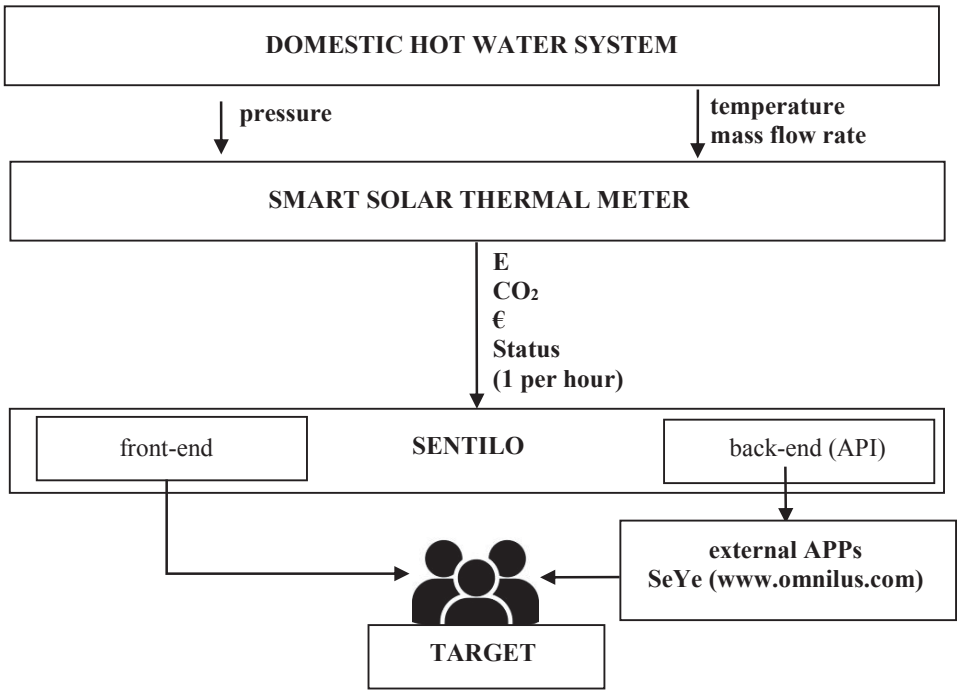

Fig. 2: Scheme of the data communication flow from the DHWS to the TARGET through the smart solar thermal meter and Sentilo.

4. Results

The open data solar thermal meter for smart cities presented in this paper has already been installed in more than 30 different plants located in the area of Barcelona.

As an example, results of plants located in the city of Terrassa will be here presented by making use of the front-end platform provided by Sentilo. The geolocation and some basic data of the solar thermal meter are shown in Fig 3. The solar thermal meter is located in a map among other meters in the area using a symbol made of a green circle with a white sun in it. By clicking on the solar meter symbol, basic data of the sensors are shown.

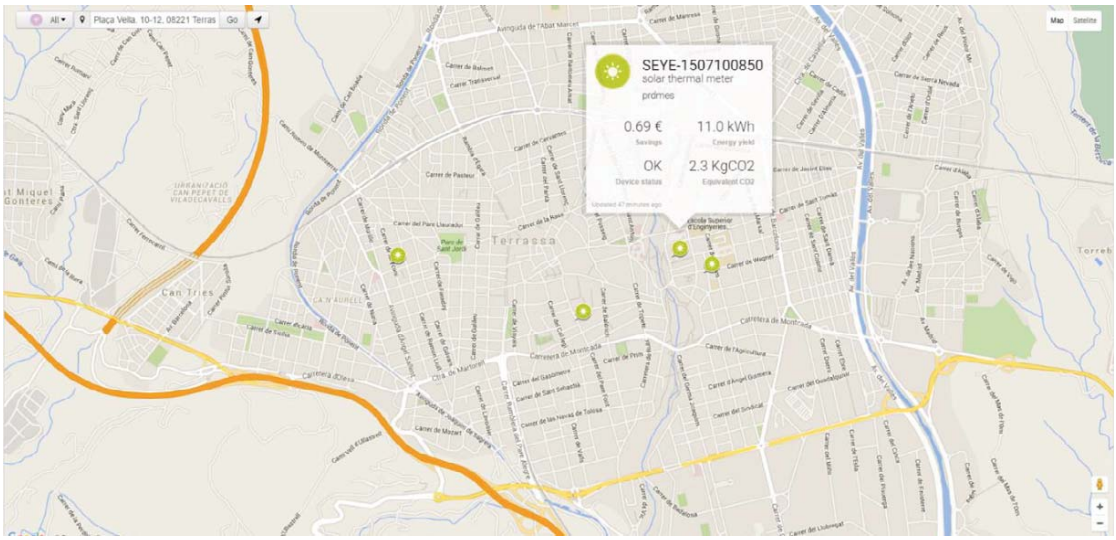

Fig. 3: Geolocation and basic data of the smart solar themal meter as shown on the front-end Sentilo platform.

Some historical data is also stored in the Sentilo platform. Real time value and historical data of the energy yield and the installation status as presented by the Sentilo front-end platform are shown in Figure 4 and 5 respectively.

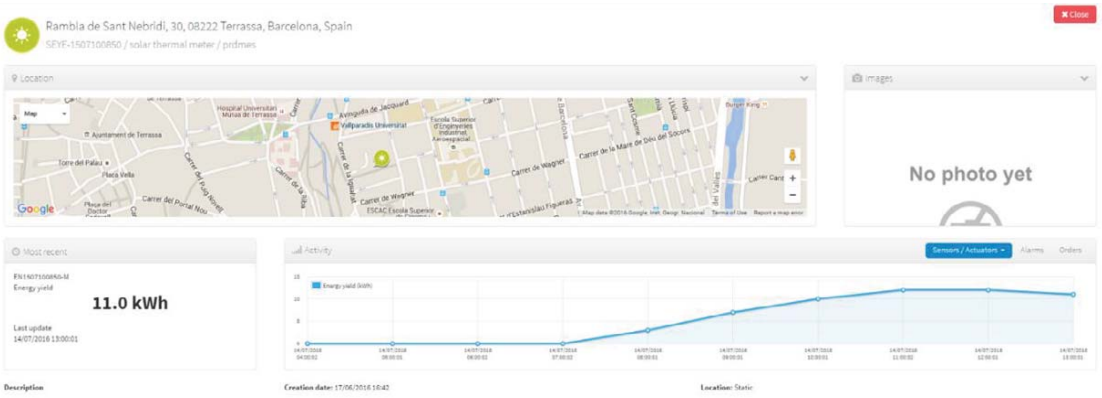

Fig. 4: Geolocation and some historical data of the energy yield as shown on the front-end Sentilo platform.

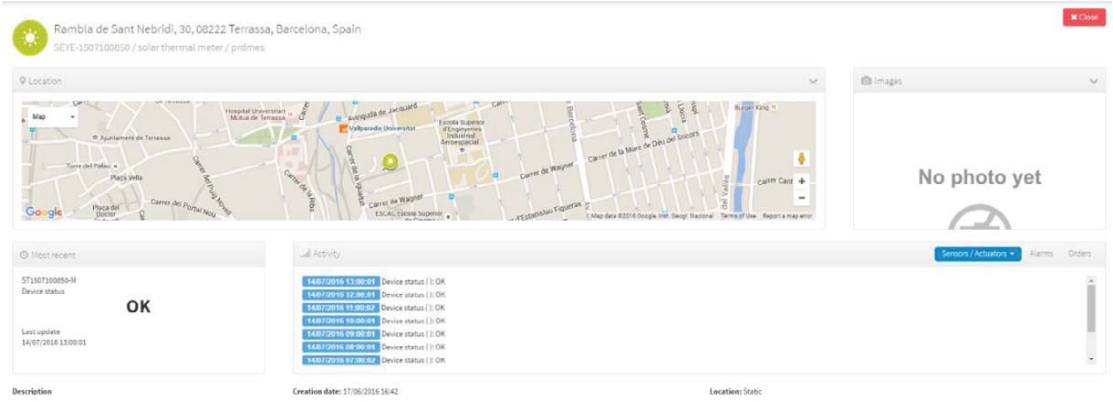

Fig. 5: Geolocation and some historical data of the installation status as shown on the front-end Sentilo platform.

5. Conclusions

With the introduction of the solar city concept, the market is now demanding for meters and sensors of relevant city activities connected to open data platforms. Solar thermal sector must be aware of that, and must provide solutions to publish the data of the domestic hot water systems installed in cities in the open data platforms.

The authors have designed a smart solar thermal meter connected to the open data platform Sentilo where the volume of transferred data is minimized in order to reduce communication and devices costs. The paper describes in some detail the smart solar thermal meter and the procedure adopted to send real time values of the energy yield, CO_2 equivalent emissions reductions, economical savings and plant status to Sentilo.

6. Acknowledgements

This work has partially been financially supported by the Agency for Management of University and Research Grants (AGAUR) of the Generalitat de Catalunya, under the Industrial Doctorates programme DI-2015.

7. References

González Valero, A., Cadafalch, J., Consul, R., Ruiz, R., 2016. "Equipo contador térmico telemático generador de alertas con un volumen bajo de datos de telecomunicación". Spanish Patent P201630319.

http://connecta.bcn.cat, 2016, Barcelona Sentilo platform.

http://www.sentilo.io, 2016, Sentilo platform main site.

http://sentilo.terrassa.cat, 2016, Terrassa Sentilo platform.

http://www.omnilus.com, 2016, Cloud platform OmniluS.

Conference Proceedings

EuroSun 2016
Palma de Mallorca (Spain), 11 - 14 October 2016

Energetic and economic comparison of different energy concepts based on solar energy for residential buildings

Thomas Duschner[1], Michael Klärner[1] and Wilfried Zörner[1]

[1] Institute of new Energy Systems, Technische Hochschule Ingolstadt (Germany)

Abstract

This paper investigates the benefit of the combination of solar thermal systems and photovoltaic systems for residential buildings. In this study, different solar energy supply concepts were modelled in the Matlab/Simulink toolbox CARNOT. The simulations were conducted with changing ratios of installed solar thermal and photovoltaic surface. Each concept was equipped with an optional battery storage. The results indicate an advantage of a combination of both solar systems with respect to the percentage of self-consumption. Economically, solar thermal plants affect the investment costs adversely because of higher unit prices compared to PV modules. Nonetheless, a combination of both systems is useful for some concepts.

Keywords: *solar thermal, photovoltaic, residential building, energy concept;*

1. Introduction

The EU guideline EPBD (Energy Performance of Building Directive), which came into effect in 2010, requires stricter building standards for new construction. To comply with this directive, all new buildings from 01.01.2021 onwards must fulfill at least the "nearly zero-energy building"-standard (European Union, 2010). For this purpose, the majority of the energy demand must be provided by renewable energies. The resulting significantly lower heat demand, however, means that the current demand ratio for thermal and electrical energy in residential buildings will change. Until now, electricity has only represented 16 % of the energy consumption in German households while 84 % was used for thermal purposes, in which room heating required 69 % and domestic hot water 15 % (Deutsche Energie-Agentur, 2015). As a result of this lower heating demand, the ratio between requirements for room heating and domestic hot water will also converge until they are almost balanced. Accordingly, greater priority must also be given to the domestic hot water demand.

In new buildings photovoltaic systems are primarily used as a solar renewable energy. This is reinforced also by the fact that in recent years the investment costs for photovoltaic systems have declined (Wirth and Schneider, 2016). Solar thermal systems have not experienced such a steep learning curve and as a result the investment cost has remained constant. In addition, the economy of PV systems is easier to identify. The energy production depends only on the irradiation and, in contrast to solar thermal systems, is not user related. The generated and fed energy is remunerated with a fixed sum. The federal government implemented a "flexible ceiling" for these feed-in tariffs which makes it more difficult to operate grid-connected PV systems economically. One key to more economical operation is self-consumption. In 2012, grid parity was reached as a consequence of the steady reduction of the feed-in remuneration and the increase of electricity prices for households (Quaschning et al., 2012). This was the turning point where the use of generated PV power became more cost-effective then the consumption of grid electricity. This development leads to new options for the use of photovoltaic energy in single-family homes. Covering the heat demand with electric energy becomes an interesting opportunity for increasing self-consumption. One possibility is to combine photovoltaic systems

doi:10.18086/eurosun.2016.04.02 Available at http://proceedings.ises.org

with heat pumps in order to cover the heat demand of single-family houses. As a result, heat generation with PV competes with other heat generation systems, in particular with solar thermal systems. The objective of this paper is to analyze this competition between and evaluate the combination of solar electric and solar thermal systems in residential buildings.

2. Methodology

The presented studies were performed in Matlab/Simulink (The MathWorks Inc., 2016). In addition, the expansion Blockset CARNOT (Conventional And Renewable Energy System Optimization Blockset) was used (Hafner et al., 1999). CARNOT contains predefined Simulink blocks from the fields of building and supply technology and has been conceived to perform detailed simulations and analyses in building energy supply.

2.1. Concepts

Four different concepts are implemented in Matlab/Simulink with different backup-heating systems. First, with a fossil fuel-boiler and a biomass-boiler, two systems are applied which operate independently from the electrical grid. Furthermore, two concepts based on power-to-heat (p2h) are part of the investigation: an electrical heating rod and a heat pump.

Due to the focus on solar energy supply, both photovoltaic and solar thermal systems were considered in each model. Based on the simulation model, a 50 m² roof was analyzed for the use of either solar thermal collectors, PV modules, or a combination of both. The ratio of installed PV modules and solar thermal collectors is varied in steps of 10 m². The results were then compared to the pure use of each solar technology, i.e. only solar thermal collectors or PV modules. In addition, the influence of energy storage for each concept was investigated. The capacity of the electrical as well as thermal storage was adjusted according to system sizes. For each kW_{peak} of installed photovoltaic power, a battery capacity of 1 kWh is used. The thermal storage has a defined basic volume of 250 l, which increases by 500 l per 10 m^2 solar thermal collector.

2.2 Database and control parameters

Meteorological data are an important aspect for solar energy simulations. Especially for photovoltaic and solar thermal systems, a temporally high resolution of the weather data is desired. For this investigation the climate data of Ingolstadt, Germany are used. The data were generated with the software Meteonorm (Meteonorm, 2016). The weather data set has to be adapted and extended for use in CARNOT. After this modification, the data now includes relevant parameters such as the direct and diffuse radiation on a horizontal surface and also location-based parameters such as hour angle, zenith angle and declination angle of the sun.

The analysis is exclusively carried out for detached single-family houses. Within the IEA-SHC Task 44, reference buildings were defined for the simulation setting which ensure the same conditions for all simulations to allow for comparison between investigated concepts (Dott et al., 2013). These buildings do not differ in geometry but solely in their U-values for the walls and therefore building types with different energy standards arise. Three building types are further defined: SFH15, SFH45 and SFH100. SFH stands for Single Family House and the additives 15, 45 and 100 indicate the specific heating demand in kWh/(m²*a). SFH15 represents a building envelope with very high energy efficiency, SFH45 represents current legal requirements or a renovated building with a building envelope of good thermal quality, and SFH100 represents a non-renovated existing building (Dott et al., 2013). Because of the higher heat demand, the SH100 building type requires radiator heating. All other boundary conditions (weather data, building orientation, roof slope and orientation) of the simulation remain the same. The building is oriented south and the roof pitch is 45°.

The thermal load of the building arises from the building parameters in the model and the weather conditions. The domestic hot water tapping profile is generated according the VDI-guideline 4655 (reference load profiles of single-family and multi-family houses for the use of CHP systems). The guideline includes standardized load profiles for 10 typical days for 15 different climate regions. These typical days differ depending on the day of the week, the temperature and the cloudiness. The average daily temperature determines whether it is a summer, winter, or a transition day. Regarding the cloudiness, a fine and a cloudy day can be distinguished. A

combination of all possibilities would yield 12 typical days, but no distinction is made according to the cloudiness of the summer typical days. Public holidays are treated like Sundays. To determine the public holidays, 2015 is chosen as the reference year. Using the meteorological data, profiles for the annual simulation are generated. Based on the guideline, which provides a domestic hot water demand of 500 kWh/person/a, results for the assumed 4-person household indicate an annual hot water demand of 2,000 kWh/a. The electrical load profile can be generated in a similar fashion. Contrary to the assumption of 1,750 kWh/person/a, a value of 1,000 kWh/person/a is assumed here. Especially in newer buildings, much more efficient components are installed. This leads to annual electricity consumption of 4,000 kWh/a for a 4-person household.

For the reference building in the IEA Task 44, a room temperature of 20°C is set, wherein a hysteresis of ± 0.5°C is set for activation of the heating circuit. The inlet temperature is regulated depending on the outside temperature. The maximum value for floor heating is 35°C and for radiator heating 55°C. The domestic hot water is mixed to a temperature of 45°C. The inflowing cold water, used for mixing, has a constant temperature of 10°C. The combined thermal storage tank is divided into two areas. The upper part is kept in a temperature range between 48°C and 52°C (SFH15 and SFH45). For the SFH100 this area is heated up 62°C. During the winter months, the lower part of the thermal storage is kept at a minimum temperature of 35°C in the case of floor heating. In case of radiator heating, this part is reserved for the solar thermal system. The loading of the upper part has thereby priority within the control. The biomass-powered boiler differs from fossil-fueled boiler with regard to start-up and switch-off times. Due to the somewhat sluggish overall system, the system is booted up slowly when reaching the lower threshold value and accordingly the power is lowered already slowly just before the maximum permissible temperature.

3. Energetic evaluation

The simulation results are evaluated in terms of energy coverage. The electrical coverage for the PV-system is the PV generation E_{PV} less the feed-in energy $E_{\mathrm{PV,feed\text{-}in}}$ relative to the total energy consumption $E_{\mathrm{el,total}}$.

$$C_{\mathrm{el}} = \frac{E_{\mathrm{PV}} - E_{\mathrm{PV,feed\_in}}}{E_{\mathrm{el,total}}} \qquad \text{(eq. 1)}$$

The total energy demand results from the household electricity demand $E_{\mathrm{el,HH}}$ and the electrical demand for heating $E_{\mathrm{el,heat}}$.

$$E_{\mathrm{el,total}} = E_{\mathrm{el,HH}} + E_{\mathrm{el,heat}} \qquad \text{(eq. 2)}$$

For the solar thermal system the thermal coverage can be determined in a similar manner by setting the thermal energy generated by the solar thermal system E_{ST} in a relation to the total thermal energy demand $E_{\mathrm{therm,total}}$.

$$C_{\mathrm{therm}} = \frac{E_{ST}}{E_{\mathrm{therm,total}}} \qquad \text{(eq. 3)}$$

The total energy demand is calculated from the sum of energy for domestic hot water $E_{\mathrm{therm,dhw}}$, the demand for space heating $E_{\mathrm{therm,heat}}$ and the thermal losses $E_{\mathrm{therm,loss}}$.

$$E_{\mathrm{therm,total}} = E_{\mathrm{therm,dhw}} + E_{\mathrm{therm,heat}} + E_{\mathrm{therm,loss}} \qquad \text{(eq. 4)}$$

In addition, the electric self-consumption of the photovoltaic system is assessed. These are calculated similarly to coverage only that in this case, the used photovoltaic energy is set in a relation to the total generated power of the PV system.

$$SC_{\mathrm{el}} = \frac{E_{\mathrm{PV}} - E_{\mathrm{PV,feed\_in}}}{E_{\mathrm{PV,total}}} \qquad \text{(eq. 5)}$$

Tab. 1 shows the annual thermal electrical energy amounts results from the simulated systems and the predetermined load profiles. All other annual amounts vary with the collector area, because the run-times of the backup-systems depends on the energy generated from the solar thermal system.

Tab. 1: Annual energy amounts of the reference buildings SFH15, SFH45 and SFH100

	SFH15 Values in kWh/a	**SFH45** Values in kWh/a	**SFH100** Values in kWh/a
Annual electricity consumption			
household	4.090	4.090	4.090
Annual heating demand			
domestic hot water	2.100	2.100	2.100
space heating	3.100	8.010	21.200

If one calculates the specific heat demand for the simulated annual space heating demand and an assumed floor area of 140 m^2, one obtains the values 22 kWh/m2/a, 57 kWh/m2/a, and 152 kWh/m2/a. These values differ from the defined values 15 kWh/m2/a, 45 kWh/m2/a and 100 kWh/m2/a. This is mainly due to the different weather dataset for Ingolstadt. To determine the defined values the weather data set for Strasbourg was used. The annual average outdoor temperature is in Ingolstadt with 8.8°C below the temperature in Strasbourg with 11°C. The radiated energy on the 45° inclined surface is with 971 kWh/m2/a 20 % smaller than that of the referenced weather data set (1,227 kWh/m2/a). The designations are retained hereinafter.

3.1. Concepts without electrical energy storage

As already described in the methodology, different ratios of the installed photovoltaic modules to solar thermal panels are compared and evaluated. This examination is carried out for various concepts and building standards. Fig. 1 shows the result for the SFH15 building type. The electrical coverage is lower in systems with p2h combined with PV systems, because the total electrical consumption is higher. Due to the even higher electrical demand when using a heating rod, the electrical coverage is about 20 %, slightly below the heat pump (23 %). The electrical self-consumption percentage changes accordingly (34 % compared to 26 %). Due to the higher electrical energy demand, a higher self-consumption can be achieved with these two systems in comparison to the boiler systems.

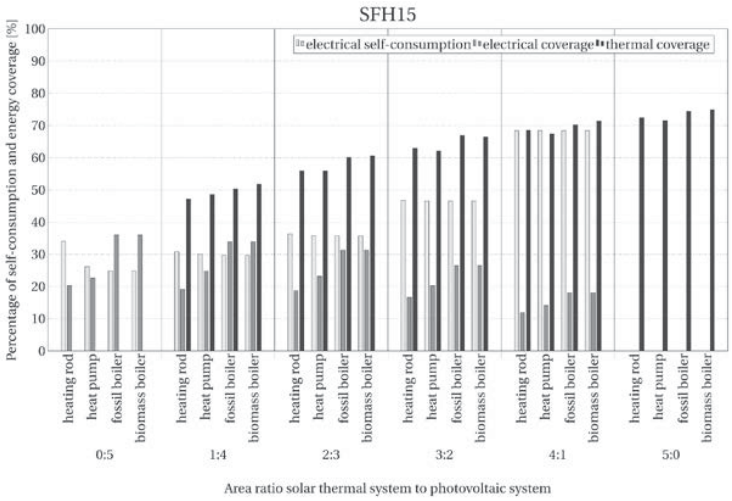

Fig. 1: Percentage coverage and self-consumption at different area ratio and backup systems for the building standard SFH15

Through the addition of a solar thermal system, lower operation time for the backup-systems is required. Moreover, the solar thermal system is now simultaneously active with the photovoltaic system and the produced photovoltaic power is used to cover the domestic electrical demand primarily. Thus, the electrical self-consumption of all concepts increases and the electrical coverage decreases. However, this is also due to the now-smaller photovoltaic surface. With this decrease, it is possible to consume a higher percentage of the generated energy. For the fossil fuel boiler and for the biomass boiler, the electrical characteristic values are the same, as they both operate independently of the power and only the domestic electricity demand is covered.

For the thermal coverage, a maximum value of 75 % can be achieved. If one increases the solar thermal surface from 30 m^2 to 50 m^2, the thermal coverage hardly changes. The heat demand of the SFH15 building is too low as the possible heat, generated by a 40 m^2 or 50 m^2 solar thermal system, can be used. The system is oversized and is therefore often in stagnation.

For the SFH45 building type, the results are similar to SFH15 (cf. Fig. 2). The electrical characteristic values for the fossil system and the biomass system remain unchanged by the independence of their power production. The heating demand of the SFH45 is higher, which results in a higher utilization of the heating system. With a heating rod or a heat-pump can thus be increased the self-consumption of the photovoltaic power. But this also means that the total power consumption of the building is higher and hence the electrical coverage decreases. Also the thermal coverage is lower than for the SFH15 because of this higher heat demand.

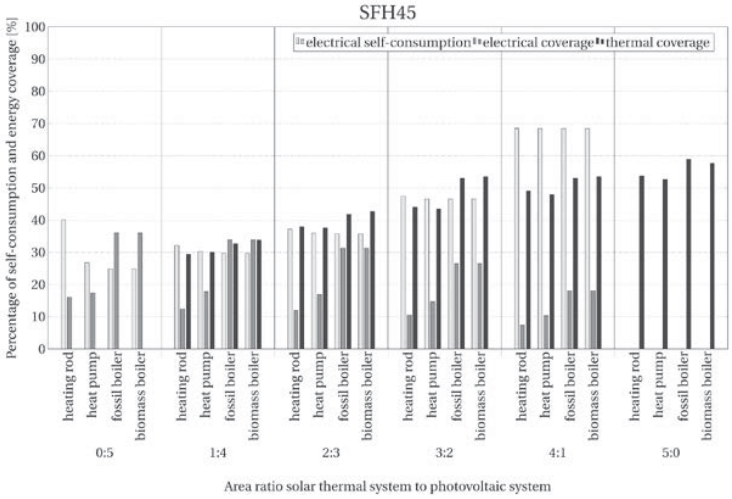

Fig. 2: Percentage coverage and self-consumption at different area ratio and backup systems for the building standard SFH45

When a vastly poorer building standard is considered (cf. Fig. 3), the results change once more. Here, the percentage of self-consumption with a photovoltaic-only system in combination with a heat pump is as high as with a heating rod. This is because heat pump operation and photovoltaic production occurs simultaneously more often due to the higher heat demand. The heat pump's higher electrical coverage of 15 %, compared to the heating rod with 8 %, is a result of the total energy demand as well as the electric energy demand of the heat pump, which is lower due to its coefficient of performance.

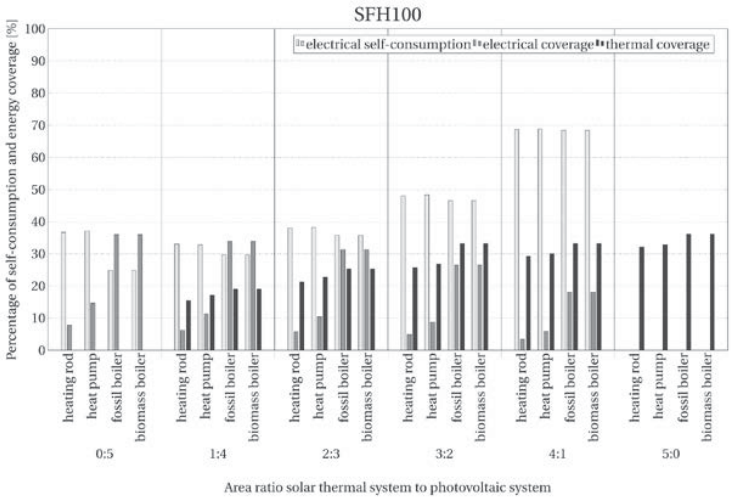

Fig. 3: Percentage coverage and self-consumption at different area ratio and backup systems for the building standard SFH100

This examination also shows that the electrical coverage of p2h-systems reacts similarly sensitive to the building standard as the solar thermal system. When the heat pump at a ratio of 3:2 is used as an example, the percentage of thermal coverage falls from 70 % (SFH15) to 53 % (SFH45) to 33 % (SFH100). In contrast, the percentage of electrical coverage drops from 20 % (SFH15) to 15 % (SFH45) to 9 % (SFH100). This corresponds to a deterioration of 55 % from building standard SFH15 to SFH100 for the electrical coverage and a decrease of 53 % for the thermal coverage. It is also seen that even for the SFH100, despite the increased heating demands little improvement of the thermal coverage can be achieved by increasing the solar thermal plant of 30 m² to 50 m².

3.2. Concepts with electrical energy storage

For the electrical characteristic values other results are obtained when an energy accumulator is integrated as a buffer for the electrical energy. Fig. 4 shows the simulation outcome for the SFH15. By the electrical storage, it is possible to achieve a balance between production and demand, thus a higher electrical self-consumption as well as a higher electrical coverage can be reached.

An electrical storage is beneficial for systems with heat pump technology and a photovoltaic system. It can be used a similar energy quantity with a heating rod as well as with a heat pump but due to the lower overall electrical energy demand of the heat pump the electrical coverage is higher. The influence of the electrical storage deceases with a reduction of the photovoltaic area. In combination with a 50 m^2 photovoltaic system a doubling of the self-consumption to the system without an electrical storage can be attained. Even the electrical coverage can be doubled with a battery storage and a large photovoltaic system. By contrast, increases in self-consumption for smaller photovoltaic systems are lower, for example about ten percentage points (20 m^2 photovoltaic system) or about four percentage points (10 m^2 photovoltaic system) with a heating rod, as this represents an increase of about 37 % and 25 %. The rise in electrical self-consumption is less, too. An electrical storage results not in a change of the thermal characteristic values.

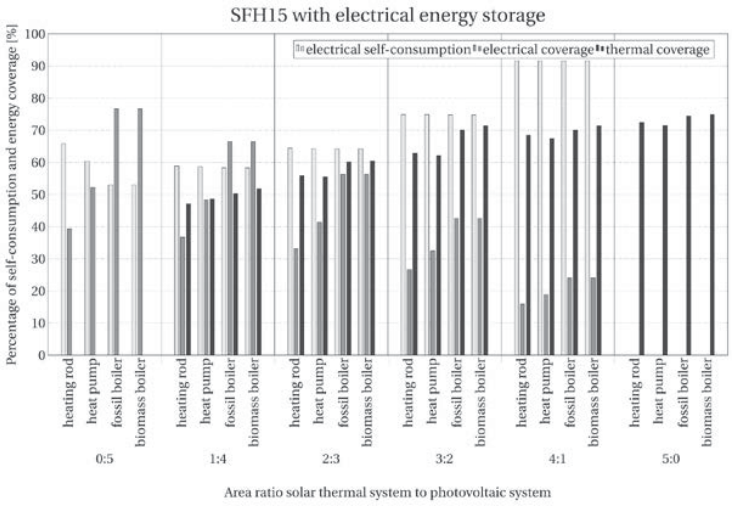

Fig. 4: Percentage coverage and self-consumption at different area ratio and backup systems for the building standard SFH15 and a battery storage

Owing to the higher thermal energy demand of the SFH45 the situation is somewhat different here (cf. Fig. 5). Although the battery storage maximum leads to a doubling of the electrical self-consumption, only lower electrical coverage can be accomplished here by the use of a heating rod or a heat pump, even though the electrical self-consumption remains almost the same. Again, the reason is the higher total energy demand of the building with poorer energy standard, which also has the consequence that a lower thermal coverage by solar thermal system is possible. The values for boiler systems, however, are again independent of the building standard.

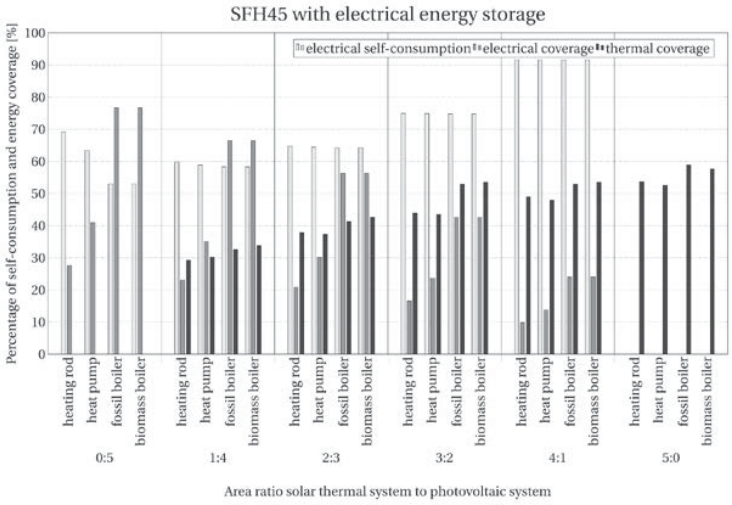

Fig. 5: Percentage coverage and self-consumption at different area ratio and backup systems for the building standard SFH45 and a battery storage

The same can be observed for the SFH100, whose results are shown in Fig. 6. Again approximately similar electrical self-consumption rates are achieved. However, the coverage ratio of the electrical energy at the total energy demand for electrical backup systems decreases.

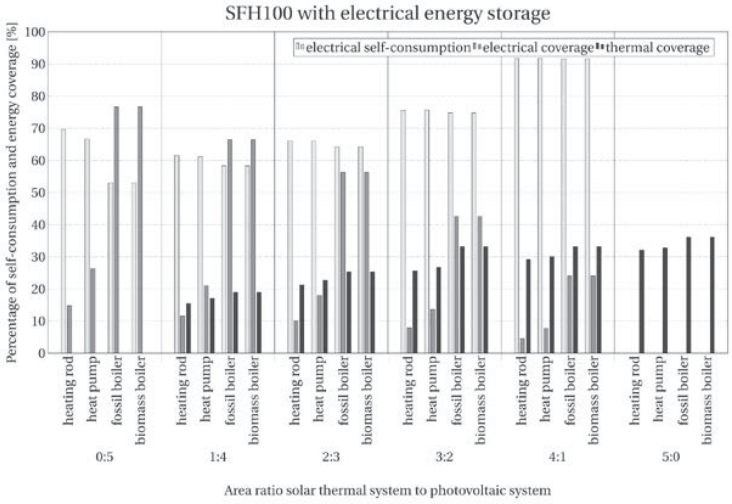

Fig. 6: Percentage coverage and self-consumption at different area ratio and backup systems for the building standard SFH100 and a battery storage

4. Economic evaluation

For the economic evaluation of the different concepts, the VDI-guideline 2067 is used. The method suggests summarizing the one-time investment costs and the ongoing payment during the period under consideration in equal annual payments, the so-called annuities. This approach allows a comparison of different system concepts. The annuity A_N of a system is calculated from the sum of the annuity of capital related costs, the annuity of needs related costs and operational related costs minus the annuity of the revenues (Lopez et al., 2011):

$$A_N = (A_{N,K} + A_{N,V} + A_{N,B}) - A_{N,E} \quad \text{(eq. 6)}$$

with: $A_{N,K}$ = annuity of capital related costs
$A_{N,V}$ = annuity of needs related costs
$A_{N,B}$ = annuity of operational related costs
$A_{N,E}$ = annuity of the revenues (e.g. grid feed-in)

To calculate the annuities some assumptions regarding the observation period, the costing interest as well as rates of price change must be taken. The adopted actuarial mathematical parameters and assumptions about the energy are summarized in Tab. 2.

Tab. 2: Boundary conditions for the calculation of the profitability

Parameter	Value	Explanation/Reference
Observation period	20 years	VDI 2067
Interest rate	3 %	-
Price change	2 %	-
Electricity price	29.16 ct/kWh	BMWi, 2016
Gas price	7.06 ct/kWh	BMWi, 2016
Firewood price	4.46 ct/kWh	DEPV, 2016
Feed-in remuneration	12.31 ct/kWh	Bundesnetzagentur, 2016

The investment costs of the different components are shown in Tab. 3. The costs for the thermal components are based on the Viessmann pricelist 2016. For the components which are variable in size (e.g. solar thermal system, photovoltaic system and battery storage) cost functions are used.

Tab. 3: Investment costs for different area ratio

	0/50	10/40	20/30	30/20	40/10	50/0
Heating rod				400 €		
Heat pump				6,000 €		
Gas-boiler				5,000 €		
Pellet boiler				12,000 €		
Thermal Storage	1,000 €	1.400 €	2,000	2,500 €	3,000 €	3,600 €
Solar thermal system	--	3,000 €	6,000 €	9,000 €	12,000 €	15,000 €
Photovoltaic system	7,500 €	6,000 €	4,500 €	3,000 €	1,500 €	--
Battery storage (lead)	9,240 €	7,280 €	5,600 €	3,640 €	1,680 €	--

Tab. 4 shows the total investment cost of each considered energy concept. The heating rod with its low investment costs shows in particular an economical advantage while concepts with a solar thermal system and without a battery storage have the higher investment costs. The high price of the pellet boiler increases the investment costs for these concepts. A battery storage compensates the higher cost of solar thermal collectors compared to photovoltaic modules and there is, with regard to various area ratios, only a small difference in the investment costs.

Tab. 4: Investment costs of the considered energy systems with and without battery storage

	0/50	10/40	20/30	30/20	40/10	50/0
Systems without battery storage						
Heating rod	8,900 €	10,800 €	12,900 €	14,900 €	16,900 €	19,000 €
Heat pump	14,500 €	16,400 €	18,500 €	20,500 €	22,500 €	24,600 €
Gas-boiler	13,500 €	15,400 €	17,500 €	19,500 €	21,500 €	23,600 €
Pellet boiler	20,500 €	22,400 €	24,500 €	26,500 €	28,500 €	30,600 €
Systems with battery storage						
Heating rod	18,140 €	18,080 €	18,500 €	18,540 €	18,580 €	19,000 €
Heat pump	23,740 €	23,680 €	24,100 €	24,140 €	24,180 €	24,600 €
Gas-boiler	22,740 €	22,680 €	23,100 €	23,140 €	23,180 €	23,600 €
Pellet boiler	29,740 €	29,680 €	30,100 €	30,140 €	30,180 €	30,600 €

4.1. Concepts without electrical energy storage

Contrary to the investment costs the system with gas-boiler has the lowest degree of annuities (c.f. Tab. 5). One the one hand, this is due to the relatively low investment cost of the gas boiler and on the other hand it is mainly up to the currently low gas price. The high cost of a pellet-boiler means that this system has the highest annuities for buildings with low heating demand (SFH15). For SFH45 and SFH100 standard are the mains supply costs for the heating rod however so high, that this concept has the highest annuities. For concepts based on power-to-heat the area ratio of 10/40 has the lowest annuity for the building standard SFH15 and SFH45. Here, the higher investment costs of the solar thermal system is compensated by the less electricity purchases form the grid. That the annuities of these systems greatly depend on the power consumption can be seen for example at SFH100 standard. There, the ratio of 20/30 has the lowest annuity because of the higher heating demand and therefore higher power consumption for thermal purposes.

Systems without thermal use of electricity have the lowest annuities by the ratio of 0/50 and increases with the enhancement of solar thermal collector area. These systems are also significantly more independent from the building standard. While here the annuities only rises between 10 %-20 %, these can double in power-to-heat-systems.

Tab. 5: Comparison of the total annuities of different concepts and building standards for various area ratios

	0/50	10/40	20/30	30/20	40/10	50/0
SFH15						
Heating rod	2,822 €/a	2,485 €/a	2,663 €/a	2,930 €/a	3,252 €/a	3,672 €/a
Heat pump	2,437 €/a	2,433 €/a	2,770 €/a	3,116 €/a	3,509 €/a	3,962 €/a
Gas-boiler	1,810 €/a	1,989 €/a	2,316 €/a	2,695 €/a	3,126 €/a	3,605 €/a
Pellet boiler	3,111 €/a	3,365 €/a	3,717 €/a	4,110 €/a	4,537 €/a	5,037 €/a
SFH45						
Heating rod	4,462 €/a	4,040 €/a	4,114 €/a	4,308 €/a	4,567 €/a	4,894 €/a
Heat pump	3,243 €/a	3,209 €/a	3,483 €/a	3,817 €/a	4,184 €/a	4,578 €/a
Gas-boiler	2,153 €/a	2,302 €/a	2,608 €/a	3,018 €/a	3,376 €/a	3,821 €/a
Pellet boiler	3,317 €/a	3,561 €/a	3,898 €/a	4,280 €/a	4,701 €/a	5,182 €/a
SFH100						
Heating rod	9,039 €/a	8,427 €/a	8,362 €/a	8,444 €/a	8,615 €/a	8,891 €/a
Heat pump	5,143 €/a	5,147 €/a	5,407 €/a	5,711 €/a	6,071 €/a	6,492 €/a
Gas-boiler	2,919 €/a	3,081 €/a	3,380 €/a	3,738 €/a	4,135 €/a	4,601 €/a
Pellet boiler	3,821 €/a	4,062 €/a	4,389 €/a	4,766 €/a	5,180 €/a	5,658 €/a

4.2. Concepts with electrical energy storage

When a battery storage is taken into consideration, the overall result of the different concepts does not change (c.f. Tab. 6). The concept with a gas-boiler has still the lowest annuity and the concepts with the pellet-boiler (SFH15) and with the heating rod (SFH45 and SSFH100) correspondingly the highest. For large-scale photovoltaic-systems, the annuity raises significantly and decreases depending on the size, what is owed to high investment costs of the battery storage. Therefore, the annuity for the area ratio 50/0 remains unchanged. However, this means that the economically optimum ratio shifts to larger solar thermal systems when higher heating demand exists. Is the optimum ratio for SFH15 standard still at 10/40, so it is at 30/20 for SFH45 standard and even at 40/10 for SFH100 standard. The advantage of an increased self-consumption is equalized by the high costs of the battery storage. In addition, the self-consumption cannot be increased as high that the savings in grid-consumption recoup the investment costs of the electrical storage. Especially for buildings with lower energetic standard, the mains supply can only be reduced about approximately 10 %.

Accordingly, a battery storage in combination with a conventional regulation is from an economical perspective not worthwhile. Only when the investment costs continue to fall, or the service life will be improved, changes may arise. Another improvement could cause an intelligent control strategy which considers forecasts of production and demand.

Tab. 6: Comparison of the total annuities of different concepts with battery storage and building standards for various area ratios

	0/50	10/40	20/30	30/20	40/10	50/0
SFH15						
Heating rod	3,804 €/a	3,149 €/a	3,280 €/a	3,331 €/a	3,445 €/a	3,672 €/a
Heat pump	3,410 €/a	3,231 €/a	3,393 €/a	3,517 €/a	3,703 €/a	3,962 €/a
Gas-boiler	2,828 €/a	2,788 €/a	2,931 €/a	3,096 €/a	3,320 €/a	3,605 €/a
Pellet boiler	4,129 €/a	4,164 €/a	4,331 €/a	4,511 €/a	4,731 €/a	5,037 €/a
SFH45						
Heating rod	5,471 €/a	4,730 €/a	4,734 €/a	4,711 €/a	4,761 €/a	4,894 €/a
Heat pump	4,179 €/a	3,983 €/a	4,124 €/a	4,216 €/a	4,379 €/a	4,578 €/a
Gas-boiler	3,172 €/a	3,101 €/a	3,222 €/a	3,418 €/a	3,569 €/a	3,821 €/a
Pellet boiler	4,335 €/a	4,360 €/a	4,512 €/a	4,680 €/a	4,895 €/a	5,182 €/a
SFH100						
Heating rod	10,009 €/a	9,110 €/a	8,981 €/a	8,848 €/a	8,809 €/a	8,891 €/a
Heat pump	6,148 €/a	5,948 €/a	6,026 €/a	6,115 €/a	6,266 €/a	6,492 €/a
Gas-boiler	3,938 €/a	3,879 €/a	4,226 €/a	4,138 €/a	4,329 €/a	4,601 €/a
Pellet boiler	4,839 €/a	4,861 €/a	4,423 €/a	5,167 €/a	5,374 €/a	5,658 €/a

5. Conclusion

The simulation-based study reveals that in terms of energy consumption it is possible to increase the electrical self-consumption with electric heating systems. The higher total electric energy demand is decreasing the electrical coverage and it must be obtained more energy from the grid. When using a heat pump the electrical coverage is slightly higher due to the better efficiency. With the addition of solar thermal systems for these systems the electrical self-consumption declines because then simultaneously with the solar electric energy also solar thermal energy is available and thus the photovoltaic power can often be used only to cover the household´s electricity demand. The use of a battery storage has only impact on the photovoltaic system and therefore only on the characteristic values of the electrical components. These values can be improved by the electrical storage. It turns out, however, that simultaneity is a crucial factor which is not always made possible by the battery storage.

From an economic view the conventional concept with a gas-boiler is the best system. In addition to the lowest investment costs are the running costs very low due to current gas prices. The economic viability of power-to-heat systems depends on the photovoltaic plant. Only if a large proportion of the electrical demand is generated by the photovoltaic system, the purchase of a heat pump is worthwhile. Otherwise, the improved efficiency of the heat pump cannot offset the high electricity costs. An electrical storage is no advantage because the invest costs are too high and savings in power supply costs are also too low. The acquisition pays off only if the costs of the battery storage decline, the costs of electricity increase or the feed-in tariff decreases.

The presented results are based on a simple system control and occurring simultaneity. Therefore, the impact of an energy management system on the self-consumption, thermal and electrical coverage will be examined in a next step. For this purpose a prediction of the expected production and load are included in the regulation in order to optimize the runtimes of the backup system.

6. References

BMWi-Bundesministerium für Wirtschaft und Energie, 2016. Zahlen und Fakten Energiedaten. National und Internationale Entwicklung, Berlin.

Bundesnetzagentur, 2016. Datenmeldung und EEG-Vergütungssätze für Photovoltaikanlagen. [online] http://www.bundesnetzagentur.de/cln_1432/DE/Sachgebiete/ElektrizitaetundGas/Unternehmen_Institutionen/ErneuerbareEnergien/Photovoltaik/DatenMeldgn_EEG-VergSaetze/DatenMeldgn_EEG-VergSaetze_node.html#doc405794bodyText4 [Accessed: 28/07/2016].

DEPV-Deutscher Energieholz- und Pellet-Verband e.V., 2016. Entwicklung des Pelletpreises in Deutschland. [online] http://www.depv.de/de/home/marktdaten/pellets_preisentwicklung/ [Accessed: 28/07/2016].

Deutsche Energie-Agentur (DEA), 2015. Wer verbraucht in Deutschland die meiste Energie? Energieverbrauch der Heizung oftmals unterschätzt. [online] http://www.dena.de/fileadmin/user_upload/Presse/Medienbibliothek/Bilder/Gebaeude/Wer_verbraucht_in_Deutschland_2015.jpg [Accessed: 12/07/2016].

Dott, R., Haller, M., Ruschenberg, J., Ochs, F. and Bony, J., ,2013. The Reference Framework for Systems Simulations of the IEA SHC Task 44 / HPP Annex 38, Part B: Buildings and Space Heat Load. Energy Agency (IEA) / Institut Energie am Bau - Fachhochschule Nordwestschweiz, Switzerland.

European Union, 2010. DIRECTIVE 2010/31/EU OF THE EUROPEAN PARLIAMENT AND OF THE COUNCIL of 19 May 2010 on the energy performance of buildings (recast), Brussels.

Hafner, B., Plettner, J., Wemhöner, C. und Wenzel, T., 1999. Conventional And Renewable eNergy systems OpTimization Blockset Blockset User's Guide, Juelich.

Lopez, J. U., Klesse A., Wagner, H.-J., 2011. Solares Heizen und Kühlen in Niedrigenergie- und Passivhäusern, Berlin.

Meteonorm. Global Meteorological Database Version 7. [online] http://www.meteonorm.com/images/uploads/downloads/mn71_software.pdf [Accessed: 12/07/2016].

The MathWorks Inc. Simulink. [online] http://de.mathworks.com/help/simulink/index.html [Accessed: 12/07/2016].

Quaschning, V., Weniger, J. und Tjaden, T., 2012. Der unterschätzte Markt. BWK, p. 25–28 (Bd. 64 Nr. 7/8).

Wirth, H. und Schneider, K., 2016. Aktuelle Fakten zur Photovoltaik in Deutschland, Freiburg.

Conference Proceedings

EuroSun 2016
Palma de Mallorca (Spain), 11 - 14 October 2016

Modelling of a Modular Indirect Natural Convection Solar Dryer

Maytham A. Al-Neama[1] and István Farkas[2]

[1]Mechanical Engineering Doctoral School /Szent István University, Gödöllő, Hungary

[2]Department of Physics and Process Control /Szent István University, Gödöllő, Hungary

Abstract

Nowadays, solar drying is becoming more important than ever before around the world. If more people use solar energy to dry agriculture and others products, our environment would be cleaner and the drying process will be more efficient. This paper discusses the performance and energy analysis of natural convection indirect solar drying system. The study rig that used consists from three main parts; flat plate air solar collector, dryer cabin and chimney. This system has been instilled in the laboratory of Szent IstvánUniversity in Gödöllő city in Hungary with collector tilt angle is 45° to the south according Budapest region, to get on the maximum amount of solar radiation. MATLAB software program has been developed to model the parts of this system, according the basic heat energy balance equations. The equations have been validated with many experimental results for different agricultural products. The experimental results showed the temperature and *RH* during drying period and the losses of water and moisture of the products.

Keywords: *solar collector, dryer, energy balance, performance*

1. Introduction

The use of the solar energy is getting a greater importance especially in the agriculture products drying. At the same time, the quality control and quality preservation technology becomes also very important technologies for processing of agricultural products than before. The Traditional application and very widely used product preservation is the drying process. Solar drying technology has many features upon the traditional dry technologies, it is low cost process and clean. In the past, the Agricultural and other products have been dried by the direct sun and wind in the open air for thousands of years. A typical solar dryer improves upon the simple open-air sun system, many main features:

- Products can be dried in a shorter period of time than the simple systems. Solar dryers improve drying process time by two methods. The first, by enhancing the translucent cover (the glass cover over the heat collection area inside the solar collector to raising the temperature of the air) and enhancing absorber plate area by increasing heat transfer area. Secondly, the flexibility of improving the solar collection area allows for greater amount of the solar radiation energy.
- Solar dryers more efficient than open-air sun system. The products can be dried faster, less possibility will be lost to spoilage immediately after harvest. This is especially for products that require immediate drying such as fresh grain with high moisture content.
- Control features, the control on the drying process parameters such as air temperatures, product and air moisture content, air velocity, etc. are better than the open-air sun dryers.

According to the brief review for many literatures the performance of drying process depend mainly on the performance of solar collector. So, the improvement of solar collector will improve the dryer work also (Mahendra et al., 1987). At the same time, some products do not need for high air temperature because it will damage such as fish, meats, etc. So, the control on the process parameters, air temperature, moisture content for air and product and air speed are very important.

Othieno (1986) explained solar cabinet dryer, it was very simple structure, and consists basically from small box has been made from wood. A transparent glass sheet was used as cover at upper edges surface. The box sides and bottom surfaces can be constructed from metal sheet (Aluminium) or wood. To circulate air through

doi:10.18086/eurosun.2016.04.19 Available at http://proceedings.ises.org

the system, holes has been made on the sides of the drier for this purpose. Indirect solar dryers also made of wood and plywood as presented by Amouzou et al. (1986). 10–15 kg of product can dried by drying chamber in 3 days. The absorber plate for solar collector is made galvanized sheet metal painted black to get selective surface.

Madhlopa et al. (2002) studied a solar dryer system had composite absorber plate systems on the principles of psychometric. The dryer consists of a flat plate solar collector, absorber plate approved with wire mesh, glass cover, chimney and insulated drying chamber. The drying chamber and solar collector box were made from wood sheets. The solar collector was connected to a drying chamber for product dehumidification.

Simate (2003) presented a comparison of optimized mixed-mode dryer and indirect-mode with natural convection solar dryers for maize. The two solar drying simulation models were validated against results from a laboratory solar dryer with experiments carried out under a solar simulator at the University of Newcastle, UK. They reported that, in both types, the collector and dryer width are the same. Airflow in the system is driven by buoyancy force. The drying cost with the mixed-mode dryer system using was 12.76 $/ton which was about 26% less than the indirect-mode system using; the quantity of dry grain obtained from the mixed-mode dryer for the one year was approximately 2.81 tones and was less than that from the indirect mode dryer by 15%.

Halewadimath et al. (2015) studied and fabricated an indirect forced- natural convection solar air dryer to estimate its performance under dry and hot weather conditions of Hubli, Karnataka, India. The system has been tested experimentally for both natural and forced convection. The performances of natural and forced convection systems are compared. The system consists of solar flat plate collector, drying chamber and a chimney. There are six baffles (fins) attached to the absorber plate to increases the turbulence of flow and increase heat transfer area for heated air in the collector which. Also, a mathematical model was developed by Ramos et al. (2015) to simulate solar drying of grapes, the heat and mass transfer models are solved by an explicit finite differences method, by considering changing boundary conditions. Many experiments were performed on a mixed mode solar dryer located in the North of Portugal, with amount pre-blanched grapes. Simulations showed with the developed model can be good to estimate accurate drying times and then to design, control and optimize the production of foods.

Then, according to the above brief review for many literatures, the performance of drying process depend mainly on the performance of solar collector. And the improvement of solar collector will improve the dryer work also. But, some products do not need for high air temperature because it will damage such as fish, meats, etc. So, the control on the process parameters, air temperature, moister content for air and product and air speed very important. In the recent paper, mathematical analysis of passive indirect solar drying system, consists from main parts: flat plate air solar collector, dryer chamber and chimney.

2. Description of the dryer

The study represented the performance of simple convective solar dryer (distributed solar dryer with natural convection), shown in Fig. 1. The test rig is constituted of two main parts; a flat plate air solar collector. It is composed of the flat aluminium plate used as an absorber surface, covered from the above by a glass sheet was fixed on the upper edges of collector box, and collector box that insulated from all sides to decrease heat losses. There is a space between the absorber surface and the glass sheet cover. This narrow space used as an air flow duct through the solar collector and integrated with the second part.

The second part is the drying chamber made with support many trays where the product is placed. Drying chamber has been insulated and painted with black paint to decrease the losses by radiation to the surrounding. As mentioned, the study was by free convection, the movement of air was by bouncy force with using a long chimney, which permits to have a good air speed by free convection and homogeneous distribution of the heated air inside the drying chamber, it allows also having better control of the drying process.

Fig. 1: Solar dryer test unit

The drying system is energized by the sun's rays (solar radiation energy) passing through the collector glazing cover. The trapping of the solar radiation (short waves) is enhanced by the inside surfaces of the solar collector that were painted black to change it to heat energy (long waves). Then, the heat energy will transfer from the black absorber plate to the air which passing inside the collector by convection. The last energy collection method is called the greenhouse. The air current will flow through the drying chamber by the effect of green house in the solar collector. Energy exchange (heat and mass transfer) between products items and hot air inside the dryer chamber. Then, the moist and hot air rises and escapes from the upper vent in the drying chamber (chimney) while cooler air at ambient temperature enters through the lower vent in the solar collector. Therefore, an air current movement is maintained, as cooler air at a temperature ($T_{collector,in}$) enters through the lower suction vent and hot air at a temperature ($T_{chimney,out}$) leaves through the upper chimney vent.

When the dryer is empty (no products in it), the entering air at a temperature T_{in} with relative humidity X_{air} and the discharged air at a temperature T_{exit}, has a relative humidity X_{exit}. With the dryer contains no item, the inlet relative humidity X_{in} higher than exit X_{exit} because T_{exit} higher than T_{in}. As referred before, there is tendency for the hot exit air to get more moisture within the dryer, as a result of the moisture difference occurs between X_{air} and X_{exit}.

For flat-plate solar collector, it is always tilted in such a way that it receives maximum solar radiation during the day and to be perpendicular with solar radiation rays at noon. Based on Duffie and Beckman (2013), the best stationary orientation is due south in the northern hemisphere and due north in southern hemisphere. Therefore, solar collector in this work is oriented facing south and tilted at 45° to the horizontal according to the solar chart for Budapest region (Budapest 47.5° N, 19.05° E).

3. Modelling assumptions

According to the classical way to modelling, the physical base with many assumptions are used the performance for every thermal system generally and drying systems especially. To simplify physical model, there are many assumptions have been taken before modelling, as following:

1. Drying system performance works with steady state condition.
2. Air flow distribution through system components is assumed homogeneous.
3. Mass and heat transfer are one-dimensional inside system components (always with air flow direction).
4. There is one-dimensional heat flow through back insulation for solar collector.
5. Dust and dirt effects on the flat plate solar collector are negligible.
6. Wind speed is approximately constant.
7. Connecting air channels is assumed to be with no leakages and without heat losses.
8. Products items initial moisture is uniform throughout the mass of the product.

9. Product size and distribution of product items assumed uniform inside the drying chamber.
10. Product surface moisture content of the sample items instantaneously reaches to the equilibrium state with the surrounding air.
11. Surface resistance to the mass transfer at the product surface is negligible compared to internal resistance of the sample.

4. Energy balance calculations

In this section, the energy balance relations are described for the main components of drying unit as solar collector and drying chamber.

4.1. Solar collector

The solar collector has the size of 2 m x 0.5 m x 0.2 m. The solar collector with about 1 m^2 absorber plate area integrated to the dryer chamber to heat air flow that will enter the chamber. It has a transparent glass cover fixed on the top edges of the collector box and thermal insulation at the bottom base side of the metal box. For the better energy collection a black absorber plate was put on the half height of the collector body box. As mentioned, the solar collector in this work is oriented facing south line and tilted at 45° to the horizontal according to the solar chart for Budapest region. To get more absorption of solar radiation and radiation reflection reduction, absorber plate painted with matt black colour.

The energy balance on the absorber plate is obtained by equating the total radiation gained from the sun rays through the glass cover with transmittance (τ) to the total heat loosed from the absorber plate of the solar collector. Therefore:

Solar radiation per unit area = useful heat +heat losses+ reflected losses.

If τ is the transmittance of the top glazing cover sheet, I is the total solar radiation incident on the top surface of the solar collector and A_c is the area of absorber plate, then mathematically the solar radiation per unit area will be:

$$Solar\ radiation\ per\ unit\ area = \tau\ I\ A_c.$$

The solar radiation represented the total solar radiation, beam, diffuse and ground reflected radiation. Experimentally, it can be measuring by simple calibrated solar measurement device. Theoretically, according the position (Gödöllő) and the time, MATLAB software program has been developed to estimate it. For beam (direct) radiation component on the collector surface, calculated according ASHREA 2005 standard. For the diffuse (indirect) and ground reflected solar radiations, depending on Al-Joboory (2012) has been estimated.

The same for the reflected radiation from the collector, the mathematical expression reflected energy from the absorber surface is given by the following expression:

$$Reflected\ losses = \rho\ \tau\ I\ A_c,$$

where ρ is the reflection coefficient of the absorber surface plate. By the Substitution of solar radiation and reflected losses expressions in the general energy balance equation for the absorber plate, will get:

$$\tau\ I\ A_c = useful\ heat + heat\ losses + \rho\ \tau\ I\ A_c.$$

By rewriting the above relation:

$$Useful\ heat = \tau\ I\ A_c.\ (1-\rho) - heat\ losses.$$

For an absorber plate, according to Duffie and Beckman $(1-\rho) = \alpha$ and then:

$$Useful\ heat = (\alpha\tau)\ I\ A_c - heat\ losses.$$

The above expression represents the energy balance equation for the absorber plate surface. For this study, it is very important to estimate air temperature rise thorough the collector. The change of air temperature through it depend on how much energy that absorbed (collected) by the absorber plate. So the above energy balance is not enough useful to show the behaviour of air temperature.

In the direction of air stream, the inlet ambient air to the collector carried sensible heat energy also depend on its mass m^o and temperature $T_{c,i}$. The same for the outlet air, it will catch the heat from stored absorber plate energy by convection, then it will leave the solar collector with the same mass flow rate and new temperature equal to $T_{c,o}$. Then by considering the heat energy content for inlet and outlet air, the final energy balance for the air solar collector system will be:

Useful heat = $(\alpha\tau)\ I\ A_c$ – heat losses+ inlet air heat content – outlet air heat content.

Mathematically:

$$M\ C_p \frac{dT_{c,o}}{dt} = (\alpha\tau)\ I\ A_c - U\ A_c\ (T_c - T_a) + m^o\ C_p\ T_{c,i} - m^o\ C_p\ T_{c,o}. \quad \text{(Eq. 1)}$$

Then by rewriting Eq. (1), get:

$$\frac{dT_{c,o}}{dt} = \frac{1}{M.C_p}\left[(\alpha\tau)\ I\ A_c - U\ A_c\ (T_c - T_a) + m^o\ C_p\ T_{c,i} - m^o\ C_p\ T_{c,o}\right], \quad \text{(Eq. 2)}$$

where M is the mass of air inside collector duct in (kg), T_a is the temperature of ambient air in (K), T_c is the average temperature of the absorber plate in (K), C_p is an air specific heat at constant pressure in (J/kgK), $\tau\alpha$ is called transmittance-absorptance product for glazed collector, and it was for black colour absorber plate about 0.87 (considered for this study) according to Anderson et al. (2009) and U represents to the total energy losses from the flat plate solar collector: top U_t, back (bottom) U_b and side edges U_s heat losses. It means:

$$U = U_b + U_s + U_t. \quad \text{(Eq. 3)}$$

The bottom heat loss coefficient and by the basic of conduction heat transfer resistance for the wall or material layer with thickness equal X_b and material thermal conductivity equal K_b, the back heat loss coefficient U_b will be as follow in Eq. (4):

$$U_b = \frac{K_b}{X_b}. \quad \text{(Eq. 4)}$$

The same for collector edges heat loss coefficient U_s, but with multiplying by the area ratio between collector side edges area to the solar collector area as shown in Fig. 2. Then, U_s for collector length L, width W and depth X will when the side edges have K_s as a thermal conductivity and side thickness equal X_s, will be:

$$U_s = \frac{K_s}{X_s}\left[\frac{X.(L+W)}{L.W}\right]. \quad \text{(Eq. 5)}$$

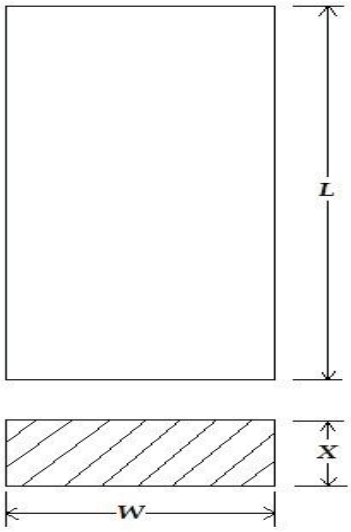

Fig. 2: Solar collector dimensions

The estimation of top energy loss coefficient for most solar collectors is complicated with using basic heat transfer relations. However, with good designed system, the collector loss should be low so that it is not necessary to predict it with great accuracy. To estimate the value of tope loss coefficient, as Kalogirou mentioned in his book an empirical useful formula is used by depending on number of covers, absorber plate temperature, and ambient temperature, etc. as follow:

$$U_t = \left[\frac{N}{\frac{C}{T_c}\left[\frac{T_c - T_a}{N+f}\right]^e} + \frac{1}{h_w}\right]^{-1} + \frac{\sigma(T_c+T_a)(T_c^2+T_a^2)}{\frac{1}{\varepsilon_p+0.0059N.h_w} + \frac{2N+f-1+0.133\varepsilon_p}{\varepsilon_g} - N}. \quad \text{(Eq. 6)}$$

where N represents to the covers number, h_w is an wind heat transfer coefficient, σ is Stefan-Boltzmann constant, ε_p and ε_g are the absorber plate and glass cover emissivity, and each of C, f and e are constants and calculated from Eq. (7) as follow:

$$C = 520\ (1-0.000051\ \beta^2).$$
$$f = (1+0.089\ h_w - 0.1166\ h_w \varepsilon_p)\ (1+0.07866\ N). \quad \text{(Eq. 7)}$$
$$e = 0.43\ (1-100/T_c).$$
$$h_w = 2.8+3V.$$

where β is a bulk coefficient of expansion of air in K^{-1} and V represents to the ambient wind velocity in m/s.

4.2. Dryer

The drying chamber (the dryer) with 7 trays for the different products items. The drying cabin dimensions are 0.8 m x 1 m x 0.65 m. The drying chamber is integrated with the solar collector by a small duct (indirect drying). The heated air exit from the collector will enter the chamber with high temperature and low moisture content. The total energy required for drying process for given quantity of any type of products items can be determined by using the basic energy balance equation for the evaporation of water. According to the schematic diagram for the dryer, the basic energy balance equation (mass + heat), as written below:

$$Q_{air,inlet} + Q_{product,inlet} = Q_{air,outlet} + Q_{product,outlet} + energy\ losses\ .$$

For perfect system insulated, the value of energy losses from the dryer will be very small, so it can be neglected. Then, the latent energy of the evaporated water from the product with mass W_v and latent heat of vaporization equal L_v will equal the heat lost from the air which flowed through the dryer. Mathematically:

$$W_v\ L_v = m^o\ C_p\ (T_{d,i} - T_{d,o}), \quad \text{(Eq. 8)}$$

where $T_{d,i}$ and $T_{d,o}$ are inlet and outlet temperatures through the dryer. The inlet dryer temperature $T_{d,i}$ equal to the outlet temperature of the solar collector $T_{c,o}$ by assuming that is no heat losses through connection small duct between the solar collector and dryer. Where the mass of water evaporated from the product W_v calculated from Eq. (9):

$$W_v = m_i \frac{w_i - w_f}{100 - w_f}, \quad \text{(Eq. 9)}$$

where m_i is the initial mass of product in (kg), w_i is the initial moisture content and w_f is the final moisture content. During drying process, water at the surface layer of the product evaporates and water in the inner part transfer gradually to the surface to get evaporated. The ability of this water movement depends on the porosity of the product item material and the surface area available.

The basic theory of drying process was described by Lewis (1921) based on the partial similarity with Newton's law of cooling and is often used to mass transfer in thin-layer drying as follow in Mahedra et al. (1987):

$$\frac{dw}{dt} = -k\ (w - w_e), \quad \text{(Eq. 10)}$$

where k represents drying process constant, w_e is an equilibrium mass, by solving the above differential Eq. (10) for these conditions, (at $t = 0$, $w = w_o$) and (at $t = \infty$, $w = w_e$), get:

$$\frac{w_t - w_e}{w_o - w_e} = -e^{-kt}. \quad \text{(Eq. 11)}$$

The above term in Eq. (11) called moisture ratio (MR), then:

$$\frac{w_t - w_e}{w_o - w_e} = MR\ . \quad \text{(Eq. 12)}$$

A product material stills for a long time at a fixed temperature and relative humidity then will eventually gradually reach a moisture content that is in equilibrium with the moist air. The equilibrium state does not mean that the product item and the air have the same moisture content. It simply means that an equilibrium condition exists such that there is no net exchange of moisture (latent heat) between the product material and the heated air. This equilibrium moisture content (w_e) is a function of the temperature, the relative humidity, and the type of the product.

Finally, to estimate the efficiency for all the system (solar collector and dryer chamber), the following relation represent the ratio between input energy and output energy to the totally system has been calculated. The system efficiency indicates the overall thermal performance of a drying system including the efficiency of a solar collector, the drying chamber and any other supplement add to the system:

$$Totalefficiency = \frac{W_v \, L_v}{I \, A_c}. \quad \text{(Eq. 13)}$$

As known to increase heat transfer by convection, turbulence of air should increase. So, the effects of free convection will be enhanced by adding a long chimney in which exiting air is heated even more by friction and enhance the buoyant flow of air. Some studies showed that the installation of three small fans and a photovoltaic cell is equivalent to the effect of chimney with 12 m length.

5. Results for validation

In this section a validation of the energy relation are performed based on the measured results for different products drying and environmental variables. The solar drying experiments were carried out between April and May 2006 at Gödöllő, Hungary (Farkas et al., 2006).

5.1. Environmental variables during the experiments results

This section shows the conditions of temperature and relative humidity during the drying period for different products as carrot, apple and potato (Tables 1-3 and Figs 3-4).

Table 1: Relative humidity (RH) and average inlet and outlet temperatures for carrot

Day	RH ext, %	Temp, ºC ext	RH int, %	Temp, ºC, int
1				
2	16,89	22,71	15,13	23,07
3	11,49	20,5	11,04	21,65
4	7,59	22,64	7,15	22,59
5	8,84	21,14	12,74	21,74
6	13,88	14,7	14,56	21,39
7	29,92	19,78	28,52	23,22
8	74,87	13,22	77,37	16,43
9	61,16	11,33	57,11	16,8

Table 2: Relative humidity (RH) and average inlet and outlet temperature for apple

Days	RH ext, %	Temp, ºC ext	RH int, %	Temp int, ºC
1				
2	59,6	17,98	66,44	21,23
3	33,22	24,27	31,04	34,05

Table 3: Relative humidity (RH) and average inlet and outlet temperature for potatoes

Days	RH ext, %	Temp, ºC ext	RH int, %	Temp int, ºC
1				
2	32	26	28,6	38,5
3	32,5	28,5	26,2	43,4

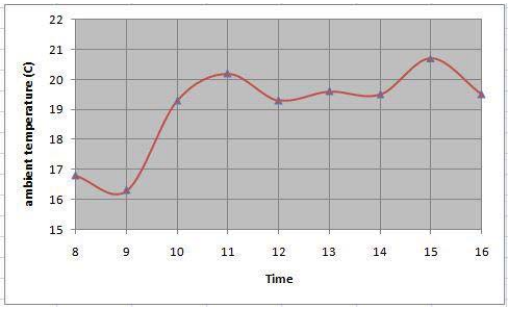

Fig. 3: Average daily ambient temperature during drying period of 8 days

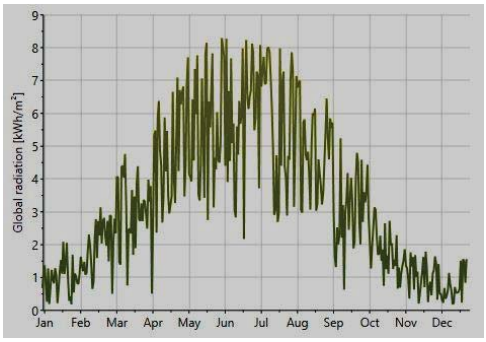

Fig. 4: The global solar radiation for 2006

5.2. Loss of water

In Figs 5-7 the changes in mass of the carrots, placed in different trays, are represented through the drying period. In Fig. 5 it can be seen that after 4 days the carrots lost 87% of the initial weight. In Fig. 6 it can be seen that after 24 hours the apples lost 84% of the initial weight. In Fig. 7 it can be seen that after 24 hours the apples lost 83,5% of the initial weight.

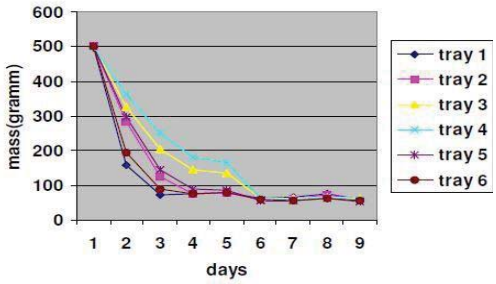

Fig. 5: Loss of water during the drying period for the carrot

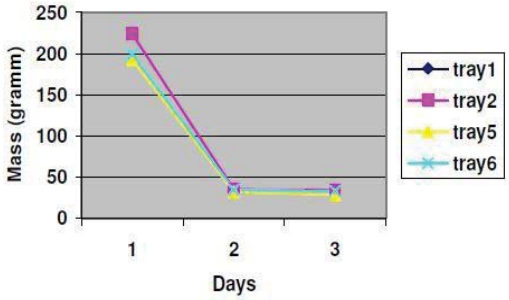

Fig. 6: Loss of water during the drying period for the potatoes

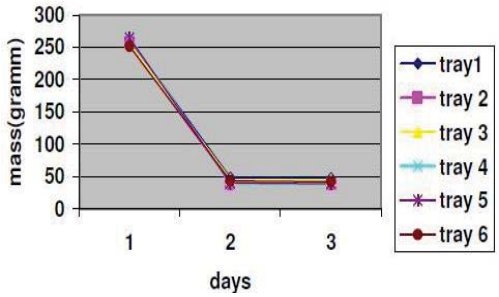

Fig. 7: Loss of water during the drying period for the apple

5.3. Temperature distribution

Figs 8-10 show for the products the distribution of the temperature outside and inside the dryer between 8 a.m. and 4 p.m. Fig. 8 shows that for the carrots there is no difference in temperature among the trays and inside the chamber is higher than outside in the second part of the day (12-16) hours. For the apples the temperature inside the chamber is always higher than that outside. This difference is more evident between 11-16 hours. The Fig. 10 shows, that for the case of potatoes there is difference in temperature among the trays in particular in the first tray where the temperature is higher than that other trays and the temperature inside the chamber is always higher than that outside.

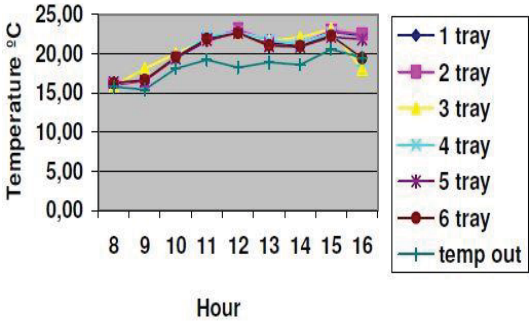

Fig. 8: Temperature distribution outside and inside the dryer for the carrots

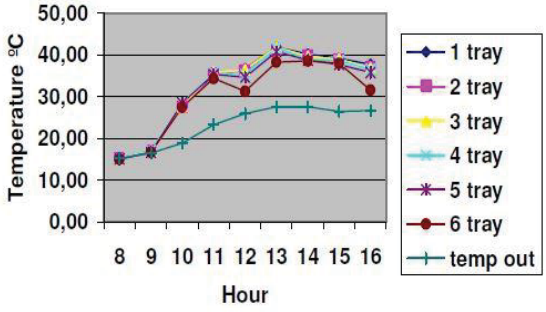

Fig. 9: Temperature distribution outside and inside the dryer for the apples

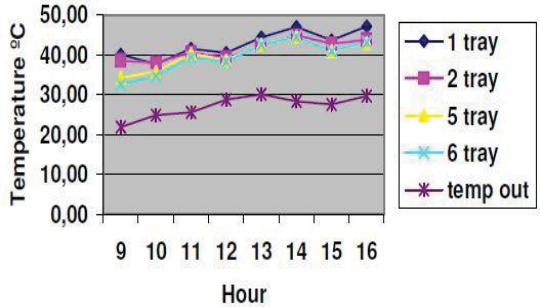

Fig. 10: Temperature distribution outside and inside the dryer for the potatoes

6. Conclusions

The temperature of air inside the system (drying chamber and solar collector) is much higher than the surrounding temperature during most times of day. That means, these systems better performance than open-air sun drying systems. The control on the drying parameters such as air velocity, temperatures, moisture contents, etc. are not complicated and not expensive.

Drying process with using solar heater, depends on the temperature and moisture content difference between an air stream and product items inside the insulated chamber. It is very important to know the type of product item, to estimate the temperature rang that is suitable to save it from damaging during drying process. With some drying products like fish, meat, yam chips, etc., over heating must be avoided to save the quality of the product.

Also that is many methods to enhance these types of dryers, such as heat transfer area is increasing, air turbulence increasing, and improvement the insulating of the system, etc. for this study, a long chimney is integrated with the drying chamber to increase air velocity during drying process. The increasing of air velocity will improve the rate of water evaporated from the product item. Also, the very important point in this dryer, it is very economic process (low costs of constructions), simple design and efficient control.

7. References

1. Al-Joboory A.N., 2012, Analytical appraisal and experimental verification of the ASHRAE cooling load calculations methods for a hot arid climate, Ph.D. thesis, Baghdad university, Baghdad.
2. Anderson T., Duke M., Carson J., 2009. Performance of colored solar collectors, The first international conference on applied energy, Hong Kong.
3. American society of heating refrigeration & air conditioning engineers, “ASHRAE HVAC applications Handbook”, Chapter 33, 1999.
4. Amouzou K., Gninin vani M., Kerim B., 1986. Solar Drying Problem in Togo, research and development solar drying in Africa, In Proceedings of a Workshop held in Daka, 21-24 July, Dakar, Senegal, 252–271.
5. Duffie J., Beckman W., 2013. Solar Engineering of Thermal Processes, Fourth edition, John Wiley & Sons, New Jersey, USA.
6. Halewadimath S., Subbhapurmath P., Havaldar N., Hunashikatti K., Gokhale S., 2015. Experimental analysis of solar dryer for agricultural products, International Research Journal of Engineering and Technology, 02(03),1517-1523.
7. Kalogirou S.A., 2009. Solar energy engineering: process and systems, First edition, Elsevier's science and technology department in Oxford, England.
8. Farkas, I., Kocsis, L., Romano, G., 2006. Temperature and moisture distribution during solar drying of vegetables and fruits, Research Report, Department of Physics and Process Control, Szent István University Gödöllő, No 39, May 2006, p. 28.
9. Madhlopa A., Jones S.A., Saka J., 2002. A Solar Air Heater with Composite-Absorber Systems for Food Dehydration, Renewable Energy Journal, 27, 27–37.
10. Mahendra S., Narendra K., Kumar A., Pradeep K., Malik M.A.S. 1987. Solar crop drying, CRC press, Florida, USA
11. Othieno H., 1986. Circulation of Air in Natural-Convection Solar Dryers, research and development solar drying in Africa, Proceedings of a Workshop held in Dakar, 21-24July, Dakar, Senegal, 47–59.
12. Ramos N., Brandao R.S., Silva L.M., 2015. Simulation of solar drying of grapes using an integrated heat and mass transfer model, Renewable Energy Journal, 81, 896-902.
13. Simate IN., 2003. Optimization of mixed-mode and indirect-mode natural convection solar dryers, Renewable Energy Journal, 28, 435–453.

8. Acknowledgements

This paper was supported by the Stipendium Hungaricum Programme and the Mechanical Engineering Doctoral School at the Szent István University, Gödöllő, Hungary.

Conference Proceedings

EuroSun 2016
Palma de Mallorca (Spain), 11 - 14 October 2016

Global Aging and Lifetime Prediction of Polymeric Materials for Solar Thermal Systems – Part 2: Polyamid 66 Glass-fiber Reinforced Absorbers for Integrated Storage Collectors

Michael K. Grabmann[1], Gernot M. Wallner[1], Thomas Ramschak[2], Georg Ziegler[3], Reinhold W. Lang[1]

[1] Institute of Polymeric Materials and Testing, University of Linz, Linz, Austria

[2] AEE Intec, Gleisdorf, Austria

[3] GREENoneTEC, St. Veit/Glan, Austria

Abstract

The paper deals with the lifetime estimation of black-pigmented, glass-fiber reinforced polyamide (PA-GF) absorber grades for absorber/storage tanks of pressurized, non-pumped hot water systems at different sites (Athens, Fortaleza, Pretoria). The annual absorber time/temperature distributions were simulated. Global aging data were gathered by exposure of specimens in hot water at elevated temperatures (115 and 135°C) and analytical and mechanical characterization after aging. Lifetime assessment for the absorber/storage-tank material was done by combining the time/temperature loading profiles, extrapolated endurance times from aging tests and assuming cumulative damages. Depending on the chosen aging indicator, glass fiber content and climate zone, the lifetimes varied between 35 and 47 years with lowest values for the hot-and-humid climate zone. The grade with 30 m% glass-fibers exhibited a slightly better long-term performance than the grade with 35 m%.

Keywords: *Polypropylene; Solar thermal collector; Absorber; Lifetime*

1. Introduction

Fiber-reinforced polymer composites represent an important material class for solar thermal systems (Wallner and Lang, 2005). Material properties like low weight, high mechanical strength, thermal, dimensional and chemical stability as well as mass production capability are of paramount importance for cost-efficient pressurized non-pumped systems based on integrated storage collectors (Celina et al., 2005; Kahlen et al., 2010). Today for solar thermal collectors a lifetime of up to 20 years or even more is mandatory (Köhl et al., 2005). In previous research the opportunities and limitations of injection moulding technologies for the production of absorbers of integrated storage collectors were evaluated (Brunold et al., 2012). It was shown that glass-fiber reinforced polyamides exhibit a high potential for such applications.

A main task of current research work is the lifetime assessment of these novel absorber materials for more cost-efficient and reliable collector systems. Hence, the main objective of the paper is to investigate the aging behavior and to assess the lifetime of various glass-fiber reinforced polyamide 66 grades for pressurized, non-pumped integrated storage collector systems. Therefore, temperature loading profiles were estimated for three different climate locations (Mediterranean (Athens, Greece), hot-and-humid (Fortaleza, Brazil) and hot-and-dry (Pretoria, South Africa)) with maximum temperatures up to 95°C. The technological parameter stress-at-break and the analytical parameter area crack density were determined for standardized specimens after exposure to hot water at elevated temperatures (115 and 135°C). Using an Arrhenius approach endurance times at service-relevant temperatures ranging from 5 to 95°C were calculated. For lifetime

doi:10.18086/eurosun.2016.04.03 Available at http://proceedings.ises.org

assessment a recently published approach based on calculated temperature loading profiles, extrapolated endurance times and cumulated damages was used (Wallner et al., 2016).

2. Methodological approach

2.1 Collector design and modelling of service relevant conditions

The investigated solar thermal integrated collector storage (ICS) (s. Fig. 1) combines the thermal absorber and the storage tank in one component. The system consists of cylindrical tubes with a diameter of about 150 mm and a thickness of 3 mm. These tubes are friction welded out of injection molded half shells and subsequently connected in series. Reinforced ribs and insulation are applied to fulfill mechanical and thermal properties. Under service conditions the tubes are permanently filled with drinking water under a given pressure, while the outside of the tubes remain dry. Consequential the tubes are loaded under permanent stress while recurring temperature changes lead to complex and superimposed conditions (Geretschläger, 2015).

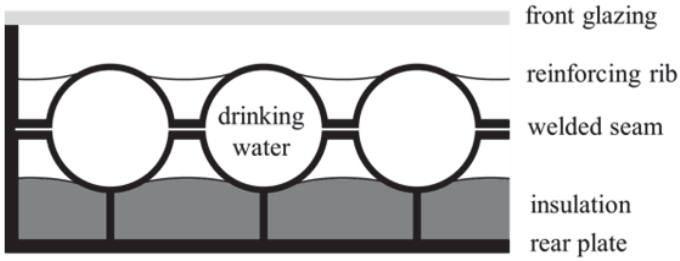

Fig. 1: Cross section of the ICS collector with injection molded absorber/storage tank made from half-shells [Geretschläger, 2015].

Based on the study by Kaiser et al. (2013) and prevalent market potentials, three different climatic conditions (Mediterranean (Athens, Greece), hot-and-humid (Fortaleza, Brazil) and hot-and-dry (Pretoria, South Africa)) are taken into account for this work. Based on Meteonorm-data, relevant climatic parameters (e.g. air temperature, relative humidity, global radiation) are established on an annual basis. In a further step for all three climate zones market-based polymeric collectors for hot water preparation in single family houses are defined and evaluated. By theoretical modeling using the software tool SHW (Streicher et al., 2004), annual time/temperature distributions for the absorber are obtained.

2.2 Materials, aging conditions and characterization

Based on established property requirements for materials of pressurized absorbers/storage-tanks aliphatic polyamide 66 grades with glass-fiber contents of 30 and 35 m% and carbon black pigmentation were selected for the investigations. The long term hydrolytic stability was characterized at elevated temperatures of 115 and 135°C. Therefore standardized dumbbell specimens were exposed in water filled pressure cooker autoclaves and withdrawn at defined intervals.

As global aging indicators, the technological parameter stress-at-break and the analytical parameter area crack density were monitored. Limit values of these aging parameters were defined on basis of maximum mechanical loads and material key-properties of an ICS. Tensile tests were carried out at 23°C using a screw-driven universal testing machine with a test speed of 50 mm/min. The lower limit as aging indicator for stress-at-break values was defined at 25 MPa. Microscopic investigations on surface defects were achieved by using a conventional microscope with a 5x-objective (2.0x2.8 mm²). Area crack density was calculated by the ratio of single cracks on the surface relative to the size of the picture. The limit value for failure was the first appearance of cracks on the surface of the specimen. A similar methodological approach dealing with the aging characterization of glass-fiber reinforced polyamides in hot water and air was carried out successfully by Geretschläger and Wallner (2016).

2.3 Lifetime assessment

For lifetime estimation a cumulative damage approach was used established by Wallner et al. (2016) for

black-pigmented PP solar absorber materials. The main elements of the approach are the simulation of temperature loading profiles, the extrapolation of aging data and the cumulation of damages of different temperature levels (Fatemi and Yang, 1998). The experimental global aging data gathered at elevated temperatures were extrapolated to service-relevant temperatures. Therefore, the log(t)/(1/T)-linear Arrhenius approach was applied assuming a specific degradation mechanism in the temperature range. Additionally, a constant endurance time of 50 years was assumed according to Leijström and Ifwarson (1998) to ensure not to overrate lower temperatures. The lifetime was deduced by weighting the temperature dependent endurance times with the loading profiles according to ISO 13760. This lifetime modelling approach neglects superimposed static and cyclic mechanical loads induced by temperature changes that are to be expected during operation of the ICS collector.

3. Results and discussion

3.1 Service relevant loading conditions

Fig. 2 illustrates the simulated absorber surface temperatures profiles for mediterranean (Athens), hot-and-humid (Fortaleza) and hot-and-dry (Pretoria) climate conditions. Two different situations (with hot water consumption and stagnation) are considered. The solid curve represents the stagnant condition whereby no water is used from the integrated storage collector. For the consumption condition, an assumed daily use of 110 litres at 45°C is taken into account. A maximum of hot water draw is assumed mainly in the morning (6am to 8am) and in the evening (7pm to 9pm) while a reduced water abstraction is given during day. Regarding the temperature loading profiles maximum temperatures of about 90°C are obtained for the collector system in Fortaleza. Slightly lower values are calculated for Pretoria and Athens. Also the maximum of the time/temperature distribution is significantly dependent on the installation site. The high temperature loads between 70 and 90°C are more pronounced for Fortaleza while minimum temperatures of about 30°C are obtained. Athens reveals lowest collector temperatures of about 5°C. In all locations the stagnant conditions lead to a slight shift of the profile curve towards higher temperatures. Hence, stagnant condition is selected to calculate a worst case scenario for lifetime modelling.

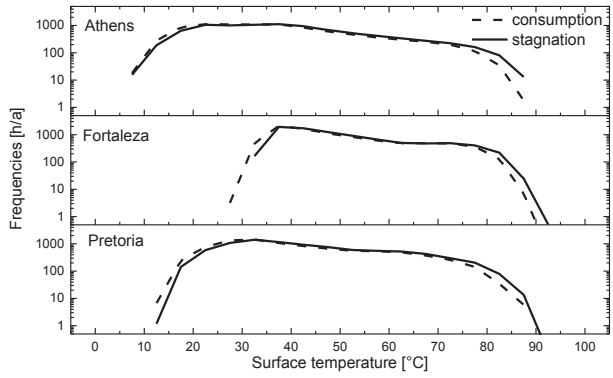

Fig. 2: Annual ICS absorber surface temperature profiles for three different climate zones with and without hot water consumption.

3.2 Aging behavior at elevated temperatures

Fig. 3 shows the stress-at-break values and the area crack density of the investigated GF-reinforced PA66 grades as a function of aging time in hot water at 115 and 135°C. Ultimate failure with stress-at-break values below 25 MPa are indicated with open symbols in the chart. The limit value for area crack density is the first visible appearance of cracks. Aging in hot water led to a steady decrease of stress-at-break values. Limit values of 25 MPa were obtained after about 750 h and 5000 h at 135 and 115°C, respectively. The aging behavior of the investigated grades was slightly differing. First cracks on the surface were detected within 350 h and about 2500 h at 135 and 115°C. Hence, this aging indicator was more sensitive and critical. The amount of cracks per area increased significantly for ongoing exposure. A higher tendency of crack formation was observed for PA66-GF35 and therefore a worse hydrolytic stability. Both materials exhibited

a regular crack pattern primarily oriented perpendicular to the fiber direction i.e. line of injection (s. Fig. 4).

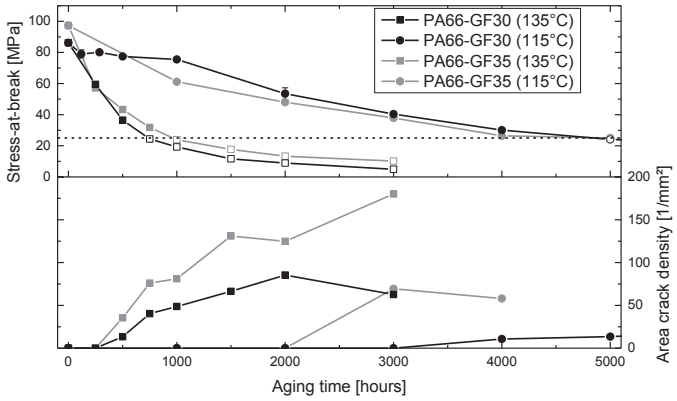

Fig. 3: Stress-at-break values (top layer) and area crack density (bottom layer) for glass-fiber reinforced PA66 specimens as a function of aging time exposed to hot water at 115 and 135°C.

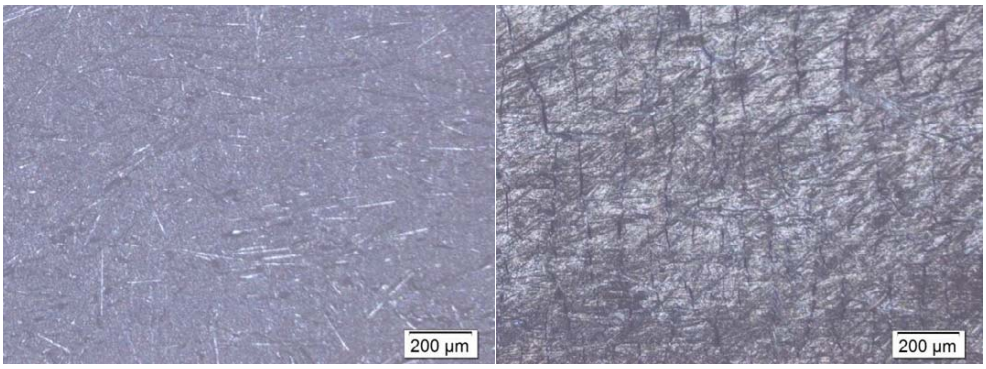

Fig. 4: Unaged (left) and degraded/cracked (right) surface of PA66-GF30 after exposure to hot water at 135°C for 750 h.

3.3 Extrapolated endurance times and estimated lifetimes for glass-fiber reinforced PA66 specimen

The derived Arrhenius plots for material endurance time estimation is presented in Fig. 5. The filled symbols represent the stress-at-break limit values while the open symbols depict crack formations on the surface of the samples for 115 and 135°C in hot water. The experimental data were fitted using an Arrhenius approach and extrapolated to service-relevant temperatures ranging from 5 to 95°C. A similar methodological approach dealing with the assessment of long-term mechanical performance of glass fibre reinforced polyester composites in aqueous environments was carried out by Carra and Carvelli (2015).

Due to the fact, that PA66-GF35 exhibited a slightly less drop of the strength at 135°C and a comparable aging behavior at 115°C, the extrapolated curves of both investigated grades intersect resulting in a worse aging behavior for PA66-GF35 below 115°C. To examine this phenomenon, additional exposure tests are ongoing at 125 and 105°C.

The shorter failure times for the aging indicator area crack density results in left shifted extrapolated curves with lower endurance times. The material with the higher glass-fiber content exhibited a more pronounced formation of cracks and therefore a worse aging behavior. For the assumed 50 years cut-off a temperature threshold of 74 and 68°C was deduced for PA66-GF30 and PA66-GF35, respectively.

Table 1 depicts the deduced lifetimes which are ranging from 35 years in the hot and humid climate of Fortaleza up to 47 years for the less critical mediterranean climate of Athens. Comparable maximal lifetimes of 47 years were deduced for the hot-and-dry climate condition of Pretoria. However, all results were significantly affected by the 50 years cut-off. Lower lifetime values were obtained for the grade with 35 m% glass fibers. This can be attributed to differences in the stabilization packages. For both materials the aging

indicator area crack density exhibited slightly lower lifetimes (less than 10% deviation).

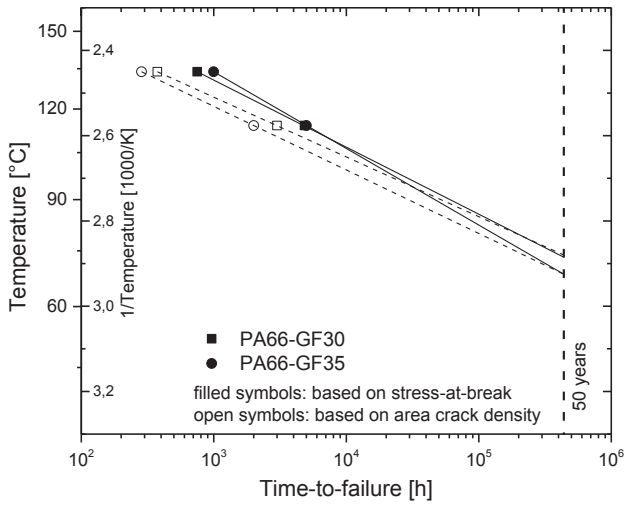

Fig. 5: Experimental failure times for glass-fiber reinforced PA66 based on stress-at-break and area crack density as limit values with extrapolated endurance times in the service relevant temperature range.

Tab. 1: Estimated lifetimes for the investigated glass-fiber reinforced PA66 grades for integrated storage collectors at the installation sites Athens, Fortaleza and Pretoria.

Aging indicator	Material	Predicted lifetimes in years		
		Athens mediterranean	**Fortaleza** hot and humid	**Pretoria** hot and dry
Stress-at-break	PA66-GF30	47	44	47
	PA66-GF35	44	38	43
Area crack density	PA66-GF30	47	43	47
	PA66-GF35	42	35	41

4. Summary and conclusion

Lifetime estimation was established for two black-pigmented glass-fiber reinforced PA66 grades used for integrated storage collectors for hot water preparation. Therefore, temperature loading profiles for three different climate zones were determined based on climatic input data. As experimental failure limits, the drop of stress-at-break below 25 MPa and the appearance of cracks on the surface of the specimen was defined. These aging indicators were observed for exposition in hot water at 115 and 135°C. Furthermore, endurance times at service relevant temperatures (5 to 95°C) were extrapolated using an Arrhenius approach. A model of cumulative damages (Miner's rule) was applied to assess lifetimes for the investigated materials.

Absorber temperature loading profiles ranging from 5 to 95°C were obtained. The profile was dependent on the installation site with longer exposure times at higher temperatures for Fortaleza. The stagnant condition led to a shift of the loading profile towards higher temperatures for all three locations. Thus, these temperature loading profiles were used for lifetime assessment.

Hot water exposure of the investigated grades at elevated temperatures resulted in a decrease of stress-at-break values with ultimate failure times of 750 and 5000 h at 135 and 115°C, respectively. Crack formation started after 350 h at 135°C and 2500 h at 115°C. Both materials showed a regular crack pattern primarily oriented perpendicular to the fiber direction with a higher tendency for crack formation for the PA66-GF35 grade.

The obtained lifetime values were ranging from 35 to 47 years. The Mediterranean climate in Athens and

hot-and-dry climate in Pretoria exhibited highest calculated lifetimes, while the hot and humid climate in Fortaleza led to shorter lifetimes (4 to 7 years lower). PA66-GF35 exhibited lower lifetimes, which was attributed to differences in the stabilization package. To assure the extrapolated endurance times and the deduced lifetime values exposure tests at 125 and 105°C are carried out additionally.

5. Acknowledgment

This research work was performed in the cooperative research projects SolPol-4/5 entitled “Solar-thermal systems based on polymeric materials” (www.solpol.at). The projects were funded by the European Commission within the Seventh Framework Programme as well as the Austrian Climate and Energy Fund (KLI:EN) within the programme "Neue Energien 2020", which is administrated by the Austrian Research Promotion Agency (FFG).

6. References

Carra, G., Carvelli, V., 2015. Long-term bending performance and service life prediction of pultruded Glass Fibre Reinforced Polymer composites, Composite Structures 127 (2015) 308–315.

Celina, M., Gillen, K.T., Assink, R.A., 2005. Accelerated aging and lifetime prediction: review of non-Arrhenius behavior due to two competing processes. Polymer Degradation and Stability 90 (3), 395–404.

EN ISO 13760, 1998. Plastics Pipes for the Conveyance of Fluids under Pressure –Miner’s Rule – Calculation Method for Cumulative Damage.

Fatemi, A., Yang, L., 1998. Cumulative fatigue damage and life prediction theories: a survey of the state of the art for homogeneous materials, International Journal of Fatigue 20 (1998) 9–34.

Geretschläger, K.J., 2015. Characterization of pigmented and reinforced polymeric materials for solar energy technologies, doctoral thesis, University of Linz, Austria.

Geretschläger, K.J., Wallner G.M., 2016. Aging characteristics of glass fiber-reinforced polyamide in hot water and air, Polymer Composites.

Kaiser, A., Fink, C., Hausner, R., Ramschak, T., Streicher, W., 2013. Leistungsanforderungen an Polymermaterialien in solarthermischen Systemen. Erneuerbare Energie 2013-1, 12–17.

Kahlen, S., Wallner, G.M., Lang, R.W., 2010. Aging behavior of polymeric solar absorber materials – Part 1: Engineering plastics. Solar Energy 84 (9), 1567–1576.

Köhl, M., Jorgensen, G., Brunold, S., Carlsson, B., Heck, M., Möller, K., 2005. Durability of polymeric glazing materials for solar applications, Solar Energy 79 (2005) 618–623.

Brunold, S., Papillon, P., Plaschkes, M., Rekstad, J., Wilhelms, C., 2012. Collectors and Heat Stores, in: Köhl, M., Meir, M.G., Papillon, P., Wallner, G.M., Saile, S., Polymeric Materials for Solar Thermal Applications, Wiley-VCH, Weinheim, pp. 301–317.

Streicher, W., Dittmann, A., Höller, P., 2004. Solaranlagensimulation in Vaillant WinSoft basierend auf SHW. In: 14. Symposium Thermische Solarenergie, 371-376.

Wallner, G.M., Lang, R.W., 2005. Guest editorial, Solar Energy 79 (2005) 571–572.

Wallner, G.M., Povacz, M., Hausner, R., Lang, R.W., 2016. Lifetime modeling of polypropylene absorber materials for overheating protected hot water collectors, Solar Energy, 125, 324-331.

Conference Proceedings

EuroSun 2016
Palma de Mallorca (Spain), 11 - 14 October 2016

Towards a Solar Hybrid Solution for Heating and Cooling

Daniel Neyer[1], Florian Gritzer[1], Alexander Thür[1], Stefan Luger[2], Jürgen Furthner[2], Patrik Kefer[3] and Hilbert Focke[3]

[1] University of Innsbruck, Unit for Energy Efficient Buildings, Innsbruck (Austria)

[2] ENGIE Kältetechnik GmbH, Lauterach (AUSTRIA)

[3] FH OÖ Forschungs und Entwicklungs GmbH, Wels (Austria)

Abstract

Solar electrical and thermal driven systems are promising for a sustainable supply of heat and cold demand. The target of the Austrian research project SolarHybrid is the optimization of both. Thermal and electrical systems are combined in solar hybrid systems to utilize advantages of each (sub-) system. The evaluation of the steps toward the hybrid solution including system design and control strategies, are performed with detailed component models. The dynamic simulation studies are supplemented with Hardware-in-the-Loop laboratory measurements.

Initial design optimization for photovoltaic and solar thermal driven system include dimensioning, control strategies and energy cascade usage. Cost savings will be achieved by common used components e.g. for the electrical and thermal driven chillers. A demonstration of such arrangements is realized with specifically designed and adapted chillers in the laboratory and investigated under dynamic tests. The controllers get further enhanced by mathematical methods and the implementation of predictive control.

The so far optimized solar thermal driven systems can achieve up to 60% non-renewable primary energy savings with a cost ratio of 1.1 compared to a simple reference system with natural gas boiler and vapor compression chiller. If an electrical driven system with a reversible heat pump is applied as benchmark, savings remain at 50%, but the cost ratio drops to 0.9. Further improvements and comparisons of the photovoltaic and solar thermal driven systems as well as the hybrid solutions will be performed in detail within the course of the project.

Keywords: *solar hybrid, solar heating and cooling, simulations, DHW preheating, Hardware-in-the-Loop*

1. Introduction

Solar technologies are promising for a sustainable heat and cold supply. An increase of solar cooling systems is observed by Mauthner et al (2016). Solar includes both technologies solar thermal and photovoltaic driven systems. Several IEA Tasks are related to this topic, one of them is IEA SHC Task 53. The objective is to assist PV and solar thermal driven systems to a sustainable market development (http://task53.iea-shc.org/).

Several studies of the previous year's show the competitiveness of solar thermal and solar electrical driven systems. The advantage of each system configuration depends on the boundary conditions. Different boundary conditions try to carve out these advantages. Magnitudes of efficiency or rather primary energy savings and costs can be equal for both technologies.

These controversial statements are taken up by the Austrian project SolarHybrid. The major target of SolarHybrid is to develop and evaluate economic, efficient and reliable solar hybrid systems. Hybrid includes solar electric (PV) and solar thermal supported heating and cooling systems in different combinations. Effective solar hybrid systems can be realized if the underlying base technologies are

doi:10.18086/eurosun.2016.04.23 Available at http://proceedings.ises.org

optimized and when they are adapted for a certain kind of applications.

In a first step both technologies were enhanced regarding the economical and energetic efficiency. The potentials have to be utilized before solar hybrid systems are examined. Only when optimized single technologies are used, solar hybrid systems lead to success. Both technologies are optimized by the mean of optimization tools. The optimization of the single systems is a basis for the hybrid ones. An automatic optimization of the control strategy supports the improvement of different parameters.

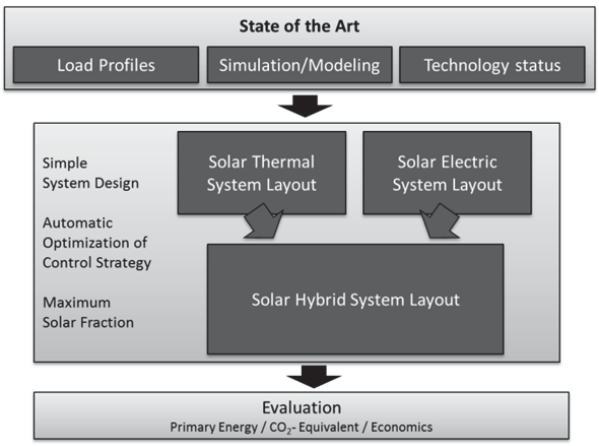

Fig. 1: Methodological approach and workflow of SolarHybrid

Optimization and development of the solar hybrid system is based upon the same methodology. Dynamic simulations are built up, taking a minimized number of components and enhanced schemes into account. The systems and their control strategies are designed using automated algorithms. The complex minimization problems lead to ideal efficiency. Applying these minimized schemes with combined used components, the solar hybrid systems allow interesting economic alternatives. The performance of this development will be proven in hardware-in-the-loop laboratory measurements.

2. Steps towards a solar hybrid solution

In this section all main steps carried out in the course of SolarHybrid are described including ideas, methodologies, highlights and results.

2.1. Assessment

The assessment follows the method of IEA SHC Task 48 and Task 53 (Neyer et al. 2015b). The main figures are non-renewable Primary Energy Ratio for the entire system (PER_{NRE}) and a pre-defined reference system (PER_{ref}). Derived from the comparison of these PER's, non-renewable Primary Energy Savings ($f_{sav\text{-}NRE}$) are calculated. The two main primary energy conversion factors used in this assessment are electricity (ε = 0.4 kWh_{el}/kWh_{prim}) and backup fuel (natural gas with ε=0.9 kWh_{end}/kWh_{prim}).

For the economic evaluation the annualized costs for investment, replacement & residual value, maintenance, energy and water costs are calculated with pre-defined values, representing cut off values derived in the Tasks. Levelized costs of energy (space heating-SH, domestic hot water-DHW, cooling-C and domestic electricity) are derived for both, the entire system and the reference system. The ratio of these levelized costs of energy (CostRatio) is used for assessing and presenting the effect of the simulation studies.

The standard reference system consists of a natural gas boiler as heat source and a vapor compression chiller as cold source. For further comparison a specific reference system was defined. The system boundary for technical and economic analysis includes all energy demands of the entire study: space heating, domestic hot water, pool heating, cooling and domestic electricity.

- Seasonal Performance Factor (SPF)

The SPF is the ratio of useful energy (out: energy supplied to the application) to energy effort from external sources. It is distinguished between thermal and electrical performance.

$$SPF_{th} = \frac{\sum Q_{out}}{\sum Q_{in}}, \; SPF_{el} = \frac{\sum Q_{out}}{\sum Q_{el,in}} \qquad \text{(eq. 1)}$$

- Non-renewable Primary Energy Ratio (PER_{NRE})

The PER converts all energy inputs of the system into primary energy equivalents. This provides appropriately comparable quality ratings for energy derived from alternative electricity, solar and fossil fuel heat energy sources. The PER_{NRE} is also calculated for the entire reference system.

$$PER_{NRE} = \frac{\sum Q_{out}}{\sum\left(\frac{Q_{el}}{\varepsilon_{el}} + \frac{Q_{EC}}{\varepsilon_{EC}}\right)} \qquad \text{(eq. 2)}$$

- Fractional Saving (f_{sav})

f_{sav} represents the non-renewable primary energy saving due to the entire SHC system compared with a reference system.

$$f_{sav-NRE} = 1 - \frac{PER_{ref}}{PER_{sys}} \qquad \text{(eq. 3)}$$

- Cost Ratio (CR)

The cost ratio is determined with the levelized costs of energy for the SHC system ($C_{tot.SHC}$) and the levelized costs of the reference system ($C_{tot.REF}$). The levelized costs ($EUR/kWh_{useful\ energy}$) are calculated including the sum of the annualized costs (invest, replacement, maintenance, energy, etc.) and the delivered energy flows of the application.

$$CR = \frac{C_{tot.SHC}}{C_{tot.REF}} \qquad \text{(eq. 4)}$$

2.2. Simulation model adaption

Crucial models in the system analysis are the component models for the vapor compression- and the absorption chiller. An ordinary effort was prosecuted to reach reliable and realistic results especially in part load conditions. Beside the chillers, other component models (e.g. cooling tower) were analyzed and adapted.

- Vapor compression chiller

Three types of compression chillers ((1) on/off screw, (2) on/off double scroll, (3) part load controlled turbo compression) are taken into account. For each compressor type a suitable simulation model was set up. Operating conditions, which remain uncovered by manufacturer data, were extrapolated using the Thin-Plate-Spline method. Fig. 2 shows this limitation due to the operation range and the limitation due to the available data.

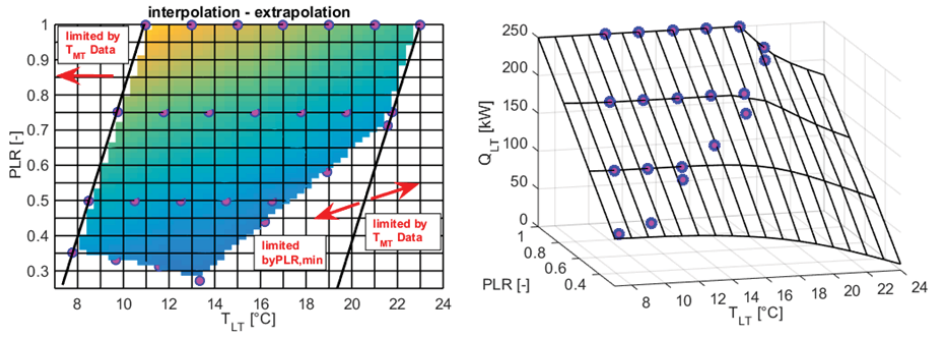

Fig. 2: Interpolation and extrapolation of boundaries for the vapor compression chiller for the turbo compressor (PLR…part load ratio, LT…chilled water, MT…cold water)

Several publications (e.g. Fillard 2009, Bettanini 2003) suggest modeling the part load energy efficiency ratio (EER) of compression chillers as function of the part load factor (PLF). While this approach correlates with the performance map for the chiller #1, major deviations from the part load behavior of the other models (especially the turbo-chiller) could be observed.

For the double compressor chiller (chiller #2) the PLF-model is valid at constant heat rejection temperature within an error interval of 1%. Thus the chillers have been modelled by a normalized lookup-table containing the performance data.

Dynamic effects were modeled by adding a thermal capacity to the output and taking the start-up time of the chillers into account. For the model of the turbo compression chiller (chiller #3), the minimum part load due to the operating range of the compressor have to be considered. Lower cooling capacities have to be provided by on/off switching.

- Absorption chiller

In case of hybrid systems, solar thermal cooling can represent a good alternative to electrical driven chillers. Therefore the influence of the usage of ammonia/water absorption chillers is investigated by simulations and assisted by real measurements of an appropriate chiller prototype. For simulations the physical models were developed for a single- and half-effect chiller (SE- and HE-chiller) and were used to create the data base for a simplified lookup-table model (Hannl 2012). Both lookup-tables are used by a newly developed TRNSYS Type (Type 1005). The data provided by the lookup-tables are interpolated accordingly. The model reflects the SE-chiller's performance curves as a function of 6 input variables (3 temperatures and 3 mass flow rates). The HE-chiller is currently implemented with 3 independent temperature input variables, volume flows are constant (Tab. 1). The mode (HE or SE) can be switched manually. Either single mode can be used in the simulations or a proper control strategy can be implemented according to the actual requirements of the entire heating and cooling system.

Tab. 1: Matrix for the characteristic curve diagrams for the SE- and HE-chiller

Parameter	Unit	SE	HE
T_{HT}	°C	75 – 80 – 85 – 90 – 95	75 – 80 – 85 – 90 – 95
T_{MT}	°C	24 – 28 – 32 – 36	25 – 28 – 31 – 34 – 37 –40
T_{LT}	°C	6 – 9 – 12 – 15	-6 – -3 – 0 – 3 – 6 – 9 – 12
$\dot{V}_{HT}$	m³/h	1 – 2 – 3 – 4 – 6	2 (GEN1 und GEN2)
$\dot{V}_{MT}$	m³/h	1 – 1,5 – 3 – 4.5 – 6 – 9	5/4/3 (ABS1, ABS2, CON)
$\dot{V}_{LT}$	m³/h	1 – 2 – 4.5 – 7	3.5

The model provides a very realistic start/stop-behavior and includes the electricity demand of the solvent pump. The chiller is scalable due to the integrated normalized data lookup-table. The Type is validated by steady state and dynamic measurements of the absorption chiller prototype at different operation modes.

2.3. System concepts

The simulations are set up in TRNSYS & MATLAB and are based on a load file concept. This concept enables the separation of building- and HVAC-simulation.

- Building profile

The building-simulation was set up in TRNSYS with a four-star Hotel (Gritzer 2016). This hotel has a capacity of 240 beds and an area of 10'080 m². Internal loads and geometry are based on different standards (e.g. SIA, etc.). The south oriented building has a high quality thermal envelope. Shading is achieved by construction and active shading elements. The hotel includes the following usage zones: accommodation, reception, lobby, bar / restaurant, kitchen and spa area with a pool. Geometry, design and control strategies determine the load profiles and energy demand for space heating, pool heating, domestic hot water and

cooling accordingly. The profiles are defined on a daily basis and change monthly. Ventilation includes heat recovery. Air change rates and specified temperatures correlate with each usage zone. Depending on the boundary condition, heat and cooling loads arise for each usage zone. These assumptions result in the following details for the Innsbruck climate profile, which is investigated in detail here.

Tab. 2: Energy demand and loads for the hotel profile in Innsbruck

Application	Demand (MWh)	Load (kW)
Space heating	271.2	190
Pool heating	766.1	208
Domestic hot water	562.5	260
Air conditioning	85.7	80
Domestic electricity	517.5	

Demand and different system configurations are evaluated separately by focusing on the profile of interest and neglecting the others.

- Thermal driven systems

The scope of the simulation study with the solar thermal driven heating and cooling systems is to survey following points as listed in Table 3.

Tab. 3: Matrix for the characteristic curve diagrams for the SE- and HE-chiller

Main Problem	Explanation / Examples
(1) System design issues	Optimization of the solar thermal heating and cooling system due to design and control strategies. Comparisons of PV driven systems simultaneously. E.g. variable collector area, hot /cold water storage tanks, ACM and VCC capacities depending on a variety of load files (pool off, SH off, cooling 100%, DHW 100% and 25%).
(2) Cascade energy use	The temperature level of re-cooling of the ACM and VCC enables possibilities of usable energy cascades. E.g. rejected heat for DHW pre-heating
(3) Common used components	Commonly used components can be forced for economic reasons, but also when refurbishing system common used components enables potential E.g. Serial or parallel use of ACM and VCC in MT- and LT-circuits
(4) Multiple use of components	Solar parts, but also the thermal driven chillers are main investment cost drivers. The multiple usage of these and other components should increase the economic competitiveness. E.g. ACM used as heat pump, combined with low temperature heating/cooling

Selected results for the (1) step are e.g. the optimization of the DHW only solar thermal systems (ST) and the comparison with PV driven heat pump (HP) systems. The solar thermal driven system is shown in Figure 3. The solar collectors feed the hot storage, back upped with a natural gas boiler. The applications for the first studies are reduced to DHW and cooling. The solar energy driven absorption chiller is running in parallel to a vapor compression chiller. Both are keeping the cold storage tank at a certain temperature to fulfill the needs of the load profile.

For the design of the ST system two different hot storage sizes are considered: 30 and 50 l/m² solar thermal collector area. The size of the solar collector is designed that 10 h of stagnation are observed. The DHW consumption is scaled from 100% down to 25% in four steps. The smaller tank volume combined with a moderate collector size (0.5-1.5 m²/person, depending on DHW demand) was chosen to be best for further applications. Solar fractions of 20-25% are reached at cost ratios of 1.25-1.1 for the standard reference system.

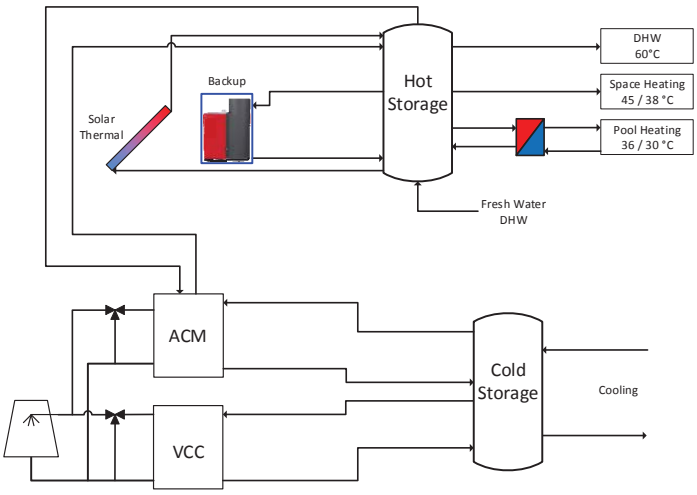

Fig. 3: Solar thermal system layout with hot and cold backups

Compared to a simple heat pump, a cost ratio of 0.82 can be reached. Because of the low solar fraction the non-renewable primary energy savings reach 17%. Hence, the solar collector area was increased to reach a cost ratio of 1. Finally, a collector field of 720 m² was determined with a f_{sav} of 0.39 compared to the heat pump. If the heat pump is equipped with a PV, 140 kW_p would be necessary to reach the same primary energy savings as the thermal driven system. Simultaneously the cost ratio drops down to 0.7. Main reason is the DHW application at its 60°C set temperature that enforces a low EER of the HP system.

With these findings a second simulation study, including the cooling demand, was started. Result of this study is an optimized control strategy and a system design. Solar fractions of 55% can be obtained with this configuration. Compared to the standard Task 53 reference primary energy savings of 49% and a cost ratio of 1.11 can be achieved. The optimization is e.g. reflected in the auxiliary electricity demand of the system.

In Figure 4 the carpet plots of the electrical efficiency SPF_{el} are shown and include the annual trend (x-axis: days of the year, y-axis: hours per day, color of each pixel: SPF_{el}). The maximum value of thermal cooling has a SPF_{el} of 21.5 and the vapor compression chiller of 5.7. The maximum for the thermal cooling efficiency appears simultaneously with small loads whereby the chiller is driven with hot water stored in the tank (mainly at night). The maximum for the vapor compression chiller appears during minimal loads. On an average, the electrical efficiency of absorption and electrical cooling results in a value of 4.

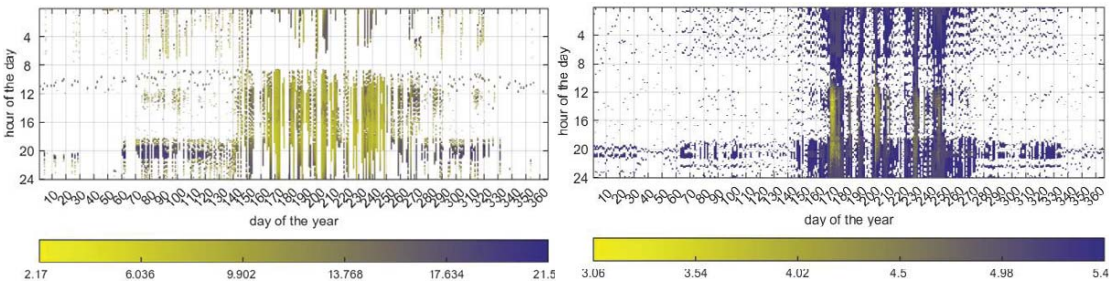

Fig. 4: Carpet plots of the electrical efficiency for the thermal cooling- (left) and vapor compression chiller (right)

The so far optimized solar heating and cooling system was used to integrate ideas of cascade energy usage (2). The heat rejection of the chillers (absorption and electrical) with temperatures around 25-40°C enables the use of this energy flux for DHW pre-heating (Fig. 5). The heat exchangers for the fresh water (DHW) pre-heating are situated in the cooling tower circuits. Thus, the hydraulic of each rejection circuit has to be extended with one mixing valves (V_{MT}) and one bypass (V_{CT}).

The first valve is used to keep a certain set point for the chiller re-cooling inlet temperature. This set point can change according to the different control strategies of the system (e.g. chilled water set temp., etc.). If the

outlet temperature of the cooling water after the heat exchanger (HX) drops below the set point, the cooling tower will be bypassed.

In Table 4 all results for DHW only and DHW&C are presented for the total DHW demand (1) and for the smallest demand (0.25). Accordingly, the ratio of C/DHW changes and affects the results.

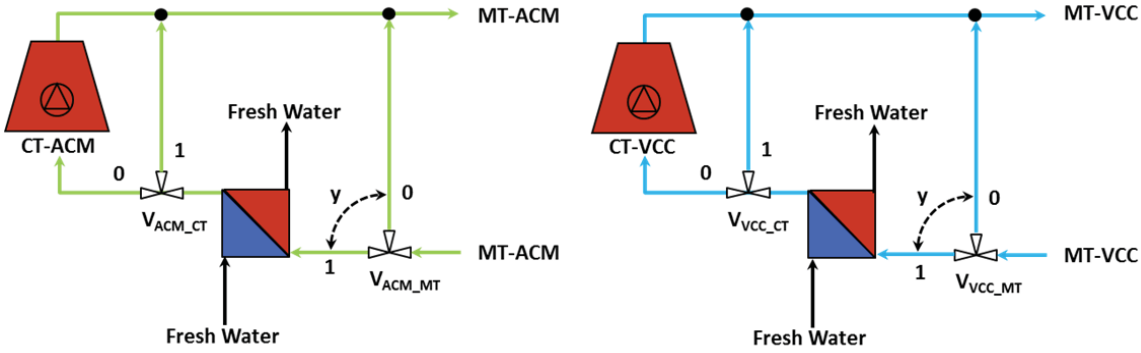

Fig. 5: DHW-pre-heating in the heat rejection circuits of the ACM (left) and VCC (right)

When DHW pre-heating is activated, the fractional savings increase from 49% to a level of 53% (DWH=1) and from 55% to 57% at low DHW demands respectively. At the same time the Cost Ratio decreases from 1.11 to 1.09 (DHW=1) and from 1.44 to 1.43 (DHW=0.25). This can be explained when the energy balance for the hot storage is disposed. All energy used for preheating, as it is arranged in continuous flow mode, reduces the affordable energy input. When the system is compared to the specific reference system (HP), the savings arise to 50% with a corresponding CR of 0.91 (65%/1.4 for DHW 0.25).

Tab. 4: Comparison of achievable cost ratio (CR) and primary energy savings (f_{sav}) for different applications of solar thermal systems

Results	Additional information	DHW only		DHW&C		DHW&C preheating	
Collector area	m²	420	131	720	431	720	431
DHW load	-	1	0.25	1	0.25	1	0.25
Solar fraction	-	0.25	0.19	0.55	0.75	0.55	0.74
f_{sav} – T53	Ref: natural gas boiler & VCC	0.25	0.19	0.49	0.55	0.53	0.57
CR – T53		1.10	1.25	1.11	1.44	1.09	1.43
f_{sav} spec.	Ref: heat pump	0.17	0.11	0.46	0.63	0.50	0.65
CR spec.		0.82	0.88	0.93	1.41	0.91	1.40

The differences in the savings and the cost ratio between highest and lowest DHW demand, derive from the specific collector area and the ratio of investment to overall costs. The 25% DHW is equipped with a greater collector area. Thus solar fraction, primary energy savings, costs and the cost ratio increase accordingly.

- Electrical driven systems

Considering the high electric loads, the integration of PV-panels or PVT-panels can lead to a decrease of primary energy consumption. Depending on the amount of low temperature thermal energy demand and on the internal heat transfer coefficient of the panel PVT or PV are used. Especially the internal heat transfer is critical for the low temperature thermal efficiency and improvement of the electric efficiency of the PVT compared to a PV panel. The PVT panels are simulated by using the model of Bertram (2012). This model takes the effective solar cell characteristic for the electrical part and the thermal model from EN 12975 (now EN ISO 9806) into account.

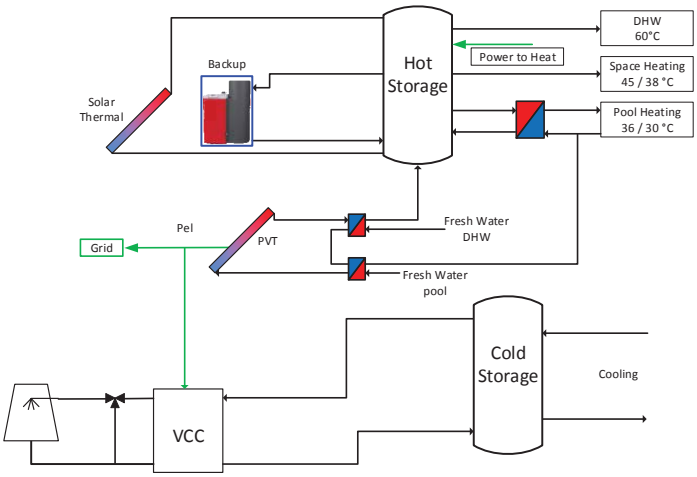

Fig. 6: Integration of PVT panels for DHW pre-heating or pool heating

The available load profile of the hotel contains a high demand of freshwater for DHW and the pool at low temperatures (around 12°C). Thus different feed in points for PVT are studied (Fig. 6). Regardless of the decision for PV or PVT, the produced electric energy is a dimensioning factor for the amortization (ecological or economical). Power to heat can only be an option if excess electric energy is produced and variable feed-in tariffs are considered. In this case it can be better from an economical point of view to store the energy in the system.

Other components, such as chillers, could also benefit from this low temperature energy demand as sink for rejection heat. This energy exchange is addressed at first in the design process. Secondly, the optimization process, which is part of the control strategy, determines the energy flow at runtime with respect to the above mentioned optimization problem amongst others (compare chapter 2.2).

The achieved results are used to show the impact of PVT collectors on the seasonal performance factor, the primary energy ratio and the Cost Ratio.

2.4 Optimization

The optimization problem described and used in the project is used to find the optimal strategy to operate the introduced systems (solar thermal and PV driven systems). Improvements of the system itself (e.g. size of the hot storage, etc.) are not considered here.

Solar hybrid systems consist of several components to fulfill specific targets. A typical configuration is a solar thermal collector and a hot backup for domestic hot water preparation, an absorption chiller and a vapor compression chiller to meet the cooling demand. To run such a system, several control loops have to be designed. The satisfaction of the energy demand is given high priority and thus complicating the above described system with three options to provide hot water, and two options for chilled water. Numerical optimization routines can help to find the operating strategy of the system, which leads to a specific minimum of a quantity. The design could e.g. aim at minimizing the primary energy demands.

The strategy of the control system is as follows: If a (course, control oriented) mathematical model of each component is given, the overall system can be described as $\dot{x} = f(x,u)$, $y = g(x,u)$ where x is the system state, u are the inputs (control signals, e.g. pump speed) and y are the control outputs. At any given time instance k, the model is used to make a *prediction* into the near future (e.g. oncoming 24 hours), which depends on u. An optimization algorithm can be used to find the optimal control signal u^* for the following 24 hours. Therefore, the primary energy usage is minimized. After implementing the first element of this optimal time series, the horizon is shifted, $k \rightarrow k+1$ and the optimization problem is formulated and solved again.

The optimization problem can be solved efficiently by using standard tools. Depending on the structure of the models, nonlinear optimization techniques are a particular solution. However, their solution takes usually a long time and the result might be only a local minima. If the system can be approximated with local linear models with reasonable accuracy, the optimization problem boils down to a linear one for which the global optimum can be found within a fraction of the time-constants of such systems.

The predictive nature of the control system requires a prediction of the energy production of the PV and solar collector, which in turn requires a prediction of the irradiation and temperature. Such values are easy to access and quite accurate over a 24 hour time window.

2.5. Chiller prototypes

According to the original idea of designing a hybrid (absorption/vapor compression) ammonia/water (NH_3/H_2O) chiller comprehensive studies were undertaken. The main difficulty in realization represents the separation and purity of the different substances (ammonia, water and oil) needed for the diverse circuits. Therefore the decision was made to combine the absorption and vapor compression chiller externally via hydraulic connections of the water circuits. Both chillers are based on ammonia and have the same capacity.

- Absorption chiller

In another research project at University of Innsbruck (DAKtris 2012) a new generation of absorption chiller was designed and adapted to the use of dry cooling tower and the resulting high re-cooling temperatures. The development is based on the existing single-effect chiller (PC19), which got improved by analyzation further investigations. This new absorption chiller concept includes a switchable half- and single-effect (HE, SE) combination, flat plate heat exchangers for the evaporator, absorber and generator, enforced throughput of the generator, a new injection nozzle and an adapted internal control strategy.

Correspondingly a prototype of this chiller was built and investigated by measurements at different modes and boundary conditions. This includes the variation of volume flows and chiller inlet temperatures at single- and half-effect, shown in Tab.5.

Tab.5: Set-point variations for measurements of the absorption chiller

Circuit	ACM-Mode	T_{in} (°C)	$\dot{v}_{min}$ (m^3/hr)	$\dot{v}_{mid}$ (m^3/hr)	$\dot{v}_{max}$ (m^3/hr)
LT / evaporator	SE	12,18	1.5	2	3
	HE				
MT / condenser & absorber	SE	20,25,30,35	4.25	5	6.5
	HE	20,25,30,35,40,45			
HT / generator	SE	80,85,90	3	3,5	4.5
	HE				

The prototype runs stable and delivers satisfactory capacities and EER's. Recording of the chiller performance map was performed by steady state measurements executed with equivalent settling time and a moving average exercised on data.

One characteristic diagram of the absorption chiller at HT temperature of 85°C, LT temperature of 18°C on the left and 12°C on the right side is shown in Fig. 7. Reached capacities are printed in the upper charts with related energy efficiency ratios, beneath corresponding to the MT inlet temperature. Especially the course of capacity shows the potential of the HE chiller mode at higher MT inlet temperatures. Regarding the costs SE has to be preferred due to the higher thermal efficiency. Depending on the overall system other operation modes can have advantages.

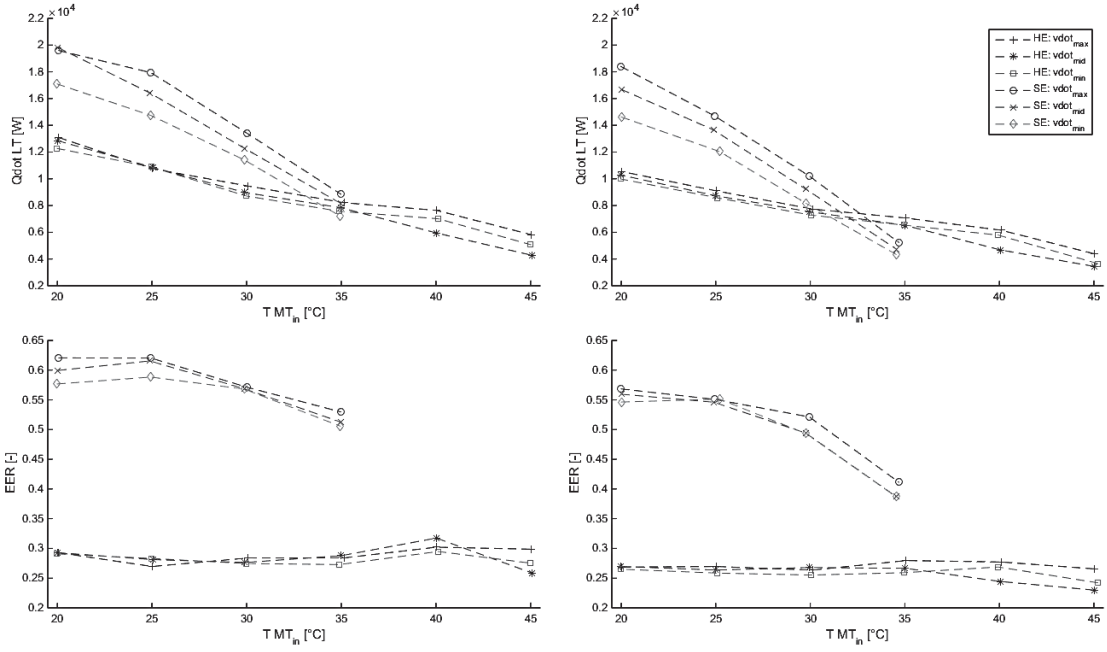

Fig. 7: Measured performance of the new SE/HE ammonia/water chiller with flat plate heat exchangers. LT temperature of 18°C (left) and 12°C (right)

Additionally to the steady state measurements, dynamic hardware-in-the-loop tests take place to evaluate the influence of fluctuating operation and different system setups especially in combination with the vapor compression chiller prototype.

- Vapor compression chiller

The vapor compression chiller L7KW 2T PP, produced by Engie Kältetechnik GmbH, is a water cooled liquid chiller and uses the natural refrigerant R717 (ammonia). The system is built up on the principle of a flooded evaporator in thermosiphon. Nominal cooling capacity is 20 kW (ϑeva = 4°C, ϑcond = 50 °C). The compressor can be continuously controlled by an inverter from 100 to 50%. The range of capacity control is enlarged by a hot-gas by-pass. The chilled water temperature at the evaporator outlet side can vary between 5 °C and 15 °C. On the condenser side the inlet temperature can diversify from 20 °C to 42 °C. These limits are mainly based on the compressor limits.

The theoretical EER varies between 14.59 at the highest evaporator outlet temperature and the minimum condensing temperature and 4.02 at the lowest evaporating and the highest condensing temperature. The chiller will be measured extensively in steady state and dynamic test in the Hardware-in-the-Loop environment of University of Innsbruck in individual operation but also in combination with the absorption chiller.

3. Conclusions

The project SolarHybrid aims to show how solar thermal and solar electrical driven heating and cooling systems can get more efficient and economical viable. This idea implies several optimization steps and comprehensive studies. It becomes obvious that a hybrid solution will benefit from single optimization of the different systems and components.

Detailed models for the adapted absorption and vapor compression chillers are used in the complex HVAC simulations. Huge effort was taken to realize models with data lookup tables, which enable realistic performance even under dynamic conditions, especially in part load. The system simulation model built up in TRNSYS & Matlab, is able to handle the multitude of the different and switchable energy cascades. Several sensitivity studies and the control strategies of the simulation variants were optimized.

The solar thermal systems show promising results for DHW but also for solar thermal cooling. The ST driven system can achieve up to 60% non-renewable primary energy savings with a cost ratio of 1.1 compared to a simple reference system with natural gas boiler and vapor compression chiller. If an electrical driven system with a reversible heat pump is applied as benchmark, savings remain at 50% but the cost ratio drops to 0.9. This magnitude of savings and costs can only be reached with domestic hot water pre-heating in the re-cooling circuit of the chillers (energy cascade).

The integration of PVT collectors benefit from the low temperature levels of the used load profile (hotel with pool). First results show an increased electrical output of roughly 10% compared to ordinary PV yield. Different hydraulic schemes with various temperature levels are under investigation. The effect on non-renewable primary energy savings and the cost ratio will be detailed in future developments.

The optimization procedure is arranged and first tests with solar thermal systems are successful. Additional solar thermal cooling will be set up and tested with integrated models for the chillers (ACM, VCC), hot and cold storage tanks as well as collectors (PV and ST). Finally, the hybrid solution will be optimized accordingly.

Two prototypes, an absorption chiller and a vapor compression chiller, were adopted to the boundary conditions due to the solar hybrid application. The absorption chiller is able to handle re-cooling temperatures up to 45°C under various generator temperatures. The new concept shows promising energy efficiency ratios under the investigated conditions. The vapor compression chiller is designed for the combined operation and especially adapted for large part loads. The laboratory measurements will show this operation mode and the advantages of the new developed chiller concept.

In the following course of the project the steps towards the hybrid solution and the final results will be discussed in detail. A high non-renewable primary energy saving and cost effective solution is expected after the successful first steps.

4. Acknowledgement

The presented work refers to the project SolarHybrid, which is carried out in collaborative work by the University of Innsbruck, FH OÖ Forschungs und Entwicklungs GmbH and the companies Engie Kältetechnik GmbH and Pink GmbH. The project is funded by the Austrian Climate and Energy Fund and is carried out within the framework of the Energy Research Program 2013.

5. References

Bettanini, E., Gastaldello, A., Schibuola, L., 2003. Simplified models to simulate part load performances of air conditioning equipment, Eighth International IBPSA Conference Eindhoven; Netherlands August 11-14, 2003

DAKTRis, 2012. Dynamic operational behavior of Absorption Refrigerators in Trigeneration Systems, goverment-funded project, Stadt der Zukunft, FFG Nr. 840650, Vienna, Austria

Filliard, B., Guiavarch, A., Peuportier, B., 2009. Performance evaluation of an air-to-air heat pump coupled with temperate air-sources integrated into a dwelling, IBPSA Conference Jul 2009; Glasgow (UK), pp.2266-2273

Focke, H., Neyer, D., Neyer, J., Thür, A., 2015. SolarHybrid - Project Overview and First Results, SAC 2015, Rom, Italy

Gritzer, F., Neyer, D., Streicher, W., 2016. unpublished Master Thesis, Solarhybride Energiebereitstellung für Hotelgebäude, University of Innsbruck, Austria

Hannl, D., Rieberer, R., 2012. Analyse einer Ammoniak/Wasser Absorptionskaelteanlage – Betriebserfahrungen und Simulationsmodellbildung, DKV-Tagung 2012, Wuerzburg

Mauthner, Franz; Weiss, Werner; Spörk-Dür, Monika, 2016. Solar Heat Worldwide; Global View on solar Heating and Cooling: Market, Industry and Policy – Webinar; June 29, 2016

Neyer D., Neyer J., Thuer A., Fedrizzi R., Vittoriosi A., White S., Focke H., 2015. Collection of criteria to quantify the quality and cost competitiveness for solar cooling systems, Solar Heating and Cooling Programme, Task 48, 2015.

Neyer, D., Neyer, J., Thür, A., Brychta, M.; Streicher, W., 2014. Simulation based optimization of dynamic power control for small capacity chillers, EUROSUN 2014; Aix-les-Baines (FR), Sep 16th - 19th, 2014

Neyer, D., Ostheimer, M., Hauer, N., Halmdienst, C., Pink, W., 2016. Evaluating heat rejection units for CHP and solar driven single or half effect absorption chiller using Hardware-in-the-Loop Testing, Eurosun 2016, Palma de Mallorca, Spain

SolarHybrid, 2014. Solare Hybridsysteme zum Heizen und Kühlen - Mit Optimierungen zu minimierten und kostengünstigen Systemkonzepten, goverment-funded project, Energy Mission Austra, e!Mission 2013, FFG Nr. 843855, Vienna, Austria

Stegmann, M., Bertram, E., Rockendorf, G., Janßen, S., 2012. Modell eines unverglasten photovoltaisch-thermischen Kollektors basierend auf genormten Prüfverfahren, 22. Solarthermisches Symposium, 9.-11. Mai 2012, OTTI e. V., ISBN 978-3-941785-89-2

Zondag, H., Bakker, M., Van Helden et.al., 2006. “PVT ROADPAMP, A European guide for the development and market introduction of PV- Thermal technology, PV Catapult (SES6), ECN, 2006

Conference Proceedings

EuroSun 2016
Palma de Mallorca (Spain), 11 - 14 October 2016

COMBINATION OF SOLAR THERMAL COLLECTORS AND HORIZONTAL GROUND HEAT EXCHANGERS AS OPTIMIZED SOURCE FOR HEAT PUMPS

Fabian Hüsing, Hauke Hirsch and Gunter Rockendorf

Institut für Solarenergieforschung Hameln GmbH (ISFH), Emmerthal (Germany)

Abstract

Heat pumps coupled to thermal ground sources, such as Horizontal Ground Heat Exchangers (HGHX), represent an efficient option to supply heating demands of single- and multi-family houses. However, the high land-use yet often prevents HGHXs from installation. The combination with solar thermal energy promises reduction of the HGHX area while retaining high system efficiencies. Our contribution studies the combination of HGHXs and solar thermal collectors, focusing on solar thermal regeneration of the soil. This is analyzed through both numerical modelling and experimental investigations. Modelling rests on a novel TRNSYS type for the HGHX, developed at ISFH. A test facility, installed on the premises of ISFH in Lower Saxony / Germany is used to validate the model. System simulations extrapolate the perceptions on differently configured heating systems.

Keywords: *horizontal ground heat exchanger, TRNSYS Type, system simulations, regeneration, bivalent source, HGHX area reduction*

1. Introduction

HGHX systems are integrated into the shallow subsurface at depth of 1-2 meters below surface. They represent flat, extended heat exchangers which extract naturally stored energy from the ground. To withdraw the heat from ground, heat pumps (HP) are used, which face the HGHX system as cold heat source and the buffer storage of a supplied building as heat sink. Characteristic performance quantity is the temperature shift between cold and hot ends of the heat pump. Especially, the coefficient of performance of the heat pump is related to this shift. One advantage of ground coupled heat pumps over ambient-air based systems is the fact that the temperature shift changes little during the course of the year as a result of the thermal inertia of the ground, provided that the HGHX size is properly designed. The existing technical guideline in Germany (VDI 4640-2) is presently under revision. The current draft (Verein Deutscher Ingenieure 2015) gives advice for the design of HGHX systems: The size (land-use) of an HGHX system for a given heating demand, soil type and climate zone. However, for typical heat pump systems in residential buildings the land-size recommended often exceeds the existing potential.

The combination of HGHX and solar thermal collectors provides a solution, as the land-use of the HGHX can be reduced significantly while maintaining high system efficiencies. This contribution deals with the investigation of this combination, analyzing solar regenerated HGHX heat pump systems through both numeric modelling and experimental investigations. A model of the HGHX developed at ISFH as a type for the modelling suite TRNSYS (Klein et al. 2010) and it's validation are presented. The validation is performed using a 150 m^2-sized HGHX, installed on the premises of ISFH in Lower Saxony / Germany as part of a test facility. We explain the model and evaluate different system configurations studied.

doi:10.18086/eurosun.2016.04.18 Available at http://proceedings.ises.org

2. Horizontal ground heat exchanger model

2.1 Numerical model

To represent the dynamic behavior of a HGHX precisely, the model includes the following physical components: It is based on a two dimensional formulation of transient conductive heat transport problem. Fourier's Law is employed to model conductive heat transport from and to soil, which is in contact to a pipe axially streamed by a heat carrier fluid. The model reduces the heat transport between soil and pipeline to a plane perpendicular to the pipe, see Figure 1. The plane is discretized by a rectilinear mesh, which refines towards the pipe and the soil surface. The selected boundary conditions are adiabatic to the lateral edges of the plane (as explained below), radiative heat exchange and convective heat transport at the surface edge and a constant temperature at the lower edge of the plane. The interior boundary to the pipe domain is represented by a convective heat transfer condition which takes into account the carrier flow regime. The temperature of the fluid results from an axial energy balance of the pipeline. The transport equations for soil and pipe are numerically solved by the method of (explicit) finite difference, coupled through the thermal conditions at the interior boundary between soil and pipeline.

The TRNSYS type distinguishes two soil domains, see Figure 1. Soil domain A represents an inner segment of the HGHX, which is enclosed by adjacent pipes. Symmetry is assumed and thus left and right boundaries are adiabatic, which leads to significantly lower computational effort. Soil domain B represents a fluid pipe at the HGHX edge or a supply pipe. In contrast to soil domain A, it extends to a variable distance (parameter b) on one side, which can be considered as undisturbed soil if parameter b is chosen sufficiently large.

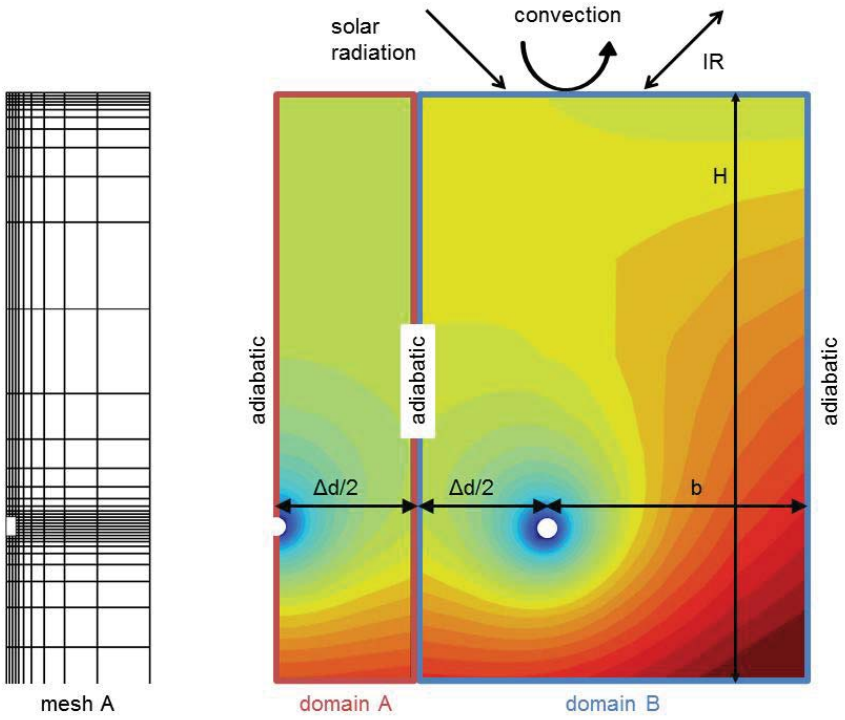

Fig. 1: Soil domain and discretization of HGHX model. Left: Discretization of soil domain A. Right: Charactersitic temperature contour plots for both soil domain A and B as well as indicated boundary conditions.

In comparison to previously published HGHX models (e.g. by Giardina 1995, Ramming 2007 or Glück 2009), the presented model has the advantage of combining all of the following properties:

- Sufficiently fine discretization of the soil domain
- Modelling of latent heat extraction and change of soil properties during freezing
- Consideration of the fluid capacity inside the HGHX, in both situations with and without massflow

- Consideration of heat gains through HGHX lateral edges
- Implementation as computation time optimized TRNSYS Type

An extended experimental validation for the presented model was conducted at ISFH for which exemplary results are presented in the following paragraph.

2.2 Model validation

For validation of the numerical model under static and dynamic operation conditions, a test facility was installed on the premises of ISFH, Figure 2 (left). It includes a shallow horizontal ground heat exchanger covering 150 m², a compressor heat pump and a resistant heater to emulate heat generation by solar thermal collectors. On the condenser side of the HP, a load module is installed, which emulates pre-defined thermal load profiles. Monitoring equipment is installed at the test facility to measure soil, brine and water temperatures, as well as meteorological data (ambient air temperature, solar irradiation, and infrared radiation (IR)) during and also between individual test runs.

Different experiments were performed to assess the quality of the model. For the simulations, measured operation data (heat transfer rate at the HPs evaporator, mass flow, and start temperature of the soil domain) and meteorological data are used as inputs to the model. The results for a selected experiment and the associated simulation are shown in Figure 2. The experiment is conducted using only a single out of four fluid circuits of the HGHX. The pipe length is 65 m. Constant mass flow of 0.278 kgs^{-1} and a heat extraction rate of 1.2 kW were the operating conditions of the experiment. The setup is chosen to validate the ability of the HGHX model to represent impacts of lateral heat gains at HGHX edges. Two model configurations are compared: A 2d model, using only soil domain A (neglecting HGHX edges) and a virtual 3d model, using a series connection of soil domain A and B and thus taking into account HGHX edges.

For both model configurations, Figure 2 confirms acceptable coincidence between measurement and simulation at the beginning of operation (see inset subfigure for first half hour). Especially for long periods of heat extraction the effects of the border segments are of significant magnitude. The virtual 3d model allows an accurate representation of this effect, as the deviation is only 0.2 K after 80 hours of operation.

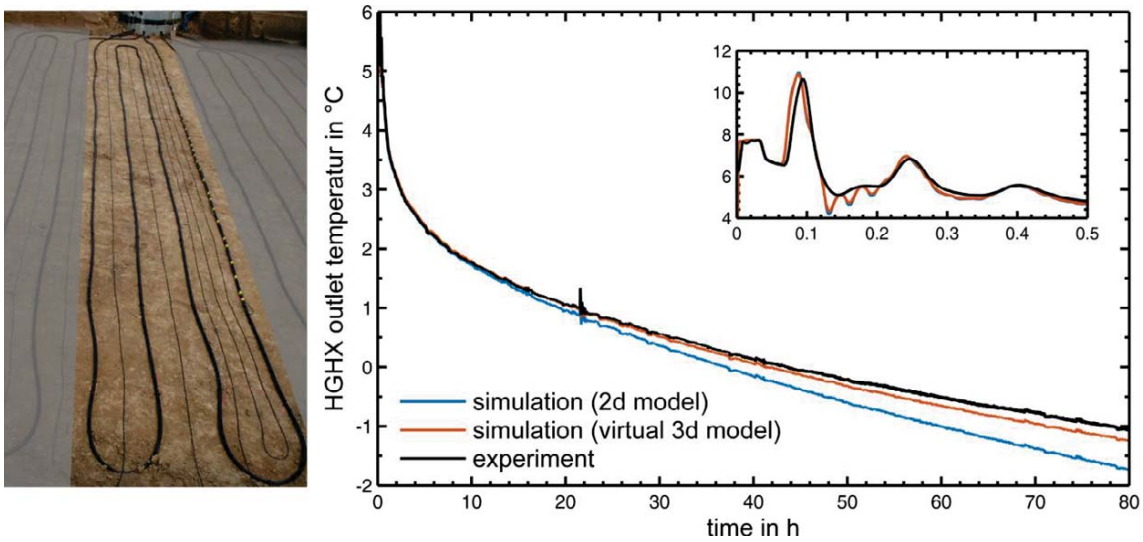

Fig. 2: Experimental setup and comparison of measured and simulated temperatures

Therefore the TRNSYS-Type can be regarded as a precise model for a HGHX for application in heat pump coupled system simulations. Further information on the HGHX model can be found in Hirsch et al. 2016.

3. System simulations

To investigate performance and efficiency of HGHX supplied heat pump systems and subsequent integration routes of solar thermal energy, TRNSYS simulations employing the presented HGHX model are evaluated.

3.1 Boundary conditions

The boundary conditions of the system simulation model are, in large part, taken from the Task 44 (Solar and Heat Pump Systems) of the Solar Heating and Cooling (SHC) program of the International Energy Agency (IEA) (Haller et al. 2012). This concerns the examined reference buildings (a newly constructed building: SFH45 and an existing building: SFH100) as well as internal load profiles for heat gains (Dott et al. 2012). The SFH45 uses a floor heating system while the SFH100 is equipped with radiators. At the chosen location of Zurich the buildings have annual heating demands of approximately 8500 kWh (SFH45) and 18000 kWh (SFH100), respectively. The domestic hot water tapping cycle adds an annual heat demand of approximately 2200 kWh. Supply configurations are equipped with two zone buffer storages for domestic hot water (DHW) and space heating (SH), each of which can be supplied with the connected heat pump.

The subsurface is characterized by three soil types according to 2015's draft of VDI guideline 4640-2 (Verein Deutscher Ingenieure 2015). Table 1 gives an overview over the properties of the three soil types used as parameters for the HGHX model. The total simulation time period is two years for each configuration, while only the data of the second year is used for evaluation.

Tab. 1: Parameters of the soil types used for the simulations

Soil nr.	1	2	3
Soil type (acc. to USDA)	Sand	loam	sandy clay
λ in $Wm^{-1}K^{-1}$ (unfrozen)	1.2	1.52	1.76
λ in $Wm^{-1}K^{-1}$ (frozen)	1.37	2.35	2.85
c_p in $Jkg^{-1}K^{-1}$ (unfrozen)	802	1218	1319
c_p in $Jkg^{-1}K^{-1}$ (frozen)	687	880	886
ρ in kgm^{-3}	1512	1815	1820
h_F (heat of fusion) in Jkg^{-1}	17648	51457	65977

3.2 System configurations

Two different HGHX-equipped supply configurations are studied, with and without solar thermal system, as shown in Figure 3. The HGHX is installed at a depth of 1.5 m in all cases. The simulations employ type 401 to model the heat pump. Parameters are taken from data determined by experimental testing of a commercially available heat pump at ISFH by Pärisch et al. 2014.

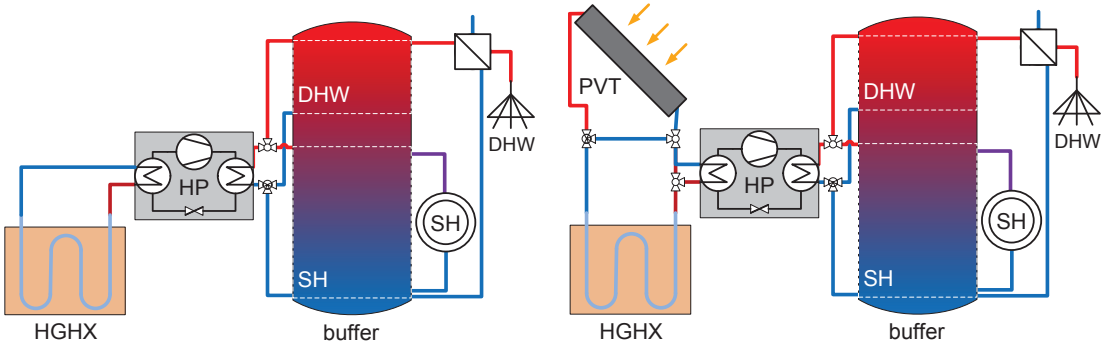

Fig. 3: System schemes for configurations without (left) and with (right) use of solar thermal energy on the source side

An unglazed photovoltaic thermal hybrid collector (PVT) is assumed as solar thermal supply system. The hydraulic layout allows different operation modes: (1) stand-alone HP/HGHX, while there are no (sufficient) solar thermal gains; (2) serial connection of the PVT and HGHX/HP, while heat demand and solar thermal gains coincide; (3) recharging of the HGHX by PVT (at lower mass flow), if solar thermal gains allow regeneration of HGHX and there is no present heat demand. The state of the system is monitored during the simulations and the specific operation mode is selected by a controller developed for this purpose. The upper limit of 25 °C for fluid entering the HGHX is observed in all operation modes to avoid overheating of the

ground.

3.2 Performance indicators

To assess the quality of the simulated system configurations a set of performance indicators is defined. For a ground coupled heat pump system there are two classes of quality to assess: efficiency and sustainability.

Sustainability of a HGHX means to avoid states of exhaust as well as securely avoiding critical frost conditions. An HGHX is exhausted if the temperature of the carrier fluid on influx to HP evaporator falls below -5 °C during operation. This is the temperature at which the HP is no longer operated and an electric auxiliary heater is used instead. Accordingly the amount of heat supplied by the auxiliary heater (Q_{aux}) is used as an indicator for HGHX exhaustion. The critical frost conditions affect the biosphere as well as important soil properties like rainfall infiltration etc. To detect states of induced frost two gauges are implemented, vertical and horizontal. The "vertical" frost indicator, referred to as vertical FI, is activated once the frost around the HGHX pipe collides with the surface frost. The horizontal frost indicator, referred to as ISFH FI, is activated once the frozen domains around adjacent HGHX pipes grow horizontally into contact, in absence of surface frost.

The efficiency of a heat pump system is assessed by the seasonal performance factor of the system (referred to as SPF_{SHP} following a definition by D'Antoni (2013)). This indicator takes into account the useful heat divided by the total electric energy spent for its generation:

$$SPF_{SHP} = \frac{\text{useful heat}}{\text{electric energy}} = \frac{\int (\dot{Q}_{DHW} + \dot{Q}_{SH})dt}{\int (P_{HP\_compressor} + P_{aux} + P_{pumps} + P_{control})dt} \qquad \text{(Eq. 1)}$$

3.3 Results

Figure 4 depicts the seasonal performance factor for different soil types as function of HGHX area. The results are based on the spacing between HGHX pipes (dx) recommended for each soil by 2015's draft of VDI guideline 4640-2 (Verein Deutscher Ingenieure 2015) for laminar flow. The size recommended for each soil type by the guideline is marked by a black diamond. Furthermore the occurrence of critical frost conditions is displayed by the frost indicators for vertical and ISFH criteria.

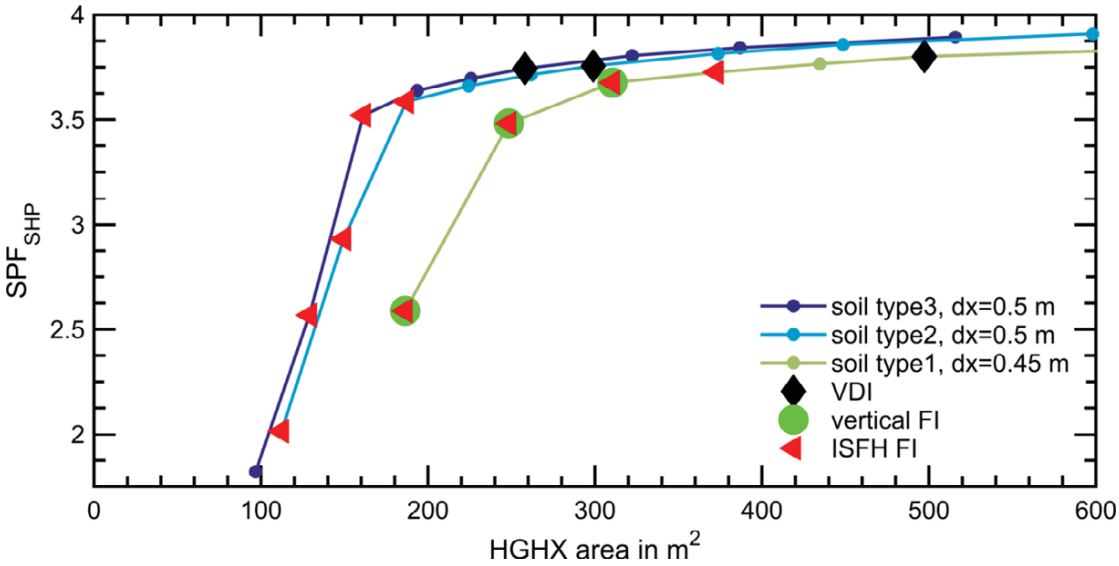

Fig. 4: Seasonal performance factor SHP for different soil types over HGHX area

The shapes of the graphs are characteristic of HGHX systems. From their curvatures follows, that the reduction of the HGHX area below a critical size causes significant degradation of the system performance, while beyond this critical value only moderate efficiency wins are possible. The designs recommended by the VDI guideline are always well beyond the critical size, securely avoiding critical frost conditions and reaching seasonal performance factors of approximately 3.75. The ISFH frost indicator is the strongest frost criteria limiting small HGHX areas. The vertical frost indicator is only activated for soil type 1 (sand), which

has the lowest enthalpy of fusion (h_F).

To analyze the underlying effects responsible for the characteristic shape of these graphs, the auxiliary power and energetically weighted evaporator inlet temperatures are plotted as function of the HGHX area in Figure 5. The occurrence of high demands for auxiliary power, Figure 5 (left), correlates with the significantly reduced seasonal performance factors below the critical systems size. Because electric auxiliary heaters have a lower thermal efficiency than heat pumps, exhausted HGHX systems cause break-in of overall system efficiency. The VDI 4640-2 avoids the necessity for auxiliary heating for all three soil types by sufficiently large design recommendations.

The energetically weighted mean evaporator inlet temperature, defined in Eq. 2, takes into account which amounts of energy are extracted at which temperature. Therefore it represents a good indication of the averaged condition of the heat source during heat pump operation throughout the year.

$$\overline{T}_{evap,\ energetically\ weighted} = \frac{\int (T_{evap}(t) \cdot \dot{Q}_{evap}(t))dt}{\int \dot{Q}_{evap}(t)dt} \qquad \text{(Eq. 2)}$$

The energetically weighted mean evaporator inlet temperature over HGHX area is shown in Figure 5 (right). For small HGHX areas, where auxiliary power demands cannot be avoided, the temperature stays in an interval from 0 to 1 °C, uncorrelated to HGHX area variations. This is explainable, as the extraction of heat from the HGHX is limited by states of exhaustion. Additionally produced heat near the state of exhaustion mainly originates from latent heat extraction at constant temperatures. Above the critical size, the increase of HGHX area increases the source temperature levels. Here, the natural soil temperature is the theoretical limit for the evaporator inlet temperature; hence the decreasing slopes of the respective curve branches. The small size-sensitivity of the source temperature for larger HGHX sizes is reflected by the HP performance. The detected performance gains are in agreement with values published earlier by Pärisch et al. 2014. The designs according to VDI recommendations reach energetically weighted mean evaporator inlet temperatures in a range from 3 to 4 °C.

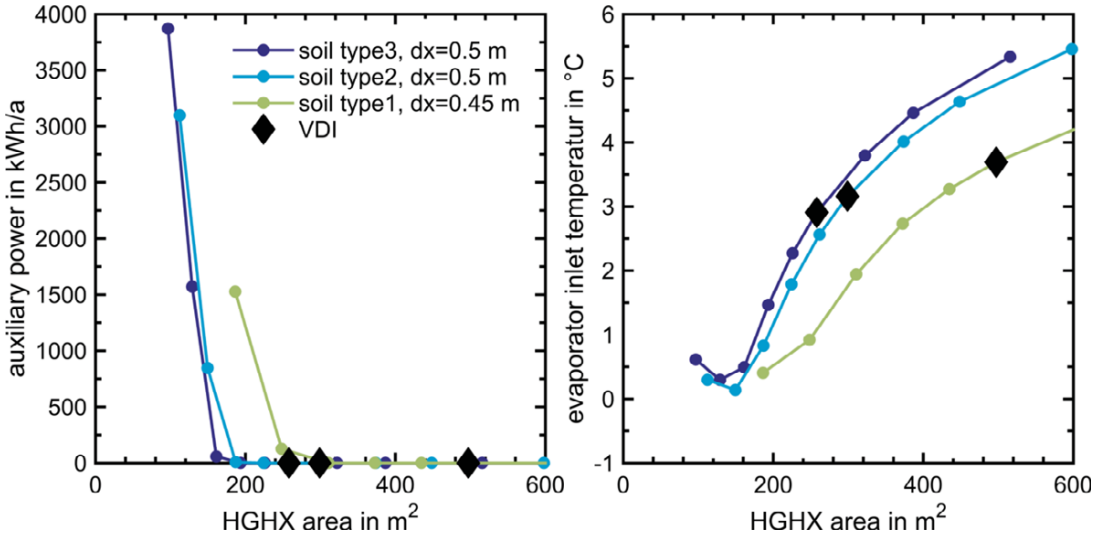

Fig. 5: Auxiliary power and energetically weighted evaporator inlet temperature for different soil types over HGHX area

Figures 6 and 7 present the seasonal performance factors for soil type 2 (loam) as function of the HGHX area, parametric in the pipeline spacing and for ascending sizes of the PVT collector. The VDI 4640 design recommends, under assumption of laminar flow, a pipeline spacing of 0.5 m. Figure 6 (left) shows the results for a system without solar thermal regeneration. The shapes of the graphs are therefore similar to the ones shown in Figure 4. All plots confirm that narrower pipeline spacing enables higher efficiencies in general. We see that a size reduction of 28 % (A_{HGHX} from 311 m² to 224 m²) of the HGHX relative to the VDI 4640 design recommendation may be tolerated at almost missing efficiency losses.

In the second diagram (Figure 6 right) results for systems equipped with 6.7 m² of PVT collector area are

depicted. To focus on the thermal/regeneration process, electrical energy yield of the PVT collector is not included in the calculation of seasonal performance factors at this time. At high HGHX areas, the seasonal performance factors are lowered, due to the added electric energy demand of the collector pumps. At lower HGHX areas the seasonal performance factors increase. The main reason therefor is that the HGHX is less frequently exhausted and thus the demand for auxiliary power is lower. Also the occurrence of critical frost conditions is slightly limited.

With increasing PVT collector areas (Figure 7), the described trends proceed, until at 26.6 m² of PVT collector area critical frost conditions are completely prevented, even for the smallest HGHX areas simulated. At this PVT collector size the HGHX area may be as much as 64 % smaller (A_{HGHX} from 311 m² to 112 m²), while achieving almost the same system efficiency as an unsupported system. Only 5 % efficiency losses (SPF_{SHP} from 3.76 to 3.60) are predicted in this case.

Similar results are obtained for soil types 1 and 3. For narrower spacing between the HGHX pipes and with solar thermal regeneration the simulations predict possible HGHX size reductions between 49 to 66 %, taking into account limited efficiency losses below 5 %. Note that Soil type 3 (sandy clay) has greater potential for area reductions (66 %) than soil type 1 (sand, 49 %) due to both higher heat conductivity and higher heat capacity.

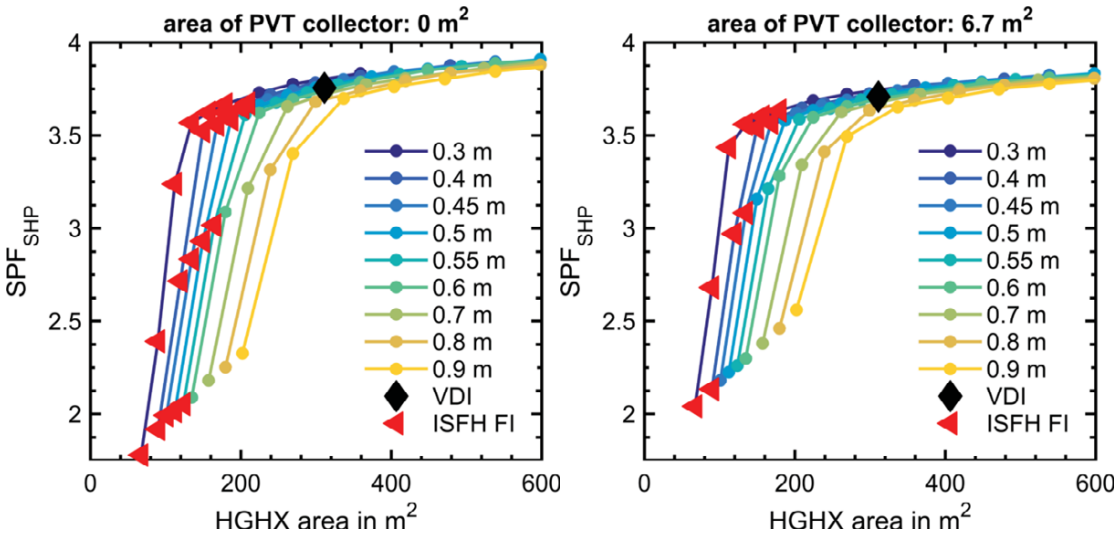

Fig. 6: Seasonal performance factor for soil type 2 over HGHX area for different spacing between HGHX pipes

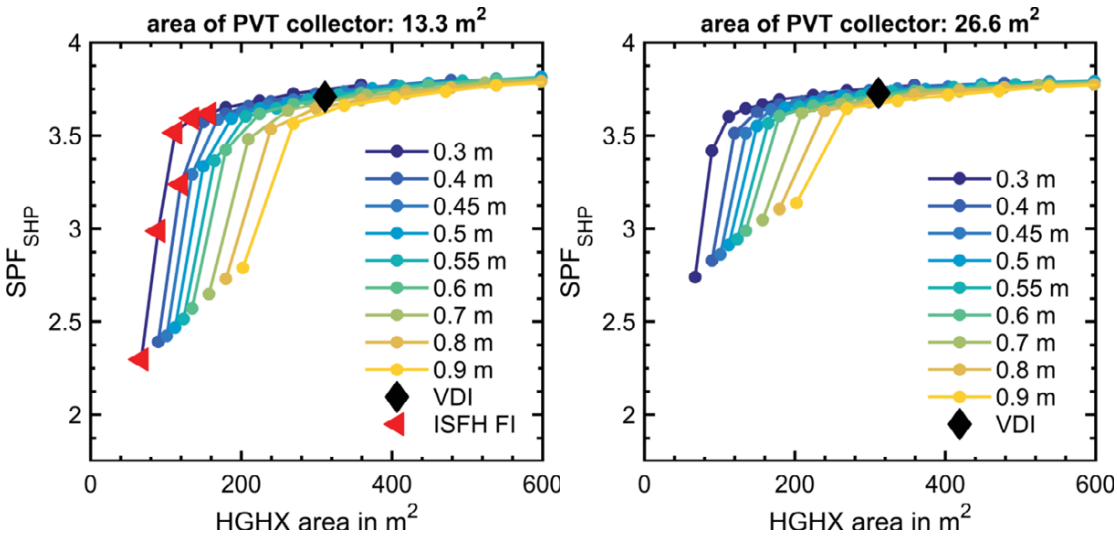

Fig. 7: Seasonal performance factor for soil type 2 over HGHX area for different spacing between HGHX pipes

In the following we analyze the operation of the HGHX fluid cycle with and without solar thermal regeneration. For this purpose the progression of energy quantities of the HGHX and the PVT collectors is considered in time on a monthly basis. The considered HGHX system has a size of 134.6 m^2 comprising a pipe separation of 0.3 m. It is supported by PVT collectors of two selected sizes (13.3 and 26.6 m^2).

Figure 8 provides the monthly net heat extraction from the HGHX with and without the PVT collectors of respective sizes. Net heat extraction is defined as heat extraction subtracted by solar thermal heat supplied to the soil. For the system without active solar regeneration (purple graph), the net heat extractions resembles a typical domestic HP heat demand progression. High heat demands in the winter oppose low demands in the summer, when domestic hot water preparation is the only demand.

Systems with solar thermal regeneration (blue and green graphs) show a slightly different progression. While the differences in net heat extraction are reduced for October (month 10) to December (month 12), i.e. the beginning of the heating season, the difference grows significantly larger towards March (month 3). Solar regenerated systems exhibit negative net heat extractions, once more heat is fed into the HGHX than extracted. The model predicts maximum regeneration heat inputs between March (month 3) and July (month 7), dependent on the size of the PVT collectors.

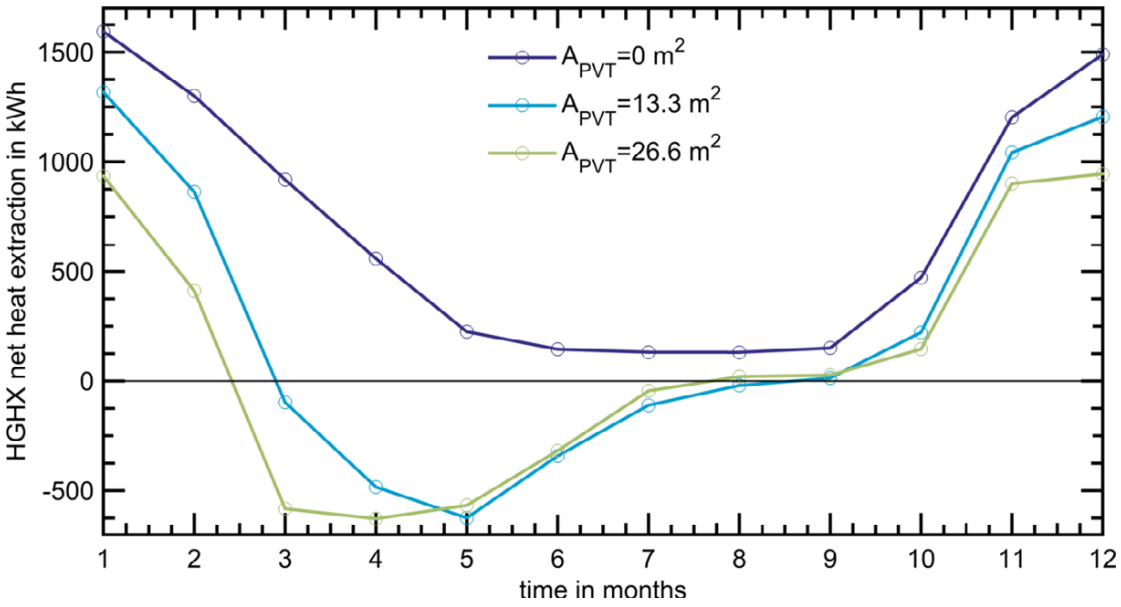

Fig. 8: Monthly distribution of HGHX net heat extraction

Figure 9 provides the monthly progression of the related solar yields, the quantity thereof fed to the soil (regeneration heat) and the solar irradiation on the collector plane. The maximum yield occurs in March (month 3, for A_{PVT} = 26.6 m^2) and April (month 4, for A_{PVT} = 13.3 m^2), respectively and coincides with the lowest net heat extractions shown in Figure 8. This shows that regeneration mainly takes place at the end of the heating season, when the HGHX tends to be exhausted.

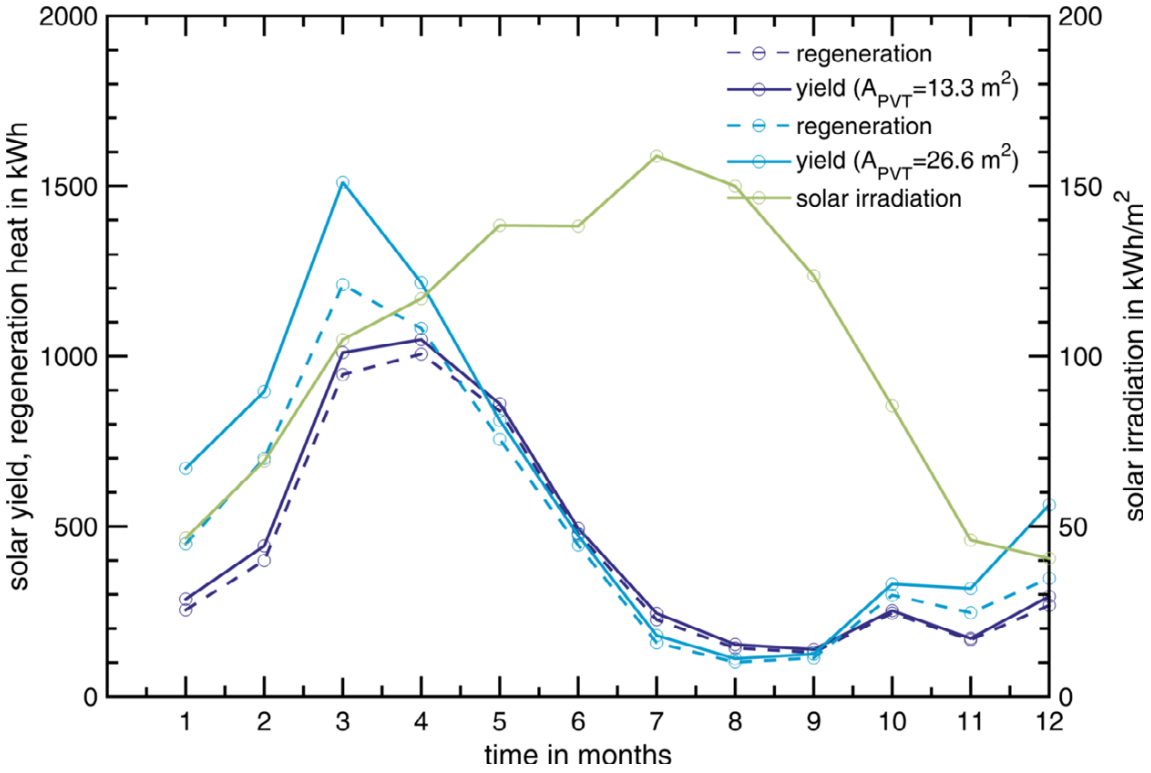

Fig. 9: Monthly distribution of solar yields, regeneration heat and insolation

For the smaller PVT collector area (A_{PVT} = 13.3 m^2) almost the entire solar yields are used for soil regeneration. Only systems with the larger PVT collector size exhibit tangible differences between solar thermal yield and regeneration heat from November (month 11) to April (month 4). In this case, the solar yield suffices to directly supply the heat pump during the heating season.

Comparing the yield and solar irradiation curves over the year, we see that significant solar irradiations (from May (month 5) to October (month 10)) remain unused in configurations connected only to the HGHX. The time period during October (month 10) to May (month 5) offers great potential for using solar thermal yields at low temperatures efficiently. Furthermore optimal synergy conditions exist for the solar/HGHX system, because of reduced competition between direct use and HGHX recovery.

Figure 10 illustrates the effects of regenerating a possibly undersized HGHX system. It shows energy quantities in the fluid carrier cycle along with auxiliary energy and energetically weighted evaporator inlet temperatures on a yearly basis. A HGHX system with a size of only 89.7 m^2 with a pipe separation of 0.3 m is considered.

The blue column represents the energy extracted from the fluid carrier cycle in the heat pumps evaporator (symbol Q_evap). This quantity scales with the PVT collector area size, because the source is less often exhausted. The auxiliary power demand (symbol E_aux, red column) shows the opposite behavior. This quantity scales inverse to the PVT collector area size. The second column shows the heat quantities delivered from the HGHX to the evaporator (symbol Q_HGHX->evap / dark green), from the PVT collectors to the evaporator (Q_PVT->evap / light green) and from the PVT collectors to the HGHX (symbol Q_PVT->HGHX / yellow). The diagram shows that while the system without PVT collector extracts the entire heat from the HGHX, the PVT supplied system may use the solar yields partially in the evaporator. Hence the heat extraction from the HGHX can be reduced, while most of the solar yields are used to actively regenerate the HGHX. The energetically weighted evaporator inlet temperature increases from -0.74 °C without PVT collectors to 2.32 °C with a PVT collector size of 26.6 m^2.

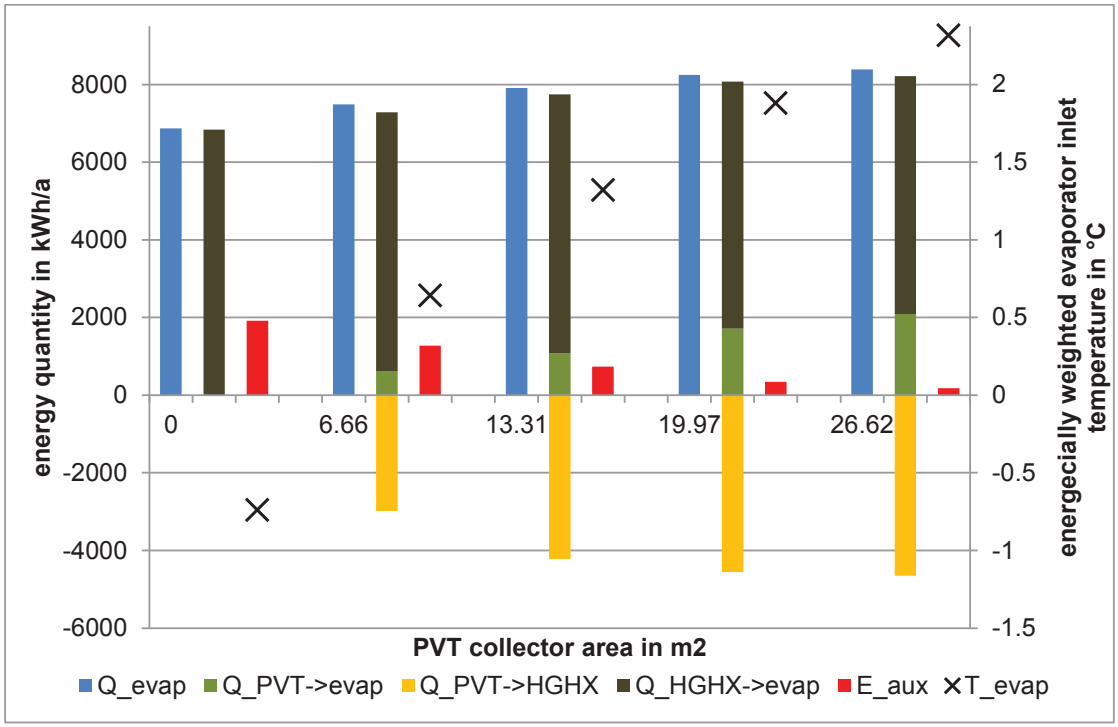

Fig. 10: Energy quantities of the source cycle, auxiliary energy and evaporator temperatures over PVT collector area

The simulations predict that the integration of 26.6 m² of PVT collectors on the source side allows the seasonal performance factor of an undersized HGHX (~29 % of VDI's recommendation) to be increased from 2.4 to 3.4. When taking into account the potential of electricity co-generation of the PVT modules (using only electricity obtained from grid for the calculation of the seasonal performance factor) the overall systems seasonal performance factor may even reach 3.7, which means the PVT-supported, undersized HGHX system is as efficient as the standard VDI design – but two thirds smaller.

4. Conclusion and prospect

A TRNSYS model for HGHX has been developed and successfully compared against measurement data. For analysis of system configurations including a heat pump and solar thermal regeneration it is successfully integrated into a system model. The ability to use the model in differently configured heat supply systems in TRNSYS allows a variety of future applications.

The presented results of system simulations show that critical frost conditions and exhaustion are the limiting factors in lowering the area of a HGHX. Solar thermal regeneration is able to avoid critical frost conditions and strongly limit exhaustion at small HGHX areas, if smaller separation between the HGHX's pipes is used.

Analysis of monthly solar yields and HGHX heat extraction reveals that a HGHX is not a seasonal storage. Still its comparatively large heat capacity allows to smoothen solar thermal heat generation and supply peak loads as a combined source for a heat pump. Unglazed and presumably even low-end collectors can be used, because of the low temperatures needed. As a result promising applications for solar thermal heat at low temperatures are enabled, while only sparsely affecting the potentials to directly use yields in the summer.

Ongoing research concerns the utilization of low-end and façade integrated collectors for regeneration of HGHXs as well as an additional connection to the buffer storage to make direct use of possible solar yields in the summer. For these configurations suited control strategies are being developed.

After demonstrating the technological potential of the combination of solar thermal collectors and HGHXs, analysis of the feasibility of differently configured solutions is the next important step towards a comprehensive assessment.

5. Acknowledgement

The project “Ground collectors and solar collectors as optimized bivalent heat sources for high efficiency heat pump systems (Terra-Solar-Quelle)”, FKZ 03ET1275A, was carried out in cooperation with the companies tewag-Technologie-Erdwärmeanlagen-Umweltschutz GmbH and Bundesverband Wärmepumpe (BWP) e.V. and funded by the German Federal Ministry for Economic Affairs and Energy on the basis of a decision of the German Federal Parliament. The authors are grateful for the financial support. The content of this publication is the sole responsibility of the authors.

6. Reference list

D’Antony, M., 2013. Presentation of System Performance Calculation Educational Material - A technical report of Subtask D - Report D1

Dott, R., Haller, M.Y., Ruschenburg, J., Ochs, F., Bony, J., 2012. The Reference Framework for System Simulations of the IEA SHC Task 44 / HPP Annex 38 – Part B: Buildings and Space Heat Load - A technical report of subtask C. Report C1 Part B

Giardina, J., 1995. Evaluation of ground coupled heat pumps for the state of Wisconsin, MSc Thesis, University of Wisconsin, Madison

Glück, B., 2009. Simulationsmodell “Erdwärmekollektor” zur wärmetechnischen Beurteilung von Wärmequellen, Wärmesenken und Wärme-Kältespeichern. Rud. Otto Meyer-Umwelt-Stiftung, Hamburg

Haller, M.Y., Dott, R., Ruschenburg, J., Ochs, F., Bony, J., 2012. The Reference Framework for System Simulations of the IEA SHC Task 44 / HPP Annex 38 – Part A: General Simulations Boundary Conditions - A technical report of subtask C. Report C1 Part A

Hirsch, H., Hüsing, F., Rockendorf, G., 2016. Modellierung oberflächennaher Erdwärmeübertrager für Systemsimulationen in TRNSYS, Proceedings of BauSIM 2016, Dresden

Klein, S.A., et al., 2010. TRNSYS 17: A Transient System Simulation Program, Solar Energy Laboratory, University of Wisconsin, Madison, USA, http://sel.me.wisc.edu/trnsys

Pärisch, P., Mercker, O., Warmuth, J., Tepe, R., Bertram, E. and Rockendorf, G., 2014. Investigations and model validation of a ground-coupled heat pump for the combination with solar collectors, Applied Thermal Engineering 62 (2014) 375-381, Elsevier

Ramming, K., 2007. Bewertung und Optimierung oberflächennaher Erdwärmekollektoren für verschiedene Lastfälle, PhD Thesis, Technische Universität Dresden, Dresden

Verein Deutscher Ingenieure, 2015. VDI: Guideline VDI 4640 Part 2 - Thermal use of the underground – Ground source heat pump systems, draft 05/2015, Düsseldorf

Conference Proceedings

EuroSun 2016
Palma de Mallorca (Spain), 11 – 14 October 2016

ISES EuroSun 2016

Design of Portable and Sustainable Solar Refrigerator

Joanna Juárez[1], Dolores Durán[1], Cuauhtémoc Palacios [1], Iván Martínez [1]

[1] Universidad Autónoma del Estado de México, Facultad de ingeniería, Toluca (México)

Abstract

This paper is presented as a preliminary design of a portable solar refrigerator, which uses a solar adsorption system. The aim is to achieve a sustainable design that includes not only the materials but also considerations for the useful life of the equipment and its final disposition.

This equipment has been considered as an economical solution for rural communities where there is no electricity, and whose food goods need to be preserved.

The suggested design considers a CPC as primary source of energy for the coolant fluid, which its three analyzed substances are: water, methanol and biogas, obtained from the bovine manure and organic domestic trash (wastage).

Vegetal carbon is recommended, for this project, as adsorbent material that is usually used in several researches around world as substitute of activated coal.

Keywords: *Solar cooling, adsorption cycle, CPC.*

---

1. Introduction

Cooling is one of the basic principles of food safety around the world because food slows degradation (Das Surah, 2010).However, according to the International Institute of Energy, approximately 15% of all electricity produced in the world it is used for cooling processes (Kim DS, 2008). Currently the most widely used are vapor-compression refrigeration systems, which work with synthetic materials, such as CFCs, HCFCs or HFCs. When released into the atmosphere, such refrigerants affect the ozone layer and contribute to the greenhouse effect. JA Edmunds et. al (1987), estimated that emissions from synthetic refrigerants, during operation or after life represent 33.3% of the greenhouse effect (Fernandes, 2012). As an immediate response care environment, various protocols, such as the Montreal Protocol (1987) and the Kyoto Protocol (1997), were established in order to eliminate or at least significantly reduce emissions of these gases. (Gupta, 2013 and Gutierrez, 2013).

Countries around the world have made some efforts to make the change or elimination of the use of HCFCs. According to SEMARNAT (Secretariat of environment and natural resources) in Mexico in 2010 was totally eliminated in the country consumption of chlorofluorocarbons (CFCs), substances used in refrigeration, air conditioning, aerosols and polyurethane foams and raised under the framework of the "National Plan for Elimination of hydro-chlorofluorocarbons (HCFC) ", which aims to eliminate 30% of consumption of HCFCs by 2018. Despite efforts in some countries, after 29 years of being created the Montreal Protocol, the situation continues to claim the development of alternative technologies that operate with friendly substances to the environment, mainly due to increased emissions of HFCs, although the emission of CFCs and HCFCs have been declined since 1980s. (Metivier, 2003 and Hassan, 2012).

doi:10.18086/eurosun.2016.04.10 Available at http://proceedings.ises.org

Computational fluid dynamics (CFD) modelling would be a viable choice, which can reduce experiments (Y Ge et al, 2010). Many studies have shown that CFD modelling is a promising and valuable tool to improve refrigeration efficiency in terms of energy savings and the required temperature maintenance. (Foster et al, 2005)

Based on the above, it may be noted that it is important to developed cooling systems that consume no electricity, because electricity usually comes from fossil sources; also, it is necessary that this system do not use refrigerants CFCs that affect the ozone layer and produce greenhouse effect. Therefore, the purpose of this research project is to design a refrigerator that uses solar energy for cooling and food preservation, particularly seafood, operating with a CPC collector and adsorption system, using natural refrigerants; proposing the analysis between three pairs of adsorbent-adsorbate: coal - water, coal -methanol and coal-biogas, and selecting the best option for the design of the prototype. As already it mentioned that the solar refrigerator would be used for seafood, thus is proposed that the design be portable for to be used in rural communities with no electricity for the conservation of their food.

Nomenclature

Quantity	Symbol	Unit
Collector diameter	*c1*	*c*m
Condenser diameter	*c2*	cm
Diameter of cylinder between condenser and evaporator	*c3*	cm
Evaporator inner diameter	*c4*	cm
Energy	*Q*	kJ
Heat of desorption	*H*	kJ kg^{-1}
Latent heat	*L*	kJ kg^{-1}
Latent heat of fusion of ice at 273 K	*L**	kJ kg^{-1}
Mass	*m*	kg
Specific heat	*Cp*	kJ kg^{-1} K^{-1}
Temperature	*T*	K
Total solar energy input to the system during the day	*QI*	kJ
Concentration of refrigerant	*X*	kg adsorbate kg^{-1} adsorbent

SUBSCRIPTIONS

Adsorbent carbon	ac
Condenser	c
Evaporator	e
Refrigerant	r
Saturation	s
Points in Clapeyron diagram	A, B, C, D
Total	T

2. Solar adsorption refrigeration system

The principles of operation of the adsorption refrigeration system are described by the ideal cycle in the Clapeyron diagram (ln *P* versus–1/*T*). See Fig. 1.

Isosteric heating. At sunrise, sunlight falls in the parabolic solar collector, which contains the activated carbon saturated with methanol at the focal line. The mixture is heated until its pressure reaches a level that enables refrigerant to be desorbed (state B).

Desorption and condensation. Between B and D addition of heat from the solar energy results in desorption of vapor refrigerant, which condenses in the condenser by the air surrounding it. In an ideal cycle, the condensation pressure remains constant. At state D, when the maximum temperature of adsorbent is reached, solar irradiance starts to decrease.

Isosteric cooling. At state D, the temperature and pressure decrease. Meanwhile, the liquid refrigerant is being collected in the evaporator.

Adsorption and evaporation. The adsorbent continues decreasing its temperature and pump the refrigerant. This evaporates and extracts heat from the evaporator generating a cold atmosphere. At sunrise the next day, the temperature of the collector is minimal and reaches the value at state A., the cycle is said to be intermittent because the cold production happens during the night.

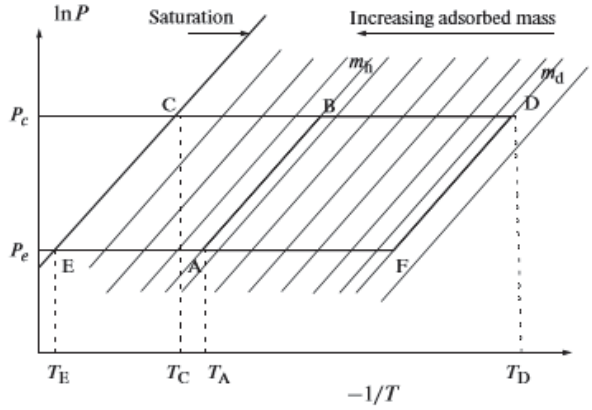

Fig. 1: Clapeyron diagram of ideal adsorption cycle. (Tashtoush et al., 2010)

The operation and principle of the solar adsorption refrigeration system is shown in Fig. 2. The system is composed of a sorption bed, which locates at the focal line of a solar collector, a condenser, and an evaporator that acts like a refrigerator. The adsorbent and the adsorbate are in a closed and vacuumed system. The collector is supplied with carbon, which is adsorbed with natural refrigerant (methanol, water or biogas). During the daytime Fig. 2a, the adsorbent (carbon) and the natural refrigerant is heated in the collector. The natural refrigerant evaporates from the adsorbent and then is cooled by the condenser and stored in the evaporator. In the nighttime Fig. 2b, the ambient air cools the collector and the temperature of the adsorbent reaches a minimum. In this period, natural refrigerant begins to evaporate by adsorbing heat from the water to be frozen and is adsorbed by the adsorbent. As the evaporation of the natural refrigerant continues, the water temperature decreases until it reaches 273 K, where ice starts to be formed. An ideal cycle assumes the use of valves to connect the collector, condenser, and the evaporator. In real unit, this can be avoided and we may depend on the pressure difference to move the refrigerant.

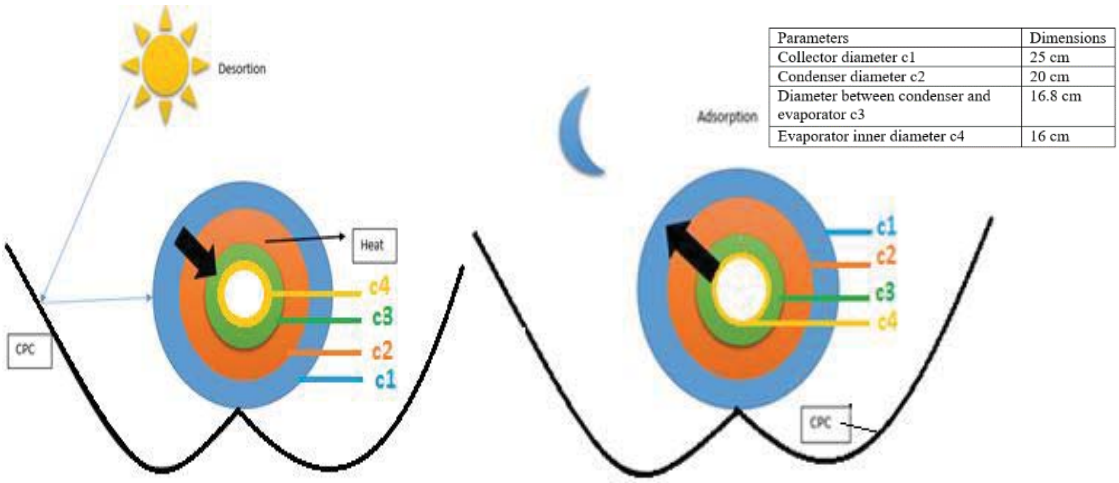

Parameters	Dimensions
Collector diameter c1	25 cm
Condenser diameter c2	20 cm
Diameter between condenser and evaporator c3	16.8 cm
Evaporator inner diameter c4	16 cm

(a) Daytime (heat/desorption) **(b) Nighttime (evaporation/adsorption)**

Fig. 2: Operation principle of solid adsorption refrigeration system using solar heat. A- sorption bed (solar collector); B condenser, C- evaporator and D- cold area.

3. Description of the design

The prototype consists of four concentric cylinder, called c1, c2, c3, c4; c1 is considering that larger diameter and below cylinder c4 is smaller diameter. (Fig.2). The first space formed by c1 and c2, forms the area called collector, wherein the pair adsorbate-adsorbent is placed. The second space formed by the c2 and c3 is the space where a serpentine is located and water to form the condenser; the space formed by c3 and c4 are the evaporator.

The condenser and evaporator are connected by a small serpentine, which performs the function of expansion valve.

It is important to mention that c1 should be a material with high thermal conductivity, so that the solar radiation concentrated by the CPC is absorbed; c2 must be an insulating material to completely separate the area of the collector and the condenser; c3 should also be an insulating material separates the condenser and the evaporator; however c4 must have a high conductivity to extract energy from the area to be cooled, in which food will be located; finally rejoins the evaporator with the manifold by a pipe; in Figure 3 shows the configuration proposed.

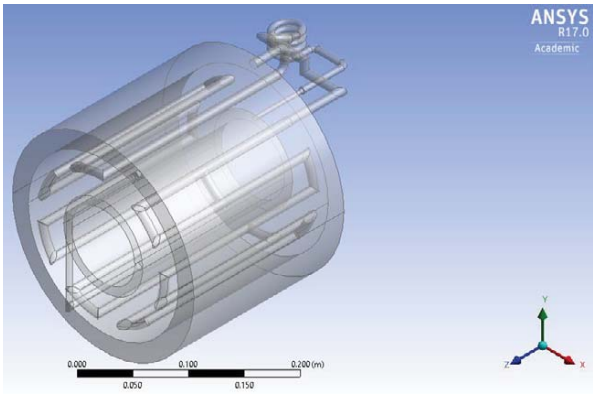

Fig. 3: Solar Refrigerator demonstration system

4. Adsorption capacity of different materials

As part of the project, we have analyzed the adsorption capacity of different materials because this is the first and fundamental part for thermal calculation and the subsequent design of the solar refrigerator. Jaraba (2012), made a comparison of adsorption capacity between orange peel and orange peel modified with chitosan for removal methyl of orange, of that investigation it was found that orange peel is best adsorbent that material orange peel modified (Metivier, 2003).

On the other hand, in 2008, E. Gonzalez, analyzed the percentage of adsorption for two particle sizes of 0.425 mm and 0.5 mm, managed to obtain maximum removal percentage of 66.8% and 62.5%, concluded that smaller particles are more adsorption capacity (Incar, 2014).

In Mexico and Malaysia, there are extensive analysis of materials with different adsorption capacities, such analysis has concluded that in order to make a sustainable adsorption system it is necessary to analyze local organic materials from the place they are used.[9], [10]. According to the analysis capacity of adsorption and desorption for proposals mixtures, tests were performed by analyzing the adsorption capacity of methylene blue, these tests were proposed by Xialong Zhang and Vargas with a stirring time of 24 hours and 48 hours respectively, which adsorption capacities were determined with efficiencies up to 60%. (Anisur, 2013 and Fernandes, 2014)

For testing, the following parameters shown in table 1 were considered. (Xialong, 2015).

Table 1: Testing parameters

Parameter	Specification
Reactive	Methylene blue
Volume of solute	10 mL
Concentrations	(2- 50 mg/L)
Temperature to generate coal	350°C
Types of organic material to generate coal	-Tangerine peel -Orange peel -Tomato peel -Shell “huaje”
Mass of adsorbent	4 mg

The results of capacity of adsorption they show in fig. 4 and it can be seen that the types of coal which has higher adsorption capacity in descending order they are: huaje, tomato and orange, but it is important to note that these three samples have higher adsorption capacity than activated coal for fishbowl, this preliminary result is very important because if we do not activate the coals we would not use substances as phenolphthalein or oxalic acid and therefore waste pollutants are reduced by the project.

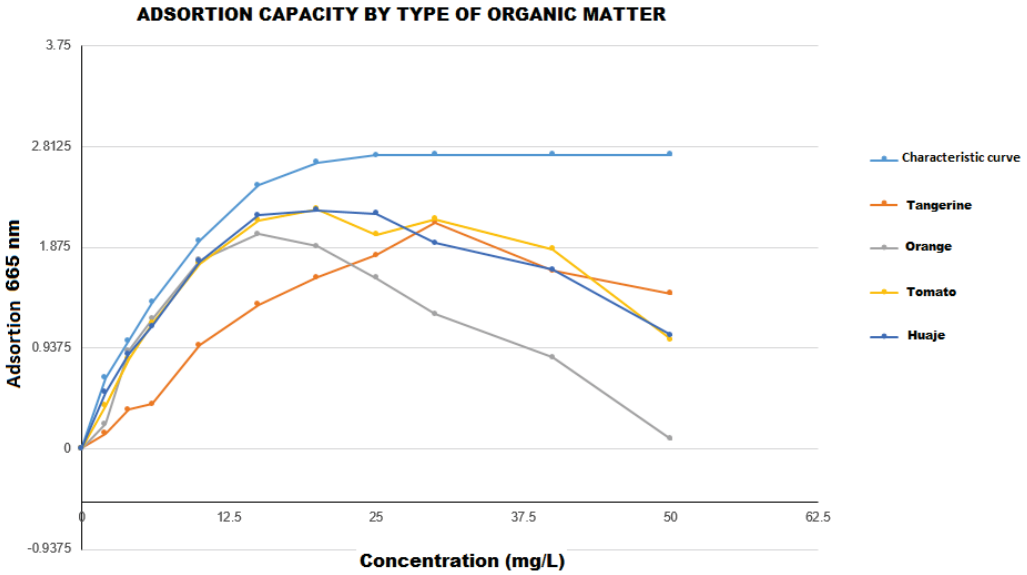

Fig. 4: Comparison of adsorptivity between organic materials

Regarding the materials used as adsorbates, it is important to point out that the biogas to be analyzed shall be deemed like methane for analysis in Ansys (CFD) and the other two adsorbates to analyze are H_2O and methanol, for the properties adsorbates are considered the values of the database of CFD.

5. Thermodynamics and transfer design procedure

The cycle begins at point A (see fig. 1) where the adsorbent bed is at law temperature T_A and at law pressure $P_e = P_s\ (T_e)$. During the daylight, AB represents the heating of the pair. The system follows the isotherm $X_A = X(T_A, P_e)$. (Tashtoush et al., (2010)

Pressure increases until it reaches the value $P_c = P_s\ (T_c)$ at point B. Thus, the energy used to raise the temperature of both the adsorbent (ac) and adsorbate (r) from point A to B is given by:

$$Q_{AB} = m_{ac} C_{pac} (T_B - T_A) + m_{ac} X_{r-A} C_{pr} (T_B - T_A). \quad \text{(eq.1)}$$

Additional heating of the adsorbent from B to D causes some adsorbate to desorbed and its vapor to be condensed at pressure P_c. When the adsorbent reaches its maximum temperature T_D, desorption stops, and the adsorbate accumulates into the evaporator. The energy used for the additional heating of the adsorbent to point D and desorption of the adsorbate is given by:

$$Q_{BD} = m_{ac} C_{pac} (T_D - T_B) + m_{ac} \left(\frac{X_{r-A} + X_{r-D}}{2}\right) C_{pr} (T_D - T_B) + m_{ac} (X_g) H. \quad \text{(eq. 2)}$$

The total energy gained by the system during the daytime will be:

$$Q_T = (Q_{AB} + Q_{BD}). \quad \text{(eq.3)}$$

During the night-time, the temperature decreases from D to F, therefore, decreasing the pressure from P_c to P_e. Then the adsorption and evaporation occur while the adsorbent is cooled from F to A. During this period, heat is withdrawn to decrease the temperature of the adsorbent and to withdraw adsorption heat. The total heat released during the cooling period will be the heat of vaporization of adsorbate, this is given by:

$$Q_{e1} = m_{ac}(X_{r-A} - X_{r-D})L_r. \quad \text{(eq. 4)}$$

From heat transfer equation, the energy necessary for cooling the liquid adsorbate from the temperature at which it is condensed to the temperature at which it evaporates is given by:

$$Q_{e2} = m_{ac}C_{pr}(X_{r-A} - X_{r-D})(T_c - T_e). \quad \text{(eq. 5)}$$

And thus the net energy actually used to produce cold area will be:

$$Q_e = Q_{e1} - Q_{e2}. \quad \text{(eq. 6)}$$

The performance of the adsorption refrigeration can be expressed in terms:

The collector efficiency $\eta_1 = Q_T/Q_I$. (eq. 7)

The evaporator efficiency $\eta_2 = Q_{ice}/Q_e$. (eq. 8)

The cycle COP = Q_{el}/Q_T. (eq. 9)

The net COP = Q_{ice}/Q_I. (eq. 10)

6. CFD simulation

The software SolidWorks is used to build up the geometry model of the constructed component. Smooth transition is introduced at the junctions. Structured tetrahedrons elements are applied for meshing. The commercial code FLUENT is employed as the equation solver to solve the governing equations. The SIMPLE algorithm is selected to compute the velocity, pressure and temperature, and the calculations are performed in single precision.

In the CFD simulation about radiation and natural convection, the model used is surface to surface (S2S) for the analysis assumes that all surface are gray and diffuse, the type is pressure- based, and consider that the radiation is constant around of diameter c1. And the method of the assembly meshing is tetrahedrons, using 836 nodes for fig. 5 and 19850 nodes for the fig. 6.

The CFD simulation is about of the heat transfer in collector, it is considered that the outlet temperature is constant with a value of 421K and a model of radiation-convection is applied. The properties of the working fluid are shown in table 2

Table 2: Fluids adsorbates properties

Fluid	Density (kg m^{-3})	Specific heat (J kg^{-1} K^{-1})	Thermal conductivity (W m^{-1} K^{-1})	Viscosity (kg m^{-1} s^{-1})
Methanol	*785*	2532	.2022	.0005495
H_2O	*998.2*	4182	.6	.001003
Biogas	*0.6679*	2222	.0332	1.087e-05

The comparison of the temperature profile for each working fluid are shown in Fig. 5. The range of temperatures is 381 K to 421 K. The dimensions are the same for the three analyses.

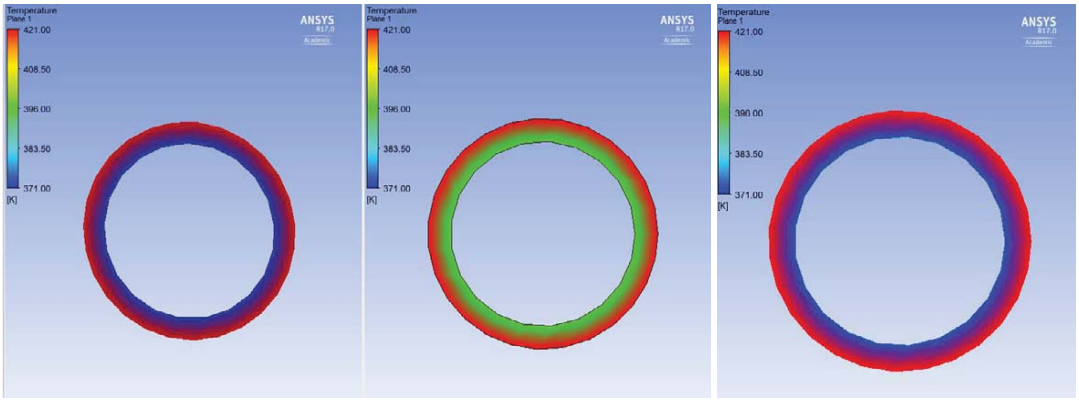

(a) Collector (Fluid methanol) **(b) Collector (Fluid H_2O)** **(c) Collector (Fluid Biogas)**

Fig. 5: Ansys radiation and natural convection with adsorbate: a) Methanol, b) H_2O and c) Biogas.

In the preliminary design, the pressure in the prototype is very important according to the Clapeyron diagram. Fig. 6 shows the pressure profile in the collector and the evaporator for each case.

Is it may be observed when the working fluid is water, the pressure decreases dramatically in the collector. Nevertheless if methanol or Biogas is used the pressure remains constant in the collector and decreases along the evaporator.

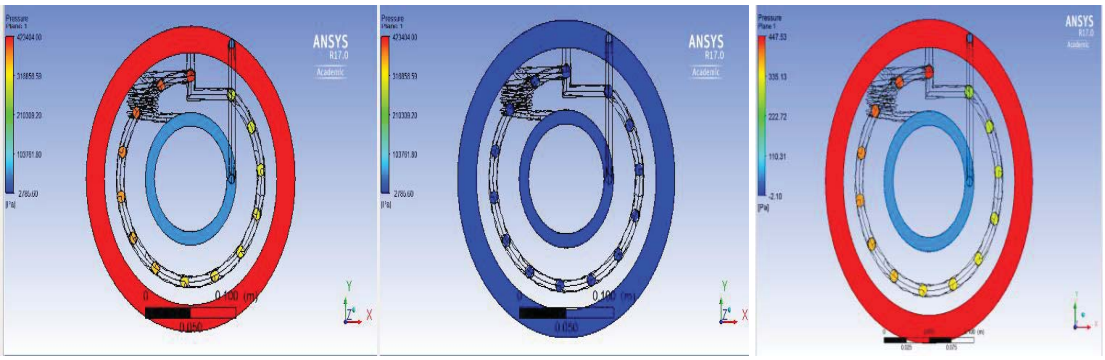

(a) Prototype (Fluid methanol) **(b) Prototype r (Fluid H_2O)** **(c) Prototype (Fluid Biogas)**

Fig. 6: Variation of pressure.

7. Results and discussion

7.1. Results of thermal analysis

In this preliminary design it was proposed assembly of four concentric cylinders, the main restriction of the design are the commercial dimensions found in the national market of alluminium tube and nylamid. The length of the cylinders are 50 cm and the dimensions in order descendent with commercial units are 6",5",3" and 1 1/2".

The function of the cylinder of 6" is be the absorber of the solar concentrator and the function of the cylinder 1 1/2" is be the wall of contact between evaporator and cold area therefore the material of the these two cylinders are alluminium cedule 40, because of termic conductivity is around of 168 W/(m K) and on these two wall is neccesary a high termic conductivity.

The function of the cylinder of 5" is be the wall of separation between the termic compressor and condenser and the function of the cylinder of de 3" is be the wall of separation between the condenser and the evaporator, the caracteristic principal of these tubes are that the material is non conductor and the material select is nylamid with a termic conductivity of 0,29 W/ mK.

The volume in the cold area is to achieve freeze approximately 0,5 liter of water. It was considered an initial ambient temperature of 15 ° C and the temperature goal of -5 °C. The initial conditions of latent and sensible heat are obtained from the total heat extracted from the cold area the which is 203,15 kJ. The mass of the refrigerant is of 0,25 kg considering that the adsorption capacity is of 0,58 kg adsorbate/kg adsorbent and the mass of adsorbent is of 0,30 kg.

The average solar radiation considered is 700 W/m2 and the captation area is 0,70 m2, through free convection was calculated superficial temperature of the absorber of 120 °C and heat transfer of 294 W.

The general equation of heat conduction is used to determine the internal temperature which is 118 °C.

Boiling inside the termic compressor has a mass flow of 0,00117 kg/s so it will take time to evaporate around of one hour, ten minutes.

The length of the tube for the condenser is at least 20 cm for evaporate all volume of refrigerant.The cooling fluid is water to condense to the refrigerant. The coefficient of convection of water is 48,99 W/m2 K

The condensation time considered was 15 minutes and the diameter between the B and C is 9.58 mm. The CPC material was considered to be aluminum with a reflectance of 0.8.

Whit the thermal analysis shown in section 5, the amounts of adsorbent- adsorbate pair were obtained. The table 2 shows the amounts obtained for the preliminary design. Also it was obtained the COP and it was observed that this value id between ranges 0.1-0.4 which is suggested for some authors (Fernandes, 2014).

Table 2: Design parameters

Parameters	Dimensions
Collector diameter c1	25 cm
Condenser diameter c2	20 cm
Diameter between condenser and evaporator	16.8 cm
Evaporator inner diameter c4	16 cm
Condenser tubes	22
Adsorbate mass	50g
Adsorbent mass	70g
CPC opening capture	0.60 m^2
COP	0.22

7.2 Discussion of CFD results

At the beginning of calculation, all the parameters took the values defined at point A. The boundary conditions used are shown in table 3.

Table 3: Boundary conditions

Parameter	Value
Condenser pressure inlet	423 kPa
Evaporator pressure inlet	103 kPa

In the Fig. 5 show the difference of the temperature are based in the specific heat of each fluid and the variation of temperature determined the change of phase of the fluids. These results are very important for the final design because is necessary the change of temperature for each element of the refrigeration cycle also the pressure change in each element propose for the prototype.

8. Conclusion

In this work it is observed that the proposed design of the portable solar adsorption refrigerator is feasible. In this design it is proposed that all the elements are together as concentric cylinders, according to the determined dimensions it was observed that this proposal is achievable.

Also in this paper adsorptivity values of charcoal obtained from different waste organic matter were analyzed. It was observed that the waste of the local product “huaje” has the major adsorption capacity, even more than the values obtained with activated charcoal.

As a result of the thermal analysis it was determined the adsorbent and adsorbate quantity required for the design proposed. The values obtained were 50g of adsorbate and 70g of adsorbent, for 1 liter of water. These values are considered suitable for a portable design. Also it was obtained the COP of the system and this value is similar to the suggested by different authors.

A CFD analysis was made in order to obtain the temperature profiles for the evaporator and condenser. It was observed that the best results are obtained with biogas and methanol. This results reinforces the proposal of using biogas as working fluid.

In future works it is proposed to compare the theoretic and experimental results with the CFD simulations and also to prove the portable solar refrigerator in rural communities.

9. References

A. Foster, M. Madge, J. Evans, The use of CFD to improve the performance of a chilled multi-deck retail display cabinet, International Journal of Refrigeration, 28 (2005) 698-705.

Anisur MR, MH Mahfuz, MA Kibria, R. Saidur, Metselaar IHSC, TMI Mahlia. Curbing global warming with phase change materials for energy storage. Renewable and Sustainable Energy Reviews, 18 (2013), pp. 23-30.

Das Surah. Review solar refrigeration cycle adsorption. IJMET, 1 (1) (2010), pp. 190-226.

Fernandes, M. E. (2012). The activated carbon developed from orange peels: Lot and | adsorption competitive dynamics of basic dyes. Buenos Aires: Elsevier.

Gupta, V. K. (2013). Potential activated carbon from waste tire rubber for adsorption of phenolic compounds: Effect of pretreatment conditions. India: Elsevier.

Gutiérrez1, A. F. (2013). Assessment power biosorbent orange peel for removing heavy metals, Pb (II) and Zn (II). Yucatan: University of Yucatan.

H. Metivier-Pignon, (2003) .The dye adsorption in activated carbon fabrics: approach adsorption mechanisms and coupling ACC ultrafiltration for treating wastewater colors.

HZ Hassan, AA Mohamad. A comment for the production of solar cooling through absorption technology. Renewable and Sustainable Energy Reviews, 16 (2012), pp. From 5331-5348.

INCAR. (2014). The adsorption of dyes with different molecular properties on activated carbons prepared from lignocellulosic waste by the Taguchi method. Spain-Mexico: Elsevier.

Jaraba, L. E. (2012). Evaluation of Adsorption Capacity orange peel. Cartagena: Cartagena University.

Kim DS, C. I. (2008). Solar cooling options - a review of the state of the art. Austria: IIR.

KR Ranjan, S. K. (2014). Thermodynamic and economic viability of solar ponds for various thermal applications: a comprehensive review. India: RENEW.

Mohand Berdja et al.(2014) Design and realization of a solar adsorption refrigeration machine powered by solar energy. Energy Procedia, pages2026-2035. Elsevier. Tipaza, Algerie.

M.S. Fernandes, G. B. (2014). Review and future trends of the solar adsorption refrigeration systems. Renewable and Sustainable Energy Reviews, Volume 39, Pages 102-123

G. M. Tashtoush, M. Jaradat, and S. AlBader (2010), Thermal Design of Parabolic Solar Concentrator Adsorption Refrigeration System. Solar Energy Concentrators.

T. Shaikh, YJ Morabiya. Revision of the solar absorption cooling using water and LiBr simulate system performance IJAERS, vol. II (. Item II) (2013), pp. January-March 57-60.

Xialong Zhang (2015). The activated carbon adsorbent coated palygorskite as activation and adsorption of methylene blue. Chine. Elsevier.

Y. Ge, S. Tassou, A. Hadawey, Simulation of multi-deck medium temperature display cabinets with the integration of CFD and cooling coil models, Applied Energy, 87 (2010) 3178-3188.

Conference Proceedings

EuroSun 2016
Palma de Mallorca (Spain), 11 - 14 October 2016

Using TRNSYS in a graduate course on solar energy engineering

Michaël Kummert

Polytechnique Montréal, Dept. of Mechanical Engineering, Montréal (Québec), Canada

Abstract

This paper presents a graduate solar energy engineering course which relies on the TRNSYS simulation tool to engage the students in the learning process through design and analysis activities. The learning objectives, course structure, and teaching and assessment methods are discussed. Student feedback has been overwhelmingly positive on the use of TRNSYS, and on the fact that the course combines theoretical notions with practical, simulation-based design exercises. The main criticism against the use of the simulation tool is the lack of training material specific to the subject, which leads to difficulties in selecting and configuring the appropriate TRNSYS components.

Keywords: education; teaching; solar energy; simulation; modeling; TRNSYS

1. Introduction

Most university-level courses on renewable energy are taught at the graduate[1] level, either as part of a program focusing on that topic, or as elective courses in more general programs (Kandpal and Broman, 2014). Renewable energy education at Polytechnique Montréal followed the general trend in North America, where renewable energy education in universities took off in the late 20th century, in the wake of the oil crises. Solar energy was often among the first graduate courses created, with many instructors adopting the seminal "Solar Engineering of Thermal Processes" textbook currently available in its 4th edition (Duffie and Beckman, 2013). At the beginning of the 21st century, dwindling research and education funding had resulted in only about 10 US universities offering regular solar energy courses, down from around 150 in the early 1980s (Goswami, 2001). The solar energy course at Polytechnique again followed that trend; it was not taught for about 10 years before being reinstated in 2011.

The course described in this paper is known as MEC 6214 – "Énergie Solaire et Applications" (Solar energy and applications). It is taught once a year, during the winter term (January to May). The current course contents and teaching methods are the results of 6 years of trial and error by the author, although the basic structure and the learning objectives remained the same. As pointed out by Kandpal and Broman (2014), "*the scope and contents of a course essentially depend upon the expertise, interest(s) and biases of the course teacher*". The course described in this paper is no exception: both the theoretical aspects addressed in the first part of the course and the practical, simulation-based approach are a result of the author's experience and level of comfort with the selected topics and tools. As a consequence, this paper does not pretend to represent the best practice in teaching solar energy engineering. It represents the author's contribution to the sharing of teaching methods and materials, and an example of how a detailed simulation program as TRNSYS can enrich a solar energy course and help engage students in the learning process.

Note: The author has made some teaching material available on an open website accompanying this paper: https://moodle.polymtl.ca/course/view.php?name=mec6214p (most material is in French at this time)

[1] "graduate" in the paper title and in the text refers to the level of a student who has graduated from a university-level "undergraduate" program, often a Bachelor's degree (~4 years). The term is frequently used in the USA and in Canada, while "postgraduate" is often used with the same meaning in Europe and some other countries.

doi:10.18086/eurosun.2016.04.05 Available at http://proceedings.ises.org

2. Prerequisites

The general policy at Polytechnique Montréal is to have no prerequisites for graduate courses. While most students taking the course have completed or are about to complete a Bachelor's degree in mechanical engineering, students from other engineering branches and sometimes other backgrounds (architecture, economics, physics) have also taken the course. The required prior knowledge is limited to basic thermodynamics and heat transfer: energy balance of closed and open systems, conduction, convection and radiation heat transfer, heat exchangers. Reading material is provided to cover these topics, e.g. Chapter 3 in (Duffie and Beckman, 2013) or thermodynamics and heat transfer textbooks, but no special tutorial sessions are organized. No prior knowledge of the software tools (especially TRNSYS) is expected, but a small number of students have typically been exposed to them in other undergraduate or graduate courses. In particular, TRNSYS is used to some extent in many of the core courses given at the school on building physics, HVAC systems, building energy modeling, and other renewable energy systems (i.e. geothermal).

3. Learning objectives

After taking the course, the students should be able to:

- Describe the environmental and economic context relevant to solar energy engineering
- Assess the solar energy resource of a site
- Calculate the solar radiation incident on a surface (beam, diffuse and ground-reflected components)
- Explain the principles of solar collectors and solar energy systems
- Calculate the performance of solar collectors
- Analyze the economic and energy performance of solar energy systems*
- Design and simulate the performance of solar energy systems
- Justify the use of given renewable energy technologies (wind, solar thermal, solar photovoltaic) in particular applications

*It should be noted that, adopting the approach of Duffie and Beckman (2013), the course focuses on solar thermal systems but also covers more briefly solar photovoltaic (PV) systems and wind energy systems.

Using Bloom's revised taxonomy (Anderson and Krathwohl, 2001), some learning objectives listed above fall in the lowest 3 categories of educational objectives in Figure 1: remember, understand, and apply (where the "remember" objective is not mentioned explicitly but implied). These categories are more present in the first part of the course ("fundamentals" part, see below).

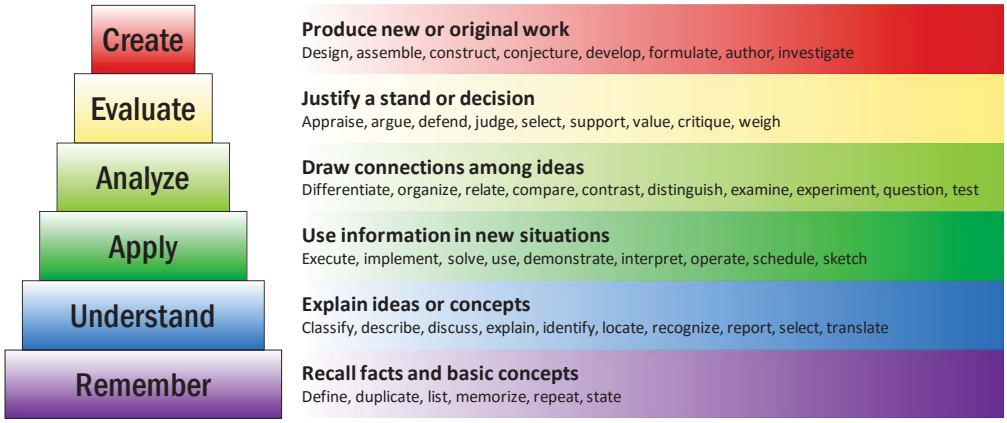

Figure 1: Bloom's revised taxonomy, adapted from (Armstrong, 2016)

The upper categories (Analyze, Evaluate and Create) rely on performance simulation with TRNSYS: students learn how to design solar energy systems first by analyzing the performance of pre-defined systems, by assessing the impact of design changes, and then by proposing and comparing different designs. In theory, it would be possible to perform these activities without relying on software tools, e.g. by using monthly

design methods such as F-Chart (Klein, Beckman and Duffie, 1976). However, using simulation programs such as TRNSYS allows to consider a much larger variety of systems combining different technologies (e.g. solar thermal, solar PV, and wind); it also allows investigating the dynamic behavior of complex systems and control strategies.

4. Teaching and assessment methods

The course follows the typical pattern for graduate courses at Polytechnique Montréal, which consists of a weekly 3-hour lecture (there are normally 13 lectures per term). There are no formal labs or tutorials, but the students are expected to dedicate time to the course at home for personal study, homework assignments and exam preparation, for a total of 96 hours. The total theoretical workload for students is 135 h over the teaching term, which corresponds to 3 credits at Polytechnique Montréal. It can be loosely translated to 5 or 6 ECTS (European Credit Transfer and Accumulation System).

The course is based on "Solar Engineering of Thermal Processes" (Duffie and Beckman, 2013), which has been one of the most popular textbooks to teach solar energy engineering since the 1970's, in North America and throughout the world. The course mainly relies on the first 6 chapters for the "fundamentals" part (see below), which is taught in conventional lectures with homework assignments.

Engaging students

There is increased evidence that traditional lectures are not the most efficient at maximizing learning and course performance in Science, Technology, Engineering and Mathematics (Freeman *et al.*, 2014). Students benefit from active learning, which is defined by the adoption of instructional practices that engage students in the learning process, such as collaborative, cooperative, and problem-based learning (Prince, 2004). While promoting student engagement is an unquestionable objective, it can be challenging to realize in a course with 39 hours of faculty-students contact and a relatively large number of students (the average course enrollment is above 30 students per term, with an upward trend).

The first approach taken to engage students in this course is to try and bring some collaborating learning in the biweekly homework assignments. Students solve the assignments and submit their results individually, but a significant part of the next lecture (roughly one hour) is taken to discuss the problem and the results. The students and instructor diagnose the errors in submitted results. In many cases, students work on different datasets, which was originally intended to prevent plagiarism, but has proven useful in transforming individual efforts into a form of teamwork, where all students contribute one part of a larger parametric analysis.

The second approach to engage students relies on simulation-based problems (assignments or intermediate steps of the final project). During the second half of the term, the time spent giving conventional lectures is considerably reduced, to approximately 1 teaching period (50 min). This leaves two periods for participative activities. Instead of the conventional classroom used for the first part of the term, the course takes place in a computer lab, which allows students to perform simulations during the class. They can analyze their results and diagnose their problems with the help of the instructor, within the constraints imposed by the number of students (i.e. each student gets relatively little time for individual assistance).

Assessment methods

The assessment relies on individual homework assignments (biweekly individual assignments, worth 1/3 of the final mark together), on a written exam (individual, 1/3 of the final mark), and the final project (groups of 2 or 3 students, 1/3 of the final mark). The weight of these different assessments have evolved over time, in response to student feedback that the initial weight for the exam (40 %) did not give a fair share to the other activities. The exam is organized as a mid-term assessment, which comes after the lecture-based "fundamentals" part of the course. It is a conventional written exam, during which students only have access to a 2-page document that they have created themselves and to a non-programmable calculator. In terms of Bloom's taxonomy, the learning objectives assessed in the exam mostly fall in the lower 3 categories (remember, understand, apply), with some attempts to reach levels 4 and 5 (analyze and justify), e.g. with questions asking to define a solar fraction that would apply to a particular system. The homework

assignments ask for numerical answers but also in many cases for a report with some analysis and critique of the results and assumptions, which can be seen as pertaining to categories 4 and 5: analyze, and evaluate. This is especially true for the assignments that use TRNSYS simulations. But to really attain the highest category of educational goals ("create", i.e. design, formulate and investigate), the course relies on simulation-based exercises, and this level is probably only reached during one or two assignments, and the final project, which is a group activity (2 or 3 students).

A practical exam using TRNSYS was introduced in 2012 and 2013. This 2-hour exam was taking place right after the conventional written exam, and was originally intended to test whether students had gained a sufficient understanding of how the program can be used to analyse solar systems, but it proved difficult to test more than basic TRNSYS skills, which was not in line with the learning objectives, so that exam was withdrawn in 2014 and for following years.

5. Use of TRNSYS and other software tools

Literature review: courses using TRNSYS

The literature on teaching solar energy with TRNSYS (or with other simulation tools) is scarce. A few papers report on successful attempts in universities across the world to use TRNSYS in teaching various subjects, from building energy systems to solar energy engineering.

TRNSYS is used in several courses at Polytechnique Montréal, from 4th year (BEng) courses in building heating and cooling mechanical systems to graduate courses on geothermal systems and solar energy (the course described in this paper). It is also used in a graduate course on building energy modeling (Bernier *et al.*, 2016). Students in graduate programs such as the recently created course-based Master in energy engineering are likely to take several of these courses (if not all), which offers synergies and reduces the student effort to learn the software.

Megri (2014) discusses the use of TRNSYS in the department of Architectural Engineering at North Carolina A&T State University. The paper presents a methodology for students to build their own model, perform numerical experiments, and analyze the results. The selected case study is a solar-assisted ground-source heat pump system coupled to a multizone building. According to the author, students prefer easier-to-use programs such as EQuest, but TRNSYS has the benefit of not restricting the type of systems which are analyzed. The instructor needs to master the TRNSYS program and the subject areas.

Charles and Thomas (2009) use TRNSYS in undergraduate courses for engineering and architecture students. The program is coupled with CONTAM for bulk airflow analysis, and other tools are used for climate analysis and Computational fluid Dynamics (CFD). The focus is on encouraging teamwork and benefitting from complementary experience, and simulation is not performed by all class students but rather by an external expert, the instructor, or a few volunteer students. The authors report that students find TRNSYS difficult and are more attracted towards the CFD software. The latter can produce visually attractive results and the authors express that using a little bit of "colorful fluid dynamics" is a necessary evil to generate interest. In spite of the difficulties, the authors conclude that simulation helps students understand the iterative nature of the design process and makes them aware of various physical phenomena. It is also a common platform to support collaboration.

Gómez-Moreno (2015) describes how TRNSYS is used in an undergraduate course on HVAC systems in Industrial Engineering at Universidad de Jaén. Transient simulations are used to help students understand the dynamic behavior of HVAC systems, enhancing the knowledge of steady-state performance that they have gained through more conventional teaching methods. The program is also used to introduce renewable energy in a course that otherwise focuses on air-conditioning systems. The authors state that a software program like TRNSYS is the ideal tool for the students to acquire new competencies and to understand the dynamic behavior of complex systems. It also has the benefits to promote student engagement and increase the motivation. They present the results of a student survey showing that 80 % or more of the students have found that the simulation tool is useful to complement the lectures, help understand the operation of HVAC and solar systems, increase their interest in the course, and improve the quality of teaching.

Gravagne *et al*. (2008) report on the use of TRNSYS in a graduate elective course on solar energy in the department of mechanical engineering at Baylor University. The authors mention the use of TRNSYS for LEED certifications of buildings and for SRCC certifications of solar thermal systems as key aspects in support of selecting the program, as well as a series of features introduced in version 16 that made the software more relevant to classroom use. TRNSYS was only used midway through the class, and it was used to revisit problems that had been solved by hand or with generic software such as Excel or Matlab. One benefit of this approach is that students had a deeper understanding of the software assumptions and results. They could identify spurious results more easily after developing intuition by obtaining results the "hard way". TRNSYS was then used as a design tool in the final project. This allowed students to perform activities (design) for complex systems that they would not have been capable of analyzing without the program. The "mixed quality" of the documentation required a careful preparation by the instructor, so that students are not frustrated by hard-to-find information. Cryptic error messages, and non-standard units, such as the use of kJ/h for energy rates, are also pointed out as weaknesses. But overall, TRNSYS improved the learning experience and most students expressed their wish to start using TRNSYS earlier in the course.

These examples show that TRNSYS can be used successfully for teaching solar energy engineering and other topics. But there is a need for a larger body of shared knowledge about how the tool can be used efficiently for teaching and learning, and there is also a need for publicly available material to support that objective. This paper and the accompanying website is the author's attempt to contribute to that material.

Why was TRNSYS selected?

Ideally, an engineering course should be tool-independent. However, the pursuit of this noble objective quickly faces practical problems: can the instructor master all the tools involved? is the time invested in software installation and basic learning justified? can all the licenses be obtained without investing too much time and money? As discussed below, the students taking this course sometimes felt that using different programs would have been beneficial, while attempts to be tool-independent (and therefore using several different tools) can lead to students being frustrated at the time and energy involved to install and master these software tools (Beausoleil-Morrison and Hopfe, 2016). In many cases – as well as in this course – students also express the need for more software training material adapted to the course (Gravagne and Van Treuren, 2008; Beausoleil-Morrison and Hopfe, 2016). Over the years, a course instructor can reasonably build specific training material adapted to a particular course for a software program, but creating and maintaining that material for several different tools seems impractical.

As indicated in the introduction, the choice of TRNSYS came naturally to the course instructor, as he was very familiar with the program and confident that he could not only use the program to obtain simulation results but also investigate its assumptions and algorithms. When teaching an engineering discipline, being able to examine the actual source code of the software is a great advantage that few commercial programs offer, and open-source alternatives are not always available. Numerous validation studies including TRNSYS have been published, such as the BESTEST inter-model comparison (ASHRAE, 2014). TRNSYS is also used as a reference tool in international standards (ISO, 2013) and certification programs (Burch *et al.*, 2012; SRCC, 2015), which is a testimony to the software relevance for solar energy systems.

TRNSYS' main advantage is probably its flexibility, which comes from its modular structure and from the well-developed libraries of component models. Components can be connected together to form a system, and then configured by modifying the relevant parameters. Assessing different system configurations only requires to add/remove components from the libraries and modify the connections, without modifying the equations and algorithms used in the model. The program flexibility is also expressed by the fact that many different *domains* (Clarke, 2001) can be analyzed together: thermal processes and electrical flows within buildings, HVAC systems and renewable energy systems can form one coupled system. This is a great advantage over some easier-to-use tools which are generally restricted to a single domain or technology (e.g. solar thermal systems for hot water production, or solar photovoltaic systems).

Flexibility has a cost: students can be overwhelmed by the numerous components and libraries, and they can define wrong connections that will result in meaningless results without being flagged as errors. If students do not know how a system operates, i.e. if they do not understand the physical processes involved and the

control strategies, they will not be able to create a TRNSYS model of that system. In that respect, it is the author's point of view that TRNSYS is fully aligned with the learning objectives of a graduate course on solar energy systems engineering.

How TRNSYS and other tools are used

During the first part of the course, students are encouraged to use generic software tools such as spreadsheets and EES (Klein, 2014) to solve sun-earth geometry and solar radiation calculation problems (e.g. anisotropic tilted radiation calculation) and radiative heat transfer problems (e.g. spectral transmittance and absorptance).

TRNSYS (Klein *et al.*, 2014) is used from the beginning for homework assignments, in parallel with hand calculations or generic tools. This is intended to familiarize students with the program and to provide practical examples of the notions defined during the lectures. Examples of assignments include assessing the incident radiation incident for different slope and azimuth angles in TRNSYS using different tilted radiation models (isotropic vs. Perez), comparing the sun position, extraterrestrial, terrestrial and tilted radiation values calculated by TRNSYS to hand-calculated values. Other authors use this two-step approach to help the students develop an understanding of underlying assumptions and algorithms, and intuition (or skepticism) when analyzing simulation results (Gravagne and Van Treuren, 2008; Bernier *et al.*, 2016). Simple solar thermal systems are also introduced (without requiring students to actually build them in TRNSYS) so that students can study the "instantaneous" (i.e. time-step) efficiency of solar collectors, and compare these values to the efficiency curve provided by manufacturers or certified performance tests. Later homework assignments include simple design exercises, mostly involving changing component sizes and control parameters. During the final project, the design exercise can be related to the "create" level in Bloom's taxonomy, as the students start with a clean sheet and a realistic set of constraints and objectives (e.g. reach a given solar fraction, attain the net-zero objective, or design a stand-alone system). In most cases the load (thermal and/or electrical) that the system must meet is provided to the students in data files or calculated using simple methods, so that the students can focus on the solar system itself.

Over the years, specific assignments were introduced which relied on other tools dedicated to PV systems and solar thermal systems, but this led to mixed feedback by students (it is good to experience different tools, but students need more time to learn how to use each of them), and to some uncomfortable situations for the instructors involving crippling software bugs and licensing problems. These problems can happen with any program, including TRNSYS, but it is obviously less demanding to deal with the peculiarities and limitations of one program than to do it for several tools, especially when the instructor and his/her team are using that one program for research on a regular basis.

Teaching how to use a program vs. using a program to teach

As shown in section 3, the course learning objectives are related to understanding and applying solar engineering principles, as well as simulating, analyzing and designing solar systems. "Mastering TRNSYS" (or any other tool) is not one of the learning objectives. Other university-level courses using simulation generally share that approach (Gravagne and Van Treuren, 2008; Megri, 2014; Beausoleil-Morrison and Hopfe, 2016; Bernier *et al.*, 2016). The emphasis should be on underlying assumptions and algorithms, and results analysis, rather than expertise with a particular tool. The key to applying simulation effectively for design and analysis is to develop confidence in the simulation while keeping a critical mind.

One approach to avoid the difficulties of using the software is to employ "simulation specialists" who do the modelling work while students focus on proposing design alternatives. Successful applications of this approach for teaching to engineering and architecture undergraduate students have been reported by Charles and Thomas (2009), who compare cases where the simulation specialist is an external expert, the instructor, or a subset of volunteer students. Reinhart *et al.* (2012) also relied on a pool of "simulation experts" to perform the simulation in a design exercise that they transformed into a game where students compete to obtain the lowest energy use intensity within predefined cost limits. The game was useful in teaching how to interpret simulation results and use them in an iterative design process, and also served as a teaser.

In a later paper, Reinhart *et al*. (2015) describe how the same "learning by playing" approach was applied to a group of 18 undergraduate and graduate students who performed the simulations themselves. The course

included a series of simulation exercises culminating in a game where the students competed to design the building with the lowest greenhouse gas emissions. The authors report overwhelmingly positive student feedback, but insist on the need to keep the complexity of input files provided to the students at a reasonable level. They insist that instructors must be intimately familiar with the strengths and weaknesses of the programs used, so that they can detect and explain wrong results caused by user errors or software limitations. They mention that for larger classes, the teaching staff (one instructor and a teaching assistant) will need to increase and the use of online tutorials may be required to complement lectures and lab sessions.

The approach taken by the author in the course described in this paper is to have students use TRNSYS themselves, individually (for homework assignments) and in groups of 2 or 3 (for the final project). The software is introduced right from the first assignment, and the emphasis is placed on obtaining and analysing results during the first weeks. Later assignments and the final project are actual design exercises of increasing complexity.

6. Course structure

An example of course schedule is provided on the accompanying website (see first page).

Part 1: fundamentals

After the introduction lecture, the first part of the teaching term (approximately six 3-hour lectures over 6 weeks) follows the topics presented in (Duffie and Beckman, 2013). Table 1 shows the topics and examples of assignments.

Table 1: Topics and example of assignments for course part 1 (Fundamentals)

Topics	Examples of homework assignments
Course objectives, context, introduction to TRNSYS Example of successful solar energy systems Worldwide context : energy and environment, solar (thermal and photovoltaic) resource and markets	**First contact with TRNSYS** Run existing solar thermal project Configure an output component (printer) Examine the impact of collector slope and azimuth Obtain and analyze results
Extraterrestrial solar radiation Solar geometry, sun position angles, equation of time	
Available solar radiation Measurement of solar radiation, clear sky radiation, beam and diffuse radiation, isotropic and anisotropic models for incident radiation on tilted surfaces	**Tilted radiation, SDHW system balance** Calculate incident radiation on a tilted surface Compare results with TRNSYS for different anisotropic models Perform an energy balance of a Solar Domestic Hot Water (SDHW) system using TRNSYS
Radiation characteristics of opaque materials Kirchhoff's law, spectral distribution of solar and long-wave radiation, absorptance, reflectance and emittance	**Collector absorptance and emittance, collector shading** Calculate α and ε from spectral properties and solar spectrum In TRNSYS, optimize collector rows (azimuth, slope, spacing).
Radiation transmission through transparent surfaces Reflection, absorption, and transmission, spectral and angular dependence of properties, transmittance-absorptance product ($\tau\alpha$)	**Collector stagnation temperature and efficiency** Calculate (by hand) the stagnation temperature of a collector In TRNSYS, examine the dynamic collector efficiency and compare to the performance curve. Students must use certified performance (ISO or SRCC) to configure the TRNSYS components.
Flat-plate solar collectors Collector energy balance, overall heat loss coefficient, collector heat removal factor and flow factor, Hottel-Willier equation, collector testing and performance data.	

Example of collaborative learning through individual assignments

In some of the assignments, students are given different conditions, which are then combined by the instructor during the feedback session to provide a complete picture. One simple example is the slope and azimuth of solar thermal collectors in an SDHW system. Students are provided the TRNSYS project shown in Figure 2 and are asked to assess its performance for a given slope and azimuth angle. All student answers are then combined and used to draw plots of the collector useful energy (Figure 2, top right) and collector efficiency (Figure 2, bottom right) for all slopes and azimuth angles. This is used to discuss the fact that the collector output is not necessarily maximum at the maximum of incident radiation (not shown in the figure) and that the collector efficiency does not really show where the system output will be maximum.

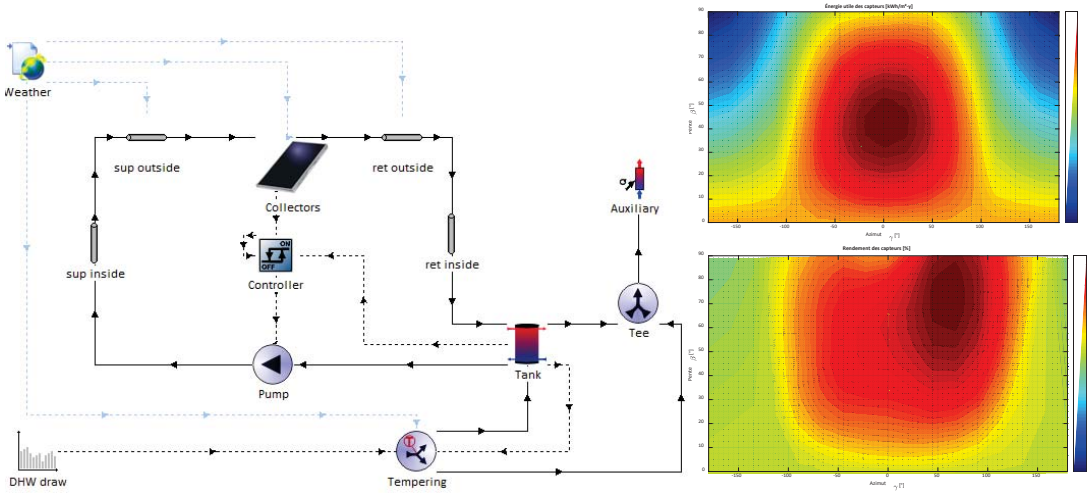

Figure 2: TRNSYS model of an SDHW system and example of results for different orientations and slopes

Part 2: applications

The second part of the teaching term (approximatively six 3-hour sessions) combines short lectures with practical design exercises. The course focuses on solar thermal applications for domestic hot water and space heating, but concentrating solar power generation and solar cooling are also covered. Photovoltaic systems are considered from a design perspective in combination with solar thermal systems, e.g. to design net-zero buildings. Occasionally wind energy is also introduced in the design of stand-alone systems. The subjects covered are sometimes adapted to make room for a graduate student who presents his/her work. Past examples include solar thermal/photovoltaic collectors, and control / fault detection of solar thermal systems.

This part of the course strongly relies on a series of homework assignments and on the final project, which all use TRNSYS. Examples of assignments and projects are again available on the accompanying website (see first page). The following paragraph briefly describe a few examples.

Design of solar thermal systems: thermal load, collectors, thermal storage

Generally, the load is provided for assignments and for the project, but for one assignment students are asked to use 2 weeks of measurements from a real site to extrapolate the design load used in a simulation. The importance of sizing the thermal storage in a solar system is shown by various examples. One assignment asks the students to compare the system performance for various collector areas and thermal storage capacities. This is also used to introduced parametric studies in TRNSYS, and student are developing the classical solar fraction vs. collector area and storage volume curves.

Photovoltaic and PV-T systems

The theory of photovoltaic system is covered briefly, the focus being on system-level design and on the interaction with other renewable energy technologies.

Examples of assignments are to design a stand-alone PV-powered system for a bike-sharing company (inspired by the actual systems in Montréal), and to design an off-grid house powered by wind and PV (optimization between the two renewable energy sources and the battery capacity).

Economic Analysis for renewable energy systems

Basics of engineering economic analysis (cash-flow, discounted payback time, internal return rate, etc.) are briefly covered. The concept of levelized life cycle cost is introduced to compare different renewable and non-renewable energy technologies. Economic analysis is typically integrated into the last two homework assignments, while the first ones focus on energy performance only. This is generally combined with exercises asking the students to perform and present energy balances, e.g. through Sankey diagrams.

Concentrating Solar Power and solar cooling

Due to time constraints, these applications, which are less relevant for the Montréal context, are typically covered in a descriptive manner through a lecture presenting the principles and successful applications. These topics generate a significant interest among the students so the possibility of offering optional final project topics is being investigated.

Putting it all together: the final project

The final project is intended to be a comprehensive design exercise where students must optimize the performance of their proposed configuration through an economic analysis. The energy performance is defined by the levelized life cycle cost of energy, or specified through targets such reaching a given solar fraction, net-zero energy, or stand-alone operation. Examples of final projects are:

- Design of an SDHW system for a building serving food to homeless people (this project used data from a real project including on-site DHW draw measurements, mechanical room and roof space constraints and local shading). Students were using different weather data, transposing the real site into different contexts.
- Design of a solar combisystem with a 75 % solar fraction for a residential building (students were allowed to select any city and exact location, including local shading).
- Design of a stand-alone polar research station (latitude higher than 75°) powered by solar thermal, PV and wind with a 90 % renewable energy fraction.

One difficulty of the final project is providing detailed feedback to the students, as it is typically due at the end of the exam session. Oral presentations were used during some years but the number of students make it difficult to organize during the last weeks of the term. The project start has been moved earlier in the term (typically before the mid-term exam), and intermediate deliverables are used to provide some feedback.

7. Student feedback and lessons learned

Formal independent surveys (2011 – 2016)

Polytechnique Montréal has a formal assessment program where students fill out anonymous evaluation forms which are collected by an independent school department (“bureau d’appui pédagogique”, teaching support group). Professors then receive the compiled evaluation results in the form of percentages of agreement to some 20 questions. Two questions are related to the use of TRNSYS: one on the clarity of homework instructions (it was noticed that complaints were mostly related to difficulties with the TRNSYS files), and one on “equipment, materials, and software”. Table 2 shows responses to both questions.

Table 2: Answers to independent student surveys (in % over the 6 years, total number of respondents = 150 over 180 students)

Question	Strongly disagree	Disagree	Agree	Strongly agree
Instructions for homework assignments are clear	0.5 %	4.5 %	45 %	55 %
Equipment, materials, and software used are useful	0 %	0 %	14 %	86 %

In addition to these questions, students are asked to comment on the course in a dedicated space. All answers are again collected by the independent department and then communicated to the instructor. The question is formulated to ask students if they have suggestions to improve the course, but some students use the space to identify the parts that they especially like. The most frequent or relevant comments are summarized below:

- An overwhelming number of students write positive statements on the course as a whole and the fact that it mixes theoretical aspects (the “fundamentals” part) with practical design applications. The fact that these

practical applications are simulation-based design exercises is very often mentioned as a positive point.

- The use of TRNSYS is appreciated, and a few students have suggested also using other programs that would be more likely to be used by consultants.
- Some students have complained that the gap between homework (where "ready-made" TRNSYS projects are provided most often) and the final project (for which students start from a clean sheet) was too large.
- Some students have suggested to spend more time on how to use TRNSYS, or to organize a specific course on the program at the beginning of the term. They have also mentioned that it would help to have more online tutorials available.
- A few students have also suggested increasing the time spent in class using the software (i.e. reducing the lectures). In one extreme case, a student complained about the "fundamentals" part with "equations that we will probably never use in our engineering career", and he/she suggested replacing it with more simulation-based case studies with economic analysis.
- During the years when other programs were used, some students appreciated the mix of programs but many complained that there was not enough time to learn how to use the different programs.
- Over the years, a few students also complained specifically about the place of TRNSYS in the course, and that the course was on simulation rather than on solar energy (2 students over 6 years). One specific comment was that TRNSYS was "irrelevant in the real world", being "much too complicated".

In-class specific survey in 2016

In addition to the formal surveys, the instructor asked some specific questions at the end of the course in 2016. The written survey was anonymous, but answers were collected and processed directly by the instructor. 30 students (over 35) responded to the survey, which had 3 closed questions and was also asking for any other suggestion to improve the course. Table 3 presents the results of the closed questions.

Table 3: Answers to specific student survey in 2016 (in %, total number of respondents = 30 over 35 students)

Question	Strongly disagree	Disagree	Agree	Strongly agree
Simulation-based applications are an important part of the course	0 %	0 %	3 %	97 %
It is a good idea to use TRNSYS, which is flexible and forces users to understand how systems operate, instead of other programs that would be easier to use	0 %	0 %	37 %	63 %
Even if the course is mostly about solar thermal systems, it is a good idea to also cover solar photovoltaic systems and wind energy conversion, even briefly, and to use PV and/or wind in the final project.	0 %	0 %	4 %	96 %

The suggestions to improve the course were wide-ranging, and the most significant ones are summarized below (the numbers in bracket indicate the number of students who made the suggestion (there were 24 comments in total for 30 respondents, and 4 of these comments repeated that TRNSYS was a good tool to understand how systems operate, which was already covered by the second question):

- (5) There should be a separate course (or some periods in the solar class) dedicated to TRNSYS.
- (3) The instructor should provide more explanations on specific TRNSYS components before they are used for the first time in homework or in the project.
- (3) More practical sessions should be devoted to TRNSYS during the course.
- (3) Other easier-to-use programs should be presented as well.
- (3) TRNSYS homework should insist more on creating systems (not just using "pre-canned" systems).
- (2) More TRNSYS tutorials and exercises should be available online.
- (1) TRNSYS documentation should be available in French

Lessons learned

Student feedback has been overwhelmingly positive on the use of TRNSYS, and most student seem satisfied that the course combines theoretical notions (through hand-written exercises and exam) with practical, simulation-based design exercises. The choice of TRNSYS is approved by the vast majority of students, even though they realize that other programs exist which would be easier to use. The second question of the 2016 survey was especially formulated to validate that hypothesis. Some students would like to be exposed to other programs, but they do see value in using a more flexible program even if it is more complicated.

The students generally suggest to spend more time teaching how to use TRNSYS, either in the solar course or in a dedicated training course. They also point at the lack of suitable online examples and tutorials. This illustrates the challenge of teaching solar energy engineering with TRNSYS rather than teaching how to use TRNSYS – it does not seem possible to avoid "software training courses" completely, whether they happen during the class or they are provided elsewhere. The students also indicated a need to evolve more progressively from the first homework assignments, which are very simple and rely on using ready-made projects, to the final project where students must create their system model from scratch. In particular, the difficulty of knowing which components to use and how each component should be used is insufficiently addressed in the present course structure. Again, training material specifically adapted to the course should be developed and provided, either as part of the course material or as online tutorials.

Although not directly indicated by survey answers, anecdotal evidence gained during the attempts to use other programs suggests that the level of comfort and expertise of the instructor with the software is critical to its successful use in teaching. It the instructor uses the program on a regular basis for teaching and research, he/she will know the software limitations and quirks. Even if the problems cannot be fixed, students can be warned about misleading indications, bugs and other problems before they get frustrated with them, which will completely change the dynamics of the exercise. In the author's experience, just quickly trying a few examples before an assignment using a program that is only used once a year for teaching is asking for trouble, even with commercial programs.

8. Conclusions

This paper presents a graduate solar energy engineering course which relies on the TRNSYS simulation tool to engage the students in the learning process through design and analysis activities. The learning objectives, course structure, and teaching and assessment methods are discussed. TRNSYS is used for assignments during the entire teaching term, in order to help students gain confidence in the program and in their skills using it. Some assignments compare hand-calculated values to simulation results to encourage the developments of intuition and skepticism toward simulation results. Student feedback has been overwhelmingly positive on the use of TRNSYS, and on the fact that the course combines theoretical notions (through hand-written exercises and exam) with practical, simulation-based design exercises. Students appreciate the fact that TRNSYS encourages them to think about the design and operation of solar systems before being able to model them, even if they realize that other tools might be easier to use and deliver results faster. The main criticism against the use of the simulation tool is the lack of training material specific to the subject, which leads to difficulties in selecting and configuring the appropriate TRNSYS components. An accompanying website provides examples of course schedule, assignments and projects.

9. Acknowledgement

I wish to thank Sandy Klein and Bill Beckman from the University of Wisconsin-Madison Solar Energy Lab, who provided material that was very helpful when I started teaching this course – and more importantly inspired me with their passion for teaching and research in solar energy.

10. References

Anderson, L. W. and Krathwohl, D. R. (2001) *A taxonomy for learning, teaching, and assessing : a revision of Bloom's taxonomy of educational objectives*. Edited by L. W. Anderson and D. R. Krathwohl. New York, NY: Longman.

Armstrong, P. (2016) *Bloom's Taxonomy*. Nashville, TN, USA: Vanderbilt University. Available at:

https://cft.vanderbilt.edu/guides-sub-pages/blooms-taxonomy (Accessed: 26 September 2016).

ASHRAE (2014) *Standard Method of Test for the Evaluation of Building Energy Analysis Computer Programs (Standard 140-2014)*. Atlanta, GA, USA: American Society of Heating, Refrigerating and Air-Conditioning Engineers.

Beausoleil-Morrison, I. and Hopfe, C. J. (2016) 'Developing and testing a new course for teaching the fundamentals of building performance simulation', in *Proceedings of eSim 2016: the 9th conference of IBPSA-Canada, May 3-6*. Hamilton, ON, CAN, pp. 22–33.

Bernier, M., Kummert, M., Sansregret, S., Bourgeois, D. and Thevenard, D. (2016) 'Teaching a building simulation course at the graduate level', in *Proceedings of eSim 2016: the 9th conference of IBPSA-Canada, May 3-6*. Hamilton, ON, CAN, pp. 34–45.

Burch, J., Huggins, J., Long, S. and Thornton, J. (2012) 'Revisions to the SRCC Rating Process for Solar Water Heaters', in *Proceedings of the World Renewable Energy Forum, May 13-17*. Denver, CO, USA, pp. 1–8.

Charles, P. P. and Thomas, C. R. (2009) 'Four approaches to teaching with building performance simulation tools in undergraduate architecture and engineering education', *Journal of Building Performance Simulation*. Taylor & Francis, 2(2), pp. 95–114.

Clarke, J. A. (2001) 'Domain integration in building simulation', *Energy and Buildings*, 33(4), pp. 303–308.

Duffie, J. A. and Beckman, W. A. (2013) *Solar Engineering of Thermal Processes*. 4th Ed. Hoboken, NJ: Wiley.

Freeman, S., Eddy, S. L., McDonough, M., Smith, M. K., Okoroafor, N., Jordt, H. and Wenderoth, M. P. (2014) 'Active learning increases student performance in science, engineering, and mathematics.', *Proceedings of the National Academy of Sciences of the United States of America*. National Academy of Sciences, 111(23), pp. 8410–5.

Gómez-Moreno, A., Palomar Carnicero, J. M. and Cruz-Peragón, F. (2015) 'Teaching different types of air conditioning systems using simulation software', in *Proceedings of INTED2015: the 9th International Technology, Education and Development Conference, Mar 2-4*. Madrid, ESP, pp. 5183–5192.

Goswami, Y. D. (2001) 'Present status of solar energy education', in *Proceedings of the 2001 American Society for Engineering Education Annual Conference & Exposition, Jun 24-27*. Albuquerque, NM, USA, p. 6.803.1-6.803.15.

Gravagne, I. A. and Van Treuren, K. (2008) 'On the Use of TRNSYS in a Solar Energy Technical Elective', in *Proceedings of the 2008 ASEE Gulf-Southwest Annual Conference, Mar 26-28*. Albuquerque, NM, USA, p. 17.4.1-17.4.9.

ISO (2013) *Solar heating - Domestic water heating systems - Part 4: System performance characterization by means of component tests and computer simulation. ISO 9459-4:2013*. Geneva, CHE: International Organization for Standardization.

Kandpal, T. C. and Broman, L. (2014) 'Renewable energy education: A global status review', *Renewable and Sustainable Energy Reviews*, 34, pp. 300–324.

Klein, S. A. (2014) 'EES - Engineering Equation Solver'. Madison, WI, USA: F-Chart Software.

Klein, S. A., Beckman, W. A. and Duffie, J. A. (1976) 'A design procedure for solar heating systems', *Solar Energy*. Pergamon, 18(2), pp. 113–127.

Klein, S. A., Beckman, W. A., Mitchell, J. W., Duffie, J. A., Duffie, N. A., Freeman, T. L., Mitchell, J. C., Braun, J. E., Evans, B. L., Kummer, J. P., Urban, R. E., Fiksel, A., Thornton, J. W., Blair, N. J., Williams, P. M., Bradley, D. E., McDowell, T. P., Kummert, M. and Duffy, M. J. (2014) 'TRNSYS 17 – A TRaNsient SYstem Simulation program, User manual. Version 17.2'. Madison, WI: University of Wisconsin-Madison.

Megri, A. C. (2014) 'TRNSYS as an Education Tool to Predict Indoor Environment Temperature for Undergraduate Students', in *Proceeding of the 121st ASEE Annual Conference, Jun 15-18*. Indianapolis, IN, USA, p. 24.1282.1-24.1282.12.

Prince, M. (2004) 'Does Active Learning Work? A Review of the Research', *Journal of Engineering Education*, 93(3), pp. 223–231.

Reinhart, C. F., Dogan, T., Ibarra, D. and Samuelson, H. W. (2012) 'Learning by playing – teaching energy simulation as a game', *Journal of Building Performance Simulation*. Taylor & Francis, 5(6), pp. 359–368.

Reinhart, C. F., Geisinger, J., Dogan, T. and Saratsis, E. (2015) 'Lessons learned from a simulation-based approach to teaching building science to designers', in *Proceedings of Building Simulation 2015:14th Conference of International Building Performance Simulation Association, Hyderabad, India, December 7-9*. Hyderabad, IND, p. 2468.1-2468.8.

SRCC (2015) *Solar Thermal Component Test and Analysis Protocol. SRCC Document TM-1-2015-10*. Cocoa, FL, USA: Solar Rating & Certification Corporation.

ISES EuroSun 2016

End-Users Decision Making Factors for Heating and Cooling Systems

Stefano Lambertucci

European Solar Thermal Industry Federation

Brussels (Belgium)

Abstract

This paper aims at showing the results of a survey carried across users of heating and cooling systems, done in order to identify what key decision factors are influencing consumers' behavior when it comes to buying a heating and cooling system. The results are analyzed and presented with a particular focus on the respondents having installed a solar thermal system in the residential sector.

Keywords: *renewable heating and cooling; solar thermal; consumers; decision making factors.*

1. Introduction

The objective of the survey carried out under the European FROnT project (Fair Renewable Heating and Cooling Options and Trade) was to identify end-users' decision making factors for heating and cooling systems in five European countries (NL, PL, PT, ES, UK), in order to understand consumer behavior and to facilitate stakeholders at European and national level to provide better and transparent information to consumers.

Although the survey has been carried out in three different sectors – residential, non-residential, industrial – this paper focuses its analysis on the residential sector, as it is the one in which more data analysis has been carried out.

The paper is structured as follows: it first gives a background on the FROnT project, describing the relation between the survey and the rest of the project areas. It outlines the survey objectives, and then goes into the details of the methodology underpinning the whole exercise, and describes the characteristics of the sample. Then, the paper will present the structure of the survey itself, describing the different steps and their specific aims. Finally, the paper will present the general results of the survey, and then the specific results for solar thermal residential owners, drawing some conclusions at the end.

2. Background of the survey – the FROnT Project

The FROnT project, co-funded by the European Union through the Intelligent Energy Europe programme, aims to develop strategies for a greater deployment and to advance the penetration of renewable energy sources for heating and cooling (RES-HC) technologies by providing a better understanding of how to deploy renewable heating and cooling technologies in the market and of the costs of such technologies[1].

In pursuit of this goal, the project aims at understanding the main barriers that are hampering the deployment of RES-HC installations and analyzes how to possibly overcome them. The project is proposing a set of short and long-term policy recommendations to address these barriers. It analyses both existing support schemes and end user decision factors, in order to help establishing strategic policy priorities for RES-HC.

Specific objectives of the project are:

- To support a better insight of the value of the energy supplied by RES-HC systems, promoting transparency and clarity towards end-users and other stakeholders

[1] More information at www.front-rhc.eu.

doi:10.18086/eurosun.2016.04.07 Available at http://proceedings.ises.org

- To improve the understanding of the end-users decision making process with regard to heating and cooling systems in order to develop tailored approaches and facilitate adequate measures enhancing the uptake of RES-HC
- To facilitate the setting-up of improved and sustainable RES-HC integrated support schemes
- To promote the implementation at national and European level of strategic policy priorities that can contribute to efficiently and cost-effectively implement the NREAPs

In order to improve the understanding of how end-users decide which heating and cooling system to use/acquire, and to map this decision making process across different countries and sectors (residential, non-residential, industrial), a survey has been foreseen, as part of an information and data collection exercise which involved all project countries[2].

The project is led by a consortium gathering European industry associations representing the solar thermal, geothermal, aerothermal and biomass technologies, and national energy agencies from Spain, Portugal, The Netherlands, Poland, and UK, assisted by the Austrian Institute of Technology, CREARA (consulting and energy management company), and Quercus (a non-profit environmental organisation based in Portugal).

3. Objectives of the Survey

The main objective of this report is to identify end-users' decision making factors when making choices about heating and cooling systems in the five participating European countries covered by the FROnT project. These countries are: The Netherlands, Poland, Portugal, Spain and the United Kingdom.

Specific objectives of the survey are:

- Identify end-user decision making factors for H/C systems (Renewable and fossil fuels)
- Understanding the decision process when deciding on a H/C system
- Obtain the Key Purchasing Criteria (KPC) which will provide information on "Willingness to Pay"
- Comparison among countries – a list of KPC weighting the criteria will be obtained in each country. Results must be comparable

To achieve these objectives a national survey has been carried out in each country under the coordination of the respective national energy agency and project partner.

The surveys, conducted in three different sub-sectors: residential, non-residential and industrial, allows the project to identify key purchasing criteria (KPC) across the whole sector. These surveys have addressed the heating and cooling sector as whole, not only renewable energy solutions.

4. Methodology and sample characterization

Questionnaires for each analyzed sector (residential, non-residential and industrial) were developed by all the partners, under the supervision of Quercus, in order to use a homogenous tool and get comparable results. The execution time for this activity, excluding subcontracting launch period, was around 2 months.

The number of interviews conducted at European level was: 4,195 in the residential sector, 896 in the non-residential sector and 585 in the industrial sector.

The details per country, and related representativeness of each group is described in the Figure 1 below. The overall confidence level on the representativeness of the sample is 95%.

[2] The full results of the survey, as well as detailed analyses per country, are available in the project portal http://www.front-rhc.eu/library/.

SECTOR	COUNTRY	NUMBER OF QUERIES	CONFIDENCE LEVEL	SAMPLE ERROR
RESIDENTIAL	NETHERLANDS (NL)	560	95%	4.14%
	POLAND (PL)	960	95%	3.16%
	PORTUGAL (PT)	900	95%	3.27%
	SPAIN (ES)	1,250	95%	2.77%
	UNITED KINGDOM (UK)	525	95%	4.28%
NON-RESIDENTIAL	NETHERLANDS (NL)	15	95%	25.29%
	POLAND (PL)	150	95%	7.97%
	PORTUGAL (PT)	250	95%	6.16%
	SPAIN (ES)	300	95%	5.62%
	UNITED KINGDOM (UK)	181	95%	7.25%
INDUSTRY	NETHERLANDS (NL)	35	95%	16.55%
	POLAND (PL)	100	95%	9.78%
	PORTUGAL (PT)	100	95%	9.78%
	SPAIN (ES)	250	95%	5.62%
	UNITED KINGDOM (UK)	100	95%	9.78%

Figure 1 Sample confidence level per country, per sector

A common methodology among partners has been agreed, concerning sample definition and size: error, confidence level, balance of the sample, timing of the application, form of application: by phone, on line, etc. Questions have been based on studies on consumer behavior, external influences, energy labelling, Building Performance Certificates, etc.

The main features of the sample interviewed in the residential sector are shown in Figure 2. This sample is balanced compared with the relative figures of the participating countries (in terms of age, gender, level of education, etc.). Additionally, the sample is balanced in each Member State.

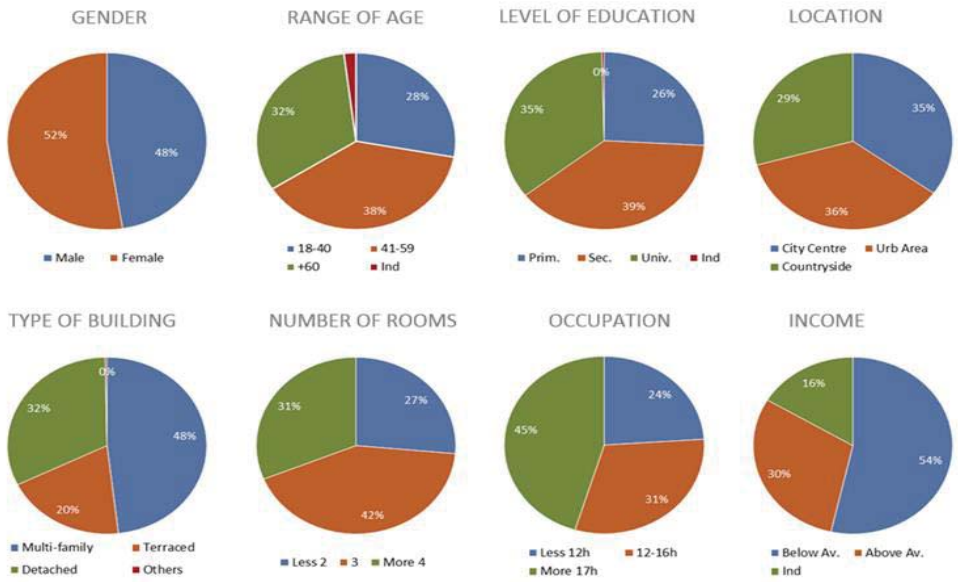

Figure 2 Sample characterisation

5. Structure of the Survey

The survey on the residential sector has addressed consumers on the heating and cooling sector, not only renewable energy solutions. The survey foresees a filter question on ownership of the house. Negative responses lead to the termination of the survey. Results are thus only including residential owners, in order to

simplify analysis.

The survey includes a first part on general information in order to characterize the sample (age, gender, education level, occupation, household income), a second part on the description of the building (location, type of building, number of bedrooms), a third part on heating and cooling system description and, the level of satisfaction with the systems, the main information source, awareness about renewable heating and cooling, adequacy of RES-HC and identification key purchasing criteria and provided information about "willingness to pay", including environmental and social parameters.

The flow diagram in Figure 3 below summarizes the structure of the survey.

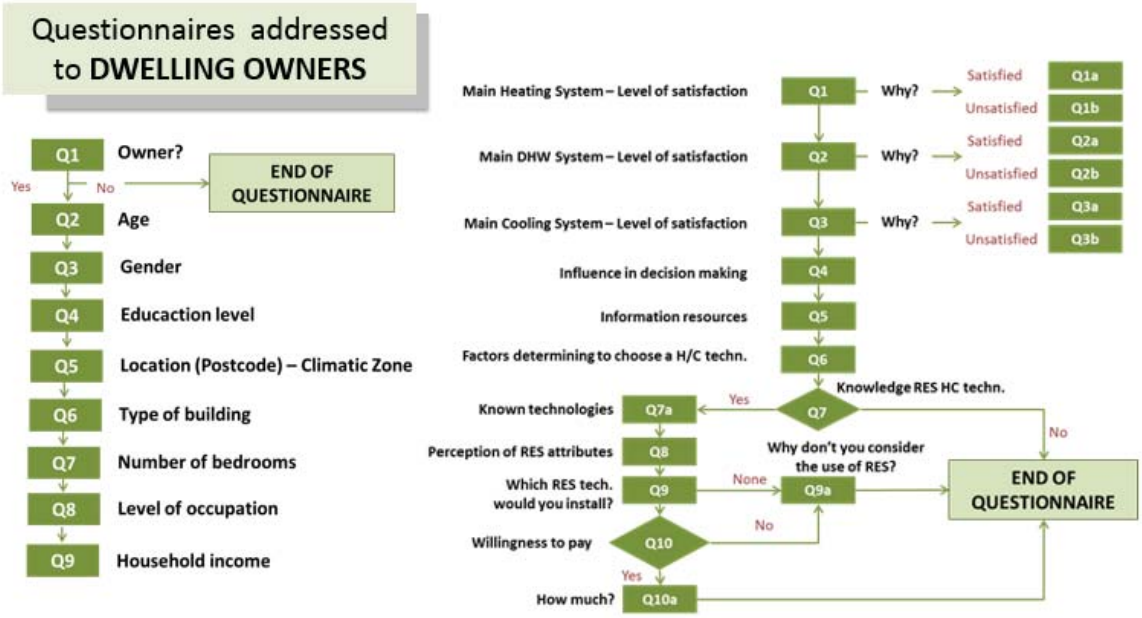

Figure 3 Flow Diagram of the questionnaire in the residential sector

6. General results of the survey

According to the results of the surveys[2], the main energy source employed in all sectors is natural gas followed by electricity. There is also a considerable variability in the industrial sector.

In general, the main information source is professionals' opinions. However, its influence is more relevant in the non-residential and industrial sectors than in the residential sector, where there are other important information sources such as the Internet or relatives.

Regarding key purchasing criteria, total economic savings is the most important criterion for the residential sector while for the non-residential sector it is reliability, followed by total economic savings. The industrial sector presents the same pattern as the non-residential sector.

In particular, in the residential sector, total economic savings is the most important criterion to choose H&C systems (84% of respondents) followed by comfort level (78%). Initial investment is also important (75% of respondents). Total economic savings is the most important criterion in Poland. Comfort level is the most important factor in Spain, the Netherlands and Portugal (followed in these three countries by total economic savings). Reliability and safety is the major factor in the United Kingdom. In general, architectural integration and environmental reasons are more relevant for women than for men. Economic savings, investment and maintenance are more important for people between 41 and 59 years-old than for young people. The importance of savings and recommendations from relatives for those who have primary education (higher than the average) is remarkable.

[2] To access the full results of the survey and the dataset, as well as detailed analyses per country, see http://www.front-rhc.eu/library/.

The non-residential sector presents the greatest level of RES technology awareness followed by the industrial sector, making the residential sector the least aware. In the residential sector, 65% of respondents declared being aware of RES-HC options, of those 96% quoted solar thermal as a familiar technology (against 49% for biomass, 40% for heat pumps, 42% for geothermal)[3]. Women, people over 60 years-old, those with primary education, people from countryside and income below the average know less about RES than the rest. The perception of RES-HC technologies is very similar in all sectors: it is considered to require high investment costs and to deliver high economic savings.

The main rejection reason for RES technologies in the residential sector is the high investment required, followed by structural changes involved and the need of approval by neighbors or superiors. In the non-residential sector, the latter has less weight than the two former. The main rejection factor in the industrial sector is, by far, the high investment required.

Considering the total sample of the respondents in the residential sector who are familiarised with RES-HC (65%), 50% of them would be willing to make a higher initial investment, 39% would not, and 11% did not answer this question. According to the results, 12% of respondents would pay up to 5% more for an RES-HC system, 15% would pay between 5 and 10%, 12% would pay between 10-25%, 6% would pay between 25-40% and 5% did not answer this question.

In general, men, young people and those with university a university level education are more willing to pay more for a RES-HC system than the rest. This is also the case for people who live in the countryside. The willingness to pay is lower in Portugal than in the rest of countries (28%).

The industrial sector is most willing to pay for RES-HC, compared to residential and non-residential sectors.

7. Specific results of the survey – Solar Thermal

By analysing the dataset of the survey results, it is possible to isolate the answers originating from people using solar thermal systems, and assess their answering patterns, as opposed to the general ones. A specific analysis of the solar thermal results per country is more difficult, as the difference in available data across countries is quite considerable (see paragraph 7.1). As for the non-residential and industrial sectors, further data analysis is required in order to process the dataset and draw some specific solar thermal conclusions there too.

For this reason, this section focuses on the residential sector, analyzing the sum of solar thermal users across the five project countries.

7.1. Solar Thermal sample

Out of the 4195 people surveyed in the residential sector, a total of 94 people declared using solar thermal as their heating and cooling system, that is 2.25% of the total sample. In particular solar thermal users are distributed as follows across countries: 16 in Spain, 48 in Portugal, 20 in the UK, 1 in Poland, 9 in the Netherlands.

Out of the 94 solar thermal users, 16 declared using it for space heating, 69 for domestic hot water (DHW), 9 for both. None was using solar thermal for cooling application. Auxiliary system for users of solar thermal for space heating is as follows: 5 electric heater, 2 gas boilers, 1 biomass, 1 heat pump, 1 geothermal, 6 ‘other’. Auxiliary system for users of solar thermal for domestic hot water is as follows: 21 gas boiler, 12 electric heaters, 5 biomass, 5 heat pumps, 5 oil boilers, 2 coal, 1 LPG, 18 none.

In terms of general sample characterization, solar thermal users are depicted in the Figure 4 below. Overall, if

[3] Data should be interpreted as the 96% of the respondents familiarised with RHC (65%) would be familiarised with solar thermal energy for heating uses. It means that 62% (0.65 x 0.96) of the total sample would be familiarised with solar thermal energy. Behavioral biases and confusion with solar photovoltaic might need to be taken into account in explaining this result vis-á-vis the other technologies.

compared with the general sample (4195 respondents), they result distributed in more rural areas (+6% countryside, -14% city centre), mostly on detached buildings (+35% detached buildings), and with a slightly higher level of income (-7% below average) and education (+5% university) than the overall average.

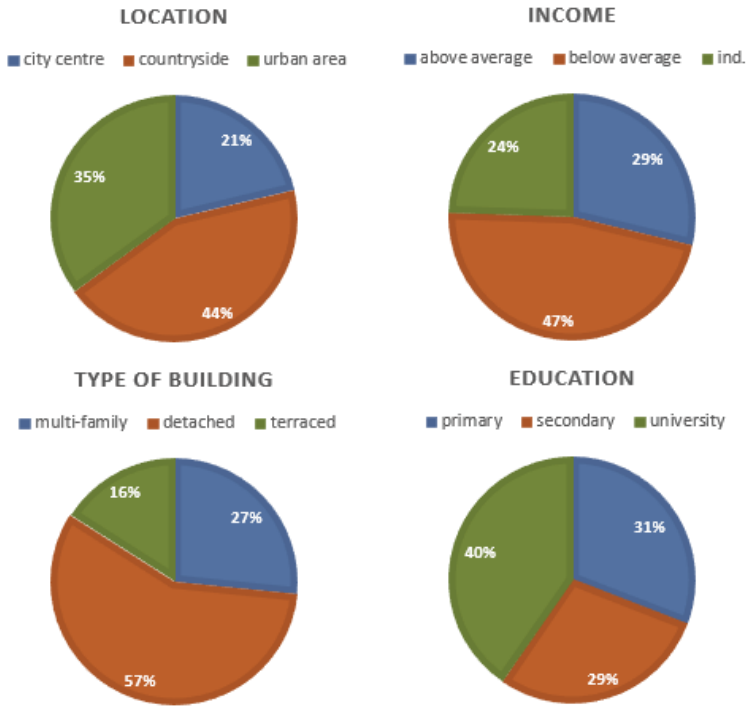

Figure 4 Sample characterisation for solar thermal users

7.2. Satisfaction with Solar Thermal

Satisfaction levels related to the use of solar thermal are relatively high, with 15 out if 16 solar thermal space heating users being satisfied of their systems, 61 out of 69 for domestic hot water users, and 7 out of 9 combi-systems users.

When asked about the reasons of their satisfaction with the solar thermal system, top four respondents answers were comfort, environmental friendliness, fuel price and reliability and safety for both space heating and DHW users (though the order slightly varies). The detailed answers to this open question (multiple choices possible) are depicted in the Figure 5 below.

Satisfaction of solar thermal users is consistent with the general answers of the full sample, as the general satisfaction level is high (satisfied – 90%; no answer – 9%; dissatisfied: 1%) and the main satisfaction reasons are: comfort levels (54%) and easy use, reliability and safety (39%). The different features of the sample (age, gender, etc.) are not really influential.

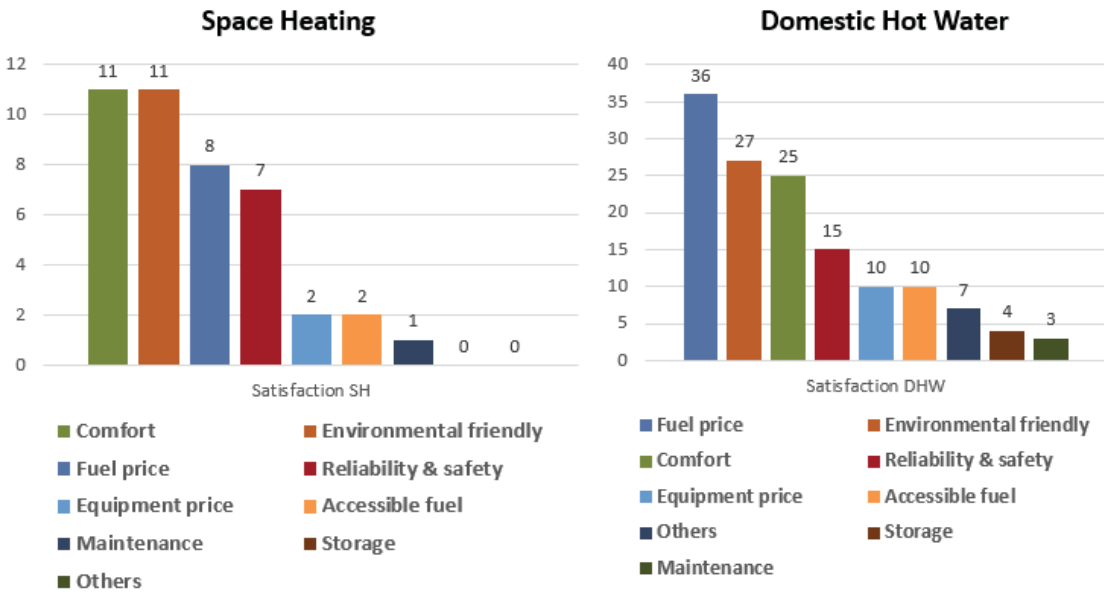

Figure 5 Satisfacion reasons for solar thermal users

7.3. Influence in decision making and information resources

Solar thermal owners did opt for those solutions for space heating or DHW because the system was already existing, because of incentives, because of the cheap cost of the system or of the fuel. Detailed answers are shown in Figure 6 below.

This is again more or less in line with the average response of the full sample, where the main reason to use current heating and DHW systems in dwellings is because they already exist there (52% and 50%, respectively). Other reasons given by respondents are: access and fuel costs (18% – 15% in the case of DHW systems) and equipment price (11% in both cases). Legal obligation is not a predominant reason to support the installation of heating and DHW systems.

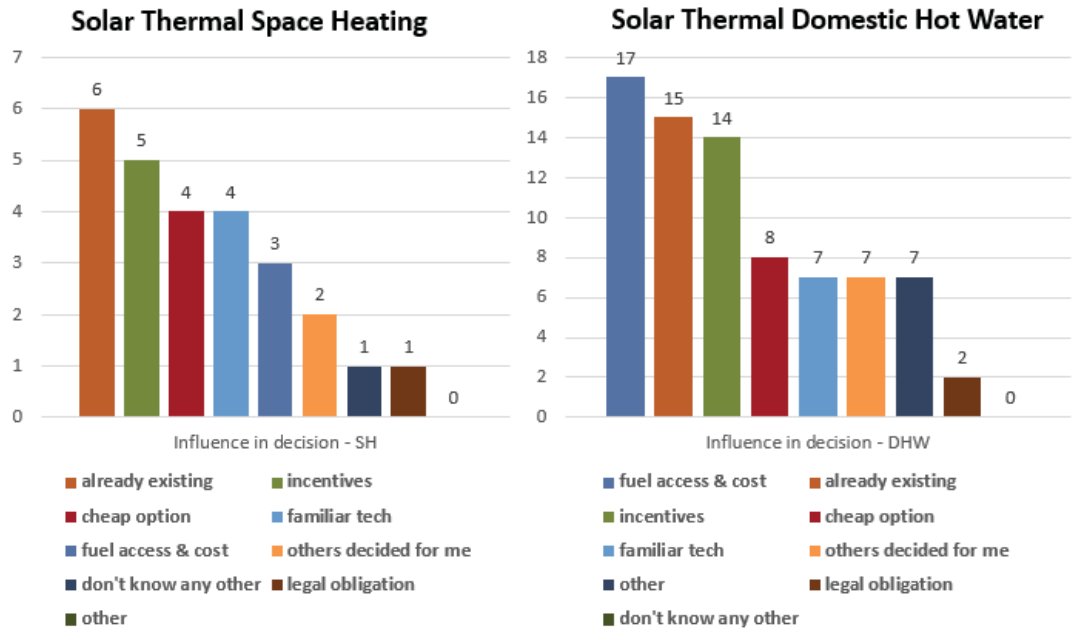

Figure 6 Influence in decision making for solar thermal users

In order to decide which system to opt for, solar thermal users used predominantly professionals as source of information, distanced by sales agents, internet, and family or friends' advices. The predominant role of installers in channeling information to consumers seems therefore confirmed.

Comparing those results with the general sample, it is to be observed an increased relevance of sales agents (+12%), and of consumers/ environmental NGOs (+9%). The detailed preferences in terms of sources of information are displayed in Figure 7 below.

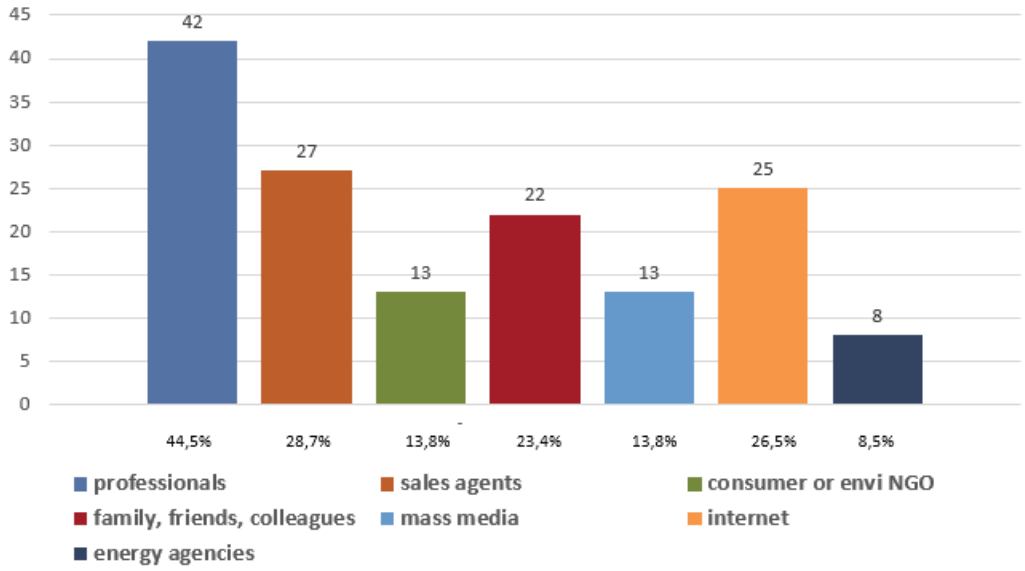

Figure 7 Information sources for solar thermal users

7.4. Key decision factors for Solar Thermal

When asked 'Which factors do you take into account when you buy new heating/cooling/DHW equipment?', solar thermal users did mention savings and comfort as their top two decision factors, with initial investment, reliability and safety, environmental reasons and reliable brand following afterwards.

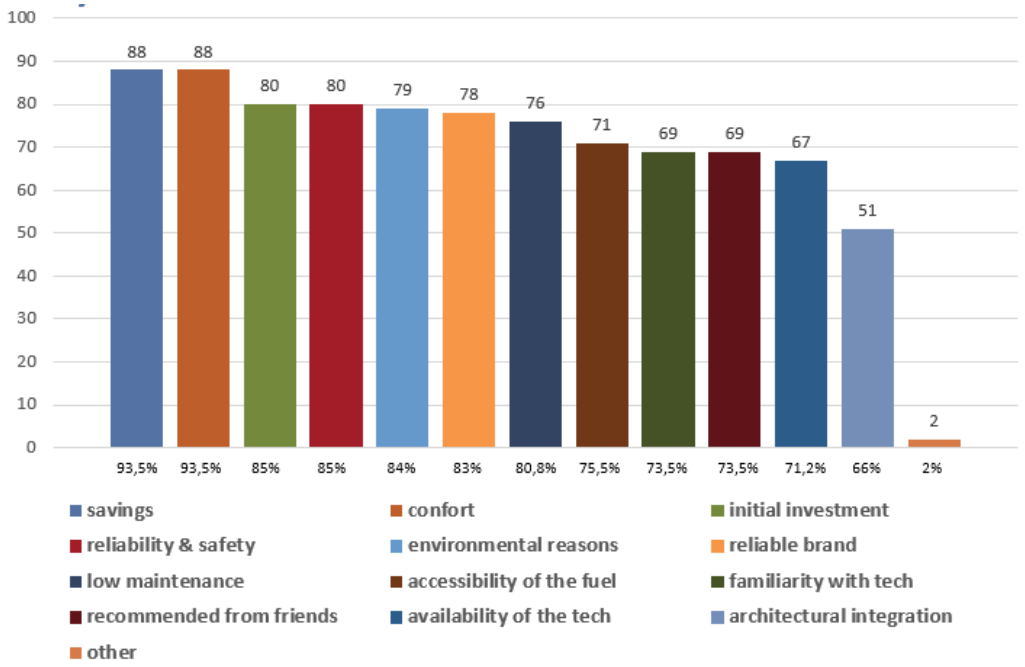

Figure 8 Key Decision Factors for solar thermal users

The detailed preferences in terms of key decision factors are displayed in Figure 8 above. In this case it is interesting to notice the differences between those results, and the overall results from the full sample. Several decision factors seem to be more relevant for solar thermal users, than the average respondents. Most notably, environmental reasons are quoted +23% than the average of the full sample, and reliable brand +26%.

8. Conclusions

The survey shows very interesting results when it comes to identify the end-users' decision making factors. Several key observations can be made both analyzing the general results of the survey, and the specific results from solar thermal users.

For the general results:

- ✓ There is an overall positive satisfaction with current heating systems in Europe;
- ✓ Professionals, sale agents and the Internet are the preferred sources of information;
- ✓ Guarantee of comfort and savings are the main key decision factors in all the participating countries;
- ✓ The awareness about RES-HC is high in Europe (63-79%). RES technologies are more familiar for heating than cooling uses. Solar Thermal the most known technology;
- ✓ Surveyed consider that RES-HC technologies are more expensive, but they provide more savings;
- ✓ Around 60% of the surveyed in Europe considered RES suitable for their heating systems.

For the solar thermal results:

- ✓ Solar thermal is less deployed in city centers and in non-detached houses;
- ✓ Solar thermal is bought by slightly higher income and higher education people;
- ✓ Solar thermal is bought mostly for domestic hot water, with gas as auxiliary space heater;
- ✓ Professionals and sales agents are the main information sources;
- ✓ Vast majority of solar thermal owners unaware of solar thermal cooling;
- ✓ Solar thermal is perceived as reliable, safe technology, providing high level of comfort and with a reasonable initial investment;
- ✓ Comfort, fuel price, environmental friendliness and reliability & safety top reasons for consumers' satisfaction with their solar thermal systems; savings and comfort also being the top two key decision factors for buying solar thermal;
- ✓ Environmental matters are very important for solar thermal buyers. Incentives do also play an important role;
- ✓ Brand reliability does matter for solar thermal buyers!

More interesting results could be extracted from the dataset, as time and resources limited the scope of the FROnT project in this area. However, the dataset will be made publicly available, and more research can be carried on by interested stakeholders. Most important areas of further analysis would be to compare results across different countries, and to cross results according to sample characteristics (gender, age, income...). Such analysis could provide additional information on consumers' behaviour on heating and cooling appliances choices, as well as important marketing and social considerations.

Conference Proceedings

EuroSun 2016
Palma de Mallorca (Spain), 11 - 14 October 2016

Linear tube solar receiver as stratified flow vapor generator/separator for absorption machines using $NH_3/LiNO_3$

Antonio Lecuona-Neumann[1], Rubén Ventas-Garzón[1] Ciro Vereda-Ortiz[1] Mathieu Legrand[1]

[1] Dep. Ingeniería Térmica y de Fluidos, Grupo ITEA, Universidad Carlos III de Madrid, Leganés, Madrid (Spain)

Abstract

Straight receiver tubes of either parabolic trough or Fresnel solar collectors can substitute the vapor generator and the solution separator of an absorption machine for producing cold/heat/power, so that no intermediate thermal fluid is required for transporting heat from the collector field to the machine. This way more compact and simpler layouts are possible. Medium temperature solar collectors are attractive for activating innovative cycle absorption machines for producing cold, pumping heat or producing electricity either single or combined.

Solar heat is absorbed directly by the solution that internally slides in the lower segment of an inclined tube by the effect of gravity yielding refrigerant vapor and concentrated solution in a stratified two-phase flow configuration.

The paper in his first part offers an introduction to this innovative technology and I its second part presents a numerical model for the performance evaluation of the concept, highlighting heat transfer issues. Integral 1D steady-state balances are used to establish equations in a simplified form to accelerate pre-design duties and capture main influencing parameters.

Results indicate that this concept is attractive and offers the potential for reducing the cost and burden of nowadays solar facilities in the small and intermediate size range.

Keywords: *Solar cooling, Two-phase flow, receiver tube, parabolic trough, Fresnel, Medium temperature solar collector, stratified flow, direct vapor production.*

1. Introduction

Solar heating and cooling (SHC) concept has been established as a current technology and is well supported by basic studies, such as (Duffie & Beckman, 1980) among others. Recent reviews confirm its interest, e. g. (Mauthner & Weiss, 2013), (The European Technology Platform on Renewable Heating and Cooling, 2014), as well as its potential in different countries has been analyzed, e. g. (CTAER. Solar Concentra., 2015). Nowadays medium temperature (150 – 250 ºC) solar collectors (MTC) e.g. (Jradi & Riffat, 2012) attract much attention because they enable new solar applications for small and medium scale applications. They offer higher flexibility than fixed geometry low-temperature collectors and enjoy the advances in the technology of high-temperature parabolic troughs collectors (HTC) used in large solar power plants.

Solar cooling by a heat pump consumes the solar heat in a thermal machine, generally following an absorption cycle, (Herold, et al., 1996). Some recent studies confirm its interest for industry and for buildings, e. g. (Henning, 2007) (Baniyounes et al., 2013). Typical application is for air conditioning, such as presented in (Henning, 2007), showing a good efficiency of the cycle owing to the mixture Water/Lithium Bromide used as working fluid. Water freezing limits extracting heat below 0 ºC, as water is used as a refrigerant. Ammonia as refrigerant offer the possibility of refrigerating even below -20 ºC and much experience has been accumulated on its use. Ammonia is a natural refrigerant, widely accepted in industry for its reduction capability of greenhouse and ozone depletion gasses (Danfoss, 2015). The absorption cycles using this refrigerant need higher temperatures on the driving source of energy, making medium temperature solar collectors ideal for that.

Currently, ammonia based absorption machines use the mixture Ammonia/Water (Wu et al., 2014). Several studies have performed on-the-field performance evaluation driving the machine with heated fluid through MT solar collectors (Wang, et al., 2015).

doi:10.18086/eurosun.2016.04.11 Available at http://proceedings.ises.org

Ammonia is good for solar energy storage in combination with absorbents, either solid or liquid, e. g. (Yu, et al., 2013), enhancing its interest in SHC.

Machines using Ammonia/Water need a rectification tower to purify the ammonia vapor reducing minute proportions of water. The solution of Ammonia into Lithium Nitrate salt ($NH_3/LiNO_3$) offers to eliminate this bulky and expensive component, but salt crystallization at the inlet of the absorber must be avoided. This solution offers a lower risk of corrosion than Ammonia/Water. Several studies confirm the potential of this working fluid (Ventas et al., 2010). Some operating test results are available (Hernández-Magallanes, et al., 2014). Even pre-industrial prototypes are now operative (Zamora et al., 2014).

The current layout of a solar cooling facility includes an outdoor primary circuit of a heat transfer fluid (HTF) including anti-freeze capability, a secondary indoor circuit, typically of water, including a heat storage tank and a tertiary circuit of cold water, (Kalogirou S. , 2004) (Lecuona et al., 2009). A heat rejection circuit is also needed when the machine is not air cooled. This leads to a high complexity and high procurement, high maintenance costs and the need of professionals for this. The end result is an increase in the Levelized Cost of Energy (LCOE). In addition, there appears some reluctance to invest, reinforced by the tailored character of every facility. Some studies confirm this appreciation, e. g. "*The lack of an optimized solution is the most critical barrier for rural or off-grid application of CSP*", in (The Carbon Thrust, 2013). Meaning "CSP" Concentrated Solar Power.

Direct steam production is an objective in large solar power plants, e.g. (Eck, et al., 2003) and (Kalogirou et al., 1997) always underpinning the objective of simplification, cost reduction, and higher energy efficiency. In solar cooling facilities, this can also be explored. The working fluid of the absorption machine has to flow partially filling the solar collector receiver tube, this way simplifying the facility and drastically eliminating the cost of heat exchangers, piping, and HTFs. In absorption machines, the liquid phase evaporates only some % of mass. This precludes the dangerous dry-out and rewetting processes. Refrigerant vapor separation is not needed at the outlet as it happens spontaneously thanks to the density difference. Stratified flow favors this, as the liquid phase flows falling under gravity effect in the lower part of an inclined tube, while the vapor phase flows upwards in the opposite direction, already separated, see Fig. 1 as it is progressively heated by the wall. This layout allows reducing the tube peripheral temperature gradients in Fresnel collectors and in parabolic trough ones near midday (Lecuona-Neumann et al., 2016).

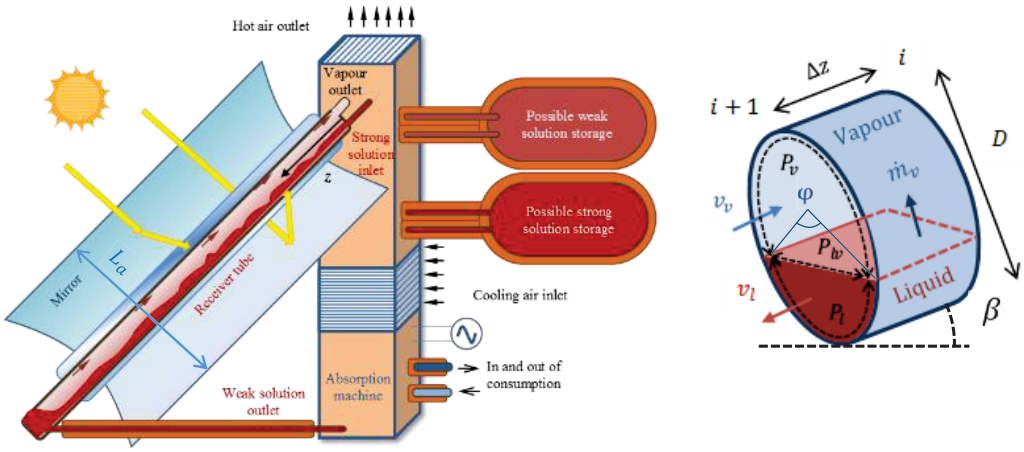

Fig. 1: Left: Scheme of an elementary solar cooling layout with gravity stratified flow in the receiver tube and attached air cooled absorption machine, eventually incorporating energy storage. Right: 1D flow discrete element.

The proposed layout is shown in Fig. 1. It includes an air-cooled absorption machine attached to the solar collector ensemble. This way no indoor building space is consumed for the machine room. Freezing/crystallization of the $NH_3/LiNO_3$ solution is no problem down to around -15 ºC ambient temperature with no specific measures.

The higher driving temperature with MTCs allows the application of advanced cycles (Ventas et al., 2016). This way several opportunities appear to reduce the Levelized Cost of Energy (LCOE) and increase coverage of the user demand: i) cooling capacity boost consuming electricity with the same machine (Vereda et al., 2014),

ii) directly produced or pumped heat production in winter, iii) increased COP using double stage/double effect (Ventas et al., 2016) and iv) even allowing electricity production in periods when neither heat nor cold is needed. NH_3 is suitable for this purpose as it generates high-pressure differentials between condenser and evaporator, allowing expanders to produce work. Small scale MT solar collectors can be built with stationary receiver tubes, thus eliminating the extra cost to avoid NH_3 leaks that are typical in large format high-temperature parabolic trough solar collectors that use articulated tubing.

This paper addresses the basic analysis of the vertically stratified flow using a simplified 1D modeling of the solar collector receiver tube of a circular cross-section, following a sequential calculation process. Stratified flow is assumed. The low velocities involved precludes either annular flow or appreciable effect of waves on the free surface of the liquid, excepting an effective roughness increase, as the inclination of the receiver tube ranges from several degrees up to the local latitude plus solar declination (Wallis, 1969). Application of the model to the promising mixture $NH_3/LiNO_3$ is performed and consequences are obtained aiming at pre-design and optimization duties.

2. Numerical model assumptions

The stratified or wavy-stratified nature of the flow is supported by the moderate mass flux and the relatively high void fraction in the flow, according to (Turgut et al., 2016) among others. Here the liquid phase is gravity driven, such as in (Faccini et al., 2015). Even this, here both flows are counter-current, differently to the most analyzed layout of co-current pressure driven two-phase flow inside typically small diameter tubes, e. g. (Issa R. I., 1988).

The slenderness of the receiver tube(s) of a parabolic trough or Fresnel type solar collector facilitates 1D modeling as a separated stratified flow with no liquid holdup, allowing separate equations and flow variables for both flows (Wallis, 1969). There the full set of governing equations applicable to the opposite direction flows is described in a generic way, as well as the single interphase jump conditions. One difficulty in the proposed layout is that the single outlet of the vapor flow is the accumulation of the opposite liquid flow vapor production and heat transfer, both with the tube wall and the interphase. In addition to that, there is mutual friction at the interphase free surface with the added complication of evaporation. This coupling makes necessary solving a large number of simultaneous equations for balances, fluid properties, and momentum plus heat transfer, when applied to a discrete number of finite elements of the tube along z, Fig.1. This would mean around 10 to 15 equations per element. Momentum and heat balances are not a closed issue when establishing 1D equations across a surface where there is evaporation because the 1D flow is represented by a single average velocity, density, temperature and NH_3 mass fraction. Some issues can be found in (Wallis, 1969) and a complete treatment is presented in (Issa, 1988) for co-current laminar (Ullmann et al., 2004) and turbulent flow with wavy interphase (Ullmann & Brauner, 2006). Fortunately, heat and momentum transfer to the liquid from the vapor flow can be considered negligible without much loss in accuracy for our case, as is supported below.

1D governing equations are coherent with heat and mass transfer correlations for respectively Sherwood and Nusselt numbers, especially when both concentrations and temperatures can safely be averaged in a cross section.

Nusselt number Nu for the liquid and vapour flow are of the same order of magnitude, as well as hydraulic diameters and wall contact areas, but for extreme cases. Thermal conductivity of NH_3 vapour is one to two orders of magnitude less than that of the liquid solution, yielding the heat transfer coefficients in the same proportion. Thus heat transfer from vapour to liquid $\dot{q}_{vl}$ can be considered negligible in front of wall-to-liquid heat transfer rate $\dot{q}_{wl}$. In addition to that the smaller heat capacity of NH_3 makes this flow approaching the wall average temperature $T_w\langle z\rangle$ faster than the liquid, so that $\dot{q}_{wl} \gg \dot{q}_{wv}$. From now on $\langle\ \ \rangle$ means functional dependence. As a consequence the net absorbed, solar heat will be applied only to the liquid as a first approximation.

Friction stress across the interphase is continuous. At the indicated pressure ~ 15 bar one finds $\rho_l \sim 10^2 \rho_v$, the vapor production is about Δx =3-8% in mass. The chosen void fraction $\alpha = A_v/A_l$ is large to minimize ammonia inventory for safety reasons. This makes $v_v \sim v_l$ by mass conservation; actually at the liquid outlet $v_v = 0$ and at the vapor outlet $v_v = \frac{\Delta x}{1-x}\frac{\rho_l}{\rho_v}\frac{v_l}{\alpha}$, see Fig. 2 to 5. This is in contrast with the much studied two-phase co-current flow in evaporators and boilers, whose mission is oriented toward either the full or a substantial phase change, implying significant acceleration near the shared outlet, with the frequent result of

liquid hold up. Friction factors $f_l \sim f_v$ as Reynolds numbers are of the same order of magnitude, mainly owing to the much larger hydraulic diameter of the vapor flow on which they are based, $Re_l \sim Re_v \rightarrow \frac{1}{2}\rho_l(v_l - v_{lv})^2 f_l = \frac{1}{2}\rho_v(v_l + v_{lv})^2 f_v$, the velocity of the interphase v_{lv} is near the liquid velocity v_l. For the case indicated in Fig. 2, at $z = 0$ $Re_l = 3{,}8 \times 10^3$ and $Re_v = 4{,}6 \times 10^3$. In This means that the liquid surface can be considered free of viscous stress with not much loss in accuracy. According to this, the pressure loss of the vapour flow is negligible in front of the tube pressure, which is determined by the saturation pressure of pure ammonia in the condenser of the absorption machine $p_s\langle T_c\rangle$, in the order of 5-20 bar when T_c is atmospheric temperature plus 5 to 10 K. Only needing standard commercial information of the collector is another advantage of this approach.

Similar reasoning will lead to considering limiting the heat transfer coefficient α_v in the mutual heat transfer at the interphase.

According to (Cussler, 2009) p. 504, mass diffusion relaxation time τ in turbulent flows is controlled by the summation of two mutually independent relaxation times, the first one is for the formation of packets of size l and the second one is for molecular diffusion into these packets with coefficient D_{diff}; this datum is obtained from (Infante-Ferreira, 1985). This leads to total a relaxation length L_τ:

$$\left.\begin{array}{r} \tau = \frac{D^2}{4E} + \frac{l^2}{4D_{diff}};\ L_\tau = v_l\tau \\ Pe = \frac{Dv_l}{E} = 2 \\ v_l \approx 2\frac{\mathrm{m}}{\mathrm{s}};\ D \approx 5\ \mathrm{cm} \\ l \sim 30\ \mu\mathrm{m};\ D_{diff} \sim 10^{-5}\frac{\mathrm{cm}^2}{\mathrm{s}} \end{array}\right\} \rightarrow E \approx 500\frac{\mathrm{cm}^2}{\mathrm{s}} \left.\right\} \rightarrow L_\tau = \left(\frac{D^2}{4E} + \frac{l^2}{4D_{diff}}\right) = (0{,}013\ \mathrm{s} + 0{,}2\ \mathrm{s})2\frac{\mathrm{m}}{\mathrm{s}} = 0{,}4\ \mathrm{m} \qquad \text{(eq.1)}$$

With collector length of 4-20 m this indicates that assuming negligible transversal concentration gradients in the liquid bulk is assumable, thus saturation can be accepted at the vapor pressure as a first approximation. Pure NH_3 forms the vapor flow, thus the mass diffusion resistance is null for this vapor flow. For temperature through the interphase, a jump is accepted between both well-mixed vapor and liquid flows as a reasonable assumption, in the turbulent regime for the resultant Reynolds numbers Re. No hydraulic pressure is considered in the liquid.

As a consequence, and in order to develop a comprehensive model, the simplifying assumptions are steady state and well mixed fully developed flows, flat free interphase with a rough surface owing to low amplitude waves, saturation equilibrium at the adiabatic interphase for liquid flow, but diabatic for vapor flow at constant pressure. Radiation and buoyancy are negligible effects inside the tube. Friction of the gas phase is negligible for the liquid flow. Constant liquid central angle φ ($\varphi = \pi$ for diameter) derives into constant falling velocity v_l $\forall z \in [0, L]$. Constant wall temperature T_w is assumed around the tube periphery, but variable along z. Solar radiance is constant along z.

Comprehensive models have been developed for the local efficiency of the parabolic trough solar collector and the subsidiary calculation of the tube wall temperature, e. g. (Forristal, 2003). For the lower optical concentration that MTCs have in comparison with HTCs and for liquid flow, the temperature average difference between wall $\bar{T}_w$ and fluid $\bar{T}$ is small, in the order of 20 ºC. This allows using the local average wall temperature instead of the fluid temperature averaged from inlet to outlet, not hindering the accuracy of the model. On the other hand this reduces the computing load substantially and allows to use available commercial information in solar collector performance. For simplicity it is acceptable using the reduced characteristic efficiency equation (no wind, no axial incidence, steady-state) determined according to standards such a (ISO/DIS 9806, 2016). As the characteristic curve is quite horizontal at the usual values of T not compromising error is expected. This curve is reduced to:

$$\eta\langle T_w\rangle = a_0 - \frac{a_1(T_w - T_{amb}) - a_2(T_w - T_{amb})^2}{G_{Tb}} \qquad \text{(eq.2)}$$

G_{Tb} is the tilted beam irradiance.

3. Numerical model setup

Terminal liquid velocity is assumed to happen just at the inlet. As a consequence average falling velocity

derives from the balance between gravity and wall friction, resumed into a Darcy friction factor $f_{D_{h,l}}$, function of the liquid hydraulic diameter through the liquid flow Reynolds number Re_l and the relative roughness of the wall $\varepsilon_r = \varepsilon/D_h$, where ε is the absolute equivalent roughness.

$$v_l^2 = \frac{2g\sin(\beta)D_{hl}\langle\varphi\rangle}{f_{D_{hl}}\langle Re_l,\epsilon_r\rangle};\ D_{hl}\langle\varphi\rangle = \frac{4A_l\langle\varphi\rangle}{P_l\langle\varphi\rangle};\ A_l\langle\varphi\rangle = \frac{D^2}{8}(\varphi - \sin\varphi);\ P_l\langle\varphi\rangle = \frac{D}{2}\varphi\ ; Re_l = \frac{4\dot{m}_l}{\mu_l\langle x,T\rangle D_{hl}} \quad \text{(eq.3)}$$

This expression neglects the momentum transfer by evaporation (Wallis, 1969), negligible in our case. This is an approximation that fits well into other analytical approximations, such as (Hetsroni, 1982) p. 2-84, originally by (Taitel & Dukler, 1976), although that considers the coflowing configuration. An implicit continuity equation allows solving for liquid central angle $\varphi\ \forall z\ \epsilon\ [0, L]$ for a given liquid mass flow $\dot{m}_l$, applied to the inlet ($_{in}$):

$$\rho_l\langle x_{in}, T_{in}\rangle v_l A_l\langle\varphi\rangle = \dot{m}_l \quad \text{(eq.4)}$$

The liquid density ρ_l is function of the local NH_3 mass fraction x and liquid temperature T. At the liquid inlet $z = 0$ ($_{in}$) pressure p is equal to the saturation of pure ammonia at the machine condenser $p_{s,NH_3}\langle T_c\rangle$. At the same point we consider, saturated inlet of the liquid solution. Subcooled or superheated solution is not considered here. Constancy of pressure both across the interphase and along z in addition to the saturation condition allow determining the NH_3 mass fraction x at any axial location z, including the outlet $z = L$ ($_{ou}$), $i = n$ when T were determined for any z:

$$p_l\langle x_{in}, T_{in}\rangle = p_l\langle x_{ou}, T_{ou}\rangle = p_l\langle x, T\rangle = p_{s,NH_3}\langle T_c\rangle \doteq p \quad \text{(eq.5)}$$

The machine condensation temperature T_c is the ambient temperature T_{amb} plus 5º to 10 ºC, depending on the heat rejection parameters. This assumption neglects the pressure decrease towards $z = 0$ because of friction and gravity and also because of the accelerating vapour flow that appears as a consequence of the accumulation of evaporation from $z = L$ down to $z = 0$. Its order of magnitude is $\rho_v v_v \frac{\partial v_v}{\partial z} L \sim \rho_v \left[\frac{(x_{in}-x_{ou})\dot{m}_l}{\rho_v A_v}\right]^2$, negligible in front of p.

As a consequence of constant pressure and saturation both x and T for the liquid are related this way:

$$\mathrm{d}p\langle x, T\rangle = 0 = \frac{\partial p}{\partial x}\mathrm{d}x + \frac{\partial p}{\partial T}\mathrm{d}T \rightarrow \frac{\mathrm{d}x}{\mathrm{d}T} \doteq x_T\langle x, T\rangle = -\frac{\partial p}{\partial T}\Big/\frac{\partial p}{\partial x} \quad \text{(eq.6)}$$

Only transversal heat transfer is considered, neglecting it in the z direction. Wall temperature tangential and radial gradients are considered negligible. Wall temperature T_w can be determined along z assuming that all the absorbed heat is transferred to the liquid, through a heat balance, where the heat transfer coefficient is α_{wl} and the aperture width of the mirror is L_{ap} (Fig. 1) on which a beam irradiance G_{Tb} is normal:

$$T_w = T_{amb} + \frac{\left(b^2+4a\right)^{0.5}-b}{2}\ ;\ a = (T - T_{amb})c + \frac{G_{Tb}a_o}{a_2};\ b = \frac{a_1}{a_2} + c\ ;\ c = \frac{P_{tl}\alpha_{wl}}{a_2 L_{ap}}\ ;\ P_{tl} = P_l \quad \text{(eq.7)}$$

For the local heat transfer coefficient α, either for liquid or vapour flow, a Gnielinski correlation (Gnielinski, 1976) has been chosen for the Nusselt number Nu in the turbulent regime ($2{,}300 < Re_{D_h}$) including the Prandtl number $Pr = c_p\mu/k$ and the friction factor from (Haaland, 1983) ($4{,}000 < Re_{D_h}$). Correction for the entrance region has been chosen from (Al-Arabi, 1982), referred in (Sigalés, 2003) p. 645. Correction for vapor transpiration at the interphase is neglected.

$$\alpha = Nu\frac{k}{D_h};\ Nu = \frac{\frac{f}{8}\left(Re_{D_h}-1000\right)Pr}{1+12.7\left(\frac{f}{8}\right)^{\frac{1}{2}}\left(Pr^{\ 2/3}-1\right)}\underbrace{\left(1 + 2.8(1-0.8)\left(\frac{D}{z}\right)^{0.8}\right)}_{C_{en}}\ ;\ f = -1.8\log\left(\left(\frac{\epsilon_r}{3}\right)^{1.11} + \frac{6.9}{Re_{D_h}}\right) \quad \text{(eq.8)}$$

The entry length correction C_{en} is for local Nu, here considered on the high side of the several formulae found in the literature, but not the highest. No correction has been implemented in α_{lv} because of vapour blowing out of the liquid free surface ($\dot{m}_v$) as it is of low magnitude (Sigalés, 2003).

The explicit (eq.4) allows calculating T progressively from inlet to outlet through the net solar heat received by a finite element Δz, between control surfaces i and $i + 1$. Using an Euler explicit advancing scheme this leads to:

$$T_{i+1} = T_i + \frac{L_{ap} G_{Tb} \eta \langle T_w \rangle}{\dot{m}_{l,i}(c_l - c_x)_i} \Delta z \; ; c_x = x_T \frac{\partial h}{\partial x} ; T_0 = T_{in} \quad \text{(eq.9)}$$

$c_x < 0$ takes into account the evaporation, acting as an increased effective specific heat c_l for the liquid. The increase in temperature leads to a decrease in x and the corresponding production of vapour at each element $\dot{m}_v$:

$$x_{i+1} = x_i + x_T(T_{i+1} - T_i) \; ; z = L \; \rightarrow x_{ou} = x_n \quad \text{(eq.10)}$$

In order to check the validity of assuming constant φ and v_l, local liquid mass flow can be corrected by:

$$\dot{m}_{l,i+1} = \dot{m}_{l,i} - \dot{m}_{v,i+1} \quad \text{(eq.11)}$$

And verify that the loss in mass can be just up to around 3%-8% along L. The accumulated vapour at point i can be calculated afterwards. The vapour velocity could be calculated when its temperature T_v is previously calculated:

$$\dot{m}_{av,i} = \sum_{j=n}^{j=i} \dot{m}_{v,j} \; ; \; n = \frac{L}{\Delta z} \; ; v_v = \frac{\dot{m}_{av,i}}{\rho_v \langle p, T_v \rangle} \quad \text{(eq.12)}$$

T_v at station i, is the result of mixing from $j = n$ down to $j = i$ and the cumulative heating from the walls and free surface of the liquid. Both of them must result in a negligible figure in front of the heat transferred from walls to the liquid for the simplifying assumptions to be valid. Assuming an average $c_{p,v}$ in the mixing process:

$$T_{v,i-1} = \frac{\dot{m}_{v,i} T_{v,i} + \frac{\left[\alpha_{wv,i}\left(T_{w,i} - T_{v,i}\right) P_v + \alpha_{v,i}\left(T_i - T_{v,i}\right) P_{lv}\right]}{c_{pv,i}}}{\dot{m}_{av,i} + \dot{m}_{v,i}} \; ; T_{v,n} = T_n \quad \text{(eq.13)}$$

4. Fluid properties

Ammonia properties are evaluated using the FluidMAT® software (Kretzschmar, Stoecker, Kunick, & Blaeser, 2015), mainly based on Tillner-Roth formulation (Tillner–Roth et al., 1993).

Ammonia/Lithium Nitrate solution properties are not so well documented. The properties of (Libotean et al., 2007) and (Libotean, et al., 2008) were used, extended for lower ammonia mass fraction and higher temperatures from data of the same source, still to be published. These results were checked against (Farshi et al., 2014) for enthalpy, correcting the reference datum. Thermal conductivity was obtained from (Cuenca et al., 2014). Crystallization boundary data, originally from (Infante Ferreira, 1984) were reported in (Wu et al., 2013). The adaptation was performed to formulate the boundary line in a more convenient form for the model.

5. Results

First, some characteristic data are presented and then a parametric study shows the results. Maximum representative irradiance has been taken into account $G_{Tb} = 800$ W m^{-2}, no wind and steady-state operation with an ambient temperature $T_{amb} = 30$ ºC.

The model can be applied to a representative MTC, in this case, the Abengoa PT-1 small scale MTC, shown in Tab. 1 (Solar Rating & Certification Corp., 2014).

Tab. 1: Basic data for the representative concentrating MTC Abengoa-IST PT-1. Effects of wind, sky infrared radiation and incidence are ignored. * for reported net aperture surface.

L_{ap} * [m]	L * [m]	$a_0 \equiv F'(\tau\alpha)_{en}$ [-]	a_1 [W m^{-2}K^{-1}]	a_2 [W m^{-2} K^{-2}]	Original fluid	T_{max} allowed [ºC]
2.2	6.0	0.71	0.3581	0.0019	water	250

For the inlet conditions, the condenser temperature chosen is $T_c = T_{amb} + 10$ K. This corresponds to $p = 15.5$ bar. Choosing an inlet temperature $T_{in} = 100$ ºC this corresponds to $x_{in} = 0.428$, thus no subcooling is considered in this case, neither the presence of bubbles at the inlet. A large inclination angle $\beta = 40$ º will be near optimum for capturing sun rays at mid-latitudes, for a collector oriented toward the equator, e. g. Madrid (Spain). $G_b = 800$ W m^{-2}, this is a compromise between the highest expected with the adequate collector inclination β around noon during a clear day and tracking the sun with a single axis, around 1.000 W m^{-2}, and an average figure because of some longitudinal incidence and cloudiness.

The flow evolution for this case is shown in Fig. 2 with some extra data indicated in the caption. It is worth to highlight:

- The evolution of the flow variables is linear, excepting wall and to a lower extent vapor temperatures. This is a consequence of the increase of α_l; α_v and α_{lv} in the entry region, around 0.5 to 1.0 m. Eliminating this correction in α (eq.8) eliminates these non-linearities. This would occur in a second additional collector located downstream the first one, Fig. 3.
- The downstream increase of T_w, does not substantially affect the local efficiency of the collector η, owing to its high stagnation temperature. This supports using the characteristic efficiency curve with T_w (eq. 2) instead of calculating the collector heat losses. The resulting average efficiency is $\eta_{av} = 0.64$.
- T_l increases up to 136 ºC in this case. This implies: a) a lower rate of the decrease downstream (decrease along z) of the vapor temperature T_v, as it is the result of mixing of vapor produced upstream b) wall heating near the exit and cooling near the inlet c) liquid cooling all along. In order to indicate the proportion of cooling by the liquid, $T_{v,a}$ indicates exclusion of any heat transfer. $T_{v,ou} = 117$ º; $T_{va,ou} = 115$ ºC. These temperatures are higher than the liquid inlet wall temperature at the same station, $T_{w,in} = 109$ ºC.
- There is a fairly constant difference between wall and liquid temperatures downstream the entrance region, 9 ºC at the inlet and around 15 ºC downstream the entrance length.
- $x_{ou} = 0.344$, meaning an 8.41% decrease from the inlet. This means a crystallization temperature of 15 ºC.

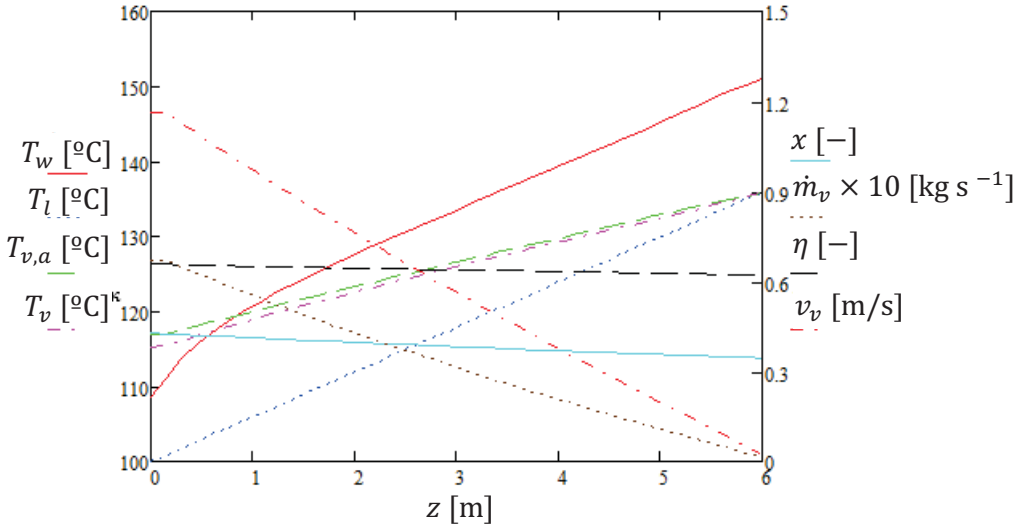

Fig. 2: Evolution along z of flow variables with $L = 6$ m; $D = 3$ cm; $m_l = 0.0833$ kg s^{-1}; $\beta = 40$ º; $\varepsilon = 0.1$ mm; $\varphi = 90$ º; $v_l = 1.32 \frac{\text{m}}{\text{s}}$.

One interesting question is how the length of the collector L affects the performance for constant mass flow. Fig. 3 uses the same input condition than Fig. 2 (ceteris paribus) but doubles the length of the collector, $L = 12$ m. The cooling of the vapour now is, $T_{v,a} - T_v = 6$ ºC. $x_{ou} = 0.28$, resulting in a crystallization temperature of 47 ºC, thus impeding operation of the absorption machine unless mass flow rate is increased. This is the logical choice as the solar power will be around twice. Fig. 4 shows the results of doubling the mass flow ceteris paribus; $x_{ou} = 0.343$.

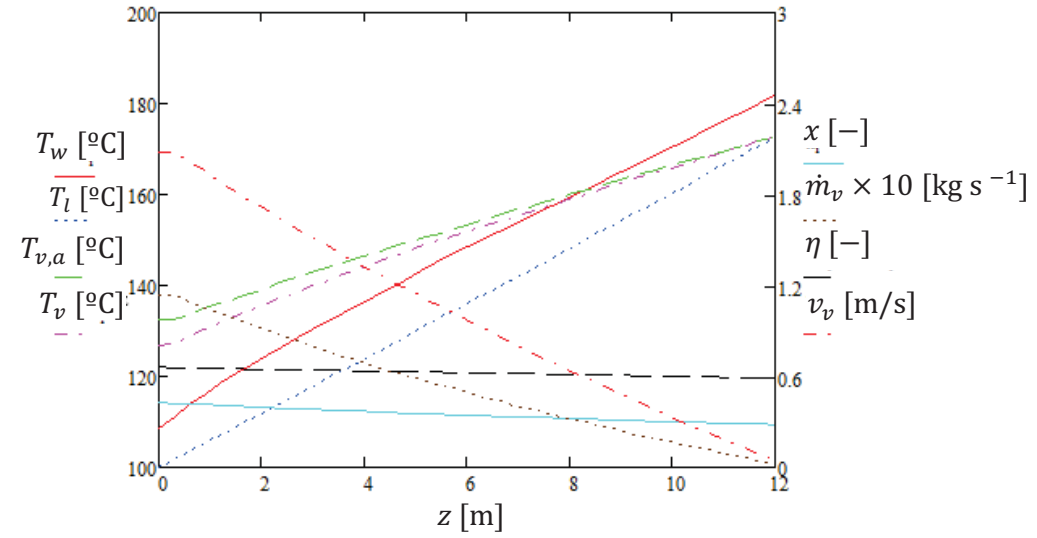

Fig. 3: Evolution along z of flow variables with $L = 12$ m $D = 3$ cm; $m_l = 0.0833$ kg s^{-1}; $\beta = 40$ º; $\varepsilon = 0.1$ mm; $\varphi = 90$ º; $v_l = 1.32 \frac{\text{m}}{\text{s}}$.

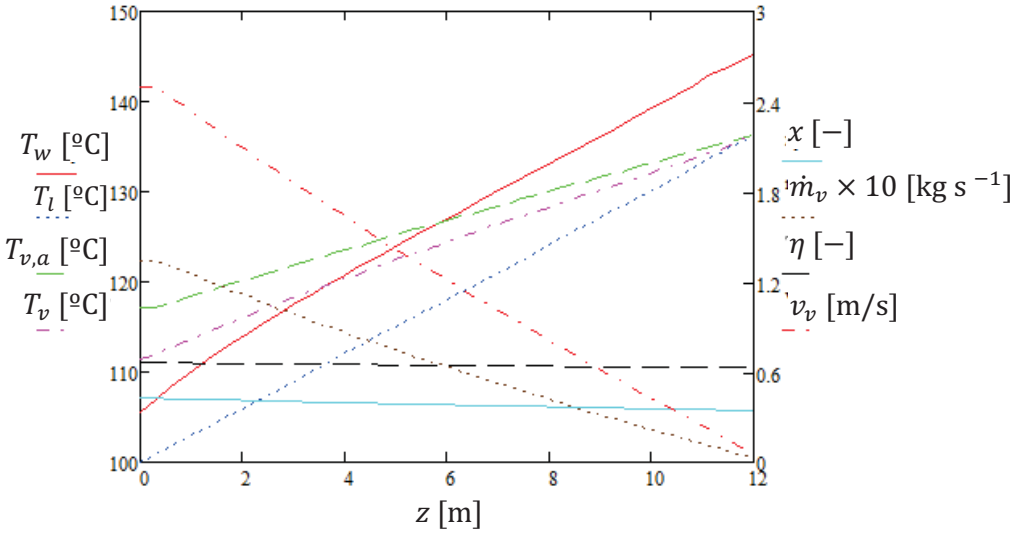

Fig. 4: Evolution along z of flow variables with $L = 12$ m $D = 3$ cm; $m_l = 0.167$ kg s^{-1}; $\beta = 40$ º; $\varepsilon = 0.1$ mm; $\varphi = 108$ º; $v_l = 1.61 \frac{\text{m}}{\text{s}}$.

The possibility of selecting different inclination facilitates the installation in different ceiling surfaces of buildings. Thus the effect of changing inclination angle β is interesting. Fig. 5 shows decreasing down to 5 º. This is valid for equatorial locations with the same G_b, but lower values should be expected at higher latitudes. The result is partially similar to the ones presented in Fig. 2, $x_{ou} = 0.344$; this means the same vapour production with the 40 º inclination, ceteris paribus, but the wall temperature is higher, although not affecting η. This is an interesting results as it indicates that the inclination angle can be widely changed. Now vapor suffers a small net heating.

Simplifying hypothesis now do not hold so well owing to the increased φ implying an increase in depth of the liquid vein that would limit reaching near NH_3 equilibrium in the bulk liquid flow. The lowest Reynolds number is for this case, $Re_l = 3{,}780$.

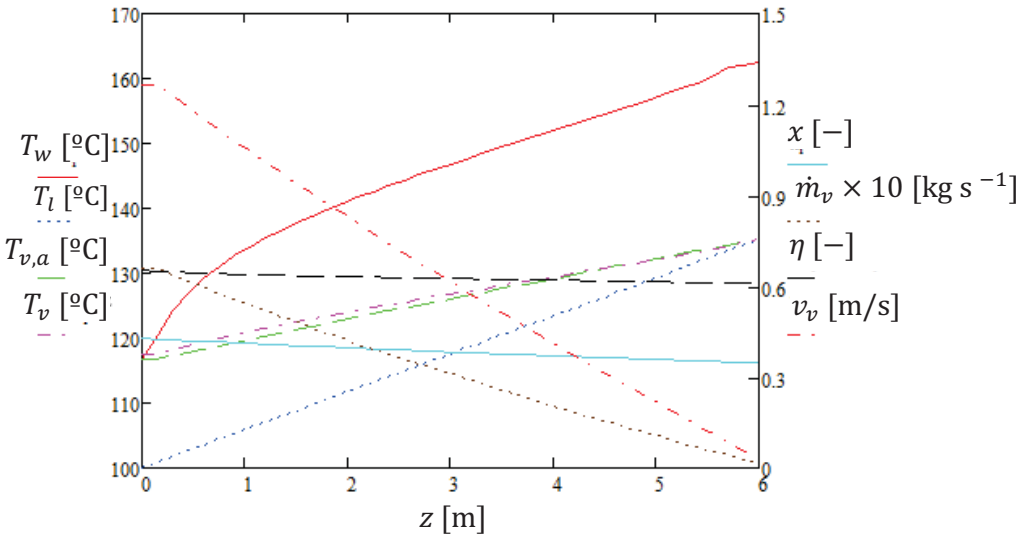

Fig. 5: Evolution along z of flow variables with $L = 6$ m; $D = 3$ cm; $m_l = 0.0833$ kg s^{-1}; $\beta = 5$ º; $\varepsilon = 0.1$ mm; $\varphi = 116$ º; $v_l = 0.67 \frac{\mathrm{m}}{s}$.

6. Conclusions and further work

Reasonable simplifications lead to the development a comprehensive 1D model of the flow evolution along the receiver tube of a parabolic trough solar collector under separated stratified two-phase flow. This model allows a sequential calculation that almost avoids iterations, excepting the liquid angle φ single equation calculation. The results support the simplifying assumptions. The model emphasizes the heat transfer process under evaporation in a MT solar collector.

The moderate heat flux from wall to liquid, always below 10 kW/m^2, the large interphase surface and temperature differences between the wall and liquid smaller than 5 K allow to be confident on the absence of significant bubble formation, thus nucleate boiling does not have to be taken into account excepting the lowest inclination angle, such as $\beta = 5$ º, Fig. 4 (Ghoshhdastidar, 2004). This large temperature difference, in spite of the low heat flux, is due to the small heat conductivity of the solution $k_l \approx 0.3$ W m^{-1}K^{-1} in comparison to water.

The innovative operation of a solar collector here described is meant for its application as a vapor generator and separator of an integral absorption machine using the promising solution $NH_3/LiNO_3$. This allows cold production at subzero temperatures using medium temperatures of the driving heat in the range of 100-200 ºC. This working fluid allows other possibilities, such as COP larger than 1.0 if double effect is used, electric backup if a hybrid cycle (Vereda, et al., 2014) is used and presumably electricity production using an expander in the refrigerant branch of the cycle.

The counter-flow layout allows minimizing heating of the vapor, owing to the cooling effect by the liquid and also by the wall near the liquid inlet. This is favorable for the operation of the absorption machine as a chiller, reducing the load of the condenser and increasing the collector efficiency. For producing power an alternative coflowing layout would be favorable because the higher is the vapor temperature the higher is the enthalpy at the inlet of the expander. Thus the enthalpy jump is higher.

Further work will likely include the effects of the mass transfer resistance in the liquid and the non-uniform transversal temperature in the tube wall, using newly developed simplified calculus (Lecuona-Neumann et al., 2016). Another line of work would be to study the evolution when the solution enters the tube subcooled or superheated. The inclusion of some correction for the interphase heat transfer in eq. 9 will increase the accuracy of the model. Experimental validation is under work.

7. Acknowledgements

The partial funding of the research project “Tecnologías energéticas térmico-solares y de aprovechamiento de calores residuales a baja y media temperatura integradas en la red eléctrica”, ENE2013-45015-R from the

Spanish Ministerio de Economía y Competitividad is greatly appreciated.

8. References

Al-Arabi, M.,1982. Turbulent Heat Transfer in the Entrance Region of a Tube. *Heat Transfer Engineering, 3*(3), 76-83. doi:10.1080/01457638108939586.

Baniyounes, A. M., Ghadi, Y. Y., Rasul, M. G., & Khan, M., 2013. An overview of solar assisted air conditioning in Queensland's subtropical regions, Australia. *Renewable and Sustainable Energy Reviews, 26*, 781–804. doi:10.1016/j.rser.2013.05.053.

CTAER. Solar Concentra., 2015. *Mercado Potencial En España y Aplicaciones en Tecnologías Solares de Concentración de Media Temperatura. Informe económico.* Sevilla, Spain: CTAER.

Cuenca, Y., Salavera, D., Vernet, A., Teja, A., & Vallés, M., 2014. Thermal conductivity of ammonia+lithium nitrate and ammonia+lithium nitrate+water solutions over a wide range of concentrations and temperatures. *International Journal of Refrigeration, 38*, 333–340. doi:10.1016/j.ijrefrig.2013.08.010.

Cussler, E., 2009. *Diffusion Mass Transfer in Fluid Systems 3rd ed.* Cambridge, UK: Cambridge University Press.

Danfoss., 2015. *De los HFC/HCFC al amoníaco en la refrigeración industrial. Una guía breve sobre el cambio al amoníaco.* Danfoss Group Global. Copenhaguen: Danfoss A/S. Retrieved November 11, 2015, from www.danfoss.com/IR-tools.

Duffie, J., & Beckman, W., 1980. *Solar Engineering of Thermal Processes 3rd ed.* Hoboken, New Jersey, USA: Wiley.

Eck, M., Steinmann, W.-D., & Rheinländer, J., 2004. Maximum temperature diff erence in horizontal and tilted absorber pipes with direct steam generation. *Energy, 29*, 665–676. doi:10.1016/S0360-5442(03)00175-0.

Eck, M., Zarza, E., Eickhoff, M., Rheinlander, J., & Valenzuela, L., 2003. Applied research concerning the direct steam generation in parabolic troughs. *Solar Energy, 74*, 341-351. doi:10.1016/S0038-092X(03)00111-7.

Faccini, J. L., Cunha-Filho, J., De Sampaio, P., & Su, J., 2015. Experimental and Numerical Investigation of Stratified Gas–Liquid Flow in Downward-Inclined Pipes. *Heat Transfer Engineering, 36*(11), 943-951. doi:10.1080/01457632.2015.972729.

Farshi, L., Infante Ferreira, C. A., Mahmoudi, S., & Rosen, M. A., 2014. First and second law analysis of ammonia/salt absorption refrigeration systems. *International Journal of Refrigeration, 40*, 111-121. doi:10.1016/j.ijrefrig.2013.11.006.

Forristal, R., 2003. *Heat Transfer Analysis and Modeling of a Parabolic Trough in Engineering Equation Solver.* Office of Scientific and Technical Information. Oak Ridge: US Department of Energy. Retrieved November 11, 2015, from http://www.ntis.gov/ordering.htm.

Ghoshdastidar, P. S., 2004. *Heat Transfer*, New Delhi, India, Oxford University Press.

Gnielinski, V., 1976. New Equations for heat and Mass Transfer in Turbulent Pipe and Channel Flow Int. *Chemical Engineering, 16*, 359-368.

Haaland, S., 1983. Simple and Explicit Formulas for the Friction Factor in Turbulent Flow. *Journal of Fluids Engineering*, 89–90. doi:10.1115/1.3240948.

Hausen, H., & Düwel, L., 1959. Frage nach dem gleichwertigen Durchmesser bei der Wärmeübertragung in einseitig beheizten Spalten. *Kältetech, 11*, 242-249.

Henning, H., 2007. Solar assisted air conditioning of buildings—an overview. *Applied Thermal Engineering, 27*, 1734–1749. doi:10.1016/j.applthermaleng.2006.07.021.

Hernández-Magallanes, J., Domínguez-Inzunza, L., González-Urueta, G., Soto, P., Jiménez, G., & Rivera, W., 2014. Experimental assessment of an absorption cooling system operating with the ammonia/lithium nitrate mixture. *Energy, 78*, 685-692. Retrieved from http://dx.doi.org/10.1016/j.energy.2014.10.058.

Herold, K., Radermacher, R., & Klein, S., 1996. *Absorption chillers and Heat Pumps.* New York: CRC Press.

Hetsroni, G. e., 1982. *Handbook of Multiphase Systems.* (G. Hetsroni, Ed.) New York, New York, USA: McGraw-Hill.

Infante Ferreira, C., 1984. Thermodynamic and physical property data equations for ammonia-lithium nitrate and ammonia sodium thiocyanate solutions. *Solar Energy, 32*(2), 231–236.

Infante-Ferreira, C., 1985. *Vertical Tubular Absorbers for Ammonia-salt Absorption Refrigeration Ph.D. Thesis.* Delft, The Netherlands: Laboratory for Refrigeration and Indoor Climate Technology, University of Delft. Retrieved August 27, 2016, from uuid:2118f67a-c5ea-4aa3-af23-45e679908eff.

ISO/DIS 9806., 2016. *Solar energy. Solar thermal collectors. Test methods.* ISO. Retrieved August 25, 2016, from http://www.iso.org/iso/catalogue_detail.htm?csnumber=67978.

Issa, R., 1988. Prediction of turbulent, stratified, two-phase flow in inclined pipes and channels. *International Journal of Multiphase Flow, 14*(2), 141-154.

Jradi, M., & Riffat, S., 2012, October. Medium temperature concentrators or solar thermal applications. *International Journal of Low-Carbon Technologies, 0*, 1-11. doi:10.1093/ijlct/cts068.

Kalogirou, S., 2004. Solar thermal collectors and applications. *Progress in Energy and Combustion Science, 30*, 231–295. doi:10.1016/j.pecs.2004.02.001.

Kalogirou, S., Lloyd, S., & Ward, J., 1997. Modelling, optimisation and performance evaluation of a parabolic trough solar collector steam generation system. *Solar Energy, 60*(1), 49-59. doi:10.1016/S0038-092X(96)00131-4.

Kretzschmar, H., Stoecker, I., Kunick, M., & Blaeser, A., 2015, November 5. Property Library for Ammonia. FluiMAT. Zittau, Görlitz, Germany. Retrieved from www.thermodynamics-zittau.de.

Lecuona, A., Ventas, R., Venegas, M., Zacarías, A., & Salgado, R., 2009. Optimum hot water temperature for absorption solar cooling. *Applied Energy, 83*(10), 1806–1814. doi:10.1016/j.solener.2009.06.016.

Lecuona-Neumann, A., Rosner, M., & Ventas-Garzón, R., 2016. Transversal temperature profiles of two-phase stratified flow in the receiver tube of a solar linear concentrator. Simplified analysis. *EUROSON 2016* (p. in press. Palma de Mallorca: ISES.

Libotean, S., Martín, A., Salavera, D., Valles, M., Esteve, X., & Coronas, A., 2008. Densities, Viscosities, and Heat Capacities of AmmoniLithium Nitrate and Ammonia + Lithium Nitrate + Water Solutions between (293.15 and 353.15) K. *Journal of Chemical Engineering Data, 53*(10), 2383–2388. doi:10.1021/je8003035.

Libotean, S., Salavera, D., Valles, M., Esteve, X., & Coronas, A., 2007. Vapor−Liquid Equilibrium of Ammonia + Lithium Nitrate + Water and Ammonia + Lithium Nitrate Solutions from (293.15 to 353.15) K. *Journal of Chemical Engineering Data, 52*(3), 1050–1055. doi:10.1021/je7000045.

Mauthner, F., & Weiss, W., 2013. *Solar Heat Worldwide. Markets and Contribution to the Energy Supply 2011.* International Energy Agency. Paris: International Energy Agency. Solar Heating and Cooling Programm.

Roldán, M., Valenzuela, L., & Zarza, E., 2013. Thermal analysis of solar receiver pipes with superheated steam. *Applied Energy, 103*, 73–84. doi:/10.1016/j.apenergy.2012.10.021.

Sigalés, B., 2003. *Transferencia de Calor Técnica* (Vol. I). Barcelona, Barcelona, Spain: Reverté.

Solar Rating & Certification Corp., 2014. *Certification #10001821 SRCC Standard 600-2013-01 in accordance with EN12975.* Cocoa: Solar Rating & Certification Corporation. Retrieved November 11, 2015, from www.solar-rating.org.

Taitel, Y., & Dukler, A., 1976. A model for predicting flow regime transitions in horizontal and near horizontal gas-liquid flow. *AIChE, 22*, 47-55.

The Carbon Thrust., 2013. *Small-scale Concentrated Solar Power. A review of current activity and potential to accelerate deployment.* London: The Carbon Thrust.

The European Technology Platform on Renewable Heating and Cooling., 2014. *Solar Heating and Cooling. Technology Roadmap.* Brussels. Retrieved November 11, 2015, from www.rhc-platform.org.

Tillner–Roth, R., Harms–Watzenberg, F., & Baehr, H., 1993. Eine neue fundamentalgleichung für Ammoniak. *20th DKV–Tagungsbericht Heidelberg, II*, 167-185.

Turgut, O., Coban, M., & Asker, M., 2016. Comparison of Flow Boiling Pressure Drop Correlations for Smooth Macro tubes. *Heat Transfer Engineering, 37*(6), 487-506. doi:10.1080/01457632.2015.1060733.

Ullmann, A., & Brauner, N., 2006. Closure relations for two-fluid models for two-phase stratified smooth and stratified wavy flows. *International Journal of Multiphase Flow, 32*(1), 82–105. doi:10.1016/j.ijmultiphaseflow.2005.08.005.

Ullmann, A., Goldstein, A., Zamir, M., & Brauner, N., 2004. Closure relations for the shear stresses in two-fluid models for laminar stratified flow. *International Journal of Multiphase Flow, 30*, 877-900. doi:10.1016/j.ijmultiphaseflow.2004.03.008.

Ventas, R., Lecuona, A., Vereda, C., & Legrand, M., 2016. Two-stage double-effect ammonia/lithium nitrate absorption cycle. *Applied Thermal Engineering, 94*, 228–237. Retrieved from http://dx.doi.org/10.1016/j.applthermaleng.2015.10.144.

Ventas, R., Lecuona, A., Zacarías, A., & Venegas, M., 2010. Ammonia-Lithium Nitrate Absorption Chiller With An Integrated Low-Pressure Compression Booster Cycle For Low Driving Temperatures. *Applied Thermal Engineering, 30*, Volume 30, Iss1351-1359. doi:10.1016/j.applthermaleng.2010.02.022.

Vereda, C., Ventas, R., Lecuona, A., & López, R., 2014. Single-effect absorption refrigeration cycle boosted with an ejector-adiabatic absorber using a single solution pump. *International Journal of Refrigeration, 38*, 22-29. doi:10.1016/j.irefrig.2013.10.010.

Wallis, G., 1969. *One-Dimensional Two-phase Flow.* New York: McGraw-Hill Book Co.

Wang, F., Feng, H., Zhao, J., Li, W., Zhang, F., & Liu, R., 2015. Performance assessment of solar assisted absorption heat pump system with parabolic trough collectors. *Energy Procedia, 70*, 529 – 536. doi:10.1016/j.egypro.2015.02.157.

Wu, W., Wang, B., Shi, W., & Li, X., 2013. Crystallization Analysis and Control of Ammonia-Based Air Source Absorption Heat Pump in Cold Regions. *Advances in Mechanical Engineering, 5*, 140341. doi:10.1155/2013/140341.

Wu, W., Wang, B., Shi, W., & Li, X., 2014. An overview of ammonia-based absorption chillers and heat pumps. *Renewable and Sustainable Energy Reviews, 31*, 681–707. doi:http://dx.doi.org/10.1016/j.rser.2013.12.021.

Yu, N., Wang, R., & Wang, L., 2013. Sorption thermal storage for solar energy. *Progress in Energy and Combustion Science, 39*, 489-514. doi:10.1016/j.pecs.2013.05.004.

Zamora, M., Bourouis, M., Coronas, A., & Vallés, M., 2014. Pre-industrial development and experimental characterization of new air-cooled and water cooled ammonia/lithium nitrate absorption chillers. *International journal of refrigeration, 45*, 189-197. doi:10.1016/j.ijrefrig.2014.06.005.

Conference Proceedings

EuroSun 2016
Palma de Mallorca (Spain), 11 - 14 October 2016

Transversal Temperature Profiles of Two-Phase Stratified Flow in the Receiver Tube of a Solar Linear Concentrator. Simplified Analysis

Antonio Lecuona-Neumann[1], Maximilian Rosner[2] Rubén Ventas-Garzón[1]

[1] Dep. Ingeniería Térmica y de Fluidos, Grupo ITEA, Universidad Carlos III de Madrid, Leganés, Madrid (Spain)

[2] Dep. Ingeniería Térmica y de Fluidos, Universidad Carlos III de Madrid, Leganés, Madrid (Spain), ERASMUS student from University of Applied Sciences Technikum Wien

Abstract

A steady-state analytical-numerical heat conduction model has been developed for the peripheral temperature profile in the wall of a straight receiver tube applicable to either parabolic trough or Fresnel solar collectors using innovative counterflow two-phase flow. It uses the slender 1D fin model of heat conduction along the tube wall periphery, which gives an analytical solution to be coordinated with boundary conditions. Constant heat transfer and solar incident irradiance are assumed on finite angle sectors of the tube periphery. This allows consideration for irradiance inhomogeneities and/or two-phase internal flows.

The model has been applied using parameters representative of medium temperature collectors of innovative design. Inside them, a sliding liquid film is established under the effect of gravity vertically stratifying a liquid/vapor two-phase flow. This flow configuration is considered for direct vapor generators/separators for advanced solar driven absorption machines and power plants.

The results show that for a circular tube with wall thicknesses large enough for withstanding typical pressures the peripheral temperature inhomogeneity is reduced. The inhomogeneity increases in the non-central hours of the day above the inhomogeneity found in the central hours of the day. This is so especially if the liquid film is shallow and for parabolic trough solar collectors.

Keywords: *Solar cooling, receiver tube wall, parabolic trough, Fresnel, Medium temperature solar collector,*

1. Introduction

1.1 Solar thermal

Solar heating and cooling (SHC) concept has been established as a current technology but still developing. It is well supported by basic studies, such as (Duffie & Beckman, 1980) among others. Nowadays medium temperature (150 – 250 ºC) solar collectors (MTC) e.g. (Jradi & Riffat, 2012) attract much attention because they enable new solar applications for small to medium scale applications. They offer higher flexibility than fixed geometry low-temperature collectors and enjoy the advances in the technology of high-temperature collectors (HTC) of either parabolic trough or Fresnel type collectors used in large solar power plants.

1.2 Absorption and working fluids

Producing cold with the solar heat is an attractive technology, especially for the synchronicity of sun and cold demand.

Absorption machines consume the heat collected from the sun and work as a thermochemical heat pump, following a thermodynamic cycle. They can work either as chillers or as heaters when respectively the useful effect is evaporating or condensing a refrigerant vapour, the same as in mechanical compression cycles (Herold, et al., 1996).

doi:10.18086/eurosun.2016.04.17 Available at http://proceedings.ises.org

Ammonia as refrigerant offer the possibility of refrigerating even below -20 ºC and much experience has been accumulated on its use. Ammonia is a natural refrigerant, widely accepted in industry for its capability of reducing greenhouse and ozone depletion gasses (Danfoss, 2015). The absorption cycles using this refrigerant need higher temperatures on the driving source than with water as a refrigerant when the working fluid is the solution Water/LiBr. This makes medium temperature solar collectors ideal for application to ammonia absorption cycles.

Currently, ammonia based absorption machines use the mixture Ammonia/Water as working fluid (Wu et al., 2014). Several studies have performed on-the-field performance evaluation driving the machine with heated fluid through MT solar collectors (Wang, et al., 2015).

Machines using Ammonia/Water need a rectification tower to purify the ammonia vapor for reducing minute proportions of water. The mixture Ammonia/Lithium Nitrate ($NH_3/LiNO_3$) does not need this bulky and expensive component, but salt crystallization at the inlet of the absorber is a risk. The absence of water reduces corrosion. Several studies confirm the potential of this working fluid (Ventas et al., 2010). Some operating test results are available (Hernández-Magallanes, et al., 2014). Even pre-industrial prototypes are now operative (Zamora et al., 2014). Ammonia as refrigerant implies pressures in the order of 15 bar in the vapour generator.

The current layout of a solar cooling facility includes: a) an outdoor primary circuit of a heat transfer fluid (HTF) including anti-freeze capability, b) a secondary indoor circuit, typically using water, including a heat storage tank and c) a tertiary circuit of chilled water for cold delivery, (Kalogirou S. , 2004) (Lecuona et al., 2009). A heat rejection circuit is also needed when the machine is not air cooled. This leads to a complex facility and the corresponding high procurement and maintenance costs, frequently requiring professionals for maintenance. Efforts toward improving competitivity seem of value for the dissemination of solar polygeneration technology.

1.3 Direct steam production

Direct steam production has been explored and continues to be explored in large solar power plants, e.g. (Eck, et al., 2003) and (Kalogirou et al., 1997). In solar cooling facilities, this can also be of interest, although there is not much work available on that in the open literature. For direct refrigerant vapour production in an absorption machine one proposal would be that the working fluid slides freely inside an inclined receiver tube along its length, partially filling it, see Fig. 1. Stratified two-phase flow favors vapour separation, as the liquid phase flows falling under gravity effect in the lower part of an inclined tube (angle β in Fig. 1) progressively evaporating the refrigerant in a fairly homogeneous way. As a consequence the vapour phase flows upwards in the opposite direction, already separated. In (Lecuona et al., 2016) the details and advantages of this layout are described.

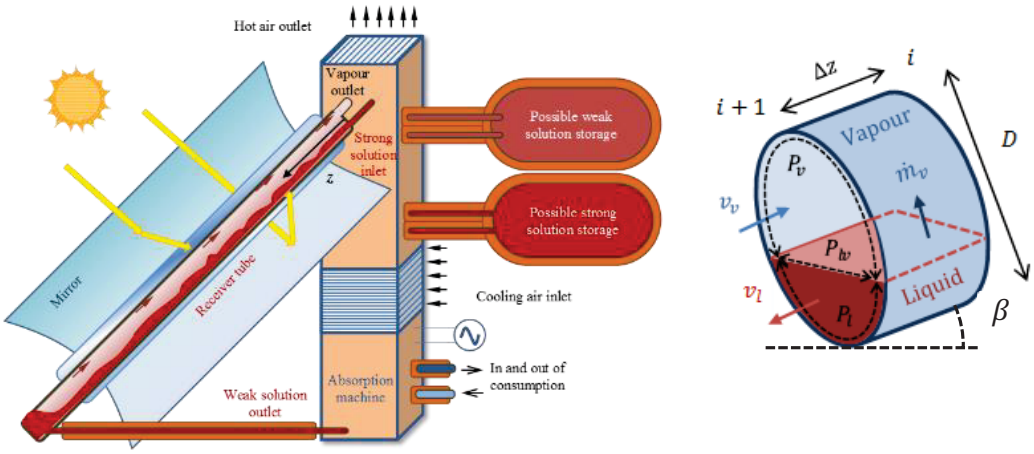

Fig. 1: Left: Scheme of an elementary solar cooling layout with stratified flow in the receiver tube and attached air cooled absorption machine, eventually incorporating two external storage tanks for energy storage. Right: 1D flow discrete element.

The higher driving temperature attainable with MTCs allows reaching innovative solar systems using advanced cycles (Ventas et al., 2016). This way, several opportunities appear to reduce the payback period of the solar system and increase coverage of the user demand. As a result cooling capacity can be boosted consuming electricity with the same machine (Vereda et al., 2014). In winter solar direct and/or pumped heat can be produced. Increased *COP* can be attained using double stage/double effect (Ventas et al., 2016). In addition to that production of electricity is possible in periods when neither heat nor cold is needed. The vapors of NH_3 are suitable for this purpose as it generates high-pressure differentials between condenser and evaporator of the absorption machine, allowing to easily produce work using expanders or turbines. Small scale MT solar collectors can be built using stationary receiver tubes, thus eliminating the extra cost to avoid NH_3 leaks. This is one risk in large format high-temperature parabolic trough solar collectors as they use articulated tubing.

1.4 Objectives of the paper

The receiver tube in linear solar thermal concentrators, such as parabolic trough or Fresnel types, is subjected to bending because of the differential heating between the concentrated sun-irradiated part and the non-irradiated part, typically the upper sector along the tube. This framework can be complicated if a two-phase flow develops inside the tube. Boiling regime is sometimes established when direct steam production is searched for, in conventional solar/electric power plants. This will imply a non-constant peripheral heat transfer to the flow. A higher inhomogeneity develops for a stratified two-phase internal flow. This unconventional flow distribution appears in a novel research area, above described.

There is not much information on the transversal temperature distribution on the wall with this particular flow and irradiation configuration, excepting for other applications, such as (Logie et al., 2015), (Eck et al., 2004), among others. One can expect that when the concentrated solar rays impact on the lower sector of the tube the liquid will evacuate heat at a higher pace that the vapor does in the upper non-irradiated sector of the tube (excepting secondary optics effect). This way there is a compensating effect. In a parabolic trough collector during the morning and afternoon, the sun impacts on the tube laterally so that there is the possibility of overheating as a high irradiance can impact on a vapor flow region. As described in (Lecuona et al., 2016) for the layout described above and schematized in Fig. 1, the vapor can have a lower temperature than the tube wall, but also a higher temperature; thus a practical procedure for calculating the temperature profile around the tube geometry seems useful.

The simulation of the whole solar cooling installation is generally pursued, becoming a complex but accurate model, as complex CFD codes and large computers are required, e. g. (Lobón et al., 2014). Some efforts on simplification are evident (Ahmed, 2014). In order to reduce modeling cost, there is an interest on low order models that keep the relevant physics, thus valid for preliminary studies.

The calculation of the temperature distribution on the wall of the receiver tube is well addressed decomposing the tube wall perimeter in a numerous ensemble of finite elements and applying the combined tangential-radial 2D heat conduction equation, including heat application and/or heat transfer in the radial direction. Axial heat conduction is frequently neglected owing to the much lower temperature gradient in this direction, excepting near brackets. The resolution of a large set of algebraic linear governing equations is performed in a standard way, delivering precise enough temperatures. Reducing the problem to 1D allows considering tangential conduction on top of the radial conduction, thanks to the linearity of the governing equations.

This paper addresses the simplified calculation of the temperature distribution on the periphery of the tube. In order to avoid the excessive computer load of a finite elements calculation, at each axial stage of the tube, the exact 1D analytical solution of the heat conduction equation is invoked. This is typically called the fin approximation (Incropera, De-Witt, 1990). A single explicit algebraic equation is needed for each peripheral segment with constant heat transfer, either toward the ambient or towards the inner fluid and constant irradiance. The fins are each other connected to complete the periphery of the tube. Solving a set of

simultaneous linear equations gives the temperature distribution. This can be done analytically in order to get an explicit overall solution, but excepting the simplest cases, the expression gets too large. Consequently, numerically solving the linear system yields a fast and numerically stable solution.

This paper describes a simplified calculation scheme for the steady-state peripheral distribution of the thickness-wise average temperature in the wall of a receiver tube of a linear solar collector with especial emphasis on MT collectors. The external net irradiance is assumed known as well as the heat transfer coefficients in different perimeters of the internal flow.

1.5 Preliminary considerations

From now on $\langle \quad \rangle$ indicates functional dependence. The longitudinal distribution of temperature $T\langle x\rangle$ by conduction along the length L in extended surface bodies that are geometrically slender $\frac{L}{A^{0.5}} \gg 1$ and thermally slender $\frac{\alpha t}{k} \ll 1$ accepts a 1D analytical approximation for some cross sectional area $A\langle x\rangle$ distributions. Such are pins and fins, not having to be straight, but with central line curvature radius $r_{av} \gg t$, being t the material thickness. Additional requirements are constant: a) heat conductivity k, b) lateral heat transfer coefficient α and c) heat added/generated per unit of lateral area g. Although the wall in our case exhibits varying temperature along its periphery it is usual to use a constant average heat transfer coefficient from experimental correlations for a single-phase flow, even in the case of adiabatic portions of the wall. Although under different operational conditions (Yang et al., 2012) indicates low inhomogeneities in the Nusselt number of a collector tube. With this generalized practice, only care must be taken to register the adequate hydraulic and thermal diameters of the cross section and eventually to correct if they are different (Sigalés, 2003) and (Lecuona et al., 2016) among others.

This extended surface theory is much used in basic texts, such as (Incropera & DeWitt, 1990) and with more detail in (Sigalés, 2003), among others. A single ordinary linear differential equation results for the temperature T distribution along the large coordinate x:

$$\frac{\mathrm{d}^2 T\langle x\rangle}{\mathrm{d}x^2} - \frac{\alpha P}{kA}\left(T\langle x\rangle - T_\infty\right) + \frac{g}{k} = 0 \qquad \text{(eq.1)}$$

P is the wetted perimeter and T_∞ the unperturbed fluid temperature used for α.

This model is used for determining the peripheral wall temperature of the receiver tube, assuming $x = r\phi$, where ϕ is the circumpherential central angle, thus neglecting curvature effects besides considering that the inner radius is smaller than the outer radius. A fin is used for every segment of periphery where the conditions are fulfilled, actually constant α, T_∞ and g. These segments will fulfill the boundary conditions with the neighbor ones in order to complete the full periphery. These boundary conditions fully determine the problem and require the simultaneous resolution of a small number of linear algebraic equations. The peculiarities of our case are:

- There are two temperatures T_∞, for heat transfer: internal T_i for either liquid ($_l$) or vapor ($_v$) and external for losses to ambient T_e. Each one has its own heat transfer coefficient, respectively α_i and α_e.
- On the external side, there is a concentrated incident solar irradiance, affected by optical losses, determining an equivalent per unit volume heat generation g.

This simplification is relevant for larger models, such as of an entire solar collector. In these models ease of use, simplification and speed of calculation are important, not neglecting the stability of the numerical algorithm. In our case of stratified two-phase flow, it serves as a tool for preliminary optimization.

2. Numerical model development

The one-dimensional heat transfer for the wall temperature T along the periphery central angle ϕ , Fig. 2, is given by reformulating eq. 1 using the internal and external heat transfer coefficients α_i and α_e. Wall thickness is t and average receiver tube radius, assumed circular, $r_{av} = r_i + \frac{t}{2}$; $w = \frac{t}{r_i}$:

$$\frac{\mathrm{d}^2T}{\mathrm{d}\phi^2} - m^2T = -T_\mathrm{I};\ m^2 = \frac{r_{av}[\alpha_i+\alpha_e(1+w)]}{kw};\ T_\mathrm{I} = \frac{T_i\alpha_i+(T_e\alpha_e+G_{bT}S)(1+w)}{kw} \quad \text{(eq. 2)}$$

Tilted incident solar irradiance on the aperture of the collector is G_{bT} and $S = Ca_0$ is the number of incident suns on the receiver tube; it is the product of the purposely defined geometric concentration $C = L_{ap}/P_s$ times the total optical efficiency of the solar collector a_0. L_{ap} is the mirror(s) aperture width, perpendicular to the axial coordinate z. P_s is the total perimeter of the receiver tube radiated; thus in a first approximation the irradiance on the tube is considered constant either concentrated, direct ($C = 1$) or null, see Tab. 1. Extension to more elaborate layouts is straightforward.

There are widely used codes for the calculation of the external heat transfer coefficient α_e, e. g. (Forristal, 2003), among others as it the series and parallel composition of radiation, conduction, and combined convection heat transfers. Here a practical way is adopted, needing only commercial information, widely available, without needing to know details of the construction and materials of the collectors.

For a three-term efficiency standard curve of the solar collector, according to (ISO/DIS 9806, 2016), with an estimated overall averaged wall temperature T_{est} and an ambient temperature T_e it follows that under nominal steady-state operating conditions with no wind and no axial incidence, α_e can be estimated as:

$$\alpha_e = \frac{[a_1+a_2(T_{est}-T_e)]L_{ap}}{2\pi r_e} \quad \text{(eq.3)}$$

Further corrections are possible, according to the standard prescriptions.

We assume all parameters in eq. 2 constant, excepting dependent variable T and angle independent variable ϕ. This makes the differential equation linear non-homogeneous, admitting a well-known analytical solution as the addition of a general exponential solution plus a particular solution T_{pj}, Tab. 1. For a generic segment j can be expressed as:

$$T_j\langle\phi\rangle = T_{C1j}e^{m\phi} + T_{C2j}e^{-m\phi} + \underbrace{\frac{(T_e\alpha_e+G_{bT}S)(1+w)}{\alpha_i+\alpha_e(1+w)}}_{T_{pj}} \quad \text{(eq. 4)}$$

The peripheral temperature distribution $T\langle\phi\rangle$ is determined by imposing temperature continuity and energy balance by peripheral conduction at both ends of each peripheral sector using this analytical solution that linearly depends on two boundary constants, actually characteristic temperatures, T_{C1j} and T_{C2j}. They are free boundary conditions for segment j, Fig. 2. Namely:

$$T_{j-1} = T_j;\ \left.\frac{\mathrm{d}T}{\mathrm{d}\phi}\right|_{j-1} = \left.\frac{\mathrm{d}T}{\mathrm{d}\phi}\right|_{j} \quad \text{(eq. 5)}$$

Fig. 2 represents the application case of a single parabolic trough solar collector in a generic non-symmetrical case, corresponding to an out-of-noon solar position and vertically stratified flow of liquid and vapor, a most challenging stratified regime. The circular periphery is divided into 5 sectors, j = Ia, II, III, IV, Ib, as Fig. 2 depicts. The temperature distribution follows the five equations in Tab. 1.

Unknowns are ten inter-boundary temperatures T_{cjk}. The five boundary conditions necessary for determining these unknowns and thus the temperature distribution are indicated in Tab. 2.

3. Results and discussion

As the parabolic trough solar collectors incorporate a rotatable mirror for sun tracking, the irradiance can impact on the side of the receiver, suggesting the larger temperature inhomogeneities than with Fresnel type collectors of similar receiver tube layout.

Tab. 3 indicates the chosen common parameters as a base case for the application of the model to some representative cases of a parabolic trough collector, varying remaining parameters. This corresponds to a clear day of the year #100 in Madrid (Spain) corresponding to 10th March of a non-leap year, as some kind of overall year representation. No changes in α_i have been considered for changes in wall temperature T as the bulk and wall temperatures are not dissimilar enough for the low concentrated irradiance on the wall of a MT

solar collector, in the order of 10^4 W m^{-2}.

The first study performed analyzes the effect of variations in the tracking angle γ_M along the day around the base case $\gamma_M = 0$ corresponding to solar noon. This implies *ceteris paribus*; meaning this "all other parameter unchanged". This implies the same G_{bT} along the day, what is really extreme. Fig. 3 shows the results. The data corresponds to a really shallow liquid depth $h_l = 5$ mm and a void fraction near to one. Low liquid heights are recommended to minimize the ammonia inventory for safety reasons. For the afternoon parabola orientation, $\gamma_M = 35$ deg, the solar irradiance affects laterally the receiver wall in contact with vapor flow, inducing a local moderate overheating of 35 K and increasing the difference of maximum to minimum temperature from 14 K to 53 K. One has to note the displacement of the high temperature peak down the liquid flow angles owing to heat conduction. These temperature increases will not happen so intensively with a Fresnel collector neither with a higher liquid height h_l.

Fig. 4 shows the effect of varying the mirror aperture angle α_M around the base case $\alpha_M = 120$ deg and sun tracking angle measured from zenith (asymmetry) $\gamma_M = 35$ deg in order to show the effect of sun radiance concentration on one side on the temperature side peak. Decreasing the aperture angle α_M reduces wall temperatures below 420 K as a result of a concentration reduction, so that thermal stresses and tube deformations diminish. Increasing the aperture angle causes a higher displacement of the high temperature arch toward either the liquid or the vapor arches, and vice versa, with respect to Fig. 3(B). Geometrical sun concentration increases up to 43 as G_{bT} is considered constant irrespective of the changes in these angles.

Fig. 5 shows the effect of increasing the liquid level h_l above the base case, by an increase of the liquid central angle ϕ_l, indicated in Fig. 2(B) in order to show the effect of liquid convection on the side temperature peak. Velocity of both fluids change as the liquid is falling freely under the sole action of gravity against friction with the wall (Lecuona et al., 2016). The vapor velocity results from the variation in vapor production and the reduction of the cross section. These effects mean a mass flow increase for both phases and a reduction of the void fraction. The results indicate the beneficial effect of a larger liquid angle ϕ_l from the point of view of limiting temperature differences in the wall, so that with $h_l = 20$ mm the wall temperature approaches the corresponding phase temperature, irrespective to γ_M, owing to α_l is much larger and α_v. This case is extreme as more than half the tube cross section is filled with liquid and the high counter-flowing vapor velocity will deform the interphase free surface forming waves. Other effects are considered in (Lecuona et al., 2016).

Tab. 1. Expressions for the temperature distribution along the periphery of the receiver tube wall for Fig. 2.

Sector *j*	Specifics	Equations
I	$\alpha_i = \alpha_l$ $T_i = T_l$ $S = a_o C$	**Ia**: $T_{1a}\langle\phi\rangle = T_{C11a}e^{m_1\phi} + T_{C12a}e^{-m_1\phi} + T_{p1}$
		Ib: $T_{1b}\langle\phi\rangle = T_{C11b}e^{m_1(\phi-\phi_4)} + T_{C12b}e^{-m_1(\phi-\phi_4)} + T_{p1}$
		$m_1^2 = \frac{r_{av}[\alpha_l + \alpha_e(1+w)]}{kw}$; $T_{p1} = \frac{T_l\alpha_l + T_e\alpha_e(1+w) + G_{bT}a_oC(1+w)}{\alpha_l + \alpha_e(1+w)}$
II	$\alpha_i = \alpha_v$ $T_i = T_v$ $S = a_o C$	$T_2\langle\phi\rangle = T_{C21}e^{m_2(\phi-\phi_1)} + T_{C22}e^{-m_2(\phi-\phi_1)} + T_{p2}$
		$m_2^2 = \frac{r_{av}[\alpha_v + \alpha_e(1+w)]}{kw}$; $T_{p2} = \frac{T_v\alpha_v + T_e\alpha_e(1+w) + G_{bT}a_oC(1+w)}{\alpha_v + \alpha_e(1+w)}$
III	$\alpha_i = \alpha_v$ $T_i = T_v$ $S = a_o$	$T_3\langle\phi\rangle = T_{C31}e^{m_3(\phi-\phi_2)} + T_{C32}e^{-m_3(\phi-\phi_2)} + T_{p3}$
		$m_3^2 = \frac{r_{av}[\alpha_v + \alpha_e(1+w)]}{kw}$; $T_{p3} = \frac{T_v\alpha_v + T_e\alpha_e(1+w) + G_{bT}a_o(1+w)}{\alpha_v + \alpha_e(1+w)}$
IV	$\alpha_i = \alpha_l$ $T_i = T_l$ $S = a_0$	$T_4\langle\phi\rangle = T_{C41}e^{m_4(\phi-\phi_3)} + T_{C42}e^{-m_4(\phi-\phi_3)} + T_{p4}$
		$m_4^2 = \frac{r_{av}[\alpha_l + \alpha_e(1+w)]}{kw}$; $T_{p4} = \frac{T_l\alpha_l + T_e\alpha_e(1+w) + G_{bT}a_o(1+w)}{\alpha_l + \alpha_e(1+w)}$

Tab. 2. Development of the boundary conditions to determine the characteristic temperatures, Fig. 2. Exponents < 2π.

$\phi_d = 2\pi$	$T_{1b} = T_{1a}$	$T_{C11b}e^{m_1(\phi_d-\phi_4)} + T_{C11b}e^{-m_1(\phi_d-\phi_4)} + T_{p1} = T_{C11a} + T_{C12a} + T_{p1}$
	$\frac{dT_{1b}}{d\phi} = \frac{dT_{1a}}{d\phi}$	$m_1T_{C11b}e^{m_1(\phi_d-\phi_4)} - m_1T_{C11b}e^{-m_1(\phi_d-\phi_4)} = m_1T_{C11a} - m_1T_{C12a}$

$\boldsymbol{\phi = \phi_1}$	$T_{1a} = T_2$	$T_{C11a}e^{m_1\phi_1} + T_{C12a}e^{-m_1\phi_1} + T_{p1} = T_{C21} + T_{C22} + T_{p2}$
	$\frac{dT_{1a}}{d\phi} = \frac{dT_2}{d\phi}$	$m_1 T_{C11a}e^{m_1\phi_1} - m_1 T_{C12a}e^{-m_1*\phi_1} = m_2 T_{C21} - m_2 T_{C22}$
$\boldsymbol{\phi = \phi_2}$	$T_2 = T_3$	$T_{C21}e^{m_2(\phi_2-\phi_1)} + T_{C22}e^{-m_2(\phi_2-\phi_1)} + T_{p2} = T_{C31} + T_{C32} + T_{p3}$
	$\frac{dT_2}{d\phi} = \frac{dT_3}{d\phi}$	$m_2 T_{C21}e^{m_2(\phi_2-\phi_1)} - m_2 T_{C22}e^{-m_2(\phi_2-\phi_1)} = m_3 T_{C31} - m_3 T_{C32}$
$\boldsymbol{\phi = \phi_3}$	$T_3 = T_4$	$T_{C31}e^{m_3(\phi_3-\phi_2)} + T_{C32}e^{-m_3(\phi_3-\phi_2)} + T_{p3} = T_{C41} + T_{C42} + T_{p4}$
	$\frac{dT_3}{d\phi} = \frac{dT_4}{d\phi}$	$m_3 T_{C31}e^{m_3(\phi_3-\phi_2)} - m_3 T_{C32}e^{-m_3(\phi_3-\phi_2)} = m_4 T_{C41} - m_4 T_{C42}$
$\boldsymbol{\phi = \phi_4}$	$T_4 = T_{1b}$	$T_{C41}e^{m_4(\phi_4-\phi_3)} + T_{C42}e^{-m_4(\phi_d-\phi_3)} + T_{p4} = T_{C11b} + T_{C12b} + T_{p1}$
	$\frac{dT_4}{d\phi} = \frac{dT_{1b}}{d\phi}$	$m_4 T_{C41}e^{m_4(\phi_d-\phi_3)} - m_4 T_{C42}e^{-m_4(\phi_d-\phi_3)} = m_1 T_{C11b} - m_1 T_{C12b}$

Tab. 3: Base parameters for the simulations.

Tube parameters	Flow parameters ($_l$ liquid, $_v$ vapor)	Solar parameters
r_{av} = 17.5 mm; t = 1.5 mm; k = 18.5 W K^{-1} m^{-1}. ϕ_1 = 44.4 deg.	α_l = 2,080 W K^{-1} m^{-2};α_v = 100 W K^{-1} m^{-2}; α_e = 15 W K^{-1} m^{-2}; h_l = 5 mm T_l = 377 K; T_v = 400 K; T_e = 287 K	G_{bT}= 817 W m^{-2}; S = 21; α_M = 120 deg; a_0 = 0.7

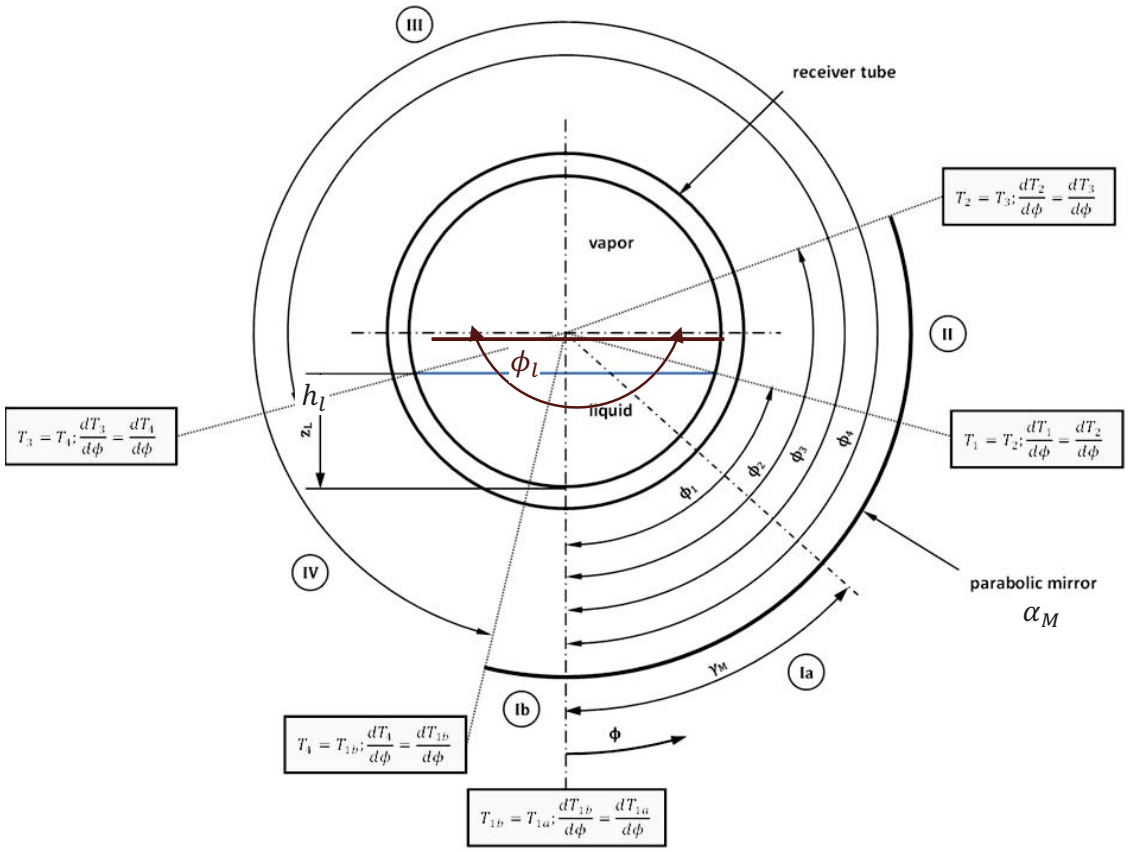

Fig. 2: Scheme of the peripheral thermal layout and boundary conditions for a parabolic trough, not to scale. γ_M represents the sun tracking angle. h_l represents the liquid flow depth.

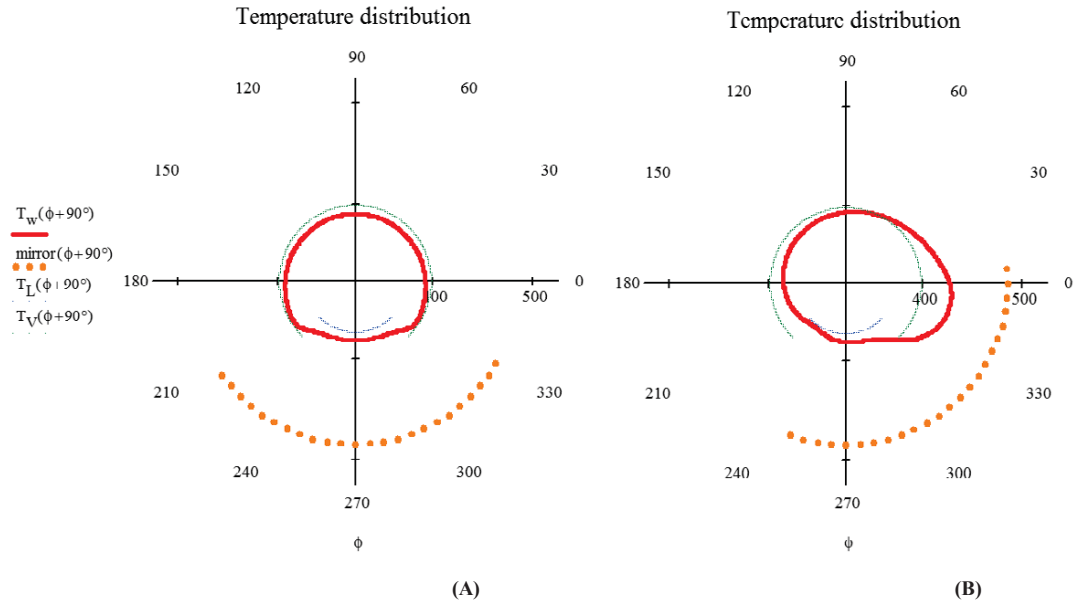

Fig. 3: Temperatures of the wall as a continuous red line, liquid temperature as continuous violet line and vapor temperature as a continuous green line [K] versus central angle ϕ [deg]. Yellow dots represent the aperture angle $\alpha_M = 120$ deg of the parabolic trough mirror. Sun tracking angle A) $\gamma_M = 0$, base case. B) $\gamma_M = 35$ deg, ceteris paribus.

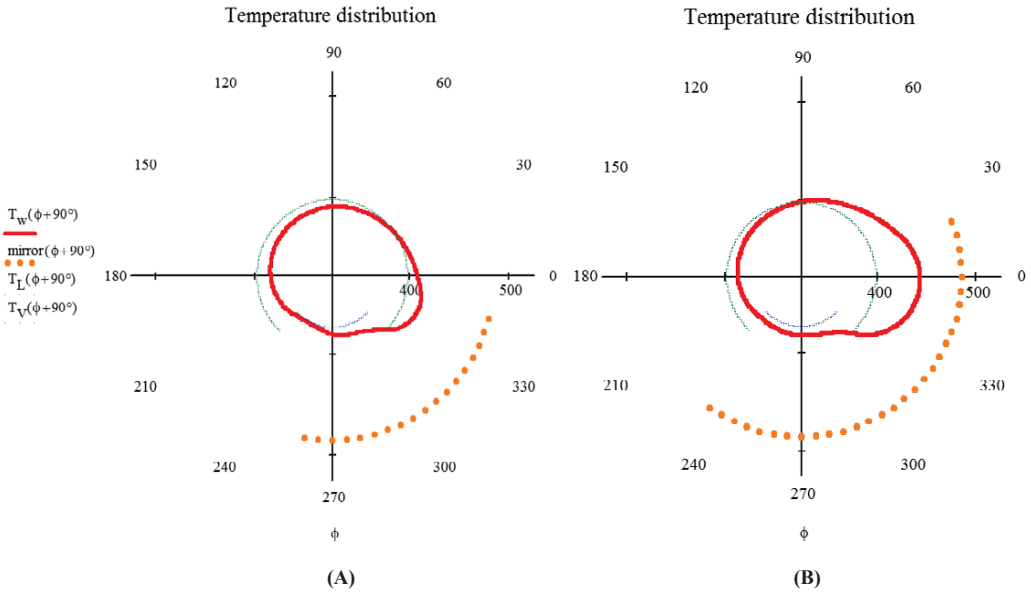

Fig. 4: Temperatures of the wall as a continuous red line, liquid temperature as continuous violet line and vapor temperature as a continuous green line [K] versus angle ϕ [deg]. Yellow dots represent the aperture angle of the parabolic trough mirror. Sun tracking angle $\gamma_M = 35$ deg. A) $\alpha_M = 90$ deg; B) $\alpha_M = 150$ deg, ceteris paribus.

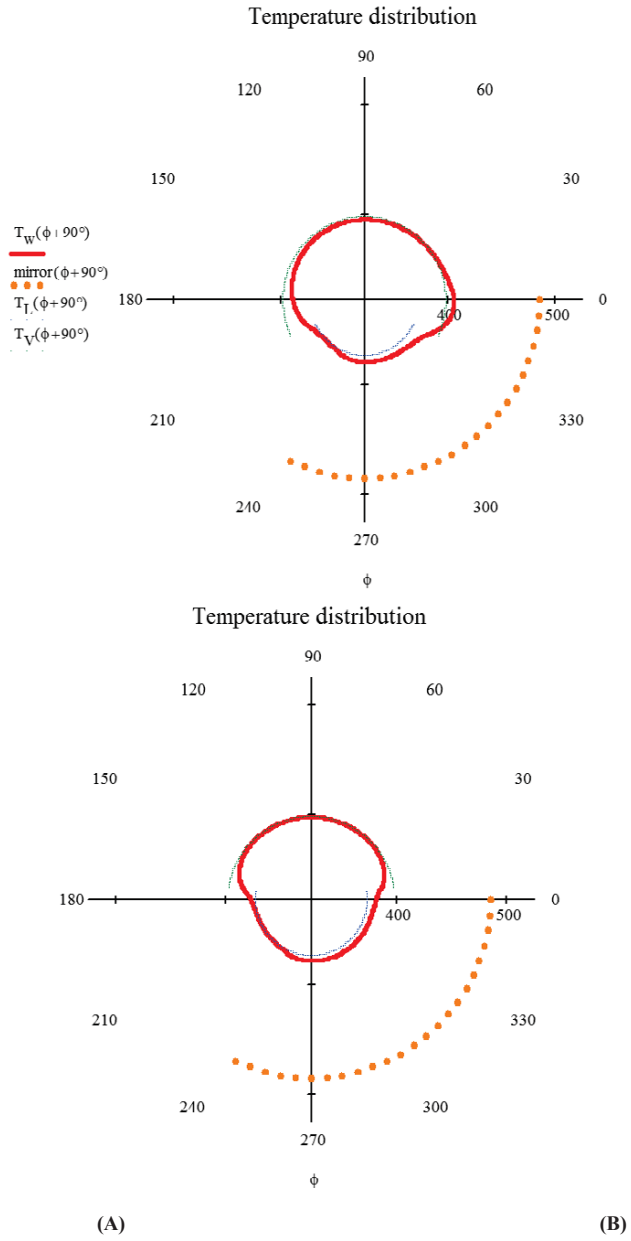

Fig. 5: Temperatures of the wall as a continuous red line, liquid temperature as continuous violet line and vapor temperature as a continuous green line [K] versus angle ϕ [deg]. Yellow dots represent the aperture angle $\alpha_M = 120$ deg of the parabolic trough mirror. Sun tracking angle $\gamma_M = 35$ deg. A) $h_l = 10$ mm; B) $h_l = 20$ mm, ceteris paribus.

4. Conclusions

A simplified method has been developed to estimate the wall temperature peripheral distribution on the circular section of the receiver tube of linear solar collectors, typically of the parabolic trough and Fresnel types. The more complex layout of a vertically gravity stratified counter-current two-phase flow has been studied.

This method relies on an exact solution of the 1D conduction heat transfer, thus more precise than its discretization on finite 1D elements.

The application has been performed to data from a representative medium temperature (MT) parabolic trough collector as it can present the most noticeable temperature inhomogeneities. Results indicate that the

temperature differences can be of concern when either/both the liquid phase central angle ϕ_l is small compared with the mirror aperture angle α_M. This is more pronounced when a parabolic trough type collector points to the sun when it is out of zenith, $\gamma_M \neq 0$. This caveat is of much lower importance for Fresnel collectors, even lower with secondary optics.

Matching the angle of the liquid sector ϕ_l to the mirror aperture angle α_M and even setting it with a larger angle benefits the temperature homogeneity of the receiver tube wall. But having a lower liquid angle is of not much concern during the morning and afternoon, as the irradiance G_{bT} decreases going away from midday, just when wall temperature inhomogeneity tends to increase in parabolic trough collectors.

The data obtained allow developing mass and heat transfer simulations of the innovative layout of direct vapor production using stratified two-phase flows with liquid film driven by gravity. This is of relevance for advanced absorption cycles for polygeneration. They allow also to ascertain the bending of the tube to avoid overstressing and touching the glass envelope.

5. Acknowledgements

The partial funding of the research project "Tecnologías energéticas térmico-solares y de aprovechamiento de calores residuales a baja y media temperatura integradas en la red eléctrica", ENE2013-45015-R from the Spanish Ministerio de Economía y Competitividad is greatly appreciated.

6. References

Ahmed, M. 2014. *Two Dimension Numerical Modeling of Receiver Tube Performance for Concentrated Solar Power Plant*. Energy Procedia, 57, 551 – 560. doi: 10.1016/j.egypro.2014.10.209

Danfoss. 2015. *De los HFC/HCFC al amoníaco en la refrigeración industrial. Una guía breve sobre el cambio al amoníaco.* Danfoss Group Global. Copenhagen: Danfoss A/S. Retrieved November 11, 2015, from www.danfoss.com/IR-tools.

Duffie, J., & Beckman, W., 1980. *Solar Engineering of Thermal Processes 3rd ed.* Hoboken, New Jersey, USA: Wiley.

Eck, M., Steinmann, W.-D., & Rheinländer, J., 2004. Maximum temperature difference in horizontal and tilted absorber pipes with direct steam generation. *Energy, 29*, 665–676. doi:10.1016/S0360-5442(03)00175-0.*Eck, M., Zarza, E., Eickhoff, M., Rheinlander, J., & Valenzuela, L., 2003. Applied research concerning the direct steam generation in parabolic troughs. *Solar Energy, 74*, 341-351. doi:10.1016/S0038-092X(03)00111-7.

Forristal, R., 2003. *Heat Transfer Analysis and Modeling of a Parabolic Trough in Engineering Equation Solver.* Office of Scientific and Technical Information. Oak Ridge: US Department of Energy. Retrieved November 11, 2015, from http://www.ntis.gov/ordering.htm.

Hernández-Magallanes, J., Domínguez-Inzunza, L., González-Urueta, G., Soto, P., Jiménez, G., & Rivera, W., 2014. Experimental assessment of an absorption cooling system operating with the ammonia/lithium nitrate mixture. *Energy, 78*, 685-692. Retrieved from http://dx.doi.org/10.1016/j.energy.2014.10.058.

Herold, K., Radermacher, R., & Klein, S., 1996. *Absorption chillers and Heat Pumps.* New York: CRC Press.

Incropera, F., & DeWitt, D. 199). *Introduction to Heat Transfer* 2nd ed. New York, New York, USA: John Wiley.

ISO/DIS 9806., 2016. *Solar energy. Solar thermal collectors. Test methods.* ISO. Retrieved August 25, 2016, from http://www.iso.org/iso/catalogue_detail.htm?csnumber=67978.

Jradi, M., & Riffat, S., 2012, October. Medium temperature concentrators or solar thermal applications. *International Journal of Low-Carbon Technologies, 0*, 1-11. doi:10.1093/ijlct/cts068.

Kalogirou, S., 2004. Solar thermal collectors and applications. *Progress in Energy and Combustion Science, 30*, 231–295. doi:10.1016/j.pecs.2004.02.001.

Lecuona, A., Ventas, R., Venegas, M., Zacarías, A., & Salgado, R., 2009. Optimum hot water temperature for absorption solar cooling. *Applied Energy, 83*(10), 1806–1814. doi:10.1016/j.solener.2009.06.016.

Lecuona-Neumann, A., Rosner, M., & Ventas-Garzón, R., 2016. Transversal temperature profiles of two-phase stratified flow in the receiver tube of a solar linear concentrator. Simplified analysis. *EUROSON 2016* (p. in press. Palma de Mallorca: ISES.

Logie, W., Asselineau, C., Pye, J., & Coventry, J. (2015). *Temperature and Heat Flux Distributions in Sodium Receiver Tubes*. 2015 Asia Pacific Solar Research Conference, (p. 10). Queensland. Retrieved September 10, 2016, from https://energystoragealliance.com.au/event/asia-pacific-solar-research-conference-2/

Lobón, D., Valenzuela, L., & Baglietto, E. (2014). *Modeling the dynamics of the multiphase fluid in the parabolic-trough solar steam generating systems*. Energy Conversion and Management, 78, 393–404. doi:10.1016/j.enconman.2013.10.072

Sigalés, B., 2003. *Transferencia de Calor Técnica* (Vol. I). Barcelona, Barcelona, Spain: Reverté.

Ventas, R., Lecuona, A., Vereda, C., & Legrand, M., 2016. Two-stage double-effect ammonia/lithium nitrate absorption cycle. *Applied Thermal Engineering, 94*, 228–237. Retrieved from http://dx.doi.org/10.1016/j.applthermaleng.2015.10.144.

Ventas, R., Lecuona, A., Zacarías, A., & Venegas, M., 2010. Ammonia-Lithium Nitrate Absorption Chiller With An Integrated Low-Pressure Compression Booster Cycle For Low Driving Temperatures. *Applied Thermal Engineering, 30*, Volume 30, Iss1351-1359. doi:10.1016/j.applthermaleng.2010.02.022.

Vereda, C., Ventas, R., Lecuona, A., & López, R., 2014. Single-effect absorption refrigeration cycle boosted with an ejector-adiabatic absorber using a single solution pump. *International Journal of Refrigeration, 38*, 22-29. doi:10.1016/j.irefrig.2013.10.010.

Wang, F., Feng, H., Zhao, J., Li, W., Zhang, F., & Liu, R., 2015. Performance assessment of solar assisted absorption heat pump system with parabolic trough collectors. *Energy Procedia, 70*, 529 – 536. doi:10.1016/j.egypro.2015.02.157.

Wu, W., Wang, B., Shi, W., & Li, X., 2014. An overview of ammonia-based absorption chillers and heat pumps. *Renewable and Sustainable Energy Reviews, 31*, 681–707. doi:http://dx.doi.org/10.1016/j.rser.2013.12.021.

Yang, X., Yang, X., Ding, Y., Shao, Y., & Fan, H. (2012). *Numerical simulation study on the heat transfer characteristics of the tube receiver of the solar thermal power tower*. Applied Energy, 90, 142–147. doi:10.1016/j.apenergy.2011.07.006.

Zamora, M., Bourouis, M., Coronas, A., & Vallés, M., 2014. Pre-industrial development and experimental characterization of new air-cooled and water-cooled ammonia/lithium nitrate absorption chillers. *International journal of refrigeration, 45*, 189-197. doi:10.1016/j.ijrefrig.2014.06.005.

Conference Proceedings

EuroSun 2016
Palma de Mallorca (Spain), 11 - 14 October 2016

Simulated Evaluation of Combined Use of Building Thermal Mass and Thermal Storage in Solar Hybrid Heat Pump System for Demand Response

Kyoung-ho Lee[1], Jae-hyeok Heo[1], Soon-myoung Lee[1], Moon-chang Joo[1]

[1] Solar Thermal Laboratory, New and Renewable Energy Research Division, Korea Institute of Energy Research

Abstract

In this study, TRNSYS simulations were employed to evaluate simple strategies for controlling energy demand response by utilizing building thermal mass and daily and weekly solar thermal storage. All control setpoints (i.e., for the building indoor space temperature, for heat pump on/off controls, and for pump and valve control for the weekly storage tank) were adjusted before and during the demand response period. Simulation results showed that a significant reduction in electric energy consumption could be achieved through combined use of thermal storage.

Keywords: *Demand response, Thermal storage, Solar heating, Heat pump, Weekly thermal storage, Setpoint adjustment*

1. Introduction

Demand response (DR) is an effective tool to reduce peak electric consumption of a national power grid when power supply is lower than demand. Energy storage systems can be utilized effectively to mitigate peak electric consumption during on-peak periods. In the case of electric heating systems combined with thermal energy storage, thermal energy storage systems are directly coupled with electric energy systems. Effective and intelligent use of thermal storage can therefore contribute to mitigating the electricity burden on the power grid. There has been significant research into DR technologies to reduce electric energy consumption during on-peak periods using thermal storage (Arteconi et al., 2016). However, most studies have focused on the summer period, when electric consumption due to space cooling is significant. Peak electric demand could also occur during winter time if electric heating systems (such as electric heaters or electric heat pumps) are widely used. During the heating season, solar thermal energy (through thermal storage) could be used for DR (Lee et al, 2015). In this study, we consider a solar hybrid electric heat pump system in an office building, with additional weekly thermal storage to use stored solar thermal energy, in order to reduce electric consumption related to heat pump operation for space heating. We consider combined use of thermal storage (such as building thermal mass, thermal storage connected to heat pumps, and weekly solar storage) for various control strategies.

2. Description of system and control strategy

Thermal storage systems could potentially contribute to managing response to electric load demand. They are activated by a control signal from electric utilities. The purpose of this control is to reduce peak demand on the power grid system. In this study, electric load shifting was evaluated by using a solar heating system with a ground-source heat pump and additional weekly thermal storage (ST_W); this is shown in Fig. 1.

doi:10.18086/eurosun.2016.04.16 Available at http://proceedings.ises.org

Weekly solar thermal storage can be feasible in office buildings because, during there is generally nearly no heating demand during weekends and surplus solar heat energy can be stored in the weekly storage tank on Sundays. A daily thermal storage tank(ST_D), used for heating domestic water and supplying energy for space heating, was connected with solar collectors and the heat pump. During weekends, the surplus solar yield was stored in the weekly storage tank. This stored thermal energy, together with building thermal mass control, could then be utilized for DR control during the following week. In this study, TRNSYS system simulation was used to evaluate the control strategy for load shifting to meet DR control. For DR with the weekly solar storage tank, the hot water in the ST_W tank was set to flow through the ST_D, so that the fluid temperature at the location controlled by the heat pump in the tank was maintained as high as possible during the DR period. In addition, the setpoint of the heat pump was set higher and lower than normal prior to and during the DR period, respectively. In this study, this control strategy was termed Solar DR (Demand Response). Simultaneously, the building indoor setpoint temperature can be set higher than conventionally the case before the DR period, to an upper limit temperature within the thermal comfort range; afterwards, the setpoint is reduced to a lower temperature within the thermal comfort range during the DR period. In this way, the building thermal mass and daily and weekly solar storage tanks could be utilized in combination to reduce the duration of heat pump operation as much as possible during the DR period. In this study, this control strategy was termed BC (Building Control). In addition, prior to the DR period, the storage setpoint temperature monitored by the heat pump can be set to an upper temperature higher than conventionally the case; subsequently, the setpoint is lowered to an allowable lower temperature suitable for space heating. This control strategy was termed HPC (Heat Pump Control). The three different control strategies can be employed either separately or simultaneously for combined use of thermal energy storage to maximize reduction of peak electric consumption.

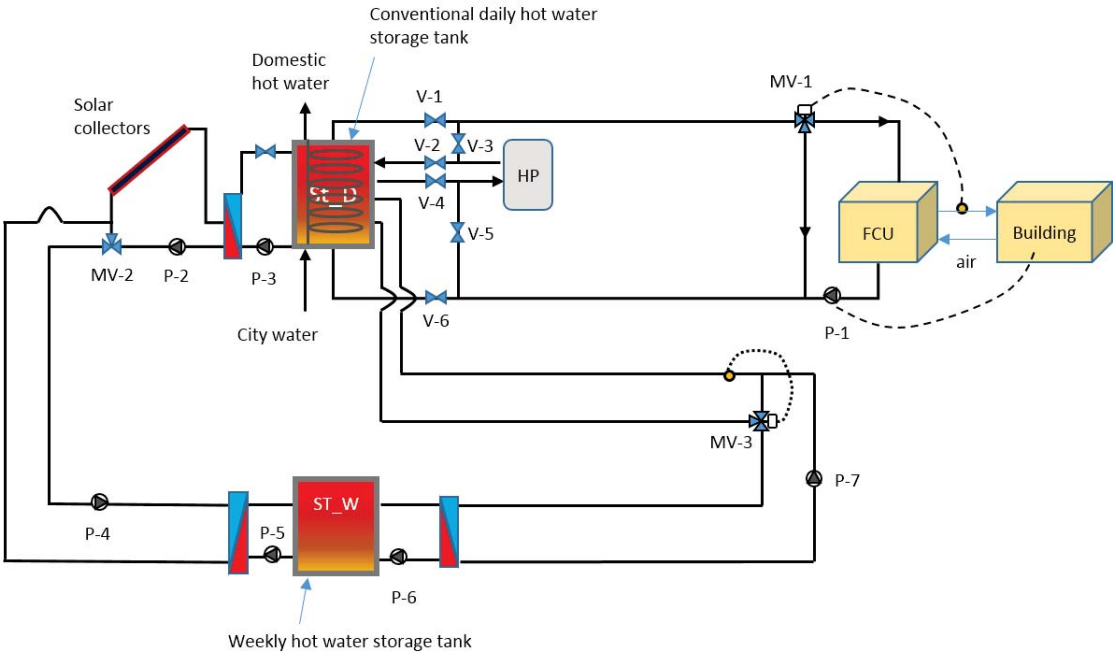

Fig. 1: Schematic diagram of solar hybrid heat pump system with daily and weekly storage tanks.

3. Simulation method and results

3.1. Simulation method

TRNSYS (SEL, 2013) simulation software was used to model the heating system. A simple capacitance and

resistance model was employed for the building thermal load. A small office building was modeled for this study with total floor area of 150 ㎡. Type 88 module in TRNSYS was used for the building model with 150,000kJ/K of thermal capacitance and thermal loss coefficient of 2.2kJ/hr-㎡-K. The building model parameters were calibrated using measured load data from an actual office building. Fig. 2 compares simulated TRNSYS model and actual measured data for space heating load and domestic hot water on a monthly basis. In this study, demand response was requested from 10 am to 12 pm and from 5 pm to 7 pm, for four hours. For simulation convenience, the Thursday of every week from December to February was selected for employment of the control strategy. The ratio of the solar collector area to the total building area was 0.04 ㎡/㎥, the ratio of the volume of the daily solar storage tank to the area of the solar collector area was 83 L/㎡, and the ratio of the volume of the weekly solar storage tank to the solar collector area was 25 L/㎡. The weekly storage tank is designed to be smaller than the daily storage tank, taking into consideration the fact that the weekly storage tank is used for one day (Sunday) per week, while the daily storage tank is used on Saturdays.

3.2. Simulation results

The annual solar fraction was estimated at approximately 10%. Figs. 3 and 4 show simulation results resulting from the application of diverse control strategies. For the purpose of the simulated evaluation, it was assumed that a DR signal is called on Thursday each week from December to February. The resultant values are averaged on a monthly basis for comparison. 'Nonsolar' indicates use of only the heat pump heating system, without solar collectors and weekly storage. 'CC' refers to conventional control. The control strategy using the weekly solar storage tank is termed DR_Solar, while HPC and BC indicate heat pump setpoint control and building thermal mass control, respectively. It was found that electric energy consumption of the solar heating system, with DR control, was reduced on average by 45.3%, 84.2%, 82.7%, and 99.4% for Solar DR control, DR_Solar+HPC, DR_Solar+BC, and DR_Solar+BC+HPC, respectively, over the three-month period. In addition, it was found that solar irradiation conditions over weekends contributed significantly to performance of solar DR control. Figs. 5 and 6 represent the performance over a day with the highest electric energy consumption due to space heating over the year. The results are similar to yearly average performance, with significant reduction of electric energy consumption during DR periods through combined use of thermal storage. However, it should be also noted that electric energy consumption over whole days could be increased by employing thermal storage control, due to the efficiency of thermal storage between thermal charge and discharge periods. This increase in energy consumption on a whole daily basis could be compensated by different hourly electric rate structures. In general, the electric charge rate during the DR period is much higher than during other periods. Fig. 7 compares the variation of heat pump electric consumption for 'Nonsolar', 'Solar(CC)', and 'DR_Solar+BC+HPC' according to time of day with highest electric consumption. It should be noted that heat pump almost does not operate during on-peak periods for the control strategy using combined thermal storage, including weekly solar thermal storage, daily thermal storage, and building thermal mass.

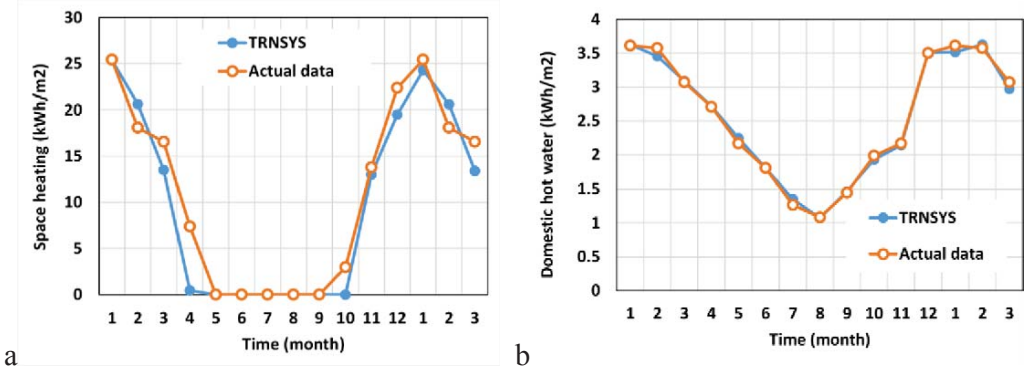

Fig. 2: Comparison of calibrated TRNSYS simulation results with measured data for monthly load of space heating and domestic hot water

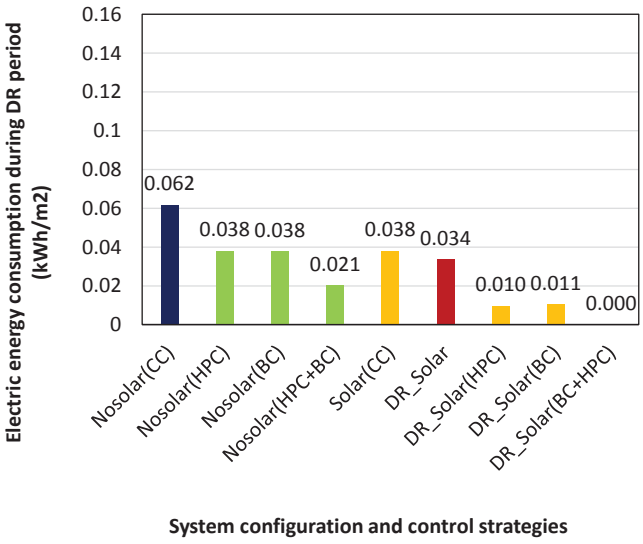

Fig. 3: Average electric energy consumption of solar hybrid heat pump system during the demand response period

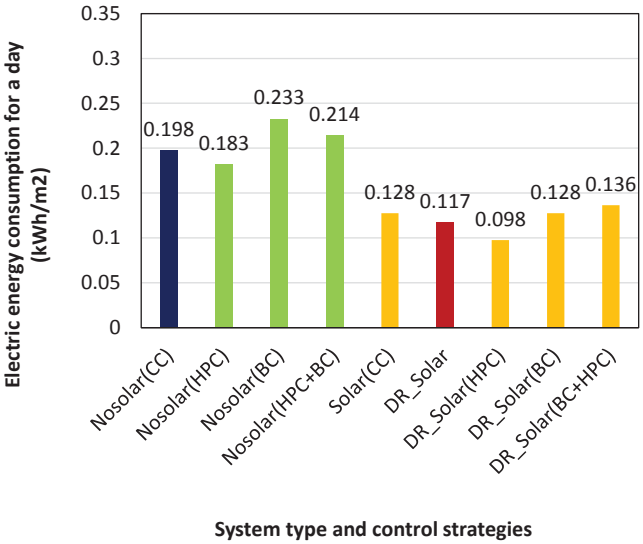

Fig. 4: Average electric energy consumption of solar hybrid heat pump system for whole day of demand response control implementation

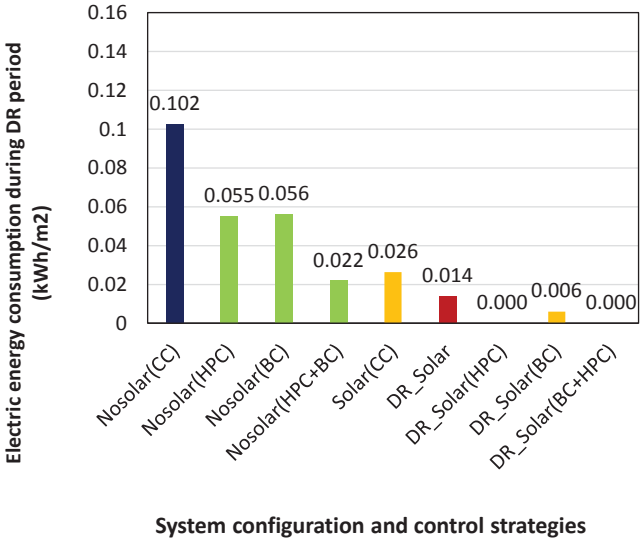

Fig. 5: Electric energy consumption of solar hybrid heat pump system during the demand response period on the day with highest electric energy consumption throughout the year

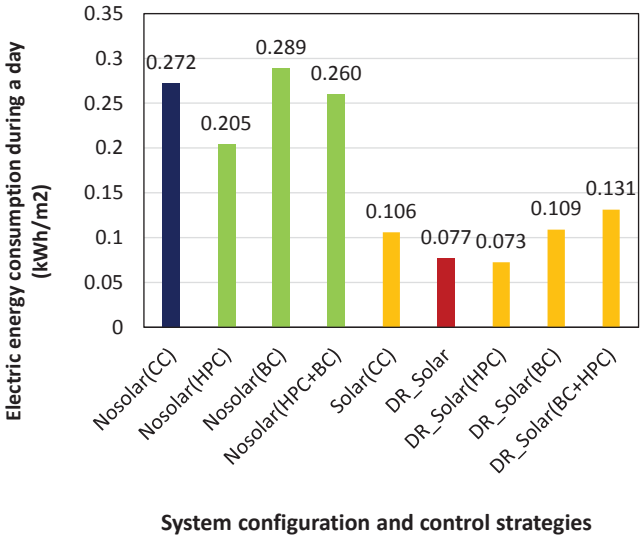

Fig. 6: Whole-day electric energy consumption of solar hybrid heat pump system on the day with highest electric energy consumption throughout the year

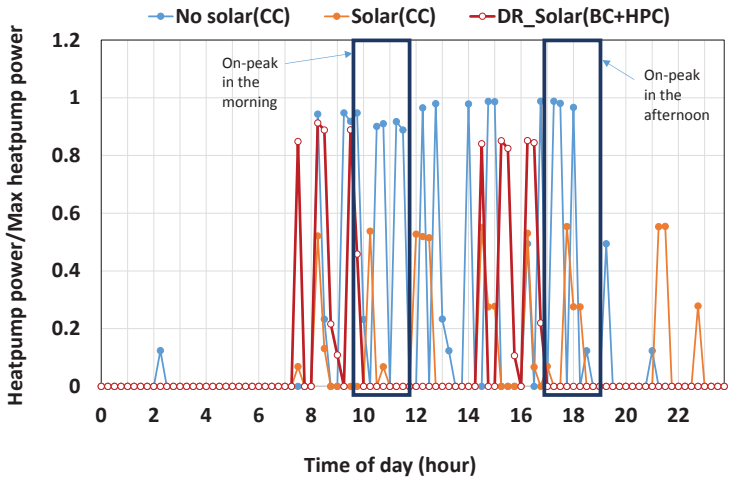

Fig. 7: Comparison of heat pump power according to time for control strategies during the day with highest electric energy consumption

4. Conclusion

The study evaluates the performance of a simple control strategy using a combination of building thermal mass and daily and weekly solar thermal storage. The TRNSYS simulations for the system indicated significant reduction in electric energy consumption of the heating system during the DR period. It was assumed that the control was called every Thursday from December to February from 10 am to 12 pm and 5 pm to 7 pm. On average, when using combined thermal storage, 99.4% of electric energy consumption during the DR control period could be shifted to the period before DR control. Based on simulation results, it can be concluded that weekly solar thermal energy storage can be used for electric demand management during space heating periods for electric heating systems installed in office buildings. The effect of demand management in solar hybrid heat pump systems can be enhanced by combined use of building thermal mass, conventional daily thermal storage, and weekly solar thermal storage.

5. References

Arteconi A., Xu, J., Ciarrocchi, E., Paciello, L., Comodi, G., Polonara, F., Wang R., 2016, Demand side management of a building summer cooling load by means of a thermal energy storage, EnergyProcedia, 75, 1637-1656.

Kyoung-ho Lee, Joo, M.-c., Baek, N.-c., 2015, Experimental evaluation of simple thermal storage control strategies in low-energy solar houses to reduce electricity consumption during grid on-peak periods, Energies, 8, 9344-9364.

SEL(Solar Energy Laboratory), TRNSYS 17, 2013, University of Wisconsin at Madison.

Acknowledgment

This work was conducted under the framework of the Research and Development Program of the Korea Institute of Energy Research(KIER) (B5-2509).

Conference Proceedings

EuroSun 2016

Palma de Mallorca (Spain), 11– 14 October 2016

Study Case of Solar Thermal and Photovoltaic Heat Pump System for Different Cities in Turkey

Andreu Moià-Pol[1], Ramon Pujol-Nadal[1],Víctor Martínez-Moll[1], Nima Bonyadi[2], Derek Baker[2]

[1] University of Balearic Islands, Physics department, Mechanical Engineering Area (ME) Palma de Mallorca (Spain)

[2] Mechanical Engineering (ME) & Center for Solar Energy Research and Applications (GÜNAM), Middle East Technical University- METU, (TURKEY)

Abstract

The combination of solar thermal, photovoltaic, and heat pump technologies is a welcome advancement in countries with large solar resources such as Turkey. These systems could have similar efficiencies throughout the year for different locations in Turkey if we adjust the solar storage according to the weather conditions. In this paper, solar heating with a heat pump system for buildings have been designed to achieve different values of the fraction of primary energy saved using Flat Plate Collectors (FPC) and solar photovoltaic (PV) technology, and having a high system efficiency resulting in net zero energy for thermal production.

Keywords: *Solar thermal; heat pump; photovoltaic; geothermal; combisystems.*

1. Introduction

Turkey has large solar resources as shown in Figure 1 and a relatively large population. This country has the second largest newly installed solar thermal capacity worldwide in 2014, and this has made Turkey the largest European solar thermal market [1]. The solar combisystems are becoming popular for villas [1], where for arrive to a high comfort and efficiency we need a system with heating and Domestic Hot Water during all the year with a large solar systems.

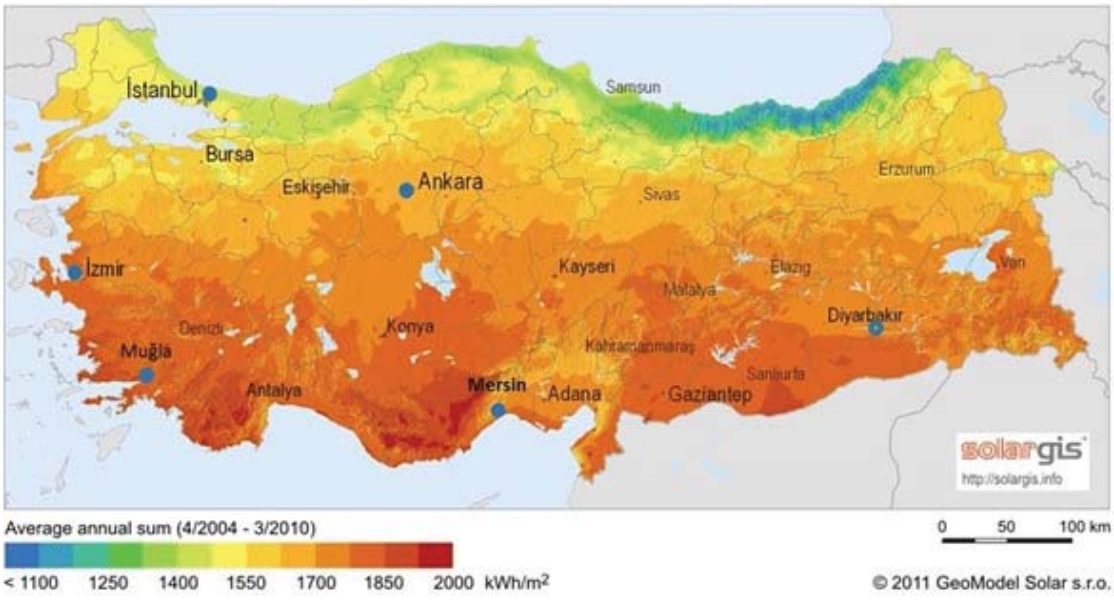

Fig. 1 Solar Radiation in Turkey and location of the studied cities. SolarGis [2]

Selection and/or peer review under responsibility of Scientific Committee
doi:10.18086/eurosun.2016.04.22 Available at http://proceedings.ises.org

The actual prices of PV systems and mature technology of Flat Plate Collectors (FPCs) and water-to-water heat pump for ground-coupled applications have provided a new model: solar-electric heat pump assisted with solar-thermal collectors. These systems have been integrated in some software programs as Polysun. This article shows that these systems will be cheaper and easier to install than the shallow geothermal systems.

2. Description and results

Six different locations in Turkey (see Figure 1) have been simulated with FPC, PV and heat pumps (Water-water) as presented in Table 1. The used software Polysun [3] includes solar thermal, photovoltaics, heat pumps and geothermal systems. The PV system has been simulated as well with PVsyst[4] for adjust the power. The proposed system can operate with outside temperatures lower than 0ºC with a high solar fraction and with a high efficiency of the solar collector [5]. The storage is changing during the year according to the external temperature, in order to obtain higher efficiency from the thermal collector, PV and work with the maximum efficiency of the heat pump.

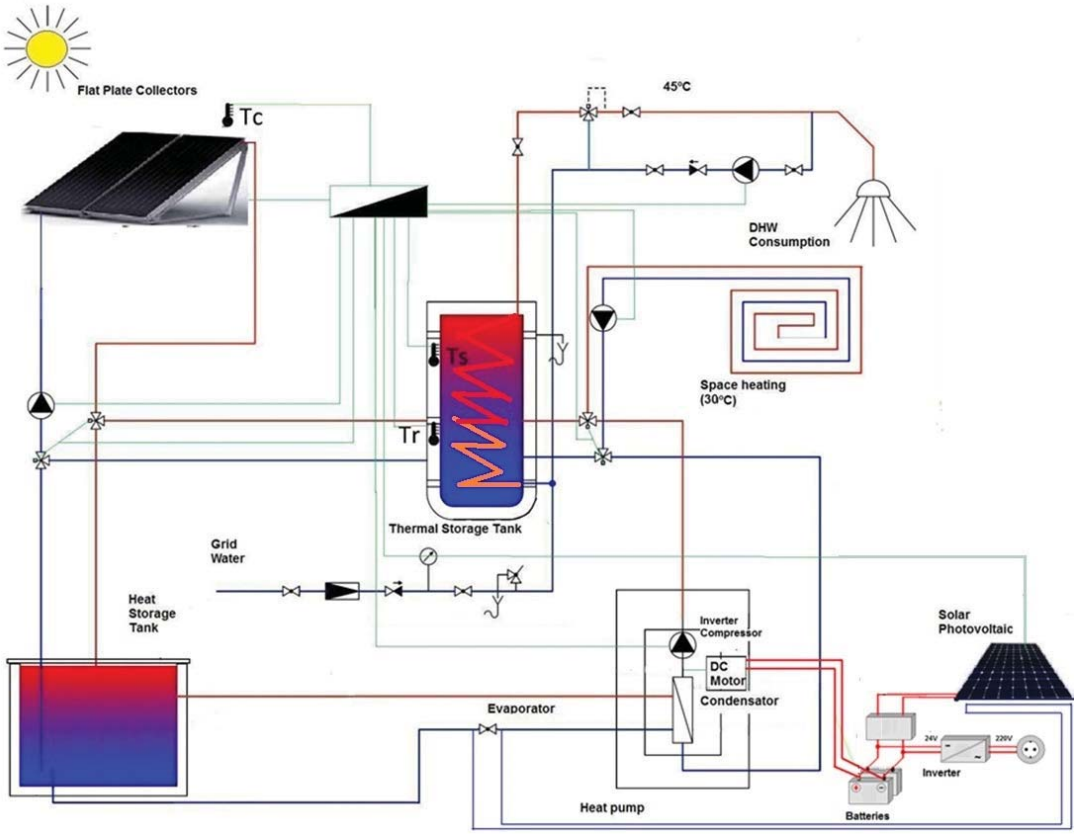

Fig. 2 : Simulation of the thermal system.

One interesting combination is for houses with swimming pool or with rain storage tank, where we can save the investment of the buffer storage tank using an isolated pool with thermal cover. In Mediterranean areas many Villas with pool or rain water storage tank have solar collectors to use the pool in autumn months. The heat can be dumped into a swimming pool in the autumn months, and the swimming pool used like a big buffer tank in the cooler days, being more efficient than the geothermal systems [9].

ST Collector Efficiency $\eta = 0{,}807 - 3{,}075(Tm\text{-}Ta)/G - 0{,}022((Tm\text{-}Ta)/G)^2$ (eq. 1)
Coefficient of Performance Heat Pump = 4.2423+0.087 T (eq. 2) ($T_{max\ evap}$=15ºC)

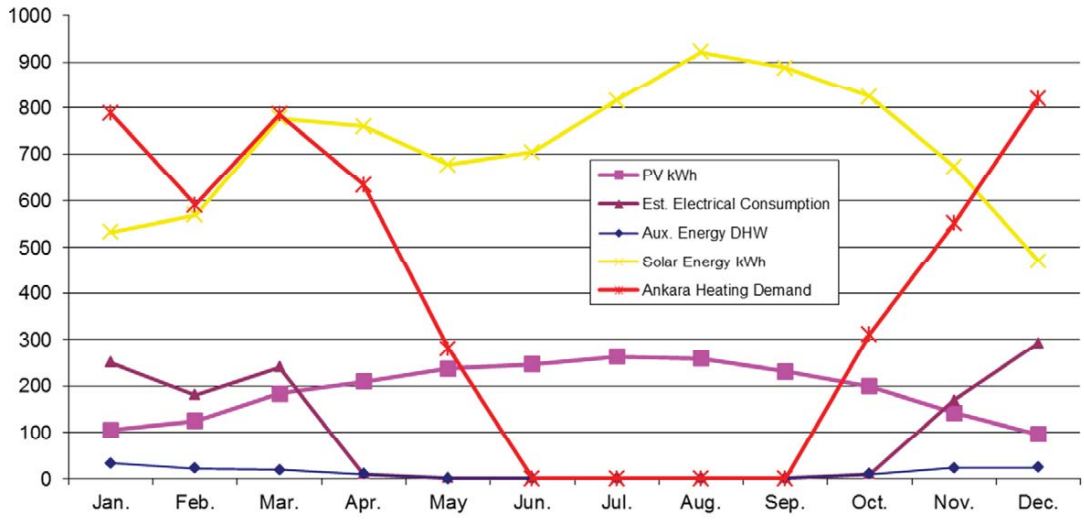

Fig. 3 : Annual Thermal demand (in kWh) with ST and PV production for Ankara

Simulating the whole year system we reach different solar fractions for the different locations, due to the efficiency of the system, the working temperature of the storage system, and the different COP of the heat pump. This system can have a very high Coefficient of Performance and adapt its efficiency to a variety of conditions. It is ideal for both cold and mild climates, and therefore for a country like Turkey with different weather conditions in the biggest cities.

Tab. 1: Results of one year simulation in three locations for DHW and Space Heating.

Location , Latitude	Thermal Energy Demand (kWh)	Solar Energy kWh/m^2	Electric Energy kWh	Solar Thermal Fraction	Average FPC Efficiency	PV installed power (Wp)	FPC (m^2)
Ankara, 39.9º	6370	1702	2284	88%	72%	1400	8
Mersin, 36.7º	3385	1486	524	93%	72%	360	6
Mugla,37.2º	4132	1798	1239	96%	74%	750	6
Izmir, 38.4º	3340	1697	1051	95%	74%	750	5
Diyarbakir, 37.9º	3993	1865	1423	96%	74%	750	5
Istanbul, 41º	2269	1486	529	94%	71%	520	4

There are some heat pump manufacturers that sell a hybrid air +PV system, and geothermal and air system for heating applications, in order to reduce the initial cost of the borehole and piping system, they have been analyzed, only shallow geothermal with PV. The size of the system is not very large for Turkey, and the maximum surface needed is less than 20m^2 if we take in account than these houses have a roof of 80 m^2 , these system fit perfectly. If there is any case without sufficient roof space, PVT technologies can be used, when it used for low temperatures with limited space is a good option, these collectors are good for low temperature heating systems, like fan coils or floor heating.

Recently, hybrid photovoltaic solar thermal collectors (PVT) became a topic of many research projects because of the possibility to gain heat and electricity simultaneously. PVT represents the alternative to separate PV panels and solar thermal collectors by integrating the two into one device [7]. Other studies have evaluated different possibilities to integrate PVT collectors in an air to water heat pump system and to compare the results with the combination of an air to water heat pump system together with a PV-system. The system P/S (PVT + heat pump in parallel and serial connection) in combination with a High Thermal Conductivity collector type turned out to be the most efficient and promising way to integrate uncovered PVT [8] collectors in a system at different locations. As the PVT collector serves essentially as a heat source for the heat pump (and is thus independent of solar radiation), the useful heat gains of the collectors occurs at the same time as heat is needed in winter. The rear insulation of the PVT collector is

in terms of best possible heat absorption from ambient air rather obstructive for such a system configuration.

FPC and PV with heat pump systems are a good solution for familiar households, both technologies are necessary in order to arrive to the future scenarios of zero emissions for net-zero energy building for Turkey.

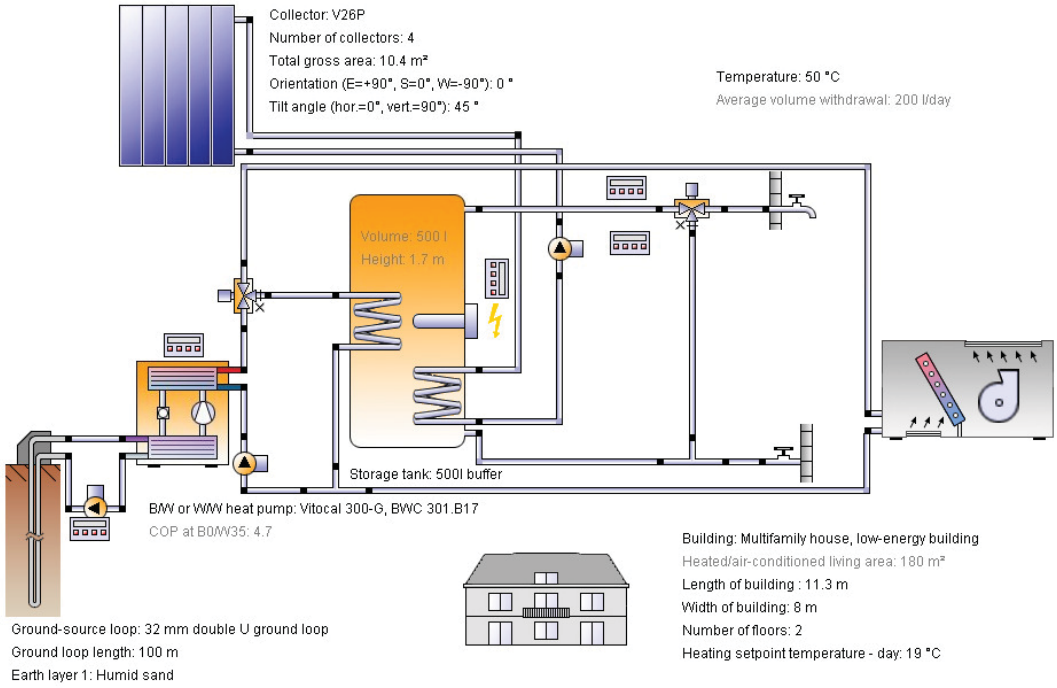

Fig. 4 : Diagram with Ground source+ Solar Thermal [3] for Istanbul.

The main problem of the geothermal is in some places the composition of the soil very uncertain, and the environmental barriers. They need a detailed geological analysis and sometimes they need some borehole, making the initial investment very high. In the analyzed case two boreholes of 120 meters were assumed. The results are presented in Table 2, standard commercial list prices of the different elements, the operational cost and maintenance hasn't been studied, supposing that is similar in both cases.

Tab. 2: Comparing cost of the system vs. Geothermal in Turkey

	Estimated cost		**Estimated cost**
Heat Pump + PV system	7 050 €	Heat Pump + PV system	7 050 €
Solar Thermal + Pipes	2 100 €	Borehole + Pipes	13 300 €
Thermal Storage Tanks	4 500 €	Thermal Tank	1 815 €
Total	**13 650 €**		**22 165 €**

The analyzed solar thermal-PV system is cheaper and has a similar efficiency than the Geothermal system, which gives an advantage. The only disadvantage will be for cooling, the geothermal will be easy to change in contrast with the Solar Heat Pump which will be needed a dry cooler or some auxiliary system in the heat pump in order to cool the house.

3. Conclusions

The analyzed solar thermal-PV system is cheaper and has a similar efficiency to the geothermal system, which gives an advantage. The only disadvantage will be for cooling, the geothermal will be easy to change in contrast with the Solar Heat Pump which will be needed a dry cooler or some auxiliary system in the heat pump in order to cool the house.

4. Acknowledgements

The authors acknowledge the financial support from Programa Pont “La Caixa”. Caixabank, S.A,”

5. References

[1]http://www.estif.org/
[2] http://solargis.info
[3] Polysun. http://velasolaris.com
[4] http://www.pvsyst.com/
[5] Andreu Moià-Pol, Víctor Martínez-Moll, Julian David Hertel,Rashid Nazmitdinov, Pavel Gladyshev. Solar and heat pump systems, analysis of several cases in Russia. Proceedings of the Solar World Congress 2015, Daegu, Korea.
[6] A. Moia-Pol, V. Martinez-Moll, R. Nazmitdinov, R. Pujol-Nadal. Study Case of Solar Thermal and Photovoltaic Heat Pump System for Different Weather Conditions. Aix-les-Bains. France. doi:10.18086/eurosun.2014.03.21
[7] A. Abdul-Zahra, T. Faßnacht, A. Wagner. Evaluation of the Combination of Hybrid Photovoltaic Solar Thermal Collectors with Air to Water Heat Pumps. Aix-les-Bains. France .EuroSun 2014.
[8] F. Ille, M. Adam, R. Radosavljevic, H. Wirth .Market and Simulation Analysis of PVT Applications for the Determination of New PVT Test Procedures. Aix-les-Bains. France. doi:10.18086/eurosun.2014.16.09
[9] Andreu Moià Pol, Víctor Martínez Moll, Miquel Alomar Barceló, Ramon Pujol Nadal. Solar and heat pump systems. An analysis of several combinations in Mediterranean areas. Proceedings of the Eurosun 2012, Rijeka, Croatia

ISESEuroSun 2016

A set of key performance indicators for solar heating and cooling systems

Marco Beccali[1], Maurizio Cellura[1], Sonia Longo[1] and Daniel Mugnier[2]

[1] University of Palermo – Department of Energy, Information Engineering and Mathematical Models, Palermo (Italy)

[2] Tecsol, Perpignan Cedex (France)

Abstract

The application of solar heating and cooling systems for building air-conditioning actually shows a significant potential of exploitation, particularly in sunny regions. The choice whether or not to apply such technologies in different climates should be based on the assessment of their energy/environmental, economic and social sustainability, as well as their technical characteristics as reliability, durability and energy efficiency. To support researchers and decision-makers in the selection of the best solar air-conditioning solution in a specific geographic and energy context, the paper proposes a set of technical, economic, energy/environmental and social key performance indicators. The research activity was developed within the Task 53 "New generation solar cooling & heating systems (PV or solar thermally driven systems)" of the International Energy Agency.

Keywords: *Solar heating and cooling, sustainability, key performance indicators, energy*

1. Introduction

The selection of the best performing solar heating and cooling (SHC) system for satisfying the cooling and heating demand of buildings in a specific location is a complex task (Beccali et al., 2012; 2014; 2016), which has to include different assessment criteria (costs, environmental impacts, etc.). This is particularly relevant for the assessment of new generation technologies, which need to be carefully evaluated for their subsequent inclusion in the market.

This topic was investigated within the International Energy Agency SHC Programme - Task 53 "New generation solar cooling & heating systems (PV or solar thermally driven systems)" aiming to the definition of a set of key performance indicators (KPIs) (Mugnier, 2013), which can be useful for helping researchers and decision-makers to have a complete overview of the performance of different SHC technologies.

2. A set of key performance indicators for solar heating and cooling systems

The set of KPIs is based on a multi-disciplinary approach that takes into account the three pillars of sustainability: environmental (including energy), economic and social sustainability (Ardente et al., 2016; Sala et al., 2015). Furthermore, a fourth element is added, describing the technical performance of the SHC technology.

In all, the set includes 19 KPIs, each of which is synthesized by using an "ad hoc" format, including the following sections:

- KPI name: it indicates the name of the KPI and its acronym.
- Typology: it specifies if the KPI is an economic, energy, environmental, social or technical indicator.
- Type of assessment: it clarifies the qualitative or quantitative nature of the indicator.
- Unit of measure: only for quantitative KPIs.
- Description: it includes a brief description of the indicator.
- Performance target: it defines the target to be achieved for improving the performance of the system under investigation for the selected KPI.

doi:10.18086/eurosun.2016.04.14 Available at http://proceedings.ises.org

- Measurement process: it describes the process or the methodology used for measuring the value of the indicator.

In detail, the following KPIs where identified for describing the SHC systems:

- Energy KPIs: global energy requirement (Table 1), energy payback time (Table 2), energy return ratio (Table 3).
- Environmental KPIs: global warming potential (Table 4), acidification potential (Table 5), eutrophication potential (Table 6), ozone depletion potential (Table 7), photochemical ozone creation potential (Table 8), GWP payback time (Table 9).
- Economic indicators: money savings during the operation (Table 10), initial cost ratio (Table 11), operation/maintenance costs ratio (Table 12), payback period (Table 13).
- Social indicators: customer satisfaction (Table 14), ease of use of the system (Table 15).
- Technical indicators: useful life of the system (Table 16), thermal performance coefficient of the ab/adsorption machine (Table 17), electrical COP (Table 18), reliability of the system (Table 19)..

Tab. 1: Energy KPI: Global Energy Requirement

KPI name	Global Energy Requirement (GER)
Typology	Energy indicator
Type of assessment	Quantitative
Unit of measure	MJ
Description	GER represents the entire (renewable and non-renewable) energy demand, valued as primary energy, which arises in connection with the production, use and disposal of an economic good (product or service).
Performance target	Percentage reduction of GER during the life cycle of the system (to be fixed case by case).
Measurement process	The KPI can be calculated following a life cycle approach with the formula: $GER = GER_M + GER_U + GER_{RD}$ (eq.1). GER_M is the primary energy consumed during the manufacture (including energy and raw materials supply) of a product or a service; GER_U is the primary energy consumed during the use of a product or a service; GER_{RD} is the primary energy consumed during the end-of-life of a product or a service (recycling or disposal).

Tab. 2: Energy KPI: Energy Payback Time

KPI name	Energy Payback Time (EPT)
Typology	Energy indicator
Type of assessment	Quantitative
Unit of measure	Years
Description	EPT is defined as the time during which the SHC system must work to harvest the additional primary energy required for its manufacturing and end-of-life, if compared with a conventional system. The harvested energy is considered as net of the energy expenditure for the system operation.
Performance target	EPT lower than the useful life of the system
Measurement process	The KPI can be calculated with the formula: $EPT = \left(GER_{SHC-system} - GER_{Conventional-system}\right) / E_{year}$ (eq.2). $GER_{SHC\text{-}system}$ is the GER related to the life cycle of the SHC system except for the operation phase; $GER_{Conventional\text{-}system}$ is the GER related to the life cycle of the conventional system except for the operation phase; E_{year} is the net yearly primary energy saving due to the use of the SHC system in replacement of a conventional one.

Tab. 3: Energy KPI: Energy Return Ratio

KPI name	Energy Return Ratio (ERR)
Typology	Energy indicator
Type of assessment	Quantitative
Unit of measure	-
Description	ERR represents how many times the energy saving overcomes the primary energy consumed during the manufacturing and the end-of-life of the SHC system.
Performance target	N.A.
Measurement process	The KPI can be calculated with the formula: $ERR = E_{overall} / GER_{SHC-system}$ (eq.3). $GER_{SHC\text{-}system}$ is the GER related to the life cycle of the SHC system except for the operation phase; $E_{overall}$ is the net primary energy saving during the overall lifetime of the SHC system.

Tab. 4: Environmental KPI: Global Warming Potential

KPI name	Global Warming Potential (GWP)
Typology	Environmental indicator
Type of assessment	Quantitative
Unit of measure	kg CO_{2eq}
Description	GWP is a measure of the relative, globally averaged, warming effect arising from the emissions of a particular greenhouse-gas. The GWP represents the time-integrated commitment to climate forcing from the instantaneous release of 1 kg of a trace gas expressed relative to that from 1 kg of carbon dioxide.
Performance target	Percentage reduction of GWP during the life cycle of the system (to be fixed case by case).
Measurement process	The KPI can be calculated following a life cycle approach with the formula: $GWP = \sum_1^n (m_i * CF_i)$ (eq.4). m_i is the mass of the substance *i* emitted; CF_i is the characterization factor that reflects the relative contribution of the substance *i* to the impact on GWP.

Tab. 5: Environmental KPI: Acidification Potential

KPI name	Acidification Potential (AP)
Typology	Environmental indicator
Type of assessment	Quantitative
Unit of measure	kg SO_{2eq}
Description	AP measures the impact generated by the emission of airborne acidifying substances (as nitrogen oxides and sulphur dioxide). Acidification refers literally to processes that increase the acidity of water and soil systems by hydrogen ion concentration.
Performance target	Percentage reduction of AP during the life cycle of the system (to be fixed case by case).
Measurement process	The KPI can be calculated following a life cycle approach with the formula: $AP = \sum_1^n (m_i * CF_i)$ (eq.5). m_i is the mass of the substance *i* emitted; CF_i is the characterization factor that reflects the relative contribution of the substance *i* to the impact on AP.

Tab. 6: Environmental KPI: Eutrophication Potential

KPI name	Eutrophication Potential (EP)
Typology	Environmental indicator
Type of assessment	Quantitative
Unit of measure	kg $PO_4^{3-}{}_{eq}$
Description	EP is defined as the potential of nutrients to cause over-fertilization of water and soil which in turn can result in increased growth of biomass. For example, it causes excessive plant growth like algae in rivers which causes severe reductions in water quality and animal populations.
Performance target	Percentage reduction of EP during the life cycle of the system (to be fixed case by case).
Measurement process	The KPI can be calculated following a life cycle approach with the formula: $EP = \sum_1^n (m_i * CF_i)$ (eq.8). m_i is the mass of the substance *i* emitted; CF_i is the characterization factor that reflects the relative contribution of the substance *i* to the impact on EP.

Tab. 7: Environmental KPI: Ozone Depletion Potential

KPI name	Ozone Depletion Potential (ODP)
Typology	Environmental indicator
Type of assessment	Quantitative
Unit of measure	kg $CFC\text{-}11_{eq}$
Description	ODP indicates the potential for emissions of chlorofluorocarbon compounds and other halogenated hydrocarbons to deplete the ozone layer in the stratosphere, where it shields the earth from harmful ultraviolet radiation.
Performance target	Percentage reduction of ODP during the life cycle of the system (to be fixed case by case).
Measurement process	The KPI can be calculated following a life cycle approach with the formula: $ODP = \sum_1^n (m_i * CF_i)$ (eq.7). m_i is the mass of the substance *i* emitted; CF_i is the characterization factor that reflects the relative contribution of the substance *i* to the impact on ODP.

Tab. 8: Environmental KPI: Photochemical Ozone Creation Potential

KPI name	Photochemical Ozone Creation Potential (POCP)
Typology	Environmental indicator
Type of assessment	Quantitative
Unit of measure	kg C_2H_{4eq}
Description	POCP is related to the potential for volatile organic compounds and oxides of nitrogen to generate photochemical or summer smog in the presence of heat and sunlight.
Performance target	Percentage reduction of POCP during the life cycle of the system (to be fixed case by case).
Measurement process	The KPI can be calculated following a life cycle approach with the formula: $POCP = \sum_1^n (m_i * CF_i)$ (eq.8). m_i is the mass of the substance *i* emitted; CF_i is the characterization factor that reflects the relative contribution of the substance *i* to the impact on POCP.

Tab. 9: Environmental KPI: GWP Payback Time

KPI name	GWP Payback Time (GWP-PT)
Typology	Environmental indicator
Type of assessment	Quantitative
Unit of measure	Years
Description	GWP-PT is defined as the time during which the avoided GWP impact due to the use of the SHC system in replacement of a conventional system is equal to GWP impact caused during its manufacturing and end-of-life.
Performance target	GWP-PT lower than the useful life of the system.
Measurement process	The KPI can be calculated with the formula: $GWP-PT=\left(GWP_{SHC-system}-GWP_{Conventional-system}\right)/GWP_{year}$ (eq.9). $GWP_{SHC\text{-}system}$ is the GWP related to the life cycle of the SHC system except for the operation phase; $GWP_{Conventional\text{-}system}$ is the GWP related to the life cycle of the conventional system except for the operation phase; GWP_{year} is the net yearly avoided GWP due to the use of the SHC system in replacement of a conventional system.

Tab. 10: Economic KPI: Money savings during the operation

KPI name	Money savings during the operation (MSDO)
Typology	Economic indicator
Type of assessment	Quantitative
Unit of measure	€
Description	MSDO represents the money saving during the useful life of the SHC system due to its lower energy (electricity and natural gas) consumption if compared with a conventional system.
Performance target	Lower than the cost of energy (electricity and natural gas) consumed by the SHC system during its useful life.
Measurement process	The KPI can be calculated with the formula: $MSDO=\sum_1^n\left(\begin{array}{l}\left(NG_{Conventional-system-i}-NG_{SHC-system-i}\right)*NG_{price-i}+\\+\left(EL_{Conventional-system-i}-EL_{SHC-system-i}\right)*EL_{price-i}\end{array}\right)$ (eq.10). $NG_{Conventional\text{-}system\text{-}i}$ is the natural gas consumption of the conventional system in the year *i*, expressed in MJ or in kWh; $NG_{SHC\text{-}system\text{-}i}$ is the natural gas consumption of the SHC system in the year *i*, expressed in MJ or in kWh; $NG_{price\text{-}i}$ is the price of natural gas in the year *i*, expressed in €/MJ or in €/kWh; $EL_{Conventional\text{-}system\text{-}i}$ is the electricity consumption of the conventional system in the year *i*, expressed in MJ or in kWh; $EL_{SHC\text{-}system\text{-}i}$ is the electricity consumption of the SHC system in the year *i*, expressed in MJ or in kWh; $EL_{price\text{-}i}$ is the price of electricity in the year *i*, expressed in €/MJ or in €/kWh.

Tab. 11: Economic KPI: Initial cost ratio

KPI name	Initial cost ratio (ICR)
Typology	Economic indicator
Type of assessment	Quantitative
Unit of measure	-
Description	ICR is the ratio between the price set by supplier/vendor in their price list when the customer purchases the SHC system from them and the corresponding price of the conventional system.
Performance target	Lower than 1
Measurement process	The KPI can be calculated with the formula: $ICR = P_{SHC-system} / P_{Conventional-system}$ (eq.11). $P_{SHC-system}$ is the price of the SHC system defined by the supplier/vendor; $P_{Conventional-system}$ is the price of the conventional system defined by the supplier/vendor. Both $P_{SHC-system}$ and $P_{Conventional-system}$ can be found by the customer in the price list given by the supplier/vendor.

Tab. 12: Economic KPI: Operation/maintenance cost ratio

KPI name	Operation-maintenance cost ratio (OMC)
Typology	Economic indicator
Type of assessment	Quantitative
Unit of measure	-
Description	OMC is the ratio between the cost to the customer during the useful life of the SHC system for its operation and maintenance (regular maintenance and repair) and the corresponding cost of the conventional system.
Performance target	Lower than 1
Measurement process	The KPI can be calculated with the formula: $OMC = \frac{\left(NG_{SHC-system-i} * NG_{price-i} + EL_{SHC-system-i} * EL_{price-i} + M_{Cost-SHC-system-i}\right)}{\left(NG_{Conv.-system-i} * NG_{price-i} + EL_{Conv.-system-i} * EL_{price-i} + M_{Cost-Conv.-system-i}\right)}$ (eq.12). $NG_{SHC-system-i}$ is the natural gas consumption of the SHC system in the year *i*, expressed in MJ or in kWh; $NG_{Conv.-system-i}$ is the natural gas consumption of the conventional system in the year *i*, expressed in MJ or in kWh; $NG_{price-i}$ is the price of natural gas in the year *i*, expressed in €/MJ or in €/kWh; $EL_{SHC-system-i}$ is the electricity consumption of the SHC system in the year *i*, expressed in MJ or in kWh; $EL_{Conv.-system-i}$ is the electricity consumption of the conventional system in the year *i*, expressed in MJ or in kWh; $EL_{price-i}$ is the price of electricity in the year *i*, expressed in €/MJ or in €/kWh; $M_{Cost-SHC-system-i}$ is the cost for the maintenance of the SHC system in the year *i*; $M_{Cost-Conv.-system-i}$ is the cost for the maintenance of the conventional system in the year *i*.

Tab. 13: Economic KPI: Payback period

KPI name	Payback period (PP)
Typology	Economic indicator
Type of assessment	Quantitative
Unit of measure	Years
Description	PP is the time in which the initial cash outflow of an investment for the SHC

	system is expected to be recovered from the economic benefit (positive cash flow) generated by the investment.
Performance target	PP lower than the useful life of the system
Measurement process	The formula to calculate the KPI depends on whether the economic benefit (positive cash flow) per period is even or uneven. In case it is even, the formula to calculate the KPI period is: $PP = P_{SHC-system} / B_{annual}$ (eq.13). $P_{SHC-system}$ is the price of the SHC system defined by the supplier/vendor; B_{annual} is the net annual benefit (positive cash flow) due to the use of the SHC system in replacement of a conventional one in terms of decrement in expenditure for electricity and natural gas. When the economic benefit is uneven, it is needed to calculate the cumulative net cash flow for each period and then use the following formula for the KPI: $PP = A + B/C$ (eq.14). A is the last period with a negative cumulative cash flow; B is the absolute value of cumulative cash flow at the end of the period A; C is the total cash flow during the period after A.

Tab. 14: Social KPI: Customer satisfaction

KPI name	Customer satisfaction (CS)
Typology	Social indicator
Type of assessment	Qualitative
Unit of measure	N.A.
Description	CS indicates how satisfied the client is with the SHC system
Performance target	Positive value of CS
Measurement process	The KPI can be estimated by using the following qualitative judgments: • Totally satisfied (positive value); • Mostly satisfied (positive value); • Neither satisfied nor dissatisfied (neither positive nor negative value); • Mostly dissatisfied (negative value); • Totally dissatisfied (negative value).

Tab. 15: Social KPI: Ease of use of the system

KPI name	Ease of use of the system (EUS)
Typology	Social indicator
Type of assessment	Qualitative
Unit of measure	N.A.
Description	EUS indicates the ease of use of the SHC system
Performance target	Positive value of EUS
Measurement process	The KPI can be estimated by using the following qualitative judgments: • Very easy to use (positive value); • Easy enough to use (positive value); • Neither easy nor difficult to use (neither positive nor negative value); • Not very easy to use (negative value); • Not easy to use (negative value).

Tab. 16: Technical KPI: Useful life of the system

KPI name	Useful life of the system (ULS)
Typology	Technical indicator
Type of assessment	Quantitative
Unit of measure	Years
Description	ULS indicates the period during which the system is expected to be usable for the purpose it was acquired.
Performance target	N.A.
Measurement process	The KPI can be estimated based on the indications given by the supplier/vendor.

Tab. 17: Technical KPI: Thermal Performance Coefficient of the ab/adsorption machine (Boudéhenn et al., 2013)

KPI name	Thermal Performance Coefficient (COP_{th}) of the ab/adsorption machine
Typology	Technical indicator
Type of assessment	Quantitative
Unit of measure	-
Description	COP_{th} is the ratio between the thermal cooling energy supplied by the evaporator and the thermal heat energy supplied to the generator of the sorption machine.
Performance target	To be fixed case by case
Measurement process	The KPI can be calculated with the formula: $COP_{th} = Q_{Cool-Ev} / Q_{Heat-generator}$ (eq.15). $Q_{Cool-Ev}$ is the thermal cooling energy supplied by the evaporator; $Q_{Heat-generator}$ is the thermal heat energy supplied to the generator of the sorption machine.

Tab. 18: Technical KPI: Solar Electric Performance Coefficient of the system (Boudéhenn et al., 2013)

KPI name	Solar Electric Performance Coefficient ($COP_{Elec-sol}$) of the system
Typology	Technical indicator
Type of assessment	Quantitative
Unit of measure	-
Description	$COP_{Elec-sol}$ corresponds to the ratio of the system's useful solar energy to auxiliary consumption.
Performance target	To be fixed case by case
Measurement process	The KPI can be calculated with the formula: $COP_{Elec-sol} = ESU / E_{Aux-sol}$ (eq.16). ESU refers to the thermal solar energy exploited by the system integrating thermal losses from hot and cold storage; $E_{Aux-sol}$ Electricity consumption of the solar system auxiliaries.

Tab. 19: Technical KPI: Reliability of the system

KPI name	Reliability of the system (RS)
Typology	Technical indicator
Type of assessment	Quantitative
Unit of measure	%
Description	RS at time *t* is the probability that the system will perform its function without failure under stated conditions in the interval [0, *t*).
Performance target	RS higher than 90%
Measurement process	The KPI can be calculated with the formula: $RS(t) = P(X > t)$ (eq.17). X is a random variable that represents the time to occurrence of system failure.

3. Conclusions

A complete evaluation of SHC systems should be based on the assessment of their economic, energy/environmental and social sustainability, as well as their technical characteristics.

The proposed set of KPIs gives a complete picture of the SHC system, aimed at measuring different aspects of its sustainability and technical performance. It can be useful for enabling researchers and decision-makers to take sustainably-based decisions in the field of SHC technologies, starting from a comprehensive investigation of the technical, economic, energy/environmental and social performance of the systems along their life cycle.

4. References

Ardente, F., Cellura, M., Longo, S., Mistretta, M. 2016. Life Cycle Assessment of Solar Technologies, in Dewulf, J., De Meester, S., Alvarenga, R. (Eds.), Sustainability Assessment of Renewables-Based Products: Methods and Case Studies. Wiley, pp. 241-258.

Beccali, M., Cellura, M., Longo, S., Nocke, B., Finocchiaro, P., 2012. LCA of a solar heating and cooling system equipped with a small water–ammonia absorption chiller. Solar Energy 86, 1491-1503.

Beccali, M., Cellura, M., Finocchiaro, P., Guarino, F., Longo, S., Nocke, B., 2014. Life Cycle performance assessment of small solar thermal cooling systems and conventional plants assisted with photovoltaics. Solar Energy 104, 93-102.

Beccali, M., Cellura, M., Longo, S., Guarino, F., 2016. Solar heating and cooling systems versus conventional systems assisted by photovoltaic: Application of a simplified LCA tool. Solar Energy Materials and Solar Cells 156, 92–100.

Boudéhenn, F., Hands, S., White, S., Zahler, C., Gammoh, F., 2013. Task 48 - Deliverable M-C4.3 – Final report Measurement and Verification Procedures, http://task48.iea-shc.org/.

Mugnier, D., 2013. Task 53 New generation solar cooling & heating systems (PV or solar thermally driven systems) - Task description and Work plan, http://task53.iea-shc.org/.

Sala, S., Ciuffo, B., Nijkamp, P., A systemic framework for sustainability assessment. Ecological Economics 119, 314–325.

Conference Proceedings

EuroSun 2016
Palma de Mallorca (Spain), 11 - 14 October 2016

Assessment of Solar Heating and Cooling – Comparison of Best Practice Thermal and PV Driven Systems

Daniel Neyer[1], Jacqueline Neyer[1], Alexander Thür[1], Bettina Nocke[2], Pedro Vicente[3] and Daniel Mugnier[4]

[1] University of Innsbruck, Unit for Energy Efficient Buildings, Innsbruck (Austria)

[2] AEE INTEC, Gleisdorf (Austria)

[3] Universidad de Miguel Hernández, Elche (Spain)

[4] TECSOL, Perpignan (France)

Abstract

Assessing the performance of Solar Heating and Cooling (SHC) systems, especially cooling systems using solar thermal or PV driving energy, in a common comparable format, is complicated by the numerous, alternative energy sources and design possibilities. A generalized technical and economic assessment methodology was developed and tested in the course of IEA SHC Task 53.

At a glance seven best practice plants were analyzed and compared in a comprehensive format. All systems can achieve non-renewable primary energy savings greater than 50%, but none is reaching a cost ratio lower than 1 compared to a reference system. The results might not be representative but show interesting trends. There is almost no difference between solar thermal and PV driven systems. Both technologies can succeed the same magnitude of savings with similar cost ratios. Plants that are achieving or aiming higher primary energy savings turn out to be more expensive.

Finally the assessment shows that solar heating and cooling can achieve cost competitiveness with an appropriate design and solar fraction if investment costs can be decreased simultaneously.

Keywords: *assessment and benchmarking, new generation solar heating and cooling, IEA SHC Task 53*

1. Introduction

A tremendous increase in the global market for air-conditioning can be observed, especially in developing countries. The results of the past IEA SHC Tasks and the ongoing activities on solar cooling show the enormous potential of this technology for building air-conditioning, particularly in sunny regions. However, solar thermal cooling faces barriers to emerge as an economically competitive solution. Thus, there is a strong need to stimulate the solar cooling sector for efficient and cost effective small and medium sized systems.

IEA SHC Task 53, which builds up on earlier IEA SHC work in this field, is working to find solutions to make solar driven heating and cooling systems cost competitive and helps to build a strong and sustainable market for solar, photovoltaic and new innovative thermal cooling systems. These objectives are tackled through five activities:

1. Investigation of new small to medium size PV & solar thermal driven cooling and heating systems, as well as development of best suited cooling and heating systems technology with a focus on reliability, adaptability and quality.
2. Demonstration of cost effectiveness of the above mentioned solar cooling and heating systems.
3. Investigation on life cycle performances on energy and environmental terms (LCA) of different options.
4. Assistance with the market deployment of new SHC systems for buildings worldwide.

doi:10.18086/eurosun.2016.04.04 Available at http://proceedings.ises.org

5. Increasing energy supply safety and influencing the virtuous demand side management behaviors.

The Task's scope is technologies for the production of cold/hot water or conditioned air by means of solar heat or solar electricity. Therefore, the Task starts with the solar radiation reaching the collectors or the PV modules and ends with the chilled/hot water and/or conditioned air transferring to the application. It is focused on solar driven systems for both cooling (ambient and food conservation) and heating (ambient and domestic hot water).

The following work deals with the economic and technical (energetic) evaluation of different configurations and technologies of New Generation Solar Heating and Cooling.

Tab. 1: Nomenclature and Subscripts

Subscripts			
C	Cooling	out	Output
DHW	Domestic hot water	NRE	Non-renewable
EC	Energy Carrier	ref	reference system
el	Electrical	SH	Space heating
equ	equivalent	sys	Overall system (C & DHW & SH)
Nomenclature			
ACM SE	Absorption chiller, single effect	PER_{NRE}	Primary Energy Ratio (-)
CR	Cost ratio (-)	SEER	Seasonal Energy Efficiency Ratio (-)
ε	Primary Energy Factor (kWh/kWh_{PE})	SPF_{equ}	Seasonal Performance Factor (-)
$fsav_{\_NRE}$	Fractional savings (-)	VCC	Vapour compression chiller

Several studies in the past years show the competitiveness of solar thermal and PV driven systems. Depending on the boundary condition each system configuration shows appropriate advantages. Existing simplifying studies (e.g. Streicher (2010), but also more detailed studies (e.g. Henning (2010), Eicker (2012), Wiemken et al. (2013)) are evaluating both technologies under different boundary conditions.

The results of these studies depend on climatic conditions (ambient temperature, irradiation) as well as on the type of application (DHW, C, etc.), size and operation hours of the system, etc. Furthermore they show that reasonable system configurations (base or peak load design) and different control strategies have a crucial impact on reachable non-renewable primary energy savings. Even under various economic considerations the results can differ significantly. But in general in common controversy PV driven systems get more positive remarks than solar thermal driven systems. Often quoted arguments are regarding efficiency, costs and handling of surplus energy.

Selected performance indicators for evaluating technical and economic quality and cost effectiveness are fully discussed and defined in Neyer et al. (2015) during the course of IEA SHC Task 48 (http://task48.iea-shc.org/). The procedure is valid for thermal driven plants with vapor compression chillers (VCC) as cold backup. If a compression chiller is the main component and is supported by PV or other renewable electricity, the methodology has to be adapted.

This adaptation was performed under the course of IEA SHC Task 53 and is described in this paper. Furthermore numerous realized systems with in-situ monitoring or rather simulation studies of solar thermal (ST) driven and photovoltaic (PV) driven systems with different capacities and applications are shown. The plants are evaluated with the tool developed in Task 53 and are benchmarked among each other with technical and economic key figures. Sensitivity analysis of four plants show the impact of specific boundary conditions (primary energy factor, costs, etc.) on the performance and the difference between ST and PV driven systems.

2. Methodology

The assessment and evaluation tool of Task 48 was generalized and extended, with the focus on new generation of solar heating and cooling with either solar thermal or photovoltaic driven systems. It enables the assessment for a wide range of systems available on the global market. Systems can contain bivalent heating and/or cooling devices (boiler or chiller respectively). The component base information includes technical as well as economic data to evaluate and benchmark the systems. Multiple usage of each component in the entire system (energy flows) can be added and analyzed.

In Figure 1 the overview of all components and main energy flows is presented in an energy flow chart, invented in IEA SHC Task 44 based on work of Frank et al. (2010). Traded energies include electricity and other energy carriers and are arranged on the left (displayed in grey); free energy sources including solar and other ambient source/sinks on the top (in green); the application and its heating (in red), cooling (in blue) and electricity demand (in grey) on the right.

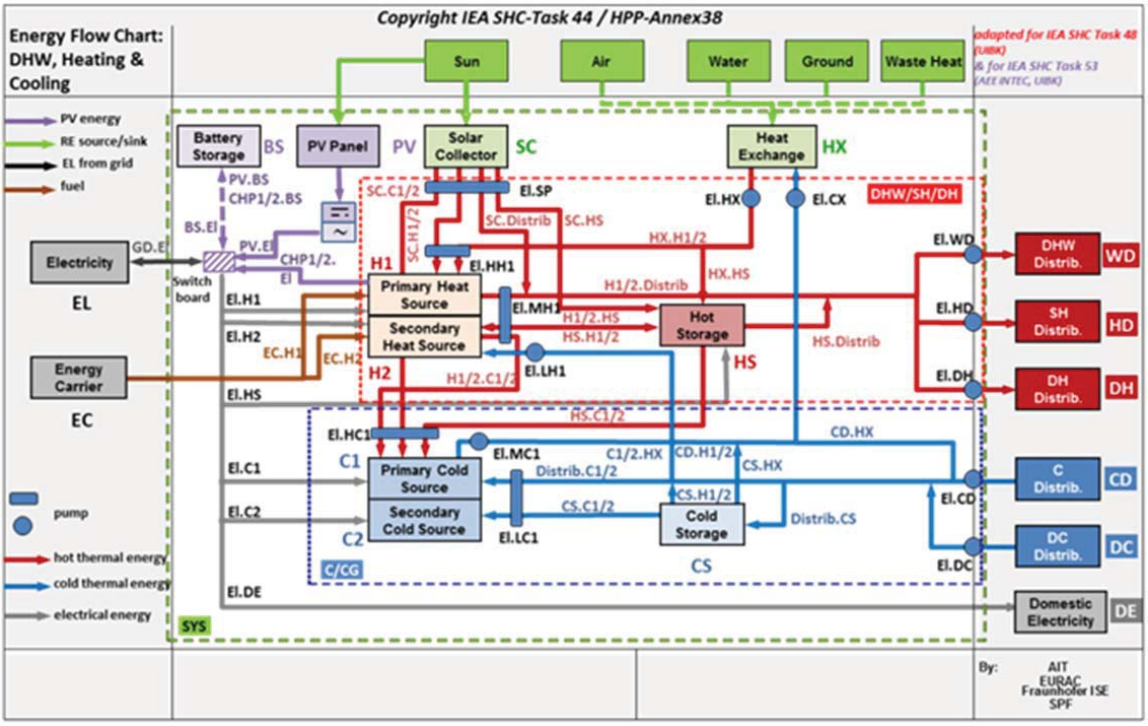

Fig. 1: Energy flow chart including all possible components for the technical and economic assessment of IEA SHC Task 53

Due to the dependency of the results on the system boundaries, it is obvious to display them in the energy flow chart. All components and auxiliary pumps can be identified easily. Within the Tool for each demand (DHW, SH, etc.) a separated assessment can be performed for the entire solar fraction and the overall performance; resulting in a maximum of five subsystems including further five solar sub boundaries and one overall system assessment.

The component selection includes reversible heat pumps (electric or thermal driven), chillers (air/water cooled VCC, SE/DE absorption, etc.), several boiler types (natural gas, CHP, oil, pellets, etc.) and storages (thermal, electrical). The database for the single components include either cut off or standardized (minimum) performance and cost indicators. For eight countries (Austria, Australia, France, Germany, Italy, P.R. China, Spain and Singapore) all input values, if applicable, were collected (primary energy factor, energy costs, etc.) and can be used for country specific assessments.

Nevertheless, these values are subjects of permanent changes, either driven by political decisions or technical issues. Furthermore the values depend on the choice of energy trading company or even on the territory. Therefore the tool enables the implementation/creation of self-calculated or investigated values, valid for a specific region or configuration / analysis. The assessment tool calculates and indicates regularly one set of

Task 53 (T53) standard Key Performance Indicators (KPI) and one set of specific (standard country or own choice) KPI's. The T53 Standard KPI's are based on a pre-defined reference system (natural gas boiler and air cooled vapor compression chiller) and the appropriate cost and primary energy factors. It allows the comparison of different plants under the same boundary conditions. In this study all KPI's are related to the T53 standard.

2.1. Technical assessment

The Seasonal Performance Factor (SPF), for a given system boundary, is generally defined as the ratio of useful energy (supplied to satisfy the needs of the application) to energy effort from any source. The SPF can include several auxiliary components within the defined boundary and is calculated over a defined period of time (e.g. annual or monthly). Well known SPFs are based upon thermal or electric energy inputs.

However, the electrical SPF_{el} can be misleading when a system with different energy inputs (thermal and electrical) is analysed. The SPF_{el} might show high results even when large amounts of fossil fuel (e.g. gas) back up is consumed with overall poor environmental performance. Therefore the Primary Energy Ratio (PER) and derivative key figures like the electrical equivalent SPF_{equ} and fsav are calculated and provide a better base for assessing different SHC systems.

- Non-renewable Primary Energy Ratio (PER_{NRE})

The non-renewable Primary Energy Ratio converts all non-renewable energy flows into primary energy equivalents. This provides appropriately comparable quality ratings for energy derived from alternative electricity, solar and fossil fuel heat energy sources. It is defined in eq. 1 as the ratio of useful energy (ΣQ_{out} supplied to satisfy the needs of the building) to non-renewable primary energy (electricity and other energy carriers). Certain primary energy conversion factors (ε) for each type of energy source have to be provided to calculate the PER_{NRE}. The primary energy factors depend on local conditions (e.g. the source from which local electricity is derived).

$$PER_{NRE} = \frac{\sum Q_{out}}{\sum\left(\frac{Q_{el}}{\varepsilon_{el}} + \frac{Q_{EC}}{\varepsilon_{EC}}\right)} \quad \text{(eq. 1)}$$

A high value for PER indicates that the heating and cooling services can be obtained with a relatively small amount of fossil derived energy and is therefore an environmentally friendly system. However, values for PER_{NRE} (in a magnitude of ca. 1 to 2.5) are not directly comparable with any widely available industry figures of merit such as the EER or SEER of a vapor compression chiller.

- Fractional saving (f_{sav})

A further key performance indicator is the so called fractional saving (f_{sav}). This represents the percentage reduction in non-renewable primary energy for the application compared with a reference (business as usual) system. Thereby the reference system can also be another renewable system. The PER_{ref} uses the same calculation as PER but takes the standardized component information to calculate its non-renewable Primary Energy demand. The non-renewable primary energy savings ($f_{sav\text{-}NRE}$) in comparison to a reference system can be calculated as follows (eq. 2).

$$f_{sav-NRE} = 1 - \frac{PER_{ref}}{PER_{sys}} \quad \text{(eq. 2)}$$

The f_{sav} cannot exceed a value of 1 but can be negative, depending on the choice of reference system (standard or renewable) and the performance of the SHC system (auxiliary electricity demand and fossil backup). A high f_{sav} indicates that a high solar fraction is given in the entire SHC system. The application's primary energy consumption has been eliminated by substitution with solar energies (solar thermal or photovoltaic).

These savings are used to generate a labeling to express the quality of the SHC systems. The labelling is based on the European energy labelling guideline 2010/30/EU (2010). The rating levels start from A+++ (best rating) to G (worst rating). If the considered SHC system has a lower primary energy demand than the reference system, the f_{sav} is greater than zero. The energy label is calculated for all subsystem (SH, DHW, C etc.) and the total system. The rating levels are kept in ten percent steps.

- Electrical Equivalent Seasonal Performance Factor (SPFequ)

Another technical key figure that is used to compare the systems is an "Electrical Equivalent SPF" (SPF_{equ}), which combines all non-renewable final energy sources (both electrical and energy carrier), by converting them into primary energy flows expressed in electrical equivalent units. This is achieved by using the relevant non-renewable primary energy factors for electricity (ε_{el}) and energy carrier (any kind of fuel) input (ε_{EC}). The SPF_{equ} is calculated following the unit conversion and ending up in eq. 3.

$$SPF_{equ} = \frac{PER_{NRE}}{\varepsilon_{el}} = \frac{\sum Q_{out}}{\sum\left(Q_{el} + \frac{Q_{EC}}{\varepsilon_{EC}} * \varepsilon_{el}\right)} \quad \text{(eq. 3)}$$

The electrical equivalent Seasonal Performance Factor for a subsystem (e.g. cooling $SPF_{equ\text{-}C}$) can thus be used to compare the application performance with a commonly used SEER value, even when hot backup is used as part of the heat supplied to a thermal chiller. The SEER declares the efficiency of a component under standardized testing conditions. The actual system performance is often much lower than these SEER values (cf. Wiemken et al. (2013), Nocke et al. (2014) and many more). Same SPF_{equ}'s indicates finally an equal primary energy demand, although the systems are supplied by different energy quantities.

However, when the building has a small solar cooling system relative to the size of a backup VCC system, the good performance of the solar cooling system may be undermined by the large fraction of cooling done by the conventional backup chiller. In this case, the SPF_{equ} of the solar subsystem can be used to represent the quality of SHC systems.

2.2. Economic assessment

Under the consideration of specific investment, replacement, operation and consumption based costs, the annualized costs for the entire system can be calculated by using the annuity method. Therefore derivative key figures (e.g. PE avoidance costs, etc.) are calculated easily.

All economically influencing parameters are pre-defined for the T53 Standard and country specific. Some of the values influencing the economical calculation are challenging and details could be discussed extensively. The aim of these calculations and definitions is to generate cut off values indicating a reasonable magnitude of economic effects. The results present best known averages and may differ from specific values.

If desired, own, project specific values can be implemented in the calculation. E.g. this is necessary if the application is serving domestic, commercial or industrial usage. Domestic prices are higher, but are mainly based on energy consumption. Commercial and industrial prices have low energy based costs, but can include capacity prices.

The economics that are defined prior for T53 and the eight countries are reaching from period under consideration, credit period, inflation rate, market discount rate, credit interest rate, inflation rate for energy prices electricity, inflation rate for energy prices, fraction of initial investment without financing up to the public funding's rate. Their main influence is visible when the different cost assets are discounted.

The consumption based costs are electricity and energy carrier prices for both energy and capacity or yearly costs. Water consumption costs are also defined as well as feed-in tariff for PV and for CHP with and without subsidies. The economic analysis is performed under the T53 standards. Main energy costs and economics are listed below. The prices are rather valid for commerce and industry and thus challenging for solar heating and cooling systems.

- Period under consideration (25 a), credit period rate (10 a)
- Inflation rate, market discount rate and inflation for energy prices (3%)
- Electricity energy prize (0.1 €/kWh) and electricity peak prize (80 €/kW)
- No subsidies, feed-in tariff for PV (0.03€/kWh)
- Natural gas energy prize (0.05€/kWh) and annual allowance (80 €/a)
- Water consumption (2.50 €/m²)

Not included are water treatment, distribution and heat / cold supply system costs.

Specific costs for each component include economy of scale prices. The greater the capacity of a certain component is the cheaper are the specific investment costs. Examples for different types of chillers are included in Figure 2. The investment curves indicate typical average and cut off values mainly valid for Central Europe. For each component the estimated lifetime, costs for maintenance, service and inspection is defined under consideration of VDI 2067. It has to be noted, that significant deviations to specific projects may occur. Therefore all values may be changed and user defined values can be implemented in the Excel Tool.

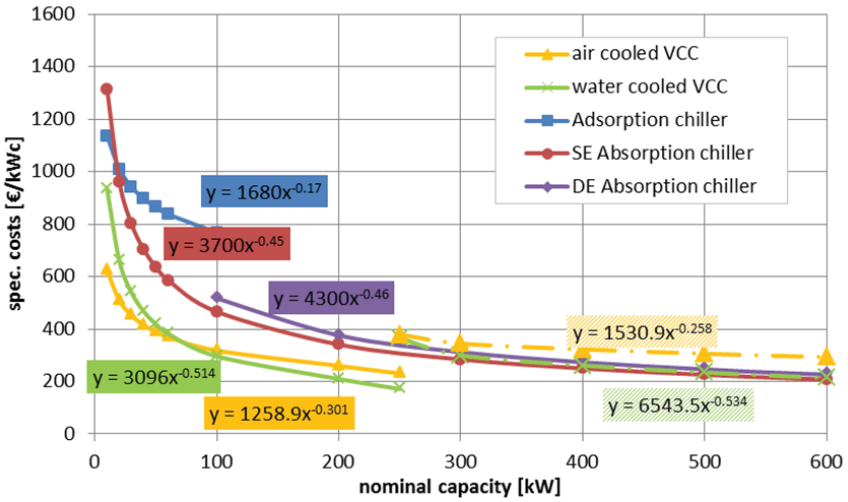

Fig. 2: Example of specific investment costs used for T53 standard calculation of investments for thermal and electrical driven chillers

The costs for each category are summed up and discounted to an annualized value according to the defined economics. The total annualized cost is the sum of yearly annualized investment, replacement and residual values, maintenance, electricity (auxiliary and if applicable domestic), energy carrier and water costs using the set of standard costs in the assessment tool. The Levelized costs of the SHC and also the one of the reference system are the ratio of annualized costs to the overall useful energy provided to the application.

Nevertheless, to avoid the discussion of absolute costs (e.g. when only taking sub systems into assessment) a cost ratio is calculated by comparing the Levelized costs of energy of the renewable systems with the Levelized costs of the reference systems.

$$CR = \frac{C_{tot.SHC}}{C_{tot.REF}} \qquad \text{(eq. 3)}$$

3. Analyzed best practice examples

The requirement for an annual cost analysis is the availability of annually measured or simulated data. There are many plants as demo- or research project in operation, but only a few were able to contribute with data. Therefore, the analyzed plants are a small selected group of photovoltaic driven and solar thermal driven systems.

Three PV and four ST systems, including some calculated derivatives, are presented and analyzed here. The most important facts are summarized in Table 2. The summary contains information of the status (monitored or simulated), the application (SH, DHW, C) and corresponding demand, solar technology used with capacity/size (ST in m², PV in kW_{peak}) and achieved solar fraction, the boiler and chiller type and its nominal capacity. The sizes vary from small scale (2 kW) up to large scale (1.5 MW). Main applications are domestic hot water combined with cooling

Regarding the design a differentiation between "full load" and "base load" is reasonable. In this sense the definition and explanation is as following.

- Base load: the solar heating and cooling system is design for assisting a larger auxiliary heating or cooling system, typically solar fraction appear between 20 to 60% appear in these bivalent systems.
- Full load: there is no backup for the solar heating and cooling system. Solar satisfies 100% of the energy demand of the according application.

None of the plants is intended for pure full load design. 6 of the example feature more than one application. The design often aims to satisfy one application by solar 100% whereas the second one runs in base load.

If there is no information available for the entire auxiliary heating / cooling system (no overall demands measured), the plants economic analysis appears to be a full load design. Two examples (#2, #3) are used to show the effect of full/base load design. A solar fraction is assumed for both and the key figures are recalculated. The derivations of these plants are marked with subscripts (3a, 5a).

Tab. 2: Fact sheet of examples

Plant	Status	demand		Solar technology			Boiler		Chiller		Source
	Monitored (MON) Simulated (SIM)	DHW/SH/C	Energy (MWh)	ST/PV	ST: Area (m^2) PV: peak capcaity (kWp)	Base or full load / magnitude SF [%]	Type	Capacity (kW)	Type	Capacity (kW)	
1	MON	SH C	175.2 15.5	ST	65	base / 20 full / 100	Pellets	300	ACM-SE	19	Nocke 2014
2	MON	DHW C	133.2 9.3	ST	240	full / 80 base / n.a.	Natural gas	70	ACM-SE	35	Mugnier 2015
2a						full / 80 base / 5			ACM-SE VCC	35 500	
3	MON	DHW C	143 949	ST	3800	full / 100 base / n.a.	-	-	ACM-SE	1500	Neyer 2013
3a						full / 100 base / 20			ACM-SE VCC	1500 5600	
4	SIM	DHW C	562.2 82.1	ST	720	base / 60 base / 30	Natural gas	270	ACM-SE VCC	20 70	Neyer 2016
5	SIM	DHW C	562.2 82.1	PV	70	base / 25	Heat pump	500	VCC	80	
5a				-	-	-					
6	MON	DHW	2.2	PV	0.47	base / 50	Split unit	2	-	-	Aquilar 2016
7	SIM	SH DHW	6.7 2.2	-	-	-	Brine heat pump	10	-	-	Thür 2016
7a				PV	2.5	base / 10					
7b				PV	2.5	base / 40					

4. Results

The assessment follows the above mentioned method of Task 53 and uses the standardized costs resulting in the following figures.

Figure 3 shows the breakdown of the total annualized cost of all plants and derivative calculations. Main cost driver are the investment cost; they aggregate between 40-60% of the overall costs. The ratio of investment cost is higher when the plants are smaller (#6, #7) or the information of the entire total system is missing (#2,#3). Second largest cost fraction are the energy cost (energy carrier or electricity). If PV surplus is feed in, the total costs reduce only slightly in #7a and #7b and up to 10% in #5. In the majority maintenance and replacement and residual value sums up to 20%.

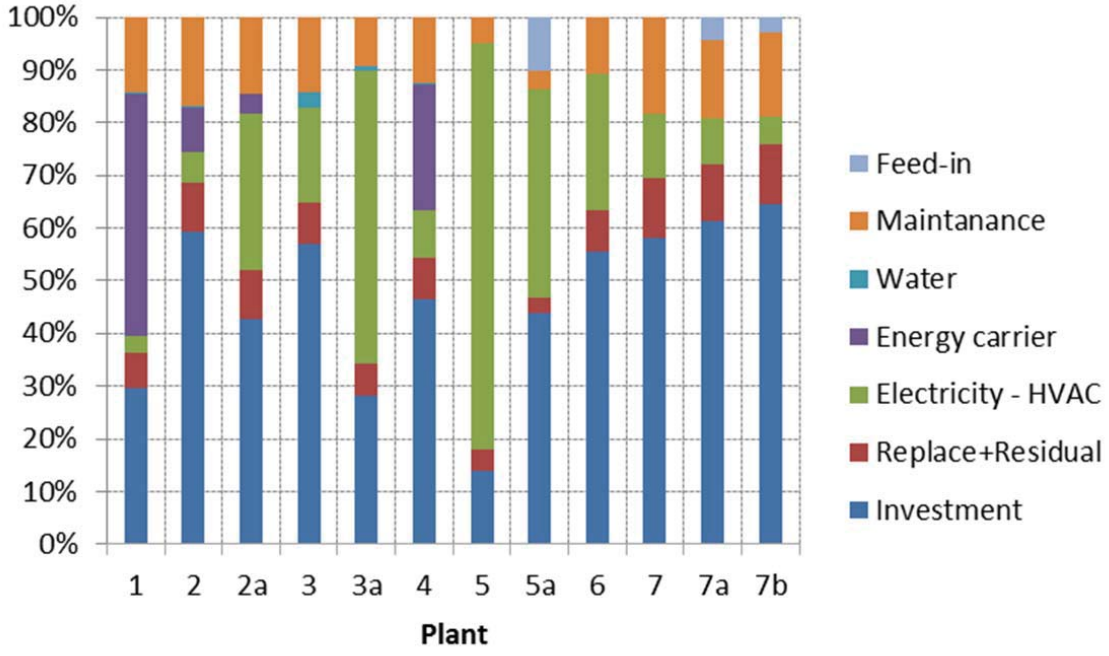

Fig. 3: break down of total annualized cost for al plants calculated with the T53 standard values.

The combined influence of non-renewable savings (f_{sav}) and the Cost Ratio (CR) is shown in Figure 4. The CR is displayed in reversed order on the y-axis in Fig. 4. A cost ratio of one is highlighted as bold line and is the value to be beaten by the solar driven heating and cooling systems. Values lower than 1 indicate that the entire SHC system is economical viable and thus cheaper than the T53 standard reference system (natural gas boiler, vapor compression chiller).

Each marker represents one plant. The target is a high non-renewable primary energy saving at affordable costs. The area in the upper right side represents that target. None of the analyzed plants can reach that area nor beat the CR of one. The trend shows, that more savings result in higher cost ratios and thus more expensive plants. Vice versa, the higher the investments are the more savings can be achieved – at least for these best practice examples.

All plants can achieve savings greater than 50% against the standard reference system. If another reference system would be chosen (e.g a heat pump system like #5a), the base is shifted accordingly (dashed lines). The average linear trend of PV and ST is displayed with a bold dotted line (PV) and a bold chain dotted line (ST).

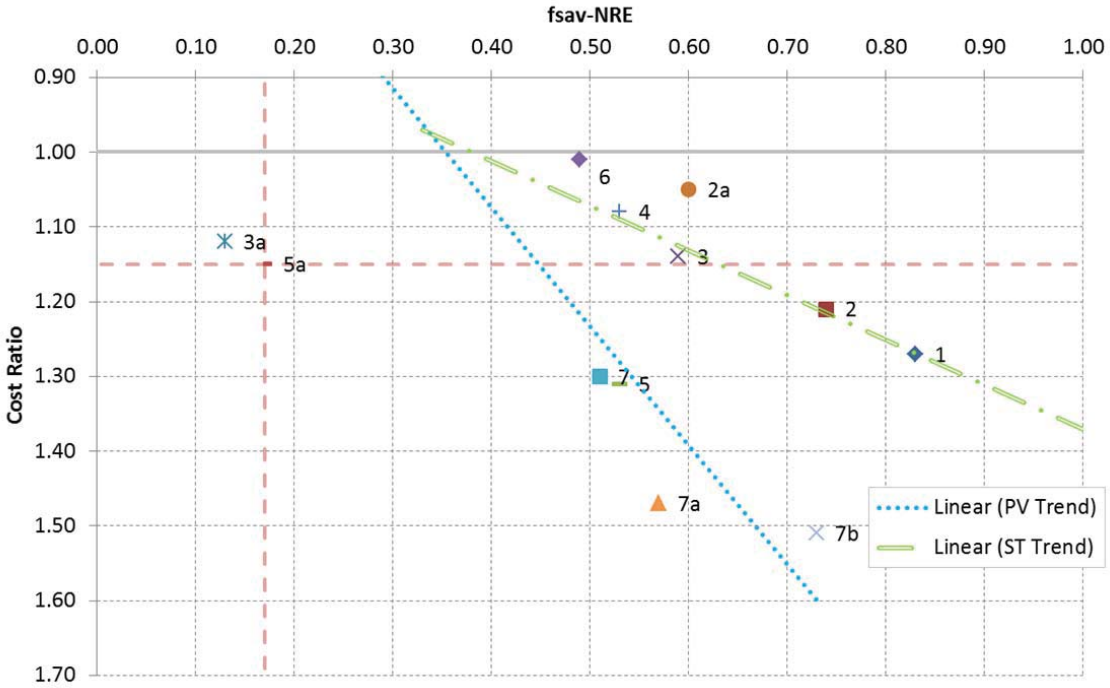

Fig. 4: Cost Ratio vs. non-renewable primary energy savings of the analyzed plants (1-7) and trends observed by PV and ST driven systems

Some findings of this line up are listed below. Including only 7 plants in the compilations, this is not representative, notwithstanding the trends are from interest and give a general view of solar heating and cooling.

- If 5a would be the reference (bold dashed lines), some examples would achieve cost competitiveness; one derivative example would decrease to negative savings.
- The plants with space heating (#1, #7a, 7b) are more expensive and can achieve higher savings.
- Heat pump systems (#5, #7) are more expensive than others.
- There is hardly any effect of the system size visible (cf. #6 – 2 kW & #3 1.5 MW).
- Type of heat pump system is shown clearly (#5 - DHW vs. #7 - SH)
- Climatic conditions are negligible.
- If gas back up is used, the f_{sav} is slightly smaller than the solar fraction (#3, #4)
- Against the common arguments the trend of PV and ST express that the sum of all solar thermal driven systems shows a smaller cost ratio with higher reachable savings than the PV driven systems.
- In this summary the economic parity of PV and ST can be reached below 40% savings.

After analyzing Figure 3 questions, especially regarding the boundary conditions of the comparison, are arising: What are the driving parameters for this constellation and how do they affect the results?

The sensitivity analysis was carried with four plants (ST: #1, #2 & PV: #5, #6). Following parameters were varied in the mentioned range.

- Primary energy factor (ε_{el}) 70 – 160% of ε_{el} = 0.4 kWh_{el}/kWh_{prim}
- Investment costs (invest) 50 – 130% for solar components
- Electricity costs (C_{el}) 50 – 150% of C_{el}=0.10 €/kWh
- Electrical efficiency ($Q_{el.sys}$) 70 – 130% of auxiliary electricity demand

The results are presented in Figure 5. The primary energy conversion factor for electricity is only affecting the non-renewable primary savings and results in horizontal lines. The investment cost and the electricity cost are only affecting the cost ratio, consequently resulting in vertical lines. An effect on both key figures is achieved by the change of the electricity demand of the entire system. This can be interpreted either as an improvement of the electrical efficiency of the heat pump or the reduction of the auxiliary electricity demand.

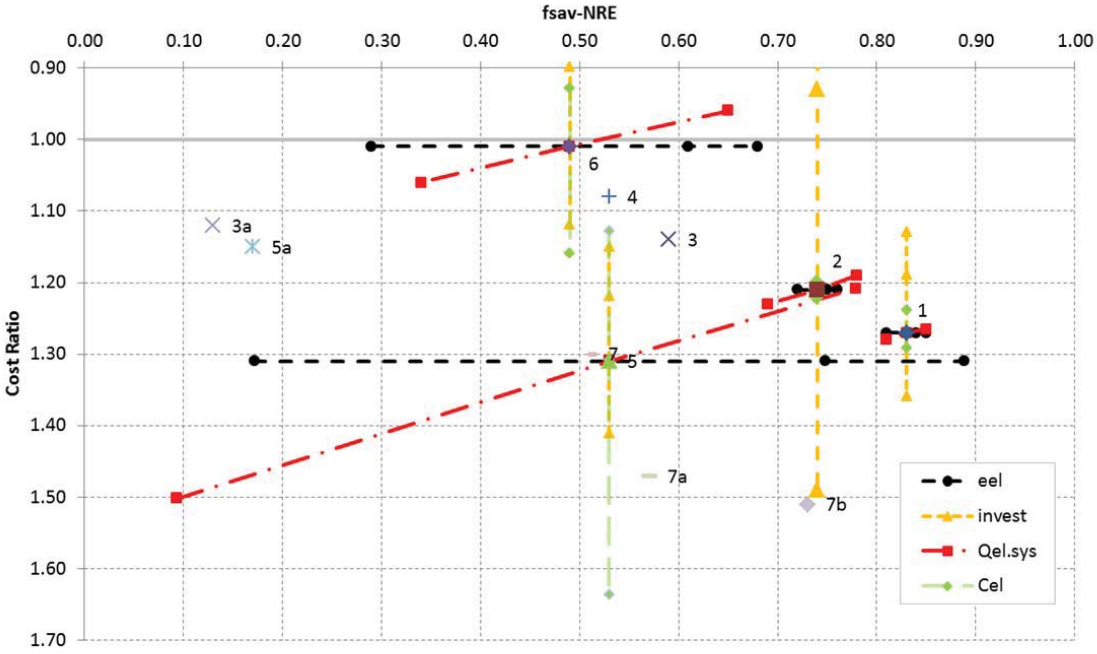

Fig. 5: Sensitivity analysis of two PV and two solar thermal driven plants

The two solar thermal plants (#1, #2) are less sensitive on the electric parameters (ε and SPF_{el}). Both thermal systems were designed and optimized regarding the auxiliary electricity demand. Thus the influence of changing input values is lower than for electrical driven systems.

The variation of ε_{el} results in a change of ±0.05 in the f_{sav} for the solar thermal plants but ±0.3 for the PV driven plants. The influence is less for ST because they are optimized towards low auxiliary electricity consumption. Thus electricity driven system are more sensitive the less the solar fraction.

Electrical efficiency is an important issue for PV supported systems. Only if the heat pump systems are optimized the systems get economical viable. Increasing the PV area increases the savings but also the cost ratio although the surplus energy rises and the revenues due to feed-in are increasing. If a system is optimized to a high standard, the less it can be influenced by varying input parameters.

Investment costs have a higher influence on the results of the solar thermal plant, due to the fact that the ratio of investment cost to all other costs is higher. Plant #6 and #2 could reach a cost ratio of 1 with lower investment costs. Plants #5 and #1 would reach affordable economics.

The sensitivity analysis shows that PV and ST are cutting across with the same trends (e.g. #2 and #5 if electricity demand is optimized). To reach cost competiveness lower investment costs have to be derived first, followed by the efficiency of the system. The chosen (or rather standardized) primary energy conversion factors have a great influence on the results and need to be stated clearly to interpreter correctly.

5. Conclusions

A comprehensive tool was developed in the course of IEA SHC Task 53 and is available for the analysis and assessment of new generation of solar heating and cooling systems. The key figures that are calculated allow a benchmarking and simplify the comparison of different system configurations. The Tool can be used to benchmark against a standardized reference systems or against other renewable heating and cooling technologies. Still, the comparability is challenging if applications and configurations are mixed. Nevertheless, a trend wise comparison of magnitudes can definitely be achieved. The tool can be downloaded at http://task53.iea-shc.org/.

One figure, that can be used to compare the application performance with a commonly used SEER value based on electricity, is the electrical equivalent Seasonal Performance Factor (SPF_{equ}). This key figure summarizes the performance even when both, electricity and heat is used to supply the entire system.

The presented plants show good performances resulting in non-renewable primary energy savings of more than 50%. None of the plants can reach a cost ratio below 1. The trend shows, that more savings result in higher cost ratios and thus more expensive plants. The four solar thermal plants show a lower gradient in the comparison than the three PV driven systems resulting in higher costs per saving.

The sensitivity analysis displays that PV and ST are cutting across with the same trends. Lower costs have to be derived first, followed by the efficiency of the system. Cost competiveness is achievable for both technologies! Change of conversion factors equals PV and ST driven systems even more, independently of the total system. Both technologies have their advantages and are desirable.

More comprehensive collection of annual data will be carried out in the ongoing Task 53 and will be presented within those activities.

6. References

Aguilar F.J., Aledo S., Quiles, P.V, 2016. Experimental study of the solar photovoltaic contribution for the domestic hot water production with heat pumps in dwellings, Applied Thermal Engineering, Volume 101, 25 May 2016, Pages 379-389, ISSN 1359-4311

Eicker, U., 2012. Solar thermal or Photovoltaic Cooling?, presentation at Intersolar Europe 2012, Munich, Germany

Frank, E., Haller, M., Herkel, S., Ruschenberg, J., 2010, Systematic classification of combined solar thermal and heat pump systems. Proc. of the International Conference on Solar Heating, Cooling and Buildings 2010, Graz, Austria

Henning, H-M., 2010. Solar air-conditioning and refrigeration – achievements and challenges, keynote at Eurosun 2010, Sept.28th -Oct.2nd 2010,Graz

Mugnier, D., 2015. DHW/cooling hybrid strategy for solar cooling: two successful year monitoring results, 6th International Conference Solar Air Conditioning. Roma, Italy, September 25th-27th, 2013. Regensburg: OTTI - Ostbayerisches Technologie-Transfer-Institut, ISBN 978-3-943891-54-6, S.89-93

Neyer D., Neyer J., Thuer A., Fedrizzi R., Vittoriosi A., White S., Focke H., 2015. Collection of criteria to quantify the quality and cost competitiveness for solar cooling systems, Solar Heating and Cooling Programme, Task 48, 2015.

Neyer, D., Gritzer, F., Thür, A., Kefer, P., Focke, H., 2016. Towards a solar hybrid solution for heating and cooling, Eurosun 2016, Palma de Mallorca, Spain

Neyer, D.; Schubert, M., 2013. Practical experience and simulation of a large solar thermal driven cooling plant in Singapore, 5th International Conference Solar Air Conditioning. Bad Krozingen, Germany, September 25th-27th, 2013. Regensburg: OTTI - Ostbayerisches Technologie-Transfer-Institut, ISBN 978-3-943891-21-8, S. 319 - 324.

Nocke, B., Preisler, A., Brychta, M., Neyer, D., Thür, A., Pucker, J., Focke, H., Podesser, E., Hannl, D.,

Schubert, M., 2014. Primärenergetische Optimierung von Anlagen zur solaren Kühlung mit effizenter Analgentechnik und innovativen Regelstrategien, Vienna, Austria

Streicher, W., Neyer, D., Weissensteiner, T., 2010. Practical experience of two small scale cooling plants and cost comparison to PV driven chillers, Eurosun 2010, Graz, Austria

Thür, A., Calabrese, T., Streicher, W., 2016. Smart Grid and PV driven Heat Pump as Thermal Battery in Small Buildings for optimized Electricity Consumption, Eurosun 2016, Palma de Mallorca, Spain

Wiemken, E., Safarik, M., Zachmeier, P., Hagel, K., Wittig, S., Schweigler, C., Nienborg, B., Petry Elias, A., 2013. EVASOLK – Schlussbericht – öffentlicher Teil, Germany

Conference Proceedings

EuroSun 2016
Palma de Mallorca (Spain), 11 - 14 October 2016

Performance Testing and Optimization of Solar Assisted Heating Systems for Multi-Family Houses

Sonja Helbig[1], Jan Steinweg[1], Daniel Eggert[1], Mario Adam[2]

[1] Institut für Solarenergieforschung Hameln (ISFH), Am Ohrberg 1, 31860 Emmerthal (Germany)

Phone: +49 5151 999 642, E-Mail: s.helbig@isfh.de

[2] Hochschule Düsseldorf (HSD), ZIES, Münsterstraße 156, 40476 Düsseldorf (Germany)

Abstract

The variety of designs for solar assisted heating systems (also called solar combisystems) in multi-family houses is wide and has not been evaluated systematically. Functional insufficiencies, resulting from unfavorable device combinations as well as improper control design place significant market barriers for the application of this technology. Using hardware-in-the-loop tests, functional aspects of the most common system designs are investigated and evaluated. Further dynamic system simulations on an annual basis allow an energetic evaluation and later a comparison of the different design options. In this contribution we present the results for the first tested solar assisted heating system. Furthermore, the study suggests the introduction of a novel evaluation parameter referred to as the *performance factor of the central heating facility,* and a novel reference parameter referred to as the *demand-specific collector area*. A newly developed benchmark procedure is comparing the central heat demand of the building to the maximum solar thermal gain of the solar circuit in order to calculate the maximum performance factor possible for an idealized central heating facility. Using this benchmark procedure, optimization potentials are exemplarily disclosed for the tested solar combisystem. The results highlight a high optimization potential of the system control and the process layout of central heating facilities, achievable with low cost at the same time.

Keywords: *solar combisystem, hardware-in-the-loop, whole system testing, system simulation, benchmark*

1. Introduction

The high theoretical potential for the reduction of final energy demand through the use of solar assisted heating systems was pointed out in earlier studies (e.g. Papillon, 2010). But there is a difference between theoretical potential and real final energy savings. One reason for the divergence are significant insufficiencies of the yield and the efficiency of solar assisted heating systems as result of inadequate hydraulic installation (Letz et al., 2010). Moreover, there is a wide and largely un-evaluated variety of available hydraulic designs for solar combisystems, especially for multi-family houses (MFH). Such systems combine the components solar thermal collectors, thermal storage tank(s), heat source(s) and distribution circuits. The research project "solar assisted heating systems for multi-family houses" (SUW-MFH) intends to identify the most efficient system design based on a functional, energetic and economic evaluation of these systems.

Selected common designs of large central solar combisystems are tested as integrated systems by hardware-in-the-loop (HIL) measurements to identify insufficient controller, valves, hydraulic connections and interaction between components. Besides functional evaluation of the investigated systems, the results of HIL measurements serve as data base for the validation of dynamic simulation models. Based on simulation results an energetic evaluation is performed by comparing the results to a newly developed benchmark procedure. An economic evaluation and comparison of the diverse system designs will be performed at a later stage of the project and respective results will be reported in future communications.

doi:10.18086/eurosun.2016.04.13 Available at http://proceedings.ises.org

Nomenclature		
A_{col}	collector area	[m²]
a_{dsc}	demand-specific collector area	[m²/MWh]
CPF	performance factor of the central heating facility	[-]
E_{final}	final energy demand	[kWh]
n_{HS}	number of heat sinks	[-]
$Q_{central}$	central heat demand of the building	[kWh]
Q_{circ}	heat losses due to domestic hot water circulation	[kWh]
Q_{DHW}	heat demand for domestic hot water draw	[kWh]
Q_{dist}	heat losses due to distribution of heat within the building	[kWh]
Q_{SH}	heat demand for space heating	[kWh]
$Q_{sol,eff}$	effective solar thermal gain	[kWh]
$Q_{sol,max}$	maximum solar thermal gain	[kWh]
$Q_{sol,pot}$	potential solar thermal gain	[kWh]
T_m	mean temperature	[°C]

2. Methodology of performance testing and evaluation

2.1. Hardware-in-the-loop measurements and dynamic system simulation

In order to standardize boundary conditions for performance tests of solar combisystems, only the central components of these systems (in the following referred to as *central heating facility*) are integrated into HIL tests. These central components may be thermal storage tank(s), a solar heat transfer station, an auxiliary heater, central fresh water station(s) and respective hydraulic connections. The components are implemented factory-set and connected to several emulators which serve as solar heat source and building heat sink (space heating, domestic hot water draw and circulation). The behavior of the emulators and their interaction with the central heating facility is calculated by real-time simulations in TRNSYS. Employing a time discretization of one minute, measured data of the HIL test is given as an input to the simulation environment which then adjusts the present set-values of the emulators. Therefore, the emulators are allowed to react to the instant behavior of the central heating facility rather than just follow a predetermined load profile. Weather conditions and solar thermal collectors as well as the building are part of the dynamic simulation model to ensure equal conditions for all solar combisystems under consideration in this work (see Table 1).

Tab.1: Boundary conditions for hardware-in-the-loop measurements and dynamic system simulation

	Description	**Values**
weather data	Meteonorm, location: Zurich, Switzerland	• days for HIL measurements: 38, 71, 99, 112, 175, 230, 250, 356
solar thermal circuit	solar thermal collectors as well as pipes between roof and central heating facility	• collector area: variable between 0 m² and 32 m² • inclination: 45°, orientation: south • total pipe length: 53.5 m
space heating and distribution	multi-family house in Germany with a construction year between 1958 and 1968 and an energy-focused refurbishment according to the standards of EnEV 2009	• multi-zone simulation model (52 thermal zones) • number of flats: 8 or 16 (depends on the size of the tested system) • detailed distribution network with more than 100 pipe sections (for a house with 8 flats) • size of a flat: 65 m² • heating system: radiators
domestic hot water draw	draw profile generated with DHWcalc (Jordan, Vajen, 2014)	• 55 litre per flat and day (assumption of 1.8 inhabitants per flat)
domestic hot water circulation	constant circulation 24 hours a day	• 19 litre per hour and flat (according to a maximum temperature difference in the flow line of 5 K)

HIL measurements are performed for eight individual days capable of representing typical meteorological patterns during the course of a year. The days are selected in order to cover all possible load situations of the systems which can occur over a year. Related approaches exist on the literature, e.g. a good prediction of the annual thermal performance (Haller et al., 2013), but have turned out to be inadequate for the HIL method employed in this work. The chosen day sequences include sunny and cloudy days in all seasons as well as extreme climate settings for winter and summer. The respective HIL tests are measured separately, always regarding both pre- and post-conditioning of the system and the related simulation model to ensure defined start conditions for devices and model and to allow the calculation of thermal capacity changes.

A new HIL test facility has been developed and implemented at the ISFH, capable of emulating up to 20 flats in a MFH. Figure 1 provides an overview of this test facility. It shows the first tested solar combisystem during operation.

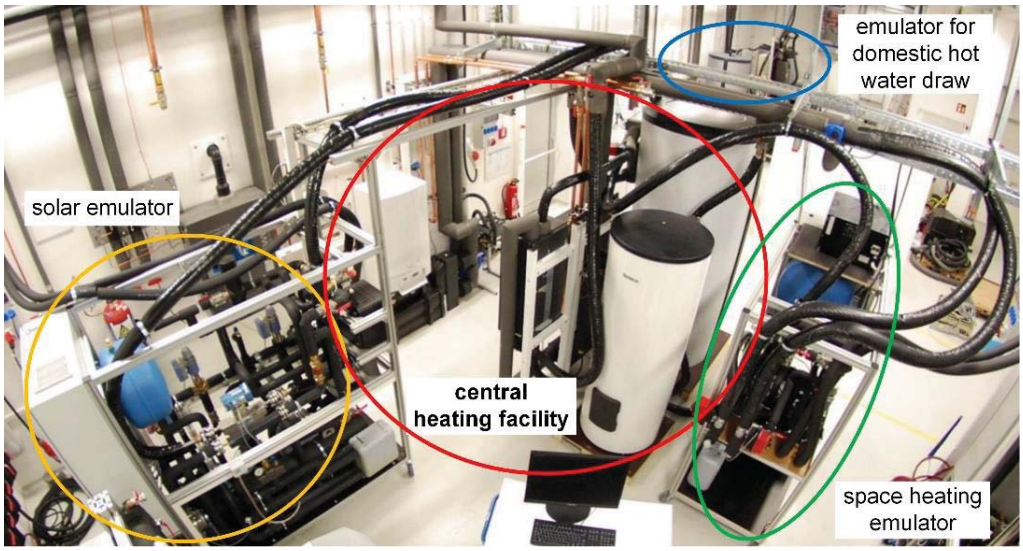

Fig. 1: Hardware-in-the-loop test facility developed for the emulation of up to 20 flats in a MFH and 60 kW solar thermal collector power, equipped with a central heating facility (red encircled), space heating emulator (green), solar emulator (yellow) and emulator for domestic hot water draw (blue)

For simulations of the complete solar assisted heating systems, the dynamic simulation model is extended by the components of the central heating facility. The added components of the model are parametrized and validated by using datasets from the HIL tests. Firstly, by qualitative comparison of measured and simulated temperature and mass flow curves, respectively, to ensure adequate implementation of control strategies and control hysteresis. Secondly, by quantitative comparisons of the energy balances of both individual components and the overall system, to guarantee the eligibility of the simulation model for further energetic evaluations of the solar assisted heating system. Therefore, the validation procedure can ensure high quality of simulated values on the one hand while allowing fast variations and optimizations of the control system, hydraulic connections or components on the other hand. The performed system simulations are covering a complete annual period, discretized by minutes, thus allowing to assess the specific system dynamics.

2.2. Energetic evaluation of solar assisted heating systems

Figure 2 shows the system boundaries employed for balancing a solar assisted heat supply for MFH. Of particular interest are the boundaries of the central heating facility comprising the solar thermal and final energy inputs and the heat loss and central heat demand as output. The final energy input covers fossil fuel and electricity whereas the central heat demand of the building ($Q_{central}$, see Equation 1) considers the heat demand for space heating (Q_{SH}) and distribution heat losses (Q_{dist}) as well as the heat demand for domestic hot water draw (Q_{DHW}) and circulation (Q_{circ}). Distribution heat losses as well as heat losses caused by domestic hot water circulation address heat demands to the central heating facility such that, the central heat demand of the building must not be equalized with useful energy.

$$Q_{central} = Q_{SH} + Q_{DHW} + Q_{dist} + Q_{circ} \quad \text{(eq. 1)}$$

A part of distribution and circulation heat losses can be credited as heat gains if they are localized inside the boundary of useful energy in Figure 2. By occurring outside of the boundary of a central heating facility it is not of further interest for an energetic evaluation of a central heating facility. For an overall evaluation of the heat supply of a MFH, which is not part of this paper, heat gains have to be taken into account.

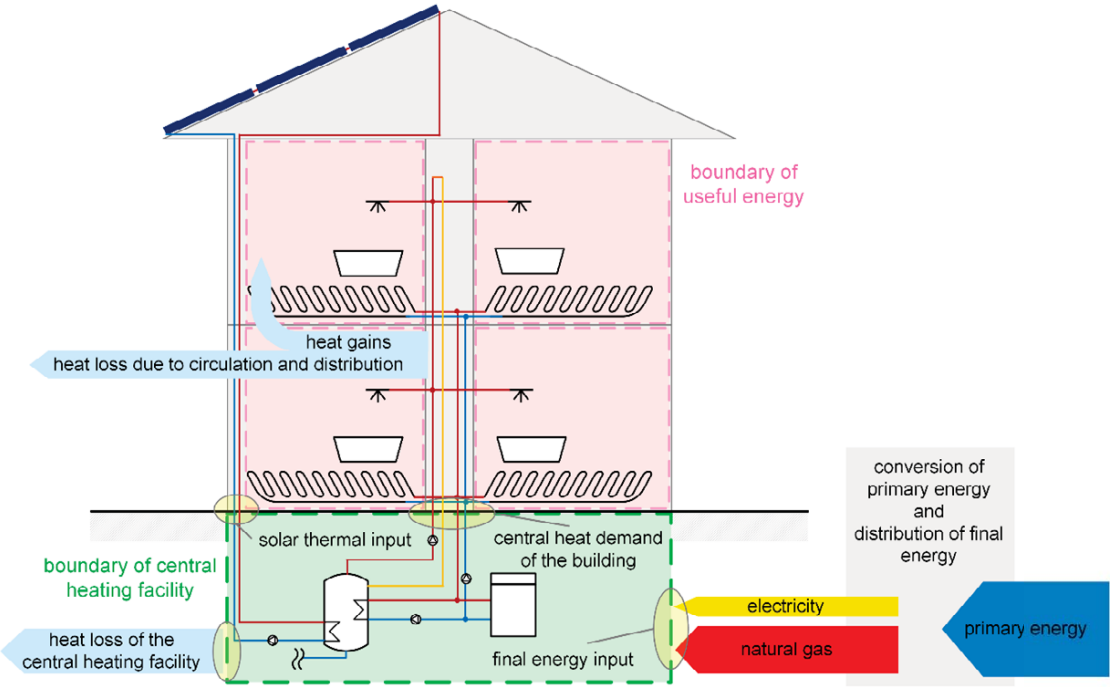

Fig. 2: Definition of system boundaries for the energetic evaluation of central heating facilities as part of solar combisystems in multi-family houses

To evaluate and compare different designs of solar assisted heating systems a novel evaluation parameter is introduced, referred to as the *performance factor of the central heating facility* (CPF, see equation 2). It is defined by the ratio between the central heat demand of the building as energetic benefit and the final energy input (E_{final}) as energetic effort.

$$CPF = \frac{Q_{central}}{E_{final}} \qquad \text{(eq. 2)}$$

The interpretation of the CPF is comparable to the seasonal performance factor (SPF) of solar heat pump systems as of IEA SHC TASK 44 (Malenković et al., 2013). In extension to this, the CPF is applicable to all central heating facilities of solar assisted heating systems owing to proper definition of system boundaries. Note that in the specific case of a solar combisystem without a central heating facility, or 100 % solar fraction, it is not advisable to use the CPF as evaluation parameter.

The CPF if highly dependent on the defined boundary conditions of performance testing (solar thermal circuit, weather and building properties). In consideration of this, and to ensure a wide comparability of systems, we also suggest a novel reference parameter, referred to as *demand-specific collector area* (a_{dsc}). It is defined as the ratio between collector area and central heat demand of the building:

$$a_{dsc} = \frac{A_{col}}{Q_{central}} \qquad \text{(eq. 3)}$$

2.3 Benchmark procedure

A benchmark procedure has been developed to estimate the effective solar thermal gain ($Q_{sol,eff}$) which can be utilized by an idealized central heating facility. The procedure extends an approach by Steinweg et al. (Steinweg et al., 2016) and employs the calculation of a maximum possible CPF. The method is comparable to the FSC procedure of IEA SHC TASK 26 (Letz, 2002). In contrast to the FSC method the benchmark procedure used here matches the central heat demand of the building with the maximum solar thermal gain of

the solar circuit ($Q_{sol,max}$) rather than the solar thermal potential. Both approaches rely on monthly energy data. However, it turned out that taking into account the efficiency of the solar thermal collectors and heat losses between collectors and central heating facility yields to a more realistic estimation of the CPF. Central assumptions and boundary conditions of the benchmark procedure are:

- monthly correlation of maximum solar thermal gain and central heat demand of the building (idealized thermal storage tank)
- no heat losses and no parasitic energy (electricity) consumption of the central heating facility
- conversion of final energy without losses
- characteristics of solar thermal collector, weather conditions and central heat demand of the building are boundary conditions

Main part of the benchmark calculation is the determination of the effective solar thermal gain which represents the solar thermal input to the central heating facility. Basis of this is on the one hand the calculation of the maximum solar thermal gain for different mean temperatures (T_m) of the collector fluid with the chosen collector specification (see Figure 3). On the other hand the central heat demand of the building needs to be separated into different heat sinks with their mean temperatures (see Figure 4).

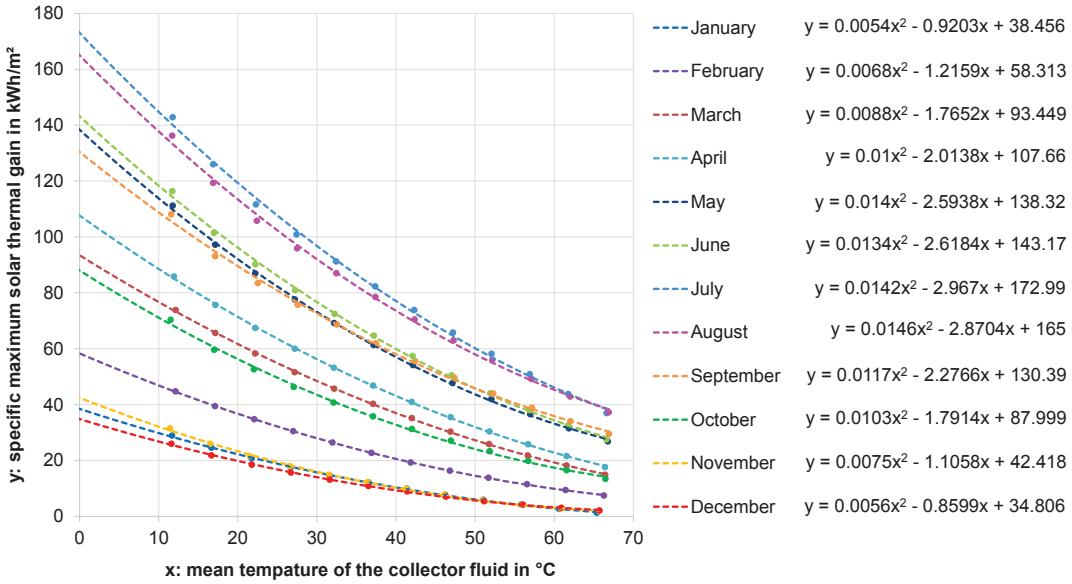

Fig. 3: Specific maximum thermal gain of the solar circuit over the mean temperature of the collector fluid on a monthly base accompanied by formulas of the trend lines (weather: Zurich)

Figure 3 shows the area specific maximum gain of the solar thermal circuit as function of the mean temperature of the collector fluid. The functions are correlated for every month in the year based on dynamic system simulations performed with TRNSYS, regarding an area specific mass flow rate of 50 kg/(h·m²) and Meteonorm climate data for the city of Zurich. The correlated functions (second degree polynomial) are provided in the figure. The functions allow the direct calculation of the maximum solar thermal gain for each month, once the collector area and the mean temperature of the individual heat sinks are set.

Figure 4 exemplifies for a selected month (March), how the central heat demand of the building may be split up into different heat sinks. The same procedure is used for the other months of a year. The figure regards three heat sinks: space heating (SH: red), domestic hot water draw (DHW: green) and domestic hot water circulation (circ: blue). For these heat sinks the specific heat demand and the temperature interval at which the demand occurs are indicated. Inspection shows that the respective temperature intervals for space heating and DHW circulation are quite small (7 K and 4 K, respectively), but the one for DHW draw is much higher (56 K: from 10°C to 66°C), than a standard solar thermal collector could possibly provide. Standard solar devices are typically capable of temperature shifts of about 15 K (with some degree of type- and operation-strategy-

specific variety). To adjust a system to this interval, heat sinks comprising larger temperature intervals may be subdivided accordingly. For example in Figure 4, the domestic hot water demand is subdivided into four separate heat sinks which sum up to the same total demand, while the temperature intervals of the individual sink is adjusted to a level of about 14 K, maintaining the following temperature level order:

- $T_{m,i} < T_{m,(i+1)}$: $T_{m,DHW,1} < T_{m,SH} < T_{m,DHW,2} < T_{m,DHW,3} < T_{m,DHW,4} < T_{m,circ}$

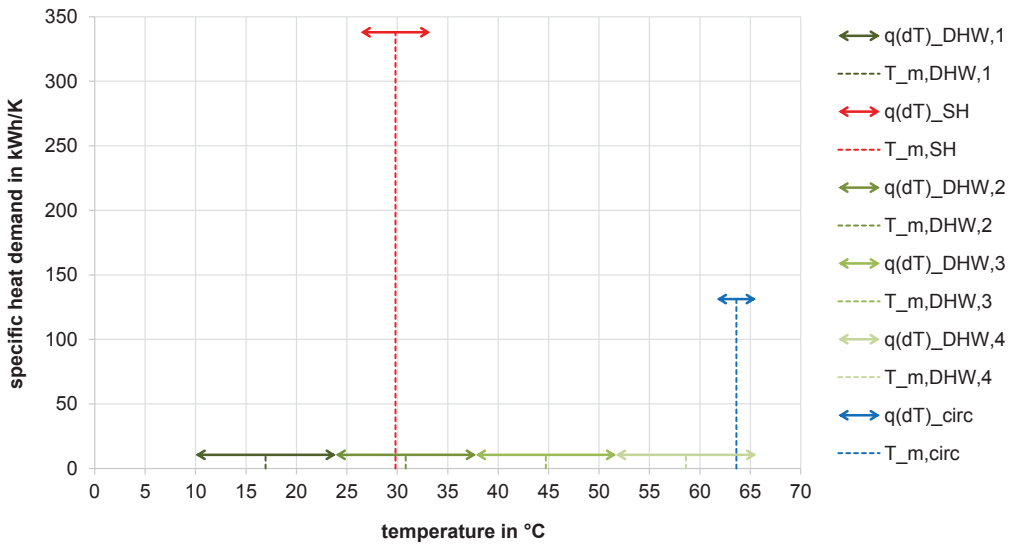

Fig. 4: Specific heat demand (q) over the corresponding temperature intervals (dT) and the resulting mean temperature (T_m), exemplified for the month March and for different heat sinks considered: hot water circulation (circ), space heating (SH) and domestic hot water draw (DHW,1-4: divided into four heat sinks)

The effective solar thermal gain is calculated on monthly basis ($Q_{sol,eff,k}$) by the following procedure: Firstly, the heat demand of the heat sink ($Q_{hs,i}$), which appears at the lowest temperature level is matched with the maximum solar thermal gain at this temperature ($Q_{sol,max}(T_{m,i})$). If the heat demand of the first heat sink is lower than the maximum solar thermal gain, the remaining solar gain is offered to the next heat sink in the temperature range. This procedure may be repeated until the maximum number of heat sinks (n_{hs}) is reached, or the maximum solar thermal gain is exploited. The potential solar thermal gain ($Q_{sol,pot}$) is an auxiliary quantity and not subject of further reflection:

$$Q_{sol,eff,k} = \sum_{i=1}^{n_{hs}} Q_{sol,eff,k,i} \qquad \text{(eq. 4)}$$

with: $Q_{sol,eff,k,i} = min\left(Q_{sol,pot,k,i}, Q_{hs,k,i}\right)$

$i = 1$: $Q_{sol,pot,k,i} = Q_{sol,max,k}\left(T_{m,i}\right)$

$i > 1$: $Q_{sol,pot,k,i} = Q_{sol,max,k}\left(T_{m,i}\right) \cdot \left(1 - \frac{Q_{sol,eff,k,(i-1)}}{Q_{sol,pot,k(i-1)}}\right)$

month: $1 \leq k \leq 12$

heat sinks: $1 \leq i \leq n_{hs}$ with $T_{m,i} < T_{m,(i+1)}$

The maximum possible CPF (benchmark) can be derived from the sums of the monthly central heat demand and effective solar thermal gain under consideration of the assumptions mentioned above:

$$CPF_{benchmark} = \frac{\sum_{k=1}^{12} Q_{central,k}}{\sum_{k=1}^{12}(Q_{central,k} - Q_{sol,eff,k})} \qquad \text{(eq. 5)}$$

3. Evaluation and optimization potential of the first tested solar assisted heating system

3.1. Description of the system and validation of the simulation model

The tested solar combisystem represents a conventional central heating facility upgraded by a solar thermal unit. A simplified hydraulic layout is sketched in Figure 5. Solar complemented parts (besides the solar thermal circuit) are a solar thermal storage tank, a solar station and a fresh water economizer. Solar thermal heat is fed into the system only through the solar thermal storage tank, from where the heat is distributed for preheating of cold freshwater and for shifting the temperature of the return flow to the boiler. The boiler is providing heat either for space heating or for the domestic hot water tank with priority for the latter. Both thermal storage tanks are equipped with internal heat exchangers without stratified charging devices. The emulated hydraulic circuits of the system are indicated by yellow background color in Figure 5. Beside the hydraulic circuits two temperature sensors are emulated by electrical resistor cascades. These are the ambient temperature sensor, used by the boiler for calculating the heating curve and the collector temperature sensor which is important for the operation of the solar station.

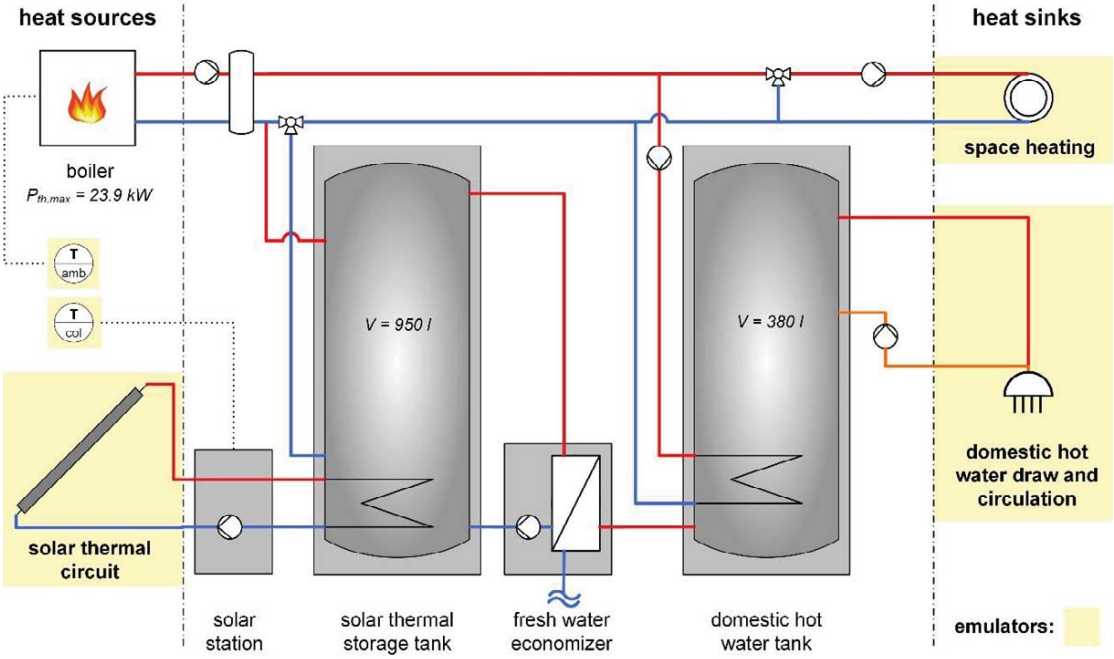

Fig. 5: Simplified hydraulic layout of the tested central heating facility with attached emulators (yellow)

The tested solar assisted heating system is dynamically simulated in TRNSYS. The validation of the model shows good results in the qualitative as well as in the quantitative comparison, see Table 2. These results have been calculated using the system boundary of the central heating facility indicated in Figure 2. The calculation considers the sequence of eight representative days during the course of the year, as explained earlier. As it turned out, for the day which represents an extreme, hot summer day, the allowed operation temperature of the solar thermal emulator was exceeded and therefore, this specific day had to be excluded from the results. Electricity as parasitic energy for the operation of electric devices like pumps and system control has not been measured and is therefore not part of the comparison in Table 2. But being a simulation result, the electricity consumption will be considered for the energetic evaluation based on the annual simulation results.

Tab. 2: Comparison of energy balances between HIL measurement and simulation of the first tested central heating facility as cumulated values of seven analyzed days (without extreme summer day)

			HIL measurement [kWh]	**simulation** [kWh]	**difference** [%]
input	final energy input	natural gas	2893	2894	0
	solar thermal input		173	169	-3
output	central heat demand of the building	SH + dist	-2408	-2428	1
		DHW	-95	-97	2
		circ	-113	-115	1
	heat losses		-65	-45	-30

The differences between simulated and measured cumulated energy amounts are lower than 4 % (relative value). There is one exception of this: the heat losses of the central heating facility exhibit a deviation of -30 %, which, however, results from the heat loss measurement and not from the simulation. The heat losses represent not a directly measured quantity but is calculated from the energy balance of the individual components of the central heating facility. In this situation, related measurement errors are superimposed as heat loss which leads to overestimation of the true value. Despite of this, the absolute divergence between simulated and measured heat losses amounts to 20 kWh. Compared to the total central heat demand of the building of 2617 kWh (measured), the heat loss deviation between HIL measurement and simulation can be tolerated.

3.2. Functional analysis

HIL measurements of the tested solar assisted heating system disclose two functional insufficiencies of the control system:

- The boiler controller is not working properly.
- A restricted interaction between the boiler controller and the controller of the solar thermal storage tank leads to a limited usage of solar thermal heat.

The boiler comprises a modulating burner with a nominal heat output between 4.8 kW and 23.9 kW (in condensing mode). As long as heat is solely produced for space heating, the burner is modulating perfectly within this power range. However, when supplying heat for the domestic hot water tank, the boiler is operating like having a single stage burner at maximum heat output. Due to a limited heat transfer capacity of the internal heat exchanger in the domestic hot water tank, the burner displays a high number of start-stop-cycles. Although this behavior does not entail efficiency loss, reduced durability of the burner device must be expected.

Another insufficiency of the tested system is the limited usage of solar thermal energy. As it is shown in Figure 5, there is a hydraulic connection (via the hydraulic separator) for using solar heat from the solar thermal storage tank to heat up the domestic hot water tank (under consideration of temperature levels). But the control system is not allowing an exclusive usage of solar thermal energy for charging the domestic hot water tank. Instead, the boiler is running the whole year, providing heat which could also be taken partly from the solar thermal storage tank without using any fossil fuel.

3.3. Identification of optimization potential by means of the benchmark procedure

The energetic analysis is based on dynamic system simulations covering a complete annual period. Among other possible parameters the evaluation is focused on the performance factor of the central heating facility as a function of the demand-specific collector area (see Figure 6). Therefore, several simulations with a variable collector area (between 0 m² and 32 m²) and a constant central heat demand of the building were performed. A comparison between the tested system installed factory-set and the benchmark allows to assess the optimization potential. A detailed analysis with a simulative approach identifies thereby single limitation sources.

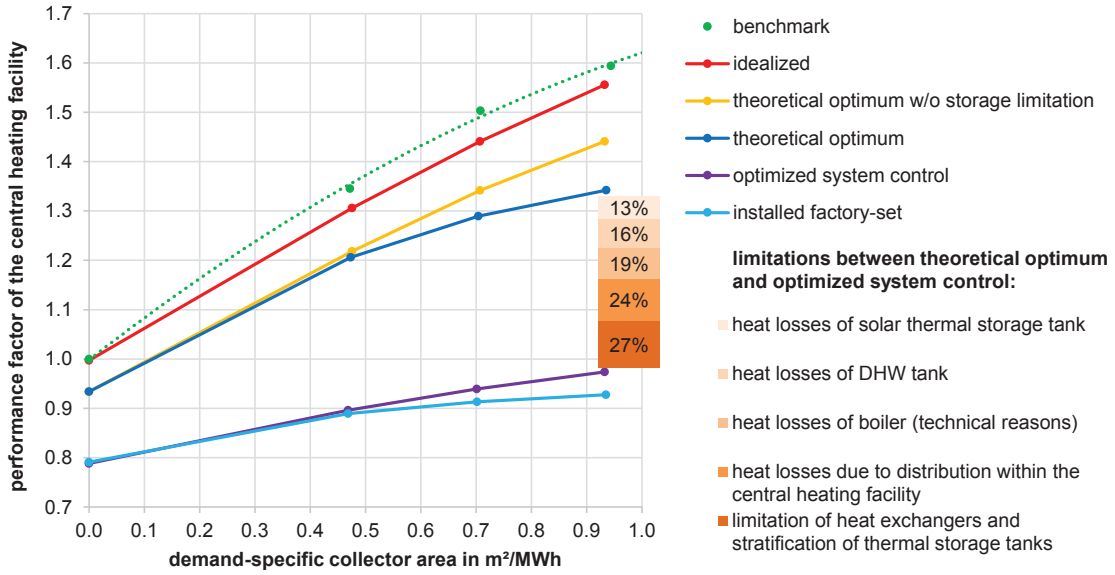

Fig. 6: Comparison between the benchmark and the CPF of the tested central heating facility (installed factory-set) by analyzing the different limitation sources

In the first place, the control system is optimized by eliminating the functional insufficiencies of the system which have been described earlier. This optimization can be done without any financial or material effort. The larger the demand specific area, the higher the optimization potential of the CPF by an improved usage of solar thermal energy. A second optimization series has been simulated, called "theoretical optimum". Therefore, different technical and chemical possible optimizations have been done, without changing any system components. The single limitation sources between "optimized system control" and "theoretical optimum" and their percentage influence for the improvement of the CPF are shown in Figure 6. The limitation of heat exchangers and a limited stratification of the thermal storage tanks have the largest influence on the CPF. Whereas the heat losses of the thermal storage tanks show the lowest limitation, the heat losses due to distribution within the central heating facility comes up to be the second highest deficit. Heat losses of the boiler only consider technical limitations caused by radiation losses and combustion inefficiency. Another limitation of the analyzed system, compared to the benchmark, is the limited storage capacity of the solar thermal storage tank. The impact of an increased solar thermal storage tank from ca. 1 m³ to 10 m³ is shown with the yellow curve. Thereby the improvement of the CPF is getting bigger, as the demand specific collector area increases. It has to be considered that all optimizations done before are maintained, like no heat losses of the storage tanks and an idealized stratification.

After optimizing the system it is idealized in a final step. For this purpose the parasitic energy demand of electric devices (e.g. pumps) is neglected and a complete utilization of the higher calorific value of fossil fuel is assumed. Both approaches are neither technical nor chemical possible. The simulation results of the idealized version of the tested solar heating system are almost approaching the benchmark. The remaining difference between these two curves can be explained with the fundamental limitation of the hydraulic connection of the analyzed system. Heat from the solar thermal circuit can only be fed into one heat sink: the solar thermal storage tank. In contrast, in the benchmark procedure the single heat sources are supplied with solar heat in sequence of their temperature level.

4. Conclusion and prospect

HIL measurements offer the possibility of functional evaluations of solar assisted central heating systems under standardized test conditions. The HIL results of the first tested central heating facility showed major insufficiencies concerning the control system causing a restricted usage of solar thermal energy. First results of the second evaluated system disclose also functional deficits in the control system. Managing the interaction of the different system components is one of the most important tasks and offers a lot of possibilities for the

improvement of system performance with low financial or material effort. Functional evaluations of further systems will show, if this result can be confirmed and therefore be generalized.

The results of the HIL measurements provide also the basis for further investigations concerning the energetic efficiency of systems. With validated dynamic simulation models a high quality of simulation results can be assured. For the analysis of annual simulation results a new parameter - *performance factor of the central heating facility* - is introduced. The parameter is applicable to all central heating facilities due to the clear definition of system boundaries. Together with the new reference parameter - *demand specific collector area* - they allow an objective comparison of different analyzed solar combisystems, which will be done in the course of the project in order to identify the most efficient system design under consideration of functional, energetic and financial aspects.

A newly developed benchmark procedure is matching the central heat demand of the building with the maximum solar thermal gain of the solar circuit to determine the maximum performance factor possible of an idealized central heating facility. For a detailed analysis of the single systems a comparison to the benchmark and an itemization of single limitation sources showed to be a good procedure for the identification of optimization potential. This approach disclosed the limitation of heat exchanger and a limited stratification of thermal storage tanks to be the largest limitation factor besides the heat loss due to distribution within the central heating facility. Furthermore the restriction of efficiency due to insufficiencies in the control system is numbered and compared to the impact of the remaining limitation sources.

5. Acknowledgement

The project SUW-MFH presented in this paper is funded by the German Federal Ministry for Economic Affairs and Energy based on a decision of the German Federal Parliament (reference number: 03ET1212B). The project is carried out in cooperation with the University of Applied Sciences Düsseldorf. The authors are grateful for the financial support and responsible for the content.

6. References

Haller, M.Y., Haberl, R., Persson, T., Bales, C., Kovacs, P., Chèze, D., Papillon, P., 2013. Dynamic whole system testing of combined renewable heating systems – The current state of the art. Energy and Buildings, 66, p.667–677

Jordan, U., Vajen, K., 2014. Manual DHWcalc – Tool for the Generation of Domestic Hot Water (DHW) Profiles on a Statistical Basis, Version 1.20, Universität Kassel, Institut für Thermische Energietechnik

Letz, T., 2002. Validation and background information on the FSC procedure. A Report of IEA SHC – Task 26 – Solar Combisystems. ASDER, France

Letz, T., Cholin, X., Pradier, G., 2010. Solar Combisystems Promotion and Standardization – D4.4: Comparison of results of all monitored plants, INES Education, Le Bourget-du-Lac

Malenković, I., Pärisch, P., Eicher, S., Bony, J., Hartl, M., 2013. Definition of Main System Boundaries and Performance Figures for Reporting on SHP Systems – IEA SHC TASK 44 – Subtask B1

Papillon, P., 2010. Solar Combisystems Promotion and Standardization – Final Report, pp. 10, CEA-INES, Le Bourget-du-Lac

Steinweg, J., Eggert, D., Rockendorf, G., Backes, K., Adam, M., 2016. Leistungsbewertung und Optimierung von solar unterstützten Wärmezentralen in Mehrfamilienhäusern, 26. Symposium Thermische Solarenergie, Bad Staffelstein

Conference Proceedings

EuroSun 2016
Palma de Mallorca (Spain), 11 - 14 October 2016

ISES EuroSun 2016

Annual Performance of a Solar Active House Prototype – Comparing Measurement and Simulation

Jan Steinweg[1] and Gunter Rockendorf[1]

[1] Institut für Solarenergieforschung Hameln, Am Ohrberg 1, 31860 Emmerthal

Abstract

A new concept for solar active houses is being tested under practical conditions. While conventional solar house concepts combine large collector areas with large storage volumes (up to 10 m³ in a single family house) in order to achieve solar fractions above 50 %, our new concept only needs small storage volumes (1 m³). To substitute the lack of storage capacity, the new system design uses thermally activated concrete elements directly fed by the solar collector. After having been dimensioned and tested by several simulation studies, a prototype building, equipped with the new heating system, has been constructed and extensively monitored.

The first year of operation already revealed the concept´s functionality. During a first monitoring period from April 2015 to March 2016 the recorded data exhibit good agreement with the simulations (based on historical weather data) while storage heat losses are identified as too high. Nonetheless, the annual overall end energy demand for domestic hot water and space heating is 8 kWh/m². This contribution analyses the first year of operation, also covering a peak load test.

Keywords: *solar active house, energy storage, thermally activated concrete elements, TABS, ground heat exchanger, heat pump, experimental study, prototype measurement*

1. Introduction

Previous solar active house concepts combine large collector areas (30…40 m²) and storage tanks (up to 10 m³) with wood stoves as auxiliary heater in order to achieve a combination of high solar thermal fraction (> 50 %) and low primary energy consumption. The new concept presented in this work is aiming at the same high energy efficiency at largely reduced buffer storage volume towards common sizes of about 1 m³, thus allowing buffer installations in the utility rooms, which is particularly favorable in case of energetic retrofit of buildings. As a matter of fact, this approach saves expensive building space, and any maintenance is now possible since all system components fit into standard utility rooms.

The resulting lack of storage capacity is substituted by direct solar thermal activation of already existing masses in the building's concrete slabs. This approach of direct solar thermal room heating has already been evaluated in the 1990´s by Papillon (1993) and generates significant advantages. Due to the characteristically low operation temperature of thermally activated building slabs (TABS), a high collector efficiency even at low irradiance levels can be achieved, which is important during the winter months.

The backup heat is provided by a heat pump (HP) coupled to a slender ground heat exchanger (GHX) which receives regeneration by solar thermal heat. Moreover, the GHX is used for the prevention of stagnation during the summer months, thus permanently obtaining the collector's energy delivery readiness. The concept is covering an innovative control strategy for temperature optimized solar heat distribution which has been

doi:10.18086/eurosun.2016.04.12 Available at http://proceedings.ises.org

designed regarding component and system simulations by Glembin (2012, 2013, and 2014) who has theoretically proven the concept's functionality. For practical testing of this concept, a test building has been planned, built and equipped with the system hydraulics developed according to the outcomes of the simulation studies. The present paper reports results of the first measurement period from April 2015 to March 2016 considering function and performance at monthly and annually scales.

2. System concept and prototype building

Fig. 1 displays the designed energy flows of the solar thermal collector, the heat pump and the different sinks for solar and backup heat. In contrast to simple solar thermal systems, the collector supplies heat to three different heat sinks. A new control strategy developed within the project is applied to utilize the heat fluxes with respect to an optimal effect on the system´s end energy savings, see Glembin (2014). According to this strategy both TABS and storage tank may experience positive demand signals, for example during the transitional periods of spring and autumn. The controller then determines the appropriate sink for which the collector is able to gain maximum efficiency. In this case, this may be either a sink provided with a higher priority or a lower demand temperature. As a result of this, the collector can be conducted with very low temperatures starting at 20 °C in cases where the TABS are supplied, and even lower temperatures down to 5 °C in cases of GHX regeneration.

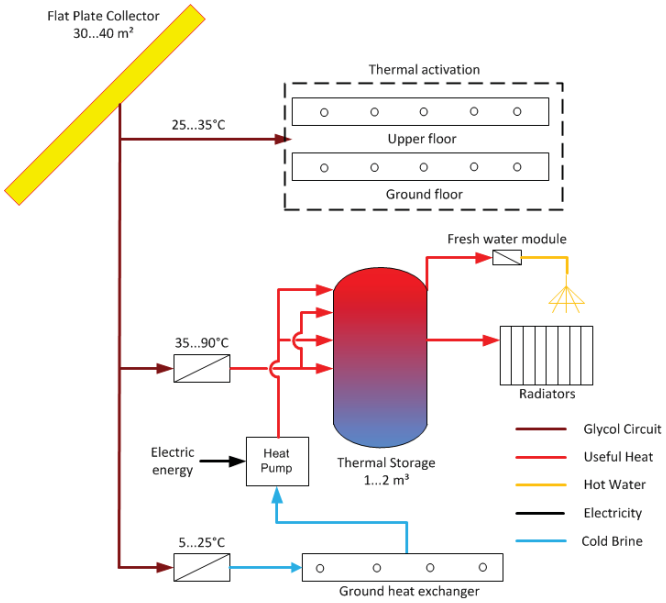

Fig. 1: Scheme of the solar thermal heating system (the lines indicate energy flows)

The test building is located in the urban area of Hanover, Germany, comprising a heated area of 270 m² on three floors; basement (BA) ground (GF) and first floor (FF), and with a nominal annual space heat demand of 39 kWh/m². The building is equipped with a solar collector area of 30 m², facing south with an inclination of 45°. TABS layers, which have been designed for maximum performance with minimum effort using component simulations according to Glembin (2012), are placed in GF and FF. To keep them highly efficient and cost effective, only one distribution loop with central temperature control is used for each floor. The utility room houses a simple buffer storage of 1 m³ from which the domestic hot water preparation (DHW) as well as the space heating demand (SH) are supplied, the letter via conventional radiators. The buffer storage is fed by the solar collector as well as an auxiliary heater, which is a ground coupled compression heat pump. A small horizontal ground heat exchanger with an area of 170 m² serves both as the heat source for the HP and the heat sink for the solar collector´s overcapacities during summer. Accordingly, the solar collector can remain in standby for further heat production throughout the summer and experiences almost absent stagnation. Correspondingly, the ground heat exchanger experiences intense regeneration. Therefore, it can be dimensioned significantly smaller than compared to standard design, e.g. due to the German guideline VDI 4640 (2010). A sketch of the concept and a picture of the realized building is displayed in Fig. 2.

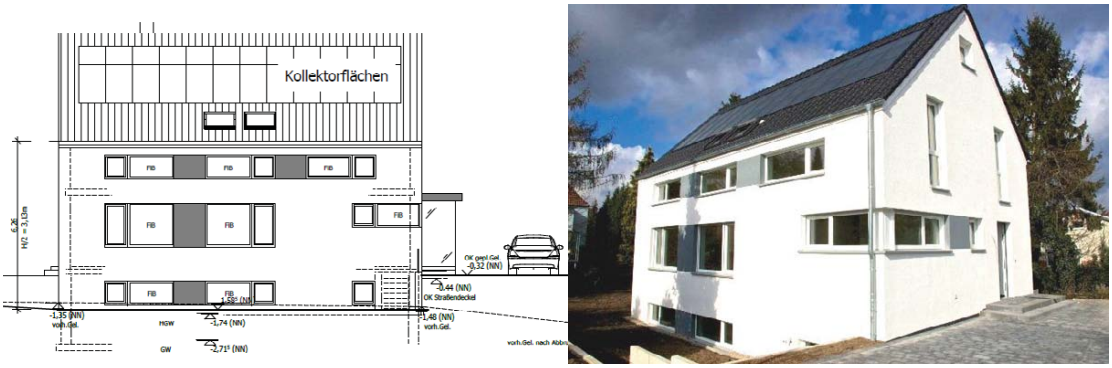

Fig. 2: Sketch of the experimental building during conception (left) and photo of the competed building after the commissioning in January 2015

A central ventilation unit has not been installed so it is up to the inhabitants to set the air change rate by window ventilation. The windows of the GF are equipped with non-automatic external mounted shading elements on the south, east and west façade, as well as the bath and sleeping room windows at the eastern and western façades of the FF. The other windows are (partially) equipped with self-mounted internal shadings. Throughout the phase of measurement, the experimental building has been inhabited by two persons. Further facts of the most important components are given in Tab. 1

Tab. 1: Generic parameters of the main system components of the experimental house

Solar thermal collector	Roof integrated, south, 45° inclination, aperture area 30 m²
Heat pump (HP)	Brine water compression HP, 8 kW nominal power at 2 kW compressor power
Ground heat exchanger (GHX)	170 m² area with four distribution circuits (excluding supply pipes), polyethylene pipes with 0.5 m distance
Thermally activated building slabs (TABS)	Approx. 160 m crosslinked polyethylene pipe per slab (ground and upper floor) with 0.5 m distance, bifilar installation, direct connection to glycol circuit of solar collector

3. Measurement and analysis

Measurement concept

The monitoring concept is regarding 65 sensors placed inside and outside the test building and its hydraulic system to gain information about the building´s boundary conditions as well as the heating system´s performance. The recorded data is evaluated firstly to prove the technical integrity of the concept, including the system controller, the component´s interaction and the identification of system and installation issues. Secondly, the system performance will be analyzed by means of indicators such as solar yield Q_{sol} and solar fraction f_{sol}, end energy demand Q_{EE} and the seasonal performance factor SPF of the HP. These quantities are defined by:

$$Q_{sol} = Q_{St} + Q_{TABS,GF} + Q_{TABS,FF} + Q_{GHX} \quad \text{(eq. 1)}$$

$$f_{sol} = \frac{Q_{St} + Q_{TABS,\mathrm{GF}} + Q_{TABS,FF}}{Q_{St} + Q_{BTA,EG} + Q_{BTA,OG} + Q_{HP,St}} \quad \text{(eq. 2)}$$

$$Q_{EE} = W_{el,HP,con} + W_{el,HP,aux} + W_{el,Pump} + W_{el,c} \quad \text{(eq. 3)}$$

$$SPF = \frac{Q_{HP,St}}{W_{el,HP,con} + W_{el,HP,aux}} \quad \text{(eq. 4)}$$

Q_{sol}	Solar energy gain from collector in kWh
Q_{St}	Solar energy to storage tank in kWh
$Q_{TABS,GF/FF}$	Solar energy to TABS in GF and FF in kWh
Q_{GHX}	Solar energy to GHX in kWh
$Q_{HP,St}$	Energy of HP to storage tank in kWh
$W_{el,HP,con}$	Electrical energy consumption of HP compressor in kWh
$W_{el,HP,aux}$	Electrical energy consumption of HP auxiliary heater in kWh
$W_{el,Pump}$	Electrical energy consumption of the hydraulic pumps in kWh
$W_{el,c}$	Electrical energy consumption of the controller, including energy for all valves in kWh

The system components, the overall hydraulic scheme and the system boundaries regarded by the energy balances are provided in Fig. 3. Technically, the energy flux is balanced through combined mass flux and temperature measurements, calibrated as pairs. The heat sinks (space heating and hot water preparation, blue areas in Fig. 3) are measured by heat meters and the electricity demand of the heat pump, all hydraulic pumps, valves and controllers is measured by electric meters. The thermal comfort of the building is rated through temperature sensors in representative rooms as well as CO_2 and moisture sensors on each floor as indicators for the level of air change due to window ventilation. The data scan interval for all sensors is set to 30 seconds.

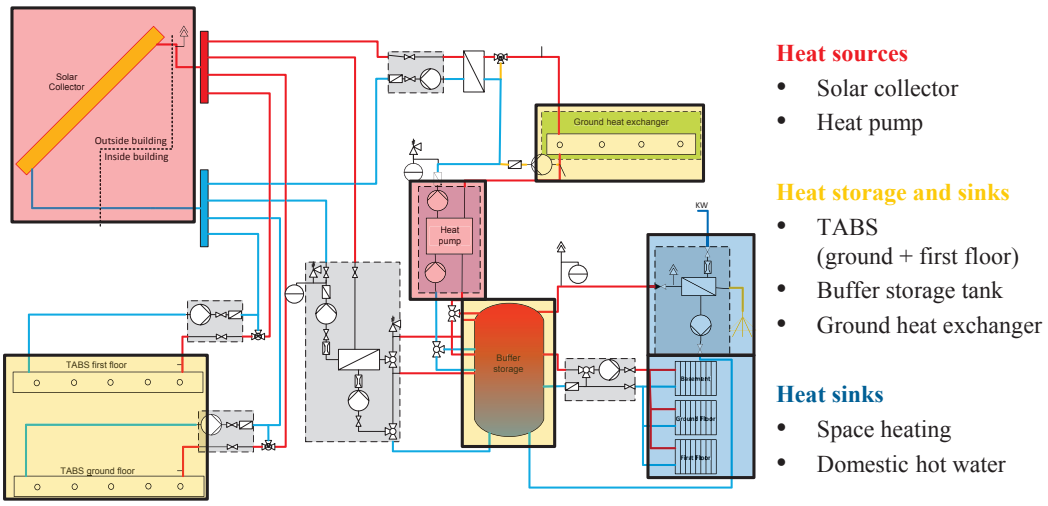

Fig. 3: Scheme of the hydraulic concept of the experimental building including the main components energy balance rooms.

Data analysis concept

We present the system indicators measured during the time period between April 2015 and March 2016 at annual and monthly scales. For further analysis, measurements will be compared to the results of system simulations based on a set of equivalent, historical weather data which had been identified from measurements in the same region during 1989 - 2001. This approach was mandatory for the following reasons:

- Some meteorological data required for the simulation were not measured with the test building, e.g. the ratio of diffuse and direct irradiation, sky temperature, wind speed and ground temperatures.
- Over the course of a year, partially shading of the solar collector and the irradiation sensor occurs, effecting localized signals to sensors and the collector.
- Missing reliable data for the inhabitant's behavior. Room temperatures are not measured building-wide, air change or shading cannot be registered directly at all.

- Some sensor values are considered to be representative for a large area or a component with a wide spread. Examples are again room temperatures but also the core temperatures of the buildings slabs, which are measured with a single sensor and assumed to be equal for the whole room or component.

Hence, to provide consistent simulation parameters, suitable historical weather data are used. As similarity indicators the annual irradiation (on the 45° south inclined surface), the mean ambient temperature and the degree-day numbers are employed and the similarity of the historical and in-situ data are judged by means of least square fit. As result, the best fit was assigned to the weather data of year 1994 which also shows good comparability at monthly scale; hence the 1994 weather data is used as climate environment for the simulations in the sequel. The respective similarity indicators are given in Tab. 2. The remaining differences between the two periods is small indeed, but has to be kept in mind when concluding the results.

Tab. 2: Comparison of the indicator values of the measured year 2015/16 and the historical weather data of Hanover 1994

	Measurement 2015/16	Hanover 1994
Irradiation (45°)	1146 kWh/m²	1185 kWh/m²
Degree-day number	3382 Kd	3312 Kd
Mean temperature	10,3 °C	10,7 °C

The useful energy demand, i.e. the energy emitted via the radiators and the domestic hot water, applied to the simulations is adjusted to the measured useful energy of the test building. The simulated space heating energy demand is adapted based on a mean room temperature. To compensate for the situation of partially heating of the building during the monitoring period, the simulations regard a slightly reduced indoor temperature of 19.1 °C. The resulting useful energy demand for space heating (via the radiators) is 5360 kWh/a. The amount of tapped hot water has not been measured. Instead the existing standard domestic hot water demand profile according to IEA Task 44 in Weiss (2003) and Dott (2012) has been adapted to match the respective energy demands of measurement and simulation. Again to adjust to the situation of reduced building usage, the demand profile was scaled by a factor of 0.46 (original data refer to four inhabitants). The resulting energy demand for domestic hot water preparation is 995 kWh.

4. Measurement and simulation results

The following analysis considers measurement and simulation outcomes of the new solar house concept. The comparison is conducted following the method described above. In the first step, annual calculations of the main indicators are compared. In the second part further details are outlined at monthly scale. The following section also concludes the experiences of the peak load tests, which were conducted during February and March 2016.

Annual results

Tab. 3 compares some of the main indicators of both the measured and the simulated building concept which characterize the system performance.

While the overall annual collector yield of ca. 275 kWh/m²a differs slightly only (by 1 %) between measurement and simulation, the spatial supply distribution of the produced solar heat exhibits some differences. The measured energy delivered to TABS contributes by 48 % to the overall solar heat produced, while in the simulation the same share is 64 % (a difference of about 1300 kWh). Analysis of the test building´s runtimes shows that TABS are fed by the collector about 25 % shorter than in the simulation. The reasons might be a lower collector performance, larger dead band temperatures or more frequent lock waits due to room temperatures exiting the controller´s high limit cut out during the measurement phase.

The lower energy input in TABS in the test building is then compensated by a higher energy input to the storage tank. Consequently, a respective difference of 1300 kWh occurs between measured and simulated storage input, too, such that in sum, the overall energy transfer between TABS and storage input are compensated. The remaining difference of the overall annual data of 1% is leveled by a slightly higher amount

of energy transferred to the GHX while runtimes are almost equal. The stagnation time of the solar collector is 48 h for the simulated system. This only occurs in rare events of GHX outlet temperatures exceeding 25 °C (which is the maximum evaporator inlet temperature of the HP). Since the collector temperature has not been measured, stagnation hours could not be detected directly during the monitoring period.

Tab. 3: Annual results of measurement from April 2015 to March 2016 and simulation based on Hanover weather data of 1994 for the new solar house concept

	Measurement 2015/16	Simulation 1994	Difference
Total solar collector yield	8525 kWh (274 kWh/m²)	8610 kWh (276 kWh/m²)	+1 %
To TABS ground floor	1949 kWh (23 %)	2893 kWh (34 %)	+48 %
To TABS first floor	2150 kWh (25 %)	2593 kWh (30 %)	+21 %
To storage	2844 kWh (33 %)	1573 kWh (18 %)	-45 %
To GHX	1295 kWh (15 %)	1094 kWh (13 %)	-16 %
Solar fraction	52 %	54 %	+4 %
Energy HP → Storage	6438 kWh	6006 kWh	-7 %
Total electricity demand	2173 kWh	1875 kWh	-14 %
SPF	3,45	3,69	+7 %

Little deviations exists for the solar gains. The difference between solar fraction of measured and simulated test house is 4%. Slight difference occurs for the energy delivered to the storage by the HP (-7%). Accordingly, the SPF of the HP is 7 % higher in reality than simulated and for the same reason, the total electricity demands differ by 14 %. The difference of the SPF can be explained by the following reasons:

- During October and November 2015, the system controller caused a problem which lead to unnecessary HP running on high temperature level. A major part of that energy got lost via the solar collector to ambient which may explain the 400 kWh higher storage input.
- As of Tab. 2 there are some residual differences in the weather data used for simulation. The mean annual ambient temperatures differ by 0.4 K only, however, between October and March the differences are slightly higher (about 0.7 K). This influences the demand of SH energy and also affects the GHX temperatures.
- The space heating zone inside the storage tank exhibits a mean temperature which is 3.8 K higher during the monitoring 2015/16 as compared to the simulations. This is most likely caused by a lower stratification efficiency of the real storage tank compared to its model. Additionally, the slightly lower ambient temperature mentioned above also has a little impact on the demand supply temperature level of the SH which is calculated with regard to the ambient temperature.

All despite this, the remaining energy demand is very low, especially when considering the sometimes imperfect performance of the system during the first year due to its commissioning. The overall electricity demand (including all electric loads necessary for the annual heat supply) is 2173 kWh or 8 kWh per m² of heated area. Considering primary energy demand, this is passive house level although the measurement period includes commissioning tests and dysfunctions during the first months in 2015 as well as peak load tests during February and March 2016.

Monthly results

To rationalize why a significantly higher share of solar energy is delivered to the storage and how this affects the system performance, Fig. 4 displays diagrams of the monthly solar energy yield distributed to the storage tank and the TABS.

The diagram on the left refers to simulation results which have been concluded in Tab. 3. These are based on a specific parameterization of the storage tank through the design heat loss rate of 5.2 W/K and also taking into account heat losses by thermal bridges and internal recirculation flows according to Wilhelms (2008). The diagram of Fig. 4 (left) shows a pronounced deviation of storage energy inputs between measurement and

simulation during the summer months: here, the measured energy input is 45 % higher between May and August than simulated. Since in this time period the only heat demand results from DHW tapping, which is the same amount at measurement and simulation, the difference must be the consequence of significantly deviating heat losses of the storage tank.

As consequence of this, the test house´s storage heat loss rate has been calculated to 7.8 W/K. Some physical reasoning for this could be identified: Considerably circulating flows between the storage tank and its adjacent components (HP and fresh water unit) were located. These flows have been detected with help of the analysis of detailed measurement data and occurred despite the installation of heat traps at the related storage connections. Although further evaluation of thermal bridges supported by thermography did not show any additional indications, other heat loss paths cannot be excluded completely, either. Given by the adverse position of the temperature and mass flow sensors, heat losses of the solar heat transfer unit and the piping are also included in the measured energy delivered to the storage. In consequence to that, the simulation model has been adapted considering these additional heat losses.

The measured overall energy delivered to TABS according to Tab. 3 is almost 1400 kWh lower than in the simulation. As Fig. 4 displays, this difference essentially occurs during the spring and autumn months. This deviation may be rationalized by taking into account passive solar gains and air change rates. The simulated building has an automatic external shading of all east, south and west oriented windows with a threshold total irradiation of 300 W. The air change rate is 0.4 h^{-1} with an optional night ventilation of 2 h^{-1} once the room temperature exceed 26 °C. The monitored test building, in contrast, has to be shaded manually and additional, not all of the windows are equipped with effective external shadings. On the other hand, the real air change is low as a consequence of the reduced building usage. As consequence, the simulated passive solar gains are underestimated while the heat losses due to ventilation are overestimated. Though, the TABS threshold room temperature in both cases is 24 °C. If the temperature hysteresis between room and threshold room temperature is lowered by higher solar gains and lower air change the potential for energy delivery by TABS is lowered as well. In sum, this explains the higher active solar energy input to the simulated building.

Taking into account adjusted storage heat losses, improved simulation results are displayed in the right diagram of Fig. 4. We see that the mean deviation between measured and simulated solar energy inputs to the storage tank from May to August has now decreased to 10 %. The measured system performance indicators used in Tab. 3 are again given in Tab. 4 and compared to the new simulation results of the model with matched storage heat losses including the losses of the solar heat transfer station.

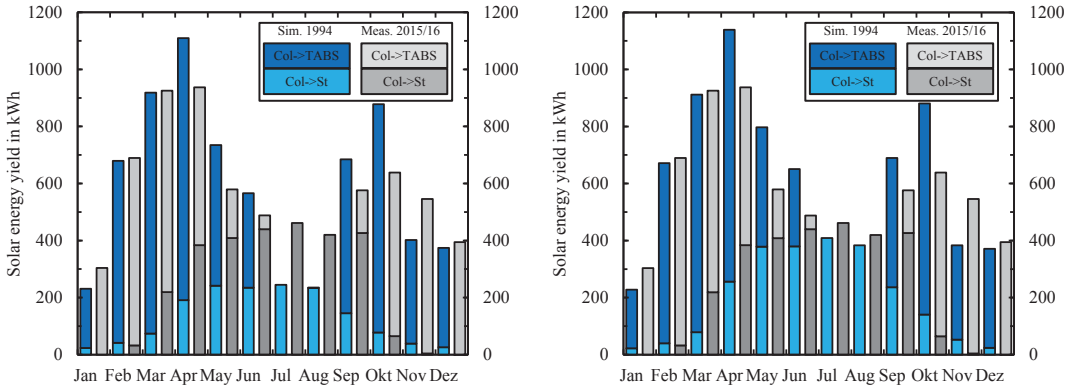

Fig. 4: Comparison of monthly solar energy distribution to storage (St) and TABS for simulation (blue bars) and measurement (grey bars), simulated with design storage heat loss rate (5.2 W/K, left diagram) and heat loss rate of the measured storage (7.8 W/K, right diagram) including heat losses of the solar heat transfer unit

When comparing Tab. 3 and Tab. 4 a slight increase of the solar collector yield is visible. Also the distribution of the solar heat to TABS and storage has changed. The improved results indicate TABS get a 6 % lesser share while the storage supply rises by 9 %. Due to elevated heat losses regarded by the new parameters, the heat transferred to the storage by heat pump also increases by more than 250 kWh. Together with a slight decrease of HP efficiency, the total electricity demand rises by 100 kWh. The solar fraction of eq. 2, in this case it yet

rises to 55 % since the solar yield rises stronger than the heat supplied by HP.

Compared to the measurements, it can be concluded that the difference in solar collector yield increases while the distribution of the solar energy to the different sinks now fits much better. With a solar yield now being a little higher than measured, the performance of the HP, its heat delivered to the storage tank and the total annual electricity demand moves closer to the measured results. Although the shares of the solar heat sinks do not fit perfectly, the order of the heat distribution can be approximated quiet well by the simulation. The remaining difference is most likely caused by the different shading and air change parameters.

Tab. 4: Annual results of measurement 2015/16 and simulation (Hanover, 1994) for the new solar house concept with matched storage heat losses

	Measurement 2015/16	Simulation 1994 (matched storage losses)	Difference
Total solar collector yield	8525 kWh (274 kWh/m²)	8891kWh (285 kWh/m²)	+4 %
To TABS ground floor	1949 kWh (23 %)	2610 kWh (29 %)	+34 %
To TABS first floor	2150 kWh (25 %)	2503 kWh (28 %)	+16 %
To storage	2844 kWh (33 %)	2402 kWh (27 %)	-16 %
To GHX	1295 kWh (15 %)	920 kWh (10 %)	-29 %
Solar fraction	52 %	55 %	+6 %
Energy HP → Storage	6438 kWh	6260 kWh	-3 %
Total electricity demand	2173 kWh	1974 kWh	-9 %
SPF	3,45	3,66	+6 %

Peak load tests

From February 23rd to March 29th, the new solar active house system of the test building has been stressed by a peak load test. It was aiming at the evaluation of the remaining thermal backup of the system, especially of the HP and its GHX source as auxiliary heat supply, under practical conditions. A higher load shall be obtained by increasing the room set temperature on the one hand while reducing the available GHX area by 50 % to about 85 m² on the other. This leads to a more frequent HP operation while the heat pump´s energy source is significantly smaller.

For the realization of a higher room set temperature the inhabitants have been instructed to adjust the radiator´s thermostats by a certain amount. The remaining heating circuit parameters have not been changed, so the threshold room temperature of the TABS remains 24 °C. The resulting mean daily room temperatures of BA, GF and FF during the peak load test are displayed in the right diagram of Fig. 5.

The distribution of the room temperatures remains the same as before the peak load tests. Due to the higher temperature of the utility room situated in the basement, this floor shows the highest temperatures, followed by the GF. As only few rooms of the FF are heated, it has the lowest temperature level. The mean overall temperature ($T_{r,m}$) increases by almost 2.5 K to 22 °C. A related simulation study reveals that this higher room temperature means an increase of the energy demand for SH of 36 %.

The diagram on the right of Fig. 5 displays the soil temperatures ($T_{soil,m}$) measured between the GHX pipes, the daily minimum of the GHX in- and outlet temperatures ($T_{GHX,in,min}$ and $T_{GHX,out,min}$) and the ambient temperature (T_{amb}) during the peak load test. The beginning of the test is clearly remarkable since the daily minimum temperatures of GHX in- and outlet decrease by almost 2 K. Both minimum temperatures remain below zero for the whole test period. While the mean runtime of the HP remains around 20 minutes, the number of cycles of HP operation increases. The reduced GHX area has been achieved by a reduced number of parallel circuits has also been reduced from four to two. This leads to a higher mass flow through the remaining circuits which, in combination with the lower heat exchanger area, also leads to a decrease of fluid temperatures. It is remarkable that the mean soil temperature measured right between the GHX pipes which are arranged with a distance of 0.5 m shows hardly no affection by this temperature decrease. Its temperature runs in closer

accordance to the ambient temperature.

However, the soil temperature at the beginning of the peak load test is almost exactly the same as at the end of the test which most reasonably is caused by the further increasing ambient temperature at the beginning of March. The grey area of the right diagram shows the slowly decreasing amount of energy which is withdrawn from the GHX while the blue area of the left diagram indicates that a significant share of SH energy is already delivered by TABS. In effect, the system withstands the higher thermal loads despite the significantly smaller GHX area very well. Nonetheless, it has to be concluded that the test has been performed quite late in the heating season and with insufficient load demand for a significant stress of the auxiliary heater to its limit. Anyway, the test clarified that the system concept provides considerably heating reserves, which corresponds to recent outcomes of system.

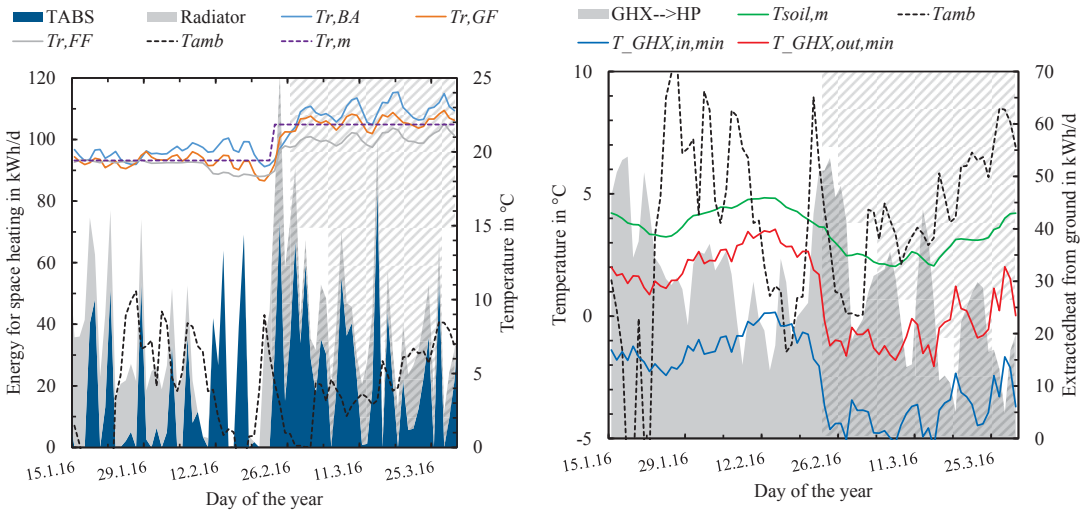

Fig. 5: Room and GHX temperatures during the peak load test, test period in both diagrams marked with hatching Room temperatures during peak load tests (left): Energy transferred to space heating from TABS and radiators, room temperatures in basement (*Tr,BA*), ground floor (*Tr,GF*), first floor (*Tr,FF*) and mean temperature (*Tr,m*), Ground temperatures during peak load tests (right): Energy transferred from GHX to HP (GHX→HP), mean soil temperature (*Tsoil,m*), ambient temperature (*Tamb*), minimum in- (*T_GHX,in,min*) and outlet temperature (*T_GHX,out,min*)

Conclusion and outlook

The measurement results of the first year show that the new solar active house concept is already working very satisfying although several initial malfunctions and issues which had to be solved lowered the systems performance. The measured solar fraction of 52 % is already within the expectations. With a remaining overall electricity demand of 8 kWh/m² the primary energy demand is very low. The comparison to system simulations shows a good correspondence but also reveals higher storage heat losses than expected. The losses can mainly be affiliated to unwanted circulating flows through heat pump and fresh water unit. Though heat traps have been provided by the installer as well as a good pipe and component insulation, backflow preventers in the prefabricated components hydraulics were missing almost completely.

The peak load test which has been performed at the end of the heating season was not intensive enough to show the backup heaters limit. Anyway, the current system configuration appears to be well prepared for seasons with higher energy demands. The GHX area might prospectively be further reduced which should be object of further simulation studies.

The missing backflow preventers have now been added, the improvements of controller algorithms, parameters, hydraulics and different performance tests are finished. The GHX temperature has been fully recovered after the end of the peak load test within two months. Since June 2016 a second measurement period is running. The aim is to get results of a full year´s period with optimized system performance and no further interference to identify the concepts full potential under practical conditions.

5. Acknowledgement

The project SH-T-Opt Exp (FKZ 032559) is funded by the German Federal Ministry for Economic Affairs and Energy based on a decision of the German Federal Parliament. Project partners of the ISFH are *HELMA Eigenheimbau AG, Lehrte* and *RESOL Elektronische Regelungen GmbH, Hattingen*. The authors are grateful for the financial support. The content of this paper is in the responsibility of the authors.

6. References

Dott, R. et al., The Reference Framework for System Simulations of the IEA SHC Task44/HPP Annex 38, PartB: Buildings and Space Heat Load, a technical report of subtask C, Report C1 Part B, University of Applied Sciences Nordwestschweiz, Muttenz, 2012

Glembin et al., Development of a Concept for the Temperature-Optimized Heat Production in Solar Active Houses, Proceedings of Eurosun Conference, September 18th-20th 2012, Rijeka, Croatia

Glembin et al., Solar Active Building with Directly Heated Concrete Floor Slabs, SHC 2013, International Conference on Solar Heating and Cooling for Buildings and Industry, September 23rd-25th 2013, Freiburg, Germany

Glembin et.al., New Control Strategy for Solar Thermal Systems with Several Heat Sinks, Proceedings of Eurosun 2014 Conference, September 16th-19th 2014, Aix-les-Bains, France

Palillon P., Souyri B., Achard G., A new concept for the direct solar floor heating system, proceedings of ISES Solar World Congress, 23.-27. August, Budapest, pp 2328/2234, 1993

Verein Deutscher Ingenieure, VDI 4640 Blatt 1 - Thermische Nutzung des Untergrunds - Grundlagen, Genehmigungen, Umweltaspekte, Beuth Verlag GmbH, 10772 Berlin, Dezember 2011

Weiss, W. (ed.). Solar Heating Systems for houses, a design handbook for solar combisystems, James & James Ltd, London, 2003

Wilhelms, C., et al.: Serienverschaltung von Solarspeichern - eine sinnvolle Systemtechnik?, 18. Symposium OTTI Solar-thermie, Bad Staffelstein, 2008

Conference Proceedings

EuroSun 2016
Palma de Mallorca (Spain), 11 - 14 October 2016

Review of Solar Thermal Systems and Their Potential in Lithuania

Rokas Valančius, Andrius Jurelionis and Juozas Vaičiūnas

Kaunas University of Technology, Faculty of Civil Engineering and Architecture, Kaunas (Lithuania)

Abstract

Solar thermal systems with a total solar panel area varying from 2 to 204 m^2 have been installed in Lithuania for over 20 years. The market of such systems is slowly growing and the trend continues towards larger domestic hot water systems in multifamily buildings, hospitals, hotels and other large complexes. Nevertheless, there's still lack of performance reviews and analysis of these systems. The aim of this paper was to analyze medium size solar thermal systems from the perspective of energy production and economic benefit as well as to outline the differences of their actual performance compared to the numerical simulation results. A number of different solar thermal systems in Lithuania were selected for the study, and both financial analysis and performance analysis by means of simulation software were performed. Solar thermal domestic hot water (DHW) systems in question produce up to 528 kWh per year per one square meter of solar collector absorber area. However, the performance of these systems depends on the type of energy users, design solutions, equipment used and maintenance of these systems. Calculation of internal rate of return showed that a grant is required in most cases for solar thermal project to be fully profitable.

Keywords: *solar thermal systems, domestic hot water, energy prices*

1. Introduction

Renewable energy share continued to grow worldwide in recent years alongside with the increasing global energy consumption, particularly in developing countries, and a dramatic decline in global fossil fuel prices in last two years. Renewable energy provided an estimated 19.2% of global final energy consumption in 2014, and growth in capacity and generation continued in 2015.

Global capacity of glazed and unglazed solar thermal collectors rose by more than 6% in 2015, despite a market slowdown due primarily to the continued contraction of markets in China and Europe. China accounted for about 77% of newly installed solar water heater capacity, followed by Turkey, Brazil, India and the United States. Cumulative capacity of water collectors reached an estimated 435 GWth by year's end (with air collectors adding another 1.6 GWth), enough capacity to provide approximately 357 TWh of heat annually. Market development varied widely from country to country. Denmark, Israel, Mexico, Poland and Turkey reported significant growth. By contrast, low oil and gas prices in Europe and the ongoing slowdown in housing construction in China dampened these markets (REN21, 2016).

In 2014, the European market underwent a reduction in the newly installed capacity. In 2014, the market amounted to 2 GWth (approximately 2.9 million m²). This represents a decrease of 7.1 % in comparison with the previous year. The total installed capacity registered a net increase of 1.6 GWth, now reaching 31.8 GWth (45.4 million m²). This represents an increase of 5.3 % compared with the total installed capacity at the end of 2013. Only about 10400 m² (7280 kWth) of glazed solar collectors were installed by the end of 2014 in Lithuania, and the applications were mostly limited to single-family buildings (ESTIF, 2015). Only in recent years the trend continued towards larger DHW systems in multifamily buildings, hospitals, hotels and other large complexes, due to support from the government, EU and other funds. In 2016 more than 1500 m² solar collectors in over 15 hospitals will be installed for DHW and other needs.

Selection and/or peer review under responsibility of Scientific Committee
doi:10.18086/eurosun.2016.04.15 Available at http://proceedings.ises.org

The major part of thermal energy used in public and multi-family buildings in Lithuania is supplied via the district heating network. 72.4% from all district heating produced energy was used for household purposes in 2012 (LSTA, 2012) and the price in different Lithuanian cities varies in the range from 0.044 Eur/kWh to 0.095 Eur/kWh (01.06.2016). In the last two years, district heating energy price dropped by 9.2% (LSTA, 2016). Quite frequently, natural gas, bio fuel or electricity are used for building heating systems. Switching from natural gas to bio fuel reduced the district heating energy price significantly within last two years. Due to a dramatic decline in oil and natural gas prices, conventional fuel prices decreased up to 35% in last five years as well.

The aim of this study was to review the existing medium-scale solar thermal (ST) systems and their potential in Lithuania in relation to traditional energy prices and government policies.

2. Review of Solar Energy Potential and Market in Lithuania

Average global solar irradiation in Lithuania is similar to the irradiation levels in such countries as Germany, Austria, Denmark, Poland, Latvia and Estonia with the annual potential of solar energy yield of approx. 1000 kWh/m². The daily potential in the country varies from 0.55 kWh in January to 5.8 kWh from one square meter in June; therefore, almost the whole irradiated solar energy can be collected during the warm period of the year (from April till end of October). Due to this fact, solar hot water (SHW) systems are most efficient in DHW applications in Lithuania (Kytra, 2006). Nevertheless, technical-economic potential of solar heat energy production in the country reaches up to 1.5 TWh/year (129 ktoe). The values of expected solar energy yield are increasing during the last decade as solar irradiation increased by 7% during the years of 2005 to 2014 compared to the long-term statistical data (Valancius et al., 2015b).

According to ESTIF 2014 statistics about 64 % of installed solar thermal systems in Lithuania were equipped with evacuated tube collectors. In fact the evacuated tube collectors are mostly used in small projects. Several studies showed that despite the fact that both evacuated tube and flat plate collectors are considered suitable for solar heating in Central European Climates, the evacuated tube collectors do not reach the additional expected energy yield (Trinkl et al., 2005). Flat plate collectors and evacuated tube collectors produce the same amount of energy from effective area during the summer season in Lithuania, but flat plate collector installations require much lower investment costs in most cases (Ambrulevicius, 2005; Jonynas et al., 2011; Sarka and Streckiene 2014). In recent years, the price of good quality evacuated tube collectors is slowly decreasing followed by the increase of the usage of this technology, yet there is still a lack of real efficiency and life span data at the moment. According to the European standard EN 15459:2006 the life span of solar collectors are from 15 to 25 years, but the actual life span of the vacuum varies from collector to collector, anywhere from 5 years to 15 years (Bhatia, 2014).

Some studies in Lithuania and in other countries of similar climate showed that small and medium-scale solar DHW systems with flat plate or evacuated tube collectors can produce from 335 to 523 kWh/m² of thermal energy per year, and the payback time of these systems is over eight years without the subsidies. The potential of ST systems is quite high; however, the support from government and EU funds is still necessary in most cases to achieve reasonable payback (Adomavicius, 2010; Ayompe and Duffy, 2013; Hugo and Zmeureanu, 2012; Jonynas and Valancius, 2010; Perednis et al., 2007; Valancius et al., 2015a; Valancius et al., 2015b). In Lithuania, some limited subsidy systems and funds for renewable energy installations exist since 2005. Depending on a project, it is possible to apply for a subsidy covering from 30 to 100% of initial costs. For example it is possible to get a subsidy up to 30 % for single family building, up to 40% for multifamily building and up to 100 % for hospitals. Such subsidies can be applied for solar thermal systems as well as other renewable energy installations. Evidence that the most important factor for users is the payback time and only two systems (Table 1) analyzed in this report were installed without any subsidies.

Some studies showed that relation between installation costs and area of the flat plate solar collectors (including heat storage tanks and auxiliary equipment) can vary in the range from 600 to 150 Eur/m² in SHW from 10 m² to 10000 m². The installation costs, annual maintenance and repair costs vary in wide range depending on the type of solar collectors and other components, but in general, larger SHW installations are relatively cheaper to maintain than small-scale SHW systems (Andrews et al., 2012; Leutgöb and

Rammerstorfer, 2013). Additional costs for design of the systems in Lithuania add up to 8% from the installation costs. In some cases, the costs of SHW installations in existing buildings can be up to 20% higher compared to new buildings (Valancius et al., 2015b).

The number of medium-scale SHW systems in Lithuania is still relatively low and represent the potential direction for development of these systems. There is a number of medium-scale SHW systems installed in the country varying from 60 to 204 m² of total solar panel area. Most of these systems are installed within the past few years in public buildings, hospitals and industrial facilities. The oldest still operational SHW system 77 m² was installed in 2002 in children sanatorium "Žibutė" (Kačerginė). However, it took 10 ten years for the first SHW system to be installed in multi-family building, as the first such system was launched only in 2012 (Katinas et al., 2013; Karbauskaite and Perednis, 2011; Valancius et al., 2015a; Valancius et al., 2015b).

Fig. 1: The first solar thermal system 60 m² in multi-family building in Panevėžys city and the biggest solar thermal system 204 m² in Plungė town hospital (till the end of 2015).

Some studies in Lithuania showed that public and multi-family buildings represent one of the major potential for SHW installation, as it is one of the best renewable energy alternatives for these buildings (Adomavicius, 2010; Diliunaite, 2013; Perednis et al., 2007; Valancius et al., 2015b;). More uniform DHW usage during the day is common for public or multi-family buildings, compared to the single-family houses. It is related to variability of occupants and their hot water consumption habits, and this aspect brings out a higher solar energy share without adding additional volume to the accumulation tank. Moreover, DHW consumption throughout the day presents the possibility to keep lower temperatures in solar collectors even during periods of high solar radiation. Public or multi-family buildings provide a possibility to connect several users to the same combined SHW system; therefore, the heat losses due to transformation and transportation of hot water will be incurred to a lesser extent during the system operation (Zandeckis et al., 2011).

3. Review and Analysis of Medium-Scale Solar Thermal Systems in Lithuania

Ten different ST systems in different Lithuanian cities were evaluated in this review. Most of these systems were designed for DHW applications. Flat plate or evacuated tube collectors and other equipment produced by different manufacturers were used for these projects. All of these systems are in operation for up to 5 years. Only some of the systems are equipped with heat meters or monitoring systems. Technical and economical characteristics of the analyzed systems are presented in Table 1.

Three different ST systems 4F, 5F and 3E (Fig. 3) were evaluated. All these systems are in operation from 2011 and are equipped with heat meters and monitoring systems. All of the analyzed systems have individual operational features that impacts their produced energy amounts. System 4F performs continuously from the start of the exploitation. System 5F was stopped for three weeks in August during pool renovation works. Performance of system 3E was interrupted for a few times due to system upgrades.

The measured performance of the existing ST systems was compared to the theoretical values obtained by means of simulation software "Polysun 8.1" (Velasolaris, 2015). All technical parameters of the existing systems such as inclination angle, orientation, energy demands and characteristics of the installed equipment were used as boundary conditions for the simulations.

Tab. 1: Technical and economical characteristics of the analyzed ST systems.

Description of ST systems			Total gross / absorber area, m^2	Investment per 1 m^2 gross area, Eur	Annual energy production per 1 m^2 gross area, kWh
Flat plate solar collectors	1F	SHW, main energy source – natural gas	25 / 23	519	512 (2015)
	2F	SHW, main energy source – district heating	40 / 37	516	382 (2015)
	3F	SHW, main energy source – district heating	72 / 67	418	n/a
	4F	SHW, main energy source – electricity*	114 / 106	479	488 (2013)
	5F	Indoor swimming pool heating and SHW. Main energy source – natural gas**	166 / 155	701	411 (2013)
Evacuated tube solar collectors	1E	SHW, main energy source – electricity	27 / 15	571	528 (2014)
	2E	SHW, main energy source – district heating	36 / 33	692	414 (2015)
	3E	Preheating the return water in the district heating network***	82 / 72	1079	343 (2013)
	4E	SHW, main energy source – district heating*	90 / 63	621	n/a
	5E	SHW, main energy source – district heating	145 / 77	320	n/a

* Approximate investment costs per 1 m² gross area.
** System was not in operation for three weeks during August 2013.
*** System was upgraded few times due to improper operation, therefore approximate value of the total investment is presented.

Financial analysis was performed for ten different ST systems. In this study, the assumption was made that the entire cost of the ST systems is covered during the installation and the systems were installed without any subsidies. The life span of the ST systems is considered to be 20 years. Parameters used for financial assessment of the ST systems are presented in Table 2.

Tab. 2: Parameters used for the simulations of ST systems.

Life span of ST systems, years	20
Specific district heating energy price (average), Eur/kWh	0.041
Specific energy from natural gas price (average), Eur/kWh	0,076
Specific electricity costs (standard), Eur/kWh	0.129
Index for energy prices, % per year	3.0
Interest capital, %	2.5
Running costs, %	1.5

4. Results of analysis

Analysis showed that the relation between installation costs and area of the flat plate and evacuated tube solar collectors (including heat storage tanks and auxiliary equipment) varies in the range of 320 – 1079 Eur/m² in ST systems from 25 m² to 166 m² gross area. Average price of flat plate solar collector systems is 527 Eur/m², but the investment for evacuated tube solar collector systems per 1 m² gross area varies in a wide range of 320 – 1079 Eur/m², with the average price of 657 Eur/m². Compared to the analysis made ten years ago (Perednis et al., 2007), prices of ST systems have not changed significantly.

The results of the analysis showed that ST systems with solar flat plate and evacuated tube collectors can produce from 343 to 528 kWh/m², and almost the whole irradiated solar energy – approximately 80% – can be collected during the warm period of the year (Fig. 3).

Simulations showed that analyzed ST systems in Lithuania can reduce greenhouse gas emissions from 49 to 232 kg $CO_2/m^2_{absorber}$ per year. However, CO_2 reduction per absorber area can vary in the wide range depending on the type of the system and an alternative source of energy production.

Price composition of the analyzed ST systems is presented in Figure 2. The price of solar collectors and mounting systems comprises 51 % of the total system price in cases when evacuated tube collectors are used, for example ST system 3E (Table 1).

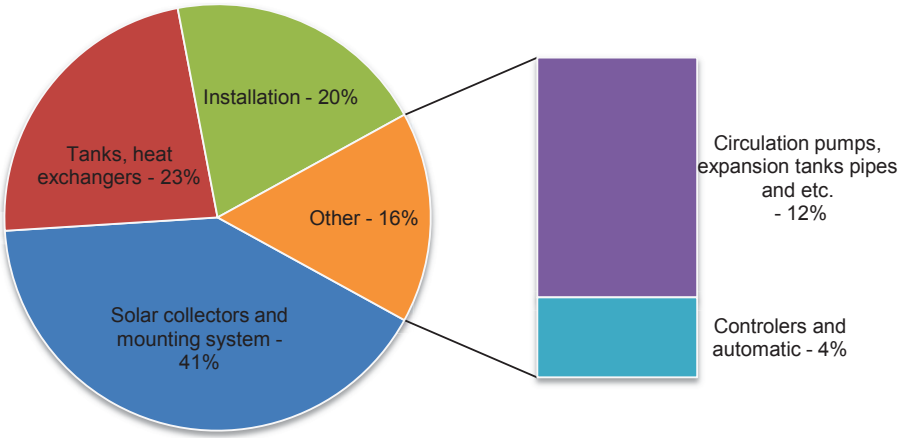

Fig. 2. Price composition of equipment in analyzed ST systems.

The financial analysis showed that heat energy generated by analyzed ST systems is not competitive in most cases in comparison with district heating (payback period from 11 to 40 years) and natural gas applications (payback period from 24 to 27 years). However, the projects were fully profitable (payback period from 6 to 10 years) in cases when electrical energy was used as an alternative to energy produced by SHW systems (Table 1). Average solar energy cost (life span is 20 years) in the analyzed cases was – 0.073 Eur/kWh.

Measured annual efficiency of the analyzed systems reached up to 44 % (4F) 39 % (5F) and 24 % (3E). The measured values of global irradiation in Kaunas city and the amount of energy produced in the analyzed systems per month are presented in Figure 3.

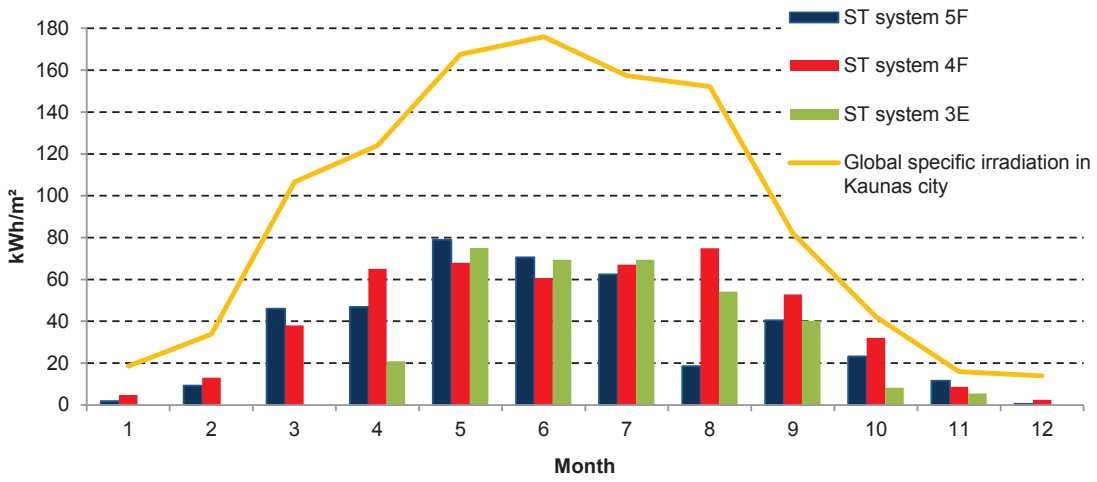

Fig. 3. Produced energy in the analyzed ST systems (kWh/m² $_{absorber}$) per month and measured global irradiation in Kaunas city (2013).

The gap between measured and modelled data of heat energy produced by SHW systems was approx. 11 % in the analyzed cases. It can either be caused by differences in actual solar irradiation compared to the standard average data, or some peculiarities of the design and maintenance of the SHW systems.

5. Discussions and conclusions

Average price of flat plate solar collector systems was 527 Eur/m² in the analyzed cases, but the investment for evacuated tube solar collector systems per 1 m² gross area varied in a wide range of 320 – 1079 Eur/m², with the average price of 657 Eur/m².

ST systems with evacuated tube collectors do not reach significant additional expected energy yield. ST systems with solar flat plate and evacuated tube collectors can produce from 343 to 528 kWh/m² of thermal energy and reduce greenhouse gas emissions from 49 to 232 kg $CO_2/m^2_{absorber}$ per year.

The results of the analysis showed that in the analyzed cases the gap between measured and modeled data of heat energy produced by ST systems was approx. 11%. From the economic perspective, the system with flat type solar collectors used for DHW production is profitable if compared with the electrical energy as an alternative.

The most expensive equipment in ST systems are solar thermal collectors. In the analyzed cases, from 28% (flat plate collectors) to 51% (evacuated tube collectors) of initial investment is required to cover the costs of solar collectors itself.

The market growth of ST systems in Lithuania and other countries depends on the policy of the governments. The payback period of ST systems in most cases is too long (from 6 to 40 years) to ensure the stable growth of ST applications without the governmental grants. Despite the long payback period the market of ST systems is slowly growing and the trend continues towards larger DHW in multifamily buildings, hospitals, hotels and other large complexes due to support from EU and other funds.

6. References

Adomavičius, V., 2010. Atsinaujinančiųjų energijos išteklių naudojimo galimybės daugiabučiuose namuose. Lietuvos taikomųjų mokslų akademijos darbai: tarptautinis inovacinis taikomųjų mokslo darbų žurnalas 6, 107-122.

Ayompe, L., Duffy, A., 2013. Analysis of the Thermal Performance of a Solar Water Heating System with Flat Plate Collectors in a Temperate Climate. Applied Thermal Engineering 58, 447-454.

Ambrulevičius, R., 2005. Saulės kolektorių sistemų eksploatavimo ypatumai. LŽŪU ŽŪI Instituto ir LŽŪ Universiteto mokslo darbai 37, 54-69.

Andrews, D. et al., 2012. Background Report on EU-27 District Heating and Cooling Potentials, Barriers, Best Practice and Measures of Promotion. EC Joint Research Centre. Luxembourg: Publications Office of the European Union [accessed 12 July 2016]. Available from Internet: https://setis.ec.europa.eu/system/files/JRCDistrictheatingandcooling.pdf

Bhatia, S.C., 2014. Advanced Renewable Energy Systems, CRC Press, pp. 124.

Diliūnaite, A., 2013. Atsinaujinančių energijos šaltinių panaudojimo daugiabučiuose gyvenamuosiuose namuose tyrimas. 16-oji Lietuvos jaunųjų mokslininkų konferencija "Mokslas - Lietuvos ateitis" 2013 metų teminė konferencija "Statyba", 2013 m. kovo 20-22 d., Vilnius, Lietuva, 1-7.

ESTIF, 2015. European Solar Thermal Industry Federation. Solar Thermal Markets in Europe. Trends and Market Statistics 2014. June 2015.

EN 15459:2006. Energy Efficiency for Buildings — Standard economic evaluation procedure for energy systems in buildings, pp. 28

Hugo, A., Zmeureanu R., 2012. Residential Solar-based Seasonal Thermal Storage Systems in Cold Climates: Building Envelope and Thermal Storage. Energies 5(10), 3972-3985.

LSTA 2012. Lietuvos Šilumos tiekėjo asociacija. Šilumos tiekimo bendrovių 2012 metų ūkinės veiklos apžvalga. Vilnius. [accessed 14 July 2016]. Available from Internet: http://www.lsta.lt/files/statistika/19493_LSTA_Ukines%20veiklos%20apzvalga_2012_WEB.pdf

LSTA 2016. Lietuvos Šilumos tiekėjo asociacija. Vidutinė šilumos kaina gyventojams (po perskaičiavimų) [accessed 14 July 2016]. Available from Internet: http://lsta.lt/lt/pages/apie-silumos-uki/silumos-kainos

Jonynas, R., Valančius, R., 2010. The Comparison of Two Different Solar Collectors Systems. Proceedings of 8th EuroSun Conference of ISES Europe. 28 September – 1 October, 2010, Graz, Austria, 1-8.

Jonynas, R., Valančius, R., Šuksteris, V., Perednis, E., Mekas, G., 2011. Study of medium scale solar water heating plants in Lithuania. Proceedings of ISES Solar World Congress 2011, 28 August – 2 September, 2011, Kassel, Germany, 921-927.

Karbauskaitė, J., Perednis E., 2011. Kačerginės vaikų sanatorijos šilumos energijos vartojimo mažinimo galimybės. Energetika 57(1), 20-25.

Katinas, V., Karbauskaitė, J., Perednis, E., Valančius, R., 2013. Efficiency Analysis of Combined Biomass and Solar Energy in Lithuania. Clean Technologies and Environmental Policy 15(4), 667-676.

Kytra, S., 2006. Atsinaujinantys energijos šaltiniai, Technologija. Kaunas.

Leutgöb, K., Rammerstorfer, J., 2013. Implementing the Cost-optimal Methodology in EU Countries. Case study Austria. BPIE.

Perednis, E., Kavaliauskas, A., Plikšienė, V. 2007. Karšto vandens ruošimo naudojant saulės kolektorius efektyvumo tyrimai. Energetika 1, 34-38.

REN21, 2016. Renewables 2016 Global Status Report, Paris: REN21 Secretariat. [accessed 3 July 2016]. Available from Internet: http://www.ren21.net/wp-content/uploads/2016/06/GSR_2016_Full_Report _REN21.pdf

Šarka, J., Streckienė, G. 2014. Vienbučio pastato karšto vandens ruošimo plokščiaisiais ir vakuuminiais saulės kolektoriais ekonominis vertinimas. 17-oji Lietuvos jaunųjų mokslininkų konferencija "Mokslas - Lietuvos ateitis" 2014 metų teminė konferencija "Pastatų inžinerinės sistemos", 2014 m. balandžio 11-12 d., Vilnius, Lietuva, 103-108.

Trinkl, C., Zörner, W., Alt, C., Stadler, C., 2005. Performance of Vacuum Tube and Flat Plate Collectors Concerning Domestic Hot Water Preparation and Room Heating. Proceedings of 2nd European Solar Thermal Energy Conference, Juni 21-22, 2005, Freiburg, Germany.

Valančius, R., Jurelionis, A., Jonynas, R., Katinas, V., Perednis, E., 2015a. Analysis of Medium-Scale Solar Thermal Systems and Their Potential in Lithuania. Energies 8(6), 5725-5737.

Valančius, R., Jurelionis, A., Vaičiūnas, J., Perednis, E., 2015b. Dimensioning of Solar Thermal Systems for Multi-Family Buildings in Lithuania: an Optimisation Study. Journal of Sustainable Architecture and Civil Engineering 11(2), 32-40.

Žandeckis, A., Timma, L., Blumberga, D., Rochas, C., 2011. Possibilities for Utilization of Solar Thermal Energy in Multi-family Buildings in Latvia. Environmental and Climate Technologies 6(1), 138-146.

Heating, cooling and ventilation with the solar-assisted heat pump based on the air solar collector

Andrii Zakovorotnyi

Lucerne University of Applied Sciences and Arts

Abstract

A new concept for solar-assisted heat pumps based on an air solar collector is discussed in this paper. The main objectives of the system have been set on a partial covering of the cooling demand of a building during summer season and simultaneous charging of the thermal storage for domestic hot water usage. Beside this, the proposed system fully covers the ventilation need of the building. The current paper presents the performance results of proposed concept for different weather conditions. The results demonstrate that such system is competitive with the existed solar-assisted heat pumps in terms of technical simplicity to cover broad range of tasks simultaneously.

Keywords: *air solar collector, heat pump, air conditioning, air cooling, thermal storage*

1. Introduction

Past decades brought various technologies based on renewable energy sources, which are promising alternatives to the dominant use of fossil fuels, including wind power, hydropower, waste energy, geothermal energy, bio energy and solar energy. Herein, solar energy has proven itself as a clean source for electricity and heat generation in the building sector. However, its performance strongly depends on time and local weather conditions which are not completely predictable. This time shift leads further to the issue of the decreased self-consumption of the solar power, especially, of the PV-plants. Use of energy storage (electrical batteries and thermal storage such as hot water boiler or others) can increase the fraction of harvested solar energy and shift gained energy to demand time zone (Tanguy et al., 2014). Another common way of increasing of the self-consumption of the electricity produced by solar PV-cells is to use a heat pump (HP) for storing the electrical energy in thermal storage for further electricity and heat production (Dumont et al., 2015).

On the other hand, the consequences of global climate change more and more shift the focus from covering of heat demand during the winter to providing the necessary cooling power to buildings during the summer season. Jurt et al. (2016) showed that the number of overheating hours will increase by 50 % to 100 % in the next 30 years, depending on building type.

In addition, there are compulsory requirements for the mechanical ventilation systems (Swiss Norms, 2006) in office and industrial buildings.

Summarizing the requirements, it is clear that in order to get high efficiency of all systems in building all the above mentioned tasks should be considered together. Typical combination of the water solar thermal collector and water-based HP which use the water tank as a daily or weekly thermal storage is presented by a number of research papers (Bucker and Riffat, 2016, Poppi et. al., 2016). Although the combination of system components varies greatly and generally increases the COP of a HP up to 6, however, these cases can be considered only for the solution of two tasks such as covering the heat load and increasing the consumption of the installed PV cells (Fischer et al., 2016).

Combination of ventilation system and HP for covering the cooling and heat load is presented by widely spread air-to-air and air-to-water HPs, which also increase self-consumption of the electricity produced by PV-cells. However, their application for covering the heating demand during winter has lower efficiency due to the lower temperature of the air. Use of thermo-chemical (Tanguy et al., 2014), sensible or latent (Kapsalis and Karamanis, 2016) seasonal heat storage provides an opportunity to increase efficiency during winter, but such systems suffer of a high technical complexity (Tanguy et al., 2014).

doi:10.18086/eurosun.2016.04.09 Available at http://proceedings.ises.org

Ventilation system based on solar air collector (SAC) also partially covers the building's heat demand and is not sophisticated. Sicre et al. (2015) measured and analyzed the efficiency of a 24 m^2 SAC as a system which simultaneously fulfills the ventilation requirements and heats up the indoor air. With an average energy conversion efficiency of 60 % this system covers only 28 % of the heat demand of typical factory building in Luzern, Switzerland, due to the obvious lower solar gains during winter. Air collector was also used as a cooling device during night using the sky radiation effect; the resulting cooling capacity was restrained to as little as 1 kWh per night. Another way to actively cool down incoming air using air solar collector is achieved by using a desiccant cooling wheel (Eicker et al., 2010). COP of such system is up to 3.2, but hygienic aspects may rise concerns.

Summarizing different concepts of system, combination of solar thermal plant such as SAC for assistance, of the standard air-to-water HP powered by PV-plant and coupled to a thermal storage is promising. The focus of the present paper is set on the design of such system that will cover simultaneously ventilation, domestic hot water (DHW) production and partially cooling. The goal of current research is to estimate the efficiency and working ability of a solar-assisted HP based on the SAC with an evaporator, which cools down the inlet air provided into the room during summer season, and a condenser, which simultaneously charges domestic hot water tank or other heat storage that is discharged later by consumer.

2. System concept

The proposed solar-assisted HP based on SAC can be well explained using the scheme of principle in fig. 1.

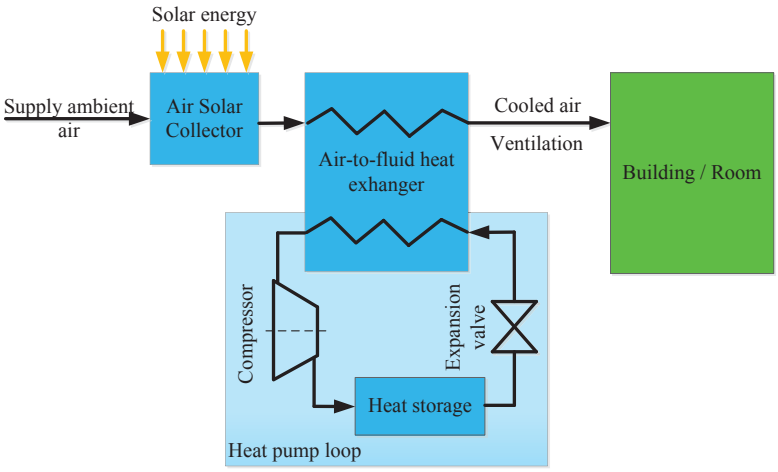

Fig. 1: Scheme of the system operation during summer season

Basically such system represents a solar-assisted air-to-water HP. Besides provision of cooling and heating, it also fulfils the function of building ventilation. During the summer season SAC sucks and heats the outside air, which is further passed through the heat exchanger, where the refrigerant of the HP evaporates. The resulting, relatively cold outlet air is sent to the rooms. On the other side, evaporated refrigerant from the heat exchanger is compressed by the compressor and supplied to the thermal storage, that may be a DHW tank or another thermal storage, which will be discharged later by consumer.

During the winter season HP can be used in combination with the SAC in a way described in Karagiorgas et al. (2010), where SAC serves during winter as an energy collector for the air-to-water HP. This solution allowed increasing the COP of the air-to-water HP by 30-50 % depending on the ambient temperature and available solar radiation.

SAC can be used alone without HP during autumn and spring to cover low heat demand (Sicre et al., 2015). Other way to cover the heat demand during winter is to use accumulated energy during summer; however seasonal thermal storage with high energy capacity is required.

Thermodynamic cycle of a HP in T-S diagram is presented in fig. 3. As a working refrigerant of the HP cycle tetrafluorethan (R134a) was chosen, due to its widespread application in cooling technologies and its critical temperature of 101,06 °C is acceptable for the investigated cycle (Lemmon et. al, 2013).

For the pressure raise simple one-stage piston compressor is used with the efficiency of 60 % (Bitzer Ecoline, 2016). Expansion of the mixture through the expansion valve assumed to occur with a constant enthalpy. In order to increase efficiency of the system the compression ratio of the compressor is changeable from 1.8 to 4.6 and depends on water temperature in storage, however, the evaporation temperature of the tetrafluorethan maintains constant and equals to 10 °C (fig. 3). But for the comparison purpose with existed systems, constant compression ratio of 4.6 is used in present paper (fig. 3 - cycle with highest compression ratio). The volume flow rate of the working fluid in a HP loop is regulated in a way that provides outlet air temperature equals to 21 °C. Technically it is fulfilled using variable speed compressor and adjustable expansion valve. Since the COP is proportional to the source temperature, the SAC HP will perform better in the summer when temperature of incoming air is increased by solar radiation in the SAC.

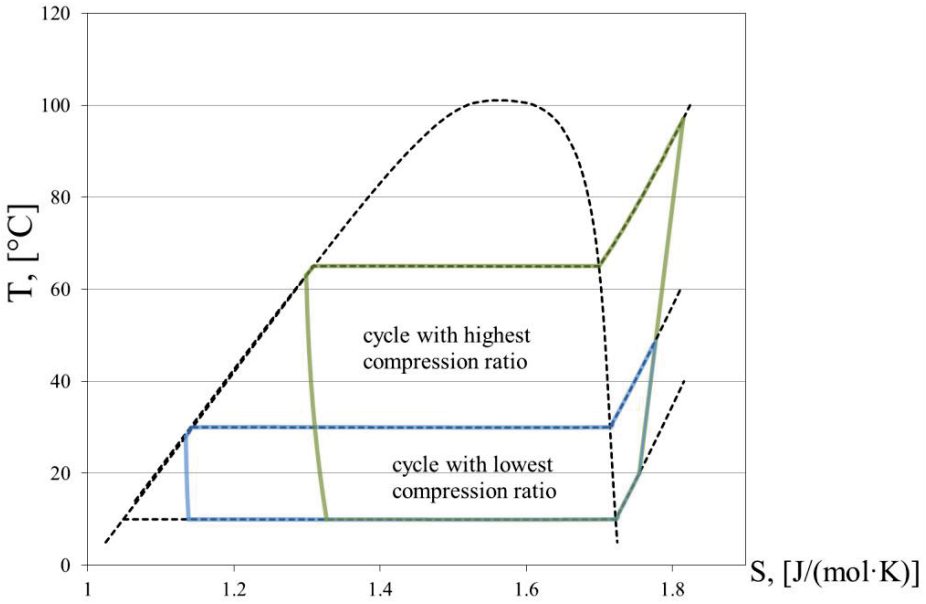

Fig. 3: T-S diagram of a HP loop

It is important to mention two running boundaries for the described system. On one hand, HP is not allowed to cool down the incoming air from the SAC below the set point temperature for the room (in present paper, 21 °C). If the ambient temperature is higher than a high room temperature limit (in present paper 26.5 °C according to Swiss Norms, 2014), use of SAC for further cooling purpose has less efficiency than direct cooling of the ambient air with the HP. Therefore, during summer operation of investigated system has lower limit of 21 °C of its outlet temperature and upper limit of 26.5 °C of the ambient temperature.

The standard characteristic of the HP cycle such as COP will be described in this case as follows:

$$COP_{cycle} = \frac{P_{heating}}{P_{compressor}+P_{ventilator}}, \qquad \text{(eq. 1)}$$

where $P_{heating}$ is energy absorbed by thermal storage, $P_{compressor}$ – electrical energy provided for the compression the working fluid in the cycle, $P_{ventilator}$ – electrical energy provided to the ventilator for the maintenance of the required volume flow rate through the ventilation channel.

3. Performance calculation

Since proposed system can be applied for the residential, office or industrial building (Sicre et al., 2015, Peci et al., 2016); and ventilation systems and requirements vary greatly, building thermal simulation will not help to achieve the goal of covering all possible options. Instead one may try to estimate the heat production of 1 m^2 area of the surface of the SAC in dependency of the geographical location.

Area of SAC is dimensioned according to the required air exchange rate in the building. According to Sicre et al. (2015) 1 m^2 of the air collector surface provides 50 m^3/h with acceptable pressure losses in ventilation channel.

For the description of the air collector performance, following equation was used:

$$\frac{Q_{SAC}}{A} = G_{90} - 9.1 \cdot (T_{SAC} - T_{air}) - 1.87 \cdot 10^{-8} \cdot \left(T_{SAC}^4 - T_{sky}^4\right) - 537 \cdot \frac{d(T_{SAC})}{d\tau}, \quad \text{(eq. 2)}$$

where Q_{SAC} – useful energy produced by the SAC, A – surface area of the SAC, T_{SAC} – mean calculated temperature of the SAC, T_{sky} – sky temperature, T_{air} – ambient temperature.

Obtained temperature of the SAC and outlet temperature of tetrafluorethan from the condenser is used for the calculation of the volume flow rate of the working fluid needed to cool down the inlet air to 21 °C. Volume flow rate is further used for the calculation of the charging power of the water boiler.

System was simulated for 8 geographical locations, which represent Mediterranean, Atlantic and Continental climates of Europe. The annual weather data for the mentioned locations was generated using software package Meteonorm 7.

In order to evaluate system's profitability, it is compared with the reference case, in which HP cycle is not changed, but inlet air in the evaporator zone is provided directly from the environment and not from the SAC. In order, to make equal $P_{heating}$ for both cases without changing the cycle, the volume flow rate of the air for reference case is increased properly due to the lower inlet air temperature. It will lead to the higher power consumption of the ventilator and lower COP of the reference system.

4. Results

Both investigated and reference systems were simulated for summer season (92 days) with the time step of 6 seconds with the mentioned boundary conditions. Comparison of the average seasonal performance factor (SPF) of the investigated and reference systems during working days with low cloudiness are shown in figure 4. For such days the SPF of the reference system is higher in southern regions due to the higher ambient temperatures – which leads to the lower air volume flow rate through the evaporator of HP.

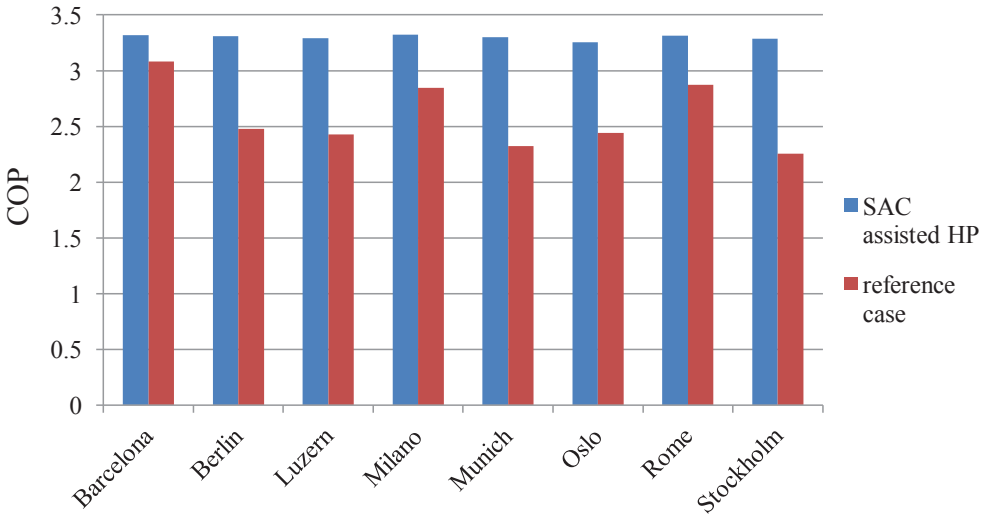

Fig. 4: Comparison of the average COP of the investigated and reference system for different geographical locations

The SPF of the investigated system is approximately the same for all geographical locations and equals 3.3. It occurs due to the application of the same governing equation (eq. 2) for the SAC in all cases with the same air volume flow rate. However, heat production of the systems in absolute values varies on geographical locations (fig. 5). The difference between average daily production per summer season and average production per cloudless day depends on the amount of the sunshine hours of each geographical location.

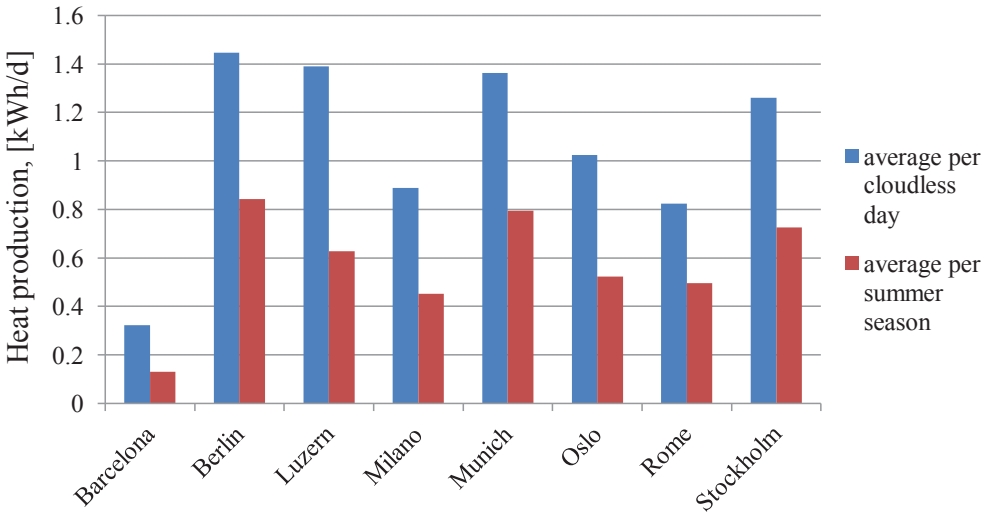

Fig. 5: Comparison of the average heat production of the investigated system with SAC area of 1 m^2 on cloudless day

From the figure 5 it can be seen that application of the SAC system has the highest production in central Europe. In the southern locations like Barcelona, Milano, Roma, ambient temperature is higher than the higher temperature set point (26.5 °C) and conventional cooling is needed. Due to this reason amount of hours during which investigated system can work is limited. On the other hand, solar radiation is lower in northern locations (Oslo and Stockholm). Useful fraction of the harvested solar energy in summer is shown in figure 6 and varies from 17 % to 26 % for office buildings, which use investigated system 5 days per week, and from 24 % to 36 % for residential buildings, which use investigated system each day.

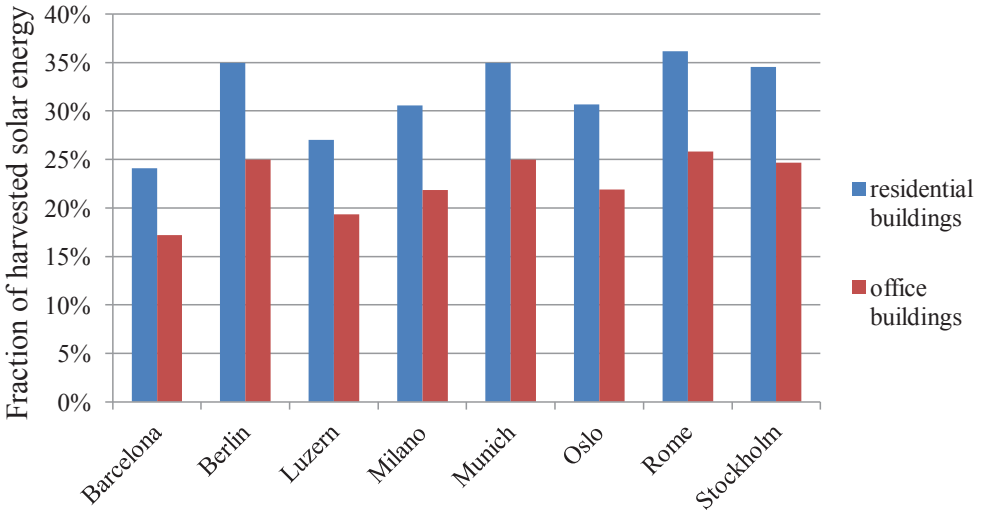

Fig. 6: Comparison of the fraction of harvested solar energy by the investigated system for different geographical locations

5. Conclusions and Discussion

This paper proposes an air-to-water heat pump cycle, which is assisted by solar air collector. Such system is handling several tasks simultaneously during summer season: ventilation and partial cooling of the rooms with internal gains, charging a thermal storage such as water tank and increasing the self-consumption of available PV-plants. It was shown that the $SPF_{heating}$ (which does not consider useful cooling energy produced by the system but only the heating up of the storage) of such system during summer season for cloudless days equals to 3.3. In comparison, the $SPF_{heating}$ of a HP-reference system would be 2.5 for central Europe.

The highest heat production can be achieved in central Europe and equals in average to 1.4 kWh/d for 1 m^2 of the solar air collector for cloudless days, which corresponds to 30 liters of water heated from 20 °C to 60 °C. The useful fraction of the harvested solar energy by the investigated system varies from 17 % to 36 % depending on the type of energy consumer (residential or office buildings). During the heating season system can run into two different modes. SAC can run standalone to cover low heating demand during autumn and spring or SAC can be used as a low temperature source for the existed heat pump which will further heat the rooms. Since the amount of energy produced by solar collector is relatively high, and the area of SAC is dimensioned according to the ventilation requirements, the amount of the heat production can be excessive and not be consumed at the same time. Therefore, accumulating of such energy also for the space heating can be promising. However, calculations should be made separately for specific building.

6. References

Bitzer Ecoline. Semi-hermetic reciprocating compressor, 2016. https://www.bitzer.de/sz/en/products /Technologies/Reciprocating-Compressors/Semi-hermetic/For-standard-refrigerants/ECOLINE/. Last date of access: 03.10.2016.

Buker, M.S., Riffat, S.B., 2016. Preliminary performance test of a combined solar thermal roof system with heat pump for buildings. Energy Procedia. 91, 421-431.

Dumont, O., Quoilin, S., Lemort, V., 2015. Experimental investigation of a reversible heat pump/organic Rankine cycle unit designed to be coupled with a passive house to get a Net Zero Energy Building. Eicker, U., Schneider, D., Schumacher, J., Ge, T., Dai, Y., 2010. Operational experiences with solar air collector driven desiccant cooling systems. Applied Energy. 87, 3735-3747.

Impact of PV and variable prices on optimal system sizing for heat pumps and thermal storage. Energy and Buildings. 128, 723-733.

Jurt, D., Zakovorotnyi, A., Seerig, A., 2016. Einfluss des Klimawandels auf die Wirkung von Kühlabgabesystemen in Bürobauten. Neunzehnter Status-Seminar «Forschen für den Bau im Kontext von Energie und Umwelt». Bern

Kapsalis, V., Karamanis, D., 2016. Solar thermal energy storage and heat pumps with phase change materials. Applied Thermal Engineering. 99, 1212–1224.

Karagiorgas, M., Galatis, K. Tsagouri, M., Tsoutsos, T., Botzios-Valaskakis, A., 2010. Solar assisted heat pump on air collectors: A simulation tool. J. of Solar Energy. 84, 66-78.

Lemmon, E.W., Huber, M.L., McLinden, M.O., 2013. NIST Standard Reference Database 23: Reference Fluid Thermodynamic and Transport Properties-REFPROP, Version 9.1. National Institute of Standards and Technology.

Peci, F., Ruiz de Adana, M., Comino, F., Berlanga, F.A., 2016. Installing Opaque Ventilated Facades for Energy Saving in Old Buildings. Proceedings of the 12th REHVA World Congress „CLIMA 2016".

Poppi, S., Bales, C., Heinz, A., Hengel, F., Chèze, D., Mojic, I., Cialani, C., 2016. Analysis of system improvements in solar thermal and air source heat pump combisystems. Applied Energy. 173, 606-623.

Sicre, B., Zakovorotnyi, A., Zwahlen, M., 2015. Performance analysis of solar air heating systems for the refurbishment of commercial buildings. Conference Proceedings of the 10th Energy Forum „Advanced Building Skins", 218-226.

Swiss Norms, 2006. SIA Merkblatt 2024, Standard-Nutzungsbedingungen für Energie- und Gebäudetechnik. Zürich.

Swiss Norms, 2014. SIA 382/1, Lüftungs- und Klimaanlagen – Allgemeine Grundlagen und Anforderungen. Zürich.

Tanguy, G., Wyttenbach, J., Stephan, L, 2014. Thermochemical seasonal storage demonstrator for a single-family house: simulation and dimensioning. ISES Conference Proceedings of "Eurosun 2014".

Conference Proceedings

EuroSun 2016
Palma de Mallorca (Spain), 11 - 14 October 2016

Compulsory Policies of Installing Solar Water Heating Systems and Normative Construction Procedure in China

Ruicheng Zheng[1], Bojia Li[1], Min Wang[1], Xinyu Zhang[2] and Tao He[2]

[1] China Academy of Building Research, Beijing (China)

[2] National Center for Quality Supervision and Testing of Solar Heating Systems, Beijing (China)

Abstract

In recent years many local governments in China have implemented compulsory policies of installing solar water heating systems integrated in new buildings. So system quality and capacity becomes a very important problem. Therefore a complete supervision system for quality control to solar water heating systems integrated in buildings during whole construction procedure has been formed gradually in China. This system includes technical code for design and acceptance, performance requirement to products of solar collectors and a normative construction procedure etc.

In this paper it is given the background of compulsory policies of installing solar water heating systems integrated in new buildings and introduced a normative construction procedure for solar water heating system. The procedure runs through design, product selecting, construction, acceptance and evaluation. As most of buildings are tall buildings in China's cities some installation types for solar collector integrated in buildings and better operation measures for central solar water heating systems to suitable special condition of China are also given in the paper.

Key-words: *compulsory policies; technical code for design and acceptance; construction procedure for solar water heating system*

1. Background

In recent years many local governments in China have implemented compulsory policies of installing solar water heating systems integrated in new buildings, and some cities publish different preferential policies, such as give financial subsidy to star green residencies which should take certain technical measures including installation of solar water heating systems etc. But some problems occur when practice, such as substandard product quality and completion inspection of projects etc. As it has influenced the health developing of these polices, for quality control and capacity promotion of the solar water heating systems, a completed supervision system has been formed gradually in China.

The system includes three important aspects. The first is national standards for products, such as "Evacuated tube solar collectors" and "Flat plate solar collectors" etc. The second is technical code for design and acceptance, such as "Technical code for solar water heating systems of civil buildings" and "Evaluation standard for solar water heating system of civil buildings" etc. The third is a normative construction procedure. Only following this construction procedure a solar water heating system integrated in building with higher quality and better effect can be completed. The procedure has 4 main steps: design, installation, acceptance and evaluation.

2. Design, examining and approving for design drawing

Engineering design in China must follow a stipulate procedure and the design for solar water heating systems

doi:10.18086/eurosun.2016.04.20 Available at http://proceedings.ises.org

integrated in buildings should also follow it. The most important step for the procedure is examining and approving to design drawing by another qualified authority after design is finished by original design authority.

2.1. Design

Design for solar water heating system integrated in building shall be done by an authority which has a certain design qualification. Design must follow the all stipulation in China's national standard "Technical code for solar water heating systems of civil buildings" GB 50364. This code has finished revision during 2014-2015 and many terms in revision version of the standard can give stronger supporting to guarantee the design quality.

For example, the term for calculating solar collector areas used in system stipulates strictly that yearly average efficiency of the solar collector shall be calculated according to the instantaneous thermal efficiency equation of a solar collector which is tested by a qualified testing authority and computation method is given in this term. The computation method of this term gives the detail selecting principle for computation parameters, such as how to select solar irradiance, ambient temperature and inlet water temperature of collector in reduced temperature difference of the thermal efficiency equation.

The revision version of the standard gives a lot of basic data used for design, such as yearly total solar irradiation and average daily total solar irradiation on horizontal and slope plane in 31 cities of China etc. In appendixes of the standard some computation methods are given, such as computation for wind load to a solar water heating system which installs on the roof of a tall building. So the revision version of the standard is a more useful design tool and can raise future design level of solar water heating system in China.

2.2. Examining and approving for design drawing

After the design for solar water heating system be finished all design materials including design drawings, calculation documents etc must be examined and approved by another authority which has a certain level of drawing check qualification.

The focus of design examining by the drawing check authority are following:

• If the design meets all stipulations in national standard " Technical code for solar water heating systems of civil buildings" GB 50364, such as various safety requirements, calculation for solar collector areas and volume of water tank etc, type selection for equipments of pump and heat exchanger etc.

• If the performance of the solar collector used in the system meets the technical requirement in concerned national standard, such as exposure and pressure-resisting etc safety performance, zero-loss collector efficiency and collector overall heat loss coefficient etc thermal performance.

• If having the reliable and flexible automatic control measure and it can prevent effectively occurring of safe faults, such as overheating and freeze of the system etc. And the control measure can give precedence to use solar energy heating water etc, so to guarantee energy saving effect of the system.

• To check the analysis for energy saving effect and economical efficiency of the system design and if it meets the original requirement.

Only an approved design scheme can be used for construction of a solar water heating system integrated in building.

3. Requirement for installation and acceptance of system construction

Requirement for installation and acceptance of a solar water heating system is stipulated in "Technical code for solar water heating systems of civil buildings" GB 50364 and acceptance is a key factor. In the revision version of the standard GB 50364, more contents are added in the chapter of acceptance for solar water heating systems, so the operability to an engineering acceptance for a solar water heating system is stronger and clearer than before, therefore the engineering quality and the effect of the solar water heating system will also has a better guarantee than before.

The standard stipulates that acceptance shall be divided into acceptance for itemized project and completion acceptance and system commissioning must be finished before completion acceptance. Acceptance for concealed work, such as embedded parts for collector installation foundation etc, must be certificated by supervision personnel of the project before concealing. After each acceptance for itemized project finished, linkage debugging to the system shall be carried out and then system commissioning must be done as practical working condition in continuous 3 days which shall be one clear day at least. When linkage debugging, temperature, flow rate and working pressure of the system shall meet the design requirement at the rated condition in which flow rate and temperature of hot water supplying equals design value.

When completion acceptance, some necessary documents, such as completion drawings, qualified certificate or performance testing reports of the main materials and equipments, records for system debugging and commissioning, testing record for thermal performance of the system etc must be given. Testing for thermal performance of the system shall be done in 4 days when having different solar daily irradiation at least, the distribution range of solar daily irradiation (shown in Table 1) and testing method shall meet the requirement in China's national standard "Evaluation standard for application of renewable energy in buildings" GB / T 50801. Only passed the completion acceptance, the engineering of a solar water heating system can transfer to users.

Tab. 1: Distribution of solar daily irradiation for thermal performance testing of a solar water heating system

days	the first day	the second day	the third day	the fourth day
daily irradiation (H)	H＜8 MJ/m^{2}d	8 MJ/m^{2}d≤H＜12 MJ/m^{2}d	12 MJ/m^{2}d≤H＜16 MJ/m^{2}d	H＞16 MJ/m^{2}d

The defects liability period for engineering quality of a solar water heating system is two years. In this period if some quality problems occur, the construction authority shall take maintenance and the responsible party shall undertake concerned economical duty.

4. Some better technical measures for solar water heating systems

As most of buildings are tall buildings in China's cities, so installation types for solar collector integrated in buildings and operation measures shall be suitable to this special condition.

4.1. Installation types for solar collector integrated in buildings

As roof area is not enough to install solar collectors which can meet demand of solar water heating system for a tall building, two main installation types are used generally in China, collectors close putting on a support structure of the roof (Fig.1 left) and collector instead of board of balcony (Fig.1 right).

Fig. 1: Two main installation types for solar collectors integrated in buildings

For installation type of collectors close putting on a support structure of the roof, in general the system can provides enough solar hot water supply to whole building which has 24 floors. As collector frame can shelter incidence sunlight, the another advantage of this installation type is to decrease the roof temperature

in summer, according to testing to a real project in Shenzhen City the roof temperature is 2℃ lower than common building, so it is favor to decrease energy consumption for air conditioning in summer.

Fig. 2: View of real projects using these two installation types for solar collectors

For installation type of solar collector instead of board of balcony the tilt angles of the collector installation are different in north part with higher latitude and in south part with lower latitude of China. In north part with higher latitude, such as Heilongjia Province etc, the tilt angles of the collector can be 90^0 (Fig.1 right), but in south part with lower latitude, such as Jiangsu Province etc, the tilt angles of the collector shall be smaller than 90^0 (Fig.2 right), so can get more incidence sunlight.

4.2. Operation measures for a central solar water heating system

For increasing energy saving effect of a central solar water heating system, it is necessary to decrease heat loss in circulation pipes of hot water supplying. So a common operation measure for hot water circulation in pipes used in China is to start circulation only when temperature of hot water is lower than a set value in the past. But now a better operation measure for hot water circulation is used in some residential buildings, circulation starting only when a user wants to use hot water. If a user in the building wants to use hot water, he/she can put a push-button on the wall of an apartment to start circulation (push-button flashing) and then use hot water till the push-button no flashing, as it (push-button no flashing) means that the temperature of hot water has reached the set value and can be used for bath etc, not only energy saving but also water saving.

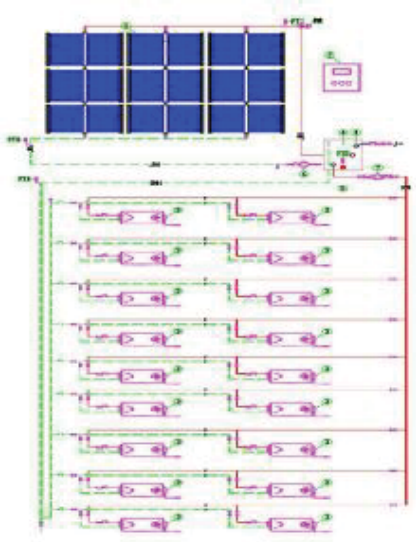

Fig.3 shows a popular central solar water heating system which is named collective-individual hot water supply system. Solar collector array of this system is installed on the roof of a tall building, and the hot water storage tanks are installed in each apartment of the building, but a small solar hot water tank is on the roof. Solar hot water is supplied into heat exchanger of water storage tank in the apartment and water in the tank is heated. The main advantage of this system is to make easier for payment of hot water using. The increasing cost for solar water heating system can be included in sale price of the apartment, the resident family need only take cold water payment when using solar hot water, so heat metering of the system can be canceled. As a possible problem of the system is unbalances heat exchange between various water storage tanks, so developed an auto-control measure to solve it. Every time heat exchange is only taken between users of selecting numbers (adjustable as real condition), not all users.

Fig. 3: Collective-individual hot water supply system

At the first round when water temperature of these tanks raise 5℃ (adjustable as real condition, in general it is 5-10℃), the hot water input valve of heat exchangers close automatically and heat exchange turn to next sets of same number's tanks for heat exchange, repeating till finishing heat exchange of all tanks, then to the

second round, so guarantee to get same solar energy for all users basically.

5. Effectiveness

Since following this normative construction procedure for solar water heating systems, many projects of solar water heating system get better effects than before in China. For spreading successful experience of better projects, China Academy of Building Research undertook a task for compiling drawing volume of excellent cases of solar water heating systems which is given by the Ministry of Housing and Urban-Rural Development of PRC in 2015. China Academy of Building Research investigated a lot of projects and National Center for Quality Supervision and Testing of Solar Heating System (Beijing) tested some projects for volume compiling and 18 engineering cases of solar water heating system are selected to put into the drawing volume.

These 18 engineering cases are located in 9 Provinces including Beijing Anhui Hebei Shandong Jiangsu Zhejiang Hainan Xinjiang Ningxia and cover 4 different weather areas of severe cold zone, cold zone, hot summer and cold winter zone, hot summer and warm winter zone in China. The system types of the cases are 7 collective hot water supply systems, 6 collective-individual hot water supply systems and 5 individual hot water supply systems. So the cases have a wide-ranging representativeness. The average solar cost of the cases is 0.11Yuan/kWh and the payback period of steady state is all smaller than 5 years, economical efficiency is very nice.

Tab.2 and Tab.3 shows a fine effect of an understanding case in the drawing volume. It is a central solar collective and hot water supply system in a living building for staff of Yimin Company, located in Nanpi County, Cangzhou City, Hebei Province, designed and installed by Jiangsu Sunrain Solar Energy Co.,Ltd which is exclusive quoted company in solar thermal field of China. Total solar collector areas of the system are 620m^2, except solar hot water supply to the building, surplus solar hot water will be transported to ground heat exchanger of a ground-souse heat pump system which is for space-heating of this building. As soil temperature will be raised through heat exchange with solar hot water, unit COP of ground-souse heat pump can be raised, so system efficiency will be also increased.

Tab. 2: Testing data for thermal performance of the project in Yimin Company Ltd

Day	Outdoor temperature ℃	Daily solar irradiation MJ/m^2	Daily solar heat gain MJ	Common energy consumption MJ	System efficiency %	Solar fraction %
1	-3.2	16.52	4241.5	0	47.7	100
2	-2.8	14.83	3983.4	0	49.9	100
3	-1.1	11.54	2545.1	804.5	41.0	76.0
4	-0.3	6.38	1234.8	2114.8	36.0	36.9

Tab. 3: Analysis results for energy saving and environment effects of this project in Yimin Company Ltd

Items	Unit	Value
Solar fraction in one year	%	81.6
Average system efficiency in one year	%	44.2
Quantity instead of common energy	tce/year	127.5
Decreasing quantity of CO_2 discharge	t/year	314.9
Solar cost	Yuan/kWh	0.04
Saving cost in one year	Yuan	498,978.00
Payback period of steady state	Year	1.4

From Tab.2 we can know that this system can get fine thermal performance even in winter. When sunny day solar fraction of the system is still attain 100%. From Tab.3 the energy saving effect and economical efficiency of the system is also very nice. Solar fraction of the system in one year is over 80%, solar cost is only 0.04 Yuan/kWh and payback period of steady state is 1.5 year, very short. The drawing volume of excellent cases of solar water heating systems will be published and as a teaching material for training. So we can believe that solar water heating systems integrated in buildings will be developed better and more healthy in China.

6. References

[1] National Standard of PRC GB 50364, Technical code for solar water heating system of civil buildings. 2006.

[2] National Standard of PRC GB / T 50604, Evaluation standard for solar water heating system of civil buildings. 2011.

[3] National Standard of PRC GB / T 50801, Evaluation standard for application of renewable energy in buildings. 2013.

05. Solar Assisted District Heating and Cooling and Large Scale Applications

Conference Proceedings

EuroSun 2016
Palma de Mallorca (Spain), 11 - 14 October 2016

Techno-economic Analysis of Solar Options for a Block Heating System

Martin Andersen[1, 2], Chris Bales[1] and Jan-Olof Dalenbäck[2]

[1] Solar Energy Research Center (SERC), Dalarna University, Borlänge, Sweden

[2] Chalmers University of Technology, Gothenburg, Sweden

Abstract

An innovative small solar district heating system with one central heating plant and four solar substations has been built in Vallda Heberg, Sweden, to supply a new housing area with passive houses. The target solar fraction was 40% and the total system design, including heat distribution in the buildings, was based on previous experience and aimed to be simple and cost-effective. The main aim of this study was to determine whether the system can be designed in a more effective manner by change of distribution system and load density. TRNSYS models were calibrated against measured data and then used to predict the energy performance. Results indicate that lower distribution heat losses can be obtained by change to a distribution concept with lower operating temperatures, while potentially reducing cost. Changes in heat density cause reduced distribution losses and boiler supplied heat demand, with only minor effects on solar system yield.

Keywords: solar thermal, district heat, hot water circulation, simulation

1. Introduction

EKSTA Bostads AB (municipal housing company) has built and operates a number of solar assisted heating plants in small residential building areas, the first ones from the 1980's. The heat supply is managed via small district heating systems based on wood chips and/or wood pellet boilers and roof-integrated solar collectors of different generations, i.e. 100% heating by renewables. The buildings, commonly small multifamily buildings, have always had a bit lower heat demand than required by the Swedish building code.

The new residential area in Vallda Heberg comprises multifamily buildings, as well as single family buildings. All buildings are designed as passive houses according to the Swedish standards, i.e. well insulated buildings with air tight envelopes, and supply and exhaust ventilation with heat recovery is applied in all buildings. The whole area is supplied with heat from a small district heating system with pellet boiler and solar thermal, with a targeted solar fraction of 40% (Nielsen et al., 2014). This system (see Figure 2) comprises one central heating plant (HP) with a wood pellet boiler (and an oil boiler for back-up) and four sub-stations (SS1-4). Buffer storage tanks are installed in the central heating plant and in each sub-station. There are 108 m^2 evacuated tube solar collectors (ETC) on the heating plant and 570 m^2 flat plate roof-integrated solar collectors in connection to the sub stations. Heat is supplied from the sub-stations to the buildings with a so called GRUDIS 2-pipe system (Zinko, 2004) where hot water is circulated in plastic (PEX) pipes, similar to a standard DHW circulation system (Figure 1). This allows a very simple and inexpensive solution for transfer of heat in each building, reducing costs for the total heating system (Gudmundson, 2003): district heat and heat distribution within the buildings. However, as all buildings are passive houses, a large share of the supplied heat is lost in culverts and sub-stations, which adds to the running costs.

The main aim of this study is to determine whether it is possible to make the design of the whole heating system more efficient. In future work, costs will also be taken into account to determine the most cost-effective solution.

Figure 1 shows a schematic overview of the heating system at Vallda Heberg, with the boiler central to the right, substation in the middle and a passive single-family house to the left.

doi:10.18086/eurosun.2016.05.12 Available at http://proceedings.ises.org

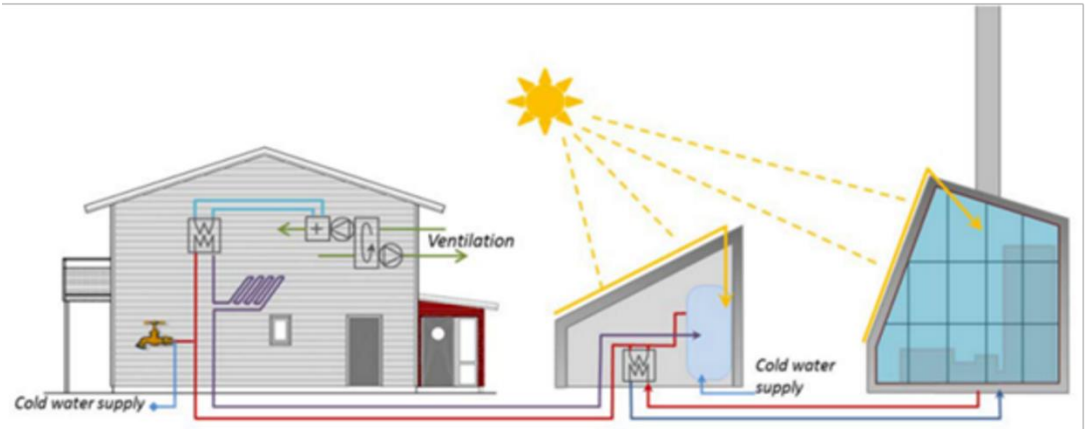

Figure 1: Simple schematic of the technical system in Vallda Heberg. (Based on figures from Markgren Arkitektur AB and Mats Abrahamssons Arkitektkontor AB).

2. Method

The main parts of the Vallda Heberg system, including buildings, have been modelled in TRNSYS and calibrated with measured data from the system. These include the single and multi-family houses, substation, primary and secondary distributions systems as well as the solar fields and central boiler plant. In order to simplify the overall system model, common "blocks" such as buildings and substations have been multiplied to give a heat load similar to that of the real Vallda Heberg system. Distribution pipes have also been lumped together to give the same heat losses as the real system. This system is then the benchmark for other system configurations where choice of culvert system and load density are varied.

3. System description

Figure 2 shows an overview of the Vallda Heberg residential area, including heat supply units and color-coded distribution pipelines. Flat-plate collectors (FPC) supply heat to storage tank through the solar heat culvert (SHC). This heat is used to pre-heat domestic hot-water (DHW) and its circulation (DHWC) flow.

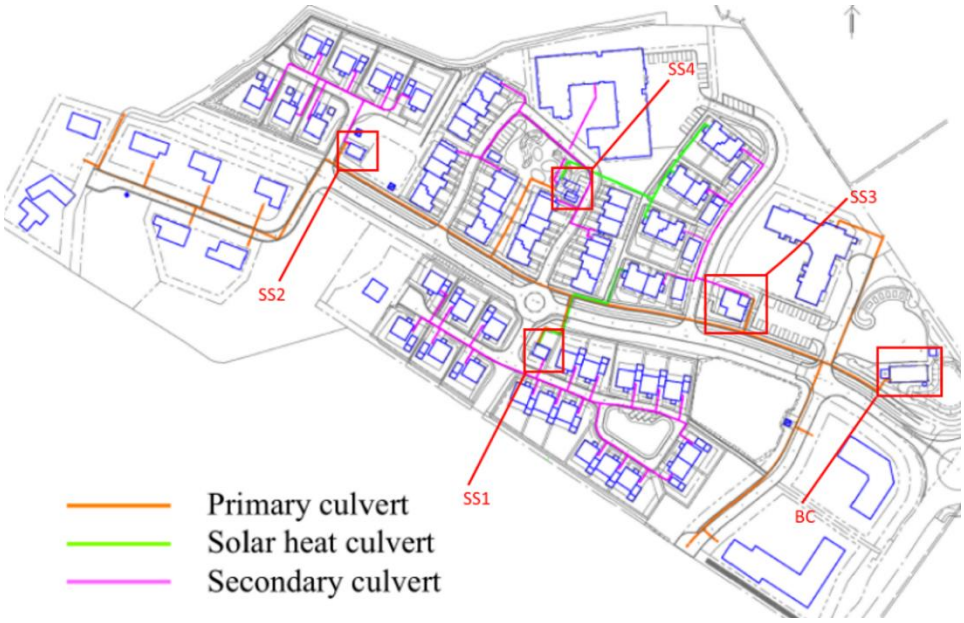

Figure 2: Residential area of Vallda Heberg with denoted substations (SS) and central heating plant (denoted BC) in red, together with color coded distribution pipelines.

Heat generated in the main heating plant (HP) by the wood pellet boiler (WPB) and evacuated-tube solar collectors (ETC) is distributed through the primary culvert (PC) to the substations. Here it acts as auxiliary heating for the DHW and/or DHWC to reach the target supply temperature to the building stock. The DHW and/or DHWC is then delivered to the residents through the secondary culvert (SC). More details on the heating system is given in the following sections.

3.1 Heat demand and distribution system

The system at Vallda Heberg supplies 128 living units, of which 16 are apartments in multi-family houses (MFH) and 64 are apartments in a senior (SEN) living facility. The remaining 48 living units are single-family houses (SFH) and row houses (RH). The heat demand of the different living units differ according to the building characteristics (Table 1), but all buildings are designed according to the Swedish passive house standard.

Table 1 shows the characteristic specific energy consumption of the buildings at Vallda Heberg, based on calculations and prognosis values as stated in a performance assessment made in 2014 (Fahlén et al., 2014).

Table 1: The characteristic specific energy consumption of the buildings at Vallda Heberg for the year April 2013 – 2014 March. The percentage value given refers to the share of total energy use in the building (including electricity).

Load	SH		DHW		Total	DHW/SH
Unit	[kWh m^{-2}]	[%]	[kWh m^{-2}]	[%]	[kWh m^{-2}]	[-]
SFH	30	58	17	32	47	0.55
RH	65	79	12	15	77	0.18
MFH	50	63	22	28	72	0.44
SEN	37	64	9	16	46	0.24

The table values have been read out of graphs for the most part and thus are somewhat uncertain. Specific demand for SH based on measurements varies significantly, as does that for DHW and the ratio of DHW to SH energy. An overview of the system characteristic demand based on measured heat consumption for 2015 and the ratio of specific energy demand presented above (Table 1), is presented below (Table 2), together with the respective collector area (CA) and storage volume (SV) for each substation:

Table 2: Characteristic demand, collector area and storage volume of the Vallda Heberg system for the year 2015

Quantity	SS1	SS2	SS3	SS4		System tot.
Load served	19 SFH	7 SFH	4 MFH (16 APT)	64 SEN APT	6 RH (22 APT)	128
Demand [kWh]	107647	44864	84599	204416	117623	559149
DHW [kWh]	38197	15919	25850	39994	18331	138292
SH [kWh]	69450	28945	58749	164422	99292	420857
CA [m^2]	142	48	64	316		570
Specific CA [m^2/MWh]	1.32	1.07	0.76	0.98		1.02
SV [m^3]	15	5	6	28		54
Specific SV [m^3/MWh]	0.139	0.111	0.071	0.087		0.10

The heat demand is supplied from the main HP to the substations through the primary culvert (PC) in regular district heating twin-pipes, but with an additional DC200 casing insulation made from expanded polystyrene (EPS) of density 30 kg/m^3 and thickness 100 mm. Pipe dimensions vary according to the load served in the different parts of the system, but the majority (~90%) of primary network pipe length is of dimension DN65, DN80 and DN100. The secondary distribution of heat from the substations to the living units is done in an EPSPEX-culvert, which consists of PEX-piping placed in an EPS-casing. These PEX-pipes are of dimensions DN32 – DN65, although the vast majority (~90%) are of dimension DN50 and DN65.

For the year April 2013 – March 2014, the losses attributed to secondary distribution were 25% and 30%, for SS1 and SS2, respectively. For the whole system, total losses were 28% for one single month (March 2014), of which about one third (10%-points) were attributed to the secondary distribution, including substations. The rest was attributed to the primary distribution and losses in HP (Nielsen et al., 2014). Two other studies estimate the heat losses during March 2014 to be around 10% each for the BC and PC (Fahlén et al., 2014; Olsson and Rosander, 2014). However, these values are highly uncertain, as the temperature difference at the heat meters used to calculate the quantities in the energy balance were small (occasionally very small, <3 °C).

3.2 Heating plant

The heat supply consists of a boiler central for which the details are listed below (Table 3). Further down, a schematic of the HP is shown in Figure 3, depicting the PC heat exchanger (HX), storage tanks, solar heat exchanger (HX), wood-pellet boiler (WPB) and oil boiler (OB). The installed solar system utilizes an ETC from Ritter XL Solar, with constant volume flow in both solar loop and charge loop. The anti-freeze system from Paradigma utilizes pure water and heat from the accumulator tanks to heat collectors and outside piping when water in loop gets near to freezing point, although the exact temperature control is unknown. The measured annual solar yield for the year April 2013 – March 2014, as well as for year 2015, was about 57 MWh/a, corresponding to about 8% and 10% of total heat demand, respectively.

Table 3: Details of the heating plant at Vallda Heberg

Boiler Central	
Installed storage volume	15 m^3
Installed collector area	108 m^2 (ETC)
Collector Slope (β)/Azimuth (γ)	70°/30°
PC design operating temperatures (S/R)	75°C/50°C
PC pipe diameter $Ø_{PC}$	100 mm
Load capacity biomass boiler	300 kW
Load capacity oil boiler (back-up)	500 kW

The installed storage volume consists of three buffer tanks of 5 m^3 each. These are connected top-to-bottom, to act as one large tank (Figure 3). The solar loop pump starts/stops when the temperature in the collector is >30°C/<25°C. When the temperature difference between the solar loop (S13) and the temperature in the bottom of the "cold" tank (S8) is >5K/<2K, the charge pump starts/stops.

Solar heat is delivered to the storage tanks according to temperature level, either through valve 1 to the "hot" tank (>75°C) or through valve 2 to the "warm" tank (<75°C).

There are two operating modes - one for winter and one for summer (boiler control sensors in parenthesis):

- Summer mode - valve 3 is open and 4 closed. The "warm" and "cold" tanks are mostly by-passed. The solar system is the preferred heat supply, with the boiler augmenting according to demand (S3, S4).
- Winter mode - valve 4 is open and 3 closed. All tanks are used, as the heat demand is larger and solar resource is less than in summer. The solar system acts as a pre-heater for the boiler (S4, S6).

The summer mode is chosen according to the availability of solar energy and the size of heat demand, and hence may commence/terminate in different months from year to year.

Figure 3 shows a schematic of the heating plant at Vallda Heberg, including all relevant temperature sensors (denoted S1 – S17) and control valves (denoted 1 – 4).

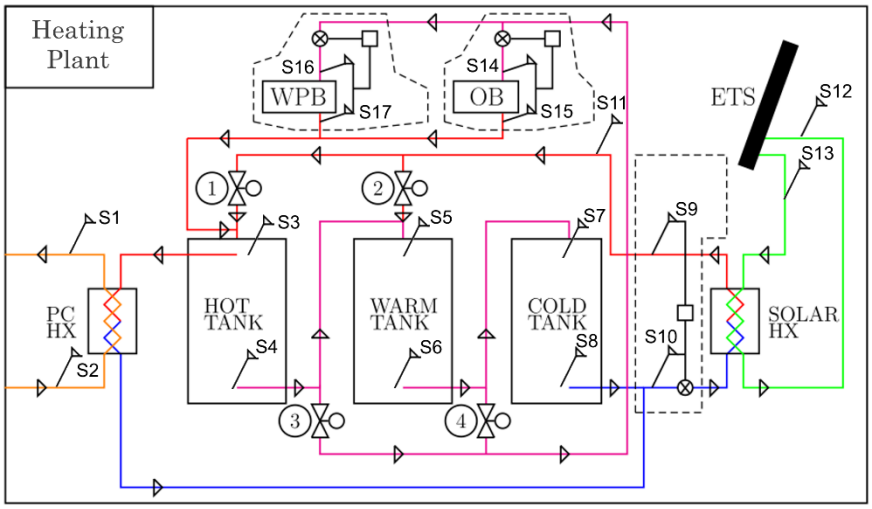

Figure 3: Schematic of the boiler central at Vallda Heberg (Olsson and Rosander, 2014)

A modulating WPB of 300 kW from Osby Parca (turndown ratio 13) supplies heat to the "hot" tank (Figure 3) when the temperature in the tank(s) falls below the target value. The flow rate of the boiler supply pump is adjusted to give an outlet temperature of maximum 95°C. There is an additional 500 kW boiler (OB) which works as reserve. Hot water supply from the tank to the PC HX is controlled to ensure a constant supply set-temperature of 70°C, increasing the flow rate if the outlet temperature to the PC (S1) is <70°C and vice versa. Note that this temperature differs from the design supply temperature (Table 3), and that the stated value is assumed based on the measured inlet temperature of SS3 and SS1). The control system is configured to start the boiler according to the temperature in the "top" and "bottom" of the tank(s), which refers to the placement of the temperature sensors in the storage. The placement of the sensors varies with operating mode, which will be explained further in the next section describing the monitoring system.

3.3 Sub-stations

The majority of sub-stations (SS1 – SS3) at Vallda Heberg have the same design, the differences being the connected load, collector area and storage volume (see Table 2). SS4 has a different design, as it supplies the senior living quarters, where SH is supplied by a radiator system, and thus is separated from DHWC.

A schematic of one of the sub-stations (SS1) used to supply a collection of 19 SFH is shown in Figure 4:

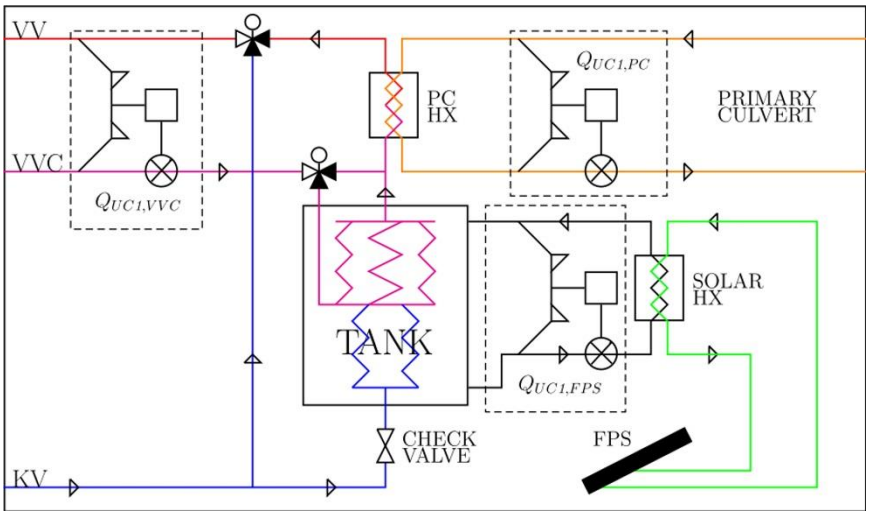

Figure 4: Schematic of SS1 at Vallda Heberg (Olsson and Rosander, 2014)

The sub-stations work as distribution units for the heat delivered by the PC and the FPC's, but also act as hydraulic separation between the higher pressure/-temperature primary distribution and the lower pressure/-temperature secondary distribution. This is important, as the pressure of the secondary distribution GRUDIS loop, must be low enough to allow for tapping of DHW.

Warm water is circulated between the buildings (the load) and the SS in the DHWC loop (denoted VVC). If storage is sufficiently warm (dT +5/+2 K), the flow is routed through the upper half of the storage through an internal HX, but only when the exiting temperature remains below a limit of 62°C. When DHW is tapped in the houses, make-up cold water (CW) enters the bottom half of the storage in an internal HX, where it is pre-heated. In the event of DHWC heating through storage, the pre-heated DHW is mixed with the DHWC flow, before entering the second internal HX. Auxiliary heat is supplied by PC HX when necessary to achieve a target supply temperature of 57°C.

3.4 Monitoring system

The monitoring system at Vallda Heberg uses flow meters from manufacturers Landis+Gyr and Kamstrup (Christensson, n.d.), with the majority coming from the former. In the HP, meters are installed at the boilers (S14 – S17) and in the charge loop (S9, S10) by the solar HX (see Figure 3). No measurements are made of the energy leaving the HP – the additional sensors (S1, S2) installed are used for system control purposes only. In SS1, they are installed in the PC loop, in the charge loop and in the circulation loop (Figure 4). SS4 monitors delivered heat to the radiator circuit in the SEN and heat from PC, whereas the remaining sub-stations (SS2, SS3) only monitor heat from PC. According to previous studies of the system, the flow meters installed in the system have large errors associated with the measured energy when the temperature differential (dT) is small between in- and outgoing flow (Fahlén et al., 2014; Olsson and Rosander, 2014).

The accuracy of heat meters is governed by European Standard EN1434, which states the methods for calculation of accuracy and their boundaries. According to EN1434, the calculated uncertainty of the heat meter is the arithmetic sum of part uncertainties - one part for the calculator, one part for the temperature sensors and one part for the flow meter. For the heat meter installed in conjunction with the WPB, about 25% of the logged temperature measurements for 2015 are below that of the operation threshold of the meter (3K < dT < 120K) (Landis+Gyr, 2015). The measurement uncertainty of the temperature component alone for these measurements is >3.5%. The average total error calculated for all measurements in the WPB is 7.5% for 2015, based on the logged temperature and flow values. This does not take into account any measurement errors in the charge loop.

For the substations, dT over the flow meter is relatively large for the majority of the values, compared to that of the lower threshold value, which means that the uncertainty is not as high as for the boiler. Nonetheless, calculations show that for SS1, about 15% of all measurements in 2015 had an uncertainty above 10%, which is still significant.

4. Model description

4.1 Overall system

Two models have been made in TRNSYS: one modelling SS1 supplying 19 SFH and one modelling the HP supplying SS1 – SS4. In order to simplify the system model when modelling the whole system, the total load was modelled as consisting of SFH only and that this load was supplied by sub-stations identical to SS1. This was done by connecting the model of SS1 (putting it in a macro) with the model of the HP in TRNSYS. By using a set of equations, the load on the SS1 model was scaled (multiplied) up by a factor giving the total system heat demand. This demand was then used to calculate the necessary mass flow in PC, depending on the inlet supply temperature and assuming a return temperature equal to that of the inlet flow in the PC HX of the SS (100% efficiency of HX).

In order to assess the differences between the demands in the different sub-stations, the demand of each sub-station was normalized to that of SS1, as shown below (Table 4):

Table 4: Overview of the heating demand of the different sub-stations at Vallda Heberg normalized to the demand of SS1. The given factor values represent the ratio between SH and DHW demand.

	SS1	SS2	SS3	SS4	Total
Load served [SFH]	19	7.9	14.9	56.8	98.7
Load factor	1.0	0.4	0.8	3.0	5.2
DHW factor	0.355	0.355	0.306	0.181	0.247
SH factor	0.645	0.645	0.694	0.819	0.753
DHW [l/day]	2630	1096	2067	7868	13676

The total heat demand of the whole heating system equals about 98.7 SFH or about 5.2 times that of SS1. In modelling the system, the number of houses modelled (24.6) were chosen so that the scale factor was exactly 4.0 with a specific collector area for the sub-station equal to the average specific collector area of 1.02 for the whole system (see Table 2).

4.2 Buildings

The SFH are modelled using a two-zone building model (type 56). One zone is heated, if necessary, by a water-air HX (with glycol anti-freeze) in the air supply duct of the mechanical ventilation system with heat recovery – the other by floor heating. Floor heating has a fixed flow rate, resulting in heating year round due to the supply temperature of around 57°C, whereas the air heating is controlled by a room sensor. The target inside temperature is 19.5°C.

The house is modelled to have low heat losses and infiltration, based on design information. Inputs for outer area of walls in different directions, air volume of different nodes etc. have been modelled based on drawings of the house. Windows and shading (provided by roof overhang and balcony) are accounted for. Internal gains are added to the main area (i.e. not bathroom) based on known electricity consumption (70 % is expected to be gained as heat) and the average number of inhabitants.

The floor heating in one zone of the building is modelled with a pipe heat load (type 682, TESS) with a 100W

constant demand based on static calculation at design conditions, which are the conditions that are dominant throughout the year. The return temperature from this model is calculated and given as input to the SC.

Active SH is supplied by pre-heating of supply air by means of heat recovery (type 667, TESS) from exhaust air, in addition to auxiliary heating by an air-fluid HX (type 670, TESS) utilizing glycol as the heat transfer fluid. The glycol circuit is supplied with heat from the SC by a fluid-fluid HX (type 5b).

4.3 DHW

The DHW consumption profile is calculated with DHWcalc (Jordan and Vajen, 2003), using a 3 minute random distribution based on the annual monitored volume for the year April 2013 – March 2014 for SS1. The base of the profile is the statistical distribution profile of a SFH, the input being the total amount of water used in one day (11676 l/day) for the whole system and the day of maximum (monitored) water load (347). The cold water supplied to the residential area of Vallda Heberg is supplied from a nearby lake. The temperature of the inlet water thus is expected to follow an annual temperature curve corresponding to a sinus function, with an average temperature of 12°C and an amplitude of 4°C (January being the coldest).

The DHW consumption profile is used as input for a data reader (type 9). Two equations are dedicated to dividing the total flow in the SC into one SH component and one DHW component, directing the correct flow to the SH and subtracting the consumed DHW from the total flow before returning to the SC return pipe.

4.4 Sub-station

The substation is modelled using the following non-standard components:

- Storage (type 340, multiport model (Drück, 2006))
- Solar collectors (type 832 QDT multi-node model (Haller et al., 2012))

The parameters for the custom made storage have been supplied by technical drawings of the sub-substation and through communication with the engineering company in charge of its design (Andersson & Hultmark – A&H). The storage has been modelled with two internal HX, one in the top of the tank and one in the bottom, which is a simplification over the real system that has six in the top of the tank and three in the bottom. This has been taken into account by sizing the top heat HX volume to be double that of the bottom HX. The solar collector parameters were taken from the supplier of the custom made collectors in this system.

The DHWC pump, storage charge pump and solar loop pump are modelled using standard components (type 3b). Pump manufacturer brand and model name has been supplied by the engineering company in charge of design (A&H), allowing to derive pump operation curve parameters from the pump datasheet. Nominal volume flow rates originated from technical drawings of the substations, but were chosen to achieve harmony between measured and simulated values during calibration. Internal piping is modelled with standard components (type 31) and heat losses from these represent the whole substation, avoiding the need of a separate building model. The UA values have thus also been chosen to allow for harmony between simulated and measured values for the SS loss in the calibration phase. All pipes with negligible flows (i.e. < 0.02 l/s) and by-pass valves have been ignored as these are irrelevant for normal operation. The PC HX and the solar HX were modelled using standard components (type 5b), with parameters supplied from technical drawings. The UA value of these was assumed to be the nominal power of the HX divided by the design temperature difference over the HX (from "hot" side inlet to "cold" side outlet).

4.5 Heating Plant

The heating plant is modelled using the following non-standard components:

- Storage (type 340, multiport model, non-standard (Drück, 2006))
- Solar collectors (type 538, evacuated tube solar collector with modulating flow, TESS)
- Boiler (type 659, auxiliary heating, TESS)
- Boiler feeding pump (type 741, variable speed pump, TESS)
- PC HX- and PC supply pump (type 742, user specified flowrate, TESS)
- PC HX (type 805, domestic hot water HX, hot side flow is output, non-standard (Haller, 2006))

Storage is modelled as one large tank instead of three small, without internal HX. Charging is done through assigned double ports according to the principle explained earlier (see section *3.2 Heating plant*). The surface-

to-volume ratio of the original storage has been maintained in scale-up of storage. The double-port feature is also used to distinguish between ports used for boiler return according to operating mode, leaving a set of ports unused for parts of the year. The switching between summer and winter mode is done with a forcing function (type 14h) in combination with a flow diverter, flow being directed to ports according to the season.

Solar collectors parameters are taken from the summary of EN12975 test results by TÜV Rheinland, annex to the Solar KEYMARK Certificate. The listed incidence angle modifiers (IAM) are compiled in a file and used as input to the model.

Boiler parameters are derived from the datasheet from the boiler manufacturer, values utilized mainly being the rated power, set-point temperature and max temperature of the boiler. The minimum flow rate is ignored, as it is considered irrelevant for modelling purposes. The boiler control is ON/OFF, as opposed to in reality where it is modulating. The modulating behaviour is imitated by implementing differential boiler control with short on/off cycles, resulting from small temperature dead-bands, much in the same way as pulse-width-modulation (PWM). Boiler control target temperature is 82°C, one differential controller checking the tank bottom and one checking the tank bottom – if both are below dead-band (1.5°C and 2°C) the boiler is ON.

The boiler feeding pump is modelled as variable speed, making modulating operation possible at a later time by implementation of a PID-controller. At present it is modelled as running when boiler is on, with the flow rate being the nominal flow rate. The PC HX pump flow rate is given as an input from the PC HX, which calculates the necessary "hot side" inlet flowrate to achieve the target "cold side" outlet temperature of 70°C. For the PC supply pump, the flow rate is given as the return flow rate from the PC, equal to the "cold side" outlet of PC HX. All pumps are modelled with a maximum flow rate taken as the nominal flow rate found in technical drawings.

Heat losses in the HP are modelled by single pipe ducts using standard components (type 31), for which the DN has been derived from the technical drawings and the dimensions have been derived from EN1057 (European Comitee of Standardization, 2006). There is one pipe for the supply from boiler to storage and one from storage to PC HX. For the solar loop, there are four pipes: two pipes for collector supply and two pipes for collector return. There is one "inside" pipe and one "outside" pipe for each of the two-pipe segments, intended to model the solar pipe heat loss to ambient. Ambient outside temperature is given by the weather data, whereas the ambient inside temperature is assumed to be a constant 25°C, as this is the target temperature for the ventilation system in the HP according to control system description.

4.6 Distribution

According to previous studies, the PC route length is 1007 m, divided into the different pipe diameters. The route length of SC connected to SS1 is 469 m, and consisted of a mix between pipes of DN32 - 63 (Olsson & Rosander 2014). To estimate the remaining length of the secondary culvert, measurements were conducted using satellite images (i.e. Google Maps). Assuming that half of the SC connected to SS1 was DN63 pipes and assigning one fourth to DN50, with the remaining being DN40 (20%) and DN32 (5%) pipes, modeling the whole load at Vallda Heberg as consisting of SFH only, the length of distribution pipes will be divided as shown below (Table 5):

Table 5: Overview of measured and estimated culvert dimensions at Vallda Heberg

Culvert dimensions							
DN [mm]	32	40	50	65 (*63)	80	100	Total
PC Length [m]	15	20	44	602	187	139	1007
SC Length [m]	56	223	278	557*	0	0	1114

The modelled PC length is divided into four pipe sections (PC1 – PC4), serving the four different sub-stations (SS1 – SS4) in the original system (see Figure 2). As can be seen, the amount of PC culvert length of DN32 – 50 is small compared to the total PC length (~8%), so that it was chosen to model the PC as consisting of DN65 – 100 pipe sections only in order to simplify the model. The section serving SS2 is also serving an area of larger SFH not currently connected to the network, and thus the length of this element was dimensioned to account for heat losses in the section. It is further assumed that the pipe diameter decreases with distance from the HP, so that SS4 and SS2 are served by DN65 pipes (600 m in total), whereas SS1 and SS3 are served by DN80 (200 m) and DN100 (150 m) piping, respectively. For the simulations, however, the four pipe elements are modelled as one pipe connected to the load (SS) at the far end.

The consequence of this simplification is that the temperature of the flow delivered to the SS is a little lower than it would be in reality. This is made up for in the model by increasing the flow through the SS, to be able to deliver the required heat. Such a simplification is considered appropriate, as the focus of this study is on accumulated energy and does not consider energy flux specifically.

Distribution pipes are modelled by use of type 951 (buried horizontal pipe, twin-pipe system). For the PC, the pipe parameters were taken from the manufacturer datasheet (Powerpipe AB, 2016), including the insulation (rigid polyurethane - PUR) parameters. For the secondary culvert, the pipe dimensions were derived as explained earlier (Table 5). Following the assumption made for the mix of pipe dimensions for the SC, the average weighted DN would be 54 mm. The insulation parameters were taken from the manufacturer datasheet for the EPS casing (Elgocell AB, 2013). Because the original EPS casing has a square/rectangular cross-section and the pipe model takes cylindrical dimensions only, the casing diameter had to be calculated assuming that the cross-sectional area of the casing was circular.

4.7 Model calibration

The two models used in this study were developed separately and then calibrated towards measured data. The SS1-model was developed using meteorological- and monitored data for the sub-station and connected houses for the year April 2013 – March 2014. Optimally, the system heat losses would be modelled separately, but due to bad quality of measurements, the total losses from SS1 and SC1 were matched to difference between delivered energy to SS (PC HX and FPC) and end-use consumption. SH demand was calibrated by changing house UA value and house set-temperature. The PC delivered heat was calibrated mainly by adjusting losses in storage heat loss. The resulting deviation between measured and simulated values after calibration was in the range 0.4 – 1.2% (absolute values), for the energy consumption of SH, DHW, distribution losses, storage charged energy and PC delivered heat.

The HP model was developed using meteorological- and monitored for the calendar year 2015. Heat delivered from PC to the sub-stations (SS1 – SS4) was used as input to a pipe heat load (type 682, TESS), calculating the return temperature to the PC HX. Calibration was done mainly by adjusting the insulation parameters and UA values of pipes, to get the appropriate heat losses. The resulting energy balance showed negligible deviations, and most of the simulated values (solar heat, heat losses) deviated only slightly (<3%) from the measured. However, there were significant deviations in the simulated boiler energy (~9% lower than measured on annual basis). Attempts to calibrate the model by assuming tenfold thermal conductivity of the EPS and threefold thermal conductivity of the PUR could not reduce the discrepancy to an acceptable level (i.e. below 5%). Studies showed that the losses of the HP and PC appeared to be underestimated for the winter months, though no explanation for this could be found. Reducing the measured boiler energy by 10% gave good correspondence between simulated and measure values, implying that the discrepancy was a consequence of the large uncertainties in measurements by the installed flow meters in the HP (7.5%) and partly in the sub-stations (up to 8%), as the monitored values from these were used as input.

4.8 Model variations – parametric studies

The parametric studies made in this study are related to the type of distribution system and the load/linear heat density (LD). There has been two types of distribution system modelled:

- Original Vallda Heberg: PC distribution, substations, and SC distribution GRUDIS
- Modified Vallda Heberg: All GRUDIS system, DHW-circulation from the HP and to the load

In the modified Vallda Heberg, the sub-station is kept and the PC HX in the HP is removed, connecting the boiler directly to the PC HX in sub-station. This allows for a more direct comparison of the distribution pipe influence on the heat losses. This in turn influences the harvested solar energy and supplied boiler energy. The model has been altered by reducing the PC length from 950 m to 0 m, and increasing the SC by the same length. The length of the pipes supplying solar heat have been assumed to be one third of the original PC length (950 m), meaning that the solar collectors are modelled as placed on the house roofs as close to the HP as possible to minimize pipe heat losses. However, one major simplification is that the pipes are modelled as being above ground, and not buried as would often be the case.

By variation of the distribution pipe length, a parametric study was made for 0.5LD, 1LD and 2LD, to show how the parameter influences the system heat losses, supplied boiler energy and the harvested solar energy.

5. Results

5.1 Distribution concept

Figure 5 depicts the simulated annual energy balance for the system at Vallda Heberg according to choice of distribution concept, showing a significant reduction in heat demand for the two simulated cases. By choosing an all GRUDIS distribution system, the supplied boiler energy was reduced by 99.5MWh (13%) mainly due to a reduction in the total pipe distribution losses by 112MWh (43%). The heating plant (HP) loss also decrease by about 5 MWh (6%) which is mainly due to reduced storage heat loss, particularly during spring and autumn months. The change in stored solar energy from FPC (HP solar) was lower by about 27MWh (17%), assumed to be due to increased solar-pipe length and -losses. Heat from ETC on the HP is about the same in both cases. The sub-station (SS) loss is similar in both cases, with minor differences. It should be noted that the house heat demand is about 1.6% lower in the all GRUDIS case, which affects the results, but not by much.

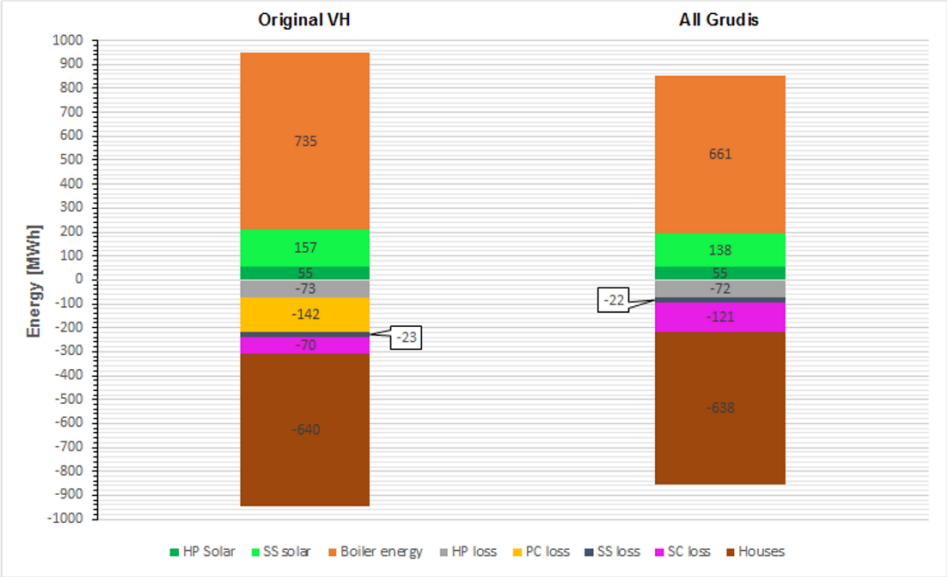

Figure 5: Simulated annual energy balance for the system at Vallda Heberg (VH) for two different choices of distribution concept. Abbreviations used: heating plant (HP), sub-station (SS), primary culvert (PC) and secondary culvert (SC).

5.2 Parametric study

Below (Figure 6) is an overview of the result from the parametric studies for the simulations conducted with the original distribution concept at Vallda Heberg, utilizing a combination of conventional DH twin pipes, sub-stations and GRUDIS.

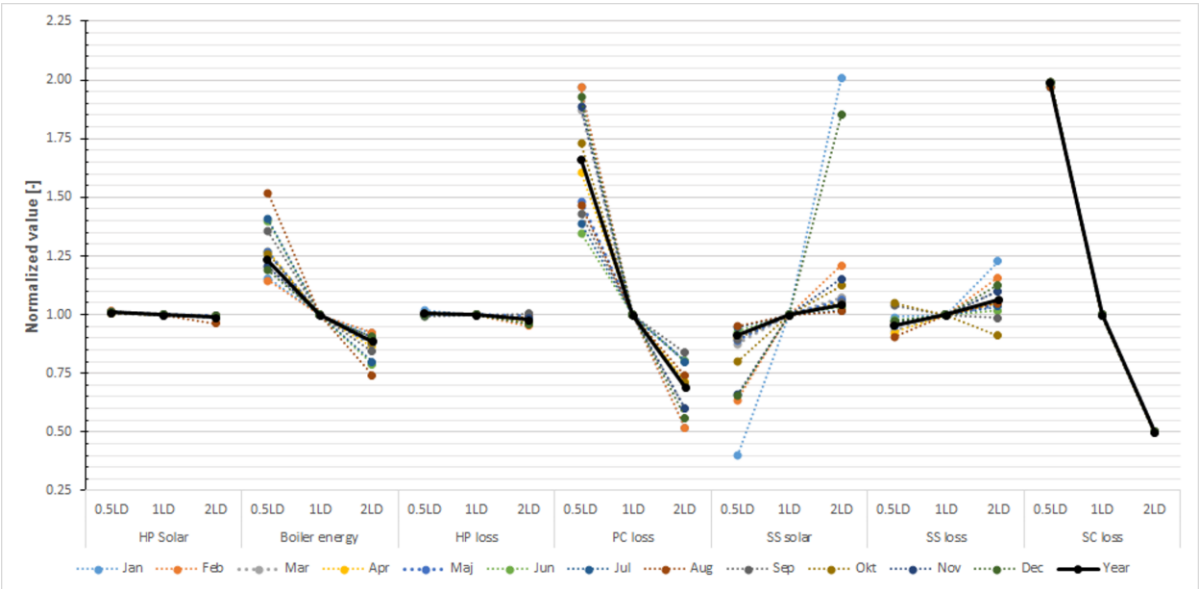

Figure 6: Influence of linear heat density on different parameters in simulation of the original distribution concept at Vallda Heberg. The values have been normalized to the simulated values for 1LD. Abbreviations used: heating plant (HP), sub-station (SS), primary culvert (PC) and secondary culvert (SC).

As can be seen, the boiler energy and distribution losses are the parameters most affected by the change in culvert length, and hence linear heat density. The SS solar energy (from FPC) varies moderately. This is expected as these parameters are directly dependent on the pipe length. The HP solar energy (from ETC) and HP loss is relatively unaffected, whereas SS loss varies moderately - mostly during winter due to higher loads and operating temperatures. For the All GRUDIS case, the influence of linear density is almost the same as that for the original system.

5.3 Discussion

In simulating the all GRUDIS system, some major simplifications were made in the model. For one, the substation was kept in the model, assuming that the available storage is divided between the HP and SS, instead of having larger stores in the HP. Doing this, the loss coefficients and stores are assumed the same for both simulated cases, instead of modelling the all GRUDIS system with a new design for a complete HP including all stores and DHWC connections. It is likely that the total losses would be lower if the HP was modelled as one unit. Secondly, the solar pipes from the FPC to the SS are not buried insulated twin pipes, but assumed to be above-ground, which overestimates the losses. Taking these two simplifications into account, the differences observed in choice of distribution concept would most likely be even greater.

Another simplification is modelling only one SS and assuming that the load is only made up of SFH. This means that the heat distribution in all buildings is the same and split between uncontrolled, year round floor heating and the heat to air supply is the same for the whole area. In the real system, there are different loads installed, many of which have a different characteristic heat demand (Table 1, Table 2 and Table 4). In contrast to the other dwellings in the system, the elderly home (SEN) has an installed radiator system with design operating temperatures of 60/40 which leads to a little lower return temperature from SS4 than for the other SS and this has not been taken into account. Furthermore, the lower ratio of DHW to SH in the RH and MFH means that the circulation flow to these buildings will be higher than in the case for SFH, which would influence the heat losses in SS3 and SS4 with associated distribution lines.

The observed pipe distribution losses in the simulations of an all GRUDIS distribution system are significantly lower than those in the original configuration. This may partly be attributed to the lower operating temperatures of the GRUDIS network and partly to the model of the SC. The modelled average ground temperature is 9°, which means that by assuming an average supply temperature of 56°C in SC and 70°C in PC, the difference in dT (47K/61K for SC/PC, respectively) is about 30%. In the twin-pipe model, the thermal conductivity of the *fill insulation* (PUR in PC and EPS in SC) surrounding the pipes is the most influential parameter for the heat losses, whereas the *gap material* (EPS for PC and clay for SC) is less influential. The PC model was calibrated to a fill insulation value 3-4% higher than that of the SC. Because the temperatures are higher in the PC, this might have a large influence on the heat losses.

The cost of distribution pipes is significantly different for PEX and conventional PUR coated steel pipes. As can be seen below (Table 6), the specific cost of SC is close to half that of the PC, whereas the trench cost is the same for both.

Table 6: Overview of the approximate costs for distribution pipes and trench work for the system at Vallda Heberg. All pipe costs are total costs including connections, welding and EPS insulation. (Andersson-Jessen, 2016; Magnus Klingheim, 2016)

		Length [m]	Price culvert [SEK/m]	Price trench [SEK/m]	Total price [10^6 SEK]
Original VH	PC	1007	1150	1600	2.8
	SC	1114	650	1600	2.5
	SUM				5.3
All GRUDIS	EPSPEX	2121	650	1600	4.8
	Solar culvert	336	1150	0	0.386
	SUM				5.2

In the all GRUDIS case, the solar culvert (SCU) length is assumed to be a third of that for PC and to be of same cost as the PC (i.e. same pipe type). It is furthermore assumed that the trench cost only applies once, with no additional trench costs for SCU going to the HP (i.e. EPSPEX and SCU in same trench). Thus, the total price of an all GRUDIS system would be about the same (-2%) as the original system cost, but with lower heat losses.

The cost of having an all-in-one HP is not calculated, but would be substantially lower than having a smaller HP and 4SS as is the present case.

The parametric study reveals it is mostly beneficial with a high linear heat density (LD), which is expected as it cuts distribution loss and consequently boiler energy. Changing the distribution pipe length has the effect of changing the LD, which is sufficient for simulation purposes, but has some practical issues in reality. Assuming that the total distribution pipe length (PC + SC) and total land area is kept the same, the implication of assuming that all living units (LU) are SFH means that more houses would need to fit in the same space. The LD would thus still be the same, but the built area would increase (i.e. higher building density). Now, if the LD is to increase, in order to get space enough for the same population living in SFH, a larger area would be needed. If the area is to be kept the same as in the original VH, increasing LD is equivalent of replacing SFH with MFH (although with the same demand characteristics as SFH). Conversely, decreasing the LD would imply having the houses further apart which, again, would require a larger area. If the space is to remain the same, then in effect, decreasing the LD implies having MFH (with the same demand characteristics as SFH) spaced further apart. Alternatively, the increase/decrease in LD can be seen as building SFH denser/sparser without limits on the area size.

5.4 Conclusions

The whole block-heating system of Vallda Heberg has been modelled in TRNSYS with some simplifications, utilizing one building model to simulate all buildings and one sub-station to simulate all sub-stations. Two distribution systems were modelled: the original system with primary culvert, substations and secondary culvert – and one all GRUDIS system using DHW-circulation piping for distribution. Results indicated a significant reduction in heat losses can be obtained by employing an all GRUDIS distribution system, while at the same time potentially reducing cost. Changes in heat density show that the distribution losses and supplied boiler energy decrease with increased heat density, and vice versa. This is as expected, as these parameters are directly related to the distribution network length. Future work should concentrate on investigating the influence of different load heat demand characteristics, as well as placement of solar collectors and type of solar collector technology.

6. References

Andersson-Jessen, P.-E., 2016. Per-Erik Andersson Jessen, Andersson & Hultmark AB. Pers. Commun. 2016-09-27.

Christensson, N., n.d. Eng. Tech. Eksta AB. Pers. Commun.

Drück, H., 2006. Transsolar: Type 340 - MULTIPORT Store Model for TRNSYS.

Elgocell AB, 2013. Behåll värmen... ...spara pengar! - Broschure.

European Comitee of Standardization, 2006. En 1057.

Fahlén, E., Olsson, H., Sandberg, M., Löfås, P., Kilersjö, C., Christensson, N., Jessen, P.A., 2014. Vallda Heberg - Sveriges största passivhusområde med förnybar energi. Göteborg.

Gudmundson, T., 2003. Svensk Fjärrvärme - EPSPEX-kulvert: UTVECKLING , UTFÖRANDE OCH UPPFÖLJNING.

Haller, M., 2006. TYPE 805: DHW heat exchanger.

Haller, M., Perers, B., Bales, C., Paavilainen, J., Dalibard, A., Fischer, S., 2012. TRNSYS Type 832 Dynamic Collector Model.

Jordan, U., Vajen, K., 2003. Tool for the Generation of Domestic Hot Water (DHW) Profiles on a Statistical Basis Version 1.10.

Landis+Gyr, 2015. EAT ® T550-UH50 Flow sensor manual.

Magnus Klingheim, E.A., 2016. Tech. Elgocell AB. Pers. Commun.

Nielsen, C., Haegermark, M., Dalenbäck, J.O., 2014. Analysis of a Novel Solar District Heating System. Eurosun 2014 16–19. doi:urn:nbn:se:du-15517

Olsson, H., Rosander, A., 2014. Evaluation of the Solar-Assisted Block Heating System in a Passive House Residential Area - A Master ' s Thesis in Sustainable Energy Systems Chalmers University of Technology.

Powerpipe AB, 2016. Powerpipe product catalogue.

Conference Proceedings

EuroSun 2016
Palma de Mallorca (Spain), 11 - 14 October 2016

A numerical model to evaluate the flow distribution in large solar collector fields in different operating conditions

Federico Bava, Janne Dragsted and Simon Furbo

DTU Civil Engineering, Technical University of Denmark, Kgs. Lyngby (Denmark)

Abstract

A numerical model to evaluate the flow distribution in a large solar collector field was developed in Matlab and is presented in this study. Model and measurements from a solar collector field were compared and a good agreement was found. The model was then used to study the flow distribution in different array layouts. Balancing valves proved to be an effective way to achieve uniform flow distribution also in conditions different from those for which the valves were regulated, as well as in case of irregular layouts with different compositions of the collector rows. A Tichelmann connection gave a uniform flow distribution, especially if the distribution pipe diameter is reduced so to give a constant pressure drop gradient. The reduction in power output from the collector field was approximately proportional to the square of the root-mean-square deviation of the flow distribution, but was generally small, at least under the considered assumptions.

Keywords: *solar collector, solar collector field, flow balancing, flow distribution, parallel connection.*

1. Introduction

1.1. Background

An increasing number of large scale solar collector fields have been built in Europe in the last years. Of the total collector area installed at the end of 2014, 77% was located in Denmark (Mauthner et al., 2016). The development in this country has been driven by specific factors, such as high taxation on fossil fuels and widespread use of district heating (DH), to which large collector areas can be connected (Furbo et al., 2015). More than 800,000 m^2 of collector fields were installed in Denmark at the end of 2015 and this number is expected to grow in the next future (Mauthner et al., 2016). Also the size of the collector fields has been increasing. The current largest field in Vojens has a collector area of 70,000 m^2 (Mauthner et al., 2016), but by the end of 2016 a 150,000 m^2 collector field should be completed in Silkeborg (EnergySupply, 2016).

The larger the collector fields and the higher the number of collector rows, the larger the risk of non-uniform flow distribution. Non-uniform flow distribution cause non-uniform temperature distribution across the collector field, so decreasing the thermal performance. The negative effect of flow maldistribution on the thermal performance was investigated by Chiou (1982), who treated this effect in a single collector with parallel channels. He presents a method to determine how much the collector efficiency is penalized by the flow maldistribution. Defined a *flow nonuniformity parameter* as the root mean square deviation of the channels flow rates, he concludes that the deterioration of the collector efficiency is proportional to the 1.8^{th}-1.9^{th} power of such parameter. Wang and Wu (1990) presented a model to calculate the flow distribution in collector arrays with vertical pipes, both in U- and Z-configuration. The U-configuration presents a higher maldistribution than the Z-configuration. Fan et al. (2007) investigated through CFD calculations the flow and temperature distribution in a large collector for solar assisted DH plants. Model results and measurements are compared. The authors conclude that the flow distribution is driven by friction (and so buoyancy can be neglected), if the velocity in the collector pipes is high compared to the temperature rise across the collector. Bava and Furbo (2015) propose a numerical model to calculate the pressure drop and flow distribution in a U-type harp collector. Based on the conclusions of Fan et al. (2007), the authors argue

Selection and/or peer review under responsibility of Scientific Committee
doi:10.18086/eurosun.2016.05.05 Available at http://proceedings.ises.org

that in large collector fields for DH applications the relation between the fluid velocity in the absorber pipes and the temperature rise in the collector is such that buoyancy can be neglected. The model was compared against measurements carried out on a collector for solar assisted DH plants and good agreement was found.

Ideally, the layout of a collector array should be with short pipe lengths and uniform flow distribution. Though, it is not possible to optimize both these aspects simultaneously, so a compromise must be found. Rohde and Knoll (1976) analyzed different options to minimize the flow maldistribution in a collector field of 12 rows connected in parallel. The options included various size manifolds, manifold area changes, different locations of the inlets and exits to the manifolds, orifices and balancing valves. The last two are presented as the best solutions, both in terms of performance and cost. It is observed that a specific configuration of valve settings maintains the desired flow distribution only at a specific total flow rate. The topic of flow distribution in collector fields is also treated by Knabl et al. (2014). Maintaining a constant and large diameter in the distribution pipes or adopting a Tichelmann configuration (Fig. 6.b) improves the flow distribution. However, both options have higher costs due to the longer/larger pipes. Balancing valves are another possibility, but these increase the cost, installation time and maintenance (in case of defective valves). A cheaper solution is to install differently sized pipes in the collector rows, but the hydraulic design must be calculated in advance and very precisely, as a later adjustment would be very expensive.

In Danish solar collector fields, the pipe diameter of the distribution pipes is progressively reduced, as fluid is diverted to the collector rows. Balancing valves are then installed in each row to obtain a uniform flow distribution. These are regulated to achieve the desired flow distribution in full-load conditions (high flow rate, high solar radiation, nominal inlet/outlet temperatures), so that the outlet temperature from all rows is the same. This is done by supplying the different rows with flow rates proportional to the collector row area.

1.2. Sizing distribution pipes and balancing valves in solar collector fields: HySelect software

The design of the hydraulic network of a solar collector array can be a time-consuming and cumbersome procedure to be carried out manually. Hence, software able to carry out the same task can be extremely useful, making the job of planners and designers much easier. A program which can be used for this purpose is the commercial software *HySelect* from IMI Hydronic Engineering (IMI Hydronic, 2014). The software can be used to design and balance generic hydraulic networks, and so solar collector fields as well, in terms of pipe size, pump head, types and settings of balancing valves. The software returns the valve type and valve settings which should be applied to achieve a user-defined flow distribution. Additionally, it makes easy to optimize the pipe diameters (based on several pipe dimension standards) to fulfill fluid velocity or pressure gradient constraints. The software also contains built-in libraries of the thermophysical properties of a variety of fluids, including those most commonly used in solar heating systems, such as water and ethylene/propylene glycol-water mixtures. When designing a branched system, the program automatically adds and considers the pressure drop caused by the resulting tee junctions and bends. HySelect is intuitive to use and extremely fast in returning the results.

Despite these strengths, the software has some limitations. First of all, its reduced flexibility. As mentioned above, the program returns the valve setting configuration which guarantees a certain flow distribution. It does not calculate the flow distribution itself. Consequently, once a system has been balanced for specific boundary conditions (e.g. total flow rate and fluid temperature), it is not possible to analyze how the flow distribution varies, if the boundary conditions are changed. Secondly, the fluid temperature is assumed constant throughout the system. This approximation does not seem very accurate when designing solar collector fields for DH application, where the temperature rise across the collector field can be 40-50 K. Furthermore, the thermophysical properties (especially viscosity) of glycol-water mixtures are known to be strongly dependent on the temperature (see Section 2.1.2). Thirdly, complex layouts, having for example a common return pipe such as in Fig. 3, cannot be designed. Finally, the correlations used for evaluating the pressure drop in tee junctions are not in agreement with the literature (Idelchik, 1994). No reference to a literature source is provided and the used correlations are not stated in the software manual (IMI Hydronic, 2014). The difference between HySelect and Idelchik's correlations for pressure drops in tee junctions is shown in Fig. 1. The diagram was obtained assuming a distribution pipe from which 10 parallel circuits parted. The distribution pipe and the circuit pipes had diameter of 81 mm and 36 mm respectively. The system was supplied with a total flow rate of 20 $m^3 h^{-1}$, uniformly distributed in the 10 parallel circuits.

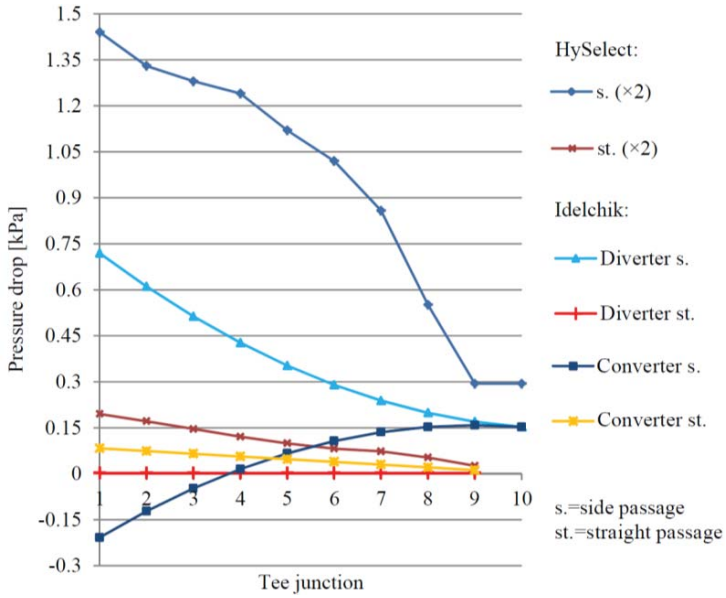

Fig. 1: Comparison between HySelect and Idelchik's correlations for pressure drop in tee junctions.

The fluid was water at 75 °C. Looking at Fig. 1, it is first of all noted that HySelect does not show the different contributions of the diverging and converging tee junctions, but only the overall pressure drop. Secondly, comparing the pressure drops in the diagram, it can be seen that for the straight passage the combined pressure drops from HySelect are approximately twice as large as the pressure drops that Idelchik's correlations give for the straight passage of the converging tee. On the other hand, the pressure drop in straight passage of the diverging tee junction predicted by Idelchik is negligible compared to that in the converging tee junction. Consequently, it could be neglected in the calculations without introducing a significant error. Regarding the side passages, the combined pressure drop from HySelect is between two and four times higher than Idelchik's pressure drop for the side passage of the diverging tee junction.

2. Material and method

2.1. Numerical model

2.1.1. Pressure drop correlations

To calculate how a fluid flow distributes in a branched system, it is necessary to know the relation between flow rate and pressure drop across each component. In fact, the fluid flow distributes in such a way that the pressure difference between two points is the same, regardless of the hydraulic path which connects one to the other. Because the relation between pressure drop and fluid velocity depends on factors such as Reynolds number, flow regime, etc., the flow distribution in a branched system may vary in different conditions.

In a collector field three main categories of hydraulic components can be identified: solar collectors, pipes and fittings (bends, tee junctions, valves, etc.).

The pressure drop characteristic of a solar collector is not always given in the technical datasheets and - even when provided - it usually refers to a specific fluid type and temperature. Different fluids and/or temperatures can affect the pressure drop. In this study the model proposed by Bava and Furbo (2016) was used to evaluate the pressure drop across each solar collectors, more specifically a HTHEATStore 35/08 from Arcon-Sunmark A/S (SP, 2016a). The HTHEATStore 35/08 is a flat plate harp collector with 18 U-connected absorber pipes. The pipes are 5.80 m long and have an inner diameter of 7.3 mm. The two manifolds are 2.24 m long and have an inner diameter of 32.9 mm. The collector gross area is 13.57 m^2 and its efficiency coefficients are η_0=0.757, a_1=2.2 W m^{-2} K^{-1} and a_2=0.007 W m^{-2} K^{-2} with respect to the collector gross area. Fig. 2 shows the modeled pressure drop for a 35% propylene glycol/water mixture, whose physical properties were evaluated through (Eq. 5) and (Eq. 7).

The friction loss along the distribution pipes was calculated by the Darcy-Weisbach equation (Eq. 1):

$$\Delta p = \lambda \frac{l}{D_h} \frac{\rho w^2}{2} \qquad \text{(Eq. 1)}$$

In (Eq. 1) Δp [Pa] denotes the pressure drop; λ [-] the Darcy friction factor; l [m] the pipe length; D_h [m] the pipe hydraulic diameter, which equals the inner diameter for a full flow circular pipe; ρ [kg m^{-3}] the fluid density and w [m s^{-1}] is the mean fluid velocity.

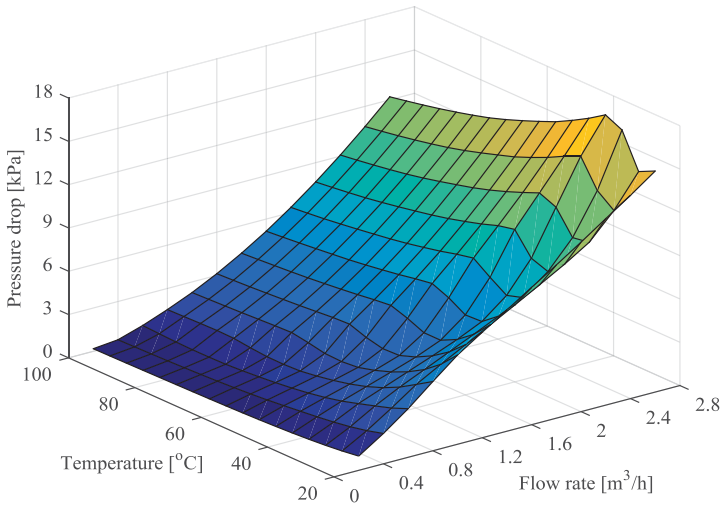

Fig. 2: Pressure drop in a HTHEATstore 35/08 collector as function of temperature and flow rate for 35% propylene glycol/water mixture.

Laminar regime was assumed for Reynolds numbers Re<2300, while turbulent regime was assumed for Re>4000 (Holman, 2002). According to the flow regime, the friction factor was calculated through the Hagen-Poiseuille law (Eq. 2) and the Haaland (1983) correlation (Eq. 3) respectively. The roughness of steel pipes was assumed to be ε=10^{-4} m. In the transition region (2300<Re<4000) the friction factor was evaluated by linearly interpolating the value obtained from (Eq. 2) at Re=2300 and that from (Eq. 3) at Re=4000.

$$\lambda = 64/Re \qquad \text{(Eq. 2)}$$

$$\lambda^{-1/2} = -1.8 \log_{10}\{[\varepsilon/(3.7\, D_h)^{1.11} + 6.9/Re]\} \qquad \text{(Eq. 3)}$$

Correlations from Idelchik (1994) were used to estimate the local losses in fittings, such as bends, tee junctions, changes of flow section area, etc. Regarding the balancing valves, the manufacturers usually provide the pressure drop characteristic as flow factor K_v (Eq. 4):

$$K_v = V \cdot [SG/(\Delta p \cdot 10^{-5})]^{1/2} \qquad \text{(Eq. 4)}$$

In (Eq. 4), V [m^3 h^{-1}] represents the volume flow rate and SG [-] the fluid specific gravity.

The flow factor is mainly function of the valve setting. However, deviations from the nominal K_v value can be expected with fluids different from water and flow rates significantly smaller than the valve nominal flow rate (IMI Hydronic, 2015). In these cases, the nominal K_v value should be corrected. In this study, valves from IMI-Hydronic were used and their corrected flow factors were evaluated through HySelect software.

2.1.2 Fluid properties

Propylene glycol/water mixtures with glycol concentration of 30-40% (Windeleff and Nielsen, 2014) are normally used as heat transfer fluid in solar assisted DH plants. In this study, the thermophysical properties of these mixtures were evaluated using the correlations proposed by Conde (2011).

$$\rho = 508.4 - 0.1824x + 965.8T^* + 0.2803xT^* - 472.2 \cdot (T^*)^2 \qquad \text{(Eq. 5)}$$

$$c_p = 4476 + 608.6 - 715.0T^* - 1939xT^* + 478.7 \cdot (T^*)^2 \qquad \text{(Eq. 6)}$$

$$\ln \mu = -1.028 - 0.1003x - 19.94T^* + 0.1464xT^* + 14.6205 \cdot (T^*)^2 \qquad \text{(Eq. 7)}$$

When comparing the thermophysical properties of propylene glycol reported in literature (Conde, 2011; DOW, 2008; George and Sastry, 2003; Melinder, 2007), a large variability was found. So, for the model validation, a sample of propylene glycol/water mixture was taken from the collector field and its properties were determined with an Anton Paar DMA4100 densimeter and an Anton Paar AMV200 viscometer. The sample (35% glycol) was tested every 10 °C in the range 20-80 °C. The following correlations were found:

$$\rho = 1038.3 - 0.4419T - 1.940 \cdot 10^{-3} T^2 \quad \text{(Eq. 8)}$$

$$\mu = \begin{cases} -1.449 \cdot 10^{-8} T^3 + 3.066 \cdot 10^{-6} T^2 - 2.337 \cdot 10^{-4}\, T + 7.289 \cdot 10^{-3} & if\ T < 38\,°C \\ 0.1803 T^{-1.232} & if\ T > 38\,°C \end{cases} \quad \text{(Eq. 9)}$$

In (Eq. 5)-(Eq. 9), ρ [kg m^{-3}] denotes the density, c_p [J kg^{-1} K^{-1}] the specific heat, μ [Pa s] the dynamic viscosity, x [%] the mass concentration of propylene glycol in the mixture, while T* is a factor defined as T*=273.15/(T+273.15), where T [°C] is the fluid temperature.

2.1.3 Matlab implementation

Based on the above mentioned correlations, a numerical model was developed in Matlab, to calculate the flow distribution in a solar collector field. The layout of the collector field, the collector pressure drop, valves types and settings, dimensions of distribution pipes, fittings and the operating conditions (fluid type, field flow rate and fluid inlet temperature) need to be specified in the model. The temperature profile along the collector rows can be evaluated in two ways. The first is that a unique outlet temperature, equal for all collector rows, is defined in input and a linear temperature profile is assumed along the collector row. The second option requires the collector efficiency parameters, solar irradiance and ambient temperature. The temperature profile in each row is given by the solution of (Eq. 10), which assumes steady state conditions.

$$\dot{m}\, c_p \frac{dT}{dA} = G\, \eta_0\, K_\theta - a_1 \cdot (T - T_{amb}) - a_2 \cdot (T - T_{amb})^2 \quad \text{(Eq. 10)}$$

In (Eq. 10), $\dot{m}$ [kg s^{-1}] is the mass flow rate, A [m^2] is the gross/aperture collector area, G [W m^{-2}] is the hemispherical solar irradiance on the collector plane, η_0 [-] is the peak efficiency of the solar collector coherent with the definition of A, K_θ [-] is the incident angle modifier, a_1 [W m^{-2} K^{-1}] and a_2 [W m^{-2} K^{-2}] are the first and second order heat loss coefficients coherent with the definition of A, T [°C] is the fluid temperature and while T_{amb} [°C] is the ambient temperature.

To determine the actual distribution, the set of equations (Eq. 11) is solved iteratively. (Eq. 11) imposes both the mass conservation across the collector field (first line in (Eq. 11)) and the uniformity of pressure drop along the different hydraulic paths (from second line downward):

$$\begin{pmatrix} 1 & 1 & 1 & 1 & 1 & 1 \\ k_{1,j} \cdot \dot{m}_{1,j} & -k_{2,j} \cdot \dot{m}_{2,j} & 0 & 0 & 0 & 0 \\ 0 & k_{2,j} \cdot \dot{m}_{2,j} & -k_{3,j} \cdot \dot{m}_{3,j} & 0 & 0 & 0 \\ \vdots & \vdots & \vdots & \vdots & \vdots & \vdots \\ 0 & 0 & 0 & 0 & k_{N-1,j} \cdot \dot{m}_{N-1,j} & -k_{N,j} \cdot \dot{m}_{N,j} \end{pmatrix} \begin{pmatrix} \dot{m}_{1,j+1} \\ \dot{m}_{2,j+1} \\ \dot{m}_{3,j+1} \\ \vdots \\ \dot{m}_{N,j+1} \end{pmatrix} = \begin{pmatrix} \dot{m}_{tot} \\ 0 \\ 0 \\ \vdots \\ 0 \end{pmatrix} \quad \text{(Eq. 11)}$$

In (Eq. 11), k [kg^{-1} m^{-1}] is a hydraulic resistance coefficient; the subscripts 1, 2, ..., N denote the collector row and N is the total number collector rows; the subscript *tot* refers to the total flow rate supplied to the solar collector field and the subscript j denotes the iteration number. The factor k_i is defined so that the product $\left(k_i \cdot \dot{m}_i{}^2\right)$ represents the pressure drop along the entire i-th hydraulic path. The value of k_i takes into account both the pressure drop along the i-th collector row, proportional to the square of the row flow rate $\dot{m}_i$, and the pressure drop along the portion of distribution pipes and tees included in the i-th hydraulic path, properly normalized to the flow rate $\dot{m}_i$.

The system (Eq. 11) is iteratively solved until the maximum difference in the collector row flow rates between two consecutive iterations is lower than 0.1%.

2.2. Description of the solar collector field and experimental setup

The developed model was based on the layout of the solar collector field installed near Høje Taastrup (Denmark). The layout is shown in Fig. 3. The collector field (gross collector area of 3257 m^2) consisted of

two subfields of 12 collector rows each. The rows consisted of 10 HTHEATStore 35/08 collectors each and were 5.5 m apart from each other. Because near the collector field there was no auxiliary heating plant, the control strategy aimed at reaching an outlet temperature from the collector field which was approximately the DH supply temperature. Nominal inlet and outlet temperatures of the field were 50-55 °C and 90-95 °C respectively, and the flow rate ranged between 8 and 50 $m^3 h^{-1}$, depending on the solar irradiance.

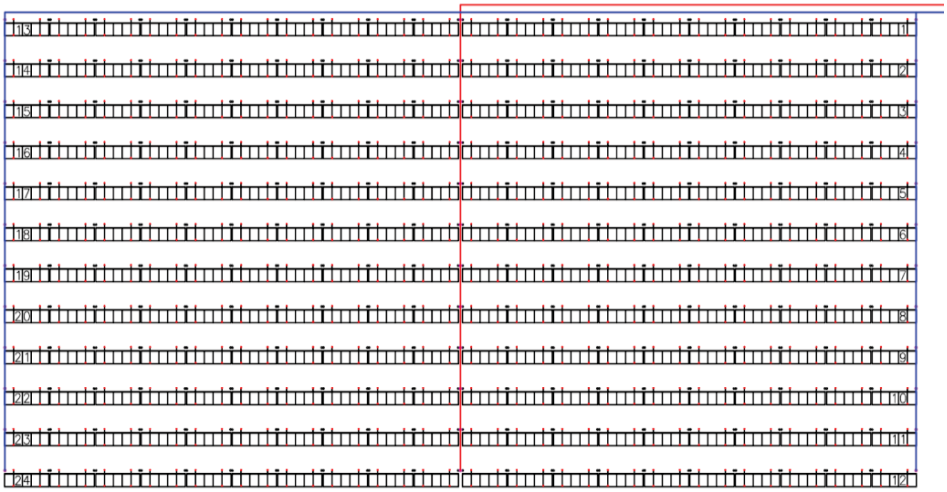

Fig. 3: Layout of Høje Taastrup solar collector field: blue and red lines represent supply and return pipes respectively (adapted from Arcon-Sunmark A/S).

The distribution pipes were made of preinsulated steel pipes. The largest inner diameter was 10.7 cm and it progressively became smaller as more fluid was diverted to the collector rows. At the inlet of each row a balancing valve was installed. In the middle of the field, the flows from each couple of row outlets were merged and then directed into the return pipe. The heat transfer fluid was a 35% propylene glycol/water mixture (Section 2.1.2).

To measure the flow distribution in the collector field, a differential pressure sensor TA-SCOPE from IMI Hydronic was used. The balancing valves have two measuring points, one before and one after the valve member. By measuring the pressure drop across the valve, the flow rate can be calculated through (Eq. 4). Specifying the type of fluid in the device, this calculates the fluid density and viscosity thanks to the built-in temperature sensor and corrects the valve flow factor. The maximum relative error when measuring the flow rate with this method is shown in Fig. 4. The error increases rapidly for low valve settings, so it is recommended to use settings higher than two. In Høje Taastrup collector field the lowest setting was 2.2.

The volume flow rate to the field was measured by an electromagnetic flow meter with accuracy of 0.5%.

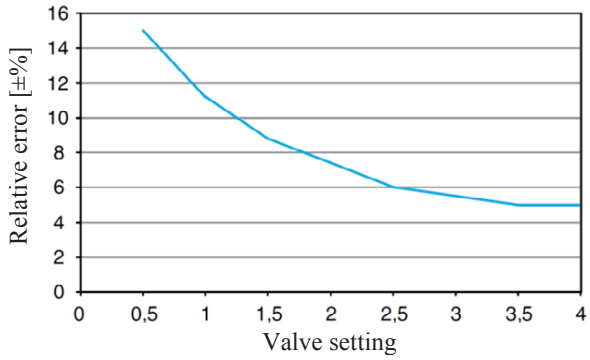

Fig. 4: Relative error on the measured flow rate across a STAD valve as function of the valve setting (IMI Hydronic, 2015).

At first, the flow distribution was measured keeping the same valve settings as in normal operation. However, the difference in the row flow rates was lower than the measurement error. Hence, the measurements were repeated after changing the setting of the first 10 valves in the eastern subfield, so to

introduce a higher maldistribution, which could be more easily detected. The flow distribution across the collector field was measured for a total flow rate of 50.3±0.3% $m^3\ h^{-1}$. The test was carried out in a cloudy day, so that the temperature across the field was constant (45.0±1.3 °C) during the entire duration of the test.

3. Results and discussion

3.1. Validation of the model

To compare the flow distributions at different field flow rate, the dimensionless row flow rate was introduced. The dimensionless flow rate V_i' in the *i*-th collector row is defined by (Eq. 12) as:

$$V'_i = \frac{V_i}{(\sum_{i=1}^{N} V_i)\cdot A_{row,i}/A_{field}} \qquad \text{(Eq. 12)}$$

In (Eq. 12), V [$m^3\ h^{-1}$] is the row flow rate, A [m^2] is the collector area, subscript *i* denotes the collector row number and N is the total number of collector rows. So, the dimensionless flow rate V'_i represents the ratio between the actual flow rate in the *i*-th collector row and the ideal flow rate in case of uniform distribution.

The measured and modeled flow distributions in terms of dimensionless flow rate are shown in Fig. 5. It is easy to recognize the effect that the change in first 10 valve settings had on flow distribution in the eastern subfield (rows 1-12) compared to the western subfield (rows 13-24). In the eastern subfield the row flow rates decreased progressively in the first 10 rows, only to return to their nominal value in the last two rows, whose valves were not changed. In the western subfield, where the valve settings were not modified, the row flow rates were much more similar to each other.

The agreement between model and measurements was evaluated through the root-mean-square deviation (*RMSD*) (Eq. 13).

$$RMSD = \sqrt{\frac{\sum_{i=1}^{N}(\hat{V}_i' - V_i')^2 \cdot b_i}{N}} \qquad \text{(Eq. 13)}$$

In (Eq. 13), V_i' [-] is the dimensionless form (Eq. 12) of measured flow rate in the *i*-th collector row in case of the model validation, while V_i'=1 in case of the investigated scenarios (Section 3.2); $\hat{V}_i'$ is the dimensionless form (Eq. 12) of modelled flow rate in the *i*-th collector row. The parameter b_i is a weight defined by (Eq. 14). If all rows are identical, *b*=1.

$$b_i = A_{row,i}/(A_{field}/N) \qquad \text{(Eq. 14)}$$

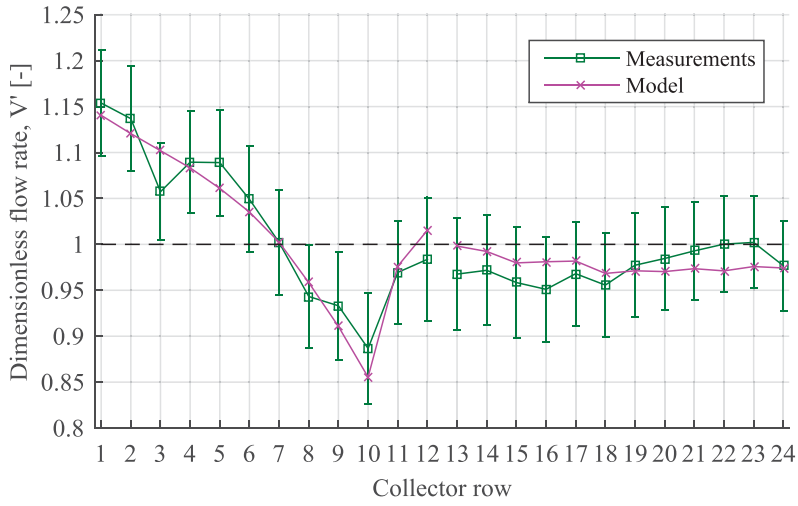

Fig. 5: Comparison between measured and modeled flow distribution for a field flow rate of 50.3 $m^3\ h^{-1}$.

Measurements and model showed an overall good agreement, with a RMSD of 0.022. In the eastern subfield the measured and modeled flow distribution profiles had the same trend, except for the third row, characterized by the highest deviation between measurement and model. In fact, the measured flow rate was

significantly lower compared to the neighboring rows. This deviation was most likely caused by additional flow resistance in this collector row, maybe due to some obstruction or dirt clog. Also the original setting of its balancing valve was larger (and hence the valve more open) than the valve settings of neighboring rows. So, already when balancing the flow at the start-up phase of the collector field, it was noted that, in order for the third row to receive the design flow rate, its valve had to be opened more than expected.

3.2. Investigated scenarios

Using the developed model, the flow distribution across a solar collector field was evaluated in different scenarios. A 35% propylene glycol/water mixture was assumed as collector fluid and its fluid properties were evaluated through (Eq. 5-Eq. 7). The following scenarios were investigated:

- Case 1. The operating conditions used for the simulation were similar to those actually used in Høje Taastrup collector field. The inlet temperature was 55 °C and the solar irradiance on the collector plane was varied with the flow rate so that the outlet temperature was about 95 °C (Eq. 10). The same balancing valves settings as those used in Høje Taastrup collector field in normal operation were used in the model.
- Case 2. As shown by the experience of the first solar collector fields built in Sweden in 80'-90', good flow distribution can be achieved without balancing valves in case of collector array with regular geometry and constant diameter of the distribution pipes. To see the effect that a more complex geometry would have on the flow distribution in case of no balancing valves, the layout of the collector field was modified as shown in Fig. 6.a. The 24 rows were now connected all in parallel and they had a different number of collectors. Because in this case the collectors were 204 instead of 240 (case 1), the highest field flow rate was proportionally decreased from 50 m^3 h^{-1} to 42.5 m^3 h^{-1}. Two different subcases were considered. In case 2.2 the diameter of the supply and return pipes decreased as fluid was diverted to the collector rows. In case 2.1 the pipe diameter of the distribution pipes was kept constant and equal to 10.7 cm, i.e. the largest diameter in subcases 2.2. Pipes commercially available for this kind of application (Logstor, 2005) were used. The field inlet and outlet temperature was 50 °C and about 85 °C respectively.

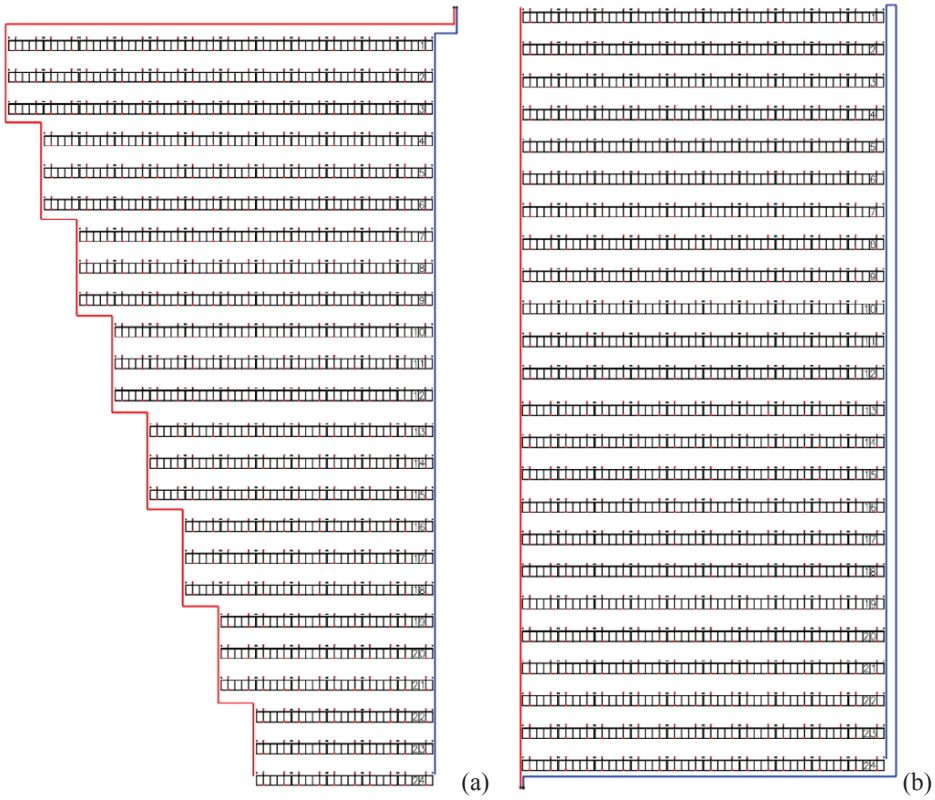

Fig. 6: Layout of the collector field assumed in case 2 (a) and in case 3 (b) (adapted from Arcon-Sunmark A/S).

- Case 3. This scenario used a Tichelmann connection (Fig. 6.b), which is expected to give a fairly uniform configuration due to the identical length for each hydraulic path. Hence, no valves were installed. As in case 2, two subcases were considered: case 3.1, having a constant pipe diameter of the distribution

pipe, and case 3.2, with decreasing pipe diameter according to the flow rate in each pipe segment. As in case 1, the inlet temperature was 55 °C and field outlet temperature was about 95 °C.

3.2.1. Case 1: normal operating conditions

The flow distribution in this case is shown in Fig. 7 for different field flow rates.

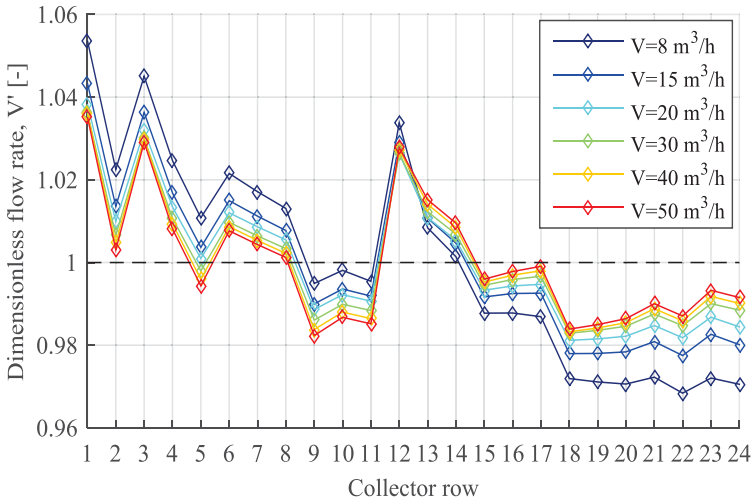

Fig. 7: Modeled flow distributions in Høje Taastrup solar collector field for different field flow rates, assuming normal operating conditions (case 1).

Also in the simulated scenarios the RMSD was used as the main parameter to quantify the level of maldistribution. Though, as no measurements were carried out for the simulated scenarios, the uniform distribution profile was now taken as term of comparison and hence z=1 in (Eq. 13) for any value of i.

Fig. 7 shows that the higher the flow rate, the more uniform the flow distribution. For $V \geq 30$ m^3 h^{-1}, the RMSD was approximately constant and equal to 0.015. At lower flow rates this value increased up to 0.025 for a flow rate of 8 m^3 h^{-1}. This was expected, as the balancing valves were set to give a uniform distribution at the nominal field flow rate, i.e. the highest flow rate the collector field operates at. The highest deviation between row flow rates and perfectly uniform flow distribution was lower than 6%, and the maximum difference between highest and lowest row flow rates was within 8%. Hence, the flow distribution can be considered acceptable for all the considered flow rates, as it differs from the ideal case less than 10%, which is considered the maximum acceptable deviation according to the German standard (VDI, 2004).

3.2.2. Case 2: Collector rows with different number of collectors

This scenario considered only cases where no balancing valves were installed, as these would give uniform flow distribution when properly regulated. The flow distribution in the two investigated subcases is shown in Fig. 8, with the subcase 2.1 characterized by much stronger maldistribution than subcase 2.2.

Given the field layout (Fig. 6.a), the collector rows became shorter while getting farther away from the pumping station. As the collector row represented the main contribution in terms of pressure drop along a hydraulic path, rows with fewer collectors had a much lower hydraulic resistance. So, in absence of balancing valves, these rows diverted flow rates higher than their design value. In case of constant pipe diameter in the distribution pipes (case 2.1) the flow maldistribution was higher with the RMSD ranging between 0.40-0.43 depending on the flow rate. The maximum deviation occurred in the last three rows, with flow rates about twice as high as the nominal value. The distribution was not very uniform, but still considerably better, in case 2.2, where the diameter was progressively decreased. In this case, the maximum deviation was only 40% and the RMSD was in the range 0.18-0.20. In fact, in case of constant diameter the fluid velocity progressively decreased in the pipe segments, making their contribution to the pressure drop of the entire hydraulic path very small. In order for all hydraulic paths to give the same pressure drop, the flow rate in the rows with fewer collectors had to increase significantly. Conversely, decreasing the pipe diameter gave similar pressure gradient in the different pipe segments. This increased the resistance of the hydraulic

paths of the collector rows which lay farther away, resulting in a more uniform flow distribution.

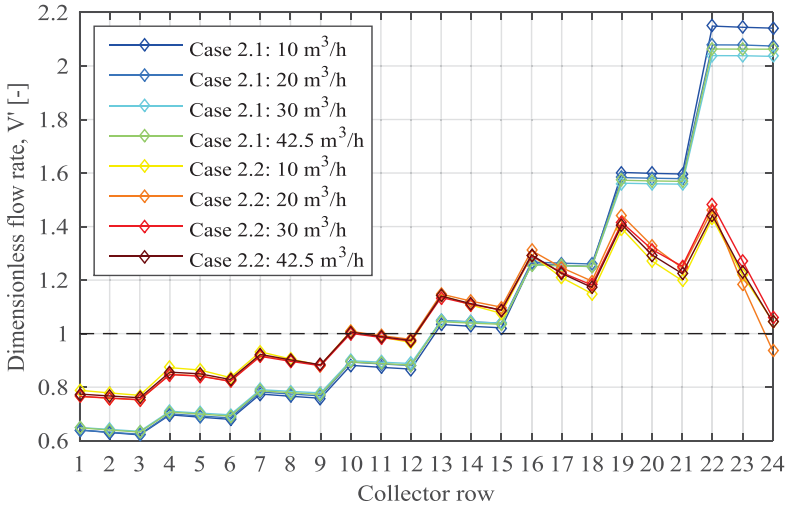

Fig. 8: Modeled flow distributions for different field flow rates in case 2.

3.2.3. Case 3: Tichelmann connection

Fig. 9 shows the flow distribution in the subcases 3.1 and 3.2. For sake of clarity, for each subcase only two flow rates, which gave the most and least uniform distribution, are shown. In both scenarios the Tichelmann connection assured a good flow distribution with deviations from the perfectly uniform case no larger than 4%. Subcase 3.2 achieved a slightly better distribution (RMSD=0.008-0.010) compared to subcase 3.1 (RMSD=0.014-0.016). In the latter, the choice of keeping a constant pipe diameter resulted into a U-shape flow distribution profile. In fact, although the pipe length was the same for each hydraulic path, the paths in more central position (rows 9-13) were supplied with lower flow rates. This was due to the fact that these paths included distribution pipes segments with higher flow rates (and hence higher pressure drop) compared to the more peripheral paths. In subcase 3.2 the distribution pipe diameter was progressively varied, so that the fluid velocity was similar in all pipe segments. This resulted in similar pressure drops and hence a more uniform flow distribution. Varying the pipe diameter also saved pipe material (steel and insulation), reducing cost and thermal losses. The main drawback of a Tichelmann connection is the longer pipe length.

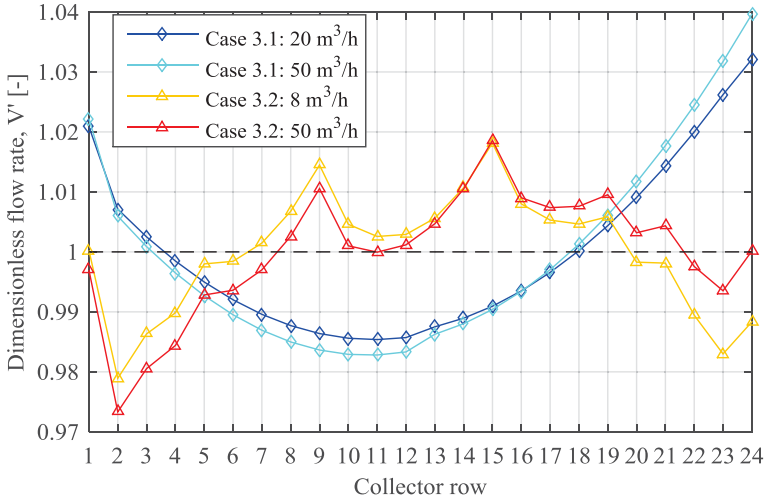

Fig. 9: Modeled flow distributions for different field flow rates in case 3.

3.3. Effect of the flow maldistribution on the thermal performance of the collector field

Modifying the row composition of the collector field shown in Fig. 6.a, different degrees of flow maldistribution were caused. The effect on the power output of the collector field is shown in Fig. 10 for two collector types, a HTHEATStore 35/08 (SP, 2016a) (Section 2.1.1) and a HTHEATBoost 35/08 (SP, 2016b)

(η_0=0.786, a_1=2.97 W m^{-2} K^{-1} and a_2=0.009 W m^{-2} K^{-2}). The collectors differed only for the presence of a polymer foil, working as convection barrier, between glass cover and absorber in the HTHEATBoost model. The loss in power output was calculated with respect to the case where the collector row flow rates were exactly proportional to the collector row area. The power output, P_{out} [W], was calculated through (Eq. 15):

$$P_{out} = \sum_{i=1}^{N} \left(\dot{m}_i \cdot c_{p,i}(\bar{T}_i) \cdot \left(T_{out,i} - T_{in} \right) \right) \qquad \text{(Eq. 15)}$$

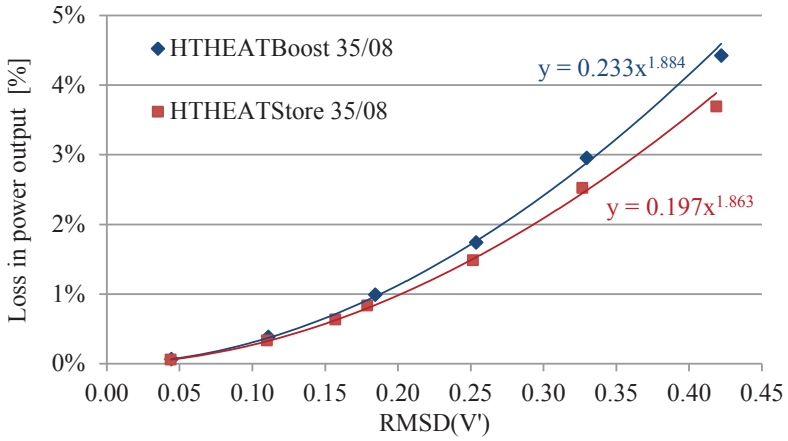

Fig. 10: Maximum reduction in power output of a solar collector field as function of the flow maldistribution.

It can be seen that the reduction in power output is proportional to the RMSD of the flow distribution to the 1.9th power, very similar to the result of Chiou (1982) for a single collector (Section 1.1). The loss in power output is relatively small, within 5% for RMSDs up to 0.4. However, it should be noted that in the current study pipe losses were neglected and the collector efficiency was assumed independent of the collector flow rate. In reality, lower efficiency is expected at low flow rates, especially if these cause laminar regime in the absorber pipes (Bava and Furbo, 2014). Slightly stronger effect on the power output would result, if these aspects were taken into account too. As expected, the performance of the collector field made of HTHEATBoost modules was more affected by the flow maldistribution. In fact, given the higher heat loss coefficients of this collector, its efficiency was more penalized in those rows which were supplied with lower flow rates and hence reached unnecessarily higher temperatures.

4. Conclusions

A model for calculating the flow distribution in a solar collector field was developed. The model results were compared against measurements and a good agreement was found.

The model was used to study different scenarios. Balancing valves in each collector row guaranteed good flow distribution in all the operating conditions. Although the valves were set in full load conditions, the deviations occurring at different operating conditions were still within the range of ±10%.

A Tichelmann connection gave a good flow distribution also without balancing valves. Reducing the pipe diameter of the distribution pipes was a good measure to improve the distribution and decrease the pipe cost.

In case of irregular field layout with collector rows having a different number of modules, balancing valves seemed to be the only way to reach uniform flow distribution.

5. Acknowledgements

The authors are thankful to the Marie-Curie Actions - Initial Training Network research programme of the European Union which supported the first author through the SolNet-SHINE project. The authors are also grateful to the company Arcon-Sunmark A/S and the DH company Høje Taastrup Fjernvarme for providing useful information necessary to develop the model and for granting access to the solar collector field.

6. References

Bava, F., Furbo, S., 2016. A numerical model for pressure drop and flow distribution in a solar collector with horizontal U-connected pipes. Solar Energy 134, 264–272.

Chiou, J.P., 1982. The effect of nonuniform fluid flow distribution on the thermal performance of solar collector. Solar Energy 29, 487–502.

Conde, M., 2011. Thermophysical properties of brines – Models, Conde Engineering, Zurich.

DOW, 2008. Engineering and Operating Guide for DOWFROST and DOWFROST HD Inhibited Propylene Glycol-based Heat Transfer Fluids.

EnergySupply, 2016. Danmarks største solenergianlæg. http://www.energy-supply.dk/article/view/235192/.

Fan, J., Shah, L.J., Furbo, S., 2007. Flow distribution in a solar collector panel with horizontally inclined absorber strips. Sol. Energy 81, 1501–1511.

Furbo, S., Perers, B., Bava, F., 2015. Thermal performance of solar district heating plants in Denmark, in: Conference Proceedings of EuroSun 2014. Aix-les-Bains (France).

George, J., Sastry, N. V., 2003. Densities, Dynamic Viscosities, Speeds of Sound, and Relative Permittivities for Water + Alkanediols (Propane-1,2- and -1,3-diol and Butane-1,2-, -1,3-, -1,4-, and -2,3-Diol) at different Temperatures. Journal of Chemical and Engineering Data 48, 1529–1539.

Haaland, S.E., 1983. Simple and Explicit Formulas for the Friction Factor in Turbulent Flow. Journal of Fluids Engineering (ASME) 105, 89–90.

Holman, J.P., 2002. Heat transfer, 9th ed. McGraw-Hill, New York.

Idelchik, I.E., 1994. Handbook of hydraulic resistance, 3rd ed. CRC press, Boca Raton.

IMI Hydronic, 2015. STAD Balancing valves DN 15-50. IMI Hydronic Engineering. Online at http://www.imi-hydronic.com/en/products-solutions/balancing-and-control/balancing-valves/.

IMI Hydronic, 2014. HySelect User Manual. IMI Hydronic Engineering. Online at http://www.imi-hydronic.com/en/knowledge-tools/hydronic-tools-software/balance-control/ta-select-4/.

Knabl, S., Fink, C., Ohnewein, P., Mauthner, F., Hausner, R., 2014. Requirements and guidelines for collector loop installation, Deliverables of IEA-SHC Task 45 Large scale solar heating and cooling systems. Online at http://task45.iea-shc.org/fact-sheets.

Mauthner, F., Weiss, W., Spörk-Dür, M., 2016. Solar Heat Worldwide. Markets and Contributions to the Energy Supply 2014. Online at http://www.iea-shc.org/solar-heat-worldwide.

Melinder, Å., 2007. Thermophysical Properties of Aqueous Solutions Used as Secondary Working Fluids. Royal Institute of Technology, KTH.

Rohde, J.E., Knoll, R.H., 1976. Analysis of a solar collector field water flow network. Lewis Research Center, Cleveland (Ohio, USA).

SP - Technical Research Institute of Sweden, 2016a. Solar Keymark Certificate No. SP SC0842-14: HTHEATstore 35/08 . Borås (Sweden). Online at http://www.solarkeymark.dk/.

SP - Technical Research Institute of Sweden, 2016b. Solar Keymark Certificate No. SP SC0840-14: HTHEATboost 35/08 . Borås (Sweden). Online at http://www.solarkeymark.dk/.

VDI, 2004. VDI-Richtlinie: VDI 6002 Blatt 1 Solare Trinkwassererwärmung - Allgemeine Grundlagen - Systemtechnik und Anwendung im Wohnungsbau.

Wang, X.A., Wu, L.G., 1990. Analysis and performance of flat-plate solar collector arrays. Solar Energy 45, 71–78.

Windeleff, J., Nielsen, J.E., 2014. Solar District Heating in Denmark.

Reviewing the dysfunctions of large solar thermal system: a classification of sub-systems reliability

Gaëlle Faure[1,2], Mathieu Vallée[1,2], Cédric Paulus[1,2] and Tuan Quoc Tran[1,2]

1 Univ. Grenoble Alpes, INES, F-73375 Le Bourget du Lac, France

2 CEA, LITEN, 17 rue des Martyrs, F-38054 Grenoble, France

Abstract

All technical processes are subject to dysfunctions during their lifespan, and large solar thermal systems (LSTS) are no exception to this rule. In order to deal with them and minimize their impact, a good knowledge of dysfunctions affecting LSTS is a major issue. In this way, the return on investment can be increased and the competitiveness of solar thermal energy could be also improved.

This paper presents a study of the dysfunctions which can affect LSTS. We first conducted a literature review and found out that more studies are necessary to obtain some up-to-date reliability data on the dysfunctions. To complete the available information, our methodology combines a top-down approach based on a Failure Modes, Effects and Criticality Analysis (FMECA) with a bottom-up approach based on a survey for domain experts. Thanks to the merging of various sources, we propose a ranking of sub-systems reliability, showing in particular that the less reliable solar sub-systems are the controller (control and sensors) and the primary transport (hydraulic components of the primary loop). Other sub-systems are less prone to failure, but the status of solar collection is particularly interesting. While previous studies often point it out as a critical sub-system, our results tend to show that it is more reliable in recent LSTS.

Keywords: *Failure Modes Effects and Criticality Analysis, large solar thermal system.*

1. Introduction

Large solar thermal systems (LSTS) can provide renewable and low cost energy to district heating networks and industrial processes. Over the last 25 years, many of them have been developed mostly in Northern European countries. At the end of 2015, the total area of LSTS installations in operation in Europe reached 1 million m^2 (Mauthner et al., 2016). In France, the first two installations (about 800m^2) started operating in 2014 (Renaude, 2016), and more installations are planned.

All technical processes are subject to dysfunctions during their lifespan, and large solar thermal systems (LSTS) are no exception to this rule. A dysfunction refers to the interruption of the system's ability to perform a required function under specific operating conditions. This interruption can be permanent or intermittent, abrupt or progressive. In any case, dysfunctions can entail a degradation of the production yields and/or additional maintenance costs. This can significantly hinder the return on investment and the competitiveness of solar thermal energy. Fortunately, the scaling increase of large systems enables more monitoring, which should be used to detect early and diagnose precisely many dysfunctions. However, few works have already been proposed to build fault detection and diagnosis (FDD) methods especially suited for LSTS (Ohnewein et al., 2006; Shahbazfar et al., 2012).

In order to develop a FDD method, a good overview of the type of dysfunctions that can affect the plant is a major prerequisite. In particular, FDD approaches can be developed with various aims, from short term detection of severe faults to long term detection of specific components wearing or fouling. Moreover, there is often a trade-off between detection of all possible faults (completeness) and precise diagnosis of the fault sources (resolution) (Venkatasubramanian et al., 2003). As a consequence, classifying the types of dysfunctions, their occurrence rate and their criticality provides useful information about which FDD method can give the most interesting results for LSTS systems.

In this paper, we present a study of dysfunctions of large-scale solar thermal systems (LSTS). Our methodology combines a top-down approach based on a Failure Modes, Effects and Criticality Analysis with a bottom-up approach based on a survey for domain experts, and provided us qualitative data about the main dysfunctions in LSTS. In section 2, we will first describe the state-of-the art of studies on dysfunctions in LSTS. In section 3, we introduce the methodology we adopted for this study. In section 4, we detail and discuss our results, from a

doi:10.18086/eurosun.2016.05.01 Available at http://proceedings.ises.org

global perspective to more precise results on the most frequent and critical dysfunctions. At last, section 5 summarizes our conclusions and opens perspectives on the development of new FDD methods.

2. State of the art

In this section, we introduce the current state of the art about dysfunctions of large scale solar systems. We first briefly present the system we consider, especially by defining the main relevant sub-systems (subsection 2.1). Please note that this description intends to be the most representative of LSTS configurations. We then report on our initial literature study (subsection 2.2).

2.1. System description

In this study, we consider LSTS with a total collector area above 500m², for the production of hot water at low and medium temperatures (80-120°C) with a focus on the production up to the feed-in. Other restrictions are applied in order to decrease the number of allowed layout while keeping the most common ones:

- Auxiliary heating: not studied ;
- System: pressurized, filled with water-glycol mixture ;
- Solar collector: no active tracking ;
- Storage: systems without storage are included. Only daily water, with passive stratification storages are taken account. Bi-energy storages are not considered in this study.

The remaining system is divided in five sub-systems to simplify the analysis as presented in Fig. 1:

- *Solar collection*: solar collectors, connections between collectors, fastening system.
- *Primary transport*: hydraulic components between solar field and first heat exchanger or storage (if no external heat exchanger).
- *Storage*: storage tank and internal heat exchangers if there are any.
- *External heat exchanger(s)*: if any.
- *Secondary transport*: hydraulic components between first heat exchanger or storage (if no external heat exchanger) and the feed-up.
- *Controller*: control-command components and sensors.

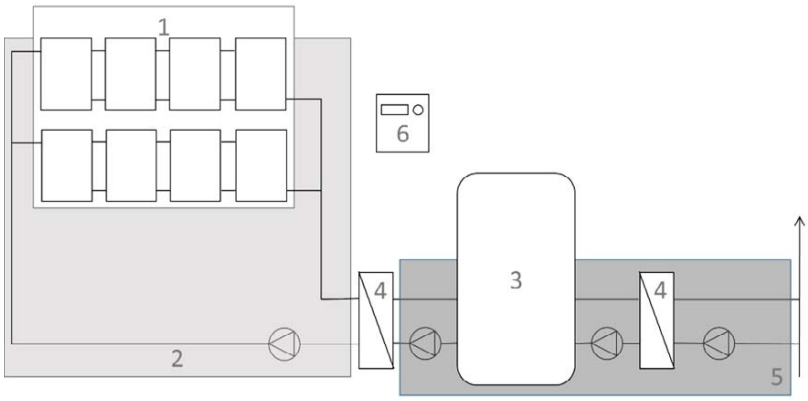

Fig. 1: Example of division of a LSTS plant in five sub-systems: solar collection (1), primary transport (2), storage (3), external heat exchanger(s) (4), secondary transport (5) and controller (6).

2.2. Literature review

Keeping in mind the characteristics of the system we have described in the previous section, we conducted a review of the literature dealing with the reliability of LSTS, with a specific focus on studies that provided data on the type and frequency of dysfunctions for each sub-system.

We can first notice that the most complete research studies on reliability of solar thermal systems date back from several decades ago (Chopra, 1980; Jorgensen, 1984). Some recent examples are the Solarthermie2000 and Solarthermie2000plus studies (Peuser et al., 2005), which are also based on solar systems in operation since the early 80's. Although these studies provide interesting inputs in terms of methodology, their results are difficult to exploit nowadays, since many of the considered technologies have been improved or are not in use anymore.

More recent studies are rather focused on small scale systems and solar domestic hot water (SDHW) system. They have especially been conducted in relation with governmental programs fostering the installation of solar

thermal systems, and sometimes provide data based on monitoring results (ADEME, 2008; Cholin, 2011). Although some findings of these studies can be applied to LSTS, there are many differences in terms of size, kinds of sub-systems and overall installation and maintenance policies, which strongly affect the type and occurrence of potential dysfunctions. As an example, problems with the solar panels' fastening system are often reported in SDHW, but will likely be not as significant in LSTS due to the standardization of the components.

A main drawback of available studies is also the lack of feedback data about the actual occurrence rate of dysfunctions. Although one older study provides occurrence data for some defaults (Jorgensen, 1984), a similar study conducted 25 years later concluded in the lack of precision and reliability of available data (Menicucci, 2009). One important issue is the lack of consistency between databases, which often yields biases and contradictory results depending on the information source.

Despite the lack of recent and reliable data on dysfunctions in LSTS, we can highlight several important conclusions from this literature review:

- **Primary transport** consistently appears to be the most impacted sub-system. In particular, insulation is often lacking or not adequate, especially to resists UV rays and bird attacks. Leaks are a usual source of dysfunction, as well as pressure loss and air bubbles, which can also result from leaks. Finally, especially in large-scale installations, a bad hydraulic balancing between the solar subfields is sometimes reported.
- **Regulation and controllers** can have a high number of dysfunctions, often related to poor installation and parameter tuning, as well as wrong placement of sensors. Especially temperature sensors yielding wrong measurement strongly impact the performance of the system.
- **Solar collection** may have some dysfunction, but is less frequently cited. Moreover, some of the problems appearing in earlier studies have been fixed in more recent products.
- **Secondary transport and heat exchanger** appear to have much less dysfunctions, primarily because these are well-known, classical systems.
- **Storage** also appears to have few dysfunctions, for the same reasons. However, this could differ in large-scale systems with unusual storage sizing and technologies.

Based on this literature review, we decided to conduct a new study in order to better assess the type, occurrence rate and criticality of dysfunctions in LSTS.

3. Methodology

This part describes the methodology used to study the dysfunctions that can affect a LSTS. Subsection 3.1 gives a description of the chosen method: the Failure Modes, Effects and Criticality Analysis. In order to apply the procedure, we collected more data thanks to a survey (subsection 3.2). The last section presents the determination of an important figure, the Failure Risk Priority Number, based on the collected data. This number is a way to emphasize dysfunctions that are critical for the system.

3.1. Failure Modes, Effects and Criticality Analysis (FMECA)

In order to study the dysfunctions that can affect LSTS, we applied a standard methodology: the Failure Modes, Effects and Criticality Analysis (Isermann, 2006; Laronde, 2011; Villemeur, 1988). FMECA is a formalized method, developed in the 60's and commonly used in industry nowadays to evaluate the dysfunctions that can occur on a system. It consists of doing the inventory of the components, their functions and the ways they cannot perform these functions (failure modes). The analysis can be extended by adding possible causes of the failures and their effects on the whole system. Finally a Failure Risk Priority Number (FRPN) can be estimated to show the criticality of different failures. The results of this work is a large table as illustrated in Tab. 1.

Tab. 1: Extract of the resulting FMECA table.

Component	Function	Failure mode	Effects	Possible causes	Properties of the causes	Detection method	FRPN
Primary pump	Set the heat transfer fluid in motion	Never start	No energy production	Pump not connected	Installation error	No flow when sunshine and demand	25
			Overheating of the primary loop	Electricity grid failure	Environment		

In practice, we made a first analysis based on prior knowledge, discussions with local experts and the literature review presented in the previous section. However, the amount of collected information was insufficient to

estimate the FRPN. In particular, no specific data about the failure occurrence rate was available. We then decided to conduct a survey with a larger panel of experts, as described in the following subsection.

3.2. Survey of domain experts

The survey was emailed to 23 experts in the field of LSTS. It was deliberately based on open-ended questions and consisted in:

- listing, for each sub-system, the dysfunctions that can affect it;
- giving a rough estimation of the occurrence rate for each listed dysfunction by choosing between "low", "medium" and "high";
- adding any significant information (cause, effect, detection…).

A sample of the survey form is given in Fig. 2. 90% of the surveyed experts returned an answer, and we collected results from a total of 21 experts from 7 countries and 20 different organizations (research institutes, consulting engineers, solar manufacturers, LSTS managers, training organizations). These additional information helped completing the FMECA and computing the FRPN as described in the next section.

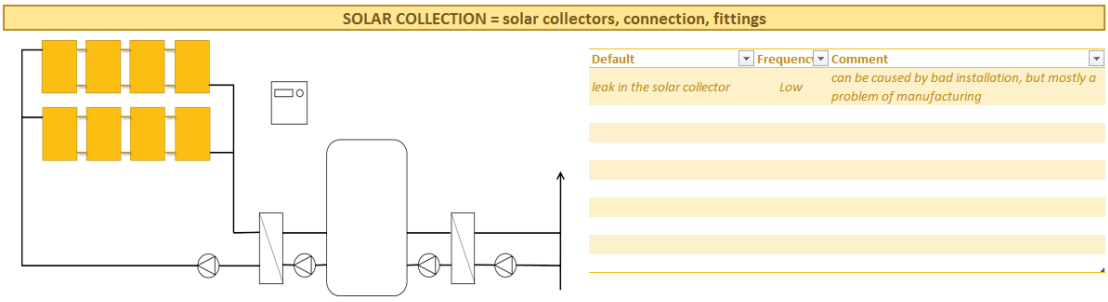

Fig. 2: Part of the survey concerning the solar collector sub-system. The same presentation is used for the other sub-systems.

3.3. Determination of the Failure Risk Priority Number (FRPN)

The Failure Risk Priority Number gives an indication of the criticality of a given failure mode for the system. It is computed for each failure i using equation *(eq. 1)*:

$$FRPN_i = ON_i \times EN_i \qquad \textit{(eq. 1)}$$

where ON_i (Occurence Number) is a number representing the occurrence rate of failure i, EN_i (Effect Number) is a number describing the effects of failure i on the system. ON_i and EN_i are ranking values with a scale from 1 to 5. FRPN is itself a ranking number with a scale from 1 to 25, 1 standing for the less critical failure modes.

To compute ON_i we first derive a raw "occurrence rate" value O_i from the results of the survey and the state of the art using *(eq. 2)*:

$$O_i = 0{,}45 * N_i + 0{,}45 * \frac{3 * Nhigh_i + 2 * Nmed_i + Nlow_i}{6} + 0{,}1 * b_i \qquad \textit{(eq. 2)}$$

N_i is the total number of citations of a failure i in the survey. $Nhigh_i$, $Nmed_i$ and $Nlow_i$ are respectively the number of "high", "medium" or "low" frequency qualifications for this failure. b_i is a value ranked between 0 and 2 describing if the failure is often reported in the literature. We obtain ON_i by scaling O_i to an integer between 1 and 5 (the higher the number, the more probable the failure occurrence).

To compute EN_i, we estimated the effect of each failure based on its description and experts comments. Possible effect numbers are given in Tab. 1, and range from 1 ("No effect") to 5 ("No more solar production").

Tab. 1 : Criteria to estimate EN_i, the rank of a failure according to its effects on the system.

EN_i	Effect on the system
1	No effect - client does not notice anything
2	Slight and stable drop in yield
3	Progressing drop in yield
4	Significant drop in yield with immediate risk of substantial degradation of the system
5	No more solar production

The resulting FRPNs allow classifying the reported failure modes from the less critical ones, which have a low occurrence rate and no effect, to the most critical ones, which have both high occurrence rates and severe consequences on the system integrity. It has to be noticed that although the computation of the ONs and the FRPNs depend on the coefficients used in *(eq. 2)*, a sensitivity analysis showed that their value have a low impact on the results of the study. More specifically, using different sets of coefficients in *(eq. 2)* does not affect the ranking of failure modes along their FRPNs.

4. Results and discussion

We identified 130 possible failure modes or dysfunctions. One failure mode is the result of one or more causes, and leads to 392 independent causes or basic events. The main characteristics of these causes are presented in subsection 4.1. We also worked at the failure modes level, first by observing the distribution of the computed ranking values (subsection 4.2), then by focusing on the more critical failure modes (subsection 4.3).

4.1. Types of causes

This first subsection is dedicated to the study of the main causes of the failure modes. The causes that leads to failure modes with a very low occurrence rate are not taken into account. After this selection, 326 independent events remain. The literature concerning faults (Isermann, 2006; Villemeur, 1988) proposes different ways to describe and classify the failure modes and their causes:

(a). The sub-system affected by the cause.

(b). The origin of the cause, which can be a design fault, an installation error, a wrong operation (missing maintenance, wrong manipulation…) or the ageing of the components. Causes resulting from environment (weather conditions, power cut…) are also distinguished.

(c). The appearance's time, showing whether this cause is already existing during the commissioning stage or whether it appears during the operation.

(d). The time's dependency, distinguishing between abrupt (stepwise), progressive (drift-like, incipient) and intermittent causes, as defined by Isermann.

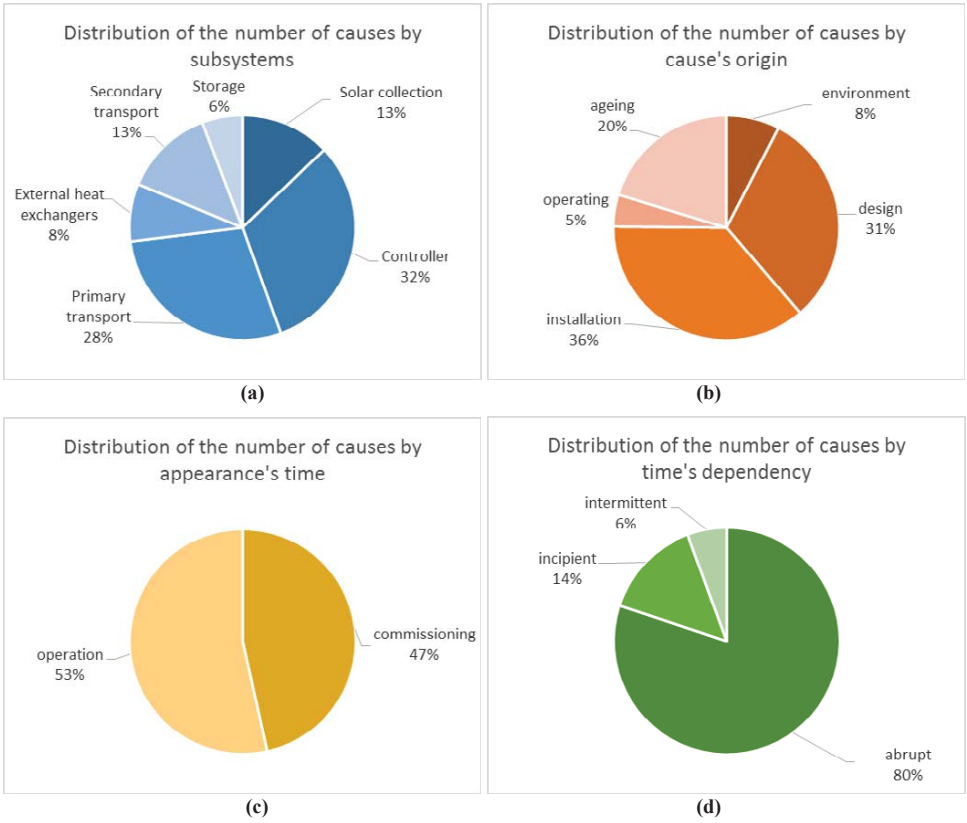

Fig. 3: Distribution of the number of found causes along some criteria: (a) sub-system, (b) cause's origin, (c) appearance's time, (d) time's dependency.

Fig. 3 presents the classification of the causes along these criteria. According to pie chart Fig. 3.a, controller and primary transport concentrate the largest number of causes of failure (60% together). Solar collection and secondary transport concerns both 13% of the inventoried causes. Storage and heat exchanger are less subject to failure. The results are in good agreement with the literature review of subsection 2.2. The pie chart Fig. 3.b shows that the main causes are design and installation problems (67%). Ageing is also a significant factor of failure. Operating and environment are less critical, in one hand because the system's environment is not extreme, and in other hand because the system is fully automatized and is designed to require few maintenance. Due to the high rate of design and installation dysfunctions, 47% of the causes are already present at the commissioning (Fig. 3.c). The pie chart Fig. 3.d teaches us that if mainly dysfunctions appears suddenly (80% of the causes), 14% are progressive, which is not negligible. The part of intermittent causes is quite low.

This first part does not take into account the criticality of the failure mode and the causes associated. It speaks about "what can happen". In the next parts, the criticality of the failure mode will be studied in order to work about "what is likely to happen".

4.2. Distribution of the failures along the key ranking numbers

Fig. 4 shows the distribution of the ranking number representing the occurrence rate (ON_i), the effect on the system (EN_i) and criticality ($FRPN_i$) of the failure modes or dysfunctions. The histogram plotted on Fig. 4.a reveals that there are few frequent failure modes. This is in accordance with some general commentaries made by experts when then reply to the survey: "defaults are rather occasional.", "a large scale solar thermal plant does not need much effort to secure an operation without failure", "we identified few defaults on solar plants". On the contrary, the impact of the failures on the global system is significant: histogram Fig. 4.b shows that more than 75% of the dysfunctions implies at least a progressing drop in solar yield ($EN_i \geq 3$), with a high risk of material degradation for almost 35% of them ($EN_i \geq 4$). Due to the low frequency of most of failure modes, the criticality is generally low (histogram Fig. 4.c). We can however show off one dysfunction with the maximal criticality ($FRPN_i = 25$). It will be detailed in the next sub-section.

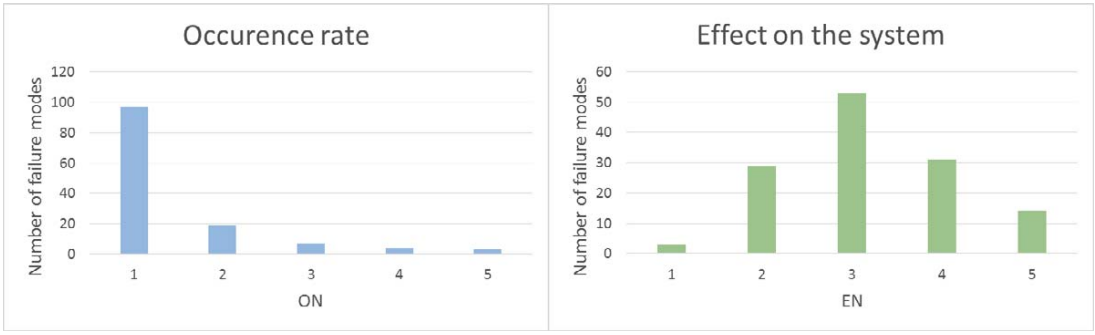

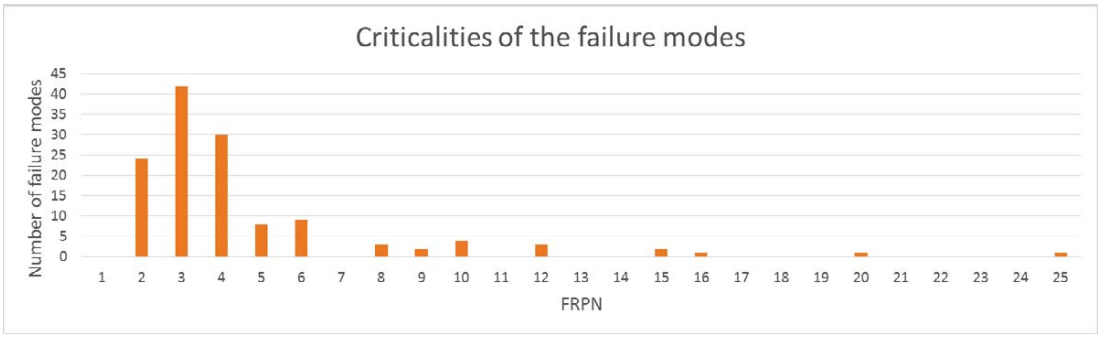

Fig. 4: Distribution of the failure modes along (a) their probability of occurrence, (b) their effect on the system, (c) their criticality.

Tab. 2 confirms that the distribution of the couples (ON_i, EN_i) follow the tendencies previously discussed: on the one hand, failure modes have in general a low probability of occurrence apart from their effect on the whole system; on the other hand the effect is mostly medium independently of their frequency.

Tab. 2: Distribution of the pairs (ON_i, EN_i).
The area delimited by a bold border includes the most critical failure modes which are studied afterwards.

		EN_i					
		1	**2**	**3**	**4**	**5**	**Total**
ON_i	**1**		22	42	25	8	97
	2	2	4	7	3	3	19
	3		2	2	1	2	7
	4	1		2	1		4
	5		1		1	1	3
	Total	3	29	53	31	14	130

4.3. Critical dysfunctions

Tab. 3 shows the most critical failure modes: those which have a Failure Risk Priority Number ($FRPN_i$) equal or above 8. This threshold represents the area delimited by a bold border in Tab. 2. This area is the lower-right corner of the table corresponding to the highest $FRPN_i$ without the pairs (1,5) which are less representative of a high criticality event, since an EN_i of 1 is "No effect - client does not notice anything" (see Tab. 1) and an ON_i of 1 can be achieved with only one citation. The failure modes are sorted along sub-systems, then along their $FRPN_i$. The most affected sub-systems are at the beginning of the table.

Tab. 3: Failure modes with a Failure Risk Priority Number equal or above 8.

Sub-system	Component	Failure mode	ON_i	EN_i	$FRPN_i$
Controller	Solar collector temperature sensor	Wrong measure	5	4	**20**
	Heat exchanger input/output temperature sensor	Wrong measure	4	4	**16**
	Solar collector temperature sensor	No more measure	3	5	**15**
	Heat exchanger input/output temperature sensor	No more measure	2	5	**10**
	Pyranometer	No more measure	2	5	**10**
	Controller	Breakdown	2	5	**10**
	Controller	Non-optimal control	3	3	**9**
Primary transport	Solar pump	Never starts	5	5	**25**
	Hydraulic connectors	Leak	4	3	**12**
	Heat transfer fluid (mixture of water and propylene- or ethylene-glycol)	Bubbles in the heat transfer fluid	3	4	**12**
	Pipes	Leak	3	3	**9**
	Pipes	Bad hydraulic balancing	2	4	**8**
	Expansion vessel	Too low pressure	2	4	**8**
	Solar pump	Too low flow	2	4	**8**
Secondary transport	Pumps	Never starts	3	5	**15**
Storage	Storage tank	Heats less than expected	4	3	**12**
Solar collection	Solar collector	Produces less energy than expected	5	2	**10**

These results have to be analyzed qualitatively more than quantitatively. Indeed, they are the results of a bibliography and a survey, which are far less accurate than an experimental test or the assembly of a large amount of representative data. For example, we can pick up on some bias on the reported occurrence rate (ON_i) for the failure mode "solar collector produces less energy than expected". ON_i is maximum for this dysfunction and seems overestimated, given the literature review (see subsection 2.2). Since the solar collector is the main component of a solar system, and one of the most complex, we can assume responders had a tendency to focus on reporting dysfunctions on this component first. Actually, additional interviews showed that the first quoted dysfunctions concerned the solar panels, even if the experts added later that these dysfunctions are uncommon. Moreover, solar collection appeared as the first item in the survey form, which could be an additional source of bias.

Generally, Tab. 3 is in line with the bibliography (subsection 2.2). Two sub-systems are more likely to fail: controller and primary transport with both 7 critical failure modes. Secondary transport, storage and solar collection have one critical failure mode each. External heat exchangers are not present in the results.

5. Conclusion and perspectives

In this paper, we report on a study concerning the dysfunctions that can affect large solar thermal systems (LSTS). We began with a review of the state of the art and noticed that there are few up-to-date information about large solar installations. Therefore, we performed a Failure Mode Effects and Criticality Analysis and completed it with an expert survey in order to obtain more elements. We finally presented the results of this analysis with a focus on the typology of the causes of failure and on the more critical dysfunctions. An important result is the fact at the commissioning almost half of the causes of the dysfunctions can already occurred. As a consequence, if a fault detection method is applied to a solar system, it cannot suppose that the plant works well at the beginning of the monitoring. As far as the risk of failure is concerned, although the majority of the dysfunctions is quite occasional, their impact on the efficiency and the degradation of the system is high. An automatic detection and a diagnosis of these problems are then of interest. In particular we demonstrated that two sub-systems are particularly subject to dysfunctions: the controller and the primary transport. Other sub-systems are less prone to failure, but the status of solar collection is particularly interesting. While previous studies often point it out as a critical sub-system, our results tend to show that it is more reliable in recent LSTS.

Based on the results of this study, our future work will focus on the development of FDD methods for specific sub-systems, starting with controllers, primary transport and solar collection. We can note that many available FDD methods work well for the controller part, but the two other sub-systems are less well covered. In particular, the detection, diagnosis and localization of dysfunctions on the primary transport sub-system and on solar collector are more complicated to perform, but are of prime importance due to the size of the solar field.

Additionally, we can mention that the study presented here could be a preliminary step for a complete reliability analysis of LSTS. A study like the one done by (Laronde, 2011) for the solar photovoltaic systems or the ANL Solar Reliability and Materials Program conducted by the Argonne laboratory in the late 70s (Chopra et al., 1978; Waite et al., 1979) could provide reliability data such as lifespan and failure rate of the main components of a LSTS. These data would be useful not only for the development of fault detection and diagnosis (FDD) algorithms but also for the design of the products and the optimization of the preventive maintenance.

6. Acknowledgement

This project has received support from the State Program "Investment for the Future" bearing the reference (ANR-10-ITE-0003). A special thanks goes to the experts who participated in the study. Their contribution was invaluable.

7. References

ADEME, 2008. Audit des installations de chauffe- eau solaires individuels - Principaux résultats et recommandations pour la mise en oeuvre des installations. ADEME.

Cholin, X., 2011. Retour d'expérience installations solaires thermiques - ASDER.

Chopra, P.S., 1980. Why do solar systems fail ? Sol. Eng. Mag. 14–21.

Chopra, P.S., Cheng, C.F., Wolosewicz, R.M., 1978. Preliminary Evaluation of Selected Reliability, Maintainability, and Material Problems in Solar Heating and Cooling Systems. Department of Energy, Energy and Environmental Systems Division.

Isermann, R., 2006. Fault-Diagnosis Systems - An Introduction from Fault Detection to Fault Tolerance.

Jorgensen, G.J., 1984. AN ASSESMENT OF HISTORICAL R&H DATA FOR SDHW SYSTEMS.

Laronde, R., 2011. Fiabilité et durabilité d'un système complexe dédié aux énergies renouvelables - Application à un système photovoltaïque. Institut des Sciences et Techniques de l'Ingénieur d'Angers.

Mauthner, F., Weiss, W., Spörk-Dür, M., 2016. Solar Heat Worldwide - Markets and Contribution to the Energy Supply 2014 (No. 2016 edition), Solar Heating and Cooling Programme. International Energy Agency.

Menicucci, D., 2009. Assembly and comparison of available solar hot water system reliability databases and information. Sandia Rep. SAND 2757, 2009.

Ohnewein, P., Dröscher, A., Schgaguler, K., Feichtner, F., Meißner, E., Luidolt, P., Köstinger, A., Heimrath, R., Jaindl, M., Streicher, W., 2006. IP-Solar: Development of a Web-Based Monitoring and Diagnostics Tool for Solar Thermal Systems, in: Eurosun 2006.

Peuser, F.-A., Remmers, K.-H., Schnauss, M., 2005. Installations solaires thermiques : Conception et mise en oeuvre. Le Moniteur Editions, Berlin, Allemagne : Paris.

Renaude, F., 2016. Monitoring results for the two firsts solar plants on district heating network in France: Balma Gramont and Juvignac. Presented at the 4th International Solar District Heating Conference, Billund, Denmark.

Shahbazfar, R., de Keizer, A.C., Kuethe, S., Jordan, U., Vajen, K., 2012. Fault detection and fault diagnosis for large scale solar thermal systems, in: Proc. of Eurosun 2012, Croatian Solar Energy Association. International Solar Energy Society (ISES), Rijeka, Croatie.

Venkatasubramanian, V., Rengaswamy, R., Yin, K., Kavuri, S.N., 2003. A review of process fault detection and diagnosis: Part I: Quantitative model-based methods. Comput. Chem. Eng. 27, 293–311. doi:10.1016/S0098-1354(02)00160-6

Villemeur, A., 1988. Sûreté de fonctionnement des systèmes industriels, Collection de la Direction des Etudes et Recherches d'Electricité de France. Eyrolles.

Waite, E., Patterson, D., Prucha, L., Singh, H., Wolosewicz, R., Chopra, P.S., 1979. Reliability and Maintainability Evaluation of Solar Control Systems (No. SOLAR/0903-79/70; ANL/SDP-TM-79-5). Argonne National Lab., IL (USA).

Conference Proceedings

EuroSun 2016
Palma de Mallorca (Spain), 11 - 14 October 2016

IMPACT OF FORM AND DENSITY ON THE URBAN OUTDOOR SPACE COMFORT IN HOT AND DRY CLIMATE

Zahra Ferhat[1], Noureddine Zemmouri[1], Houda Saddok[1] and Mohamed El-Hadi Matallah [1]

[1] **Laboratory of architecture and environmental design (Lacomofa)**
University of Biskra, Algeria.

Abstract

In recent years, rapid urbanization and a tremendous increase in population have exerted pressure on urban developments in developing countries. The strategy adopted by most governments in the past twenty years in Algeria was that of densification. New and different urban forms have evolved from this strategy, but resulting in a loss of public green spaces and creating new problems in terms of environmental issues.
The present paper examines the relationships between forms and resulting environmental parameters such as temperature, ventilation, relative humidity.
The investigation is carried out by using the three dimensional numerical model « Envi-met 4.0 » which simulates the microclimatic parameters within urban environment and neighborhood. Models calculations are run for typical summer day 'Design Day July 21st ' in Biskra, south East of Algeria (34,48° N, 5,4° E), a region characterized by a hot and dry climate.
The aim of this study is to develop guidelines for architects and urban designers in order to develop new strategies and urban forms for a better and sustainable urban space.

Keywords: *hot and dry climate, outdoor space comfort, urban density, urban form, urban microclimate*

Introduction

Cities' planning and design has been conditioned throughout history by many and diverse factors including political, environmental, cultural, social, etc.
There are two main challenges related to the design of modern cities; the first is linked to global climate change, urban morphology (shape, density, vegetable and mineral volume, atmospheric air pollution, energy consumption ... etc.) is achieved in a context of rapid climate change (Vinet, 2000).
The second issue concerns the specific microclimate of cities. The phenomenon of urban heat island "UHI" is known for decades as a direct consequence of urbanization (Claverie, 2011). A sharp warming in air temperature of city centers, caused mainly by pollution from industries and transport. It has been defined (Oke, 1987) as the temperature difference between the city center and the surrounding countryside.
The urban heat island is the most dramatic manifestation of the global climate change consequences. It can be very drastic and leads to a temperature difference of the order of 10°C to 15°C between urban and surroundings areas (Musy, 2014).
Urban heat island is responsible for an increased mortality during heat waves periods. The elderly are mostly among the worst affected (Campbell, 2009).
It can also cause discomfort, weakness, and disorders of consciousness, cramps, syncope and heat stroke or exacerbate pre-existing chronic diseases such as diabetes, respiratory failure, and cardiovascular disease, cerebrovascular, neurological or renal, to the point of death (Filiatreault, 2015).

doi:10.18086/eurosun.2016.05.04 Available at http://proceedings.ises.org

1-City configuration and heat island risk

The structural and morphological characteristic of the city allows storing and trapping heat from solar radiation. Different parameters can increase or decrease the storage capacity or heat dispersion; several factors contribute to the increase in the appearance of the urban heat island as given in table 1:

Factors	Parameters
Climate	Sky state, wind speed and direction
Geographic	City location
Energy	Heat rejection from energy consumption
Morphology	Building density, mineral and vegetal surfaces
Policies	Land management practices
Structural	City size, plot ratio

Table 1: factors favoring the urban heat island.

According to Bozonnet (Bozonnet, 2005) the heat island phenomenon is linked to cities expansive increase of energy consumption see figure 1.

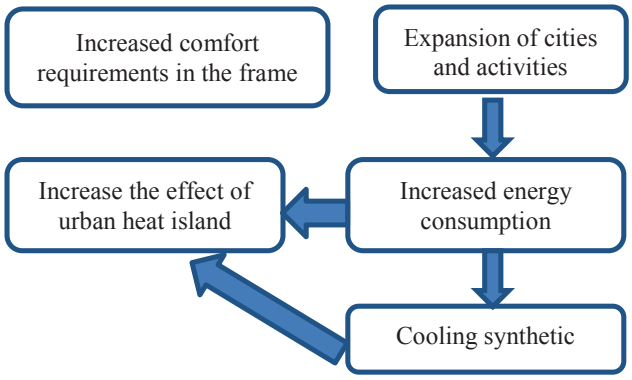

Figure 1: The relationship between the urban heat island and energy consumption (Bozonnet, 2005).

The present research examines the relationships between cities' forms and resulting environmental parameters such as temperature, air speed, and relative humidity.

2- Case study description

The city of Biskra, located in Algeria, is chosen for its hot and arid climate of the country. It has a rigorous climate characterized by very hot, dry summer and mild winter.

Meteorological data of Biskra show that the average temperature ranges from maximum of +44, 9°C and a minimum value of−2.1°C with high insolation exceeding 3500h/year and intense direct sunlight which can reach 900 to 1100 W/m² on a horizontal plane, relative humidity values vary between 25% to 40% with rare and irregular rainfall. This city is characterized by violent seasonal sandstorms (Khelil, 2015).

3-Methodology and approach

In order to assess the effect of urban configuration on the heat island risk in Biskra, a series of simulations has been performed using the Envi-met "*Environment- Meteorology*" version 4.0 code.

ENVI-MET is multidisciplinary simulation consultancy with a core services portfolio including architecture, building physics and microclimate; landscape architecture and garden design; it also includes urban planning and climate change adaption and human comfort and health.(Envi-met, 2014)
A simulation has been performed specially for the 21st July 2011 as it represents the hottest day of the year 2011. At 4 p.m, the air temperature reached almost 53°C.

4 -Urban typologies modelization

Biskra is an urban configuration with a variety of typologies: traditional, colonial and post-colonial. Creating a very diverse urban landscape, see figure 2.

(1)

(2)

(3)

Figure 2: Different typologies of Biskra: (1 traditional, (2) colonial and (3) post-colonial.

In order to assess the risk of heat island in this specific town, we have selected typical typologies (4 cases) representing a general trend form and typology of new urban developments, described in table 2.

Case	Total surface (m²)	Sb (m²)	Nb	Plot ratio	D (m)	Total plant area (m²)
1	12800	400	12	3.75	10	300
2	12800	400	10	3.125	10	300
3	12800	400	8	2.5	10	300
4	12800	400	6	1.875	10	300

kTable 2: Biskra urban typologies characteristics.

In order to assess the natural environment, a specific species of trees has been selected in order to be incorporated in the modelization process. The tree species is widely planted in the region and known as *Abies Alba* see figure 3.

Figure 3: The species of the tree *Abies Alba.* Source (http://www.lesarbres.fr/sapin.html)

This tree is characterized by:

- Height: 30m to 50 m
- Width: 10m to 15 m
- The leaves are needle-like, flattened, 1.8–3 centimetres (0.71–1.18 in) long and 2 millimetres (0.079 in) wide by 0.5 millimetres (0.020 in) thick

4- Simulation process

The four cases selected urban configuration representing Biskra urban landscape as described in table 2, have been used as models for the simulations.

- Case 1 consisting of 12 detached blocs aligned in result grid.
- Case 2 is 10 blocs configuration with a central courtyard.
- Case 3 consisting of 8 blocs aligned in U form.
- The last case, case 4 is 6 blocs urban composition evenly distributed over the surface area.
- Two green belts of *Albies Alba* tree have been added on the models on the East and West orientation as given in figure 4, 5 and 6.Wich a total vegetal density 0.1875 given by: vegetal density **(Vd)** = total plant area / total area
  Vd = [30 x 10 x 8] / 12800 =
  0, 1875

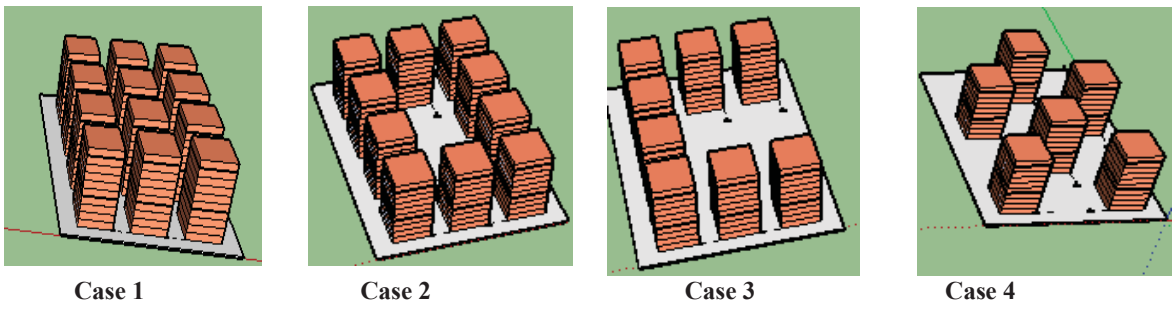

Figure 4: Generics models via Skeutchup.

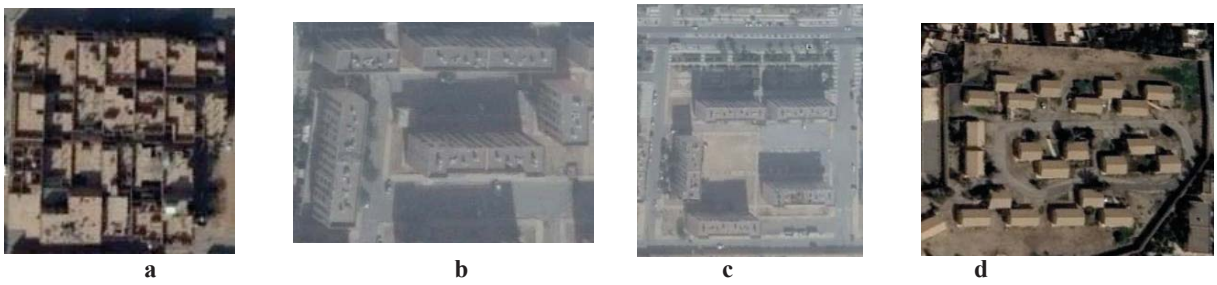

Figure 5: Different urban configuration in Biskra. a: city 1000 lodgements, b: city 500 lodgements, c: city 300 lodgements, d: city Bab Al Dherb.

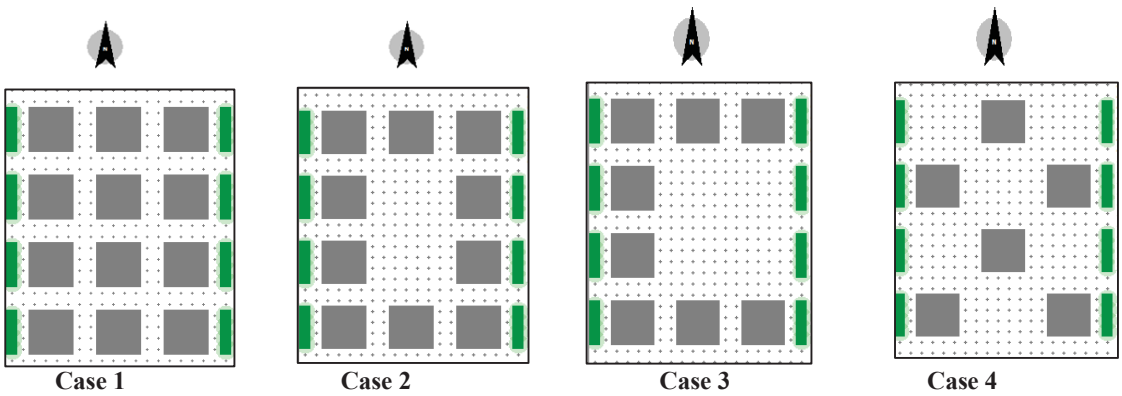

Figure 6: Generics models via Envi-met 4.

5- Results and discussion

From the results shown in figures 7 to 9 and tables 3 to 5 it is clear that, air temperature, air speed and relative humidity varies differently from one urban configuration to another.

3-1- Air temperature

Air temperature inside the models decreases with increasing plot ratio and vice versa.

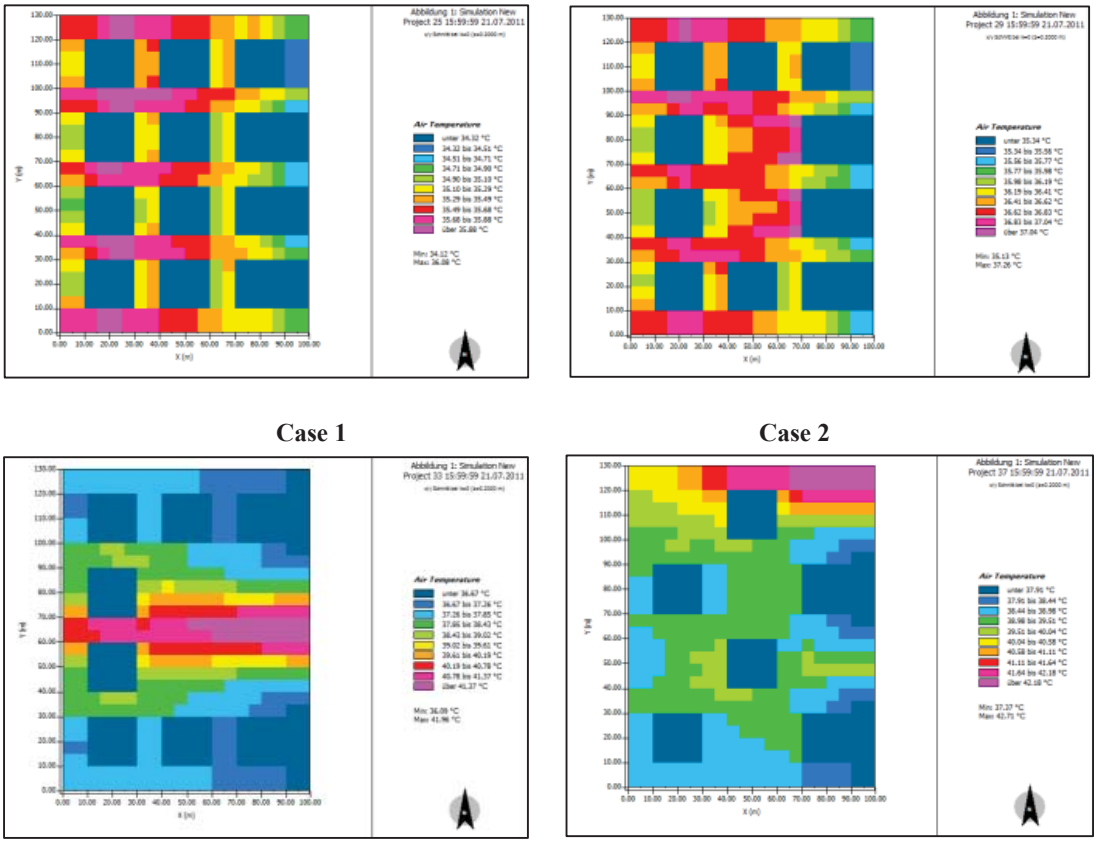

Figure 7: Air temperature variety results for each configuration

T°c	Case 1	Case2	Case3	Case4
Tmin	34.12	35.13	36.09	37.37
Tmax	36.08	37.26	41.96	42.71

Table 3: Max and Min values of air temperature inside each configuration.

The increase in the number of blocs on the same surface area helps to decrease the outside air temperature.
The effects of shadowing bloc to bloc reduce the blocs surfaces exposed to direct sun heat. The same effect can be seen on case 2 and 3.
The outside air temperature rises as the number of blocs decreases.
However, the orientation and the green belt have different subsequent results as seen in case 2, 3 and 4, see figure 5.

3-2- Air speed

It has been reported that during anticyclonic periods and during the months of July and August reduced wind speed 2 m/s to 3 m/s (APUR, Bigorgne, 2012), combined to a clear sky increases the risk of creation of urban heat island.

Figure 8 and table 4 shows the results of the simulations for the wind speed factor for the four typical urban configurations.

The air speed is quite uniform for all the four configurations with slight differences between the reference case (case 1) and case 4. The risk of heat island is more probable for case 4.

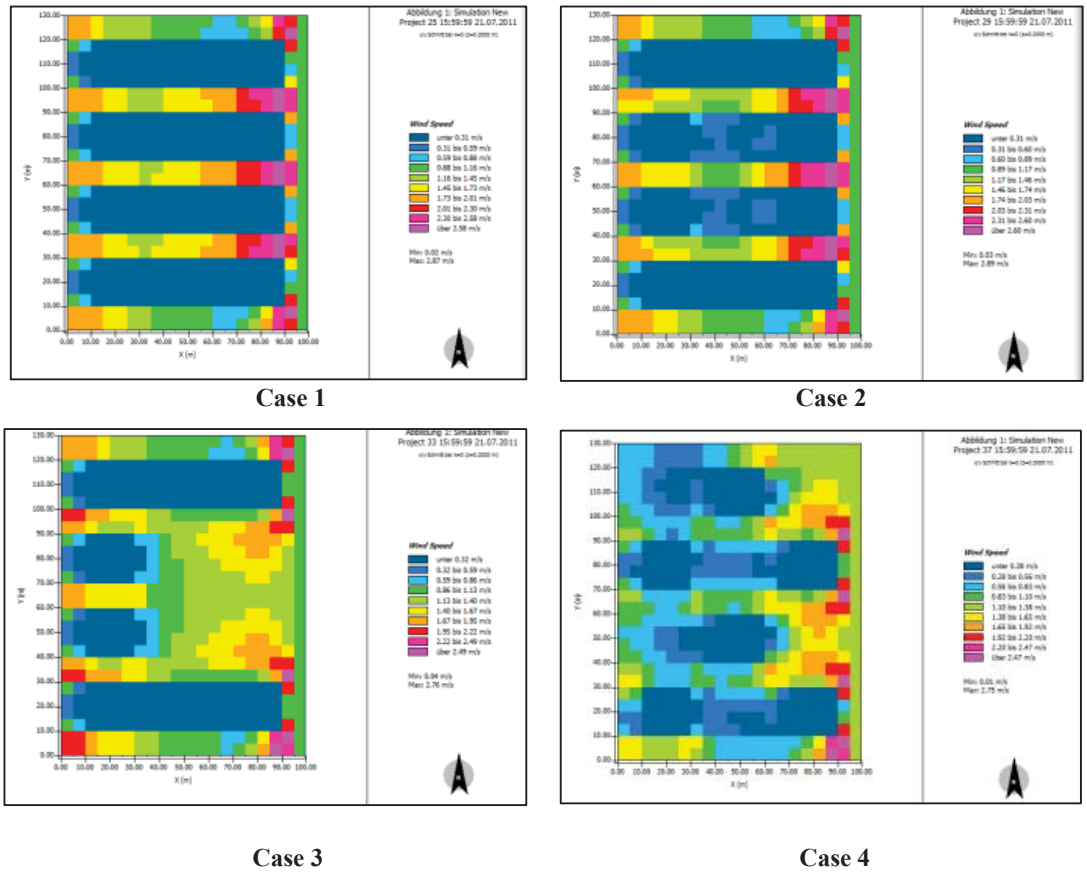

Figure 8: Air speed variety results for each configuration.

V (m/s)	Case1	Case2	Case3	Case 4
V min	0.02	0.03	0.04	0.01
V max	2.87	2.89	2.76	2.75

Table 4: Max and Min values of air speed inside each configuration.

3-3- Relative humidity

Relative humidity values could influence the risk of the urban heat island.

When humidity is low, climate becomes too dry promoting water and energy consumption. The evapo-transpiration phenomenon “green and water spaces” helps to reduce outside air temperature.

However, it could be pointed out that excessive increases in relative humidity reduce comfort temperature.

From figure 9 and table 5, we can deduce that relative humidity values are at their highest in cases 3 and 4. On the East orientation in case 4 and evenly distributed all over the urban configuration in case 3.

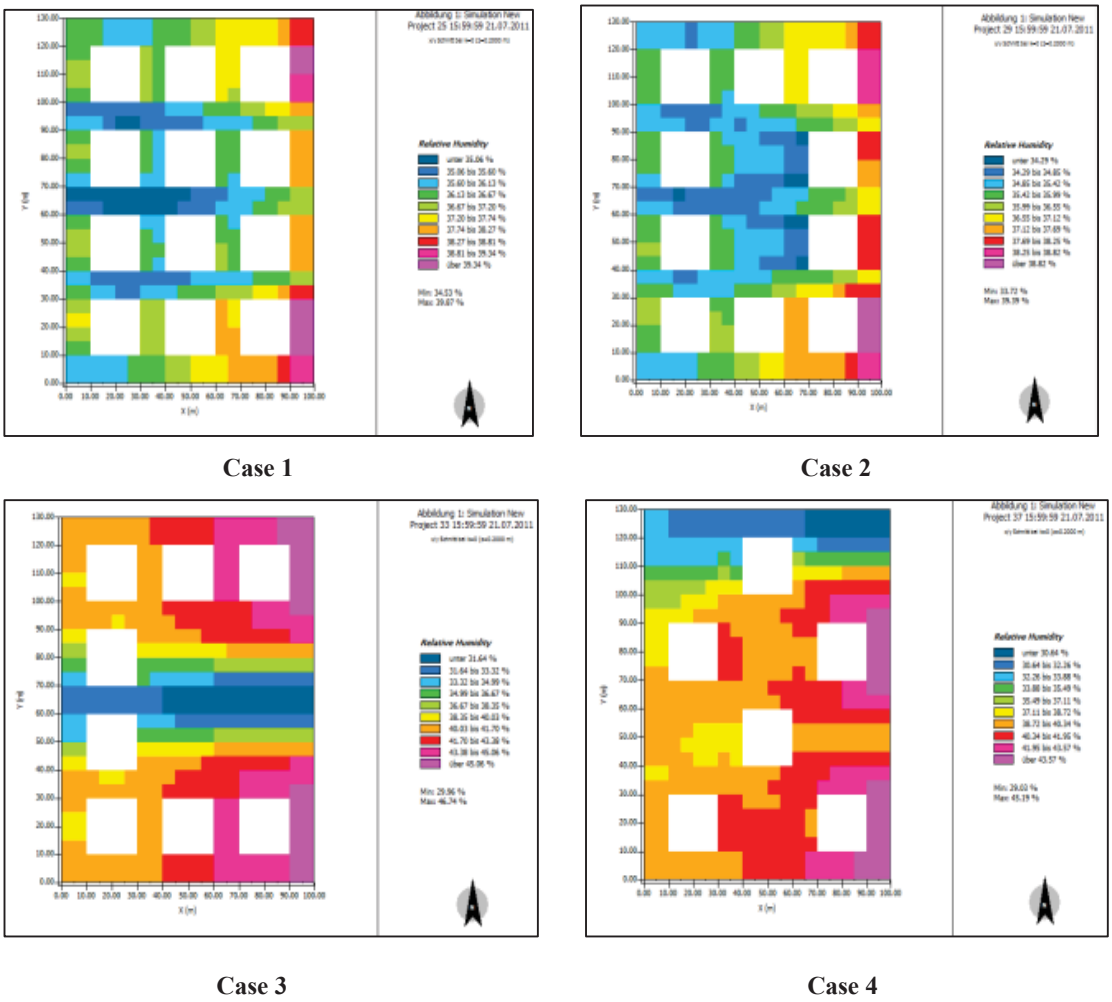

Figure 9: Relative humidity variety results for each configuration

RH%	Case1	Case2	Case3	Case4
RH min	34.53	33.72	29.96	29.03
RH max	39.87	39.39	46.74	45.19

Table 5: Max and Min values of relative humidity inside each configuration.

Conclusion

The results show that in hot and dry climate; the urban density creates a microclimate on the urban outdoor spaces by the diminution of air temperature and the urban heat island risk.
Urban typology has a great effect on the urban heat island risk. Designers of new urban development should take into account all the factors influencing urban morphology such as: form, geometry, density and orientation in the design of new towns and districts.
A sustainable architecture or urban design, should take into account all the variables which could influence positively the resulting urban climate.
A holistic approach could constitute a fundamental strategy for resolving nowadays urban issues and problem.

References

[1] Jérôme Vinet, contribution à la modélisation thermo-aéraulique du micro climat urbain, université de Nantes, 2000.
[2] Emmanuel Bozonnet, impact des microclimats urbains sur la demande d'énergie des bâtiments cas de la rue canyon, université de la Rochelle, 2009.

[3] Remy Claverie, caractérisation de l'îlot de chaleur urbain par mesure dynamique embarquée, université de Nancy, 2011.
[4] Ysabelle Filiatreault, changements climatiques et îlot de chaleur, université de Sherbrooke, 2015.
[5] Sara Khelil, Biomimicry, towards a living Architecture in hot and arid regions, université de Biskra, 2015.
[6] Marjorie Musy, coord, une ville verte, les rôles du végétal en ville, édition Quae, 2014.
[7] Julien bigorgne, les îlots de chaleur urbains à Paris cahier 1, apur, Décembre 2012.
[8] Sean Campbell, 2003 European Heat Wave, 2009.
[9] www.envi-met.com
[10] www.lesarbres.fr
[11]https://www.wunderground.com/history/station/60525/2015/11/1/MonthlyHistory.html?&reqdb.zip&reqdb.magic&reqdb.w o

Conference Proceedings

EuroSun 2016
Palma de Mallorca (Spain), 11 - 14 October 2016

ISES EuroSun 2016

Flexibility of Large-Scale Solar Heating Plant with Heat Pump and Thermal Energy Storage

Katarzyna M. Luc[1], Alfred Heller[1] and Carsten Rode[1]

[1] Department of Civil Engineering, Technical University of Denmark, Kongens Lyngby (Denmark)

Abstract

In the future energy system, based wholly on renewable energy sources, biomass is likely to become a scarce resource because of high demand especially by the transport sector. The current paper investigates, what is the possibility of utilizing excess electrical energy from renewable generation to decrease biomass use in a district heating system. The paper focuses on the renewable energy-based district heating system in Marstal, Denmark, with heat produced in central solar heating plant, wood pellet boiler, heat pump and bio-oil boiler. The plant has been the object of research and developments since its construction in 1996 and its operation is well documented. In the first part of the paper, the background of the current study is explained and the system in question is presented. Subsequently, the methodology of the study is explained and the model used in the study is described. Due to lack of widely accepted definition of a metrics for comparing system flexibility the paper proposes such an indicator. It was concluded, that cheap electricity can partially replace scarce biomass for heat production for district heating system.

Keywords: *Central Solar Heating Plant, District Heating, Heat Pump, Integrated Energy System*

1. Introduction

1.1. Background

The goal of the Danish energy system, including electricity, heating, industry and transport, is to wholly transition to renewable energy resources by 2050. In contrast to fluctuating renewable energy sources such as solar and wind energy, biomass offers generation flexibility on similar level as traditionally used fossil fuels. However, there is a number of considerations that need to be taken into account in case of evaluating environmental impact of biomass use for energy purposes. Removal of biomass can impact soil, hydrology and water quality, and habitat resources (Abbas et al., 2011). Reijnders (2006) lists a number of conditions that are required for sustainable biomass-for-energy production: levels of soil, organic matter and nutrients should not decrease over time, erosion and water usage should not exceed additions to soil and water stocks and the use of virtually non-renewable phosphate ores and fossil fuels should be significantly reduced. The author states also, that meeting such conditions requires major effort and most likely leads to relatively low productivity per hectare (estimated for around 3 metric tons per hectare per year of woody biomass, both in the temperate and tropical areas (Pimentel et al., 2008)). In Denmark, realistic biomass potential for energy purposes was estimated supply by Danish Energy Agency to be 20-25% of current total energy supply (Lund, 2007). Additionally, in the future energy system based wholly on renewable energy sources, in some development scenarios biomass is expected to be in high demand by the transport sector (Lund, 2007). Thus, its availability for heat production is going to decrease. It is also expected, that with increasing share of wind in electricity sector, periods when electricity generation exceeds the demand will occur more and more often. Thus, utilizing this excess electrical energy can provide an opportunity to simultaneously decrease biomass use for heating purposes and provide cost-effective heat generation.

doi:10.18086/eurosun.2016.05.10 Available at http://proceedings.ises.org

1.2. Aim of the study

The aim of the study was to investigate, to what degree the biomass use in the a large-scale solar heating plant with seasonal storage could be reduced through the use of heat pump during the periods with excess electrical energy generation from the fluctuating renewable sources. It was expected, that the central solar heating plant remains the main heat source for the system.

2. Methodology

2.1. Investigated system

The system investigated in the study is the district heating system in Marstal, Denmark. The system supplies heat to around 1,600 consumers. 50-55% of heat production comes from solar energy, 40% from a wood pellet boiler, 2-3% from a heat pump and the rest from a bio-oil boiler (Marstal Fjernvarme). Three solar collector fields sizing respectively, 9,000 m^2, 9,300 m^2 and 15,000 m^2. The plant has the thermal capacity of 23,300 kW_{th} and is equipped with water thermal energy storages of the size of 2,100 m^3 (steel tank), 10,000 m^3 and 75,000 m^3 (pit heat storages). The storage can act both as diurnal storage and seasonal storage. The plant runs with an adjustable flow both on the primary and secondary side. Thanks to this, it is possible to ensure requested outlet temperature through regulating the flow, using the efficiency curve for the solar collectors and taking into account sun radiation and return temperature to the collectors (PlanEnergi, 2013a). The first heat pump uses R290 as refrigerant and has the power use of 100 kW. The second heat pump uses CO_2 as a refrigerant and has the power use of 475 kW and thermal output of 1.5 MW_{th}. The 4 MW wood chip boiler includes thermal oil boiler for ORC and has a heat output of 3.25 MW (PlanEnergi, 2013a). The diagram of the existing system is shown in Figure 1.

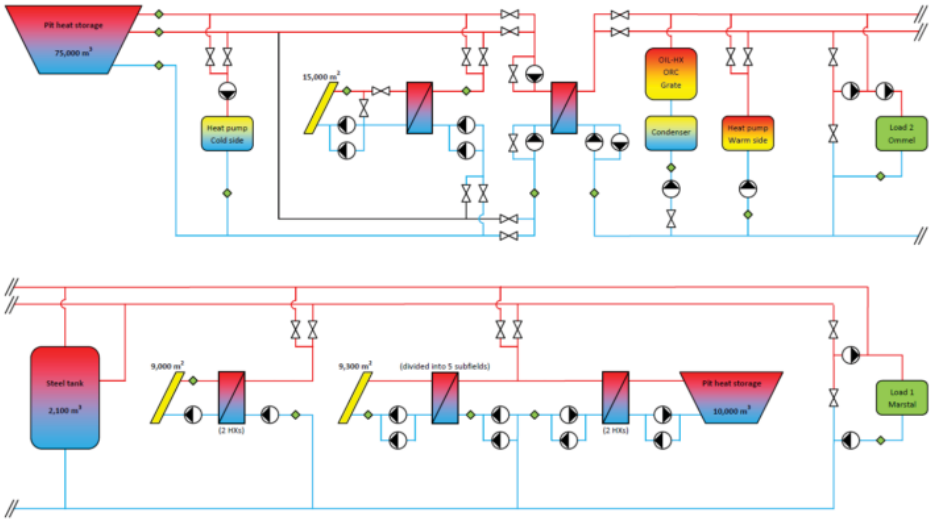

Figure 1. System diagram of the Solar District Heating plant in Marstal (PlanEnergi, 2013b)

The system was chosen as the subject of investigation, as has been the object of research and developments since its construction in 1996 and its operation is well documented (Fan et al., 2009; Heller, 2000; Heller and Dahm, 1999; Sørensen et al., 2012). Moreover, it is entirely based on renewable energy sources and therefore it is interesting in the context of developing such systems in the future.

2.2. Model

2.2.1. Model with simple electric heater

The model of the energy system in question was created by the Danish consultant company PlanEnergi in the TRNSYS software (Solar Energy Laboratory, 2014). The system was modelled in a simplified way, with the demand side represented in an aggregated way and certain simplifications on the supply side. The collector fields were modelled by using three separate 2nd-Order Incidence Angle Modifier (Type 1b) components representing the three collector fields. The largest pit heat storage was modelled in TRNSYS using the non-

standard XST- Seasonal Ground Heat Storage component (Type 342) (Mazzarella and Holst, 1992). Two smaller storages were modelled as non-standard Type 340 (Multi-port water storage) (Drück, 2006). The heat pumps were modelled by a set of equation, not with the use of an existing TRNSYS heat pump component. The annual heat load was set at 32,000 MWh/year, the number of degree-days at 81834.3936 and the GAF ratio at 0.709. GAF is the part of heat demand dependent on the weather conditions (degree days) and the ratio expresses the share of heat demand dependent on the number of degree days in the total heat demand. The electricity prices used in the simulation were Elspot prices for DK-Vest for year 2009 ("Nord Pool Spot," 2016). Elspot is the day-ahead market for electrical energy operated by Nord Pool Spot. Nord Pool Spot is the market for electrical energy that operates in Denmark, Finland, Norway, Sweden, Estonia, Latvia, Lithuania, Germany and the UK ("Nord Pool Spot," 2016). Supply and return temperatures were set based on the measurements in the system. The supply temperatures are between 72 and 77 °C and the return temperatures between 33 and 41 °C. Bio oil boiler was modelled in a simplified way as an Auxiliary heater (Type 6) with the maximum heating rate of 10 MW. The ORC was set to operate from October 7th (280th day of the year) to June 6th (160th day of the year), to avoid using it in the summer period. Both heat pumps already existing in the system were set to operate from September 30th to April 1st (91st day of the year).

The reference model, was then validated by PlanEnergi (PlanEnergi, 2013a) by comparing the results from the model with the measurements taken in the year 2009. The new parts of the installation were disabled in the simulation (thus, no heat pumps or wood chip boiler were taken into account), as it was done before the expansion of the heating plant. The system in its current form and resulting mix of heat production technologies were taken as the reference.

The heat pumps or a potential electric boiler were identified as the elements of the systems that can be used to connect electrical and thermal energy systems. To investigate the possibility of decreasing the biomass use in favour of heat pumps during the low electricity price periods, the above model of the existing system was then modified to simulate the future application.

In an initial phase of the investigation, the system was expanded by a simple electrical heater placed before the wood chip boiler. This was done just to investigate how an additional heating source influences operation of the plant without introducing additional "disturbances" to the simulations. The efficiency of the heater was set to 1 and heat losses in this component were not accounted for. The electrical heater was set to operate during the periods, when the electricity price was below a certain set point. The same way as the ORC, additional electric heater was set to operate from October, 7th to June, 6th, to avoid using it in the summer.

A parameter variation on a) the size of the electric heater b) limit electricity price for the heater operation was carried out by simulation with the above TRNSYS model. The initial investigation for the data from 2009 was performed for electric heater sizes between 0.01 MW and 10 MW and for the price limit for electric heater operation between 0 and 300 DKK/MWh. Then, the range of analyzed electric heater sizes was limited to the range between 0.1 MW and 7.5 MW. This was done, as the smallest of the investigated heat sources did not have any significant influence on the system's operation. On the upper end of the parameter scale, the largest value is chosen to be able to supply the max demand of the whole district heating system. Results showed that values the 10 MW additional heater had power overshooting the largest observed load. Moreover, no significant increase in energy delivered by electrical heater was observed after increasing the heater size from 7.5 MW to 10 MW.

Then, influence of different price levels on the energy delivered by electrical heater (and subsequent reduction in biomass use by ORC unit) was investigated by running the simulations with the Nordic Elspot electricity prices from four different years (Energinet.dk, 2015). This was done to investigate sensitivity of the results concerning the amounts of biomass saved to the electricity prices, with respect to the variation in prices during the last years. Data from 2009 were used for the reference case. For the other three cases, data from 2006 (to represent a year with very high electricity prices), 2013 (a year with high electricity prices) and 2015 (a year with relatively low electricity prices) were used. Price curves for the years between 2000 and 2015 are shown below in Figure 2. The highest prices were not shown in the graph, as they occur for a very short period and do not influence the results of the investigation. It was assumed, that the heat demand was independent from the electricity prices and was the same in all analyzed cases.

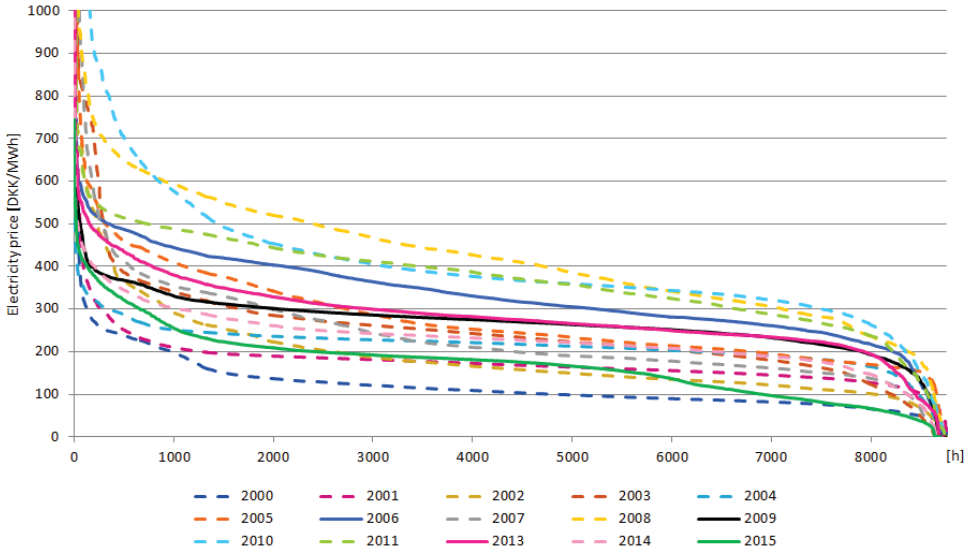

Figure 2. Elspot price curves for the period from 2000 to 2015 (Energinet.dk, 2015)

2.2.1. Model with heat pump

In the above simulation a simplified model with idealizes electrical heater was applied to find the overall potential for substituting part of the biomass use by the excess electricity. In the second model the heat pump was placed in the same spot in the system as the heater. Two sizes of the heat pump were investigated – the first one was chosen to correspond to the 1.25 MW electric heater, the second one to 3.25 MW electric heater. The absorbed power rating for the first heat pump was set at 350 kW and for the second one at 1050 kW.

The general control system in the modified model was not changed compared to the original model applied by PlanEnergy in 2013. The same way as the electric heater before, the heat pump was set to operate from October 7th to June 6th, to avoid using it in the summer period and so its operation substitutes the operation of ORC unit. As the data used is in 1-hour resolution, the concerns about the heat pump compressor turning on and off frequently for very short periods was not considered to be relevant. It was assumed the heat pump is a ground source heat pump. However, as the TRNSYS heat pump component (Type 927) requires more detailed input than the one that could be provided based on the model used, the heat pump was modelled using a set of equations, as two other heat pumps in the system. The equations used were based on the ones used for the propane heat pump. The investigation, due to its general character, was not aimed at optimizing the heat pump operation. It was assumed, that the mass flow through the warm side of the heat pump stays the same as the mass flow directed to boiler. To prevent circular reference, caused by making COP depend on the outlet temperature that at the same time can depend on the COP, the outlet temperature from the previous step was used, the same way it was done for CO_2 heat pump. The resulting COP levels correspond to the ones indicated in "Technology Data for Energy Plants" from Energinet.dk (Energinet.dk, 2012).

$$Q_{warm} = P_{HP} \cdot 3600 \cdot COP_{AHP\ warm} \cdot HP_{ON?} \quad \text{(eq. 1)}$$

$$T_{WS\ out} = min(T_{setpoint} + 5, T_{WS\ in} + \frac{Q_{warm}}{c_{p\ water} \cdot m_{WS\ out}}) \quad \text{(eq. 2)}$$

$$COP_{AHP\ warm} = 0.6 \frac{T_{WS\ out} + 273.15}{T_{WS\ out} - T_{CS\ in}} \quad \text{(eq. 3)}$$

where: Q_{warm} – heat output of a heat pump [kWh], P_{HP} – electrical power used [kW], $COP_{AHP\ warm}$ - Coefficient of Performance of the heat pump operating as a heat source, $HP_{ON?}$ - is the heat pump on (1 if yes, 0 if no), $T_{WS\ out}$ – output temperature on the warm side [°C], $T_{setpoint}$ – setpoint temperature [°C], $T_{WS\ in}$ – input temperature on the warm side [°C], $m_{WS\ out}$ – mass flow on the warm side of the heat pump [kg/h], $T_{CS\ in}$ – input temperature on the cold side [°C].

The TRNSYS model of the modified system with a heat pump can be seen in Figure 3. The figure shows only the water loops of the model – layers with control systems, weather files and outputs were switched off to make the schematics clearer.

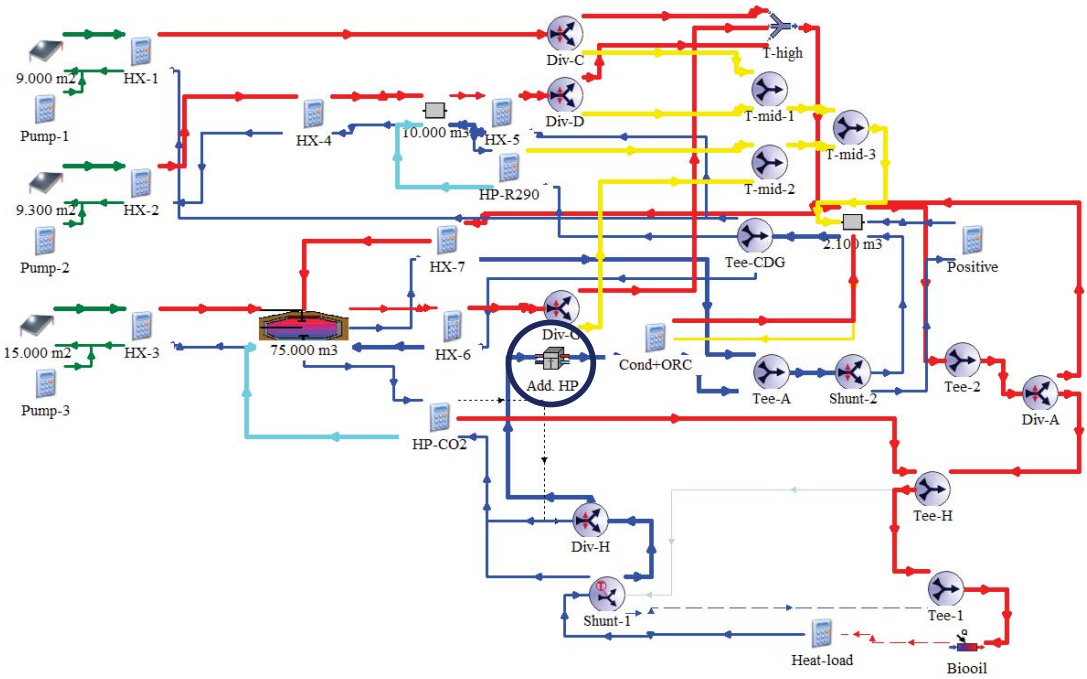

Figure 3. Model of the water loops in TRNSYS after modification. Left side of the model represents solar collector fields, connected to the rest of the system with the use of heat exchangers; followed by the storages (labeled "75..000 m3" and "2.100 m3" and "10.000 m3"); the black circle indicates additional heat source in the system added in the current investigation, "Cond+ORC" represents the woodchip boiler and ORC unit

2.3. Biomass use

The biomass savings were calculated in a simplified way, to estimate the amount of biomass saved thanks to substitution of ORC unit by the heat pump. First, the biomass burned to generate 1 MWh of heat was calculated. The fuel efficiency of the wood chip boiler in the ORC unit depends on the temperature of the cooling water, which is the return temperature from the district heating system. The return temperatures in the district heating system are between 33 and 41 °C, with the average return temperature of 36 °C. So, based on the information from the report by PlanEnergi (2013a), it was assumed the efficiency of the boiler is $\eta = 108\%$. The heating value of the wood chips at 45% of moisture content was estimated as LHV = 2.63 kWh/kg, using the information from (WoodEnergy.ie, 2015). The amount of biomass saved, $m_{biomass\ saved}$, was calculated using eq. 4.

$$m_{biomass\ saved} = \frac{Q_{boiler\ ref} - Q_{boiler}}{\eta \cdot LHV} \qquad \text{(eq. 4)}$$

where: $m_{biomass\ saved}$ – mass of biomass saved [kg], $Q_{boiler\ ref}$ – heat output of the boiler in the reference scenario [kWh], Q_{boiler} – heat output of the boiler [kWh], η – efficiency of the boiler, LHV - lower heating value of the wood chips [kWh/kg]

2.4. Flexibility indicator

There is no one single, universal way of defining flexibility in literature (Alizadeh et al., 2016; Lund et al., 2015). Cochran et al. (2014) used the definition of flexibility as "the ability of a power system to respond to change in demand and supply". While flexibility is often defined as the ability of the system to shift the use of certain amount of energy in time (Nuytten et al., 2013; Six et al., 2011), it can relate to its ability to utilize different energy sources.

Based on the definitions from literature, in the context of this study, the energy flexibility of the system in question was defined as its ability to utilize different energy sources, also called fuel shifting. So, the energy

in MWh that can be shifted over a year in an analysed scenario was used as an indicator of system's flexibility.

3. Results

3.1. Results for the model with electric heater

3.1.1. Change in production distribution and in biomass use

Results of the initial simulations done with the data for 2009 can be seen in Figure 4. The graph shows annual energy production by the biomass boiler in the Organic Rankine Cycle (ORC) unit and electric heater (added to the existing system) in MWh for different electric heater sizes and limit price set-points. It can be seen, that there is a significant increase in energy generation from the electric heater between the limit price of 200 DKK/MWh and 250 DKK/MWh. This is related to the shape of the electricity price curve and elaborated on in the further in the Discussion chapter. It should be noted, that for the heaters greater than 1.5 MW for limit price higher than 225 DKK/MWh temperature in one of the storages exceeded 100 °C. Heat delivered by the ORC and electric heater for these cases was not shown in the graph.

Additionally, the ratios between annual energy generation and heater size were compared for heaters of different sizes at different price limit levels. The results of this comparison indicated, that for the heaters up to 1.25 MW, this ratio remained constant and above that size gradually decreases. However, the smaller heaters were not able to replace significant part of the heat generation from the ORC unit – for the limit price of 225 DKK/MWh, electric heater of the size of 1.25 MW delivered 5.6% of energy generation of ORC unit (1,018 compared to 1,8087 MWh). Hence these sizes are excluded from further analysis.

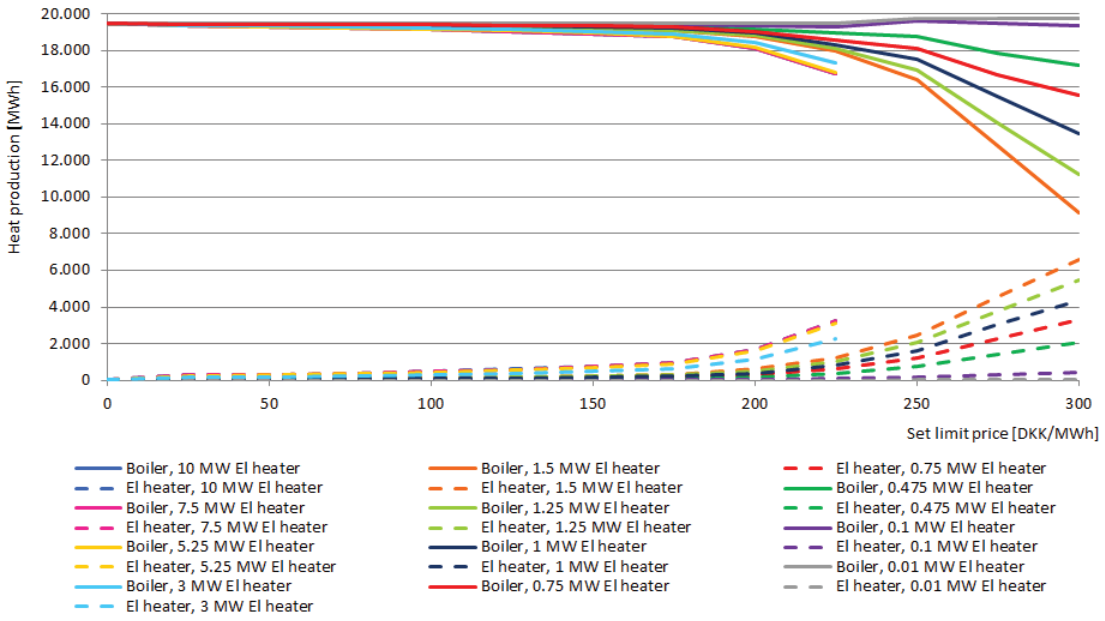

Figure 4. Heat generation by ORC unit and electric heater for different sizes of the heater and different levels of limit price for electricity prices from 2009

Subsequently, the following simulations were run for identical range of limit prices as above, but for the reduced range of heat source sizes 0.1 - 7.5 MW, using the electricity prices for year 2006, 2013 and 2015. Figure 5 shows how much heat can be delivered to the system by 1.25 MW electric heater for different limit price levels for electricity prices from different years. It can be seen that for 2015, a year with relatively low prices (Figure 2), energy delivered increases significantly at much lower limit price than in case of three other years. It can be seen that, as expected, electricity prices during the year have significant impact on the level of substituting biomass by electricity. For example, for the prices from 2006, for the limit price of 225 DKK/MWh, 1.25 MW electric heater delivered 948 MWh, and for the prices from 2013 - 928 MWh.

However, for the price levels from 2015, a heater of the same size delivered 5,981 MWh, so significantly more than both in 2006 and 2013. Additionally, small changes in the limit price may have significant influence on the substitution level, also due to the shape of the price curve. This can be seen for example for the data from 2015, where the energy delivered to the system by electrical heater at the limit price of 200 DKK/MWh is 201% of the energy delivered at the limit price of 175 DKK/MWh for the heaters between 0.1 MW and 1.5 MW.

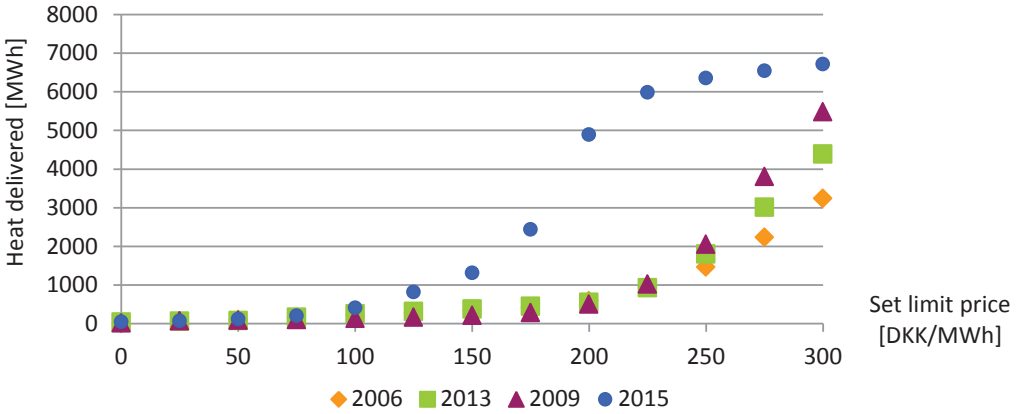

Figure 5. Heat delivered to the system by 1.25 MW electric heater for different limit price levels for electricity prices from different years

Figure 6 shows duration curves for the load, the ORC unit, the oil boiler and electrical heater (in case of the modified systems). All curves are based on results of simulations run with the electricity prices from 2009. Three cases of the systems with additional heater installed were shown: 1.25 MW heater with limit price of 225 DKK/MWh, 1.25 MW heater with limit price of 250 DKK/MWh and 3 MW heater with limit price of 225 DKK/MWh. It can be seen again that the slight increase in limit price resulted in significantly greater number of operation hours for the electric heater. Reduction in ORC unit operation occurred for all three shown cases, the greatest for the case with 1.25 MW heater and limit price of 250 DKK/MWh. The differences between cases with 1.25 MW heater and different limit prices is greater than between the case with 3 MW and 1.25 MW at the same limit price. However, it should also be noticed that the use of bio oil boiler is greatest for the case with highest degree of ORC unit substitution. This is caused by the fact that the operation of the electric heater prevents ORC unit from turning on, but the heat supplied is not sufficient to cover the system demand.

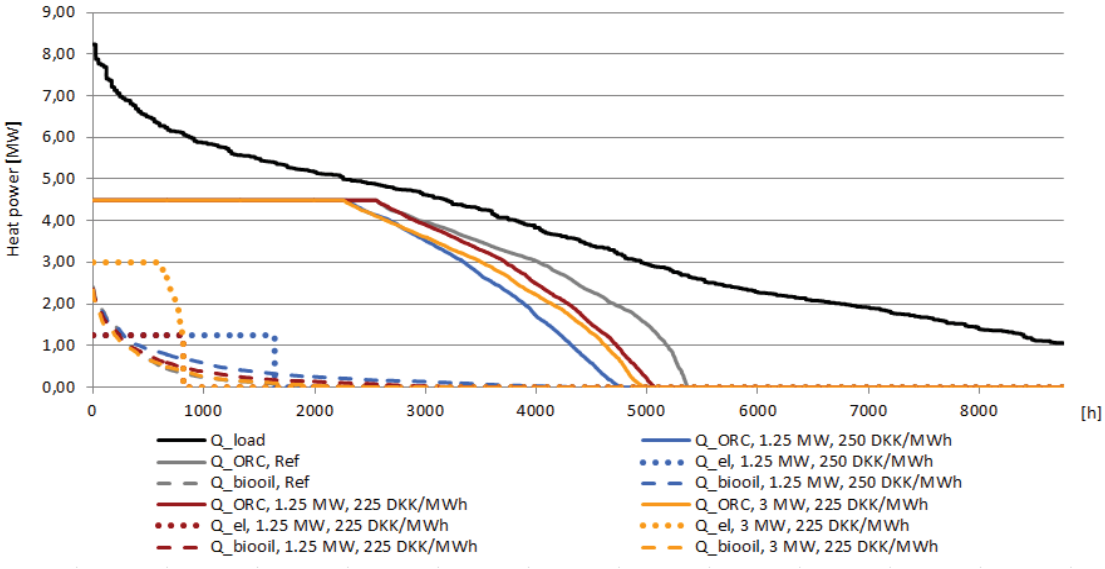

Figure 6. Duration curves for the load, the ORC unit and the oil boiler for the reference system

It was observed, that heater size at which the heat delivered by bio oil boiler changes the least between 2.70 - 3.25 MW. Thermal output of the ORC unit is 3.25 MW. This is caused by the fact that the operation of the electric heater prevents ORC unit from turning on, but the heat supplied is not sufficient to cover the system demand. Another problem at the investigated system configuration is the injection of the heated up water to the cold part of the 2,100 m^3 storage tank. This is also the reason of the overheating in 10,000 m^3 tank that occurs in systems with large supplementary electric heater at high limit prices, so if the heater operates for many hours during a year (exact level of the limit price depends on the price levels in a given year). Table 1 shows more detailed information about heat delivered by different technologies in the system and about calculated heat losses from heat storages. All the results presented in the table were calculated using electricity prices from 2009.

Table 1. Heat delivered by different technologies and thermal losses from heat storages

	Reference	5.25 MW, 100 DKK/MWh	5.25 MW, 175 DKK/MWh	1.5 MW, 100 DKK/MWh
	MWh/year	MWh/year	MWh/year	MWh/year
9,000 m^2 collector field	3.341	3.339	3.337	3.341
9,300 m^2 collector field	3.647	3.644	3.637	3.656
15,000 m^2 collector field	6.412	6.411	6.410	6.412
Collectors total	13.400	13.394	13.384	13.409
Propane heat pump	219	219	218	219
CO_2 heat pump	1.043	1.043	1.043	1.043
Heat pump total	1.262	1.261	1.261	1.262
2,100 m^3	-132	-132	-132	-131
10,000 m^3	-525	-525	-527	-524
75,000 m^3	-2.475	-2.476	-2.483	-2.475
Storage losses total	-3.132	-3.133	-3.142	-3.130
ORC	19.476	19.166	18.778	19.328
Electrical heater	-	438	903	158
Bio oil	996	873	816	973
Total	32.002	32.000	32.000	32.000

	1.5 MW, 225 DKK/MWh	1.25 MW, 100 DKK/MWh	1.25 MW, 225 DKK/MWh	0.75 MW, 275 DKK/MWh
	MWh/year	MWh/year	MWh/year	MWh/year
9,000 m^2 collector field	3.325	3.342	3.321	3.293
9,300 m^2 collector field	3.742	3.656	3.736	3.795
15,000 m^2 collector field	6.421	6.412	6.416	6.464
Collectors total	13.489	13.410	13.473	13.552
Propane heat pump	217	219	218	210
CO_2 heat pump	1.043	1.043	1.043	1.043
Heat pump total	1.260	1.262	1.260	1.253
2,100 m^3	-130	-131	-130	-128
10,000 m^3	-515	-524	-513	-513
75,000 m^3	-2.434	-2.475	-2.502	-2.315
Storage losses total	-3.079	-3.130	-3.144	-2.956
ORC	18.087	19.349	17.954	16.188
Electrical heater	1.018	133	1.219	2.282
Bio oil	1.224	976	1.236	1.679
Total	31.997	32.000	31.998	31.999

After this initial observation, additional simulations were run with the electric heaters at sizes between 1.5 and 5.25 MW. It was observed, that heater size at which the heat delivered by bio oil boiler changes the least between 2.70 - 3.25 MW. Thermal output of the ORC unit is 3.25 MW. This is caused by the fact that the operation of the electric heater prevents ORC unit from turning on, but the heat supplied is not sufficient to cover the system demand. Another problem at the investigated system configuration is the injection of the heated up water to the cold part of the 2,100 m^3 storage tank. This is also the reason of the overheating in 10,000 m^3 tank that occurs in systems with large supplementary electric heater at high limit prices, so if the heater operates for many hours during a year (exact level of the limit price depends on the price levels in a given year).

It was decided that for the needs of this study, the configuration of the system will not be modified. However, if the additional heat source is to be installed in the suggested place in the system, modification of the system and adjustment of the control scheme is necessary. This is further elaborated on the in the Discussion section.

3.1.3. Sizing of the supplementary heat source

Based on the initial investigation, two sizes of the heat pump were proposed 1.25 MW and 3.25 MW. The 1.25 MW heat pump was chosen, as it was the largest electric heater size for which the ratio between annual energy generation and heater size remained the same as for all smaller heaters. The 3.25 MW heat pump was chosen to investigate the situation where the supplementary heat pump has the same thermal output as the ORC unit.

3.2. Results of the simplified heat pump investigation

Schematic of the system with heat pump in question is shown in Figure 3. Results of the performed simulations can be seen in Figure 7. Heat generation by ORC unit and additional heat pump for different sizes of the heat pump and different levels of limit price for electricity prices from 2009 The graph shows annual energy production by the biomass boiler in the Organic Rankine Cycle (ORC) unit and heat pump in MWh for two heat pump sizes and different limit price set-points. It can be seen, that there is a significant increase in energy generation from the heat pump between the limit price of 200 DKK/MWh and 250 DKK/MWh, similarly as it was for the simplified electric heaters. It should be noted, that for the larger heat pump 250 DKK/MWh temperature in one of the storages exceeded 100 °C, similarly as it was in case of the electric heater. Energy delivered by the ORC and electric heater for these cases was not shown in the graph.

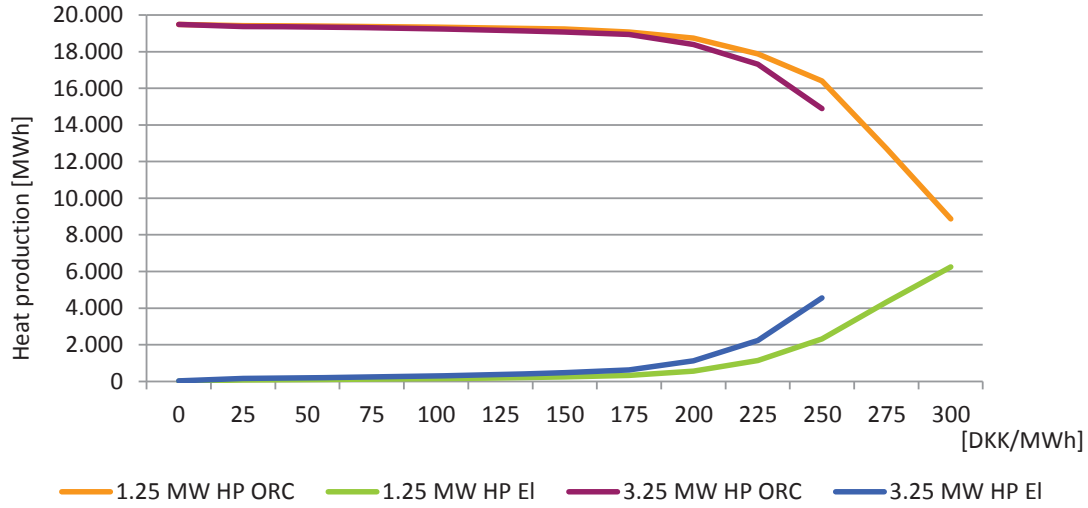

Figure 7. Heat generation by ORC unit and additional heat pump for different sizes of the heat pump and different levels of limit price for electricity prices from 2009

3.2.1. Change in production distribution and in biomass use

Figure 8 shows the energy production in each month both for the reference case and for two heat pump cases, with the share coming from bio oil use and delivered by heat pump highlighted (yellow parts). It can be seen, that they do not constitute significant part of the production. However, introducing the heat pump to the system leads to the decrease in heat production from biomass boiler in the ORC unit that is directly substituted by the heat pump. This shows the potential for biomass savings due to a combination of low electricity prizes and the potential of the heat pump installed. It can be seen, that this potential in the proposed setup is not significant compared to the energy output of the whole system.

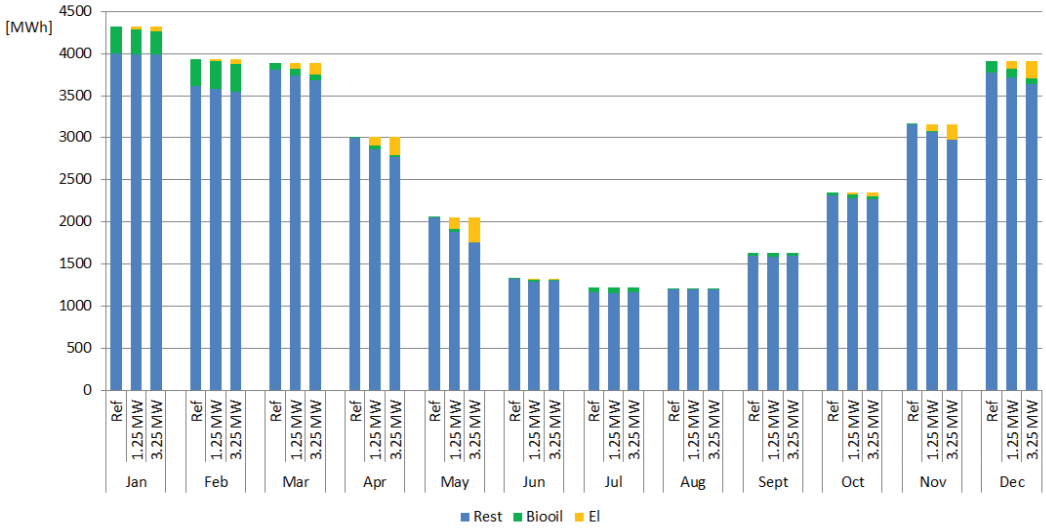

Figure 8. Monthly heat production for the reference case and two heat pump cases with the production from bio oil boiler and additional heat pump highlighted

Amount of biomass saved annually thanks to the use of heat pump for two investigated heat pump sizes at different limit prices is presented in

Table 2.

Table 2. Biomass saved for two investigated heat pump sizes at different limit price levels

Limit price [DKK/MWh]		25	50	75	100	125	150	175	200	225	250	275	300
Biomass replaced by electricity [tonne]	1.25 MW HP	18	26	35	47	64	84	145	260	563	1080	2381	3734
	3.25 MW HP	36	46	62	82	110	143	189	381	759	1613		

3.3. Flexibility of the system

Finally, the flexibility of different systems was compared. We decided to use the energy in MWh that can be shifted over a year as an indicator of system's flexibility under chosen control conditions. System's flexibility understood that way increases with the increase in the size of additional heat source. For the system with 1.25 MW heat pump was calculated to be 153 MWh annually for the set limit price of 100 DKK/MWh, 320 MWh for 175 DKK/MWh and 2324 MWh for 250 DKK/MWh. For the system with 3.25 MW heat pump it was calculated to be 301 MWh annually for the set limit price of 100 DKK/MWh, 630 MWh for 175 DKK/MWh and 4552 MWh for 250 DKK/MWh. After adjusting the system control to cope with additional large heat source, the flexibility indicators independent of the control scheme and set limit price should be established. This is further elaborated on in the Discussion.

4. Discussion

One of the assumptions made in the analysis is related to the use of electricity prices as an input for control system. In the study, electricity prices from Nordic Elspot market were used as a control signal for the additional electricity-based heat source, with a constant price limit indicating whether the electric heater / heat pump should turn on or not. Low electricity prices occur in periods when expected demand is relatively low compared to the expected supply. Very low electricity prices in Denmark are frequently associated with periods of high electricity production by wind turbines. However, middle-sized district heating utilities are not participating in trade at Nord Pool. So, in the current conditions, proposed solution brings no economic benefit for the district heating plant and is beneficial only from the perspective of energy system as a whole.

It was assumed, that the heat demand was identical for all analyzed cases for different electricity prices and thus, indirectly, that heat demand and electricity prices are fully independent. This is a simplification. However, it was decided that electricity market prices are influenced by numerous factors not connected to the local heat demand and that such an assumption provides a good way of investigating the influence of electricity prices during a year on the analysis' results.

Another factor that significantly influences the results is the set limit price and market electricity prices. As it was discussed in section 3.1, the exact energy delivered to the system by additional electricity-based heat source during a year is very sensitive to the set limit price and price levels on the electricity market. This causes trouble in case of a potential economic analysis, when estimating e.g. Net Present Value of the system's modification. Additionally, results of such analysis would be also heavily influenced by assumptions on future energy market and taxation.

In the proposed system setup, operation of the additional heat source competes with the operation of ORC unit. So, if the district heating utility benefits from selling electricity generated by the ORC unit, adding additional heat source in proposed configuration decreases this profit. However, it can be argued, that generating electricity during the low-price periods does not benefit energy system as a whole and should be avoided.

As it was mentioned in section 3.1.1, it was decided that for the needs of this study, the configuration of the system will not be modified. However, if the additional heat source is going to be installed in the system, adjustment of the setup and control strategy would be necessary. Such an adjustment would have to include connections between the electric heater / heat pump, boiler and ORC unit and heat storages. Moreover, it should be assured that the operation of the additional heat source does not result in increase in energy delivered by the bio oil boiler – both for economic and for environmental reasons. After this adjustment, also the flexibility indicator for a given system configuration should be estimated, by calculating theoretically possible heat production by the additional electrical heat source when the set limit price is higher than highest electricity price during a year.

5. Conclusions

We showed in the paper that cheap electrical energy can replace scarce biomass in a large-scale solar heating plant with large storage capacities. However, location of the additional heat source in the system and control scheme for the new setup need to be carefully considered, as there is a risk the new heat source will destabilize system's operation, as it was shown. Increasing the size of additional heat source increases also system's flexibility, understood as the ability to utilize different energy sources, but makes incorporating in the existing system more difficult and results in high investment costs. Results of the performed study indicate, that for the system in question the potential for such a replacement is not significant. Additionally, results are characterized by large uncertainties due to the significant influence of the level of electricity prices on the results in the proposed control strategy. While the investigation was made based on the solar district heating plant and renewable-based district heating system in Marstal, Denmark, we believe that such solution can also be applicable for other similar systems, where biomass is used as supplementary heat source.

In further work, we will investigate the possibility of replacing biomass that may become a scarce resource, by cheap electricity from renewable sources for a district heating system with seasonal storage based on different energy sources than solar energy. This will be done for a generic model also with that will be

applied on concrete city districts.

6. Acknowledgement

The authors thank Danish EUDP EnergyLab Nordhavn for funding. Additionally, the authors would like to thank Niels From and Per Alex Sørensen from PlanEnergi for their input, provided model of the system and information about the solar district heating plant.

References

Abbas, D., Current, D., Phillips, M., Rossman, R., Hoganson, H., Brooks, K.N., 2011. Guidelines for harvesting forest biomass for energy: A synthesis of environmental considerations. Biomass and Bioenergy 35, 4538–4546. doi:10.1016/j.biombioe.2011.06.029

Alizadeh, M.I., Moghaddam, M.P., Amjady, N., Siano, P., Sheikh-El-Eslami, M.K., 2016. Flexibility in future power systems with high renewable penetration: A review. Renew. Sustain. Energy Rev. 57, 1186–1193. doi:10.1016/j.rser.2015.12.200

Cochran, J., Miller, M., Zinaman, O., Milligan, M., Arent, D., Palmintier, B., O'Malley, M., Mueller, S., Lannoye, E., Aidan, T., Kujala, B., Sommer, M., Holttinen, H., Kiviluoma, J., Soonee, S.K., 2014. Flexibility in 21 st Century Power Systems.

Drück, H., 2006. MULTIPORT Store - Model for TRNSYS - Type 340.

Energinet.dk, 2015. Download of market data [WWW Document]. URL http://www.energinet.dk/en/el/engrosmarked/udtraek-af-markedsdata/Sider/default.aspx (accessed 9.17.16).

Energinet.dk, 2012. Technology data for energy plants. doi:ISBN: 978-87-7844-940-5

Fan, J., Chen, Z., Furbo, S., Perers, B., Karlsson, B., 2009. Efficiency and lifetime of solar collectors for solar heating plants. Proc. ISES Sol. World Congr. 2009 Renew. Energy Shap. Our Futur. 331–340.

Heller, A., 2000. 15 Years of R&D in central solar heating in Denmark. Sol. energy 69, 437–447. doi:10.1016/S0038-092X(00)00118-3

Lund, H., 2007. Renewable energy strategies for sustainable development. Energy 32, 912–919. doi:10.1016/j.energy.2006.10.017

Lund, P.D., Lindgren, J., Mikkola, J., Salpakari, J., 2015. Review of energy system flexibility measures to enable high levels of variable renewable electricity. Renew. Sustain. Energy Rev. 45, 785–807. doi:10.1016/j.rser.2015.01.057

Marstal Fjernvarme, n.d. Marstal Fjernvarme [WWW Document]. URL http://www.solarmarstal.dk/firmaprofil (accessed 4.5.16).

Mazzarella, L., Holst, S., 1992. Multi-flow Stratified Thermal Storage Model with Full-mixed Layers.

Nord Pool Spot [WWW Document], 2016. URL http://www.nordpoolspot.com/ (accessed 9.20.16).

Nuytten, T., Claessens, B., Paredis, K., Van Bael, J., Six, D., 2013. Flexibility of a combined heat and power system with thermal energy storage for district heating. Appl. Energy 104, 583–591. doi:10.1016/j.apenergy.2012.11.029

Pimentel, D., Herz, M., Glickstein, M., Zimmerman, M., Allen, R., Evans, J., Hussan, B., Sarsfeld, R., 2008. Energy : 19 Renewable Current and Potential Issues 52, 259–276.

PlanEnergi, 2013a. Design of the Overall Energy System of the Demonstration Plant at Marstal Fjernvarme.

PlanEnergi, 2013b. Summary technical description of the SUNSTORE 4 plant in Marstal [WWW Document]. URL http://www.solarmarstal.dk/media/2854117/summary-technical-description-marstal.pdf (accessed 8.24.16).

Reijnders, L., 2006. Conditions for the sustainability of biomass based fuel use. Energy Policy 34, 863–876. doi:10.1016/j.enpol.2004.09.001

Six, D., Desmedt, J., Van Bael, J., Vanhoudt, D., 2011. Exploring the Flexibility Potential of Residential Heat Pumps Combined with Thermal Energy Storage for Smart Grids. 21st Int. Conf. Electr. Distrib.

Solar Energy Laboratory, 2014. TRNSYS: Transient System Simulation Tool.

Sørensen, P.A., Jensen, M.V., From, N., 2012. Smart district heating using the SUNSTORE concept.

Strojarstvo 54, 455–461.

WoodEnergy.ie, 2015. Frequently asked questions [WWW Document]. URL http://www.woodenergy.ie/frequentlyaskedquestions/ (accessed 10.1.15).

Solar multi-generation in the Mediterranean area, the experience of the STS-MED project

Alaric C. Montenon[1], Filippo Paredes[2], Alberto Giaconia[3], N. Fylaktos[1], Silvana Di Bono[2], Costas N. Papanicolas[1] and Fabio Montagnino[2]

[1] The Cyprus Institute, Aglantzia (Cyprus)

[2] Consorzio ARCA, Palermo (Italy)

[3] ENEA Casaccia Research Center, Rome (Italy)

Abstract

A solar multi-generation approach has been implemented through four demonstrative plants in Italy, Cyprus, Jordan and Egypt based upon solar concentrating collectors. Different design options have been developed, including technologies that have been adapted and downsized from the utility scale of CSP plants, with the aim to be integrated at building, settlement and community scale. Demo plants have been conceived as living labs in order to support the further development of the technologies in a real-life environment, supporting the local smart specialization strategies in collaboration with SMEs, local stakeholders and citizens.

Keywords: *multi-generation, solar thermal, CSP, storage, concentrating solar collectors, solar cooling, building integration, smart specialization, living labs*

1. Introduction

Global space cooling energy consumption increased by 60% between 2000 and 2010, reaching 4% of global consumption (OECD/IEA Report 2013), meanwhile the production of heat accounts for more than 50% of global final energy consumption (OECD/IEA Report 2014). The seasonal switch among the winter demand of heat and the summer demand of cold is already a characteristic of the solar belt regions, including the Mediterranean area. Therefore, specific efforts are needed in piloting innovative approaches to cover the complex mix of heat, electricity, cold and other energy driven services by an optimized harvest, storage and conversion of the solar radiation. As a matter of fact, seasonal demand can be holistically managed at a settlement level by multi-generative solar concentration systems; the collection of high quality solar radiation, mostly available in summer periods, can feed a solar cooling system in the hot days, while the same collectors can cover the moderate heat demand in winter-time. Electricity can be generated from small turbines or integrated PV panels. Residual heat can be used to drive other services, as the purification of brackish, waste water or sea water desalination. Since November 2012, such a challenge is undertaken through the Small scale Thermal Solar district units for Mediterranean communities (STS-Med) project, supported by the ENPI- CBCMED program, with the construction of 4 pilot plants:

- in Palermo, Italy, led by Consorzio ARCA - coordinator of STS-Med - in the campus of the University of Palermo, in partnership with the Italian National Agency for New Technologies, Energy and Sustainable Economic Development (ENEA) for the Thermal Energy Storage (TES) system,
- in Aglantzia, Cyprus, led by the Cyprus Institute (CyI), in the campus of the institute,
- in Markaz Belbes, Egypt, at Sekem Hospital, led by Academy of Scientific Research and Technology (ASRT) and built by Elsewedy Electric,
- in Irbid, Jordan, led by Al Balqa Applied University (ALBUN) and built by Millennium Energy Industries.

The 4 plants demonstrate that a smart integration and optimization of both commercially available and innovative solar technologies can open a way towards the goal of "zero energy" communities in the Mediterranean region (Rashad et al. 2015 and Kiwan et al. 2016).

doi:10.18086/eurosun.2016.05.06 Available at http://proceedings.ises.org

Figure 1. Novel Technologies Laboratory (left), rooftop of the University College in Irbid (right)

The buildings concerned self-produce the energy they need through sustainable systems, integrated at a settlement level, with a significant reduction of CO_2 emissions and consumption especially in seasonal peak. The design of each demo site has been adapted accordingly with the result of specific energy audits and the availability of either ground or roof space for the collectors. Local communities have been involved in awareness activities and local SMEs have been invited to take part into educational activities during the preparatory and erection phases.

In Italy, the collectors are installed in a field nearby the building and the plant is generating electricity by an existing ORC (Organic Rankine Cycle) and heat/cold with the help of an absorption chiller integrated on the HVAC system. The case-study in Cyprus is located in the premises of the Cyprus Institute in Aglanzia (district of Nicosia), Cyprus. The objective of the plant is to support the heating, cooling and hot water system of the Novel Technologies Laboratory (NTL, Figure 1, left) by reducing the use of the existing electric heat-pumps. NTL was designed to be a "near to zero energy" building (Papanicolas 2015 et al.) by a specific selection of the materials and orientation of the windows and walls, which minimize the energy demand for air-conditioning. A 14.5 kW peak power photovoltaic generator covers a part of its electricity consumption. In Jordan the collector is installed on the roof of one of the buildings at University College in Irbid (Figure 1, right). As for the Cypriot plant, the system is installed on the roof a public building (Figure 2, right). The objective of the plant is to provide heating and cooling to classrooms of the university and hot water in case of over-production. A small steam turbine can be activated to generate electricity. The pilot plant in Egypt is located in Belbes to support Sekem medical center HVAC, at 60 km from Cairo city center as the crow flies. The collector is installed on plain field next to the hospital. A small ORC turbine is generating electricity balancing the seasonal demand of cold.

2. Solar collectors

As shown in Figure 2 and Figure 3, solar fields in Cyprus, Egypt and Italy are based on North-South aligned Linear Fresnel Collectors (LFC) or Linear Fresnel Reflectors (LFR). The installed LFRs, specifically designed for integration in built environments, have been developed by Idea (Vasta 2013 et al.), an Italian company affiliated to Consorzio ARCA. In Jordan the plant relies on a Parabolic Tough Collector (PTC, Figure 3) manufactured by the Italian company Soltigua. The characteristics of the collectors are detailed in Table 1. Platforms are located at different latitudes, from 30°25'05.5"N in Egypt to 38°06'01.0"N in Italy.

Figure 2. LFR at Palermo, Italy (left) and Nicosia, Cyprus (right)

Figure 3. PTC at Irbid, Jordan (left) and LFR at Egypt Markaz Belbes (right)

Table 1. Characteristics of the solar fields

	Cyprus	Egypt	Italy	Jordan
Location	Aglantzia, on the roof of a school, next to the NTL	Markaz Belbes, nearby the Sekem medical center	University of Palermo, on the ground at ARCA premises	Irbid, roof a building of the Balqa University College
Latitude *Longitude* *Elevation (Above the sea level)*	*35°08'28.1"N* *33°22'50.7"E* *176m*	*30°25'05.5"N* *31°38'07.8"E* *35m*	*38°06'01.0"N* *13°20'37.3"E* *50m*	*32°29'13.2"N* *35°53'24.0"E* *648m*
Average DNI per year (Source: SolarGis)	2142 $kWh.m^{-2}$	1958 $kWh.m^{-2}$	1703 $kWh.m^{-2}$	2377 $kWh.m^{-2}$
Type of collector	LFR - Idea	LFR - Idea	PTC - Soltigua	LFR
Global aperture area	184.32 m^2	299.50 m^2	483.84 m^2	163.2 m^2
Thermal oil, Heat Transfer Fluid (HTF)	Duratherm 450	Therminol 66	Paratherm NF	Seriola eta 32 - Total Lubmarine
Peak thermal power	70 kW	115 kW	190 kW	85 kW
Total receiver length	32 m	52 m	84 m (3 x 28 m receivers rows)	38.56 m
Working temperatures (outlet)	170°C	140°C	280°C	240°C

All the collectors are working with thermal oil as heat transfer fluid (HTF) at different temperature: from 140°C to 280°C. The total thermal peak power of the plants is 460kW. The platform in Palermo is the main contributor with 190kW with 3 identical LFC parallel loops. Figure 4 shows a simplified layout of the solar plant installed in Sicily.

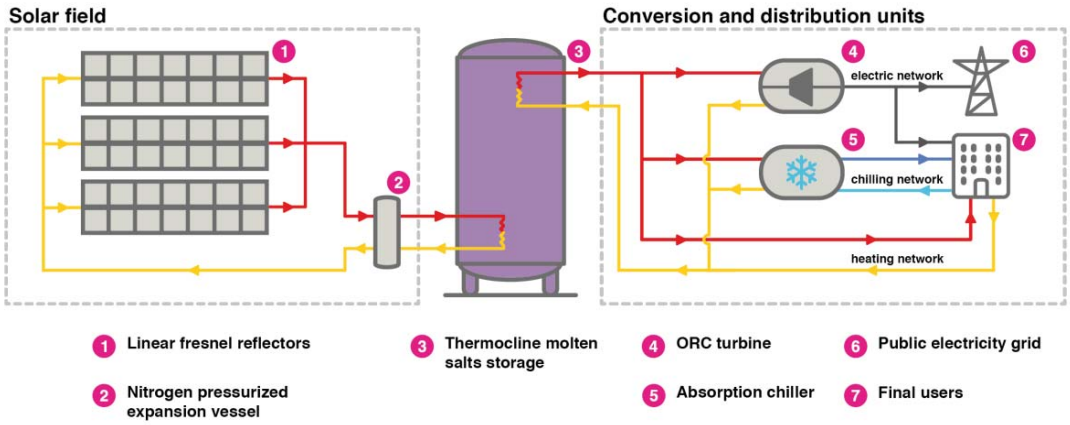

Figure 4. Layout of the field at ARCA (Sicily)

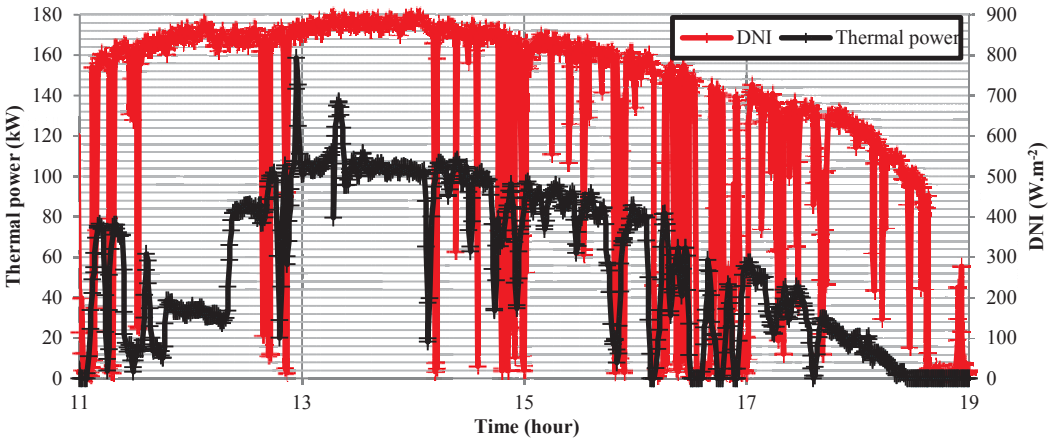

Figure 5. DNI and thermal power on the 6th of September 2016 (Italy)

The thermal power and DNI on the 6th of September 2016 are shown in Figure 5. A peak of 160kW was achieved at 12.30PM. In Cyprus 70kW peak power is installed. On the 26th of July 2016, the Fresnel collector was commissioned. Thermal power and DNI are show in Figure 6. The output power reached 68.7 kW with a DNI of 800 $W.m^{-2}$ at 12.52PM.

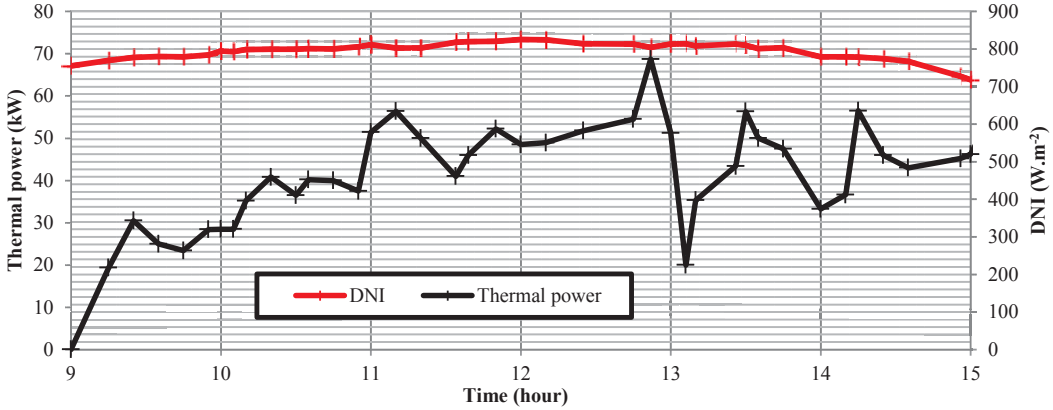

Figure 6. DNI and thermal power on the 26th of July 2016 (Cyprus)

The peak power installed in Egypt is 115kW and 85kW in Jordan. All the 4 for plants are equipped with a vacuum receiver and with the association of a secondary reflector for the LFRs in Cyprus, Egypt and Italy with estimated 90% optical efficiency. DNI is the highest in Jordan with 2377$kWh.m^{-2}$ per year. DNI in Cyprus is 2142$kWh.m^{-2}$ per year and in Egypt 1958$kWh.m^{-2}$ (Source: SolarGis Imaps, Beták et al. 2012). DNI in Palermo is the lowest with 1703 $kWh.m^{-2}$ per year. The solar fields were all completed in September 2016. Dimension of the mirrors of the 3 LFRs are identical: 0.32m x 2.000m. Cypriot LFR was the first to be installed on the island (Montenon and Fylaktos 2016). It is composed of 288 mirrors with a reflective area of 184.32 m^2, driven by 72 DC motors (4 mirrors per motor). In Egypt, the system is composed of 468 mirrors and the reflective area is 299.52 m^2, but driven by 13 DC motors (36 mirrors per motor). The Italian field is hybrid: 2 LFC modules are configured as in Egypt and the third collector is configured according to the Cypriot model. In this way it is possible to lead comparisons between the two strategies. On the one hand in Cyprus the flexibility of the field is higher but requires more maintenance due to larger number of motors: if one motor fails, the system will be only slightly impacted and can continuously operate with the rest of the 71 motors. On the other hand, the Egyptian collector relies on fewer motors, so requiring less maintenance, but if one motor has to be changed a larger area of the solar field will be impacted; furthermore, tracking angles of the motors is not independent and the whole field cannot be placed in flat position for cleaning purpose for instance. In Cyprus and Italy, HTF loops are separated from the thermal storage medium. Nonetheless, small buffers are installed in the HTF loops in order to stabilize the temperatures.

Figure 7. HTF Loop at CyI (Cyprus) : oil loop (left) and pressurized vessel (right)

As shown on the main layout (Figure 4), in Sicily, on the field installed at ARCA a buffer tank is also integrated in the HTF loop with a total volume of 800L containing 500L of thermal oil (Paratherm NF) pressurized with nitrogen at 3bar (for a thermal storage capacity of 22kWh). In Cyprus the thermal oil (Duratherm 450) is stored temporarily in an 800L tank (containing 425L of oil), pressurized with nitrogen at 3bar (Figure 7). A 3kW electric heater is wrapped around the tank to pre-heat the oil in case of cold start-up. The role of these tanks is also to stabilize the outlet temperature of the piping. Pre-heating the oil decreases the viscosity of the HTF and increases the Reynolds number to maintain it above 10,000 (turbulent flow). Based on experience, the solar absorber pipe bends at low ranges of the Reynolds number, due to thermal gradients, and it may get in contact and break the external glazing pipe. As soon as the oil inside the buffering tanks is heated to a satisfactory value, the inverter pump of the HTF loop starts. The control of the platforms in Cyprus and Italy aims to correlate the output with the real time value of the DNI. To that end, two pyrheliometers are installed on the respective sites (Figure 8).

Figure 8. Pyrheliometers at ARCA (left) and the Cyprus Institute (right)

3. Thermal storage

Thermal storage is a key element of the four platforms. It permits to buffer the production for some minutes to several hours. Details of the thermal storage in use in the 4 platforms are exposed in Table 2. In the plants built in Jordan and Egypt, the HTF is directly stored respectively at 240°C and 140°C. In both Cyprus and Italy, a heat-exchanger transfers the heat from the oil to TES system. In Cyprus thermal storage is based on water pressurized with nitrogen up to 146°C ensuring 2 hours of autonomy for cooling in summer or 4 hours for heating in winter. The same nitrogen tank is used to pressurize the thermal oil (Figure 9). Storage with water is a low cost technology and vessels are available on Cypriot market.

Table 2. Thermal storages

	Cyprus	Egypt	Italy	Jordan
Medium	Pressurized water	Thermal oil (Therminol 66)	Ternary molten salts mixture	Thermal oil (Seriola eta 32 - Total Lubmarine)
Storage Volume	2.0 m^3	2.8 m^3	8 m^3	1.3 m^3
Storage capacity	100 kWh	21 kWh	400 kWh	30 kWh
Average temperature	146°C	140°C	260°C	240°C

Figure 9. Buffer of oil, expansion vessel, thermal storage tank (left to right) at CyI (left) and molten salts storage, oil storage and expansion tank (left to right) at ARCA (right)

Safety relief-valves are installed on the tank in case of over-pressure. The developed TES integrated in the pilot plant built in Sicily includes innovative features. Different options have been reviewed. TES systems commonly applied in conventional CSP plants operate with "solar salts" (molten nitrates mixture $NaNO_3/KNO_3$ 60%/40% of weight distribution), in two-tanks heat storage system operating from 290°C (cold tank) to 385°C (hot tank) when oils are used as HTF in the solar field (Lovegrove and Stein 2012). In small CSP plants (lower than 1MW range) it is rather difficult to replicate such a complex scheme due to the lower operative temperatures (280°C maximum in Sicily) and principally due to the need of expert personnel to manage molten salts loops too. Therefore, an innovative TES system has been specifically developed in STS-Med project. It is also based on molten salts, but the management of the TES is eased. This is lower than the melting point "solar salts", which is around 220°C (Serrano et al. 2013). Hence, the temperature range is much more compatible with the above-mentioned small-medium CSP temperatures (up to 300°C). Also the "two-tanks" configuration is replaced by a single-tank system avoiding any external pumping of the molten salts and the critical management of pipelines against freezing. In the developed TES at ARCA, all the typical operations of a CSP plant of charging and discharging are achieved inside the single buffer tank where given temperature gradients and molten salts circulation are easily determined. Therefore, besides lower equipment volume and cost reduction potentials, the plant operator does not have to manage molten salts flows. Thus, the developed TES is tailored for residential users and fits into the STS-Med requirements. The developed TES system is represented in Figure 10. The operation concept is based on the properties of unmixed molten salts in the tank to thermally stratify along the vertical axis, as an effect of their low thermal conductivity and the density variability with temperature. Two heat exchangers are immersed in the zones where the temperature is lower (bottom) and higher (top) to be operated during the charging and discharging phases. In a conventional two-tanks TES systems with the high temperature tank at $T_{S\text{-}high}$ = 385°C (and the low temperature tank at $T_{S\text{-}low}$ = 290°C) about 280 m^3 of "solar salts" shall be loaded to store 20 MWh thermal energy, to drive a steam Rankine cycle.

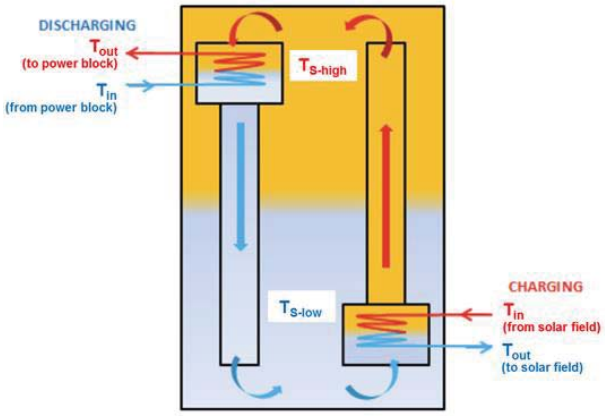

Figure 10. Optimized TES system developed for STS-Med: general scheme with explanatory working conditions (left) and prototype drawings (right)

The same principle can be applied to a smaller TES system with maximum temperature of 300°C, combined with an Organic Rankine Cycle. In the pilot plant in Sicily, TES is filled up with about 7 m^3 of eutectic ternary salt mixture (42%/15%/43% of weight distribution). Considering the reduction of the overall amount of salt, the use of a single tank instead of two tanks and the avoidance of external molten salt pumps and pipelines, the cost (€/kWh thermal) of this optimized heat storage system developed can compete with the large scale CSP benchmark.

In the framework of the STS-Med project a small TES prototype of 0.96 m^3 has been designed, built, installed and successfully tested at ENEA-Casaccia research center (Rome) in order to validate the concept before the installation in the pilot plant in Sicily. Loading, mixing, and melting procedures of the salts in the TES have been studied. The experimental results and concept validation with the prototype enhanced the design of an up-scaled TES for the demonstration plant in Palermo. Specifically, further optimizations and improvements have been performed in a "new" version of the TES installed in the STS-Med pilot plant in Sicily. This upgraded prototype is designed to work in a thermal range of 160-280°C. It is characterized by an inner volume around 8.0m^3 (1.8m diameter, 4m height) corresponding to effective heat capacity of about 400kWh (thermal). The charging/discharging thermal power averages 250/125 kW (thermal). The tank has been insulated with a 20cm coating of rock wool.

4. Cooling, heating and hot water

4.1. Cooling

Cooling is the central task of all the STS-Med platforms, due to climate considerations in the Mediterranean areas concerned by the project. The 4 plants rely on absorption chillers (Figure 11) to provide chilled water at 7°C. The global cooling capacity of the platforms averages 110.1kW. Chillers in Cyprus, Egypt and Italy are LiBr (Lithium Bromide) based, while in Jordan it is ammonia based. In Cyprus, the model used is YAZAKI WFC-SC10. It is water-fired at low temperature (88°C inlet, 83°C outlet). Its cooling capacity is 35kW with a COP (Coefficient of Performance) of 0.7.

Table 3. List of absorption chillers

	Cyprus	Egypt	Italy	Jordan
Model	YAZAKI WFC-SC10	YAZAKI SH10	Broad BCT 23	Robur ACF 60-00 HT
Type	LiBr – Single effect	LiBr – Single effect	LiBr – Double effect	Ammonia – Single effect
Firing medium	Water	Thermal oil	Thermal oil	Thermal oil
Cooling capacity	35 kW	35 kW	23 kW	17.1 kW
Inlet temperature	88°C	88°C	200°C	240°C
COP cooling	0.7	0.7	1	0.6
Heating capacity		48.3 kW	23 kW	

Figure 11. Absorption chiller and cooling tower at CyI (left) and at ARCA (right)

The heat is transferred to the absorption chiller from the thermal storage medium through a heat-exchanger (pressurized-water and water). Then the heat is stored in a 500L tank of water. This stabilizes the inlet temperature for the chiller. A cooling tower dissipates the heat from the absorber and condenser chambers (Figure 11). In Egypt the same capacity chiller is used but the heat medium is thermal oil instead of water. In Italy, the double effect absorption chiller is the most performant with a COP of 1 and it includes its own cooling tower (Figure 12). The cooling capacity is 23kW. The Jordanian chiller is a Robur HT model with a cooling capacity of 17.1kW at COP 0.6. Its working temperature is 240°C.

4.2. *Heating and hot water*

The absorption chillers in Egypt and Italy are also heating in winter with better COP than cooling. Heating capacity is 48.3 kW in Sekem and 23 kW in Palermo (Figure 11). In Cyprus the absorption chiller is simply by-passed to heat directly two water stratified tanks (2000L each). The heat is supplied to the Air Handling Units (AHU) and the Fan Coil Units (FCU) for the offices of the NTL. In Jordan, the absorption chiller is also by-passed in winter. If the available solar energy exceeds the cooling and electricity generation demands, the excess heat is released to hot water network through shell and tubular heat-exchanger. The heated water is then stored in a tank. If the excess heat exceeds the storage capacity, it is dissipated by dry cooling.

5. Electric power units

Platforms in Egypt and Italy (Figure 12) cogenerate with ORCs (Organic Rankine Cycles) fired with thermal oil. They both have an electric capacity of 10 kW and gross efficiency of 10% (Table 4) and need a cooling tower to dissipate the heat rejection. They produce electricity in parallel with heating or cooling. The ORC in Egypt works with inlet temperatures of 125°C to 150°C. In Jordan the oil exchanges its heat with a steam loop to operate a demonstrative steam turbine of 1.2kW of electric power (Figure 12).

Table 4. Power units in Egypt, Italy and Jordan

	Egypt	Italy	Jordan
Element	ORC	ORC	Steam turbine
Electric power	10 kW	10 kW	1.2 kW
Medium	Thermal oil	Thermal oil	Steam

Figure 12. Steam turbine during the installation in Irbid (left) and ORC Rank turbine in Palermo with cooling tower (right)

6. Conclusions

Nowadays solar concentration platforms are designed to produce several thermal MW and generally for electricity generation in desert places. STS-Med project demonstrated the possible application of solar concentrating technologies within integrated multi-generative plants at small/middle scale in built environment either on the ground (Egypt and Italy) either on roofs (Jordan and Cyprus). Production of heat to directly drive absorption chillers through thermal energy storage permits to avoid the stage of transformation to electricity. The residual heat can be used for electricity production with the help of ORCs. Thus, the co-generation of heat and electricity reduces the global balance of the energy consumption of

buildings and not only the electric part. The thermal storage permits to shift the production at peak load with good flexibility. In the plant built in Sicily an innovative thermal energy storage system based on the use of molten salts and specifically tailored for small scale concentrating solar applications has been integrated. The main limitation to downscale solar cooling is the lack of commercial small scale absorption chillers and ORCs. At the same time COP of absorption chiller, even with double-effect, is still poor if compared to electric heat-pumps. Efficiency of small ORC turbine is also poor and their application at the project scale (5-10 kW) can be considered as demonstrative of larger (50-100kW) applications. In this scope, the 4 plants have been conceived as living labs, introducing the technology mix into different real-life environments acting as showcases for the respective local communities. Comparative studies of design options and subsystems will permit to identify the best strategies for the overall optimization of both efficiency and cost; at the same time the local academic and technical communities will have a joint and open access to the demo facilities as platforms for future collaborations and developments.

7. Acknowledgments

The Small Scale Thermal Solar District Units for Mediterranean Communities (STS-MED) project was financed by CrossBorder Cooperation initiative funded by the European Neighbourhood and Partnership Instrument (ENPI). In its scope, the project aimed to raise 4 pilot solar plants for air-conditioning and electricity generation in four different locations: Cyprus, Jordan, Egypt and Sicily. We would like to thank the European Neighbourhood and Partnership Instrument, as well as the 14 partners in the project (Consorzio ARCA, ENEA, Sicilian Region, CEEI, CEA, IASA, Egyptian new and Renewable energy ministry, ASRT, Elsewedy Electric, Jordanian Ministry of Energy and Mineral Resources, ALBUN, Millenium Energy Industries, Cyprus Chamber of Commerce and Industry and CyI).

8. References

Beták, J., Šúri, M., Cebecauer, T., Skoczek, A., Proc. 27th European Photovoltaic Solar Energy Conference and Exhibition, Solar resource and photovoltaic electricity potential in EU Mena Region, Frankfurt, Germany, 24-28 Sep., 2012, pp. 4623-6.

Kiwan, S., Damseh, R., Venezia, L., Montagnino, F.M., Paredes, F., Techno-Economic Performance Analysis of a Concentrated Solar Polygeneration Plant in Jordan, GCREEDER 2016 at Amman, Jordan.

Lovegrove, K., Stein, W., Concentrating Solar Power Technology, 1st Edition, Principles, Developments and Applications, Woodhead Publishing, pp 370, 19 October 2012

Montenon, A., Fylaktos, N., First solar air-conditioning system in Cyprus supported by a Fresnel collector. 5th International Conference on Renewable Energy Sources & Energy Efficiency - New Challenges, 5-6th of May 2016, Nicosia, Cyprus.

OECD/IEA Report "Transition to Sustainable Buildings: Strategies and Opportunities to 2050, Paris, 2013.

OECD/IEA Report "Heating without Global Warming: Market Developments and Policy Considerations for Renewable Heat, Paris, 2014.

Papanicolas, C., Lange, M. A., Fylaktos, N., Montenon, A., Kalouris, G., Fintikakis, N., Santamouris, M. (2015), Design, construction and monitoring of a near-zero energy laboratory building in Cyprus. Advances in Building Energy Research, 1–11

Rashad, M., El-Samahy, A., Daowd, M., Amin, A., A comparative study on photovoltaic and concentrated solar thermal power plants. EUROSUNMED Symposium, Advanced materials and technologies for renewable energies (AMREN-1), EMRS Conference, Lille, France, 14-15 May 2015

Serrano-López, R., Fradera, J., Cuesta-López, S., Molten salts database for energy applications, Chemical Engineering and Processing: Process Intensification, 73, 87-102, 2013.

Vasta, S., Frazzica, A., Freni, A.,Venezia, L., Buscemi, A., Paredes, F., Montagnino, F. M., A concentrating–based solar cooling system for agri-food industry, Acts of 5th International Conference Solar Air-conditioning, Germany, 2013

Conference Proceedings

EuroSun 2016
Palma de Mallorca (Spain), 11 - 14 October 2016

A CSP plant combined with biomass CHP using ORC-technology in Brønderslev Denmark

Bengt Perers[1], Simon Furbo[1], Guofeng Yuan[1], Zhiyong Tian[1], Federico Bava[1], Peter Kvist[2], Jan Holst Rothmann[2] , Thorkil Neergaard[3] , Jørgen Røhr Jensen[4] , Per Alex Sørensen[5], Niels From[5]

Fabienne Sallaberry[6]

[1] Department of Civil Engineering, Technical University of Denmark, Lyngby (Denmark)

[2] Aalborg CSP, Aalborg (Denmark)

[3] Brönderslev Varme, Brönderslev (Denmark)

[4] NIRAS, Frederikshavn (Denmark)

[5]PlanEnergi, Skørping (Denmark)

[6]CENER, Pamplona (Spain)

Abstract

A new CSP plant combined with biomass CHP, using ORC technology, will be built and taken into operation in Brønderslev, Denmark during spring 2017. The price for Biomass is expected to increase with more and more use of this very limited energy source and then CSP will be cost effective in the long run, also in the Danish climate. Oil is used as heat transfer fluid instead of steam giving several advantages in this application for district heating at high latitudes. Total efficiencies and costs, competitive to PV plants, are expected.

Keywords: *CSP, ORC, CHP, Biomass.*

1. Introduction

In the report "ORC og dampmotor til små flisfyrede varmeværker" [1] the potential for installing ORC-units in Danish district heating plants with wood chip boilers, is calculated to approximately 30 utilities with more than 20,000 MWh in yearly heat production. The first Danish plant (4 MW heat and 0.75 MW electricity) was implemented in December 2011 in Marstal. Aalborg CSP has developed a concentrating solar collector that has been demonstrated in pilot plants. 800m^2/0.6MW in Thisted, 1350m^2/0.8MW in Brønderslev and 4000m^2 / 2.8MW in a Combi plant in Tårs.

The Technical University of Denmark (DTU) has evaluated the performance of the parabolic trough array design in these plants at temperatures up to 350°C [2, 4]. The result was an array efficiency curve with a maximum efficiency of 0.75 and a total heat loss coefficient of only 0.04-0.06 W/m^2/K, in the temperature range 100-350 °C.

The Brønderslev district heating company expects lack of biomass in the future, resulting in higher prices. They therefore want to implement a CSP-plant, to supply the ORC with hot oil from a CSP collector array in periods with enough DNI (Direct Normal Irradiance).

doi:10.18086/eurosun.2016.05.02 Available at http://proceedings.ises.org

2. The Plant Technology

The Italian Company Turboden will deliver the ORC-units for the CSP plant. In the last 15 years Turboden has implemented ORC-units in approximately 300 places. Of these, around 250 plants are heated up with oil from biomass boilers and of these 250 plants, 170 are placed in Germany, Italy and Austria. One plant using solar energy as heat source (parabolic trough) was implemented in Morocco in 2010 and 3 new plants using hot oil from parabolic troughs (PTC) are under implementation or planning in Italy. The technical efficiency when using solar as heat source is higher than 15%. Solar power with ORC is thus as efficient as photovoltaic systems.

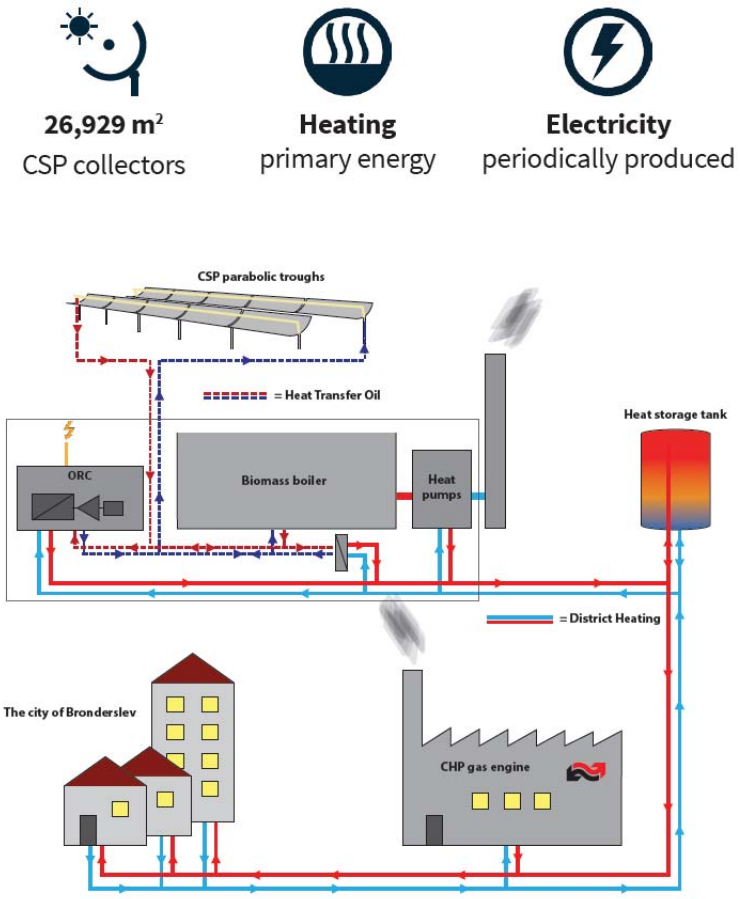

Fig.1. Flow duagram of the biomass CHP-plant with ORC-power unit and feed-in of solar thermal energy both to the ORC and District heating network. Drawing from http://www.aalborgcsp.com/

.

Compared to steam systems, ORC has the following advantages:

1) Low mechanical stress (lower pressure and temperatures in the turbine).
2) No corrosion of turbine blades. Simple start procedure.
3) No demand from continuous supervision.
4) Easy maintenance.
5) Long lifetime (more than 20 years).
6) No use of demineralized water.
7) Possible with maintenance guarantee (95 % of running hours guaranteed).

Disadvantages are the low electrical efficiency (19 – 20 %) compared to a high pressure steam turbine. Thus ORC is a proven technology and when the heat production from the cold side of the ORC unit is utilized – as it is from most biomass fueled plants – also an efficient technology.

CSP (Concentrated Solar Power) plants operating by temperatures higher than 300°C and producing power are already installed in Southern Europe. Aalborg CSP has installed several of these plants already and knows the technology.

The pilot CSP-plant in Thisted, in northern Denmark, was monitored and evaluated for high end district heating temperatures up to 120°C during July 2013 [2] see figure 2. The result was a maximum zero loss collector array efficiency of 75 % and an array heat loss coefficient as low as 0.04 W/m^2/K. Later higher temperature operation was investigated in the pilot test in Brønderslev 2015 [4] at up to 350°C giving the collector parameters 0.75 respectively 0.06 W/m^2/K.

Thus at a temperature difference of 300 K above ambient, assuming a heat loss coefficient of 0.06 W/m^2/K will mean a total heat loss as low as 18 W/m^2. Even if the direct radiation level is as low as 100 W/m^2 the net production will still be 100 W/m^2 *0.75 – 0.06 W/m^2/K *300K = 57 W/m^2. Therefore the plant will be able to deliver 300°C also with low DNI levels. Normal clear sky irradiation levels are in the range of 600-900 W/m^2. The main reason is the selective vacuum tube absorber, a very precise tracking mechanism, and stiff enough mirror- plus absorber support to keep the focal line on the absorber all the time.

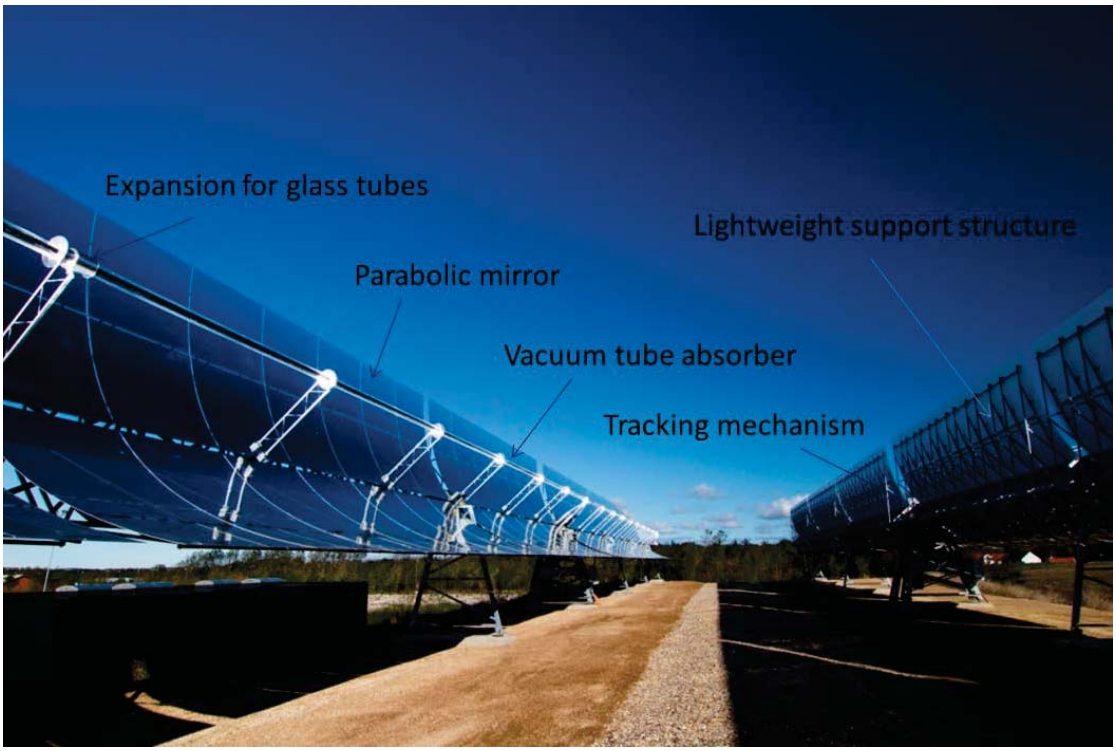

Fig.2. Close up of the Aalborg CSP concentrating collector array in Thisted (Ref. 2).

The Bøndereslev plant is now under intensive construction. See figure 3 and 4. Small improvements of the collectors have been done during the final design and construction phase of the plant that will improve the performance.

Fig 3. Photo of the CSP collector field, under construction. The collector rows are 240 m long and a total length of 480m of collectors are series connected in each series loop. (No absorbers or connecting pipes are installed in this photo).

Fig 4. Close up of one mirror element of the CSP collectors. The width is almost 6 m. Glass mirrors are used. The metal structure is optimized for low material use, but till enough stiffness in windy conditions.

3. Collector field modelling

A detailed TRNSYS model has been developed for the full size collector field, so that control and performance can be investigated in detail. The TRNSYS model is based on the modelling experiences for the 0.8 MW pilot plant in Brønderslev.

Later when the plant is in operation the model will be precisely validated and then used to check and optimize the whole plant operational performance. Then effects of for example weather and operating conditions like deviations in operating temperature from design, can be exactly taken into account and a true performance check of the collector field can be made. Also the 30 degree offset of the tracking axis from south can be accurately taken into account.

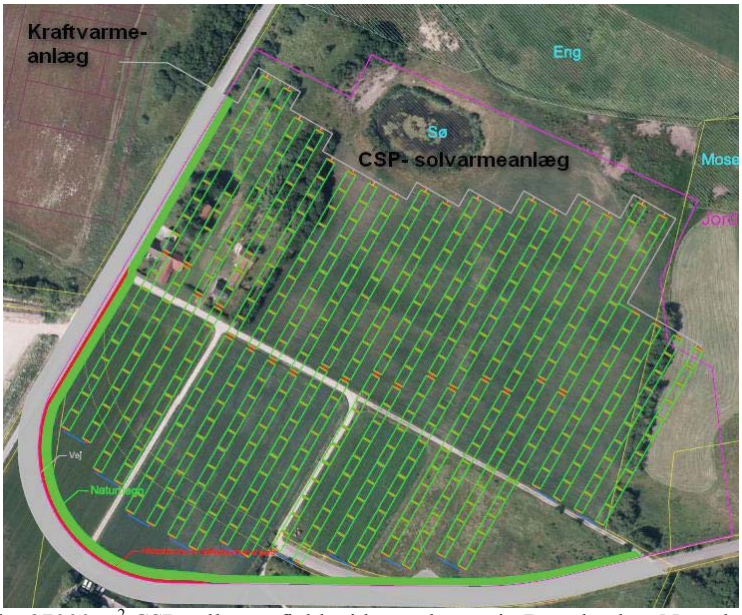

Fig 5. Photo of the 27000 m^2 CSP collector field with row layout in Brønderslev. Note that the troughs are turned approximately 30 degrees from south to match the available land area. This has been found to reduce the annual performance relatively little and was a finding in [2] giving a large flexibility in installation of such plants.

The simulation tool in TRNSYS see fig 6 and 7, is now up and running, but we await further final design information, after the construction of the plant is finished. The aim of the TRNSYS tool is also to be able to use the TRNSYS setup for continuous plant performance check and optimization of control and operation.

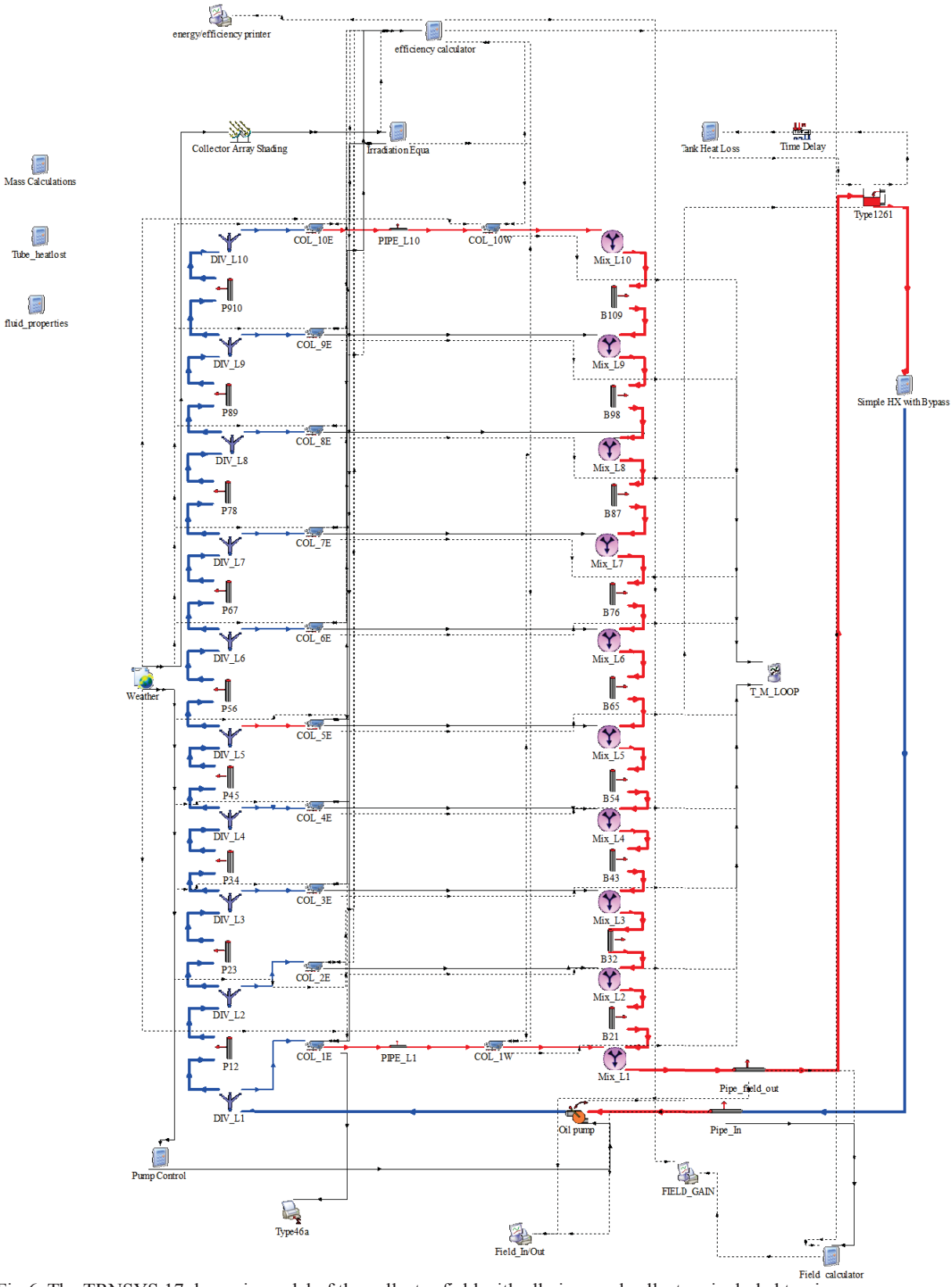

Fig 6. The TRNSYS 17 dynamic model of the collector field with all pipes and collectors included to give a very realistic simulation including transient behavior under variable weather conditions.

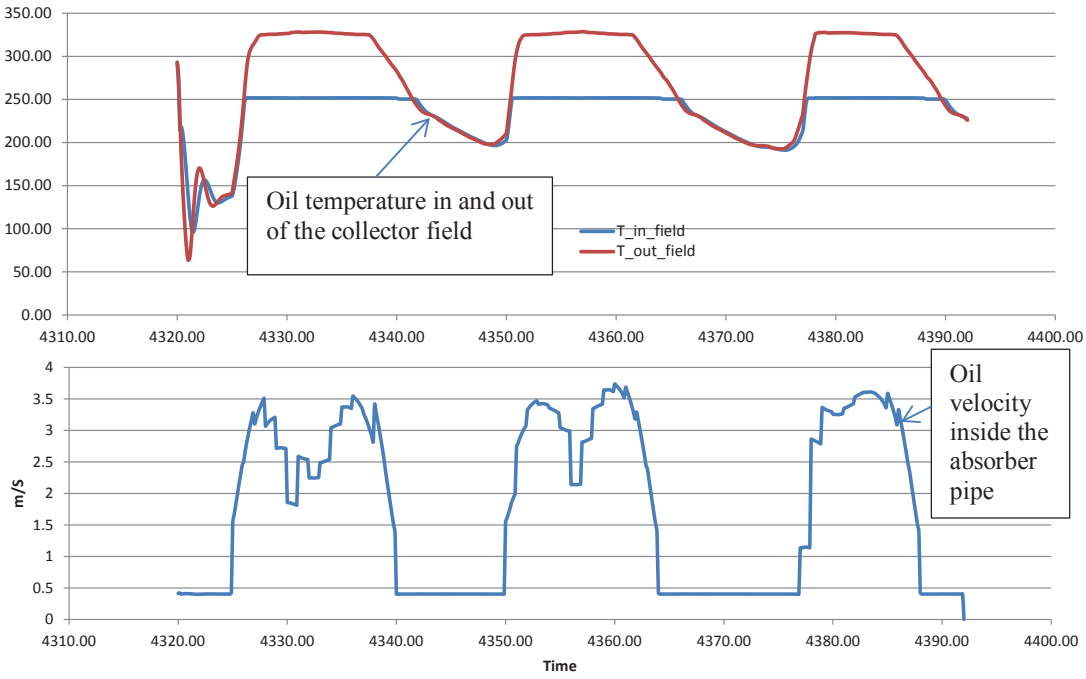

Figure 7: Simulation results for a few days in summer with variable solar radiation during the days. The flow control (lower curve) gives a constant output temperature of 330 °C (upper curve) by varying the flow according to the available radiation level and collector design parameters.

4. Conclusions

The CSP, ORC and CHP technology will be evaluated together in the Brønderslev plant in Denmark. The previous demonstration plants built in other climates indicates favorable long term performance and economy.

Pilot testing of a 0.8 MW sub array of the plant [4], show very good performance, even at these very high operating temperatures, above 300°C, in the Danish climate.

The construction work is ongoing and can be seen online [6].

5. References

[1] ORC og dampmotor til små flisfyrede varmeværker. Jan. 2011. Udført af Plan Energi for Dansk Fjernvarme 2011.

[2] Thermal performance of concentrating tracking solar collectors. Bengt Perers, Simon Furbo and Janne Dragsted. DTU Byg report R-292. August 2013.

[3] Theoretical analysis of the combination of CSP with a biomass CHP-plant using ORC-technology in Central Europe. Solar PACES 2013. R. Sterrer et al.

[4] Verification of high temperature performance for the 0.8 MW CSP test plant at Brønderslev. Bengt Perers, Simon Furbo and Janne Dragsted. DTU Byg repo6rt SR-15.03. August 2015.

[6] Web camera at Brønderslev showing the construction work.

http://www.bronderslevforsyning.dk/da/Aktuelt/solvarmeogbiomasseanlaeg.aspx

Conference Proceedings

EuroSun 2016
Palma de Mallorca (Spain), 11 - 14 October 2016

Optimal solar district cooling harvesting scenarios

Nicolas Perez-Mora[1,2], Paolo Lazzeroni[3], Vincent Canals[2], Maurizio Repetto[4] and Victor Martinez-Moll[2]

[1] SAMPOL Ingeniería y Obras, Palma of Majorca (Spain)

[2] University of Balearic Islands, Palma of Majorca (Spain)

[3] Istituto Superiore sui Sistemi Territoriali per l'Innovazione, Torino (Italy)

[4] Politecnico di Torino, Torino (Italy)

Abstract

In the Southern European countries solar thermal energy is harvested few moths per year as heating, thus, solar cooling is a suitable option to increase the yield of solar fields that supports tri-generation power plants. In this kind of facilities solar cooling integration is achieved with the use of absorption chillers and appropriated energy generation management strategies. These strategies depend on the resource availability, primary energy price and energy storage facilities.

Sizing these generation systems or planning modifications on existing ones, requires detailed studies and deep knowledge on the particular boundary conditions of the site and the possible scenarios that the power plant can be subjected at. In this work a comparison between solar system and CHP system is carried out for different repowering scenarios of an existing power plant. Different tilt angles are tried out in order to obtain the most cost-effective solution over useful life for a solar system which is size to harvest solar for cooling purposes.

Keywords: *Solar thermal, CHP, Cooling, District heating and cooling, Absorption, Optimization*

1. Introduction

Worldwide the energy panorama is rapidly changing; the appearance of renewable energies is gaining relevance in despite of conventional technologies based on fossil fuels. Nevertheless energy consumption is increasing in amount and in forms such as heating, cooling and electricity. This three forms of energy are considered the threefold of energy consumption in residential, public and commercial buildings (Sivak, 2009). Furthermore, in warm environments, the demand of cooling as form of energy is exponentially increasing, especially in developed countries where as the life standards improve the demand increases. In such places it is common to find heating demand for domestic hot water (DHW) coexisting with cooling demand for space cooling.

In warm environments solar thermal energy can be harvested few moths per year as heating, therefore solar cooling is a suitable option to increase the yield of solar fields as heating and cooling demands are complementary along the year. Such fields are usually connected to a hybrid generation plant to soften its generation variability and uncertainty.

In hybrid power plants, solar cooling integration is achieved with the use of absorption chillers, thus, enduring the power plant with poly generation. These hybrid poly generation power plants require an appropriated energy generation management strategies to maximize energy generation.

doi:10.18086/eurosun.2016.05.07 Available at http://proceedings.ises.org

Given a complex generation system, the plant manager bases management strategies on appropriated tools to support optimal decisions. Such tool shall include information regarding non-dispatchable thermal energy forecast, prices for primary energy and power plant efficiency on the different performance points.

Once the generation is sorted out, the demands can be aggregated and centralized by means of a distribution network, in those cases a District Heating and Cooling (DHC) network fulfils the transportation requirements of a centralized generation point supplying energy consumers located in various locations.

This paper present two repowering options and their possible working scenarios and it is organized as follows: next section provides an overview of the problem description. Section 3 describes the methodology used to approach the problem. Section 4 presents the result obtained and the conclusions from those are given in Section 5.

2. Problem description

The hybrid poly generation plant under study in this work is located in Majorca, Spain and constructed in 2000. The generated energy is provided to the Balearic Islands University and the Innovation centre of Balearic Islands "Parc Bit" through a DHC. The customers are the university facilities, including the student house and the sports centre and office buildings from the innovation park; in total the system provides heating and/or cooling to 25 different customers with different load profiles. The DHC network is detailed explained in (Perez-Mora et al., 2016b).

The actual cooling generation system comprises two absorption chillers of almost 2.0MW_c, two electric chillers summing 2.5MW_c, plus cooling towers and dry coolers for condensing purposes.

In the other hand, the heating generation system comprises an existing solar thermal installation with 864m^2 of solar collectors, two Combined Heat and Power (CHP) engines of 1360kW_e, biomass burner and a diesel burner as auxiliary summing 3.0MW_t. The system includes, as well, energy storages for heating and cooling; there are four tanks of 100m^3, two for cooling and two for heating. The system schematic can be seen in Fig. 1 and the generators figures and technologies can be seen in Tab. 1.

Currently the solar collector field generation is quite decreased due strong deterioration and the proper ageing of a 16 years old solar collector (Fan et al., 2009).

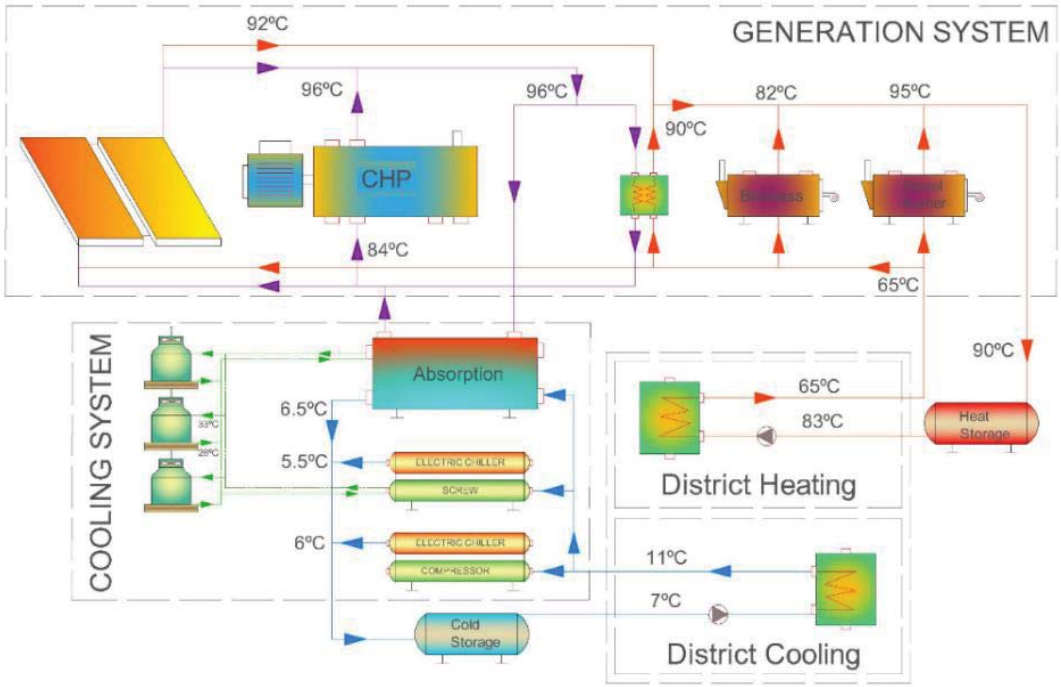

Fig. 1: Current energy generation system schematic.

Tab. 1: Current figures of installed generators at Parc Bit.

	Element	Technology	Installed Figure	Design parameters
Generation	IC Motor (2)	Diesel	2 x 1.36 MW_e	η_e=0.415; η_t=0.43
	Solar Collectors	Flat Plate	864m^2	η_0=0.76; a_1=3.5; a_2=0.002
	Biomass	Wood chip	1 MW_h	η_t=0.95
	Burner (2)	Diesel	1.2+0.8 MW_h	η_t=0.9
Cooling	Absorption (2)	Single. Li-Br	1.32 + 0.64 MW_c	η_c=0.6
	Electric Chiller	Compressor	1.2 MW_c	η_c=3.5
	Electric Chiller	Screw	1.3 MW_c	η_c=3.5
	Cooling Tower (3)	Open	3 x 4m^3	-
Storage	Heat Storage	Water	2 x 100 m^3	η_t=0.998
	Cold Storage	Water	2 x 100 m^3	η_t=0.999

2.1. Repowering scenarios

As mentioned before the hybrid poly generation power plant providing energy to the DHC was built more than 16 years ago and therefore its lifetime is coming to an end. This work studies possible scenarios that could be carried out in order to repower the existing power plant. In those scenarios only the main heating generator change is proposed, keeping the use of the auxiliary, cooling, storage and distribution systems.
In the repowering scenarios the following assumptions are taken:

- Heating system is backed up by the existing auxiliary diesel boiler,
- Biomass burner, solar collector field and CHP engines are decommissioned,
- The existing installation can be used and only the generator has to be replaced,
- Only one technology is considered at once, either CHP or solar thermal system,
- Absorption and electric chillers are able to work at any load with a fixed COP,
- The cooling towers are sufficient to fulfil the condensing requirements at any time,
- Energy storages have a fixed heat loss expressed in stored energy by hour,
- The inertia of the DHC is not taken into consideration at simulation time step,
- The heating generation temperatures matches the absorption chiller requirements,
- Heating and cooling demands must be matched by all means,
- Energy demands are measured at generation point and not at customer location, therefore delay or inertia is not taken into consideration,
- Selling electricity price from CHP is equal to the market at the feed in hour,
- Purchasing electricity price for the power plant is equal to the market plus fees and taxes,
- There is not governmental incentive for green energy generation, neither electric nor thermal,
- Requested land area is considered as part of the existing power plant and there is not extra rent cost.

The proposed repowering thermal generation system is designed to harvest the required amount of energy requested by the absorption chillers during the summer simulation. Therefore it is dimensioned so its peck generation fulfils the requirements from the existing absorption chillers. This design aims to boost solar cooling as main supplier of the District Cooling (DC) and its power calculation explained in equation 1.

$$P_{sys} = \frac{P_{abs}}{COP} = \frac{2.0MW}{0.6} \approx 3.33MW \rightarrow 3.4MW \qquad \text{(eq. 1)}$$

2.2. Solar thermal system

The proposed solar thermal system is designed to harvest the required amount of energy during the summer simulation at the first year of installation, without taking into consideration any performance loss due ageing. Therefore the collector area and tilt are dimensioned so its peck generation fulfils the requirements set form the existing absorption chillers. To do so, the collector field present the following features and design data summarized as:

- Range of tilt angle used: 20º - 65º,
- Azimuth angle used: 0º South.
- Collector performance figures are η_0=0.816; a_1=2.418; a_2=0.085,
- Collector area installed depends on the tilt angle; installation land free of charge and available,
- IAM = 1, albedo = 0.2,
- Mean temperature inside collector is 75ºC, as return from the DH or absorption can be considered 60ºC and flow to either of the options is fixed in 90ºC,
- Peak generation in summer week = 3400 kW,
- Operation and Maintenance (O&M) cost is fixed in 1€/MWh generated,
- Approximated cost of installation = 248€/m^2,(Bava et al., 2015)
- Useful life: 25 years.

Accordingly, solar generation can be used either directly for heating along the year for the customers in the District Heating (DH) or for cooling being converted with absorption chillers for the users in DC. In addition to the solar generation field, the existing heating and cooling storages are kept to improve solar performance. The heating storage being used as buffer, is able to provide a constant output temperature to the DH or the absorption chiller, meanwhile, the cooling storage helps increasing system reliability and improving cooling generation performance. Moreover, the solar generation is backed up by the diesel auxiliary boiler which provides the energy shortages that may occur during operation. In the same way, electric chillers back up cooling generation in case of shortage. In figure 2 the location for new solar collector field is shown, the total area of the addressed land is about 20.000m^2.

Solar generation forecast is required during the power plant daily optimization, to acquire such information generation forecast can be made by using historical data related with climatic information. The most relevant information can be extracted from irradiation and temperature at the power plant site and it is used to improve forecasting accuracy (Inman et al., 2013; Perez-Mora et al., 2015)(Perez-Mora et al., 2015).

Fig. 2: New solar system location.

2.3. CHP system

The proposed diesel CHP system is, as well, designed to harvest the absorption chiller requested heating energy during the summer simulation. Therefore the heat to be recovered fulfils the requirements set form the existing absorption chillers. The CHP system is designed with generation flexibility by adding two

engines of half of the required power instead of a single unit. The CHP system present the following features and design data summarized as:

- 2 CHP diesel engines of 1700kW$_t$,
- CHP performance figures are η_e=0.45; η_t=0.45,
- Installation site and pipework already existing and free of charge,
- Flue smokes recovered at a heat exchanger which output temperature is 90ºC,
- High temperature circuit heat recuperation output temperature is 90ºC,
- Nominal heating generation = 3400 kW$_t$,
- Nominal electricity generation = 3400 kW$_e$,
- O&M cost is fixed in 20€/MWh$_e$ generated, overall maintenance included,
- CHP electricity price equal to the wholesale market,
- Approximated cost of installation = 265€/kW$_t$,
- O&M stops not included on the simulation. Motor availability = 100%,
- Useful life: 25 years, including overall,
- Capital cost of installation turnkey = 900.000€.

In the same way as in solar, the heating generation can be used in both DH directly or in DC once is converted by the absorption chillers. In addition to the CHP system, the existing heating and cooling storages are kept to improve power plant performance. Moreover, the diesel boiler and electric chillers as kept as auxiliary systems in case of power shortage.

In this case the fuel price uncertainty impacts harder than in the previous case since is the only and main energy source for heating generation at the power plant. This system is tied, as well, to the wholesale energy price which variations affect in two ways to the generation; positively when selling electricity from the CHP and negatively when generating cooling with the electric chillers.

2.4. Proposed scenarios

In order to study several cases where the two proposed systems can be compared and evaluated the scenarios are created by the variation of selected figures. The following ranges and variables are modified:

- Tilt angle and collector area. The tilt is ranged from 20º to 65º in 5º step. The area is calculated so the peak power in the summer week is equal to 3400kW$_t$.
- Fuel price, the variability of the Brent crude oil price impacts strongly on CHP generation, moreover when the auxiliary system is fed with diesel as well.
  The purchase diesel prices used range from 0.3€/l to 1.0€/l with a 0.1€/l step; such values depend on Brent crude oil price and national taxes. As an example, for a given Brent price of 50$ the price per litre is 0.4€/l and 150$ correspond to 1.0€/l. These variations bring a huge uncertainty for the power plant manager and energy consumers.
- Wholesale price, OMIE, hourly values of electric energy price. The average price of OMIE has been increasing rapidly in the past decade. The values vary hourly and there are great price differences among seasons, even though the daily trend is similar. The values for the selected weeks are shown in figure 3. To create new scenarios the shape of curve and trend are kept the same and the hourly figures are increased by a percentage. The value of increasing percentages range from 0% to 50% increase with a 5% step.

To compare the different scenarios four weeks, considered standard demand wise, are selected. Such weeks are considered representative for the whole year, and thus, its demand is used as annual demand once is multiplied by an annual conversion factor. Figure 3 shows wholesale energy price, heating and cooling demand on the selected weeks. In table 2 the energy loads for the different weeks are shown.

Tab. 2: Heating and cooling demands in the DHC

Week	Dates	Heating	Cooling
Winter	19/1/15 – 25/1/15	219.68MWh	3.50 MWh
Spring	20/4/15 – 26/4/15	76.70 MWh	10.66 MWh
Summer	20/7/15 – 26/4/15	8.15 MWh	142.53 MWh
Autumn	19/10/15 – 25/10/15	39.23 MWh	33.76 MWh
TOTAL	Annual	4481 MWh	2483 MWh

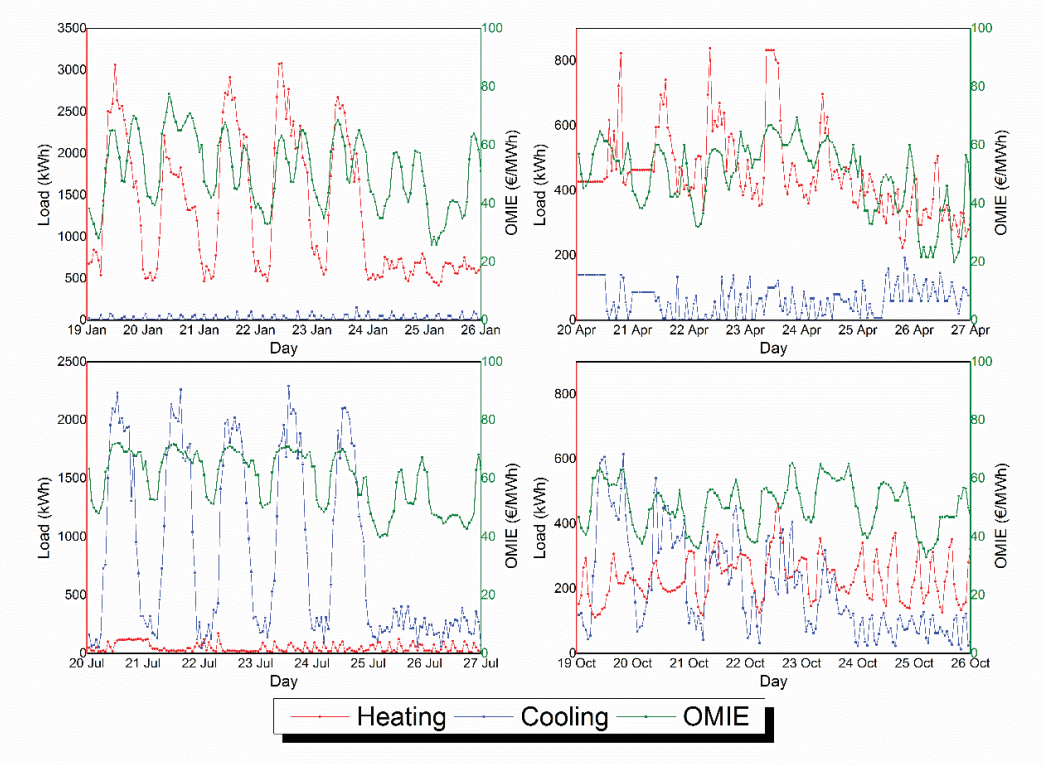

Fig. 3: Typical week loads and OMIE price.

3. Methodology

The methodology followed to compare the different scenarios and systems is explained in this section. To study the proposed scenarios it is necessary to develop an optimization tool to find the best fitting between generation and demand. Besides the detailed generation knowledge of the power plant, to achieve a proper energy curve fitting, an accurate estimation of the solar thermal generation, cooling energy demand and wholesale price of electricity is required; in this work, to run simulations of scenarios, historical values are used from the year 2015.

Creating a plant simulator to include such information into the model attempts to improve the generation strategies by reducing expenses and maximizing revenues. Once this model is operational and includes the requested information, a decision maker tool, based on Mixed Integer Linear Programming (MILP) (Carpaneto et al., 2015), is used. This tool supports the plant manager decision process while aiming to optimize heating and cooling energy generation.

In this work a tool is proposed to optimize the generation of a hybrid poly generation plant. The tool, XEMS13, has been developed in the Energy Department of Politecnico di Torino (Italy) and some parts have been developed in collaboration with the company Sampol Ingenieria y Obras (Spain). The tool is extensively explained on (Perez-Mora et al., 2016a).

The optimization tool is used to set new scenarios and configurations for heating and cooling generation and to seek optimal demand matching. The savings coming from primary energy consumptions are compared with the investment cost of such system modification during its lifetime to determine the suitability of the investment. In particular, four relevant weeks are selected, one for each season of the year. These four weeks represent the whole year in terms of demand diversity, and therefore, the economic results calculated in the simulations can be extrapolated to a whole year.

In a first instance, different tilt angles are used to create different solar generation scenarios. The tilt angle ranges from 20º to 65º, covering from summer to winter solar generation optimization. Once those scenarios are set with different angles and a range of fuel and wholesale energy prices, the best tilt angle is selected for the purpose by looking to the economic expenses along the year.

Accordingly, to calculate the generation during the useful life of the solar system the annual generation is multiplied times the useful life, without taking into account the effects of ageing.

The better optimized solar system is then compared with the CHP system to calculate savings on O&M. Those savings are, afterwards, compared with the capital cost of both systems in order to find the scenarios where each system is more interesting. Such comparison brings then the conclusions for the different systems and its influences from scenarios.

To compare the results, Interest Rate of Return (IRR) of the system cost, fuel or primary energy price increases are not considered during the systems useful life. Energy price and fuel are modified to generate different scenarios, but they fixed along the useful life of the system.

4. Results

In this section the results obtained by the optimization tool, XEMS 13, are shown.
At first the solar generation calculated using the different tilt angles presented along with the calculated collector area for each scenario. Using the solar generation and DHC demand profiles, the power plant optimization is carried out to compare the influence of a field optimized for summer, winter or annual generation. From the studied options the one serving better the purpose of this work is selected.
The final economic results from the solar collector field is then compared with the results given by the CHP system and their investment costs.

4.1. Solar generation

The first obtained results are the solar generation depending on the tilt angle used. As mentioned before, the solar collector area is dimension so its peak generation on the summer week is equal to 3400kW$_t$. This procedure brings along a calculation of the required solar collector area for each tilt angle. Obviously, the collector area increases with the increase of tilt angle since the lower angles provide its maximum generation during summer. In figure 4 it is show as well the weekly generation of the proposed solar system for each tilt in MWh. The generation shown is by means of total collector installed area. This fact is the reason why the summer week generation is more or less steady comparing with the winter generation which increases rapidly with the increase of tilt.

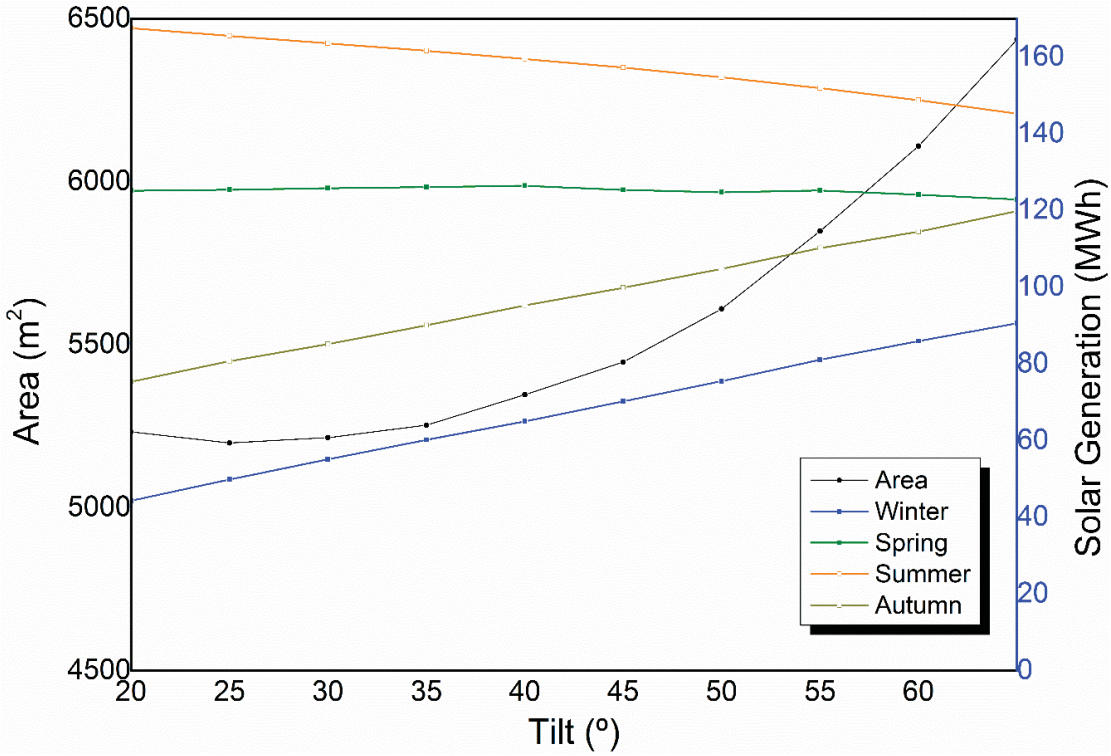

Fig. 4: Solar generation and collector area depending on tilt angle.

The largest solar collector area calculated for any tilt is 6436m^2, being the lower solar collector area equal to 5198m^2, both collector field sizes are able to fit in the proposed land. A larger solar collector area increases linearly the initial investment on the system.

4.2. Solar optimization

Once the solar generation is calculated for the different tilts, the system optimization is carried out. In this optimization the whole system is simulated, including cooling, auxiliary systems and storages. As result, the economic cost of running the plant is given, this result is influenced by the different scenarios proposed in which wholesale energy market and fuel prices are modified.

From those simulations the results show the generation cost for the selected four weeks as a 3D map, as could be obvious, the higher the fuel and energy price is the higher the operation of the power plant becomes. In figure 5 the O&M cost for the selected four weeks on the ten proposed cases are shown and it is possible see how the O&M cost varies in the different scenarios. The figure shows as well how the variation of fuel and wholesale price affects in the same way to all the scenarios, and thus, the result maps are parallel surfaces. The result surfaces of the different scenarios decrease their generation cost with the increase of solar tilt angle, being the most expensive O&M for a 20º tilt angle and the cheapest for 65º tilt angle. It is possible notice than the fuel price increase has a stronger impact in the final power plant operation cost than the wholesale energy price increase.

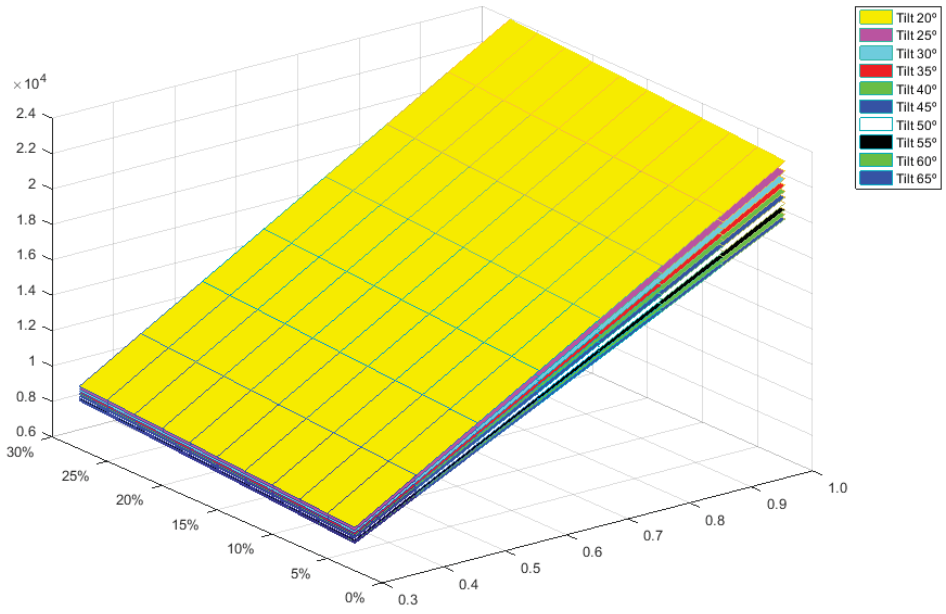

Fig. 5: Solar system tilts generation cost.

The cost for power plant operation is calculated as the sum of solar O&M cost plus the O&M cost of auxiliary systems at the power plant and is shown in figure 6. Solar O&M is fixed in 1€/MWh$_t$ generated at the collector field. The scenario selected to show the power plant generation cost in figure 6 is the one corresponding with the situation nowadays, the figures for the wholesale market correspond to the 0% price increase and the cost per litre of fuel is 0.4€/l. Nevertheless, this value does not influence how the final result looks like, as has been shown the generation cost are parallel surfaces for the different tilt angles, therefore, the only significant variable is the tilt angle. In the figure 6 is shown how the increase of annual solar generation increases, and thus, the solar O&M cost with the increasing tilt angle; this is due the increase of solar collector area. In the other hand, the operation cost decreases with increasing tilt angle, this is due the increase of annual solar yield. Figure 6 also shows the final cost of the solar collector field repowering plus the O&M cost of the whole power plant, including solar field, calculated for a useful life of 25 years and

excluding ageing impact. The cheapest solution taking into consideration generation cost and initial investment is given for a tilt angle of 45º. In this scenario the solar annual yield is 5449MWh which represents a solar fraction of 63.22% of the total heating and cooling demand. The total installed area of solar collectors is equal to 5446m^2 which corresponds to a investment cost of 1.352.000€.

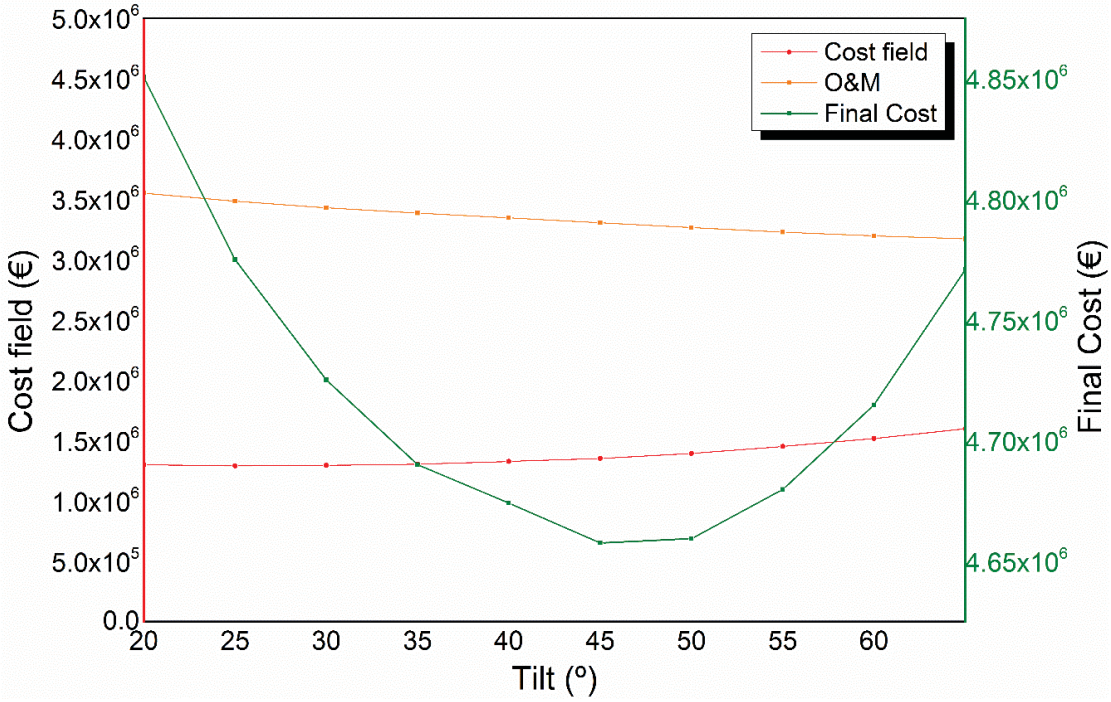

Fig. 6: Solar system total cost over useful life.

4.3. Repowering scenarios comparison

At last, the two proposed system are compared in this section. As shown in the previous section the tilt angle case which provides the most cost effective solution is 45º, therefore, this scenario is compared against the CHP scenario. To do so, systems operation costs through their useful life plus the capital cost of purchasing the systems are compared. For both systems the assumed useful life is 25 years.

In figure 7A, is shown the O&M cost over a year of the CHP system ($O\&M_{CHP}$), in the proposed scenarios and in figure 7B, the O&M cost over a year for the solar system are shown ($O\&M_{sol}$). In figure 7A it is possible notice that for some scenarios the cost of O&M in the CHP is negative, this means that it is profitable to run the CHP even when the thermal energy is not used. Those scenarios occur when the fuel is very cheap and the wholesale energy market price, OMIE, is very high, as happens for instance when the CHP generation is subsidized by electric generation.

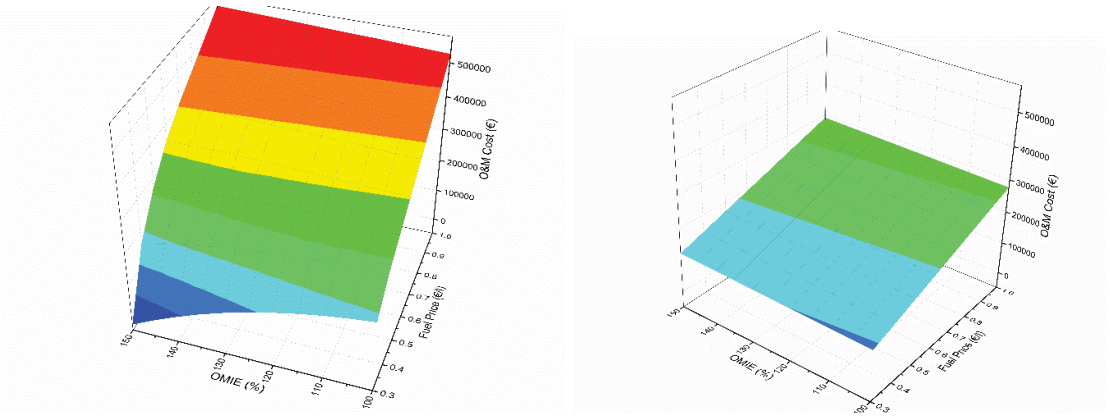

Fig. 7: O&M cost over a year for different scenarios for A) CHP system and B) Solar system.

In figure 8 the final cost of the systems over their useful life are compared, the calculation is done according to equation 2. The result given by equation 2 is positive for any scenario where it is more profitable to install a CHP system instead of a solar system. The useful life for both systems is fixed in 25 years. Figure 8 shows how most of the scenarios give negative values, this means that the solar generation system is more profitable than the CHP scenarios. The purple line is used as break-even point to separate scenarios where it is better to install a CHP system or solar system. The scenarios when is better to install a CHP system have, at least, a minimum increase of electricity price of 20% and the maximum fuel cost of 0.4€/l.

$$Result_{sys} = \left(C_{sol} + \sum_{n=1}^{25} O\&M_{sol_n}\right) - \left(C_{CHP} + \sum_{n=1}^{25} O\&M_{CHP_n}\right) \qquad \text{(eq. 2)}$$

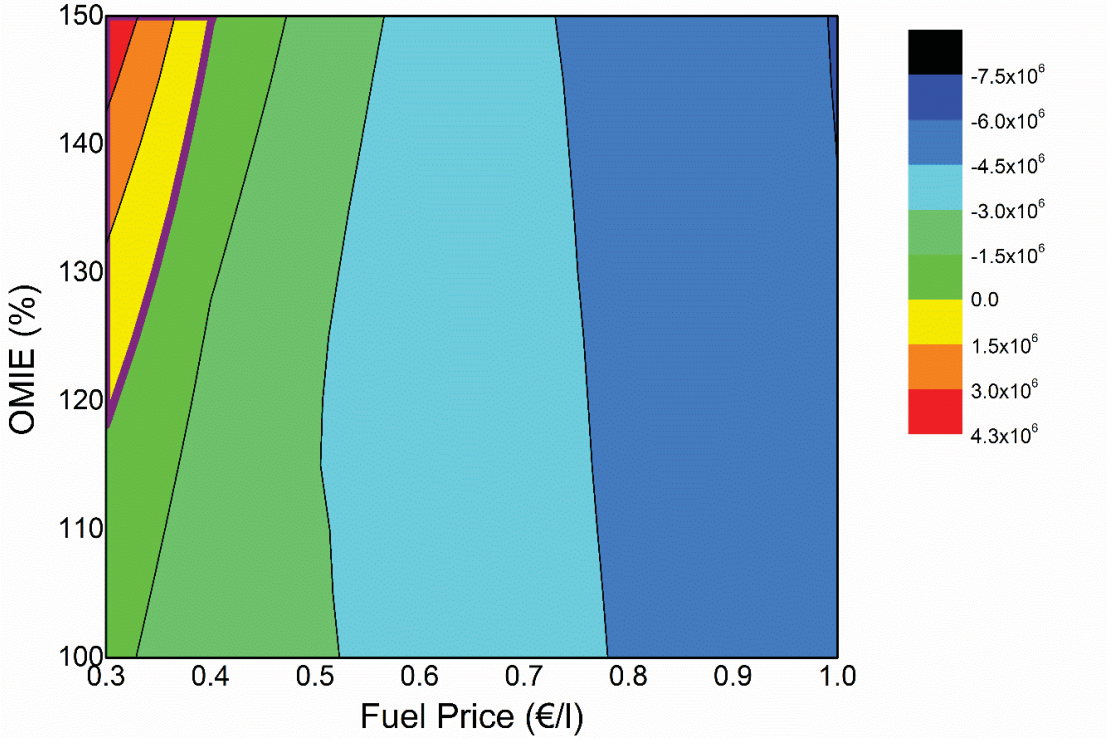

Fig. 8: Total cost comparison over useful life.

5. Conclusions

In the present work a comparison between different repowering scenarios for an existing power plant has been carried out. The different scenarios include solar system configurations and a CHP system. The comparison is made with help of an energy optimizer, XEMS13, by means of generation cost of the whole system.

The first step taken is to select the optimum tilt angle of the solar collector field, to do so, the system is optimized using four typical weeks. The best performing tilt angle, in annual minimum generation cost, is 45º, followed closely by 50º, therefore, it can be concluded than, for the given demands in this case, the system is more economic when it is annually optimized. Even if the power is dimensioned to fulfil cooling requirements in summer, the presence of storage motivates the annual optimization over the summer optimization. The large collector area required to fulfil cooling requirement when the system is winter optimized makes it very expensive comparing with the other optimization cases.

In solar system calculation over its useful life, ageing is not taken into consideration as it is very difficult to estimate the real efficiency drop on the collectors and how it will affect the system performance. In the same way, the cost of land renting for the new solar collector field is not accounted in the calculations as it is considered part of the existing power plant land. If those two factors are taken into consideration the

comparison with CHP system shown in figure 8 would present more scenarios where the CHP system overrules the installation of a solar collector field.
Nevertheless, figure 8 shows how most of the scenarios suggest the installation of a solar collector field against a CHP system. This is mainly due a high O&M cost for the CHP system which represent almost twice the cost of the solar system O&M, the relation can be seen in figure 7, and the fact that the solar system cost, 1.352.000€ is greater than the CHP system, 900.000€, but the difference pays of along its useful life. The cost of energy, regardless if heating or cooling in a mix like the given on this DHC, on a scenario as the current one where the cost of the fuel can be considered 0.4€/l and the wholesale price is taken from year 2015, is for the solar system 19.52€/MWh and for CHP system 32.19€/MWh. These values evidence that currently and with no subsidies were taken into account, it is better to repower the power plant with the installation of a solar system over a CHP system.

6. Acknowledgements

This work is supported by the European Union under FP7 grant contract 'Solar Heat Integration Network' (SHINE) and the fellowship at Sampol Ingeniería y Obras S.A. (317085) in the framework of Marie-Curie initial research training network (ITN).

References

Bava, F., Furbo, S., Perers, B., 2015. Simulation of a Solar Collector Array Consisting of two Types of Solar Collectors, with and Without Convection Barrier. Energy Procedia 70, 4–12. doi:10.1016/j.egypro.2015.02.091

Carpaneto, E., Lazzeroni, P., Repetto, M., 2015. Optimal integration of solar energy in a district heating network. Renew. Energy 75, 714–721. doi:http://dx.doi.org/10.1016/j.renene.2014.10.055

Fan, J., Chen, Z., Furbo, S., Perers, B., Karlsson, B., 2009. Efficiency and lifetime of solar collectors for solar heating plants. Proc. ISES Sol. World Congr. 2009 Renew. Energy Shap. Our Futur. 331–340.

Inman, R.H., Pedro, H.T.C., Coimbra, C.F.M., 2013. Solar Forecasting Methods for Renewable Energy Integration. Prog. Energy Combust. Sci. 39, 535–576. doi:10.1016/j.pecs.2013.06.002

Perez-Mora, N., Canals, V., Martínez-Moll, V., 2015. Short-Term Spanish Aggregated Solar Energy Forecast, in: Advances in Computational Intelligence. Springer-Verlag Berlin Heidelberg 2011, Palma de Mallorca, pp. 307–319. doi:10.1007/978-3-319-19222-2_26

Perez-Mora, N., Lazzeroni, P., Repetto, M., 2016a. XEMS13 : An Hybrid-Energy Generation Management System. IEEE eXpress 6.

Perez-Mora, N., Martinez-Moll, V., Canals, V., 2016b. DHC Load Management Using Demand Forecast. Energy Procedia 91, 557–566. doi:10.1016/j.egypro.2016.06.198

Sivak, M., 2009. Potential energy demand for cooling in the 50 largest metropolitan areas of the world: Implications for developing countries. Energy Policy 37, 1382–1384. doi:10.1016/j.enpol.2008.11.031

Conference Proceedings

EuroSun 2016
Palma de Mallorca (Spain), 11 - 14 October 2016

Renewable District Heating and Cooling in a Technology Park in Catalonia

Saad Saleem, Alaia Sola, Laura Sisó and Jaume Salom

Thermal Energy and Building Performance Area, IREC, Sant Adrià del Besòs (Spain)

Abstract

As part of the SmartReflex project, supported by the Intelligent Energy Europe Programme, the region of Catalonia is performing a study to increase the number of smart and flexible district heating and cooling (DHC) systems with a high percentage of renewable energy sources (RES). This regional strategy includes analysis of case studies for development of new DHC and the integration of renewable energy in existing DHC.

One case study is of a Commercial Technology Park. A detailed study to design a new DHC plant, including DHC demand characterization, shall be carried out using energyPRO, incorporating combinations of several renewable energy technologies comprising biomass, geothermal heat exchanger and solar cooling.

The objective is to evaluate the environmental, technical and economic feasibility of the RES DHC and which combination of renewable energies is best suited for this new DHC.

Keywords: *Solar cooling, district heating and cooling, smart cities, energy infrastructure*

1. Introduction

The region of Catalonia is located in north east Spain, next to the Mediterranean Sea and bordering France at the Pyrenees. Having various climatic zones, Catalonia has different characteristics that justify the demand of establishing district heating and cooling (DHC) networks over its territory. As of 2015, Catalonia had 84 district heating and cooling networks, according to the Spanish association of district heating and cooling (ADHAC). Majority of the networks are small heating networks and four of them provide heating and cooling simultaneously. Biomass is the main renewable energy source used in the small networks.

As part of the SmartReflex project (Smart and Flexible 100 % Renewable District Heating and Cooling Systems for European Cities, 2016), supported by the Intelligent Energy Europe Programme, the region of Catalonia (along with five other European regions) is pursuing different activities to increase the number of smart and flexible district heating and cooling systems with a high percentage of renewable energy sources including solar, biomass, biogas and geothermal energy. One of the activities is the performance of studies to promote the construction of new networks by proving their technical and economic feasibility.

This paper presents the results of the case study named “Parc de l´Alba”, which is a Technology Park in Cerdanyola del Vallès (near Barcelona) in Catalonia, Spain. Currently, the Park comprises of a Particle Accelerator (Synchrotron), a data center and some office buildings. In the coming years, there is a forecast of construction of several non-residential buildings, implying an increase in the cooling, heating and electricity demands. The new consumers shall be mainly office buildings and data centers. An existing Combined Heat and Power plant (ST-4) satisfies the present day demand of the existing DHC network. The components of ST-4 plant are shown in Fig. 1. A new plant (ST-5) shall be built in the future along with an extension of the DHC network in order to accommodate the increased demand. By 2020, there will be a total of 9 buildings with total floor area being 112,230 m^2 . The large area indicates a high demand of cooling and heating and thus is an encouragement to integrate renewable energy in the district heating and cooling plant.

doi:10.18086/eurosun.2016.05.11 Available at http://proceedings.ises.org

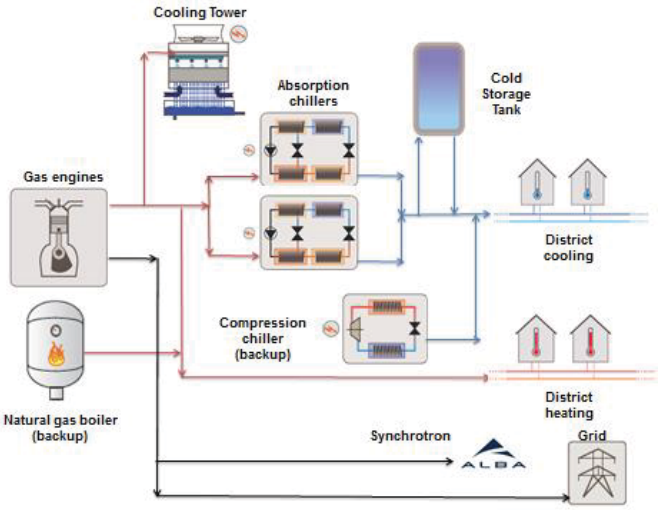

Fig. 1 Scheme of operation of the existing ST-4 plant at Parc de l'Alba

A detailed study to design the new DHC plant is carried out using the EnergyPRO (EMD International A/S, 2016) software, by performing simulations from present day (2016) till 2020. The plant will incorporate several combinations of renewable energy technologies.

2. Objectives and Methodology

The main objective is to determine if the construction of a new RES DHC is an environmental, technical and economically feasible option and which combination of renewable energies is best suited for this new DHC. The most feasible options(s) shall be decided by several Key Performance Indicators (KPIs), namely the Net Present Value (NPV), primary energy consumption and carbon dioxide (CO_2) emissions obtained in each scenario.

Two key goals must be fulfilled to reach this objective:

- To model the energy demand growth until 2020, including demand characterizations of space heating, space cooling and Domestic Hot Water (DHW) of the new consumers
- To create 5-years scenarios incorporating several renewable energy sources (RES) in the DHC plants comprising biogas, biomass, geothermal heat pumps and solar thermal cooling.

3. Base model validation

As an initial step, a base model was created in 2015 by obtaining real data from the plant (from 2014); validation was done by comparing simulation results with the real plant operation. This was done to ensure that analysis of future scenarios will be accurate.

EnergyPRO (version 4.4) is a powerful and flexible computing tool to model district heating and cooling systems. On the basis of several inputs such as the demand profile, meteorological conditions, efficiencies and capacities of various energy conversion units and tariffs, energyPRO calculates annual productions in steps of typically one hour, giving a comprehensive output on economics, emissions and operational strategy. Instead of the traditional approach of chronological hour-by-hour calculations of energy production, energyPRO is able to place productions in the most favorable time periods of the year, i.e., in the cheapest production unit /tariff combination, and so on, until the complete demand is met or there is no more production capacity left of the energy conversion units in the model.

Time Series, which are data sets of typically 8,760 time steps, are an integral part of the energyPRO software. Hourly temperature and solar irradiation data for Barcelona were input to the software as Time Series, along with some other time series to generate the Spanish electricity markets (to consider the changes

in electricity pool price). For the base model, Tab. 1 shows the details of the energy conversion units which were provided as input to the software.

Tab. 1 Details of energy conversion units and cold storage unit at Parc de l' Alba presently (2015)

Unit type	Quantity	Specifications (each unit)	Comments
Cogeneration Engines	3	3.28 MW_{th}; 3.35 MW_e; η_{el} = 44.9%	Turned on simultaneously whenever electricity spot markets are high
Single Effect Absorption Chiller	1	3 MW_c; COP = 0.7	Driven by hot water from the engines at 90 ºC
Double Effect Absorption Chiller	1	5 MW_c; COP = 1.3	Driven by exhaust gases of the engines at 398 ºC
Natural gas boiler	1	5 MW_{th}; η_{th} = 60%	Back-up
Compression Chiller	1	5 MW_c; COP = 5	Back-up
Cold water storage tank	1	4000 m^3; 21 MWh_c	
Total plant capacity: 8.0 MW_c , 9.8MW_{th} and 10.1 MW_e			

Tab. 2 shows the various revenues generated by the ST-4 plant in 2015, while Tab. 3 and Tab. 4 show the expenses incurred. Details of the two consumers served by the plant, i.e. Synchrotron facilities and an office building (referred to as "Plot 1") are shown in Tab. 5.

Tab. 2 Prices for heating, cooling and electricity sales at Parc de l'Alba for base model (2015)

Payment	Value for heating	Value for cooling	Value for electricity (Synchrotron)	Value for electricity (grid)
Connection payment	48.21 €/kW_{th} connected	145.77 €/kW_c connected	-	-
Capacity payment	13.98 €/kW_{th}/ year	23.01 €/kW_c /year	617,132 €/year	529,193 €/year
Variable price	34.84 €/MWh_{th} sold	34.84 €/MWh_c sold	114.24 €/MWh_e sold	113.20 €/MWh_e sold

Tab. 3 Fuel expenditure at Parc de l' Alba for base model (2015)

Fuel	Value
Natural gas	0.402 €/m^3
	37.78 €/MWh
Electricity imported	40.73 €/MWh_e

Tab. 4 Maintenance expenditure at Parc de l'Alba for base model (2015)

Maintenance type	Value
Fixed maintenance	245,064 €/year
Variable maintenance	13.27 €/MWh_e from gas engines
Overhaul of engines	6.83 €/hour operation

Tab. 5 Energy demands at Parc de l' Alba for base model (2015)

Type of demand	Consumer	Value
Cooling demand	Synchrotron	21,710 MWh_c
	Plot 1	651 MWh_c
Heating demand	Synchrotron	895 MWh_{th}
	Plot 1	532 MWh_{th}
Electricity demand	Synchrotron	20,419 MWh_e
	In-house consumption and losses	5,314 MWh_e

4. Key Performance Indicators

After the base model validation, simulation models were created for the years 2016, 2017, 2018 and 2020 (2019 is assumed to have identical performance as 2018) incorporating new demands. Different combinations of RES were used to satisfy this demand. The best combination was evaluated on the basis of CO_2 emissions, Primary Energy consumption and Net Present Value (NPV)

The CO_2 emissions were calculated by the software simulation once the user had entered specific emission factors of each fuel, while primary energy consumption was calculated by multiplying the fuel consumption with their respective primary energy factors (PEFs). Specific emission factors and PEFs were taken from a Joint Resolution of the Ministries of Industry, Energy and Tourism and Ministry of Development (Resolución conjunta de los Ministerios de Industria, Energía y Turismo, y Ministerio de Fomento, 2016) of Spain. They are shown in Tab. 6.

Tab. 6 Specific emission factors and Primary Energy Factors for fuels used in Parc de l' Alba

Fuel	Specific emission factor (kg CO_2/unit fuel)	Primary Energy Factor
Imported Electricity	0.357 kg/kWh	2.368
Natural gas	2.681 kg/m^3	1.195
Biogas	0.62 kg/m^3	0.500
Biomass	0.0621 kg/kg	0.034

The NPV is basically the difference in the between present value of cash inflows and present value of cash outflows. A positive NPV indicates that the projected earnings exceed the expected costs, while it is the other way around for a negative NPV. To calculate NPV for each scenario, an extensive economic calculation is done by construction of Profit and Loss (P & L) sheets from the present year (2016) up to the end of concession period (2037) for each scenario, as explained by Ross et al. (2014) in Fundamentals of Corporate Finance. The NPV is calculated by eq. 1.

$$NPV = -C_0 + \sum_{t=1}^{T} \frac{C_t}{(1+i)^t} \quad \text{(eq. 1)}$$

Where

C_0 (€) = Free Cash Flow in year zero, i.e., in 2016

T (years) = Lifetime of technology (21 years)

i (%) = Interest rate (assumed as 10%)

C_t (€) = Free Cash flow in year‘t’

The Free Cash Flow in each year is calculated by eq. 2.

$$Free\ cash\ flow = Operating\ Cash\ Flow - Increase\ in\ Working\ capital - CAPEX \quad \text{(eq. 2)}$$

CAPEX refers to the capital expenditure. The inflation applied to natural gas prices, variable and fixed prices of heating and cooling was 7.48%, which is the increase in gas prices in Spain in the past 13 years according to International Energy Agency (IEA, Energy Policies of IEA countries – Spain 2015 Review). Similarly, an inflation of 9.72% was applied to variable price of electricity, as per IEA. For all other revenues and expenses, the inflation was assumed as 2%, according to the European Central Bank. Information of taxes for 2016 was received from Parc de l'Alba; they are the IAE (city council tax for business activity), IBI (city council tax for property), IS (national corporation tax), tax on electricity export (7% of total export earnings) and tax on natural gas consumption (0.00234 €/kWh gas consumed).

5. Demand characterization

The demands of Parc de l'Alba from 2016 till 2020 are shown in Tab. 7.

Tab. 7 Present and future energy demands of Parc de l' Alba

	2016	2017	2018	2020
Cooling demand (MWh_c/year)	23,600	25,368	26,048	31,848
Heating demand (MWh_{th}/year)	1,426	2,386	2,738	3,398
Electricity demand (MWh_e/year)	22,847	22,768	23,921	48,429

The main consumers are the Synchrotron facilities (cooling and electricity), office buildings (cooling and heating) and data centers (cooling and electricity). The Synchrotron has a cyclic operation throughout the year and hence its cooling and electricity demand was modelled accordingly (shown in Fig. 2), as per information received from Parc de l' Alba. For offices, the cooling demand was modelled according to the Barcelona Energy Improvement Plan (Pla de Millora Energètica de Barcelona, 2002), while the heating demand was based on a study by Pedersen and Ulseth (2006), as shown in Fig. 3. Finally, the cooling and electricity profiles of data centers (Fig. 4) were modelled on the basis of real data (operation of IT loads throughout the day) simulated in the Renew IT project (European Union, 2013).

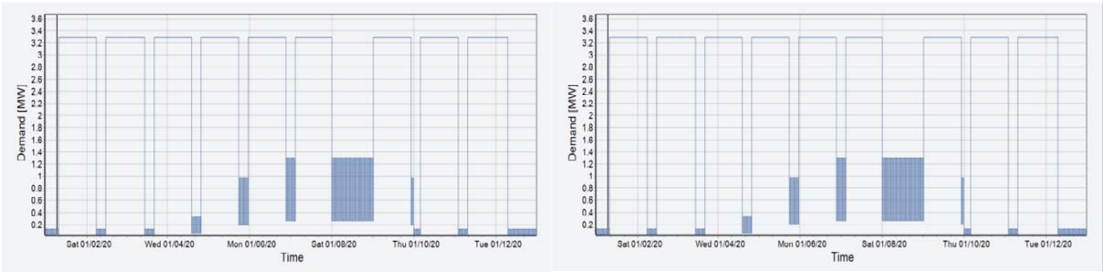

Fig. 2 Annual cooling (left) and annual electricity (right) demand profiles of Synchrotron facilities

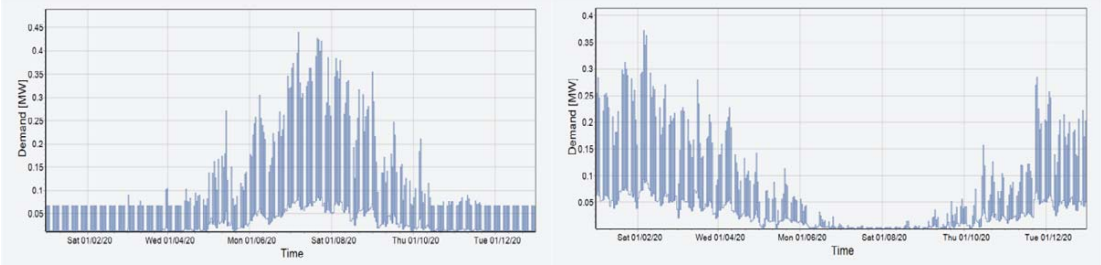

Fig. 3 Annual cooling (left) and annual heating (right) demand profile of office buildings

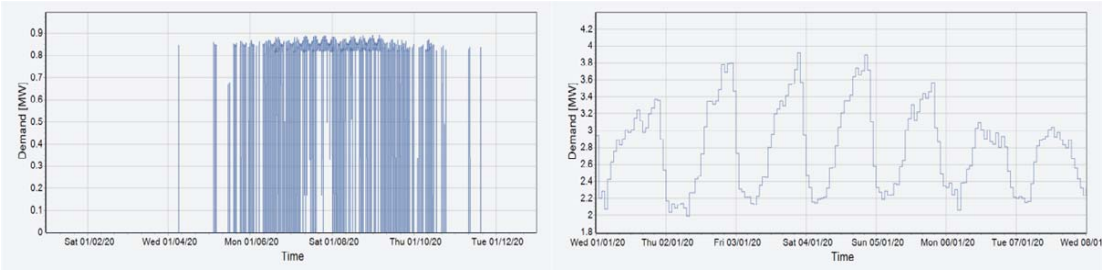

Fig. 4 Annual cooling (left) and weekly electricity (right) demand profile of data centers

6. Supply modeling

In order to supply the growing energy demand of Parc de l' Alba, three different scenarios have been considered, namely:

- Scenario 1: Solar cooling and Biomass cooling (SCBC)
- Scenario 2: Ground Source Heat Pumps (GSHPs)
- Scenario 3: Business As Usual (BAU)

All three scenarios involve the incorporation of a biogas boiler in the ST-4 plant from 2017 till 2019, while for 2020 each of the scenarios incorporates different energy conversion technologies in the new ST-5 plant. Each scenario shall be described in detail, including specifications of the energy conversion units and CAPEX (capital expenditures). Common to all scenarios are some miscellaneous investment costs (engineering, monitoring, permits, legalization etc.) which are taken as 25 % of the total physical investment of the equipment, as recommended in the guide published by the Catalan Energy Institute (Institut Català d'Energia, 2010). In the SCBC and GSHPs scenarios, it is assumed that electricity for new data centers is purchased from the grid and sold to the data centers. For the BAU scenario, the new gas engines installed at the ST-5 plant are used to directly sell electricity to the new data centers while any excess is exported to the grid. The costs of fuels in 2020 for all scenarios are shown in Tab. 8. The prices of energy sales after transformation are according the ones in Tab. 2 updated by inflation.

Tab. 8 Fuel costs in 2020 (all scenarios)

Fuel	Cost (€/MWh)
Imported electricity	60-68
Natural gas	50
Biomass	33

For the biogas boiler, all information is received from the Parc de l' Alba management. The fuel used is landfill gas, with a current price of 8 €/MWh and a calorific value of 6.2 kWh/m^3. The percentage of methane in this gas is 60 %, the specific emission factor of CO_2 is 0.62 kg/m3 and the PEF is 0.5. The biogas boiler has a capacity of 1.5 MW_{th} and currently costs € 147,500. The aim is to use this boiler to substitute the existing 5 MW_{th} natural gas (backup) boiler since it is oversized for heating demands till 2020.

6.1. Scenario 1: Solar cooling and biomass cooling (SCBC)

For the SCBC scenario, a part of the rooftop of the ST-5 plant was used for installing Parabolic Trough Collectors (PTCs) that would be connected to a double effect absorption chiller. For the remainder (major) cooling demand, a biomass boiler connected to another absorption chiller was used.

Currently, EnergyPRO can only model flat plate or evacuated tube solar collectors. Because of this, TRNSYS software was used to model the PTCs, with TRNSYS Type 536 (Linear Parabolic Concentrating Solar Collector with Capacitance and Flow Modulation). Data for the simulations was acquired from the Swedish manufacturer "Absolicon Solar Collector AB". The chosen collector model for simulations was

T160 by Absolicon. Data on the solar collectors' field simulated on TRNSYS are shown in Tab. 9

The output of the TRNSYS simulation was an hourly time series of the heating energy produced by the solar field, with 8,760 time steps. This time series was then provided to EnergyPRO as the heat input to the double effect absorption chiller.

Tab. 9 Parameters for modeling parabolic trough collectors for solar thermal cooling in Parc de l' Alba

Parameter	Value
Aperture area of each collector	10.37 m^2
Total number of collectors	105
Total aperture area	1088 m^2
Outlet temperature from collectors	180°C
Return temperature to collectors	160°C

According to the manufacturer, the present day cost of the PTCs is approximately 300 €/m^2 while the cost of the absorption chiller was assumed as 640 USD/kW_c (570 €/kW_c), as quoted by Shirazi et al. (2016). The total investment for the solar thermal cooling system was calculated by doubling the sum of the cost of the collectors and chiller, assuming that roughly 50% of the total system cost is of the buffer storage tank, piping connections, cooling tower, control system, etc. For the biomass boiler, the investment cost was taken from a study conducted by IREC for a project, while costs of the large absorption chillers were provided by the Parc de l' Alba management.

Tab. 10 Details of energy conversion units and storage units modelled for SCBC scenario

Unit type	Quantity	Specifications (each unit)	Cost
Parabolic trough collectors	1	1,088 m^2 ; 298 kW_{th} (417 kW_c)	€ 353,468
Absorption chiller (connected to solar collectors)	1	450 kW_c; COP = 1.4	€ 277,449
Biomass boiler	1	2,500 kW_{th}; η_{th} = 90%	€ 1,171,659
Absorption chiller (connected to biomass boiler)	1	3,300 kW_c; COP:1.4	€ 658,616
Cold water storage tank	1	6,400 m^3; 29.8 MW_c	€ 1,394,574
Hot water storage tank	1	200 m^3; 5.8MW_{th}	€ 97,419
Total plant capacity: 3,717 kW_c and 2,500 kW_{th} **Total CAPEX: € 5,730,128**			

6.2. Scenario 2: Ground Source Heat Pumps (GSHPs)

For the GSHPs scenario, the cooling and heating demands are served by ground source heat pumps that simultaneously produce cooling and heating. For every unit of electricity input, 3.2 units of cooling are produced (Energy Efficiency Ratio: 3.2) while 4.2 units of heating are produced (Coefficient of Performance: 4.2). The COP and EER are similar to the ones calculated for ground source heat pumps in Mollet hospital near Barcelona, as part of the Green Hospital project (European Commission, 2015). For Parc de l'Alba, the GSHPs are oversized in terms of heating capacity since cooling demand is higher than heating demand but the units have a heating output higher than the cooling output (for the same electricity input). The investment cost of the GSHPs for Parc de l'Alba was assumed as 1,583 €/kW_{th}, in accordance with a study done in France by Boissavy (2015). Additionally, the rooftop of the plant was used to install mono crystalline solar photovoltaic (PV) panels, manufactured by Suntech Power. Costs of this PV system were taken from IEA.

Tab. 11 Details of energy conversion units and storage units modelled for GSHPs scenario

Unit type	Quantity	Specifications (each unit)	Cost
Solar PV system	1	1800 m^2; 275 kW_e; η_{el} = 15.4%;	€ 389,675
Ground Source Heat Pumps	1	Input: 1,214 kW_e ; Output: 3,900 kW_c and 5,113 kW_{th}	€ 8,761,075
Cold water storage tank	1	6400 m^3; 29.8 MW_c	€ 1,394,574
Hot water storage tank	1	200 m^3; 5.8MW_{th}	€ 97,419
Total plant capacity: 3,900 kW_c and 5,113 kW_{th} **Total CAPEX: € 13,303,429**			

6.3. Scenario 3: Business As Usual (BAU)

In this scenario, cogeneration engines are installed at the new plant so as to directly sell electricity to the data centers connected in 2020. The exhaust heat of the engines would be used to serve the heat demand and to power an absorption chiller to serve the cooling demand. A backup boiler is also installed.

Tab. 12 Details of energy conversion units and storage units modelled for BAU scenario

Unit type	Quantity	Specifications (each unit)	Cost
Cogeneration engine	3	3.28 MW_{th}; 3.35 MW_e; η_{el} = 44.9%	€ 4,931,299
Double effect absorption chillers	1	5 MW_c; COP = 1.3	€ 997,902
Natural gas boiler (backup)	1	5 MW_{th}; η_{th} = 60%	€ 123,214
Cooling tower	1	-	€ 493,812
Cold water storage tank	1	6,400 m^3; 29.8 MW_c	€ 1,394,574
Hot water storage tank	1	200 m^3; 5.8MW_{th}	€ 97,419
Total plant capacity: 5,000 kW_c, 9,840 kW_{th} and 10,050 kW_e **Total CAPEX: € 10,047,775**			

7. Results

The important results obtained from the energyPRO simulations and economic analyses are presented in this section. The results from 2016 till 2018 are shown first, and then results for 2020 are shown for all scenarios.

7.1. Energy Performance of the three scenarios

From 2016-2018, the simulation models of each year are the same for all three scenarios. Tab. 13 shows the energy balance of all scenarios from 2016 till 2018. Energy demand can be checked in Tab. 7.

Tab. 13 Energy balance at Parc de l'Alba from 2016 to 2018 (MWh/year)

	2016	2017	2018
Energy Consumption			
Imported Electricity	16,842	16,957	17,525
Natural gas	92,890	94,854	92,378
Biogas	-	9,176	9,107
Primary Energy Consumption			
Imported electricity	39,881	40,154	41,499
Natural gas	111,004	113,348	110,391
Biogas	-	4,588	4,554
Total	150,885	158,090	156,444

In 2020, increase in demand is enough to implement the new plants according to the different scenarios (SCBC, GSHPs and BAU). The energy distribution depending on the scenarios is shown in Tab. 14.

Tab. 14 Energy balance at Parc de l'Alba in 2020 (MWh/year)

	SCBC	GSHPs	BAU
Energy Consumption			
Imported Electricity	41,383	44,964	10,067
Natural gas	93,528	98,304	288,712
Biomass	13,756	-	-
Primary Energy Consumption			
Imported electricity	97,995	106,475	23,838
Natural gas	111,765	117,473	345,010
Biomass	468	-	-
Total	210,228	223,948	368,848

From Tab. 14, it can be noticed that biomass contributes with primary energy nearly zero and heat pumps have slightly higher electricity consumption in comparison to SCBC scenario. The BAU scenario consumes a large amount of natural gas in comparison to the two RES based scenarios. This higher consumption is due to the fact that cogeneration engines at the ST-4 plant are running more hours than they were in the SCBC and GSHPs scenarios, since there are no RES-based energy conversion units (in BAU scenario). Also, in the BAU scenario, the backup boiler at the ST-4 plant is now allowed to operate throughout the whole year and not only in winter months like SCBC and GSHPs scenarios, where RES are prioritized. Finally, the ST-5 plant now has three cogeneration engines and another backup boiler, implying further use of natural gas.

7.2. Environmental assessment of the three scenarios

Tab. 15 shows the CO_2 emissions of all scenarios from 2016 till 2018, while emissions produced in 2020 for each scenario are shown in Tab. 16

Tab. 15 CO_2 emissions in Parc de l' Alba from 2016 till 2018

	2016	2017	2018
CO_2 emissions (tons/year)	29,418	30,872	30,443

Tab. 16 CO_2 emissions in Parc de l' Alba for 2020 (all scenarios)

	SCBC	GSHPs	BAU
CO_2 emissions (tons/year)	38,588	40,822	76,342

Tab. 16 clearly shows that the BAU scenario produces almost three times the amount of CO_2 when compared to the RES based scenarios, only because it is burning much more natural gas because of the new cogeneration engines, new backup boiler and the longer running hours of the old engines and old boiler.

7.3 Economic assessment of the three scenarios

Tab. 17 shows the main economic indicators of all scenarios from 2016 till 2018.

Tab. 17 Economic indicators of Parc de l' Alba from 2016 till 2018

	2016	2017	2018
Revenues	€ 7,651,061	€ 8,819,717	€ 10,155,051
Operating Costs	€ 5,079,909	€ 5,603,887	€ 5,887,325
EBITDA	€ 2,571,152	€ 3,215,829	€ 4,267,726
Free Cash Flow	€ 629,143	€ 1,962,362	€ 2,722,148

EBITDA refers to the earnings before interest, taxes, depreciation, and amortization. The main economic indicators of 2020 for each scenario are shown graphically in Fig. 5 and in tabular form (with NPV and CAPEX) in Tab. 18.

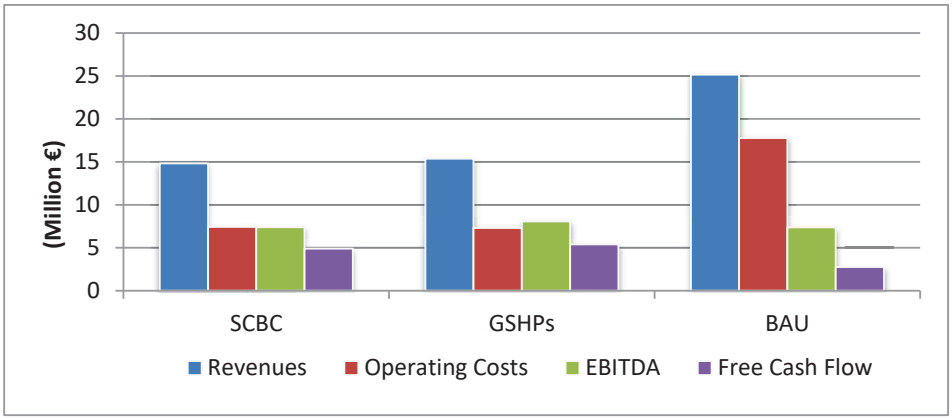

Fig. 5 Economic indicators of Parc de l' Alba for 2020 (all scenarios)

Tab. 18 Economic indicators of Parc de l' Alba for 2020 (all scenarios)

	SCBC	GSHPs	BAU
Revenues	€ 14,824,125	€ 15,371,743	€ 25,153,832
Operating Costs	€ 7,433,577	€ 7,299,363	€ 17,779,229
EBITDA	€ 7,390,549	€ 8,072,380	€ 7,374,604
Free Cash Flow	€ 4,894,266	€ 5,403,243	€ 2,765,192
NPV	€ 62,629,325	€ 61,226,405	€ 60,680,186
CAPEX	€ 5,730,128	€ 13,303,429	€ 10,047,775

Tab. 18 shows that the most profitable scenario is the SCBC scenario with the highest NPV and lowest CAPEX, followed by the GSHPs scenario and finally the least profitable being the BAU scenario. As mentioned in section 6 (page 7), the GSHPs were oversized in terms of the heating capacity since there is not a balanced demand between heating and cooling. The main consumers of Parc de l'Alba, located in a Mediterranean climate, are offices and data centers and hence cooling demand is significantly higher than heating. Hence, the option of using GSHPs is perhaps more profitable when there is a large demand of heating; the heat that is being 'wasted' to the soil could then have been sold to bring additional revenues. GSHPs have average energy efficiency roughly four times better than boilers burning biomass and using heat in absorption chillers of SCBC scenario. However, price of electricity is double the price of biomass and CAPEX of GSHPs is nearly three times higher than CAPEX of SCBC. Another important conclusion that can be drawn, in the case of Parc de l'Alba, is that it is apparently more profitable to import electricity from the grid and then sell it to the data centers at a profit, rather than self-production by cogeneration engines. Basically, the BAU scenario has higher taxes because of higher electricity export to the grid and higher natural gas consumption and hence it has a lower free cash flow.

Conclusions can be summarized in Fig. 6, which shows the environmental benefits and economic cost-effectiveness together. It is clear that the solution with the best results is the system with solar thermal cooling and biomass with absorption chillers (SCBC scenario).

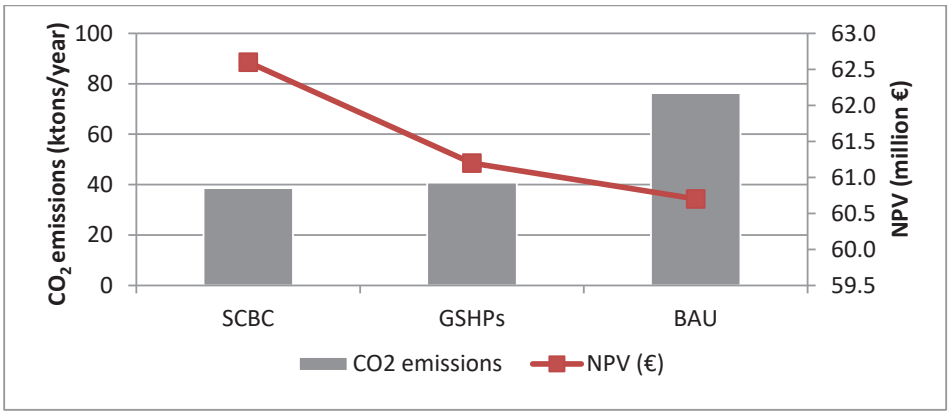

Fig. 6 Relation of environmental and economic key indicators for different scenarios in 2020

8. Conclusion

In this study, a comprehensive feasibility study has been performed to integrate renewable energy systems in the district heating and cooling network at Parc de l' Alba, a technology park in the region of Catalonia in Spain. Three 5-year projection scenarios were created on the energyPRO software, after validating a base model, in order to simulate the energy demand and supply of Parc de l'Alba from 2016 till 2020.

The projected cooling, heating and electricity demand of Parc de l'Alba were modelled on the software in accordance with the nature of the consumers, which were mainly offices, data centers and a particle accelerator. For all scenarios, data for the KPIs, namely primary energy consumption, CO_2 emissions and NPV, was collected by literature review and personal communications with relative authorities. All three scenarios incorporated a biogas boiler in the existing plant from 2016 till 2019. In 2020, different technologies were used to model the energy supply by the new plant. In scenario 1 (SCBC), a biomass boiler connected to an absorption chiller was mainly used to supply the cooling and heating demands. A small part of the cooling demand was provided by the solar thermal collectors installed on the roof of the plant connected to a small absorption chiller. Scenario 2 (GSHPs) mainly utilized ground source heat pumps that simultaneously provided heating and cooling, and the plant rooftop was used for installing solar photovoltaic panels to cater for some in-house electricity consumption of the plant. Scenario 3 (BAU) relied on cogeneration engines, an absorption chiller and a natural gas (backup) boiler to serve not only the cooling and heating demands of Parc de l'Alba, but also the electricity demands of the new data centers.

The results of the simulations and economic evaluation showed that the SCBC scenario is the most feasible option in comparison to the GSHPs scenario, due to its lower primary energy consumption (210,228 MWh/year vs. 223,949 MWh/year), lower CO_2 emissions (38,588 tons/year vs. 40,822 tons/year) and higher NPV (€ 62,629,325 vs. € 61,226,405) with lower CAPEX.

When talking about the SCBC scenario, solar thermal cooling has a great potential for primary energy savings and savings in CO_2 emissions (no combustion of any kind), but in the case of Parc de l'Alba, the limited roof area availability was the reason that solar thermal cooling could only contribute very little in the large cooling demand. Only 2% of the cooling demand of 2020 came from solar thermal cooling. This was expected because the maximum output of the system was 417 kW of cooling, while the total cooling capacity of ST-5 plant was 3,717 kW.

In the GSHPs scenario, the units are producing heating and cooling simultaneously, the former being larger in quantity than the latter, i.e. each kW of electricity (input to compressor) produces 4.2 kW of heating and 3.2 kW of cooling. For Parc de l'Alba, this excess heat has to be rejected to the soil and cannot be taken profit of. Hence, implementation of this technology is not so feasible for offices and data centers located in

the Mediterranean climate (Catalonia) where cooling is the major requirement and not heating. Moreover, digging of boreholes to install GSHPs requires large areas of land, which is an additional investment.

In contrast to the solar thermal cooling system and the ground source heat pumps, biomass boilers (burning woodchips) connected to double effect absorption chillers appear to be the most favorable solution in this study. Not only is cost of the fuel low compared to importing electricity for GSHPs (for example in 2020, woodchips cost 33 €/MWh while electricity was imported at an average price of 60 €/MWh), but also there are large savings in primary energy consumption (wood chips have a PEF of 0.034 while for electricity it is 2.368). Additionally, for the same cooling capacities, biomass boilers and absorption chillers require less land space for installation compared to GSHPs and solar thermal cooling systems.

To conclude, in the frame of this study, biomass boilers connected to absorption chillers with support from solar thermal cooling are the most feasible renewable energy systems technology for the large district heating and cooling network of Parc de l'Alba.

9. References

Ajuntament de Barcelona, Agència d'Energia de Barcelona, 2002. Pla de Millora Energètica de Barcelona.

Boissavy, C., 2015. Cost and Return on Investment for Geothermal Heat Pump Systems in France. Proceedings World Geothermal Congress 2015, Melbourne, Australia.

EMD International A/S – EnergyPRO, 2016. Available at http://www.emd.dk/energypro/. (Accessed 17th September 2016)

European Union, 2013. Advanced concepts and tools for renewable energy supply of IT Data Centers (RenewIT). Available at http://www.renewit-project.eu/requirement_it_equipment/. (Accessed 18th September 2016)

Gobierno de España - Ministerio de Industria, Energía y Turismo, y Ministerio de Fomento, 2016. Factores de Emisión de CO2 y coeficientes de paso a energía primaria de diferentes fuentes de energía final consumidas en el sector de edificios en España. Available at http://www.minetur.gob.es/energia/desarrollo/EficienciaEnergetica/RITE/Reconocidos/Reconocidos/C%20_%2020140720_Factores%20emision%20CO2%20y%20E%20%20Final_Primaria-CorrErrata_con%20portada.pdf. (Accessed 17th September 2016)

Institut Català d'Energia (ICAEN), 2010. Guia de desenvolupament de projectes de xarxes de Districte de Calor i Frio, Barcelona.

Intelligent Energy Europe, 2016. Smart and Flexible 100 % Renewable District Heating and Cooling Systems for European Cities (SMARTREFLEX). Available at https://ec.europa.eu/energy/intelligent/projects/en/projects/smartreflex. (Accessed 17th September 2016)

International Energy Agency (IEA), 2016. Energy Policies of IEA Countries - Spain 2015 Review. Available at https://www.iea.org/publications/freepublications/publication/IDR_Spain2015.pdf. (Accessed 17th September 2016)

Pedersen, L., Ulseth, R., 2006. Method for Load Modeling of Heat and Electricity Demand. Proceedings of the 10th International Symposium on District Heating and Cooling, Hanover, Germany.

Ross, S., Westerfield, R., Jordan, B., 2014. Fundamentals of Corporate Finance, 11th ed. McGraw-Hill, New York.

Shirazi, A., Taylor, R.A., White, S.D., Morrison, G.L., 2016. A systematic parametric study and feasibility assessment of solar-assisted single-effect, double-effect, and triple-effect absorption chillers for heating and cooling applications. Energy Conversion and Management, 114, 258-277.

European Commission, 2015. Web-based energy management system for the optimization of the energy consumption in Hospitals (Green@Hospital). Available at https://ec.europa.eu/digital-single-market/en/content/greenhospital-making-hospitals-healthier-and-greener. (Accessed 25th September 2016)

Conference Proceedings

EuroSun 2016
Palma de Mallorca (Spain), 11 - 14 October 2016

Thermoeconomic Analysis of Cogeneration Systems Assisted with Solar Thermal Heat and Photovoltaics

Eduardo A. Pina[1], Miguel A. Lozano[1], Luis M. Serra[1]

[1] GITSE I3A, Universidad de Zaragoza, Maria de Luna 3, 50018, Zaragoza, Spain

Abstract

This work aims to perform a thermoeconomic analysis of a cogeneration system assisted with solar thermal heat and photovoltaic power, and determine the daily optimal operation taking into consideration the effects of thermal energy storage (TES) and hourly variations of solar radiation, energy prices and energy demands. The system is considered to be interconnected to the national electric grid, thus purchase and selling of electricity are possible. A linear programming model was developed to represent the hourly operation of the system. The results presented herein correspond to the optimal operation for a representative day in April. It was shown that the cogeneration module operates at full load throughout the day and the system sells electricity to the grid for a total of 8 hours. The marginal cost analysis showed the different situations in which heat is charged/discharged to/from the TES and how it affects the unit cost of the heat produced. It has been proposed a thermoeconomic model that incorporates a new set of equations to contribute towards a better understanding of the charge and discharge in different time periods in the TES. The obtained unit costs for internal flows and products showed that the electricity and heat produced by the cogeneration system are always cheaper than the separate conventional production (43-53% cheaper for the electricity and 19-67% cheaper for the heat).

Keywords: *cogeneration, thermal storage, solar thermal energy, photovoltaics, thermoeconomics*

1. Introduction

The increasing world energy demand as a consequence of society development, along with a growing concern about environmental issues and fossil fuel depletion have motivated the development of more efficient energy systems and that consume a greater share of renewable energy. Conventionally, the electricity consumed by buildings is purchased from the national electric grid and the heat demand is covered by onsite production, e.g. in a natural gas boiler. The building sector accounts for 40% of total energy use in the European Union. The Directive 2010/31/EU on energy performance of buildings set the framework for energy efficiency in buildings and nearly zero-energy buildings and states that new buildings must assess the technical, environmental and economic feasibility of incorporating high-efficiency alternative systems such as cogeneration (Combined Heat and Power, CHP) and of producing energy from renewable energy sources (e.g. solar thermal heat and photovoltaic power).

In CHP systems, electric (and/or mechanical) and thermal energy are produced from the same primary energy source. This combined production allows for primary energy savings and a reduction of pollutant emissions relative to the conventional separate production. By incorporating CHP systems in buildings, a shift from centralised to distributed generation takes place, which is accompanied by benefits such as reduction in transmission and distribution costs, reduction in energy dissipation, increase in energy efficiency of the system (Serra et al., 2009; Mancarella, 2014). In order to achieve the benefits described, two fundamental issues must be addressed (Lozano et al., 2010; Yokoyama et al., 2015): (i) the synthesis of the plant configuration (equipment number and capacity for each type of technology employed) and (ii) the operational planning (equipment operational strategy, energy flow rates, purchase or selling of electricity, etc.). However, the variability of energy demands in buildings as opposed to the simultaneous and often constant production in

doi:10.18086/eurosun.2016.05.03 Available at http://proceedings.ises.org

industry impose some issues to the optimal operation of the system. Moreover, the same reasoning applies to the incorporation of renewable energy sources (RES), such as photovoltaic panels and solar thermal collectors, which are characterised by low predictability and non-simultaneity between production and consumption. Therefore, it becomes convenient to incorporate thermal energy storage units, allowing a decoupling of production and consumption, reducing heat wasting to the environment and enhancing the overall performance of the system (Ashouri et al., 2013; Buoro et al., 2014).

The objective of the present work is to perform a thermoeconomic analysis of a cogeneration system assisted with solar thermal heat and photovoltaic power. A linear programming model was formulated, taking into consideration only the operational planning of the system. The daily optimal operation for a representative day in April was determined, considering the effects of thermal energy storage and hourly fluctuations of solar radiation, energy services prices and energy demands. The cost of internal flows and products of the system were assessed by analysis of marginal costs and thermoeconomic unit costs calculation.

2. System description and data elaboration

The cogeneration system analysed in the present work (Fig. 1) consists of the following productive units: (i) a cogeneration module CM, which includes a natural gas reciprocating engine and a hot water heat recovery system, producing electricity W_c and heat Q_c; (ii) an oil-fired auxiliary boiler AB, producing heat Q_a; (iii) a thermal energy storage TES that can be either charging Q_{in} or discharging Q_{out}; (iv) photovoltaic panels PV for electricity production W_{pv}; and (v) solar thermal collectors ST for heat production Q_{st}. All energy flows (in bold) are given in kW, except for the energy stored in the TES Sq, which is given in kWh.

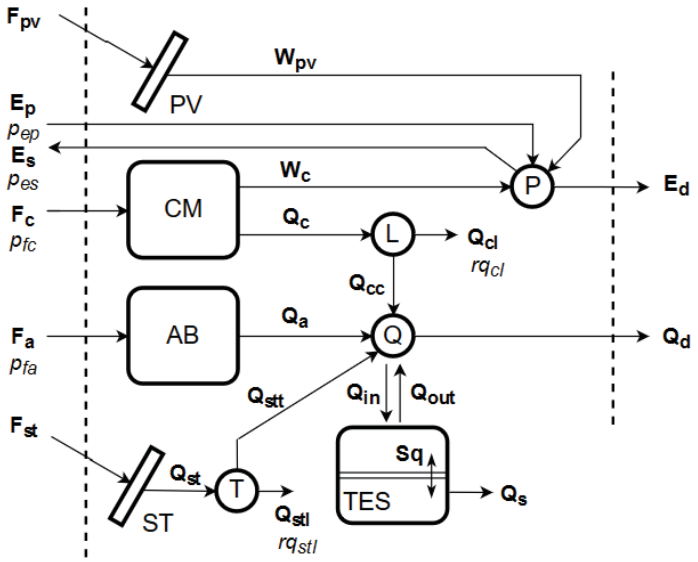

Fig. 1: Diagram of the cogeneration system

Tab. 1: Technical parameters and capacity limits of the cogeneration system's equipment

Equipment	Technical parameters	Capacity limits
Cogeneration Module (CM)	$\alpha_w = W_c/F_c = 0.35$ $\alpha_q = Q_c/F_c = 0.40$	$W_{max} = 400$ kW
Auxiliary Boiler (AB)	$\eta_q = Q_a/F_a = 0.80$	$Q_{max} = 600$ kW
Photovoltaic Panel (PV)	$P_{pv} = 0.300$ kW, $A_{pv,m} = 1.93$ m² $\eta_{pv} = 0.1538$, $\mu_T = -0.0035$ K^{-1}	$A_{pv} = 700$ m²
Solar Thermal Collector (ST)	$k_0 = 0.8170$, $k_1 = 2.2350$ W/(m²·K) $k_2 = 0.0135$ W/(m²·K²)	$A_{st} = 700$ m²
Thermal Energy Storage (TES)	$\eta_{TES} = 0.99$	$V_{max} = 1200$ kWh

Tab. 1 presents the technical parameters and capacity limits of each of the system's components. The cogeneration system was designed to attend all the electric E_d and thermal Q_d demands of a consumer centre (e.g. multifamily building). For the present work, the energy demands of a representative day in April were considered, being the total daily electric and thermal values 10,100 kWh and 19,200 kWh, respectively. As can be seen in Tab. 2, the demands and the daily operation of the system are described by 24 consecutive periods of 1-hour duration.

The system is considered to be interconnected to the national electric grid, therefore electricity can be purchased, E_p, at a price p_{ep} = 0.100 €/kWh, and sold, E_s, at a price p_{es} = 0.080 €/kWh. Natural gas and fuel oil are purchased from the market at prices p_{fc} = 0.025 €/kWh and p_{fa} = 0.020 €/kWh, respectively. There is the possibility of wasting cogenerated heat Q_{cl} and solar thermal energy Q_{stl} without cost ($rq_{cl} = rq_{stl} = 0$).

The PV and the ST are characterised by their surface areas (A_{pv} and A_{st}, respectively) and hourly specific productions (x_{pv} and x_{st}, respectively). The photovoltaic electricity W_{pv} and solar thermal Q_{st} productions can be obtained by multiplying the respective equipment area by its specific production. In order to evaluate x for each hourly period, the hourly ambient temperature T_a and the hourly radiation over tilted surface Q_r must be determined. The Erbs' correlation for ambient temperature (Erbs et al., 1983) was used to calculate the hourly T_a, using the monthly mean temperatures for the month of April from the *Guía Resumida del Clima en España 1981-2010* (AEMET, 2010). The hourly radiation Q_r over tilted surface (beam, diffuse and total) is calculated using the isotropic sky model (Duffie and Beckman, 2013). The sky clearness index can be obtained from the average daily horizontal radiation and the extraterrestrial radiation, which depends on the city latitude and the date. This index is used to calculate the daily diffuse radiation with Erbs' correlation (Erbs et al., 1982). The total horizontal radiation is hourly distributed with the Collares-Pereira and Rabl (1979) correlation, and the diffuse horizontal radiation is hourly distributed with Liu and Jordan (1960) correlation. The difference between total radiation and diffuse radiation is the direct (beam) horizontal radiation. Specific data required are: the monthly average of daily solar radiation on a horizontal surface (AENOR, 2007), latitude (41.6º for Zaragoza), surface azimuth angle (0º), reflectance of the ground (0.2) and tilt (35º for both PV and ST).

For each hourly period, x_{st} was determined by Eq. 1 using the performance coefficients from the manufacture's catalog (Tab. 1), the hourly data of the solar radiation over tilted surface Q_r, and the hourly temperature difference ΔT between the collector $T_{c,st}$ and the ambient T_a. Only the positive values of collected heat are considered. Further, $T_{c,st}$ is considered constant throughout the day and equal to 60 ºC.

$$x_{st}(h) = Max(k_0 \cdot Q_r(h) - k_1 \cdot \Delta T(h) - k_2 \cdot \Delta T(h)^2; 0) \quad \text{(Eq. 1)}$$

For each hourly period, x_{pv} was determined by Eq. 2 according to the methodology described in Duffie and Beckman (2013). The maximum power P_{pv}, the surface area $A_{pv,m}$, the module efficiency η_{pv}, and the temperature coefficient of power μ_T, were obtained from the manufacture's catalog (Tab. 1). Irradiation and cell temperature at SRC conditions are $Q_{r,SRC}$ = 1 kW/m² and $T_{c,SRC}$ = 25 ºC, respectively. Irradiation, cell temperature and ambient temperature at NOCT conditions are $Q_{r,NOCT}$ = 0.8 kW/m², $T_{c,NOCT}$ = 47 ºC and $T_{a,NOCT}$ = 20 ºC, respectively. The efficiency of power-conditioning equipment, η_e, is 0.9. The hourly cell temperature $T_{c,pv}$ and the hourly temperature correction factor F_{top} were obtained by solving Eqs. 3 and 4.

$$x_{pv}(h) = \left(P_{pv}/A_{pv,m}\right) \cdot \left(Q_r(h)/Q_{r,SRC}\right) \cdot F_{top}(h) \cdot \eta_e \quad \text{(Eq. 2)}$$

$$F_{top}(h) = 1 + \mu_T \cdot \left(T_{c,pv}(h) - T_{c,SRC}\right) \quad \text{(Eq. 3)}$$

$$T_{c,pv}(h) = T_a(h) + \left(T_{c,NOCT} - T_{a,NOCT}\right) \cdot \left(Q_r(h)/Q_{r,NOCT}\right) \cdot \left[1 - \left(\eta_{pv} \cdot F_{top}\right)/0.9\right] \quad \text{(Eq. 4)}$$

3. Optimal operation model

In order to determine the hourly operation modes that minimise the daily cost of meeting the energy demands, a linear programming model was developed and solved, as described in the following sub-sections. The LINGO modelling language and optimiser was used (LINGO, 2011).

3.1. Objective function and restrictions

The objective function is set to minimise the daily operation cost *DC* (€/day) of meeting the energy demands,

$$DC = \sum_{h=1}^{NP} HC(h) \quad \text{(Eq. 5)}$$

which is the sum of the hourly operation costs *HC(h)* of the 24 periods (*NP*) of 1-hour duration (*NHP*) that comprise the day,

$$HC(h) = \left(p_{ep}(h) \cdot E_p(h) + p_{fc}(h) \cdot F_c(h) + p_{fa}(h) \cdot F_a(h) - p_{es}(h) \cdot E_s(h)\right) \cdot NHP(h) \quad \text{(Eq. 6)}$$

subject to

Capacity limits:

CM_Wmax: $W_c(h) \leq W_{max}$ (Eq. 7)

AB_Qmax: $Q_a(h) \leq Q_{max}$ (Eq. 8)

Sqi_Vmax: $Sq_i(h) \leq V_{max}$ (Eq. 9)

Equipment efficiency:

CM_W: $\alpha_w \cdot F_c(h) - W_c(h) = 0$ (Eq. 10)

CM_Q: $\alpha_q \cdot F_c(h) - Q_c(h) = 0$ (Eq. 11)

AB_Q: $\eta_q \cdot F_a(h) - Q_a(h) = 0$ (Eq. 12)

PV_W: $A_{pv} \cdot x_{pv}(h) - W_{pv}(h) = 0$ (Eq. 13)

ST_Q: $A_{st} \cdot x_{st}(h) - Q_{st}(h) = 0$ (Eq. 14)

Balance equations:

P: $W_c(h) + W_{pv}(h) + E_p(h) - E_s(h) - E_d(h) = 0$ (Eq. 15)

L: $Q_c(h) - Q_{cc}(h) - Q_{cl}(h) = 0$ (Eq. 16)

Q: $Q_a(h) + Q_{cc}(h) + Q_{stt}(h) + Q_{out}(h) - Q_{in}(h) - Q_d(h) = 0$ (Eq. 17)

T: $Q_{st}(h) - Q_{stt}(h) - Q_{stl}(h) = 0$ (Eq. 18)

TES: $Q_{in}(h) - Q_{out}(h) - Q_s(h) + (Sq_i(h) - Sq_f(h))/NHP(h) = 0$ (Eq. 19)

The cyclical characteristic of the TES operation means that the energy stored at the beginning of an hourly period equals the energy stored at the end of the previous period (Eq. 20). Likewise, the energy stored at the beginning of the day (h = 1) must be equal to the energy stored at the end of the previous day (h = 24) (Eq. 21). The heat losses Q_s in each hourly period is a function of the TES efficiency η_{TES} and the stored energy at the beginning of the hourly period Sq_i (Eq. 22).

$$Sq_i(h) = Sq_f(h-1) \quad \text{(Eq. 20)}$$

$$Sq_i(1) = Sq_f(24) \quad \text{(Eq. 21)}$$

$$Q_s(h) = (1 - \eta_{TES}) \cdot Sq_i(h) \quad \text{(Eq. 22)}$$

3.2. Optimal operation and marginal costs

Tab. 2 presents the main flows of the system's optimal operation, for each hourly period, that brings the minimum total daily cost of 848.50 €. Positive Q_{TES} values correspond to the charged energy flow Q_{in} whereas negative values correspond to the discharged flow Q_{out}. The CM operates at full load throughout the day, while the AB modulates as needed. The daily photovoltaic production reaches 483.90 kWh, about 5% in relation to the total CM electricity production (9600 kWh). From hours 6 to 13 the system is able to sell 110.42 kWh/day of electricity to the grid, resulting in an income of 8.83 €/day; in all other hours the system purchases electricity from the grid, except for hour 5, in which the CM power production matches the electric energy demand.

Concerning the heat production, it can be seen that the solar thermal energy production peaks at hour 13, 308.42 kWh, adding up to a total daily production of 1894.70 kWh, about 17% in relation to the total cogenerated heat produced (10,971.40 kWh). Such production displaces the operation in the AB, avoiding 47.37 €/day of fuel consumption. Regarding the TES operation, for this representative day in April, it is most charged by the end of hour 4, with 416 kWh, about a third of its storage capacity. Attention should be paid to the different scenarios in which charging takes place:

Tab. 2: Optimal operation for a representative day in April

Hour	E_d[1]	Q_d[1]	T_a[2]	Q_r[3]	x_{pv}[3]	x_{st}[3]	E_p[1]	E_s[1]	W_c[1]	Q_c[1]	Q_a[1]	Sq_i[4]	Q_{TES}[1]	F_c[1]	F_a[1]	W_{pv}[1]	Q_{st}[1]
1	410	300	10.2	0	0	0	10.0	0	400	457.1	0	0	157.1	1142.9	0	0	0
2	408	300	9.6	0	0	0	8.0	0	400	457.1	0	155.6	157.1	1142.9	0	0	0
3	405	400	9.1	0	0	0	5.0	0	400	457.1	0	309.6	57.1	1142.9	0	0	0
4	402	400	8.6	0	0	0	2.0	0	400	457.1	0	363.1	57.1	1142.9	0	0	0
5	400	600	8.1	0	0	0	0	0	400	457.1	0	416.0	-142.9	1142.9	0	0	0
6	400	800	7.9	3.4	0.5	0	0	0.4	400	457.1	163.7	270.4	-179.2	1142.9	2.4	0.4	0
7	404	1000	8.1	91.3	13.4	0	0	5.4	400	457.1	600.0	90.3	57.1	1142.9	63.9	9.4	0
8	410	1200	9.0	227.1	32.8	36.4	0	13.0	400	457.1	600.0	146.0	-117.4	1142.9	159.0	23.0	25.5
9	420	1200	10.6	375.8	53.2	163.6	0	17.2	400	457.1	600.0	28.3	-28.3	1142.9	263.1	37.2	114.5
10	425	1200	12.6	516.1	71.5	285.3	0	25.1	400	457.1	543.1	0	0	1142.9	361.3	50.1	199.7
11	435	1000	14.5	625.7	85.2	381.7	0	24.6	400	457.1	275.7	0	0	1142.9	438.0	59.6	267.2
12	445	1000	16.2	685.7	92.2	436.3	0	19.5	400	457.1	237.4	0	0	1142.9	480.0	64.5	305.4
13	459	700	17.4	685.7	91.8	440.6	0	5.3	400	457.1	0	0	65.6	1142.9	480.0	64.3	308.4
14	461	600	18.3	625.7	84.0	394.5	2.2	0	400	457.1	0	64.9	133.3	1142.9	438.0	58.8	276.2
15	455	700	18.8	516.1	69.9	306.8	6.1	0	400	457.1	0	196.2	-28.1	1142.9	361.3	48.9	214.8
16	439	800	18.9	375.8	51.6	192.3	2.9	0	400	457.1	41.8	166.4	-166.4	1142.9	263.1	36.1	134.6
17	425	1000	18.4	227.1	31.7	69.2	2.8	0	400	457.1	525.6	0	31.2	1142.9	159.0	22.2	48.4
18	418	1000	17.3	91.3	13.0	0	8.9	0	400	457.1	600.0	30.9	57.1	1142.9	63.9	9.1	0
19	413	1000	15.9	3.4	0.5	0	12.7	0	400	457.1	600.0	87.2	57.1	1142.9	2.4	0.4	0
20	412	1200	14.5	0	0	0	12.0	0	400	457.1	600.0	142.9	-142.9	1142.9	0	0	0
21	413	900	13.3	0	0	0	13.0	0	400	457.1	442.9	0	0	1142.9	0	0	0
22	414	700	12.3	0	0	0	14.0	0	400	457.1	242.9	0	0	1142.9	0	0	0
23	416	600	11.6	0	0	0	16.0	0	400	457.1	142.9	0	0	1142.9	0	0	0
24	411	600	10.9	0	0	0	11.0	0	400	457.1	142.9	0	0	1142.9	0	0	0
Day[4]	10,100	19,200	-	5050.2	691.3	2706.7	126.5	110.4	9600	10,971.4	6358.8	-	24.9	27,428.6	3535.14	483.9	1894.7

given in: [1] kW, [2] ºC, [3] W/m^2, [4] kWh.

- Excess heat production: in hours 1 to 4, 13 and 14 the heat production from solar thermal collector and cogeneration module surpasses the thermal energy demand. The surplus heat stored for later consumption allows a reduction in the conventional heat production;
- Conventional heat required: in hours 7 and 17 to 19 the system must store energy in order to guarantee supply in hours of peak thermal demand (1200 kWh), e.g. hours 8, 9 and 20. Therefore, the AB is put into operation at the closest feasible period to the discharge, as to reduce heat losses to a minimum.

Dual prices obtained from the linear programming model help to unravel the marginal costs of internal flows and products, and to evaluate the economic impact of changes in demand or operational condition of the equipment (Lozano et al., 2009b).

Regarding the optimal operation, from hours 6 to 13, when the system is selling electricity to the grid, supplying an additional unit of electricity to the consumer centre means reducing selling by the same amount, therefore its marginal cost equals the selling price ($\lambda E_d = p_{es} = 0.080$ €/kWh); on the other hand, when the system matches the electric demand (hour 5) or purchases electricity from the grid (the rest of the time), the marginal cost of the electricity corresponds to the purchasing price ($\lambda E_d = p_{ep} = 0.100$ €/kWh).

Supplying an additional unit of heat to the consumer centre will always result in an increase in the production of the AB because solar thermal energy is a non-dispatchable resource and the CM already operates at full load throughout the day. Therefore, the important thing to notice is when this production takes place. Fig. 2 presents the 24 hourly periods and their respective marginal costs in €/kWh. The grey circles represent periods in which the AB is modulating. In such periods, the additional unit of heat is produced and consumed at the same hourly period, thus its marginal cost is the cost of producing 1 kW in the AB ($\lambda Q_d = p_{fa}/\eta_{AB} = 0.025$ €/kWh). The red circles indicate periods in which the dispatchable equipment (CM and AB) are not able to increase their productions (CM and AB operate at full load) and thus the deficit of heat must be produced in an earlier period and stored. In these cases, the AB will have to produce more than 1 kW as to compensate for the storage heat losses, resulting in a marginal cost that equals the cost of producing 1 kW plus heat losses in the AB. The blue circles correspond to periods of excess heat. Consuming an additional unit of heat in such periods means that one less unit is stored in the TES, so, in a later period, the AB will have to increase its production in not 1 kW, but less. Thus, the marginal cost will be the cost of producing 1 kW minus heat losses in the AB. The marginal costs of interconnected periods (red and blue circles) can be calculated by Eq. 23, which relates the cost of producing 1 kW in the AB, the TES efficiency and the storage time between the period k of AB production and the period h of additional unit of heat consumption.

$$\lambda Q_d(h) = \left(p_{fa}/\eta_{AB}\right) \cdot \eta_{TES}^{(k-h)} \qquad \text{(Eq. 23)}$$

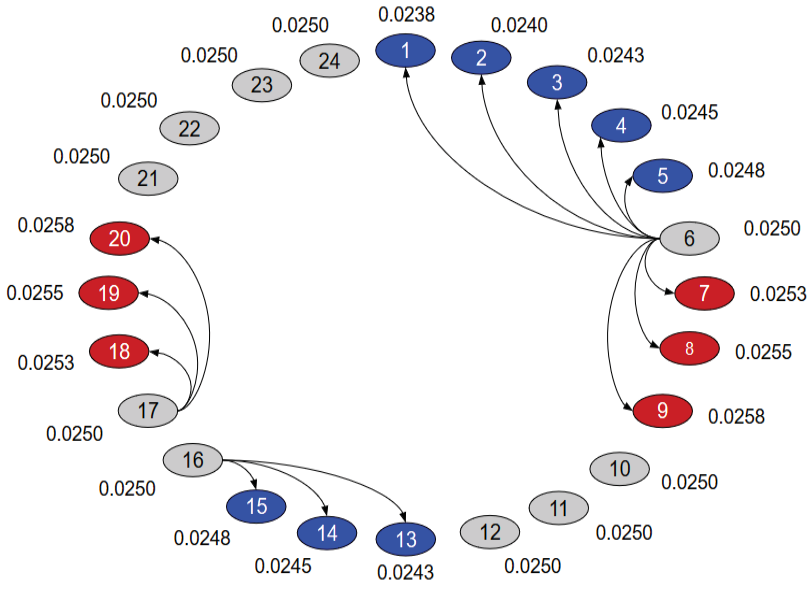

Fig. 2: Hourly marginal costs of the heat supplied to the consumer centre in €/kWh

4. Interconnection Between Hourly Periods

As stated by Chicco and Mancarella (2009), the effective combination of the different alternatives of production can bring forward enhanced benefits in terms of economic profitability, among others. In the analysed system, the thermal energy demand can be met by heat production in the CM, AB and/or ST at different productions costs. Because of the TES, heat can be produced and consumed at the same hourly period or produced and stored for later consumption. Therefore, as important as evaluating how much energy must be charged and discharged from the TES at each period, is knowing its source period. Only then the cost of the discharged flow can be traced back up to its production.

The optimal operation model described in section 3.1 gives the amount of heat that must be charged or discharged into the TES in each hourly period. In order to broaden this view and allow for a better understanding of how charge and discharge periods are interconnected through the TES, it was proposed to include a new set of equations in the model. It should be noted that such considerations do not change the results obtained; only more detailed information about the optimal processes of heat charge and discharge is revealed.

The diagram presented in Fig. 3 can be taken as example to clarify the interconnection between charging and discharging periods: the heat discharged in period z, $Q_{out}(z)$, is composed of virtual energy flows originated in three different earlier periods: OUT(i,z), OUT(j,z) and OUT(k,z) (Eq. 24); the pair (i,z) meaning i as the source period and z the destination period. Therefore, the heat stored in period i, $Q_{in}(i)$, may be divided into several virtual flows IN(i,x) that are going to be discharged in later periods, OUT(i,x) (Eq. 25). On account of heat losses, the discharge flow is always lower than the charge one (Eq. 26). The heat losses LOSS are assessed at the end of each period for each pair, and are proportional to the stored volume and duration (Eq. 27); the notation (i,z,j) means i as the source period, z as the destination period, and j the period in which the heat losses are being assessed. Thus, the longer the storage duration, the greater the heat losses along the pair, as can be seen by comparing pairs (i,z) and (k,z), the former with three LOSS flows and the latter with only one. The total heat losses of each period Q_s can be calculated as the sum of all LOSS flows in that period (Eq. 28), thus replacing Eq. 22.

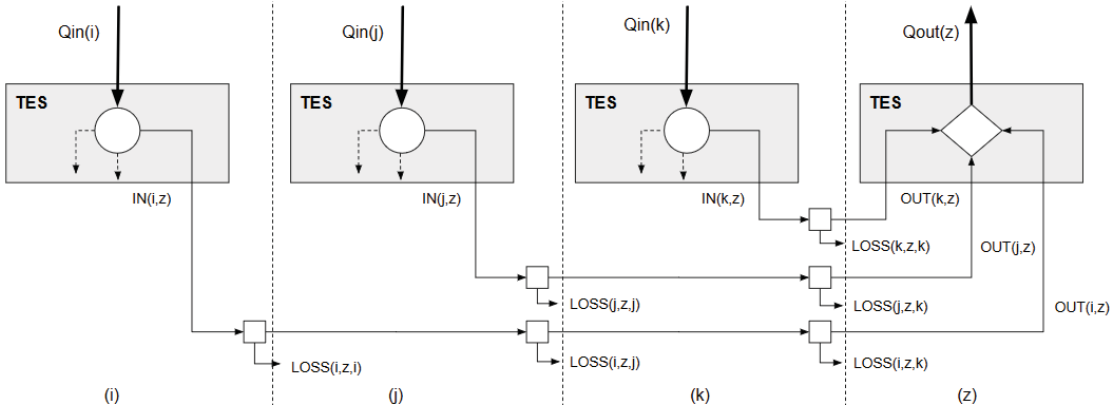

Fig. 3: Diagram for the charging and discharging of the TES

$$Q_{out}(h) = \sum_{i \neq h} OUT(i,h) \quad \text{(Eq. 24)}$$

$$Q_{in}(h) = \sum_{z \neq h} IN(h,z) \quad \text{(Eq. 25)}$$

$$IN(i,z) = OUT(i,z) + \sum_{h=i}^{z-1} LOSS(i,z,h) \quad \text{(Eq. 26)}$$

$$\sum_{h=i}^{j} LOSS(i,z,h) = IN(i,z) \cdot \left(1 - \eta_{TES}{}^{(j-i+1)}\right) \text{ for all } j = i, \ldots\ldots, z-1 \quad \text{(Eq. 27)}$$

$$Q_s(h) = \sum_{i,z} LOSS(i,z,h) \quad \text{(Eq. 28)}$$

The chart in Fig. 4 presents, for each relevant pair of periods (j,k), the charged energy IN, the discharged energy OUT and the heat losses LOSS between them. Because heat losses increase with storage time, as explained earlier, the model seeks to keep energy stored for the minimum time necessary in order to guarantee supply, meaning that the first unit of energy to be charged must be the first unit of energy to be discharged. Even though the model may infringe this rule once in a while, e.g. pairs (1,9) and (2,6), the optimal operation still stands, as both pairs form a loop in a way that shortening a pair and extending the other, e.g. (1,6) and (2,9), would provide equivalent heat losses.

Pair (j,k)		1	2	3	4	5	6	7	8	9	10...12	13	14	15	16	17	18	19	20	21...24
(1,5)	IN, OUT	148,72				142,86														
	LOSS	1,49	1,47	1,46	1,44															
(1,9)	IN, OUT	8,43								7,77										
	LOSS	0,08	0,08	0,08	0,08	0,08	0,08	0,08	0,08											
(2,6)	IN, OUT		128,22				123,16													
	LOSS		1,28	1,27	1,26	1,24														
(2,8)	IN, OUT		6,87						6,46											
	LOSS		0,07	0,07	0,07	0,07	0,07	0,07												
(2,9)	IN, OUT		22,06							20,56										
	LOSS		0,22	0,22	0,22	0,21	0,21	0,21	0,21											
(3,8)	IN, OUT			57,14					54,34											
	LOSS			0,57	0,57	0,56	0,55	0,55												
(4,6)	IN, OUT				57,14		56,01													
	LOSS				0,57	0,57														
(7,8)	IN, OUT							57,14	56,57											
	LOSS							0,57												
(13,16)	IN, OUT											65,56			63,62					
	LOSS											0,66	0,65	0,64						
(14,15)	IN, OUT												28,38	28,10						
	LOSS												0,28							
(14,16)	IN, OUT												104,91		102,82					
	LOSS												1,05	1,04						
(17,20)	IN, OUT															31,21			30,28	
	LOSS															0,31	0,31	0,31		
(18,20)	IN, OUT																57,14		56,01	
	LOSS																0,57	0,57		
(19,20)	IN, OUT																	57,14	56,57	
	LOSS																	0,57		
Qin(z)		157,1	157,1	57,1	57,1	0,0	0,0	57,1	0,0	0,0	0,0	65,6	133,3	0,0	0,0	31,2	57,1	57,1	0,0	0,0
Qout(z)		0,0	0,0	0,0	0,0	142,9	179,2	0,0	117,4	28,3	0,0	0,0	0,0	28,1	166,4	0,0	0,0	0,0	142,9	0,0
Qs(z)		1,6	3,1	3,7	4,2	2,7	0,9	1,5	0,3	0,0	0,0	0,7	2,0	1,7	0,0	0,3	0,9	1,4	0,0	0,0

Fig. 4: Heat flows between relevant pairs of periods through the TES

5. Thermoeconomic Analysis and Cost Allocation

In energy systems, resources are consumed in order to produce certain qualities to the internal flows until the desired final products are obtained. Thermoeconomics allows the cost formation process to be transparent throughout the system, from energy resources to final products (Lozano and Valero, 1993).

In the cogeneration system analysed herein (Fig. 1) the possibility of selling electricity to the grid provides an income ($p_{es} \cdot E_s$) that reduces the operation cost. As the CM and the PV are the two productive units that can produce electricity, it was proposed to proportionally distribute E_s between both equipment according to their power productions. By doing so, the benefit of selling electricity to the grid could be incorporated to the internal flow costs of cogenerated W_{cc} and photovoltaic W_{pvv} electricity produced by the system. For each hourly period, the parameter γ, defined by Eq. 29, was used to determine the cogenerated E_{cs} and photovoltaic E_{pvs} electricity sold to the grid.

$$\gamma(h) = W_{pv}(h)/\left(W_{pv}(h) + W_c(h)\right) \quad \text{(Eq. 29)}$$

$$E_{pvs}(h) = \gamma(h) \cdot E_s(h) \quad \text{(Eq. 30)}$$

$$E_{cs}(h) = (1 - \gamma(h)) \cdot E_s(h) \quad \text{(Eq. 31)}$$

In order to properly carry out a thermoeconomic analysis, it is essential to identify the correct productive structure of the system (Lozano et al., 2011). Fig. 5 presents the productive structure devised for the thermoeconomic analysis, showing the energy flows in bold, the market prices of the resources in italic and the unit costs of internal flows and final products.

For each hourly period, all energy flows of the system and the prices of the commercial energy sources consumed are known (p_{ep} = 0.100 €/kWh, p_{es} = 0.080 €/kWh, p_{fc} = 0.025 €/kWh, p_{fa} = 0.020 €/kWh). There is no cost related to the dissipation of heat to the ambient (rq_{cl} = 0 and rq_{stl} = 0) and to the heat losses in the TES

(c_{Qs} = 0). The solar resource is obtained at zero cost (c_{Fst} = 0 and c_{Fpv} = 0). Thus, there remain 9 unit costs to be determined (c_{Wpvv}, c_{Wcc}, c_{Qcc}, c_{Qa}, c_{Qstt}, c_{Qin}, c_{Qout}, c_{Ed}, c_{Qd}).

Applying the cost conservation principle as described in Lozano et al. (2009a) to PV+V, ST+T, AB and P brings c_{Wpvv}, c_{Qstt}, c_{Qa} and c_{Ed}, respectively. There remain 5 unit costs to be determined (c_{Wcc}, c_{Qcc}, c_{Qin}, c_{Qout}, c_{Qd}). To complete the calculation of unit costs the following auxiliary equations are proposed.

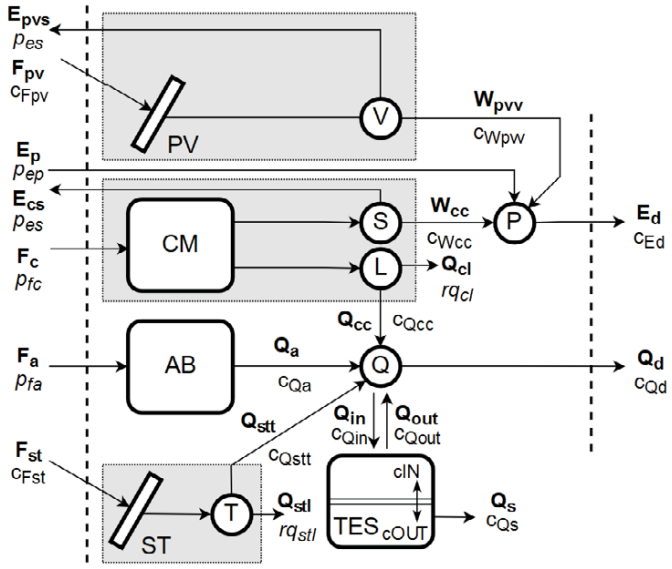

Fig. 5: Productive structure of the cogeneration system for the thermoeconomic analysis

Apart from the cost balance in CM+S+L, another equation is needed in order to determine the unit costs of the cogenerated products (c_{Wcc} and c_{Qcc}). The cogeneration subsystem is characterised by concurrent production of energy services, which is achieved through the energy integration of the process occurring in the equipment. Such a high level of integration hinders the determination of a unique distribution of the resource consumed F_c towards the obtained products W_{cc} and Q_{cc}. Considering an equal share of benefits, it was proposed (Lozano et al., 2011) to apply the same discount d to both products of the cogeneration subsystem (see Fig. 5) with respect to the cost of their conventional separate production: the purchasing price of electricity, $(c_w)_{ref} = p_{ep}$ = 0.100 €/kWh, for W_{cc}, and the cost of producing heat in the AB, $(c_q)_{ref} = p_{fa}/\eta_{AB}$ = 0.025 €/kWh, for Q_{cc}.

$$d(h) = 1 - c_{Wcc}(h)/(c_W)_{ref} = 1 - c_{Qcc}(h)/(c_Q)_{ref} \quad \text{(Eq. 32)}$$

$$c_{Wcc}(h)/p_{ep} = c_{Qcc}(h)/(p_{fa}/\eta_{AB}) \quad \text{(Eq. 33)}$$

The cost balance in junction Q will change according to the operation of the TES. When the TES is charging, an accepted rule can be applied, which establishes that the unit cost of several flows obtained from a homogeneous flow is the same (Lozano and Valero, 1993). This same rule can be applied to distribute c_{Qin} between the virtual IN flows (see section 4). Hence, Eq. 34 follows:

$$c_{Qin}(h) = c_{Qd}(h), \text{ when } Q_{in}(h) > 0 \quad \text{(Eq. 34)}$$

When the TES is discharging, the cost balance in Q gives c_{Qd}. In this case, the unit cost of the discharged flow c_{Qout} must be known. It can be determined by applying the cost conservation principle to Eq. 24.

$$c_{Qout}(h) = (\sum_{i \neq h} c_{OUT}(i,h) \cdot OUT(i,h))/Q_{out}(h), \text{ when } Q_{out}(h) > 0 \quad \text{(Eq. 35)}$$

The unit cost of the discharged energy c_{OUT} in a pair (h,j) (see section 4) can be determined by considering the increase in the unit cost of the charged energy c_{IN} in the same pair due to heat losses:

$$c_{IN}(h,j) = c_{Qin}(h) \quad \text{(Eq. 36)}$$

$$c_{OUT}(h,j) = c_{IN}(h,j) \cdot IN(h,j)/OUT(h,j), \text{ when } OUT(h,j) > 0 \quad \text{(Eq. 37)}$$

Tab. 3 presents the unit costs obtained for internal flows and products of the system. It was verified that the

unit costs of the final products c_{Ed} and c_{Qd} are always lower than the cost of their separate production.

Tab. 3: Unit costs of the main internal flows and products of the system, in €/kWh

Hour	cEd	cWcc	cWpvv	cQd	cQa	cQcc	cQin	cQout	d[1]
1	0.0566	0.0556	-	0.0139	-	0.0139	0.0139	-	0.4444
2	0.0564	0.0556	-	0.0139	-	0.0139	0.0139	-	0.4444
3	0.0561	0.0556	-	0.0139	-	0.0139	0.0139	-	0.4444
4	0.0558	0.0556	-	0.0139	-	0.0139	0.0139	-	0.4444
5	0.0556	0.0556	-	0.0140	-	0.0139		0.0145	0.4444
6	0.0555	0.0555	-0.0001	0.0163	0.0250	0.0139		0.0144	0.4446
7	0.0540	0.0553	-0.0011	0.0202	0.0250	0.0138	0.0202	-	0.4470
8	0.0518	0.0550	-0.0025	0.0194	0.0250	0.0137		0.0174	0.4504
9	0.0498	0.0548	-0.0033	0.0181	0.0250	0.0137		0.0149	0.4522
10	0.0479	0.0545	-0.0047	0.0165	0.0250	0.0136	-	-	0.4555
11	0.0468	0.0545	-0.0045	0.0131	0.0250	0.0136	-	-	0.4551
12	0.0466	0.0547	-0.0035	0.0122	0.0250	0.0137	-	-	0.4527
13	0.0476	0.0553	-0.0009	0.0083	-	0.0138	0.0083	-	0.4466
14	0.0487	0.0556	-	0.0087	-	0.0139	0.0087	-	0.4444
15	0.0502	0.0556	-	0.0094	-	0.0139		0.0087	0.4444
16	0.0513	0.0556	-	0.0111	0.0250	0.0139		0.0087	0.4444
17	0.0530	0.0556	-	0.0189	0.0250	0.0139	0.0189	-	0.4444
18	0.0553	0.0556	-	0.0202	0.0250	0.0139	0.0202	-	0.4444
19	0.0569	0.0556	-	0.0202	0.0250	0.0139	0.0202	-	0.4444
20	0.0569	0.0556	-	0.0202	0.0250	0.0139		0.0203	0.4444
21	0.0570	0.0556	-	0.0194	0.0250	0.0139	-	-	0.4444
22	0.0571	0.0556	-	0.0177	0.0250	0.0139	-	-	0.4444
23	0.0573	0.0556	-	0.0165	0.0250	0.0139	-	-	0.4444
24	0.0568	0.0556	-	0.0165	0.0250	0.0139	-	-	0.4444
Day	0.0532	0.0554	-0.0020	0.0162	0.0250	0.0138	0.0141	0.0145	0.4464

[1] Discount applied to the cogenerated products, nondimensional.

Photovoltaic production and/or selling of electricity contribute to reducing c_{Ed}. In fact, at hour 12, when the system is selling electricity to the grid and the PV production is highest, c_{Ed} reaches its lowest value, 53% cheaper than p_{ep}. On the other hand, c_{Ed} peaks at hour 23, when there is no PV production and the system is purchasing electricity from the grid. Then, c_{Ed} is only 43% cheaper than p_{ep}. Considering the unit cost of the heat supplied to the consumer centre, it plunges at hour 13, when solar thermal production is highest, attaining a 67% reduction relative to the cost of producing heat in the AB. The highest c_{Qd} takes place at hour 20, when there is no solar thermal production, the AB works at full load and the TES is in discharging mode. At this hour, the reduction in c_{Qd} is of about 19%.

Regarding the products of the cogeneration subsystem, c_{Wcc} and c_{Qcc}, their unit costs are aprox. 45% cheaper than the cost of their conventional separate productions. This is due to the discount d applied, as explained earlier. The discount values increase between hours 6 and 13 because of the selling of cogenerated electricity to the grid. The income associated with the selling of E_{cs} is incorporated into the cogenerated products, reducing their unit costs and increasing the discount in those hours, as can be seen from Tab. 3.

By considering free of charge the solar resource, the income due to the selling of photovoltaic electricity to the grid results in negative unit costs of the photovoltaic electricity supplied to the system c_{Wpvv}, which contributes to lowering even further c_{Ed}.

Similar to Fig. 4, Fig. 6 presents the internal costs of the charged and discharged heat from the TES, for each pair (j,k) and for each hourly period z.

Pair (j,k)	1	2	3	4	5	6	7	8	9	10...12	13	14	15	16	17	18	19	20	21...24
(1,5) cIN, cOUT	0,0139				0,0145														
(1,9) cIN, cOUT	0,0139								0,0151										
(2,6) cIN, cOUT		0,0139				0,0145													
(2,8) cIN, cOUT		0,0139						0,0148											
(2,9) cIN, cOUT		0,0139							0,0149										
(3,8) cIN, cOUT			0,0139					0,0146											
(4,6) cIN, cOUT				0,0139		0,0142													
(7,8) cIN, cOUT							0,0202	0,0204											
(13,16) cIN, cOUT											0,0083			0,0085					
(14,15) cIN, cOUT												0,0087	0,0087						
(14,16) cIN, cOUT												0,0087		0,0088					
(17,20) cIN, cOUT															0,0189			0,0195	
(18,20) cIN, cOUT																0,0202		0,0206	
(19,20) cIN, cOUT																	0,0202	0,0204	
cQin(z)	0,0139	0,0139	0,0139	0,0139	0,0000	0,0000	0,0202	0,0000	0,0000	0,0000	0,0083	0,0087	0,0000	0,0000	0,0189	0,0202	0,0202	0,0000	0,0000
cQout(z)	0,0000	0,0000	0,0000	0,0000	0,0145	0,0144	0,0000	0,0174	0,0149	0,0000	0,0000	0,0000	0,0087	0,0087	0,0000	0,0000	0,0000	0,0203	0,0000

Fig. 6: Internal costs of charged and discharged heat from the TES

As can be seen from Fig. 6, the unit cost of the heat discharged from the TES c_{Qout} is always lower than the cost of its separate production (p_{fa}/η_{AB} = 0.025 €/kWh). Looking into each section (j,k), it can be noted the considerable variation of c_{Qout} throughout the day, which reaches a 133% difference between its highest and lowest values. Such variations are due to the nature of the charged heat. Different system equipment produce heat at different unit costs, e.g. c_{Qa} = 0.025 €/kWh, c_{Qcc} = 0.0139 €/kWh and c_{Qstt} = 0 €/kWh. Because the CM operates at full load at all hourly periods, the unit cost of the charged heat will be closer or farther from c_{Qcc} depending on its share in the total heat produced. For example, for hours 1 to 4, $c_{Qin} = c_{Qcc}$ because all the thermal energy produced by the system comes from the CM. In hours 7 and 17 to 19, there is a higher share of conventional than cogenerated heat (e.g. 57% Q_a and 43% Q_{cc}, for hour 7), resulting in a c_{Qin} closer to c_{Qa}. On the other hand, in hours 13 and 14 the free solar resource allows the c_{Qin} to be lower than c_{Qcc} (e.g. 62% Q_{cc} and 38% Q_{stt}, for hour 14).

6. Closure

Cogenerated Heat and Power systems have been progressively used in commercial and residential buildings in order to reduce primary energy consumption and costs of the energy services relative to the separate conventional production. The present work proposed to analyse a cogeneration system assisted with solar thermal heat and photovoltaics, located in Zaragoza (Spain). The daily optimal operation for a representative day in April was obtained by a linear programming model developed in LINGO.

The marginal cost analysis evinced the fundamental difference between (i) storing excess heat for later consumption because it is a better option than wasting it into the environment, and (ii) producing heat to be stored in order to guarantee supply in a later period.

Thermoeconomic analysis was used to determine the cost of internal flows and final products of the system. It has been shown that the electricity and heat produced by the cogeneration system were always cheaper than the separate conventional production, e.g. electricity purchase from the national electric grid and onsite heat production in an auxiliary boiler. However, it must be noted that the way in which costs are allocated to products will influence the consumer's behaviour. The incorporation of a TES adds a new dimension to the cost allocation problem: not only it requires to know from which equipment the heat produced comes from, but also in which time period it was produced.

7. Acknowledgments

This work was developed in the frame of the research project ENE2014-57262-R, partially funded by the Spanish Government (Energy Program), the Government of Aragon (Spain) and the European Union (FEDER Program). The authors also want to acknowledge the program "Ciência sem Fronteiras" offered by CNPq (Brazil).

8. References

AEMET, 2010. Guía Resumida del Clima en España 1981-2010 [WWW Document]. URL http://www.aemet.es/en/conocermas/recursos_en_linea/publicaciones_y_estudios/publicaciones/detalles/guia_resumida_2010 (accessed 8.30.16).

AENOR, 2007. Norma UNE 94003: Datos climáticos para el dimensionado de instalaciones solares térmicas.

Ashouri, A., Fux, S.S., Benz, M.J., Guzzella, L., 2013. Optimal design and operation of buildings services using mixed-integer linear programming techniques. Energy, Vol. 59, pp. 365-376.

Buoro, D., Pinamonti, P., Reini, M., 2014. Optimization of a distributed cogeneration system with solar district heating. Applied Energy, Vol 124, pp. 298-308.

Chicco, G., Mancarella, P., 2009. Distributed multi-generation: A comprehensive view. Renew. Sustain. Energy Rev. 13, 535–551.

Collares-Pereira, M., Rabl, A., 1979. The average distribution of solar radiation: correlations between diffuse and hemispherical and between daily and hourly insolation values. Solar Energy, Vol. 22, pp. 155–184.

Directive 2010/31/EU of the European Parliament and the Council of 19 May 2010 on the energy performance of buildings. Official Journal of the European Union 18.06.2010.

Duffie, J.A., Beckman, W.A., 2013. Solar Engineering of thermal processes, 4th Ed. Wiley.

Erbs, D.G., Klein, S.A., Duffie, J.A., 1982. Estimation of diffuse radiation fraction for hourly, daily and monthly-average global radiation. Solar Energy, Vol. 28, pp. 293–302.

Erbs, D.G., Klein S.A., Beckman, W.A., 1983. Estimation of degree-days and ambient temperature bin data from monthly-average temperatures. ASHRAE J. 25, 60–65.

LINGO, 2011. The modeling language and optimizer. Lingo Systems [WWW Document]. URL http://www.lindo.com/ (accessed 8.11.16).

Liu, B.Y.H., Jordan, R.C., 1960. The interrelationship and characteristic distribution of direct diffuse and total solar radiation. Solar Energy Vol. 4, pp. 1–19.

Lozano, M.A., Valero, A., 1993. Theory of the exergetic cost. Energy, Vol. 18, pp. 939-960.

Lozano, M.A., Carvalho, M., Ramos, J.C., Serra, L.M., 2009a. Thermoeconomic analysis of simple trigeneration systems. Int. J. Thermodyn. 12, 147–153.

Lozano, M.A., Carvalho, M., Serra, L.M., 2009b. Operational strategy and marginal costs in simple trigeneration systems. Energy 34, 2001–2008.

Lozano, M.A., Ramos, J.C., Serra, L.M., 2010. Cost optimization of the design of CHCP (combined heat, cooling and power) systems under legal constraints. Energy, Vol. 35, pp. 794-805

Lozano, M.A., Carvalho, M., Serra, L.M., 2011. Allocation of economic costs in trigeneration systems at variable load conditions. Energy and Buildings, Vol. 43, pp. 2869-2881.

Mancarella, P., 2014. MES (multi-energy systems): An overview of concepts and evaluation models. Energy 65, 1–17.

Serra, L.M., Lozano, M.A., Ramos, J.C., Ensinas, A.V., Nebra, S.A., 2009. Polygeneration and efficient use of natural resources. Energy, Vol. 34, pp. 575-586.

Yokoyama, R., Shinano, Y., Taniguchi, S., Ohkura, M., Wakui, T., 2015. Optimization of energy supply systems by MILP branch and bound method in consideration of hierarchical relationship between design and operation. Energy Conversion and Management, Vol. 92, pp. 92-104.

Conference Proceedings

EuroSun 2016
Palma de Mallorca (Spain), 11 - 14 October 2016

Solar Driven Organic Rankine cycle (ORC) – A Simulation Model

Florian Theede, Andrea Luke

Institute of Technical Thermodynamics, University of Kassel, Kassel (Germany)

Abstract

In this work, an ORC-process driven by solar heat is simulated, analyzed and dimensioned for reliable electricity generation in remote areas, especially for refugee camps. The most common fluid for ORC-systems is R245fa. In 2022 this fluid will not be available because of the f-gas decree from 2015. Butane, pentane, R1233zd(e), R1234ze(z) are fluids with low global warming potential and are simulated in the ORC-process to analyze the performance and potential to replace R245fa. From the performance results, R1233zd(E), R1234ze(z) and n-butane have the potential to replace R245fa in organic Rankine cycles with low temperatures. Evacuated tube collector with the heat pipe system in low flow is found to be the best collector type for this application. 60 m² ETC collector area is needed for the generation of 2 kW electrical power. The increasing thermal efficiency of the ORC with higher source temperatures has more influence than the decreasing collector efficiency. In conclusion, the solar driven organic Rankine cycle is a potential alternative off-grid power technology to generate reliable electricity in remote areas in the sunbelt area. The whole system as a container concept is simple, robust, low-maintenance, mobile and can power, for example, a medicate centrum and public light with 2kW.

Keywords: *Organic Rankine cycle, low temperature waste heat, working fluid, solar thermal energy*

1. Introduction

In many remote areas exist no electricity grid or it is very unreliable. The international energy agency reported 1.2 billion people without access to electricity in the world (WEO, 2015). According to the general secretary Ban Ki Moon, all people should have universal access to modern energy sources. People in developing countries should have access to renewable and environmentally friendly energy sources (se4all, 2016). Electricity is necessary to develop the economy and to improve the health and education situation. Many people without electricity live in the rising refugee camps. In the end of 2015, 63.5 million people refuge from war, poverty and religious or political persecution, increasing tendency (UNHCR, 2015). A big part of the refugees live in camps, with until 400000 people in one camp. The greatest camps are located in countries like Kenya, Ethiopia, Jordan, Gaza Strip, Mauritania, South Sudan, Uganda, Tanzania and India. In refugee camps 90 % of people have no access to electricity. (Leach, 2015) Big problems in these camps are the medical care without a reliable electricity supply and the dark nights without light and high criminal violation.

The most less-developed countries are located equatorial respectively in the sunbelt of the earth, therefore solar energy represents a big potential for these countries. A big problem by using the sun for electricity generation with photovoltaic is the unreliability in times without sun and high priced power stores. An alternative is to heat up water by solar collectors and store it in a boiler, to save energy for the few hours without sun. An organic Rankine cycle (ORC) generates reliable electricity with the heated water out of the storage. ORC-processes in connection with solar heating and a heat reservoir have the potential for safe and environmental friendly electricity-generation in these camps and remote villages. With the right dimensioning of collector field and heat reservoir it is possible to generate enough electricity for medical equipment and light supply. Also a thinkable task is the stability of isolated electricity grids (rotated masses and black start) and energy supply in public buildings, server rooms and hospitals. Many new projects exist at the moment in modernization and new building of hospitals in less-developing countries in Africa.

A study on a 3kW solar driven ORC with concentrated collectors and temperatures around 150°C is published by Orosz et al. (2009). Organic Rankine cycles have usually small thermal efficiencies, because of the usage of

doi:10.18086/eurosun.2016.05.08 Available at http://proceedings.ises.org

low temperature heat sources with a small exergetic part of energy like solar thermal systems. The design of the components and the choice of a suitable working fluid are important to ensure a proper working process without any losses in the efficiency. Studies on the fluid selections for ORC-processes especially driven by a solar heat source are made from researchers like Tchanche et al. (2008), Rayegan and Tao (2011), Delgado-Torres and Garcia-Rodrigez (2010). They all did not analyzed new environmental friendly refrigerants like R1233zd(e) and R1234ze(z).

The biggest challenge to design an ORC-process is the selection of the working fluid and the design of the heat exchanger for the application in dependence of specified temperature levels. In this work, the heat source is solar energy and usually bounded in temperatures between 20°C and 180°C, depending on collector type, without considering concentrated systems.

In this paper, an ORC driven by solar heat is simulated, analyzed and dimensioned for reliable electricity generation in remote areas especially for refugee camps. The whole system should be simple, robust, with a low-maintenance and mobile with 2kW electric power for a medicate centrum and public light. The most common fluid for ORC-systems is R245fa. In 2022 this fluid will not available because of the f-gas decree from 2015 (EG-VO 517, 2014). Different working fluids in the ORC-process for the temperatures of a designed solar system are simulated to analyze the performance of low GWP working fluids for the potential replacement of R245fa.

2. System description and dimensioning

The whole system is dependent from the climate and weather conditions. Refugee camps located in the sunbelt and offer a high potential in the usage of solar energy. As reference in this paper, Aleppo is chosen from meteonorm software. The ambient temperature and the radiation in hour values are relevant. The system schematic is shown in figure 1. On the right side, the ORC is illustrated; on the left side the solar system. The systems are connected by the evaporator as heat exchanger and a storage tank for the compensation of hours without sun. It is also possible to operate directly without storage in hours with maximum turbine power output and high sun radiation to raise the efficiency.

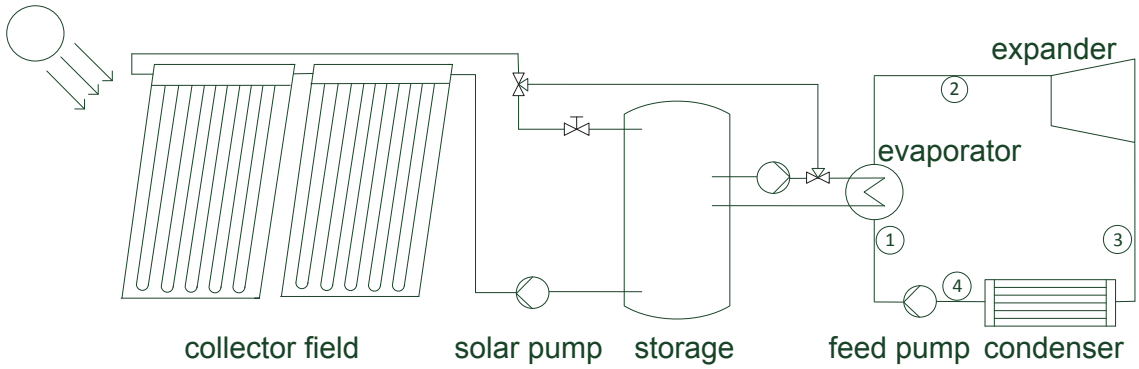

Fig. 1: Overview of the electricity-generation-system with solar heat and ORC

Solar collector:

Because of the limitation in Carnot efficiency and the dependence of exergetic and thermal efficiency on temperature [Theede and Luke, 2016], higher temperatures are preferable for the ORC. To avoid complex collectors with concentrated systems and to use water for a simple system, an evacuated tube collector (ETC) with the heat pipe system is chosen. This collector type has a high operation safety because of the easy replaceable tubes, need less space than flat collectors, has a freezing protection and has a higher performance at high temperatures, because of the better isolation. Collector outlet temperatures are in the rage of 80°C and 140°C. The usage of water at temperatures of 140°C results in a pressure level of maximum 4 bar to avoid evaporation with low heat transfer coefficients. The low flow operation is chosen to generate high temperatures in a big solar system. In this work, the mass flow is calculated to 0.28kg/s in the simulation with an assumed flow rate of 20 l/m²h and a first evaluated collector area of 55m². The fluid velocity is fixed at 1 m/s to avoid high pressure losses in the pipes. The commercial solar collector named Vitosol-T SPA is chosen for the dimensioning and simulation. It is an ETC working on the heat pipe principle. Other collector data with the optical efficiency and heat loss coefficients for the calculation of the collector efficiency are listed in table 1.

The collector efficiency is calculated in

$$\eta_{Coll} = \eta_{op} - \frac{a_1 \cdot (T_m - T_a)}{G} - \frac{a_2 \cdot (T_m - T_a)^2}{G} \qquad \text{(eq. 1)}$$

and depends on the collector a_1, a_2 and η_0 data on the mean average fluid temperature in collector T_m, the ambient temperature T_a and the sun radiation G.

In Figure 2, the characteristic of the ETC is shown. The efficiencies are calculated with radiations between 200 W/m² and 1200 W/m² and an average ambient temperature of 18°C in Aleppo. The collector efficiency decreases with higher collector temperatures and lower sun radiation. The less strong decreasing efficiency of the ETC in comparison to the decreasing efficiency with higher collector temperature in common flat collectors is conspicuous. Because of the good insulation with the vacuum, this is a big advantage of this collector type.

The product of the hour values of sun radiation from meteonorm and calculated collector efficiencies are taken and summarized to the solar thermal heat energy per square meter. In Aleppo, this value was 1875 kWh/m²a in 2003. This value shows the big potential in the usage of solar thermal energy in this region.

Organic Rankine Cycle:

The ORC-process consists of four components similar to the conventional Rankine cycle, but uses a refrigerant as working fluid to enable the generation of electricity from heat with low temperatures. The feed pump raises the pressure for the evaporation. The fluid is heated up, evaporated completely and superheated in the evaporator. The turbine expands the vapor and generates work, which is transferred in the generator in electricity. Finally, the vapor is condensed at the lower pressure.

The ORC-process should have 2kW of electrical power and generate electricity with a source temperature between 80°C and 130°C. The temperature spread in heat exchangers are 10 K and the evaporator is designed with superheat of 5 Kelvin. The evaporator uses a coaxial heat exchanger because of the simple construction. A tube bundle heat exchanger is not worth because of the slow fluid velocity in the solar process.

Tab. 1: collector data (VITOSOL 200-T SPA)[Q]

gross surface	4.62 m²
absorber surface	3.03 m²
aperture surface	3.13 m²
width	2.061 m
height	2.241 m
optical efficiency η_0	0.81
heat loss coefficient a_1	1.103 W/m²K
heat loss coefficient a_2	0.007 W/m²K
permissible pressure	6 bar

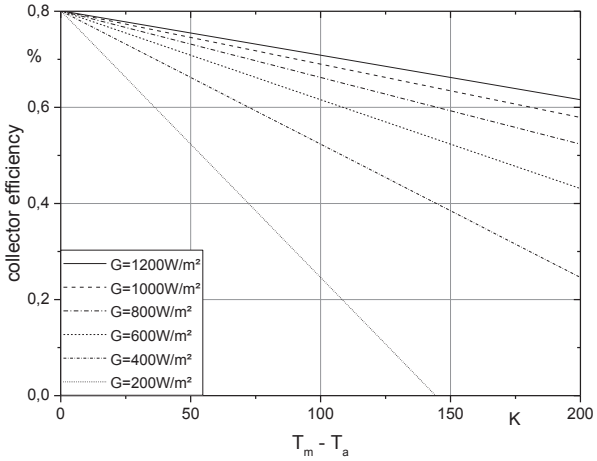

Fig. 2: collector efficiency characteristic of ETC

turbine inlet temp.: 130°C power output: 2 kW isentropic efficiency: 80%	evaporator type: coaxial heat exchanger	condenser type: tube bundle with cross streamed air
feed pump isentropic efficiency: 70%	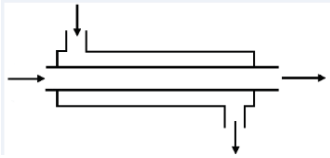	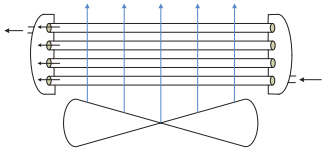
heat source (solar) fluid: water inlet temp.: 140°C pressure: 4 bar velocity: 1 m/s mass flow: 0.28 kg/s	super-heat: 5K velocity: 2 m/s ambient conditions temp.: 18°C pressure: 1 bar	number of tubes: 100 (shifted) inner diameter: 0.5 cm distance between tubes: 1 cm Condensation temp.: T_a+10K air velocity: 20 m/s

A tube bundle heat exchanger with cross streamed air is chosen for the condenser, because of the lack of water as a coolant in remote areas. So the re-cooling temperature is the average ambient air temperature (18°C in Aleppo) plus the temperature spread in the heat exchanger. Many fluids are reviewed in the temperature range until 90°C [Theede]. The best fluids are found to be R245fa and n-butane. This fluids, n-pentane and two new environmental friendly fluids R1233zd(e) and R1234ze(z) with a low global warming potential are analyzed in this paper. The design conditions are summarized in table 2.

3. Simulation tool

The simulation, realized with the engineering equation solver (EES), is based on change of state in the thermodynamic cycle and is calculated with energy balances, equations of states and the definitions of the isentropic performance of expander and feed pump in equation (3) until (8).

turbine: $P_T = \dot{m} \cdot (h_3 - h_2)$ (eq. 3) $\eta_{s,T} = \frac{h_3 - h_2}{h_{3s} - h_2}$ (eq. 4)

feed pump: $P_P = \dot{m} \cdot (h_1 - h_4)$ (eq. 5) $\eta_{s,P} = \frac{h_{1s} - h_4}{h_1 - h_4}$ (eq. 6)

condenser: $\dot{Q}_C = \dot{m} \cdot (h_3 - h_4)$ (eq. 7)

evaporator: $\dot{Q}_E = \dot{m} \cdot (h_2 - h_1)$ (eq. 8)

where P is power of turbine or feed pump, $\dot{Q}$ is heat transfer rate, $\dot{m}$ is the mass flow of the working fluid, h is the enthalpy in the points of the process, calculated with the equation of states of the fluids. The pressure losses are neglected and evaporation and condensation are assumed to be isobaric. The heat exchangers are simulated according to the kinetic. The simplified simulation structure for the main process is shown in figure 3. The code calculates all working conditions and the parameters of the components.

The results of the thermodynamic process in equation (3-8) are used to calculate the thermal and exergetic efficiency:

$$\eta_{th} = \frac{P_T}{\dot{Q}_E + P_P} \quad \text{(eq. 9)}$$

$$\eta_{ex} = \frac{P_T}{\frac{T_3 - T_a}{T_3}\dot{Q}_E + P_P} \quad \text{(eq. 10)}$$

T_3 is the turbine inlet temperature and T_a is the ambient temperature. The other simulation parameters are reported in table 2. The operating conditions of the heat source are taken from the solar collector calculations.

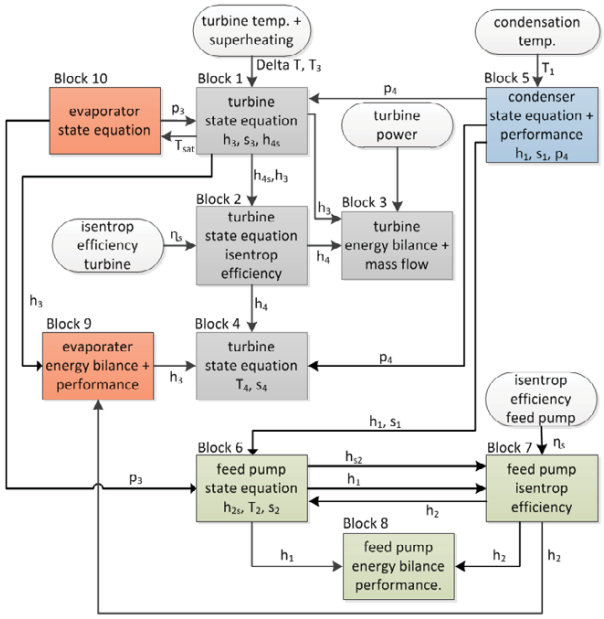

Fig. 3: simplified simulation structure of the ORC

A coaxial heat exchanger is set for pre-heating, evaporation and super-heating and a tube bundle condenser with cross streamed air for desuperheating and condensation. The thermodynamic parameters of the heat exchangers are numerically calculated with a segment-method. The different heat transfer coefficients are calculated and generate the overall heat transfer coefficient for the cell with

$$\frac{1}{k} = \frac{d_o}{d_i \cdot \alpha_{prim}} + \frac{d_o}{2 \cdot \lambda_{Co}} \cdot ln\frac{d_o}{d_i} + \frac{1}{\alpha_{sec}} \qquad \text{(eq. 11)}$$

for each cell with a default length, where k is the overall heat transfer coefficient, d_o outer diameter, d_i inner diameter, α_{prim} heat transfer coefficient inside the pipe, α_{sec} heat transfer coefficient on the outside of the pipe and λ_{Co} the thermal conductivity of copper. At the same time, conditions for the next segment like the new temperatures, vapor quality and the heat flux are calculated. The heat flux in the first segment is simulated with a loop of the first cell that compares the heat fluxes of two consecutive loop cycles until the error is negligible.

In this work, correlation of Steiner (Kind and Saito, 2013) are chosen to calculate the heat transfer coefficients for flow boiling inside the evaporator and the correlation of Gnielinski (2013) for pre- and super-heating plus the heat transfer in the gap (solar fluid) in the coaxial heat exchanger are chosen. The condensation correlation from Thome et al. (2003) is used in the inner tube flow condensation and Gnielinski (2013) for the circulated flow of the air around the tubes. The desuperheater is calculated by Gnielinski (2013) for flow in tubes.

4. Results and discussion

Some primary results of the simulation and conditions of the fluids are reported in table 3. The critical point of the fluids is between 150.1°C and 196.5°C. The differences in the critical temperature of R245fa, n-butane, R1233zd(e) and R1234ze(z) lie in a small range of 15.5 K. R245fa is in many reviews the best and common refrigerant for ORC-process with low temperature heat sources. The F-gas decree from the January 1st, 2015 [EG-VO 517, 2014] prohibits the use of refrigerants with a GWP higher than 150 at 2022. So R245fa will not available for ORC projects in future. The GWP from n-butane, n-pentane, R1233zd(e) and R1234ze(z) are 5 or lower and could be an alternative to replace R245fa.

The pressure levels in evaporation and condensation in the design point are presented in table 3. Pressure levels in evaporation in dependence of the turbine inlet temperature are shown in figure 4. The evaporation and condensation pressure level of the fluids are similar. Only n-pentane has a significant lower vapor pressure curve. The mass flow of process and of different fluids in design point are between 25 g/s (pentane) and 89 g/s (R1234ze(z)). The differences in mass flow are due to the enthalpy difference in the turbine between the given condensation and evaporation pressure level in equation 3. The enthalpy range of the hydrocarbons is higher than the other fluids. R1234ze(z) with the highest mass flow has a significant small enthalpy difference in the turbine. A high mass flow requires bigger components and more use of material, but in this case all mass flows are very low. The feed pump depends on the pressure difference between low and high pressure and the mass flow.

The heat exchanger are the biggest elements of the ORC. Depending on the working fluid, the evaporator and condenser have different heat transfer areas. In figure 5 the evaporator heat transfer surface in dependence of the turbine inlet temperature is shown. The differences in the volume of the evaporator depend mainly in the heat transfer coefficient. In evaporation, the pressure level has the biggest effect in the value of heat transfer coefficient. The increasing evaporation pressure with higher turbine inlet temperatures (see fig. 4) results in a decreasing heat transfer surface in the evaporator with increasing temperatures (see fig. 5). Butane and R1234ze(z) with the highest evaporation pressures have the smallest evaporator. The fluid properties, in particular the thermal conductivity, have the biggest influence on heat transfer coefficient in condensation.

Tab. 3: ORC results of the simulation and fluid conditions on the design point

Fluid	critical temp.	pressure evap.	pressure cond.	massflow	pump power	HX(evap.) surface	HX(cond.) surface	GWP
[-]	[°C]	[bar]	[bar]	[kg/s]	[W]	[m^2]	[m^2]	[-]
R245fa	154	21.25	1.65	0.052	53.1	0.181	3.723	1030
n-butane	152	24.13	2.68	0.027	70.1	0.175	3.695	4
n-pentane	196.5	9.98	0.77	0.025	26.2	0.199	3.274	5
R1233zd(e)	165.6	17.33	1.44	0.051	45.2	0.194	3.662	1
R1234ze(z)	150.1	22.32	1.98	0.089	60.3	0.175	3.603	< 1

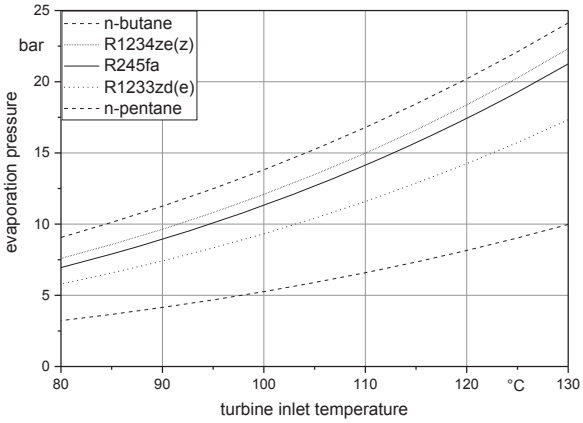

Fig. 4: evaporation pressure in dependence of turbine inlet temperature

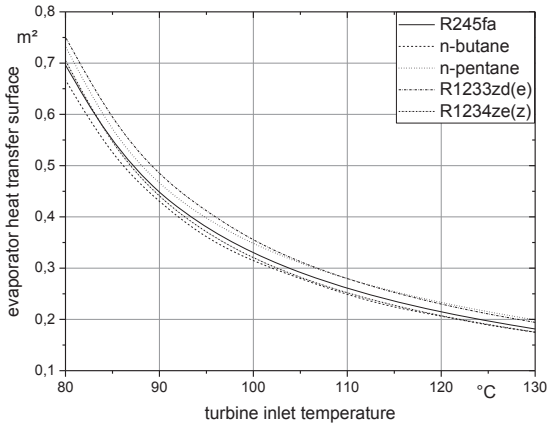

Fig. 5: evaporator heat transfer surface in dependence of the turbine inlet temperature

The design point of the evaporator can be fixed at medium collector temperatures. In ORC-operation driven by the heat of the boiler with lower temperatures, the extra pump can produce (see fig. 1) a higher heat transfer coefficient on the secondary side of the heat exchanger by raising the mass flow.

In table 4 the efficiency results of the ORC, the needed thermal power and energy for 2kW turbine power plus the efficiency of the whole system and the resulting collector area in the design point at 140 degrees source temperature is shown. The thermodynamic efficiency of the ORC-process in dependence of the turbine inlet temperature is shown in figure 6. The thermal efficiency depends on the turbine power, feed pump power and the transferred heat in the evaporator and increases with a slight digressive trend. The difference between the thermal efficiency of the best fluid (R1234ze(z)) and the worst fluid (n-pentane, R245fa) in design point is about 3.85%. These small differences are due to the similar physical characteristics of the fluid. R1234ze(z) has the best thermal efficiency (15.6%) because of the smallest difference of the evaporation temperature to the critical point. So the relation between specific heat capacity and the evaporation enthalpy is the smallest.

Tab. 4: The results of the simulation on the design point

Fluid	thermal efficiency (ORC)	exergetic Efficiency (ORC)	heat flux evaporator	thermal energy	system efficiency* (ORC+solar)	collector area
[-]	[%]	[%]	[kW]	[MWh/a]	[%]	[m²]
R245fa	15.0	53.5	13.27	116.25	9.59	61.99
n-butane	15.2	53.9	13.10	114.76	9.71	61.19
n-pentane	15.0	53.8	13.28	116.32	9.61	62.02
R1233zd(e)	15.4	54.8	12.98	113.68	9.82	60.62
R1234ze(z)	15.6	55.5	12.76	111.80	9.97	59.61

* sun radiation 800 W/m²

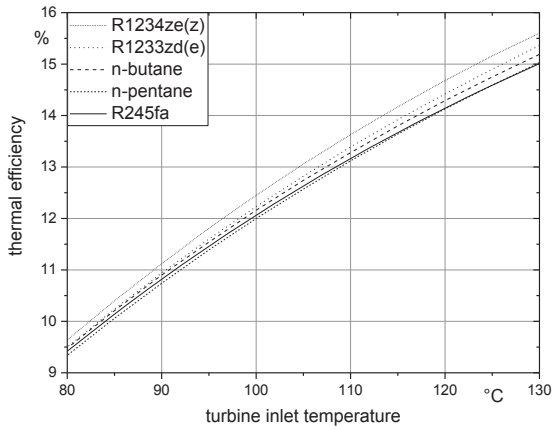

Fig. 6: thermal efficiency of the ORC-process in dependence of the turbine inlet temperature

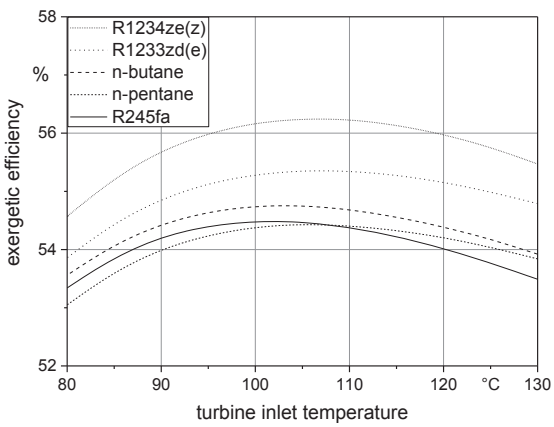

Fig. 7: exergetic efficiency of the ORC-process in dependence of the turbine inlet temperature

The exergetic efficiency of the fluid in dependence of the turbine inlet temperature is shown in figure 7. The exergetic efficiency in equation 10 includes the quality of the heat source (solar) in relation of the ambient temperature. With increasing temperature, the exergetic efficiency increases first, because the increasing exergetic part of the transferred heat is higher than the efficiency loss than the increasing pump power. After the point with the maximal exergetic efficiency at ca. 105°C, the increasing pump power has more influence in the exergetic efficiency and the value decreases. All differences in exergetic efficiency of the fluids with fixed turbine power and fixed ambient temperature depend on the feed pump power and the transferred heat in the evaporator (preheating, evaporation, superheating). The difference between the exergetic efficiency of the best fluid (R1234ze(z)) and the worst fluid (R245fa) in design point is about 3.60%. R245fa has the worst exergetic efficiency because of a combination of a higher relation of specific heat capacity and evaporation enthalpy, a higher feed pump power and a high enthalpy difference between high and low pressure combined with more preheating. The performance data of R1233zd(E) and R1234ze(z) in the respective temperature range are comparable to or better than the performance data of R245fa. R1233zd(E) and R1234ze(z) shows well performance results in figure 6 and 7 to have the potential to replace R245fa in ORC future.

The solar thermal energy of the chosen collector in Aleppo (2003) calculated with hour values in the design point equals 1875.35 kWh/m²a. Other thermal energy values for different collector outlet temperatures are listed in table 5. The thermal energy increases with lower temperatures, because of the rising collector efficiency (see in equation 1).This quantity of thermal energy is in good agreement with other works [Kalogirou, 2002]. The required heat to generate 2kW electricity over the whole year is reported in table 4. The quotient of the thermal energy and the solar thermal energy per m² equals the needed collector area. The collector area in dependence of the source temperature is plotted in figure 8. The collector area decreases with higher temperatures because of the rising thermal efficiency of the ORC. The trend is digressive because of the decreasing collector efficiency with higher collector temperatures.

Tab. 5: solar thermal energy

temperature	solar thermal energy
[°C]	[kWh/m²a]
140	1875.35
130	1899.33
120	1921.90
110	1942.97
100	1962.54
90	1980.61

Tab. 6: collector and system efficiency in design point for R1234ze(z)

sun radiation	collector efficiency	system efficiency
[W/m²]	[%]	[%]
600	59.61	9.13
800	63.92	9.97
1000	67.15	10.48

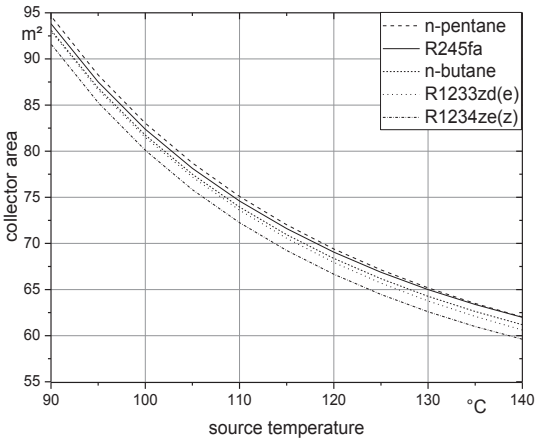

Fig. 8: collector area in dependence of the source temperature

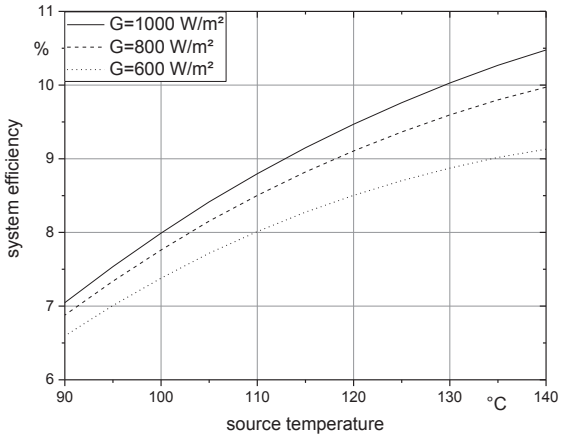

Fig. 9: system efficiency in dependence of the source temperature

In table 6 the collector efficiencies and the system efficiencies in three cases of sun radiation are listed. The values are generated in the design point and for the fluid R1234ze(z). Values for other fluids are listed in table 4 with a fix sun radiation of 800 W/m². The product of the collector efficiency and the thermal efficiency of the ORC equals the system efficiency. The system efficiency increases with higher sun radiations because of increasing collector efficiency. The dependence of the system efficiency with varying source temperature is plotted in figure 9. The system efficiency increases with the source temperature.

The trend is digressive because the collector efficiency is the product of the collector efficiency and the thermal efficiency of the ORC equals the system efficiency. The system efficiency increases with higher sun radiations because of increasing collector efficiency. The dependence of the system efficiency with varying source temperature is plotted in figure 9. The system efficiency increases with the source temperature. The trend is digressive because the collector efficiency is decreasing with higher temperatures. So the influence of the increasing thermal efficiency of the ORC in figure 6 is higher than the decreasing collector efficiency in figure 2. The trend of the system efficiency is more digressive with lower radiations because of the relation of the strong degreasing collector efficiency with lower sun radiation (figure 1). The trend of the system efficiency with 600 W/m² radiation is more decreasing and reaches nearly the maximum point.

In the design point with the selected ETC the system needs 59.6 m² collector absorber area with the fluid R1234ze(z). The absorber area of a ETC has 3.03 m² with 24 heat pipes (see table 1). So the whole system needed 20 ETCs, respectively 480 heat pipes to generate 2 kW electricity over the year. That's a value of 29.8 m²/kWe.

The whole system should be designed simple, robust, low-maintenance and mobile for refugee camps in remote areas. Solar thermal energy and the orc system are much tested and both systems need, with a good control engineering system, no supervision personnel. To make the system simple and mobile an ISO-container is most suitable (see in figure 10). The solar system is installed on the roof of the container and the ORC-process and water boiler are installed in the container. The transport goes by ship and truck. An ISO-container has a volume of 67.4 m² and a roof area of 28.3 m² (12.032 m length, 2.352 m width, 2.382 m high).

An optimal collector slope is the geographic latitude minus ca. 10 degree (Eicker, U., 2011). Aleppo with geographic latitude of 36.2 degree has an optimal collector slope of 26.2 degree. With a space factor of 2.2, four collectors take place on one container in the operation. With an installed rail system 10 collectors take place on one container. Two containers get enough space for a collector field of a 2 kW solar-ORC-power-system. The boiler can be free scaled, because there is enough space in the container. The ORC and boiler take place in one container and the other container can use for service quantities and other technical systems to compensate the hours were no electricity is needed. A potential technology is a water treatment system.

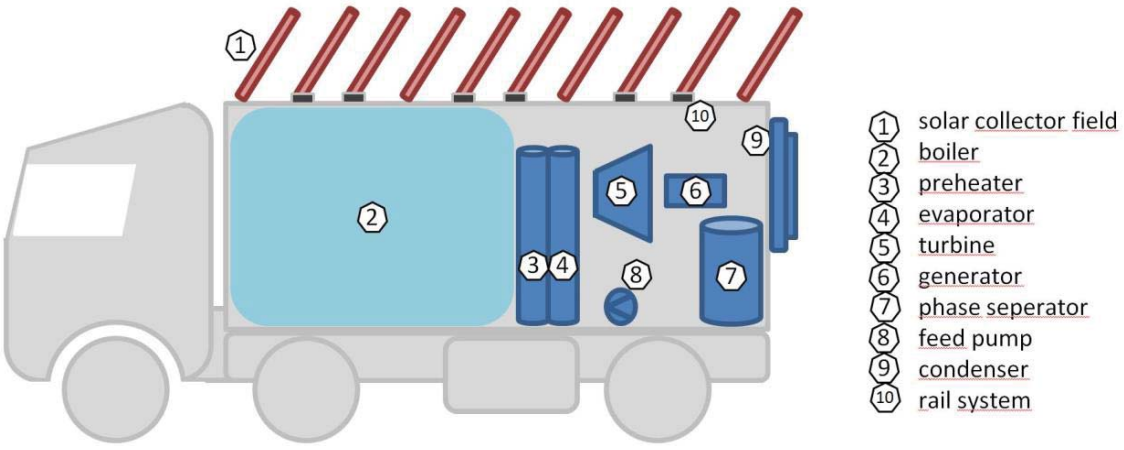

Fig. 10: schematic drawing of the solar driven ORC as container system

5. Conclusions

An ORC-process driven by solar heat is simulated, analyzed and dimensioned in this work for reliable electricity generation in remote areas, especially for refugee camps. ORC-processes in connection with solar heating and a heat reservoir plus a high value of sun radiation in remote areas in the sunbelt have the potential for safe and environmental friendly electricity-generation. The whole system as a container concept is simple, robust, low-maintenance, mobile and can power for example a medicate centrum and public light with 2kW. Evacuated tube collectors with the heat pipe system in low flow are chosen as the best collector type for theses application because of the easy replaceable tubes, higher performance at high temperatures (better isolation). 60 m² ETC collector area is needed for the generation of 2 kW electrical power. This value increases with lower temperatures. The system efficiency is increasing with higher source temperatures. Therefore the increasing thermal efficiency of the ORC with higher source temperatures has more influence than the decreasing collector efficiency. The most common fluid for ORC-systems is R245fa. In 2022 this fluid will not be available because of the f-gas decree from 2015. Four different fluids (n-butane, n-pentane, R1233zd(e), R1234ze(z)) with low GWP for the temperatures of a designed solar system are simulated in the ORC-process to analyze the performance and potential to replace R245fa. All fluids produce similar results in terms of evaporation pressure and thermal respectively exergetic efficiency. Only n-pentane has lower efficiencies and evaporation pressures in comparison to the other fluids. A local maximum point for the exergetic efficiency is found. After this point, the increasing pump power with higher temperatures has more influence as the raising exergetic part of solar heat. R1234ze(z) offer a high mass flow because of the low enthalpy difference between high and low pressure in the turbine. From the in performance results R1233zd(E), R1234ze(z) and n-butane have the potential to replace R245fa in organic Rankine cycles with low temperatures. Other analysis concerning thermal stability, security and economical aspect should be made in future. Also, the pressure losses should be analyzed. In conclusion, the solar driven organic Rankine cycle is a potential alternative off-grid power technology to generate reliable electricity in remote areas in the sunbelt.

6. References

Delgado-Torres, A.M., Garcia-Rodriguez, L., 2010. Analysis and optimization of the low-temperature solar organic Rankine cycle (ORC). Energy Conversion and Management 51, 2846-2856

EG-VO 517-2014, 2014. F-gas decree of the European Union

Eicker, U., 2011. Solarthermische Anlagen. Taschenbuch für Heizung+Klimatechnik, ISBN 3835632027, 75th edition 2011/2012, Oldenbourg Industrieverlag GmbH, Kapitel 5.2 Kollektoren

Galloni, E., Fontana, G., Staccone, S., 2015. Design and experimental analysis of a mini ORC (organic Rankine cycle) power plant based on R245fa working fluid. Energy 90, 268-775

Gnielinski, V., 2013. Durchströmte Rohre & Querangeströmte einzelne Rohrreihen und Rohrbünde. VDI Wärmeatlas, Springer (Berlin), 11. Aufl., G1 & G7

Orosz, M.S., Mueller, A., Quolin, S., Hemond, H., 2009. Small scale solar ORC system for distributed power. SolarPaces conference, Berlin, Germany

Kalogirou, S., 2002. The potential of solar industrial process heat applications. Applied Energy 76, 337-361

Kind, M., Saito, Y., 2013. Strömungssieden gesättigter, reiner Flüssigkeiten. VDI Wärmeatlas, Springer (Berlin), 11. Aufl., H3.4

Leach, Anna, 2015. Clean energy in refugee camps could save millions of dollars. theguardian

Rayegan, R., Tao, Y.X., 2011, A procedure to select working fluids for Solar Organic Rankine Cycles (ORCs). Renewable Energy 36, 659-670

se4all, Sustainable Energy for all, 2016. Strategic framework for results 2016-21

Tchanche, B.F., Papadakis, G., Lambrinos, G., Frangoudakis, A., 2009. Fluid selection for a low-temperature solar organic Rankine cycle. Applied Thermal Engineering 29, 2468-2476

Theede, F., Luke, A., 2016. A simulation model of an ORC-process driven by low temperature waste heat. Heat Powered Cycles 2016 Conference Proceedings

Thome, J. R.: Condensation in horizontal tubes, part 2. New heat transfer model based on flow regimes. Int. J. of Heat and Mass Transfer 46, 3365-3387

UNRA, The UN Refugee Agency, 2015. UNHCR Global Trends 2015

WEO, World Energy Outlook, 2015. WEO 2015 Electricity access database
URL: http://www.worldenergyoutlook.org/resources/energydevelopment/energyaccessdatabase/ (22.09.2016)

7. Nomenclature and symbols

a	heat loss coefficient [W/m²K]
d	diameter [m]
G	sun radiation [W/m²]
h	enthalpy [kJ/kg]
k	overall heat transfer coefficient [W/m²K]
$\dot{m}$	mass flow [kg/s]
P	power [W]
$\dot{Q}$	heat transfer rate [W]
T	temperature [K]
η	efficiency [-]

Subscripts

a	ambient
C	condenser
Co	copper
Coll	collector
E	evaporator
ex	exergetic
I	inner
o	outer
op	optical
P	feed pump
prim	primary
s	isentropic
sec	secondary
T	turbine
th	thermal

Conference Proceedings
EuroSun 2016
Palma de Mallorca (Spain), 11 – 14 October 2016

Integration of solar thermal systems in existing district heating systems

Carlo Winterscheid[1], Jan-Olof Dalenbäck[1] and Stefan Holler[2]

[1] Chalmers University of Technology, Gothenburg (Sweden)

[2] HAWK University of Applied Science and Arts, Göttingen (Germany)

Abstract

The integration of large solar heating systems in district heating (DH) networks with large combined heat and power (CHP) plants is rarely considered. This is often due to low costs for heat but also due to subsidies for the electricity by CHP plants. Possible changes in subsidies and requirements in the reduction of fossil fuel based CO_2 emissions raise an awareness of improving the operational flexibility of fossil fuelled CHP plants. This paper provides a rather simple but detailed methodology of including large solar heating systems in an existing district heating system, where heat is supplied by a large CHP plant. It uses hourly data of load and temperature patterns as well as radiation data and collector efficiency data to determine collector field size and storage size. The possibility of largely independent operation of sub-networks is analysed, which allows different system temperatures. A feasibility study indicates specific heat generating costs for different collector types. It is demonstrated that a sub-network can operate without a back-up boiler and that both network parts benefit from the interaction.

Keywords: *district heating, solar district heating, solar thermal systems*

1. Introduction

The integration of solar thermal systems in DH systems is a more and more common practice in some countries; however, few studies have been performed on methodologies and benefits of integrating solar thermal systems in DH systems that are mainly supplied by large scale CHP plants with low heat generation costs.

The general idea behind including solar collector fields in DH networks is to lower or even completely supply the low heat demand of a DH network during the summer months. Since the 1980s Denmark and Sweden have built many solar heating plants (Fisch et al. 1998). In some of these cases a seasonal storage is used to provide a solar share even above 50 % of the total system demand. The high taxation of primary energy sources supported the ambitions in Denmark that lead to seasonal storages which are only feasible in a very large scale (Meißner et al. 2012). In comparison to the Danish and Swedish developments solar DH systems in Germany started to be built later, at the beginning of the 1990s.

The large DH systems in Germany are generally supplied by large CHP plants. These plants are often operating as base load power producers and can supply heat and electricity at a cost-efficient level during summer and winter due to funding through the CHP production law (KWKG) (Berberich et al. 2015). In addition to the availability of low-cost heat, high and very high system temperatures in the DH systems also prevented solar heat generating systems (Urbaneck et al. 2015). In the case of the DH system Chemnitz, only a large change in the system structure in one district made a change feasible. Possibilities of including solar collector systems in existing DH networks that are not about to change radically and are using large scale CHP plants as a main heat source were rarely analysed. Despite of the higher specific generation costs a solar collector field can also bring several advantages to systems of the mentioned kind.

doi:10.18086/eurosun.2016.05.09 Available at http://proceedings.ises.org

This paper presents aspects where a solar collector field can be beneficial for a DH system based on a large scale CHP plant and how such a collector field can be included. The work was carried out by evaluating the load pattern of a part of an existing DH system in Germany. In the given case the system analyse was based on the following conditions:

- A fixed supply temperature in a connected sub-network that is not needed in the whole system
- A long connection pipeline between the main network plant and the connected sub-network
- A reduction of the primary energy factor (PEF)
- A reduction in CO_2 emissions

Taking into account the interests of the network owner different methodologies of including a solar collector field were developed. In the given case a solution without a local backup boiler is preferred; instead a daily reheat of a storage from the large CHP plant was suggested.

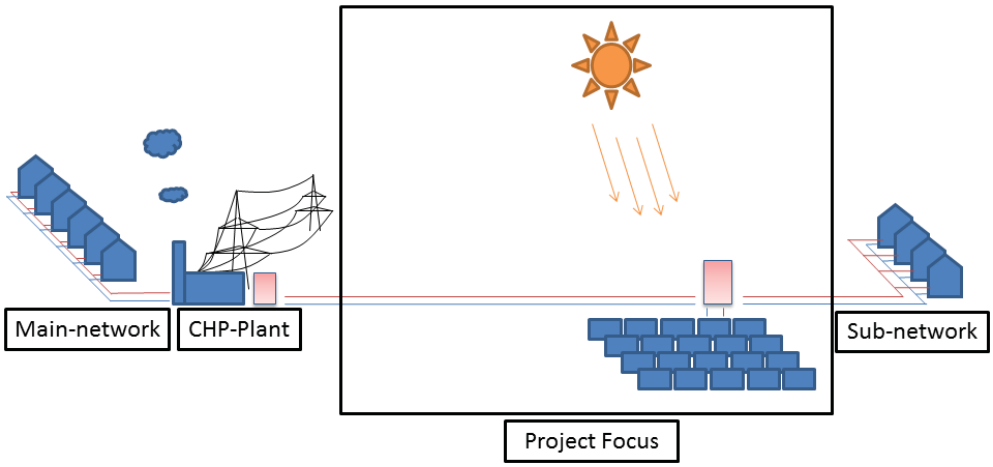

Figure 1. Project focus: The solar thermal field and the thermal storage are located between main-network and sub-network

2. Methodology

The calculations for this project have been performed in MATLAB and are based on four years of measurements of heat consumption, volume flow and flow temperatures. Values in 15 min time steps for the solar radiation of an average day of each month were imported from PVGIS (European_Commission) for the specific location. Additional weather evaluation has been performed using outdoor temperature data from 1974 to 2014 from Germany's National Meteorological Service (DWD) (Deutscher Wetterdienst).

Figure 2 below visualizes the methodology in a flow-chart starting with the input over a decision in solar share, resulting in collector areas, storage sizes and finally an energy flow overview and a storage operation visualization.

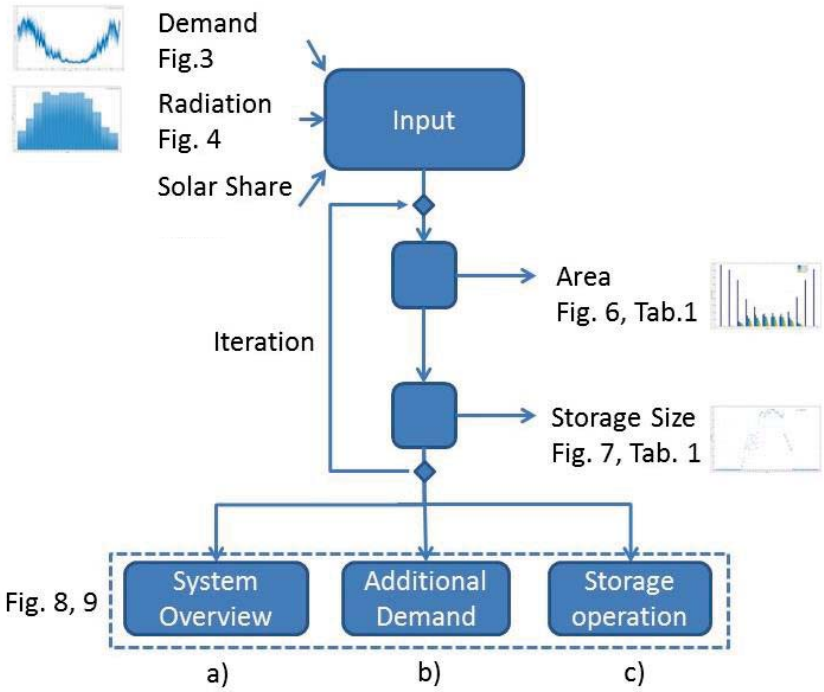

Figure 2. Methodology for the integration of solar heat into existing DH systems

Figure 3 shows the average heat load $Q_{dem,av}$ of the given consumer, the sub-network of the years 2013-2015. The following figure 4 shows the solar radiation during a year on a surface tilted south with an angle of 35°.

Based on the smoothened outdoor temperature line of the average outdoor temperature from 1974 to 2014 given by DWD (Deutscher Wetterdienst) and a graph displaying the required supply temperature to the sub-network, the time span from hour 3241 to hour 6337 of a year was calculated when the supply temperature is at its allowed minimum (Figure 5). In this time span the DH main-network could further decrease the supply temperature, if it could operate independently of the sub-network. The focus of this project was how the sub-network can be supplied by a solar heating system during this period.

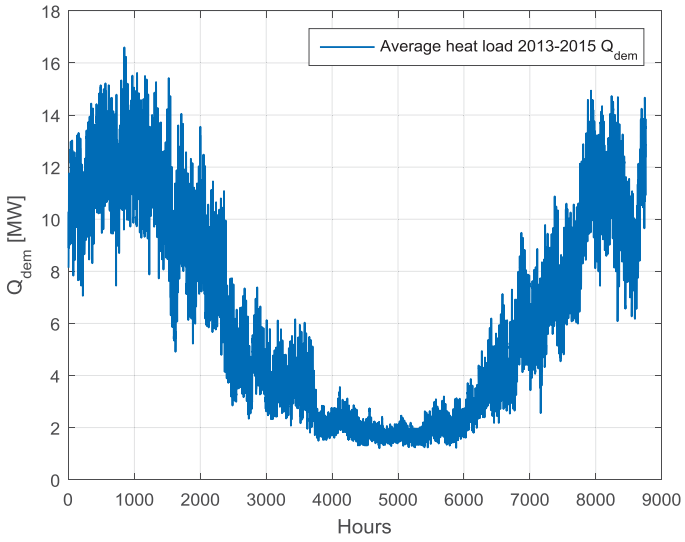

Figure 3. Example of annual the heat load curve in a sub-network

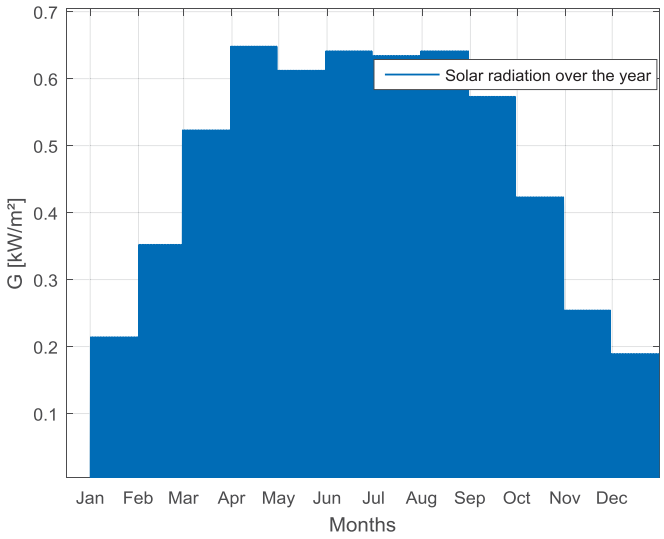

Figure 4. Example of maximum solar radiation on an average day on a south oriented 35° tilted surface in southern Germany

The efficiency of solar collectors η_c was calculated according to the European Standard EN 12975 (Kovacs 2012) as follows:

$$\eta_c(t) = \eta_0 - a_1 \frac{(T_m(t) - T_a(t))}{G(t)} - a_2 \frac{(T_m(t) - T_a(t))^2}{G(t)} \quad \text{(Eq. 1)}$$

$$T_m(t) = \frac{(T_{out}(t) + T_{in}(t))}{2} \quad \text{(Eq. 2)}$$

η_0 Collector zero-loss efficiency (-)

a_1 First degree coefficients of the collector heat losses (W/Km²)

a_2 Second degree coefficients of the collector heat losses (W/Km²)

G Global radiation (W/m²)

T_m Hourly medium temperature (K)

T_a Hourly ambient temperature (°C)

T_{out} Hourly collector outlet temperature (°C)

T_{in} Hourly collector inlet temperature (°C)

Accordingly, the net solar gain $Q_{sol}(t)$ is:

$$Q_{sol}(t) = \eta_c(t) * G(t) \quad \text{(Eq. 3)}$$

As the average global irradiance ins given in 15 minute steps the resolution was reduced to hourly steps in order to use the actual DH return temperature as collector inlet temperature T_{in} and the DH supply temperature as the collector outlet temperature T_{out} if it was above 80 °C, otherwise T_{out} was set to 80°C. The ambient temperature T_a was taken from PVGIS as well. The collector dependent values η_0, a_1 and a_2 were taken from collector datasheets of a Arcon HT-HEATboost 35/10- flat plate collector (FPC) and a RitterXL XL 19/49P evacuated tube collector (ETC).

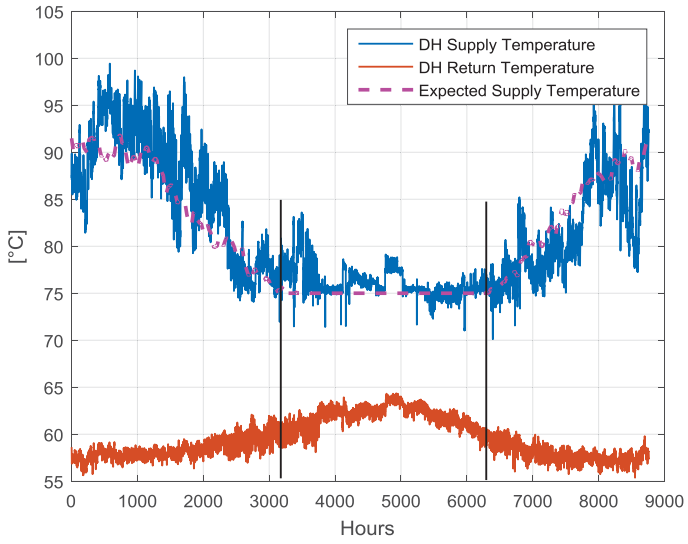

Figure 5. Average supply and return temperature and expected supply temperature of the sub-network

2.1 Area selection

Field sizes were calculated depending on different annual solar shares of 5 %, 10 %, 15 % and 20 % of the total annual heat consumption. Additionally, one approach aims to supply the heat consumption of July completely, which corresponds to 14 % solar share, because this is the month with the lowest consumption throughout the year. The following calculation steps are used to receive the actual collector aperture area in m²:

$$Rel(t) = \frac{Q_{dem,m}(t)}{Q_{dem,tot}} \quad \text{(Eq. 4)}$$

$$Q_{sol,m}(t) = Q_{sel} * Rel(t) \quad \text{(Eq. 5)}$$

$$A = \max\left(\frac{Q_{sol,m}(t)}{q_{sol,m}(t)}\right) \quad \text{(Eq. 6)}$$

Rel Relative monthly energy demand (-)

$Q_{dem,m}$ Monthly energy demand by the sub-network (kWh)

$Q_{dem,tot}$ Annual energy demand by the sub-network (kWh)

$Q_{sol,m}$ Monthly energy to be supplied by solar (kWh)

Q_{sel} Annual energy chosen to be supplied by solar (kWh)

$q_{sol,m}$ Specific net solar gain per month (kWh/m²)

A Aperture area needed (m²)

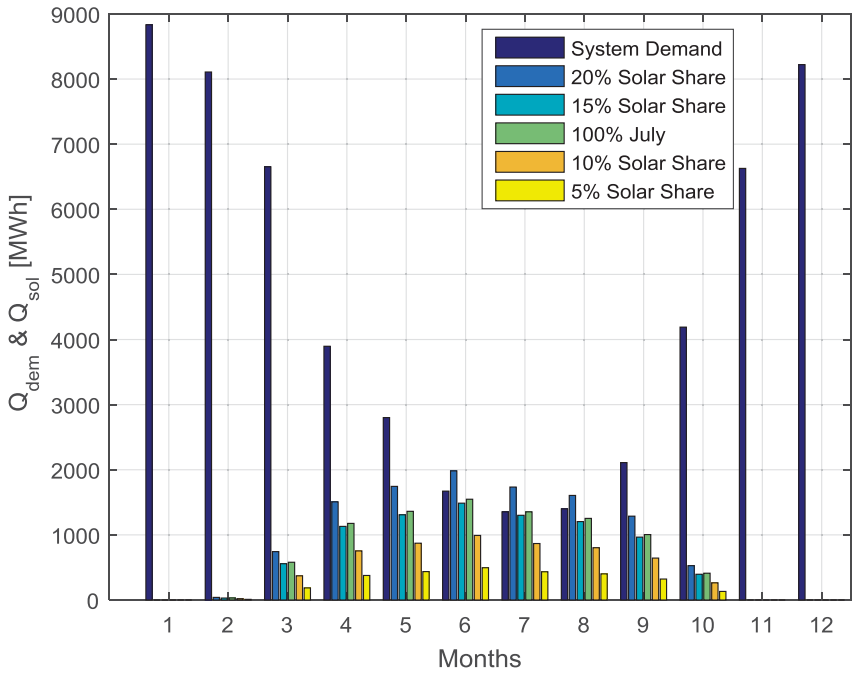

Figure 6. Net solar gain compared to demand for different solar share variations

Figure 6 shows an overview of the different solar shares compared to the monthly energy demand. At an annual solar share of 14 % the solar heat energy fully covers the heat demand in the month of lowest demand (July). A higher annual solar share provides a surplus of solar heat during the summer that cannot be used.

Table 1 shows an overview of the calculated variations with the collector area, the relative storage dimension and the achieved CO_2 savings.

Table 1. Calculation results for different annual solar share

Solar share	Collector area (m²)	Specific storage volume (l/m²)	Storage volume (m³)	CO_2 savings (t/a)
5 %	6507	7.3	50	480
10 %	13029	30.3	403	961
14 %	18319	39.5	728	1348
15 %	19536	40.5	802	1424
20 %	26044	46.2	1220	1725

2.2 Storage dimensioning

For this project it was required to store only the surplus solar heat that can be received within a single day and dimension the storage size accordingly. Figure 7 shows the solar surplus of each day that can be received when having an average load and a solar collector field size corresponding to the July demand (annual solar share of 14 %).

The conversion from MWh storage capacity to m³ water in storage capacity was performed according to the following formula:

$$V = \frac{Q_{st}}{\varrho * c * (T_{max} - T_{min})} \qquad \text{(Eq. 7)}$$

V Storage volume (m³)

Q_{st} Storage energy capacity (MWh)

ϱ Density of water (kg/m³)

c Heat capacity of water (Wh/(kg*K))

T_{max} Maximum storage temperature (°C)

T_{min} Minimum storage temperature (°C)

T_{min} is the maximum return temperature measured, 63 °C and T_{max} is the maximum allowed temperature in the storage 95 °C.

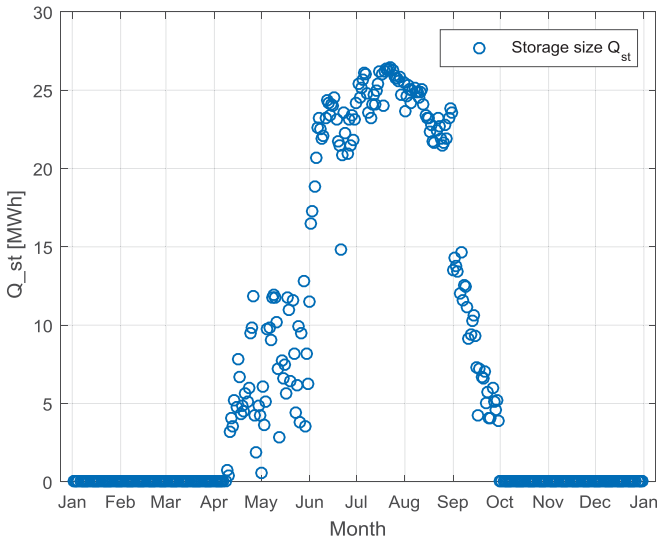

Figure 7. Needed storage capacity to store the solar surplus energy

2.3 Storage operation

To enable the sub-network to operate as independently as possible without having a backup boiler it is considered that the storage is reheated once per day. In this scenario the recharge from the main-network is set to be done every evening at 21.00 h with a supply temperature of 80 °C. This means that during summer time 3 different temperature zones will develop in the storage; one with the DH return temperature, one with 80 °C from the CHP plant and one with a maximum of 95 °C from the collector field.

2.4 Iteration

At this point an iteration is needed because the collector efficiency calculation depends on the DH supply and return temperatures that influence the collector inlet and outlet temperatures. To utilize the thermal storage to its maximum the storage temperature was set to a maximum of 95 °C. For the days that the storage is charged to its maximum the collector outlet temperature needs to be at least 95 °C. With the adjusted temperatures and thereby changed efficiencies the area and storage calculation was repeated.

3. Results

The first thing to realize throughout the calculation was that the needed storage size to store a solar surplus was below 50 l/m² collector area. A relatively small dimensioned storage is also recommended by Meißner et al.. Meißner et al. also points out that a solar storage is normally not used for the largest part of the year. This statement is also visually confirmed in Figure 7.

Figure 8a shows the supply and demand curves for the summer season if a recharge every evening is done for a solar collector area of 18,319 m² which corresponds to 14 % solar share. Figure 8 b) shows the additional demand of the system, meaning the heat power that is needed at some hours to cover the demand of the sub-network if the storage is empty and not enough direct solar energy is available. Equation (8) below shows the relation between the different heat power terms:

$$\dot{Q}_{dem} = \dot{Q}_{sol,dir} + \dot{Q}_{dis} + \dot{Q}_{add} \quad \text{(Eq. 8)}$$

$\dot{Q}_{dem}$	Heat load of the sub-network	(MW)
$\dot{Q}_{sol,dir}$	Directly used solar heat rate	(MW)
$\dot{Q}_{sol,stor}$	Stored solar heat rate	(MW)
$\dot{Q}_{dis}$	Storage heat discharge rate	(MW)
$\dot{Q}_{add}$	Additional heat supply rate	(MW)
Q_{re}	Daily storage heat energy recharge	(MWh)
Q_{ch}	Level of storage charge	(MWh)

Figure 8c and 9c display the storage charge and the energy the storage is charged with during the reheating process. In Figure 9a it can also be seen that when the storage is recharged, $\dot{Q}_{dem}$ of the sub-network at that moment is covered by the main-network, too.

While Figure 8 presents the complete summer season of a system with 14 % solar share, Figure 9 shows the supply and demand for the same system but this time only for 4 days. In Figure 9c, the excerpt of Figure 8c, it becomes visible that a regular evening recharge enables a projectable operation of main- and subnetwork. When analysing the red state of charge line in Figure 8c one can see that a daily recharge is not even needed every day.

The optimal system choice is therefore an offset between a system that needs as little additional energy during the summer season as possible, with the aim to let the main-network operate as independent as possible and a system that has a collector area as little as possible to reduce the system costs as well as to reduce the losses during the summer due to storage limitations.

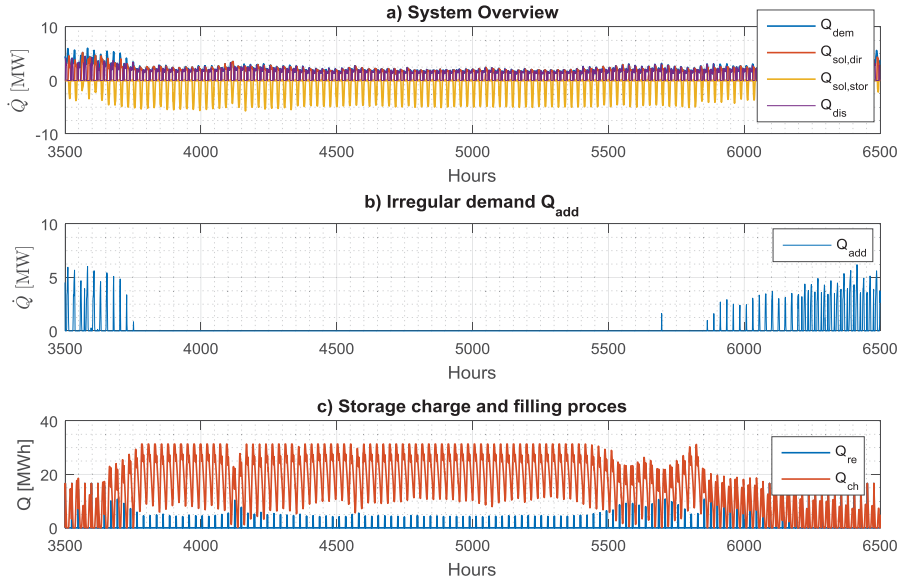

Figure 8. Supply and demand curves (a), additional heat power demand (b) and storage charging (c) during the summer season with 14 % solar share

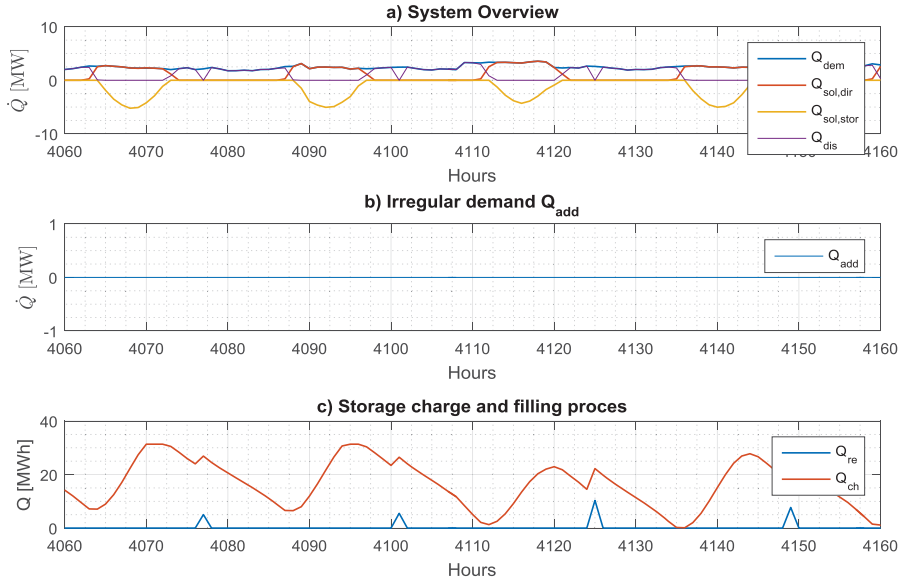

Figure 9. Zoomed in 4 days of supply and demand for the scenario with 14 % annual solar share

$\dot{Q}_{dem}$	Heat load of the sub-network	(MW)
$\dot{Q}_{sol,dir}$	Directly used solar heat rate	(MW)
$\dot{Q}_{sol,stor}$	Stored solar heat rate	(MW)
$\dot{Q}_{dis}$	Storage heat discharge rate	(MW)
$\dot{Q}_{add}$	Additional heat supply rate	(MW)
Q_{re}	Daily storage heat energy recharge	(MWh)
Q_{ch}	Level of storage charge	(MWh)

Figure 8 shows that a system of the given specification can supply the sub-network's demand during the summer season to a large extent independently of the main-network if an overnight charging of the storage to 80 °C is given. An increase from 14 % solar share to 20 % solar share will reduce the need for additional energy supply from the main network during the summer season but will also increase the losses of solar energy as the storage is not emptied for the largest part of the summer season. Furthermore, the difference in the collector area between 14 % and 20 % solar share is 7725 m² and will also have a large economic impact.

Additionally, a decrease in CO_2 emissions, as visible in Table 1, is possible by up to 1725 t CO_2 per year in the case of 20 %.

4. Feasibility study

The economic analysis of the calculated system is based on the main components as collectors, storage and the cost of land. Additional costs as control technology, system technology, construction works, planning and costs for system integration were added in percentage on the sum of the costs of the main components according to Schmidt & Deschaintre. The discounting of the investment costs is performed over 25 years and an interest rate of 4 % is applied. The collector costs used are 200 €/m² (Trier 2015) for flat plate collectors and 340 €/m² (AGFW 2013) for evacuated tube collectors. Cost of land were in this calculation set to 9 €/m² and the specific costs for the thermal storage were set to 140 €/m³(Maripuu & Dalenbäck 2011).

Additional subsidies based on German legislation were taken into account for this example system. According to (Pauschinger) 40 % of the collector costs and 30 % of the storage cost can be subsidized in Germany.

The following figure 10 shows the specific heat generating costs depending on the collector costs. The turn in both collector type lines at about 15 % solar share can be explained with the maximal capacity of the short-term thermal storage. If the collector area is too large the solar gains per day exceed the demand of the DH network per day.

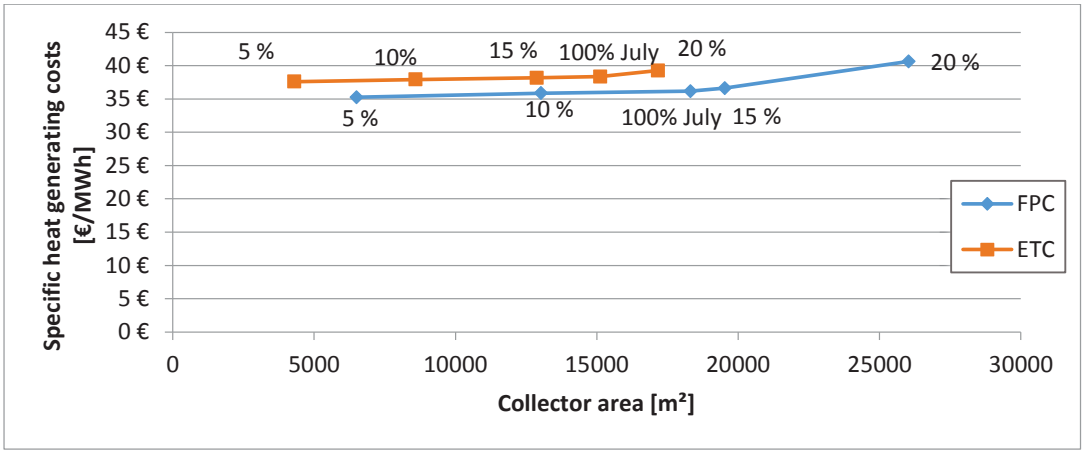

Figure 10. Specific heat generating costs dependent on the collector area for both collector types.

Figure 11 shows that the annual cost per amount of CO_2 reduced develop rather linear for both collector types until about 15 % when the issue of the storage limitation and too low network demand change the balance.

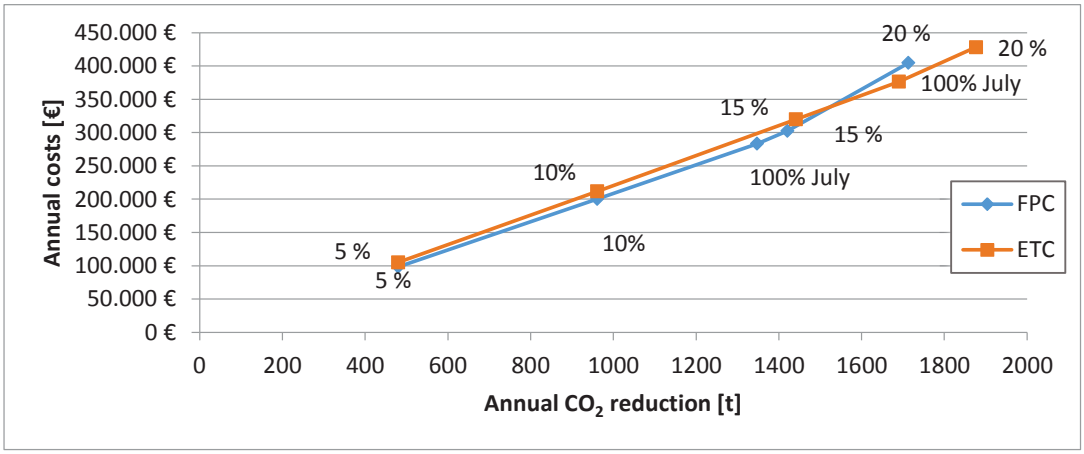

Figure 11. Annual system costs depending on the annual achievable CO2 emission reduction

5. Discussion

The comparison of the presented results against results of a freeware calculation tool (SDH Online-Calculator (Solites & AGFW)) with similar input data shows a generally good validity of the method. However, due to different methodological approaches the results cannot be compared to each other directly.

Firstly, the irradiation on the collector field was about 16 % higher in this project. This is due to a different location that was chosen but most of all due to the different meteorological data source of both calculations.

Secondly, it has to be mentioned that losses in the piping system and the storage of about 5 to 10 % have to be added.

Thirdly, results in the CO_2 savings differ in this project compared to the SDH-Online tool as the CO_2-emission factor of 172 g/kWh for the given example DH system was used.

The reader also has to be aware that small variations on the specific collector price [€/m²] have huge influence on the overall costs as the collector costs account for 70% of the whole system costs. The collector prices are changing depending on the system size, the location and are also expected to change over time.

6. Conclusion

The integration of solar heat into existing DH systems brings benefits to a fossil CHP plant based system such as CO_2 reduction, primary energy factor improvement and a larger operational flexibility. The possibility to supply a sub-network for certain periods of the year mainly by solar heat, allows an increasing efficiency of the CHP plant in the main network for the time that the temperatures can be lowered.

Furthermore, a solar thermal system enables the whole DH network to react better on future changes in the German electricity price market when it may be economically beneficial to decrease the energy production of the plant from an electricity production point of view.

The study shows that the accuracy of dimensioning a solar district heating system highly depends on the quality of the input data used. Calculations on the basis of annual data provide a rough idea on the necessary collector area and storage volume for a given heat demand. However, an exact dimensioning can only be done by using hourly-data of solar radiation and heat load for a whole year period.

The methodology for the integration of solar heat into DH systems that is presented in this paper leads to more detailed results and avoids over-dimensioning of solar fields and storage volume.

The example calculation shows that a solar thermal DH sub-network with a thermal storage and an annual solar share of 14 % can be realized without auxiliary gas or biomass boiler, if the main-network can adapt to a lack of heat power in the sub-network. The option of a regular recharge of the storage makes the operation of the centralized CHP plant more predictable. During the summer months the solar heat gains cover the total heat demand of the sub-network for long periods, whereas in other times of the year the main-network provides the additional heat. A short-term storage with a specific volume below 40 l/m² is sufficient under the here give load pattern.

7. Outlook

The results of the presented calculations can be improved by optimizing the storage recharging time and level as well as by adding the piping system as a temporary storage. In the example of a DN300 pipe without extractions an additional specific volume of 78 m³/km can be taken into account to store water at 80 °C for a short time once a day. In this case a focus will also have to be put on the losses over the pipeline.

Finally, the methodology needs to be applied on an operating SDH system.

8. References

AGFW, 2013. Transformationsstrategien Fernwärme, Frankfurt am Main.

Berberich, M. et al., 2015. SOLAR-KWK Entwicklung multifunktionaler Systeme zur solar unterstützten Kraft-Wärme-Kopplung – solare Fernwärme und saisonale Wärmespeicher für die Energiewende, Stuttgart.

Deutscher Wetterdienst, DWD Deutscher Wetterdienst. Available at: http://www.dwd.de/DE/leistungen/klimadatendeutschland/klimadatendeutschland.html [Accessed May 10, 2016].

European_Commission, PV GIS. Available at: http://re.jrc.ec.europa.eu/pvgis/apps4/pvest.php# [Accessed May 10, 2016].

Fisch, M., Guigas, M. & Dalenbäck, J.-O., 1998. A review of large-scale solar heating systems in Europe. Solar Energy, 63(6), pp.355–366. Available at: http://www.sciencedirect.com/science/article/pii/S0038092X98001030.

Kovacs, P., 2012. A guide to the standard EN 12975, Borås.

Maripuu, M. & Dalenbäck, J.-O., 2011. SUNSTORE 4 WP5 - European level concept study Feasibility / simulation studies, Göteborg.

Meißner, R. et al., 2012. Sinn und Unsinn von Solarspeichern. FEE Heizungsjournal - Special, pp.1–6.

Pauschinger, T., 2015. Solnet BW Solare Wärmenetze für Baden-Württemberg Grundlagen | Potenziale | Strategien, Stuttgart.

Schmidt, T. & Deschaintre, L., 2013. SDH online-rechner. Available at: http://www.sdh-online.solites.de/Content/media/SDH-Online-Rechner.PDF. [Accessed May 10, 2016]

Solites & AGFW, SDH Online-Calculator. Available at: www.sdh-online.solites.de [Accessed May 10, 2016].

Trier, D., 2015. Solare Fernwärme in Dänemark - Entwicklungen und Trends. Erneuerbare Energie, 3. Available at: www.aee.at/aee/index.php?option=com_content&view=article&id=870&Itemid=113.

Urbaneck, T. et al., 2015. Solar District Heating in East Germany – Transformation in a Cogeneration Dominated City. Energy Procedia, 70, pp.587–594. Available at: http://www.sciencedirect.com/science/article/pii/S1876610215002866.

06. Testing & Certification

Selective Absorber Coatings Qualification - ISO 22975-3:2014 Full Application

T. C. Diamantino[1], A. Nunes[1], R. Gonçalves[1], S. Páscoa[1], T. Chambino[1] and M. J. Carvalho[1]

[1] LNEG - Laboratório Nacional de Energia e Geologia. Estrada do Paço do Lumiar, 1649-038 Lisboa, Portugal

Abstract

The main R&D challenges in the development of Solar Thermal Collectors are focused on increasing reliability and long-term performance stability. Absorber coatings have a major role in conversion of solar radiation into thermal energy. For this reason, testing procedures for qualification were developed and are described in ISO 22975-3:2014. Full application of the test methodologies proposed in ISO 22975-3:2014 is seldom referred for commercial absorber coatings commercially available. This work reports the results of the full tests to five absorber coatings (commercially available), two obtained by physical vapor deposition (PVD) and three by air spray with selective paints. Additional results, obtained with different accelerated aging tests including salt spray and/or sulfur dioxide and nitrogen dioxide as contaminants, are presented. The advantages and limitations of the methodologies proposed in ISO 22975-3:2014 will be discussed, as will be analyzed and proposed new methods of accelerated aging tests.

Keywords: *Solar thermal collectors, Absorber coatings, Qualification tests*

1. Introduction

Countries with high solar resource and a significant amount of coastal regions are the places with the highest population density, constituting a large and prospective market for solar thermal technology and a challenge in terms of reliability and durability for solar thermal technology. Solar thermal collectors (STC) have to withstand stress conditions like high temperatures, high humidity, ultraviolet irradiance or wind and snow loads depending on the geographic location. Literature points out to dependence on other influences like prevailing wind conditions, contaminants like chlorides, SO_2 and NO_x, global solar irradiation, wetness time and precipitation (Köhl, M., et al, 2004; Slamova, K et al, 2016).

Most of the absorbers materials are metallic, copper or aluminium, with different types of coatings obtained by different application methods (Mihelčič M.et al, 2015). Metallic materials are particularly susceptible to corrosion due to combined effect of the different atmospheric parameters namely chloride ions, sulphur dioxide, temperature and relative humidity.

For absorber coatings, due to its major role in conversion of solar radiation into thermal energy, testing procedures for qualification were developed (ISO 22975-3:2014). This international standard specifies a scheme of accelerated ageing tests for qualification of absorber surfaces. Three types of degradation processes are considered: high temperature degradation, degradation by the action of condensed water and degradation caused by high humidity in air containing a small concentration of sulphur dioxide (SO_2). Although SO_2 is one of the dominating airborne pollutants for atmospheric corrosion, the consideration of SO_2 as main corrosion factor for absorber surfaces may be disputable for collectors placed in marine environments as chloride ion from sodium chloride is considered to be major corrosion agent in these regions (Slamova, K et al, 2016; Diamantino, T et al, 2017). Additionally, nitrogen oxides levels have remained constant or even increased with urban NO_x levels higher than SO_2 levels in most cities (Castãno et al, 2007).

In this work, commercially available absorbers with different substrate materials and coatings, PVD - Physical Vapor Deposition and PC – Paint Coatings, were submitted to the full set of tests of ISO 22975-3:2014 and to additional accelerated aging tests with different atmospheric contaminants. The objective of this study allowed the test laboratories involved to gain experience in the application of the tests, but also to identify the advantages and limitations of the methodologies proposed in ISO 22975-3:2014.

doi:10.18086/eurosun.2016.06.01 Available at http://proceedings.ises.org

2. Experimental

2.1. Selective solar absorber coatings

In this study five selective absorber coatings applied on aluminum were considered, 2 coatings obtained by PVD are commercially available and were acquired from STC manufacturers (PVD 1 - commercial name *mirotherm*® and PVD 2 - commercial name *eta plus*®); 3 selective paint coatings (two PCs thickness sensitive spectrally selective (TSSS) with silicone binders (PC1 and PC2) which commercial names are SUNCOLOR TS S Black and SOLKOTE HI/SORB-II ™, respectivelly; 1 PC thickness insensitive spectrally selective (TISS) with a poly(urethane) binder (PC3) which commercial name is SUNCOLOR PUR Black. All the paints used were aquired from the selective paints commercially available. The paints were applied according with the technical instructions of the products on aluminum substrates. Before the application of the paints, all the aluminum samples were subjected to a pre-treatment without chromium. Firstly the panels were acid degreased/deoxidized with Gardacid P 4307 and Gardoclean 450B for 10 min at ambient temperature. Then the specimens followed to a passivation stage with Gardobond X 4707 for 45-60s at ambient temperature. For application by air spray it was used a gravity fed spray gun with a 1.5 mm nozzle and air compressor settled to 2 bar pressure.

The samples evaluated have a dimension of 50 X 50 mm for tests under ISO 22975-3:2014 (section 2.2) and 65 x 140 mm for tests describe in 2.3 and 2.4..

2.2. Methodologies for Solar Absorber Surfaces Qualification (ISO 22975:2014)

2.2.1. Optical properties

All the selective solar absorber samples used specifically in this study were optically characterized by measurement of solar absorption (α_s) and thermal emittance (ε_t). The solar absorption (α_s) was determined based on the solar absorption hemispherical solar spectral irradiance (incident on a 37° tilted plane, equator-facing) and the reflectance measurements were done on Perkin Elmer's Spectrophotometer Lambda 950 UV/VIS/NIR with a 150 mm integrating sphere. The thermal emittance (ε_t) was determined with a portable emissometer, Devices & Service Company model AE-AD3, which measure a surface emittance at 80 °C of temperature and compared later with measurements using a Spectrophotometer Frontier IR/NIR of Perkin Elmer, with integrating sphere For measurement of the spectral reflectance between 2,5 and 20 μm a diffuse gold coating reference calibrated by Avian Technologies LLC was used.

Evaluation of absorber coatings according to ISO 22975-3:2014 is based on a performance criterion (Pc) dependent directly on the optical properties of the collector and which is defined according to equation (1).

$$Pc = -\Delta\alpha_s + 0{,}5\,\Delta\varepsilon_t \quad (1)$$

Where $\Delta\alpha_s$ is the change of solar absorptance during an aging test and $\Delta\varepsilon_t$ the change in thermal emittance in the same test. In order to an absorber coating be qualified the value of Pc shall be lower or equal to 0.05.

Optical properties, like solar absorptance and thermal emittance are also the main quantitative values for comparison of absorber coatings and its selection for use in STC. Roberts, D. E., 2013 introduces a figure of merit (FM) based on these optical properties with the purpose of making the selection of solar absorber coatings easier. This figure of merit (FM) is given by equation (2).

$$FM = \alpha_s - 0{,}44\varepsilon_t \quad (2)$$

2.2.2. Coating Adhesion

The coating adhesion of all absorber surfaces were evaluated by pull-off method according to ISO 4624:2002 for deformable substrates. A tensile tester INSTRON 4467 with a load cell of ± 5KN was used. Steel test dollies used have a nominal diameter of 20 mm. The adhesive selected was a cyanoacrylate glue.

2.2.3. Assessment of thermal stability

The assessment of thermal stability of the different solar absorber coatings was performed according ISO 22975-3:2014. The equipments used were an HERAEUS LUT 6050 until temperatures of 250ºC and a Heratherm Oven OMH100 for higher temperatures, until 330ºC. The temperature in the chambers is uniform within the range of ±1 °C.

2.2.4. Resistance to condensed water

The qualification scheme and the conditions for resistance to condensed water were according to ISO 22975-3:2014. Binder MKF 240 was used as test chamber with sample holders and cooling block as shown in Figure 1.

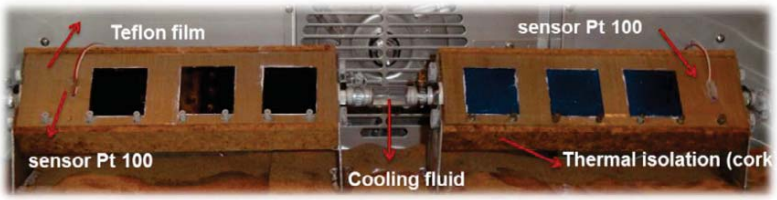

Fig. 1 - Combined sample holder and cooling block for condensation test

2.2.5. Resistance to high humidity air containing sulfur dioxide

The test procedure involves exposure in circulating air of a relative humidity of 95% RH, temperature of 20°C, a sulfur dioxide volume fraction of 10^{-6} and a linear flow rate of air in the range between 1mm/s and 5mm/s. This test is performed according to ISO 10062:2006. According to this standard, the corrosion rate of zinc is considered as a measure for severity of environmental stress on absorber surfaces. During this test, 6 samples of zinc with known initial mass were used. The mass loss was determined for specific time periods, after 90h, 180h and 360h while measuring 2 samples for each time period. Assuming that mass loss rate is linear with testing time, it is possible to calculate the zinc corrosion rate (r_{Zn}), in mg/m^2/h, by linear fitting (Least squares method). The average corrosion rate of zinc obtained (0.014g/m^2/h) is used to determine the shortest acceptable failure times in hours:

- For a type A solar collector: Shortest acceptable failure time, $t_{f,A} = 2.5/r_{Zn}$
- For a type B solar collector: Shortest acceptable failure time, $t_{f,B} = 7.5/r_{Zn}$

Since the solar absorber surfaces studied could be use in either type of solar collectors, it was decided to submit them to both failure times. According to the determined chamber corrosivity for Zinc, for a type A solar collectors, 180h, and for a type B solar collector, 540h, were respectively considered. A WEISS WK3-340/0-BSB chamber was used.

2.3. Methodologies of accelerated aging tests with continuous exposure of contaminants

2.3.1 Neutral salt spray test

A continuous neutral salt mist spray with a concentration of 50g/l ± 5g/l of sodium chloride in demineralized water, pH value of the solution between 6.5-7.2 and test chamber temperature between 35°±2°C was used (ISO 9227:2012).The inclination of test samples was 20º±5° from the vertical. The duration of the test was 120 hours with observations and evaluation of optical properties after 24, 48, 72, 96 and 120 hours. 6 replicates were used. The chamber used is an Erichsen Model 606/400L. This test was chosen because it is the oldest and most widely used method for laboratory accelerated corrosion testing.

2.3.2 Saturated atmosphere in the presence of sulfur dioxide

A test in a saturated atmosphere in the presence of sulfur dioxide according with ISO 3231:1993 during 5 cycles (24 hours each cycle) was performed. Each cycle consists of 8 h at 40ºC±3°C and 100% of RH (SO_2 – 0.2L) and 16 h at 18-28ºC and RH max 75% (test chamber vented). 6 replicates were used. The chamber used is a VLM Model CCT 400-Air CTD-A. This test was selected because is widely used to evaluate and qualify metallic and organic coatings for anticorrosive protection to industrial atmospheres with a higher concentration of sulfur dioxide than the test proposed by ISO 22975-3:2014.

2.4 Methodologies of accelerated aging tests with cyclic variation of corrosion promoting gases, higher humidity, salt spraying and drying

This study began applying a methodology of ISO 21207:2015 (Method A) that involves exposure of the test objects to the following test cycle: a) neutral salt spray testing (ISO 9227:2012 for 2 h in a mist of a salt solution containing a mass fraction of 5 % of sodium chloride at 35 °C, followed by drying for 22 h in a

standard laboratory climate; b) exposure for 120 h in a test atmosphere containing a mixture of corrosion-promoting gases, volume fraction of NO_2 equal to 1.5×10^{-6} and of SO_2 equal to 0.5×10^{-6}, at a relative humidity of 95 % and at a temperature of 25 °C, followed by drying for 24 h in a standard laboratory climate. The climatic chambers used were a WEISS WK3-340/0-BSB for mixture of corrosion-promoting gases and a Erichsen (Model 600-400L) for salt spray environment. All the tests performed with solar absorber surfaces were simultaneously monitored with reference materials to evaluate atmosphere corrosivity. The optical properties were evaluated after 2, 3 and 4 test cycles. This method was chosen because is recommended for the qualification of coatings, as well as, to predict the lifetime of electronic equipments and is also suitable for comparative testing (ISO/TR 16335:2013).

2.5 Evaluation the corrosivity of accelerated aging tests chambers

The corrosivity of the different accelerated aging test chambers were performed with Zinc standard samples (reference material 99.95%) simultaneously with absorber coatings. Two replicates (section 2.2.5) or three replicates were used for each test period (section 2.3 and 2.4). The samples are rectangular plates with dimensions 100 mm x 150 mm, and a thickness of 1 mm. After exposure, corrosion products were removed in accordance with ISO 8407:2009. The corrosion rates were obtained by weight loss per unit area during exposure periods of different accelerated aging tests.

3. Results and Discussion

3.1. Solar Absorber Surfaces Qualification (ISO 22975-3:2014)

Table 1 resumes the initial optical properties, figure of merit (FM) and adhesion of coatings. These values of optical properties are the average value of thirty samples (50 x 50 mm) and the corresponding standard deviation is also indicated (σ_α for solar absorptance and σ_ε for thermal emmitance). PVDs have similar values of solar absorptance and thermal emittance. The Paint Coatings PC1 and PC2 have also similar values of solar absorptance and thermal emittance values, but with lower solar absorptance and higher thermal emittance than PVDs. PC3 has the lower solar absorptance and the higher thermal emittance. Except for PVD1 that has a lower adhesion, all other coatings have very similar rupture resistance values.

All absorber coatings were submitted to the full tests according to ISO 22975-3:2014. In Table 2 a summary of results obtained is shown. Figure 2 shows the optical properties converted in results of performance criteria (Pc) and Figure of Merit (FM) of the different selective coatings during the different accelerated aging tests indicated in ISO 22975-3:2014 for surfaces qualification.

All the absorber coatings were qualified for the test in saturated atmosphere in the presence of sulfur dioxide, in terms of optical properties and adhesion of coatings. In terms of thermal stability PVD1 did not qualify due to the changes in optical properties (performance criteria - Pc>0,05). PC3 also did not qualify but due to low adhesion of coating (ruptures resistance < 0,15MPa).

Tab. 1 – Initial optical properties, adhesion and figure of merit (FM) of PVDs and PC coatings

Absorber reference	**Optical initial values**		**Coating Adhesion** (rupture resistance – Mpa) (σ)	**FM**
	Solar absorptance $\alpha \pm \sigma_\alpha$	**thermal emittance** $\varepsilon \pm \sigma_\varepsilon$		
PVD1	0.96±0.00(1)	0.11±0.00(2)	0.9 (0.3)	0.91
PVD2	0.96±0.00 (1)	0.11±0.00(3)	3.9 (2.1)	0.91
PC1	0.94±0.00(2)	0.46±0.04	4.0 (0.6)	0.74
PC2	0.94±0.00(1)	0.50±0.03	3.7 (1.7)	0.72
PC3	0.92±0.01	0.58±0.03	4.8 (1.4)	0.66

Tab. 2 – Overall durabilityresults of PVDs coatings and PCs according to ISO 22975-3:2014

	Thermal Stability	Condensed Water	High humidity air containing sulfur dioxide
PVD1	NQ *(optical properties)*	Q*	Q
PVD2	Q	Q*	Q
PC1	Q	Q*	Q
PC2	Q	Q*	Q
PC3	NQ *(adhesion loss)*	Q*	Q

Q – qualified; NQ – not qualified; *require confirmation with thermal conditioning

In terms of resistance to condensed water all the coatings were qualify. However, the results require confirmation because the tests were performed with samples without conditioning. This conditioning considered in ISO 22975-3:2014 consists in submiting each test the sample for at least 5 hours at maximum absorber temperature. The thermal stability tests were performed with samples without and with conditioning. The test of resistance to high humidity air containing sulfur dioxide was performed with all samples condicionated.

Table 3 shows the photographic records of selective solar absorber coatings after exposure to 180 hours and 540 hours to high humidity air with sulfur dioxide. In all coatings (PVDs and PCs) no visual degradation (Table 3) nor significant changes in the optical properties were observed (Figure 2 – e) and f)).

Tab. 3 – Photographic records of PVDs (PVD1 and PVD2) and PCs (PC1, PC2 and PC3) after 180h and 540h of exposure to high humidity air containing sulfur dioxide, according to ISO 22975-3:2014

PVD1		PVD2	
			
180 hours	540 hours	180 hours	540 hours

PC1		PC2		PC3	
					
180 hours	540 hours	180 hours	540 hours	180 hours	540 hours

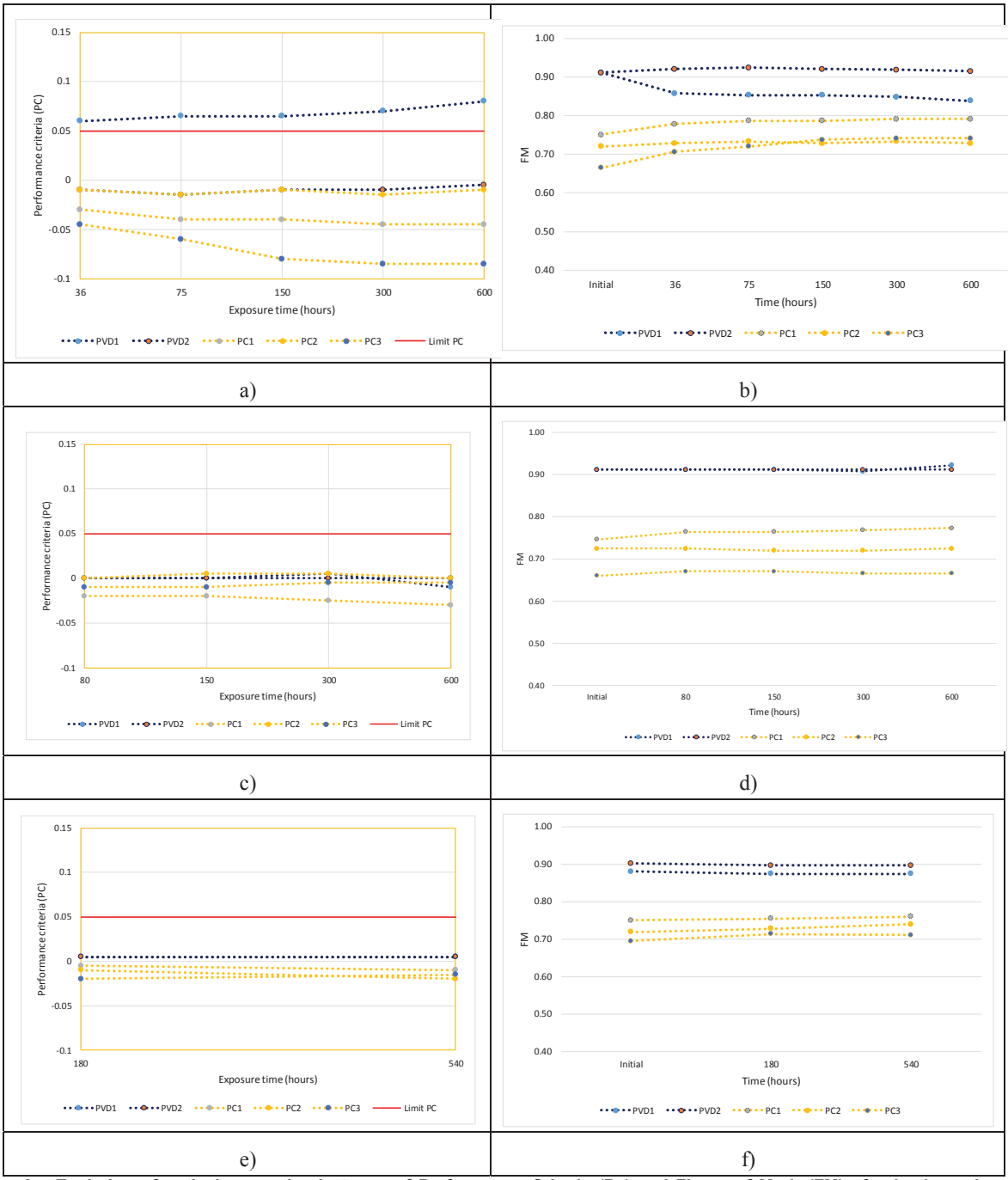

Fig. 2 – Evolution of optical properties in terms of Performance Criteria (Pc) and Figure of Merit (FM) of selective solar absorber coatings after thermal stability test (a) and b)), condensed water test (c) and d)) and test of resistance to high humidity air containing sulfur dioxide (e) and f))

3.2. *Accelerated aging tests with continuous exposure of contaminants*

Figure 3 and Table 4 show, respectively the results of the optical properties and visual degradation of the different selective solar absorber surfaces after the exposure to accelerated aging tests with continuous exposure of contaminants (salt spray and sulfur dioxide). Neutral salt spray led to a higher degradation in PVDs than in PCs. Considering only PVDs, PVD2 showed higher degradation than PVD1. For PCs, PC3 showed the best behaviour in terms of anticorrosive protection and optical properties (lower Pc and higher FM). For the sulfur dioxide resistance test opposite results are observed, i.e., the PCs showed higher degradation than PVDs. No significant changes were observed between the 2 PVDs and the 3 PCs.

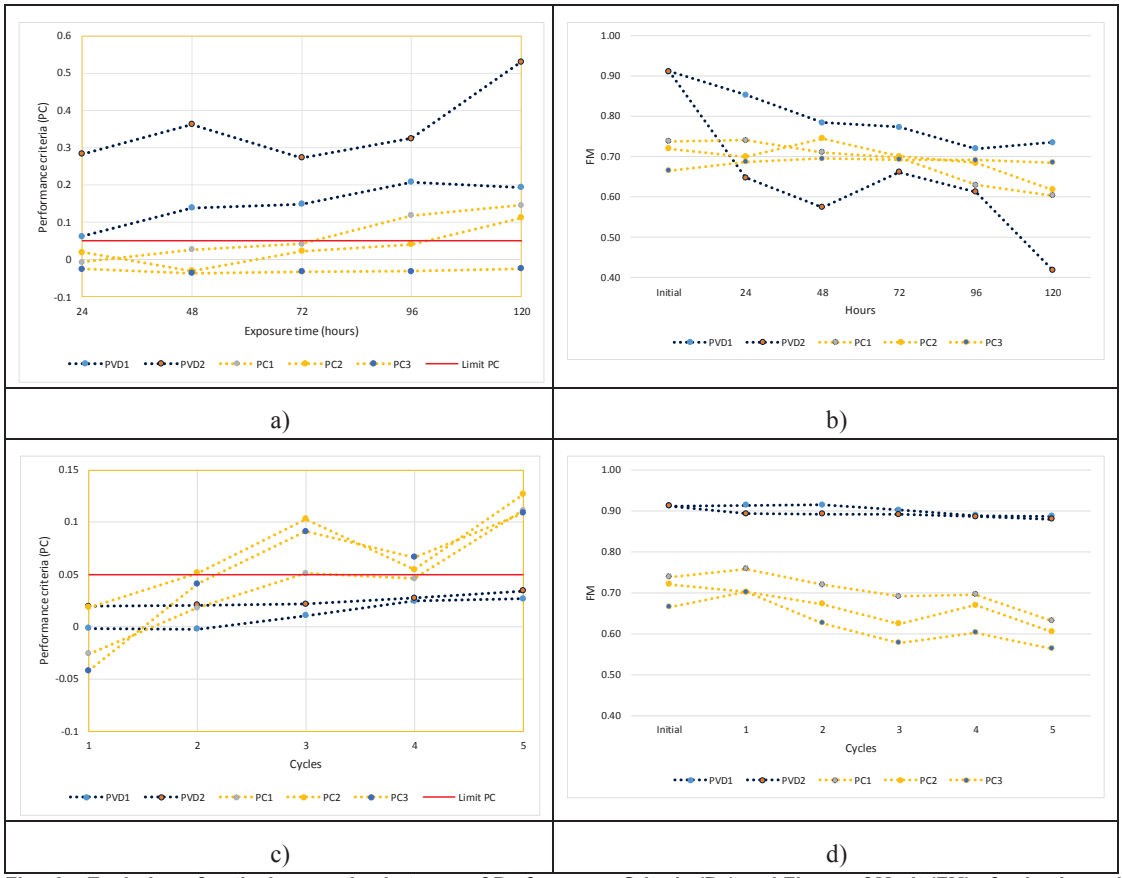

Fig. 3 – Evolution of optical properties in terms of Performance Criteria (Pc) and Figure of Merit (FM) of selective solar absorber coatings after neutral salt spray test (a) and b)) and to humid atmospheres containing sulfur dioxide (c) and d))

Tab. 4 – Photographic records of PVDs (PVD1 and PVD2) and PCs (PC1, PC2 and PC3) of exposure to neutral salt spray during 120 hours (ISO 9227:2012) and to humid atmospheres containing sulfur dioxide during 5 cycles (ISO 3231:1993)

Solar absorber coating	Neutral salt spray (24h, 48h, 72, 96 and 120h)	Sulfur dioxide (0.2L) (1, 2, 3. 4 and 5 cycles)
PVD1		
PVD2		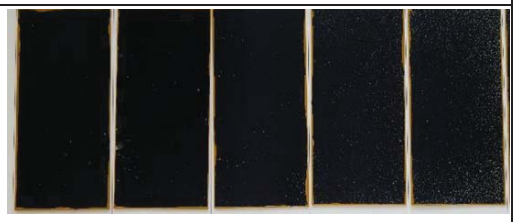
PC1		
PC2		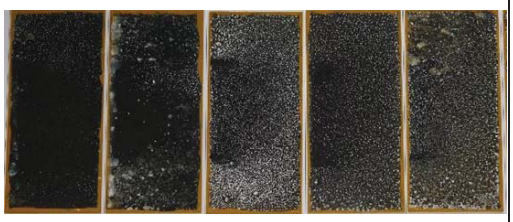
PC3	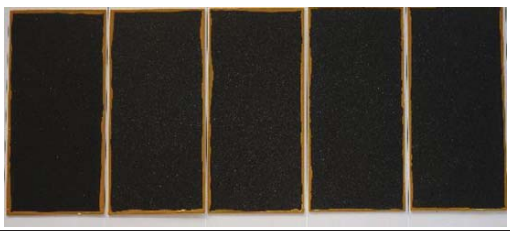	

3.3. *Accelerated aging tests with cyclic variation of corrosion promoting gases, higher humidity, salt spraying and drying*

Figure 4 and Table 5 show, respectively the results of the optical properties and visual degradation of the different selective solar absorber surfaces during the 4 weeks (4 cycles – Method A) of exposure to accelerated aging tests with cyclic variation of corrosion promoting gases, higher humidity, salt spraying and drying.

PVD2 showed higher corrosion which is accompanied with the higher reduction of FM (decrease of absorptance and increase of emittance) and a Pc higher than 0.05. PCs showed also higher degradation, namely PC1 and PC2 reaching values of FM similar to PVD2.

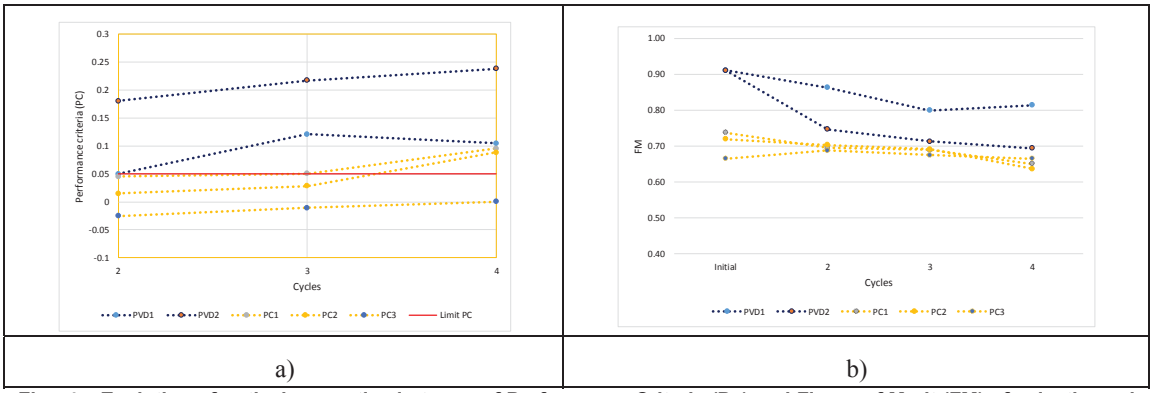

Fig. 4 – Evolution of optical properties in terms of Performance Criteria (Pc) and Figure of Merit (FM) of selective solar absorber coatings during exposure (4 cycles – 4 weeks) to accelerated aging test with cyclic variation of corrosion promoting gases, higher humidity, salt spraying and drying

Tab. 5 – Photographic records of PVDs (PVD1 and PVD2) and PCs (PC1, PC2 and PC3) during exposure (4 cycles – 4 weeks) to accelerated aging test with cyclic variation of corrosion promoting gases, higher humidity, salt spraying and drying (ISO 21207:2015)

2, 3 and 4 cycles		
PVD1	PVD2	
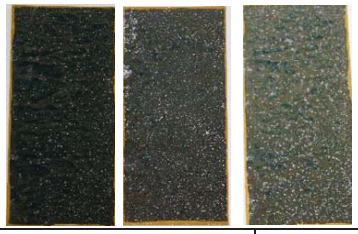		
PC1	PC2	PC3
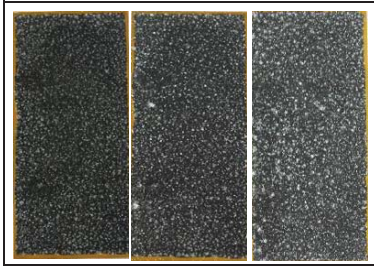	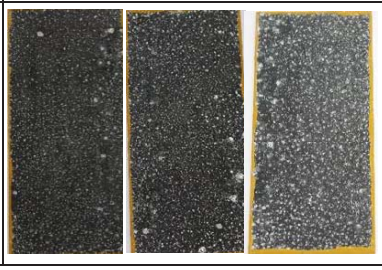	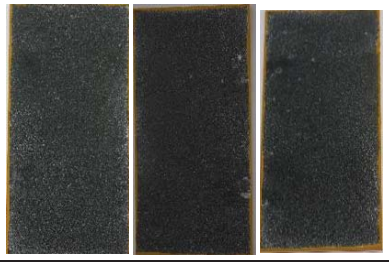

The results obtained with this methodology show results similar to those presented by Diamantino et al, 2017 with the same solar absorber coatings exposed to outdoor exposure testing sites with different corrosivity (urban test site with marine influence – medium corrosivity and an industrial/marine test site with very high /extreme corrosivity) in terms of the ranking of Pc, FM and anticorrosive protection. PVD2 showed the higher Pc and PVD1 the higher FM in both OET sites as seen in this accelerated aging test. PC3 showed the best anticorrosive protection and PVD2 the lower in both OET sites, as well as, from results obtained by electrochemical impedance spectroscopy (Fernandes et al, 2017), as well as in this test method.

3.4. Zinc corrosivity in accelerated aging tests chambers

In order to compare the different corrosivity of accelerated aging tests presented, Table 6 resumes the values obtained experimentally and from literature, assuming that mass loss rate is linear with testing time. Neutral salt spray is clearly the higher corrosive test followed the SO_2 resistance test based on ISO 3231:1993.
According to ISO 22975-3:2014 the atmospheric corrosivity at the bottom part of the solar collector under service conditions may typically correspond to a corrosion rate of zinc of 0.1 or 0.3 g/m^2 per year depending of the type of collector. Other authors (Slamova et al, 2016) evaluated collectors under stagnation conditions obtaining a zinc corrosion rate of 19.72g/m^2 per year. Carvalho, M. J. et al, 2017 obtained zinc corrosion rates, in different type of collectors with different solar absorber surfaces under stagnation exposed in same atmosphere, of 4.5 g/m^2 and 99.9 g/m^2 per year. So, the corrosivity of the SO_2 resistance test proposed in ISO 22975-3:2014 seems to be insufficient to guarantee durability of 25 years for solar selective absorber surfaces.

Tab. 6 – Zinc corrosion rate (g/m^2/day) in the different accelerated aging tests

Accelerated aging tests	**Corrosion rate (g/m^2/day) (range)**
SO_2 (ISO 22975-3:2014)	0.34 (0.26-0.39)
Neutral salt spray (ISO 9227:2012)	25 (12.5-50)[(1)]
SO_2 (ISO 3231:1993)	1.25 (1.13-1.37)
Cycles (ISO 21207 - Method A:2015)	0.81 (-)[(2)]

[(1)] Value assuming that mass loss rate is linear with testing time. The value indicated in ISO 9227:2012 is 50±25g/m^2 (48 hours)

[(2)] Value assuming that mass loos rate is linear with testing time. The value indicated in ISO 21207:2015 (Method A) is 40g/m^2 (4 weeks or 4 cycles)

4. Conclusions

It was the main objective of this work the implementation of standardized test methods for qualification of different solar absorber coating surfaces. The tests according to ISO 22975-3:2014 were implemented and applied to 5 absorber coatings that were commercially available (two PVDs and three PCs).

All absorber coatings were qualified for resistance to sulfur dioxide. PVD1 was not qualified in terms of thermal resistance due to optical properties and PC3 was equally not qualified but due to loss of coating adhesion. All surfaces are qualified relatively to resistance to condensed water. However the paint and PVD coatings require confirmation because the study was performed only with samples without previous thermal conditioning. Temperature can lead to some adhesion and optical weakness in the organic and PVDs coatings respectively during the exposure to condensed water.

The methodologies of accelerated aging tests with continuous exposure to contaminants (salt spray and sulfur dioxide) revealed that PVDs are more susceptible to degradation induced by chloride rather than sulfur dioxide and PCs suffer further degradation with sulfur dioxide than chlorides. Countries with high solar resource and amount of coastal regions with high population density constitute a large and prospective market for STC and a challenge in terms of reliability and durability. The results obtained with the methodology describe in ISO 21207: 2015 considering an accelerated aging test with cyclic variation of corrosion promoting gases (SO_2 and NO_2), higher humidity, salt spraying and drying reveal similar results to those presented by Diamantino et al, 2017 with the same solar absorber coatings exposed to outdoor exposure testing sites with different corrosivity (urban test site with marine influence – *medium corrosivity* and an industrial/marine test site with *very high /extreme corrosivity*) in terms of the ranking of Pc, FM and anticorrosive protection. PVD2 obtained the higher Pc and PVD1 the higher FM in both OET sites and in accelerated aging according to ISO 21207:2015 (Method A). PC3 showed the best anticorrosive protection and PVD2 the lower in both OET sites, in accelerated aging test according to ISO 21207:2015 and from results obtained by electrochemical impedance spectroscopy (Fernandes et al, 2017).

The methodologies proposed in ISO 22975-3:2014 are an important tool for qualification of selective absorber

coatings. However these tests require many hours and don't reflect the environments where the collectors are exposed. These results showed that the accelerated aging test for qualification of selective solar absorber coatings must include at least sulfur dioxide and chloride as contaminants, beyond the resistance to temperature and humidity condensation. Additional studies are ongoing, namely to study the degradation mechanism of solar selective surfaces under the influence, separately and combined, of SO_2, NO_2 and chlorides in a defined temperature and humidity, with and without dry cycles and UV radiation under the cover. The procedures of accelerated aging tests to qualified coatings guaranteeing high durability should have gas with low concentrations together with a proper choice of temperature and relative humidity, salt spray, radiation and air flow to generate the degradation that have been observed in well characterized field environments with a specific atmospheric corrosivity.

5. Acknowledgements

This work was carried out under the Project FCOMP-01-0124-FEDER-027507 (Ref. FCT RECI/EMS-ENE/0170/2012) and the Project POCI-01-0145-FEDER-016709 FCT (PTDC/EMS-ENE/0578/2014). The authors would like to thank to industrial partners (FogãoSol, Hempel, OpenPlus and Permasolaris), by the supply of samples and the means for performing this work. Thanks are due also to Laboratory of Materials and Coatings team in particular to Ana Soares Vieira, Isabel Nascimento Alves and Soraia Páscoa.

6. References

Castaño J. G., D. de la Fuente, M. Morcillo, 2007. A laboratory study of the effect of NO2 on the atmospheric corrosion of zinc. Atmospheric Environment 41 (2007) 8681–8696 http://dx.doi.org/10.1016/j.atmosenv.2007.07.022

Diamantino, T. C. , R. Gonçalves, A. Nunes, S. Páscoa, M. J. Carvalho. Durability of different selective solar absorber coatings in environments with different corrosivity. Solar Energy Materials and Solar Cells, (2017) 166, 27-38 https://doi.org/10.1016/j.solmat.2017.03.004

Carvalho M. J., S. Páscoa, R. Gonçalves N. Mexa and T. C. Diamantino. Influence of maritime/industrial atmosphere on solar thermal collector's degradation. EUROSUN Proceedings, 2017.

Fernandes, J. C. S., Ana Nunes, M. João Carvalho, Teresa C. Diamantino. Degradation of Selective Solar Absorber Surfaces in Solar Thermal Collectors – An EIS Study. Solar Energy Materials and Solar Cells, (2017) 160, 149-163 https://doi.org/10.1016/j.solmat.2016.10.015

ISO 3231:1993. Paints and varnishes - Determination of resistance to humid atmospheres containing sulfur dioxide

ISO 4624:2002 Paints and varnishes -- Pull-off test for adhesion. 2002

ISO 9227:2012. Corrosion tests in artificial atmospheres -- Salt spray tests

ISO 8407:2009 Corrosion of metals and alloys - Removal of corrosion products from corrosion test specimens. 2009

ISO 10062:2006. Corrosion tests in artificial atmosphere at very low concentrations of polluting gas(es)

ISO/TR 16335:2013 Corrosion of metals and alloys -- Corrosion tests in artificial atmospheres - Guidelines for selection of accelerated corrosion test for product qualification. 2013

ISO 21207:2015 - Corrosion tests in artificial atmospheres — Accelerated corrosion tests involving alternate exposure to corrosion-promoting gases, neutral salt-spray and drying.

ISO 22975-3:2014(E), Solar Energy – Collectors components and materials – Part 3: Absorber surface durability

Köhl, M., Carlsson, B., Jorgensen, G. J., Czanderna, A. W. (Editors), Performance and Durability Assessment. Optical Materials for Solar Thermal Systems. 2004, Elsevier (ISBN 0-08-044401-6)

Mihelčič M., V. Francetič, J. Kovač, A. Šurca Vuk, B. Orel, R. Kunič, D. Peros. Novel sol–gel based selectivecoatings: From coil absorber coating to high power coating. Solar Energy Materials & Solar Cells 140 (2015) 232–248 http://dx.doi.org/10.1016/j.solmat.2015.04.010

Roberts, D. E., A figure of merit for selective absorbers in flat plate solar water heaters, Solar Energy 98 (2013) 503-510 http://dx.doi.org/10.1016/j.solener.2013.10.012

Slamova, K., I. Duerr, T. Kaltenbach, M. Köhl, 2016. Degradation effects of maritime atmosphere on metallic components of solar collectors. Solar Energy Materials and Solar Cells 147, 246–254 http://dx.doi.org/10.1016/j.solmat.2015.12.011

Conference Proceedings

EuroSun 2016
Palma de Mallorca (Spain), 11 - 14 October 2016

CLASSIFICATION OF SOLAR DOMESTIC HOT WATER SYSTEMS

José Luis Duomarco

A.I.U. Montevideo (Uruguay)

Abstract

For commercial reasons it is becoming more and more necessary to have an effective way of classifying solar domestic hot water systems. Customers need a quick advice before shopping and impartial information printed on a label may help. Two indexes are defined, the energy factor and the figure of merit, that can serve this purpose. The energy factor is the rate between the volume of hot water produced in one year and the auxiliary heat needed, (L/kWh), calculated when the daily extraction is 2/3 of the storage volume, (2Vs/3), and the temperature is T_{DN} = 60°C. The figure of merit is the ratio of the energy factor to a theoretical reference yield; in turn, ratio of the total annual volume of hot water produced, at T_{DN} = 60°, to its content in sensible heat. A Transient System Simulation program (TRNSYS) model and new software, (ISO), have been developed on the guidelines of the International Standard ISO 9459-2, as simulation software on which they can be calculated. The draw-back of such procedures result from observing that the values obtained are site-dependent. An alternative classification way is presented, based on a non-dimensional number that is totally site-independent.

Keywords: *solar domestic hot water systems, international standards, solar systems classification.*

1. Introduction

For commercial reasons it is becoming more and more necessary to have an effective way of classifying solar domestic hot water (SDHW) systems. Customers need a quick advice before shopping and impartial information printed on a label may help.

The qualification test procedures are well established and are of the pass-fail type (ISO 9806-2, 1995). Instead, energy performance information adapts easily to a numeric or eventually to a color scale. At least two simulation procedures have given the raw material for such a scale. The Solar Energy Laboratory of the University of Wisconsin, UW-SEL, has developed a modular method, where each module is tested separately. The parameters obtained are then fed into especial software where annual performance is calculated. The f-chart and TRNSYS, works on these trends (Duffie & Beckman, 1991). The solar Collector and System Testing Group, CSTG, has followed a track quite different because no reference is made to components parameters. The system is characterized from the start as a black-box with input-output parameters that are determined by an all-day test (ISO 9459-2, 1995).

Until now, the main quantity used to evaluate the energetic performances of SDHW systems has been the solar fraction; defined as the percentage of the total load supplied by the sun. Solar fraction values specific to the collector area are also used (FSEC, 2002) (INMETRO, 2012). But this information should not be enough for a customer that wants to use a constant daily volume of hot water, V_D, at a specified temperature, T_D, all through the year . The auxiliary costly energy requirement is very important and should be a part of the energy performance information.

Two indexes, the energy factor (EF) and the figure of merit (FOM) are adequate. The EF is the rate of the

doi:10.18086/eurosun.2016.06.09 Available at http://proceedings.ises.org

volume of hot water produced, to the auxiliary heat used in one year (L / kWh), calculated when the only daily evening time extraction is 2/3 of the storage volume ($2V_S/3$), and the temperature is T_{DN} = 60°C. The FOM is the ratio of the EF to a theoretical reference yield (TRY); in turn ratio of the total annual volume of hot water produced, at T_{DN} = 60ºC, to its content in sensible heat or total auxiliary energy not-sun-assisted needed. The higher their values the better, as more hot water is produced with the unit of auxiliary energy.

The T_{DN} = 60ºC reference temperature, has been chosen in behalf of domestic uses.

The $V_{DN}=2V_S/3$ reference volume has been arbitrarily selected with the only restriction of being less than the storage volume V_S. It is shown in figure 3 that extractions greater or equal than V_S, tend to fade out differences between the y values of collectors, due to the cold water intrusion in the tank.

2. Method

Two different simulation procedures are used in the evaluation of the EF and the FOM:

1. ISO simulation in 2.2 (B. Bourgues, *et al*, 1991) (M. J. Carvalho & D. J. Naron, 2000) (J.L. Duomarco, 2015).
2. TRNSYS simulations in 2.3 (TRNSYS,2000)

2.1 Equations defining the EF and the FOM

- The ratio of the total annual volume of hot water produced, at T_{DN} = 60ºC, to the total sun-assisted auxiliary energy, and its inverse, are written as:

$$v_{AUX} = \frac{365\,V_D}{\sum_{i=1}^{365} Q_{AUX,i}} = \frac{1}{q_{AUX}} \qquad \text{(eq. 1)}$$

- The ratio of the total annual volume of hot water produced, at T_{DN} = 60º, to its content in sensible heat, are written as:

$$v_{DN} = \frac{365\,V_D}{\sum_{i=1}^{365} Q_{DN,i}} = \frac{365\,V_D}{\sum_{i=1}^{365} V_D c_{p\omega}\rho_{\omega}\left(T_{DN} - T_{MAIN,i}\right)} = \frac{1}{q_{DN}} = TRY \qquad \text{(eq. 2)}$$

- The ratios x and y :

$$x = \frac{V_D}{V_S} \qquad \text{(eq.3)}$$

$$y = \frac{q_{AUX}}{q_{DN}} = \frac{v_{DN}}{v_{AUX}} = \frac{\sum_{i=1}^{365} Q_{AUX,i}}{\sum_{i=1}^{365} Q_{DN,i}} \qquad \text{(eq.4)}$$

- The energy factor:

$$EF = v_{AUX} \qquad when \quad V_D = V_{DN} = \frac{2V_S}{3} \qquad \text{(eq. 5)}$$

- The figure of merit:

$$FOM = \frac{v_{AUX}}{v_{DN}} = \frac{EF}{TRY} = \frac{1}{y} \qquad when \quad V_D = V_{DN} = \frac{2V_S}{3} \qquad \text{(eq.6)}$$

2.2 The ISO simulation.

A detailed description of the test method can be found in the text of the standard ISO 9459.2. The system characterization is obtained by the fulfillment of 4 steps:

- input-output diagram,
- draw-off temperature profiles,
- store overnight heat loss coefficient,
- long term performance prediction (LTPP).

The calculation details of LTPP include two load patterns:

- Load pattern 1: determined by the volume of daily hot water consumption,
- Load pattern 2: determined by a minimum useful temperature limit for the hot water consumption. When the outlet temperature is lower than this minimum value, no water is extracted.

The new ISO software has been developed with a different load pattern:

- Load pattern 3: modeled for a nominal temperature and a nominal hot water volume production, both constant during the year, with only one daily draw-off. According to the daily climate conditions and daily hot water demand, the draw-off temperature and draw-off volume may be under or above the nominal values. If overheating is present, the excess energy over the nominal is calculated and discarded. If solar heating is under the nominal value, the auxiliary heat necessary to reach nominal settings is calculated. The calculation is extended only to 365 days assuming an annual periodicity,
- Case study systems: The performance of three different systems, System5, System8 and Baxiroca, were calculated and compared. The typical data of System 5 and System 8 were obtained from work at the Solar Collectors and Systems Laboratory from the National Research Centre Demokritos (Athens, Greece)(Belessiotis & Harambopoulos, 1993) and similar data for Baxiroca150, from a test report emitted by the "Escuela Superior de Ingenieros" (Seville, Spain) (LCS, 2009).The values are listed in Table 1, the draw-off profiles and the input-output plots are shown in Fig.1. The daily climate data for Belo Horizonte, Salto, Montevideo, Boston, Edinburgh and Punta Arenas were obtained from project "Surface Meteorology and Solar Energy" (NASA, 2010). Simultaneous daily global solar radiation on horizontal surface, maximum and minimum temperature series for year 2010, were used in the simulation.

Table 1 - Experimental results (Belessiotis & Harambopoulos, 1993), (LCS, 2009).

System name	a1 (m^2)	a2 (MJ / K / d)	a3 (MJ / d)	Ac (m^2)	Vs_{tk} (L)	ls_{tk} (length) (m)	Ds_{tk} (diameter) (m)
System 5	1.58	0.45	-1.37	3.41	200	1.67	0.39
System 8	0.96	0.47	-1.37	2.05	160	1.34	0.39
Baxiroca	1	0.27	-0.61	1.92	150	1.25	0.39
System name	δo=a1/Ac	δ1=a2/Ac (MJ/K/m^2/d)	δ1=a2/Ac (W/K/m^2)	a3/a2 (K)	As_{tk} (m^2)	Us_{tk} (W/K)	U_{SCtk} (W/K)
System 5	0.4633	0.1320	1.5274	-3.04	2.2902	2.6	2.93
System 8	0.4683	0.2293	2.6536	-2.91	1.8799	1.81	1.87
Baxiroca	0.5208	0.1406	1.6276	-2.25	1.7773	3.23	-
System name	Number of collectors	Storage Type	Heat exchange	Operation type	V_{DN} = 2/3Vs (L/d)	T_{DN} (ºC)	Yield in MVD (L/kWh)
System 5	2	Horizontal	Tube	Thermo-siphon	133	60	56.3
System 8	1	Horizontal	Double wall	Thermo-siphon	107	60	33.6
Baxiroca	1	Horizontal	Tube	Thermo-siphon	100	60	51.1

ISO 9459-2 - eq. (2) - a_1,a_2,a_3 - determined from test results by least-squares fitting methods, Q_T net solar energy gained by the storage tank in the day, T_a ambient air temperature, T_S cold water supply temperature, A_C collector's aperture area, A_S store-tank's surface, V_S store-tank's volume, l_S store-tank's length, D_S store's tank diameter

$$Q_{T_i} = a_1 G_T + a_2 (T_a - T_S) + a_3 = G_T A_C (\delta_0 - \delta_1 z)$$

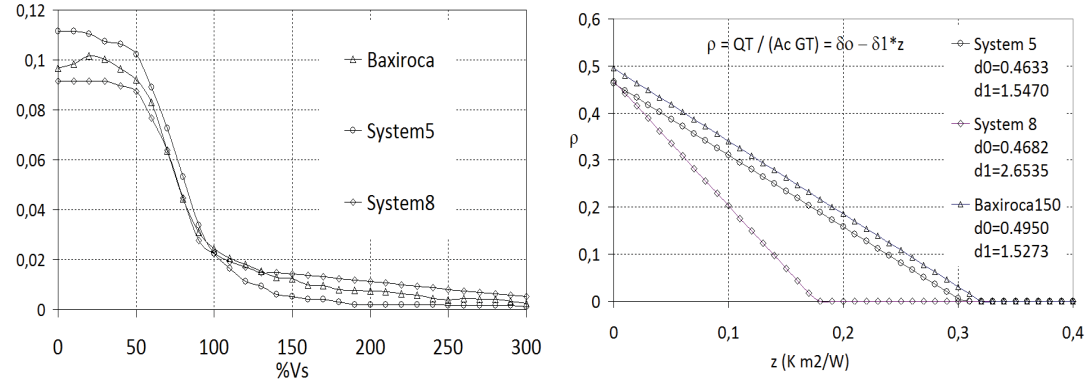

a) b)

Fig. 1: Normalized draw-off temperature profiles a), and input-output diagram b) ,for Baxiroca, System5 and *System8.*

2.3 The TRNSYS simulation .

A TRNSYS model (TRNSYS, 2000) has been built around component Type 45a and is shown in Fig.3. It requires, 39 parameters, 10 inputs and produces 12 outputs. This component models the thermo-siphon solar collector system. The system consists of a flat-plate solar collector, a stratified storage tank (either vertical or horizontal cylinder) located physically above the collector plate, a check valve to prevent reverse flow, and water as the working fluid. The tank's stratification is modeled with the plug-flow concept.
Global horizontal hourly solar radiation and simultaneous hourly ambient temperature for one year are needed. Two such databases, from Montevideo (Ewenson, 1979) and Salto (LES, 2015) are used. The daily routine consists in evaluating the storage sensible heat at 19h after a day's recollection, making the constant volume draw-off at 20h after fixing its temperature by adding auxiliary heat or discarding overheat and calculating the heat remains in the storage tank. Fig. 2a shows hourly energy variations on May 21 when auxiliary heat is necessary, Fig. 2b similarly for January 5 when overheat is present in the city of Salto and Table 2 lists some parameters, inputs and outputs present with their definitions.

3. Results

In Fig. 4, eight graphs show the index y as function of x.

The reference systems, Baxiroca in 4.1, System5 in 4.2, and System8 in 4.3, are evaluated in the six reference cities, Belo Horizonte, Salto, Montevideo, Boston, Edinburgh and Punta Arenas.

The reference systems, Baxiroca, System5, and System8, are evaluated jointly, with ISO simulation, in Boston 4.4, Salto 4.5, Montevideo 4.6, and with TRNSYS simulation, in Montevideo 4.7, and Salto 4.8

For small values of x, cold climate cities begin with high values of y, around 60%, while mild and warm climate cities begin with y values between 5% and 20%. A null y value stands for no auxiliary heat needed. When draw-off volume V_D, exceeds the storage tank volume V_S, (V_D>V_S), all y functions asymptotically get near 100%, or q_{AUX} gets near q_{DN} from below.

When systems are evaluated in the same place, for V_D less than V_S (V_D<V_S), System5 leads Baxiroca and Baxiroca leads System8, in the sense that they need less auxiliary energy to heat up one liter of water. In the trend of classifying solar collector systems with only one number, we selected arbitrarily a constant daily extraction volume $V_{DN} = 2V_S/3$. In Fig. 5, Fig.6 and Table 3, EF and FOM values, are calculated and plotted.

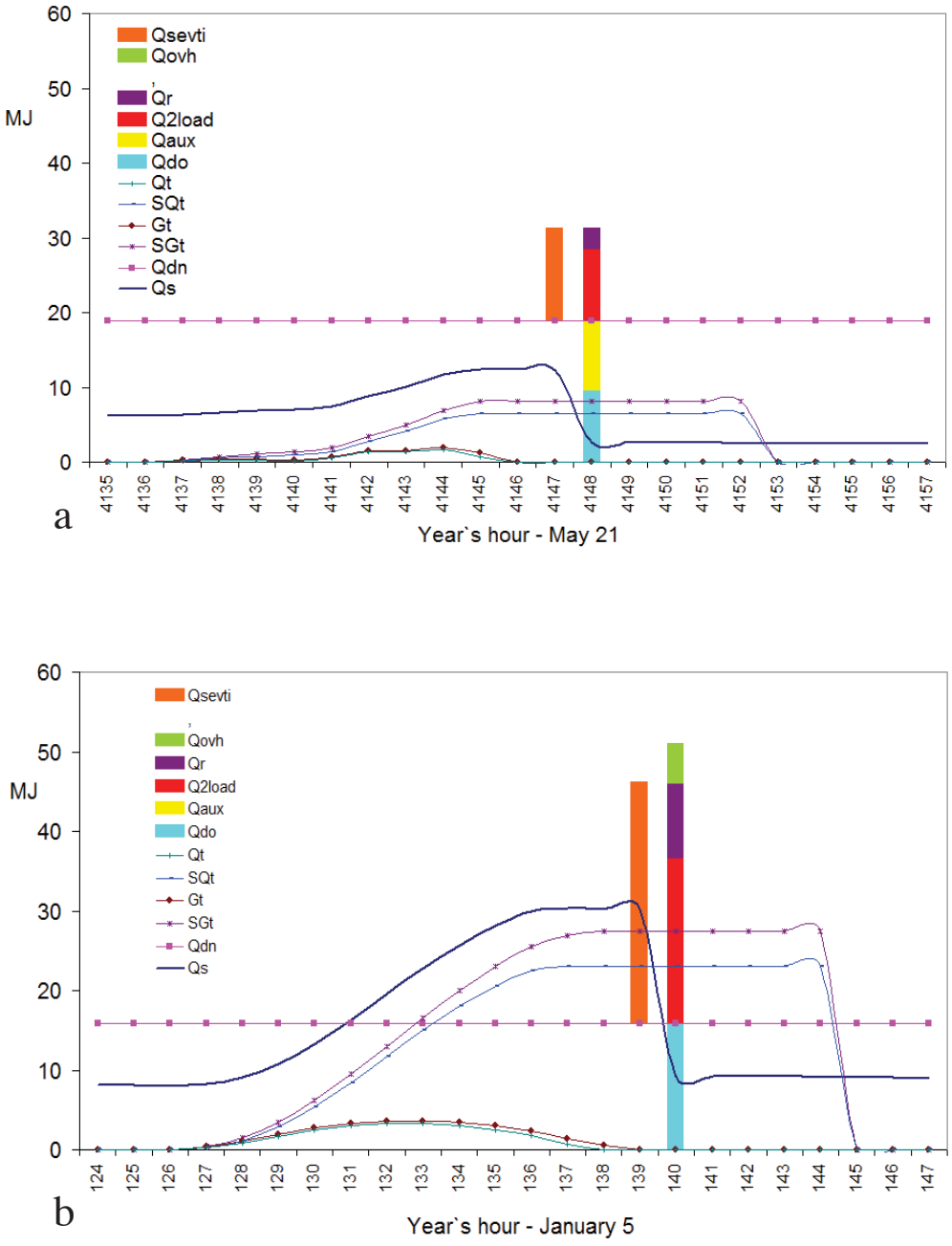

Fig. 2: TRNSYS simulation hourly energy variations in Salto on: a) May21, with auxiliary heat and b) January 5, with overheat

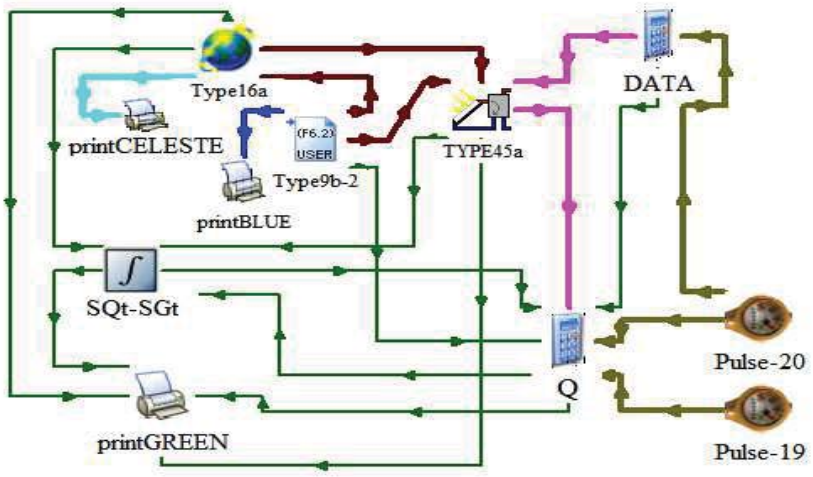

Fig.3: TRNSYS model built around a thermo siphon collector-storage subsystem (Type 45a).

Table 2 - Energy daily transactions in TRNSYS simulation

Hourly events	
Q_{DN}	Daily energy reference settings $Q_{DN,i} = V_D . 4.1868 . (T_{DN}-T_{main,i})$ - kJ
Q_S	Sensible heat in storage tank - kJ
Q_T	The rate of energy transfer from the heat source to the storage tank - kJ/h
SQ_T	$\int Q_T \, dt$ Accumulated daily energy transfer from the heat source to the storage tank - kJ
G_T	Radiation on the tilted surface (beam + sky diffuse + ground reflected diffuse) - kJ /h m^2
SG_T	$\int G_T \, dt$ Accumulated daily radiation on the tilted surface - kJ/d m^2
Evening time events, at 19h and 20h	
Q_{SEVT}	Sensible heat in storage at evening-time , 19 h - kJ
Q_{2LOAD}	total heat to load, 20h - kJ
Q_{OVH}	Overheat discarded - 20h - kJ
Q_{AUX}	Auxiliary heat to load - 20h - kJ
Q_{DO}	Q_{2LOAD}-Q_{OVH} Energy removed from the tank to supply the load - 20h - kJ
Q_R	SQ_{SEVT} -SQ_{2LOAD} - kJ Remains of sensible heat in storage, after draw-off - 20h - kJ

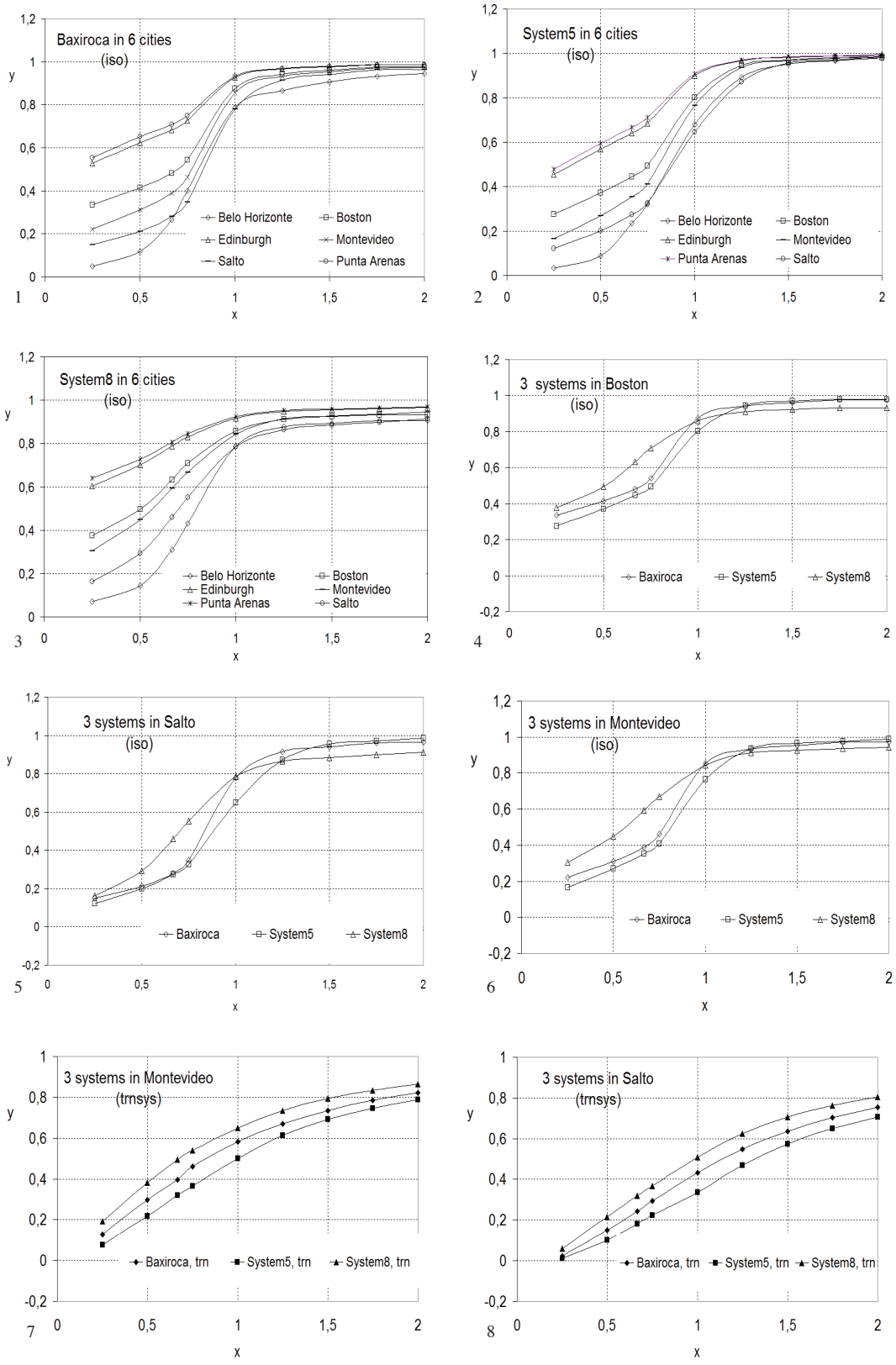

Fig. 4: Ratio y = qaux / qdn as function of ratio x = Vd / Vs, for System 5, System 8 and Baxiroca, using ISO and TRNSYS simulation procedures, in Belo Horizonte, Salto, Montevideo, Boston, Edinburgh and Punta Arenas

Table 3 - Calculation of the EF, FOM and q for System 5, System 8 and Baxiroca by the ISO simulation procedure in Punta Arenas, Edinburgh, Boston, Montevideo, Salto and Belo Horizonte and by the TRNSYS simulation procedure in Montevideo and Salto.

V_{DN} = 2Vs/3 T_{DN} = 60 °C	System 5 V_{DN} = 133.3.. L/d			System 8 V_{DN} = 106.6… L/d			Baxiroca V_{DN} = 100 L/d		
City	EF L/kWh	q_5 kWh /100 L	FOM %	EF L/kWh	q_8 kWh/100L	FOM %	EF L/kWh	q_{bax} kWh/100L	FOM %
iso									
Punta Arenas	22.9	4.354	150	19.0	5.257	124	21.6	4.616	141
Edinburgh	26.0	3.843	156	21.1	4.721	127	24.4	4.093	147
Boston	37.0	2.698	224	26.1	3.828	158	34.3	2.910	208
Montevideo	56.2	1.777	282	33.5	2.979	168	51.1	1.955	256
Salto	77.7	1.285	365	46.3	2.155	218	75.5	1.322	355
Belo Horizonte	94.6	1.056	425	72.1	1.386	324	84.4	1.184	379
trnsys									
Montevideo	62.7	1.595	314	40.3	2.477	202	50.3	1.989	251
Salto	116.6	0.857	547	66.9	1.495	314	87.2	1.146	409

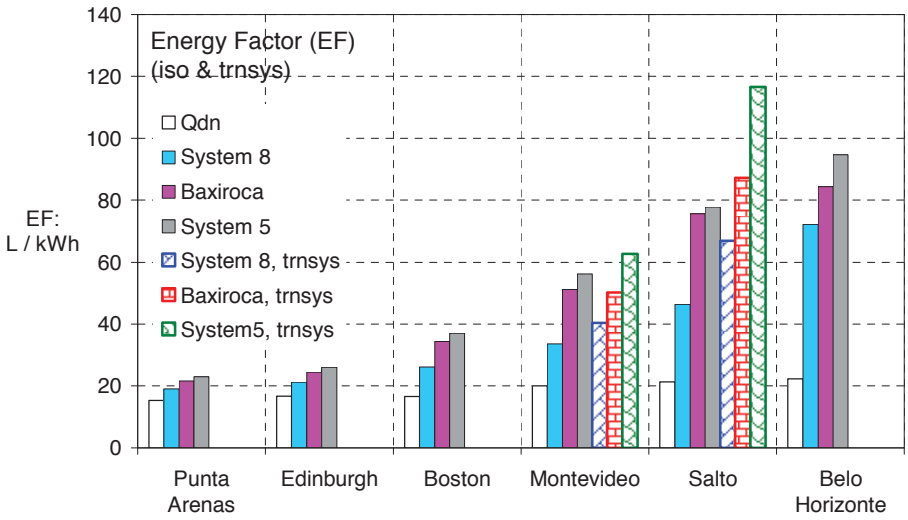

Fig. 5: Theoretical Reference Yield (TRY) and Energy Factor (EF) for 6 different cities, with ISO and TRNSYS simulations.

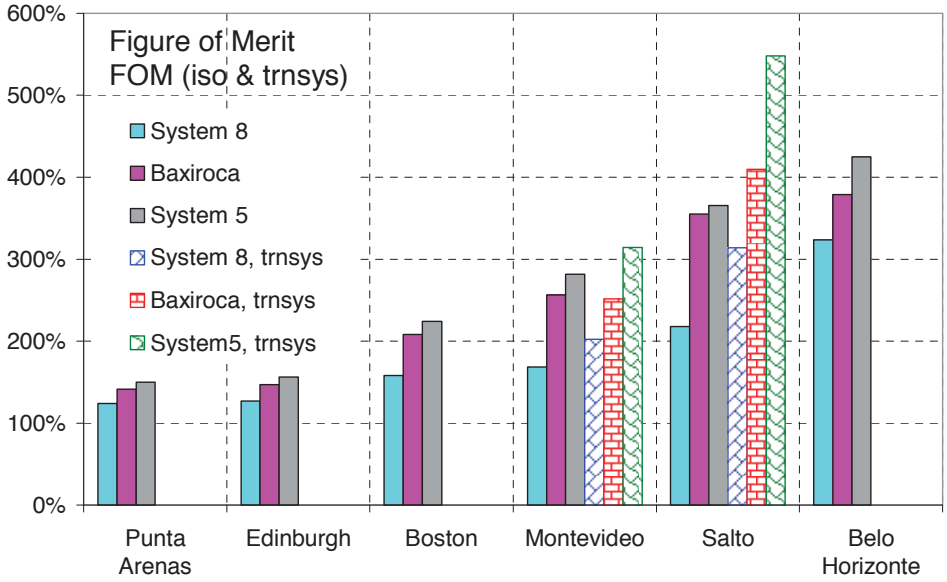

Fig. 6: Figure of Merit FOM for 6 different cities with ISO and TRNSYS procedures.

4. Site-independent figure of merit

From what has been said before, both EF and FOM depend on location. This hinders a universal classification of solar systems based on these indexes. It's desirable to classify SDHW systems in an intrinsic way, only dependent on their characteristics and not on their locations. Commercial confusion is likely to happen when equal indexes may address different SDHW systems measured in different places not properly recorded. An alternative classification procedure has been studied, based on a non-dimensional number γ_0 that gets together all three loss mechanisms,

$$\gamma_0 = 100^* \log_{10}\left[\frac{\delta_0^2}{2\delta_1\lambda_S}\left(\frac{G_0}{\Delta T_0}\right)^2\right] = 100^* \log_{10}\left[\frac{a_1^2 A_S}{2a_2 A_C U_S}\left(\frac{G_0}{\Delta T_0}\right)^2\right] \quad \text{(eq. 7)}$$

where

1. $\lambda_S = U_S / A_S$ with units (W/m^{2}K), characterize the heat loss of the storage tank,
2. $\delta_1 = a_2 / A_C$ with units (W/m^{2}K), characterize the heat loss of the collector,
3. $\delta_0 = a_1 / A_C$ measures the collector's optical efficiency,
4. $\delta_0^2 / (2\delta_1\lambda_S)$ gets together losses and is proportional to the surface under the input-output diagrams,
5. $(G_0/\Delta T_0)^2$ with Go= 1367 W/m^2 and ΔT = 100 K is a theory-related constant with dimensions,
6. logarithm is taken to smooth-out big variations,
7. calculation of our reference systems is shown in Table 4.

Table 4 - Site-independent non-dimensional figure of merit γ_0

System 5	System 8	Baxiroca
106	90	91

5. Conclusions

The energy factor EF (L/kWh), depends only on end points in the line; hot water production (L), and auxiliary energy to be paid-for (kWh). Free solar energy acts indirectly as a means to improve the EF. The figure of merit FOM is a non-dimensional quantity used to characterize the SDHW system relative to its basic without sun's boosting, alternative.

The simulation program must be specified. Two such simulation programs have been used. TRNSYS models require numerous modules connected with plenty of parameters, acting as input and output data, between them. Sometimes it is cumbersome to set such a simulation. On the other hand, ISO has a black-box-layout, needs fewer experimental results and is easier to use.

EF as FOM are site-dependent and so, meaningless if measuring place is not reported. From an international commerce point of view, it would be helpful to classify SDWH systems in a site-independent way. Three independent loss mechanisms may always be identified: optical efficiency, day collector-thermal-loss and night storage-thermal-loss. Improving these three characteristics, results in a increased non-dimensional γ_0 number with the additional advantage of being site-independent.

6. Reference

V. Belessiotis and D. Harambopoulos, 1993. Testing solar water heating systems in Athens, Greece. Solar Energy 50, No. 2, pp167-177.

B. Bourgues, A. Rabl, M.J. Carvalho & M. Collares-Pereira, 1991. Accuracy of the European solar water heater test procedure. Part 1 & Part 2. Solar Energy, vol. 47 no.1, pp 1-25.

M. J. Carvalho & D. J. Naron, 2000. Comparison of test methods for evaluation of thermal performance of preheat and solar-only factory made systems. Solar Energy, vol 69 (Suppl.) no 1-6, pp. 145-156

Duffie & Beckman,1991. Solar Engineering of Thermal Process. Wiley-Interscience. New York.

J.L. Duomarco, 2015. Figure of merit for solar domestic hot water systems. Solar Energy, Vol. 111, pp. 151- 156.

I.W. de Ewenson, Facultad de Ingenierìa, UdelaR, 1979. Serie horaria de radiación global de Montevideo, Uruguay

Florida Solar Energy Center (FSEC), 2002. Operation of the Collector Certification Program. FSEC-GP-6-80-Florida.

INMETRO, 2012. Regulamento da qualidade para equipamento de aquecimento solar de agua. Brasil.

ISO 9459-2:1995. Solar heating. Domestic water heating systems- Part 2: Outdoor test methods for system performance prediction of solar-only systems.

ISO 9806-2, 1995. Test Methods for Solar Collectors – Part 2: Qualification Test Procedures.

Laboratorio de Captadores Solares (LCS), Escuela Superior de Ingenieros, 2009. Test Report, Baxiroca STS 150. Seville, Spain.

Laboratorio de Energìa Solar (LES), UdelaR, 2015. Serie horaria de radiaciòn global de Salto, Uruguay

NASA, 2010. Surface meteorology and Solar Energy. http://eosweb.larc.nasa.gov/sse/

Transient System Simulation Program, TRNSYS, 2000. Version 16.00.0037, Solar Energy Laboratory of the University of Wisconsin–Madison.

ISES International Solar Energy Society

Conference Proceedings

EuroSun 2016

Palma de Mallorca (Spain), 11 – 14 October 2016

Assessment of Elastomeric Components of a Solar Thermal Collector

M.C. Ferreira, A.R. Rosado, M.J. Carvalho and T.C. Diamantino

National Laboratory of Energy and Geology, Lisbon (Portugal)

Abstract

Elastomeric components play important functions in solar thermal collectors (STC's) as sealings, fittings or absorbers, being important that they maintain their properties along STC lifetime. In what ageing is concerned, current standards for assessment of elastomeric materials put emphasis on the effect of heating.

The results presented in this paper refer to the evaluation of the effects of exposure to heating as well as to solar radiation by means of accelerated tests on two ethylene propylene diene terpolymer (EPDM) components of a commercial STC both carbon black filled compounds. At the current stage of the study, results showed that the effect of solar radiation may be relevant for the assessment of the components and, for that reason, should be considered along with temperature.

Keywords: *solar thermal collectors, elastomeric components, ageing, accelerated tests*

1. Introduction

Environmental factors cause degradation of polymers (Massey, 2007), in particular UV radiation induce photo-oxidation reactions. Even polymers with low unsaturation as is the case of EPDM, which is extensively used in outdoor applications, are prone to such reactions (Maecker and Priddy, 1991). EPDM formulations for those applications are designed to minimise photodegradation. Nevertheless changes in crosslink density, hardness, tensile properties and appearance are referred (Aimura and Wada, 2006; Zhao et al., 2007).

The work whose results are presented in this paper is part of a study aiming at evaluating the suitability of the accelerated ageing tests specified in standards ISO 9808:1990 and ISO 9553:1997 for the assessment of elastomeric components of STC's operating in high UV radiation environments and contributing to design accelerated ageing tests more capable of reproducing those environments whenever the standards are not adequate. To that end different components of STC's are characterised after the heating test described in those standards and after laboratory exposure to radiation as well as after exposure in two outdoor exposure sites. Detailed characterization of these sites can be found in Diamantino et al. (2017). The results here reported refer to the evaluation of the effects of the laboratory tests – resistance to heating and exposure to xenon-arc and to UV radiation - on two components of a commercial STC, a fitting with the function of isolating inlet and outlet connections and the glazing sealant, both carbon black filled EPDM compounds.

2. Methods

For the tests fittings were used as such while the sealing was cut in segments with a length of approximately 200 mm.

2.1 Resistance to heating test

The test was carried out at 175 ºC for 14 days according to ISO 9808:1990 and ISO 9553:1997 based on the stagnation temperature of the collector (150ºC) in an oven with forced air circulation. Complementary tests were performed at 150 ºC and 125 ºC to investigate the thermal behaviour of the components also at lower

doi:10.18086/eurosun.2016.06.03 Available at http://proceedings.ises.org

temperatures.

To evaluate the effects of the heating on the components the relative variations of total mass and dimensions were calculated, thermogravimetric analyses and mechanical tests were done.

The internal diameter of the fittings was determined with a caliper rule, three measures being taken for each sample. The length of the fractions of the sealing was determined with a scale. Relative variation of mass and dimensions was calculated for a minimum of five samples according to equation 1:

$$\text{Relative variation (\%)} = \frac{\text{Final value} - \text{Initial value}}{\text{Initial value}} \times 100 \qquad \text{(eq. 1)}$$

Thermogravimetric analyses were done according to ASTM D6370-99 in a Setaram equipment, model Setsys, with around 10 mg of sample in a platinum crucible. The first heating from room temperature to 560 ºC was carried out in argon atmosphere and the second heating from 300 ºC to 800 ºC was carried out in air atmosphere.

Mechanical tests were done with a Testing Machine Instron 4467 at 100 mm/min for fittings and 500 mm/min for sealing according to ISO 37:2011. The shape of the samples made impossible determining the cross-sectional area, so the maximum force was determined, instead of tensile strength. Elongation at break was determined according to ISO 37:2011. The initial distance between grips in the test of sealing was 10 mm. Five specimens of each component were tested.

2.2 Exposure to radiation sources

Exposure to xenon-arc radiation was done according to ISO 4892-2:2013, cycle nº 4, in an Atlas Weatherometer Ci35A with daylight (borosilicate) filters. Each cycle is composed of a dry period of 1.7 h at a spectral irradiance level of 0.51 W m^{-2} nm^{-1} at 340 nm with black panel temperature of 63±3 ºC, chamber temperature of 38±3 ºC and a relative humidity of 50±10% followed by 0.3 h of water spray at the same spectral irradiance. Samples were collected after 72, 168, 336, 668, 1030, 1436, 1922, 2234 and 3240 h of exposure.

Exposure to UV fluorescent radiation was done according to ISO 4892-3:2013, cycle nº 2, in a chamber Q-Lab, QUV spray with a UVA-340 lamp type. Each cycle is composed of a dry period of 8 h at a spectral irradiance level of 0.76 W m^{-2} nm^{-1} at 340 nm with black panel temperature of 50±3 ºC, followed by 0.25 h water spray and 3.75 h condensation without radiation and black panel temperature of 50±3 ºC during the condensation period. Samples were collected after 84, 180, 348, 732, 1080, 1404, 1752, 2076, 3240 and 4320 h of exposure.

The effect of the radiation on the components was assessed by colour difference evaluation, mechanical tests and glass transition temperature determination.

Colour difference, ΔE^*_{ab}, was determined according to ISO 11664-4:2011 with a spectrocolorimeter X-Rite 948. A minimum of five specimens were used in each determination. With the objective of showing the contribution of the variation of each of the coordinates to ΔE^*_{ab}, average values of ΔL^*, Δa^* and Δb^* were calculated.

Mechanical properties were evaluated as referred above.

Glass transition temperature, T_g, was determined in a TA Instruments DSC Q2000 equipment with a refrigeration system TA Instruments Refrigerated Cooling System 90. A mass of 5 mg was used in each test that was put in an aluminium crucible. Two cycles were carried out between -90 ºC and 100 ºC at a heating rate of 20 ºC/min, the values of the second cycle being taken.

3. Results

3.1 Resistance to heating test

Relative variations of mass and dimensions of the fitting and of the sealing after the resistance to heating test at 125 ºC, 150 ºC and 175 ºC are shown in Figure 1.

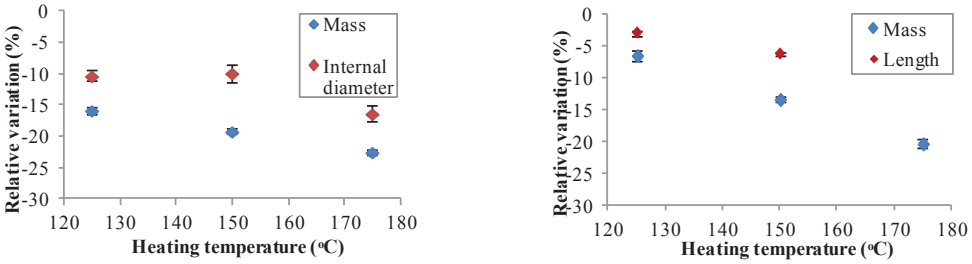

Fig. 1: Relative variations of mass and internal diameter of the fitting (left) and of mass and length of the sealing (right) after resistance to heating tests carried out at 125 ºC, 150 ºC and 175 ºC (bars representing standard deviation).

It was observed mass loss of the fitting in the three tests, variation increasing with the increase of the test temperature. The fitting lost 16% of the mass in the test at 125 ºC, 19 % of the mass at 150 ºC and 22% at 175 ºC. Internal diameter of the sealing decreased 10% after the tests at 125 ºC and 150 ºC and 16% after the test at 175 ºC. ISO 9808:1990 does not indicate an upper limit for volatiles loss.

The sealing lost 6% of the mass in the test at 125 ºC, 13% at 150 ºC and 20% at 175 ºC. The mass loss of the sealing was higher than the sum of maximum of volatiles lost (1%) and volatiles condensable (0.1%) for all the temperatures tested, which is the upper limit value admissible by ISO 9553:1997. The length of the sealing decreased 3% after the test at 125 ºC and 6% at 150 ºC. The length of this component was not determined after the test at 175 ºC as the samples were deformed and brittle.

The results of thermogravimetric analyses in the zone of heating in inert atmosphere of the fitting and of the sealing are shown in Table 1. The thermograms of the unheated components showed two zones of mass loss. The first zone begun in the region typically designated by “highly volatile matter”, referring to compounds of low boiling points (approximately 300 ºC or lower) such as oil, plasticizers, curatives, antioxidants and antiozonants, and ended already in the region designated “medium volatile matter”, referring to medium volatility material such as processing oil and processing aid (Sircar, 1992). The second zone was also included in the region of medium volatile matter where EPDM is found (Paroli et al., 1991; Sircar, 1992).

Tab. 1: Temperature range of mass loss and mass loss of the fitting and of the sealing unheated and after the heating tests at 150 ºC and 175 ºC determined in the zone of heating in argon atmosphere

Component	Heating test temperature (ºC)	Temperature range of mass loss (ºC)	Mass loss (%)
Fitting	Unheated	178 - 421	25
		421 - 500	29
	150	236 - 514	42
	175	243 - 519	36
Sealing	Unheated	171 - 418	23
		419 - 502	24
	150	276 - 501	34
	175	256 - 505	28

The thermograms of the fitting and of the sealing heated at 150 ºC and 175 ºC showed only one zone of mass loss during inert heating beginning in the region of “highly volatile matter” but at significantly higher temperatures than the observed in the first mass loss for the unheated sample indicating that compounds with lower boiling points were removed during the heating tests. In the case of the fitting while above mentioned additives and elastomer corresponded to 54 % of the mass of the unheated sample they corresponded to 42 % and 36 % of the mass of the samples heated at 150 ºC and 175 ºC, respectively. In the case of the sealing additives and elastomer corresponded to 47% of the mass of unheated sample, while they corresponded to 34% and 28% of the samples heated at 150 ºC and 175 ºC, respectively.

Figure 2 shows maximum force and elongation at break of the fitting and of the sealing unheated and after the

resistance to heating test. No appreciable variation of maximum force was observed for the fitting after the heating test at 125 ºC, but a decrease of elongation at break occurred. Maximum force clearly decreased after the tests at 150 ºC and 175 ºC. Elongation at break of this component after the heating tests at these higher temperatures was not determined due to brittleness of the samples. Maximum force of the sealing did not also change appreciably after the heating test at 125 ºC but a decrease of elongation at break occurred. Brittleness of the samples after heating at higher temperatures made impossible carrying out mechanical tests.

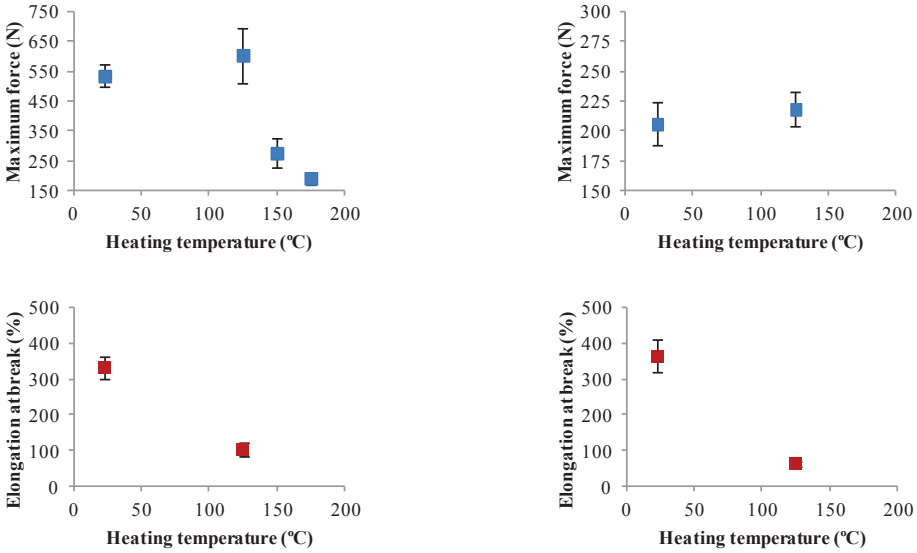

Fig. 2: Maximum force and elongation at break of the fitting (left) and of the sealing (right) unheated and after resistance to heating tests (bars representing standard deviation). Lack of data for 150 ºC and 175 ºC was due to brittleness of the samples.

3.2 Exposure to radiation sources

Colour difference, $\Delta E^*_{ab,}$ and average values of ΔL^*, Δa^* and Δb^* of the fitting and of the sealing after different exposure times to xenon-arc and to UV radiation are shown in Figures 3 and 4, respectively.

Exposure to xenon-arc radiation and water spray caused slight change of samples colour. Regarding the fitting, the final value was practically reached after 336 h of exposure. After this period, the difference in colour was mainly due to an increase of the coordinate L^* meaning the samples were lighter, with a smaller contribution of the b^* coordinate that varied towards the yellow. The colour difference of the sealing was more pronounced the most accentuated difference occurring in the first 72 h of test, after what the colour practically did not change. As observed with the fitting, the difference in colour was mainly due to the increase of coordinate L^*.

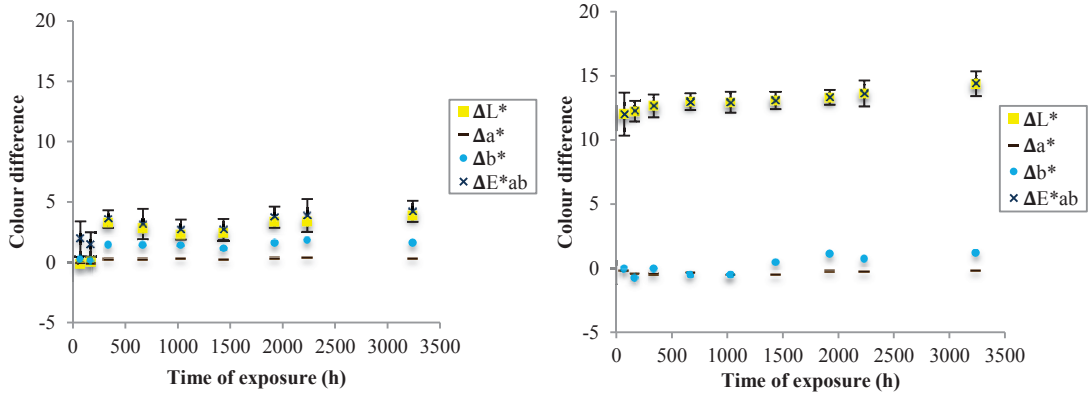

Fig. 3: Colour difference, $\Delta E^*_{ab,}$, and average values of ΔL^*, Δa^* and Δb^* of the fitting (left) and of the sealing (right) after exposure to xenon-arc radiation with water spray(bars representing standard deviation).

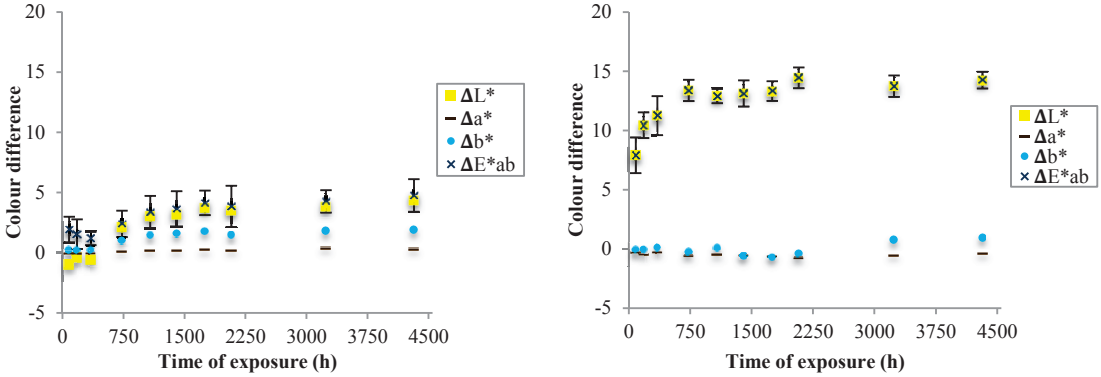

Fig. 4: Colour difference, ΔE^*_{ab}, and average values of ΔL^*, Δa^* and Δb^* of the fitting (left) and of the sealing (right) after exposure to fluorescent UV radiation with condensation and water spray (bars representing standard deviation).

Exposure to UV fluorescent radiation with condensation and water spray caused also slight change of samples colour, the variation in the final of the test being similar to the values determined at the end of the exposure to xenon-arc radiation. The main contribution to the difference of colour of the fitting was from ΔL^*, that until 348 h had negative values, meaning the samples were slightly darker, and after 732 h changed to positive values meaning the samples were lighter. There was also a small variation of the coordinate b^* after 732 h towards yellow. The most pronounced difference of colour of the sealing was observed in the first 72 h but difference of colour still increased, although less sharply until 732 h of test. The difference in colour was mainly due to the increase of L^*.

Maximum force and elongation at break of the fitting and of the sealing after exposure to xenon-arc radiation with water spray are shown in Figure 5.

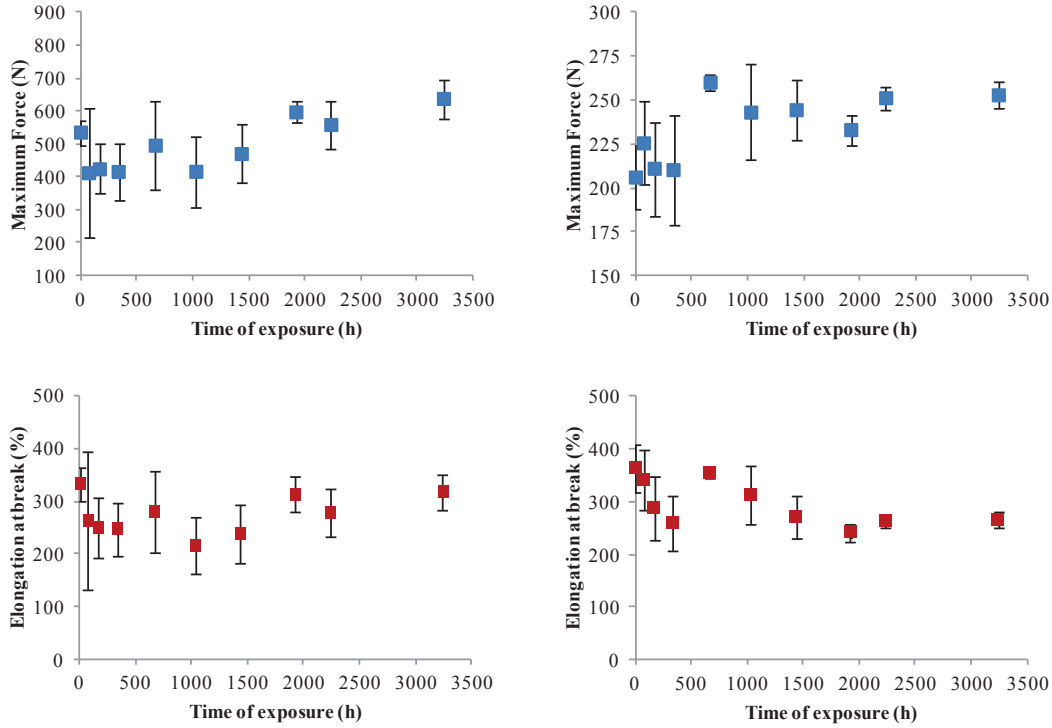

Fig. 5: Maximum force and elongation at break of the fitting (left) and of the sealing (right) after exposure to xenon-arc radiation and water spray (bars representing standard deviation).

Despite the relevant figures of standard deviation mainly due to specimen variability, changes of mechanical properties were noticed. The fitting showed a decrease of maximum force and elongation at break at early

stage of exposure followed by an increasing. The maximum force of the sealing increased after an initial period of no defined tendency while the elongation at break decreased at early stage and after a reverse in this tendency decreased again. EPDM rubber undergoes both chain scission and crosslinking upon xenon-arc weathering (Maecker and Priddy, 1991). Although the changes observed may not be straightforwardly related to those polymer changes due to the chemical complexity of compounded EPDM rubber products, the increase of maximum force of the sealing and decrease of elongation at break for longer periods of exposure relatively to the initial values is compatible with formation of crosslinks.

The patterns of maximum force and elongation at break of the fitting after exposure to UV fluorescent radiation with water spray and condensation (Figure 6) resemble in general with those observed after exposure to xenon-arc test. However the more pronounced decrease of maximum force and elongation at break at early stages of exposure seems to indicate that chemical changes were intensified in the UV test. General patterns of maximum force and elongation at break of the sealing are also similar to those observed after exposure to xenon arc radiation. However, at the early stage of exposure a decrease of maximum force was observed.

Glass transition temperatures, *Tg*, of the two components determined along the exposure to xenon-arc radiation with water spray (Figure 7) and to UV fluorescent radiation with water spray and condensation (Figure 8) showed only slight variations. The trend that was observed in the fitting to increasing at longer periods of exposure to xenon-arc radiation means that the system became stiffer. Glass transition temperature of the sealing practically did not change along exposure indicating that this parameter was not sensible to the chemical changes that occurred in the system.

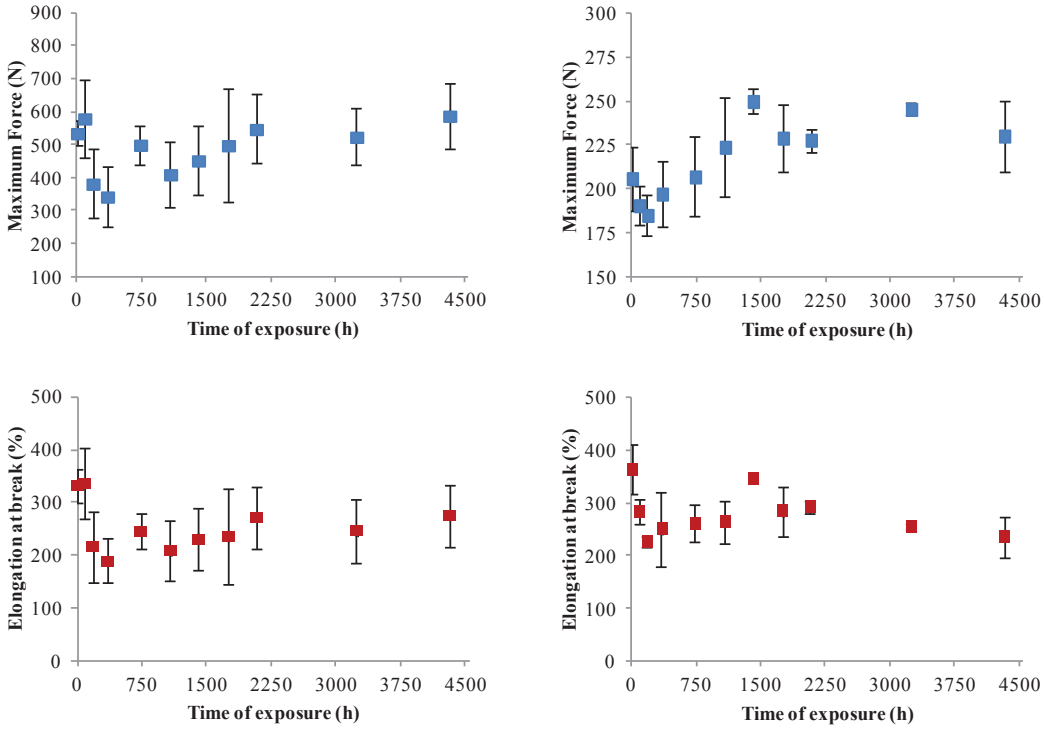

Fig. 6: Maximum force and elongation at break of the fitting (left) and of the sealing (right) after exposure to UV fluorescent radiation with water spray and condensation (bars representing standard deviation).

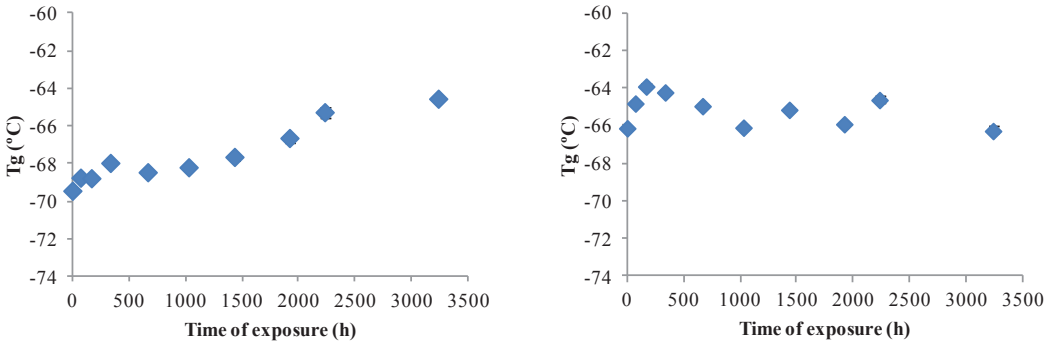

Fig. 7: Glass transition temperatures, T_g, of the fitting (left) and of the sealing (right) after exposure to xenon-arc radiation with water spray(bars representing standard deviation).

Glass transition temperatures of the fitting tended to increase at the beginning of the exposure to UV fluorescent radiation meaning that changes leading to stiffness of the system occurred. This trend was reversed after around 1050 h of test and then recovered at the end of the exposure time. Glass transition of the sealing practically did not change along exposure as observed after xenon-arc radiation.

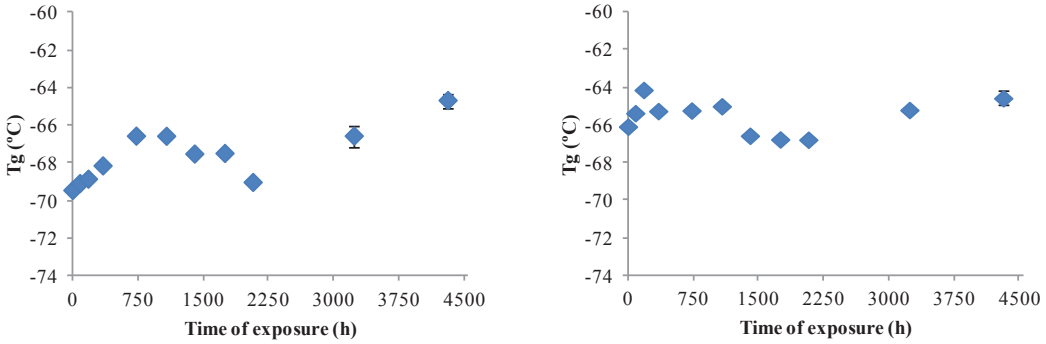

Fig. 8: Glass transition temperatures, T_g, of the fitting (left) and of the sealing (right) after exposure to UV fluorescent radiation with water spray and condensation (bars representing standard deviation).

4. Conclusions

The accelerated ageing tests - resistance to heating, exposure to xenon arc radiation and exposure to UV fluorescent radiation - performed with two elastomeric components of a solar thermal collector, a fitting and a sealing, caused chemical changes indicating that during the operation these components will be affected by high temperature and solar radiation. Resistance to heating tests performed at the temperature indicated by ISO 9808:1990 and ISO 9553:1997 and complementarily at lower temperatures led to significant mass loss and shrinkage of the fitting and the sealing, the variations being more pronounced with the increase of test temperature. Loss of mechanical performance was also clearly observed. Exposure to xenon-arc and to UV fluorescent radiation led to change of mechanical properties, the effects induced by UV fluorescent radiation being more pronounced. It is expected that those changes will be accelerated at the temperature of operation of the collector. The decrease in dimensions and mechanical performance of the fitting and of the sealing will result in poor isolation and higher permeability to atmospheric aggressions, changing the environment inside the collector. Results showed that the effect of solar radiation may be relevant for the assessment of the components and, for that reason, should be considered along with temperature.

5. Acknowledgements

This work was carried out under the Project FCOMP-01-0124-FEDER-027507 (Ref. FCT RECI/EMS-ENE/0170/2012) and the Project POCI-01-0145-FEDER-016709 FCT (PTDC/EMS-ENE/0578/2014).

Authors thank the companies that made available the samples for test. Thanks are also due to the Laboratory of Materials and Coatings team in particular to A.S. Vieira for the support in the accelerated ageing tests and to J.A. Coelho for the collaboration in the mechanical tests.

6. References

Aimura, Y., Wada, N., 2006. Reference materials for weathering tests on rubber products. Polym. Test. 25, 166-175.

ASTM D6370-99:2014. Standard Test Method for Rubber Analysis by Thermogravimetry (TGA).

Diamantino, T.C., Gonçalves, R., Nunes, A., Páscoa, S., Carvalho M. J., 2017. Durability of different selective solar absorber coatings in environments with different corrosivity. Sol. Energy Mat. Sol. Cells 166, 27-38.

ISO 37:2011. Rubber, vulcanized or thermoplastic -- Determination of tensile stress-strain properties.

ISO 4892-2:2013. Plastics -- Methods of exposure to laboratory light sources -- Part 2: Xenon-arc lamps.

ISO 4892-3:2013. Plastics -- Methods of exposure to laboratory light sources -- Part 3: Fluorescent UV lamp.

ISO 9553:1997. Solar energy — Methods of testing preformed rubber seals and sealing compounds used in collectors.

ISO 9808:1990. Solar water heaters - Elastomeric materials for absorbers, connecting pipes and fittings - Method of assessment.

ISO 11664-4:2011. Colorimetry - Part 4: CIE 1976 L*a*b* Colour space.

Maecker, N.L., Priddy, D.B., 1991. Photodegradation of ethylene-propylene copolymer and ethylene-propylene-ethylidenenorbornene terpolymer. J. Appl. Polym. Sci. 42, 21-33.

Massey, L.K., 2007. The Effects of UV Light and Weather on Plastics and Elastomers, second ed. William Andrew Publishing, New York.

Paroli, R.M., Dutt, O, Delgado, A.H., Mech, M.N., 1991. Termochim. Acta 182, 303-317.

Sircar, A.K., 1992. Analysis of elastomer vulcanizate composition by TG-DTG techniques. Rubber Chem. Technol. 65, 503-526.

Zhao, Q., Li, X., Gao, J., 2007. Aging of ethylene-propylene-diene monomer (EPDM) in artificial weathering environment. Polym. Degrad. Stabil. 92, 1841-1846.

Conference Proceedings

EuroSun 2016
Palma de Mallorca (Spain), 11 - 14 October 2016

Global Aging and Lifetime Prediction of Polymeric Materials for Solar Thermal Systems – Part 1: Polypropylene Absorbers for pumped Systems

Michael K. Grabmann[1], Gernot M. Wallner[1], Thomas Ramschak[2], Robert Buchinger[3], Reinhold W. Lang[1]

[1] Institute of Polymeric Materials and Testing, University of Linz, Linz, Austria

[2] AEE Intec, Gleisdorf, Austria

[3] Sunlumo Technology GmbH, Perg, Austria

Abstract

Part 1 of the paper series deals with the lifetime estimation of black-pigmented polypropylene (PP) absorber grades for pumped solar thermal hot water systems at different sites (Antalya, Mumbai, Phoenix). Absorber temperature loading profiles were calculated using the simulation tool SHW. Furthermore, global aging experiments in hot air or heat carrier fluid were carried out on specimen level for a commercial black-pigmented PP grade. The aging indicator strain-at-break was measured and endurance times at elevated temperatures (up to 135°C) were extrapolated to service relevant temperatures (maximum 105°C). The lifetime was assessed by weighting the temperature dependent endurance times with the loading profiles assuming cumulative damages. Depending on the extrapolation method, system specific parameters (i.e., collector size and storage tank volume) and installation site, lifetimes ranging from 20 to 45 years were obtained.

Keywords: *Polypropylene; Solar thermal collector; Absorber; Lifetime*

1. Introduction

The amount of polymers used in pumped or non-pumped solar thermal collector systems steadily increases. For polymeric solar thermal absorber materials a long-term stability in hot heat carrier fluid or hot air environment is of prime importance [Kahlen et al., 2010a, 2010b]. To meet high demands in terms of efficiency and lifetime, special attention is given to control the maximum stagnation temperature and pressure level. Based on research work in IEA SHC Task39 [Köhl et al., 2014] and collaborative projects different concepts for polymer-based collector systems have been established and successfully introduced into the market. According to Köhl et al. (2005) for solar thermal collectors a service lifetime of 20 years is required. Polymeric flat-plate collectors for pumped systems are usually operated at maximum temperatures up to 120°C and maximum pressure levels below 3 bar [Lang et al., 2013]. For overheating protection, various measures such as controlled back-cooling or venting are implemented. Novel glazed, flat-plate collector concepts allow for cost-efficient polymeric absorber materials such as black-pigmented polypropylene (PP).

At elevated temperatures some polyolefin pipe grades (e.g. polypropylene) do not exhibit the stress dependent Region II characterized by quasi-brittle failure (Ifwarson and Leijström, 1992). Hence, it is of utmost importance to investigate and characterize primarily the large scale aging and brittle failure. A main task of current research work is the lifetime assessment of these novel absorber materials for more cost-efficient and reliable collector systems. The main objective of Part 1 of the paper series is to investigate the aging behavior and to assess the lifetime of a selected PP grade for a pumped collector systems for hot water

Selection and/or peer review under responsibility of Scientific Committee
doi:10.18086/eurosun.2016.06.06 Available at http://proceedings.ises.org

preparation in single family houses at selected sites. Therefore, the "One World Solar Collector" of Sunlumo Technology was used.

2. Methodological approach

2.1 Materials, aging conditions and characterization

A commercial black-pigmented polypropylene grade (PP-Bα), commonly used in swimming pool absorbers, was selected for the investigations. The amount of carbon black in the investigated grade is about 2 wt.%. The PP grade is stabilized with a stabilization package commonly used in piping applications. The specific amount and type of stabilizers are described and discussed in Povacz (2014).

Based on compression molded 2 mm thick plates, 0.1 mm thick micro-sized specimens were automatically manufactured using an adapted CNC-milling technique [Grabmayer et al., 2015]. The specimens were aged in hot air and hot heat carrier fluid in a Binder FED 53 (Tuttlingen, Germany) heating chamber with forced circulation at 95, 115 and 135°C. The hot air aged specimens were freely suspended on a grid. Hot water aging was carried out in closed stainless steel vessels with integrated sample holder to prevent contact between the samples. At least three specimens were removed and characterized per aging interval.

To assess the aging behavior, tensile tests were carried out at 23°C using a screw-driven universal testing machine with a test speed of 50 mm/min. The strain-at-break values were obtained over the aging period. Embrittlement was defined and classified when strain-at-break values dropped below strain-at-yield value ($\varepsilon_b < \varepsilon_y$). The ε_y values were 8% for PP-Bα

2.2 Modeling of service relevant loading conditions

Based on the study by Kaiser et al. (2013) and prevalent market potentials, three different climatic conditions (mediterranean (Antalya/Turkey), hot and dry (Phoenix/USA), hot and humid (Mumbai/India)) were taken into account for this work. Based on Meteonorm-data, relevant climatic parameters (e.g. air temperature, relative humidity, global radiation) were established on an annual basis. In a further step for all three climate zones market-based polymeric collector systems based on the Sunlumo "One World Solar Collector" for hot water preparation in single family houses were defined and evaluated. By theoretical modeling, annual time/temperature distributions for the absorber were obtained, which were significantly dependent on the location and the associated climatic conditions.

2.3 Lifetime assessment

For lifetime estimation a cumulative damage approach was used established by Wallner et al. (2016) for black-pigmented PP solar absorber materials. The main elements of the approach are the simulation of temperature loading profiles, the extrapolation of aging data and the cumulation of damages of different temperature levels. Endurance time extrapolation was carried out using a theoretical Arrhenius approach and an empirical extrapolation approach assuming a specific degradation mechanism in the temperature range. Various aging processes and changes of degradation mechanism of polymeric materials described by several authors [Gugumus, 1999; Kahlen et al., 2010a, 2010b] may result in an invalid use of the Arrhenius approach. Hence, an additional empirical extrapolation approach was used in this study which is based on an S-shaped degradation curve derived for polypropylene grades with comparable stabilizer packages by Gugumus (1999). Endurance times at service relevant temperatures were calculated by adapting and shifting aging data published by Gugumus (1999) to recorded failure times of the investigated materials. Additionally, a constant endurance time of 50 years at lower temperatures was assumed according to Leijström and Ifwarson (1998).

As endurance time limits the aging indicator time-to-ultimate-failure of the specimen was characterized by tensile testing. Expected endurance times in the service relevant temperature range from 5 to 105°C (in 5 K intervals) were determined using Arrhenius and Gugumus approach. A cumulative damage model according to ISO 13760 was used for lifetime assessment. It is assumed, that each effect caused by a constant service condition is proportional to the duration of the exposure and furthermore the damage from different service conditions can be added cumulatively. The lifetime is deduced by weighting the temperature dependent

endurance times with the frequency distribution of the temperature loading profiles (Miner's rule).

3. Results and discussion

3.1 Service relevant loading conditions

Table 1 presents the used technical parameters for the simulation of temperature loading profiles for three different locations. The collector areas vary between 3.6 m² in Mumbai and 5.4 m² in Phoenix per single household. The simulated absorber temperatures are strongly influenced by the environment and the storage system. Fig. 1 illustrates the simulated time/frequencies of the absorber temperatures in the polymeric collector system for hot water preparation in single family houses at three different locations. Maximum stagnation temperature values of 95°C for Mumbai or up to 105°C for Phoenix were deduced. However, differences between the collector systems can be observed by the frequencies at temperatures above 75°C, which occur more often for Phoenix and Mumbai. In the temperature range between 20 and 75°C all three locations show comparable curve shape with frequencies of about 400 h/a. While in the hot and humid location Mumbai the lower limit of the temperature profile is about 10°C, all other locations show minimum temperatures of 5°C with higher frequencies. The frequency maxima are in the temperature range between 10 and 30°C with a shift to higher temperatures of about 25°C in hot and humid sites such as Mumbai.

Tab. 1: Specific parameters of pumped collector systems for hot water preparation in single family houses at different sites.

		Antalya	Mumbai	Phoenix
Collector	Area [m²]	4.4	3.6	5.4
	Inclination [°]	36.9	19	34
	Orientation [-]	South	South	South
Storage	Volume [l]	300	150	300
	Height [m]	1.8	1.2	1.8
	Required temperature [°C]	55	45	60
	Hot water consumption [l/d]	160	120	250

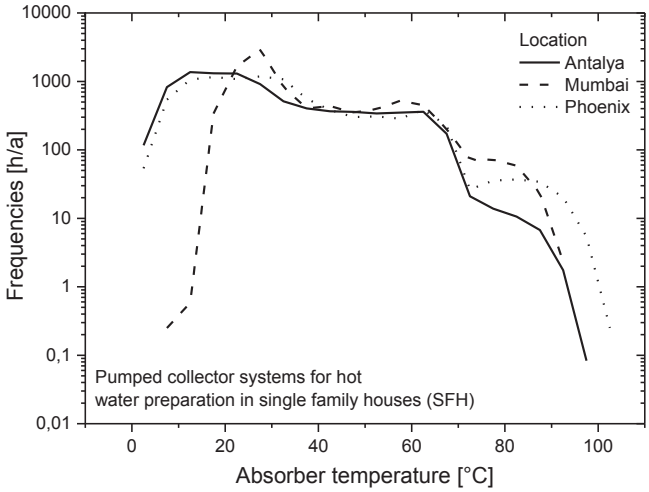

Fig. 1: Time/frequencies (h/a) of the absorber temperatures in polymeric pumped solar thermal collectors at different sites.

3.2 Aging behaviour at elevated temperatures

As reported and discussed in previous research work by Povacz (2014), for the investigated PP grade a more critical aging behavior in hot air than in hot heat carrier fluid was deduced at 95, 115 and 135°C. Based on

these results only hot air aging behavior is discussed and the aging data in hot air is used for lifetime assessment in this study. Fig. 2 shows the strain-at-break values of the black-pigmented PP-Bα as a function of aging time in hot air at 95,115 and 135°C. Ultimate failure with strain-at-break values below yield point is indicated with open symbols in the chart.

Unaged specimens reveal a highly ductile behavior with strain-at-break values of about 70. A significant decrease in strain-at-break values are obtained for PP-Bα at 135°C with ultimate failure within 2350 h. At 115 and 95°C, an initial drop appears within 150 h, presumably related to physical aging effects such as recrystallization. At longer hot air aging times the material behavior is characterized by a plateau of about 15 and 50% with ultimate failure appearing after 8400 and 26500 h for 115 and 95°C, respectively.

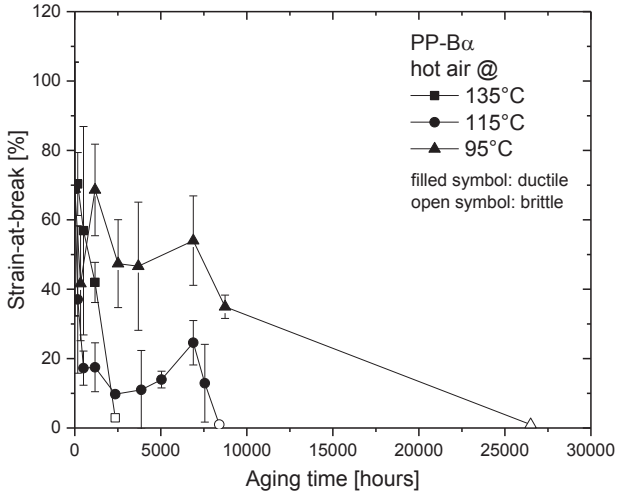

Fig. 2: Strain-at-break values for 100 µm micro-sized black-pigmented PP-Bα specimen exposed in hot air at 135, 115 and 95°C as a function of aging time.

3.3 Extrapolated endurance times and estimated lifetimes for micro-sized PP specimen

Fig. 3 illustrates the reciprocal temperature (K^{-1}) over the derived endurance limits for the investigated PP grade. The experimental embrittlement times at elevated temperatures were fitted using an Arrhenius approach (top layer) as well as the Gugumus approach (bottom layer). All extrapolated curves exhibit sufficient high coefficient of determination. The dashed vertical line depicts the assumed 50 years cut-off limit. Experimental data examined and published by Gugumus (1999) are shown in the bottom layer of Fig. 3. Two different antioxidant stabilizer packages (AO-1 and AO-7) are illustrated to show the S-shaped curve of endurance limits. In this study, average values of these curves are considered to establish endurance time limits at service relevant temperatures.

For PP-Bα the linear Arrhenius approach results in endurance limits of about 4 years (1500 days) at 90°C and of about 13 years (4650 days) at 75°C. By using the Gugumus approach, the endurance limits at 90°C are in the same range of about 4 years. The obtained endurance limits of about 5 years (1790 days) at 75°C are significantly lower compared to the Arrhenius extrapolation approach. Hence, the Gugumus approach results in more conservative behavior due to the S-shaped curve. Compared to the homopolymer grades investigated by Gugumus (1999) a much better behavior is obtained for the black copolymer grades of this study.

Lifetime estimation is deduced for the investigated black-pigmented specimens according to an optimistic upper bound scenario (Arrhenius approach) and a conservative scenario (Gugumus approach) for three different climate zones. Table 2 shows the calculated lifetimes which are ranging from 20 to 45 years for the investigated black-pigmented PP grade. Highest lifetimes are achieved for Antalya due to the mild mediterannean climate. Using the Arrhenius approach, the lifetimes are significantly affected by the constant endurance time of 50 years that is assumed for temperatures below 60°C. Due to the S-shaped curve of the Gugumus approach, this effect is even less pronounced and particularly shifted to shorter endurance times.

Hence, for all climate locations the predicted lifetimes using the Gugumus approach are much lower, ranging from 20 to 24 years. The estimated lifetime is reduced due to harsher climate conditions (hot and humid) in Mumbai to about 20 years.

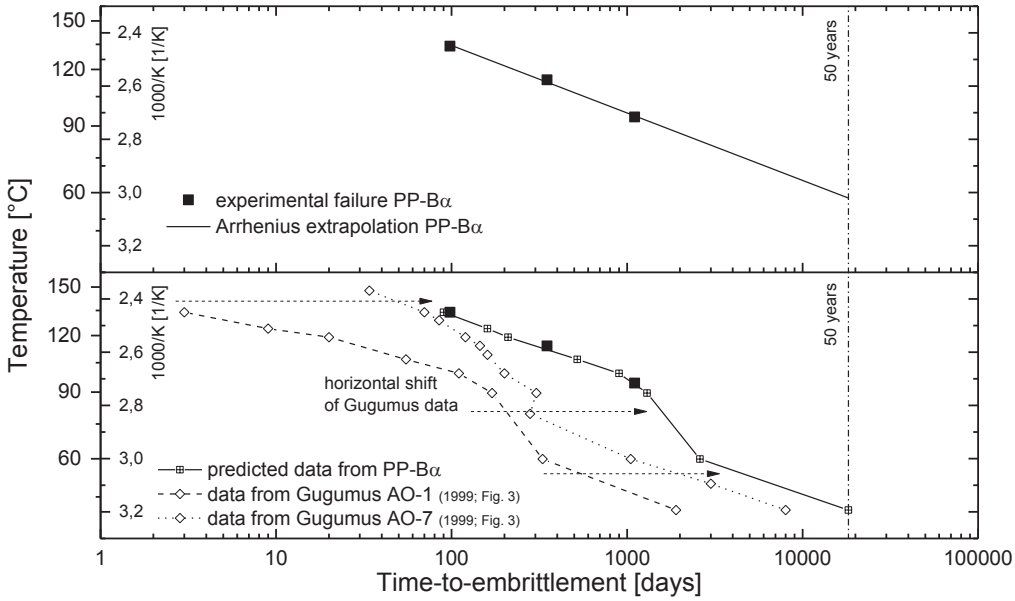

Fig. 3: Experimental failure times for micro-sized black-pigmented PP-Bα specimens and extrapolated endurance times at service relevant temperatures using an Arrhenius approach (top) and the Gugumus approach (bottom).

Tab. 2: Estimated lifetimes for PP-Bα absorber materials in pumped flat-plate collector systems at three different sites for the Arrhenius and Gugumus extrapolation approach.

Location	Climate zone	Estimated lifetimes in years	
		Arrhenius	Gugumus
Antalya	mediterranean	45	24
Mumbai	hot and humid	41	20
Phoenix	hot and dry	41	23

4. Summary and conclusion

To assess the lifetime of a black-pigmented PP absorber grade for pumped solar thermal hot water systems, temperature loading profiles for three different climate zones were established based on climatic input data. Strain-at-break values as experimental failure data were determined after exposure to hot air and hot heat carrier fluid at elevated temperatures ranging from 95 to 135°C of micro-sized specimen with a thickness of 100 µm. Due to the pronounced aging behavior in hot air, these data were used for lifetime estimation. Furthermore, endurance times at service relevant temperatures (5 to 105°C) were extrapolated using a linear Arrhenius approach (optimistic upper boundary) and a S-shaped Gugumus approach (conservative scenario). Subsequently a model of cumulative damages (Miner's rule) was applied to assess lifetimes for the investigated black-pigmented PP absorber materials.

Depending on the installation site and the system type, annual time/frequency curves over the collector temperature were simulated for polymeric hot water systems in single family houses. The absorber temperature was ranging between 5 and 105°C for the investigated climate zones with comparable curve shape between 20 and 75°C at frequencies of about 400 h/a. However, differences between the three systems were observed with pronounced frequencies at low temperatures (< 20°C) for Antalya (mediterranean) and Phoenix (hot and dry) as well as at high temperatures (> 75°C) for Mumbai (hot and humid) and Phoenix (hot and dry).

The unaged specimens exhibited ductile material behavior with strain-at-break values of about 70% for PP-Bα. Hot air aging at 135°C resulted in a steady decrease of strain-at-break values till ultimate failure appeared within 2350 h. The estimated lifetimes for the PP absorber material was ranging from 20 years (Mumbai, Gugumus approach) to 45 years (Antalya, Arrhenius approach). The calculated lifetimes were significantly depending on the used extrapolation method. As an optimistic upper boundary scenario, the linear Arrhenius approach showed estimated lifetimes higher than 41 years for all climate zones, strongly affected by the endurance cut-off limit of 50 years. Contrary, the non-linear Gugumus approach as a conservative lifetime assessment resulted in lifetimes ranging from 20 to 24 years.

5. Acknowledgment

This research work was performed in WP-03 of the cooperative research project SolPol-4/5 entitled ‘‘Solar-thermal systems based on polymeric materials” (www.solpol.at). This project is funded by the Austrian Climate and Energy Fund (KLI:EN) within the programme ‘‘Neue Energien 2020” and administrated by the FFG. The authors wish to express their acknowledgements to Susanne Kahlen, Kurt Stubenrauch and Andreas Meinecke (Borealis, Linz, A) for the cooperation, especially for making available the compounds.

6. References

Grabmayer, K., Beißmann, S., Wallner, G.M., Nitsche, D., Schnetzinger, K., Buchberger, W., Schobermayr, H., Lang, R.W., 2015. Characterization of the influence of specimen thickness on the aging behavior of a polypropylene based model compound. Polymer Degradation and Stability 111, 185-193.

Ifwarson, M., Leijström, H., 1992. What controls the lifetime of plastic pipes and how can the lifetime be extrapolated. Studsvik Polymer AB, Sweden, Polymer Exova Report. C1/1-1-16.

Kahlen, S., Wallner, G.M., Lang, R.W., 2010a. Aging behavior and lifetime modeling for polycarbonate. Solar Energy 84 (5), 755–762.

Kahlen, S., Wallner, G.M., Lang, R.W., 2010b. Aging behavior of polymeric solar absorber materials – Part 2: commodity plastics. Solar Energy 84 (9), 1577–1586.

Kaiser, A., Fink, C., Hausner, R., Ramschak, T., Streicher, W., 2013. Leistungsanforderungen an Polymermaterialien in solarthermischen Systemen. Erneuerbare Energie 2013-1, 12–17.

Köhl, M., Jorgenson, G., Brunold, S., Carlsson, B., Heck, M., Möller, K., 2005. Durability of polymeric glazing materials for solar applications. Solar Energy 79, 618–623.

Köhl, M., Saile, S., Piekarczyk, A., Fischer, S. 2014. Task 39 exhibition – Assembly of polymeric components for a new generation of solar thermal energy systems. Energy Procedia 48, 130-136.

Lang, R.W., Wallner, G.M., Fischer, J., 2013. Solarthermische Systeme aus Polymerwerkstoffen: Das Großforschungsvorhaben SolPol. erneuerbare energie 2013-1, 7–11.

Povacz, M., 2014. Black-pigmented Polypropylene Absorber Materials – Aging Behaviour and Lifetime Modelling, doctoral thesis, University of Linz, Austria.

Wallner, G.M., Povacz, M., Hausner, R., Lang, R.W. 2016. Lifetime modeling of polypropylene absorber materials for overheating protected hot water collectors. Solar Energy 125:324-331.

Conference Proceedings

EuroSun 2016
Palma de Mallorca (Spain), 11 - 14 October 2016

Methodology for the Evaluation of Solar Thermal Energy Projects' Sustainability in Peru

Miguel Hadzich[1], Juan José Muñoz[2], Emilio Bautista[2]

[1]Sección Ingeniería Mecánica, Pontificia Universidad Católica del Perú.

[2]Escuela Técnica Superior de Ingenieros Industriales, Universidad Politécnica de Madrid

Abstract

This paper presents a new methodology to evaluate the sustainability of projects which involve any renewable energy equipment that take place in rural areas. By using the Star of Sustainability method we are able to see, visually and efficiently, the process of sustainability of technology projects.
The study includes the results of six appropriate technologies and technology transference projects with solar thermic energy done by the GRUPO PUCP during the last five years.
These validated technologies refer to the generation of heat through solar energy, such as Parabolic Cookers, Greenhouse-type dryers, Trombe Walls, Scheffler-type concentrators for coffee and cocoa and Hot Air Parabolic Concentrators for black tea drying; all of them using local materials and labor.

Keywords: *Sustainability, evaluation, qualitative methods, solar thermal energy,solar dryers*

---

1. Introduction

The Rural Sector Support Group GRUPO PUCP is an operating unit of the Department of Engineering at the Pontificia Universidad Católica del Perú (PUCP) and has made several designs and implementations of equipment in various areas of Peru. This study considers the results of six case studies conducted by GRUPO PUCP in Peruvian territory during the last five years.

The technologies evaluated are: Parabolic Cookers, Greenhouse-type dryers, Indirect Solar Dryers, Trombe Walls, Scheffler-type concentrators for coffee and cocoa and Hot Air Parabolic Concentrators for black tea drying

Star of Sustainability method that allows us to see, visual and efficiently, the technology projects process sustainability will be used.

Conclusions are analyzed by the QCA method (QUALITATIVE Comparative Analysis), using KIRQ as support free software, these methods are used due to the existence of five qualitative variables: Technology, Economics, Politics, Social and Environmental for each the cases studied.

doi:10.18086/eurosun.2016.06.08 Available at http://proceedings.ises.org

2. GRUPO PUCP

The Rural Sector Support Group GRUPO PUCP is an operating unit of Engineering Department at Pontificia Universidad Catolica del Peru (PUCP). Since 1992 we have been carrying out development projects for rural communities, related to applied scientific research, technology transfer and innovation, dissemination and promotion of appropriate technologies and conservation activities natural environment using renewable energy

Our goal is to improve the quality of life of the rural population in the areas of energy, water, agriculture and housing; through the dissemination and application of appropriate technologies to contribute to sustainable development of the rural sector of Peru.

3. Methodology used.

The proposed method, Sustainability Star, allows us to analyze the sustainability process of technology projects and provides us with a clear view to either decide the continuity of the projects or their cancelation. The Star has 5 tips that analyze the Technology (T), Economy (E), Politics (P), Social (S) and Environmental (A) factors which from now own we will refer to as TEPSA (in Spanish) or 5E`s (in English).

We believe it is a good tool to be used in all projects with a technological and political base in their development processes.
This method could also be used in other situations where projects have been completed technological base and gives us a good insight to decide the continuation or closure thereof.

SUSTAINABILITY DEVELOPMENT: TEPSA oR 5 E´s			
T	Tecnología	**E**	Engineering
E	Economía	**E**	Economics
P	Política	**E**	Ethical
S	Social	**E**	Equity
A	Ambiental	**E**	Environment

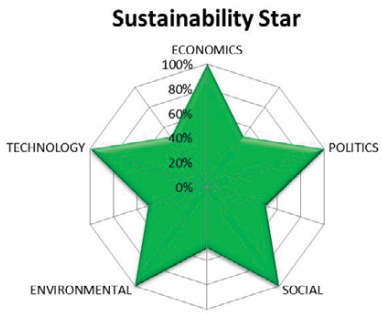

Fig 1: Factors of sustainable development in the Sustainability Star

To analyze the index that corresponds to each tip of the Star, a 25 question survey is made, defining the break percentage of the shape. These surveys refer to TECHNOLOGY (utility, sustainability, operation, reliability, maintenance), ECONOMY (income, employment, savings, affordability, innovation), POLITICS (political interest, acceptance, legal, promotion, and distribution), SOCIAL (compatibility, motivation, life improvement, participation and capacity) and ENVIRONMENTAL (friendly, climate, pollution, awareness, and health).

If all surveys questions have positive answers then the star will be perfect without any break, as shown in Fig. 1 and the project will be considered as 100% SUSTAINABLE .

In order to decide the percentage corresponding to each point of the star we use a survey of 25 questions - see Table 1 - which defines the percentage of the Star break. Negative responses from the survey will fall inside the star percentage values that indicate the failure of the project in each of TEPSA factors.

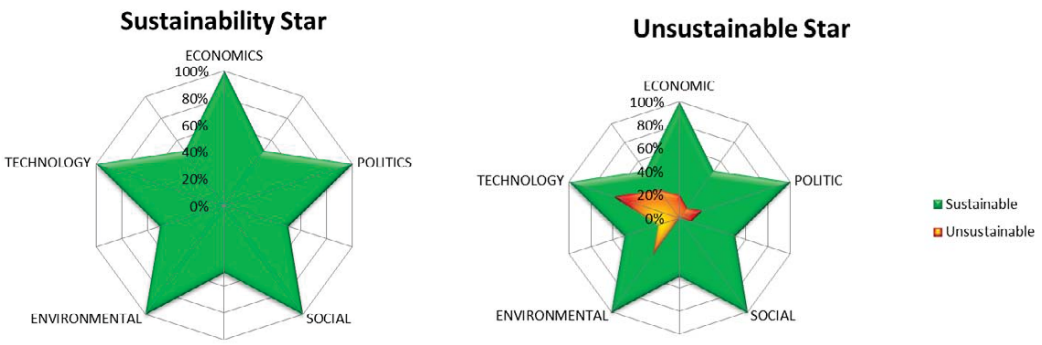

Fig 2: Example of Sustainability Stars – Perfect (left) and Broken (right).

4. Case Studied

We will analyze six case studies of technology projects related to heat generation, such as Parabolic Solar Cookers COCISOL, Indirect Solar Dryers SECASOL, Solar Greenhouse Indirect Dryers INVER, Trombe Walls TROMBEPUCP, Scheffler Concentrators for coffee and cocoa CONSOL and Hot Air Parabolic Concentrators for black tea drying CONPAR.

4.1. Hot Air Parabolic Concentrators for black tea drying – CONPAR

The project "Development and Integration of a Cogeneration System With Solar Thermal Energy for Processing of Black Tea in the Cusco region" was developed in partnership with the company AGROINKA. The company AGROINKA - Herbi brand tea producer - is located in a rural area of the department of Cusco with poor access to other possibilities of energy resources and weak technologies for various processes in the production chain. It is an area dedicated to the processing of tea to supply 80% of the market in the country and works with 750 families dedicated to tea production.

The design sought to solve the problem of shortage of fuel for drying processing in a producing factory for black tea, through the use of solar thermal concentration with the adaptation of the receiver tube of a linear parabolic concentrator for heating air. This is the design of a pilot project to develop and implement in tea enterprise AGROINKA a prototype cogeneration system with solar thermal energy consisted of 6 lines of 10 concentrators (60 linear concentrators). There is a paper describing the behavior of hot air in the receiver tube along a line of 10 concentrators in Reference 30.

Fig 3: Picture of 60 linear parabolic concentrators in AGROINKA tea factory.

Table 1: Model of survey: results for the case of Parabolic Solar Cookers.

					PARABOLICS SOLAR COOKERS
					TECHNOLOGY SUSTAINABILITY
					Survey about machines or project operation
	YES		NO		
1.-	x				**Do you tkink that the machine is going to be useful?**
2.-			x		**Technology (or machine) is constantly being used during the last year?**
3.-	x				**Do you think the machine can easily operate?**
4.-			x		**Do you think is a reliable technology?**
5.-	x				**Do you think that local technicians can repair, copy or modify -all or part- of this machine?**
					ECONOMIC SUSTAINABILITY
					Survey about machines and project cost
	YES		NO		
6.-			x		**Do you see an economic improvement in your life or business when using this technology?**
7.-			x		**It has generated work for someone with the use of this technology in the community?**
8.-	x				**You think that you have saved on fuel or electricity when using this renewable technology?**
9.-	x				**Do you (or your neighbors) purchase or install a similar machine?**
10.-	x				**Do you think that this technology can be produced and sold in your community in the future?**
					SUSTAINABILITY POLICY
					Survey on political and organizational project management
	YES		NO		
11.-			x		**There has been interest in the project or the machine by any political authority?**
12.-	x				**The authorities of the community accept the project? There are requests from the community to some authority?**
13.-	x				**The project complies with the laws and regulations of the community and technical institutions ?**
14.-	x				**Do you believe that the government, person, or institution should promote this technology to other Peruvians?**
15.-	x				**The people of the town know the project?**
					SOCIAL SUSTAINABILITY
					Survey on the perception of the community about the project
	YES		NO		
16.-	x				**The project is accepted "normal way" for the community?**
17.-	x				**There is interest in the community or their neighbors for the proposed technology?**
18.-			x		**The project has improved the standard of living of someone in the community ?.**
19.-	x				**The people have participated in some part of the project or activity?**
20.-	x				**There are people in your community with the necessary capabilities for operation and maintenance?**
					ENVIRONMENTAL SUSTAINABILITY
					Survey on the impact of the project or the machine on the environment
	YES		NO		
21.-	x				**The project is seen as a friendly environment technology ?**
22.-	x				**You do you think this machine is good for our Earth planet?**
23.-			x		**The project has created some kind of contamination in the environment?**
24.-	x				**Mind that this technology is clean rather than other similar package?**
25.-			x		**The use of this technology affects your health?**

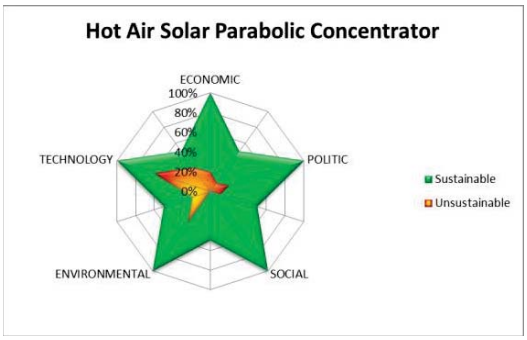

Fig 4: Sustainability Star in Hot Air Solar Parabolic Concentrator.

Sustainability Analysis: In the years 2013 and 2014, GRUPO PUCP has carried out investigations about concentrated solar thermal linear technologies, obtaining good results for toasted black tea. The mistakes observed in the star of sustainability are especially technological due to multiple failures in electronic solar trackers in the project area, especially by the highly voltage fluctuation of electricity.

4.2. Scheffler Concentrators for coffee and cocoa - CONSOL

This new technology is being investigated by the GRUPO PUCP in various applications since 2010, when Dr. Damien Puigserver of France came to Peru for an academic exchange and the first solar concentrator 2.7 m2 Scheffler cooking was built. Later PUCP funded the project to roast coffee with support from Dr. Francois Veynandt, Ing. Julien Delcol, Ing. Juan Pablo Pérez, Ing. Sandra Vergara and industrial designer Luis Miguel Hadzich.

As the results of this research were very positive, we won an announcement FINCYT in 2013 but for roasting cocoa and producing chocolate.
Currently there are two concentrators 8 m2 for this latest project and it is spreading in La Convencion Valley 300 km from Cusco city, with good results. In 2016, with the support from the university PUCP we are working on a prototype of 16 m2 for making orange and pineapple jam .

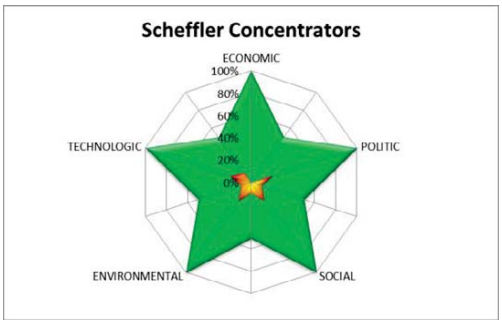

Fig 5: Sustainability Stars in Scheffler-type concentrators for coffee and cocoa

Sustainability Analysis: Since 2013, GRUPO PUCP is researching this concentrated solar thermal technology, reaching good results for roasted coffee and cocoa. We are still working on the improvements on the electronic parts, monitoring of solar concentrator design to improve efficiency. The main difficulty lies in the intermissions of climate due to the rains and the presence of clouds.

4.3. Solar Greenhouse Indirect Dryers - SECASOL

For over 20 years we have had good results with solar corn and oragano (wild marjoram) dryers in Moquegua and Tacna in southern of Peru, but one of the drawbacks is due to the low capacity of direct and indirect dryers.

A project that was relatively successful is the one on the use of solar coffee dryers promoted by the technical American institution cooperation USAID since 1990. These dryers were installed in jungle areas in the north and west of Peru in the departments of Cajamarca, Amazonas, San Martín and Piura with good results.

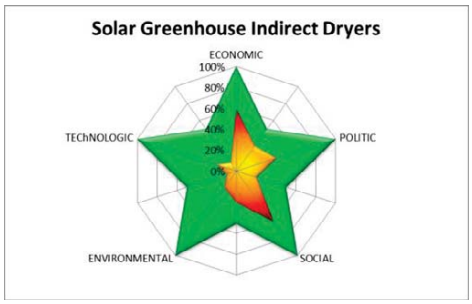

Fig 6: Sustainability Stars in Indirect Solar Dryers

Sustainability Analysis: This technology continues in an experimetal phase according to the capacity of the dryers and quantities of the product. The most used are small and medium dryers because they are cheaper for farmers. We are currently investigating the linear parabolic concentrators for drying tea and aromatic and medicinal herbs and the results will be shown in the coming years.
Research to improve higher production capacities and automatic controllers shoul be on going.

4.4. Solar Greenhouse Dryers - INVER

The glass and plastic greenhouses are having very good diffusion in highlands of Peru where the cold is very intense: its use is mainly dedicated to growing vegetables such as lettuce, tomato, pepper, chili and herbs. The lack of control of the temperature inside the greenhouses as well as the difficult control of automatic irrigation systems within them (for lack of electricity) have made this technology to be not as important as it is in other parts of the world. The material used (glass, plastic) has also been one of the obstacles for the successful dissemination and replication. In an analysis of our travels throughout Peru it can be clearly noted that greenhouse projects only last as long as the plastic degrading life timespan.

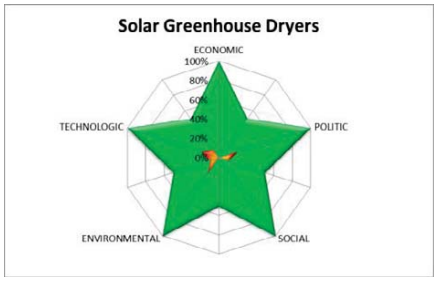

Fig 7: Pictures and Sustainability Star in Solar Greenhouse Dryers

Sustainability Analysis: The star shows us that the political component should mainly be fixed, and technological and economic aspects partially to make it perfect in its execution; It tells us that we need more presence of political authorities to replicate this project for drying coffee, cocoa, fruits in the region of the jungle of Peru. The process of the project was done with the method of participatory design or design thinking method. (Salgado, 2010).

4.5. *Trombe Walls - TROMBEPUCP*

It is a type of greenhouse that is placed on the side walls of the houses to transfer heat from the sun to the inside of the housing, there are those using plastic, polycarbonate and glass materials.
The evolution of this technology by GRUPO was very successful in its dissemination, especially due to the social adaptability of this technology as a counteract against frost and cold spell in the highlands due to climate change. Since 2008 GRUPO has installed more than 600 houses in the departments of Cusco and Puno and is expected to be a model for broadcast as a government policy in the highlands throughout Peru.

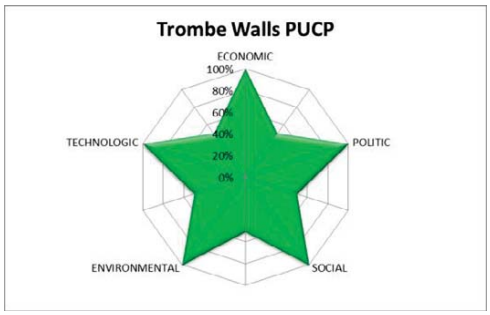

Fig 8: Example of Sustainability Stars in Trombe Walls

Sustainability Analysis: One of the ways to measure the sustainability of a product is the feedback of the beneficiaries, in this case the requests for this technology are increasing day by day due to inclement frost and cold spell in the highlands of Cusco and Puno, in southern of Peru.
The combination of four technologies: Sealing doors and windows, improved kitchen, false ceiling burlap and Trombe walls, enable us to reach a difference in average temperatures between the inside and outside of 10 ° C, which is making this technology one of the most successful projects of GRUPO PUCP and with many opportunities to be part of its replicability by the Peruvian government.

4.6. *Parabolic Solar Cookers - COCISOL*

Parabolic solar cookers have been introduced in Peru since 1982 and there have been attempts made to massify their application by several NGOs as GIZ, SOLARTEC in areas of Huancayo, Cusco, etc. The first design came to GRUPO PUCP in 1995 thanks to GIZ which funded part of the cost (50%); the cost of these kitchens was 150 US $. Later in 2004 this technology's demonstration was the starting point for a project with the NGO IAA in Yanaoca, Cusco area where 4 people were trained in the subject but none came to replicate the model.
Currently the only one that can offer this technology is the Renewable Energy& Hassan company that builds kitchens on request, but so far has not received massive orders. In 2012 several of these kitchens were installed in Pisco and Huancavelica by the PROSINERGY company as demonstration centers.

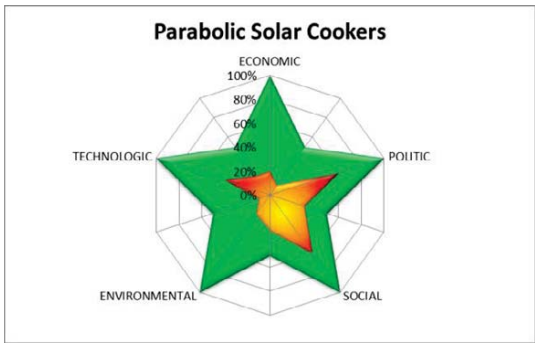

Fig 9: Pictures and Sustainability Stars of Parabolic Solar Cookers

Sustainability Analysis: These kitchens are easy to build and are easy to assemble, but do not have a good reception from women, especially by cultural reasons.
This technology will be sustainable if used in places where there is no wood or manure, when women accept it as alternative, when their costs are lowered and when they can be sold by credit.
The approximate cost of these kitchens is US $ 150, which makes it very difficult for the inhabitants of poor areas to acquire it. The introduction of gas stoves, subsidized by the state, also threaten the spread of this technology.The project is environmentally friendly, the only thing that makes interferes is the climatic variabilities that may occur when operating the kitchens, for example it can start raining or get cloudy or foggy which may result in having food left on it half cooked – this generates distrust in the population towards this technology.

5. Results Obtained

Other than using the star of sustainability that helps us to understand sustainability from 5 views TEPSA there are several versions of software for qualitative analysis to help us in numerical calculations and have been validated in social projects. These are QCA, QCA fs, KIRQ, Tosmana, etc. We decided to use the free software KIRQ due to its simplicity and effectiveness in assessing our case responses. This software is a form of QCA (Qualitative Comparative Analysis) and is suitable for cyclical factors, identifying the necessary and sufficient conditions to enable the performance of some activity by analyzing the probabilities for this to happen. It is used when the variables are dichotomous (YES / NO) as has been developed in the survey of this work.

The methodology allows us to compare the Case Studies and draw probabilities of occurrence with few variables; in this case we will rely on the KIRQ software which has been validated in similar social projects.

The results with the database of surveys give us the following table:

Table 2. Sorted Data Base of sustainability of the 6 case studies.

TECNOLOGIA	UTIL	CONT	OPER	CONF	MANT	ING	EMPL	AHOR	ASEQ	INNO	IPOL	ACEP	~LEGA	DISE	VISI	COMP	MOTI	MEJO	PART	CAPA	AMIG	EDUC	~CONTA	ECOL	~SALU	
CONPAR	1	0	1	1	0	1	1	1	0	0	1	0	1	1	1	1	1	0	0	1	1	0	1	1	1	17
CONSOL	1	0	0	1	1	1	1	1	1	0	1	0	1	1	1	1	0	0	1	0	1	0	1	1	1	17
SECASOL	1	1	1	1	1	1	0	1	0	1	1	0	1	0	0	1	0	1	1	0	0	0	1	1	1	16
INVER	1	1	1	1	0	1	1	1	1	0	1	0	1	0	1	0	0	0	1	0	1	0	1	1	1	16
TROMBEPUC	1	1	1	1	1	0	0	0	1	1	1	0	1	0	1	0	0	0	1	0	1	0	1	1	1	15
COCISOL	1	0	1	0	0	0	0	1	1	0	0	1	1	1	1	1	0	1	0	1	0	1	1	1	1	15

Table 2 gives us some interesting results, such as that the technologies that are transferred to companies are those with the highest index of sustainability and technologies that have been donated by public institutions or NGOs are the ones with worst sustainability acceptance.

From the technological point of view, the best machines turned out to be the ones massively distributed such as the Solar Dryers and Trombe walls for heating homes in highlands. Economically, politically and socially the best technologies proved to be those where local materials and communities where involved during their construction and development, respectively. From the environmental point of view every case resulted to be good for the environment but none of them passed the survey as totally clean.

6. Conclusions

The influence of the 5 factors TEPSA (Technology, Economy, Politics, Social and Environmental) in each of the cases presented has its relative importance in the final results of sustainability, since, in one way or another it influences the success of the implementation of technological projects in poor rural areas of Peru.

The proposed methodology for the evaluation of technological projects has proven to be a good tool for decision making, since it allows us to evaluate the results of a project by analyzing it's sustainability.
The evaluation of the sustainability of projects depends not only on technological and economic conditions of the equipment that works with renewable energy but also depends heavily on the social and political situations of the places where these projects are to be implemented.

7. Bibliography

- Adriaanse, A., 1999. Environmental Policy Performance Indicators .INFOPLAN Environment Consultans The Haag Holland . Cartesius Institute Library TME 5376
- Butera, F., 1990. *Fuentes energéticas renovables en los países en vías de desarrollo. Éxitos y fracasos en la transferencia y difusión de tecnología*. SEMTA La Paz, Bolivia
- Clancy, J., 1998. SADC Rural energy planning and environmental management training programme TDG Library
- Commission of the European Communities, 1984. Energy and Development. What Challenges Which Methods?. Lavoisier Publising INC Boston UK. TDG Library Vob 200 Ener
- Congress of United States, 1994. Perspectives on the role of science and technology in Sustainable Development. US Congress, Office of Technology Assesment. Cartesius Library TME 5574; Internet www.wws.princeton.edu
- EIA Energy Information Administration. PERU Country Analysis Brief *www.eia.doe.gov*
- Fecko, S., Janek, F., Ismmek, P., 2000. The concept of Sustainability in the Development of Electroenergetics. Slovak Technical University. www.worldenergy.org
- GEF, 2002. The Challenge of Sustainability. Global Environment Facility. www.gefweb.org
- Hadzich M., Ortiz I., Muñoz J.J., Bautista E., 2014. *Metodología para la evaluación de la sostenibilidad de innovaciones tecnológicas en ambientes rurales.* Tesis doctoral Escuela Técnica Superior de Ingenieros Industriales, Universidad Politécnica de Madrid.
- Hadzich M., 2013, Excel Software to design Sustainability Star http://miguelhadzich.com/cocinas-solares-parabolicas/
- Hadzich, M., 2000. Conflicts to Renewable Energy in Peru. Presentation to World Renewable Energy Congress. http://www.cnfl.go.cr/ CLER/conferencias/ conferencias/MHadzich.htm
- Hislop, D., 1992. Energy options: An introduction to small scale renewable energy technologies. IT Publications, UK
- ITDG Peru: Rural Electrification http://rru.worldbank.org/ Documents/ PaperLinks/ 549.pdf
- Malhotra, P., Dutta, S., Ramana, V., 1998. Participatory Rural Energy Planning. Tata Energy Research Institute. TDG Library Vob 207 – Part
- Martinot, Eric, 2002. Renewable Energy Markets in Developing Countries, Indicators of Renewable Energy in the World.pdf www.martinot.info
- NREL, 1998. Renewables for Sustainable Village Power NREL village power. Pdf www.rsvp.nrel.gov
- Oelert, G., Auer, F., Pertz, K., 1987. Economics issues of Renewable Energy Systems. GTZ, Eschborn Germany TDG library Vob 206 – 20 – Econ
- Ramani, K., Reddy, A., Islam, M. 1995. Rural Energy Planning. A government-Enabled Market-Based Approach GTZ, Eschborn. Germany TDG Library Vob 200 1 RURA
- REPP, 2004. Renewable Energy Policy Projects www.crest.org
- Rogers, E., Diffusion of Innovations, 5th Edition. Free Press Simon & Schuster Inc.
- SADC, 2002. Matching Energy Supply and Energy Demand: The rationale of matching energy needs to potential solutions. Rural energy planning and environmental management training programme. www.meeti.org.za/sadc/sadc_courses.htm
- Scott, S., Nolan, B., Fahey, T., 1996. Formulating Environmental and Social Indicators for sustainable development. The economic & social research institure ESRI Dublin. Cartesius Institute Library TME 5855
- Sectoral policy document of Development Cooperation SPDDC, 1999. Sustainable Energy economy. Cartesius Institute Library TME 4105 www.metabase.net
- UNEP, 2000. Natural Selection: Evolving Choices for Renewable Energy Technology and Policy http://www.uneptie.org
- UNIDO Initiative on Rural Energy for Productive Use Rural Energy Unido.pdf
- United Nations, 1991. Global Climate Change. The role of Technolgy Transfer. A report for the United Nations Conference on Environment and Development. Touche Ross management Consultants . Cartesius Institute Library TME 4085
- Vergara, S., 2016. Analysis of results of a parabolic concentrator's pipe receiver to heat air for the drying process of black tea in Cusco, Perú. ISES EUROSUN 2016 Conference Procedings
- Wilkings, Gill, Technology Transfer for Renewable Energy - Overcoming Barriers in Developing Countries www.conae.gob.mx
- World Bank. Financing of the energy sector in developing countries www.worldbank.org
- World energy Council and FAO, 1999. The challenges of rural energy poverty in developing countries. Word Energy Council London W1R6LE, UK TDG Library Vob 203 – 50 – Cha. Internet www.worldenergy.org/wec-geis/

Conference Proceedings

EuroSun 2016
Palma de Mallorca (Spain), 11 - 14 October 2016

OTSun Project: Development of a Computational Tool for High-resolution Optical Analysis of Solar Collectors

Ramon Pujol-Nadal[1*], Víctor Martínez-Moll[1], Andreu Moià-Pol[1], Gabriel Cardona[2], Julian D. Hertel[1] and Francesc Bonnín[1]

[1] Departament de Física, Universitat de les Illes Balears, Ctra. de Valldemossa km 7,5, 07122 Palma de Mallorca, Illes Balears, Spain

[2] Departament de Ciències Matemàtiques i Informàtica, Universitat de les Illes Balears, Ctra. de Valldemossa km 7,5, 07122 Palma de Mallorca, Illes Balears, Spain

*Corresponding Author, ramon.pujol@uib.es

Abstract

The OTSun project is a research project co-funded by the Spanish Ministry of Economy and Competitiveness, with the reference number ENE2015-68339-R, where the main goal is to develop a computational tool for high-resolution optical analysis of solar collectors. The project is runs from 2016 to 2018 and is composed of eight tasks. The main motivation of the project is to develop an open source code that serves as reference to simulate optical systems for solar energy applications where the most important optical effects are being considered. In order to achieve high-resolution results the radiation-matter interaction effects, the dependence of the incident angle on absorptive and anti-reflective surfaces, and also the dependence of the wavelength will be taken into account. The tool is based on the Monte Carlo ray-tracing method, and a useful software interface will be provided allowing the user to create, or import, the solar collector geometry. A data base of solar materials will be provided with the tool. Finally, the optical efficiency and the energy distribution on the receiver will be calculated by the program.

Keywords: *Ray-tracing, optical characterization, optical simulation, FreeCAD*

1. Introduction

Computational tools with the aim to simulate the optical performance of solar collectors are of utmost importance for optimization of a real system or during the design state of new systems. Moreover, the use of these tools produce economic savings in experimental validations, testing, and manufacturing (Osório et al., 2016); and also can be used to determine the optical behavior at different incidence angles (Hertel et al., 2016a, 2015). Nowadays there are many programs able to analyze the optical behavior of solar energy systems, such as STRAL, TieSol, ISOS, HFLCAL and HFLD. These programs are commercially available and are designed for the analysis of central tower plants with heliostats (Bode and Gauché, 2012). Programs that are available for free are SolTrace ("NREL," n.d.) and Tonatiuh (Blanco et al., 2009, 2005). Since OTSun is a project with the aim to develop an open source code with free availability, a briefly description of the specifications of the SolTrace and Tonatiuh softwares is exposed below.

SolTrace is a software tool developed at the National Renewable Energy Laboratory (NREL) to model concentrating solar power (CSP) systems and analyze their optical performance. Although ideally suited for solar applications, the code can also be used to model and characterize many general optical systems. SolTrace is free and can be downloaded from the NREL website. As for the ray-tracing methodology, the solar radiation distribution can be considered as a Gaussian, punctual or user defined models. For the optics of materials the "optical element definition" model is used to characterize any optic element of the system;

doi:10.18086/eurosun.2016.06.04 Available at http://proceedings.ises.org

this element is adjusted by parameters in order to consider mirrors or glasses, such as: the reflectivity (with incidence angle dependence), the transmissivity, the slope error, the specularity error, and the refractive index. In the case of refraction, the Fresnel equation is handling the reflection and refraction at interfaces (angular variation). SolTrace has a graphical user interface (GUI) for the visualization of the scene.

Tonatiuh is an open source code written in C++ and designed for the analysis of the optical behavior and energy distribution of radiation in concentrating solar power (CSP). Similar to SolTrace, Tonatiuh supports multiple geometric shapes and has a GUI. However, the analysis and the processing results should be treated with an external program such as Mathematica or R. Tonatiuh has a Universal GNU Public License, which allows free access to the code for any user and contribute to its development. About the ray-tracing methodology, the solar radiation distribution can be considered as a pillbox, or as the Buie model (Buie et al., 2003). As for the optics of materials, Tonatiuh considers refractive materials (e.g. glass covers) and specular materials (e.g. mirrors). The refractive materials are defined by the transmittance (a constant value), and the slope error. It should be noted that the electromagnetic Fresnel optics equations are not implemented. The reflective materials are defined by the reflectivity and the slope error.

Despite the variety of programs meant for optical simulation of solar systems, there is no open source software capable of taking into account the most relevant effects of the radiation-matter interaction that occur in solar energy systems, such as: electromagnetic Fresnel optics equations, the real behavior of dielectric materials, the wavelength dependence, the incidence angular dependence of selective and anti-reflective materials, the multivariate Gaussian function for the reflection direction, the volume scattering effects, among others. For this reason, the authors of this study are developing an open source code to simulate the optical behavior of solar collectors that takes into account the most relevant optical effects in optical solar systems.

To achieve the goals of the project, first a study of the most relevant effects related with the radiation-matter interaction of the common materials used to construct solar concentrating collectors has been conducted. Results are presented in another study at the EuroSun 2016 (Hertel et al., 2016b). All the interaction effects should be modeled by the Monte Carlo approach in order to consider the stochastic nature in the energy harvesting process of solar collectors.

On the other hand, a GUI will be provided with the tool to facilitate the visualization of the scene, and also be able to import the geometry of the solar collector from other formats. The interface software should allow working with open file formats such as STEP, STL, DXF, and OBJ.

An important part of the project is the availability under an open source license (GPL, freeBSD or similar). Finally it can be mentioned that the project is supported by the Plataforma Solar de Almería (PSA), the Spanish institute Instituto para la Diversificación y Ahorro de la Energía (IDAE), The solar Energy Research Center (CIESOL), TECNALIA Corporation, and SOLARUS Sunpower Sweden AB.

2. Previous results in ray-tracing analysis

The team of the project has a lot of experience in ray-tracing simulations. It can be noted that the first code developed was implemented in 2006 (Martínez Moll et al., 2006; Pujol et al., 2006) where the Fixed Mirror Solar Concentrator (FMSC) (Russell John L., 1977) was analyzed with simple optical models. The results showed the most interesting geometries of the FMSC based on two design parameters (the number of mirrors and the focus/width ratio). The simulations were conducted with simple models, such as a point source for the sun model, ideal specular reflectivity for mirror surfaces, a constant value for the transmittance of the cover, and a constant value for the absorptance of the receiver surface. As for the code, the geometry of the system only could be defined by triangles with ASCII files. Hence, only one algorithm was required to detect the intersection between a line and a triangle in 3D space. The algorithm used is the one exposed in the book (David H. Eberly, 2006). About the ray-tracing program developed at 2006, it can be concluded that the ray blocking effect was the most important phenomenon for the analysis of the optical efficiency of the solar collector. The code was implemented in FORTRAN.

It was not until 2012 when the first results with a more accurate ray-tracing model were presented by the

authors (Pujol Nadal and Martínez Moll, 2012). The major improvements implemented at this stage were: the Fresnel equations for the electromagnetic waves (Hetch and Zajac, 1999), the Buie model for the solar radiation distribution (Buie et al., 2003), the incidence angle dependence for the absorptance surfaces according to the model exposed in (Tesfamichael and Wäckelgård, 2000), and a one-dimensional radial distribution for the normal deviations from an ideal specular reflection (Johnston, 1995). All the effects were modeled with the Monte Carlo methods. The tool was used to analyze the FMSC and its curved mirrors version, the Curved Slats Fixed Mirror Solar Concentrator (CSFMSC) (Pujol Nadal and Martínez Moll, 2013). The most promising geometries of both designs were identified for medium temperatures ranges in other works (Pujol-Nadal et al., 2013; R Pujol-Nadal and Martínez-Moll, 2014).

It can be noted that a difference of 25% was observed between the optical efficiency calculated by simple models (studies presented in 2006) and the one based on more accurate models (presented in 2012). Even though the more promising geometries were in both cases very similar. Hence, if it is true that simulations with simple optical models can be used to compare different designs of the same concept (the FMSC and the CSFMSC), the absolute value of the energy collected by the system can only be determined if the simulations take into account accurate models which are based on the most important effects in the energy harvesting process of the solar collectors.

In order to evaluate the importance of a high-resolution ray-tracing model with respect to a simple ray-tracing tool, an optical simulation of a parabolic through collector (PTC) has been conducted. The PTC chosen for the analysis was the NEP PolyTrough 1800 collector exposed in (Sallaberry et al., 2015). The simulations have been done using two different models: Model 1 and Model 2. The first one takes into account the Buie model for the Sun (Buie et al., 2003), one-dimensional radial distribution for the normal deviations from an ideal specular reflection (Johnston, 1995), Fresnel optics equations for electromagnetic waves, the extinction coefficient of the glass tube for the transmittance, and the angular dependence of the absorber surface (Tesfamichael and Wäckelgård, 2000). On the other hand, Model 2 considers a point source model for the sun, ideal specular reflectivity, a constant value for the transmittance of the glass tube, and a constant value for the absorptance of the receiver. The results are shown in Fig. 1, for transverse and longitudinal angles of incidence. It can be seen that if a simple model for the radiation-matter interaction is considered in a ray-tracing simulation, an overestimation of the optical efficiency is obtained.

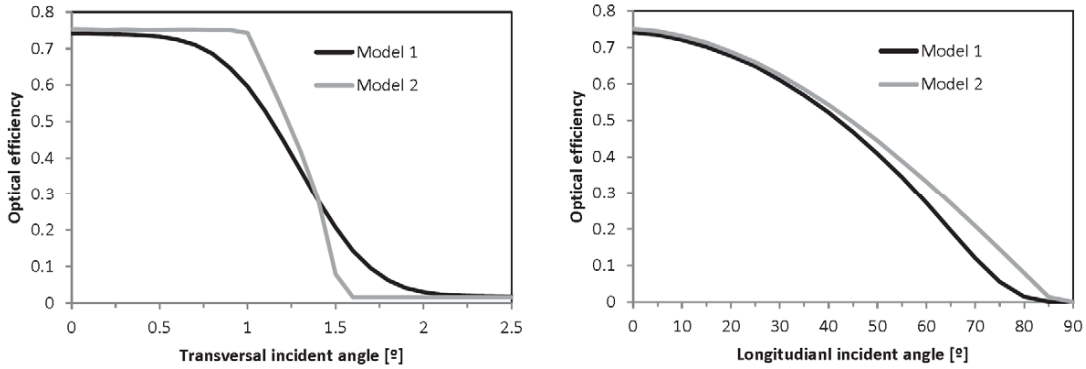

Fig. 1: Ray-tracing results of a PTC for transverse and longitudinal planes using simple and more accurate models

3. The ray-tracing code

The current code, written in FORTRAN, is under development. New models from 2012 are implemented in order to consider optical models based on the interaction of light and matter. The main description of the code in the actual state is described below.

In the current version the geometry has to be defined by surface objects. In a subsequent step different physical models with its respective parameters can then be assigned to each surface object.

For any type of model, the lay of energy conservation is always satisfied. There are consequently only three

possible ways of interaction. The incident ray can be either reflected, transmitted, or absorbed according to Eq. 1.

$$R(\theta_i, \lambda) + T(\theta_i, \lambda) + A(\theta_i, \lambda) = 1 \quad (1)$$

All coefficients depend on the wavelength, the incidence angle and the polarization of the light. With Eq. 1 in mind it is possible to classify common materials of solar concentrating collectors into three different groups: Reflective (mirrors), transparent (envelope, covers etc.) and absorbing (receiver) materials. As illustrated in Fig. 2, the simplifying assumptions are zero transmittance for reflective and absorptive materials, and zero absorptance for transparent materials. The latter only goes for the surface itself, because in the medium (after passing through the interface) there will be absorptance of the propagating electromagnetic wave, see Fig. 3.

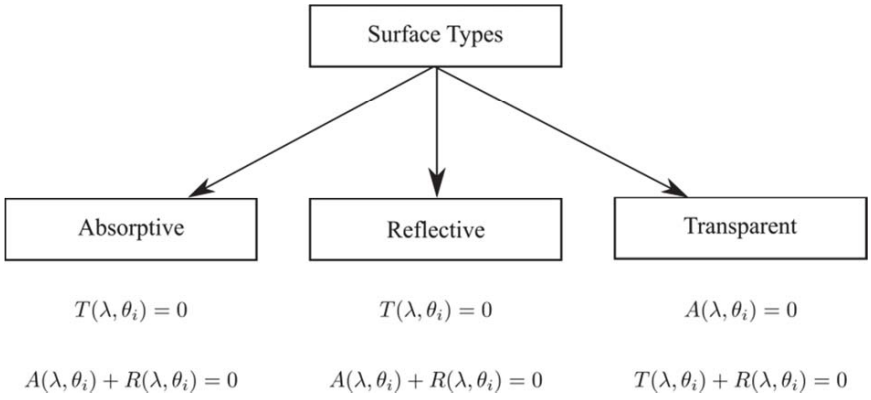

Fig. 2: Classification of typical solar thermal material: absorptive material (receiver), reflective material (mirrors) and transparent material (covers, envelopes)

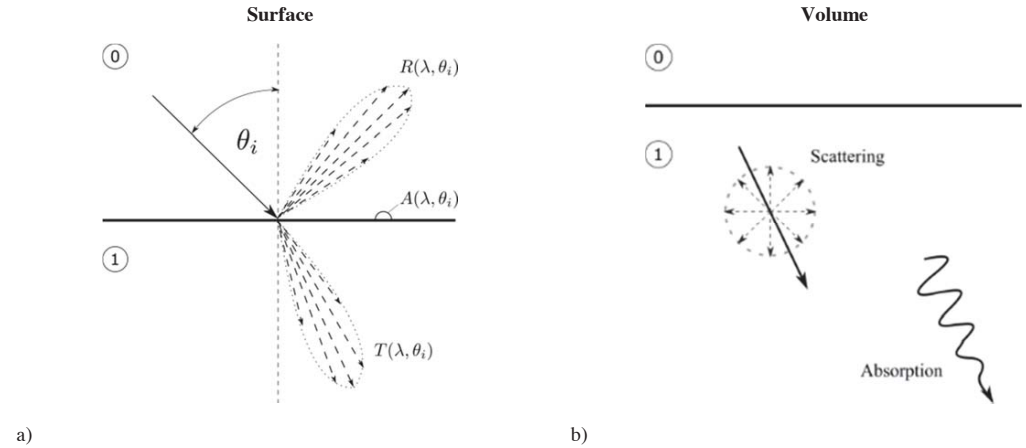

Fig. 3: Radiation-matter-interaction phenomena: a) Reflection, transmission and absorption on surfaces. b) Scattering and absorption within volume (Hertel et al., 2016b)

As far as conservation of energy goes, the interaction of an incident ray with a surface can be fully described by a surface reflectance model. What is then still missing for a more accurate description is the spatial dispersion of the reflected energy due to random microscopic surface textures. This phenomenon called

scattering can be described by a scattering model.

In summary, all radiation-matter interaction models that our ray-tracing code contains can be categorized into:

- Surface effects
  - Reflectance models
  - Scattering models
- Volume effects (only transparent material):
  - Volume absorption.

3.1 Reflectance models

Fig. 4 shows all surface reflectance models, which are currently implemented in the OTSun ray-tracing code. For more details see (Hertel et al., 2016b). It is important to comment here on the accuracy of the reflectance model. As mentioned before, the surface reflectance is a function of the wavelength and the incidence angle of the ray, as shown in Eq. 1. Depending on the purpose of the study, the surface reflectance can also be defined as a constant value, only depending on the incident angle, or depending on both the incidence angle and the wavelength.

In any case, sufficient experimental data has to be available. As for selective materials, often manufacturers provide a constant value. If such a value is not available, (Tesfamichael and Wäckelgård, 2000) proposed an empirical model of $R(\theta_i)$. This model was derived from measurements of an Al2O3-Ni/Al2O3 and NiO3-Ni-composite selective surfaces. Unfortunately, there was no other data obtained apart from these two samples. The model of (Grena, 2010) is a good alternative to derive the incidence angle dependence if the absorption coefficient is known for normal incidence.

Alternatively, accurate information about reflectance can be obtained from refractive index data bases. Based on this information, the Fresnel equations for single interfaces or the Transfer-Matrix method for more complex multi-layers (coatings) are common approaches in other fields such as PV or optics design (Macleod, 2010).

3.2 Scattering models

At the moment there are three options for scattering implemented: no scattering, Lambertian (isotropic) or Gaussian scattering (Fig.). Isotropic dispersion is typical for matte surfaces, while a Gaussian curve describes the reflection pattern of specular surfaces such as mirrors. In reality, the result is often a combination of isotropic and specular reflection and is described by a bidirectional reflectance distribution function (BRDF).

In solar concentrating applications the Gaussian model was found to be sufficiently accurate to describe the reflection of mirrors. OTSun uses a more general superposition of two bivariate normal distributions (Eq. 2).

$$f = Ke^{\left(-\frac{\varphi^2}{2\sigma_{21}^2}-\frac{\varphi^2}{2\sigma_{22}^2}\right)} + (1-K)e^{\left(-\frac{\varphi^2}{2\sigma_{11}^2}-\frac{\varphi^2}{2\sigma_{12}^2}\right)} \quad (2)$$

with K the ratio between distributions, σ_{ij} the respective variances and φ the acceptance angle. Moreover, it is possible to define wavelength and incidence angle dependent data for the variances σ_{ij} such as defined e.g. by (Good et al., 2016).

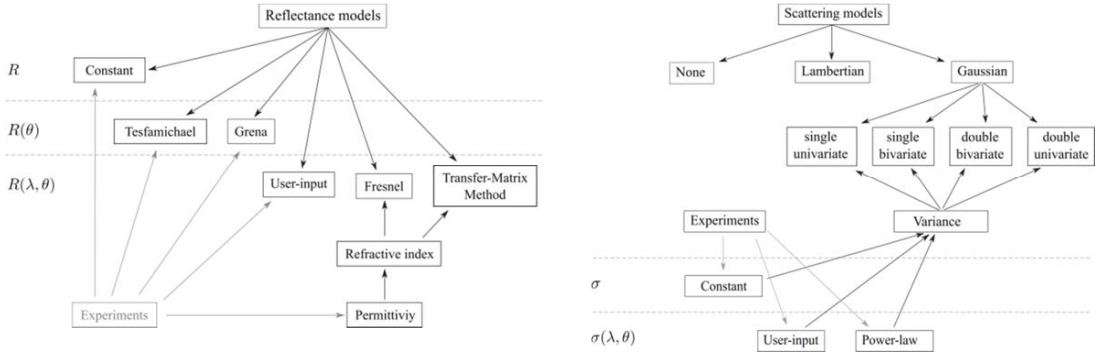

Fig. 4: Schematic of implemented reflectance (left) and scattering models (right) in the current version of the OTSun ray tracing code

4. Objectives and methodology

The improvement of the FORTRAN code is the first task of the OTSun project. The optical models are first proved and validated in the FORTRAN code, and then they will be implemented in the new version of the program.

The general objectives covered by the OTSun project are:

- Developing a computational tool for the high-resolution optical analysis of solar collectors.
- Validating the computational tool by comparison with theoretical and experimental results.
- Applying the computational tool in real cases.
- Distributing the tool as an open source code.

To achieve the general objectives, the next set of tasks will be developed during the project:

- Task 1: Current Status and improvements of the actual ray-tracing tool (FORTRAN).
- Task 2: Implementation of new algorithms of ray-intersection.
- Task 3: Implementation of a general algorithm for the energy distribution on the receiver.
- Task 4: Types of sources, spectrum and its implementation.
- Task 5: Models for specular reflective surfaces.
- Task 6: Radiation-matter interactions of materials.
- Task 7: Simulation of real cases.
- Task 8: Web and documentation platform.

General requirements for the simulation tool are a graphical interface for the visualization of the scene (GUI), and a programming language accessible to future improvements and developers. With this in mind, during the initial stage of the project we explored possible tools to start from; tools that were already developed with regard to these specifications. It should be clear that it is not beneficial to develop a visualization tool from scratch, but rather incorporate the physical models into an already existing visualization tool. Such a tool could be a computer aided design software (CAD), or any other 3D data visualization programs.

As discussed in previous sections, the geometry of the system only can be introduced by triangles in the actual FORTRAN code. It is possible to generate any geometry with the desired precision at the expense of an increasing number of triangles. Consequently, constructing curved surfaces with triangles has the disadvantage of requiring a large number of elements, which means increasing computation time. For this reason we explored new algorithms for ray-intersection with surfaces in task 2.

In view of the general specifications, and the need to reduce the CPU time, we explored the FreeCAD software (“FreeCAD,” n.d.). FreeCAD is a parametric 3D modeler made primarily to design real-life objects of any size. Parametric modeling allows to easily modifying the design by going back into the model history and changing its parameters. FreeCAD is open source and highly customizable, scriptable and extensible, it

runs on multiple platforms (Windows, Mac and Linux), and supports many open file formats such as STEP, IGES, STL, SVG, DXF, OBJ, IFC, DAE among others. It has the great advantage that almost all of FreeCAD's functionalities are accessible to Python, hence it is possible to easily extend these functionalities, automatize them with scripts, build self- made modules, or even embed FreeCAD in your own application.

Finally, it can be noted that Python is a widely used high-level, general-purpose, interpreted, and dynamic programming language, and that FreeCAD has implemented methods for the intersection between faces and lines (very useful for the ray-intersection problem mentioned above and to decrease the CPU time). For all of these reasons, we decided to develop the OTSun project as an extension of the FreeCAD software.

5. First results using the FreeCAD software

A ray-tracing simulation of a solar collector using the FreeCAD software has been conducted and validated. To do so, first the creation of the geometry of the NEP PolyTrough 1800 collector exposed in (Sallaberry et al., 2015) was modeled using the functions available in the *Part Module* of FreeCAD. Then, the skeleton of a simple ray-tracing procedure written in Python was implemented and executed. Only simple effects of optics have been implemented in this stage of the project. The main objective of this work was to evaluate the extensibility of FreeCAD software for ray-tracing simulations applied to solar collector systems.

5.1. Creating a PTC in FreeCAD

The *Part module* of FreeCAD allows accessing and using the OpenCasCade objects and functions. OpenCascade is a software development platform providing services for 3D surface and solid modeling, CAD data exchange, and visualization ("Open CASCADE Technology: Overview," n.d.). Most of its functionality is available as C++ libraries.

The *Part Module* has implemented tools for creating primitive objects, such as: box, cone, cylinder, torus, parabola and sphere among others. The ones that we used for creating the PTC were the parabola, the circle and the cylinder. Then, the *Part Module* has also implemented tools for modifying existing objects in the document, such as: booleans, union, common, extrude and cut among others. The extrude tool was used to create the parabolic mirror and the absorber tube from the primitives mentioned above. Since the glass tube has volume effects from the optical point of view, it was generated using the cut tool subtracting one cylinder from another. This way a solid object was obtained for the glass cover of the evacuated tube. A Python package with all the instructions mentioned above was written to create the geometry of the PTC in FreeCAD. Figs. 5 and 6 show the PTC created. Note that the parabolic mirror and the absorber cylinder are faces, but the glass tube is a solid.

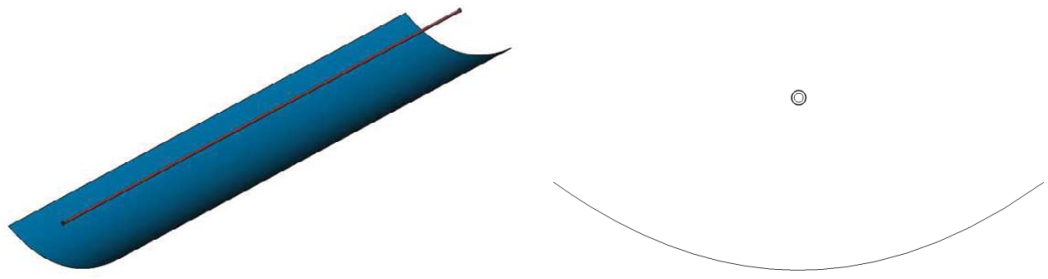

(a) (b)

Fig. 5: (a) General view of the PTC. (b) Frontal view of the PTC

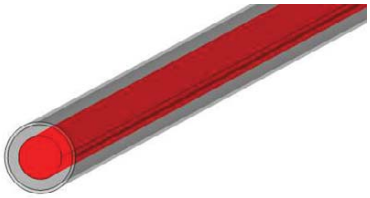

Fig. 6: Evacuated tube of the PTC

5.2. The ray-tracing procedure

The program calculates ray trajectories originating from one source (called sun window) that emits rays to all surfaces of the system. We have created a Python package that uses the classes provided by FreeCAD and extends them in order to model scenes and implement the ray-tracing procedure.

At this stage of the project, the core of the computation is implemented via three main classes, Scene, Ray and SolarCollector. An object of the class Scene collects all the information related to the physical objects present in the active document (the solar collector constructed).The physical objects are represented using *Shapes* in FreeCAD with some extra information regarding their materials. At this stage of the project, only simple models for the optics are considered.

An object of the class Ray collects the path that a solar ray describes while it interacts with the objects present in its scene; it is initialized by giving its source and direction. For now, only a punctual source is considered. We have implemented algorithms to compute, step by step, the points that the object passes through while it is reflected, refracted or absorbed in the surfaces present in the scene. These two classes are used by the third; SolarCollector, that implements the overall computation of the optical efficiency of the scene as a solar collector, making an estimation of the overall energy that it gets absorbed when the scene is exposed to the source.

5.3. Ray-tracing simulations

Fig. 7(a) shows a visualization of a ray-tracing simulation of the NEP PolyTrough 1800 collector done with the package mentioned above. This simulation was done emitting 100 rays, and it can be see how the sun window emits rays to the solar collector system. In Fig. 7(b) a front projection of the same ray-tracing simulation is shown. Also visible are the path trajectories of the rays according to the refraction law. Another case is shown in Fig. 8, for the longitudinal angle equal to 45º.

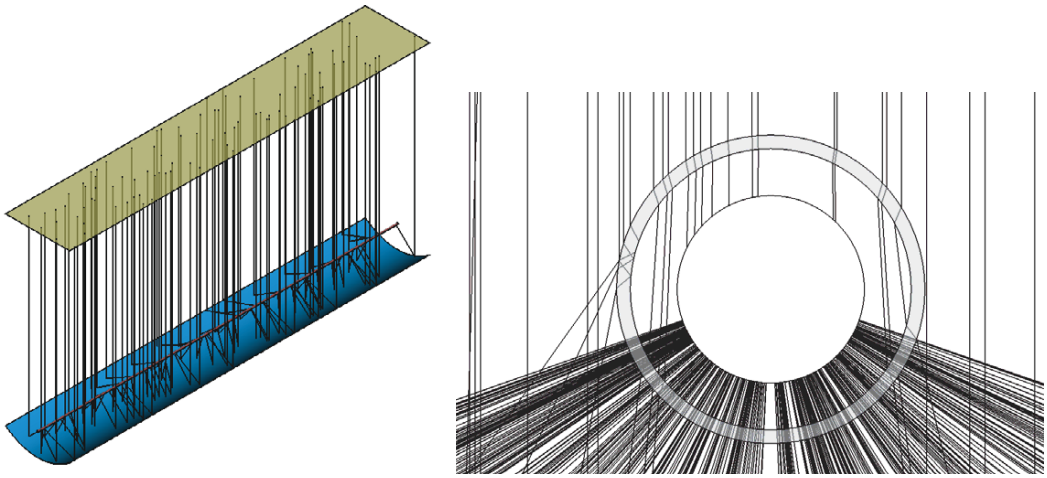

(a) **(b)**

Fig. 7: Ray-tracing simulation with 100 rays emitted. (a) Total view of the concentrator, sun rays, and sun window. (b) Frontal projection of the same ray-tracing in the region of the receiver.

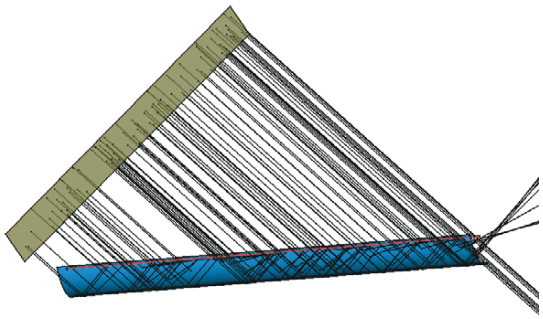

Fig. 8: Ray-tracing simulation with 100 rays emitted for the case of longitudinal angle equal to 45º

In order to validate the results of the new code generated, a simulation with 20000 rays has been conducted considering the same assumptions of Model 2 in Section 2. In Fig. 9 the optical efficiency obtained with the new code (OTSun_FreeCAD) and with the FORTRAN code (OTSun_FORTRAN) is shown. In view of the results, we can conclude that the new OTSun code calculates the optical efficiency with same accuracy as the FORTRAN version. Moreover, as the FORTRAN version was validated with experimental results in (Pujol-Nadal et al., 2015; Ramon Pujol-Nadal and Martínez-Moll, 2014), hence the code implemented in FreeCAD is also validated.

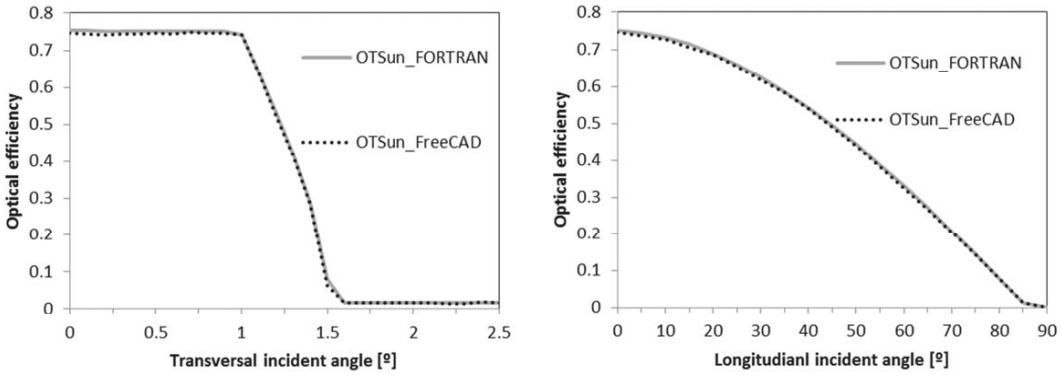

Fig. 9: Ray-tracing results of a PTC for transverse and longitudinal planes using simple models with FORTRAN and FreeCAD versions.

6. Conclusions

Ray-tracing simulations show great benefit for the optical analysis of solar collectors, and in order to achieve high-resolution results the consideration of the radiation-matter interaction is needed. In this contribution the authors describe the OTSun project, where the main goal is to develop a computational tool for high-resolution optical analysis of solar collectors. The tool will be developed under a free license (GPL, freeBSD or similar). Due to the general requirements for the tool, the authors decided to develop the OTSun project as an extension of the FreeCAD software which has the advantage that almost all of its functionalities are accessible to Python. A Python package has been written in order to explore the viability of making a ray-tracing simulation of a solar concentrating collector using the FreeCAD functions. In view of these experiences, it has been demonstrated that the FreeCAD program is suitable to extend its functionality and use it for a ray-tracing simulation of solar energy systems.

7. Acknowledgements

This work was supported by the Spanish Ministry of Economy and Competitiveness (MINECO) and the European Funds for Regional Development (ERDF) [ENE2015- 68339-R], and the European Union [call FP7-PEOPLE-2012-ITN, grant number 317085]. The authors would also like to acknowledge the support provided by the *Plataforma Solar de Almería* (PSA), the Spanish institute *Instituto para la Diversificación y*

Ahorro de la Energía (IDAE), CIESOL, TECNALIA Corporation, and SOLARUS Sunpower Sweden AB.

8. References

Blanco, M.J., Amieva, J.M., Mancilla, A., 2005. The Tonatiuh Software Development Project: An open source approach to the simulation of solar concentrating systems, in: Proceedings of the ASME Computers and Information in Engineering Division. ASME, pp. 157–164. doi:10.1115/IMECE2005-81859

Blanco, M.J., Mutuberria, A., Garcia, P., Gastesi, R., Martin, V., 2009. Preliminary validation of Tonatiuh. SolarPACES 2009 Int. Conf.

Bode, S., Gauché, P., 2012. Review of optical software for use in concentrating solar power systems. South African Sol. Energy Conf. ….

Buie, D., Dey, C.J., Bosi, S., 2003. The effective size of the solar cone for solar concentrating systems. Sol. Energy 74, 417–427. doi:http://dx.doi.org/10.1016/S0038-092X(03)00156-7

David H. Eberly, 2006. 3D Game Engine Design, Second Edition: A Practical Approach to Real-Time Computer Graphics (The Morgan Kaufmann Series in Interactive 3D Technology). Morgan Kaufmann Publishers Inc. San Francisco.

FreeCAD [WWW Document], n.d. URL http://www.freecadweb.org/index.html

Good, P., Cooper, T., Querci, M., Wiik, N., Ambrosetti, G., Steinfeld, A., 2016. Spectral reflectance, transmittance, and angular scattering of materials for solar concentrators. Sol. Energy Mater. Sol. Cells 144, 509–522. doi:10.1016/j.solmat.2015.09.057

Grena, R., 2010. Optical simulation of a parabolic solar trough collector. Int. J. Sustain. Energy 29, 19–36. doi:10.1080/14786450903302808

Hertel, J.D., Martinez-Moll, V., Pujol-Nadal, R., 2016a. Influence of thermal losses on the incidence angle modifier factorization approach. Sol. Energy 135, 50–58. doi:10.1016/j.solener.2016.05.035

Hertel, J.D., Martinez-Moll, V., Pujol-Nadal, R., 2015. Estimation of the influence of different incidence angle modifier models on the biaxial factorization approach. Energy Convers. Manag. 106, 249–259. doi:10.1016/j.enconman.2015.08.082

Hertel, J.D., Martínez-Moll, V., Pujol-Nadal, R., Bonnín, F., 2016b. State of the art of radiation-matter interaction models applied for the optical characterization of concentrating solar collectors.

Hetch and Zajac, 1999. Optica.

Johnston, G., 1995. On the analysis of surface error distributions on concentrated solar collectors. J. Sol. Energy Eng. Trans. ASME 117, 294–296.

Macleod, H.A., 2010. Thin-Film Optical Filters. CRC Press.

Martínez Moll, V., Pujol Nadal, R., Moià Pol, A., Schwiger, H., 2006. Analysis of a Stationary Parabolic Linear Concentrator With Tracking Absorber, in: Technologies, 13th International Symposium on Concentrated Solar Power and Chemical Energy (Ed.), . CIEMAT. Servicio editorial., Av. Complutense 22. E-28040 Madrid, Spain.

NREL [WWW Document], n.d. URL http://www.nrel.gov/csp/soltrace/

Open CASCADE Technology: Overview [WWW Document], n.d. URL https://www.opencascade.com/doc/occt-7.0.0/overview/html/index.html

Osório, T., Horta, P., Larcher, M., Pujol-Nadal, R., Hertel, J., van Rooyen, D.W., Heimsath, A., Schneider, S., Benitez, D., Frein, A., Denarie, A., 2016. Ray-tracing software comparison for linear focusing solar collectors. AIP Publishing, p. 20017. doi:10.1063/1.4949041

Pujol, R., Martínez, V., Moià, A., Hans, S., 2006. Analysis of stationary Fresnel like linear concentrator with tracking absorber, in: 13th Solar Paces Symposium.

Pujol Nadal, R., Martínez Moll, V., 2013. Optical analysis of a curved-slats fixed-mirror solar concentrator by a forward ray-tracing procedure. Appl. Opt. 52, 7389–98.

Pujol Nadal, R., Martínez Moll, V., 2012. Optical Analysis of the Fixed Mirror Solar Concentrator by Forward Ray-Tracing Procedure. J. Sol. Energy Eng. 134, 31009. doi:10.1115/1.4006575

Pujol-Nadal, R., Martínez-Moll, V., 2014. Parametric analysis of the curved slats fixed mirror solar concentrator for medium temperature applications. Energy Convers. Manag. 78, 676–683. doi:http://dx.doi.org/10.1016/j.enconman.2013.11.032

Pujol-Nadal, R., Martínez-Moll, V., 2014. Optical characterization of a fixed mirror solar concentrator prototype by the ray-tracing procedure. J. Renew. Sustain. Energy 6, 43105. doi:10.1063/1.4890219

Pujol-Nadal, R., Martínez-Moll, V., Moià-Pol, A., 2013. Parametric Analysis of the Fixed Mirror Solar Concentrator for Medium Temperature Applications. J. Sol. Energy Eng. 136, 11017–11019. doi:10.1115/1.4026098

Pujol-Nadal, R., Martínez-Moll, V., Sallaberry, F., Moià-Pol, A., 2015. Optical and thermal characterization of a variable geometry concentrator using ray-tracing tools and experimental data. Appl. Energy 155,

110–119. doi:10.1016/j.apenergy.2015.06.005
Russell John L., J., 1977. Principles Of The Fixed Mirror Solar Concentrator. Proc. SPIE 0085, Sol. Energy Util. II, 139 139–145. doi:10.1117/12.954950
Sallaberry, F., Pujol-Nadal, R., Larcher, M., Rittmann-Frank, M.H., 2015. Direct tracking error characterization on a single-axis solar tracker. Energy Convers. Manag. 105, 1281–1290. doi:10.1016/j.enconman.2015.08.081
Tesfamichael, T., Wäckelgård, E., 2000. Angular solar absorptance and incident angle modifier of selective absorbers for solar thermal collectors. Sol. Energy 68, 335–341.

Conference Proceedings

EuroSun 2016
Palma de Mallorca (Spain), 11 - 14 October 2016

INFLUENCE OF THE INPUT PARAMETERS ACCURACY DEFINED IN THE STANDARD ISO 9459-5 FOR A DOMESTIC WATER HEATING THERMOSIPHON

Jonathan Vera[1]*, Isidoro Lillo[2], Laima Reina[2] and Sara Moreno[2]

[1] Solar Thermal Energy Department, National Renewable Energy Centre (CENER), Sarriguren, Spain

[2] Group of Thermodynamic and Renewable Energies (GTER), University of Seville, Seville, Spain

*Corresponding Author, jvera@cener.com

Abstract

The International Standard ISO 9459-5 describes the characterization of thermal performance for domestic water heating systems. The objective of this paper is to analyze the influence of measurement accuracy of some input parameters (inlet water temperature, outlet water temperature and solar radiation) during the test sequences on resulting solar fraction of a domestic water heating system, type thermosiphon, on the different European reference locations (Athens, Davos, Würzburg and Stockholm). A study of the measurement accuracy according to Standard ISO 9459-5 and other values has been carried out. The long-term prediction (solar fraction) for each of the input measurements was determined, and according to these results, a less restrictive measurement accuracy could be propose for a future revision of Standard ISO 9459-5.

Keywords: *solar system, dynamic testing, certification*

1. Introduction

According to the Spanish Technical Building Code (CTE) and Ministerial Order ITC/71/2007, all solar thermal systems on the Spanish market must be homologated by the Ministry of Industry to be eligible for government subsidies. For this reason, they must pass the EN 12976-1 and -2 (2006) European Standard tests. This Standard stipulates durability, safety and efficiency tests and user and installer documents checking.

The CENER (National Renewable Energy Centre) and GTER (Group of Thermodynamic and Renewable Energies) Accredited Solar System Testing Laboratory in Seville has been performed all the tests for factory-made solar thermal systems according to the European Standard since 2008. Before that, solar systems had been tested in this laboratory for 25 years. The European Standard efficiency test refers to two ISO Standards, ISO 9459-2 (2008) (CSTG method) and ISO 9495-5 (2007) (DST method). The CSTG method "Complete System Testing Group" makes use of an input-output method, while the DST method, called the "Dynamic System Test", makes use of dynamic software for parameter identification of the system characterization.

These International Standards provide information about measurement accuracies for each experimental measure (ambient temperature, inlet water temperature, outlet water temperature, flow-meter and solar radiation). The objective of this paper is to analyze the influence of measurement accuracy of some input parameters (inlet water temperature, outlet water temperature and solar radiation) on solar fraction in four different locations (Athens, Davos, Würzburg and Stockholm) for a factory made solar heating system, type thermosiphon, testing according to Standard ISO 9459-5.

doi:10.18086/eurosun.2016.06.07 Available at http://proceedings.ises.org

2. Description of testing method (ISO 9459-5)

The efficiency test of the DST method (also called dynamic method) consists in several test sequences with different system behaviors: S-Sol for characterizing the collector array performance at high efficiencies and acquire information about store heat losses and collector array performance at low efficiencies, S-Store for characterizing store heat losses and S-Aux for determining the heat losses and the volume fraction of the auxiliary heated portion of the storage tank. All the significant parameters (solar radiation, inlet and outlet water temperature, ambient temperature and flow-meter) are recorded. The mathematical model of the system energy output is based on a partial differential equation.

2.1. S-Sol Sequence

The aims of these sequences are to characterize the collector array performance at high efficiencies and acquire information about store heat losses and collector array performance at low efficiencies. The tests consists in conditioning the system and then letting the solar system operates normally for several days and finally the system is conditioned again to make uniform the tank temperature. Those sequence types are the called Test A and Test B. During those sequences, a series of 5 (Test A) or 7 (Test B) draw-offs are executed with different durations according to the system characteristics and at different times of the day. The Test A is supposed to let the system work at high efficiencies with enough closed draw-offs to not let the collectors heat too much. The Test B is supposed to let the system work at low efficiency leaving the tank as warm as possible.

Within those sequences, there should be a minimum of valid days with enough daily solar radiation and outlet temperature higher than a minimum for Test B.

2.2. S-Store Sequence

This sequence aims to characterize the store heat losses parameter of the system. It consists of a Test B sequence for at least 2 days and a cooling period of between 36 and 48 h.

2.3. S-Aux Sequence

This sequence aims to characterize the volume fraction of the auxiliary heated portion of the store. But it is not used in the tests of solar-only system.

2.4. Identification of system parameters and prediction of long-term performance

The identification of the characteristics parameters of the system is done using all the measured data recorded during the whole testing sequences. It is made by the validated commercial software InSitu (version 2.7) referred in the Standard ISO 9459-5. Figure 1 shows the flow chart of InSitu program

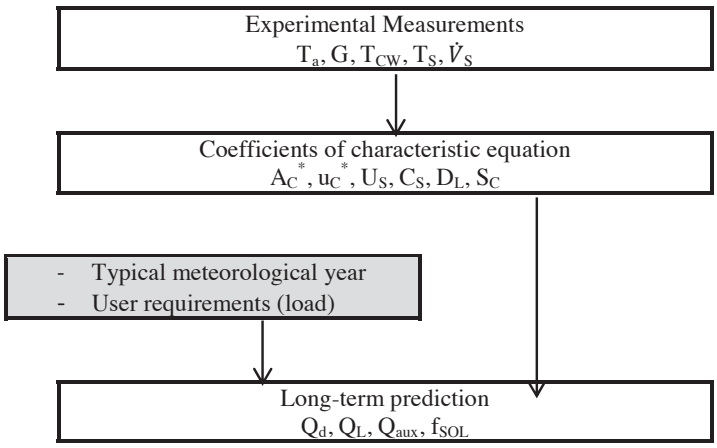

Fig. 1: Flow chart, InSitu program

The results consist in the coefficients A_c* (effective collector area), u_c* (effective collector loss coefficient), U_s (total store heat loss coefficient), C_s (total store heat capacity), D_L (mixing constant), Sc (store stratification). Each of those parameters is a coefficient of the terms in the physical model used for the thermosiphon.

The same software is used to calculate the yearly performance of the system for different reference locations and load demand using hourly meteorological data [H, T_a].

The solar fraction (f_{SOL}) is defined as the energy supplied by the solar part (Q_L) divided by the total system load (Q_D = heat demand).

3. Description of influence of the input parameters measurement accuracy

This section analyzes the influence of measurement accuracy of some the input parameters (inlet water temperature, outlet water temperature and solar radiation) on solar fraction in four different locations (Athens, Davos, Würzburg and Stockholm) for a factory made thermosiphon solar system. Table 1 shows the measurement accuracies according to Standard ISO 9459-5, as well as the accuracies proposed for this analysis. A prediction of long-term performance for each of the measurement accuracies has been carried out.

Tab. 1: Measurement accuracies

Parameter	Measurement accuracy according to Standard ISO 9459-5	Measurement accuracy analysed in this study
Inlet temperature	± 0.1 ºC	± 0.2 ºC, ± 0.5 ºC
Outlet temperature	± 0.1 ºC	± 0.2 ºC, ± 0.5 ºC
Solar radiation	± 1.0 %	± 1.5 %, ± 3.0 %

4. Influence of the input parameters measurement accuracies

4.1 Testing sample

A thermosiphon system with a storage tank of a volume of 300 l. and 2 flat-plate collectors with an aperture area of 4.46 m^2 is selected for analyzing the influence of input parameters measurement accuracies.

The results of these system parameters obtained according to Standard ISO 9459-5 are shown in Table 2

Tab. 2: System parameters

Parameter	Value	Unit
A_C*	2.619	m^2
u_C*	8.191	$Wm^{-1} K^{-1}$
U_S	2.504	$W K^{-1}$
C_S	1.114	$MJ K^{-1}$
D_L	0.125	--
S_C	0.515	--

The results of the long-term performance are presented in the following graphs

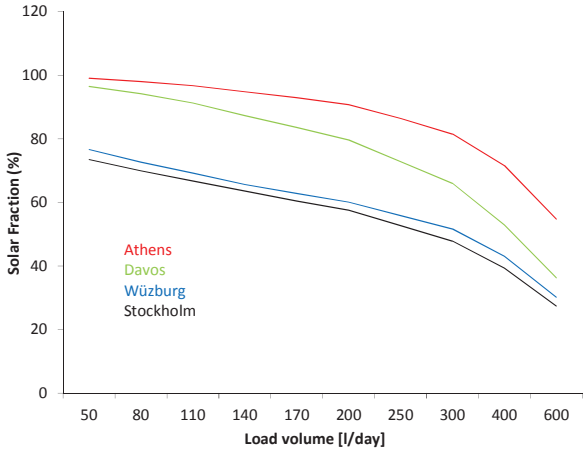

Fig. 2: f_{SOL} results

4.2 Comparative analysis

This section describes the variation on the solar fraction as a function of the load volume for every reference locations in order to modify the measurement accuracy of each parameter proposed in Table 1. Similarly, the average relative error of the solar fraction in every input parameter will be represented.

a. Inlet temperature

As shown in Figure 3, the maximum difference of the solar fraction obtained between the results to testing sample and the results in all intlet temperature measurement accuracies (table 1) is lower than 0.9 % in different reference locations. The maximum difference in variation on solar fraction is lower than 0.7 % to measurement accuracies according to Standard ISO 9459-5 (± 0.1 ºC) and 0.9 % to other measurement accuracies proposed (± 0.2 ºC, ± 0.5 ºC).

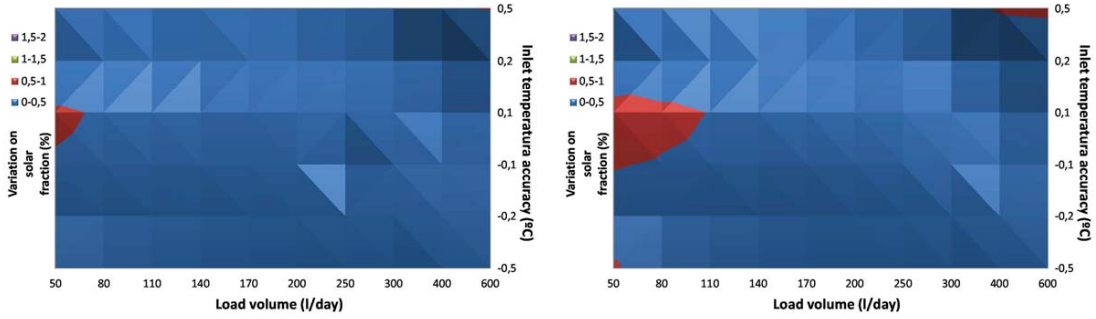

(a) **(b)**

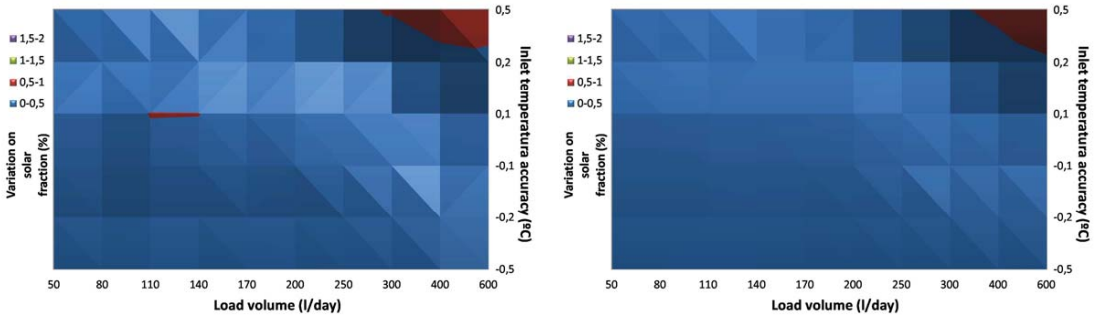

(c) (d)

Fig. 3: Variation on f_{SOL} to modify inlet temperature measurement accuracy in Stockholm (a) Würzburg (b) Davos (c) and Athens (d)

Figure 4 shows the average relative error of solar fraction with respect to inlet temperature accuracy in all reference locations. The maximum average relative error on solar fraction is lower than 0.6 % for all measurement accuracies studied (table 1). The minimun values of average relative error on solar fraction occurs on Athens location.

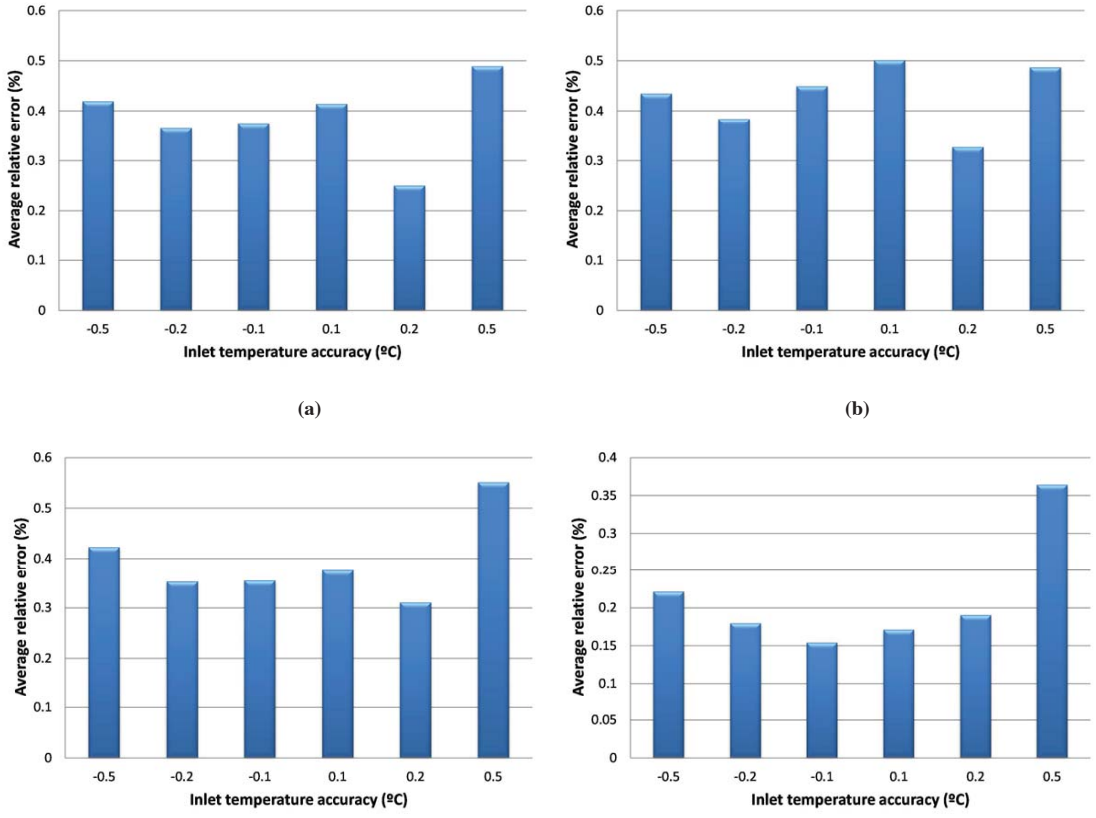

(a) (b)

(c) (d)

Fig. 4: Average relative error on solar fraction to modify inlet temperature measurement accuracy in Stockholm (a) Würzburg (b) Davos (c) and Athens (d)

b. Outlet temperature

As shown in Figure 5, the maximum difference of the solar fraction obtained between the results to testing sample and the results in all outlet temperature measurement accuracies (table 1) is lower than 1% in different reference locations. The maximum difference in variation on solar fraction is lower than 0.4% to measurement accuracies according to Standard ISO 9459-5 (± 0.1 ºC) and 1% to other measurement accuracies proposed (± 0.2 ºC, ± 0.5 ºC).

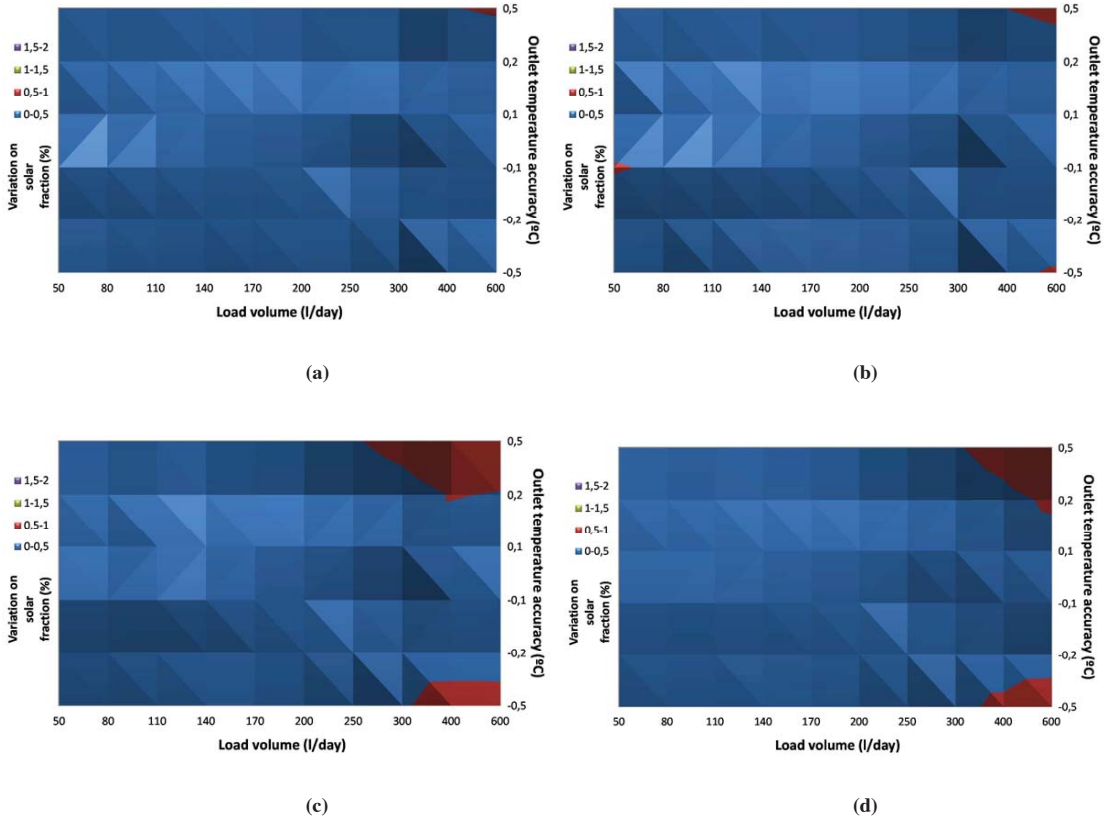

Fig. 5: Variation on f_{SOL} to modify outlet temperature measurement accuracy in Stockholm (a) Würzburg (b) Davos (c) and Athens (d)

Figure 6 shows the average relative error of solar fraction with respect of outlet temperature accuracy in all reference locations. The maximum average relative error on solar fraction is lower than 0.4% for the measurement accuracies according to Standard ISO 9459-5 (± 0.1 ºC) and 0.7% for other measurement accuracies analized (± 0.2 ºC, ± 0.5 ºC). The minimun values of average relative error on solar fraction occurs on Athens location.

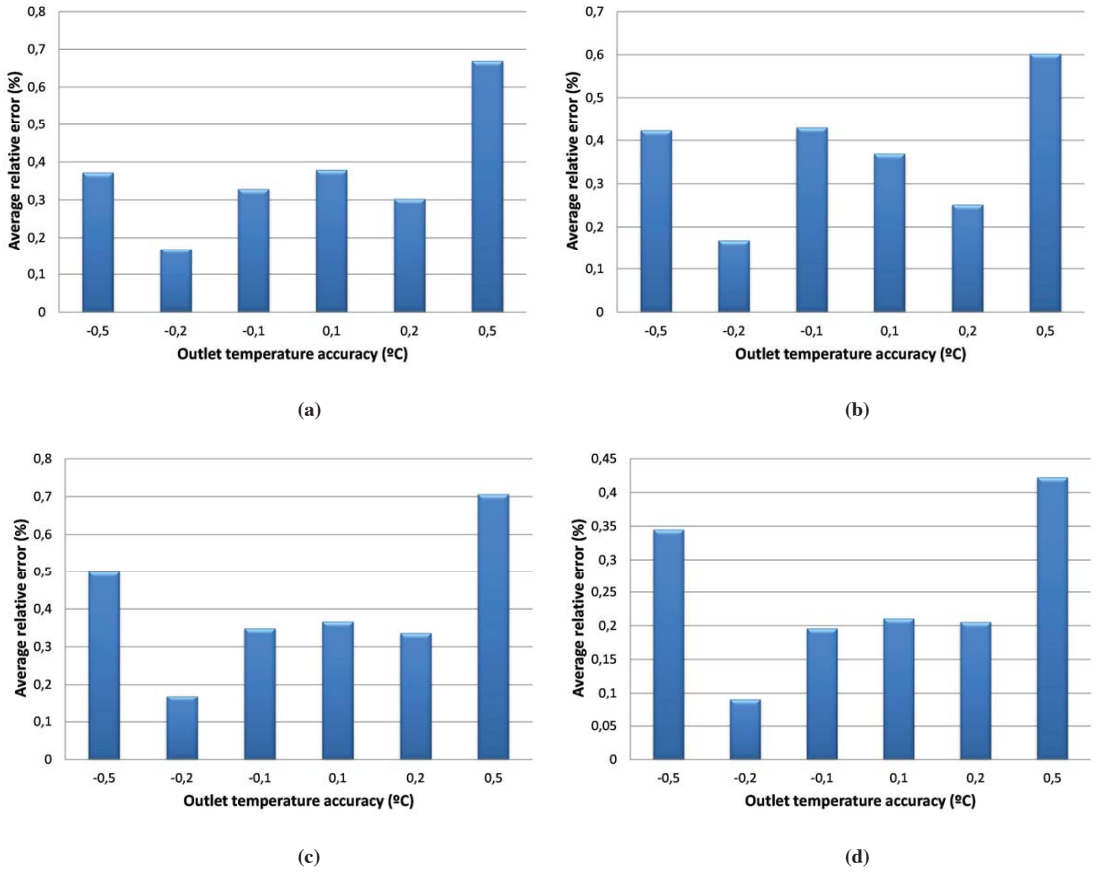

Fig. 6: Average relative error on solar fraction to modify outlet temperature measurement accuracy in Stockholm (a) Würzburg (b) Davos (c) and Athens (d)

c. Solar radiation

As shown in Figure 7, the maximum difference of the solar fraction obtained between the results to testing sample and the results in all solar radiation measurement accuracies (table 1) is lower than 1.3% in different reference locations. The maximum difference in variation on solar fraction is lower than 0.7% to measurement accuracies according to Standard ISO 9459-5 (± 1.0 %) and 1.3% to other measurement accuracies proposed (± 1.5 %, ± 3.0 %).

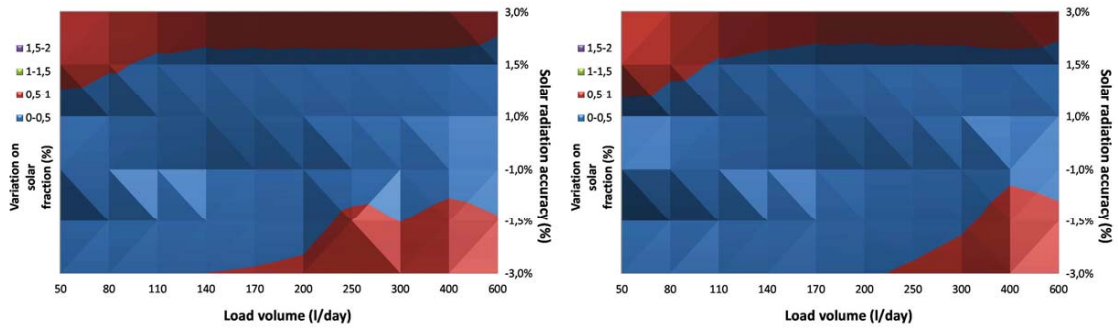

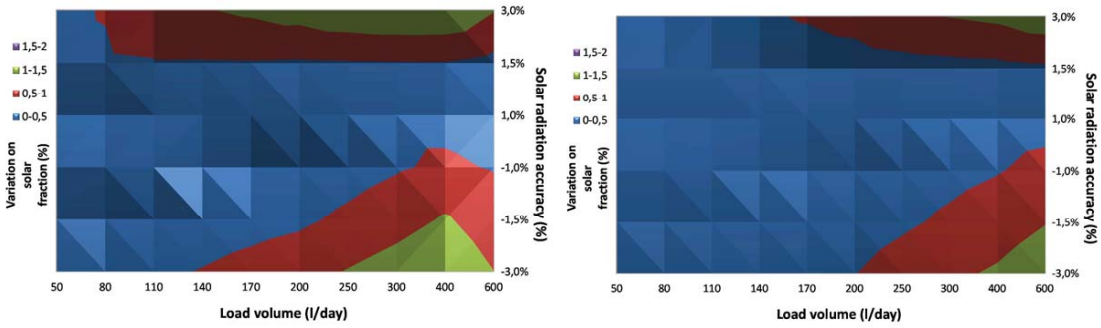

(c) (d)

Fig. 7: Variation on f_{SOL} to modify solar radiation measurement accuracy in Stockholm (a) Würzburg (b) Davos (c) and Athens (d)

Figure 8 shows the average relative error of solar fraction with respect of solar radiation accuracy in all reference locations. The maximum average relative error on solar fraction is lower than 0.5% for the measurement accuracies according to Standard ISO 9459-5 (± 1.0 %) and 1.6% for other measurement accuracies proposed in this study (± 1.5 %, ± 3.0 %).

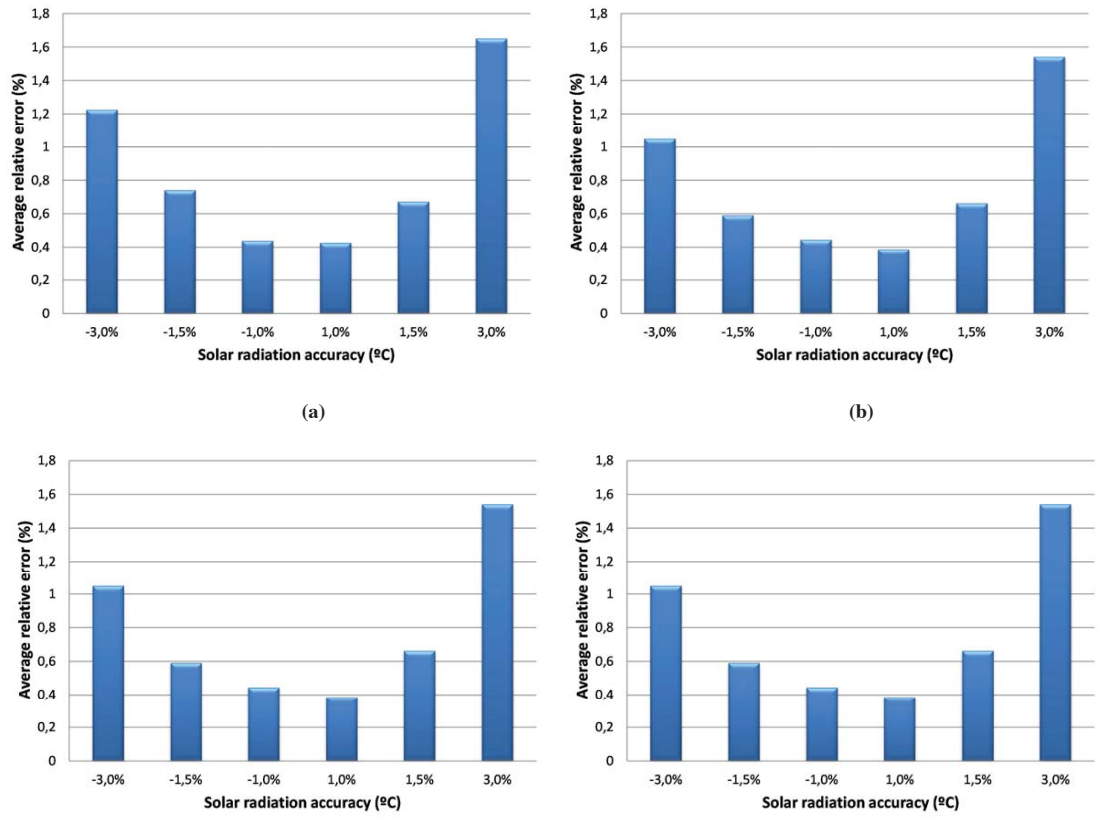

(a) (b)

(c) (d)

Fig. 8: Average relative error on solar fraction to modify solar radiation measurement accuracy in Stockholm (a) Würzburg (b) Davos (c) and Athens (d)

5. Conclusion

The influence of measurement accuracies of some input parameters is analyzed (inlet water temperature, outlet water temperature and solar radiation) obtaining the following conclusions:

- The maximum differences on solar fraction when using the measurement accuracy according to Standard ISO 9459-5 varies between 0.4% (for the outlet temperature) and below than 0.7% (for the inlet temperature and solar radiation) considering all load volumes in the reference locations.
- The maximum differences on solar fraction when using the new measurement accuracies proposed in this study varies between 1% approximately (for the inlet temperature and outlet temperature) and 1.6% (for the solar radiation) considering all load volumes in the reference locations.
- The maximum average relative error on solar fraction when using the measurement accuracy according to Standard ISO 9459-5 is approximately 0.5% (for the inlet temperature, outlet temperature and solar radiation) in the reference locations.
- The maximum average relative error on solar fraction when using the new measurement accuracies proposed in this study varies between approximately 0.6% (for the inlet temperature and outlet temperature) and 1.6% (for the solar radiation) in the reference locations.
- This study shows that it is possible to increase the measurement accuracies range required in Standard ISO 9459-5 without losing effectiveness on the results obtained in long-term prediction (solar fraction).

6. Nomenclature

Symbol	Quantity	Unit
A^*	effective collector area	m^2
C_S	total store heat capacity	MJ/K
D_L	mixing constant	--
f_{SOL}	solar fraction	--
G	solar irradiance	W/m^2
H	solar radiation	MJ/m^2
T_a	ambient temperature	ºC
T_{cw}	inlet water temperature	ºC
T_S	outlet water temperature	ºC
Q_{aux}	parasitic energy (electricity)	MJ
Q_d	head demand	MJ
Q_L	heat delivered by the solar heating system	MJ
S_C	store stratification	--
u_C^*	effective collector loss coefficient u_C^*	W/m K
U_S	total store heat loss coefficient	W/K
$\dot{V}_S$	flow-meter	l/min

7. Reference

EN 12976-1: 2006, Thermal solar systems and components. Factory made systems –Part 1: General requirements.

EN 12976-2: 2006, Thermal solar systems and components. Factory made systems –Part 2: Test methods.

ISO 9459-2: 2007, Solar heating – Domestic water heating Systems. Part 2: Outdoor test methods for system performance characterization and yearly performance prediction of solar-only systems.

ISO 9459-5: 2007, Solar heating – Domestic water heating Systems. Part 5: System performance characterization by means of whole-system tests and computer simulation.

Conference Proceedings

EuroSun 2016
Palma de Mallorca (Spain), 11 - 14 October 2016

A Comparison Study of Solar Thermal Collector Performance in the Tropics

Arifeen Wahed[1] and Thomas Reindl[1]

[1] Solar Energy Research Institute of Singapore, Singapore

Abstract

Over the recent years, awareness on integration of a solar thermal system for industrial process heating applications has been increased. In the Tropics, a huge potential on similar applications has been identified due to availability of abundant solar energy throughout the year. However, challenges lie on selection of an appropriate solar thermal collector for supplying required thermal energy to the industrial processes in tropical conditions with fluctuation irradiance and ambient high moisture air.

A test methodology has been developed in order to evaluate the solar thermal collector efficiency via measured data, a model based time resolved simulation analysis. In this analysis, collectors were tested at an outdoor test facility in the tropical condition. Collector model was developed and optimized the collector parameters for validating the experimental results. The validated collector model was then utilized to determine the efficiency parameters of the collector. Thus, the proposed method of comparing the collector performance would provide a valuable basis for selection of the appropriate collector technology to be utilized in a large-scale solar thermal system for industrial heating applications.

Keywords: *Solar thermal collector performance, tropics, industrial process heat.*

1. Introduction

Solar energy has emerged as a competitive source of energy compare to the conventional source of fossil energy due to concern of economic and environmental considerations. Utilization of solar thermal energy for industrial heating applications is one such targeted areas. At present, about two hundred large scale solar heating plants have been identified for industrial heating applications [SHIP] all around the world. Solar thermal collector is one of the key components of solar heating systems. Thus, selection of right type of solar thermal collector is crucial for industrial heating applications.

Collector thermal performance is generally tested either by steady-state test (SST) method or by quasi-dynamic test method. Researchers have been working on development of new and more effective test methods [Amer et al., 1997; Perers, 1997; Kratzenberg et al., 2006; Kong et al., 2012a, 2012b; Xu et al., 2012] that could predict the collector performance more accurately. In general, solar thermal collectors are certified by a specific test standard such as ISO 9806. This certificate provides the general basis for comparing different collector performances. However it is of particular interest to compare different collector performance for a particular condition such as the tropical climatic conditions in Singapore, where fluctuation irradiation and high humidity exists. The present study of the collector performance is thus not to redefine the existing test methods; rather to develop a test methodology for comparing the collector performance by outdoor testing over a period of time in the tropical climate. Thus the proposed study provides input for selection of the right type solar thermal collector, which is very much important for industrial heating applications.

In this study, solar thermal collectors' outdoor performance has been tested; and an evacuated model based on time resolved simulation has been developed to evaluate the collector thermal performance from the dynamic test performances. This method is an effective way of comparing collector outdoor thermal performance in the

doi:10.18086/eurosun.2016.06.02 Available at http://proceedings.ises.org

tropics, where a high fluctuation of irradiation has been observed.

2. Collector outdoor test

An experimental test facility, as shown in Fig. 1 of a solar thermal collector system has been installed at the roof top of the Solar Energy Research Institute of Singapore (SERIS).

Fig. 1: Solar Thermal collector testing system at the roof top of the Solar Energy Research Institute of Singapore (SERIS). Three different solar thermal collectors were installed for the test operation.

2.1. Experiments setup

For collector testing, three different collectors were setup in parallel. Other components of the test facility were a thermostat system including water tank, chiller, heater and temperature controller, three water flow pumps with variable speed drive for each collector, power control panel and data acquisition system. The testing collectors comprise of different technologies – (i) flat plate collector incorporated with evacuated technology, (ii) evacuated tube collector, and (iii) evacuated tube with heat-pipe technology. Testing area of each collector was approximately 4 to 5 m^2.

During experiments, the heat generated by these solar thermal collectors was discharged via the thermostat. The thermostat, controlled by the temperature controller via temperature sensors was heated up or cooled down the water in the storage tank, if required. Collector pre-set input water temperatures were supplied to the collectors from the storage tank. Water flow through each collector was controlled by the variable speed driven water pump. To measure water temperature and water flow, temperature sensors and water flowmeters were installed at the different positions of the system. A silicon sensor and a temperature sensor were installed to measure radiation and ambient temperature respectively. During test operation, data acquisition, processing and system control were achieved by utilizing the National Instrument systems through LabVIEW program.

For measurements, instruments such as (i) four-wire Class A type PT100 Resistance Temperature Detectors (RTD) for temperature measurement, (ii) magnetic flowmeters with low volumetric flow rate in the range of 0 to 1 $m^3.h^{-1}$ for flow measurement, (iii) silicon sensor (transducer set range 0 – 70 mV) for irradiance measurement and (iv) National Instrument (NI) equipment for control, data acquisition and processing were installed for test operation. A graphical user interface (GUI) of the solar thermal test system was developed in the LabVIEW for the purpose of the data processing, analyses and control with high flexibility. For data acquisition, one (1) second time resolution was set for all experiments.

Calibration of these sensors was performed in order to achieve a higher accuracy of the measured data. RTD temperature sensor, water flow meter and silicon sensors were calibrated before deployed for experiments. RTD (PT-100, 4-wire, Class A) sensors correction had been performed against a calibrated Platinum Resistance Thermometer (PRT). The magnetic flowmeter and the silicon sensor were also calibrated with a correction formula for higher accuracy. Even though the sensors were calibrated, there were systematic uncertainties in the systems. Tab. 1 lists the sensors' systematic uncertainties to be considered.

Tab. 1: Measuring sensors systematic uncertainties

Parameters	Sensor type	Range	Uncertainty
1. Temperature	RTD (PT-100, 4-wire, Class A)	0 to 200 ºC	0.02 ºC *
2. Water flow	Magnetic flowmeter (Rosemount 8732)	0 to 0.9 m^3/h	max. deviation ±0.025% of max. reading +
3. Solar irradiance	Silicon sensor (Mono-Si PV Cell)	0 to 1600 W/m^2	± 2.0% #
4. Data logging	NI analog input connector	4 to 20 mA	Gain error (reading): 0.76%

* Based on calibration report by A* Star Metrology Centre
\+ Flowmeter calibration test report by POLYCONTROLS
\# Test report – precision measurement of a PV irradiance sensor, Fraunhofer ISE

2.2. Test procedures

In order to determine the yield of the solar thermal collectors – in particular comparing the yield of different type of collectors in parallel against each other, an experimental test procedure, 'constant collector flow', had been followed. Under the experimental boundary conditions, collector flow was fixed but different minimum flow rates through each collector type according to the recommendation of the manufacturer. And the inlet temperature was same for all collectors during experiment and could be varied in the range of 80 to 100°C.

Tab. 2: Experiments conditions for fixed flow and constant inlet temperature for each collector

Collector	Irradiation, W/m^2	Ambient temperature, ºC	Water flow, m^3/h	Collector inlet water temperature, ºC		
Collector A	Ambient condition 100 - 1000	Ambient condition 30 - 34	0.10 – 0.12	80	90	~ 100
Collector B			0.17 - 0.20			
Collector C			0.13 – 0.16			

As observed from Tab. 2, the inlet water temperature boundary condition was relatively high during experiments, 80 to 100°C. Because the collectors were tested for industrial process heating application and such inlet water temperature range could represent the actual industrial process heating applications. Collector yield performance results were discussed in Section 4.2.

2.3. Stagnation test

In a tropical climate, supply of solar thermal heat may far exceed the heat demand due to the stagnation condition of the solar thermal system. This may raise the collector temperature above 200°C. Increasing stagnation temperature may lead to thermal stress of the collector. In order to determine the collector performance after such stagnation condition, tests were performed on the collectors.

For stagnation test, collector pumps were switched off and all three collectors were exposed to the ambient irradiance condition for continuously seven days. During this stagnation test, all the collector loops were filled with water.

After the stagnation test, a visual inspection had been performed to figure out any physical damage, wear and tear of the collectors including the corresponding joints. No visual defects including any wear and tear had been observed on these collectors. After visual inspection, experiments were performed with the same boundary conditions for all three collectors, as stated in the Tab. 2

3. Solar collector model

In order to evaluate the collector efficiency via measured data, model based time resolved simulation analyses have been developed. The method is well adapted to the fluctuating solar radiation conditions in the tropics. It allows for determining various collector parameters under non equilibrium conditions.

3.1. Collector mathematical model

During experiments three different technologies were investigated – (i) Collector A: flat plate vacuum solar thermal panel, (ii) Collector B: evacuated tube collector, and (iii) Collector C: evacuated tube collector with heat pipes. Even though these collectors use different technologies to absorb solar thermal heat, the mechanism of harnessing solar thermal heat is almost similar – evacuated technology and selective absorbers are used for all these collectors. In case of Collector A and Collector B, solar thermal heat is conducted by the absorbers directly to the collector fluid. In case of Collector C collector solar thermal heat is conducted indirectly to the collector fluid through heat pipe.

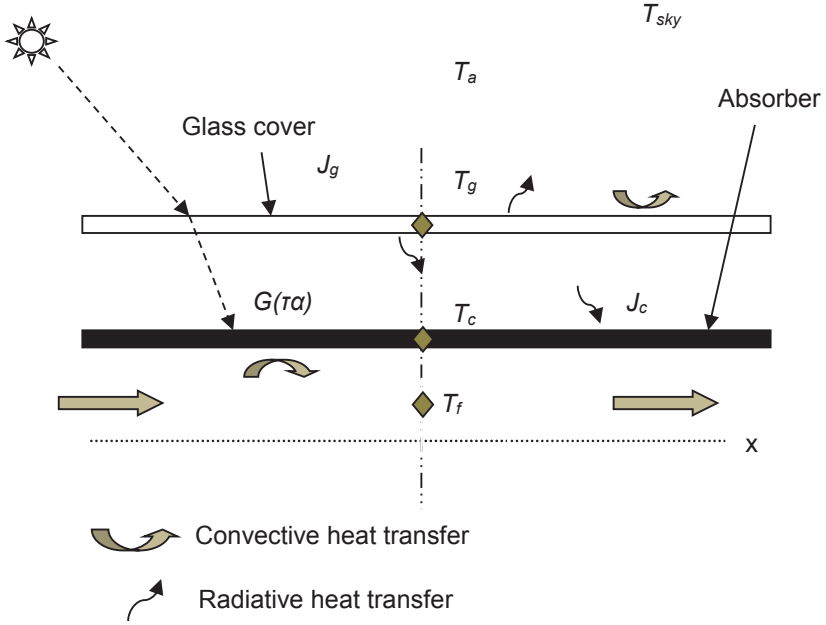

Fig. 2: Evacuated tube collector model. T_g, T_c, and T_f are the temperature of glass, absorber and fluid respectively. T_a is the ambient temperature and T_{sky} is the radiation temperature of the sky. G is the solar irradiance, α is the optical absorptance and τ is the transmittance coefficient. J_g and J_c are the heat capacity of glass and absorber respectively

An evacuated collector model as shown in Fig. 2 is considered to describe the different types of heat energy coupling between the absorber of the collector and the fluid applied for heat transfer. The assumption for these simplifications is the sufficiently accurate conformance between measured and modelled (simulated) time series of collector data, as shown in Section 4. Additional assumptions in the model are – (i) flow of the heat transfer fluid is unidirectional, along one axis (ii) properties of glass and absorber are independent of temperature (constant) (iii) thermo-physical properties of the water are temperature dependent (iv) no heat is supposed to be transported in the fluid moving direction by heat conduction (v) effect of the varying incidence angle of the solar radiation on the collector performance is neglected (vi) infrared emissivity of the sky is one (ε_{sky}=1).

As shown in Fig. 2, radiated heat transfer between the sky and the glass cover is taken into account. Heat transfer between the back cover and the ambient is assumed to be dominated by convection (radiative and conductive heat transfer is neglected here). Since there is almost no medium (vacuum) between the cover and the absorber, the heat transfer between these two components is assumed to be purely due to radiation.

Evacuated tube collector modelling is done following the publication of Praene et al. (2005). The model consists of 3 thermal nodes, namely, the transparent glass cover, the absorber plate and the heat transfer fluid. It is considered that the temperature of the fluid is a function of x (flow direction along x - axis) and the fluid is moving in an effective single channel with a velocity u (u=function of distance x, and time, t). Thus the thermal nodes can be expressed as,

For the transparent glass cover:

$$J_g \rho_g \frac{dT_g}{dt} = \varepsilon_g \sigma(T_{sky}^4 - T_g^4) + h_{g,a}(T_a - T_g) + \frac{\varepsilon_c \varepsilon_g}{\varepsilon_c + \varepsilon_g - \varepsilon_c \varepsilon_g} \sigma(T_c^4 - T_g^4) \quad \text{(eq. 1)}$$

The sky temperature of (eq. 2) can be obtained from the ambient temperature by using Swinbank's formula [Deacon, 1970],

$$T_{sky} = 0.0552 T_a \quad \text{(eq. 2)}$$

For the absorber plate:

$$J_c \rho_c \frac{dT_c}{dt} = G(\tau\alpha) + \frac{\varepsilon_c \varepsilon_g}{\varepsilon_c + \varepsilon_g - \varepsilon_c \varepsilon_g} \sigma(T_g^4 - T_c^4) + h_{f,c}(T_{fx,t} - T_c) \quad \text{(eq. 3)}$$

For the heat transfer fluid:

$$C_f \rho_f \frac{\pi d_{in}^2}{4} \left(\frac{dT_{f\,x,t}}{dt} + u \frac{dT_{f\,x,t}}{dx} \right) = \pi d_{in} h_{f,c}(T_c - T_{f\,x,t}) \quad \text{(eq.4)}$$

The collector heat removal channel is modelled as a single fluid channel, which is divided into N segments. The temperature values $T_f(x,t)$, $T_g(t)$ and $T_c(t)$ at every segment are obtained by solving the equations- (eq. 1), (eq.2), (eq.3) and (eq.4).

3.2. Collector parameter identification and model validation

Input parameters for identification in the model are (i) infrared emissivity of glass cover, (ii) glass heat capacity (specific heat of glass times glass thickness), (iii) absorber tube diameter, (iv) heat transfer co-efficient between glass and ambient, (v) heat transfer co-efficient between water and absorber, (vi) infrared emissivity of absorber, (vii) transmittance-absorptance co-efficient of the absorber, and (viii) absorber heat capacity (specific heat of absorber times absorber thickness). Tab.3 shows the input values obtained from data sheets (Engineering toolbox) and own assessment (Mahbubul 2013) for sensitivity analysis.

Tab. 3: Input parameter values for sensitivity analysis

Input parameter	Unit	Value
Collector absorber specific Heat capacity	J/kg K	400
Collector absorber thickness	m	0.001
Collector absorber emissivity	-	0.09
Collector absorber pipe diameter	m	0.0135
Heat transfer coefficient absorber-fluid	W/(m^2 K)	10
Transmittance-absorptance coefficient		0.86
Collector glass specific heat capacity	J/kg K	840
Collector glass thickness	m	0.0025
Collector glass emissivity	-	0.9
Heat transfer coefficient glass-air	W/(m^2 K)	9

The following steps are considered to identify the corresponding collector parameters in order to validate the model with experimental results (water is used as heat transfer fluid).

Step 1: Set the constant parameters (i) collector dimensions, (ii) collector glass and absorber densities, (iii) water properties as function of temperature, (water properties are determined for the mean fluid temperature T_m (average water temperature of collector inlet and collector outlet) at any time, using interpolation in the

water properties table.

Step 2: Input the experiment's data (time resolution one minute) into the model (i) mass flow rate, (ii) ambient temperature, (iii) irradiance, (iii) collector inlet water temperature.

Step 3: Perform sensitivity analysis of the identified parameters on the model (detailed discussion on the top of this section). Only the sensitive parameters – change of RMSE $\leq$ 1K with respect to the change of input parameter values in the range of ±10%, are considered for the optimization process. Else, input the parameter values (as constant) in the model.

Step 3a: In the optimization process, input an upper range value and a lower range value for each parameter selected for optimization. After optimization, input the optimized values to the model.

Step 4: Run the model. Compare the collector outlet temperature (simulated values) with the corresponding experimental values of the collector outlet temperature

Step 5: Calculate the root mean square (RMSE) of collector outlet temperature between the simulation value and the experiment value. Set the stopping criteria 10-6 K (a threshold to terminate the iteration when the successive iteration of the defined RMSE function does not satisfy the condition). This iteration process continues until the stopping criteria are satisfied.

Step 6: After optimization, the parameter values of the validated model are checked with another set of experimental data and step 4 and step 5 are repeated. If this condition is satisfied, the optimized parameters of the model are identified; else, repeat the procedures outlined in step 3a to step 6.

The parameter identification and model validation approach was adopted for three different collectors analysed – Collector A, Collector B and Collector C. The corresponding results obtained are discussed in the Section 4.2.

3.3. Collector efficiency parameter

In a dynamic model, the collector efficiency is defined as a ratio of the useful energy gain to the incident solar radiation power, as mentioned in (eq. 5),

$$\eta(t) = \frac{\dot{m} C_f(t)[T_o(x,t) - T_i(x,t)]}{G(t)A} \qquad \text{(eq. 5)}$$

The water temperature at the collector inlet, $T_i(x,t)$ and the collector outlet, $T_o(x,t)$ are obtained from the valid model, (eq. 4).

In a stationary model, the collector efficiency is usually defined as the function of collector efficiency parameters (η_0, a, and b) as mentioned in (eq. 6),

$$\eta = \eta_0 - a\frac{(T_m - T_a)}{G} - b\frac{(T_m - T_a)^2}{G} \qquad \text{(eq. 6)}$$

Collector validated dynamic efficiency model of (eq. 1) to (eq. 5) were used to determine the efficiency parameters η_0, a, and b of the stationary model from (eq. 6). By applying a multiple linear regression method on the simulation results these coefficients (η_0, a, and b) can be determined. The corresponding results for three different collectors – Collector A, Collector B and Collector C, are discussed in Section 4.2.

4. Results and discussions

Outdoor testing of the collectors was performed over a period of time. Collector experiment results were used to validate the collector models via fitted identified parameters. The collector models were then utilized to identify the efficiency parameters for collector performance analysis.

4.1. Outdoor test performance

According to the test procedures described in Section 2.2, experiments were performed for each of the three collector for three months. After that testing, a stagnation test as described in Section 2.3 followed by each collector performance test were performed.

During experiments, collector flows were maintained at the minimum flow condition recommended by the collector manufacturers as shown in Tab. 2. Minimum flow condition of the collector had been chosen to attain maximum temperature gain across the collectors. Since each collector technology has different specifications, minimum flow condition recommended by the manufacturer had been considered for experiments.

Thermal performances of the each collector, as shown in Fig. 3, were recorded by measuring the collector water temperature at the inlet and at the outlet. As observed from Fig. 3 collector inlet temperatures were maintained constant at ~80°C and the collector outlet temperature varies due to the fluctuation of irradiance during operation. Similar experiments with different collector inlet temperatures such as 90°C and ~100°C as described in Tab. 2, had also been performed.

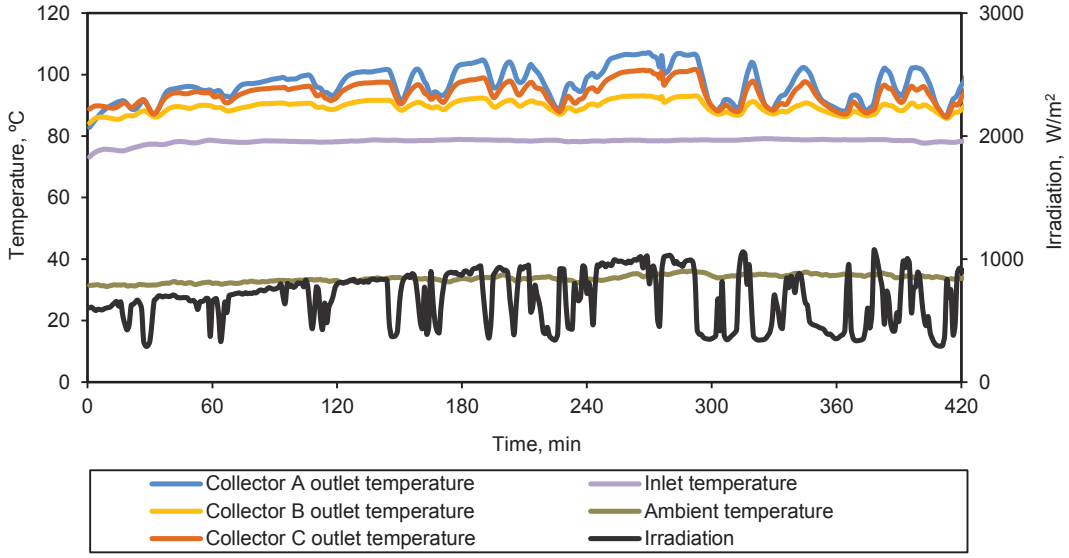

Fig. 3: Solar thermal collector performance for maintaining of the inlet water temperature of each collector at ~80°C. Collector outlet water temperatures, irradiation and ambient air temperature are shown in the figure. Caveat: "0 minute" considers the starting time of the experiments measurement. This time is generally between 9:30 to 10:00 a.m.

Since aperture area and water flow of each collector are different, the collector thermal performance could not be compared with this data alone. Therefore, collectors yield energy, i.e., thermal energy gain per unit collector aperture area has been analysed, as shown in Fig. 4.

As observed from Fig. 4, thermal energy gain per unit aperture area is different for each collector. Collector A is more responsive to the fluctuating irradiation followed by Collector B and Collector C. Collectors' materials properties and heat transfer mechanism of each collector attributes the difference of thermal energy gain of each collector. This comparison study provides the required data to consider the appropriate collector for industrial solar heating application in the tropics.

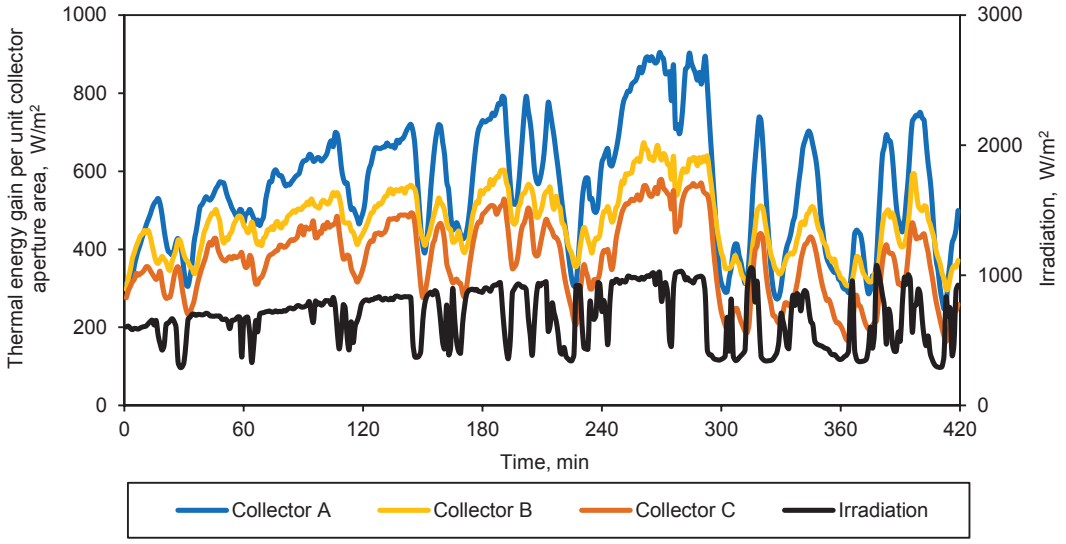

Fig. 4: Solar thermal collector thermal energy per unit collector aperture area when each collector inlet water temperature was maintained at ~80°C. Collector thermal energy gain per unit collector aperture area and irradiation are shown in the figure.
Caveat: "0 minute" considers the starting time of the experiments measurement. This time is generally between 9:30 to 10:00 a.m.

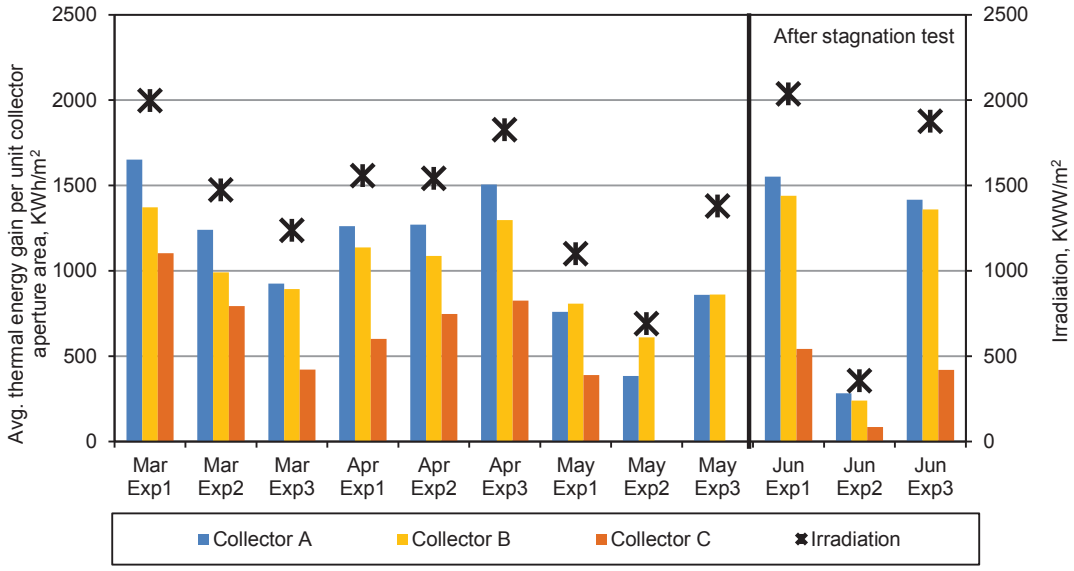

Fig. 5: Tested solar thermal collector thermal energy gain per unit collector aperture area when each collector inlet water temperature was maintained at 80°C (Exp1), 90°C (Exp2), 100°C (Exp3) on the month of March, April, May and June. June experiments were conducted after the stagnation test. Operating conditions of these experiments are given in Tab.2.
Caveat: Due to to technical failure some expermient results could not be recorded properly. Therefore, those data were not considered for analysis.

4.2. Outdoor test performance

Solar yield performance of the three collectors were analysed based on the experimental results. Average solar thermal gain for each month has been considered for this analysis. In the later part, collector efficiency parameters are compared on a monthly basis.

Yield energy

According to EN 12975 standard, the best way to compare different types of collectors is to compare the useful energy from a square meter of collector under equivalent circumstances (Standard 12975). Even though the present experiments of the three different types of collectors would not comply with the procedures of the mentioned standard, thermal energy gain per unit aperture area of each collector has been calculated for analysis purposes.

Fig.5 presents the comparison of thermal energy gain per unit collector aperture area among the three collectors under different operating conditions. As defined, the thermal energy gain by the collector depends on two factors – collector water temperature rise (delta T) and collector flow. Collector water temperature rise (delta T) is attributed to the solar irradiation absorbed and the collector heat losses. In the experiments, collector minimum flow according to manufacturer was attained for maximum temperature gain across the collector (highest delta T). It is observed from Fig.5 that the performance of the collector A and Collector B was the significantly higher than Collector C thermal performance under those boundary conditions. The difference of the collector performance would be due to the difference of technologies of heat gain and heat losses of these collectors. After stagnation test, Collector C performance was decreased significantly. Thus, the experimental findings would provide yield performance of the collectors before and after the stagnation test. But, these results would not be sufficient for comparison of the collector performance. For this reason, collector efficiency parameters had been analysed in the later sections.

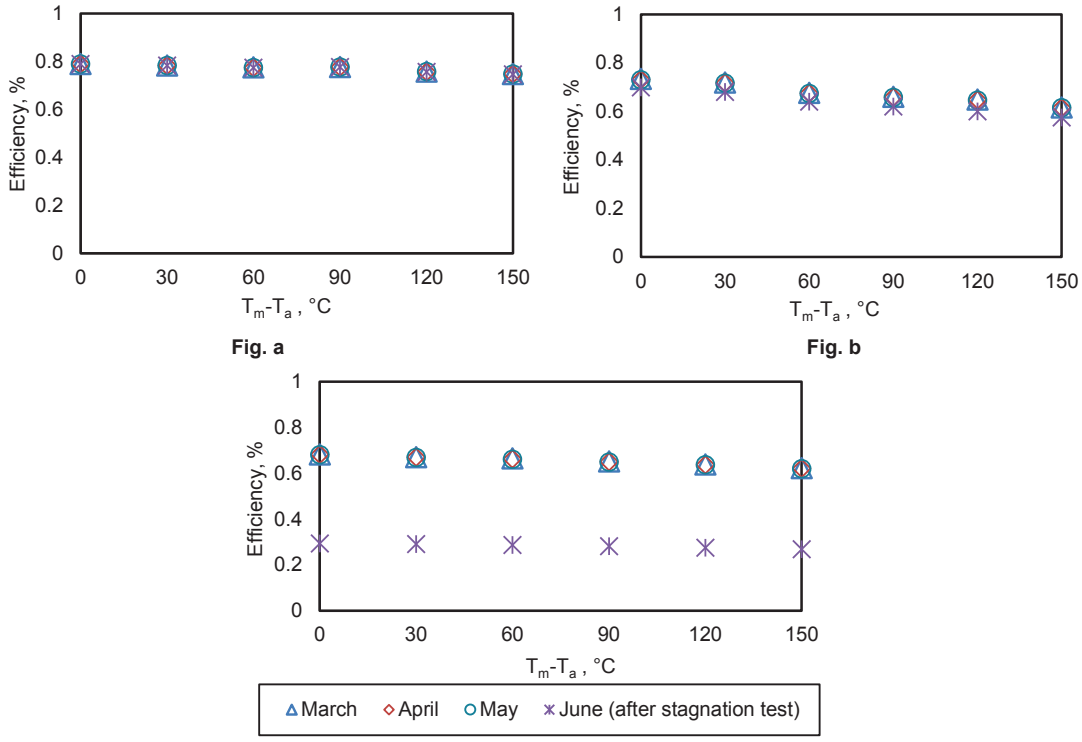

Fig. a

Fig. b

Fig. c

Fig. 6: Comparison of η vs (T_m-T_a) curve for unit aperture area and solar irradiance (G = 1000 W/m^2) values for testing months (March, April, May and June) of the collectors – Collector A (Fig. a), Collector B (Fig. b) and Collector C (Fig. c). June results present the collectors performance after the stagnation test.

Collector efficiency

The solar thermal collector models were validated with the experimental results, as discussed in section 3. In order to validate the collector models, the comparison of the collector outlet temperature between experimental and simulated values for the three different collectors were performed. The root mean square error (RMSE) of

the collector outlet temperature values between the simulated models and the experiments were found RMSE≤ 1K, which is not significant. The validated collector models, as presented in Section 3.3, were used to determine the efficiency parameters η_0, a, and b of the stationary model from (eq. 6). Applying the least squares approach, the coefficients η_0, a and b were determined for analysis of collectors performance

Fig.6 shows the calculated collector efficiency of the three different collectors for the temperature difference ($T_m - T_a$) when solar irradiance G=1000 W/m^2 on the collector plane. The efficiency functions are a result of a least square fit of the simulated values with a second order polynomial. This efficiency functions takes into account that the heat loss coefficient of the collectors is a function of temperature.

Comparison of the Collector A efficiency, as shown in the Fig. 6(a), revealed no degradation of the collector performance during testing from March to May. Even after the stagnation test on June, Collector A performance degradation has not been observed.

Comparison of the Collector B efficiency, as shown in the Fig. 6(b), revealed no degradation of the collector performance during the actual testing from March to May. After the stagnation test, a small order of degradation of the collector performance has been observed. After stagnation test, no defects were noted from outer inspection during collector operation. Thus, it might suspect that the collector materials, presumably the absorbent layer, could have degraded due to the high temperature of the stagnation test.

Comparison of the Collector C efficiency, as shown in the Fig. 6(c), revealed that here was a significant degradation of the performance after stagnation test. In this collector field, there are heat pipes which could be damaged and/or spoiled due to the excess heat during stagnation test. Because of this, the Collector C performance degraded after stagnation test.

Though the analyses of these collectors provide an insight of the collector performances for the given duration of the outdoor testing in Singapore, degradation of the collector performances for a longer period of operation could not be determined from these analyses.

5. Summary

This paper describes a test methodology for comparing collector performance in tropical climatic conditions like Singapore. An outdoor test facility has been setup at the roof top of SERIS facility, where different collectors performance can be tested side-by-side for different operating conditions. Experimentally measured data is used to validate the collector dynamic model. The model is then utilized to identify the collector efficiency parameters.

In this paper, three different collectors- Collector A, Collector B and Collector C were studied. Based on the experiments and simulation results of the three collectors, the following findings can be summarized:

- Solar thermal yield (energy performance) of the Collector A and the Collector B are higher than the solar yield (energy performance) of the Collector C.
- There was no degradation of the Collector A, Collector B and Collector C performance was observed during first three months of outdoor testing (before stagnation test). The reason is that three months outdoor testing would not enough duration to observe any collector performance degradation.
- After the stagnation test, no degrading of the Collector A had been noticed. The Collector B performance showed some degradation of collector performance, while the Collector C showed a considerable performance degradation.

Performance analyses of the three different collector show that the Collector A and Collector B could consider for industrial heating applications in Singapore.

Finally, the present analysis of the collector performances for outdoor testing in Singapore provides a valuable basis for the selection of the relevant collector technologies for a large-scale solar thermal systems. Other factors such as, relevant costs associated with the collector (including installation and maintenance costs) and the long-term durability have to be considered though in order to design, implement and operate a large scale solar thermal installation.

6. Acknowledgement

The work is supported by a project with a multinational pharmaceutical company.

7. References

Amer, E.H., Nayak, J.K., Sharma, G.K., 1997. Transient test methods for flat-plate collectors: review and experimental evaluation. Sol. Energy 60 (5), 229–243.

Deacon, E.L., 1970. The derivation of Swinbank's long-wave radiation formula. Q.J.R.Meterol.S. 96(408); 313-319.

IEA SHC Task 49, The Solar Heat for Industrial Processes – SHIP online database contains a worldwide overview on existing solar thermal plants for different industry sectors. < http://ship-plants.info/>, !8 September, 2016.

Kong, W.Q., Wang, Z.F., et al., 2012a. Theoretical analysis and experimental verification of a new dynamic test method for solar collectors. Sol. Energy 86 (1), 398–406.

Kong, W.Q., Wang, Z.F., et al., 2012b. An improved dynamic test method for solar collectors. Sol. Energy 86 (6), 1838–1848.

Kratzenberg, M.G., Beyer, H.G., Colle, S., 2006. Uncertainty calculation applied to different regression methods in the quasi-dynamic collector test. Sol. Energy 80 (11), 1453–1462.

Material properties <www.engineeringtoolbox.com>; DOI: 30 August, 2015.

Mahbubul, M., 2013.Optimization of solar thermal collector systems for the tropics, M.S. Thesis, National University of Singapore.

Praëne, J.P. , Garde, F., et al., 2005. Dynamic modelling and elements of validation of a solar evacuated tube collector, Building Simulation, 953-960.

Perers, B., 1997. An improved dynamic solar collector test method for determination of non-linear optical and thermal characteristics with multiple regression. Sol. Energy 59 (4-6), 163–178.

Xu, L., Wang, Z.F., et al., 2012. A new dynamic test method for thermal performance of all-glass evacuated solar air collectors. Sol. Energy 86 (5), 1222–1231.

Quality assurance in solar heating and cooling technology. A guide to the standard EN12975 <www.estif.org/fileadmin/estif/content/projects/QAiST/QAiST_results/QAiST%20D2.3%20Guide%20to%20EN%2012975.pdf> DOI: 18 September, 2016.

Appendix: **UNITS AND SYMBOLS**

Table 1: Symbols and units

Quantity	Symbol	Unit
Area	A	m^2
Global heat loss coefficient	a	$W\ m^{-1}\ K^{-1}$
Temperature dependent of global heat loss coefficient	b	$W\ m^{-2}\ K^{-2}$
Specific heat	c	$J\ kg^{-1}\ K^{-1}$
Diameter	d	m
Global irradiance	G	$W\ m^{-2}$
Heat transfer coefficient	h	$W\ m^{-2}\ K^{-1}$
Heat capacity	J	$J\ m\ kg^{-1}.K^{-1}$
Mass flow rate	$\dot{m}$	$kg\ s^{-1}$
Temperature	T	K or °C
Velocity	u	$m\ s^{-1}$
Absorptance	α	
Emittance	ε	
Density	ρ	$kg\ m^{-3}$
Transmittance	τ	
Efficiency	η	
Stefan-Boltzmann constant	σ	$W\ m^{-2}\ K^{-4}$

Table 2: Subscripts

Quantity	Symbol
Ambient	a
Absorber	c
Fluid (water)	f
Glass	g
Inlet	i
nner	in
Outlet	o
Optical	o
Mean	m
Sky	sky

Conference Proceedings

EuroSun 2016
Palma de Mallorca (Spain), 11 - 14 October 2016

Erosion experimental system design and experimental research of high temperature molten salt

Yao Fan[1], Bi Qincheng[1]

[1] The State Key Laboratory of Multiphase Flow in Power Engineering, Xi'an Jiaotong University, Xi'an 710049, China

Abstract

The erosion behavior of two types of stainless steel in mixtures of sodium nitrate ($NaNO_3$) and potassium nitrate (KNO_3) is presented. The erosion resistance can be used to evaluate the lifetime of heat exchange tubes for solar thermal applications. A molten salt erosion experimental system was established for this purpose. Erosion tests were conducted for approximately 750 hours with type 304 and 321 stainless steel at 500 ºC and 400 ºC with different molten salt wash velocities, ranging from 1.09 m/s to 2.98 m/s. Erosion rates were determined by mass losses, and the results indicate that short-term erosion rates of the two types of stainless steel can be described in term of parabolic kinetics. The annual rates of metal loss were measured to be 10.8 to 18 μm/year for 304 stainless steel at 500 ºC depending on the wash velocities. Metal loss for 321 stainless steel at 500 ºC is about 7.68 to 10.92 μm/year. Based on these results, we confirm that the erosion resistance performance of 321 stainless steel is better than that of 304, which may be related to the titanium in 321 stainless steel.

Keywords: *Erosion behavior, molten salt, 321stainless steel, 304stainless steel*

1. Introduction

The two primary components of Concentrated Solar Power (CSP) are the receiver and heat exchanger. In a CSP system, the receiver structure consists of tubing panels through which heat transfer fluid circulates as it is heated by sunlight focused by an array of computer-controlled mirrors. The heat exchanger constitutes of a number of tubes transferring heat in fluid cross-flow tube banks that is steam cooled on the tube side. It has been suggested that a higher performance material should be used to construct these devices, such as stainless steel. We chose to study 300 series stainless steels; previous work has demonstrated that they exhibit good corrosion resistance and no degradation in mechanical properties after relatively long-term exposure to molten nitrates at the temperatures of interest.

The chosen heat transfer fluid is one of the most important aspects of a successfully operating power plant. Solar Two utilizes a molten salt consisting of 60 wt.% $NaNO_3$ and 40 wt.% KNO_3 as the heat transfer fluid, which has a melting point of 238 ºC and an intended working range of 290 ºC to 560 ºC. This mixture optimizes a number of important properties, including heat capacity, thermal conductivity, corrosivity, ease of handling and storage, and cost.

While the previous studies mentioned above have established the static corrosion behavior of stainless steel immersed in molten salt, there is little information regarding the dynamic erosion behavior at different flow rates of molten salt. Recent papers concerning stainless steel immersed in different mixtures of molten salt reported that pitting type corrosion occurs on the material's surface. Pitting corrosion of stainless steel is a critical form of corrosion in engineering structures and most equipment fabricated from stainless steel fail due to pitting. Moreover, the flow rates of molten salt could aggravate pitting corrosion. Therefore, the dynamic erosion behavior may be worse than static corrosion behavior. One specific goal of the current work is to address the question of molten salt velocity on corrosivity.

doi:10.18086/eurosun.2016.06.05 Available at http://proceedings.ises.org

2. System description

In order to research the dynamic erosion behavior of heat exchanger tubes at high temperature due to molten salt, the author independently designed and established a high temperature molten salt erosion experimental system, as shown in Fig. 1 and Fig. 2.

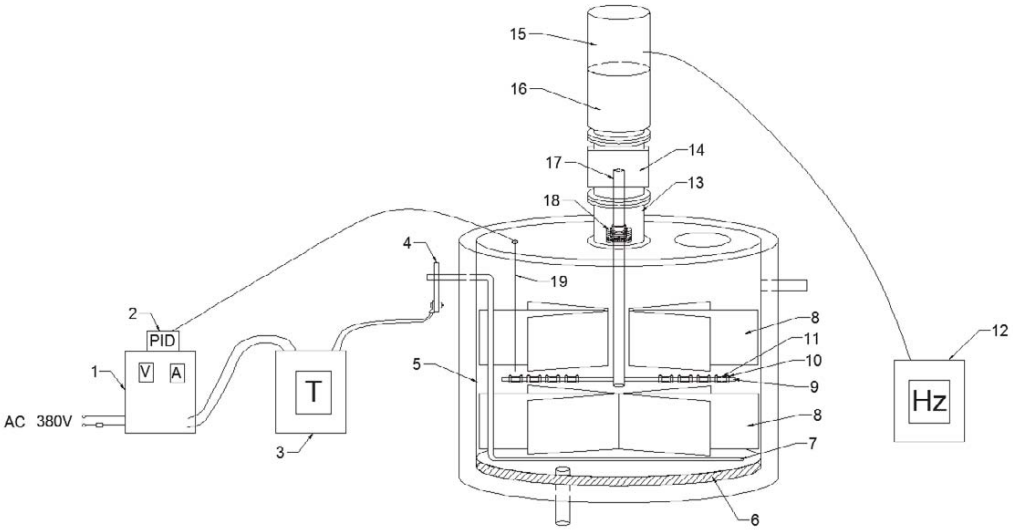

Fig. 1: Experimental system diagram 1：SCR voltage regulator；2：PID regulator；3：transformer；4：electrode plate；5：molten salt storage can；6：fire brick；7：heating element； 8：baffle；9：agitating shaft；10：ferrule ；11：experimental test；12：inverter；13：metal stent；14：reducer；15：encoder；16：motor；17：motor shaft；18：coupling；19：thermocouple

Fig. 2: Experimental system picture

The high temperature molten salt erosion experimental system consisted of an electrical heating system and erosion system. The electrical heating box was made of thick stainless steel for the internal surface, a middle layer filled with insulating cotton and an external surface containing an iron sheet. A layer of firebricks was spread on the bottom of electrical heating box. Two terminals of heating tubes were placed on the firebrick directly by welding with electrical heating plates. Ceramic tubes acted as insulators between the extension of the heating tube and electrical heating box. The transformer was connected with a silicon controlled voltage regulator by cable. One side of the cable was connected with electrical heating plates by four screws; the other side was link with a transformer. The silicon controlled voltage regulator includes a voltmeter,

amperage meter and PID controller. PID controller adjusted the output current from the silicon controlled voltage regulator in real time and controlled the heating power of the entire system by receiving a temperature signal from the sensors. The other side of the silicon controlled voltage regulator was linked to a 380 V alternating current by cable connections, which were installed with an electrical leakage protector to prevent short-circuiting. The erosion system was comprised of a motor shaft with accessory components. One side of the motor shaft was immersed in molten salt and installed as an agitating shaft. Coupons were installed on the agitating shaft according to the expected design distance are shown in Fig. 3. Both sides of the coupons were locked by card sleeves to prevent rolling while the agitating shaft was moving.

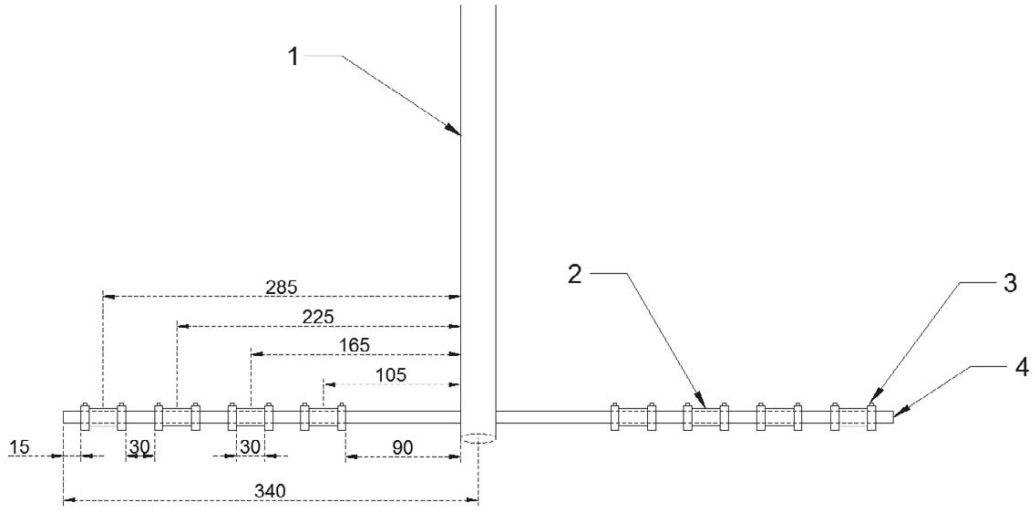

Fig. 3: Testing section distributions

1：motor shaft；2：experiment test；3：ferrule；4：agitating shaft

A coupling was installed on an extension from the motor shaft's electrical heating box. The upper side of the coupling was connected with the motor shaft using a keyway structure and a thrust bearing supported the bottom side. The motor shaft was connected with a reducer. The other side of the reducer was connected to a motor. The top of the motor was set up with an encoder, which was linked to a frequency converter, by signal wires. Baffles were installed on both sides of the agitating shaft in the electrical heating box in order to decrease the effect of turbulent flow in the vertical direction. The rotation speed of the motor was controlled by adjusting the operation panel of the frequency converter. This control allowed us to simulate the erosion behavior of stainless steels at different velocities of molten salt. In this experiment, the rotated speed of motor was set to 100 $r \cdot min^{-1}$, moreover the calculated velocities of each coupon are reported in Table 1. For maintaining precise experimental temperature, the thermocouple was installed on the same flat surface with the coupons.

Tab. 1: Locations and velocities of coupons

Number	Radius(m)	Velocity($m \cdot s^{-1}$)
1	0.105	1.099
2	0.165	1.727
3	0.225	2.355
4	0.285	2.983

Based on the commercial applications of the heat exchanger, we chose two types of stainless steel (SS) as coupons: 304SS and 321SS. The coupons, measuring approximately 30 mm × 25 mm× 3 mm in thickness, were cut from stainless steel tubes, polished, cleaned, alcohol rinsed, and weighed prior to immersion in salt. Two specimens of each alloy were immersed at 500 ºC and removed from nitrate mixtures at intervals of 168, 336, 504, and 720 hours for examination and analysis. Before starting the analysis the samples were washed

in distilled water, and cleaned ultrasonically in alcohol. The coupons were weighed after immersion to measure loss due to erosion process.

3. Data collection and discussion

Corrosion kinetics refers to the variable quantity of coupons per unit area in the experimental process. This study provides descaled mass loss measurements per unit area after conducting analysis and calculations. Mass loss measurements are an easy and direct way to represent the erosion behavior. Dissolvability of corrosion products and corrosion product adsorption onto coupons were not considered. Next, values of M are established using the descaled mass loss of metal alloys according to Equation. 1.

$$M = \frac{W_0 - W_1}{S} \qquad \text{(eq. 1)}$$

In Equation 1, M is the descaled mass loss of coupons per unit area. W_0 and W_1 represent the original mass and the post-experiment mass of coupons, respectively, and S is the surface-area of coupons. In this case, the value of S is 23.55 cm^2.

Adding the time factor to the Equation 1, the descaled mass loss of coupons per unit interval (erosion rate) is calculated according to Equation. 2.

$$V = \frac{W_0 - W_1}{S * t} \qquad \text{(eq. 2)}$$

In Equation 2, V is the erosion rates of coupons and t is the erosion time.

Fig. 4 is a plot of the average mass loss data versus time for 304SS based on different molten salt velocities. The mass losses were between 1.08 and 1.76 mg/cm^2 after 720 hours of erosion. The kinetics appear closely to follow parabolic rate laws initially and later become linear after prolonged exposures. In the absence of uniform erosion kinetics for the entire duration of coupon immersion, a conservative approach based on a linear extrapolation of the data seems warranted for estimating erosion-induced metal loss over longer timescales. For 500 ºC isothermal exposures, such linear extrapolations yield annualized mass losses of 12.96-21.12 mg/cm^2. We emphasize that these estimates are based on the flow velocity of molten salt used in this experiment.

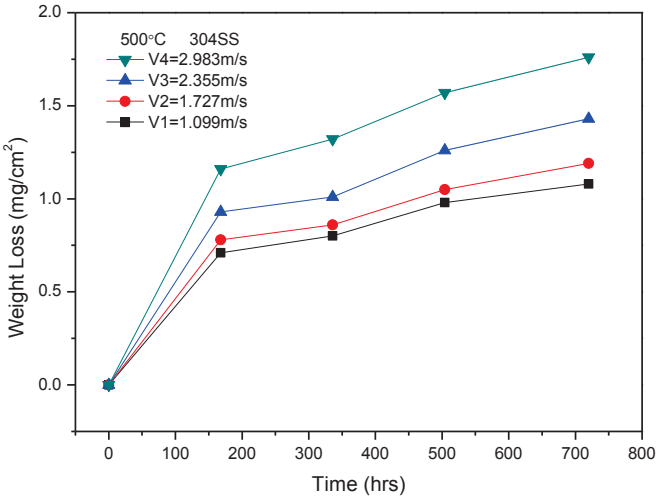

Fig. 4: Descaled weight loss measurements for 304 stainless steel specimens exposed to nitrate salt mixtures at 500 ºC

Based on Fig. 5, mass loss rate curve can be clearly observed. Mass loss velocities were $6.9 \cdot 10^{-3}$ mg·cm^2·h^{-1} after 168 hours and $2.4 \cdot 10^{-3}$ mg·cm^2·h^{-1} after 720 hours with a molten salt flow velocity of 2.983 m/s. Therefore, we hypothesize that steel erosion is based on a high corrosion rate at the beginning of the experiment and decreases slightly as time elapses. The erosion rate then became constant and dropped to a minimum erosion rate. The corrosion is possibly due to chemical or electrochemical processes that take place on the surface of the material. The electrochemical reaction is reduction and oxidation or can be simplified as a redox coupled reaction. Metal and alloy were used to form an oxide layer on the metal surface in air. The oxide layer is responsible for protecting the surface and retarding diffusion of oxidants to the reaction interface of the metal or alloy. The 304 stainless steel, with chromium and iron ions, tends to form Cr_2O_3 and Fe_2O_3 as its protective oxide layer. After a period of time, the coupons are immersed in molten salt, and anions will gather at points on the surface of coupons; moreover, certain points have negative potential. Electrons will move between certain anions points and their surroundings due to the potential difference, as if forming primary cells. The Cr_2O_3 and Fe_2O_3 of the protective oxide layer and iron atoms will exchange in an ionic state dissolved in molten salt. This reaction can induce pitting type erosion and cause an interruption or breakdown of the protective oxide film on the surface of the metal. The high corrosion rate at the beginning is likely due to impurities on the surface of coupons, such as carbon, which are prone to induce the redox reaction. After the conclusion of impurity reactions, the erosion rate is reduced with time. We hypothesize that the minimum erosion rate is achieved once the erosion rate is equal to the protective oxide layer self-regeneration.

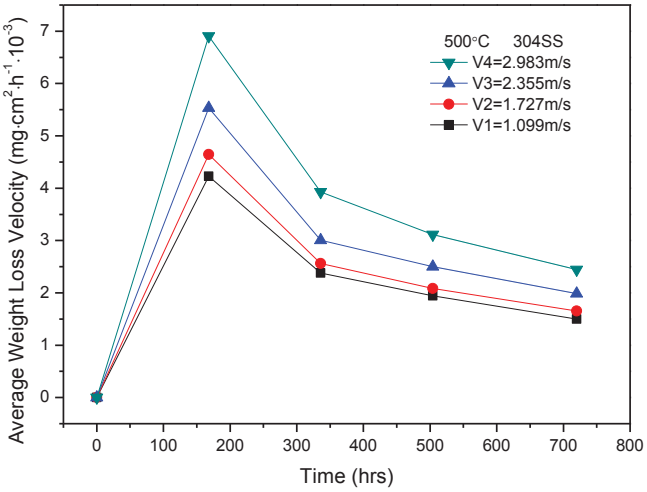

Fig. 5: Descaled weight loss velocity measurements for 304 stainless steel specimens exposed to nitrate salt mixtures at 500 ºC

Descaled mass loss measurements for 321SS coupons removed from nitrate salt mixtures at different flow velocities and 500 ºC are presented in Fig. 6. The mass losses range from 0.78 to 1.29 mg/cm^2 after 720 hours of immersion. Overall, 321SS exhibited more effective erosion resistance compared to 304SS. The mass loss data for 321SS reveal differences due to titanium. The 321 stainless steel has chromium, titanium and iron ions, which form Cr_2O_3, Ti_2O_3 and Fe_2O_3 as its protective oxide layer. According to standard electrode potentials shown in Table 2, the standard electrode potential of chromium is higher than that of titanium and the standard electrode potential of iron is highest of the three elements.

Tab. 2: Standard electrode potentials (25 ºC, 101.325kPa)

Number	Electrode process	Standard electrode potential(V)
1	Fe^{3+}+3e═Fe	-0.037
2	Cr^{3+}+3e═Cr	-0.744
3	Ti^{3+}+3e═Ti	-1.37

The higher the standard electrode potential element, the stronger its ability to capture electrons in the element's oxidation state. The Cr_2O_3 and Fe_2O_3 conduct electrochemical reaction captures electrons when the accumulation of ionic potential on the surface of coupons is higher than the equilibrium potential of chromium. This reaction deteriorates the protective oxide layer. However, this potential is too low for Ti_2O_3 to respond. The Ti_2O_3 electrochemical reaction proceeds when the accumulation of ionic potential on the surface of coupons is higher than the equilibrium potential of titanium. Therefore, the protective oxide layer of titanium has a more effective erosion resistance performance.

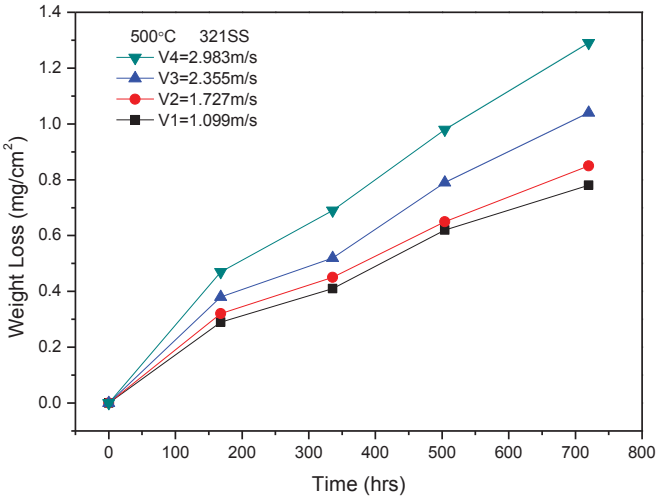

Fig. 6: Descaled weight loss measurements for 321 stainless steel specimens exposed to nitrate salt mixtures at 500 ºC

The descaled mass loss rate data for 321SS due to molten salt at different flow velocities and 500 ºC are shown in Fig. 7. Mass loss rates were $2.8 \cdot 10^{-3}$ mg·cm^2·h^{-1} after 168 hours and $1.8 \cdot 10^{-3}$ mg·cm^2·h^{-1} after 720 hours at 2.983 m/s molten salt flow velocity. The erosion rates curve for 321SS also generally shows slower rates after the initial high erosion rate. On the whole, the lower erosion rates for 321SS coupons than that of 304SS coupons potentially demonstrates that 321SS erosion resistance is stronger than 304SS erosion resistance.

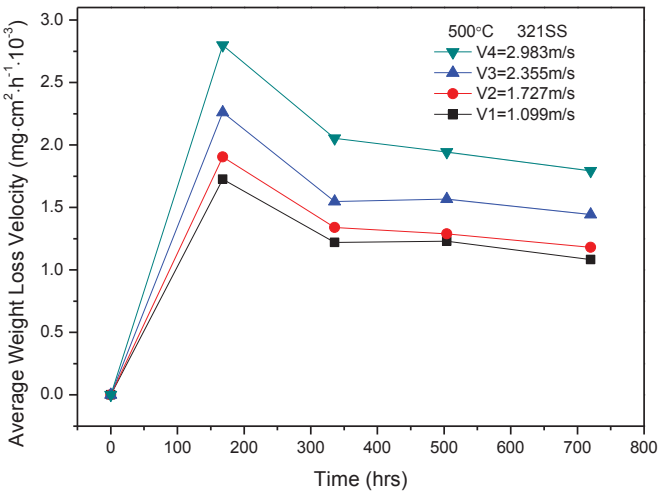

Fig. 7: Descaled weight loss velocity measurements for 321 stainless steel specimens exposed to nitrate salt mixtures at 500 ºC

4. Conclusions

The 300 series stainless steels are the most important materials to be used in solar thermal applications. The experimental data presented in this study indicate that flow velocities and temperature of molten salt play important roles in the erosion process of stainless steel. For the two sets of coupons made from different types of stainless steel, both rate of mass losses increased as flow velocities increased. However, erosion rates for SS321 were less sensitive to molten salt flow velocities than that of 304SS, due to the presence of titanium, which provides a protective oxide layer on the surface. The erosion kinetics of SS304 present a parabolic tendency, while that of SS321 exhibit approximately a linear one. Future work on the influence of different molten salt compositions on erosion behavior is warranted, in order to further develop an understanding of erosion behavior of 304SS and 321SS.

5. References

R. W. Bradshaw and R. W. Carling., 1987. A Review of the Chemical and Physical Properties of Molten Alkali Nitrate Salts and Their Effect on Materials Used for Solar Central Receivers, Sandia National Laboratories.

Cristina Prieto, Laia Miró, Gerard Peiró, Eduard Oró, Antoni Gil, & Luisa F. Cabeza, 2016, Temperature Distribution and Heat Losses in Molten Salts Tanks for CSP Plants, Solar Energy, Vol. 135, 518–526

Cabeza, L. F., & Mehling, H., 2003. Review On Thermal Energy Storage With Phase Change: Materials, Heat Transfer Analysis And Applications., Vol. 23, pp. 251-283

I.B. Singh, 1995, The Influence of Moisture on the Oxidation Rate of Iron in NaNO3 and KNO3 Melts, Corrosion Science, pp. 1981–1989

Brashaw, R. W., & Siegel, N. P., 2008. Molten Nitrate Salt Development for Thermal Energy Storage in Parabolic Trough Solar Power System, 1-7.

Ebner, M. A., Sharpe, P., & Sharpe, P. 2010. Engineering Database of Liquid Salt Thermophysical and Thermochemcal Properties Engineering Database of Liquid Salt Thermophysical.

Raade, J. W., Padowitz, D., & Vaughn, J., 2011. Low Melting Point Molten Salt Heat Transfer Fluid With Reduced Cost. I.

S. Guillot, A. Faik, A. Rakhmatullin, J. Lambert, E. Veron, P. Echegut, C. Bessada, N. Calvet, X. Py, 2012, Corrosion Effects Between Molten Salts and Thermal Storage Material for Concentrated Solar Power Plants, Applied Energy, pp. 174–181

F. Javier Ruiz-Cabañas, Cristina Prieto, Rafael Osuna, Virginia Madina, 2016, Corrosion Testing Device for In-situ Corrosion Characterization in Operational Molten Salts Storage Tanks: A516 Gr70 Carbon Steel Performance under Molten Salts Exposure, Solar Energy Materials and Solar Cells, Vol 157, 383-392

Fontana, M. G. and Green, N. D, 1967. Corrsion Engineering. New York, McGraw-Hill. 51.

Jongnotte, B. J., 2007. Stainless steel in architectural construction, beautiful but delicate.

Ma, F., 2012. Corrosive Effects of Chlorides on Metals, 178.

Wei-Jen Cheng, Ding-Jhih Chen, Chaur-Jeng Wang, 2015, High-temperature Corrosion of Cr-Mo Steel in Molten LiNO3-NaNO3-KNO3 Eutectic Salt for Thermal Energy Storage, Solar Energy Materials and Solar Cells, Vol 132, 563-569

I.B. Singh, 1992, Influence of Temperature and Sulphate Ion on Corrosion of Mild Steel in Molten NaNO3, British Corrosion Journal, pp. 299–304

I.B. Singh, 1993, The Effect of NaCI Addition on the Corrosion of Mild Steel in NaNO3 Melt, Corrosion Science, pp. 1733–1742

Taltavull, C., Shi, Z., Torres, B., Rams, J., & Atrens, A. 2014. Influence of the chloride ion concentration on the corrosion of high-purity Mg, ZE41 and ZA91 in buffered Hank's solution. Journal of materials science. Materials in medicine, 329-45.

A.G. Fernández, H. Galleguillos, & F.J. Pérez, 2014, Thermal Influence in Corrosion Properties of Chilean Solar Nitrates, Solar Energy, Vol 109, 125–134

Geoff McConohy, Alan Kruizenga, 2014,Molten Nitrate Salts at 600 and 680 °C: Thermophysical Property Changes and Corrosion of High-temperature Nickel Alloys, Solar Energy, Vol 103, 242–252

R.W. Bradshaw, S.H. Goods, Corrosion Resistance of Stainless Steels During Thermal Cycling in Alkali

Nitrate Molten Salts, SAND2001-8518
R.W. Bradshaw, S.H. Goods, Corrosion Resistance of Nickel-Base Alloys in Molten Alkali Nitrates, SAND2000-8240.
S.H. Goods, R.W. Bradshaw, M.R. Prairie, J.M. Chavez, Corrosion of Stainless and Carbon Steels in Molten Mixtures of Industrial Nitrates, SAND94-8211.

07. Solar Thermal Collectors and Solar Loop Components

Conference Proceedings

EuroSun 2016
Palma de Mallorca (Spain), 11 – 14 October 2016

Performance Testing of a Solar Thermal Fruit Dryer – A Case Study to Reduce Food Waste in Mozambique

Viktor Döhlen[1], Gustaf Bengtsson[1], Randi Phinney[2] and L. Ricardo Bernardo[1]

1 Department of Architecture and Built Environment, Division of Energy and Building Design, Lund University, Lund, Sweden

2 Department of Food Technology, Engineering and Nutrition, Lund University, Lund, Sweden

Abstract

The purpose of this project is to investigate an innovative technology for sustainable preservation of juicy fruits in developing countries with the aid of simple solar thermal drying technology. Approximately five million tonnes of citrus fruit produced in Mozambique is annually wasted (FAOSTAT, 2015). A large solar energy potential and large fruit spoilage in Mozambique present the opportunity to implement a simple method for fruit preservation, combining solar thermal drying with a semipermeable membrane bag containing fruit juice. A small-scale indirect passive solar air dryer for drying the membrane bags was constructed and evaluated in terms of drying flux as a function of temperature, relative humidity and air flow rate. Measurements were initially carried out in the laboratory and later complemented with a field study in Mozambique. The dryer achieved a temperature interval that was required for high quality fruit drying and lowered the relative humidity. However, it was further found that air flow passing over the bags acted as an important parameter in the drying meaning that an increased air flow rate increased the drying flux to a larger extent than first assumed. The findings provide insight on the drying process and on how to improve the design of the solar air dryer.

Keywords: *Solar Thermal, Indirect Solar Dryer, Semipermeable Membrane, Fruit Drying, Food Waste, Development Project.*

1. Introduction

Fruit is abundant in Mozambique, both farmed and wild, yet much of it spoils post-harvest or is never even picked due to the large amounts that ripen during a short harvesting season. Long-term storage possibilities are uncommon since industrial preservation technologies require large amounts of clean water and power – something limited in rural Mozambique (Phinney et al., 2015). One contributing solution to this problem could be the combination of solar thermal dryers with a newly developed breathable membrane bag to facilitate drying of fruit juices and purées in Mozambique. This means that juicy fruits, such as oranges and tangerines, that are difficult to dehydrate using traditional open-air sun drying, could also be dried. Preservation with the membrane bags only requires suitable ambient conditions since the drying process is largely driven by a lower relative humidity in the air surrounding the bags. The objective of using a solar dryer is to protect the bags from external disturbances and supply the process with more heat than the ambient conditions can provide (Ekechukwu and Norton, 1997), increasing the temperature and thus decreasing the relative humidity. This technological combination results in a system independent of external electric power and large amounts of clean water and thus is more suitable for rural areas lacking developed infrastructure (Ekechukwu and Norton, 1997; Otte, 2014). To ensure fruit preservation of high quality, the drying has to be performed using an adequate temperature interval. The aim of the research is to construct a solar dryer for enhancing the drying of the membrane bags and to understand the underlying mechanisms behind this drying process so that future dryers coupled with membrane bags can be properly optimised.

doi:10.18086/eurosun.2016.07.13 Available at http://proceedings.ises.org

2. Theory

2.1. Theory behind the technique

Drying is the process of removing water from a product. In this study, drying of a liquid product was achieved using a membrane bag and a technique called Solar Assisted Pervaporation (SAP) (Phinney et al., 2015). Pervaporation is a process in which a non-porous semi-permeable membrane is used to separate one or more chemical species from one or more other chemical species. The species that diffuses through the membrane also has an affinity for it, or in other words the species "wets" the membrane (Néel, 1991). In the case of Solar Assisted Pervaporation, the membrane is hydrophilic and water molecules are able to diffuse through the void spaces of the polymer molecules that make up the membrane. The membrane acts as a selective barrier, letting water vapour molecules through while keeping the liquid water and other nutrients inside the bag (Phinney et al., 2015).

The SAP process is driven by a water vapour partial pressure difference across the membrane, where the partial pressure is a function of temperature (i.e. it increases with increasing temperature) (Pervatech BV, 2014). Inside the bag, the initial water vapour partial pressure is close to the saturation pressure whereas outside the bag, the partial pressure corresponds to the relative humidity (RH) of the surrounding air. If the RH of the surrounding air is less than 100%, a water vapour partial pressure gradient across the membrane will exist and drying will proceed (Saravacos and Kostaropoulos, 2002). Solar energy enhances the process by supplying the latent heat of evaporation and reducing the RH of the air surrounding the bag. As the second law of thermodynamics states: diffusion of a species will occur as long as a difference in saturation exists, striving for an equilibrium (Cengel and Boles, 2011).

The amount of mass transferred from the bag to the surrounding air over time, $\dot{m}$ (kg·s^{-1}), due to diffusion through the membrane is a function of the overall mass transfer coefficient, K (kg·m^{-2}·s^{-1}·Pa^{-1}), the total membrane surface area, A_s (m^2), and the difference in water vapour partial pressure (with units of Pa) on the inside ($p_{w,sat\ @\ T_1}$) and outside ($p_{w,\infty\ @\ T_2}$) of the bag, where T_1 is the surface temperature and T_2 is the surrounding air temperature in degrees Celsius (Bergman et al, 2007). The heat and mass transfer phenomena taking place can be compared to the case of an open dish with water where in both cases, water vapour is assumed to be an ideal gas. Since RH is equal to the ratio between $p_{w,\infty}$ and $p_{w,sat}$ at a given temperature, the RH on the inside of the bag is 100% and in the surrounding air is $p_{w,\infty\ @\ T_2}$ divided by $p_{w,sat\ @\ T_2}$ and then multiplied by 100 (note: $p_{w,sat\ @\ T_1}$ and $p_{w,sat\ @\ T_2}$ are only equal if T_1 and T_2 are equal, which is not always the case). The main differences between our case and that of an open water dish is a resistance provided by the polymer membrane (which reduces K), and that the open dish has only one drying surface whereas the bag has two (which means A_s is twice as large for a bag of the same length and width). Equation 1 shows how the mass transfer rate is affected by the mass transfer coefficient, surface area and water vapour partial pressure. Mass transfer flux is defined as $\dot{m}/A_s$ and is the quantity referred to in the remainder of the paper.

$$\dot{m} = K \times A_s \times (p_{w,sat\ @\ T1} - p_{w,\infty\ @\ T2}) \qquad \text{(eq. 1)}$$

2.2. Temperature as a function of flow rate

As relative humidity is a function of temperature, the speed of water removal in the dryer is dependent on temperature. In addition, the quality of the end-product (e.g. related to vitamin losses) requires a set temperature interval. The small-scale solar thermal dryer's gained energy over time, absorbed by the collector, can be calculated by measuring global irradiance, G (W·m^{-2}), for an angle of incidence normal to the glass of the dryer, on the collector area, A_c, (m^2). A thermal efficiency ($\eta_{thermal}$) is introduced to include the heat losses, the material properties and the optical losses into account. This efficiency only serves as a rough estimate on how much energy is put to use in the dryer as hot air. An equation for the power transfer from the sun to the air can be written as:

$$\dot{Q}_{gain} = G \times \eta_{thermal} \times A_c \qquad \text{(eq. 2)}$$

The amount of useful energy over time can also be calculated by looking at the collector as a control volume with a temperature difference over the absorber area.

$$\dot{Q}_{gain} = A_{cs} \times v \times \rho \times c_p (T_{out} - T_{in}) \qquad \text{(eq. 3)}$$

where A_{cs} (m^2) is the cross section area, v is the flow rate normal to the cross section, ρ ($kg \cdot m^{-3}$) is the fluid's density, C_p ($J \cdot kg^{-1} \cdot K^{-1}$) is the specific heat capacity at a constant pressure, T_{in} is the temperature of the air entering the collector and T_{out} is the outlet temperature of the collector. The velocity varies spatially due to the flow profile in the collector. Therefore, a mean has to be calculated, based on reference measurement points over the cross section width, from measurement standard SS-EN-1505 (Johansson and Svensson, 1998). Combining equations 2 and 3 and isolating T_{out}:

$$T_{out} = T_{in} + \frac{G \times \eta_{thermal} \times A_c}{A_{cs} \times v \times \rho \times C_p} \qquad \text{(eq. 4)}$$

Which results in the outlet temperature as a function of the flow rate in the dryer. The flow rate can be adjusted by regulated the air outlet opening size.

3. Method

3.1. Construction of the solar dryer

A prototype small-scale solar thermal dryer was constructed in Lund before the field study was conducted. The result is presented in Figure 1 with a schematic illustration of the basic technique of natural ventilation, along with dimensions. The implementation of the solar dryer would take place in a developing country, something the design of the dryer had to account for. This means that complexity had to be minimized and user friendliness maximized. Furthermore, the design of the solar dryer had to meet the posed criteria of temperature and size. A temperature interval defined by a lower temperature of 50 ºC to prevent microbial growth and a higher limit of 65 ºC to minimise degradation of ascorbic acid was set as desirable (Rab et al, 2015). The size, presented in Table 1, is limited to a small-scale solar thermal dryer, possible to transport on conventional flights.

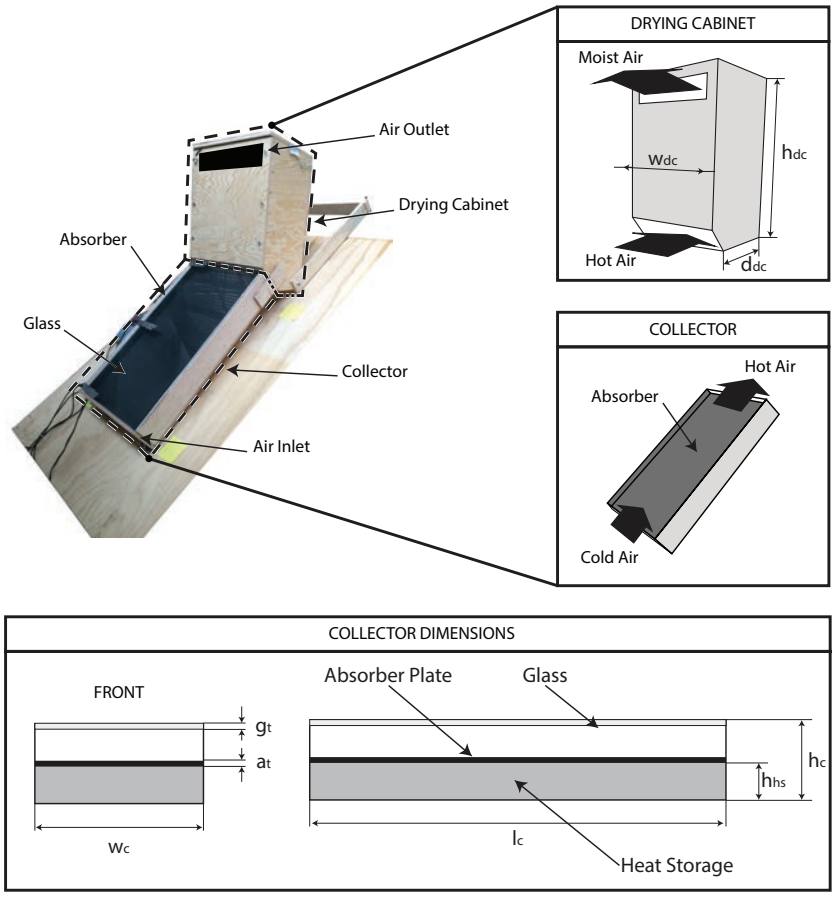

Fig. 1: Picture of the constructed solar dryer, with a schematic illustration of the collector, to illustrate the dimensions of the dryer.

Tab. 1: Table of the small-scale solar thermal dryer's dimensions.

Collector Parts	**Dimensions**
Length, l_c	0.700 m
Outer width, w_o	0.424 m
Width absorber plate, w_a	0.376 m
Height collector, h_c	0.082 m
Distance absorber-glass, $d_{a\text{-}g}$	0.035 m
Height heat storage, h_{hs}	0.035 m
Thickness absorber, a_t	0.012 m
Thickness glass, g_t	0.003 m
Drying Cabinet Parts	
Height, h_{dc}	0.500 m
Width, w_{dc}	0.400 m
Depth, d_{dc}	0.200 m

3.2. Measurement setup

The semi-permeable bag consists of a breathable polymer that is permeable to water vapour but not liquid water, as stated in the theory section. This means that during drying, all of the liquid water is contained in the bag, while water vapour is able to diffuse through the membrane and then escape to the surroundings. For a more detailed description of the procedure and SAP technique, please refer to Phinney et al., 2015. Previous

testing from the mentioned study with a bag prototype suggested a constant drying flux is achieved at the beginning of drying if the product to be dried is very watery (e.g. fruit juice). Wind speed was not found to play a crucial role in previous testing due to the nature of the equipment used where the air flow was able to pass horizontally over both sides of the bag. Figure 2 presents a picture of the membrane bags filled with water. The height of the bags are 19 cm, and width of 7.5 cm. Thickness varied depending on different amount of water in the bags, between 2 to 4 cm.

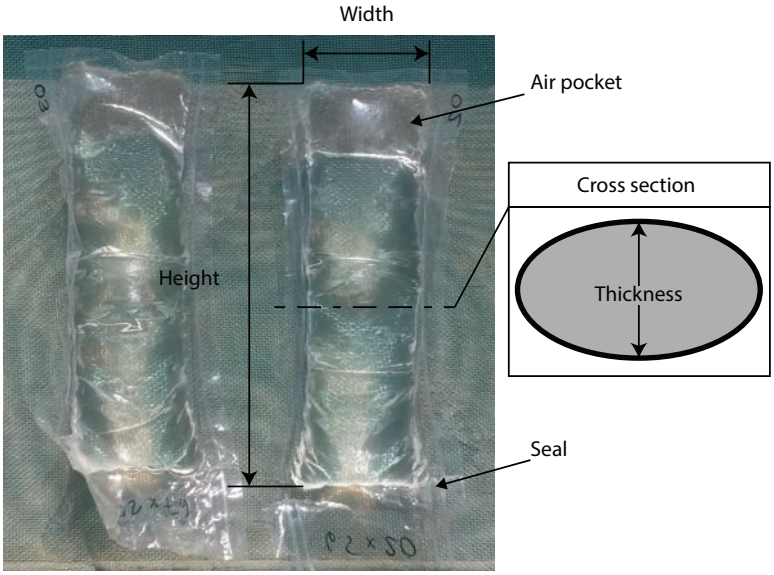

Fig. 2: Picture of the transparent membrane bags filled with water that were dried on-site in Mozambique..

The measurement equipment was setup to gather data on temperatures in the collector and drying cabinet, the relative humidity in the ambient environment and inside the drying cabinet, mass loss, wind speed and irradiance. The equipment was installed at the following points illustrated in Figure 3. The measurement points used in this article are points number 3, 9 and mass loss found by the hand scale represented at point 12.

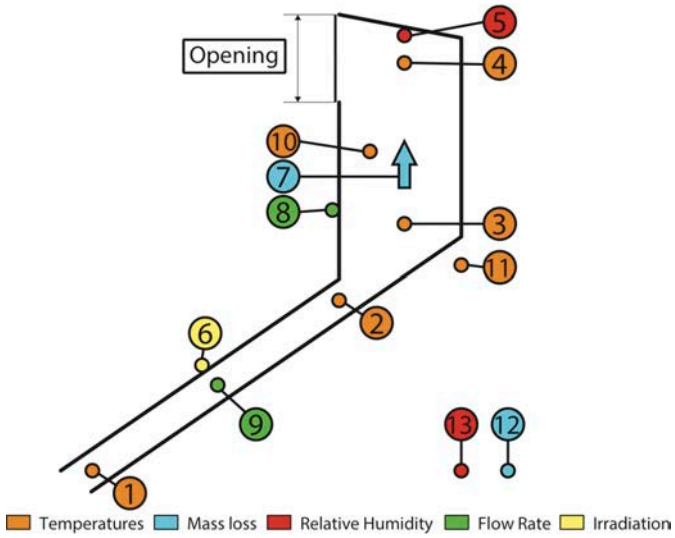

Fig. 3: A schematic figure of the measurement setup for the field testing.

3.3. Performance testing

The performance tests consisted of investigating the drying flux ($\dot{m}/A_s$) of the bags in the dryer over the course of a day. The separate tests are referred to as Run 1 to 6. The test runs begun by weighing the bags before they were inserted in the drying cabinet and ended by weighing after removal from the same space, in order to identify a linear representation of the mass loss over time per unit surface area. All membrane bags used were rectangular with dimensions of 0.19 ± 0.005 m times 0.075 ± 0005 m. The bags consisted of two sides, resulting in a total active surface area of 0.0266 ± 0.0025 m^2. The bags were filled with water, not fruit juice, since the aim of the project was to investigate how the conditions in the dryer affected the drying flux, and water was deemed easier to handle than fruit juice. The drying process of water in the bags is similar to the first stage of drying juice, otherwise known as the constant rate or constant flux period, when the water at the surface of the juice is still plentiful and internal mass transport is not yet dominating (Phinney et al., 2015).

The test aimed to reach a stable input of solar energy, by rotating the dryer along the solar azimuth angle every hour and regulating the temperature and air-flow in the dryer by adjusting the opening of the air outlet. These parameter changes are presented in Table 2. The resulting drying fluxes were later analysed to identify how drying flux could relate to temperature and air flow rate regulation in the dryer. The drying flux of the bags was later compared to a reference bag placed out in the open beside the dryer to evaluate the relative speed.

Tab. 2: Table representing the approximated amount of time each air outlet opening was used during Runs 1-6.

Opening /%	Run 1	Run 2	Run 3	Run 4	Run 5	Run 6
0	2 h					
16	2 h	1 h		3.5 h		
33	1 h	2 h		2 h		
50		2.5 h	4 h		5.25 h	3.5 h
100			3 h			2.5 h

3.4. Design changes

The dryer's design was examined after Runs 1, 2 and 3 and then the drying cabinet's volume was decreased by reducing the depth to 7 cm instead of 20 cm to increase the flow rate through the drying cabinet, illustrated in Figure 4. The hypothesis was that an increased flow rate passing the bags would increase the drying flux. The bag was hung vertically to fit in the smaller space, leading to a change in the characteristic length of flow passing over the bag.

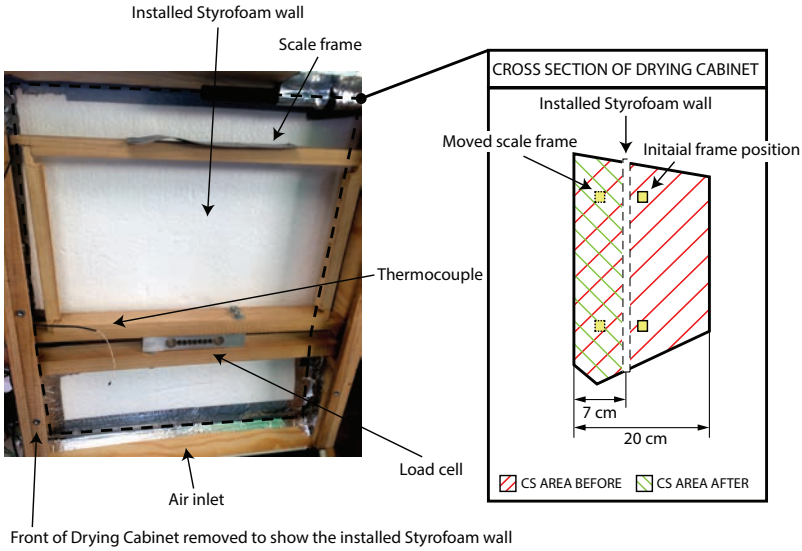

Fig. 4: Illustration of how the design change decreased the cross-sectional area of the drying.

4. Results

Table 3 presents measurement results of the drying flux of the bags as a function of the mean temperature (measurement point 3) in the drying cabinet and the air flow rate passing over the bags. Runs 1 to 6 are shown and compared to the reference bag dried at outdoor ambient conditions. Results for the drying flux are averaged over the course of a day. The results are presented ranging from the lowest to highest percentage of air outlet opening, where the first three runs represent the original design and Runs 4-6 represent the implemented design change with a smaller cross-sectional area. The air flow velocity is not corresponding entirely as it is higher for run 5 than run 6, which can be due to ambient weather conditions. Another anomaly is the drying flux for Run 2, which is not following the trend, since three bags were present in the dryer as opposed to the other runs where only one bag was present. Figure 5 and Figure 6 present the results in a graphical manner, where the values for the drying flux is plotted over air flow velocity. A linear approximation is introduced to illustrate the relationship between these variables. To be noted, the drying flux inside the dryer system never exceeded that of the reference bag, as presented in Table 3, but the run with the highest air flow rate reached approximately the same value.

Tab. 3: The results are presented ranging from the lowest to highest percentage of air outlet opening.

Test	Opening /%	Time	Drying Flux /g·m^{-2}·h^{-1}	Temperature /ºC	Air Flow Velocity /m·s^{-1}
Run 1	16 & 0	10:38-15:39	182.3	45.8	0.0190
Run 2	33 & 50	09:47-15:13	142.2	49.8	0.0436
Run 3	50 & 100	09:20-16:03	247.3	46.6	0.0783
Run 4	16 & 33	10:10-15:43	265.7	44.3	0.0871
Run 5	50	10:31-16:07	359.0	45.1	0.157
Run 6	50 & 100	10:23-16:41	369.7	50.2	0.144
Reference bag	N/A	N/A	372.0	30.0	N/A

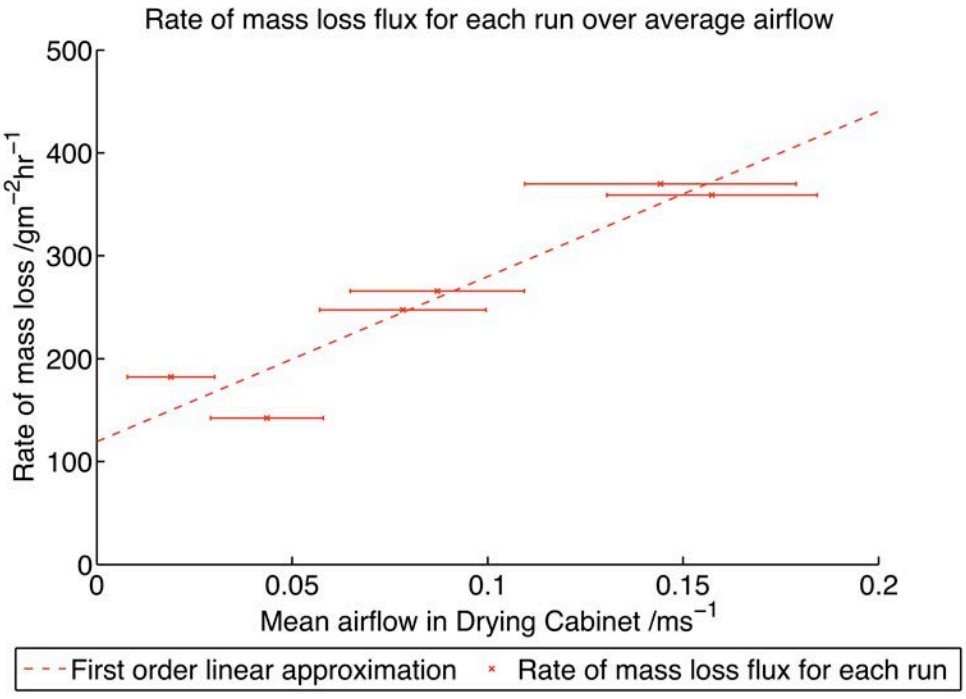

Fig. 5: Graphical representation of the drying flux versus air flow velocity from the values represented in Table 3 to identify the relationship between drying flux and flow rate. The points in Figure 5 and 6 are from corresponding runs.

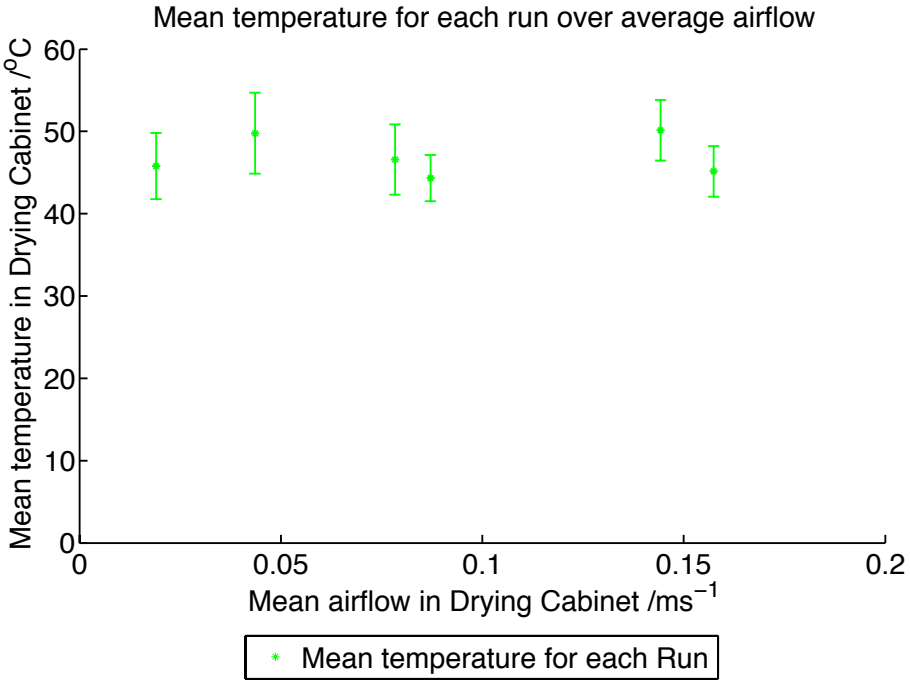

Fig. 6: Graphical representation of the temperature versus air flow velocity from the values represented in Table 3. The points in Figure 5 and 6 correspond, and with a small variation in temperature, a clear relationship between drying flux and flow rate is identified.

5. Measurement Uncertainties

Measurements with the hand anemometer to measure the air flow rate in the collector had complications due to fluctuating values with random variations in intervals. The fluctuation was affected by external wind which can create regions of turbulence and affect the measurements. The anemometer can only operate in laminar regions (Operation and Service Manual, Model 8330 VELOCICHECK 1994). The air flows measured in the collector were low, and small variations in wind led to large relative errors.

6. Discussion & Conclusion

6.1. Discussion

As can be seen in Table 3, the mass loss fluxes in the solar dryer never exceeded that of the reference bag. When this was discovered, during Runs 1 to Run 3, the driving forces of the drying process that differed between the dryer and ambient environment were analysed in order to identify the limiting factor on mass transport for the system. The temperature in the drying cabinet had increased by around 20 degrees compared to the ambient temperature, as seen in Table 3, and the relative humidity was lowered from 59.9 % (ambient) to 26.3 % (drying cabinet) on the 11th of May. This is one data point logged and the relation is similar during all performed tests. This corresponded with our predicted requirements for drying, but effectively it showed little effect. The most crucial parameters that differed between the drying cabinet and ambient environment were the direct sunlight on the reference bag in the sun and ambient wind passing over all reference bags. Direct sunlight was deemed to play a certain role in increasing the temperature of the reference bag. However, since it is transparent, it was not thought to have increased the temperature more than the 20

degrees which was the case in the drying cabinet. Ambient wind, or air flow passing over the bags, was thus investigated further.

The increased airflow velocity had a positive effect on the drying flux, as the drying flux was doubled between Run 1 and Run 6 which can be seen in Table 3 and Figure 5. If we relate the drying flux to eq. 1 in the Theory section, this suggests that the limiting factor for mass loss inside the drying cabinet was the mass transfer coefficient K, which is the only parameter dependent on airflow velocity. When the flow rate was actively increased in later test runs, the results showed an increase in drying flux. A hypothesis we suggest is that the limiting factor was not the diffusion of water through the membrane during the simulated "constant rate drying period" (i.e. when the drying flux is normally constant at the beginning of juice drying). If this was the case, an increased temperature would have led to an increased diffusion as it is driven by the difference in partial pressure as a function of relative humidity on the different sides of the membrane. However, the problem faced was not getting water to the surface of the membrane, but rather removing the already surfaced water.

6.2. Conclusion

Higher temperatures and a lower relative humidity inside the solar dryer did not increase the drying flux to the level of the reference bag placed in ambient conditions where passing wind and direct sunlight were available. A drying flux of 247.3 $g \cdot m^{-2} \cdot h^{-1}$ was reached during Run 3 compared to the drying flux of 372.0 $g \cdot m^{-2} \cdot h^{-1}$ for the reference bag. The solar dryer seemed to be missing the capacity to remove the vapour from the surface of the bag to continue the pervaporation process through the membrane. One hypothesis is that the air flow velocity was limiting the drying. A design modification, increasing the flow rate by 100%, by decreasing the volume of the drying cabinet doubled the drying flux between Runs 1 and Run 6, from 182.3 $g \cdot m^{-2} \cdot h^{-1}$ to a drying flux of 369.7 $g \cdot m^{-2} \cdot h^{-1}$. The hypothesis of air flow rate acting as an active parameter during the beginning stages of drying using Solar Assisted Pervaporation with membrane bags seems to be correct, but further research should be done to confirm this. It was concluded that the drying flux in the cabinet increased with the increased air flow rate due to a smaller cross section area, while temperature was maintained around the lower limit of the required temperature interval and a lower relative humidity than ambient was achieved.

7. Acknowledgements

We direct a large thank you to all sources of inspiration and help we have received during the project. We would like to send a special mention to Dr. Henrik Davidsson, Dr. Pia Otte and Dr. Lucas Tivana. Your academic guidance and practical knowledge have contributed greatly to the work. We also direct a thank you to our financiers, Åforsk, Kapten Hanssons minnesfond, Bengt Ingeströms stipendiefond and the Espersen Foundation. It is with their generosity this project has been made possible.

8. References

Cengel, Y. A., Boles, M. A., 2011. Thermodynamics: An Engineering Approach, seventh ed. McGraw-Hill.

Ekechukwu, O.V., Norton, B., 1997. Review of solar-energy drying systems II: an overview of solar drying technology. Energy Conversion and Management. 40, 657-667.

FAOSTAT, Food and Agriculture Organization of The United Nations Statistics Division, 2015. Food Balance Mozambique. Accessed on 07/03/2016. http://faostat3.fao. org/compare/E

Bergman, T. L., Lavine, A. S., Incropera, F. P., DeWitt, D. P., 2007. Fundamentals of Heat and Mass Transfer, volume 1, sixth ed. Michigan: John Wiley.

Johansson, P., Svensson, A., 1998. Metoder för Mätning av Luftflöden i Ventilationsinstallationer. Byggforskningsrådet, Stockholm, Sweden.

Néel J., 1991. Introduction to Pervaporation, in Pervaporation membrane separation processes, R.Y.M. Huang, Ed. Amsterdam: Elsevier, pp. 1-109

Otte, P., 2014. Solar cooking in Mozambique an investigation of end-user's needs for the design of solar cookers. Energy Policy. 24, 366-375.

Paul, S. 2013. Introduction to Food Engineering. Academic Press.

Pervatech BV. 2014. Pervaporation: An Overiew Separation Technology Articles - Chemical Engineering - Frontpage - Cheresources.com. Accessed on 18/03/2016. http://www.cheresources.com/content/articles/separation-technology/pervaporation-an-overiew?pg=1

Phinney, R., Rayner, M., Sjöholm, I., Tivana L., Dejmek P., 2015. Solar Assisted Pervaporation (SAP) for Preserving and Utilizing Fruits in Development Countries., Third Southern African Solar Energy Conference, 11-13 May 2015.

Rab A., Sajid, N, M., Bibi, F., Jan, I., Nabi, G., Najia, K., 2015. Quality changes in heat treated sweet orange fruit during storage a tlow temperature. The Journal of Animal and Plant Sciences. 25, 661-668.

Saravacos G.D., and Kostaropoulos, A.E., 2002. Handbook of Food Processing Equipment, New York: Kluwer Academic/Plenum Publishers.

TSI –Incorporated. 1994. Operation and Service Manual, Model 8330 VELOCICHECK

Appendix: **NOMENCLATURE**

Table A1: Nomenclature used in the report

Quantity	Symbol	Unit
Specific heat capacity	C_p	J kg^{-1} K^{-1}
Density	ρ	kg m^{-3}
Mass transfer rate	$\dot{m}$	kg s^{-1}
Global Irradiance	G	W m^{-2}
Mass transfer coefficient	K	kg/ m^{-2} s^{-1} Pa^{-1}
Surface Area of bag	A_s	m^2
Collector Area	A_c	m^2
Relative Humidity	RH	%
Heat gained by collector	$\dot{Q}_{gain}$	W
Air flow rate	v	m s^{-1}
Inflow Temperature (collector)	T_{in}	ºC
Outflow Temperature (collector)	T_{out}	ºC
Thermal Efficiency	$\eta_{thermal}$	%
Partial pressure of water vapour on inside of the bag at surface temperature T_1	$p_{w,sat\ @\ T1}$	Pa
Partial pressure of water vapour on outside of bag at ambient temperature T_2	$p_{w,\infty\ @\ T2}$	Pa

Conference Proceedings

EuroSun 2016
Palma de Mallorca (Spain), 11 - 14 October 2016

A Fracture Mechanics Based Lifetime Assessment Approach for Polyamide used for Integrated Storage Collectors

Patrick R. Bradler[1], Joerg Fischer[1], Mathias Schlaeger[1], Gernot M. Wallner[1] and Reinhold W. Lang[1]

[1] Institute of Polymeric Materials and Testing, Johannes Kepler University of Linz, Linz (Austria)

Abstract

A novel test method simulating the superimposed mechanical, thermal and environmental service loads representative for single-loop integrated storage collectors (ICS) was developed. Engineering polyamide (PA) grades with glass fiber reinforcement, which are of high relevance for endcaps of steel-pipe ICS absorbers and all-polymeric absorbers and storage-tanks, were characterized on laboratory specimen level. An in-situ testing facility for fracture mechanics specimen was used on an electrodynamic testing machine. By in-situ characterization in hot water, a significant decrease in crack growth resistance compared to air (same temperature) was detected. For these specific loading conditions, an extrapolation to static loading was performed to better resemble the loading situation in the ICS and to calculate critical stress levels for cylindrical pipes.

Keywords: *integrated storage collector; polyamide; superimposed loading; lifetime assessment approach; fatigue crack growth kinetics*

1. Introduction

An objective in previous research projects (e.g. SCOOP – Solar Collectors made of Polymers) was to develop and implement advanced testing methods for the evaluation of the long-term behavior of polymeric materials for solar collectors under service relevant loading conditions (Wallner et al., 2004; Kahlen et al., 2010; Köhl et al., 2012; Geretschlaeger, 2015; Geretschlaeger and Wallner, 2016; Steffen et al., 2017). To fulfill the application requirements for pressurized integrated storage collectors, maximum internal pressures of 6 bar and maximum application temperatures of 90°C should be considered (Solecrafte, 2015). While in a previous paper, fatigue crack growth kinetics of PA under superimposed mechanical, thermal and environmental loads were described properly (Fischer et al., 2016), this paper deals with a lifetime assessment approach considering the previously determined most critical crack growth behavior. Special attention is given to an extrapolation procedure simulating a static loading case, as originally proposed for plastics pressure pipes (Lang et al., 2005).

2. Background

The entire discipline of fatigue crack growth (FCG) behavior in plastics is fundamentally based on the concept of linear-elastic fracture mechanics (Hertzberg and Manson, 1980; Lang, 1980; Lang et al., 1982; Hertzberg et al., 2013). The failure mechanisms are frequently described by two different regimes, the crack initiation and the subsequent crack growth regime (Lang et al., 1997; Haager et al., 2004).

Based on cyclic tests which allow an accelerated material characterization, the calculation of FCG kinetic curves is possible. In these FCG curves three different failure modes are apparent in a double logarithmic plot (see Fig. 1). Region I represents the threshold, region II the stable crack growth region typically obeying a power law (representing a linear increase in the double logarithmic scale), and finally region III which corresponds to unstable crack growth approaching ultimate failure.

doi:10.18086/eurosun.2016.07.05 Available at http://proceedings.ises.org

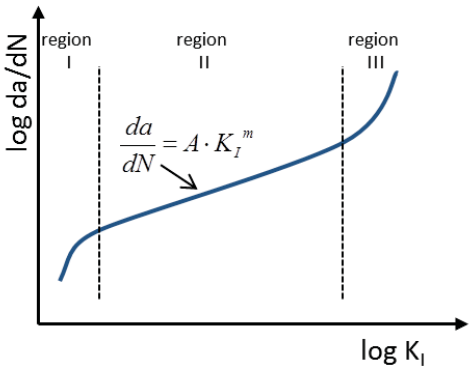

Fig. 1. Crack growth rate da/dN as a function of the stress intensity factor K_I.

However, for a lifetime prediction based on fracture mechanics, a static loading case representing creep crack growth is necessary. This requires a transformation of FCG data to static loading data with a procedure presented elsewhere (Lang et al., 2005; Frank et al., 2008; Frank et al., 2009). This procedure, in principle, also allows a prediction of lifetime of components, whereby a component and dimension dependent stress intensity factor K_I has to be simulated via finite element analysis.

3. Methodology and experimental

Materials

The test program was performed by using two semi-crystalline fiber reinforced polyamide (PA) grades. An overview of selected grade specific information as to the materials is given in Table 1. The grades are seen to vary in the glass fiber content as well as in the chemical composition. PA66-GF30 is an aliphatic PA, and PA6T/6I-GF50 is a semi-aromatic co-PA. Both material grades offer a high potential for the substitution of metals in integrated storage collectors.

Table 1. Materials with specific information

Material designation	Matrix polymer type	Glass fiber content	Commercial grade name	Manufacturer
PA66-GF30	Polyamide 66	30 w%	SCHULAMID® 66 GF 30	A. Schulmann GmbH, Germany
PA6T/6I-GF50	Polyamide 6T/6I-GF50	50 w%	Grivory HT1V-5 FWA	EMS-Chemie AG, Switzerland

Specimen and specimen preparation

The crack growth tests on the specimen level were conducted using compact-type (CT) specimens (see Fig. 2). The materials were first injection-molded to plates, which were then milled to the desired specimen geometry and subsequently notched with a razor blade for obtaining an initial crack. To cover the expected lower bound crack growth resistance of the specimens with a layered fiber orientation pattern caused by the injection molding process, the notched direction was chosen to be parallel to the main melt flow direction when injection molding the plates (Schlaeger, 2015; Fischer et al., 2016). Hence, the loading direction in these specimens is perpendicular to the main fiber orientation direction.

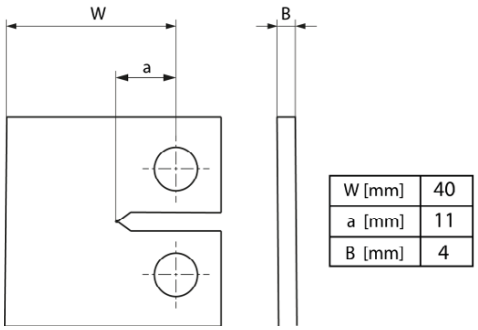

Fig. 2. Compact type (CT) specimen with test specific dimensions.

Fatigue testing and data reduction

Both PA grades were investigated in a previous research work (Fischer et al., 2016) as to their fatigue crack growth resistance under various, service relevant conditions. It has been shown that elevated temperature and liquid media are influencing and accelerating the failure kinetics of these PA-types (Hahn et al., 1982; Fischer et al., 2016). Hence, the testing conditions in this paper were chosen with a temperature of 80°C and deionized water (referred to as H_2O). In order to ensure water-saturation of grades tested in H_2O, a pre-conditioning procedure with a saturation time of 7 days in the testing-similar surrounding media was carried out (Schlaeger, 2015). To allow for extrapolation of cyclic crack growth data to static loading, the cyclic tests were performed with various R-ratios ranging from 0.1 to 0.7, with R being defined as the ratio between the minimum and maximum applied force in the sinusoidal, cyclic loading profile.

The tests were conducted in the superimposed in-situ testing media containment device originally designed and implemented by Schoeffl et al. (Schoeffl, 2014; Schoeffl et al., 2014). In contrast to tests with highly ductile materials, the camera system and the software device for crack length evaluation was especially adapted for less ductile materials. All FCG tests were conducted with an electro-dynamic testing machine of the type ElectroPlus E3000 (Instron; Nordwoos, USA) under sinusoidal loading and a frequency of 5 Hz. R-ratios were set to 0.1, 0.3, 0.5 and 0.7, respectively. To reduce overall testing times while simultaneously ensuring quasi-brittle, stable crack growth, the initial stress intensity factor levels were suitably chosen by pretesting some specimens. The calculation of the stress intensity factor K_I was done as described by Fischer et al. using eq. 1 and eq. 2 (Gross and Seelig, 2011).

$$K_I = \frac{F}{B \cdot \sqrt{W}} \cdot f\left(\frac{a}{W}\right) \qquad \text{(eq. 1)}$$

$$f\left(\frac{a}{W}\right) = \frac{\left(2+\frac{a}{W}\right)}{\left(1-\frac{a}{W}\right)^{3/2}} \cdot \left(0.886 + 4.64 \cdot \left(\frac{a}{W}\right) - 13.32 \cdot \left(\frac{a}{W}\right)^2 + 14.72 \cdot \left(\frac{a}{W}\right)^3 - 5.6 \cdot \left(\frac{a}{W}\right)^4\right) \qquad \text{(eq. 2)}$$

Lifetime assessment approach for a cylindrical ring

By using a quantitative comparison between the internal pressure loading conditions in ICS and the characterized FCG behavior, the probability of crack growth can be assessed. Therefore, calculations were carried out with eq. 3 and eq. 4 postulated by Yan (Yan and Nguyen-Dang, 1994). These equations allow a calculation of the K_I-values for a cylindrical ring under static internal pressure and small defect sizes, whereby p is the internal pressure, a the defect size and F a factor for considering different geometries relations of the cylinder. This factor contains the inner radius r of the cylinder (r=130 mm), the outer radius

R or the wall thickness. Representative values for the calculations were chosen with p=10 bar, a defect size of 0.5 mm and wall thicknesses of 2.0, 2.5 and 3.0 mm.

$$K_{I,critical} = p \cdot \sqrt{\pi \cdot a} \cdot F\left(\frac{a}{r}, \beta\right) \qquad \text{(eq. 3)}$$

$$F = 1.12 \cdot \frac{\beta^2 + 1}{\beta^2 - 1} \quad with \quad \frac{a}{r} \approx 0 \quad and \quad \beta = \frac{R}{r} \qquad \text{(eq. 4)}$$

As mentioned before, to obtain creep crack growth curves for static loading (R=1) from FCG curves, a procedure proposed by Lang et al. was followed (Lang et al., 2005; Frank et al., 2008; Frank et al., 2009). It allows for an extrapolation of FCG tests at different R-ratios to creep crack growth (CCG) curves under static load. If the K_I-values of these extrapolated CCG curves are higher than the calculated stress intensity factor K_I, FCG curves may be extrapolated back to those calculated component typical, calculated K_I-values, assuming no threshold regime occurs in the extrapolated range. In any case, this calculation remains on the safe side should such a threshold regime occur in the extrapolated range.

4. Results and discussion

The effect of R-ratio on the FCG resistance of PA66-GF30 is shown in Fig. 3 in terms of the da/dN vs. $K_{I,max}$. This illustration (rather than a ΔK diagram) was chosen as it is more prone to extrapolate the data directly to the static case. Clearly, the crack growth lines for constant R-ratios shift towards higher $K_{I,max}$-values as the R-ratio is increased.

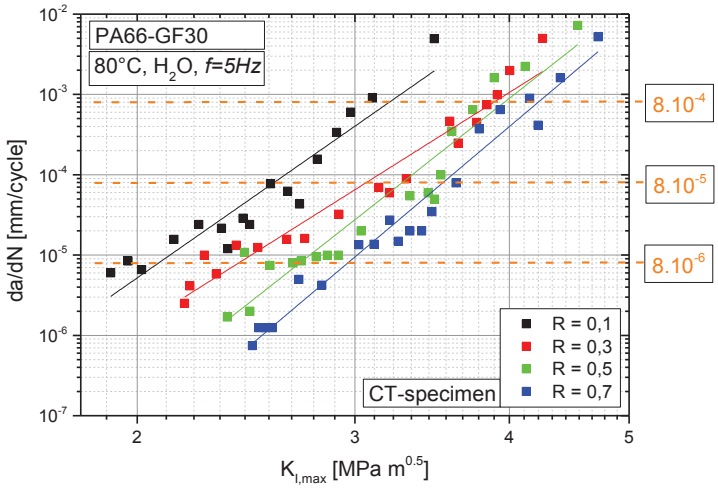

Fig. 3. Measured FCG kinetics for PA66-GF30S under various R-ratios.

In Fig. 4, the corresponding $K_{I,max}$ values at constant crack growth rates are plotted as a function of the R-ratio. Based on an exponential curve fitting and extrapolation using the existing data sets, values for the static loading conditions are achieved. The coefficient of determination R^2 was consistently above 0.9. By using the extrapolated data sets a CCG curve under static load was derived. Hence, a quantitative "synthetic" kinetic law for static loading (R=1) is obtained, which is shown in Fig. 5 together with the experimental kinetic laws at lower R-ratios. The results are in good agreement with expectations and results from previous studies with other materials (Lang et al., 2005; Pinter et al., 2007; Frank et al., 2009).

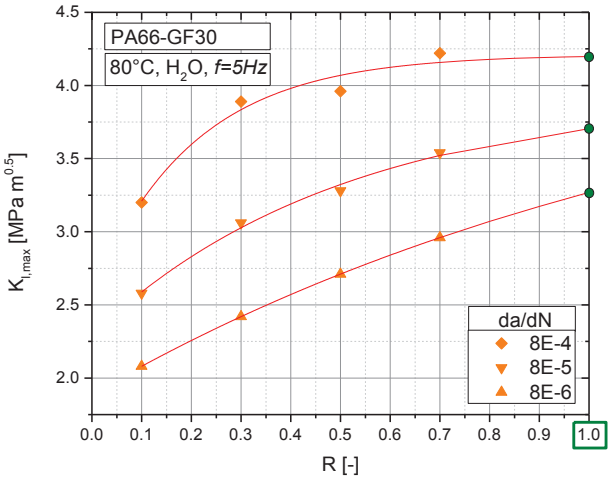

Fig. 4. Extrapolation of $K_{I,max}$-values at different R-ratios to R=1.

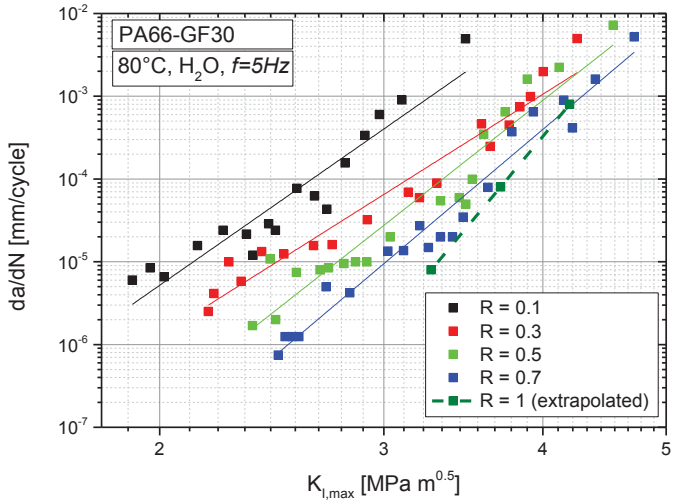

Fig. 5. Measured and calculated fatigue crack growth kinetics for PA66-GF30 under various R-ratios .

Using the assumptions for a pressurized ring component under service conditions described above (pressure p=10 bar; inner cylinder radius r of 130 mm; defect size a=0.5 mm; wall thicknesses of 2.0, 2.5 and 3.0 mm), "initial" K_I-values for the component level were calculated and are listed in Table 3.

Table 3. Calculated "initial" stress intensity factors under internal pressure for a cylindrical ring

Wall thickness (mm)	K_I-values ($MPa.m^{0.5}$)
2.0	1.47
2.5	1.17
3.0	0.97

These "initial" K_I-values are depicted in Fig. 6 together with the extrapolated "synthetic" CCG curves for both materials investigated. It appears that the CCG curves, when linearly extrapolated to lower stress intensity factors, would intersect the lines for initial stress intensity factor values at crack growth rates substantially below 10^{-8} mm/cycle. Considering that in a crack growth threshold may actually exist as one

moves towards such low crack growth rates, it is feasible to assume that the material inherent crack growth resistance may be sufficient for such an application. This conclusion, at least at this stage, does not necessarily apply to weld-bonded areas, an aspect which needs to be looked at in detail separately.

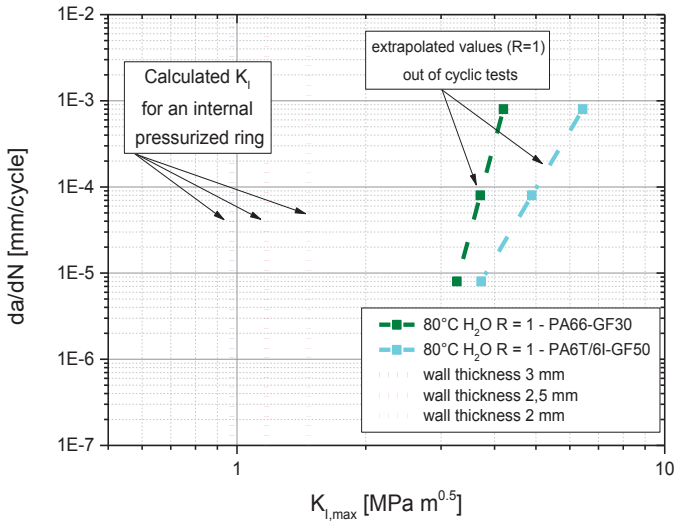

Fig. 6. Comparison of K_I-values of an internal pressurized cylinder with generated crack kinetics curves (R=1) for PA66-GF30 and PA6T/6I-GF50 at 80°C in water.

5. Summary and outlook

In this paper, based on a lifetime assessment approach for two polyamide grades with different glass fiber contents, the probability of crack growth under application conditions was investigated. Fatigue crack growth (FCG) experiments at different R-ratios (ratio of minimum to maximum force) were conducted at a temperature of 80°C in deionized water. The loading was applied to the injection molded compact-type (CT) specimens perpendicular to the main fiber orientation direction, i.e. the most critical case. Experimental data show that the FCG curves are strongly affected by the R-ratio, showing higher $K_{I,max}$-values with increasing R-ratio at a given crack growth rate. The experimental results were used to extrapolate towards a "synthetic" creep crack growth curve for both materials, which in turn were utilized to assess the long term performance capability of pressurized ring components in service such as in a single-loop integrated storage collector. While both PA material grades investigated seem to exhibit sufficient material-inherent crack growth resistance under service conditions, the crack growth resistance of weld-bonded sections remains a topic of further studies.

6. Acknowledgements

This research work was performed in the cooperative research projects SCOOP entitled "Solar Collectors made of Polymers" (www.eu-scoop.org) and SolPol-4/5 entitled "Solar-thermal systems based on polymeric materials" (www.solpol.at). The project SCOOP was funded by the European Commission within the Seventh Framework Programme. The ongoing project SolPol-4/5 is funded by the Austrian Climate and Energy Fund (KLI.EN) within the program "e!MISSION.at" and administrated by the Austrian Research Promotion Agency (FFG).

7. References

Fischer, J., Bradler, P.R., Schlaeger, M., Wallner, G.M., Lang, R.W., 2016. Novel Solar Thermal Collector Systems in Polymer Design – Part 5. Fatigue Characterization of Engineering PA Grades for Pressurized Integrated Storage Collectors. Energy Procedia 91, 27–34.

Frank, A., Freimann, W., Pinter, G., Lang, R.W., 2009. A fracture mechanics concept for the accelerated

characterization of creep crack growth in PE-HD pipe grades. Engineering Fracture Mechanics 76 (18), 2780–2787.

Frank, A., Pinter, G., Lang, R.W., 2008. A Novel Qualification Procedure for Lifetime and Safety Assessment of PE Pressure Pipes for Arbitrary Installing Conditions.

Geretschlaeger, K.J., 2015. Characterization of pigmented and reinforced polymeric materials for solar energy technologies. Doctoral Dissertation, Linz.

Geretschlaeger, K.J., Wallner, G.M., 2016. Aging characteristics of glass fiber-reinforced polyamide in hot water and air. Polym. Compos.

Gross, D., Seelig, T., 2011. Bruchmechanik. Mit einer Einführung in die Mikromechanik. Springer-Verlag Berlin Heidelberg, Germany.

Haager, M., Pinter, G., Lang, R.W., 2004. Estimation of Slow Crack Growth Behavior in Polyethylene after Stepwise Isothermal Crystallization. Macromol. Symp. 217 (1), 383–390.

Hahn, M.T., Hertzberg, R.W., Manson, J.A., Lang, R.W., Bretz, P.E., 1982. Effect of test frequency and water content on localized crack-tip heating in nylon-6,6. Polymer 23 (11), 1675–1679.

Hertzberg, R.W., Manson, J.A., 1980. Fatigue of engineering plastics. Academic Press, New York, xv, 295.

Hertzberg, R.W., Vinci, R.P., Hertzberg, J.L., 2013. Deformation and fracture mechanics of engineering materials. John Wiley & Sons, Inc, Hoboken, NJ, xxvi, 755.

Kahlen, S., Jerabek, M., Wallner, G.M., Lang, R.W., 2010. Characterization of physical and chemical aging of polymeric solar materials by mechanical testing. Polymer Testing 29 (1), 72–81.

Köhl, M., Meir, M.G., Papillon, P., Wallner, G.M., Saile, S. (Eds.), 2012. Polymeric materials for solar thermal applications. Wiley-VCH, Weinheim, XXIII, 393 S.

Lang, R.W., 1980. Applicability of linear elastic fracture mechanics to fatigue in poymers and short-fiber composites. Dissertation, Berhlehem (US).

Lang, R.W., Manson, J.A., Hertzberg, R.W., 1982. Effect of short glass fibers and particulate fillers on fatigue crack propagation in polyamides. Polym. Eng. Sci. 22 (15), 982–987.

Lang, R.W., Pinter, G., Balika, W., 2005. Konzept zur Nachweisführung für Nutzungsdauer und Sicherheit von PE-Druckrohren bei beliebiger Einbausituation. 3R International (1-2/2005), 32–41.

Lang, R.W., Stern, A., Doerner, G., 1997. Applicability and limitations of current lifetime prediction models for thermoplastics pipes under internal pressure. Angew. Makromol. Chemie 247 (1), 131–145.

Pinter, G., Lang, R.W., Haager, M., 2007. A Test Concept for Lifetime Prediction of Polyethylene Pressure Pipes. Monatsh. Chem. 138 (4), 347–355.

Schlaeger, M., 2015. Einfluss der Umgebungsbedingungen auf die mechanischen Eigenschaften von kurzglasfaserverstärktem PA 66 unter monotoner und zyklischer Belastung. Master Thesis, Linz, V, 64 Bl.

Schoeffl, P.F., 2014. Influence of Liquid Hydrocarbon Environments on High Density Polyethylene for Oil and Gas Applications. Doctoral Dissertation, Linz.

Schoeffl, P.F., Bradler, P.R., Lang, R.W., 2014. Yielding and crack growth testing of polymers under severe liquid media conditions. Polymer Testing 40, 225–233.

Solecrafte, 2015. Product brochure. http://www.solcrafte.com/sites/default/files/downloads/solcrafte_brochure_en_2015-12-1.pdf. Accessed 6 September 2016.

Steffen, R., Setyamukti, H., Wallner, G., Geretschläger, K., Röder, B., 2017. Kinetics of degradation-induced polymer luminescence. Polyamide under dry heat exposure. Polymer Degradation and Stability 140, 114–125.

Wallner, G., Weigl, C., Leitgeb, R., Lang, R., 2004. Polymer films for solar energy applications—thermoanalytical and mechanical characterisation of ageing behaviour. Polymer Degradation and Stability 85 (3), 1065–1070.

Yan, A.-M., Nguyen-Dang, H., 1994. Stress intensity factors and crack extension in a cracked pressurised cylinder. Engineering Failure Analysis 1 (4), 307–315.

Conference Proceedings

EuroSun 2016

Palma de Mallorca (Spain), 11 – 14 October 2016

Influence of maritime/industrial atmosphere on solar thermal collector's degradation

M. J. Carvalho[1] S. Páscoa[1] R. Gonçalves[1] N. Mexa[1] T. C. Diamantino[1]

[1] LNEG – Laboratório Nacional de Energia e Geologia, Lisbon (Portugal)

Abstract

Influence of atmospheric corrosivity on solar thermal collector's degradation was studied by exposure of flat plate collectors to two different corrosivity environments, one urban Outdoor Exposure Testing (OET) site with medium corrosivity (C2-C3) and a very high/extreme corrosivity (industrial and marine) (C5-CX) atmosphere highly polluted and simultaneously with highly airborne salinity. This OET site is a natural laboratory and can be considered as an accelerated test site. Results of thermal performance measurements after two years of exposure in the OET site with very high/extreme corrosivity (C5-CX) are presented, as well as the characterization of collectors inside environment with reference materials (zinc) in terms of corrosion rate.

Measurement of thermal performance of the collectors exposed in the OET site with very high/extreme corrosivity (C5-CX) are also presented for 13/14 months and 26 months of exposure. Collectors were dismantled and optical properties of the absorbers were measured.

Keywords: *Solar thermal collectors, atmospheric corrosivity, thermal performance degradation*

1. Introduction

Solar thermal collectors (STC) have to withstand stress conditions like high temperatures, high humidity, ultraviolet irradiance or wind and snow loads depending on the geographic location. Literature points out to dependence on other influences like prevailing wind conditions, contaminants like chlorides, SO_2 and NO_x, global solar irradiation, wetness time and precipitation (Köhl, M., et al, 2004; Slamova, K et al, 2016).

Although for certification of solar thermal collector (e.g. Solar Keymark, SRCC), the testing standards applied, namely ISO 9806:2013, consider a set of tests which address testing of collector resistance to most common adverse conditions when collectors are in use, these tests do not address long term collector durability.

In order to better know how different environmental conditions influence STC, as well as collector components, two OET (Outdoor Exposure Testing) sites were used to expose collectors and collector components. The two OET sites represent an urban climate (Lisboa-Lumiar) and a maritime climate with industrial influence (Sines). The results of full collector exposure will be presented in this work for one of the OET sites where the highest corrosivity levels are present.

In section 2 the collectors exposed are described, as well as the test methodology for thermal performance evaluation of the collector. In this section the method for evaluation of corrosivity inside the collectors is also presented. A short presentation of Sines OET site characterization is given based on detailed work of Diamantino, T. et al., 2016.

In section 3 thermal performances of collectors before and after exposure are presented. In this section the corrosivity inside the collectors is also presented.

Conclusions are presented in section 4.

doi:10.18086/eurosun.2016.07.04 Available at http://proceedings.ises.org

2. Exposure of STC at OET sites

STC studied were Flat Plate collectors with tempered glass cover. Their main characteristics are described in Table 1.

Tab. 1: Main collector characteristics

Reference of collector model	Main collector characteristics
A *	Aluminum absorber surface with PVD coating (mirotherm ®); Aluminum box.
B	Copper absorber surface with PVD coating (mirotherm ®); Aluminum box.
C *	Aluminum absorber surface with PVD coating (Eta plus ®); Aluminum box.
D *	Copper absorber surface with selective paint coating (SUNCOLOR TS S Black); Stainless steel box.

*one (1) replicate with zinc metal samples (reference materials)

For each collector model, two samples were exposed in each OET site (see Fig. 1).

Fig. 1: Installation of collector in OET- Maritime/Industrial

Thermal performance was measured in one collector of each collector model before exposure. For three of the models, zinc standard samples (reference materials) were installed in one of the collector samples to evaluate the corrosivity inside the collector.

2.1 STC thermal performance evaluation method

Originally it was decided that after two years of exposure, thermal performance would be measured for all collectors. However, considering the need to have a longer exposure period it was decided to measure only the thermal performance of collectors exposed at the Sines OET site since it has the highest corrosivity levels. It was decided to keep the collectors exposed at Lisboa-Lumiar for a longer period, except those with zinc standard samples (reference materials) which will be measured after completing similar exposure time as those in Sines OET site (26 months). The results of the performed measurements for collectors exposed in Sines are presented in this paper.

Thermal performance tests of solar thermal collectors were performed according ISO 9806:2013, using quasi-dynamic test method. The comparison is made based on the power curve as defined in ISO 9806:2013 for normal incident irradiance of 1000 Wm^{-2} (Direct irradiance = 850 Wm^{-2}; Diffuse irradiance = 150 Wm^{-2}).

Initial thermal performance was measured only in one collector of each reference. Final results of thermal performance were measured for all collectors exposed. The collectors with installed reference materials were dismantled for inspection and for evaluation of the corrosivity in zinc samples.

2.2 Optical properties of absorbers

Optical properties of absorbers were also measured. Information on optical properties of absorbers used in each collector exists and will also be presented and compared with the performed measurements of the absorber samples extracted from collectors.

The optical properties measured were solar absorptance (α_s) and thermal emittance (ε_t). The solar absorption (α_s) was measured using a Perkin Elmer's Spectrophotometer Lambda 950 UV/VIS/NIR with a 150 mm integrating sphere according to equation (1):

$$\alpha_s = \int_0^{\infty} \frac{[1-\rho(\lambda)]S_\lambda}{S_\lambda} d\lambda \qquad \text{(eq. 1)}$$

where S_λ is the spectral solar irradiance according to ASTM G173 – 03(2012) and $\rho(\lambda)$ is spectral hemispherical reflectance of the absorber coating between 300 and 2500 nm (ISO 22975-3:2014). For measurement of the spectral reflectance a spectralon ® coating reference not calibrated is used.

The thermal emittance (ε_t) was initially determined with a portable emissometer, Devices & Service Company model AE-AD3, which measures a surface emittance at 80°C of temperature and corrected for a temperature of 100ºC based on later measurements using a Spectrophotometer Frontier IR/NIR of Perkin Elmer, with integrating sphere. The thermal emittance is determined according to equation (2):

$$\varepsilon_t = \int_0^{\infty} \frac{[1-\rho(\lambda)]P_\lambda(T)}{P_\lambda(T)} d\lambda \qquad \text{(eq. 2)}$$

where $P_\lambda(T)$ is the Planck function for the black-body at a temperature T equal to 373 K and $\rho(\lambda)$ is spectral hemispherical reflectance of the absorber coating between 2.5 and 20 μm (ISO 22975-3:2014). For measurement of the spectral reflectance, a diffuse gold coating reference calibrated by Avian Technologies LLC is used.

2.3 STC inside corrosivity evaluation

In the collectors referenced in Table 1 with * five (5) replicates of zinc metal samples were put in the air gap between absorber and glazing according to Fig. 2, to evaluate the corrosivity of the micro-climate after approximately 2 years (26 months). Zinc metal samples are equal to the zinc metal samples placed outdoors to comparatively evaluate the atmospheric corrosivity. The corrosion categories of outdoor exposure test sites were obtained by determination of the corrosivity based on corrosion rate measurement of standard specimens (carbon steel, zinc, copper and aluminum) according to ISO 9226:2012. Three (3) replicates of standard specimens were exposed in support structures fixed with ceramic screws at an angle of 45° facing South (S). After exposure, corrosion products of each metal (inside and outside the collectors) were removed in accordance with ISO 8407:2009 and the corrosion rate was determined by weight loss according to ISO 9226:2012, considering the mass loss, total surface area and exposure period.

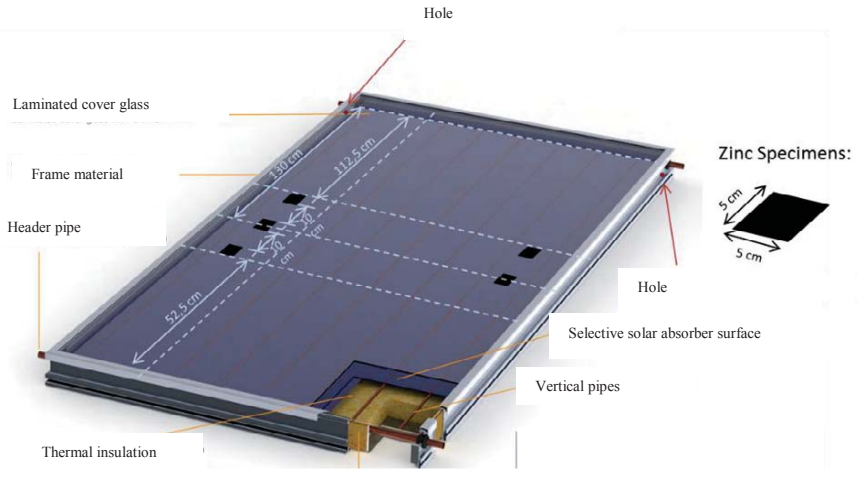

Fig. 2: Zinc specimens put in air gap between absorber and glazing.

To avoid contact with the absorber, the zinc samples inside the collector were fixed on the absorber with specially designed polymeric sample holders to ensure that the samples were galvanically isolated.

2.4 Short description of Sines OET site

Detailed description of OET site characterization can be found in Diamantino, T et al. (2016). A short description of Sines OET site is presented in Table 2. The values presented were obtained for one year (2014).

Tab. 2: Climate characterization in Sines OET site (2014) (Diamantino et al, 2016)

Location	Latitude	Longitude	Altitude [m]	Ambient temperature [°C] (average)	Solar irradiance tilt 45° G_h [W/m^2]	average relative humidity [%]	Cl^- [mg.day^{-1}.m^{-2}]	SO_2 [mg.day^{-1}.m^{-2}]
Sines, Portugal	37,95°N	8,88°W	17	16,9	351	78,7	191,8	139,1

In Table 3 are presented the results of atmospheric corrosion rates in Sines OET site. Detailed presentation of these results can be seen in Diamantino, T. et al. (2016).

Tab. 3: Corrosion rates of carbon steel, copper, zinc and aluminum and corrosion categories measured after 1 year of exposure for (exposed in 2 orientation – N and S) Sines OET site (Diamantino et al, 2016)

Sines OET site									
Reference materials		Carbon steel		Copper		Zinc		Aluminum	
Samples orientation		N	S	N	S	N	S	N	S
Corrosion rate (g/(m^2.a)*		3535.76	1346.01	82.19	76.06	57.71	89.87	1.31	3.98
Corrosion category	Category	CX	C5	CX	CX	C5	CX	C3	C4
	Corrosivity	Extreme	Very High	Extreme	Extreme	Very High	Extreme	Medium	High
	Reference values (g/(m^2.a)*	1500<rcorr ≤5500	650<rcorr ≤1500	50<rcorr ≤90		30<rcorr ≤60	60<rcorr ≤180	0,6<rcorr ≤2	2<rcorr ≤5

**corrosion rates expressed in grams per square meter per year*

3. Results of one and two years of exposure in Sines OET.

In Table 4 the periods of exposure of the collectors in Sines OET are listed, as well the exposure time (in months).

Tab: 4 – Exposure dates of STC in Sines OET site

Model (Ref.)	Installation date	Uninstallation data	Exposure time (month)
S_A1	11/04/2014	02-06-2015	14
S_A2 *	11/04/2014	01-06-2016	26
S_B1	11/04/2014	01-06-2016	26
S_B2	11/04/2014	---	Still exposed
S_C1	11/04/2014	01-06-2016	26
S_C2*	11/04/2014	01-06-2016	26
S_D1	16/06/2014	02-06-2015	13
S_D2*	16/06/2014	01-06-2016	26

*one (1) replicate with zinc metal samples

3.1 STC thermal performance results after approximately one and two years of exposure

After approximately one year of exposure (see Exposure time in Table 4) in Sines OET, two collectors were tested for thermal performance and dismantled after. Measurement of optical properties was made in one section of the absorber.

After approximately two years of exposure (see Exposure time in Table 4) in Sines OET, the collectors with zinc metal samples were also tested for thermal performance and dismantled after. Measurement of optical properties was made to one or two sections of the absorber.

One collector of type B was also tested for thermal performance. The other collector is still exposed in Sines.

Fig. 3 to 6 show the collector's power curve according to the definition of ISO 9806:2013, comparing the

thermal performances after exposure with the initial thermal performance, measured in collectors of the same type before exposure.

Fig.3 and 5 show the thermal performance after one and two years for collectors with aluminum absorbers and PVD coatings (Mirotherm ® and Eta plus ®, respectively) (Models A and C). After one year there was almost no change in thermal performance. After two years, a difference can be observed mainly due to change in optical efficiency.

Fig. 4 shows the impact of two years of exposure on a collector with copper absorber and PVD coating (Mirotherm ®) (Model B). In this case, optical efficiency does not show differences but thermal losses are higher and a loss in power for higher temperatures is visible. The collector was not dismantled and no information is yet available on optical properties of the absorber or on other degradation factors that can explain this behavior.

Fig. 6 shows the impact of two years of exposure of a collector with copper absorber and Paint coating SUNCOLOR TS S Black (Model D). Two collectors were tested after two years. The collector with installed zinc metal samples does not show significant decrease in the power curve. This collector was dismantled and information on optical properties are available in Table 5.

The collector without zinc samples was not dismantled but shows a difference on the power curve. Further analyses will be made to this collector.

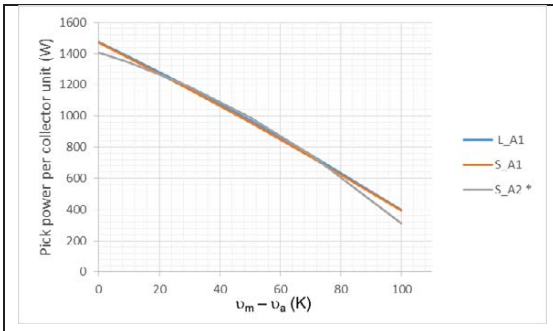

Fig. 3: Power curves of collector model A (L_A1 – initial measurement: S_A1 – measurement after one year; S_A2 * - measurement after two years).

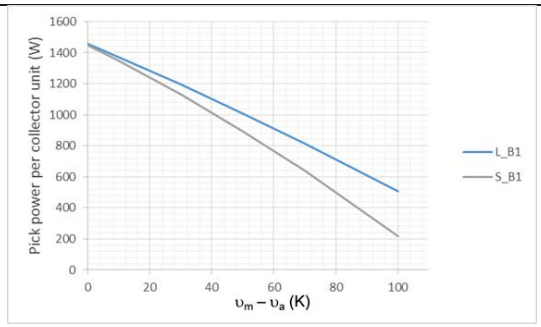

Fig. 4: Power curves of collector model B (L_B1 – initial measurement; S_B1 - measurement after two years).

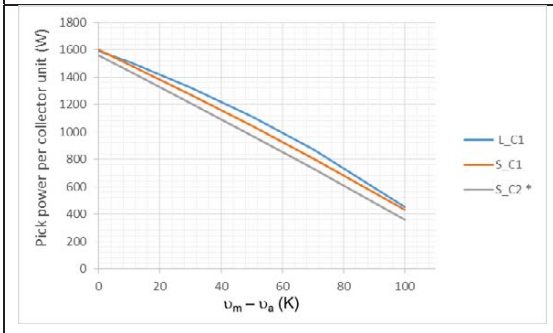

Fig. 5: Power curves of collector model C (L_C1 – initial measurement: S_C1 – measurement after one year; S_C2 * - measurement after two years).

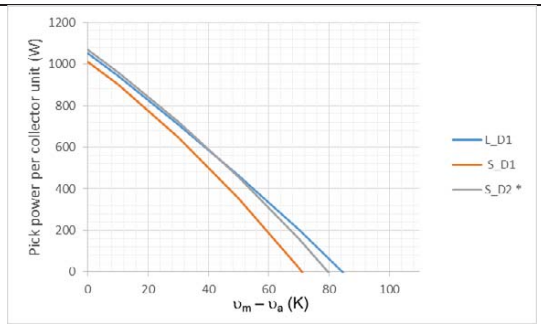

Fig. 6: Power curves of collector model D (L_D1 – initial measurement: S_D1 – measurement after one year; S_D2 * - measurement after two years).

In Table 5 the average relative difference between the power curves is presented.

Tab. 5: Average difference of power curve relative to initial peak power (%) in the temperature range 0-100 K.

Collector sample	Exposure time (month)	Average difference of power curve relative to initial peak power (%) in the temperature range 0-100 K
S_A1	14	0,6
S_A2 *	26	1,8
S_B1	26	7,7
S_C1	13	2,2
S_C2 *	26	6,2
S_D1	26	12,4
S_D2 *	26	0,0 (temp. range 0-70 K)

In Table 6 the optical properties of the absorber of the four collector models are listed. Initial values were obtained from measurement of thirty samples of the absorber used in each collector. The values after one and two years of exposure were measured in section of the collector absorber after dismantling.

The initial values of the optical properties correspond to average values of thirty samples with corresponding standard deviation. The values after 13/14 months correspond to only one measurement in one sample of the absorber of the collector dismantled. The values after 26 months correspond to values of measurements made on two different samples of the absorber (side and bottom) and, when more than one measurement was made, the standard deviation is given.

For collectors A with aluminum substrate and PVD coating, the variation in the solar absorptance is in agreement with the change in peak power (see Fig. 3). The thermal emmitance shows a higher change and after two years the bottom part of the absorber has higher thermal emittance values. For collectors C the solar absorptance does not show significative difference although some change in peak power measured (see Fig. 5) is observed. A change in glass transparency may be the reason for this. Also in this case a higher change in thermal emmitance can be observed and this change is not uniform. The bottom part of the absorber shows higher thermal emmitance values.

Tab. 6: Optical properties of collector absorber coatings.

Note: Figures in parentheses indicate that the standard deviation observed is lower than the measurement uncertainty.

Collector sample	Exposure time (month)	Location inside collector	α	σ_α	ε	σ_ε
	Initial	---	0,96	0,00(1)	0,11	0,00(2)
S_A1	14	---	0,95	---	0,11	----
S_A2 *	26	side	0,94	0,00(1)	0,13	0,01
		bottom	0,94	0,00(1)	0,12	0,00(2)
	Initial	---	0,96	0,000(2)	0,11	0,00(3)
S_C1	13	---	0,95	---	0,14	---
S_C2 *	26	side	0,95		0,11	
		bottom	0,95		0,14	
	Initial		0,95	0,00(1)	0,72	0,02
S_D2 *	26	side	0,93		0,56	
		bottom	0,93	0,00(1)	0,56	0,00(4)

The high difference of initial thermal emittance of collector D absorber when compared with the thermal emittance of absorber sections measured may result from different application procedures in initial samples and collector absorber.

3.3 Corrosivity rates

After dismantling the collectors with zinc specimens installed, the determination of the corrosivity based on corrosion rate measurement was obtained according to ISO 9226:2012 and ISO 8407:2009.

The results are presented in Table 7. Although five samples were installed, only three were used for corrosion rate measurement. The two additional samples will be used for morphological and chemical characterization of corrosion products formed. The average corrosion rate obtained inside each collector is presented in the Table below, as well as the categories obtained according to the classification described in ISO 9223:2012.

Tab. 7: Corrosion rates and corrosion categories obtained inside collectors

Collector	Corrosion rate inside collectors $r_{corr\ (g/m^2.a)\ (SD)}$	Corrosion category according to ISO 9223:2012
A	90,31 (9,53)	CX
C	99,91 (10,63)	CX
D	4,56 (0,55)	C2

Collector model A and C show corrosivity levels almost equal to outdoor (89,87 g(m^2/a) (category CX). Collector D shows low corrosivity values. These differences may be explained by different ventilation rates and higher temperatures in the collectors A and C. Further investigation will be performed on this aspect.

4. Conclusions

A first evaluation of STC exposure impact to a very high/extreme corrosivity (C5-CX) (Maritime/Industrial) was performed after one year and two years of exposure by measuring thermal performance of four collector models and comparing it with the initial thermal performance measured. Simultaneously measurement of the absorbers optical properties after dismantling of the collectors was performed. The change in thermal performance was evaluated based on the power curve of each collector for normal incidence with 1000Wm^{-2}.

In one replicate of each collector model, zinc metal samples (reference material) were installed in the air gap between absorber and glass cover. These zinc metal samples were collected after the two years of exposure of the collectors and allowed measurement of corrosion rate inside collectors.

For two of the collector models, the thermal performance was measured after one year of exposure of each collector model and did not show high impact. The average difference in the power curve relative to initial peak power (%) in the temperature range 0-100 K was of the order of 0,6 and 2,2 % for collector samples S-A1 and S-C1, respectively. The reduction in thermal performance after two years was higher for collector model C (6,2%) than for collector model A (1,8%). These differences can be correlated with the measured optical properties of the absorbers.

Collector model B showed a higher difference (7,7%) which is related with higher change in thermal losses. Future dismantling of the collector will help to identify causes for this change in thermal performance.

Collector model D showed low and high differences for the same exposure period. Also in this case for the collector showing higher difference, future dismantling of the collector will help to identify causes for the change in thermal performance.

The corrosion rate inside collectors and evaluation of the corrosion category according to ISO 9223:2012 showed for models A and C corrosion rates very close to atmospheric corrosivity measured at Sines OET site

(89,87 g(m^2/a) (category CX). For model D the corrosion rate was much lower. These differences may be explained by different ventilation rates and higher temperatures in the collectors A and C. Further investigation will be performed on this aspect.

The corrosion rates inside the collectors installed in Lisboa-Lumiar OET site will be measured for approximately the same time as for Sines OET site and will allow comparison between corrosion category inside the collectors and atmospheric corrosion for this test site.

5. Acknowledgements

This work was carried out under the Project FCOMP-01-0124-FEDER-027507 (Ref. FCT RECI/EMS-ENE/0170/2012) and the Project POCI-01-0145-FEDER-016709 FCT (PTDC/EMS-ENE/0578/2014). The authors would like to thank to industrial partners (FogãoSol, Hempel, OpenPlus and Permasolaris), by the supply of samples and the means for performing this work.

6. References

ASTM G173 – 03, 2012. Standard Tables for Reference Solar Spectral Irradiances: Direct Normal and Hemispherical on 37° Tilted Surface

Diamantino, T. C. , R. Gonçalves, A. Nunes, S. Páscoa, M. J. Carvalho, 2017. Durability of different selective solar absorber coatings in environments with different corrosivity. Solar Energy Materials & Solar Cells, Volume 166, July 2017, Pages 27–38, (https://doi.org/10.1016/j.solmat.2017.03.004)

ISO 8407:2009 Corrosion of metals and alloys - Removal of corrosion products from corrosion test specimens. 2009

ISO 9223:2012 Corrosion of metals and alloys - Corrosivity of atmospheres - Classification, determination and estimation. 2012
ISO 9226:2012 Corrosion of metals and alloys - Corrosivity of atmospheres - Determination of corrosion rate of standard specimens for the evaluation of corrosivity. 2012

ISO 9806:2013(E), Solar Energy – Solar Thermal Collectors – Test Methods

ISO 22975-3:2014, Solar energy- collector components and materials – Part 3: Absorber surface durability, ISO 2014

Köhl, M., Carlsson, B., Jorgensen, G. J., Czanderna, A. W. (Editors), Performance and Durability Assessment. Optical Materials for Solar Thermal Systems. 2004, Elsevier (ISBN 0-08-044401-6)

Performance and Durability Assessment. Optical Materials for Solar Thermal Systems. Köhl, M., Carlsson, B., Jorgensen, G. J., Czanderna, A. W. (Editors), 2004, Elsevier (ISBN 0-08-044401-6)

Slamova, K., I. Duerr, T. Kaltenbach, M. Köhl, 2016. Degradation effects of maritime atmosphere on metallic components of solar collectors. Solar Energy Materials & Solar Cells 147, 246–254 (http://dx.doi.org/10.1016/j.solmat.2015.12.011)

Conference Proceedings

EuroSun 2016
Palma de Mallorca (Spain), 11 - 14 October 2016

State of the art of radiation-matter interaction models applied for the optical characterization of concentrating solar collectors

Julian D. Hertel[1], Víctor Martínez-Moll[1], Ramon Pujol-Nadal[1], Francesc Bonnín-Ripoll[1]

1 Departament de Física, Universitat de les Illes Balears, Ctra de Valldemossa km 7,5, 07122 Palma de Mallorca, Illes Balears, Spain

Abstract

The optical modelling of concentrating solar collectors is nowadays of great importance for a variety of applications. In this study two major goals have been achieved: First, the current market of materials for solar thermal applications was reviewed; and second, the most commonly used optical models for radiation-matter interaction were summarized. In the future, the study could be interesting for ray tracing implementations in order to adequately simulate solar concentrating or PVT collectors, which employ innovative materials and show more sensitive behavior towards incidence angle and wavelength dependent input.

Keywords: *Monte-Carlo Ray Tracing, Optical Modelling, Solar Concentrating Collectors, PVT, Coatings*

Nomenclature

Quantity	Symbol	Unit
Absorptance	A	-
Superposition factor	K	-
Depolarization factor	L	-
Complex refractive index	N	-
Reflectance	R	-
Transmittance	T	-
Optical admittance of a stack	Y	S
Optical impedance of free space	Z_0	S^{-1}
Empirical constant	b_0	-
Empirical constant	c	-
Thin-film thickness	d	m
Volume fraction	f	-
Real refractive index	n	-
Porosity	p	-

Quantity	Symbol	Unit
Absorption coefficient	α	-
Solar weighted absorption coefficient	α_{SW}	-
Permittivity of free space	ε_0	Fm^{-1}
Optical admittance	η	-
Incidence angle	θ_i	rad
Extinction coefficient	κ	-
Wavelength	λ	m
Permeability of free space	μ_0	Hm^{-1}
Variance of specular reflection	σ	rad
Phase factor of plane wave	φ	-

1. Introduction

The optical characterization of concentrating solar collectors is of paramount importance. To mention only some of possible applications, such simulations are nowadays irreplaceable for designing and optimizing conventional or even completely new collector concepts; they allow to economically determining the error tolerance margins for real operating collectors or they could serve to complement testing procedures where laboratory settings cannot reproduce real conditions. Apart from these most common applications, optical modelling might gain even more importance with the increasing success of photovoltaic-thermal (PV/T) applications, which on the one hand have a wavelength sensitive receiver (PV-cells), but at the same time often have complex designs such as concentration collectors.

Undeniably, the core part of each optical simulation is the underlying mathematical radiation-matter interaction models. During the last decades a remarkable progress has been experienced in the field of solar

doi:10.18086/eurosun.2016.07.08 Available at http://proceedings.ises.org

materials research. New types of polymers, tailor designed coatings or surface structures are only some indicators for an increasingly changing market. The question is raised whether state-of the art models for radiation-matter interaction are still suitable to describe newly developed materials.

For this reason, a literature review has been conducted in order to first make a comprehensive list of commonly used solar materials and materials that show great potential to be used in the near future. The focus will be on solar thermal concentrating technologies, but the analysis applies to reflective and transparent materials used in PV and PVT collectors as well. The outcome of this review about solar materials will be presented in section 2. Section 3 will be related to section 2 describing physical models for radiation-matter interaction as they are often applied in order to simulate different materials.

A problem that was observed in this regard was to obtain reliable information about incidence angle dependent data of the material or material compounds that could serve as an input to optical models. It is not clear, what parameters a manufacturer or research group should provide in order to allow accurate simulations. We consider this a necessary debate in order to bring together the field of solar material research and development and the field of optical modelling.

2. Solar thermal material for concentrating applications

This section will provide a general overview on materials which are nowadays commonly used and such materials that show great potential to be used in the near future. Since the focus will be on concentrating solar collectors, materials are divided into the following groups: “transparent and semi-transparent”, “reflective”, “absorptive materials” and “coatings”.

2.1. Transparent and Semi-Transparent

Transparent and semi-transparent materials are mainly used as covers for protection and heat loss reduction. Doubtlessly, such covers come at the cost of a lower optical efficiency, which makes it even more important to model this part of the collector adequately.

At this point, the most employed material for covers is solar/optical glass, which is made of borosilicate with a low content of iron. One conventional example for such glass is the Schott BK-7 type (Schott, 2014). But there are also more innovative approaches to give glass more favorable properties for the use in solar applications, such as introducing gas bubbles to reduce the thermal conductivity and increase the transmittance (Cai et al., 2016).

While for a long time solar glass was the only choice for solar covers it has become more popular recently to employ semi-transparent polymeric materials. The advantages are manifold: low costs, less weight and almost no restrictions on the design. When it comes to essential optical properties such as the transmittance, polymers perform still poor in comparison to glass. However, due to its good mechanical properties polymer covers can be made extremely thin, which makes this drawback less significant. A good example for such an application is the parabolic trough collector (PTC) prototype of (Bader et al., 2011), which has a pressurized chamber with an ETFE-membrane as top-cover.

(French et al., 2011) and (Köhl et al., 2012) give an overview of polymeric materials which are promising for the use in solar thermal applications (ST). Some of them are:

- Fluoropolymers: ETFE, FEP
- Ethylene backbone polymers: PV1400 EVA
- Polyimides: Kapton H

2.2. Reflective

Reflective material is used for mirrors. To be interesting for the use in concentrating solar collectors, they need to be stable, stretch- and soil-resistant, durable and highly reflective in the wavelength range of the solar spectrum. Three types of mirrors are commercially available:

Glass mirrors

Glass mirrors are the most used type of mirrors. They usually have a 4mm thick solar glass layer with a thin reflective silver layer beneath. A paint layer protects the silver from environmental impacts such as corrosion. This type of mirror is very resistant and durable but rather expensive and heavy. Moreover, the 4 mm glass substrate reduces the mirror's reflectance. To improve optical performance there are versions with a 1mm thick substrate, which, however, comes at the cost of reduced rigidity. An additional metal sheet on the back side of this mirror can compensate this loss.

Polymer mirrors

This type of mirror comes as a thin foil. The core part of the mirror is a reflective silver or aluminum layer protected by a copper layer at the backside. Finally, a thin polymer film at the front and the back side further protects the metal stack from environmental impacts. Polymer mirrors are extremely light, flexible and cheap, but also less durable and resistant than glass mirrors. For the parabolic trough collector in (Bader et al., 2011) MyLar polymer mirrors are used.

Aluminum mirrors

Aluminum mirrors start from an anodized aluminum substrate that has either a pure aluminum or silver layer on top for reflection. To protect the reflection layer from corrosion and abrasion the mirror is also provided with a reflectance enhancing, protective coating. The advantage of aluminum mirrors is a comparably low weight at a still high rigidity. The overcoat of the mirror plays an important role for the optical performance and will be explained more in detail in the following.

2.3. Absorptive

Solar absorbers are mostly made of stainless steel, copper or ceramics (solar tower) or less common of polymeric material (pool collector or flat plate collector) (Köhl et al., 2012). The substrate of the absorber has to guarantee a high heat transfer coefficient. The most important part of the absorber is, however, its selective overcoat. This one should show high absorption in the short wavelength region (UV-Vis region), but low absorption/emission in the long wavelength region (Infra-red thermal radiation (IR)). According to Kirchhoff's law, a low absorption is equivalent to a low emission, which allows making use of most of energy of the incident radiation. The other main requirements to a selective coating are thermal stability at the operating range, good adhesion to the absorber substrate and resistance to corrosion. In fact, commercially available coatings are only designed for a specific temperature range (Selvakumar and Barshilia, 2012).

2.4. Coatings

As already mentioned in the previous sections, coatings or thin-films are single or multi-layers placed on top of a substrate with the purpose of giving a material certain optical properties. Today's processing methods allow designing coatings with a high degree of accuracy which give a lot of freedom for property design. Their importance for solar thermal technologies is paramount. In fact, nowadays coatings are employed in basically all parts of a solar thermal collector: Absorbers have a selective overcoat to allow better exploitation of energy of the incident solar spectrum; anti-reflective layers on covers reduce their reflectance and simultaneously enhance transmittance while mirrors have a high-reflectance coating to improve reflectance further sometimes to an even higher extent than the pure metal and at the same time protect the reflective layer.

Anti-reflectance and high-reflectance coating

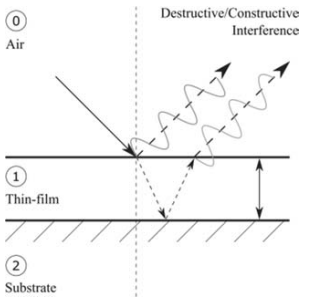

Fig. 1. Single layered optical coating: Controlled destructive or constructive interference by multiple reflections.

While anti-reflectance (AR) coatings are applied to reduce surface reflectance and enhance transmittance of covers such as e.g. the envelope of a PTC, high-reflectance (HR) coatings try to achieve exactly the contrary and are used on mirrors. Even though the effect of both coatings is exactly the opposite, their underlying principle is the same. These coatings consist of one or multiple layers. As an electromagnetic wave is propagating through the thin-film assembly it is partially reflected at the layer interfaces according to Fresnel's equations (Eq. 2). Given a specific refractive index for each layer, their thickness can be adjusted for a specific wavelength such that interference of the reflected light is either destructive (AR coating) or constructive (HR coating), as illustrated in Fig. 1. The resulting overall reflectance of the stack is then low or high. Absorption within the thin-film assembly is not desired which is why they consist of dielectrics.

The simplest version of an AR coating is a single MgF_2 of the thickness of a quarter of the target wavelength. When constructing a single HR layer on a metal surface it has to be taken into account that the substrate material has a complex refractive index (Macleod, 2010).

Coatings only perform well at the range around the wavelength and incidence angle they were designed for. In order to enable broadband AR or HR behavior for a coating, it is common practice to use multiple quarter-wavelength layers of alternating low (L) and high (H) refractive indices. In this sense, LHL…LHL would form an anti-reflective and HLH…HLH a highly-reflective structure. Commonly used dielectric materials are: MgF_2, SiO_2, TiO_2 (Choi et al., 2014; Jeong et al., 2004; Sutter et al., 2012), HfO_2, Si_3N_4, Al_2O_3 or ZnO (Macleod, 2010; Mazur et al., 2015).

Other increasingly popular low-refractive materials are sol-gels. The sol-gel process allows manufacturing porous layers with an almost tailor-designed refractive index (Atkinson et al., 2015; Prado et al., 2010; Sutter et al., 2010; Xin et al., 2013).

Selective coating

Selective coatings show low reflectance in the short wavelength range and high reflectance (low emission) in the long wavelength range. Most coatings incorporate metal which functions as an infra-red reflector, while the dielectric matrix substrate mainly absorbs in the UV-Vis spectrum. It can be distinguished between four types basic of selective surfaces: Intrinsic, metal-semiconductor tandem, metal-dielectric composite (e.g. cermets) or textured surfaces (Atkinson et al., 2015; Selvakumar and Barshilia, 2012; Soum-Glaude et al., 2013). To reduce reflection losses, selective coatings often also have an AR coating on top. The principle of textured surfaces differs from the other methods in such a way that short wavelength radiation is "trapped" in a complex structure and finally absorbed after multiple reflections (see Fig. 2).

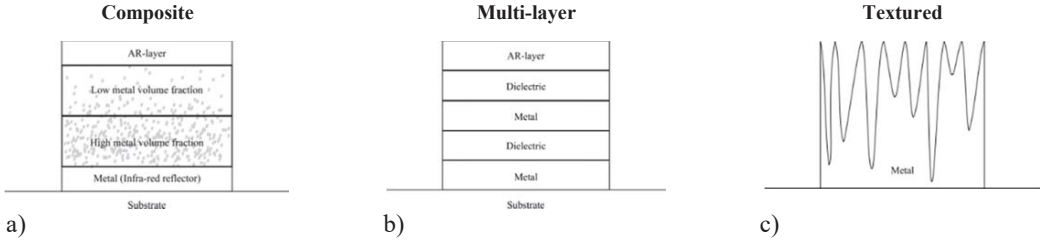

Fig. 2. Structures of selective coatings: a) dielectric-metal-composites b) dielectric-metal multi-layers c) textured surface.

The most widely used concepts nowadays are the composites or dielectric-metal multi-layers (Selvakumar and Barshilia, 2012). Selective coatings are designed for a narrow operation range. High temperature coatings are often based on Al_2O_3 as dielectric due to its high thermal resistance. Other dielectric matrix materials are: AlN, SiO and MgO (Selvakumar and Barshilia, 2012). Also possible for high-temperature resistant selective coatings is the assembly of the metallic-like TiAlN with the semiconductor TiAlON on top of a metallic IR reflective layer or directly on the substrate (An et al., 2015; Barshilia et al., 2008; Rebouta et al., 2012) or composites of $MoSi_2$ (conductor) and Si_3N_4 (dielectric)(Hernández-Pinilla et al., 2016).

Anti-soiling coating (AS)

Another positive effect of coatings is to make materials more resistant against soiling. In this light, TiO2 needs to be highlighted as a dielectric material with a couple of additional favorable properties. Not only does TiO_2 show high scratch resistance, its photocatalytic properties accelerate the decomposition of organic particles, which leads to a self-cleaning effect (Atkinson et al., 2015; Mazur et al., 2015).

3. Optical models for solar materials

After having summarized some of the most important materials and new structural concepts that are employed in concentrating solar collector nowadays, we will discuss some of the optical models in order to simulate material response on incident radiation. It will be distinguished between surface, volume and thin-film (coating) effects.

The propagation of an electromagnetic wave (radiation) through a medium is described by the Maxwell equations and the Lorentz force law. Where complex optical devices are used and results with a high degree of accuracy are needed, it is necessary to employ computational methods to solve these equations. However, if the properties of a medium are approximately constant and its dimensions are several times larger than the considered wavelength, the wave front can be represented by rays (geometrical optics). As a ray is passing through a solar thermal collector and interacting with different materials the finally absorbed energy is subject to a complex coupling of different physical correlations. The overall optical performance of a collector is then best approached by tracing an arbitrary number of rays separately according to the Monte Carlo method until the result is statistically stable. This is the principle description of how ray tracing work, the most commonly applied method for simulation of solar concentrating collectors.

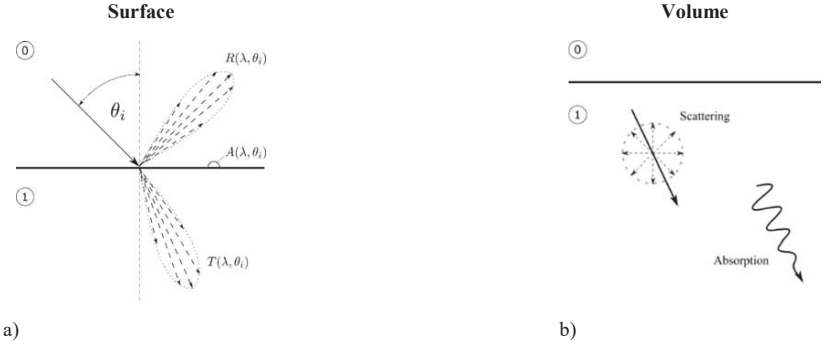

Fig. 3. Radiation-matter-interaction phenomena: a) Reflection, transmission and absorption on surfaces. b) Scattering and absorption within volume.

3.1. Surface effects:

In ray tracing, when a ray hits a surface there are only three possible ways it can interact with it. It can be either reflected, transmitted or absorbed (Fig. 3). According to the law of energy conservation all fractions over the incident energy add up to 1.

$$R(\theta_i, \lambda) + T(\theta_i, \lambda) + A(\theta_i, \lambda) = 1 \tag{1}$$

All coefficients depend on the wavelength, the incidence angle and the polarization of the incident light. Making some approximations regarding Eq. 1, helps to group the previously presented materials into different categories according to their surface type. Fig. 4 illustrates these categories. It is valid to assume zero transmission for absorptive and reflective materials such as receivers and mirrors. On the other hand, transparent materials like covers can be assumed to have zero absorption, since even if they are coated they only employ dielectric materials. This only goes for the surface itself. In the volume there will be absorption. The main advantage of this simplification is that a material is optically fully characterized when determining its reflectance beside its scattering properties, which will also be discussed.

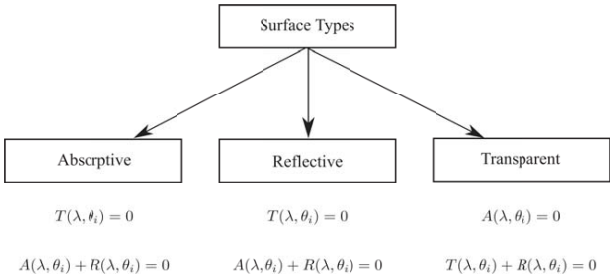

Fig. 4. Classification of typical solar thermal material: absorptive material (receiver), reflective material (mirrors) and transparent material (covers, envelopes)

Reflectance - $R(\theta_i, \lambda)$

One solution of Eq. 11 is given by the Fresnel equations, which result from the boundary condition of a balance of the electric and magnetic fields across the surface. The Fresnel equations therefore present a solution of the simplified Maxwell equations (Macleod, 2010).

$$R = \left(\frac{\eta_0 - \eta_1}{\eta_0 + \eta_1}\right)\left(\frac{\eta_0 - \eta_1}{\eta_0 + \eta_1}\right)^* \tag{2}$$

$$T = \frac{4\eta_0 Re(\eta_1)}{(\eta_0 + \eta_1)(\eta_0 + \eta_1)^*} \tag{3}$$

η is the optical admittance of the material and depends on the polarization of the incident light. It is also common to use a modified "tilted" version of the optical admittance that also incorporates the angle of propagation θ of the particular medium.

$$\eta_i = \begin{cases} \dfrac{N_i \cos\theta_i}{Z_0} & \text{, for s-polarization (TE)} \\ \dfrac{N_i}{Z_0 \cos\theta_i} & \text{, for p-polarization (TM)} \end{cases} \tag{4}$$

with Z_0 the optical impedance of free space. TE refers to a plane wave with the electric field vector perpendicular to the plane of incidence and TM with the magnetic field vector perpendicular to the plane of incidence.

$$Z_0 = \sqrt{\frac{\mu_0}{\varepsilon_0}} \tag{5}$$

And N the complex refractive index

$$N = n + i\kappa \tag{6}$$

It should be noted that the refractive index can be complex as is the case for non-dielectric matter such as metals. This becomes important for the analysis of mirrors. The refractive index and the angle of incidence are also the only non-Natural constants and hence fully describe the reflectance at an interface.

The angle of propagation of each medium θ_i is related to the angle of incidence θ_0 by Snell's law:

$$n_0 \sin\theta_0 = n_i \sin\theta_i \tag{7}$$

In the case of dielectric materials ($\kappa \neq 0$) Schlick proposed an approximation of the incidence angle dependence of the reflectance given by Eq. 2 (Schlick, 1994). Schlick's alternative equation is computationally less expensive.

$$R(\theta) = R_0 + (1 - R_0)(1 - \cos\theta)^5 \tag{8}$$

Scattering

Beside de Fresnel effect, scattering is another important phenomenon of radiation-matter interaction on a surface. While the former is the result of an energetic balance, the latter is instead due to surface texture. The microscopically random surface structure has influence on the direction of the reflected photon and disperses the energy flux spatially (see Fig. 5).

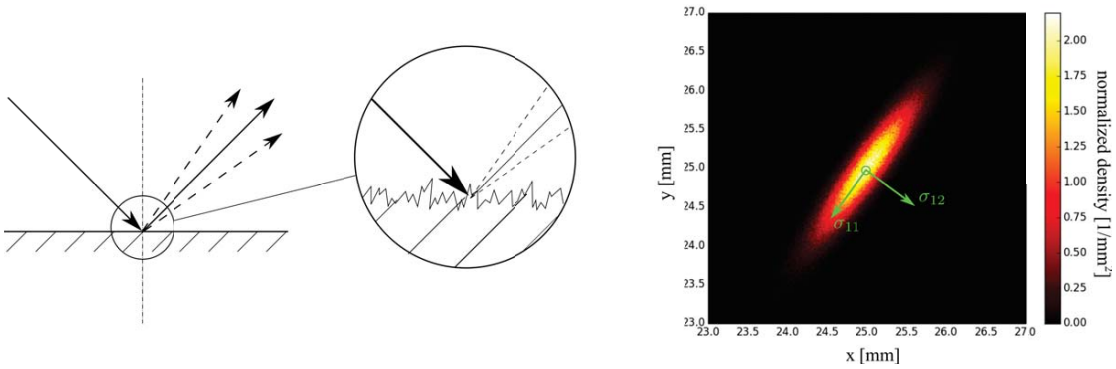

Fig. 5. Microscopic surface errors lead to narrow-angle dispersion of specular reflection (left). Right: reflection pattern on target. Due to systematic errors brought into by e.g. processing methods of the material, dispersion can have a preferred direction.

In general, it can be distinguished between two ideal cases of reflection: isotropic reflection (maximum dispersion) and specular reflection (no dispersion). In reality, the reflection pattern is a combination of both cases and is described by a bidirectional reflectance distribution function (BRDF). Many different BRDFs have been proposed to meet the variety of many different surface types (Montes and Ureña, 2012).

From the perspective of Monte Carlo ray tracing, it is necessary to express the direction of reflection in terms of probabilities. Isotropic or Lambertian reflection in this regard is the simplest case, since the probability for each reflection direction on the surface hemisphere is the same. This is the case for highly rough or matte surfaces.

Most of BRDF models are based on a Gaussian distribution. Especially when it comes to modelling the specular reflection of mirrors for solar thermal collectors, this is a well-established probability function (Gee et al., 2010; Good et al., 2016; Pettit, 1977; Sutter et al., 2016).

$$f = Ke^{\left(-\frac{\varphi^2}{2\sigma_{21}^2} - \frac{\varphi^2}{2\sigma_{22}^2}\right)} + (1 - K)e^{\left(-\frac{\varphi^2}{2\sigma_{11}^2} - \frac{\varphi^2}{2\sigma_{12}^2}\right)} \tag{9}$$

Eq. 9 essentially incorporates four basic forms of Gaussian specular reflection (Gee et al., 2010):

- Single univariate ($K = 0, \sigma_{11} = \sigma_{12}$)

- Single bivariate ($K = 0, \sigma_{11} \neq \sigma_{12}$)
- Double univariate ($K \neq 0, \sigma_{11} = \sigma_{12}$, $\sigma_{21} = \sigma_{22}$)
- Double bivariate ($K \neq 0, \sigma_{11} \neq \sigma_{12}, \ \sigma_{21} \neq \sigma_{22}$)

The multivariate Gaussian function accounts for a preferred reflection direction, which in reality appears on reflective material. It is caused by the respective processing method, so for example the rolling process in the manufacturing of aluminum mirrors. The superposition of two Gaussian distributions better represents the combined effect of microscopic and macroscopic surface errors. In practice, as long as macroscopic errors (slope, shape, alignment, tracking) are considered random, they are all summed up to a total surface variety σ_{tot} (Rabl, 1985).

$$\sigma_{tot}^2 = \sum_{i=1}^{n} \sigma_i^2 = \sigma_{spec}^2 + 4\sigma_{slope}^2 + 4\sigma_{shape}^2 + 4\sigma_{align}^2 + 4\sigma_{track}^2 \tag{10}$$

It is important to state that the dispersion itself depends on the wavelength and the angle of incident light as well ($\sigma = \sigma(\lambda, \theta)$). This dependency significantly depends on the material type (Good et al., 2016; Sutter et al., 2016). Since there is still no standardized experimental method for the complete spectral assessment of specular material (SolarPACES, 2013), little can be found on wavelength and incidence angle dependency of σ. One relation is the power law that can be derived from (Good et al., 2016) is given by Eq. 11.

$$\sigma(\lambda, \theta) = \sigma\left(\lambda_{ref}, \theta_{ref}\right) \cdot \left(\frac{\lambda}{\lambda_{ref}}\right)^{p} \cdot \left(\frac{\cos\theta}{\cos\theta_{ref}}\right)^{q} \tag{11}$$

3.2. Volume effects:

When an electromagnetic wave is propagating through a medium it will experience both scattering and absorption (Fig. 3). Scattering can be important if the medium contains particles or inclusions as for example in the case of (Cai et al., 2016). Volume scattering can also play an important role in polymeric material (French et al., 2011) or atmospheric calculations such as for solar tower applications. If the medium is mainly homogeneous, however, volume scattering in comparison to surface scattering is rather small and absorption will have most influence on the radiation intensity (Wallner et al., 2005).

The absorption coefficient α is correlated with the extinction coefficient κ – the complex part of the refractive index of a material (Eq. 6).

$$\alpha(\lambda) = \frac{4\pi\kappa}{\lambda} \tag{12}$$

A rough relation between a material's absorbance and the wavelength can be obtained by an exponential Urbach fit. However, this approximation is not accurate in all cases (French et al., 2011).

In order to get from experimental data to usable input for ray tracing, one challenge is to separate between volume and surface effects, as in reality they can only be measured together. This was also pointed out by the work of (Good et al., 2016) and (Wallner et al., 2005).

3.3. Thin-film effects (coatings):

The most common approach to model the reflectance, transmittance and absorptance of a thin-film assembly (coating) is the transfer-matrix method (TMM). Within a layer the electric and magnetic field is the sum of the total forwards and backwards (reflected) waves propagating according to a phase factor. This assumption is described by M_p, the characteristic matrix of a thin-film. Since the continuity condition of the electric and magnetic field across the boundary of the layer p and its adjacent layer is also applies here, the characteristic matrices can be multiplied. Theoretically, this can be done for an infinite number of layers. The result correlates the electric and magnetic field on top and at the bottom of the assembly (see Eq. 13) (Macleod,

2010).

$$\begin{pmatrix} B \\ C \end{pmatrix} = \left\{ \prod_{p=1}^{q} \underbrace{\begin{bmatrix} \cos\varphi_p & (i\sin\varphi_p)/\eta_p \\ i\eta_p \sin\varphi_p & \cos\varphi_p \end{bmatrix}}_{M_p} \right\} \begin{pmatrix} 1 \\ \eta_q \end{pmatrix} \tag{13}$$

with the phase factor φ_i (Eq. 14), the number of layers q (including the substrate) and the optical admittance of the substrate η_q

$$\varphi_i = \frac{2\pi N_i d_i \cos\theta_i}{\lambda} \tag{14}$$

From Eq. 13 an optical admittance of the assembly can be derived.

$$Y = C/B \tag{15}$$

And in the same way as done for the Fresnel equations, the reflectance, transmittance and absorptance of the stack can be calculated.

$$R = \left(\frac{\eta_0 - Y}{\eta_0 + Y}\right)\left(\frac{\eta_0 - Y}{\eta_0 + Y}\right)^* \tag{16}$$

η_0 is the optical admittance of the incidence medium.

$$T = \frac{Re(\eta_q)(1-R)}{Re(BC^*)} \tag{17}$$

$$A = 1 - R - T \tag{18}$$

The transmittance of the assembly is always independent of the direction of the propagation (propagation from the incidence medium to the substrate or from the substrate to the incidence medium (Abelés, 1950)). For the reflectance, however, this is only the case if there is no absorption in any of the layers (only dielectric material), which is usually satisfied for AR coatings, since here absorption is not desired.

Eqs. 13 to 18 present the basis for all thin-film performance simulations and design.

AR/HR coatings

There are many ways to design AR and HR coatings. One possibility is to make them out of multiple quarter wavelength layers. In this case the quarter wavelength condition $\varphi = \pi/2$ has to be satisfied for each layer, so that

$$d_p = \frac{\lambda}{4n\cos\theta_p} \tag{19}$$

and with a successively increasing refractive index according to

$$N_p = \sqrt[p+1]{\frac{n_0}{n_{sub}}} \tag{20}$$

It is however more common, in practice, to use layers with alternating refractive indices. Some examples for the analytical assessment of such layers are (Choi et al., 2014; Mazur et al., 2015; Sahouane and Zerga, 2014) for ST and (Saylan et al., 2015; Sikder and Zaman, 2016) for PV applications.

Especially for single layer AR coatings low refractive material are needed. Promising here are porous sol-gels, because the refractive index is related to the porosity (Prado et al., 2010; Xin et al., 2013).

$$n_p = [(1-p)(n^2-1)+1]^{1/2} \tag{21}$$

where p is the porosity volume fraction and n the refractive index of the base material.

Selective coatings

As described in the previous section, selective coatings are often based on dielectric-metal composites. Eqs. 13 to 18 are only valid for layers with homogeneous properties. It is therefore necessary to approximate the effective refractive index of the composite from the refractive indices of the base materials. This can be done by the Maxwell-Garnett relation.

$$\frac{\varepsilon_{eff} - \varepsilon_m}{L(\varepsilon_{eff} - \varepsilon_m) + \varepsilon_m} = f \cdot \frac{\varepsilon_i - \varepsilon_m}{L(\varepsilon_i - \varepsilon_m) + \varepsilon_m} \tag{22}$$

with the dielectric constants ε_m of the matrix, ε_i of the inclusions and ε_{eff} of the composite. f is the volume fraction of inclusion and matrix and L the depolarization factor.

Some examples for the analytical analysis and design of high-temperature resistant selective thin-film assemblies using the previously described transfer matrix method are (An et al., 2015; Cardenas, 2015; Hernández-Pinilla et al., 2016; Rebouta et al., 2012; Soum-Glaude et al., 2013; Yang et al., 2016).

Particularly interesting for ray tracing applications is the approach of (Tesfamichael and Wäckelgård, 2000) and (Grena, 2010). In their studies they tried to describe the absorptance (reflectance) of a selective solar receiver as a function of the angle of incidence only. Tesfamichael et al. proposed a modified version of the incidence angle modifier law for solar thermal applications (Duffie and Beckmann, 2006)

$$\alpha_{SW}(\theta_i) = \alpha_{SW}(\theta_0) \cdot b_0 \left(\frac{1}{\cos\theta_i} - 1\right)^c \tag{23}$$

Where $\alpha_{SW}(\theta_0)$ is the absorption coefficient at normal incidence.

$$\alpha_{SW}(\theta_0) = \frac{\int_0^\infty s(\lambda) \cdot \alpha(\lambda, \theta_0)\, d\lambda}{\int_0^\infty s(\lambda)\, d\lambda} \tag{24}$$

This model is able to describe different selective surfaces by adjusting the characteristic parameters b_0 and c. Unfortunately, the only available results are those provided by the authors themselves, which were those measured for a Al_2O_3-Ni/Al_2O_3 assembly and a NiO_3-Ni-composite layer.

(Grena, 2010), on the other hand, defines a more general power law based on experimental data from different selective absorption material.

$$\alpha_{SW}(\theta_i) = \alpha_{SW}(\theta_0) \cdot \left[1 - \left(\frac{2\theta}{\pi}\right)^8\right] \tag{25}$$

4. Discussion and Outlook

During the last decades significant progress has been experienced in the development of new materials and collector designs. Especially coatings have gained in importance for the use in solar thermal collector technologies due to more sophisticated processing methods and the possibility of application specific design, but also the increasing success of PV and PVT technologies make great demands on optical simulations.

In this study two major goals have been achieved: First, the current market of materials for solar thermal applications was reviewed; and second, the most commonly used optical models for radiation-matter interaction were summarized.

The outcome of this study could be particularly interesting for implementations of ray tracing optical simulation tools. It could be shown that most ray tracing programs do not consider the option of a more accurate spectral analysis. Whether such an analysis is necessary, might depend on the types of material that are employed. Glass mirrors e.g. do not show very strong variations of scattering with the wavelength, but aluminum and polymer mirrors do. It is also noticed that there is a lack of models that reflect incidence angle dependencies, most of all for selective surfaces.

The radiation-matter interaction models that were presented are a summary of what can be found in current

literature. A key parameter to optically define materials is their refractive index. There are extensive data bases that contain refractive information based on ellipsometry and dispersion relations for many different materials. Such data bases could provide valuable input to optical simulations. Nevertheless, a general problem one faces when trying to get from experimental data to usable input for ray tracing e.g., is to separate between volume and surface effects. This might be important in order to model compounds such as e.g. glass mirrors.

Acknowledgement

This work was co-funded by the European Union (call FP7-PEOPLE-2012-ITN, SHINE project, grant number 317085), and the University of the Balearic Islands.

Literature

Abelés, F., 1950. Recherches sur la propagation des ondes électromagnétiques sinoïdales dans les milieurs stratifiés. Applications aux couches minces. Ann. Phys. (Paris). 12, 596–640.

An, L., Ali, S.T., Søndergaard, T., Nørgaard, J., Tsao, Y.C., Pedersen, K., 2015. Optimization of TiAlN/TiAlON/Si3N4 solar absorber coatings. Sol. Energy 118, 410–418. doi:10.1016/j.solener.2015.05.042

Atkinson, C., Sansom, C.L., Almond, H.J., Shaw, C.P., 2015. Coatings for concentrating solar systems – A review. Renew. Sustain. Energy Rev. 45, 113–122. doi:10.1016/j.rser.2015.01.015

Bader, R., Pedretti, A., Steinfeld, A., 2011. A 9-m-aperture solar parabolic trough concentrator based on a multilayer polymer mirror membrane mounted on a concrete structure. J. Sol. Energy Eng. 133, 31016. doi:10.1115/1.4004353

Barshilia, H.C., Selvakumar, N., Rajam, K.S., Sridhara Rao, D.V., Muraleedharan, K., 2008. Deposition and characterization of TiAlN/TiAlON/Si3N4 tandem absorbers prepared using reactive direct current magnetron sputtering. Thin Solid Films 516, 6071–6078. doi:10.1016/j.tsf.2007.10.113

Cai, Q., Ye, H., Lin, Q., 2016. Analysis of the optical and thermal properties of transparent insulating materials containing gas bubbles. Appl. Therm. Eng. 100, 468–477. doi:10.1016/j.applthermaleng.2016.02.041

Cardenas, J.F., 2015. Modelling the spectral selective solar absorption properties of graphite-silica composite/aluminium structures. Thin Solid Films 586, 76–81. doi:10.1016/j.tsf.2015.04.042

Choi, J., Han, K., Kim, J.H., 2014. Enhanced near infrared reflectance of TiO2/SiO2/TiO2 multilayer structure using a base-catalyzed SiO2 film. Thin Solid Films 569, 100–103. doi:10.1016/j.tsf.2014.08.036

Duffie, J.A., Beckmann, W.A., 2006. Solar Engineering of Thermal Processes, 3rd Editio. ed. John Wiley & Sons inc., New Jersey.

French, R.H., Rodríguez-Parada, J.M., Yang, M.K., Derryberry, R.A., Pfeiffenberger, N.T., 2011. Optical properties of polymeric materials for concentrator photovoltaic systems. Sol. Energy Mater. Sol. Cells 95, 2077–2086. doi:10.1016/j.solmat.2011.02.025

Gee, R., Brost, R., Zhu, G., Jorgensen, G., 2010. An improved method for characterizing reflector specularity for Parabolic Trough Concentrators. SolarPaces Conf. 1–8.

Good, P., Cooper, T., Querci, M., Wiik, N., Ambrosetti, G., Steinfeld, A., 2016. Spectral reflectance, transmittance, and angular scattering of materials for solar concentrators. Sol. Energy Mater. Sol. Cells 144, 509–522. doi:10.1016/j.solmat.2015.09.057

Grena, R., 2010. Optical simulation of a parabolic solar trough collector. Int. J. Sustain. Energy 29, 19–36. doi:10.1080/14786450903302808

Hernández-Pinilla, D., Rodríguez-Palomo, A., Álvarez-Fraga, L., Céspedes, E., Prieto, J.E., Muñoz-Martín, A., Prieto, C., 2016. MoSi2–Si3N4 absorber for high temperature solar selective coating. Sol. Energy Mater. Sol. Cells 152, 141–146. doi:10.1016/j.solmat.2016.04.001

Jeong, S.-H., Kim, J.-K., Kim, B.-S., Shim, S.-H., Lee, B.-T., 2004. Characterization of SiO2 and TiO2 films prepared using rf magnetron sputtering and their application to anti-reflection coating. Vacuum 76, 507–515. doi:10.1016/j.vacuum.2004.06.003

Köhl, M., Meir, M.G., Papillon, P., Wallner, G.M., Saile, S., 2012. Polymeric Materials for Solar Thermal Applications. Wiley-VCH. doi:10.1002/9783527659609

Macleod, H.A., 2010. Thin-Film Optical Filters. CRC Press.

Mazur, M., Wojcieszak, D., Kaczmarek, D., Domaradzki, J., Song, S., Gibson, D., Placido, F., Mazur, P., Kalisz, M., Poniedzialek, A., 2015. Functional photocatalytically active and scratch resistant antireflective coating based on TiO2 and SiO2. Appl. Surf. Sci. 380, 165–171.

doi:10.1016/j.apsusc.2016.01.226
Montes, R., Ureña, C., 2012. An Overview of BRDF Models 1–26.
Pettit, R.B., 1977. Characterization of the reflected beam profile of solar mirror materials. Sol. Energy 733–741.
Prado, R., Beobide, G., Marcaide, A., Goikoetxea, J., Aranzabe, A., 2010. Development of multifunctional sol-gel coatings: Anti-reflection coatings with enhanced self-cleaning capacity. Sol. Energy Mater. Sol. Cells 94, 1081–1088. doi:10.1016/j.solmat.2010.02.031
Rabl, A., 1985. Active Solar Collectors and their Application. Oxford Univ. Press. New York.
Rebouta, L., Pit??es, A., Andritschky, M., Capela, P., Cerqueira, M.F., Matilainen, A., Pischow, K., 2012. Optical characterization of TiAlN/TiAlON/SiO 2 absorber for solar selective applications. Surf. Coatings Technol. 211, 41–44. doi:10.1016/j.surfcoat.2011.09.003
Sahouane, N., Zerga, A., 2014. Optimization of antireflection multilayer for industrial crystalline silicon solar cells. Energy Procedia 44, 118–125. doi:10.1016/j.egypro.2013.12.017
Saylan, S., Milakovich, T., Hadi, S.A., Nayfeh, A., Fitzgerald, E.A., Dahlem, M.S., 2015. Multilayer antireflection coating design for GaAs0.69P0.31/Si dual-junction solar cells. Sol. Energy 122, 76–86. doi:10.1016/j.solener.2015.07.049
Schlick, C., 1994. An Inexpensive BRDF Model for Physically - based Rendering. Comput. Graph. Forum. doi:10.1111/1467-8659.1330233
Schott, 2014. Optical Glass - Data Sheets.
Selvakumar, N., Barshilia, H.C., 2012. Review of physical vapor deposited (PVD) spectrally selective coatings for mid- and high-temperature solar thermal applications. Sol. Energy Mater. Sol. Cells 98, 1–23. doi:10.1016/j.solmat.2011.10.028
Sikder, U., Zaman, M.A., 2016. Optimization of multilayer antireflection coating for photovoltaic applications. Opt. Laser Technol. 79, 88–94. doi:10.1016/j.optlastec.2015.11.011
SolarPACES, 2013. Solar Paces Guideline: Parameters and Method to Evaluate the Solar Reflectance Properties of Reflector Materials for Concentrating Solar Power Technology, VERSION 2.5.
Soum-Glaude, A., Bousquet, I., Thomas, L., Flamant, G., 2013. Optical modeling of multilayered coatings based on SiC(N)H materials for their potential use as high-temperature solar selective absorbers. Sol. Energy Mater. Sol. Cells 117, 315–323. doi:10.1016/j.solmat.2013.06.030
Sutter, F., Heller, P., Meyen, S., Pitz-paal, R., Kennedy, C.E., Fernández-garcía, A., Schmücker, M., Fernández, A., Heller, P., Fernández García, A., Heller, P., Kennedy, C.E., Meyen, S., Pitz-paal, R., Schmücker, M., 2010. A new method to characterize degradation of first surface aluminum reflectors. Proc. SolarPACES 2010 1–8.
Sutter, F., Meyen, S., Fernández-García, A., Heller, P., 2016. Spectral characterization of specular reflectance of solar mirrors. Sol. Energy Mater. Sol. Cells 145, 248–254. doi:10.1016/j.solmat.2015.10.030
Sutter, F., Ziegler, S., Schmücker, M., Heller, P., Pitz-Paal, R., 2012. Modelling of optical durability of enhanced aluminum solar reflectors. Sol. Energy Mater. Sol. Cells 107, 37–45. doi:10.1016/j.solmat.2012.07.027
Tesfamichael, T., Wäckelgård, E., 2000. Angular Solar Absorptance and Incident Angle Modifier of Selective Absorbers for Solar Thermal Collectors 68, 335–341. doi:10.1016/S0038-092X(00)00029-3
Wallner, G.M., Platzer, W., Lang, R.W., 2005. Structure-property correlations of polymeric films for transparent insulation wall applications. Part 1: Solar optical properties. Sol. Energy 79, 583–592. doi:10.1016/j.solener.2005.05.006
Xin, C., Peng, C., Xu, Y., Wu, J., 2013. A novel route to prepare weather resistant, durable antireflective films for solar glass. Sol. Energy 93, 121–126. doi:10.1016/j.solener.2013.04.006
Yang, R., Liu, J., Lin, L., Qu, Y., Zheng, W., Lai, F., 2016. Optical properties and thermal stability of colored solar selective absorbing coatings with double-layer antireflection coatings. Sol. Energy 125, 453–459. doi:10.1016/j.solener.2015.12.022

Experimental and CFD investigations on full volumetric flow to a solar flat-plate glass collector

Pascal Leibbrandt, Thomas Schabbach, Michael Dölz, Martin Rhein

Institut für Regenerative Energietechnik, University of Applied Sciences Nordhausen (Germany)

Summary

In the project solar flat-plate glass collector, a new type of solar collector will be developed which, simplified, consists of 4 glass plates. As subgoal of the project the full volumetric flow and heat transfer in the fluid layer and the collector filling have been examined experimentally and numerically. The experimental setup and the CFD settings are presented. By comparison of experimental data and CFD results the simulation results were checked. It appeared that the CFD simulations are able to model the flow well, so an optimization of the flow and heat transfer in the layer can be carried out numerically.

Keywords: glass collector, fluid distribution, CFD, validation, filling process

1. Collector construction and function

In context of the research project "Nurglassolarflachkollektor" a collector with lower production costs will be developed, which consists primarily of glass. Due to the simplified construction cost intensive production steps such as the absorber welding will be unnecessary and enable an automated production process with fewer production steps. Manufacturing costs can thus be reduced by approximately 20% compared to conventional standard flat-plate collectors. Another advantage is the reduced collector height of <50 mm, which allows a simplified installation and collector field connection, so that other application areas (especially in facade) can be opened up.

The glass collector consists of four planar glass plates, which are glued and sealed by a frame and a fluid layer structure. As shown in Fig. 1 the heat transfer medium passes directly through the middle rectangular disk-space. The coatings on the glasses ensure optimal radiation absorption in the fluid layer and minimize the radiation losses due to reflection and emission, see also Leibbrandt et al. (2014). Insulating gas layers minimize convective heat losses to the front and back. As also shown in Fig.1, the heat transfer fluid has to be distributed full volumetric from the circular collector connection through the flow channel. Without adequate installations in the fluid layer a short-circuit flow would be the follow. The fluid layer structure should also be able to absorb inner/outer forces from/to the fluid layer.

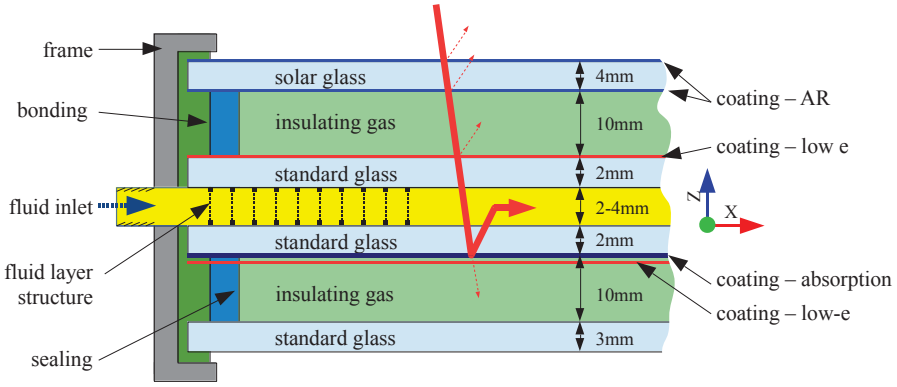

Fig. 1: Construction of the glass collector

Beside the presented problem of the fluid layer flow also the flow in the insulating gas layer, see Leibbrandt et al. (2016) and structural mechanical questions about the glass loads (Rhein et al. (2016)) are investigated in the project. With a specially developed collector test rig collector prototypes are investigated parallel to the project (see Dölz et al. (2016)).

doi:10.18086/eurosun.2016.07.02 Available at http://proceedings.ises.org

2. Full volumetric flow and heat transfer

The flow in the fluid layer should be optimized so that the absorbed radiation energy is transported ideally from the absorption layer to the heat carrier fluid. The collector efficiency factor is:

$$F' = \frac{U_{int}}{U_{int} + U_{loss}} \qquad \text{(eq. 1)}$$

U_{int} is the internal heat transfer coefficient, which describes just the forced convection in the fluid layer here, U_{loss} describes the overall heat transfer losses of the whole collector. So, F' is the theoretical ratio of the useful energy gain to the useful gain that would result if the absorbing surface would be at the fluid temperature, Duffie Beckman (2013). The collector efficiency factor is at its maximum if the flow would be full volumetric. For flat-plate collectors with a fin width of 90-120 mm, the collector efficiency factor is about 88-94%, Wesselak et al. (2013). The heat transfer is at its maximum when the flow is fully homogeneous (without flow areas with no/low flow velocity) and turbulent.

At the same time the pressure drop and the filling/drainback performance must be ensured for a potentially drainback system application.

The rectangular flow channel has a length L, a width B and a thickness of s_F (see Fig. 2). For the analysis presented here the collector size is LxB = 2000x1000 mm, the fluid layer thickness s_F varies between 2 and 10 mm. The fluid layer is inclined at an angle φ against the horizontal.

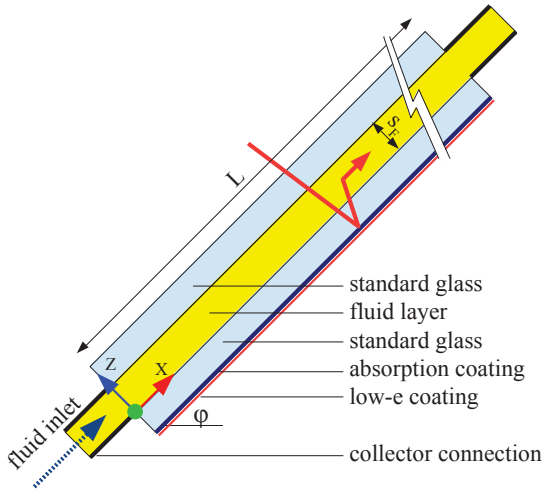

Fig. 2: Problem definition

Starting from a circular collector connection the heat transfer fluid should be distributed ideally. The flow velocity $\overrightarrow{u_i}$ at any point i of the fluid layer field consists of the flow velocity components u_i, v_i and w_i - see Fig. 3(a).

$$\overrightarrow{u_i} = \begin{pmatrix} u_i(x,y,z) \\ v_i(x,y,z) \\ w_i(x,y,z) \end{pmatrix} \qquad \text{(eq. 2)}$$

In case of homogeneous flow, the flow velocity $\overrightarrow{u_{i,opt}}$ is the same at all points of the fluid layer and consists only of velocity components in the main flow direction - see Fig. 3(b).

$$\overrightarrow{u_{i,opt}} = \begin{pmatrix} u_i(x) \\ 0 \\ 0 \end{pmatrix} \qquad \text{(eq. 3)}$$

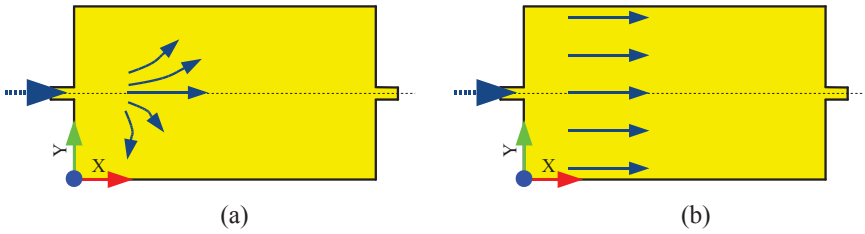

Fig. 3: Flow types in the fluid layer

For the experimental investigation of the flow behavior in the fluid layer 2 glasses in size of 2000x1000x4 mm each were glued and sealed with a 10 mm aluminum spacer in between. Later, the fluid film thickness will be reduced to up to 2-4 mm. For stabilization of the fluid layer the glasses were fixed with mounting rails in the experimental setup – see Fig. 4.

For volume flow generation and pressure control a laboratory thermostat was used, so that the fluid temperature could be adjusted and kept constant. Volume flow rate, in-/outlet temperatures and the pressure drop were determined.

The fluid was enriched with particles before the collector inlet via an injector pipe to visualize the flow behavior. The particle selection was based on a number of preliminary tests. Based on practicality, slip behavior and density expanded glass granulate, ceramic microspheres, polyester plates and soda-lime glass balls were tested. The particles had to be able to reflect the incoming light well. They should be small enough to have no effect on the flow and ensure a slip-free behavior in contrast to the fluid. Also different lighting media, such as halogen spotlights, fluorescent lighting tubes and led were tested.

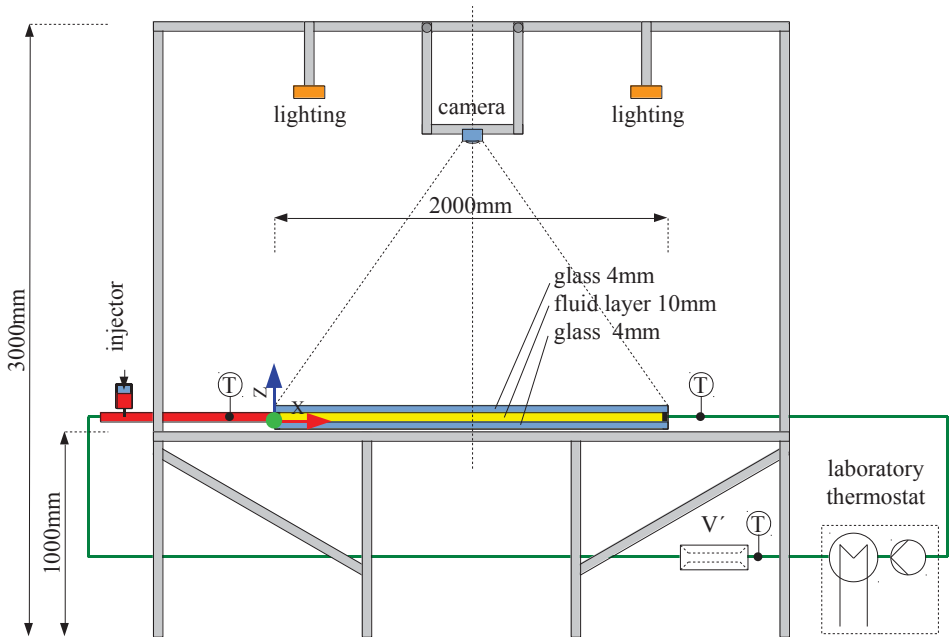

Fig. 4: Test setup full volumetric flow

The flow field was recorded with an HD-camera (50 frames/sec) from above. The generated single images were aligned, optimized and transferred to an image stack by using an image processing program. That image stack was transformed to a single image by subtraction, so it was possible to visualize the trail of the particles and to identify areas with low velocity. Ideally, the flow velocity should be identical in all points in the layer (see above).

So, three versions of different fluid layer structures (V00 - V02, see Fig. 5) were initially investigated experimentally. The inlet and outlet was located centrally on the short side of the fluid layer.

- In version V00 the fluid flows through the fluid layer without any internals.
- In version V01 the fluid is slowed right after the inlet with a central small barrier (width = 100 mm) and is so distributed sideways.
- Version V02 features a wide barrier (width = 900 mm) which directs the fluid to the long fluid layer wall.

Moreover, the experimental investigated versions V00 - V02 were simulated numerically using a simplified 2D CFD model. By preliminary investigations, the numerical discretization, the choice of flow and turbulence models and the admissibility of the 2D simplification ($z = 0$) were tested and validated. The boundary conditions were in all experimental analysis and simulations set identical to

$$\dot{V} = 140\,\frac{l}{h} \qquad p \approx 1\ bar \qquad T \approx 20°C.$$

As shown in Fig. 5, there is a good correlation between experimental and numerical data. In version V00 qualitatively similar flow swirls are identifiable. In versions V01 and V02 the distribution of the fluid to the edges agrees qualitatively in experiment and CFD results. Therefore, it can be assumed for additional versions that the CFD model provides sufficiently results and can be used to optimize the fluid distribution better than in the reference experiment V00. In addition, the option will be tested, to measure the velocity field locally with Prandtl tubes for example.

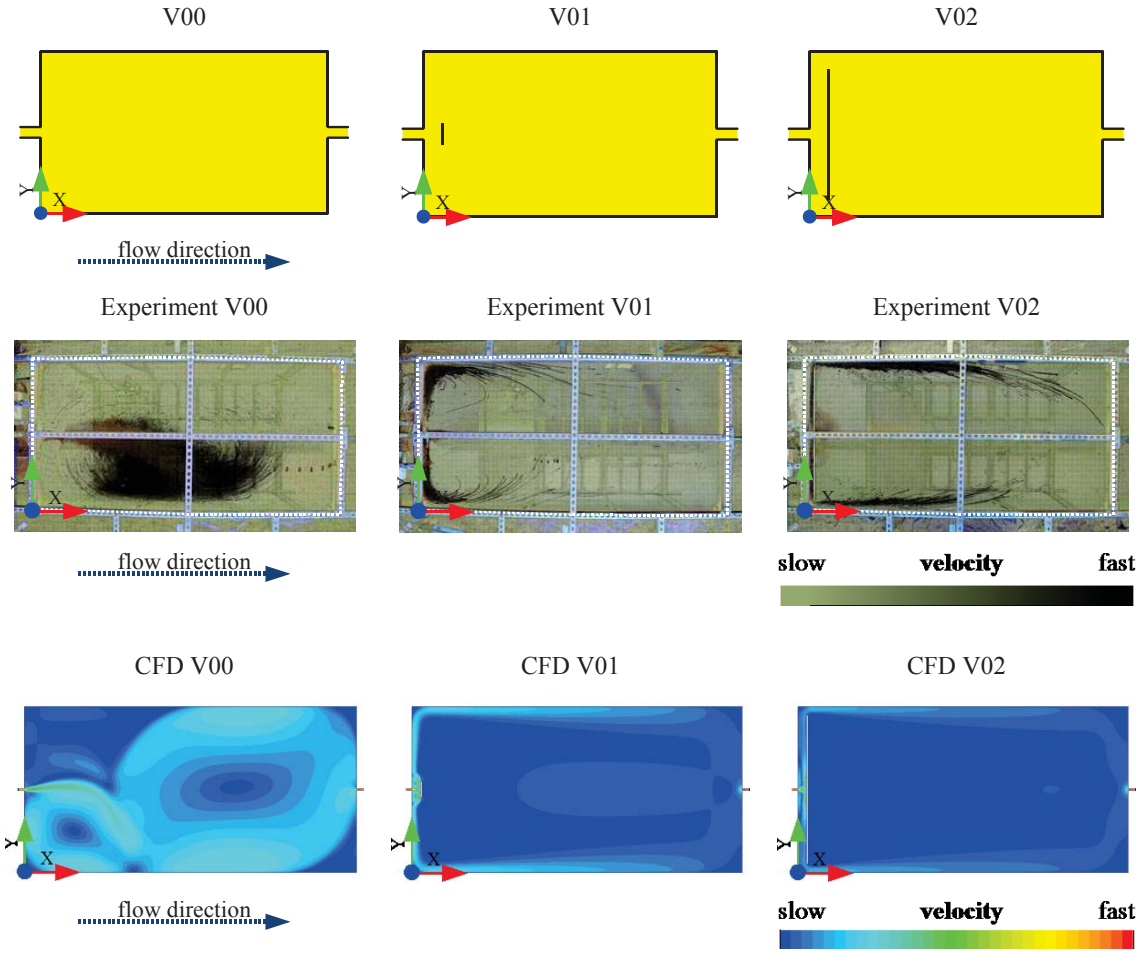

Fig. 5: Comparison of velocity distribution (middle: experiment, bottom: CFD)

After the qualitative validation of the CFD simulations additional fluid layer structures (V03-V08) were investigated numerically. So the optimization could be done more quickly. The experimental investigations took about 2-3 days per version, the simulation time was about a few hours per version.

The analysis of the homogeneity was carried out with the qualitative evaluation of flow visualization and the standard deviation of flow velocities u_i from the CFD simulations. It is:

$$std = \sqrt{\frac{1}{n}\sum_{i=1}^{n}\left(u_i - \frac{1}{n}\sum_{i=1}^{n} u_i\right)^2} \qquad \text{(eq. 4)}$$

Also the pressure loss was read from the simulation data. In these 2D simulations, the pressure loss is determined over a reference layer thickness without any boundary layer influence. It is:

$$\Delta p = p_{inlet} - p_{outlet} \qquad \text{(eq. 5)}$$

For better overview these criteria are represented relative to the reference version V00.

Tab. 1: Velocity distribution, standard deviation and pressure loss V00 – V08

V00 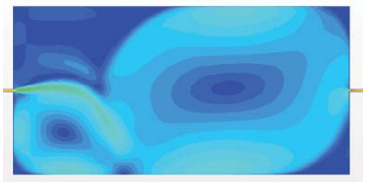 std = 100% Δp = 100%	**V01** 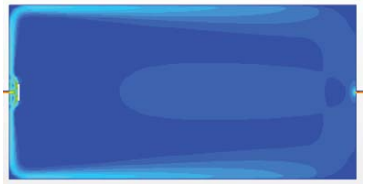 std = 100,2% Δp = 102.3%	**V02**  std = 95.4% Δp = 101.6%
V03  std = 99.2% Δp = 104.1%	**V04** 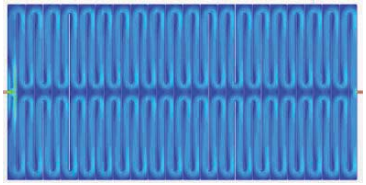 std = 82.5% Δp = 124.3%	**V05**  std = 92.5% Δp = 101.0%
V06 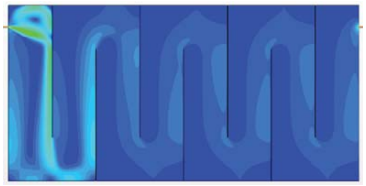 std = 98.2% Δp = 105.0%	**V07** 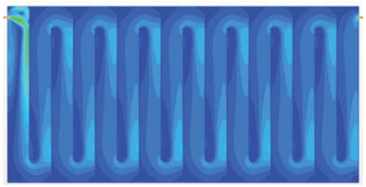 std = 88.1% Δp = 106.7%	**V08** 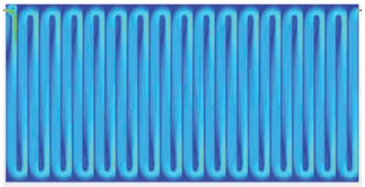 std = 77.6% Δp = 159.6%

Results:

- V00, V03: In fluid channels with central inflow on the short collector side without fluid layer structures occur a flow expansion and thus a lowering of the average flow velocity. Generally, two flow swirls arise. The main flow direction tends thereby to a collector side, the other is barely flowed. For s_F = 2 mm and ideal distribution is Re = 78.
- V01, V02 and V05: In fluid channels with central inflow on the short collector side with fluid layer structures at the collector inlet a flow distribution to the long collector sides occurs. The fluid layer structures at the inlet are not able to distribute to the fluid over the whole collector length.

- V04, V06 – V08: In fluid channels with inflow on the short collector side with fluid layer structures the fluid is distributed optimally. From reasons of material saving, manufacturability and an ease of installation, fluid layer structures with lateral inlets (V06-V08) are appropriate preferable. The choice of the resultant channel width and geometry influence can be made regarding to flow homogeneity and thus to heat transfer. For s_F = 2 mm and good distribution (V08) is Re = 1213.

Also other structures have been tested so far, which are capable to distribute the heat transfer fluid quite well. As expected the pressure loss rises for more complex fluid layer structures. Especially in the versions V04, V06-V08 the fluid layer structure is able to connect the fluid layer glasses. The result is a sandwich structure which is able to carry internal and external loads from/to the fluid channel.

The CFD optimized fluid layer structures will be investigated experimentally in the further proceeding of the project. In addition, there are first collector prototypes under construction, which also will be tested on the collector test rig. This prototype studies will be supported by additional 3D CFD and FEM investigations with regard to the fluid distribution and the glass loads analysis.

After the optimization of the fluid layer structure, the influence on heat transfer was investigated. For this purpose, a 3D CFD model with the boundary conditions, as shown in Fig. 6, was used. The fluid layers' dimension was set to LxBxs_F = 2000x1000x10 mm. The inclination of the layer was 45°. For these simulations 3 fluid layer structures, similar to versions V00, V06 and V07 were analyzed. The backside of the fluid channel has been set up with a constant heat flow density $\dot{q}_{abs}$ which corresponds to the absorbed solar radiation power. At the front convective heat transfer with a constant heat transfer coefficient and fixed ambient temperature was assumed. In reality the convective heat transfer coefficient depends on the front side temperature. The edges of the fluid channel have been supposed to be adiabatic. The fluid inlet temperature was set to 20°C; the inlet velocity was varied between 0.25 – 1.00 m/s (35 – 140 l/(m² h)).

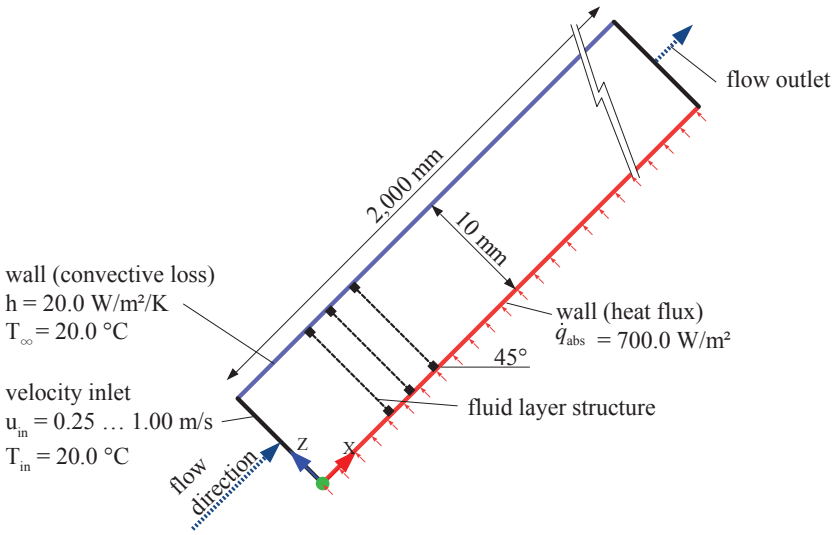

Fig. 6: CFD setup heat transfer

To rate the quality of the heat transfer through the fluid layer the useable enthalpy-flow $\dot{q}_{use}$ at the layer outlet was set into relation to mean fluid temperature difference. It is:

$$h_f = \frac{\dot{q}_{use}}{\overline{T_{abs}} - \overline{T_f}} \qquad \text{(eq. 6)}$$

To compare the collector efficiency factor of the fluid layer F_f' with standard flat-plate collectors it is assumed, that the overall loss heat transfer coefficient $U_{loss} = 4\ W/(m^2K)$. U_{loss} describes the collector heat losses over the sides and the back of the collector which are not part of the presented CFD simulations. The efficiency factor of the fluid layer F_f' is:

$$F_f' = \frac{h_f}{h_f + U_{loss}} \qquad \text{(eq. 7)}$$

Tab. 2: Influence of fluid layer structures on heat transfer (3D CFD results)

		u_{in} in m/s		
		0.25	0.50	1.00
fluid layer structure V00	$\dot{q}_{use}$ in W/m²	565.95	630.53	657.35
	h_f in W/m²/K	372.86	365.07	360.68
	$\boldsymbol{F_f'}$	**98.9%**	**98.9%**	**98.9%**
fluid layer structure V06	$\dot{q}_{use}$ in W/m²	558.99	628.45	658.76
	h_f in W/m²/K	337.87	327.60	405.85
	$\boldsymbol{F_f'}$	**98.8%**	**98.8%**	**99.0%**
fluid layer structure V07	$\dot{q}_{use}$ in W/m²	556.11	617.33	651.18
	h_f in W/m²/K	343.25	421.14	625.53
	$\boldsymbol{F_f'}$	**98.8%**	**99.1%**	**99.4%**

The temperature distribution is shown in Fig. 7. In the versions V06 and V07 a temperature inhomogeneity can be seen especially at the end of the individual fluid channels. They are formed due to the lower flow velocity and lead to local temperature maxima (hot spots). They should be minimized by a suitable flow guidance. At these hotspots the heat transfer reduces and high temperature gradients occur which also lead to stresses in the glasses.

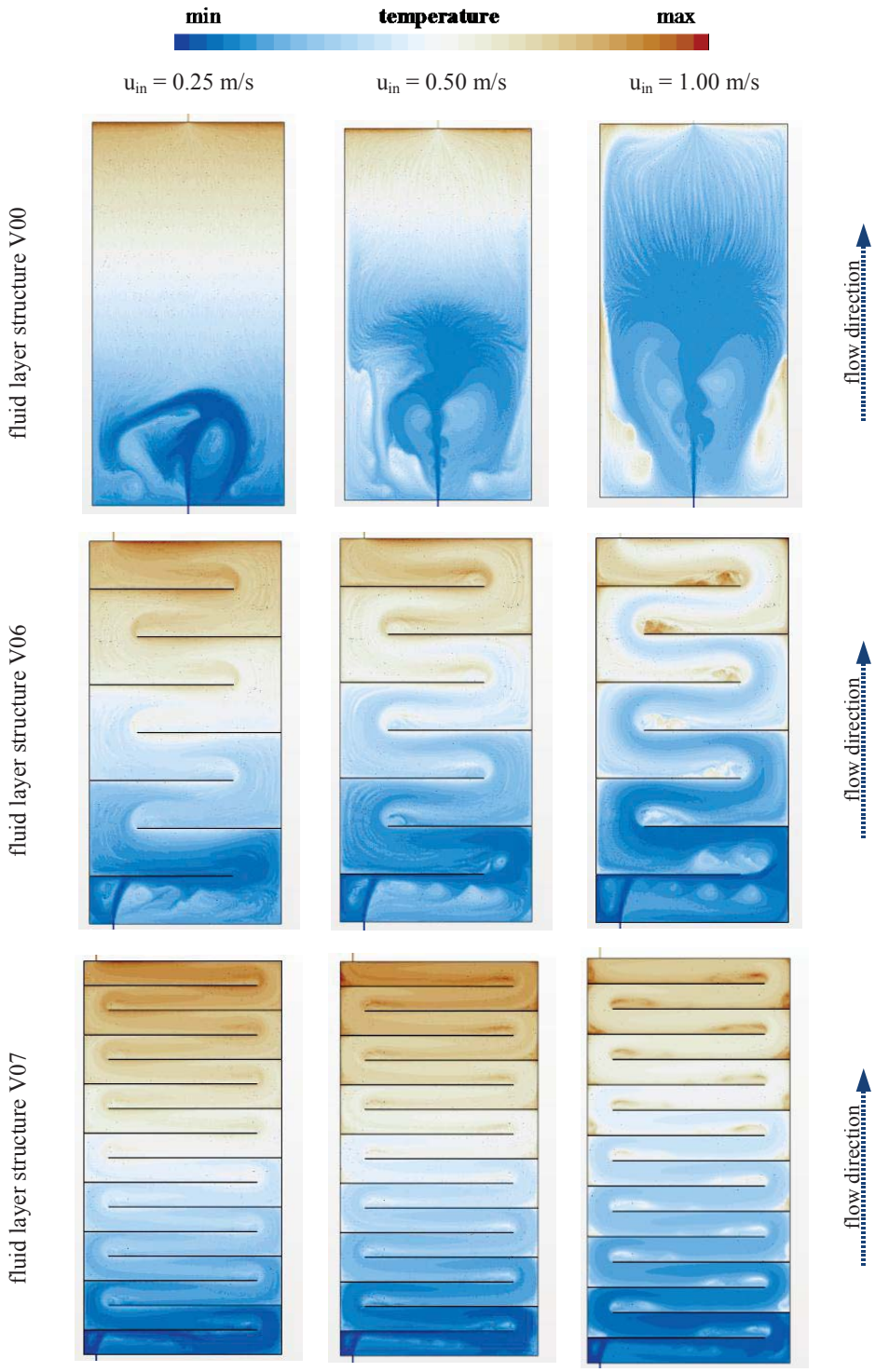

Fig. 7: Influence of fluid layer structures on temperature distribution (3D CFD results)

The versions with fluid channels as fluid layer structures lead to the best results for fluid distribution and heat transfer. This was shown by using experimental investigations and CFD simulations of the fluid layer.

These results are used as input quantities for experiments and FEM simulations to optimize structural behavior of the collector and are used as guidelines for first collector prototype design.

3. Collector filling

As mentioned above, the collector should also be suitable for a potential drain back use. The fluid layer structure should not only ensure a homogeneous flow and a good heat transfer but should also allow a fast and gas-free filling and completely emptying of the collector.

For first assessment the filling behavior was tested on a smaller version of the fluid layer with the measurement of $LxBxs_F$ = 500x250x10 mm. The fluid layer was confined with 4 mm single pane safety glass in the experiment. Target was an air-free filling in the least possible time. For this a simplified drainback system with open drainback reservoir, as shown in Fig. 8, was realized. A HD-camera gave the opportunity to have a detailed look to the fluid layer, detect gas bubbles and ascertain the filling time.

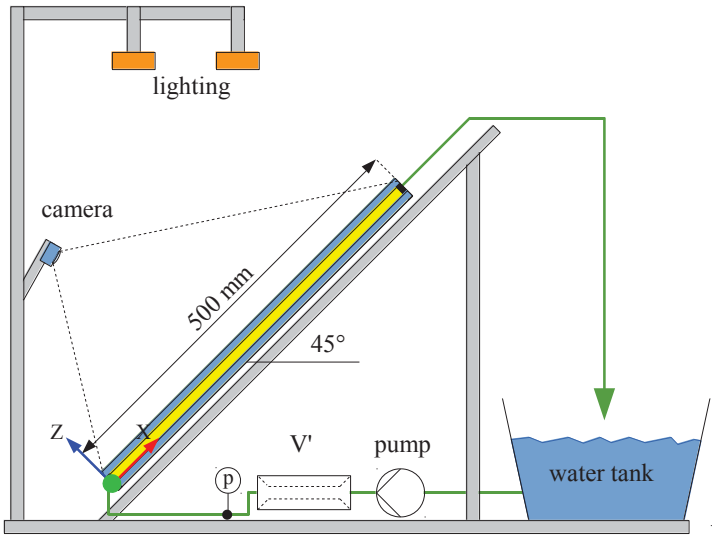

Fig. 8: Test setup collector filling

The lighting and contrast enhancement for better visualization of the bubbles were done with led spotlights and an all-around led belt on the glasses. The volume flow was generated with a pump after the drainback reservoir and was identified with an impeller counter.

The filling process is shown for different inlet velocities by single pictures in the interval of 10 seconds in Fig. 10.

- With the inlet velocity of u_{in} = 2 m/s the filling time was under 10 seconds. In addition to that, it is demonstrated, that a big amount of air bubbles is captured in the fluid layer. These air inclusions remain for several minutes in the collector. By internal flow rolls the air bubbles are circulated periodic in the fluid layer. Only by a short stop of the pump, the air bubbles can partially escape.
- With an inlet velocity of u_{in} = 1 m/s the filling time increased up to 12 seconds. The entry and circulation of air bubbles were reduced compared to the higher filling velocity. After 30 seconds of filling time there were just little bubbles at top of the fluid layer.
- Regarding to the proportionality the filling time increased up to 24 seconds with an inlet velocity of u_{in} = 0.4 m/s and after 30 seconds there are just a minimal amount of air inclusions left in the fluid layer. Compared to the higher filling velocities there was a worse venting of the upper corners to observe.

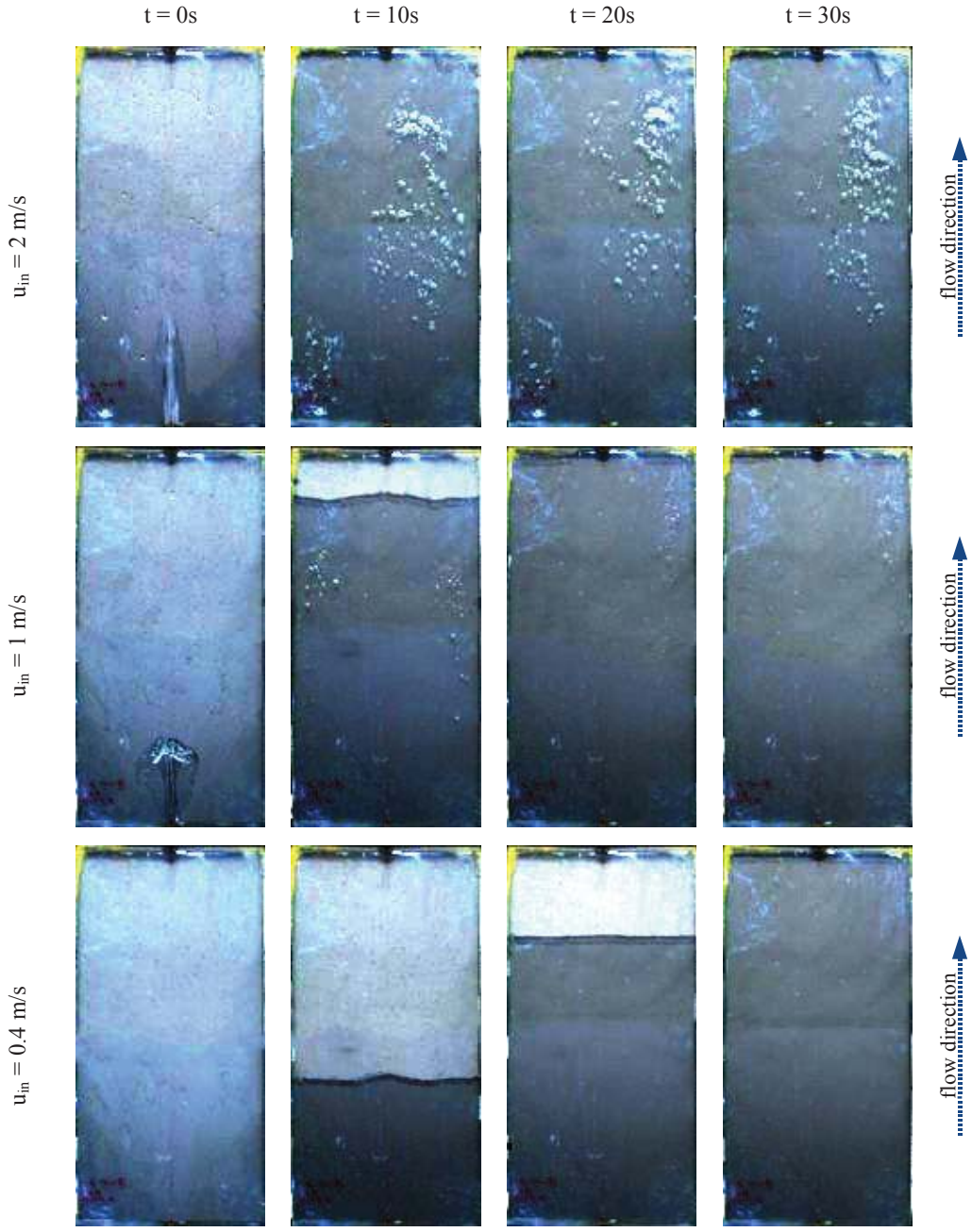

Fig. 9: Experimental results filling tests

In addition to these experimental investigations also CFD simulations on the filling behavior were carried out. In the simulations the fluid layer thickness was varied to check these influence on the filling behavior, too. For this purpose, a 3D CFD model inclined at an angle of 45° was used. Also a two-phase model which considered the interaction of the water and the air in the filling process was used. For better comparison of filling processes at different fluid layer thicknesses the fill level l_F was defined. This is the relationship of water volume in the fluid layer to the entire fluid layer volume.

$$l_F(t) = \frac{V_{water}\,(t)}{V_{total}} \qquad \text{(eq. 8)}$$

Tab. 3 and Fig. 10 illustrate the results of the filling process with different fluid layer thicknesses and variable inlet velocities. For this simulations the inlet velocities were decreased in contrast to the experiments.

Tab. 3: Influence of filling velocity and fluid layer thickness on filling level l_F (3D CFD results)

		u_{in} in m/s		
		0.25	0.50	1.00
l_F (t=140s) in %	s_F = 10 mm	99.3	98.5	87.6
	s_F = 4 mm	99.8	96.9	78.1
	s_F = 2 mm	99.1	89.5	53.3

- For s_F = 10 mm there are good filling results for the both low filling velocities. Of course the filling process takes longer for the lowest velocity. Even for this fluid layer thickness a vent at the highest filling rate is only partially possible because of the forming of circulating air bubbles – see also experimental results.
- The behavior and the trend of poor ventability is proofed for smaller fluid layer thicknesses. For s_F = 4 mm an air free filling is even not possible for medium filling velocity. An air free filling for s_F = 2 mm is only possible with quite slow filling velocity.

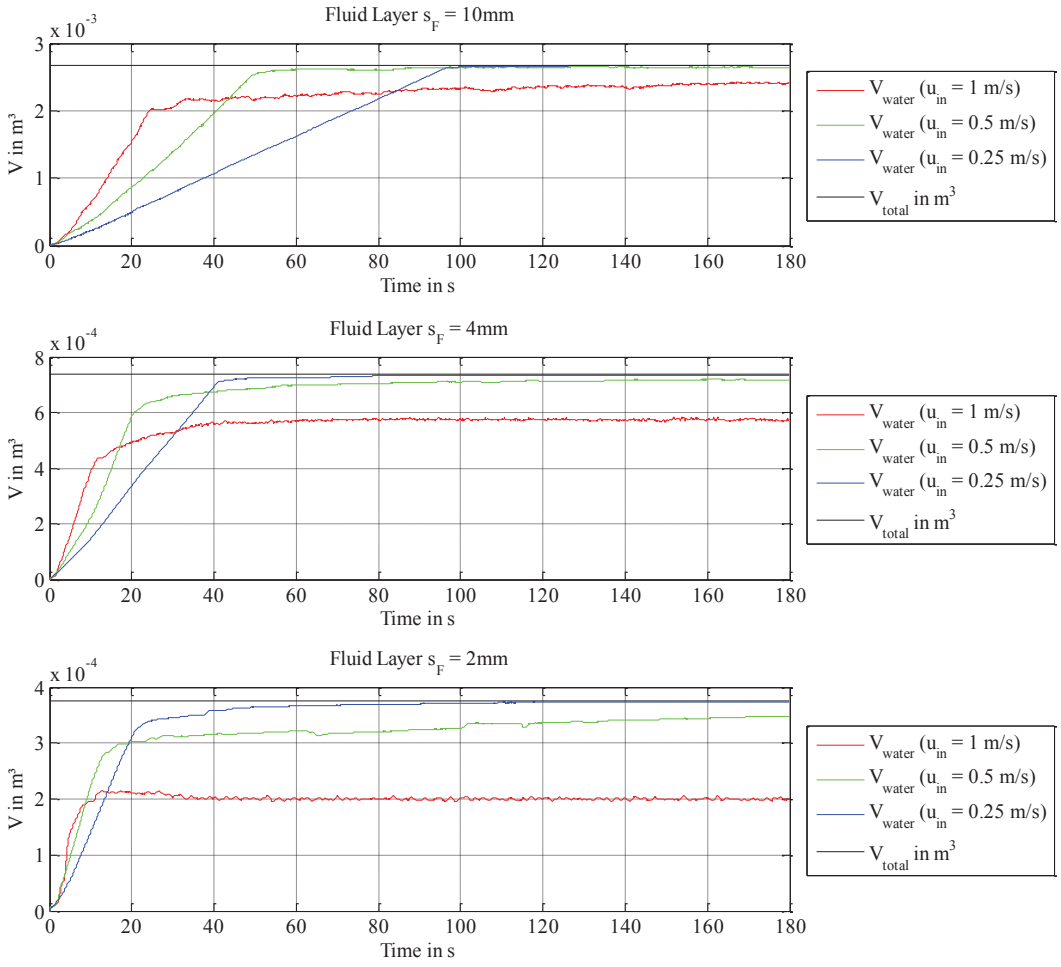

Fig. 10: Influence of filling velocity and fluid layer thickness on filling level (3D CFD results)

For the filling process therefore the lowest possible filling velocity should be chosen. In collectors and whole systems, the overall filling time will be the limiting factor. Further studies are needed to validate the filling behavior of collectors in the original scale with integrated fluid layer structure in addition to the presented results. Moreover, there will be a different filling behavior with water glycol mixture because of the varying material data.

4. Outlook

In continuation to the project additional fluid layer structures will be investigated experimentally and numerically. Target will be to increase the flow homogeneity, heat transfer and stability of the fluid layer. The pressure loss, manufacturability and long term stability must also be considered. The performance of the entire collector will be checked during QDT-testing in dependence of the different fluid layer structures. Mechanical load tests with internal and external forces will also take place.

5. Acknowledgement

The project “NUGLACOL – Development of a low cost solar flat-plate collector system based on glass”, FKZ 0325557, is carried out in cooperation with the companies Wagner Solar, Energyglas and Kömmerling and funded by the German Federal Ministry for Economic Affairs and Energy (BMWi) based on a decision of the German Federal Parliament. The authors are grateful for the financial support.

CFD analysis were carried out with the flow simulation software STAR-CCM+ by CD-adapco. Thanks for the support.

6. References

Dölz; Schabbach; Leibbrandt; Rhein, 2016. Low-Cost-Kollektorprüfstand für quasidynamische Messungen im Hochtemperaturbereich. 26. OTTI Symposium Thermische Solarenergie, Bad Staffelstein

Duffie, Beckman, 2013. Solar Engineering of Thermal Processes, fourth ed. John Wiley & Sons Inc., Hoboken, New Jersey

Leibbrandt; Schabbach; Dölz; Rhein, 2016. CFD-Untersuchungen zu konvektiven Wärmeverlusten in Scheibenzwischenräumen mit großem Seitenverhältnis. 26. OTTI Symposium Thermische Solarenergie, Bad Staffelstein

Leibbrandt; Schabbach; Weber, 2014. Flachkollektoren aus Glas – erste Untersuchungsergebnisse. 24. OTTI Symposium Thermische Solarenergie, Bad Staffelstein

Rhein; Schabbach; Dölz; Leibbrandt, 2016. Strukturanalyse eines Nurglaskollektors unter Berücksichtigung statischer und dynamischer Lasten. 26. OTTI Symposium Thermische Solarenergie, Bad Staffelstein

Stephan, F. 2016. Experimentelle Untersuchung zur vollvolumetrischen Durchströmung eines Nurglaskollektors. Hochschule Nordhausen, Bachelor Thesis

Wesselak et al. 2013. Regenerative Energietechnik, 2. ed. Springer Vieweg, Berin, Heidelberg

Conference Proceedings

EuroSun 2016
Palma de Mallorca (Spain), 11 - 14 October 2016

Effect of collector self-shading on the performance of a Biomass/Solar Micro-CHP system

Ana I. Palmero-Marrero and Armando C. Oliveira

University of Porto – Faculty of Engineering, Porto (Portugal)

Abstract

This paper describes an exhaustive study concerning solar geometry and the effect of shading between collectors in the overall performance of a new biomass/solar micro-CHP system. The system is a new prototype of a 6 kWe plant, based on a micro-cogeneration Organic Rankine Cycle (ORC) system, driven by a combination of solar thermal and biomass sources. Both sources may be used separately or combined. The solar thermal energy is obtained through medium-temperature concentrating compound parabolic solar collectors (CPC) with evacuated tubes. The system simultaneously produces electrical energy and low/medium temperature heat. In this study, five scenarios are presented: no shading; shading when the collector tilt is seasonally adjusted; and shading when the collector tilt is fixed in three positions during the year. Results of system simulation under the different operating modes are presented. Namely, a comparison of solar fractions and global electrical efficiencies of the system, with and without shading, is carried out.

Keywords: *collector shading, organic Rankine cycle, micro-cogeneration, solar energy, biomass*

1. Introduction

Micro-generation is the decentralised production of electricity, through different means with an electrical power output up to 50 kW. Micro-cogeneration, or micro-CHP, is the combination of micro-generation with useful heat (Pehnt et al., 2006). Among the several existing technological solutions for micro-cogeneration, Organic Rankine Cycle (ORC) systems are an interesting solution in cases where the heat demand is significantly larger than electricity needs, which is the case of residential and also other buildings (Oliveira et al., 2014). Micro-ORC systems driven by renewable energy sources have attracted the attention of many researchers. Either theoretical or experimental works have been carried out, including developments and improvements in system components (Facão et al., 2008), (Palmero-Marrero and Oliveira, 2009), (Quoilin et al., 2011), (Qiu et al., 2011), (Twomey et al., 2013), (Jradi et al., 2014).

A micro-cogeneration ORC system driven by a combination of solar thermal and biomass sources was simulated by the authors (Palmero-Marrero et al., 2015), (Oliveira et al, 2014). In the simulations, high efficiency vacuum-CPC solar collectors were used, and the power cycle used a highly efficient rotary lobe expander. The results obtained allowed the prediction of system annual performance. The system is under development and the prototype will be installed and tested in Benguerir (Morocco) during this year, in the framework of the REELCOOP project, funded by the EU (REELCOOP, 2015). For solar resource assessment purposes, Meteonorm software was used to generate climatic data of Benguerir.

The previous simulation of the overall system was performed considering no shading between the collectors. However, limitations in the available space may recommend shorter distances between collectors. Taking into account the dimensions of the vacuum-CPC collectors and the layout of the solar field, an extensive study about shading effects was developed.

The performance of the overall system is analyzed, taking into account the shading effects between collectors. Namely, a comparison of solar fractions and global electrical efficiencies of the system, with and without shading, is carried out. Five scenarios are presented: no shading; shading when the collector tilt is seasonally adjusted; and shading when the collector tilt is fixed in three positions during the year. When shading occurs, the reduction in incident solar radiation must be compensated by an increase in the boiler input energy. With

doi:10.18086/eurosun.2016.07.03 Available at http://proceedings.ises.org

that in mind, the biomass consumption for all scenarios was also calculated for different operating periods. In the next sections, detailed numerical simulations for specific climatic and operational conditions are presented.

2. Description of the system and numerical model considering shading

2.1 System description

A computer model of the overall system was developed by combining EES (Engineering Equation Solver) with TRNSYS software. EES was used for the power cycle calculations and TRNSYS for simulating the solar circuit and overall system. The system, including its main components, is schematically represented in Figure1 (Oliveira et al., 2014).

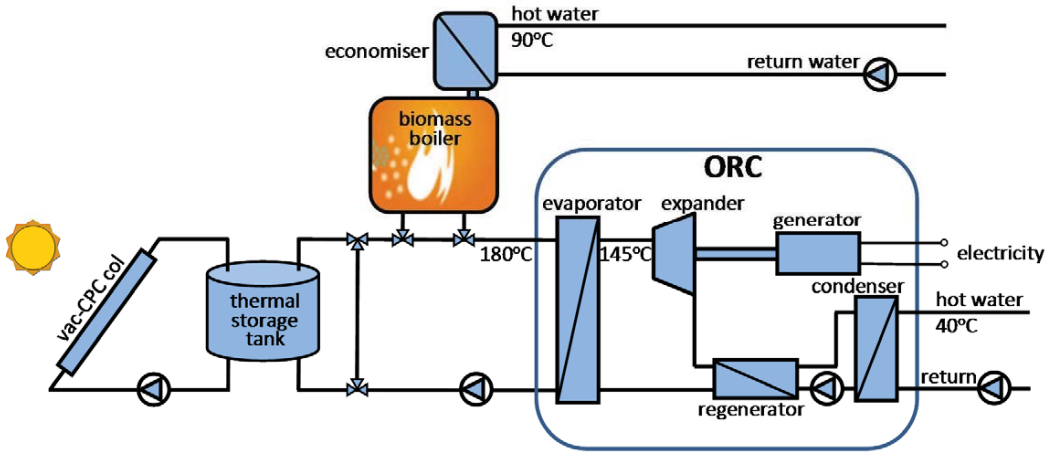

Fig. 1: System schematic representation.

The ORC/power cycle model consists of a set of algebraic equations representing the thermodynamic behavior of each ORC component. The ORC simulated by EES includes the following main components: evaporator, expander, generator, regenerator, condenser and pump. For an electrical output equal to 6 kW, a maximum temperature for the solar circuit of 180ºC is assumed. It is expected that the ORC operates under almost steady-state conditions, as the cycle driving temperature is kept approximately constant. However, the simulations in TRNSYS are transient, as they reflect changes in solar radiation and ambient temperature. The solar circuit simulated by TRNSYS includes the following main components: solar collector, boiler with economizer, thermal storage, pumps and control system. Different working fluids are used in the system: thermal oil for the solar sub-system, water for the condenser, and Solkatherm (SES36) fluid for the ORC.

The inputs of TRNSYS components and EES components are shown in Table 1.

Table 1: Definition of the inputs for each component

Programs	Components	Inputs
TRNSYS	Climatic data (Meteonorm)	Local: Benguerir (Morocco); Latitude = 32.13ºN, Longitude = 7.98ºW.
	Vacuum-CPC collectors (vac-CPC)	A_{coll} = 145.92 m^2; 32 modules (4 in series, 8 in parallel) Concentration factor (C) =2.573 Efficiency curve parameters: η_0=0.623; a_1=0.59 $Wm^{-2}K^{-1}$; a_2=0.004 $Wm^{-2}K^{-2}$ Tested flow rate = 0.0274 kg $s^{-1}m^{-2}$ Maximum total flow rate = 0.557 kg/s Collector tilt: seasonally adjusted at **51º** (from October to February), **29º** (March, April and September) and **8º** (from May to August), optimised according to period of the year and manufacture. Collector azimuth = 0º Fluid specific heat = 2620 J/kgºC (oil TERMOL 5HT) IAM data: file created through the numerical simulation of the novel CPC collector
	Thermal storage	Tank volume = 8000 l Thermal stratification modelled with 6 fully-mixed equal volume layers Tank losses: negligible Cold-side temperature (from Evaporator) = 140ºC Cold-side flowrate (from Evaporator) = 0.412 kg/s
	Boiler	Rated capacity = 60 kW Set point temperature = 180ºC Boiler efficiency = 0.9
	Pump	Maximum power = 0.6 kW
EES	Evaporator	Useful heat: 40 kW Outlet temperature = 145ºC Superheating = 5ºC
	Expander	Efficiency (η_{exp}): 0.75
	Generator	Efficiency = 0.95 Net electrical power = 6 kW
	Regenerator	ΔTmin = 10ºC Efficiency = 0.82
	Condenser	Condenser temperature = 45ºC

2.2 Climatic data

For solar resource assessment purposes METEONORM (Meteotest, 2015) was used to generate data of Global Horizontal Irradiation, GHI, solar azimuth and height, and ambient temperature (Ta), on an hourly basis for a typical year. The chosen location was Benguerir (Morocco), with a latitude = 32.13ºN and a longitude = 7.8ºW. For this city, the data from Meteonorm and local data were compared - see Fig. 2. In this case, the Meteonorm data were obtained with interpolation from nearby meteorological stations.

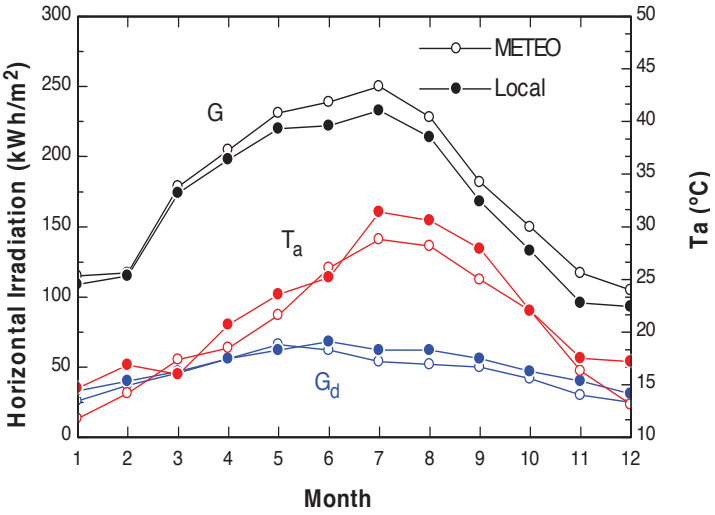

Fig. 2: Global (G) and diffuse (Gd) solar radiation on horizontal surface and ambient temperature (Ta) with Meteonorm data and local data for Benguerir.

The major differences between Meteonorm and local data concern horizontal global irradiation (G) and ambient temperature (Ta) for July, August and September (difference lower than 10% for these months).

2.2 Solar geometry analysis

A solar geometry analysis was carried out, considering the collector dimensions together with the location. Figure 3 shows the dimensions used to calculate the shading effect between the evacuated-CPC collectors, where L_{aper} is the collector aperture (L_{aper} = 0.437 m), d is the collector row separation (d = 0.7 m), tilt is the collector tilt ($tilt$ = 51°, for the most unfavourable situation) and h_{sun} is the solar altitude angle.

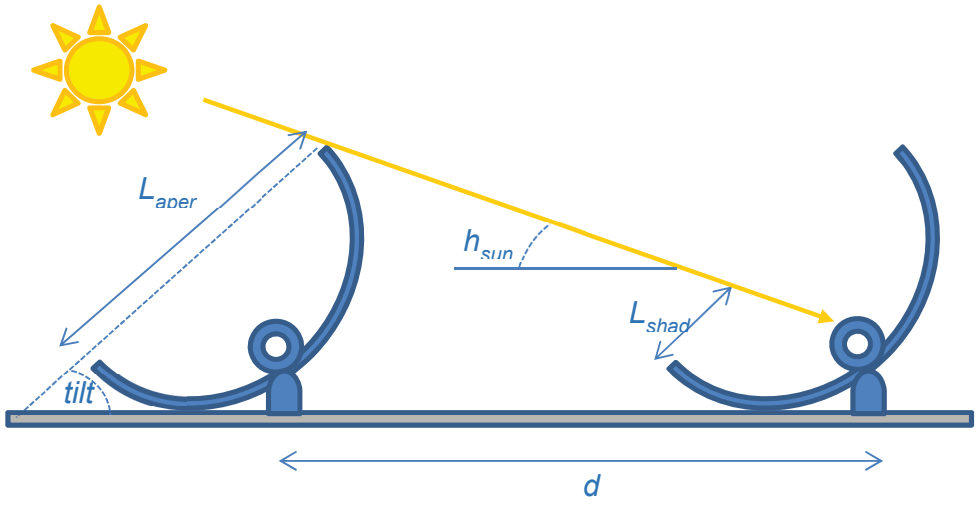

Fig. 3: Schematic view of the evacuated-CPC collectors with some parameters used for the solar geometry analysis.

Using the geometric relationship between a plane of any orientation and the incoming beam solar radiation for the specific latitude (Benguerir's latitude = 32.13ºN), it is possible to calculate the relations of the position of the sun relative to that plane. Considering the worst scenario for shading, when the solar altitude angles are lower (winter period) and the collector tilt is 51°, the shading effects were analysed, and the results will be shown in the next section.

3. Simulation results

Figure 4 shows the shaded length on the collector (L_{shad}) and the percentage of insolated length (*%insolated*) for each solar altitude angle, defined as (see eq. 1):

$$\%insolated = 100 \cdot (L_{aper} - L_{shad})/L_{aper} \quad \text{(eq.1)}$$

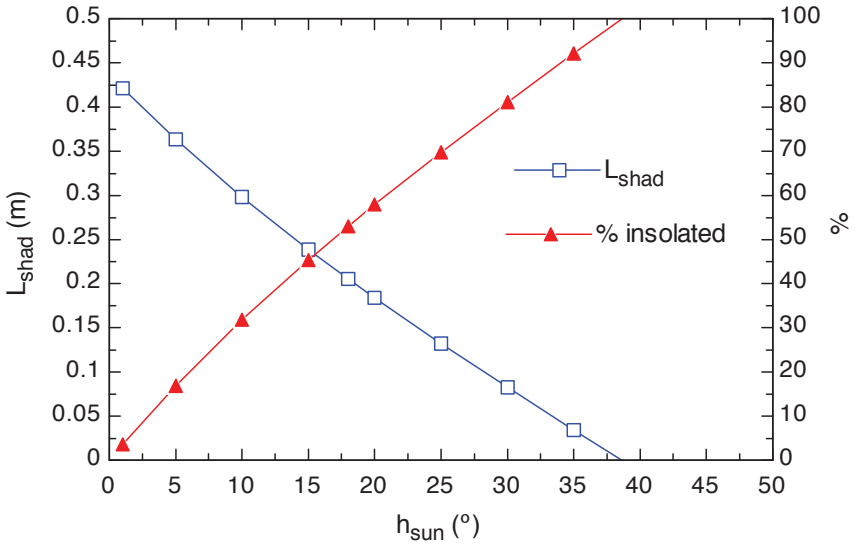

Fig. 4: Shaded length and insolated percentage on the CPC collector depending on solar altitude angle (h_{sun})

As can be seen, for the considered dimensions, the collector surface is completely insolated for a solar altitude angle above about 40º. To know in which months and hours shading occurs, it is necessary to combine the information with a solar chart (solar altitude angle and solar azimuth angle for different days and hours).

Figure 5 shows the solar chart for Benguerir, using an average day for each of the months, and results when the collector tilt is equal to 51º (from October to February).

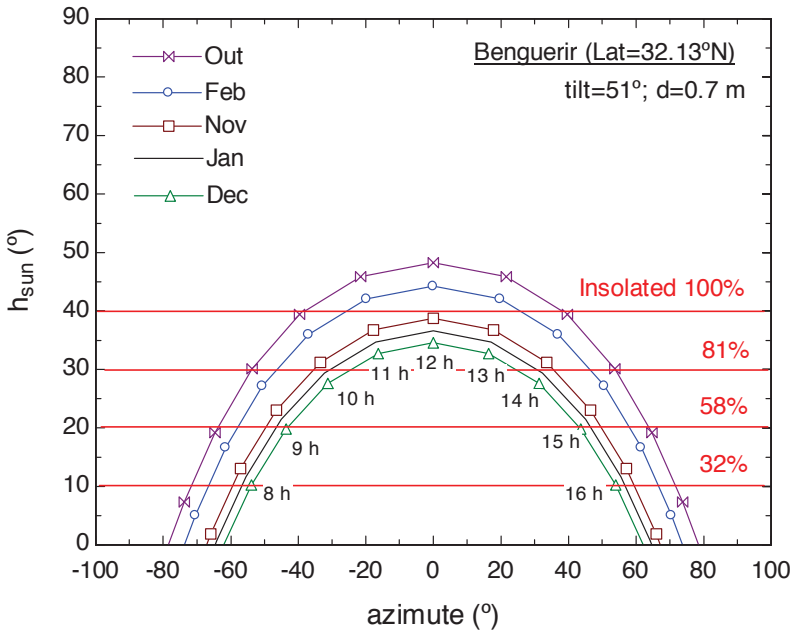

Fig. 5: Solar chart for Benguerir (months when the collector tilt is equal to 51º)

As can be seen, during the average day of November, December and January, part of the collectors behind the first row are always shaded.

Now, it is necessary to evaluate the performance of the system when the shading effect is considered. In the next section, the overall system performance is analysed.

3.1 Overall system performance

The monthly and annual performances, with and without shading, are shown in Table 2.

The table contains values of solar radiation incident on the collector surface (G_{coll}), useful heat gain on the solar collectors (Q_{usef_coll}), energy supplied by the boiler (Q_{aux}), and solar fraction (f), considering that no shading occurs and when the effect of shading is taken into account. The solar fraction can be defined as (see eq. 2):

$$f = Q_{usef\_coll}/(Q_{usef\_coll} + Q_{aux}) \quad \text{(eq. 2)}$$

Table 2: Monthly and annual performance results

Month (tilt)	G_{coll} (MWh)		Q_{usef_coll} (MWh)		Q_{aux} (MWh)		F	
	no shading	Shading	no shading	shading	no shading	shading	no shading	Shading
Jan (51º)	29.23	24.03	6.12	4.99	23.64	24.77	0.21	0.17
Feb (51º)	24.35	21.45	4.61	4.05	22.63	22.83	0.17	0.15
Mar (29º)	30.93	29.46	5.58	5.22	24.18	24.54	0.18	0.18
Apr (29º)	30.95	29.77	5.19	4.83	23.61	23.97	0.17	0.17
May (8º)	33.70	33.59	6.01	5.96	23.75	23.80	0.20	0.20
Jun (8º)	34.57	34.52	6.48	6.45	22.32	22.35	0.23	0.22
Jul (8º)	36.23	36.16	6.82	6.78	22.94	22.98	0.23	0.23
Aug (8º)	33.88	33.72	5.28	5.22	24.48	24.54	0.18	0.18
Sep (29º)	29.56	28.20	5.47	5.12	23.33	23.68	0.18	0.18
Oct (51º)	28.65	25.68	4.74	4.15	25.02	25.61	0.16	0.14
Nov (51º)	27.77	23.69	5.36	4.85	23.44	23.95	0.19	0.17
Dec (51º)	28.11	22.13	5.84	4.53	23.92	25.23	0.20	0.15
Annual	**367.91**	**342.40**	**67.48**	**62.15**	**282.92**	**288.25**	**0.19**	**0.18**

The annual thermal performance can be related to the annual net electricity generation of the power block. Assuming that the solar driven CHP plant is running non-stop throughout the year (helped by the boiler), the annual generated electricity value is 52.6 MWh, with an operating period of 24 h/day. The annual global electrical efficiency ($\eta_{electr,annual}$) is defined as the total electrical energy generated during one year (E_{elec}), divided by the sum of all annual energy inputs – boiler input energy (Q_{boiler}) plus incident solar radiation (G_{coll}), as can be seen in eq. 3:

$$\eta_{electr.annual} = E_{elec}/(Q_{boiler} + G_{coll}) \quad \text{(eq. 3)}$$

Figure 6 shows the annual solar fraction (f_{annual}) and annual global electrical efficiency for 5 scenarios: no shading, with shading when the collector tilt is seasonally adjusted (3 tilts), and when the collector tilt is fixed during the whole year at 51º, 29º and 8º.

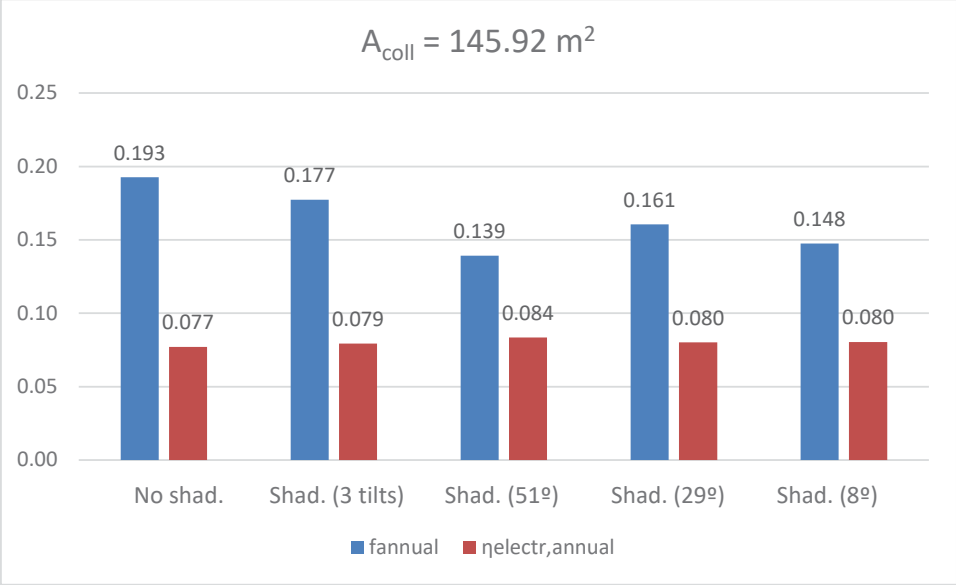

Fig. 6: Annual solar fraction and annual global electrical efficiency for the 5 scenarios.

Shading reduces the annual solar fraction from 0.193 to 0.177 (a relative reduction of 8%). When shading and solar fractions are analysed, the best scenario is when the collector tilt is seasonally adjusted (three times per year): the annual solar fraction with 3 tilts is equal to 0.177. If a single constant tilt of 29º is used, the resulting solar fraction is equal to 0.161, which means a relative reduction of 9%. This will be the best tilt for a constant inclination throughout the year.

A higher solar fraction does not imply a higher global electricity efficiency, since the reduction in incident solar radiation is compensated with an increase in the boiler input energy (with a higher efficiency). On the other hand, biomass consumption increases with the increase in boiler input energy. For that, the biomass consumption for all scenarios was also calculated. For 24 hours/day operation, the biomass consumption will be equal to 69.41 tons/year (3 tilts), 72.62 tons/year (tilt=51º), 70.82 tons/year (tilt=29º) and 71.92 tons/year (tilt=8º).

4. Conclusions

In the present paper, an exhaustive study concerning solar geometry and the effect of shading between collectors in the overall performance of a new biomass/solar micro-CHP system was presented. The performance of the overall system was analyzed, taking into account the shading effects between collectors and the location where the prototype will be installed and tested (Benguerir, Morocco). Five scenarios were considered: no shading, with shading when the collector tilt is seasonally adjusted (3 tilts), and when the collector tilt is fixed during the whole year at 51º, 29º and 8º.

Considering the worst scenario for shading, when the solar altitude angles are lower (winter period) and the collector tilt is 51º, the study shows that the collector surface is completely insolated for a solar altitude angle above about 40º. Then, during the average days of November, December and January, part of the collectors behind the first row are always shaded. To evaluate the performance of the system when shading is considered, annual solar fractions (f_{annual}) and annual electrical efficiencies ($\eta_{electr,annual}$) were assessed. The best performance corresponds to a collector tilt that is seasonally adjusted (three times per year): f_{annual} with 3 tilts is equal to 0.177 and $\eta_{electr,annual} = 0.08$. When shading occurs, the reduction in incident solar radiation must be compensated by an increase in boiler input energy, and so the $\eta_{electr,annual}$ remains practically constant for the different scenarios analysed. Biomass consumption increases with the increase in boiler input energy: for an operating period of 24 hours/day, biomass consumption will be equal to 69.41 tons/year (3 tilts), 72.62 tons/year (tilt=51º), 70.82 tons/year (tilt=29º) and 71.92 tons/year (tilt=8º). After the results, if a single constant tilt throughout the year is used, the best tilt is 29º.

Acknowledgments

The REELCOOP project receives funding from the European Union Seventh Framework Programme (FP7/2007-2013), under grant agreement nº 608466. All consortium partners are acknowledged, especially those involved with the development of this prototype: University of Evora (Portugal), IRESEN (Morocco) and MCG Solar (Portugal).

References

EES-Engineering Equation Solver, Program Manual, F-Chart Software (available at http://www.fchart.com), 2016.

Facão J., Palmero-Marrero A., Oliveira A.C., 2008, Analysis of a Solar Assisted Micro-Cogeneration ORC System, International Journal of Low Carbon Technologies, vol.3 n.4, pp.254-264.

Jradi M., Li J., Liu H., Riffat S., 2014, Micro-Scale ORC-Based Combined Heat and Power System Using a Novel Scroll Expander, International Journal of Low Carbon Technologies, Advance Access published February 20, 2014, available online (doi:10.1093/ijlct/ctu012).

Meteotest, Meteonorm Handbook, Parts I, II and III. Bern, Switzerland (available at http://www.meteotest.ch), 2015.

Oliveira A.C., Palmero-Marrero A., Soares J., Horta P., Brouwer J., Saraiva C., Frej H., Bennouna E.G and Lalami S., 2014, Presentation and Preliminary Simulation of a Biomass/Solar Micro-Cogeneration ORC System, Proceedings book of the 13th International Conference on Sustainable Energy Technologies SET2014, 25-28th August 2014, Geneva, Switzerland.

Palmero-Marrero A.I, Oliveira A.C, 2009, Economic Analysis of a Solar Assisted Micro-cogeneration Organic Rankine Cycle System, Proceedings book of the 8th International Conference on Sustainable Energy Technologies SET2009, 31st August to 3rd September, 2009, Aachen, Germany.

Palmero-Marrero A.I, Soares J. and Oliveira A.C, 2015. Numerical simulation of a new biomass/solar micro-cogeneration ORC system. Proceedings book of the 14th International Conference on Sustainable Energy Technologies – SET 2015, 25th - 27th of August 2015, Nottingham, UK.

Pehnt M., Cames M., Fischer C., Praetorius B., Schneider L., Schumacher K., Voβ Jean-P., 2006, Micro Cogeneration: Towards decentralized energy systems, Ed. Springer, Germany.

Qiu G., Liu H., Riffat S., 2011, Expanders for Micro-CHP Systems with Organic Rankine Cycle, Applied Thermal Eng, vol.31, pp.3301-3307.

Quoilin S., Orosz M., Hemond H., Lemort V., 2011, Performance and Design Optimization of a Low-Cost Solar Organic Rankine Cycle for Remote Power Generation, Solar Energy, vol.85, pp.955-966.

REELCOOP project: http://www.reelcoop.com, 2015.

TRNSYS 17 - A Transient System Simulation Program, Solar Energy Lab, University of Wisconsin-Madison, (available at http://sel.me.wisc.edu/trnsys), 2013.

Twomey B., Jacobs P.A., Gurgenci H., 2013, Dynamic Performance Estimation of Small-Scale Solar Cogeneration with an Organic Rankine Cycle Using a Scroll Expander, Applied Thermal Eng, vol.51, pp.1307-1316.

ISES International Solar Energy Society

Conference Proceedings

EuroSun 2016

Palma de Mallorca (Spain), 11 – 14 October 2016

Thermal simulation and efficiency of a hermetically sealed flat plate collector with a fully adhesive edge bond

Hermann Riess[1], Michael Klärner[1], Wilfried Zörner[1] and Richard M. Greenough[2]

[1] Institute of new Energy Systems, Technische Hochschule Ingolstadt, Germany

[2] De Montfort University, The Gateway, Leicester LE1 9BH, United Kingdom

Abstract

This research work deals with the thermal analysis of a hermetically sealed flat plate collector with a gas-filled cavity between absorber and glazing. Published scientific work in this field is discussed and compared to own laboratory testing and simulation results. The impact of the mechanical absorber deflection for small gap sizes between absorber and glazing on the collector efficiency are investigated. A parameter study for gas-filled collectors with a fully adhesive edge bond was conducted. Four different types of functional models were built and tested to validate the simulation model. Impacts affecting the thermal efficiency such as the absorber deflection of solar collectors with a fully adhesive edge bond were analysed and evaluated. A system simulation was conducted analysing the components temperatures and the annual collector yield.

Keywords: *solar thermal; absorber; gas-filled; edge bond;*

1. Introduction

In a standard flat plate solar collector, the highest heat loss is caused via the front loss (Tabor 1958, Beikircher 2009). This loss, in turn, can be split up into a radiative and a convective part. Modern collectors are equipped with a high selective coating with absorbance values of 0.95 respectively emission values of less than 0.05. This means 95 % of the short-wave sunlight is absorbed and only 5 % of the heat radiation (long-wave) emitted. Consequently, the highest loss in a flat plate collector with a high selective coated absorber is caused by the convection between absorber and glazing (Platzer 1988, Beikircher 2009, Tabor 1958). Consequently, reducing the convective heat transfer is a promising approach to increase the efficiency.

A common and successful method to reduce the convective front heat loss is the use of transparent insulation material. In particular, a transparent component is put between absorber and the ambient retarding the convection process. The measures can be classified according to their geometrical position to the absorber (Platzer 1988, Kaltenbach 2003) – structures parallel and perpendicular to the absorber, chamber structures and quasi-homogenous structures. The exhibit for a collector with a structure parallel to the absorber is the ordinary glazed flat plate collector. Yet, there were several approaches to use two or more layers to suppress free convection. Usually, plastic foils or glasses were used as layer material. Remarkable boosts in efficiency were calculated and demonstrated (Rommel et al. 2003, Beikircher 2010, Föste 2013). Absorber parallel structures such as multi-covers are finding infrequent use in solar collectors.

Structures perpendicular to the absorber are, amongst others, honeycomb structures. A wide field of valuable publications on the convective heat transfer itself and on honeycomb structures have been published. There might be still some challenges concerning the long-term stability as well as problems during stagnation but a decent performance level was demonstrated (Hollands 1965, Tabor 1969, Buchberg et al. 1976, Kessentini et al. 2013). However, due to the demanding requirements in solar collectors concerning the long-term stability and costs, these measures are not widely spread. Chamber structures are closely linked to absorber perpendicular and parallel structures and are usually made out of multiple wall sheets. The method

Selection and/or peer review under responsibility of Scientific Committee
doi:10.18086/eurosun.2016.07.07 Available at http://proceedings.ises.org

retards convection in a similar way to the other structures mentioned above but results in a deterioration of the solar transmission coefficient. Since the chambers are usually made out of plastics the negative effects of ageing and long-term stability applies here as well as on the honeycomb insulation.
Svendsen and Jensen (1987), Svendsen (1992) respectively Nordgaard and Beckman (1992) investigated the use of monolithic silica aerogel in solar collectors. Aerogel is a highly porous solid body in which more than 95 % of the volume is air. Hence, it is an outstanding insulation material. Up to date, the use of aerogel insulation in solar collectors is linked with no economic advantages, as the material costs are exorbitant.
Beside transparent insulation between absorber and glazing, the possibility of evacuating this gap was analysed as well. In theoretical studies, an efficiency of 41 % at an operating temperature of 150 °C was calculated (Eaton and Blum 1975). Benz and Beikircher (1999) concluded in a laboratory testing that the convective heat coefficient is reduced by up to 65 % in the continuum range compared to air. Buttinger et al. (2009, 2010) analysed an evacuated compound parabolic collector (CPC) and confirmed efficiencies above 50 % for working temperatures of more than 150 °C. A significant drawback of these collector types can be seen in the complex design, the high requirements concerning mechanical loads and sealing methods, which prevents a low-maintenance lifetime.
A gas-filled interspace between glazing and absorber is a promising approach in reducing the convective heat loss. Vestlund et al. (2009) analysed the thermal performance of a gas-filled solar collector at ambient pressure. In their work, a parameter analysis was carried out including the variation of the inclination angle and the gas type. Based on simulations, a considerable reduction of the overall heat loss by 20 % was shown. Despite of the discussed paths, gas-filled collectors at ambient pressure are not yet as explicitly analysed as the other discussed approaches. The charm of this measure is that there is no additional hardware needed. In return, an efficiency on the level of a well-designed collector with a honeycomb structure or even an evacuated flat plate collector needs to be proven. The aim needs to be in a collector design, which is suitable for a highly automated production with a decent performance level and a cost structure competitive to a conventional solar collector.

2. Design of a collector with an all-round supported absorber with a fully adhesive edge-bond

Within this paper, a collector with an all-round supported absorber with a fully adhesive edge bond was analysed in terms of its thermal behaviour respectively convective heat loss. The basic collector construction was intended to be simple and as similar to an insulated glazing unit as possible in order to produce the collector on a highly automated insulated glazing unit production line. A butyl sealant (primary sealing) was applied directly on the absorber sheet. Subsequently, it was bonded to the glazing to achieve a gastight cavity. During the assembly process of the absorber and the glazing, the gap was filled with an inert gas to lower the convective heat loss. Fig. 1 shows a schematic cross section of the proposed collector design.

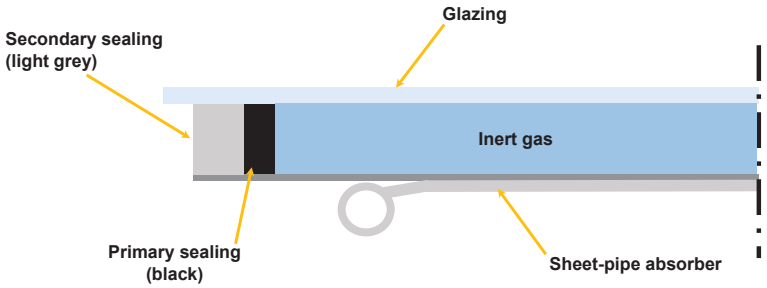

Fig. 1: Schematic cross section of the assembly group of absorber and glazing

In this work, it was favourable to achieve a short distance between absorber and glazing. On the one hand, a shorter distance between absorber and glazing reduces the adhesive costs, which cannot be ignored, as those are a considerable part of the total collector costs. On the other hand, a lower convective heat loss might be achievable by adjusting the gap size to the transition region between conduction and convection, i.e. Nusselt number is still 1 respectively very close to 1. Furthermore, it needs to be considered that less volume is enclosed between absorber and glazing and, thus, a lower mechanical load is applied on the collector

components due to the pressure change (Riess et al. 2014, Vestlund et al. 2009, 2012). Conventional flat plate collectors are designed to have a gap size between 25 and 35 mm whereas in this approach an absorber glazing distance at first of 10 mm for Argon was intended. In a later stage of the research work, gap sizes of up to 20 mm were considered and analysed as well. Even though Xenon and Krypton are allowing very short spacing distances in comparison to Argon or air (Vestlund et al. 2009), those inert gases are of no practical interest. Whilst Krypton is by a factor of 100 times more expensive than Argon, Xenon is even more costly than Krypton. An Argon filled interspace with a gap size of 15 mm for an aperture area of 2 m² causes costs of about 0.06 €. In theory, Krypton enables a shorter distance between absorber and glazing cutting the filling costs down to about 3.5 €. However, own results showed that it is not rational to achieve shorter gap sizes than 15 mm with conventional sheet-pipe absorber (Riess et al. 2014). Beyond that, it needs to be analysed whether the higher filling costs can be justified by an increased annual yield. Consequently, Argon was chosen as a filling gas in this approach whereas air served as the main reference. However, Krypton was used in some considerations as a further reference to Argon and air. Xenon was of no further interest due to its uneconomic pricing and very limited availability.

The principal theory concerning the convective heat loss in a flat plate collector is not discussed in this paper but can be found in (Eismann 2015, Hollands et al. 1976, Tabor 1959).

3. Thermal collector model

Over the decades, there have been plenty contributions in the modelling of flat plate solar collectors. In the early 1940s, Hottel and Woertz (1942) analysed the thermal performance of flat plate solar collectors and presented an analytical calculation approach of the collector efficiency. In 1958, their analytical approach was refined by Tabor (1958). In the same year, Hottel and Whillier (1958) published a linear efficiency model of the correlation between test results and analytical description. Cooper and Dunkle (1980) introduced a non-linear flat plate collector model in which the efficiency is plotted in dependence of the difference between ambient temperature and the mean fluid temperature to the solar irradiation. Klein et al. (1974) presented their investigations on the transient collector behaviour and pointed out the differences to a steady state collector model. Ultimately, the collector simulation model was refined by two heat capacities resulting in a two-node model. Matuska and Zmrhal (2008) as well as Koo (1999) published a collector simulation model that can be downloaded and used without a license fee. The mentioned models are sophisticated and established simulation approaches. A drawback of those approaches is that the component temperatures are not available at all or only very limited. In the case of a hermetically sealed flat plate collector with a fully adhesive edge bond new materials are being used. Moreover, the adhesive is by its nature sensitive to high temperature loads, i.e. temperature magnitude, period and occurrences. Against this backdrop, beside the collector efficiency it was essential to analyse the thermal loads on the components. Finally, in the mentioned freeware simulation models a gas-filled cavity cannot be simulated. Therefore, the simulation model by Reiter et al. (2015) was adapted for the conducted thermal analysis. This collector model was implemented for the development of full polymeric collectors and, hence, the temperature loads were in the focus of Reiter's research (2014). The principle equations, assumptions and simplifications used in this model can be found in Reiter et al. (2015) and, thus, are not further described. However, the convective heat transfer between absorber and glazing was modified. Reiter et al. (2014, 2015) used an approach to calculate the convective heat transfer between absorber and glazing from Matuska and Zmrhal (2009). In contrast to this, the widely used convection theory according to Hollands et al. (1976) was applied in this approach at first.

During the research program it turned out that, there is a considerable discrepancy between the applied convection theory and the laboratory testing results. The thermal influences that led to this deviation are discussed within the next chapters.

The convective heat transfer is amongst other parameters affected by the inclination angle of the collector. However, the inclination effect was not of interest within this research program. Hence, the standard inclination for testing and simulation was always set to 45°.

The inert gas properties as well as the change of the material properties such as viscosity or density depending on the present gas temperature were approximated by polynomials and can be found in the VDI Heat Atlas (Stephan 2010).

4. Thermal simulation according to the convection theory after Hollands et al. (1976)

The efficiency tests of the functional model were conducted on the institute's own indoor solar simulator according to the standard DIN EN 12975-2 (2006). During the complete research programme all parameter relating to the collector efficiency were referenced to the aperture area – unless otherwise stated.
Even though deviations between simulation results and measured efficiency curves were expected, the deviations were surprisingly high. Fig. 2 shows the simulated efficiency curve and the tested efficiency conducted on an indoor solar simulator. The collector parameters are found in Tab. 1.

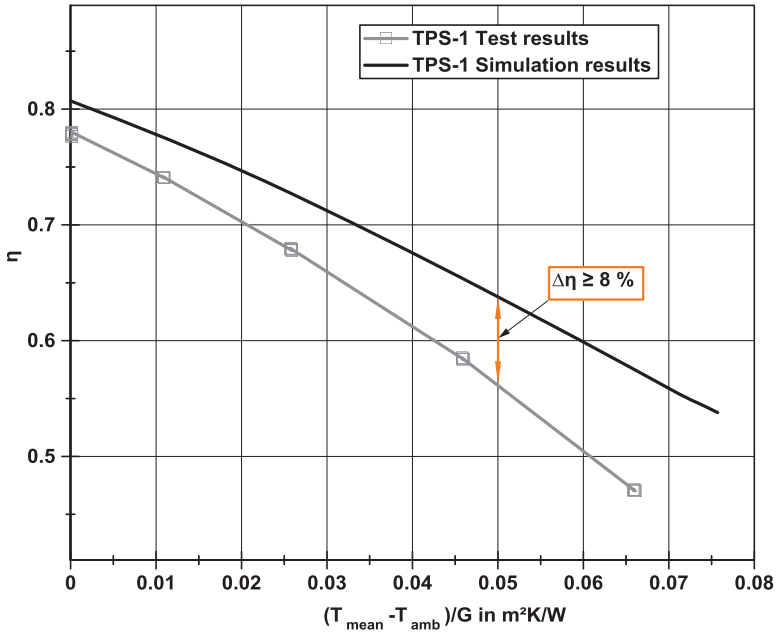

Fig. 2: Comparison between the first simulation model result of a hermetically sealed and gas-filled collector (convection theory according to Hollands et al. 1976) and the measured collector efficiency of the corresponding experimental collector

Tab. 1: Collector parameters used in both laboratory testing and simulation

Parameter	Value
Optical efficiency η_0	0.782
Linear loss coefficient a_1 in W/m²K	3.215
Quadratic loss coefficient a_2 in W/m²K^2	0.023
Aperture area in m²	1.9
Initial gap size in mm	10
Insulation thickness (back) in mm (mineral wool; λ = 0,04 W/mK)	40
Insulation thickness (side) in mm	--
Absorber type	Sheet-pipe
Absorber piping	Harp
Material absorber sheet	Aluminium
Material absorber piping	Aluminium
Gas filling	Argon

The simulated efficiency curve shows a higher performance over the complete operating range. Close to η_0 the deviation between the curves is only 2.4 %. Even though η_0 is called the optical efficiency there is also the fin efficiency F' contributing to this value and, thus, the collector heat loss is affecting this parameter as well. With rising collector working temperatures, the deviation between the two curves increases. For a typical working point of a space heating supporting solar system of $(T_{mean} - T_{ambient}) / G = 0.05$ m²K/W the deviation is more than 8 %. Reiter et al. (2015), however, validated the simulation model for a conventional collector with a double-harp absorber and a gap size of 30 mm. According to their results, the model showed a good correlation between laboratory testing and simulation results. Within this research study, the

simulation model code was modified in terms of the convective heat transfer, smaller gap sizes and gas fillings. Consequently, it can be concluded that the deviation is rather an underestimation of the actual convective heat loss or a failure in the experimental setup than a bug in the model code. At first, it seemed plausible to examine the experimental setup to exclude possible mistakes. As the institute's solar simulator is regularly checked by testing the same reference collector, it was ensured that the test rig was not faulty. Therefore, the collector was further analysed. The gas concentration of the functional model was measured thrice – right after its production, two hours later and 24 h after the production. All measurements gave values well over 95 % Argon concentration. The collector test was conducted 36 h after the production. It can be, therefore, concluded that a high Argon concentration (< 95 %) was in the interspace. However, several observations were made on the absorber. The thin absorber sheet showed a considerable deflection during collector operation. Instead of the intended 10 mm gap between absorber and glazing a mean distance between the two plates of only 6 mm was measured. It turned out that the initial absorber shape has a significant impact on the absorber deflection as its shape is magnified during collector operation (Riess et al. 2014). Consequently, this means absorber areas that had already a shorter distance than 10 mm to the glazing are getting even closer during collector operation and vice versa. Those absorber deflections were hard to spot by a visual inspection through the glazing due to the dark absorber coating and the glass reflections. Instead, holes were drilled through the back of the insulated back plate to conclude on the actual distance of the absorber to the glazing. This was possible as the collector dimensions, e.g. glass thickness and total collector height, were known and measurable. This investigation led to the result that the absorber deflection has a considerable effect on the difference of the collector efficiency prediction. Fig. 3 clarifies the impact of a small deviation in the gap size on the convective heat transfer respectively the collector efficiency for collectors with a small gap size, i.e. within the transition area between heat conduction and convection.

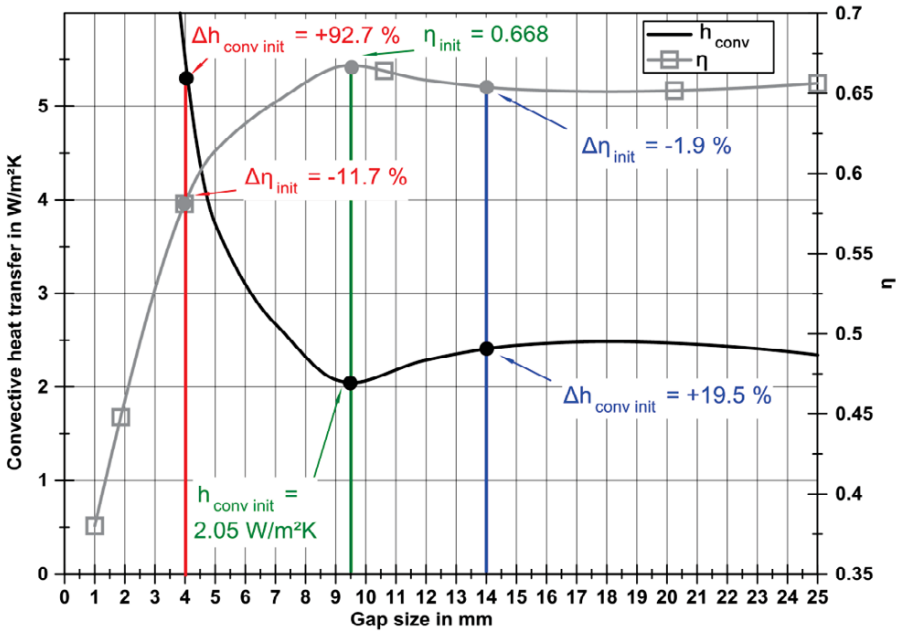

Fig. 3: Simulated change of collector efficiency depending on the gap size after the convection theory of Hollands et al. (1976) for a mean fluid temperature difference of 60 K

For a mean fluid temperature difference of 60 K and Argon as gas filling, the local minimum in the convective heat transfer is at 9.5 mm. If the gap size is decreased by only 5.5 mm the convective heat transfer is increased by almost 93 %. Ultimately, this means an efficiency loss in this typical working point of 11.7 %. In contrast to this, an increased interspace of 5.5 mm to 14 mm is followed only by a slight increase of the convective heat loss of 19.5 % which correspondents to an efficiency loss of less than 2 %. However, the interaction between absorber deflection and convective heat transfer cannot be implemented in to the applied thermal collector model. Reiter et al. (2015) showed that the simulation model was valid for conventional flat plate collector with a normal gap size; it is doubtful whether it is possible to predict the

precise convective heat loss for such short distances between absorber and glazing due to the absorber deflections. Furthermore, it is problematic if not impossible to adjust the gap between the glazing and a conventional sheet-pipe absorber to the local minimum of the convective heat transfer.
As a model validation with this experimental was not conductible another set of functional models with a wider spacing between absorber and glazing and different absorber types was produced and tested.

5. Discussion of different convection theories and model validation

Bartelsen et al. (1993) measured with an own experimental collector under various inclinations the convective heat transfer between absorber and glazing down to gap sizes of 15 mm and compared the results to the one published by Hollands. Their results showed a 25 to 60 % higher convective heat loss than the results computed according to Hollands. Föste (2013) measured the convective heat loss of a collector with a double-glazing unit. In his approach, a collector prototype was equipped with temperature sensors along the glass panes and the absorber. Subsequently, the absorber piping was perfused by hot water (> 150 °C) and the temperature difference between inlet and outlet was measured to conclude on the total collector heat loss. His results showed a deviation of the convective heat loss coefficient between the values derived by the literature and the measured results by up to 32 % between absorber and glazing unit respectively up to 15 % in the glazing interspace. Recently, Eismann (2015) published an extended correlation for the convective heat transfer in the cavity between absorber and glazing. In his study, 22 standard collectors were modelled based on the specifications provided by producers respectively test reports. As the common convection correlations were stated for isothermal plates, Eismann's focus was to extend the Hollands' equation for the convective heat loss for non-isothermal absorbers with a high selective coating. This is in particular of interest as the Hollands equation is only valid for Rayleigh numbers up to 105. The Rayleigh number, however, are by a factor of three higher in the case of coated absorber surfaces (Eismann 2015). According to the author, those facts are resulting in an underestimation of the convective heat loss in solar flat plate collectors. Eismann extended in his approach the convection equation according to Hollands by fitting it to the equation of ElSherbiny et al. (1982). This results in a better accordance for selective coated absorber surfaces.
For the author's own model validation, an experimental test was setup in which the convective heat transfer between absorber and glazing was measured. The collector 'TPS-AlCu20' was, therefore, in addition to the already applied 55 mm thick mineral wool further insulated on the back and on the side with polystyrene (t = 80 mm, $\lambda = 0.038$ W/m²K). The collector was equipped with temperature sensors to conclude on the thermal collector losses (Fig. 4).

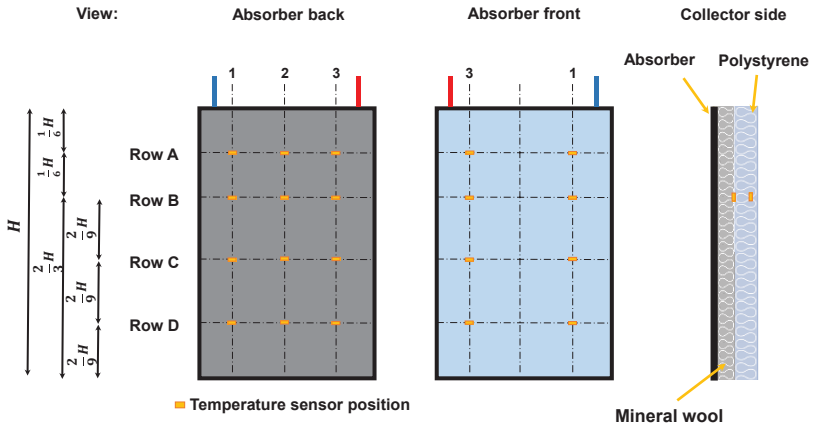

Fig. 4: Sensor positions on the experimental collector

Subsequently, the functional model was put under the solar simulator to measure the efficiency for certain collector inlet temperatures, i.e. 70, 80 and 89 °C. The testing rig is equipped with two pyranometers, a magnet-inductive flow meter and two matched PT100 sensors to log the collector inlet and outlet temperature. Hence, the useful collector energy respectively collector loss can be calculated. The conduction loss via the back insulation and the radiative absorber loss is calculated based on the collector temperature

measurements, the ambient temperature and the known physical collector properties. The sidewall losses are neglected, as the collector side surface is small compared to the collector's aperture area. Beyond that, the collector sides are very well insulated and, thus, considered as adiabatic. The collector model was enhanced by the convection equation according to Eismann (2015):

$$Nu = 1 + 1.44 * \left(1 - \frac{1708}{Ra\emptyset + 1708R_c}\right) * \left(1 - (\sin(1.8\emptyset))^{1.6} \frac{1708}{Ra\emptyset + 1708R_c}\right) + \left(\left(\frac{Ra\emptyset + 5830R_c}{5830}\right)^{0.39} - 1\right)(1 + C * R_c)$$

Eismann (2015) suggests a C-value of 0.29 with a mean deviation of ±0.17. For the here conducted calculation C was set to 0.46 whereas R_c was 1. Subsequently, the author's own convection loss measurements were compared to the calculation results according to the equations of Hollands et al. (1976) and Eismann (2015) in Fig. 5.

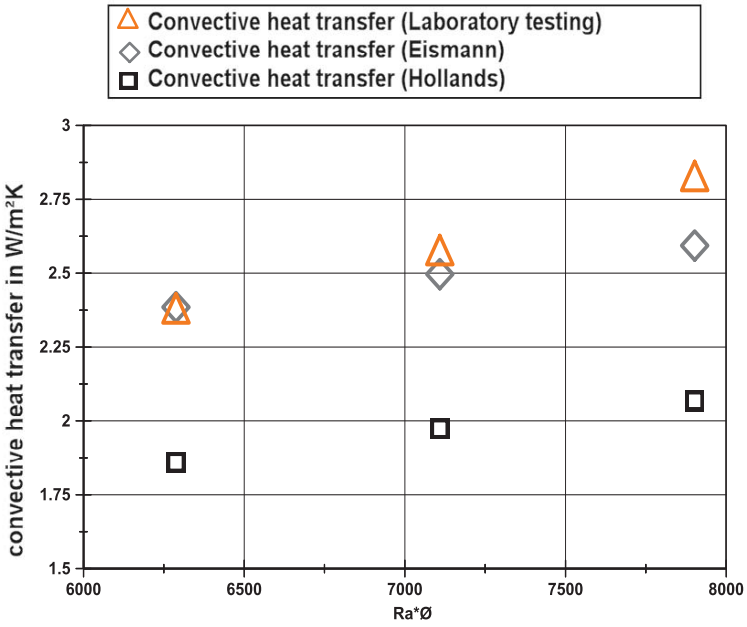

Fig. 5: Comparison of the calculated heat transfer according to Eismann and Hollands et al. and the own test results

The own results differ clearly from Hollands' approach. However, the measured deviations are in a similar range with the results obtained by Bartelsen et al. (1993) and Föste (2013). Beyond that, the results for the convective heat loss are in good accordance with the values from Eismann. The measured points with an inlet temperature of 70 °C and 80 °C are differing only -0.9 % respectively 2.5 % from the values derived by Eismann's approach. Yet, the value for the point with an inlet temperature of 89 °C differs by 7.8 %. Based on this experimental setup the used collector model was enhanced by the extended convection equation. Fig. 6 shows the tested results and the simulated efficiency curve according to Eismann's respectively Hollands' approach of the collector TPS-AlCu20 (Tab. 2).

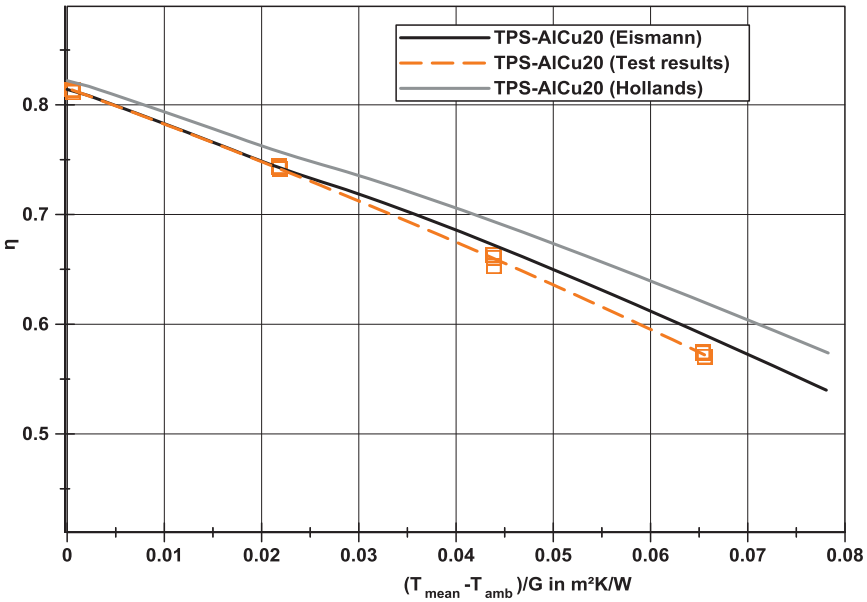

Fig. 6: Model validation by comparison of the measured and simulated collector efficiency with a calculation approach according to Eismann (2015) respectively Hollands et al. (1976)

Tab. 2: Used collector parameters in simulation

Parameter	Value
Aperture area in m²	1.84
Absorber type	Sheet-pipe
Absorber piping	Double-harp
Material absorber sheet	Aluminium (Al)
Material absorber piping	Copper (Cu)
Absorption absorber	0.95
Emission absorber	0.05
Transmission glazing	0.94
Emission glazing	0.94
Thermal conductivity Aluminium in W/m²K	235.0
Thermal conductivity Copper in W/m²K	390.0
Thermal conductivity mineral wool in W/m²K	0.035
Thermal conductivity glass in W/m²K	0.84
Glass thickness in mm	3.2
Thickness absorber sheet in mm	0.5
Fin width in mm	99
Outer diameter riser in mm	7
Absorber length in mm	1,857
Absorber width in mm	990
Insulation thickness in mm	50
Gap size in mm (unless stated otherwise)	20
Gas filling	Argon / Krypton

For the typical operation point of 0.05 m²K/W the deviation of the simulated values are 7.5 % (Hollands) respectively only 3 % (Eismann). The deviation of the complete temperature difference between the measured values and the simulated values is shown in Fig. 7.

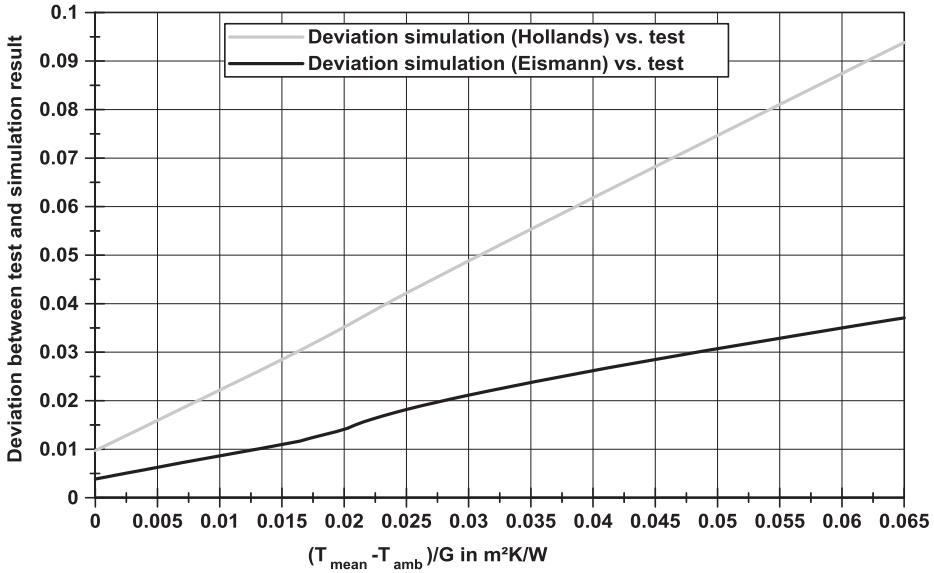

Fig. 7: Deviation between simulation and measurement results

The smallest deviation for the Hollands' approach is about 1 % in the region of the optical efficiency. Again, this is owed to the impact of the fin efficiency factor F' that affects this value. As the total collector losses are included in F' and the convection losses are slightly different, a rather small deviation exists. However, with increasing operation temperatures the deviation gets more obvious. For an ordinate value of 0.065 m²K/W the difference is almost 9.5 %. The extended correlation after Eismann shows only a deviation of 0.5 % for values close to η_0 and 3.5 % at max for higher operating temperatures. The deviation with increasing temperature ranges were also observed in the own conducted convective heat loss measurement. As the mean collector gap size varies, the convective losses differ as well. Ultimately, this behaviour is not included in an equation.

Beside the satisfying results of the efficiency comparison, the measured component temperatures showed as well a good correlation to the simulated results. In this second test setup, the functional model TPS-AlCu20 without the additional polystyrene insulation was equipped with the temperature sensors and put under the solar simulator. The collector's absorber and glazing temperatures were measured for three different inlet temperatures (70, 80 and 89 °C). During this steady-state test, the average insolation was 881.7 W/m² with a mean wind speed across the glazing of 2.5 m/s and an ambient temperature of 24.9 °C. In addition to the varying inlet temperatures, a further measurement series in dry stagnation (I = 879.8 W/m²; v_{wind} = 2.5 m/s) was conducted. Finally, the measured temperatures for absorber and glazing were averaged and compared with the simulation results. The deviation between the stagnation test and the simulated values were between -1.7 up to +0.1 % for the absorber respectively -1.7 to -0.2 % for the glazing. As for the good correlation between test and simulation results, the model is considered to be working properly and, thus, validated.

6. Efficiency analysis, thermal loads and annual yield of a gas-filled collector

Derived by the parameter study above, a gap size of 20 mm for an efficiency comparison between gas-filled collectors (Krypton, Argon) and an identical but vented collector was conducted (Fig. 8).

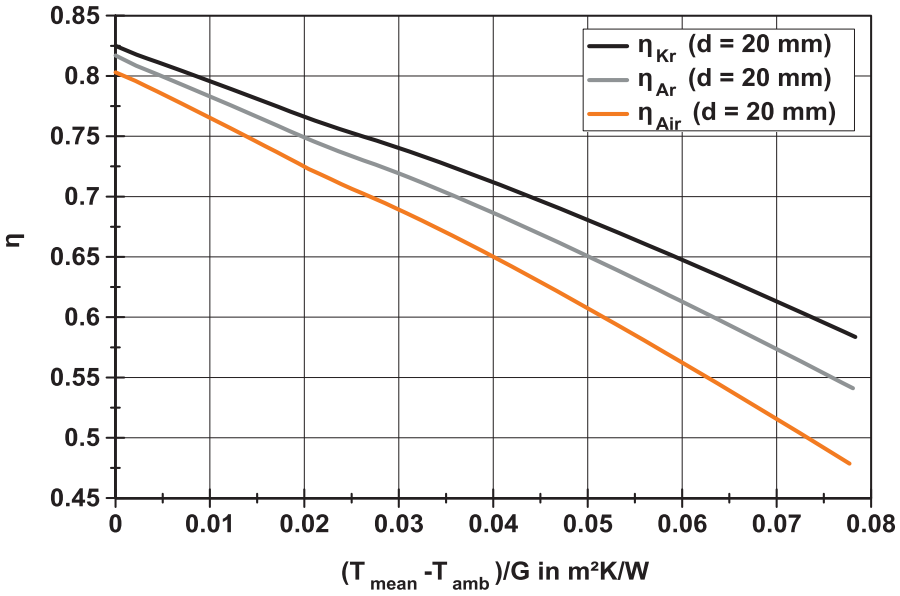

Fig. 8: Efficiency comparison of an Argon and Krypton filled respectively vented collector with a gap size of 20 mm (convection theory according to Eismann (2015))

The collector setting with the Krypton filling outruns the two other simulation results over the complete temperature range. For an ordinate value of 0.05 m²K/W, the efficiency difference between the Krypton and vented collector results in a 7.2 % higher performance whereas the second gas-filled collector version (Argon) lacks 3 % compared to the Krypton variant but outperforms the vented collector by 4.3 %. The predicted efficiency increase by Vestlund (2009, 2012) cannot be confirmed.

Beside the analyses of the collector's efficiency, a system simulation in Carnot (Hafner et al. 1999), an open source toolbox in Matlab / Simulink, and a simulation of the maximum temperature in dry stagnation was conducted. Therefore, the introduced collector model was embedded in a system simulation to derive the magnitude and occurrences of thermal loads during a normal system operation in Germany, maximum temperature during dry stagnation and the annual yield. For this evaluation, a typical solar thermal system for a single-family house in Germany was chosen and implemented in Matlab / Simulink. Since the maximum temperature occurs at the fin end (Duffie and Beckman 2009) and the edge bond was applied in this region, these absorber temperatures were analysed for the thermal load on the primary sealing. However, the edge bond temperatures are slightly lower than the simulated absorber temperatures due to higher edge losses. Yet, it is assumed that this effect is negligible as of the thick side insulation (20 mm). Tab. 3 comprises the used system parameters.

Tab. 3: Applied parameters in the system simulation

Parameter	
Location	Wurzburg (Germany)
Building	Single-family house
Annual heat energy demand in kWh	16,239
Space heating in kWh	2,539
Domestic hot water in kWh	13,700
Heating	Floor heating
Furnace	Oil (15 kW)
Domestic hot water storage volume in litre	130
Buffer storage volume in litre	1,000
Solar collectors in m²	14.4
Collector azimuth	South
Collector parameter TPS-AlCu20	
Optical efficiency	0.815
Linear heat loss coefficient in W/m²K	3.19
Quadratic heat loss coefficient in W/m²K²	0.009
Collector parameter Reference collector	
Optical efficiency	0.815
Linear heat loss coefficient in W/m²K	3.52
Quadratic heat loss coefficient in W/m²K²	0.012
Mass flow in l/m²h	40

Fig. 9 shows the maximum temperatures that occurred during a regular system operation throughout the year.

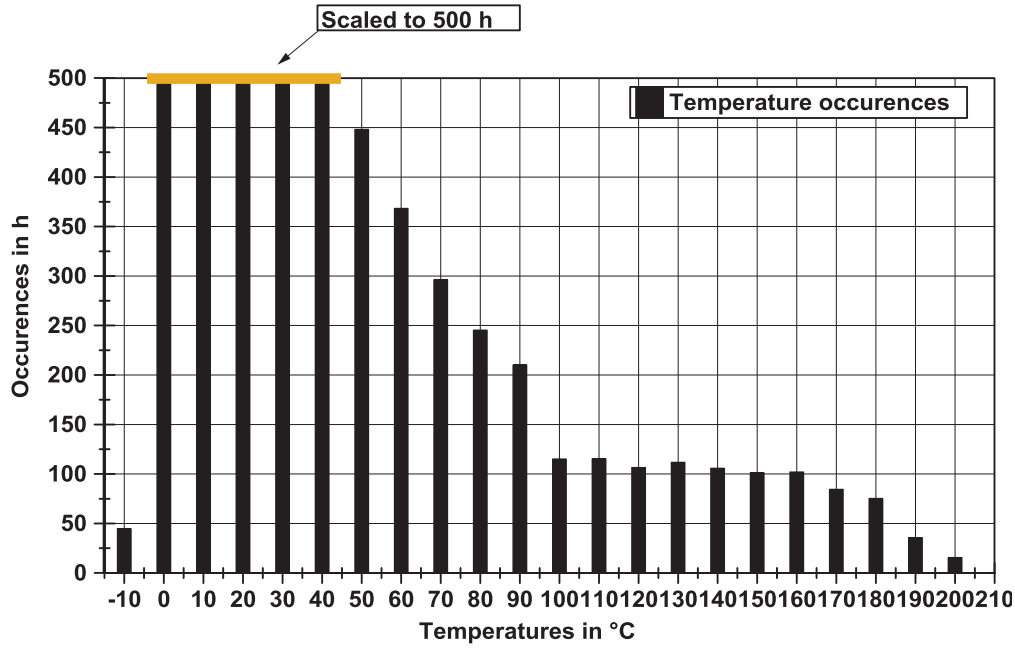

Fig. 9: Temperature load and duration of the absorber temperature during a year in system operation in Wurzburg, Germany

The adhesive service temperatures are not available in public. The temperature range between 100 and 130 °C were defined as short service temperature; however, the idle time cannot be stated. Temperatures exceeding 130 °C are critical and leading to an accelerated ageing effect. In total a dwell time for an absorber temperature between 100 to 130 °C of 449 h respectively 520 h for temperatures above 130 °C were detected. This means 5.9 % of the complete collector operation time the short-term service temperature was exceeded. The higher temperatures, i.e. > 200 °C, are badgering the adhesive more than temperatures close to

130 °C. A temperature amplitude between -13 °C and up to 207 °C was derived by the system simulation. Unlike the high temperatures, this minimal temperature is not afflicted with an ageing effect. To what dimension the temperature magnitude and periods exceeding the service temperature are affecting the material needs to be thoroughly tested, e.g. in outdoor tests.

The gas-filled solar collector achieved an annual solar yield of 5,386 kWh, which corresponds to a specific solar yield of 374 kWh/m²a. In contrast to this, the annual yield of the reference collector is 5,525 kWh (352 kWh/m²a). Further studies with Krypton as gas filling will be conducted as the Argon filled variant only shows a 6 % higher annual yield per collector area than the reference collector.

7. Summary

An existing collector simulation model was adapted, enhanced for gas-filled solar collectors and validated by laboratory testing. The convective heat transfer between absorber and glazing was analysed and compared to recent findings from other scientists. The results confirm the extended convection correlation after Eismann (2015) and show that the use of the convection calculation approach in solar collectors according to Hollands et al. (1976) underrates the heat loss. An efficiency increase of more than 4 to 7 % at a collector working temperature of 0.05 m²K/W for gas-filled collectors was demonstrated. Compared to the values stated in the literature, the efficiency increase of a gas-filled solar collector falls short of expectations (Vestlund 2009, 2012). Short gap sizes of less than 15 mm are critical due to the absorber deflection and, thus, not recommended.
In a system simulation, the thermal loads on the absorber edges and the annual yield of an Argon filled collector were derived. Whether the calculated temperature loads are critical for the adhesive needs to be analysed in a following paper. However, this collector type outruns a vented collector in terms of the annual yield by 6 %. Finally, the proposed collector is produced on a highly automated production line that offers a cost effective assembly for mass production (Riess et al. 2014a, b).

8. References

Bartelsen, B., Janßen, S. & Rockendorf, G., 1993. Heat transfer by natural convection in the air gap of flat plate collectors. Proceedings ISES Solar World Congress, pp. 267-273.

Beikircher, T., 2009. Hocheffizienter Flachkollektor mit Folienisolation und Überhitzungsschutz für höhere Betriebstemperaturen FKZ: 0329280A. Abschlussbericht, München.

Beikircher, T., 2010. Tabor, H., 1959. Radiation, convection and conduction coefficients in solar collectors. Solar Energy, Volume 3, pp. 155-176.

Benz, N., Beikircher, T., 1999. High efficiency evacuated flat-plate solar collector for process steam production. Solar Energy 65, pp. 111-118.

Buchberg, H., 1976, Design considerations for solar collectors with cylindrical glass honeycombs. Solar Energy, Volume 13, Issue 3, pp. 193-203.

Buttinger, F., 2009. Entwicklung eines konzentrierenden Vakuum-Flachkollektors zur Prozesswärmeerzeugung. Dissertation, TU München.

Buttinger, F., 2010. Development of a new flat stationary evacuated CPC-collector for process heat applications. Solar Energy, Volume 85, pp. 1166-1174.

Cooper, P.I., Dunkle, R.V., 1981. A non-linear Flat-plate collector model. Solar Energy, Volume 26 (Issue 2), pp. 133-140.

Duffie, J. A. & Beckmann, W. A., 2006. Solar engineering of thermal processess. 3. Hrsg. New York: John Wiley & Sons.

Eaton, C. B., Blum, H., 1975, The use of moderate vacuum environments as a means of increasing the collection efficiencies and operating temperatures of flat-plate solar collectors. Solar Energy 17, pp. 151-158.

Eismann, R., 2015. Accurate analytical modeling of flat plate solar collectors: Extended correlation for convective heat loss across air gap between absorber and cover. Solar Energy, Volume 122, pp. 1214-1224.

El Sherbiny, S. M., Raithby, G. D. & Hollands, K. G. T., 1982. Heat transfer by natural convection across vertical and inclined air layers. Journal of Heat Transfer-Transactions of the ASME, Band 104, pp. 96-102.

Föste, S., 2013. Flachkollektor mit selektiv beschichteter Zweischeibenverglasung. Dissertation, Universität Hannover.

Hollands, K. G. T., Honeycomb devices in flat-plate solar collectors. Solar Energy, Volume 9, Issue 3, pp. 159-164.

Hollands, K. G. T., Unni, T. E., Raithby, G. D. & Konicek, L., 1976. Free convective heat transfer across inclined air layers. Journal of Heat Transfer-Transaction of the ASME, Band 2, pp. 189-193.

Hottel, H. C., Woertz, B. B., 1942. The performance of flat-plate solar heat collector. ASME Transactions 64.

Hottel, H.C. and Whilier, A., 1958. Evaluation of Flat-Plate Collector Performance. In: Trans. of the Conf. on the Use of Solar Energy, 2 (1), pp. 74-76.

Kaltenbach, F., 2013. Transluzente Materialien: Glas – Kunststoff – Metall. 1. Auflage, Institut für internationale Architektur-Dokumentation GmbH & Co. KG, München.

Kessentini, H., Roser, C., Castro, J., Assensi, O., Chiheb, B., Three dimensional heat transfer analysis of combined conduction and radiation in honeycomb transparent insulation. Solar Energy, Volume 105, pp. 58-70.

KLEIN, S., DUFFIE, J.A. and BECKMAN, W.A., 1974. Transient considerations of flat-plate solar collectors. Trans. of ASME: Journal Engineering for Power, 96A, pp. 109-113.

KOO, J.-M., 1999. Development of a Flat-Plate Solar Collector Design Program. Published Thesis (Master of Science), University of Wisconsin-Madison.

MATUSKA, T. and ZMRHAL, V., 2009. KOLEKTOR 2.2 – reference handbook. 1st Edition. Prague (CZ): Czech Technical University.

Nordgaard, A., Beckman, W.A., 1992. Modelling of flat-plate collectors based on monolithic silica aerogel. Volume 49, Issue 5, pp. 387-402.

Platzer, W. J., 1988. Solare Transmission und Wärmetransportmechanismen bei transparenten Wärmedämmaterialien. Dissertation, Universität Freiburg.

Reiter, C., 2014. Polymeric Solar-Thermal Flat-Plate Collectors. PhD, De Montfort University

Reiter, C., Trinkl, C., Zörner, W., Hanby, V.I., 2015. A Dynamic Multinode Model for Component-Oriented Thermal Analysis of Flat-Plate Solar Collectors. Journal of Solar Energy 2015, pp. 1–16.

Riess, H., Brandmayr, S., Zörner, W. & Greenough, R., 2014a. Analysis of the mechanical behaviour of an all-round fully adhesive supported absorber. Energy Procedia

Riess, H., Brandmayr, S., Zörner, W. & Greenough, R., 2014b. A novel production techniqe for flat plate solar collectors with a fully adhesive edge bond, DOI: 10.18086/eurosun.2014.16.19, EuroSun 2014, Aix-les-Baines.

Rommel, M., Schäfer , A., Schmidt, V. & Schmitt, Y., 2003. Entwicklung neuer doppelverglaster Flachkollektoren mit Antireflex-Glas. OTTI Symposium Thermische Solarenergie.

STEPHAN, P. (2010) VDI Heat Atlas. 2nd Edition. Düsseldorf (DE): VDI-Verlag GmbH.

Svendsen, S., Jensen, K. I., 1987. Flat Plate Solar Collector with Monolithic Silica Aerogel. ISES Solar World Congress, Hamburg.

Svendsen, S., 1992. Solar collector with monolithic silica aerogel. Journal of Non-Crystalline Solids. Volume 145, pp. 240-243.

Tabor, H., 1969, Cellular insulation (honeycombs). Solar Energy, Volume 12, Issue 4, pp. 549-552.

Vestlund, J., Rönnelid, M. & Dalenbäck, J.-O., 2009. Thermal performance of gas-filled flat plate solar collectors. Solar Energy , Band 83, pp. 896-904.

Vestlund, J., Rönnelid, M. & Dalenbäck, J.-O., 2012a. Thermal and mechanical performance of sealed, gas-filled flat plate solar collectors. Solar Energy, Band 86, pp. 13-25.

Vestlund, J., Rönnelid, M. & Dalenbäck, J.-O., 2012b. Movement and mechanical stress in sealed, flat plate solar collectors. Solar Energy , Band 86, pp. 339-350.

Conference Proceedings

EuroSun 2016
Palma de Mallorca (Spain), 11 - 14 October 2016

Optical losses due to tracking on solar thermal collectors

Fabienne Sallaberry[1], Ramón Pujol-Nadal[2], Bengt Peres[3]

[1] CENER (National Renewable Energy Center), Solar Thermal Energy Department, Sarriguren (Spain)

[2] UIB (University of Balearic Islands), Physics Department. Ctra. Valldemossa km 7.5; 07122 Palma de Mallorca (Spain)

[3] DTU (Technical University of Denmark), Department of Civil Engineering, Brovej, Building 118, DK - 2800 Kgs. Lyngby (Denmark)

Abstract

For a wide range of operational temperatures, the solar thermal collectors can use optical concentration systems to optimize their efficiency. However, as optical concentration relies on direct solar radiation, it is necessary to use a solar tracker following the sun direction to maximize the amount of useful solar radiation received. The selection of the appropriate tracking systems matching the optical concentration factor is essential to achieve optimal collector efficiency. Otherwise, the concentrator would experience high optical losses due to the inadequate focusing of the direct solar radiation onto its receiver, regardless of its quality. This paper gives the state-of-the-art of the methodologies available to characterize the tracking error of a concentrating collector, a summary of different previous studies done in this subject and of the standardization regarding the tracking accuracy and its influence on the solar collector efficiency. The methodologies and results of the tracking accuracy, incidence angle modifier and optical losses due to tracking errors are presented in this paper for the five collectors studied.

Keywords: *Collector testing; Optical characterization; Solar tracking accuracy; Optical losses*

1. Introduction

Several predictions induces a change in the energy model and the one possibility for serving the world energy demand is the use of renewable and clean energies that are the only one that can support sustainable development by its inexhaustible nature, preserving the environment and distributing the resources locally. The solar energy is one of the main renewable energies with great benefit. Solar thermal energy is able to provide a considerable fraction of the current and future energy demand in both industrial and domestic sectors. This fact is reflected by the growing interest during the last decade in the design of new solar collectors in order to satisfy the increasing electricity and heating demands and replace fossil fuels.

The purpose of a solar tracker is to orient a solar system during the day in order to optimize the incident solar radiation. However, while using optical concentration devices on a solar collector, it is important to use a solar tracker with adequate precision compared to the optical concentration factor and the acceptance angle of the concentrator. Otherwise, the concentrator would sustain high optical losses due to the inadequate focusing of the solar radiation onto its receiver, despite having a good optical quality.

Even though the concentrating solar collectors are mentioned in the International Standards (ISO 9806:2013), the general testing methods cannot always be easily applied to unusual collector designs.

doi:10.18086/eurosun.2016.07.10 Available at http://proceedings.ises.org

Moreover, those testing methods consider the solar tracker as part of the solar collector so they do not characterize the impact of its precision on the overall efficiency. Additionally, the international technical committee IEC/TC 117, created in 2012, is dealing with the same issues related to thermal performance and durability of concentrating/tracking CSP systems and their components considering inputs from experts of various countries. In this committee, two working group has been created at the end of 2014 in order to define the testing standards for PTC (future standard IEC 62862-3-2) and for LFR (future standard IEC 62862-5-2), but no characterization of the tracker accuracy is proposed.

Bendt et al. (1979) considered different optical losses when calculating the flux on a receiver for a parabolic trough collector (PTC). The total effective root mean square (RMS) of a surface optical error results by adding quadratically the individual standard deviation of: the deviation of contour from design direction $\sigma_{contour}$, the imperfect specularity of reflector material $\sigma_{specularity}$, the imperfect placement of the receiver $\sigma_{displacement}$ and the imperfect tracking $\sigma_{tracking}$ as schemed in Fig. 1.

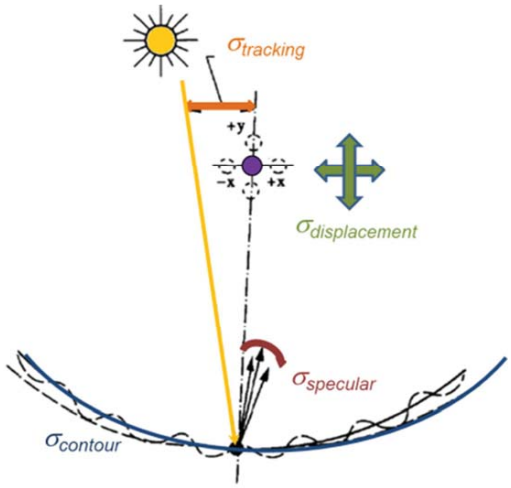

Fig. 1: Optical error from the individual standard deviation

Although the tracking error is not taken into account in current Standards for solar thermal collectors, several studies tried to characterize the tracking error. To do so, some devices could be used in a similar way to the sun-sensors on a closed-loop actuation tracker. But to qualify precisely the tracking error, an accurate electronic device is necessary. Gee (1982) defined a testing procedure and analyzed the angular pointing error on a parabolic through collector (PTC). An encoder was used to record the instantaneous tracking errors with a resolution of 0.03° and then to calculate the RMS (root mean square) of the error. Hession and Bonwick (1984) designed and tested a sun sensor composed of three photo-transistors mounted in a simple structure. This device allowed a solar tracking precision in double-axis better than 0.1°. Bhatnagar et al. (1987) measured experimentally the average tracking error of a tracking system at different solar hours. It was done using their own collector sun-sensor, which consisted in two silicon solar cells placed on either side of a rectangular plate. The error value at noon for the solar tracker characterized in this study was 0.93°. Kalogirou (1996) designed a single-axis tracker using a sun sensor made of three light-dependent resistors (LDRs). The tracking accuracy was estimated of 0.2° for cloudy days (solar radiation of 100 W/m^2) and of 0.05° for sunny days (solar radiation of 600 W/m^2). Arboiro and Sala (1997) presented an improved sun sensor and new strategies for the control unit of solar tracking, using both closed loop and open loop mode. The solar tracker prototype was monitored for one year and presented an accuracy of 0.2°. Sun et al. (2014) used a beam characterization system to evaluate the tracking error of two heliostats from a central tower plant with an estimated accuracy of better than 2% of the positioning angle measurement. Bentaher et al. (2014) analyzed a tracking system for PV panels using a sun sensor composed of two photo-resistors separated on two inclined planes.

Among all the previous studies, none has characterized the tracking error of a linear solar thermal concentrator in actual operation. Moreover, no testing procedure has been developed as the basis for a future standard. As explained before, the tracking system is a critical point of concentrating collectors. In Kalogirou

et al. (2004), the importance of an accurate tracking was clearly verified in the experiment. Those experimental data showed the influence, of the incidence angle deviation from the ideal angle, on the collector efficiency of a parabolic trough. For this PTC, a deviation of only one degree in the transversal incidence angle implies an incidence angle modifier (IAM) of 0.8, which means that the energy efficiency decreases by 20%. In some studies, the optical losses due to the tracking deviation was analyzed and discussed. In Hughes (1980), the pointing error was clearly identified as a source of efficiency reduction. The theoretical intercept factor losses due to the tracking error of a point focusing solar collector with ±0.1º error were calculated using a statistical analysis, but no experimental measurements were performed. Grass et al. (2004) mentioned that the tracking error of a collector with a small acceptance angle can have a significant effect on performance. It was also estimated in that study a value of 0.6 % for the tracking error for evacuated tubes collectors (ETC) with integrated tracking reflector, but with no more experimental details.

For all of those reasons, and the previous results mentioned in the previous sections, due to the lack of characterization test procedures, for single-axis tracking solar concentrators, a testing procedure for solar collectors with single-axis solar tracker is defined in this paper. The main objective is to determine the adequacy of the solar tracking system together with the actual concentration optics of the collector. Moreover, the optical losses due to the tracker were calculated on different concentrating tracking collectors in order to estimate the percentage of reduction on the concentrator efficiency. This study aims to contribute to the improvement of tracking errors estimation on single-axis solar trackers for a solar thermal collector, in particular linear trough collectors. And therefore, it also aims to estimate the optical losses resulting from the tracker.

2. Review of the equipments for measuring the tracking error

A review of all the commercial devices which use the “Machine-Vision” method (MV), based on image treatment. Those equipments already existing in the market are designed to characterize the deviations of the trackers and are not part of the actuator or tracking system.

The first device using MV method, the model Trac-Stat SL1 was developed by the company GreenMountain (Fig. 2a) (Pract Engineering & Consulting webpage). This system was composed of two separate independent sensors, one with a narrow acceptance angle and one with a higher acceptance angle. The first sensor has a field of view angle of 5º with an accuracy of ±0.02º. The second sensor has a field of view angle of 60º with an accuracy of ±0.5º. This device is now commercialized by the company Pract Engineering.

The model SunSpear, developed by the company Inspira and based on the patent 2008/0258051 (Heredia, et al., 2008), is a sensor for measuring the pointing error using an image sensor positioned within a collimator tube (See Fig. 2.b). According to the technical specifications, this equipment has a resolution of 1/10000th of angle with a field of view of 1º (Cervantes and Luque-Heredia, 2008; López et al., 2012; Luque-Heredia et al., 2006). Inspira S.L. was bought by the American company SolFocus.

The model TA1 is manufactured by the German company Black Photon (http://black-photon.de/) (See Fig. 2.c). According to the technical specifications, the measurement range is ± 1.2º, the linearity is ± 1.8 % of full scale and the accuracy is ± 2.4 % of full scale (for temperature between 5ºC and 45ºC). Missbach et al. (2012) presented the results of this sun sensor, with a high accuracy showing a standard deviation of 0.01% of full scale with the measurement of a stable LED (light-emitting diode) light source.

The model LAB is manufactured by the company AKKUtrack (http://akkutrack.com/lab/) (protected by the following patents: BO2010A000361, GE2014A000006, WO2011 /154872). According to technical specifications, the field of view is 4.5º per 2.9º, the resolution is ±0.01º and the relative accuracy is ±0.01º (see Fig. 2.d).

The model Heliosensor is manufactured by the German company PSE (Projects in Solar Energy) (http://www.pse.de) in collaboration with the Black Photon company (see Fig. 2.e). According to technical specifications, the field of view is 55º, the resolution is less than ± 0.02º, and the accuracy is less than ± 0.05º for angles less than 15º and less than 0.5 % for the entire acceptance angle.


(a)


(b)

(c)

(d)


(e)

Fig. 2: (a) Tract-Stat SL1 by Pract Engineering (Pract Engineering & Consulting) (b) SunSpear by Inspira (Heredia, et al., 2008) (c) Model TA1 by Black Photon (black-photon.de) (d) Model LAB by AKKUtrack (akkutrack.com/lab) (e) Heliosensor by PSE (www.pse.de)

Table 1 summarizes the specifications of the different devices exposed above. In particular, it compares the accuracy and field of view of several commercial devices

Tab. 1: Characteristics of commercial optical device for tracking error measurement

Model	Manufacturer	Accuracy	Field of view angle
Trac-Stat SL1	GreenMountain Engineering	± 0.02º ± 0.5º	5º 60º
Solar Tracker Tester	Proxima Systems S.L	±1º	20º
TA1	Black Photon	± 2.4% of full scale	1.2º
LAB	AKKU track	± 0.01º	4.5º x 2.9º
SunSpear	Inspira	1/10000th	1º
Heliosensor	PSE	± 0.05º	55º

Most of those optical devices characterize the pointing error on a double-axis tracker and could not be used for a linear concentrator because of their reduced field of view. The GreenMountain Engineering device has a field of view up to 60º but its accuracy (±0.5º) is not suitable for the characterization of the tracking error of a PTC tracker in order to estimate the optical losses.

In order to measure the tilt and orientation of a solar tracker, different sensors could be used, such as the angles sensors, the rotary encoders, the tilt sensors or inclinometers (Prinsloo and Dobson, 2015). Within the angular sensors, there are two types: the absolute encoder and the incremental or differential encoder. The main advantage of those devices is that they keep the information of the position even when the power is off. The magnetic encoders are angle sensors connected to a motor actuator drive, which convert the motor rotation pulse into tracking angles. The differential or incremental encoder record the change in the shaft position of a system, but do not keep the information if the power is off. This encoder needs a microprocessor or a software in order to calculate the position angle and to record this data. Table 2 presents the specifications of the different commercial devices.

Tab. 2: Characteristics of commercial inclinometers

Model	Manufacturer	Repeatability	Resolution	Absolute accuracy	Measure angle
IM 60-2	FIAMA	±0.05º	--	--	±60º
LCA318T-30	RION		±0.1º	±0.1º	360º
P-Series	Measurement Specialties	±0.001º	±0.02º	±5º	--
Pro 3600	MITUTOYO	--	±0.01º (from 0º to 10º)	±0.05º (from 0º to 10º)	--
DJ-1022	Mini Digital Protractor	±1º	0.1º/ 0.01%	--	4x90º
DP-90HC	ZJTM	--	±0.1 º	±0.2 º	4x90 º
ACS-360-1-SV00-VE2-PM	POSITAL FRABA	± 0.02%	±0.01º	±0.1º	360º

3. Materials

This section presents the main characteristics and particularities of the five solar collectors studied during this work. Those collectors have different tracking types and concentrating geometries. The first collector called Sunaitec, from a Portuguese company that manufacture it, is composed of several elliptical concentrators that act synchronized. The second collector is a prototype of variable geometry collector, designed and built by the university of Balearic island (UIB). It is composed of 32 parabolic mirrors, 8 sets of four receiver tubes and a structure that moves the array of receivers with a circular trajectory to maintain the focussing. The third collector is a small size PTC, commercial model PolyTrough 1800, manufactured by the Swiss company NEP Solar AG. The fourth collector was designed for the DIGESPO European project. It is a small size PTC consisting of 4 modules with 4 receivers. The last collector was designed for the EUROTrough European project. It is a large size PTC. All the experiments were carried out in different European facilities. Fig. 3 shows a map with the location of all the collectors and testing bench used during this study.

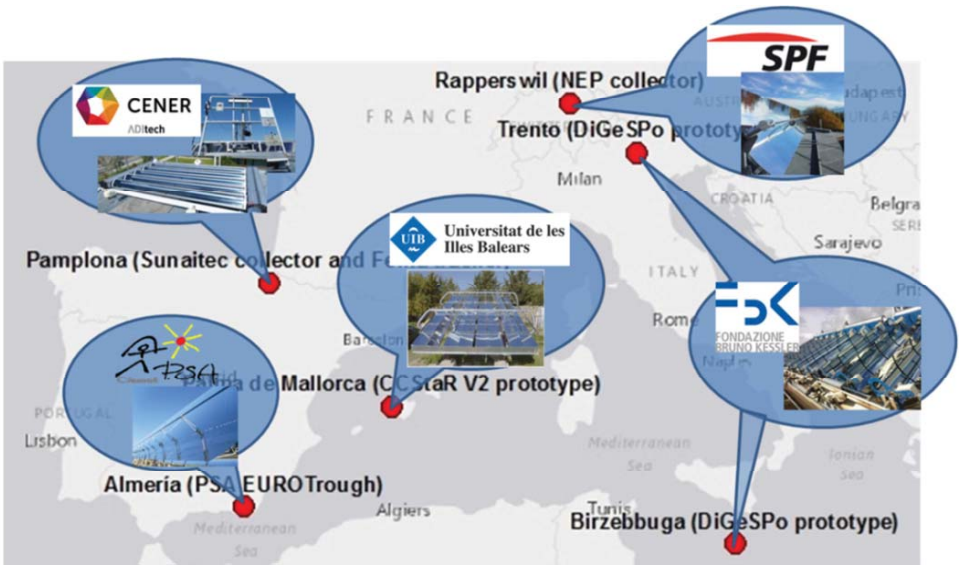

Fig. 3: Defining acceptance angle and relationship between tracking error and optical losses

Table. 3 shows a summary of the main characteristics of the solar collectors used for this study.

Tab. 3: Summary of collector characteristics studied

Solar collector	Sunaitec	CCStaR	NEP	DiGeSPo	EUROTrough
Concentrator type	Elliptic	Fixed-Mirror (fixed reflector and mobile receiver)	Small PTC	PTC with fixed receiver and mobile reflector	Large PTC
Focal length [mm]	Not specified	--	647	200	1710
Collector length L [m]	2.337	576.95 mm	10.347	2.0	75 meters
Receiver tubes	5	4*8	4	4*4	18
aperture area [m2]	1.82	37.4	19.1	12.8	409.9
Concentration factor	4.48	14.4	17.27	33.33	26.2
Actuator	Electric	Electric	Electric	Electric	Hydraulic
Command	Solar sensor (Closed loop)	Algorithm (open loop)	Algorithm (open loop)	Algorithm (open loop)	Algorithm + encoder (hybrid)
Axis and orientation	horizontal EW	tilted NS	horizontal EW	tilted polar NS	horizontal EW

4. Methodology

The optical losses due to the solar tracking are an important characteristic of a solar tracker and need to be characterized experimentally by defining a testing procedure. Thus, the main objective of this study is the characterization of those optical losses on a linear solar concentrator and unconventional collectors, for low and medium temperature applications. The test procedure is based on the angular tracking error θ_{track} and the profile of dependency of the optical efficiency on the tracking error, as scheme in Fig. 4.

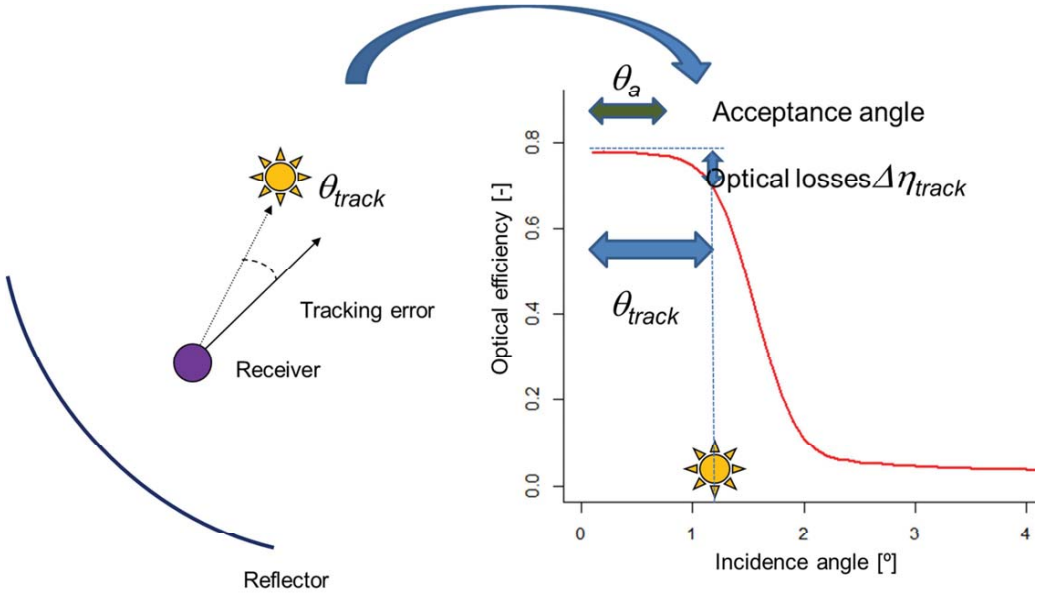

Fig. 4: Defining acceptance angle and relationship between tracking error and optical losses

To achieve this main objective, the following partial objectives were considered:

- Objective 1: Determination of the tracking error θ_{track} on a single-axis solar tracker and analysis for different environmental conditions like wind speed and wind direction. Development of a testing procedure for the characterization of this angular error.
- Objective 2: Characterization of the angular dependency of the optical efficiency to the tracking error, namely incidence angle modifier (IAM) by theoretical simulation and experiment. Demonstration of the utility of ray-tracing techniques in unconventional solar concentrators to determine its optical behavior.
- Objective 3: Calculation of the optical losses due to the tracking error. Determination of the acceptance angle, a key parameters of a solar concentrator, in order to check the accuracy required for the solar tracker to minimize the optical losses of the whole system (tracker and collector).

To reach the objective 1, different testing methodologies were described to quantify the tracking error of solar tracking in single-axis mode. The ad-equation between the precision of the device used to measure the tracking error and the accuracy of the tracker tested was determined. An experimental methodology for the tracking error characterization on a PTC, in the case of horizontal rotation axis, has been proposed, based on the international standard (IEC 62817, 2014) for the design qualification of solar trackers for photovoltaic systems. This proposal leads to the creation of a standard working group in November 2014 within the committee IEC/TC 117 (prIEC 62862-3-2). A statistical analysis was performed to estimate the mean angular error of each tracker.

To reach the objective 2, the optical efficiency was determined for different linear concentrators. The IAM parameter, regarding the beam solar irradiance $K_b(\theta_{track})$, is the one used to estimate the optical losses due to tracking error. The first method to characterize the optical efficiency was done experimentally using International Standards (ISO 9806:2013), the so-called quasi-dynamic test (QDT), monitoring the inputs and outputs of the collectors. The test benches and sensors used for the different collectors are summarized in Table 4.

Tab. 4: Summary of testing facilities

Solar collectors	Sunaitec	CCStaR	NEP	DiGeSPo	EUROTrough
Test location	Pamplona (Spain)	Mallorca (Spain)	Rappeswil (Swizerland)	Malta	Almeria (Spain)
Direct irradiance	Pyranometer - Shaded pyranometer	Pyrheliometer	Pyrheliometer	Pyranometer - Shaded pyranometer	Pyrheliometer
Diffuse irradiance	Shaded pyranometer	Shaded pyranometer	Shaded pyranometer	Shaded pyranometer	--
Temperature	Pt100	Pt100	Pt100	Pt100	Pt100
Flow	Mass flowmeter (Endress Hausser)	Volume flowmeter (Kamstrup)	Volume flowmeter (Endress Hausser)	Mass flowmeter (Micro Motion)	Flowmeter Emerson

The second method was by simulation, using a ray-tracing program OTSun that was developed in Fortran by the UIB, exposed in Pujol Nadal and Martínez Moll (2012) and compared to other commercial software in Osório et al. (2015). From the IAM profile $K_b(\theta_{track})$ was also determined the acceptance angle qa, which is an important factor of the concentrator.

To reach the objective 3, the long-term optical losses due to an imperfect tracking were estimated; an estimation of the long-term and average weighted optical losses due to the tracking error of a solar concentrator. The experimental and simulation results of the IAM on the tracking plane are used to determine the optical losses due to the tracker ($\Delta\eta_{track}$) using the transversal IAM fit $K_b(\theta_{track})$ and the tracking error (θ_{track}), according to Eq. 1.

$$\Delta\eta_{track} = \left(1 - K_b\left(\theta_{track}\right)\right) \cdot 100 \qquad \text{(eq. 1)}$$

As not all the collectors were studied in the same way, Table 5 summarized methodologies used for each sub-objective and collector.

Tab. 5: Methodologies used for each collector and objective

Sub-objetives / Solar collectors	Sunaitec	CCStaR	NEP	DiGeSPo	EuroTrough
1-Tracking error θ_T	Estimation from manufacturer	--	Experimental + Inclinometer	Optical device+ Estimation from orientation	Experimental + Inclinometer
2-IAM $K_b(\theta_T)$	Experimental	Experimental + Simulation	Simulation	Simulation	--
3-Optical losses due to tracking $\Delta\eta_{track}$	Calculation + Experimental	--	Calculation + Experimental	Estimation	--

5. Results

For the first objective, a testing procedure was defined for solar trackers by adapting a testing method from an International Standard IEC for photovoltaic double-axis trackers. The experiments were carried out using a simple procedure to determine the tracking elevation error. In Sallaberry et al. (2014a), a methodology for measuring elevation tracking error using an inclinometer has been defined and tested on a simple double-axis solar tracker at CENER. In Sallaberry et al. (2015a), the same methodology using an inclinometer has been tested on the NEP small-size PTC with EW single-axis solar tracker. In Sallaberry et al. (2015b), the same methodology using an inclinometer has been tested on the EUROTrough large-size PTC with EW single-axis solar tracker. On the DiGeSPo, a prototype device, based on the MV concept, had been designed and tested (Sallaberry, 2015d).

Second, the optical characterization of different concentrating solar collectors was performed through simulation and experiments. In particular, its dependency to the transversal incidence angle along the tracking plane is characterized. The IAM on the tracking plane was studied experimentally on the Sunaitec elliptic trough collector. In Sallaberry et al. (2015b), the IAM testing procedure for tracking collector has been defined and the asymmetrical product behavior for the Sunaitec asymmetric collector has been verified experimentally on a low concentrating/ tracking collector. In Sallaberry et al. (2015a), the IAM was obtained by simulation for the NEP collector. In Sallaberry et al. (2014b), the IAM testing procedure for the CCStaR nonconventional collector has been defined and a simulation ray tracing has been validated experimentally. A good agreement was found between the simulation and the experimental results considering the measurement uncertainties. In Sallaberry et al. (2015c), a theoretical model has been presented to specify the range of the incidence angles which should be tested on variable-geometry collectors to validate the IAM terms in the energy equation balance used on the CCStaR collector. In Sallaberry et al. (2014c) the IAM profile of the NEP collector was also determined by simulation. See Fig. 5 for IAM results in color surface by simulation and in black dot for experiment.

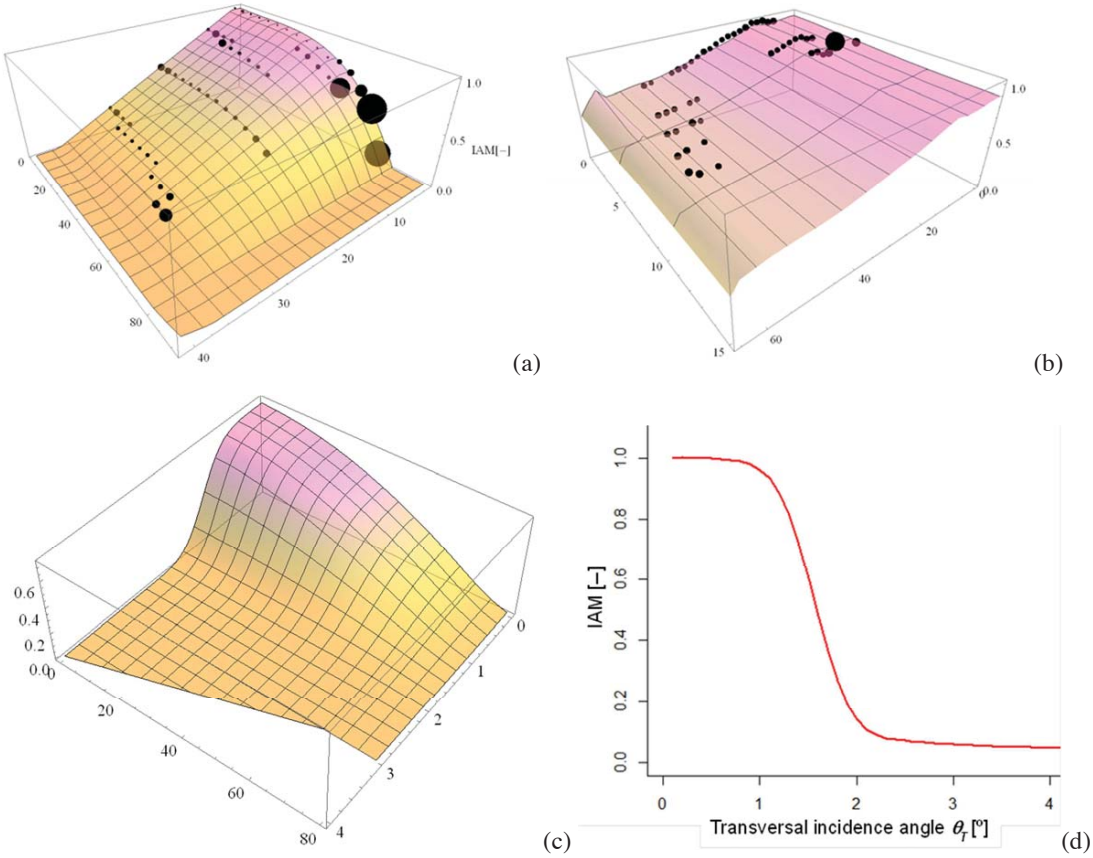

Fig. 5: IAM results by simulation (color surface and red line) and experiment (black dots) for (a) Sunaitec (b) CCStaR (c) NEP (d) DiGeSPo

Third, the long-term optical losses due to the tracking error were estimated using the transversal IAM obtained previously by raytracing simulation or by experiment, and the tracking errors distribution estimation. The impact of the maximum tracking error angle upon the optical efficiency has been determined on different concentrating/tracking collector types. In Sallaberry et al. (2015b), the long term calculation of the optical losses due to a tracker has been defined on the Sunaitec small low-concentration collector. In Sallaberry et al. (2014c), a sensitivity analysis has been performed about the possible source of tracking errors caused by an incorrect positioning of the DiGeSPo concentrating/tracking collector. In Sallaberry et al. (2015a), the average optical losses caused by the solar tracker has been calculated on the NEP small-size PTC. Table 6 summarized the results obtained for the three different sub-objectives,

Tab. 6: Summary of results

Results	Sunaitec	CCStaR	NEP	DiGeSPo	EUROTrough
1-Tracking error θ_T	Estimated ± 5°	Not estimated	± 0.4°	Experimental: between -0.6° and 0.1° / Estimation: ± 0.6°	± 0.3°
2-IAM $K_b(\theta_T)$: Acceptance angle θ_a	2.8°	Variable geometry	0.58°	0.9°	--
2- IAM $K_b(\theta_T)$: Optical efficiency η_{0b}	Experimental 67.7%	Simulation: 68.8% Experimental: 68.7% /	Simulation: 74%	Simulation: 77.7% Experimental: 30.9%	Experimental: 65.6%

3-Optical losses due to tracking $\Delta\eta_{track}$	$\Delta\eta_{track,year}$ = 1.01% 62% of data lower than 1%.	--	$\Delta\eta_{track,weighted}$ = 0.317% 95% of data less than 2.5%	$\Delta\eta_{track}$ up 0.5%	--

Finally, this work (Sallaberry, 2015e) describes the points defined in the International Standards that should be improved in order to ascertain the influence of the tracking accuracy on the overall efficiency of concentrating/tracking solar collectors. Some points have been proposed for a future Standard testing procedure on trackers for solar thermal collectors

6. Conclusions

In this work, solar collectors with different typologies have been tested; all with single-axis tracking and optical concentration (CCStaR V2 prototype with fixed reflectors and mobile receiver; Sunaitec collector with elliptic trough concentrators; NEP PTC single-axis solar tracker; DiGeSPo collector with fixed receiver tube and mobile reflectors). Unlike conventional solar collectors, such as flat plates and evacuated tubes, in the case of concentrating/tracking collectors, there is no clear specific testing procedure from a standard organisation. Furthermore, no testing procedure for the tracking precision exists and the efficiency testing procedures do not take into account all the special features of those collector types. More precisely, the IAM characterization is not completely standardized for unconventional concentrating/tracking collectors.

The main conclusions of this work, related to the three objectives in section 4 are given beneath:

- The characterization methodology of the angular error of tracking systems have been developed and validated experimentally on different solar trackers. The instantaneous angular tracking errors obtained by a simple procedure using digital inclinometer can be implemented and characterize statistically the tracking error distribution.
- The use of ray-tracing simulation has been validated for different types of concentrating solar systems, in which the optical efficiency for some solar incidence angles are difficult to obtain experimentally. Hence, the simulation by ray-tracing programs allowed determining the optical efficiency at any incidence angle. The simulation results have been compared to the experimental ones obtained during testing campaigns using the procedure presented. The agreement was very good.
- The IAM profile obtained previously has been compared to the maximum angular tracking error. In this way, the connection between the concentration optics and the tracker precision has been checked for two collectors.
- Finally, the optical losses of concentrators have been estimated using both the instantaneous angular tracking error measurements and the IAM results. Thus, valuable parameters, the weighted or the long term optical values, could be calculated to quantify the effect of the solar tracker on a concentrator performance.

7. Acknowledgements

I would like to thank the companies Sunaitec, TSC Tecnología Solar Concentradora S.L., NEP for letting me use the data of their collectors for my PhD and the institutes FBK and Ciemat-PSA for welcoming me in their facilities. Part of the experimental work on the EUROTrough collector were performed during an exchange of two weeks at PSA European Union Seventh Framework Programme (FP7/2007-2013) under grant agreement n° 609837 (Scientific and Technological Alliance for Guaranteeing the European Excellence in Concentrating Solar Thermal Energy, STAGE-STE).

8. References

AKKUtrack. Model LAB from AKKUtrack web page http://akkutrack.com/lab/ PSE AG.

Arboiro, J., and Sala, G. “Self-learning tracking": a new control strategy for PV concentrators. Progress in

Photovoltaics: Research and Applications 5, 3 (1997), 213-226.

Bendt, P., Rabl, A., Gaul, H., and Reed, K. Optical analysis and optimization of line focus solar collectors. Tech. rep., Solar Energy Research Inst., Golden, CO (USA), 1979

Bentaher, H., Kaich, H., Ayadi, N., Ben Hmouda, M., Maalej, A., and Lemmer, U. A simple tracking system to monitor solar pv panels. Energy Conversion and Management 78 (2014), 872-875.

Black Photon. Black photon web page http://black-photon.de/

Cervantes, R., and Luque-Heredia, G. Q. I. Sunspear calibration against array power output for tracking accuracy monitoring in solar concentrators. In European Photovoltaic Solar Energy Conference (2008), pp. 890-893.

Gee, R. An experimental performance evaluation of line-focus sun trackers. Tech. rep., 1982

Grass, C., Schoelkopf, W., Staudacher, L., and Hacker, Z. Comparison of the optics of non-tracking and novel types of tracking solar thermal collectors for process heat applications up to 300ºC. Solar Energy 76, 1 (2004), 207-215.

Heliosensor technical specification web page http://goo.gl/LUwQ1R

Heredia, I., Quemere, G., and Saldana, R. Equipment and process for measuring the precision of sun tracking for photovoltaic concentrators http://www.google.com/patents/US20080258051, 2008. US Patent US20080258051 A1.

Hession, P., and Bonwick, W. Experience with a sun tracker system. Solar energy 32, 1 (1984), 3-11.

Hughes, R. O. Effects of tracking errors on the performance of point focusing solar collectors. Solar Energy 24, 1 (1980), 83-92.

IEC 62817, Photovoltaic systems - design qualification of solar trackers, 2014.

IEC pr62862-3-2, Solar thermal electric plants - Part 3-2: Systems and components - general requirements and test methods for parabolictrough collectors (draft version), 2014.

ISO 9806, 2013. Solar Energy - Test method for solar collectors - Thermal performance of glazed liquid heating collectors including pressure drop.

Kalogirou, S. A. Design and construction of a one-axis sun-tracking system. Solar Energy 57, 6 (1996), 465-469.

Kalogirou, S. A. Solar thermal collectors and applications. Progress in energy and combustion science 30, 3 (2004), 231-295.

López, A. B. C., Vega, A. M., Cristobal, A., and López, A. L. Next Generation of Photovoltaics: New Concepts, vol. 165. Springer Science & Business Media, 2012

Luque-Heredia, I., Cervantes, R., and Quéméré, G. A sun tracking error monitor for photovoltaic concentrators. In Photovoltaic Energy Conversion, Conference Record of the 2006 IEEE 4th World Conference on (2006), vol. 1, IEEE, pp. 706-709.

Missbach, T., Jaus, J., Dimroth, F., Rubio, F., and Anton, I. New sensor for measuring tracking accuracy, tracker vibration, and structural deflecion. In AIP Conference Proceedings-American Institute of Physics (2012), vol. 1477, p. 262.

Osório, T., Horta, P., Larcher, M., Pujol-Nadal, R., Hertel, J., Wet van Rooyen, D., Heimsath, A., Schneider, S., Benítez, D., Frein, A., and Denarie, A. (2015) Ray-tracing software comparison for linear focusing solar collectors. In Proceedings of SolarPACES congress, CapeTown (South Africa).

Pract Engineering & Consulting. Web page model trac-stat sl1 from pract engineering (a diagnostic instrument for measuring tracker accuracy) http://static1.1.sqspcdn.com/static/f/988604/14694311/1318967247940/SL+1+Datasheet.pdf?token=Vm43qChteDpLRjQNV%2B3JQmtbPAw%3D.

Prinsloo, G., and Dobson, R. Solar Tracking, Sun Tracking, Sun Tracker, Solar Tracker, Follow Sun, Sun Position, Book November 2015, DOI: 10.13140/2.1.2748.3201

Pujol Nadal, R., and Martínez Moll, V. Optical analysis of the fixed mirror solar concentrator by forward ray-tracing procedure. Journal of Solar Energy Engineering 134, 3 (2012), 031009.

Sallaberry, F., Pujol Nadal, R., and García de Jalón, A. Direct tracking error estimation on a 1-axis solar tracker. EUROSUN Congress, Aix-les-Bains (France) (2014a), ISES.

Sallaberry, F., Pujol Nadal, R., Martínez Moll, V., Torres, J-L., Optical and thermal characterization procedure of a variable geometry concentrator: a Standard approach, Renewable Energy 68 (2014b) 842-852

Sallaberry, F., Alberti, F., Torres, J.-L., Crema, L., Roccabruna, M., and Pujol-Nadal, R. Characterization of a medium temperature concentrator for heat process - tracking error estimation. EUROSUN Congress, Aix-les-Bains (France) (2014c), ISES.

Sallaberry, F., Pujol Nadal, R., Larcher, M., and Rittmann Frank, M. Direct tracking error characterization on a one-axis solar tracker. Energy Conversion and Management 105 (2015a), 1281-1290.

Sallaberry, F., García de Jalón, A., Torres, J. L., and Pujol-Nadal, R. Optical losses due to tracking error estimation for a low concentrating solar collector. Energy Conversion and Management 92 (2015b), 194-206.

Sallaberry, F., Pujol Nadal, R., García de Jalón, A., and Martínez Moll, V. Toward a standard testing methodology for solar thermal collectors with variable-geometry: the direct radiation incidence angle modifier issue. Solar Energy 121 (2015c), 31-40.

Sallaberry, F., Valenzuela, L., García de Jalón, A., Leon, J., David Bernad, I., Towards Standardization of in-Site Parabolic Trough Collector Testing in Solar Thermal Power Plants, SolarPACES congress, Capetown (South-Africa) (2015d), SolarPACES

Sallaberry, F. Characterization of optical losses due to tracking systems on a linear solar thermal concentrator (2015e), Universidad Pública de Navarra (UPNA), Departamento de Proyectos e Ingeniería Rural, PhD Thesis.

Sun, F., Wang, Z., Guo, M., Bai, F., and Xu, Z. Determination of tracking errors with respect to the geometrical errors based on optimization algorithm. Energy Procedia 49 (2014), 2211-2220.

Conference Proceedings

EuroSun 2016
Palma de Mallorca (Spain), 11 - 14 October 2016

Performance Evaluation of scheffler Concentrator

Praveen J. Sanga[1], Arbind Kumar[2] and Sabin K. Mishra[3]

[1] Waljat College of Applied Sciences in academic partnership with Birla Institute of Technology, Muscat (Oman)

[2] Birla Institute of Technology, Mesra, Ranchi (India)

[3] Higher College of Technology, Ras-Al Khaimah (UAE)

Abstract

Scheffler concentrator, used widely for cooking purpose, is simple in design and efficient, hence performance analysis of the reflector is essential. In this regard, an experiment is conducted to evaluate its performance. A lateral section of paraboloid having fixed focus at a distance is taken as a reflector to minimize the effect of the shadow of the receiver. The water contained in a dome shaped receiver located at fixed focus, gets converted into steam and collected in the steam header until ample pressure is reached and further, it can be utilized for cooking purpose.

Keywords: *Scheffler concentrator, receiver, fixed focus, steam header, solar energy*

1. Introduction

Over the past few years solar energy has been strongly recommended as a feasible source of energy both economically and its availability in abundance. Almost all the fossil fuels (coal, wood, natural gas, oil, etc.) have originated from solar energy as they have been formed due to high pressures and temperatures over a long period of time. Also, the increasing rate of consumption of oil and gas would not be able to meet the future demand in energy. In this situation one of the alternative source of energy is solar energy, available free of cost. In recent years, solar energy is being utilized in power generation, water desalination, cooking purpose etc. (Sanga 2013). Solar energy is also pollution free and in present context it is one of the major advantages for the society.

Concentrators designed and developed by Delaney (2003) are suitable for medium temperature applications because of their ability of delivering temperature in the range of 300^0 C. One of the major properties of solar concentrator is its fixed focus, which is desirable for domestic and industrial application. Munir et al. (2010) concluded that it is possible to construct a concentrator having fixed focus for all the days of the year. In this regard, a Scheffler concentrator was constructed and tested by Solare Bruecke (2010). In the study, a thermal storage device is constructed for storing heat that could further be utilized in the evening. It has also been showed that the available energy in the cooking vessel fixed at the focal point of the reflector is approximately half of the energy falling over the reflector.

2. Experimental Description

The experimental set up consists of a dome shaped receiver, steam header, Scheffler reflector, pressure relieve valve and pressure gauge as illustrated in Fig. 1. The specification of the complete set up is mentioned in table 1. The Scheffler reflector is exclusively used for cooking application because of fixed focus and single axis tracking. The shape of the concentrator chosen is a lateral section of a paraboloid having reflectivity of 90% and

doi:10.18086/eurosun.2016.07.01 Available at http://proceedings.ises.org

above. Protection of the mirror coating has been taken into consideration at the time of fixing the mirrors. The purpose of this break is to have reflectivity equal to conventional secular's anodized finishes and resistant to ultraviolet light like glass. The axis of daily rotation of the reflector is fixed at an angle equal to the latitude angle of the site (Ranchi, India) with horizontal in north-south direction parallel to the earth axis and runs through the centre of gravity of the reflector. It helps the reflector to maintain its gravitational equilibrium, hence it requires less force to rotate it. The performance of the concentrator depends upon the efficiently utilization of tracking system coupled to a gearbox which runs with the help of digital timer and a DC motor.

Table 1: Experimental set up specification

Parameter	Specification
Inner base diameter of receiver	337 mm
Outer base diameter of receiver	355 mm
Height of the receiver	150 mm
Inlet Pipe diameter	0.5 inch
Outlet Pipe diameter	1 inch
Inner diameter of steam header	255 mm
Length of steam header	800 mm
Thickness of steam header	19 mm
Length of mirror	225 mm
Breadth of mirror	170 mm
Total mirror used	212
Total cutting mirror used	20

Table 2: Nomenclature and symbols

Quantity	Symbol	Unit
Enthalpy	h	kJ/kg
Volume	V	m^3
Density	ρ	kg m^{-3}
Beam Radiation	I_b	W m^{-2}
Concentration ratio	C	
Area	A	m^2
Efficiency	η	
Time	t	s

The steam generated in the receiver gets collected in the cylindrical steam header. The working pressure of the steam header is about 15 kg/cm^2. A Bourdon tube pressure gauge is used for measuring the pressure inside the steam header. The range of the pressure gauge used is 0 kg/cm^2 to 15 kg/cm^2. Pressure-relieve valve controls or limits the pressure, if it exceeds the desired pressure. The temperature gauge attached with steam header is having range varies from 0^0 C to 200^0 C. The interconnecting pipe between steam header and receiver is insulated with glass wool having minimum thickness of 50 mm.

The concentration ratio of the reflector is the ratio of aperture area to the receiver area and is given by Sukhatme et al. (2013).

$$C = \frac{\text{Aperture area}}{\text{Absorber area}} \qquad \text{(eq. 1)}$$

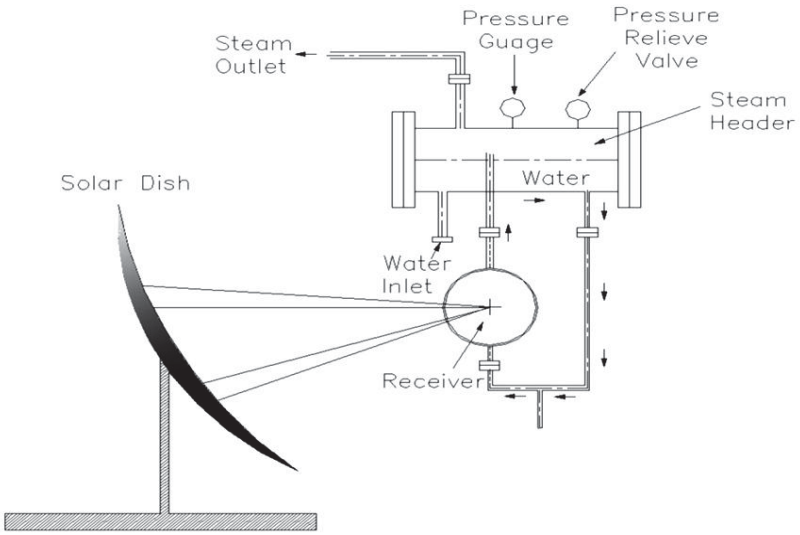

Fig. 1: Schematic of experimental set up

The effective area of the aperture is obtained by the total number of mirrors used. The enthalpy of the steam stored in the steam header is determined by steam table using linear interpolation. The experiment was carried out in February, 2015 and the average readings were taken at the time interval of 15 minutes as given in table 3. Beam and diffused radiation were measured with the help of precision pyranometer. The performance of the system is determined by the effective utilization of the reflected radiation. Therefore, efficiency of the system is defined as a ratio of energy stored in steam header to the energy reflected on the receiver.

$$\eta = \frac{h \times V \times \rho}{I_b \times C \times A \times t} \qquad \text{(eq. 2)}$$

Table 3: Experimentation reading

S.N.	Time (Hrs.)	Average Global Radiation (W/m^2)	Average Diffused Radiation (W/m^2)	Average Beam Radiation (W/m^2)	Average Pressure (kg/cm^2)	Average Temperature (^0C)
1	9.00	564	115	449	0.1	50
2	9.15	599	120	479	0.1	52
3	9.30	650	121	529	0.2	60
4	9.45	694	125	569	0.5	70
5	10.00	750	143	607	0.75	80
6	10.15	785	146	639	1	91

7	10.30	775	153	622	1.2	100
8	10.45	842	168	674	1.8	112
9	11.00	812	173	639	2	120
10	11.15	840	163	677	2.4	124
11	11.30	829	176	653	2.6	129
12	11.45	866	168	698	2.6	134
13	12.00	907	186	721	2.6	135
14	12.15	920	197	723	2.8	138
15	12.30	854	176	678	3.4	142
16	12.45	920	197	723	4	153
17	13.00	844	188	656	5	155
18	13.15	872	180	692	5.9	160
19	13.30	830	183	647	6.8	164
20	13.45	797	181	616	7.6	168
21	14.00	761	162	599	8	170

3. Results and Discussion

The variation of beam radiation and temperature with respect to time is depicted below in Fig. 2. Both of them increase with respect to time. It has been observed that there is an increase in temperature of the steam stored in header even if the beam radiation falls down.

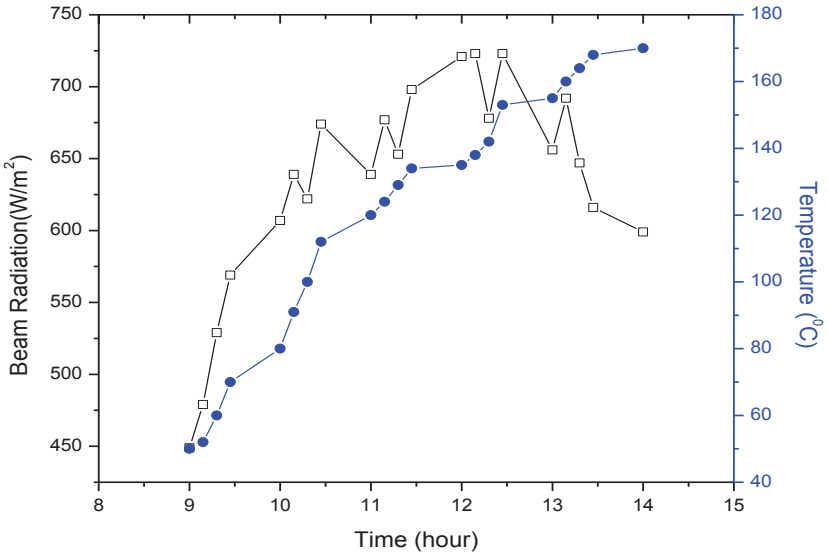

Fig. 2: Variation of beam radiation and steam temperature

The pressure and temperature of the steam collected in steam header is used to evaluate the physical state of the steam. It was also observed that the temperature of the steam is slightly more than the saturation temperature in the steam header after 12 p.m. as shown in Fig. 3, which is vital as the saturated steam has high heat transfer coefficient than the superheated steam.

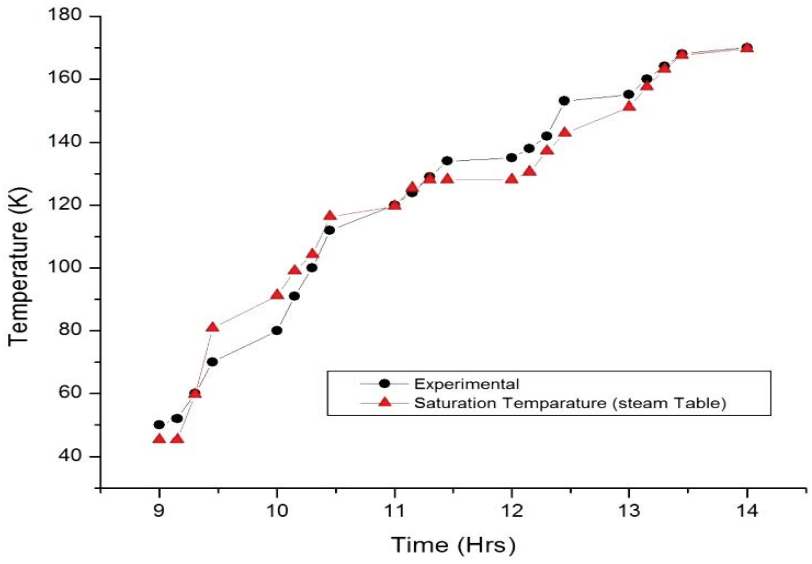

Fig. 3: Comparison of steam temperature at steam header with saturation temperature

The performance of the system is also evaluated. Maximum efficiency of the system was calculated to be 35 %.

4. Conclusion

The study suggests that the system can produce enough steam after 12 p.m. which can further be utilized for cooking purpose. It is also required to have a proper well insulated storage system to minimize the heat loss. As far as cooking place is concerned, it should be decided on the basis of the length of the pipe needed to maintain its temperature without any significant change or loss. The efficiency of the system can also be increased by minimizing heat loss.

References

Bruecke S., Scheffler W., 2006. Introduction to the revolutionary design of Scheffler. SCIs International Solar Cooker Conference.

Delaney D., 2003. Scheffler's community solar cooker.

Munir A., Hensel O., Scheffler W., 2010. Design principle and calculations of a Scheffler fixed focus concentrator for medium temperature applications. Solar energy. 1490-1502.

Sanga P.J., 2013. Solar Energy – A competitive energy source, Oman observer, 7 Dec. 2013. Print

Sukhatem S.P., Nayak J.K.., 2013. Solar energy, 3rd ed., McGraw Hill.

Conference Proceedings

EuroSun 2016
Palma de Mallorca (Spain), 11 - 14 October 2016

Theoretical Analysis of Vacuum Flat-plate Solar Collector with a Detailed Model

Viacheslav Shemelin[1,2], Tomas Matuska[1,2]

[1] University Centre for Energy Efficient Buildings, Czech Technical University in Prague

[2] Faculty of Mechanical Engineering, Czech Technical University in Prague

Abstract

Flat-plate collectors are generally designed for applications with typical working temperatures between 40 °C and 60 °C, which is mostly the case for domestic hot water systems. The major effect on the performance of flat solar collector has heat loss through glazing. The reduction of front side heat loss and consequently increasing efficiency can be achieved by using vacuum glazing. The paper presents a theoretical analysis of flat-plate solar collectors with a vacuum glazing. Different configurations of the collector have been investigated by a detailed theoretical model based on combined external and internal energy balance of the absorber. Performance characteristics for vacuum flat-plate collector alternatives have been derived. Subsequently, annual energy gains have been evaluated for a selected variant and compared with state-of-art vacuum tube collectors. The results of modeling indicate, that in case of using advanced vacuum glazing with special low-emissivity coating (emissivity 0.20, solar transmittance 0.85), it is possible to achieve efficiency parameters similar to or even better than vacuum tube collectors.

Keywords: *flat-plate collector, vacuum glazing, detailed model*

1. Introduction

Flat-plate solar collector (FPC) is the most widely used solar collector type in Europe. Simple structure, high optical efficiency, low cost, and safe operation are its main features. However, FPC is generally designed for a low temperature level between 40 °C and 60 °C, which is mostly the case for domestic hot water system. Any shifts to a higher temperature level could bring the extension of applicability range of FPC. Hence, efforts aimed to improve the performance of flat plate solar collectors are ongoing. The performance of a flat plate solar collector is largely influenced by the thermal losses from the absorber to the ambient via the transparent cover. One way to reduce this heat loss is to reduce the natural convection heat transfer in the space between the absorber and the cover by its partitioning with the use of additional glass pane, plastic film, or transparent insulation materials (TIM). Another way to reduce this heat loss is to use gas with lower thermal conductivity rather than air or by evacuating the space.

During the last 60 years a great number of research works have been done with the aim to develop new designs of solar flat-plate collector able to yield good performance at medium temperature range. The proposed designs are mainly centered around the objective to reduce heat losses, especially front side heat losses, e. g. by using transparent insulation materials (TIM), moderate vacuum, and high vacuum.

Veinberg and Veinberg (1959) investigated the use of “deep narrow meshes” as solar transparent honeycomb insulation. Further, Hollands (1965) presented the theoretical performance characteristics of a cellular honeycomb as a convection suppression device placed between the absorber and the outer glass cover of the FPC. Tabor (1969) presented a brief picture of cellular (honeycomb construction), indicating successful use of honeycomb insulation should wait for material with better physical properties and manufacturing technique. Later, Rommel and Wagner (1992) demonstrated that FPC containing 50-100 mm polycarbonate honeycomb

doi:10.18086/eurosun.2016.07.06 Available at http://proceedings.ises.org

layers function well with fluid working temperature between 40-80 °C. Higher working temperatures up to 260 °C are also possible using glass honeycombs, since plastic covers are susceptible to melting at temperatures above 120 °C. Svendsen and Jensen (1987) and Svendsen (1989) experimentally showed that solar FPC efficiency can be significantly improved by filling the air gap between absorber and cover with monolithic silica aerogel and evacuating to 10 kPa. Later, Duan (2012) studied the reduction of front side heat loss by placing the aerogel layer between the transparent cover and the absorber plate showing an increase of 21% in the collector efficiency respecting to the conventional collector.

However, most of the available transparent insulation materials are still not a good choice for high temperature flat plate collectors (Brunold et al., 1994). They either cannot withstand high temperature levels because they are made of plastics (most of honeycomb and capillary materials), they are hygroscopic and cannot withstand the humidity inside the collector (aerogels etc.), or they are very expensive (glass capillaries).

The use of a moderate vacuum in flate-plate collectors is known to reduce front side heat losses since the work of Eaton and Blumn (1975). The concept of an evacuated flat-plate collector was commercially realized and is available of the market. Apart from the higher thermal output, these collectors have the advantage of longer lifetime compared to nonevacuated collectors, because no humidity and condensation problems occur within the casing. Typical interior pressures, which can be maintained economically, lie between 1 and 10 kPa. It means that although convection losses are suppressed, gas conduction remains fully developed. Further, Benz and Beikircher (1997) constructed a prototype collector based on the commercially available flat-plate collector. To implement high thermal efficiency in the medium temperature range, the thermal losses of the absorber have been reduced using a low emissive selective absorber, a low pressure krypton filling (5 kPa) in the collector casing. The prototype collector has been dynamically tested and has showed very high efficiencies of more than 60% at 100 °C. Later Benvenuti (2005) presented a FPC, which is able to reach 300 °C. That has become possible by ultrahigh vacuum (1.33 x 10^{-7} Pa) maintained by a getter pump powered by the sun. After few years SRB Energy, with the support of CERN experts and facilities, has started the production of these collectors.

This paper presents the idea of replacing single glazing, which is used in most of flat solar collectors, with flat vacuum glazing, which, on the one hand, will show a low level of heat losses (low-emissivity coating, high vacuum) and, on the other hand, will demonstrate a high solar energy transmittance. Flat-plate solar collectors with low heat loss (at the level of vacuum tube collectors) and with a sufficiently high optical efficiency could be effectively used for integration into building envelopes (residential, industrial), which are widely available.

2. Vacuum glazing as a glazing cover of solar collector

Vacuum glazing consists of two glass sheets sealed together around the periphery. Glass sheets are supported by a pillar array arranged on a regular square grid pattern, and space between sheets is evacuated to a pressure lower than 0.1 Pa, thus effectively eliminating both gaseous conduction and convection. The pillars have a dimension of about 0.5 mm in diameter and behave like thermal bridges. Three different heat transfer mechanisms contribute to the total heat transfer coefficient $h_{g1\text{-}g2}$ of the glazing: thermal conduction through residual gas (h_{gas}), thermal conduction through spacers (h_{spac}), and radiation heat transfer between the two sheets (h_{rad}) in vacuum glazing. The total heat transfer coefficient $h_{g1\text{-}g2}$ between the glass sheets of a vacuum glazing can be approximated by the simple addition of individual heat transfer coefficients as (Weinlader et al, 2005; Collins and Simko, 1998)

$$h_{g1-g2} = h_{gas} + h_{rad} + h_{spas} = 0.8P + 4\varepsilon_{eff}\sigma T_{mean}^3 + \frac{2\lambda r}{d^2} \quad \text{(eq. 1)}$$

where P is internal pressure, σ is Stefan Boltzmann constant (5.67 x 10^{-8} W/(m^2.K^4)), T_{mean} is the average of temperatures T_1 a T_2 of the glass sheets, λ is the thermal conductivity of glass pillars, r is thr radius of glass pillars, d is the distance between pillars and, the effective emittance, ε_{eff}, is conventionally written as follows:

$$\varepsilon_{eff} = \frac{1}{\frac{1}{\varepsilon_1}+\frac{1}{\varepsilon_2}-1} \quad \text{(eq. 2)}$$

The relationship (eq. 1) is valid for the space with pressure less than 0.1 Pa, that is, high vacuum.

Vacuum glazing already appears in the portfolio of windows suppliers for use in buildings (Fig. 1). Commercially available vacuum glazing with configuration 3-0.2-3 mm has a transmittance of solar radiation of τ = 67 % and glazing center-of-glazing transmittance U value of 1.1 W/(m^2.K) (e.g. Pilkington Spacia).

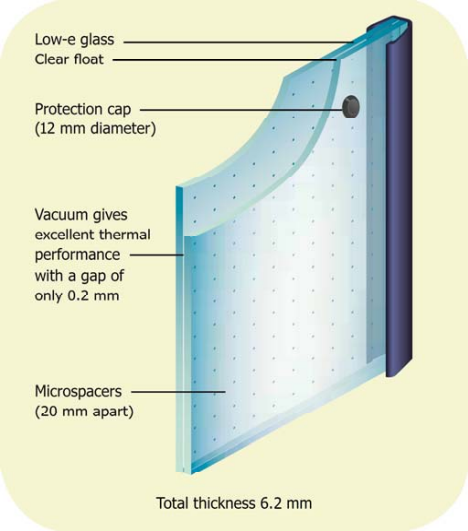

Fig. 1: Vacuum glazing (Pilkington Spacia)

Commercially available low-e coatings have been almost exclusively developed for architecture. To uphold the thermal and visual comfort in buildings, coating systems based on silver are primarily used, which can provide for extremely low emissivity (less than 0.03) and high visible transmittance (up to 0.90). Solar transmittance, however, is rarely higher than 0.60. A low solar energy transmittance, caused by reflectance of low-emissivity coating for the near infrared radiation (NIR) in the solar spectrum, is unsuitable for use in solar collectors. However, values up to 0.80 and corresponding higher emissivity (between 0.15 and 0.20) can be achieved using very thin silver layers, which have been developed in the last years for triple glazing, or with metal oxides (Fig. 2). It is also possible to use the external glass antireflection coatings on both surfaces and thus reduce reflection at the two boundary surfaces air-glass.

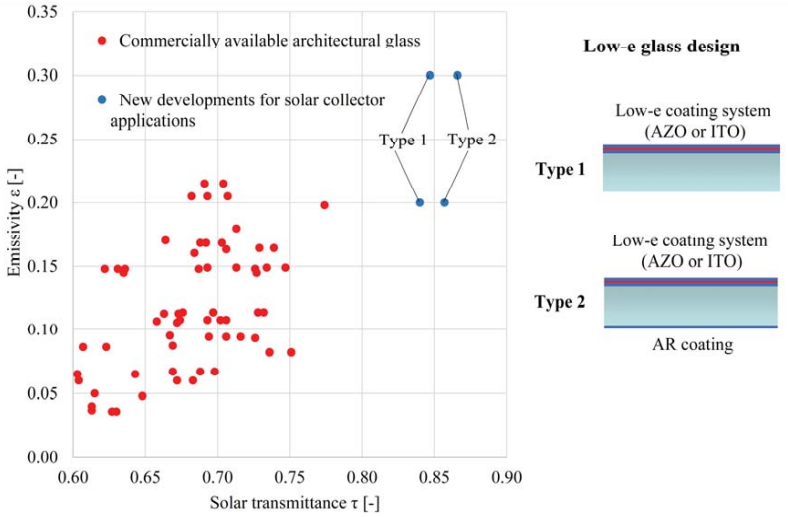

Fig. 2: Optical properties of spectrally selective glass with high solar transmittance for architecture and solar collector applications (Giovannetti et al, 2012)

To evaluate the potential of vacuum glazing application in solar thermal collector design, detailed simulations for three different variants of the collector cover glazing have been carried out. Reference variant (REF) is a simple solar low iron glass. The second variant (VG1) has a vacuum glazing based on two low iron glass without any coating. The last variant (VG2) is an advanced vacuum glazing with low-emissivity coating on

the outer surface of the inner glass (position 3). The optical properties of the coating are IR emissivity of 0.2 and solar transmittance of 0.85. Configurations of considered collector glazings are shown graphically in Fig. 3. The parameters of the cover glazings used for the comparative study are listed in Tab. 1.

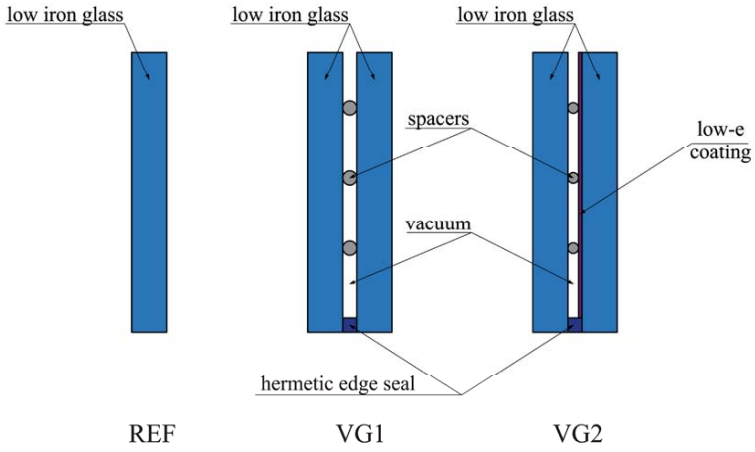

Fig. 3: Configurations of the investigated cover glazings

Tab. 1: Comparison of cover glazing physical properties

Properties	REF	VG1	VG2
Thickness of layers (mm)	4	4-0.2-4	4-0.2-4
Emissivity of surfaces (-)	0.85/0.85	0.85/0.85/0.85/0.85	0.85/0.85/0.2/0.85
Solar transmittance of glazing (-)	0.92	0.85	0.79

Since the thermal conductance is dependent on the temperature of the glazing, the heat transfer coefficient should be determined as a function of mean glazing temperature $T_{g1\text{-}g2}$ (Fig. 4)

$$h_{g1-g2} = f\left(T_{g1-g2}\right) = f\left(\frac{T_{g1}+T_{g2}}{2}\right) = h_{g0} + h_{g1}T_{g1-g2} + h_{g2}T_{g1-g2}^2 \qquad \text{(eq. 3)}$$

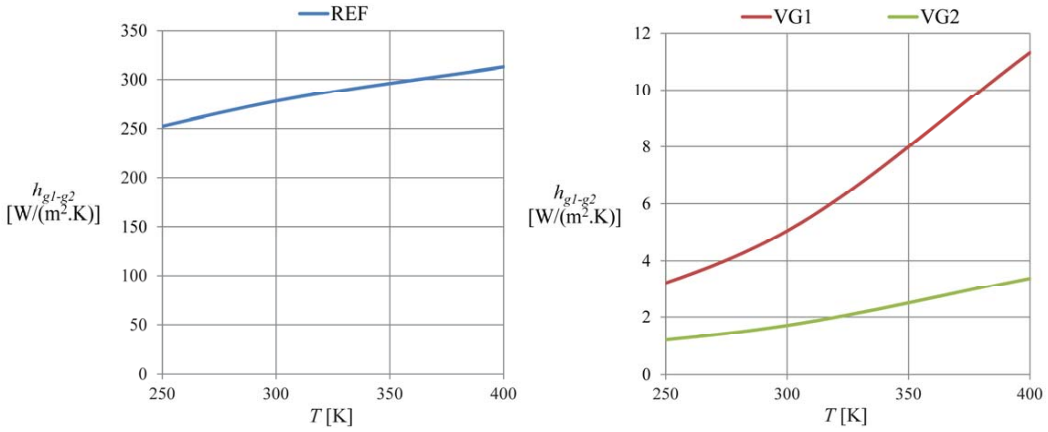

Fig. 4: Thermal conductance of the glazing as a function of mean temperature

3. Theoretical model of solar flat-plate collector

3.1. Description of the model

In order to analyze the thermal performance of FPC with considered variants of the transparent cover, a detailed theoretical model of the flat-plate collector Type 205 has been used and implemented into TRNSYS simulation software. The TRNSYS type is a successor of design tool KOLEKTOR 2.0 (Matuska and Zmrhal, 2009) originally developed as the Visual Basic program.

To compare the performance of given glazings the flat-plate collector has been considered consisting of an absorber placed in the insulated box covered with a given transparent cover. There is an air gap between the absorber and the cover and between the absorber and its back insulation, both defined by thickness and slope. The absorber is designed as a harp with distribution and riser pipes (defined by length, distance, and diameter). Transparent cover and back thermal insulation are defined by temperature dependent thermal conductance (see eq. 3).

The detailed model of flat-plate solar collector allows concluding a detailed calculation of heat transfer in the solar collector. Energy flow from the absorber surface to ambient and from the absorber surface to a heat transfer liquid, together with a temperature distribution in the collector, are calculated in the iteration loops. A solar collector can be specified by a number of detailed parameters, optical properties of glazing and absorber, and thermophysical properties of the main components of solar collector (frame, absorber, and transparent cover) in the model.

The implementation of the model in TRNSYS environment offers the parametric analysis for different construction alternatives for annual solar collector performance in the given solar system application. There is also a possibility to change a mathematical models describing the fundamental heat transfer phenomena (closed gap convection, wind convection, forced convection heat transfer in pipes etc.) and perform sensitivity analysis for selection of the models.

3.2. Basic equations

Mathematical model for solar flat-plate liquid collector solves one-dimensional heat transfer balances. Hottel and Woertz, Hottel and Whilier, and Bliss developed the simplest assumptions: thermal capacities, are neglected and a single value of collector overall heat loss coefficient is considered. Based on these assumptions and considering that the heat transfer is mainly one-dimensional and predominant in the direction normal to the absorber, Duffie and Beckman developed a simplified model (with electrical analogy) to characterize the solar collector in steady-state conditions.

The mathematical model in general consists of two parts: external energy balance of absorber (heat transfer from absorber surface to ambient environment) and internal energy balance of absorber (heat transfer from absorber surface into heat transfer fluid). The model solves the energy balance of the solar collector under steady-state conditions according to the principle Hottel-Whillier equation for usable thermal output

$$\dot{Q}_u = A_{abs} F_R [\tau_n \alpha_{abs} G_t - U(T_{in} - T_{amb})] \quad \text{(eq. 4)}$$

In this equation, A_{abs} is the absorber area, F_R is the collector heat removal factor, τ_n is the solar transmittance of the collector cover, α_{abs} is the solar absorptance of the absorber, G_t is the total solar irradiance, U is the overall heat loss coefficient of collector, T_{in} the inlet fluid temperature and T_{amb} is the ambient temperature.

The main planes of the collector are cover exterior surface (f_2), cover interior surface (f_1), absorber (abs), back insulation interior surface (b_1), back frame exterior surface (b_2), edge insulation interior surface (e_1), and edge frame exterior surface (e_2). A surface temperature is determined for each plane of collector during the calculation procedure. The main collector planes are schematically outlined in Fig. 5.

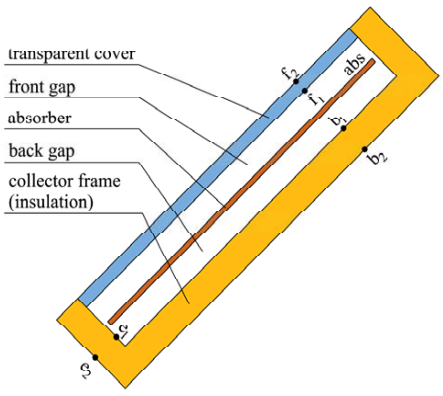

Fig. 5: Main temperature planes (surfaces) in solar collector model

Both external and internal energy balances are mutually dependent. The overall collector heat loss coefficient U as the main output from external balance is one of the inputs for internal balance. On the other side, mean absorber temperature T_{abs} as one of the outputs from internal balance is used as necessary input for external balance. Iteration loop has been introduced to transfer the results from external balance to starting internal balance and results from internal balance are put to external balance. Loop iterates as long as the difference between absorber temperatures calculated in two adjacent iteration steps higher than required minimum.

3.3. External energy balance

The external energy balance consists of:

- the heat transfer by radiation and by natural convection in the gap between absorber surface and transparent cover (respectively back insulation and edge insulation);
- the heat transfer by conduction through transparent cover (respectively back insulation and edge insulation);
- the heat transfer convection and radiation from exterior cover (respectively back frame and edge frame) surface to ambient.

To calculate the heat transfer coefficients properly (Fig. 6), temperatures for main collector planes (surfaces) should be known, but on the other side the temperature distribution in the collector is dependent on the heat transfer coefficients values. Therefore, external energy balance of absorber is solved in an iteration loop starting from first estimate of temperatures for each main surface based on given input temperature T_{in} and ambient temperature T_{amb}.

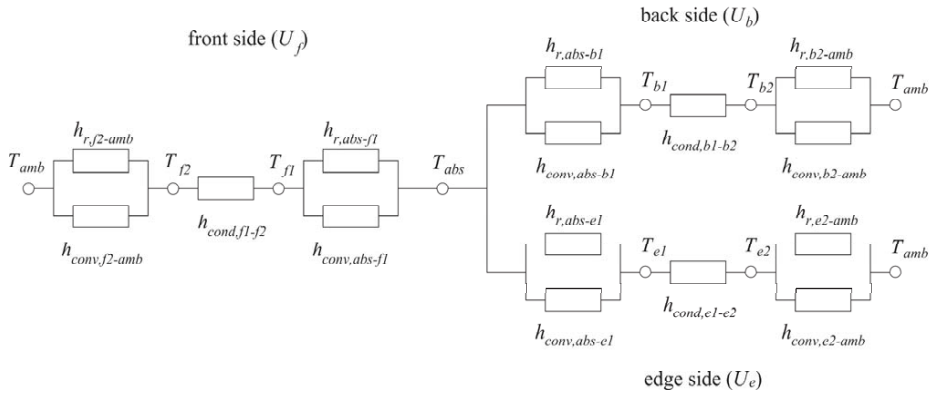

Fig. 6: Schematic detailed layout of external energy balance of absorber

3.4. Internal energy balance

The internal energy balance considers:

- the fin heat transfer by conduction;
- the heat transfer by conduction through the bond between absorber and pipes;
- the heat transfer by forced convection from interior surface of pipe to fluid.

Internal energy balance proceeds in its own iteration loop due to relationship between mean fluid temperature T_{mean} and forced convection heat transfer coefficients in absorber pipe register. The iterative calculation results of internal balance are collector efficiency factor F', collector heat removal factor F_R, usable thermal output and efficiency of solar collector.

3.5. Experimental validation

Type 205 has been experimentally validated in the frame of solar collectors testing according to European standard EN ISO 9806 in the accredited Solar Laboratory operated under University Centre for Energy Efficient Buildings, Czech Technical University in Prague. Solar thermal collectors have been tested to obtain steady state thermal output at constant operation conditions of inlet temperature (±0.05 K) and mass flow rate (±0.002 %) of heat transfer fluid (water) entering collector and at constant climatic conditions of solar irradiation (±1.4 %) and ambient temperature (±0.05 K).

Instantaneous efficiency has been calculated from collector thermal output related to total solar irradiation input (incident on collector reference area: gross area). Experimental data points of solar collector efficiency are coupled with uniform uncertainty bars in the graphs. Expanded uncertainty of efficiency and reduced temperature difference have been assessed for experimental data from both type A (statistical) and type B (instrumental) uncertainties considering the coverage factor $k = 2$ with 95% level of confidence (normal distribution).

The theoretical calculation of efficiency characteristic by the model is subjected to the uncertainty of input parameters. While geometrical parameters are easily available with high degree of confidence, the number of parameters defining the properties of collector parts is found uncertain within narrow range (e.g. absorber and glazing optical parameters, mostly ±2 %), middle range (e.g. conductivity of insulation layer dependent on its temperature and density, ±10 %), and quite broad range (e.g. emittance of absorber back side, insulation or collector frame, >10 %). Therefore, the results of theoretical calculation could be presented as two delimiting curves where the collector efficiency values can be found in reality.

The mathematical model has been validated in the field of atmospheric solar flat-plate collectors (top quality solar collectors with state-of-art copper laser welded absorber coated with a high performance selective coating and solar glazing as a transparent cover). Four different solar collectors have been used for detailed model validation. The majority of solar thermal collector parameters (e.g. thermal conductivity of insulation, the solar transmittance of the glazing, and the emissivity of the absorber) have been measured experimentally to reduce the uncertainty range. The model has also been tested in the case of various values of slope, mass flowrate, wind velocity, and incident radiation. More information about model validation could be found in (Shemelin and Matuska, 2015).

Fig. 7 shows experimentally measured efficiency points and theoretical modelled efficiency characteristics. It is evident from the results that simulated efficiency characteristics fit the measurements relatively well, which gives confidence about the developed model.

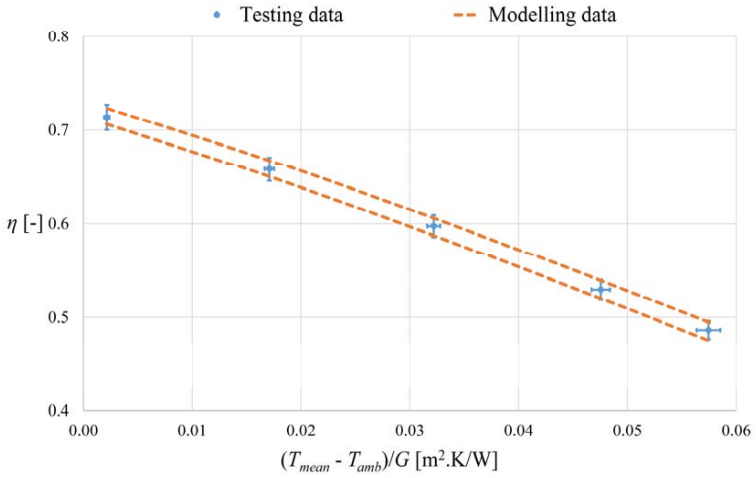

Fig. 7: Mathematical model validation

4. Results

Four configurations of FPC were modeled with dimensions 1 x 2 m. All variants have state-of-art copper laser welded absorber with a high performance selective coating with absorptivity of 0.95 and emissivity of 0.05. The thickness of the absorber is 0.2 mm and distance between pipes is 100 mm. Back thermal insulation and edge thermal insulation with thermal conductivity of 0.04 W/(m.K) have thickness 50 and 20 mm, respectively. The thickness of the air gap between absorber and glazing is 30 mm (except variant VC4, explained below). The difference between considered variants is only in the covering glazing.

The first configuration of FPC (RC) has a reference glazing (REF) as transparent cover with the parameters shown in Tab.1. The second configuration VC1 has a vacuum glazing VG1 instead of the reference glazing.

The third configuration VC2 considers variant VG2 as cover glazing. The last configuration VC3 has a principally different configuration. This variant has no gap between the absorber and the cover. Here, the absorber is bonded to the VG2 by permanently flexible, highly transparent silicone gel to reduce the whole thickness of the collector ("slim" collector alternative suitable for building envelope integration). Considered configurations of FPC collectors RC, VC1, VC2, and VC3 are shown in Fig. 8.

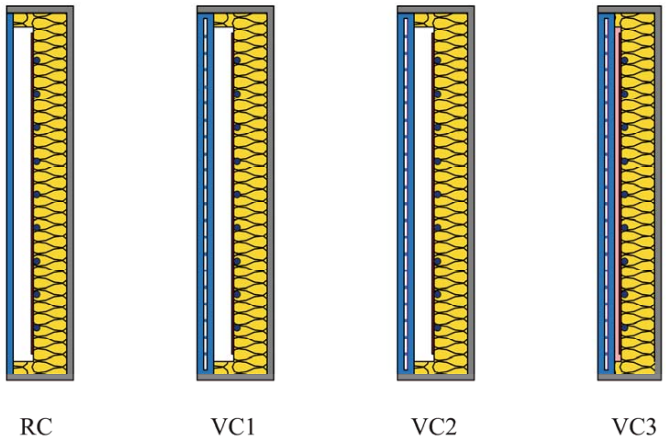

Fig. 8: Considered solar collector configurations

The graph in Fig. 9 shows the efficiency curves of considered solar collector variants. With respect to the EN ISO 9806 (2015) Standard "Solar energy-Solar thermal collectors-Test methods", the collector efficiency η is based on the collector gross area A_G. The calculations have been done with use of early described theoretical detailed model of FPC Type 205. The Graph shows the difference in energy quality of compared FPC variants. The low slope of the efficiency curve of the VC2 is due to the collector VC2 having two low-e coatings—the first inside the vacuum glazing and the second on the absorber surface. Other variants RC, VC1, and VC3 have only one low-e coating. Despite the vacuum layer, higher emittance of the glass low-e coating (0.2) in the VC3 variant instead of absorber coating with emittance 0.05 in the REF variant, brings the total top heat loss to similar value, but optical parameters of the VC3 configuration are lower (lower zero loss efficiency η_0). The resulting coefficients of efficiency characteristics η_0, a_1, and a_2 are listed in tab. 2.

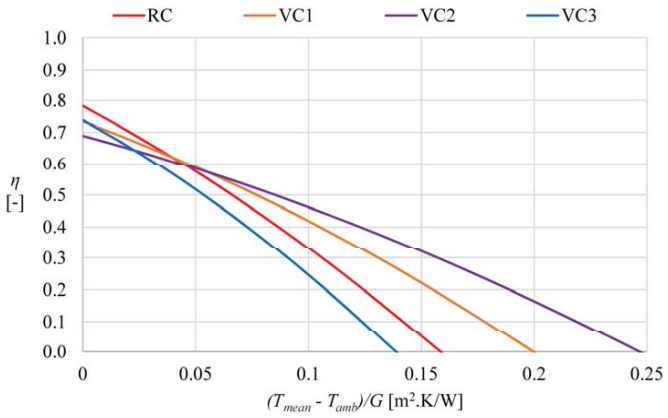

Fig. 9: Efficiency curves of different solar collector variants

Tab. 2: Summary of the collector simulation results

Collector variants	η_0 [-]	a_1 [W/(m^2.K)]	a_2 [W/(m^2.K^2)]
RC	0.783	3.788	0.006
VC1	0.734	2.634	0.004
VC2	0.689	1.919	0.003
VC3	0.738	3.890	0.009

On the other hand, solar collector variant VC3 has the lowest thickness between comparing variants – only 60 mm. Such thickness gives more possibility for integration of FPC into the building envelope because of the slim and compact design. Other variants RC, VC, and VC2 have thickness 87, 91 and 91 mm, respectively.

Fig. 10 presents the comparison of efficiency characteristics of flat-plate collector variant VC2 and vacuum tube collectors (with/without reflector, cylindrical/flat absorber) related to the gross area of collector. Thermal performance of solar flat-plate collector variant VC2 is comparable with that of vacuum tube collectors. Moreover, solar collector variant VC2 shows significantly higher efficiency than the majority of vacuum tube collectors (VT).

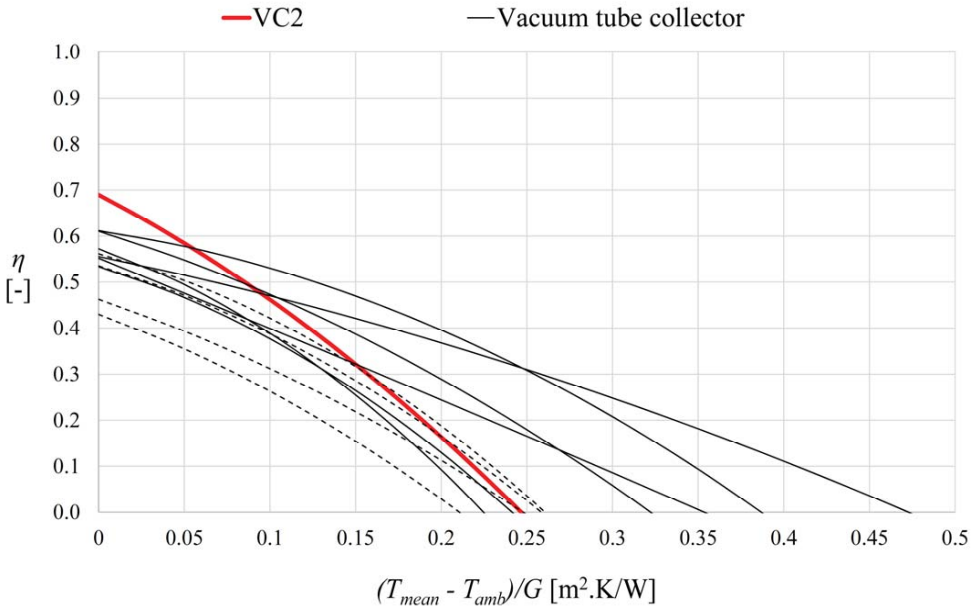

Fig. 10: Efficiency curves of different solar collector variants

To get a whole picture, the annual performance of the collector VC2 and VT collectors has been modelled using ScenoCalc software for constant operating temperatures 25, 50, 75, and 100 °C and climate conditions of Würzburg. The performance and optical characteristics of the compared collectors were used as input data. The results are shown in Tab. 3. The results of the modelling confirmed that the flat-plate solar collector variant VC2 has higher solar energy gains than the majority of vacuum tube collectors up to operating temperature 100 °C.

Tab. 3: Calculated annual solar collector gain with respect to the collector gross area

Solar gain [kWh/m^2]	25 °C	50 °C	75 °C	100 °C
VC2	697	548	422	320
VT1	653	**552**	**462**	**378**
VT2	586	480	386	303
VT3	527	465	390	308
VT4	603	511	421	**337**
VT5	616	515	416	320
VT6	577	478	386	304
VT7	**708**	**646**	**583**	**518**
VT8	607	493	400	318
VT9	626	**556**	**494**	**436**
VT10	667	**590**	**510**	**427**

5. Conclusions

Different designs of flat solar collectors based on a flat vacuum glazing have been theoretically investigated by using the detailed mathematical model to show the potential of vacuum glazing application in solar flat-plat collectors. The selected variant VC2 has been compared with state-of-the-art vacuum tube collectors by annual simulation of collector heat output in ScenoCalc. Results have shown, that there is a significant potential for increasing the efficiency of solar flat-plate collectors by using high performance vacuum glazing as a transparent cover. Collector variant VC2 shows higher performance than the majority of vacuum tube collectors up to operating temperature 100 °C.

Based on this analysis, now it is possible to proceed to the practical solution of the vacuum flat plate solar collector with vacuum glazing and low-emissivity coating (variant VC2). This collector promises to combine the low heat losses and the high solar energy transmittance.

6. Acknowledgment

This paper has been written with support by SGS16/212/OHK2/3T/12 - Modelling, control and design of environmental engineering installations.

7. References

Benvenuti C, 2005. Evacuable Flat Panel Solar Collector. PCT / EP 2004 / 000503. CERN.

Benz N., Beikircher T., 1999. High efficiency evacuated flat-plate solar collector for process steam production. Solar Energy Vol. 65, No. 2, 111-118.

Bliss J., 1959. The derivations of several “plate-efficiency factors” useful in the design of flate-plate heat collectors. Solar Energy Vol. 3, No. 4, 55-64.

Brunold, S., Frey, R., Frei, U., 1994. Comparison of three different collectors for process heat applications, Proceedings of SPIE – The International Society for Optical Engineering Optical Materials Technology for Energy Efficiency and Solar Energy Conversation XIII, Freiburg, Germany.

Collins, R. E., Simko, T. M., 1998. Current status of the science and technology of vacuum glazing. Solar energy Vol. 62, No. 3, 189-213.

Duan R., 2012. The efficiency of new solar flat-plate collectors. Advanced Materials Research, Vols. 347-353, 1337-1341.

Duffie J. A., Beckman W. A., 2006. Solar engineering of thermal processes, third ed., Wiley.

Eaton C., Blum H. A., 1975. The use of moderate vacuum environments as a means of increasing the collection efficiencies and operating temperatures of flate-plate solar collectors. Solar energy Vol. 17, 151-158.

Hottel H., Whillier A., 1955. Evaluation of flate-plate solar collector performance, Transactions of conference on the use of solar energy, 74-104.

Hottel H., Woertz B., 1942. The performance of flate plate solar collector, Transactions of ASME, No. 64, 91-104.

Holllands K. G. T., 1965. Honeycomb devices in flat-plate solar collectors. Solar energy Vol. 9, 159-164.

Rommel M., Wagner A., 1992. Application of transparent insulation materials in improved flat-plate collectors and integrated collectors storages. Sol Energy, Vol. 49, 371–380.

ScenoCalc v.5.01. Solar Collector Energy Output Calculator – a program for calculation of annual solar collector energy output. Available on https://www.sp.se/en/index/services/solar/ScenoCalc/Sidor/default.aspx

Shemelin V., Matuska T., 2015. TRNSYS type 205 – Detailed Model of Flat-Plate Solar Collector. Available

on: http://users.fs.cvut.cz/tomas.matuska/?page_id=582

Svendsen S., 1992. Solar collector with monolithic silica aerogel. Journal of Non-Crystalline Solids Vol. 145, 240-243.

Svendsen S., Jensen K. I., 1987. Flat Plate Solar Collector with Monolithic Silica Aerogel, Proceedings of ISES World Congress, Hamburg, Germany.

Matuška T., Zmrhal V. A mathematical model and design tool KOLEKTOR 2.2 reference handbook. 2009.

TRNSYS 17, TRNSYS: Transient System Simulation Tool. Available on http://www.trnsys.com/

Veinberg B. P., Veinberg V. B., 1959. Optics in equipment for the utilization of solar energy, State Publishing House of Defense Industry, Moscow (1959) [English translation]

Weinlader, H., Ebert, H.-P., Fricke J., 2005. VIG – Vacuum Insulation Glass, Proceedings of IVIS – 7th International Vacuum Insulation Symposium, Zurich-Duebendorf, Switzerland.

8. Web references

Pilkington Spacia. Available on: http://www.pilkington.com/en-gb/uk/products/product-categories/thermal-insulation/pilkington-spacia

Conference Proceedings

EuroSun 2016

Palma de Mallorca (Spain), 11 – 14 October 2016

Energy-economic Optimization of Flat-plate Collector

Viacheslav Shemelin[1,2], Tomas Matuska[1,2]

[1] University Centre for Energy Efficient Buildings, Czech Technical University in Prague

[2] Faculty of Mechanical Engineering, Czech Technical University in Prague

Abstract

The optimization of solar collector design may be based on energy, economic or energy-economic criteria. Obtaining maximum energy from a given collector area or determining the required minimum area of collector that produces a given amount of energy are examples of energy criteria. Designing a solar collector with a minimum cost is an example of economic criteria. The net present values, internal rate of return and payback period methods are examples of energy-economic criteria. This paper deals with the obtaining collector design parameters that provide the highest net present value. The following design parameters have been accepted as the decision variables: air gap size between the absorber and the cover glazing, emissivity of the absorber, frame insulation thickness, and distance between riser pipes. A detailed analysis is carried out for evaluating the thermal and optical performance, energy flows and losses for typical flat plate solar collector under given operating conditions – producing hot water for household needs. The high-quality flat-plate solar collector was chosen as a reference alternative. The results of modeling indicate that NPV value of solar collector variant with reduced to 50 mm distance between riser pipes is higher than in the reference variant, which indicates that a design change is economically justified.

Keywords: *flat-plate solar collector, optimization, sensitivity analysis, net present value*

1. Introduction

A wide spectrum of flat-plate collectors (FPC) is available on the market today, ranging from low-cost unglazed collectors to sophisticated selective-coated, single-glazed solar collectors. Up to now, a number of studies have been done in order to improve the thermal efficiency of FPC. The ways of increasing the energy performance of solar collector generally can be divided into two categories: effective absorption of solar radiation together with high rate heat transfer from the absorber to a transport media and reduction the heat loss of the collector to the minimum. The increase in optical efficiency can be achieved by application of glazing with antireflective coatings, use of extra clear low-iron glass instead of ordinary float glass together with spectrally selective absorber coatings. The heat transfer from the absorber surface can be maximized by fully wetted absorbers. Heat loss reduction can be achieved especially by using low emissivity absorber coatings, by increasing thickness of back, and by increasing thickness of the air gap between an absorber and collector glazing, alternatively using the low conductive gas instead of the air, or even by evacuating the space between absorber and cover glazing.

However, any improvement in the efficiency of solar collector has its cost. The use of new technologies and new materials always leads to an increase in collector price. Even given thickness of air gap between an absorber and covering glazing has an influence on the cost of the collector because it affects the overall depth of the collector and, thus, the amount of material used in the frame construction. On the other hand, while the solar PV modules price has dropped considerably in the last decades, the price of FPC collectors still remains high and there are no prospects for significant price reduction. Therefore, energy-economic optimization of the FPC has been taken into account in the present paper. Currently, there are not many studies in this area. A critical point, however, is that most of the published studies focused on energy optimization and did not take into account economic effects of the optimization.

doi:10.18086/eurosun.2016.07.12 Available at http://proceedings.ises.org

Furbo and Shan (2003) investigated the influence of antireflection treatment on the thermal performance of the solar system. Simulations showed that the thermal performance of SDHW systems with annual solar fractions of 25% and 60%, respectively, is increased by 10% and 4%, respectively, if a collector with a glass with an antireflective coating is used instead of a collector with a standard glass. Later, Kong et al. (2015) carried out the half-year measurement of the SDHW system with and without antireflective coating. The results show that solar gain for the system with solar fraction 75% and an antireflective coating is 2.4% higher in comparison to the solar system without an antireflective coating.

For achieving the maximum conversion efficiency, one important strategy is to use spectrally selective solar absorbers that exhibit a near-blackbody absorptance in the solar radiation region while suppressing emittance at infrared range. In particular, the new low-cost tandem absorber coatings have been extensively investigated by a number of groups. Feng et al. (2015) reported that TiAlN/TiAlSiN/Si_3N_4 coatings, deposited on stainless steel substrates can exhibit high absorptance of 0.938 and thermal emittance of 0.09. According to Liu et al. (2012), NbTiON/SiON absorber coating prepared on Cu substrate showed high selectivity with an absorptance value of 0.95 and emittance value of 0.07. Barshilia et al. (2008) studied NbAlN/NbAlON/Si_3N_4, and these tandem absorbers showed high absorptance of 0.956 and low emittance of 0.07. In a different work, Wu et al. (2015) reported that high absorptance of 0.948 and low emittance of 0.05 could be achieved by multilayered coating of Al/NbMoN/NbMoON/SiO_2 on stainless steel substrate. In another study, Zou et al. (2015) reported a CrAlN–CrAlON based tandem absorber that exhibited a high absorptance of 0.984 and a low emissivity of 0.07.

Brunold (1994) presented a prototype of a new FPC using glass capillary as transparent insulation. The results of the test indicated that an improved transparent insulated FPC could enter into competition with vacuum tube collectors. Further, Duan (2012) demonstrated that application of aerogel can greatly reduce top heat loss of FPC. Beikircher et al. (2015) presented advanced insulation methods for flat plate collectors. The collector front losses have been reduced by transparent insulation materials, the rear losses by an integrated vacuum insulation. The results of the experiment showed that the prototype with double fluorinated ethylene-propylene film and vacuum rear insulation, as well as prototype with transparent honeycomb insulation with ethylene tetrafluoroethylene film, has efficiency comparable to evacuated tube collectors.

Unfortunately, the main disadvantage of investigations presented above is a lack of cost data to show the profitability of the improvements in energy performance. The objective function for the optimization presented in the paper has been formulated according to the energy-economic criteria because it includes the investment costs (the cost of design changes) and also it includes the performance gains after design changes. The following analysis has been performed at first generally, and then in more detail for the most common application: solar domestic hot water system.

2. Variable design

To demonstrate the influence of the design changes on the collector performance, a detailed theoretical model of flat-plate collector Type 205 has been used. The detailed model of flat-plate solar collector allows a detailed calculation of heat transfer in the solar collector. Energy flow from the absorber surface to ambient and from the absorber surface into heat transfer liquid together with temperature distribution in the collector are calculated in the iteration loops. The solar collector can be specified by a number of detailed parameters, optical properties of glazing and absorber, thermophysical properties of main components of solar collector (frame, absorber, and transparent cover) in the model.

The implementation of the model in TRNSYS environment offers the parametric analysis for different construction alternatives for annual solar collector performance in the given solar system application. There is also a possibility to change mathematical models describing the fundamental heat transfer phenomena (closed gap convection, wind convection, forced convection heat transfer in pipes etc.) and perform sensitivity analysis for selection of the models.

A high-quality solar collector with solar glass as a transparent cover and selective absorber coating has been taken into account as an initial case. Specifications of the flat-plate solar collector used in the analysis are provided below.

Tab. 1: Design parameters of the FPC used in the analysis

Collector parameter	Value	Collector parameter	Value
Length	1175 mm	Air gap thickness	30 mm
Width	2017 mm	Absorber material	Aluminium
Height	87 mm	Absorber thickness	0.4 mm
Aperture area	2.25 m^2	Absorber emissivity	0.05
Absorber area	2.185 m^2	Surface treatment	PVD
Header pipe	Cu 22 x 1 mm	Number of riser tubes	11
Cover material	Solar glass	Distance between riser pipes	100 mm
Cover thickness	4 mm	Back insulation thickness	50 mm
Cover transmittance	0.92	Insulation material	Rockwool

Four decision changes in collector design have been investigated. The parameters discussed are back insulation thickness, absorber emissivity, air gap thickness, and distance between riser pipes. These parameters are known to have a significant influence both on the collector performance and on the collector price. Thus, it becomes possible to perform an energy-economic optimization aimed to reduce the payback period of flat-plate collector. For a series of simulations the evaluated parameter varies in the range of set values while the others parameters are kept fixed. The investigation provided below was based on the analysis performed by detailed theoretical model Type 205 available for TRNSYS environment.

2.1. Back insulation thickness

Nowadays, flat-plate collectors at the rear side are insulated by rock/mineral wool or similar insulation materials. Thermal conductivity of dry insulation amounts to 0.03-0.06 W/(m.K) for temperatures between 0 °C and 100 °C (see Fig. 1).

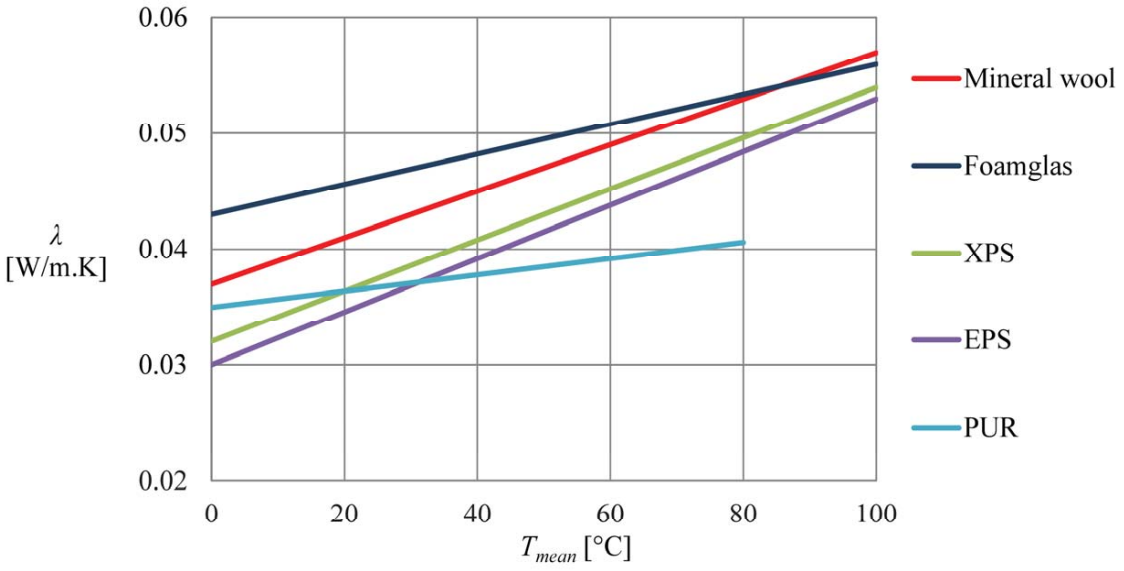

Fig. 1: Thermal conductivity as a function of mean temperature of insulation

For a typical insulation thickness of 40–60 mm, the backside collector heat losses amount to about 0.8 W/(m^2.K) from 3 to 5 W/(m^2.K) total losses. The question for the cost performance optimization is which insulation thickness is significant and which is not? Fig. 2 shows comparison of the efficiency curves for five solar collectors with the same geometrical and physical properties, but with varying thickness of the back insulation. It is apparent from the Fig. 2 that the thickness larger than 30 mm does not make significant improvement in the performance of FPC.

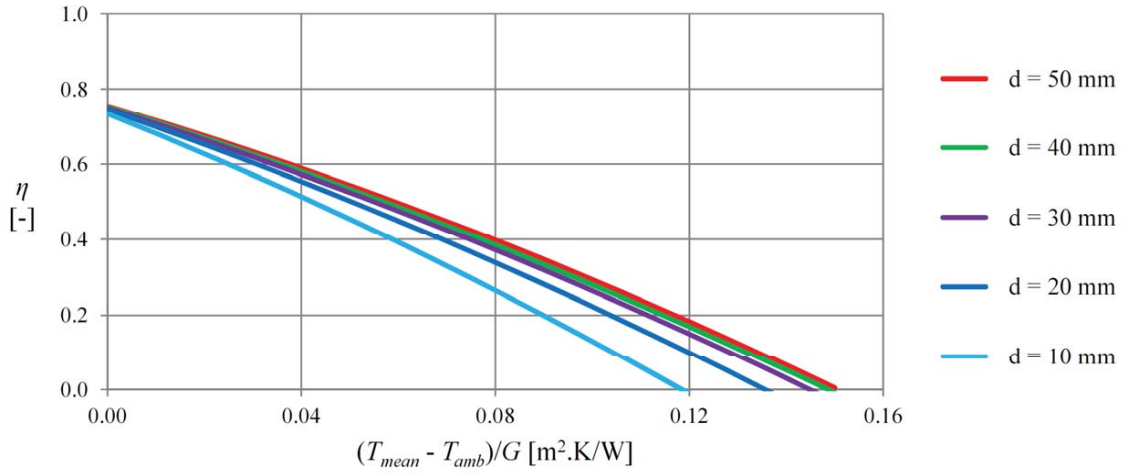

Fig. 2: Collector efficiency for considered design variants

2.2. Absorber emissivity

A solar absorber must have a high absorptivity α for solar (shortwave) radiation and a low emissivity ε for thermal (long-wave) radiation. Selective coatings are used to improve the performance of the solar collector by modifying optical properties both in the shortwave and longwave radiation ranges. For an absorber painted matt black without selective properties, absorptivity is 0.95 and IR emissivity is 0.85. Because of high ε values, such collectors have high heat losses by radiation and thus low efficiency, especially at high operation temperatures. Therefore, practically all single glazed collectors available on the market use selective coatings for the absorber (Tab. 2).

Tab. 2: Optical properties of selective coatings

Absorber coating	Absorptivity α in solar spectrum	Emissivity ε in infrared spectrum
Black chrome	0.95	0.12
Black nickel on polished nickel	0.92	0.11
Black anodized aluminium	0.93	0.07
Ceramic metal (cermet)	0.95	0.05

For the purpose of energy-economic optimization, two versions of absorbing coatings have been considered: a modern PVD coating with an emissivity of 0.05 or older and cheaper electrochemical (galvanic) coating with an emissivity of 0.12 both with the same absorptivity of 0.95. Fig. 3 shows collector efficiency characteristics of considered collector variations as a result of complex modeling. The difference between efficiency characteristics is obvious, especially at high operation temperatures.

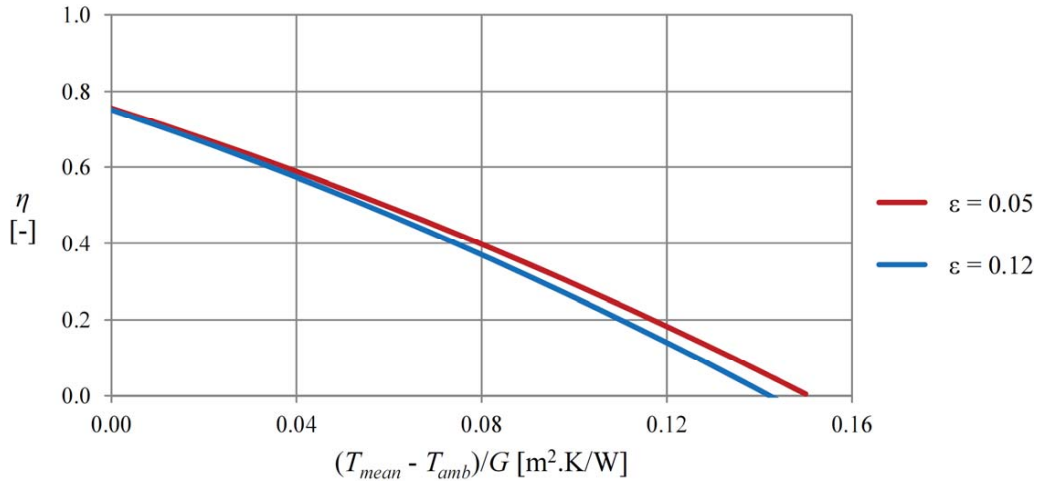

Fig. 3: Collector efficiency for the considered variants with ε = 0.05 and ε = 0.12

2.3. Air gap thickness

To have a good performance of a solar collector it is necessary to limit the thermal losses towards ambient through the front side of collector. Convective heat transfer through the air gap between the absorber surface and glazing has significant influence on these losses. The circulating air between absorber and cover, driven by temperature difference between absorber surface and interior glazing surface, transports the absorbed heat to the glazing. It depends on slope of the collector β and gap thicknesses L. The typical thickness of air gap is 30 mm. The goal is to investigate the influence of the air gap on the effectiveness of solar collector and to determine whether it makes sense to have 30 mm air gap in climatic conditions of Central Europe or the thickness of the air gap could be smaller. The graph in Fig. 4 shows natural convection heat transfer coefficient for closed layer between absorber and cover glazing as a function of the thickness of the air gap. Evidently, convection heat transfer coefficient decreases continuously with an increasing thickness of the air gap. However, Fig. 5 demonstrates a reduced influence of air gap thickness on the collector efficiency characteristics.

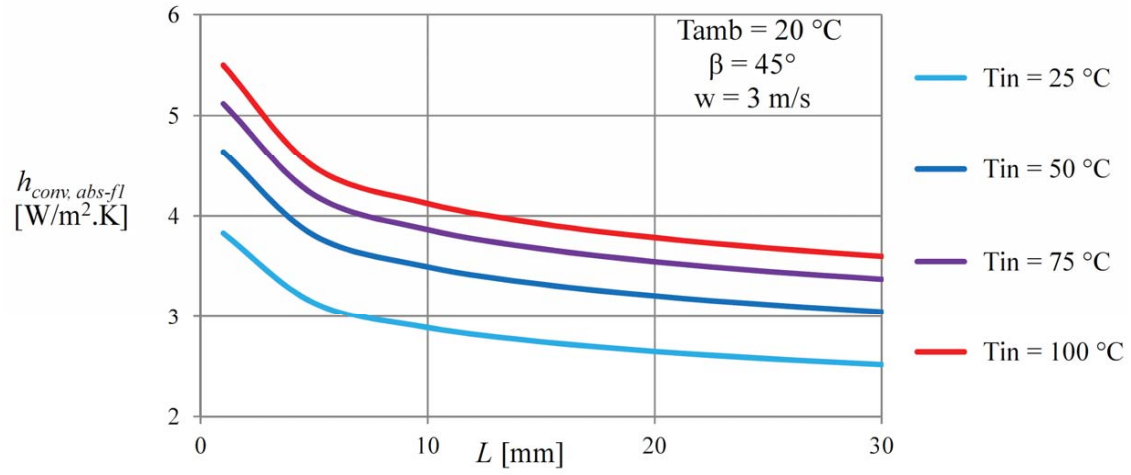

Fig. 4: Natural convection heat transfer coefficient as a function of the thickness of the air gap

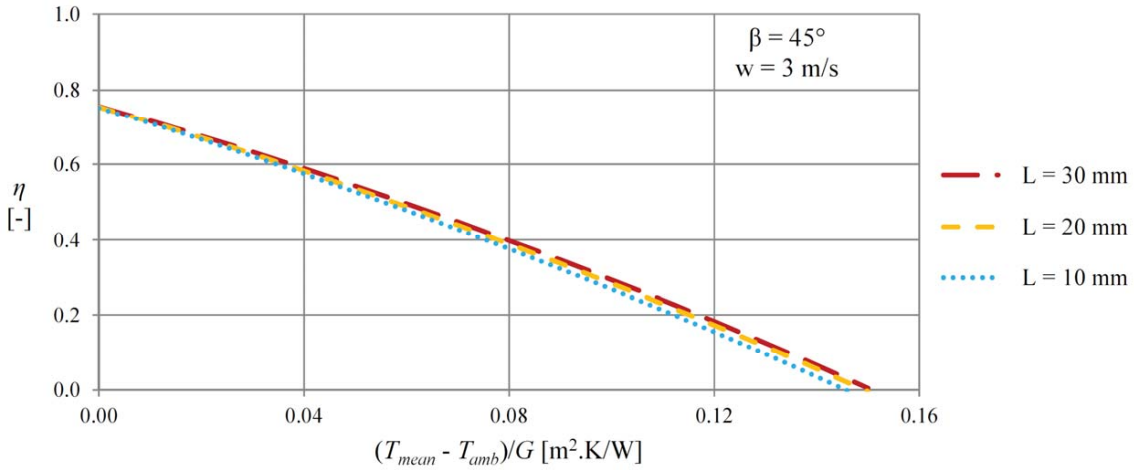

Fig. 5: Collector efficiency for the considered design variants

2.4. Distance between riser pipes

A typical design of the absorbers in solar FPC is represented by a tube and sheet configuration. Different hydraulic collector type (e.g. harp, double harp, or meander) can be used, but conductance of the sheet, conductance of the bond, forced convection heat transfer to the fluid, always have the crucial influence on the thermal performance (heat transfer from absorber surface to the fluid). As for distance between riser pipes, it has a direct impact on the heat conductance of the sheet and, therefore, on thermal performance of FPC. The typical distance between riser pipes is 100 mm. Reducing the distance between riser pipes increases fin efficiency F, collector efficiency factor F' (see Fig. 6) and consequently solar collector efficiency η (see Fig.7). As Fig. 6 shows that thermal conductivity and thickness of absorber also have a significant influence on the heat removal from absorber. For this reason,

the reduction of the distance of rising pipes from 100 mm to 50 mmin has been considered in the analysis. Fig. 7 demonstrates a significant increase in the efficiency characteristic of FPC with reduced pipe distance, especially for low operation temperature.

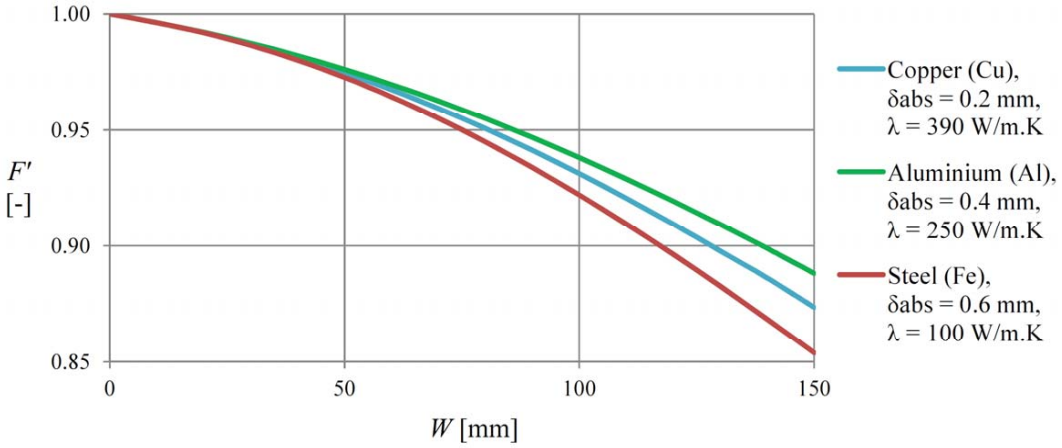

Fig. 6: Collector efficiency factor for different absorber materials as a function of pipe distance

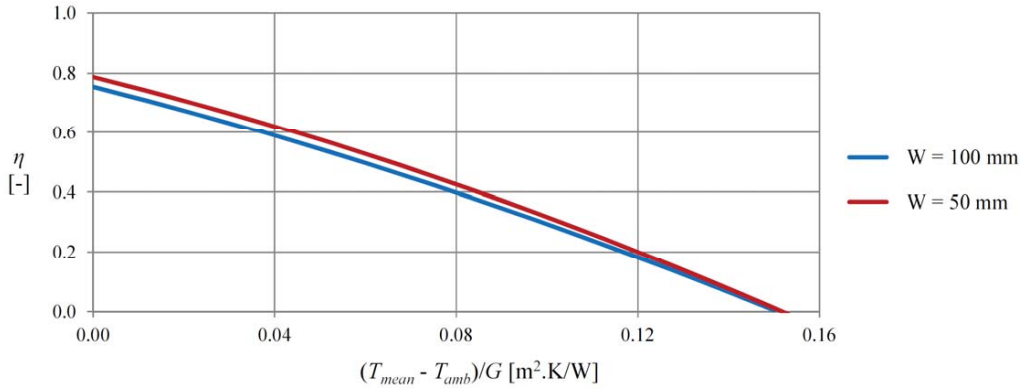

Fig. 7: Collector efficiency for the considered design variants

3. Energy analysis

The annual performance of the different solar collector variants has been evaluated by simulation of solar domestic hot water system with a given solar fraction 50 %. Scheme of the solar system is shown in the Fig. 8.

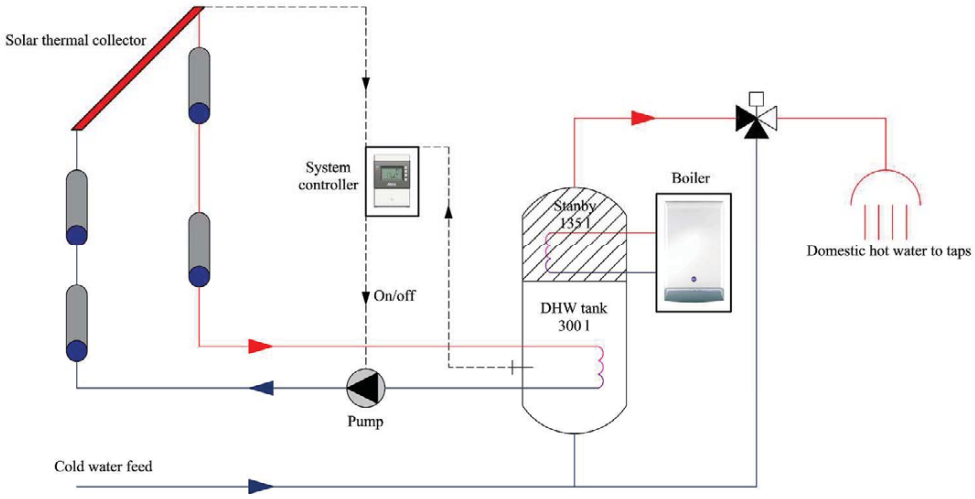

Fig. 8: Schema of simulated solar domestic hot water system

The system specification and the simulation results are shown in Table 4 and Table 5 consequently. The results show that the difference in the annual performance of compared solar collector variants decreases.

Tab. 4: Solar domestic hot water system parameters and operating conditions

Parameter	Description
Location	Athens, Würzburg, and Stockholm
Weather	TMY (Meteonorm)
Collector orientation	South, collector slope: Athens 25°, Würzburg 35° and Stockholm 45°
Collector area	Must cover 50% of domestic hot water heat demand (result between 49.5 and 50.5 %)
Reference area	Gross area
Collector mass flow rate	50 l/h.m^2
Heat transfer medium	Water
Pump control	Pump switching temperature is $\Delta T = 2$ *K* difference between collector output temperature and storage tank temperature in the area of heat transfer surface
Piping	Supply and return pipes are located in the internal and external environments: 7.5 each, DN 16 with 25 mm thermal insulation (λ = 0.04 W/m^2.K). Heat losses are determined towards the inside, respectively outside temperature.
Heat exchanger	Smooth tube heat exchanger with *UA* = 400 W/K (±15%) for 42 °C / 40 °C (outside temperature/tank storage temperature)
Tank storage	Volume: 300 l, heat loss: 2.2 W/K, height/diameter ratio: 2.5, standby volume 135 l with the temperature 60 °C
Cold water temperature	10 °C
Building interior temperature	15 °C
Hot water consumption	200 l/day (7.00 : 80 l; 12.00 : 40 l; 19.00 : 80 l), hot water temperature 45 °C, annual heat demand 2936 kWh/a

Tab. 5: Comparison of the annual energy gains for different solar collector variants

#	Collector design				Annual energy gain		
	back insulation thickness [mm]	absorber emissivity [-]	width of the air gap [mm]	distance between riser pipes [mm]	Athens [kWh/m^2.a]	Würzburg [kWh/m^2.a]	Stockholm [kWh/m^2.a]
RC	50	0.05	30	100	833	499	450
1	40	0.05	30	100	825	493	435
2	30	0.05	30	100	814	478	425
3	20	0.05	30	100	790	451	406
4	10	0.05	30	100	731	369	311
5	50	0.12	30	100	815	480	437
6	50	0.05	20	100	828	495	447
7	50	0.05	10	100	818	488	430
8	50	0.05	30	50	872	510	464

4. Economic analysis

The investigated design changes in the collector construction cause a change in the price of the collector. Based on the cooperation with the manufacturer of solar collectors, the influence of design changes on the price of the reference solar collector has been evaluated (Tab. 6). A negative value of the price change means the price

reduction, while positive value means the price increase. The energy-economic study has also been performed for three cities - Athens, Würzburg, and Stockholm.

Tab. 6: Effect of design changes on the collector price (relative to the gross collector area)

#	Collector design				Price change [€/m²]
	back insulation thickness [mm]	absorber emissivity [-]	width of the air gap [mm]	distance between riser pipes [mm]	
RC	50	0.05	30	100	0
1	40	0.05	30	100	-1.70
2	30	0.05	30	100	-3.37
3	20	0.05	30	100	-5.07
4	10	0.05	30	100	-6.78
5	50	0.12	30	100	-5.59
6	50	0.05	20	100	-0.50
7	50	0.05	10	100	-1.00
8	50	0.05	30	50	+6.07

Based on the full-year simulation results of SDHW system (Table 5) and on the effect of collector price changing (Table 6), the economic analysis has been carried out by using Net Present Value (NPV) method. NPV is a method used to determine the present value of an investment (collector price changing) by the discounted sum of all cash flows (additional energy gain, i.e. operation cost savings) received from the changed solar collector construction. A positive net present value indicates that the additional energy gain generated by a changing construction exceeds the cost of design changes. Generally, an investment with a positive NPV will be a profitable one and one with a negative NPV will result in a net loss. This concept is the foundation for the Net Present Value Rule, which dictates that the only investments that should be made are those with positive NPV values.

The formula for the discounted sum of all cash flows could be written as

$$NPV = -C_0 + \sum_{i=1}^{T} \frac{C_i}{(1+r)^i} \quad \text{(eq. 1)}$$

where C_0 is an initial investment costs, C_i is net cash inflow during period T, r is discount rate and T is time.

To calculate NPV profitability indicator, the following parameters have been assumed:

- Calculation of NPV for all collector variants has been carried out in relation to the reference variant.
- Additional energy gain multiplied by heat price has been used as a net cash inflow (Table 5).
- Collector price change has been used as an initial investment cost (Table 6).
- The following heat prices have been used in the analysis: 0.094 €/kWh for Athens, 0.085 €/kWh for Würzburg and 0.146 for Stockholm with annual growth rate 1%. These prices were derived from statistics on average natural gas prices in Greece, Germany, and Sweden (Eurostat) divided by a boiler efficiency of 0.80.
- A discount rate of 0.1% (average interest for private time accounts in Europe) has been used in the analysis.
- The service life of the collectors has been set at 20 years.

The results of calculation are shown in Table 7. The results of the modelling indicate that the only flat-plate solar collector with reduced to 50 mm distance between riser pipes has the positive value of NPV. That means that this design change is economically profitable. New PVD coatings with an emissivity of 0.05 are economically justified compared to old and cheap electrochemical (galvanic) coating with an emissivity of 0.12. Yet reducing the thickness of insulation to a level less than 50 mm or reduction of the air gap width to a level less than 30 mm, as can be seen from the results, does not make an economic sense as of today.

Tab. 7: Net present value for considered collector variants

#	Collector design				Net present value		
	back insulation thickness [mm]	absorber emissivity [-]	width of the air gap [mm]	distance between riser pipes [mm]	Athens [€/m^2]	Würzburg [€/m^2]	Stockholm [€/m^2]
RC	50	0.05	30	100	0		
1	40	0.05	30	100	-13	-8	-42
2	30	0.05	30	100	-32	-32	-69
3	20	0.05	30	100	-75	-76	-122
4	10	0.05	30	100	-183	-212	-395
5	50	0.12	30	100	-28	-30	-36
6	50	0.05	20	100	-9	-6	-8
7	50	0.05	10	100	-27	-18	-57
8	50	0.05	30	50	67	12	34

5. Conclusion

The energy-economic analysis of flat-plate collector in SDHW system with yearly solar fractions of 50% has been carried out. In order to evaluate economically profitable design changes, numerical calculations have been made corresponding to the climatic and economic conditions of Athens, Würzburg, and Stockholm. The following design parameters were used as the decision variables: air gap size between the absorber and the cover glazing from 30 mm to 10 mm with the step 10 mm, emissivity of the absorber 0.12 and 0.05, rear insulation thickness from 50 mm to 10 mm with step 10 mm, and the distance between riser pipes 100 mm and 50 mm. At the end of the analytical study, there following conclusions can be drawn:

- There is a potential for increasing efficiency of the solar flat-plate collector by reducing the distance between rising pipes and, more importantly, this collector optimization is economically reasonable.
- The energy-economic analysis also shows that using new PVD coating with emissivity 0.05 instead of the electrochemical (galvanic) coating with an emissivity of 0.12 was economically justified.
- Back thermal insulation reduction or width of air gap reduction leads to a reduction of the initial price of the collector, but in the long term does not make any economic sense.

6. Acknowledgment

This paper has been written with support by SGS16/212/OHK2/3T/12 - Modelling, control and design of environmental engineering installations.

7. References

Barshilia H. S., Selvakumar N., Rajam K. S., Biswas A., 2008. Spectrally selective NbAlN/NbAlON/Si3N4 tandem absorber for high-temperature solar applications. Solar Energy Materials and Solar Cells Vol 92, 495-504.

Brunold, S., Frey, R., Frei, U., 1994. Comparison of three different collectors for process heat applications, Proceedings of SPIE – The International Society for Optical Engineering Optical Materials Technology for Energy Efficiency and Solar Energy Conversation XIII, Freiburg, Germany.

Duan R., 2012. The efficiency of new solar flat-plate collectors. Advanced Materials Research, Vols. 347-353, 1337-1341.

Feng J., Zhang S., Lu Y., Yu H., Kang L., Wang X., Liu Z., Ding H., Tian Y., Ouyang J., 2015. The spectral selective absorbing characteristics and thermal stability of SS/TiAlN/TiAlSiN/Si3N4 tandem absorber prepared by magnetron sputtering. Solar energy Vol 111, 350-356.

Furbo S., Shah L. S., 2003. Thermal advantages for solar heating systems with a glass cover with a glass cover with antireflection surfaces. Solar energy Vol 74, 513-523.

Kong W., Han J., Peres B., Furbo S., Fan J., 2015. Side by side tests of two SDHW systems with solar collectors with and without antireflection treatment. Energy Procedia Vol 70, 462-469.

Liu Y., Wang C., Xue Y., 2012. The spectral properties and the thermal stability of NbTiON solar selective absorbing coating. Solar Energy Materials and Solar Cells Vol 96, 131-136.

Wu Y., Wang C., Sun Y., Xue Y., Ning Y., Wang W., Zhao S., Tomasella E., Bousquer A., 2015. Optical simulation and experimental optimization of Al/NbMoN/NbMoON/SiO2 solar selective absorbing coatings. Solar Energy Materials and Solar Cells Vol 134, 373-380.

Zou C., Huang L., Wang J., Xue S., 2015. Effects of antireflection layers on the optical and thermal stability properties of a spectrally selective CrAlN–CrAlON based tandem absorber. Solar Energy Materials and Solar Cells Vol 137, 243-252.

8. Web reference

Eurostat. Natural gas prices during the second semester of 2015. Available on:
http://ec.europa.eu/eurostat/statistics-explained/index.php/File:Half-yearly_natural_gas_prices_(EUR).png

1.

Conference Proceedings

EuroSun 2016
Palma de Mallorca (Spain), 11 - 14 October 2016

Electrodeposition of Co-Cr Black Coatings on Steel in an Ionic Liquid, For Solar Collection Applications

Gregorio Vargas, Ana P. García, Juanita Cerda and Jorge López

CINVESTAV-IPN, Unidad Saltillo, Calle Industria Metalúrgica No. 1062, Parque Industrial Saltillo - Ramos Arizpe, Ramos Arizpe, Coahuila, México, CP 25900

Abstract

The electrodeposition of Co-Cr black coatings on AISI 304 stainless steel substrates was studied using a solution of Co and Cr salts in an ionic liquid as electrolyte. The electrolyte was prepared employing choline chloride (ChCl) and ethylene glycol (EG) in molar ratios of 1:2, 1:8 and 1:16, as well as Co and Cr salts in molar ratios of 1:1, 2:1 and 4:1. The electrodeposition times were 30, 45 and 60 min. Cyclic voltammetry was used in order to define the potential window in an interval from -1.93 to 1.12 V. The electrodeposition was carried out by chronoamperometry. Scanning Electron Microscopy (SEM) was used to characterize the microstructure and chemical composition of the coatings. Their optical properties were characterized by using UV-Vis spectroscopy and Fourier-Transform Infrared spectroscopy (FT-IR). Homogeneous black coatings having absorptivities (α) of 0.98 and emissivities (ε) of 0.03 were obtained, which were suitable for their application in solar thermal collectors.

Keywords: *Black Co-Cr coatings, deep eutectic solvents, optical properties.*

1. Introduction

Spectrally selective surfaces for applications in solar thermal collectors must have high absorptivity (α) and low emissivity (ε) values. Electrodeposition of black Cr has been widely studied for applications in solar collectors due to their good optical properties (α = 0.97 and ε = 0.19) (Grimmer and Collier, 1981; Eugenio et al., 2011). The toxicity of Cr (VI) has incentivized the study of systems using instead Cr (III) in less toxic water-based electrolytes (Eugenio et al., 2011). However, the success of such systems has been limited by the chemical complexity of the Cr (III) ions in such solutions (Ferreira et al., 2013), as well as due to the hydrogen embrittlement underwent by the coatings (Saravanan and Mohan, 2012). Recently, a new family of ionic liquids, including Deep Eutectic Solvents (DES), has been developed (Abbott, 2006). These liquids are generally composed by two or more environmentally friendly components that are able to associate freely, often through hydrogen bonds (Abbott, 2006). The aim of the present work is to show that the electrodeposition of Co-Cr black coatings on stainless steels, using Co-Cr salts and an ionic liquid as electrolyte, allowed us to obtain spectrally selective coatings that are suitable for applications in solar thermal collectors.

2. Experimental Method

The electrolyte was prepared employing ethylene glycol (EG), choline chloride (ChCl), chromium chloride hexahydrate ($CrCl_3 \cdot 6H_2O$) and cobalt chloride hexahydrate ($CoCl_2 \cdot 6H_2O$). ChCl and EG mixtures (ethaline) were used in molar ratios of 1:2, 1:8 and 1:16, and the Co and Cr salts were used in molar ratios of 1:1, 2:1 and 4:1. The electrodeposition times were 30, 45 and 60 min. Cyclic voltammetry was used in order to define the potential window. The electrolyte was kept at a constant temperature of 60 °C. The studies were carried

doi:10.18086/eurosun.2016.07.11 Available at http://proceedings.ises.org

out using a three-electrode electrochemical cell, employing a vitreous carbon electrode (A = 0.007 cm^2), a stainless steel counter electrode (A = 0.785 cm^2) and an Ag/AgCl reference electrode. The electrodeposition was carried out on AISI 304 stainless steel substrates. Both, the electrochemical studies and the electrodeposition were carried out using a PARSTAT 4000 potentiostat/galvanostat, controlled by the Versa Studio 2.43 software. The employed electrochemical techniques were voltammetry and chronoamperometry. The optical properties of the coatings were characterized using a LAMBDA 850 UV/Vis spectrophotometer, fitted with a 150 mm integrating sphere for the determination of the absorptivity (α). The emissivity (ε) was determined employing a Frontier FT-IR spectroscope fitted with an accessory for diffuse reflectance spectroscopy, which allowed us to obtain the spectral reflectance curves (reflectance vs. wavelength) for the studied coatings.

The values of α were calculated employing equation 1 (Li, 2000):

$$\alpha = \frac{\int_{0.3\mu m}^{2.5\mu m}(1-R)I_{sol}d\lambda}{\int_{0.3\mu m}^{2.5\mu m}I_{sol}d\lambda} \qquad \text{(eq. 1)}$$

where I_{sol} is the solar radiation taken from the ASTM AM1.5 standard (ASTM AM1.5, 2012), while R and λ are reflectivity and total hemispherical wavelength, respectively.

The values of ε were calculated at 100 °C employing equations 2 and 3 (Li, 2000):

$$\varepsilon = \frac{\int_{2.5\mu m}^{25\mu m}(1-R)I_{p}d\lambda}{\int_{2.5\mu m}^{25\mu m}I_{p}d\lambda} \qquad \text{(eq. 2)}$$

$$I_p = \frac{2x10^{24}hc^2}{\lambda^5}\frac{1}{e^{\frac{10^6 hc}{\lambda kT}}-1} \qquad \text{(eq. 3)}$$

where I_P is the black body radiation at 100 °C, c is the speed of light ($2.998x10^8$ m s^{-1}), h is Planck's constant (6.628×10^{-34} J s = 4.136×10^{-15} eV s), and k is Boltzmann's constant (1.381×10^{-23} J K^{-1} = 8.617×10^{-5} eV K^{-1}).

Scanning Electron Microscopy (SEM) was used to characterize the microstructure and chemical composition of the coatings. This was carried out using a PHILIPS XL30ESEM apparatus, with a voltage of 20 KeV and a working distance of 10 mm.

3. Results and Discussion

Cyclic voltammetry allowed us to define the potential window (electrochemical stability range for the electrolyte) in an interval from -1.93 to 1.12 V (see Figure 1). At potential values higher than 1.15 V (anodic side), current density is rapidly increased, which is attributed to the decomposition of the medium, i.e., oxidation of Cl^-. At potential values smaller than -1.5 V (cathodic side), a reduction process is observed with a decrement in the current density, which indicates a reduction of hydrogen (Souza et al., 2007). An additional event occurring at 0.72 V, corresponding to the reduction of ethaline, was also identified. The potential window determined in this work agrees with previously published research (Binder, 2010) for ethaline.

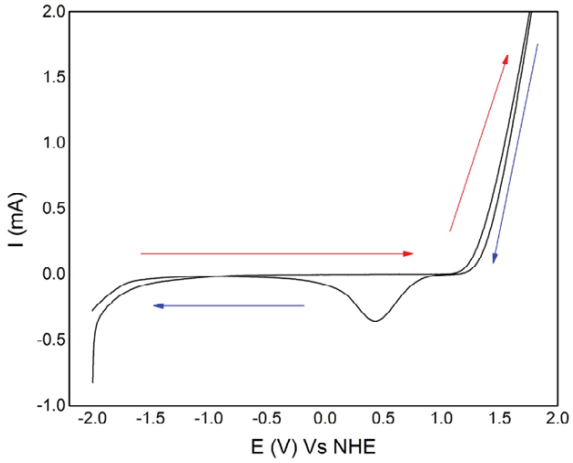

Fig. 1: Cyclic voltammetry curve of Ethaline obtained at 65 °C and V = 25 mVs^{-1} in vitreous carbon.

According to Figure 2, when $CoCl_2 \cdot 6H_2O$ and $CrCl_3 \cdot 6H_2O$ were present in a molar ratio of 2:1 in ethaline, a displacement was observed in reduction peak I (dotted line), which corresponds to reduction of ethaline, towards more anodic potentials (from 0.72 to 0.88 V), which was due to the presence of Cr (III) and Co (II) ions in the solution.

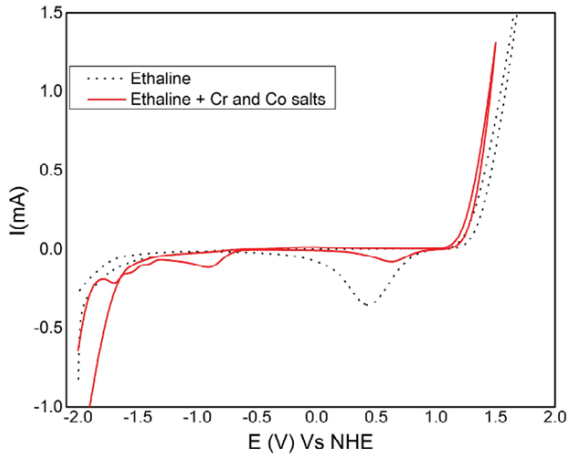

Fig. 2: Cyclic voltammetry curves of ethaline and ethaline + $CrCl_3 \cdot 6H_2O$ + $CoCl_2 \cdot 6H_2O$ obtained at 65 °C and V = 25 mVs^{-1} in vitreous carbon.

In this case, three reduction processes were observed in the potential window, which were located at -1.05, -1.38 and -1.6 V. The first one corresponded to the reduction of Cr (III) to Cr (II), the second one to the reduction of Cr (II) to Cr (0), and the third one to hydrogen embrittlement underwent by the coatings. These results are consistent with those reported by Eugenio et al. (2011).

To confirm the existence of the reduction processes observed when the electroactive species were added to ethaline, linear-sweep voltammetry tests were carried out at more electronegative potentials. Figure 3 shows the corresponding voltammetry curve in which three different processes can be appreciated: the first one was located at -1.06 V & Ag/ AgCl (1), the second one appeared at -1.38 V & Ag/ AgCl (2), and the third one was found at -1.6 V & Ag/ AgCl (3).

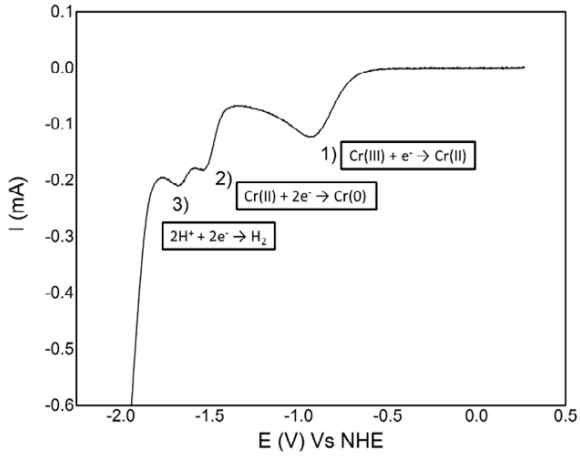

Fig. 3: Linear-sweep voltammetry curve of ethaline + $CrCl_3 \cdot 6H_2O$ + $CoCl_2 \cdot 6H_2O$ obtained at T = 65 °C with a sweep speed of 25 mVs^{-1}.

Chronoamperometric runs were carried out at the potentials identified in the voltammetric studies in order to select the working potential, which was based on the observation that uniform black deposits were obtained only at the potentials of -1.06 and -1.38 V. In contrast, black deposits were not obtained at a potential of -1.6 V due to the evolution of hydrogen at the metal surface. Furthermore, an excesive formation of bubbles was visible in the electrolitic solution in the cell, which apparently caused that the deposit layers became fractured, and thus, the electrodeposition was hindered, resulting in a damaged electrode.

Table 1 shows the factors and levels used to study the effect of the processing variables on the optical properties of the coatings.

Tab. 1. Factors and levels used in the employed L9 orthogonal array Taguchi experimental design.

Factors	Level 1	Level 2	Level 3
ChCl: EG molar ratio in the electrolyte	1:2	1:8	1:16
Co:Cr salt molar ratio	1:1	2:1	4:1
Voltage (V)	-1.06	-1.22	-1.38
Time (min)	30	45	60

Table 2 shows the employed L9 orthogonal array Taguchi experimental design, as well as the α and ε values obtained for the coatings deposited on the AISI 304 stainless steel substrates.

Tab. 2. L9 orthogonal array Taguchi experimental design.

Experiment	Independent variables				Dependent variables	
	Electrolyte	Co:Cr salt molar ratio	Voltage (V)	Time (min)	α	ε
1	1:2	1:1	-1.06	30	0.59	0.07
2	1:2	2:1	-1.22	45	0.55	--
3	1:2	4:1	-1.38	60	0.85	0.08
4	1:8	1:1	-1.22	60	0.90	0.16
5	1:8	2:1	-1.38	30	0.97	0.19
6	1:8	4:1	-1.06	45	0.95	0.18
7	1:16	1:1	-1.38	45	0.77	0.03
8	1:16	2:1	-1.06	60	0.98	0.03
9	1:16	4:1	-1.22	30	0.94	0.09

As it can be seen, the stainless steel substrates without electrochemical treatment showed an α value of 0.55, while the substrates with electrodeposited coatings achieved α values of up to 0.98. The best α values were achieved employing a deposition potential of -1.06 V for 60 min, with a ChCl:EG molar ratio of 1:16 and a

$CoCl_2$•$6H_2O$:$CrCl_3$•$6H_2O$ molar ratio of 2:1. Sample 8 showed a value of α = 0.98 and a value of ε = 0.035. The lowest ε value obtained corresponded to sample 7 (ε = 0.0309). This sample was coated using a deposition potential of -1.38 V & Ag/AgCl for 45 min, with a ChCl:EG molar ratio of 1:16 and a $CoCl_2$•$6H_2O$:$CrCl_3$•$6H_2O$ molar ratio of 1:1. However, this sample showed a value of α = 0.77. According to Malhotra and Chopra (1986), an increment in the value of α is considerably more favorable than a reduction in the value of ε. Mar et. al. (1976), in a similar previous work, reported values of α = 0.91 and ε = 0.07 (T = 100 °C). In this work, higher values of α and ε were achieved.

Sample 8, which showed the best optical properties, was characterized by SEM/EDS in order to identify and quantify the composition of the areas of interest. The SEM studies revealed that the black deposits were composed of Cr and Co oxide particles, whose chemical composition and morphology varied in the sample's cross section (Tab. **3. Results of the SEM/EDS analysis carried out in the cross-section of sample 8.**3).

Tab. 3. Results of the SEM/EDS analysis carried out in the cross-section of sample 8.

Sample	Analyzed zone	Elemental Composition (wt.%)				
		O	Cr	Co	Cu	Fe
8	I	15.97	20.3	56.28	-	7.45
	II	17.58	19.68	60.93	-	1.81

The SEM micrograph and photograph of Figure 4 correspond to sample 8. At a glance, it can be observed that the formed coating was uniformly distributed throughout the substrate surface, showing a black coloration.

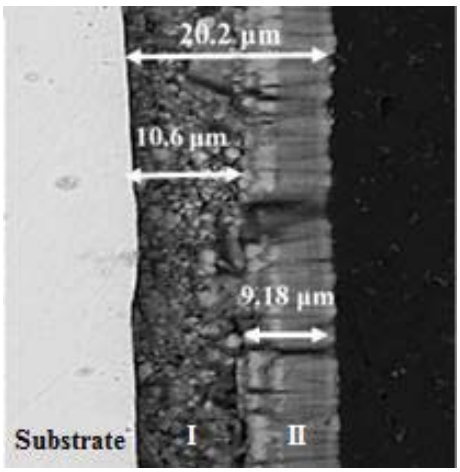

Fig. 4: SEM micrograph and photograph taken for the sample for which the best coating was obtained (sample 8).

The SEM micrograph of Figure 4 shows the morphology of the coating obtained on the surface of sample 8, in which the presence of equiaxed (zone I) and columnar (zone II) particles can be noticed. According to Table 3, it can be seen that both zones had a high content of Co and Cr, and thus, it was deduced that they were composed by a mixture of Co and Cr oxides. The main compositional difference among both zones was a higher Fe content in zone I and a higher Co content in zone II. Saravanan and Mohan (2012), who investigated a similar system, observed the formation of nodular particles. Probably in this study the variation in the composition of the used electrolyte and salts, as well as the applied potential, influenced the composition and morphology of the coatings. The coating formed on the surface of sample 8 was dense and compact, with zone I with a thickness of 10.6 µm, and zone II with a thickness of 9.18 µm. The coating thickness was dependent on the time of deposition.

4. Conclusions

The electrochemical study of the system ethaline/Co-Cr chloride salts allowed us to establish the conditions required to obtain uniform and well-adhered black Co-Cr oxide coatings on AISI 304 stainless steel

substrates, with excellent optical properties suitable for their application in solar thermal collectors ($\alpha = 0.98$ and $\varepsilon = 0.03$).

The efficiency of the process was controlled mainly by the molar composition of the electrolyte.

The conditions employed to obtain the electrochemical coating having the best optical properties were: a ChCl:EG molar ratio of 1:16, a Co:Cr salt molar ratio of 2:1, and a deposition potential of -1.06V.

The SEM characterization of the best deposited coating revealed that it was composed by two layers formed by particles with different morphologies, which probably consisted of a mixture of Co and Cr oxides. The total thickness of the coating was approximately 20 μm.

5. References

Abbott, A.P., McKenzie, K.J., 2006. Application of ionic liquids to the electrodeposition of metals. Phys. Chem. Chem. Phys. 8, 4265-4279.

ASTM G173, 2012. Standard Tables for Reference Solar Spectral Irradiances: Direct Normal and Hemispherical on 37° Tilted Surface. American Society for Testing and Materials, West Conshocken, PA, USA.

Binder, Q.A.L, 2010. Synthesis and Characterization of Choline Chloride Based Binary Mixtures. ECS Trans. 33, 49-59.

Eugenio, S., Rangel, C.M., Vilar, R., Botelho do Rego, A.M., 2011. Electrodeposition of black chromium spectrally selective coatings from a Cr(III)-ionic liquid solution. Thin Solid Films 519, 1845-1850.

Ferreira, E.S.C., Pereira, C.M., Silva, A.F., 2013. Electrochemical studies of metallic chromium electrodeposition from a Cr(III) bath. J. Electroanal. Chem. 707, 52-58.

Grimmer, D.P., Collier R.K., 1981. Black-chrome solar-selective coatings electrodeposited on metallized glass tubes. Sol. Energy 26, 467-469.

Li, L., 2000. AC anodization of aluminum, electrodeposition of nickel and optical property examination. Sol. Energy Mater. Sol. Cells 64, 279-289.

Malhotra, L.K., and Chopra, K.L., 1986. Selective Coatings for Photothermal Conversion, in: Garg, H.P. (Eds), Solar Water Heating Systems: Proceedings of the Workshop on Solar Water Heating Systems, Springer Science & Business Media, New Delhi, pp. 169-178.

Mar, H.Y.B., Peterson, R.E., and Zimmer, P.B., 1976. Low cost coatings for flat plate solar collectors. Thin Solid Films 39, 95-103.

Saravanan, G., Mohan, S., 2012. Structure composition and corrosion resistance studies of Co-Cr alloy electrodeposited from deep eutectic solvent (DES). J. Alloys Compd. 522, 162-166.

Souza, R.F., Padilha, J.C., Gonçalves, R.S., de Souza M.O., Rault-Berthelot, J., 2007. Electrochemical hydrogen production from water electrolysis using ionic liquid as electrolytes: Towards the best device. J. Power Sources 164, 792-798.

Conference Proceedings

EuroSun 2016
Palma de Mallorca (Spain), 11 - 14 October 2016

OPTICAL DESING AND SIMULATION OF A CIRCULAR TROUGH SOLAR CONCENTRATOR WITH TRAPEZOIDAL SECONDARY REFLECTOR

Eduardo Venegas-Reyes[1], Ignacio R. Martín-Domínguez[2], Ulises Dehesa Carrasco[3], Ricardo A. Pérez Enciso[4]

[1] CONACYT, Centro de Investigación en Materiales Avanzados, S.C. - Unidad Durango, Durango, Dgo. México. eduardo.venegas@cimav.edu.mx

[2] Centro de Investigación en Materiales Avanzados, S.C. - Unidad Durango, Durango, México.

[3] CONACYT, Instituto Mexicano de Tecnología del Agua, Jiutepec, Mor. México.

[4] Universidad de Sonora, Hermosillo, Son. México.

Abstract

This study presents the design and optical simulation of a circular trough solar concentrator with a trapezoidal secondary reflector using the SolTrace Software. The circular curve of this concentrator approaches the curve of a parabola with an edge angle of 45°. Due to the spherical aberration, the reflective surface introduces optical errors in such a way that it is necessary to use a second reflective stage that allows most of the rays that fall outside of the receiver to be reflected towards the latter. It is not necessary to obtain an even distribution of the concentrated solar radiation because the application of this solar concentrator is towards the generation of process heat. The ratio of rays intercepted by the cylindrical receiver to those intercepted by the primary reflector was 0.847. This study made a comparison of the collection efficiency according to the slope errors and misalignment for a parabolic trough and a circular trough collector, with and without a trapezoidal secondary reflector.

Keywords: *Solar concentrator, Circular trough, Medium temperature solar collector, SHIP,*

1. Introduction

Various processes in industry require heat in a temperature range between 90° C to 250° C (Kalogirou, 2003); solar collectors of medium temperature, such as parabolic troughs (PTC), Compound Parabolic (CPC), and Linear Fresnel (LFC) Collectors, can generate heat within this temperature range. Solar concentrators are optical systems that are subject to errors in their shape, slope, and surface, this causes a portion of the rays reflected by the concentrator not to impact the receiver. In order to increase the concentration or improve the intercept of rays, second stages of reflection are often used.

Mills (1995) presents a comparison via the ray tracing technique of different configurations of second concentration stages. In Singh et al. (1999), a linear fresnel concentrator was developed and the amount of heat absorbed by the used oil was assessed with 10, 15, and 20 mirrors; the absorber was surrounded with trapezoidal mirrors on three sides. Spirkl et al. (1997) presented a numerical optimization of the secondary reflectors for parabolic troughs using an involute and a flat section. Their performance was determined by ray tracing and by taking into account the reflective losses, shading, and the solar shape. In Chemisana et al. (2011), the development of a solar concentrator consisting of a fresnel lens, a CPC secondary concentrator, and a photovoltaic thermal module was presented; the latter was analyzed and characterized both electrically and thermally. Chen and Ho (2013) used an analytical method to obtain the geometrical shape of a secondary

doi:10.18086/eurosun.2016.07.09 Available at http://proceedings.ises.org

mirror of non-image in the application of photovoltaic with solar concentration. In Cheng et al. (2014), the ray tracing technique was used for the estimation of the concentrated irradiance using secondary reflectors of non-image. Zheng et al. (2014) developed a cylindrical solar concentrator composed of an arc-shaped fresnel lens, a fresnel mirror, and a secondary reflector. The collection efficiency of the concentrator (based on the tracking error and the longitudinal angle of incidence) was obtained using ray tracing along with a comparison with the experimental results. In Rodriguez Sanchez and Rosengarten (2015), a theoretical analysis was made on a parabolic trough with a flat secondary reflector that increased the concentration ratio (up to 80%); ray tracing was conducted to validate the developed equations. The curves of energy received in the receiver, as a function of the misalignment angle for different reflectivities, and the ratio of local concentration in the receiver were obtained. In Abbas et al. (2016) a ray tracing code was developed to compare the efficiencies of the parabolic trough technology against that of the linear Fresnel technology. The results showed that the parabolic trough is more efficient, however, the leveled cost of generation is lower than that of the linear Fresnel system.

This work presents the optical design of a Circular Trough Collector (CTC) with a trapezoidal secondary reflector by making the approximation in the paraxial region of a circular profile with a parabolic profile. It was taken into consideration that the fabrication of a rib with a circular profile is less expensive than a rib with parabolic profile, this is because the rib can be formed using a rolling process. Using the technique of ray tracing, a comparison of the collection efficiency of the circular trough and the parabolic trough is made.

2. Optical design

The PTC is one of the most developed solar concentration technologies, however, it still faces the challenge of cost reduction in its manufacturing with a good optical performance. Conversely, from the manufacturing viewpoint, it is easier to manufacture a circular section rather than a parabolic one, and a section of the circumference can be virtually indistinguishable in the paraxial region of a parabola (Hetch, 2000). Figure 1 shows both geometries. The circular section is given by

$$x = \frac{y^2}{2R} + \frac{1y^4}{2^2 2! R^3} + \frac{1 \cdot 3 y^6}{2^3 3! R^5} + \ldots \quad \text{(eq. 1)}$$

On the other hand, the normal equation of a parabola with vertex at the origin and whose focus is at a distance f towards the right is

$$y^2 = 4fx \quad \text{(eq. 2)}$$

Comparing equations (1) and (2), one can see that if $4f = 2R$ (i.e. if $f = R/2$), the first contribution in the series of equation (1) can be considered parabolic while the remaining terms are the deviation. This difference will be noticeable when y is relatively large in comparison with R.

The circumference introduces aberrations into the concentrated image, therefore, a part of the rays reflected by the circular reflective surface won't impact the focal region. Because of this, it is necessary to use a secondary reflector that redirects the rays so that most of these impact the cylindrical receiver. Figure 2 shows a diagram of the trapezoidal secondary reflector and receiver, in which the secondary reflector and the glass cover form a cavity. Additionally, Figure 2 shows an outer shell which, aside from giving support to the secondary reflector and receiver, serves as a cover whose interior space is filled with a thermal insulator.

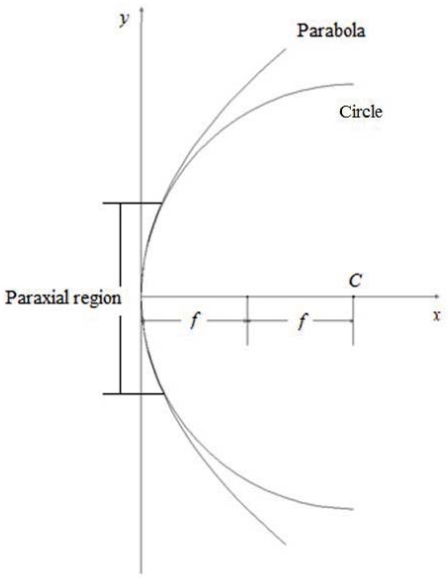

Fig. 1: Paraxial region of the circular and parabolic profiles

A way to evaluate the optical performance of a solar concentrator is by using the ray tracing technique. This study employed the Soltrace software developed by NREL. The width of the opening of the trapezoidal cavity was determined by taking into account that the image formed in the focal region should be less than the opening, thus ensuring that most of the rays pass through said opening. In addition, an almost right angle between the horizontal and lateral surfaces was used to ensure that the rays reflected by the latter strike on the receiver. The determination of the angle that should have the lateral reflectors must have with respect to the horizontal reflector was conducted in an iterative manner using the Soltrace program. To carry out the ray tracing, data from a parabolic trough developed in (Venegas et al., 2012) were used. The optical properties of the reflective surface can be seen in Table 1.

Tab. 1: Concentrator data used in the ray tracing

Variable	Quantity	Units
Circle radius R	1.432	m
Focal distance f	0.716	m
Aperture	1.21	m
Sheet curve perimeter S	1.22	m
Reflectance ρ	0.95	
Slope error σ_{slope}	3.73	mrad
Specularity error σ_{ref}	3.0	mrad
Receiver diameter	0.0254	m
Aperture of second reflector	0.08	m

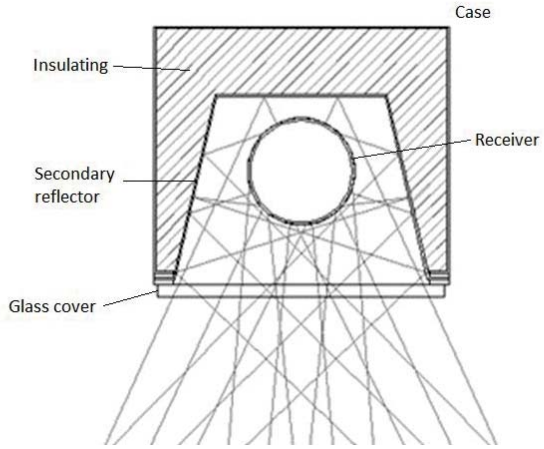

Fig. 2: Trapezoidal secondary reflector and receiver

3. Ray tracing results

Ray tracing was carried out with the Soltrace software by considering a Gaussian solar flux distribution and the data contained in Table 1. Figure 3 shows the trajectories of the ray tracing, where one can observe that most of the traced rays fall into the cavity that is formed by the secondary reflector. The intercept factor between the receiver and the primary reflector is 0.847, of which 7.8% of the incident rays in the cylindrical receiver are redirected by the trapezoidal secondary reflector. Table 2 shows a comparison of the intercept factor for different studies, where one can observe that the intercept factor was slightly higher in the proposed collector than in other developed collectors.

Tab. 2: Intercept factor for different collectors

	Intercept factor	C
This work	0.847	11.47
(Brooks et al., 2005)	0.823	15.92
(Coccia et al., 2015)	0.829	9.25

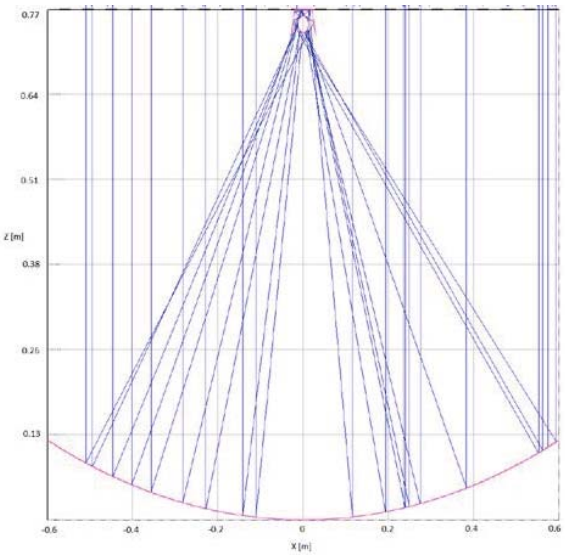

Fig. 3: Ray tracing paths of circular trough and trapezoidal reflector

Figure 4 shows the radiative flux distribution in the cylindrical receiver. The highest radiative flux density was found at the bottom of the cylindrical receiver (with peak values of approximately 25,000 W/m^2). At the top part of the receiver, one can see a slight increase in the radiative flux due to the rays that are redirected by the secondary reflector (with peak values of approximately 5,000 W/m^2). It is important to note that in Figure 4, the abscissa is zero at the top of the tube, which means that most of the amount of radiative flux impacts at the bottom part of the receiver.

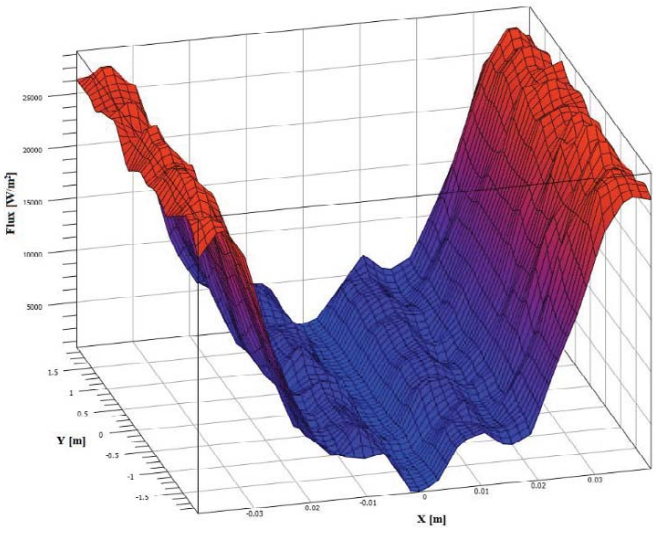

Fig. 4: Flux distribution in the receiver

The collection efficiency was obtained as a function of the slope error for a specular surface error of 3 mrad. The PTC, the CTC without a reflector, and the CTC with a trapezoidal secondary reflector were compared. It is important to note that, for the circular trough, the receiver was moved so that the opening of the secondary reflector remained in the focus, thus improving the collection efficiency. In Figure 5, one can see that the collection efficiency was greater in both the circular trough without a reflector and in the parabolic trough; however, as the slope error increased, the collection efficiency decreases in a more pronounced manner in these than in the circular trough with a secondary reflector. It is easy to observe that the trapezoidal secondary reflector reduced the optical losses due to the scattering caused by the slope error. For the case in which σ_{slope} = 10 mrad, the collection efficiencies of the PTC and CTC were close to 0.5 while the efficiency for the same slope error for the CTC with secondary reflector was 0.62 (i.e. more than 0.1). This implies that the trapezoidal secondary reflector can minimize the optical losses due to scattering caused by slope errors and other types of dispersion (e.g. profile errors).

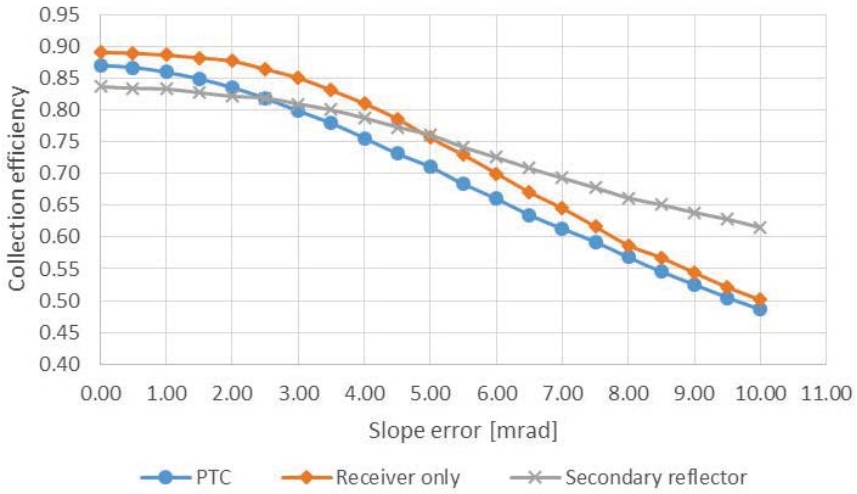

Fig. 5: Collection efficiency on the basis of the slope error

Figure 6 shows the collection efficiency as a function of the misalignment error angle for the parabolic trough collector, the cylindrical trough, and the cylindrical trough with a secondary reflector. It can be seen that the decreasing slopes were higher for both the PTC and CTC than for the CTC with a secondary reflector. It is important to note that the optical errors from Table 1 were taken into account to obtain this graph (Figure 6).

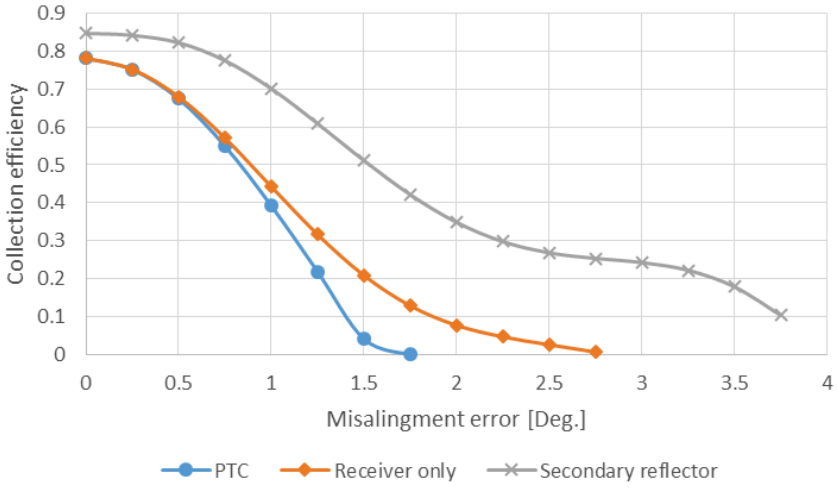

Fig. 6: Collection efficiency as a function of the misalignment angle

The collection efficiency appears with a minimal change until the misalignment angle reaches 0.3 degrees; therefore, the tracking error should be less than this value. When the misalignment angle reaches 0.5 degrees, the intercept factor goes down to 0.82, which is relatively close to 0.847 for a 0 degree angle. Even when the misalignment error angle reaches a value of 1, the collection efficiency reaches a value of 0.7 when compared to an approximate value of 0.4 for the other two configurations.

4. Conclusions

Ray tracing showed that the circular trough solar concentrator with a trapezoidal secondary reflector has an acceptable collection efficiency when compared to other devices in literature. A contribution of the present

study is to achieve a collection efficiency comparison between a parabolic trough and a substitute (so to speak), which is the CTC with a trapezoidal secondary reflector. The secondary reflector allows to reduce the losses caused by the slope error, which tends to disperse the reflected rays. At the same time, the secondary reflector allowed for a greater average misalignment error than if one only has the receiver. This demonstrated the utility of this system to minimize the dispersion effects, which improved the collection efficiency and therefore the optical efficiency of the solar concentrator under appreciable error conditions. Finally, the thermal losses of the solar concentrator are expected to be reduced than if one only has the bare receiver; this is thanks to the envelope that is formed by the secondary reflector and the glass of its opening.

5. Acknowledgments

To academic technicians of the energy area of CIMAV unit Durango M.Sc. Jorge A. Escobedo-Bretado and M.Sc. Mario Najera-Trejo for their support in ray trace simulations. We thank the support received from: ***Mexican Center for Innovation in Solar Energy*** (CeMIE-Sol), Through Project: P13 "Test laboratories for low and medium temperature. Computer-aided laboratory for the design and integration of solar thermal systems". 2013-02 Sustainable Energy Federal Research Fund: CONACYT – SENER, for the development of this work.

6. References

Abbas R., Montes M.J., Rovira A., Martínez-Val J.M. Parabolic trough collector or linear Fresnel collector? A comparison of optical features including thermal quality based on commercial solutions. Solar Energy 124 (2016) 198–215.

Brooks, M. J., Mills, I., Harms, T. M. (2005), Design, construction and testing of a parabolic trough solar collector for a developing-country application, Proceedings of the ISES Solar World Congress, Orlando, Florida, pp. 6-12. August 2005.

Chemisana D., Ibáñez M., Rosell J.I., 2011. Characterization of a photovoltaic-thermal module for Fresnel linear concentrator. Energy Conversion and Management. 52, 3234–3240.

Chen Y.T., Ho T.H. Design method of non-imaging secondary (NIS) for CPV usage. Solar Energy 93 (2013) 32–42.

Cheng Q., Chai J., Zhou Z., Song J., Su Y., 2014. Tailored non-imaging secondary reflectors designed for solar concentration systems. Solar Energy. 110, 160–167.

Coccia G., Di Nicola G., Sotte M. Design, manufacture, and test of a prototype for a parabolic trough collector for industrial process heat. Renewable Energy 74 (2015) 727-736.

Kalogirou S. A. The potential of solar industrial process heat applications. Applied Energy, 76 (2003) 337–361.

Hecht, E., 2000. Optics. Addison Wesley, Madrid, pp.184-187.

Mills D. R., 1995. Two-stage solar collectors approaching maximal concentration. Solar Energy. 54, 41-47.

Rodriguez-Sanchez D., Rosengarten G., 2015. Improving the concentration ratio of parabolic troughs using a second-stage flat mirror. Applied Energy. 159, 620–632.

Singh P. L., Ganesan S., Yadav G. C. Performance study of a linear Fresnel concentrating solar device. Renewable Energy 18 (1999) 409-416.

Spirkl W., Ries H., Muschaweck J., Timinger A., 1997. Optimized compact secondary reflectors for parabolic troughs with tubular absorbers. Solar Energy. 61, 153–158.

Venegas-Reyes E., Jaramillo O. A., Castrejón-García R., Aguilar J. O., Sosa-Montemayor F., 2012 Design, construction, and testing of a parabolic trough solar concentrator for hot water and low enthalpy steam

generation. Journal of Renewable and Sustainable Energy. 4, 053103.

Zheng H., Feng Ch., Su Y., Dai J., Ma X., 2014. Design and experimental analysis of a cylindrical compound Fresnel solar concentrator. Solar Energy. 107, 26–37.

08. PV and PVT Systems for Buildings and Industry

Conference Proceedings

EuroSun 2016
Palma de Mallorca (Spain), 11 - 14 October 2016

Pressure drop in parallel flow flat-plate PV/T collectors

Esteban Iglesias Manríquez[1,2,3], Laetitia Brottier[1,4] and Rachid Bennacer[4]

[1] DualSun, Marseille (France)

[2] École CentraleSupélec, Paris (France)

[3] Department of Electrical Engineering, Universidad de Chile, Santiago (Chile)

[4]LMT, ENS Cachan, CNRS, Université Paris Saclay, Cachan (France)

Abstract

Pressure drop is known to be an important factor for the efficacy of thermosiphon systems. Accordingly, in this paper a flat-plate PV/T solar collector is studied to predict the pressure drop over it. First, a numerical model of the collector is presented and fluid dynamic concepts are introduced. This is done in order to determine an expression of pressure drop for a given water flow rate over both the collector's channels and manifolds. Then, an algorithm is presented to predict the pressure drop over the whole collector. The effect of the manifold size on the induced pressure drop is investigated. Finally, three flat-plate solar collectors with different manifold dimensions were used as a test case in which the model was validated within 3-8% in terms of normalized root-mean-square deviation. For the case of flat-plate PV/T solar collectors to be used in thermosiphon water systems, this model can be used to investigate trade-offs between fabrication choices and the thermosiphon performance.

Keywords: *Pressure drop, PV/T collector, solar energy, heat exchanger, thermosiphon, DualSun module*

1. Introduction

A solar photovoltaic-thermal (PV/T) collector is a combination of a solar photovoltaic panel (PV) and solar thermal (T) collector which simultaneously convert solar energy into electricity and heat in one integrated system. The photovoltaic cells are in contact with a thermal collector. When the system is operating, the energy from the sun is converted to electricity by the photovoltaic cells on the front side of the panel while a coolant fluid removes heat from the cells on the back side of the panel, generating a double benefit: (1) the collected heat can be used in domestic hot water systems and (2) the cooling of the photovoltaic cells increases the total electricity output as the efficiency of the photovoltaic cells decrease as a function of temperature (Wysocki and Rappaport, 1960).

Fig. 1: A DualSun module being installed in a thermosiphon water system testbed in Marseille, France.

doi:10.18086/eurosun.2016.08.09 Available at http://proceedings.ises.org

Nomenclature:

A	cross-sectional area, m^2
D	diameter, m
f	Darcy friction factor, $-$
g	gravitational constant = 9.81 $\mathrm{m/s^2}$
H	head loss, m
K	pressure loss coefficient, $-$
L	length, m
N	number of channels, $-$
$\vec{N}$	unit normal vector, $-$
$NRMSE$	normalized root-mean-squared error, $-$
P	local pressure, Pa
Q	cumulative flow rate, m^3/s
q	flow rate, m^3/s
Re	Reynolds number , $-$
v	fluid local velocity, m/s
z	height, m

Greeks

α	flow distribution factor, $-$
ΔP	pressure drop, Pa
Δp	frictional pressure loss, Pa
ϵ	convergence error, $-$
ν	kinematic viscosity, m^2/s
ρ	fluid density, $\frac{kg}{m^3}$

Superscript

i	channel number

Subscripts

adj	adjusted
e	between two channels
exp	experiment
F	feed
f	friction
h	hydraulic
in	inlet
L	loss
M	mayor
m	minor
mod	model
new	new
out	outlet
ref	reference
T	tee junction
$Txin$	tee junction at the entrance of the channel
$Txout$	tee junction at the exit of the channel
$Tyin$	diverging-flow tee junction for the inlet manifold
$Tyout$	converging-flow tee junction for the outlet manifold
x	channel
y	manifold

Thermosiphon water systems are typically less expensive than active pump-driven systems and there is a growing interest to use PV/T collectors in thermosiphon water systems. Also, pressure drop over a solar collector gains importance since pressure drop is known to be an important factor for thermosiphon systems efficacy (Kalogirou, 2013). On the other side, flat-plate solar collectors are the usual type of collector for hybrid PV/T systems technology using water as coolant (Kalogirou and Tripanagnostopoulos, 2006). Accordingly, this paper presents a study made by DualSun on pressure drop in parallel flow flat-plate collectors in order to adapt the DualSun module, an innovative photovoltaic-thermal (PV/T) collector (Brottier et al. 2016), to be used in thermosiphon water systems. Fig. 1 shows a thermosiphon water system testbed where a DualSun module was installed in Marseille, France.

In this paper, first, a numerical model of a parallel flow collector is presented. Then, several fluid dynamic concepts are reviewed to calculate pressure drop over both the collector's manifold and the collector's channel. Next, an algorithm is used to calculate pressure distribution and pressure drop over the collector. Finally, the results of pressure drop measures over three flat-plate solar collectors with different manifold dimensions are presented and compared with the model results.

2. Mathematical Model

2.1 Variables and Flow distribution.

Parallel flow heat exchangers, or solar collectors, consist of an inlet and outlet manifold joined by a series of parallel channels where both inlet and outlet fluid flow are in the same direction, as shown in Fig. 2.

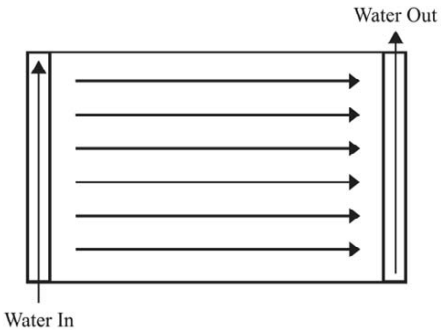

Fig. 2: Parallel flow collector diagram.

Several papers have analyzed the pressure drop over compact heat exchangers (Camilleri et al. 2015) and gas manifolds of a fuel-cell stack (Koh et al. 2003). In this paper an N-channel collector will be considered, and the channels will be numbered from the highest (1^{st}) to the lowest (N^{th}) position, where the input edge of the inlet manifold is in front of the N^{th} channel, and the output edge of the output manifold is in front of the 1^{st} channel, as shown in Fig. 3. Here $P_{in}^{(i)}$ denotes the pressure at the entrance of the i^{th} channel, $P_{out}^{(i)}$ denotes the pressure at the exit of the i^{th} channel and q_x^i is the water flow rate through the same channel. With this expression, pressure drop over each channel (i) is expressed by $\Delta P_x^{(i)}$, as shown in eq. 1.

Local pressure drop over the i^{th} inlet manifold section is expressed by eq. 2, and by eq. 3 for the case of the i^{th} outlet manifold section. Here, a manifold section (i) is defined from the entrance of the $(i-1)^{th}$ channel until the entrance of the i^{th} channel for inlet manifolds ('in' subscript and '(i)' superscript), and from the exit of the $(i-1)^{th}$ channel until the exit of the i^{th} channel for an outlet manifold section ('out' subscript and '(i)' superscript)

$$\Delta P_x^{(i)} = P_{in}^{(i)} - P_{out}^{(i)}, \quad (i = 1, \dots, N) \qquad \textit{(eq. 1)}$$

$$\Delta P_{in}^{(i)} = P_{in}^{(i)} - P_{in}^{(i-1)}, \quad (i = 2, \dots, N) \qquad \textit{(eq. 2)}$$

$$\Delta P_{out}^{(i)} = P_{out}^{(i)} - P_{out}^{(i-1)}, \quad (i = 2, \dots, N) \qquad \textit{(eq. 3)}$$

Then, cumulative flow rates $Q_{in}^{(i)}$ and $Q_{out}^{(i)}$ are defined as follows, where Q_F is the total inlet feed flow rate.

$$Q_{in}^{(i)} = \sum_{j=1}^{i} q_x^j = Q_{in}^{(i-1)} + q_x^i, \quad (i = 1, \dots, N) \qquad \textit{(eq.4)}$$

$$Q_{out}^{(i)} = \sum_{j=1}^{N} q_x^j = Q_{out}^{(i+1)} + q_x^i, \quad (i = 1, \dots, N) \qquad \textit{(eq. 5)}$$

$$Q_{in}^{(N)} = Q_F \qquad \textit{(eq. 6)}$$

2.2. Pressure Drop and Pressure Loss

In fluid mechanics, *pressure drop* is defined as the difference in pressure between two points of a fluid carrying network and which is due to the dissipation of mechanical energy into heat. Bernoulli's principle in fluid dynamics states that if there is conservation of energy, the following expression remains constant at any cross-sectional area A of a flowing fluid:

$$\int_A \left(\frac{P}{\rho} + \frac{v^2}{2} + gz\right) \rho \vec{v}.\vec{N}.\, dA \qquad \textit{(eq. 7)}$$

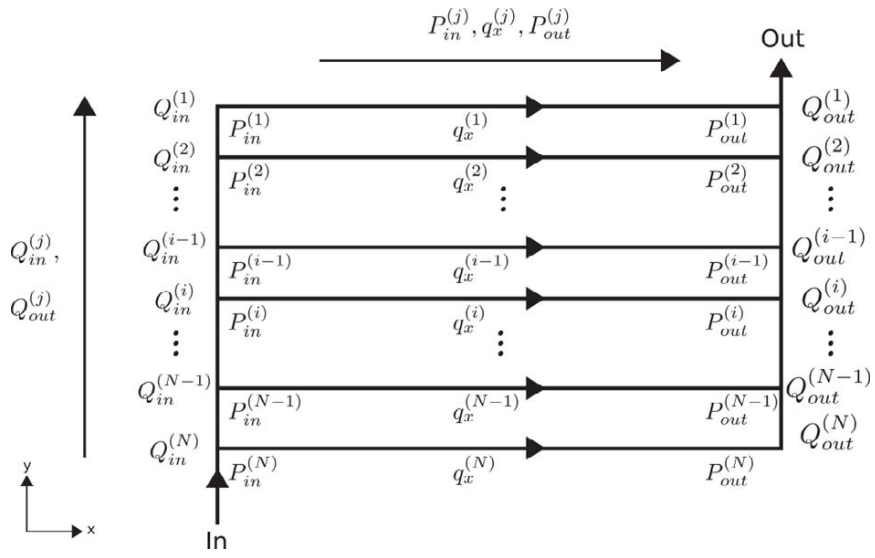

Fig. 3: Pressure and flow variables in the collector

Where P is pressure, ρ is the fluid density, v is the fluid local velocity, g is the acceleration due to gravity and z is the fluid height. Then, $\frac{P}{\rho}$ represents the flow work per unit mass, $\frac{v^2}{2}$ represents the kinetic energy per unit mass and gz represents the potential energy per unit mass. Some authors prefer to express eq. 7 in terms of energy per unit weight dividing it by the acceleration due to gravity. Considering the fluid pressure, fluid velocity and fluid height values as their mean values, along with assumed energy dissipation, the expression is no longer constant, and eq. 7 could be written in terms of energy per unit weight as:

$$\frac{\overline{P}_1}{\rho g} + \frac{\overline{\overline{v}_1^2}}{2g} + \overline{z}_1 = \frac{\overline{P}_2}{\rho g} + \frac{\overline{v}_2^2}{2g} + \overline{z}_2 + H_f \qquad \textit{(eq. 8)}$$

Here H_f represents the frictional work done per unit weight of a fluid element while moving from a point 1 to another point 2. H_f is called *head loss* and has a dimension of height. For simplicity, *frictional pressure loss* will be referred to as Δp_L , defined as:

$$\Delta p_L = \rho g H_f \qquad \textit{(eq. 9)}$$

Then, from eq. 2 we can calculate the *pressure drop*, defined as the pressure difference (in mean value) of a fluid while moving from a point 1 to a point 2, expressed then as the following:

$$\Delta P = \overline{P}_1 - \overline{P}_2 = \rho \frac{\overline{v}_2^2 - \overline{v}_1^2}{2} + \rho g(\overline{z}_2 - \overline{z}_1) + \Delta p_L \qquad \textit{(eq. 10)}$$

Pressure loss depends on any type of head loss H_f as described in eq. 9. Head losses, on their side, are divided in two main categories: *major head losses* (H_M) due to viscosity and wall friction along a pipe, and *minor head losses* (H_m) due to changes in the cross-section of the flow such as junction and bends. Major head losses can be calculated using the Darcy-Weisbach equation as shown in eq. 11, where f is the *Darcy friction factor*, L is the length of the pipe and D_h is the hydraulic diameter of the pipe. Minor head losses, for their part, depend on the *local loss coefficient K,* as shown in eq. 12.

$$H_M = f\frac{Lv^2}{2gD_h} \qquad \textit{(eq. 11)}$$

$$H_m = K\frac{v^2}{2g} \qquad \textit{(eq. 12)}$$

Having explained each type of head loss, the *total head loss* H_f is defined as the sum of major head losses and minor head losses, and total pressure loss becomes:

$$\Delta p_L = \rho g(H_M + H_m) = f\frac{\rho L v^2}{2D_h} + K\frac{\rho v^2}{2} \qquad \textit{(eq.13)}$$

Combining eq. 10 and eq. 13, pressure drop can then be written as:

$$\Delta P = \rho\frac{\bar{v}_2^2 - \bar{v}_1^2}{2} + \rho g(\bar{z}_2 - \bar{z}_1) + f\frac{\rho L v^2}{2D_h} + K\frac{\rho v^2}{2} \qquad \textit{(eq. 14)}$$

2.3. Darcy friction factor f and the loss coefficient K

The Darcy friction factor f and the loss coefficient K of the last expression (eq. 14) have been widely studied (Hager, 2010; Koch, 2000). The Darcy friction factor is a function on the dimensionless Reynolds number Re and depends on whether the flow is laminar or turbulent. The Reynolds number is defined as shown in the following equation, where ν is the kinematic viscosity of the fluid:

$$Re = \frac{vD_h}{\nu} \qquad \textit{(eq. 15)}$$

Here, an approximate way to calculate the Darcy friction factor is presented. For laminar flow ($Re < 2300$), the Darcy friction factor can be calculated as eq. 16; and for turbulent flow ($Re > 2300$), the Blasius equation is used as shown in eq.17

$$f = \frac{64}{Re}, \qquad Re < 2300 \qquad \textit{(eq. 16)}$$

$$f = 0.3164\, Re^{-0.25}, \qquad Re > 2300 \qquad \textit{(eq. 17)}$$

Koch (2000) has made a survey of available data of the pressure loss coefficient K for elbows and tees of pipework. The survey shows that in tee joints the K factor depends considerably on the tee configuration (converging flow, diverging flow) and which flow is being considered (from the branch, along the straight, etc.). The velocity used to calculate the minor head loss shown in eq. 12 is the velocity of the combined flow. For further information, see the articles listed in the Reference section.

2.4 The solar collector and pressure drop

In order to calculate pressure drop over the solar collector, an expression will firstly be given to calculate the pressure drop in each channel and in each manifold, based on the variables defined before.

Pressure drop over each channel strongly depends on the channel geometry and the presence of tee junctions or bends as explained in the previous section. If we consider the *channel flow* as the flow starting from the inlet manifold until the outlet manifold, both the tee junction diverging the flow from the inlet manifold and the tee junction converging the flow at the outlet manifold should be considered as minor head losses, each one with its own loss coefficient K. In the following, the subscript *Txin* will be used to describe the effects of the tee junction at the entrance of the channel, while the subscript *Txout* will be used to describe the effects of the tee junction at the exit of the channel. As there is no change in the flow, the fluid velocity through the channel (v_x) remains constant. Using the pressure drop expression introduced in eq. 14, and assuming that there is no change in height, eq. 1 becomes:

$$\Delta P_x^{(i)} = \Delta p_{L_{Tin}}^{(i)} + \Delta p_{L_x}^{(i)} + \Delta p_{L_{Tout}}^{(i)} = \frac{\rho}{2}\left(f_x\frac{L_x {v_x^{(i)}}^2}{D_{h_x}} + K_{Txin}^{(i)} {v_{y_{in}}^{(i)}}^2 + K_{Txout}^{(i)} {v_{y_{out}}^{(i)}}^2\right) \qquad \textit{(eq.18)}$$

Here, the fluid velocity through both intlet ($v_{y_{in}}$) and outlet ($v_{y_{out}}$) manifold are used to calculate the minor head losses since for tee junctions the velocity of the combined flow should be considered. However, the same superscript is used to simplify the solution algorithm. For the first and the last channel, the loss coefficient corresponding to elbows should be considered (Koch, 2000). Velocities are defined as the flow rate divided by the cross section flow area.

For the case of manifolds, the fluid flow rate decreases from the feeding position to the other end, with an inverse effect for the outlet manifold as the flow from each channel is sequentially added to the main flow.

Thus, the fluid velocity change should be considered. Additionally, only one tee junction will be taken into account. For simplification in the following, the subscript *Tyin* will be used to describe the effect of the diverging-flow tee junction (with flow going to the branch) for the inlet manifold, while the subscript *Tyout* will be used to describe the effect of the converging-flow tee junction (with flow coming from the branch) for the outlet manifold. Using the pressure drop expression introduced in eq. 14, and assuming that there is no change in height, eq. 5 and eq. 6 becomes eq. 19 for the local pressure drop in an inlet manifold section, and eq. 20 for the local pressure drop in an outlet manifold section, where L_e is the distance between two channels.

$$\Delta P_{in}^{(i)} = \rho \frac{\bar{v}_{y_{in}}^{(i-1)^2} - \bar{v}_{y_{in}}^{(i)^2}}{2} + \Delta p_{L_{Tyin}}^{(i)} + \Delta p_{L_y}^{(i)} = \frac{\rho}{2}\left(v_{y_{in}}^{(i-1)^2} - v_{y_{in}}^{(i)^2} + f_y \frac{L_e v_{y_{in}}^{(i)\ 2}}{D_{h_y}} + K_{Tyin}^{(i)} v_{y_{in}}^{(i)\ 2} \right) \quad \textit{(eq. 19)}$$

$$\Delta P_{out}^{(i)} = \rho \frac{\bar{v}_{y_{out}}^{(i-1)^2} - \bar{v}_{y_{out}}^{(i)^2}}{2} + \Delta p_{L_{Tyin}}^{(i)} + \Delta p_{L_y}^{(i)} = \frac{\rho}{2}\left(v_{y_{out}}^{(i-1)^2} - v_{y_{out}}^{(i)^2} + f_y \frac{L_e v_{y_{out}}^{(i)\ 2}}{D_{h_y}} + K_{Tyout}^{(i)} v_{y_{out}}^{(i)\ 2} \right) \textit{(eq. 20)}$$

2.5 Solution algorithm

In the following, a modified algorithm first introduced by Koh et al (2002) is presented to calculate pressure distribution and pressure drop over the collector.

Starting from an equally-divided channel flow rate ($q_x^{(i)} = Q_F/N$), the cumulative local flow rates in manifolds $Q_{in}^{(i)}$and $Q_{out}^{(i)}$ are obtained from eqs. 4 and 5. To continue, a reference local pressure in the outlet manifold $P_{out_{ref}}^{(1)} = P_{ref} = 0$ is defined, defining also a channel pressure drop reference $\Delta P_x^{(1)}{}_{ref}$ and a local pressure in the inlet manifold $P_{in}^{(1)}{}_{ref}$ using eqs.1 and 2. Then, sequentially, the pressure drop in outlet manifold $\Delta P_{out}^{(i)}$ and local pressure $P_{out}^{(i)}$ are calculated. $\Delta P_{out}^{(i)}$ is calculated using eq.20, while $P_{out}^{(i)}$ is calculated using eq. 3. The next step is to calculate sequentially the local pressure in the inlet manifold $P_{in}^{(i)}$ using eqs. 19 and 2.

In the following, a *flow distribution factor* $\alpha^{(i)}$ shown in eq. 22 is defined to be used as a redundant parameter in order to sequentially adjust channels flow rates in each iteration step until convergence is reached.

$$\alpha^{(i)} = \frac{P_{in}^{(i)} - P_{out}^{(i)}}{\Delta P_x^{(1)}} \quad \textit{(eq. 21)}$$

The adjustment correlation is developed from the definition of the flow distribution factor:

$$\sum_{i=1}^{N} \alpha^{(i)} = \frac{\sum_{i=1}^{N}\left[P_{in}^{(i)} - P_{out}^{(i)}\right]}{\Delta P_x^{(1)}} \quad \textit{(eq. 22)}$$

From this expression, a new value of the pressure drop over the first channel is obtained to adjust all local pressure and pressure drop values systematically as shown in the following expression:

$$\Delta P_x^{(1)} = \frac{\sum_{i=1}^{N}\left[P_{in}^{(i)} - P_{out}^{(i)}\right]}{\sum_{i=1}^{N} \alpha^{(i)}} \quad \textit{(eq. 23)}$$

By substituting the pressure drop terms, $P_{in}^{(i)} - P_{out}^{(i)}$ in eq. 23 by the equation for pressure drop over channels $\Delta P_x^{(i)}$ (eq.18), the expression becomes:

$$\Delta P_x^{(1)} = \frac{\sum_{i=1}^{N}\left[P_{in}^{(i)} - P_{out}^{(i)}\right]}{\sum_{i=1}^{N} \alpha^{(i)}} = \frac{\sum_{i=1}^{N} \Delta P_x^{(i)}}{\sum_{i=1}^{N} \alpha^{(i)}} = \frac{\sum_{i=1}^{N} \frac{\rho}{2}\left(f_x \frac{L_x v_x^{(i)^2}}{D_{h_x}} + K_{Txin}^{(i)} v_{y_{in}}^{(i)\ 2} + K_{Txout}^{(i)} v_{y_{out}}^{(i)\ 2} \right)}{\sum_{i=1}^{N} \alpha^{(i)}} \quad \textit{(eq. 24)}$$

Here, it is important not to replace the flow distribution factor by its formula, but to use the already calculated values. Once all local pressure and pressure drop values are adjusted, the flow distribution factor should be adjusted as well. Finally, new channel flow rates are then calculated from the adjusted inlet manifold pressure values using the flow rate definition (eq. 25) and eq. 18, as shown in eq. 25 and 26, whereA_x is the channel cross-sectional area.

$$q_{x\ new}^{(i)} = A_x v_{x\ new}^{(i)} \quad \textit{(eq. 25)}$$

$$q_{x\ new}^{(i)} = A_x \sqrt{\frac{D_h}{fL_x}\left(\frac{2}{\rho}\left(P_{in\ adj}^{(i)} - P_{out}^{(i)}\right) - K_{Txin}^{(i)} v_{y_{in}}^{(i)\ 2} - K_{Txout}^{(i)} v_{y_{out}}^{(i)\ 2}\right)} \quad \textit{(eq. 26)}$$

Note that the outlet manifold pressure is not adjusted because the exit pressure is known and is equivalent to the outlet reference pressure *($P_{out_{ref}}^{(1)} = P_{ref} = 0$)*. Once new channels flow rates are determined, they are compared with the initial or the previously calculated channel flow rates. The calculation continues with a new set of channel flow rates until the $q_x^{(i)}$ values are close to the old values within an error limit. The entire solution algorithm is summarized in Appendix A.

3. Experimental

Three flat-plate solar collectors as shown in Figs.4 and 5 with different manifold dimensions where used to measure pressure drop, using water columns to measure pressure and an electronic flow meter to measure the water flow rate in the collector inlet. The width and depth of the manifolds where respectively: 0.035x0.035m (collector N°1) 0.02x0.007m (collector N°2) and 0.045x0.045m (collector N°3). All other dimensions where equal as shown in Table 1.

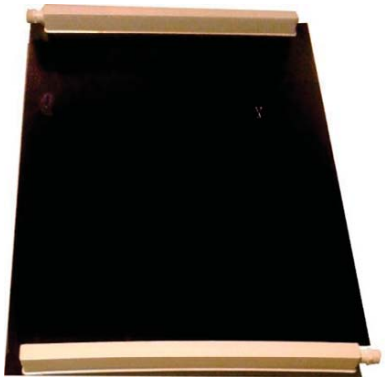

Fig. 4: Parallel flat-plate solar collector with rectangular manifold.

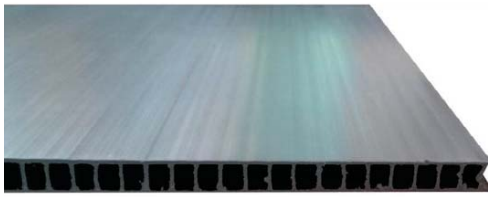

Fig. 5: Cross-sectional view of the collector channels.

Tab. 1: Manifold Dimensions

	Manifold Width [m]	Manifold Depth [m]	Manifold Large [m]	Channel Large[m]	Channel Width [m]	Channel Depth [m]	Number of Channels
Collector N°1	0.035	0.035	0.954	1.4	0.004	0.0044	165
Collector N°2	0.02	0.007	0.954	1.4	0.004	0.0044	165
Collector N°3	0.045	0.045	0.954	1.4	0.004	0.0044	165

4. Results

The three collector pressure drop measurements and simulations are compared in Fig. 6-9. The model is compared with the experiment values using the normalized root-mean-squared error (NRMSE) as defined in eq. 25. Finally, a pressure drop prediction is made for four solar collectors with different squared manifold dimensions (Fig. 4) in order to show the influence of the manifold size on the solar collector pressure drop.

$$NRMSE = \sqrt{\frac{1}{n}\sum_j^n (\Delta P_{exp} - \Delta P_{mod})^2} \,/\, (\Delta P_{mod}^{max} - \Delta P_{mod}^{min})$$

(eq. 27)

It can be seen that at some point (a=0.045m), pressure drop becomes less sensitive to increasing manifold width or depth in 0.005m when comparing to a smaller manifold (a=0.020m). This is probably because manifold size becomes proportionally less important and the analysis must be extended to the channels dimensions.

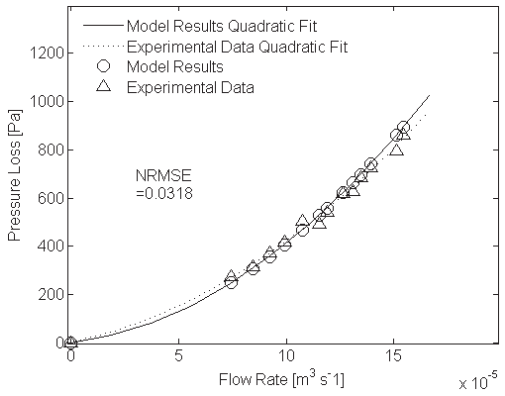

Fig. 6: Comparison of the predicted and measured pressure drop for the collector N°1

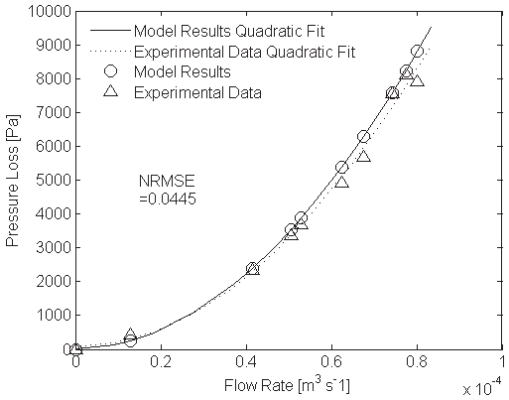

Fig. 7: Comparison of the predicted and measured pressure drop for the collector N°2

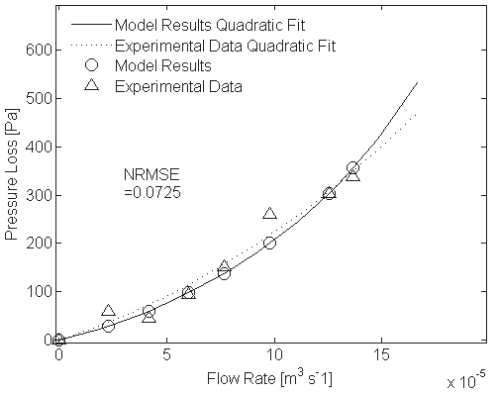

Fig. 8: Comparison of the predicted and measured pressure drop for the collector N°3

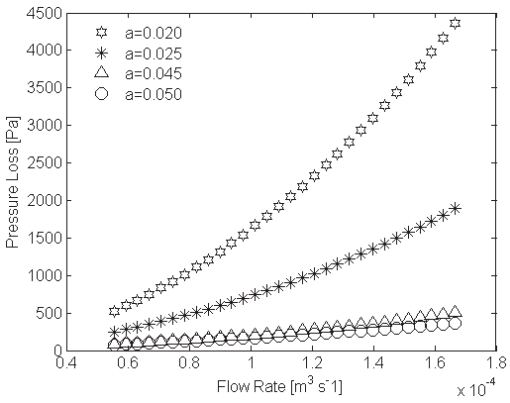

Fig. 9: Pressure drop predictions for different squared manifold dimensions (width=depth=a).

5. Conclusions

This paper presents a reliable numerical model and solution algorithm to calculate the pressure drop over parallel flow flat-plate solar collectors. The model gives the possibility to simulate pressure drop over exchangers at an early design stage and investigate the effects of geometric dimensions such as manifold or channel size. For the case of flat-plate PV/T solar collectors to be used in thermosiphon water systems, this model can be used to investigate trade-offs between fabrication choices and the thermosiphon performance.

Three flat-plate solar collectors with different manifold dimensions were used as a test case in which the model was validated within 3-8% in terms of normalized root-mean-square deviation. Also, the influence of the manifold size on the solar collector pressure drop was analyzed. It is shown that for smaller manifold size, the incremental pressure drop is higher than for larger manifolds. A channels size sensibility was not studied and should be take into account in further studies.

6. References

Brottier L., Naudin S., Veeser V., Terrom G., Bennacer R., 2016. Field test results of an innovative PV/T collector for solar domestic hot water. Energy Procedia. 91, 276-283.

Camilleri R., Howey D.A., McCulloch M.D., 2015. Predicting the flow distribution in compact parallel flow heat Exchangers. Applied Thermal Engineering. 90, 551-558, with permission from Elsevier.

Hager W.H., 2010. Losses in Flow, in: Wastewater Hydraulics, second ed., Springer-Verlag, Berlin-Heidelberg, pp. 17-54

Kalogirou S., Tripanagnostopoulos Y. 2006. Hybrid PV/T solar systems for domestic hot water and electricity production. Energy Converssion and Management. 47, 3368–3382.

Kalogirou S., 2013. Thermosiphon solar water-heating systems, in: Solar Energy Engineering, second ed., Elsevier/Academic Press, Amsterdam-London, pp 606-618.

Koch P., 2000. A survey of available data for pressure loss coefficients, z for elbows and tees of pipework. Building Services Engineering Research & Technology. 21, 153-160.

Koh J.H., Seo H.K., Lee C.G., Yoo Y.S., Lim H.C., 2003. Pressure and flow distribution in internal gas manifolds of a fuel cell stack. Journa of Power Sources. 115, 54-65.

Wysocki J. J., Rappaport P. 1960. Effect of temperature on photovoltaic solar energy conversion. Journal of Applied Physics. 31, 571–578.

Appendix: **Algorithm to calculate pressure drop over flat-plate solar collectors**

Step 1: Initial guess of channel flow rates and a reference inlet pressure drop.

$$q_x^{(i)} = \frac{Q_F}{N}, \quad (i = 1 \text{ to } N) \qquad \textit{(eq.A.1)}$$

$$v_x^{(i)} = \frac{q_x^{(i)}}{A_x}, \quad (i = 1 \text{ to } N) \qquad \textit{(eq.A.2)}$$

$$\Delta P_{x\ ref}^{(1)} = \frac{\rho}{2}\left(f_x \frac{L_x v_x^{(i)^2}}{D_{h_x}} + K_{Txin}^{(i)} v_{y_{in}}^{(i)\ 2} + K_{Txout}^{(i)} v_{y_{out}}^{(i)\ 2} \right) \qquad \textit{(eq.A.3)}$$

Step 2: Calculate flow rates and linear velocity in manifolds and Reynolds numbers.

$$Q_{in}^{(i)} = Q_{in}^{(i-1)} + q_x^i, \quad (i = 1, \dots, N) \qquad \textit{(eq.A.4)}$$

$$Q_{out}^{(i)} = Q_{out}^{(i+1)} + q_x^i, \quad (i = 1, \dots, N) \qquad \textit{(eq.A.5)}$$

$$v_{y_{in}}^{(i)}, v_{y_{out}}^{(i)}, Re_{y_{out}}^{(i)}, Re_{y_{out}}^{(i)}, Re_x^{(i)}$$

Step 3: Calculate outlet manifold pressure.

$$P_{out_{ref}}^{(1)} = P_{ref} = 0 \qquad \textit{(eq.A.6)}$$

- *Loop 3.1: For i= 2 to N:*

$$\Delta P_{out}^{(i)} = \frac{\rho}{2}\left(v_{y_{out}}^{(i-1)^2} - v_{y_{out}}^{(i)^2} + f_y \frac{L_e v_{y_{out}}^{(i)\ 2}}{D_{h_y}} + K_{Tyout}^{(i)} v_{y_{out}}^{(i)\ 2} \right) \qquad \textit{(eq.A.7)}$$

$$P_{out}^{(i)} = \Delta P_{out}^{(i)} + P_{out}^{(i-1)} \qquad \textit{(eq. A.8)}$$

Step 4: Calculate inlet manifold pressure.

$$P_{in\ ref}^{(1)} = \Delta P_{x\ ref}^{(1)} + P_{out_{ref}}^{(1)} \qquad \textit{(eq.A.9)}$$

- *Loop 4.1: For i= 2 to N:*

$$\Delta P_{in}^{(i)} = \frac{\rho}{2}\left(v_{y_{in}}^{(i-1)^2} - v_{y_{in}}^{(i)^2} + f_y \frac{L_e v_{y_{in}}^{(i)\ 2}}{D_{h_y}} + K_{Tyin}^{(i)} v_{y_{in}}^{(i)\ 2} \right) \qquad \textit{(eq.A.10)}$$

$$P_{in}^{(i)} = P_{in}^{(i-1)} + \Delta P_{in}^{(i)}, \qquad \textit{(eq. A.11)}$$

Step 5: Calculate flow distribution factors.

$$\alpha^{(i)} = \frac{P_{in}^{(i)} - P_{out}^{(i)}}{\Delta P_x^{(1)}}, \quad (i = 1, \dots, N) \qquad \textit{(eq. A.12)}$$

Step 6: Calculate a new value of the pressure drop over the first channel

$$\Delta P_{x\ new}^{(1)} = \frac{\sum_{i=1}^{N} \frac{\rho}{2}\left(f_x \frac{L_x v_x^{(i)^2}}{D_{h_x}} + K_{Txin}^{(i)} v_{y_{in}}^{(i)\ 2} + K_{Txout}^{(i)} v_{y_{out}}^{(i)\ 2} \right)}{\sum_{i=1}^{N} \alpha^{(i)}} \qquad \textit{(eq. A.13)}$$

Step 7: Adjust local inlet manifold pressure from new pressure drop over the first channel

$$P_{in\ adj}^{(1)} = \Delta P_{x\ new}^{(1)} + \Delta P_{out}^{(1)} \qquad \textit{(eq. A.14)}$$

$$P_{in\ adj}^{(i)} = P_{in\ adj}^{(i-1)} + \Delta P_{in}^{(i)}, \quad (i = 2, \dots, N) \qquad \textit{(eq. A.15)}$$

Step 8: Adjust flow distribution factors from new pressure drop over the first channel.

$$\alpha^{(i)}{}_{adj} = \frac{P^{(i)}_{in\,adj} - P^{(i)}_{out}}{\Delta P^{(1)}_{x\,new}}, \quad (i = 1, \ldots, N) \qquad \textit{(eq. A.16)}$$

Step 9: Calculate new set of channel flow rates form adjusted inlet manifold pressure.

$$q^{(i)}_{x\,new} = A_x \sqrt{\frac{D_h}{fL_x}\left(\frac{2}{\rho}\left(P^{(i)}_{in\,adj} - P^{(i)}_{out}\right) - K^{(i)}_{Txin} v^{(i)\,2}_{y_{in}} - K^{(i)}_{Txout} v^{(i)\,2}_{y_{out}}\right)}, \quad (i = 1, \ldots, N) \qquad \textit{(eq. A.17)}$$

Step 10: Check convergence.

$$ERR = \sum_{i=1}^{N} \left[\frac{q^{(i)}_{x\,new} - q^{(i)}_{x}}{q^{(i)}_{x}}\right]^2 \qquad \textit{(eq. A.18)}$$

In $ERR > \epsilon$, update $\Delta P_x^{(1)}$ and $q_x^{(i)}$, and go to Step 2. If $ERR < \epsilon$, stop.

Conference Proceedings

EuroSun 2016
Palma de Mallorca (Spain), 11 - 14 October 2016

Holographic photovoltaic-thermal module for window louvre integration: Design and simulation

Alex Moreno[1], Julia Marín-Sáez[1], Alberto Riverola[1], Daniel Chemisana[1], Jesús Atencia[2], María Victoria Collados[2]

[1] University of Lleida, Lleida (Spain)

[2] University of Zaragoza, Zaragoza (Spain)

Abstract

A building integrated holographic concentrating photovoltaic-thermal system has been optically and energetically simulated. The system has been designed to be superimposed into a solar shading louvre; in this way the concentrating unit takes profit of the solar altitude tracking, which the shading blinds already have, to increase system performance. An energetic simulation has been conducted for Avignon (France), which is a European representative location suitable for solar applications with available atmospheric parameter and irradiance experimental data sets. The simulation tool utilized has been TRNSYS, coupled with MATLAB (where the ray-tracing algorithm to simulate the holographic optical performance has been implemented). In the frame of the simulation, a comparison with a conventional photovoltaic-thermal (PVT) module installed on the blinds and with the same area than the concentrator aperture one is conducted. The concentrator achieves an annual mean optical efficiency of 43.0%, an electrical energy production of 148.2 kWh/kWp and a thermal energy of 250.4 kWh/m^2. On the other hand, the reference PVT module behaves very similar in terms of the thermal energy yielding 294.2 kWh/m^2 but almost doubles the electrical annual production with 281.7 kWh/kWp.

Keywords: *solar energy, solar concentration, photovoltaics, PVT, holographic optical elements (HOE), building integration, energy dynamic simulation.*

1. Introduction

Energy consumption in the building sector represents 40% of the total energy consumed in the European Union. The European Commission, in order to decrease energy consumption, defined (considering buildings as a priority) the directive which states the "20-20-20" objectives: greenhouse gas emissions reductions (20%), the share of renewable energy (20%) and improvements in energy efficiency (20%) (*Directive 2010/31/EU of the European Parliament and of the Council of 19 May 2010 on the energy performance of buildings.*, 2010). In this regard, building integrated solar hybrid Concentrating Photovoltaic-Thermal (CPVT) systems are a technology which perfectly addresses the objectives defined by the European Union, as may cover both the thermal and the electrical consumption needs.

CPV systems replace part of the cell area by cheaper and more environmentally friendly materials, the optical elements, which can lead to more cost-efficient systems from both, economic and environmental aspects (Menoufi et al., 2013). On the contrary, when increasing the concentration ratio the percentage which is not converted into electricity becomes much higher in absolute terms. This could cause PV overheating and thus, problems related with efficiency reduction, stress of materials, etc. arise. A strategy to profit the removal heat which negatively influences system performance is to use a hybrid Photovoltaic-Thermal (PVT) receptor. A PVT module controls PV temperature while simultaneously produces thermal energy. Another strategy to prevent the PV warming up is the spectral selection of the incident irradiance. A technology able to concentrate sunlight and at the same time to spectrally select irradiance is holography.

Among the different types of Holographic Optical Elements (HOEs), volume holograms have been studied as solar concentrators attending to some interesting properties as the high optical efficiency achieved (they can reach 100% efficiency for a selected wavelength). They may be utilized in different configurations (Collados et

doi:10.18086/eurosun.2016.08.03 Available at http://proceedings.ises.org

al., 2016): plane gratings, that are not concentrating elements but as they operate directing light toward the same area the incident irradiance is concentrated (Castillo, 2011; Castro et al., 2010; Zhang et al., 2011) or concentrating optical elements (lenses) either cylindrical (Chemisana et al., 2013; Ludman et al., 1997) or spherical (Ludman, 1982; Vorndran et al., 2015; Zhang et al., 2013).

HOEs present two main characteristics that affect their performance: angular and chromatic selectivity, in other words, their efficiency depends on the angle of incidence and the wavelength. Consequently, the solar spectrum and the spectral sensitivity range of the photovoltaic cell, among other parameters, need to be taken into account in the design of the HOE, in order to optimize its behavior for the wavelength range of interest. The chromatic selectivity of holograms provides an important advantage in comparison with refractive elements, since the concentration of undesired wavelengths on the photovoltaic cell is avoided. If the HOE is designed to diffract infrared wavelengths with very poor efficiency, the cell is prevented from overheating, which could cause a worsening on the cell's performance (Chander et al., 2015; Xiao et al., 2014). The chromatic selectivity also allows spectrum splitting, if a configuration with more than one kind of receiver (either different photovoltaic cells (Ludman et al., 1997; Zhang et al., 2013) or a hybrid photovoltaic-thermal receiver (Froehlich et al., 1993; Iurevych et al., 2012; Vorndran et al., 2015; Xia et al., 2011)) is chosen.

More specifically, regarding holographic PVT designs: Vorndran et. al. (Vorndran et al., 2015) proposed a spectrum-splitting holographic system in which a holographic lens diffracts a narrow bandwidth towards a photovoltaic cell. The transmitted spectrum is reflected on a parabolic mirror towards a thermal tube. The solar concentrator described by Froehlich et. al. (Froehlich et al., 1993) is formed by two stacked holographic lenses, each composed by a holographic grating to correct the incident direction and a holographic lens. Each holographic lens directs a different spectral range of the incoming light to a photovoltaic cell, sensitive to one of these two spectral bandwidths. The transmitted spectrum reaches a thermal absorber, which also refrigerates the PVs. Xia et. al. (Xia et al., 2011) proposed a solar concentrator formed by a holographic grating, which would split the incident spectrum into visible and infrared range, and a Fresnel lens, which would concentrate the visible spectrum onto a set of PV cells and the IR spectrum onto a heat exchanger. Iurevych et. al. (Iurevych et al., 2012) simulated the performance of a solar concentrator constituted by a reflection holographic grating. Incoming rays with wavelengths of a certain range are reflected by the HOE and the surfaces of the system, reaching a PV cell, whereas the rest are transmitted through the HOE and reach a thermal absorber.

Based on the previous studies found in the literature, it can be noted that even though there are some works conducting optical and energetic simulation of holographic concentrators, there is no research dealing with the energy simulation of the system performance in a building integrated configuration. In this regard, the present research is the continuation of that presented by the authors in (Marín-Sáez et al., 2016b) and aims at covering an important gap in the frame of Holographic Concentrating Photovoltaic-Thermal (HCPVT) solar generators, which is their dynamic energy simulation. For this purpose, the electrical and thermal energy productions of the proposed HCPVT are simulated and compared with those obtained by a conventional reference PVT system.

2. System description

The analyzed building integrated concentrating PVT system is designed to be superimposed on the blinds of a solar louvre shading system. In this manner, the concentrator is benefitted from the solar altitude tracking of the shading blinds and thus increasing the optical efficiency. Figure 1 illustrates the architectural configuration proposed, indicating in light blue the blind area where the concentrating system is placed (top-left). The blinds' size is 9 meters long by 0.4 meters wide and by 0.065 m high. The simulated building is considered to be 5.8 m height, starting the blinds at the ground floor window level (1 m height), therefore the number of blinds is 12. On the top-right, a schematic of a blind section shows the location of the holographic lenses and the PVT module, which is placed in the interior space. Both elements are assembled in a single unit forming a modular system with two parallel layers, the HOEs and the PVT module. At the bottom, a diagram of the cross section indicates the main dimensions of the module.

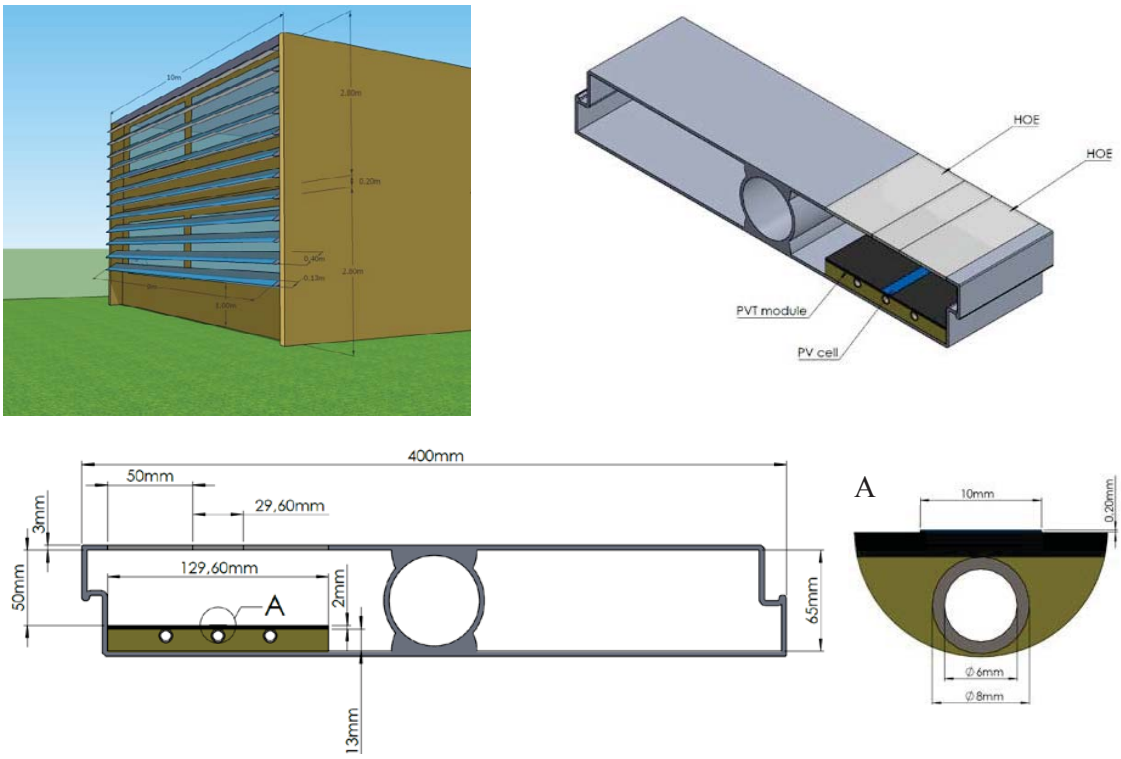

Figure 1. Architectural image of the building integrated concentrator (top-left), section of the blind where the PVT concentrator in placed (top-right) and cross-section and detail of the blind with the PVT concentrator (bottom). (Marín-Sáez et al., 2016b)

The concentrating system consists of two holographic lenses that focus incident irradiance toward the PVT module. Both lenses are attached to the same glass substrate, which at the same time closes the space between them. In figure 2a, a diagram of the ray-tracing is represented. Three different wavelengths in the range of maximum spectral response of the Si PV cell are depicted to show the rays' spatial distribution at the *YZ* plane.

2.1. Holographic optical element

A cylindrical holographic lens is chosen as a solar concentrator HOE. The recording of such lens is carried out by means of the interference of a plane wave and a cylindrical wave onto a photosensitive medium, as shown in Figure 2b. This turns into variations of the refraction index along the material.

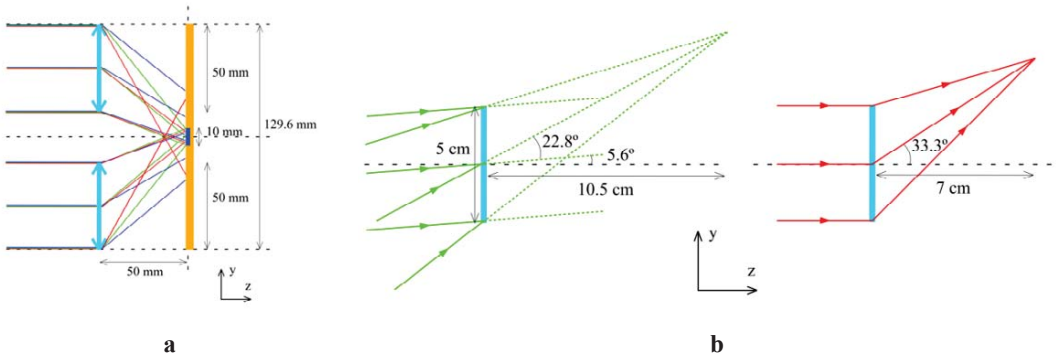

Figure 2. a) Schematic of the HCPVT generation unit (right), with ray-tracing for rays with three different wavelengths: 700 (depicted with blue lines), 800 (green lines) and 900 nm (red lines); b) Sketch of the recording (center, at 532 nm) and reconstruction (right, at 800 nm) schemes of the holographic cylindrical lens simulated in this study. (Marín-Sáez et al., 2016b)

When illuminating a volume hologram at the reconstruction stage, only two waves are found at its output: the transmitted wave and the diffracted wave. With the adequate incident conditions (wavelength and angle), the efficiency of the diffracted beam is maximal, and it can reach 100 % for a selected wavelength if the design is also optimum. When illuminating a holographic cylindrical lens with a plane wave, the resulting diffracted wave is a cylindrical one, as it is shown in Figure 2b.

The reconstruction wavelength for which the HOE will be most efficient is set at 800 nm. This value results from a compromise between the incident solar spectrum (with maximal intensity at wavelengths around 500-800 nm most of the day) and the photovoltaic cell sensitivity (optimum around 700-1000 nm for mono-Si cells). Incident light at 800 nm will focus at a line parallel to the x-axis, 7 cm away from the HOE, as it is shown in Figure 2b. However, the PVT module is placed at 5 cm away from the HOE, in order to collect more energy of the desired wavelength range, since rays with different wavelengths are led towards different directions, as it is illustrated in Figure 2a.

Holograms present higher angular selectivity when the incidence direction varies in the plane formed by the two recording beams, and lower in the perpendicular plane. Taking advantage of this effect, a cylindrical lens offers the possibility of suppressing tracking in one direction. Therefore, tracking is only necessary along the direction with higher angular selectivity.

The proposed recording material of the HOE is Bayfol HX, a photopolymer manufactured by Covestro AG (Berneth et al., 2014), adequate for holographic recording with solar photovoltaic applications (Marín-Sáez et al., 2016a).

In the configuration chosen for this study, two HOEs are placed separated in the same *XY*-plane, so that the spatial distributions of the diffracted beams are symmetrical. A glass plate located in this plane serves as a substrate for the photopolymer, covers the space between the two HOEs and is assumed to have the same refractive index as the photopolymer. The distance between the two lenses, and therefore, the position of the PV cell in the y-axis, was optimized so that it would receive more energy at the most favourable wavelength range for the cell. The ratio between the x dimension of the HOEs and the PV cell was chosen to avoid vignetting on the cell of its optimal wavelength range (700 - 1000 nm).

2.2. Hybrid photovoltaic-thermal module

The PVT module units for the holographic system are considered to be 100 cm long by 12.96 cm wide; thus every shading blind of 9 m is composed of 9 PVT modules. Every PVT module is formed by 7 cells connected in series of 14.29 cm long by 1 cm wide each. The photovoltaic cells considered in the simulation are based on commercial mono-crystalline cells by Sunways ("Sunways," n.d.), whose main electrical characteristics are summed up in table 1. The characteristics of the thermal receiver are detailed in section 3.2.

In the case of the reference PVT module, it presents the same dimensions as the HCPVT one and is considered to be composed of the same type of cells (table 1) and with the same thermal receiver characteristics. The difference between both is that the reference PVT module is placed at the same position than the optical system, thus receiving the same incident irradiance.

Table 1. Parameters of the PV cells ("Sunways," n.d.).

V_{OC} [1] (V)	J_{SC} (A/m^2)	FF (%)	γ (%/°C)	T_{NOCT} (°C)
0.635	377.6	78.4	-0.44	45

[1] V_{OC} = Open circuit potential; J_{SC} = Short circuit current density; FF = Fill factor; γ = Power temperature dependence losses; T_{NOCT} = Nominal operating cell temperature.

3. Methodology

3.1. Spectra simulation

The direct normal irradiance spectrum is calculated with the SMARTS radiative model (Gueymard, 2001), whose main atmospheric input parameters are (listed by order of importance): Air mass (AM), aerosol optical depth (τ), precipitable water (PW) and Ångström exponent (α).

Measured values of Z , τ , PW and α, can be obtained from the Aerosol Robotic Network (AERONET) database ("Aerosol Robotic Network (AERONET)," n.d.). For this study, only AERONET's level 2.0 data are used to guarantee the highest possible data quality (after cloud screening, calibration and degradation correction (Holben et al., 1998)).

Detailed information on the sunlight spectrum is required for at least a complete year in order to accurately estimate the energy output of the PVT modules. Therefore, a preliminary search on AERONET's database has been done to select only those locations and years with a high density of atmospheric retrievals. These retrievals

are performed at least every 15 minutes for AM less than 5. Following the procedure described by Chan et al. (Chan et al., 2014), measurement gaps longer than 15 minutes are considered to be caused by extended cloudiness, not computing this time for the annual yield. In addition, the selected locations should be suitable for CPVT systems and have a high direct normal irradiance (DNI).

The location has been selected according to two criteria: (i) It should provide high-quality data over an extended period of time (a constraint satisfied by only a small fraction of AERONET sites); and (ii) it should have co-located and simultaneous DNI measurements, in order to validate the simulated spectra. Based on the above criteria, Avignon, France, (2003) has been chosen.

Table 2. Characteristic parameters for Avignon.

Location	Simulated year	Lat. (°)	Long. (°)	Elevation (m)	Mean daily DNI (kWh/m^2/day) [25]	Annual mean atmospheric parameters AM | τ | PW | α
Avignon	2003	43.93	4.88	32	5-5.5	2.16 | 0.25 |1.76 | 1.37

Figure 3a illustrates the monthly variation of the most representative atmospheric parameters obtained by AERONET at the selected location. This graph conveniently displays the amplitude with which each variable varies throughout the simulation year.

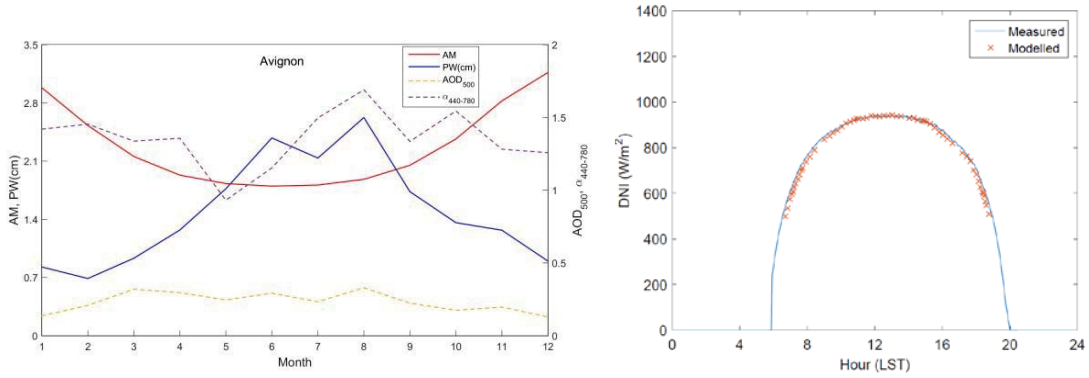

a b

Figure 3. a) Monthly-average values of the main atmospheric variables for the simulated sites, obtained from AERONET. In the case of AM, the values are limited to AM < 5, in agreement with AERONET measurements; b) DNI data validation on the 1st of August in the selected simulated year. LST: Local standard time. (Marín-Sáez et al., 2016b).

Finally, the validation of the spectra generated by SMARTS is undertaken by comparing the calculated broadband DNI to reference irradiance measurements obtained from the Baseline Surface Radiation Network (BSRN) ("World Radiation Monitoring Center – Baseline Surface Radiation Network homepage.," n.d.). A good agreement is achieved between the simulated and the measured data, as depicted in Figure 3b, showing the irradiance profiles for a cloudless typical day. The validation has been conducted using DNI data from BSRN station in Carpentras, located 28 km away.

3.2. Optical simulation

The performance analysis of the holographic lens is based on Kogelnik's Coupled Wave Theory (Kogelnik, 1969) and the approximate scalar theory established by Syms (Syms, 1985). A ray-tracing algorithm has been developed (Bañares-Palacios et al., 2015), which allows the calculation of the output directional cosines and the spectral energy associated with each ray, for the transmitted and the diffracted wave delivered to the PVT module.

The propagation wave vectors of the recording beams, $\vec{k}_1$ and, $\vec{k}_2$ with modulus $k_1 = k_2 = \frac{2\pi}{\lambda_R}$ (where λ_R is the recording wavelength), determine the grating vector $\vec{K} = \vec{k}_1 \pm \vec{k}_2$, illustrated in Figure 6. Since one of the recording beams is a cylindrical wave, its propagation wave vector has a different direction at each point along the *y*-direction, and the angle between beams is also different. Therefore, the vector $\vec{K}$, which is perpendicular

to the planes with constant refractive index variation, is spatially dependant. Its modulus is $\frac{2\pi}{\lambda}$, where Λ is the spatial period of a grating with vector $\vec{K}$, and also different at each point. Each point of the holographic lens behaves differently; thus, each point is treated as a local holographic grating.

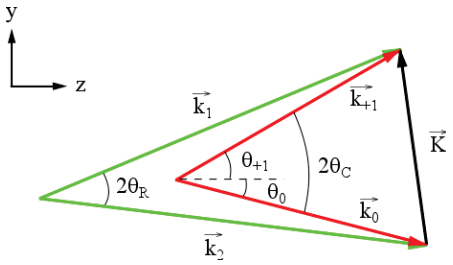

Figure 4. Sketch of the relation between the grating vector $\vec{K}$ and the wave vectors of the two recording beams, $\vec{k}_1$ and $\vec{k}_2$, and the transmitted and diffracted waves, $\vec{k}_0$ and $\vec{k}_{+1}$.

When illuminating the HOE with a wave with vector $\vec{k}_0$ and a certain wavelength λ_C, the resulting diffracted wave has a vector $\vec{k}_{+1}$, which has the same modulus as $\vec{k}_0$ and direction determined with $\vec{k}_0$ and $\vec{K}$. This relation is shown in Figure 4. Thus, if the vector $\vec{K}$ along the hologram is known, the direction of the diffracted ray originated with each incident reconstruction ray at a certain point can be calculated.

The energy of the diffracted wave from each point is calculated with equation 1:

$$\eta = \frac{\sin^2\left[\left(\nu^2 + \xi^2\right)^{1/2}\right]}{1 + \frac{\xi^2}{\nu^2}} \tag{1}$$

The parameters ν and ξ are given by:

$$\nu = \frac{\pi d \Delta n}{\lambda_C c_0 c_{+1}} \tag{2}$$

$$\xi = \frac{d\vartheta}{2c_{+1}}, \tag{3}$$

where d is the thickness of the recording material, Δn is the refraction index modulation, λ_C is the reconstruction wavelength, and c_0 and c_{+1} are the directional cosines with respect to the z-axis of the reconstruction and diffracted wave, respectively. ϑ is a parameter that determines the variation from Bragg's law, that is, the condition of maximal efficiency. Bragg's law is met when the next equation is fulfilled:

$$2\Lambda \sin\theta_C = \lambda_C, \tag{4}$$

where θ_C is the semiangle between the transmitted and the diffracted beam, shown in Figure 6. When Bragg's condition is not fulfilled the efficiency of the diffracted wave decreases, and the efficiency of the transmitted wave increases.

The energy of the transmitted wave is calculated as the remaining available energy that is not taken by the diffracted wave, at each point and for each reconstruction wavelength.

The rays entering the system through the glass plate between the two HOEs are also considered.

The simulation considers direct normal irradiance solar spectrum, generated by SMARTS, as the incident irradiance input parameter. Nevertheless, due to the implicit difficulty and computational time required, the solar semiangle and the diffuse irradiance fraction are not considered at this stage. Further research will be conducted to define the algorithm containing the particular angles of incidence and polarization constraints of the diffuse radiation, jointly with the implementation of the solar semiangle. Therefore, it should be taken into account that the irradiance delivered by the holographic concentrator is underestimated in a percentage proportional to the diffuse fraction. Losses due to Fresnel reflections on the surface and to total internal

reflection (Hecht, 1998) are taken into account in the simulations.

3.3. Energetic simulation

The energetic simulation is conducted in TRNSYS, evaluating the HCPVT performance under the weather conditions of Avignon. Figure 5 charts the monthly cumulated DNI values and the monthly average ambient temperatures. The annual cumulated DNI is 1860 kWh/m^2 and the annual mean temperature is 14.7 °C. It should be noticed that, in agreement with AERONET criteria, values with AM > 5 (solar altitude below 11.5°) are not considered and, taking into consideration the optical efficiency limitations of the concentrating system, the direct beam irradiances accepted by the HCPVT module will be significantly lower than the DNI values. Results regarding optical efficiencies are included in section 4.

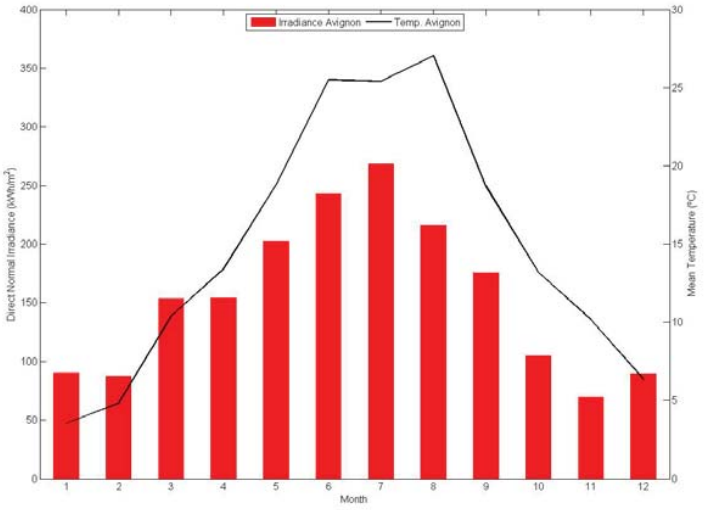

Figure 5. Monthly cumulated DNI and mean temperature values.

The optical simulation program described in subsection 3.2, which is programmed in MATLAB, is linked to TRNSYS delivering at every time step (1 minute) the irradiance impacting on the PVT module. From the irradiance received on the module, the thermal energy produced is calculated by a MATLAB code which determines the electrical power (P'_{mpp}) coupled with the thermal generator *type 1b*, as a function of the solar cell electrical parameters and the cell temperature, calculated with the following equation (5) (Marion, 2002). In the case of the reference module, the simulation is conducted in the same way but with no optical simulation.

$$P'_{mpp} = P_{mpp}\left[1+\gamma\left(T_{cell}-25\right)\right], \tag{5}$$

where P_{mpp} is the electrical power generated by a PV cell without taking into account losses due to the temperature, γ is a temperature coefficient equal to -0.44 %/°C for the PV cells considered in this study, and T_{cell} is the temperature of the cell in °C. The temperature of the cell of the PVT module is estimated with equation 6 (Amrizal et al., 2013):

$$T_{cell} = T_{in} + \frac{P_{th}}{F'U_L A}\left(1-F'\right), \tag{6}$$

where T_{in} is the input temperature of the water circulating at each module, P_{th} is the power generated by the thermal absorber, F' is the collector efficiency factor, U_L is the overall convective heat loss coefficient of the collector and A is the surface of the collector. T_{in} and P_{th} values are obtained from the previous time step, considering the error to be minimum.

The electrical power of the cell P_{mpp} without temperature effects is calculated with:

$$P_{mpp} = J_{SC}V_{OC}FF \tag{7}$$

The short circuit current, J_{SC} is calculated taking into account the spectral response curve of the mono-crystalline silicon solar cell manufacturer. The values of the open circuit voltage V_{OC} and the fill factor FF are assigned from the technical characteristics of the simulated solar cells (see Table 1).

Table 3. Parameters of the thermal collector [33].

η_0 [2] (%)	U_L (W/m^{2}K)	k_2 (W/m^{2}K^2)	$F' = \eta_0 / \tau\alpha$	ε (%)	α (%)	τ (%)
79.9	3.97	0.016	0.913	5.0	95.5	91.6

[2] η_0 = Efficiency; U_L, k_2 = Coefficients of heat loss; ε = Emission; α = Absorption; τ = Transmission and F' = Collector efficiency factor ($F' = \eta_0 / \tau\alpha$).

4. Results

The optical efficiency of the concentrating holographic system is defined in Eq. (8) as the ratio between the irradiance received at the generator surface, differentiated in the area where the PV is situated (A_{PV}) and the rest of the area where it is the thermal absorber (A_T), and the irradiance at the entrance pupil area of the system (A_E). The irradiances on the PV, thermal absorber and entrance pupil are respectively I_{PV}, I_T and I_E.

$$\eta_{opt} = \frac{I_{PV} A_{PV} + I_T A_T}{I_E A_E} . \tag{8}$$

The average optical efficiency obtained each month is presented in Figure 6. The fact that the system works better during the winter months than the summer months may seem counterintuitive. However, it is due to the lack of tracking of the system in the azimuth direction, since the maximum optical efficiency is reached when the azimuth angle, φ, is zero (at solar noon), and decreases when the absolute value of this angle increases. The azimuth angle reaches greater values in summer; therefore, the optimum incident angle range is found during less time each day, which results in lower optical efficiency, because of the angular selectivity of the HOEs.

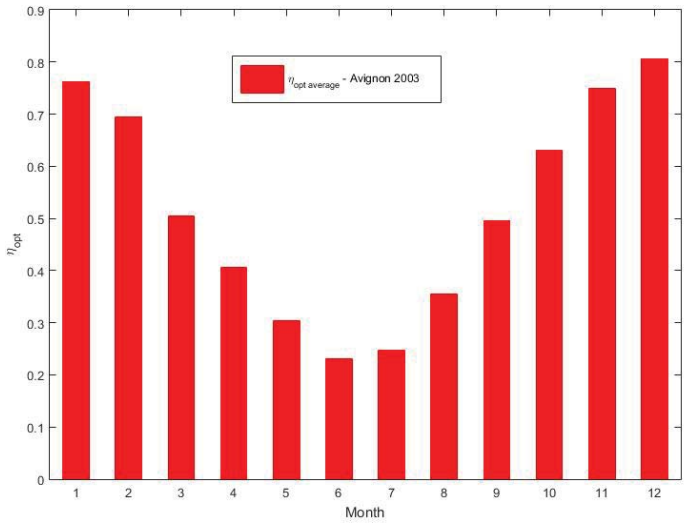

Figure 6. Average optical efficiency of the concentrating holographic system obtained each month with incident radiation of Avignon (2003).

The incident mean annual spectral irradiance received at the surface of the PV cell and at the surface of the thermal absorber, determined by means of the optical simulation described in section 3.2, is plotted in Figure 7, together with the incident solar spectral irradiance received at the entrance of the system. One of the most remarkable aspects of this graph is the shift of the peak wavelength of the spectrum that reaches the PV cell, compared to the solar spectrum. This effect is caused by the chromatic selectivity of the HOEs, which are designed to perform more efficiently around 800 nm. The shape of the spectral irradiance received by the thermal absorber is rather similar to the solar spectrum, except for the optimum wavelength range of the PV

cell.

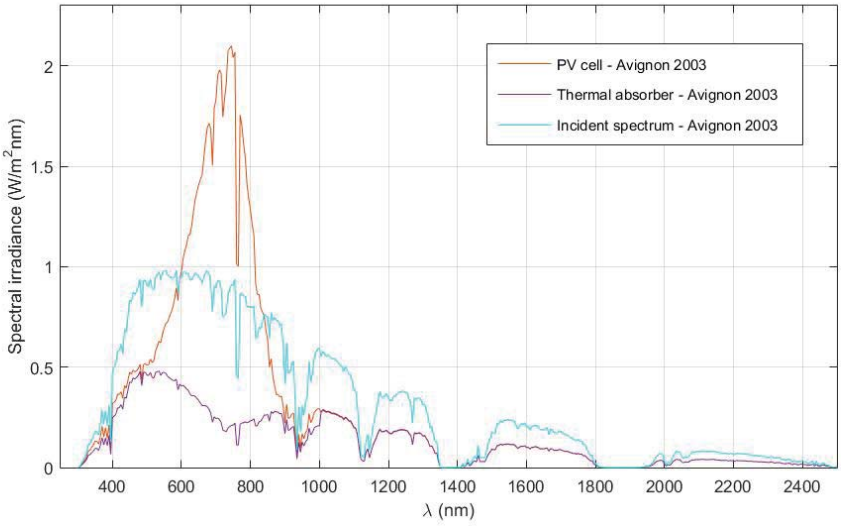

Figure 7. Average spectral irradiance at the entrance of the system, at the PV cell and at the thermal absorber at both locations.

The electrical energy produced by the HCPVT module expressed in terms of the PV cell area outperforms clearly the one delivered by the reference PVT system as it can be observed in Figure 8 a. More specifically the productions are 275.8 kWh/m^2 and 144.8 kWh/m^2 for the HCPVT and the reference PVT respectively. These values denote a mean effective optical concentration of about 2 for the whole spectrum where the PV cell is sensitive. In addition, figure 8b represents the results in a more widespread manner for PV systems that is in terms of the kilowatt pic (kWp). Conversely, in this case the energy values are the opposite: the reference system delivers almost twice the electric energy than the HCPVT (563.3 vs 296.4 kWh/kWp). This behavior is attributed to the low annual efficiency achieved by the concentrating system for all the spectral response bandwidth of the PV cell (43%) and it is a key indicator that further research in the optical design should be conducted to increase the average optical efficiency and therefore to obtain either similar or higher electrical yield values than in the reference module. On the other hand, it is worthy to mention that in terms of environmental impact the ten times reduction of the PV cell area, even the production to be the half than for the reference case in terms of kWp, reduces considerable the impact of the system as polymeric materials (used for the lenses) present in most of the cases and with all the particularities of each environmental indicator a much lower impact (Lamnatou et al., 2016).

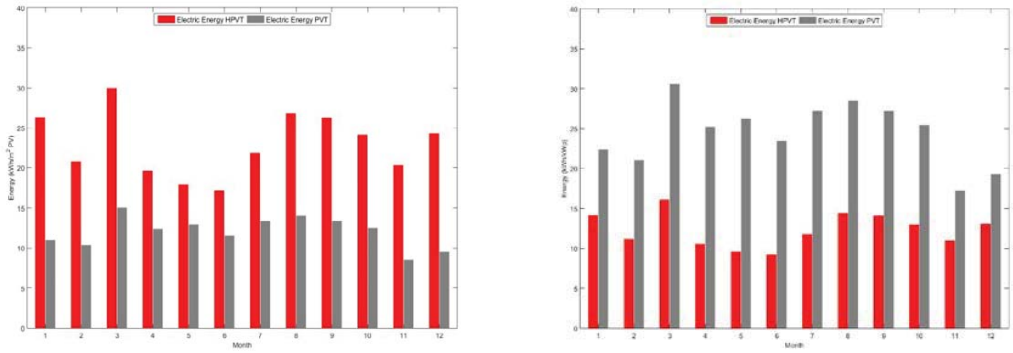

Figure 8. Electric energy output of the HCPVT system (grey bars) and the PVT system (red bars) along the year, expressed in terms of kWh/m^2 (left) and kWp (right).

The thermal energy output in both systems is quite simimilar, as it can be seen in Figure 9, reporting annual values of 250.4 and 294.2 kWh/m^2 of thermal collector area for the HCPVT and the reference PVT respectively. Therefore, the system proposed reports satisfactory values with respect to the thermal energy, however, concerning the electrical production further research is necessary not only from the energetical point of view but also considering environmental aspects.

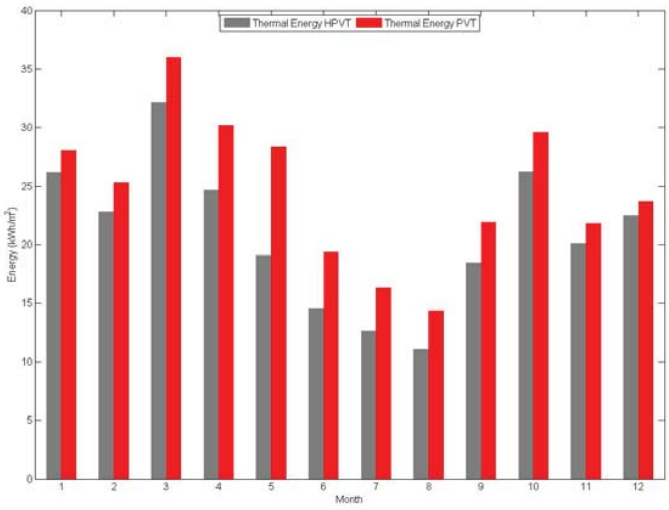

Fig 9. Thermal energy output of the HCPVT system (grey bars) and the PVT system (red bars) along the year.

5. Conclusions

A building-integrated holographic concentrating photovoltaic-thermal system has been designed and simulated. The module has been placed on the blinds of a solar louvre, which track the solar altitude movement of the sun along the day, on a south-oriented façade.

The direct normal irradiance solar spectra along one year have been calculated with the SMARTS radiative model, utilizing AERONET atmospheric parameters to test the concentrating system proposed under different spectral conditions. These spectra have been verified with direct irradiance measurements obtained from the Baseline Surface Radiation Network (BSRN), which proved the high accuracy of the simulations.

The behavior of the holographic concentrator, based on two holographic cylindrical lenses, was simulated by means of a ray-tracing algorithm. It concentrates toward the cell mainly its optimal wavelength range and also distributes the rest of the spectral irradiance on the thermal absorber, reaching a total optical efficiency. The annual average optical efficiency obtained is 43.0%.

A MATLAB-TRNSYS coupling was implemented to run simultaneously the optical, the thermal and the electrical simulations.

In the comparative study with respect to a reference photovoltaic-thermal conventional module installed with the same characteristics as the concentrating one, a similar thermal output was observed (~15% difference) but the electrical energy delivered by the reference module doubled the electricity production of the concentrating one (563.3 vs 296.4 kWh/kWp)

A future work of the present study is the improvement of the optical design to achieve higher mean optical efficiencies to obtain better electrical efficiencies mainly. In addition, environmental criteria should be considered to adequately estimate the differential performance of the holographic concentrator proposed.

6. References

Aerosol Robotic Network (AERONET) [WWW Document], n.d. URL http://aeronet.gsfc.nasa.gov/ (accessed 10.14.15).

Amrizal, N., Chemisana, D., Rosell, J.I., 2013. Hybrid photovoltaic–thermal solar collectors dynamic modeling. Appl. Energy 101, 797–807. doi:10.1016/j.apenergy.2012.08.020

Bañares-Palacios, P., Álvarez-Álvarez, S., Marín-Sáez, J., Collados, M.-V., Chemisana, D., Atencia, J., 2015. Broadband behavior of transmission volume holographic optical elements for solar concentration. Opt. Express 23, A671–A681. doi:10.1364/OE.23.00A671

Berneth, H., Bruder, F.-K., Fäcke, T., Jurbergs, D., Hagen, R., Hönel, D., Rölle, T., Walze, G., 2014. Bayfol HX photopolymer for full-color transmission volume Bragg gratings. SPIE Photonics West 2014-OPTO

Optoelectron. Devices Mater. 9006, 900602. doi:10.1117/12.2038399

Castillo, J.E., 2011. Thermal effects of the extended holographic regions for holographic planar concentrator. J. Photonics Energy 1, 15504. doi:10.1117/1.3569118

Castro, J.M., Zhang, D., Myer, B., Kostuk, R.K., 2010. Energy collection efficiency of holographic planar solar concentrators. Appl. Opt. 49, 858. doi:10.1364/AO.49.000858

Chan, N.L.A., Brindley, H.E., Ekins-Daukes, N.J., 2014. Impact of individual atmospheric parameters on CPV system power, energy yield and cost of energy. Prog. Photovoltaics Res. Appl. 22, 1080–1095. doi:10.1002/pip.2376

Chander, S., Purohit, A., Sharma, A., Nehra, S.P., Dhaka, M.S., 2015. A study on photovoltaic parameters of mono-crystalline silicon solar cell with cell temperature. Energy Reports 1, 104–109. doi:10.1016/j.egyr.2015.03.004

Chemisana, D., Collados, M.V., Quintanilla, M., Atencia, J., 2013. Holographic lenses for building integrated concentrating photovoltaics. Appl. Energy 110, 227–235. doi:10.1016/j.apenergy.2013.04.049

Collados, M.V., Chemisana, D., Atencia, J., 2016. Holographic solar energy systems: The role of optical elements. Renew. Sustain. Energy Rev. 59, 130–140. doi:10.1016/j.rser.2015.12.260

Directive 2010/31/EU of the European Parliament and of the Council of 19 May 2010 on the energy performance of buildings., 2010. . European Parliament, Strasbourg, France.

Froehlich, K., Wagemann, E.U., Frohn, B., Schulat, J., Stojanoff, C.G., 1993. Development and fabrication of a hybrid holographic solar concentrator for concurrent generation of electricity and thermal utilization, in: Lampert, C.M. (Ed.), Proceedings of SPIE. San Diego, USA, pp. 311–319. doi:10.1117/12.161971

Gueymard, C.A., 2001. Parameterized transmittance model for direct beam and circumsolar spectral irradiance. Sol. Energy 71, 325–346. doi:10.1016/S0038-092X(01)00054-8

Hecht, E., 1998. Optics. Addison Wesley.

Holben, B.N., Eck, T.F., Slutsker, I., Tanré, D., Buis, J.P., Setzer, A., Vermote, E., Reagan, J.A., Kaufman, Y.J., Nakajima, T., Lavenu, F., Jankowiak, I., Smirnov, A., 1998. AERONET—A Federated Instrument Network and Data Archive for Aerosol Characterization. Remote Sens. Environ. 66, 1–16. doi:10.1016/S0034-4257(98)00031-5

Iurevych, O., Gubin, S., Dudeck, M., 2012. Combined receiver of solar radiation with holographic planar concentrator. IOP Conf. Ser. Mater. Sci. Eng. 29, 12016. doi:10.1088/1757-899X/29/1/012016

Kogelnik, H., 1969. Coupled wave theory for thick hologram gratings. Bell Syst. Tech. J. 48, 2909–2947. doi:10.1002/j.1538-7305.1969.tb01198.x

Lamnatou, C., Baig, H., Chemisana, D., Mallick, T.K., 2016. Environmental assessment of a building-integrated linear dielectric-based concentrating photovoltaic according to multiple life-cycle indicators. J. Clean. Prod. 131, 773–784. doi:10.1016/j.jclepro.2016.04.094

Ludman, J.E., 1982. Holographic solar concentrator. Appl. Opt. 21, 3057–3058. doi:10.1364/AO.21.003057

Ludman, J.E., Riccobono, J., Semenova, I. V., Reinhand, N.O., Tai, W., Li, X., Syphers, G., Rallis, E., Sliker, G., Martín, J., 1997. The optimization of a holographic system for solar power generation. Sol. Energy 60, 1–9. doi:10.1016/S0038-092X(96)00148-X

Marín-Sáez, J., Atencia, J., Chemisana, D., Collados, M.-V., 2016a. Characterization of volume holographic optical elements recorded in Bayfol HX photopolymer for solar photovoltaic applications. Opt. Express 24, A720. doi:10.1364/OE.24.00A720

Marín-Sáez, J., Chemisana, D., Moreno, Á., Riverola, A., Atencia, J., Collados, M.-V., 2016b. Energy Simulation of a Holographic PVT Concentrating System for Building Integration Applications. Energies 9, 577. doi:10.3390/en9080577

Marion, B., 2002. A method for modeling the current-voltage curve of a PV module for outdoor conditions. Prog. Photovoltaics Res. Appl. 10, 205–214. doi:10.1002/pip.403

Menoufi, K., Chemisana, D., Rosell, J.I., 2013. Life Cycle Assessment of a Building Integrated Concentrated Photovoltaic scheme. Appl. Energy 111, 505–514. doi:10.1016/j.apenergy.2013.05.037

Schüco [WWW Document], n.d. URL www.schueco.com (accessed 5.27.16).

Solar and Wind Energy Resource Assessment (SWERA) [WWW Document], n.d. URL https://maps.nrel.gov/swera (accessed 5.27.16).

Sunways [WWW Document], n.d. URL www.sunways.eu (accessed 1.1.13).

Syms, R.R.A., 1985. Vector Effects in Holographic Optical Elements. Opt. Acta Int. J. Opt. 32, 1413–1425. doi:10.1080/713821663

Vorndran, S., Russo, J.M., Wu, Y., Gordon, M., Kostuk, R., 2015. Holographic diffraction-through-aperture spectrum splitting for increased hybrid solar energy conversion efficiency. Int. J. Energy Res. 39, 326–335. doi:10.1002/er.3245

World Radiation Monitoring Center – Baseline Surface Radiation Network homepage. [WWW Document], n.d. URL http://bsrn.awi.de/ (accessed 5.27.16).

Xia, X.W., Parfenov, A. V., Aye, T.M., Shih, M.-Y., 2011. Efficient hybrid electric and thermal energy generation, in: VanSant, K., Sherif, R.A. (Eds.), Proceedings of SPIE. San Diego, USA, p. 81080F. doi:10.1117/12.894166

Xiao, C., Yu, X., Yang, D., Que, D., 2014. Impact of solar irradiance intensity and temperature on the performance of compensated crystalline silicon solar cells. Sol. Energy Mater. Sol. Cells 128, 427–434. doi:10.1016/j.solmat.2014.06.018

Zhang, D., Castro, J.M., Kostuk, R.K., 2011. One-axis tracking holographic planar concentrator systems. J. Photonics Energy 1, 15505. doi:10.1117/1.3590943

Zhang, D., Gordon, M., Russo, J.M., Vorndran, S., Kostuk, R.K., 2013. Spectrum-splitting photovoltaic system using transmission holographic lenses. J. Photonics Energy 3, 34597. doi:10.1117/1.JPE.3.034597

Conference Proceedings

EuroSun 2016
Palma de Mallorca (Spain), 11 - 14 October 2016

THE IMPACT OF SHADING IN THE PERFORMANCE OF THREE DIFFERENT SOLAR PV SYSTEMS

Jose Francisco Contero[1,2], João Gomes[1], Mattias Gustafsson[1] and Björn Karlsson[1]

[1] University of Gävle (Sweden)

[2] University of Zaragoza (Spain)

Abstract

Partial shading decreases the performance of PV modules due to the series connection between the solar cells. In the recent years, several new technologies have emerged within the photovoltaics field to mitigate the effect of shading in the performance of the PV modules. For an accurate assessment of the performance of these devices, it is required to evaluate them comparatively in different circumstances.

Three systems with six series-connected PV modules (each containing 60 cells) have been installed at the University of Gävle. System One comprises a string inverter system with 6 PV modules; System Two features a DC-DC optimizer per panel and a string inverter; System Three incorporates three micro inverters for six modules.

A major conclusion of this study was that under partial shading of one (or more) modules both System Two (DC-DC optimizers) and System Three (micro inverters) perform considerably better than System One (string inverter), as long as the Impp of the shadowed module is lower than the Impp of the unshaded string. It is also important that the Vmpp in the shaded module is higher than the lowest allowed voltage of the DC-DC optimizer or module inverter. The economic implications of the usage of these devices were also analyzed.

Keywords: Shading; PV-cells, DC-DC, inverter, installation, Impp, Vmpp, Pmax

1. Introduction

It is well known that partial shading decreases the performance of PV modules due to the series connection between solar cells in a string. In the recent years, several new technologies and devices have emerged within the photovoltaics field to mitigate the effect of shading in the performance of the PV modules. In order to make an accurate assessment about how such devices affect the overall efficiency of the PV-systems, it is necessary to evaluate them comparatively.

1.1. A standard PV system

The investigated modules have 72 series connected cells divided into 6 columns and 12 rows. There are three by-pass diodes connected between column 1 and column 2, column 3 and column 4 and between column 5 and column 6. This means that each diode is connected in parallel with 24 cells.

1.2. How shading affects PV

There are several reasons that can lead to the reduction of produced power on PV panels such as manufacturing defects, degradation of cells, high solar cell temperatures, or partial shading (Stuart R. Wenham, 2012). This project has been focused on the significant decrease of power that can be caused by shading.

doi:10.18086/eurosun.2016.08.25 Available at http://proceedings.ises.org

A cell can be seen as a combination of a current generator and a diode. Current is generated in the reverse direction of the diode. If a cell is partially shaded, it will produces less current than a cell that is fully illuminated. Voltage is practically not affected by the level of illumination, as long as a minimal level is present. During partial shading of one cell of a string, the shaded cell will not be able to generate as much current as the remaining cells of the string. Since the photo current flows in the reverse direction of the diode the unshaded cells cannot force current through the shaded cell. This means the shaded cell will limit the output of all cells in that string. Since cells are normally series connected in a string in order to raise module voltage, this causes a significant power reduction. However, if a by-pass diode is connected over the cell this will allow the surplus current to pass through the diode permitting the unshaded solar cells of the string to produce current unrestrained by the low current production caused by the shaded solar cell.

2. Method

The effect of shading was evaluated by controlled shading of different cells in a string of six modules.

2.1 The four PV installations at Gävle University

At the University of Gävle, there are four different solar systems installed. This paper is focused on the three PV systems that are shown in the picture below. Each of these three systems has 6 EOPLLY 125M/72 200 W monocrystalline modules with 72 cells and 3 bypass diodes per module (3 circuits of 24 cells per panel). There are 18 PV modules in total.

Figure 1. Systems 1, 2 and 3 at University of Gävle

2.2.1 The PV panels

The electrical specifications are shown in the table below. Each panel measures 1580x808 mm.

Table 1 Electrical specifications of the modules (Energy, n.d.)

Open circuit Voltage Voc	45.73 V	Measured at STC: 25ºC, 1000 $\frac{W}{m^2}$
Rated Voltage Vmpp	37.00 V	
Short Circuit Current Isc	5.589 A	
Maximum Power	200 W	
Operating Temperature	-40ºC to 85ºC	
Cell Efficiency	15.67%	
Module Area	1580mm x 808mm	

2.2.2 System description and schematics

- **System One:** Comprises six standard PV modules series connected to one central inverter. The string inverter contains a Maximum Power Point Tracker (MPPT) that finds out the maximum power voltage and maximum power current (Vmp and Imp) by a trial and error algorithm for the PV array. A schematic drawing can be observed on the following picture:

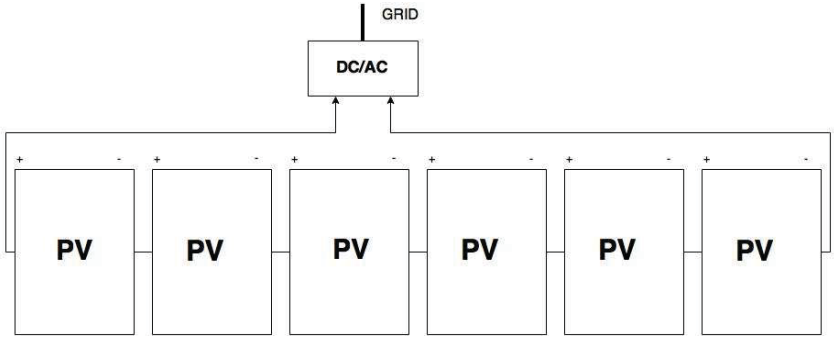

Figure 2. Schematics of System 1 (String inverter)

It is important to mention that this central inverter has a maximum DC voltage of 400V and the range of the MPP tracking in the inverter is between 100V to 320V.

- **System Two:** Comprises of the same six standard PV modules and the same string inverter as system 1. However, on this system each panel has a DC-DC optimizer. Since the output from an array of PV panels is limited by the weakest producing panel, a good solution to obtain the maximum output is to install DC-DC optimizers. They basically work as an individual MPPT for each PV panel. The DC-DC optimizers are series connected and the string inverter collects the output from the optimizers. The following figure describes how the system is connected:

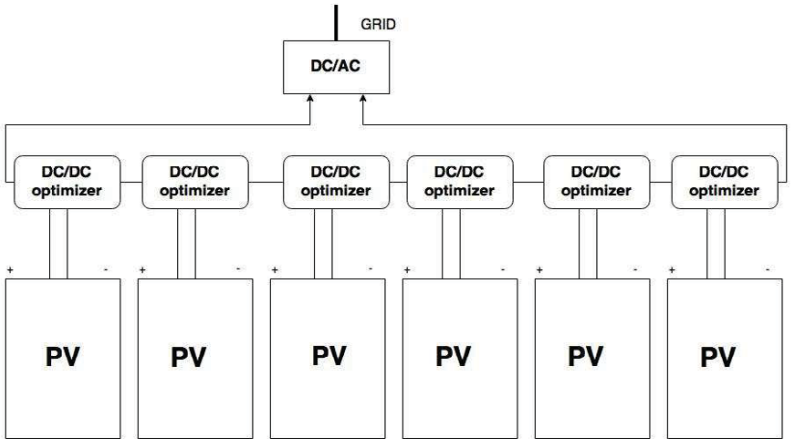

Figure 3. Schematics of System 2 (String inverter with additional DC/DC optimizers)

The following table describes the electrical specifications of the DC-DC optimizers:

Table 2. Electrical specifications for the optimizer (Tigo Eenergy, 2012)

Maximum power	375 W
Maximum Voc	52 V
Vmpp range	16-48 V
Maximum Imp	9.5 A
Maximum Isc	10 A

It is important to mention that the optimizers include a function that allows the users to monitor the power as well as the voltage and current outputs during the day on the manufacturers´ web page.

- **System Three**: Comprises three micro inverters for six modules, resulting in one micro inverter with a MPPT built-in for each two PV panels connected in parallel between themselves. The three inverters are connected to the grid like the above system. The following picture explains how the system is installed:

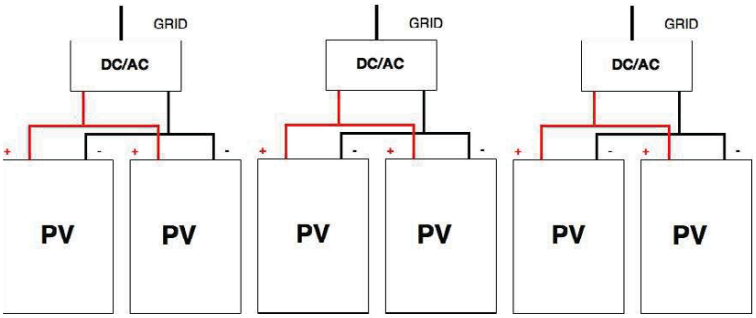

Figure 4. Schematic of system 3 (Micro inverters)

The electrical features of the micro inverters are:

Table 3. Electrical specifications of one micro inverter (Anon., n.d.)

Maximum PV power	250 W
Maximum V_{OC}	45 V
Vmp range	20-40 V
Maximum I_{SC}	10 A

- **System four:** This system was installed slightly above the location of system one, two and three at the University of Gävle. This system consists of nine thin film modules that where only utilized as reference in order to compare the output at the same irradiance level when the remaining systems were shaded.

Figure 5. System 4 (Thin film modules)

2.2.3 Components of the Systems

In order to compare the different prices of the systems that are going to be investigated, its components need to be enumerated. The table below describes each system:

Table 4. Systems components

SYSTEM	COMPONENTS
System 1	6 PV modules + 1 String Inverter
System 2	6 PV modules + 1 Maximizer Management Unit + 1 Optimizer Energy Gateway + 1 Inverter (Tigo Eenergy, 2012)
System 3	3 Micro Inverters + 6 PV Modules

2.3 Testing Procedure

In order to know how the different systems work under shading, the performance was monitored during different shading configurations. Two different procedures have been carried out:

- **Procedure 1:** System 1 was measured with the help of a solar sensor and an IV tracer which provided the IV curves. System 2 was evaluated thanks to the website of the Tigo optimizers which gave us the voltage, current and power output. Both of these systems were always evaluated with a solar irradiance

exceeding 750W/m^2. None of these procedures was available for system 3. These measurements were taken under 4 cases:

1. No shading.
2. One cell covered in one module in each system.
3. Two cells covered in different circuits in one module for all systems.
4. Three cells covered in different circuits in one module per system.

- **Procedure 2:** A data logger was collecting the power output of the three systems continuously. This data was used in a comparative analysis. Since there was no permanent pyranometer installed on site, system 4 was used as a solar radiation reference allowing us to conclude that all analyzed cases always took place during sunny days with a solar radiation exceeding 600W/m^2. The measurements were performed under 5 different cases:

1. No shading.
2. One cell shaded in one module in each system.
3. Two cells shaded in different circuits in one module for both systems.
4. Three cells shaded in different circuits in one module per system
5. 30% of a row shaded in one module per system

The following figures illustrate how the modules were shaded

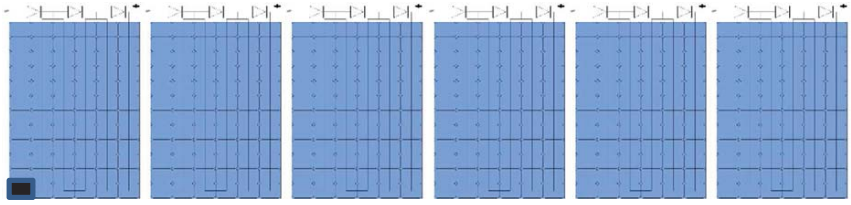

Figure 6 Case 1: No shading

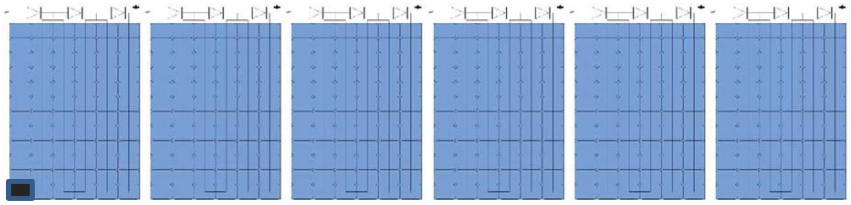

Figure 7 Case 2: One cell shaded

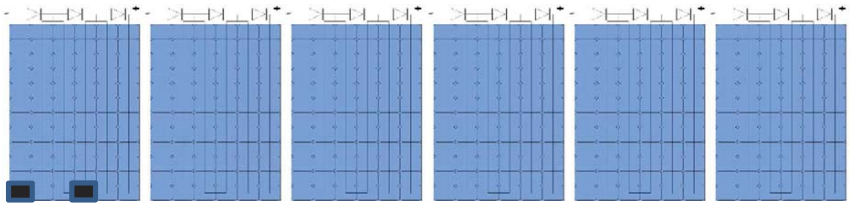

Figure 8 Case 3: Two cells shaded

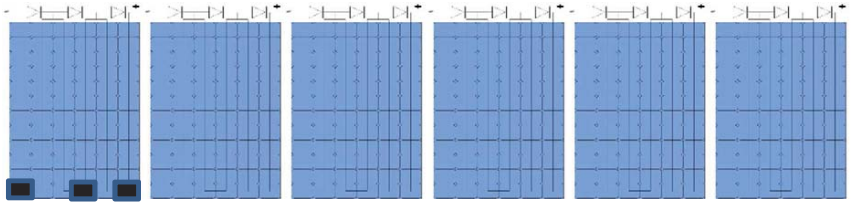

Figure 9 Case 4: Three cells shaded

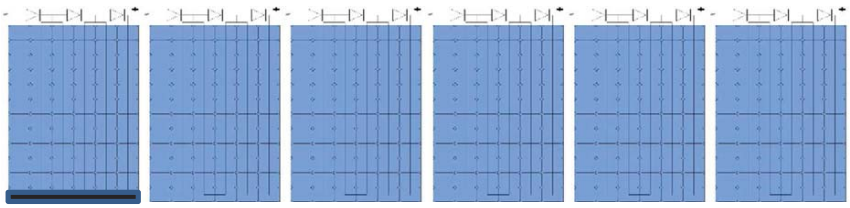

Figure 10 Case 5: 30% of a row shaded

Measurements Limitations

In order to avoid the influence of clouds, the analysis of measured data were limited to sunny days around solar noon. Only days with high output from the modules were considered. In procedure 2, the system with thin film modules were used as a reference, instead of a pyranometer.

3. Results

3.1 Procedure 1

An IV tracer was used to measure the IV curves for system 1 for each case above. For system 2, the optimizer's webpage showed the power output of the system. A solar sensor was used in order to be able to compare the results between each case and each system. Since the module current is proportional to the irradiance on the module (Alberto Dolara, 2013), it was possible to normalize the obtained results to the irradiance level of 1000 W/m^2, as shown in the following table:

Table 5. Comparison between the power output for systems 1 and 2 normalized to the same irradiation level of 1000W/m^2

28/05/2015	Irradiation level [W/m^2]	**System 1**			**System 2**	
		Normalized Power [W]	**Power relative to no shading (in %)**	Vmpp[V]	Normalized Power [W]	**Power relative to no shading (in %)**
No shading Case 1	762	1094	**100.0**	198	1089	**100.0**
1 cell shaded Case 2	815	1021	**93.3**	185	1034	**95.1**
2 cells shaded Case 3	877	948	**86.6**	171	887	**81.6**
3 cells shaded Case 4	1040	887	**81.1**	167	909	**83.6**

3.2 Procedure 2

The output during different time periods has been analyzed in order to get a comparison between the three systems which was not possible to do using procedure 1. In order to avoid influence of clouds, a careful choice

of the time periods when the output was high was made. The next graph shows the power output for the reference day with no shading based on a 10 minute resolution.

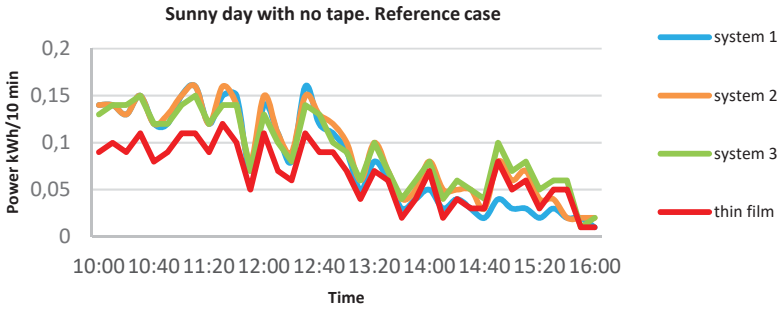

Figure 11. Power during the reference day with no shading

The following figures show the power during time periods with high power under 3 different shading cases:

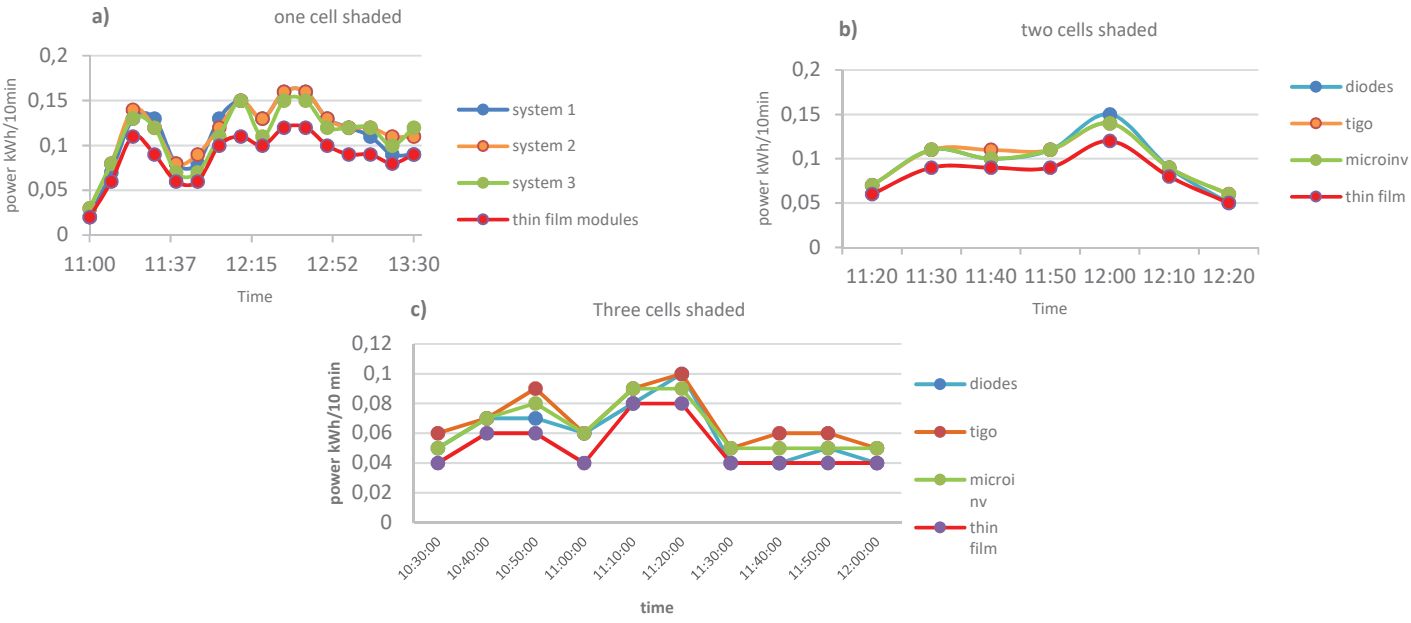

Figure 12. Power output for the cases: a) Case 2, One cell shaded, b) Case 3, Two cells shaded, c) Case 4, Three cells shaded

The following tables show the output values for each case and system. The column "percentage relative to the reference case" shows us the performance drop suffered by each system under different shading conditions. The thin film modules (system 4) where never shaded.

Table 6. Panel output in kWh during 150minutes for the case of one cell shaded in one string

ONE CELL SHADED	150 min output [kWh]			
From 11.00 to 13.30 (150 minutes)	**Reference (No tape)**	**Measurement**	**Normalized Value**	**Power relative to no shading (in %)**
System 1	1,80	1.78	1,72	**95.6**
System 2	1.89	1.85	1,78	**94.2**
System 3	1.76	1.75	1,69	**96.5**
Thin film system (reference)	1.35	1.40	1.35	**100**

Table 7. Panel output in kWh during 60 min for the case of two cells shaded in two different strings

TWO CELLS SHADED	60 min output [kWh]			
From 11.20 to 12.20	**Reference (No tape)**	**Measurement**	**Normalized Value**	**Power relative to no shading (in %)**
System 1	0.82	0.64	0.71	**86.5**
System 2	0.85	0.64	0.71	**83.5**
System 3	0.78	0.63	0.70	**89.7**
Thin film system (reference)	0.60	0.54	0.60	**100**

Table 8 90 min output. Case of three cells shaded in the three different strings

THREE CELLS SHADED	90 min output [kWh]			
From 10.30 to 12.00	**Reference (No tape)**	**Measurement**	**Normalized Value**	**Power relative to no shading (in %)**
System 1	1.33	0.6	1.12	**84.2**
System 2	1.36	0.62	1.16	**85.3**
System 3	1.28	0.59	1.10	**85.9**
Thin film system (reference)	0.97	0.52	0.97	**100**

As it can be observed in the following table, the daily output of the thin films system remains stable. This is because the measured days (the reference and the studied cases) were sunny with no clouds. Therefore, the output of the different systems in the different cases is comparable.

Table 9. Daily output with a tape covering 30% of a row in one module

30% of a row shaded	Daily output [kWh]			
Case	System 1	System 2	System 3	Thin film system
No tape (no shading)	5.9	6.0	6.2	4
Tape 30% row covered	4.9	5.6	5.8	4
Comparison to "no tape case"	83.2%	93.7%	94.6%	100%

The following table summarizes the comparison results obtained:

Table 10. Comparison between the three systems during different shading configurations

	% of the power relative to no tape		
	System 1	**System 2**	**System 3**
No tape (no shading)	100	100	100
Tape on one cell	95.6	94.2	96.5
Tape on two cells	86.5	83.5	89.7
Tape on three cells	84.2	85.3	85.9
Tape covers 30% of a row	83.2	93.7	94.6

3.3 Summary of both procedures and comparison with theoretical results:

The following table summarizes the experimental results, the relative power decrease, and compares it with the theoretically expected results.

Table 11 Percentage of the power relative to no shading. Comparison Theoretical Vs Experimental.

	Experimental results Power relative to no shading (in %)					Theoretical power relative to no shading case (in %)		
	System 1		System 2		System 3	System 1	System 2	System 3
	Procedure 1	Procedure 2	Procedure 1	Procedure 2	Procedure 2			
No shading	**100**	**100**	**100**	**100**	**100**	**100**	**100**	**100**
One cell shaded	**93.3**	**95.6**	**95.1**	**94.2**	**96.5**	**94,5**	**94,5**	**94,5**
Two cells shaded	**86.6**	**86.5**	**81.6**	**83.5**	**89.7**	**88,8**	**83,3**	**88,8**
Three cells shaded	**81.1**	**84.2**	**83.6**	**85.3**	**85.9**	**83,3**	**83,3**	**83,3**
30% of a row shaded	**---**	**83.2**	**---**	**93.7**	**94.6**	**83,3**	**95**	**95**

3.4 System costs

The performance of PV modules connected to different shading mitigation systems has been shown in the above tables. However, this is analysis would not be complete without looking into the costs.

This way, the investment cost for each system has been calculated. The following tables show the price of each component of the three systems installed at Gävle University.

Table 12. Costs of the devices

DEVICE	PRICE	PRICE [SEK]
Inverter	450£ (direct, n.d.)	5784
Optimizer Maximizer	111$ (Solar, 2015)	903
Optimizer Energy Gateway	113$ (Solar, s.f.)	918
Optimizer Energy Maximizer Management Unit	343$ (direct, s.f.)	2780
Micro inverter	249€(Anon., n.d.)	2345
PV modules	3720€(Gomes et al., 2014)	39466

Table 13 System Cost

System	Price [SEK]	Added cost
System 1	18 330	**0%**
System 2	27 446	**50%**
System 3	19 581	**7%**

4. Discussion and Conclusions

The influence of shading in solar panels is difficult to measure since both power output and the energy collected are strongly dependent on factors like the weather, time of the year, latitude and others. Table 5 shows the decrease in Vmpp for each shading case of procedure 1. The current produced by the panel, after normalization to the solar radiation, remained fairly stable and thus was not included in table 5. Therefore, in the evaluated cases, the power decrease correlates very well with the voltage decrease.

In system 1 (the string inverter), when one cell is shaded, the MPP tracker finds the point that leads to the highest power production in all the series connected PV modules, which means that the five modules are working at maximum power while the shaded module is working only at 2/3 of its maximum power. This means that the maximum current possible will pass through the six panels and one bypass diode will be activated to bypass one string. The theoretical percentage of power collected from the six panels will be 95% which corresponds to 5.67 out of six modules working at full power. The data collected from the measurements in procedure two supports the above statement. Table 6 shows the same 95% percentage of power production in all systems. Likewise, system 2 (with the DC-DC optimizers) with one cell shaded shows a similar power reduction (from 100% to 95%), as shown in table 5. This means five optimizers will collect the maximum power output from five unshaded modules while the shaded one will produce only 2/3 of its maximum power output. Finally, system 3 (parallel connected micro inverters) also shows a 5% power reduction. When one cell is shaded the DC-DC optimizer and the microverter will not increase the power and all systems will produce the same power.

In the case of two cells shaded, it can be observed that in system 1, the shaded panel only produces 1/3 of the power which corresponds to two strings producing no power. In this case, the theoretical power output is about 88% of the power collected with no shading, since 5.33 out of 6 modules are working. However, using procedure 1, it can be seen that the optimizer collects slightly lower output, about the 83% of the output collected from the unshaded case. This is shown by optimizer's webpage (procedure 1) in figure 10 where it is visible that one module (in black) is basically not working:

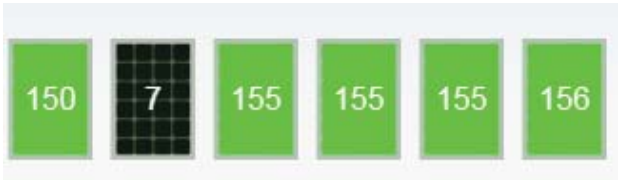

Figure 10. Power in Wp from each panel of system 2, in the case where two cells shaded. Each square represents the PV panel and the number inside is its power output in W.

This is a result of the limited Vmpp range of the optimizers being between 16-48V. If two strings in one module are shaded, the maximum voltage output is 1/3 of the PV module voltage (about 12V) which is below 16V, the minimum operating range of the optimizers. Hence the optimizer will go to a point in the IV curve where the voltage is bigger than 16 V and consequently sacrifice the current output, collecting almost no power from the PV module like shown in figure 10. It was expected that system 3 (with the micro inverters) would have the same problem since the Vmpp range is between 20-40V and the expected voltage was 12V. However, looking at table 7, the output obtained is about 90% of the output with no shading in the system which means that 5.33 out of 6 modules are working. This is probably due to the fact that the total voltage of the two mismatched parallel modules is between the Vmpp range of the MPP tracker of the micro-inverter.

In the case where three cells are shaded in each string of one module, all of them behave in the same way; Five module produce at full power and the shaded module is not working. This can be observed in table 8.

Finally, in case 5 (where a tape was covering the 30% of the module), it can be observed that the system 1 produces less output than the other two systems. In this case, the MPP tracker of system 1 has two options: to get the power output with a current about 70% of the total generated or collect the power output with five modules working while the bypass diodes of the shadowed one are working. The MPP tracker in the string inverter will take the last option since it produces more power.

This way, the main conclusions from this paper are:

1) If the shaded module gives full current at MPP then optimizers and the micro inverters will not increase the output. The module gives full current, if one of the three circuits in the module are not shaded.

2) The Vmpp range of the optimizers and inverters are important. If the Vmpp is out of range then the module will give either no or a low output.

3) The optimizers and the micro inverters will increase the output if the shaded module gives lower current than the non-shaded modules. This occurs under partial shading of all circuits in one (or more) modules. In this situation both System two (DC-DC optimizers) and System Three (micro inverters) perform considerably better than System One (string or central inverter), as long as the Impp of the shadowed module is lower than the Impp of the string. It is also important that the Vmpp in the shaded module is higher than the lowest allowed voltage of the DC-DC optimizer or module inverter.

4) There is a good agreement between the experimental results and the theoretically expected results for all cases.

From an economic perspective, considering the impact of shading, since system 2 (DC-DC optimizer) does not collect more energy that system 3 and it is 50% more expensive, it should not be selected as an option. System 1 (string inverter) is the cheapest and for this reason, it is preferable in all situations when one can be certain that there will be no shading. When one is uncertain if shading will occur, the extra 7% cost (difference between system 1 and system 3 with micro inverters) will probably be justified since the increase in annual energy produced should be superior to 7%.

5. Acknowledgements

The authors would like to thank the financial support given by the PV Applied Research and Development programs (SolEl) from the Swedish Energy Agency and Swedish industries through the Energy Research Institute.

6. References

Alberto Dolara, G. C. L. S. L. G. M., 2013. Experimental investigation of partial shading scenarios on PV. *Energy*, Volume 55, pp. 466-475.

Anon., n.d. *PVshop.eu*. [Online]
Available at: http://pvshop.eu/PV-Solar-Micro-Inverter-250W-AEConversion-INV250-45EU.html
[Accessed 17 6 2015].

direct, B. P., n.d. *Buy PV direct*. [Online]
Available at: http://www.buypvdirect.co.uk/SMA_SunnyBoy_SB1200_Solar_Inverter
[Accessed 17 June 2015].

direct, e., n.d. *eco direct*. [Online]
Available at: http://www.ecodirect.com/Tigo-MU-ESW-p/tigo-mu-esw.htm
[Accessed 17 June 2015].

Energy, E. s., n.d. *Solar Modules*. [Online]
Available at: http://www.eoplly.com/Htdocs/Html/_productsModuleDetail.asp?SolarModules_id=22
[Accessed 10 June 2015].

João Gomes, J. J. B. K., 2014. *Defining an annual energy output ratio between PV and solar thermal*. Aix-les-Bains, s.n.
SMA, n.d. *Sunny Boy 1200 / 1700 / 2500 / 3000*. [Online]
Available at: http://www.el-tec.nl/include/nl/downloads/SB1200_3000-DEN110712W.pdf
[Accessed 10 June 2015].

Solar, C., 2015. [Online]
Available at: http://www.civicsolar.com/product/tigo-energy-mm-2es50-tyco-st-dual-maximizer-w-tyco-connectors
[Accessed 17 June 2015].

Solar, C., n.d. *Civic Solar*. [Online]
Available at: http://www.civicsolar.com/product/tigo-energy-mu-gtwy-extra-gateway
[Accessed 17 June 2015].

Stuart R. Wenham, M. A. G. M. E. W. a. R. C., 2012. *Applied photovoltaics*. New South Wales: Earthscan.

Tigo Energy, I., 2012. *Tigo energy*. [Online]
Available at: http://www.tigoenergy.com/sites/default/files/attachments/mm-2es_data_sheet_1.12.2015.pdf
[Accessed 5 6 2015].

ESTIMATION OF ELECTRICITY PRODUCTION FOR A PHOTOVOLTAIC PARK USING SPECIALIZED ADVANCED SOFTWARE

[1]Alexandru Diaconu, [1]Dan Crăciunescu, [1,2]Laurentiu Fara, [1,2]Paul Sterian, [3]Cristian Oprea, [1]Silvian Fara

[1]Polytechnic University of Bucharest (Romania)
[2]Academy of Romanian Scientists, Bucharest (Romania)
[3]National Administration of Meteorology, Bucharest (Romania)

Abstract

Modeling and simulation of photovoltaic systems represent an essential task for the integration of photovoltaic panels in current power applications. At the present time, there are sizing tools of photovoltaic systems available on the market, taking into account the proposed energy consumption, site localization and system cost. Many of the specialized programs are relatively simple and allow the user to solve automatically the energy balance calculations, basing on different components of the photovoltaic system.
In this article, there were considered the most common specialized programs namely SAM, SOLARIUS PV and PVSyst; it was analysed the sizing of a photovoltaic system. The results obtained through numerical modeling were compared with the existing data from a photovoltaic park installed in the South of Romania. In this way, it was identified the most efficient program for sizing.

Keywords: *PV system, the Photovoltaic Park, simulation, modeling, software tools*

1. Introduction

In the recent years, the share of the energy produced from renewable energy sources has grown considerably. This kind of energy presents numerous advantages, which lead to the sustainable development of society, but it has a major drawback: it is very fluctuant. This drawback becomes more and more an issue, since the increase in the percentage of total energy production using renewable energy sources could have a negative impact on energy distribution equipment, as well as on the quality of energy.
In the case generated by photovoltaic systems based on small or large photovoltaic power plants, energy quality varies not only in annual cycles (different angles of the incident solar radiation depending on the season), or day-night cycle, but also depends on the spontaneous factors such as clouds, nebulosity, aerosols, etc. For these reasons, the present work proposes a comprehensive study on the most interesting software packages used for simulation and analysis of a photovoltaic system developed for energy purposes and to compare the obtained results in order to identify the most efficient way for estimations and forecasts (Fara, et al., 2009; Sharma, et al., 2014)

2. Presentation and results of the SAM software (Solar Advisory Model)

SAM, called "Solar Advisory Model" was firstly developed (for internal use only) by the National Renewable Energy Laboratory (NREL), in cooperation with the Sandia National Laboratories, in 2005 (https://sam.nrel.gov; Wagner and Gilman, 2011). NREL has released the first public version of SAM in August 2007, in order to be used by solar energy experts for the technical – economical analysis of PV systems. The program allows the performance forecasts and energy estimates for photovoltaic systems, both for grid connected or mixed photovoltaic systems, and stand alone ones, based on the technical and economical parameters to be used as input for analysis.
The aim of the program is to facilitate the decision making for persons involved in the renewable energy industry. It could be used by the project managers, researchers, engineers, financial experts and developers of new technologies (Klise and Stein, 2009; Wagner and Zhu, 2011). SAM makes performance forecasts and estimates the cost of power installations connected to the grid or stand-alone, based on the costs of installing,

doi:10.18086/eurosun.2016.08.18 Available at http://proceedings.ises.org

operating and specific design parameters. National Renewable Energy Laboratory (NREL) distributes the software SAM at: https://sam.nrel.gov. https://sam.nrel.gov/content/sam-publications
Based on this program, it is possible to calculate the electricity output of the PV systems from hour to hour; it can be exploited the performance characteristics of the system by visualization of the hourly and monthly data from the tables and graphs in order to establish the system performance and annual capacity (Wagner 2012; Gilman and Flat 2013). The input data from our study are represented by the main specifications of the Photovoltaic Park sited in the South of Romania (see **Tab. 1**); they are compared with the data obtained from numerical modeling using SAM program. The meteorological parameters interesting for the PV Park's location are: direct irradiance - 1 [kWh/m^2/day], average annual temperature – 11.5 [˚C], average annual wind speed – 3.2 [m/s] and Albedo – 0.2. These parameters were introduced to describe a general view of the site where the PV system is located. The comparative study between the measured data and simulated ones by means of specialized software programs for determination of monthly/yearly electricity production does not take into account the meteorological parameters of the analyzed existing PV Park because the simulation programs have own meteorological data and different models were used for calculation of electricity production; the authors' main objective was to interfere as little as possible in the characteristics of the simulation programs.

Tab. 1: The main specifications of the PV system for the studied PV Park

Installed power	**9934 kW**
PV panel power	245 245 Watt Suntech Power
Total number of panels	40551
Number of panels on string	21
Number of strings	1931
Number of inverters	20 - Green Power PV500
Used area	33 ha

The PV power plant is composed from 1931 strings, each string having 21 Suntech panels of 245W each. Totally there are 40551 PV panels having an installed power of 9934 kW. The solar radiation data are measured done by 2 pyranometers and 10 cells for calibration. The pyranometers are located within the weather station in the PV Park and the cells for calibration are placed at each transformation center. PV panels are made of 72 solar cells based on Si polycrystalline. The I-V characteristics of a PV module is presented in **Fig. 1.** The PV module main parameters are considered for Standard Test Conditions (STC): total irradiance of 1000W/m^2 and cell temperature of 25^{o}C (See **Tab. 2**).

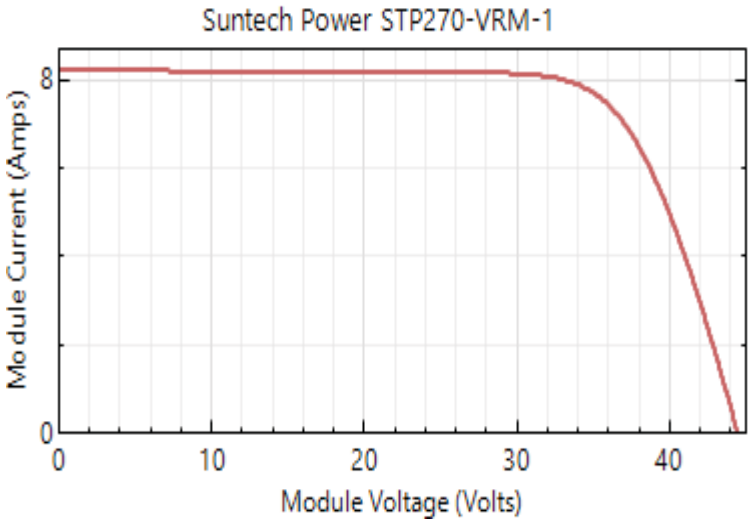

Fig. 1: I-V characteristics of the PV module

The PV system includes, too 20 Green Power inverters of PV500 type (the efficiency curve of an inverter is shown in **Fig. 2**). Each transformation center contains 2 inverters. The inverter main parameters are presented in **Tab. 3.**

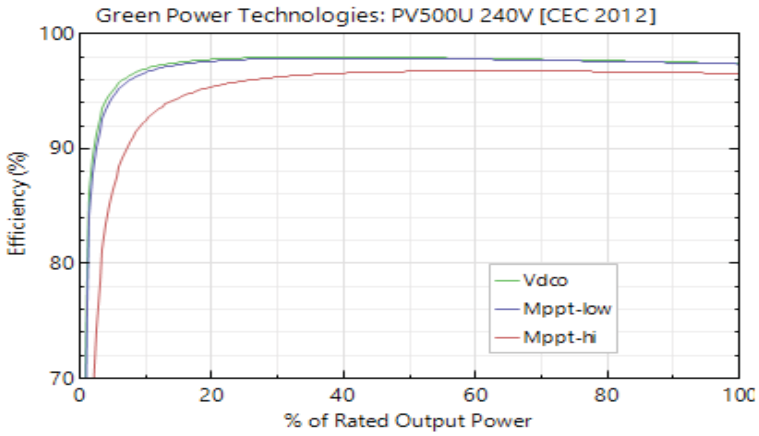

Fig. 2: The PV500 Green Power Inverter Efficiency

Tab. 2: Main parameters for PV module

PV module	
Nominal efficiency	13.9098%
Maximum power	269,850 W dc
Maximum voltage	35 V dc
Maximum current	4.8 A dc
Voltage in open circuit	44.5 V dc
Short-circuit current	8.2 A dc

Tab. 3: Main parameters for inverter

Inverter	
CEC Efficiency	97,733%
EURO Efficiency	97,656%
Max. power output ac	500000W ac
Maximum power dc	513270 W dc
Normal operating power consumption	998,728 W dc
Night operating power consumption	140.4 W ac
Nominal voltage ac	240 V ac
Maximum voltage dc	1000 V dc
Minimum current dc	1250 A dc
Minimum voltage MPPT	425 V dc
Nom. voltage 12v dc	395,616 V dc
Maximum voltage MPPT	825 Vdc

In **Fig. 3** is represented simulated monthly energy production using SAM software. The simulation was carried out over a period of a year; the results are adjusted using an annual degradation coefficient of 0.5% per year.
The losses caused by various factors-both technical, and external ones from the environment of the system location were taken into account. In order to make a comparison between actual and simulated data, the components of the existing PV system and those used in simulation are identical.
In terms of losses arising in the system functionality, the program calculates their estimates based on the existing literature and data on the technical details of the used components. In addition to the technical factors, the program estimates other type of losses that may be due to the environment in which the system is located. All of

these losses are represented in a Sankey diagram, (see **Fig. 4**) and according to this, the user can estimate the future problems and differences between the installed power of the system and the energy actually delivered to the local grid of energy distribution.

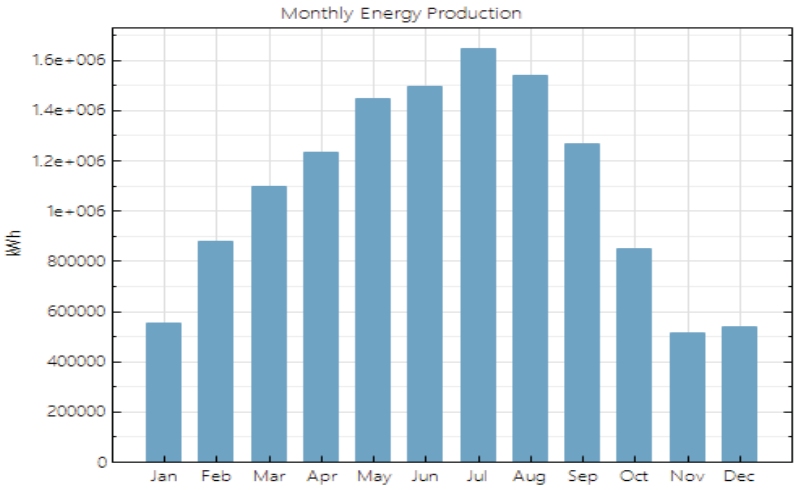

Fig. 3: SAM monthly energy production

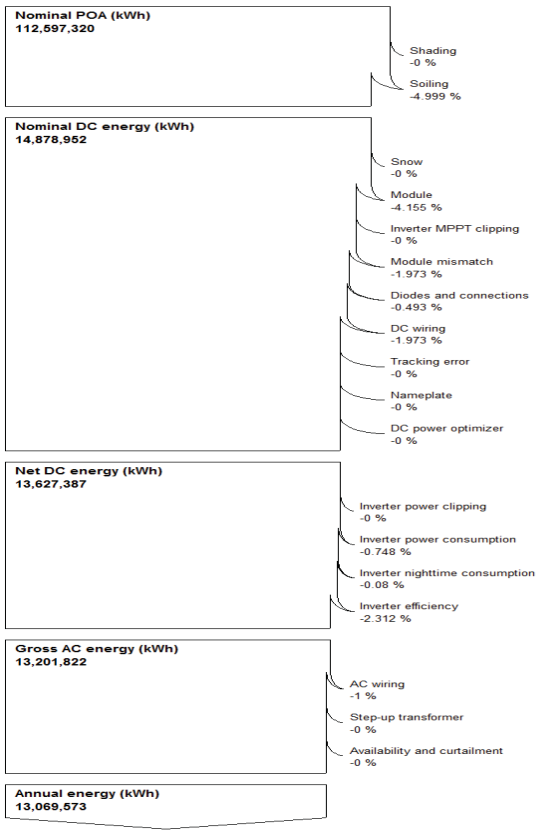

Fig. 4: Sankey diagram for energy losses

In the database relating to the sizing program, the same types of panels, strings, inverters from the studied PV Park have used. We have to mention that the weather data from the SAM software are different from those existing in the database of meteorological station of the PV Park.
The energy to be injected in SEN (National Energy System) based on the SAM software presents an annual difference of 1020 MWh compared with the actual one.

3. Presentation and results of the software SOLARIUS-PV

The program SOLARIUS – PV represents a software package for the design and simulation of energy production for PV systems connected to the grid (http://www.acca.it). It has multiple functions to be fulfilled for a better sizing (ACCA Software, Solarius PV, User's Guide, 2011):

a) **Calculator for estimation of solar irradiance.** The SOLARIUS software guides the user for the sizing process in order to obtain the best technical and financial solutions. The program provides the ability to view real-time possible benefits of changes that the user could enter. For example, the benefits obtained by the optimum changing of the tilt angle for PV panels on a monthly time period of one year, could be remarked
b) **The CAD (computer aided design) input files parameters**
c) **Calculations of the efficiency rate of the PV system.** The SOLARIUS software calculates annual and hourly energy production for a PV system. In this way there is obtained its profitability based on the recovery period that determines the PV system simulated performance (**Fig. 5**). This technical and financial evaluation is simple and fast, the program generating system yields through various charts and tables, easy to understand even for new users.
d) **Analysis of the losses**
e) **Automatic sizing and positioning of the photovoltaic panels**. The SOLARIUS software works in graphic mode to be faster and easier for understanding. The program sizes and automatically places the PV panels on the selected location (roof, fixed mounting systems or solar trackers). The panels to be used in the construction of the system can be selected from an existing archive, which can be updated easily and from which you can extract information about the technical specifications of these panels. Within the framework of appropriate size and location of the PV system, it is possible to sketch the site plan and PV panel location.
f) **Auto - size of the inverters.** The PV systems can be sized by SOLARIUS software, integrating single phase or three phase inverters or inverters based on MPPT (Maximum Power Point Tracking) technology. In order to achieve maximum efficiency, inverters can be chosen from a list of components but, depending on the characteristics of the system, the program can propose the best options to maximize the yield of the inverters.

The reflection capacity of solar energy within the incident surface is characterized by *albedo*. The albedo depends on many factors such as soil nature, its degree of roughness and soil color. In this study the albedo value was considered to be 0.2. The monthly energy production based on SOLARIUS software is shown in **Fig. 5.**

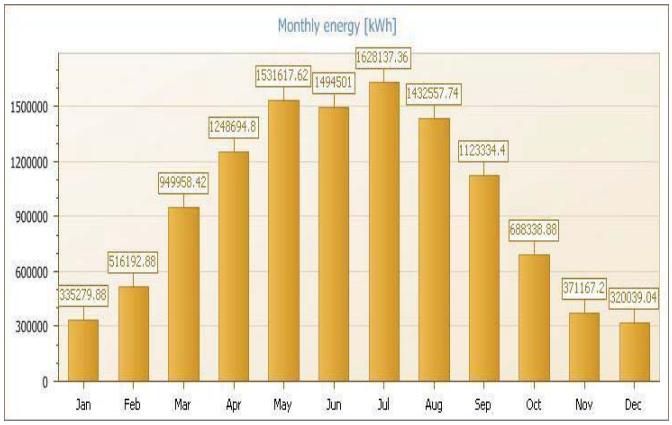

Fig. 5: SOLARIUS – PV monthly energy production

The simulated annual energy to be injected into the SEN is 11639 MWh. The BOS components are identical to those of the existing PV Park. There is a difference of 410 MWh between the simulated values and existing ones. In terms of annual energy production, we conclude that the SOLARIUS software has better results in comparison with the SAM one because the energy production value provided by SOLARIUS is approaching to the value supplied by the PV Park.

4. Presentation and results of the software PVSyst

The PVSyst software is a package intended for study, sizing and data analysis of a photovoltaic system (grid connected or stand-alone PV systems). For analysis, meteorological global database and databases containing detailed specifications of the system components are used. The software holds two expertise technical levels for sizing of a PV system, each level corresponding to different stages in the development of a real system (http://www.pvsyst.com; Chikh et al., 2011).

Preliminary Design - is appropriate to the pre-dimensioning stage. In this level, the PV system performance is assessed using the average monthly values, without detailed specification of the components of the system. For PV systems connected to the grid, in particular for BIPV systems, this level has architectural guidance, requiring information on available space, photovoltaic technology used (color, transparency, etc.), the required power and financial details (Karki et al., 2012; Iftakhar et al., 2012). For stand-alone systems, a sizing of power generated or storage batteries, taking into account the load profile and loss of load probability could be achieved (Irwan et al., 2015).

Project Design – The project aims to carry out a detailed examination using hourly simulations and selection of different specific components of PV system. The program helps the user in sizing the PV system (number of PV modules used and their layout-in series or in parallel); there are considered data related to the inverters, batteries or project needs. On this basis, the PVSyst software is developing monthly energy production (see **Fig. 6**), and losses Sankey diagram (see **Fig. 7**).

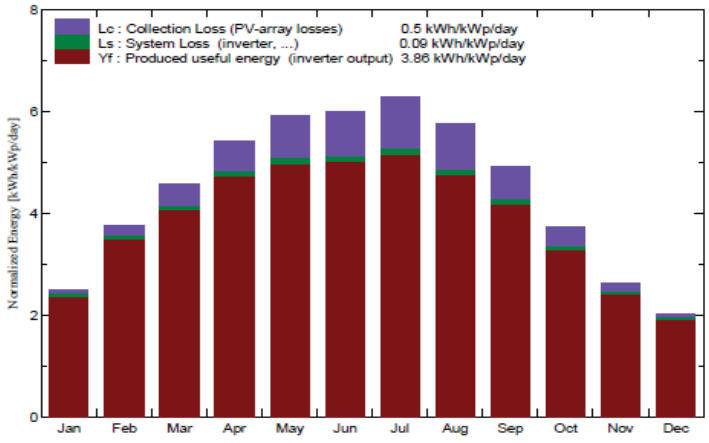

Fig. 6: PVSyst monthly energy production

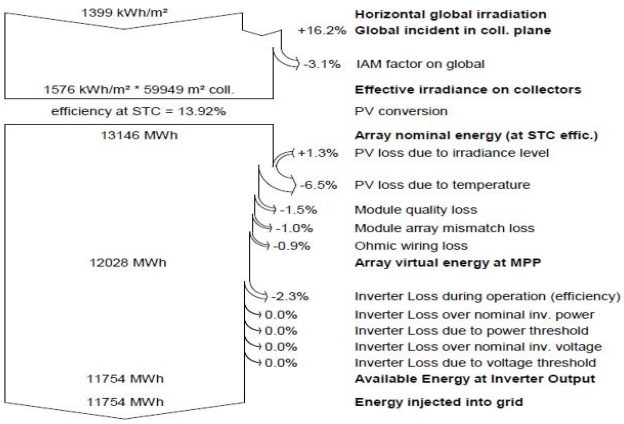

Fig. 7: Sankey diagram for energy losses

There is a difference of 395 MWh between the simulated yearly energy (injected into the SEN) and the real one supplied by the PV Park. This value of 11758 MWh obtained using the PVSyst software is the closest to the value obtained in situ, respectively 12049 MWh, thus the PVSyst software, is the most corresponding for estimation of annually energy production by a PV Park.

5. Analysis of the results

The simulated results using the three software programs: SOLARIUS, SAM and PVSyst were compared with the measured data for the studied PV Park (see **Tab. 4** and **Fig. 8**). There were obtained too, the absolute and relative errors for annual energy production estimation using the analyzed simulation programs, namely: 1) For SAM software the absolute error is 1020 MWh and the relative error is 8.47 %, 2) For SOLARIUS software the absolute error is 409.62 MWh and the relative error is 3.4 %, 3) For PVSyst software the absolute error is 290.80 MWh and the relative error is 2.41 %. According to the obtained results the PVSyst software has the smallest error in comparison with the measured data; it is the most efficient program to be used in the simulation of energy production estimation on long term (annually).

Tab. 4: Monthly/annually energy injected into to the grid: measured data and simulated results by three programs SAM, SOLARIUS and PVSyst

Month / Database	Measured energy production [MWh]	Simulated energy production with SAM [MWh]	Simulated energy production with SOLARIUS [MWh]	Simulated energy production with PVSyst [MWh]
January	347.33	556.07	335.28	613.12
February	585.39	880.84	516.19	816.08
March	1273.83	1095.69	949.96	1049.45
April	1094.03	1235.40	1248.69	1183.21
More	1442.60	1447.85	1531.61	1286.56
June	1422.56	1495.60	1494.50	1254.12
July	1507.23	1646.23	1628.14	1334.63
August	1671.89	1542.12	1432.55	1229.47
September	1197.59	1267.53	1123.33	1044.16
October	922.31	849.48	688.34	849.58
November	217.65	513.89	371.16	605.01
December	367.05	538.76	320.09	493.27
Total annual	**12049**	**13069**	**11639**	**11758**

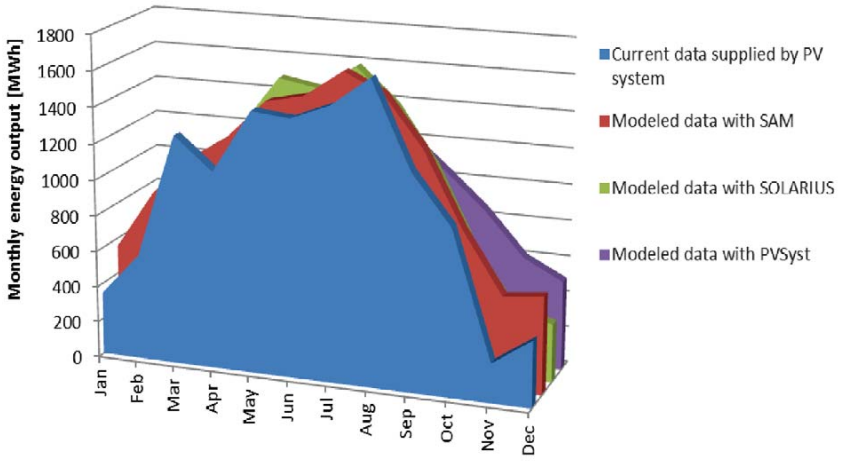

Fig. 8: Monthly energy production related to the analyzed PV Park using three specialized software (SAM, SOLARIUS – PV and PVSyst) compared with the monthly energy production registered by the PV system, all results are obtained within one year (2015)

6. Conclusions

- The comparative analysis shows that for the annual level, the closest results from the measured ones in the analyzed PV Park are based on the PVSyst software.
- The SAM Program could be recommended to optimize the existing PV Park, because it offers the highest annual simulated energy production. A reconditioning of the actual PV Park could be taken into account.
- The programs could not be used for forecasts on short and medium term because the errors are significant in these cases, but on the long term (one year) they would offer an acceptable perspective of the results.

7. References

1. *Fara, L. et al*, 2009, Physics and technology of solar cells and PV systems, Publ. House of Academy of Romanian Scientist
2. *Sharma K. D., Verma V. and Singh A. P.,* 2014, Review and Analysis of Solar Photovoltaic Softwares International Journal of Current Engineering and Technology vol. 4, no. 2
3. https://sam.nrel.gov – System Advisor Model (SAM) National Renewable Energy Laboratory – NREL site accessed as on Feb. 2016
4. *Wagner, M.J.; Gilman, P.,* 2011, Technical Manual for the SAM Physical Trough Model, 124 pp.; NREL Report No. TP-5500-51825
5. *Klise, G. T. and Stein, J. S.,* December 2009, Models used to assess the performance of photovoltaic systems, Sandia report
6. *Wagner, M.J.; Zhu, G.,* 2011, Generic CSP Performance Model for NREL's System Advisor Model: Preprint, 10 pp.; NREL Report No. CP-5500-52473
7. *Wagner, M.* 2012, Results and Comparison from the SAM Linear Fresnel Technology Performance Model: Preprint. NREL Conference Paper CP-5500-54758
8. *Gilman, P.,* Flat P. 2013, PV Module Model: Simple Efficiency Module Model, System Advisor Model Help System
9. http://www.acca.it/ photovoltaic software (Solarius-PV) site accessed as on Feb. 2016
10. ACCA Software. SOLARIUS-PV, User's Guide; ACCA Software: Montella, Italy, 2011.
11. http://www.pvsyst.com - photovoltaic software (PVsyst) site accessed as on Apr. 2016

12. *Chikh M., Mahrane A. and Bouachri F.*, 2011, PVSyst 1.0 sizing and simulation tool for PV systems. Energy Procedia, 6, 75-85
13. *Karki P., Adhikary B. and Sherpa K.,* 2012, Comparative study of grid-tied photovoltaic (PV) system in Kathmandu and Berlin using PVSyst. IEEE ICSET, Nepal.
14. *Iftakhar T.M. Uddin, et al.*, 2012, Computational modeling of a GRID connected system using PVSyst software, International Journal of Scientific & Engineering Research, vol. 3
15. *Irwan Y. M. et al.,* 2015, Stand-Alone Photovoltaic (SAPV) System Assessment using PVSyst Software International Conference on Alternative Energy in Developing Countries and Emerging Economies, Elsevier, vol.79, pp.596-603,
16. *Sterian, P. E.*, 1981, Transmision optical information, Technical Publ. House, Romania
17. *Sterian, P. E.*, 2000, Photonics, Printech, Publ. House, Romania,
18. *Sterian P. E., Toma C.*, 2000, Methods for presenting key concepts in Physics for MS students by Photon-MD Program", Bulgarian Journal of Physics; 27(4):27-30
19. *Sterian A., Sterian P. E.*, 2012, Mathematical Models of Dissipative Systems in Quantum Engineering, Mathematical Problems in Engineering, vol. 2012, Article ID 347674, 12 pages, doi:10.1155/2012/347674

Conference Proceedings

EuroSun 2016
Palma de Mallorca (Spain), 11 - 14 October 2016

Characteristics Experimental of A Photovoltaic Module in Tropical Climate

Dani Rusirawan[1], Liman Hartawan[1], Andi Juhaeri[1] and Istvan Farkas[2]

[1] Department of Mechanical Engineering, Institut Teknologi Nasional (ITENAS) Bandung Jl. PKHH. Mustapa No. 23 Bandung 40124, West Java (Indonesia)

[2] Department of Physics and Proces Control, Szent Istvan University

Pater K. u. 1., Godollo, H-2100 (Hungary)

Abstract

In the photovoltaic (PV) system, relations between current, voltage and power generated by system can be illustrated by photovoltaic characteristics, and it can be developed experimentally and/or theoretically. In this work, characterization of a PV module in Bandung – Indonesia, as one of tropical climates area, will be shown based on experimentals. Our works were carried out using a Laboratory scale PV system. Three sub systems, i.e. a PV module, measuring instruments and data acquisition, and PC for the monitoring system, were identified and determined. An Electrical Solar Module (ESM) of 50 Wp was used as the object. As an output of this work, characterization of a PV module in a tropical climate, represented by current-voltage-power relation will be shown.

Keywords: *current, voltage, power, experimental test, laboratory scale.*

1. Introduction

Presently, research in the photovoltaic (PV) field becomes interesting topic for many institutions, universities and companies, as a response to the crisis of energy and environmental problem all over the world.

Testing through experiments, modelling through numerical method or simulation using software package are typical to quantify the physical phenomenon. Testing and modelling of a PV system performance are very complicated and influenced by a variety of interactive factors related to the environment (temperature and irradiance), besides to solar cell physics (Rusirawan and Farkas, 2014).

In designing power generation system that incorporates PV modules, there is a basic requirement to accurately estimate outputs from the proposed PV system under a particular operating condition. PV modules are given a power rating at standard test conditions (STC) of 1000 Wm^{-2}, AM 1.5 and a module temperature of 25 ^{o}C, but these conditions do not represent what are typically experienced outdoor (Carr and Pryor, 2004).

A PV system (cell/module/panel/array) naturally exhibits non-linear *I-V* (current – voltage) and *P-V* (power – voltage) characteristics which vary with the radiant intensity and PV cell temperature (Tsai et al., 2008).

Referring to the state of arts of PV modules technology, currently, proven technologies in the commercial market are crystalline technology and thin film technology. From the PV module performance point of view, the eficiency of thin film technology is lower than crystalline technolgy. Nevertheless, an additional issue is the lower energy consumption for the production of thin film technology and consequently a shorter energy payback time for these technology. One should bear in mind that the total energy payback time for a given PV module does not only depend on the solar cell used, but also on the module design, e.g. framed module, glass/glass, metal foil, EVA, etc. The general features of commercial wafer based crystalline silicon and thin film are presented in the working material of Greenrhinoenergy (2012).

In this work, characterizations (*I-V-P*) of a PV module by experiments will be shown for some operating condition (solar irradiance and module temperature) in Bandung – Indonesia condition, as one of tropical/hot climate regions. As the first, characterizations of crystalline technology of PV module is performed.

doi:10.18086/eurosun.2016.08.02 Available at http://proceedings.ises.org

In the near future, characterization of thin film technology will be performed as well, therefore a comparison of two PV technologies between crystalline technology (mono and/or poly crystalline silicon) and thin film technology (amorphous silicon) can be performed.

As an outcome of this work, all required informations, especially related to characteristics of different types of PV modules technology can be acquired. Based on this outcome, a depth consideration in order to choose a type of PV module can be defined by countries in tropical region, as a response to the controversy in selecting the proper PV modules, based on their climates.

2. System Description and Methods

The photovoltaic module experiments apparatus is shown in Fig. 1 and the schematic diagram for photovoltaic module experiments along with the measuring features can be seen in Fig. 2.

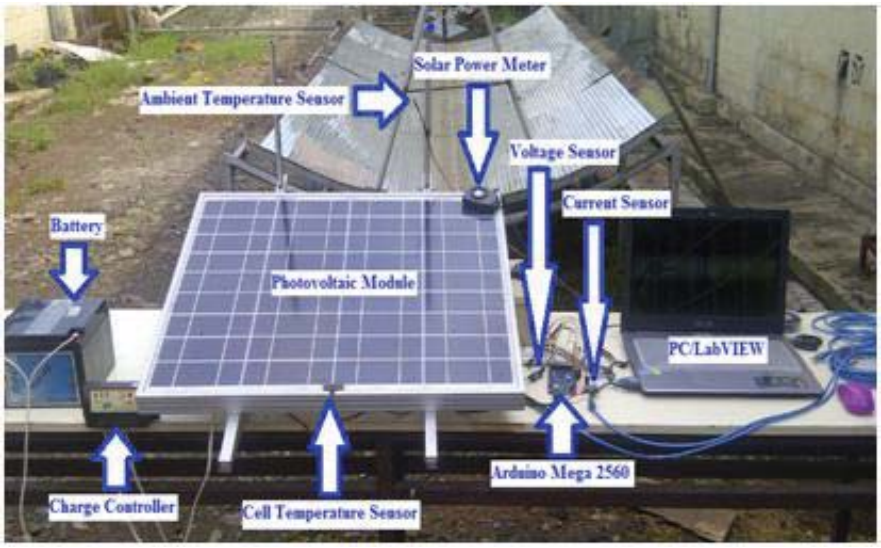

Fig. 1: The PV module experiment test

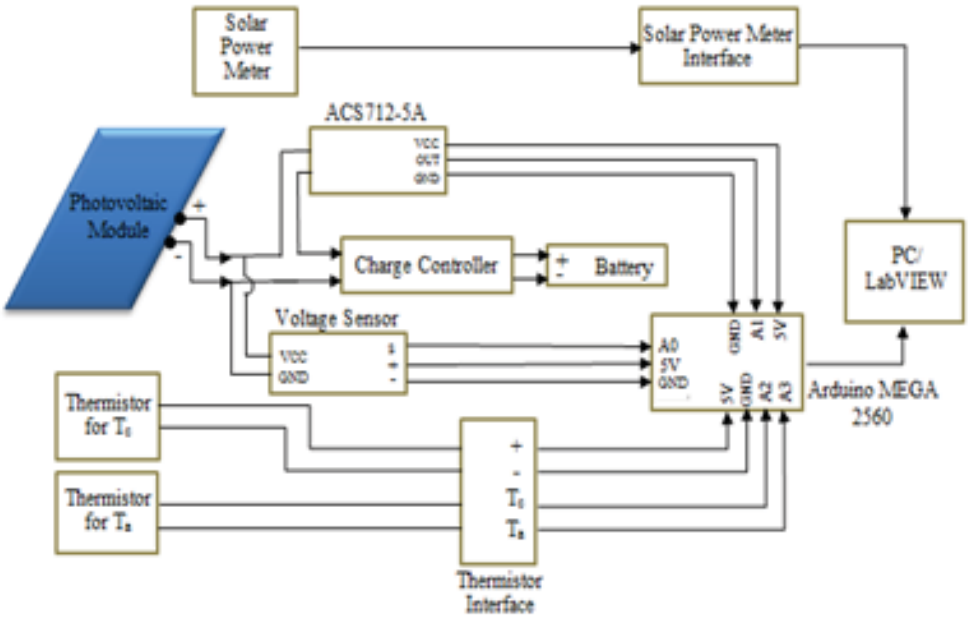

Fig. 2: Experimental test schematic diagram

The location for experiments is Bandung, West Java-Indonesia, with latitude 06°54'S and longitude 107°36'E. The type of the PV module in this research is ESM (Electrical Solar Module) 50 Wp with the optimum operation voltage 17.2 V and optimum current operation 2.91 A. The data acquisition system is Arduino

MEGA 2560 with LABVIEW Programming, and the sensors for: voltage, current and temperature are VCC<25V, ACSC712-5A, thermistor 10 kOhm, respectively. The system is equipped by solar power meter and its sensor.

Additionally, two LED lamps (with the same specification: 12 V and 3.5 W) are provided as an external load.

The specifications of all component used in the experimental test are shown in Figs 3-8.

Fig. 3: ESM PV module and Its specification

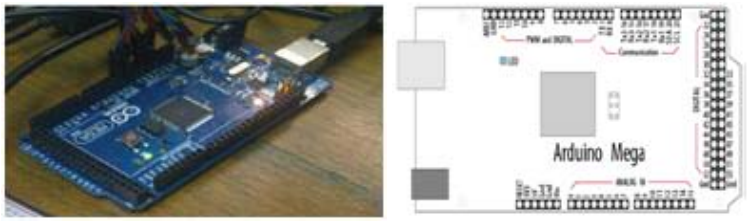

ATmega2560 microcontroller
54 Digital I/O Pins (14 PWM outputs)
256k Flash Memory

Input voltage – 7-12V
16 Analog Inputs
16Mhz Clock Speed

Fig. 4: Arduino mega 2560

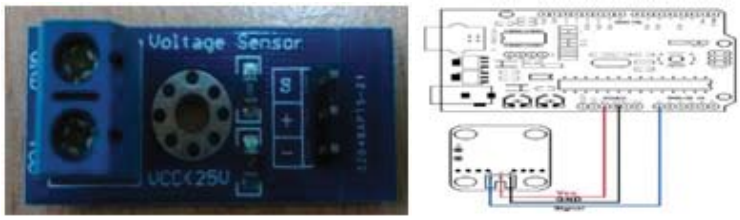

Fig. 5: Voltage censor and conection diagram to arduino

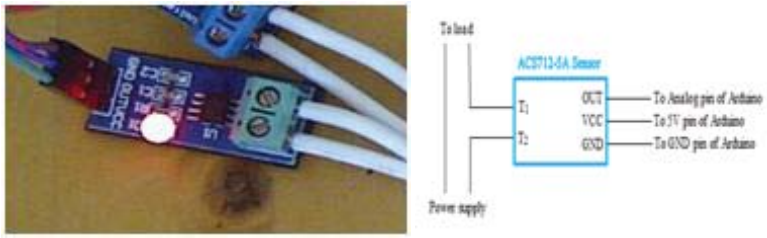

Fig. 6: Current sensor and connection diagram to arduino

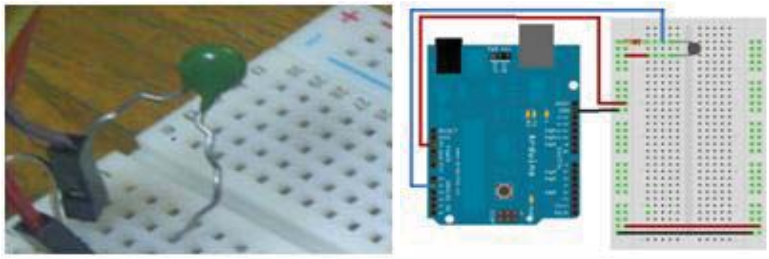

Fig. 7: Temperature sensor and connection diagram to arduino

Fig. 8: Solar power meter

Results

The PV module experimental system was installed in the ITENAS campus area in Bandung. The data acquisition was performed during 1 day experiments, January 16, 2016, from 09:00 a.m. to 05:00 p.m. The input – output parameters and the principle of measurement can be seen in Figs 9 and 10.

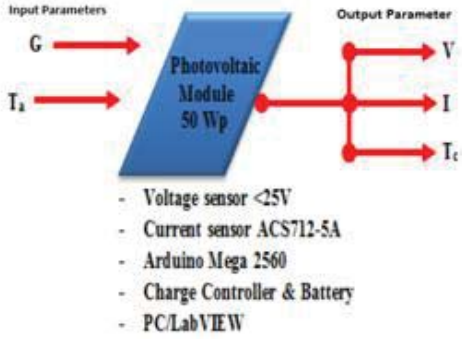

G : Global irradiance ($W.m^{-2}$)

T_a : Ambient temperature (^oC)

V : Voltage (Volt)

I : Current (Ampere)

T_c : Cell temperature (^oC)

Fig. 9: Input – output parameters

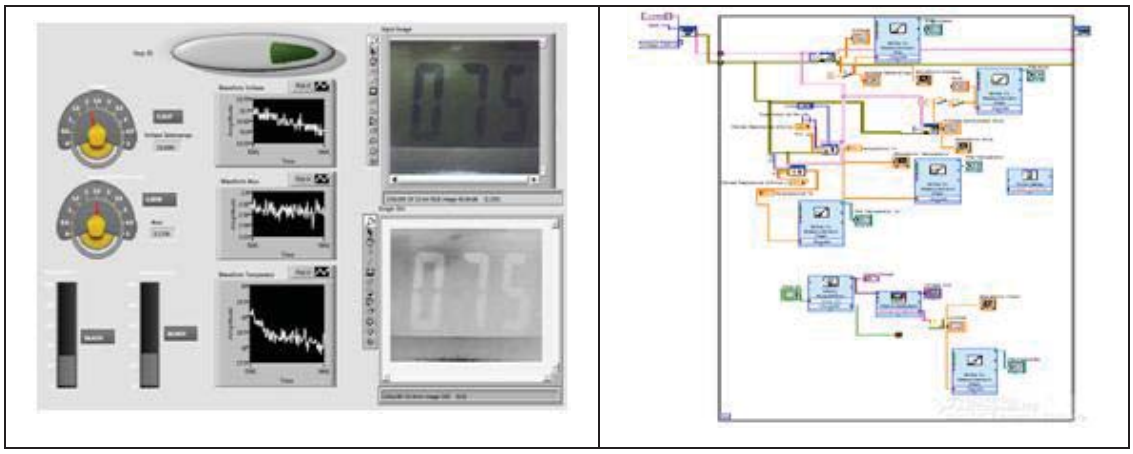

Fig. 10: Data acquisition method and block diagram

Input parameters, G, T_a and output parameters I, V, P and T_c recorded. All parameters data was taken every 3 minutes, for 8 hours (09:00-17:00), except solar irradiance data. The solar irradiance data was taken manually every hour, because the signal from solar power meter could not be processed by Lab VIEW. Figs 11-13 show the relationship between *I-V-P* data based on the experiments.The average of all data at each hour is summarized in Table 1.

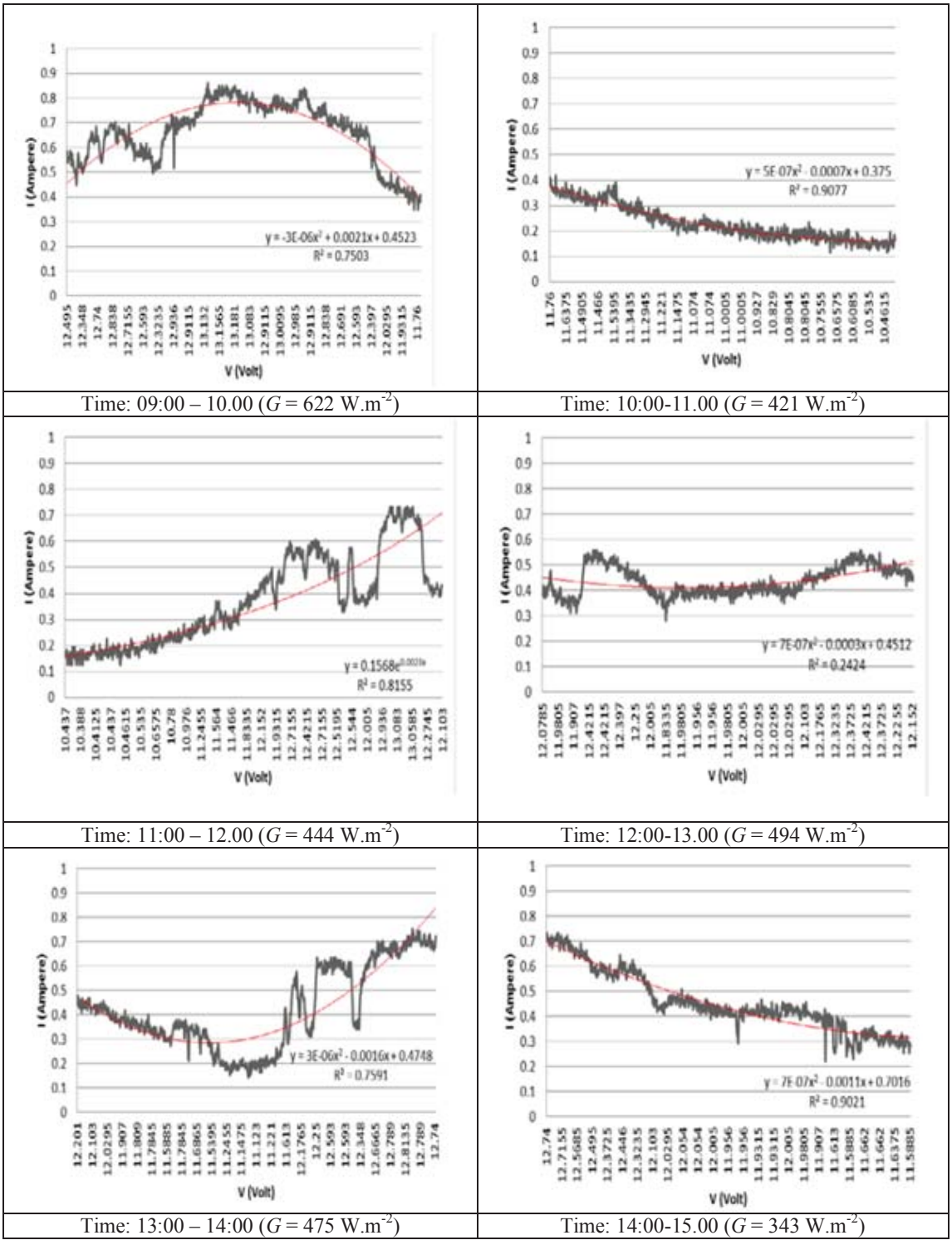

Time: 09:00 – 10.00 (G = 622 W.m^{-2})	Time: 10:00-11.00 (G = 421 W.m^{-2})
Time: 11:00 – 12.00 (G = 444 W.m^{-2})	Time: 12:00-13.00 (G = 494 W.m^{-2})
Time: 13:00 – 14:00 (G = 475 W.m^{-2})	Time: 14:00-15.00 (G = 343 W.m^{-2})

Fig. 11: *I-V* Data in interval time 09:00-15:00

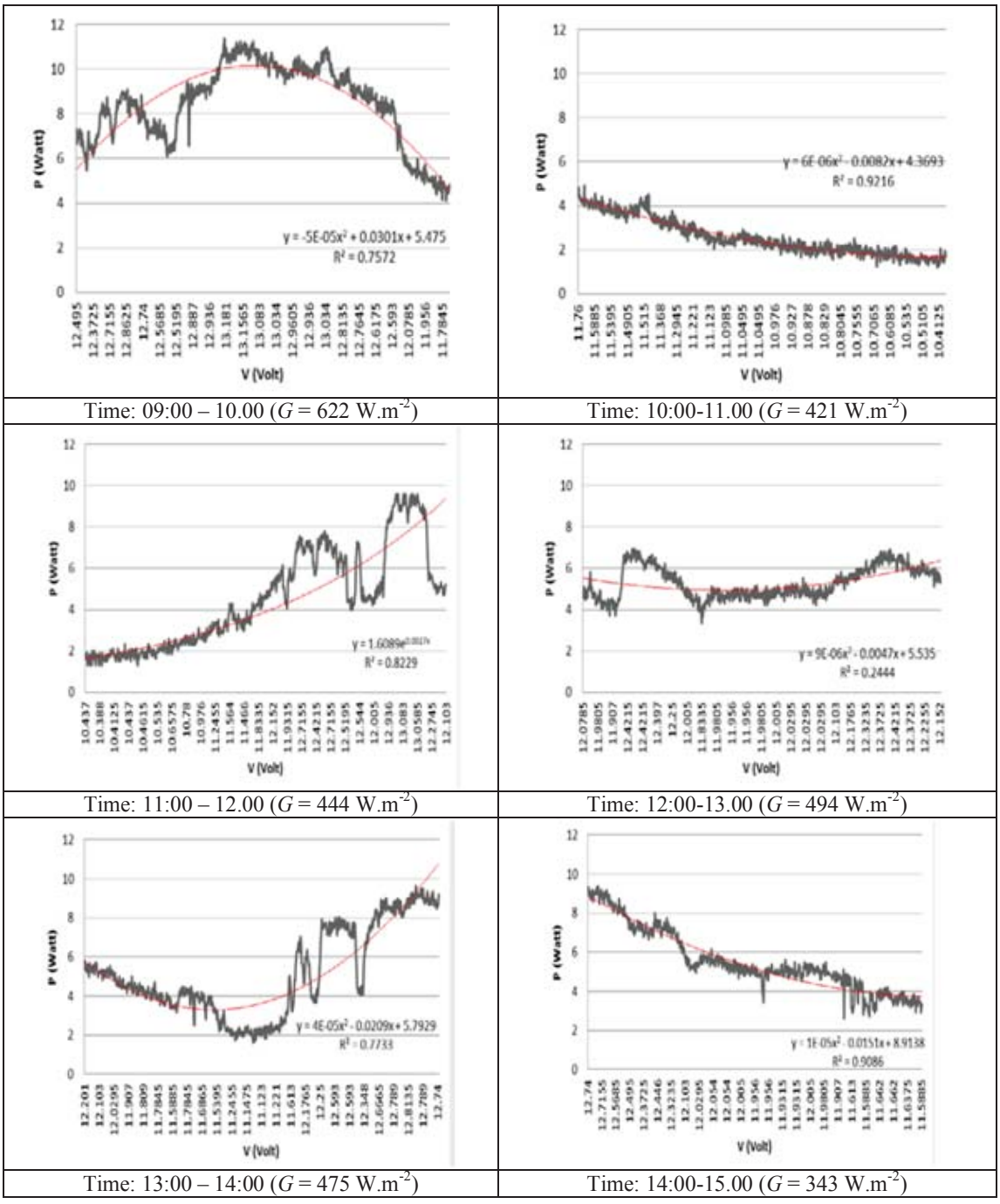

Time: 09:00 – 10.00 (G = 622 W.m^{-2}) | Time: 10:00-11.00 (G = 421 W.m^{-2})

Time: 11:00 – 12.00 (G = 444 W.m^{-2}) | Time: 12:00-13.00 (G = 494 W.m^{-2})

Time: 13:00 – 14:00 (G = 475 W.m^{-2}) | Time: 14:00-15.00 (G = 343 W.m^{-2})

Fig. 12: *P-V* Data in interval time 09:00-15:00

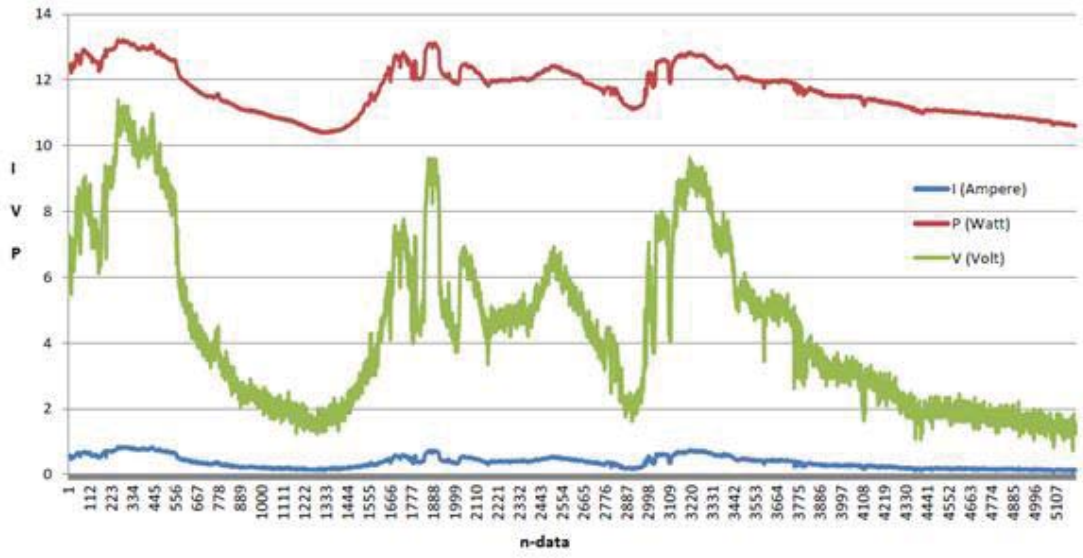

Fig. 13: *I-V-P* Data in interval time 09:00-15:00

Table 1: Experiment Results at 09.00-17.00 in Western Indonesian Time

Time	G (W/m^2)	T_a (^{o}C)	T_c (^{o}C)	V (Volt)	I (Ampere)	P (Watt)
09:00-10:00	622	33.72645	44.62749	12.7001	0.6634	8.42525
10:00-11:00	421	30.37906	35.66878	11.5366	0.2316	2.67188
11:00-12:00	444	31.10322	36.99411	11.6797	0.3731	4.35769
12:00-13:00	494	32.22211	39.10253	12.1597	0.4429	5.38553
13:00-14:00	475	32.14042	38.8852	11.9814	0.4246	5.08731
14:00-15:00	343	29.73048	35.10191	11.3350	0.1917	2.17292
15:00-16:00	295	29.06154	33.90926	11.2879	0.1624	1.83315
16:00-17:00	242	28.85283	31.60192	10.8493	0.1542	1.66729

3. Conclusions

A progress on characterization of a PV module in tropical climate is reported in this paper. The PV module observed was polycrystalline and the type was ESM (Electrical Solar Module) 50 Wp. In this preliminary experiments, characterization of the PV module was performed in the real Bandung weather condition in one day, for 8 hours. It is found that current, voltage and power of PV module is influenced by the fluctuation of temperature and solar irradiance. Conducting to main purpose, in the future work, characterization of PV modules based on thin film technology will also be performed.

4. Acknowledgement

This research is carried out with the support of the Research Institution Itenas and the Ministry of National Education of the Republic Indonesia under contract No. 146/B.05/LPPM-Itenas/VI/2016.

5. References

Carr, A.J., Pryor, T.L., 2004. A comparison of the performance of different PV module types in temperate climates, Solar Energy. 76, pp. 285–294.

Greenrhinoenergy. Solar Power – Technologies, PV cells and modules, on line at: www.greenrhinoenergy.com/solar/technologies/pv_modules.php, accessed on December 19, 2012.

Rusirawan, D., Farkas, I., 2014. Identification of model parameters of the photovoltaic solar cells. Energy Procedia. 57, pp. 39-46.

Rusirawan, D. and Farkas, I., 2014. Photovoltaic technology characteristics in hot weather conditions, Energy and the Environment, /ed. by B. Frankovic/, Croatian Solar Energy Association, Opatija, Croatia, October 21-24, 2014. pp. 151-157.

Tsai, H.L., Tu, C.S., Su, Y.J.: Development of generalized photovoltaic model using Matlab/simulink, Proceeding of the World Congress on Engineering and Computer Science (WCECS) October 22 – 24, 2008, San Fransisco, USA, 2008, 846-851.

Online at: http://www.iaeng.org/publication/WCECS2008/WCECS2008_pp846-851.pdf, accessed on September 25, 2016.

Conference Proceedings

EuroSun 2016
Palma de Mallorca (Spain), 11 - 14 October 2016

Performance Evaluation and Trial Making of a Compact Solar EV

Toru Fujisawa[1] and Takashi Kawaguchi[1]

[1] Kanagawa Institute of Technology, Atsugi (Japan)

Abstract

In this study, we built a compact solar electric vehicle (EV) converted from a Honda Gyro Canopy, which is a three wheel scooter widely used in Japan for delivery services, and installed bifacial c-Si PV modules on the surface of its delivery box. The power generated from the photovoltaic (PV) modules was controlled using a quad peak power tracker (PPT) system in the solar EV. In this paper, we discuss three types of PPT systems that can maximize the charging power from PV modules to the four valve-regulated lead-acid storage batteries. Moreover, we evaluated the energetic performance of the solar EV running on a Li-ion storage battery of 5 kg. The outdoor experiments clearly showed that four series–parallel PPT systems produce better electrical energy than the other systems. The average energy consumption by the solar EV circling a building on a flat asphalt pavement road was 1.06 kW at an average speed of 15.9 km/h (peak speed was 25.1 km/h).

Keywords: *Solar EV, EV conversion, PV system, bifacial c-Si, multiple peak power tracker.*

1. Introduction

In 2015, the number of Honda Gyro (GYRO) Canopy vehicles manufactured in Japan was over 240,000 (Honda Gyro, 2015). The GYRO is a three-wheel scooter, popular for delivery services in Japan, and has an engine displacement of under 50 cc.

Fig. 1 shows a solar electric vehicle (EV) converted from the GYRO Canopy with bifacial c-Si photovoltaic (PV) modules on its delivery box. The powertrain of the solar EV is a surface-mounted permanent magnet synchronous motor (SPMSM; outer rotor type, with 12 poles, 18 teeth, and 6 coils in parallel with a Y connection, as indicated in Table 1), as shown in Fig. 2. Its reduction gear ratio was 29.86 after the conversion.

Fig. 1: Solar EV (EV conversion of HONDA GYRO CANOPY)

Fig. 2: SPMSM

doi:10.18086/eurosun.2016.08.05 Available at http://proceedings.ises.org

Tab. 1: Specification of the blushless DC motor.

Item	Value
Core diameter	94.7 mm
Core thickness	27.0 mm
Air gap	0.85 mm
Permanent magnet	FB6B (Br = 420 mT)
Slot／Pole	18／12
Turns of 1 slot	25 turns
Wire type	Polyester enamel wire
Wire diameter	1.0 mm
Winding and Connection	3 phase 6 parallel, Y connection

2. PV system

2.1. PV cell and PV module

Fig. 3 shows the unit cell of bifacial c-Si PV produced by bSolar (2012) comprising a cut cell, laminated cell layout, and weight of the module. The laminated modules are installed on four surfaces (top, back, left, and right) of the delivery box. Table 2 lists the ratings as typical values of bifacial c-Si PV module under the standard test condition (STC) of 1kW/m^2, A.M.1.5, and 25 °C.

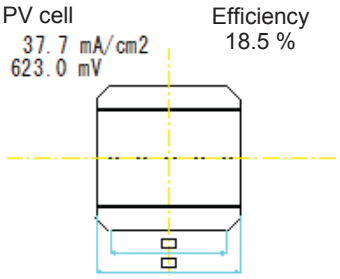

(a) 156 × 156 mm cell

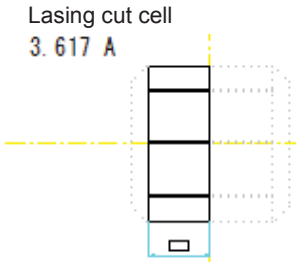

(b) 156 × 61.5 mm cut cell

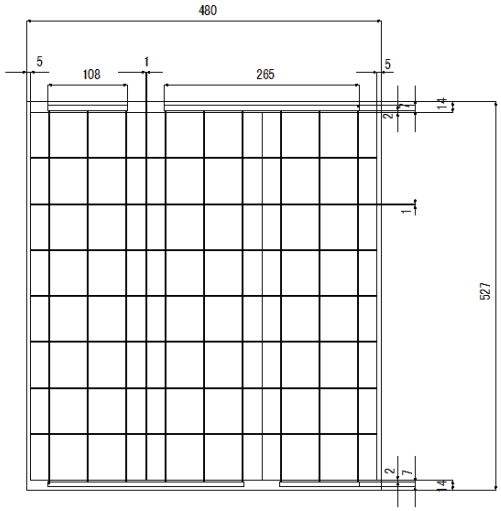

(c) Laminated PV module made from the cut cell (24 cell types)

(d) Weight of laminated module (approx. 0.5 kg for a 24-cell module)

Fig. 3: Laminated PV module of bifacial c-Si

Tab. 2: Ratings of bifacial c-Si PV module (Typical value for 24 cells)

surface	Voc [V]	Isc [A]	Vmax [V]	Imax [A]	Pmax [W]	FF [-]
Primary	14.50	3.52	11.74	3.31	38.87	0.76
Secondary	14.36	2.82	11.77	2.67	31.41	0.78

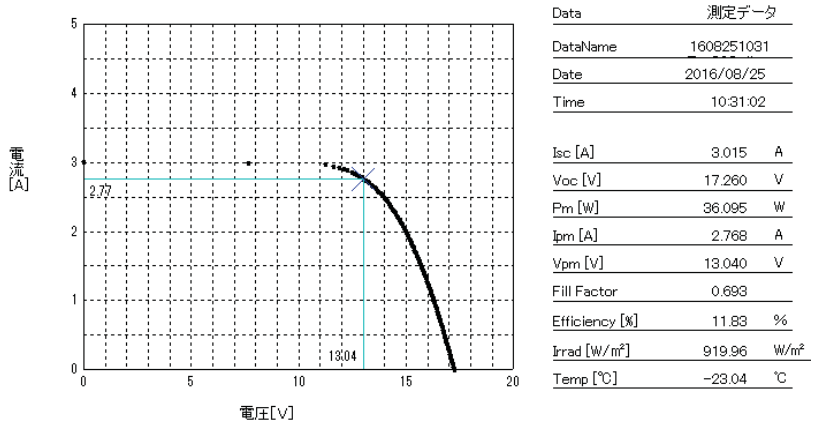

Fig. 4: I–V characteristic curve of the top 32 cells obtained from outdoor experiments (25th AUG, 2016; 10:31)

Fig. 4 illustrates the I–V characteristic curve of the 32-cells PV module on the top surface of the delivery box. A temperature sensor was not connected, and the PV module is second hand. However, a smooth curve and a peak power current of 2.8 A were obtained in outdoor (with reduced irradiance and increased temperature).

2.2. PV system (Peak Power Tracker)

On the delivery box, PV modules on the top surface consist of 32 cells, and the other three vertical surfaces (back, left, and right surfaces) have 24 cells each. We used four boost dc–dc type peak power trackers (PPTs; of one-chip and an efficiency of up to 98%, as developed by STMicroelectronics, 2012) for those PV modules (Fig. 5). A distributed PPT in stationary PV array, evaluation and introduction has discussed by Youhei et al. (2013). Takanori et al. demonstrated a distributed PPT on a racing solar car (2014). To evaluate a multiple PPT system, we tested three connections (Fig. 6). In addition, a series PPT system and series–parallel PPT system were compared through outdoor experiments at the north parking (as shown in Fig. 6). The series–parallel system consists of a pair of parallel PPTs in series with other PPTs; this arrangement is aimed at recovering lower power of the PV module by adding current to the left, right, back, and top of the delivery box.

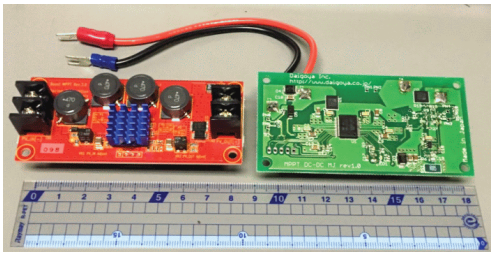

Fig. 5: Boost-type peak power tracker (SPV1020)

3. Outdoor experiments

3.1. Trial experiment of PV power generation

Fig. 7 and Table 3 show some results of outdoor experiments of the series and series–parallel PPT systems. For these experiments, the solar EV was tested at the north parking with the PV module of its back side facing the south; the measuring period was 10:30–15:30 (logging data by every 10 s). As indicated in Fig. 7 and Table 3, every output power was kept low in the trial experiments because few protection settings in the PPT circuit board, such as the input voltage, output current, and output voltage, were not suitable. Thus, the PV module's current was limited to less than 0.3 A based on the PPT settings. However, every PPT system can function for

different surfaces and irradiance conditions. In Table 3 and Fig. 7, the measured powers are normalized based on the top surface's PV module.

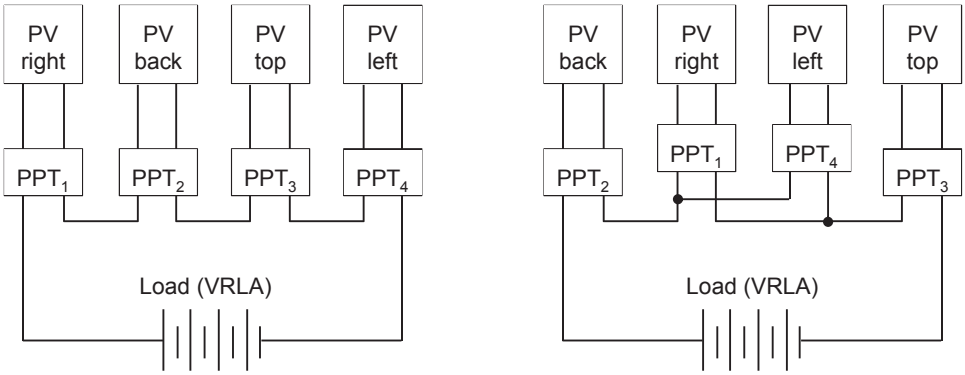

(a) Series **(b) Series–Parallel (Left//Right)**

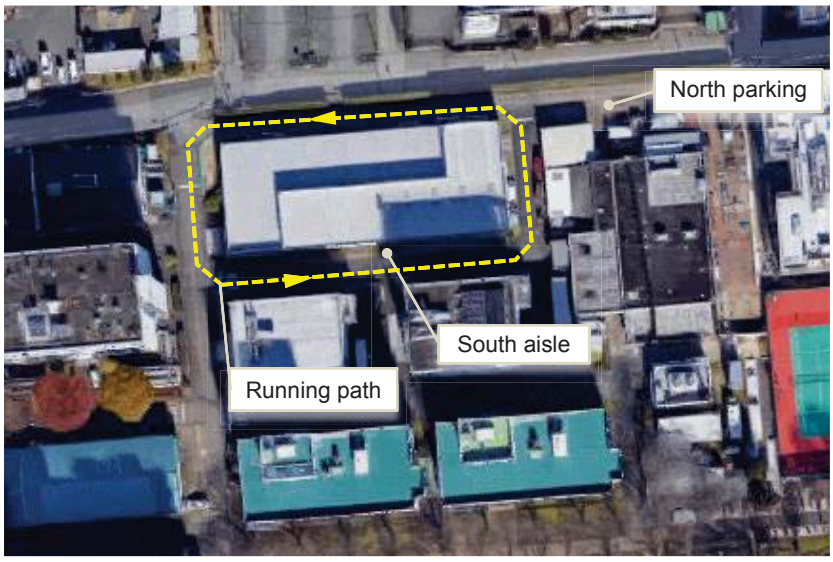

(c) Experimental location

Fig. 6: Different connections of the multiple PPT system

Tab. 3: Results of outdoor experiments at the north parking in winter from 10:30 to 15:30. (PPT outputs were limited because of the PV voltage setting)

Averaged values	Series PPT system on 9th DEC	Series–Parallel PPT system	
		Left//Right on 18th DEC	Top//back on 22nd DEC
Horizontal irradiance	377.4 W/m^2	389.9 W/m^2	344.3 W/m^2
PPT input power from the top PV	1.00	1.00	1.00
PPT input power from the left side PV	0.62	0.50	0.81
PPT input power from the right side PV	0.28	0.30	0.65
PPT input power from the back side PV	0.62	0.69	0.37
Output power of the four PV modules	2.61	2.48	2.83

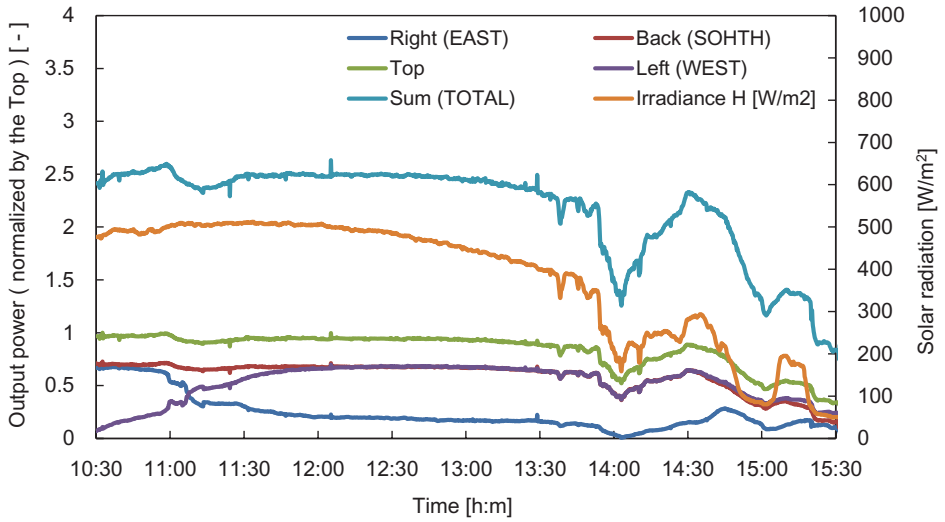

Fig. 7: Output power of PV modules on Dec 9, 2015 (Series PPT system)

3.2. Battery charging data in summer

To fix the setting problem mentioned earlier, actual charging was tested for various connections by means of the summer sunlight at the south aisle (Fig. 6). Four valve-regulated lead-acid (VRLA) batteries of 12 V/27 Ah (5 h) were connected to the PPT output as system load. Fig. 8 shows a series PPT system, in which the east PPT underwent the through-mode from the beginning, the west PPT underwent the through-mode at noon. And after 15:00, when the shadows from surrounding buildings appear on the east and south PV, at around 15:30, the overall output power decreases rapidly because of the presence of the shadows of the surrounding buildings. Fig. 9 shows the result of the series–parallel PPT system. The west and east PPTs were connected in parallel; thus, the output currents for both are confluent with those of the top and south PPT. Except after 15:00, no PPTs underwent the through-mode.

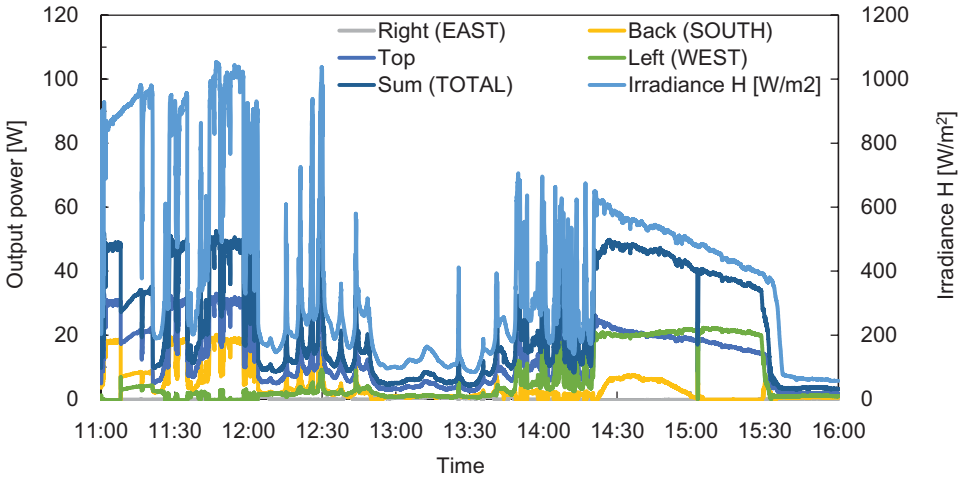

Fig. 8: Output power of PV on Sep 27, 2016 (four series PPTs for four VRLA systems)

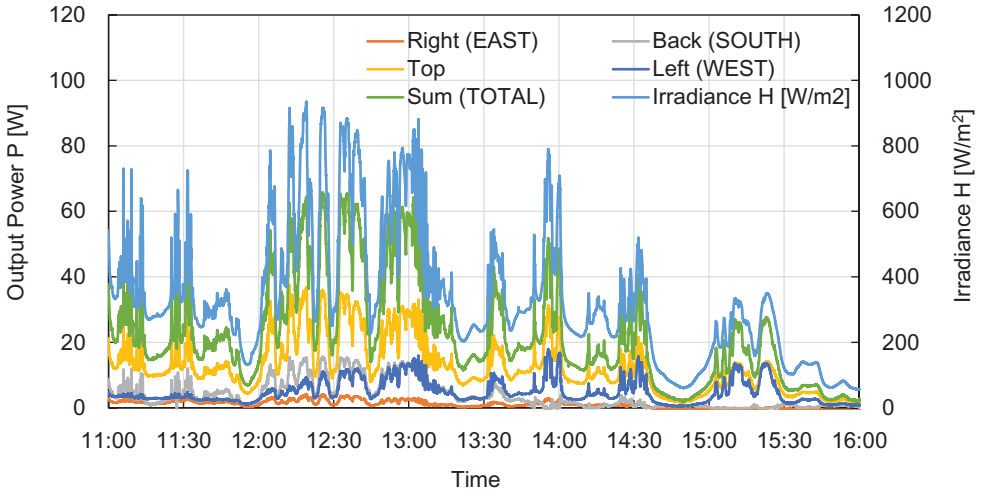

Fig. 9: Output power of PV modules in Sep 26, 2016 (Series–Parallel PPT system)

3.3. Irradiance on vertical surfaces

The output power is proportional to the PV current, which is proportional to the irradiance. Therefore, we must determine how to utilize the irradiance on three vertical surfaces. Different azimuth angles of the vertical surface imply an increase in the peak-time difference. In a calculation, it seems easy to add solar irradiance at different angles; however, in an actual system, it is difficult to collect the generated power through simple summation. This is because a low power implies low voltage output of a PPT in a system, and the load voltage is much higher than that of PV modules.

$$P \propto I_{SC} \quad \text{(eq. 1)}$$

$$I_{SC} \propto Irr \quad \text{(eq. 2)}$$

$$E = \sum Irr \quad \text{(eq. 3)}$$

$$k = \frac{E_{Hrzn}}{E_{ESW}} \quad \text{(eq. 4)}$$

where P (W) is the output power of the PV module, I_{SC} (A) is the short-circuit current of the PV module, Irr (W m^{-2}) is the solar irradiance onto the PV module, E (W m^{-2}) is the summation of the irradiance on different angled surfaces, and k is the imbalance ratio between horizontal irradiance and three vertical surfaces.

Fig. 10 shows the hourly output data of solar irradiance from METPV-11 as a standard meteorological data in Japan released by NEDO/JMA (2016). The figure shows the mean data of a clear day near the university (distance is less than 10 km) in Ebina city, with an irradiance from four directions. Yoshio (2016) recently showed energy utilization in four directions in an architectural study. To utilize a vertical surface efficiently, irradiance on the three walls can be added for collecting PV module's current in the East, South, and West (ESW) directions. As indicated in Fig. 10(b), ESW can function accurately with respect to the horizontal surface. Especially, within few hours before or after noon, the imbalance ratio of irradiance between the horizon and ESW surfaces is less than two.

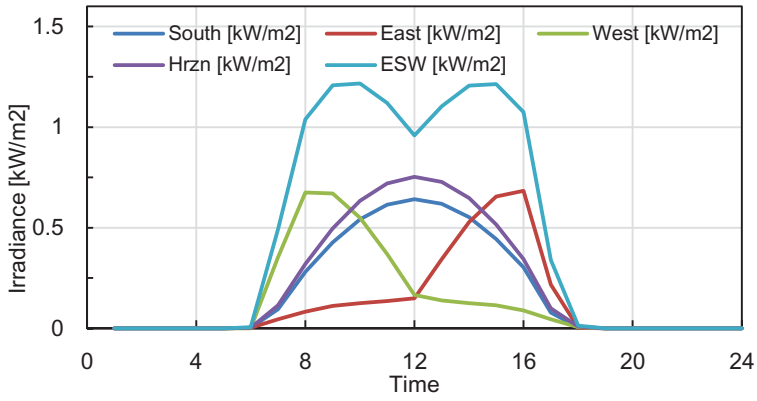

(a) Irradiance

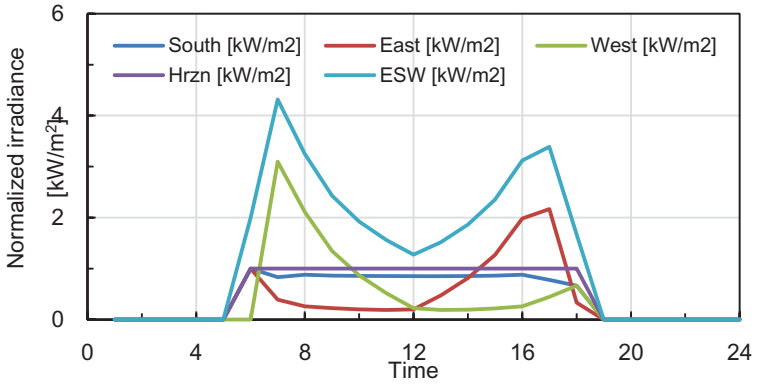

(b) Normalized Irradiance (Imbalance ratio)

Fig. 10: Meteorological data for 25th September in Ebina city (N35°26.0, E139°23.2/METPV)

When imbalance ratio is smaller, other combination circuitries of the multiple PPT system are also possible (Figs. 11 and 12). PV modules on the three vertical surfaces are connected to a single PPT in parallel. Further, for the PV module on the delivery box's top surface, another PPT is connected to the PPT in series or parallel.

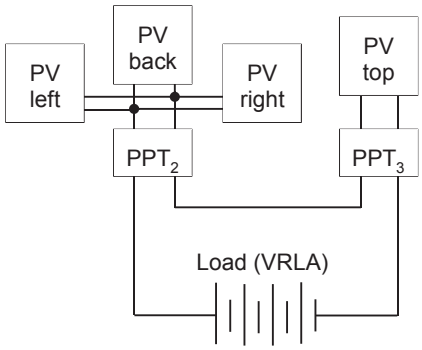

Fig. 11: Series PPT system for collecting individual current (three vertical PV modules are connected in parallel to one PPT, and another PPT is connected at the top surface)

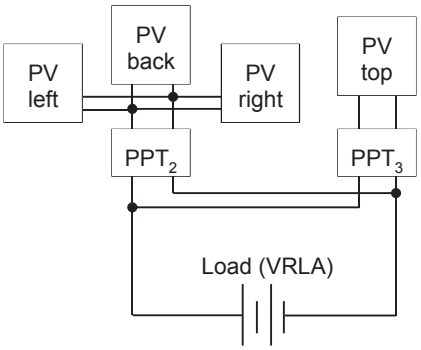

Fig. 12: Parallel PPT system to collect individual current (three vertical PV modules are connected in parallel to one PPT, and another PPT is connected at the top surface)

Fig. 13 shows the charging results of a 2-series PPT system on a fine summer day. In the figure, the load comprises four VRLA batteries in series. As shown, the system does not work well even though enough irradiance was present. The PPT output was less than 0.5 A and the boost voltage was imbalanced; thus, the PV modules were unable to operate at the peak power point. The averaged output power was 25.1 W for 5 h. Fig. 14 shows the charging results of a 2-parallel PPT system on a clear summer day; the load comprises four VRLA batteries: two units in series and two units in parallel. As shown, the output power was unstable from 11:00 to 11:10; however, this fluctuation was due to the opening of the back hatch of the delivery box. From 11:10 to 16:10, the PV system of the solar EV generated 51.1 W on an average. It was found that a 180-min

PV charge produces 150 Wh (= 540 kJ) of electrical energy into the load battery even when the irradiance decreased.

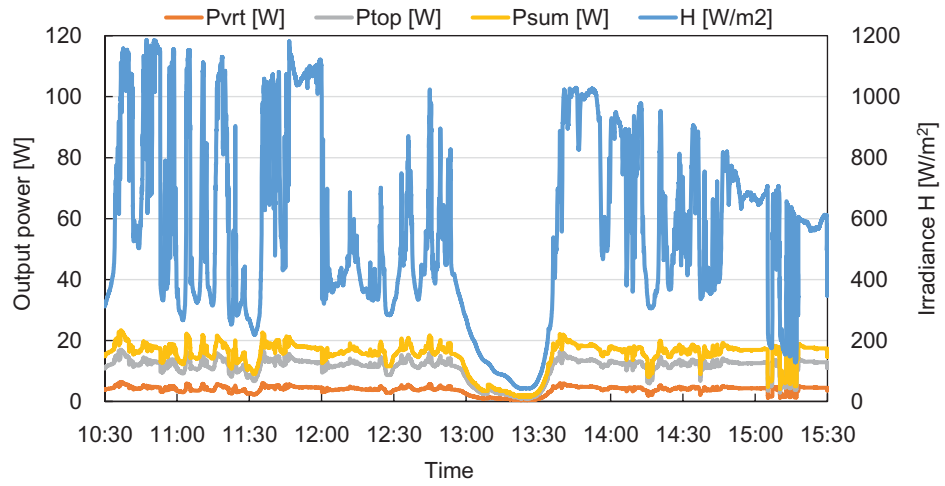

Fig. 13: Output power of PV on Aug 24, 2016 (2 series PPTs for a 4-series VRLA system)

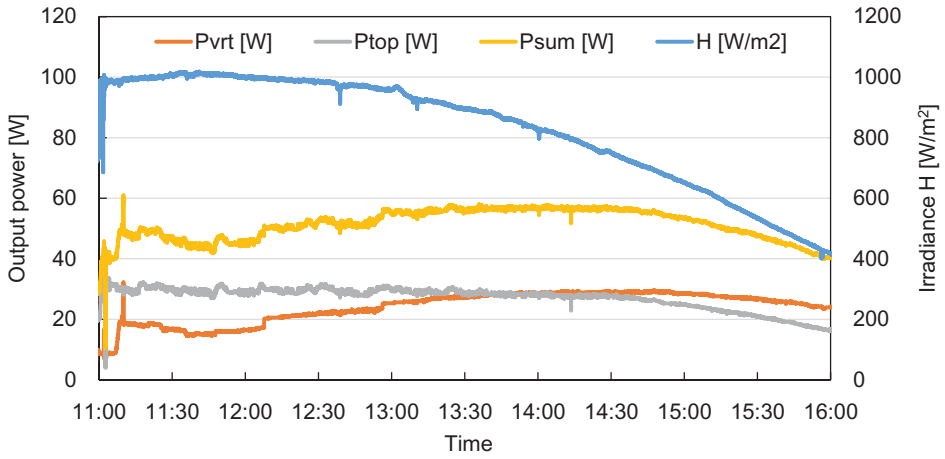

Fig. 14: Output power of PV on Aug 26, 2016 (2 parallel PPTs for a low voltage VRLA system)

Table 4 shows the results of the overall experiments at the south aisle in summer; the parallel PPT system showed a slightly better performance. However, the scattering irradiance affects the vertical surfaces, and more data must be collected to discuss an optimum system.

Tab. 4: Results of outdoor charging experiments of 5 h at the south aisle in summer.

PPT System / Average values	Series on 27th Sep	Series–Parallel (left/right) on 26th Sep	Series (top, vertical) on 24th Aug	Parallel (top/vertical) on 26th Aug
Horizontal irradiance	389.6 W/m^2	332.7 W/m^2	560.1 W/m^2	811.5 W/m^2
Charged Power	23.7 W	22.1 W	25.1 W	51.1 W
P/*H*	6.1%	6.6%	4.5%	6.3%
	(Scattering irradiance effect)			(Low voltage load)

3.4. Running experiment

Power and energy consumptions of the solar EV were measured through an experiment by using a 5 kg Li-ion rechargeable battery. Fig. 15 shows the measurement result of the scooter riding around a building on a flat asphalt road in winter. As indicated in the figure, the top speed reached 25.1 km/h and the peak current was 30 A, approximately. In addition, the average power consumption was 1.09 kW. This result shows that the solar-

energy-charging time would be at least 20 times longer than running time in fine weather.

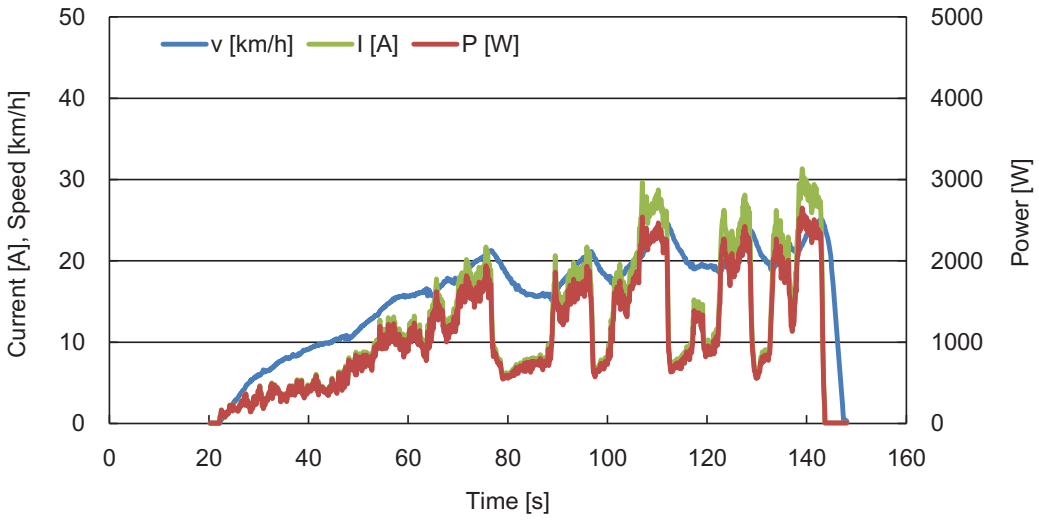

Fig.15: Test data of travelling 0–25 km/h around the building (Feb 18, 2016).

4. Conclusions

In this paper, we discussed about the solar EV converted from the three wheel scooter Honda Gyro Canopy widely used for delivery service in Japan. The limited data of outdoor experiments showed that the series–parallel PPT system produced more energy than the series or parallel PPT systems at the south aisle in summer. There is more room to discuss the optimization of a multiple PPT system. However, we must also consider the system load voltage of the VRLA battery and the effect of scattering irradiance. Experiments were conducted in which the solar EV was driven with the help of a 5 kg Li-ion rechargeable battery around a building on a flat asphalt road. The result showed that the average power consumption was 1.06 kW at an average speed of 15.9 km/h (the peak speed was 25.1 km/h), electric energy consumption ratio was 15 km/kWh.

In photovoltaic and automotive industry, 100 thousand delivery boxes with PV system for the Solar EVs means creating at least 10 MW new PV business market. With amount of 100 thousand Solar EV utilizing solar energy, if the ratio of charging time / running time was 3-4, 15-20 thousand Solar EVs are equivalent to zero energy vehicle (ZEV).

4.1. Remaining Problems

- For the PPT, both optimum connection and protective limit settings must be discussed.
- Optimum PPT control at the running state must be discussed. (Direction of sunlight and shading area will be variable.)
- The installation area of the PV modules, such as the rooftop and front fairing, must be increased.
- The vehicle's weight must be reduced, and the rolling resistance of the tires and air flow drag should be improved.
- The delivery box needs an advertisement area, and strong reflective sunlight due to the PV modules must be avoided for the benefit of other drivers.
- The merits for bifacial PV cells should be investigated.

5. References

bSolar Ltd, 2012. Electrical Characteristics, BSBF-18.5/22 Bifacial Monocrystalline Silicon Solar Cell, p. 2.

ST Microelectronics, 2012. Interleaved DC-DC boost converter with built-in MPPT algorithm, Doc ID 17588 Rev 4.

Takanori Matsuyama, Kazuhiro Igura, Hiroshi Fukukita et al., 2014. Experiment Introduction of Distributed Maximum Power Point Tracking Systems for PV System and Effect Applied to Solar Car, J. JSES, Vol. 40, No. 4, 51–60.

Yoshio Hashimoto, 2016. Aqua Innovation International Center at Shinshu University, J. IEIE Jpn. Vol. 36, No. 8, 37–40.

Youhei Takigawa, Tomoki Kinno, Kazuto Yukita et al., 2013, A Distributed MPPT introduction evaluation of solar power, Proc. JSES/JWEA Joint Conf., Vol. 100, 369–372.

Web:

HONDA GYRO, 2015, https://ja.wikipedia.org/wiki/%E3%83%9B%E3%83%B3%E3%83%80%E3%83%BB%E3%82%B8%E3%83%A3%E3%82%A4%E3%83%AD.

JMA, 2016. METPV-11, NEDO, http://app0.infoc.nedo.go.jp/

Conference Proceedings

EuroSun 2016
Palma de Mallorca (Spain), 11 - 14 October 2016

Design Options for Uncovered Photovoltaic-Thermal Glass-Glass Panels

Federico Giovannetti, Maik Kirchner and Marc Albert

Institut für Solarenergieforschung Hameln (ISFH), Emmerthal (Germany)

Abstract

The use of glass-glass photovoltaic modules in uncovered photovoltaic-thermal (PVT) panels can provide for a longer durability of the solar cells and for higher design flexibility compared to other encapsulating technologies, thus representing an attractive solution for building integration. After giving an overview of available design options and of their impact on the efficiency of the PVT, the paper presents and analyzes the thermal performance of different prototypes by means of measurements in open circuit (OC) mode according to ISO 9806. The customized panels are assembled from commercially available components and intended for the integration into ventilated glass façades. As cell technology, wafer-based crystalline silicon (c-Si) and thin film copper indium diselenide (CIS) are implemented. For the front cover, clear glass with high and low iron content as well as special low emissivity and colored glass with high solar transmittance developed for solar applications are considered. In combination with c-Si solar cells, we additionally compare the use of black enameled rear glass and multilayer black encapsulant as a solution to mask the heat exchanger. The results show the significant impact of the design on the thermal performance of the PVT panels: we report zero-loss efficiency values between 0.61 and 0.78 and heat loss coefficients $b_{1.5m/s}$, evaluated at a wind speed of 1.5 m/s, between 10.2 and 17.8 W/m²K. Concerning both performance and aesthetics, the best results are achieved with CIS photovoltaic modules and low-emissivity front glass panes.

Keywords: *photovoltaic-thermal collectors, hybrid collectors, uncovered collectors, building integration*

1. Introduction

Photovoltaic-thermal (PVT) collectors have been regarded since longer than 40 years as a promising solution to supply both for renewable electricity and heat with a single device. Compared to the common separate installation of solar thermal and photovoltaics, a higher solar yield and lower costs per unit area, a more appealing design as well as an improvement of the electrical efficiency of the solar cells in case of low-temperature applications with uncovered panels can be mentioned as main advantages. Still far away from being an established technology, PVT collectors have been receiving a renewed interest in the last time, not only in research works but also among manufacturers and end users, as a consequence of the recent development of the photovoltaic market and the energy performance requirements set by the new European building regulation.

Similarly to the case of solar thermal and photovoltaics, building integration represents a very efficient way to improve the architectural quality and reduce the cost of the installations, by replacing existing building components and their associated embodied energy with active solar ones. Both aspects represent a key approach for a successful deployment of these renewable energy systems. Most of the available design and integration options (type of cell technologies, glass, encapsulants, coatings, etc.) are known from previous experiences with photovoltaics (Farkas, 2013; Jelle et al., 2013) and their effects have been commonly investigated with regards to the electrical efficiency or to the reliability of the solar cells. Furthermore, developments aiming at improving the design of the modules are often carried out for specific commercial projects and seldom comprehensively documented in the scientific literature (Perret-Aebi et al., 2014).

doi:10.18086/eurosun.2016.08.11 Available at http://proceedings.ises.org

Nomenclature		
$b_{1.5m/s}$	collector heat loss coefficient at w = 1.5 m/s	[W/m²K]
G	hemispherical solar irradiance	[W/m²]
G"	net irradiance	[W/m²]
T_a	ambient temperature	[°C]
T_m	mean fluid temperature	[°C]
w	wind speed	[m/s]
α	solar absorptance	[-]
γ	temperature coefficient of the maximum power	[%/K]
η	thermal efficiency	[-]
η_0	zero-loss thermal efficiency	[-]
η_{el}	electrical efficiency	[%]
ε	thermal emittance	[-]
τ	solar transmittance	[-]

In the framework of a current research project we have been investigating the design and the integration of uncovered liquid-based glass-glass PVT panels into ventilated glass façades (s. Figure 1). The specific façade system consists of vertical aluminum profiles screwed to the main bearing wall and equipped with clip fasteners able to support glass claddings with different thickness, size and geometry and, thus, best suitable also for PV and PVT panels.

The glass-glass encapsulating technology can generally provide for a longer service life of the solar cells thanks to the higher mechanical durability and the improved degradation behavior, thus representing a reliable choice if combined with an additional heat exchanger as for photovoltaic-thermal applications. The wider range of design options makes it furthermore an attractive and flexible solution for building integration. As drawbacks, higher costs and a higher thermal resistance due to additional rear glass have to be taken into considerations if compared to the common use of thin plastic backsheets or to the direct lamination of the PV cells on the heat exchanger, a manufacturing approach already tested in previous research works (Rockendorf et al., 1999; Dupeyrat et al., 2010; Matuska et al. 2015).

Fig. 1: Examples of ventilated glass façades with common glass panels (left, source: Konvortec) and PV panels (center, source: Konvortec) as well as schematic representation of the ventilated façade with glass-glass PVT panels under development (right)

After giving an overview of relevant design options for glass-glass PVT panels and analyzing their correspondent impact on the collector performance, the work presents and discusses selected results of thermal efficiency measurements on different large-sized prototypes, assembled on the basis of commercially available components.

2. Overview of design options

Liquid-based, uncovered glass-glass PVT panels basically result from the combination of a glass-glass PV-module and a heat exchanger, which can be connected to each other by using different mechanical or/and adhesive fixings. This section briefly describes the single components of PVT panels, mainly considering

commercial products and focusing on the influence of possible design configurations on the thermal efficiency of the panels.

2.1. Solar cell technology

Solar cells represent the core of PVT panels and can have a strong impact both on their energy performance and their design. They are basically distinguished in wafer-based silicon and thin film cells; under this last category amorphous silicon (a-Si), cadmium telluride (CdTe), copper indium diselenide (CIS) and copper indium gallium selenide (CIGS) are the most common and commercially relevant ones. Due to the different manufacturing processes implemented, the choice of a specific technology also affects the module assembly itself, i.e. the number and type of components used, as shown in Figure 2.

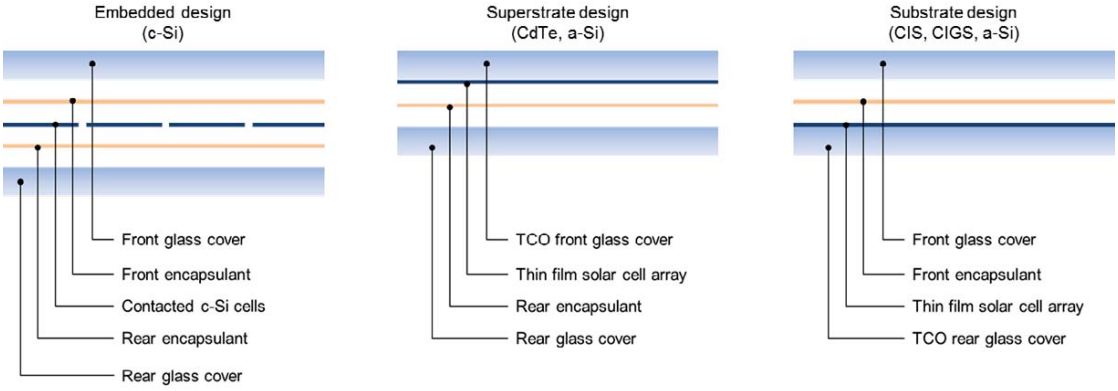

Fig. 2: Design of glass-glass photovoltaic modules for wafer-based (left) and thin film (center, right) solar cells

The photovoltaic performance is commonly characterized by the electrical efficiency η_{el} measured under standard conditions STC (irradiance: 1000 W/m²; spectrum: air mass AM 1.5; module temperature: 25°C). In commercially available PV modules it ranges between 10% (a-Si) and 16% (CdTe or CIGS) for thin films and between 16% (polycrystalline) and 20% (monocrystalline) for wafer-based silicon cells (Fraunhofer ISE, 2015). The electrical efficiency exhibits a significant temperature dependent behavior. The temperature coefficient γ, which describes the relative change of the power output of the module in %/K compared to measurements under standard conditions, roughly varies from - 0.45%/K (c-Si) to - 0.20%/K (CdTe). A lower coefficient is generally considered a negative property for common PV installations, as it can lead to lower energy production under operation. In typical applications with uncovered PVT panels, such as solar assisted heat pump systems, on the contrary, it can even be energetically advantageous, as the solar cells usually operate at temperatures below 25°C.

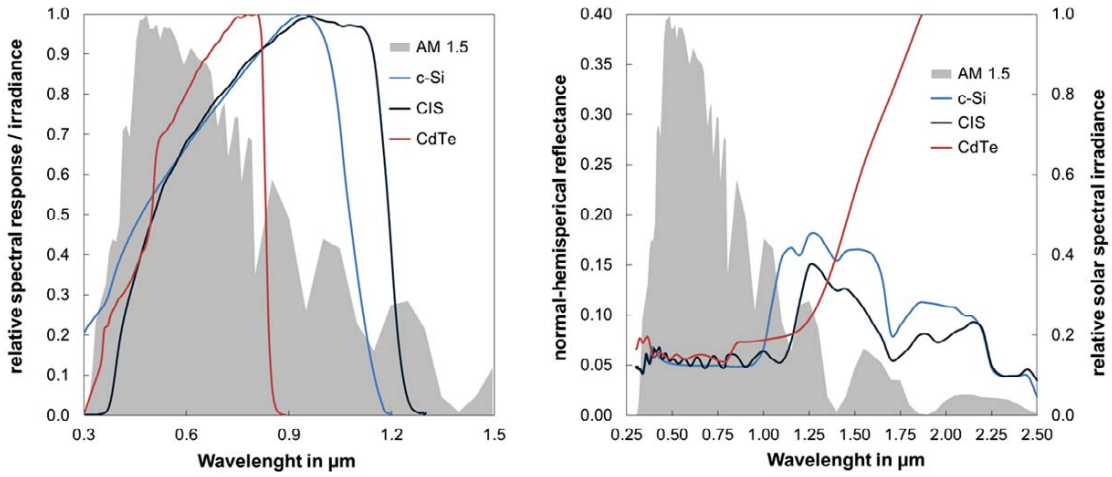

Fig. 3: Relative spectral response (left, data provided by manufacturers) and spectral reflectance (right, ISFH measurements) of PV modules based on different solar cell technologies.

To assess the impact of the PV cell as well as of other module components on the thermal performance of the PVT collector, more detailed data than the electrical efficiency are required: the spectral optical properties over the whole solar wavelength range and the spectral response of the PV module, describing the amount of current coming out of the device per incoming photon of a given energy and wavelength (or alternatively the quantum efficiency). Figure 3 compares exemplarily spectral response and reflectance of three PV modules based on different cell technologies. The modules' data were provided by manufacturers, the optical measurements were carried out at ISFH with a commercial double-beam spectrometer equipped with an integrating sphere.

The graphs show the different wavelength dependent behavior of the technologies especially in the near-infrared range, which has to be considered if combining the cells with spectral selective front covers or encapsulants. The reflectance measurements report otherwise similarly low integral values, ranging between 0.09 and 0.06, thus proving their suitability for the use as solar thermal absorbers.

The choice of a defined cell technology can also significantly influence the color and the final aspect of the module, thus playing an important role for building integration. Wafer-based silicon cells are typically available in dark blue or black and feature a homogenous or non-homogenous appearance, depending on the crystalline structure of the cell itself (mono or poly). The color is determined by the material and by the antireflective coating, which is usually optimized to achieve maximum electrical power under solar irradiation. Many research works have addressed the manufacturing of colored cells with low power losses by tuning the antireflective coating (Selj et. al., 2011; Chen et. al., 2012; Vogt et al., 2015) and several commercial products developed for building integration are already available on the market in different colors (green, red, etc., s. Figure 4). Beside the color, the shape and size of the cell still remain a limiting factor for the module design, affecting both its characteristic patterned appearance and its geometry.

Due to the specific manufacturing process, thin film technology presents a much more homogenous aspect and enables a customized and very flexible dimensioning of the modules, which make them more attractive as components of the building envelope. The cells are generally matt black, blue or brown. Different grades of transparency can be achieved by reducing the cell thickness and/or by removing small areas of the cell with laser treatment, which implies a correspondent efficiency loss. The combination of semitransparent cells with colored rear glass panes or films significantly extends the design options of this technology as shown in Section 2.3.

Fig. 4: Typical appearance of wafer-based c-Si and thin film cells. Left: common monocrystalline c-Si cell; center: colored mono- and polycrystalline c-Si cells (source: Loft Solar Corporation); right: CIGS cell

Reliability of solar cells is finally a complex and crucial aspect to be considered in the development of PVT panels, which is not specifically addressed by the present work. Manufacturers of photovoltaic modules generally guarantee 90% and 80% of the performance (power output) after 10 years and 25 years operation respectively, independently from the cell technology used. The operation in PVT systems can primarily lead to higher mechanical and thermomechanical stress, depending on the heat exchanger and bonding technology chosen. Comparative investigations on long-term reliability of PVT panels are not known to the authors. Degradation mechanisms and behavior of different PV modules are on the contrary well documented in the literature, for example in a recent work by Jordan et al. (2016).

2.2. Front and rear cover glass

The front cover of glass-glass PVT modules should provide for high mechanical stability and low optical

losses. In case of PV modules with superstrate design (s. Figure 2), it also represents the substrate for the deposition of the thin film cell array. Tempered, soda-lime glass panes with a thickness of 3 to 4 mm and low-iron content are generally used both for photovoltaic and solar thermal applications (s. Figure 5). The impact of the iron content (mainly Fe_2O_3) on the PVT module performance depends on the spectral sensitivity of the considered cell technology and on the referred spectral range, as explained in section 2.2. For monocrystalline c-Si modules a power output decrease between 1% (Fe_2O_3 = 0.1 ‰) and 10% (Fe_2O_3= 1‰) compared to an ideal iron-free glass is reported for commercially available 3.2 mm samples in a recent work (Vogt et al, 2015). The thermal efficiency of uncovered PVT is less influenced by the iron content of the glass, as part of the solar radiation absorbed in the glass bulk is transferred by thermal conduction to the fluid and contributes as secondary heat gain to an increase of the conversion factor η_0.

To further reduce the optical losses of solar modules antireflective coatings are commonly deposited on the external surface of the front cover of premium products. In most cases porous SiO_2 layer stacks are used, which can improve the efficiency of photovoltaic and thermal collectors by about 0.02 for each side.

Aiming at improving the thermal performance of PVT collectors, the use of low emissivity, high transmittance coatings to reduce the radiative heat losses represents an additional option. This approach has been already investigated in previous works for different kind of flat plate collectors (Giovannetti et al., 2014) as well as for covered PVT (Lemmle et al. 2016). To minimize the optical losses and ensure long-time reliability in uncovered collectors coatings based on metal oxides (e.g. indium, tin or zinc) are suggested. The impact of the low-e coating for low-temperature applications is strongly dependent on the specific heating system design and on the operation mode: if the collector is working as heat exchanger below ambient temperature, the use of the coating can even lead to a lower performance if compared with non-selective panels.

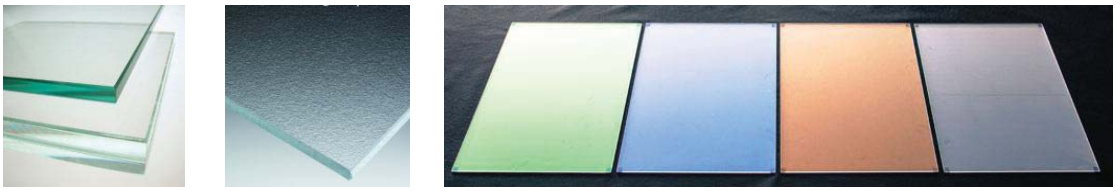

Fig. 5: Examples of front glass for solar applications. Left: clear glass with different iron content (source: Euroglas); center: textured clear glass (source: Interfloat Corporation); right: colored glass with high solar transmittance (source: Swissinso)

For architectural purpose, the use of colored or patterned glass is of high interest: most of the available products exhibit a considerably lower transmittance compared to common covers (in best case about -10%). Special spectrally selective coatings for solar glazing with improved optical properties were developed at the École polytechnique fédérale de Lausanne (EPFL) and are now manufactured by the Swiss company Swissinso (Schüler et al., 2005; Swissinso, 2016). These interference thin films can reflect a very small selected portion of the visible spectrum while letting the rest of the energy pass through. The glass panes are supplied in several colors, which according to manufacturers' data reduce the performance of thermal collectors by approximately 1% (grey) to 4% (yellow) and of photovoltaics by 2% to 6% (Swissinso, 2016). An additional light diffusing layer, achieved by etching the outside surface of the glass makes it possible to completely hide the absorber and obtain stable quality colors (s. Figure 5). Independently from the coloration, textured glasses and acid etching treatments are since long in use for solar applications with the aim of partially masking the solar absorber or the solar cells and improve the module appearance.

Rear cover glass is used similarly to front glass to ensure the durability of the glass-glass PV-modules and represents in case of PV modules with substrate design (CIS, CIGS or a-Si) the substrate for the cell deposition. The optical properties as well as the aesthetics play a role only in combination with wafer-based silicon or with semitransparent thin film cells. Colors or patterns can in these cases be used to hide the heat exchanger and better match the façade design, while affecting the solar absorptance of the glass and, thus, the thermal performance of the PVT panels.

2.3. Encapsulants

Encapsulants are primarily used in glass-glass PV modules to embed the solar cells between the glass panes and protect them from environmental stress. To provide for high performance and long-term durability several requirements have to be fulfilled, such as optical transparency, mechanical adhesion, electrical isolation, resistance to UV radiation, temperature and moisture penetration. For aesthetical purposes, colored or patterned encapsulants are also available on the market. These products are mainly combined with wafer-based silicon or semitransparent thin film cells in building integrated photovoltaics (Perret-Aebi et al., 2014) as shown in Figure 6 and can be similarly implemented in PVT panels to hide the heat exchanger. As for the glass panes, different colors result from different optical properties and can thus affect the energy efficiency of the panel.

Concerning the typical materials, ethylene vinyl acetate (EVA) represents today the most common choice for photovoltaics, thanks to its high transmittance, good durability but especially low cost. EVA films are transparent, white or black and supplied in different thickness. Silicon-, polyefine- or ionomer-based films offer alternative solutions for EVA products and exhibit even better optical performance and weatherability. Due to their higher costs, they haven't been able to gain a significant market share so far. The use of colored silicon films for solar energy applications is documented in recent research activities (Vogt et al., 2015). Finally polyvinylbutyral (PVB), commonly known as interlayer in laminated safety glass is also implemented as encapsulant material. These films are manufactured in many different colors, thus representing an attractive option for architectural applications. Furthermore, according to the current European building regulation PVB is the only material that can be integrated into façades without a special construction permit, which explains its prevalent use in building integrated photovoltaics. As relevant drawbacks, it exhibits inferior performance and durability if compared to the previously mentioned products.

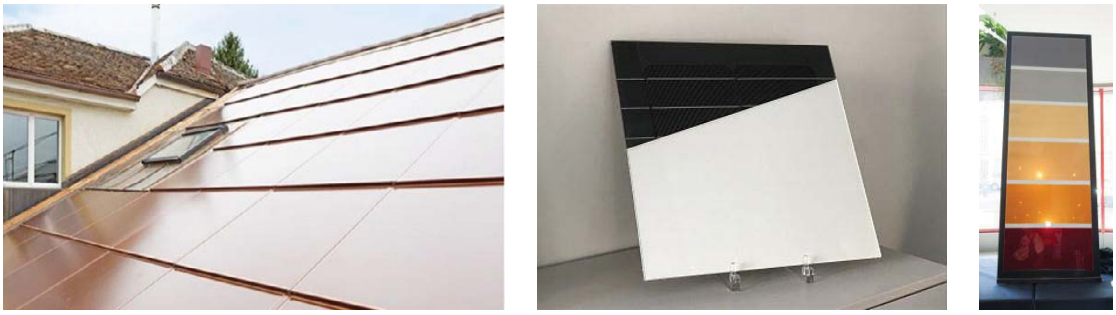

Fig. 6: Colored solutions developed for building integrated photovoltaics: Left: thin film PV with rear encapsulant as roof tile (source: NexPower). Center/right: Samples of modules with white and colored multilayer front encapsulants (source: Solaxxes)

Additionally to these standard encapsulants, special multilayer solutions embedding interference filters for tuning the color of the modules have been recently introduced to the PV market, on the basis of the research work carried out at the EPFL and at the Centre Suisse d'Electronique et Microtechnique (Perret-Aebi et al., 2015): deposited on microstructured films, these filters can selectively scatter visible light while transmitting infrared radiation, thus enabling the manufacture of perfectly homogenous colored and even white modules (Figure 6). Combined with heterojunction c-Si cells, which are particularly sensitive in the IR range, electrical power losses by about 40% were measured for white samples. For PVT applications also a significant decrease in thermal efficiency is expected.

2.4. Heat exchanger

Aim of the heat exchanger in PVT panels is to efficiently transfer the solar energy absorbed in the PV module to the fluid. For the challenging design two main aspects have to be taken into consideration: the low thermal conductivity of glass (λ = 0.8÷1.0 W/m*K), which requires a large contact area between the heat exchanger and the rear pane of the PV module in order to provide for a reasonable internal heat transfer coefficient; the combination of components consisting of different materials, which on the other side calls for an appropriate solution able to avoid critical thermo-mechanical stress under typical operation, and over the service life of the panels. One approach is to use materials for the heat exchanger exhibiting mechanical properties similar to those of glass as well as a suitable geometrical configuration. A second approach is to

fix the heat exchanger to the PV module in a way that can tolerate and/or compensate the different thermo-mechanical behavior of the components. Commercially available products adopt for the heat exchanger materials (copper, aluminum, steel and plastics) and assemblies (sheet-and-tube, roll-bond, etc.) common in solar thermal collectors as well as customized designs (s. Figure 7). For the fixing, mechanical or adhesive solutions are used (Brotje et al., 2016).

Fig. 7: Examples of heat exchangers used in commercially available uncovered PVT-panels (sources from left to right: Fototherm, AnafSolar, DualSun, Poly Solar Solutions, CGA Technologies)

3. Experimental investigations

Our investigations focused on the thermal performance of different photovoltaic-thermal glass-glass modules. This section presents the selected assemblies as well as the details of the efficiency measurements.

3.1. PVT-panel design

The prototype panels were manufactured on the basis of commercially available components. Figure 8 gives an overview of the design selected for our investigations. Additional technical data are reported in Table 1.

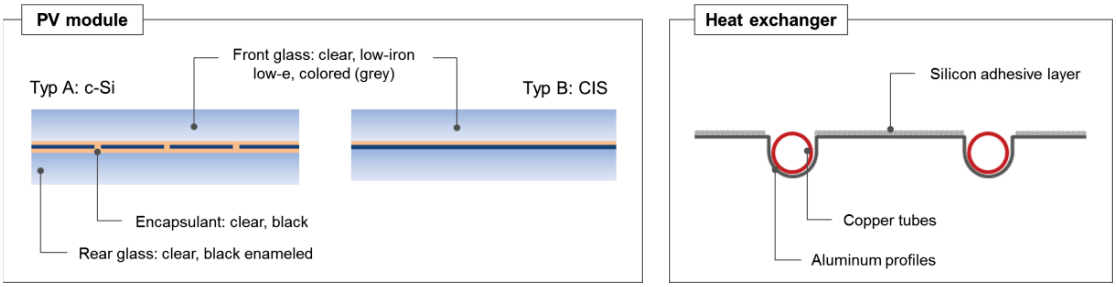

Fig. 8: Design of the investigated PVT panels

As solar cell technologies wafer-based crystalline silicon and thin film CIS were implemented. For the heat exchanger we chose a composite construction consisting of copper tubes with a serpentine geometry and aluminum omega-profiles, which enclose the tubes and are glued to the rear glass cover with a temperature resistant, two-component silicon adhesive layer (thickness about 0.8 mm; thermal conductivity λ = 0.3 W/m·K). This heat exchanger is produced by the German company Schmoele for heating and cooling panels as well as for solar absorbers of flat plate collectors. It enables an efficient and uniform heat transfer from the glass pane to the fluid and can compensate the thermo-mechanical stress originated by the different thermal expansion coefficients of glass ($\alpha = 9 \cdot 10^{-6}$ K^{-1}) and aluminum ($\alpha = 23 \cdot 10^{-6}$ K^{-1}) or copper ($\alpha = 17 \cdot 10^{-6}$ K^{-1}) more effectively than other common solutions. The long-term durability of the fixing over the expected operating temperature range has been successfully proved at ISFH both by accelerated weathering laboratory tests on small samples (Seitz M., 2015) and by outdoor exposition tests on large-sized prototypes.

Tab. 1: Selected technical data of the investigated PVT panels

Module type	Area [m²]	Nominal power [W]	Packaging factor [-]	Coeff. γ [%/K]	Area HTX / Area glass	Distance tubes [mm]
c-Si	1.26	171 ÷ 175	0.71	-0.45	0.86	0.95

CIS	0.84	91 ÷ 94	-	-0.39	0.81	0.85

To analyze the impact of the front cover glass on the thermal performance of the PVT-panels four different panes were taken into consideration. Beside common clear glass typically used in architecture and glass with low iron content, two functional glasses with high solar transmittance specially developed for solar applications and already mentioned in Section 3 were selected: a colored (grey) glass intended for building integration and a low emissivity glass for improved thermal performance. Both coatings are deposited on a substrate with low iron content. The correspondent optical properties calculated according to ISO 9050 (solar spectral range) and EN 12898 (infrared spectral range) are reported in Table 2. The data of the clear and the grey glass were supplied by the manufacturers, the low iron and low-e glass were measured at ISFH by using the equipment already mentioned in Section 2.1 and a commercial Fourier transform infrared spectrometer.

Tab. 2: Relevant optical properties of the investigated front glass covers

Cover type	Solar transmittance τ	Solar absorptance α	Thermal emittance ε
Clear glass	0.85 ± 0.01	0.07 ± 0.01	0.84 ± 0.02
Low-iron glass	0.90 ± 0.01	0.02 ± 0.01	0.84 ± 0.02
Grey glass	0.88 ± 0.01	-	0.84 ± 0.02
Low-e glass	0.86 ± 0.01	0.07 ± 0.01	0.30 ± 0.02

For the PVT-modules with crystalline silicon cells, we further investigate two alternative solutions for the standard combination clear glass + clear encapsulant, with the purpose to effectively mask the portion of the heat exchanger visible through the cell interspaces, thus providing for a more homogeneous appearance, and to increase the solar absorptance of the panel. In the first case we use an opaque black enameled glass (color RAL 9005), with the enamel layer facing the heat exchanger. In the second case, the PV module was laminated with a multilayer encapsulant consisting of a black fluoropolymer backsheet embedded between two transparent EVA films. Spectrometric measurements on the two modules report very similar results, which exclude a possible different optical impact of the films on the thermal efficiency of the PVT panels.

3.3 Performance measurements

The performance of the PVT panels was investigated by means of indoor and outdoor measurements according to ISO 9806, both in open circuit (OC) and with the PV modules operating in maximum power point (MPP). As the panels are intended for the integration into ventilated glass façades, additional measurements were carried out by closing the air cavity (40 mm) between the rear side of the test specimen and the mounting plate, which is otherwise open to allow free air circulation. The paper presents and discusses the results in OC mode, thus focusing on the impact of the design on the thermal efficiency of the panels.

For the eight prototypes, we report zero-loss efficiency values η_0 between 0.61 and 0.78 (0.58 and 0.76 if referred to the hemispherical irradiance G and not to the net irradiance G", as displayed in Figure 9 and 10) as well as heat loss coefficients $b_{1.5m/s}$ (heat loss coefficients evaluated at a wind velocity w = 1.5 m/s) between 10.2 and 17.8 W/m²K. The correspondently calculated stagnation temperature (G = 1000 W/m²; ambient temperature = 30 °C; no wind) ranges between 84 °C and 126 °C. Compared to the performance of commercially available products (Brötje et al., 2016) or to previous research works, the results attest the potential of this reliable PVT assembly, in spite of the additional thermal resistance due to the rear glass pane and show at the same time the strong impact of the considered design options. Further performance improvements are technically feasible by optimizing the thickness of the silicon-based adhesive layer or by more efficiently coupling the heat exchanger to the PV module (larger contacted area of the aluminum profiles, smaller distance of the copper tubes). For a comprehensive assessment, also economic and long-term reliability aspects are to be taken into consideration. The influence of the single design options is displayed in Figure 9 and 10 and can be summed up as follows:

- Low-emissivity coating (Figure 9, left): in comparison to an identically assembled module equipped with common low-iron glass, the use of a low-emissivity front cover improves the heat loss coefficient $b_{1.5m/s}$ of the panel by 2.0 W/m²K. Thanks to the high solar transmittance of the coated pane and the better thermal insulation, also the conversion factor η_0 is positively affected by the replacement of the cover. With refer to the specific boundary conditions (sky temperature T_{sky}) improvements up to 0.04 (0.07 if referred to the hemispherical solar irradiance G and not to the net irradiance G) are reported.

- Colored cover (Figure 9, right): the influence of grey glass was investigated on PVT modules both with c-Si and CIS solar cells. The performance results remain slightly below our expectations: In combination with c-Si cells, for example, we measured a lower η_0 than that of the module equipped with clear glass ($\Delta\eta_0$ = - 0.01), despite the higher solar transmittance declared by the manufacturer ($\Delta\tau$ = 0.03). This special combination of interference coating and light-scattering finishing proves to be an effective solution to modify the appearance of thin film modules and adapt them to the specific building design. In case of wafer-based silicon modules, on the contrary, the masking effect is not as satisfactory and the solar cells are still clearly visible under the cover. The aesthetical results are of course restricted to the selected glass and not transferable to other colors.

- Rear cover glass (Figure 10, left): non-transparent rear glass or encapsulants were used in combination with c-Si solar cells to mask the metallic heat exchanger and to enhance the solar absorptance of the PV module. The best performance was achieved by the panel equipped with a black enameled pane. Due to the higher thermal resistance between the heat sources (solar cell and black absorbing layer) and the fluid, the use of a fluoropolymer backsheet embedded between two EVA films leads to a decrease of the conversion factor by 0.04. The significant difference results not only from the position of the absorbing layer and the number of the sheets, but also from the low packaging factor of the PV module (71.4%). By using a single black EVA film as rear encapsulant and increasing the packaging factor lower deviations are expected. As further advantage of enameled glass the easier and more reliable processing has to be mentioned, which doesn't differ from the standard lamination procedure.

- Rear ventilation of the panels (Figure 10, right): Convective heat losses at the rear side of the PVT modules confirm to have a significant impact on their thermal performance. By closing the air gap and suppressing the ventilation between the modules and the mounting panel, we report a well reproducible reduction of the heat loss coefficient $b_{1.5m/s}$ between 5.6 W/m²K and 5.7 W/m²K, which corresponds to an increase of the stagnation temperature by about 15 K.

- Cell technology: due to the different size of the c-Si and CIS PV modules and the correspondently different configuration and tube distance adopted for the heat exchanger (s. Table 1), the results are not directly comparable. Assuming identical size and configuration, similar zero-loss efficiencies are expected and the discrepancy will depend more on the solution used to mask the heat exchanger in the c-Si module and on the packaging factor than on the photovoltaic technology itself. The choice of the solar cells has a much more significant impact on the aesthetics than on the performance of the panels.

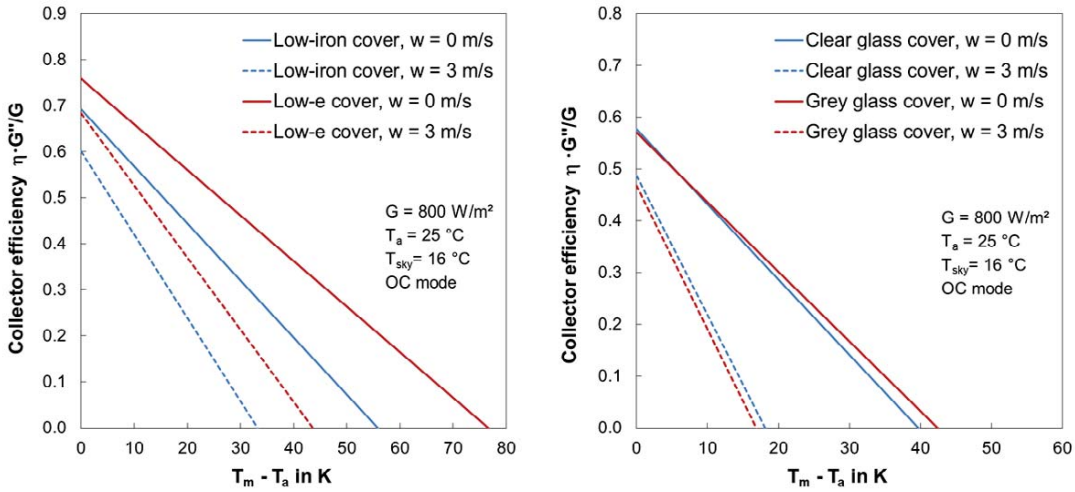

Fig. 9: Measured thermal efficiency of the investigated PVT panels. Left: comparison between prototypes with CIS PV modules featuring a low-iron and a low emissivity front glass cover (closed rear air cavity). Right: comparison

between prototypes with c-Si modules featuring a clear and a grey front glass cover (open rear air cavity). The results are displayed with refer to the hemispherical solar irradiance G and not to the net irradiance G".

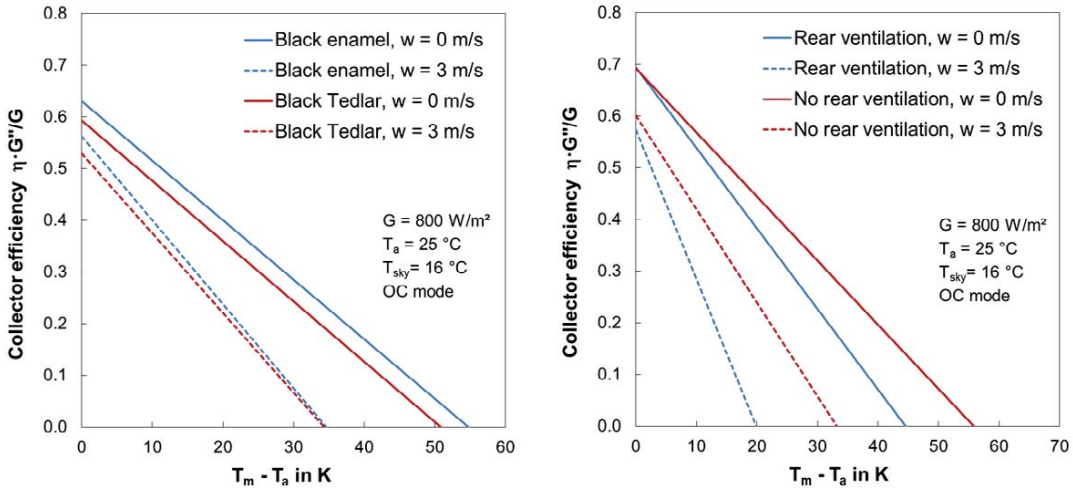

Fig. 10: Measured thermal efficiency of the investigated PVT panels. Left: comparison between prototypes with c-Si PV modules using a black enameled rear glass and a multilayer encapsulant embedding a black sheet to mask the heat exchanger (closed rear air cavity). Right: comparison between measurements on a prototype with a CIS PV module with and without ventilation of the rear air cavity. The results are displayed with refer to the hemispherical solar irradiance G and not to the net irradiance G".

4. Conclusion

Uncovered glass-glass PVT-modules offer a high design freedom by combining different types of solar cell technologies, front and rear cover glass as well as encapsulating sheets. We investigate the performance of 8 different modules by means of thermal efficiency measurements in open circuit mode. The results show the strong impact of the design options as well as the potential of this PVT assembly. We report conversion factors η_0 between 0.61 and 0.78 as well as heat loss coefficients $b_{1.5m/s}$ between 10.2 and 17.8 W/m²K. Considering both performance and aesthetics, the best results are achieved by combining a high transmittance low-emissivity front cover with a CIS thin film photovoltaic module.

5. Acknowledgments

The project underlying this publication is funded by the German Federal Ministry for Economic Affairs and Energy, on the basis of a decision of the German Federal Parliament ("Solar Glas - Development of a cost efficient solar activated glass façade for heat and electricity production", reference number: 16KN014827). The investigations are carried out in cooperation with the companies Konvortec GmbH and Energy Glas GmbH. The PV-modules were manufactured and supplied by the company Antec-Solar GmbH. The authors are grateful for the support and responsible for the content of the paper.

6. References

Brötje, S., Kirchner, M., Giovannetti, F., 2016. Performance and heat transfer analysis of unglazed photovoltaic-thermal collectors with detachable compound. Proceedings 11th EuroSun Conference.

Chen, Y., Yang, Y., Z. Feng, Z., Altermatt, P.P., Shen, H., 2012. Color modulation of c-si solar cells without significant current-loss by means of double layer anti-reflective coating. Proceedings 27th EUPVSEC Conference.

Dupeyrat, P., Ménézo, C., Rommel, M., Henning, H-M., 2011. Efficient single glazed flat plate photovoltaic–thermal hybrid collector for domestic hot water system. Solar Energy. 85, 1457-1468.

Farkas K., 2013. Designing photovoltaic systems for architectural integration - Criteria and guidelines for

product and system developers. Report T.41.A.3/2: IEA SHC Task 41 “Solar Energy and Architecture”.

Fraunhofer ISE, 2015: Photovoltaic report. https://www.ise.fraunhofer.de (access: August 2016).

Giovannetti, F., Foeste, S., Ehrmann, N., Rockendorf, G., 2014. High transmittance, low emissivity glass covers for flat plate collectors: Applications and performance. Solar Energy. 104, 52-59.

Jelle, B. P., Breivik, C., Røkenes, H. D., 2012: Building integrated photovoltaic products: A state-of-the-art review and future research opportunities. Solar Energy Materials and Solar Cells. 100, 69-96.

Jordan, D. C., Kurtz, S. R., Van Sant, K., Newmiller, J., 2016. Compendium of photovoltaic degradation rates. Prog. Photovolt: Res. Appl. 24, 978 – 989.

Lämmle, M., Kroyer, T., Fortuin, S. Wiese, M., Hermann, M., 2016. Development and modelling of highly-efficient PVT collectors with low-emissivity coatings. Solar energy materials and solar cells. 130, 161-173.

Matuska, T., Sourek, B., Jirka, V., Pokorny, N., 2015. Glazed PVT Collector with Polysiloxane Encapsulation of PV Cells: Performance and Economic Analysis. International Journal of Photoenergy.

Perret-Aebi, L-E., Ballif, C., Leterrier, Y., Roecker, C., Schüler, A. , Scartezzini, J.-L., Leibundgut, H. L., Carmeliet, J., 2014. ARCHINSOLAR - Innovative PV products for better aesthetical integration of green energies in the built environment. BFE final report SI/500474.

Perret-Aebi, L-E., Escarré, J., Li, H.-Y., Sansonnens, L., Galliano, F., Cattaneo G., Heinstein, P., Nicolay S., Bailat, J., Eberhard S., Ballif, C., 2015. When PV modules are becoming real building elements: White solar module, a revolution for BIPV. Proceedings 42nd PVSC IEEE Conference.

Rockendorf, G, Sillmann, R, Podlowski, L, Litzenburger, B., 1999. PV-hybrid and thermoelectric collectors. Solar Energy. 67, 227–37.

Schüler, A., Boudaden J., Oelhafen, P., De Chambrier, E., Roecker, C., Scartezzini, J.-L., 2005. Thin film multilayer design types for colored glazed thermal collectors. Solar Energy Materials and Solar Cells 89. 219-231.

Seitz, M., 2015. Research concerning the durability and performance of adhesive bonds in novel glass panels for the solar thermal activation of the building envelope. Internship Report Saxion University / ISFH.

Selj, J. H., Mongstad, T.T., Søndenå, R., Marstein, E.S., 2011. Reduction of optical losses in colored solar cells with multilayer antireflection coatings. Solar Energy Materials and Solar Cells. 95, 2576-2582.

Swissinso, 2016. Product information. http://www.swissinso.com/ (access: 15.09.2016)

Vogt, M. R., Hahn, H., Holst, H., Winter, M., Schinke, C., Köntges, M., Brendel, R.; Altermatt, P.P., 2015. Measurement of the Optical Constants of Soda-Lime Glasses in Dependence of Iron Content and Modeling of Iron-Related Power Losses in Crystalline Si Solar Cell Modules. IEEE Journal of Photovoltaics. 99, 1-8.

Vogt, M. R., Holst, H., Winter, M., Knoc, S., Ruppenthal, A., Köntges, M., Brendel, R., Altermatt, P. P, 2014. Optical loss analysis of colored PV modules using comprehensive ray tracing. Proceedings 6th World Conference on Photovoltaic Energy Conversion.

Conference Proceedings

EuroSun 2016
Palma de Mallorca (Spain), 11 - 14 October 2016

Profitability of Solar Photovoltaic Rooftop Systems in Buildings with Medium Sized Loads

Maria Haegermark[1], Peter Kovacs[2] and Jan-Olof Dalenbäck[1]

[1] Chalmers University of Technology, Gothenburg (Sweden)

[2] SP Technical Research Institute of Sweden, Borås (Sweden)

Abstract

In Sweden, it is generally most feasible to install solar photovoltaics (PV) primarily for self-consumption, as long as there either is a large enough load when the sun shines or that over-generation is generously compensated. Currently there are two support schemes for PV: a capital subsidy and a tax rebate for grid feed-ins. However, the latter is not available for systems above 100A, thus making self-consumption highly important for these systems. This paper studies the profitability of systems connected to loads from 100 to 700 MWh, most of them above 100A. In particular, it compares multi-family buildings to other building types. Analyses were based on measured electricity use matched to simulated PV yield and current market conditions. Calculations were conducted with and without consideration of existing roofs. In general, the supply points in multi-family buildings had less favorable load profiles than the ones in other buildings, which resulted in lower self-sufficiencies as well as relatively lower profitability and smaller system sizes. The support schemes turned out to be crucial for the profitability in most cases, but not all. For supply points in other building types with loads above 300 MWh profitable systems were found also without a subsidy. Taking areas and orientations of existing roofs into consideration drastically decreased the share of profitable systems.

Keywords: *solar photovoltaics, buildings, profitability, support schemes, Sweden, self-consumption*

1. Introduction

Sweden has a small but growing solar photovoltaic (PV) market with a majority of installations made on buildings (Lindahl, 2015). As in the rest of the world, system prices has decreased drastically the last few years, but due to low electricity prices, PV system investments are generally still in need of financial support to reach profitability. Sweden has an REC (Renewable Energy Certificates) system in place since 2003 and since 2009 there is also a direct capital subsidy program available for all PV installations connected to the grid. After a few years of discussions about a support scheme based on net billing, a tax rebate system for renewable electricity generated in small plants was introduced in 2015. A tax rebate of 0.60 SEK is achieved per kilowatt-hour electricity fed into the grid up to an equivalent amount that is bought from the grid during one calendar year. The tax rebate is only available for systems with a main fuse size of maximum 100A. After years of falling prices and with the new support scheme in place, the relevance of the investment subsidy has been questioned and there are ongoing discussions about the appropriate subsidy level for the near future.

The effects of current market conditions and support schemes were previously examined by the authors of this paper in an economic feasibility study of solar PV systems in Swedish multi-family buildings. Economic analyses were then conducted for 108 electricity supply points with loads ranging from 0 to 370 MWh and fuse sizes from 16 to 250A. The study has been presented in the article "Economic feasibility of solar photovoltaic rooftop systems in a complex setting: A Swedish case study" submitted to Energy earlier this year. Today, it is generally most feasible to install solar PV primarily for the purpose of self-consumption, as long as there either is a large enough load during hours with high insolation (in Sweden mainly daytime April – September) or over-generation of PV electricity is generously compensated. However, it was shown that the

doi:10.18086/eurosun.2016.08.10 Available at http://proceedings.ises.org

profitability of a PV system is highly affected by both building specific parameters and load characteristics.

In this paper, the profitability analysis was expanded to comprise also other types of buildings and it focuses on electricity supply points with medium sized loads (100 – 700 MWh). Most of the studied supply points have main fuses above 100A, and are therefore not entitled to the tax rebate described above. The paper examines the importance of an investment subsidy under different circumstances and aims to show how the profitability as well as self-sufficiency of a PV system is affected by the size of the load and load profile. In particular, the results of multi-family buildings are compared to the results of other buildings. Moreover, the influence and potential limitations of existing roofs were studied.

2. Method

Economic analyses were conducted for 35 PV systems based on measured electricity use matched to simulated PV electricity generation. For each of the electricity loads a PV system was sized according to highest system profitability. First, the analyses were carried out for optimally oriented systems (oriented to give a high annual yield) and thereafter consideration was taken to the slopes and orientations of existing roofs.

The method used in this paper has previously been used and described in the article "Economic feasibility of solar photovoltaic rooftop systems in a complex setting: A Swedish case study" (Haegermark, Kovacs and Dalenbäck), which was submitted to Energy 2016. Therefore, a condensed version of the methodology description is given below along with input data used in this study.

This study comprises 22 electricity supply points in multi-family buildings and 13 supply points in buildings with other types of activities (e.g. office, museum and warehouse). It was limited to supply points with yearly electricity loads between 100 and 1000 MWh and the main fuse sizes range from 80A to 750A. Some of the supply points only include electricity for facility management, while others include all electricity use within the building (e.g. electricity for facility management and household electricity).

The buildings are all situated in Gothenburg, Sweden (57° 42' N, 11° 58' E). Measured data of electricity use were collected from a database owned by the local grid company (Göteborg Energi Nät AB) with the consent of the property owners. Hourly data from 2014 were used in all cases but one. For the last supply point, data from 2013 were used.

The electricity use in each of the electricity supply points was matched to simulated electricity generation from a fictive PV system on an hourly basis. Solar electricity generation was achieved from simulations in Polysun with a poly-crystalline PV system and local climate data. A summary of the input parameters used for the simulations are shown in Table 1.

Table 1 Summary of input parameters for simulations in Polysun

Input parameter	Value	Unit
Weather data	Gothenburg	n/a
Module	Yingli YL205P	n/a
Module type	Polycrystalline	n/a
Module nominal peak power	250	W
Efficiency at STC (standard test conditions)	15.3	%
Module area	1.633m^2 (1.65m*0.99m)	m^2
Soiling losses	2	%
Cable losses	2	%
Module mismatch	1	%
Inverter	Sunny Tripower STP 25000TL-30	n/a
Inverter efficiency	93.5	%
Performance ratio	88	%
Degradation	0	%
Module orientation (base case)	0 (south)	°
Module tilt (base case)	45	°

The PV system sizes were decided according to highest system profitability. For this, net present value (NPV) (eq. 1) was used as the decisive financial metric. The NPV approach is considered appropriate when choosing between mutually exclusive investments (Berk and DeMarzo, 2014). It includes all future cash flows, considers time value of money and recognizes the size of the project.

$$\mathrm{NPV} = \mathrm{PV(benefits)} - \mathrm{PV(costs)} = \mathrm{PV(all\ project\ cash\ flows)} = \sum_{n=0}^{N}(C_n/(1+r)^n) \quad \text{(eq. 1)}$$

C= cash flow (positive or negative)
n= year of cash flow
N= total number of years of cash flows
r= discount rate

Table 2: Summary of input parameters for economic calculations. The table presents all cash flows excluding VAT.

	Input parameter	Value	Source
PV system parameters	Lifespan of PV system	30 years	
	Salvage value	0 SEK	
	Degradation of PV modules	0.5%/year	Jordan and Kurtz, 2013
General	Real discount rate	4%	
	VAT	25%	
Investment costs	PV system incl. BoS and installation (year 0)	$I_0 = 11000 + 3200 \times P^{(-0,0033 \times P)}$ (where P=peak power)	Assumptions based on Lindahl, 2015
	Meter for green certificates (year 0)	4800 SEK	
	Inverter replacement incl. installation (year 15)	15% of investment	
Annual costs	Operation and maintenance costs	0.75% of investment	Keating et al., 2015
	Grid metering fee	1500 SEK	Göteborg Energi, 2015a
	Metering fee for green certificates	Sold certificates up to 1000 SEK: 0.2 x income Sold certificates above 1000 SEK: 0.1 x income	Egen el, 2015
Value of self-consumed electricity	Green certificate trading (first 15 years)	0.20 SEK/kWh for 15 years	Energimyndigheten, 2015
	Avoided spot price	0.29 SEK/kWh (Nord Pool Spot price for SE3 2014) first year and increasing with 2.4% per year	Nord Pool Spot, 2015. Spot price assumed based on Lindahl, 2015
	Avoided grid fee	0.07 SEK/kWh	Göteborg Energi, 2015b
	Avoided energy tax	0.29 SEK/kWh	Lindahl, 2015
	Avoided green certificate fee (excl. VAT)	0.03 SEK/kWh	
	Avoided trading surcharge (excl. VAT)	0.05 SEK/kWh	
Value of sold electricity	Green certificate trading (first 15 years)	0.20 SEK/kWh for 15 years	Energimyndigheten, 2015
	Selling price	0.29 SEK/kWh (Nord Pool Spot average price for SE3 2014) and increasing with 2,4% per year	Nord Pool Spot, 2015. Sales at spot price was assumed based on Lindahl, 2015.
	Grid benefit compensation	0.037 SEK/kWh	Göteborg Energi, 2015a
Economic incentive	Investment subsidy	20% of PV system cost (maximum 800 000 SEK)	Assumption based on current subsidy (Lindahl, 2015)

The profitability was calculated from the perspective of a building owner. The costs include the initial investment, a replacement of the inverter, operation and maintenance costs, and other additional costs associated with the PV electricity generation. The basic benefits include cash inflows from sold electricity, tradeable green certificates, and savings from reduced electricity purchases from the grid. Calculations were performed with and without PV-specific benefits currently available in Sweden, that is, investment subsidy and tax rebate. All economic input parameters were chosen to reflect current market conditions.

A summary of the economic parameters used in the base case is given in Table 2. In addition, the following sensitivity analyses were conducted:

No subsidy. The current capital subsidy is available for all grid-connected PV systems. However, due to a discrepancy between supply and demand, the waiting period before a subsidy request is granted can be very long. Moreover, the subsidy scheme is today only planned to continue until 2019 and the level for upcoming years has not yet been decided. For these reasons, profitability was also calculated without a subsidy.

Value-added tax: The owners of multi-family buildings, which mainly have private customers, are generally not allowed to deduct value-added tax (VAT) from their expenses. Hence, in the base case scenarios VAT was added to all costs for these buildings. Economic calculations for buildings other than multi-family houses were conducted without value-added tax (VAT). This difference between multi-family buildings and other buildings is one of the factors that affects the system profitability. Hence, additional calculations without VAT were carried out for the multi-family buildings in the scenario with 20% subsidy in order to separate this effect from the influence of other parameters.

Tax rebate for systems ≤ 100A: There is today no plan for how long the current tax rebate program will be in place and it was therefore not included in the base case scenario. However, a sensitivity analysis including a tax rebate of 0.60 SEK/kWh during the first 10 and 30 years respectively was carried out for systems with a main fuses of 100A or less. The tax rebate is received for solar electricity fed into the grid up to a maximum of 30 MWh. However, it does not apply for more than the amount of electricity that is bought from the grid.

Discount rate: Besides the costs benefits associated with the installation of a PV system, the profitability of the investment will also vary with the chosen discount rate. In the base case scenario in this study a discount rate of 4 is used. For the systems in multi-family buildings, results from the base case were compared to scenarios with no subsidy, but a discount rate of 2 and 3 respectively.

Roof-tops: Initially, the study focuses on how the profitability of a PV system is affected by the size and type of electric load as well as current support measures. Calculations in the base case scenarios are therefore performed without consideration of the size and orientation of available rooftop areas. Instead, the economic analyses are based on a PV system oriented towards the south with a 45° slope, which gives a high yearly energy output per kilowatt peak. As a sensitivity analysis, the characteristics of existing roofs were included in the economic calculations, and reductions of PV generation and profitability due to less beneficial system orientations were determined.

3. Results

The results presented below are based on data from 35 real electricity supply points, all with unique load profiles. Some main characteristics of these loads are displayed in Figure 1. Figure 1a shows the load factor (highest hourly electricity use to yearly electricity use) as a function of yearly electricity use. Here, no difference can be seen between the supply points in multi-family buildings and other buildings. Figure 1b on the other hand, shows a divergence in how large share of the electricity use that coincide with hours of sunshine. Especially, the share of load that occurs during daytime is generally lower in multi-family buildings than in other buildings.

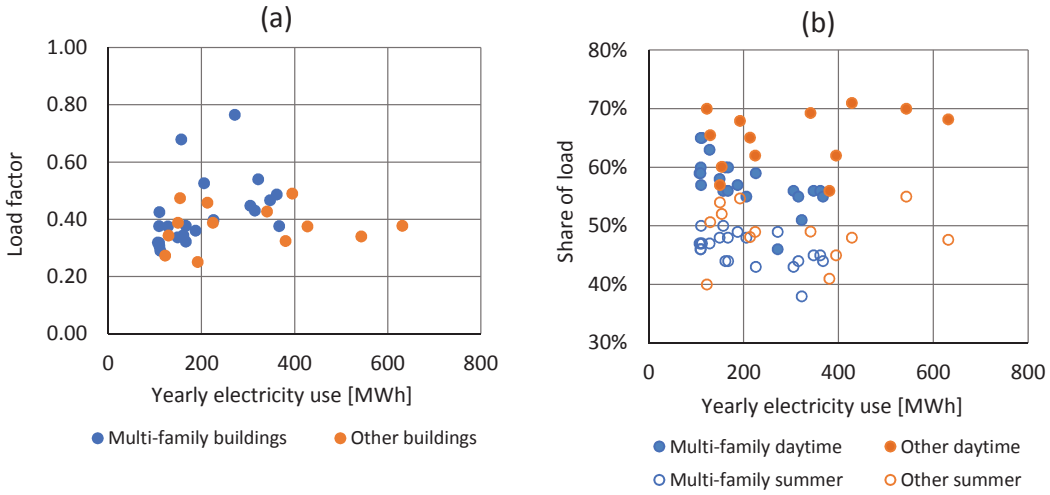

Fig.1: Characteristics of the studied electricity loads. Figure (a) shows the highest measured hourly energy as a function of yearly electricity use. Figure (b) shows the share of the load that occurs during daytime (07h-18h) and summer half-year (April – September) respectively as a function of yearly electricity use.

3.1 Profitability and sizing

This section gives the results from economic analyses with and without a capital subsidy of 20%. The highest achieved profitability (in NPV) for PV systems connected to each of the studied electricity supply points are shown in figure 2, while figure 3 shows the corresponding system sizes.

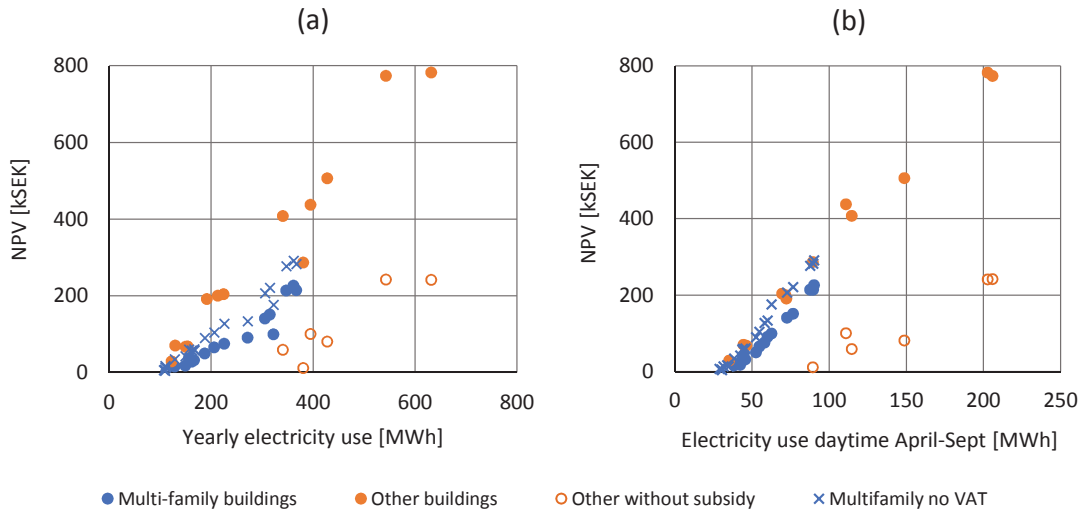

Fig. 2: The highest net present values (NPV) for PV systems connected to the studied electricity supply points. Profitability is shown as a function of (a) early electricity use and (b) electricity use during daytime (07h-18h) April – September. For multi-family buildings, the results are all with subsidy but with and without VAT. For systems in other buildings, results are shown with and without subsidy. Only systems with positive NPVs are included.

In relation to yearly electricity use, PV systems in multi-family buildings results in lower net present values (figure 2a) and lower system sizes (figure 3a) compared to the systems in other buildings. This can partly be explained by the fact that the profitability in multi-family buildings was calculated with VAT added to all cost. However, also when excluding VAT for the cost (as for other buildings), the results show lower values for multi-family buildings. It can be seen that excluding VAT makes the largest difference on optimal system size, while there is only a small increase in system profitability.

Comparing NPV or system size to the part of electricity load that occurs during daytime April through September (figures 2b and 3b) shows even stronger correlations than when comparing to the yearly load. Also, now there is no difference between multi-family buildings calculated without VAT and other buildings, indicating that the previous gap was due to differences in the load profiles (figure 1b).

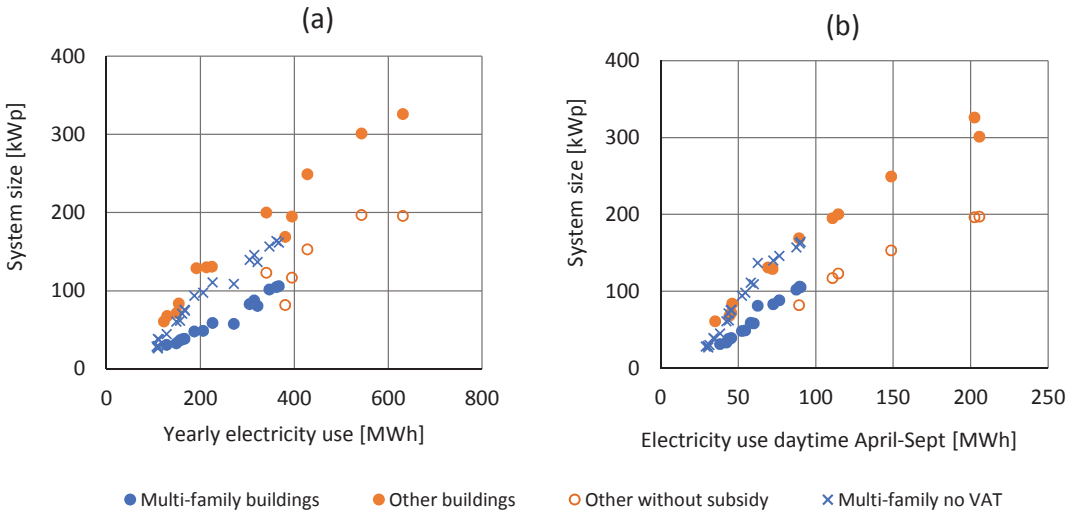

Fig. 3: Solar PV system sizes that results in the highest net present values (NPV) as a function of (a) total early electricity use and (b) electricity use that occurs during daytime (07h-18h) April – September. For multi-family buildings, the results are all with subsidy but with and without VAT. For systems in other buildings the results are shown with and without subsidy. Only systems with positive NPVs are included.

Without an investment subsidy no profitable system sizes were found for supply points in multifamily buildings, but for half of the supply points in other buildings. It can be seen that a daytime summer load of about 90 MWh, or yearly loads above 300 MWh, was required for the PV systems in other buildings to reach profitability. Regarding the supply points in multifamily buildings with yearly loads above 300 MWh, system sizes around 60 kW were close to being profitable.

3.2 Self-sufficiency and grid feed-ins

In this section, the share of the yearly electricity load that is covered by solar electricity, so called self-sufficiency, as well as solar electricity grid feed-ins are shown for the system sizes previously displayed in figure 3.

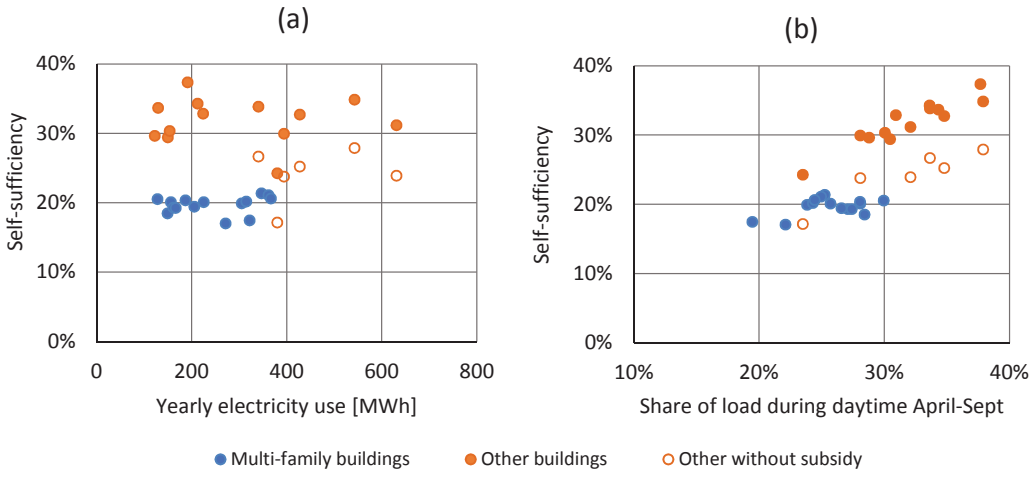

Fig. 4: Self-sufficiency (self-consumed solar electricity to total electricity use) as a function of (a) yearly electricity use and (b) share of the load that occurs during daytime (7h-18h) April-September.

Figure 4 shows that the PV systems optimally sized for supply points in multi-family buildings all result in a self-sufficiency around 20 %, while for the systems in other buildings it varies from above 20 to almost 40 %. For buildings other than multi-family houses, figure 4b shows a trend with increasing self-sufficiency with increase share of electricity load during daytime from April through September.

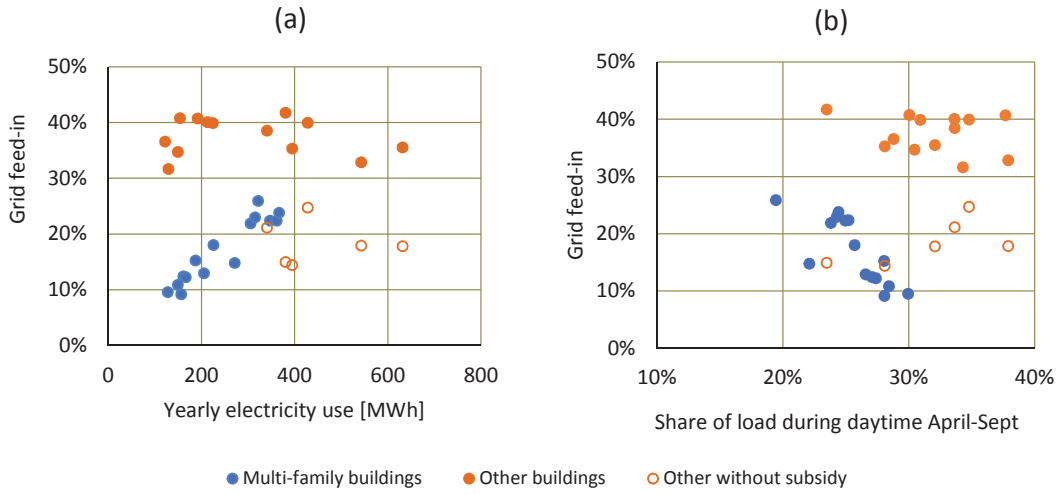

Fig. 5: Grid feed-in (over-generation of solar electricity to total solar electricity generation) as a function of (a) yearly electricity use and (b) share of the load that occurs during daytime (7h-18h) April-September.

Figure 5 shows the share of electricity that is fed to the grid, thus over-generation of solar electricity. The grid-feed-ins are about 10-25 % for systems in multi-family buildings and as much as 30-40 % for systems in other buildings (with subsidy) (figure 5). For multi-family buildings, the grid feed-ins increases with increased yearly use (figure 5a), but decreases with increased share of the load that occurs during daytime April through September. The same trends cannot be seen for other buildings.

3.3 Tax rebate

Eight of the electricity supply points in multi-family buildings and one of the supply points in other buildings have a main fuse smaller or equal to 100A, which makes them entitled to a tax rebate based on solar electricity fed to the grid (see section 2). Optimal system sizes for scenarios with 20% subsidy and tax rebate during 0, 10 and 30 years respectively are shown in figure 6.

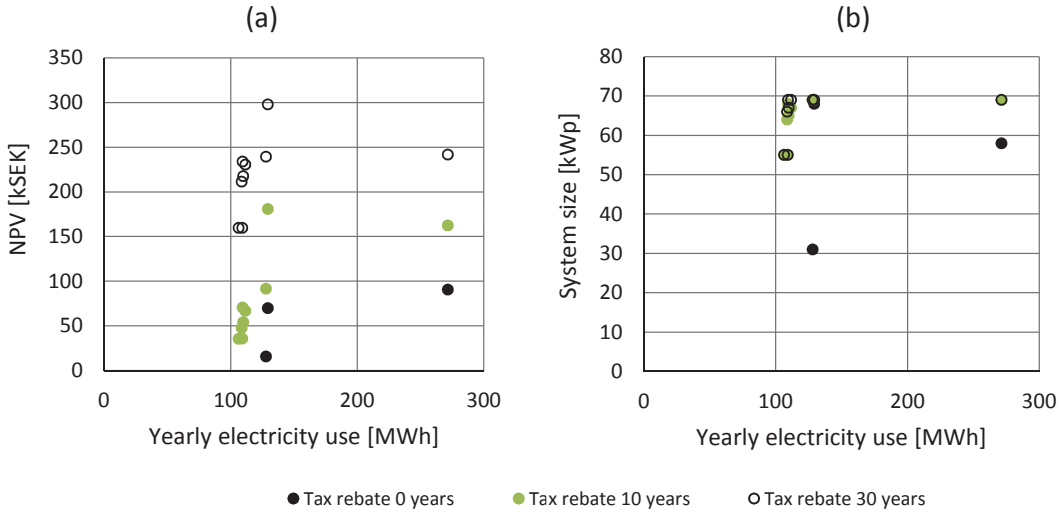

Fig. 6: Diagrams showing (a) maximum net present values (NPVs) and (b) corresponding system sizes for electricity supply points ≤ 100A, when the economic analyses are carried out with an investment subsidy as well as a tax rebate during 0, 10 or 30 years. Only systems with positive NPVs are included.

Only considering an investment subsidy, and no tax rebate, profitable PV systems were found for three of the supply points within this group (≤ 100A). With a tax rebate during 10 or 30 years on the other hand, all of the systems were profitable. As seen in figure 6, these two scenarios resulted in similar optimal system sizes, but with higher NPVs when including the tax rebate during a longer period of time.

3.4 Discount rate

A sensitivity analysis of the discount rate was carried out for all supply points in multifamily buildings. Figure 7 displays the resulting optimal system sizes and corresponding NPVs.

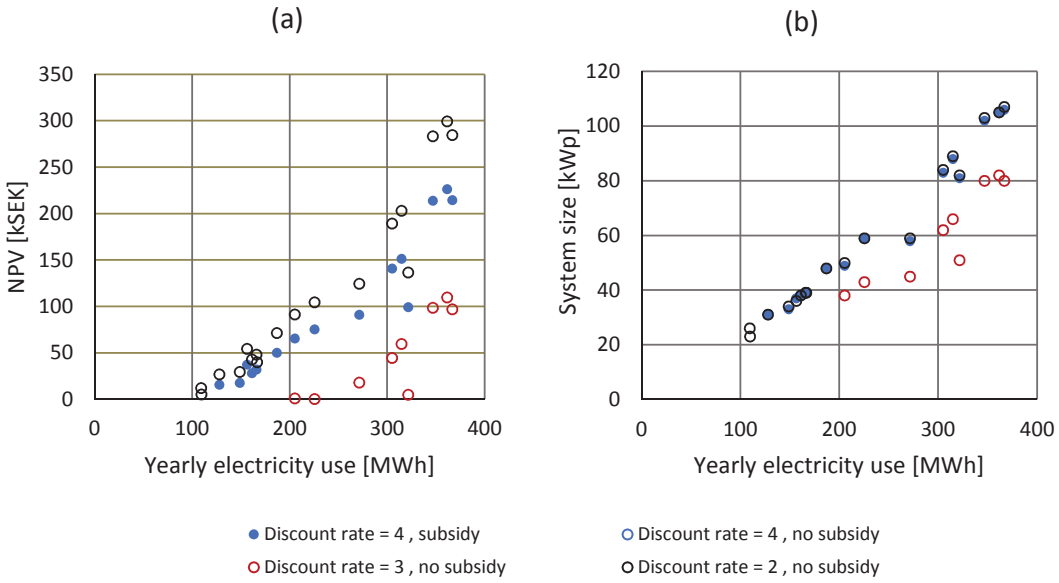

Fig. 7: Diagrams showing (a) maximum net present values (NPVs) and (b) corresponding system sizes for electricity supply points in multifamily buildings for economic analyses based on different discount rates. Only systems with positive NPVs are included.

Using a discount rate of 4 (base base), there were no profitable systems when the subsidy was excluded from the analysis. Accepting a discount rate of 3 would result in 9 profitable systems and with a discount rate of 2, twice as many are profitable. Moreover, figure 7 shows that with a discount rate of 2, the optimal same system sizes are the same as with a discount rate of 4 and a subsidy. However, the corresponding NPVs are higher in the former case.

3.4 Existing roofs

The results shown in previous sections were all were based on PV systems oriented to give a high yearly output and with an unrestricted system size. Since this is not often the circumstances in reality, this section explores the available areas offered by existing roofs and their effect on system profitability.

Figure 8 shows the optimal PV system sizes as well as the practically possible system sizes after consideration has been taken to available roof areas. The previously calculated PV system sizes for supply points in multi-family buildings (section 3.1) were generally small enough to fit the available roof areas. Only 3 out of 22 systems would have to be reduced (if sized with both subsidy and tax rebate). On the contrary, the systems sized for electricity loads in other building types were generally too large. When assuming a 15 degree module slope on flat roofs, all but one of these systems had to be downsized, 40% of them as much as 5 times or more. This is a result of relatively larger system sizes in combination with generally higher electricity use per floor area for these supply points, compared to the ones in multi-family buildings. Also, a large share of these buildings have a very small usable roof area relative to the floor area.

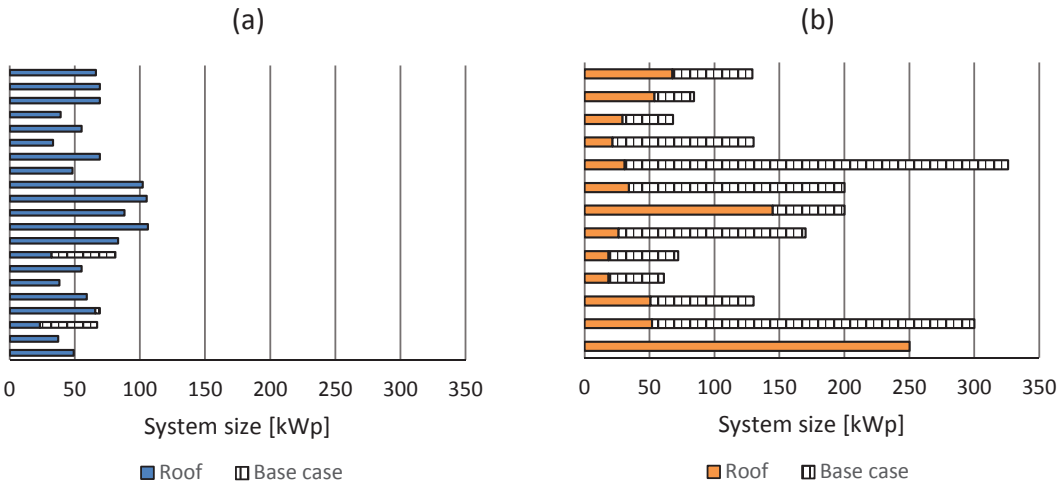

Fig. 8: System sizes before (base case) and after considering available roof areas in (a) multi-family buildings and (b) other buildings.

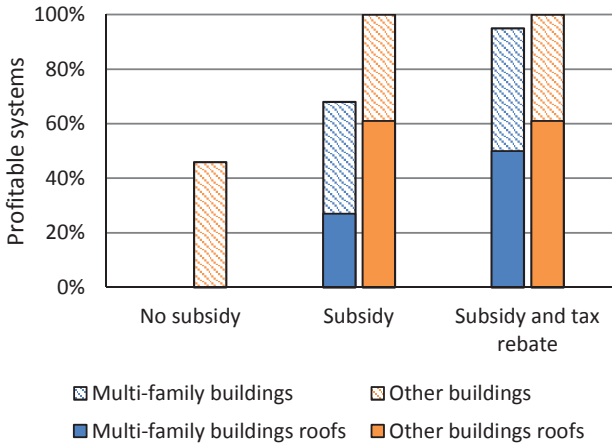

Fig. 9: Share of profitable PV systems in multi-family buildings and other buildings respectively before and after consideration of existing roofs. The results are shown for three different support scheme scenarios.

Reduced system sizes as well as adjustments of the module orientation to the slopes and directions of existing roofs affect the profitability of the PV systems. The shares of profitable systems before and after consideration of existing roofs are shown for different scenarios in figure 9. With a 20% investment subsidy, the number of profitable systems (positive NPVs) in multi-family buildings decreased from 15 to 6 and in other buildings from 13 to 8.

4. Conclusions

In general, the share of electricity use during hours of sunshine is lower for the studied multi-family buildings, compared to the buildings with other types of activities, thus giving them a disadvantage when matched to the electricity generation from a solar PV system. The effects of this difference can be seen as a lower self-sufficiency, as well as relatively lower profitability and smaller system sizes for supply points in multi-family buildings, compared to other buildings.

The currently available support schemes for solar PV in Sweden – an investment subsidy and a tax rebate based on net billing – turned out to be crucial for the profitability of a PV system investment in most of the studied buildings, but not all. Without any of the two, no profitable system sizes were found for the supply points in

multi-family buildings. Among the supply points in other building types on the other hand, the ones with a yearly electricity use above 300 MWh resulted in profitable systems also without additional financial support. With an investment subsidy of 20 %, more than half of the systems in multi-family buildings were profitable and all of the systems in other buildings. A fourth of the studied supply points had a main fuse smaller than or equal to 100A and were thereby also qualified for the tax rebate program. How much this would influence the profitability depends on the number of years that the program will be in place, which at this point is unknown. However, it was shown that with a subsidy, an additional tax rebate during either 10 or 30 years resulted in similar optimal system sizes. Taking the areas, slopes and directions of existing roofs into consideration drastically decreased the number of profitable systems both among the multi-family buildings and other buildings.

The economically optimal self-sufficiency (electricity use covered by solar electricity) was around 20 % for multi-family buildings and from 24 % up to almost 40 % for other buildings. Self-sufficiency was shown to be linked to the share of load that occurs during daytime April-September, rather than the size of the yearly load.

5. References

Berk, J., DeMarzo, P., 2014. Corporate Finance, third ed. Pearson Education Limited, Edinburgh Gate.

Egen el, 2015. Elcertifikatmätaren kan nu fås trådlös [Online], Available at: http://egenel.etc.se/ [Accessed Nov 2015] Energimyndigheten, 2015

Göteborg Energi, 2015a. Ersättningar och avgifter för produktion av el 2015 [Online], Available at: http://www.goteborgenergi.se/ [Accessed Nov 2015]

Göteborg Energi, 2015b. Elnätspriser i Göteborg 2015 [Online] Available at: http://www.goteborgenergi.se/ [Accessed Nov 2015]

Jordan, D.C., Kurtz, S.R., 2013. Photovoltaic Degradation Rates — an Analytical Review 12–29. doi:10.1002/pip

Keating, T.J., Walker, A. and Ardani, K., 2015. SAPC Best Practices in PV Operations and Maintenance Version 1.0. National Renewable Energy Laboratory, Golden, CO. Available at: http://www.nrel.gov/

Lindahl, J., 2015. National Survey Report of PV Power Applications in SWEDEN 2014. Available at: http://www.iea-pvps.org/

Nord Pool Spot, 2015. Elspot prices SE3 2014 [Online] Available at: http://www.nordpoolspot.com/ [Accessed Nov 2015

Energy Characterization and Optimization of New Heat Recovery Configurations in Hybrid PVT Systems

María Herrando[1], Ilaria Guarracino[2], Alejandro del Amo[3], Ignacio Zabalza[1], Christos N. Markides[2]

[1] Centre of Research for Energy Resources and Consumption (CIRCE),
University of Zaragoza, Zaragoza, Spain

[2] Clean Energy Processes (CEP) Laboratory, Department of Chemical Engineering,
Imperial College London, London (UK)

[3] EndeF Engineering, Zaragoza (Spain)

Abstract

The main goal of this research is to design and assess a new heat recovery (absorber-exchanger) configuration for a hybrid PVT solar panel with a geometry and from a material that maximises heat transfer while reducing weight and cost. To this end, firstly, potential configurations and materials for the absorber-exchanger unit that have the potential to meet the aforementioned aim are considered. The selected configurations (plus a benchmark reference case) are then applied to the same PVT panel in order to compare their performance. Once these configurations are defined in detail, they are modelled in 3-D finite-element and multiphysics (FEM and CFD) software, specifically COMSOL. The objectives are to: i) maximize the heat transfer performance of the different absorber-exchanger configurations, ii) obtain characteristic curves that describe the steady-state performance of the PVT panel in each case, and iii) compare the different alternatives with the reference case. The results show that a polymeric flat-box configuration is a promising alternative to commercial PVT panels, being able to achieve an improvement in the thermal performance of the PVT unit compared to the reference case (up to 5.1% higher optical efficiency and up to 48.7% lower heat loss coefficient), while also lowering the weight (up to 12%) and investment costs (up to 22%) of the PVT panel.

Keywords: *hybrid PVT panel, absorber-exchanger unit, heat transfer, energy efficiency, energy modelling*

1. Introduction

Currently, PV systems only use ~15% of the solar radiation, losing the remaining 85% as heat which, if recovered, could be used to heat a circulating fluid such as air or water. This has been the main motivation behind the development of hybrid PVT systems, which simultaneously generate electricity and a thermal output, and are considered a very promising technology for electricity and heat provision in buildings (Herrando et al., 2014). In particular, PVT-water (PVT-w) systems can increase the efficiency of PV panels by up to ~15% while generating hot water suitable to provide Domestic Hot Water (DHW) or space heating, so it is believed that this technology has an important potential in the residential sector, which accounts for 25% of the total electricity and 29% of the final energy consumption in the European Union (Antonanzas et al., 2015).

Previous research undertaken by the authors concluded that PVT-w systems can cover up to 50% of the total electricity demand and 35% to 50% of the DHW demand of a typical household located in London (the UK) (Guarracino et al., 2016c; Herrando et al., 2014), while completely covering the electricity demand and around 70% of the DHW demand if located in a household in Larnaca (Cyprus) (Guarracino et al., 2016a). Furthermore, as previous authors noted (Allan et al., 2015), the most desirable aspect of the PVT technology is the more efficient use of the roof space compared to stand-alone PV and solar collector systems.

Since their appearance, commercial PVT systems have been made available with increased in efficiency, making these panels an interesting option for integration in buildings. However, there are still very few companies worldwide that commercialise this type of PVT panel (Herrando and Markides, 2016) and most of the products available on the market do not have an optimised design for PVT applications. For this reason, the International Energy Agency (IEA), in its Task 35 for the development of PVT systems, insists on the need to optimise these systems from the manufacture and performance points of view, by developing projects that accelerate their economic viability to compete with current renewable energy technologies.

The main goal of this research is to develop an improved hybrid PVT module, with an optimal balance of energy efficiency, weight, cost, and ease of manufacturing. A number of alternative heat recovery (absorber-

doi:10.18086/eurosun.2016.08.22 Available at http://proceedings.ises.org

exchanger from now on) configurations are designed and compared with a reference case, all of them integrated in the same panel, for which a 3-D model is developed in COMSOL to model their energy performance, obtain their corresponding characteristic curve, and finally identify the design parameters which optimise the performance. The main focus is the study of a new absorber-exchanger configuration made of polymer and with a geometry that maximises heat transfer, while reducing the cost and weight of the PVT panel.

A detailed 3-D model of the PVT module is required to predict the non-uniform temperature distribution on the solar cells. In a previous work of Guarracino et al. (2016a), the 3-D PVT model showed a temperature gradient on the surface of a sheet-and-tube PVT module of ~10 °C during normal operating conditions, which led to a 5% drop in cell efficiency at the hot spots compared to cooler points, with a consequent loss in the PVT panel electrical performance. Therefore, the aim here is to achieve a uniformly cooled PVT module through the identification in the 3-D PVT model of the solar cells' hot spots and their elimination as far as possible.

In this work, a commercially available PVT sheet-and-tube collector (ECOMESH panel) model is implemented in COMSOL and validated with experimental results provided by the panel manufacturer, EndeF Engineering. COMSOL allows the investigation of more complex geometries which are not easy to model mathematically without a graphic tool, thus once the COMSOL model of the commercial PVT panel is validated, the model can be used with confidence to evaluate the temperature distribution and the thermal performance of different geometries of absorber-exchanger of the PVT unit. Specifically, a flat-box configuration is investigated in the present paper, and other more complex geometries will be considered in future work.

2. Hybrid PVT panel selection

In the last decades, significant research has been undertaken giving rise to a large number of PVT water (PVT-w) system configurations, both in terms of material and geometry. Copper is the most widespread material used for several reasons, such as its high thermal conductivity. Among all the absorber-exchanger configurations found in literature, parallel tubes (sheet-and-tube) is the most common (Chow, 2003; Chow et al., 2007; Herrando et al., 2014; Kalogirou, 2001; Tripanagnostopoulos et al., 2005; Zondag et al., 2003), also used in various commercially available PVT panels. Regarding the PVT panel cover, several configurations have been studied: uncovered, with one or two covers, with or without gap between the cover and the PV cells, as well as different filling gases: air, inert gases or vacuum. The authors decided to use as benchmark reference case a commercial copper parallel tubes PVT panel, ECOMESH (EndeF Engineering), with an innovative Transparent Insulating Cover (TIC), with which the thermal efficiency is significantly improved while maintaining the electricity generated (Antonanzas et al., 2015; del Amo et al., 2016).

On the other hand, other authors (Chow et al., 2006, 2007; He et al., 2006) have studied other PVT configurations, such as the flat-box structure made of extruded aluminium alloy, with the aim to improve the fin efficiency and bonding quality, and hence the heat transfer. Therefore, as a first alternative to the reference case, aluminium flax-box is considered in an attempt to reduce the weight and cost of the absorber-exchanger unit, while improving (or at least maintaining) the thermal efficiency of the panel.

However, the main innovation and focus of this work is the study of a new absorber-exchanger configuration made of polymer, as it is believed that some polymeric materials such Polycarbonate (PC) or Polyamide (PA) have several properties that make them an interesting option for PVT collectors, such as (Cristofari et al., 2009): low density, mechanical strength, no special surface treatment required, no corrosion, ease of manufacturing at mass production as there are fewer components to assemble, and lower production cost because the material is generally cheaper and the manufacturing time is reduced. Nonetheless, there are also some disadvantages, such as the low thermal conductivity, large thermal expansion and limited service temperature. Specifically, the ideal polymer for this application should have the following properties: UV protected, high thermal conductivity, water-resistant and glycol-resistant, good thermal range of utilization (-10/+150°C), a good mechanical strength and be chemically stable (Cristofari et al., 2002, 2009, 2012). Bearing in mind this, two types of polymer are considered in the present research: Polycarbonate (PC), as suggested by previous authors (Cristofari et al., 2002, 2012; Huang et al., 2001) and Polyamide (PA) without and with additives to improve its thermal conductivity (Ghaffari Mosanenzadeh et al., 2015). Regarding the geometry, flat-box structure is the most common configuration studied with different channel dimensions. Examples are Huang et al. (2001) who considered channels of 6×4 mm (W×H), or Cristofari et al. (2009) who studied bigger channels of 10×10 mm (W×H), based on the results of parametric analysis undertaken in previous research (Cristofari et al., 2002), which concluded that the highest thermal energy gain is achieved with a fluid layer

thickness of 1 mm. The study also concluded that, to collect more than 90% of this energy, the collector should have a fluid layer thickness smaller than 10 mm.

Although some of the absorber-exchanger configurations proposed in this work were studied previously, this research is innovative in the following aspects: i) these configurations were not implemented in high efficiency PVT units such as the one proposed (ECOMESH panel), but in PVT panels uncovered or covered with an air gap; ii) none of the studies found proposed a detailed study through 3-D FEM and CFD software of the absorber-exchanger alternatives considered in this work, integrated in the same PVT panel; iii) so far it has not been found any work that studied Polyamide with additives for the absorber-exchanger unit.

3. Methodology

Firstly, each absorber-exchanger configuration is defined in detail (geometry, technical specifications, etc.), integrated in the same PVT panel, and the energy balance of the PVT unit considering radiation, convection and conduction heat exchanges among the layers is developed. The reference PVT unit is then graphically implemented in COMSOL, together with its parameters and physics associated. Thanks to the symmetry of this sheet-and-tube geometry, only one riser tube of the PVT unit is implemented, significantly lowering the computation time and computational resources required by the 3-D model. The performance curve obtained is then compared with the empirical results provided by the PVT panel manufacturer (EndeF Engineering). Once the detailed 3-D model is validated, the different absorber-exchanger configurations are modelled to obtain the characteristic curve that describes the steady-state performance of the PVT panel in each case, i.e., the value of the optical efficiency (η_o) and linear and quadratic heat loss coefficients (a_1 and a_2). Finally, a simple cost analysis is undertaken to evaluate the different configurations studied from a cost perspective.

3.1 PVT panel modelling

The two main components of the PVT unit are the PV module and the rest of the solar collector, which can be further divided into the glazing, the thermal absorber and the riser water tubes (referred to, in the present work, as the absorber-exchanger or heat recovery unit) and the insulation layer (see Figure 1). Similarly to previous work by the authors (Herrando et al., 2014) and other PVT modelling attempts (Notton et al., 2005; Zondag et al., 2003), energy balances were written in order to evaluate the heat fluxes and temperatures throughout the unit. The equations were applied separately to each layer of the unit, instead of using global equations to find the average absorber plate temperature and energy flows (Kalogirou, 2004; Zondag et al., 2002). This allowed an estimation of the average temperatures of all the separate unit layers. Figure 1 shows the main heat transfer mechanisms of the PVT unit as well as the section with the different layers considered in the present work.

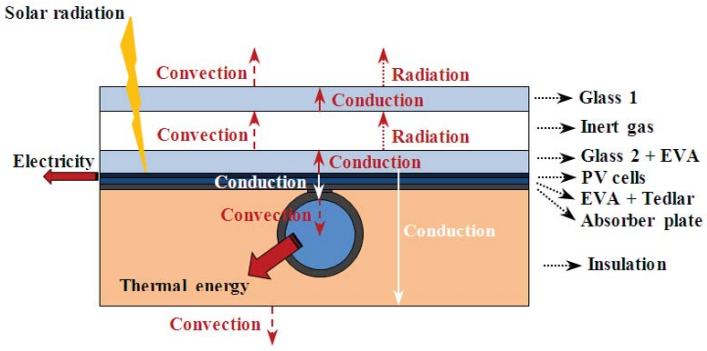

Fig. 1. PVT collector cross-section.

The PVT model was developed under the following main assumptions: i) Solar radiation is absorbed only by the collector (Agarwal and Garg, 1994); ii) the fraction of solar irradiance that is not converted into electricity in the PV cells and is not lost to the environment, is transmitted and absorbed in the absorber plate (Chow, 2003; Cristofari et al., 2009; Zondag et al., 2002, 2003), where most of it heats the water flowing through the collector and the rest is lost as heat (Agarwal and Garg, 1994); iii) the ambient temperature is considered uniform around the module (Cristofari et al., 2009; Notton et al., 2005) and heat transfer (losses) at the sides of the PVT collector are negligible (Notton et al., 2005), iv) the heat capacities of the PVT panel components (PV cells, Tedlar and insulation) are negligible compared to the heat capacity of water (Tiwari and Sodha, 2006); v) the water mass flow-rate is divided equally among all tubes of the collector (Bhattarai et al., 2012; Cristofari et

al., 2009), the water flow-rate within the collector tubes is uniform and heat is transferred to the tubes by forced convection; and vi) radiative thermal exchanges between the sides of the solar collectors' channels are neglected (Chow, 2003; Cristofari et al., 2009; Sandnes and Rekstad, 2002; Zondag et al., 2002). The model was run under steady state conditions (Tiwari and Sodha, 2006; Zondag et al., 2003).

To compare the performance of the different absorber-exchanger configurations studied, the thermal efficiency of the PVT unit is calculated, following both the ASHRAE method (ASHRAE Standard, 2013) and the ISO method (ISO, 2013) for the performance testing of solar thermal collectors, as there is currently no standard method to assess the performance of a PVT collector (Allan et al., 2015).

The former is used to determine the heat removal factor (F_R) and the overall heat loss coefficient (U_L) of the PVT collector (Allan et al., 2015), by measuring or calculating (as in this case) the thermal efficiency of the collector at different inlet temperatures in steady state conditions (Antonanzas et al., 2015; Collins and Zondag, 2009; Sandnes and Rekstad, 2002; Vokas et al., 2006),

$$\eta_{th} = \frac{q_u}{G_i} = F_R(\alpha\tau)_{PV} - F_R U_L \frac{T_{in}-T_a}{G_i}; \qquad \text{(Eq. 1)}$$

where η_{th} is the thermal efficiency of the PVT unit, q_u is the useful thermal energy extracted (W/m^2), G_i is the Incident irradiance (W/m^2), $(\alpha\tau)_{PV}$ is the combined transmission-absorption coefficient, T_{in} is the inlet water temperature and T_a is the ambient temperature.

Alternatively, in the ISO method, the PVT collector is also tested under steady state conditions but in this case the difference between the mean fluid temperature (T_{fm}) and the ambient temperature (T_a) is considered (Allan et al., 2015; Antonanzas et al., 2015; del Amo et al., 2016),

$$\eta_{th} = \frac{q_u}{G_i} = \eta_o - a_1 \frac{T_{fm}-T_a}{G_i} - a_2 G_i \left(\frac{T_{fm}-T_a}{G_i}\right)^2; \qquad \text{(Eq. 2)}$$

with $T_r = \frac{T_{fm}-T_a}{G_i}$; (Eq. 3)

where η_o is the optical efficiency, a_1 is the heat loss coefficient which accounts for the linear heat loss variation, a_2 is the temperature dependence of the heat loss coefficient which accounts for the quadratic heat loss variation, T_{fm} is the mean fluid temperature and T_r is the reduced temperature.

One of the main limitations of detailed CFD-FEM 3-D simulations is the significant amount of both time and computational resources required, especially in problems involving multiple processes, e.g. thermal, fluid flow, etc. This is the case of hybrid PVT panels, where heat transfer and fluid-dynamic equations should be solved simultaneously. Furthermore, surface-to-surface radiation should also be considered to properly model covered PVT units, which adds an extra complexity to the model. Consequently, to lighten the problem without simplifying the physics (which would reduce the accuracy of the 3-D model), some simplifications are required. In the configurations studied in the present research, both the reference case (parallel riser tubes) and flat-box collectors have in common that all the riser pipes behave likewise, as the water mass flow-rate is divided equally among all tubes of the collector (Bhattarai et al., 2012; Cristofari et al., 2009), therefore symmetry can be applied to solve this problem. As consequence, only one pipe was implemented in COMSOL, applying symmetry boundary conditions on both sides of the model. However, even though the 1-pipe 3-D model worked for an uncovered PVT collector, when the Transparent Insulating Cover (TIC) was implemented, together with the physics involved (heat transfer in fluids in the gap and surface-to-surface radiation between PV glass and glass cover), the problem became too heavy to compute. Consequently, an additional symmetry was applied, considering half of the pipe with its corresponding half fin width (see Figure 2). To ensure the validity of this assumption, the results obtained in COMSOL for half pipe were validated with those of an entire pipe for the uncovered PVT panel.

Fig. 2. (Left) Cross section of a pipe and its fin and (right) half a pipe modelled in COMSOL Multiphysics

In the case of the flat-box structure, the geometry is simpler so it was possible to model a whole channel (20×10 mm, 40×10 mm), or two in the case of smaller dimensions (10×10 mm, 6×4 mm and 3×2 mm).

Examples of the type of results obtained from the COMSOL simulations are presented in Figure 3, where it is possible to observe on the left the PV layer temperature distribution and on the right 10 slices at different collector lengths of the temperature profile of the PVT layers throughout half of a pipe's fin, for the reference case. The results obtained for the reference PVT unit in the COMSOL model where validated with the experimental performance curve provided by the PVT panel manufacturer (EndeF Engineering).

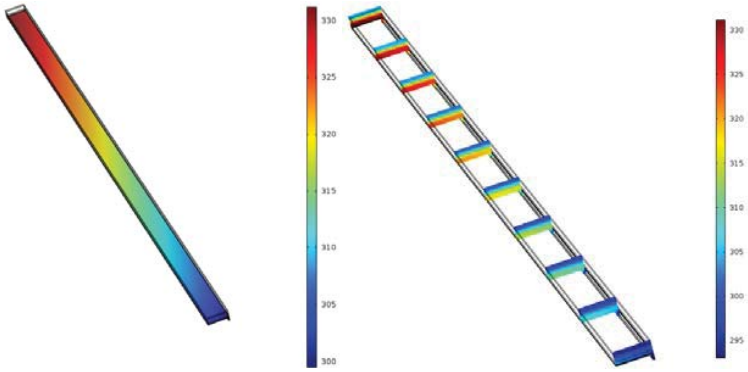

Fig. 3. (Left) PV layer temperature and (right) slices of the temperature profile in the different layers.

3.2 PVT unit parameters

The PVT unit taken as the reference case and modelled in this paper is the commercially available ECOMESH panel (EndeF Engineering), which consists of (from top to bottom): a Transparent Insulating Cover (TIC) comprising a transparent cover (glass) and an insulating gas (del Amo et al., 2016), a poly-crystalline (pc-Si) PV module, an EVA encapsulating film, an absorber-exchanger which transforms the solar radiation to heat and transfers it to the collector fluid (heat recovery unit), and a layer of insulation material at the bottom (see Figure 1). The absorber-exchanger unit consists of a sheet-and-tube heat exchanger in which water flows in (nine) copper parallel pipes (Antonanzas et al., 2015). The main PVT panel features are shown in Table 1. In order compare the different absorber-exchanger configurations studied in the present research, all the PVT parameters of the different layers were kept constant (panel dimensions, cover layers, PV cell, etc.), varying only the absorber-exchanger unit.

Tab. 1. Technical specifications of the PVT unit modelled (single module) (ECOMESH Panel) (EndeF Engineering)

Nominal power	240	W_p
Total gross area	1.64	m^2
Total aperture area	1.55	m^2
Recommended flow-rate range (nominal)	10-50 (30)	L/h
Reference PV module efficiency	14.7	%
Temperature coefficient of cell power (β_0)	-0.45	%/K
Normal Operating Cell Temperature (NOCT)	47	°C
Type of solar cell	Poly-crystalline (pc-Si)	

Tab. 2. Physical properties of the different polymeric materials considered

Properties	**PC**[*]	**PA**	**PA90-15**[+]	**PA30-33**[+]	**PA ideal**[$]
hBN load	-	-	15 vol.%	33.3 vol.%	Max.
Density (ρ) (kg/m^3)	1,180	1,140	1,170	1,390	1,390
Thermal Conductivity (k) (W/(m·K))	0.775	0.26	1.2	3.6	30
Heat capacity (c_p) (J/(kg·K))	1,200	1,700[†]	1,700[†]	1,700[†]	1,700[†]

[*] *(Cristofari et al., 2009, 2002);* [+] *(Ghaffari Mosanenzadeh et al., 2015);*

[†] *The same heat capacity is considered for all Polyamides (PAs) as the addition of hBN does not significantly influence this physical property and its effect on the absorber-exchanger performance (within this order of magnitude) is negligible.*

[$] *An hypothetical polymer with a high thermal conductivity (30 W/(m·K)) is considered to study to which extent it is possible to improve the thermal performance of the absorber-exchanger unit with additives.*

As alternative to the reference case, flat-box structure was considered. First of all, aluminium alloy was studied with two different channel dimensions, 20×10 mm (*W*×*H*) as suggested by several authors (Chow et al., 2006, 2007; He et al., 2006), and 10×10 mm (*W*×*H*), both with wall thickness of 2 mm. The properties of the aluminium alloy considered as those provided by Chow et al. (2006) (c_p = 903 J/(kg·K), ρ = 2702 kg/m^3, k = 237 W/(m·K)). Regarding polymeric materials for the absorber-exchanger unit, two main types of polymers were considered: Polycarbonate (PC) and Polyamide (PA), studying also some variations of the latter with different loadings of hexagonal Boron Nitride (hBN) particles (additive) (Ghaffari Mosanenzadeh et al., 2015). Table 2 summarizes the physical properties of different polymers considered.

Table 3 summarises all the geometric absorber-exchanger configurations considered in the present research.

Tab. 3. Summary of the absorber-exchanger configurations studied

Copper	Aluminium	Polymer		
3×2 mm 10×10 mm	10×10 mm 20×10 mm	3×2 mm • PC • PA30-33 6×4 mm • PC • PA30-33	10×10 mm • PC • PA • PA90-15 • PA30-33 • PA ideal	20×10 mm • PA • PA30-33 40×10 mm • PA • PA30-33

All the PVT configurations detailed in Table 3 as well as the reference case are studied at steady state with the same initial conditions, detailed in Table 4. It should be noted that, even though according to the PVT manufacturer of the reference case the nominal flow-rate for the sheet-and-tube configuration is 0.0083 kg/s (30 L/h), the same collector flow-rate than for the flat-box configurations has been considered in this study to compare the alternatives under the same operating conditions.

Tab. 4. Initial conditions and other important constant system parameters

G_i	Incident solar irradiance	1000	W/m^2
T_a	Ambient temperature	25	°C
v_w	Wind velocity	1	m/s
T_{in}	Mains water temperature	20.2	°C
$\dot{m}_c$	Collector flow-rate	0.00533[†]	kg/s

[†]*Optimum flow-rate for the 10×10 mm flat-box configuration according to Cristofari et al. (2002, 2009)*

To complete the technical assessment, a simple cost analysis was undertaken in which the investment cost of each configuration was estimated, and the electricity and heat generation were converted to the same unit (€/h per PVT panel), so as they can be added up. To this intend, the actual electricity and natural gas price (€/kWh) in Spain were considered (see Table 5).

Tab. 5. Cost factors for the economic analysis

Cost analysis		Reference
Natural gas price	€/kWh	0.0508
Electricity price	€/kWh	0.14
Polymer cost	€/kg	2.3-3*
Additive (hBN) cost	€/kg	150
Aluminium 20×10 mm flat box cost	€/m	2.33
Ratio copper/aluminium cost	-	1.27
Extrusion production cost	€/m	2

**Price varies slightly between this range for PA, PA30, PA90 and PC*

The aim of the economical assessment is the estimation of the payback time (PBT) of the panels with Eq. (4) from the cost savings (€/h per PVT panel) and the investment costs (C_0). The payback time is estimated at constant weather conditions (Table 4) and represents a simple figure that can be used for comparison. The

investment cost of the polymeric absorber-exchanger configuration is estimated from the cost of the raw polymeric material and the cost of adding the additive (hBN) where applicable, including also an estimation of the extrusion production cost. For the aluminium configurations, the price of off-the-shelf square channel tubes was considered, which was then extrapolated to the copper square channels considering the price ratio of both materials (Table 5).

$$PBT = \frac{C_0}{cost\ savings \cdot 24} \quad \text{(Eq. 4)}$$

4. Results and discussion

4.1 Model Validation

The 3-D model developed in COMSOL was validated against a manufacturer's performance curve. In Figure 4 the thermal efficiency (η_{th}) is plotted against the reduced temperature (T_r). The 3-D model fits the experimental results with an average error of 19%, when the inlet water temperature is in the range 10-80°C, being the thermal performance overestimated with the largest deviation at high temperatures of operation. It should be noted that for inlet water temperatures lower than 30°C, the error is below 10%. This suggests that the heat losses are underestimated in the model. It should be noted that the model assumes a perfect thermal contact between the PV module and the rear copper sheet, and between the absorber and the pipe which are bonded, both assumption might explain the overestimation of the thermal performance. Guarracino et al. (2016b) found that that a poor thermal contact between the PV module and the thermal absorber, which resulted in an insulating air gap between the layers, reduces the thermal performance of the module up to 30%.

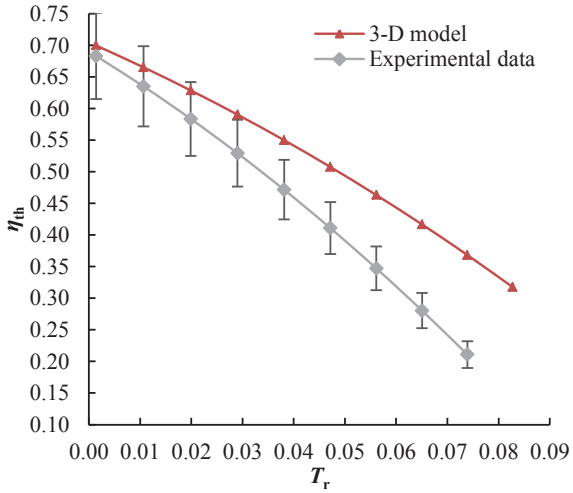

Fig. 4. Performance curves of the reference sheet-and-tube PVT unit for the COMSOL model, as well for the commercial ECOMESH panel (EndeF Engineering)

Regarding the heat transfer from the copper absorber to the tubes, a uniform bond made of copper and with fixed dimensions throughout the pipe is assumed, and both parameters influence the heat removal factor (F_R) and the overall heat loss coefficient (U_L) and hence the linear (a_1) and quadratic (a_2) heat loss coefficients. However, in reality depending on the bonding method (welding, ultrasounds, etc.) these will vary and hence the heat conduction will be achieved at lower or higher extent. Furthermore, lateral losses are not considered in the theoretical models. Finally, it should be noted that to obtain the experimental performance curve, the different experimental points are plotted in a T_r vs. η_{th} graph obtaining a cloud of points, and depending on which ones are selected to fit the curve, this might considerably vary .

4.2 Performance curve analysis

From the different PVT configurations studied and detailed in Table 3, first of all the effect of the material on the thermal efficiency of the PVT panel was assessed for the same channel dimensions (10×10 mm). First of all, it should be noted that, even though the thermal conductivity of all the polymers considered is lower than the one for copper, the heat transfer area between the polymer and the fluid is significantly larger than the sheet-and-tube configuration where the pipe is in contact with the copper only thought the bond. Furthermore, while for the sheet-and-tube collector the temperature on the PV cells reaches a maximum between two pipes, the temperature distribution on the PV surface is more uniform for the flat-box configuration, resulting in lower

thermal losses (top thermal losses for the sheet-and-tube q_{top} = 138.06 W/m^2, while for the copper 10×10 flat box, q_{top} = 95.04 W/m^2). This is in agreement with the results found by previous studies that used polymeric flat-box absorber-exchanger units (Cristofari et al., 2009; Sandnes and Rekstad, 2002). As consequence, Figure 5 left shows that all flat-box configurations have better thermal performance than the sheet-and-tube collector, with a higher optical efficiency (η_o) (up to 4.3% better) and significantly lower heat loss coefficient (a_1) (up to 28.4% lower) in all the cases.

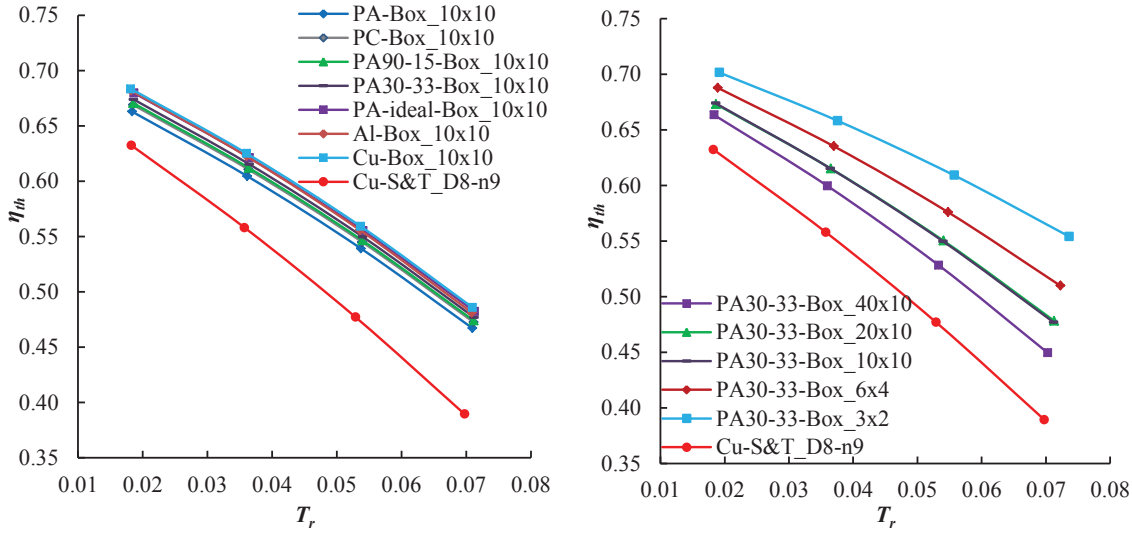

Fig. 5. Performance curves of the different PVT configurations studied for (left) same channel dimensions with different materials and (right) same material with different channel dimensions. In the legend, Cu-S&T_D8-n9, refers to 9 copper pipes of 8 mm external diameter.

It can also be observed that for the same channel dimensions, the difference in the performance curves between the best configuration (made of copper) and the worst one (made of Polyamide) is less than 5%, which implies that in this type of configuration the material selected is not determinant in the thermal performance of the PVT collector. This can be attributed to the small thickness of the polymeric absorber plate (1 mm).

On the other hand, Figure 5 right shows that the channel dimensions (for the same material) have a significantly higher influence on the thermal efficiency of the PVT panel. It is possible to observe that the smaller the channel is, the higher optical efficiency (η_o) (up to 5.1% better) and the lower heat loss coefficient (a_1) (up to 48.7% lower) compared to the reference case. The reason is that, as the total collector flow-rate was maintained constant in all the cases, the water velocity through smaller channels is higher as well as the convention heat transfer coefficient (which depends on the hydraulic diameter for laminar flows) (h = 1,141 W/(m^2·K) for the best case (3×2 mm) *vs*. h = 171 W/(m^2·K) for the worst case (40×10 mm)), so more heat can be extracted.

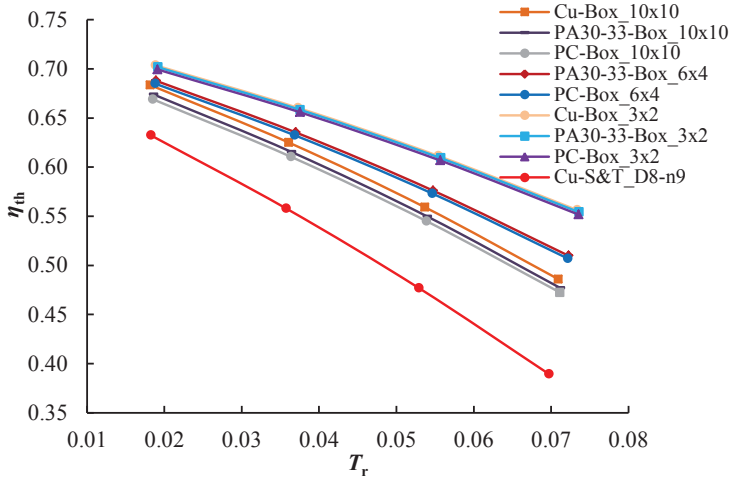

Fig. 6. Performance curves of the most promising PVT configurations studied.

In Figure 6, the most promising PVT configurations studied are presented, which are for channel dimensions of 10×10 mm or lower. These results corroborate that the channel dimensions are determinant in the thermal

performance of the PVT panel, while the material does not influence as much. Consequently, it is believed that, in the case of polymeric materials, the higher complexity and costs of loading the polymer with additives might not be outweighed with the increase in thermal performance of the PVT unit. Besides, even though the copper flat-box configuration has the highest thermal performance, the improvement achieved compared to off-the-self polymers (such as Polycarbonate (PC) or Polyamide (PA)) for the same channel dimensions is considerably small. Therefore, a techno-economic analysis is required to bring into consideration other factors such as investment cost and weight to draw conclusions.

4.3 Techno-economic analysis

Table 6 shows a summary of the techno-economic results obtained for the different PVT configurations studied. The heat removal factor (F_R) and the overall heat loss coefficient (U_L) are obtained with Eq. (1), plotting the thermal efficiency (η_{th}) for different water inlet temperatures (T_{in}), and fitting the points to a line (in all fittings, R^2 is higher than 0.997). The results obtained are equivalent to those shown in Figures 5 and 6, with the lowest heat loss coefficient (U_L) and the highest heat removal factors (F_R) in the PVT configurations with smaller channels.

Tab. 6. Summary of the techno-economic results of the different PVT configurations studied.

Configuration	F_R (-)	U_L (W/m^2-K)	T_{PV} (K)	T_{out} (K)	ΔT (K)	w_e (W/m^2)	q_u (W/m^2)	η_e (%)	η_{th} (%)	PBT (days)
Cu-S&T_D8-n9	0.677	-5.739	325.5	336.1	43.1	121.2	632.2	12.1%	63.2%	208
Cu-Box_3x2	0.766	-3.212	318.6	338.3	45.3	125.5	703.6	12.5%	70.4%	236
Cu-Box_10×10	0.738	-4.464	318.3	336.6	43.6	125.7	683.5	12.6%	68.4%	284
Al-Box_10×10	0.743	-4.501	318.3	336.7	43.7	125.6	681.9	12.6%	68.2%	246
Al -Box_20×10	0.744	-4.427	318.7	337.1	44.1	125.4	682.1	12.5%	68.2%	228
PC-Box_3×2	0.761	-3.240	320.3	339.7	46.7	124.4	699.3	12.5%	70.2%	152
PC-Box_6×4	0.748	-3.964	320.6	338.8	45.8	124.2	684.9	12.4%	68.5%	155
PC-Box_10×10	0.729	-4.492	322.5	338.0	45.0	123.1	669.0	12.3%	66.9%	159
PA-Box_10×10	0.722	-4.521	324.2	337.6	44.6	122.0	662.9	12.2%	66.3%	159
PA-Box_20×10	0.723	-4.474	324.2	337.7	44.7	122.0	664.0	12.2%	66.4%	158
PA-Box_40×10	0.711	-4.987	323.7	337.0	44.0	122.3	654.5	12.2%	65.4%	159
PA90-15-Box_10×10	0.731	-4.485	322.0	338.1	45.1	123.3	670.5	12.3%	67.0%	177
PA30-33-Box_3×2	0.764	-3.227	319.4	339.8	46.8	125.0	701.6	12.5%	70.2%	187
PA30-33-Box_6×4	0.751	-3.949	319.6	339.0	46.0	124.8	687.9	12.5%	68.8%	191
PA30-33-Box_10×10	0.734	-4.471	321.1	338.2	45.2	123.9	673.8	12.4%	67.4%	200
PA30-33-Box_20×10	0.734	-4.430	321.5	338.2	45.2	123.7	673.2	12.4%	67.3%	193
PA30-33-Box_40×10	0.721	-4.946	321.4	337.5	44.5	123.7	663.4	12.4%	66.3%	190

The highest average temperature of the PV cells (T_{PV}), and hence the lowest electrical output (w_e) and electrical efficiency (η_e), are obtained for the reference case, which is operating at lower collector flow-rate than the recommended one by the manufacturer, while if it is operated at the nominal flow-rate (0.0083 kg/s (30 L/h)), the PV temperature decreases to 318 K, value lower than for the rest of the configurations. Regarding the flat-box configurations, as expected, the highest PV cell temperatures are reached for the Polyamide (PA) absorber-exchanger, as it has the lowest thermal conductivity (see Table 2). In terms of channel dimensions, the electrical output and electrical efficiency increases as the channel dimensions decreases, as more heat can be extracted (higher useful heat obtained (q_u)) and hence lower PV temperature is reached. On the other hand, it is observed that outlet water temperature (T_{out}) and hence the increment in the water temperature throughout the PVT collector (ΔT) is higher for all flat-box configurations compared to the sheet-and-tube panel, as more heat can

be extracted (higher q_u), thanks to the higher heat transfer area of the channels.

Figure 7 shows the total cost savings (€/h) *vs*. the total investment cost (€) of each PVT panel alternative. It is possible to observe that there are two points which differ significantly from the rest (red diamonds) which correspond to the copper flat-box configurations, due to the significantly higher investment cost (as the cost of copper is higher than the aluminium and polymer costs) which is not outweighed by the higher cost savings. Similar results are obtained for the aluminium configurations (green squares). The lowest investment costs are for the polymers without additives, as expected, due to the lower cost of the raw material (dots on the left of the graph), and among them, the best results are obtained for the Polycarbonate (PC) flat-box configuration, in particular the 3×2 mm and 6×4 mm (upper and lower purple triangles respectively) with which high cost savings are achieved, compared to the rest of the channel configurations.

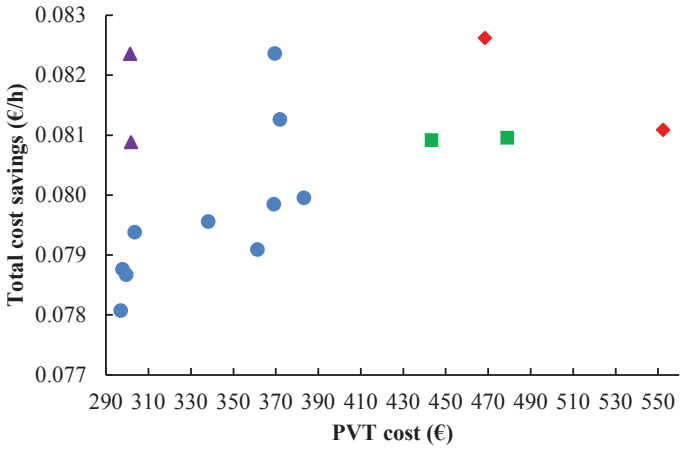

Fig. 7. Total savings (€/h) *vs*. total investment cost of the PVT panel for the different configurations studied. (Red diamonds = copper flat-box, green squares = aluminium flat-box, purple triangles = PC 3×2 mm and 6×4 mm flat-box configurations).

Finally, it is noted that the weight of all polymeric panels can be reduced by 7.5-12%, while the weight of the aluminium flat-box panels increase by 6% and 12% for the 20×10 mm and 10×10 mm configurations, and of the copper flat-box by 48% and 59% for the 3×2 mm and 10×10 mm configurations respectively, compared to the reference case; the absorber-exchanger unit accounts for 17.3% of the total PVT panel weight in the reference sheet-and-tube panel.

5. Conclusions

In this work, 17 different flat-box configurations for the absorber-exchanger unit (plus a benchmark reference case) are applied to the same PVT-w panel in order to compare their performance. The results show that all flat-box configurations have better thermal performance than the copper sheet-and-tube (reference) collector, which is attributed to the larger heat transfer area between the absorber and the fluid in the former configurations. Furthermore, with the flat-box configurations proposed, the temperature distribution on the PV surface is more uniform, avoiding the maximum PV cell temperatures reached between two pipes that appear in the sheet-and-tube collector. As a consequence, although the thermal conductivity of all the polymers considered is lower than the one for copper, all of them achieve a higher optical efficiency (η_o) (up to 5.1% better) and a lower heat loss coefficient (a_1) (up to 48.7% lower) compared to the reference case.

Amongst the different flat-box configurations studied, the results show that for the same channel dimensions, the material does not significantly affect the thermal performance of the PVT collector, with a variation of less than 5% in the performance curves between the best (copper) and worst (Polyamide) configuration. Conversely, the channel dimensions (for the same material) have a significantly higher influence on the thermal efficiency of the PVT panel, varying from around 7% at low water inlet temperatures up to 25% at higher temperatures, between the best (3×2 mm) and worst configuration (40×10 mm). This is attributed to the significantly higher heat transfer coefficient of the water flowing through the channels in the former case (nearly 7 times higher).

Finally, a basic economic consideration of the PVT panels showed that the slightly better thermal performance of the copper and aluminium flat-box configurations do not outweigh their significantly higher investment costs (as the cost of copper and aluminium are higher than the polymer costs). Similarly, among the different polymeric absorber-exchanger alternatives studied, it is observed that the loading of additives considerably

increases the investment costs, while only achieving marginal cost savings. Consequently, it can be concluded that the polymeric flat-box configuration is a promising alternative to commercial PVT panels, being able to achieve an improvement in the thermal performance of the PVT unit, while also lowering the investment costs (by up to 22%) and weight (up to 12%) of the PVT panel. However, further work is required to study the thermal expansion of these configurations and its effects on the PV module as well as the performance of the PVT panels under real weather conditions at short and medium term.

Acknowledgement

This work was developed during an international placement of the PhD Candidate Ms. María Herrando at Imperial College London, which was partially funded by University of Zaragoza, Fundación Bancaria Ibercaja and Fundación CAI under the CAI-Ibercaja Program of Research Placements [reference number IT9/16].

References

Agarwal, R.K., Garg, H.P., 1994. Study of a Photovoltaic-Thermal system - Thermosyphonic solar water heater combined with solar cells. Energy Convers. Manag. 35, 605–620.

Allan, J., Dehouche, Z., Stankovic, S., Mauricette, L., 2015. Performance testing of thermal and photovoltaic thermal solar collectors. Energy Sci. Eng. 3, 310–326. doi:10.1002/ese3.75

Antonanzas, J., del Amo, A., Martinez-Gracia, A., Bayod-Rujula, A.A., Antonanzas-Torres, F., 2015. Towards the optimization of convective losses in photovoltaic–thermal panels. Sol. Energy 116, 323–336. doi:10.1016/j.solener.2015.04.013

ASHRAE Standard, 2013. Standard 93-2003 Methods of testing to determine the performance of solar collectors.

Bhattarai, S., Oh, J., Euh, S., Krishna, G., Hyun, D., 2012. Simulation and model validation of sheet and tube type photovoltaic thermal solar system and conventional solar collecting system in transient states. Sol. Energy Mater. Sol. Cells 103, 184–193. doi:10.1016/j.solmat.2012.04.017

Chow, T.T., 2003. Performance analysis of photovoltaic-thermal collector by explicit dynamic model. Sol. Energy 75, 143–152. doi:10.1016/j.solener.2003.07.001

Chow, T.T., He, W., Ji, J., 2006. Hybrid photovoltaic-thermosyphon water heating system for residential application. Sol. Energy 80, 298–306. doi:10.1016/j.solener.2005.02.003

Chow, T.T., Ji, J., He, W., 2007. Photovoltaic-Thermal Collector System for Domestic Application. J. Sol. Energy Eng. 129, 205. doi:10.1115/1.2711474

Collins, M., Zondag, H., 2009. Recommended standard for the characterization and monitoring of PV/Thermal systems, Task 35 - Solar Heating and Cooling Programme (SHC).

Cristofari, C., Canaletti, J., Notton, G., Darras, C., 2012. Innovative patented PV/TH Solar Collector: optimization and performance evaluation. Energy Procedia 14, 235–240.

Cristofari, C., Notton, G., Canaletti, J.L., 2009. Thermal behavior of a copolymer PV/Th solar system in low flow rate conditions. Sol. Energy 83, 1123–1138. doi:10.1016/j.solener.2009.01.008

Cristofari, C., Notton, G., Poggi, P., Louche, A., 2002. Modelling and performance of a copolymer solar water heating collector. Sol. Energy 72, 99–112. doi:10.1016/S0038-092X(01)00092-5

del Amo, A., Martínez-Gracia, A., Bayod-Rújula, A.A., Antoñanzas, J., 2016. An innovative urban energy system constituted by a photovoltaic/thermal hybrid solar installation: Design, simulation and monitoring. Appl. Energy. doi:10.1016/j.apenergy.2016.07.011

EndeF Engineering, 2016. Technical Datasheet ECOMESH panel.

Ghaffari Mosanenzadeh, S., Liu, M.W., Osia, A., Naguib, H.E., 2015. Thermal Composites of Biobased Polyamide with Boron Nitride Micro Networks. J. Polym. Environ. 23, 566–579. doi:10.1007/s10924-015-0733-8

Guarracino, I., Freeman, J., Ekins-daukes, N., Markides, C.N., 2016a. Performance assessment and comparison of solar ORC and hybrid PVT systems for the combined distributed generation of domestic heat and power. International Conference on Heat Transfer, Fluid Mechanics and Thermodynamics.

Guarracino, I., Freeman, J., Markides, C.N., 2016b. Experimental validation of a 3-D dynamic solar- thermal collector model under time-varying environmental conditions. The 29th International Conference On Efficiency, Cost, Optimization, Simulation And Environmental Impact Of Energy Systems.

Guarracino, I., Mellor, A., Ekins-daukes, N.J., Markides, C.N., 2016c. Dynamic coupled thermal-and-electrical modelling of sheet-and-tube hybrid photovoltaic / thermal (PVT) collectors. Appl. Therm. Eng. 101, 778–795. doi: 10.1016/j.applthermaleng.2016.02.056

He, W., Chow, T., Ji, J., Lu, J., Pei, G., 2006. Hybrid photovoltaic and thermal solar-collector designed for natural circulation of water. Appl. Energy 83, 199-210. doi:10.1016/j.apenergy.2005.02.007

Herrando, M., Markides, C.N., 2016. Hybrid PV and solar-thermal systems for domestic heat and power provision in the UK: Techno-economic considerations. Appl. Energy 161, 512–532. doi:10.1016/j.apenergy.2015.09.025

Herrando, M., Markides, C.N., Hellgardt, K., 2014. A UK-based assessment of hybrid PV and solar-thermal systems for domestic heating and power: System performance. Appl. Energy 122, 288–309. doi:10.1016/j.apenergy.2014.01.061

Huang, B.J., Lin, T.H., Hung, W.C., Sun, F.S., 2001. Performance evaluation of solar photovoltaic / thermal systems. Sol. Energy 70, 443–448.

ISO, 2013. ISO 9806:2013 (e) Solar energy - solar thermal collectors - test methods.

Kalogirou, S.A., 2004. Solar thermal collectors and applications. Prog. Ener. Comb. Science 30, 231-295. doi:10.1016/j.pecs.2004.02.001

Kalogirou, S.A., 2001. Use of TRNSYS for modelling and simulation of a hybrid pv–thermal solar system for Cyprus. Renew. Energy 23, 247–260. doi:10.1016/S0960-1481(00)00176-2

Notton, G., Cristofari, C., Mattei, M., Poggi, P., 2005. Modelling of a double-glass photovoltaic module using finite differences. Appl. Therm. Eng. 25, 2854–2877. doi:10.1016/j.applthermaleng.2005.02.008

Sandnes, B., Rekstad, J., 2002. A photovoltaic/thermal (PV/T) collector with a polymer absorber plate. Experimental study and analytical model. Sol. Energy 72, 63–73. doi:10.1016/S0038-092X(01)00091-3

Tiwari, A., Sodha, M.S., 2006. Performance evaluation of solar PV/T system: An experimental validation. Sol. Energy 80, 751–759. doi:10.1016/j.solener.2005.07.006

Tripanagnostopoulos, Y., Souliotis, M., Battisti, R., Corrado, A., 2005. Energy, cost and LCA results of PV and hybrid PV/T solar systems. Prog. Photovoltaics Res. Appl. 13, 235–250. doi:10.1002/pip.590

Vokas, G., Christandonis, N., Skittides, F., 2006. Hybrid photovoltaic – thermal systems for domestic heating and cooling — A theoretical approach. Sol. Energy 80, 607–615. doi:10.1016/j.solener.2005.03.011

Zondag, H.A., de Vries, D.W., van Helden, W.G.J., van Zolingen, R.J.C., van Steenhoven, A.A., 2003. The yield of different combined PV-thermal collector designs. Sol. Energy 74, 253–269. doi:10.1016/S0038-092X(03)00121-X

Zondag, H.A., de Vries, D.W., Van Helden, W.G.J., Van Zolingen, R.J.C., Van Steenhoven, A.A., 2002. The thermal and electrical yield of a PV-thermal collector. Sol. Energy 72, 113–128. doi:10.1016/S0038-092X(01)00094-9

Conference Proceedings

EuroSun 2016
Palma de Mallorca (Spain), 11 - 14 October 2016

Horticultural crop production in plant factories with translucent solar cells and improvement of crops' marketability via supplementary monochromatic lighting

Akira Horibata[1] and Toshiro Matsumoto[1]

[1] Faculty of Biol.-oriented Sci. and Tech., Kindai Univ., Kinikawa, Wakayama (Japan)

Abstract

The rapid ageing of the population of Asian countries presents a demand for increased agricultural labor productivity. We are currently investigating the potential of a renewable energy-operated, energetically autonomous, sunlight combination-type plant factory for meeting this demand. In the factory, electricity is generated from translucent solar cells (TSCs) while improving the marketability of the horticultural crops cultivated within by supplementing the crops with monochromatic light using a portion of the generated power. Evaluation of the energy characteristics in a model glasshouse using TSCs revealed that sufficient electricity could be secured for supplementary monochromatic illumination. Subsequently, ultraviolet radiation–induced color change in chrysanthemum flowers and red light–induced early maturation of pea plants were investigated to evaluate the potential improvement of crop marketability from monochromatic light irradiation. The results demonstrated that the products' marketability could be improved with only minute power consumption.

Keywords: *crop marketability, monochromatic lighting, plant factory, translucent solar cell*

1. Introduction

Traditional family farming with low labor productivity has historically been practiced in many Asian countries, including Japan. However, as the population of Asian countries is aging rapidly, increasing the labor productivity of agriculture is a pressing issue. To solve this issue, the automation of agriculture, that is, the widespread use of plant factories, will become necessary. We have previously investigated the realization of a renewable energy-operated, energetically autonomous, sunlight combination-type plant factory (Watanabe *et al*., 2005). A conceptual diagram is shown in Figure 1. In this plant factory, translucent solar cells (TSCs) are installed in the roof of a glasshouse. Part of the incident solar energy is harnessed for power generation, while the light energy that passes through is used for by crops for photosynthesis. The electricity generated is used for management of the cultivation environment, such as ventilation of the glasshouse and operation of monochromatic lighting.

Plants use light not just for photosynthesis, but also as a signal of changes in their surroundings. Making use of this latter characteristic, we previously investigated the effect of supplemental blue light (460 nm) on the production of functional components in perilla planted in an unheated glasshouse, and found that the content ratio of a functional component, perillaldehyde, in plants grown with blue light was 60% higher than in control (Horibata *et al*., 2013). In this way, sunlight supplemented with additional monochromatic lighting has been shown to improve crops' marketability. Based on research revealing the specific photoreceptors present in plants, ultraviolet light (Christie *et al*., 2012), blue light (Ahmad *et al*., 1998, Christie *et al*., 1999), red light, and far-red light (Butler *et al*., 1959) are candidate wavelengths for supplementary monochromatic light expected to favorably affect crops. Crop marketability indicates superiority quality or value added in the market, such as early harvest time, unique flower color, excellent taste, or good nutritional properties. The specific properties important in the market depends on the type of crop, which span diverse categories such

doi:10.18086/eurosun.2016.08.08 Available at http://proceedings.ises.org

as flowers and ornamental plants, fruits and vegetables, or medicinal plants. Therefore, it is necessary to examine the effect of different kinds of supplementary lighting on various kind of crops with different economic values in order to refine and spread the use of supplementary monochromatic light.

In this study, we investigated the effect of supplementary monochromatic lighting in chrysanthemum flowers and pea plants for improving crop marketability, as well as the energy use characteristics of a sunlight combination-type plant factory equipped with TSCs.

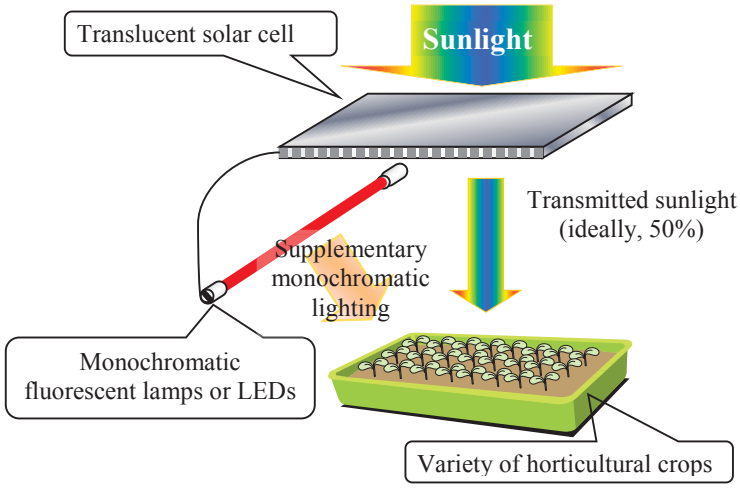

Figure 1. Conceptual diagram for divided use of solar energy in horticulture.

2. Material and Methods

2.1 Measurement of power output using a model glasshouse equipped with translucent solar cells

A model glasshouse (width 3.0 m, length 2.0 m, height 2.6 m; Kinokawa, Wakayama, Japan) was set up to evaluate the energy characteristics of a sunlight combination-type plant factory equipped with TSCs. As shown in Figure 2, TSCs totaling 6 square meters were mounted on the roof of the model glasshouse. Six plate of TSC model KN38 (Taiyo Industrial Co., LTD., Osaka, Japan) were used in this study. KN38 is originally a kind of the TSCs for building use and has been used for the outer wall of Suwon City Labor Welfare Center in Korea. Since numerous narrow slits (0.1 mm width) are in the non-transparent amorphous silicon layer at intervals of 8 mm × 1 mm, the overall light transmittance is about 10%. The output characteristics in one unit of about 1 square meter are as follows; the maximum power voltage is 54.5 V, the maximum power current is 0.66 A, and the maximum power is 36 W. Thus, the electromotive force of the entire 6 square meter panel is calculated at 3.96 A, 54.5 V. In terms of crop cultivation, a light transmittance of 10% is quite low, but as this was a preliminary model and as the incident scattered light from the normal-glass sides of the glasshouse may also be used in photosynthesis, tests were carried out in this light transmittance for the time being. In addition to the slit TSCs used in the present study, other TSCs designs with fine pores in the amorphous silicon solar cell (Takeoka *et al*., 1993) or using an organic thin-film solar cell (light transmittance 50%) (Lin *et al*., 2012) have been developed, but these were not yet available at the time that the present glasshouse was designed.

We performed model studies on the relation between insolation and power output and other parameters. A set of sensors for measuring solar operating current, solar operating voltage, amount of solar radiation, ambient air temperature, and humidity was affixed to the glasshouse. Data from each respective sensor were acquired at 10-minute intervals and transmitted to a monitoring system via wireless LAN. Unfortunately, due to system malfunctions, we were able to obtain the data of a consecutive few days only in March, August,

November, and December in 2015. Despite this, however, we were able to establish approximate trends for the amount of power generated by the TSCs over one year.

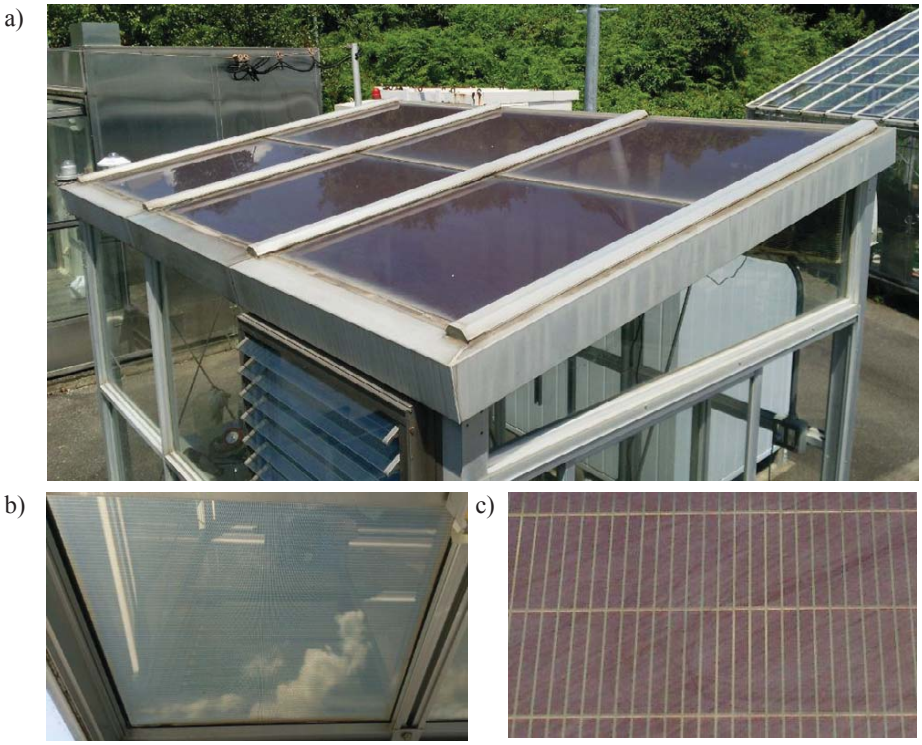

Figure 2. Model glasshouse used in this study.

a) Translucent solar cells installed in the roof of the glasshouse.
b) Light transmittance of the TSC (blue sky is visible through the solar cell).
c) Narrow slits in the amorphous silicon layer.

2.2 Improvement of marketability of horticultural crops by monochromatic lighting

2.2.1 Improvement of flower color of spray-type chrysanthemum by UV irradiation

Following this, we investigated the effects of supplementary monochromatic lighting on horticultural crops' marketability. Our first subject of investigation was flower color improvement in spray-type chrysanthemums (*Chrysanthemum morifolium* Ramat.), a flower with a history of symbolism tied to Japan. Spray-type chrysanthemums, as shown in Figure 3, are a category of cut flower that are tufted and of medium size. Colors range from reddish colors (purple, red, pink) generated anthocyanin-related pigments, yellowish colors (yellow, cream) generated by carotenoid-related pigments, orange colors, generated by both pigments, and white, without either pigment. Anthocyanin have superior antioxidant function and so are sometimes accumulated at high concentrations in tissues to be protected, such as young leaves. Biosynthesis of anthocyanin is particularly induced with oxidative stress due to UV irradiation (Chalker-Scott, 1999, Zhou *et al*., 2007). In light of these findings, we considered that darker color in chrysanthemum flowers would be induced by

UV irradiation.

Figure 3. Spray-type chrysanthemum.

Preliminary studies in red, red-purple, and yellow chrysanthemum varieties showed that flower color darkens upon UV irradiation in only those varieties that owe their color to anthocyanin-related pigments (red and red purple). Change in flower color was not observed at all in yellow carotenoid-related color varieties (data not shown). From this, the present study was targeted at anthocyanin-related chrysanthemums and two experiments were conducted to clarify the timing and intensity of UV irradiation required to induce a change in flower color.

In the first experiment, UV light of various intensity was used to irradiate buds before blooming and flowers after blooming in order to observe changes in flower color. A pink chrysanthemum variety, 'Elite Pink', was used, and 50 flowers cut at time of shipping, when the top terminal flower was just flowering (before-blooming) or at 1 week before shipping (after blooming) were obtained from Kinosato Agricultural Cooperative (Kinokawa, Wakayama, Japan). Before UV irradiation, in the before-blooming plot, all already-opened flowers were excised to retain the buds only, and in the after-blooming plot, all buds and partially opened flowers were excised to retain the newly bloomed flowers only. Here, different UV intensity conditions were effected by placing cut flowers at various distances from a single blacklight (FL40SBLB; Toshiba Lighting & Technology Co., Yokosuka, Japan; wavelength 270–430 nm, peak wavelength 350 nm). The UV irradiation intensity of the high- and medium- intensity plots were four and two times that of the low-intensity plot, respectively. UV irradiation was performed for 3 h (4–7 AM) daily. Petal color was evaluated from day 3 to day 12 after beginning UV irradiation in the before-blooming plot, and from day 1 to day 12 after beginning irradiation in the after-blooming plot. Color evaluation was performed using a fiber multichannel spectrometer (USB-4000; Ocean Optics Inc., Dunedin, USA) and the light reflected off petals upon irradiation with a standard halogen lamp was analyzed spectroscopically. Red color index was evaluated by using the relative intensity of red (wavelength; 645 nm) against green (wavelength; 500 nm) in the reflected light.

Based on findings that UV irradiation of buds was effective in changing flower color, in the following experiment, we attempted to assess the most effective developmental stage for inducing color change in flowers with UV irradiation in order to explore whether more efficient use of UV light could reduce irradiation. In this experiment, we used a different, pink-colored chrysanthemum variety, 'Kyonkyon'. A total of 150 flowers cut 2 weeks before shipping were obtained from Kinosato Agricultural Cooperative.

We designed 6 experimental plots, which each received 4 consecutive days of UV irradiation beginning at either 6, 8, 10, 12, 14, or 16 days before blooming; additionally, a control plot that received no irradiation was established. Due to the shorter UV irradiation period compared to the previous experience, the irradiation intensity and exposure hours per day were increased. Irradiation intensity was doubled by using two of the aforementioned 40 W blacklights, and exposure hours per day was doubled to 6 hours per day; however, this time was divided into three 2-h periods (5–7 AM, 1–3 PM, 9–11 PM) due to concerns about tissue damage caused by continuous UV exposure. After 5 days of blooming, redness of petals was evaluated as in the previous experiment.

2.2.2 Accelerated flower formation in pea plants using red light

Our second subject of investigation is the acceleration of flower formation in garden peas (*Pisum sativum* L.). This variety of pea is the same species as green peas, but is eaten at a slightly more mature phase of development. In Japan, forced pea culture is practiced using incandescent lamps, allowing for harvest to occur from early spring to early summer. Earlier flower formation leads to earlier harvesting and shipment, as well as higher market value due to the ability to supply a savored spring vegetable to expectant consumers earlier in the season. Flower formation in plants is controlled by the length of the continuous dark period. When plants are exposure to light for a short duration during the night, the continuous dark period is interrupted and shortened, falsely creating conditions that mirror the arrival of spring. In the case of peas, this manipulation leads to flower formation. One red light receptor pigment, phytochrome, plays a principal role

in measurement of the length of the continuous dark period, and we therefore attempted to accelerate flower formation in peas by exposure to red light at nighttime.

In this experiment, we used two pea varieties, 'Kishu-usui' and 'Kinokagayaki'. 'Kinokagayaki' is an improved variety of 'Kishu-usui' developed for with earlier flower formation. An LED array (1200 × 600 mm) was established using 230 high-brightness Flux LEDs (CH-LB3B-2; Peace Co., Koshigaya, Japan; 645 nm) as the red light source. A series of test plots with different red light intensity was established by placing 8 parallel plant containers (700 × 300 mm) at various regularly spaced intervals from the array, with the closest at 1500 mm. A control plot was also placed in an unexposed location. A total of 8 pea seeds were planted in each container on October 28th, and days from seeding to first bloom was observed. All experimental plots were irradiated with red light for 3 h nightly (1–4 AM), resulting in a continuous dark period of less than 8 hours, which is even shorter than the dark period on the shortest night of the year, the summer solstice.

3. Result and Discussion

3.1 Power output measurement using a model glasshouse equipped with a translucent solar cell

Figure 4 shows the monthly insolation for an average year in Wakayama, Japan, and the estimated amount of power generation calculated based on this solar radiation and the standard parameters of the TSCs provided by the supplier. The maximum estimated monthly power generated was 20 kWh in August, and the minimum was 8 kWh in December. Figure 5 shows the diurnal variation in power generation measured during 4 consecutive days in August or December, 2015. The maximum value of power generated in one day reached about 40 W in summer and about 20 W in winter. Of course, power generated on cloudy and rainy days was lower than that generated on days with clear weather.

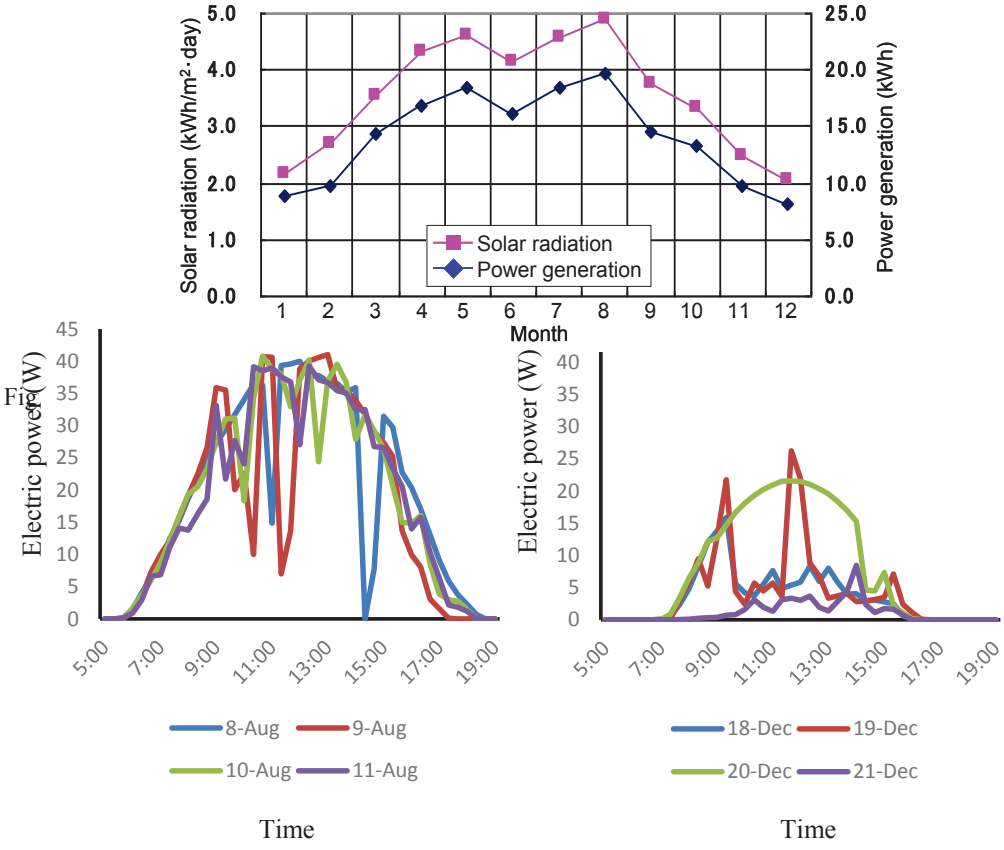

Figure 5. Diurnal variation of power obtained from TSCs at Kinokawa, Wakayama.

Table 1 shows the amount of global solar radiation and daily power generation measured for 2 or 4 consecutive days in March, August, November, and December, 2015. Global solar radiation shown is based on the public database of the regional meteorological observatory located closest to the experimental site, in Osaka, Japan (Japan meteorological agency website, http://www.data.jma.go.jp/gmd/risk/obsdl/). On a clear day, the amount of daily power generated was 0.827 kWh in summer (8 August) and 0.351 kWh in winter (20 December). On a cloudy/rainy day, daily power generated declined to as low as 0.051 kWh (21 December). Figure 6 shows the correlation of the amount of global solar radiation and the amount of daily power generation. The amount of daily power generation increased proportionately to the amount of global solar radiation. The conversion efficiency of the entire apparatus was calculated to be about 2%.

Table 1. Global solar radiation and daily power generation measured in continuous 2 or 4 days in March, August, November and December 2015.

Date	Global solar radiation (MJ/m^2・day)	Daily power generated (kWh)
28 March	22.80	0.618
29 March	4.49	0.120
8 August	23.96	0.827
9 August	25.78	0.760
10 August	22.74	0.821
11 August	23.30	0.813
13 November	5.13	0.131
14 November	3.24	0.080
15 November	7.12	0.192
16 November	13.10	0.401
18 December	6.16	0.149
19 December	8.42	0.183
20 December	11.34	0.351
21 December	2.20	0.051

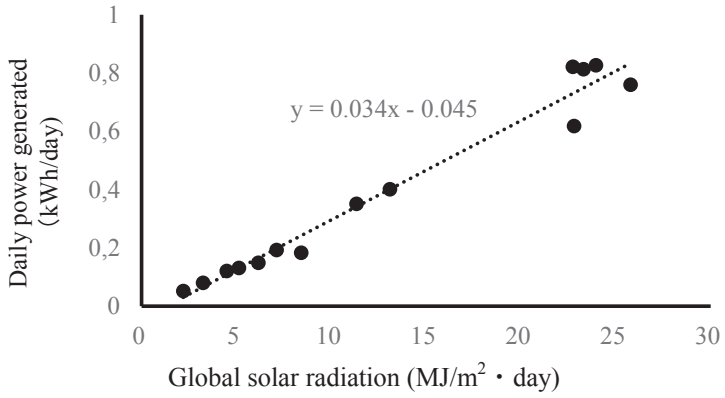

Figure 6. Correlation between the amount of global solar radiation and the amount of daily power generation.

3.2 Improvement of flower color in spray chrysanthemums by UV irradiation

Figure 7 shows the flower color of chrysanthemums subjected in various intensities of UV irradiation before or after blooming. For the group irradiated before blooming, the color of the high- and medium-intensity plots, but not the weak-intensity plot, was significantly more intense than that of the control plot. In contrast, in group irradiated after blooming, no significant differences in flower color were observed between any of the plots and the un-irradiated control. These results suggest that UV irradiation before blooming is necessary for induction of change in flower color in chrysanthemums.

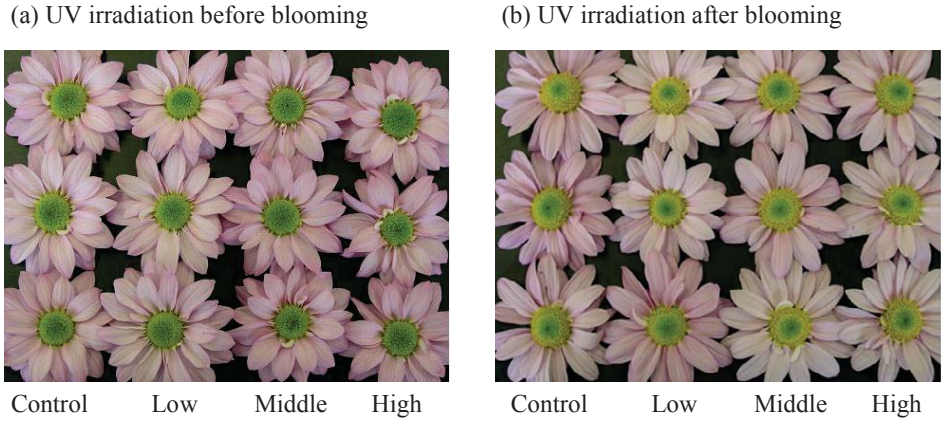

Figure 7. Flower color of chrysanthemums subjected to different intensities of UV irradiation before blooming (a) or after blooming (b).

In light of this result, we irradiated buds with UV light for 6 h/day for 4 consecutive days beginning between 19 and 6 days before blooming. Figure 8 shows the change in flower color in each plot. UV irradiation 13 to 10 days before blooming or 11 to 8 days before blooming resulted in significant change in flower color compared to the control plot. Taken together, this indicates that the period of 11 to 10 days before blooming, the overlapped period of these two plots, results in marked change in flower color. Because this period is equal to a few days prior to the general shipment time for cut flowers, it is economically preferable to perform UV irradiation for cut flowers harvested at a slightly earlier time than performing UV irradiation for an entire greenhouse.

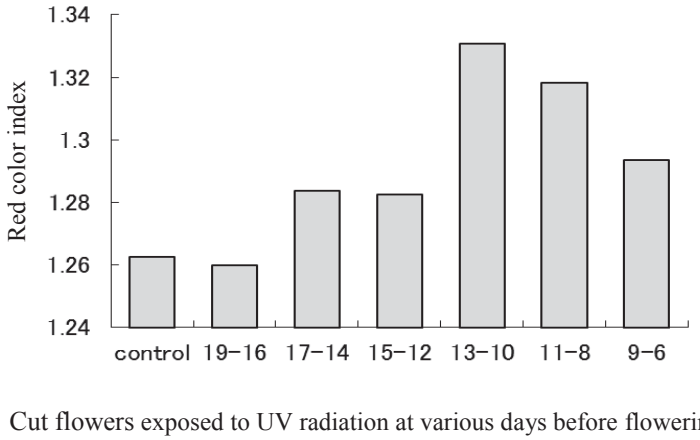

Figure 8. Flower color of chrysanthemums when buds were exposed to 4 days of UV irradiation at different developmental stages.

3.3 Accelerated flower formation in pea plants using red lighting

Figure 9 shows the effect the intensity of red light used for dark period interruption on the duration from seeding to blooming of the first flower cluster. In 'Kishu-usui', days to blooming was approximately 150 days in the control group, which was reduced by 10 days by dark period interruption. In 'Kinokagayaki', this reduction of the days to blooming in groups with dark period interruption was about 20 days. In both varieties, this reduction was maximized by irradiation intensity of 2 μmol/m^2/s, but no further effects were observed when the intensity increased beyond this point up to about 10 μmol/m^2/s. This suggests that the

minimum value of the red light intensity used in dark period interruption required to accelerate flower formation in peas is as low as 2 μmol/m^2/s.

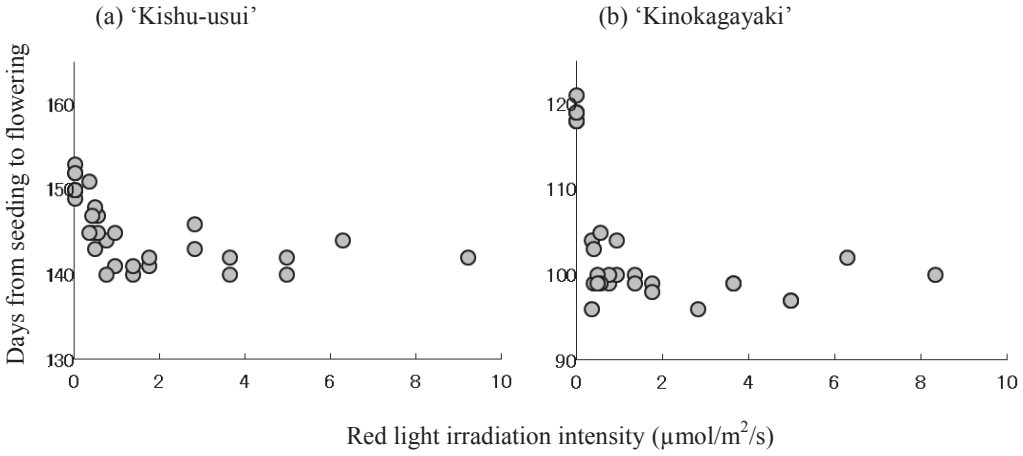

Figure 9. Effect of intensity of red light used for dark period interruption for promoting flowering in pea plants.

4. Conclusion

The power output of the model glasshouse equipped with TSCs, as investigated in 2015, was greatest on 8 August, at 0.827 kWh/day, and lowest in 21 December, at 0.051 kWh/day. In comparison, 0.240 kWh/day (40 W × 6 h/day) of electricity was used to induce chrysanthemum flower color change and 0.099 (33 W × 3 h/day) kWh/day was required to accelerate pea plant flower formation. Because we used a 40 W fluorescent tube (blacklight) with relatively high power consumption for chrysanthemum experiments, power consumption per day was as high as 0.240 kWh/day. However, since it was possible to narrow the irradiation period to only 4 days, the power supplied over multiple days would still be sufficient to power the lights for 4 days, even in winter, if appropriate energy-storage systems are available. For peas, we used daily irradiation consuming 0.099 kWh/day of electricity; however, as the required irradiation intensity necessary for acceleration was determined to be 2 μmol/m^2/s, the actual amount of electricity needed is estimated to be only 0.050 kWh/day. The present TSCs are capable of supplying this amount of electricity, and generally speaking, are fully capable of providing energy within this range.

The TSCs used in our study were amorphous solar cells with slits to give 10% transmittance; however, to grow healthy crops under TSCs, light transmittance of around 50% is desired. As stated by Lin *et al*. (2012), although TSCs with around 50% transmittance have been produced experimentally, their power generation performance is corresponding lowered as light transmission is increased. In the future, we must investigate the economic performance of our cultivation method when higher transmittance units are used.

The average amount of solar radiation in the plain part of Japan is about 1300 μmol/m^2/s. In contrast, up to about 800 μmol/m^2/s can only be used for photosynthesis of crops. Excessive solar radiation will increase leaf temperature, accelerate respiration, inhibit growth of the crop, and cause various obstacles due to production of active oxygen species. Therefore, in this study, we proposed to convert a part of excessive solar energy into electric energy by TSCs. And we expected to obtain some economic benefits by irradiating crops with red light that regulates the circadian rhythm of plants, or with ultraviolet light that induces the production of secondary metabolites. As a result of this study, we have shown that characteristics of horticultural crops can be changed by minute photostimulation of plants. The electricity required for these processes was obtainable from TSCs equipped within the cultivation facility. The marketability of products from sunlight combination-type plant factories can be expected to improve when these methods are used.

References

Ahmad, M., Jarillo, J. A., Cashmore, A. R., 1998. Chimeric proteins between cry1 and cry2 *Arabidopsis* blue light photoreceptors indicate overlapping functions and varying protein stability. The Plant Cell 10(2), 197-207

Butler, W.L., Norris, K.H., Seigelman, H.W., Hendricks, S.B., 1959. Detection, assay, and preliminary purification of the pigment controlling photoresponsive development of plants. Proc. Natl. Acad. Sci. USA 45, 1703–1708.

Chalker-Scott, L., 1999. Environmental significance of anthocyanins in plant stress responses. Photochemistry and Photobiology 70(1), 1-9.

Christie, J. M., Arvai, A. S., Baxter, K. J., Heilmann, M., Pratt, A. J., O'Hara, A., Kelly, S. M., Hothorn, M., Smith, B. O., Hitomi, K., Jenkins, G. I., Getzoff, E. D., 2012. Plant UVR8 photoreceptor senses UV-B by tryptophan-mediated disruption of cross-dimer salt bridges. Science 23, 1492-1496.

Christie, J. M., Salomon, M., Nozue, K., Wada, M., Briggs, W. R., 1999. LOV (light, oxygen, or voltage) domains of the blue-light photoreceptor phototropin (nph1): Binding sites for the chromophore flavin mononucleotide. Proc. Natl. Acad. Sci. USA 96, 8779-8783

Horibata, A., Matsukawa, T., Itoh, T., Watanabe, T., Matsumoto T., 2013. A novel cropping method for production of high functioning crops by utilizing on-site solar energy. Energy Procedia 57, 1502-1507.

Japan meteorological agency website, http://www.data.jma.go.jp/gmd/risk/obsdl/.

Lin, H., Chen, Y., Huang, Z., Chen, C., Lin, L., Lin, F., Wong, K., 2012. Highly efficient bifacial transparent organic solar cells with power conversion efficiency greater than 3% and transparency of 50%. Organic Electronics 13, 1722-1728.

Takeoka, A., Kouzuma, S., Tanaka, H., Inoue, H., Murata, K., Morizane, M., Nakamura, N., Nishiwaki, H., Ohnishi, M., Nakano, S., Kuwano, Y., 1993. Development and application of see-through a-Si solar cells. Solar Energy Materials and Solar Cells 29(3), 243-252.

Watanabe T., Matsumoto, T., Itoh, T., Horibata, A., 2005. High efficient use of solar cell power for supplemental fluorescent blue light in green house. Mem, School of Biol. Oriented Sci. and Tech. Kinki University. 16, 53-58.

Zhou, B., Li, Y., Xu, Z., Yan, H., Homma, S., Kawabata, S., 2007. Ultraviolet A-specific induction of anthocyanin biosynthesis in the swollen hypocotyls of turnip (*Brassica rapa*). Journal of Experimental Botany 58(7), 1771-1781.

.

Conference Proceedings

EuroSun 2016
Palma de Mallorca (Spain), 11 - 14 October 2016

Forecasting Models for an Intelligent Use of Renewable Energy Based on the Prediction of PV Energy

Alexander-Nicolai Köhler[1], Markus Fischer[1] and Steven Lambeck[1]

[1]University of Applied Sciences Fulda, Fulda (Germany)

Abstract

Renewable energy has many advantages, such as low environmental impact and endless resources. However, there are also some disadvantages. For example, such energy can be highly weather-bound and therefore not always available. This sometimes makes it necessary to store this time-dependent energy. On the other hand, it would be ideal to adjust the power consumption to the power generation. Forecasting the produced energy in order to plan its use in advance is thus highly advantageous. In photovoltaic technology (PV), forecast-based operation is very helpful to both electricity suppliers and plant operators. It prevents both the unwanted load peaks and the economic losses of the system. In this paper, a mathematical forecasting model is presented and validated. The main focus is on the forecast of energy production with PV systems. Electrical load forecasts are not examined here.

Keywords: *forecasting models, prediction, PV energy*

1. Introduction

Renewable energy has many advantages, such as low environmental impact and endless resources. However, there are also some disadvantages. For example, such energy can be highly weather-bound and therefore not always available. This sometimes makes it necessary to store this time-dependent energy. On the other hand, it would be ideal to adjust the power consumption to the power generation. Forecasting the produced energy in order to plan its use in advance is thus highly advantageous. In photovoltaic technology (PV), forecast-based operation is very helpful to both electricity suppliers and plant operators. Through the rapid expansion of PV and the fluctuating amount of electricity, the existing electricity network increasingly pushes its limits. To avoid damaging power peaks in the electricity network, various laws to limit the maximum feed-in capacity and to regulate the expansion of PV systems have been agreed upon in Germany. The operator of plants for generating electricity with PV are obliged to operate in accordance with feed-in management regulations or to limit the maximum active power feed to 70 percent of the installed capacity at the network transfer point. (EEG, 2014) Limiting the output means economic losses for the plant operator. This could be avoided by a forecast-based operating method of the PV system. Thus the energy consumption of the produced energy can be tracked by PV forecasts and suitable activation of electric loads. This prevents both the unwanted load peaks and the economic losses of the system. The basis for forecast-based operations are particular methods of predicting the PV production in order to plan the usage of the generated energy better. In this paper, a mathematical forecasting model is presented and validated. The main focus is on the forecast of energy production with PV systems. Electrical load forecasts are not examined here.

2. Forecasting methods

A forecast is defined as a statement about one or more events, conditions or developments in the future, based on information in the past (Theil, 1966). This information is usually in the form of time series, which are needed to calculate future values of the process (Schlittgen, 2001). Forecasts of load profiles of energy

doi:10.18086/eurosun.2016.08.04 Available at http://proceedings.ises.org

consumption and power generation are very important in the energy sector. Because the production and consumption of energy in the electricity grid have to be in balance at all times, forecasting methods are used to predict the energy consumption.

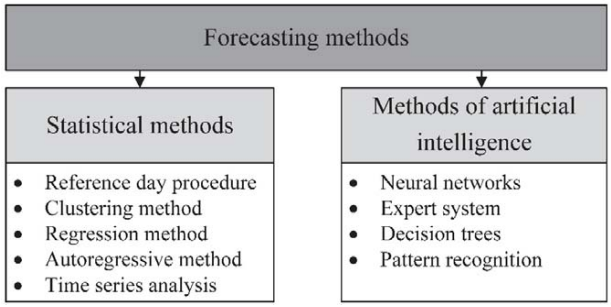

Fig. 1: Overview of typical forecasting methods

As shown in Figure 1, there are two typical types of forecasting methods. Statistical methods use mathematical combinations of historical data combined with information on the influencing variables to predict the behavior of consumers. However, if, due to the lack of information about influencing factors, no expedient prediction can be made, it could be helpful to use methods of artificial intelligence. Some artificial intelligence processes involve learning patterns of behavior with the help of historical data and project these patterns as a function of the expected operating conditions into the future. To select the optimal forecasting method for a particular application, it is also important to look for the required time horizon of the forecast. Short-term forecasts (forecast horizon of one day) can be created on the basis of measurements and current data. In contrast to long-term forecasts (forecast horizon of several months), mostly methods of artificial intelligence are used. These learn the different patterns of behavior based on historical data and project them into the future. Various forecasting methods can work differently depending on the influencing factors, such as climate or weather. Because of this, combined or cascaded models are increasingly used. Each of them operate for certain input variables and complement each other. A combination of different methods for a forecast can improve accuracy. (Prokhorova and Heimel, 2013)

3. Forecast of the PV capacity

The production of energy with a PV system is, in contrast to the electric load profile of a building, not affected by stochastic factors and can be described mathematically. A forecast of PV capacity can be done on the basis of weather forecasts and the characteristics of the PV system (type of assembly, module orientation, location, ...). The output of the generating PV system depends mainly on the available solar radiation at the place of installation, the installed modules and the efficiency of the inverter. The necessary basics for the calculation of the solar radiation range and the related performance calculation will be explained in the following sections with reference to Quaschning, 2015, Blank, 2005 and Schumacher, 2005.

3.1. Global radiation

The extra-terrestrial irradiance E_e varies due to the non-constant distance between sun and earth, which is between 1321 $\frac{W}{m^2}$ and 1412 $\frac{W}{m^2}$. Therefore, methods for the calculation must be chosen with care. An exact calculation of E_e is possible via the factor of eccentricity E_0, which can be determined by Duffie/Beckmann (Baehr and Stephan, 1994). The extraterrestrial irradiance is reduced by various influences as it passes through the earth's atmosphere. The horizontal extra-terrestrial irradiance $E_{e,hor}$ is reduced by the terrestrial atmosphere because of

- reduction by reflection at the atmosphere
- reduction by absorption of the atmosphere,
- reduction by Rayleigh scattering,
- reduction by Mie scattering.

All these influences can be analyzed though the transmittance τ. Determining the size of the influences is usually difficult, so it is possible to substitute the influences with a factor of the clearness index k_T. This is the ratio of the global irradiance $E_{G,hor}$ and the extra-terrestrial irradiance parallel to the surface of the earth $E_{E,hor}$.

The light on the surface of the earth is composed of a direct radiation component and a diffuse radiation component. Direct radiation $H_{dir,hor}$ comes directly from the sun and strikes in a certain point. The diffuse radiation $H_{diff,hor}$ is caused by scattering and reflection in the atmosphere and reaches a certain point indirectly. The sum of direct and diffuse radiation results the global radiation $H_{G,hor}$.

3.2. Calculation of the solar altitude

The current position of the sun, which is relevant for many calculations, can be determined for any place on earth. For this determination, two angles, the sun height γ_S and the solar azimuth α_S, are needed. According to DIN5043, the height of the sun is defined as the angle between the center of the sun and the horizon from the observer's perspective. The solar azimuth is the angle between geographic north direction and the vertical circle by the center of the sun (Fig. 2a).

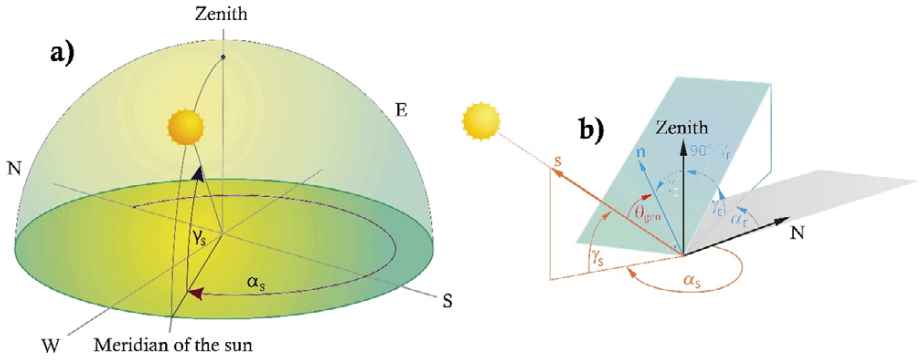

Fig. 2: Overview of typical forecasting methods (Figures based on Quaschning, 2011)

The height of the sun and the sun's azimuth also depend on date and time. The angle between the center of the sun and the celestial equator, also known as the solar declination δ, is an important variable. The position of the sun can be calculated with various algorithms. Some examples are SUNAE (Walraven, 1978), SOLPOS and SPA (Reda, 2008). In this paper, a method according to DIN 5034-2 is used to calculate the position of the sun. For each given point in time, it yields the height of the sun and the azimuth as a function of longitude λ and latitude φ.

To calculate the angle of incidence θ_{gen} at an oblique plane, the angle of inclination γ_E and the angle of rotation α_E is needed (Fig. 2b). Depending on the orientation of the generator surface and the angle of incidence of the sun, it is possible to calculate the direct radiation θ_{gen} on the PV modules. For this, the direction of irradiation $\vec{s}$ and the normal vector $\vec{n}$ of the surface are determined. The angle of incidence θ_{gen} can be calculated on the dot product of the two vectors $\vec{s}$ and $\vec{n}$. For detailed information, please refer to Fischer, 2016.

3.3. Radiation on oblique and aligned surfaces

The global irradiance $E_{G,gen}$ on an oblique plane is composed of a direct, a diffuse and a reflective component:

$$E_{G,gen} = E_{dir,\mathrm{gen}} + E_{diff,gen} + E_{refl,gen} \qquad \text{(eq. 1)}$$

Because it is a geometric problem, the determination of the direct irradiance $E_{dir,gen}$ on the oblique plane can be solved mathematically based only on the sun. The direct irradiance can be determined on the geometric relationships below (Fig. 2b), where $E_{dir,\mathrm{hor}}$ is the direct horizontal irradiance:

$$E_{dir,\mathrm{gen}} = E_{dir,\mathrm{hor}} \cdot \frac{cos\theta_{gen}}{sin\gamma_S} \qquad \text{(eq. 2)}$$

The calculation of the diffuse irradiance $E_{diff,gen}$ on an oblique plane differentiates between an isotropic and anisotropic approach. The isotropic approach means that there is always the same proportion of sky radiation in all directions. The radiance is neglected. For an exact calculation, the anisotropic approach is needed, because the radiance, especially in a clear sky, is very different. For this, Temps and Coulson, 1977, Klucher 1979 and Perez, 1987 proposed some calculation models. Temps/Coulson's anisotropic radiation model for a clear sky was expanded by Kulcher, who introduced the weather factor F_K for general sky conditions. Several studies, such as Jakhrani, 2016, show that this model provides good results when calculating diffuse irradiation. Therefore, the calculation of the radiation components is based on the Temps/Coulson/Klucher model.

The reflected radiation $E_{refl,gen}$ of the ground depends on the reflectivity of the surface and can be determined by using the albedo value A. The albedo value describes the reflectivity of the surface, which depends on its texture. Blank, 2005 provides an overview of different albedo values.

3.4. Calculation of performance

The performance of PV modules is specified in watt peak (Wp). This is achieved under standard test conditions (STC) and corresponds to the rated output of a module. The STCs are defined by DIN EN 60904-3 and correspond to an irradiance of $1000\frac{W}{m^2}$ and a module temperature of 25°C. Under normal conditions, the specified power value is rarely achieved in Germany. Despite this, it can sometimes be exceeded. How high the power value depends on the method of installation, module temperature, season and ambient temperature. The influence of the spectral distribution of light and the reduction in performance by shadowing and pollution is neglected in the model.

Deviation of the temperature is a crucial factor. If it deviates from STC, the performance will vary. The temperature coefficient that describes the deviation of the STC is about $-0.43\frac{\%}{K}$ on current PV modules (Fischer, 2016).

The dimensions of a PV system a usually chosen so that the nominal DC output is higher than the nominal AC output. This is common because the theoretical generator power under (STC) is achieved only a few days of a year. In addition, system losses like cable resistances between modules and inverters have to be taken into account. Because of this, it is common to make the power of the inverter smaller than the power of the generator.

4. Verification of the forecast

In order to verify the forecasts of the PV simulation program, the comparison of the results with measurements of real systems is necessary. In this case, the measurements are from a conventional single-family house in the center of Germany. In the following, the results of the PV forecast are compared with the real measurements and the results achieved are evaluated.

The weather data "global radiation" and "temperature" required for the simulation are available at local weather stations that are provided by Weather Underground, 2016. In each case, a summer and a winter day are used to compare simulation and measurements of the PV system. A disadvantage is that there are no forecast data for global radiation and temperature for the periods in which measurements of PV systems are available. Instead of this, the actual weather data is used in each case.

The measurement (measuring station 1) of the global radiation takes place very close to the aforementioned building. This provides an optimum condition for the verification of the PV forecasting model. The data can be measured in the immediate vicinity of the generator field and thus represent the global radiation that exists near the generator field.

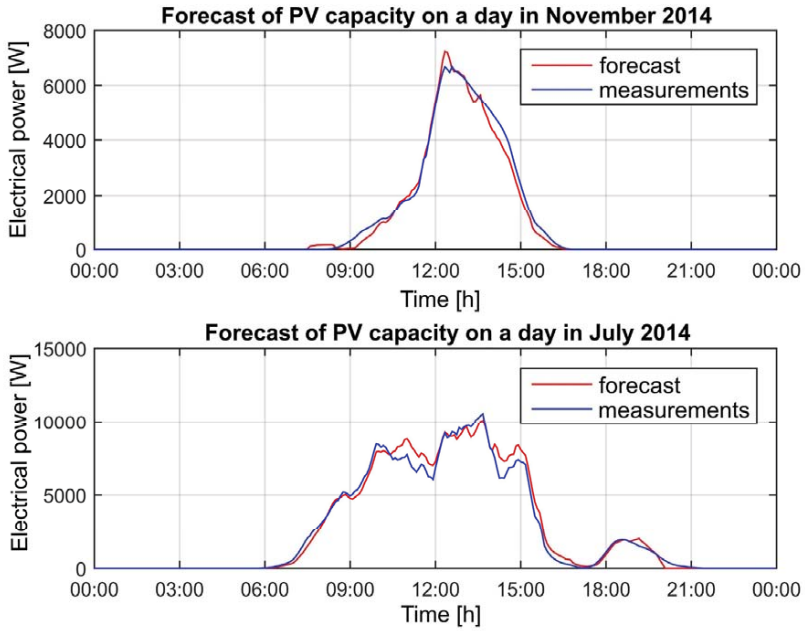

Fig. 3: Comparison between simulation and measurements on two days

Figure 3 shows the results of the forecast for a winter day (top) and a summer day (bottom) compared to the measured power values of the PV system. It can be seen that the calculated forecasts and the measured power curve correspond closely. The basic course of the calculated curve corresponds to the measured curve. Since the global radiation measurements were taken immediate vicinity of the PV system, it can be concluded that the existing minor forecast errors are caused by the calculation model or inaccurate measurements.

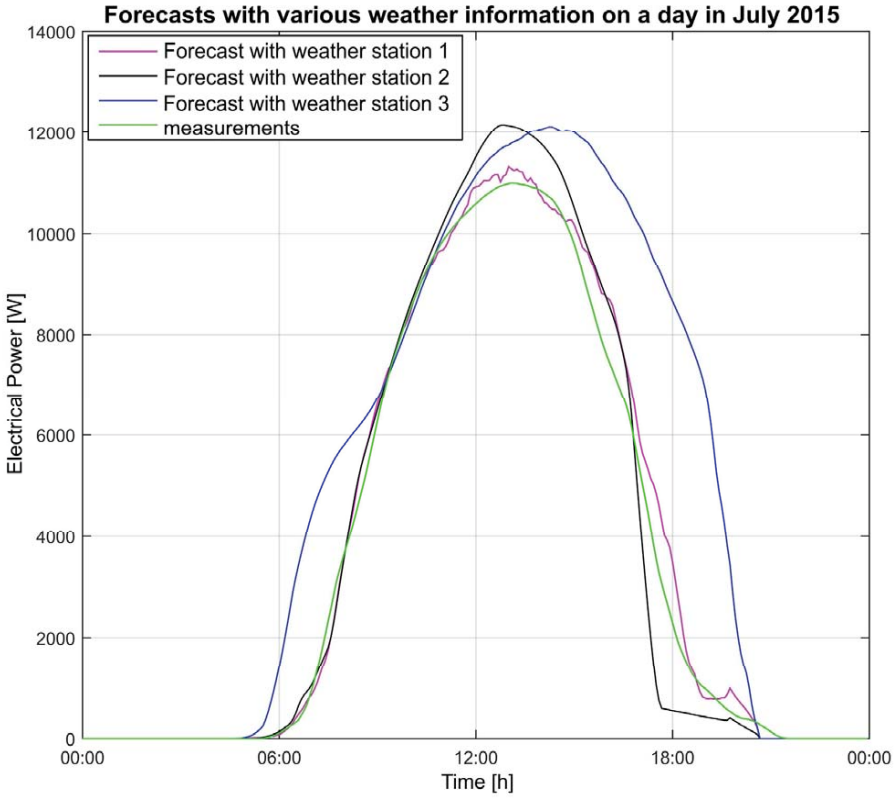

Fig. 4: Comparison between different forecasts depending on different weather stations

The above forecast with weather data from three different stations is useful for investigating the effects of the global radiation values on the forecast result. Figure 4 shows the measured curve of the power (green), and the forecasts based on the measurements of station 1 (magenta), station 2 (black) and station 3 (blue). It can be seen that the power curve of the forecast based on the measurements of station 1 is best predicted. The influence of the global radiation on the forecast results are clearly recognizable in the different weather stations. If the station is further away from the PV system, the differences between the measurements and the forecast are larger.

5. Conclusion and prospect

Due to the verification of the forecast model with data from the immediate vicinity of the PV system, it can be seen that the power curve of the PV system can be accurately predicted if the measurements and forecast data are of equivalent quality. The simulation program developed for the current paper makes it possible to predict the power of a PV system for a day with sufficient accuracy. In a near-optimal forecast, only negligible differences occur between forecast and real value. The simulations of a real pilot house at various summer and winter days clearly show that the forecasting model is highly dependent on the global radiation or temperature data.

Deviations between the forecast data and real measurement can be explained by simplifications in the calculation model, the neglect of shading losses and pollution and measurement inaccuracies. However, these deviations were not significant and the forecasting model is sufficient for the scope and requirements of this paper. Furthermore, since the input for and characteristics of a PV system are variable, a flexible and universal forecasting model such as the one developed for the current paper is also necessary and appropriate in other contexts and will be used in a further paper in conjunction with forecast data of global radiation and temperature.

6. References

Baehr, H.-D., Stephan, K., 1994. Wärme- und Stoffübertragung. Springer-Verlag. Berlin-Heidelberg.

Blank, T., 2005. Modellierung und Verifikation von Photovoltaikanlagen im Verteilnetz. Diploma thesis TU Munich.

Fischer, M., 2016. Untersuchung von prognosebasierten Verfahren für den effizienten Einsatz von erneuerbaren Energien in Verbindung mit Energiespeichern. Master thesis. University Fulda. Fulda.

EEG, 2014. Gesetz für den Ausbau erneuerbarer Energien (Erneuerbare-Energien-Gesetz). Bundesministerium für Wirtschaft und Energie. Berlin.

Jakhrani, A. Q., 2016. Selection of Models for Calculation of Incident Solar Radiation on Tilted Surfaces. World Applied Sciences Journal Vol 22.

Klucher, T. M., 1979. Evaluation of models to predict insolation on tilted surfaces. Solar Energy Vol. 23.

Perez, R., 1987. A new simplified version of the Perez diffuse irradiance model for tilted surfaces. Solar Energy Vol. 39.

Prokhorova, A., Heimel, S., 2013. Prognoseverfahren für die Energiewirtschaft: Klassifizierung und Anwendungsbereiche verschiedener Modelle. Zeitschrift für Energiewirtschaft Recht Technik und Umwelt. Edition ½.

Quaschning, V., 2011. Regenerative Energiesysteme – Technik, Berechnung, Simulation. 7th Edition. Carl Hanser Verlag. Munich.

Quaschning, V., 2015. Regenerative Energiesysteme. 9th Edition. Carl Hanser Verlag. Munich.

Reda, I., 2008. Solar Position Algoritm for Solar Radiation Applications. Technical Report NREL-Golden. Colorado.

Schumacher, J., 1991. Digitale Simulation regenerativer elektrischer Energieversorgungssysteme. PhD-Thesis. University Oldenburg.

Schlittgen, R., 2001. Zeitreihenanalyse. 9th Edition. Oldenbourg Verlag. Munich.

Temps, R. C., Coulson, K. L., 1977. Solar radiation incident upon slopes of different orientations. Solar Energy Vol. 19.

Theil, H., 1966. Applied Economic Forecasting. 2nd Edition. Amsterdam.

Conference Proceedings

EuroSun 2016
Palma de Mallorca (Spain), 11 - 14 October 2016

Heat Pump System Performance with PV System Adapted Control

Tomas Matuška [1,2], Jan Sedlář[1], Bořivoj Šourek[1]

[1] University Centre for Energy Efficient Buildings, Czech Technical University in Prague

[2] Faculty of Mechanical Engineering, Czech Technical University in Prague

Abstract

Combination of heat pumps with PV systems could significantly reduce the use of grid electricity from external supplier for space heating and hot water application. The paper presents an analysis of using PV adapted control for heat pump operation in two different alternatives and compares such advanced approach with conventional static approach. Both alternatives of the adapted control for the heat pump system achieve high solar fraction about 39 % compared to conventional approach (16 %) and more than 30 % higher seasonal performance factors.

Keywords: *heat pump, PV system, adapted operation*

1. Introduction

There is a number of measures to increase the energy performance of modern buildings today. Space heating demand has been minimized to limits of technical and economical possibilities in case of passive houses (envelope insulation, triple glazings, ventilation heat recovery, etc.). Domestic hot water systems use energy saving showers, insulation of hot water piping, time and temperature control of hot water circulation run, etc. Further savings can be expected with use of heat recovery from waste water. Electricity demand has been continuously reduced with an introduction of appliances with energy class A and better and implementation of modern daylighting principles together with proper control of LED artificial lighting.

Logical step ahead to decrease the energy demand in buildings is application of renewable energy sources. Heat pumps use the renewable energy from ambient environment, however they also need grid electricity to valorise the renewable heat to useful temperature level for space heating and hot water preparation. Grid electricity in Europe in general has high primary energy conversion factors (Molenbroek, 2011) dependent on the share of renewables in the grid in each country. The grid electricity in Czech Republic originates from non-renewable fuels (brown coal and nuclear power plants) which disqualifies the use of such electricity in heating applications within the frame of building certification. Simultaneously, the associated high CO_2 emission factor for electricity (Ecometrica, 2011) has a direct impact on the environmental assessment of the heating systems in subsidy schemes. Both implications lead to the effort of minimizing grid electricity use as an energy carrier for space heating and hot water preparation, despite the fact that costs of electric heating systems are the lowest.

Current trend in increasing the effectiveness of electricity use by the heat pumps is complemented by local production of renewable electricity by PV systems. The supply of local electricity production to a public grid has been complicated in several countries already (huge administration, negligible feed-in tariffs) and new installations are focused on the local use of renewable electricity from PV systems integrated into buildings. Production of electricity by PV systems and use of electricity by heat pumps seems to be an ideal combination to significantly reduce the external supply of electricity from public grid for space heating and hot water systems (IEA, 2014). However, the reality is not that simple as can be evident on first sight. The paper shows the potential of conventional state-of-art heat pump systems to use local PV electricity to increase the effectiveness of space heating and hot water preparation.

doi:10.18086/eurosun.2016.08.06 Available at http://proceedings.ises.org

2. Family house

Energy efficient family house under construction (2016) has been chosen for an analysis of potential to combine the heat pump and PV system under climate of Czech Republic. Family house has two floors with a space volume of 935 m^3 and total living floor area 190 m^2. Family house has a passive house concept, *U*-values of individual envelope constructions meet the recommended values for such high performance buildings. Saddle roof has a slope of 40° with south-north orientation. Design heat loss of the house is 4.5 kW. Low temperature floor space heating system has been used with design flow/return water temperatures 40/35 °C. Ventilation is provided by air handling unit with maximum flowrate 275 m^3/h using a heat recovery.

Ground source heat pump unit has been designed for the heat supply to house. Investor considered the PV system installation to increase the energy independency of the house operation. Analysis of different size of PV system and different control of heat pump operation has been performed by computer simulation to provide maximum use of electricity production from PV system to cover the heat pump needs and thus to minimize external supply from public grid. System simulations have been performed in TRNSYS with use of detailed mathematical models of building (type56), storage tank (type340) and heat pump (type250) with a borehole (type451). Simulation has been performed with time step of 2 minutes to evaluate the match between the the electricity load by heat pump and electricity production by PV system properly. Two subsequent identical years of system operation have been simulated to provide the balance in the ground source, only second year has been used for evaluation.

3. Conventional static approach

Conventional solution for the improvement of energy effectivity for heat supply in considered passive house has been based on combination of ground source heat pump of capacity 5.5 kW without speed control and PV system. PV system has been considered in different alternatives of installed nominal power without any advanced system control to adapt the operation of the heat pump according to available PV production. Heat pump is hydraulically connected to combined water storage tank with volume 900 l. Bottom part of the storage is connected to space heating system (SH zone) and is charged to required flow temperature according to outside air temperature (OTC control). Storage tank involves the integrated tube heat exchanger with surface area 6 m^2 for hot water preparation. Top part of the storage tank is dedicated to water heating (HW zone) and maintained at required temperature at minimum required set-point the whole year.

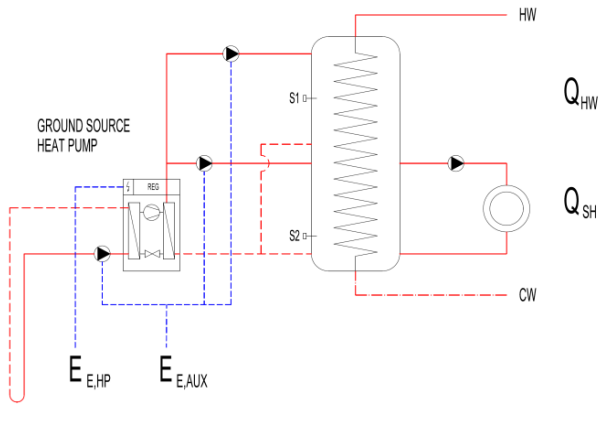

Fig. 1: Scheme of the conventional ground source heat pump system

The heat pump system delivers 3429 kWh/a of heat for space heating and 3063 kWh/a of heat for hot water to satisfy the energy demand of house. The heat loss of the storage tank amounts more than 550 kWh/a which degrades the performance of the whole system. Electricity use of the heat pump system is 2446 kWh/a, i.e. system seasonal performance factor *SPF* is 2.7. This is a value common for heat pump applications in passive houses because annual effectiveness is significantly influenced by high ratio of hot water preparation demand (47 % in given case) to be supplied at high required temperature 45 °C at any part of the year. Such temperature available at integrated heat exchanger output results in hot water set-point for HW zone permanently 55 °C.

Improvement of the system performance could be achieved by a combination with PV system. The PV electricity production can partially cover electricity use of the heat pump system. Tab. 1 presents the results of computer simulation in TRNSYS for different alternatives of PV system size: 1 kW_p, 3 kW_p and 6 kW_p. Except the grid electricity use and *SPF* the parameters monitored and evaluated were solar fraction f_{PV} (coverage of electricity use by PV system) and degree of PV electricity utilization r_{PV} (ratio of used PV electricity to produced PV electricity). The results show that installation of PV system slightly improves the total effectiveness of heat supply, however utilization of PV electricity is very low, at level of several percents. The explanation can be shown in two profiles of the electricity load and production including the temperatures in the storage tank for two typical weeks, first for summer season (see Fig. 2) and second for winter season (see Fig. 3).

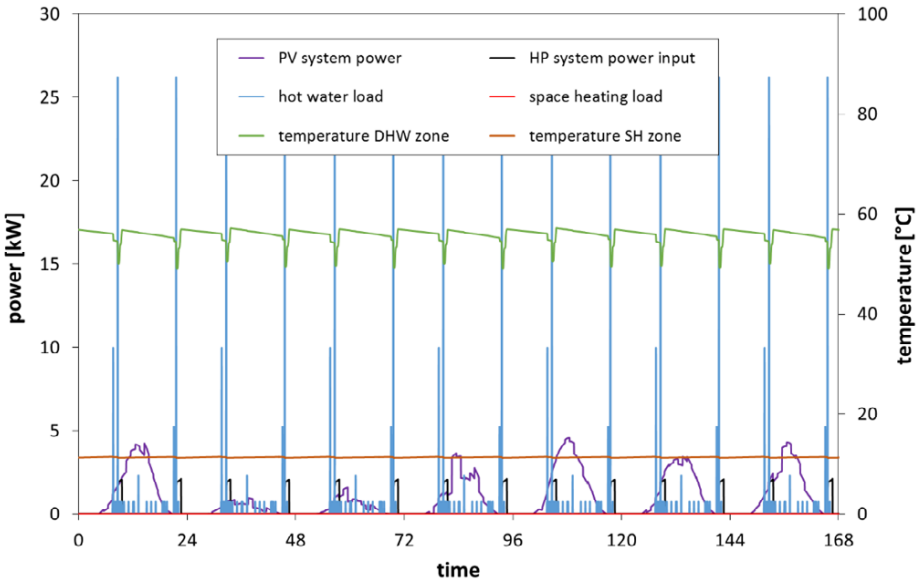

Fig. 2: Production and load profile of the conventional PV heat pump system in summer (6 kW_p)

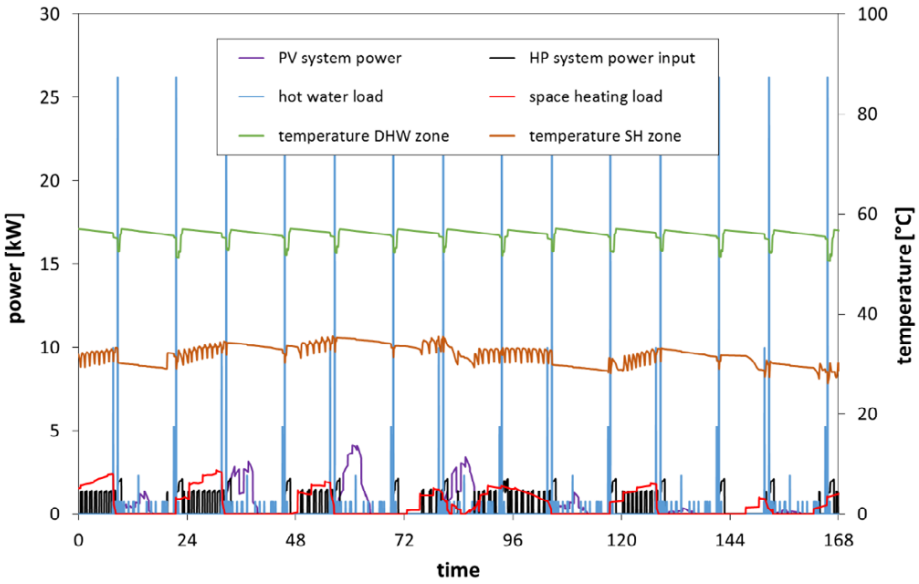

Fig. 3: Production and load profile of the conventional PV heat pump system in winter (6 kW_p)

As shown in Fig. 2 for summer season, the heat pump starts and uses electricity if temperature in HW zone decreases due to hot water load. Hot water load has the morning peak and the evening peak. Match between time of PV electricity production and electricity load by heat pump happens only partially during the HW zone

charging by heat pump after morning peak of hot water load (in optimum case).

Tab. 1: Results of TRNSYS simulation of PV heat pump system with conventional approach

Parameter	Reference alternative (no PV)	Alternative 1 kW_p (4 modules)	Alternative 3 kW_p (12 modules)	Alternative 6 kW_p (24 modules)
Electricity from grid W_{el} [kWh/a]	2446	2370	2217	2061
System *SPF* [-]	2.7	2.7	2.9	3.1
Solar fraction f_{PV} [%]	-	3	9	16
PV utilization r_{PV} [%]	-	8	8	6

From the point of the match between heat pump electric load and PV system electricity production (see Fig. 3) the situation is not more favourable in winter. Heat pump for space heating starts and uses electricity if temperature in SH zone decreases due to space heating load. The space heating in passive house occurs practically only during the night because the heat loss of the passive house is effectively compensated by solar heat gains during the day. Morning and evening hot water peak loads occur mostly within the time periods with no PV production.

4. Advanced approach – PV adapted operation of heat pump

An adaptation of heat pump operation to time period of PV system production ca be used in order to increase the utilization of PV electricity to cover heat pump electricity use. If the PV system actual power overcomes at given time a certain power threshold, algorithm of the system controller shifts the set-point for charging the storage tank and thus forces the heat pump to start. It practically means that in case of sufficient PV electricity production the heat pump is started, heats up the defined volume of storage tank to higher temperature than the required set-point (zone overcharging). The heat produced by the heat pump is stored in the combined storage tank for later use. The question of optimization process is the value of the power threshold for adapted operation of the heat pump system to minimize the annual electricity demand of the system. There were two alternatives for the control by set-point shift considered:

- PV-HW – alternative where the control shifts the required temperature 55 °C to 60 °C (considering the temperature limit of the heat pump) in the hot water zone of storage tank and sensor S3 is used as relevant temperature sensor (see Fig. 4 left) to enlarge the heated volume of the HW zone in storage tank;
- PV-SH – alternative where the control shifts the required temperature to 50 °C in the space heating zone of storage tank (see Fig. 4 right).

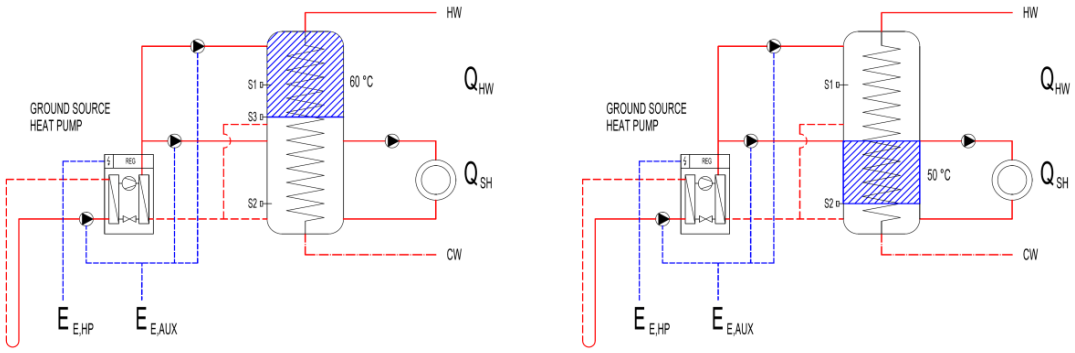

Fig. 4: Alternatives of adaptive control for heat pump system: PV-HW (left) and PV-SH (right)

To find an optimum power threshold for both adapted control alternatives a parametric analysis has been

performed. The results are shown in Fig. 5 and Fig. 6. While the system power input in regime of overheating the storage to high temperatures 50 to 60 °C overcomes the value of 2 kW, the optimum threshold found for both alternatives ranges around 1.0 kW for 3 kW_p PV system and around 1.25 kW for 6 kW_p PV system. Analysis for PV system with installed power 1 kW_p wasn't considered.

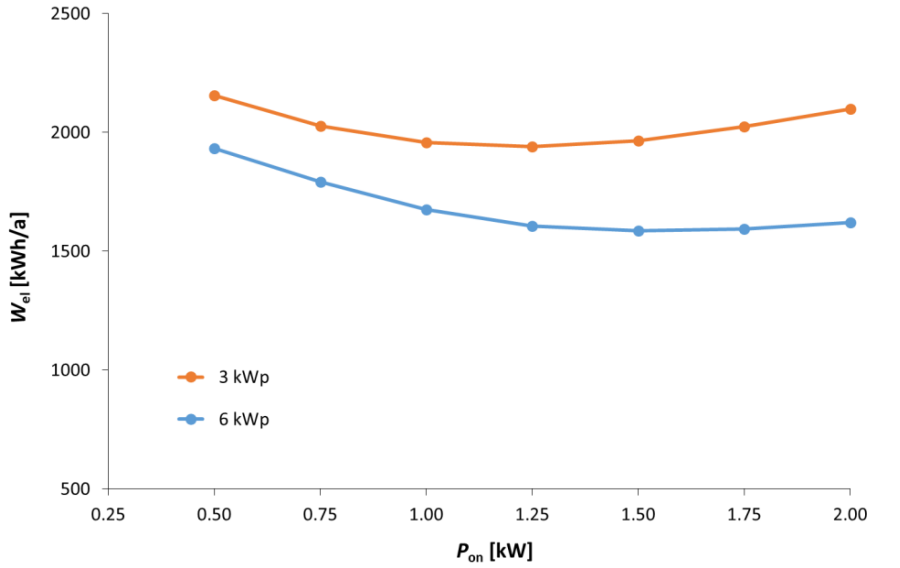

Fig. 5: Optimum value of power threshold for alternative PV-HW

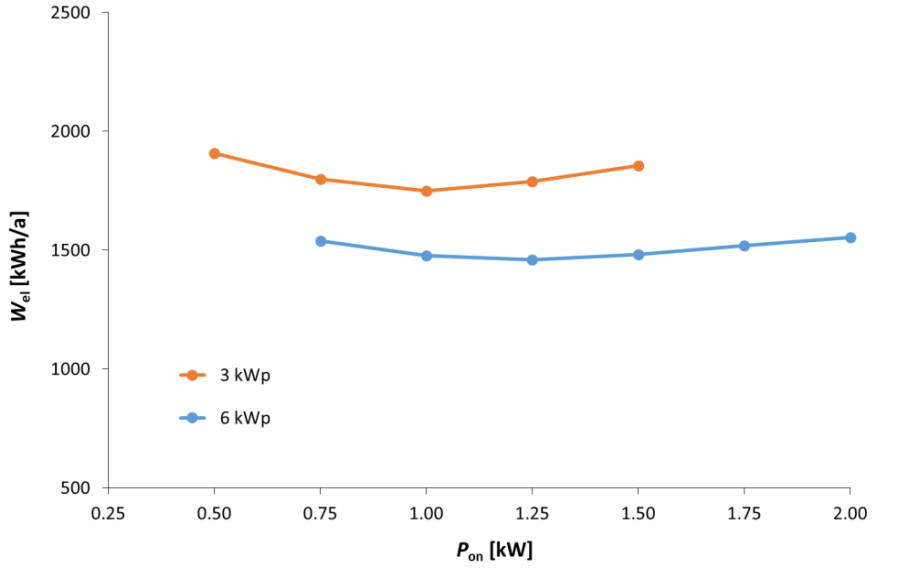

Fig. 6: Optimum value of power threshold for alternative PV-SH

Results of simulations with optimized thresholds are presented in Tab. 2 for both alternatives of the adaptive control and PV systems with nominal power 3 kW_p and 6 kW_p. Fig. 7 and 8 shows the profile of the electricity load and production, including the temperatures in the storage tank for adaptive system alternative PV-HW in the identical two typical weeks as it has been shown for reference system with PV system of nominal power 6 kW_p. Compared to the reference (shown in Fig. 2), there is obvious shift of heat pump operation to the daytime with PV electricity production due to adaptive control in summer season (see Fig. 7). Increased temperature and larger heated volume has a direct consequence that despite the evening and morning hot water peak load from the storage, the temperature in the HW zone of the storage (required temperature sensor) doesn´t decrease under the standard set-point value and the heat pump doesn´t start out of the daytime. Only the days without available power of PV system sufficient to forced starting the heat pump show the decrease

of required temperature in the HW zone in the evening hours and operation of the heat pump consuming the grid electricity. Similar function can be seen within the winter season (see Fig. 8 and compare it with Fig. 3), but with respect to lower PV system production the charging of HW zone in the storage tank to higher temperatures is not so frequent.

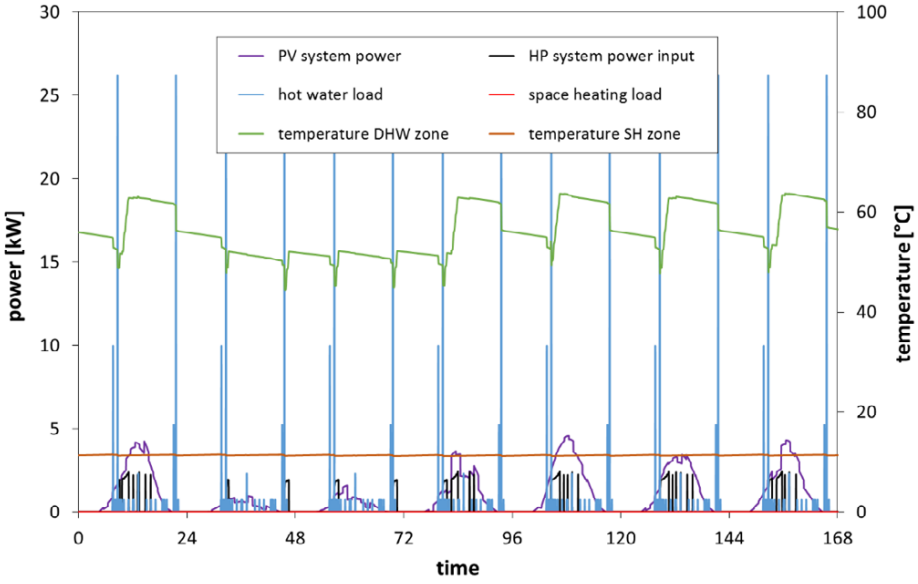

Fig. 7: Production and load profile of the PV heat pump system in summer (6 kW_p) – alternative PV-HW

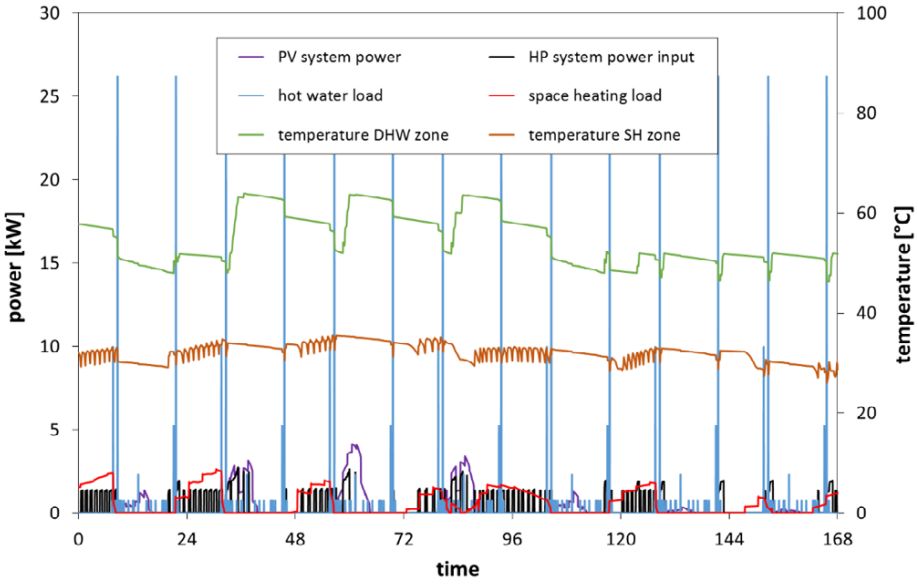

Fig. 8: Production and load profile of the PV heat pump system in winter (6 kW_p) – alternative PV-HW

Similar trend in system operation can be monitored also in adaptive control alternative PV-SH. Heat pump charges the SH zone of the storage tank to 50 °C whole year if the sufficient PV power is available. Hot water is preheated by integrated tube heat exchanger already in the SH zone. Therefore the temperature in HW zone doesn´t decrease significantly during the hot water loads (see Fig. 9 and 10). A very detailed comparison is shown in Fig. 11 where the PV system power and electric power input of the system for selected sunny winter day are presented for a conventional alternative without adaptation (above) and for PV-SH alternative with adapted control (below). Use of the PV electricity for overcharging of the storage tank by heat pump can shift significant amount of "night demand" of grid electricity to daytime and cover it from PV system. Temperatures shown in graphs belongs to temperature sensors positions dedicated to control of storage tank charging in both

zones (HW, SH).

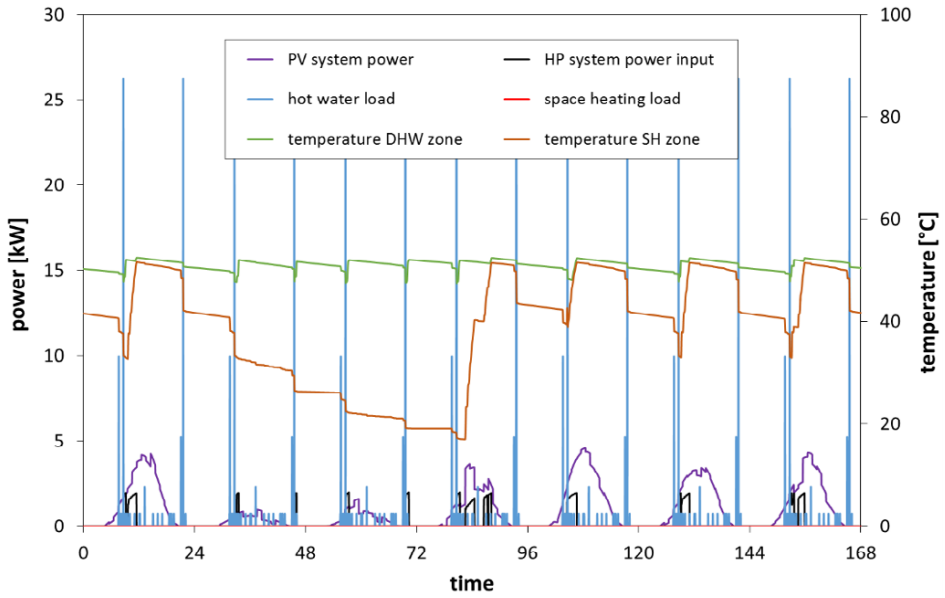

Fig. 9: Production and load profile of the PV heat pump system in summer (6 kW_p) – alternative PV-SH

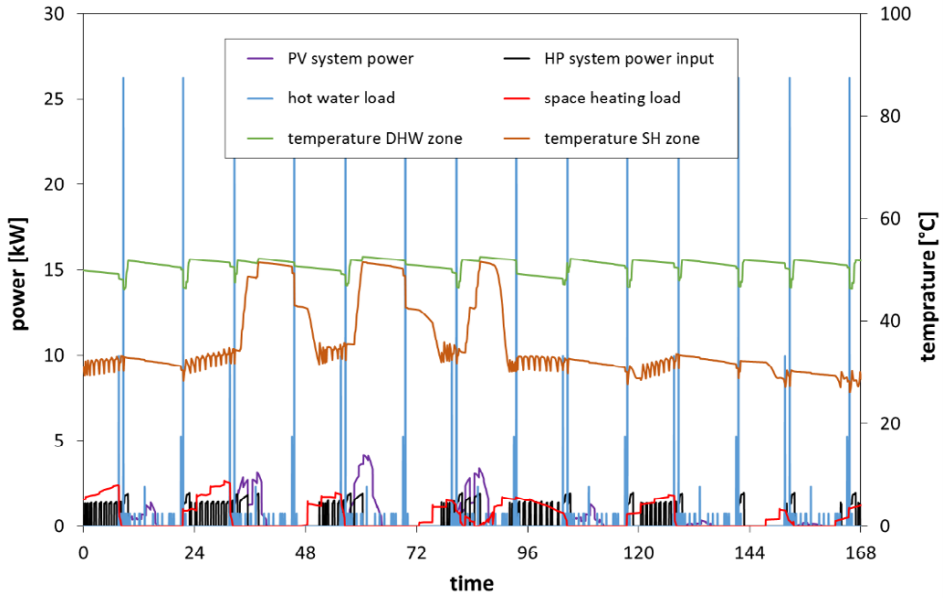

Fig. 10: Production and load profile of the PV heat pump system in winter (6 kW_p) – alternative PV-SH

Tab. 2: Results of TRNSYS simulation of PV heat pump system with adaptive control

Parameter	Alternative PV-HW		Alternative PV-SH	
	3 kW_p	6 kW_p	3 kW_p	6 kW_p
Electricity from grid W_{el} [kWh/a]	1941	1586	1749	1459
System *SPF* [-]	3.3	4.1	3.7	4.4
Solar fraction f_{PV} [%]	26	41	32	44
PV utilization r_{PV} [%]	22	19	27	19

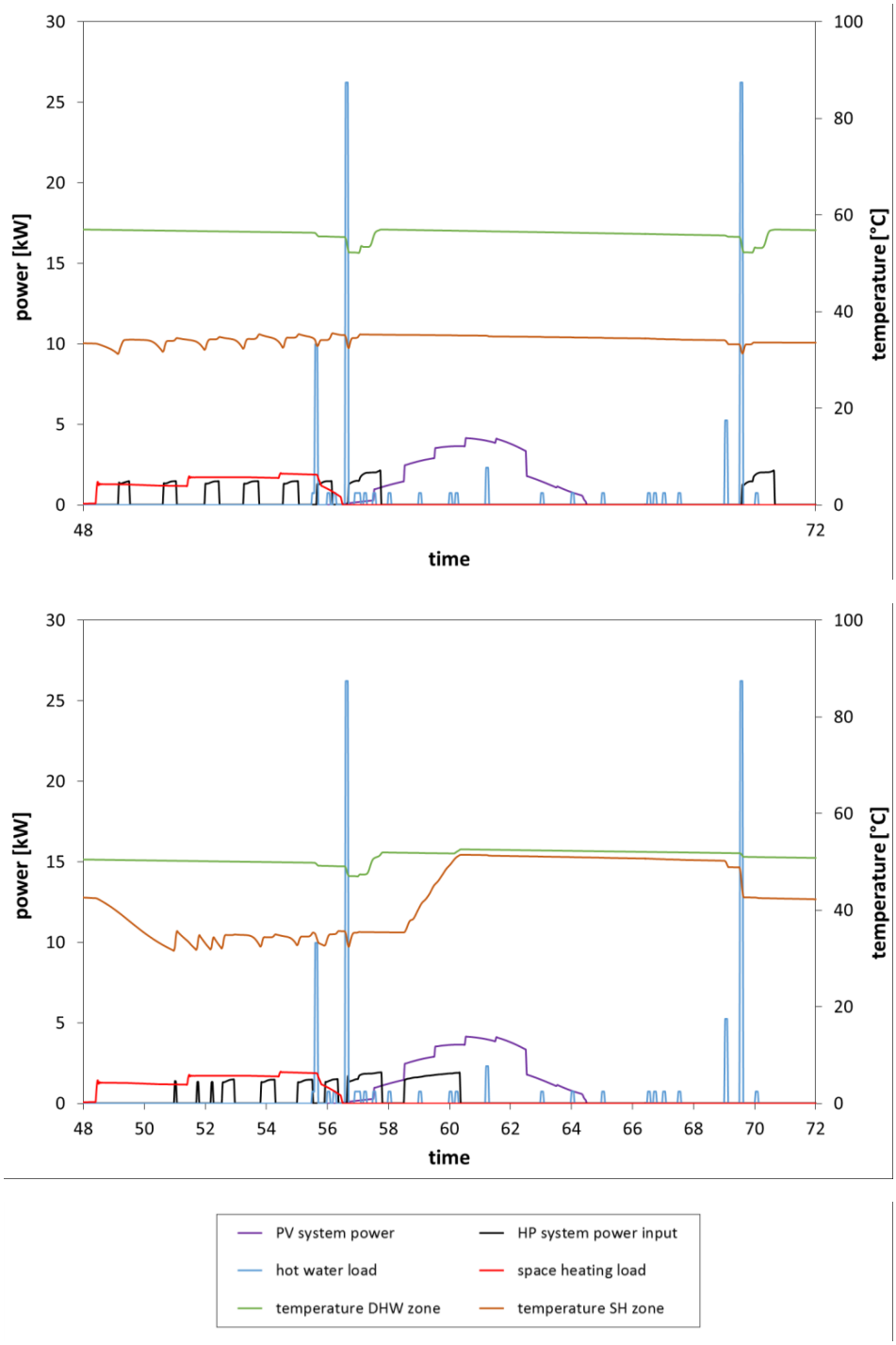

Fig. 11: Detailed comparison of production and load profile of the PV heat pump system in winter for conventional alternative and adapted PV-SH alternative (6 kW_p)

Computer simulations have shown that both alternatives of adapted control can significantly reduce the grid electricity use of heat pump system combined with PV system. The alternative PV-SH with overcharging the SH zone of the storage tank is more favourable thanks to lower annual use of grid electricity and higher seasonal performance factor *SPF* of the system for both PV systems with installed power 3 kW_p and 6 kW_p. Heat pump system alone works more effectively in time of using PV electricity due to charging the storage volume to lower temperature (50 °C) and finally the larger volume of the storage tank which is charged due to natural convection too.

5. Conclusions

Paper has indicated possibility of combination of heat pump and PV system by means of advanced adaptive control which already appears on the market. Computer simulation in TRNSYS has shown the benefits in energy performance of the PV heat pump systems for space heating and domestic hot water preparation. Simple adaptive control allows a significant increase in solar PV fraction and reduction of grid electricity use when compared with static control of conventional system. I has been shown that power threshold for adapted operation of heat pump to PV system lies significantly lower than maximum power input of the system. PV-SH control alternative with overcharging of space heating zone in storage tank has shown better results for the energy performance of the system at conditions of given passive house than alternative with overcharging of the hot water zone.

6. Acknowledgment

The analysis has been supported by Technology Agency of Czech Republic in the frame of research project TA04021243 Sustainable energy source for nearly zero energy buildings.

7. References

Molenbroek, E., Stricker, E., Boermans, T. (2011). Primary energy factors for electricity in buildings. Toward a flexible electricity supply. Ecofys.

Ecometrica (2011). Electricity-specific emission factors for grid electricity.

International Energy Agency (2014). Task 44/Annex 38 - Solar and Heat Pump Systems SHC Position Paper.

Transient System Simulation Tool - TRNSYS 17.1 (2014), The University of Wisconsin, Madison, http://sel.me.wisc.edu/trnsys.

Conference Proceedings

EuroSun 2016
Palma de Mallorca (Spain), 11 - 14 October 2016

Effect of Ambient Conditions on Monthly Performances of Three Different PV Arrays

Talat Özden[1,2], Bülent G. Akınoğlu[3,4], Raşit Turan[2,3]

[1] Electrical and Electronics Engineering, Gümüşhane University, Gümüşhane (Turkey)

[2] The Center for Solar Energy Research and Applications (GÜNAM), METU, Ankara (Turkey)

[3] Department of Physics, METU, Ankara (Turkey)

[4] Earth System Science Program, METU, Ankara (Turkey)

Abstract

Solar PV cells may be mainly divided into two parts as crystalline and thin film. Mono-crystalline silicon (e.g. Mono-Si) and microcrystalline based amorphous silicon and other thin films (e.g. µc-Si/a-Si and CdTe thin films) are widely used PV cells in the arrays. The outdoor performances of these systems depend on some climatic parameters and conditions, and it is important to understand how the monthly efficiencies vary with these parameters. In the present study, the data obtained from three grid connected PV arrays of Mono-Si, a-Si/µc-Si and CdTe thin film that were operated for 41 months in Ankara-Turkey is analyzed. The results showed that Mono-Si array performance depends on the 5 parameters of outdoor climatic conditions while a-Si/µc-Si and CdTe thin film arrays performances are not significantly affected by the variation of the climatic parameters. The possible reasons are discussed in details.

Keywords: *Photovoltaic system, climatic parameters, efficiency*

1. Introduction and Methodology

Performances of solar PV systems are affected by meteorological parameters and ambient climatic conditions. Some examples from the literature are: (Bhattacharya et al., 2014; Sabri et al., 2007). In fact, all these references mainly discuss the temperature and wind speed variations of the PV system performances and with relatively for a period of short term data. Present study is the monthly performance variations of three PV systems installed in Ankara, Central Anatolia, with 5 monthly averages of climatic parameters, using a data set of 41 months. To the best of our knowledge, such an extended study for the monthly averages did not appear in the literature, both in terms of the length of the time period and number of climatic parameters analyzed. Such works are important in simulating feasible and optimum PV installations, toward the transition to clean energy policies for the decision makers, investors and end-users.

Fig. 1: Mono-Si, micro-crystalline based amorphous silicon and CdTe grid connected PV systems.

The specifications of the systems are as follows: The first one is Mono-Si array of 1.14 kWp and its total area is 7.584 m^2; the second one is µc-Si / a-Si array (thin film) with installed capacity of 1.26 kWp and its total area is 14.4 m^2 and the last one is CdTe thin film of 1.215 kWp and its total area is 12.96 m^2. There are

doi:10.18086/eurosun.2016.08.21 Available at http://proceedings.ises.org

three inverters connected to each PV array. The inverters are identical and the outputs are directly connected to the grid. The systems and the inverter specifications are presented in Table 1 and 2, respectively.

Tab.1: Mono-Si, CdTe and µc-Si / a-Si thin film PV systems properties.

Specifications	Mono-Si	CdTe	µc-Si / a-Si
Module brand	IBC	Abound	Kaneka
Module type	190 MS	AB1-67B	U-EA105
P_{MAX} [W]	190	67.5	105
V_{OC} [V]	45.2	46.6	71
I_{SC} [A]	5.56	2.2	2.4
V_{MPP} [V]	36.6	36.1	53.5
I_{MPP} [A]	5.19	1.9	1.96
Connection	6 series	6 series x 3 parallel	4 series x 3 parallel

Their performance and degradation analysis were carried out and presented before (Ozden et al., 2015 and 2016). As mentioned above in the present work, we analyzed the variation of the monthly performances of the arrays with respect to different climatic parameters. These parameters are monthly averages of ambient temperature (T_a, °C), relative humidity (RH, %), air mass at the noon of the average day (M) and solar irradiation on tilted arrays (H_t, kWh/m2). In this paper we present only the effects of two of these parameters: T_a and H_t.

Tab.2: Inverter properties.

Specifications	Energy Input Values [DC]	Energy Output Values [AC]
Inverter Brand	SMA	
Inverter type	SB 1200	
V_{MAX} [V] / V_{nom} [V]	400	105
V_{MPP} [V] / f_{nom} [Hz]	100-320	50/60
I_{MAX} [A] / I_{nom} [A]	12.6	5.2
--- / P_{nom} [V]	---	1200

Monthly efficiency (η) calculations are carried out using the hourly values I_t of solar irradiation on tilted panels and the hourly outputs of the systems by the equation:

$$\eta = \frac{\sum_j^N \left(\sum_i^{day} (hourly\ output)_i\right)_j}{\sum_j^N \left(\sum_i^{day} (hourly \quad I_t)_i\right)_j} \qquad \text{(eq. 1)}$$

where N is the number of days in the month and i and j are the indices that stand for the hour in a day and day in a month, respectively. The output and input in equation 1 are inserted in unit of kWh/m^2. In the previous analysis (Ozden et al., 2017, 2015) and in the present study, the calculation of hourly solar irradiation on tilted panels using anisotropic sky model HDKR, as named in (Duffie and Beckman, 2013), is used as it was demonstrated to be relatively better among one isotropic and another anisotropic model (Ozden et al., 2017, 2015).

Monthly performance ratio, R_P is defined as the ratio of the final monthly energy yield of the PV system, Y_f, to the monthly estimated reference yield, Y_r:

$$R_p = \frac{Y_f}{Y_r} \qquad \text{(eq. 2)}$$

In this equation, Y_f is calculated as the ratio of the monthly yield (Wh) of the PV array, E_{out}, to the installed array's rated output power P_{STC} (Wp), provided by the manufacturer. Y_r is calculated by dividing the total monthly tilted PV surface irradiation (Wh/m^2) E_t by the reference irradiance G_{STC} = 1000 W/m^2.

Variations of the monthly efficiency and performance ratio with the parameters H_t, T_a, M and RH are analyzed using IBM SPSS software package. The calculations of the monthly parameters H_t, T_a ve RH are simply carried out by averaging the hourly values in a full month. We used the noon air mass for a specific month calculated at the average day of the month (Duffie and Beckman, 2013).

Next section gives the graphical results and the discussion of these results. Section 3 is conclusion and future prospects.

2. Results and Discussions

2.1. Variation with temperature

Figure 2a and 2b depict the efficiency and performance ratio variation with respect to T_a. As it can be seen clearly, the temperature has negative effect on the monthly efficiency of the PV system with mono crystalline cells as expected. This is mainly due to the well-known band gap decrease with the increasing temperature which mainly affects the open circuit voltage and thus decreasing the efficiency.

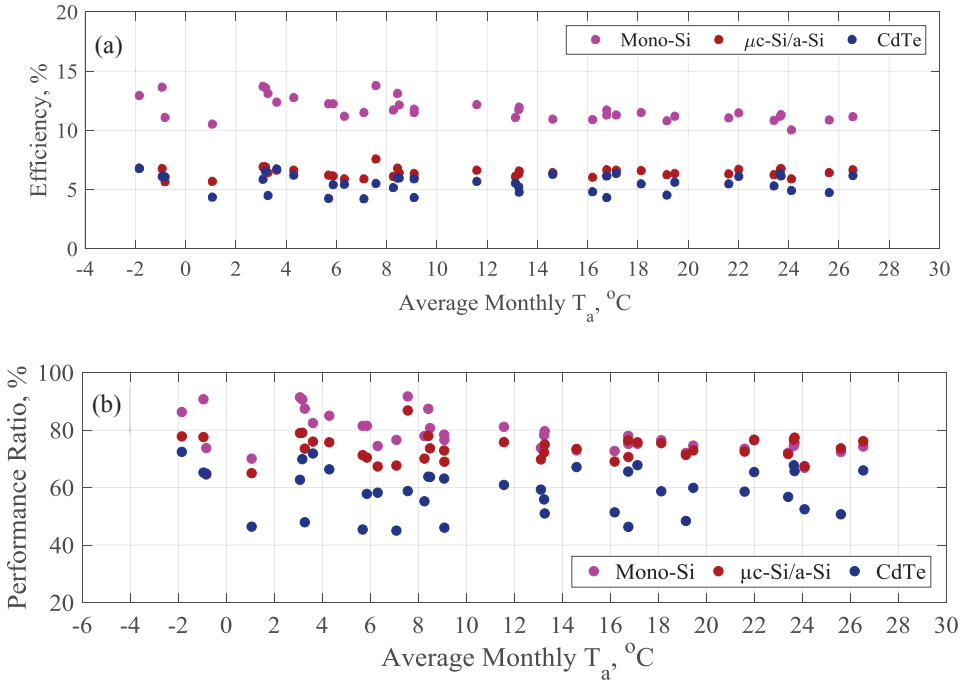

Fig. 2: Variation with temperature for Mono-Si, micro-crystalline based amorphous silicon and CdTe grid connected PV systems, (a) efficiency and (b) performance ratio.

For the systems with thin film solar cells however, the variation of the performances with the temperature is not that obvious as can be seen from Fig. 2. Although this is an unexpected result, we should note that the figure is obtained using the monthly performances and monthly average ambient temperature. Another reason may be the relatively narrower range of monthly average ambient temperatures in the outdoor testing conditions. We should note that in the laboratory, efficiency experiments with wider ranges of ambient temperatures (ambiance of the laboratory) would reveal the temperature variation clearly.

2.2. Variation with solar irradiation on tilted arrays

Similar to the variations with the temperature can be observed in the variation of the performances with the incident monthly average solar irradiation on tilted array as can be observed in Figure 3a and b. This can be attributed to the increase in the temperature of the ambient with the increase in solar irradiation. However, it seems that the thin film systems, especially in the variation of the performance ratio are also affected, as the monthly average incident solar irradiation is increased the performance ratio seems to decrease. To clarify, we calculated coefficient of Pearson correlation for all the variations and present in Tables 3 and 4. In the first columns of Table 4 one can observe that this variation is clearly revealed and the significance of correlation values given in Table 4 are also noteworthy. We discuss this result in the following sub-section.

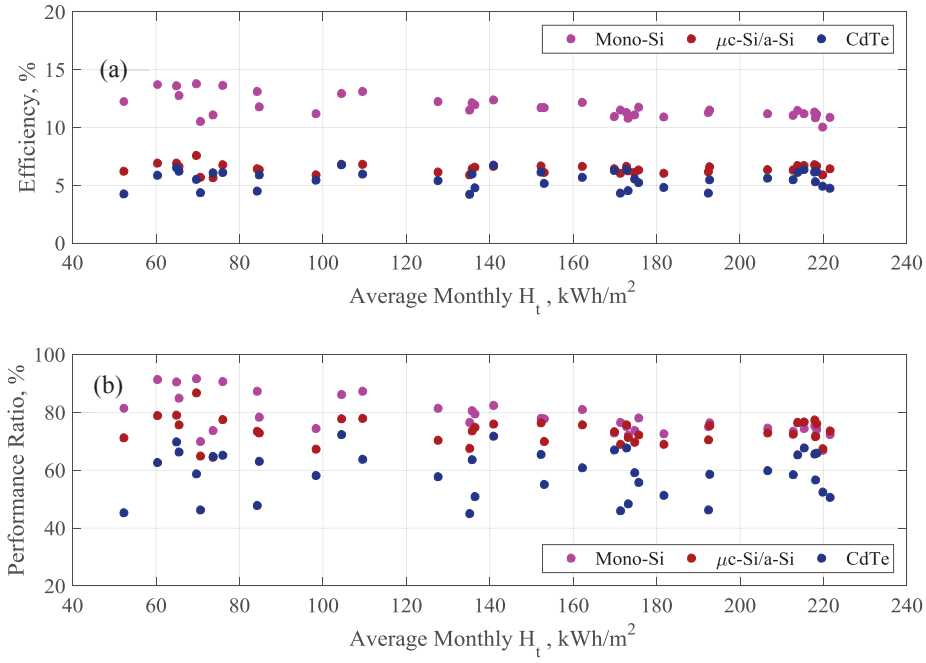

Fig. 3: Variation with solar irradiation on tilted arrays for Mono-Si, micro-crystalline based amorphous silicon and CdTe grid connected PV systems, (a) efficiency and (b) performance ratio.

2.3. Variation with air mass

Figures 4a and b present the variations with monthly average noon air mass. These variations follow very similar trends as in the variations with H_t. This conclusion can also be reached using Table 4 again. Of course, it is also a validation of the observed variation with H_t since it is clear that larger the air mass means the morning and evening hours so is smaller the solar irradiation and the ambient air temperature, and so increased performance. We should here note that these dependences of the thin film systems performances on H_t and M could not be clearly revealed in the efficiency variations (Figure 3a and 4a). Although this situation needs further test data and analysis to clarify, one might attribute it to the obvious difference between the laboratory test conditions and outdoor climate conditions.

Tab. 3: Coefficient of Pearson Correlation for grid connected PV systems (efficiency).

Module type	Pearson Correlation Coefficients				Significant of Correlations			
	H_t	T_a	RH	M	H_t	T_a	RH	M
Mono-Si	-0.682	-0.637	0.546	0.666	0.000	0.000	0.000	0.000
µc-Si / a-Si	-0,067	0.027	-0.060	0.112	0.683	0.868	0.718	0.498
CdTe	0.071	-0.054	-0.034	-0.062	0.669	0.746	0.839	0.708

Tab. 4: Coefficient of Pearson Correlation for grid connected PV systems (performance ratio).

Module type	Pearson Correlation Coefficients				Significant of Correlations			
	H_t	T_a	RH	M	H_t	T_a	RH	M
Mono-Si	-0.460	-0.468	0.324	0.446	0.003	0.002	0.037	0.003
µc-Si / a-Si	-0.271	-0.262	0.141	0.278	0.082	0.094	0.372	0.075
CdTe	-0.250	-0.282	0.141	0.277	0.110	0.071	0.375	0.075

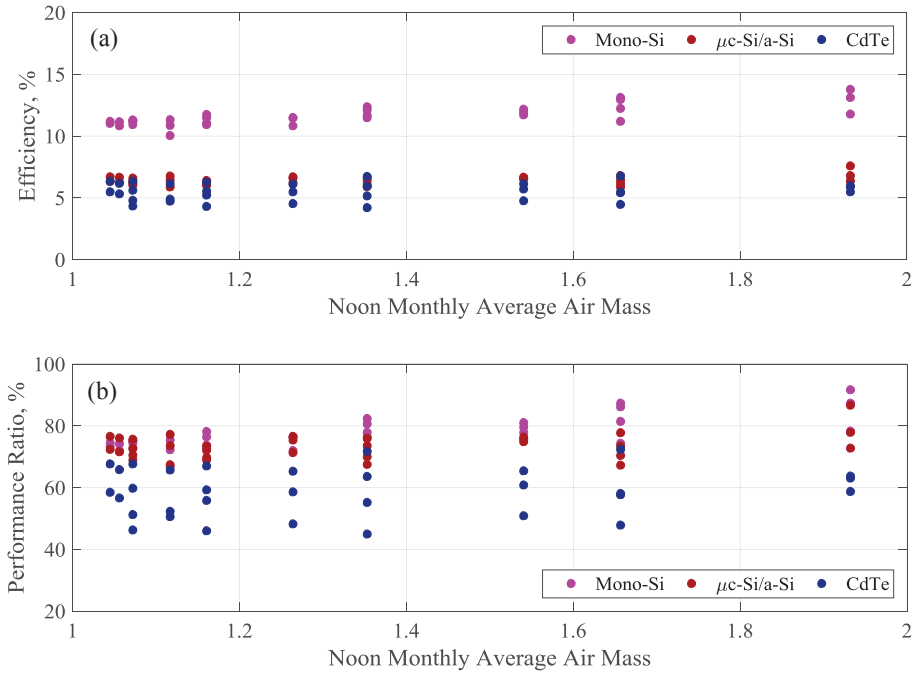

Fig. 4: Variation with air mass for Mono-Si, micro-crystalline based amorphous silicon and CdTe grid connected PV systems, (a) efficiency and (b) performance ratio.

2.4. Variation with relative humidity

Figures 5a and b are the variations of the monthly performance with the average monthly relative humidity. It is quite interesting that for the mono-Si system there exist considerable correlation between RH and system performance (Figure 5a and b, and see also Table 3 and 4). However, this can be attributed to the correlation between the monthly average ambient temperature and relative humidity as depicted in Figure 6.

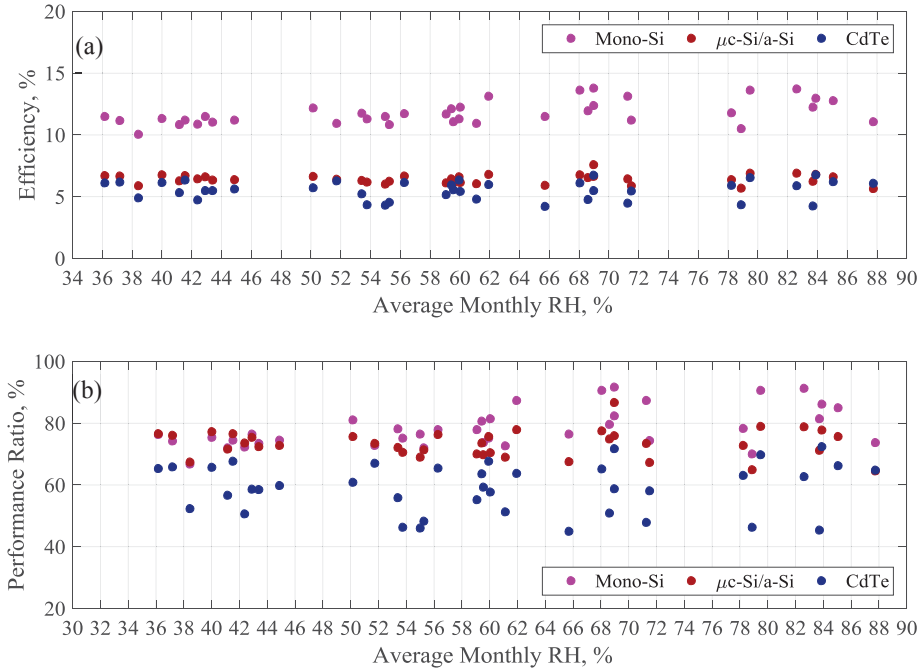

Fig. 5: Variation with relative humidity for Mono-Si, micro-crystalline based amorphous silicon and CdTe grid connected PV systems, (a) efficiency and (b) performance ratio.

The nature of this relation between T_a and RH is specific to the region of the installations and therefore, the correlation between performance and RH for mono-Si system should not be treated to be a physical effect of RH on the performance. That is, the correlation with RH for mono-Si is rather an artificial one which results due to increase in temperature with decreasing RH of the location. In any case, further data and analysis are needed to reach clearer conclusions. Similar to the T_a independence of the performance of the thin film systems, no considerable dependence on RH can be observed (Figure 5, and Table 3 and 4).

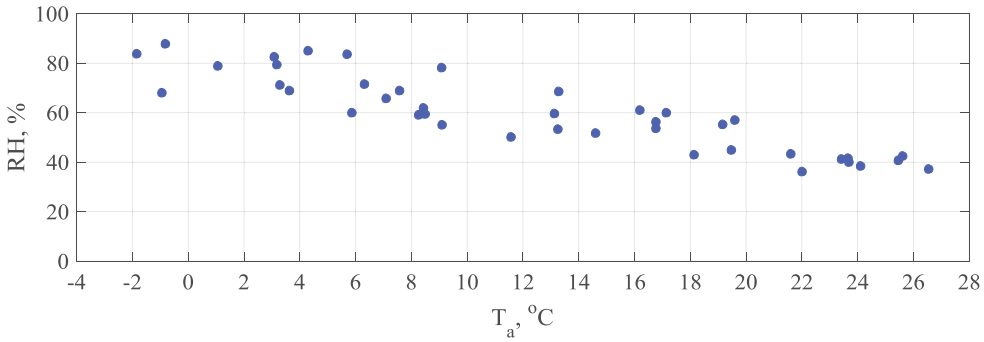

Fig. 6: RH with respect to T_a.

3. Conclusion

In this work, we analyzed the effects of all aforementioned monthly performance variation with climatic parameters and discuss the possible reasons of obtained correlations. As mentioned above, Mono-Si array performance depends on the outdoor climatic conditions while a-Si/µc-Si and CdTe thin film arrays performances are not significantly affected. Although one would expect decrease in efficiency with increasing temperature, we demonstrated that, a-Si/µc-Si and CdTe thin film array performances seems independent of T_a, while a decrease in the efficiency can be clearly observed for Mono-Si array. Similarly, H_t value affects the efficiency of Mono-Si while does not effect a-Si/µc-Si and CdTe thin film array efficiencies. In fact, Pearson's correlation coefficients for H_t independence are in accord with these findings for a-Si/µc-Si and CdTe thin film array monthly efficiencies. However for the performance ratio R_p, it seems that there is rather a significant correlation with H_t and we attributed this dependence to the obvious differences between the laboratory and outdoor climatic conditions. Air mass dependences of the performances are in accord with T_a and H_t dependences. There exists a dependence of the performances on the relative humidity RH however, this dependence should not be due to some unobvious physical effects but instead, it should be due to the interdependence of the T_a to RH specific to the region.

The results of the present work are important in planning and deciding the large scale PV installations to the regions with dry continental climate as in Central Anatolia. Further analysis of efficiency, performance and degradation of some larger number of different types of PV modules at the outdoor conditions of Ankara-Turkey are our future prospects.

4. Acknowledgments

The authors would like to thank B. Aksoy and MGM for the supply of meteorological data. The helps of Mr. C. Güvenç Oğulgönen, Mr. Harun Tanık and Mr. Ugur Yardım during installation, maintenance and data handling are acknowledged. One of the authors thanks to TUBITAK for the support from 2218 program.

5. References

Bhattacharya, T., Chakraborty, A.K., Pal, K., 2014. Effects of Ambient Temperature and Wind Speed on Performance of Monocrystalline Solar Photovoltaic Module in Tripura , India 2014, 1–5.

Duffie, J.A., Beckman, W.A., 2013. Solar engineering of thermal processes, 4th ed. John Wiley and Sons, New York. doi:10.1002/9781118671603

Ozden, T., Akinoglu, B.G., Turan, R., 2017. Long term outdoor performances of three different on-grid PV arrays in central Anatolia – An extended analysis. Renew. Energy 101, 182–195. doi:http://dx.doi.org/10.1016/j.renene.2016.08.045

Ozden, T., Yardım, U., Akınoğlu, B.G., Turan, R., 2015. Outdoor efficiency analyses and comparison of on-grid CdTe and μc-Si/a-Si thin-film pv systems for three years in Ankara-Turkey. Phys. Status Solidi.

Sabri, L., Benzirar, M., Student, P.G., 2007. Effect of Ambient Conditions on Thermal Properties of Photovoltaic Cells: Crystalline and Amorphous Silicon. Int. J. Innov. Res. Sci. Eng. Technol. (An ISO Certif. Organ. 3297, 17815–17821. doi:10.15680/IJIRSET.2014.0312010

Conference Proceedings

EuroSun 2016

Palma de Mallorca (Spain), 11 – 14 October 2016

MONITORING OF SOLAR DOMESTIC HOT WATER SYSTEM WITH GLAZED LIQUID PVT COLLECTORS

Nikola Pokorny[1,2], Tomas Matuska[1,2], Vladimir Jirka[1], Borivoj Sourek[1]

[1]University Centre for Energy Efficient Buildings, Czech Technical University in Prague

[2]Faculty of Mechanical Engineering, Czech Technical University in Prague

Abstract

Glazed liquid photovoltaic-thermal collectors with polysiloxane encapsulation of photovoltaic cells have been developed and fabricated to generate both electric and heat energy simultaneously. The purpose of this study is to present the monitoring of the solar domestic hot water system with the new photovoltaic-thermal collector prototypes and compare the results with data simulated by a dynamic mathematical model of glazed liquid photovoltaic-thermal collector. The detailed dynamic model enables the optimization of the construction design and has been implemented into TRNSYS as a new type to allow the system simulations. Experimental measurement of solar domestic hot water system with two glazed photovoltaic-thermal collectors has been done for 6 days. Thermal energy difference for whole measured period of monitoring was less than 1.5 % compare to dynamic model. Difference between measured electric energy output and modelled was 8.1 %.

Keywords: *Solar energy, glazed PVT collector, SDHW system*

1. Introduction

Hybrid solar photovoltaic-thermal (PVT) collectors have attracted a large interest in last decade. Increase of energy production from given receiving area at the building envelope can bring higher solar fractions both for electricity and heat demand. While unglazed PVT collectors show excellent electric yields, their poor thermal performance results in lower total energy production when compared with combination of conventional PV modules and photothermal collectors(Matuska, 2014). Glazed PVT collectors could offer a good compromise between electricity and heat production, the total energy production is higher than for conventional combination of identical area (Matuska et al., 2015). The principle barrier for the glazed PVT collectors development is the weak resistance of common ethylene-vinyl acetate (EVA) encapsulation to excessive thermal exposure. Maximum operation temperature of EVA laminate is around 85 °C (Zondag et al., 2002) while the stagnation temperature for glazed solar collectors ranges from 120 to 180 °C. At these temperatures EVA encapsulation decomposes to acetic acid, which causes the corrosion of PV cell contacts, delamination and degradation of layer transparency. Nevertheless, majority of published papers focused on development of new glazed PVT collectors consider PV cells encapsulated in EVA lamination (Zondag et al., 2002; Chow et al., 2006; Dupeyrat et al., 2011). Research in the area of glazed PVT collectors resulted into two approaches. One is focused on the increasing heat losses during stagnation period (Lammle et al., 2016) and second focuses on the temperature resistant material as replacement for EVA lamination (Matuska, 2014). In this paper new concept of solar PVT collectors is presented where PV cells are encapsulated between double glazing and metal heat exchanger by means of polysiloxane gel. Polysiloxane gel as PV encapsulant offers a large range of operation temperatures (from -60 to +250 °C), high transparency for solar radiation and allows the compensation of thermal dilatation stresses thanks to low modulus of elasticity (Poulek et al., 2012).

Developed PVT collector presented in this paper uses temperature resistant material as encapsulant for PV cells. Moreover, the paper presents a detailed numerical model convenient for the optimization of glazed PVT collector design. Several glazed solar PVT collector prototypes based on the polysiloxane encapsulant have

doi:10.18086/eurosun.2016.08.20 Available at http://proceedings.ises.org

been fabricated. Prototypes have been tested in outdoor conditions and under conditions of artificial sun. The developed mathematical model has been validated for steady-state conditions (Pokorny et al., 2015) both for electrical and thermal performance and it has been implemented into TRNSYS as a new type. Reason of the implementation to the TRNSYS was to have a model which includes sufficient amount of parameters for the optimization in the PVT collector design process (glazing properties, dimensions and physical properties of sheet and tube absorber, properties of insulation etc.). Currently available types in TRNSYS is type 563 (unglazed) and type 50 (glazed). Only type 50 is suitable for glazed PVT collectors but type 50 do not consider a detailed construction parameters of the collector as well as do not consider change of important collector parameters during the varying operation conditions. Several steady-state models (Bergene and Løvvik, 1995; Zondag et al., 2002)and dynamic models of glazed PVT collector (Chow, 2003; Haurant et al., 2015; Guarracino et al., 2016) were published but not available for TRNSYS. The work presented here extends the steady-state model by a dynamic term to allow the system performance simulations at realistic conditions. The new type has been used for the simulation of solar domestic hot water system and the results were compared with an experimental installation of solar DHW system equipped with the developed glazed PVT collectors.

2. Theoretical model of glazed liquid PVT collector

In order to optimize construction of the glazed PVT collector, a detailed mathematical model has been developed and implemented into the TRNSYS. The advantage of implemented model is that model calculates energy flow from PVT absorber surface to ambient and energy flow from PVT absorber surface to liquid, all in every time step. The detailed model of glazed PVT collector allows to define a number of construction and physical parameters of collector configuration. Inputs of the model are climatic and operation conditions. Main outputs of the model are: thermal output, electric output, absorber temperature and outlet temperature. For instance, type 50 available in TRNSYS has effective heat loss (eq. 3) constant for whole simulation. Equally collector efficiency factor (eq. 4) is constant because model does not consider variable forced convection in pipes. Also type 50 does not consider thermal capacity of the PVT collector. Mathematical model of glazed PVT collector has been developed on the basis of Florschuetz approach (1979)). A detailed calculation of the heat transfer from the collector absorber to ambient (heat loss) and from the collector absorber to the heat transfer liquid (internal balance) is performed within the iterative loops. The model inputs are the detailed geometrical, thermal, electrical and optical properties (about 40 parameters) of individual segments of the PVT collector together with operation and climatic conditions. Temperature distribution in the solar collector is calculated in the iteration loops. Original steady-state model has been extended to a dynamic model by the introduction of the effective thermal capacity term available from testing or calculation. The dynamic term is used for the thermal calculations, the calculation of the electric output doesn't consider dynamic change of the temperature in the PVT collector so far. Moreover, non-uniform distribution of PV cells temperature which could have impact on the electric performance is not taken into account in the electric part of the model.

The photoelectric efficiency to establish electrical performance in Florschuetz approach is estimated as a function of ambient temperature t_a, using the relation of the form

$$\eta_a = \eta_{ref}\left[1-\beta_{ref}(t_a - t_{ref})\right] \qquad \text{(eq. 1)}$$

where β_{ref} [-] is the temperature coefficient of the PV cells, η_{ref} is the reference efficiency of PV cells, and t_{ref} [°C] is the reference temperature, all at standard testing conditions (STC). The incident solar energy converted to heat can be calculated as

$$\tilde{S} = G \cdot \alpha \cdot \tau_g \cdot \left(1 - \frac{\eta_a \cdot r_c}{\alpha}\right) \qquad \text{(eq. 2)}$$

where G [W·m^{-2}] is the incident irradiance, α [-] is the solar absorptance of the PVT absorber, τ_g [-] is the transmittance of the glass cover and r_c [-] is the packing factor (related to aperture area).

Effective heat loss coefficient of the PVT collector can be calculated as

$$\tilde{U} = U - r_c \eta_{ref} \tau_g G \beta_{ref} \qquad \text{(eq. 3)}$$

where U [W·m^{-2}·K^{-1}] is the PVT collector heat loss coefficient from absorber to ambient related to aperture area. The collector efficiency factor $\tilde{F}'$ [-] for upper bond of absorber to riser pipes is given as

$$\tilde{F}'=\frac{1/\tilde{U}}{W\cdot\left[\frac{1}{\tilde{U}\left[2a+(W-2a)\cdot F\right]}+\frac{1}{C_b}+\frac{1}{h_i\cdot\pi\cdot D_i}\right]} \quad \text{(eq. 4)}$$

where W is distance between risers, C_b [W·m^{-1}·K^{-1}] is bond thermal conductance, a [m] is the average bond width and h_i [W·m^{-2}·K^{-1}] is forced convection heat transfer coefficient in the riser pipe.

Heat removal factor $\tilde{F}_R$ [-] is defined as

$$\tilde{F}_R=\frac{\dot{m}\cdot c}{A_a\cdot\tilde{U}}\left[1-\exp\left(-\frac{A_a\cdot\tilde{U}\cdot\tilde{F}'}{\dot{m}\cdot c}\right)\right] \quad \text{(eq. 5)}$$

where $\dot{m}$ [kg·h^{-1}] is the mass flow rate, c [J·kg^{-1}·K^{-1}] is the specific heat capacity of the fluid and A_a [m^2] is the aperture area. Thermal output $\dot{Q}_t$ [W] is given by

$$\dot{Q}_t=\tilde{F}_R\cdot A_a\left[\tilde{S}-\tilde{U}\cdot(t_{in}-t_a)\right]-C\cdot A_a\cdot\frac{dt_m}{d\tau} \quad \text{(eq. 6)}$$

where t_{in} [°C] is the inlet fluid temperature to the collector, C [J.m^{-2}.K^{-1}] is the effective thermal capacity of PVT collector, t_m [°C] is mean fluid temperature, and $d\tau$ is time step of simulation. Electric output $\dot{Q}_e$ [W] is given by formula

$$\dot{Q}_e=\tau_g\cdot G\cdot A_A\cdot r_c\cdot\eta_a\cdot\left\{1-\frac{\beta_{ref}\cdot\eta_{ref}}{\eta_a}\cdot\left[\tilde{F}_R(t_{in}-t_a)+\frac{\tilde{S}}{\tilde{U}}\left(1-\tilde{F}_R\right)\right]\right\} \quad \text{(eq.7)}$$

3. Steady-state testing of prototypes and model validation

The prototypes of glazed liquid PVT collector have been developed and constructed based on the new concept (Matuska, 2014)to be further investigated and used for the validation of the mathematical model. The construction is based on sandwich structure with monocrystalline PV cells encapsulated in the polysiloxane gel layer between double glazing (see Fig. 1) and copper sheet with pipe register (conventional solar thermal absorber technology). Double glazing with a gap between glass panes 24 mm filled with argon has been used. No optical coatings have been applied for glass surfaces. Transmittance of the glazing is 0.91 and emissivity of the PVT absorber is 0.84. Average absorptance of the PVT absorber is 0.93. In total 6 x 11 polycrystalline PV cells at size 125 x 125 mm have been used. Gross area of the collector has been filled with PV cells for 60 % (packing factor related to gross area). Absorber has been made from copper sheet (0.2 mm) soldered to pipe register made from risers of 8 mm in diameter with thermal conductivity 200 W.m^{-1}.K^{-1}. Distance between the copper risers was 50 mm. Absorber has been insulated by 30 mm of mineral wool on the back, edge side was insulated by 10 mm of mineral wool (thermal conductivity 0.04 W.m^{-1}.K^{-1}). The frame of the PVT collector has been made of aluminum profiles.

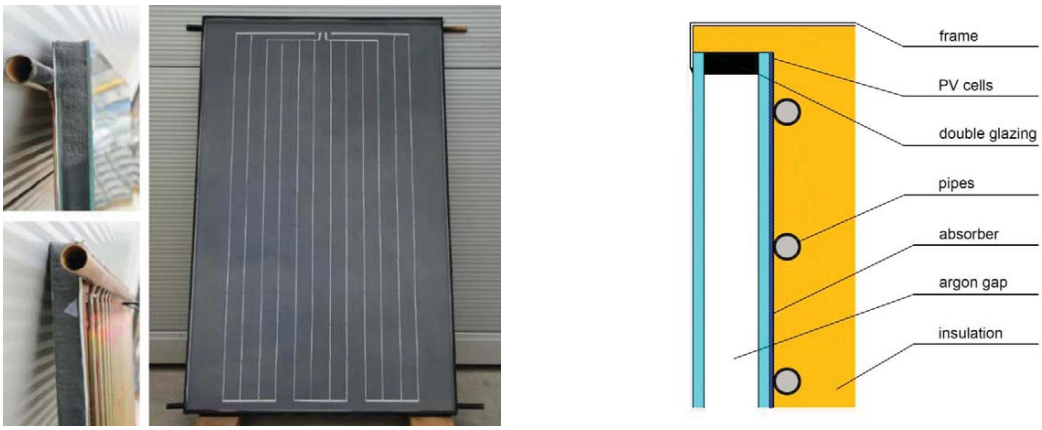

Fig. 1: Compact sandwich of double glazing, encapsulated PV cells and copper heat exchanger (left) and the schematic layout of the whole PVT collector (right)

The sample of developed glazed PVT collector have been tested at Solar laboratory (UCEEB CTU) with use of indoor solar simulator. Solar simulator consist of 8 metal halide lamps with power 4.5 kW. Solar simulator can achieve irradiance up to 2000 W.m^{-2} with guaranteed homogeneity 5 % on the area 1 x 2 m. Required inlet temperature to the collector is supplied by thermostat with tolerance ±0.03 K. The thermal performance has been determined according to EN ISO 9806. Required accuracy of measurement according to EN ISO 9806 was respected. Characteristic of thermal efficiency has been tested in two modes. In the hybrid mode, the PV part was connected to MPP tracker with measured load. In open circuit mode, the PVT collector thermal performance was tested without electric load. Thermal and electric characteristics have been related to gross area of the PVT collector which is 1.71 m^2 (1.04 m x 1.64 m). The global irradiance was kept at the average value 931 W.m^{-2} during the test. The collector tilt angle was set up to 45°. Ambient temperature was fixed at 17 °C. Collector zero loss thermal efficiency was evaluated 65 % and the electrical efficiency 9.1 % (both related to gross area). Moreover, the thermal capacity of the PVT collector was assessed 14.5 kJ.m^{-2}.K^{-1} by the testing.

Individual electric test of the PV part of PVT collector was carried out with PASAN tester at standard test conditions (G = 1000 W.m^{-2}, t = 25 °C, AM1,5). The results of the PV test are: U_{OC} = 40.7 V, I_{SC} = 5.1 A, U_{MPP} = 31,4 V, I_{MPP} = 4.81 A, P_{MPP} = 151 W, η_{STC} = 8.8 %.

To validate the mathematical model the thermal and electric efficiency characteristics have been modelled and compared to steady-state tested data. There is natural uncertainty in the parameters data for the model, e.g. real thermal conductivity of the insulation, real transmittance of the cover glazing, real absorptance and emissivity of the full absorber area, etc. For example, uncertainty of thermal conductivity value for the insulation could be considered about 10 % if not determined from special testing, transmittance of cover glazing was considered with uncertainty about 2 % according to datasheet of the manufacturer, etc. Therefore the efficiency characteristics have been modelled as two boundary lines expressing the full range of parameters uncertainty and creates the model uncertainty band for given PVT collector. This band could be diminished if there is a knowledge of the parameters with better precision. The experimental data derived for steady-state laboratory test of the PVT collector in hybrid mode lie within the model uncertainty band (see Fig. 2, red lines), however there is still potential to improve the model further.

The measurement uncertainty of thermal efficiency was determined by methodology published in (Mathioulakis et al., 1999). Results of experimental uncertainties are in Tab 1. Uncertainty of the model is much bigger compare to uncertainties of the measurement. For this reason uncertainties were not plotted in the chart in Fig. 2.

Tab. 1: Measurement uncertainties for thermal efficiency (related to gross area)

	η	η + σ	η - σ
η_0 [-]	0,645	0,649	0,640
a_1 [W.m^{-2}.K^{-1}]	5,391	5,141	5,640
a_2 [W.m^{-2}.K^{-2}]	0,011	0,008	0,014

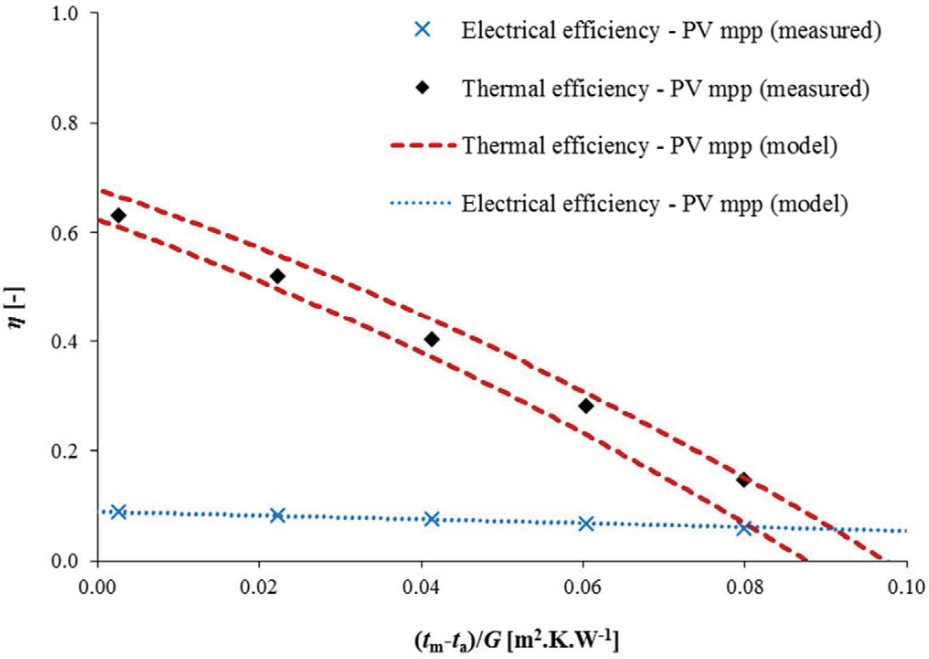

Fig. 2: Measured and calculated thermal and electrical performance in hybrid mode under steady state conditions

4. Solar system with glazed PVT collectors

Solar domestic hot water system with glazed nonselective PVT collectors has been realized to prove the applicability of the technology in real environment. Moreover, the developed dynamic model has been used for parallel simulation of the energy output in TRNSYS to continue with the validation process. PVT collectors were installed in the outdoor part of Solar laboratory on the roof of the Faculty of Mechanical Engineering, CTU in Prague and rest of the technology was placed in the adjacent room. Scheme of the system is shown in Fig. 3. Solar system consists of two glazed PVT collectors with gross area 3.42 m^2, storage water tank with volume 400 l, basic control components (circulation pump, closing and safety fittings, pressure and temperature sensors) and pipelines with thermal insulation. Heat transfer fluid was water. PVT collectors were installed on the metal construction of south orientation with tilt angle 45°. Solar system is dedicated to the preparation of domestic hot water in central storage tank but it does not fit to realistic design (high volume of the storage to collector area ratio). It was set up as laboratory system to provide the experimental testing of continuous PVT collectors operation under realistic climate conditions with dynamic behavior. Solar PVT collectors are directly connected to storage water volume, hot water is taken from integrated tube heat exchanger (similar to combined storage tanks). Conventional controller has been installed with the monitoring of the temperature difference and switching on and off the circulation pump of the system. Mass flow in the collector loop was set to 180 l.h^{-1}. Hot water load has been emulated by time-controlled electromagnetic valve representing the tapping device. Simple hot water load profile consisted from 4 loads with duration from 5 to 10 minutes was used at flowrate 5 l.min^{-1}. Daily hot water draw off was 200 l to provide sufficient load for the storage. Solar system works as solar only system for water preheating and auxiliary heater was not installed. For measurement was used pyranometer Kipp & Zonen (type CMP 6), wattmeter Hioki Power HiTester -3334, magnetic flowmeter TCM 142/02/3715, anemometer, and temperature sensors Pt100. For the electric part there

is hybrid inverter INV (with MPP tracker), two batteries BATT (24 V x 140 Ah = 3360 Wh) and continuous electric load (see Fig. 3) for PV electricity. Energy from batteries was used continually in order to avoid full charged battery and reduction of useful PV electricity generation.

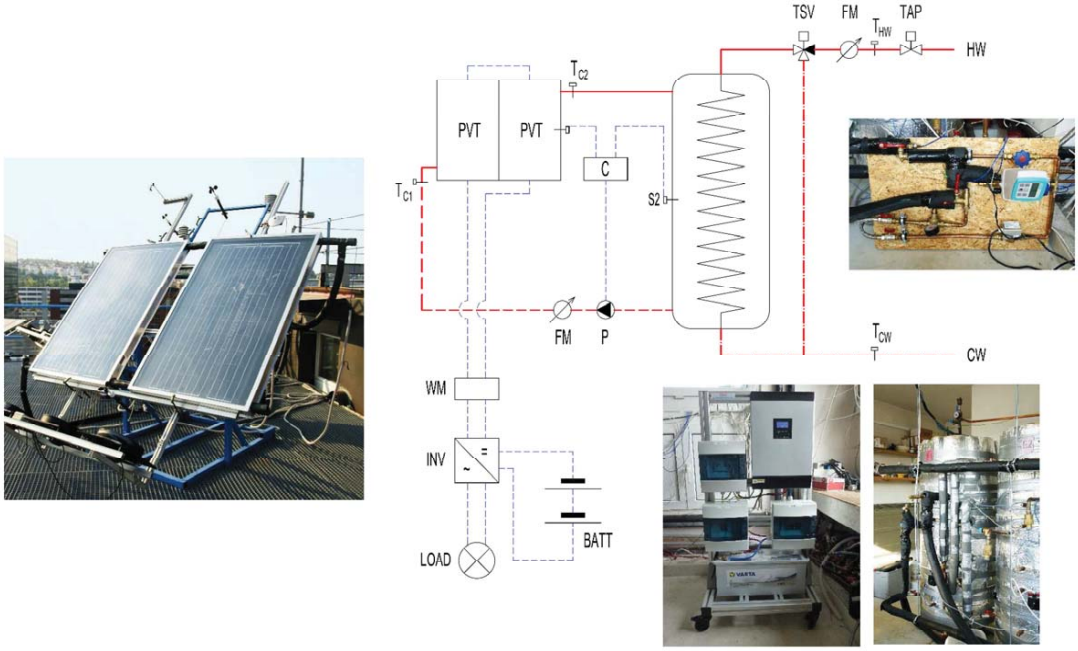

Fig. 3: Scheme of the solar DHW system with PVT collectors

5. Comparison between measured and simulated data

Thermal and electric output generated by solar PVT collector field has been evaluated for 6 days (from 18.5.2016 to 23.5.2016). Electric power, collector flowrate and temperatures at input and output of the collector field has been monitored in 30s time step together with climatic data (solar irradiance, ambient temperature, wind velocity). Electric power of PVT collectors was measured by digital wattmeter WM. Flowrate was measured by electromagnetic flowmeter FM and temperatures were monitored with Pt100 sensors.

Measured thermal and electric output data typical for clear and cloudy day is shown in Fig. 4 and Fig. 5. Heat output peaks are caused by switching the circulation pump on and off. For example at 9.00 am mean fluid temperature in the collector is higher compare to temperature in storage therefore pump is turned on. Although in short time temperature in collector is cooled because irradiation is not sufficient high, the same phenomena is during the evening. Fluctuation of thermal performance during the day is caused by cloudiness. These dynamic states are convenient for observation of the dynamic behavior and comparison with the steady state and dynamic model. During the clear day the heat output peaks are present only at morning and evening. Cloudy day leads to frequent heat output peaks during the whole daytime.

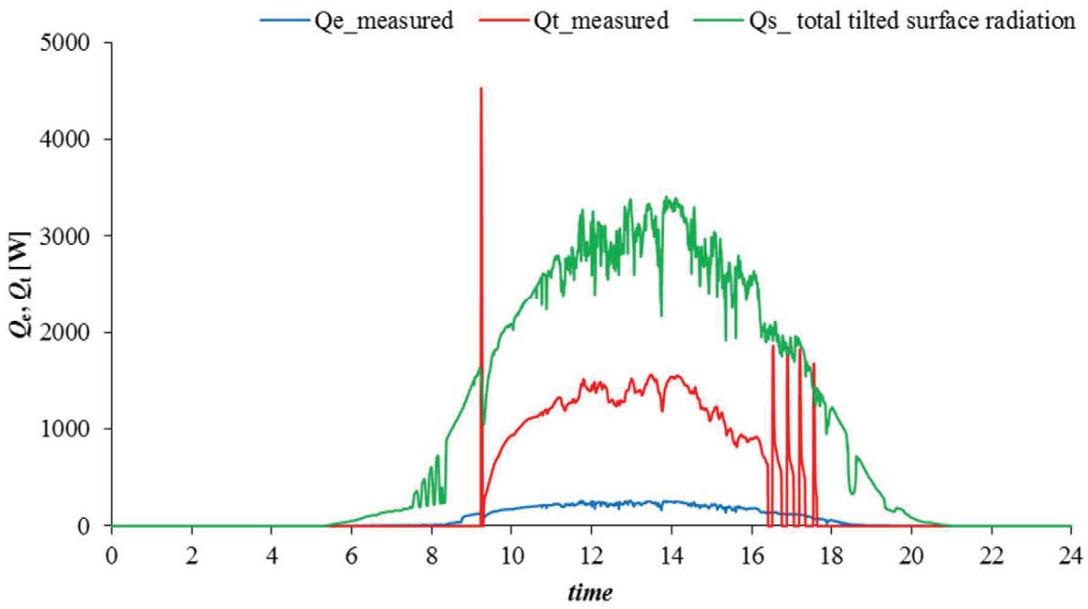

Fig. 4: Thermal and electric performance during clear day (22.5.2016)

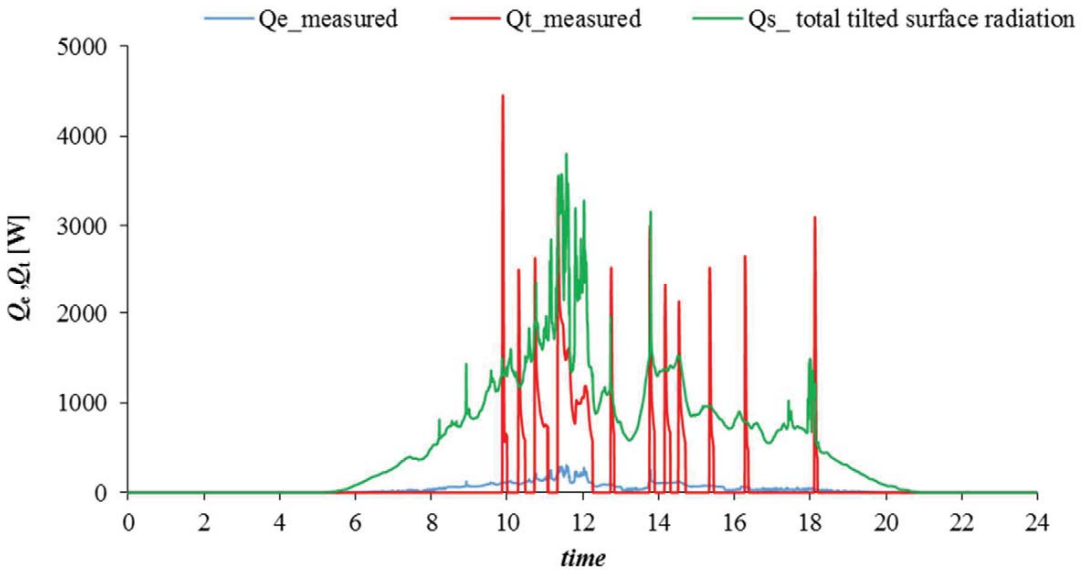

Fig. 5: Thermal and electric performance during cloudy day (18.5.2016)

Tab. 2: Measured data on the SDHW system with PVT collectors (for area 3.42 m^2)

Date	Incident solar irradiation Q_s [kWh]	Measured electric gain Q_e [kWh]	Electric efficiency η_e [%]	Measured heat gain Q_t [kWh]	Thermal efficiency η_t [%]
18. 5. 2016	12,8	0,91	7,1	2,93	22,9
19. 5. 2016	17,4	1,18	6,8	5,84	33,6
20. 5. 2016	16,6	1,17	7,0	4,98	29,9
21. 5. 2016	19,3	1,41	7,3	6,46	33,4
22. 5. 2016	24,3	1,76	7,2	9,05	37,2
23. 5. 2016	16,7	1,23	7,4	5,80	34,6

Tab. 2 shows the measured data from SDHW system. Daily thermal and electric gain was evaluated and daily efficiency of the collectors related to gross area has been determined. Tab. 3 shows the theoretically determined data by simulation model (steady-state, dynamic) and differences between modeled and measured values. Thermal energy difference for whole 6 days period of testing was -7 % for steady-state model and less than 1.5 % for dynamic model. Difference in modelled and measured electric energy was 8.1 % for the whole testing period. Maximum daily difference of the heat output are present during cloudy days but still less than 10 % for dynamic model, while quite large difference has been monitored for the steady-state model. Maximum difference between electric output modelled and measured is 15.7 %. This overestimation of electricity production by the model especially for cloudy days could be caused not only by quality of the model but also by operation out of the range of used hybrid inverter and power point tracker. This will be further investigated.

Tab. 3: Simulated daily energy output by model including difference from measured energy

Date	$Q_{e,stac}$ [kWh]	$\Delta_{e,stac}$	$Q_{t,stac}$ [kWh]	$\Delta_{t,stac}$	$Q_{t,dyn}$ [kWh]	$\Delta_{t,dyn}$
18. 5. 2016	1,02	12,3 %	1,83	-37,5 %	3,17	8,5 %
19. 5. 2016	1,37	15,9 %	5,60	-4,2 %	5,93	1,5 %
20. 5. 2016	1,30	11,0 %	4,22	-15,2 %	5,21	4.7 %
21. 5. 2016	1,48	5,6 %	5,95	-7,8 %	6,36	-1,5 %
22. 5. 2016	1,83	3,8 %	9,20	-1,6 %	9,03	0,2 %
23. 5. 2016	1,28	3,7 %	5,83	0,7 %	5,76	-0,5 %

Fig. 6 shows a detailed comparison between measured and modeled data for part of the clear day. To show the difference the steady-state and dynamic modeled data are put together with measured data in the graph. Dynamic model corresponds to measured data quite well in the whole period including the heat output peaks at the end of the day. Heat gain modelled with steady-state model without PVT collector capacity term oscillates during the operation and this results in worse precision of the model when compared to measured data.

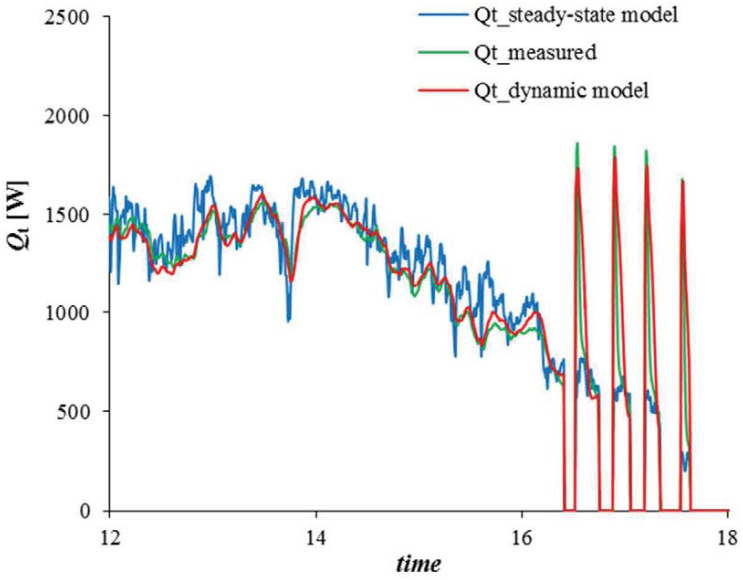

Fig. 6: Comparison between measured and modelled thermal performance (22.5.2016)

Fig. 7 shows the comparison of measured and modeled electric output. Significant differences of electric output are obvious particularly during the morning and evening. One possible reason of discrepancy is that hybrid

inverter works out of his range as mentioned above. Due to this fact measured electric output is lower than modeled electric output. However the electric model could be improved further. Currently, the electric model does not consider non-uniform temperature distribution across the collector plane. Temperature difference between the area close to inlet and the area close to outlet can be more than 5 K.

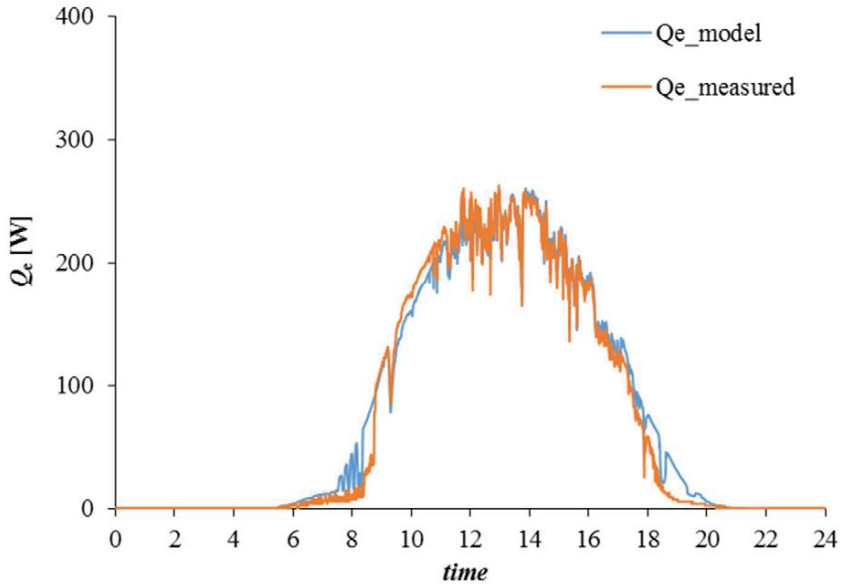

Fig. 7: Comparison between measured and modelled electric performance (22.5.2016)

6. Conclusion

The detailed mathematical model of new concept of glazed PVT collector has been validated by steady-state testing and further extended to dynamic model. The prototypes of the developed glazed PVT collectors has been fabricated and used in laboratory system for domestic hot water preparation. The performance PVT collectors in the system has been monitored and results have been compared with a simulation using the developed dynamic model implemented into TRNSYS. The comparison has shown a good agreement for the thermal part of the model (compared to steady-state model) and relatively good agreement with electrical part during the sunny days.

Main findings

- Prototype of PVT collector with durable lamination over high operating temperatures
- Dynamic model of PVT collector implemented into the TRNSYS as a new type

Acknowledgement

The analysis has been supported by Technology Agency of Czech Republic in the frame of research project TA04021195 Energy active curtain walling façade and by the Ministry of Education, Youth and Sports within National Sustainability Programme I, project No. LO1605.

References

Bergene, T., Løvvik, O.M., 1995. Model calculations on a flat-plate solar heat collector with integrated solar cells. Sol. energy 55. doi:10.1016/0038-092X(95)00072-Y

Dupeyrat, P., Menezo, C., Rommel, M., Henning, H.M., 2011. Efficient single glazed flat plate photovoltaic-thermal hybrid collector for domestic hot water system. Sol. Energy 85, 1457–1468. doi:10.1016/j.solener.2011.04.002

Florschuetz, L.W., 1979. Extension of the Hottel-Whillier model to the analysis of combined photovoltaic/thermal flat plate collectors. Sol. Energy 22, 361–366. doi:10.1016/0038-092X(79)90190-7

Guarracino, I., Mellor, A., Ekins-Daukes, N.J., Markides, C.N., 2016. Dynamic coupled thermal-and-electrical modelling of sheet-and-tube hybrid photovoltaic/thermal (PVT) collectors. Appl. Therm. Eng. 101, 778–795. doi:10.1016/j.applthermaleng.2016.02.056

Chow, T.T., 2003. Performance analysis of photovoltaic-thermal collector by explicit dynamic model. Sol. Energy 75, 143–152. doi:10.1016/j.solener.2003.07.001

Chow, T.T., He, W., Ji, J., 2006. Hybrid photovoltaic-thermosyphon water heating system for residential application. Sol. Energy 80, 298–306. doi:10.1016/j.solener.2005.02.003

Lammle, M., Thoma, C., Hermann, M., 2016. A PVT Collector Concept with Variable Film Insulation and Low-emissivity Coating, in: Energy Procedia. pp. 72–77. doi:10.1016/j.egypro.2016.06.174

Mathioulakis, E., Voropoulos, K., Belessiotis, V., 1999. Assessment of uncertainty in solar collector modeling and testing. Sol. Energy 66, 337–347. doi:10.1016/S0038-092X(99)00034-1

Matuska, T., 2014. Performance and economic analysis of hybrid PVT collectors in solar DHW system, in: Energy Procedia. pp. 150–156. doi:10.1016/j.egypro.2014.02.019

Matuska, T., Sourek, B., Jirka, V., Pokorny, N., 2015. Glazed PVT Collector with Polysiloxane Encapsulation of PV Cells: Performance and Economic Analysis. Int. J. Photoenergy 2015. doi:10.1155/2015/718316

Pierrick, H., Christophe, M., Leon, G., Patrick, D., 2015. Dynamic numerical model of a high efficiency PV-T collector integrated into a domestic hot water system. Sol. Energy 111, 68–81. doi:10.1016/j.solener.2014.10.031

Pokorny, N., Matuska, T., Sourek, B., 2015. Modeling of glazed liquid PV-T collector with use of detail model, in: 14th International Conference of IBPSA - Building Simulation 2015, BS 2015, Conference Proceedings.

Poulek, V., Strebkov, D.S., Persic, I.S., Libra, M., 2012. Towards 50 years lifetime of PV panels laminated with silicone gel technology. Sol. Energy 86, 3103–3108. doi:10.1016/j.solener.2012.07.013

TRNSYS Manual, 2006. TRNSYS 16 a TRaNsient SYstem Simulation program. In: Mathematical Reference, vol. 5. Solar Energy Laboratory, University of Winconsin–Madison.

Zondag, H.A, Van Helden, W.G.J. 2002. Stagnation temperature in PVT collectors. PV in Europe, Rome (Italy).

Zondag, H.A., Db e Vries, D.W., Van Helden, W.G.J., Van Zolingen, R.J.C., Van Steenhoven, A.A., 2002. The thermal and electrical yield of a PV-thermal collector. Sol. Energy 72, 113–128. doi:10.1016/S0038-092X(01)00094-9

Conference Proceedings

EuroSun 2016
Palma de Mallorca (Spain), 11 - 14 October 2016

INVESTIGATION OF PV/THERMAL COLLECTOR MODELS FOR USE WITH GROUND SOURCE HEAT PUMPS IN TRANSIENT SIMULATIONS

Michele Pressani[1], Nelson Sommerfeldt[2] and Hatef Madani[2]

[1] Politecnico di Milano, Milan, Italy

[2] KTH Royal Institute of Technology, Stockholm, Sweden

Abstract

Photovoltaic-thermal (PVT) collectors are commonly designed for use in domestic hot water systems, however it can be interesting to incorporate them into ground source heat pump (GSHP) systems. Because of the historically narrow use case, many PVT models are created with a collection of assumptions which may not apply to novel collectors designed for use in PVT+GSHP systems. The aims of this study are to review existing PVT collector models for use in TRNSYS, identify any potential error sources, and test for possible improvements. Type 560 is found to be the most promising theoretical model, however two potentially limiting features are identified; the radiation absorption model and the confinement to sheet-and-tube configurations. The absorption is tested using a recreation of Type 560 in Matlab where two alternative models developed specifically for PV modules are compared. The results show a marked increase in power during low angle, low light hours, and a 14.36% increase in electrical energy and a 10.91% for the thermal energy over the course of a day with one of the models. Collector geometry is tested by creating a 1D model in EES and comparing it to several geometries in Type 560. A method of packing as many tubes as possible together is shown to give comparable results as the 1D model. The results of these simulations will be compared with empirical data from currently ongoing testing.

Keywords: Solar PV/thermal, Transient Simulation, State-of-Art Review, Collector Geometry

1. Introduction

With the increasing interest in improving the energy efficiency of buildings, solar assisted heat pumps (SAHP) have been gaining attention. There are numerous potential configurations, but one of particular interest to heating dominated climates combine photovoltaic-thermal (PVT) hybrid solar collectors with ground source heat pumps (GSHP). Series configurations, where the solar collector is integrated on the source side of the heat pump, have been identified as a promising systems solution for PVT (Hardorn, 2015).

In this case, working fluid temperatures may often be lower than the ambient air which can lead to some non-conventional operating cases. For example, the collector can also be used as an air-to-water heat exchanger, capturing heat from the air in sensible and latent forms. The lower temperatures can also lead to lower PV cell temperatures, which may result in higher electricity production. Being on the source side may also limit the acceptable temperatures to be delivered to the evaporator, meaning higher flow rates during times of high irradiance may be necessary to avoid overheating.

Since these operating conditions are significantly different from PVT used for domestic hot water or direct space heating, it stands to reason that typical PVT designs may need to be modified for use with a GSHP. For example; larger or alternative flow channels from fin-and-tube, enhanced heat exchange on the rear of the panel rather than insulation, or accommodations for condensation.

Because of the interactions between components, it is critical to use a comprehensive modeling tool when designing hydraulic configurations and testing control strategies for a PVT+GSHP system. TRNSYS is a widely used and accepted, transient simulation tool for solar energy systems with many additional models for additional building components (Klein et al., 2009). Several solar thermal, PV, and PVT models have been

doi:10.18086/eurosun.2016.08.19 Available at http://proceedings.ises.org

incorporated, however they were developed with more traditional usage cases in mind and may not be as appropriate for PVT+GSHP applications. Therefore, the objective of this study is to develop a state-of-the-art PVT collector model for use in TRNSYS which can be incorporated into GSHP systems.

To meet this objective, a comprehensive review of existing PVT models is made with a focus on those which have already been implemented in TRNSYS. The study is limited to theoretical models rather than experimental since it is the general modeling of PVT that is of interest, rather than a particular module. Any critical limitations that are identified are tested by building new models or co-simulating with modifications to existing types in Matlab and EES, or using a combination of TRNSYS Types to overcome limitations to stand-alone models. The impact of the modifications will be tested against the existing TYPEs. Steady-state as well as quasi-steady state simulations are performed. The nomenclature used throughout is given in Tab. 1.

Tab. 1. List of nomenclature

Quantity	Symbol	Unit
Collector Area	A_c	m^2
PV air mass coefficient	a_k	-
Air mass	AM	-
Incidence angle modifier coefficient	b_o	-
Bond conductance	C_b	$Wm^{-1}\,K^{-1}$
Specific heat at constant pressure	c_p	$Jkg^{-1}K^{-1}$
External diameter of the tubes	D	m
Hydraulic diameter	D_h	m
Collector efficiency factor	F'	-
Collector heat removal factor	F_R	-
Total radiation on horizontal surface	G	Wm^{-2}
Beam radiation on horizontal surface	G_b	Wm^{-2}
Beam radiation on tilted surface	$G_{b,T}$	Wm^{-2}
Diffuse radiation on horizontal surface	G_d	Wm^{-2}
Total radiation on tilted surface	G_T	Wm^{-2}
Convective heat transfer coefficient on the top of the PVT collector	$h_{conv-top}$	$Wm^{-2}K^{-1}$
Convective heat transfer coefficient on the back of the PVT collector	$h_{conv-back}$	$Wm^{-2}K^{-1}$
Heat transfer coefficient between the fluid and the tube wall	h_{fl}	$Wm^{-2}K^{-1}$
Radiative heat transfer coefficient	h_{rad}	$Wm^{-2}K^{-1}$
Length of a collector	L_1	m
Width of a collector	L_2	m
Thickness of the rectangular water layer	L_3	m
Air mass modifier	M	-
Mass flow rate	$\dot{m}$	$kg\,s^{-1}$
Number of tubes	N_{tubes}	-
Electrical power gain	Q_{el}	W
Thermal power gain	Q_{th}	W
Conductivity thermal resistance	R	m^2KW^{-1}
Solar absorbed radiation	S_{abs}	Wm^{-2}
Temperature	T	K
Ambient temperature	T_a	K
Temperature around the tube	T_b	K
Mean fluid temperature	$\overline{T_{fl}}$	K
Inlet fluid temperature	T_{fi}	K
Outlet fluid temperature	T_{fo}	K
Sky temperature	T_{sky}	K
Overall thermal loss coefficient	U_L	$Wm^{-2}K^{-1}$
Top loss coefficient	U_t	$Wm^{-2}K^{-1}$
Wind velocity	v_{wind}	$m\,s^{-1}$

Greek	Symbol	Unit
Absorptance	α	-
Slope of the collector	β	◦
Type 50 temperature coefficient	β_a	K^{-1}
Incidence angle modifier	$K_{\tau\alpha}$	-
Emissivity	ε	-
Electrical efficiency	η_{PV}	-
Thermal efficiency	η_{th}	-
PV module efficiency (-) when $T_{PV}=T_a$	η_a	-
Stefan-Boltzmann constant	σ	$Wm^{-2}K^{-4}$
Transmittance	τ	-
Packing factor	ξ	-
Angle of incidence	θ	◦
Zenith angle	θ_z	◦
Ground reflectance	ρ_g	-
PV module temperature coefficient	γ	K^{-1}

Subscripts and abbreviations	Symbol	Unit
Beam	*b*	-
Building Integrated Photovoltaic-Thermal	*BIPVT*	-
Diffuse	*d*	-
Ethylene Vinyl Acetate	*EVA*	-
Ground reflected	*g*	-
Ground Source Heat Pump	*GSHP*	-
Radiation component	*i*	-
Incidence angle modifier	*IAM*	-
Normal	*n*	-
Photovoltaic Panel	*PV*	-
Photovoltaic-Thermal	*PVT*	-
Standard Test Condition	*ref*	-
Solar Assisted Heat Pump	*SAHP*	-
Modified	*	-

2. Review

PVT modeling in TRNSYS is by-in-large based on solar thermal collectors with the PV layer added to the front. This section reviews these models in detail as they have been applied to PVT models, as well as modifications made by succeeding authors.

2.1. Type 50

Type 50 is a modification of the Hottel-Whillier (1955) model used in Type 1 and is presented by Florscheutz (1979). It is available in the default TRNSYS library, can be used with glazed and unglazed modules, and is the most widely used PVT Type (Pressiani, 2016). The model is built on the assumption that the PV cells are laminated directly to the absorber plate, and thus the cells and the absorber are considered to have the same temperature.

The electrical power output Q_{el} is calculated with eq. 1.

$$Q_{el} = A_c \tau G_T \eta_a \left\{1 - \beta_a \left[F_R\left(T_{fi} - T_a\right) + \frac{S_{abs}}{U_L}(1 - F_R)\right]\right\} \quad \text{(eq. 1)}$$

Eq. 2 defines the useful thermal output Q_{th} of the combined collector.

$$Q_{th} = F_R A_C [S_{abs} - U_L (T_{fi} - T_a)] \quad \text{(eq. 2)}$$

Where F_R is the collector heat removal factor shown in eq. 3.

$$F_R = \frac{\dot{m} c_p}{A_c U_L} \left[1 - \exp\left(- \frac{U_L F' A_c}{\dot{m} c_p} \right) \right] \quad \text{(eq. 3)}$$

The absorbed radiation S_{abs} is calculated using eq. 4.

$$S_{abs} = G_T \left(1 - \frac{\eta_a}{\alpha} \right) (\tau\alpha) \quad \text{(eq. 4)}$$

There are eight different operational modes: modes 1 to 4 simulate flat-plate collectors with an increasing level of complexity in the heat loss calculations, modes 5 to 8 are used to model concentrating solar collectors, which is outside the scope of this study. In mode one the heat loss coefficient (U_L) and the angular dependence of ($\tau\alpha$) are set as constant values. This mode is recommended for all cases except those for which the assumption may introduce significant error in the calculated performance. Mode two calculates U_L as a function of the operating temperatures, the wind speed and the collector geometry using Klein's equation (1975). In mode three U_L is set as a constant and τ is considered using Hottel-Woertz (1944). Mode four is a combination of modes two and three, however it can only be used with glazed collectors.

Shortcomings of Type 50 have been noted by several authors over the years. A significant source of error is the lumped temperature of the absorber and the PV cells, which when measured was found to be up to 12K different and result in electric overproduction of 10% (Raghuraman, 1981). Later simulations would demonstrate that the temperature gradients between cooling tubes are much higher when a thermal resistance is added between the layers, also identifying a greater average temperature difference (Mazara, 2009). The collector efficiency factor (F') in eq. 3 is an input in Type 50 and constant throughout the simulation, even though it is a function of irradiation, wind speed, and internal temperature of the collector layers. This assumption may be appropriate for glazed collectors, but will likely lead to greater errors in unglazed PVTs (Bilbao and Sproul, 2012). An issue directly related to the PVT+GSHP concept is the calculation of the top loss coefficient (U_t), which uses the mean absorber temperature rather than the fluid temperature, potentially causing increased errors when the fluid temperature is lower than ambient (Bilbao and Sproul, 2012). Type 50 doesn't consider the thermal resistance of the bond between absorber and the tube ($C_b = \infty$).

The algorithm used in Type 50 may also be a source of error. The Florscheutz model requires multiple iterations to converge on a solution. Type 50 is hard coded to perform only three iterations, which may not be enough to reach an acceptable convergence (Bilbao and Sproul, 2012). Additionally, a floating point error can cause the simulation to fail (Collins, 2009).

2.2. Type 560

Type 560 has been created as a dedicated unglazed PVT model using heat transfer equations derived by Duffie-Beckman (1991) based on energy balances of the PV layer, absorber fins, and absorber tubes. Like Type 50, it uses an iterative approach to solve the analytical equations until convergence is reached and is also based on a fin-tube absorber design.

The electrical power output Q_{el} is defined with eq. 5.

$$Q_{el} = (\tau\alpha)_n (IAM) G_T \eta_{PV} A_c \quad \text{(eq. 5)}$$

The thermal power output Q_{th} is calculated with eq. 6.

$$Q_{th} = \dot{m} c_p (T_{fo} - T_{fi}) \quad \text{(eq. 6)}$$

The outlet fluid temperature T_{fo} can be written using eq. 7.

$$T_{fo} = \left(T_{fi} + \frac{C_1}{C_2} \right) exp\left(\frac{N_{tubes} C_2 L}{\dot{m} c_p C_3} \right) - \frac{C_1}{C_2} \quad \text{(eq. 7)}$$

The coefficients C_1, C_2, and C_3 are based on the fin-tube geometry and material properties, as well as the heat transfer coefficients with the surroundings.

A notable feature of Type 560 is that it considers the PV and absorber layers separately, allowing the user to

define the thermal resistance between them. It also considers convection coefficients as inputs. In Type 50, wind speed is an input and the convection coefficient on the front of the collector is calculated using the linear relationship defined by McAdams (1954). This allows users to calculate convection externally using Type 1232 or a custom equation. Convective and radiative heat transfer is also considered on the back side of the module in Type 560, which is of particular interest in a PVT without insulation.

2.3. Modifications to Type 50 and 560

Upon the identification of limitations to Type 50, a small library of modified Types were created as a part of the IEA Solar Heating and Cooling Task 35 and are freely available for download (Collins, 2009). Type 250 is the flat plate, water cooled model in the library and is a modification of Type 50d. Modifications to the model include the correction of the floating point error which lead to a division by zero and the correction of an error in the PV efficiency equation related to the temperature coefficient.

Several authors have created their own versions of Type 50 by connecting their own PV electrical equations with Type 1. For calculating PV output, Elswijk et al. (2004) used a linear temperature relationship similar to Types 50 and 560 and used the mean fluid temperature from Type 1 to determine cell temperature. Kalogirou and Tripanagnostopoulos (2006) use the same linear relationship to temperature, however they use a combination of standalone PV module temperature models with the PVT fluid temperature to determine cell temperature.

Type 563 is an alternative version to 560 which relies on the same thermodynamic model but is intended for building integrated PVT. The modification connects the back side temperature to the interior air node in a multi-zone building model. This allows the building model to take into consideration the heat transfer of the PVT modules on the building energy balance.

2.4. Other PVT Types

A number of researchers have created custom PVT models in recent decades using a variety of approaches. Some of these have been adapted for use in TRNSYS. Kalogirou (2001) created Type 49 based on the work of Bergene and Lovvik (1995). Their approach is similar to Duffie-Beckman but use a 2D steady state model which considers temperature gradients in the surface plane of the module. Like Type 50, temperature gradients through the thickness of the PV and absorber are not considered. Fraisse et al. (2007) used an electrical current analogy applied to heat transfer to create Type 105. The model is capable of glazed and unglazed PVT collectors and is described by 12 nodes with heat capacities that handle the dynamic behavior of each layer. Bilbao and Sproul (2012) developed Type 850 which is mathematically similar to Type 50 in that it assumes the PV cell temperature is the same as the absorber, however it uses a numerical solving approach and a top heat loss coefficient model by Akhtar and Mullick (1999). Dupeyrat et al. (2014) use Type 832, a thermal collector model original developed by Perers and Bales (2002) and extended most recently by Haller et al. (2012) which relies on experimental data to determine its coefficients. They modify it to include the electrical portion using an experimentally derived relationship between temperature and PV power.

2.5. Review conclusions

There have been numerous studies towards the goal of modeling PVT collectors, many of which are directed towards use in TRNSYS due to its ability to model complete solar energy systems. The vast majority of work has been based on the original solar thermal model by Hottel-Whillier and integrated into Type 50. As noted above, Type 50 has a number of computational shortcomings as well as physical limitations. Two significant issues are the matching PV cell temperature with the absorber layer and the limited modeling capabilities of heat transfer with the surroundings. In PVT collectors where the PV cells are laminated directly to the absorber with very high conductivity, then the single temperature assumption is more reasonable. However, this limits the type of collectors which can be explored. Similarly, the heat transfer with the surroundings is unique with PVT+GSHP systems given the potential for collector temperatures well below ambient. These issues limit the applicability of Type 50 and its derivatives to PVT+GSHP system models.

Type 560 offers a multi-layered model which solves the major shortcomings of Type 50. Surprisingly, it is not used by nearly as many researchers as Type 50, and there is little documentation to validate its performance with experimental data. However, the theoretical foundations make it a more promising tool for use with novel PVT collector designs in GSHP system simulations.

Nevertheless, Type 560 does have artifacts which may be a source of error for unglazed and uninsulated PVT

collectors. There are several which have been identified (Pressiani, 2016), only two are discussed here. First, the model used for absorbed radiation is derived from a glazed thermal collector, rather than an unglazed PV module. Second, the model is entirely based on the traditional fin-tube design, which may not be representative of other configurations, such as roll bond construction, that could have other flow patterns.

3. Models and Results

In consideration of the artifacts listed above regarding Type 560, alternative models are tested to see if there are any impacts on electric and/or thermal production. The alternative models are only tested against the default 560 model. To make the modifications, the Fortran code from Type 560 has been recreated in Matlab and EES.

3.1. Absorbed radiation

Testing the absorbed radiation is performed with transient simulations over the course of one day, using TMY2 weather data for Stockholm-Arlanda from June 1st, and a time step of 10 minutes. The model used to calculate the total amount of incident radiation absorbed by the PV surface in Type 560 is based on Liu and Jordan's (1963) isotropic sky method and represented by eq. 8.

$$S_{abs} = (\tau\alpha)_n (IAM) G_T = (\tau\alpha)_n \left(G_{b,T} K_{\tau\alpha,b} + G_d K_{\tau\alpha,d} \frac{1+\cos\beta}{2} + G\rho_g K_{\tau\alpha,g} \frac{1-\cos\beta}{2} \right) \quad \text{(eq. 8)}$$

Where $K_{\tau\alpha,i}$ is represented by eq. 9.

$$K_{\tau\alpha,i} = 1 - b_0 \left(\frac{1}{\cos\theta_i} - 1 \right) \quad \text{(eq. 9)}$$

And $G_{b,T}$ with eq. 10.

$$G_{b,T} = G_T - G_d \frac{1+\cos\beta}{2} - G\rho_g \frac{1-\cos\beta}{2} \quad \text{(eq. 10)}$$

While developing an improved PV generation model, De Soto (2004) proposes a PV specific absorption term described in eq. 11.

$$S_{abs} = (\tau\alpha)_n M (IAM) G_T = (\tau\alpha)_n M \left(G_{b,T} k_{\tau\alpha,b} + G_d k_{\tau\alpha,d} \frac{1+\cos\beta}{2} + G\rho_g k_{\tau\alpha,g} \frac{1-\cos\beta}{2} \right) \quad \text{(eq. 11)}$$

Where $K_{\tau\alpha,i}$ is represented by eq. 12. that defines light refraction passing through a single pane of glass without an air gap on the other side. This better represents a standard PV module, similar to what would be found in an unglazed PVT.

$$K_{\tau\alpha,i} = \frac{(\tau\alpha(\theta_i))_i}{(\tau\alpha)_n} \quad \text{(eq. 12)}$$

$G_{b,T}$ is also modified and shown in eq. 13.

$$G_{b,T} = G_b R_b = \frac{\cos\theta_b}{\cos\theta_z} (G - G_d) \quad \text{(eq. 13)}$$

A new term, *M*, represents the air mass modifier to account for changes in spectral distribution due to air mass, and is described with eq. 14 (King et al., 2004). The coefficients a_k are constants based the cell material (De Soto et al., 2006).

$$M = \sum_{k=0}^{4} a_k (AM)^k \quad \text{(eq. 14)}$$

For zenith angles between 0° and 60°, the air mass is represented with eq. 15, and for angles beyond 60° is described by Kasten and Young (1989).

$$AM = \frac{1}{\cos(\theta_z)} \quad \text{(eq. 15)}$$

In most absorption models, the PV cell is the only material considered even though there are gaps and busbars which are also present. Santbergen and van Zolingen (2008) consider the absorptivity of the multiple surfaces of a PV module using a dedicated optical model. The absorptivity model is represented by eq. 16.

$$\alpha = \tau\left(\xi\alpha_{cell} + (1-\xi)\alpha_{space\ between\ cells}\right) \quad \text{(eq. 16)}$$

$G_{b,T}$ is calculated using eq. 10 and the effective absorptivity with eq. 17. The packing density ξ is the ratio of the module area that are active PV cells to the total area of the module.

$$S_{abs} = \alpha\left(G_{b,T} + G_d\frac{1+\cos\beta}{2} + G\rho_g\frac{1-\cos\beta}{2}\right) \quad \text{(eq. 17)}$$

The three radiation absorption models (Type 560, De Soto, Santbergen) are tested using identical conditions and input values where possible. In cases where model specific terms are considered, values representing a typical mono-crystalline PV module are used.

The results in Fig. 1 show that Type 560 has the lowest electrical power output. Relative to 560, the De Soto model is higher across the entire day, while Santbergen has notably higher output during the morning and evening hours when there are low incident angles. The peak difference occurs in both models during the morning, with De Soto being 38.1% greater and Santbergen 44.5%. During the midday when there is much greater production, the De Soto model is about 13% greater. In terms of electrical energy generation, Type 560 produced 1.692 kWh, De Soto 1.798 kWh, and Santbergen 1.975 kWh for the day, suggesting that over a year there could be significant differences in this portion of the model.

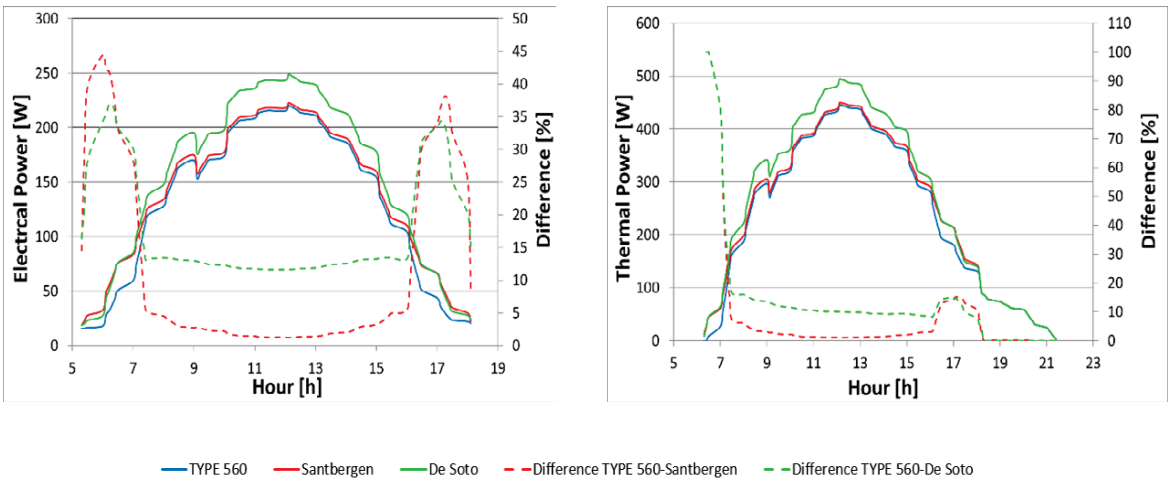

Fig. 1. Electrical and thermal output comparison of Type 560, De Soto, and Santbergen radiation absorption models

The thermal output results show once again that De Soto is shown to have significantly higher output throughout most of the day. The differences in the early and late hours are less pronounces as in the electrical generation, particularly in the later hours where all three models match exactly. During the midday, De Soto gives a 10-18% higher output while Santbergen is usually under 5% greater. Total thermal production for the day from each model is 3.575 kWh for Type 560, 3.713 kWh for De Soto, and 4.012 kWh for Santbergen.

3.2. Alternative Collector Geometry

One of the main limitations of Type 560 is that the only absorber design is a sheet and tube, represented by Fig. 2a. If another geometry is considered, like the rectangular channel absorber in Fig. 2b, then it is possible to use the hydraulic diameter. In Type 560 there's the assumption that the temperature (T_b) around the tube is uniform. This may not be true for all types of design, for example with a single channel like in Fig. 2c where there is direct contact on one side and no insulation on the rear, $T_{b,1}$ could have a significantly different value from $T_{b,2}$.

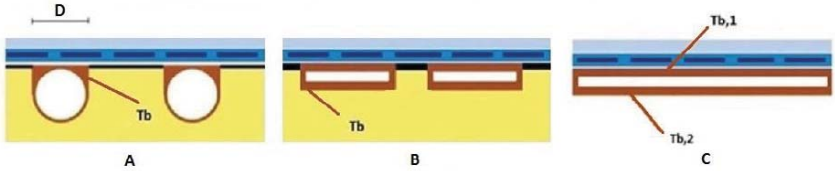

Fig. 2. Different absorber geometry

A 1D steady state model is built with EES in order to simulate the geometry with one single rectangular channel (Fig. 2c). The single channel configuration is used as a way to examine designs which do not have large gaps between the parallel tubes. The proposed model is then compared with several configurations of Type 560 which attempt to mimic the single channel design. A cross section of the layered construction which the 1D model is based on is shown in Fig. 3, and is based on a prototype collector currently in development. The model is built using energy balances over multiple layers within the collector; the top glass, PV, bottom glass, and the metal back layer.

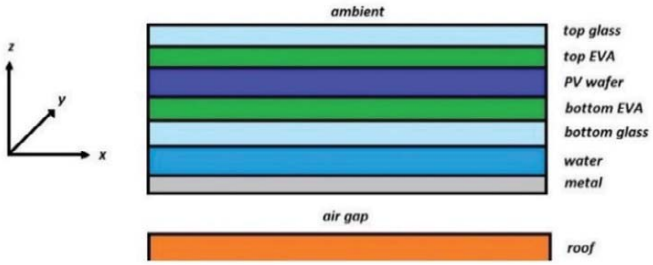

Fig. 3. PV/T collector representation

The energy balance on the top glass cover is given by eq. 18.

$$\frac{T_{PV} - T_{top-glass}}{R_{top-glass} + R_{top-eva} + R_{PV}} - h_{rad}\left(T_{top-glass} - T_{sky}\right) - h_{conv-top}\left(T_{top-glass} - T_a\right) = 0 \quad \text{(eq. 18)}$$

Where h_{rad} is represented with eq. 19:

$$h_{rad} = \varepsilon_g \sigma \left(T_{top-glass} + T_{sky}\right)\left(T_{top-glass}^2 + T_{sky}^2\right) \quad \text{(eq. 19)}$$

Eq. 20 gives the energy balance on the PV cells.

$$S_{abs} - \frac{T_{PV} - T_{top-glass}}{R_{top-glass} + R_{top-eva} + R_{PV}} - \frac{T_{PV} - T_{bottom-glass}}{R_{bottom-eva} + R_{bottom-glass}} - \frac{Q_{el}}{A_c} = 0 \quad \text{(eq. 20)}$$

Where Q_{el} is represented with eq. 21. S_{abs} is described with eq.8.

$$Q_{el} = G_T \eta_{\mathrm{PV,ref}}\left[1 - \gamma\left(\mathrm{T_{PV}} - \mathrm{T_{PV,ref}}\right)\right] A_c \quad \text{(eq. 21)}$$

The energy balance on the bottom glass is given by eq. 22.

$$\frac{T_{PV} - T_{bottom-glass}}{R_{bottom-eva} + R_{bottom-glass}} - h_{fl}\left(T_{bottom-glass} - \overline{T_{fl}}\right) = 0 \quad \text{(eq. 22)}$$

Eq. 23 and 24 represent the energy balance on the metallic backing on the fluid channel.

$$\frac{\left(T_{back} - T_{metal}\right)}{R_{metal}} - h_{fl}\left(T_{metal} - \overline{T_{fl}}\right) = 0 \quad \text{(eq. 23)}$$

$$h_{conv-back}\left(T_{amb} - T_{back}\right) - \frac{\left(T_{back} - T_{metal}\right)}{R_{metal}} = 0 \quad \text{(eq. 24)}$$

The convective heat transfer coefficients $h_{conv-top}$ and $h_{conv-back}$ follows Cole and Sturrock's formula (1977).

The average working fluid temperature in the collector $\overline{T_{fl}}$ is calculated with eq. 25.

$$\overline{T_{fl}} = \frac{\frac{T_{bottom-glass} + T_{metal}}{2} - T_{fi}}{\frac{2h_{fl}L_1L_2}{\dot{m}cp}}\left(\exp\left(-\frac{2h_{fl}L_1L_2}{\dot{m}cp}\right) - 1\right) + \frac{T_{bottom-glass} + T_{metal}}{2} \quad \text{(eq. 25)}$$

The convective heat transfer coefficient h_{fl} is calculated for laminar and turbulent flow using Nusselt correlations.

The final output for thermal power Q_{th} is given by eq. 26.

$$Q_{th} = \dot{m}cp\left(T_{fo} - T_{fi}\right) \quad \text{(eq. 26)}$$

Where the outlet temperature T_{fo} is given by eq. 27:

$$T_{fo} = \left(T_{fi} - \frac{T_{bottom-glass} + T_{metal}}{2}\right)\exp\left(-\frac{2h_{fl}L_1L_2}{\dot{m}cp}\right) + \frac{T_{bottom-glass} + T_{metal}}{2} \quad \text{(eq. 27)}$$

There are three configurations of Type 560 tested; a single tube approach (I), a packed tube approach (II), and a typical collector design (III). The single channel approach considers one tube with a diameter equal to the width of the module, which is similar to the adaptation that can be made for designs like Fig. 2b. The packed channel approach places the tubes directly next to each other across the entire width, effectively removing the fins, which is represented in Fig. 4. The typical collector uses 10 tubes with diameters of 0.015 m in parallel, which result in absorber fins between them much like Fig. 2a, and is included as a control.

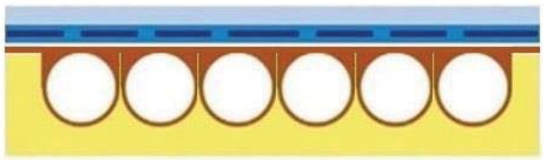

Fig. 4. Approximation of a rectangular water channel using the packed tube approach

To represent the single fluid channel directly in contact with the rear glass, the bond conductance between the tubes and absorber plate in all of the Type 560 models is set very high (10^{10}) and the thickness very low (10^{-10}). The resistance of the back glass in the 1D model is then incorporated into the absorber plate conductivity setting. The front and back convection coefficients in Type 560 are set to match the values used in the proposed 1D model. This means adding resistance to the front since Type 560 does not consider the glass and EVA layers on top of the PV. The convection coefficient inside the tubes are set using eq. 28 and 29.

$$h_{fl} = \frac{h_{fl}^{*} D_h}{D} \quad \text{(eq. 28)}$$

$$h_{fl}^{*} = f\left(Nu(D_h)\right) \quad \text{(eq. 29)}$$

The four geometries are run using steady state simulations across a range of operating conditions. A range of inputs are considered for three external variables; wind velocity, ambient temperature, and mass flow rate. The default value for the wind is 1 m/s, ambient temperature is 10 °C, and the flow rate is 0.05 kg/s.

The electrical and thermal production results are shown in Fig. 5, with electrical on the left and thermal on the right. In both cases the packed tube approach (II) is the closest to the 1D model. The difference in electric output is only 0.63% and in thermal output 3.77%. The greatest difference is found in the traditional collector design, highlighting the differences between the design concepts.

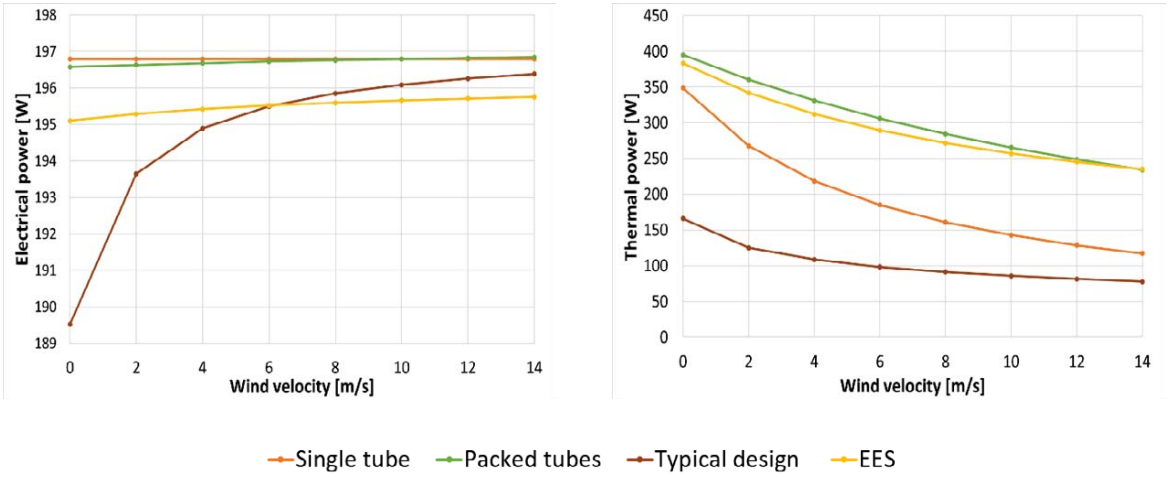

Fig. 5. Electrical and thermal power outputs with wind velocity variation for multiple geometries

The relationship between power and ambient temperature are shown in Fig. 6. Once again the packed tube concept and 1D concept are best matched in both thermal and electrical output. The average difference is 1.20% for electrical and 8.36% in thermal. In this case the traditional collector had the greatest error again, but this time is significantly greater, with a variation of 59.92% for the thermal part.

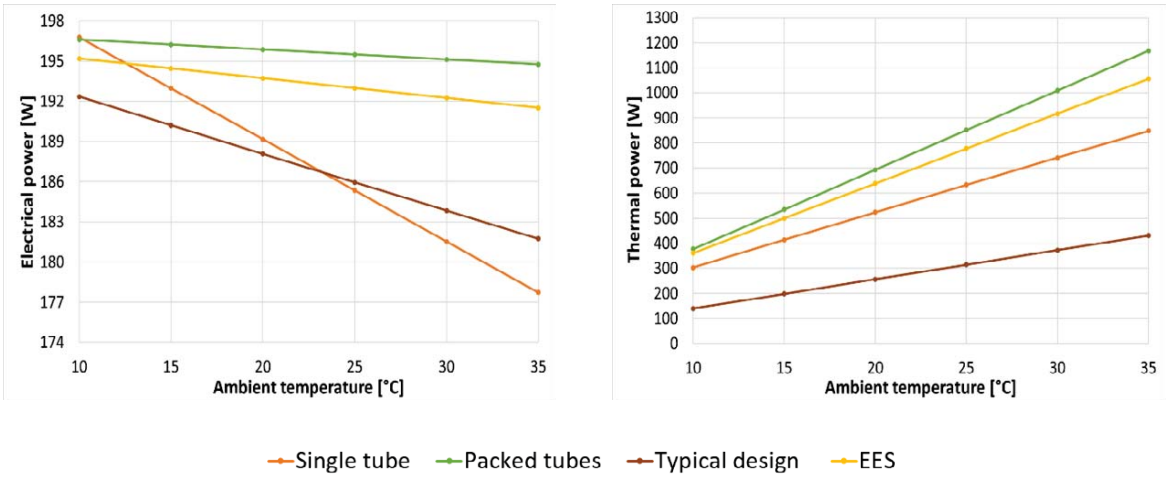

Fig. 6. Electrical and thermal power outputs with ambient temperature variation for multiple geometries

Fig. 7 shows the trends in output related to mass flow rate.

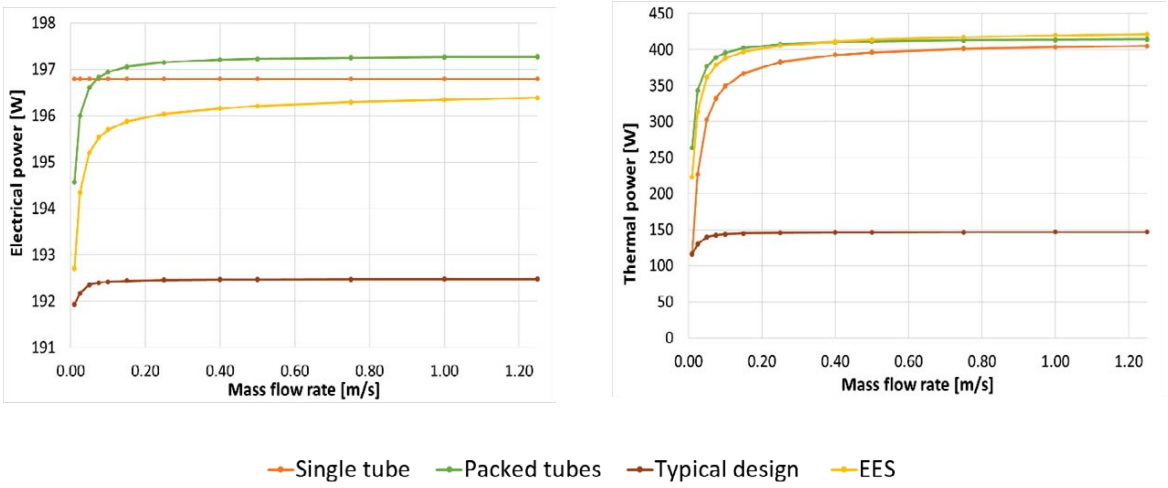

Fig. 7. Electrical and thermal power outputs with mass flow rate variation for multiple geometries

The difference in electric production is small between each geometry, but again the packed tubed concept (II) matches the 1D model most closely. There's a difference of 0.62% for the electrical power output and 3.62% for the thermal one. A notable feature in these results is the deviation of the single tube concept (I) from the patterns of the others at low flow rates. This may be caused by an error in the way the convection coefficient is being calculated for the single tube. Once again in thermal output, the traditional collector geometry is significantly lower than the others, with a 62.07% of deviation.

3 Discussion and Conclusions

Upon review of the two most prominent TRNSYS models for PVT collectors, Type 50 and Type 560, the later model has been identified as the most promising representation for novel PVT designs. Type 850, which incorporated the thermal model Type 832 would also be a good choice, however it requires the construction and testing of a collector prior to use. Type 560 is a theoretical model and provides the most flexibility and control. Type 50 and its derivations are limiting by not considering resistance between the absorber and PV cells and the relatively basic convection interaction with the environment.

For exploring novel PVT collectors Type 560 is not without limitations, however, two of which have been explored here; radiation absorption and collector geometry. Two absorption models dedicated to PV modules demonstrated significant differences in electrical and thermal power output during low angle, low light conditions. One of the models, from De Soto (2004) showed increased power output during nearly all hours of the day. These differences require most testing given the limited results presented here. The impact on annual or lifetime production should be investigated. Validation with experimental data is also necessary.

The collector geometry limitation has been tested considering two possibly modifications with Type 560 and compared with a 1D model created in EES. The results showed that collector geometry has significant impact on output, and that is must be taken into consideration in the model. A method which places as many working fluid tubes together as possible gave the most similar results between Type 560 and the 1D model, and are close enough to recommend 560 for use in this collector design. This is beneficial since construction of a new Type can be a lengthy and difficult process.

A limitation to this work is that all of the results presented here are theoretical. Development and testing of a prototype PVT collector specifically for use with GSHP systems is currently being performed. Once completed, the results from this modeling can be compared to the empirical data to confirm and validate the models.

6. Acknowledgement

This research has been funded by Mistra Innovation (project no. MI15.18) for which the authors are grateful.

7. References

Akhtar, N., Mullick, S.C., 1999. Approximate method for computation of glass cover temperature and top heat-loss coefficient of solar collectors with single glazing. Sol. Energy 66, 349–354. doi:10.1016/S0038-092X(99)00032-8

Bergene, T., Løvvik, O.M., 1995. Model calculations on a flat-plate solar heat collector with integrated solar cells. Sol. energy 55, 453–462. doi:10.1016/0038-092X(95)00072-Y

Bilbao, J., Sproul, A., 2012. Analysis of flat plate photovoltaic-thermal (PVT) models. World Renew. Energy Forum 95–102.

Cole, R.J., Sturrock, N.S., 1977. The convective heat exchange at the external surface of buildings. Build. Environ. 12, 207–214. doi:10.1016/0360-1323(77)90021-X

Collins, M., 2009. A review of PV, solar thermal, and PV/thermal collector models in TRNSYS, IEA SHC - Task 35.

De Soto, W., 2004. Improvement and Validation of a Model for Photovoltaic Array Performance. University of Wisconsin-Madison.

De Soto, W., Klein, S. a., Beckman, W. a., 2006. Improvement and validation of a model for photovoltaic array performance. Sol. Energy 80, 78–88. doi:10.1016/j.solener.2005.06.010

Duffie, J.A., Beckman, W.A., 1991. Solar Engineering of Thermal Processes, Second. ed. John Wiley & Sons, Inc., Hoboken, NJ.

Dupeyrat, P., Ménézo, C., Fortuin, S., 2014. Study of the thermal and electrical performances of PVT solar hot water system. Energy Build. 68, 751–755. doi:10.1016/j.enbuild.2012.09.032

Elswijk, M.J., Jong, M.J.M., Strootman, K.J., Braakman, J.N.C., de Lange, E.T.N., Smit, W.F., 2004. Photovoltaic/thermal Collectors in Large Solar Thermal Systems, in: 19th European Photovoltaic Solar Energy Conference and Exhibition. Paris.

Florschuetz, L.W., 1979. Extension of the Hottel-Whillier model to the analysis of combined photovoltaic/thermal flat plate collectors. Sol. Energy 22, 361–366. doi:10.1016/0038-092X(79)90190-7

Fraisse, G., Ménézo, C., Johannes, K., 2007. Energy performance of water hybrid PV/T collectors applied to combisystems of Direct Solar Floor type. Sol. Energy 81, 1426–1438. doi:10.1016/j.solener.2006.11.017

Haller, M.Y., Perers, B., Bales, C., Paavilainen, J., Dalibard, A., Fischer, S., Bertram, E., 2012. TRNSYS Type 832 v5.00, Dynamic Collector Model by Bengt Perers: Updated Input-Output Reference.

Hardorn, J.-C. (Editor), 2015. Solar and Heat Pump Systems for Residential Buildings, First. ed. Ernst & Sohn GmbH & Co., Berlin.

Hottel, H.C., Whillier, A., 1955. Evaluation of flat-plate solar collector performance, in: Transcript of the Conference on the Use of Solar Energy, The Scientific Basis, Vol. II, Part 1, Section A. University of Arizona Press, Tucson, Arizona, pp. 74–104.

Hottel, H.C., Woertz, B.B., 1944. Performance of Flat-Plate Solar-Heat Collectors. ASME Trans. 64, 91.

Kalogirou, S.A., 2001. Use a TRNSYS for modelling and simulation of a hybrid pv-thermal solar system for Cyprus. Renew. Energy 23, 247–260. doi:10.1016/S0960-1481(00)00176-2

Kalogirou, S. a., Tripanagnostopoulos, Y., 2006. Hybrid PV/T solar systems for domestic hot water and electricity production. Energy Convers. Manag. 47, 3368–3382. doi:10.1016/j.enconman.2006.01.012

Kasten, F., Young, A.T., 1989. Revised optical air mass tables and approximation formula. Appl. Opt. 28, 4735–4738. doi:10.1364/AO.28.004735

King, D.L., Boyson, W.E., Kratochvill, J.A., 2004. Photovoltaic Array Performance Model. Sandia National Laboratories, SAND2004-3535.

Klein, S.A., 1975. Calculation of flat-plate collector loss coefficients. Sol. Energy 17, 79–80.

Klein, S., Beckman, W.A., Mitchell, J., Duffie, J.A., Freeman, T., 2009. TRNSYS 17, A Transient System Simulation Program.

Liu, B.Y.H., Jordan, R.C., 1963. A Rational Procedure for Predicting The Long-Term Average Performance of Flat-Plate Solar-Energy Collectors. Sol. Energy 7, 53–74. doi:10.1016/0038-092X(63)90006-9

Mazara, A., 2009. Analisi termica di collettori cogenerativi fotovoltaici-termici. Politecnico Milano.

McAdams, W.H., 1954. Heat Transmission, Third. ed. McGraw-Hill, New York.

Perers, B., Bales, C., 2002. A Solar Collector Model for TRNSYS Simulation and System Testing, IEA SHC Task 26.

Pressiani, M., 2016. Photovoltaic/thermal hybrid solar collectors: TRNSYS analysis and possible improvements. Politecnico Milano.

Raghuraman, P., 1981. Analytical Predictions of Liquid and Air Photovoltaic/Thermal, Flat-Plate Collector Performance. J. Sol. Energy Eng. 103, 291–298. doi:10.1115/1.3266256

Santbergen, R., van Zolingen, R.J.C., 2008. The absorption factor of crystalline silicon PV cells: A numerical and experimental study. Sol. Energy Mater. Sol. Cells 92, 432–444. doi:10.1016/j.solmat.2007.10.005

Conference Proceedings

EuroSun 2016
Palma de Mallorca (Spain), 11 - 14 October 2016

Control algorithms for PV and Heat Pump system using thermal and electrical storage

Emmanouil Psimopoulos[1,2], Lorenz Leppin[1], Rasmus Luthander[2], Chris Bales[1]

[1] Energy Technology, Dalarna University, Borlänge, Sweden

[2] Department of Engineering Sciences, Uppsala University, Uppsala, Sweden

Abstract

In this study a detailed model of a single-family house with an exhaust air heat pump and photovoltaic system is developed in the simulation software TRNSYS. The model is used to evaluate three control algorithms using thermal and electrical storage in terms of final energy, solar fraction, self-consumption and seasonal performance factor. The algorithms are tested and compared with respect to energetic improvement for 1) use of the heat pump plus storage tank for domestic hot water and space heating, 2) use of the electrical storage in batteries and (3) use of both electrical and thermal storage. Results show the highest increase of self-consumption to 50.5%, solar fraction to 40.6% and final energy decrease to 6923 kWh by implementing the third algorithm in a system with 9.36 kW PV capacity and battery storage of 10.8 kWh. The use of electrical energy storage has higher positive impact compared to the thermal storage with the settings and component sizes used. The combined use of thermal storage and batteries leads to final energy savings that are nearly the same as the combined savings of thermal storage and batteries separately, showing that they are mostly independent of one another for the settings of this study.

Keywords: Photovoltaics, heap pump, thermal storage, electrical storage, solar fraction, self-consumption

Nomenclature

COP	Coefficient of performance
DHW	Domestic hot water
FE	Final energy
HP	Heat pump
SC	Self-consumption [%]
SF	Solar fraction [%]
SH	Space heating
SPF	Seasonal performance factor
PV	Photovoltaics

1. Introduction

The energy consumption in the building sector has increased steadily in developed countries for several years, reaching 20-40% of the total energy consumption with Sweden in the upper end of the scale in 2015 (Heier et al., 2015; Pérez-Lombard et al., 2008; Swedish Energy Agency, 2015a). Domestic hot water (DHW) and space heating (SH) accounted for more than half of the sector's total energy use (Swedish Energy Agency, 2015a). There are several options for supplying thermal energy for DHW and SH in the

doi:10.18086/eurosun.2016.08.13 Available at http://proceedings.ises.org

building stock, including district heating, electric heating, biofuels and fossil fuels. In Swedish single-family houses electric heating is the most common option with a share of 45% of the total heat demand in the sector in 2014 (Swedish Energy Agency, 2015b). For houses with electric heating, a heat pump (HP) combined with a hot water storage tank is an efficient way to lower the electricity demand for heating in an electrically heated house (Hirvonen et al., 2016; Swedish Energy Agency, 2015a).

1.1 Energy management in buildings

There are two ways to reduce the need of buying electricity in a household: either using solutions for energy savings or producing own electricity. This paper focuses on the latter method to lower the need of buying electricity from a retailer by using photovoltaics (PV) for in-house electricity production. PV for residential applications is becoming more popular in Sweden due to lower prices for turnkey systems and enhanced economic supporting schemes for micro-producers of electricity (Lindahl, 2016). The cumulative installed PV capacity in Sweden has increased remarkably during the past years, from a total of 11 MW in 2010 to 127 MW at the end of 2015, of which 30% was residential grid-connected PV systems.

With an electric HP more of the PV electricity can be used in the house in comparison to non-electric heated houses. This can be an advantage both from an economical point of view and from a power system's perspective. If the buying prices of electricity exceed the selling prices, it is more profitable to replace bought electricity by own PV electricity than to sell the excess production to the power grid. A higher use of the PV electricity also lowers the excess electricity from the PV system, which might reduce the stress on the power grid in areas with a large penetration of PV.

Apart from converting electricity to heat via a heat pump, batteries for electricity storage or load shifting of electric appliances can be used to increase the use of PV electricity in the house (Castillo-Cagigal et al., 2011; Widén, 2014). The advantage of batteries is the possibility to store electricity for later use, while heat pumps can convert electricity into heat but not back again. Heat pumps can, however, have a higher thermal output than electric output, known as the coefficient of performance (Binder et al., 2012). This means that the efficiency of converting and storing electric energy as thermal energy can exceed 100% whereas the efficiency of battery storage always is below 100% due to conversion and storage losses. By time-shifting electric appliances such as washing and drying machines to times when there are high PV production, both self-consumption and solar fraction can be improved. The economic benefit for load shifting in the Swedish single-family building stock might, however, be low. A study of 200 houses in Sweden showed the economic benefit of load shifting to be maximum 20 Euro per house and year (Widén, 2014).

1.2 Final energy, solar fraction, self-consumption and seasonal performance factor

Apart from the electricity production, there are three measures that are useful to evaluate the energy performance of a residential PV system, namely, final energy consumption, self-consumption and solar fraction. Furthermore, a heat pump can be evaluated based on its seasonal performance factor.

Final energy (FE) consumption refers to the energy supplied to a customer (European Environment Agency, 2016). In this study the final energy is the electricity that needs to be bought from an electricity retailer over the studied year. Self-consumption is defined as PV electricity production that is directly consumed in the house, i.e. self-consumed electricity, relative to the total PV electricity production (Baetens et al., 2012). Solar fraction is defined as the self-consumed PV electricity production relative to the total load (Lund, 2005).

A mathematical description of self-consumption and solar fraction can be found in Luthander et al. (2015). If $L(t)$ denotes the instantaneous electric load including appliances, heat pump and auxiliary heater, and $P(t)$ is the instantaneous power from the PV system, the directly consumed PV power $M(t)$ can be defined as

$$M(t) = \min\{L(t), P(t)\} \quad (1)$$

if no electric storage is used. When adding battery storage to the system, this can be extended to

$$M(t) = \min\{L(t), P(t) + S(t)\} \quad (2)$$

where $S(t) < 0$ denotes power to storage (charging) and $S(t) > 0$ denotes power from storage (discharging). The final energy for the simulation period is equal to the electric load that cannot be supplied by PV

electricity:

$$FE = \int_{t_1}^{t_2} L(t)\,dt - \int_{t_1}^{t_2} M(t)\,dt \quad (3)$$

Self-consumption and solar fraction can then be defined as:

$$SC = \frac{\int_{t_1}^{t_2} M(t)\,dt}{\int_{t_1}^{t_2} P(t)\,dt} \quad (4)$$

$$SF = \frac{\int_{t_1}^{t_2} M(t)\,dt}{\int_{t_1}^{t_2} L(t)\,dt} \quad (5)$$

Strategies for improving PV self-consumption and solar fraction in residential buildings are a rapidly expanding research field (Luthander et al., 2015). The majority of the studies focus on PV in combination with battery storage but heat pumps plus hot water storage have also attracted some interest in recent years (Binder et al., 2012; Hesaraki and Holmberg, 2013; Hirvonen et al., 2016; Luthander et al., 2015; Thygesen and Karlsson, 2014).

Seasonal performance factor (SPF) is a measure of the efficiency of the heat pump, defined as the heat output relative to the electric input. In this study two definitions are used, the first SPF_{HP} includes only the HP compressor electric input and the second SPF_{HP+aux} includes both the HP compressor electric input and the auxiliary input. Since the use of a heat pump system in cold regions is higher in the winter months when the solar irradiance and thus PV electricity production is low, the SPF of the heat pump may have a large impact on the yearly final energy. SPF can be defined as:

$$SPF_{HP} = \frac{\int_{t_1}^{t_2} [Q_{SH}(t) + Q_{DHW}(t)]\,dt}{\int_{t_1}^{t_2} P_{el,HP}(t)\,dt} \quad (6)$$

$$SPF_{HP+aux} = \frac{\int_{t_1}^{t_2} [Q_{SH}(t) + Q_{DHW}(t)]\,dt}{\int_{t_1}^{t_2} [P_{el,HP}(t) + P_{el,aux}(t)]\,dt} \quad (7)$$

Where $Q_{SH}(t)$ is the instantaneous heating power for the SH and the $Q_{DHW}(t)$ is the instantaneous heating power for the DHW respectively. $P_{el,HP}$ denotes the instantaneous power of the HP's compressor and $P_{el,aux}$ the instantaneous power of the auxiliary input.

1.3 Aim and novelty

In this paper, control algorithms for residential PV, heat pump and battery storage systems are evaluated for a single family house in Sweden in terms of self-consumption, solar fraction and final energy. A detailed model of a new single-family house with a typical grid connected PV system, exhaust air heat pump and hot water storage tank is defined and modelled on the simulation software TRNSYS 17. The model is further developed by regulating the heat pump based on PV power production and by using battery energy storage.

The aim of the study is to maximize the self-consumption and solar fraction and to minimize the final energy by using control algorithms for the heat pump and battery storage. The novelty of this study is the combined use of a detailed and validated house model, measured high-resolution weather data and detailed load profiles for both DHW and electric load. The stochastical load patterns are based on monitoring data for single family houses (Widén et al., 2012, 2009). All these are implemented in the simulation software TRNSYS where the components are designed to meet the specifications of existing products of a house, heat pump, hot water tank and battery storage available on the market today.

2. Models and boundary conditions

This section describes the models of the house and PV system, heat pump and hot water storage tank, battery storage as well as the boundary conditions of the whole system.

2.1 House model and boundary conditions

The modelled house is a typical Swedish single floor, single family house (SFH) with a gabled roof, an overall U-value of 0.2 W m^{-2} K^{-1} and 143 m^2 heated floor area, see Tab. 1. A detailed model of the house

with six zones using space heating, developed in the simulation software TRNSYS, is described in detail and validated by Persson and Heier (2010). TRNSYS' type 56 is used for the house model. A schematic figure of the house with its zones is found in Fig. 1. The set temperatures in the zones (rooms) differ from 20°C in zone 3, 5 and 6, 21°C in zone 1 and 2, and 22°C in zone 4 (Persson and Heier, 2010). The SH is switched on when the temperature falls 1°C below the set temperatures in either of the zones.

Tab. 1: Geometrical and thermal properties of the studied house (Persson and Heier, 2010)

	Total area [m^2]	**U-value [W m^{-2} K^{-1}]**
Outer walls	107	0.23
Roof	153	0.09
Floor	143	0.10
Windows	24	1.27
Doors	5	0.54
Mean U-value		0.20

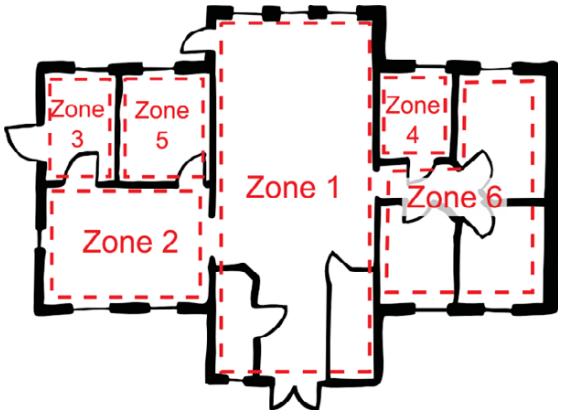

Fig. 1: Schematic figure of the house and the temperature zones (Persson and Heier, 2010)

The location of the house is Norrköping, Sweden (58.6°N, 16°2E). Measured high-resolution (one minute) meteorological data by the Swedish Meteorological and Hydrological Institute (SMHI) from the year 2007 in Norrköping is used in the simulations. The weather data is used both for calculation of the PV electricity production and for calculations of energy gains and losses in the house.

Fresh water temperature, which affects the heating demand, is dependent on the time of the year and modelled on a function described by Heimrath and Haller (2007). Two adults and two children are living in the house, and the internal heat energy gain, assumed to be the same as the electricity consumption for appliances, are calculated using a Markov-chain model for occupancy and energy use described in Widén et al. (2009). The DHW demand is derived from the MacSheep project and adjusted for this study, see Table 2 (Bales et al., 2015). All variables are in a 2 minute resolution over the period of one year.

Tab. 2: DHW and appliance data (Bales et al., 2015)

2979	Discharge energy [kWh $year^{-1}$]
70.9	Discharge volume [m^3 $year^{-1}$]
45	Discharge temperature [°C]
194.2	Daily Average draw-off [kg]
2.44 – 972.2	Flow [kg h^{-1}]
3437	Electricity for appliances [kWh $year^{-1}$]
5650	Max load for appliances [W]

2.2. Hot water storage tank, heat pump and auxiliary heater

A variable speed, exhaust air HP delivers heat both for SH and DHW but cannot supply them both at the same time. The HP model is based on the performance map of the HP, with heat capacity and power input as dependent variables together with inlet air temperature, inlet air flow rate and compressor speed as independent variables. SH is turned on in each zone when the room temperature falls below a lower limit, see Section 2.1. This means that the SH can be on for one zone but not for the rest. A hot water storage tank of 180 litres is used for DHW whereas the SH is supplied by the HP through a buffer store of 25 litres. The HP is activated according to a heating curve and compensatory control algorithm dependent on the SH supply temperature. An electric auxiliary heater is activated when the thermal power provided by the heat pump is insufficient to meet thermal power need. The auxiliary heater is inactivated during the predefined summer period. Preferences that are used for this study of the DHW storage, heat pump and auxiliary heater can be found in Table 3. The models for HP including storage and control algorithms are based on one of the most common commercial products on the market.

Tab. 3: Specifications of hot water storage tank, exhaust air heat pump and auxiliary heater

Preference	Quantity/name
DHW storage tank capacity [litre]	180
Electric compressor power [kW]	0.27-2.05
Thermal power of HP [kW]	1.14 – 4.99
Heat pump COP	2.4 – 4.7
Electric auxiliary heater [kW]	0.5 – 6.5

2.3. Battery storage and PV system

Three PV system sizes and three battery storage sizes are used to study the impact on the performance in terms of self-consumption, solar fraction and final energy, see Tab. 4. The tilt angle is defined by the roof of the building whereas the azimuth angle is chosen to optimize the yearly PV electricity production. The PV panels, inverter and batteries are modelled on products available on the market.

Tab. 4: Specifications of the PV system and battery storage

Preference	Quantity/name
Capacity PV [kW]	3.12, 5.7, 9.36
Inverter efficiency [%]	97.7
PV tilt [°]	27
PV azimuth [°]	0
Capacity battery [kWh]	3.6, 7.2, 10.8
Battery technology	Lithium-ion
Battery losses [%]	10%

3. Control algorithms for increased self-consumption

A base case and three control algorithms for improving the energy performance of the system are developed and evaluated:

- The base case includes the house equipped with a PV system and a heat pump for DHW storage and SH. The HP is controlled solely by the need of SH and the temperature in the DHW storage tank.
- First control algorithm is applied to the base case system. The heat pump is controlled by excess PV production to increase self-consumption.

- Second control algorithm is applied to the base case system with added battery storage. Charging and discharging of the batteries are controlled by excess PV production to increase self-consumption whereas the HP is controlled solely by the need of SH and temperature in the DHW storage tank.
- Third control algorithm is for the base case system with usage of both thermal storage and batteries. Excess PV power production is first used to charge the batteries, thereafter the HP is switched on if possible.

A flow chart showing the control scheme for on-off control of the HP for the case of algorithm 3, can be found in Figure 2. Moreover, since the algorithm 3 is the combination of algorithm 1 and 2 the flow chart contains all the three algorithms.

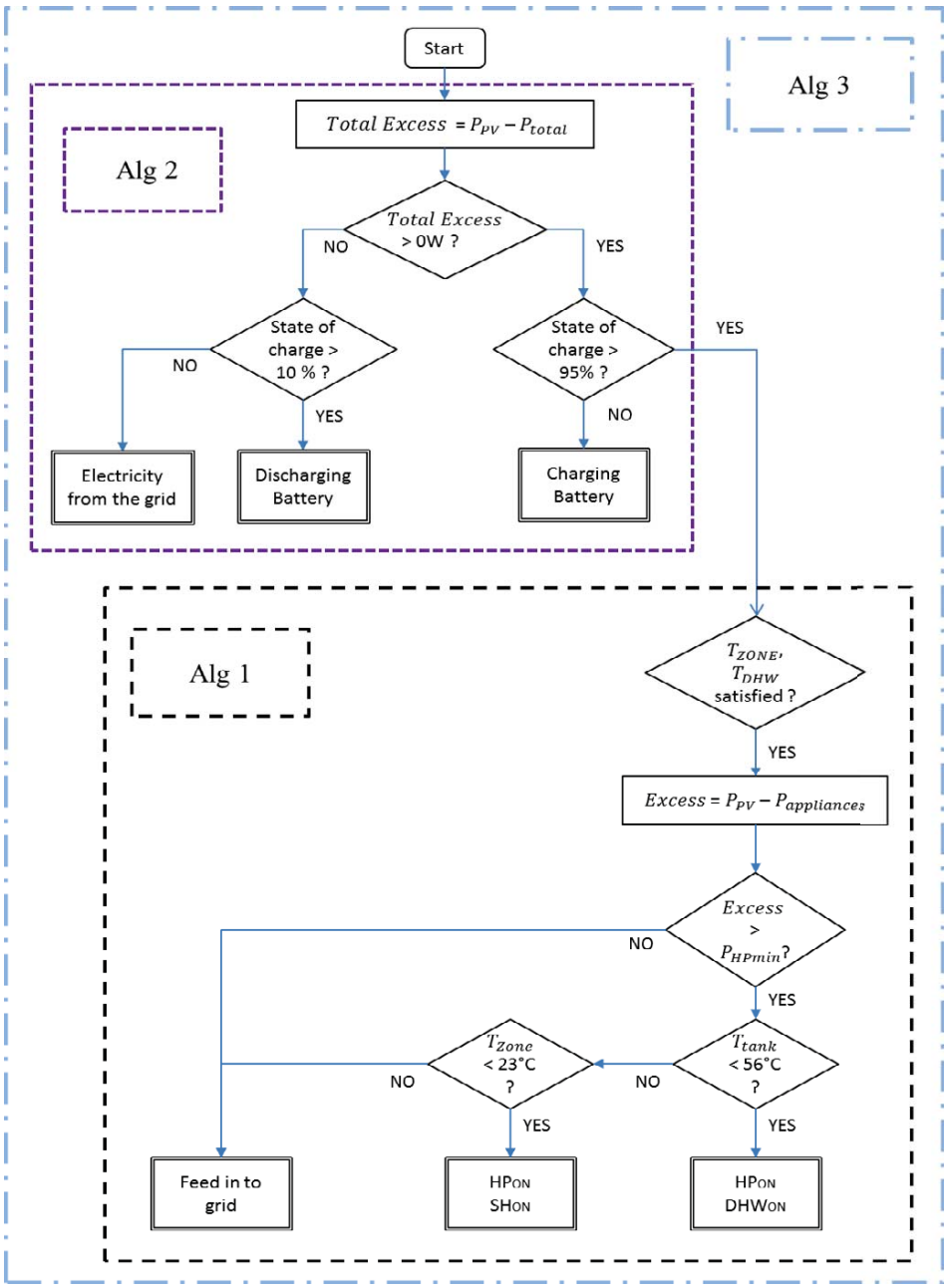

Fig. 2: Flow chart for control scheme to utilize excess PV power combining electrical with thermal storage (algorithm 1-3).

In algorithms 1 and 3, excess PV power production can switch on the HP even if no SH is needed and the DHW storage temperature is above the lower temperature limit. This is used to increase the self-consumption of PV electricity production and lower the demand of buying electricity at later times. The temperature in the DHW storage must be below than the upper temperature limit as well as the maximum allowed individual zone temperature, to allow the HP to be operated based on PV excess production. In order for the HP to be activated and increase the thermal storage either by DHW or by SH a minimum power limit of the excess PV electricity is required which is the P_{HPmin}.

4. Results

A comparison of the key figures such as self-consumption, solar fraction and final energy is given in Table 6 for base case, while Table 5 gives the heat and electricity use of the building and its occupants. For the base case system the self-consumption varies from 43 to 23% while solar fraction varies from 12 to 19% with increasing PV size. The SPF of the HP is 2.67 while that for the system (HP plus auxiliary electrical heater) is only 2.35 due to the relatively large amount of auxiliary energy used.

Tab. 5: Heat and electricity use of the base case

Electrical energy	**kWh year-1**
Electrical appliances	3437
Heat pump	6506
Auxiliary heater	1380
Thermal energy	**kWh year-1**
SH load	14923
DHW load	2979
DHW tank losses	669

Tab. 6: Key results for the base case system

PV capacity	3.1kW	5.7kW	9.3kW
Electrical energy		**kWh year-1**	
PV production AC	3123	5914	9370
Measure		**Quantity**	
PV SC (annual)	43%	30.6%	23.3%
PV SF (annual)	11.9%	16%	19.3%
Final energy	9981	9499	9116

The system was simulated for each of the algorithms with the three different PV sizes, each with its own storage size chosen according to the PV capacity (3.1 kW/3.6 kW, 5.7 kW/7.2 kWh, 9.3 kW/10.8 kWh). The results can be seen in Figure 3, where FE, SC and SF are shown for the base case and the three algorithms for all three PV sizes. Algorithm 2 (batteries) gives far greater savings (reduction in FE compared to base case) than algorithm 1 (thermal storage), and this difference is greater for larger PV sizes. For the largest PV size, algorithm 2 saves three times as much FE as algorithm 1 does. The savings for algorithm 3 are only slightly less than the sum of the savings of the algorithms 1 and 2 separately. This shows that the two algorithms are compatible and additive and hardly competing for the PV electricity. The savings in final energy for algorithm 3 (compared to base case) are 837, 1573 and 2193 kWh for the 3.1, 5.7 and 9.3 kW PV sizes respectively.

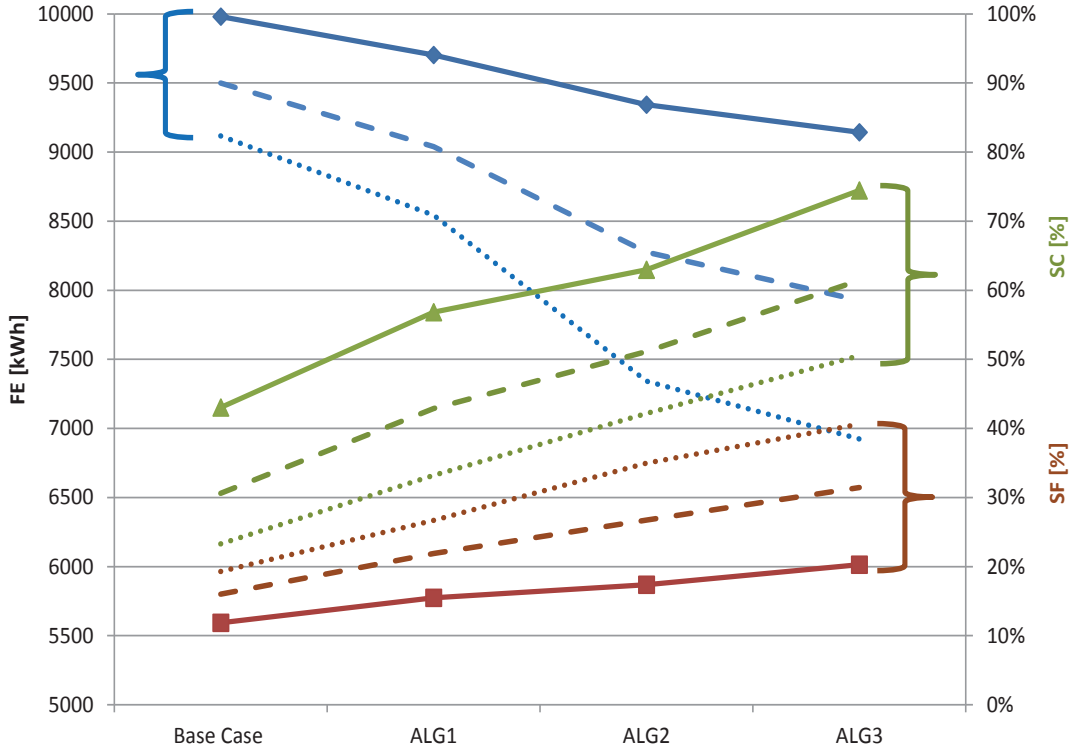

Fig 3: Comparison of the key figures between the base case and the control algorithms 1, 2 and 3. Final energy in blue (diamonds), self-consumption in green (triangles) and solar fraction in brown (squares). The PV sizes are denoted with solid lines (3.1 kW), dashed lines (5.7 kW) and dotted lines (9.3 kW).

The annual electricity production is 3120 kWh for a system of 3.1 kW. Key figures for the base case and the same PV system size using the third algorithm are presented in Table 7. SPF_{HP} is lower for algorithm 3 than for the base case, while the values for SPF_{HP+aux} are the same. This is because the algorithm using thermal storage leads to increased operating temperatures in the HP, reducing the COP. However, the auxiliary does not have to supply as much energy, which in this case happens to cancel out the negative effect of lower COP.

Tab. 7: Key figures for the base case system of 3.1 kW PV and the control algorithm 3 with 3.1 kW PV.

	Base case	Alg3
Electrical energy	**kWh year-1**	
PV production AC	3123	
Heat pump	6506	6805
Auxiliary heater	1380	1223
Measure	**Quantity**	
PV SC (annual)	43%	74.5%
PV SF (annual)	11.9%	20.3%
Final energy	9981	9144
SPF_{HP}	2.67	2.59
SPF_{HP+aux}	2.35	2.35

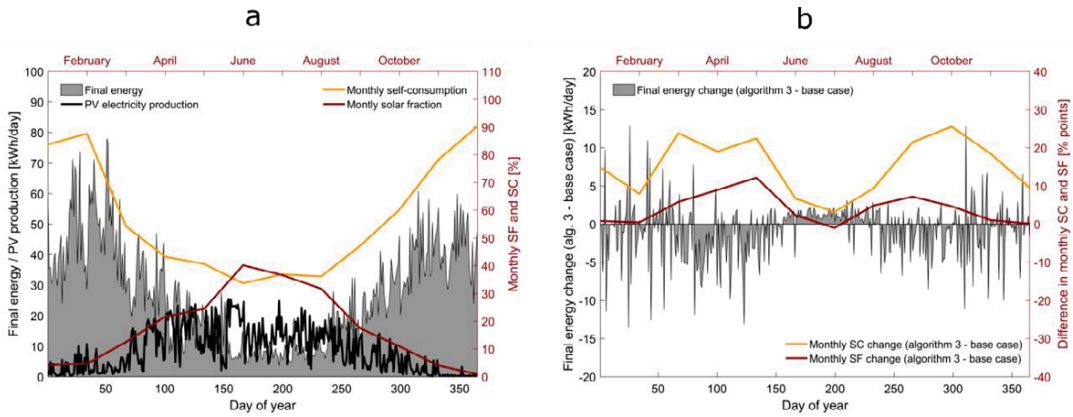

Fig 4: Daily final energy and production and monthly solar fraction and self-consumption for the base case (a) and the result with the third algorithm applied (b).

The monthly solar fraction varies much over the year, reaching 40% in June but is below 10% in November to February as seen in Figure 4a. With the third algorithm the solar fraction, as well as self-consumption, can be improved, most notably in the spring, see Figure 4b. Solar fraction, self-consumption and final energy are calculated with minute values of production and consumption. If aggregated monthly values would be used instead for the calculations, the solar fraction would get near to 100% in the summer.

5. Discussion

In order to increase the self-consumption, the temperature in the DHW tank is sometimes exceeding the set temperature during periods with high excess PV power production. Although the total electricity consumption by the HP is increasing due to higher heat losses, the final energy will be reduced due to a lower need of HP operation during periods without excess PV production.

Figure 4b shows that there are times during the year when the final energy is greater with algorithm 3 than for the base case, but for the whole year there are significant savings (837 kWh for 3.1 kW PV system). This shows that there is still some potential for improving the algorithms.

The climate conditions in Sweden with negative seasonal correlation between irradiance and outdoor temperature make it difficult for a regular single-family house to be completely independent of the power grid. For an off-grid system either large storage units or a drastically changed behavior are needed. Therefore, a reliable power grid that can handle both high power demand as well as high power production is needed for a larger integration of PV in the Swedish power system.

The performance map of the HP is defined for constant water flow rate, but in practice the system flow for SH and DHW is variable, which will affect both the capacity and COP of the HP. This effect has not been taken into account in the study.

To minimize the final energy the solar fraction should be high and to minimize excess PV electricity production the self-consumption should be high. The highest PV power production occurs in the summer which coincides with low electricity demand, see Figure 4. The need of thermal energy for space heating is low in the summer but there is still a need of DHW. For the Swedish climate and indoor temperature of 22 °C in the bathroom, there is only a short period when no heating is required. The heat pump and thermal storage can therefore be operated to minimize both final energy and excess PV electricity

6. Conclusion

This study shows the potential of increasing the self-consumption of a residential PV system and reducing the final energy. The base case with a PV system of 3.1 kW and a heat pump operating independently of PV excess power production has a self-consumption of 43%, final energy of 9981 kWh and solar fraction of 12% for the simulated year.

- The use of the existing thermal storage gives a decrease in final energy of 279 to 573 kWh per year for the PV sizes of 3.1 to 9.3 kW.
- The use of battery gives far greater decreases in FE than the use of the thermal storage, with the used settings and sizes of components.
- The combined use of thermal storage and batteries leads to final energy savings that are nearly the same as the combined savings of thermal storage and batteries separately, showing that they are mostly independent of one another for the settings of this study.

7. References

Baetens, R., De Coninck, R., Van Roy, J., Verbruggen, B., Driesen, J., Helsen, L., Saelens, D., 2012. Assessing electrical bottlenecks at feeder level for residential net zero-energy buildings by integrated system simulation. Appl. Energy 96, 74–83. doi:10.1016/j.apenergy.2011.12.098

Bales, C., Betak, J., Broum, M., Chèze, D., Cuvillier, G., Haberl, R., Hafner, B., Haller, M., Hamp, Q., Heinz, A., Hengel, F., Kruck, A., Matuska, T., Mojic, I., Petrak, J., Poppi, S., Sedlar, J., Sourek, B., Thissen, B., Weidinger, A., 2015. Optimized solar and heat pump systems, components and dimensioning: MacSheep - New Materials and Control for a next generation of compact combined Solar and heat pump systems with boosted energetic and exergetic performance [WWW Document]. URL http://www.macsheep.spf.ch/ (accessed 9.20.16).

Binder, J., Williams, C.O., Kelm, T., 2012. Increasing PV Self-Consumption, Domestic Energy Autonomy and Grid Compatibility of PV Systems Using Heat-Pumps, Thermal Storage and Battery Storage. 27th Eur. Photovolt. Sol. Energy Conf. Exhib. 4030–4034. doi:10.4229/27THEUPVSEC2012-5AV.1.55

Castillo-Cagigal, M., Caamaño-Martín, E., Matallanas, E., Masa-Bote, D., Gutiérrez, A., Monasterio-Huelin, F., Jiménez-Leube, J., 2011. PV self-consumption optimization with storage and Active DSM for the residential sector. Sol. Energy 85, 2338–2348. doi:10.1016/j.solener.2011.06.028

European Environment Agency, 2016. Final energy consumption by sector and fuel [WWW Document]. URL http://www.eea.europa.eu/data-and-maps/indicators/final-energy-consumption-by-sector-9 (accessed 7.14.16).

Heier, J., Bales, C., Martin, V., 2015. Combining thermal energy storage with buildings – a review. Renew. Sustain. Energy Rev. 42, 1305–1325. doi:10.1016/j.rser.2014.11.031

Heimrath, R., Haller, M., 2007. The Reference Heating System, the Template Solar System of Task 32 [WWW Document]. URL http://archive.iea-shc.org/publications/downloads/task32-Reference_Heating_System.pdf (accessed 3.30.16).

Hesaraki, A., Holmberg, S., 2013. An investigation of energy efficient and sustainable heating systems for buildings: Combining photovoltaics with heat pump, in: Smart Innovation, Systems and Technologies. pp. 189–197. doi:10.1007/978-3-642-36645-1_18

Hirvonen, J., Kayo, G., Hasan, A., Sirén, K., 2016. Zero energy level and economic potential of small-scale building-integrated PV with different heating systems in Nordic conditions. Appl. Energy 167, 255–269. doi:10.1016/j.apenergy.2015.12.037

Lindahl, J., 2016. National Survey Report of PV Power Applications in Sweden 2015 - IEA PVPS.

Lund, P.D., 2005. Sizing and applicability considerations of solar combisystems. Sol. Energy 78, 59–71. doi:10.1016/j.solener.2004.07.008

Luthander, R., Widén, J., Nilsson, D., Palm, J., 2015. Photovoltaic self-consumption in buildings: A review. Appl. Energy 142, 80–94. doi:10.1016/j.apenergy.2014.12.028

Pérez-Lombard, L., Ortiz, J., Pout, C., 2008. A review on buildings energy consumption information. Energy Build. 40, 394–398. doi:10.1016/j.enbuild.2007.03.007

Persson, T., Heier, J., 2010. Småhusens framtida utformning : Hur påverkar Boverkets nya byggregler? [How

do the new Swedish building codes affect detached houses of the future?]. Region Gävleborg, Gävle, Sweden.

Swedish Energy Agency, 2015a. Energy in Sweden 2015.

Swedish Energy Agency, 2015b. Energistatistik för småhus 2014 [Energy statistics for detached houses 2014].

Thygesen, R., Karlsson, B., 2014. Simulation and analysis of a solar assisted heat pump system with two different storage types for high levels of PV electricity self-consumption. Sol. Energy 103, 19–27. doi:10.1016/j.solener.2014.02.013

Widén, J., 2014. Improved photovoltaic self-consumption with appliance scheduling in 200 single-family buildings. Appl. Energy 126, 199–212. doi:10.1016/j.apenergy.2014.04.008

Widén, J., Lundh, M., Vassileva, I., Dahlquist, E., Ellegård, K., Wäckelgård, E., 2009. Constructing load profiles for household electricity and hot water from time-use data - Modelling approach and validation. Energy Build.

Widén, J., Molin, A., Ellegård, K., 2012. Models of domestic occupancy, activities and energy use based on time-use data : deterministic and stochastic approaches with application to various building-related simulations. J. Build. Perform. Simulation, Taylor Fr. 5, 27–44.

Conference Proceedings

EuroSun 2016
Palma de Mallorca (Spain), 11 - 14 October 2016

Experimental characterisation of a flat panel integrated collector-storage solar water heater featuring a photovoltaic absorber and a planar liquid-vapour thermal diode

Adrian Pugsley[1], Mervyn Smyth[1], Jayanta Deb Mondol[1], Aggelos Zacharopoulos[1], Luigi Di Mattia[2]

[1] Ulster University, Faculty of Art, Design and the Built Environment, Centre for Sustainable Technologies, Belfast (UK)

[2] University of Naples "Federico II", Dept. Energy Applied Thermal Fluid Dynamics & Environmental Influences, Naples (Italy)

Abstract

A flat panel Integrated Collector-Storage Solar Water Heater (ICSSWH) incorporating a photovoltaic-thermal (PVT) absorber and a Planar Liquid-Vapour Thermal Diode (PLVTD) was fabricated. Tests indicate zero temperature rise instantaneous thermal and electrical efficiencies of 60% and 9% respectively, dropping to 40% and 6% under nominal intended operating conditions (600 Wm^{-2} irradiance, 50°C storage tank, 20°C ambient temperature). Measured overall heat loss coefficient was 0.85 $Wm^{-2}K^{-1}$ and thermal diode conductances were typically 45 $Wm^{-2}K^{-1}$ during solar collection periods and 1.7 $Wm^{-2}K^{-1}$ during heat retention periods. The work demonstrates that ICSSWH, PVT and PLVTD concepts can be successfully combined to create a scalable flat panel solar collector suitable for integration within a multifunction building facade.

Keywords: *Integrated-Collector-Storage Solar Water Heater (ICSSWH), Photovoltaic-Thermal (PV/T), Building Integrated Solar Thermal (BIST), Building Integrated Photovoltaic (BIPV), Thermal Diode*

1. Introduction

This paper presents key findings of experimental investigations undertaken to characterise behaviour of a flat panel Integrated Collector-Storage Solar Water Heater (ICSSWH) incorporating a photovoltaic-thermal (PVT) absorber and a Planar Liquid-Vapour Thermal Diode (PLVTD). This new hybrid solar collector type is intended for integration within multifunction building façades to provide low temperature hot water and electrical power to buildings. The paper briefly introduces the concept and cites influential prior work. The theoretical basis for the concept is outlined and modelling results are presented which demonstrate how collection, retention and diurnal thermal efficiencies are influenced by diode thermal conductances. Methodology and results of the experimental investigation are presented. Measurement results are compared to those typically achieved by comparable collector types and recommendations are made for future work.

1.1. Thermal and photovoltaic solar collectors

The Renewable Energy Directive (EU, 2009) sets a target of 20% of EU gross final energy consumption to be supplied from renewables by 2020. Increasing solar energy utilization plays a key role in meeting the target. Solar Thermal (ST) systems are expected to make a significant contribution to renewable heat targets in addition to renewable electricity supplied by already popular PhotoVoltaic (PV) systems. Traditionally, building mounted ST competes with PV for suitable roof or façade space. Combining technologies gives rise to PhotoVoltaic-Thermal (PVT) solutions which deliver low to medium temperature solar heat at efficiencies marginally lower than conventional ST collectors and generate electricity similar to standard PV modules.

doi:10.18086/eurosun.2016.08.14 Available at http://proceedings.ises.org

Careful design is necessary as most building thermal demands require heat to be delivered at temperatures significantly above ambient which reduces both thermal and electrical efficiencies. Domestic hot water, space heating and cooling systems which combine, ST, PV or PVT collectors with heat pumps appear to be a promising development area and a popular subject for current applied research (Good et al., 2015; Aguilar et al., 2016; Calise et al., 2016; Poppi et al., 2016; Qu et al. 2016).

Zondag (2008) gives a comprehensive review of PVT collector development, covering both air and water heating variants. More recent reviews are given by Michael et al. 2015 and Besheer et al. 2016. Santbergen et al. (2010) and Dupeyrat et al. (2011) specifically examine module design, construction, and heat transfer aspects of PVT-water collectors for domestic hot water production. Most PVT-water collectors take the form of photovoltaic cell laminates glued or bonded to sheet-and-tube, flow channel, or roll-bond type solar thermal absorbers. Packing Factor (PF) is the ratio of PV cell area to total absorber area. Thermal efficiency is maximized by ensuring absorber substrates are matt black or selectively coated to maximize solar thermal input. Bonding layers between PV cells and absorber substrates should be thin and thermally conductive. Convective heat transfer within the working fluid should be promoted. Zondag (2008) cites PVT-water collector examples featuring overall cell-to-fluid conductances in the range 40 to 250 $Wm^{-2}K^{-1}$. Low conductances increase PV cell temperatures which reduce both electrical and thermal efficiencies. Thermal efficiencies of PVT collectors are typically lower than those of dedicated ST collectors due to lower absorption coefficients of encapsulated PV cells ($0.7 \lesssim \alpha \lesssim 0.9$ as opposed to $\alpha=0.95$ for matt black surfaces) and also because some of the available energy ($15<\eta_{E(0,mpp)}<20\%$ typically for crystalline silicon cells) is extracted as electricity. Silicon cells produce a nominal voltage of 0.55V per cell but this reduces significantly with increasing temperature (~0.45%/°C) and falls markedly under low irradiance conditions (below about 200 Wm^{-2}). Photovoltaic current is directly proportional to irradiance and only slightly temperature dependent. Temperature nonuniformities across PVT absorber surfaces can significantly reduce electrical efficiency if cells are connected in parallel but generally have minimal effect on series connected cells.

Smyth et al. (2006) present a thorough review of Integrated Collector-Storage Solar Water Heaters (ICSSWH). These collectors can be significantly more cost effective than conventional ST systems because they have fewer components and require less floor space for water storage tanks. However, inherent exposure of the thermal storage to the outdoor environment (via the absorber surface) means that ICSSWH collectors suffer from heat loss at night and during periods of low insolation, particularly if installed in cold and windy climates. Most ICSSWH designs utilize one or more transparent covers to reduce heat loss. Various researchers have examined the use of novel techniques to improve heat storage effectiveness in ICSSWH collectors, including use of reflectors, concentrators, inlet diffusers, baffles, sleeves, phase change materials and thermal diodes. A recent review by Singh et al. (2016) attempts to categorise ICSSWH designs according to whether they are non-concentrating (eg flat plate or tank box systems), concentrating (eg compound parabolic) or employing phase change materials. Performance comparisons between different ICSSWH collectors are commonly made by considering collection efficiencies (typically $15<\eta_{col}<50$ %), overall heat loss coefficients (typically $2<U_{sys}<7$ $Wm^{-2}K^{-1}$), and maximum daily stored water temperatures (typically $30<T_{max}<60$°C).

Façade mounted Building Integrated (BI) solar collectors (BIST, BIPV and BIPVT) offer viable alternatives to bolt-on roof mounted collectors if structural, functional, aesthetic and cost considerations are addressed holistically to achieve high quality architecturally integrated solutions. Combining façade integrated BIPVT with improved ICSSWH technology potentially offers attractive and cost effect solutions for new buildings and refurbishments, particularly in multi-tenanted dwellings, hotels, and hospitals which have significant demands for low temperature heat and typically have limited roof-space available for solar collectors.

1.2. Thermal diodes and development of the PVT-PLVTD-ICS concept

A thermal diode is a unidirectional heat flow device analogous to an electrical semiconductor diode which offers low resistance to heat flow in one direction and higher resistance in reverse. Most studies involving thermal diodes focus on liquid convective devices (Kolodziej et al., 1997; Mohamad, 1997; Chen et al., 1998; Smyth et al., 1999; Faiman et al., 2001; Sopian et al., 2004; Fang & Xia, 2010; Rhee et al., 2010) but few consider phase change diode concepts. De Beijer (1998) proposed a horizontal cylindrical building integrated roof-ridge ICSSHW employing a liquid-vapour-liquid phase change thermal diode. Studies from Ulster

University (Quinlan et al., 2008; Quinlan, 2010; Souliotis et al., 2011) fabricated and tested similar devices in both horizontal and vertical orientations. The best of several ~25 L/m^2 prototypes investigated by Quinlan (2010) was DVICS Mark VI which achieved η_{col} =38 %, T_{max}=44°C and U_{sys}=1.3 Wm^{-2}K^{-1} during solar simulator tests. These performances (particularly heat loss coefficients) compare favourably with values reported in Section 1.1. Calculations based on Quinlan's results suggest that the x≈25mm wide thermal diode in DVICS Mark IV offered U_{12f}≈20 Wm^{-2}K^{-1} during collection periods and U_{12r}≈2 Wm^{-2}K^{-1} during retention periods. Boreyko et al. (2011) and Boreyko & Chen (2013) investigated planar jumping-drop liquid-vapour-liquid thermal diodes primarily aimed at microelectronics cooling applications, but recognised their potential use in solar collectors. High conductances of U_{12f}=40500 Wm^{-2}K^{-1} and U_{12r}≈165 Wm^{-2}K^{-1} were reported, seemingly enabled by highly effective evaporator wetting, thorough removal of non-condensable gases, and small diode cavities (x≈2.5mm). Thermal diode behavior is eminently suited to ICSSWH applications which inherently require rapid heat transfer from absorber to storage tank during sunny daytime periods (collection/forward mode) and thermal insulation to minimise tank heat losses during cloudy and overnight periods (retention/reverse mode). Unfortunately, the reverse mode conductances achieved by Boreyko et al. are unlikely to be beneficial in reducing tank heat losses. Recent work at Ulster University has progressed the patented vertical cylindrical liquid-vapour-liquid phase change thermal diode ICSSWH concept (Smyth, 2015) and evaluated commercial feasibility (Solaform, nd). Several design variants are currently evolving, aimed at cost reduction, improved evaporator wetting, and flattened forms compatible with PVT and building façade integration (Smyth et al., 2015 & 2016; Pugsley, 2017). The present paper details results of tests undertaken on the first truly flat panel prototype, the design of which is shown in Figure 1. Unlike previous design variants, the prototype examined in this study features resin-bonded PV cells and the liquid-vapour thermal diode has a much wider cavity (x=70mm) than any others encountered in the literature with the aim of reducing overnight heat losses. The diode is planar in form to facilitate building façade integration and features a novel internal support structure similar to that employed in vacuum glazing (Fang et al., 2004).

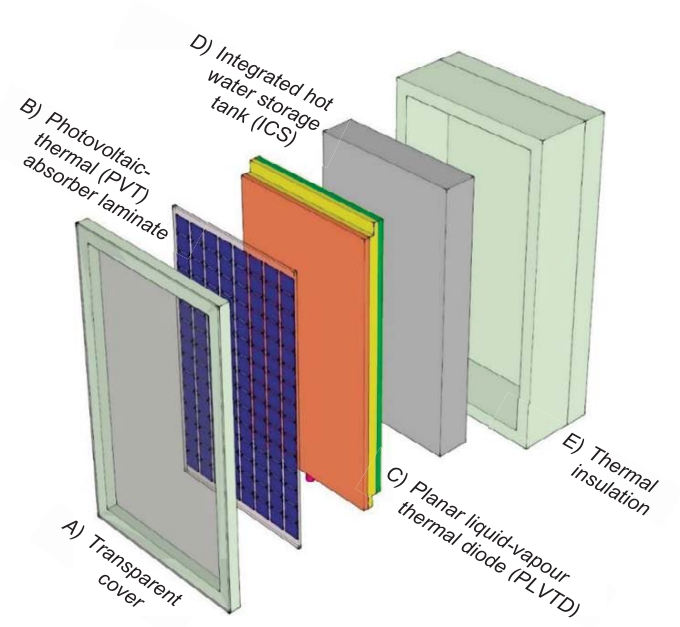

Figure 1 – General arrangement of a PVT-PLVTD-ICS solar collector

2. Theory

Heat collection (η_{col}) and retention (η_{ret}) efficiencies and system heat loss coefficients (U_{sys}) for ICSSWH collectors can be defined (after Smyth et al., 1999 and Faiman et al. 2001) using Equations 1 to 3 based on total heat capacity (C_{tot}), water storage tank temperatures ($T_{3[t]}$) at dawn ($t=t_0$), dusk ($t=t_0+t_{col}$) and the subsequent dawn ($t=t_0+t_{col}+t_{ret}$), retention period average ambient temperatures ($\tilde{T}_a$), collection period average

incident irradiance ($\tilde{G}$), and collector area (A). The overall diurnal efficiency ($\eta_{T+E,24}$) of a PVT-ICSSWH can be expressed in terms of the product of the collection and retention efficiencies plus the electrical efficiency, as per Equation 4, where instantaneous electrical power is determined from the product of current (I) and voltage (V) supplied to an electrical load. Diurnal thermal efficiency is a relative performance measure where $\eta_{T24}=1$ indicates perfect solar thermal collection and retention without losses and $\eta_{T24}=0$ implies either no heat collection, total overnight heat loss, or both. Values of $0<\eta_{T24}<1$ indicate potential for useful net heat gain provided that Equation 5 is satisfied.

$$\eta_{col} = \frac{C_{tot}\left(T_{3[t=t_0+t_{col}]} - T_{3[t=t_0]}\right)}{\tilde{G}A} \quad \text{(eq. 1)}$$

$$\eta_{ret} = \frac{T_{3[t=t_0+t_{col}+t_{ret}]} - \bar{T}_a}{T_{3[t=t_0+t_{col}]} - \bar{T}_{a[t=t_0+t_{col}]}} \quad \text{(eq. 2)}$$

$$U_L = \frac{C_{tot}}{A.t_{ret}} \ln \frac{1}{\eta_{ret}} \quad \text{(eq. 3)}$$

$$\eta_{T+E,24} = \eta_{T24} + \eta_{E24} = \eta_{col}\eta_{ret} + \frac{\int_{t_0}^{t_0+t_{col}+t_{ret}} IV}{\tilde{G}A} \quad \text{(eq. 4)}$$

$$\eta_{T24}\tilde{G}A + C_{tot}\left(\overline{T_{3[t=t_0]} - T_a}\right)(\eta_{\text{ret}} - 1) > 0 \quad \text{(eq. 5)}$$

Equations 6, 7 & 8 describe how ICSSWH collector instantaneous thermal efficiencies ($\eta_{T,col}$ during collection and $\eta_{T,ret}$ during retention periods) are determined by the solar power input (GA); transmission-absorption product ($\tau\alpha$); and the absorber (T_1), tank (T_3), and ambient (T_a) temperatures. These equations were derived by Pugsley (2017) based on a lumped parameter model which considers the thermal resistances associated with absorber-to-tank heat transfer ($R_{123}=R_{12}+R_{23}$), absorber-to-ambient heat loss (R_{1a}) and insulated tank envelope heat losses (R_{3ia}). Conductance $U_{12}=1/(A\cdot R_{12})$ describes diode behaviour and conductance $U_{23}=1/(A\cdot R_{23})$ represents water storage tank natural convection. Conductance $U_{1a}=1/(A\cdot R_{1a})$ represents combined radiative heat transfer and air mass natural convection effects occurring between the absorber and its transparent insulating cover, and also between the transparent cover and the external environment.

$$\eta_{T(col)} = \frac{{}^{(T_1-T_3)}/_{R_{123}} - {}^{(T_3-T_a)}/_{R_{3ia}}}{GA} \quad \text{(eq. 6)}$$

$$\eta_{T(ret)} = \frac{C_{tot}(T_3-T_a) + t_{ret}\left[{}^{(T_3-T_a)}/_{R_{123}} - {}^{(T_3-T_a)}/_{R_{3ia}}\right]}{C_{tot}(T_3-T_a)} \quad \text{(eq. 7)}$$

$$T_1 = \frac{R_{123}T_a + R_{1a}T_3}{R_{1a}+R_{123}} = \frac{R_{123}R_{1a}\tau\alpha GA + T_aR_{123} + T_3R_{1a}}{R_{123}+R_{1a}} \quad \text{(eq. 8)}$$

The theoretical relationship between diurnal thermal efficiency and water storage tank temperature is shown on Figure 2 for various diode performance scenarios. The analysis was undertaken by calculating the product of Equations 6 & 7 for nominal G=500 Wm^{-2}, t_{ret}=64800s, A=1m^2, $\tau\alpha$=0.81, and U_{3ia}=0.3 $Wm^{-2}K^{-1}$ using temperature dependent values of $3<U_{1a}<5$ $Wm^{-2}K^{-1}$ and $100<U_{23}<1000$ $Wm^{-2}K^{-1}$ which were evaluated using well known Rayleigh-Nusselt convection and Stefan-Boltzmann radiation heat transfer equations (Cengel, 2006). Equilibrium absorber temperatures (T_1) during collection periods were found by iteration to satisfy Equation 8. Temperature dependent collection/forward mode (U_{12f}) and retention/reverse mode (U_{12r}) diode conductances (see legend of Figure 1) were determined from experimental and theoretical work on PLVTDs by Pugsley (2017). Figure 2 indicates that the benchmark single glazed collector with no thermal diode (A) achieves η_{T24}=37% when the tank temperature is low (close to a zero daytime heat loss operating condition $[T_3-T_a]/G=0$) and a nominal mild-climate night-time heat loss condition $[T_3-T_a]$=15°C occurs. Performance decreases with increasing tank temperature such that η_{T24}=9% occurs for a hypothetical daytime condition of $[T_3-T_a]/G=0.1m^2KW^{-1}$ followed by a cold night-time period where $[T_3-T_a]$=70°C. Addition of a basic thermal diode (B) yields a 1.5 times improvement in low temperature performance (η_{T24}=56%) and doubles the high

temperature performance (η_{T24}=18%). Use of a high performance diode (E) yield a 1.7 times improvement in low temperature performance (η_{T24}=61%) and a 2.3 times improvement in high temperature performance (η_{T24}=21%). These improvements in diurnal thermal efficiency are primarily due to improved (reduced) reverse mode conductance (D) which improves heat retention efficiency, rather than increased forward mode conductance (C) which has only a limited effect on collection efficiency.

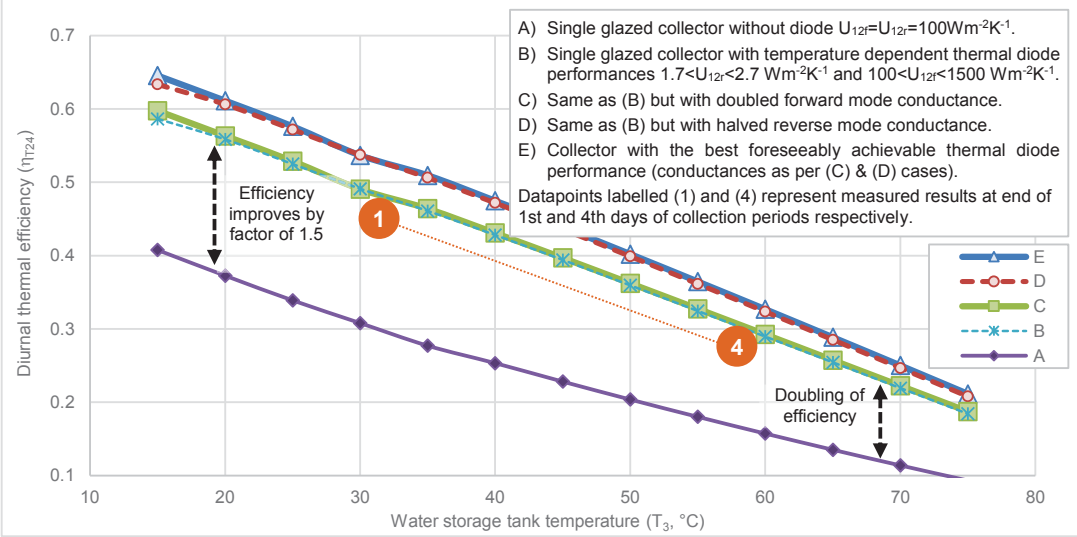

Figure 2 – Effect of diode thermal conductance upon diurnal thermal efficiency of an ICS collector

3. Experimental methodology

A prototype taking the form shown in Figure 1 was fabricated. The thermal diode and water storage tank (see Figures 3, 5a and Table 1) were formed of folded and welded stainless steel sheet supported internally by an array of stainless steel tubular struts. A welded vacuum flange was added to enable working fluid addition and chamber evacuation through the top of the unit. A stainless steel manifold plate was welded to the bottom to enable connection of the evaporator wetting mechanism (Intellectual Property considerations prevent us from describing this in detail). The completed steelwork was tested for storage tank water leaks and diode vacuum leaks (Figure 5c). The PVT absorber was then formed on the diode's absorber-evaporator plate (see Figure 4, 5b and Table 1) using matt black paint, double-sided adhesive foam tape, quartered mono-crystalline silicon cells, transparent silicone resin, and transparent Perspex cover plates. The series-parallel interconnected PV cells were connected to a 5.2Ω resistive load bank. Prior to resin casting, T-Type Thermocouples (TTC) producing measurement results with standard uncertainty ±0.3°C in the range 0 to 100°C were attached to the rear of four PV cells (T_0) and to the absorber-evaporator plate surface at twelve locations (T_1). Fourteen TTCs were bonded to the condenser-tank plate surface (T_2) within the tank, along with five TTCs mounted along a thin vertical wire suspended in the water (T_3). Thirteen TTCs were bonded to outer surfaces of diode sidewalls (T_4) and sump (T_S) and three were placed in shaded and sheltered locations to measure ambient temperatures (T_a). All TTCs were connected to a Delta-T Devices DL2e datalogger sampling continuously and recording average temperatures at 5 minute intervals. Thermally insulating polystyrene foam was applied to the rear and sides of the prototype along with a transparent Perspex sheet to cover the absorber.

The diode was filled with 1 kg of working fluid and evacuated to ~2.5 kPa (close to saturated vapour pressure of water at 20°C) using an Edwards XDS5 scroll vacuum pump and a Druck DPI-104 vacuum pressure gauge. The completed prototype was initially tested for heat retention performance by filling the tank with hot water at T_3=70°C and measuring the rate of temperature reduction overnight. The test was repeated with additional polystyrene insulation over the absorber which enabled tank back and sides heat loss to be quantified as U_{3ia}=1.1 $Wm^{-2}K^{-1}$ at 70°C and U_{3ia}=0.6 $Wm^{-2}K^{-1}$ at 40°C (estimated standard uncertainty ±0.2 $Wm^{-2}K^{-1}$). The tank was then drained and the prototype moved to Ulster University's solar simulator facility (Zacharopoulos et al., 2009). The main tests under the simulator followed similar methodologies and procedures to those used

by Quinlan (2010) and Smyth et al. (2015) although the test duration was significantly extended to account for the relatively high volume-to-absorber area ratio (100 L/m^2) of the prototype:

1. Adjust solar simulator for irradiance of G≈600 Wm^{-2} by taking readings at locations across the entire absorber surface with a Kipp and Zonen CMP6 pyrometer.
2. Fill tank with cold mains water. Activate evaporator wetting mechanism and remove temporary shading from absorber.
3. Disconnect resistive load bank from PV terminals. Measure characteristic IV performance curve of PV module using Daystar DS1000 tracer. Reconnect resistive load bank.
4. Repeat Step 3 after 2, 4 & 6 hours of illumination then immediately switch off the solar simulator and leave to cool overnight.
5. Repeat Steps 1 to 5 on subsequent days until no significant day-to-day change in daily minimum and maximum tank temperature occurs.

The procedure featured 6 hour collection periods (t_{col}=21600s) and 18 hour retention periods (t_{ret}=64800s) repeated over four consecutive 24 hour periods. Recorded temperature time history results were error-checked and spatially averaged to determine overall average values of T_0, T_1, T_2, T_3, T_4, T_S and T_a. These results were then used to determine heat transfer rates, corresponding thermal conductances and subsequently to determine thermal efficiencies according to Equations 1, 2 & 3. Photovoltaic performance results (V_{oc}, I_{sc}, V_{mpp}, I_{mpp}, Q_{Empp} and FF) were produced directly by the Daystar DS1000 along with characteristics IV curves.

Table 1 – Specifications of the prototype

Parameter		*Value*		*Basis / Reason*
Tank and diode envelope and structure construction material		**Stainless steel**		High strength, low vacuum outgassing, relatively low thermal conductivity and emittance.
Diode cavity depth	$x = x_w = x_s$	*mm*	70	Optimum value for compromise between forward and reverse mode performance.
Absorber-evaporator & condenser-tank plates height and width	z	*mm*	1400	Slender cavity aspect ratio (z/x=20) and modest plate aspect ratio (y/z=0.5) to minimise reverse mode vapour convection and optimise high temperature liquid-vapour-liquid conductance.
	y	*mm*	700	
Plate thickness	x_1	*mm*	1.2	Chosen for compromise between structural integrity, cost and weight, whilst minimising number of struts.
Sidewall thickness	z_w	*mm*	0.9	Chosen for compromise (z_w≈0.1x_w) between structural integrity and minimal sidewall thermal conductance, rounded up to nearest available gauge.
Centre-centre spacing of struts	d_{ss}	*mm*	70	Chosen to be similar to cavity depth and strut length
Strut tube diameter	d_s	*mm*	8	Compromise between structural integrity and minimising structure thermal conductance.
Strut tube wall thickness	d_{sw}	*mm*	0.9	
Mass of diode and tank	m_{1234s}	*kg*	8.1	Construction material and liquid masses determined from dimensions given above together with densities for stainless steel and liquid water (7900 and 1000 kg·m^{-3} respectively).
Mass of diode working fluid	m_{Lv}	*kg*	1.0	
Mass of water stored in tank	m_{3L}	*kg*	100	
Total mass	m_{tot}	*kg*	131	
Photovoltaic cells		**Monocrystalline silicon**		Bosch M-2BB high efficiency pseudo-square cells.
Number of cells	N	8 x 15 = 120		Formed of 30 whole cells cut into quarters.
Cell size	A_0	*m*^{2}	78 x 78	Quarter of a standard 6x6 inch whole cell.
Wiring scheme & voltage	V_{oc}	*V*	23	Series-parallel configuration of 8 cells per string with 3 strings connected in parallel to form each bus (V_{oc} ≈ 4.5V). Module consists 5 buses in series.
Cell packing factor	PF	%	72%	Thermo-electrical efficiency compromise. Absorber surface behind PV cells was painted matt black.
Encapsulation		**Silicone resin PlatSil® 71-20**		Low cost, highly transparent, pourable resin, resists UV degradation and high temperatures.
Bonded cover (on top of encapsulation) **Thermal cover (for air gap)**		**Clear Perspex**		Low cost, robust, resistant to UV degradation.
Thickness of encapsulation and bonded cover (x_{15}=x_{01}+x_{05})	x_{15}	*mm*	5	Perspex sheet minimum 2mm available thickness. Resin thickness determined by pour viscosity and adhesive foam tape spacer thickness.
	x_{01}	*mm*	1.5	
	x_{05}	*mm*	3.5	
Thickness of thermal cover	x_6	*mm*	2	
Thickness of air gap	x_{56}	*mm*	35	

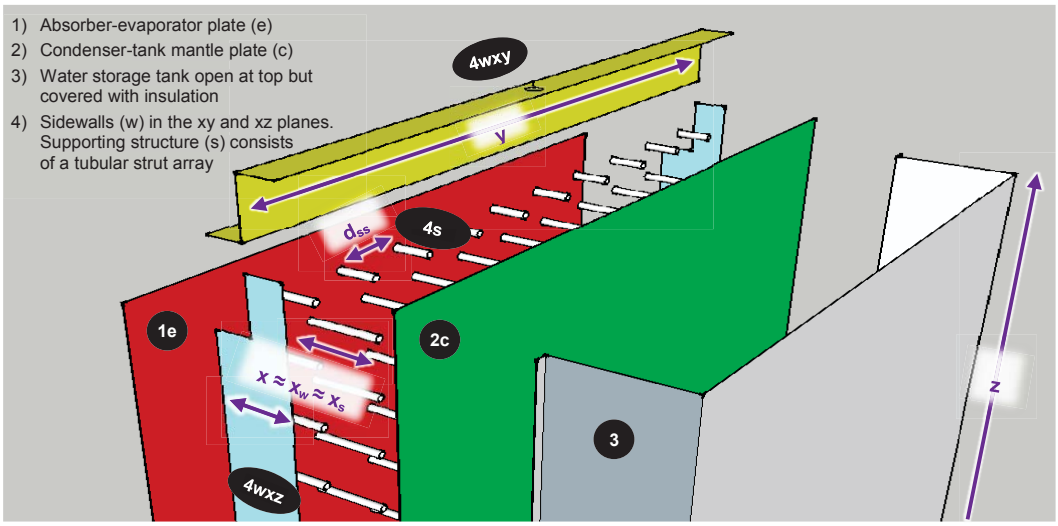

Figure 3 – Construction of the thermal diode and tank

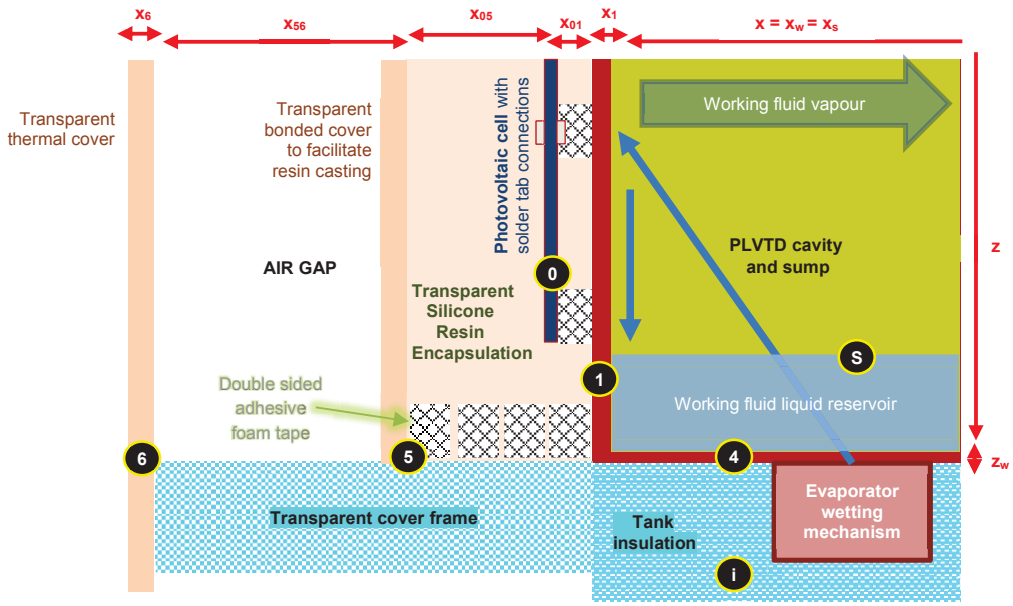

Figure 4 – Cross section through absorber laminate and transparent covers (scale exaggerated)

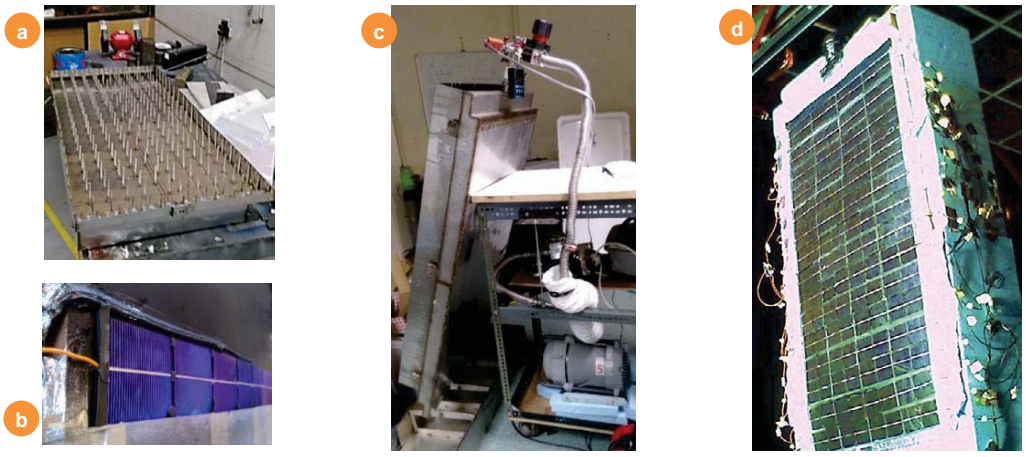

Figure 5 – Photographs showing steelwork & PVT absorber fabrication (a & b), leak testing (c), solar simulator testing (d)

4. Results and discussion

Recorded temperature time histories are shown on Figure 6. Tests began with T_3=17°C tank temperature which rose by 21°C during the first collection period and fell by only 5°C during the first overnight retention period. The final (fourth) day of collection saw only 11°C gain before reaching T_3=57°C. This gain was almost entirely lost during the fourth overnight retention period. Ambient temperatures were T_a≈25±5°C during collection and T_a≈20±3°C during retention periods. Instantaneous thermal and electrical efficiencies were 60% and 9% respectively at zero increased temperature (T_3-T_a=0), dropping to 40% and 6% respectively at a nominal intended operating condition ~0.05 m^2KW^{-1} corresponding to T_3≈50°C, T_a≈20°C and G≈600 Wm^{-2}.

Dependence of the instantaneous thermal and electrical efficiencies upon the water storage tank temperature are shown on Figure 7 to be reasonably linear. Scatter in the data is primarily a manifestation of absorber heat-up and cool-down transients which occurred at the beginning and end of each collection period due to the diode's significant thermal mass (sensible and latent). These transients were observed to affect PV module efficiency as well as absorber heat loss and diode thermal conductance. Electrical efficiencies recorded at the start of each day of testing, immediately after illumination whilst the absorber was cool ($T_1 \lesssim T_a$+15°C), were consistently higher than values recorded at other times when the absorber was warmer (typically $T_1 \approx T_3$+8°C). Recorded collection efficiencies each day were η_{col}=65, 46, 44 and 40%. Overnight retention efficiency was η_{ret}=71% with corresponding overall loss coefficient U_{sys}=0.85 $Wm^{-2}K^{-1}$ (estimated standard uncertainty ±0.1 $Wm^{-2}K^{-1}$). With reference back to Figure 2, diurnal thermal efficiencies recorded for Days 1 and 4 were slightly lower than predicted because of poorer than expected forward mode diode thermal conductances, but as predicted, were significantly higher than for the benchmark ICSSWH without thermal diode.

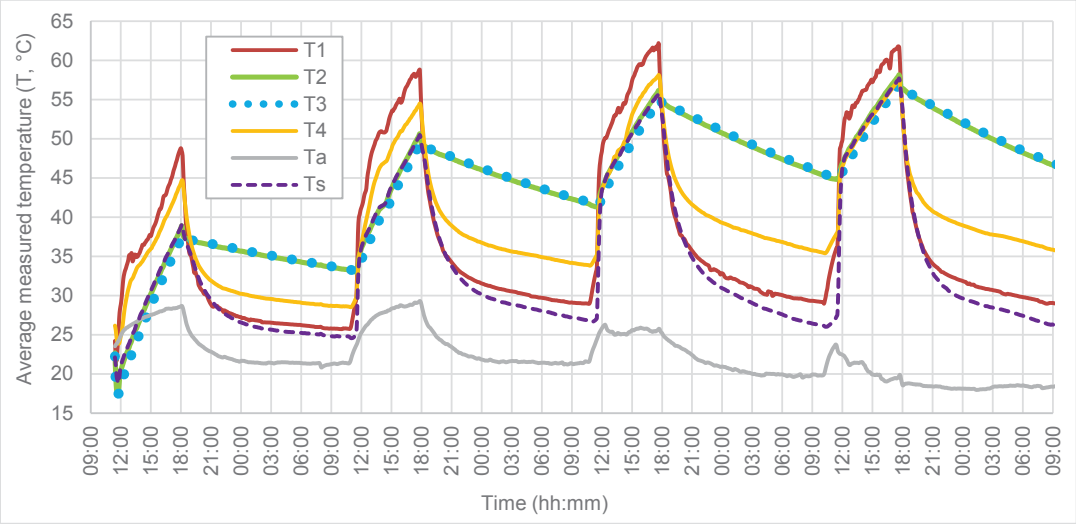

Figure 6 – Recorded temperature time history

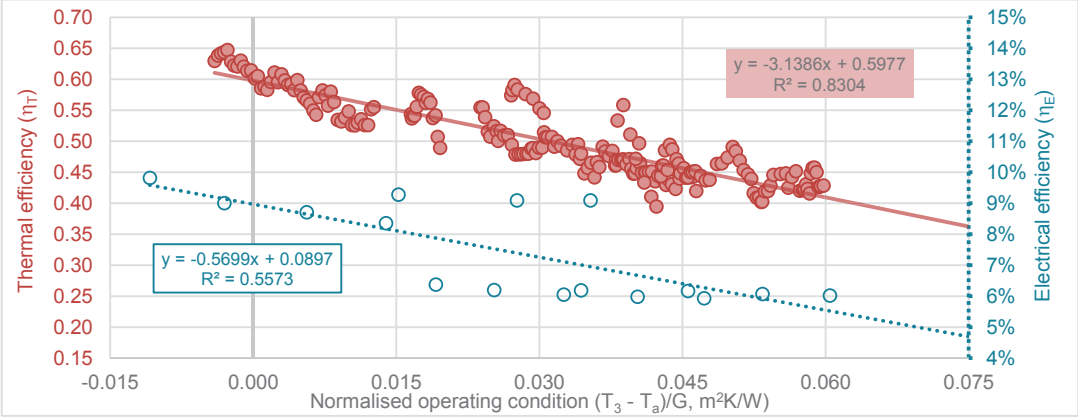

Figure 7 – Instantaneous thermal and electrical efficiencies

Table 2 – Comparison of measured photovoltaic characteristics against manufacturers data

Characteristic	***Manufacturer's data for single cell***	***Expected module performance***	***Actual module performance*** *(with encapsulation and bonded cover*)*
Maximum Power at STC (Q_{Empp}, W)	4.24	127	83*
Cell efficiency at STC ($\eta_{E(0,mpp)}$, %)	17.6%	17.6%	11.4%*
Module efficiency at STC ($\eta_{E(ec,mpp)}$, %)	-	13.7%	8.9%*
Open Circuit Voltage at STC (V_{oc}, V)	0.616	24.6	24.1*
Short Circuit Current at STC (I_{sc}, A)	8.9	6.7	4.8*
Fill Factor (FF, %)	78% (G=1000 Wm^{-2})		74% (G=610)
Voltage temperature coefficient (%V_{oc}/K)	-0.37%		-0.37%
Current temperature coefficient (%I_{sc}/K)	+0.03%		-0.19%
Maximum power temperature coefficient (%Q_{Empp}/K)	-0.49%		-0.55%

** Photovoltaic performance was measured under a variety of irradiances (G=350, 610 and 870 Wm^{-2}) and a variety of temperatures, with the transparent thermally insulating cover removed. No measurements were made under strict Standard Test Conditions (STC) of G=1000 Wm^{-2} and T_0=25°C but the data obtained enabled STC open circuit voltage, short circuit current, maximum power, and efficiency values to be determined by extrapolation.*

Forward mode diode thermal conductances were typically an order of magnitude lower (worse) than expected, but the predicted temperature dependence was clearly apparent with U_{12f}=30 $Wm^{-2}K^{-1}$ occurring when the water storage tank was cold, rising to U_{12f}=70 $Wm^{-2}K^{-1}$ when it was hot. Considerable spatial variation in absorber surface temperature was observed during collection periods. Detailed investigations (Pugsley, 2017) found that the relatively poor forward mode diode performances were primarily caused by poor evaporator wetting. Wetted parts of the absorber-evaporator plate were typically observed to be $T_1 \approx T_3$+3°C (as expected) whereas "dry spots" were markedly hotter (typically $T_1 \approx T_3$+30°C) due to the lack of evaporative cooling.

Reverse mode diode thermal conductances were generally slightly lower (better) than predicted being typically U_{12r} =1.7 $Wm^{-2}K^{-1}$. Other measured forward and reverse mode conductances were broadly as expected, being typically U_{23f}=250 $Wm^{-2}K^{-1}$ and U_{23r}=100 $Wm^{-2}K^{-1}$ within the water storage tank; U_{1af}=3.5 $Wm^{-2}K^{-1}$ and U_{1ar}=2.5 $Wm^{-2}K^{-1}$ between the absorber and ambient; and $U_{01} \approx$100 $Wm^{-2}K^{-1}$ through the silicone resin encapsulation bonding the PV cells to the absorber. Water storage tank thermal conductances (U_{23}) and absorber heat loss thermal conductances (U_{1a}) were higher during forward mode than during reverse mode because heat fluxes and plate temperatures were inherently higher during solar collection periods than they were during retention periods. The estimated combined standard uncertainty of the aforementioned thermal conductance results is about ±30%.

Measured PVT absorber electrical performance is summarised in Table 2. Short circuit current (I_{sc}), maximum electrical power yield (Q_{Empp}), and efficiency (η_E) were all 30-35% lower than expected, despite results of pilot tests on individual cells being broadly consistent with manufacturer's data. Measured temperature coefficients for whole-module power (%Q_{Empp}/K) and short circuit current (%I_{sc}/K) were also notably worse than manufacturers single-cell values. Analysis described in detail by Pugsley (2017) identifies several potential causes for the poor current yield, of which the most significant is accidental cell damage (to approximately a quarter of all cells) which occurred during absorber laminate fabrication. Cell fractures function as electrical resistances which limit (or completely eliminate) the flow of current between broken cell fragments and the main body of each cell. Detailed inspection of the test data indicated an abrupt worsening of current loss above $T_1 \approx$45°C which is thought to be due to absorber thermal expansion widening fractures and increasing associated electrical resistances. In addition to cell fractures, the following effects are also likely to have contributed to current and power loss:

- Uneven distribution of light emitted by the solar simulator (±10% for high irradiance tests) causing some cells to produce less current than others, thereby limiting overall string currents.
- Optical losses associated with delamination of the encapsulation material, which was particularly notable in locations where the aforementioned hot "dry spots" occurred.

- Non-uniform absorber surface temperatures which caused voltage mismatches between parallel connected cell strings. The hot "dry-spots" on the absorber-evaporator plate were observed to be most pronounced when the absorber and/or the tank were cool and irradiance levels were high.

Despite the lower than expected diode forward mode thermal conductance and underperforming PV cell array, the solar thermal collection and retention performances of the prototype are amongst the highest reported anywhere in the ICSSWH literature (see Sections 1.1 & 1.2) providing strong evidence that incorporation of a planar liquid-vapour thermal diode yields a significant performance benefit. This finding is echoed in the comparative study reported by Smyth et al. (2016).

5. Supporting analyses

In addition to the work presented above, a considerable amount of additional experimental and theoretical work and supporting analyses have been undertaken as part of this study (Pugsley, 2017) and will be the subject of several anticipated future papers:

- **Theoretical behavior of PLVTDs:** A lumped parameter thermal resistance model enabling prediction of PLVTD heat transfer was developed and experimentally validated. The model was used to undertake a parametric study examining PLVTD behaviour under different heat flux, temperature, and tilt angle conditions. The model was also used to optimize the PLVTD design in respect of material choices; working fluid types and flow rates; dimensions and aspect ratios.
- **Economics:** Materials for the prototype cost £600/m^2. This cost is comparable to typical retail prices of flat plate and evacuated tube solar thermal collectors and is considerably less than most commercially available packaged solar water heaters. Estimated labour costs were very high (£2000/m^2) due to reliance on labour intensive processes required to fabricate a one-off prototype. Significant value engineering and manufacturing process optimization would be required to make the device commercially viable and mass-manufacturable.
- **Building integration:** Feasibility studies were undertaken to examine how the PVT-PLVTD-ICSSWH concept might be integrated into different building façade constructions, allowing for key considerations such as structural loading and aesthetic/dimensional compatibility with building structural grids. The compatibility of the device in respect of integration into building electrical and heating services systems was also examined.

6. Conclusions

A flat panel Integrated Collector-Storage Solar Water Heater (ICSSWH) incorporating a photovoltaic-thermal (PVT) absorber and a Planar Liquid-Vapour Thermal Diode (PLVTD) was fabricated and tested under Ulster University's solar simulator. The collector primarily consisted of a sealed evacuated thermal diode and a vented water storage tank, both constructed of welded and folded stainless steel sheet. The absorber-evaporator plate was painted black and 120 quartered monocrystalline photovoltaic cells were encapsulated and bonded to it using clear silicone resin. Cells were interconnected in a series-parallel configuration to produce an open circuit voltage of ~24V. The absorber was insulated by a transparent Perspex cover and air gap. Collector rear and sides were insulated by polystyrene foam.

Test results indicate instantaneous thermal and electrical efficiencies of 60% and 9% respectively under zero temperature rise conditions (when stored water temperature equals ambient temperature), dropping to 40% and 6% at the nominal intended operating condition (~0.05 m^2KW^{-1} at 20°C ambient). Water temperature of 57°C was achieved in the 100 Litre tank after four days of consecutive 6-hour collection periods (G=610Wm^{-2} irradiance on ~0.95m^2 absorber) and 18 hour retention periods (T_a≈20±3°C). Daily solar thermal collection and overnight heat retention efficiencies of η_{col}=65% and η_{ret}=71% were achieved, corresponding to diurnal thermal efficiency of up to $\eta_{T+E,24}$=46% and an overall heat loss coefficient of U_{sys}=0.85 $Wm^{-2}K^{-1}$. Measured thermal diode conductances were typically U_{12f}=45 $Wm^{-2}K^{-1}$ in forward mode (during collection periods) and U_{12r}=1.7 $Wm^{-2}K^{-1}$ in reverse mode (during retention periods). These thermal performances are comparable to

the best ICSSWH collector designs encountered in the literature. Photovoltaic performance was lower than expected, primarily owing to accidental damage to PV cells during fabrication, together with temperature and irradiance non-uniformities, and optical losses associated with delaminated encapsulation.

Overall, the work demonstrates that ICSSWH, PVT and PLVTD concepts can be successfully combined to create a scalable flat panel solar collector suitable for integration within a multifunction building facade. Changes to fabrication procedures could reduce or eliminate breakage of PV cells. Improved evaporator wetting, reduced PV cell encapsulation thickness, and better bonding of PV cells to the absorber plate would all increase conductance during collection periods yielding improvements to both thermal and electrical efficiencies. It is recommended that further work focusses on implementing the aforementioned improvements and undertaking further studies to optimize the design for building façade and services systems integration.

7. Nomenclature

Meanings of symbols:

A	Area
α	Solar absorption coefficient
C	Heat capacity
d	Distance or dimension
FF	Fill Factor of current-voltage characteristic curve
G	Irradiance or solar power flux
η	Efficiency with subscripts $_{E, T, col, ret, 24, 0, ec, mpp}$
I	Current (subscript $_{sc}$ for "short circuit")
m	Mass with subscripts $_{Lv, 3L, 1234s, tot}$
N	Number of PV cells
PF	Packing Factor of PV cells
Q	Power (Q_{Empp} = electrical at maximum power point)
R	Thermal resistance with subscripts $_{12, 123, 1a, 23, 3ia}$
t	Time or duration with subscripts $_{0, col, ret}$
T	Temperature with subscripts $_{0, 1, 2, 3, 4, a, s}$
τ	Optical transmittance
U	Thermal conductance with subscripts $_{12f, U12r, 23f, 23r, 1af, 1ar, 3ia, sys}$
V	Voltage (subscript $_{oc}$ for "open circuit")
x	Distance parallel to collector depth with subscripts $_{01, 05, 1, 15, 56, 6, s, w}$
y	Distance parallel to collector width
z	Distance parallel to collector height (subscript $_{w}$ for "sidewall thickness")

Meanings of subscripts:

a	Ambient
col	Collection
E	Electrical
f	Forward mode / collection periods
Lv	Diode working fluid at liquid-vapour saturation
r	Reverse mode / retention periods
ret	Retention period
s	Strut
S	Sump
sys	System heat loss coefficient
tot	Total
T	Thermal
0	Photovoltaic cells (T_0, A_0) or Start of period (t_0)
1	Absorber-evaporator plate
2	Condenser-tank mantle plate
3	Water in storage tank
4	Diode sidewalls
5	Absorber laminate bonded cover plate surface
6	Transparent thermally insulating cover
12	Between Plates 1 and 2
123	Between absorber and bulk of stored water
1a	Between absorber and ambient
23	Between Plate 2 and bulk of stored water
24	Diurnal value over a 24 hour period
3ia	Between "3" and "a" via foam insulation
56	Air gap between absorber & transparent cover

8. References

Aguilar, F., Aledo, S. Quiles, P., 2016. Experimental study of the solar photovoltaic contribution for the domestic hot water production with heat pumps in dwellings. App. Therm. Eng. 101, 379–89

Besheer, A., Smyth, M., Zacharopoulos, A., Mondol, J., Pugsley, A. 2016. Review on recent approaches for hybrid PV/T solar technology. Int. J. Energy Res. DOI: 10.1002/er.3567

Boreyko, J., Zhao, Y., Chen, C., 2011. Planar jumping-drop thermal diodes. Appl. Phys. Lett. 99, 234105

Boreyko, J. and Chen, C., 2013. Vapor chambers with jumping-drop liquid return from superhydrophobic condensers. Int. J. Heat & Mass Trans. 61, 409–18

Calise, F., d'Accadia, M, Figaj, R., Vanoli, L., 2016. A novel solar-assisted heat pump driven by photovoltaic/thermal collectors: Dynamic simulation and thermoeconomic optimization. Energy 95, 346-66

Cengel, Y., Boles, M., 2006. Thermodynamics an Engineering Approach, 5th Edition. McGraw-Hill, New York.

Chen, K., Chailapo, P., Chun, W., Kim, S., Lee, K., 1998. Dynamic behavior of a bayonet-type thermal diode. Sol. Energy 64, 257–63

De Beijer, H., 1998. Product development in solar water heating. Ren. Energy 5, 201-4

Dupeyrat, P., Menezo, C., Rommel, M., Henning, H., 2011. Efficient single glazed flat plate photovoltaic-thermal hybrid collector for domestic hot water systems. Sol. Energy 85, 1457-68

Faiman, D., Hazan, H., Laufer, I., 2001. Reducing the Heat Loss at Night from Solar Water Heaters of the Integrated Collector-Storage Variety, Sol. Energy, 71, 87-93

Fang, Y., Hyde, T., Arya, F., Hewitt, N., Eames, P., Norton, B., Miller, S., 2014. Indium alloy-sealed vacuum glazing development and context. Renewable and Sustainable Energy Reviews 37 (2014) 480–501.

Fang, X., Xia, L., 2010. Heating performance investigation of a bidirectional partition fluid thermal diode. Ren. Energy 35, 679–84

Good, C., Andresen, I., Hestnes, A., 2015. Solar energy for net zero energy buildings – A comparison between solar thermal, PV and photovoltaic–thermal (PV/T) systems. Sol. Energy 122, 986–96

Kolodziej, A., Jaroszynski, M., 1997, Performance of liquid convective diodes. Sol. Energy 61, 321-6

Michael, J., Iniyan, S., Goic, R., 2015. Flat plate solar photovoltaic–thermal (PV/T) systems. Ren. & Sus. Energy Rev. 51, 62–88

Mohamad, A., 1997. Integrated Solar Collector-Storage Tank System with Thermal Diode. Sol. Energy, 61, 211-8.

Pugsley, A., 2017. Theoretical and experimental analysis of a novel flat photovoltaic-thermal solar water heater with integrated energy storage via a Planar Liquid-Vapour Thermal Diode. Ulster University PhD Thesis. Available at: <http://ethos.bl.uk/SearchResults.do>

Poppi, S., Bales, C., Haller, M., Heinz, A., 2016. Influence of boundary conditions and component size on electricity demand in solar thermal and heat pump combisystems. App. Energy 162, 1062–73

Qu, M., Chen, J., Nie, L., Li, F., Yu, Q., Wang, T., 2016. Experimental study on the operating characteristics of a novel photovoltaic/thermal integrated dual-source heat pump water heating system. App. Therm. Eng. 94, 819–26.

Quinlan, P., 2010. The Development of a Novel Integrated Collector Storage Solar Water Heater (ICSSWH) Using Phase Change Materials and Partial Evacuation. PhD Thesis, University of Ulster.

Quinlan, P., Smyth, M., Griffiths, P., Conway, S. and Filippi, A., 2008. Novel Integrated Collector Storage Solar Water Heater Utilising Phase Change Materials. Proceedings World Renewable Energy Conference, 19-25 July 2008, Glasgow, UK.

European Union (EU) Directive 2009/28/EC on the promotion of the use of energy from renewable sources and amending and subsequently repealing Directives 2001/77/EC and 2003/30/EC (Text with EEA relevance). Official Journal of the European Union.

Rhee, J., Campbell, A., Mariadass, A., Morhous, B., 2010. Temperature stratification from thermal diodes in solar hot water storage tank Sol. Energy 84, 507–511.

Santbergen, R., Rindt, C., Zondag, H., Van Zolingen, R., 2010. Detailed analysis of the energy yield of systems with covered sheet-and-tube PVT collectors. Sol. Energy 84, 867–78.

Singh, R., Lazarus, I., Souliotis, M., 2016. Recent developments in integrated collector storage (ICS) solar water heaters: A review. Ren. & Sus. Energy Rev. 54, 270-98.

Smyth, M., 2015. A solar water heater. Patent WO2010052010.

Smyth, M., Eames, P., Norton, B., 1999. A comparative performance rating for an integrated solar collector/storage vessel with inner sleeves to increase heat retention. Sol. Energy 66, 291–303.

Smyth, M., Eames, P., Norton, B., 2006. Integrated Collector Storage Solar Water Heaters. Ren. & Sus. Energy Rev. 10(6), 503-38.

Smyth, M., Besheer, A., Zacharopoulos, A., Mondol, J., Pugsley, A., Novaes, M., 2015. Experimental evaluation of a Hybrid Photovoltaic/Solar Thermal (HyPV/T) Façade Module. Proceedings EURO ELECS Conference 21-23 July 2015, Guimarães, Portugal.

Smyth, M., Pugsley, A., Hanna, G., Zacharopoulos, A., Mondol, J., Besheer, A., 2016. Experimental performance comparison of a Hybrid Photovoltaic/Solar Thermal (HyPV/T) Façade Module with a flat ICSSWH module. Proceedings BIRES 2017 Conference 6-10 March 2016, Dublin, Ireland.

Solaform, nd. SolaCatcher Innovative, cost effective solar water heating system. http://solaform.com/ [accessed 2016-19-09].

Sopian, K.,Syahri, M., Abdullah, S., Othman, M.,Yatim, B., 2004. Performance of a non-metallic unglazed solar water heater with integrated storage system. Ren. Energy 29, 1421–30.

Souliotis, M., Quinlan, P., Smyth, M., Tripanagnostopoulos, Y., Zacharopoulos, A., Ramirez, M., Yianoulis, P., 2011. Heat retaining integrated collector storage solar water heater with asymmetric CPC reflector. Sol. Energy 85, 2474–87.

Zacharopoulos, A., Mondol, J., Smyth, M., Hyde, T., O'Brien, V., 2009. State of the Art Solar Simulator with Flexible Mounting. Proceedings ISES Solar World Congress, 11-14 October 2009, Johannesburg, South Africa, pp 854-863.

Zondag, H., 2008. Flat-plate PV–thermal collectors and systems: a review. Ren. & Sus. Energy Rev. 12, 891–959.

Conference Proceedings

EuroSun 2016
Palma de Mallorca (Spain), 11 - 14 October 2016

Optimization Methods for Optimal Power Flow in Microgrid Non-Autonomous Mode

Luis O. Polaco Vasquez[1], Cristian A. Carreño Meneses[1], Alejandro Pizano Martínez[1], Juana López Redondo[2], Manuel Pérez García[2] and José Domingo Álvarez Hervás[2]

[1] University of Guanajuato, Irapuato-Salamanca Campus, Guanajuato (Mexico)

[2] University of Almería, Agrifood Campus of International Excellence (ceiA3)
CIESOL Joint Centre University of Almería -CIEMAT, Almería (Spain)

Abstract

In this work, the Optimal Power Flows (OPF) for the tertiary control problem in microgrid is studied. The objective is to find the optimal dispatch of energy which maximize the benefit. Such energy can come from renewable sources, storage devices or the main power grid. To this aim, a unified model of the microgrid, which is operated in non-autonomous mode, has been developed. This model is composed by basic submodels of the distribution system, the photovoltaic panels, the wind turbines and the batteries for energy storage. The optimization problem is solved using three different methods provided by the optimization toolbox of MATLAB®. More precisely, an interior point method, a genetic algorithm and the direct search method have been considered. The performance of those optimization methods is analyzed in terms of efficiency and effectiveness. Some good results are depicted. The case study considers the microgrid connected to the main power system with the photovoltaic panels, the wind turbines and the batteries for energy storage. In this test, the power supplied by the grid is mostly due to the size of each renewable source, but it is possible to see the contribution of the microgrid in the cost graphics.

Keywords: *optimal power flow, microgrid, distributed power systems*

1. Introduction

Nowadays the electricity sector worldwide is subject to meet strict environmental policies that promote the use of renewable energy sources, with the aim to contribute with the environmental and global energy sustainability. The operation modes of a microgrid are two: i) non-autonomous (connected to the main power grid) and, ii) autonomous (not connected to the main power grid) [Olivares, 2014]. In any of these operation modes, the microgrid is controlled through a three-level hierarchical control system which can be split in a primary controller, a secondary controller and tertiary one [Bidram, 2012]. This work is part of the tertiary controller of the microgrid operating in non-autonomous mode. In this scenario, the objectives that are mainly considered for the tertiary controller are the minimization of the energy cost from the main grid and the optimization of the voltages profile within the microgrid among others, through different optimization methods [Katiraei, 2008]. As a result, Optimal Power Flows (OPF) analysis is the cornerstone of the tertiary controller. Taken it into account, this paper is particularly focused in implement a model of optimal power flows of the microgrid for non-autonomous operating mode and three different optimization methods for the resolution of OPF. Based on the profiles of electric demand curves and solar radiation from the cities of Salamanca and Guanajuato, Mexico, and the predicted wind speed for a period of time T, the analysis of optimal power flows can be used to determine the optimum dispatch for the energy storage devices and the optimal quantity of power imported from the main grid, with the aim of maximizing the benefit of the energy generated by the Distributed Energy Sources (DES) installed in the microgrid and, at the same time, reducing the cost of the energy imported from the main grid [Levron, 2013]. In a microgrid framework,

doi:10.18086/eurosun.2016.08.24 Available at http://proceedings.ises.org

different models of optimal power flow, optimization algorithms and strategies for the energy management have been proposed [Olivares et al 2014, Levron et al 2013, Gill et al 2014]. Despite this, there is not any strategy of optimal power flows that can be considered as the ultimate tool for the implementation of a tertiary controller. Therefore, the problem of optimal flows for microgrids is a topic of current research and of relevant importance in this context.

This work presents three different optimization methods for a unified model of optimal power flow for microgrids, which considers basic models of the elements of the distribution system, photovoltaic panels, wind turbines, as well as batteries for energy storage. The model is solved by three different methods of optimization: i) interior point, ii) genetic algorithm and, iii) direct search provided by the optimization toolbox included in MATLAB®. The solutions obtained allows us to evaluate the optimal dispatch of energy storage devices and the optimal amount of power imported from the main grid. The mathematical basis of this work and the generic model of OPF for microgrid are presented in the Section 2. Section 3 shows the mathematical models of the different components of the microgrid as a wind turbine, photovoltaic module, battery, load, and the components of the distribution lines. In Sections 4 and 5 the explicit model of OPF and its solution are described, respectively. In Section 6 are described, showed and compared the results obtained with the different methods of optimization for the proposed case study. Finally, the conclusions of this work are presented in Section 7.

2. Generic model of OPF for Microgrid

For electric demand curves, solar radiation and predicted wind speed for an interval of time T, the general model of OPF is given by eqs. 1-4. It should be noted that, in this model, it is considered that the period of time T is composed of a set of time stages t_z ($\forall z = 1,..., end$), such that $T = [t_1,..., t_{end}]$.

$$\text{Minimize} \quad F_T = \sum_{t_z=1}^{t_{end}} f^{t_z}(\boldsymbol{y}^{t_z}) \qquad \text{(eq. 1)}$$

$$\text{Subject to} \quad \boldsymbol{h}^{t_z}(\boldsymbol{y}^{t_z}) = \boldsymbol{0}\ ;\ \forall t_z \in T \qquad \text{(eq. 2)}$$

$$\boldsymbol{g}^{t_z}(\boldsymbol{y}^{t_z}) \le \boldsymbol{0}\ ;\ \forall t_z \in T \qquad \text{(eq. 3)}$$

$$\underline{\boldsymbol{y}} \le \boldsymbol{y}^{t_z} \le \overline{\boldsymbol{y}}\ ;\ \forall t_z \in T \qquad \text{(eq. 4)}$$

Taking into account that, t_z represents the *z-th* time stage, the description of the terms of the model, eqs. 1-4, is as follows: F_T is the objective function to optimize along the interval T, $\boldsymbol{h}(\boldsymbol{y})$ is a set of equality constraints, which represents the balance equations of active power and reactive on all the nodes in the microgrid, as well as other operating conditions that must be fulfilled unconditionally, $\boldsymbol{g}(\boldsymbol{y})$ is a set of constraints of inequalities that represents the physical limits and operating of the elements that make up the microgrid, $\boldsymbol{y}$ is the set of decision variables (to be optimized) composed of subsets $\boldsymbol{y}_{RD}$, $\boldsymbol{y}_{MF}$ and $\boldsymbol{y}_B$ such $\boldsymbol{y}=[\boldsymbol{y}_{RD}, \boldsymbol{y}_{MF}, \boldsymbol{y}_B,]$. Where $\boldsymbol{y}_B$, $\boldsymbol{y}_{RD}$ and $\boldsymbol{y}_{MF}$ represent batteries variables, distribution grid and photovoltaic modules, respectively. The upper and lower limits, $\overline{\mathbf{y}}$ and $\underline{\mathbf{y}}$, of these variables are formulated through the inequality constraints, see eq. 4.

3. Model for microgrids components

The models for microgrid components presented in this section are considered to formulate explicitly the unified model of OPF for microgrid presented in Section 4.

3.1. Points of Common Coupling

It is considered that the microgrid operates in non-autonomous mode, such that is connected to the main grid in N_{pac} ($N_{pac} \ge 1$) Points of Common Coupling (PCC). It is assumed that each PCC is electrically robust and is an interface for the unlimited exchange of both, active and reactive power between the microgrid and the main grid. In this context, the PCC are modeled as generation sources that operate at voltage levels

magnitude $V_j^{t_z}$ and angle $\theta_j^{t_z}$ within the limits given by eq. 5:

$$\left.\underline{V}_j \le V_j^{t_z} \le \overline{V}_j ; \underline{\theta}_j \le \theta_j^{t_z} \le \overline{\theta}_j \right\} \forall t_z \in T \;\; ; \;\; \forall j \in PAC \qquad \text{(eq. 5)}$$

For time t_z, the cost of active total power exchanged through the PCC is modeled by eq. 6. Where a_j, b_j and c_j are weight constant coefficients for the *j-th* PCC. The variable $P_{RPj}^{t_z}$ means the power exchanged through the *j-th* PCC. The decision variables associated with the PCC are $\left[V_j^{t_z}, \theta_j^{t_z}, P_{RPj}^{t_z}\right] \in \boldsymbol{y}_{RD}$ ($\forall t_z \in T, \forall j \in PCC$).

$$f^{t_z}(\boldsymbol{y}^{t_z}) = \sum_{j=1}^{N_{pac}} a_j + b_j (P_{RPj}^{t_z}) + c_j (P_{RPj}^{t_z})^2 \quad ; \; \forall t_z \in T \qquad \text{(eq. 6)}$$

3.2. Feeders

Each feeder is modeled as a line of transmission, as is illustrated in Fig. (1) Where $\boldsymbol{I}_i$ and $\boldsymbol{E}_i$ are the phasors of the injected electricity and voltage, respectively, on the node i ($i = k,m$) of the microgrid. R, L and B_c represent the parameters of resistance series, inductance series and shunt susceptance, respectively, of the feeder. The relationship electricity-voltage of the equivalent circuit is given by eq. 9 [Acha, 2004]. Where admittance matrix elements are evaluated in eq. 8 and eq. 9.

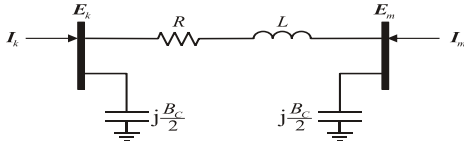

Fig. 1: π circuit for the feeders

$$\begin{bmatrix} \boldsymbol{I}_k^{t_z} \\ \boldsymbol{I}_m^{t_z} \end{bmatrix} = \begin{bmatrix} \boldsymbol{Y}_{kk} & \boldsymbol{Y}_{km} \\ \boldsymbol{Y}_{mk} & \boldsymbol{Y}_{mm} \end{bmatrix} \begin{bmatrix} \boldsymbol{E}_k^{t_z} \\ \boldsymbol{E}_m^{t_z} \end{bmatrix} \quad \forall t_z \in T \qquad \text{(eq. 7)}$$

$$\boldsymbol{Y}_{kk} = \boldsymbol{Y}_{mm} = (\boldsymbol{y}_{km} + j0.5Bc) = G_{kk} + jB_{kk} ; \boldsymbol{Y}_{km} = \boldsymbol{Y}_{mk} = -\boldsymbol{y}_{km} = G_{km} + jB_{km} \qquad \text{(eq. 8)}$$

$$G_{km} = R/R^2 + (\omega L)^2 ; B_{km} = -\omega L/R^2 + (\omega L)^2 \qquad \text{(eq. 9)}$$

Starting from Fig. 1 and eq. 7 it is possible to obtain expressions that model the injection of active and reactive power, eq. 10 and eq. 11 respectively, on the node i ($i = k, m$) at each moment $t_{T \in} z$ [Acha, 2004]. Where $j = k, m$, being $j \neq i$. The variables $V_n^{t_z}$ and $\theta_n^{t_z}$ ($n=i, j$) represent the magnitude and the angle of the nodal voltage phasor $\boldsymbol{E}_i$.

$$P_{inyi}^{t_z} = (V_i^{t_z})^2 G_{ii} + V_i^{t_z} V_j^{t_z} \left[G_{ij} Cos(\theta_i^{t_z} - \theta_j^{t_z}) + B_{ij} Sin(\theta_i^{t_z} - \theta_j^{t_z}) \right] \qquad \text{(eq. 10)}$$

$$Q_{nyi}^{inj\ t_z} = -(V_i^{t_z})^2 B_{ii} + V_i^{t_z} V_j^{t_z} \left[G_{ij} Sin(\theta_i^{t_z} - \theta_j^{t_z}) - B_{ij} Cos(\theta_i^{t_z} - \theta_j^{t_z}) \right] \qquad \text{(eq. 11)}$$

The decision variables associated to these feeders correspond to the nodal voltages in its terminals $\left[V_k^{t_z}, V_m^{t_z}, \theta_k^{t_z}, \theta_m^{t_z}\right] \in \boldsymbol{y}_{RD}$ ($\forall t_z \in T$).

3.3. Transformer

The primary winding is considered an ideal transformer with relation of complex tap T_v:1 and T_i:1 in series with the impedance Z_p (refers to Fig. (2)). Where $\boldsymbol{T}_v = \boldsymbol{T}_i^* = T_v \angle \phi_{tv}$, the symbol * denotes complex conjugate. The secondary winding is also represented as an ideal transformer with relation of complex tap $\boldsymbol{U}_v$:1 and $\boldsymbol{U}_i$:1 in series with the impedance $\boldsymbol{Zs}$. Where $\boldsymbol{U}_v = \boldsymbol{U}_i^* = U_v \angle \phi_{uv}$. The relationship between voltage $\boldsymbol{V}_p$ and electricity $\boldsymbol{I}_p$ of the primary winding and the voltage $\boldsymbol{V}_s$ and electricity $\boldsymbol{I}_s$ of the secondary one is given by eq. 12 [Acha, 2004].

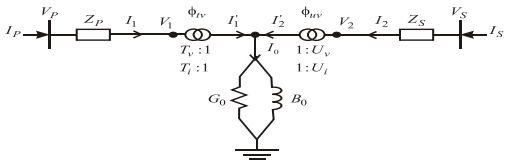

Fig. 2: T model for the transformers

$$\begin{bmatrix} \boldsymbol{I}_p^{t_z} \\ \boldsymbol{I}_s^{t_z} \end{bmatrix} = \begin{bmatrix} G_{PP}\ G_{PS} \\ G_{SP}\ G_{SS} \end{bmatrix} + j \begin{bmatrix} B_{PP}\ B_{PS} \\ B_{SP}\ B_{SS} \end{bmatrix} \begin{bmatrix} \boldsymbol{V}_p^{t_z} \\ \boldsymbol{V}_s^{t_z} \end{bmatrix};\ \forall t_z \in T \qquad \text{(eq. 12)}$$

where:

$$G_{PP} = \frac{F1(U_v^2 + R1) + F2R2}{F1^2 + F2^2},\ B_{PP} = \frac{F1R2 - F2(U_v^2 + R1)}{F1^2 + F2^2}$$

$$G_{SS} = \frac{F1(T_v^2 + R3) + F2R4}{F1^2 + F2^2},\ B_{SS} = \frac{F1R4 - F2(T_v^2 + R3)}{F1^2 + F2^2}$$

As the feeders, the injections of active and reactive power in the connection nodes *i* and *j*, where *i = p, s; j = p, s; i≠j,* are represent by eqs. 10 and 11, but considering the conductance and susceptance matrices of eq. 12. It is important to highlight that, the decision variables associated with transformers correspond to the nodal voltages in its terminals $\left[V_p^{t_z}, V_s^{t_z}, \theta_p^{t_z}, \theta_s^{t_z}\right] \in \boldsymbol{y}_{RD}$. ($\forall t_z \in T$).

3.4. Batteries

The batteries are elements that can operate in charge or discharge mode to provide or consume a net amount of active power in their connection node. Then, the *j-th* battery is represented by two sources of active power, as shown in Fig. 3 [Gill, 2014]. One of them represents the charge power $P_{Bc\,j}^{t_z} \leq 0$ and the other the discharge power $P_{Bd\,j}^{t_z} \geq 0$, the sum of both powers represents the net power $P_{Bn\,j}^{t_z}$ provided or consumed by the battery in their connection node.

$$P_{Bn\,j}^{t_z} = P_{Bc\,j}^{t_z} + P_{Bd\,j}^{t_z};\ 0 \leq P_{Bd\,j}^{t_z};\ P_{Bc\,j}^{t_z} \leq 0;\ \forall t_z \in T \qquad \text{(eq. 13)}$$

In addition, the voltage phasor in the connection node is represented by its magnitude $V_j^{t_z}$ and its angle $\theta_j^{t_z}$. Thus, the decision variables of the *j-th* battery are $\left[P_{Bd\,j}^{t_z}, P_{Bc\,j}^{t_z}\right] \in \boldsymbol{y}_B$ ($\forall t_z \in T$), while $[V_j^{t_z}, \theta_j^{t_z}] \in \boldsymbol{y}_{RD}$ ($\forall t_z \in T$). Moreover, the State Of Charge of the *j-th* battery (SOC) in the time t_z ($SOC_{B\,j}^{t_z}$) can be approximated by means of eq. 14.

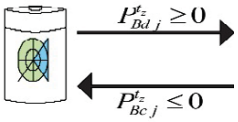

Fig 3. Battery model

$$SOC_{B\,j}^{t_z} = SOC_{B\,j}^{t_0} - \frac{\varepsilon_{c\,j}\Delta t}{E_{Bnom\ j}} \sum_{t=1}^{t_z} P_{Bc\,j}^{t} - \frac{\Delta t}{E_{Bnom\ j}\,\varepsilon_{d\,j}} \sum_{t=1}^{t_z} P_{Bd\,j}^{t} \qquad \text{(eq. 14)}$$

It is assumed that the energy provided by the batteries has not cost, since it is absorbed and provided in the same node of connection. However, since the optimization algorithm will manage the power, batteries will be charged in periods of low-cost energy and it will be discharged in periods of high cost. This fact involves an economic benefit in the operation of the microgrid.

3.5. Wind turbine

For the aim of the stationary analysis, the wind turbine can be considered like a source of non controlled

active power $P_{Aj}^{t_z}$, depending on its density δ_w, wind speed $S_w^{t_z}$, as well as of the area A_w covered by the blades of the wind turbine [Wang, 2009]

$$P_{Aj}^{t_z} = \delta_w A_w \left(S_w^{t_z}\right)^3 \Big/ 2, \forall t_z \in T \qquad \text{(eq. 15)}$$

Since it is considered that the power delivered by the wind turbine is not controllable; this element does not introduce decision variables. However, eq. 16 is required to assess the contribution of the power *j-th* of the wind turbine for a wind speed curve, $S_w^{t_z}\ \forall\ t_z \in T$, density, δ_w, and area, A_w, given. Clearly, the magnitude $V_j^{t_z}$ and angle $\theta_j^{t_z}$ of the voltage phasor of the connection node are considered as decision variables, such that $[V_j^{t_z}, \theta_j^{t_z}] \in \boldsymbol{y}_{RD}$ ($\forall t_z \in T$). Finally, it is assumed that the energy provided by the wind turbine has no cost. In addition, it is considered available a good forecast for wind speed curves.

3.6. Photovoltaic modules

Figure 4 shows the schematic model of a photovoltaic module connected to the node *k-th* through a converter DC/AC 4 [Bellini, 2009]. The implicit expression eq. 16 models the behavior of the current DC in $I_{CD\,k}^{t_z}$ panel terminals. Where I_{ph}, I_0, $V_{CD\,k}^{t_z}$, R_s, n_s and n_p represent the current of the panel photovoltaic, the current of saturation, the DC voltage in the module terminals, the resistance in series, and the number of cells in series and in parallel, respectively. The term R_s is evaluated from eq. 17, where V_{oc}, V_{mp}, I, I_{mp} represent the open circuit voltage, the voltage of the point of maximum power, short circuit electricity and maximum power point electricity, respectively. Terms I_{sc} and V_{oc} are evaluated through eq. 18 and eq. 19, respectively. Where $I_{sc,\,stc}$, G, G_{stc}, k_i, T, T_{stc}, $V_{oc,\,stc}$, and k_v represent the short circuit electricity standard under conditions of test, irradiance under test, electricity temperature coefficient, temperature of the panel, standard temperature under test, standard low open circuit voltage conditions test and voltage and temperature coefficient, respectively.

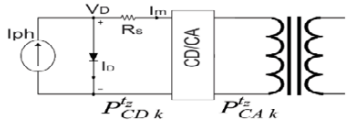

Fig. 4 Schematic model of a photovoltaic module

$$I_{CDk}^{t_z} = \left[I_{ph} - I_0 \left(\exp\left(\frac{\frac{V_{CD\,k}^{t_z}}{n_s} + \frac{I_{CDk}^{t_z}}{n_p} R_s}{V_{CD}^{t_z}} \right) - 1 \right) \right] n_p; \forall t_z \in T \qquad \text{(eq. 16)}$$

$$R_s = \frac{\frac{V_{oc} - V_{mp}}{n_s} + V_{CD}^{t_z} \ln\left(\frac{I_{sc} - I_{mp}}{I_{sc}}\right)}{\frac{I_{mp}}{n_p}} \qquad \text{(eq. 17)}$$

$$I_{sc}(T,G) = I_{sc,stc} - \frac{G}{G_{stc}}\left[1 + \frac{k_i}{100}(T - T_{stc})\right] \qquad \text{(eq. 18)}$$

$$V_{oc}(T) = V_{oc,stc}\left[1 + \frac{k_v}{100}(T - T_{stc})\right] \qquad \text{(eq. 19)}$$

In this work, the photovoltaic module parameters involved in eqs.16-19 were taken from the features of the polycrystalline module Solartec S60PC-250 [Bellini, 2009]. Moreover, a good forecast of solar irradiance curves is considered available.

According to the model of the Fig. 4, the injected power in DC terminals (generated by module) can be expressed directly as:

$$P_{CD\,k}^{t_z}\left(V_{CD\,k}^{t_z},\, I_{CD\,k}^{t_z}\right) = I_{CD\,k}^{t_z} V_{CD\,k}^{t_z};\ \forall t_z \in T \qquad \text{(eq. 20)}$$

Moreover, the balance of power between the terminals of AC and DC of the inverter must also be fulfilled. If the losses of the converter are rejected:

$$P_{CA\,k}^{t_z}\left(V_k^{t_z}, V_m^{t_z}, \theta_k^{t_z}, \theta_m^{t_z}\right) = P_{CD\,k}^{t_z}\left(V_{CD\,k}^{t_z}, I_{CD\,k}^{t_z}\right);\ \forall t_z \in T \qquad \text{(eq. 21)}$$

where $P_{CA\,k}^{t_z}$ is the active power injected at the terminals of the primary transformer coupling module. $V_k^{t_z}$ and $\theta_k^{t_z}$ are the magnitude and the angle, respectively, of the voltage phasor for such terminals. $V_m^{t_z}$ and $\theta_m^{t_z}$ represent the same but for the secondary terminals. Therefore, $P_{CA\,k}^{t_z}$ in eq. 21 is formulated explicitly by means of eq. 11, but considering the matrix of conductances and susceptances of eq. 13. It is important to mention that, due to it is considered a DC/AC converter multipulse with 48 pulses, the following relationship must also keep [Zúñiga, 2006]:

$$V_{CD\,k}^{t_z} = \frac{\pi}{16} V_k^{t_z};\ \forall t_z \in T \qquad \text{(eq. 22)}$$

It is important to highlight that, the decision variables introduced by the photovoltaic module are $\left[V_{CD\,k}^{t_z} I_{CD\,k}^{t_z}\right] \in \boldsymbol{y}_{MF}$ ($\forall t_z \in T$), whereas $[V_k^{t_z}, V_m^{t_z}, \theta_k^{t_z}, \theta_m^{t_z}] \in \boldsymbol{y}_{RD}$ ($\forall t_z \in T$).

3.7. Electrical load

Energy consumption in load nodes of the microgrid is represented by a model of constant power for any interval of time T. The power *i-th* $\boldsymbol{S}_{li}^{t_z}$ complex consumed in the node is then represented by eq. 23. Where $P_{li}^{t_z}$ and $Q_{li}^{t_z}$ represent the power consumption active on that node at the instant t_z, respectively.

$$\boldsymbol{S}_{li}^{t_z} = P_{li}^{t_z} + jQ_{li}^{t_z}\ \ \forall t_z \in T \qquad \text{(eq. 23)}$$

Model of energy demand does not introduce decision variables to the optimization problem, but the magnitude $V_i^{t_z}$ and angle $\theta_i^{t_z}$ of the connection node phasor voltage must be considered as decision variables, such as $[V_i^{t_z}, \theta_i^{t_z}] \in \boldsymbol{y}_{RD}$ ($\forall t_z \in T$). In addition, it is considered that a good forecast of the energy demand curves is available ($\boldsymbol{S}_{li}^{t_z} \forall i, t_z \in T$).

4. Explicit model of OPF

Models of the microgrid components described in Section 3 are considered in this section to formulate explicit model of OPF for non-autonomous microgrid. For this purpose, is considered one generic microgrid composed of a number of N_{bAC} nodes in AC, N_{bCD} nodes in DC, N_{Al} feeders, N_T transformers, N_B battery, N_A wind turbines, N_{MF} photovoltaic modules and N_{CE} electrical loads. Noted that, the N_{pac} points of common coupling are a subset of the N_{bAC} nodes in AC. In addition, the nodes in DC represent DC terminals of the photovoltaic modules, such N_{bCD}=N_{MF}.

4.1. Objective function

The intention is to minimize eq. 1, which is formulated explicitly taking into account eq. 6, as follows:

$$F_T = \sum_{t_z=1}^{t_{end}} \sum_{j=1}^{N_{pac}} a_j + b_j\ (P_{RP\,j}^{t_z}) + c_j\ (P_{RP\,j}^{t_z})^2 \qquad \text{(eq. 24)}$$

Note that eq. 24 denotes that the objective is to minimize the cost of the total energy imported through the PCC during the period of time T to supply the demand curves predicted $\boldsymbol{S}_{li}^{t_z} \forall i, t_z \in T$.

4.2. Equality constraints

The set of equality constraints **h(y)** in eq. 2 is expressed explicitly as follows. The constraints of power active, $\Delta P_{RDi}^{t_z}$, and reactive, $\Delta Q_{RDi}^{t_z}$, balance corresponding to the nodes of the microgrid in AC are written in the first block of eq. 25.

$$\boldsymbol{h}^{t_z}(\boldsymbol{y}^{t_z})=\left\{\begin{array}{c}\left.\begin{array}{c}\Delta P^{t_z}_{RD\,i}=P^{t_z}_{RP\,i}+\sum\limits_{\forall j\in i}P^{t_z}_{Bc\,j}+\sum\limits_{\forall j\in i}P^{t_z}_{Bd\,j}+\sum\limits_{\forall j\in i}P^{t_z}_{A\,j}+\\ \sum\limits_{\forall j\in i}P^{t_z}_{CD\,j}-\sum\limits_{\forall j\in i}P^{t_z}_{lj}-\sum\limits_{\forall j\in i\,|\,j\in N_{AI},N_T}P^{t_z}_{inj\,j}(\boldsymbol{V},\boldsymbol{\theta})=0,\\ \Delta Q^{t_z}_{RD\,k}=-\sum\limits_{\forall j\in k}Q^{t_z}_{lj}-\sum\limits_{\forall j\in k}Q^{t_z}_{inj\,j}(\boldsymbol{V},\boldsymbol{\theta})=0\\ i=1,2,\ldots,N_{bAC}\;;\;k=1,2,\ldots,N_{bAC}\,|\,\forall k\notin N_{GEN}\end{array}\right\}\\ \left.\begin{array}{c}\Delta I^{t_z}_{CD\,k}=I^{t_z}_{CD\,k}-f_{CD}(V^{t_z}_{CD\,k},I^{t_z}_{CD\,k})=0,\\ \Delta P^{t_z}_{CD\,k}=P^{t_z}_{CAk}(\boldsymbol{V},\boldsymbol{\theta})-P^{t_z}_{CD\,k}(V^{t_z}_{CD\,k},I^{t_z}_{CD\,k})=0,\\ \Delta V^{t_z}_{CD\,k}=V^{t_z}_{CD\,k}-(\pi/16)V^{t_z}_{k}=0\\ k=N_{bAC}+1,\ldots,N_{bAC}+N_{bCD}\end{array}\right\}\forall t_z\in T\end{array}\right. \qquad \text{(eq. 25)}$$

4.3. Inequality constraints functions

According to the elements models introduced in Section 3, the only inequality constraints function $\boldsymbol{g}(\boldsymbol{y})$ in eq. 3 corresponds to the batteries, as follows. The batteries have finite capacity of charge and discharge. With this point in mind, the SOC is modulated over the period of time T through eq. 26 [Gill, 2014].

$$\boldsymbol{h}^{t_z}(\boldsymbol{y}^{t_z})=\left\{SOC^{\min}_{B\,j}\le SOC^{t_z}_{B\,j}\le SOC^{\max}_{B\,j}\right\}\forall j\in N_B;\forall t_z\in T \qquad \text{(eq. 26)}$$

4.4. Equality constraints variables

Should be taken into account that, the decision variables must acquire admissible values, otherwise, the solution provided by the OPF model could not make sense from a practical point of view. For this reason, the decision variables $\boldsymbol{y}$ are limited during the interval of time T by means of the constraints set in eq. 27.

$$\left\{\begin{array}{c}\underline{\boldsymbol{y}}_{RD}\le\boldsymbol{y}^{t_z}_{RD}\le\overline{\boldsymbol{y}}_{RD}\\ \underline{\boldsymbol{y}}_{MF}\le\boldsymbol{y}^{t_z}_{MF}\le\overline{\boldsymbol{y}}_{MF}\\ \underline{\boldsymbol{y}}_{B}\le\boldsymbol{y}^{t_z}_{B}\le\overline{\boldsymbol{y}}_{B}\end{array}\right\}\forall t_z\in T \qquad \text{(eq. 27)}$$

5. Solution of the OPF model

The OPF model eqs. 24-27 corresponds to a non-linear optimization model with constraints, which could be not continuous or differentiable. For this reason, is solved by means of three different optimization methods provided by MATLAB® optimization toolbox. The methods are: i) interior point method, ii) genetic algorithm and, iii) direct search method. For this purpose, the objective function, eq. 24, and the constrains, eqs. 25-27, are written in two separate functions, which are provided as input arguments to the above-mentioned functions. For the interested reader a detailed description of the use of these tools can be found in [MathWorks et al 2002, MathWorks et al 2013].

5.1. Interior Point Method

The interior point method is applied through the *fmincon* function which belongs to the MATLAB® 'Optimization Toolbox' [MathWorks, 2002]. It is considered as a tool for local search with constraints for non-linear multivariable functions. Therefore, it fits well for the OPF problem in microgrids.

5.2. Direct Search Method

The direct search method is applied through the function *patternsearch* which belongs to the MATLAB® 'Direct Search and Genetic Algorithm Toolbox' [MathWorks, 2013] and, like *fmincon*, can be classified as a tool for local search with non-linear constraints for multivariate functions such as the OPF problem in microgrids.

5.3. Genetic Algorithm Method

The genetic algorithm method is applied through of the *ga* function which belongs to the MATLAB® 'Direct Search and Genetic Algorithm Toolbox' and is especially thought for the optimization of global non-linear problems with or without constraints. Also, provides a great flexibility since contains multiple parameters of configuration.

6. Results

In this section, the analysis of optimal power flows for the microgrid showed in Fig. 5 is presented with the aim of showing and comparing the different optimization methods used in this work. The microgrid is connected to the main grid through the only PCC (node 1). Note that, the elements of the network between pair of nodes 1-2, 3-6, 4-7 and 5-8 are transformers. The other elements are feeders. The parameters of the network distribution models, photovoltaic module, wind turbine components, as well as the cost coefficients of associated at the energy import are presented in the Appendix. For the case of study has been considered the unit variables in per unit (pu), for which it took a base power and voltage of 100 VA and 100 V, respectively.

For the analysis, the forecasted curves of active power demand, wind speed and solar irradiation from the city of Salamanca (Mexico) are considered. These signals are displayed in Fig. 6a, 6b and 6c, respectively, and were provided by the Center for Atmospheric Sciences of the University of Guanajuato. The limits of the magnitudes for the AC voltage for all nodes in the microgrid are 0.95≤V≤1.05 pu. The limits of batteries SOC are 0.2 ≤SOC (t_z) ≤0.95 (in %) while the initial SOC is $SOC(t_0)$ = 0.2 (in %). The results, which have been obtained with a PC DELL with 8 GB of RAM and an Intel processor i5 - 3230 M CPU @ 2.40 GHz, from the solution of the OPF model are shown and discussed below.

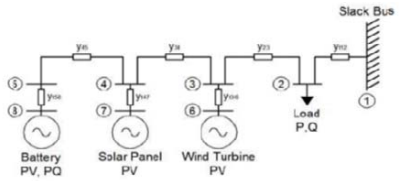

Fig. 5 Microgrid scheme

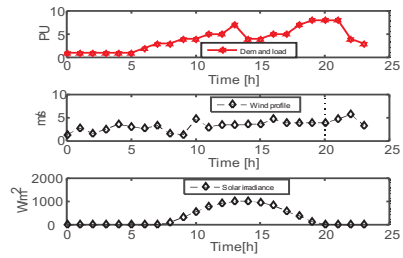

Fig. 6 Forecasted signals: a) active power demand, b) wind speed, c) solar irradiance

Figure 7a shows the active power provided by the battery, wind turbine, module PV and the imported one from the main grid. There is a greater percentage of the demand curve, see Fig. 6a, which is supplied from the main grid. It is important to highlight that, the panel photovoltaic has a relevant role in the contribution of energy between the 10:00 and 18:00 hours, which coincides with the period of high irradiation, see Fig. 6c. It is clear that the power provided by the wind turbine has a similar shape than the wind speed shown in Fig. 6b. The battery experiences periods of charge ($P_{Bnj}^{t_z} < 0$) and discharge ($P_{Bnj}^{t_z} > 0$). In particular, it is possible to see that in periods with high wind power generation (e.g. at hours 4 and 10) the battery is charged ($P_{Bnj}^{t_z} < 0$). This power is useful to reduce the energy cost in hours of peak demand (e.g. at hours 13 and 20). This fact fits with the battery SOC shown in Fig. 7b

Figure 7c shows the cost in $/h of the total energy imported from the main grid. It is clear that the cost varies depending on the imported power from main grid and has its highest value around the 20 hour, which is

where the high peak demand happens. Moreover, in the same figure it is possible to compare the energy cost if there would be no renewable power sources, clearly, without renewable sources the energy cost increases.

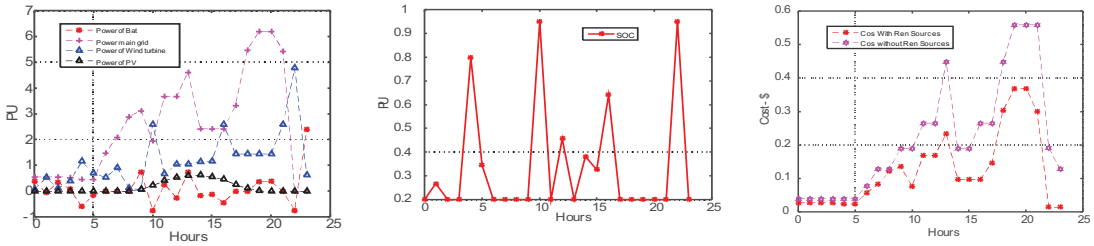

Fig. 7 Case study solved with the interior point method a) generated power b) battery SOC c) cost of the energy from the main grid

These results were obtained by means of the interior point method. In this work, the solution of this problem will be analyzed with the three different optimization methods explained in the section below.

6.1 Results of the different methods of optimization

To carry out this study, tests have been done taking into account the following points:

- It has been repeated several times the execution of each configuration and have taken into account all the results through the arithmetic mean and the standard deviation.
- It has been evaluated the most important parameters and those ones that fit better to this problem, maintaining fixed the rest.
- For each tool, it has been selected for this study those parameters that are relevant to the problem, setting the rest to their values by default.

6.1.1 Interior Point Method (fmincon)

Because this is a deterministic method for a given problem, its performance depends mainly of the initial condition. However, the initial condition for the OPF problem for the tertiary control of microgrids is completely defined, so arbitrary modification makes no practical sense. However, it is possible determine the CPU time required for the complete execution of the OPF analysis and the value of the objective function ("fitness") associated. The last results will serve as reference like comparison with them associated to them methods meta-heuristics. In this case, the convergence, the solution provided by the interior point method is associated to a fitness of $3 units currency, while the time of computation is of approximately 3630 s.

6.1.2. Direct Search (patternsearch)

As can observe in Figs. 8a and 8b for the parameter *Pollingorder* of the function *patternsearch*, the option *Consecutive* is the one that obtains best results in the fitness value. But, in cost time terms, the option that is the fastest is *Random*. On the other hand, Figs 9a and 9b show the effect of the parameter *Pollmethod*. In this case the option that gives best results for both, as in fitness values as at runtime, is *MADSPositiveBasisNp1* that is the option will be used during the optimization.

Fig. 8 Effect of *PollinfOrder* parameter: a) value of the fitness function b) time spent

Fig. 9 Effect of *PollMethod* parameter: a) value of the fitness function b) time spent

6.1.3. Genetic Algorithm (GA)

As is shown in Fig. 10a and 10b, in general to increase the population size gets a better result in the fitness value but, at the same time, it implies a higher computational time. Therefore, searching a tradeoff between fitness value and computational cost, the population size has been set to 25. Figure 11a and 11b show the evaluation of the parameter *selectionFCN* where is possible to see that for both, the fitness value and the computational cost, the best option is *selectiontournament*. Finally, in Figures 12a and 12b evaluate the parameter *crossoverFCN* where it is shown that the best result for the fitness value is the option *crossoverscartered* whereas the option *crossoverheuristic* is the best one in computational cost terms. Since in this work the execution time of the algorithm is a priority the last option, *crossoverheuristic*, will be selected.

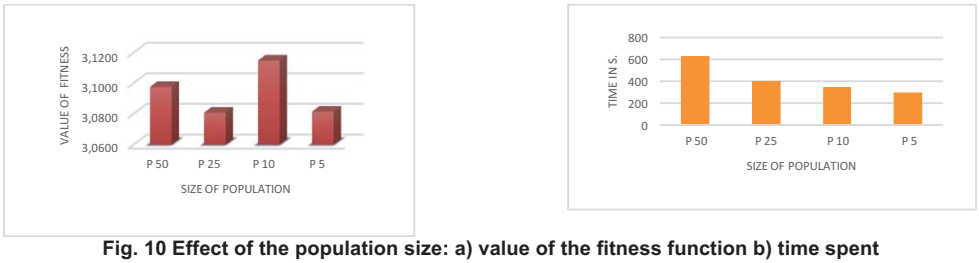

Fig. 10 Effect of the population size: a) value of the fitness function b) time spent

Fig. 11 Effect of *selectionFCN* parameter: a) value of the fitness function b) time spent

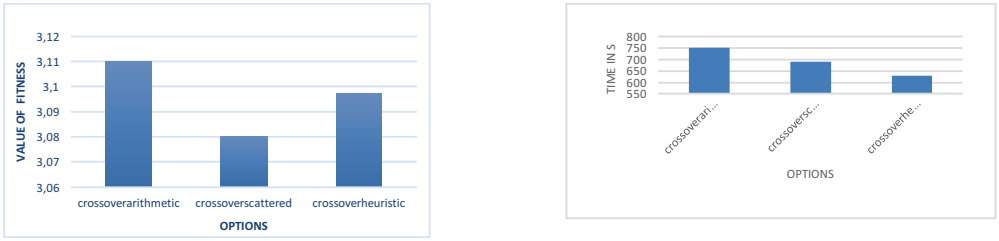

Fig. 12 Effect of *crossoverFCN* parameter: a) value of the fitness function b) time spent

6.1.4. Comparison of results between the different methods

As is possible to see in Fig. 14 the method that achieves the best result in the fitness value is the interior point through the *fmincon* function. In computational time terms the genetic algorithm method is the one that obtains a smaller computational cost. Finally, the direct search method through the *patternsearch* function is the one that gets a worst value for the fitness value and intermediate results in computational cost. Therefore, three different methods have been tested and can be used to solve the optimization problem of OPF in micro-grids each one with its advantages and disadvantages. It is important to note that, the interior point method is the one that best result obtains in the fitness function and its value will be used for continuous functions, but also, the genetic algorithm can solve not continuous fitness functions which is important since can evaluate cost functions which different behaviors between day and night.

Fig. 14 Comparison of the different optimization methods: a) value of the fitness function b) time spent

Figure 15 shows the results of the optimization of the microgrid presented in Fig. 5 with the three methods, Fig. 15a depicts the power of the main grid whereas Fig. 15b the costs of the imported power compared to the cost of the total energy load. It is important to highlight that, the solutions given for the three methods varying only in a percentage of 2% for the genetic algorithm and a percentage of 4% for the direct search method with respect to the interior point one.

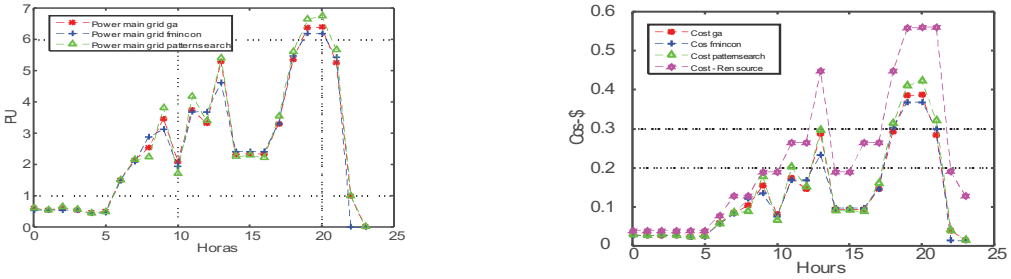

Fig. 15 Results obtained with the three optimization methods: a) Comparison of power main grid b) Comparison of cost of the imported power compared to the cost of the total energy load

7. Conclusions

In this work a model for the analysis of OPF microgrids is presented. The model allows us to manage the energy storage elements to improve the economic operation of the microgrid. Likewise, through it is possible to determine the optimal amount of power imported from the main grid. The model considers basic models of the elements of the distribution system, photovoltaic panels, wind turbines, as well as batteries for energy storage. The model is solved by three different optimization methods: i) interior point, ii) genetic algorithm and, iii) direct search. The presented numerical results illustrate the potential analysis of OPF to determine values that could be used as a reference by the secondary controller of a microgrid. In addition, the validation of the optimization methods has been performed through the evaluation of a case study which has been efficiently solved.

8. Acknowledgments

This work has been possible thanks to the collaboration of CONACYT in conjunction with the University of Guanajuato Mexico and the CIESOL center of the University of Almeria Spain. Luis O. Polaco Vásquez, Cristian A. Carreño Meneses, Alejandro Pizano Martínez are fellows of Universidad de Guanajuato and CONACYT. This work has been funded by grants from the Spanish Ministry of Economy and Competitiveness (TIN2015-66680-C2-1-R and ENERPRO DPI 2014-56364-C2-1-R), Junta de Andalucía (P11-TIC7176 and P12-TIC301). Juana López Redondo and José Domingo Álvarez Hervás are fellows of the Spanish ‘Ramón y Cajal’ contract program, co-financed by the European Social Fund.

9. References

Acha, E., Fuerte C. R., Ambriz H., Camacho C., 2004 "FACTS Modelling and Simulation in Power Network", 1nd ed., England: John Wiley & Sons LTD, 117-125.

Acosta R., Potencial eólico en México. Comisión Federal de Electricidad, México, [Online]. Available in: http://www.conae.gob.mx/work/sites/CONAE/

Bellini, A., Bifaretti, S., Iacovone, V., Cornaro, C., September 2009., "Simplified model of a photovoltaic module," in Applied Electronics, 2009. AE 2009, 1(47-51), 9-10.

Bidram, A., Davoudi, A., December 2012, "Hierarchical Structure of Microgrids Control System," in Smart Grid, IEEE Transactions on, 3(4), 1963-1976.

Bose, B.K., March 2010, "Global Warming: Energy, Environmental Pollution, and the Impact of Power Electronics," in Industrial Electronics Magazine, IEEE , 4(1), 6-17.

Doniz-Gonzales V.V, Montaño-Fernández, C., Espinosa-Bustamante E., September 2006, Prospectiva del Sector Eléctrico 2005–2014, Dirección General de Planificación Energética, México, [Online]. Available in: http://www.sener.gob.mx/webSener /Electrico_2005_2014.pdf

Gill, S., Kockar, I., Ault, G.W., January 2014, "Dynamic Optimal Power Flow for Active Distribution Networks," in Power Systems, IEEE Transactions on, 29(1), 121-131.

Katiraei, F., Iravani, R., Hatziargyriou, N., Dimeas, A., May-June 2008, "Microgrids management," in Power and Energy Magazine, IEEE, 6(3), 54-65.

Larsen, P., Energy Policy Toolkit on System Integration of Wind Power Experiences from Denmark. Low Carbon Transition Unit, Denmark, [Online]. Available in: http://www.ens.dk/.

Levron, Y., Guerrero, J.M., Beck, Y., August 2013, "Optimal Power Flow in Microgrids with Energy Storage," in Power Systems, IEEE Transactions on, 28(3), 3226-3234.

Olivares, D.E., Cañizares, C.A., Kazerani, M., July 2014, "A Centralized Energy Management System for Isolated Microgrids," in Smart Grid, IEEE Transactions on, 5(4), 1864-1875.

The MathWorks Inc., 2002, "Matlab Optimization Toolbox", Users Guide Version 2, [Online], Available in: http://www.mathworks.com.

The MathWorks Inc., 2013, "Genetic Algorithm and Direct Search Toolbox™ 2", Users Guide Version 2, [Online], Available in: http://cda.psych.uiuc.edu/matlab_pdf/gads_tb.pdf

Wang L., Yeh T., Lee W., Zhe C., May 2009., "Benefit Evaluation of Wind Turbine Generators in Wind Farms Using Capacity-Factor Analysis and Economic-Cost Methods," in Power Systems, IEEE Transactions on, 24(2), 692-704.

Zúñiga Haro P., 2006. "Analysis and control of a series compensator", Ph.D. dissertation, Dept. Electrical Power Systems, CINVESTAV Gdl., Guadalajara, México, [Online]. Available in: http://orion.gdl.cinvestav.mx/~jramirez/Tesis_pavel2006.pdf

Appendix

This appendix shows the parameters of the microgrid components which are the following:

Table A. 1. Number of nodes and the microgrid components

Node	Lines	Battery	Loads	WT	Panel S.V.	Node slack grid
8	6	1	1	1	1	1

Performance data of the microgrid components

$$P_{eolico} = 400\ w\ , -100 < Q_{eolico} > 150VA$$

$$P_{bateria} = 300\ w$$

$$P_{red} = 800\ , -100 < Q_{red} > 150VA$$

$$P_{panel\ solar} = 75\ w$$

Grid cost coefficients

$$a = 0.014, b = 0.020, c = 0.0060$$

Voltage general bounds

$$Min = 0.95\ pu, \qquad Max = 1.05\ pu$$

Table A. 2. feeders

Node sent	Node receiving		R (P.U.)	T (P.U.)	BC (P.U.)
3	2		0.00029	0.00086	0
4	3		0.00029	0.00086	0
5	4		0.00029	0.00086	0
1	2		0.00029	0.00086	0
6	3		0.00029	0.00086	0
5	8		0.00029	0.00086	0

ENERGY EFFICIENCY AND PERFORMANCE EVALUATION OF HYBRID PHOTOVOLTAIC SYSTEM FOR FAN-PAD OF GREENHOUSES

Eduardo Ríos U.[1], Eugenio Romantchick K.[1], Felipe Sánchez C.[1], José Reyes S.[1], Elisa Sánchez C.[2]

[1] Autonomous University of Chapingo, State of Mexico (Mexico).

[2] Metropolitan Autonomous University, Mexico City (Mexico).

Abstract

This research is oriented towards improving energy efficiency in the cooling of greenhouses equipped with pad fan system. Once the least amount of energy was achieved, it was installed and evaluated the performance of a hybrid photovoltaic system inexpensive. Two of the most important branches of research related to agricultural greenhouses were unified to achieve the objective, namely, 1) the mathematical modeling of greenhouse climate and 2) experiments of solar energy for greenhouses. The results of the mathematical model allowed selecting the adequate ventilation rate and avoiding unnecessary consumption of electrical energy in the exhaust fans. After determining the optimal ventilation rate, it was calculated the energy required by fans depending on the hours of operation. A hybrid photovoltaic system with backup was evaluated with a solar resource of 5.5 kWh per day (Central region of Mexico). The main objective of the hybrid system is not to provide all the energy required for extraction fans, but reduce the power consumption from the local grid. The reduction of energy consumption was 32% and the total cost of hybrid system was USD $3,400.00.

Keywords: *agricultural greenhouse, photovoltaics, mathematical modeling, saved energy*

1. Introduction

In general, mathematical models applied to agricultural greenhouses have two main objectives: 1) to get knowledge about greenhouses systems, without the need to reproduce expensive experiments, 2) to optimize the greenhouses processes of operation and management. In literature, mathematical models predict variables such as natural ventilation rate, temperature, relative humidity, carbon dioxide concentration, growth of crops, among others (Tiwari, 2003). However, their practical application to solving real specific problems of agricultural engineering is limited by their low reliability. On the other hand, photovoltaic systems are a source of electrical power also with low reliability, mainly because generated energy is variable along the day and year (Duffie, 1993). The above objections foster distrust the implementation of photovoltaic systems in greenhouses. The objective of this work is to solve these problems in order to reduce the electric power consumed by the cooling system of a greenhouse. First, a mathematical model is used to predict the energy required by the cooling system and its reliability is increased by validating with experimental data. After, the performance of a hybrid photovoltaic system that supplies electric energy for fans from solar panels and local grid was evaluated.

Greenhouses without cooling systems often have 11 °C higher indoor temperatures than the surrounding environment. The detrimental effects of high temperatures on crops are characterized by loss of strength in the stem, reduced flower size, delay flowering, among other (ASABE, 1995). The pad fan system can lower the temperature of incoming air by about 80 percent of the difference between the dry and wet bulb temperatures, by example, air at a dry bulb temperature of 32 °C and relative humidity of 20%, the wet bulb temperature would be of 17 °C and the pad fan system could lower temperature to approximately 20 °C. To generate the cooling effect, it is required a ventilation rate created by exhaust fans located on the opposite side wall of the evaporative pad. There are different technical methods based on experience for calculating this ventilation rate, for example, the National Greenhouse Manufacturers Association (NGMA) indicates in its 1993 standards for cooling greenhouses that a rate of removal of 13.6 m^3 per hour per m^2 is sufficient. Nelson (1998) suggests a method of applying correction factors to the previous value considering, elevation

doi:10.18086/eurosun.2016.08.16 Available at http://proceedings.ises.org

above sea level of greenhouse, light intensity and distance between fans and evaporative pad. Likewise, several authors have shown that steady-state mathematical models describe with high level of accuracy the thermal behavior of a greenhouse with pad fan system (Jain et al (2002), Ganguly, Kittas (2001)). In the field of energy efficiency applied to pad fan systems, Franco and Valera (2014) used a steady state model to describe the operation parameters of three different materials for evaporative pads. Since that results they concluded that evaporative cooling boxes are better option than cellulose pads for cooling non-hermetic greenhouses such as those most frequently used in the Mediterranean basin. The use of steady-state models has yielded practical results for the improvement of operation of greenhouses.

In reference to the use of photovoltaic systems in greenhouses, Al-Helal (2004) realized a study of pad-fan performance for a photovoltaic application and his results showed that electricity consumption increased non-linearly as the ambient temperature increased, only through experimentation and without modeling. Ahmed (2011) evaluated a standalone photovoltaic system for cooling a greenhouse, he proposed the design of isolated photovoltaic system to supply power to the fans of greenhouses in remote areas, however, the system is expensive and its main objective is to provide all energy, since it is off-grid and electrical loads are inductive decreases the reliability of the battery bank, jeopardizing the control of the depth of discharge and decreasing the life of the same. There are several studies related to photovoltaic for cooling greenhouses, Al-Shamiry et al (2007), Carlini et al (2012), Ganguly et al (2010), Al- Ibrahim et al (2006), however, none of them involves mathematical modeling to calculate electrical energy consumed by the fans, i.e. that the dimensioning of the photovoltaic system is not a function of the greenhouse temperature or ventilation rate.

2. Materials and methods

2.1 Instrumentation for greenhouse climate study.

The experiment was conducted in an experimental even-span greenhouse equipped with a pad-fan system (height: 5 m, length: 30 m and width: 11 m) of the Center for Plant Breeding Research of Autonomous University of Chapingo, located in Texcoco, Mexico (19.30 °N, 98.53 °W). The greenhouse is equipped with two fans located on the opposite side to the pad and their function is exhaust air, sucking there through pad. The rated power of each electric fan motor is 1.125 kW, and the electric motor of the water pump is 0.375 kW, all them work at 220 V. Greenhouse instrumentation was performed to measure air temperatures inside the greenhouse on a typical day at high temperatures (01/03/2015). Campbell Scientific datalogger (CR1000) was used. Variables recorded were: air temperatures (seven sensors, model108, Camp. Sc.) (before and after the pad and along the greenhouse), relative humidity (four sensors, model HMP50, Camp. Sc.). For measurements of solar radiation a sensor CMP3 (Camp. Sc.) was used.

2.2 Thermal modelling for energy demand.

In order to predict the thermal behavior inside agricultural greenhouses when ventilation rate varies, different mathematical models have been studied. Jain and Tiwari (2002) developed a detailed model in order to predict the temperatures inside the greenhouse divided in two zones (Eqs. 1-2), where $T_{r,i}$: temperatures of zones, I_i: solar radiation on various walls and roof (W/m^2), V_1: volume of greenhouse under zone-I (m^3), $\boldsymbol{H_{z2}}$: height of walls in zone II, $\boldsymbol{A_{nw1}}$: area in north wall (m^2), $\boldsymbol{U_i}$: overall heat transfer coefficient from cover zone-II to ambient air, A_i: area of walls and roofs of greenhouse (m^2) , $\boldsymbol{T_a}$: ambient temperature (°C), $\boldsymbol{h_{r1r2}}$: convective heat transfer coefficient of air from zone-I to zone-II (W/m^2°C), $\boldsymbol{A_g}$: area of floor under greenhouse (m^2) , $\boldsymbol{T_{r2}}$: room air temperature in zone-II (°C) , L: length of greenhouse (m) , a: constant value , $T_{r2,0}$: room air temperature in zone-II at 0 m (°C) . The model can be simplified and applied for the greenhouse of case study of this research which is equipped with pad-fan system (Eq. 3), from an energy balance Kittas (2001) developed the model solution. Ganguly and Ghosh (2006) compared the results of this model with other similars, demonstrating that steady state models described with acceptable accuracy the interior temperatures of greenhouses.

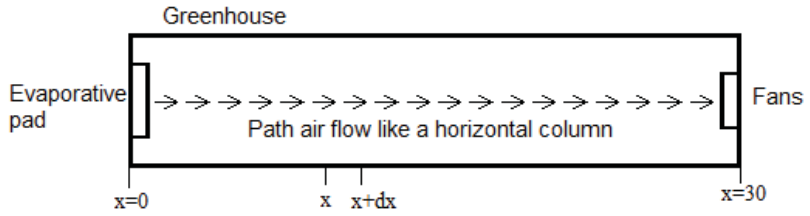

Fig.1. Greenhouse cross section scheme used for mathematical modeling. The main assumption is that air flow moves only in the horizontal direction. No temperature gradients in the vertical direction.

$$\boldsymbol{T_{r,1}} = \frac{I_1 V_1 + I_2 H_{z2} A_{nw1} + (U_{r2a} A_{nw1} + \sum U_i A_i) T_a + h_{r1r2} A_g T_{r,2}}{h_{r1r2} A_g + \sum U_i A_i + U_{r2a} A_{nw1}} \qquad \text{(eq. 1)}$$

$$T_{r,2} = \frac{1}{L}\int_0^L T_{r,2}\,dx = \frac{F(t)}{a}\left[1 - \frac{1 - e^{-aL}}{aL}\right] + T_{r,2,0}\,\frac{1 - e^{-aL}}{aL} \qquad \text{(eq. 2)}$$

Where $F(t) = \frac{T_{r2}}{dx} + aT_{r2}$, and the simplified model applied to this case study is:

$$T_{in}(x) = \left[T_o + \frac{\tau(1-\alpha)R_o w_{gh}}{K_c L_{cov}}\right]\left[1 - e^{-\left(\frac{K_c L_{cov}}{\dot{V}\rho C_p}[x]\right)}\right] + T_{pad}\, e^{-\left(\frac{K_c L_{cov}}{\dot{V}\rho C_p}[x]\right)} \qquad \text{(eq. 3)}$$

In Eq. 3, $T_{in}(x)$ is the interior temperature at x position (Fig. 1), T_o is exterior dry bulb temperature, τ is transmissivity of the plastic cover; α: coefficient representing the fraction of radiation incident on the plant that is directly converted into latent heat by transpiration and losses of radiation through soil, R_o: outside solar radiation in W/m^2, w_{gh}: greenhouse width en m, K_c: coefficient of sensible heat losses through the plastic cover in $W/m^2\,°C$, L_{cov}: length of cover proportional to the width of greenhouse to obtain the differential heat transfer area, $\dot{V}$: ventilation rate generated by fans; C_p: heat capacity of air in $J/kg°C$; ρ is air density, T_{pad} is air temperature when leaves evaporative pad.

This model can describe the temperature of a completely sealed greenhouse without evaporative pad, this is achieved when the ventilation rate, $\dot{V}$, approaches zero, this way the temperature is not a function of x, and there is only one temperature along greenhouse:

$$T_{in} = \left[T_o + \frac{\tau(1-\alpha)R_o w_{gh}}{K_c L_{cov}}\right] \qquad \text{(eq. 4)}$$

The term x represents the length of the greenhouse, that is, the distance between the pad and the fans. This term is limited by the exponential function, so it is expected that the model cannot be applied to great lengths greenhouses because the exponential function generates an asymptote and the value of the temperature would be the same. This asymptote is physically correct. Since for large distances between the evaporative pad and the fans, there would be no cooling effect inside the greenhouse. In general, the model describes physically a greenhouse with or without pad fan system. The main results of interest for research will be the temperature depending on the ventilation rate. That is, it is necessary to know the ventilation rate required to obtain a given temperature of 25 °C, which is most recommended for crops.

2.3 Hybrid photovoltaic system.

The amount of energy obtained from the mathematical model served as the first parameter design of a hybrid system. The hybrid system consists of four PV modules of 200 W each one, one hybrid inverter charger of 3.0 kW and four batteries of 150 Ah each one. The operation mode of Fig. 2 is described below:

t1: To ensure the battery is at full capacity, when the inverter is turned ON, the CPU will execute the bypass

mode automatically connecting the AC main to the load. In the meantime, it will activate both the AC charger and solar charger to simultaneously charge the batteries.

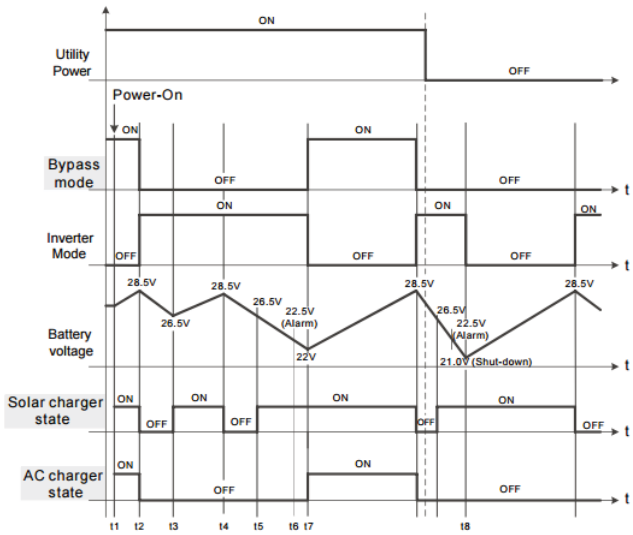

Fig. 2. Diagram of hybrid photovoltaic system mode control logic.

t2: When the batteries are full (battery voltage around 28.5 V), both the AC and solar charger will be turned OFF by the CPU to prevent overcharging and reducing battery lifetime. The CPU will also switch to inverter mode and the AC electricity provided to the loads will be coming from the batteries.

t3: When the batteries are depleted to around 90% of their capacity (battery voltage around 26.5V), CPU will start up the solar charger but not the AC charger to achieve the goal of energy saving.

t4: If the energy provided by the solar panels is larger than the load requirement, voltage of the battery bank will increase gradually until reaching battery voltage around 28.5 V and then the solar charger will shut off to prevent the batteries from overcharging.

t5: When the capacity of batteries goes down to battery voltage around 26.5 V, solar charger will restart and begin charging.

t6: If the energy provided by the solar panels is lower than consumed by the loads, voltage of the battery bank will decrease gradually to battery voltage around 22.5 V. The built-in buzzer will sound to inform the user that battery power is very low.

t7: If the power consumption of the loads does not decrease and the AC main is normal, the CPU will detect this and the unit will be transferred to "bypass mode." The utility will provide electricity to the loads and charge the battery bank at the same time in order to prevent the unit from shutting off. If the solar current is higher than 3 A, the CPU will not activate the AC charger and just let the solar changer charge the batteries to achieve energy saving target.

t8: When there is no AC main, the CPU will shut down the whole system if the external battery bank voltage is less than 21 V in order to prevent over-discharging and reducing its lifetime. After shutdown, the CPU will still provide LED indication so the user knows why the inverter has shut off.

Fig. 3: PV array and hybrid inverter with battery bank.

Fig. 4: View of PV system outside greenhouse.

3. Results and discussion

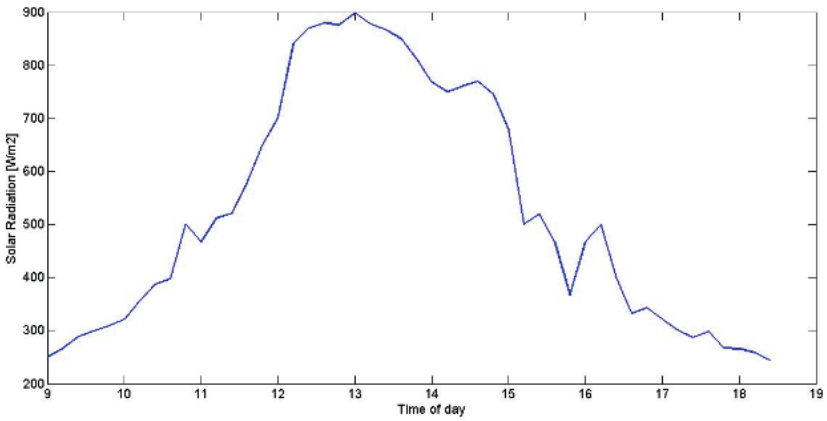

Fig. 5: Variation of exterior solar radiation on experimentation day (03 june 2015)

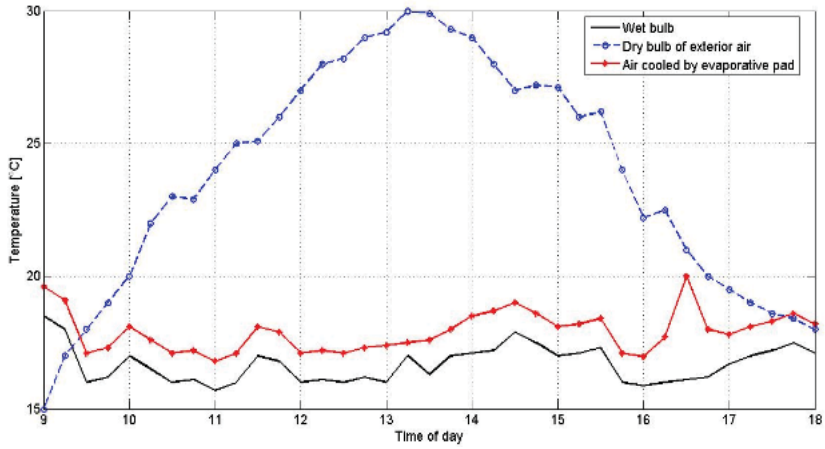

Fig. 6: Operation air temperatures involved in performance of evaporative pad on experimentation day.

The mathematical model does not include factors such as partial cloudy, rain and outside wind speed and these represent sources of random errors that generates uncertainty of non-reproducible measurements. For that reason, it was taken a specific day with the least influence of these factors, environmental conditions and operation temperatures of evaporative pad are shown in Figs. 5 and 6.

MatLab software was used to program solution. Figures 5 and 6 shows that when exterior dry bulb temperature was 30 °C the outside solar radiation achieve 890 W/m^2, and the wet bulb temperature was 17 °C. The average dry bulb air temperature leaving the pad was 18 °C. That means 85% of pad efficiency. This value is less than the common pads and could rise with an increase in ventilation rate, however the temperature of 25 °C is reached successfully with the current rate of ventilation. Here lies the importance of implementing energy efficiency plan to avoid consuming more energy than necessary.

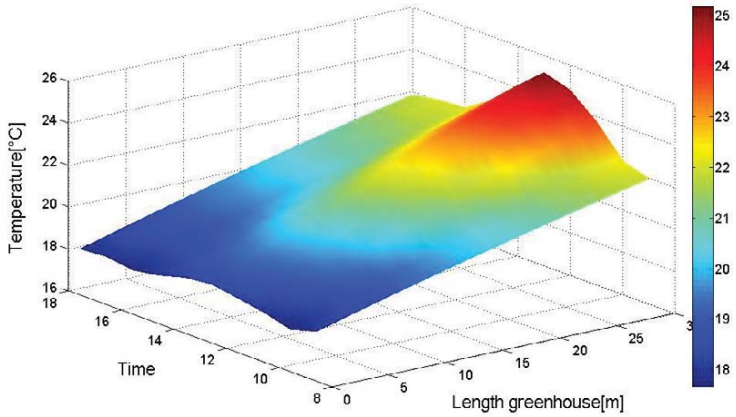

Fig. 7: Spatial temperature distribution inside the greenhouse during experimentation.

With the steady-state model it can obtain a spatial temperature distribution inside the greenhouse along the day when operating the evaporative wall and exhaust fans. To determine the temperature versus time, experimental data of radiation was used in the model along the day while keeping constant the ventilation rate. Fig. 7 shows the spatial temperature distribution inside the experimental greenhouse along the experimentation day. Fig. 8 shows predicted temperature inside greenhouse at x = 30 m, ie maximum temperatures at outlet in fans.

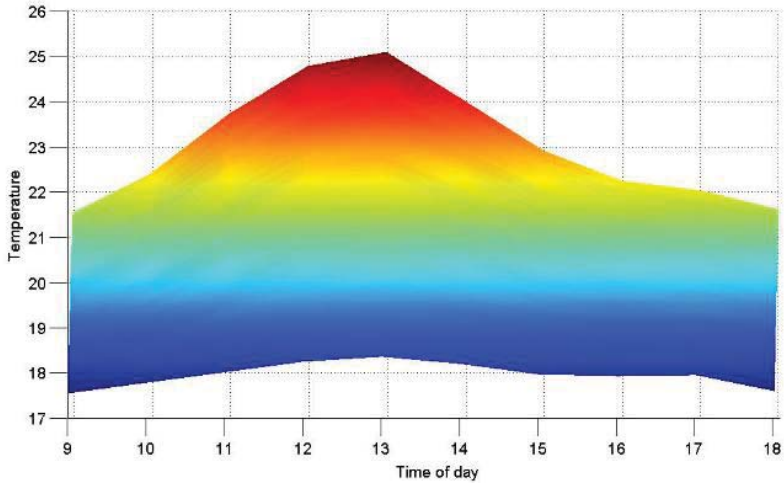

Fig. 8: Predicted temperature inside greenhouse at x= 30 m, ie maximum temperatures at outlet in fans.

To improve the energy efficiency of exhaust fans is necessary to determine the value of adequate ventilation rate, then to know the number of fans and power to meet that ventilation rate. As an example, in Table 1, three models of fans are proposed:

Tab. 1: Characteristics of three models of fans commonly used for pad fan system

Model	Power W	Airflow rate $m^3/h - m^3/s$
1	563	24666 - 6.9
2	746	27630 - 7.7
3	1119	31663 - 8.9

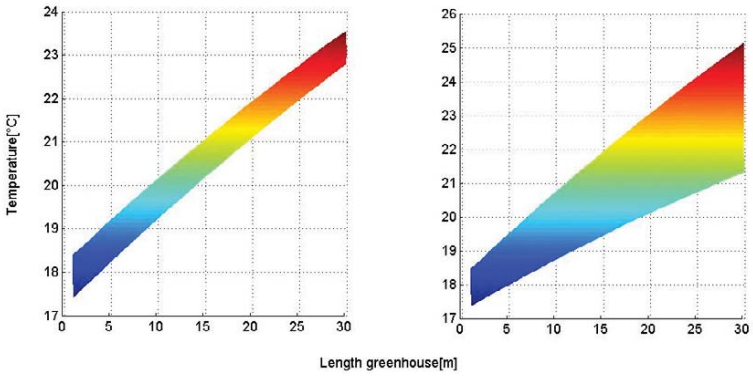

Fig. 9: Temperature profiles along greenhouse with 16 m^3/s (left) and 14 m^3/s (right).

Under same exterior conditions but different ventilation rate, it can obtained different temperature profile. It is expected that energy consumed is proportional to cooling effect. Fig. 9 shows two different temperature profiles generated from two ventilation rates. It is necessary to select fans to meet these ventilation rates of 16 and 14 m^3/s from the models proposed in table1. Table 2 shows results:

Tab. 2: Fans selected for different ventilation rates

Ventilation Rate [m^3/s]	Maximum temperature obtained at x=30 [°C]	Fans selected	Energy consumed in 1 hour kWh
16	23.5	Two fans of model 3	2.22
14	25	Two fans of model 2	1.49

In order to create a flow as uniform as possible, ASABE (2008) suggest that the fans should have the same air flow capacity and technical features, that is, they are the same model. For that reason, it is important to select just necessary ventilation rate, it would be creating more cooling effect than necessary for crops. Also, it would be wasting electrical energy. The ventilation rate of 14 m^3/s is sufficient to maintain 25 °C or lower temperature. If we use this design parameter, for 5 hours of operation of the pad fan system during the hottest part of the day, the energy consumed would be 7.45 kWh/day.

Fig. 10. Fans in opposite face to evaporative pad.

Theoretically energy generated by solar panels at Central Region of Mexico during experimentation is 3.3 kWh per day (5.5 sunshine hours equivalent to 1000 W/m^2 multiplying 600 W of power pv array). However, the energy measured with a Power Quality Analyzer (Fluke 434 Three phase power) during the 30 days of 2015 summer, the percentage of energy saving was 32%. The specific technical characteristics and unit prices of all major components shown, including also expenses for construction and installation of the support tower of photovoltaic modules, electrical cables, and labor. The total cost of the installed system was USD$3,400.00 and the recovery time is 10.5 years. After that the system will have an estimated 15 years additional life.

4. Conclusions

If a pad works at maximum efficiency, it does not guarantee that energy consumption is minimal. The increased pad efficiency could cause unnecessary energy consumption, this is because the optimum temperature inside a greenhouse can be obtained with a ventilation rate lower than that corresponding to the maximum ventilation pad efficiency. Consequently, the power of the fans must be lower and energy consumption as well. After this energy analysis, a hybrid photovoltaic system of low cost and high reliability was obtained. Energy savings of nearly a third of the total are obtained by keeping the greenhouse temperature close to 25 °C during the hours of maximum solar radiation. 32% of the energy saved is the best choice because other settings create more cost and time of return is achieved close to the life of the system. Even when AC utility is available, the main source of power will still be solar, AC utility will supplement only when necessary. This type of design cuts back the use of paid electricity thus reaching the goal of energy conservation.

5. References

G. N. Tiwari, 2003. Greenhouse Technology for Controlled Environment, Alpha Science, Pangbourn England.

Duffie, J. A. and Beckman, W. A., 1991. Solar engineering of thermal processes, John Wiley and Sons, New York.

ASABE, 2008. Heating, ventilating and cooling greenhouses. ASABE standards. ANSI /ASAE EP406.4 JAN2003 (R2008). St. Joseph, American Society of Agricultural and Biological Engineers

Nelson V.P., 1998. Greenhouse operation and management. 5th ed. Prentice Hall, pp. 144-154. ISBN 0-13-374687-9

D. Jain, G. N. Tiwari, 2002. Modeling and optimal design of evaporative cooling system in controlled environment greenhouse. Energy Conversion and Management 43. 2235–2250

Ganguly, S. Ghosh. Modeling and analysis of a fan–pad ventilated floricultural greenhouse, Energy Build, vol.39, pp. 1092-1097, December 2007.

Kittas C., Bartzanas T., 2001. Greenhouse evaporative cooling: measurements and data analysis. Transactions of the ASAE. 44 (3), 683-689.

A. Franco, D. L. Valera. 2014. Energy Efficiency in Greenhouse Evaporative Cooling Techniques: Cooling Boxes versus Cellulose Pads, 2014 Energies, 7, 1427-1447; doi:10.3390/en7031427.

Al-Helal , N. Al-Abbadi. 2004. A study of fan-pad performance for a photovoltaic powered greenhouse in saudi arabian summer. International Agric. Engineering Journal 2004, 00:1-14.

N. M. Ahmed, H. M. Farghally. 2011. A Modified Cooling System for Stand Alone PV Greenhouse in Remote Areas. International Conf. on Renewable E. and Power Quality.

Al-Shamiry F., Ahmad D., Mohamed S., Aris I., 2007. Design and development of a photovoltaic power system for tropical greenhouse cooling. American Journal of Applied Sciences 4 (6): 386-389, 2007

Carlini MHT., Castellucci S. Photovoltaic greenhouses: Comparison of optical and thermal behavior for energy savings. Math Probl Eng 2012:1–10.

Ganguly A, Misra D, Ghosh S. Modeling and analysis of solar photovoltaic electrolyze-fuel cell hybrid power system integrated with a floriculture greenhouse. Energy Build 2010; 42:2036–43.

Al-Ibrahim A, Al-Abbadi N. PV greenhouse system, system description, performance and lesson learned. Acta Hortic (ISHS) 2006; 710:251–6

ASABE, 2008. Heating, ventilating and cooling greenhouses. ASABE standards. ANSI /ASAE EP406.4 JAN2003 (R2008). St. Joseph, American Society of Agricultural and Biological Engineers.

NOMENCLATURE

C_p	heat capacity of air $[J/kg°C]$
K_c	coefficient of sensible heat losses through the plastic cover $[W/m^2\ °C]$
L_{cov}	length of polyethilene cover proportional to greenhouse width to obtain the differential heat transfer area $[m]$
$\dot{m}$	mass airflow generated by fans $[kg/s]$
$\dot{Q}_{accum}$	heat rate accumulated in greenhouse $[J/s]$
R_o	outside solar radiation $[W/m^2]$
T_{in}	interior temperature $[°C]$

T_o	outside temperature $[°C]$
T_{pad}	air temperature cooled by pad of cellulose corrugated $[°C]$
$\dot{V}$	ventilation rate $[m^3/s]$
w_{gh}	greenhouse width $[m]$
τ	coefficient transmissivity of the plastic cover
α	coefficient of losses that involves transpiration and radiation through soil
ρ	air density $[kg/m^3]$

Conference Proceedings

EuroSun 2016
Palma de Mallorca (Spain), 11 - 14 October 2016

Effect of the phase change material's melting point on the thermal behaviour of a concentrated photovoltaic system in a tropical dry climate

Jawad Sarwar[1], Brian Norton[2] and Konstantinos E. Kakosimos[1]

[1] Sustainable Energy and Clean Air Research Laboratory, Department of Chemical Engineering, Texas A&M University at Qatar, 23874, Doha, Qatar

[2] Dublin Energy Lab, Dublin Institute of Technology, Grangegorman, Dublin 7, Ireland

Abstract

In this work, we investigated temperature regulation of concentrating photovoltaic (CPV) and thermal energy storage using solid-liquid phase change material (PCM) under tropical dry climatic conditions. A finite element based heat transfer model is developed that includes the optical behavior of incident irradiance, solar to electrical conversion and online calculation of heat loss coefficients. The model's results are in good agreement (±3 ºC) against indoor experimental results. The validated model is used to predict the thermal behavior of PV and CPV incorporating PCM by varying melting point (35 ºC to 75 ºC), ambient temperature (30 ºC to 50 ºC) and concentration ratio (2× - 4×). It is found that a PCM with melting temperature in the range of 45 ºC to 65 ºC is suitable for temperature regulation and thermal energy storage for a CPV system in a tropical dry climate for up to ~ 4×. The choice of an appropriate PCM in melting temperature range of 45 ºC – 65 ºC depends on energy utilization requirement. The overall efficiency of the CPV system with a PCM makes it an attractive choice for a CPV thermal application in a tropical dry climate.

Keywords: *Phase change material, concentrated photovoltaic, finite element, heat transfer*

1. Introduction

Concentrating solar radiation onto photovoltaic (PV) cells generates more electricity but concomitantly raises the PV cell operating temperature thereby decreasing solar to electrical conversion efficiency by 0.08 %/K for crystalline silicon PV (Radziemska, 2003). Solid-liquid phase change material (PCM) is a promising technology to regulate the temperature of PV along with enabling thermal storage of energy (Hasan et al., 2015). A PCM stores energy during phase change otherwise acts as a sensible heat storage material. The absorption, storage and releasing capability of a PCM depends on its geometrical configuration and its thermophysical properties (Sarwar and Mansoor, 2016). A comprehensive review of integration of a PCM for thermal management of photovoltaic has shown that the PCM is not only useful for non-concentrating PV but has particular potential for temperature regulation of concentrated photovoltaic (CPV) application (Browne et al., 2015).

Recently, several researchers have experimentally and numerically investigated the performance enhancement of CPV using a PCM. For example, an in-door experimental investigation of a low concentrated, geometrical concentration ratio of 2.7, building integrated CPV containing a paraffin wax (RT42) has been carried out. It is reported that the PCM effectiveness depends upon the incident irradiance intensity and the integration of PCM reduces module center temperature by an average of 3.8 ºC (Sharma et al., 2016). An outdoor investigation of another low concentrated CPV system integrated with a paraffin wax (melting temperature of 47 ºC) has shown a decrease in PV temperature and increase in solar to electrical conversion efficiency (Ceylan et al., 2016). A theoretical investigation of application of a PCM in a photovoltaic-thermoelectric system has

doi:10.18086/eurosun.2016.08.12 Available at http://proceedings.ises.org

been undertaken to determine PCM influence on electrical conversion (Cui et al., 2016). The results are compared with a photovoltaic-thermoelectric system without a PCM. It is reported that introduction of a PCM increases the electrical conversion efficiency and mitigates the temperature fluctuations of a PV cell. It is also discussed that the selection of an appropriate PCM depends on desired operating temperature conditions (Cui et al., 2016). A combination of heat spreading and PCM cooling method has been employed to experimentally investigate the temperature regulation of a PV cell under concentrated irradiance (optical concentration ratio of 4). It is reported that the introduction of PCM (Fatty acids and salt hydrates) reduces the peak PV cell temperature in the range of 9 ^{o}C – 20 ^{o}C (Sarwar et al., 2013). An indoor and outdoor investigation of a CPV using a V-trough as a concentrator and a PCM having melting temperature of 57 ^{o}C has also reported the temperature regulation ability of the PCM (Maiti et al., 2011).

Although, temperature controlling ability of a PCM is well established but selection of an appropriate PCM is critical to design an efficient system that can work over the whole year. The PCM used should have a large latent heat of fusion, reversible phase change and melting point within a range of operation (Cabeza et al., 2011). On the other hand, ambient conditions play an equally important role in selection of a PCM in extreme conditions such as a tropical dry climate (i.e. Qatar, Middle East). Nocturnal ambient or radiative cooling temperatures must fall below the melting temperature to solidify the PCM for operation the next day. A multi-year (1978-2012) analysis of the weather data for Qatar showed that during summer night, temperature can go as high as up to 32 ^{o}C while peak temperature during summer day can reach up to 50 ^{o}C. In this preliminary analysis we considered the effect of ambient temperature (e.g. no humidity) and melting temperature. Therefore, we consider PCMs with a melting point in the range of 35 - 75 ^{o}C for the temperature regulation and calculate the electrical and thermal energy storage performance of selected system. The ambient temperature is considered in the range of 30 - 50 ^{o}C while the concentrated flux intensity is considered up to 4 kWm^{-2}.

2. Optical-thermal model

A finite element based heat transfer model is coupled with an optical model to evaluate the thermal, optical and electrical behavior of a photovoltaic cell integrated with a phase change material. The schematic illustration of different physical phenomena within the system is shown in Fig. 1.

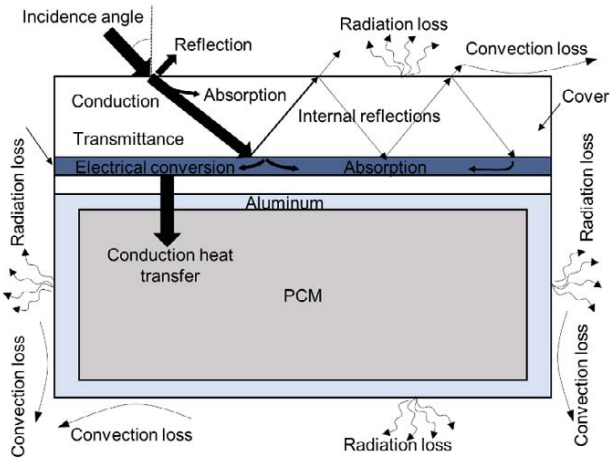

Fig 1: Physical phenomena within the photovoltaic/phase change material system

The principles of the optical-thermal model are as follows:

- A 2D differential heat diffusion equation is used to develop the finite element based heat transfer model. The weak formulation is developed using a test function and integrating it over the domain and its boundary. Green-Gauss theorem and divergence theorem are used to simplify the formulation. An 8-node Serendipity element is used to transform physical coordinates to natural coordinates. The elements are assembled using direct addition of components method to form the domain of the system.

- Latent heat of fusion effect is introduced via an effective heat capacity method.
- The temporal discretization is carried out using a Crank-Nicholson method.
- Convection and radiation losses are considered on all sides of the system.
- Reflectance, transmittance and absorptance is calculated using Fresnel equations method.
- Angle of incidence of sun's irradiance is found via a methodology proposed by Hoang et al. (2014).
- Temperature dependence of electrical conversion is considered for calculations of electrical power generation by incident irradiance.

The following assumptions are made to simplify the calculations:

- Multiple reflections up to 3 are considered in the cover.
- Incident diffuse and direct radiations are considered un-polarized.
- Effective thermal conductivity of the PV cell is used instead of using thermal conductivity of each layer of the PV cell.
- Only conduction heat transfer in the PCM is considered.

2.1 Thermal model

A two-dimensional differential heat diffusion equation governing transient heat transfer in the system shown in Fig. 1 is as follows:

$$\rho c \frac{\partial T}{\partial t} - \left[\frac{\partial}{\partial x_i}\left(k_{ij}\frac{\partial T}{\partial x_j}\right)\right] = 0 \qquad \text{(eq. 1)}$$

The convection and radiation heat losses at the boundary of the system are given by following equations:

$$H = h_c A \Delta T \qquad \text{(eq. 2)}$$

$$R = h_r A \Delta T \qquad \text{(eq. 3)}$$

The energy balance of the system is obtained using equation eq. 1 – eq. 3 and multiplied by a test function δT and integrated over the domain to get its weak formulation. The Green-Gauss theorem and divergence theorem is applied on the relevant equations to obtain simplified form of the weak formulation which is given as:

$$\int_\Omega \delta T \rho c \frac{\partial T}{\partial t} \partial\Omega + \int_\Omega \left[k_{11}\frac{\partial \delta T}{\partial x_1}\left(\frac{\partial T}{\partial x_1}\right) + k_{22}\frac{\partial \delta T}{\partial x_2}\left(\frac{\partial T}{\partial 2}\right)\right]\partial\Omega - \int_\Gamma \delta T q \partial A + \int_\Gamma \delta T (H+R)\partial A = 0 \qquad \text{(eq. 4)}$$

The differential of temperature and test functions are transformed from physical coordinates into natural coordinates by using chain rule and an 8-node Serendipity element. After transformations, the energy balance equation becomes as:

$$\mathbf{M}\dot{T} + \mathbf{K}T - \boldsymbol{q} + (\mathbf{H}+\mathbf{R})T = 0 \qquad \text{(eq. 5)}$$

where $\dot{T}$ is the time derivate of temperature while **M**, **K**, **H**, **R** and $\boldsymbol{q}$ are the mass, conductivity, convection, radiation and irradiance matrices. These matrices are calculated as:

$$\mathbf{M} = \int_{-1}^{1}\int_{-1}^{1} \rho c N^T N |J| h \partial\xi_1 \partial\xi_2 \qquad \text{(eq. 6)}$$

$$\mathbf{K} = \int_{-1}^{1}\int_{-1}^{1} B^T k B |J| h \partial\xi_1 \partial\xi_2 \qquad \text{(eq. 7)}$$

$$\mathbf{H} = \int_{-1}^{1} h_c N^T N |J_i| h \partial\xi_{1\ or\ 2} \qquad \text{(eq. 8)}$$

$$\mathbf{R} = \int_{-1}^{1} h_r N^T N |J_i| h \partial\xi_{1\ or\ 2} \qquad \text{(eq. 9)}$$

$$\mathbf{q} = \int_{-1}^{1} q N^T N |J_i| h \partial\xi_{1\ or\ 2} \qquad \text{(eq. 10)}$$

N represents an 8-node Serendipity element, B is the B-operator, ξ is the natural coordinates, J is Jacobian matrix and h is the width of the system. The physical discretization of the domain is obtained by assembling

the elements using direct addition of components method. The temporal discretization of the system is carried out using a Crack-Nicholson scheme. The convection and radiation heat transfer coefficients are calculated at each time step using following equations:

$$h_c = 2.9v + 4.5 \quad \text{(eq. 11)}$$

$$h_r = \sigma \varepsilon F \left(\frac{T^4 - T_a^4}{T - T_a}\right) \quad \text{(eq. 12)}$$

Where v is the velocity of the air, σ is the Stefan-Boltzmann constant, ε is the emissivity and T_a is the ambient temperature. In current calculations, the ambient temperature is considered equal to the sky temperature (Kumar and Mullick, 2012) and view factor is considered as 1. For indoor calculations, velocity of the air is considered as zero. The latent heat effect of the PCM is introduced using an effective heat capacity method (Lamberg et al., 2004) which is as follows:

$$c_e = \begin{cases} c_s & T < T_1 \\ c_s + \frac{L}{T_2 - T_1} & T_1 \le T \le T_2 \\ c_l & T > T_2 \end{cases} \quad \text{(eq. 13)}$$

Where c_e is the effective heat capacity of the PCM, c_s and c_l are the heat capacities of solid and liquid PCM respectively. L is latent heat of fusion while T_1 and T_2 are the melting onset and solidification temperature respectively.

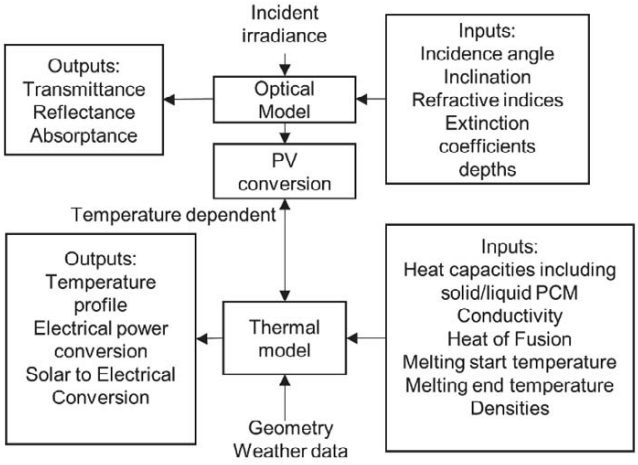

Fig. 2: Flow chart representation of the optical-thermal model

2.2 Optical model

The irradiance incident on the PV cover goes through the series of reflections and absorptions in the cover, as shown in Fig. 1, before absorbing in the PV cell. The reflectance, absorptance and transmittance in the system is calculated using Fresnel equations (Hecht, 2002).

$$\begin{aligned} &\rho = \tfrac{1}{2}(\rho_\parallel + \rho_\perp) \quad \rho_\perp = -\frac{sin(\theta_i - \theta_t)}{sin(\theta_i + \theta_t)} \quad \rho_\parallel = \frac{tan(\theta_i - \theta_t)}{tan(\theta_i + \theta_t)} \\ &\tau = \tfrac{1}{2}(\tau_\parallel + \tau_\perp) \quad \tau_\perp = \tau_a \left(\frac{1-\rho_\perp}{1+\rho_\perp}\right)\left(\frac{1-\rho_1^2}{1+\rho_1^2\tau_a^2}\right) \quad \tau_\parallel = \tau_a \left(\frac{1-\rho_\parallel}{1+\rho_\parallel}\right)\left(\frac{1-\rho_\parallel^2}{1+\rho_\parallel^2\tau_a^2}\right) \\ &\alpha = \tfrac{1}{2}(\alpha_\parallel + \alpha_\perp) \quad \alpha_\perp = (1-\tau_a)\left(\frac{1-\rho_\perp}{1+\rho_\perp\tau_a}\right) \quad \alpha_\perp = (1-\tau_a)\left(\frac{1-\rho_\perp}{1+\rho_\perp\tau_a}\right) \\ &\tau_a = e^{\frac{-Kx}{cos\theta_t}} \end{aligned} \quad \text{(eq. 14)}$$

A transmittance angle (θ_t) is calculated from an incident angle (θ_i) by using Snell's refractive law. For indoor calculations, the incident irradiance is assumed normal to the cover but for the outdoor calculations, the incident angle is found using a methodology available in literature (Hoang et al., 2014). The formulae for

calculations of incidence angle, sun declination angle (δ) and hour angle (ω) are presented in eq. 15.

$$\cos\theta_i = \sin\delta \times \sin l \times \cos s - \sin\delta \times \cos l \times \sin s \times \cos\varphi + \cos\delta \times \cos l \times \cos s \times \cos\omega + \cos\delta \times \sin l \times \sin s \times \cos\varphi \times \cos\omega + \cos\delta \times \sin s \times \sin\varphi \times \sin\omega$$
$$\delta = 0.38 + 23.26 \sin\left(\frac{2\pi J'}{365.24-1.395}\right) + 0.37 \sin\left(\frac{4\pi J'}{365.24-1.457}\right) \quad \text{(eq. 15)}$$
$$\omega = 15 \times \left(H_l - \Delta H_l + \Delta H_g - E - 12\right)$$
$$E = 7.5 \times \sin\left(2\pi \frac{J'}{365.24} - 0.03\right) + 0.99 \times \sin\left(4\pi \frac{J}{365.24} + 0.35\right)$$

Where J' is the rank of the day after the first of January 2013 while J is the Julian day of the year. The local time is represented by H_l, time lag between the given time zone and UTC is represented by ΔH_l and time lag due to the longitude variation is denoted by ΔH_g.

2.3 Coupling of optical-thermal model

The flow chart representation of the optical-thermal model is shown in Fig. 2. The irradiance available at the PV after going through series of reflections and absorption losses in the PV cover is obtained via following equation:

$$q_{aol} = (1 - \rho - \alpha) q_i \quad \text{(eq. 16)}$$

The part of the irradiance available at the PV is converted in to electricity while rest is converted in to heat. The irradiance after accounting for electrical conversion is shown in equation 17.

$$q = q_{aol} - [\eta + \mu(T - T_a)] q_{aol} \quad \text{(eq. 17)}$$

Where η is the efficiency and μ is the power output temperature coefficient of the PV cell under standard test conditions.

The irradiance (q) is updated at every time step to include temperature dependence properties of the PV cell and incidence angle variations over the day. The electrical power produced from the PV cell is calculated using following correlation:

$$P = q_{aol}\, A\, \eta\, [1 - \mu(T - 298)] \quad \text{(eq. 18)}$$

Furthermore, the thermal efficiency of the CPVPCM system is calculated by calculating the ratio of thermal energy stored in the PCM (Hasan et al., 2015) to the incident energy.

2.4 Input parameters of the optical-thermal model

The electrical, thermal and optical properties of the materials that serve as an input in the optical-thermal model are presented in table 1.

Tab. 1: Thermal parameters of the materials used in the system for the optical-thermal model

	Thermal parameters of the materials					
	ρ (kg m^{-3})	k ($Wm^{-1}K^{-1}$)	c ($kJkg^{-1}K^{-1}$)	ε	H ($kJkg^{-1}$)	T_m (K)
Perspex	1190	1.9	1.3	0.9	×	×
PV	2205	125.4	0.8	0.9	×	×
Aluminium	2700	205.0	0.9	×	×	×
PCM	880	0.2	1.3 (s) 1.8 (l)	×	190	303 - 323
	Electrical characteristics					
	η			μ ($^oC^{-1}$)		
	12.7			-0.005		
	Optical parameters of the materials					
	n		K (m^{-1})		x (m)	
Perspex	1.5		10		3×10^{-3}	
PV	4		4710		5×10^{-4}	

A clear sky broadband solar radiation model (Bird and Hulstrom, 1981) is used to simulate the direct beam and global horizontal irradiance. The latitude and longitude of the selected location (Education city, Doha, Qatar) are 25.314779° N and 51.43978° E respectively. Four days (January 1, March 30, June 29 and September 29) belonging to each season of a year 2015 are selected to predict the electrical, thermal and optical behaviour of the selected system. The weather data including wind speed and ambient temperature for the selected days is obtained from experimentally measured data by meteorological department, Qatar. The variations in irradiance, ambient temperature and wind speed on selected days are shown in Fig. 3. Thermal and electrical output of the system under concentrated irradiance, referred as CPVPCM in subsequent text, is predicted and compared with non-concentrated PV. The inclination angle of the PV for non-concentrated system is considered equal to the latitude of the location while dual-axes tracking is considered for CPVPCM system with an error of ±0.1°.

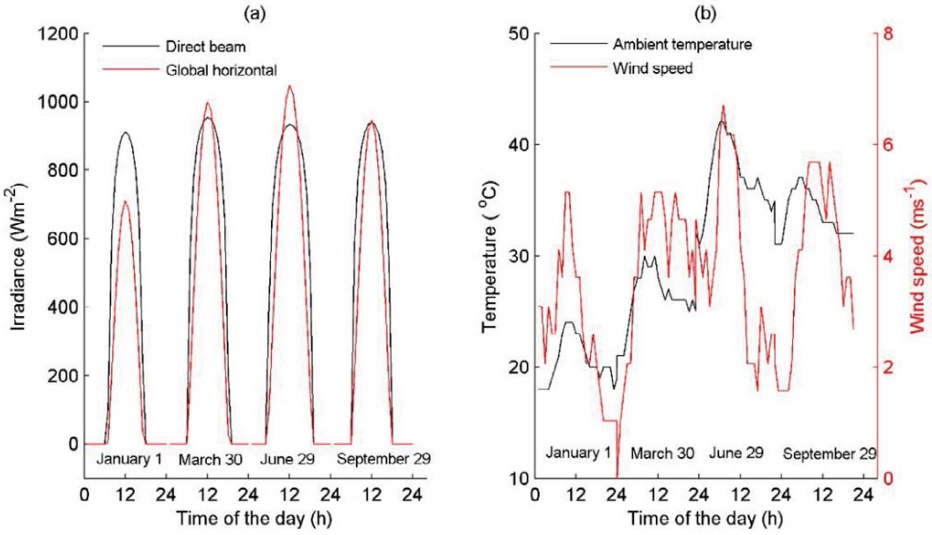

Fig. 3: The irradiance, ambient temperature and wind speed variations on selected days

3. Experimental setup and model validation

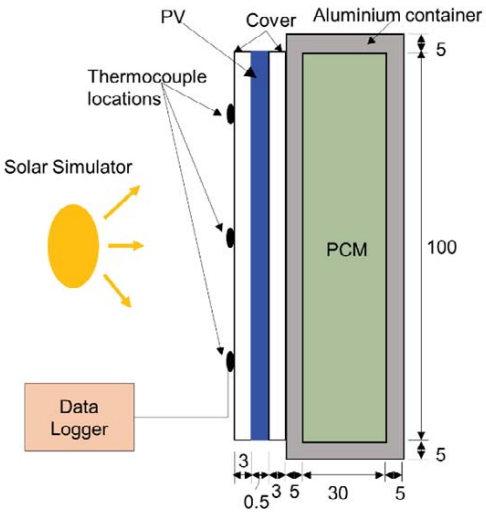

Fig. 4: Schematic illustration of the experimental setup

The schematic illustration of experimental setup is shown in Fig. 4. Polycrystalline silicon PV cell, Suntech power STP065-12/Sb, (Solar, 2013) with the dimensions of 100 mm × 100 mm × 0.5 mm encapsulated in a 3 mm thick Perspex imitated the PV cell. The volume of PCM required for temperature regulation of the PV cell, was calculated using an energy balance equation presented by Huang et al. (Huang et al., 2004) by

considering RT20 as a PCM. A 5 mm thick aluminium sheet was used to fabricate a 30 mm thick aluminium container encapsulating a PCM having a volume of 0.3 litres. Five T-type copper-constantan thermocouples with a maximum measurement deviation of ±0.2 °C were attached to the front surface of the system to measure the temperature at a sampling rate of 100 Hz using a data logger. The system is irradiated at 1000 Wm^{-2} using a Griven GR262 solar simulator and the flux is measured using a Kipp & Zonen CM6B pyranometer. The height of the solar simulator and PV cell was adjusted to keep the irradiance normal to the centre of the PV cell. The experiments were performed three times to ensure repeatability and to quantify the uncertainty in the experimental results. The average of the measured experimental PV cell temperature along with error bars depicting uncertainty was compared with numerically predicted temperature under same irradiance to validate the numerical model.

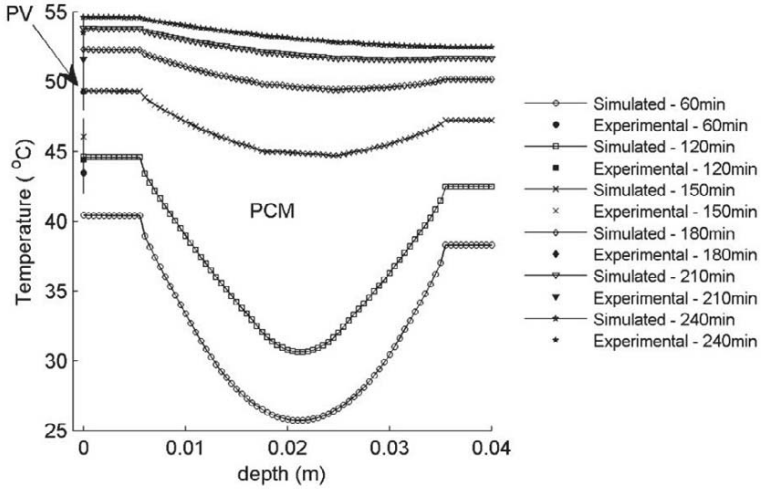

Fig. 5: Comparison of experimental and numerical temperature along with melting behavior of a phase change material

It is shown in figure 5 that the temperature of the PV cell is in agreement with numerically predicted temperature. The experimental temperature of the PV cell increases to 43.4 °C in one hour while it increases to 53.9 °C while exposed to 1000 Wm^{-2} for four hours. The corresponding numerical temperatures are 41 °C and 54.6 °C respectively. A maximum standard deviation of ±3 °C is achieved between experimental and numerical temperatures thereby, validating the optical-thermal model. The melting behavior of the system is also shown in Fig. 5 which indicates that heat is transferred to the PCM from both front and back side. Although irradiance is incident on the PV cell only but heat is transmitted to the back of the container fast through the aluminum containment due to its high thermal conductivity. Therefore, the melting of the PCM starts from each side of the container and completes in the center of the container.

4. Results and Discussion

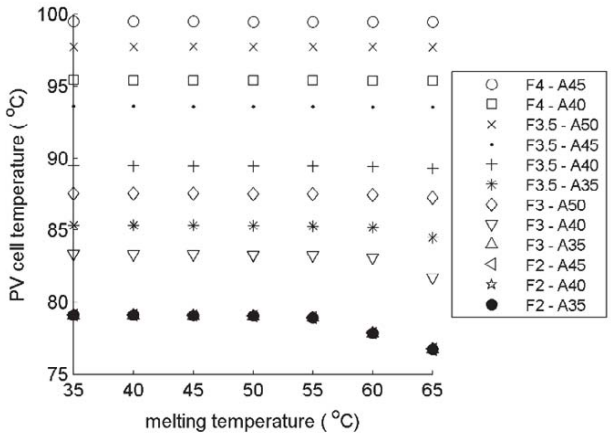

Fig. 6: Temperature of the CPVPCM system under variable concentrated irradiance, ambient and melting temperature

The temperature of the CPVPCM system under in-door conditions has been investigated using developed optical-thermal model for variable incident concentrated irradiance up to 4 kWm^{-2}. The ambient temperature has been varied in the range of 35 ºC – 50 ºC while melting temperatures of the PCM are varied in the step of 5 ºC from 35 ºC to 65 ºC. The result is shown in Fig. 6.

The temperature of the PV cell increases with the increase in ambient temperature and increase in concentrated irradiance. The PV cell temperature decrease with the increase in the melting temperature but the difference is more pronounced at lower concentrated irradiance up to 3 kWm^{-2}. The temperature of the PV cell in the CPVPCM system can be maintained below 85 ºC up to concentrated irradiance of 3.5 kWm^{-2} under indoor conditions. To investigate the electrical and thermal behavior of the CPVPCM system under out door conditions, the temperature evolution and electrical output of the system is simulated for PCM melting temperatures of 45 ºC and 65 ºC. The simulated irradiance, ambient temperature and wind conditions, as shown in Fig. 3, of selected days of a year 2015 are used for that purpose. The incident concentrated and non-concentrated irradiance on the CPVPCM system and PV only after optical losses is shown in Fig. 7(a) while corresponding temperature evolution is shown in Fig. 7(b).

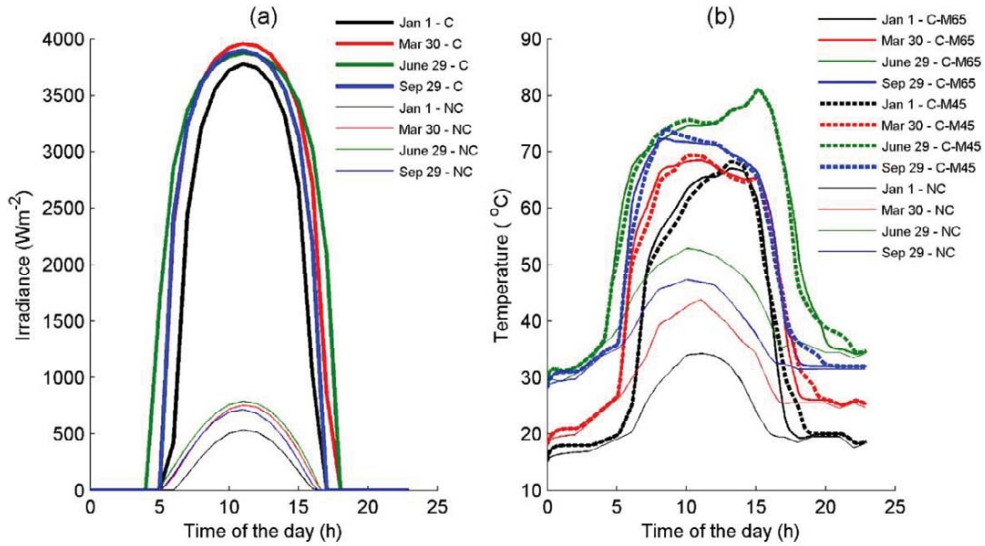

Fig 7: (a) Concentrated and non-concentrated irradiance after optical losses (b) Temperature evolution of the selected system and PV only

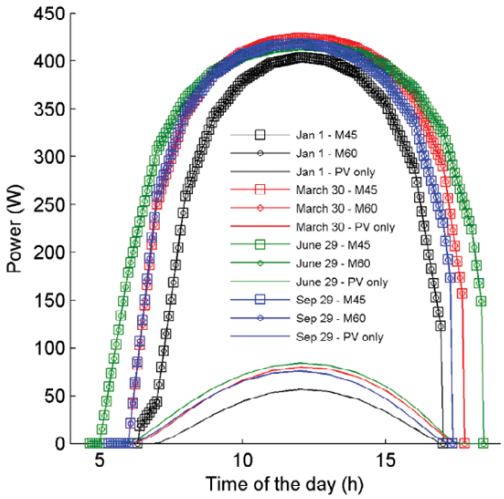

Fig 8: Electrical output of the system and PV only for a unit cell area

The peak concentrated irradiance varies in the range of 3.7 kWm^{-2} – 3.9 kWm^{-2} while non-concentrated irradiance varies in the range of 534 Wm^{-2} – 787 Wm^{-2}. The peak temperature of ~81 ºC for the CPVPCM system is found in June while minimum peak temperature of ~68 ºC is found in January. The change in melting

temperature of the PCM results in slight temperature increase of ~2 ºC for the melting temperature of 45 ºC. The peak temperature of PV only system varies in the range of 35 ºC – 53 ºC for selected days of the year. The hourly averaged incident irradiance and ambient temperature are used in the current investigations and the peak hourly average ambient temperature is ~ 40 ºC in June. The difference between peak PV temperature for PV only system and ambient temperature is ~ 13 ºC for incident irradiance of 787 Wm^{-2}. This difference is reasonable compared to a previous outdoor simulated analysis carried out by author, where the temperature difference between ambient to PV cell is obtained as 22 ºC for peak incident irradiance of ~ 980 Wm^{-2} (Hasan et al., 2015). There is a peak shifting in the temperature of the PV cell in the CPVPCM system is observed which is due to the integration of the PCM. This behavior is also consistent with previously reported experimental and simulated results (Hasan et al., 2015). The electrical output of both systems is investigated using equation 18 and result of electrical output is shown in Fig. 8. It is found that the electrical output of the system integrated with PCM remains almost same. The peak output of 424 W is obtained in March while peak output of 84 W is obtained for PV only system in June. The electrical output of the concentrated systems increases disproportionally with the increase in the incident irradiance. The incident irradiance increases by ~ 7 times but corresponding increment in electrical output is just ~5 times which is due to the temperature effect of the PV cell. Nevertheless, in current configuration, the electrical output remains unchanged by changing melting temperature from 45 ºC to 60 ºC but thermal behavior changes with the change in melting temperature of the PCM as shown in Fig. 9.

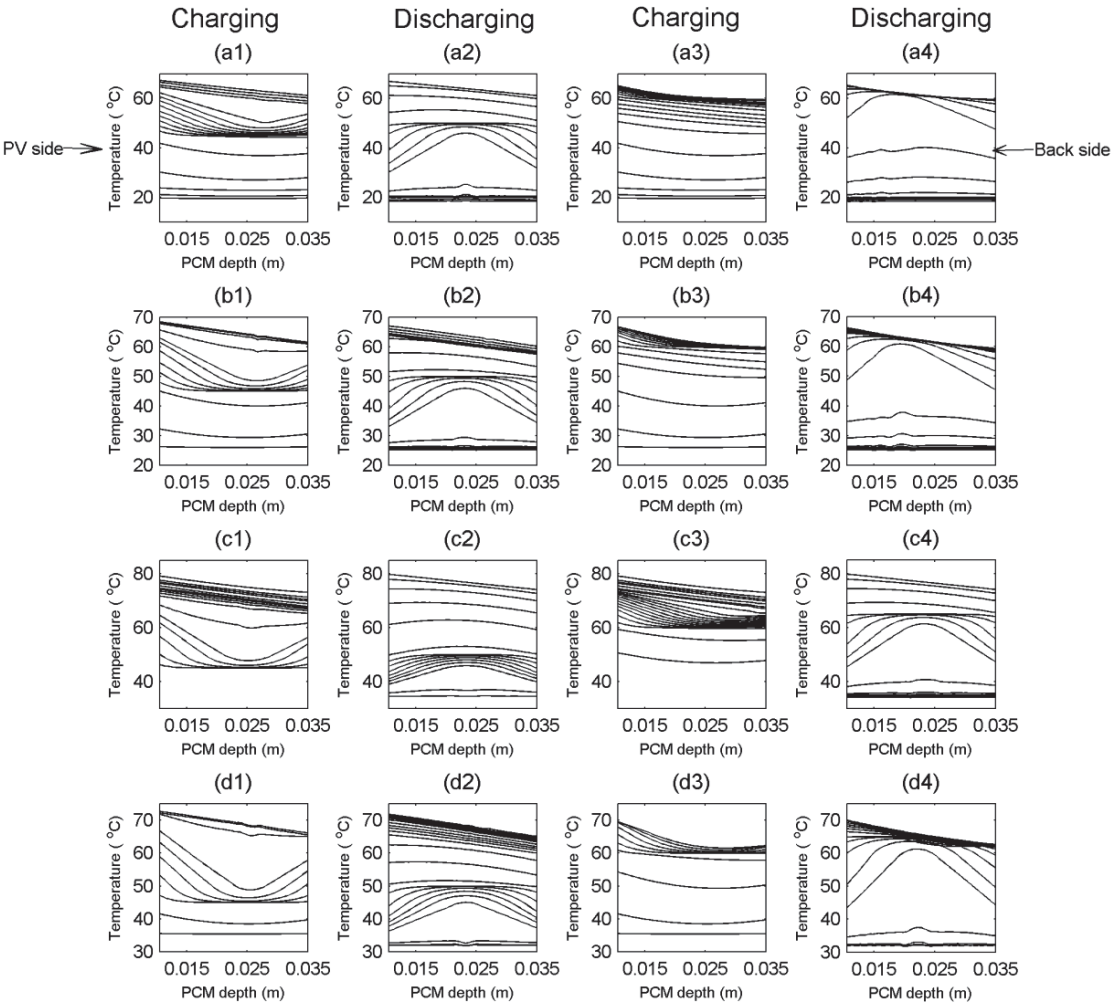

Fig. 9: Temperature curves in the PCM for every 30 minutes during charging and discharging (a) January 1 (b) March 30

(c) June 29 (d) September 29

The thermal energy storage in the PCM takes place at the melting temperature of the PCM as shown in Fig. 9. For the PCM, having melting temperature of 45 ºC, the temperature curves in the PCM shows energy storage and an extended temperature maintenance in the melting temperature range of 45 ºC – 50 ºC. The similar behavior is shown in Fig. 9 for the PCM having melting temperature of 65 ºC. This result shows that the PCMs having melting temperatures in between 45 ºC to 65 ºC are suitable for temperature regulation of a CPVPCM system. Thus, the selection of a PCM, in current configuration, also depends upon energy utilization requirement of the system. For example, if stored energy is required to be extracted at 45 ºC than PCM with a melting temperature of 45 ºC is appropriate and so on. The results of the electrical and thermal efficiencies of the systems are shown in Fig. 10.

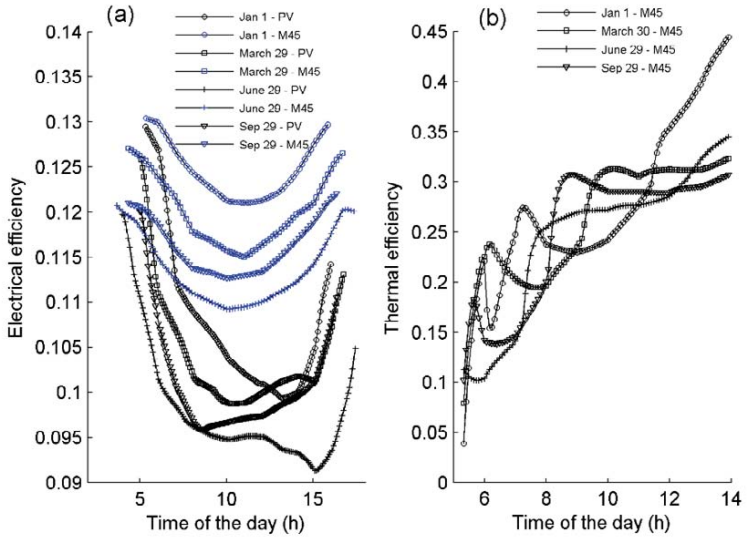

Fig. 10: (a) Electrical efficiency of the PV only and the system having PCM (b) thermal efficiency of the system

Despite increase in electrical power output for a unit area of CPVPCM system as compared to PV cell (as shown in Fig. 8), the overall electrical efficiency of the CPVPCM system decrease by ~16.5% than the PV system. But, the storage of thermal energy provides an advantage for the CPVCPM system and its thermal efficiency is found up to 45% during charging (Fig. 10). Therefore, the overall efficiency of the CPVPCM system is higher than the PV only system that makes it an attractive choice for a hybrid concentrated photovoltaic thermal application. Further studies are required to investigate the combined effect of other parameters of the CPVPCM system such as thermophysical properties of PCMs, geometry, containment thickness etc.

5. Conclusions

Following conclusions can be drawn from this work:

1. Developed optical-thermal model is a suitable tool for optical, thermal and electrical behavior of the system.
2. Ambient temperature and concentrated irradiance intensity effects the selection of a suitable PCM. A PCM with melting temperature in the range of 45 ºC to 65 ºC is suitable for temperature regulation and thermal energy storage for a CPV system in a tropical dry climate.
3. The utilization of stored energy from a PCM is another criterion for the selection of a PCM under limiting ambient and concentrated irradiance conditions.
4. The overall efficiency of a CPV system integrated with a PCM makes it an attractive alternative to a conventional PV system.

Acknowledgements

This publication was made possible by a PDRA award [PDRA2-1105-14044] from the Qatar National Research Fund (a member of The Qatar Foundation). The statements made herein are solely the responsibility of the authors. The HPC resources and services used in this work were provided by the IT Research Computing group in Texas A&M University at Qatar. IT Research Computing is funded by the Qatar Foundation for Education, Science and Community Development (http://www.qf.org.qa).

References

Bird, R. E. and R. L. Hulstrom (1981). Simplified clear sky model for direct and diffuse insolation on horizontal surfaces, ; Solar Energy Research Inst., Golden, CO (USA)**:** pp. Medium: ED; Size: Pages: 46. (1981).

Browne, M. C., B. Norton and S. J. McCormack (2015). "Phase change materials for photovoltaic thermal management." Renewable and Sustainable Energy Reviews **47**: 762-782.

Cabeza, L. F., A. Castell, C. Barreneche, A. de Gracia and A. I. Fernández (2011). "Materials used as PCM in thermal energy storage in buildings: A review." Renewable and Sustainable Energy Reviews **15**(3): 1675-1695.

Ceylan, İ., A. E. Gürel, A. Ergün and A. Tabak (2016). "Performance analysis of a concentrated photovoltaic and thermal system." Solar Energy **129**: 217-223.

Cui, T., Y. Xuan and Q. Li (2016). "Design of a novel concentrating photovoltaic–thermoelectric system incorporated with phase change materials." Energy Conversion and Management **112**: 49-60.

Hasan, A., S. J. McCormack, M. J. Huang, J. Sarwar and B. Norton (2015). "Increased photovoltaic performance through temperature regulation by phase change materials: Materials comparison in different climates." Solar Energy **115**: 264-276.

Hecht, E. (2002). Optics. San Francisco [etc.], Addison Wesley.

Hoang, P., V. Bourdin, Q. Liu, G. Caruso and V. Archambault (2014). "Coupling optical and thermal models to accurately predict PV panel electricity production." Solar Energy Materials and Solar Cells **125**: 325-338.

Huang, M. J., P. C. Eames and B. Norton (2004). "Thermal regulation of building-integrated photovoltaics using phase change materials." International Journal of Heat and Mass Transfer **47**(12-13): 2715-2733.

Kumar, S. and S. C. Mullick (2012). "Glass cover temperature and top heat loss coefficient of a single glazed flat plate collector with nearly vertical configuration." Ain Shams Engineering Journal **3**(3): 299-304.

Lamberg, P., R. Lehtiniemi and A.-M. Henell (2004). "Numerical and experimental investigation of melting and freezing processes in phase change material storage." International Journal of Thermal Sciences **43**(3): 277-287.

Maiti, S., S. Banerjee, K. Vyas, P. Patel and P. K. Ghosh (2011). "Self regulation of photovoltaic module temperature in V-trough using a metal–wax composite phase change matrix." Solar Energy **85**(9): 1805-1816.

Radziemska, E. (2003). "The effect of temperature on the power drop in crystalline silicon solar cells." Renewable Energy **28**(1): 1-12.

Sarwar, J., M. Browne, S. McCormack, M. J. Huang and B. Norton (2013). Experimental investigation of temperature regulation of concentrated photovoltaic using heat spreading and phase change material cooling method. The 2nd International Conference on Sustainable Energy Storage (IC-SES), Dublin, Ireland.

Sarwar, J. and B. Mansoor (2016). "Characterization of thermophysical properties of phase change materials for non-membrane based indirect solar desalination application." Energy Conversion and Management **120**: 247-256.

Sharma, S., A. Tahir, K. S. Reddy and T. K. Mallick (2016). "Performance enhancement of a Building-Integrated Concentrating Photovoltaic system using phase change material." Solar Energy Materials and Solar Cells **149**: 29-39.

Solar, I. (2013). "Solar modules - polycrystalline, Suntech power STP040-12/Rb, STP065-12/Sb, STP085-12/Bb." Retrieved September 20, 2016, from http://www.fibat.ro/energie_neconv/panouri_ibc_solar/6.pdf.

Conference Proceedings

EuroSun 2016
Palma de Mallorca (Spain), 11 - 14 October 2016

SOLAR PV FOR SWEDISH PROSUMERS – A COMPREHENSIVE TECHNO-ECONOMIC ANALYSIS

Nelson Sommerfeldt

KTH Royal Institute of Technology, Stockholm, Sweden

nelson.sommerfeldt@energy.kth.se

Abstract

Like many countries around the world, Sweden is experiencing an exponential growth in PV installations, driven largely by building mounted systems. As prosumers become significant actors in the electricity market, questions about how to integrate them technically, economically, and politically are becoming more critical. A recently concluded, three-year research effort dedicated to the techno-economic analysis of PV prosumers has identified some of the major challenges for multi-family housing owners in designing PV systems in light of uncertainty in the market and policies. This paper highlights the primary results and conclusions from the project, including; PV system sizing, strategies for electricity metering to maximize revenues, a Monte Carlo analysis to understand market and policy risks, and several case studies. The overall conclusion is that PV installations can be a profitable investment in Swedish multi-family houses, however it is important to have a roof with good solar resources, a well designed and installed system, and to capture as many available economic support programs as possible. While primarily focused on multi-family houses, much of this work can be used as a practical guide for many Swedish prosumers towards developing practical systems integration solutions and increasing renewable energy usage in buildings.

Keywords: Solar PV, Techno-economic, Monte Carlo analysis, Systems integration, Self-consumption

1. Introduction

The continued reduction in the cost of solar photovoltaics (PV) is making it increasingly easier for building owners to turn their properties into small scale, renewable energy power plants. These new actors in the energy system are transitioning from being solely consumers to both consumers and producers, often called prosumers. As subsidies continue to be reduced in parallel with reduced costs, prosumers will increasingly be subject to market conditions which will likely come with increased risk, particularly in the deregulated markets commonly found in Europe.

The PV market in Sweden is often overlooked given its small size, however the trend has been towards exponential growth (Lindahl, 2015). Solar PV is only 0.1% of total electricity generation, but it is popular with the public and if trends continue could significantly influence the power system, particularly in buildings. The low cost of electricity but high consumption and VAT taxes make prosumers the most economically interesting installation point under the current market structure.

From the prosumer's perspective, there is considerable uncertainty both inherent in the deregulated electricity market, as well as the rapidly changing policies. When considering a PV investment, there are several economically related questions which can come to mind:

- What size should the PV system be?
- What is the chance I will make a profit on my investment?
- How have others done it?
- Are there any special considerations with regards to the building?

Selection and/or peer review under responsibility of Scientific Committee
doi:10.18086/eurosun.2016.08.01 Available at http://proceedings.ises.org

There are many concerns around designing and building a PV system, and it is important to prepare and execute in the best possible way to boost the chances of profitability. For example, sufficient pre-studies to ensure good solar resources, keeping costs down, and capitalizing on available subsidies. Multi-family houses (MFH) can be particularly challenging due to the coordination of tens if not hundreds of actors (Muyingo, 2015). A recently concluded, three-year study has examined PV opportunities and risks for Swedish MFH prosumers in detail (Sommerfeldt et al., 2016). This paper is a summary of the primary results and conclusions, and covers issues regarding system sizing and electricity metering with regards to self-consumption, market and policy risks, and case studies from some first movers in this emerging market.

2. Background

Multi-family housing makes up 51% of all households in Sweden, of which 41% are resident-owned cooperatives and 59% are corporate owned and rented to tenants (Statsitics Sweden, 2013). Building electricity usage can be split into two categories; communal and private. Communal electricity consists of HVAC, exterior and stairwell lighting, garages, and laundry rooms. Private electricity is that which is used inside of apartments. Under the European Commission's energy efficiency directive (2012/27/EU), all apartments must have individual electricity meters, however billing methods can vary. Some MFH will own the apartment meters and include electricity usage with other utilities in a monthly fee, while others will allow the apartments to have electricity contracts directly with utilities and thus have their own meter. The aggregating of meters has the advantage of only one connection point with the utility that covers the entire load of the building, thus making the MFH one large customer which can save on fixed network connection fees. Independent metering gives apartment owners the freedom to select their own electricity supplier and contract to fit their needs.

Electricity supply in Sweden is dominated by hydro and nuclear power, with wind and biomass fueled co-generation plants making up the majority of the balance (Swedish Energy Agency, 2015). Demand peaks during the winter months due to a high fraction of electric heating. The wholesale and retail electricity markets are both deregulated. Most electricity is traded on the wholesale market, Nord Pool Spot, where it is purchased by retailers and delivered to end users. A variety of economic pressures have been placed on the nuclear industry, both in the market and by the government, which is likely to lead to the premature closure of several reactors (World Nuclear Association, 2015). Renewable energy development is primarily supported through a technology neutral quota system, where demand is set by the government and prices for green certificates are set by the market based on supply. This program has largely benefited the wind and biomass industries (Swedish Energy Agency, 2015).

The Swedish solar market is relatively small compare to many others in Europe. In 2015, 47 MW_p were installed resulting in a cumulative total of 127 MW_p. Fig. 1a shows how the market has expanded rapidly in recent years, which is correlated with the rapid decline in costs (shown in Fig. 1b) and favorable financial support from the government. Solar PV systems can qualify for a 20-30% capital rebate (depending on the owner), earn green certificates to sell on the quota market, and earn a 0.06 €/kWh feed-in bonus on over-production sold to the network. The future of the feed-in bonus is highly uncertain, placing emphasis on self-consumption as a way to maximize revenues. A PV system in Sweden facing south with little shading can usually expect to produce 900-1000 kWh/kW_p.

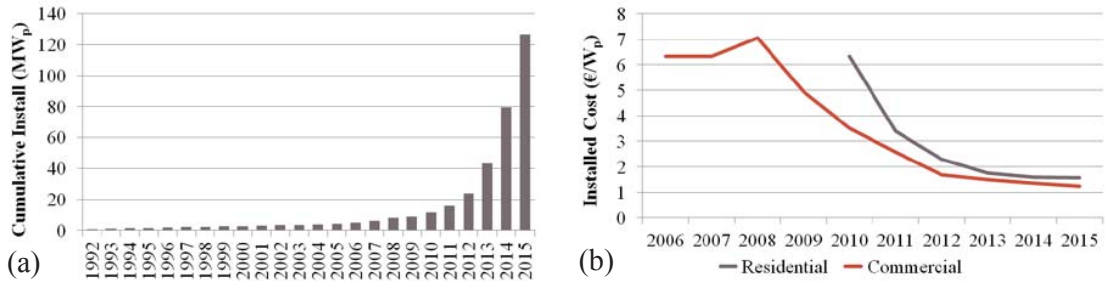

Fig. 1. Cumulative installations (left, a) and installed cost (right, b) for PV in Sweden (Lindahl, 2016)

3. System Sizing

Sizing a PV system for maximum economic benefits is difficult to generalize across buildings. Differences in building load profile, system orientation, or personal economic factors can all play a role in sizing optimization. To demonstrate this, two buildings with the same annual load but significantly different load profiles are presented with a sizing sensitivity analysis. Measured building load data is used and compared to modeled PV production values from System Advisor Model (Blair et al., 2014) using TMY2 climate data from Gothenburg, Sweden. The PV systems are set facing south with a 30° tilt and no shading, resulting in an annual production of 970 kWh/kW_p. The loads for each building are given in Tab. 1. with the key difference being that building one has a laundry rooms while two does not. The system sizes are increased in 1 kW_p increments until reaching 100% load coverage. Net present value (NPV) is used as the key performance indicator and is reported as a function of self-consumption, demand coverage, and system size.

Tab. 1: Building parameters for sensitivity analysis

Building	Laundry	Annual Demand	Maximum Size
1	Yes	27,490	28 kW_p
2	No	27,974	29 kW_p

The results are shown in Tab. 2 and Fig. 2 using three discount rates, where it can be seen that the discounting has a significant effect on optimal sizing of the PV systems. For example, the optimal size for building 1 moves from 11 kW_p to 17 kW_p to 28 kW_p with a change from 3% to 1.5% to 0% discounting, respectively. The wide range signifies the difficulty in generalizing rules for all owners. Even if those owners have nearly identical buildings, they could have different discounting preferences.

Comparing the two buildings, it is clear the optimal system sizes and corresponding demand coverage varies considerably between them. This highlights the difficulty of recommending a rule of thumb for all buildings based on a single load value, even if those buildings are of the same type like a MFH. The optimal self-consumption values are much more consistent however, which is logical since self-consumption rates scale with system size and directly affect revenues whereas demand coverage is only a sizing indicator. The curves in Fig. 2 are notably flat, with optimal size ranges being approximately ±50% of the peak to remain within 5% of the maximum NPV. However, the ranges between the two buildings do not overlap.

Tab. 2. Optimal PV system sizing results comparing a MFH with and without laundry rooms

Building	Discount Rate	Optimal System Size	Demand Coverage	Self-Consumption	Size Range Within 5% of NPV Max.
1	3.0%	11 kW_p	39%	75%	8.5 - 14 kW_p
1	1.5%	17 kW_p	60%	59%	12 - 23.5 kW_p
1	0%	28 kW_p	99%	42%	19 - 28 kW_p
2	3.0%	3 kW_p	10%	75%	2 - 4 kW_p
2	1.5%	4 kW_p	14%	64%	3 - 6 kW_p
2	0%	8 kW_p	28%	39%	5 - 13 kW_p

While it is difficult to extract a hard rule of thumb, some broad guidelines can be suggested for early stage design. In MFH with laundry rooms, the PV system can be sized such that annual production is between 30-50% of the annual demand, which will often correlate with 60-80% self-consumption. In buildings without laundry, a 15-35% ratio can be sought for similar self-consumption rates, however more care must be taken not to oversize since NPV declines more rapidly with increases in system size. In summary, before any final system decisions it is important to review hourly demand and production profiles to estimate self-consumption. It may also be the case that the investors are more focused on goals other than economic optimization. For example, in a case where an owner wishes to maximize their solar production, they could choose to cover 70-80% of their demand and still have a positive NPV, even if it is not the maximum value. More detailed analysis can be found in the project's final report (Sommerfeldt et al., 2016).

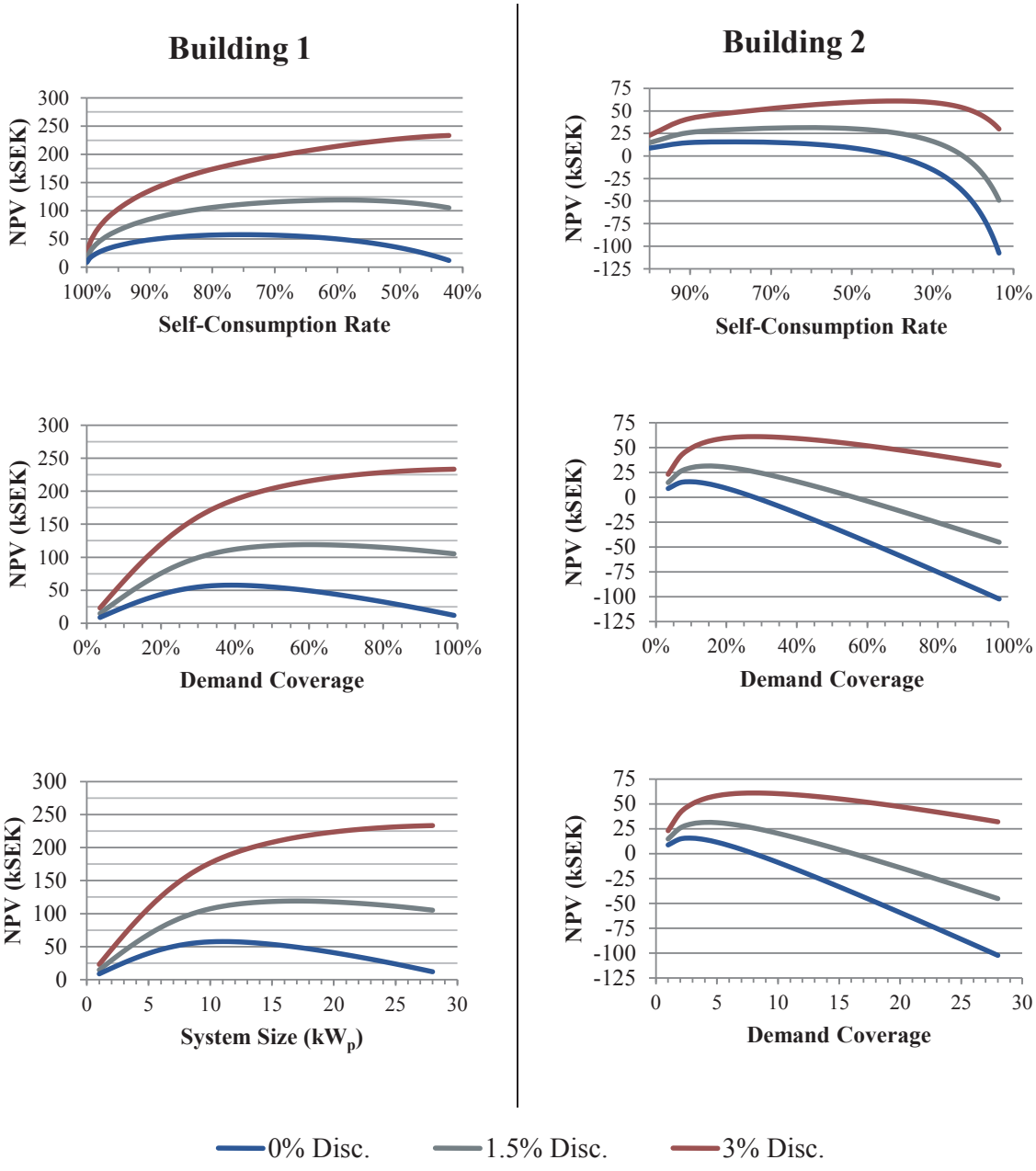

Fig. 2: PV system sizing sensitivity results for two buildings with similar demand but different load profiles

4. Electricity Metering

As mentioned in the background, MFH have options for how their building and apartments are metered by electric utilities; aggregated or independent. The metering configuration determines load volumes and profiles, which was shown in the previous section to impact PV system sizing and profitability due to changes in self-consumption. The effect of metering is tested for a six building housing cooperative considering four configurations, which are visualized in Fig. 3 and described as followed:

- Default: each building is metered separately and includes only communal loads
- Horizontal: all buildings are metered together and includes only communal loads
- Vertical: each building is metered separately and includes communal and apartment loads
- Combined: all buildings and all loads are combined into a single load

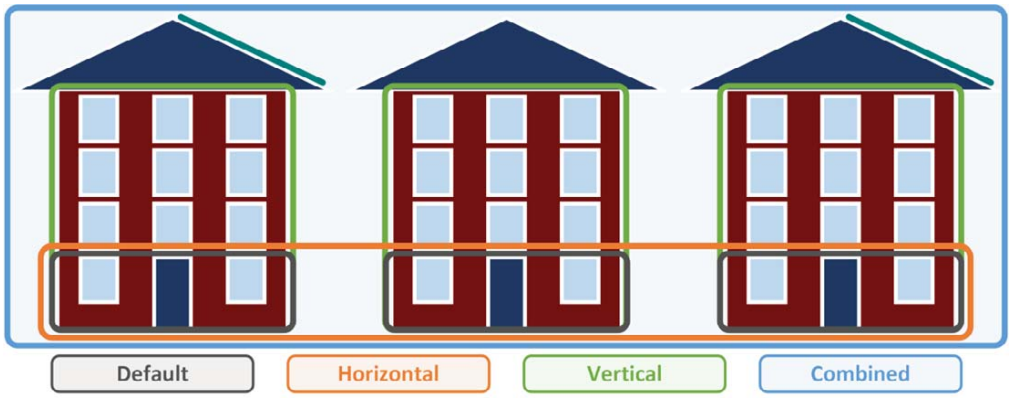

Fig. 3. Diagram of the tested metering configurations (Sommerfeldt, 2015)

Two years of measured communal load data is averaged together to create a single load curve for each of six buildings. Apartment loads are created using a Markov chain model developed by Widén and Wäckelgård (2010). Total communal and apartment demand is 264 MWh-yr^{-1} and 705 MWH-yr^{-1}, respectively. Solar production is modeled using System Advisor Model (Blair et al., 2014) with TMY2 climate data from Gothenburg, Sweden for a PV system facing due south with a 30° tilt. The buildings have identical 16 kW$_p$ systems producing 15.5 MWh-yr^{-1} each and 93 MWh-yr^{-1} in total. The economic impacts of metering are compared to the three prominent subsidies currently available in Sweden; capital rebate, green certificates, and the feed-in bonus.

Increasing self-consumption is the primary motivation for changing metering schemes, and it is found that a vertical scheme is more effective than horizontal. The default self-consumption is 60% whereas the horizontal configuration increases to 77% and the vertical to 97%. This is not entirely surprising given the significantly greater load found in the apartments. When combined the self-consumption rate reaches 100%. The effect on profitability is shown in Fig. 4, where NPV is shown to increase by €60,000 in the vertical configuration. This is significantly more than any of the subsidies which are €44,000 when combined (the subsidies are added cumulatively moving from left to right).

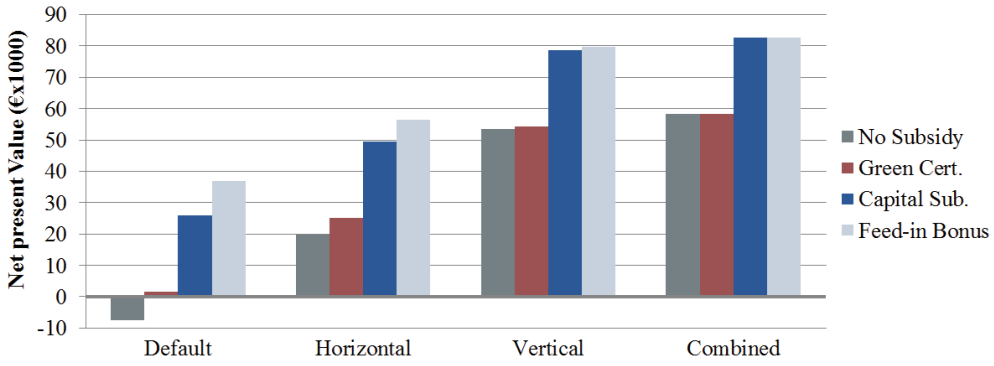

Fig. 4. Net present value of each metering scheme compared to various subsidies (Sommerfeldt, 2015)

Vertical and combined metering configurations are not entirely uncommon in Sweden due to the savings on network fees. However many MFH would need to convert, which would require the replacement of utility meters with those owned by the cooperative. The cost of this conversion would be approximately €35,000 which significantly reduces the benefit as it relates to the PV installation, but should also be compared to the saving in network fees which must be done on a case by case basis. The results also place the importance of metering in context with state subsidies. If it were easier to share generation between prosumers and consumers (i.e. removing tax and market structure barriers), then it might be possible to save on direct subsidies. Alternatively, energy service companies could see this as an opportunity to create micro-grids on housing campuses with solar PV. A more complete analysis can be found in a recent ISES Solar World Congress paper (Sommerfeldt, 2015).

5. Monte Carlo Analysis

Monte Carlo analysis (MCA) is a mathematical modeling method which uses traditional performance indicators but selects inputs at random from predefined distributions to perform repeated iterations and create a distribution of results. The MCA process can be viewed like an outer layer surrounding the inner deterministic layer, as shown in Fig. 5. Presenting the results as a distribution rather than a point value is an improvement over common sensitivity analyses in that it can give the results in a way that tells the investor *what is likely to happen* rather than *what could happen*. This is particularly relevant for PV and other renewables, which are typically subject to long payback times.

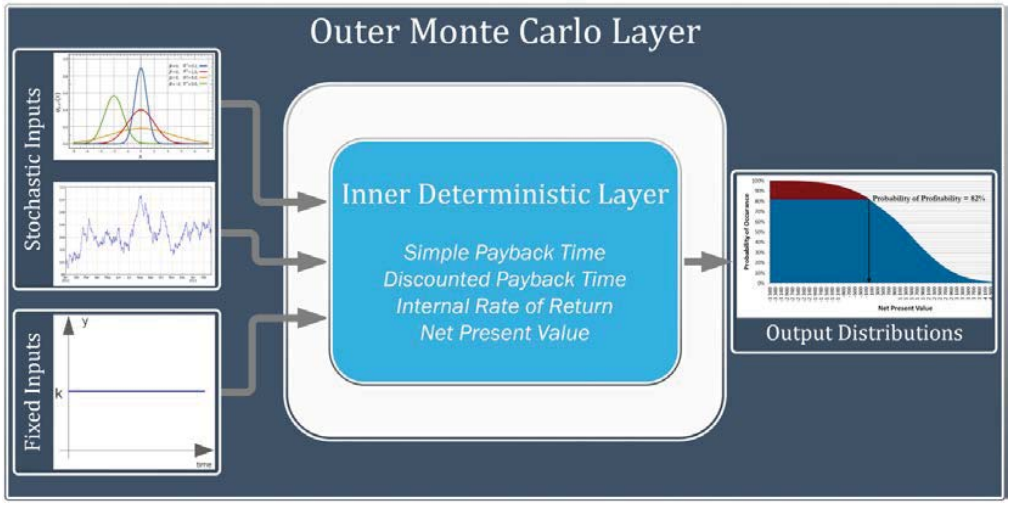

Fig. 5: Diagram of the MCA method in relation to traditional deterministic methods (Sommerfeldt and Madani, 2016)

At the core of the probabilistic method are the traditional deterministic, cost-benefit calculations based on discounted cash flows (Short et al., 1995). The outer MCA layer selects input values at random from a distribution to be fed into the deterministic models. Only the most critical factors are considered for probabilistic input, which includes electricity price, installation cost, annual generation, self-consumption rate, system lifetime, and the real discount rate. Electricity price is treated with a novel geometric Brownian motion model, while the remaining inputs are given distributions.

The output from the MCA is a distribution of NPV values. This is used to create two metrics; the probability of profitability (PoP) and probability of principle return (PPR). Profitability in this case is defined as earning the desired real discount rate (in this case a 3% real return), and thus the PoP represents the chance that NPV will be greater than zero. PPR is found the same way, however with the discount rate at 0% and thus representing only the return of the original investment.

The case presented here is intended to be representative of the most common PV installations currently in Sweden. Nominal values are annual generation at 900 kWh/kW$_p$, an installation cost of 1.81 €/kW$_p$, a system lifetime 30 years, and a self-consumption rate of 60%. The primary subsidies (capital rebate, green certificates, and the feed-in bonus) are examined in three policy scenarios, shown in Tab. 3, to give a practical assessment from the prosumer perspective. They are also examined separately to identify their individual impact.

Tab. 3: Policy scenario descriptions

Scenario	Capital Rebate	Green Certificates	Feed-In Bonus
Unsubsidized	None	None	None
Common Case	15%	Overproduction	5 Years
Best Case	20%	All production	15 Years

The results in Fig. 6 show that under a common case of policy support, a prosumer with a well-designed and well-oriented system has an approximately 70% chance of earning a profit. Without subsidies the probability falls to 8% and in a best case scenario there is a 97% chance of profit. Interestingly, the PPR is 100% in all cases, even without any policy support.

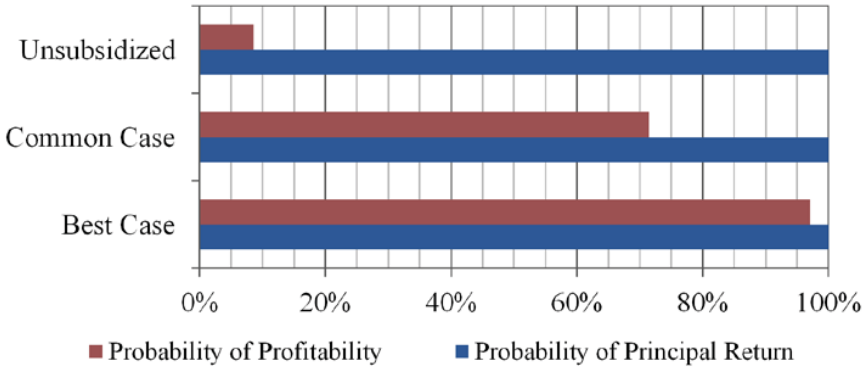

Fig. 6: Probability results for the policy scenarios (Sommerfeldt and Madani, 2016)

Comparing results from the various policies, shown in Fig. 7, indicates that the capital subsidy is the strongest tool for profitability in Sweden. The 20% capital subsidy alone is capable of lifting the PoP from 8% to nearly 60%. The feed-in bonus is the next valuable while green certificates are the least, however the feed-in bonus' future remains highly uncertain. The impact of the capital subsidy on profitability is in large part due to the immediate payment, which has no discounting applied and thus carries more value to the investor than payments extending into the future.

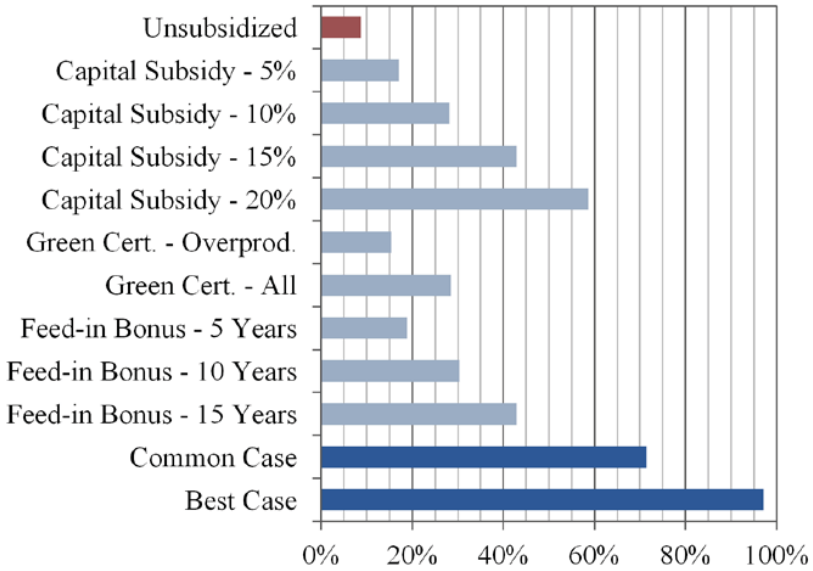

Fig. 7: PoP values for a range of subsidy levels for the most direct PV support policies (Sommerfeldt and Madani, 2016)

It is important to note that the applicability of these results are limited to the assumptions and models used, most important of these being the current market structure. There are a number of possible exogenous risks which are not easily incorporated into a single MCA which could significantly alter the probabilities presented here. These abbreviated results and further detailed analysis is presented in a recently submitted article currently under review (Sommerfeldt and Madani, 2016).

6. Case Studies

Like the remainder of the Swedish market, the number of MFH installing solar PV systems is small but growing. The boards of directors from three early adopting MFH cooperatives agreed to interviews to discuss their experiences and are used as case studies to learn about the ideation, planning, execution, and conclusions about installing a PV system. The results are summarized here and a more complete description can be found in (Sommerfeldt and Muyingo, 2015).

In all cases, the motivation for installing a PV system is rooted in a desire to improve the economic position of the cooperative. This would primarily be achieved through reduced energy costs, but in some cases it was believed that the system would create a positive image for the cooperative and subsequently improve property prices. All of the cooperatives were presented with a financial analysis from an outside party prior to construction; in two cases from the contractor installing the system and in the other the economics were simply estimated without calculation. Naturally these reports indicated positive returns for their investment such that they wanted to move forward. Since the time of the original analyses, the electricity prices collapsed by 40% and significantly altered the economic outlook. In one case it is highly unlikely that they will earn a return and may even lose some principle.

The unforeseen downturn has not dissuaded the boards from considering their projects a success. This could be because economic factors are not as critical as originally claimed, or that their opinion is biased since they have little choice but to accept the installations. The boards also see their PV as positive advertisement for their community, which has been confirmed by two of the cases being given awards by the Solar Energy Association of Sweden for their pioneering efforts (Solar Energy Association of Sweden, 2015). All of the communities have received media attention in some form, which could very well result in higher property prices since the environmental awareness in Sweden is relatively high (TNS Opinion & Social, 2014).

These cases highlight the challenges that can arise with early adopters and there is a need for improved financial assessment for PV, particularly in deregulated markets like Sweden where forecasts have a high uncertainty. However the general attitude towards PV suggests a continued increase on installations, particularly if environmental and social benefits are highlighted. As one chairman put it, “the long term sustainability of the cooperative is more important than the short term economics.”

7. Conclusions

While the volume of the Swedish PV market is still small, awareness and interest are growing such that more and more building owners are considering becoming prosumers. The results here show that PV investments can be profitable, but without dedicated policy support the chances of earning an acceptable return are low. Even with positive investment indicators, it is important for prosumers to keep in mind that PV is a long term investment and that a well design and installed system are necessary. Policy towards prosumers is highly uncertain, however high levels of self-consumption have been identified as a good way to hedge against policy changes and maintain profitability.

From a policymaker’s perspective; of the policies currently in place, the capital rebate is the most powerful and valuable to the prosumer. The receipt of the money earlier in the investment results in less discounting costs and in less uncertainty about the value. By comparison, green certificates can be earned for 15 years and have a moving price based on market conditions. Green certificates and the feed-in bonus can also act against the development of flexibility via storage or demand response. Policies should support the transition to a flexible electricity system. Therefore emphasis should be placed on the capital rebate with a long term, transparent plan for phase out that encourages stability for investing.

8. Acknowledgements

This research is funded by the Swedish Research Council Formas (no. 2012-256) and performed in conjunction with Riksbyggen, Sustainable Innovation, and the KTH School of Architecture and the Built Environment.

9. References

Blair, N., Dobos, A.P., Freeman, J., Neises, T., Wagner, M., Ferguson, T., Gilman, P., Janzou, S., 2014. System Advisor Model, SAM 2014.1.14: General Description.

Lindahl, J., 2016. National Survey Report of PV Power Applications in Sweden 2015.

Muyingo, H., 2015. Organizational Challenges in the Adoption of Building Applied Photovoltaics in the Swedish Tenant-Owner Housing Sector. Sustainability 7, 3637–3664. doi:10.3390/su7043637

Short, W., Packey, D.J., Holt, T., 1995. A Manual for the Economic Evaluation of Energy Efficiency and Renewable Energy Technologies. Golden, CO, USA.

Solar Energy Association of Sweden, 2015. Solenergipriset [WWW Document]. URL http://www.svensksolenergi.se/omoss/solenergipriset (accessed 9.7.15).

Sommerfeldt, N., 2015. On the economic effects of metering schemes in community owned residential PV systems, in: 2015 ISES Solar World Congress. Daegu, South Korea.

Sommerfeldt, N., Madani, H., 2016. Revisiting the techno-economic analysis process for building mounted, grid-connected solar photovoltaic systems: Part Two - Application. Renew. Sustain. Energy Rev. Ms. Ref. No.: RSER-D-16-01501.

Sommerfeldt, N., Muyingo, H., 2015. Lessons in community owned PV from Swedish multi-family housing cooperatives, in: 31st European Photovoltaic Solar Energy Conference and Exhibition. Hamburg.

Sommerfeldt, N., Muyingo, H., af Klintberg, T., 2016. Photovoltaic Systems for Swedish Prosumers. KTH Royal Institute of Technology, Stockholm, Sweden.

Statsitics Sweden, 2013. Yearbook of Housing and Building Statistics 2012. Stockholm.

Swedish Energy Agency, 2015. Energy in Sweden: Facts and Figures [WWW Document]. URL http://www.energimyndigheten.se/Statistik/Energilaget1/ (accessed 9.6.15).

TNS Opinion & Social, 2014. Climate change: Special Eurobarometer 409. European Commission.

Widén, J., Wäckelgård, E., 2010. A high-resolution stochastic model of domestic activity patterns and electricity demand. Appl. Energy 87, 1880–1892. doi:10.1016/j.apenergy.2009.11.006

World Nuclear Association, 2015. Nuclear Energy in Sweden [WWW Document]. Ctry. Profiles. URL http://www.world-nuclear.org/info/Country-Profiles/Countries-O-S/Sweden/ (accessed 9.25.15).

Conference Proceedings

EuroSun 2016
Palma de Mallorca (Spain), 11 - 14 October 2016

REVIEW OF SOLAR PV/THERMAL PLUS GROUND SOURCE HEAT PUMP SYSTEMS FOR EUROPEAN MULTI-FAMILY HOUSES

Nelson Sommerfeldt*, Hatef Madani

KTH Royal Institute of Technology, Stockholm, Sweden

*Corresponding author: nelson.sommerfeldt@energy.kth.se

Abstract

The combination of photovoltaic-thermal (PVT) hybrid modules with ground source heat pumps (GSHP) has the potential to increase renewable fractions of heating, cooling and power generation in buildings. The concept benefits each component in the system; the solar collector can be more efficient; collected heat can be stored in the boreholes and recovered in both short and long term; and the elevated temperatures of the boreholes improves the efficiency of the heat pump. System optimization is challenging due to the number of possible configurations, options in component designs and system control, and the close interrelation of performance between components. This study presents several system configurations which are designed to be a balance of performance, practicality, and cost. The designs are based on a state-of-the-art literature review from multiple fields (solar collectors, heat pump controls, seasonal thermal storage, and solar assisted heat pumps) and consultations with heat pump and PVT collector manufacturers.

Keywords: Solar PV/thermal, Ground Source Heat Pump, Seasonal Thermal Storage, Systems Integration

1. Introduction

In light of environmental challenges, throughout Europe there is an increased interest in integrating solar power with the built environment. At the same time, heat pumps are often considered an environmentally sound method for producing heat or domestic hot water and are often part of low-energy or net zero energy building (NZEB) concepts (Cao et al., 2016). The combination of the two, known as a solar assisted heat pump (SAHP), has been investigated for decades (Andrews, 1981a; Freeman et al., 1979; Threlkeld, 1953) with the idea that the two technologies can complement each other and improve the system as a whole. Recently, research on the subject has accelerated as environmental and regulatory pressures to reduce energy demand in buildings increase.

SAHP systems are complex both in design and operation. For the heat pump, there are multiple potential heat sources (air, ground, water, aquifer, solar) and sinks for delivering space heating and domestic hot water (hot water tanks, traditional radiators, floor heating, combi-stores, etc.) that result in a multitude of design options. Likewise, solar collectors have several designs and configurations, such as thermal and/or photovoltaic, insulated (glazed) or not, and liquid or air based. The hydronic connection can be done in series, parallel, or both and can also include regeneration of a seasonal thermal store. All together, the options are quite broad.

The recently concluded IEA project on solar assisted heat pumps (Solar Heating and Cooling Task 44 / Heat Pump Program Annex 38, hereafter referred to as T44A38) resulted in a useful handbook for guiding engineers and researchers (Hardorn, 2015). While successful examples of most configurations could be found, the most promising solutions tended towards insulated (glazed) solar collectors working in parallel with the heat pump. At the same time, the best examples also tended to be the ones where components were specifically designed for a SAHP configuration and where the control strategy was well planned.

doi:10.18086/eurosun.2016.08.15 Available at http://proceedings.ises.org

The majority of the IEA project research, and the research on SAHP in general, has been done considering solar thermal collectors in single family houses (Haller et al., 2014). However, as noted in the handbook, photovoltaic/thermal (PVT) hybrid collectors are an interesting prospect that merit further investigation. The co-generation of heating, cooling, and electricity can produce more renewable energy per roof area than other solar solutions and will likely result in alternative control strategies to thermal-only systems (Dott et al., 2012). Multi-family houses (MFH) are often overlooked since 90% of European heat pumps are installed in single family houses (EHPA, 2015), even though 40% of Europeans live in multi-family houses (Eurostat, 2015). Space for heat sources, in particular ground sourced systems, is a common limitation for MFH which are often located in denser urban areas. Regenerating the ground with solar heat could make ground source heat pumps (GSHP) a possibility for more MFH with limited space (Reda, 2015).

A recently initiated research project at KTH Royal Institute of Technology aims to fill a research gap for PVT plus ground source heat pump (GSHP) systems in MFH (Sommerfeldt, 2016). As a first step in the project, this study's objective is to identify PVT+GSHP systems with a high probability of implementation through improved performance, ease of integration, and cost efficiency. This is done primarily through a state of the art review. However given the relative lack of examples for this type of system, guidance must be inferred from similar SAHP systems as well as reviewing the relevant literature of each component.

The application for this system is in heating dominated climates, therefore less inspiration is taken from systems with significant cooling loads given their different operating conditions. There is also considerable interest in the ability to store the excess of solar energy from the summer to the winter, which is made easier with the use of boreholes in the GSHP. Direct-expansion collectors, i.e. those which use the PVT as the heat pump evaporator, are not considered due to their relatively low technology readiness for commercial use, higher cost, and risk for environmental impact. The strengths, weaknesses, and motivations for each design will be presented and the study concludes with an outline of the future work planned for the chosen systems.

2. State-of-the-Art Review

The investigation of PVT+GSHP systems dates back to 1981, where series, parallel, and even ground regeneration were all considered (Andrews, 1981b). The conclusions were that in no case could PVT be economically justified over solar thermal due to the lower thermal efficiency and that all or most of the electricity is degraded into heat. It's important to note, however, that PV modules in 1981 had a typical efficiency of 6-10% and cost 25 USD/W_p. Today's commercial PV modules can routinely be 15% efficient for 0.75 USD/W_p (Fraunhofer ISE, 2015).This rapid decline in the cost of PV has significantly altered the approach designers take in adding solar generation to buildings, and could have a similar impact in the economics of SAHP systems.

Perhaps the most comprehensive review of SAHPs comes from Haller et al. (2014), which summarized the studies performed under T44A38 and was then adapted for the SAHP handbook. As previously mentioned, solar thermal systems working in parallel with heat pumps of any source typically have the best energy performance. This correlates with the types of product available on the market, which are dominated by glazed solar thermal collectors working in parallel with air or ground source heat pumps (Hardorn, 2015).

Kamel et al. (2015) reviewed the fundamentals of SAHP systems and corresponding collector designs with an objective of identifying promising systems for cold climates. Their focus was drawn towards PVT collectors, where it was found that most studies consider the collector as the evaporator (direct-expansion) and that most SAHP systems in cold climates use liquid as the working fluid. Buker and Riffat (2016) performed a review of SAHP for low temperature water heating with a focus on system classification and performance. They concluded that an optimal configuration cannot be identified for a given climate and application due to the wide range of possible system designs and methods for measuring performance, which is similar to the conclusions from T44A38. In light of this, they call for developing a standardized method for defining performance that can capture all designs.

The work performed under T44A38 is extremely helpful as a foundation, but additional input is necessary to guide system design. The remainder of this chapter will review specific PVT+GSHP systems, as well as relevant literature which can give important insights.

2.1. PVT + GSHP Systems

Although not as common as solar thermal systems, there have been several PVT+GSHP studies performed in recent years. To be certain, there are several other SAHP oriented studies which have included PVT collectors and are not considered here. This is due to the structures of those studies not lending themselves as well to be used for system design inspiration.

Bertram et al. (2011) studied the measurements from a single family house near Frankfurt, Germany with 39 m^2 of unglazed PVT collectors, a 12 kW GSHP, and 225m (3 x 75 m each) of borehole heat exchangers (BHE) for delivering space heating and DHW. Fig. 1 shows how the PVT collectors are connected in series to the BHE loop after the heat pump, thus delivering heat to the ground first and then to the evaporator. The measurements showed that heating demands were underestimated, thus resulting in an undersized BHE. TRNSYS simulations were used to estimate long term performance. After 20 years, the system without solar showed temperature degradation in the BHE whereas the solar equipped system did not, resulting in a 13% improvement in the seasonal performance factor (SPF) in year 20. Had the BHE been sized correctly however, the improvement would only be 6%. The electrical output of the PVT was also compared to uncooled PV modules on the same roof, which showed the PVT to produce 4% more electricity.

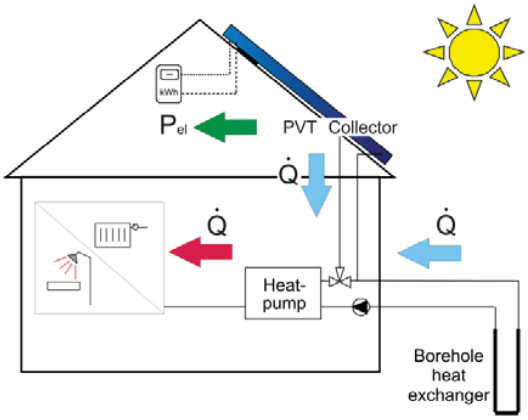

Fig. 1: PVT used to boost brine temperatures to the BHE (Bertram et al., 2011)

Another single family house in Montreal, Canada was simulated by Brischoux and Bernier (2016), shown in Fig. 2, which included a 140 m BHE with independent dual u-tube circuits, where one tube was connected to a 10 m^2 unglazed PVT array and the other to a 10 kW heat pump. The annual SPF only increased from 2.82 to 2.88. The mild performance increase was attributed to the unglazed collectors providing little benefit during the heating season, only having a single borehole (such that it could not act as a seasonal store), and that the BHE was appropriately sized. The cooled PV cells produced 7.7% more electricity than a traditional PV module. It is also worth noting that when the system boundaries are moved to include the PV production the SPF improves by 18%. This demonstrates the importance of defining relevant performance indicators, particularly when considering electrical and thermal co-generation.

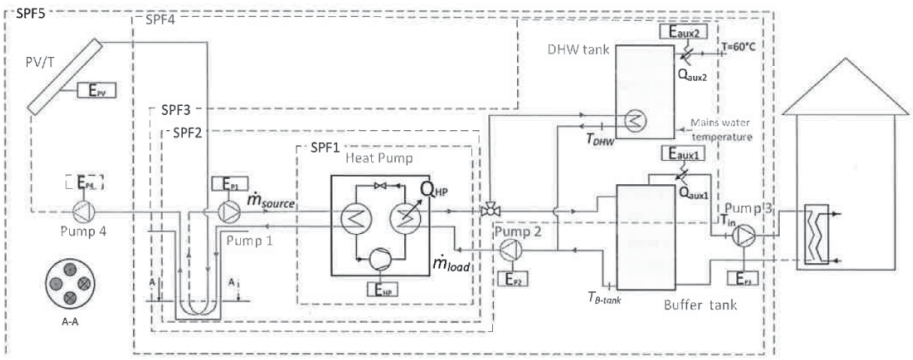

Fig. 2: PVT+GSHP concept using dual u-tubes in a single family house (Brischoux and Bernier, 2016)

In Switzerland, a low-exergy building concept presented by Meggers et al. (2012) and Baetschmann and Leibundgut (2012) includes unglazed PVT collectors combined with a novel dual-depth BHE where there are a set of 400 m boreholes for higher temperatures and a set of 200 m boreholes for lower temperatures. As shown in Fig. 3, the PVT collector heat can be used directly (in parallel) as a boost for the heat pump (in series) or to recharge the boreholes (regeneration). The concept focuses on low temperature differences between all components in the building energy system and requires a specially designed low-lift heat pump. The simulations suggest that the average coefficient of performance (COP) could be near eight and an SPF during the heating season of six. This is about double what is typically expected in European GSHP systems and highlights the performance opportunities in taking a systems approach to building energy supply.

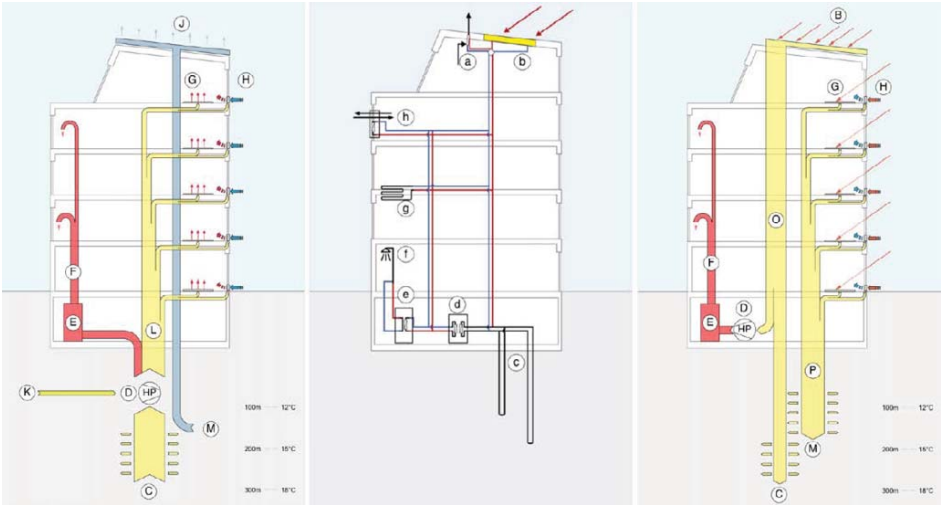

Fig. 3: Low exergy building concept configuration (center) in heating (left) and cooling modes (right) (Meggers et al., 2012)

2.2. PVT Collectors

PVT collectors come in an extremely varied range of configurations and designs (Michael et al., 2015; Riffat and Cuce, 2011; Tyagi et al., 2012; Zondag, 2008). In building applications, flat plat collectors using a liquid working fluid are the most common, leaving the primary categorization in designs being between glazed and unglazed (Kamel et al., 2015). A glazed collector typically has greater thermal efficiency but lower electrical efficiency than unglazed, so the design choice is partially influenced by which energy form is more important. In the case of unglazed collectors, there is also the choice to insulate the rear side of the panel.

The operating condition of the collector in conjunction with the GSHP is an important factor since temperatures can fall outside the typical operating conditions (Haller et al., 2012). In a series or regenerative configuration, collector temperatures can be below ambient thus making glazing or insulation a barrier to added heat gains from the ambient air. Bunea et al. (2012) tested four collector designs (flat plat, evacuated tube, unglazed-insulated, unglazed-uninsulated) with low inlet temperatures. The results show that unglazed collectors have higher efficiency during periods of low temperature or irradiance. They also showed that condensation gains can be a significant portion of the energy gains during periods of low or no incident radiation. This can be particularly helpful during winter months when heating demands are highest, but on an annual basis condensation is not likely to be a significant heat source (Bertram et al., 2010). From a product reliability standpoint, condensation does need to be attended to.

2.3. Borehole Thermal Energy Storage

Several SAHP studies have shown that borehole regeneration using a single BHE is not energy efficient due to the heat dissipating too rapidly in the earth (Bertram, 2014; Bertram et al., 2012a, 2012b; Kjellsson et al., 2010). Additionally, appropriately sized boreholes (i.e. those which would operate successfully without solar regeneration) do not significantly benefit the heat pump's SPF (Kjellsson et al., 2010; Reda, 2015). In a MFH, it is usually expected that there will be multiple boreholes and thus there is the opportunity for creating a borehole thermal energy store (BTES). The design of these stores depends on many local factors, but some general design principles can be garnered from previous work.

Most solar BTES have been designed for low mean temperatures (10-40 °C), are usually supplied by glazed solar thermal collectors, and are used in combination with heat pumps (Dalenbäck, 1990; Rad and Fung, 2016). These systems are usually designed for a high solar fraction (50-90%) and often have relatively short boreholes (30-65 m) in order to give a compact volume for minimizing heat losses. Thermal stratification, which is done radially rather than vertically as in a hot water tank, is helpful for reducing losses and improving collector efficiency but can be difficult to achieve in the ground (Dalenbäck, 1990). Nordell and Hellström (2000) state that the heat losses, and thus the efficiency, of a BTES depend primarily on the size and shape of the store, average cycle temperature (more specifically, the temperature at the boundary of the store), and the thermal properties of the ground. The optimal BTES volume is highly dependent on size of the heating demand and the desired supply temperature, and the most efficient conditions are with large loads and low temperatures (Nordell, 1994; Pahud, 2000). It is suggested that only systems with high thermal loads (greater than 500 MWh/yr) can be built cost effectively (Dalenbäck, 1990; Pahud, 1996).

Drake Landing, a solar community of 52 single family houses in Alberta, Canada, uses flat plate collectors with a high temperature BTES that feeds directly to the buildings (McClenahan et al., 2006; Wong et al., 2006). The BTES is a 35,000 m^3 cylinder with 144, 35 m deep boreholes, 2.5 m spacing, six boreholes in series, a maximum storage temperature of 80 °C and was expected to have an efficiency of 40%. Measurements after five years show that the system is performing very close to the simulations and the BTES has an efficiency of 36% with an operating temperature range of 45-70 °C (Sibbitt et al., 2012).

Chapuis and Bernier (2009) examine a redesign of Drake Landing by lowering the store temperature to have a range of 10-16 °C and then combine with a GSHP. The solar collector area is reduced by 75% and the BTES volume enlarged nearly 300% by increasing the borehole spacing to 4.5 m. The result is greater collector efficiency (58% vs. 23%) due to the lower inlet temperatures and reduced heat losses by over 70%. This configuration does require significantly more auxiliary energy input (144 vs. 11 MWh) thus lowering the solar fraction to 78% from 98%. Unfortunately no economic comparison was performed to compare the savings from the solar collectors to the cost of the heat pump and electricity.

In addition to the BTES, Drake Landing uses short term thermal storage in the form of two hot water buffer tanks with a total volume of 240 m^3. A buffer tank is a common component in a solar thermal system, and Pohud (1996) identified that a BTES only becomes economically interesting when targeting solar fractions higher than 60%. Since some solar collectors are capable of producing heat faster than the BTES can absorb it, the buffer tanks can play an important role in the control of the system and increase the efficiency of the storage system as a whole. The size of the buffer tank is predominantly linked to the collector area, and less so with the heating load type and the size of the BTES (Pahud, 2000).

2.4. Control Strategies

With the increased deployment of solar PV in buildings, there has been a decrease in financial support schemes in many countries which make it less profitable to sell overproduced electricity to the grid. It can also be the case that high penetrations of PV in a power grid will erode the tariffs during these hours and thus reduce profitability. Therefore increasing self-consumption of solar generation using load shifting and/or energy storage is likely to be increasingly important in coming years (Luthander et al., 2015).

The use of a heat pump makes it possible to convert excess electricity into thermal energy for use in the building later on, and is a concept which has seen increasing research interest. Thygesen and Karlsson (2014) compared the cost effectiveness of storage using a hot water tank with a direct electric element for DHW to lead acid batteries. For an equivalent increase in self-consumption for both technologies (from 56% without storage to 88% with) the PV + battery system was found to cost double the PV + thermal storage. Thygesen and Karlsson (2016) went on to study a weather forecasting control for the GSHP, foregoing any direct electric storage. In this case self-consumption increased from 56% without predictive control to 63% with, however heat pump demand also increases due to additional running time called for by the controller.

Control systems, particularly with a complex hydronic configuration such as in a PVT+GSHP, can create difficult optimization problems. Salpakari and Lund (2016) presented a non-linear, cost-optimization algorithm considering appliance load shifting, battery storage, and GSHP control for a single family NZEB in Helsinki. The method was compared to a baseline building without controls and found to perform

significantly better, with self-consumption increasing by as much as 30 percentage points and annual electricity costs decreasing 13-25%. A simpler rule based control algorithm was also tested and increased self-consumption, but usually resulted in higher annual costs due to increased storage losses and less efficient heat pump operation. The best performance was found with combined thermal and battery storage, however investments were not considered in a cost-benefit analysis. Storage was found to be more effective than load shifting towards improving PV self-consumption, which correlates with previous work (Widén et al., 2009).

Dar et al. (2014) compared several simple air source heat pump control strategies with PV in Oslo, considering; self-consumption maximization, electricity cost minimization, and grid import/export limitations. For a given system configuration, it was found that self-consumption could be improved by six percentage points and as much as 12 points if larger thermal stores were considered. Using spot price signals as a control input, the annual electricity cost could be reduced by up to 19%. These two objectives are currently at odds with each other, as the lowest electricity prices are currently during the night when there is no solar production. It was also shown that SPF of the heat pump was made worse in every case by 10-20% and that self-consumption by the heat pump is limited to about 35% without the use of seasonal storage.

3. Resulting System Configurations

Prior to the review, there were some design features which were planned to be a part of the system, such as the use of PVT modules, a GSHP, and a BTES. The method(s) in which these components would be connected and controlled however was unknown. In light of the review, it is clear that the complexity of the system makes objectively selecting a single best SAHP design difficult if not impossible. There are some overarching design principles which guide system design in this study to help identify a configuration. The focus is techno-economic, meaning that cost-optimized solutions are important, not only performance optimized. This places emphasis on relatively simple components and configurations, which has been previously highlighted as a design goal for future SAHP systems (Dalenbäck, 1990).

The design process can begin with the PVT collectors and the decision to use glazed versus unglazed. Glazed collectors can be more thermally efficient at the expense of electrical efficiency, but are likely to be restricted to the sink side of the heat pump (parallel configuration) due to the risk of condensation inside the collector from the low inlet temperatures of the BHE loop. Unglazed collectors have the advantage of acting as an air-to-water heat exchanger during periods of low irradiance, having lower cost due to less materials and can more easily integrate with PV systems (physically and aesthetically).

Having access to seasonal storage via the BTES is a major element in the design considerations. The elevated temperatures will supply the heat pump higher source temperatures, thus improving efficiency, but not without limits. The BTES core temperatures should be planned to be low enough such that it can continue to work with the heat pump during the summer when temperatures are highest. Integrating the collectors on the source side makes it easier to access the BTES for regeneration. It also has the advantage of being relatively easy to integrate into existing systems, as there would be no need to change the hydronic system between the heat pump and the building. A series configuration also pairs well with the unglazed PVT collectors, since much of the time outlet temperatures from the PVT will likely be too low to supply the building directly.

Considering the economic goals of the system and the inclusion of a seasonal BTES, a series/regenerative configuration is chosen for this project. Not using the solar energy directly may lead to a less energy or exergy efficient system (Haller and Frank, 2011), however it may be that the cost efficiency will be greater. The integration of the PVT collectors to the BHE loop remains an open question, and there are several possibilities to do this that are difficult to rank without more information. Therefore the following four design concepts will be simulated to determine performance and cost effectiveness; PVT-in-loop, heat exchanger, buffer tank, and dual u-tube.

The first concept, shown in Fig. 4 places the PVT collector in the same hydronic circuit as the connection between the heat pump and BHE, similar to the system presented by Bertram et al. (2011). The strengths of this configuration are its simplicity and low cost, where only one three-way and one check valve are required. The weaknesses include lack of control over flow rate or fluid properties, as the PVT collector is directly bound to the requirements of the heat pump and BHE.

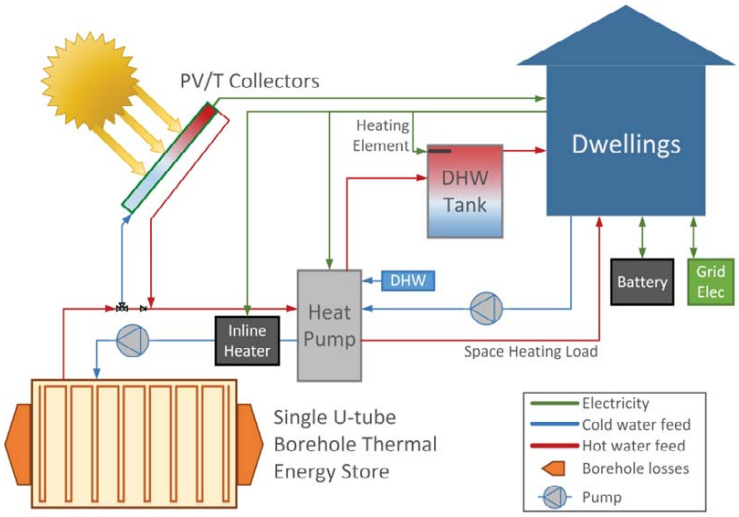

Fig. 4: Concept One using PVT in the BHE loop to boost incoming fluid temperature to the HP

There are two additional components that appear in every concept; batteries and an inline heater connected to the BTES. These allow the storage of electricity with the batteries being short term chemical storage and the BTES being long term thermal storage. While there may be large amounts of exergy destruction by heating the BTES with electricity, the heat is reducing the need for electricity from the heat pump in the winter thus acting as a method for storing electricity rather than simply converting it to heat. It can also test the cost efficiency of the BTES in comparison to selling electricity to the market.

Another consideration for all concepts is the connection point for the PVT collectors, which can go in either the supply or return lines from the BHE to the heat pump. Thermodynamically it would be the most logical to use the heat to boost the temperature supply into the heat pump, however they have a source temperature limit that could cause faults. Therefore a pre-study will need to be made to determine the appropriate connection point, which will then be used in all concepts.

Concept two uses a liquid-to-liquid heat exchanger to integrate the PVT collectors, as shown in Fig. 5. This configuration overcomes a weakness of concept one by allowing the PVT circuit flow rate to be controlled independently from the BHE circuit. It also allows for a separate working fluid, which may be important in later years when the BTES is fully charged and it's possible to reduce the fractions of antifreeze in the BHE circuit. The primary weaknesses are the additional cost of a heat exchanger and the higher pumping demands due to the additional pressure drop. From a practical standpoint, the integration of this concept into the physical system should be similar to concept one and does not require a prohibitive amount of space.

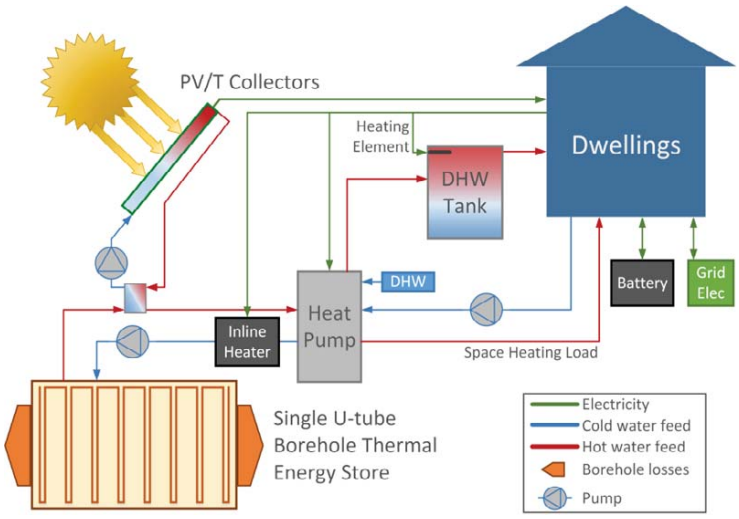

Fig. 5: Concept two using a liquid-to-liquid heat exchanger to boost incoming fluid temperatures to the HP

In concept three, the heat exchanger in concept two is replaced with a buffer tank as shown in Fig. 6. This concept's strength is that it could result in more efficient use of the solar heat by avoiding delivery to the BTES until there is an excess of solar energy beyond daily use, as recommended by Pahud (1996). The control of the buffer may require forecasting to decide when to release the heat into the BTES. This concept has the potential for improved control options over concept two, but has the weakness of the cost and space for space for the tank.

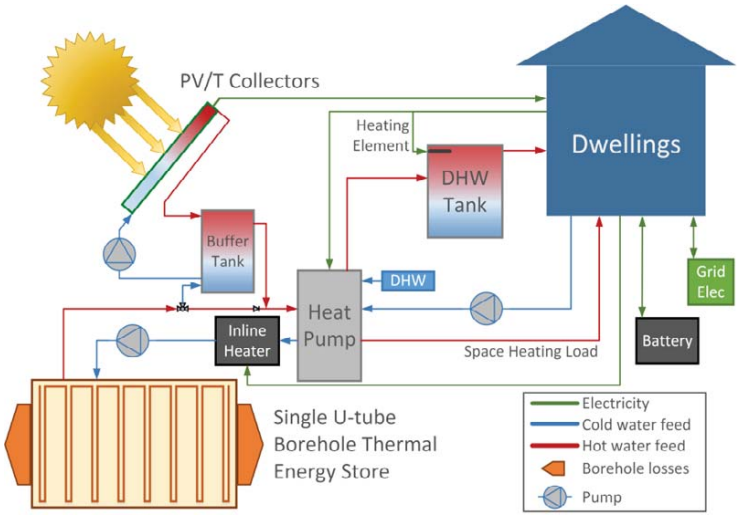

Fig. 6: Concept three using a storage tank to boost incoming fluid temperatures to the HP

Concept four, shown in Fig. 7, uses the BHE as the heat exchanger for the PVT collectors and the heat pump via a dual u-tube, similar to Brischoux and Bernier (2016). This configuration has the same strengths as concepts two and three, where independent working fluids and flow rates can be used. It also removes the need for valve control strategies since the circuits are completely separate and can be controlled independently. The greatest weakness for this concept is that it applies predominantly to new systems, since many existing systems only use a single u-tube and adding a second tube may be prohibitively expensive or impractical. There will also be high pumping losses in the PVT circuit since it includes the BTES as well.

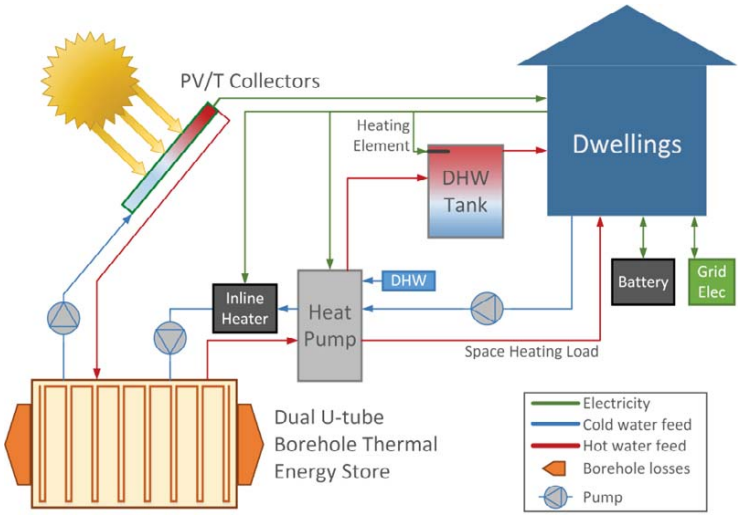

Fig. 7: Concept four using dual u-tubes as a heat exchanger and regeneration method

Recent market trends have seen new solar thermal system installations decline with the rise of solar PV, particularly on rooftops. PVT collectors have traditionally been used to create DHW directly but have never had a significant market share. In this application it is interesting to ask if the additional thermal energy collection justify the costs. Therefore a fifth concept, shown in Fig. 8, is considered which only uses PV

collectors that are coupled to the BTES. This concept tests the marginal value of adding a thermal component to the PV collectors and the associated hydronic complexities. In this concept, the battery acts as short term storage, similar to a thermal buffer tank, while the BTES is used as long term seasonal storage.

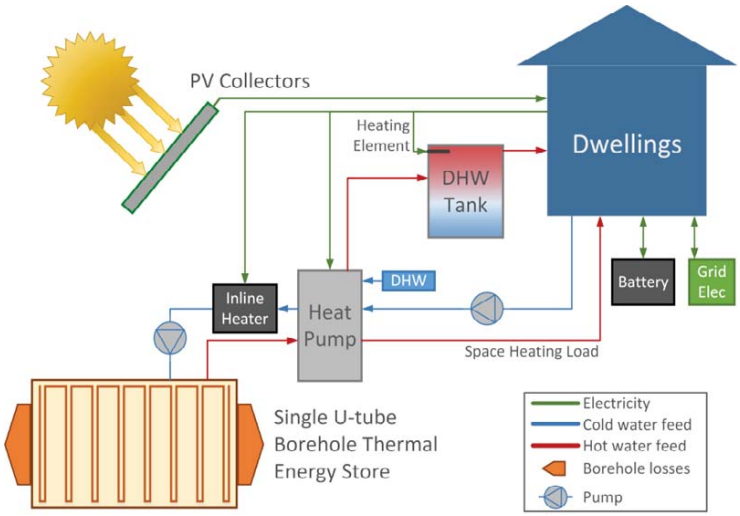

Fig. 8: Concept only considering PV and borehole regeneration

4. Discussion

A significant challenge when reviewing SAHP systems, particularly when comparing thermal to PV systems, is the lack of consistency between metrics used in studies (Buker and Riffat, 2016). Many authors use traditional key performance indicators (KPI) such as SPF, solar fraction, self-consumption, self-sufficiency, or renewable fraction, however the system boundaries are often not defined or do not capture the performance of the entire system as it relates to the owner. For example, if the indicator boundaries are limited to the heating system, the value of the PV generation to the rest of the building loads can be missed. The traditional indicators are still valuable to SAHP analysis, however care must be taken not to emphasize any particular one to the detriment of the others (Dar et al., 2014).

An extensive discussion surrounding the selection and use of KPI can be found in the SAHP handbook (Hardorn, 2015), and the top level systems definition of SPF is given by eq. 1. In the numerator is the total space (Q_{SH}) and domestic hot water (Q_{SH}) energy supplied to the building. The denominator includes the electricity used by the heat pump (E_{HP}), all auxiliary heaters ($E_{AUX,H}$), and all auxiliary pumps ($E_{AUX,P}$). One missing factor in this definition is electricity supplied from PV. In PV-HP literature there is often a focus on self-consumption and the definition for SPF is the same as in a non-solar HP, however as noted earlier, PV generation can make a significant improvement to SPF (Brischoux and Bernier, 2016).

$$SPF_{sys,grid} = \frac{\int Q_{SH} + Q_{DHW}}{\int [E_{HP} + \sum E_{AUX,H} + \sum E_{AUX,P}]} \qquad \text{(eq. 1)}$$

In a SAHP with PVT cogeneration, the handling of the electricity generation raises interesting questions about KPI. What fraction of PV generation should be applied to the heat pump? Is it necessary to make such a distinction in SPF? Are there other KPI (or combination of indicators) which would be more useful to the owner? Environmental or economic indicators can often be important to the purchaser of energy related equipment. In an economic KPI, it is important to capture the impact PV generation has on the entire building load and not limit it to the SAHP system. It is also necessary to capture all costs and benefits in order to make a fair comparison between options. Further research and careful consideration will be made towards the selection of KPI to ensure fair and relevant evaluation of the PVT+GSHP systems.

5. Summary and Future Work

Solar assisted heat pumps are complex in design, operation, and analysis. The review presented in this paper briefly captures some of the facets to be considered in the design of a PVT+GSHP system, including; collector design, borehole thermal energy storage, hydronic configurations and control strategies. The four PVT system concepts presented are focused on simplicity and practicality, and are of the series/regenerative configuration with various integration methods for the PVT into the BHE hydronic loop. They are designed primarily to maximize cost efficiency with the expectation that energy or exergy performance may not be as high as other designs. The marginal benefit of collecting heat from a PV array will also be tested by simulating a PV-only system which can also feed into the BTES.

The next steps in the project are to create system models in TRNSYS, finalize the remaining questions about system configuration, and identify appropriate ranges of component sizes. Input from component manufacturers for PVT collectors, heat pumps, and boreholes will be used to ensure that the practical limits of the components are respected and to identify opportunities for designs specific to this application. Care will be taken to ensure that most representative costs are used for the installed system, which is particularly important given the uniqueness of the concept. Control strategies will also be tested to optimize the use of the batteries, heat pump compressor speed, circulation pumps, etc. Effort will also go into defining meaningful KPI to evaluate and optimize systems that are relevant to the system owners. The primary area of application is in the Nordic region, therefore building construction, usage, and GSHP system designs will be taken from regional norms.

6. Acknowledgements

This research is funded by the Swedish Energy Agency through the Effsys Expand program, for which the authors are most grateful. Appreciation is also given to the private companies contributing to the project, including; Danfoss heat pumps, Solybrid i Småland, HP Borringar, Geobatteri, Bengt Dahlgren, Nowab AB, Avanti Drillers Association, housing cooperative Moranvikan, and housing cooperative Timmermannen 2.

7. References

Andrews, J.W., 1981a. Ground coupled solar heat pumps: Analysis of four options, in: Amercian Society of Mechanical Engineers (Ed.), 4th ASME Solar Energy Division Conference. Amercian Society of Mechanical Engineers, Reno, Nevada.

Andrews, J.W., 1981b. Evaluation of Flat-Plate Photovoltaic / Thermal Hybrid Systems for Solar Energy Utilization, U.S. Department of Energy.

Baetschmann, M., Leibundgut, H., 2012. LowEx Solar Building System: Integration of PV/T Collectors into Low Exergy Building Systems. Energy Procedia 30, 1052–1059. doi:10.1016/j.egypro.2012.11.118

Bertram, E., 2014. Solar Assisted Heat Pump Systems with Ground Heat Exchanger – Simulation Studies. Energy Procedia 48, 505–514. doi:10.1016/j.egypro.2014.02.060

Bertram, E., Glembin, J., Rockendorf, G., 2012a. Unglazed PVT collectors as additional heat source in heat pump systems with borehole heat exchanger. Energy Procedia 30, 414–423. doi:10.1016/j.egypro.2012.11.049

Bertram, E., Glembin, J., Scheuren, J., Rockendorf, G., 2010. Condensation heat gains on unglazed solar collectors in heat pump systems, Proceedings of the EuroSun 2010 Conference. Graz, Austria.

Bertram, E., Pärisch, P., Tepe, R., 2012b. Impact of solar heat pump system concepts on seasonal performance-Simulation studies, Eurosun 2012 - ISES-Europe Solar Conference. Rijeka, Croatia.

Bertram, E., Stegmann, M., Rockendorf, G., 2011. Heat pump systems with borehole heat exchanger and unglazed PVT collector, in: ISES Solar World Congress. Kassel, Germany, pp. 1170–1179.

Brischoux, P., Bernier, M., 2016. Coupling PV/T Collectors with a Ground-Source Heat Pump System in a Double U-tube Borehole, in: 2016 ASHRAE Winter Conference. ASHRAE, Orlando, Florida, p. OR-16-C046.

Buker, M.S., Riffat, S.B., 2016. Solar assisted heat pump systems for low temperature water heating applications: A systematic review. Renew. Sustain. Energy Rev. 55, 399–413. doi:10.1016/j.rser.2015.10.157

Bunea, M., Eicher, S., Hildbrand, C., Bony, J., 2012. Performance of solar collectors under low temperature conditions: Measurements and simulations results, in: Eurosun 2012 - ISES-Europe Solar Conference. Rijeka, Croatia.

Cao, X., Dai, X., Liu, J., 2016. Building energy-consumption status worldwide and the state-of-the-art technologies for zero-energy buildings during the past decade. Energy Build. 128, 198–213. doi:10.1016/j.enbuild.2016.06.089

Chapuis, S., Bernier, M., 2009. Seasonal storage of solar energy in borehole heat exchangers, in: Eleventh International IBPSA Conference. Glasgow, pp. 599–606.

Dalenbäck, J.-O., 1990. Central Solar Heating Plants with Seasonal Storage - Status Report (D14:1990). IEA Solar Heating and Cooling Programme - Task VII.

Dar, U.I., Sartori, I., Georges, L., Novakovic, V., 2014. Advanced control of heat pumps for improved flexibility of Net-ZEB towards the grid. Energy Build. 69, 74–84. doi:10.1016/j.enbuild.2013.10.019

Dott, R., Genkinger, A., Afjei, T., 2012. System Evaluation of Combined Solar & Heat Pump Systems. Energy Procedia 30, 562–570. doi:10.1016/j.egypro.2012.11.066

EHPA, 2015. European Heat Pump Market and Statistics Report 2015. Brussels.

Eurostat, 2015. Housing Statistics [WWW Document]. URL http://ec.europa.eu/eurostat/statistics-explained/index.php/Housing_statistics#Further_Eurostat_information (accessed 9.12.16).

Fraunhofer ISE, 2015. Current and Future Cost of Photovoltaics. Long-term Scenarios for Market Development, System Prices and LCOE of Utility-Scale PV Systems.

Freeman, T., Mitchell, J., Audit, T., 1979. Performance of combined solar-heat pump systems. Sol. Energy 22, 125–135.

Haller, M.Y., Bertram, E., Dott, R., Afjei, T., Ochs, F., Hadorn, J.-C., 2012. Review of Component Models for the Simulation of Combined Solar and Heat Pump Heating Systems. Energy Procedia 30, 611–622. doi:10.1016/j.egypro.2012.11.071

Haller, M.Y., Carbonell, D., Mojic, I., Winteler, C., Bertram, E., Bunea, M., Lerch, W., Ochs, F., 2014. Solar and heat pump systems - summary of simulation results of the IEA SHC task 44/HPP annex 38, in: 11th IEA Heat Pump Conference. Montreal, pp. 1–12.

Haller, M.Y., Frank, E., 2011. On the potential of using heat from solar thermal collectors for heat pump evaporators, in: ISES Solar World Congress. Kassel, Germany, pp. 1–10.

Hardorn, J.-C. (Editor), 2015. Solar and Heat Pump Systems for Residential Buildings, First. ed. Ernst & Sohn GmbH & Co., Berlin.

Kamel, R.S., Fung, A.S., Dash, P.R.H., 2015. Solar systems and their integration with heat pumps: A review. Energy Build. 87, 395–412. doi:10.1016/j.enbuild.2014.11.030

Kjellsson, E., Hellström, G., Perers, B., 2010. Optimization of systems with the combination of ground-source heat pump and solar collectors in dwellings. Energy 35, 2667–2673. doi:10.1016/j.energy.2009.04.011

Luthander, R., Widén, J., Nilsson, D., Palm, J., 2015. Photovoltaic self-consumption in buildings : A review. Appl. Energy 142, 80–94. doi:10.1016/j.apenergy.2014.12.028

McClenahan, D., Gusdorf, J., Kokko, J., Thornton, J., Wong, B., 2006. Okotoks: Seasonal Storage of Solar Energy for Space Heat in a New Community, in: ACEEE Summer Study on Energy Efficiency in Buildings. Pacific Grove, pp. 121–132.

Meggers, F., Ritter, V., Goffin, P., Baetschmann, M., Leibundgut, H., 2012. Low exergy building systems implementation. Energy 41, 48–55. doi:10.1016/j.energy.2011.07.031

Michael, J.J., Iniyan, S., Goic, R., 2015. Flat plate solar photovoltaic – thermal (PV / T) systems : A reference guide. Renew. Sustain. Energy Rev. 51, 62–88. doi:10.1016/j.rser.2015.06.022

Nordell, B., 1994. Borehole heat store design optimization. Luleå University of Technology. doi:10.1007/s13398-014-0173-7.2

Nordell, B.O., Hellström, G., 2000. High temperature solar heated seasonal storage system for low temperature heating of buildings. Sol. energy 69, 511–523. doi:10.1016/S0038-092X(00)00120-1

Pahud, D., 1996. Simulation of Central Solar Heating Plants Using a Duct Store: An Application for Switzerland. Lund University.

Pahud, D., 2000. Central solar heating plants with seasonal duct storage and short-term water storage: Design guidelines obtained by dynamic system simulations. Sol. energy 69, 495–509. doi:10.1016/S0038-092X(00)00119-5

Rad, F.M., Fung, A.S., 2016. Solar community heating and cooling system with borehole thermal energy storage – Review of systems. Renew. Sustain. Energy Rev. 60, 1550–1561. doi:10.1016/j.rser.2016.03.025

Reda, F., 2015. Long term performance of different SAGSHP solutions for residential energy supply in Finland. Appl. Energy 144, 31–50. doi:10.1016/j.apenergy.2015.01.059

Riffat, S.B., Cuce, E., 2011. A review on hybrid photovoltaic/thermal collectors and systems. Int. J. Low-Carbon Technol. 6, 212–241. doi:10.1093/ijlct/ctr016

Salpakari, J., Lund, P., 2016. Optimal and rule-based control strategies for energy flexibility in buildings with PV. Appl. Energy 161, 425–436. doi:10.1016/j.apenergy.2015.10.036

Sibbitt, B., McClenahan, D., Djebbar, R., Thornton, J., Wong, B., Carriere, J., Kokko, J., 2012. The Performance of a High Solar Fraction Seasonal Storage District Heating System – Five Years of Operation. Energy Procedia 30, 856–865. doi:10.1016/j.egypro.2012.11.097

Sommerfeldt, N., 2016. Solar energy and ground source heat pumps for Swedish multi-family housing [WWW Document]. URL http://tinyurl.com/KTH-PVT-GSHP (accessed 8.25.16).

Threlkeld, J.L., 1953. Solar energy as a potential heat source for the heat pump (Phd Thesis). University of Minnesota.

Thygesen, R., Karlsson, B., 2014. Simulation and analysis of a solar assisted heat pump system with two different storage types for high levels of PV electricity self-consumption. Sol. Energy 103, 19–27. doi:10.1016/j.solener.2014.02.013

Thygesen, R., Karlsson, B., 2016. Simulation of a proposed novel weather forecast control for ground source heat pumps as a mean to evaluate the feasibility of forecast controls' influence on the photovoltaic electricity self-consumption. Appl. Energy 164, 579–589. doi:10.1016/j.apenergy.2015.12.013

Tyagi, V.V., Kaushik, S.C., Tyagi, S.K., 2012. Advancement in solar photovoltaic/thermal (PV/T) hybrid collector technology. Renew. Sustain. Energy Rev. 16, 1383–1398. doi:10.1016/j.rser.2011.12.013

Widén, J., Wäckelgård, E., Lund, P.D., 2009. Options for improving the load matching capability of distributed photovoltaics: Methodology and application to high-latitude data. Sol. Energy 83, 1953–1966. doi:10.1016/j.solener.2009.07.007

Wong, W.P., Mcclung, J.L., Kokko, J.P., Snijders, A.L., 2006. First large-scale solar seasonal borehole thermal energy storage in Canada, in: Proceedings of Ecostock Conference. Stockton.

Zondag, H., 2008. Flat-plate PV-Thermal collectors and systems: A review. Renew. Sustain. Energy Rev. 12, 891–959. doi:10.1016/j.rser.2005.12.012

Conference Proceedings

EuroSun 2016
Palma de Mallorca (Spain), 11 - 14 October 2016

FINE-TUNING OF MULTI-JUNCTION SOLAR CELLS: A THEORETICAL ASSESSMENT

Laurène Parent[1], Alberto Riverola[2], Daniel Chemisana[2], Alain Dollet[1] and Alexis Vossier[1]

[1] Laboratoire Procédés, Matériaux et Energie Solaire- PROMES-CNRS UPR8521, Odeillo/Perpignan (France)

[2] Universitat de Lleida, Lleida (Spain)

Abstract

The typical number of subcells comprised in multijunction solar cells steadily increased over the last 25 years to achieve higher electrical efficiencies. However, these cells typically show increased sensitivity to the spectral content of sunlight, and the efficiency under real conditions can be significantly affected. This study investigates whether or not fine-tuning of MJ solar cells could lead to significant improvement in the energy yield of CPV systems comprising a high number of subcells. The average incident spectrum in several cities is obtained with SMARTS, using as an input the main atmospheric parameters from AERONET database. The optimal combinations of bandgaps for all the selected locations and cell architectures comprising up to 10 subcells was derived. In particular, the improvement in the energy output achieved when using fine-tuned MJ solar cells to a mean annual spectrum in a located area is investigated. Implications for future generations for multi-junction solar cells are also discussed.

Keywords: *Multi-junction solar cells, spectral distribution, fine-tuning, energy yield, optimization,*

1. Introduction

Multi-junction solar cells could potentially achieve ultra-high solar-to-electricity conversion efficiency (Pérez-Higueras and Fernández, 2015) and are seen as one of the most promising options toward affordable solar electricity. Cells comprising up to 5 different subcells have been reported in the litterature with efficiencies currently approaching 50%. Today, the world record is held by a quadruple-junction solar cell with a conversion efficiency of 46% under concentrated sunlight (Green et al., 2015).

Increasing the number of *pn* junctions with appropriate band gaps leads to a more efficient utilization of the solar spectrum and consequently better conversion efficiencies. Nonetheless, the spectral distribution of the light reaching the cells may affect dramatically the ability of MJ cells to efficiently convert sunlight into electricity. The photovoltaic conversion efficiency is usually provided assuming a spectral distribution of the incoming light described by the AM1.5 reference spectrum. However, the spectral distribution of light is likely to vary significantly due to changes in the atmospheric parameters, and the ability of MJ cells comprising a high number of subcells to accommodate changes in the spectral distribution was recently questioned (Chan et al., 2014; Vossier et al., 2015). In particular, the energy output of CPV systems was shown to be highly dependent on the climatic conditions to which it is exposed. Fine-tuning of solar cells is often mentioned as a promising strategy toward increasing the efficiency with which solar energy is converted into electricity: Fine-tuning basically consists in tailoring the combination of electronic gaps comprised in the MJ stack to the spectral distribution characteristic of a particular location. This raises the question of whether or not CPV systems involving fined-tuned MJ solar cells are likely to outperform conventional MJ cells designed according to the AM1.5D reference solar spectrum, taking into account the typical variations in working conditions over a long period of time.

doi:10.18086/eurosun.2016.08.23 Available at http://proceedings.ises.org

2. Method

In order to tackle this question, the mean spectral distribution of the light received in several locations around the world was first assessed, using long time series of actual measurements of the main atmospheric variables at widely different sites. The locations investigated here were chosen for being representative of the large range of climatic conditions on the planet. They cover a wide range of latitudes (see details in Table 1), extending from Nauru (near the equator) to Palaiseau (near Paris, France). Xianghe (China) is characterized by a high pollution level resulting in systematically large AOD. Nauru is a tropical site with high PW, as opposed to arid sites, such as Sede Boqer. The latter is characterized by intermediate values of all variables, with however large daily excursions in AOD and α in the wake of regional dust storm activity.

The direct normal irradiance spectrum was calculated with SMARTS radiative model (Gueymard, 2001) whose main input parameters are the Air Mass (AM), the Aerosol Optical Depth (AOD), the Precipitable Water (PW), the Angstrom exponent (α),. The AM values were evaluated in SMARTS from the solar zenith angle (Z) for the location and time considered. Simultaneous values of Z, AOD, PW, α, were obtained from the Aerosol Robotic Network (AERONET) database (http://aeronet.gsfc.nasa.gov). From this set of data, the mean annual solar spectra were derived for each selected location, and compared to the AM1.5D (AM=1.5, AOD_{500} = 0.084 and PW = 1.416 cm) solar spectrum (from ASTM G173) commonly used as an input solar spectrum when designing solar cells.

Table 1: Characteristic parameters for the selected locations

Location	Simulated year	Lat. (°)	Long. (°)	Elevation (m)	Mean daily DNI (kWh/m2/day) [Source: (SWERA)]	Annual mean atmospheric parameters AM | AOD | PW |α
Nauru	2011	-0.52	166.92	7	6-6.5	1.72 | 0.09 | 4.17 |0.26
Sede Boqer	2004	30.86	34.78	480	6-6.5	1.92 | 0.18 | 1.34 |0.86
Xianghe	2009	39.75	116.96	32	2.5-3	2.07 | 0.53 | 1.01 |1.12
Palaiseau	2012	48.71	2.21	156	3–3.5	2.29 | 0.16 | 1.44 |1.15

Fig. 1 depicts the spectral distribution of the mean annual solar spectrum for each city investigated in this study, using the method described above. Some spectra are shown to deviate drastically from the AM1.5D Spectrum (bold purple curve). Places characterized by low latitudes and favorable climatic parameters (such as Sede Boqer or Nauru) show relatively high annual mean intensities. Conversely, places characterized by high latitudes (such as Palaiseau) and/or poor atmospheric parameters (i.e Xianghe), demonstrate modest values of the mean annual solar spectrum. Such a representation, however, does not allow a convenient analysis of the extent with which each range of wavelength is altered.

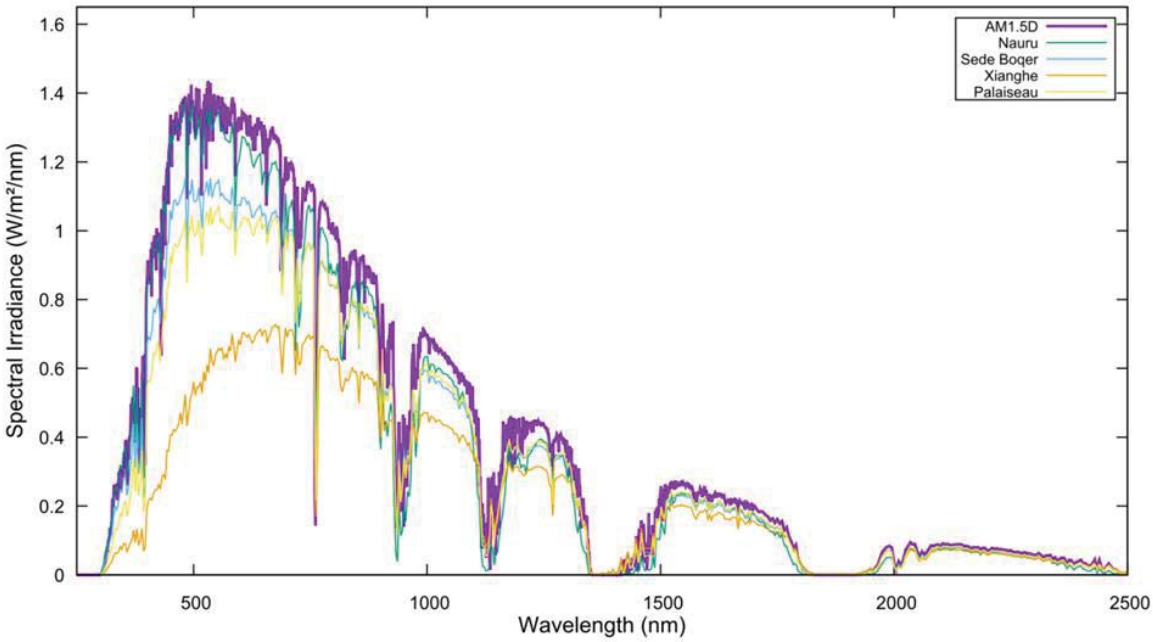

Fig. 1: Mean annual solar spectrum for each investigated city

For sake of clarity, the relative residual of the mean annual spectrum with the AM1.5D spectrum is reported in Figure 2. The spectra are normalized so that the total solar irradiance corresponding to each spectrum equals the power corresponding to AM1.5D solar spectrum (900W/m²). The deviation relative to the AM1.5 solar spectrum is represented as a red curve for each city investigated. The regions of the spectra corresponding to the absorption bands were removed from the graphs (the very low spectral irradiance values associated with these regions gave rise to high levels of noise). Several statements can be drawn from Fig. 2:

- First, for Xianghe and Palaiseau, the mean annual spectrum, calculated using the method described above, shows lower irradiance values in the UV-Vis range relative to the AM1.5D solar spectrum. From these first preliminary data values, it is expected that a fine-tuning of the MJ cells will lead to an optimal combination of subcells characterized by lower values of their electronic gaps, when compared to AM1.5-optimized MJ cells. On the other hand, Nauru exhibits higher values in the UV-Vis range and consequently higher electronics gaps are expected. The solar spectrum is mostly attenuated in this range by the air mass and the AOD which are particularly low in this city. Sede Boqer presents a spectrum similar to AM1.5 and significant differences in the bandgaps are not expected.

- Second, the amplitude of the spectrum alteration over a full year varies drastically from one place to the other. If Nauru and Sede Boker show modest variations in the annual spectral distribution of light (relative to AM1.5 spectrum), Palaiseau and Xianghe demonstrate significant changes in the spectral content of the light, and fine-tuned MJ cells should could lead to a noticeable improvement in the electrical efficiency of CPV systems in these locations.

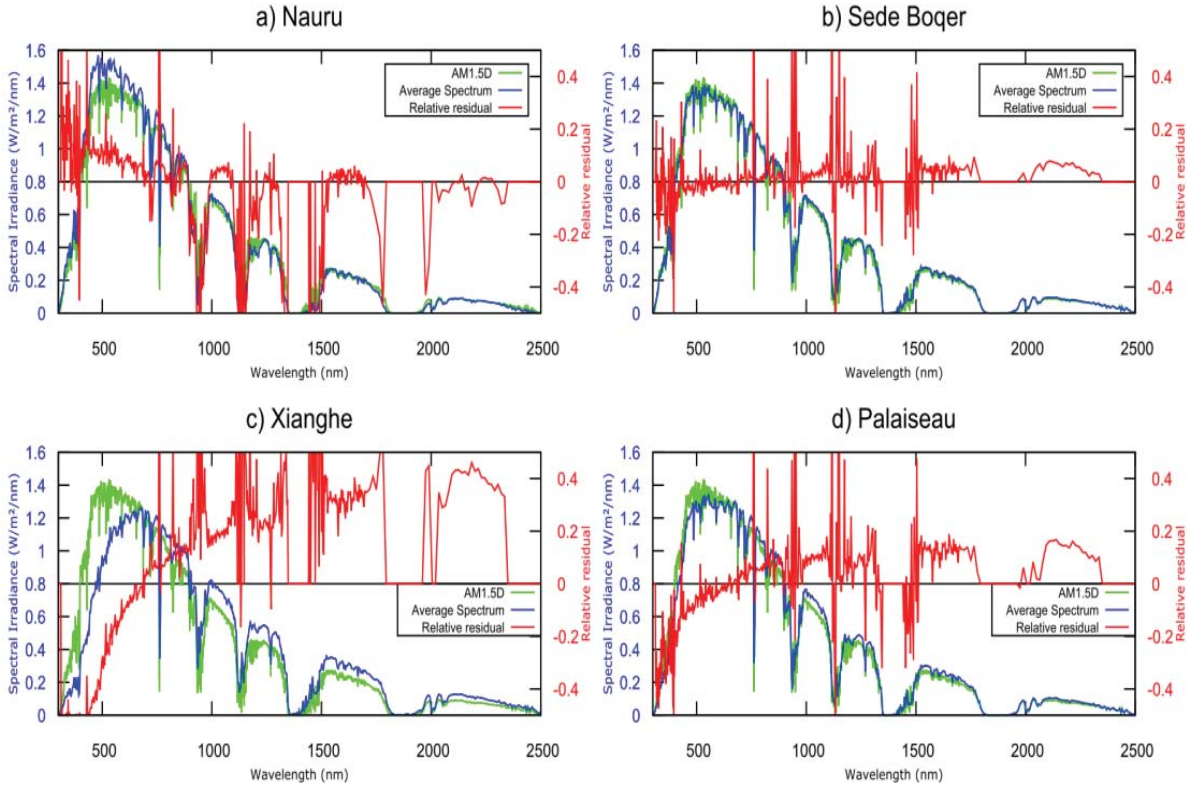

Fig 2: Relative residual of the normalized mean annual spectrum of each city (in red) compared to reference spectrum AM1.5D (in green) and the mean annual spectrum of each city (in blue)

The optimal combination of electronic gaps leading to the highest conversion efficiency was derived using the Shockley and Queisser (SQ) model with the mean annual spectra as an input spectrum for each selected location. The model considers the following assumptions:

- Each absorbed photon generates one single electron-hole pair
- There is no absorption of photons with energy less than the semiconductor band gap
- The only recombination process within the cell is radiative recombination; the other non-radiative processes (SRH, Auger) are thus neglected
- There are no resistive losses
- The cell temperature is kept equal to the ambient temperature (298 K).

The numerical method used here is based on the detailed balance model originally suggested by SQ. The conversion efficiency of these MJ cells was calculated using the detailed balance formalism (Brown and Green, 2002; Vossier et al. 2015) which only requires as an input a reduced set of parameters, namely the sun and the cell temperature, the spectral distribution of the light absorbed, and the electronic gaps of the semi-conductor materials used in the cell.

Basically, the maximum electrical power that can be extracted from a solar cell is obtained as the difference between the absorbed and emitted radiation. Both are conveniently described by the generalized Planck's law, as pointed out in (Brown and Green, 2002).
The maximum current (I) extractable from the cell can be obtained from:

$$I/q = \dot{N}_S - \dot{N}_R \quad (1)$$

where q is the elementary charge, and $\dot{N}_S$ and $\dot{N}_R$ are the current contributions associated with the absorption and emission of photons, which both are a function of the semiconductor bandgap, cell and sun temperatures, and other parameters, as described in (Vossier et al. 2015).

Using the SQ limit, the ultimate efficiency is given by:

$$\eta_{SQ} = \frac{\left\{qV\left[\dot{N}_S(\mu=0) - \dot{N}_R(\mu=qV)\right]\right\}_{\max}}{P_{in}} \quad (2)$$

where P_{in} is the incident power.

The optimal combination of electronic gaps leading to the highest solar→electricity conversion efficiency was investigated using a genetic algorithm, taking into account the current-constraint between each subcell (introducing such a constraint imposes the current generated by each individual subcell to be equal).

3. Results

The optimal bandgaps and the corresponding conversion efficiencies for MJ solar cells comprising up to ten subcells under the AM1.5D, 298K and 1 sun were obtained in (Vossier et al., 2015 b), and are reported here as a reference to show how the optimal bandgaps change as a function of the selected spectrum for the optimization (Table 2)

Table 2: Optimum efficiencies for MJ solar cells ten subcells comprising up to ten subcells under the AM1.5D spectrum of every city and 1-sun illumination.

Spectrum	Nb. Cells	E_{g1}	E_{g2}	E_{g3}	E_{g4}	E_{g5}	E_{g6}	E_{g7}	E_{g8}	E_{g9}	E_{g10}	Efficiency (%)
AM1.5D	1	1.14										33.2
	2	1.57	0.94									45.1
	3	1.75	1.18	0.7								50.7
	4	1.94	1.44	1.05	0.7							54.4
	5	2.07	1.61	1.26	0.99	0.7						56.6
	6	2.18	1.74	1.44	1.17	0.95	0.68					58.7
	7	2.27	1.85	1.56	1.33	1.12	0.92	0.7				59.8
	8	2.29	1.88	1.59	1.37	1.16	0.96	0.74	0.5			60.8
	9	2.35	1.96	1.69	1.47	1.26	1.09	0.94	0.74	0.53		61.4
	10	2.41	2.03	1.77	1.56	1.39	1.21	1.05	0.92	0.74	0.55	62

Table 3 summarizes the bandgap combinations for MJ cells optimized considering the mean annual spectra of every location investigated, rather than the AM1.5D reference spectrum.

As mentionned before, Xianghe and Palaiseau present lower bandgaps in the UV-Vis range than those obtained considering the AM1.5D spectrum. These 2 cities are located well above the equator and therefore the AM effect over the UV-Vis range is noticeable. In addition, Xianghe presents high pollution levels and thus even lower irradiance in this particular wavelength range.

The normalized average spectrum for Sede Boqer, depicted in Figure 2, shows negligeable differences compared to the AM1.5D reference spectrum. As a consequence, the optimized combination of bandgaps only shows slight variations relative to the AM1.5-optimized reference case, and fine-tuning would not bring any significant gain in the energy output for this location.

On the other hand, the optimized bandgaps for Nauru are energetically higher than the reference case for almost all the wavelengths considered. Nauru is practically located over the equator and characterized by low pollution levels (low AOD) but, as a tropical city, presents high PW. The water vapor absorption bands are mainly located in the near-infrared and infrared regions of the spectrum, accounting for the relative residual drops which can be seen in Figure 2 at around 940, 1100 and 1400 nm. Since the irradiance in the UV-Vis region is higher, the bandgap energies tend to be higher to enhance the conversion for these photon frequencies.

Table 3: Optimum efficiencies for MJ solar cells comprising up to ten subcells under the average spectrum of every city and 1-sun illumination.

Spectrum	Nb. Cells	E_{g1}	E_{g2}	E_{g3}	E_{g4}	E_{g5}	E_{g6}	E_{g7}	E_{g8}	E_{g9}	E_{g10}
Sede Boqer	**1**	1.14									
	2	1.57	0.94								
	3	1.74	1.18	0.71							
	4	1.93	1.45	1.06	0.70						
	5	2.07	1.61	1.26	0.99	0.70					
	6	2.19	1.75	1.45	1.19	0.96	0.70				
	7	2.27	1.86	1.57	1.35	1.13	0.93	0.71			
	8	2.29	1.88	1.59	1.37	1.16	0.97	0.75	0.52		
	9	2.35	1.97	1.69	1.48	1.26	1.10	0.95	0.74	0.53	
	10	2.42	2.03	1.77	1.57	1.40	1.22	1.05	0.93	0.74	0.55
Xianghe	**1**	1.12									
	2	1.34	0.72								
	3	1.59	1.12	0.71							
	4	1.74	1.31	0.99	0.70						
	5	1.81	1.41	1.12	0.80	0.54					
	6	1.94	1.57	1.31	1.11	0.92	0.71				
	7	1.97	1.60	1.35	1.14	0.94	0.73	0.52			
	8	2.03	1.69	1.44	1.24	1.06	0.91	0.74	0.55		
	9	2.11	1.77	1.54	1.37	1.20	1.04	0.89	0.74	0.55	
	10	2.13	1.81	1.58	1.41	1.23	1.09	0.96	0.79	0.69	0.52
Nauru	**1**	1.38									
	2	1.63	0.94								
	3	1.90	1.36	0.79							
	4	2.01	1.51	1.12	0.71						
	5	2.15	1.68	1.34	1.00	0.69					
	6	2.26	1.83	1.51	1.22	0.98	0.71				
	7	2.32	1.91	1.62	1.39	1.16	0.94	0.70			
	8	2.35	1.94	1.66	1.42	1.19	0.98	0.75	0.51		
	9	2.40	2.01	1.75	1.53	1.32	1.15	0.96	0.75	0.54	
	10	2.44	2.08	1.82	1.62	1.44	1.24	1.08	0.94	0.74	0.53
Palaiseau	**1**	1.13									
	2	1.54	0.94								
	3	1.69	1.16	0.70							
	4	1.91	1.45	1.12	0.74						
	5	2.06	1.63	1.33	1.04	0.75					
	6	2.10	1.68	1.40	1.15	0.93	0.69				
	7	2.22	1.82	1.55	1.33	1.14	0.94	0.71			
	8	2.25	1.85	1.58	1.37	1.17	0.98	0.76	0.53		
	9	2.32	1.94	1.69	1.49	1.31	1.16	1.00	0.80	0.69	
	10	2.32	1.94	1.70	1.50	1.33	1.17	1.01	0.81	0.70	0.51

The conversion efficiency for the MJ solar cell architectures reported in the previous Table 3 and for the corresponding annual mean spectrum are depicted together with the efficiency under the same spectrum but using the gaps optimized for AM1.5D in Figure 3.

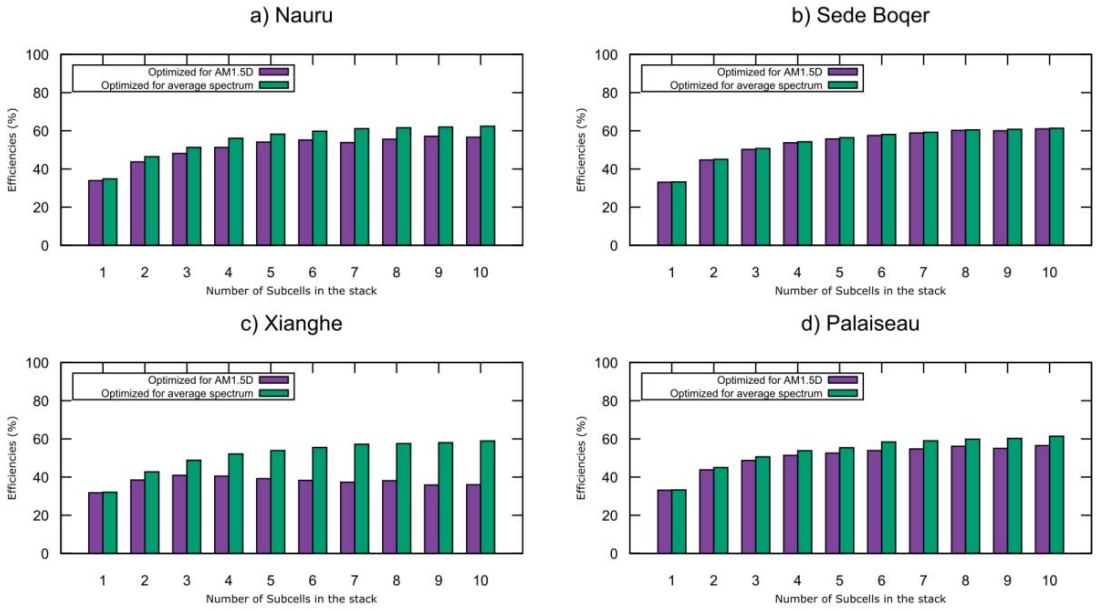

Fig 3: Efficiencies for MJ solar cells comprising up to 10 subcells with gaps optimized for AM1.5D (pink bars) or for average spectrum in every city (green bars)

Fig. 3 illustrates the potential benefits for fine-tuning in different locations around the world: some noticeable improvement in the conversion efficiency can be obtained with fine-tuned MJ solar cells, relative to the "reference" conversion efficiency achieved with AM1.5-optimized cells. However the extent to which fine-tuning may lead to noticeable improvement in the cell efficiency largely depends on the location. The benefit for fine-tuning is particularly strong in Xianghe: because of the noticeable alteration in the spectral distribution of light relative to the reference AM1.5 spectrum, fine-tuning is shown to lead to significant improvement in the cell efficiency, in particular for cell architectures involving a high number of subcells. Nauru and Palaiseau show a modest improvement in the cell efficiency with fine-tuned solar cells, as a result of the minor difference between the mean annual spectral distribution of light and AM1.5 reference spectrum. Finally, the gain in efficiency for fine-tuned solar cells appears to be very weak in Sede Boqer, the mean annual distribution of light and AM1.5 solar spectrum being very close. It should be finally stressed that all the selected locations tend to achieve maximum efficiencies around 60% for the 10 subcells stack, suggesting that fine-tuning of solar cell is a promising way to achieve ultra-high conversion efficiencies for a broad range of climatic and atmospheric conditions.

It was previsouly shown that the higher the number of subcells in the stack, the narrower the range of spectral characteristics for which the cells performs optimally (Vossier et al, 2016). To better grasp the spectral dependence of MJ cells as the number of subcells increases, the relative residual between the optimized and non-optimized efficiencies in the case of Xianghe is plotted in Figure 4 (see Eq. (3)). The relative residual grows sharply with increasing number of subcells, underlining the strong impact of AOD and the fundamental inability of MJ solar cells comprising more than 3 subcells to accommodate spectral variations. The relative residual is higher than 20% with more than 3 junctions and reaches 60% for 10 junctions. Thus, the benefit for tailoring the gaps in this specific case could lead to an efficiency increase of 60% with 10 gaps.

$$Relative\ residual(\%) = 100\left(\frac{Efficiency\ \ for\ the\ optimized\ gaps - Efficiency\ for\ the\ AM1.5D\ gaps}{Efficiency\ for\ the\ AM1.5D\ gaps}\right) \quad (3)$$

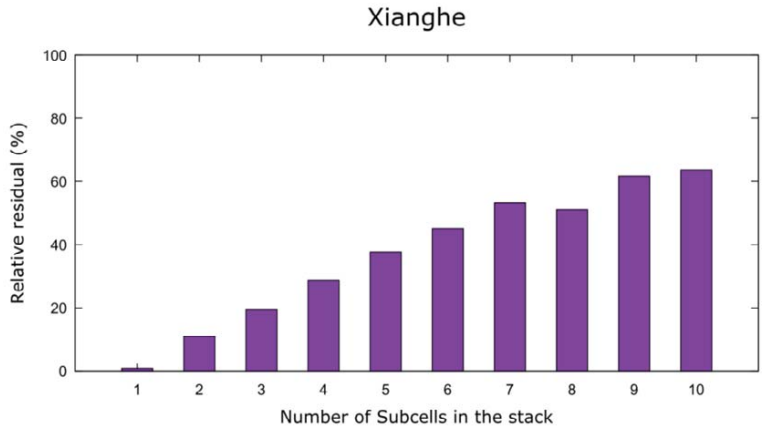

Fig 4: Efficiency relative residual in the case of Xianghe

4. Conclusions

Fine-tuning of solar cells can potentially increase the efficiency with which solar energy is converted into electricity, by tailoring the combination of electronic gaps to the spectral distribution characteristic of a particular location. The present results suggest that increasing the number of subcells in a MJ stack leads to increased conversion efficiency. However, locations characterized by a strong alteration in the mean annual spectral distribution relative to AM1.5 solar spectrum only show modest improvement in the maximum conversion efficiency achievable, when designing the cells using AM1.5 as a reference spectrum. In this work, we showed that fine-tuning of MJ solar cells may allow a significant increase in the cell conversion efficiency. The amplitude of the efficiency gain associated with fine-tuning largely depends on the variation in the mean distribution of light relative to AM1.5 spectrum. Locations characterized by minor difference in the spectral distribution of the light (relative to AM1.5) show a very weak improvement in the conversion efficiency of fine-tuned MJ solar cells. Conversely, locations characterized by a noticeable modification in the spectral distribution of light demonstrate a strong improvement in the efficiency of fine-tuned MJ cells. Finally, it was demonstrated that the maximum conversion efficiency achievable with fine-tuned MJ cells is around 60% for the 10 subcells stack, suggesting that this approach is a promising way to achieve ultra-high conversion efficiencies for a broad range of climatic and atmospheric conditions.

References

Aerosol Robotic Network (AERONET) homepage. http://aeronet.gsfc.nasa.gov

Brown, A.S., Green, M.A., 2002. Limiting efficiency for current-constrained two-terminal tandem cell stacks. Prog. Photovolt: Res. Appl 10, 299–307.

Chan N.L.A., Brindley H.E., Ekins-Daukes N.J., 2014. Impact of individual atmospheric parameters on CPV system power, energy yield and cost of energy. Prog. Photovolt: Res. Appl 22, 1080–1095.

Green, M.A., Emery, K., Hishikawa, Y., Warta, W., Dunlop, E.D., 2015. Solar cell efficiency tables (version 47), Prog. Photovolt: Res. Appl. 24, 3-11

Gueymard C.A., 2001. Parameterized transmittance model for direct beam and circumsolar spectral irradiance. Sol. Energy 71, 325–346.

Pérez-Higueras P., Fernández E.F., 2015. High Concentrator Photovoltaics, Springer International Publishing, Cham.

Shockley W, Queisser HJ., 1961. Detailed balance limit of efficiency of p-n junction solar cells. J. Appl. Phys. 32, 510–519.

Solar and Wind Energy Resource Assessment (SWERA) https://maps.nrel.gov/swera (accessed May 27, 2016).

Vossier A., Al Alam E., Dollet A., Amara M., 2015. Assessing the Efficiency of Advanced Multijunction Solar Cells in Real Working Conditions: A Theoretical Analysis. IEEE J. Photovolt. 5, 1805–1812.

Vossier A., Riverola A., Chemisana D., Dollet A., Gueymard, C.A, 2016. Should energy output be preferred over conversion efficiency to qualify advanced multi-junction solar cells?. Under revision in Prog. Photovolt: Res. Appl

Conference Proceedings
EuroSun 2016
Palma de Mallorca (Spain), 11-14 October 2016

Thermal Behavior of Photovoltaic-Thermal Hybrid Collector

Hiro Yoshida, Shigetoshi Daidouji, Kazutaka Itako and Naoto Hagino
Kanagawa Institute of Technology, Atsugi (Japan)

Abstract

Thermal behavior of the PV-T hybrid collector was examined using a simulator, where the PV cell is backed by the thermal collector. Heating effect of the PV cell (Joule heating by internal currents) was a main interest in this study. For the hybrid PV-T system, the thermal collector coefficient was prone to be larger in the case without external electric loads (open PV circuit) than in the case with the loads (closed PV circuit). Such trend was able to be explained analytically in terms of the internal heating phenomenon of PV. Results of field experiment by Sandnes and Rekstad (2002) show similar trend to the present one. The maximum heating power of the PV cell was confirmed to be equivalent to the maximum electric power of it. This result seems quite reasonable from the physical point of view. In the present PV-T configuration, the thermal collector coefficient drops significantly due to the shade effect of the PV cell placed in front of the thermal collector.

Keywords: *Photovoltaic cell, Joule heating, thermal collector, PV-T hybrid collector / simulator*

1. Introduction

The solar energy gives us an irreplaceable benefit. It is well known that a part of the energy is converted into electricity by the photovoltaic (PV) cells. The conversion rate of the cells will be practically 10-20 %. Regarding the remaining 80 % of the solar energy, our choice for now seems to be confined to using it as heat. Thus not only the electricity but the clever application of the heat is important. In many cases, the electricity and the heat are collected by the separate surfaces to each. It is natural that people come to an idea of collecting both electricity and heat by one common surface. Such device generally called photovoltaic and thermal (PV-T) hybrid collector. In the hybrid collector PV cell is often backed by the thermal collector.

The first publication on the PV-T hybrid model appeared about 40 years ago (Florschuetz, 1978). Up to now, many papers, mostly on the field experiments, have been published (for example, Chen and Riffat, 2011, Ito and Miura, 1993, Ibrahim, Othman, Ruslan, and Sopian, 2011, Sandnes and Rekstad, 2002). In one of the latest international conferences, EuroSun 2014 for example, discussions on the PV-T hybrid system was very active. To date, however, the performance of the PV-T hybrid system is not necessarily well understood (Yandri, Hagino, Itako, and Yoshida, 2012). Namely, the thermal coefficients of the hybrid collector showed different trend depending on whether the PV cell was connected to the external electric loads or not, where the electric loads are the household appliances such as TV, air-conditioner or lighting equipment (Yandri, Hagino, Itako, and Yoshida, 2012, Sandnes and Rekstad, 2002). It has been suggested that the internal heating (Joule heating) of the PV cell is supposed to affect the thermal characteristics of the hybrid collector (Yoshida, Daidouji, Itako, and Hagino, 2013). Based on the field experiment data, Sandnes and Rekstad (2002) also commented qualitatively on an excess heat generated by PV cell. Here, it might be interesting to ask what occurs in the PV cell under the irradiation when the cell is not connected to the loads (i.e. electricity generated is not properly taken out). In any case, direct observation of such phenomenon will be important for quantitative discussion.

In this study, aiming at further understanding about the thermal behavior of the PV-T hybrid system accompanying the PV internal heating, the authors tried to measure directly the heating effect of PV cell. For this purpose, a compact PV-T hybrid simulator was employed (Yandri, Hagino, Itako, and Yoshida, 2012).

doi:10.18086/eurosun.2016.08.17 Available at http://proceedings.ises.org

Through a series of experiments by the simulator, the behavior of the hybrid system was able to be examined more quantitatively.

2. Photovoltaic-thermal (PV-T) hybrid collector simulator

Figure 1 shows the schematic diagram of the PV-T simulator. It consists of the light source, the water supplying unit, and the PV cell (KIS Co.Ltd., model GT434, mono-crystalline type) backed by the thermal collector unit. The size of the PV cell is 1 mm thick (or less) and 378 x 349 mm^2 surface area. Side of the PV cell and the thermal collector were heat insulated by a 5 mm thick styrene foam sheet. In the precise measurement of the PV internal heating (section 4.4), the back surface of the thermal collector was covered by a 20 mm thick foam rubber. The heat conduction coefficients of the styrene foam and the foam rubber are 0.03 J/(mK) (JSME Data Book, 2009). In the preliminary experiment in section 4.1, the foam rubber was not set. The normal maximum output of the PV module is 13 W at 25 ^oC under the sun light. The 16 halogen bulbs (Ushio, model JDR110V40W LW/K) were used as the light source. The bulbs are arranged in a 4 x 4 matrix at equal intervals in the light source plane. The light source was placed underneath the PV-T collector surface facing downwards (Fig.1). Such arrangement (collector top - light source bottom) was adopted for the convenience of arranging cooling pipes and temperature sensors. Actually, due to this arrangement, the temperature field on the PV back surface was easily monitored by an infrared thermal view camera (Yoshida, 2010). The thermocouples for T_{in} and T_{out} (Fig.1) were attached through brass T-joints to a silicon rubber tube for cooling water. The thermocouple for T_{in} was placed at 1 m tube length from the inlet of the thermal collector and that for T_{out} was at 0.3 m from the outlet of the collector (Fig.A1 in Appendix). The outer and inner diameters of the silicon rubber tube were 11 mm and 5 mm, respectively. The light collecting surface is 0.38 m x 0.35 m area. The base structure of the simulator is the same as Yandri, et al (2012). In the present setup, a few improvements were added: 1) A center aperture was made at the center of the thermal collector unit to monitor PV temperature correctly (Fig.2); 2) The thermal collector unit was replaced by an aluminum plate with machined channel of cooling water (Yoshida,Daidouji, Itako, and Hagino, 2013). The imbedded channel is covered with a flat aluminum plate. A sheet of silicon rubber is placed between the channel and the aluminum plate (Fig.2). A flat surface is easy to manage heat transfer and heat insulation. Due to those modifications, temperatures of the PV unit and the thermal collector were able to be monitored

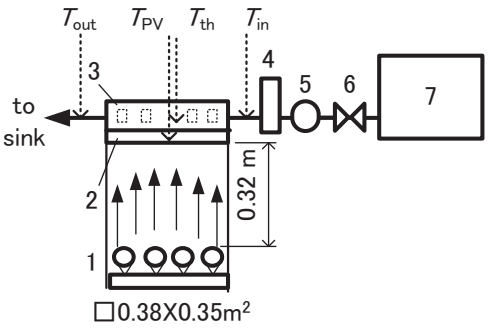

Figure 1 Schematic diagram of PV-T simulator: 1, light source (halogen light bulbs); 2, PV unit of 0.38 m x 0.35 m cross section; 3, thermal collector unit with cooling water channel; 4, flow meter; 5, circulating pump; 6, gate valve; 7, water tank. T_{in}, T_{out}, T_{th}, and T_{PV} are the temperatures of water at thermal collector inlet, outlet, center of the thermal collector and PV unit, respectively.

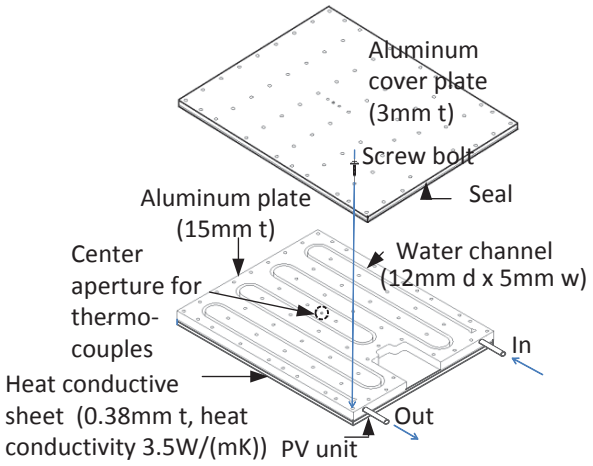

Figure 2 Aluminum plate thermal collector with cooling water channel. The center aperture was made for temperature measurement of PV and thermal collector.

simultaneously and correctly. Because the authors focused on the phenomena of internal heating of PV cell, effect of the light source position on the thermal collector performance was not examined.

Thermocouples of type T class 2 (CHINO, model 1STF013, precision measured by the authors was in the order of ∓0.2 ^{o}C) and a pyranometer (EKO INSTRUMENTS, model MS-42, internal resistance 500 Ω) were used for the temperature and the irradiation measurement, respectively. A float type flow meter (KOFLOC, RK1710-500/MIN) and a magnet pump for cooling water flow (SANSO, PMD-331B6K, 45W, 3L/min) were used. The temperature measurement was done when the simulator was under thermally steady state condition.

Regarding the convection heat transfer between the light source and the PV surface, the convection stream up to the PV surface was negligibly small, i.e. less than 0.3 m/s. As far as the light source and PV-T set (units 1 and 3 in Fig.1) was concerned, convection heat transfer was considered to be negligible. The effects of the room temperature and the convections on the piping tubes, attachments of thermocouples, and water tank (units 4 – 7 in Fig.1) will be concretely discussed later (section 4.4 and Appendix).

3. Thermal collector coefficient under additional heating in PV

In this section, we examine theoretically the thermal collector coefficient of the PV-T hybrid system for the case with an additional internal heating in the PV unit. It is quite reasonable to consider that the internal current in PV is prone to bring Joule heating effect. This effect is supposed to be maximized especially when the PV unit is not connected to the external electric loads. In the following, let us consider the thermal collector coefficient. The net thermal energy absorbed by the thermal collector unit, Q_{net}, is given as:

$$Q_{net} = Q_c - Q_{loss} \tag{1}$$

, where Q_c and Q_{loss} are the total thermal energy absorption and the total loss of the thermal collector unit, respectively. Referring to Huang and Du (1991), Q_c and Q_{loss} are defined as

$$Q_c = \alpha A I_0 \tag{2}$$

and

$$Q_{loss} = U\left(T_{out} - T_a\right) \tag{3}$$

In Eqs.(2) and (3), α, A, I_0, U, T_{out}, and T_{a} are, respectively, the non-dimensional effective solar absorptance, the collector surface area, the irradiation intensity incident upon the surface of the PV-T system, the coefficient of total heat loss, the temperature of water flowing out from the thermal collector unit, and the ambient temperature. In the present experiment, we took room temperature T_{room} as T_{a}. If there is an additional internal heating in the thermal collector, i.e. Joule heating in the PV unit, Eqs(2) and (3) can be modified as

$$Q_c^{'} = \alpha A\left(I_0 + \delta I\right) \tag{4}$$

$$Q_{loss}^{'} = U\left[\left(T_{out} + \delta T\right) - T_a\right] \tag{5}$$

, where δI and δT are the increments of the apparent irradiation and the water temperature at the thermal collector exit, respectively. Thus the thermal coefficient of the thermal collector, η'_{th}, under the additional heating is given as

$$\eta_{th}^{'} = \left(Q_c^{'} - Q_{loss}^{'}\right)/\left(AI_0\right) = \alpha^{'} - U^{'}\left(T_{out} - T_a\right)/I_0 \tag{6}$$

, where a' and U' are

$$\alpha^{'} = \alpha\left(1 + \delta I / I_0\right) \tag{7}$$

$$U^{'} = U\left[1 + \delta T /\left(T_{out} - T_a\right)\right] \tag{8}$$

In Eq.(6), let us name the term $(T_{out}\text{-}T_a)/I_0$ the temperature parameter. On the other hand, the thermal coefficient without the internal heating, η_{th}, , is given as

$$\eta_{th} = (Q_c - Q_{loss})/(AI_0) = \alpha - U(T_{out} - T_a)/I_0 \quad (9)$$

Comparing Eqs.(7) and (8), we easily see that

$$\alpha' \geq \alpha \text{ and } U' \geq U \quad (10)$$

Relationship (10) suggests that, if we plot η_{th} as a function of the temperature parameter $(T_{out}\text{-}T_a)/I_0$, the thermal coefficient of PV-T collector with the internal heating tends to be higher than that without it. More specifically, the inclination of the coefficient curve is steeper for the case with internal heating than that without it. This analytical examination will be confirmed experimentally in section4.3.

4. Experimental results

4.1 Starting behavior and various coefficients of PV-T simulator (*preliminary experiment*)

In this section a rough image of the general performance of the PV-T simulator was examined. In the experiment, back surface of the thermal collector was not covered by the rubber sheet. Effect of the room temperature will be discussed precisely in section 4.4. The irradiation intensity, I_0, was kept 1000 W/m^2 constant at the center of the PV surface, which was set 0.32 m above the light source (Fig.1). Distribution of irradiation intensity on the PV surface was measured by the pyranometer. On the surface, the irradiation was the largest at the center and smaller in peripheral area. The difference was less than 10 % (Takahashi and Nishiwaki, 2012).

Figure 3 shows temperature traces of PV unit for various cooling water flow rates, i.e. 100 – 600 cc/min. For those flow rates, the PV-T simulator reaches steady condition within an hour. After the steady condition, the temperature fluctuations around the mean value were less than ∓3 % for the flow rates of 100 cc/min and 200 cc/min, ∓6 % for 400 cc/min, and ∓10 % for 600 cc/min. The transition time of the present simulator is longer than that of the previous one (Yandri, Hagino, Itako, and Yoshida, 2012). However, as far as the steady state behavior is concerned, this is not the essential obstacle in the present study. To investigate non-steady behavior of the PV-T system, precise adjustment of the heat capacity of the collector will be necessary.

The PV power generation coefficient η_{PV} and the thermal collector coefficient η_{th} are compared in Fig.4, where η_{total} is the sum of them. The irradiation intensity was the same as the case of Fig.3, i.e. I_0=1000 W/m^2. In Fig.4, the coefficients at various PV temperatures 30.9, 32.7, 33.6, and 38.2 ^{o}C were obtained under the flow rates of 600, 400, 200, and 100cc/min, respectively. The higher flow rate tends to cause the lower PV temperature. In this figure, η_{PV} is about 0.05 for the temperatures considered and η_{th} ranges 0.4 to 0.55. As a result the total coefficient was around 0.5 – 0.6. It is clear that η_{th} is prevailing over η_{PV}. Although results are

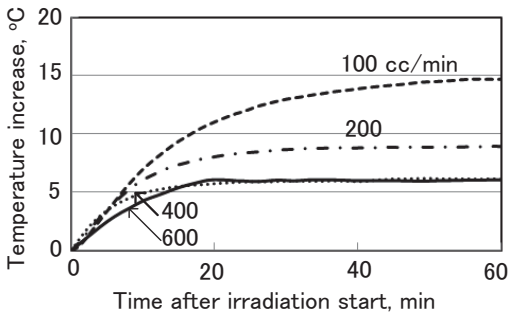

Figure 3 TempErature increase of PV unit after the irradiation start for various cooling water flow rate. Irradiation intensity is 1000 W/m^2.

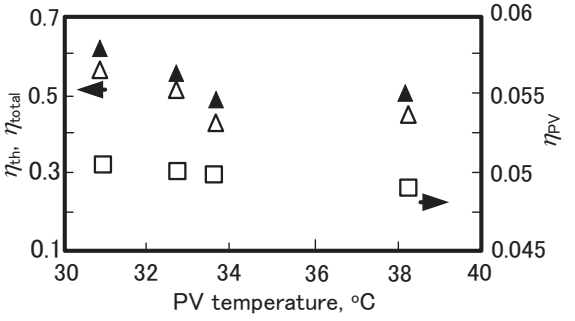

Figure 4 η_{PV}, η_{th}, and η_{total} vs PV temperature. Coefficients η_{PV}, η_{th}, and η_{TotaL} are designated by the symbols of open square, open triangle, and closed triangle, respectively. Irradiation intensity is 1000 W/m^2.

not shown here, our another experiment without PV cell in front of the thermal collector showed that η_{th} was above 80 % under the same flow rates and the irradiation conditions. Thus, in the present PV-T configuration, the thermal collector coefficient with PV cell dropped by roughly 40 % due to the shade effect of PV cell. This result seems quite understandable. The shading effect of the hybrid system is significant subject in future.

4.2. Internal (Joule) heating of PV cell

Hereafter, the open PV circuit and the closed PV circuit mean that the PV is connected to and not connected to the proper outside electric loads, respectively. Table 1 gives the measured data which are plotted in Figs.5 and 6. The irradiation intensity was set I_0=1000 W/m^2 constant as hitherto. Thus the actual irradiation input to the PV cell is 1000 W/m^2 x 0.378 m x 0.349 m = 132 W. The background temperature at each experiment was equal to the room temperature of the day. As can be read in Table 1, the temperature increase (T_{out}-T_{in}) for the open PV is larger than that for the closed PV by 0.2 ^{o}C - 1.2 ^{o}C for the flow rates considered. Those temperature increases are compared in Fig.5. As can be seen in this figure, the temperature increment in the open PV is distinguishable within the present experimental precision. At this stage, however, we can merely say that the Joule heating of PV may be detected. Amount of the Joule heating and effect of the room temperature will be discussed and handled more quantitatively in section 4.4.

Table 1 Data of PV open and closed, I_0=1000W/m^2

PV open

Flow rate	T_{PV}	T_{th}	T_{PV}-T_{th}	T_{in}	T_{out}	T_{out}-T_{in}	T_{room}	Power	$(T_{out}-T_{room})/I_0$	η_{th}
cc/min	^{o}C	^{o}C	^{o}C	^{o}C	^{o}C	^{o}C	^{o}C	W	^{o}C/(Wm^2)	
100	37.5	33.5	4.0	25.9	35.2	9.3	26.7	0	0.0085	0.49
200	31.1	27.0	4.1	22.9	28.2	5.3	24.2	0	0.004	0.55
400	29.9	26.0	3.9	23.9	26.7	2.8	23.2	0	0.0035	0.59
600	30.8	26.9	3.9	25.4	27.5	2.1	25.5	0	0.002	0.66

PV closed

Flow rate	T_{PV}	T_{th}	T_{PV}-T_{th}	T_{in}	T_{out}	T_{out}-T_{in}	T_{room}	Power	$(T_{out}-T_{room})/I_0$	η_{th}
cc/min	^{o}C	^{o}C	^{o}C	^{o}C	^{o}C	^{o}C	^{o}C	W	^{o}C/(Wm^2)	
100	38.2	34.5	3.7	27.5	36	8.5	28.2	6.52	0.0078	0.44
200	33.6	29.9	3.7	26.8	30.9	4.1	26.4	6.61	0.0045	0.43
400	32.7	29.0	3.8	27.3	29.7	2.4	25.8	6.61	0.0039	0.50
600	30.9	27.2	3.7	26.2	28	1.9	25.5	6.71	0.0025	0.57

Influence of the heat transfer between the simulator and the ambient air is considered as follows: The PV cell is irradiated in front surface. It transfers the heat to the ambient air in the room through the side surface and to the thermal collector through the back surface. If the coefficients of the heat transfer among PV, the ambient air, and thermal collector are the same in each experiment, it is reasonable to consider that the magnitudes of the heat releases from PV unit to the room and to the thermal collector must be proportional to the temperature differences i.e. (T_{PV}-T_{room}) and (T_{PV}-T_{th}). Thus amount of heat leaving from the side and the back surfaces of the PV unit can be estimated by A_s(T_{PV}-T_{room}) and A_b(T_{PV}-T_{room}), respectively, where A_s is the area of the side surface (1 mm thick x 2 x (378+349) mm periphery) and A_b is that of the back surface (378 mm wide x 349 mm height) of the PV unit. Using the data in Table 1, ratio of A_s(T_{PV}-T_{room}) and A_b(T_{PV}-T_{room}) was calculated as 0.02 – 0.03. That is, the heat release from the side surface of the PV unit is negligible compared to that from the back surface. The heat leaving from the thermal collector to the room is estimated by using the thermal property and geometry of the heat shield (section 2) and the temperature differences. Based on the above discussion and the data in Table 1, the heat loss from the back surface was calculated as 1 – 4 % of the thermal output, which was calculated by (mass flow rate) x (specific heat) x (measured T_{out}-T_{in}). On the other hand, the excess heat (difference of thermal outputs between open and closed PV cases) was 9 – 29 % of the thermal output in each experiment. Possibly, this result suggests that the internal (Joule) heating effect of PV might be maximized when it is not connected to the external electric loads.

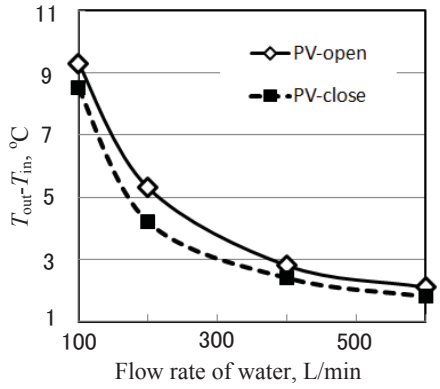

Figure 5 Temperature increase due to the internal heating of PV.

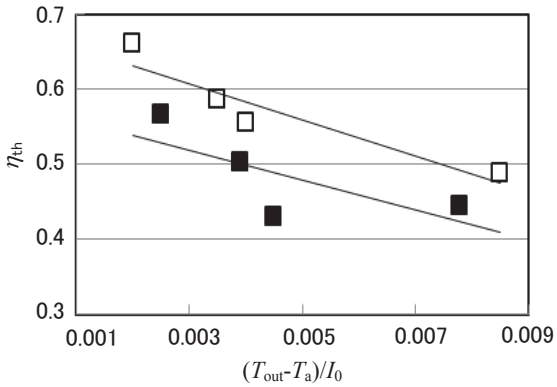

Figure 6 Thermal collector coefficient vs temperature parameter. Open and closed symbols indicate the cases of open and closed PV circuit, respectively.

The convection heat transfers were neglected and not taken into account in the present discussion. Effect of the room temperature and heat transfers including the convections will be discussed statistically in section 4.4 and Appendix.

In the case of the closed PV, the electric resistance of the circuit was controlled by the MPPT (Maximum Power Point Tracking) algorism (Itako, 2013) to generate maximum power output for various irradiation intensities. This algorism has been commonly applied already in the ordinary PV generation system.

4.3 Thermal collector coefficient with/without internal (Joule) heating of PV

The thermal coefficients of the open and the closed PV circuits are shown in Fig.6. As was forecasted in section 3, the coefficient of the open circuit is larger than that of the closed one. The regression lines in Fig.6 are: for the open circuit

$$\eta_{th} = 0.68 - 24(T_{out} - T_a)/I_0 \qquad (11)$$

, and for the closed circuit

$$\eta_{th} = 0.58 - 20(T_{out} - T_a)/I_0 \qquad (12)$$

In Eqs.(11) and (12), the ambient temperature T_a means the room temperature T_{room} in this study. Those equations indicate that $\alpha' = 0.68$, $U' = 24$ and $\alpha = 0.58$, $U = 20$, thus $\alpha' > \alpha$ and $U' > U$. This result is just the same as what suggested by Eq.(10). We can confirm that the experimental results by Sandness and Rekstad (2002) (Fig.5 in their paper) show the similar trend to the present results shown in Fig.6. Considering the Joule heating effect of the PV cell, we understand the reason of the trend of the thermal collector coefficient.

4.4 Joule heating and electricity output

In this section we examine the relationship between the thermal output of the PV cell when it is not connected to the outside electric loads (open PV) and the electric power output of it when it is properly connected to the loads (closed PV). To evaluate more correctly the heat generation by PV itself, influence of the room temperature on T_{in} and T_{out} (Fig.1) must be minimized. For this purpose the heat insulation of the thermal collector was improved: the back side of the thermal collector placed behind the PV cell was heat shielded by a foam rubber (section 2). Silicon rubber tubes connecting the inlet and the outlet of the thermal collector (Fig.A1) were left as they were. Three irradiation intensities of 800, 1000, and 1100 W/m^2 were chosen as I_0. At each irradiation the temperatures measured at least five times. The volume flow rate of cooling water was kept 200cc/min constant for each experiment. In Table 2 and 3 are given the measured raw temperatures and the modified temperature difference ($T'_{in} - T'_{out}$), where the effect of the room temperature was minimized. The procedure of calculation of the modified temperatures and the minimization is given in Appendix.

The data in Tables 2 and 3 are plotted in Figs.7 and 8. In Fig.7 are compared the raw temperature differences $\Delta T = (T_{out} - T_{in})_{open} - (T_{out} - T_{in})_{closed}$ and the corresponding modified temperature differences $\Delta T' = (T'_{out} - T'_{in})_{open} - (T'_{out} - T'_{in})_{closed}$. The suffixes "open" and "closed" indicate temperature differences under the open and the closed PV circuits, respectively. In the plot of ΔT and $\Delta T'$, the 1-σ (a standard deviation) error bars are superimposed. We can see in Fig.7 that both the raw ΔT (closed squares) and the modified $\Delta T'$ (open squares) tend to be positive. In the modified $\Delta T'$, a much clear dependency on I_0 can be seen. Those results indicate that the PV appreciably generates heat when it is not connected to the external electric loads. Figure 8 compares the thermal output of PV under unconnected circuit and the corresponding maximum electric power output under connected circuit. Within the present measurement precision, we can say that internal current of PV generates an appreciable amount of heat when it is not connected to the external electric loads. In other words, the maximum thermal output of unconnected PV is almost the same order of magnitude as the maximum electric power output of it under the same irradiation condition.

Table 2 Experimental data, reduced temperatures and thermal output for open PV circuit under 200 cc/min flow rate

I_0, W/m^2	T_{room}, °C	T_{PV}, °C	T_{in}, °C	T_{out}, °C	T_{out}-T_{in}, °C	$P_{th\text{-}o}$, W	T'_{out}-T'_{in}, °C	$P'_{th\text{-}o}$, W
800(1)	25.4	32.8	24.0	29.4	5.4	76.0	5.4	75.5
800(2)	23.4	31.8	23.3	28.3	5.0	69.3	5.2	72.7
800(3)	23.3	30.8	21.9	27.1	5.2	72.5	5.2	72.1
800(4)	22.3	30.3	21.6	26.9	5.2	73.2	5.3	74.9
800(5)	19.8	27.5	18.8	24.2	5.5	76.6	5.5	77.3
1000(1)	25.6	35.1	24.4	31.0	6.7	93.2	6.7	94.2
1000(2)	24.9	34.3	23.7	30.1	6.4	90.2	6.5	91.0
1000(3)	24.1	33.6	23.3	29.3	6.1	85.3	6.2	87.0
1000(4)	20.8	33.2	23.4	29.2	5.7	79.9	6.6	92.2
1000(5)	21.8	31.3	20.7	27.2	6.4	90.2	6.5	91.4
1100(1)	25.1	35.7	24.3	31.2	7.0	97.4	7.1	99.8
1100(2)	26.7	36.6	24.8	31.9	7.1	99.3	7.0	98.6
1100(3)	24.5	33.7	22.1	29.2	7.1	99.7	7.0	97.4
1100(4)	21.5	32.7	21.6	28.4	6.8	94.8	7.1	99.9
1100(5)	25.3	37.6	27.2	33.3	6.1	85.4	6.8	95.6

Table 3 Experimental data, reduced temperature and difference of thermal outputs for closed PV circuit under 200cc/min flow rate

I_0, W/m^2	T_{room}, °C	T_{PV}, °C	T_{in}, °C	T_{out}, °C	T_{out}-T_{in}, °C	$P_{th\text{-}c}$, W	T'_{out}-T'_{in}, °C	$P'_{th\text{-}c}$, W	P_{el}, W	$P'_{th\text{-}o}$-$P'_{th\text{-}c}$
800(1)	25.5	32.5	24.4	29.3	4.9	68.0	4.9	68.0	5.33	8.0
800(2)	23.3	31.3	23.6	28.1	4.5	63.3	4.8	67.2	5.28	6.0
800(3)	23.6	31.1	23.0	27.6	4.6	64.4	4.7	65.6	4.98	8.1
800(4)	22.7	29.6	21.6	26.3	4.6	64.8	4.6	64.9	5.24	8.4
800(5)	19.5	26.8	18.6	23.6	5.0	70.3	5.1	71.1	5.27	6.3
1000(1)	26.8	34.7	24.6	30.8	6.2	87.2	6.0	84.7	7.22	6.0
1000(2)	24.0	33.0	23.1	29.0	6.0	83.9	6.1	85.2	7.09	6.3
1000(3)	24.0	32.8	23.3	28.8	5.5	77.3	5.7	79.2	7.05	8.0
1000(4)	20.7	30.8	21.3	26.9	5.7	79.5	6.1	85.3	7.09	0.4
1000(5)	22.6	30.6	20.5	26.5	6.0	84.0	5.8	81.9	7.18	6.2
1100(1)	25.0	34.4	23.7	30.0	6.3	88.2	6.3	88.6	8.11	9.2
1100(2)	26.6	36.1	25.4	31.8	6.3	88.5	6.4	89.3	7.99	10.8
1100(3)	23.7	31.0	20.0	26.5	6.5	91.3	6.0	84.6	7.89	8.4
1100(4)	21.5	31.9	21.6	27.7	6.2	86.2	6.5	90.8	7.92	8.5
1100(5)	25.9	36.3	26.8	32.4	5.6	78.5	6.1	85.2	7.83	6.9

.

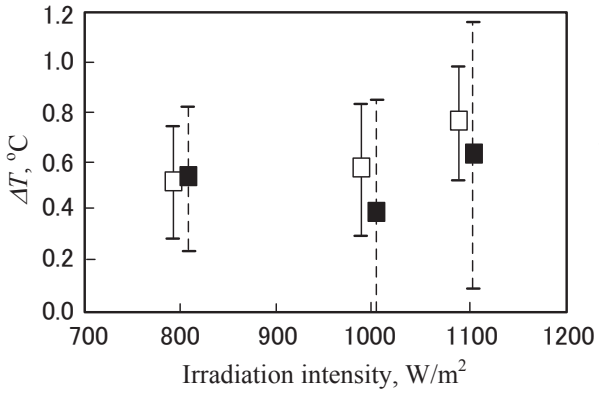

Figure 7 Temperature difference ΔT between (T_{out}-T_{in}) for the open and the closed PV circuits vs the irradiation intensity. ΔT =(T_{out}-T_{in})$_{open\ PV}$-(T_{out}-T_{in})$_{closed\ PV}$. Open and closed square symbols denote the results with and without modification of the room temperature, respectively. 1-σ error bars are superimposed on the both ΔT results.

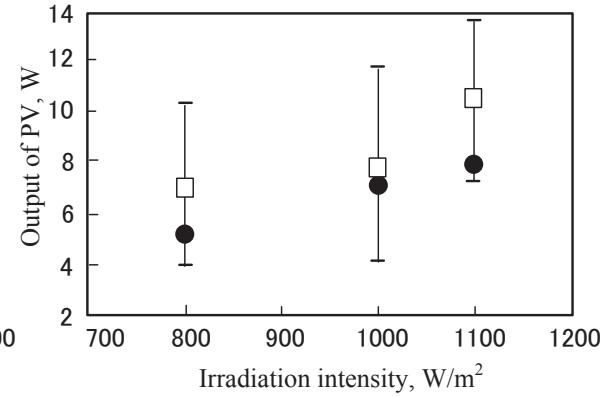

Figure 8 Thermal and electric Output Of P vs the irradiation intensity. Open square and closed circle symbols denote thermal output for open PV circuit and electric output of PV for closed PV circuit, respectively. 1-σ error bars is superimposed on the thermal output.

5. Concluding remarks

The thermal behavior of the photovoltaic-thermal (PV-T) hybrid collector was examined using a simulator, especially focusing on the cases when PV cell was connected to (closed) and not connected to (open) external electric loads. The main results are summarized as follows:

1) For the hybrid PV-T system: it was confirmed that the thermal collector coefficient was prone to be larger in the case without the external electric loads (open PV) than the case with them (closed PV). Such trend was well explained in terms of the internal heating phenomenon (Joule heating) of the PV cell. Field experiment by Sandnes and Rekstad (2002) show the similar trend to the present one. In the present PV-T configuration, thermal collector coefficient drops significantly due to the shade effect of the PV cell. Overcoming such defect and improving total coefficient may be an important subject in future study.

2) For the Joule heating of the PV cell: the heating phenomenon was directly observed by the simulator. The maximum heating power of the PV cell was confirmed to be equivalent to the maximum electric power of it. This result seems quite reasonable from the physical point of view.

In the last the authors would like to express their sincerer thanks to Messes E.Yandri, N.Nishiwaki, K.Takahashi, and S.Ono for their help in the experiments. The present study was performed under the special grant of Kanagawa Institute of Technology.

6. References

Chen,H. and Riffat,S.B., Development of photovoltaic thermal technology in recent years: a review, International Journal of Low-Carbon Technologies, Vol.6 (2011), pp.1-13.

EuroSun 2014, International Conference on Solar Energy and Buildings was held in September 16-19, 2014, in Aix-le-Bains, France. In addition to the session on the PV-T hybrid system, some commercial products of PV-T system were displayed.

Florschuetz L.W., Extension of the Hottel-Whillier model to the analysis of combined Photovoltaic/thermal Flat-Plate collectors, Solar Energy, Vol.22, pp.361-366, 1978.

Huang, B. J. and Du, S. C., A performance test method of solar thermosyphon systems, Transactions of the ASME, Journal of Solar Energy Engineering, Vol.113 (1991), pp.172-179.

Ibrahim, A., Othman, M.,Y., Ruslan, M.H., Mat, S., and Sopian, K., Recent advances in flat plate photovoltaic/thermal (PV/T) solar collectors, Renewable and Sustainable Energy Reviews, Vol.15, pp.325-365, 2011.

Imada, H., Hagino, N., and Yoshida, H., Field experiment of solar thermosyphon, Transactions of the JSME B, Vol.79 (2013), No.801, pp.809-813 (in Japanese).

Itako, K., New I-V Characteristics Scan-Type MPPT Control Method for PV Generation System" Journal of Technology Innovations in Renewable Energy (USA),Vol.1, (2013), No.2,pp.87-91.

Ito, S. and Miura, N., Solar air collector using photovoltaic modulus as the cover, Proceedings of ISES Solar World Congress, Budapest, Vol.3 (1993), pp.271-276.

JSME Data Book: Heat Transfer, 5th edition (2009), p.290, Maruzen, Tokyo (in Japanese).

Peuser, F. A., Remmers, K.-H., and Schnauss, M., Solar Thermal Systems (2002), Solarpraxis Berlin.

Sandnes B., and Rekstad J., A photovoltaic/thermal collector with a polymer absorber plate, experimental study and analytical model, Solar Energy, Vol. 72 (2002), No.1, pp. 63-73.

Takahashi,K. and Nishiwaki,N., PV-T simulator, Kanagawa Institute of Technology graduate thesis, 12YSD03 (2012) (in Japanese).

Tamaura, Y., et al, Solar Energy – front of effective utilization – (2008), NTS (in Japanese).

Yandri, E., Hagino, N., Itako, K., Yoshida, H., Basic characteristics of a compact PV/T simulator, ASME ICONE20-POWER2012 (2012), Paper No.54216.

Yoshida, H., Annual Report of 2010 (No. 4), Solar Energy System R & D Center, Kanagawa Institute of Technology, pp.7-11 (in Japanese).

Yoshida,H., Daidouji,S., Itako,K., Hagino,N., Characteristics of photovoltaic-thermal collector tested by a simulator, JSME, 23rd Kankyo Kogaku Symposium (2013), No.13-15, 405, pp.286-287 (in Japanese).

Appendix

1. Effect of room temperature and heat losses

We consider in section 4.4 that effect of the room temperature on T_{out} - T_{in} mainly originated from the heat exchange through the silicon rubber tubes of 0.3 m long and 1 m long. Shorter one is for the outlet and the longer one for the inlet of the thermal collector, respectively. The situation considered is depicted in Fig.A. Heat exchanges through the other units except those tubes are considered to be negligible. The thermal entrance region (length) of the tubes was estimated to be over 1.5 m in the present experimental condition. For a reference, Reynolds number and Prandtl number were ≈ 900 - 1100 and ≈ 5 - 7, respectively. Exact analytical approach for deciding the temperatures without the room temperature effect seemed difficult. Thus a statistical but mathematically reasonable method of data analysis was adopted in the following.

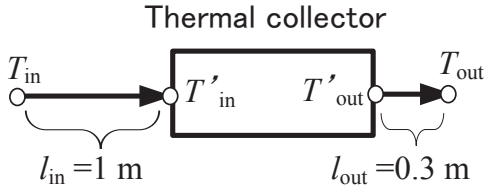

Figure A1 Silicon rubber tubes connected to the inlet and the outlet of the thermal collector. The main heat exchange between the simulator and the ambient is supposed to occur through the tubes.

Based on the observed data, we assume $T_{room} < T'_{in} < T_{out} < T'_{out}$ simply as an aid in the following procedure. The temperatures T_{room}, T_{in}, and T_{out} are the measured ones and T'_{in}, and T'_{out} are the modified ones, in which the room temperature effect is minimized. It is obvious that this

inequality assumption on the temperatures does not violate the validity of the present approach.

1. Heat transfer between the silicon tubes and the ambient

Let the heat transfers through the tube l_{in} and l_{out} be Q_{in} and Q_{out}, respectively. It seems reasonable to assume that those heat transfers are given as Eqs. (A1) and (A2):

$$Q_{in} = A_{in}h_{in}\left[\left(\frac{T_{in}+T_{in}^{'}}{2}\right)-T_{room}\right] \quad \text{(A1)}$$

$$Q_{out} = A_{out}h_{out}\left[\left(\frac{T_{out}+T_{out}^{'}}{2}\right)-T_{room}\right] \quad \text{(A2)}$$

, where h_{in} and h_{out} are empirical coefficients of heat transfer evaluated statistically and A_{in} and A_{out} are the surface area of the tubes given as Eq. (A3).

$$A_{in} = l_{in}\pi d,\ A_{out} = l_{out}\pi d \quad \text{(A3)}$$

, where d is the outer diameter of the silicon tube. Using mass flow rate m and specific heat C of the cooling water, Eqs.(A1) and (A2) are rewritten as

$$Q_{in} = mC\left(T_{in}-T_{in}^{'}\right) \quad \text{(A4)}$$

$$Q_{out} = mC\left(T_{out}-T_{out}^{'}\right) \quad \text{(A5)}$$

From Eqs. (A1), (A2), (A4), and (A5), modified temperatures T'_{in}, and T'_{out} are decided as follows,

$$T_{in}^{'} = \frac{-\left(\frac{1}{2}-\frac{mC}{ak}\right)T_{in}+T_{room}}{\left(\frac{1}{2}+\frac{mC}{ak}\right)} \quad \text{(A6)}$$

$$T_{out}^{'} = \frac{-\left(\frac{1}{2}+\frac{mC}{k}\right)T_{out}+T_{room}}{\left(\frac{1}{2}-\frac{mC}{k}\right)} \quad \text{(A7)}$$

, where a factor a is the ratio of the tube lengths $l_{in}/l_{out} \approx 3.3$ and a parameter k is given as $k = \pi d l_{out} h$, respectively. In Eqs.(A6) and (A7), we can easily confirm that $T'_{in} \rightarrow T_{in}$ and $T'_{out} \rightarrow T_{out}$ when $k \rightarrow 0$.

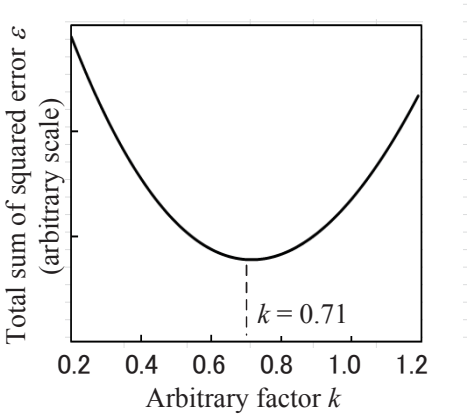

Figure A2 Total sum of squared errors vs k

2. Calculation of k and $T'_{out} - T'_{in}$

Using Eqs.(A6) and (A7), we can define the error in $T'_{out} - T'_{in}$ for experiments i and j done under the common irradiation condition. The error ε_{ij} and sum of squared ones ε are defined as

$$\varepsilon_{ij} = \left(T_{out}^{'}-T_{in}^{'}\right)_i - \left(T_{out}^{'}-T_{in}^{'}\right)_j \quad \text{(A8)}$$

$$\varepsilon = \sum_{i,j}\varepsilon_{ij}^{2} \quad \text{(A9)}$$

The factor k was calculated so as to minimize ε. In Fig.A2 is plotted ε for all temperature data given in Table 2 and 3 as a function of k. As can be seen in this figure, we find the error is minimum at $k \approx 0.71$. Using the relationship $k = \pi d l_{out} h$, the corresponding heat transfer coefficient h is evaluated to be $\approx$ 70 W/(m^2 K). The temperatures $T'_{out} - T'_{in}$ in Table 2 and 3 are calculated by using Eqs. (A6) and (A7) with k = 0.71.

3. Symbols for quantities

Quantity	Symbol	Unit
Area	A	m^2
Specific heat	C	J kg^{-1} K^{-1}
Diameter of tube	d	M
Heat transfer coefficient	h	W m^{-2} K^{-1}
Irradiation intensity	I	W m^{-2}
A parameter (Appendix)	k	W K^{-1}
Length of tube (Appendix)	l	M
Mass flow rate	m	Kg s^{-1}
Heat flow rate	Q	W
Temperature	T	K
Coefficient of total heat loss	U	W K^{-1}
Effective absorptance	α	0
Difference	δ	0
Error (Appendix, Eq.(A8))	ε_{ij}	K
Error (Appendix, Eq.(A9))	ε	K^2
Efficiency	η	0

4. Subscripts

Quantity	Symbol
Ambient condition	*a*
Total energy	*c*
PV with electric loads	*closed*
Inlet condition	*in*
Loss	*loss*
Net energy	*net*
Outlet condition	*out*
PV without electric loads	*open*
Photovoltaic cell	*PV*
Thermal collector	*th*
Reference value	0

5. Superscripts

Quantity	Symbol
Relating additional heating or reduced, modified quantities	‘

Conference Proceedings

EuroSun 2016
Palma de Mallorca (Spain), 11 - 14 October 2016

Economic analysis of renewable energy production with photovoltaic- and solar thermal systems for small and medium-sized enterprises

Maximilian Zarte[1] and Agnes Pechmann[1]

[1] University of Applied Sciences, Emden (Germany)

Abstract

The economic benefits that photovoltaic and solar thermal renewable energy (RE) producers offer under Germany's current legislative conditions (EEG 2014) have been investigated for two cases involving small and medium-sized enterprises (SMEs). The energy demands of the case SMEs are very distinct in volume, type, and profile. With the aid of a simulation, the direct consumption of the expected RE generation and the resulting energy exchange with the grid have been calculated. The results have been analyzed from an economic standpoint using economic indicators and the LCCA (life-cycle cost analysis) method. For the two cases, the results are presented with their indicator values and the designs of the PV and solar thermal systems.

Keywords: Renewable energy; small and medium-sized enterprises; simulation; cost analysis; life-cycle cost analysis

1. Introduction

While energy supply is a constant subject of discussion, focus on it has intensified due to factors such as the prediction regarding the depletion of fossil fuels or nuclear accidents. The current driver of the discussion is climate change. Approximately 80% of the world's primary energy supply comes from fossil fuels that emit greenhouse gases such as CO_2 (International Energy Agency (IEA), 2015). CO_2 and other greenhouse gases modify the planet's absorption and emission of solar radiation and are associated with the observed warming of the climate and other serious environmental problems (Pachauri and Mayer, 2015). To initiate and maintain a decrease in CO_2 emissions, several targets have been set worldwide. For instance, for 2020, the European Union has set the 20/20/20 targets. These entail reducing greenhouse gas emissions by 20% (in comparison to the 1990 levels), increasing the share of renewable energy (RE) sources in final energy consumption by 20%, and increasing energy efficiency by 20% (European Commission, 2010). Installing RE plants could improve the first two targets but would result in further challenges. One such challenge involves the change of predominantly centralized energy systems into bi-directional, decentralized ones which integrate RE producers. Another challenge involves handling the fluctuating behavior of RE producers such as photovoltaic systems (PV) and/or wind stations (WS) due to their weather dependency. Energy production is difficult to predict. The fluctuating behavior and forecast errors would lead to instabilities in the grid, resulting in higher management control efforts. Like that of many other countries, the infrastructure of the German energy system must be modified to manage such challenges; such efforts will incur major costs. To finance them, several levies and taxes have been established based on the Renewable Energy Sources Act (EEG) (Deutsche Bundestag, 2014).

The German EEG manages the expansion of RE producers and sets tariffs for the feed-in of RE into the grid for new RE producer installations. The EEG was first introduced in 2000. Initially, investors benefit from the high feed-in tariffs and lower taxes. But the regulations are constantly revised over the years. Certain conditions have drastically reduced and restricted the feed-in tariffs, bringing self-consumption into focus.

doi:10.18086/eurosun.2016.08.07 Available at http://proceedings.ises.org

For SMEs which are willing to invest in RE, a complex decision problem has to be solved. Once the technical and legal feasibility of installing and operating one or more RE producers has been verified, the issue of how the optimal RE system fits the SME's energy demand and profile has to be decided: Does it consist of one type of RE producer or of different types of RE producers? In what combinations do they occur, and of what size are they? To what extent does the RE satisfy the energy demand? How is overproduction handled? Is it suitable to store it or can it be injected into the grid – and under which conditions are such efforts possible?

This paper investigates the optimal design of a PV and solar thermal system that will supply an SME consumer with electrical and thermal RE and fit its energy demand and profile. These results are compared with the original situation, which involves the 100% feeding of RE into the grid, to illustrate the higher benefits that self-consumption offers. Two distinct cases are investigated under the rubric to achieve the best financial return for the investment within the restrictions of Germany's 2014 EEG.

The optimal design of a RE producer is highly critical for maximizing energy cost savings. Tools have been developed to calculate the economic effects of RE producers. Available tools, such as pv@now (Deutsche Gesellschaft für Sonnenenergie (DGS)), base their calculations on average yearly values for RE production and company demand. Though the results are useful for rough estimations, they neglect the seasonality of RE generation and company demand, leading to considerable deviations in efforts to balance RE supply and demand and, consequently, to differences between the expected and true economic effects. To solve this problem, the research group, "Energy Efficiency in Production," at the University of Applied Sciences Emden/Leer has developed the agent-based simulation, PREmdeK (Pechmann). It simulates a local energy system that consists of one major industrial consumer (e.g., an SME), a multi-source renewable power plant (PV, wind station, CHP, solar heat), and storage entities. The simulation runs on data produced at 15-minute intervals for the duration of a year. For the two cases, historical data regarding energy demand and local weather conditions were used (Pechmann et al., 2016). The simulation employed various PV and solar thermal machine designs that were calculated to balance RE generation with the company's consumption while using storage entities and the grid. The scenarios served as input for an economic analysis that employed economic indicators and the LCCA (life-cycle cost analysis) method. The results of the economic analysis include supplying solutions that will maximize the SMEs' energy cost savings.

In the subsequent section, related work is discussed. Next, section three presents background information on "energy" business models (BM) for SMEs that are feasible under the German EEG 2014, the two case SMEs and energy supply scenarios, and the calculation methods that are applied in the economic analysis. Section four evaluates the case SMEs' results. Then the article ends with a conclusion and a description of possible future work, followed by the references.

2. Related Work

Choosing the right machine design is very important when investing in an RE plant for full or partial self-supply to achieve maximum energy cost savings. It is not sufficient to solely consider energy production costs per plant though they have been researched widely and calculated (Michaelis et al., 2013; Balks and Breloh, 2014; Oliveira e Silva and Hendrick, 2016).

Several conditions affect the benefits that the RE producer offers and should be analyzed for each specific consumer. An overview of possible methods is presented and reviewed in the recent article, "Decision-Making in Renewable Energy Investments," by Strantzali and Aravossis (2016). This literature review shows that the choice of the method mostly depends on the preferences of the decision-maker and the analyst. Industrialists prefer the use of economic indicators for decision-making, and LCCA is dominant in the fields of energy policy and management (Strantzali and Aravossis, 2016). To calculate the economic indicators and the LCCA value, the right input parameters (e.g., investment, installation, and operational costs) must be defined, depending strongly on the types and sizes (designs) of the RE producers and necessary storage devices. Studies on the methodologies that define the input parameters associated with the design and size of the RE producer exist as well (Baños et al., 2011; Erdinc and Uzunoglu, 2012). There is a need for case examples that present the technical design of the RE producer in relation to costs and benefits during the

operation of the system. Though there are a few such case studies, they focus on private households and buildings (Achtnicht, 2011; Marszal et al., 2012). Case studies that focus on manufacturing SMEs with real data are not publicly available. SMEs account for half of the industry's power consumption (BMWI, 2016). It is therefore expected that the results of this study will be of great interest to SMEs that are looking for ways to reduce their energy costs with RE.

3. Background and Methods

3.1 Feasible business models under the German EEG 2014

Generally speaking, the operator of an electrical RE producer has different ways to handle RE (see Figure 1): as a mix of self-consumption and feeding into the grid (BM1), as self-consumption alone (BM2), and as feeding into the grid alone (BM3–BM5). This paper investigates BMs for supplying an SME consumer within the operational scope; therefore, it does not take into further consideration the BM of selling to a third person. Only BM3 (market premium model) is considered to compare the benefits of self-consumption and those of 100% grid feed-in under the current EEG.

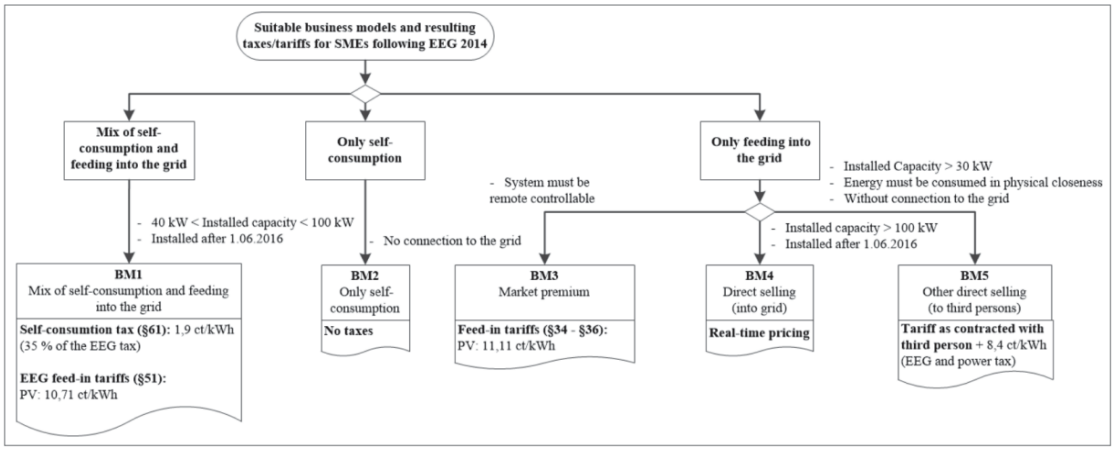

Figure 1: The range of possible applications for RE according to the German EEG

In **BM1**, the operator has the following options for using the electrical RE produced (P_{elRE}) (see Equation 1): consuming the RE ($P_{elRE\text{-}elC}$) and/or feeding the RE produced into the grid ($P_{elRE\text{-}G}$). Additionally, it is possible to temporarily save the energy in electrical storage ($P_{elRE\text{-}elS}$) for its later consumption and/or feeding in. According to the EEG 2014, BM1 is only possible if the machine design value of the RE producer is lower than 100 kW.

$$P_{RE} = P_{elRE-G} + P_{RE-ES} + P_{RE-elC} \quad \text{(eq. 1)}$$

Equation 2 calculates the cash inflows for BM1 (C_{BM1}). The operator gets the tariff for feeding RE into the grid from to §51 ($P_{elRE\text{-}G} * c_{RE,i}$). The self-consumption of electrical RE saves energy costs less the tax for own consumption of energy (($P_{elRE\text{-}elC} + P_{ES\text{-}elC}$) * ($c_{el}$ - c_{EEG})) according to §61. For electrical storage systems, special conditions are applied. The self-consumption tax must be paid twice: for charging the electrical storage and for discharging it.

$$C_{BM1} = P_{elRE-G} * c_{elRE,i} + (P_{ES-elC} + P_{elRE-elC}) * (c_{el} - c_{EEG}) + P_{elRE-ES} * c_{EEG} \quad \text{(eq. 2)}$$

If the machine design value is greater than 100 kW, the option of consuming and/or feeding the RE into the grid is not allowed. For **BM2**, the RE plant may not be connected to the grid. Therefore, in the event of the overproduction of electrical energy, it cannot be injected into the grid. If the consumer makes no demand and is not able to store the energy, it will be wasted. ($P_{elRE\text{-}EO}$) (see Equation 3).

$$P_{elRE} = P_{elRE-EO} + P_{elRE-ES} + P_{elRE-EC} \quad \text{(eq. 3)}$$

The advantage of BM2 over BM1 is that the tax for self-consumption does not apply to it. The operator saves the full purchasing costs for its own consumption of electrical energy ($P_{elRE\text{-}elC} * c_{el}$). The disadvantage lies with the overproduction: It is wasted. Hence, it does not lower any costs ($P_{elRE\text{-}EO} * 0$). Equation 4 calculates the cash inflows for BM2 (C_{BM2}).

$$C_{BM2} = P_{elRE-EO} * 0 + (P_{elRE-elS} + P_{elRE-EC}) * c_{el} \quad \text{(eq. 4)}$$

For the thermal RE producer, no regulation is in place due to the EEG 2014. The thermal energy supply via local and/or district heating grids is not considered in this paper. Because of this, no thermal energy is fed into a grid, and the calculations are made in analogy to those for BM2 (see Equations 5 and 6).

$$P_{thRE} = P_{thRE-EO} + P_{thRE-TS} + P_{RE-thC} \quad \text{(eq. 5)}$$

$$C_{BMTh} = P_{thRE-EO} * 0 + (P_{RthE-thS} + P_{thRE-EC}) * c_{th} \quad \text{(eq. 6)}$$

In the case of the market premium model (**BM3**), the grid operator must have access to remote control of the RE producers. The RE produced is completely fed into the grid (see Equation 7).

$$P_{elRE} = P_{elRE-G} \quad \text{(eq. 7)}$$

The operator gets a tariff according to §34 - §36 ($c_{PM,i}$). In case of a shutdown by the grid operator (for various reasons), the amount for the non-fed-in energy is reimbursed as it would have been if it were feed-in. Equation 8 calculates the cash inflows for BM3 (C_{BM3}).

$$C_{BM3} = P_{elRE-G} * c_{PM,i} \quad \text{(eq. 8)}$$

3.2 Characterization of case companies and scenarios

For two case SMEs, the capital and operating costs for energy supply are investigated for several scenarios for the year 2014. For each SME, the scenarios are then compared. All scenarios are technically feasible and applicable. The energy demand (see Table 1) is known, and load metering data from the SMEs' energy provider is used. Additionally, individual load metering is performed on the most energy-intensive machines using metering devices. The installation of these devices is part of a long-term effort by the PREmdeK Project (Ernst et al., 2013).

Tab. 1: Yearly energy demand of the case SMEs considered for 2014

SME	1	2
El. demand in [kWh] (day)	199.099	3.454.636
El. demand in [kWh] (night)	47.363	934.972
Th. demand [kWh]	1.236.802	-

SME 1 is a small production company that specializes in fruit processing. The company fills 10.000 bottles of different types of fruit juice per hour for five workdays in a one-shift system. The main energy consumer on the production floor is the bottle cleaning system, which cleans reusable glass bottles. The system works at water temperatures between 40 °C and 95 °C, and it is feasible to integrate thermal RE into it. The integration details are not relevant to the investigation and, therefore, are not explained further here.

SME 2 is a medium-sized manufacturing company that specializes in metal processing. The company produces mainly small to medium-sized product series with some repetitive orders on a five-day week in a two-shift system. The main energy consumers in production are big smelters. The smelters need to achieve about 1.500 °C to melt the metal and account for most of the energy costs (purchase of foundry coal, gas, and power). Because of the required high temperature level, the use of thermal RE is not feasible. In addition, the company has a waste heat system in place. Because of this, the amounts of gas and foundry coal used, and the location of the company site, this paper only considers the electrical supply and the demand side of the

company.

For the investigation, in addition to the load profiles of the SMEs, the weather conditions at the company sites are necessary for calculating energy generation. The PREmdeK simulation uses the following meteorological data: air temperature, air moisture, air pressure, global radiation, wind speed, and wind direction. The weather data is measured by a local weather station that the University of Applied Sciences Emden/Leer operates. The data is aggregated to 15-minute intervals (Ernst et al., 2012). Different scenarios for the RE supply have been investigated for the SMEs. The scenarios differ in terms of the composition of the RE plant (PV and solar thermal systems), the use of storage systems, and the machine design value (see Table 3 for elements used in the RE plant).

3.3 Cost calculation data and methods

For both SMEs, Table 2 lists the actual energy supply costs for 2014 and the $LCCA_{Reff}$ value. The costs are the product of the energy demand and the specific energy cost.

Tab. 2: Actual energy costs of the case SMEs in 2014

	Energy price c_i [ct/kWh]	**SME 1 [Euro]**	**SME 2 [Euro]**
El. energy cost (day)	20,5	40.752	707.095
El. energy cost (night)	18,5	8.747	172.671
Th. energy cost	6,5	56.892	-
Total cost	-	106.391	879.766
$LCCA_{Reff}$	-	1.172.275	9.693.702

For the alternative supply (according to the investigated scenarios) and for each RE producer and storage system different suppliers have requested offers related to machine design value (see Table 3), which industry experts have verified. Based on the weather and energy demand data (split into electrical demand data and thermal demand data), simulations have been run with scenarios involving different combinations and designs. For each scenario, the PREmdeK simulation gives values for the energy generated according to plant type, storage usage, and energy exchange with the grid.

Tab. 3: Overview of the capital and operating costs for the RE producer

RE producer	**Supplier**	**Machine design value (P_i)**	**Capital cost (CC_i)**	**Operating cost (OC_i)**
Photovoltaic	Heckert Solar NeMo 60P	40–2.000 kW	1036,9 * P_{PV} + 7309,6	2% of the capital cost
Solar heat	Paradigma Aqua Plasma 19/50	5,01–1002 m²	801,69 * P_{SH} + 63,934	2% of the capital cost
El. Storage	EP Solarpower EnergieS 18	18,4 kWh	26.983,09 Euro	-
	EP Solarpower EnergieS 55	55,2 kWh	59.769,20 Euro	
	EP Solarpower EnergieS 110	110,4 kWh	120.758,17 Euro	
Th. Storage	Paradigma Aqua Expresso ll 110	441–4410 kWh	13,831 * P_{ThS}	-

Based on these results, the following indicators have been calculated for the three BMs considered: net present value (NPV), internal rate of return (IRR), payback period (n_{dyn}), and life-cycle cost analysis (LCCA) value. The calculations of the indicators and the LCCA values are explained below. The NPV is used in capital budgeting to analyze the profitability of an investment ($CC_{RE\ plant}$) for a certain time (here k = 20a) at a specific discount rate (here j = 6.5%) (see Equation 9) (Poggensee, 2009).

The NPV is the difference between the present value of cash inflows and the present value of cash outflows ($C_{BMi} - OC_{RE\ plant}$).

$$NPV = \sum_{k=0}^{k=20} \frac{(C_{BMi} - OC_{RE\ Plant}) - CC_{RE\ Plant}}{(1+j)^k} \quad \text{(eq. 9)}$$

The IRR is the discount rate, where the NPV of all cash flows from a particular project equals zero. IRR calculation (see Equation 10) is similar to NPV calculation (Poggensee, 2009) but sets the NPV at zero.

$$NPV = 0 = \sum_{k=0}^{k=20} \frac{(C_{BM} - OC_{RE\ Plant}) - CC_{RE\ Plant}}{(1+IRR)^k} \quad \text{(eq. 10)}$$

The discounted payback period gives the number of years it takes to break even after undertaking the initial investment by discounting future cash flows and considering the value of money in relation to time (see Equation 11) (Poggensee, 2009).

$$NPV = 0 = \sum_{k=0}^{n_{dyn}} \frac{(C_{BM} - OC_{RE\ Plant}) - CC_{RE\ Plant}}{(1+j)^{n_{dyn}}} \quad \text{(eq. 11)}$$

The LCCA value takes into account all cash outflows related to future activities and the business model but does not consider cash inflows (Fuller and Petersen, 1996). The following cash outflows are considered: operation costs, taxes for self-consumption, and electrical and thermal energy costs. All costs are discounted and total to an NPV (see Equation 12).

$$LCCA = \sum_{k=0}^{k=20} \frac{CC_{RE\ Plant} + \text{cash outflows}}{(1+i)^{-k}} \quad \text{(eq. 12)}$$

For the evaluation, the ratio of the LCCA for the RE plant to the reference LCCA has been calculated (see Equation 13).

$$LCCA\ ratio = 100\% * \frac{LCCA}{LCCA_{Reff}} - 100\% \quad \text{(eq. 13)}$$

4. Evaluation of the Scenarios for the Case SMEs

4.1 Results of the economic indicators and LCCA for SME 1

Figure 2 shows the electrical RE self-consumption ratio in relation to the PV machine design value and the electrical storage capacity for SME 1. As expected, the self-consumption ratio increases as the storage capacity increases and decreases as the PV machine design value increases.

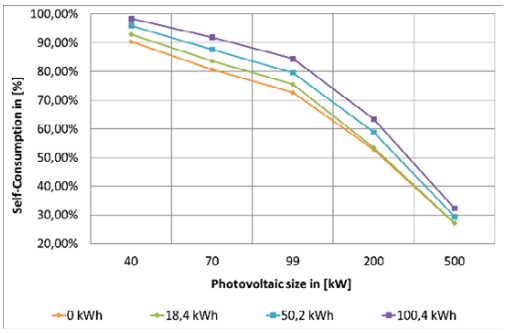

Fig. 2: Self-consumption ratio of the electrical RE for SME 1

Figure 3 shows the results for the IRR and payback period in relation to the PV machine design value and BM for SME 1. For easier comprehension, the figures only show the results for the electrical storage capacity of 18 kWh. It is not necessary to show all the results because the conclusion is the same for all the storage capacities. As expected, a comparison of BM1 and BM2 with BM3 shows that BM1 and BM2 offer higher benefits. Only with higher machine design values can BM3 achieve better benefits, but this is not applicable to SMEs. Typically, the SMEs do not have a sufficiently large free area for bigger PV machine design values and for the efforts required to operate big RE plants. BM2 has the best IRR and payback period at 40 kW. As Figure 2 shows, there is also a maximum point for the self-consumption ratio. BM1 has the best IRR and payback period at 70 kW. The combination of the high self-consumption ratio and RE overproduction feed-in lead to an enhanced benefit. In both BMs (BM1 and BM2), using storage systems leads to lower profitability. As Figure 2 shows, it is possible to increase the self-consumption of the electrical RE with storage systems, but that cannot compensate for the higher capital cost and higher taxes for self-consumption (BM1 alone).

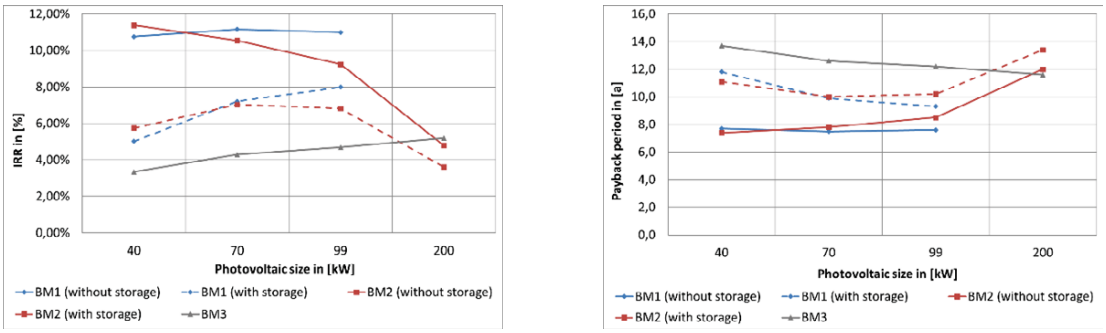

Fig. 3: Relationship between PV machine design value and IRR (left) and between PV machine design value and payback period (right) for SME 1 and all BMs

Figure 4 shows the results of the NPV and LCCA ratio in relation to the PV machine design and BM for SME 1. As Figure 3 shows, the profitability of BM3 and of the systems that have storage is lower than that of BM1 and that of BM2. In contrast to the IRR and payback period, the NPV achieves the maximum points at different machine design values: BM1 at 99 kW and BM2 at 70 kW. For BM1, the profit is higher because more electrical RE is fed in, and for BM2, more electrical energy is saved in total compared to the scenarios involving lower machine design values. Higher machine design values save more electrical energy in total, but the higher profit cannot compensate for the higher capital and operation costs, leading to a lower IRR. The LCCA ratio has the best value in BM2 at 70 kW. At this point, the combination of high cost savings and no taxes for self-consumption leads to a low operating cost for the electrical energy supply for SME 1.

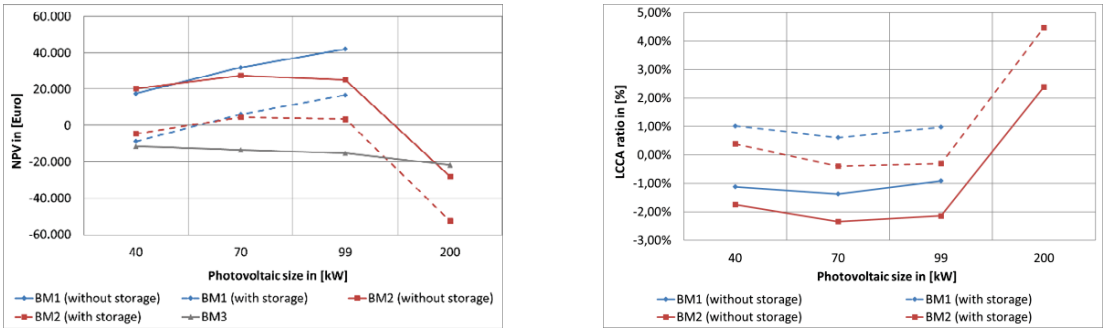

Fig. 4: Relation between PV machine design value and NPV (left) and between PV machine design value and LCCA ratio (right) for SME 1 and all BMs

Figure 5 shows the thermal RE self-consumption ratio in relation to the solar thermal machine design value and the thermal storage capacity for SME 1. As expected, the self-consumption ratio increases with the rise in the storage capacity and falls with the rise in the solar thermal machine design value.

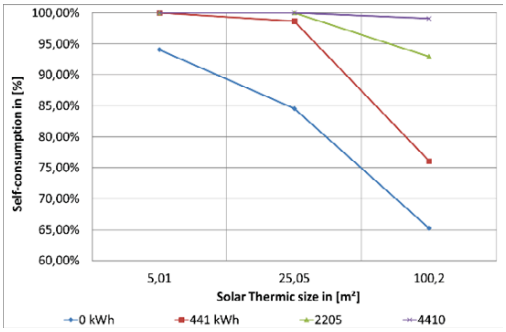

Fig. 5: Self-consumption ratio of the thermal RE for SME 1

Figure 6 shows the results for the IRR and payback period in relation to the solar thermal machine design value for SME 1. Contrary to expectations, the profitability of the thermal RE producer is in the negative range. In comparison to the PV system, the maximum point is experienced with this system, which has the highest self-consumption ratio. Moreover, the storage usage shows that the higher benefits due to higher self-consumption do not compensate for the higher capital costs.

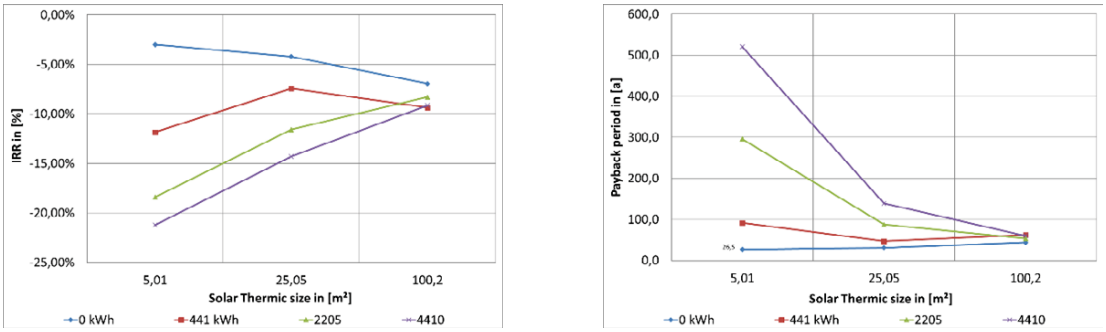

Fig. 6: Relation between solar thermal area and IRR (left) and between solar thermal area and payback period (right) for SME 1 and all BMs

Figure 7 shows the results of the NPV and LCCA ratio in relation to the solar thermal machine design value for SME 1. The NPV is like the IRR, and the payback period is in the negative range. The operation costs are at the lowest point (0,4 % higher than they would be without the solar thermal system). The problem is the low cost savings due to the low gas price. In comparison to the electrical energy price (20,5 ct/kWh), the thermal energy price (6,5 ct/kWh) is significant lower, which leads to lower profits.

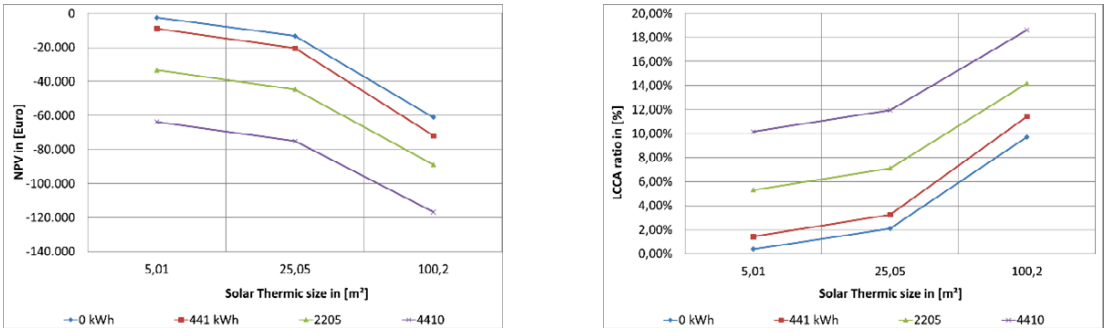

Fig. 7: Relation between solar thermal area and NPV (left) and between solar thermal area and LCCA ratio (right) for SME 1 and all BMs

4.2 Results of the economic indicators and LCCA for SME 2

Figure 8 shows the electrical RE self-consumption ratio in relation to the PV machine design value and electrical storage capacity for SME 2. As expected, the self-consumption ratio rises with the increase in the storage capacity and falls with the increase in the PV machine design value. In comparison to that for SME 1, the increase is lower because of the higher total electrical energy consumption.

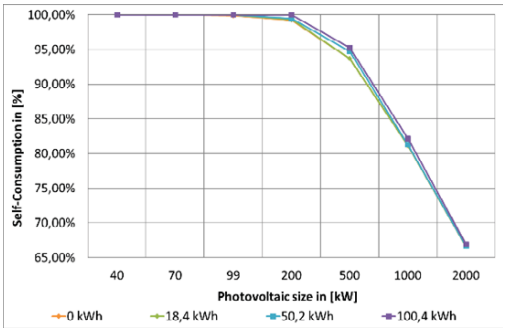

Fig. 8: Self-consumption ratio of the electrical RE for SME 2

Figure 9 shows the results of the IRR and payback period in relation to the PV machine design value and BM for SME 2. For easier comprehension, the figures for SME 2 only show the results for the electrical storage capacity of 55 kWh. In contrast to SME 1, BM2 always offers the best benefits. The advantage due to BM1's feeding of overproduced RE into the grid is not applicable because the self-consumption ratio (Figure 8) is still 100% for the 99-kW PV system. The best IRR and payback period are achieved at 200 kW. The results for the storage system are similar to those for SME 1.

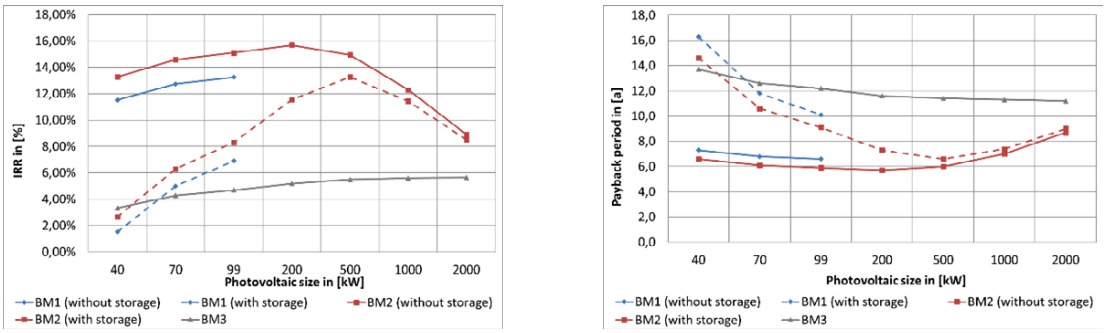

Fig. 9: Relation between PV machine design value and IRR (left) and between PV machine design value and payback period (right) for SME 2 and all BMs

Figure 10 shows the results of considering the NPV and LCCA ratio in relation to the PV machine design value and BM for SME 2. Similarly to those for SME 1, the best NPV and LCCA ratio occur at a different machine design value (like the IRR and payback period). The best NPV and LCCA ratio occur with the

1,000-kW PV machine design value.

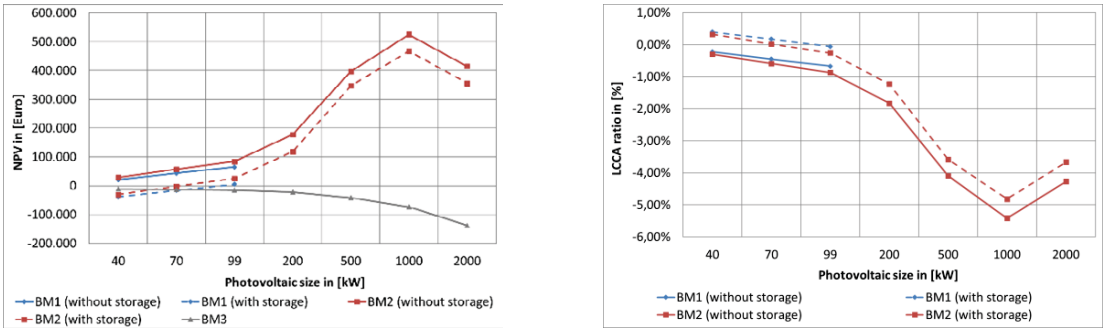

Fig. 10: Relation between PV machine design value and NPV (left) and between PV machine design value and LCCA ratio (right) for SME 2 and all BMs

5. Conclusion

The comparison of all investigated systems and BMs shows that the most beneficial scenarios are always the ones with high, direct, self-consumption of electrical RE from PV systems and the ones with minimal use of storage systems or no storage systems. The benefits that BM3 (which solely involves the feeding of RE into the grid) offers are too low to compete against those that BM1 (self-consumption and/or feeding into the grid) and BM2 (self-consumption alone) offer. The main reason for this is that the feed-in tariffs (10,7 ct/kWh) for the RE from PV systems are low compared to the cost savings due to self-consumption of electrical RE (20,5 ct/kWh). The use of storage systems in BM1 and BM2 is not economically reasonable. Though it is possible to increase RE self-consumption with a storage system, the following factors make it less profitable than a situation that involves no storage: The main problem in BM1 and BM2 is the high capital cost. The benefits due to higher self-consumption are too low to compensate for the higher capital costs. Another factor concerns BM1 alone: German´s EEG "double tax" for electrical storage systems decreases their profitability. Under the investigated conditions, if the PV system is optimally designed for RE self-consumption, no storage systems are required. For demand-side management or other applications, new analyses must be undertaken regarding the need for storage systems.

The use of solar thermal energy to decrease the SME's thermal energy cost makes cannot be recommended, the cost savings (6,5 ct/kWh) are too low to have a satisfying effect on overall energy costs.

Considering the currently electrical energy prices (including taxes and levies) and the political conditions that the EEG 2014 for RE producers promotes, SMEs warrant PV systems for self-consumption with no storage systems. The choice between BM1 and BM2 and the design of a PV system depends on the company's size and on the amount of energy that is consumed. The final decision regarding the most ideal machine design and BM should be analyzed individually for each SME.

6. Future Work

The legislation regarding RE and the grid system is in a state of constant change, at least with respect to the German EEG. The next version, EEG 2017, is currently under preparation and will need to be taken into account in future research. Controllable demand (e.g., demand-side management) and other business models (e.g., real-time pricing or selling to third persons) should also be considered in the future. This will become possible with a new PREmdeK simulation design. The verification of measured data and the easy use of historical local weather data via a direct connection and databases should constitute another future task.

7. References

Achtnicht, M., 2011. Do environmental benefits matter? Evidence from a choice experiment among house owners in Germany. Ecological Economics 70 (11), 2191–2200.

Balks, M., Breloh, P., 2014. Auswirkungen des neuen Erneuerbare-Energien-Gesetzes auf Offshore-Wind-Investitionen. Wirtschaftsdienst 94 (7), 520–523.

Baños, R., Manzano-Agugliaro, F., Montoya, F.G., Gil, C., Alcayde, A., Gómez, J., 2011. Optimization methods applied to renewable and sustainable energy. A review. Renewable and Sustainable Energy Reviews 15 (4), 1753–1766.

BMWI, 2016. Energiedaten: Gesamtausgabe. http://www.bmwi.de/BMWi/Redaktion/PDF/E/energiestatistiken-grafiken,property=pdf,bereich=bmwi2012,sprache=de,rwb=true.pdf. Accessed 11 August 2016.

Deutsche Bundestag, 2014. Gesetz für den Ausbau erneuerbaren Energien - (Erneuerbare-Energien-Gesetz -EEG 2014). http://www.gesetze-im-internet.de/eeg_2014/. Accessed 28 June 2016.

Deutsche Gesellschaft für Sonnenenergie (DGS). PV@now. https://www.pv-now.de/registration/registration.xhtml?windowId=dd6. Accessed 13 May 2017.

Erdinc, O., Uzunoglu, M., 2012. Optimum design of hybrid renewable energy systems. Overview of different approaches. Renewable and Sustainable Energy Reviews 16 (3), 1412–1425.

Ernst, S., Hackmann, R., Pechmann, A., Schöler, I., 2012. A Concept for an Energy Management System. In: D. A. Dornfeld und Barabara, in: Dornfeld, D.A., Linke, B.S. (Eds.), Leveraging technology for a sustainable world. Proceedings of the 19th CIRP Conference on Life Cycle Engineering, University of California at Berkeley, Berkeley, USA, May 23 - 25, 2012 ; [LCE 2012]. Springer, Berlin, pp. 525–532.

Ernst, S., Hackmann, R., Pechmann, A., Schöler, I., 2013. A simulation based feasibility study to satisfy the energy demand of SME production sites by their own multi-source renewable power plants. IEEE International Workshop.

European Commission, 2010. EUROPE 2020: A strategy for smart, sustainable and inclusive growth. http://eur-lex.europa.eu/LexUriServ/LexUriServ.do?uri=COM:2010:2020:FIN:EN:PDF. Accessed 5 July 2016.

Fuller, S.K., Petersen, S.R., 1996. Introduction to Life-Cycle Cost Analysis, in: Fuller, S.K., Petersen, S.R. (Eds.), Life Cycle Costing Manual. for the Federal Energy Management Program, 1-1 bis 1-3.

International Energy Agency (iea), 2015. Key World Energy STATISTICS. https://www.iea.org/publications/freepublications/publication/KeyWorld_Statistics_2015.pdf. Accessed 5 July 2016.

Marszal, A.J., Heiselberg, P., Lund Jensen, R., Nørgaard, J., 2012. On-site or off-site renewable energy supply options? Life cycle cost analysis of a Net Zero Energy Building in Denmark. Renewable Energy 44, 154–165.

Michaelis, J., Junker, J., Wietschel, M., 2013. Eine Bewertung der Regelenergievermarktung im Power-to-Gas-Konzept. Z Energiewirtsch 37 (3), 161–175.

Oliveira e Silva, G. de, Hendrick, P., 2016. Lead–acid batteries coupled with photovoltaics for increased electricity self-sufficiency in households. Applied Energy 178, 856–867.

Pachauri, R.K., Mayer, L. (Eds.), 2015. Climate change 2014. Synthesis report. Intergovernmental Panel on Climate Change, Geneva, Switzerland, 151 pp.

Pechmann, A. PREMDEK. Hochschule Emden/Leer. www.hs-emden-leer.de/premdek.html. Accessed 13 May 2017.

Pechmann, A., Schöler, I., Ernst, S., 2016. Possibilities for CO2-neutral manufacturing with attractive energy costs. Journal of Cleaner Production.

Poggensee, K. (Ed.), 2009. Investitionsrechnung. Grundlagen - Aufgaben - Lösungen, 1st ed. Gabler, Wiesbaden, 401 pp.
Strantzali, E., Aravossis, K., 2016. Decision making in renewable energy investments. A review. Renewable and Sustainable Energy Reviews 55, 885–898.

09. Solar Resources and Energy Metereology

Conference Proceedings

EuroSun 2016
Palma de Mallorca (Spain), 11 - 14 October 2016

Estimation of Global Solar Radiation from Air Temperature using Artificial Neural Networks based on Reservoir Computing

Miquel L. Alomar[1], Vincent Canals[1], Josep L. Rosselló[1] and Víctor Martínez-Moll[1]

[1] University of Balearic Islands, Palma de Mallorca (Spain)

Abstract

Solar radiation data are crucial for the design and evaluation of solar energy systems. For locations where measurements are not available, models to estimate solar radiation from more readily available data are required. In this paper, we introduce the use of the reservoir computing (RC) technique to model daily global solar radiation (GSR) as a function of air temperature. RC is a type of artificial neural network (ANN) with closed loops (recurrent neural network, RNN) particularly suited to process time-dependent information. The novelty of this work is the use of a recurrent network for modeling solar radiation, which allows including temporal correlations between the input and output variables. The proposed approach is used to estimate GSR using weather data from a location in Almeria, Spain. The results show higher accuracy than those obtained with conventional regression models.

Keywords: *Global solar radiation, modeling, artificial neural networks, reservoir computing*

1. Introduction

Reliable knowledge of solar radiation availability and variability is essential for the efficient and economical development and implementation of solar energy applications such as photovoltaic, solar thermal and passive solar systems. Long-term real measurements at the site of the proposed solar system are the ideal database for the simulations required to evaluate the performance of such application. However, solar radiation measurements are made at few locations due to the high cost of the equipment. This makes necessary the use of accurate models for locations where measured values are not available.

A number of empirical formulas have been developed to estimate solar radiation from more commonly available data at weather stations. A review of such models for global, beam and diffuse radiation is presented in Wong and Chow (2001). In the present paper, we focus on the estimation of daily global solar radiation (GSR) on the horizontal surface. Several methods for decomposing direct and diffuse irradiance from GSR can be found in the literature (Lam and Li, 1996).

The empirical models for the assessment of GSR use historical weather data of the location under study. The meteorological observations typically employed are sunshine, cloud and temperature. As cloud is routinely detected by satellites and strongly influences solar radiation, numerous accurate models have been proposed to estimate GSR through satellite images (Janjai et al., 2009). Nonetheless, sunshine and satellite-based cloud observations are not readily available in most locations. On the other hand, air temperature is measured (usually along with humidity and precipitation) in any weather station worldwide and has been shown to be an important meteorological parameter for the modeling of GSR (Almorox et al., 2011). This motivates the research to find precise models for GSR based only on the geographical location and in commonly available temperature measurements, such as maximum and minimum temperature registers.

Apart from standard regression models (see Almorox et al., 2011 for a review of empirical temperature-based GSR models), artificial neural networks (ANNs) have also been employed in recent years for the estimation of GSR from other available meteorological parameters (Rehman and Mohandes, 2008; Behrang

doi:10.18086/eurosun.2016.09.13 Available at http://proceedings.ises.org

et al., 2010). Conventional regression models are based on the use of empirical equations that define a relationship between the desired output function (daily GSR, H) and some input variables (for example, the extraterrestrial GSR, H_0, and the daily maximum, T_{max}, and minimum temperature, T_{min}). Some empirical coefficients in these equations need to be calibrated for the site under study with available measurements by means of a mathematical regression. On the contrary, ANNs represent a methodology that allows fitting an output function without a predefined structure (black box modeling). In this approach, a network of so-called artificial neurons with configurable connections is used to learn from data the desired nonlinear output function.

ANNs can be essentially classified into feed-forward neural networks (FFNNs) and recurrent neural networks (RNNs). A FFNN has its neurons organized in layers with no feedback or lateral connections. The input signal propagates through the network in a forward direction, on a layer-by-layer basis. On the other hand, RNNs present loops, feedback connections between neurons. Thus, information can propagate forward and backwards. The major advantage of RNNs over FFNNs is that they can implicitly learn temporal tasks. That is to say, an output function can be learnt such that it does not only depend on the current value of the input signal but also on the input history. In other words, RNNs are appropriate for processing time series.

A number of works have already proposed the use of FFNNs to model GSR (Mohandes et al., 1998; Rehman and Mohandes, 2008; Benghanem et al., 2009; Behrang et al., 2010). Here, however, we propose the use of a RNN for that purpose. More specifically, we make use of reservoir computing (RC, Lukosevicius and Jaeger, 2009), a particular approach for building and training RNNs that presents a conveniently simple learning algorithm. As records of GSR represent time-series values, we hypothesize that the RNN's capability of learning temporal features from the data may improve the accuracy of the GSR estimations. This idea was already suggested by the empirical model of Bristow and Campbell (Bristow and Campbell, 1984) where the estimated radiation at current time does not only depend on the current temperature value, but also on that at a different time step.

2. Methods

2.1. Empirical models

Among the existing methods that use empirical relationships to estimate GSR, two of them have been chosen as representative for comparing the accuracy of our RC-based proposed model with conventional regression ones. Namely, the Hargreaves model (Hargreaves and Samani, 1982) and the Bristow-Campbell model (Bristow and Campbell, 1984).

Daily total extraterrestrial radiation (H_0) is included in both models together with maximum (T_{max}) and minimum temperature (T_{min}) or other quantities derived from them. H_0 can be calculated using standard geometric procedures as described in Almorox et al. (2011). The only inputs required to calculate this value is the day of the year and the latitude of the location.

The equation to estimate daily GSR according to the Hargreaves model can be expressed as follows:

$$H = H_0 \cdot [A_{HG}(T_{max} - T_{min})^{\frac{1}{2}}] \qquad \text{(eq. 1)}$$

where A_{HG} is an empirical coefficient that usually ranges between 0.16 and 0.17, but must be derived for the particular site using the available data.

The Bristow-Campbell model is based on a function (ΔT) of the maximum and minimum temperatures and on three empirical parameters (A, B and C):

$$H = H_0 \cdot A \cdot [1 - \exp(-B \cdot \Delta T^C)] \qquad \text{(eq. 2)}$$

where ΔT is defined as the next function (i corresponds to the current day and $i+1$ to the next day):

$$\Delta T = T_{max,i} - (T_{min,i} + T_{min,i+1})/2 \qquad \text{(eq. 3)}$$

Typical values for the empirical coefficients are $A=0.7$, $B=0.004\text{-}0.001$ and $C=2.4$, but they can be determined using solar radiation data.

2.2. Reservoir computing approach

Artificial neural networks (ANNs) are a computational tool inspired by the way our brain seems to process information. Basically, an ANN is an interconnected group of processing nodes (neurons) that can be used to estimate or approximate functions that depend on a number of inputs. As in biological neural networks, ANNs can learn from experience adjusting the strength of the connections (weight values). That is, they learn from examples (data) constructing an input-output mapping without explicit derivation of the model equation. ANNs can be used for many different applications, such as pattern recognition (in speech, handwriting, etc.), optimization problems, prediction and control among others.

Reservoir computing (RC) is a particular type of ANN characterized by a recurrent network architecture with a high number of interconnected nodes as illustrated in Fig.1 (a). Contrary to conventional RNNs, where all connections need to be adapted, all connection weights in an RC system are randomly chosen and kept fixed except for a linear output layer, which is the only configurable part of the network. This design reduces the complex RNN training to a simple linear regression problem, which facilitates the practical application of RNNs.

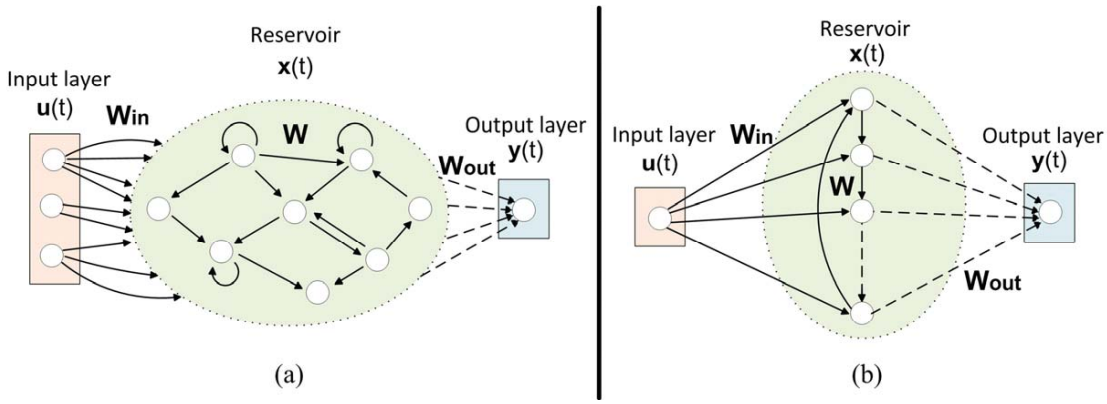

Fig. 1: (a) General architecture of an RC system. All connections are randomly chosen and kept fixed except the ones coupling the reservoir on the output layer (dashed arrows). (b) Particular RC architecture where the reservoir units are organized in a cycle.

An RC system consists of two clearly differentiated parts (apart from the input signals):

- The reservoir, a recurrent network that is randomly generated and remains unchanged.
- The output layer, a simple linear combination of the reservoir states. The weights of such combination are obtained through linear regression using a training set of data.

The general expression to estimate the neuron states in the reservoir at current time, $\boldsymbol{x}(t)$, as a function of the (multidimensional) input signal, $\boldsymbol{u}(t)$, and of the reservoir states at the previous time step, $\boldsymbol{x}(t\text{-}1)$, is given by eq. 4:

$$\boldsymbol{x}(t) = \boldsymbol{f}[\boldsymbol{W_{in}} \cdot \boldsymbol{u}(t) + \boldsymbol{W} \cdot \boldsymbol{x}(t-1)] \qquad \text{(eq. 4)}$$

where ***Win*** refers to the strength of the connections coupling the input signals with the reservoir and ***W*** corresponds to the reservoir internal weights (both matrixes of weight values are, in general, randomly generated). ***f*** denotes the nonlinear transfer function employed for the neurons. When a sigmoidal function is used for ***f***, such as the hyperbolic tangent function (it is the case of the present work), the reservoir is called an echo state network (ESN).

The output layer units (***y***) in RC (readouts) are computed as a simple linear combination of the reservoir states (***x***):

$$\boldsymbol{y}(t) = \boldsymbol{W_{out}} \cdot \boldsymbol{x}(t) \qquad \text{(eq. 5)}$$

where ***Wout*** corresponds to the matrix of output connection weights.

The recent study of Rodan and Tino (2011) shows that a simple reservoir where the neurons are organized in a cycle as illustrated in Fig.1 (b) is practically equivalent to the original reservoir structure with random connections of Fig.1 (a). The connections between internal units in the reservoir have the same weight value *r*. The input layer is fully connected to the reservoir with a connection weight that is positive or negative with equal probability and with the same absolute value for the weight (*v*). Parameters *r* and *v* must be scanned in order to find the best performing weight configuration. This conveniently simple RC topology, known as the simple cycle reservoir (SCR) is the one employed in the present article. For more details about this approach, see the work by Rodan and Tino (2011) or that by Alomar et al. (2016).

RC can be viewed as an expansion (or kernel) method similar to the support vector machine (SVM) approach (Burges, 1998) where the input signal is projected to a higher dimensional state space through the nonlinear dynamics of the reservoir recurrent network. The expanded feature vector (***x***) composed of the reservoir states can be finally readout with a linear method to get an estimation (***y***) of the desired output function. However, it must be noted that apart from producing a nonlinear transformation of the input signals, RNNs (unlike SVMs or FFNNs) have the capability to learn a temporal task. That is, to set a relationship between the desired output value and the input history.

2.3. Data description

A 5-year recording (from 1 July 2007 to 30 June 2012) of GSR and temperature values derived from satellite data for a location in Almeria has been used for training and testing the different models (conventional regression models and RC networks). These data are freely available on the internet (SolarGis, 2016). The original data provided with a 15-minute time basis have been integrated to obtain daily values. The resulting time-series are shown in Fig. 2 and Fig. 3. All input signals (T_{max}, T_{min}, H_o) have been normalized to the [0, 1] range before being processed by the RC network. The first 4 years of data have been used as training set for calibrating the models while the last year has been employed for testing them.

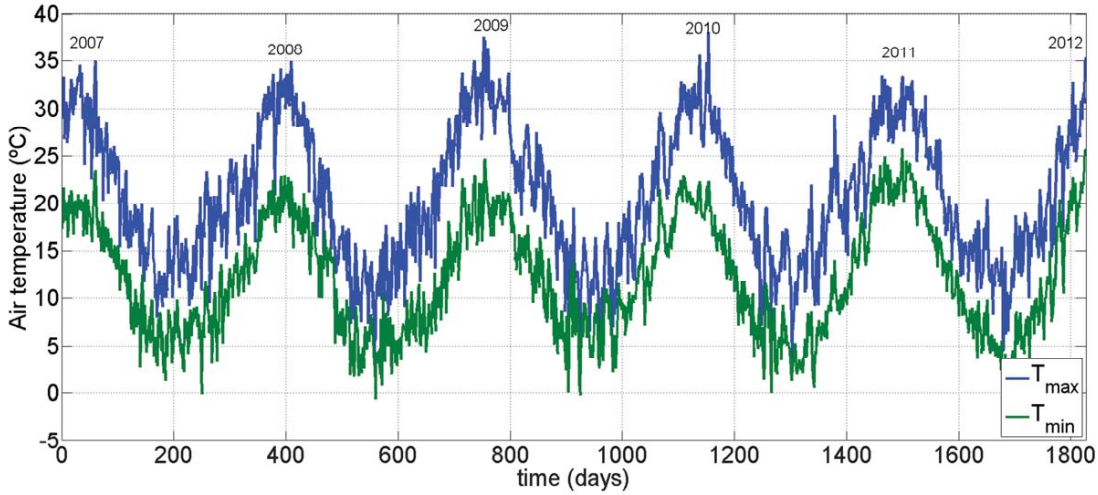

Fig. 2: Daily maximum and minimum temperature values employed as input data to estimate the GSR.

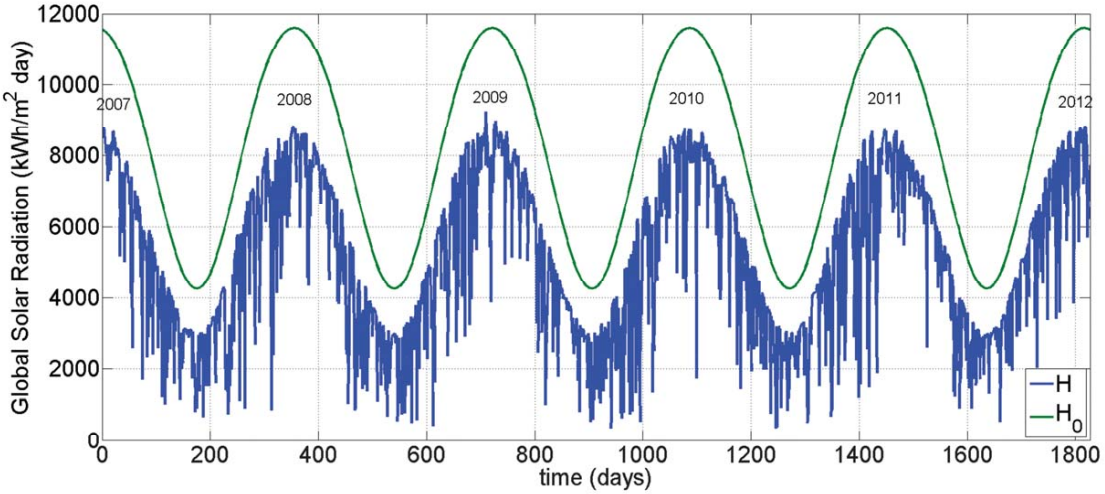

Fig. 3: Observed daily GSR (*H*) along with the daily total extraterrestrial radiation (H_0) calculated using standard geometric procedures from the latitude of the location.

3. Results

A number of network combinations using different parameters as inputs (T_{max}, T_{min}, T_{mean}, $\delta T=T_{max}$,- T_{min}, H_0) and different numbers of units (30, 50, 70 and 100 neurons) have been tested. The performance of the various models has been assessed according to various statistical errors: normalized mean-square error (NMSE), normalized root mean-square error (NRMSE), coefficient of determination R-squared (R^2), root mean-square error (RMSE), mean-square error (MSE), mean absolute error (MAE) and mean bias error (MBE).

Two network configurations have been found to perform the best, both using 50 neurons. The first model (which we call "RC-1") employs a single input (δT) to estimate the ratio H/H_0 (desired output). That is, a linear dependence between H and H_0 is assumed. The second model ("RC-2") utilizes two input signals (δT and H_0) for modeling H as output function. Any other combination of variables used as input signals have resulted in less accurate estimations. The test error results of both RC-based models compared to those of the standard regression methods are presented in Tab.1 where "Regress1" corresponds to the Hargreaves model and "Regress2" to the Bristow-Campbell model. It can be appreciated that both RC-based models are practically equivalent, which indicates that assuming that H is directly proportional to H_0 seems adequate.

On the other hand, it can be observed that, as expected, the proposed RC-based models exhibit a higher accuracy than the conventional regression-based empirical methods. Only for the case of the MBE one of the conventional models provides a lower error than the RC-based models. However, it must be mentioned that the MBE is not a good indicator of the estimations' accuracy but just of the error bias.

The function fitting performed by one of the proposed models ("RC-1") is finally illustrated for the test set (one year of data) in Fig.4.

Tab. 1: Statistical evaluation of the conventional (regression-based) and proposed (RC-based) models for the test data set.

Model	NMSE	NRMSE	R^2	RMSE ($Wh/m^2 \cdot day$)	MSE ($(Wh/m^2 \cdot day)^2$)	MAE ($Wh/m^2 \cdot day$)	MBE ($Wh/m^2 \cdot day$)
Regress1	0.2467	0.4967	0.7533	1053.90	$1.18 \cdot 10^6$	836.82	237.61
Regress2	0.2201	0.4691	0.7799	995.35	$9.93 \cdot 10^5$	823.73	535.26
RC-1	0.1940	0.4404	0.8060	934.49	$8.76 \cdot 10^5$	745.03	407.08
RC-2	0.1940	0.4404	0.8060	934.48	$8.76 \cdot 10^5$	771.49	426.06

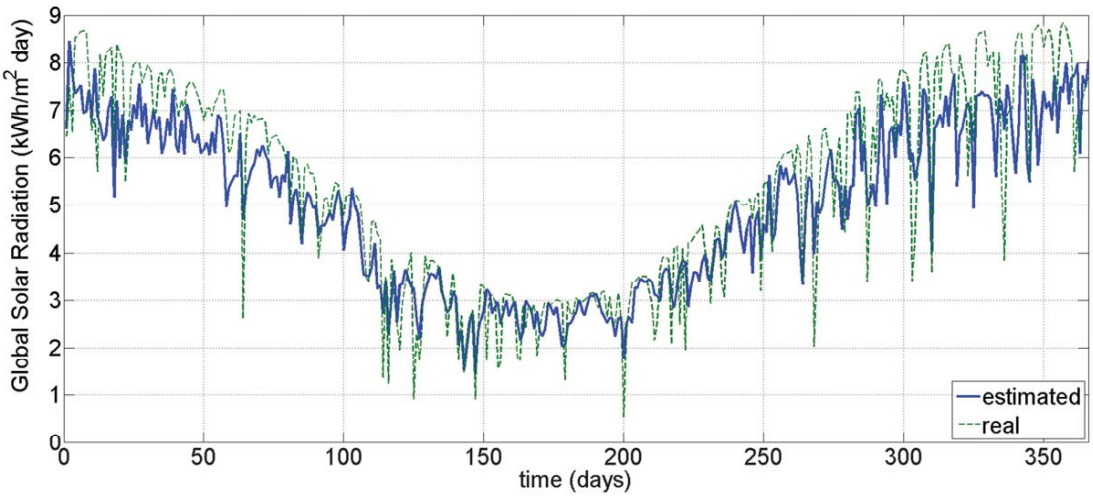

Fig. 4: Estimated and observed GSR for the test data set using an RC-based model that employs Tmax-Tmin as input signal.

4. Conclusions and future work

In this paper, we have proposed a convenient model for estimating daily global solar radiation (GSR) using temperature measurements commonly available at weather stations. The model is based on reservoir computing (RC), a particular type of recurrent neural network (RNN), which allows implicitly learning from time-series data the relation between the input and output signal. We have shown that the proposed neural approach outperforms other conventional empirical methods. The RC-based model can be calibrated for any particular desired location, which makes it useful for the simulation of solar energy systems.

Nevertheless, it is worth highlighting that the validity of the proposed approach has been tested using meteorological data derived from satellite observations assuming that such values present a similar complexity to those that might be obtained from direct physical measurements at a weather station. Therefore, it would be of high interest to further validate the proposed methodology with measured data.

Furthermore, although the presented RC models have been compared with standard methodologies (adjustable empirical equations), they have not yet been demonstrated to outperform other simpler kernel approaches, such as feed-forward neural networks (FFNNs). Finally, it could be an interesting step for the future analyzing whether GSR estimations can be improved by including other input parameters different from temperature, such as humidity and precipitation, which are also often available at most weather stations.

5. References

Almorox, J., Hontoria, H., Benito, M., 2011. Models for obtaining daily global solar radiation with measured air temperature data in Madrid (Spain). Applied Energy 88, 1703-1709.

Alomar, M. L., Canals, V., Perez-Mora, N., Martínez-Moll, V., Rosselló J. L., 2016. FPGA-based stochastic echo state networks for time-series forecasting. Computational Intelligence and Neuroscience 2016, 1-14.

Behrang, M. A., Assareh, E., Ghanbarzadeh, A., Noghrehabadi, A. R., 2010. The potential of different artificial neural network (ANN) techniques in daily global solar radiation modeling based on meteorological data. Solar Energy 84, 1468-1480.

Benghanem, M., Mellit, A., Alamri, S. N., 2009. ANN-based modeling and estimation of daily global solar radiation data: A case study. Energy Conversion and Management 50, 1644-1655.

Bristow, K. L., Campbell, G. S., 1984. On the relationship between incoming solar radiation and daily maximum and minimum temperature. Agricultural and Forest Meteorology 31, 59-166.

Burges, C. J. C., 1998. A tutorial on support vector machines for pattern recognition. Data Mining and Knowledge Discovery 2, 121-167.

Hargreaves, G. H., Samani, Z. A., 1982. Estimating potential evapotranspiration. Journal of Irrigation and Drainage Engineering 108(IR3), 223-230.

Janjai, S., Pankaew, P., Laksanaboonsong, J., 2009. A model for calculating hourly global solar radiation from satellite data in the tropics. Applied Energy 86, 1450-1457.

Lam, J. C., Li, D. H. W., 1996. Correlation between global solar-radiation and its direct and diffuse components. Building and Environment 31(6), 527-535.

Lukosevicius M., Jaeger, H., 2009. Reservoir computing approaches to recurrent neural network training. Computer Science Review 3, 127-149.

Mohandes, M., Rehman, S., Halawani, T. O., 1998. Estimation of global solar radiation using artificial neural networks. Renewable Energy 14(1-4), 179-184.

Rehman, S., Mohandes, M., 2008. Artificial neural network estimation of global solar radiation using air temperature and relative humidity. Energy Policy 36, 571-576.

Rodan, A., Tino, P., 2011. Minimum Complexity Echo State Network. Trans. Neural Netw. 22(1), 131-144.

SolarGis web-page, last accessed Apr. 2016. http://solargis.info/doc/climdata-samples.

Wong, L. T., Chow, W. K., 2001. Solar radiation model. Applied Energy 69, 191-224.

6. Ackowledgements

This work has been supported by the Spanish Ministry of Economy and Competitiveness (MINECO) under Grant Contract TEC2014-56244-R, and a fellowship (FPI/1513/2012) financed by the European Social Fund (ESF) and the Govern de les Illes Balears (Conselleria d'Educació, Cultura i Universitats).

Conference Proceedings

EuroSun 2016
Palma de Mallorca (Spain), 11 – 14 October 2016

The influence of Sahara dust particles in the direct normal irradiance estimation through a total sky camera

Joaquín Alonso-Montesinos[1, 2], Javier Barbero[1], Gabriel López[3], Jesús Ballestrín[4], Jesús Polo[5], Aitor Marzo[6, 7] and Francisco Javier Batlles[1, 2]

[1] Department of Chemistry and Physics, University of Almería, 04120 Almería, Spain

[2] CIESOL, Joint Centre University of Almería-CIEMAT, 04120 Almería, Spain

[3] Department of Electrical and Thermal Engineering, Design and Projects, University of Huelva, 21004, Huelva, Spain

[4] Concentrating Solar System Unit (Plataforma Solar de Almería, CIEMAT), 04200 Almería, Spain

[5] Photovoltaic Solar Energy Unit (Renewable Energy Division, CIEMAT), 28040 Madrid, Spain

[6]Antofagasta Energy Development Center (CDEA), 02800 Antofagasta, Chile

[7] Solar Energy Research Center (SERC-Chile), Santiago (Chile)

Abstract

To properly operate Central Tower Solar Power (CTSP) plants, collection systems must work under appropriate weather conditions. Therefore, knowing the state of the atmosphere, and more specifically the level of incident radiation, is a very valuable information for the operation, to adapt the system for electricity production to atmospheric conditions. Sky cameras have emerged as terrestrial point technologies that can observe the changes produced in short-time intervals. In this work, we have estimated Direct Normal Irradiance (DNI) using a total sky camera (TSI-880 model) under high dust load to study its effect in the DNI estimation, for next compare the results with a cloudless day without these attenuator particles. Furthermore, a CL-51 Vaisala ceilometer was used to identify the presence of this dust concentration in the atmosphere.

Keywords: *Solar radiation estimation, Atmospheric attenuation, Central tower solar power plants, Sky camera, LIDAR*

1. Introduction

The great majority of CTSP plants are in areas with low or medium probability of occurrence of clouds, but high probability of occurrence of episodes of high concentrations of aerosols or dust intrusion. That is why it is necessary to include both factors of a correct evaluation and prediction of the values of direct radiation in the receiver of the tower.

Sky cameras have been used to characterize the atmosphere from a terrestrial point. Its technology makes can be installed in any geographical location, providing a hemispheric view of the sky in real time. Subsequently, many researchers have used these cameras for cloud detection (Alonso et al., 2014) and solar irradiance estimation (Alonso-Montesinos and Batlles, 2015). In that case, atmospheric constituents play also an important role in the radiation attenuation and must be take into account in the solar irradiance estimation.

On 22nd February 2016, an intense episode of Sahara dust intrusion took place in almost all of the Iberian Peninsula, reducing visibility drastically and producing a remarkable dust deposition. In the southeast, Almería was particularly affected by the event (Alonso-Montesinos et al. 2016). Having a sky free of clouds, the DNI estimation was carried out, obtaining a results very distant than in a normal cloudless sky.

doi:10.18086/eurosun.2016.09.05 Available at http://proceedings.ises.org

Therefore, in this work, we present the influence of the concentration of dust particles in the DNI estimation using a total sky camera (TSI-880 model). To ensure the presence of this dust deposition in the lower atmosphere layers, LIDAR data were used from a CL-51 Vaisala ceilometer, obtaining different atmospheric parameters for the days studied.

2. Data

Radiation data were obtained from a radiometric station placed at CIESOL at the University of Almería, Spain (36.8ºN, 2.4ºW, at sea level), at the same time that total sky images (from TSI-880 sky camera) have also collected. The hemispheric vision was represented in JPEG (joint photographic expert group) images, with a 352x288 pixel-image resolution. Furthermore, CL51 Vailasa data were used. Fig. 1 shows the instrumentation in the rooftop of the CIESOL building.

Fig. 1: Total sky camera, TSI-880 model and CL51 Vaisala ceilometer placed in the rooftop of the CIESOL building at the University of Almería

3. Methodology and results

In this section, a particular episode occurred in the southeast of Spain is presented where dust particles appeared over Almería, provoking a decrease in the Direct Normal Irradiance (DNI). Therefore, a case study was performed for estimating DNI using a total sky camera under this special situation. The estimations for this turbid day were compared with the estimations for a clear day, obtaining representative conclusions. Furthermore, CL51 Vaisala ceilometer data were used to contrast the causes of the DNI decreasing.

The importance of this study comes from the special interest of CTSP plants, which need to measure the DNI attenuated in the lower layers of the atmosphere. Therefore, one of the main goal of these plants is to model the irradiance losses between the heliostats and the receiver placed at the top of the tower.

3.1 Turbid day vs clear day

As the idea of this paper is to determine the influence of dust particles in the estimation of DNI with total sky cameras, two contrasted days were selected. The first day was conditioned by a high concentration of Saharan dust particles in the atmosphere (22nd February 2016). For the second day, we tried to choose a clear day in the same date but in other years, obtaining it on 22nd February 2012. Fig. 2 shows the difference of DNI measurements for both days:

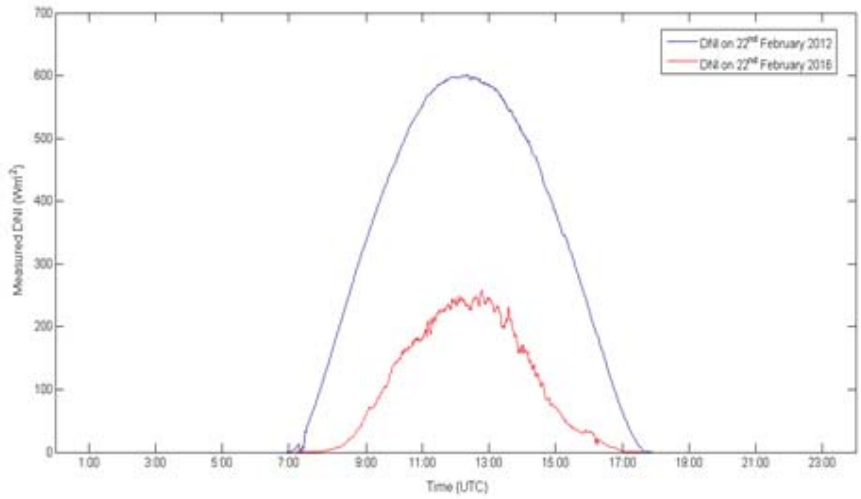

Fig. 2: Representation of measured DNI curves for the days 22nd February 2012 and 22nd February 2016

As seen, the DNI measured for the two days presented an important difference along the day. This difference was also captured by the total sky camera where the digital image levels were also very different. Fig. 3 shows the difference between the two sky camera images:

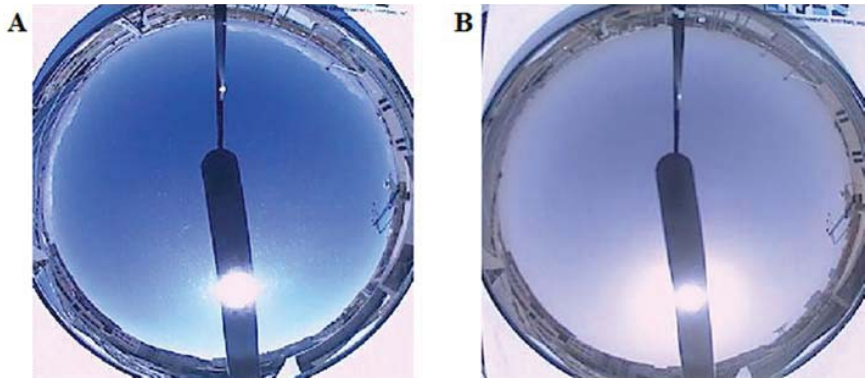

Fig. 3: Sky representation using a TSI-880 sky camera. The image A represents the sky on 22nd February 2012 at 12:00 Universal Coordinated Time (UTC), and image B on 22nd February 2016 at 12:00 UTC.

In the previous images, the blue sky presents a different appearance: in the picture A the sky appears in a more intense blue; whereas in the picture B, the sky appears with another blue tone (cloudier). Having this difference, the objective was to study the influence of the dust presence in the DNI estimation. Subsequently, the idea was to see how the atmosphere was composed in the lower layers with the CL51 Vaisala ceilometer. As Vaisala was installed in the CIESOL building in 2014, there was not data available from 2012. Then, a day with similar DNI was searched, finding 1st March 2016 like the most suitable. Figure 4 represents the DNI curves for 22nd February 2012 and 1st March 2016 to see that the DNI values had a similar trend in the two days:

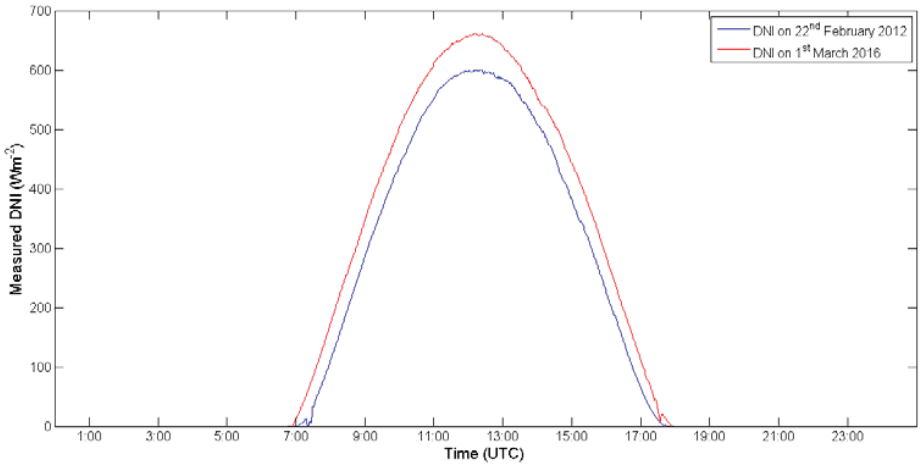

Fig. 4: Representation of measured DNI curves for the days 22nd February 2012 and 1st March 2016

The DNI on 1st March presented higher values than 22nd February, indicating a clearer day. Therefore, the first day of March was selected like the clear sky for comparing with 22nd February 2016 (dust episode). Figure 5 shows an image for the selected day, where blue sky does no present any perturbation in the atmosphere due to dust particles apparently.

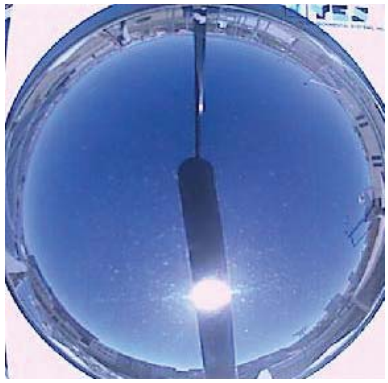

Fig. 5: Image from TSI-880 sky camera on 1st March 2016 at 12:00 (UTC)

3.2 DNI estimation using a total sky camera

According to methodology presented in Alonso-Montesinos and Batlles, (2015) and Alonso-Montesinos et al., (2015), the DNI was estimated using TSI-880 sky images for the two studied days: 22nd February 2016 and 1st March 2016. The first one presented the concentration of Sahara dust particles; whereas the second one was a cloudless sky where dust particles do not appear.

Digital image levels are used to estimate a DNI value. For DNI, not all pixels are processed; only pixels in the sun area. As the sun area has not always the same size, a radius which covers the solar area is obtained in function of the solar altitude angle (α), following the next expression:

$$Radius = -0.9646\,\alpha + 99.2986 \qquad \text{(eq. 1)}$$

Figure 6 represents the solar area detected for a cloudless moment, where the red circle represents the sun area to estimate the DNI.

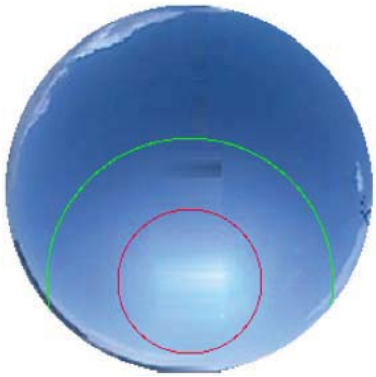

Fig. 6: Image from TSI-880 sky camera, where different areas are established to do the estimation of radiation.

After that, using digital image level correlations and the solar altitude angle, each pixel belonging to the red circle acquires a DNI value following the methodology described in the previous cites. Finally, the mean value of the total pixel estimations represents the DNI.

From sunrise to sunset, images from the sky cam were processed every minute. For all results, different parameters were obtained: RMSE given by Eq. (2) and expressed in (Wm^{-2}); nRMSE given by Eq. (3) in (%); MBE given by Eq. (4) and expressed in (Wm^{-2}); nMBE given by Eq. (5) in (%) and R given by Eq. (6) (dimensionless):

$$RMSE = \sqrt{\frac{1}{N}\sum_{i=1}^{N}(DNI_{est} - DNI_{mea})^2} \quad \text{(eq 2)}$$

$$nRMSE = \left[\frac{RMSE}{DNI_{max} - DNI_{min}}\right] 100 \quad \text{(eq 3)}$$

$$MBE = \frac{1}{N}\sum_{i=1}^{N}(DNI_{est} - DNI_{mea}) \quad \text{(eq 4)}$$

$$nMBE = \left[\frac{MBE}{DNI_{max} - DNI_{min}}\right] 100 \quad \text{(eq 5)}$$

$$R = \frac{\sigma_{DNI_{est}DNI_{mea}}}{\sigma_{DNI_{est}}} \quad \text{(eq 6)}$$

where DNI_{est} is the DNI estimated, DNI_{mea} is the DNI measured, DNI_{max} is the maximum observed DNI value, DNI_{min} is the minimum DNI value, $\sigma_{DNI_{est}DNI_{mea}}$ is the covariance of the two input data sets (the estimated and measured radiations), $\sigma_{DNI_{est}}$ is the standard DNI_{est} deviation and $\sigma_{DNI_{mea}}$ is the standard DNI_{mea} deviation. Tab. 1 shows the numerical results:

Tab. 1: DNI estimation results for the two day analyzed: 22nd February 2016 (turbid day) and 1st March 2016 (clear day).

Day	RMSE (Wm^{-2})	nRMSE (%)	MBE (Wm^{-2})	nMBE (%)	R
22nd February 2016	192.87	50.36	-141.35	-36.91	0.27
1st March 2016	137.68	16.17	50.13	5.89	0.95

As seen, the results on February presented an nRMSE value higher than on March in a value of 30%. Furthermore, the nMBE presented a high difference; on February, the DNI was underestimated, with a mean value of -37%; whereas on March, the value was lower than 6%. The underestimation was consequence of the classification of pixels. In the February's case, the pixels were classified like overcast due to the digital image level of the pixels that belong to the red circle, and therefore, the DNI estimation was done for an overcast day. As seen, the DNI estimation model is only based on the image digital values without considering atmospheric measurements. By this reason, in a free cloud day, the appearing of dust situations provokes that the model presents results very far than for typical cloudless skies. Therefore, CL51 Vaisala ceilometer data were used to see the behavior of the atmosphere, having another tool which could improve the solar radiation estimation.

3.3 Determination of atmospheric factors using a LIDAR ceilometer

CL51 Vaisala ceilometer with LIDAR technology, provides atmospheric information (from 0 to 4 kilometers) related to aerosol presence and visibility, and gives indirect information to calculate some atmospheric factors. Therefore, with the data collected, it is possible to identify the main attenuation factors helping to improve the solar radiation estimation models.

In the case of study of this paper, the profiles for the two analyzed days were studied, and the complete distributions are presented in Fig. 7, where it is shown the evolution along the whole day of the attenuated backscatter intensity (ABI) profiles from ground up to 4 km:

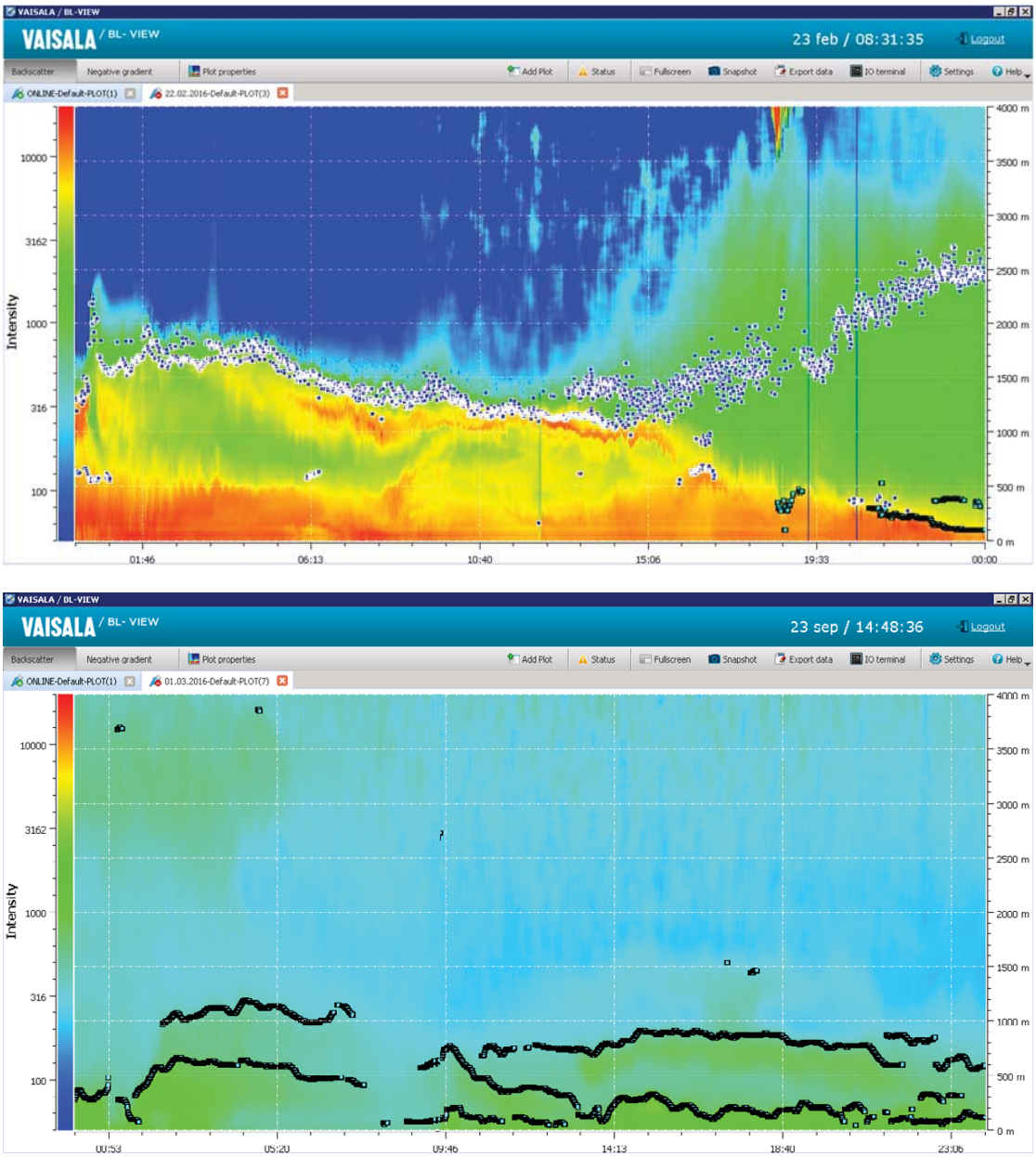

Fig. 7: CL51 Vaisala ceilometer profiles: the upper image represents the profiles on 22nd February 2016, and the other one represents the profiles on 1st March 2016

In this figure, important information is extracted for the two days. In the case of 22nd February, the most relevant data are presented below:
A nearly static dust layer 500 meters thick appears. With the sunrise, the surface temperature rises and this layer expands up to the boundary layer. Another thin layer, in the upper limit of the residual boundary layer appears floating on the boundary layer. From 16:00 UTC to the end of the day, the two layers precipitate progressively, appearing an expanding region of intermediate Attenuated Backscatter Intensity (ABI) values (in green) reaching up to 4 km in altitude.
For the analyzed case on 1st March, the atmosphere presents clear profiles (low intensity values) along the day. Perhaps, from 14:00 hours to midnight, a higher concentration of particles appears in the lower atmospheric layers (from 0 to 250 meters) but in a lower degree than on 22nd February. However, this first day of March can be considered like a very clear day.

As seen, the most important successes occurs in the lower layers (being more representative from 0 to 250 meters, approximately). Taking into account the interest of CTSP plants in the study of the sky conditions in these lower atmospheric layers to quantify the DNI losses between the heliostats and the receiver placed at the top of the central tower, these layer are analyzed. Furthermore, the first 250 meters are enough to measure the losses, covering the higher towers built in the plants.

Therefore, the inclusion of LIDAR information in DNI estimation models can improve the accuracy of that. For this reason, different atmospheric factors have been obtained from LIDAR measurements. Subsequently, ABI has been analyzed with the aim to determine the Meteorological Optical Range (MOR) and the Aerosol Optical Thickness (AOT) from 0 to 250 meters. Concretely, the profiles were obtained at midday (12:00 UTC) for an average time of 20 minutes in the two selected days.
The extinction coefficient (K_{ext}) is obtained solving the ceilometer equation, for a given profile, taking a particular Lidar Ratio (LR). The LR is a variable which depends on the aerosols and the water vapor, being 33 $(Wm)^{-1}$ for a cloudless sky by the manufacturer. Figure 8 represents the K_{ext} coefficient on 22nd February.

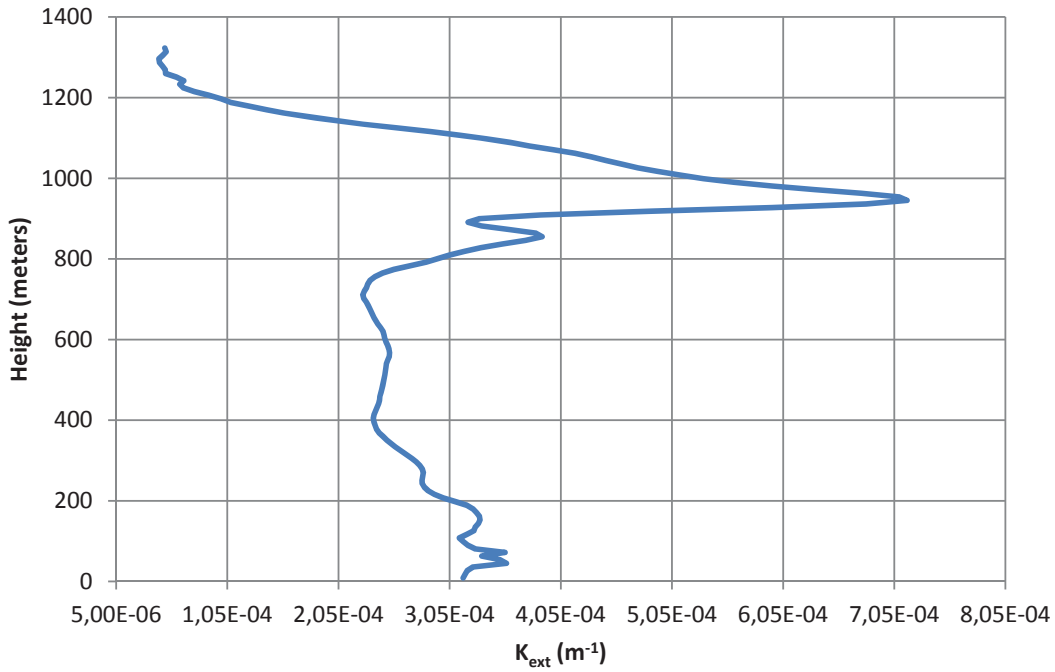

Fig. 8: K_{ext} profile obtained from CL51 Vaisala ceilometer on 22nd February 2016 at 12:00 UTC

Analyzing the graph, the coefficient shows similar values in the lower atmospheric layers (until 500-600 meters approximately), having a high dispersion from 800 to 1300 meters. It means that the atmospheric composition was homogenous in the low layers with a K_{ext} coefficient value between $2.5E^{-04}$ and $3.5E^{-04}$; and next, the homogeneity changed significantly. For comparing this day with the clear studied day, Figure 9 shows the K_{ext} profile on 1st March 2016:

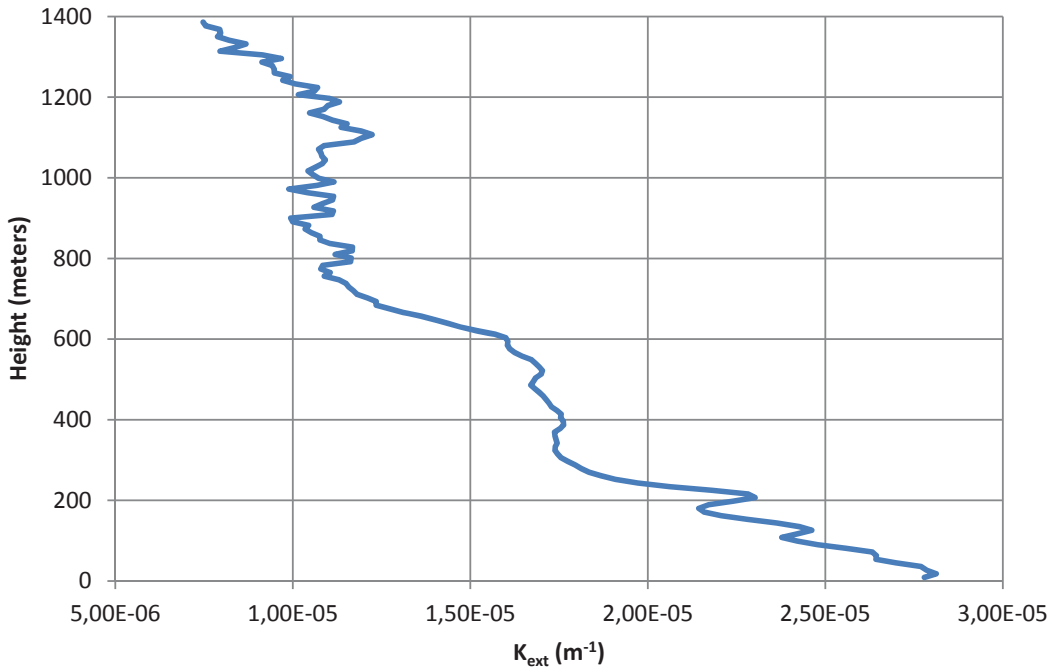

Fig. 9: K_{ext} profile obtained from CL51 Vaisala ceilometer on 1st March 2016 at 12:00 UTC

In this case, the K_{ext} values were lower than the values registered on February. For the first 250 meters, the K_{ext} values presented a decrease, reaching values between $2.8E^{-05}$ for 9 meters and $1.9E^{-05}$ for 250 meters.

The MOR (expressed in meters) was also calculated following the next equation:

$$MOR = \frac{3}{K_{ext}} \qquad \text{(eq 7)}$$

Together with the averaged K_{ext} values and the MOR parameter, the AOT was obtained integrating the K_{ext} into the first 250 meters. As the CL51 ceilometer profiles are retrieved every 9 meters, we integrated the coefficient from ground to 252 meters (multiple of 9). Table 2 shows the summary of variables for the two days:

Tab. 2: Atmospheric variables obtained from CL51 Vaisala LIDAR ceilometer from ground to 252 meters

Day	K_{ext} (m^{-1})	MOR (Km)	AOT (910nm)
22nd February 2016	$3.19E^{-04}$	9.40	$8.04E^{-02}$
1st March 2016	$2.40E^{-05}$	125.00	$6.05E^{-03}$

The results show a significant difference between the two analyzed days: in the case of 22nd February, the K_{ext} coefficient was higher than on March, and consequently, the MOR was different too. In the case of February, the dust particles provoked that the MOR decreased until 10 Km approximately, whereas for the case of March, with a clean atmosphere, the MOR was higher than 120 Km. The AOT obtained at 910 nm was also lower under a clear sky, presenting a value of $8.04E^{-02}$ with the presence of dust particles, and $6.05E^{-03}$ for a very clear atmosphere in the lower layers.

Therefore, considering LIDAR measurement, the DNI estimation can be improved taking into account the attenuation coefficients in the processing of total sky images. The coefficients calculated can help to determine the optical properties of sky cam images depending on the contamination degree which appears in the digital image levels. With that, the interpretation of the pixel like cloudless or overcast is improved, and the consequent DNI estimation too.

4. Conclusions

In this work, a Sahara dust episode occurred the last 22nd February 2016 has been studied and compared with a totally clear day (1st March 2016) using a TSI-880 total sky camera and a CL51 Vaisala ceilometer with LIDAR technology.

The DNI was estimated using the TSI camera for the two studied days using the digital image levels. On 22nd February, where the intensity of dust particles was very high, the nRMSE value was higher than 50%, whereas the nMBE value presented an underestimation of 37%. The other day, 1st March 2016, presented an atmosphere free of dust particles, and the DNI estimation presented better results, where the nRMSE value was of 16% and the nMBE was lightly overestimated, with a value of 6%. In this case, the R coefficient presented also good values. Therefore, the results show that the nRMSE can differ in more than 30% under cloudless skies, if particular episodes, like the scenarios presented on February, appear.

LIDAR data from the CL51 Vaisala ceilometer have been used to obtain atmospheric parameters. K_{ext}, MOR and AOT were obtained for the turbid and for the clear day, showing a high difference. In the case of K_{ext} and AOT the values were lower in the clear day, and the MOR presented lower values in the turbid day.

As seen, dust particles have an important impact in the solar irradiance. Depending on the particle load, the attenuation of solar radiation can be more or less important. Theferore, the DNI estimation with sky cams can be improved using LIDAR data, where the atmospheric parameters are quantified, helping to identify the correct classification of pixels and, consequently, improving the solar irradiance estimations.

Acknowledgments

Financial support by the Education and Competitiveness Ministry of Spain, PRESOL project “Forecast of solar radiation at the receiver of a solar power tower” with references ‘ENE2014-59454-C3-1-R1, 2 and 3’. Also, the authors acknowledge the generous financial support provided by the Education Ministry of Chile Grant PMI ANT1201, the Fondecyt Project 3160190, as well as CONICYT/ FONDAP/ 15110019 "Solar Energy Research Center" SERC-Chile.

5. References

Alonso J., Batlles F. J., Ternero A., López G., 2014. Sky camera imagery processing based on a sky classification using radiometric data. Energy. 68, 599-608.

Alonso-Montesinos J., Batlles F. J., 2015. The use of a sky camera for solar radiation estimation based on digital image processing. Energy. 90, 377-386.

Alonso-Montesinos J., Batlles F. J., Portillo, C., 2015. Solar irradiance forecasting at one-minute intervals for different sky conditions using sky camera images. Energy Conversion and Management. 105, 1166-1177.

Alonso-Montesinos, J., Polo, J., López, G., Barbero, J., Bosch, J.L., Ballestrín, J., Batlles, F.J., 2016. Modelling clear sky DNI under extreme aerosol loading: the case of Saharan outbreak in south-east Spain. Proc. EuroSun2016 Conf., Palma de Mallorca (Spain).

Conference Proceedings

EuroSun 2016
Palma de Mallorca (Spain), 11 – 14 October 2016

Modelling clear sky DNI under extreme aerosol loading: the case of Saharan outbreak in south-east Spain

Joaquín Alonso-Montesinos[1, 2], Jesús Polo[3], Gabriel López[4], Javier Barbero[1], Juan Luis Bosch[4], Jesús Ballestrín[5] and Francisco Javier Batlles[1, 2]

[1] Department of Chemistry and Physics, University of Almería, 04120 Almería, Spain

[2] CIESOL, Joint Centre University of Almería-CIEMAT, 04120 Almería, Spain

[3] Photovoltaic Solar Energy Unit (Renewable Energy Division, CIEMAT), 28040 Madrid, Spain

[4] Department of Electrical and Thermal Engineering, Design and Projects, University of Huelva, 21004, Huelva, Spain

[5] Concentrating Solar System Unit (Plataforma Solar de Almería, CIEMAT), 04200 Almería, Spain

Abstract

In this work we analyze the impact of a strong Saharan dust intrusion on the DNI registered at two sites in the southeast of Spain: University of Almería (UAL) and Almería Solar Platform (PSA) located in Tabernas (Almería). Direct normal irradiance (DNI) modelling with ESRA procedure presents high Linke turbidity values, being extremely high at the first site. DNI simulations using SMARTS code in the PSA emplacement, using AERONET data from PSA and maximum desert aerosol type, show a great accordance with the measured DNI values. In the UAL emplacement, SMARTS simulation of DNI values seems also to be compatible with maximum desert aerosol type aerosols. Visibility values are in good accordance with the extinction coefficients derived from the CL51 ceilometer profiles.

Keywords: *Aerosol optical depth, solar irradiance estimation, DNI simulation, atmospheric attenuation*

1. Introduction

On 21st and 22nd February 2016, an intense episode of Saharan dust intrusion took place in almost all of the Iberian Peninsula, reducing drastically the visibility and producing a remarkable dust deposition. Southeast, where the University of Almería (UAL) and the Almería Solar Platform (PSA) are located, was particularly affected by the event. Fig. 1 shows that relevant entrance of dust in the coast of Almeria region.

doi:10.18086/eurosun.2016.09.10 Available at http://proceedings.ises.org

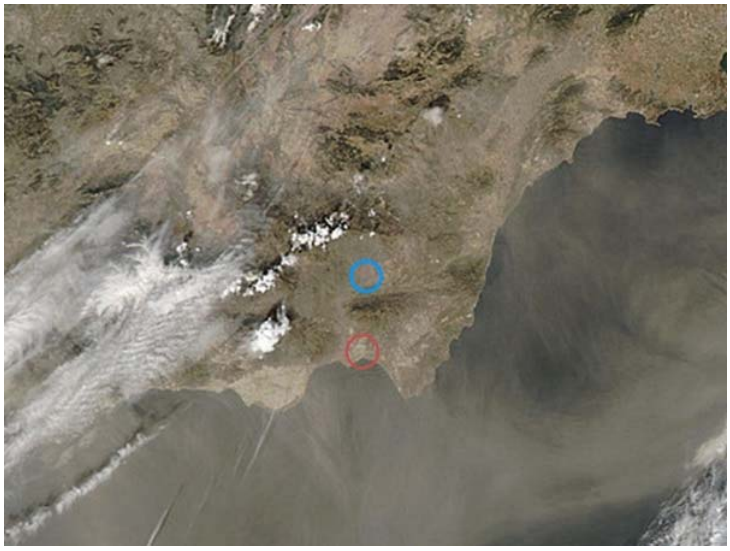

Fig. 1: MODIS satellite image for Almeria and surroundings on 22nd February 2016. Blue circle denotes PSA site. Red circle, the UAL site.

Observing the previous image, an evidence mineral dust load comes from the south, reaching a higher concentration of dust particles in the coast than in the PSA site. This feature can be also seen in the next image, where the sun reaches a heliostat and the sun's reflection is attenuated gradually due to the presence of concentrated Saharan dust.

Fig. 2: This figure shows the low visibility and the light scattered by the large particles in the atmosphere on 22nd February 2016 at 14:30 in PSA. Solar radiation reflected by the heliostats is attenuated by scattering.

Other African-dust episodes reaching Europe, even at high latitudes have been described so far (Kambezidis et al, 2012). 22nd February was a clear day, almost from sunrise to 14:00 h (when some high clouds appeared, affecting the DNI measurements), and this work analyzes the influence of the high turbidity on the DNI values for both sites. Figure 3 shows the HYSPLIT predicted back-trajectories for the studied area. The HYSPLIT model results corroborate the evidence of an air mass with coarse aerosols particles that enters the Iberian Peninsula from the Sahara desert.

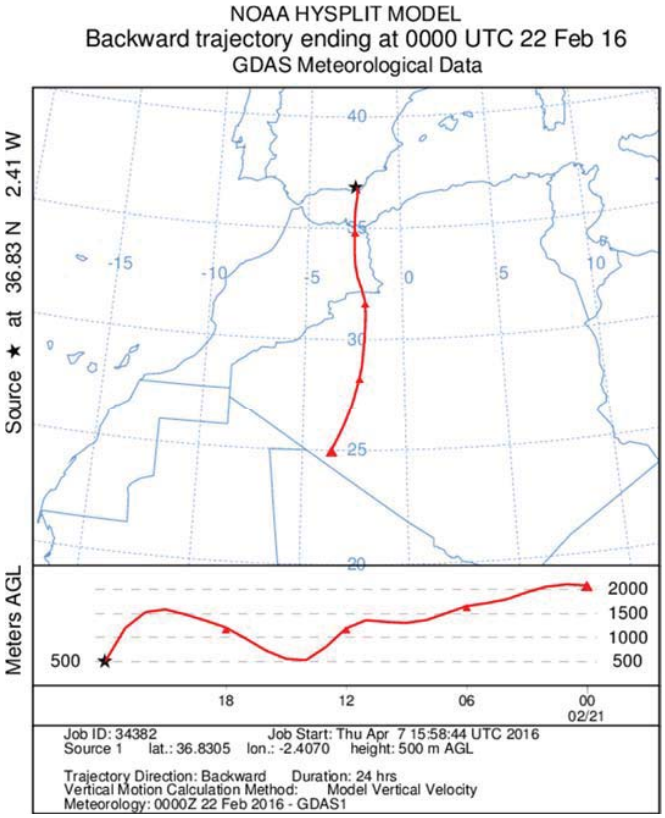

Fig. 3: HYSPLIT back trajectories

2. Data

DNI was measured at UAL station (36.8304º N, 2.4071º W, 0 m above sea level (ASL)), whereas, measurements at PSA (37.0949º N, 2.3614ºW, 550 m ASL) comprised both DNI and aerosol optical thickness (AOT) from the AERONET station.
Figure 4 shows the DNI ground measurements registered during 22nd February in both sites.

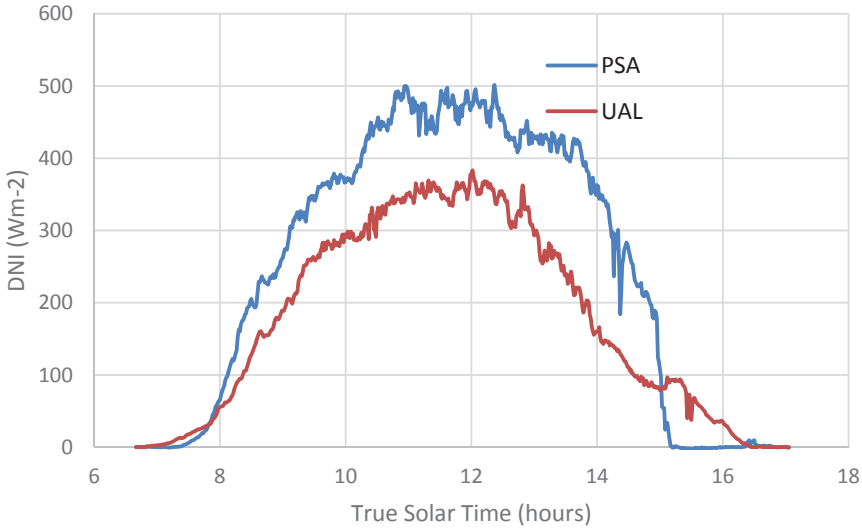

Fig. 4: DNI from PSA and UAL on 22nd February 2016

DNI values show that the daily profiles do not correspond to a clear sky situation for the whole day. After noon there is a clear decrease in DNI not related with an increase of dust concentration (as showed in Figure 4); when upper clouds appeared in the atmosphere. Figure 5 shows the presence of clouds in the solar area and in the surroundings at 16:00 True Solar Time (TST).

Fig. 5: Total sky image on 22nd February 2016 at 16:00 TST

In Figure 6, we show the evolution along the whole day 22nd of the attenuated backscatter intensity (ABI) profiles from ground up to 4 km registered by a CL51 ceilometer (Vaisala), located at the UAL.

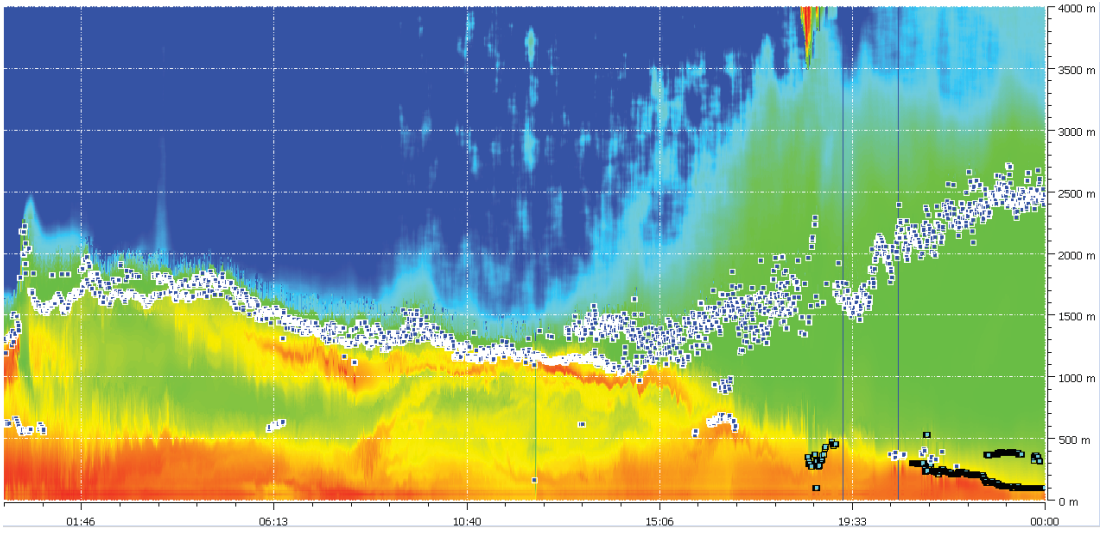

Fig. 6: Attenuated backscatter profiles from CL51 ceilometer at Almeria University

In this figure we observe:

- A nearly static dust layer 500 m thick from the previous day and through sunrise. As the surface temperature rises, this layer expands into the boundary layer.
- Another thin layer, in the upper limit of the residual boundary layer of the previous day, floating on the day 22nd boundary layer. Both layers together, progressively precipitate from 16:00 h through the end of the day.
- An expanding region of intermediate ABI values (in green) reaching up to 4 km in altitude.

3. Methodology and results

In this section the study of a particular case of Saharan dust is presented for two southeastern Spain locations: PSA and UAL.

Figure 7 shows the evolution of Aerosol Optical Thickness (AOT) at PSA site, where the measurements were offered by the AERONET station at 1.5 level for 22nd February.

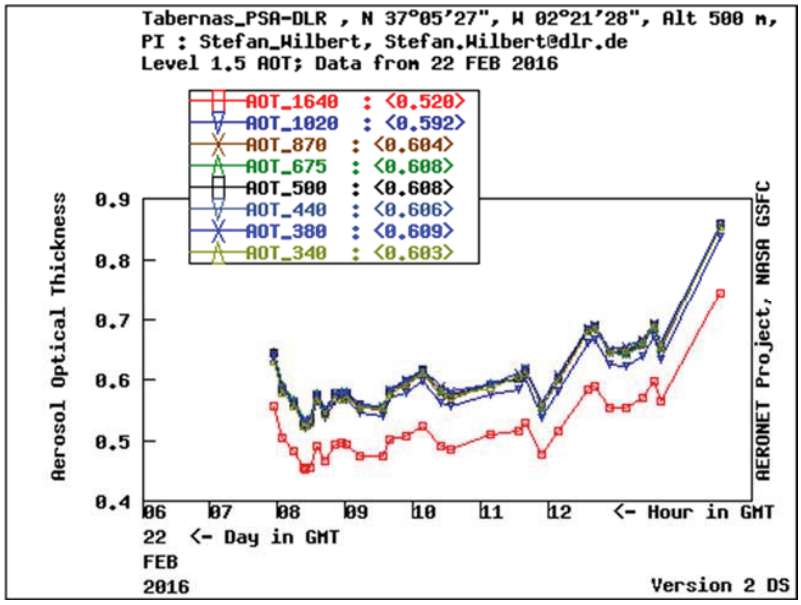

Fig. 7: AERONET AOT at 1.5 level measured at PSA

From the AERONET data, the mean daily value for the Angström turbidity parameter was $\beta \sim 0.6$, indicating an important load of coarse mode aerosols. According to Fig. 7, the AOT values showed an increasing trend along the day.

After that, the first goal was to determine the Linke Turbidity (T_L) under these particular sky conditions. Subsequently, the ESRA clear sky model (Rigollier et al., 2000) was used to obtain a representative T_L factor according to DNI values from PSA. The air mass was set to 2 and the results showed an average T_L of 8.2 (Fig. 8).

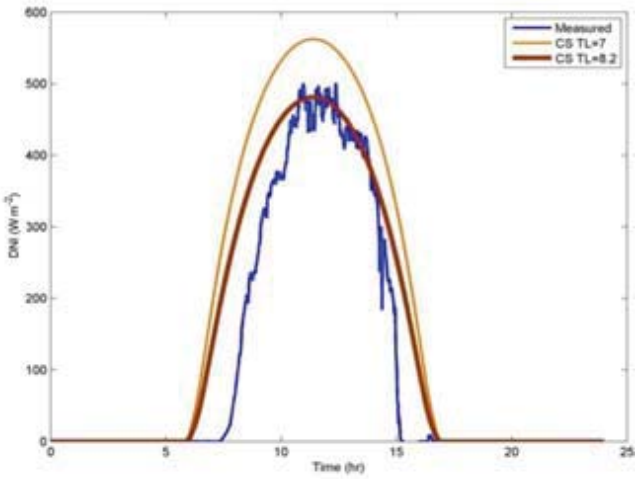

Fig. 8: PSA DNI and ESRA clear sky model using T_L factor of 7 and 8.2 for PSA site on 22nd February 2016

The use of ESRA model for computing Linke turbidity at air mass 2 is required for comparing the results with the estimation of T_L at air mass 2 from the AOT and water vapor using the Ineichen approach (Ineichen, 2008). The estimation of Linke turbidity from inverting the ESRA model is in agreement with the AERONET data. Thus, using the Ineichen model, T_L is computed from AOT and water vapor. AERONET measurements resulted in a mean T_L value of 7. The differences between the estimations of T_L from DNI data and from AERONET are expected taking into account the strong dynamism of the aerosol loading phenomena and the different time stamp between AERONET and pyrheliometer measurements.

Analyzing this factor at UAL emplacement, the estimated T_L was of 10.5, which is an extremely high value. Fig. 9 represents the measured and estimated DNI values using the T_L factor estimate of 10.5.

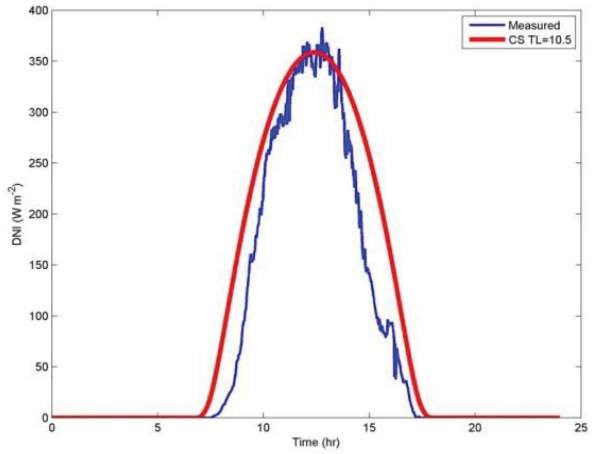

Fig. 9: UAL DNI and ESRA clear sky model using T_L factor of 10.5 for UAL site on 22nd February 2016

3.1 SMARTS simulations

Figure 10 shows the evolution of the AOT at 500 nm and the Angström exponent at (440-675) nm for 4 consecutive days, starting on 22nd February, date where the dust intrusion took place. The AOT values for 22nd February are extremely large, around 0.6, indicating the high aerosol concentration. After two days, the AOT levels diminish to values of about 0.05 corresponding to the clean conditions at the PSA. The atmospheric dust has a large attenuating effect on the solar energy reaching the ground, with a reduction of about 50%. To note, the effect of turbidity is only observed on the first half of the day. In the afternoon, the cloudiness fully blocks DNI, showing values near 0 Wm^{-2}. Besides, the Angström exponent provides useful information about the size distribution of aerosols (Eck et al., 1999). α- values obtained from the spectral band (440-675) nm close to 0 are mainly associated with desert dust. From Fig. 8 it is observed the temporal evolution of α, where zero values appear for the beginning of the dust intrusion increasing until reaching typical values of 1.2-1.3 on 25th February.

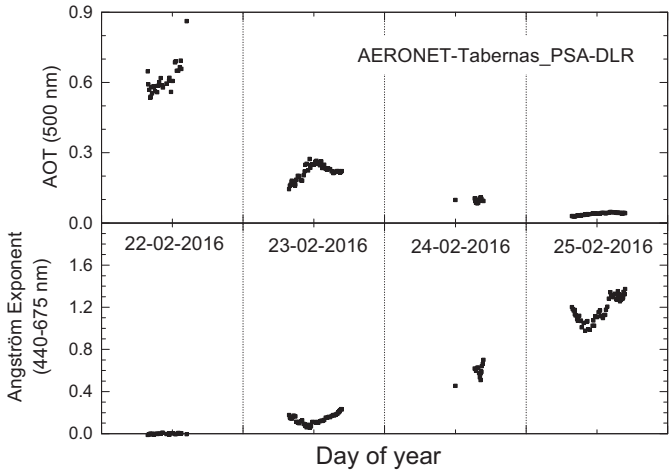

Fig. 10: Time-series of AOT at 500 nm (upper panel) and Angström exponent at (440-675) nm (lower panel) obtained with the AERONET-Cimel at Plataforma Solar de Almería (Spain). Cimel data are AERONET level 1.5 data.

To investigate the type of aerosol, DNI simulations using the SMARTS code (Gueymard, 1995) were carried out. Four different aerosol models available in SMARTS were selected (Tab. 1): the tropospheric aerosol model defined by Shettle and Fenn –"S&F Tropospheric"-, the Maritime aerosol model of the IAMAP preliminary standard atmosphere –"SRA Maritime"-, the "Desert_min" option corresponding to normal conditions in desert areas and "Desert_max" corresponding to extremely turbid conditions.

Tab. 1: Daily mean values of the Angström exponent and the meteorological optical range (MOR) given by SMARTS for the 4 aerosol models considered in this work and corresponding to 22nd February.

Aerosol model	α	MOR (km)
S&F Tropospheric	1.3	14
SRA Maritime	0.24	12
Desert_min	1.13	14
Desert_max	0.0	11

The turbidity coefficient was the AOT (500 nm) given by AERONET. Precipitable water data derived from the sunphotometer (Cimel) was also used. Atmospheric pressure measurements were available from the PSA radiometric station. The atmospheric profile and total column amounts of other atmospheric constituents are those specified by the Mid-Latitude Summer Atmosphere. Tab. 1 shows the daily averaged mean Angström exponent and the Meteorological Optical Range (MOR) obtained from SMARTS for the four aerosol models. The MOR is similar for the four options, however the Angström exponent is different.
The S&F Tropospheric and Desert_min models are not suitable to describe the existing size distribution of aerosols since the values are 1.3 and 1.13 respectively. To compare clear and turbid skies, Fig. 11 shows the DNI measured at PSA for the very turbid day 22nd February and for the day 25th February with the clean atmosphere.

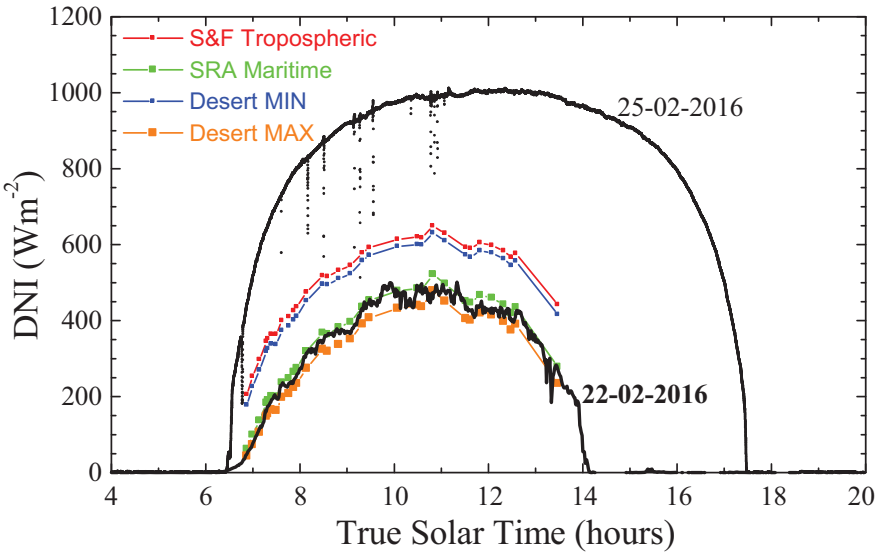

Fig. 11: DNI measured at PSA for the days 22nd February and 25th February (black dots). Simulations using Smarts code corresponding to four different aerosol models are included for the day 22nd February

In addition, the estimated DNI values using the four aerosol types for the 22nd February are also included. The DNI estimates corresponding to the two aerosol models with Angström exponent values close to the measured zero values, i.e. SRA Maritime and Desert_max, show a good agreement with the experimental pyrheliometric measurements. Since the simulated α value corresponding to the Desert_max model matches better the experimental one, this aerosol model is then selected to be representative of the main type of aerosol prevailing in this event.

In the case of UAL site, the Desert_max aerosol model was also used like in PSA site. We also used SMARTS for estimating DNI by using the AOT values derived from the Linke Turbidity factor. Using a MidLat-Summer atmosphere type, and atmospheric pressure and humidity data from the meteorological station placed at UAL, we have checked the influence on the DNI in the aerosol type:

Tab. 2: Cases for the simulation with SMARTS code of the event at UAL.

Aerosol type	AOT (500)	α	MOR (Km)
Desert_max	0.7	0.0	9.4

After obtaining direct normal irradiance values from SMARTS, the model was validated from sunrise to midday, because next to this moment the clouds appeared and SMARTS model works only under cloudless skies.

Estimated and measured values for the complete day are presented in the graph in Fig. 12:

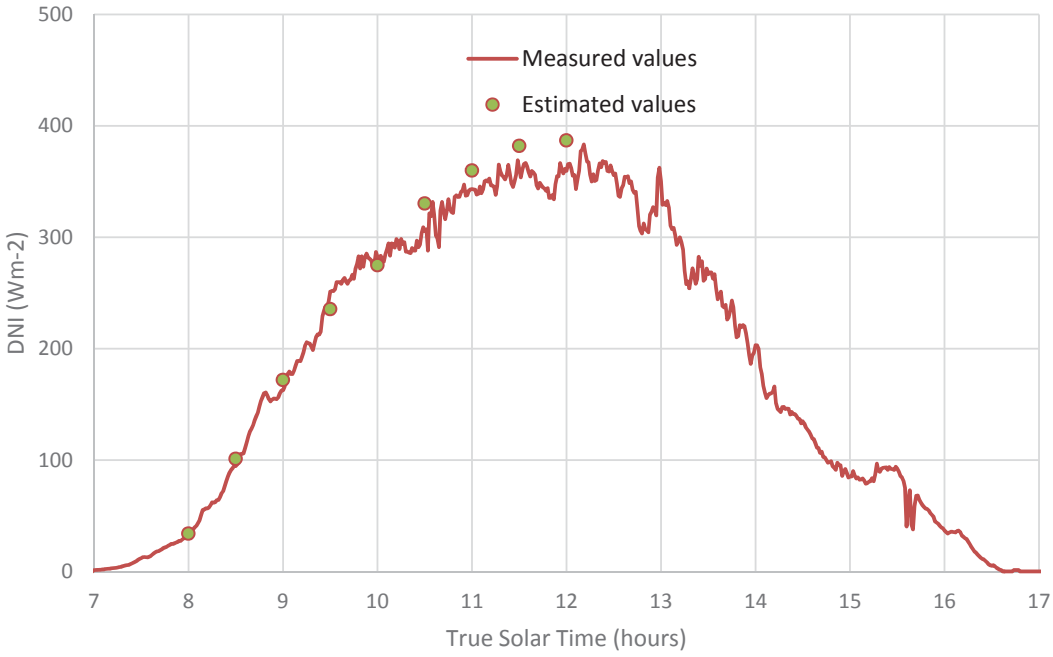

Fig. 12: DNI measured and estimated at UAL using Smarts code

Therefore, estimated DNI values show a good agreement with the measured ones in both cases, having a higher difference at 11:00 and 12:00. In these cases, the estimated values from SMARTS (green dots) presented a higher value than measured values (red line). Mainly, this difference was produced by the appearing of very thin clouds (see Fig. 1); for this reason, the DNI curve presented a different trend from sunrise to midday than from midday to sunset. Due to Saharan dust coming from the south, the saturation was higher at UAL than at PSA.

4. Conclusions

In this work we have made an exhaustive study for 22nd February 2016, with a high presence of dust particles from Sahara desert.

Linke turbidity factor was estimated for PSA and UAL through ESRA clear sky model and the measured DNI data in both sites. In the case of PSA, the best approximation was a TL value of 8.2, whereas for UAL the best value was 10.5, which are expected values for this type of phenomena.

DNI values were analyzed and estimated using SMARTS code by using AOT (500nm) measured at PSA, and desert type aerosols. Subsequently, DNI values were estimated for UAL using the Smarts code, also using desert type aerosols successfully.

In general, we have characterized an episode of turbidity using terrestrial measurements and simulations based on a clear sky radiative transference model in two south-east Spain sites, representing with satisfactory results the type of aerosol which appeared, and accurately modeling the direct normal irradiance during this phenomena. Furthermore, with the correct reproducibility of this extreme episode, the DNI estimation procedure acquires confidence and reliability under this particular sky condition.

Acknowledgments

Financial support by the Education and Competitiveness Ministry of Spain, PRESOL project “Forecast of solar radiation at the receiver of a solar power tower” with references ‘ENE2014-59454-C3-1-R1, 2 and 3’. Also, we thank to the AERONET staff for their support.

5. References

Gueymard, C., *Report 1995. SMARTS2, Simple Model of the Atmospheric Radiative Transfer of Sunshine: Algorithms and Performance Assessment*. Florida Solar Energy Center.

Ineichen, P., 2008. Conversion function between the Linke turbidity and the atmospheric water vapor and aerosol content. Solar Energy 82, 1095–1097. doi:10.1016/j.solener.2008.04.010

Kambezidis, H.D., Paliatsos, A.G., Kappos, N. and Kasselouri, B. 2012. A *Case of African Dust Transport over Athens Captured by a Ceilometer*. In Advances in Meteorology, Climatology and Atmospheric Physics, Springer Atmospheric Sciences, # Springer-Verlag Berlin Heidelberg, 1011-1018.

Rigollier, C., Bauer, O., Wald, L., 2000. On the clear sky model of the ESRA - European Solar Radiation Atlas - with respect to the heliosat method. Solar Energy 68, 33–48. Doi: 10.1016/S0038-092X(99)00055-9

Conference Proceedings

EuroSun 2016
Palma de Mallorca (Spain), 11 - 14 October 2016

STUDY OF SOILING ON PYRANOMETERS IN DESERT CONDITIONS

Dunia Bachour[1], Daniel Perez-Astudillo[1] and Luis Martin-Pomares[1]

[1] Qatar Environment and Energy Research Institute (QEERI), HBKU, Qatar Foundation, Doha (Qatar)

Abstract

This work presents a study of the degree of soiling on pyranometers in Qatar, a region with high amounts of dust in the atmosphere. The experiment was performed during several months including a dusty season. It consists of using two pyranometers to measure the global horizontal irradiance: one of the pyranometers was considered the reference sensor and was cleaned on a daily basis, and the other pyranometer was used as the testing one, on which different frequencies of cleaning were tested. In order to evaluate the losses in the measurements due to dust/dirt accumulation on the sensor dome, the ratio of the daily average of global horizontal irradiance measured by both sensors was calculated and analysed in function of the time passed after the last cleaning of the testing sensor. From day to day, the changes in this ratio are between 0.3% and 0.5% *per day* depending on the soiling environment of each season, with increasing changes towards summer. The relative errors (RMSE and bias) of the output of the testing sensor as compared to the reference one were also studied and show a linear increase with the time passed since the last cleaning, for the period under study. It is concluded that a schedule of daily, or every 2 days, cleaning of the pyranometer dome is advisable in order to avoid noticeable errors in the measurements. This study helps to develop an adapted quality assurance programme for sensors installed at remote sites in the desert, including an adapted cleaning schedule which takes into account the local environmental conditions.

Keywords: *solar radiation, solar measurements, pyranometers, soiling, GHI.*

1. Introduction

As solar-based projects multiply across the planet, the need for high-quality assessment of the available solar resources also increases. Solar resource assessment is needed throughout the lifetime of solar power projects, from the prefeasibility studies to the operation of the final system. Knowledge of the historical (long-term) solar climatology at the selected site is fundamental for plant sizing and bankability studies, and such historical solar data are usually obtained with the aid of long-term satellite observations site-adapted with direct, ground measurements. Real-time solar input data during the plant operation goes directly into the calculation of plant performance, as well as into forecasting methodologies. It is, therefore, evident that the solar measurements have to be accurate and trustable enough for the cited purposes.

Currently, the most accurate measurements of the solar resource can be obtained with thermoelectric radiometers. For projects based on photovoltaic (PV) technology, the solar resource is usually measured on the horizontal plane, in the form of the so-called global horizontal irradiance, using thermopile pyranometers. This type of radiometers is the one recommended by the International Organization for Standardization (ISO) and the World Meteorological Organization (WMO), to measure the global solar radiation. Pyranometers typically have one or two curved optical glass domes covering the sensor for protection and reduction of dirt or rain drop deposition. When they are used for solar resource assessment studies, the radiometers are usually installed at remote sites and left unattended to achieve continuous measurements. The instrument is exposed to the weather conditions and might accumulate substantial amounts of dirt on its dome, especially in desert

doi:10.18086/eurosun.2016.09.08 Available at http://proceedings.ises.org

regions; this is problematic since it affects the quality of the measurements and thus the resource assessment studies and solar projects relying on these data.

To obtain accurate measurements, two checks should be done daily on the sensors: alignment and cleaning of the dome. However, when the sensor is located at remote sites, it is usually difficult to follow this ideal maintenance schedule or at least to control that it is done the right way. Therefore, the study and quantification of soiling will result in a better management of a solar radiation network distributed across remote sites, and will help in terms of setting optimum rules for the frequency of sensor cleaning and for correcting the data before final processing.

While studies of the effect of soiling on PV panel performance are common (see, e.g., Urrejola et al., 2016; Maghami et al., 2016; a recent PV soiling study was carried out in Qatar by Abdallah et al., 2016), sensor soiling studies are not so abundant, but several examples can be found, like Hammond et al. (1997) in Arizona, Maxwell et al. (1999) in Saudi Arabia, Geuder and Quaschning (2006) in Spain and Morocco, Pape et al. (2009), and Wolfertstetter et al. (2014) in the north of Africa. Most of these studies focus on only determining a sensor cleaning frequency for specific sites; Geuder and Quaschning (2006) propose a method to correct for soiling which, however, requires the measurement of the beam, global and diffuse radiations and, along similar lines, Pape et al. (2009) describe an additional accessory to determine soiling rates. In a report of IEA SHC Task 46 (Wilbert et al., 2015), the soiling of a rotating shadow band irradiometer (RSI) and a pyrheliometer was studied during a period of one month in Almeria, Spain. After one month of not cleaning both sensors at this location, they found that the relative error of the uncleaned pyrheliometer follows a linear trend with an increase of around 0.7% per day, whereas the relative error of DNI measurements of the uncleaned RSI varies within the range of the reference uncertainty of ±2 %.

This work focuses on the study of pyranometer soiling and its characteristics in a region where dust is highly present in the atmosphere, and dust storms occur frequently. Qatar is embarking on its journey of using solar energy for power production and, to measure its solar resources, a network of 13 solar radiation monitoring stations will be deployed throughout the country (Mohieldeen et al., 2015). Due to the location of the stations in the desert, the sensors will be highly susceptible to soiling, thus affecting the accuracy and reliability of the measurements. In the present work, a methodology is described to determine the effects of soiling on the output of the pyranometer.

2. Methodology

The total or global horizontal irradiance (G) can be measured using a thermopile pyranometer mounted on a horizontal surface. In this work, two Kipp & Zonen CMP11 pyranometers mounted on the same horizontal platform, each provided with a ventilation unit and located at the same site in Doha, Qatar, are used (Perez-Astudillo and Bachour, 2014); one of the radiometers is considered the reference, on which the cleaning and alignment check are done on a daily basis, and the other pyranometer is used for testing, where only the alignment check is done every day, and the cleaning frequency followed different scenarios. During the first week of the experiment, both sensors were cleaned on a daily basis for calibration purposes to ensure that for the soiling study both sensors provide the same measured values. For the next three consecutive weeks, the testing sensor was left without any manual cleaning, only somewhat washed by some rain events. Afterwards, the cleaning frequency of the testing sensor varied following the schedule in Table 1, which shows the days when this sensor was cleaned. Note that for the month of July, the *reference* sensor was not cleaned from the 3rd until the 14th of July; these days are excluded from the data analysis of this soiling study.

Tab.1: Cleaning schedule of the testing sensor from March until September 2016. Note that the reference sensor was cleaned every day including the days shown in the table. *See also note for July in the text.

Dates of cleaning						
March	April	May	June	July*	August	September
12	1	--	--	2 & 15	1 & 21	25

It can be seen from Table 1 that the longest period in which the test sensor was left without cleaning is from

April through June (90 consecutive days without cleaning), followed by the period from August 21 until September 25 (35 days). The shortest period was in the second half of July (16 days). In March and August, the testing periods were of 19 days. For simplicity, the testing periods are called herein: A (Mar), B (Apr-Jun), C (Jul), D (1st half of Aug) and E (Aug-Sep). A future scenario consists of not cleaning the sensor for several months to test whether the losses due to soiling will reach a plateau.

The analysis of the difference between the two measurements under the different cleaning regimes stated above will be used to quantify the soiling of pyranometers and to understand its characteristics and the change of associated errors with time. This analysis will consequently lead to the establishment of independent benchmarks and procedures to control the data and the sensors, due to soiling in desert regions.

3. Results and discussions

3.1. Calibration of the two sensors

Since the current soiling study relies on the measurements of two independent sensors, it was deemed necessary to calibrate the sensors relatively to each other, in order to eliminate sources of errors related to a drift or variations in the response of the sensors and to ensure that for the same conditions, the data from both sensors are comparable.

The calibration was performed using the days when both sensors were cleaned, which consist of all days during the first week of the experiment and several other days representing different seasons across different months: one day in April, two days in July, two days in August and one day in September. Fig. 1 shows in black, for the calibration days, the 1-minute values G_test measured by the testing pyranometer (the one to be kept without cleaning afterwards) versus G_ref, measured by the reference pyranometer (the one used as a control, with daily cleaning). The testing pyranometer slightly underestimates G. This underestimation can be fitted using a linear function, shown in blue on the graph. The linear fit relates G_test to G_ref through the following equation:

$$G\_test = 0.996547 * G\_ref - 3.99292 \qquad \text{(eq.1)}$$

Equation 1 was then used to calibrate G_test, for the following data analysis.

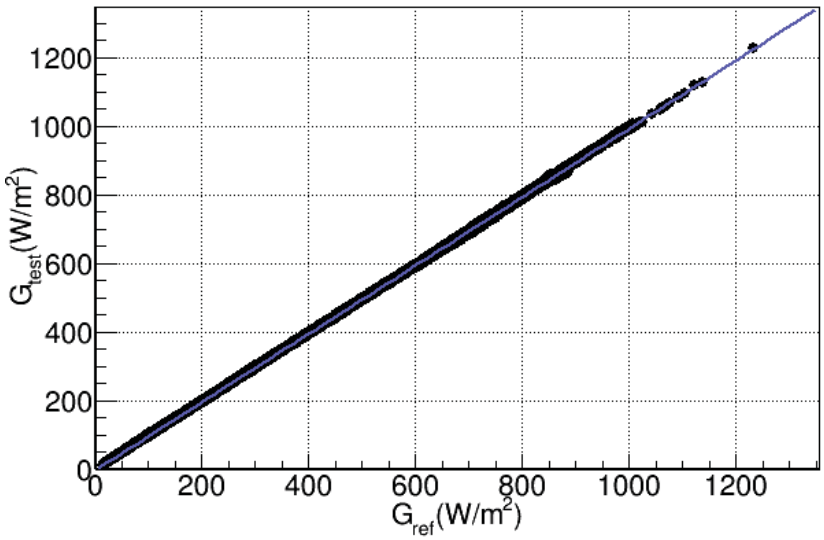

Fig. 1: Comparison of the G values (W/m2) measured by the testing and reference pyranometers.

3.2. Effect of pyranometer soiling on measured G

In order to study the effect of the soiling with the time passed since the last cleaning of the test sensor, the errors in terms of daily relative root mean square error (rRMSE) and relative bias (rBias) were studied for each of the testing periods. Fig. 2 and Fig. 3 show, respectively, rRMSE and rBias as function of time.

In Fig. 2, each point represents the relative RMSE between the two sets of 1-minute measurements during one day. It should be noted that the errors are calculated after calibration of the testing sensor against the reference one, as described in Section 3.1. The relative RMSE is calculated as

$$rRMSE = \frac{\sqrt{\frac{\sum_0^N (G\_test - G\_ref)^2}{N}}}{G\_ref_{mean}}, \qquad \text{(eq.2)}$$

where G_ref and G_test are the 1-minute values within one day, measured respectively by the reference pyranometer and the testing one. N is the total number of included minutes during that day and G_ref_{mean} is the mean value of G_ref during that same day.

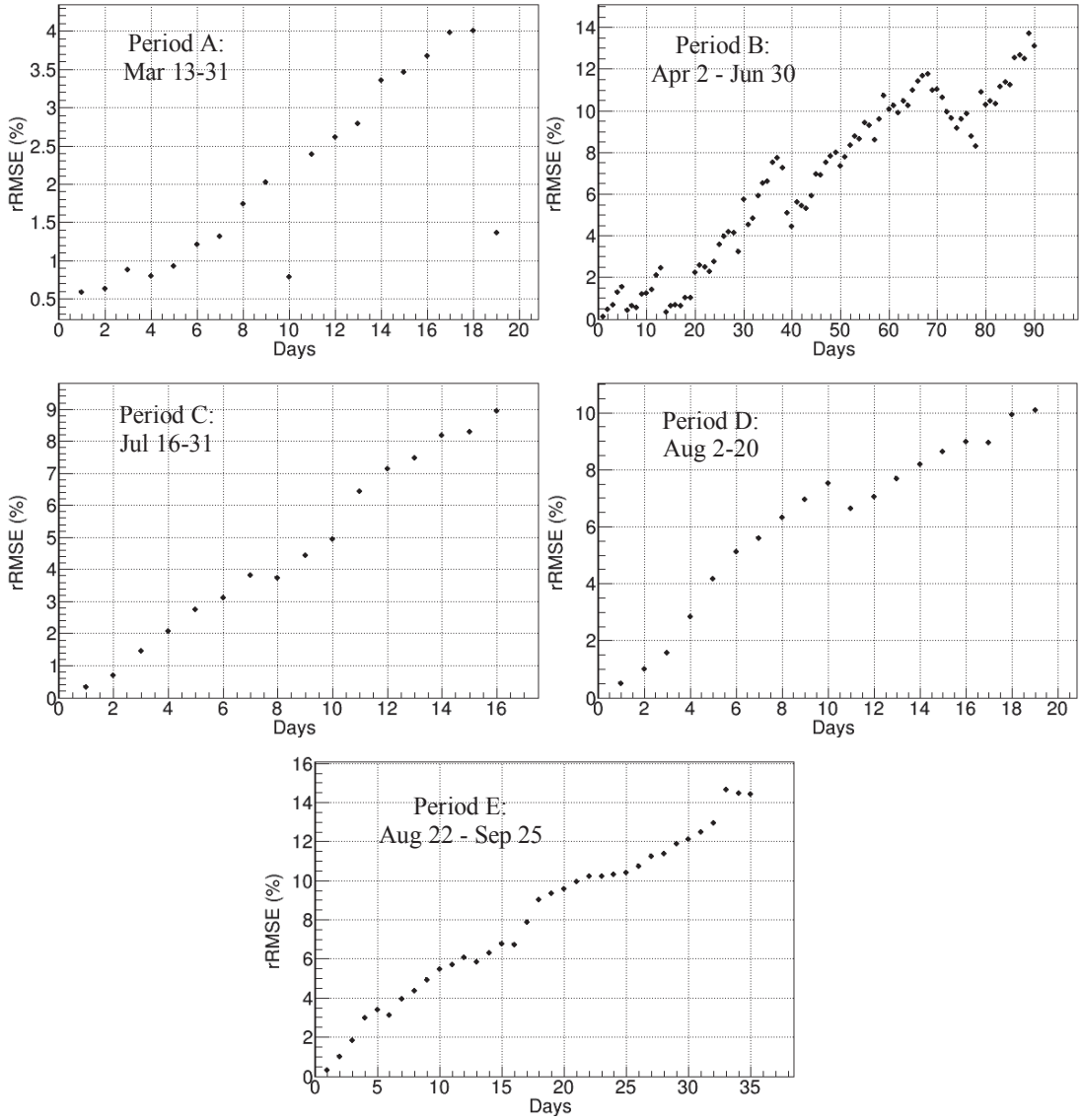

Fig. 2: Daily values of relative RMSE between G_test and G_ref for several days after cleaning the testing sensor, for different testing periods (shown on each of the plots).

It can be seen that for each of the testing periods the error due to soiling is continuously increasing with time; points showing deviation from the increasing trend correspond to rain events. The magnitude and speed of the increase in the error are different between the testing periods and depend on the season. For instance, the error in period 'A' grew at slower rate than in periods 'D' and 'E': it reached 4% after 17 days since the last cleaning in period 'A', whereas in period 'E' it reached the same level after 7 days. This is most probably due to more stable weather conditions, i.e., mostly clear days, in the summer months, but also due to the increasing dust

levels in the atmosphere during summer. It is to be noted that for each of the testing periods, the error due to the pyranometer soiling starts increasing from 0 (see Fig. 2 and 3), which means that the calibration factors were the same at the start of each period; in other words, after each cleaning event of the testing sensor, the signal is brought to the same level of the signal of the reference sensor.

In order to better understand this behaviour and be able to compare the differences in rRMSE within different periods, the average rRMSE for a span of 15 days after the last cleaning was calculated for each of the testing periods and is shown in Table 2.

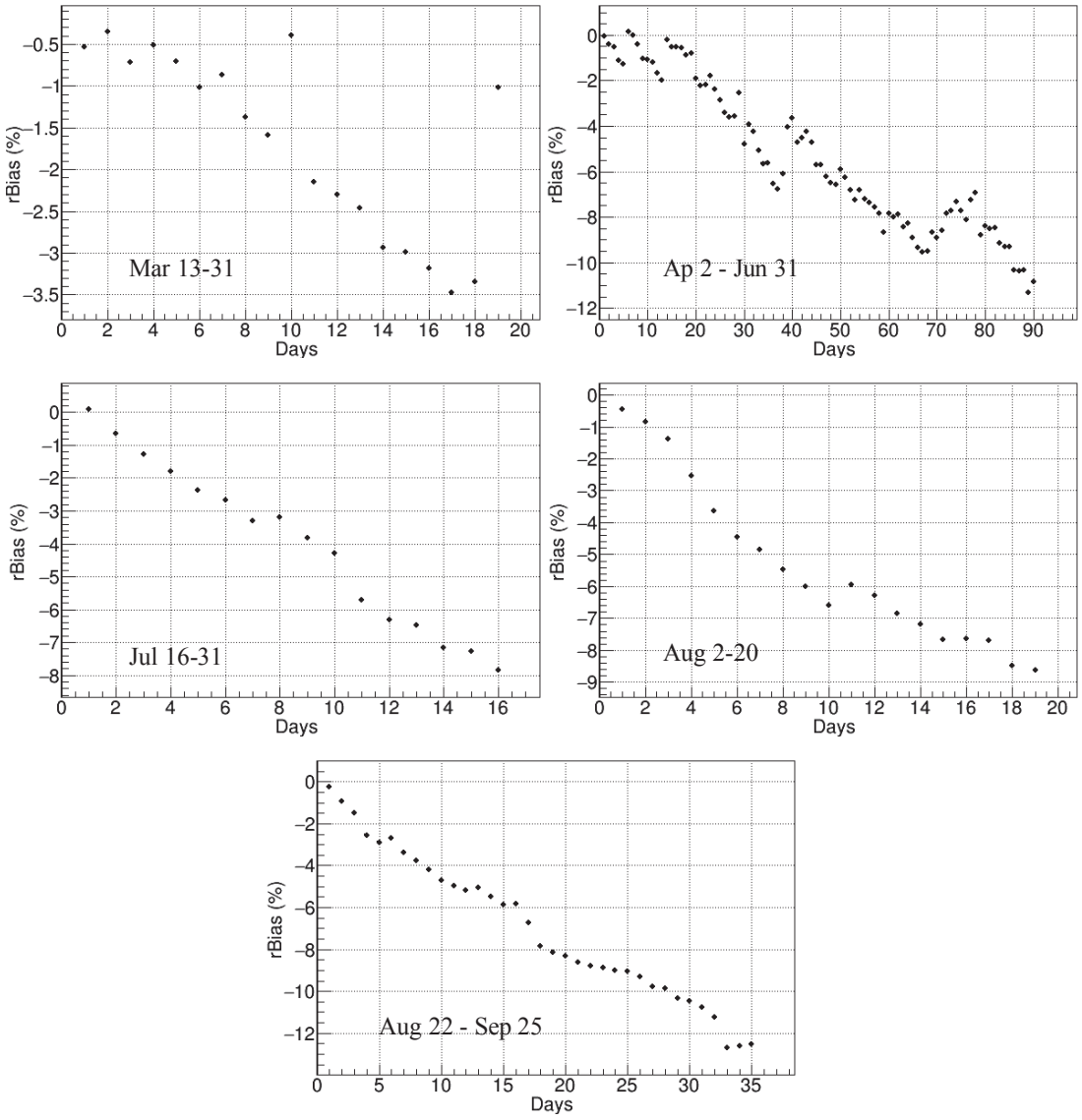

Fig. 3: Daily averages of relative Bias between G_test and G_ref for several days after cleaning the testing sensor, for different testing periods (shown on each of the plots).

Tab.2: Average of relative RMSE during 15 days after cleaning the testing sensor, for each of the testing periods.

rRMSE (%)				
March	April	July	Aug (first half)	Aug-Sep
1.71	0.99	4.32	5.32	4.13

Comparatively, it is noticeable that the averaged rRMSE during the first 15 days since the last cleaning is higher in the summer months. The low value of the averaged error in April is due to the frequent rainy days during this period, which resulted in a low average of rRMSE.

For comparison purposes also, Table 3 shows the quantification of the level of increase of rRMSE per day due to soiling, for each of the studied periods. These values were determined by establishing a linear relation between rRMSE and the days since the last cleaning, separately for each period. Although finding the relation was not straightforward due to changing weather conditions, especially in period 'B', an average rate was calculated using different series of consecutive clear days. The dependency of the soiling effect on the season is clear: the average increase of rRMSE is lower in March and April and higher in July and August, when dust is more abundant in the local atmosphere.

Tab.3: Average increase in relative RMSE, per day, for each of the testing periods.

rRMSE/day (%)				
A	**B**	**C**	**D**	**E**
0.25	0.33	0.6	0.5	0.4

In Fig. 3, each point represents the relative bias error between the two sets of measurements during one day, calculated using Equation 3, after calibration of the testing sensor against the reference one.

$$rBias = \frac{\frac{\sum(G_{test} - G_{ref})}{N}}{G\_ref_{mean}} \qquad \text{(eq.3)}$$

As expected, rBias increases as a function of time and this increase more or less follows the trend of the rRMSE. This can be explained by looking closely to the plot in Fig. 4, which shows the relative bias of each 1-minute pair (G_test vs. G_ref) as a function of time for the testing period 'E'. For clarity, the data shown were limited to minutes between hours 9 and 14 (local time). It is clear that the mean relative bias increases with time, similarly to Fig. 3, but it is noted too that the amplitude of each individual U-shaped curve (corresponding to one day) also increases with time and remains more or less constant after a certain time. The shape of each day's rBias depends on the spatial distribution of dust on the dome, as dust accumulates more on the top than on the sides of the dome, thus obstructing more direct sunlight (resulting in larger bias) when the sun is higher in the sky. The increasing amplitude with time contributes to the growing trend of the relative daily RMSE (as seen in Fig. 2).

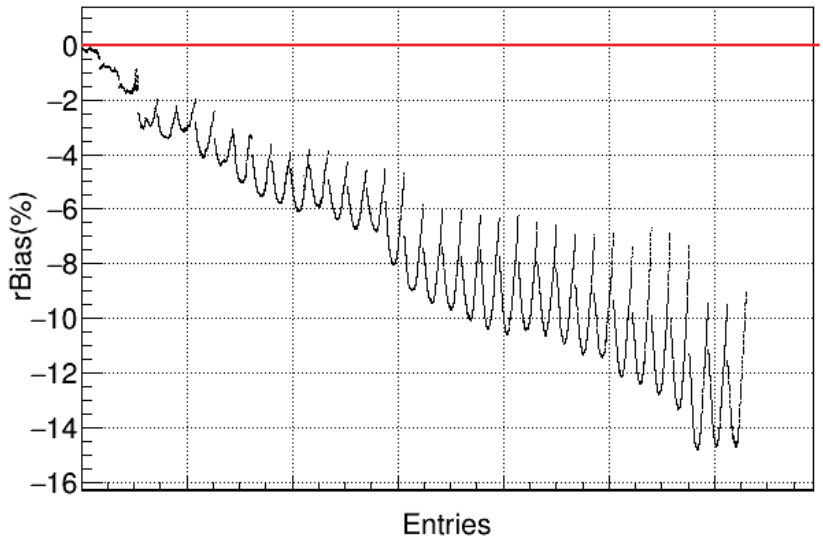

Fig. 4: Relative Bias of each one-minute value of G_test relative to G_ref for several days after cleaning the testing sensor, during the last testing period (22 Aug to 25 Sep).

Tab.4: Average change of relative bias, per day, for each of the testing periods.

rBias/day (%)				
A	**B**	**C**	**D**	**E**
-0.22	-0.3	-0.53	-0.43	-0.38

Table 4 shows the averaged increase per day of the relative bias due to soiling, for each of the studied periods. Similarly to the determination of the increase of rRMSE per day, this was determined by fitting a linear function on the plots in Figure 3, using consecutive clear days and excluding days with rain events. Here also, the rate of increase of the relative bias per day is higher in the summer months of July and August.

To obtain a quantitative evaluation of the loss in G due to sensor soiling, the ratio of the daily average of G_soil to G_ref (hereby called 'cleanliness') as a function of time since the last cleaning, is studied (shown in Figure 5, for period 'C'). The correlation between the cleanliness and time (the linear fit function shown in red) gives the value of the loss in output signal per day due to soiling. As in the previous cases, the loss was easily determined in periods of clear days. In periods with unstable conditions, it was determined using the average of the loss of one or several series of consecutive clear days (if found). As a result of this test, the loss per day in the global radiation due to soiling is around 0.2 to 0.3% in periods 'A' and 'B', from March to June, and is evaluated as 0.5% and 0.4% in July and August, respectively.

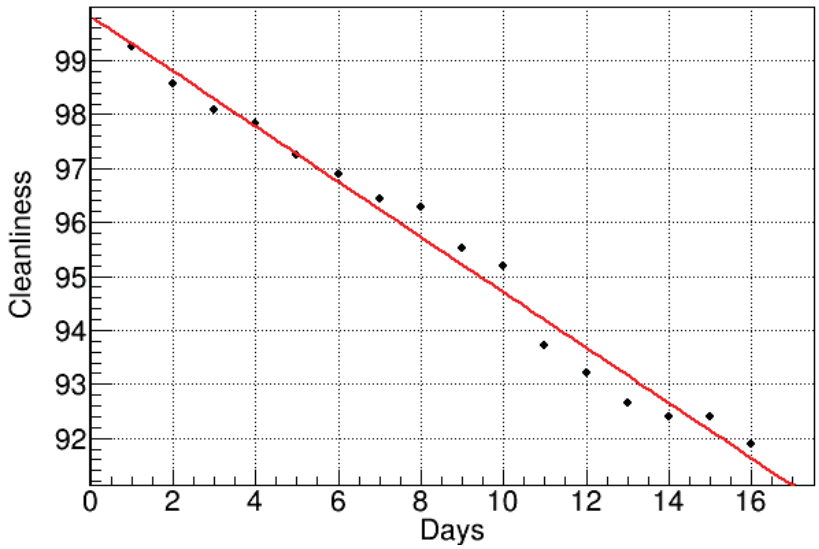

Fig.5: Decrease of measured global horizontal radiation per day due to sensor soiling, in period C. The red line is the fit of the cleanliness with time.

4. Conclusions

For the deployment of solar projects using photovoltaic systems, one of the key parameters to determine is the global horizontal irradiance, G, as part of the solar resource assessment studies for the project. G is usually measured on the horizontal plane using thermopile pyranometers. In this type of radiometers, the sensor is protected from the elements by a transparent dome, which only allows solar radiation to reach the sensor. Because the dome is exposed to the elements, it gets dirty, or soiled, as time passes, due to deposition of atmospheric dust and particulates, rain, snow, bird droppings, etc. This soiling obstructs the passage of sunlight to the sensor, resulting in erroneously low measurements, more obviously at locations with high amounts of dust in the atmosphere. Therefore, an important part of the routine maintenance of the sensor is the periodic cleaning of the dome. Ideally, this cleaning should be done daily; however, this is not always possible, for example, at remote unmanned sites, and also the costs (personnel, transportation, etc.) have to be considered, so in practice the instrument cleaning is commonly done at longer intervals, sometimes extending several

weeks or even months. The optimal cleaning frequency depends on each site's conditions, which are highly variable depending on atmospheric and any other surrounding events.

In this work, the assessment of the soiling rate of pyranometers was evaluated using two sensors: one with daily cleaning and another one following a cleaning schedule with varying intervals. The results show that the measurement errors due to soiling increase linearly with time, and the increase varies depending on the weather conditions, with a seasonal dependency. The average increases in rRMSE and rBias are, respectively, around 0.4% per day and 0.37% per day, for the studied period.

The actual decrease in the signal due to accumulation of dust on the dome of the pyranometer is evaluated as around 0.2 to 0.3% per day for the winter season, and around 0.4% to 0.5% per day for the summer season. This shows that the effect of dust and soil on the pyranometer signal is not negligible in dusty environments even in short intervals, frequent cleaning of the glass dome of the instrument should be followed in order to avoid dust accumulation and consequently larger errors on the measured data. According to the analysis shown here, and in order to ensure low deviations from the correct measurement (on the order of 1 to 2 %) in dusty regions, the pyranometer dome should be cleaned daily, or every 2 days.

Although the results presented here cannot be universally applied due to varying soiling conditions between different sites, they may be useful in regions with similar weather conditions.

5. References

Abdallah, A., Martinez, D., Figgis, B., El Daif, O. 2016. Performance of Silicon Heterojunction Photovoltaic modules in Qatar climatic conditions. Renewable Energy 97, 860-865. doi.org/10.1016/j.renene.2016.06.044

Geuder, N., Quaschning, V. 2006. Soiling of irradiation sensors and methods for soiling correction. Solar Energy 80, 1402-1409. doi:10.1016/j.solener.2006.06.001

Hammond, R., Srinivasan, D., Harris, A., Whitfield, K. 1997. Effects of soiling on PV module and radiometer performance. 26th PVSC, Sept. 30-0ct. 3, 1997, Anaheim, CA.

Maghami, M.R., Hizam, H., Gomes, C., Radzi, M.A., Rezadad, M.I., Hajighorbani, S. 2016. Power loss due to soiling on solar panel: A review. Renewable and Sustainable Energy Reviews 59, 1307-1316. doi:10.1016/j.rser.2016.01.044

Maxwell, E.L., Wilcox, S.M., Cornwall, C., Marion, B., Alawaji, S.H., bin Mahfoodh, M., Al-Amoudi, A. 1999. Progress Report for Annex II - Assessment of Solar Radiation Resources In Saudi Arabia 1993 - 1997. NREL/TP-560-25374

Mohieldeen, Y., Pomares, L., Perez-Astudillo, D., Bachour, D., Wahadj, S. 2015. Qatar dynamic solar atlas and solar resource assessment. ISES Solar World Congress, Nov. 8-12, 2015, Daegu, Korea.

Pape, B., Batlles, J., Geuder, N., Zurita Piñero, R., Adan, F., Pulvermueller, B. 2009. Soiling Impact and Correction Formulas in Solar Measurements for CSP Projects. Proceedings of the SolarPACES 2009 Conference. doi:10.13140/2.1.4355.0406

Perez-Astudillo, D., Bachour, D., 2014. DNI, GHI and DHI Ground Measurements in Doha, Qatar. Proceedings of the 2013 SolarPACES Conference, Energy Procedia 49, 2398-2404. doi:10.1016/j.egypro.2014.03.254

Urrejola, E., Antonanzas, J., Ayala, P., Salgado, M., Ramirez-Sagner, G., Cortes, C., Pino, A., Escobar, R. 2016. Effect of soiling and sunlight exposure on the performance ratio of photovoltaic technologies in Santiago, Chile. Energy Conversion and Management 114, 338-347. doi:10.1016/j.enconman.2016.02.016

Wolfertstetter, F., Pottler, K., Geuder, N., Affolter, R., Merrouni, A.A., Mezrhab, A., Pitz-Paal, R. 2014. Monitoring of mirror and sensor soiling with TraCS for improved quality of ground based irradiance measurements. Energy Procedia 49, 2422-2432. doi:10.1016/j.egypro.2014.03.257

Wilbert, S., Geuder, N., Schwandt, M., Kraas, B., Jessen, W., Meyer, R., Nouri, B. 2015. Best practices for solar irradiance measurements with Rotating Shadowband Irradiometers. A report of IEA SHC Task 46, Solar

Resource Assessment and Forecasting. https://www.iea-shc.org/data/sites/1/publications/INSRSI_IEA-Task46B1_BestPractices-RSI_150819.pdf. Last accessed 4/Oct/2016.

Detailed information on irradiance characteristics in Central Africa (Rwanda) from a dedicated network of ground stations for characterizing statistics of the irradiance field and validation of satellite derived data

Hans Georg Beyer[1], Fabien Habyarimana[1,2]

[1]Inst. Of Engineering, University of Agder, Grimstad (Norway)

[2]Department of Physic, University of Rwanda, Kigali (Rwanda)

Abstract

In Rwanda as in most of the countries in central Africa in-situ empirical data on solar irradiance are sparse. This presents an obstacle for an increased application of solar energy to the coverage of the (increasing) energy needs of the country. These needs are given by both, the wish to increase the share of PV to bulk electricity and the application of PV for off-grid rural electrification. Required for a proper planning of both on- and off-grid applications are information beyond the knowledge of annual or monthly irradiance sums. For the layout of the off-grid systems the respective knowledge of the temporal variability is essential for e.g. the sizing of batteries. For on-grid systems the time and space characteristics of the irradiance field effect the interaction of PV-power plants with the conventional generation park. In Rwanda a new dedicated network of meteorological stations, that are logging the irradiance with a 5min time resolution has been set up to close this gap. For a more comprehensive approach the data from this network can be used to calibrate the satellite derived irradiance data for the continuous coverage of this region. This paper gives a short view on the use of the data for these two fields of application.

Keywords: *irradiance data, irradiance statistics, satellite derived data, ground station network*

1. Introduction

To increase the knowledge of the agro- and energy-meteorological conditions, the government of the Central African country of Rwanda initiated the setup of a fleet of Basic meteorological stations. The map in fig.1 shows the distribution of these stations operated by the Rwanda Environment Management authority (REMA) [Meteo Rwanda, 2014]. In operation since mid of 2013 (stable data delivery since mid of 2014). The stations are equipped with - among others sensors for the registration of the horizontal irradiance. The data are logged with a time resolution of 5min.

Fig. 1: Map of the network of Automatic weather stations setup in in Rwanda (Meteo Rwanda, 2014).

doi:10.18086/eurosun.2016.09.15 Available at http://proceedings.ises.org

This set offers - beyond the countywide information on the general solar potential - on one hand, information on the detailed statistics of the irradiance field in time and space needed as input for the detailed assessment of the performance of both, on-grid and off-grid solar energy systems. In addition these data form a unique basis for the check of the quality of satellite derived irradiance data extracted for this region. In the present paper exemplary applications of this data set should show its usefulness for these two fields of applications.

2. Quality of Data set

As initial analysis, the quality of the ground data set was checked by its consistency to the outcome of a clear sky model. As can be seen in the example given in Fig. 2 , the measured data are well in accordance with a clear sky irradiance calculated (Kasten 1983) for a Linke turbidity of 3.

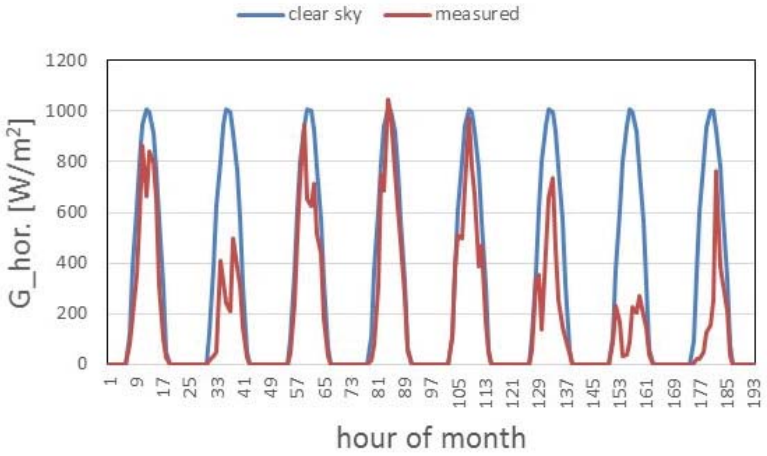

Fig. 2: Data quality from the weather stations in Rwanda, shown by consistency to modelled clear sky data (Linke turbidity:3) . Section of a time series of measured data from Location Gikomera, data from July 2014.

3. Analysis of irradiance statistics

As examples for more in depth analysis of the data sets, two examples are given here. The first concerns the investigation into short term statistics of the irradiance series that effect the performance of both on- and off-grid systems. For on-grid systems the magnitude and persistence of the irradiance fluctuations may challenge the stability of the grid. For off-grid systems the fluctuations cause stress to the storage devices.

3.1. Temporal statistics of short term data

From the 5min ground station data, the temporal variability of the irradiance re analysed. This is done here by extracting the daily standard deviation of the 5 min clear sky index (csi). Fig.3 gives for the location Kigali the daily standard deviation of the csi in dependence of the daily mean csi for the month of December 2013 and July 2014. It can be observed that there is no unique coupling of the daily standard deviation to the daily mean. This may call for a revisiting of both, schemes for the generation synthetic data sets based on daily averages (see e.g. Remund, Kunz 2004) and respective tools for the analytics system design (see e.g. Beyer, Langer 1996). In addition the autocorrelation coefficient of these csi series are inspected, indicating a general high correlation of the fluctuations on this time scale (Fig.4) which e.g. effects the cycling characteristics of the storages.

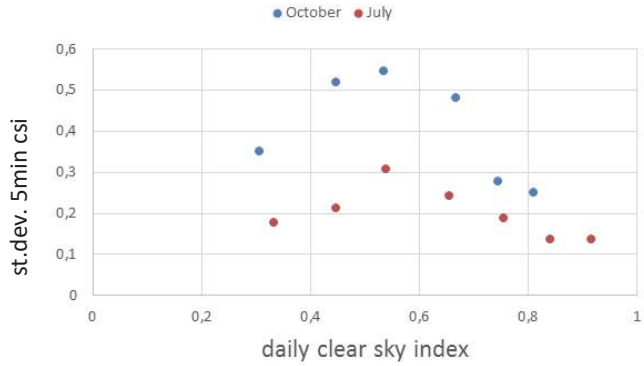

Fig. 3: Standard deviation of the 5 min clear sky indices csi, depending on the daily clear sky index for the location Kigale, month December 2013 and July 2014.

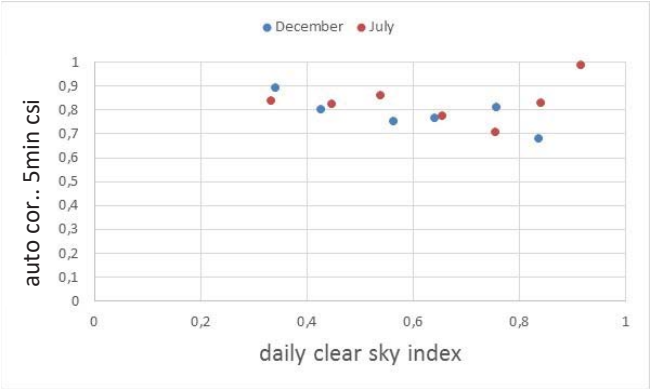

Fig. 4: Temporal correlation of 5 min. clear sky indices csi auto- correlation depending on daily clear sky index location Kigali, July and December - similar structure for both month indicate persistence of cloud situation for periods > 5min. Same data base data as Fig.3.

3.2. Spatial statistics of daily and hourly data

A second approach to investigate the details of the variability of the irradiance field with relevance for the large scale country wide integration of photovoltaics focusses on the large scale spatial correlation. Fig. 5a and 5b give a first qualitative view on the homogeneity of the irradiance field by showing the monthly time series of the daily clearness index for the months of July and December for 4 stations dispersed over the country (see map in fig.1).

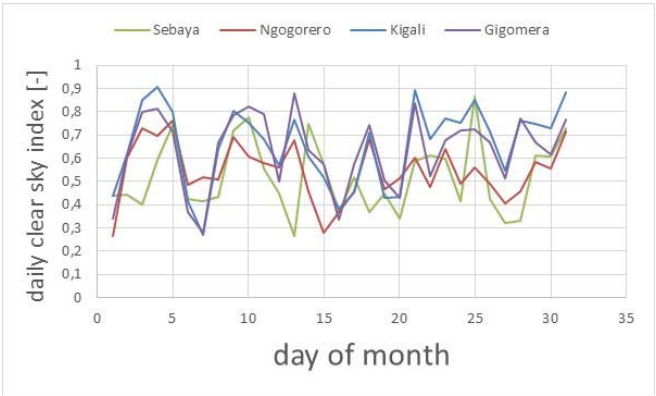

Fig. 5a:. : Monthly time series of the daily clear sky index at 4 stations (see map in fig.1). Given are the data for (July 14 5a)

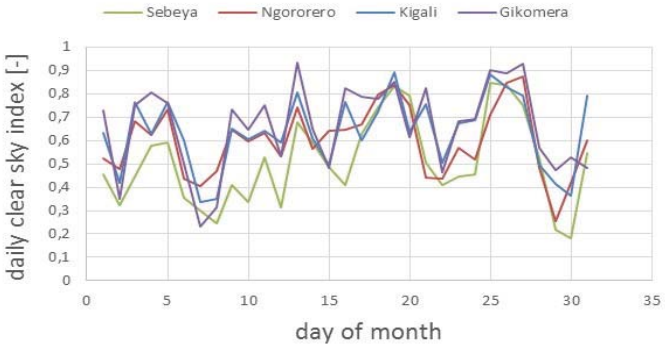

Fig. 5b: Same as fig.5 but for December 14 (5b)

It can be observed that days with an either completely clear of completely covered sky at all of the stations are rare. Thus it has to be expected, that a county wide PV-fleet will only rarely challenge the grid by delivering the rated power of all systems at one. The more fractures spatial structure of the irradiance field in Rwanda is also visible when looking at the cross-correlation of the hourly clearness index for pairs of stations.
Fig. 6 gives the correlation coefficients for pairs of stations in dependence of the interstation distances. Data for the month of July and December are analyzed. The strong decay with distance can be observed. For comparison, the characteristic of the decay of the interstation correlation (annual average) extracted from data sets for Germany (Wiemken et. al. 2001) are given. This indicates, that the fluctuations of the irradiance field in Rwanda show less spatial coherence that in northern Europe – leading to a more pronounced smoothing of the relative fluctuations of lumped power output from dispersed stations as compared to the fluctuations in single station data.

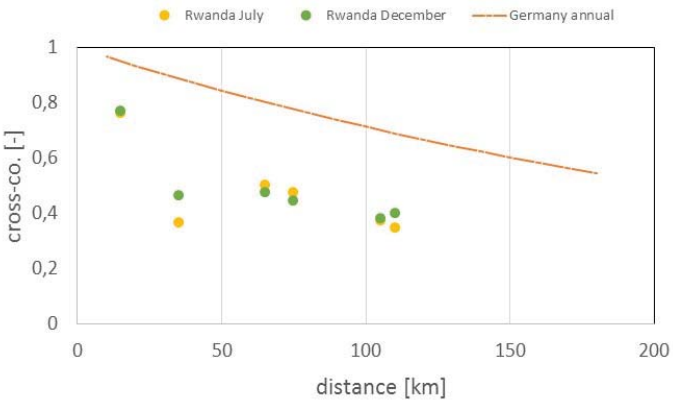

Fig. 6: Cross correlation of hourly clear sky indices compared to the correlation derived from a respective set from stations in Germany (Wiemken et al. 2001).

4. Application for the quality check of satellite derived data

A first qualitative assessment of the quality of satellite derived data for Rwanda had been done by Habyarimana, Beyer 2015. With the by then absence of time parallel ground and satellite data there was a comparison of the trace of monthly means for 5 years of satellite data (Geomodell 2013) with the 2014 ground data for the station of Kigali. It can be remarked that the satellite derived data are for most of the month clearly superior to that ground data.

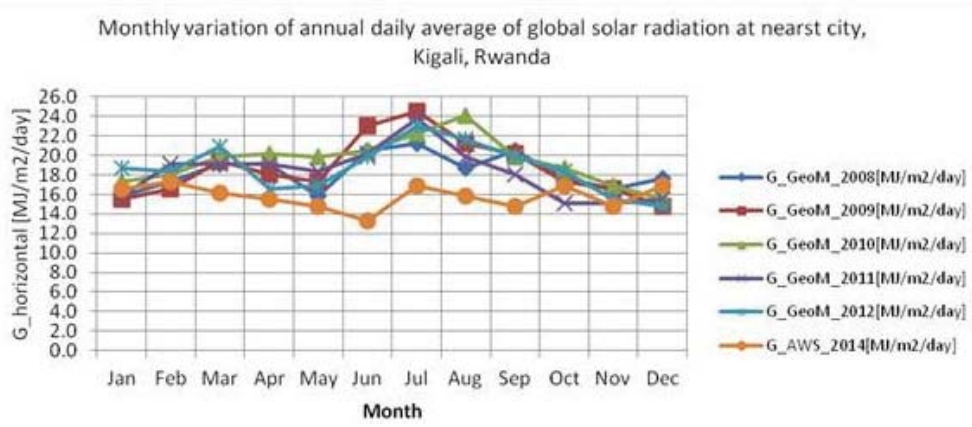

Fig. 7: Comparison of yearly traces of the monthly irradiance sum for Kigali from the 2014 ground data and 2008-2012 satellite derived data from Geomodel 2013.

This comparison is taken up here with the use of now available datasets with worldwide coverage offered by the SARAH service (Müller et al 2015). The following results refer to that source.
Fig.8 gives data for the station. Here the increase of the cumulative irradiance sum for the month of October is given. It can be observed that the satellite derived data give an overestimation of ~20%. A pattern that is qualitatively repeated for the month of November and December (fig. 9 and fig. 10).
For an explanation of this overestimation a first guess would call for an inspection of the assumptions taken for the estimation of the clear sky irradiance used in the calculation scheme for the satellite derived data. To get a qualitative impression of the influence of the assumptions on clear sky irradiance, it is assumed that a tuning of the clear sky irradiance may result in but a scaling of the modelled irradiance. Applying this assumption, one may test the use of a scaling to matching the final monthly irradiance sum.
The results of this procedure applied to the monthly sets are added in the figs.8-10.

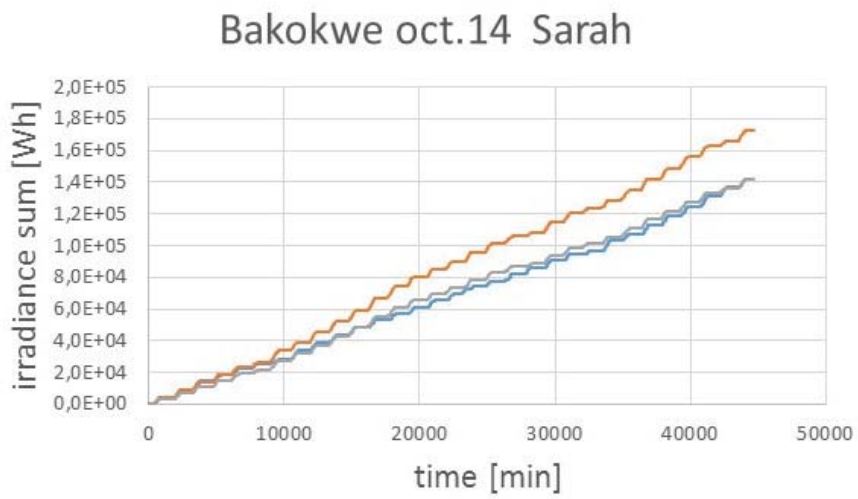

Fig. 8: Cumulative irradiance sum for the data from the station Bakokwe, month of October14 - Red line: satellite derived data, blue line: ground data, grey line: satellite derived data matched to meet the final monthly irradiance sum (see text).

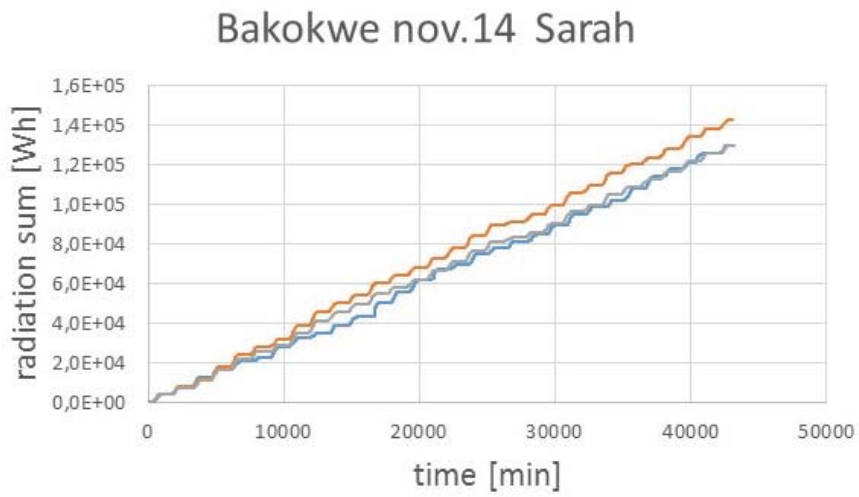

Fig. 9: Same as fig.8, but for the month of November 14.

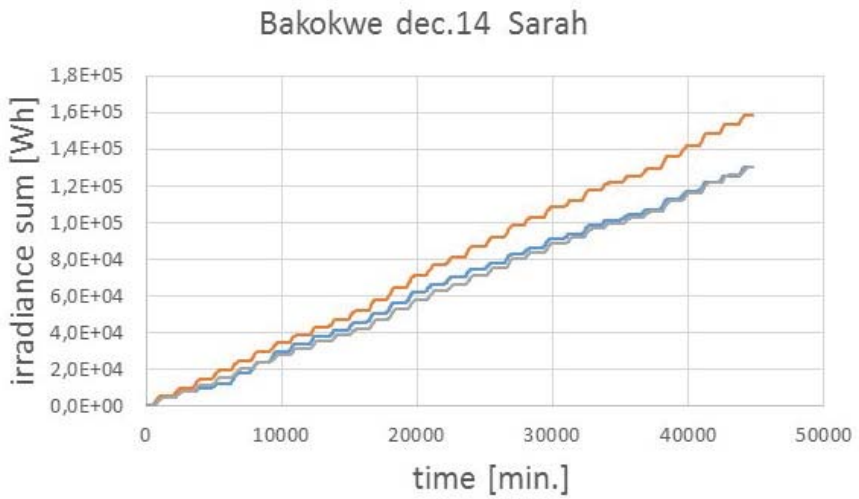

Fig. 10: Same as fig.8, but for the month of December 14.

In the figures 8-10 the grey lines present this adopted irradiance sums - a perfect match with the line for the ground data would indicate that errors are due to but a faulty scaling, i.e. incorrect assumptions on clear sky irradiances. As can be observed this is most likely the case for the December and October data. For November further inspection would be needed.

5. Conclusions

In view of the general lack of detailed irradiance data in central Africa, the opportunities offered by a network of meteorological stations in Rwanda logging highly time resolved respective data sets are obvious. This could be discussed for both, the application for the layout (e.g. sizing of storage) of small stand-alone PV systems and the assessment of large scale application of grid-connected PV-power stations with repercussion in the country wide power grid. An additional benefit of the set discussed is given by its applicability for the quality assessment of satellite derived information on irradiance. Here, a need for improved information on the local atmospheric turbidity could be identified.

6. Acknowledgement

Thanks are due to Meteo Rwanda for granting access to the ground data. The SARAH data are kindly supplied by Thomas Huld from JRC, Ispra, Italy.

7. References

Beyer, H.G. Habyarimana, F. 2015, Assessment of the quality of satellite derived irradiance data for Rwanda by comparison with data from a fleet of automated ground stations

Beyer, H.G., Langer, C., 1996, A method for the identification of configurations of pv/wlnd hybrid systems for the reliable supply of small loads, Solar Energy, 98, 381-391

GeoModel, 2013. http://geomodelsolar.eu/home as of 15.05.2014

Kasten, F., 1983, Parametrisierung der Globalstrahlung durch Bedeckungsgrad und Trübungsfaktor, Annalen der Meteorologie, Neue Folge 20

Meteo Rwanda, 2014. http://www.meteorwanda.gov.rw

Müller, R.; Pfeifroth, U.; Träger-Chatterjee, Ch; Cremer, R.; Trentmann, J.; Hollmann, R.. 2015: Surface Solar Radiation Data Set - Heliosat (SARAH) - Edition 1. Satellite Application Facility on Climate Monitoring. DOI:10.5676/EUM_SAF_CM/SARAH/V001. http://dx.doi.org/10.5676/EUM_SAF_CM/SARAH/V001

Remund, J., Kunz, S., 2004. METEONORM Version 5.1, http://www.meteonorm.com

Wiemken, E. et.al, 2001, Power characteristics of PV ensembles: experiences from the combined power production of 100 grid connected PV systems distributed over the area of Germany, Solar Energy, 70

Conference Proceedings
EuroSun 2016
Palma de Mallorca (Spain), 11 – 14 October 2016

Short-term solar irradiance prediction using Time series analysis and Neural Networks for Green Energy Park Photovoltaic Plant.

Abdelkrim Bouabbou[2*], Abdellatif Ghennioui[1], Sébastien Vaudreuil[2] and Zakaria Naimi[1]

[1] The Research Institute for Solar Energy and New Energies IRESEN – Rabat, Morocco

[2] The Euro-Mediterranean University of Fez - Morocco

Abstract

Short-term solar irradiance forecasting is of great importance for optimal operation and grid integration of photovoltaic (PV) plants. Morocco's Green Energy Park (GEP) of Benguerir is investigating the possibility of providing accurate solar forecasts for its own PV plant. However, to overcome the variability of solar resources under changing weather conditions, a reliable forecasting model is needed. In this context, this work provides a detailed research in short-term solar irradiance forecasting, an implementation and a technical analysis were performed in this study for a suitable and a reliable Global horizontal irradiance (GHI) forecasting model. Comparing the performance of different models such as ARIMA, Multiple linear regression, curve fitting and artificial neural networks, gave valuable information for further development of the final model. This final model is based on NARX ANN. In order to achieve meaningful results when comparing these different approaches as well as for NARX ANN model assessment, a standardized methodology for evaluation is used. NARX model outperformed all the approaches carried out in this study and it gave very satisfying results of 4,57 % MAPE error for Clear-sky and 14,67% MAPE error for Cloudy weather conditions.

Keywords: GHI, Forecasting, *ARIMA, MLR, Curve Fitting, ANN, NARX*

1. Introduction

Solar power generation is gaining substantial prominence worldwide, especially Photovoltaic (PV) power technologies, with an average yearly growth rate of 50% over the last ten years (Jäger-Waldau, 2015), making PV one of the fastest growing industries at the present. However, while PV output is dependent on solar irradiance, natural intermittency and variability of solar resources poses limitations for a more stable grid integration. Furthermore, this variability of solar technologies output at higher grid penetration levels induces problems economically, regarding dispatchability, generation, and grid reliability in general (Rich H. Inman, 2013). While energy storage in large amounts on-site is very problematic, this limitation can be tackled by accurate solar irradiance forecasting, which is crucial for efficient integration of solar energy into the electric power grid and for improving its proportion in total energy consumption.

Solar irradiance at the ground level are highly variable mostly due to weather related variables like clouds coverage variability and their motion, and to a lesser extent aerosols and gases in the atmosphere. However, thanks to solar meteorology for renewable generation, a number of promising approaches for prediction have been developed in the past few years, such as Remote sensing based Numerical weather prediction (NWP) methods (Diagne, 2013) (Lima, 2016), Regression methods, Machine learning and artificial intelligence (AI) forecasting using data acquired by local sensing instrumentation such as total sky imager (Chi Wai Chowa, 2011) , pyranometers and local weather instrumentation (Rich H. Inman, 2013).

Regressive methods are not new to forecasting, beginning with pre-stochastic algorithms like Multiple Linear Regression (MLR), and Curve Fitting (CF) to newly developed nonlinear stochastic algorithms. Hard computing techniques like MLR and Curve fitting predict different types of data, the authors of (Jain, 2012) have carried out these techniques on variables like temperature, humidity and "day type" parameters to recognize load patterns in short-term load forecasting. Also, authors in (Sahin, 2012) have compared MLR based model with Artificial Neural networks (ANN) for estimating solar radiation, and they are generally very simplistic while maintaining the ability to model non-linear patterns. Nonetheless, a lot of models were developed based on Box-Jenkins model ARMA, such as ARIMA (Zhang, 2003) taking into consideration external information to the time-series under analysis. Also we can find many variations of such model like ARMAX and ARIMAX with the same philosophy.

doi:10.18086/eurosun.2016.09.02 Available at http://proceedings.ises.org

For solar radiation, many works have incorporated these methods like (Aguiar RJ, 1989) used clearness index K_t to model daily sequences of hourly irradiance with ARMA techniques, where K_t was obtained by multiplying a clear sky index values by a non-stationary fluctuation, with probability depending on the hour of the day.

Since the late 1990s, ANNs have seen an increase in solar forecasting applications. Several works proposed in literature modeled solar irradiance using various ANN's internal topologies, different inputs and for several time scales (Lopez, 2005) (Koca, 2011) .Al-Alawi and Al-Hinai used weather variables as inputs to an ANN to predict monthly values of Global Horizontal Irradiance (GHI) over a year (Al-Alawi S, 1998). Authors in (A. Di Piazza, 2013) have acquired very satisfactory forecasts using a feedforward Time delay Neural Networks called NARX. In addition, In the work of (Vaz, 2015) PV output forecast have been generated using NARX by employing meteorological variables as exogenous inputs and assed the influence of multiple PV neighboring systems.

In this context, a thorough methodology was undertaken for short-term global horizontal irradiance forecasting using local meteorological measurements. This paper is organized as follows. In section 2, the study overview and experimental data collection were presented. The methodology is illustrated in Section 3. Results and discussion in section 4 and finally this paper ends with a conclusion.

2. Study overview and Experimental setup

2.1 Overview and Objective.

The Research Institute for Solar Energy and New Energies (IRESEN) was established in 2011 to lead and promote Moroccan R&D in the field of renewable energy through applied R&D projects. To expand this leadership further, a research platform called "Green Energy Park" (GEP) was set-up in Benguerir by IRESEN and the OCP Group in 2014. The goal of this technical platform is to provide the means to characterize various PV technologies in local weather conditions and investigate their long-term behavior. The GEP's PV plant is facing the same limitations in regards to the export of electricity to the grid. Thus, the aim of this work is to provide a precise model for a short-term solar irradiance forecasting for optimal operation and a prospect grid integration in Morocco.

2.1 Experimental solar irradiance data

In the present study, we have selected some weather related variables that are directly or indirectly influencing global horizontal irradiance (GHI). GEP PV Plant is equipped with a Meteo-Station measuring accuratly various weather related variables like wind speed, temprature, pressure, ...etc. Also, a very accurate SOLYS2 solar monitoring station and it is composed of two pyranometers, one directly exposed to the sun and measures Global Horizontal Irradiance, one with a shading ball to help measure DHI the diffuse Diffuse Horizontal Irradiance and finally, one pyrheliometer measuring Direct Normal irradiance (DNI). When solar data are logged, they are sent via a Modbus data logger to GEP Servers. These data is then treated and organized in a SQL database. Data quality is checked and calibrated according to World Meteorological Organization (WMO).

For this study GHI data were aggregated with time, temprature and relative humidity. As an example Fig.1 present data of three days, 21th, 22th, 23th of april 2016 with 10 minutes lag.

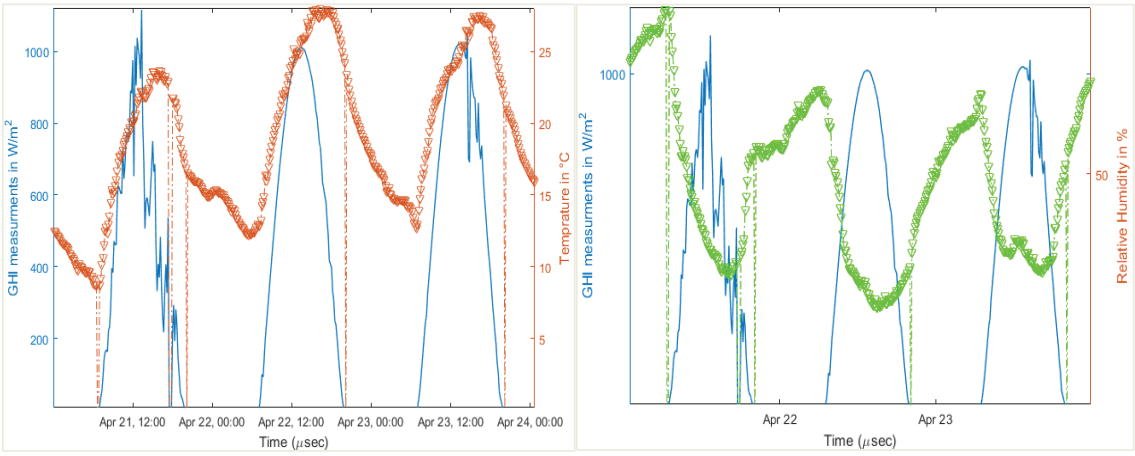

Fig. 1: Variability comparison of Temperature (Left) in red and relative humidity (Right) in green with GHI in blue.

Several datasets were created in order to investigate the influence of lags on the computation time, forecast error and finaly the choice of forecasting method.

3. Approach and implementation

3.1 Forecasting approach

The methodology undertaken was to choose two of the extreme scenarios (Clear-Sky and cloudy) of data and test them using ARIMA and time series analysis with different lags (1 min, 10 min, 1 hour) to assess the quality of forecast and for different forecast horizons. The developed ARIMA model was tuned up to see its capabilities for 48h forecast horizon.

The next step was to determine a suitable model from the different methods that deal with local sensing data, in order to do so, a MATLAB program was developed to benchmark 2 stochastic methods and one of the soft computing based on neural networks (Fig. 2).

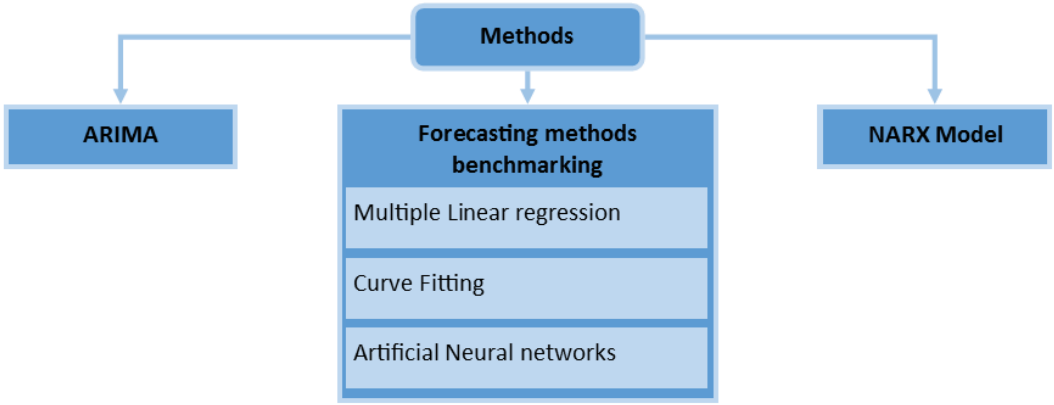

Fig. 2: Forecasting methods involved in this study.

3.2 ARIMA

Unlike the stationary model ARMA, ARIMA is a non-stationary regressive model. Non-linear methods would enable powerful structures with the ability to accurately describe complex non-linear behavior problems (Suykens JAK, 1996). This model has 3 orders, and it is known as ARIMA (p,I,q), AutoRegressive (AR), Moving average (MA) and I for the integrative part and it means that the model take into account the difference between response variable data, which is suitable for non-stationary values. This makes the model look like the following:

$$Y_t = (1-L)^d X_t \qquad \text{(eq. 1)}$$

With Y_t being forecasted values, L the lag, d seasonality exponent and X_t actual values. In a wide sense it can be written as such:

$$\left(1 - \sum_{i=1}^{p} \emptyset_i L^i\right) Y_t = \left(1 + \sum_{i=1}^{q} \beta_i L^i\right) \varepsilon_t \qquad \text{(eq. 2)}$$

Where β_j are Moving average ***MA*** coefficients and $\emptyset_i$ are AutoRegression ***AR*** coefficients. This equation creates a multitude of forecasting models, determining the orders of ARIMA was carried out by computing ACF and PACF functions provided by *autocorr* and *parcorr* in MATLAB, also this model was tuned up using an optimization for parameters like, ***SAR*** (Seasonal AutoRegression Coefficents), ***SMA*** (Seasonal MovingAverage coefficents) and Variance. Using *optimset* function in Matlab help estimate these coefficients by incorporating a nonlinear iterative optimization algorithm called Sequential quadratic programming (SQP).

3.3 Forecasting models benchmarking

For the sake of comparison a program had been developed to select the most suitable approach for our data‘s behavior. The program compares two well-known statistical methods against one based on Artificial Neural Network.

3.3.1. Multiple Linear regression (MLR) Model

In order to be able to predict accurately, and to fit data in the best way possible, regression models are often constructed based certain conditions that must be verified. The basic linear model is a simple linear regression

between dependent and independent variables. Linear regression model fits the data to a model of the following form:

$$y_i = \beta_0 + \beta_1 x_i + \varepsilon_i \qquad \text{(eq. 3)}$$

Where i is the number of measurements, (β_0, β_1) are coefficients and ε is a random error.

The term ε is a catch-all for differences between predicted and observed values of y. These differences are due to process fluctuations (changes in β), measurement errors (changes in x) and model misspecifications (for example, nonlinear relationships between x and y). It is usually assumed that ε is generated by an unobservable innovations process with stationary covariance $\Omega_t = Cov(\varepsilon_1, \ldots \varepsilon_t)$.

If the model has more than one independent variable, it will become a multiple linear regression model and will be in this form:

$$y_i = \beta_0 + \beta_1 x_i + \beta_2 x_i^2 + \beta_3 x_i^3 + \cdots + \beta_k x_i^k + \varepsilon_i \qquad \text{(eq. 4)}$$

Where β_i ($i = 1,2,3, \ldots, k$) are the coefficients of the model, this method is used to analyze the effect of more than one independent variable ($x_1, x_2, x_3, \ldots, x_k$) on the dependent variable (Solar Radiation). For a given dataset ($y, x_1, x_2, x_3, \ldots, x_k$) the multiple linear regression fits the dataset to the model according to (eq.4).

Assuming that ε are independent and identically distributed as normal random variables with $\overline{\varepsilon_i} = 0$ and the unknown variance of these random errors $\sigma^2 = Var(\varepsilon_i)$. In Order to minimize the $\|\varepsilon_i\|$ with respect to β_i, we solve the function:

$$\frac{\delta\, \varepsilon_i^T \varepsilon_i}{\delta \beta_i} = 0 \qquad \text{(eq. 5)}$$ Where ε_i^T is the transposed errors vector.

Which leads to the optimal coefficients $\hat{\beta}$ that are being estimated from the vector β by least squares method:

$$\begin{bmatrix} \widehat{\beta_0} \\ \vdots \\ \widehat{\beta_k} \end{bmatrix} = (X^T X)^{-1} X^T \qquad \text{(eq. 6)}$$

Matlab provides script driven tools to carry out multiple linear regression, the regression used returns a p-by-2 matrix of 95% confidence intervals for the coefficient estimates. The inputs were designed to bring about seasonality features in solar irradiance and to make sure that our forecasts revolve around the average of each hour.

3.3.2. Curve Fitting Model

Curve fitting finds an appropriate mathematical model that expresses the relationship between dependent and the independent variables and the parameters are estimated using nonlinear regression.

Using the historical data to find coefficients of an equation is the basic principle of Curve fitting; the equations could be multiple sin waves, Fourier or polynomial equations, etc. Matlab Curve fitting GUI is a good way to find the potential of this Model. In our case, our equation is fourier8 of the form (eq. 7):

$$Fit_{model}(x) = a_0 + a_1\cos(x * w) + b_1\sin(x * w) + a_2\cos(2 * x * w) + b_2\sin(2 * x * w) + a_3\cos(3 * x * w) + b_3\sin(3 * x * w) + a_4\cos(4 * x * w) + b_4\sin(4 * x * w) + a_5\cos(5 * x * w) + b_5\sin(5 * x * w) + a_6\cos(6 * x * w) + b_6\sin(6 * x * w) + a_7\cos(7 * x * w) + b_7\sin(7 * x * w) + a_8\cos(8 * x * w) + b_8\sin(8 * x * w) \qquad \text{(eq. 7)}$$

This model uses the same inputs in MLR model and all coefficients a_n, b_n and c_n will be found using "fit" function in Matlab.

3.3.3. Artificial neural network (ANN)

Artificial intelligence techniques use a symbolic approach to intelligent systems, it is a processing architecture based on the human brain focusing on information representation by its ability to learn and adapt. ANNs are constituted by a mathematical model of biological neuron called perceptron arranged in nodes and connected by weigh vectors or simply called weights (Fig.3).

ANNs can model any actual data variations by constantly changing the weights between the nodes based on information flow through the network during the learning phase.

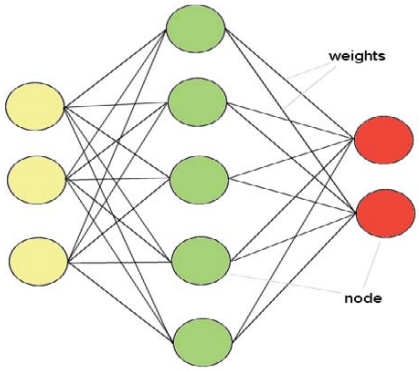

Fig. 3 : ANNs incorporate the two components of biological neural nets: Neurones (nodes) and Synapses (weights), inputs layer is in yellow, hidden layer in green and output nodes are in red.

ANN is well suited for modeling complex relationships between inputs and outputs with an ability to construct a map without explicit analytical equation, which is at the same time a very powerful tool to model nonlinear statistical data. The basic mathematical model of ANNs is shown below.

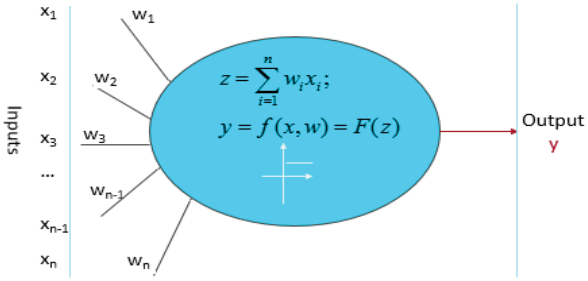

Fig. 4 : Neurons work by processing information as they receive and provide it in form of spikes.

(Fig.4) present the McCullogh-Pitts model, where x_i is an input vector, w_i are weights values, $f(x,w)$ an activation function and y is the output. The architecture used in this study is a feedforward neural network and is designed in a way to acquire a forecasts error less or equal to the error imposed by the user via a constraint imposed in a loop, so the program can reiterates until it finds the forecast with the minimum error. The training algorithm used is Levenberg-Marquardt, Training, Test and Validation dataset are divide randomly from the original data, the best results were acquired for 5 hidden neurons with a logistic sigmoid activation function and one output neurons with an adaptive linear function.

3.4 NARX model implementation

The Nonlinear AutoRegressive with eXogenoues inputs model or NARX in short, is a specific type of recurrent neural architecture (RNN), it was derived from derived from Autoregressive exogenous (ARX) model commonly used in time-series modeling. It is a recurrent dynamic network, with feedback connections enclosing several layers of the network. It has limited feedback architectures that come only from the output neuron instead of from hidden neurons.

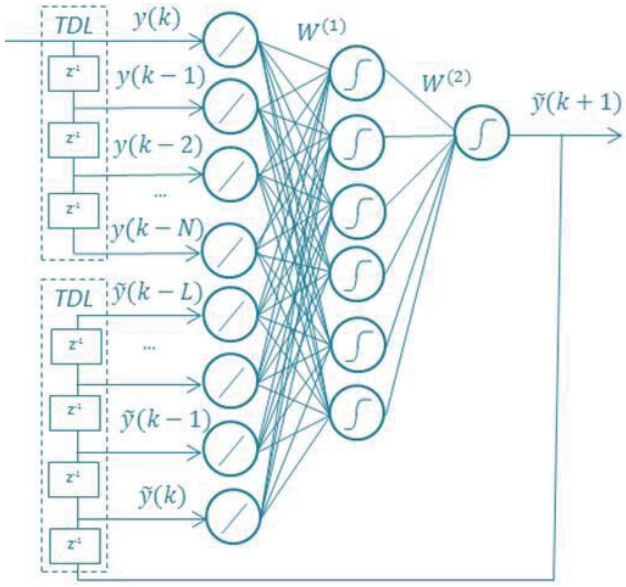

Fig. 5: NARX NEURAL NETWORK (Mladenov, 2013)

The NARX neural network structure is shown in Fig. 5 is equipped with both a tapped delay line (TDL) at the input y and global recurrent feedback connections $\tilde{y}$. It represents a Dynamic Multilayer Perceptron. The input vector can be written as such:

$$x(k) = [y(k) \dots y(k-N) \;\; \tilde{y}(k) \dots \;\; \tilde{y}(k-L)]^T \qquad \text{(eq. 8)}$$

Where N is the order of the input tapped delay and L is the order of the feedback tapped delay line. Long-term dependencies that solar radiation has with other exogenous input was the reason for choosing an ANN that uses TDL.

The output is then generalized by:

$$\tilde{y}(k+1) = g(\sum_j w_j{}^{(2)}(f(\sum_i w_i{}^{(1)} x_i))) \qquad \text{(eq. 9)}$$

Where $w^{(1)}$ and $w^{(2)}$ are weights of the hidden and output layers, $f(.)\ and\ g(.)$ are activation functions respectively of the hidden and the output layers.

NARX use taps to set-up the delays across the inputs. Also, it incorporates the past values of the output. Recurrent networks have loops within intermediate layers and incorporate memory via these loops.

The inputs for the NARX ANN are GHI time serie and as exogenous inputs we have chosen what might reflect the changes in GHI, variables like *relative humidity* and *ambient temperature* were often mentioned in literature as exegenous inputs for NARX ANN and as the fig.2 shows they follow to a certain extent solar irradiance‘s seasonality.

Also, we have divided our dataset to inputs and targets, target series are what we compare the response of the neural network to. So the first group is used to train the Neural Network while the second group of variables are Validation series, this new data is used for simulation. For this model we have used a 10 min resolution time-series from 1st of January 2016 to 1st of February 2016.

For learning process, ANNs training uses mathematical procedures to adjust the network’s weights and biases. The training function necessitates a global algorithm that affects all the weights and biases of our network. The algorithm used is *Levenberg-Marquardt algorithm* found in NN toolbox in Matlab. And then we have divided our dataset into 3 parts, Training, validation and test datasets by setting up ratios respectively 60%, 20%, 20% of input vectors. The training performance function is Mean squared error (MSE), minimizing this error while our network learns the dataset behavior. Also, we assigned *Tansig* activation function for hidden layers and *Purelin* for the output layer. Number of the hidden layers is determined by trial and error until the program converges at an error less or equal to the desired error entred by the user. The evaluation of each trial is carried out by Mean Absolute Percent Error (MAPE).

4. Results and discussion

4.1 Forecasting evaluation metrics:

A standardized performance evaluation was adopted to asset the accuracy of each model involved in this study, the metrics used are RMSE and MSE because they give more weight to the largest error and MAE was used to give the average of the magnitude of forecast error. Also we have used MAPE as a constraint over forecast iterations in our programs.

We define the forecast error: $e_i = y_{i,forecasted} - y_{i,observed}$ (eq. 10)

where $y_{i,forecasted}$ is the i[th] forecasted value, $y_{i,observed}$ the i[th] actual value and N is the length of the test dataset.

$$RMSE = (MSE)^{\frac{1}{2}} = \left(\frac{1}{N}\sum_{i=1}^{N} e_i^2\right)^{\frac{1}{2}} \quad \text{(eq. 11)}$$

$$MAE = \left(\frac{1}{N}\sum_{i=1}^{N}|e_i|\right) \quad \text{(eq. 12)}$$

$$MAPE = \left(\frac{1}{N}\sum_{i=1}^{N}\frac{|e_i|}{y_{i,observed}}\right) * 100 \quad \text{(eq. 13)}$$

4.2 ARIMA

The first set of experiments was carried out for intra-day forecasts with the horizon of 30 minutes. The two datasets used for clear-sky and cloudy day have a 1 min resolution. Running ARIMA gave us an error less than 5% MAPE for clear-sky and 10% cloudy day after the beginnig of each day. The dataset used was only one day of GHI. However, it seems very problematic if the program is supplied with more than two days of data. Taking into account the computing power of the processor (4 CPU 1.6 GHz, 8G RAM), running time average in this case around 15 to 30 seconds. If the dataset is too large, computation takes a lot more time to produce results. So we have concluded that it is best to reason with the length of the dataset, not with its duration.

For a Days-ahead forecast, we have begun the procedure by estimating the model through ACF and PACF, calculating residuals, testing residuals, running simulation and finally comparing results for the three data sets chosen. A constraint in the program has been integrated in order to stop it from running if the calculation was going to take a lot of time, this is the reason behind the poor results acquired for larger datasets.

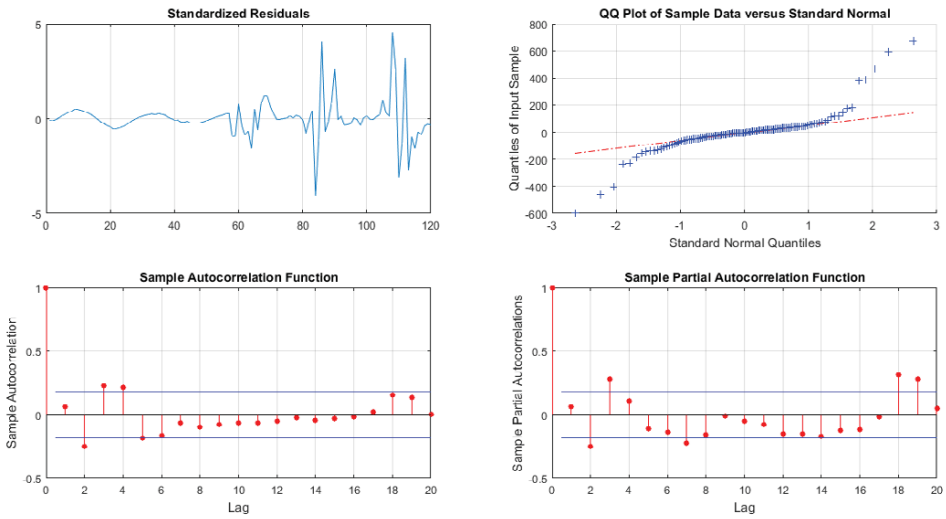

Fig. 6: Tuned up ARIMA Standarized Residuals and QQplot (1 Week 1 Hour)

After optimizing the process of getting ARIMA coefficient, we have noticed a reduction in standardized residuals amplitude and the evenly distributed quantiles on the references line (Fig. 6 Standarized residuals plot). However, there are fractions that indicate that our forecasted values is still greatly different from real measurements (Fig.6 QQ plot).

ARIMA results were evaluated and are presented in (Tab. 1):

Tab. 1: Tuned-up ARIMA Model results for the 3 chosen datasets

	1 Week 1 Hour	1 Week 10 minutes	1 Month 1 Hour
MAE W/m²	98,78	159,67	335,769
MSE W/m²	2,47E+04	7,85E+04	2,05E+05
RMSE W/m²	157,19	280,14	453,64

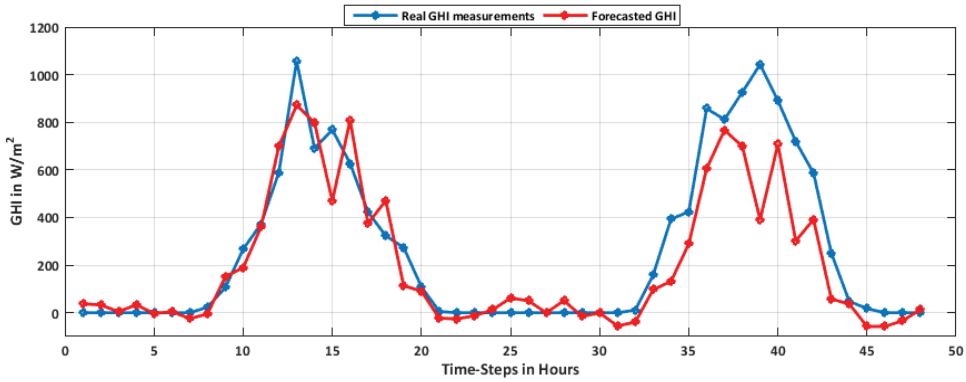

Fig. 7: Forecasted GHI results using 1 Week of data with 1 Hour resolution

The best results were recorded for one week of solar data with one hour resolution presented in (Fig. 7), the larger the dataset is the more time the computer takes to produce forecasts. A constraint over computational time was however put in place to have some rapidity while maintaining the same reliability. This constraint had largely increased the error on one Month dataset with the resolution of one hour. But it still gives relatively acceptable results if compared to the other datasets. In either ways, ARIMA seems incapable of producing reliable forecast for long periods. One limitation of ARIMA models is that they often overlook the physical behavior of time series objects, in our case sunrise and sunset. A study by (Moreno-Munoz, 2008) showed that ARIMA can accurately forecast hourly irradiance levels using data from a few previous hours. However, due to the discontinuity of solar irradiance, forecasts immediately adjacent to sunrise and sunset are problematic and increase forecast errors.

4.3 Benchmarking Program Results and Analysis

For this task we have used a year of historical GHI data with the resolution of 1 hour, the results are compared for clear-sky and cloudy conditions as presented in Fig.8:

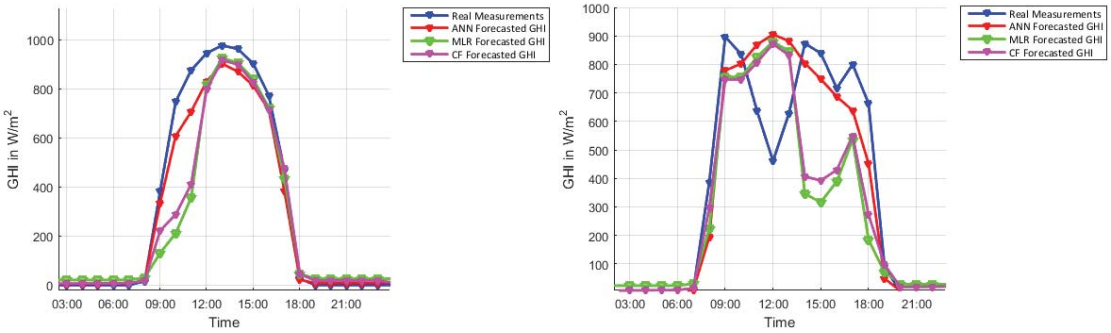

Fig. 8: Forecasting Benchmark results of a clear-sky day and cloudy day

Using the daily and hourly averages of solar irradiance of the previous day imposes that our MLR model to mimic yesterday's behavior, the choice of this procedure was taken because generally adjacent days follow relatively the same behavior. MLR model gave 56.352% MAPE for Validation dataset, this Error was reduce to 22.733% Using Curve Fitting model. ANN model is seeeminly independent of adjecent days but gives relatively satisfying results of 16, 264% MAPE.

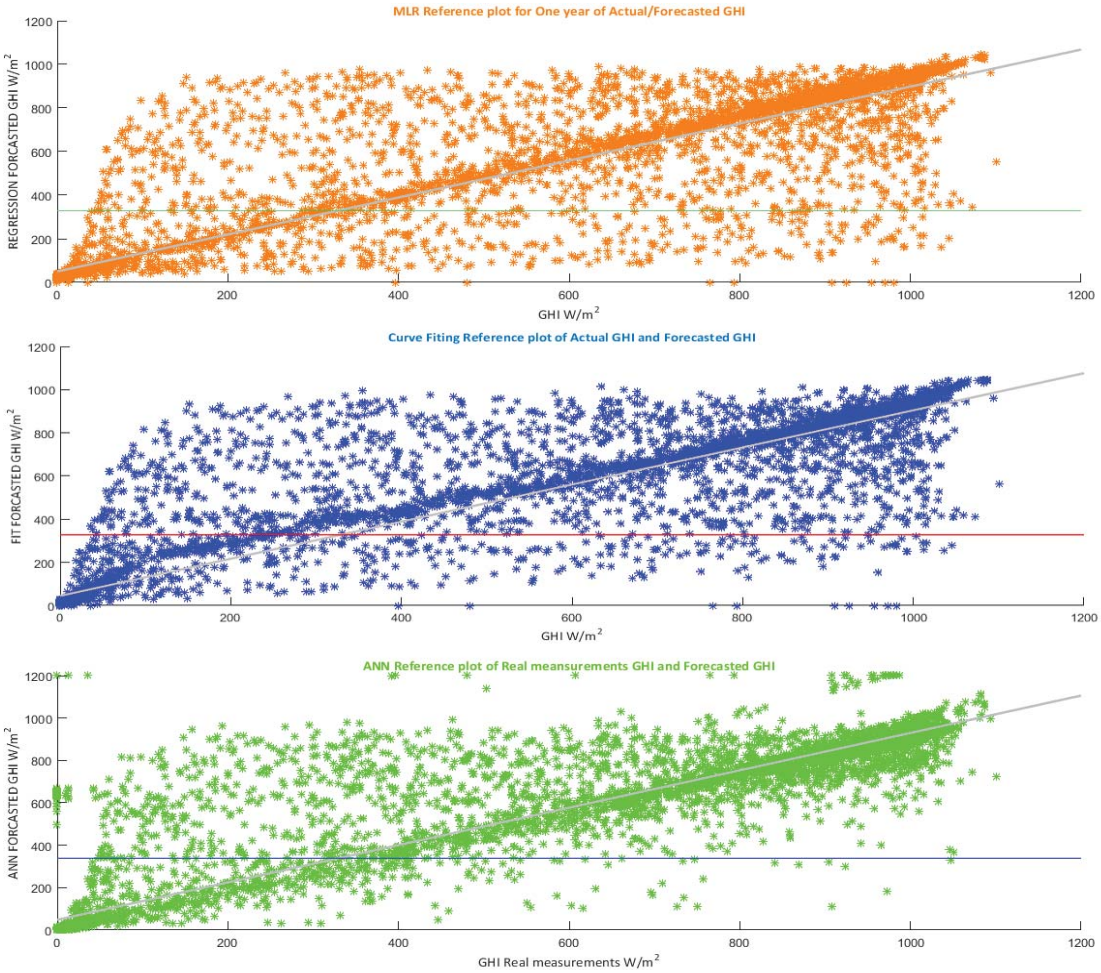

Fig. 9: Reference plot of the three benchmarked methods using 1 year of GHI with 1 hour resolution

For visual comparison we present in (Fig. 9) reference plot for MLR model in orange, Curve Fitting in blue and ANN model in green, horizontal line represent mean value, and the inclined line represent least-squares line.

If the diffenrence between forecasted and measured values was smaller the dots tend to be close to the least-square line, so we can notice that ANN response fits GHI historical data better than MLR and CF models, which is verified by (Tab.2) of Metrics presented in section 4.1:

Tab. 2: Benchmarking forecasting models evaluation using 1 year of GHI with 1 hour resolution

	Curve Fitting		Multiple Linear Regression		ANN	
	Validation Error	Historical Error	Validation Error	Historical Error	Validation Error	Historical Error
MAE W/m²	23,35	81,1673	29,94	75,57	20,77	66,87
MSE W/m²	1,05E+03	2,42E+04	1,48E+03	2,21E+04	0,77E+03	3,38E+04
RMSE W/m²	32,58	155,57	38,3	148,513	22,1	183,729
MAPE	22.733%	44.644%	56.352%	123.045%	16, 264%	331,11%

While regression barely gave admissible results, improving it with fitting curve has considerably enhanced it. But between the three combined models, the best is Artificial Neural Networks model as the Validation MAPE error indicates, even with the high error of historical GHI due the learning phase and night time values. Ergo tuning up Neural Networks model will surely produce a robust forecasting engine.

4.4 NARX ANN model

Mean squared Error MSE gives a huge proportion to the difference between predicted and real values, using it in as performance function in learning phase helped reduce the error drastically. However evaluating regression models is often done by MAE or MAPE as they only evaluate the difference between two data values. The

simulation were carried out and the Neural Network stopped training with ten layers at a delay of 2, in (Fig. 10) the NARX ANN is presented.

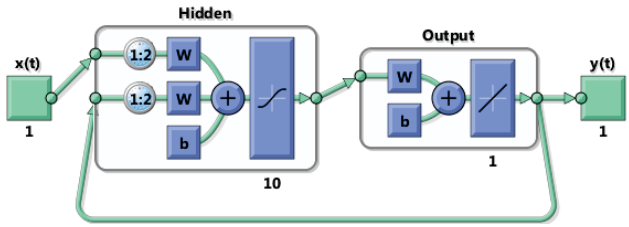

Fig. 10: NARX ANN Model architecture.

x(t) is a matrix containing historical data lagged by 10 minutes from 15th of April to 15th of May of GHI, Relative humidity and ambient Temperature and as an output y(t) is forecasted GHI. The choice of the input matrix was taken for examining various meteorological variables and how they change with GHI (Fig. 2).

We have tried this model for three Forecast Horizons, one day, two days and three days ahead results are shown in (Fig. 11) below:

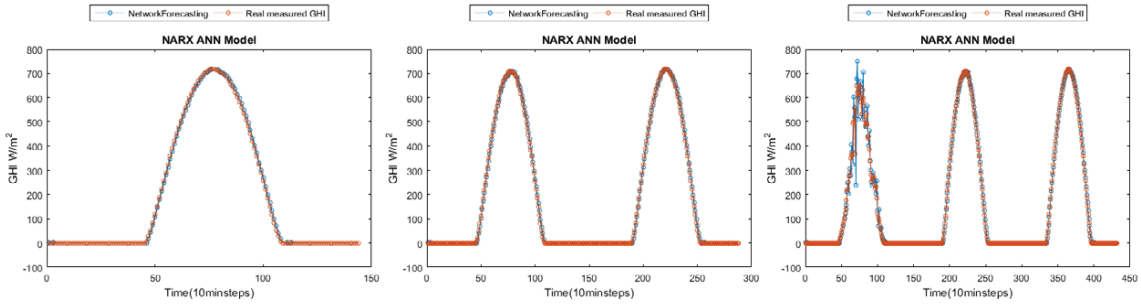

Fig. 11: Plot of forecasted values and real measurements of NARX model for the three Forecast Horizons

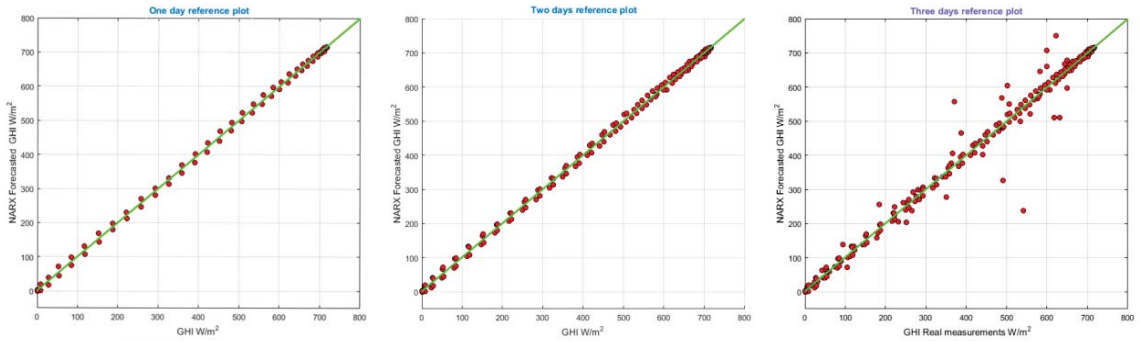

Fig. 12: Reference Plot of NARX model for the three Forecast Horizons

For a clear sky conditions, the results are near perfect as shown in (Fig.12) for one and two days forecast horizon, with less than 4,57 % MAPE error, however for cloudy day the minimum error acquired was 14,67% which by far less than the other models previously developed in this study. Also, as presented in (Tab. 3) we noticed that when the Forecast Horizons gets bigger the accuracy decreases, it was the same for all models, however for NARX model this lost of accuracy is really subtle and relative to cloudy days presence, but for clear sky the forecast is very good which demonstrates the robustness for NARX model.

Tab. 3: Evaluation metrics results for NARX model

	1 Days ahead	2 Days ahead	3 Days ahead
MAE W/m²	8,82	9,3126	4,21E+01
MSE W/m²	1,47E+02	1,64E+02	1,71E+04
RMSE W/m²	12,10	12,81	130,95

The results in Tab. 3 shows that NARX ANN model outperforms all the other models, and the best way to make a neural network learn seasonality and the trend is to make a construct of inputs that are related to each other to a certain extent, temperature and relative humidity gave better results if compared with clearness index.

For Clear-sky day the forecasted values seem to be close to real measurements as they follow the least squared error line, as for cloudy days the majority of values are near real measurements, the other minority have bigger differences from real measurements.

5. Conclusion

In this paper, a methodology has been undertaken for short-term globale horizontal irradiance forecasting for the case of Green Energy Park of benguerir. An ARIMA model was developed and showed its efficiency in Intra-hour forecasts and its inability to produce reliable forecasts for longer horizons. Other stochastic methods were also developed for the sake of comparison. Multiple linear regression (MLR) and curve fitting were compared with artificial neural networks. We also have demonstrated that MLR barely has the ability to determine the general trend of used solar data but it cannot model data non-linearities, MLR was tuned with curve fitting by trying to find coefficients for the Fourier polynomial equation, the improvement seen were barely noticeable. However, for ANNs, the results were promising and it was a better choice for further developments. For this reason, a new forecasting model was developed based on NARX ANN, the results were very satisfying as the forecast error (MAPE) was decreased to 4,57 % for Clear-sky day and 14,67% cloudy day.

To make a good use of enhancements made in GEP's forecasting model, using SANDIA PV library in Matlab, we have succeeded in modeling 12 photovoltaic systems with different photovoltaic technologies from different PV modules manufacturers. This precise model will be used as conversion process for solar irradiance forecasts to acquire DC power output predictions of GEP's PV power Plant.

6. Future work

In order to make the model developed in this study more reliable, a hybrid model based on satellite images and NWP is under development. As for the GEP PV power plant model, some enhancement are underway to make the model more responsive to real weather conditions.

7. References

A. Di Piazza, M. D. (2013). Solar radiation estimate and forecasting by neural networks-based approach. *XIII Spanish Portuguese Conference on Electrical Engineering*.

Aguiar RJ, C.-P. M. (1989). The modeling of daily sequences of hourly radiation through autoregressive methods. *Proceedings of the congress of the international solar energy society*, vol. 3. p. 2107e11.

Al-Alawi S, A.-H. H. (1998). An ANN-based approach for predicting global radiation in locations with no direct measurement instrumentation. *Renewable Energy* .

Chi Wai Chowa, B. U. (2011). Intra-hour forecasting with a total sky imager at the UC San Diego solar energy testbed. *Solar Energy - Elsevier*, 2881–2893.

Diagne, M. (2013). Review of solar irradiance forecasting methods and a proposition for small-scale insular grids. *Renewable and Sustainable Energy Reviews Volume 27,* , 65–76.

Jäger-Waldau, A. (2015). *PV Status Report.* Publications Office of the European Union, European Commission. Joint Research Centre.

Jain, M. B. (2012). Curve fitting and Regression line method based seasonal short term load forecasting. *IEEE*.

Koca, A. O. (2011). Estimation of solar radiation using artificial neural networks with different input parameters for Mediterranean region of Anatolia in Turkey. *Expert Systems with Applications -Volume 38, Issue 7*, 8756–8762.

Lima, F. J. (2016). Forecast for surface solar irradiance at the Brazilian Northeastern. *Renewable Energy 87*, 807-818.

Lopez, G. B.-P. (2005). Selection of input parameters to model direct solar irradiance by using artificial neural networks. *Energy 30*, 1675–168.

Mladenov, V. (2013). Artificial Neural Networks and Machine Learning-. *Springer proceedings of the 23rd international conference of AI and machine learning*.

Moreno-Munoz. (2008). Short term forecasting of solar radiation. *IEEE International Symposium on Industrial Electronics*, pp. 1537–1541.

Rich H. Inman, H. T. (2013). Solar forecasting methods for renewable energy integration. *Progress in Energy and Combustion Science*, 535-576.

Sahin, M. (2012). Comparison of ANN and MLR models for estimating solar radiation in Turkey using NOAA/AVHRR data . *Elsevier - Advances in space research turkey*.

Suykens JAK, V. J. (1996). Artificial neural networks for modeling and control of non-linear systems. *Kluwer Academic*.

Vaz, A. (2015). An artificial neural network to assess the impact of neighbouring photovoltaic systems in power forecasting in Utrecht, the Netherlands. *Renewable energy 85 Elsevier*, 631-641.

Zhang, G. (2003). Time series forecasting using a hybrid ARIMA and neural network model. *Neurocomputing 50* , 159 - 175.

Conference Proceedings

EuroSun 2016
Palma de Mallorca (Spain), 11 - 14 October 2016

ISES EuroSun 2016

Experimental validation of a novel methodology for fast an accurate analysis of solar energy yields based on cluster analysis

Luis Guerreiro[1], Carlos M. Fernández-Peruchena[2], Afonso Cavaco[1], Martin Gastón[2] and Manuel Collares Pereira[1]

[1] Renewable Energy Chair, University of Evora, Palacio do Vimioso, P - 7002 Evora

[2] CENER, Department of Solar Thermal Energy, E – 41092 Sevilla

Abstract

The design and optimization of solar power systems requires a detailed knowledge of the dynamic behavior of the meteorology at the site of interest, usually assess by one typical meteorological year (TMY). Even with today's technology, the computational effort to simulate solar energy system performance with one year of data at high frequency (as 1-min) may become colossal if a multivariable optimization has to be performed. This work evaluates a methodology based on cluster analysis for selecting number of individual days able to represent the long-term performance of a solar energy system. This procedure permits to drastically reduce computational effort related to the calculation of a solar power plant energy yield by simulating a reduced number of days from a TMY, facilitating a fast and optimal design of the plant.

Keywords: Cluster, Day selection, STE (Solar Thermal Electricity), Optimization

1. Introduction

Concentrating Solar Thermal Power (CSTP) technologies collect and concentrate the Direct Normal Irradiance (DNI) incident on the earth's surface to heat a working fluid and afterward producing electricity through a thermodynamic cycle. The mean power produced by a CSTP system often determines the viability of the Solar Power Project, which is calculated from energy yield simulation computer programs requiring weather data input to drive the optical and thermal models within the simulation tools.

The feasibility analysis of a CSTP plant project requires the estimation of the amount of energy that it will be able to deliver to the grid during its lifetime. A detailed knowledge of the Direct Normal Irradiation (DNI) is a critical point to perform an economical feasibility analysis of these plants, as it is the most determining variable in the final energy yield. This knowledge comprises a deep understanding of the availability and dynamics of the solar resource over different temporal scales (intraday, day, month, year) (Vignola et al., 2012). To achieve this, long time series of meteorological data are usually condensed into shorter series that typify the meteorological conditions at a specific location with the aim of data volume reduction and speeding-up of energy system simulations, considered as representative of the location of interest.

Currently, the typical year approach is by far the most widely used among the scientific and industry communities for the design and optimization of solar power plants. These datasets hold 8,760 hourly meteorological values that typify conditions at a specific location throughout a longer period. Accordingly, simulations are usually performed using one hour simulation steps, either with steady state models or somehow

Selection and/or peer review under responsibility of Scientific Committee
doi:10.18086/eurosun.2016.09.03 Available at http://proceedings.ises.org

taking into account system dynamics to more accurately simulate the performance of the plant. Also, worst cases of solar resource availability are often analyzed in order to ensure the viability of the project. Frequently, these worst cases are evaluated by probability of exceedance scenarios, which provide an estimate of electric generation output that the solar resource consultant expects to be exceeded in any given year over the life of the debt with 90% confidence (P90) and 99% confidence (P99) (C.M.F. Peruchena et al., 2016).

TMY approach seems to be appropriate for rather detailed simulations of a specific solar power plant. Notwithstanding, DNI exhibits a great variability at high-frequency due to the dynamic effects of passing clouds, which is a key issue in the design and performance analysis of a CSTP system, given its nonlinear response to DNI caused by various thermal inertias due to their complex response characteristics (Fernández-Peruchena et al., 2015). DNI series of sub-hourly resolution (in the range of 1 to 10 minutes) permit an accurate modeling and analysis of transient processes in some CSTP technologies. For example, parabolic troughs with direct steam generation could be particularly sensitive to the cloud transients (Eck and Hirsch, 2007; Montes et al., 2009), and, therefore, better analyzed using DNI series with frequency resolutions much lower than 1-h (Meyer, 2010). This kind of simulations provides more accurate representation of the plant performance at the cost of larger computational effort leading to longer simulation times. Thanks to the powerful computers currently available, these transient simulations are being used not only for detailed simulations of the short term performance of the plant to improve the design and operation of specific aspects of the system, but also for the energy yield estimation over long periods of the plant (e.g. year simulation or even multi-year simulations) for a specific final plant design.

During the optimization of the large number of plant parameters before a final design is reached, a huge number of simulations are required. The computational effort to simulate a CSTP plant performance with 1-year series at high frequency (as 1-min) may become colossal if a multivariable optimization has to be performed. To overcome this problem, several approaches have been presented for reducing or condensing the data, as the Short Reference Year (SRY) (Hallgreen, 1983), which divides the calendar year into periods. However, in this approach, the selection of the representative days is left to the designer expertise, or they are selected emblematic days like the solstices. More recently, a novel approach based on cluster analysis has been proposed to optimally select individual days able to represent meteorological conditions at a site (Carlos M. Fernández Peruchena et al., 2016). The goal of this contribution is to apply this methodology in a location with high-quality and long term validated measurements, in order to evaluate if selected days can represent the performance of a CSTP plant throughout the complete year.

2. Experimental data and method

2.1. Experimental data

A 12-year series of hourly solar irradiance and meteorological parameters measured in Evora, Portugal by the University of Évora has been selected for this study. Table 1 below presents details about the location of the station, its pyrheliometer and the climatic conditions of the station location, according to the Köppen-Geiger classification (Peel et al., 2007).

Tab. 1: Radiometric station selected for this study.

Location (Country)	Coordinates (º)	Altitude (m)	Pyrheliometer	Period	Climate (Köppen classification)
Évora (Portugal)	38.567 N 7.911 W	290	Kipp&Zonen CHP1	2003-2015	Mediterranean (Csa)

The measured data set covers a 12-years period. The data has been recorded every 5 seconds and averaged every 10 minutes. DNI is measured with a Kipp&Zonen Pyrheliometer (model CHP1), a WMO First Class Pyrheliometer with an associated estimated uncertainty at daily scale of <1%. The pyrheliometer is calibrated every 2 years according to the standard ISO9059:1990.

2.2. Energy yield simulations

A 50 MWe Fresnel type power plant without thermal-energy storage and with a primary mirror area of 193.000 m^2 has been designed for Évora, Portugal. The software TRNSYS V.17 (www.trnsys.com) has been used for the estimation of hourly values of the energy produced by this system. TRNSYS is a validated, time-series simulation program that can simulate the performance of photovoltaic, concentrating solar power, water heating systems, and other renewable energy systems using hourly resource data (Wagner, J. M. and Gilman, P., 2011).

2.3. Day selection

In this work, a TMY series is generated from measured series available at the location. For selecting specific days of this yearly series, the following parameters have been calculated to characterize individual days: daytime mean temperature; daily cumulative DNI value; sum of the product of DNI · cos (SZA), being SZA the solar zenith angle; a wind-dependent variable that is zero if maximum daytime wind speed is lower than 12 m/s, 2 if percentile 90 of daytime wind speed is higher than 12 m/s, and 1 in any other case.

Cluster analysis comprises a wide variety of techniques for delineating natural groups (clusters) in data sets, so that observations within each group are similar to one another with respect to variables or attributes of interest and the groups themselves stand apart from one another. This technique is useful for summary and discovery:

- *Summary* refers to the reduced representation of the full data;
- *Discovery* refers to finding out patterns into the original data series.

In this work, the objective of applying cluster analysis is summarizing the data, by means of selecting a small number of days to represent the complete year.

Finally, the clustering method used in this work is the K-medoids algorithm, which selects points analyzed as the center of the clusters. Also, the gap statistic method (Tibshirani et al., 2001) is used for estimating the number of clusters (groups) in the daily series. The idea behind this technique is to find a benchmark (i.e., a *null distribution*) and to compare the observed value of W (the within-cluster variability) with the expected value under the null distribution (being large deviations from the mean evidence against the null hypothesis).

2.4. Method relevance

The aim of this method, using groups of data as clusters is to enable a faster analysis of a wide range of options when designing a Solar Plant. With today's computer processing capability this might seem outdated. However, engineers that design big plants usually do not have plenty of time to run multiple scenarios and in multiple locations. For that reason, reducing the computing time for one set of data for a specific location is an advantage specially in the pre-design phase. With the cluster analysis the computing effort in time is reduced in a magnitude of 15 to 20 times, thus enabling many other alternatives and configurations to be studied.

3. Results

3.1. Optimal number of days

In fig. 1 it is represented the gap statistics for the TMY at Évora, where 3 number of clusters cases are highlighted: 15 days (blue), 18 days (green) and 22 days (orange). These cases represent the maximum value of the gap functions in 5-clusters intervals (10-15 clusters; 15-20 clusters; 20-25 clusters), and they are candidates to be the optimal number of clusters to represent the TMY.

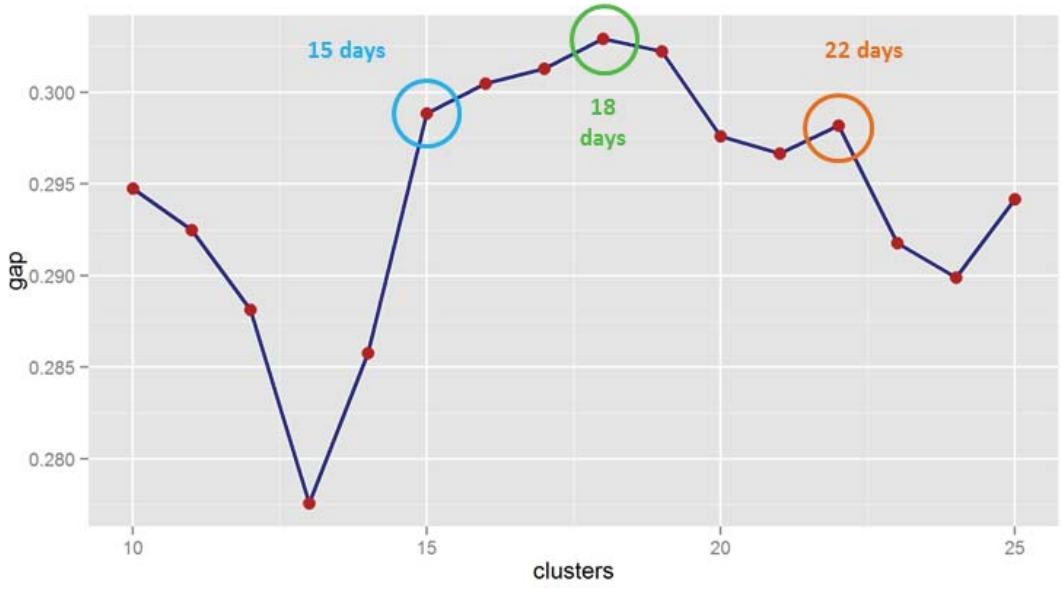

Fig. 1: Gap statistics for day selection

In the analysis carried out, the medoid of each cluster is selected as the most representative days, and also each of the 365 days of the TMY are assigned to one of these clusters. Table 2 shows the 18 selected days selected for representing the TMY at the site (this is expected to be the optimal case, as it reaches the highest Gap value), their DNI value and the number of days represented. This table also shows the maximal and average dissimilarity (max_diss and av_diss, respectively) between the observations in the cluster and the cluster's medoid, as well the *isolation* of the clusters: the maximal dissimilarity between the observations in the cluster and the cluster's medoid, divided by the minimal dissimilarity between the cluster's medoid and the medoid of any other cluster.

Tab. 2: Cluster parameters for the TMY representation

Specific days selected of TMY (1-365)	Daily DNI (kWh/m^2)	Number of days represented	max_diss	av_diss	Isolation
301	1.55	23	2.60	1.56	0.98
2	2.97	28	2.45	1.31	0.93
328	6.23	25	4.00	1.45	1.76
17	4.71	20	6.34	1.88	1.64
8	0.97	15	2.38	1.21	0.68
326	5.81	28	2.64	1.17	1.16
276	3.88	20	2.84	1.54	1.18
60	7.89	19	2.98	1.56	1.09
282	2.46	11	2.70	1.96	0.76

103	10.34	16	3.15	1.92	0.69
86	1.72	7	2.36	1.03	0.98
289	6.76	23	2.91	1.65	1.13
186	9.72	31	2.54	1.38	1.13
287	7.22	17	2.83	1.33	1.10
165	11.34	20	3.14	1.38	1.40
228	4.50	14	3.36	1.97	0.67
237	9.22	26	4.35	1.93	1.24

In fig. 2 it is plotted the selected days, representing its own typical DNI value varying along a 24h period. Clusters are numbered from 1 to 18, and also color-coded. As expected in a Mediterranean climate, most days of summer are represented by clusters 14-18 (characterized by high DNI values as well as long days), and most of winter days are represented by clusters 1-5 (characterized by shorter days and higher DNI variability).

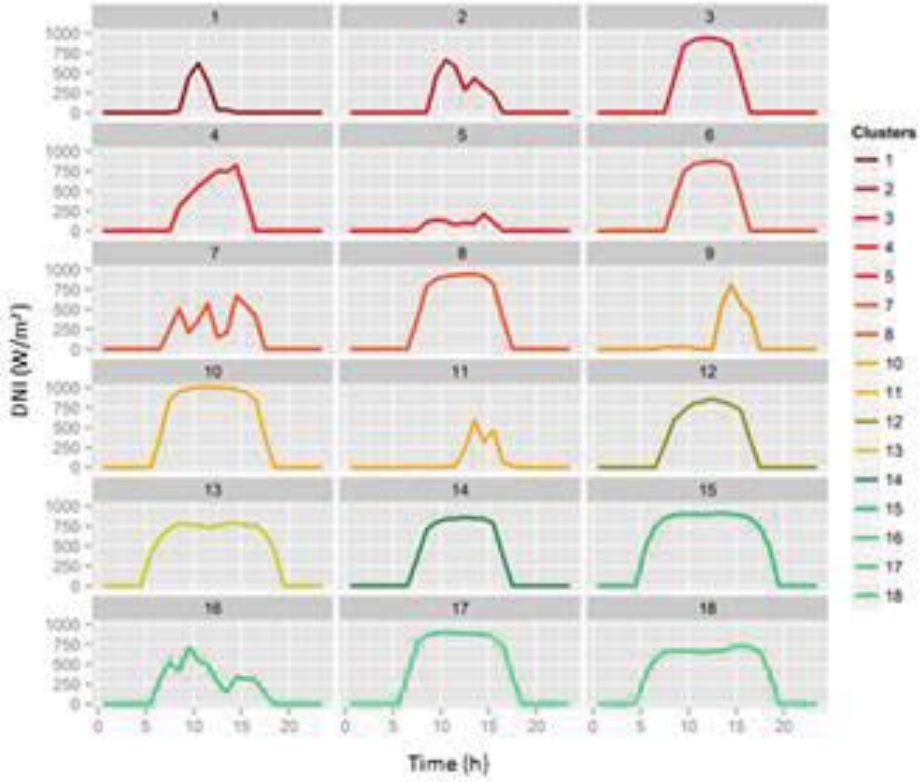

Fig. 2: left, days selected representative of the 18 clusters calculated for the TMY at Évora

This variability across the year can be observed in fig. 3 where which of the 18 typical days are represented throughout the whole year.

From fig. 3, it is clear that from November to February the representation is mainly obtained with clusters 1 to 6, while March, April and October are transition months with clusters 7 to 12 representing most of the period.

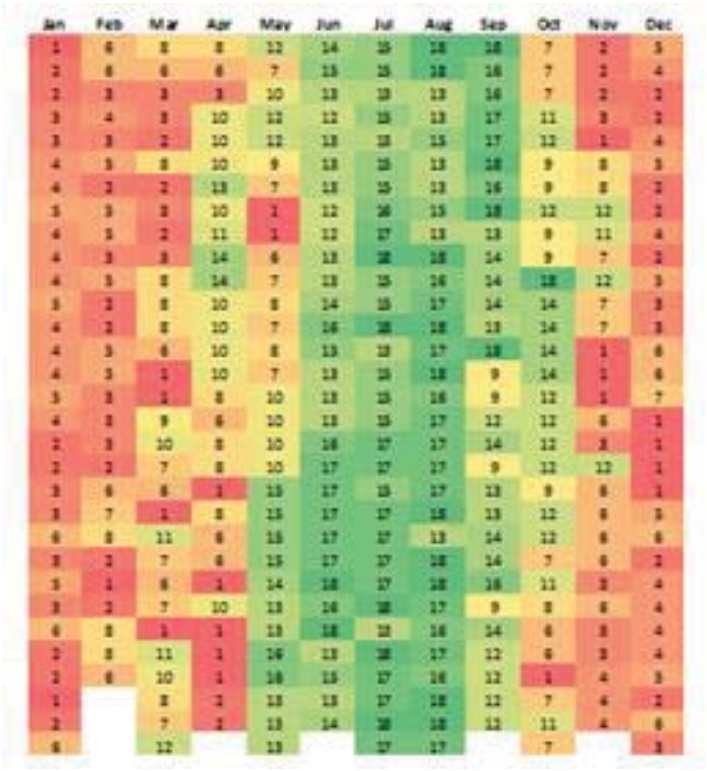

Fig. 3: Days throughout the year (January to December) represented by the selected days (#18 days)

The comparison of the annual energy yield provided by the days selected, multiplied by the number of days represented by each one of the cluster days, has been compared with the solar energy yield of the 365 days of the TMY, and their differences are shown in fig. 4 as a function of the number of clusters selected (from 10 to 183 days). These differences tend to decerase at increasing number of days selected, as expected. Very low differences (<1%) are found even for the selection of few days (15 or less).

Peaks are found in almost the whole range analyzed, as expected as a trend, the amplitude decays with an increasing number of days.

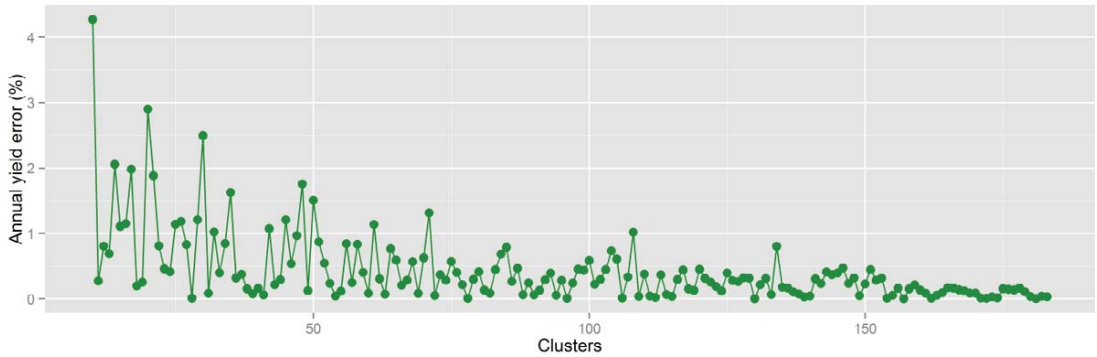

Fig. 4: Difference between annual energy yield calculated with clusters and TMY, as a function of the number of clusters selected

Even if a univocal relation between Gap function and accuracy of annual energy yield cannot be fully established, it has been found a more clear correlation by grouping clusters into intervals. Table 3 shows the optimal number of days selected as a function of the maximum number of days allowed in the cluster analysis, in 5-days intervals. It is shown the difference between TMY and days-selected electric yield, as a function of the maximum number of clusters allowed, showing a clear correlation between Gap function and accuracy in yield estimation.

Tab. 3: Results of cluster analysis as a function of the maximum number of clusters allowed

Maximum number of days allowed for the cluster	15	20	25
Optimal number of days selected	15	18	22
Gap function value	0.2959222	0.2996370	0.2949644
Difference between electric yield production using TMY data and using cluster selected days	1,1%	0,2%	0,8%

4. Conclusions

The methodology presented in this work allows a very significant reduction in the computational effort related to the calculation of a STE plant energy yield by simulating a reduced number of days from a high frequency TMY (90% of computing time can be reduced if 18 days are selected for representing the TMY). These days are the medoids of clusters selected according to gap statistic.

The energy yield produced by these selected days facilitates a fast and accurate, evaluation of the annual energy production of a STE plant. Concurrently, in the optimization phase of a solar plant design, many more configurations can be explored using these 18 days than using the whole TMY production analysis (with the same computing cost / time).

The computational effort of this evaluation depends on the uncertainty allowed: a tradeoff between inaccuracy (which is given at low numbers of clusters selected) and computational effort (which is given at low numbers of clusters) must be carried out in each specific analysis as it was shown for the specific location of Evora, Portugal where a STE research facility has been built, the EMSP (Evora Molten Salt Platform).

5. Acknowledgments

The authors would like to thank to ICT-Uni.Evora (Prof. Paulo Canhoto and Prof. Heitor Reis) for enabling the usage of solar radiation collected data, to project DNI approved by IPES (Portuguese Solar Energy Institute), as well as to the H2020 Program which funded Project PreFlexMS, the trigger for the study presented.

6. References

Eck, M., Hirsch, T., 2007. Dynamics and control of parabolic trough collector loops with direct steam generation. Sol. Energy 81, 268–279. doi:10.1016/j.solener.2006.01.008

Fernández-Peruchena, C.M., Blanco, M., Gastón, M., Bernardos, A., 2015. Increasing the temporal resolution of direct normal solar irradiance series in different climatic zones. Sol. Energy 115, 255–263. doi:10.1016/j.solener.2015.02.017

Hallgreen, L., 1983. Short Reference Year, SRY, in: Palz, W. (Ed.), Solar Radiation Data, Solar Energy R&D in the European Community Series F. Springer Netherlands, pp. 40–48.

Meyer, R., 2010. Recommendations for bankable meteorological site assessments for solar thermal power plants, in: Proceedings of the SolarPACES Symposium. Perpignan, France.

Montes, M.J., Abánades, A., Martínez-Val, J.M., 2009. Performance of a direct steam generation solar thermal power plant for electricity production as a function of the solar multiple. Sol. Energy 83, 679–689. doi:10.1016/j.solener.2008.10.015

Peel, M.C., Finlayson, B.L., McMahon, T.A., 2007. Updated world map of the Köppen-Geiger climate classification. Hydrol Earth Syst Sci 11, 1633–1644. doi:10.5194/hess-11-1633-2007

Peruchena, C.M.F., García-Barberena, J., Guisado, M.V., Gastón, M., 2016. A clustering approach for the analysis of solar energy yields: A case study for concentrating solar thermal power plants, in: AIP Conference Proceedings. Presented at the SOLARPACES 2015: International Conference on Concentrating Solar Power and Chemical Energy Systems, AIP Publishing, p. 70008. doi:10.1063/1.4949155

Peruchena, C.M.F., et al, 2016. A statistical characterization of the long-term solar resource: Towards risk assessment for solar power projects. Sol. Energy 123, 29–39. doi:10.1016/j.solener.2015.10.051

Tibshirani, R., Walther, G., Hastie, T., 2001. Estimating the number of clusters in a data set via the gap statistic. J. R. Stat. Soc. Ser. B Stat. Methodol. 63, 411–423. doi:10.1111/1467-9868.00293

Vignola, F., Grover, C., Lemon, N., McMahan, A., 2012. Building a bankable solar radiation dataset. Sol. Energy, Progress in Solar Energy 3 86, 2218–2229. doi:10.1016/j.solener.2012.05.013

Wagner, J. M., Gilman, P., 2011. Technical Manual for the SAM Physical Trough Model.

Estimation of diffuse component for two locations in Turkey

Abdullah Bugrahan Karaveli[1] and Bulent G. Akinoglu[1,2]

[1] Earth System Science Program, Graduate School of Natural and Applied Sciences/Middle East Technical University, Ankara (Turkey)

[2] Department of Physics, Faculty of Arts and Sciences/Middle East Technical University, Ankara (Turkey)

Abstract

In analyzing the solar energy systems, the first step is the accurate measurements/estimations of the input in the long term: solar irradiation incident on the panels. The measurements are lacking in many places so the estimation procedures should be developed using the measured data of the locations having similar climates and close in latitudes. In most life cycle assessments, monthly averages of daily values are utilized in the form of typical meteorological year or simply with the averages of a year or for a number of consecutive years. Although the beam component of the solar irradiation is usually higher than total of all diffuse components except in highly cloudy and overcast sky conditions, estimation of diffuse components is vital especially to determine the solar irradiation on tilted solar panels. In this study, with the final aim of developing the best procedures to estimate diffuse solar radiation component for all the locations of Turkey, we carried out a preliminary comparison and reached a best procedure of estimation for two locations in Central Anatolia. Our procedure is to compare a model based on a physical formalism developed before with four methods of estimation appeared in the literature, together with the data obtained by Meteonorm Software. As a result, our model has given one of the two best results together with Meteonorm Software when compared to measured values. It is in fact the best one according to the RMSE value.

Keywords: *Total, beam and diffuse solar radiation; solar energy; Turkey; MBE; RMSE*

1. Introduction

By courtesy of being in solar belt (EPIA, 2010), Turkey is a high potent country to utilize solar energy for daily needs of public body, such as heating, cooling, hot water and in particular electricity, *inter alia*. In that vein, there is an opportunity for developing countries like Turkey to meet their needs in more economical, social and environmental way in parallel to the necessities of sustainable development. Even if the current position of Turkey on solar electricity production is still low with 562 MW PV installed power which was just 249 MW in the beginning of the year (TEIAS, 2016), it carries huge potential when compared to global leaders. For instance, while 1 kW PV system installed at the south part of Germany, a region that has got the highest solar potential in the country, is able to produce 1190 kWh electricity annually, it ranges between 1350-1750 kWh in Turkey from north to south (SMS and Fraunhofer, 2015). Considering the leadership role of Germany throughout the development process of solar energy market, this situation in Turkey is an obvious measure of the potential of Turkey.

As for hot water production via solar energy, Turkey's performance is devastating as being world number 3 together with Germany after China and USA with respect to solar water heating collector capacity (REN 21, 2016).

On the other hand, Turkey has got increasing electricity production demand. Current electricity demand which is around 280 TWh is estimated to be 424 TWh by the year 2023 with more than 50% increase rate (DG for Renewable Energy, 2014). Furthermore, Turkey is obliged to condemn the pledges under Paris Agreement a legally binding document ratified in order to tackle with climate change.

Consequently, solar energy usage in various fields has vital importance for the country. Moreover, its sharply decreasing marginal costs and rapidly increased technological development strengthen the use of solar energy against its counterparts. To look more closely at the development on solar technologies and their prices, together with annual reduction of marginal cost of wafer-based silicon PV modules of about 9% since 1990 (Fraunhofer, 2016) it is expected to be declined 59% more till 2025 (IRENA, 2016). Furthermore, the

doi:10.18086/eurosun.2016.09.04 Available at http://proceedings.ises.org

efficiency of them is increased about 5% in the last 10 years (Fraunhofer, 2016).

In this manner, there are two necessities to be known accurately that can be identified by making correct calculations after defining appropriate estimation procedures. The first necessity is to know the solar potential which is directly depended on solar insolation exposure. Second is related to defining the methods/ways to exploit/utilize the potential. In other words, there is a need to make feasible, bankable, technically efficient projects to install solar energy systems for various purposes (Karaveli et al., 2015). In this respect, Karaveli et al. made calculation of monthly mean solar irradiation for horizontal and tilted surface for Konya province Karapinar district which has one of the highest solar potential in the country and owns Energy specialized industrial zone specific to solar energy . Then, solar photovoltaic system designed in an appropriate manner and compared it with nuclear power plant planned to be installed in Turkey. Consequently, this study has lead in showing the appropriate way to define the solar potential and the feasibility of solar energy (Karaveli et al., 2015).

In order to be able to attain these above mentioned two necessities, the most important step is to make accurate estimations of the input of the system with its all components. For solar energy, this input is the solar irradiation falling on tilted surfaces of solar energy systems; mainly its components: beam (direct) and diffuse (scattered) ones.

Of course, the most accurate way to know the solar radiation with its components is long-term measurements of it at each location taken into account. However, this option is not used for a current situation and not possible in a short-run. Moreover, this option may not be economically feasible and physically possible. Therefore, the possibility of using measurements of one location to estimate the irradiation values for another location which has similar coordinate (latitude) and climate features can make it possible to estimate the feasibilities of the applications. Accordingly, by using currently measured long-term solar irradiation values of some locations to attain the best estimation procedures of the solar energy for the other locations, on tilted panels are an important and a possible way to reach feasibilities of the solar systems.

The estimation procedures of solar irradiation incident on tilted surfaces necessitate the calculation of beam and diffuse components of solar irradiation on horizontal surface (Duffie and Beckman, 2006). There are quite a large number of methods developed in the literature as reviewed by (Khorasanizadeh and Mohammadi, 2016). In addition many comparative studies are carried out using the measured data set of a location or at most a region [see for example (Tasdemiroglu and Sever, 1991)]. The results of our preliminary comparisons showed that it is very important to determine the best procedure(s) for Turkey and for different regions of the country, due to the highly complicated nature of the diffuse component. We present here our preliminary results of these comparisons of various models using the data of two locations in Central Anatolia, as a preliminary work. We also compared a model that we developed based on a physical modeling approach that was outlined before by Akinoglu (1993, 2008) and updated by Karaveli and Akinoglu (2016).

We chose a pair of locations to work on this study located in Central Anatolia: Eskisehir (39.78^{o} N) and Ankara (39.95^{o} N). The climates of the two locations are semi-dry continental and typically similar in terms of mean temperatures, rainfall and hot and cold waves spatial distributions (SMS, 2016). The distance between these two locations is 235 km. and altitudes are 792 m and 938 m, respectively. The data is obtained from State Meteorological Service (SMS) of Turkey.

The correlations that we used for comparisons are as follows: The first expression was derived for twelve locations in Central Anatolia by Aras et al. (2006). They concluded that a cubic expression is relatively better than others. Ulgen and Hepbasli conducted similar analysis and proposes another cubic expression and they both depended on monthly average daily bright sunshine hours per day length ratio (n/N) and monthly average daily solar irradiation on horizontal surface divided by monthly average daily extraterrestrial solar irradiation on horizontal surface, that is clearness index (Ulgen and Hepbasli, 2009). Tasdemiroglu and Sever utilized experimental data of mean solar irradiation on horizontal surface and obtained forth order polynomial function for the diffuse ratio with respect to clearness index (Tasdemiroglu and Sever, 1991). In comparisons, we also used the expression obtained by Erbs et al. who utilized hourly pyrheliometer and pyranometer data of US locations and derived clearness index and sunset hour angle depended equation (Erbs et al., 1982, Duffie and Beckman, 2006).

Moreover, one of the most famous databases/methodologies used by some of the commercial software programs which are heavily used for solar system design in Turkey, namely Meteonorm, is also used for comparisons in this study. The aim is to find the accuracy that this software can reach in their performance

calculations of solar energy systems.

Lastly, we obtained linear correlations between monthly average diffuse ratio and monthly average daily fractional bright sunshine hours to estimate the diffuse component of monthly average daily solar irradiation, based on a physical modeling developed by Akinoglu (1993, 2008). In fact, we obtained a linear correlation for one of the locations: Eskisehir, and used this correlation to estimate the diffuse solar irradiation for Ankara.

In the view of above information, this study takes into account all the options to obtain the best estimation method for the diffuse part of solar irradiation. The results will be used in the short term and long term feasibility studies of the solar energy systems to be installed in the mentioned regions of the country.

The data used and exploited in the study provided from State Meteorological Service (SMS) of Turkey is as minute by minute values of total, diffuse solar irradiation and bright sunshine hours. These are the data measured through pyranometers and pyrheliometers in SMS measurement stations in the unit of watts per minute. Then, the measured data taken from the beginning of 2011 till the end of 2015 are analyzed and unreliable data are extracted. Moreover, the unit of the data is converted into MJ m^{-2} d^{-1} as needed for the models used in this study. Finally, the monthly averages of the compiled data are calculated and assigned as the value for monthly mean daily amounts.

In the comparisons, we used Mean Bias Error (MBE) and Root Mean Square Error (RMSE) values for the estimations of each procedure. MBE is a measure of under or over-estimation while RMSE can get high values even if the estimation only for one of the months considerably deviates from its measured value. Therefore, for both error values closer the value to 0 means better the estimation.

2. Solar Radiation Calculations

The study is on the estimation of monthly average daily solar irradiation on horizontal surface. To this aim, we calculated monthly average of daily extraterrestrial solar irradiation on horizontal surface using the equation given in Duffie and Beckman (Duffie and Beckman, 2006). Then, the diffuse component of the solar irradiation reaching the Earth on a horizontal surface after passing through the atmosphere is calculated using the aforementioned models.

These models (equations) are depended on H_0, H, H_d, n and N where H_o symbolizes daily value of the extraterrestrial (outside the atmosphere) irradiation incident on a horizontal surface; H is the estimated daily global solar irradiation; H_d is the daily values of diffuse component; n is daily bright sunshine hours (sunshine duration) and N is day length. The over-bar of the mentioned symbols refers to monthly average values. The models used in comparisons are given in Table 1.

In addition to these equations, to retrieve data from Meteonorm, the software is installed on the desktop. Ankara is selected from the tool bar. The diffuse solar radiation data for Ankara is given in the following screen that is revealed in Figure 1.

Tab. 1: Defined equations to find diffuse component of solar irradiation

Equation	Reference
$\frac{\bar{H}_d}{\bar{H}} = 1.6932 - 8.2262(\frac{\bar{H}}{\bar{H}_0}) + 25.5532(\frac{\bar{H}}{\bar{H}_0})^2 - 37.8070(\frac{\bar{H}}{\bar{H}_0})^3 + 19.8178(\frac{\bar{H}}{\bar{H}_0})^4$	Tasdemiroglu and Sever, 1991
$\frac{\bar{H}_d}{\bar{H}} = 1.7111 - 4.9062\frac{\bar{H}}{\bar{H}_0} + 6.6711\left(\frac{\bar{H}}{\bar{H}_0}\right)^2 - 3.9235\left(\frac{\bar{H}}{\bar{H}_0}\right)^3$ and $\frac{\bar{H}_d}{\bar{H}_0} = 0.2427 - 0.0933\left(\frac{\bar{n}}{\bar{N}}\right) + 0.1846\left(\frac{\bar{n}}{\bar{N}}\right)^2 - 0.2184\left(\frac{\bar{n}}{\bar{N}}\right)^3$	Aras et al., 2006
$\frac{\bar{H}_d}{\bar{H}} = 0.981 - 1.9028(\frac{\bar{H}}{\bar{H}_0}) + 1.9319(\frac{\bar{H}}{\bar{H}_0})^2 - 0.6809(\frac{\bar{H}}{\bar{H}_0})^3$ and $\frac{\bar{H}_d}{\bar{H}_0} = 0.1437 + 0.2151\left(\frac{\bar{n}}{\bar{N}}\right) - 0.1748\left(\frac{\bar{n}}{\bar{N}}\right)^2 + 0.0697\left(\frac{\bar{n}}{\bar{N}}\right)^3$	Ulgen and Hepbasli, 2009
$\frac{\bar{H}_d}{\bar{H}} = 1.391 - 3.560(\frac{\bar{H}}{\bar{H}_0}) + 4.189(\frac{\bar{H}}{\bar{H}_0})^2 - 2.137(\frac{\bar{H}}{\bar{H}_0})^3$	Erbs et al., 1982

From the table revealed in Figure 1, monthly mean daily diffuse solar radiation amount, as needed, is reckoned by dividing irradiation in the second column in the Table with the number of days in the specific month. The results are given in Table 3.

ANKARA TU

Radiation | Temperature | Precipitation | Sunshine duration

Daily global radiation | Daily temperature | Data table

	Gh kWh/m²	Dh kWh/m²	Bn kWh/m²	Ta °C	Td °C	FF m/s
January	52	28	63	-0,5	-3,9	1,9
February	66	37	66	1,5	-3,4	2,2
March	98	58	72	6,2	-1,3	2,7
April	140	66	121	11	2,5	2,5
May	164	72	138	16,1	6,2	2,3
June	192	82	165	20,5	8	2,6
July	201	78	189	24,1	9,2	2,9
August	176	76	153	24,1	9,7	2,7
September	127	64	107	18,5	6,9	2,2
October	89	46	90	12,8	4,6	1,9
November	65	31	91	6,3	1,5	1,6
December	55	28	77	1,3	-1,9	1,8
Year	1422	665	1332	11,8	3,2	2,3

Fig. 1: Meteonorm data for Ankara

3. Linear Equation Derivation

As mentioned in previous parts of this article, the physical formalism derived and applied in this study was developed in Akinoglu (1993 and 2008) and adopted for the diffuse component by Karaveli and Akinoglu (2016). The development of the aforementioned model is launched by the consideration of the instantaneous fractional clear sky period n_i. Then the beam solar irradiation directly reaching the Earth's surface during n_i period, I_B, can be given as:

$$I_B = I_0 \tau n_i \qquad \text{(eq. 1)}$$

where I_0 is the extraterrestrial solar irradiation falling on horizontal surface during that certain time interval and τ is atmospheric transmission coefficient for clear-sky. In the mentioned time interval, there is not only beam but also diffuse part (sky and circumsolar) reaching to the surface that can be expressed as:

$$I_{D1} = I_0 (1-\tau) \beta' n_i \qquad \text{(eq. 2)}$$

where β' is the atmospheric forward scattering coefficient. The time remaining after n_i period is called as cloudy period. This period, as is nature, has diffuse radiation, I_{D2}, that can be expressed as:

$$I_{D2} = I_0 \tau \tau' (1-n_i) \qquad \text{(eq. 3)}$$

where τ' is a transmission coefficient of the clouds.
Then the linear model expression for the global solar irradiation [Akinoglu, 1993, 2008] is attained by adding Eqns. (1) to (3). Moreover, adding Eqns. (2) and (3) results in a linear expression for the diffuse part as:

$$I_D = I_0 (1-\tau) \beta' n_i + I_0 \tau \tau' (1-n_i) \ . \qquad \text{(eq. 4)}$$

We may then write equation (4) for daily integrated and then monthly averaged values of diffuse solar irradiation by assuming that the forms would not change and by replacing the coefficients with their effective monthly counterparts (Akinoglu, 1993, 2008 and Karaveli and Akinoglu, 2016). While structuring this approach, we should also consider that the ratio of monthly average of daily sunshine duration to day-length n/N will replace the fractional time period n_i. Accordingly, I_D and I_0 will be replaced with their monthly average daily values of $\overline{H}_D$ and $\overline{H}_0$. If these replacements are carried out, a linear correlation for the monthly average of daily diffuse irradiation from Eqn. (4) can be reached as:

$$\overline{H}_D / \overline{H}_0 = a_1 + a_2 (\overline{n} / \overline{N}) \qquad \text{(eq. 5)}$$

where $\overline{H}_D$ is monthly average daily diffuse solar irradiation, $\overline{H}_0$ is extraterrestrial solar irradiation, $\overline{n}$ is the monthly average daily bright sunshine hours and $\overline{N}$ is monthly average day length. In this approach, the parameters a_1 and a_2 can be written as:

$$a_1 = \tau_e \tau_e' \quad \text{and} \quad a_2 = \beta_e' (1-\tau_e) - \tau_e \tau_e' \ .$$

The sub-index e stands to indicate that the coefficients are monthly effective counterparts of the coefficients defined before. Accordingly, τ_e and τ_e' are effective monthly parameters of the transmission coefficient of the atmosphere during clear-sky condition and the transmission coefficients of the clouds, respectively, and β_e' is effective monthly forward scattering coefficient of the clear atmosphere.

In this modeling approach, knowing the value of the global and diffuse component for a location and by assigning a value to β_e' one can reach the monthly values of a_1 and a_2. Thus, in the present study we also used the calculated monthly values of a_1 and a_2 for one location to estimate the diffuse component of solar irradiation of the other location.

In fact, linear equation for the monthly-mean daily total solar irradiation, and monthly average daily fractional bright sunshine hours can also be obtained using this physical modeling approach as presented in ref. Akinoglu, 1993.

Applying above mentioned procedure and using measured SMS values for Eskisehir, we have found the constants specific to Eskisehir to calculate diffuse solar irradiation falling on a horizontal surface, namely a_1, and a_2 as presented in Table 2.

Tab. 2: Monthly specific constants for linear equations

Months	Constants	
	a_1	a_2
January	0.41	-0.26
February	0.28	-0.13
March	0.32	-0.18
April	0.33	-0.19
May	0.35	-0.21
June	0.28	-0.15
July	0.37	-0.24
August	0.33	-0.19
September	0.38	-0.24
October	0.39	-0.22
November	0.37	-0.21
December	0.28	-0.10

Then by using constants given in Table 3, we calculate diffuse solar radiation of Ankara as given in Table 3. Table 2 also gives the estimated values by the models together with the measured SMS data.

4. Results

The diffuse solar radiation values for Ankara calculated by using all the options to be compared are compiled in Table 3. So as to ease the comprehension of Table 3, models are numbered. Model 1 is reserved for the first equation coming from reference Aras et al. (2006), while Model 2 is the second equation of the same reference. Model 3 is the result of the first equation coming from reference Ulgen and Hepbasli (2009), while Model 4 is the second equation of the same reference. Model 5 and 6 constitutes the methodology of the references Tasdemiroglu and Sever (1991) and Erbs et al. (1982), respectively. Model 7 is reserved for Meteonorm values and finally Model 8 for the results coming from the procedure developed and used in this study.

Tab. 3: Diffuse solar radiation in MJ m^{-2} reckoned through all the models

Months	Models								Measured
	1	2	3	4	5	6	7	8	
January	3.45	3.47	2.88	2.87	3.43	3.05	3.25	5.24	3.93
February	4.53	4.54	4.31	4.23	4.96	4.05	4.76	4.73	5.68
March	5.94	6.06	5.92	5.68	6.59	5.88	6.74	6.79	8.14
April	7.29	7.49	7.65	7.43	8.13	7.33	7.92	8.21	9.52
May	8.20	8.57	8.90	8.54	9.15	8.33	8.36	10.06	11.17
June	7.85	8.55	9.82	9.43	8.76	8.37	9.84	7.73	9.02
July	6.64	7.76	9.99	9.50	7.60	7.62	9.06	8.13	9.32
August	5.88	6.79	9.02	8.62	6.77	6.80	8.83	7.02	8.15
September	5.07	5.58	7.31	7.07	5.74	5.71	7.68	6.22	7.13
October	4.60	4.72	5.10	5.02	5.13	4.70	5.34	5.99	5.70
November	3.52	3.54	3.60	3.56	3.91	3.18	3.72	4.41	4.89
December	3.12	3.11	2.72	2.71	3.24	2.77	3.25	3.41	3.98

Then, the results of the comparisons with respect to MBE and RMSE statistical comparison methods are tabulated in Table 4.

Tab. 4: The results of the comparisons for diffuse solar radiation values

Option	MBE	RMSE	Reference
1	-1.71	1.87	Aras et al., 2006
2	-1.37	1.51	Aras et al., 2006
3	-0.78	1.36	Ulgen and Hepbasli., 2009
4	-1.00	1.44	Ulgen and Hepbasli., 2009
5	-1.10	1.22	Tasdemiroglu and Sever., 1991
6	-1.57	1.68	Erbs et al., 1982
7	-0.66	1.20	Meteonorm value
8	-0.72	**1.05**	Procedure derived in this study

5. Outcomes and Discussions

On the way to structure a formalism to determine specific equations for Turkey, the preliminary steps are carried out in this study by identifying equations for diffuse solar irradiation calculations for Eskisehir and estimating the diffuse component for Ankara by utilizing obtained monthly coefficients a_1 and a_2 for Eskisehir. Then, its accuracy is examined by comparing its results with other options in order to get estimations with the least error values.

Checking the results of the comparisons tabulated in Table 4, it can be clearly observed that the procedure used in this study is one of the two best methods. In fact, pursuant to RMSE comparison the procedure derived and used in this study is the best one. The larger value of RMSE for Meteonorm is due to quite high deviation of its estimation for the month May with the measurement as can be seen from Table 3.

The rationale behind this result can be identified with following reasons: The two previous methods (Aras et al., 2006 and Ulgen and Hepbasli, 2009) proposed for the estimation of diffuse irradiation was not derived using measured data of diffuse irradiation. And, the method proposed by Erbs et al. was derived using hourly pyrheliometer and pyranometer data from four U.S. locations and therefore, its lesser accuracy for locations in Turkey is reasonable. Although the model proposed by Tasdemiroglu and Sever was derived from the measured data of five different locations from various climates in Turkey, it is not better than the procedure explained and used in this study. This is because the equation of Tasdemiroglu and Sever, using regression analysis, obtained one equation that fits all the months however the linear equation derived in this study provides an opportunity to assign month-specific correlations.

Therefore, we concluded that better results we obtained by the procedure we used are reasonable and may be the procedure we should choose at the end. The results of Meteonorm Software are also good for diffuse values but our observations showed that global solar irradiation values of Meteonorm considerably deviate from the measured values. Nevertheless, some further analysis should be carried out to reach concrete conclusions.

As a result, our formalism has given one of the two best results together with Meteonorm Software when compared to measured values. It is in fact the best one according to the RMSE comparison. By sticking to the method derived in this study if this study is applied to all regions/locations/provinces in Turkey, the most accurate total and diffuse solar radiation results can be gathered/acquired for all over the Turkey. This paves the way for us to see the exact potential and enables to define the most feasible ways to utilize solar radiation.

Our further prospects are first to extend the present analysis to different locations covering all the climates/regions of Turkey to reach the best procedure(s) to be used in estimation of diffuse component of solar irradiation. Secondly, we will use these procedures to estimate the solar irradiation on tilted panels and evaluate the long term performances of solar energy systems.

6. References

Akinoglu,B.G., 1993. A physical formalism for the modified angstrom equation to estimate solar radiation. Tr. J. of Physics. 17, 345-55.

Akinoglu B.G. Chapter 5: Recent advances in the relations between bright sunshine hours and solar irradiation. In: Badescu V., editor. 2008. Modeling solar radiation at the earth surface. Springer Verlag Berlin Heidelberg; p. 115-143.

Aras, H., Balli, O., Hepbasli, A., 2006. Estimating the horizontal diffuse solar radiation over the Central Anatolia Region of Turkey. Energy Conversion and Management. 47: 2240-49

DG for Renewable Energy (former EIE), 2014. Turkey National Renewable Energy Action Plan (Türkiye Ulusal Yenilenebilir Enerji Eylem Planı) (in Turkish). Avaliable in: http://www.eie.gov.tr/duyurular_haberler/document/Turkiye_Ulusal_Yenilenebilir_Enerji_Eylem_Plani.PDF. (Last Accessed on: 26/08/2016)

Duffie, J.A., Beckman, W.A., 2006. Solar engineering of thermal processes, third ed. New York: John Wiley and Sons.

Erbs, D.G., Klein. S.A., Duffie. J.A., 1982. Estimation of the diffuse radiation fraction for hourly, daily and monthly-average global radiation. Solar Energy. 28(4): 293-302

Fraunhofer ISE, 2015. Current and Future Cost of Photovoltaics. Available in: http://www.fvee.de/fileadmin/publikationen/weitere_publikationen/15_AgoraEnergiewende-ISE_Current_and_Future_Cost_of_PV.pdf. (Last Accessed on: 26/08/2016)

Fraunhofer ISE, 2016. Photovoltaics Report. Avaliable in: https://www.ise.fraunhofer.de/de/downloads/pdf-files/aktuelles/photovoltaics-report-in-englischer-sprache.pdf. (Last Accessed on: 26/08/2016)

Karaveli, A.B, Soytas. U, Akinoglu, B.G., 2015. Comparison of large scale solar PV (photovoltaic) and nuclear power plant investments in an emerging market. Energy. 84:656-65

Karaveli, A.B, Akinoglu, B.G., 2016, Comparison of quadratic and linear models on the estimation of diffuse solar radiation for location in Turkey, Proc. Of SEEP 2016: 9th Int. Conf. On Sustaianble Energy and Environmental Protection

Khorasanizadeh, H., Mohammadi, K., 2016. Diffuse solar radiation on horizontal surface: reviewing and categorising emprical models. Renewable and Sustainable Energy Reviews. 43: 338-62

IRENA, 2016. The power to change: Solar and Wind Cost Reduction Potantial to 2025. Avaliable in: http://www.irena.org/DocumentDownloads/Publications/IRENA_Power_to_Change_2016.pdf. (Last Accessed on : 26/08/2016)

REN 21, 2016. Renewables 2016 Global Status Report, Key Findings 2016. Avaliable in: http://www.ren21.net/wp-content/uploads/2016/06/GSR_2016_KeyFindings1.pdf. (Last Accessed on: 26/08/2016)

SunPowerEurope (former EPIA), 2010. Unlocking the sunbelt potantial of photovoltaics. Avaliable in: http://www.mesia.com/wp-content/uploads/2012/08/EPIA-Unlocking_the_Sunbelt_Potential-of-PV.pdf (Last Accessed on : 26/08/2016)

State Meteorological Service, 2015. Official Statistics Reports (in Turkish) Avaliable in: mgm.gov.tr/veridegerlendirme/il-ve-ilceler-istatistik.aspx?k=C (Last Accessed on: 07 04 2016)

State Meteorological Service (SMS), Official web-site, Avaliable in: http://www.mgm.gov.tr/iklim/iklim-siniflandirmalari.aspx. (Last Accessed on: 01/09/2016)

The Official Web-Site Turkish Electricity Transmission Company (TEIAS), Avaliable in: www.teias.gov.tr/yukdagitim/kuruluguc.xls (Last Accessed on: 26/08/2016)

Tasdemiroglu, E., Sever, R., 1991. Estimation of monthly average daily, horizontal, diffuse radiation in Turkey. Energy. 16(4):787-90

Ulgen, K., Hepbasli, A., 2009. Diffuse solar radiation estimation models for Turkey's big cities. Energy Conversion and Management. 50(1), 149-56

Conference Proceedings

EuroSun 2016
Palma de Mallorca (Spain), 11 - 14 October 2016

COMPARISON OF THE FUTURE RESIDUAL LOAD IN FIFTEEN COUNTRIES AND REQUIREMENTS TO GRID-SUPPORTIVE BUILDING OPERATION

Konstantin Klein[1], Sven Killinger[1], David Fischer[1], Christoph Streuling[1], Doreen Kalz[1], Jaume Salom[2], Eduard Cubi[3]

[1] Fraunhofer Institute for Solar Energy Systems ISE, Heidenhofstr. 2, 79110 Freiburg, Germany

[2] IREC - Catalonia Institute for Energy Research, Jardins de les Dones de Negre 1, 08930 Sant Adrià de Besòs (Barcelona), Spain

[3] University of Calgary, 2500 University Dr NW, Calgary, Canada

Abstract

Many countries in the world plan to increase their share of wind and solar power. In order to efficiently utilize large amounts intermittent renewable power, flexible consumers such as buildings with heat pumps and chillers may play a crucial role. However, it is not clear how heat pumps and chillers should be operated in order to make the best use of the volatile renewable energy. For this purpose, the residual loads of 13 European countries, Great Britain, and Alberta in the year 2030 were simulated and analyzed. The term "residual load" refers to the electricity demand that is not covered with intermittent renewable systems and that, therefore, must be met by dispatchable electricity generation units. It was calculated as the difference of the wind and PV generation simulated as part of this study, and the electric load of 2011.

The results show a high relative variability in the residual load in almost all analyzed countries. In winter, the lowest residual loads (i.e. the most favorable times for electricity consumption) occur either around noon (particularly in the countries with the highest amount of wind and solar power), or at night. In summer, the residual loads are usually lowest around noon, which coincides well with the typical cooling load profile of a building. PV-dominated countries show stronger daily variations in the residual load, which can be managed even with relatively small storage capacities as typically found in buildings. In contrast, in wind-dominated countries, the residual load fluctuates on longer time scales, which requires larger storages.

Keywords: *energy system, residual load, energy scenario, demand response, heat pumps*

1. Introduction

In an effort to reduce the emissions of greenhouse gases and combat climate change, intermittent renewable energy sources such as wind and photovoltaics (PV) are gaining in importance in many countries of Europe and throughout the world. A large share of intermittent renewable energy in the electricity mix presents serious challenges to power systems, as load and generation must match at any time. However, the generation of intermittent renewables depends on the current weather conditions and, unlike in conventional plants, cannot be dispatched and controlled at will.

In order to promote an efficient integration of a large share of intermittent renewables into the electric energy system, a part of the electric consumers can be made flexible such that their consumption follows the renewable generation. This concept is known as 'demand response'. Demand response has been identified by (IEA, 2003) as a viable alternative to traditional supply side remedies and the most cost effective solution to integrate large amounts of renewable in the energy mix.

doi:10.18086/eurosun.2016.09.07 Available at http://proceedings.ises.org

Presently, many international research activities (e.g. as part of IEA EBC Annex 67) study how buildings can be used for demand response purposes by implementing special control strategies for heat pumps, chillers, CHP units and other technical systems in order to support the electric energy system.

Efforts in the recent years have been made to understand the interaction between buildings and grid, particularly with buildings that incorporates on-site renewable energy systems. Thus Salom et al. (2014) analyzed several indicators to study grid interaction of prosumer buildings, particularly Net Zero Energy Buildings and Cubí et al. (2015) proposed a method to incorporate GHG emissions intensity changes due to grid variability into building environmental assessment with the objective to encourage building systems that reduce electricity use during peak periods. Several solutions have already been investigated how buildings can be providers of flexibility in the grid and demand response agents. Hedegaard et al. (2012) studied the potential of individual heat pumps, using heat accumulation tanks or passive heat storage in the construction, for increasing wind power utilisation and providing cost-effective fuel savings in the Danish energy system. Results show that by displacing less efficient heating technologies and increasing electricity demand, the installation of heat pumps alone can contribute to the integration of wind power, providing significant reductions in excess electricity production and fuel consumption.

However, the load profiles that ideal flexible buildings should follow are unique for each country, because each country or region has a different combination of amount of wind and solar power to be integrated in the energy system, electric load profile, as well as weather conditions. Furthermore, the amount of energy that can be stored and shifted by buildings depends on the dynamics of the thermal load, which is influenced by the ambient temperature and irradiation and thus changes with the geographical location. It is thus relevant to analyze and compare the availability of renewable energy generation as well as thermal demand and deduce requirements to grid-friendly heating and cooling strategies in buildings for each location.

In the current paper, 15 geographies (more accurately: 13 European countries, Great Britain (i.e. UK sans Northern Ireland, which is part of the Irish power grid), as well as the Canadian province of Alberta, which is similar in population to the smaller European countries), are compared in terms of the projected residual load in the year 2030. The residual load is here defined as the electric load minus the generation of intermittent renewable plants (wind and PV). Therefore, it is the electric power that needs to be provided by conventional dispatchable plants in order to balance generation and demand, and can be used as an indication of the relative demand for conventionally-produced electricity.

2. Methodology

The methodological procedure and structure of this paper is illustrated in Fig. 1.

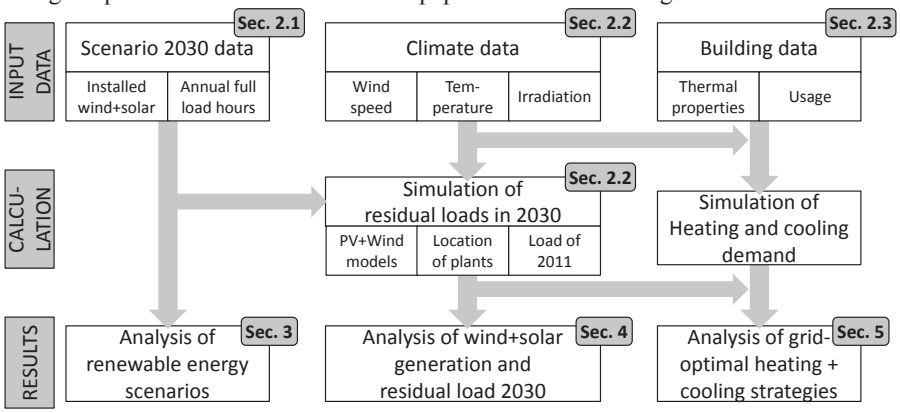

Fig. 1: Process flow, data and models used for this study.

The assumed scenario data are introduced in sec. 2.1, the climate data and models used for the simulation of renewable wind and PV generation in 2030 and calculation of the residual load are discussed in sec. 2.2. Building data and assumptions used for the simulation of thermal demand are given in sec. 2.3. The evaluation is done in three steps: First, the assumed energy systems of 2030 in the individual countries are characterized in terms of the installed capacity of solar and wind plants, as well as the share of renewable

energy generation in the energy mix (sec. 3). Following this, the residual loads for the year 2030 are analyzed in terms of their daily and seasonal characteristic (sec. 4). Finally, requirements to grid-supportive heat pump operation (in heating mode and in cooling mode) in the respective countries are deduced (sec. 5)

2.1 Scenario data for wind and PV energy in 2030

The assumed installed capacities of wind and PV plants in 2030 are mostly based on (Agora, 2016). For nearly all of the countries considered as part of the current paper, the assumed values from said study match (closely, if not exactly) with the "Vision 3" assumptions of (ENTSO-E, 2014). Some differing figures were used for the following countries. The complete data are given in Table 1 in the Appendix.

- For Germany installed capacities of 73.5 GW wind power and 66.3 GW PV power in 2030 were chosen according to the latest Grid Development Plan (Bundesnetzagentur, 2016; scen. B2030).
- For Denmark, there was a big mismatch between the assumed solar generation capacity in (Agora 2016) and (ENTSO-E, 2014). After consultation with Danish researchers which are familiar with the latest status in Danish energy policies, a third source was chosen (Energienet.tk, 2016).
- For Greece, assumptions from (ENTSO-E, 2014) were used as the country was not included in (Agora, 2016).
- For Alberta, a wind generation capacity of 5.5 GW was assumed in accordance with (Canadian Wind Energy Association, 2016). The province neither has nor plans to acquire significant amounts of solar generation power.

2.2 Simulation of wind and PV generation

The renewable energy generation is simulated using historic weather data of the numeric weather model COSMO-EU, run by the German Weather Service (DWD). COSMO-EU has a high spatial (average distance 7 km) and temporal (hourly) resolution and predicts the area of Europe. The meteorological values of irradiance, wind speed and temperature are allocated to a NUTS3 level, which covers different national counties. The processed weather data forms the basis of a PV and wind turbine power production estimation by additionally including their technical characteristics. In the case of PV, the simulation differs between azimuth and inclination angles as well as installation and module types. To represent the wide variety of wind turbines in reality, different power curves and hub heights are used and result in 61 individual specifications. Furthermore the roughness length of the ground is used to transform the wind speed to the individual hub height. The simulation procedure has already been employed with the COSMO-DE model on a national scale by (Killinger et al. 2015).

In order to simulate the total renewable energy generation of a country, it is assumed that the total installed capacity is evenly distributed over the NUTS3 regions, meaning that the regions are weighted by their area. The installed capacities of wind and PV plants assumed according to sec. 2.1.

Figure 2, left and right, show the simulated full load hours of wind and PV power in the examined European countries, respectively. Although these values are further aggregated and processed in order to derive the residual load within a country, the figures show clearly the large fluctuation within Europe. The full load hours of PV range between 700 in the North and 1489 in the South. In terms of wind power, this variability between the NUTS3 regions is even increased and differs between 174 and 4080 full load hours per year with the best locations close to the sea in the northern parts of Europe.

As becomes evident from Fig 2, the annual full load hours of wind and PV plants are highly inhomogeneous even within the respective countries. Since it is not known how the future installed capacity of wind and PV plants will be allocated to the individual NUTS3 areas, the following assumptions are made: First, it is assumed that the renewable generation units are distributed homogeneously throughout the country (i.e. proportional to the size of the NUTS 3 area).

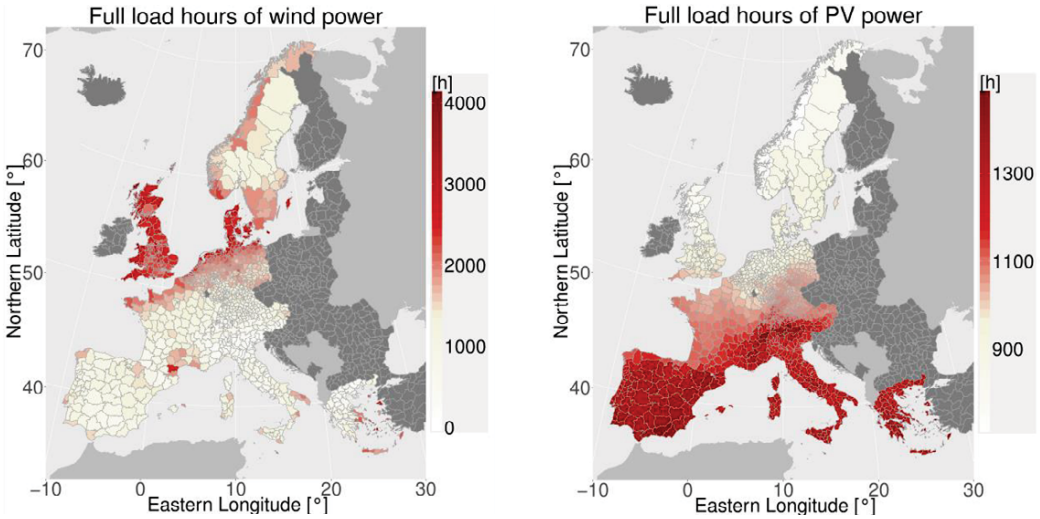

Fig. 2: Full load hours on NUTS3-level of PV (left) and wind power (right) based on the numeric weather model COSMO-EU and a power simulation with different technical specifications.

This procedure will in tendency underestimate the wind and PV yield potential, because in reality, the locations with the best conditions (i.e. most sunshine hours, most steady wind) will be preferred. In order to account for this, the generation curve is in a second step corrected by a factor such that the full load hours of wind and PV plants match those assumed by the national renewable energy plants of 2020 (European Commission, 2008).

For the load, data of the year 2011 from the European Network of Transmission System Operators for Electricity (ENTSO-E, 2016) are used, assuming that the oppositional effects of economic growth and advances in energy efficiency will lead to a similar electricity demand in 2030 as today. The ENTSO-E load data are corrected by a factor such that the official electricity consumption according to Eurostat is matched. For Alberta, which is not contained in ENTSO-E, the load data are obtained from the Alberta Electric System Operator (AESO, 2016).

2.2 Simulation of heating and cooling demand for an office building in each country

In order to analyze how a buildings should be heated or cooled in order to promote the integration intermittent renewable energy, the thermal energy demand must be known. Evidently, the heating and cooling demand differs between the studied countries depending on the ambient temperature and irradiation.

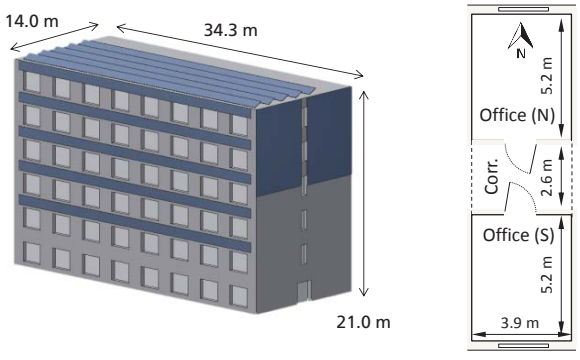

a) b)

	value	unit
U-value walls	0.24	W/m2·K
U-value baseplate	0.3	W/m2·K
U-value roof	0.2	W/m2·K
U-value window	1.0	W/m2·K
g-value window	0.58	(-)
shading factor	0.4	(-)

c)

Fig. 3: Bulding model used for determination of thermal demand in each country. a) outside view of the building, b) geometry of the internal space usage, c) thermal properties of the building

The heating and cooling demand in the considered geographies is quantified using a simple single-zone model of a generic office building with a useful area of approximately 2430 m^2, which was described in

(Klein et al, 2015). It is assumed that the building is composed of two-person offices on the Northern and Southern façade with a connecting corridor in between. The building is modeled as a resistor-capacitor network in compliance with the ISO 13790 modeling standard. The insulation standard is based on the German building code EnEV 2014. The assumptions for usage (occupancy on weekdays from 7 a.m. to 6 p.m., six full-occupancy hours per day), the control of the external shading devices (activated above 200 W/m^2 irradiation onto the façade, deactivated below 150 W/m^2), the heat gains by human occupancy and appliances (100 W/pers. and 7 W/m^2, respectively), as well as the mechanical ventilation (30 m^3/hr·pers. during occupancy, heat recovery factor 0.75) are based on the DIN-V 18599 standard (DIN-V 18599, 2011). The interior temperature of the building is controlled using an ideal heater, such that the interior temperature does not fall below 20°C in heating operation and does not exceed 26°C in cooling operation. If the interior temperature assumes a value between these two limits (e.g. in the intermediate periods, spring and autumn), the building is neither heated nor cooled.

3. Characteristics of energy systems in 2030

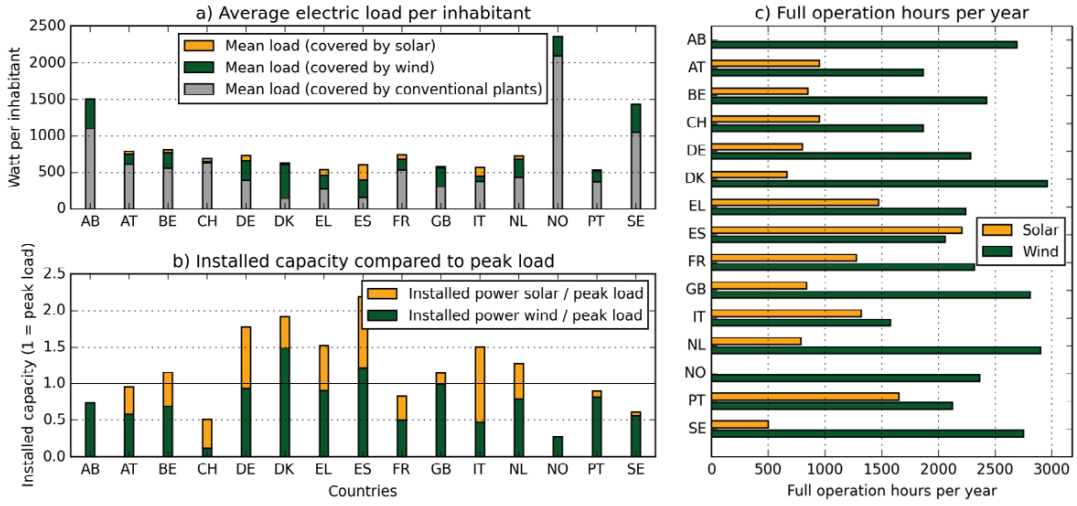

Fig. 4: Characteristics of the energy systems under evaluation. a) Mean electric load and share of solar and wind power in energy mix. b) installed power of solar and wind plants compared to peak load, c) annual full operation hours of solar and wind plants (from (European Commission, 2008)).

Fig. 4 a) shows the average electric power used by each inhabitant, which can be interpreted as an indication of how much a society relies on electricity. A glossary of the country codes is provided in Table 1 in the appendix. It becomes evident that Norway has the highest per capita electricity load, followed by Sweden and Alberta. The reasons for this are on the one hand the electricity-intensive heavy industries (notably the steel and aluminum production in Norway and Sweden, oil and gas industries in Alberta), and on the other hand the high share of electricity-based heating. Most other countries have a significantly lower mean load per inhabitant in the order of 500-700 W/person because they rely more on fossil fuels. Fig 4 a) also illustrates that Denmark and Spain are the countries with the highest share of intermittent renewable electricity, followed by Germany, Great Britain, the Netherlands and Sweden. Norway has a relatively large share of conventional electricity, however, is shall be noted that the renewable, but non-intermittent hydroelectric power accounts for nearly all of the conventional generation.

Fig 4 b) indicates the installed capacity of wind and solar plants in comparison to the peak load (determined here as the 98th percentile of the electric load). Interestingly, 10 out of the 15 countries have installed capacities close to or larger than the peak load. In Denmark, Spain and Germany, the installed wind power alone exceeds the peak load, closely followed by Great Britain and Greece.

In all countries except Spain, wind power provides more full operation hours per year than solar power, which is why it produces more electricity in proportion to the installed capacity than solar power. That said, the number of full load hours of both solar and wind varies greatly between the considered countries. The

countries along the North Sea reach close to 3000 full load hours per year, whereas Italy reaches just over half that number. Sweden gets around 500 full load hours for solar plants, while Spain, Portugal and Greece get nearly three times as many. Spain's exceptionally high solar full load hours are partly due to the fact that Spain plans to build concentrated solar power plants with storages which operate during part of the night.

4. Wind and solar generation and residual load in 2030 in 15 countries

4.1 Wind and PV generation in 2030

The aggregated daily profiles of the electric load are given in Fig. 5. The daily aggregation has been performed for the sample months January, April, July and October illustrating seasonal variations: the generation curve for January is most representative of the heating season, while July is most representative of the cooling season. April and October represent the intermediate seasons, spring and autumn.

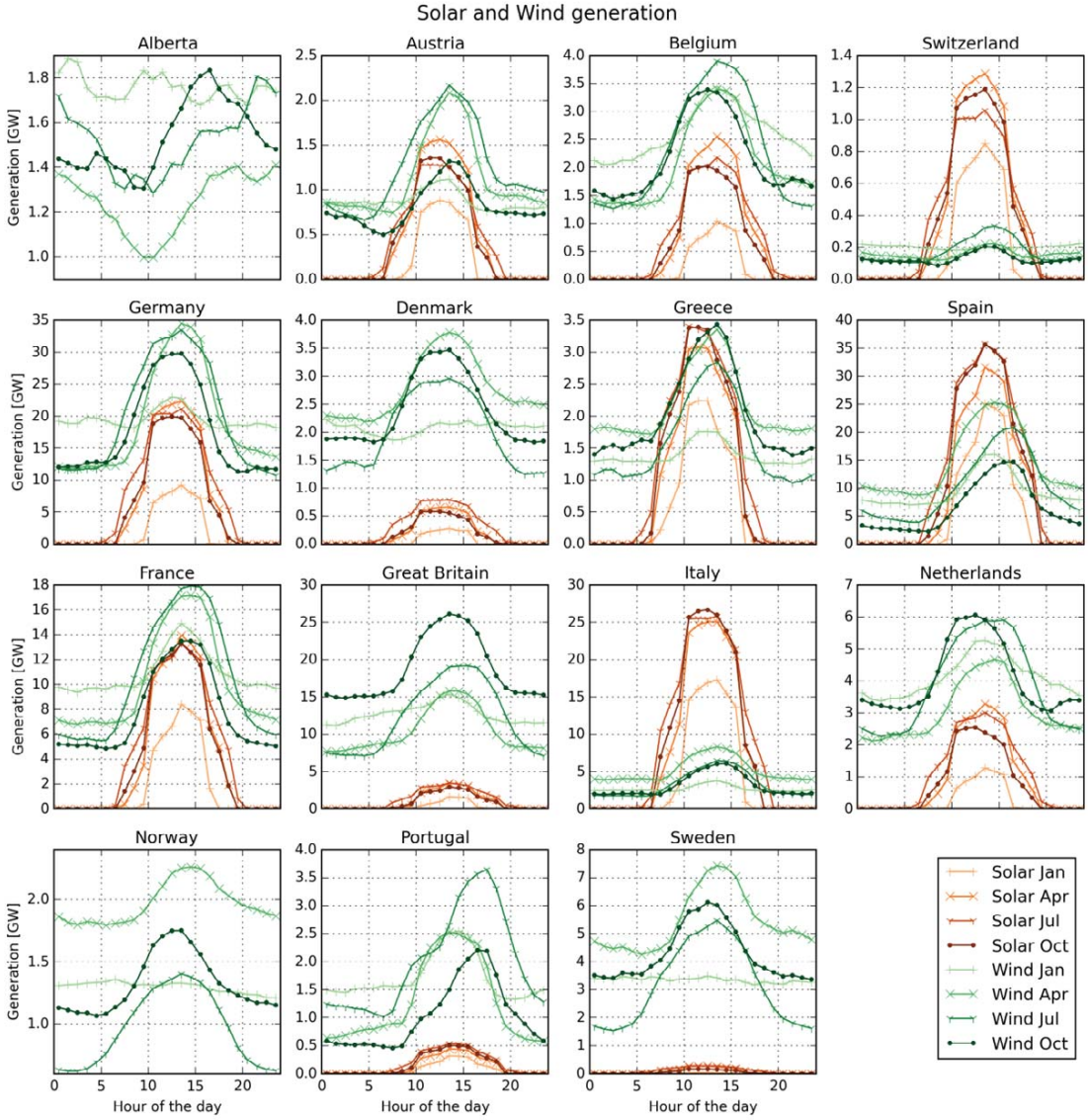

Fig. 5: Aggregated daily profiles of solar and wind generation 2030 for the months January, April, July and October.

As expected, solar generation peaks around noon and is highest in quantity in July, with April and October close behind. The Solar generation in January typically amounts to 50-70% of the generation in July. The time delay between the solar noons of Austria and Portugal due to their different longitudes is visible in the solar generation peaks. Note that Alberta and Norway have no solar plants and thus no generation.

Wind generation also peaks in the day and thus shows a high coincidence with solar generation, although a base generation usually occurs throughout the night. The daily generation peak is more pronounced in the summer than in the winter due to the larger share of solar irradiation in summer. Wind power seems to be partly overestimated during day in the summer. The explanation can be found in the methodology itself for two reasons. The wind speed is provided by COSMO-EU for a height of 10m, which is interpolated to the hub height by only including the roughness length of the ground. Nightly inversions in summer will strongly affect this ground layer and lead to almost no wind, although in reality there is significant wind potential close to hub height. Furthermore the stability of the atmosphere is unknown, but influences the growth of the wind speed with an increasing height. Unstable atmospherical conditions, which are likely to occur in the summer, will lead to an overestimation of the wind speed at hub height and the generated power as well (Focken and Heinemann, 2003).

4.2 Electric load

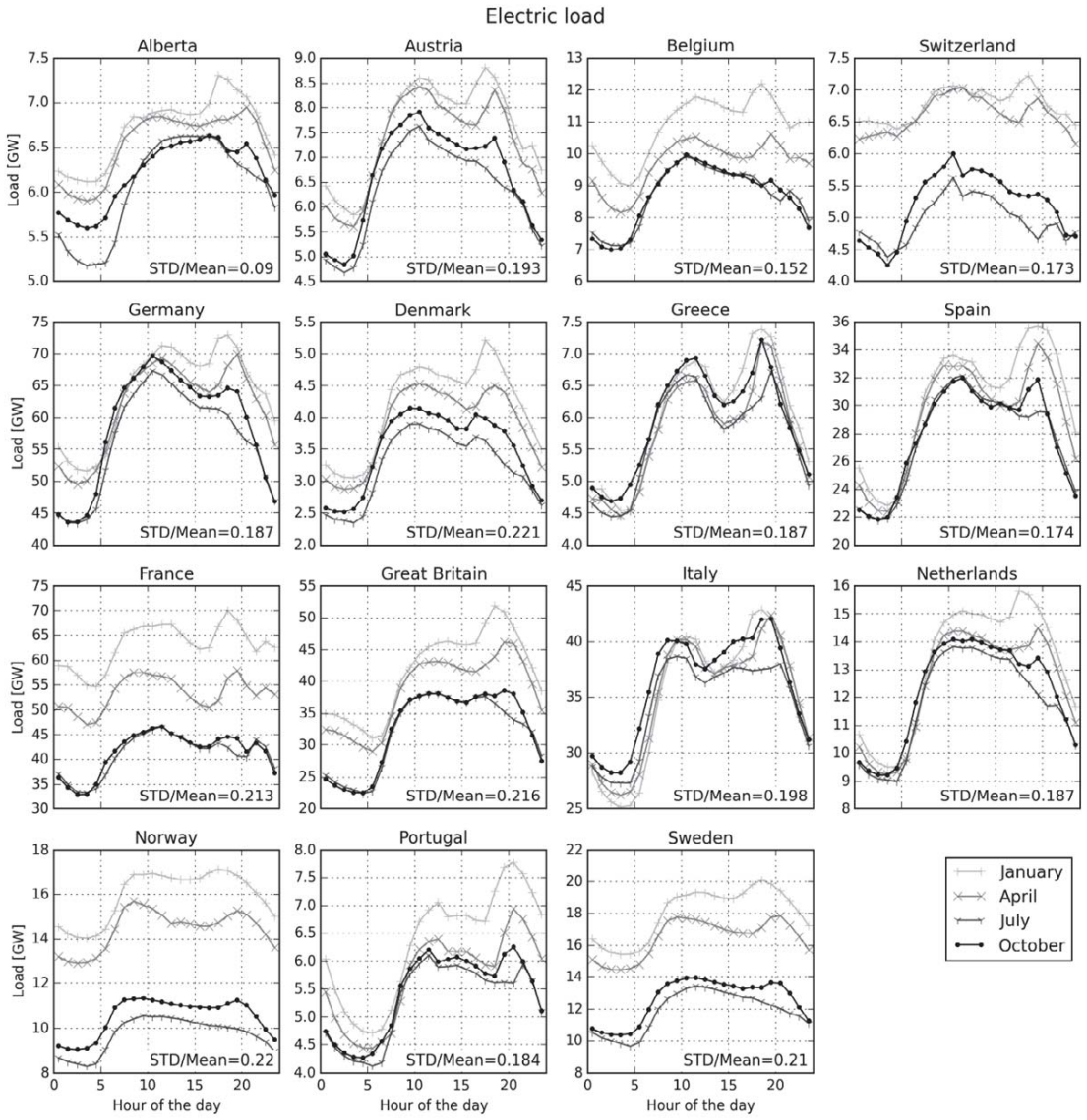

Fig. 6: Aggregated daily profiles of the electric load in 2011 for the months January, April, July and October.

The aggregated daily profiles of the electric load of 2011 are given in Fig. 6 for the same sample months as previously. The load of 2011 is used for the calculation of the residual load of 2030. In all considered countries, the electric load is significantly higher during the day than in the night. Typically, two demand peaks occur in the morning and in the evening. In some countries (Norway, Sweden, Switzerland, France,

Belgium) a notable seasonal difference in the electric load is observed, which is mainly attributable to a high share of electricity-based space heating using heat pumps or direct-electric heaters and a larger lighting demand due to longer nights in winter, while other countries (Greece, Italy) have a nearly identical load profile in the evaluated months. The relative fluctuation of the load, quantified here by the standard deviation (STD) of the load in relation to its mean value, assumes relatively similar values between 0.09 (Alberta) and 0.22 (Denmark, Norway). In absence of significant renewable energy capacities in a traditional energy system, the load is equal to the residual load. The relative fluctuation of the load is thus similar to the level of variability that most energy systems (and markets) were designed to deal with.

4.3 Residual load

The daily curve of the projected residual load 2030 for the four sample months is given in Fig. 7.

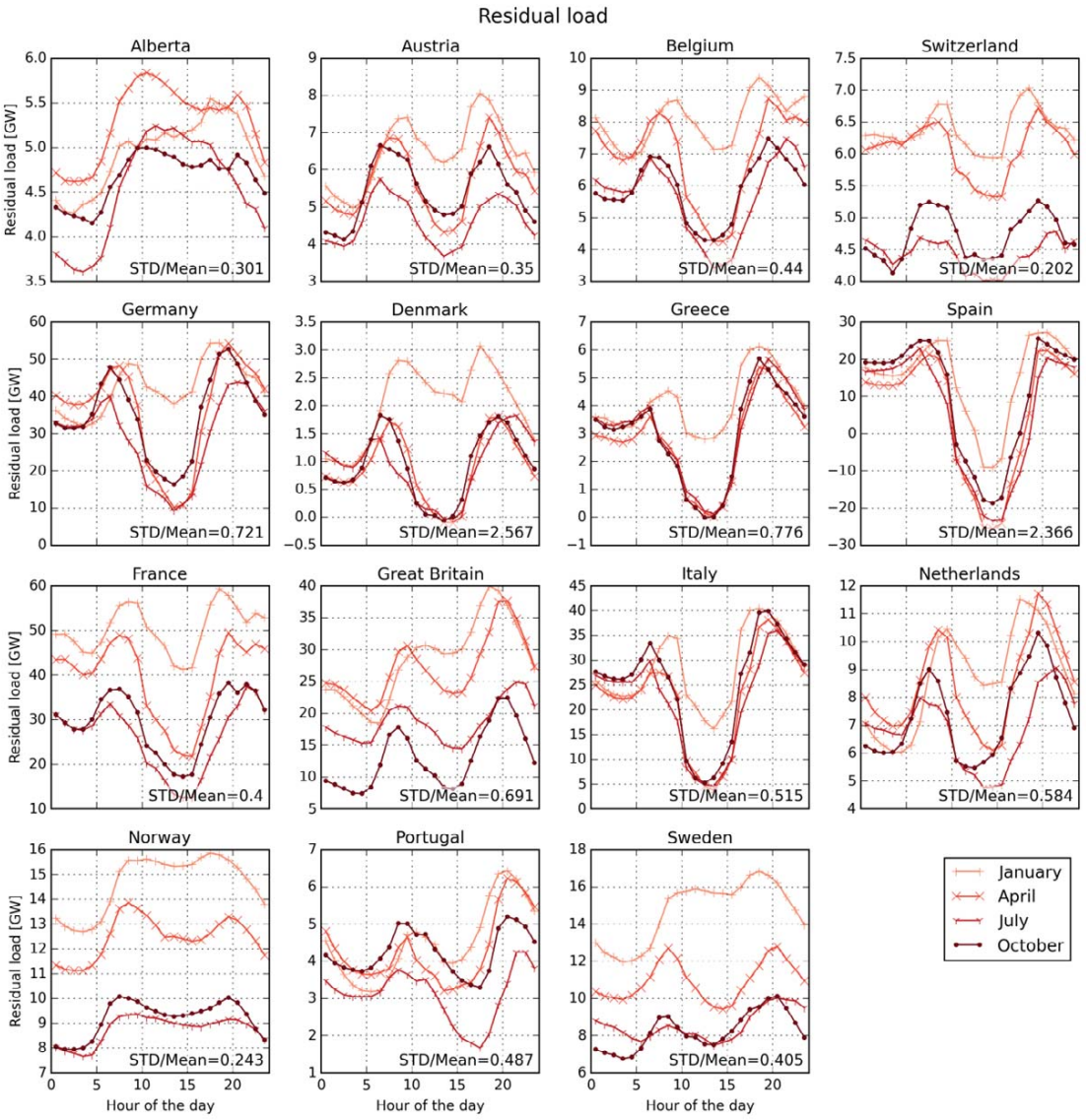

Fig. 7: Aggregated daily profiles of the residual load 2030 for the months January, April, July and October.

In most countries, the residual load shows its lowest values around noon as a consequence of peak solar and (on average) wind generation, as well as lower loads compared to the morning and evening. Even in the aggregated form shown in Fig. 7, residual loads close or below zero occur in Spain, Denmark, Greece and

Italy. This means that during especially sunny and/or windy days, extreme surpluses of renewable electricity (emission-free and at zero marginal cost) are expected. Storing this surplus or making it useful by demand response will be a major challenge and builds a strong case for considering variable grid conditions in heat pump and chiller control strategies.

Moreover, the residual loads in the analyzed countries show significant seasonal differences: they are typically lower and more volatile in summer than in winter. This is largely due to higher solar and wind generation and lower electric loads in summer. This means that daily variations in the availability of electricity, which justify grid-supportive building operation, are most prevalent during the cooling season.

Finally, it is noteworthy that the residual loads of 2030 of most of the analyzed countries have a much higher relative fluctuation (standard deviation/mean value) than the respective loads (Fig. 6). Particularly in the countries with the highest share of intermittent renewable energy, Denmark and Spain, the standard deviation of the residual load is over twice as large as its mean value, indicating rapid and substantial changes in the relative demand for electric energy – and thus the value of electricity. The relative fluctuations in residual load are up to ten times larger than those for the electric load – which underlines the necessity of demand response and other new measures to integrate intermittent renewables.

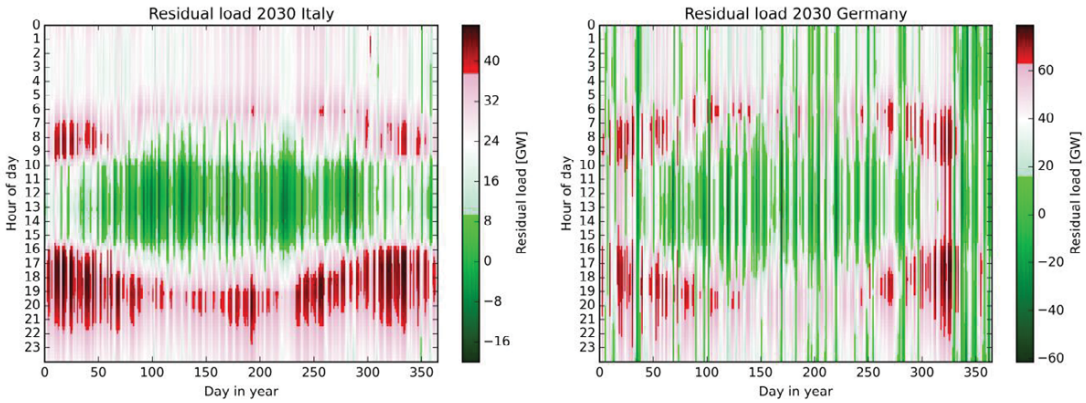

Fig. 9: Carpet plot diagrams of the residual load 2030 in Italy and Germany. For visual reference, highlighted areas residual loads above 80% of the peak load (red) and below 20% of the peak load (green).

Fig. 9 shows the residual loads of Italy and Germany in carpet plot diagrams For visual reference, the periods with very high demand (residual load > 80% of the peak load) and low relative demand (residual load < 20% of the peak load) are highlighted in red and green, respectively. It becomes clear that in Italy, which is characterized by a high amount of solar power, the relative demand for electricity varies very strongly and regularly within one day, between peak demands in the morning and evening and generation surplus around noon. This provides a strong incentive for intraday storage and load shifting. Germany, in contrast, has both a high amount of solar generation, which produces a similar pattern as in Italy, and additionally a significant amount of wind power generation, which causes sequences of entire operating days with surplus electricity. In addition, Germany has a stronger seasonal load variation than Italy, which leads to fewer peak load situations in summer. In such a situation, electricity needs to be stored for longer time periods, which is more challenging for conventionally designed building energy systems.

5. Requirements to grid-supportive heating and cooling

The annual heating and cooling energy consumption as well as the thermal peak loads (based on the 98th percentile) for are given in Fig. 10. Alberta, Norway and Sweden have both the highest heating energy consumption and the highest heating load. Greece has the highest highest cooling energy consumption and cooling load, followed by Italy and Spain. Portugal is the country with the lowest combined annual thermal demand of about 18 W/m^2·a, as well as the lowest combined heating and cooling load.

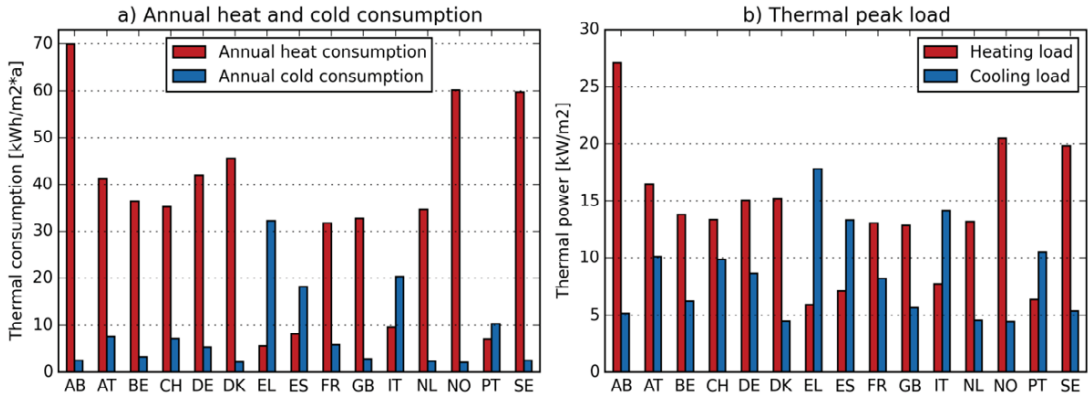

Fig. 10: Annual thermal consumption and peak heating and cooling loads

Figure 11 shows the aggregated thermal loads and the grid-optimized thermal generation trajectories for January (heating, red) and July (cooling, blue), i.e. the operation periods during the hours of the day with the lowest residual load. For calculation of the latter, 25% overdimensioned heating and cooling systems (according to Fig. 10 b)) and sufficient thermal storage capacity for intraday load shifting were assumed.

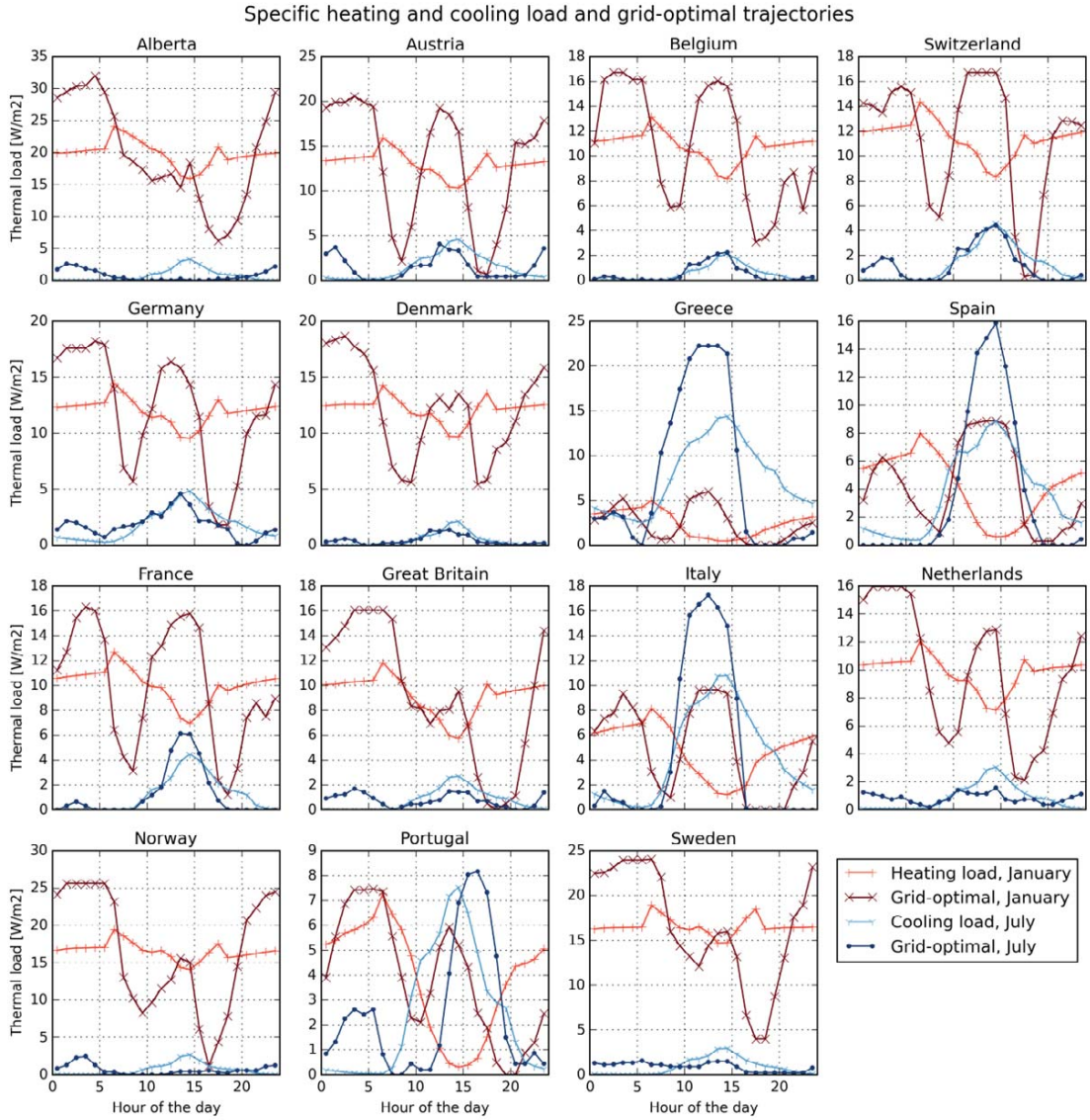

Fig. 11: Specific thermal loads and grid-optimal heating and cooling trajectories for January and July

As expected, the cooling loads assume their highest values around noon due to the high ambient temperatures and irradiation intensity. In nearly all countries, this coincides well with the generation and wind and PV and thus the residual load, which is why the grid-optimized cooling trajectory is similar to the load profile. Notable exceptions are Norway and Alberta, which lack solar generation and whose grid-optimal operation is scheduled at night when the load and residual load are lowest.

The heating load profile of the considered reference building is nearly constant throughout the day in the colder countries (e.g. Alberta, Norway, Denmark, Germany) and is more variable in warmer countries (Portugal, Spain), with the highest heating load occurirng in the morning (due to an increase in ventilation rate at the beginning of occupancy in the morning, when ambient temperatures are low) and the lowest heating loads occurring in the afternoon. The grid-optimal heating trajectory depends on the renewable energies mix: in wind-dominated regions such as Alberta, Norway and Sweden, it peaks in the night hours, whereas in PV-dominated countries such as Spain, it peaks around noon. Most countries, however, have a combination of wind and PV power, leading to two peaks in the grid-optimal heating profile at night and in the middle of the day. Their relative size depends on the mix of wind and PV in the energy system and the weather conditions of the individual day, which affects the thermal demand as well as wind and PV generation. This makes it difficult to derive general rules for grid-optimal scheduling of heat pump operation only based on the hour of the day. Note that for CHP units, which unlike heat pumps are electric generators rather than loads, the conclusions for grid-optimal scheduling of heating must be reversed: the most favorable times of the day for heating with CHP units are usually in the morning and evening.

6. Conclusions

This paper analyzes the dynamics of future renewable electricity generation and electricity demand profiles in a range of 15 geographies. The future scenarios (2030) are forecasted based on the current dynamics of the systems in combination with claims or commitments on PV and wind power installed capacities stated in the corresponding energy plans. At the core of this analysis, the “residual load” is defined as the electricity demand that must be met by conventional dispatchable electricity generation systems. This study explores short term and long term variability in the residual load, as a first step towards assessing the role that demand response systems (such as controls of heat pumps in buildings) might have in mitigating such variability and maximizing use of renewable generation.

Results show that, if the energy plans materialize, residual loads will be highly variable in 2030. The magnitude and variability of residual load varies across countries. However, some general trends can still be identified:

- Residual loads are lower and more variable in summer than in winter. In summer, electricity demand is generally lower (which helps lower residual load), and renewable generation is larger (which also contributes to reducing residual load, but adds variability)
- In summer, the lowest residual loads are seen around noon. This is good news, as the use of electricity in space conditioning devices (chillers, heat pumps) during the hottest periods of the day coincide in time with the lowest residual loads (i.e., when electricity use is the least disturbing for the electricity system)
- In winter, the lowest residual loads are either around noon or at night, none of which coincides well with the typical peak heating demand of a building. If heat pumps were to be used as a demand response system to accommodate variability in the grid, they would likely have to be accompanied by a thermal storage system.

It is interesting to note that one of the factors that make a difference in the dynamics of the residual load is the relative capacities of solar and wind power. In the European geographies, wind power peaks during daytime. However, unlike solar, generation does not necessarily drop to zero at night. Large solar generation capacities lead to strong daily variations in residual load, which can be more easily managed with short term storage systems. In contrast, variability of wind power is often in a longer time scale (days or even weeks). Managing variability in a longer time scale would require storage systems of higher capacity. The relative share of solar vs. wind power can, to some extent, be determined by the local jurisdictions. Electricity management and the opportunities for demand response could (and arguably, should) be among the criteria in defining renewable energy policies.

Acknowledgement

This paper was created as part of IEA EBC Annex 67. It was primarily funded by the German Federal Ministry of Economic Affairs and Energy via project *FlexControl* (promotional reference: 03ET1359A).

References

Alberta Electric System Operator, 2016. http://www.aeso.ca/

Agora Energiewende, Fraunhofer IWES, 2015. The European Power System in 2030: Flexibility Challenges and Integration Benefits.

Bundesnetzagentur, 2016. Genehmigung des Szenariorahmens für die Netzentwicklungspläne Strom 2017-2030. http://data.netzausbau.de/2030/Szenariorahmen_2030_Genehmigung.pdf

Canadian Wind Energy Association, 2016. Wind energy in Alberta. http://canwea.ca/wind-energy/alberta/

Cubi, E., Doluweera, G., Bergerson, J, 2015, Incorporation of electricity GHG emissions intensity variability into building environmental assessment, Applied Energy, Volume 159, pp 62-69,

DIN V 15599:2011-12: Energetische Bewertung von Gebäuden – Berechnung des Nutz-, End- und Primärenergiebedarfs für Heizung, Kühlung, Lüftung, Trinkwarmwasser und Beleuchtung.

Energienet.tk, 2016. PV and Batteries in Denmark. http://energinet.dk/SiteCollectionDocuments/Danske%20dokumenter/Klimaogmiljo/Solceller%20og%20batterier.pdf

ENTSO-E, 2014. Scenario Outlook & Adequacy Forecast (SO&AF) 2014-2030. www.entsoe.eu/publications/system-development-reports/adequacy-forecasts/soaf-2014-2030/Pages/default.aspx

ENTSO-E, 2016. Consumption Data. http://www.entsoe.eu/data/data-portal/consumption/

European Commission, 2008. National Renewable Energy Action Plans. https://ec.europa.eu/energy/en/topics/renewable-energy/national-action-plans

Focken, U., Heinemann, D., 2003: Influence of Thermal Stratification on Wind Profiles for Heights up to 140m. Proc. European Wind Energy Conference EWEC, Madrid.

Hedegaard , K., Mathiesen, B.V., Lund, H., Heiselberg, ,P., 2012, Wind power integration using individual heat pumps - Analysis of different heat storage options, Energy, Volume 47, pp. 284-293, http://dx.doi.org/10.1016/j.energy.2012.09.030

IEA (2003). The Power to Choose: Demand Response in Liberalised Electricity Markets, OECD Publishing, Paris.

Killinger, Sven; Mainzer, Kai; McKenna, Russell; Kreifels, Niklas; Fichtner, Wolf: „A regional optimisation of renewable energy supply from wind and photovoltaics with respect to three key energy-political objectives“. Energy 84(2015), p. 563-574

Klein, K., Kalz, D., Herkel, S., 2016. Numerical study on load shifting strategies for the heating and cooling of an office building considering variable grid conditions. CLIMA 2016, Aalborg, Denmark

National Grid, 2011. UK Future Energy Scenarios. http://www2.nationalgrid.com/WorkArea/DownloadAsset.aspx?id=24676

Salom, J., Marszal, A.J., Widén, J., Candanedo, J., Lindberg, K.B., 2014, Analysis of load match and grid interaction indicators in net zero energy buildings with simulated and monitored data, Applied Energy, Volume 136 , pp. 119–131, http://dx.doi.org/10.1016/j.apenergy.2014.09.018

Appendix

Table 1: Country codes and installed wind and PV generation capacities in 2030 assumed in this study

	Alberta	Austria	Belgium	Switzerland	Germany	Denmark	Greece	Spain	Frane	Great Britain	Italy	Netherlands	Norway	Portugal	Sweden
Abbreviation	AB	AT	BE	CH	DE	DK	EL	ES	FR	GB	IT	NL	NO	PT	SE
Wind capacity [GW]	5.5	5.5	8.54	0.9	73.5	7.79	7.8	46.1	36.6	51.0	22.1	13.0	5.0	6.34	12.1
PV capacity [GW]	0	3.5	5.74	3.0	66.3	2.24	5.3	37.0	24.1	8.27	48.9	8.0	0	0.72	1.0

Conference Proceedings

EuroSun 2016
Palma de Mallorca (Spain), 11 - 14 October 2016

Multiscale Characterization of French Polynesia Climate for Dynamic Simulation of Buildings

Franck Lucas, Marania Hopuare, Charlotte Besnard and Pascal Ortega

Laboratoire GePaSud, Université de la Polynésie française, FAA'A Tahiti (French Polynesia)

Abstract

Performance assessment of buildings in tropical climates requires annual meteorological data files for an "energy approach" of air-conditioned buildings. It also requires localized climatic sequences allowing a real estimation of the natural ventilation potential of the sites for a "comfort" approach of non-air-conditioned buildings. The absence of this type of weather data in Polynesia considerably limits designer analysis means. This article presents two methods to establish meteorological sequences for both energy and comfort approaches. The first aims developing annual typical weather files from a reduced number of ground measurements. The missing meteorological variables are completed using a global to diffuse decomposition model of the solar irradiance. The second is based on a mesoscale climate model and a downscaling to obtain a characterization of localized natural ventilation potential and climatic data on a fine mesh. The weather sequences generated are used to perform energy calculation for air conditioned classrooms and wind potential and comfort assessment for cross ventilated classrooms of a primary school located in French Polynesia.

Keywords: *Weather data, tropical climate, dynamic simulations, natural ventilation.*

1. Introduction

The design of very low energy buildings or net zero energy buildings requires sophisticated analysis and forecasting tools. For assessing energy performance of buildings during the design phase, dynamic thermal simulation codes are now the most commonly used tools. These codes simulate building behavior using a physical description and weather data. Design methods have evolved in the last decades. At the beginning, the buildings performance analysis supposed steady states outside conditions, for example: the method of "outside based conditions" or the "Degree Days method". The more recent dynamics simulation tools propose building energy calculation on hourly or even lower time step. They account for a large number of input variables and parameters. Nevertheless, there are significant differences between energy performance of buildings estimated by dynamic simulation codes during the design phase and the real performance of the operating building. In his thesis, C Spitz (2012) evaluates all sources of uncertainty between the design and operating phase. Of course, "Design" phase calculations generate errors due to the assumptions on the building and its components description. But Spitz noted that the quality of meteorological data used in numerical simulations is also an important source of error that can cause deviations of up to 30% of the estimated consumption of an air conditioning system. To be representative of the building external loads meteorological data used by designers must meet specific standards. Several types of data can be used:

- "multi-year" data sets: they bring together all the meteorological data required for the simulation of buildings and over several years. They are complicated to use because of the large number of values they have. Example: SAMSON database 1961-1990 (NCDC 1993).

Selection and/or peer review under responsibility of Scientific Committee
doi:10.18086/eurosun.2016.09.11 Available at http://proceedings.ises.org

- Typical weather annual files: the most commonly used data to estimate the average performance of a building. Example: Typical Meteorological Year (TMY), Weather Year for Energy Calculation (WYEC), Test Reference Year (TRY)...
- Short representative weather sequences: They can be used to study extreme weather conditions (very hot or cold, very sunny or very wet ...), localized weather (considering the influence of the relief on meteorology), the design of specific technical solutions (studying the potential for natural ventilation of a building) or the design of building components ("design day" sequences for the sizing of air conditioning systems).

The type of weather data to use and therefore generate, depends on the objectives for the design process. The French Polynesia like all island territories is facing a difficult situation because of energy supply difficulties and operating constraints of a non-interconnected electricity grid. The ambitious political commitment is to achieve a 50% renewable energy for electricity supply in 2020. Thus, an energy regulation is being drafted. This thermal regulation will target energy ratio for air-conditioned buildings but will also state minimum comfort performance for naturally ventilated buildings. In both cases, specific weather data are needed. For energy approach, annual weather sequences will assess the energy consumption of buildings. Short sequences are dedicated to the comfort evaluation. This paper presents the study to provide both types of meteorological data for French Polynesia. The first part addresses the creation of typical meteorological year for the energy approach. The chosen method uses a reduced meteorological database obtained from ground measurements. For the "comfort" approach, it is necessary to consider the high spatial variability of the meteorological inputs. In the second part, we use a climatic model to generate climate data on a fine mesh (around 1.3 km) compatible with the needs of dynamic simulations of buildings operating in natural ventilation. These weather sequences will then be applied to energy calculation and comfort evaluation for air conditioned classrooms and cross ventilated classrooms in French Polynesia.

2. Energy calculation with typical annual weather file

2.1 File Constitution

In preparation for the implementation of a thermal regulation in French Polynesia, the climatic sequences that seem most important and most urgent are the annual weather files. These sequences are very often used by building designers. They bring together all hourly climate variables needed for dynamic simulation of buildings for a period of one year. There are several possibilities to obtain these annual typical sequences. The first is based on the selection of the most representative month made in a database developed with ground measurements over long periods (between 10 and 30 years). The ground measurements are usually obtained from forecast utilities. For all the French territories, the first 200,000 digital values are provided free of charge for the public institutions by the French forecast utility Meteo France. Beyond, the data are charged. The second method is based on the use of stochastic models that generate time series climate data by extrapolation of measured data by ground stations. These tools are often called "weather generators." Developed by research laboratories since the 1980s (Van Passen, 1979) (Knight, 1990) (Adelard, 2000), (David, 2010), these methods were taken over by private providers for commercial services. Among them, for example Meteonorm (Remund, 2004) and Type 54 from TRNSYS (TRNSYS 2000) are commonly used by designers.

The annual typical weather data sets generated from ground measurements are the most widespread. It has been developed in several formats. The main ones are:

- TRY (Test Reference Year): One of the first weather data sets, developed in 1976.
- TMY (Typical Meteorological Year) developed from TRY format by especially adding global horizontal irradiance data. The TMY dataset includes measurements selected over the periods from 1945 to 1973. It evolved in 1995 in the TMY2 format by adding new weather variables such as direct solar irradiation and using more recent weather data (1961 to 1990). Then, the TMY3 format is built up with even more recent years, up to 2005.
- WYEC (Weather Year for Energy Calculation) were developed by ASHRAE. As for the TMY format, WYEC2 version was made from the WYEC files by adding additional variables, including the characterization of natural lighting.

Drury's study for US climates (Drury 1998) analyzes the estimation of the energy performances of a building according to the type of the weather files used. The performances are compared to the results of simulations with real weather data collected over 30 years. It notes that the climate data used in dynamic simulation of buildings can have a significant influence on the energy performance assessment and concluded by recommending the use of TMY2 formats (or TMY3) and the WYEC2. These two types of data sets are developed by selecting twelve typical meteorological months (TMM) from a multi-year weather database. The difference between the TMY and WYEC files comes with the TMM selection process. For TMY files, Hall (Hall 1978) presents a method for selecting the representative month by analyzing four climatic variables (global solar radiation, air dry temperature, dew-point air temperature, wind velocity) supplemented by daily maximum, daily minimum, daily mean air dry temperature and dew point temperature, daily maximum and daily mean wind speed, and daily global solar radiation. A total of 9 variables are required for the selection process. Each of these variables is weighted according to its importance on the behavior of buildings. The selection of each typical meteorological month in the database is operated following the Finkelstein-Shaffer statistical method. The weighting of each leads to several variants of the method (Hall 1978) (Yang 2007) (Yang, 2011). The drawback of this method is that the weighting process may seem subjective, but above all, it requires a large number of values in the selection database (over 1 million, just for the process selection). Crow (Crow 1984) proposes a method to generate annual typical weather files kinds requiring a smaller database for the selection of the TMM. It is based solely on the study of the dry air temperature. The selected representative month is the one whose monthly average dry bulb temperature is within a range of ± 0.3 ° C of the monthly average dry bulb temperature over the entire database. The choice of the TMM is done according to:

$$dx = \left| \overline{T}_x^i - \overline{T}^i \right| \qquad \text{(eq. 1)}$$

$\overline{T}_x^i$: Monthly average temperatures for the month i in year x.

$\overline{T}^i$: Monthly average temperatures for every month i on the entire database.

The selection process is carried out using only the values of the monthly average temperature over a period of 10 to 30 years. Once the TMM selection made, the values bought from the forecast utility to form the typical annual weather file are limited to the climatic hourly meteorological variables of the selected months. The total number of values required for the selection process is 360 and the file includes less than 44,000 values. On the available database for French Polynesia from 1997 to 2007, the weather typical year was formed by the months given in the table below:

Table 1: Selection of the TMM for the typical annual weather file for French Polynesia.

	J	F	M	A	M	J	J	A	S	O	N	D
Selected year	2006	2002	2001	1998	1997	1998	1999	1998	2001	1998	2004	1999

The meteorological data requested for each TMM are the hourly values of the following variables: dry air temperature, relative humidity, wind speed, wind direction, horizontal global irradiation. From these TMM a "Polynesian typical meteorological year" (PTMY) is then generated using the Matlab conversion tool "Weather xls to TMY2". However, the horizontal diffuse radiation has not been continuously measured by Meteo France in Polynesia and is no longer measured since 2006. It is, therefore, necessary to estimate the diffuse and direct irradiation form the other variables available.

a. Post processing of data: Decomposition of global irradiance

The creation of the typical annual weather file requires determining the diffuse and direct solar irradiance using the global horizontal irradiance. A decomposition model adapted to the climate of Polynesia is then necessary. A number of models are available in the literature. They are generally based on the use of the

index clearness index K_t and diffuse fraction K_d given by: $K_t = \frac{G_h}{G_o}$ and $K_d = \frac{G_{d,h}}{G_h}$

Where, G_h is the global horizontal solar irradiance, G_o is the extraterrestrial solar irradiance, and $G_{d,h}$ is the diffuse solar irradiance on a horizontal plane. Among the available models, a pre-selection of four mathematical models was made: Orgill & Hollands (Orgill 1977), Li Lam (Lam 1996), Erbs (Erbs 1982) and Reindl (Reindl 1990). This series model is complemented by the DIRINT model established by Perez (Perez 1992) which is available through a Matlab toolbox or in Python. An additional model was established in this study. It is derived from a correlation established by Meteo France. This latter model, designated "PF model" whose interest is to be simple and valid throughout the interval 0<kt<1 is given by:

$$K_d = \frac{1}{1 + \exp(c_0 K_t + c_1)} \qquad \text{(eq. 2)}$$

c_0 and c_1 are coefficients determined from the diffuse radiation measurements available in Polynesia. The global and diffuse radiation measurements of 1993, 199, 1998 and 1999 were previously screened by the method of BSRN (Long 2002) and c_0 and c_1 are determined by the least squares method. The values obtained are: c_0 =7.122 and c_1 = - 3.511.

The comparison between the measurements for the years when diffuse radiation is available (1993, 1997, 1998, and 1999) and the different models is given in the table below by the value of the relative root mean square error (rRMSE).

Table 2: relative root mean square error between measurements and the different models.

rRMSE (%)	Erbs	Lam & Li	Reindl	Orgill & Hollands	Perez	PF Model
1993	43,0	37,7	43,6	44,3	42,6	32,0
1997	38,0	35,0	39,4	39,8	37,9	27,6
1998	37,3	32,0	38,7	38,8	37,2	25,7
1999	46,4	39,7	48,0	48,2	46,1	30,9
Average	41,175	36,1	42,425	42,775	40,95	29,05

3. Downscaling of climate models

Climate models are a numerical representation of the climate system based on the physical, chemical and biological properties of its components and their interaction processes. It calculates all climatic parameters with a very fine spatial resolution. Weather and Research Forecasting (WRF) climate model (Skamarock 2008) used in this study is a non-hydrostatic limited area model to zoom in on a particular region. WRF is known to have high bias and isn't the best method and model for solar resource assessments. WRF is parameterized with localized convective scheme and thus, can show some discrepancies when assessing solar radiation. Anyway, it is a useful tool for estimating coherent coupled climatic variables (temperature humidity, wind and also radiation). It is, therefore, adapted to provide climatic weather sequences. A realistic parameterization of the subgrid processes has been assessed for French Polynesia by Heinrich. (2009). An experimental comparison is also provided by Hopurare. (2016) which compare small scale prediction with ground measurements.

The method used consists in increasing the resolution within an area of interest by embedding other smaller domains. We get what is called a "downscaling cascade" with increasing resolution nested domains until the desired spatial resolution is obtained in the inner domain (Fig. 1). The spatial resolution is the dimension in km of a grid. The calculations have been carried out on three interacting grids, with horizontal resolutions of 20, 4, and 1.33 km, respectively. The use of a mesoscale model provides short weather sequences to address specific building design issues. This study presents a specific analysis on wind regimes in Tahiti with the objective of a fine-scale characterization of the natural ventilation potential for low energy buildings.

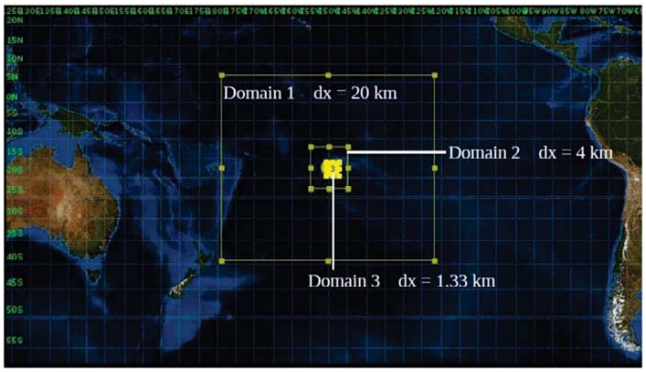

Fig. 1: Diagram of the downscaling with WRF positioned on a large central Pacific area, 20 km resolution and boundary conditions as the Interim reanalysis Era. A second domain is implemented with 4 km resolution centered on French Polynesia. A final domain (domain 3) is implemented in the domain 2 with a resolution of 1.3 km and centered on Tahiti.

3.1 Synoptic wind regimes in Tahiti and Moorea

ERA Interim dataset (http://apps.ecmwf.int/datasets) is a reanalysis product provided by the European Centre for Medium-Range Weather Forecasts (ECMWF). In this study, Era Interim reanalysis data were processed to identify the regimes of most frequent winds in Tahiti. A statistical method on a time series of 31 years (1979 to 2009) has highlighted six main synoptic wind regimes (fig. 2).

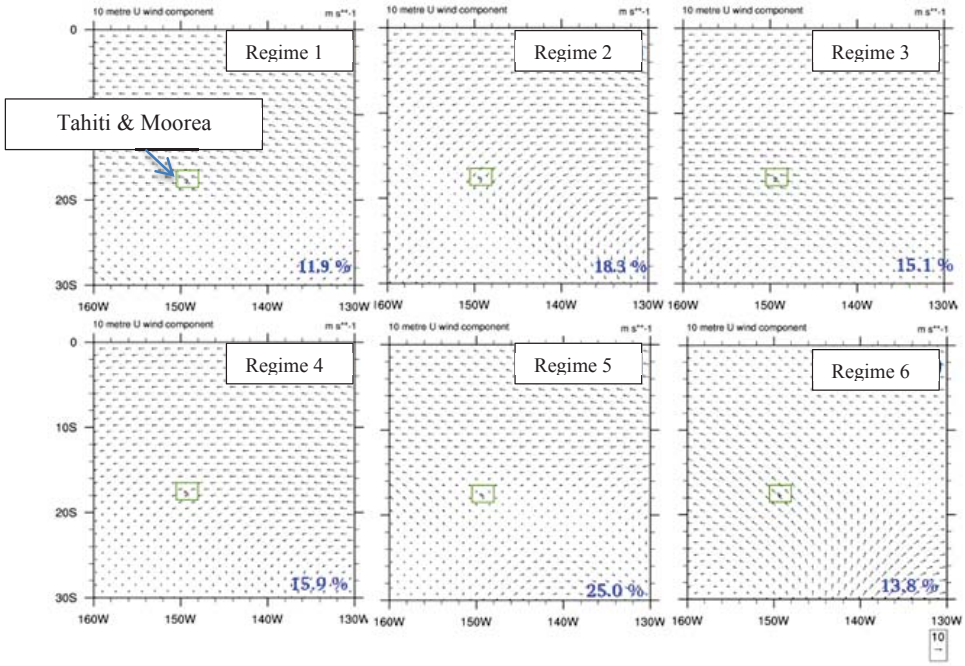

Fig. 2: Synoptic wind regime over French Polynesia obtained with 10m Era Interim reanalysis. The green square locates Tahiti.

The wind regime can be observed both on Tahiti and Moorea Islands with the following frequency of occurrence : Regime 1 (11,9%); Regime 2 (18,3%); Regime 3 (15,1%); Regime 4 (15,9%) ; Regime 5 (25,0%); Regime 6 (13,8%). It appears that at least 25% of a year, for the days of wind regime 5, the potential of natural ventilation is weak. The downscaling technique focused on a restricted area with a higher resolution gives a better estimate of the natural ventilation potential.

3.2 Downscaling

The Era Interim Reanalyzes data for five days for each of the six wind regimes were recovered and applied as boundary conditions of the WRF model domains. This provides five daily weather sequences simulated for each wind regime. The wind cartography for each regime at 1.3 km resolution is obtained by averaging the five days. The consideration of the relief is essential for small scales. Figure 3 shows the orographic

description considered by the model for Tahiti and Moorea Islands. The relief description level remains coarse as the maximum altitude considered is 1200m while the highest point of Tahiti is actually 2240 m. However, greater finesse requires very long calculation times.

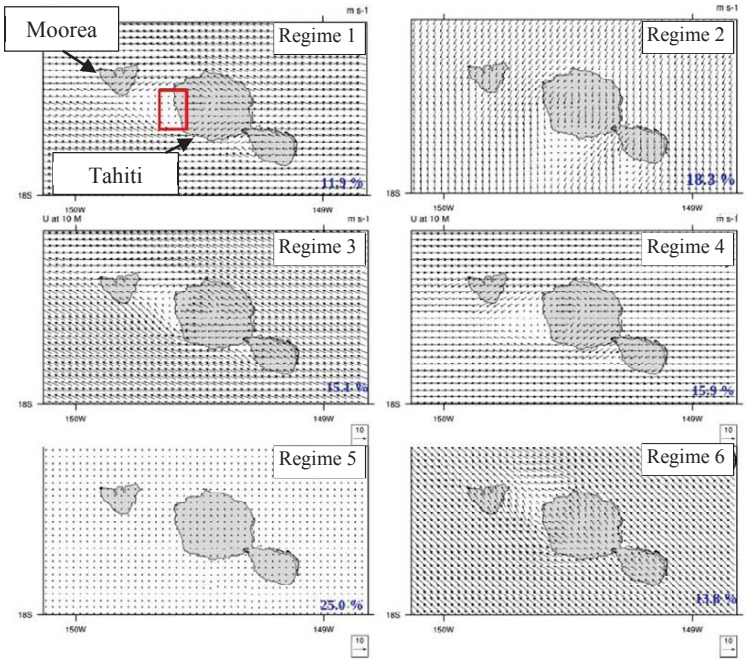

Fig. 3: Wind cartography at fine resolution (1.3 km) focused on Tahiti and Moorea islands and simulated with WRF model for the six wind regimes.

The downscaling with WRF has resulted in a more accurate and reliable wind cartography, showing the windward and leeward contrast for northeast, east and southeast wind regimes and is north. This study has highlighted the potential of natural ventilation throughout the islands of Tahiti and Moorea. It confirms that the main wind direction is South East with a frequency of 40% (regime 1, 3 and 6) and that for synoptic wind regime 5, natural ventilation of building might not be ensured as wind is very low. Moreover, for each coastal area, it evaluates the time percentages with light wind (<2.5 m/s) moderate wind (2.5 <wind <11 m/ s) and strong wind (> 11 m/s). The results are as follows:

- North and East Coasts: low wind 25%, moderate wind 34.2%; strong wind 40.8%
- South Coasts: low wind 43.3%, moderate wind 15.9%; strong wind 40.8%
- West Coasts: low wind 67.9%, moderate wind 13.8%; strong wind 19.3%

The downscaling approach provides also fine scale short weather sequences (typically one day) for each wind regime as the example shown on fig 4. These hourly sequences include all meteorological data needed for dynamic simulations of naturally ventilated building.

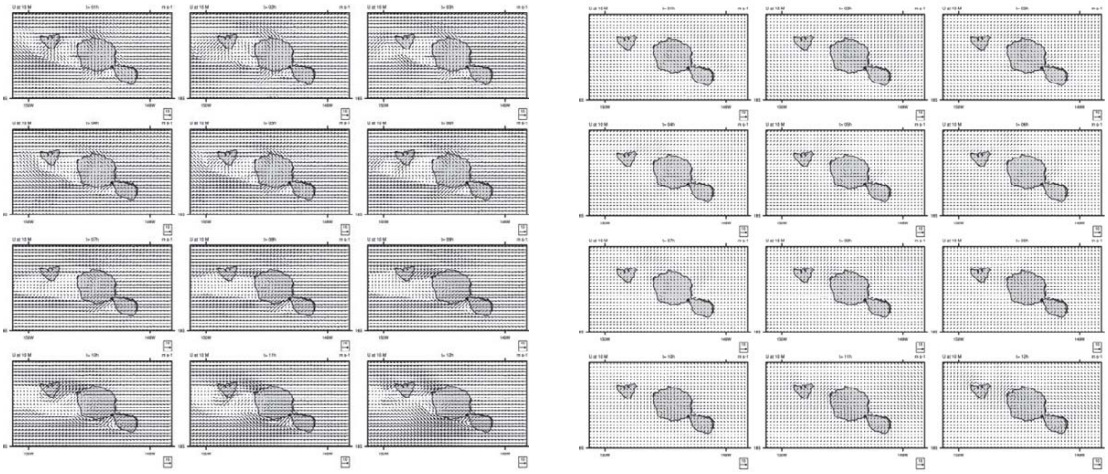

Fig. 4 : Example of hourly fine scale weather sequences. Hour by hour wind cartography for one day (from 0am to 12am) for a windy day (regime 1, on the left) and for day with low wind (regime 5, on the right)

4. Case study : building performance assessment using weather files

To compare the result of the weather sequences presented in this article, dynamic simulations using Energyplus software (Drury 2001) were carried out on a building located at Papetoai on the northwest coast of Moorea Island. (Fig 5). This building is a primary school building including 11 identical classrooms. Some classrooms are air conditioned whereas some are cross ventilated. Two different kinds of simulations where performed. The first simulations aim to compare the energy consumption of the air conditioned classrooms estimated with the PTMY weather file presented above and an annual weather file produced by Meteonorm. The second set of simulation includes simulations for each wind regime in order to estimate the comfort condition for the naturally ventilated classrooms. The one-day weather sequences used are generated hour by hour by the mesoscale model which perform a downscaling over Papetoai. All the simulations assess the classrooms are occupied with 20 people and their design is adapted to the tropical climate (solar shading, roof insulation, large openings equipped with louvers on opposite walls…) and to the operating mode. For the simulations of ventilated classroom the openings are supposed open all the time. For air conditioned rooms, these openings are closed and, according to sanitary regulations, mechanical ventilation provides 15m^3/h per person of outside air. The air conditioning system has a rated COP of 2.6 and the set point temperature is 26°C.

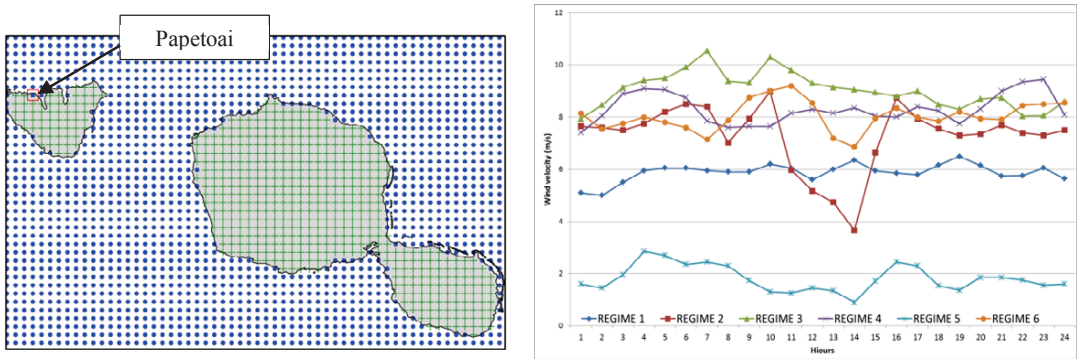

Fig. 5 : Location of the building under study on the north coast of Moorea plotted on the resolution grid of 1.33 km (left) and wind velocities for the short hourly sequences of the 6 wind regimes (right).

According to the Spitz's study mentioned in the introduction, the comparison of annual weather file will focus on the energy consumption and the cooling demand of the air conditioned classrooms. The output variables studied are the Air Conditioning sizing cooling load (kW), the annual cooling energy (kWh/year) and the annual electricity consumption of the AC system (kWh/year). The results are presented in table 3. The deviations observed are in the range of 10% for annual energies but rise to 18% for the cooling power required in the zone to reach the set point temperature. Consequently, the choice of the input weather file can

lead to overestimate the air conditioning system size.

Table 3: Cooling rate, cooling energy and electricity consumption for the two weather files

Weather file	System sizing cooling load (kW)	Annual cooling energy (MJ/year)	Annual electricity consumption of AC system (MJ/year)
Meteonorm	10.5	28 519	12 711
PTMY	8.6	25 603	11 397
Deviation (%)	18.0%	10.2%	10.3%

To ensure comfort in buildings, natural ventilation has two objectives: one is to evacuate thermal loads from the building and the second is to generate air velocity on occupants. The simulations performed for non-air conditioned classrooms aim to verify if natural ventilation can be an effective solution for building design in French Polynesia especially when the potential of ventilation is weak. As mentioned above, synoptic wind is low everywhere on Tahiti and Moorea the days of wind regime 5. It is also low on leeward coasts for all other wind regimes. Then, natural ventilation may not be sufficient to ensure comfort. The building studied being located on the North West coast; one can suppose that it is not exposed to the main synoptic South-East trade winds. However, the specific weather sequences generated for this location show that the wind velocity is most of the time moderate (Fig. 5). For these simulations, the effect of cross ventilation in the classrooms is estimated by the temperature difference between interior and exterior (overheating) and by the airflow rates through the zone. The target values for airflow rates depend on many parameters and among them the main one would be the population habits and their expectation in terms of comfort. Few targets values can be found in the literature for the populations in the islands of the Pacific Ocean. Le Bars (2010) mentions that an average airflow rate of 15 ach/h limits the overheating at only 4 to 5°C for an office building. To reduce the overheating to 2°C the airflow rate must be at least 20 to 30 ach/h. For classrooms, the same airflows and overheating values can be targeted if building design is adapted.

The simulation results (Fig.6) confirm that the natural ventilation potential is weak for wind regime 5, as the wind velocity is always less than 3m/s (the average during the day is 1.8 m/s) and the overheating goes up to 3°C (average is 1.5°C and the maximum is 3.26°C at 2pm). The airflow rate is always less than 25 ach/h (the average is 13 ach/h). The other wind regimes lead to moderate wind velocities with averages during the day ranging from 5.8 to 8.3 m/s. The average airflow rates range between 37 to 58 ach/h. The average overheating is less than 1°C, but its maximum values stay high (from 1.7°C to 2.8°C).

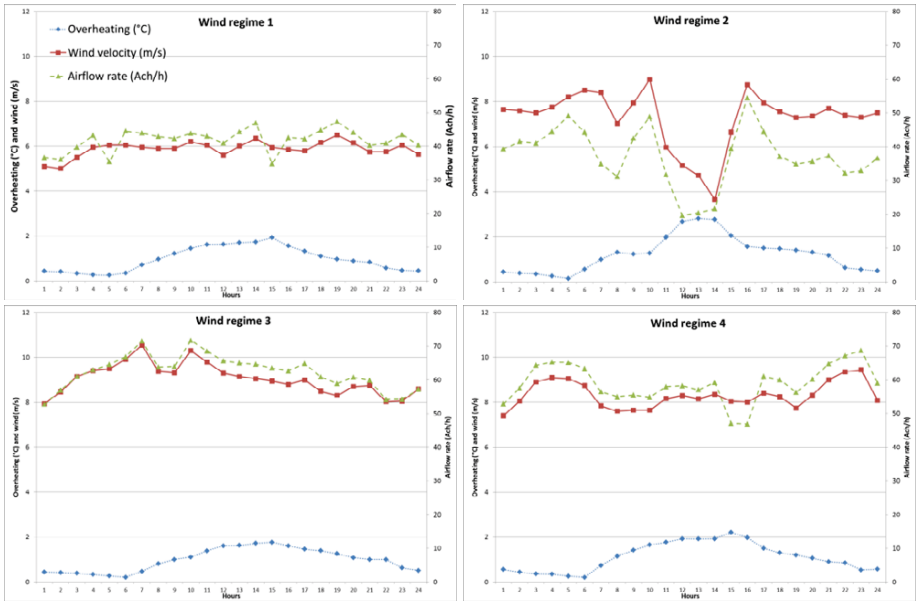

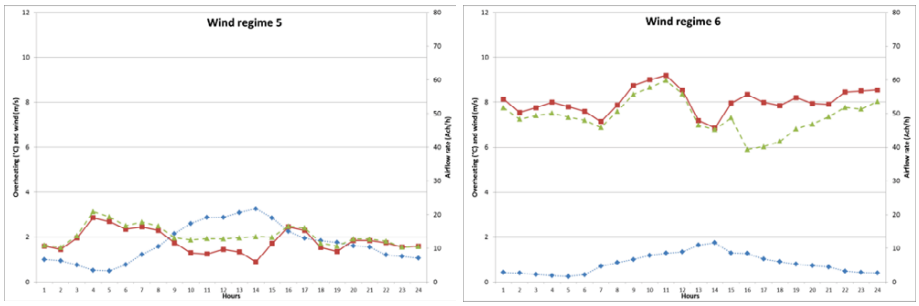

Fig. 6 : Simulation results with overheating, wind velocity and airflow rate for the 6 synoptic wind regimes

The use of localized short weather sequences shows that although the building is not located on the windward coast of Moorea, the local wind is most of the time moderate (between 2.5 and 11 m/s) and can be usable for effective natural ventilation. Thus, the airflows generated through the building are significant and overheating can be limited under 3°C all the days except for days of wind regime 5. Most of the time, comfort might be acceptable in ventilated classrooms, providing that the building design is suitable. From 1pm to 3pm during days of wind regime 5, the inside conditions are hot. In this case, ensuring an air velocity on occupants could be a solution to improve thermal comfort. The thermal simulation with Energyplus doesn't give access to air velocity in the thermal zone. Therefore a coupling with a CFD model should be investigated. At the last resort, ceiling fans could be added in the zone to generate the required air velocity.

5. Conclusion

Appropriate meteorological data is the first decision making tool that should be provided to building designers. This article presents the methods used to obtain climate data for addressing the building design in French Polynesia by following two approaches: an energetic approach for air conditioned buildings and a qualitative approach of comfort for naturally ventilated buildings. For the energy approach, the presented method proposes to establish a "Polynesian typical meteorological year" from a reduced ground measurement database. To complete the meteorological measurements on the ground, a global to diffuse decomposition model for solar irradiance was developed. This model presents interesting performances because it is easy to use by designers and has satisfactory accuracy. To carry out a qualitative analyzes of comfort in naturally ventilated buildings a climate model was used. This has highlighted six main synoptic wind regimes on Tahiti and Moorea Islands. The downscaling of this model has helped develop the wind cartography over a 1.33 km mesh and generate short weather sequences for each wind regime and for each point of the mesh. The weather sequences provided in this study have been used for energy calculation and wind potential assessment of a primary school building located in Moorea. For energy calculation, the "Polynesian typical meteorological year" is compared to an annual weather file from Meteornorm. The simulations of natural ventilation show that the fine mesh short weather sequences give a better evaluation of localized wind potential. To go further in this study, two directions must be investigated. The first is to carry on the downscaling toward a finer resolution (typically 100m) to better consider the orography and very localized climatic phenomenons. The second is to estimate the air velocities inside the building with CFD calculations using localized wind velocities as input. Considering the air velocities on the occupant will significantly improve the comfort assessment in the zone.

6. References

Spitz C. Analyse de la fiabilité des outils de simulation et des incertitudes de métrologie appliquée à l'efficacité énergétique des bâtiments. Other. Université de Grenoble, 2012. French. <NNT : 2012GRENA004 >. <tel-00768506 >

NCDC (1993). Solar and Meteorological Surface Observation Network, 1961-1990, Version 1.0, September 1993. Asheville, North Carolina: National Climatic Data Center, U.S. Department of Commerce.

Drury B. Crawley. 1998. Which Weather Data Should You Use for Energy Simulations of Commercial

Buildings? ASHRAE TRANSACTIONS 104 Part 2

Adelard L., Boyer H., Garde F.,. Gatina J.-C. 2000. Detailed weather data generator for building simulations. Energy and Buildings. 31, 1. 75-88

Van Paasen A. H. C., Dejoing A. G. 1979. « The Synthetical Rference outdoor climate ». Energy and Buildings. Vol (2). P 151-161.

Knight K.M., Klein S.A., Duffie J.A. 1991 « A methodology for the synthesis of hourly data », Solar Energy, Vol. 46, N°2, pp.109-120.

M. David et al. 2010. A method to generate Typical Meteorological Years from raw hourly climatic databases. Building and Environment 45, pp 1722‑1732.

Remund J, Kunz S. METEONORM. handbook. Bern: METOTEST; 2004.

TRNSYS. A transient simulation program. USA: Solar Energy Laboratory, University of Wisconsin-Madison; 2000.

Hall IJ, Prairie RR, Anderson HE, Boes EC. 1978. Generation of typical meteorological years for 26 SOLMET stations. SAND 78e1601. Albuquerque, New Mexico: Sandia National Laboratories;

Yang L, et al. 2007. « An analysis of the typical meteorological years in different climates in China". Energy Conversion Management. 48:654-68.

Yang L. et al. 2011. "A new method to develop typical weather years in different climates for building energy use studies". Energy 36. 6121-6129

Orgill, J.F., and K.G. Hollands. 1977. "Correlation equation for hourly diffuse radiation on a horizontal surface". Solar Energy 19, Vol. 4, pp. 357–359.

Erbs, D.G., S.A. Klein, and J.A. Duffi. 1982. "Estimation of the diffuse radiation fraction hourly, daily, and monthly-average global radiation". Solar Energy, Vol. 28, No. 4, pp. 293–304.

Reindl D.T., Beckman W.A., and Duffie J.A.. "Diffuse fraction correlations ». Solar Energy, 45:1–7, 1990

Lam JC, Li DHW. 1996. "Correlation between global solar-radiation and its direct and diffuse components." Building and Environment ; 31(6):527–35

Perez, R., P. Ineichen, E. Maxwell, R. Seals, and A. Zelenka. 1992. "Dynamic globalto-direct irradiance conversion models". ASHRAE Transactions Research, 3578(RP-644), pp. 354–369.

Long, CN, and EG Dutton. 2002. "BSRN Global Network Recommended QC Tests, V2. X." http://epic.awi.de/30083/1/BSRN_recommended_QC_tests_V2.

Skamarock, W. C., et al. (2005). A description of the advanced research WRF version 2 (No. NCAR/TN-468+ STR). National Center For Atmospheric Research Boulder Co Mesoscale and Microscale Meteorology Div.

Heinrich, P., Blanchard, X. 2009. Simulation of atmospheric circulation over Tahiti and of local effects on the transport of 210Pb. Monthly Weather Review, 137(6), 1863-1880.

Marania Hopuare et al.2016. High resolution wind regimes over Tahiti, French Polynesia, using the WRF-ARW mesoscale model. CLIMA 2016 - proceedings of the 12th REHVA World Congress: volume 9..

Drury B. Crawley, et al. 2001. Energy Plus: Creating a new-generation building energy simulation program, Energy and Buildings, 33, pp 319-331.

Le Bars Y and al. 2010. Energy for the development of New Caledonia. IRD, ISSN 1633-9924 978 -2-7099-&692-9

Conference Proceedings

EuroSun 2016
Palma de Mallorca (Spain), 11 - 14 October 2016

COMPARISON OF ATACAMA DESERT SOLAR SPECTRA vs. ASTM G173-03 REFERENCE SPECTRA FOR SOLAR ENERGY APPLICATION

Aitor Marzo[1,2] *, Pablo Ferrada[1,2], Felipe Beiza[1], Joaquín Alonso-Montesinos[3,4], Jesús Ballestrín[5], Roberto Román[2]

[1] Centro de Desarrollo Energético Antofagasta (CDEA), University of Antofagasta (Chile)

[2] Solar Energy Research Center (SERC-Chile), Santiago (Chile)

[3] Department of Chemistry and Physics, University of Almería, Almería (Spain)

[4] CIESOL, Joint Centre of the University of Almería-CIEMAT, Almería (Spain)

[5] Plataforma Solar de Almería (PSA), Centro de Investigaciones Energéticas, Medioambientales y Tecnológicas (CIEMAT), Almería (Spain)

Abstract

Knowledge of the solar spectrum is essential for the design and study of numerous technologies based on the use of the solar resource. In spite of the fact that the Atacama Desert is in the spotlight of solar industry, there is not enough information about the spectral irradiance present on it. This fact and the special atmospheric conditions of Atacama cause an increasing interest of solar industry to know the spectral differences with other places of the world. Using a standard spectrum may represent very different results from the true. In this paper, direct and global tilted Atacama Desert Solar Spectra are derived from mean values of available satellite and model retrievals databases. Results are compared against the ASTM G173-03 Reference Spectra in order to know if the information provided by the standard is useful for solar energy applications. For that, solar spectra derived from SMARTS atmospheric transfer model in combination with the atmospheric information from the available databases are previously compared with several spectral irradiance measurements from the first spectral measurement campaign in Chile, developed on 2015. Later, the average of the atmospheric parameters for the whole Atacama Desert area is calculated from these data bases and is used to obtain the mean Global tilted Irradiance and Direct plus Circumsolar Irradiance solar spectrum.

Keywords: *Spectral Irradiance, Atacama Desert, Atmospheric Radiative Transfer Model, Solar Energy*

1. Introduction

Chile has experienced a rapid grow regarding the implementation of solar energy technologies. According to the Centre for Innovation and Promotion of Sustainable Energy (CIFES), the cumulative installed photovoltaic (PV) capacity in the country surpassed 1.5 GWp in June 2016, where 0.78 GWp will be added next. Concentrated Solar Power (CSP) is also reported with a 110 MW plant currently under construction (CIFES, 2016). Many of these solar projects are located in the Atacama Desert.

The Atacama Desert is located along the Pacific coast in South America. It has a hyper arid climate with annual precipitations lower than 50 mm (Larraín and Escobar, 2012). Characteristic mean temperatures range from 10ºC to 20ºC in winter and 20ºC to 30ºC in summer, whereas the air temperature keeps below 38ºC (McKay et al., 2003). In terms of chemical composition, nitrates represent 28% of the soil and water-soluble salts such as perchlorates and iodides. These salts rarely exist anywhere else (Navarro-González et al., 2003).

doi:10.18086/eurosun.2016.09.01 Available at http://proceedings.ises.org

Under clear sky conditions, the spectral distribution of solar radiation strongly varies during the day, mainly due to the distance that light must travel through the atmosphere, or air mass (M). It also depends on the climate conditions, which are responsible for the variation of the spectrum from one day to another and throughout the year. The most important parameters affecting the solar spectrum are the Solar Zenith Angle (SZA) related to M, cloudiness, the Total Ozone Column (TOC), the Precipitable Water (PW), the Aerosol Optical Depth (AOD), and the reflectance from the ground or albedo.

The Atacama Desert Solar Spectrum and environmental conditions can differ from what is usually found in northern hemisphere. The key factors responsible for these spectral differences are the high mean altitude, a large number of days with clear skies and low absorption ozone and water vapour columns (Cordero et al., 2016). Thus, this location receives highest surface irradiation. It was determined that the Global horizontal irradiation (GHI) can reach more than 8 kWh/m^2 per day resulting in more than 2500 kWh/m^2 per year (Escobar et al., 2014).

Knowledge of the solar spectrum at the earth surface can be important for the application of any solar energy technology but also for other disciplines. A spectral treatment of solar radiation can provide more accuracy since it incorporates more physical phenomena. The spectral irradiance can be essential for spectral, narrow-band and broadband applications. Among the spectral applications, the precise determination of the solar spectrum can be used for quantifying atmospheric parameters, for testing the performance of spectroradiometers, for defining a reference spectrum to certify PV technology, and for obtaining accurate spectra in the UV part of the spectrum. Narrow-band and broadband applications include UV radiation, illuminance and luminous, photosynthetically active radiation, filter radiometry as well as circumsolar radiation for pyrheliometers, assessment of broadband radiation models, turbidity determination from irradiance data and mapping and predictions of radiation fluxes (Gueymard, 2005).

Reference spectra were first generated as independent norms as E-891-82 and E-892-82, for the direct normal and global tilted irradiance, respectively. From June 1999 on, the subcommittee G3.09 of the American Society for Testing and Materials (ASTM) combines these two documents in the "Standard Tables for Reference Solar Spectral Irradiance at Air Mass 1.5: Direct Normal and Hemispherical for a 37 Degree Tilted Surface". This norm is based only on E891 and E892 standards and has the ISO 9845-1 certification. In January 2003, the G159 norm was reviewed and replaced by the G173-03. The current G173-03 was created by the North American PV industry together with ASTM (http://www.astm.org/) and research centers of the US government. They developed and defined two standard distributions of the ground solar spectrum. These spectra are the standards for direct normal and global tilted (at 37º) spectral irradiances (Myers, D. R.; Emery, K.; Gueymard, 2004).

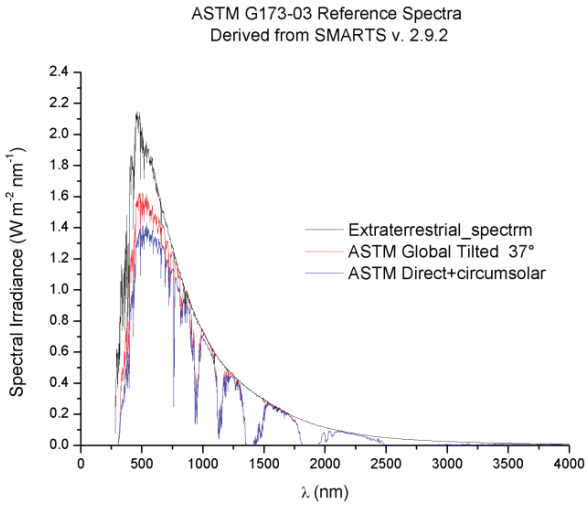

Fig. 1: ASTM G173-03 Reference Spectra Derived from SMARTS v.2.9.2, available in (American Society for Testing and Materials, 2012; Gueymard, 2004; Gueymard et al., 2002; NREL, 2015)

The calculation of the standard spectral irradiances was performed by means of the Simple Model of the Atmospheric Radiative Transfer of Sunshine (SMARTS) (Gueymard, 2001, 1995). SMARTS is a spectral model based in the Fortran programming language which can determine solar spectral irradiances under clear sky conditions for a set of given atmospheric parameters.

The ASTM G173 spectra, available in (NREL, 2015), represents the solar spectral irradiance at the earth surface which falls on a plane with specific orientation and specific atmospheric parameters. This spectrum provides the only reference for the evaluation of PV materials studied under natural and artificial light with different spectral distributions. However, the chosen atmospheric conditions were thought for the US during one year. Therefore, the tilt angle as well as the atmospheric conditions correspond to the national average values (Berman et al., 1999).

As the actual sunlight and environments, where PV systems operate, can be very different to those defined by standard testing conditions (STC), PV modules may not produce the maximum power output, as they should. The spectral effects need to be considered (Simon and Meyer, 2011; Topi et al., 2007). As reported in (Bücher, 1997) the efficiency of PV devices can differ up to 35% with respect to what is rated under STC due to the spectral differences. In order to demonstrate the relevance of the spectra, the photovoltaically active fraction (PAF) was defined (Berman et al., 1999). The effect of the solar spectrum was observed when using semiconductors with different bandgap energy. In order to quantify that impact on the absorbing materials, another parameter was defined, namely the useful fraction (UF) (Gottschalg et al., 2003). According these results, the need for a representative spectrum for Atacama Desert becomes clear.

In order to ensure optimal performance of PV technologies under specific conditions such as those of the Atacama Desert, PV module materials, solar cells and modules can be adapted and designed. Advances in this matter have been reported in (Cabrera et al., 2016, 2015; Ferrada et al., 2017) where different module materials were combined with several solar cell configurations and considering a preliminary calculated Atacama Solar Spectrum.

In order to achieve the aim of this paper, the Simple Model of the Atmospheric Radiative Transfer of Sunshine, or SMARTS (Gueymard, 2001, 1995), was chosen to estimate mean direct an global spectral irradiances for the Atacama Desert. Firstly, SMARTS model and the selected data bases were validated by comparison against global horizontal spectral irradiance measurements in north of Chile. Subsequently, the astronomic factors and long-term atmospheric parameters, available in satellite databases, were averaged for Atacama Desert area. Then, results were used to calculate mean solar spectra. Finally, the estimated Atacama spectra were compared with the ASTM G173-03 Reference Spectra.

2. Comparison with ground measurements

The SMARTS code is used for many applications in the solar industry and previously it has been widely validated by researchers. Some examples are (Eltbaakh et al., 2013; Gueymard, 2008, 2005, 2004, 1995; Kocifaj and Gueymard, 2011; Myers, D. R.; Emery, K.; Gueymard, 2004). However, estimated spectra derived from SMARTS and the available databases were compared against ground spectral measurements in order to know if it is reliable the use of SMARTS and the selected databases in this work.

A first campaign of solar spectral measurements supported by CIFES (CIFES, 2016) was performed in February 2015. The campaign focused on the spectral global horizontal measurement of solar irradiance at several places from Antofagasta and Iquique Regions, in north of Chile. The resulting information from the measuring campaign was not enough to obtain mean solar spectral irradiances for the Atacama Desert, because of the short time period of measurement at each place, around three days per each location, and the short covered area. However, the spectral measurements play an important role to validate the performance of atmospheric radiative transfer models and satellite databases..

The measurement campaign were carried out with a Bentham DTMS300 double monochromator spectroradiometer and a probe to measure the solar spectral global horizontal irradiance (G_λ), as described in (Cordero et al., 2016). The spectroradiometer measured the spectral irradiance between 290 and 1800 nm wavelengths, and took nearly 10 minutes to measure in this range. Consequently, only measurements taken under clear and stable sky conditions were considered. The measurement uncertainty was estimated around ±10% for the UV-B spectral range [290, 315] nm and ±4% for upper wavelengths, obtained from the comparison of the integral values for each spectral range, as reported by authors. Authors also point out that higher uncertainties may be found in atmospheric absorption bands but they did not quantity them.

To compare the estimation of solar spectral irradiances with the measurements, three places where chosen according to the availability of ground and satellite databases. Antofagasta, Calama and Caldera were the selected locations; and Era Interim (ECAD, 2016), Giovanni (NASA and Kempler, 2016) and the ground database of the National Air Quality Information System, SINCA (SINCA, 2015), were the consulted databases.

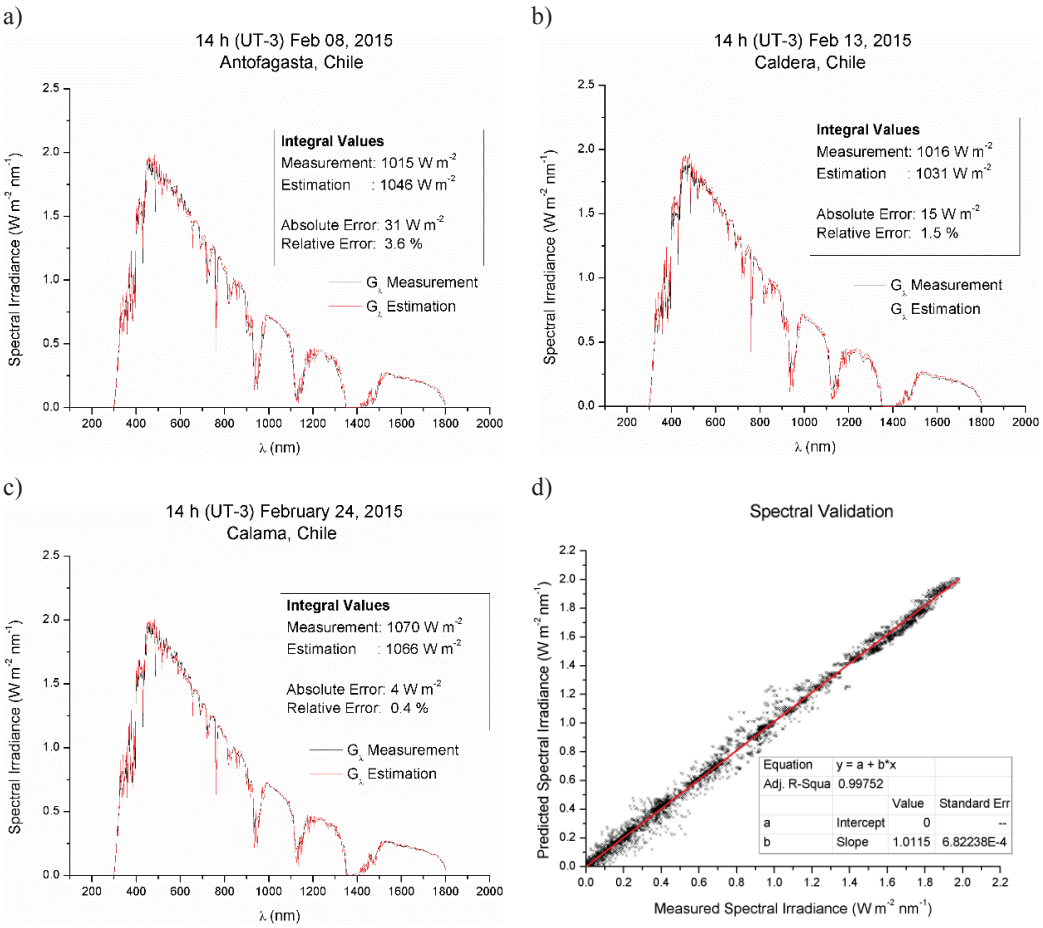

Fig. 2: Spectral global horizontal measurements (black) and spectral irradiance calculations using SMARTS (red) for Antofagasta (a), Caldera (b) and Calama (c). (d) Linear fit of the measured spectral irradiances against the calculations obtained with SMARTS model.

An example of the validation test for each place is shown in Fig. 2, as well as the fit of predictions and measurements for the spectral irradiance values (Fig. 2-d).

As shown in Fig. 2, some differences are presented in the bands relating to the water vapour and ozone absorption. This fact is in agreement with ground measurement reported by authors. A slight deviation can be

observed also at short wavelengths, where predictions overestimate the measurements. These differences may be due to the radiative transfer model or, aerosols or instrument uncertainty. An in-depth investigation will be developed in future works in order to improve the estimations. However, if the instrument uncertainty is taken into account, the results of the SMARTS predictions are in agreement with the measurements shown in Fig. 2 d, and Tab. 1.

Tab. 1: Averaged relative errors for the validation test according to the integration spectral range.

Spectral Range	**Comparison** *Relative error*	*Instrumental Relative* **Error**
[290, 316]	±3%	±10%
[316, 400]	±3%	±4%
[400, 700]	±1%	±4%
[700, 1800]	±3%	±4%
[290, 1800]	±2%	±4%

3. The Atacama Desert Solar Spectra

On one hand, several inputs, most of them characterized with a high temporal and spatial variability, are needed to predict or calculate a solar spectrum. On the other hand, different criteria can be considered to estimate the average values to calculate a representative spectrum for the area of interest. For these reasons, it is difficult to affirm that an average solar spectral irradiance is the representative mean spectra for a specific place, mainly for the direct normal component of the solar irradiance. However, this work intends to highlight the importance of considering local atmospheric parameters in spectral studies related to solar energy technologies instead of the global reference spectra.

The inputs considered to calculate an average of the Atacama Desert Solar Spectrum were: temperature, relative humidity, precipitable water, ozone, pressure, altitude at ground, carbon dioxide, turbidity (AOD at 550 nm), albedo, and surface tilt angle. Each one of the mentioned inputs was changed individually with respect the ASTM G173-03 Reference Spectra. The remaining inputs were left as the default values: Air Mass (M) and Shettle & Fenn aerosol model (rural). All atmospheric parameters were averaged for the area of interest before to be introduced as inputs in SMARTS to estimate mean solar spectral irradiances for Atacama Desert.

The surface tilt angle, β, for PV panels was calculated according to the following expression (Gallegos and R. Righini, 2012):

$$\beta = 3.7 + 0.69\,\phi \qquad \text{(eq. 1)}$$

where β results 18º when the ϕ value is 20.7º.

The average elevation of the area of interest for solar technologies in Atacama Desert is approximately 2 km. This value is derived considering that the elevated places, over 3.5 km, are not suitable for the installation of solar power plants due to their complex orography with steep slopes, difficult access, long distances to the distribution network and villages, and the disadvantages of working at height: altitude sickness, low atmospheric density and strict national safety regulations for these places. The atmospheric pressure value, 804.3 hPa, corresponds to the value of pressure at 2 km altitude for a sub-tropical reference atmosphere considering a pressure of 1013.25 hPa at sea level (Gueymard, 1995).

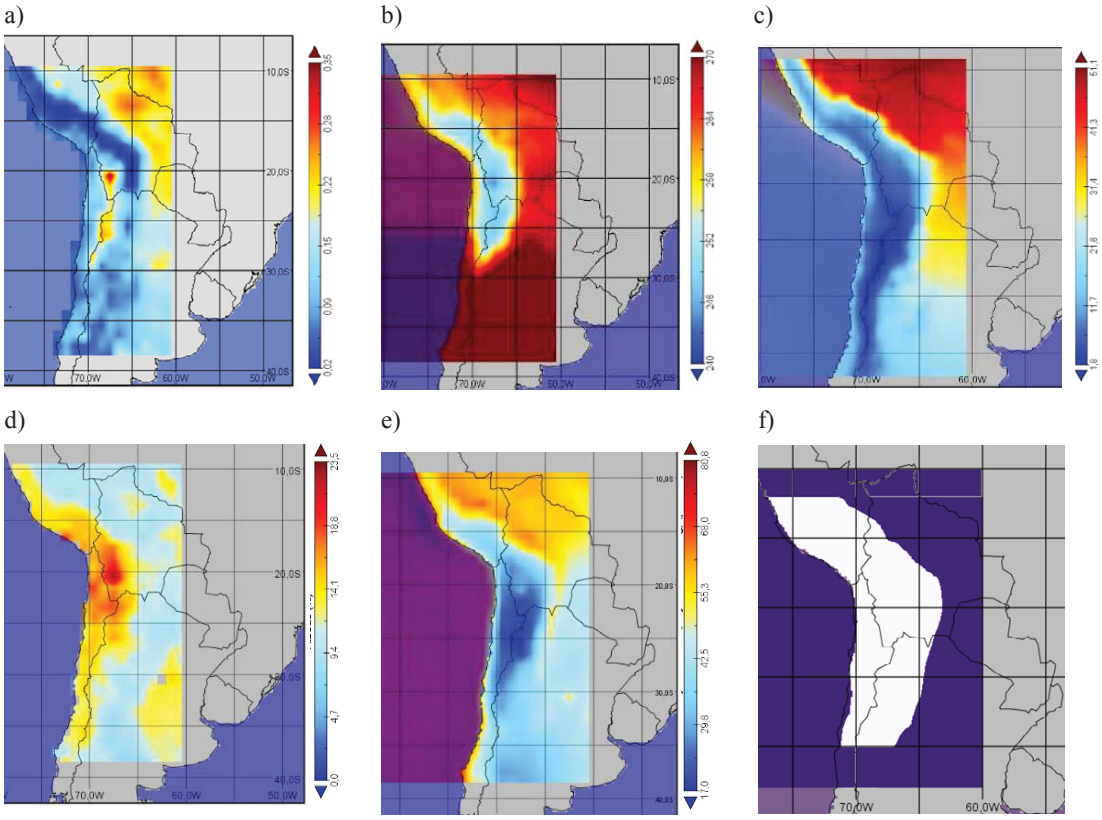

Fig. 3: a) Aerosol Optical Depth at 550 nm [no units]; b) Ozone Total Column [DU]; c) Precipitable Water Vapor [cm]; d) Albedo [no units]; e) Relative Humidity [%]; all parameters were averaged for a time-period of 10 years. f) The white region represents the area where parameters were averaged.

Other atmospheric parameters derived from long-term satellite databases were averaged for Atacama Desert area (Fig. 3), which is represented as a white region in figure 4 f. All parameters plotted in Figure 4 are available in (NASA and Kempler, 2016). Figure 4a and 4c show the MODIS retrievals for Atacama Desert Aerosol Optical Depth (AOD) at 550 nm and Precipitable Water (PW) values averaged from January 2006 to January 2016 (Bellouin et al., 2013; Kato et al., 2011; Remer et al., 2005). Figure 4b shows the Ozone Total Column (TOC) values over the Atacama Desert and figure 4e the Relative Humidity (RH), both from AIRS/Aqua L3 Daily Standard Physical Retrieval (Wang et al., 2012). Albedo (Figure 4d) was obtained from Global Land Data Assimilation System Version 2, bases on temporal averaging of the 3-hourly reprocessed data. It contains a set of land surface parameters simulated from the Noah Model 3.3 (Rodell and Beaudoing, 2015). Albedo values were calculated as an average for dates from January 1999 to January 2010.

Results of the average and the remaining inputs are shown in the table of Figure 4.

As results shows, low levels of TOC and PW are achieved. These results are in agreement with the ground measurements at several points of north of Chile (Cordero et al., 2016; Dirección Meteorológica de Chile, 2015; Galewsky et al., 2011; Kerber et al., 2014, 2012; McKenzie et al., 2015; Patat et al., 2010).

The Atacama Desert spectra derived from SMARTS and the average values of the atmospheric conditions are shown in Figure 4.

PARAMETER	VALUE	UNITS
P	804.3	*(hPa)*
T	22.54	*(C)*
RH	38	*(%)*
T_{MEAN}	14.25	*(C)*
PW	1.5	*(cm)*
TOC	257	*(DU)*
CO_2	400	*(ppmv)*
AOD at 550 nm	0.102	*(--)*
ALBEDO	0.18	*(--)*
β	18	*(°)*
M	1.50	*(--)*

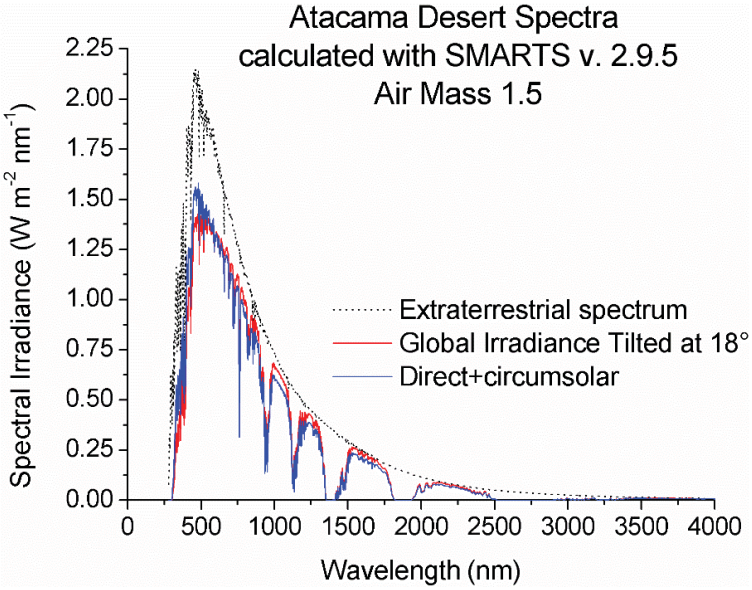

Fig. 4: At left, a table with the inputs resulting from data processing, considered to calculate the Atacama Spectra. Right, Atacama Spectra derived from SMARTS v 2.9.5. Black line represents the extra-terrestrial solar spectrum (Gueymard, 2004), the red line is the global irradiance for a tilted surface at 18°, and the blue line represents the direct and circumsolar irradiance assuming a half aperture angle of a simulated spectroradiometer of 2.5°.

4. Comparison with the ASTM G173-03 Reference Spectra

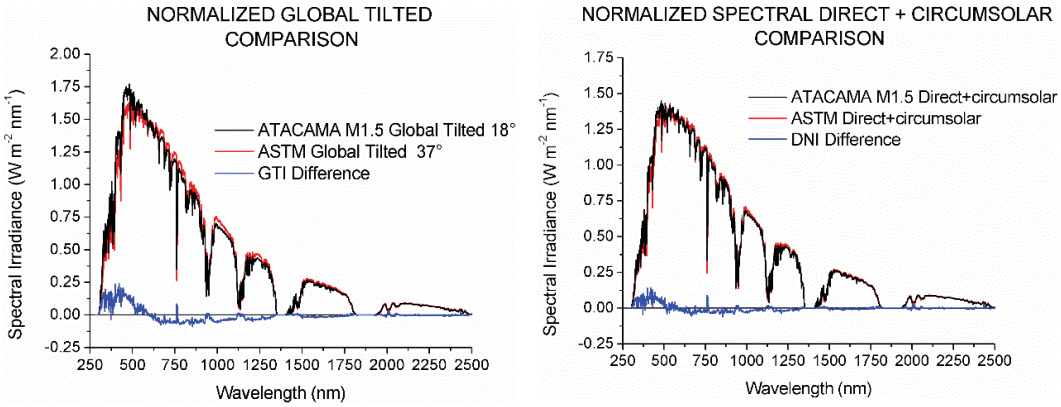

Fig. 5: Right, comparison of Atacama (black) and Reference (red) global spectral irradiances over a tilted surface at 18° and 37° respectively. Left, comparison of Atacama (black) and Reference (red) direct and circumsolar spectral irradiances.

Under the previously defined atmospheric and astronomic conditions, the integral values of the solar spectral global and direct plus circumsolar irradiances estimated for Atacama Desert were 893 and 903 W m^{-2} respectively, while the reference spectra have 1000 W m^{-2} and 900 W m^{-2}. The main different occurs in the global tilted spectrum and it is mainly due to the difference in the tilted angle of the surface where solar radiation is impinging on. A higher tilt angle permits a higher amount of solar radiation reflected from the ground to achieve the surface.

In order to show the differences on how the solar power is distributed along the electromagnetic spectrum, figure 5 shows the comparison of the normalized Atacama Desert spectra with the ASTM G173-03 reference for each solar irradiance component, namely Global (left) and Direct + Circumsolar (right), for M equal to 1.50. Normalization was performed to the integral values of the global tilted and direct plus circumsolar

spectral irradiances of the standard, 1000 W m^{-2} and 900 W m^{-2} respectively. In general, the greatest differences occur in the spectral range from 250 to 600 nm. Elevation above sea level (Pressure), AOD and TOC play an important role in light transmission at wavelengths below approximately 600 nm. The low levels of atmospheric ozone which play an important role in the atmospheric transmittance below the 340 nm, lead to higher UV-B irradiances, as ground measurements have shown, e.g. see (Dirección Meteorológica de Chile, 2015).

In the framework of solar energy technologies, the differences per wavelength do not play a role as important as the power distribution differences inside broadband ranges, excluding those processes, which occur at a given wavelength, such as for water treatment.

Figure 6 shows how much power there is in the ultraviolet (UV), visible (VIS) and near-infrared (NIR) ranges for each spectrum. In other words, it shows how the solar power is distributed for each spectral range. For that purpose, the integral of the spectral irradiance in each range was calculated and compared with the integral for the whole range in two cases: from 280 to 1200 nm (Fig. 6 left) and from 280 to 2500 nm (Fig. 6 right). Both spectral ranges were selected to provide useful information for Concentrated Solar Power (CSP) and Photovoltaic (PV) technologies, respectively.

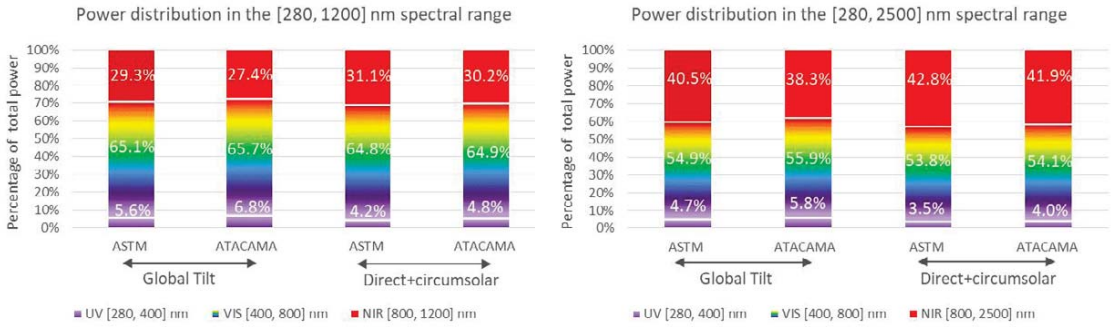

Fig. 6: Solar power distribution for each spectral irradiance according to the UV [290, 400] nm (violet colour), VIS [400, 800] nm (rainbow colour) and NIR [800, 2500] nm (red colour) ranges. Left: results for the [280, 1200] nm spectral range. Right: results for the [280, 2500] nm spectral range.

As figure 6 at left shows, 6.8% of the total hemispherical power received by a 18° tilted surface in Atacama Desert, is confined in the UV spectral range. Paying attention to the irradiance values in this spectral range, 58 W m^{-2} for Atacama and 46 W m^{-2} for the ASTM. It means that the predicted spectrum for Atacama differs 24% from the ASTM, and the difference is 93% higher if the same comparison is done in the UVB spectral range. Similar values can be obtained if the comparison is done for the direct plus circumsolar irradiance, 17% and 67%, respectively.

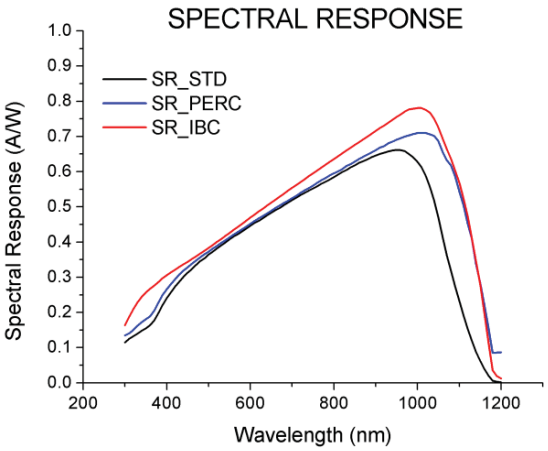

Fig. 7 Spectral Response of standard, PERC and IBC photovoltaic technologies

In order to know how these differences affect the development of solar technologies, three PV cells are studied under the influence of the solar global tilted reference spectrum and the average spectral irradiance estimated for Atacama Desert. The technologies used in this study were: a standard solar cell (STD), a passivated emitter and rear contact solar cell (PERC) and an interdigitated back contact solar cell (IBC) with spectral responses (SR(λ)) shown in Fig. 7.

A good indicator that helps to know about the influence of the solar spectrum shape on solar PV cells or devices is the spectral mismatch factor (MM). The MM is defined in the IEC 60904-7 norm (IEC, 2008) and describes the procedure for correcting the bias error introduced in the testing of a photovoltaic device, caused by the mismatch between the test spectrum and the reference spectrum and by the mismatch between the spectral responses (SR) of the reference cell and of the test specimen. The MM factor is defined in this work as follows:

$$MM = \frac{\int E_{ref}(\lambda) S_{Std}(\lambda) d\lambda \int E_{Ata}(\lambda) S_{sample}(\lambda) d\lambda}{\int E_{Ata}(\lambda) S_{Std}(\lambda) d\lambda \int E_{ref}(\lambda) S_{sample}(\lambda) d\lambda} \quad \text{(eq. 2)}$$

Where $E_{ref}(\lambda)$ is the irradiance per unit bandwidth at a particular wavelength, of the reference spectral irradiance; $E_{Ata}(\lambda)$ is the irradiance per unit bandwidth at a particular wavelength, of the spectral irradiance distribution estimated for Atacama; $S_{Std}(\lambda)$ is the spectral response of the standard PV device; $S_{sample}(\lambda)$ is the spectral response of the test PV device. The relative error (ΔMM) is calculated as a deviation from 1. Results are shown in table 2.

Tab. 2: Spectral mismatch (MM) and relative error of the spectral mismatch (ΔMM) in comparison with the reference global tilted spectrum and reference photocell

CELL	MM	ΔMM (%)
PERC	0.9989	0.11%
IBC	1.0004	0.04%

The calculations show low MM values, 0.998 and 1.000, and ΔMM values, 0.11% and 0.04%, for PERC and IBC solar cells, respectively. These low ΔMM values indicate that the changes in the shape of the spectra, estimated for the specific conditions previously defined in this work, are not significant for the PV cells performance.

The photo-generated current (J_{ph}) is defined as the maximum theoretical current that can be generated by a PV device. It is calculated as (Ferrada et al., 2017):

$$J_{ph} = \int E(\lambda)\, SR(\lambda)\, d\lambda \quad \text{(eq. 3)}$$

Where $SR(\lambda)$ is the spectral response of the considered PV device, E_λ is the incident solar spectral irradiance, and λ is the wavelength. The calculations were performed for both normalized and non-normalized solar spectra estimated for Atacama, and the reference solar spectrum. Results are shown in Fig. 8.

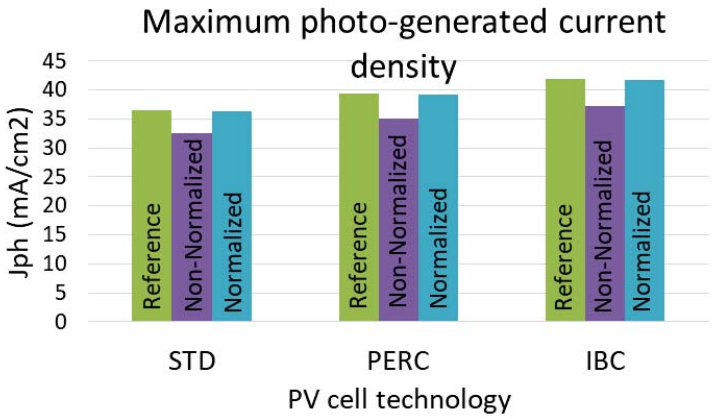

Fig. 8 Maximum photo-generated current (Jph) for different solar cells (STD, PERC and IBC). The green bar indicates the Jph calculated with the reference global tilted spectrum, the violet bar is the Jph for the Atacama Desert global tilted spectrum without normalization, and the cyan bar represents the Jph calculated with the normalized solar spectrum estimated for Atacama Desert.

The results indicate that the maximum difference occurs if the calculation is performed for a non-normalized spectrum, around 11%. On the contrary, the difference is minimum, less than 0.6%, if the comparison is done with normalized solar spectra. This result therefore agrees with the result of the MM comparison, indicating that the shape of the spectrum is not as important as the total amount of incident solar power, at least under the atmospheric and air mass conditions used in this work.

From the point of view of thermal processes, the differences in the energy distribution of the solar radiation do not play a major role. In CSP technologies, the aim is the production of process heat from the incident solar radiation. For this purpose, the receivers play an important role. In this context, receivers are designed to absorb the maximum of the incident solar power, which means pursuing absorptance values close to 1, usually in the 300-2500 nm spectral range. However, the aging of materials used may become a factor to be considered, especially at mirrors and receivers.

5. Conclusions

An estimation of the local solar irradiance spectrum for the Atacama Desert was conducted by deriving relevant atmospheric parameters from satellite databases, and then using those parameters as inputs for the SMARTS model. The atmospheric values were averaged for the area of Atacama Desert. These estimates represent a spectral distribution of the solar power for the specific conditions defined in this work.

The estimated spectra show changes with respect the world reference. These changes are in the amount of solar power and in the shape of the spectral power distribution. Changes are mainly due to the difference in the angle of the tilted surface and also because of the differences in the atmospheric parameters.

The main difference is found for short wavelengths, especially in the UV spectral range. The solar irradiance confined in the UV spectral range for the Atacama calculations resulted in 24 percentage points higher than the reference spectra for the global tilted component.

On one hand, the differences found in the shape of the solar spectrum, are not relevant for the solar technologies. The spectral mismatch calculation for three different solar cell types shown that the relative deviation from 1 is less than 0.11%. The maximum photo-generated current calculations indicates a relative error less than 0.6% respect the reference for the normalized spectrum calculated for Atacama. Both results are in agreement with themselves.

On the other hand, if the maximum photo-generated current calculations are performed with the non-normalized spectrum for Atacama, the relative error is around the 11%. This result indicates that what matters is the amount of energy and not the shape of its spectral distribution, at least under the specific conditions detailed in this paper which takes into account the same air mass than that defined for the world reference (M=1.5).

From the review of the available databases, it was noted that ground-based measurements of long-term atmospheric parameters in Atacama Desert is still necessary. The calculated spectral irradiances through SMARTS were in agreement with the spectral horizontal global measurements. However, an in-depth investigation is required in order to improve estimations, including more measurements for the improvement of the statistical methodology.

6. Acknowledgments

The authors acknowledge the generous financial support provided by the Education Ministry of Chile Grant PMI ANT1201, the Fondecyt Project 3160190, as well as CONICYT/ FONDAP/ 15110019 "Solar Energy Research Center" SERC-Chile.

We also grateful the Financial support by the Education and Competitiveness Ministry of Spain, PRESOL project “Forecast of solar radiation at the receiver of a solar power tower” with references ‘ENE2014-59454-C3-1-R1, 2 and 3’.

7. References

American Society for Testing and Materials, 2012. ASTM G173 - 03 Standard Tables for Reference Solar Spectral Irradiances: Direct Normal and Hemispherical on 37° Tilted Surface [WWW Document]. URL https://www.astm.org/Standards/G173.htm (accessed 9.9.16).

Bellouin, N., Quaas, J., Morcrette, J.J., Boucher, O., 2013. Estimates of aerosol radiative forcing from the MACC re-analysis. Atmos. Chem. Phys. 13, 2045–2062. doi:10.5194/acp-13-2045-2013

Berman, D., Faiman, D., Farhi, B., 1999. Sinusoidal spectral correction for high precision outdoor module characterization. Sol. Energy Mater. Sol. Cells 58, 253–264. doi:10.1016/S0927-0248(99)00002-1

Bücher, K., 1997. Site dependence of the energy collection of PV modules. Sol. Energy Mater. Sol. Cells 47, 85–94. doi:10.1016/S0927-0248(97)00028-7

Cabrera, E., Schneider, A., Rabanal Arabach, J., Ferrada, P., Cordero, R., Fuentealba, E., Kopecek, R., 2015. Advancements in the development of “AtaMo”: a solar module adapted for the climate conditions of the Atacama Desert in Chile, in: Conference: 31nd European Photovoltaic Solar Energy Conference and Exhibition (EU PVSEC). Hamburg, Germany.

Cabrera, E., Schneider, A., Wefringhaus, E., Rabanal Arabach, J., Ferrada, P., Thaller, D., Araya, F., Marzo, A., Trigo, M., Olivares, D., Haas, J., Fuentealba, E., Kopecek, R., 2016. Advancements in the Development of “‘AtaMo’”: A Solar Module Adapted for the Climate Conditions of the Atacama Desert in Chile - The Impact of Soiling and Abrasion, in: Conference: 32nd European Photovoltaic Solar Energy Conference and Exhibition (EU PVSEC). Munich, Germany. doi:10.4229/EUPVSEC20162016-5BO.11.5

CIFES, 2016. Renewable Energy in the Chilean Electricity Market.

Cordero, R.R., Damiani, A., Seckmeyer, G., Jorquera, J., Caballero, M., Rowe, P., Ferrer, J., Mubarak, R., Carrasco, J., Rondanelli, R., Matus, M., Laroze, D., 2016. The Solar Spectrum in the Atacama Desert. Sci. Rep. 6, 22457. doi:10.1038/srep22457

Dirección Meteorológica de Chile, 2015. Indice UV-B observado y pronosticado [WWW Document]. URL http://www.meteochile.cl/radiacion_uv.php (accessed 6.15.16).

ECAD, 2016. Daily data [WWW Document]. URL http://apps.ecmwf.int/datasets/data/interim-full-daily/levtype=sfc/ (accessed 7.16.16).

Eltbaakh, Y.A., Ruslan, M.H., Alghoul, M.A., Othman, M.Y., Sopian, K., 2013. Measurements of spectral-band solar irradiance in Bangi, Malaysia. Sol. Energy 89, 62–80. doi:10.1016/j.solener.2012.11.016

Escobar, R.A., Cortés, C., Pino, A., Pereira, E.B., Martins, F.R., Cardemil, J.M., 2014. Solar energy resource assessment in Chile: Satellite estimation and ground station measurements. Renew. Energy 71, 324–332. doi:10.1016/j.renene.2014.05.013

Ferrada, P., Marzo, A., Cabrera, E., Chu, H., del Campo, V., Rabanal, J., Diaz-Almeida, D., Schneider, A., Kopecek, R., 2017. Potential for photogenerated current for silicon based photovoltaic modules in the Atacama Desert. Sol. Energy 144, 580–593. doi:10.1016/j.solener.2017.01.053

Galewsky, J., Rella, C., Sharp, Z., Samuels, K., Ward, D., 2011. Surface measurements of upper tropospheric water vapor isotopic composition on the Chajnantor Plateau, Chile. Geophys. Res. Lett. 38, n/a-n/a. doi:10.1029/2011GL048557

Gallegos, H.G., R. Righini, 2012. Ángulo Óptimo Para Planos Colectores De Energía Solar Integrados a Edificios. Av. en Energías Renov. y Medio Ambient. 16, 1–7.

Gottschalg, R., Infield, D.G., Kearney, M.J., 2003. Experimental study of variations of the solar spectrum of relevance to thin film solar cells. Sol. Energy Mater. Sol. Cells 79, 527–537. doi:10.1016/S0927-0248(03)00106-5

Gueymard, C.A., 2008. Prediction and validation of cloudless shortwave solar spectra incident on horizontal, tilted, or tracking surfaces. Sol. Energy 82, 260–271. doi:10.1016/j.solener.2007.04.007

Gueymard, C.A., 2005. Interdisciplinary applications of a versatile spectral solar irradiance model: A review. Energy 30, 1551–1576. doi:10.1016/j.energy.2004.04.032

Gueymard, C.A., 2004. The sun's total and spectral irradiance for solar energy applications and solar radiation models. Sol. Energy 76, 423–453. doi:10.1016/j.solener.2003.08.039

Gueymard, C.A., 2001. Parameterized transmittance model for direct beam and circumsolar spectral irradiance. Sol. Energy 71, 325–346. doi:10.1016/S0038-092X(01)00054-8

Gueymard, C.A., 1995. SMARTS, A Simple Model of the Atmospheric Radiative Transfer of Sunshine: Algorithms and Performance Assessment. SMARTS.

Gueymard, C.A., Myers, D., Emery, K., 2002. Proposed reference irradiance spectra for solar energy systems testing. Sol. Energy 73, 443–467. doi:http://dx.doi.org/10.1016/S0038-092X(03)00005-7

IEC, 2008. IEC 60904-7:2008 Photovoltaic devices - Part 7: Computation of the spectral mismatch correction for measurements of photovoltaic devices. 60904–7:2008.

Kato, S., Rose, F.G., Sun-Mack, S., Miller, W.F., Chen, Y., Rutan, D.A., Stephens, G.L., Loeb, N.G., Minnis, P., Wielicki, B.A., Winker, D.M., Charlock, T.P., Stackhouse, P.W., Xu, K.-M., Collins, W.D., 2011. Improvements of top-of-atmosphere and surface irradiance computations with CALIPSO-, CloudSat-, and MODIS-derived cloud and aerosol properties. J. Geophys. Res. 116, D19209. doi:10.1029/2011JD016050

Kerber, F., Querel, R.R., Rondanelli, R., Hanuschik, R., van den Ancker, M., Cuevas, O., Smette, A., Smoker, J., Rose, T., Czekala, H., 2014. An episode of extremely low precipitable water vapour over Paranal observatory. Mon. Not. R. Astron. Soc. 439, 247–255. doi:10.1093/mnras/stt2404

Kerber, F., Rose, T., Chacón, A., Cuevas, O., Czekala, H., Hanuschika, R., Momany, Y., Navarette, J., Querel, R.R., Smette, A., van den Anckera, M., Curé, M., Naylorf, D.A., 2012. A water vapour monitor at Paranal Observatory, in: SPIE Astronomical Telescopes+ Instrumentation. Proc. SPIE 8446,. doi:10.1117/12.924340

Kocifaj, M., Gueymard, C.A., 2011. Theoretical evaluation of errors in aerosol optical depth retrievals from ground-based direct-sun measurements due to circumsolar and related effects. Atmos. Environ. 45, 1050–1058. doi:10.1016/j.atmosenv.2010.07.054

Larraín, T., Escobar, R., 2012. Net energy analysis for concentrated solar power plants in northern Chile. Renew. Energy 41, 123–133. doi:10.1016/j.renene.2011.10.015

McKay, C.P., Friedmann, E.I., Gómez-Silva, B., Cáceres-Villanueva, L., Andersen, D.T., Landheim, R., 2003. Temperature and Moisture Conditions for Life in the Extreme Arid Region of the Atacama Desert: Four Years of Observations Including the El Niño of 1997–1998. Astrobiology 3, 393–406. doi:10.1089/153110703769016460

McKenzie, R.L., Bernhard, G., Madronich, S., Zaratti, F., 2015. Comment on "Record solar UV irradiance in the tropical Andes, by Cabrol et al." Front. Environ. Sci. 3, 26. doi:10.3389/fenvs.2015.00026

Myers, D. R.; Emery, K.; Gueymard, C.C.., 2004. Revising and Validating Spectral Irradiance Reference Standards for Photovoltaic Performance Evaluation. ASME. J. Sol. Energy Eng. 126, 567–574. doi:10.1115/1.1638784

NASA, Kempler, S.J., 2016. Giovanni [WWW Document]. URL http://giovanni.sci.gsfc.nasa.gov/giovanni/ (accessed 9.9.16).

Navarro-González, R., Rainey, F.A., Molina, P., Bagaley, D.R., Hollen, B.J., de la Rosa, J., Small, A.M., Quinn, R.C., Grunthaner, F.J., Cáceres, L., Gomez-Silva, B., McKay, C.P., 2003. Mars-Like Soils in the Atacama Desert, Chile, and the Dry Limit of Microbial Life. Science (80-.). 302.

NREL, N.R.E.L., 2015. Reference Solar Spectral Irradiance: Air Mass 1.5 [WWW Document]. URL http://rredc.nrel.gov/solar/spectra/am1.5/ (accessed 9.10.16).

Patat, F., Moehler, S., O'Brien, K., Pompei, E., Bensby, T., Carraro, G., Postigo, A. de U., Fox, A., Gavignaud, I., James, G., Korhonen, H., Ledoux, C., Randall, S., Sana, H., Smoker, J., Stefl, S., Szeifert, T., 2010. Optical atmospheric extinction over Cerro Paranal. doi:10.1051/0004-6361/201015537

Remer, L.A., Kaufman, Y.J., Tanré, D., Mattoo, S., Chu, D.A., Martins, J. V., Li, R.-R., Ichoku, C., Levy, R.C., Kleidman, R.G., Eck, T.F., Vermote, E., Holben, B.N., Remer, L.A., Kaufman, Y.J., Tanré, D., Mattoo, S., Chu, D.A., Martins, J. V., Li, R.-R., Ichoku, C., Levy, R.C., Kleidman, R.G., Eck, T.F., Vermote, E., Holben, B.N., 2005. The MODIS Aerosol Algorithm, Products, and Validation. J. Atmos. Sci. 62, 947–973. doi:10.1175/JAS3385.1

Rodell, M., Beaudoing, H.K., 2015. NASA/GSFC/HSL (2015), GLDAS Noah Land Surface Model L4 monthly 1.0 x 1.0 degree V2.0, version 2.0, Greenbelt, Maryland, USA [WWW Document]. Goddard Earth Sci. Data Inf. Serv. Cent. (GES DISC). URL http://disc.sci.gsfc.nasa.gov/datacollection/GLDAS_NOAH10_M_2.0.html (accessed 8.20.16).

Simon, M., Meyer, E.L., 2011. The effects of spectral evaluation of c-Si modules. Prog. Photovoltaics Res. Appl. 19, 1–10. doi:10.1002/pip.973

SINCA, 2015. Sistema de Información Nacional de Calidad del Aire, Ministerio del Medio Ambiente, Gobierno de Chile [WWW Document]. URL http://sinca.mma.gob.cl/index.php/ (accessed 5.16.16).

Topi, M., Brecl, K., Sites, J., 2007. Effective efficiency of PV modules under field conditions. Prog. Photovoltaics Res. Appl. 15, 19–26. doi:10.1002/pip.717

Wang, H., Zou, X., Li, G., Wang, H., Zou, X., Li, G., 2012. An Improved Quality Control for AIRS Total Column Ozone Observations within and around Hurricanes. J. Atmos. Ocean. Technol. 29, 417–432. doi:10.1175/JTECH-D-11-00108.1

Conference Proceedings

EuroSun 2016
Palma de Mallorca (Spain), 11 - 14 October 2016

Impact Assessment of Short-Term Temporal Variability of Solar Power in Rajasthan Using SRRA Data

Sujit Kumar Tripathy [1], Indradip Mitra [2], Detlev Heinemann [3], Godugunur Giridhar [4], S. Gomathinayagam [4], Aravindakshan Ramanan [2]

[1] Department of Energy & Environment, TERI University, New Delhi (India)

[2] GIZ GmbH, New Delhi (India)

[3] Energy Meteorology Group, University of Oldenburg, Oldenburg (Germany)

[4] National Institute of Wind Energy, Chennai (India)

Abstract

During the last decade, worldwide deployment of solar photovoltaic power plants has registered an unprecedented growth owing to – initially – politically motivated support programs and – finally – economic competitiveness. India has also witnessed an exponential growth in solar PV installation during the recent years and has set an ambitious target of 100 GW solar PV installed capacity by 2022. In Rajasthan alone, a solar power capacity of around 5.8 GW is aimed to be achieved by that time. However, short-term solar variability can be a hindrance in the process of large scale solar power deployment, as this makes operation of large solar PV plants difficult and management of power grid challenging.

Here, the aim is to study the impact of short-term temporal variability of solar power in Rajasthan. Also, another motive is to observe the effect of spatial smoothing and to quantify the suppression of variability due to the same. The data sets used consist of 1-min solar irradiance data measured at ten time-synchronized solar radiation resource assessment (SRRA) sites dispersed across Rajasthan. The methodology includes calculation of clear sky index (K_t*) using Bird clear sky model, computation of site-pair correlation using the parameter 'Change in clear sky index' (ΔK_t*), evaluation of proposed parameter 'Percentage change in generation' to observe Dispersion-Smoothing effect and sample calculation of parameter 'Diversity Filter' to estimate suppression of variability due to regional smoothing.

Key Words: *Short-term temporal variability, Spatial smoothing, PV power ramps.*

1. Introduction

India, a country of around 1.3 billion population, is power starved. Today still around 22% of the Indian population has no access to electricity (The World Bank, 2015). The Indian government (GOI) has recognized the fact that renewable energy (RE) will play a very important role in reducing the percentage of people, who are deprived of electricity, by providing easier access to clean energy and is working assiduously to create a conducive environment for renewable energy infrastructure growth in the country. Last sexennial, India has witnessed an unprecedented growth in green energy installations. As of June 2015, India's net grid-connected RE capacity stood at 36.47 GW, of which almost 65 % came from wind, while solar PV contributed to nearly 11 % of total RE installed capacity (MNRE, 2015a). Though contribution of solar PV has been meagre compared to the share from wind previously, the scenario is about to change. By the year 2022, the GOI aims to achieve an updated target of 100 GW of solar PV capacity under its Jawaharlal Nehru National Solar Mission (JNNSM) program. In Rajasthan alone, the target is to achieve solar PV power installed capacity of 5.8 GW (MNRE, 2015b).

doi:10.18086/eurosun.2016.09.14 Available at http://proceedings.ises.org

However, short-term solar variability may be an impediment to the large scale solar deployment. Solar variability, which – on the very short-term time scale – happens mainly due to the movement of clouds, can drive a PV power plant from generation at rated power to nearly no generation mode or vice versa in matter of seconds. An array of cloud structures passing in front of the sun can cause an abrupt change in power generation, thus making the operation of solar PV power plants difficult and the management of electrical grids challenging.

In addition, a sudden variation in solar generation due to short-term solar resource variability can be a source of unprecedented challenges for power generation companies, transmission companies and distribution system operators (DSOs). Changes in solar irradiance over a short time scale (seconds) can create power quality problems like voltage flicker & harmonic distortion etc., which may be detrimental to critical, sensitive loads at consumer end. Serious grid level problems like issues with power quality and network outages may occur, when, due to sudden variation in solar power generation and unavailability of sufficient ramping capability, the grid fails to cater to system load. In addition to this, variable PV generation can also have a serious impact on local feeders and substations, which are highly specific to local conditions like demand profile, grid distribution and existing system constraints (CAT Projects, 2015). Tab. 1 lists different impacts on power system due to variable solar generation (IEA, 2015). The grid operator may sometimes need to take corrective actions like using voltage limiters, ensuring availability of ample operating reserve and ramping capability and load following etc.

Tab. 1: Potential impact on power system due to short-term solar variability (IEA, 2015)

Time interval of change in solar irradiance	Potential impact on power system
Seconds	Voltage fluctuation
Minutes	Regulation reserves
Minutes to hours	Load following

Hence, short term solar variability is a very important parameter to study, as the outcome of the study may throw light on the extent to which variability can be experienced and the balancing resources needed to lessen its impact. In recent years, this topic has attracted attention of a large number of researchers and there have been numerous publications on this topic, most notably by (Hoff & Perez, 2010, 2012a, 2012b), (Mills & Wiser, 2010) and (Perez et al, 2015). For most of these studies, synthetic data or satellite data has been used to evaluate the impact of short-term variability over a wide area. (Mills & Wiser, 2010) used ground measured irradiance data from 23 time-synchronized stations to study the event of solar variability in the Southern Great Plains area.

Here, a short-term solar variability study for the state of Rajasthan is conducted using 1-min resolution irradiance data, measured at the Solar Radiation Resource Assessment (SRRA) stations. This is the first time, a wide-area study on assessing the impact of solar variability has been conducted for any state in India using high-quality ground measured irradiance data sets. Also, another motive behind this study is to observe the effect of spatial smoothing and to quantify the suppression of variability due to spatial smoothing. The main rationale behind choosing Rajasthan for this study is the proposed development of solar energy infrastructure in the state in the coming years. Recently, the Indian government has proposed setting up of ultra-mega solar power farms at Sambhar, Bhadla and Jaisalmer of Rajasthan. In the years to come, Rajasthan is going to witness a steep increase in solar power generation and in that context, the selection of Rajasthan for a variability study can be justified.

2. Methods

2.1. Quantifying solar variability for a single site, for a fleet of solar generators & suppression of variability

For properly quantifying variability, the parameters needed to be defined are: (a) the physical quantity that varies (b) the time interval over which it varies and (c) the time period of variation.

The most important physical quantity under assessment can be solar PV power generated from a single site or from a fleet of PV plants, as it is of the highest concern for a solar power producer or grid operator. Solar power generated is also a linear function of solar resources available. Hence, researchers study variability of global horizontal irradiance (GHI) or direct normal irradiance (DNI) in case of unavailability of power generation data. Studying variability of DNI is more relevant for concentrating technologies, while the former is more important for non-concentrating flat plate solar systems. Short-term GHI variability considers variation due to both predictable solar geometry and unpredictable cloud motion. The effect of predictable

components can be excluded by analysing the clear sky index K_t^*, the ratio of GHI to clear sky GHI. This parameter is calculated by applying a clear sky irradiance model with a specific set of atmospheric parameters as input. K_t^* as a normalized quantity then clearly shows any deviation from this highly predictable clear sky situation – especially any cloud induced variability. In this work, the clear sky index K_t^* is used based on the clear sky irradiance model from (Bird, 1984; Myers, 2013).

Time interval (Δt) is the time over which the selected physical quantity, K_t^*, varies. ΔK_t^* is defined as the change that the clear sky index undergoes during the time interval Δt. The time interval can vary from few seconds to hours depending on the concern of the user. For large PV generators or regional grid operators, solar variability over few seconds may not be a serious matter to worry about, but it will be troublesome for a small PV generator or for a single site.

Time period is the time span over which variability is studied. Time span is always a multiple of time interval. Here, for this work, the time period of study is one year.

Now, a nominal variability metric for a single site can be defined as the standard deviation of the change in clear sky index ΔK_t^* during a time interval Δt over the selected time period (Perez & Hoff, 2013).

$$\sigma\ (\Delta Kt^*_{\Delta t}) = \sqrt{Var(\Delta Kt^*_{\Delta t})} \quad \text{(eq.1)}$$

The quantity $\sigma\ (\Delta K_t^*)$ is a normalized dimensionless quantity. This variability is directly proportional to the standard deviation of the change in generated power. Absolute power output variability is expressed by:

$$\sigma(\Delta P_{\Delta t}) = \sqrt{Var(\Delta P_{\Delta t})} \quad \text{(eq.2)}$$

Where $\Delta P_{\Delta t}$ = change in power generated during time interval Δt.

Again, normalized power variability is given by:

$$\sigma(\Delta P_{\Delta t})_{Norm} = \sqrt{Var(\Delta P_{\Delta t})}\ /P_{installed} \quad \text{(eq.3)}$$

Where $P_{installed}$ = net installed capacity at the site under study.

Ideally,

$$\sigma(\Delta Kt^*_{\Delta t}) = \sigma(\Delta P_{\Delta t})_{Norm} \quad \text{(eq.4)}$$

For a fleet of solar generators, the absolute power variability of N plants is given by (Perez & Hoff, 2013):

$$\sigma_{\Delta t}^{fleet} = \sqrt{Var(\sum_{n=1}^{N} \Delta P_{\Delta t}^{n})} \quad \text{(eq.5)}$$

Where $\Delta P^n_{\Delta t}$ = change in generation at n^{th} site during time interval Δt.

For a special case, when all the plants in the fleet have the same installed capacity, exhibit the same variability and their power output time series are uncorrelated, the above equation simplifies to:

$$\sigma_{\Delta t}^{fleet} = \sqrt{(N * Var(\Delta P_{\Delta t}))} \quad \text{(eq.6)}$$

For this special case, the relative normalized power variability for the fleet of generators is given as follows:

$$(\sigma_{\Delta t}^{fleet})_{Norm} = \sqrt{(N * Var(\Delta P_{\Delta t}))}\ /(N * P_{installed}) \quad \text{(eq.7)}$$

Where $P_{installed}$ is the net installed capacity of an individual power plant.

Hence, the relative variability for a fleet of identical generators with their power output time series uncorrelated, experiencing same variability equals each individual plant's relative variability divided by square root of the number of plants N (Perez et al, 2015).

$$\text{Fleet Relative Variability} = (\text{Single Relative Plant Variability})/\sqrt{\text{N}} \quad \text{(eq.8)}$$

Hence, the following equation mentioned in terms of clear sky index (K_t*) can be applied to the relative variability for a fleet of identical generators:

$$(\sigma_{\Delta t}^{fleet})_{\text{Norm}} = \sigma_{\Delta t}^{1}/\sqrt{N} \quad \text{(eq.9)}$$

Here, $(\sigma_{\Delta t}^{fleet})_{\text{Norm}}$ is the fleet's normalized variability and $\sigma_{\Delta t}^{1}$ is a single location's nominal variability. This event of suppression of variability is also known as spatial smoothing effect, which signifies suppression of power variability experienced (by a factor of 1/√N) at a single PV generator when integrated to a fleet of similar but uncorrelated PV power plants. The above equations hold good for a fleet of identical uncorrelated generators, but in actual case, there will be a correlation among any two sites under study, which is a function of distance between them, the time interval and the time period of analysis. Therefore, the key parameter to find is the site-pair correlation (ρ).

Now, considering a pair of identical stations with site-pair correlation ρ, (eq. 9) can be re-written as:

$$(\sigma_{\Delta t}^{pair})_{\text{Norm}} = \frac{\sqrt{(\rho+1)}}{\sqrt{2}} * \sigma_{\Delta t}^{1} \quad \text{(eq.10)}$$

This site-pair correlation parameter for a pair of sites can be evaluated by deriving the weighted mean of each individual day's correlation. Again individual day's correlation is found by correlating the change in clear sky index values between a pair of stations for different time intervals. The weighting factor is the day's variability quantified by the daily variance of ΔK_t* (Perez et al, 2012).

$$\rho_{\Delta t}^{L} = \frac{\sum_{j=1}^{n}(\rho_{\Delta t,j}^{L} * Var(\Delta Kt_{\Delta t}^{*}))}{\sum_{j=1}^{n} Var(\Delta Kt_{\Delta t}^{*})} \quad \text{(eq.11)}$$

Where $\rho_{\Delta t}^{L}$ = Site-pair correlation for a pair of sites separated by a distance L for a time interval Δt,
n = total number of station days analyzed.

In this work, the site-pair correlation between any two sites has been evaluated for n = 365 with Δt varying from 1 minute to 60 minutes and L ranging from 47 km to 532 km.

For a fleet of identical PV generators (whether correlated or uncorrelated), absolute power variability is given by the expression:

$$\sigma_{\Delta t}^{fleet} = \sqrt{Var(\sum_{n=1}^{N} \Delta P_{\Delta t}^{n})} = \sqrt{(\sum_{i=1}^{N}\sum_{j=1}^{N} \text{Cov}(\Delta P_{\Delta t}^{i}, \Delta P_{\Delta t}^{j}))} \quad \text{(eq.12)}$$

Relative Power Variability for a fleet of identical generators can be expressed as:

$$(\sigma_{\Delta t}^{fleet})_{\text{Norm}} = \sigma_{\Delta t}^{fleet}/(N * P_{installed}) \quad \text{(eq.13)}$$

$$(\sigma_{\Delta t}^{fleet})_{\text{Norm}} = \sqrt{(\sum_{i=1}^{N}\sum_{j=1}^{N} \sigma_{\Delta t}^{i}\sigma_{\Delta t}^{j}\ \rho_{\Delta t}^{i,j})} \quad \text{(eq.14)}$$

To quantify the suppression of variability, a factor termed as Diversity Filter (Mills & Wiser, 2010) has been introduced. Diversity Filter denotes the factor by which spatial smoothing takes place. It is expressed by the ratio of agglomerated variability of all sites to the sum of variability at individual sites.

$$\text{Diversity Filter} = \text{D} = \frac{\sigma_{\Delta t}^{fleet}}{\sum_{i=1}^{N} \sigma_{\Delta t}^{i}} \quad \text{(eq.15)}$$

So, for a group of N uncorrelated sites with same variability, Diversity Filter (D) is 1/√N, which is the theoretical maximum by which suppression of variability, for a group of PV generators, can take place. But, for a group of correlated sites the diversity factor can be calculated by using (eq. 15). In our study, we have evaluated Diversity Filter values for ten SRRA sites for time intervals, Δt = 1 minute, 5 minute, and 15 minute on a highly variable 165th day of the year 2014. This value signifies the suppression of variability that can be achieved, by combining outputs from PV plants at these ten different sites and feeding them to a common regional grid.

2.2. Experimental data

2.2.1. SRRA Stations

For this work, we have collected ground measured environmental parameter data-sets from ten solar radiation resource assessment (SRRA) stations in Rajasthan. SRRA stations are automatic stand-alone systems consisting of several high quality/high resolution instruments, which measure available solar radiation (global horizontal irradiance (GHI), diffuse horizontal irradiance (DHI), and direct normal irradiance (DNI)) along with other weather parameters like ambient temperature, relative humidity, atmospheric pressure, and wind speed etc. at a temporal resolution of 1 minute. In the year 2011, the erection and commissioning of 51 SRRA stations was started by the National Institute of Wind Energy (NIWE) with funding from the Ministry of New & Renewable Energy (MNRE), Government of India and technical assistance from the Deutsche Gesellschaft für Internationale Zusammenarbeit (GIZ GmbH) under the SolMap Project. The SolMap project was initiated under Indo-German Bilateral Cooperation and was supported by the German Ministry for Environment, Nature Conservation and Nuclear Safety (Bundesministerium für Umwelt, Naturschutz, Bau und Reaktorsicherheit, BMUB).

In the second phase, NIWE has established 60 more SRRA stations in 28 states and 3 union territories. As of May 2015, there is a total of 121 SRRA stations operating all over India being maintained by NIWE (Fig 1). The SRRA network with 121stations is one of the world's largest pyrheliometric networks and ensures the availability of a solid database of ground measured solar radiation data essential for the deployment of solar power plants in India.

All station data quantifying global, direct and diffuse irradiance as well as other environmental parameters are acquired at SRRA stations and stored in a server at Central Receiving Station (CRS) established at NIWE. The raw data sets are further processed by applying different quality control algorithms. If any errors or inconsistencies are detected, then corresponding data points are flagged. Quality control algorithms are based on Baseline Surface Radiation Network (BSRN) rules set by the World Meteorological Organization (WMO). The radiation data obtained is also compared to modelled clear sky irradiance and to the physical limits. Once, the data points have cleared all the tests, they are cached in another server at CRS (Kumar et al., 2014). For this work, the archived datasets for the year 2014 measured at some selected SRRA stations in Rajasthan, have been extracted from CRS.

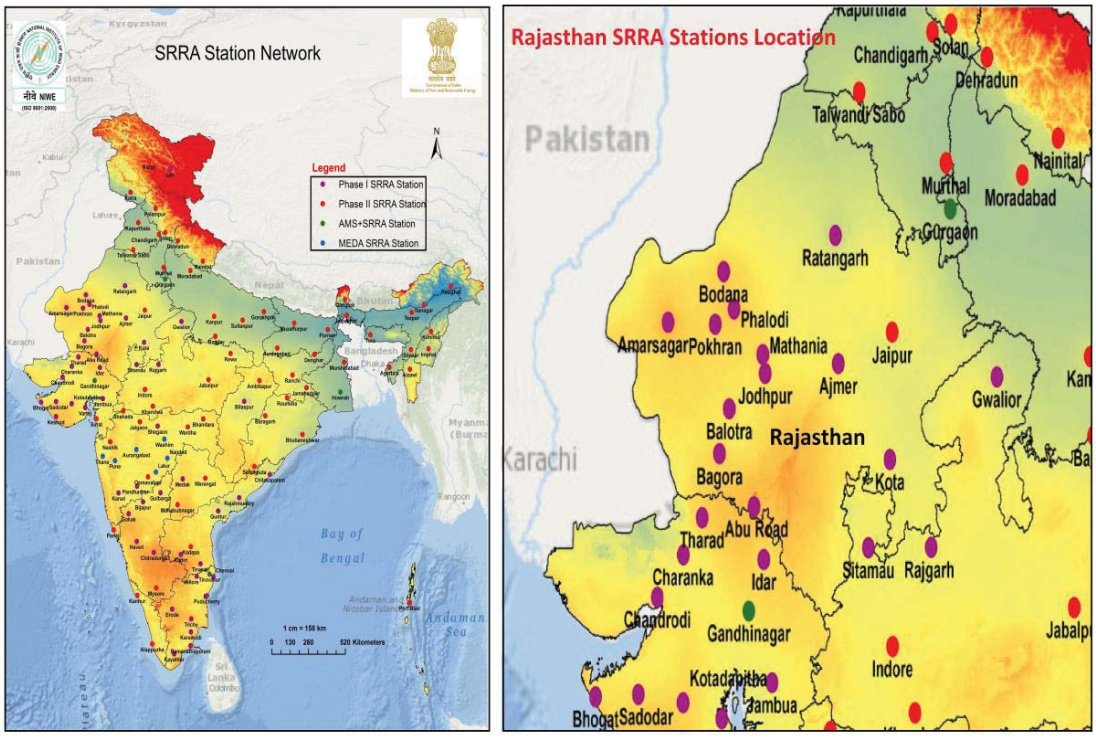

Fig.1: Map of the full SRRA network (left) and the SRRA stations in Rajasthan (right), as of May 2015.

2.2.2. Specification of used data sets

Mentioned below are different environmental parameters studied:

- Temperature (in deg. C), relative humidity (in %) and pressure (in hPa) data sets measured at ten different SRRA stations across Rajasthan for calculating clear sky GHI values.
- Measured GHI (in W/m2) values for calculating the clear sky index (K_t*).

Tab. 2 gives additional details about the quality, temporal resolution and time period of data sets used. As can be seen from the table, the data sets acquired from ten SRRA stations are of high quality as 98.62 % i.e. almost 99% of the meteorological data points pass the quality control tests (Kumar et al., 2014). The use of such high quality radiation data corroborates the authenticity and the validity of the study. Tab. 3 and Fig. 1 (right) provide more detailed information regarding the location of the SRRA stations under observation. Fig. 2 depicts different SRRA stations in Rajasthan. Tabled values of latitude, longitude and elevation at each location have been used to evaluate the Bird model clear sky GHI values, which are subsequently used to calculate the clear sky index (K_t*) at each time step (Bird, 1984; Myers, 2013).

Tab. 2: Detailed Specification of SRRA data sets used.

Details	Specification
Parameters studied	Temperature (in deg. C), relative humidity (in %), pressure (in hPa) and GHI (in W/m2).
Temporal resolution of data sets	1 Minute
Temporal horizon	1 year (analysis done for the year 2014)
Quality control statistics (Percentage of error free values)	98.62 %

Tab. 3: SRRA Stations under study.

SRRA Stations	Latitude (North)	Longitude (East)	Elevation (m amsl)
Aburoad	24º51'57.8" N	72º49'58.0" E	362
Ajmer	26º24'01.6"N	74º39'38.2"E	501
Amarsagar	26º56'30.89"N	70º52'27.28"E	288
Bagora	25º12'50.6"N	72º1'03.3"E	91
Balotra	25º48'19.35" N	72º14'12.95"E	126
Kota	25º08'27.3" N	75º48'35.1" E	304
Mathania	26º16'15.8" N	72º59'7.2' E	271
Phalodi	27º7' 03.6" N	72º20' 43.0" E	242
Pokhran	26º54'58.4" N	71º55'39.5" E	293
Ratangarh	28º4'43.32" N	74º37'18.84" E	312

Fig.2: SRRA stations at Bagora (top left), at Balotra (top right), at Kota (middle left), at Mathania (middle right), at Ajmer (bottom left) & at Phalodi (bottom right).

3. Results

The objective here is to understand site-pair correlation and the factors upon which it depends. Another intention behind the study is to observe the effect of spatial smoothing and to quantify the factor by which suppression of variability takes place due to spatial smoothing.

3.1. Evaluating site-pair correlation

As mentioned before, site-pair correlation value is a very important parameter to evaluate, as it will help in understanding the impact of aggregation of outputs from several PV sites. Here in our study, we have obtained site-pair correlation values among different SRRA sites at Rajasthan for a time interval of 1 minute, 5 minutes, 15 minutes, 30 minutes, and 60 minutes with the time period of the study being one year.

Fig. 3 shows the correlation of change in the clear sky index across the time scales of 1 minute to 60 minutes for pair of sites at different distances from one another. Fit curves, as function of distance between the pair of sites and time interval, can be drawn for all these scattered plots and the equation of the curve can be used to find correlation for intermediate/other distance values.

In Fig. 3, a near-zero correlation for the 1-minute time interval is observed between all ten sites in SRRA network in Rajasthan. Even the closest sites in the network, separated by a distance of 47 km, exhibit zero correlation of change in the clear sky index values (of time interval of 1 minute). Similarly, for the 5-minute time interval, site-pair correlation values are almost zero. Hence, for 1 minute and 5-minute time intervals the ten sites under SRRA networks are almost uncorrelated. Now, if output from PV generators with the same installed capacity at these sites is combined and the power variability at these sites is identical, a smoothing by a factor of $1/\sqrt{N}$ (with N = number of PV generators) will take place. But for the 15-minute time interval, a slight increase in site-pair correlation values is observed with percentage correlation values hovering around 3% - 5% and for 30 and 60-minute time intervals, higher correlation between sites are more evident.

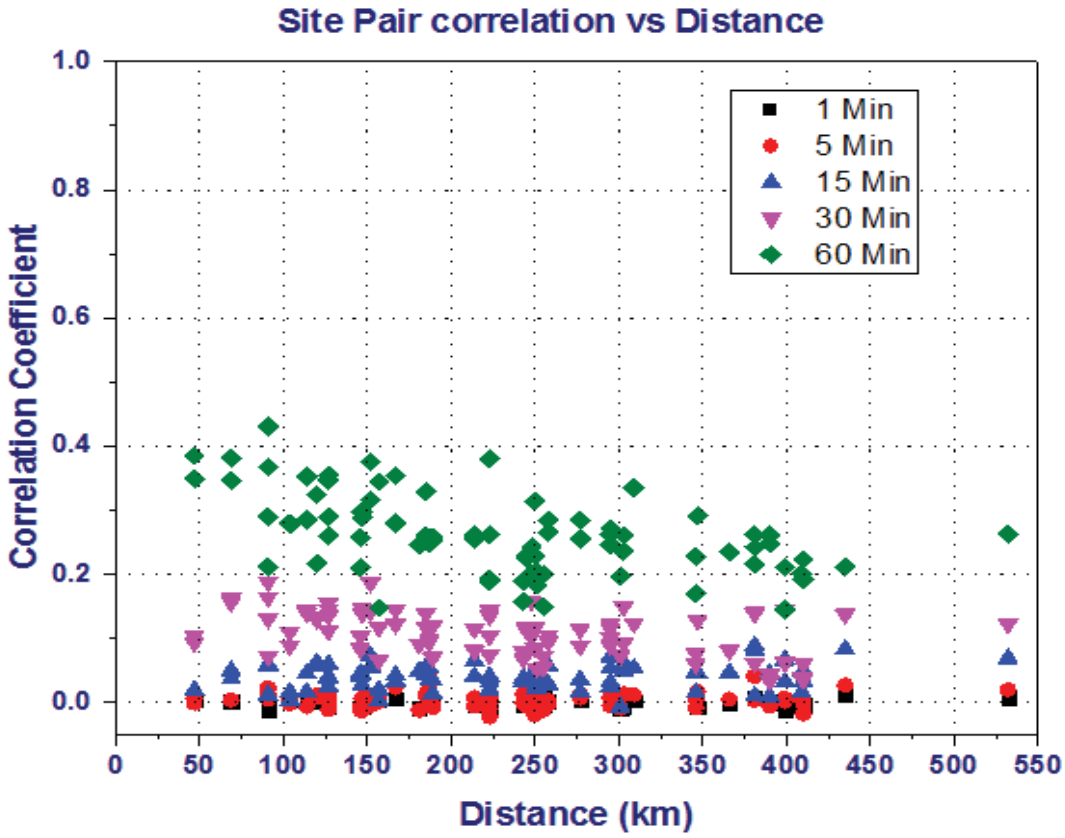

Fig. 3: Site-pair correlation as a function of distance for time intervals Δt = 1min, 5 min, 15 min, 30 min, and 60 min.

3.2. Dispersion-smoothing effect

To observe the pattern of spatial smoothing over a wide area with geographical diversity for a highly variable day, a parameter titled 'Percentage Change in Generation' has been introduced.

The 'Percentage Change in Generation' parameter is defined as:

$$\text{Percentage Change in Generation} = (GHI_2 - GHI_1) / GHI_1 * 100 \qquad \text{(eq. 16)}$$

Where, GHI_1 = GHI measured at time t_1
GHI_2 = GHI measured at time t_2
$t_2 > t_1$, Time Interval, $\Delta t = t_2 - t_1$

The above parameter is analogous to ramp rate (rate of change of power generation in a certain time) as change in solar resources results change in PV power generated and hence, the higher the 'Percentage Change in Generation' value, the higher will be the ramp rate. So, it is an appropriate parameter to demonstrate the effect of smoothing. The above equation has not been used for situations when, $(GHI)_1$ is equal to zero or of extremely small value as the calculation of 'Percentage Change in Generation' parameter would lead to infinity or an unrealistically high value.

We have calculated the 'Percentage Change in Generation' parameter for several days in the year 2014 and here, we have included our observations on a highly variable 165th day of the year i.e. on 14-06-2014. In Fig. 4, the 'Percentage Change in Generation' value for a single site is compared with the same quantity for all 10 sites combined for a certain 'time block' to observe the spatial smoothing effect over a wide area. The term 'time block' has been taken from Central Electricity Regulatory Commission (CERC) documents (CERC, 2011) and describes a time interval of 15 minutes. This value received increasing importance after

modification of the bidding time block from one hour to 15 minutes in the day-ahead market. Scheduling is also done on a 15-minute time interval.

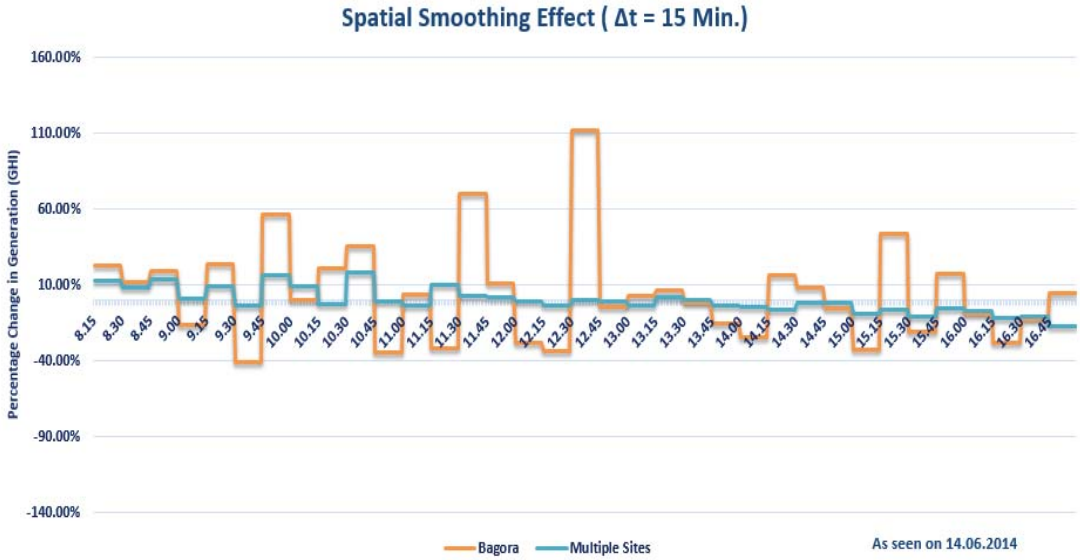

Fig. 4: Spatial smoothing effect observed for multiple sites for the time interval Δt = 15 min.

3.3. Results from sample calculation of diversity filter on a highly variable day

For the day chosen (day 165th of the year 2014), diversity filter values for 1 min., 5 min., and 15 min. time intervals have been calculated. Mentioned below are outcome of these evaluations:

3.3.1. Diversity filter calculation for Δt = 1 min.

Diversity Filter (considering 10 uncorrelated sites with the same variability) = $1/\sqrt{10} = 0.316$.

The theoretical maximum smoothing is achieved for a Diversity Filter of 0.316 i.e., around 68.4% of the variability will be suppressed.

Diversity Filter (considering the site-pair correlation obtained from graph) = 0.341, i.e., almost 65.9% of variability is suppressed. The small difference in the Diversity Filter value indicates that for a time interval of 1 minute the sites are nearly uncorrelated.

3.3.2. Diversity filter calculation for Δt = 5 min.

Diversity Filter (considering the site-pair correlation obtained from graph) = 0.365, i.e. almost 63.5% of variability is suppressed. Again, the small difference in the Diversity Filter value indicates that for a time interval of 5 minutes the sites are nearly uncorrelated.

3.3.3. Diversity filter calculation for Δt = 15 min.

Diversity Filter (considering the site-pair correlation obtained from graph) = 0.392, i.e., almost 60.8% of variability is suppressed. Also for a time interval of 15 minutes, only a slight increase in correlation is observed.

4. Discussion

The analysis that has been done to understand site-pair correlation leads to several points to ponder upon. Firstly, site-pair correlation values decrease with increasing distance between a pair of stations for a specific time interval. This means as the distance between a pair of sites increase, changes in output from PV plants at these locations become less correlated and outputs vary in an independent manner. When solar generation varies independently, maximum smoothing will occur when outputs from these plants are fed to a common grid. Also reduction in site-pair correlation signifies less Diversity Filter value, which indicates higher suppression of variability when the PV plants at sites under study are connected as a fleet. Secondly, site-pair correlation values increase with increasing time interval for a pair of sites. This denotes the significance of

selecting the time interval, which actually depends on the concern of the user. For a regional grid operator, solar variability during a time interval of a few seconds may not matter much, but it will be a reason to worry for a small PV plant. So, it is of utmost importance to study the site-pair correlation to estimate solar variability for a group of PV plants, whether clustered over a small area or dispersed over a wider region.

Another important observation has been the effect of spatial smoothing or dispersion-smoothing effect. As an example, the 15-minute time interval from 12.30 PM to 12.45 PM in Fig. 4 shows 'Percentage Change in Generation' values of +110% and +3% for the single site Bagora and for multiple sites, respectively. That is, a significant spatial smoothing for the time interval of 15 minute is observed, when generation from all ten sites is combined. This also means a substantial reduction in ramp rates for a wider control area compared to that for a single site, which can lead to the conclusion that, from better grid management point of view, wider control area holds greater significance compared to a single generator at a site.

We have also evaluated Diversity Filter values on a highly variable day for time intervals 1, 5, and 15 minutes. Here, the Diversity Filter value signifies the percentage by which variability is suppressed when the output from individual sites are fed to a common regional grid. For the 1-minute time interval, almost 66 % of variability was suppressed, while for 5 and 15-minute time intervals, the percentage values by which suppression took place were estimated to be around 64% and 61%, respectively. The values obtained from the sample calculation also denote the importance of considering the effect of smoothing while estimating reserves for balancing operation. Ignoring the same may lead to an overestimation of balancing requirements and hence, to extra costs.

Previously, we discussed several impacts of short term solar irradiance variability on power system. The same can be addressed by strengthening the grid and by efficient control and management of the power network. A strong, reinforced grid will facilitate evacuation of power from areas with high solar resources to locations where there is a power scarcity and will also enable grid operators to access a wide variety of flexible resources to manage ramps. In India, currently efforts are underway in this direction under the 'Green Energy Corridors (GEC)' project to build an advanced, robust grid infrastructure. Under this project, in addition to improved transmission facilities, it has also been proposed to establish, locate Renewable Energy Management Centers (REMCs) along with load dispatch centers where challenges pertaining to system operation, managing variable resources can be addressed through day-ahead forecasting, improved scheduling and ancillary services. Day-ahead solar power forecasting along with real time solar generation information can prepare grid operators for controlling ramps effectively, while ancillary services can compensate for the operating reserves. Also under GEC project, policies are being formulated to bring market reforms and strengthen power market for improving coordination, cooperation along balancing areas.

In the end, commenting about the usefulness of solar radiation data sets measured at SRRA stations, the high resolution 1-min solar irradiance data shows an excellent value and can be used for a Pan-India level solar variability study. If combined with satellite-based resource information and ground-based sky imagers at few selected sites, this could provide an invaluable information source for studying various aspects of solar power grid integration.

5. Acknowledgements

The work described here was funded by the Deutsche Gesellschaft für Internationale Zusammenarbeit GmbH (GIZ GmbH) on behalf of the Federal Government of Germany under Green Energy Corridors (GEC) of the Indo-German Energy Program (IGEN). The authors would also like to thank the National Institute of Wind Energy (NIWE), Chennai, and the Ministry of New and Renewable Energy (MNRE), Government of India, for providing environmental parameter data sets measured at the Solar Radiation Resource Assessment (SRRA) stations in Rajasthan.

6. References

Bird, R. E., 1984. A simple, solar spectral model for direct-normal and diffuse horizontal irradiance. Solar Energy. 32, 461-471.

CAT Projects & ARENA for public distribution, 2015. Investigating the Impact of Solar Variability on Grid Stability. <http://arena.gov.au/files/2015/03 /150302-Impact-of-Variability-Report-for-public-release.pdf>

Central Electricity Regulatory Commission (CERC), 2011. Suo- Motu Petition No. 127 /2011. <http://www.cercind.gov.in/2011/May/signed_order_in_suo _motu_pet_No_127-2011.pdf>

Hoff, T.E. & Perez, R., 2010. Quantifying PV Power Output Variability. Solar Energy. 84 (10), 1782 –1793.

Hoff, T.E. & Perez, R., 2012a. Modelling PV Fleet Output Variability. Solar Energy. 86 (8), 2177–2189.

Hoff, T.E. & Perez, R., 2012b. Predicting Short-Term Variability of High-Penetration PV. Proc. World Renewable Energy Forum. Denver, CO.

IEA, 2015. Characterization of the Spatio-Temporal Variations and Ramp Rates of Solar Radiation and PV, IEA PVPS Task 14, Subtask 1.3, Report IEA-PVPS T14-05:2015.

Kumar, A., Gomathinayagam, S., Giridhar, G., Mitra, I., Vashistha, R., Meyer, R., Schwandt, M. & Chhatbar, K., 2013. Field experiences with the operation of solar radiation resource assessment stations in India, Energy Procedia 49 (14), 2351 – 2361.

Mills, A., Wiser, R., 2010. Implications of Wide-Area Geographic Diversity for Short-Term Variability of Solar Power. Lawrence Berkeley National Laboratory Technical Report. LBNL-3884E.

MNRE, Govt. of India, 2015a. Programme/ Scheme wise Physical Progress in 2015-16 (During the month of June, 2015). < http://mnre.gov.in/mission-and-vision-2/achievements/ >

MNRE, Govt. of India, 2015b. Tentative State-wise break-up of Renewable Power target to be achieved by the year 2022. < http://mnre.gov.in/file-manager/UserFiles/Tentative-State-wise-break-up-of-Renewable-Power-by-2022.pdf>

Myers, D. R., 2013. Solar Radiation Practical Modelling for Renewable Energy Applications. Energy and the Environment. CRC Press: Taylor & Francis Group.

Perez, R., David, M., Hoff, T., Kivalov, S., Kleissl, J., Lauret, P. & Perez, M., 2015. Spatial and temporal variability of solar energy. <http://asrc.albany.edu/people/faculty/perez/2015/SEVAR.pdf>

Perez, R. & Hoff, T., 2013. Solar Resource Variability. In: Kleissl, J. (ed.). Solar Resource Assessment and Forecasting. Elsevier, pp. 133-148.

Perez, R., Kivalov, S., Schlemmer, J., Hemker Jr., K. & Hoff, T. E., 2012. Short-term irradiance variability: Preliminary estimation of station pair correlation as a function of distance. Solar Energy. 86. 2170–2176.

The World Bank, 2015. Access to electricity (% of population). <http://data.worldbank.org/indicamyerstor/EG.ELC.ACCS.ZS >

On the linear relationship between daily relative sunshine duration and daily mean cloud cover

Heinrich Morf, Senior Member ISES

Buechraiweg 47, 5452 Oberrohrdorf, Switzerland

Abstract

This paper explores the relationship between daily relative sunshine duration – *S* and daily mean cloud cover – *C*. A theoretical model that leads to the idealized linear relationship *S=1-C* often encountered in literature is derived, based on well-defined simplifying assumptions. We demonstrate the application of the theoretical model to vertical visibility and cloud cover readings by ceilometer. We explore the deviations from linearity in the real world in the context of the theoretical model. An estimate of the relationship between measurements of *S* and *C* based on sunshine recorders, ground based human observers, and ceilometers is given.

Keywords: ceilometer, climatology, cloud cover, sunshine, stochastic modeling

1. Introduction

The opinion that the relationship between daily relative sunshine duration – *S* and daily mean cloud cover – *C* would be *S=1-C* under ideal conditions is often encountered in literature. This is a very convenient assumption because it opens the way for many elegant mathematical simplifications. However, in reality a non-linearity between S and C is observed. See Biga and Rosa (1980), Brabec et al. (2016), Gueymard et al. (1995), Hoyt (1977), Rangarajan et al. (1984), and Sarkar (2016). To our knowledge, no convincing description of the conditions leading to *S=1-C* was ever given. This paper fills this argumentation gap. First, the linear relationship is theoretically derived, based on well-defined simplifying assumptions. Then reasons for the non-linear relationship encountered in the real world are given.

We base our theoretical considerations on the stochastic solar irradiance model by Morf (2013). In this model cloud cover – *cc(t)* is modeled as a strictly stationary stochastic process that is invariant to the observation area. Then, sunshine – *ss(t)* is generated in a random experiment with probability *1-cc(t)*. We demonstrate that, over the period from sunrise to sunset – T_d, the mean of *ss(t)* – *S* can be approximated by the mean of *1-cc(t)* – *1-C*. As *S* and *1-C* are both random variables, this implies that ideally also their probability distributions are the same.

Our theoretical model takes a strict nadir view of the sky, and clouds have no vertical extent. To the contrary, real world observations take a single point view of the sky dome. In consequence, sunshine and cloud cover observations are affected by the vertical extent of clouds and the height of the cloud layers in the sky. This disrupts the ideal conditions assumed by the theoretical model and leads to the observed non-linear relationship between *S* and *C*.

2. Problem statement

Prior to going into details, some definitions are necessary.

Definition of daily relative sunshine duration – *S*:

$$S = \frac{\int_{SR}^{SS} ss(t)}{T_d} \qquad \text{eq. (1)}$$

ss(t) is the stochastic insolation function. As an indicator function, it is 1 when the sun is shining and 0 when the sun is hidden behind clouds. T_d is the time between sunrise – *SR* and sunset – *SS*.

doi:10.18086/eurosun.2016.09.09 Available at http://proceedings.ises.org

Definition of daily mean cloud cover – C:

$$C = \frac{\int_{SR}^{SS} cc(t) \cdot dt}{T_d} \qquad \text{eq. (2)}$$

$cc(t)$ is cloud cover. This is the fraction of the sky that is covered by clouds; 0 represents a completely cloudless sky, 1 a fully cloud covered sky. T_d is the time between sunrise – SR and sunset – SS.

Our objective is to demonstrate that the following approximation holds true:

$$S = \frac{\int_{SR}^{SS} ss(t) \cdot dt}{T_d} \approx 1 - C = \frac{\int_{SR}^{SS} (1 - cc(t)) \cdot dt}{T_d} \qquad \text{eq. (3)}$$

For this purpose, we prove that

$$\frac{\int_{0}^{T} ss(t) \cdot dt}{T} \sim \frac{\int_{0}^{T} (1 - cc(t)) \cdot dt}{T} \quad T \to \infty \qquad \text{eq. (4)}$$

The equation states that the two terms converge with increasing observation time T.

We then verify up to what degree the approximation by eq. (3) is met, when delimiting T by T_d in eq. (4).

3. A theoretical interpretation for the linear relationship between daily relative sunshine duration and daily mean cloud cover

We will prove eq. (4) by demonstrating that the expectation – μ of its first term is equal to its second term. Then, we will show that the variance – σ^2 of the first term converges towards 0 with growing T. The leading idea is that a random variable with zero variance is a certainty. Thus, the result of the two terms in eq. (4) must finally match.

For the proof we take a discrete approach, in concordance with the model of Morf (2013), where the random experiment for sunshine is periodically executed with a time interval Δt, corresponding to the minimum time resolution for sunshine encountered in the real world.

Morf (2013) models sunshine by executing a random experiment that generates sunshine from cloud cover with a probability equal to the complement to one of cloud cover:

$$P_{ss=1}(t) = 1 - cc(t) \qquad \text{eq. (5)}$$

$P_{ss=1}(t)$ is the probability for sunshine. $cc(t)$ is cloud cover.

Expectation and variance of $ss(t)$:

$$\begin{aligned} \mu(ss(t)) &= 0 \cdot cc(t) + 1 \cdot (1 - cc(t)) = 1 - cc(t) \\ \mu(ss^2(t)) &= 0 \cdot cc(t) + 1 \cdot (1 - cc(t)) = 1 - cc(t) \\ \sigma^2(ss(t)) &= \mu(ss^2(t)) - \mu^2(ss(t)) = (1 - cc(t)) \cdot cc(t) \end{aligned} \qquad \text{eq. (6)}$$

Integrating the expectation of $ss(t)$ over T and normalizing by T leads to the proof of the first proposition:

$$\mu\left(\frac{\int_{0}^{T} ss(t) \cdot dt}{T}\right) \approx \mu\left(\frac{\sum_{n=1}^{N} ss_n}{N}\right) = \frac{\sum_{n=1}^{N} (1 - cc_n)}{N} \approx \frac{\int_{0}^{T} (1 - cc(t)) \cdot dt}{T} \qquad \text{eq. (7)}$$

whereby $N = T/\Delta t$.

To demonstrate the convergence of the variance of the first term of eq. (4) towards zero we proceed as follows:

$$\sigma^2\left(\frac{\int_0^T (ss(t))\cdot dt}{T}\right) \approx \sigma^2\left(\frac{\sum_{n=1}^{N} ss_n}{N}\right) = \frac{\sum_{n=1}^{N}(1-cc_n)\cdot cc_n}{N^2} \qquad \text{eq. (8)}$$

whereby $N=T/\Delta t$. With increasing N the variance given by eq. (8) converges towards zero. Thus, one may write:

$$\frac{\int_0^T ss(t)\cdot dt}{T} \sim \frac{\int_0^T (1-cc(t))\cdot dt}{T} \quad T\to\infty \qquad \text{Q.E.D.} \qquad \text{eq. (9)}$$

As the two terms of eq. (9) converge, so will also their probability distributions. We refer the reader to Morf (2011) for an analysis and to Morf (2014) for an analytical expression of this probability distribution.

Executing the random experiment for sunshine every 30 seconds (corresponding roughly to the minimum time resolution of sunshine in the real world) in the model described by Morf (2013) leads to a spread in the plot of *S* against *C* that is smaller than *0.05* for both, *S* and *C*. Thus, on a daily basis, eq. (3) may be used with little loss of accuracy. See Fig. 1.

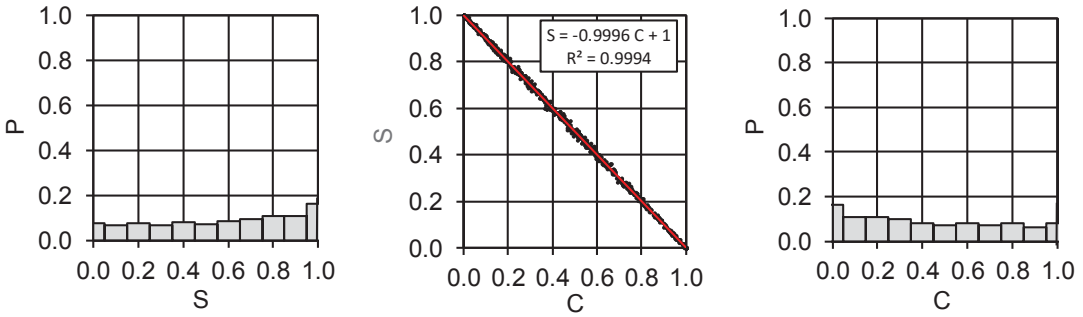

Fig. 1: Simulated plot *S=g(C)* of daily relative sunshine duration – *S* as a function of daily mean cloud cover – *C* and the probability bar charts of *S* and *C*. Observe the little spread of the plot, the high correlation coefficient of the least square fit, and the equality of the probability bar charts of *S* and *1-C*.
Simulation results for Payerne, Switzerland, in July. 300 points, roughly the July-days of 10 years, are shown. A time resolution of 30s was used for the simulation.

4. Vertical visibility and ceilometer readings

The model of Morf (2013) that generates sunshine – *ss(t)* by a random experiment with probability equal to the complement to one of cloud cover – *1-cc(t)* (which is the basis of our theoretical considerations) is an approximation of another model given by Morf (2011). It generates vertical visibility – *vv(t)* with a probability equal to the complement to one of cloud cover – *1-cc(t)*. *vv(t)*, as defined by Morf (2011), describes the state of the sky (0 for covered, 1 for clear) at the observer's zenith. The only difference between the two models is that one is defined for sunshine – *ss(t)* and the other for vertical visibility – *vv(t)*. As *vv(t)* takes a strictly zenithal view, the observations are not affected by the vertical extent of clouds. Therefore, it fits the theoretical model better than *ss(t)*.

Thus, under the assumptions of our theoretical model one may write for eq. (9):

$$\frac{\int_0^T vv(t)\cdot dt}{T} \sim \frac{\int_0^T (1-cc(t))\cdot dt}{T} \quad T\to\infty \qquad \text{eq. (10)}$$

The equation states that the two terms converge with increasing observation time *T*.

Returning to eq. (3), we write:

$$S_{vv} = \frac{\int_{SR}^{SS} vv(t) \cdot dt}{T_d} \approx 1 - C_{vv} = \frac{\int_{SR}^{SS} (1 - cc(t)) \cdot dt}{T_d} \qquad \text{eq. (11)}$$

S_{vv} is the daily relative vertical visibility duration.[1]

vv(t) also corresponds to the reading of a ceilometer that indicates either 0 (covered) or 1 (clear). Thus, eq. (10) is the fundamental equation for the estimation of cloud cover by ceilometer readings.

Cloud cover by ceilometer readings is calculated as the complement to one of the moving average of the ceilometer readings over the period *T*. Thus, it is the moving average of *cc(t)* over *T*, and not *cc(t)*. The integration time – *T* of a ceilometer is small in comparison to the rate of change of cloud cover. Therefore, the difference between the two values is negligible.[2] Daily mean cloud cover derived from ceilometer readings – C_c is then the mean over T_d of the moving average of *cc(t)* over *T*. Note that this procedure, contrary to eq. (11), will deviate from reality, even under the ideal conditions of the theoretical model.

The automatic determination of cloud cover by ceilometer is established practice. In the USA, it has replaced cloud cover observations by ground-based human observers at the end of the twentieth century.

5. The non-linearity

The non-linearity under discussion is an upward bend of the straight line for *S=g(C)* in Fig. 1. See also the least square fits for $S_s=g(C_g)$ in Fig. 2.

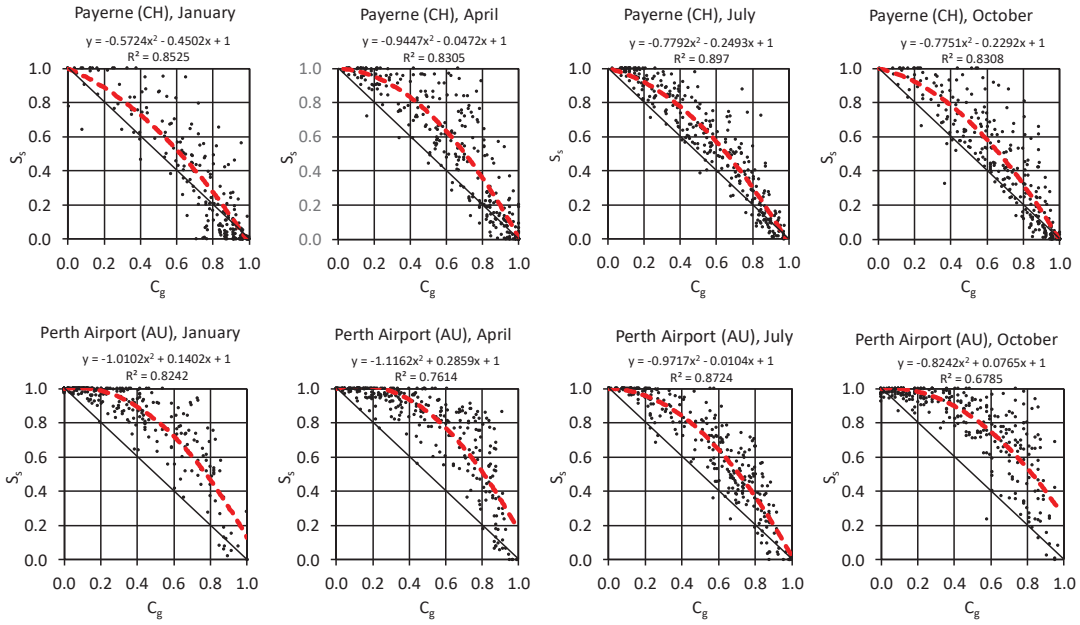

Fig. 2: Plots $S_s=g(C_g)$ of daily relative sunshine duration measured by sunshine recorder – S_s as a function of daily mean cloud cover reported by ground based human observers – C_g. Observe the slight upward bend of the least square fits.

Observe the subscripts introduced for *S* and *C* in Fig. 2. The subscript *s* indicates that a value was derived from sunshine recorder readings, and the subscript *g* indicates that it was derived from cloud cover observations by ground-based human observers.

[1] For the sake of compatibility with the theoretical model, we prefer to use the mnemonic S_{vv} (instead of, for example, *V*) for daily relative vertical visibility duration.
[2] For the determination of cloud cover, ceilometers use a sampling interval – Δt of about 30 seconds and an integration time *T* of about 30 minutes.

It is worth the while to have a closer look at the two variables S_s and C_g:

- Daily relative sunshine duration from the traces of sunshine recorders – S_s: This is the daily relative sunshine duration from sunrise to sunset, measured by a sunshine recorder at a single point on earth, in the line of sight to the sun. It is well known that the free line of sight to the sun depends on the elevation of the sun in the sky due to the vertical extent of clouds and the height of the cloud layers in the sky (Lund and Shanklin, 1971).
- Daily mean cloud cover from observations by ground-based human observers – C_g: The objective is to determine the proportion of the sky dome that is obstructed by clouds when seen from a single point on earth – $cc_g(t)$. Every single cloud cover observation – $cc_g(t)$ is an instant average of cloud cover over the entire sky dome. Daily mean cloud cover – C_g is then the mean of cloud cover – $cc_g(t)$ from sunrise to sunset.

These two variables are not related by the linear relation $S=1-C$, but by the slightly up bent curves of the least square fits depicted in Fig. 2. It is well known that for a function of two random variables $Y=g(X)$ – here $S_s=g(C_g)$ – the probability density functions (*pdfs*) – $f(x)$ and $f(y)$ are related by:

$$f(y)\cdot|dy| = f(x)\cdot|dx| \qquad \text{eq. (12)}$$

The vertical bars indicate absolute values.[3]

Thus, in consequence of the up-bent function $S_s=g(C_g)$, the pdf of S_s as well as of C_g will be skewed towards higher values than in the linear relationship $S=1-C$. Hence, the mean of S_s becomes greater than the mean of $1-C_g$.

Fig. 3 depicts probability bar charts of S_s and $1-C_g$ with the corresponding means for selected calendar months in Payerne, Switzerland and Perth Airport, Australia. It follows from the foregoing paragraph that the pdf of S_s is skewed to the right and the one of $1-C_g$ to the left. As to be expected, the mean of S_s is always greater than the mean of $1-C_g$. (Means are marked with overbars.)

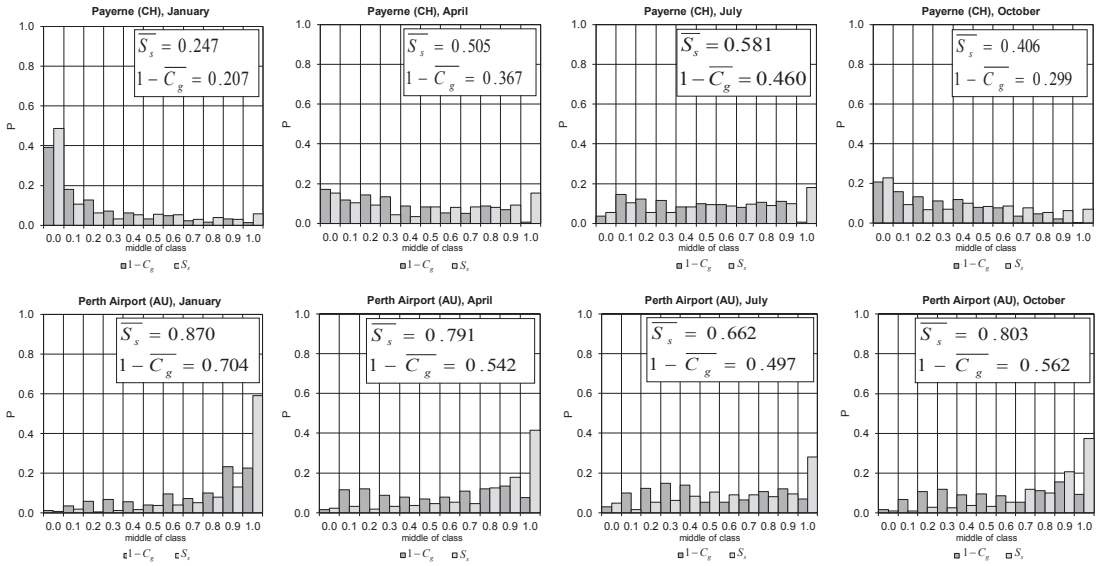

Fig. 3: Comparison of the probability bar charts of daily relative sunshine duration measured by sunshine recorder – S_s and the complement to one of mean daily cloud cover measured by ground based human observers – 1-C_g. Observe that the mean of S_s is higher than that of $1-C_g$. Overbars indicate means.

A concentration of readings of $1-C_g$ around *0.1 ... 0.4* keeps the mean of $1-C_g$ low. Cloud cover observations by ground-based human observers seem not to reflect properly the free line of sight to the sun through open cloud fields. A further disturbance that keeps the mean of $1-C_g$ low is caused by the reluctance of ground

[3] As an alternative, to the least square regressions for $Y=g(X)$ in Fig. 2, one may obtain a regression line for $Y=g(X)$ from $f(x)$ and $f(y)$, based on eq. (12). It brings $f(x)$ and $f(y)$ in proper relation. Although the objectives of the two regression methods are different, they lead to only slightly different results here.

based human observers to declare minimum cloud cover of 0 okta (tenth), because they are instructed to do so only when the sky is absolutely clear. On the other hand, excessive readings for $S_s=1$ keep the mean of S_s high. Hoyt (1977) attributes this effect to thin cirrus clouds: while a ground based human observer would see a covered sky, a sunshine recorder would still register sunshine.

6. Delimiting results

As for the relation $S=1-C$ of the theoretical model, imagine that corresponding to daily relative cloud cover from observations by ground based human observers – C_g, there is daily relative sunshine duration – $S_g=1-C_g$. Likewise, imagine that corresponding to daily relative sunshine duration from sunshine recordings – S_s, there is mean daily cloud cover – $C_s=1-S_s$. Consequently, for the case of the up bent relation $S_s=g(C_g)$ encountered in the real world, the following inequalities hold true: [4]

$$1-\overline{S_s} < \overline{C} < \overline{C_g} \;,\; 1-\overline{C_g} < \overline{S} < \overline{S_s} \;,\; \textit{whereby} \;\; \overline{C}=1-\overline{S} \qquad \text{eq. (13)}$$

The overbars indicate that the values are expectations. $\overline{C}$ and $\overline{S}$ correspond to the theoretical model; they might have been estimated from vertical visibility readings – *vv(t)* by ceilometer. Fig. 4 depicts the inequality for $\overline{C}$ at Payerne, Switzerland and Perth Airport, Australia.[5]

The inequalities may be helpful for data cross checks and to estimate a parameter when others are known. Each of the three results – $C_s=1-S_s$, $C=1-S$, and $C_g=1-S_g$ – is also correct in its own right. One might as well chose data of that observation method whose results fit best a specific problem at hand. For example, Morf (2011) suggests to use cloud cover observations by ground based human observers when the emphasis is on diffuse irradiation and data from traces of sunshine recorders when the interest concentrates on good results for direct irradiance. Climatologists might prefer data from zenithal views by ceilometer.

Hoyt (1977), analyzing data from 72 locations in the USA, concludes that $1-S_s$ is a better estimate for C than C_g. He reasons that $1-S_s$ comes closer to cloud cover estimates from satellite observations. This result must be viewed with caution, because the viewing angle of satellites down to earth is mostly not in strict nadir direction.

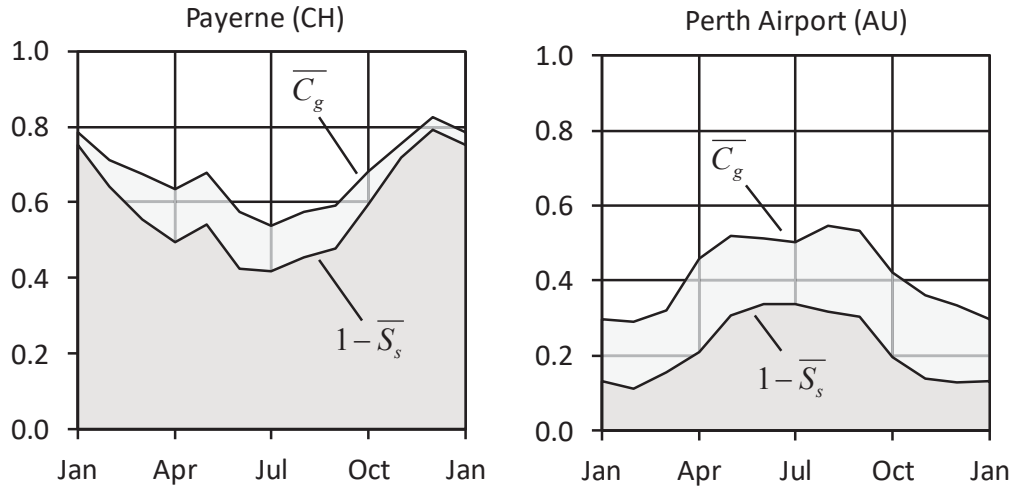

Fig. 4: Delimiting the expected daily mean cloud cover – $\overline{C}$.
The value of $\overline{C}$ must lie within the upper boundary $\overline{C_g}$ and the lower boundary $1-\overline{S_s}$.

[4] Moriarty (1991) predicts a down bent relationship for $S_s=g(C_g)$ at high latitudes. The inequalities would have to be modified to cover this case. So far, we have not encountered this effect in the real world.
[5] The irregularity in May for Payerne is a consequence of the outbreak of the volcano Eyjafjallajökull in April 2010.

7. Verification of the inequalities

So far, we could not thoroughly verify the inequalities of Section 6 in the real world, because there are few records of the three variables that have been taken at the same location, at the same time, and over a sufficiently long time-period. However, Neske (2014)[6] presents two data cloud diagrams of daily relative sunshine duration – S as a function of daily mean cloud cover – C that have been taken at two stations that are both representative for the area of Hamburg, Germany.

- One was taken from 2004 to 2011 at the NDR Transmitter Mast in Hamburg Billwerder by the Meteorological Institute of the University of Hamburg. S_s was calculated from pyranometer readings and C_c from ceilometer readings.
- The other was taken from 1996 to 2011 at Hamburg Airport by the German National Meteorological Service – DWD. S_s was derived from the recordings of an electronic SONI sunshine switch and C_g from observations by ground-based human observers.

The S_s values of the two stations are statistically undistinguishable, whereas the C values are different. For Hamburg Airport the function $S_s=g(C_g)$ has the characteristic upward bend as in Fig. 2. For Hamburg Billwerder the linear relation $S_s=1.088-0.9088 \cdot C_c$ is a good fit. As expected, the use of the ceilometer data at Hamburg Billwerder instead of the estimates by ground-based human observers has brought the relation more within reach of the relation $S=1-C$ of the theoretical model.

8. Concluding remarks and outlook

The findings in this work contribute to the understanding of the stochastic behavior of sunshine and cloud cover, and indirectly also of solar irradiance. We hope that they will facilitate the estimate of model parameters (Morf, 2011; Morf, 2013), and will give new impulses to the challenge of generating realistic two-dimensional cloud cover patterns as a function of time (Morf, 2011). As already brought to attention in Morf (2014), there seems to be one single Markov process that drives most cloud related dynamic processes. We hope this observation will give rise to interest for further investigations.

As a byproduct, this paper provides support for the approach by Morf (2011) of modeling cloud cover as a strictly stationary stochastic process that is invariant to the observation area. Otherwise, determining cloud cover from single point ceilometer readings would be impossible.

The relationship between the differing results given in form of inequalities in Section 6. might be helpful for a seamless transition from historical records of cloud cover estimates by ground based human observers to the automated cloud cover estimates based on ceilometer readings being introduced starting at the end of the last century.

Our proof that the mean of cloud cover converges to the mean of relative sunshine duration with increasing length of the observation period deserves further mathematical evaluation and exploration. It describes a transition of a random variable to a certainty.

In mathematical terms:

Given an indicator function $ind(t)$ with probability $P_{ind=1}(t)$, then

$$\frac{\int_0^T ind(t) \cdot dt}{T} \sim \frac{\int_0^T P_{ind=1}(t) \cdot dt}{T} \quad T \to \infty \qquad \text{eq. (14)}$$

The equation states that the two terms converge with increasing observation time – T.

As a simple example, consider the discrete case of tossing a coin. Then the probability of receiving *head* – $P_{ind=1}(t)$ will be 0.5, and with increasing number of tosses the probability to have a *head* in the tosses will

[6] Caution must be taken in Neske (2014): The paper uses an uncommon linear scale for daily mean cloud cover – C with a value of 0 for a totally cloud free sky and a value of 0.8 for a fully cloud covered sky.

turn into certainty. The consequences of this statement cannot be overestimated. The reasoning "if the probability for an event is infinitely small, then it will never happen" should rather be exchanged against the statement "even if the probability for an event is infinitely small, it will certainly happen".

9. Data

Publicly available data sets of the following locations are used in this paper:

- Payerne, Switzerland, 46.80 N / 6.93 E, for the years 2001-2010
- Perth Airport, Australia, 31.93°S / 115.98° E, for the years 1998-2007

From both stations, records of daily sunshine duration from sunshine recorders are used. The rare days with unreliable or missing data were removed. The time between sunrise and sunset was set to the duration of the period where the sun is more than 5° above the horizon.

From both stations, cloud cover data observed by ground-based human observers are used. At both stations, observations are taken every three hours starting at zero hours local time. The rare days with unreliable or missing data were removed. Cloud cover observations of 9 okta were changed to 8 okta. Daily mean cloud cover was calculated as the average of cloud cover from sunrise to sunset using linear interpolation; the result in *okta* was converted to *tenth*, dividing by 8. For every calendar month, local time for sunrise and sunset was determined based on the average maximum possible sunshine duration.

Conflict of Interests

The author declares that there is no conflict of interests regarding the publication of this paper.

Acknowledgements

The author wishes to thank the Western Australian Climate Service Centre for the supply of a ten-year data set of Perth Airport, containing daily sunshine duration, daily global irradiation, and total cloud cover observations.

The author wishes to thank the Swiss Federal Office of Meteorology and Climatology – Meteo Swiss for the supply of a ten-year data set of Payerne, containing daily sunshine duration, daily global irradiation, and total cloud cover observations.

Nomenclature

Capital Letters

C	daily mean cloud cover [-]
	without index it corresponds to the theoretical model, or it applies generically
N	counter limit [-]
P	probability [-]
R^2	regression coefficient
S	daily relative sunshine duration [-]
	without index it corresponds to the theoretical model, or it applies generically
SR	sunrise [s]
SS	sunset [s]
T	time, duration [s]
V	daily relative vertical visibility duration [-]

Small Letters

cc	cloud cover [-]
g	generic function
f	probability density function – pdf
ind	generic indicator function
n	generic counter [-]
ss	sunshine [-]
t	time [s]
x	generic variable
y	generic variable
vv	vertical visibility [-]

Special Characters

$\lvert\ \rvert$	absolute value
$\bar{}$	expectation, mean
$\sim$	convergence
$\approx$	approximation

Greek Letters

μ	mean, expectation
σ^2	variance

Subscripts

c	derived from ceilometer readings
d	from sunrise to sunset
g	derived from cloud cover by ground based human observers
s	derived from sunshine recorder readings
vv	derived from vertical visibility

References

Biga, A.J., Rosa, R., 1979. Contribution to the study of the solar radiation climate of Lisbon. Solar Energy 23, 61–67.

Brabec, M., Badescu, V., Paulescu M., Dumitrescu, A., 2016. A new perspective on the relationship between cloud shade and point cloudiness. Atmospheric Research 172-173, 136-146.

Gueymard, C., Jindra, P., Estrada-Cajigal, V., 1995. A critical look at recent interpretations of the Ångström approach and its future in global solar radiation prediction. Solar Energy 54, 357-363.

Hoyt, D.V., 1977. Percent of possible sunshine and the total cloud cover. Monthly Weather Review 105, 648–652.

Lund, I.A., Shanklin M.D., 1971. Universal methods for estimating probabilities of cloud-free lines-of-sight through the atmosphere. Journal of Applied Meteorology 12, 28-35.

Morf, H., 2011. The stochastic two-state cloud cover model STSCCM. Solar Energy 85, 985-999.

Morf, H., 2013. A stochastic solar irradiance model adjusted on the Ångström-Prescott regression. Solar Energy 87, 1-21.

Morf, H., 2014. The parameterization of cloud cover. Energy Procedia 57, 2014, 1293-1298.

Moriarty, W.W., 1991. Cloud cover as derived from surface observations, sunshine duration, and satellite observations. Solar Energy 47, 219-222.

Neske, S., 2014. About the relation between sunshine duration and cloudiness on the basis of data from Hamburg. Journal of Solar Energy, 2014, Article ID 306871, 7 pages.

Rangarajan, S., Swaminathan, M.S., Mani, A., 1984. Computation of solar radiation from observations of cloud cover. Solar Energy 12, 553-556.

Sarkar, N.I., 2016. Estimation of solar radiation from cloud cover data of Bangladesh. Renewables: water, wind, and solar 3:11, 1-15.

Conference Proceedings

EuroSun 2016
Palma de Mallorca (Spain), 11-14 October 2016

Influence of air pollutants on spectral regions from ultraviolet to visible solar radiation

Marie Opálková[1], Michal Burda[2], Martin Navrátil[1] and Vladimír Špunda[1]

[1] Department of Physics, Faculty of Science, University of Ostrava, Ostrava (Czech Republic)

[2] Institute for Research and Applications of Fuzzy Modeling, CE IT4Innovations, Division of the University of Ostrava, Ostrava (Czech Republic)

Abstract

The dependencies of spectral regions of incident solar radiation in ultraviolet and visible spectra on concentrations of air pollutants were studied. We used two different approaches to conduct linear model analyses. First, linear models with different meteorological factors as explanatory variables were made for the entire data set without division according to solar elevation angle. These models showed no apparent influence of air pollutants on incident solar radiation but did reveal an effect of air pollutants on incident solar radiation in combination with relative air humidity. Secondly, after eliminating the major effect of solar elevation angle, linear models showed a spectrally dependent influence of dust particles PM_{10} and NO_x and increasing effects of the other air pollutants on at least one of the studied spectral regions. Dust particles PM_{10} caused a significant reduction in almost all spectral regions. We found that air pollutants affect the spectral composition of incident solar radiation, but it is difficult to identify the direct and indirect impacts of air pollutants on solar radiation in its different spectral regions.

Keywords: *linear regression, pollutants, solar elevation angle, solar radiation*

1. Introduction

Air pollutants created during anthropogenic activities are important compounds in the atmosphere's boundary layer. In addition to their impact on human health (e.g. Pedersen et al., 2006; Sram et al., 2013), they contribute to changes in incident solar radiation, particularly in its intensity, proportions of direct and diffuse radiation (Rooba, 2009), and spectral composition (Jacovides et al., 1997). The absorption and scattering caused by air pollutants are the main physical mechanisms which influence incident solar radiation (Charlson et al., 1992). Absorption of solar radiation is mainly by ozone, water vapour, and compounds of nitrogen and/or carbon (Thuillier et al., 2003). Black and brown carbon particles are the main effective absorbents of ultraviolet and visible solar radiation, and subsequent thermal radiation emission can induce cloud evaporation (Moosmüller et al., 2009) and thus increase the penetration of solar radiation to the Earth's surface. Radiation scattering, especially in the spectral range from 550 to 700 nm, causes an increase in diffuse radiation (Jacovides et al., 1997). These effects have a strongly regional character because of the prevailing influence of local sources of air pollution, pollutant properties, and removal mechanisms (Esteve et al., 2014). The spatial variability of air pollutants is the primary cause of different irradiances in urban versus rural areas when the sky is clear (Jacovides et al., 1997). Various air pollutants selectively affect different spectral regions of solar radiation. For example, UVB radiation is mainly absorbed by ozone (O_3) and sulphur dioxide (SO_2). UVA radiation is absorbed by nitrogen dioxide (NO_2), which has no influence on the transmission of UVB (World Meteorological Organization, 2011). Air pollution has been found to have a significant influence on both ultraviolet and visible regions of the solar spectrum, decreasing in longer wavelengths in urban areas (under cloudless conditions the attenuation of visible radiation reaches 18% in very polluted air; Jacovides et al., 1997). This effect is most important at low latitudes and during summer months (Zhou & Savijärvi, 2014.

doi:10.18086/eurosun.2016.09.06 Available at http://proceedings.ises.org

In this contribution, we used two different approaches to describe the influence of air pollution and other meteorological parameters on the intensity and spectral composition of incident ultraviolet (UV) and visible (VIS) solar radiation. The influence of particular air pollutants on individual spectral regions of UV and VIS spectra is not well known. We first analysed the influence of other meteorological factors, and secondly we studied the influence of individual air pollutants on particular spectral regions of incident solar radiation. We hypothesized that air pollutants significantly influence incident solar radiation and that air pollutants reduce short-wave spectral regions (UVB, UVA, blue radiation) more so than longer-wave spectral regions (green and red radiations) of incident solar radiation (according to Jacovides et al., 1997).

2. Material and methods

Two identical systems of sensors for solar radiation measurements were situated in the botanical gardens of the University of Ostrava (49°49.64873' N, 18°19.56197' E). Data from the first system were used for analysis. Data from the second system were used as a control of measurement reliability. Both systems consist of UVA and UVB sensors (Skye, UK), sensors measuring at wavelength intervals 400–700 nm (VIS), 510–700 nm, and 600–700 nm, and a sensor for global radiation (EMS Brno, Czech Republic). Spectral regions of VIS were calculated from the following interval measurements: blue (400–510 nm), green (510–600 nm), and red (600–700 nm). The systems also contain sensors for measuring air temperature and relative air humidity (EMS 33R, EMS Brno). Air pollution (hourly concentrations of PM_{10}, NO, NO_2, NO_x, SO_2, O_3, and CO) and hourly values for air pressure were taken from the website www.ims-msk.cz (provider: Public Health Institute Ostrava; their own data). Hourly values for visibility were taken from the website https://www.wunderground.com/history/airport/LKMT/2013/5/8/DailyHistory.html?req_city=NA&req_state=NA&req_statename=NA (meteorological data from airports). Data were divided according to weather into three categories – cloudy, partly cloudy, and sunny days. Only data for sunny days were used for analyses in order to eliminate the influence of clouds, which is difficult to define.

We used two different approaches to data analysis by linear regression. First, we analysed the influence of meteorological factors and air pollution on the spectral composition of incident solar radiation. We used solar elevation angle (SA), relative air humidity (Hum), air pressure (AirPress), and visibility (Vis) as meteorological factors and air pollutants (PCpol) as one variable using the first principal component equation $-0.33\ PM_{10} - 0.38\ NO - 0.41\ NO_2 - 0.44\ NO_x - 0.36\ SO_2 + 0.32\ O_3 - 0.39\ CO$ because of very high correlation among concentrations of individual air pollutants. We created a total of 15 linear models for each measured spectral region of incident solar radiation using different explanatory variables and their combinations (Tab. 1). We compared the coefficients of determination (R^2) for the final linear models. The main aim was to determine those factors which contributed significantly to improving the correspondence of the linear models with the measured data. We hypothesized a significant influence of air pollutants on incident solar radiation. These linear models were made for data in 2014, 2015, and the first half of 2016. In total, we used 615 hourly measurements from 179 days.

Secondly, we analysed the relationship between the intensity of incident solar radiation (UVA, UVB, blue, green, and red radiations) and concentrations of air pollutants (PM_{10}, NO, NO_2, NO_x, SO_2, tropospheric O_3, and CO). Each linear model had only two explanatory variables – solar elevation angle and one air pollutant (because of highly correlated concentrations of air pollutants; Tab. 2). In order to reduce the effect of varying solar elevation angle on solar irradiance, data obtained for the period when the solar elevation angle was within intervals 15–25° and 25–35° were analysed separately. These intervals were chosen according to the maximum solar elevation angle during winter months. If we were to use data with a greater solar elevation angle, we would lose winter data which are important because the highest concentrations of some air pollutants occur during winter. We compared the significances of each air pollutant's influence according to the p-values from the linear models. The main aim was to determine whether particular air pollutants influenced the spectral regions of incident solar radiation during different radiation conditions (given by two intervals of solar elevation angle). We hypothesized a significant reduction of incident solar radiation due to air pollutants. These linear models were made for data in 2014 and 2015. In total, we used 313 hourly measurements from 63 days.

The statistical analyses were performed in the R statistical environment version 3.3.0 (R Core Team, 2016).

3. Results and discussion

First, we studied linear models for spectral regions of incident solar radiation made using different combinations of explanatory variables. Solar elevation angle and relative air humidity were revealed as the most important explanatory variables (Tab. 1). The linear model with only solar elevation angle as the explanatory variable accounted for 62.53% of variability in UV radiation and 57.56% of variability in VIS radiation. Relative air humidity was the only explanatory variable to show an opposite effect – it explained variability in VIS radiation (36.55%) better than variability in UV radiation (29.33%; Fig. 1). The linear model with solar elevation angle and relative air humidity as explanatory variables exhibited the best explained variability among all models (71.72% for UV radiation, 72.00% for VIS radiation). The addition of other variables did not improve the linear models in a significant way. The addition of air pollutants to the linear model with solar elevation angle and relative air humidity as explanatory variables increased the explained variability of linear models by 0.74% for UV and by 1.04% for VIS radiation (Tab. 1, Fig. 1). However, the addition of air pollutants to the linear model with only solar elevation angle as the explanatory variable increased the explained variability of linear models imperceptibly (0.035% for UV and 0.057% for VIS radiation). These results demonstrate that the influence of air pollutants is important in combination with relative air humidity.

Tab. 1: Coefficients of determination (in %) for different types of linear models for measured spectral regions. SA = solar elevation angle, Hum = relative air humidity, Vis = visibility, AirPress = air pressure, PCpol = principal component of air pollutants. Bold values are displayed in Fig. 1.

	UVB	UVA	Blue	Green	Red
SA+Hum+Vis+AirPress+PCpol	71.61	73.34	73.16	73.65	72.71
SA+Hum+AirPress+PCpol	71.57	73.31	73.15	73.62	72.70
SA+Hum+Vis+PCpol	71.46	73.10	72.92	73.35	72.31
SA+Hum+PCpol	**71.42**	**73.07**	**72.90**	**73.32**	**72.30**
SA+Hum+Vis+AirPress	71.21	72.69	72.34	72.97	71.70
SA+Hum+AirPress	71.16	72.66	72.32	72.94	71.68
SA+Hum+Vis	71.06	72.46	72.11	72.68	71.31
SA+Hum	**71.01**	**72.42**	**72.08**	**72.64**	**71.29**
SA+Vis	63.90	62.45	58.37	59.62	57.21
SA+AirPress+PCpol	63.61	62.17	58.04	59.34	57.05
SA+AirPress	63.58	62.15	57.99	59.27	57.03
SA+PCpol	63.36	61.77	57.60	58.84	56.41
SA	**63.32**	**61.74**	**57.54**	**58.75**	**56.39**
Hum	**26.97**	**31.68**	**36.69**	**36.01**	**36.94**
AirPress	0.22	0.36	0.40	0.47	0.59

These linear models were created from all data without division into intervals according to solar elevation angle, which is the main factor determining the intensity of incident solar radiation. This fact could be the reason why other meteorological factors showed only a small improvement in linear models and our hypothesis about the significant influence of air pollutants on incident solar radiation was not proven. From these results it is difficult to quantify the exact influence of meteorological factors and air pollutants on incident solar radiation.

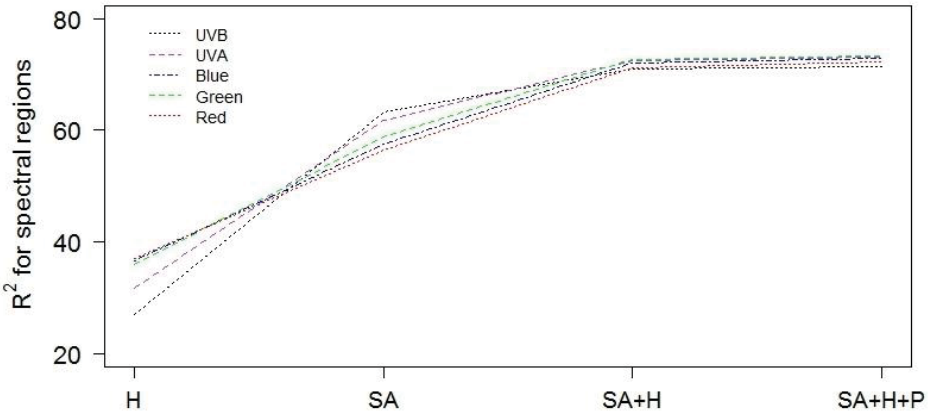

Fig. 1: Coefficients of determination (in %) for selected linear models for measured spectral regions. H = relative air humidity, SA = solar elevation angle, P = principal component of air pollutants. Only linear models with significant improvement of explained variability are shown.

Next, we studied the different influences of particular air pollutants on individual spectral regions of incident solar radiation during varying intervals of solar elevation angle. Each linear model had only two explanatory variables – solar elevation angle and one air pollutant (Tab. 2).

The air pollutant PM_{10} had the most significant reducing effect on all studied spectral bands except for the green band (Tab. 2). This effect was expected because dust particles cause a reduction of incident solar radiation (Rooba, 2009). However, the results surprisingly showed that the influence of PM_{10} on incident solar radiation was spectrally dependent insofar as PM_{10} had no significant influence on green radiation. Nitrogen oxides had a significant negative effect only on the intensities of some spectral bands, particularly blue radiation (Tab. 2). They showed surprisingly positive effects on green radiation at higher solar elevation angles. The effects of NO_x are more significant for visible than ultraviolet radiation. Palancar et al. (2013) reported that NO_2 significantly absorbs UV radiation, but our results did not confirm that.

Tab. 2: Statistical significances (p-values) of linear models of radiation dependencies on air pollutants. Bold number indicates significant dependence (i.e. p-value < 0.05). Grey colour denotes a positive effect.

Radiation	UVB		UVA		Blue		Green		Red	
Solar angle (°)	15–25	25–35	15–25	25–35	15–25	25–35	15–25	25–35	15–25	25–35
PM_{10}	**< 0.001**	**< 0.001**	**< 0.001**	**< 0.001**	**< 0.001**	**0.010**	0.827	0.987	**0.003**	**< 0.001**
NO	0.067	0.131	**0.044**	0.162	**< 0.001**	0.065	0.516	**0.037**	**0.003**	0.665
NO_2	0.651	0.107	0.956	0.133	**0.004**	**0.001**	0.108	**0.035**	0.243	0.141
NO_x	0.182	0.116	0.217	0.174	**< 0.001**	**0.005**	0.730	**0.014**	**0.015**	0.405
SO_2	**0.007**	0.649	**0.001**	0.805	0.164	0.055	**< 0.001**	0.055	**<0.001**	0.675
O_3	0.245	0.101	0.448	0.167	**0.001**	**< 0.001**	**0.023**	**< 0.001**	0.102	0.610
CO	0.187	0.679	0.057	0.974	0.682	0.157	**0.004**	0.096	0.331	0.945

Sulphur dioxide had a significant positive effect on UVB, UVA, green, and red radiation at lower solar elevation angles (Tab. 2). These results contradicted our expectations. Such positive effects might be caused by multi-scattering of radiation on these molecules or could be connected with other climatic factors which accompany higher SO_2 concentrations. The fact that this effect occurred only during low solar elevation angles can be connected with the higher SO_2 concentration during winter months (there are usually lower SO_2 concentrations when solar elevation angle is higher).

Tropospheric ozone had no significant effects on UV radiation but a significant positive effect on blue radiation and a significant negative effect on green radiation (Tab. 2). These results also contradicted our expectations, based on the general knowledge that ozone absorbs light with a wavelength shorter than 300 nm (e.g. Lu & Khalil, 1996). Although it had been thought that ozone does not absorb light with a wavelength longer than 350 nm (e.g. Kudish and Evseev, 2011), in reality it also absorbs visible light in the Chappius band with absorption peaks at 575 and 603 nm (e.g. Jodpimai et al., 2016). This fact could explain the significant reduction in green radiation, but the absence of effect on UV radiation was rather surprising. Carbon monoxide had a significant effect only in a single case – on green radiation in combination a lower solar elevation angle (Tab. 2). It seems that CO has no special influence on incident solar radiation.

Although studies about the general reduction of solar radiation by anthropogenic aerosol are quite common (e.g. Rooba, 2009; Esteve et al., 2014), detailed analyses are not available. To the best of our knowledge, there are no scientific reports regarding the influence of individual air pollutants on incident solar radiation in the spectral regions we have studied.

4. Conclusions

The results of this study were dependent upon the approach used. Linear models on data which were not divided according to solar elevation angle did not confirm our hypothesis about the significant influence of air pollutants on incident solar radiation. That was due to the dominant effect of solar elevation angle on incident solar radiation. The influence of air pollutants in combination with relative air humidity, however, was noticeable. After eliminating the major effect of solar elevation angle, linear models showed a significant influence of individual air pollutants on particular spectral regions of incident solar radiation. The spectrally dependent influence of PM_{10} and NO_x and positive influence of SO_2 on incident solar radiation were the main findings of this study. It is evident that air pollutants affect the spectral composition of incident solar radiation, but it is difficult to recognize the direct (especially absorption) and indirect impacts of air pollutants on absorption and scattering characteristics of the atmosphere for spectral regions of incident solar radiation with different wavelength ranges.

5. Acknowledgement

This work was financially supported by grants COST CZ LD14005 and SGS06/UVAFM/2016 (specific university research grant) and by EU structural funding Operational Programme Research and Development for Innovation, project no. CZ.1.05/2.1.00/19.0388. We thank to English Editorial Services for English language assistance.

6. References

Charlson, R.J., Schwartz, S.E., Hales, J.M., et al., 1992. Climate forcing by anthropogenic aerosol. Science 255, 423-430. DOI: 10.1126/science.255.5043.423

Esteve, A.R., Estellés, V., Ultrallas, M.P., Martínez-Lozano, J.A., 2014. Analysis of the aerosol radiative forcing over a Mediterranean urban coastal site. Atmos. Res. 137, 195-204. DOI: 10.1016/j.atmosres.2013.10.009

Jacovides, C.P., Timbios, F., Asimakopoulos, D.N., Steven, M.D., 1997. Urban aerosol and clear skies spectra for global and diffuse photosynthetically active radiation. Agr. For. Meteorol. 87, 91-104. DOI: 10.1016/S0168-1923(97)00031-2

Jodpimai, S., Boonduang, P., Limsuwan, P., 2016. Inline ozone concentration measurement by a visible absorption method at wavelength 605 nm. Sensor. Actuat. B-Chem. 222, 8-14. DOI: 10.1016/j.snb.2015.08.028

Kudish, A.I., Evseev, E.G., 2011. The analysis of solar UVB radiation as a function of solar global radiation, ozone layer thickness and aerosol optical density. Renew. Energy 36, 1854-1860. DOI: 10.1016/j.renene.2010.12.008

Lu, Y., Khalil, M.A.K., 1996. The distribution of solar radiation in the Earth's atmosphere: The effects of ozone, aerosols and clouds. Chemosphere 32, 739-758. DOI: 10.1016/0045-6535(96)00028-8

Moosmüller, H., Chakrabarty, R.K. & Arnott, P., 2009. Aerosol light absorption and its measurement: A review. J. Quant. Spectrosc. Ra. 110: 844-878. DOI: 10.1016/j.jqsrt.2009.02.035

Palancar, G.G., Lefer, B.L., Hall, S.R. et al., 2013. Effect of aerosols and NO_2 concentration on ultraviolet actinic flux near Mexico City during MILAGRO: measurements and model calculations. Atmos. Chem. Phys. 13, 1011-1022. DOI: 10.5194/acp-13-1011-2013

Pedersen, M., Vinzents, P., Petersen, J. H. et al., 2006. Cytogenetic effects in children and mothers exposed to air pollution assessed by the frequency of micronuclei and fluorescence in situ hybridization (FISH): A family pilot study in the Czech Republic. Mutat. Res. 608, 112-120. DOI: 10.1016/j.mrgentox.2006.02.013

R Core Team, 2016. R: A language and environment for statistical computing. R Foundation for Statistical Computing, Vienna, Austria. URL: https://www.R-project.org/

Robaa, S.M., 2009. Urban-rural solar radiation loss in the atmosphere of Greater Cairo region, Egypt. Energ. Convers. Manage. 50, 194-202. DOI: 10.1016/j.enconman.2008.06.024

Sram, R.J., Binkova, B., Dostal, M. et al., 2013. Health impact of air pollution to children. Int. J. Hyg. Envir. Heal. 216, 533-540. DOI: 10.1016/j.ijheh.2012.12.001

Thuillier, G., Hersé, M., Labs, D. et al., 2003. The solar spectral irradiance from 200 to 2400 nm as measured by the SOLSPEC spectrometer from the ATLAS and EURECA missions. Sol. Phys. 214, 1-22. DOI: 10.1023/A:1024048429145

World Meteorological Organization, 2011. Scientific Assessment of Ozone Depletion: 2010. Global Ozone Research and Monitoring Project – Report No. 52. Geneva, Switzerland.

Zhou, Y. & Savijärvi, H., 2014. The effect of aerosols on long wave radiation and global warming. Atmos. Res. 135-136, 102-111. DOI: 10.1016/j.atmosres.2013.08.009

Conference Proceedings

EuroSun 2016
Palma de Mallorca (Spain), 11 - 14 October 2016

ANALYSIS OF MEASURED AND MODELED SOLAR RADIATION AT THE TÅRS SOLAR HEATING PLANT IN DENMARK

Zhiyong Tian, Bengt Perers, Simon Furbo and Jianhua Fan

Department of Civil Engineering,Technical University of Denmark, Kgs.Lyngby, Denmark

Abstract

A novel combined solar heating plant with tracking parabolic trough collectors (PTC) and flat plate collectors (FPC) has been constructed and put into operation in Tårs, 30 km north of Aalborg, Denmark in August 2015. To assess the operation performance of the plant, detailed parameters, such as solar radiation, inlet and outlet temperature for the solar collector field, flow rate and pressure, ambient temperature, wind speed and wind direction were measured. Global horizontal radiation, direct normal irradiation (DNI) and total radiation on the tilted collector plane of the flat plate collector field have been measured in Tårs solar heating plant. To determine the accuracy of modeled and measured solar radiation in Tårs solar heating plant, monthly comparisons of measured and calculated radiation using 6 empirical models have been carried out. Comparisons of measured and modeled total radiation on the tilted surface with different methods were also studied. The results have shown that the DTU model could be used to calculate the diffuse radiation on horizontal surface and the anisotropic models (Perez 1988 model and Perez 1999 model) with only 1% and 2% disagreement with measured data respectively were the most accurate to be used for the calculation of total radiation on the tilted collector surface under Danish climate conditions only based on global horizontal radiation.

Keywords: Tårs solar heating plant, solar radiation, diffuse radiation, total radiation on tilted surfaces, measurements, calculations

1. Introduction

Solar radiation data are the best source of information for estimating thermal performance of solar thermal systems and necessary for design and assessment of solar thermal systems. However, a drawback, common for solar energy systems is the unpredictable nature and variability of solar radiation. Solar heating systems are strongly dependent on weather conditions. The accuracy of the solar radiation is valuable for design and evaluation of the solar energy systems. In the past, in most cases cheap and low accurate solar radiation meters were used to measure solar radiation in solar heating plants. Acquiring information about correct and typical solar irradiation available at potential plant sites is of high importance for controlling and planning of the solar heating plants to improve the thermal performance of the solar thermal systems.

Generally, climate stations only measure global radiation and only in rare cases DNI or diffuse solar radiation. Therefore, total tilted surface irradiation in most cases is calculated by using measured global horizontal irradiation by means of empirical models for general use.

A novel combined solar heating plant with a 4039 m^2 parabolic trough collector field and a 5960 m^2 flat plate collector field in Tårs has been put into operation in August 2015 (Aalbog CSP.2016). To evaluate the thermal performance of the plant and the accuracy of modeled solar radiation, detailed solar radiation, such as, DNI, global (total) horizontal radiation and total titled solar radiation are measured. In addition, a weather station was also constructed nearby the solar heating plant to make sure that the pyranometers in the plant have correct values to reduce systemic errors and to measure the direct normal irradiance. South facing flat

doi:10.18086/eurosun.2016.09.12 Available at http://proceedings.ises.org

plate collectors were installed with 50° tilt in the solar heating plant. Pyranometers were adhered to the flat plate collector with the same tilt to measure the total radiation on the tilted surface. Calibrated high class solar sensors were used.

Previous empirical models for conversion of global solar radiation may not be applicative under Danish climate conditions with high accuracy. A DTU model has been developed to calculate the diffuse radiation on horizontal surface under Danish climate conditions based on the global radiation (J. Dragsted,et al. 2012). DTU model was used to calculate the diffuse radiation on horizontal surface and 5 empirical models were used to investigate the total radiation on the tilted surface in this paper. The difference between measured solar radiation and modeled total radiation on the tilted surface estimated by the empirical formulas under Danish climate conditions were shown. Calculated total tilted radiation only based on the global horizontal radiation and based on both the global horizontal radiation and beam radiation were discussed, which could provide a new method to calculate total tilted radiation with less measurements under Danish climate conditions and maybe the proposed method can be extended to other Nordic area with similar weather conditions.

2. Monitoring equipments

As is shown in the figure 1, Denmark has 6 climate zones. The Tårs plant is located in the first climate zone, in the northern part of Denmark. Figure 2 illustrates the locations of the weather station and the pyranometers in the flat plate collector field in Tårs solar heating plant. The weather station is next to the solar heating plant. There are several pyranometers to measure the global solar radiation on horizontal surface and the tilted plane of the flat plate collectors in the middle of the flat plate collector field to reduce systematic errors (figure 3). The latitude of the plant is 57.39 °N and the longtitude is 10.11°E respectively.

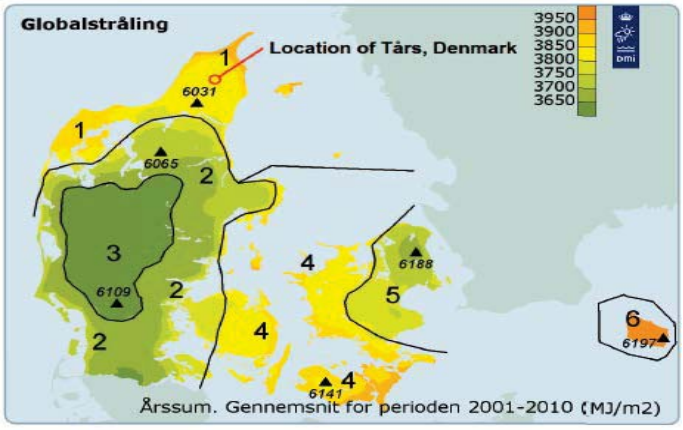

Fig.1. Location of Tårs in Denmark.

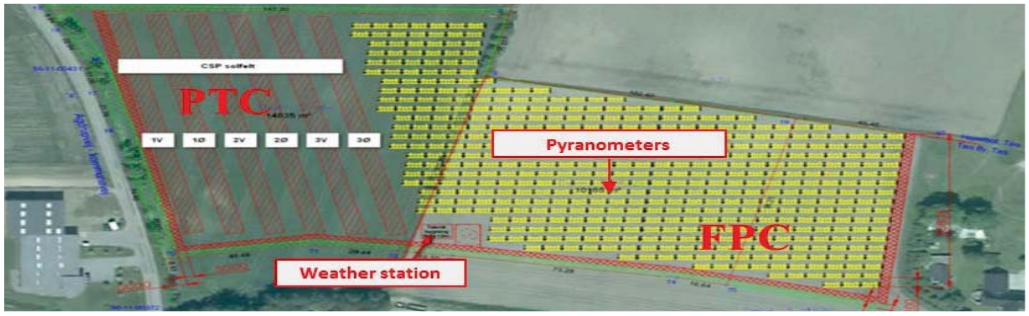

Fig.2. Location of the weather station and pyranometers

Fig.3. Pyranometers in the middle of flat plate collector field

As is shown in figure 2 and figure 3, five pyranometers with a tilt 50° were installed in the middle of the flat plate collector field. One is installed on a horizontal surface. Four pyranometers were installled on the tilted collector plate. Global solar radiation on the horizontal surface and solar radiation on the titled collector plane were measured with Kipp&Zonen SMP11. DNI was measured with a PMO6-CC pyrheliometer with the sun tracking platform Sunscanner SC1 in the weather station next to the solar heating plant, see Fig.2 and 4. Table 1 and 2 show the technical specifications of Kipp&Zonen SMP11 pyranometer and PMO6-CC pyrheliometer. It is estimated that that the uncertainty of the measured solar radiation is about 2%.

Fig.4. Weather station and pyrheliometer at Tårs solar heating plant

Table 1. Specifications of Kipp & Zonen SMP11 Pyranometer

Parameters	Values
Spectral range (50% points)	285 to 2800 nm
Response time (63%)	< 0.7 s
Response time (95%)	< 2 s
Zero offset A	< 7 W/m²
Zero offset B	< 2 W/m²
Directional response (up to 80° with 1000 W/m² beam)	< 10 W/m²
Temperature dependence of sensitivity (-20 ºC to +50 ºC)	< 1 %
Analogue output (-V version)	0 to 1 V
Analogue output (-A version)	4 to 20 mA

Table 2. Specifications of PMO6-CC pyrheliometer

Parameters	Values
Dimension	80 x 80 x 230 mm
Mass	2.15 kg
Field of view (full angle)	5°
Slope angle	1°
Range	up to 1400 W/m^2 (Or custom design available)
Traceability to WRR	< 0.1%
Operating temperature range	-25 °C to +50 °C

3. Models

Solar radiation, including DNI, global horizontal radiation and total solar radiation on a tilted south facing surface of 50° parallel to flat plate collectors have been measured with high time resolution: 2 minutes time steps. Hourly mean values are calculated based on the measurements. Six solar radiation models using the hourly mean data are used to calculate the diffuse radiation on horizontal surface and total solar radiation on the tilted surfaces. The DTU model was used to calculate diffuse radiation on the horizontal surface. And five empirical models for general use were used to calculate the total solar radiation on the tilted surface (Beckman W A.,et al. 1990-2012). Calculation methods of five empirical models were investigated (Beckman W A.,et al. 1990-2012). Ground reflectance was assumed to be 0 in the calculation of modeled solar radiation in the solar heating plant, which is the fair value when shadow between collectors is taken into consideration in the calculations.

4. Results and Discussions

Based on the measurements, total radiation on the tilted flat plate collectors has been investigated with different models. Further, accuracies of the different mentioned models on the calculation of total radiation on the tilted surface have been figured out. The TRNSYS platform was used to set up the mentioned models. Monthly comparisons of modeled and measured solar radiation on horizontal and tilted surface are presented.

4.1 Total radiation on 50° tilted surface facing south

To investigate the total radiation on the tiled surface and accuracy of the different empirical models, calculated total radiation on the tilted surface by the isotropic and anisotropic models based on measured total horizontal radiation and measured beam radiation are shown in figure 6. Because the tilt of the flat plate collectors is 50°, all the mentioned tilted surfaces are 50° tilt surfaces towards south.

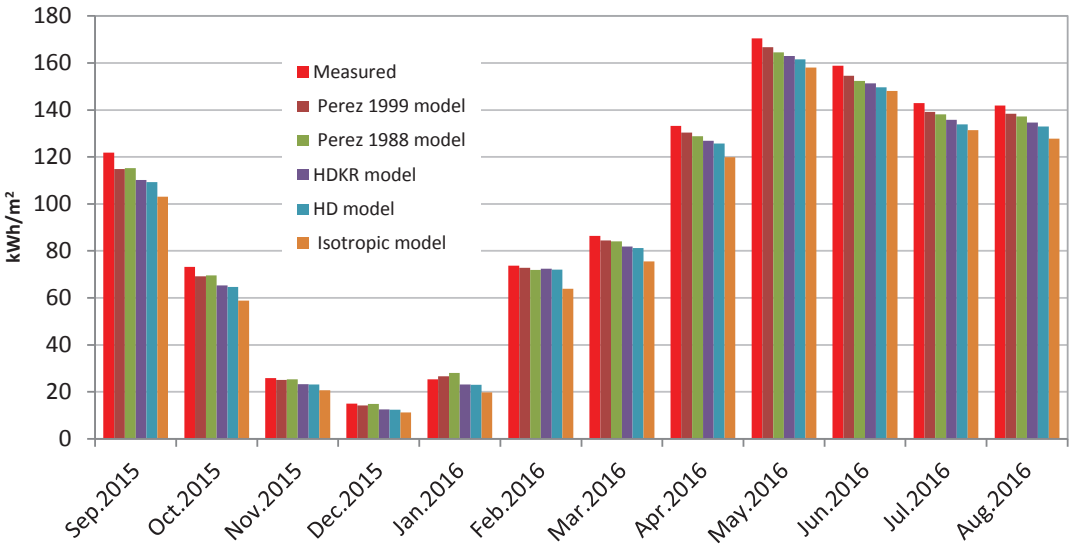

Fig.5. Modeled and measured monthly total radiations on 50° tilted surface facing south (Sep.2015 – Aug.2016)

Fig.5 illustrates measured and modeled total radiation on the tilted surface. The modeled total radiation by isotropic model is lower than the measured values obviously. For the four anisotropic models, the modeled total tilted radiations of the Perez 1999 model and Perez 1988 model are the closest to the measured values with only average -3% and -1% difference between the modeled and measured values, which is the same as reported by Andersen E., et al (Andersen E., et al,2004).

4.2 Measured and calculated total tilted radiation

Normally the total radiation on tilted surfaces is not measured in solar heating plants. Calculated total radiation on tilted surfaces only based on measured global radiation on horizontal surface is useful. By the DTU model, calculated diffuse radiation and beam radiation are obtained only based on measured global radiation on horizontal surface. Because the anisotropic models (Perez 1999 model and Perez 1988 model) are closest to measured value in section 4.1, the anisotropic models (Perez 1999 model and Perez 1988 model) were selected to calculate the total radiation on the tilted surface based on the calculated diffuse radiation and calculated beam radiation. The calculated total tilted radiation by the Perez 1988 model and Perez 1999 model are only 1% and 2% respectively larger than the measured one from Sep.2015 to Aug.2016, see figure 6. Calculated total tilted solar radiation by the Perez 1999 model mainly is a bit higher than measured values in the summer (Fig.6.b.). The Perez 1988 model has the best agreement with measurements of the investigated two empirical models. Compared to the calculated total tilted radiation based on the measured global radiation and measured beam radiation, the accuracy of calculated total tilted radiation only based on the measured global radiation also has high accuracy (the anisotropic model -Perez 1999 model and Perez 1988 model).

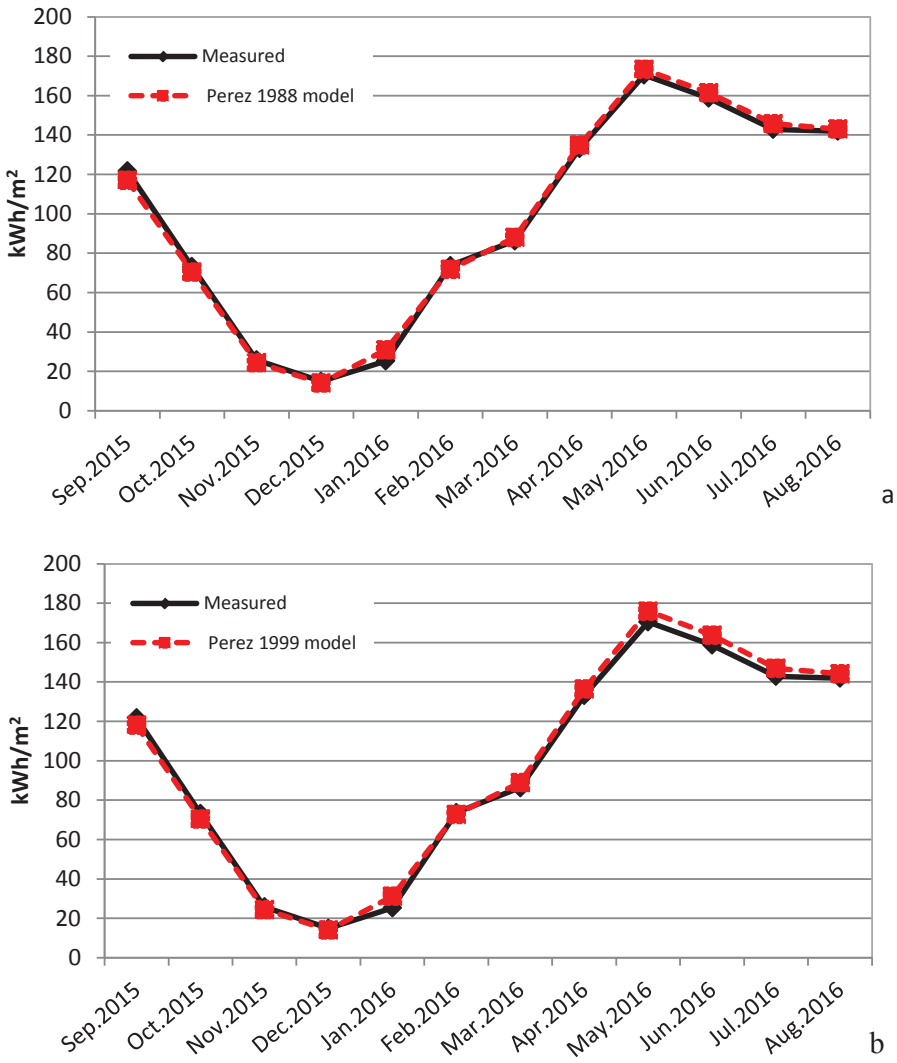

Fig.6. Measured and calculated monthly total radiation on 50° tilted south facing surface (Sep.2015 – Aug.2016: a-Perez 1988 model, b- Perez 1999 model.)

5. Conclusions

Measured and modeled solar radiation in a demonstration solar heating plant in Denmark were analyzed. The main purpose of this paper is to present a new calculation method to determine tilted total radiation on tilted flat plate collectors for large solar heating plants in Denmark. Calculated total tilted solar radiation only based on measured global horizontal radiation was investigated. Furthermore, an isotropic model and four anisotropic models for general use have been investigated for calculation of total radiation on tilted surfaces under Danish climate conditions.

It is suggested that the anisotropic model can be used to calculate total radiation on the tilted surface with better accuracy than the isotropic model under Danish climate conditions. The anisotropic models (Perez 1999 model and Perez 1988 model) are the most suitable empirical model for the calculation of total radiation on the tilted surface under Danish climate conditions. Calculated tilted solar radiation based on the anisotropic models and DTU model only based on the global horizontal radiation can be a new method to predict the total radiation on tilted surfaces accurately under Danish climate conditions.

6. Acknowledgements

Special thanks are expressed to Aalborg CSP for the information provided. The first author also really appreciated the financial support of China Scholarship Council for the PhD study at DTU (No.201506120074).

References

[1] AalborgCSP: http://www.aalborgcsp.com/
[2] J. Dragsted, S. Furbo. Solar radiation and thermal performance of solar collectors for Denmark. DTU Civil Engineering Report R-275 (UK) October 2012.
[3]. Klein S A, Beckman W A. Trnsys 17-a TRaNsient SYstem Simulation program. Programmer'Guide[J]. Solar Energy Laboratory, University of Wisconsin-Madison, 2012.
[4]. Reindl D T, Beckman W A, Duffie J A. Diffuse fraction correlations[J]. Solar energy, 1990, 45(1): 1-7.
[5]. Reindl D T, Beckman W A, Duffie J A. Evaluation of hourly tilted surface radiation models[J]. Solar energy, 1990, 45(1): 9-17.
[6]. Duffie Jone A, Beckman William A. Solar engineering of thermal process[J]. John Wiley& Sons Inc,2013.
[7]. PMO6-CC pyrheliometer. https://www.pmodwrc.ch/pmod.php?topic=pmo6
[8]. Kipp&Zonen SMP11. http://www.kippzonen.com/Product/202/SMP11Pyranometer#.V35QMvl95mM
[9]. Sunscanner SC1. http://www.black-photon.de/products/sunscanner-s
[10]. Andersen E, Lund H and Furbo S. The influence of the solar radiation model on the calculated solar radiation from a horizontal surface to a tilted surface, in proceedings of EuroSun 2004 Congress, Freiburg, Germany, 2004.

10. Solar Education

Conference Proceedings
EuroSun 2016
Palma de Mallorca (Spain), 11 – 14 October 2016

Rear Wheel Steering System for Racing Solar Cars

Toru Fujisawa and Takashi Kawaguchi
Kanagawa Institute of Technology, Atsugi (Japan)

Abstract

Some of our students study energy by producing racing solar cars. Of course, they are concerned with solar energy and how to use it efficiently, however they must also study total energy system for making good solar cars. In solar education we try to provide them with an opportunity for learning engineering technologies around the solar energy to realize that solar power is related to other fields and branches. For example, it is important to reduce resistance to motion of a car to save the energy. So they designed a rear wheel steering system and a narrow spat in order to make the drag force be small. The spat is a kind of cover for a tire. They showed the rear wheel steering caused the width of the spat to be more narrow. The drag force, which is a part of the resistance to motion, on two front spat was estimated. From the result, they calculated the total energy saving over the route of the 2013 World Solar Challenge. It is recognized that adding the rear steering system to the car is useful for the race.

Keywords: *Solar Education, Energy Education, Mechanical Engineering, Racing Solar Car, Drag Force Coefficient, Rear Wheel Steering System, World Solar Challenge*

1. Introduction

Solar energy is origin of other forms or types of energy on the earth. When we teach energy to our students, we may have to make them consider that solar energy plays a significant role in many fields and understand that solar power is related to other fields and branches.

One of main purposes of solar education is getting and using solar energy effectively. In our racing solar car team, students have found out the power density of solar radiation is low. So they improve the car with various techniques. The work for their improvement suggests the using solar energy is related to other fields and many technological knowledge is needed for the using that energy effectively. Now teachers try to show the students recognizing that solar energy is included in total system and emphasizing that using energy in the system is related to many fields.

An example of the improvement of the solar car was introducing a rear wheel steering system to the car. This improvement was effective way for reducing the drag force to save the energy, because that force depends on a width of a vehicle spat covering a tire. The knowledge of other fields, example for vehicle dynamics and fluid dynamics, was used to utilize solar energy.

2. The racing solar cars

The racing solar car, which is shown in Fig.1, was designed by our students for the World Solar Challenge (WSC) and participated in the 2013 WSC adventure class. It has a 1.3 kW photovoltaic (PV) system, a 5.2 kWh rechargeable Lithium-ion (Li-ion) battery system, a carbon fiber monocoque, two front tires and one rear tire which contains an in-wheel motor. The motor is a 2.0 kW direct drive one.

After the 2013 WSC, the solar car team members tried to improve the car. For example, reducing resistance to motion of the car became their aim, because it is important for saving energy to reduce the resistance. The

doi:10.18086/eurosun.2016.10.04 Available at http://proceedings.ises.org

members thought that one of the solutions to the reducing is adding a rear wheel steering system to the solar car.

When a vehicle turns left or right, for a given turning radius, the larger the steer angle of a rear tire is, the smaller that of the front tires is. So steering a rear tire can make the width of a vehicle spat covering a front tire be more narrow. The fact suggests that the spat's drag force, which is included by the resistance to motion, may be small.

Fig. 1: KAIT (Kanagawa Institute of Technology) racing solar car participated in the 2013 WSC

3. Turning radius and steer angle

We consider the relation between turning radius and steer angle in this section. If a steady-state turning at very low speed is assumed, centrifugal force doesn't act on the car, lateral forces are not needed, and side-slip angle is 0 while front and rear wheels travel in the heading direction of the car and make a circular motion (Abe and Manning, 2009), as shown in Fig.2. α, γ, W and T are given.

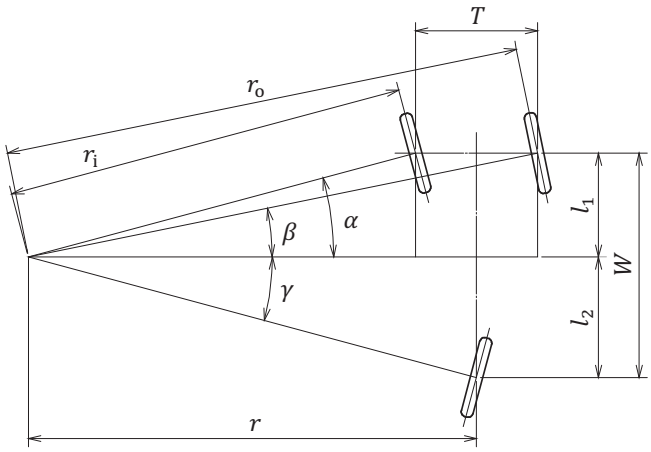

Fig. 2: Turning radius and steer angles (α, β : front; γ : rear) for steady–state turning at low speed

We start by

$$W = l_1 + l_2 = (r - T/2)\tan\alpha + r\tan\gamma = -T\tan\alpha/2 + r(\tan\alpha + \tan\gamma) \quad \text{(eq. 1)}$$

then

$$r = (W + T\tan\alpha/2)/(\tan\alpha + \tan\gamma)\ . \quad \text{(eq. 2)}$$

And from Fig. 2,

$$\tan\beta = l_1/(r+T/2) = (r-T/2)\tan\alpha/(r+T/2) = (1-1/(r/T+1/2))\tan\alpha\ , \qquad \text{(eq. 3)}$$

$$r_o/T = (r+T/2)/(T\cos\beta) = (r/T+1/2)/\cos\beta\ . \qquad \text{(eq. 4)}$$

Putting

$$p \equiv r/T + 1/2 = (W/T + \tan\alpha/2)/(\tan\alpha + \tan\gamma) + 1/2\ , \qquad \text{(eq. 5)}$$

we obtain

$$\tan\beta = (1-1/p)\tan\alpha\ , \qquad \text{(eq. 6)}$$

and a dimensionless radius :

$$r_o/T = p/\cos\beta = p/\cos\tan^{-1}\big((1-1/p)\tan\alpha\big)\ . \qquad \text{(eq. 7)}$$

For the racing solar car, $W = 2000$ mm, $T = 1300$ mm , so $W/T = 1.54$. Figure 3 presents the dimensionless radius : r_o/T for both the inside front steer angle α and the rear one γ at $W/T = 1.54$.

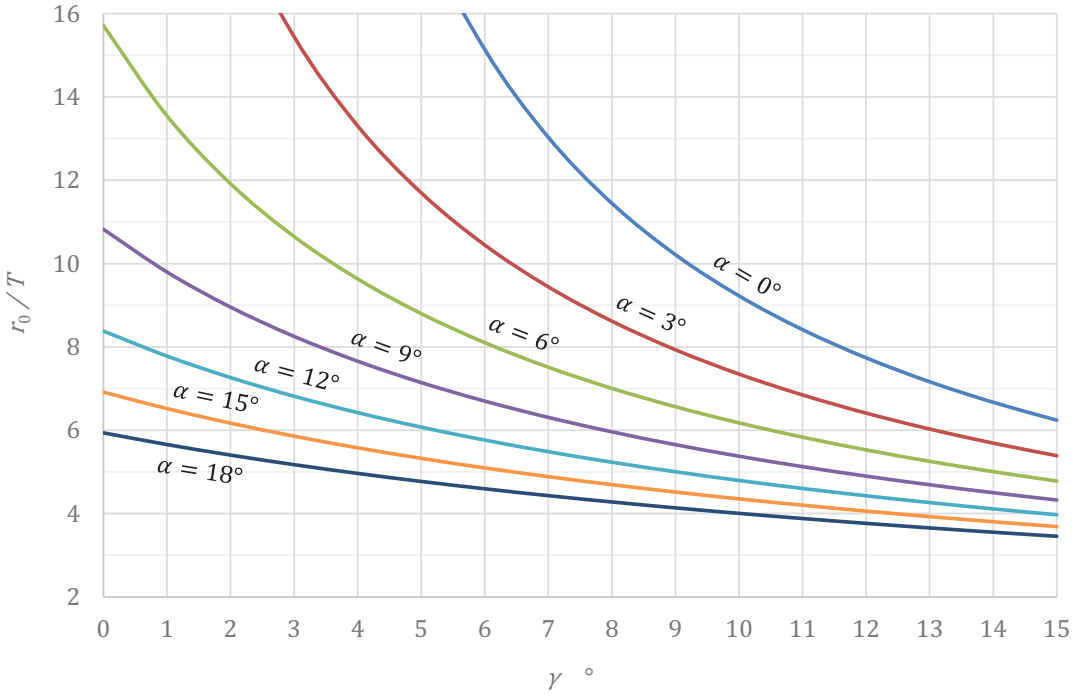

Fig. 3: Dimensionless turning radius r_o/T , inside front steer angle α and rear one γ for steady–state turning at low speed at *W/T* = 1.54

According to regulations for the 2013 WSC, the Solar car must be able to make a U-turn in either direction within a 16 m lane, kerb to kerb. If the car has no rear wheel steering system, the maximum value of inside front steer angle α must be 18° or more in order to observe the regulations, because of $r_o/T < (16/2)/1.3 = 6.15$ and Fig. 3. However we can satisfy the regulations at that angle $\alpha = 7.5°$, if the car has the rear steering system and rear steer angle γ is 9°.

4. Drag force on the front spat

In the previous section, we know that the rear wheel steering system is effective against the reducing the front steer angle. So the width of the spat, which covers a tire, may become narrow and the drag force on the narrow spat is smaller than that on the wide one. We assume that the shape of the spat is a streamlined two-dimensional cylinder, and we are going to guess the drag coefficient C_D by the procedure shown in Fig.4.

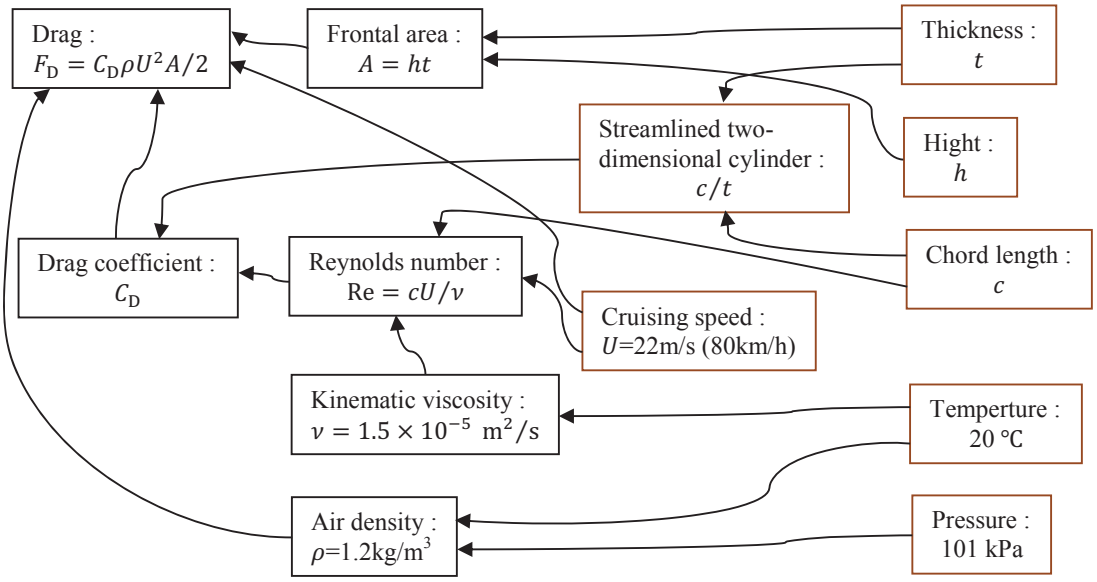

Fig. 4: Procedure for determining drag from the shape of the spat, the cruising speed, air temperature, atmospheric pressure

Reynolds number is defined here by

$$Re \equiv cU/\nu \qquad \text{(eq. 8)}$$

where c is the longitudinal length of the spat, U is the cruising speed of the car and ν is kinematic viscosity of air . The chord length c is approximately 1200 mm. Let the air temperature, atmospheric pressure, the cruising speed be 20℃ , 101 kPa and U =22 m/s (80km/h) respectively. So the kinematic viscosity $\nu = 1.5 \times 10^{-5}$ m^2/s, the air density ρ=1.2 kg/m^3. Then Reynolds number is

$$Re = 1.2 \times 22/(1.5 \times 10^{-5}) = 1.8 \times 10^6 \ . \qquad \text{(eq. 9)}$$

The diameter of the front tire of the solar car $D = 552$ mm and the width of it $B = 103$ mm, then

$$D \sin\alpha + B \cos\alpha = \begin{cases} 174 \text{ mm} & \text{for } \alpha = 7.5° \\ 269 \text{ mm} & \text{for } \alpha = 18° \end{cases} \qquad \text{(eq. 10)}$$

is needed for width of inside spat cavity. If there exists the rear wheel steering system, that is, $\alpha = 7.5°$, the outside width of spat is $t = 190$ mm. On the other hand no rear one, that is, $\alpha = 18°$, the outside width of spat is $t = 285$ mm. Then

$$t/c = \begin{cases} 0.16 & \text{for } \alpha = 7.5° \\ 0.24 & \text{for } \alpha = 18° \end{cases} . \qquad \text{(eq. 11)}$$

We obtain the drag coefficient

$$C_D = \begin{cases} 0.082 & \text{for } \alpha = 7.5° \\ 0.075 & \text{for } \alpha = 18° \end{cases} \qquad \text{(eq. 12)}$$

from Fig. 5 (Granger, 1995; Goldstein, 1965; Shames, 1992; White, 2011). Figure 5 gives drag coefficients for Reynolds number $= 10^6$, and our one : 1.8×10^6 is not that, however it is likely that the drag coefficient for Reynolds number $= 1.8 \times 10^6$ is nearly equal to that for $Re = 10^6$. Generally, the drag coefficient of bluff forms depends on the span, but on low-drag forms the effect of aspect ratio is considerably smaller than that on bluff forms (Goldstein, 1965). So the effect of the aspect ratio on the drag coefficient is negligible.

The drag force F_D is expressed by

$$F_D = \frac{1}{2} C_D \rho U^2 A \qquad \text{(eq. 13)}$$

where A is the frontal or projected area. Let the spat height be 308 mm, then

$$F_{\mathrm{D}} = \begin{cases} 0.082 \times 1.2 \times 22^2 \times 0.190 \times 0.308/2 = 1.4\mathrm{N} & \text{for } \alpha = 7.5° \\ 0.075 \times 1.2 \times 22^2 \times 0.285 \times 0.308/2 = 1.9\mathrm{N} & \text{for } \alpha = 18° \end{cases} \quad \text{(eq. 14)}$$

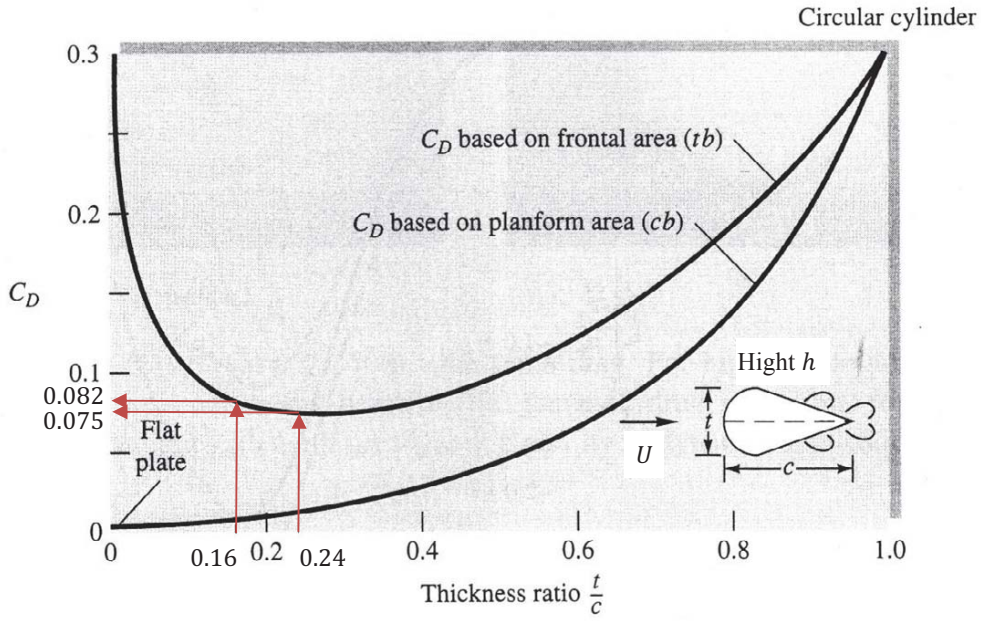

Fig. 5: Drag coefficients for a streamlined two-dimensional cylinder at *Re* = 10^6 (White, 2011)

5. Energy consumption of the rear wheel steering system

The rear wheel steering system consists of a DC 12V geared motor, a screw driven liner actuator, a stroke sensor, a microcontroller. The motor is controlled by feedback. The actuator can push or pull the swing arm of the rear wheel. A part of the system is shown in Fig. 6.

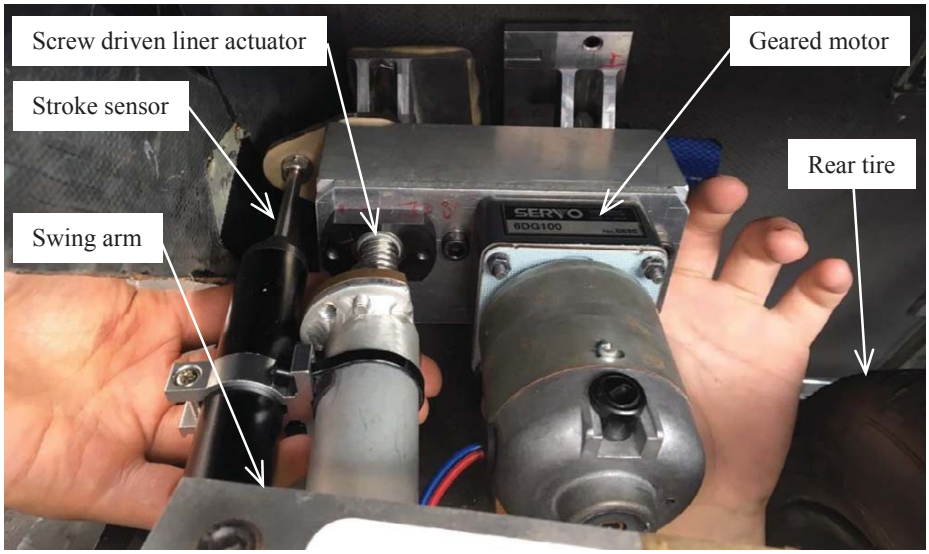

Fig. 6: Putting the rear wheel steering system to the solar car

The solar car team member measured the current of the steering system and Fig. 7 shows the result. The current was approximately 1A, so electric power was 12W and it took 2×6s=12s for one cornering operation.

Then 12×12s=144J is needed for one that operation. Since it is likely that the efficiency of the electric power is 70%, the energy consumption of the rear wheel steering system is $144/0.7 = 206$J. They also researched the number of turning that required the rear wheel steering on the 2013 WSC route. The turnings were 26, so the total energy consumption of the rear wheel steering system is $206 \times 26 = 5.36 \times 10^3$J throughout the race.

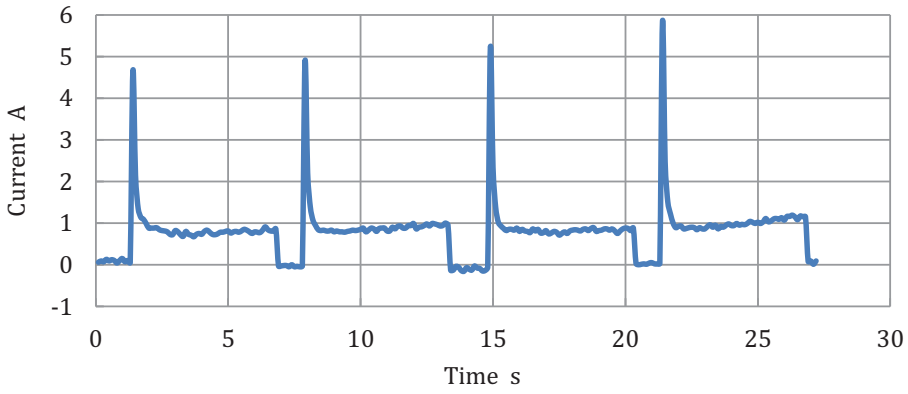

Fig. 7: Current consumed by the rear wheel steering system

6. Effect of the rear wheel steering

We consider the effect of rear wheel steering system here. The travelling distance by no rear steering operation in the WSC route is approximately 3008km. The merit in the rear wheel steering is reducing the resistance to motion. It saves the energy : $2 \times (1.9 - 1.4) \times 3008 \times 10^3 = 3 \times 10^6$J, because front spats are two. The demerit is the consumption of electric power of the rear steering system : 5.36×10^3J for the result of previous section. Now we can guess the effect. It is $3 \times 10^6 - 5.36 \times 10^3 \cong 3 \times 10^6$ J energy saving in the race.

7. Conclusions

The racing solar car has been improved. The rear wheel steering system added to the car may make the total driving energy consumption be reduced throughout the WSC. We obtained the following.

If the solar car has the rear wheel steering system and rear steer angle γ may be 9°, we can satisfy the 2013 WSC regulations at the inside front steer angle $\alpha = 7.5°$.

The drag force on the front spat with the rear wheel steering system may be 1.4 N at the cruising speed = 22 m/s (80 km/h). But with no that system the force is 1.9 N.

The effect of the rear wheel steering system throughout the WSC, we estimated, is 3×10^6 J energy saving. Effective solar energy usage induces our students to study many fields related to solar energy practically.

8. References

Abe, M., Manning, W., 2009. Vehicle Handling Dynamics, Elsevier.

Granger, R.A., 1995. Fluid Mechanics, Dover Publications.

Goldstein, S., 1965. Modern Developments in Fluid Dynamics Volume Ⅱ, Dover Publications, New York.

Shames, I.H., 1992. Mechanics of Fluid, third ed. McGraw-Hill.

White, F.M., 2011. Fluid Mechanics, seventh ed. McGraw-Hill.

Conference Proceedings

EuroSun 2016
Palma de Mallorca (Spain), 11 - 14 October 2016

Using TRNSYS in a graduate course on solar energy engineering

Michaël Kummert

Polytechnique Montréal, Dept. of Mechanical Engineering, Montréal (Québec), Canada

Abstract

This paper presents a graduate solar energy engineering course which relies on the TRNSYS simulation tool to engage students in the learning process through design and analysis activities. The course learning objectives are discussed in relation to Bloom's revised taxonomy. The paper then presents an overview of the course contents, as well as teaching and assessment methods. Student feedback has been overwhelmingly positive on the use of TRNSYS, and on the combination of theoretical notions and practical, simulation-based design exercises. The students also pointed out the lack of software training material specific to the subject, which leads to difficulties in selecting and configuring the appropriate components.

Keywords: education; teaching; solar energy; simulation; modeling; TRNSYS

1. Introduction

Most university-level courses on renewable energy are taught at the graduate[1] level, either as part of a program focusing on that topic, or as elective courses in more general programs (Kandpal and Broman, 2014). Renewable energy education at Polytechnique Montréal followed the general trend in North America, where renewable energy education in universities took off in the late 20th century, in the wake of the oil crises. Solar energy was often among the first graduate courses created, with many instructors adopting the seminal "Solar Engineering of Thermal Processes" textbook currently available in its 4th edition (Duffie and Beckman, 2013). At the beginning of the 21st century, dwindling research and education funding had resulted in only about 10 US universities offering regular solar energy courses, down from around 150 in the early 1980s (Goswami, 2001). The solar energy course at Polytechnique again followed that trend; it was not taught for about 10 years before being reinstated in 2011.

The course described in this paper is known as MEC 6214 – "Énergie Solaire et Applications" (Solar energy and applications). It is taught once a year, during the winter term (January to May). The current course contents and teaching methods are the results of 6 years of trial and error by the author, although the basic structure and the learning objectives remained the same. As pointed out by Kandpal and Broman (2014), "*the scope and contents of a course essentially depend upon the expertise, interest(s) and biases of the course teacher*". The course described in this paper is no exception: both the theoretical aspects addressed in the first part of the course and the practical, simulation-based approach are a result of the author's experience and level of comfort with the selected topics and tools. As a consequence, this paper does not pretend to represent the best practice in teaching solar energy engineering. It represents the author's contribution to the sharing of teaching methods and materials, and an example of how a detailed simulation program as TRNSYS can enrich a solar energy course and help engage students in the learning process.

Note: The author has made some teaching material available on an open website accompanying this paper: https://moodle.polymtl.ca/course/view.php?name=mec6214p (most material is in French at this time)

[1] "graduate" in the paper title and in the text refers to the level of a student who has graduated from a university-level "undergraduate" program, often a Bachelor's degree (~4 years). The term is frequently used in the USA and in Canada, while "postgraduate" is often used with the same meaning in Europe and some other countries.

doi:10.18086/eurosun.2016.10.01 Available at http://proceedings.ises.org

2. Prerequisites

The general policy at Polytechnique Montréal is to have no prerequisites for graduate courses. While most students taking the course have completed or are about to complete a Bachelor's degree in mechanical engineering, students from other engineering branches and sometimes other backgrounds (architecture, economics, physics) have also taken the course. The required prior knowledge is limited to basic thermodynamics and heat transfer: energy balance of closed and open systems, conduction, convection and radiation heat transfer, heat exchangers. Reading material is provided to cover these topics, e.g. Chapter 3 in (Duffie and Beckman, 2013) or thermodynamics and heat transfer textbooks, but no special tutorial sessions are organized. No prior knowledge of the software tools (especially TRNSYS) is expected, but a small number of students have typically been exposed to them in other undergraduate or graduate courses. In particular, TRNSYS is used to some extent in many of the core courses given at the school on building physics, HVAC systems, building energy modeling, and other renewable energy systems (i.e. geothermal).

3. Learning objectives

After taking the course, the students should be able to:

- Describe the environmental and economic context relevant to solar energy engineering
- Assess the solar energy resource of a site
- Calculate the solar radiation incident on a surface (beam, diffuse and ground-reflected components)
- Explain the principles of solar collectors and solar energy systems
- Calculate the performance of solar collectors
- Analyze the economic and energy performance of solar energy systems*
- Design and simulate the performance of solar energy systems
- Justify the use of given renewable energy technologies (wind, solar thermal, solar photovoltaic) in particular applications

*It should be noted that, adopting the approach of Duffie and Beckman (2013), the course focuses on solar thermal systems but also covers more briefly solar photovoltaic (PV) systems and wind energy systems.

Using Bloom's revised taxonomy (Anderson and Krathwohl, 2001), some learning objectives listed above fall in the lowest 3 categories of educational objectives in Figure 1: remember, understand, and apply (where the "remember" objective is not mentioned explicitly but implied). These categories are more present in the first part of the course ("fundamentals" part, see below).

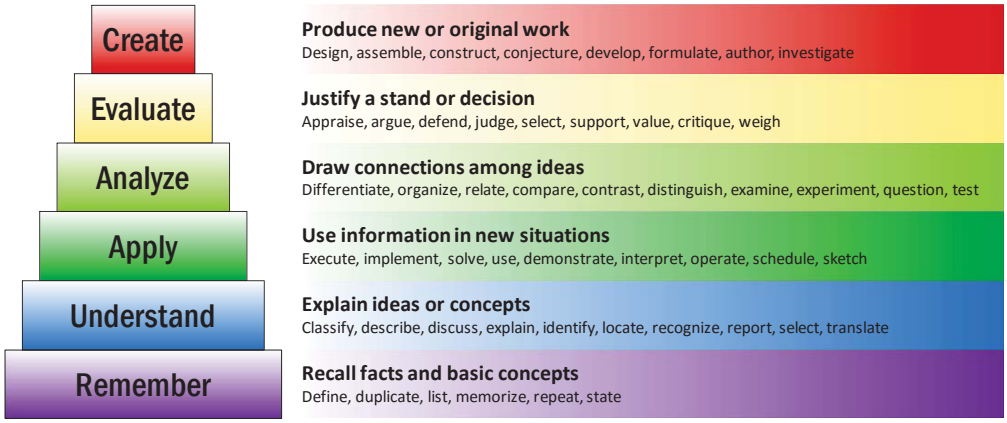

Figure 1: Bloom's revised taxonomy, adapted from (Armstrong, 2016)

The upper categories (Analyze, Evaluate and Create) rely on performance simulation with TRNSYS: students learn how to design solar energy systems first by analyzing the performance of pre-defined systems, by assessing the impact of design changes, and then by proposing and comparing different designs. In theory, it would be possible to perform these activities without relying on software tools, e.g. by using monthly

design methods such as F-Chart (Klein, Beckman and Duffie, 1976). However, using simulation programs such as TRNSYS allows to consider a much larger variety of systems combining different technologies (e.g. solar thermal, solar PV, and wind); it also allows investigating the dynamic behavior of complex systems and control strategies.

4. Teaching and assessment methods

The course follows the typical pattern for graduate courses at Polytechnique Montréal, which consists of a weekly 3-hour lecture (there are normally 13 lectures per term). There are no formal labs or tutorials, but the students are expected to dedicate time to the course at home for personal study, homework assignments and exam preparation, for a total of 96 hours. The total theoretical workload for students is 135 h over the teaching term, which corresponds to 3 credits at Polytechnique Montréal. It can be loosely translated to 5 or 6 ECTS (European Credit Transfer and Accumulation System).

The course is based on "Solar Engineering of Thermal Processes" (Duffie and Beckman, 2013), which has been one of the most popular textbooks to teach solar energy engineering since the 1970's, in North America and throughout the world. The course mainly relies on the first 6 chapters for the "fundamentals" part (see below), which is taught in conventional lectures with homework assignments.

Engaging students

There is increased evidence that traditional lectures are not the most efficient at maximizing learning and course performance in Science, Technology, Engineering and Mathematics (Freeman *et al.*, 2014). Students benefit from active learning, which is defined by the adoption of instructional practices that engage students in the learning process, such as collaborative, cooperative, and problem-based learning (Prince, 2004). While promoting student engagement is an unquestionable objective, it can be challenging to realize in a course with 39 hours of faculty-students contact and a relatively large number of students (the average course enrollment is above 30 students per term, with an upward trend).

The first approach taken to engage students in this course is to try and bring some collaborating learning in the biweekly homework assignments. Students solve the assignments and submit their results individually, but a significant part of the next lecture (roughly one hour) is taken to discuss the problem and the results. The students and instructor diagnose the errors in submitted results. In many cases, students work on different datasets, which was originally intended to prevent plagiarism, but has proven useful in transforming individual efforts into a form of teamwork, where all students contribute one part of a larger parametric analysis.

The second approach to engage students relies on simulation-based problems (assignments or intermediate steps of the final project). During the second half of the term, the time spent giving conventional lectures is considerably reduced, to approximately 1 teaching period (50 min). This leaves two periods for participative activities. Instead of the conventional classroom used for the first part of the term, the course takes place in a computer lab, which allows students to perform simulations during the class. They can analyze their results and diagnose their problems with the help of the instructor, within the constraints imposed by the number of students (i.e. each student gets relatively little time for individual assistance).

Assessment methods

The assessment relies on individual homework assignments (biweekly individual assignments, worth 1/3 of the final mark together), on a written exam (individual, 1/3 of the final mark), and the final project (groups of 2 or 3 students, 1/3 of the final mark). The weight of these different assessments have evolved over time, in response to student feedback that the initial weight for the exam (40 %) did not give a fair share to the other activities. The exam is organized as a mid-term assessment, which comes after the lecture-based "fundamentals" part of the course. It is a conventional written exam, during which students only have access to a 2-page document that they have created themselves and to a non-programmable calculator. In terms of Bloom's taxonomy, the learning objectives assessed in the exam mostly fall in the lower 3 categories (remember, understand, apply), with some attempts to reach levels 4 and 5 (analyze and justify), e.g. with questions asking to define a solar fraction that would apply to a particular system. The homework

assignments ask for numerical answers but also in many cases for a report with some analysis and critique of the results and assumptions, which can be seen as pertaining to categories 4 and 5: analyze, and evaluate. This is especially true for the assignments that use TRNSYS simulations. But to really attain the highest category of educational goals ("create", i.e. design, formulate and investigate), the course relies on simulation-based exercises, and this level is probably only reached during one or two assignments, and the final project, which is a group activity (2 or 3 students).

A practical exam using TRNSYS was introduced in 2012 and 2013. This 2-hour exam was taking place right after the conventional written exam, and was originally intended to test whether students had gained a sufficient understanding of how the program can be used to analyse solar systems, but it proved difficult to test more than basic TRNSYS skills, which was not in line with the learning objectives, so that exam was withdrawn in 2014 and for following years.

5. Use of TRNSYS and other software tools

Literature review: courses using TRNSYS

The literature on teaching solar energy with TRNSYS (or with other simulation tools) is scarce. A few papers report on successful attempts in universities across the world to use TRNSYS in teaching various subjects, from building energy systems to solar energy engineering.

TRNSYS is used in several courses at Polytechnique Montréal, from 4th year (BEng) courses in building heating and cooling mechanical systems to graduate courses on geothermal systems and solar energy (the course described in this paper). It is also used in a graduate course on building energy modeling (Bernier *et al.*, 2016). Students in graduate programs such as the recently created course-based Master in energy engineering are likely to take several of these courses (if not all), which offers synergies and reduces the student effort to learn the software.

Megri (2014) discusses the use of TRNSYS in the department of Architectural Engineering at North Carolina A&T State University. The paper presents a methodology for students to build their own model, perform numerical experiments, and analyze the results. The selected case study is a solar-assisted ground-source heat pump system coupled to a multizone building. According to the author, students prefer easier-to-use programs such as EQuest, but TRNSYS has the benefit of not restricting the type of systems which are analyzed. The instructor needs to master the TRNSYS program and the subject areas.

Charles and Thomas (2009) use TRNSYS in undergraduate courses for engineering and architecture students. The program is coupled with CONTAM for bulk airflow analysis, and other tools are used for climate analysis and Computational fluid Dynamics (CFD). The focus is on encouraging teamwork and benefitting from complementary experience, and simulation is not performed by all class students but rather by an external expert, the instructor, or a few volunteer students. The authors report that students find TRNSYS difficult and are more attracted towards the CFD software. The latter can produce visually attractive results and the authors express that using a little bit of "colorful fluid dynamics" is a necessary evil to generate interest. In spite of the difficulties, the authors conclude that simulation helps students understand the iterative nature of the design process and makes them aware of various physical phenomena. It is also a common platform to support collaboration.

Gómez-Moreno (2015) describes how TRNSYS is used in an undergraduate course on HVAC systems in Industrial Engineering at Universidad de Jaén. Transient simulations are used to help students understand the dynamic behavior of HVAC systems, enhancing the knowledge of steady-state performance that they have gained through more conventional teaching methods. The program is also used to introduce renewable energy in a course that otherwise focuses on air-conditioning systems. The authors state that a software program like TRNSYS is the ideal tool for the students to acquire new competencies and to understand the dynamic behavior of complex systems. It also has the benefits to promote student engagement and increase the motivation. They present the results of a student survey showing that 80 % or more of the students have found that the simulation tool is useful to complement the lectures, help understand the operation of HVAC and solar systems, increase their interest in the course, and improve the quality of teaching.

Gravagne *et al*. (2008) report on the use of TRNSYS in a graduate elective course on solar energy in the department of mechanical engineering at Baylor University. The authors mention the use of TRNSYS for LEED certifications of buildings and for SRCC certifications of solar thermal systems as key aspects in support of selecting the program, as well as a series of features introduced in version 16 that made the software more relevant to classroom use. TRNSYS was only used midway through the class, and it was used to revisit problems that had been solved by hand or with generic software such as Excel or Matlab. One benefit of this approach is that students had a deeper understanding of the software assumptions and results. They could identify spurious results more easily after developing intuition by obtaining results the "hard way". TRNSYS was then used as a design tool in the final project. This allowed students to perform activities (design) for complex systems that they would not have been capable of analyzing without the program. The "mixed quality" of the documentation required a careful preparation by the instructor, so that students are not frustrated by hard-to-find information. Cryptic error messages, and non-standard units, such as the use of kJ/h for energy rates, are also pointed out as weaknesses. But overall, TRNSYS improved the learning experience and most students expressed their wish to start using TRNSYS earlier in the course.

These examples show that TRNSYS can be used successfully for teaching solar energy engineering and other topics. But there is a need for a larger body of shared knowledge about how the tool can be used efficiently for teaching and learning, and there is also a need for publicly available material to support that objective. This paper and the accompanying website is the author's attempt to contribute to that material.

Why was TRNSYS selected?

Ideally, an engineering course should be tool-independent. However, the pursuit of this noble objective quickly faces practical problems: can the instructor master all the tools involved? is the time invested in software installation and basic learning justified? can all the licenses be obtained without investing too much time and money? As discussed below, the students taking this course sometimes felt that using different programs would have been beneficial, while attempts to be tool-independent (and therefore using several different tools) can lead to students being frustrated at the time and energy involved to install and master these software tools (Beausoleil-Morrison and Hopfe, 2016). In many cases – as well as in this course – students also express the need for more software training material adapted to the course (Gravagne and Van Treuren, 2008; Beausoleil-Morrison and Hopfe, 2016). Over the years, a course instructor can reasonably build specific training material adapted to a particular course for a software program, but creating and maintaining that material for several different tools seems impractical.

As indicated in the introduction, the choice of TRNSYS came naturally to the course instructor, as he was very familiar with the program and confident that he could not only use the program to obtain simulation results but also investigate its assumptions and algorithms. When teaching an engineering discipline, being able to examine the actual source code of the software is a great advantage that few commercial programs offer, and open-source alternatives are not always available. Numerous validation studies including TRNSYS have been published, such as the BESTEST inter-model comparison (ASHRAE, 2014). TRNSYS is also used as a reference tool in international standards (ISO, 2013) and certification programs (Burch *et al.*, 2012; SRCC, 2015), which is a testimony to the software relevance for solar energy systems.

TRNSYS' main advantage is probably its flexibility, which comes from its modular structure and from the well-developed libraries of component models. Components can be connected together to form a system, and then configured by modifying the relevant parameters. Assessing different system configurations only requires to add/remove components from the libraries and modify the connections, without modifying the equations and algorithms used in the model. The program flexibility is also expressed by the fact that many different *domains* (Clarke, 2001) can be analyzed together: thermal processes and electrical flows within buildings, HVAC systems and renewable energy systems can form one coupled system. This is a great advantage over some easier-to-use tools which are generally restricted to a single domain or technology (e.g. solar thermal systems for hot water production, or solar photovoltaic systems).

Flexibility has a cost: students can be overwhelmed by the numerous components and libraries, and they can define wrong connections that will result in meaningless results without being flagged as errors. If students do not know how a system operates, i.e. if they do not understand the physical processes involved and its

control strategies, they will not be able to create a TRNSYS model of that system. In that respect, it is the author's point of view that TRNSYS is fully aligned with the learning objectives of a graduate course on solar energy systems engineering.

How TRNSYS and other tools are used

During the first part of the course, students are encouraged to use generic software tools such as spreadsheets and EES (Klein, 2014) to solve sun-earth geometry and solar radiation calculation problems (e.g. anisotropic tilted radiation calculation) and radiative heat transfer problems (e.g. spectral transmittance and absorptance).

TRNSYS (Klein *et al.*, 2014) is used from the beginning for homework assignments, in parallel with hand calculations or generic tools. This is intended to familiarize students with the program and to provide practical examples of the notions defined during the lectures. Examples of assignments include assessing the incident radiation incident for different slope and azimuth angles in TRNSYS using different tilted radiation models (isotropic vs. Perez), comparing the sun position, extraterrestrial, terrestrial and tilted radiation values calculated by TRNSYS to hand-calculated values. Other authors use this two-step approach to help the students develop an understanding of underlying assumptions and algorithms, and intuition (or skepticism) when analyzing simulation results (Gravagne and Van Treuren, 2008; Bernier *et al.*, 2016). Simple solar thermal systems are also introduced (without requiring students to actually build them in TRNSYS) so that students can study the "instantaneous" (i.e. time-step) efficiency of solar collectors, and compare these values to the efficiency curve provided by manufacturers or certified performance tests. Later homework assignments include simple design exercises, mostly involving changing component sizes and control parameters. During the final project, the design exercise can be related to the "create" level in Bloom's taxonomy, as the students start with a clean sheet and a realistic set of constraints and objectives (e.g. reach a given solar fraction, attain the net-zero objective, or design a stand-alone system). In most cases the load (thermal and/or electrical) that the system must meet is provided to the students in data files or calculated using simple methods, so that the students can focus on the solar system itself.

Over the years, specific assignments were introduced which relied on other tools dedicated to PV systems and solar thermal systems, but this led to mixed feedback by students (it is good to experience different tools, but students need more time to learn how to use each of them), and to some uncomfortable situations for the instructors involving crippling software bugs and licensing problems. These problems can happen with any program, including TRNSYS, but it is obviously less demanding to deal with the peculiarities and limitations of one program than to do it for several tools, especially when the instructor and his/her team are using that one program for research on a regular basis.

Teaching how to use a program vs. using a program to teach

As shown in section 3, the course learning objectives are related to understanding and applying solar engineering principles, as well as simulating, analyzing and designing solar systems. "Mastering TRNSYS" (or any other tool) is not one of the learning objectives. Other university-level courses using simulation generally share that approach (Gravagne and Van Treuren, 2008; Megri, 2014; Beausoleil-Morrison and Hopfe, 2016; Bernier *et al.*, 2016). The emphasis should be on underlying assumptions and algorithms, and results analysis, rather than expertise with a particular tool. The key to applying simulation effectively for design and analysis is to develop confidence in the simulation while keeping a critical mind.

One approach to avoid the difficulties of using the software is to employ "simulation specialists" who do the modelling work while students focus on proposing design alternatives. Successful applications of this approach for teaching to engineering and architecture undergraduate students have been reported by Charles and Thomas (2009), who compare cases where the simulation specialist is an external expert, the instructor, or a subset of volunteer students. Reinhart *et al.* (2012) also relied on a pool of "simulation experts" to perform the simulation in a design exercise that they transformed into a game where students compete to obtain the lowest energy use intensity within predefined cost limits. The game was useful in teaching how to interpret simulation results and use them in an iterative design process, and also served as a teaser.

In a later paper, Reinhart *et al*. (2015) describe how the same "learning by playing" approach was applied to a group of 18 undergraduate and graduate students who performed the simulations themselves. The course

included a series of simulation exercises culminating in a game where the students competed to design the building with the lowest greenhouse gas emissions. The authors report overwhelmingly positive student feedback, but insist on the need to keep the complexity of input files provided to the students at a reasonable level. They insist that instructors must be intimately familiar with the strengths and weaknesses of the programs used, so that they can detect and explain wrong results caused by user errors or software limitations. They mention that for larger classes, the teaching staff (one instructor and a teaching assistant) will need to increase and the use of online tutorials may be required to complement lectures and lab sessions.

The approach taken by the author in the course described in this paper is to have students use TRNSYS themselves, individually (for homework assignments) and in groups of 2 or 3 (for the final project). The software is introduced right from the first assignment, and the emphasis is placed on obtaining and analysing results during the first weeks. Later assignments and the final project are actual design exercises of increasing complexity.

6. Course structure

An example of course schedule is provided on the accompanying website (see first page).

Part 1: fundamentals

After the introduction lecture, the first part of the teaching term (approximately six 3-hour lectures over 6 weeks) follows the topics presented in (Duffie and Beckman, 2013). Table 1 shows the topics and examples of assignments.

Table 1: Topics covered in lectures and examples of assignments for course part 1 (Fundamentals)

Topics covered in lectures	Examples of homework assignments
Course objectives, context, introduction to TRNSYS Examples of successful solar energy systems Worldwide context : energy and environment, solar (thermal and photovoltaic) resource and markets	**First contact with TRNSYS** Run existing solar thermal project Configure an output component (printer) Examine the impact of collector slope and azimuth Obtain and analyze results
Extraterrestrial solar radiation Solar geometry, sun position angles, equation of time	
Available solar radiation Measurement of solar radiation, clear sky radiation, beam and diffuse radiation, isotropic and anisotropic models for incident radiation on tilted surfaces	**Tilted radiation, SDHW system balance** Calculate incident radiation on a tilted surface Compare results with TRNSYS for different anisotropic models Perform an energy balance of a Solar Domestic Hot Water (SDHW) system using TRNSYS
Radiation characteristics of opaque materials Kirchhoff's law, spectral distribution of solar and long-wave radiation, absorptance, reflectance and emittance	**Collector absorptance and emittance, collector shading** Calculate α and ε from spectral properties and solar spectrum In TRNSYS, optimize collector rows (azimuth, slope, spacing).
Radiation transmission through transparent surfaces Reflection, absorption, and transmission, spectral and angular dependence of properties, transmittance-absorptance product ($\tau\alpha$)	**Collector stagnation temperature and efficiency** Calculate (by hand) the stagnation temperature of a collector In TRNSYS, examine the dynamic collector efficiency and compare to the performance curve. Students must use certified performance (ISO or SRCC) to configure the TRNSYS components.
Flat-plate solar collectors Collector energy balance, overall heat loss coefficient, collector heat removal factor and flow factor, Hottel-Willier equation, collector testing and performance data.	

Example of collaborative learning through individual assignments

In some of the assignments, students are given different conditions, which are then combined by the instructor during the feedback session to provide a complete picture. One simple example is the slope and azimuth of solar thermal collectors in an SDHW system. Students are provided the TRNSYS project shown in Figure 2 and are asked to assess its performance for a given slope and azimuth angle. All student answers are then combined and used to draw plots of the collector useful energy (Figure 2, top right) and collector efficiency (Figure 2, bottom right) for all slopes and azimuth angles. This is used to discuss the fact that the collector output is not necessarily maximum at the maximum of incident radiation (not shown in the figure) and that the collector efficiency does not really show where the system output will be maximum.

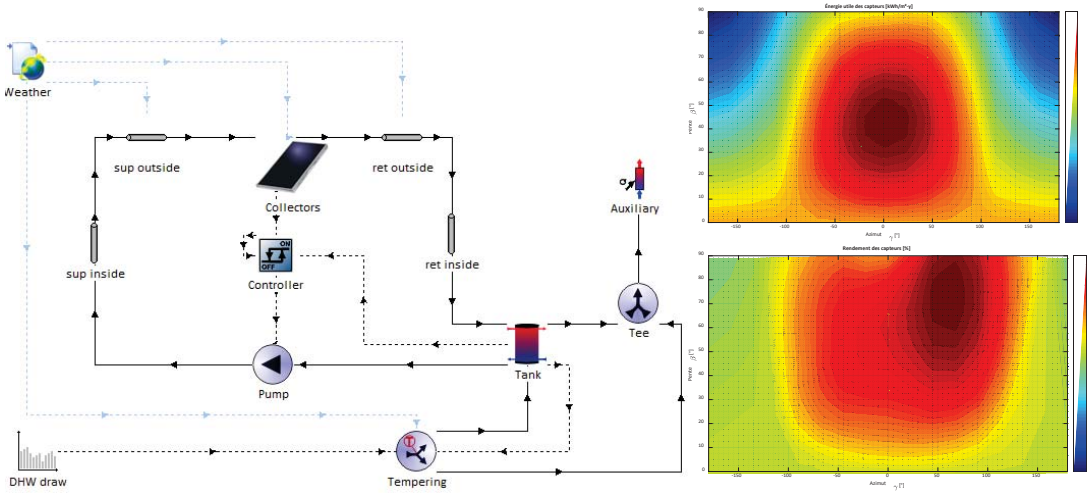

Figure 2: TRNSYS model of an SDHW system and example of results for different orientations and slopes

Part 2: applications

The second part of the teaching term (approximatively six 3-hour sessions) combines short lectures with practical design exercises. The course focuses on solar thermal applications for domestic hot water and space heating, but concentrating solar power generation and solar cooling are also covered. Photovoltaic systems are considered from a design perspective in combination with solar thermal systems, e.g. to design net-zero buildings. Occasionally wind energy is also introduced in the design of stand-alone systems. The subjects covered are sometimes adapted to make room for a graduate student who presents his/her work. Past examples include solar thermal/photovoltaic collectors, and control / fault detection of solar thermal systems.

This part of the course strongly relies on a series of homework assignments and on the final project, which all use TRNSYS. Examples of assignments and projects are again available on the accompanying website (see first page). The following paragraph briefly describe a few examples.

Design of solar thermal systems: thermal load, collectors, thermal storage

Generally, the load is provided for assignments and for the project, but for one assignment students are asked to use 2 weeks of measurements from a real site to extrapolate the design load used in a simulation. The importance of sizing the thermal storage in a solar system is shown by various examples. One assignment asks the students to compare the system performance for various collector areas and thermal storage capacities. This is also used to introduced parametric studies in TRNSYS, and student are developing the classical solar fraction vs. collector area and storage volume curves.

Photovoltaic and PV-T systems

The theory of photovoltaic system is covered briefly, the focus being on system-level design and on the interaction with other renewable energy technologies.

Examples of assignments are to design a stand-alone PV-powered system for a bike-sharing company (inspired by the actual systems in Montréal), and to design an off-grid house powered by wind and PV (optimization between the two renewable energy sources and the battery capacity).

Economic Analysis for renewable energy systems

Basics of engineering economic analysis (cash-flow, discounted payback time, internal return rate, etc.) are briefly covered. The concept of levelized life cycle cost is introduced to compare different renewable and non-renewable energy technologies. Economic analysis is typically integrated into the last two homework assignments, while the first ones focus on energy performance only. This is generally combined with exercises asking the students to perform and present energy balances, e.g. through Sankey diagrams.

Concentrating Solar Power and solar cooling

Due to time constraints, these applications, which are less relevant for the Montréal context, are typically covered in a descriptive manner through a lecture presenting the principles and successful applications. These topics generate a significant interest among the students so the possibility of offering optional final project topics is being considered.

Putting it all together: the final project

The final project is intended to be a comprehensive design exercise where students must optimize the performance of their proposed configuration through an economic analysis. The energy performance is defined by the levelized life cycle cost of energy, or specified through targets such reaching a given solar fraction, net-zero energy, or stand-alone operation. Examples of final projects are:

- Design of an SDHW system for a building serving food to homeless people (this project used data from a real project including on-site DHW draw measurements, mechanical room and roof space constraints and local shading). Students were using different weather data, transposing the real site into different contexts.
- Design of a solar combisystem with a 75 % solar fraction for a residential building (students were allowed to select any city and exact location, including local shading).
- Design of a stand-alone polar research station (latitude higher than 75°) powered by solar thermal, PV and wind with a 90 % renewable energy fraction.

One difficulty of the final project is providing detailed feedback to the students, as it is typically due at the end of the exam session. Oral presentations were used during some years but the number of students make it difficult to organize during the last weeks of the term. The project start has been moved earlier in the term (typically before the mid-term exam), and intermediate deliverables are used to provide some feedback.

7. Student feedback and lessons learned

Formal independent surveys (2011 – 2016)

Polytechnique Montréal has a formal assessment program where students fill out anonymous evaluation forms which are collected by an independent school department (“bureau d’appui pédagogique”, teaching support group). Professors then receive the compiled evaluation results in the form of percentages of agreement to some 20 questions. Two questions are related to the use of TRNSYS: one on the clarity of homework instructions (it was noticed that complaints were mostly related to difficulties with the TRNSYS files), and one on “equipment, materials, and software”. Table 2 shows responses to both questions.

Table 2: Answers to independent student surveys (in % over the 6 years, total number of respondents = 150 over 180 students)

Question	Strongly disagree	Disagree	Agree	Strongly agree
Instructions for homework assignments are clear	0.5 %	4.5 %	45 %	55 %
Equipment, materials, and software used are useful	0 %	0 %	14 %	86 %

In addition to these questions, students are asked to comment on the course in a dedicated space. All answers are again collected by the independent department and then communicated to the instructor. The question is formulated to ask students if they have suggestions to improve the course, but some students use the space to identify the parts that they especially like. The most frequent or relevant comments are summarized below:

- An overwhelming number of students write positive statements on the course as a whole and the fact that it mixes theoretical aspects (the “fundamentals” part) with practical design applications. The fact that these

practical applications are simulation-based design exercises is very often mentioned as a positive point.

- The use of TRNSYS is appreciated, and a few students have suggested also using other programs that would be more likely to be used by consultants.
- Some students have complained that the gap between homework (where "ready-made" TRNSYS projects are provided most often) and the final project (for which students start from a clean sheet) was too large.
- Some students have suggested to spend more time on how to use TRNSYS, or to organize a specific course on the program at the beginning of the term. They have also mentioned that it would help to have more online tutorials available.
- A few students have also suggested increasing the time spent in class using the software (i.e. reducing the lectures). In one extreme case, a student complained about the "fundamentals" part with "equations that we will probably never use in our engineering career", and he/she suggested replacing it with more simulation-based case studies with economic analysis.
- During the years when other programs were used, some students appreciated the mix of programs but many complained that there was not enough time to learn how to use the different programs.
- Over the years, a few students also complained specifically about the place of TRNSYS in the course, and that the course was on simulation rather than on solar energy (2 students over 6 years). One specific comment was that TRNSYS was "irrelevant in the real world", being "much too complicated".

In-class specific survey in 2016

In addition to the formal surveys, the instructor asked some specific questions at the end of the course in 2016. The written survey was anonymous, but answers were collected and processed directly by the instructor. 30 students (over 35) responded to the survey, which had 3 closed questions and was also asking for any other suggestion to improve the course. Table 3 presents the results of the closed questions.

Table 3: Answers to specific student survey in 2016 (in %, total number of respondents = 30 over 35 students)

Question	Strongly disagree	Disagree	Agree	Strongly agree
Simulation-based applications are an important part of the course	0 %	0 %	3 %	97 %
It is a good idea to use TRNSYS, which is flexible and forces users to understand how systems operate, instead of other programs that would be easier to use	0 %	0 %	37 %	63 %
Even if the course is mostly about solar thermal systems, it is a good idea to also cover solar photovoltaic systems and wind energy conversion, even briefly, and to use PV and/or wind in the final project.	0 %	0 %	4 %	96 %

The suggestions to improve the course are summarized below (the numbers in bracket indicate the number of students who made the suggestion). There were 24 comments in total for 30 respondents, and 4 of these comments repeated that TRNSYS was a good tool to understand how systems operate, which was already covered by the second question:

- (5) There should be a separate course (or some periods in the solar class) dedicated to TRNSYS.
- (3) The instructor should provide more explanations on specific TRNSYS components before they are used for the first time in homework or in the project.
- (3) More practical sessions should be devoted to TRNSYS during the course.
- (3) Other easier-to-use programs should be presented as well.
- (3) TRNSYS homework should insist more on creating systems (not just using "pre-canned" systems).
- (2) More TRNSYS tutorials and exercises should be available online.
- (1) TRNSYS documentation should be available in French

Lessons learned

Student feedback has been overwhelmingly positive on the use of TRNSYS, and most students seem satisfied that the course combines theoretical notions (through hand-written exercises and exam) with practical, simulation-based design exercises. The choice of TRNSYS is approved by the vast majority of students, even though they realize that other programs exist which would be easier to use. The second question of the 2016 survey was especially formulated to validate that hypothesis. Some students would like to be exposed to other programs, but they do see value in using a more flexible program even if it is more complicated.

The students generally suggest to spend more time teaching how to use TRNSYS, either in the solar course or in a dedicated training course. They also point at the lack of suitable online examples and tutorials. This illustrates the challenge of teaching solar energy engineering with TRNSYS rather than teaching how to use TRNSYS – it does not seem possible to avoid "software training courses" completely, whether they happen during the class or they are provided elsewhere. The students also indicated a need to evolve more progressively from the first homework assignments, which are very simple and rely on using ready-made projects, to the final project where students must create their system model from scratch. In particular, the difficulty of knowing which components to use and how each component should be used is insufficiently addressed in the present course structure. Again, training material specifically adapted to the course should be developed and provided, either as part of the course material or as online tutorials.

Although not directly indicated by survey answers, anecdotal evidence gained during the attempts to use other programs suggests that the level of comfort and expertise of the instructor with the software is critical to its successful use in teaching. If the instructor uses the program on a regular basis for teaching and research, he/she will know the software limitations and quirks. Even if the problems cannot be fixed, students can be warned about misleading indications, bugs and other problems before they get frustrated with them, which will completely change the dynamics of the exercise. In the author's experience, just quickly trying a few examples before an assignment using a program that is only used once a year for teaching is asking for trouble, even with commercial programs.

8. Conclusions

This paper presents a graduate solar energy engineering course which relies on the TRNSYS simulation tool to engage students in the learning process through design and analysis activities. The course learning objectives are discussed in relation to Bloom's revised taxonomy, showing the role of simulation in reaching the higher levels of objectives. The paper then presents an overview of the course contents, as well as teaching and assessment methods. TRNSYS is used for assignments during the entire teaching term, in order to help students gain confidence in the program and in their skills using it. Some assignments compare hand-calculated values to simulation results to encourage the developments of intuition and skepticism toward simulation results. Student feedback has been overwhelmingly positive on the use of TRNSYS, and on the fact that the course combines theoretical notions (through hand-written exercises and exam) with practical, simulation-based design exercises. Students appreciate the fact that TRNSYS encourages them to think about the design and operation of solar systems before being able to model them, even if they realize that other tools might be easier to use and deliver results faster. Students also point out the lack of training material specific to the subject, which leads to difficulties in selecting and configuring the appropriate TRNSYS components. An accompanying website provides examples of course schedule, assignments and projects.

9. Acknowledgement

I wish to thank Sandy Klein and Bill Beckman from the University of Wisconsin-Madison Solar Energy Lab, who provided material that was very helpful when I started teaching this course – and more importantly inspired me with their passion for teaching and research in solar energy.

10. References

Anderson, L. W. and Krathwohl, D. R. (2001) *A taxonomy for learning, teaching, and assessing : a revision of Bloom's taxonomy of educational objectives*. Edited by L. W. Anderson and D. R. Krathwohl. New York, NY:

Longman.

Armstrong, P. (2016) *Bloom's Taxonomy*. Nashville, TN, USA: Vanderbilt University. Available at: https://cft.vanderbilt.edu/guides-sub-pages/blooms-taxonomy (Accessed: 26 September 2016).

ASHRAE (2014) *Standard Method of Test for the Evaluation of Building Energy Analysis Computer Programs (Standard 140-2014)*. Atlanta, GA, USA: American Society of Heating, Refrigerating and Air-Conditioning Engineers.

Beausoleil-Morrison, I. and Hopfe, C. J. (2016) 'Developing and testing a new course for teaching the fundamentals of building performance simulation', in *Proceedings of eSim 2016: the 9th conference of IBPSA-Canada, May 3-6*. Hamilton, ON, CAN, pp. 22–33.

Bernier, M., Kummert, M., Sansregret, S., Bourgeois, D. and Thevenard, D. (2016) 'Teaching a building simulation course at the graduate level', in *Proceedings of eSim 2016: the 9th conference of IBPSA-Canada, May 3-6*. Hamilton, ON, CAN, pp. 34–45.

Burch, J., Huggins, J., Long, S. and Thornton, J. (2012) 'Revisions to the SRCC Rating Process for Solar Water Heaters', in *Proceedings of the World Renewable Energy Forum, May 13-17*. Denver, CO, USA, pp. 1–8.

Charles, P. P. and Thomas, C. R. (2009) 'Four approaches to teaching with building performance simulation tools in undergraduate architecture and engineering education', *Journal of Building Performance Simulation*. Taylor & Francis, 2(2), pp. 95–114.

Clarke, J. A. (2001) 'Domain integration in building simulation', *Energy and Buildings*, 33(4), pp. 303–308.

Duffie, J. A. and Beckman, W. A. (2013) *Solar Engineering of Thermal Processes*. 4th Ed. Hoboken, NJ: Wiley.

Freeman, S., Eddy, S. L., McDonough, M., Smith, M. K., Okoroafor, N., Jordt, H. and Wenderoth, M. P. (2014) 'Active learning increases student performance in science, engineering, and mathematics.', *Proceedings of the National Academy of Sciences of the United States of America*. National Academy of Sciences, 111(23), pp. 8410–5.

Gómez-Moreno, A., Palomar Carnicero, J. M. and Cruz-Peragón, F. (2015) 'Teaching different types of air conditioning systems using simulation software', in *Proceedings of INTED2015: the 9th International Technology, Education and Development Conference, Mar 2-4*. Madrid, ESP, pp. 5183–5192.

Goswami, Y. D. (2001) 'Present status of solar energy education', in *Proceedings of the 2001 American Society for Engineering Education Annual Conference & Exposition, Jun 24-27*. Albuquerque, NM, USA, p. 6.803.1-6.803.15.

Gravagne, I. A. and Van Treuren, K. (2008) 'On the Use of TRNSYS in a Solar Energy Technical Elective', in *Proceedings of the 2008 ASEE Gulf-Southwest Annual Conference, Mar 26-28*. Albuquerque, NM, USA, p. 17.4.1-17.4.9.

ISO (2013) *Solar heating - Domestic water heating systems - Part 4: System performance characterization by means of component tests and computer simulation. ISO 9459-4:2013*. Geneva, CHE: International Organization for Standardization.

Kandpal, T. C. and Broman, L. (2014) 'Renewable energy education: A global status review', *Renewable and Sustainable Energy Reviews*, 34, pp. 300–324.

Klein, S. A. (2014) 'EES - Engineering Equation Solver'. Madison, WI, USA: F-Chart Software.

Klein, S. A., Beckman, W. A. and Duffie, J. A. (1976) 'A design procedure for solar heating systems', *Solar Energy*. Pergamon, 18(2), pp. 113–127.

Klein, S. A., Beckman, W. A., Mitchell, J. W., Duffie, J. A., Duffie, N. A., Freeman, T. L., Mitchell, J. C., Braun, J. E., Evans, B. L., Kummer, J. P., Urban, R. E., Fiksel, A., Thornton, J. W., Blair, N. J., Williams, P. M., Bradley, D. E., McDowell, T. P., Kummert, M. and Duffy, M. J. (2014) 'TRNSYS 17 – A TRaNsient SYstem Simulation program, User manual. Version 17.2'. Madison, WI: University of Wisconsin-Madison.

Megri, A. C. (2014) 'TRNSYS as an Education Tool to Predict Indoor Environment Temperature for Undergraduate Students', in *Proceeding of the 121st ASEE Annual Conference, Jun 15-18*. Indianapolis, IN, USA, p. 24.1282.1-24.1282.12.

Prince, M. (2004) 'Does Active Learning Work? A Review of the Research', *Journal of Engineering Education*, 93(3), pp. 223–231.

Reinhart, C. F., Dogan, T., Ibarra, D. and Samuelson, H. W. (2012) 'Learning by playing – teaching energy simulation as a game', *Journal of Building Performance Simulation*. Taylor & Francis, 5(6), pp. 359–368.

Reinhart, C. F., Geisinger, J., Dogan, T. and Saratsis, E. (2015) 'Lessons learned from a simulation-based approach to teaching building science to designers', in *Proceedings of Building Simulation 2015:14th Conference of International Building Performance Simulation Association, Hyderabad, India, December 7-9*. Hyderabad, IND, p. 2468.1-2468.8.

SRCC (2015) *Solar Thermal Component Test and Analysis Protocol. SRCC Document TM-1-2015-10*. Cocoa, FL, USA: Solar Rating & Certification Corporation.

Conference Proceedings

EuroSun 2016
Palma de Mallorca (Spain), 11 - 14 October 2016

Solar house prototypes as *living labs in architecture* for holistic sustainability education

Torsten Masseck

Universitat Politècnica de Catalunya (UPC), Sant Cugat del Vallès (Spain)

Abstract

The LOW3 prototype solar house of UPC has been designed and built between 2008 and 2010 and converted and operated as a *Living Lab for sustainable architecture and lifestyle* since 2011 at the ETSAV campus at Sant Cugat del Vallés (Barcelona) under the responsibility of the author (www.livinglab-low3.blogspot.com)

This paper highlights the importance of *Living Labs* as innovation infrastructures in Higher Education and presents the specific educational experience of LOW3 within the institutional framework of UPC, drawing from 5 years of action research regarding pluridisciplinary, experience based sustainability education.

Keywords: *Living Labs, Education for Sustainable Development, Sustainable Lifestyle, Sustainable Architecture, Solar Architecture*

1. Background

Education at schools of architecture must attend the demand for a new profile for architects, integrating and fostering corresponding SD competences through new learning methodologies, tools and concepts (EDUCATE Project Partners 2012). A series of recent developments give relevance to the research on *Living Labs in Architecture* as new tools for a holistic Education for Sustainable Development (ESD) with a specific focus on renewable energies in housing and our daily lives:

- A new educational reality, with redefined objectives in higher education based on competence-based learning and a more transdisciplinary approach
- A new knowledge reality, with an urgent need for acquisition of new knowledge regarding specific subjects like low energy buildings, low-impact building materials and energy efficient technologies
- A new social reality, shifting towards participation, constant social innovations and a higher demand for environmental standards
- A new professional reality, requiring more interdisciplinarity, the ability to deal with complexity and uncertainty and new forms of project development processes based on collaboration

Important considerations regarding the essence of ESD are furthermore the understanding of sustainability as a (socially constructed) reality, "*... as a dynamic and/or evolving concept, as controversial and the source of conflict*", and as a "*catalyst for change*" (Wals & Jickling 2002), which in consequence needs places for its collective negotiation and definition. This might require a new form of collaborative and empathic learning in order to develop a new collective "*biospheric consciousness"* (Rifkin 2011). Finally ESD seems to require so-called "*transformative learning"* based on psychological, convictional and finally behavioral transformation (Wiek et al. 2011, Boehnert 2012). On the other hand a newly strengthened social responsibility of university towards society in the development of innovative solutions for our environmental, social and economic conflicts must lead towards new processes in teaching, research and technology transfer based on a strong interaction with their local and regional communities and society in general (Cortese 2003). Living Labs seem to play here an interesting role as collaborative multi-stakeholder platforms.

doi:10.18086/eurosun.2016.10.06 Available at http://proceedings.ises.org

2. Introduction

In the area of architecture, the ETSAV School of Architecture at Sant Cugat del Vallés can be considered a pioneering institution in understanding its campus and buildings as a laboratory to learn about energy efficiency in buildings, but also its community as an important stakeholder for a broader approach to sustainability regarding its socio-economic environment.

Solar Decathlon is an international competition for 20 selected universities to plan and build prototypes of energy self-sufficient solar houses. In 2008 a first ETSAV team under the lead of the author started the development of the first prototype solar house LOW3 at the campus in order to participate in the Solar Decathlon Europe 2010 competition in Madrid (Masseck 2011).

The LOW3 project (2008-2010) demonstrated over a 2 year period the importance and impact of a new way of education in architecture, based on the development and construction of a prototype house at the campus with a high degree of team self-organization, individual responsibility, and a strong link between teaching and research.

LOW3 has been reconstructed in 2011 and renamed *Living Lab LOW3 – Laboratory for sustainable architecture and lifestyle* at the ETSAV Campus at Sant Cugat del Vallès (Barcelona) with the objective of establishing an open platform for collaboration with companies, and an exploration of experience-based concepts for teaching, research and innovation activities.

Living Lab LOW3 adds since then value to the academic offer at UPC-Barcelona Tech through its innovative transdisciplinary educational programs, transmitting experience-based knowledge about integrated energy design in architecture and a holistic approach to sustainability. This paper argues that Architecture Living Labs like Living Lab LOW3 make a positive contribution to architectural education in its approach to sustainability including the holistic paradigm shift towards solar architecture, renewable energies and standards like Nearly Zero Energy Buildings.

3. Methodology

The concept of Living Lab LOW3 is influenced by the concept of user involvement in research and innovation, derived from the definition of Living Labs, as well as the co-creation and open innovation in real-life settings through a multi stakeholder approach (academia, companies and research entities but also local administration), understanding both students, researchers as well as citizens as the "users" of this newly generated platform. (Masseck 2013)

The concept of Living Lab LOW3 is that of an activities platform with a participatory approach to teaching and learning based on a prototype solar house, offering its spaces, its equipment and its infrastructure to diverse user groups from both inside and outside the UPC.
Teaching and learning activities take place in parallel with research projects and outreach activities in order to create synergies between sectors, people and disciplines. Finally, Living Lab LOW3 is also a place for the networking of people in order to engage in new sustainability projects and initiatives, fostering the human factor behind these activities.

Living Lab LOW3 is an educational research project under continuous development since January 2011. During almost 5 years of its existence, new teaching formats, methods and tools have been tested regarding the link between formal and non-formal learning, the exploration of the personal learning environments of participants and the synergies between teaching, research and innovation.

Living Lab LOW3 applies a mixed-methods approach with quantitative and qualitative research methods. Phenomenological research has been used in the Live-at-LOW3 experiment, evaluating the experience of students living a sustainable lifestyle in the LOW3 solar house. The tools used are surveys, questionnaires, semi-structured interviews, amongst other formats like video documentaries and participant's videos.

4. Results

Results of this innovative educational project can be described in the following areas:

- *General educational and research activities* referring to a huge amount of diverse activities regarding teaching and learning as well as research and innovation at an university campus
- *Specific Living Lab teaching formats* regarding innovative approaches to sustainability education applying a user-centered living lab approach, and
- *Activities as a higher education transition platform,* which contributes to a holistic sustainability transition of university and the society it is embedded.

4.1 Activities at Living Lab LOW3

Since 2011 3 regular Living Lab LOW3 courses, 6 innovation seminars, 2 international sustainability seminars, 1 house occupation experiment, 5 open doors days and around 25 educational visits have taken place at Living Lab LOW3, with links to different Master and PhD Programs both inside and outside the UPC and the ETSAV undergraduate program. Additionally more than 30 specific events opened up the house to user groups to disseminate knowledge to the academic community and beyond.

Fig.1 shows an educational activities map of the project, resuming the areas of knowledge; disciplinary, transdisciplinary and ESD related initiatives, as well as the corresponding formats, methods, and outcomes:

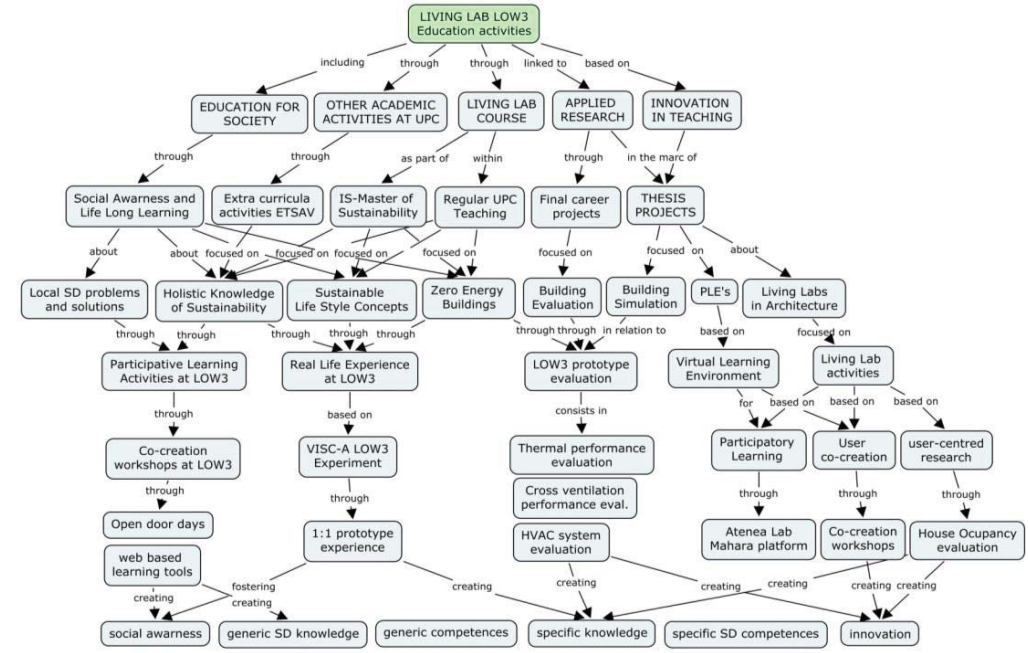

Fig. 1: Educational activities map Living Lab LOW3

4.2 Live-at-LOW3 Experiment

One of the most intensive, experience-based, transformative teaching and learning activities has been the 'Live-at-LOW3' experiment, a house occupation experiment in 2012.
The 'Live-at-LOW3' experiment was carried out within the elective course "Living Lab LOW3", linked to the Master Program Sustainability (IS.UPC) and the ETSAV undergraduate program.

This teaching and learning concept needed special commitment by the participating students. No regular timetable could be guaranteed during the course. The house-occupation experiment has been a holistic approach to user-centered research.
Two selected students evaluated and tested the prototype solar house during 14 days with the participating course students preparing, accompanying and evaluating the experiment through the monitoring and evaluation of the inhabitant's lifestyle with a holistic view on housing, consumption, food and mobility.
This course had a transformative effect on its participants, as in parallel to the generated theoretical knowledge about sustainable lifestyles, the related experience-based learning showed to be highly effective.

The experiment included:

- Monitoring energy consumption (daily consumption, relation to daily activities, comparison with solar production)
- Assessing water consumption (grey water recycling, dry toilet, water saving measures)
- Measuring waste production (daily production, type and weight)
- Assessing indoor comfort (day and night comfort in the house, privacy, air quality, noise)
- Reporting about food habits (local market, own vegetable garden and even 2 hens at the campus)
- Calculating the overall ecological footprint of the inhabitants

Results were published in course reports[1], the experiment was filmed and published through a documentary as well as local newspapers, and television showed interest in the experiment and its outcomes[2].
A holistic learning and user-centered research process was conducted in order to evaluate the LOW3 solar house, its concept, its technologies, and the resulting comfort for inhabitants. A wider engagement of the academic community, as well as society in general, could be achieved through open door days, media interest (national and local TV and radio emissions, digital newspapers) and the use of social networks and ICT (YouTube channel for video diary, documentary, live webcam).

The educational experiment was very successful, with students evaluating their participation and related learning as very positive. Nevertheless the educational format had to overcome administrative and legal issues, was time consuming for all participants, depending on a special personal commitment of all participants, and needed a certain amount of economic resources, which is the reason why this format could not be repeated since then.

4.3 The role of Living Lab LOW3 as multi-stakeholder platform

Living Lab LOW3 has shown to function as a multi-stakeholder platform for the following activities:

- Interchange between the professional and the academic world of architecture, bringing together professional associations interested in life-long learning and additional professional qualification programs, and the university (students, teachers, research groups), creating synergies between the academic and the professional world of architecture and building construction.

- Link to the productive sector of the building industry, allowing synergies in the knowledge dissemination about materials, products or services, within an environment which allows critical reflection, in-situ evaluation and as a consequence, a creative approach to innovations.

- Link to public administration, allowing collaboration between municipalities and academia regarding knowledge generation and dissemination, consultancy services, formative activities as well as specific project developments.

[1] http://www.low3.upc.edu/eng/plataforma_eng.html
[2] http://www.livinglab-low3.blogspot.com.es/2012/10/fin-del-primer-experimento-visc-low3.html#more

- Link to society, offering a place for knowledge dissemination and critical reflection, learning and experiencing different aspects related to a more sustainable lifestyle like the resource consumption in buildings, the environmental impact of materials, alternative forms of living such as co-housing, or the amount and impact of food and water consumption in private households.

- Transition Platform for the academic community, serving as a place for meeting, working and innovating for all kind of groups of the academic community (and beyond), generating synergies and allow the creation of new initiatives e.g. for HE transition projects towards SD, or community outreach projects, organized by student teams or even administrative staff. This approach reflects the idea of Living Labs as *Transition Arenas* e.g. for SD transition of HEIs. (Masseck 2016)

Figure 2 shows the diversity of uses of Living Lab LOW3 for research, teaching and outreach.

Fig. 2: Diversity of uses of Living Lab LOW3 for research, teaching and university outreach

Living Lab LOW3 today forms part of a new, emerging educational ecosystem at ETSAV, which links formal teaching with informal learning and established educational courses to a whole series of outreach initiatives supported by non-formal learning environments at the campus.

5. Conclusions

Architecture Living Labs can serve as multi-stakeholder platforms, which connect the academic world with its surrounding - the professional world of architecture and building construction, the productive sector, public administration, and last but not least, society as a whole. Through its experimental character, Living Labs can offer a place to meet, reflect, discuss, learn, explore and develop ideas, concepts and strategies with regard to sustainability in a most holistic way, not only limited to architecture but also considering the lifestyles adopted by society which include existing consumption and production models, political and economic issues, as well as social processes and innovations.

The diversity of activities related to one single platform like Living Lab LOW3, allowed the creation of many synergies among actors, programs and projects. Stakeholders have the opportunity to participate in a community of users beyond established academic structures, with transversality from high school students up to senior researchers.

In this sense Living Labs can be seen as social ecosystems within the specific context of university and with a strong link to the surrounding socio-economic context, fostering the creation of transversal educational communities.

References

Boehnert, J., 2012. The visual communication of ecological literacy: designing, learning and emergent ecological perception. University of Brighton, UK. Available at: http://visecology.wordpress.com/\nhttp://ethos.bl.uk/OrderDetails.do?uin=uk.bl.ethos.566147.

Cortese, A.D., 2003. The Critical Role of Higher Education in Creating a Sustainable Future. *Planning for Higher Education*, March-May, pp.15–22.

EDUCATE, 2012. Environmental Design in University Curricula and Architectural Training in Europe: Framework for Curriculum Development, S. Altomonte (ed.)

Masseck, T., 2011. LOW3 – a Mediterranean Net Zero Energy Building. In ISES Solar World Congress 2011- Conference Proceedings.

Masseck, T., 2013. Teaching Sustainability through Living Labs in Architecture : The case study of the UPC-LOW3 prototype solar house. In EESD 2013 – Engineering Education for Sustainable Development - Conference Proceedings. Available at: http://www-eesd13.eng.cam.ac.uk/proceedings.

Masseck, T., 2016. Teaching sustainability: living labs in architecture.
A framework proposal for living lab eco-systems for teaching, research and innovation in the field of sustainable architecture and ESD in higher education. Specific case study : Living Lab LOW3 (UPC - BarcelonaTech), Chapter 5.2.2, http://hdl.handle.net/10803/387819

Rifkin, J., 2011. The third industrial revolution - How lateral power is transforming energy, the economy, and the world, St. Martin's Press.

Wals, A.E.J. & Jickling, B., 2002. "Sustainability" in higher education: From doublethink and newspeak to critical thinking and meaningful learning. International Journal of Sustainability in Higher Education, 3, pp.221–232.

Wiek, A., Withycombe, L. & Redman, C.L., 2011. Key competencies in sustainability: a reference framework for academic program development. Sustainability Science, 6, pp.203–218

Conference Proceedings

EuroSun 2016
Palma de Mallorca (Spain), 11 - 14 October 2016

SHWwin: freeware (beta stadium) for Universities and schools for the simulation of solar thermal plants

Wolfgang Streicher[1] (Author), Dietmar Siegele[1]

[1] University of Innsbruck, Unit for Energy Efficient Buildings, Innsbruck (Austria)

Abstract

The simulation software SHWwin is being developed since 1993, first at the Institute of Thermal Engineering at Graz University of Technology, Austria and since 2009 at the Unit for Energy Efficient Buildings at the University of Innsbruck, Austria. In 2015 a new Version compatible with 64bit Operating Systems (Windows 7© and higher) was relaunched. Several new features like swimming pool, second domestic hot water store, English language, statistics on temperatures and pressure distribution, thermotrophic or back cooled collectors and others were implemented and a new layout of the graphical user interface was developed.

Like the old Version also the new Version is available for free from the author to be used for education and research. SHWwin has a large number of sets of hydraulic layouts. As all parameters of e.g. heat stores (position of in/outlets, sensors) and control can be chosen freely, it is a nice tool to show students dependencies and relevance of the parameters and allows optimizing plants. Climate data can be taken from e.g. Meteonorm (2015) or any other source.

Keywords: *Simulation Tool, Solar Thermal Systems, Freeware, Education,*

1. Introduction (SWC_Heading1)

Several tools for the simulation of solar thermal plants are on the market. Besides tools with predefined hydraulics like TSOL (2015) or Getsolar (2015) there are tools with free definable hydraulics like Polysun (2015) or TRNSYS (2015) available. SHWwin is closest to TSOL-professional but is available for free for educational and research purposes. It is being developed since 20 years and the recent update has a new GUI and several new features like swimming pool, Tank-in-Tank storage, 2nd DHW store, thermotrophic layers as collector cover, maximum allowed temperature at stagnation for the collector pump to switch on, statistics about temperatures and pressures in the system with expansion device layout, and can be run under Windows 7© or higher. There is no online help desk available, but reports on bugs are always welcome and will be repaired as fast as possible with updates to all users. Translation of the GUI in other languages or the translation of the help file from German to English (and other languages) would be welcome.

2. Functions of SHWwin

SHWwin runs on all windows platforms starting with windows 7©. Additionally the kernel (an .exe) file can run standalone using the ASCII input files normally generated by the GUI. All input and output files including weather data can be edited also manually as ASCII files. So a coupling to other tools like e.g. MatLab or GenOpt is possible. SHWwin simulates dynamically solar thermal systems. Time steps can be chosen freely, but 3 or 6 minute time step is recommended.

Climate data on a hourly base can be used either from climate date generators (e.g. Meteonorm (2015)) or from other measured or produced hourly data.

doi:10.18086/eurosun.2016.10.05 Available at http://proceedings.ises.org

The following solar thermal plant designs can be simulated:

- Domestic hot water plants
- Combined domestic hot water and space heating plants (two store systems, one store system and DHW once through heat exchanger or Tank-in-Tank)
- Both of the above can be coupled with an indoor or outdoor swimming pool
- Solar assisted district heating networks

Each plant design allows several variations e.g. the choice of:

- Internal or external heat exchangers
- Fixed pipe positions or stratifying units or two inlets/outlets at the tank.
- All positions of heat exchangers, in/outlet pairs and temperature sensors can be freely chosen
- How the auxiliary heat is delivered (immersed electric rods or external boiler). The boiler can deliver only in the buffer (space heating) store or in both stores (SH and DHW)
- Auxiliary heat to DHW store (if chosen) can be either delivered directly from boiler or via the buffer store. Additionally an electric direct heating rod is available.
- Priority for solar heat input on space heating, domestic hot water, swimming pool or to the currently lowest temperature is available

Several collector volume flow strategies are available (see Figure 7, left column bottom)

- Fixed mass flow (can be freely chosen).
- Variable mass flow with either fixed collector outlet temperature or fixed ΔT between collector outlet and highest heat sink (e.g. for district heating systems)

Figures 1 – 3 show examples for hydraulic layouts.

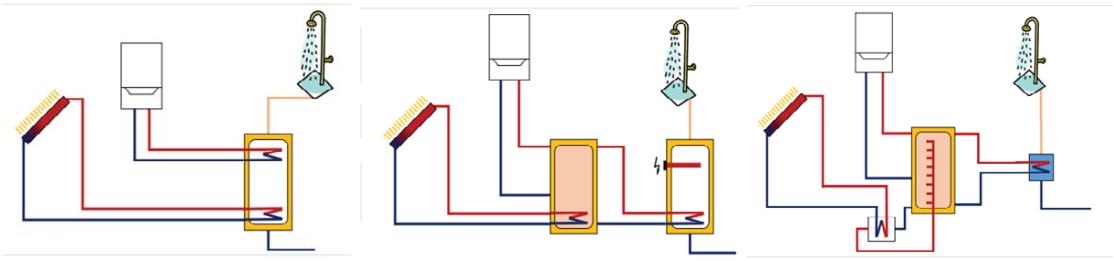

Fig. 1: Examples for hydraulics for domestic hot water (DHW) systems

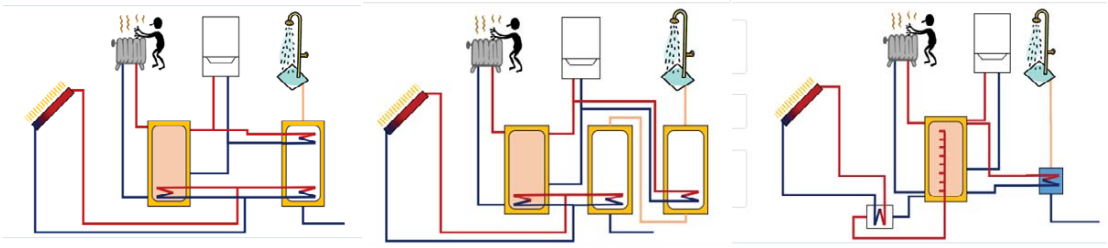

Fig. 2: Examples for hydraulics for domestic hot water and space heating systems (Combisystems)

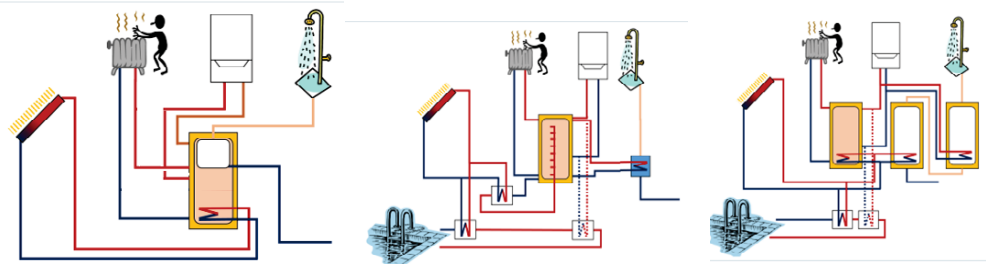

Fig. 3: Examples for hydraulics for domestic hot water, space heating and swimming pool systems

Plant Control settings

- On/Off temperature difference for the collector loop
- Blocking of state of collector loop for a specific time.
- Setting of a maximum temperature above which the collector pump cannot start to prevent the start of the collector pump during a stagnation period with steam in the collectors.
- Temperature settings of solar, boiler and electric rod input (maximum temperature, hysteresis)
- Temperature difference to load DHW store from space heating store to the domestic hot water store (if this plant design is chosen)

Additional available functions are

- Generation of statistics of temperatures and pressure in the collector loop. For this function the expansion vessel is either designed automatically or can be chosen. The volumes of each part of the solar loop have to be given by the user. For this function a coupling to Excel© is made. Results are tables and graphs, the latter are shown in Figure 4.

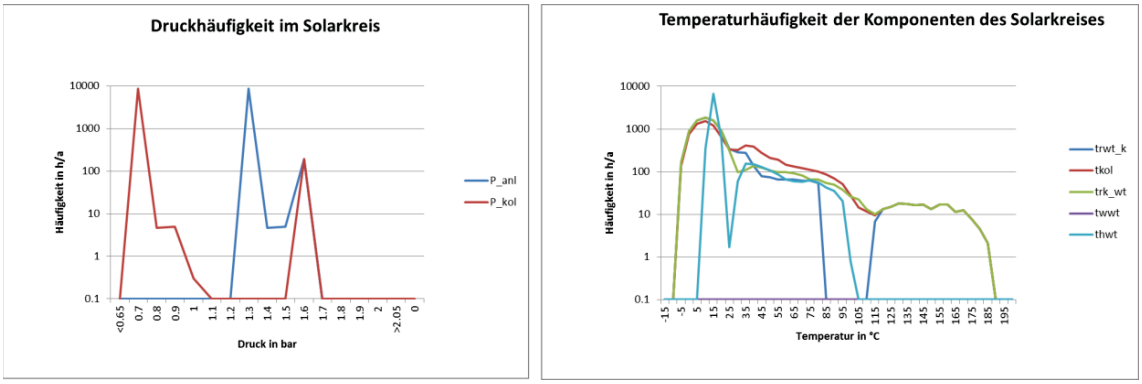

Fig. 4: Collector loop statistics of pressure and temperature in SHWwin

- If measured data of auxiliary heat input into the buffer store or the heating system, the domestic hot water demand or the space heat demand was measured in a real plant, this data can be used as input and overrules the respective simulation data.

3. Description of the SHWwin GUI

Currently the GUI is available in German and English language. To change between the languages the option button has to be clicked. When the language is changed, the program has to be shut down and restarted. The F1 online help is currently only available, if the German language is chosen.

When starting, first of all, a weather data file has to be chosen. All relevant main project data including a picture of the plant can be given (see Figure 5). Here also some general simulation values (start, end, number

of time steps per hour ...) and the specific general functions stated above can be chosen. In the standard data set of SHWwin there are already some weather files available.

The next step is to choose the hydraulic system (Figure 6). Figures 1 to 3 show examples for systems available. Then, details for all components have to be defined. First the general system can be chosen in the above part and then hydraulic details can be added in the lower klick box area. The graph on the lower right side is changing accordingly, so that the user can directly see, which configuration is chosen.

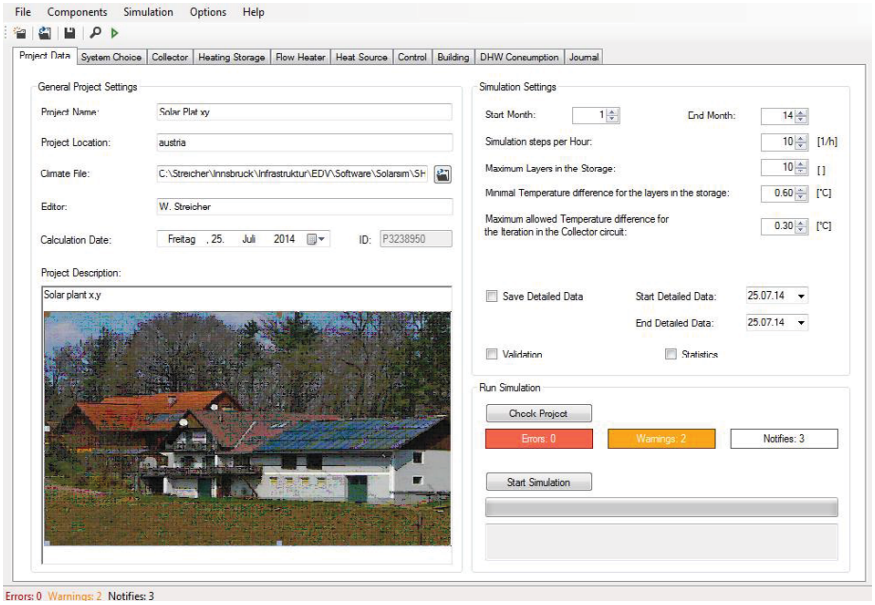

Fig. 5: System choice and visualization in SHWwin

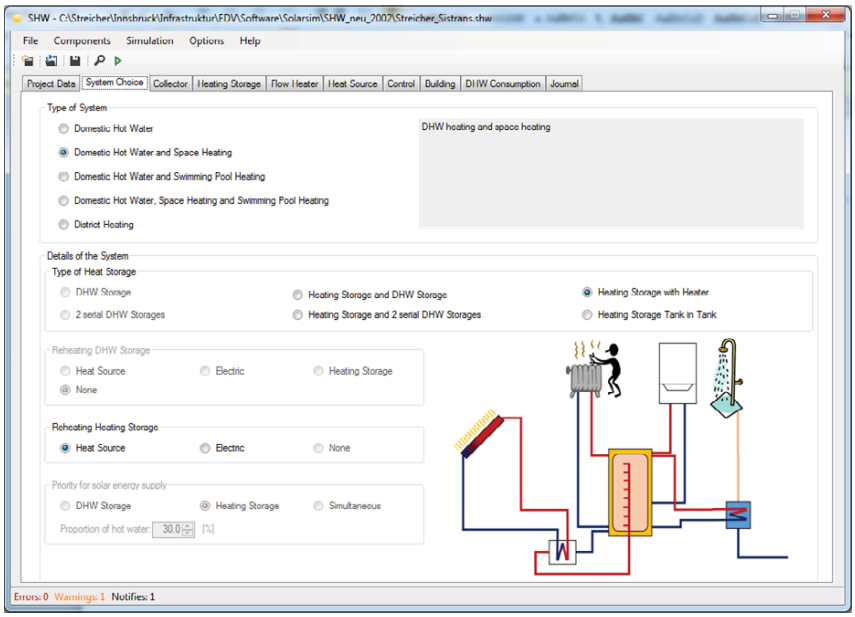

Fig. 6: System choice and visualization in SHWwin

After this, the input data of the different components have to be filled in. All fields are already prefilled with default values that allow immediately a simulation run. For many components databases are available, which are partly filled and can be edited and expanded by the user.

Figure 7 shows the inputs for the solar collector. The grey values on the left column are taken from database values (accessible by clicking on the first input box on the left column below collector). An old database from SPF Rapperswil, Switzerland is available for collectors which can be expanded by the user. Of course all values can be changed by the user clicking on "Edit Free". The input is related to key values of collector tests (parameters for the characteristic curves for efficiency and incident angle modifier and the thermal active mass of the collector).

The right column shows the volume flows through the collector to different stores. The input is given as relative value [kg/m$^2_{collector_area}$, h] grey values give the absolute resulting volume flow. Also some fixed fluid properties and the connecting tube characteristics have to be given.

On the very low right side collectors with thermotrophic layer or backside cooler for maximum temperature control during stagnation of the collector can be defined by putting in parameters for the change of the collector efficiency curve depending on the mean collector temperature. For thermotrophic layers the conversion factor c0 and for the backside cooler the heat transfer coefficient c1 are altered by an additional temperature dependent factor fc0 or fc1. Figure 7 right shows a sample dependency.

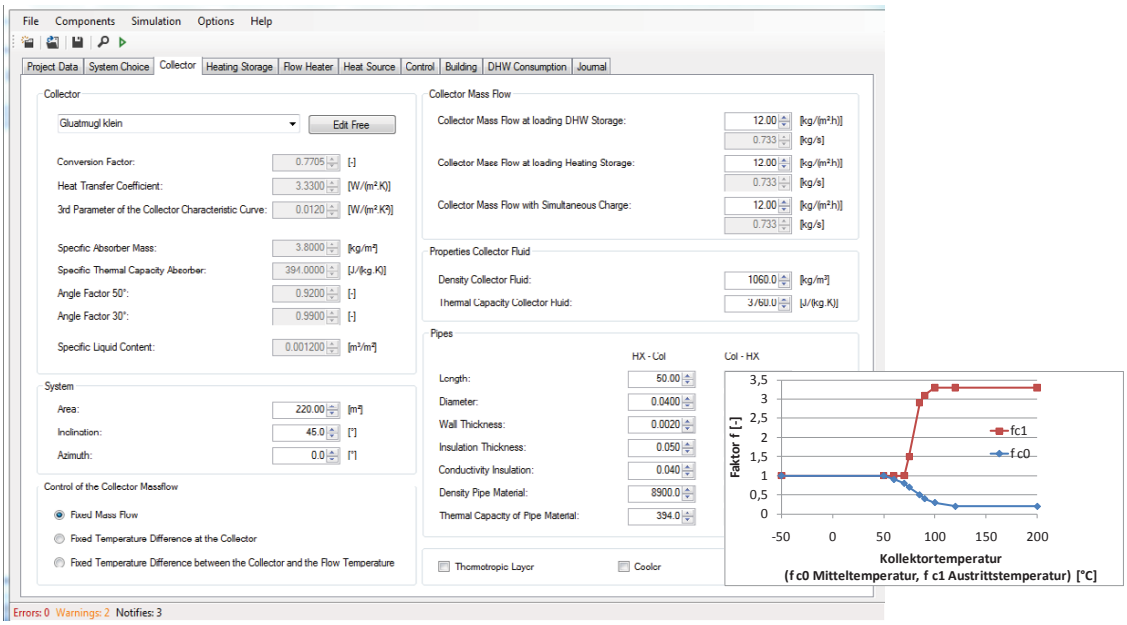

Fig. 7: Input for solar collectors and solar loop in SHWwin

Figure 8 shows the input data for domestic hot water store. All volumes, heights, insulation thickness and properties etc. can be freely chosen. The graph in the lower right is changing accordingly, thus the visual control of the store design is given. Additionally key values like volume for backup heating and solar are calculated simultaneously and shown to check the input data.

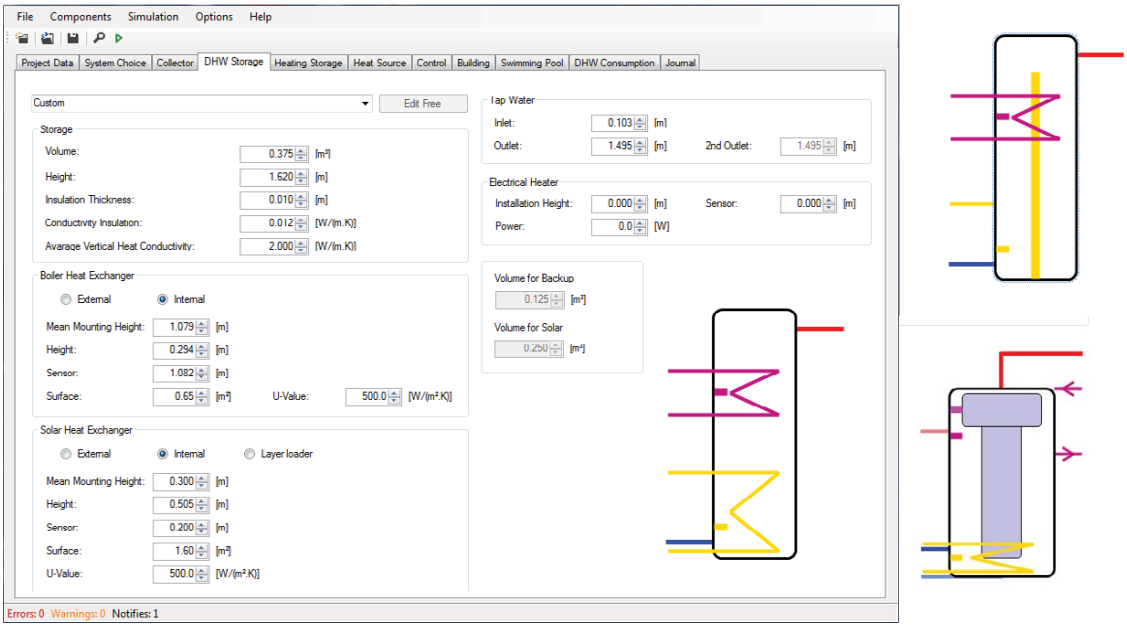

Fig. 8: Input and visualization of water stores for different types of heat input and output in SHWwin

The domestic hot water demand (Figure 9) can be given in terms of standard daily use with daily, weekly and monthly distribution. The cold water temperature can be varied via sinus curve variation over the year with the lowest temperature in February. Additionally a domestic hot water circulation can be defined.

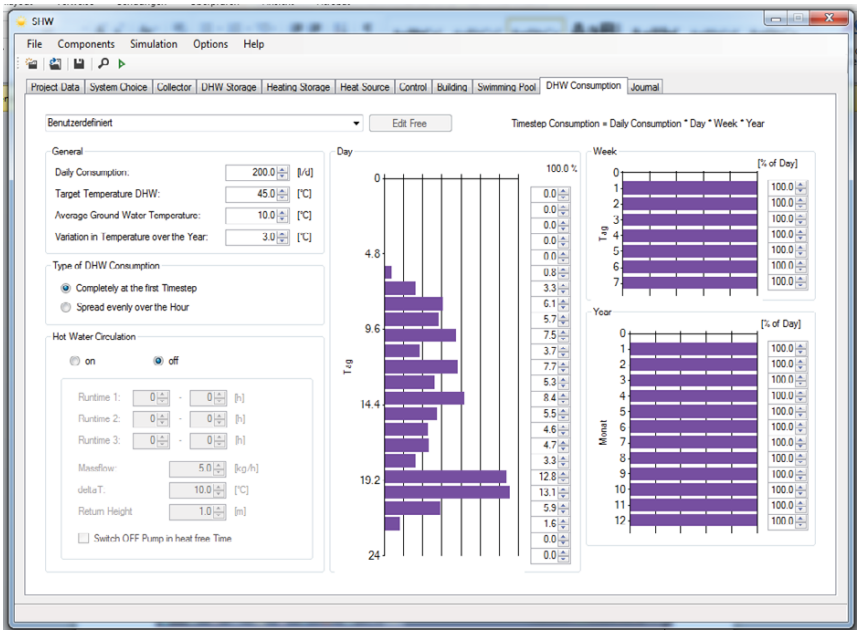

Fig. 9: Input and visualization of the domestic hot water demand in SHWwin

The space heating demand (see Figure 10) can be defined by the heat load reduced by internal gains and unheated parts as well as by the solar radiation passing up to 6 defined window areas. The flow/return temperature to the heating system is given as heating curve over the ambient temperature including a radiator exponent. The resulting curve is visualized for understanding and control purpose.

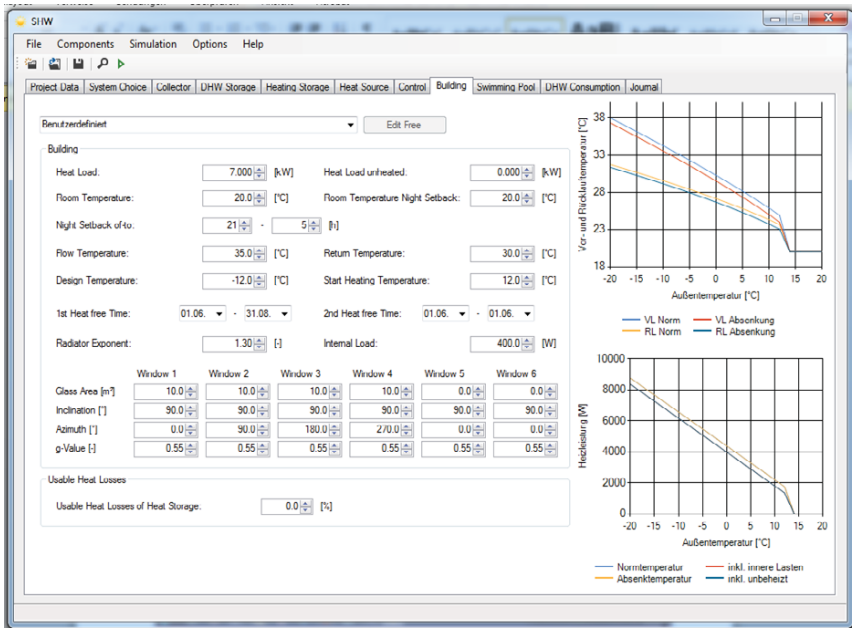

Fig. 10: Input and visualization of space heating demand in SHWwin

If a solar assisted district heating system is chosen the heat demand is defined by a space hating load and temperature curve over the ambient temperature (Figure 11). The domestic hot water demand is added to the given heat load.

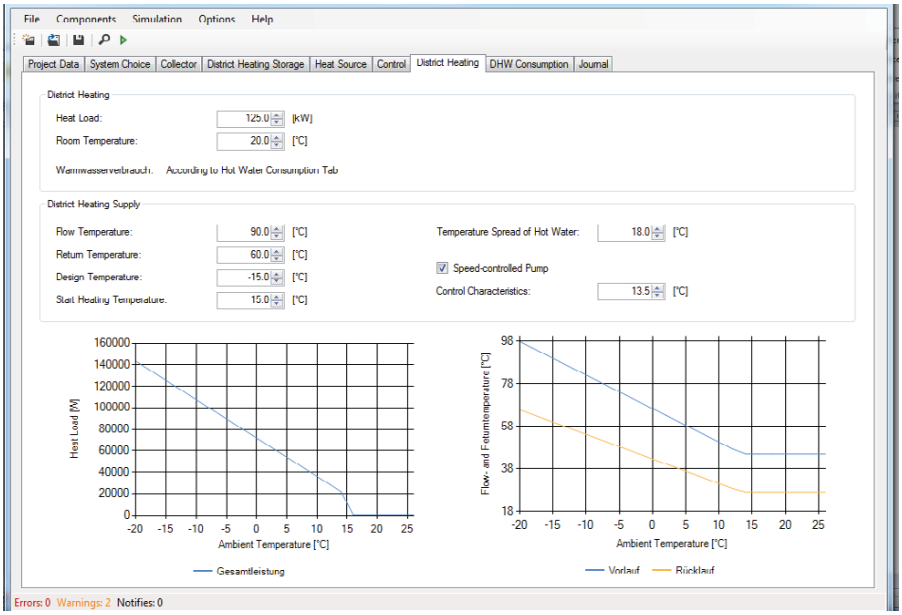

Fig. 11: Input and visualization of district heating network demand in SHWwin

An Online Help via the F1 button is available, if the German language is chosen. For every input value the online help can be invoked by clicking on the respective input button and then pressing F1. A help message with description of the value and some additional information will pop up (see Figure 12).

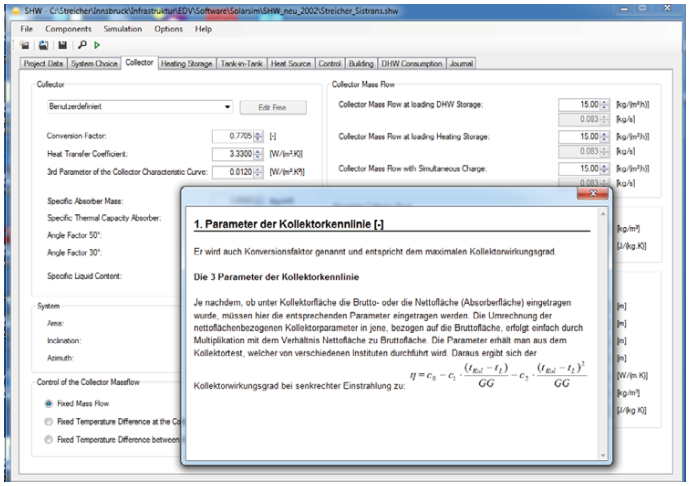

Fig. 12: Online Help via F1 in SHWwin (only if German language is chosen)

Before starting the simulation a check of the input data is performed and Errors, Warnings and Infos are delivered. This check can be invoked manually by pressing the magnifying glass. Also in the lower left edge of the window the actual number of Errors, Warnings and Infos is shown. By clicking on it, clear text messages about the nature of Error/Warning/Info (in German) show up and hints how to correct the input data are given. This is very important, as the input data can be freely chosen and e.g. heat exchangers or sensors could be placed above or below the storage. Additionally stability values are checked (e.g. if the volume turned around between an inlet/outlet pair in one time step is bigger than the volume available). The input boxes that induce the error are marked red. Figure 13 gives an example for errors occurring at a tank-in-tank buffer store inputs. As long as there are Errors in the input file (e.g. the heat exchanger is below or above the store) the simulation does not start.

Warnings give the user information about control settings that are not matching to the temperatures of the demand or too low auxiliary power. The simulation can be started despite the existence of Warnings. The respective input boxes are marked orange. Info's just give some hints on detailed system layout.

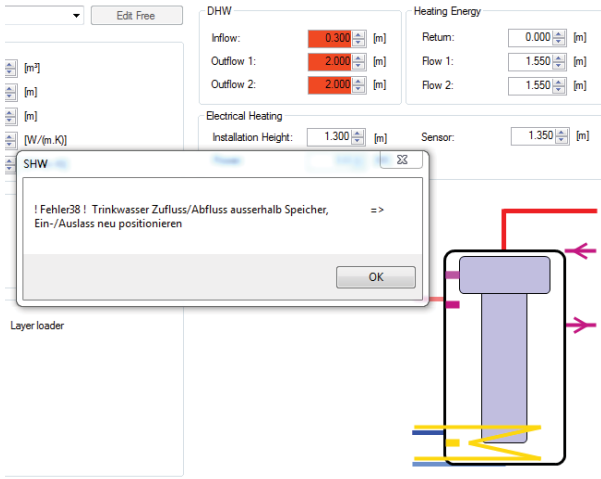

Fig. 13: Inherent input data check and display of input mistakes including suggestions for improvement

After the simulation is finished a summary with monthly and seasonal data and KPI's (key performance indicators) and some graphical and ASCII-data output is available. Additional this output includes all input data in (German) text including the units and can be seen as simulation protocol. Figure 14 shows the respective window with the first part of the output data.

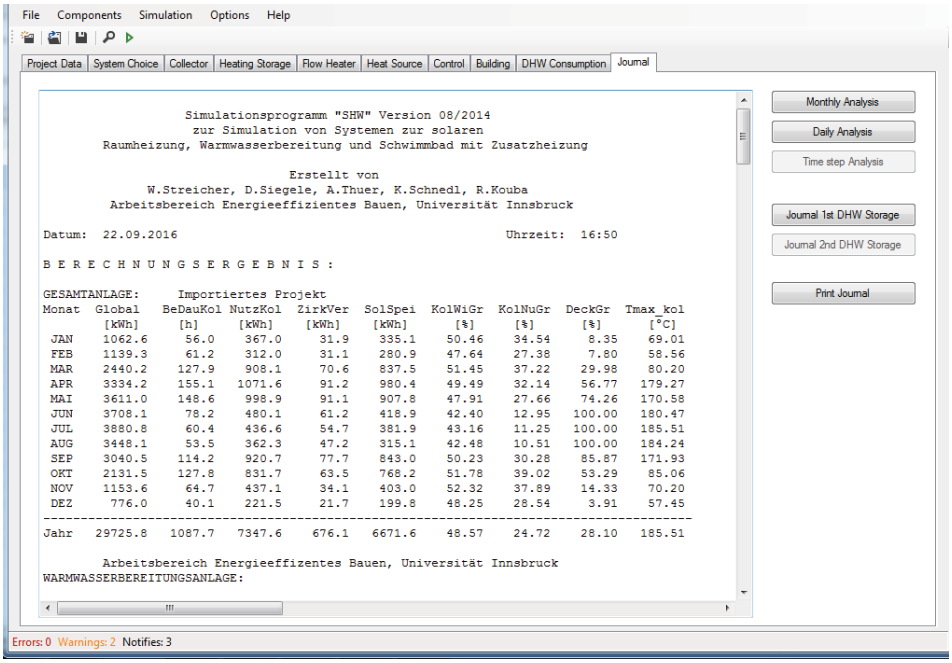


```
                Simulationsprogramm "SHW" Version 08/2014
                 zur Simulation von Systemen zur solaren
        Raumheizung, Warmwasserbereitung und Schwimmbad mit Zusatzheizung

                              Erstellt von
             W.Streicher, D.Siegele, A.Thuer, K.Schnedl, R.Kouba
          Arbeitsbereich Energieeffizientes Bauen, Universität Innsbruck

Datum:  22.09.2016                                        Uhrzeit:  16:50

B E R E C H N U N G S E R G E B N I S :

GESAMTANLAGE:      Importiertes Projekt
Monat  Global   BeDauKol NutzKol  ZirkVer  SolSpei  KolWiGr  KolNuGr  DeckGr  Tmax_kol
        [kWh]     [h]     [kWh]    [kWh]    [kWh]     [%]      [%]     [%]      [°C]
 JAN    1062.6     56.0    367.0     31.9     335.1    50.46    34.54    8.35    69.01
 FEB    1139.3     61.2    312.0     31.1     280.9    47.64    27.38    7.80    58.56
 MAR    2440.2    127.9    908.1     70.6     837.5    51.45    37.22   29.98    80.20
 APR    3334.2    155.1   1071.6     91.2     980.4    49.49    32.14   56.77   179.27
 MAI    3611.0    148.6    998.9     91.1     907.8    47.91    27.66   74.26   170.58
 JUN    3708.1     78.2    480.1     61.2     418.9    42.40    12.95  100.00   180.47
 JUL    3880.8     60.4    436.6     54.7     381.9    43.16    11.25  100.00   185.51
 AUG    3448.1     53.5    362.3     47.2     315.1    42.48    10.51  100.00   184.24
 SEP    3040.5    114.2    920.7     77.7     843.0    50.23    30.28   85.87   171.93
 OKT    2131.5    127.8    831.7     63.5     768.2    51.78    39.02   53.29    85.06
 NOV    1153.6     64.7    437.1     34.1     403.0    52.32    37.89   14.33    70.20
 DEZ     776.0     40.1    221.5     21.7     199.8    48.25    28.54    3.91    57.45
-------------------------------------------------------------------------------------
Jahr   29725.8   1087.7   7347.6    676.1    6671.6    48.57    24.72   28.10   185.51

        Arbeitsbereich Energieeffizientes Bauen, Universität Innsbruck
WARMWASSERBEREITUNGSANLAGE:
```

Fig. 14 Output from for monthly and seasonal energy balance

Additionally the values can be shown as graphs on monthly or daily bases (Figure 15) as well on a time step bases for a selected time period (one file per day). To select the time step based output, the respective values have to be set in the project register card (see Fig. 5) in the middle right. The values to be shown can be chosen, the nomenclature can be found in the (German) handbook.

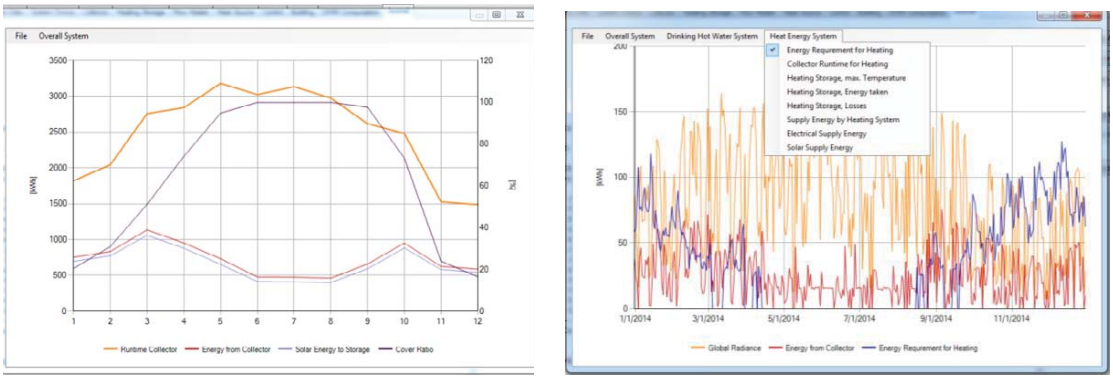

Fig. 15 Graphical output for selected values on monthly and daily bases

Input files or project files can be shared. Each project gets a number and one can save the project file at any place of your computer. This file is very small and can be sent to colleagues that can open it again with their SHWwin Version.

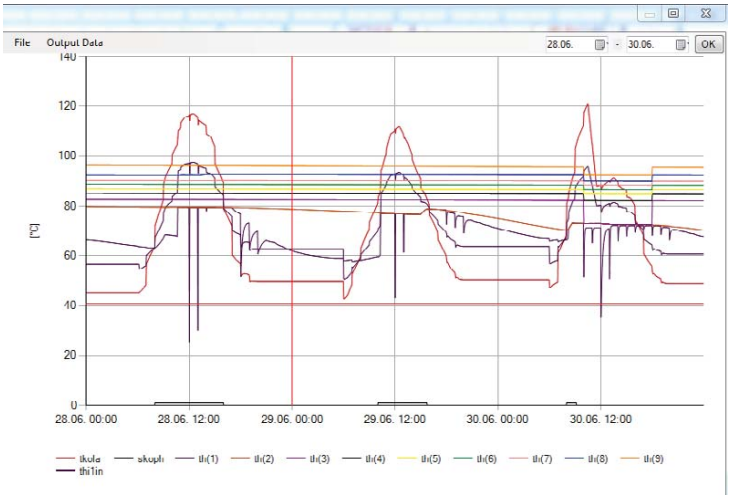

Fig. 16 Graphical output for selected values on time step bases (store temperatures, collector outlet temperature, store inlet temperature, running time collector)

The whole program is available for free for educational or research purpose at Innsbruck University. Just send an E-Mail to wolfgang.streicher@uibk.ac.at. A ZIP file will be delivered with the installation files, some weather data and a full German manual. As it is freeware, there is NO online support available. Of course, there may be some bugs in the program. The author would be happy, if you can send him a description of the bug and the respective input and weather data file.

As the full program is only available in German language and the GUI also in English language, the Authors are looking for helping hands to translate the GUI and the HELP files into other languages. As .xml structures are used for all text inputs this can be quite simply integrated. Volunteers can contact the author for more details.

No liability is taken by the authors for any results of simulations with the SHWwin program.

4. References

GetSolar, 2015, Hottgenroth Software GmbH & Co. KG, Köln, Deutschland

Meteonorm, 2015, Klimadatengenerator, Meteotest, Bern, Schweiz

Polysun, 2015, Vela Solaris AG, Winterthur, Schweiz

TRNSYS, 2015, z.B. Transsolar Energietechnik GmbH, Stuttgart, Deutschland

TSOL, 2015, Valentin Software GmbH, Berlin, Deutschland

Conference Proceedings

EuroSun 2016
Palma de Mallorca (Spain), 11 - 14 October 2016

Methodology in the teaching solar energy, IDEA

Torres Montealban Jonas

Universidad Autónoma Chapingo, Km 38.5 Carretera México-Texcoco, MEXICO

Abstract

The aim of this paper was design, apply and evaluate a teaching-learning experience in physics, by means of implementation of a methodology: integration didactic with exploration applied (IDEA), with students of precollege level. We considered for this study, solar energy applications and we worked in four stages, each one of which represents the elements of methodology: the integration of learning theories, the teaching of discipline, the exploration with worksheets and the application in prototypes. Participated in this study 47 students and we review the topic of transfer of thermal energy. Therefore, through exploring with PreTest and PostTest, during and after the intervention methodology; we get an integrating conceptual in the topics studied. Finally, was possible to achieve a significant conceptual gain in both the acquisition of cognitive and procedural elements. Accordingly, the methodology can be an alternative in the teaching-learning process of physics.

Keywords: *Physics education, worksheets, didactic integration and solar energy.*

1. Introduction

We can apply different strategies for understanding physical situations, this depend of historical moment or and theory teaching learning that is fashionable. However, there is no recipe that can be applied in solving contextual problems, or a general theory of education that give respond to different aspects of thinking of students in the classroom and their relationship in everyday life. In this sense, behavioral learning theories; Humanistic, Cognitive and Information Processing, to mention some; which develop activities that fail to be consistent with the results obtained by educational researchers in the classroom. However, they try to give an order to guide students in solving science problems (Hardin, 2013).

Based on the above, it is to reflect on: the what, the how and, what for, the problems are solved in physical situations into the classroom and these can be transferred to situations of human activity. Move from something memoristic to the critical thinking; from to simple association, to the understanding of problems in the classroom; from lab, to the problems in everyday life. We have implemented in the topic of transfer of thermal energy, for the course of pre-university physics: the IDEA methodology (by its acronym), based on the following four processes concatenated.

Integration of learning theories

In a classic sense, and with proven qualities in the teaching-learning process, we know that students can be involved them with many differences styles of strategies, as shown in Figure 1; collaborative work, the problem solving, (Mendez, 2014), active learning (Sokoloff and Thornton, 1997). Lab activities (Gros, 1990). Thus, develop of attitudes and critical point of view, about the phenomenology. With this, it was possible the achieve objectives, as: developing of skills cognitive, metacognitive and instrumentals, (Segura, 1984).

doi:10.18086/eurosun.2016.10.02 Available at http://proceedings.ises.org

Didactic of Physics

In the case of thermal energy, in which we pretend to analyze and describe the ideas that students have about the transfer of thermal energy: conduction, convection and radiation; in order to generalize the transformation and conservation of energy. The information with we begin the study, we obtained from data collection instruments, questionnaires, which is designed through reliability and validity a analysis process (Sampieri, et al., 2006). These instruments are referred to previous teaching experiences on the same theme and with discussions in academic meetings with physics teachers. With these criteria, we approach reliably to an appropriate instrument where we could observe the representation the concepts and variables that they were taken into account for the measurements, (Sampieri, et al., 2006).

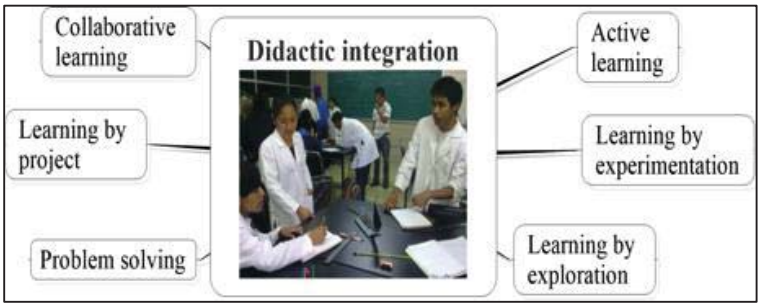

Fig. 1. Didactic integration, theoretical-experimental.

Furthermore, we also consider the concepts that students have in everyday language about the "heat" (Lara and James, 2013). And there are two points of view on how to introduce the concepts of thermal energy transfer. The first one, has to do with the systematization of the concept of energy conservation. The second one, has to see with a gradual process of knowledge nucleus, which are incorporated into the new attributes, to complete the meaning of the mechanisms of thermal energy transfers; conduction, convection and radiation, (Solbes and Tarin, 2004). The two aspects were part of the design of data collection instruments and the IDEA learning activities, It was with the aim of introducing the concept of "heat" as a measure of thermal energy transferred in a particular type of process; for our study is the use of solar thermal energy, (Sandino and Lilia, 2012).

Exploration with worksheets

Through explorations with sheets, a path didactic methodology IDEA of teaching learning is obtained in the classroom-laboratory, by way of elucidate the problems to be explored, and the analyzing the possible resolution and their documentation. With these data collection instruments, learning is monitored, the difficulties to be addressed are identified and also we make emphasized on developing thinking skills and characteristic procedure of sciences like physics, (Michelini and Stefanel, 2012).

On the other hand, for us like teachers, they became design tools and reflection, on the learning processes of students. And with that obtain instruments work and data collection, with the possibility of transforming teaching practice in a research on action. It is so, as were designed, they implemented and analyzed four PretTest and their posttest. The worksheet were designed between peers academics and open discussions. As result we have eight elements to highlight in each of these worksheets, as show on Figure 2.

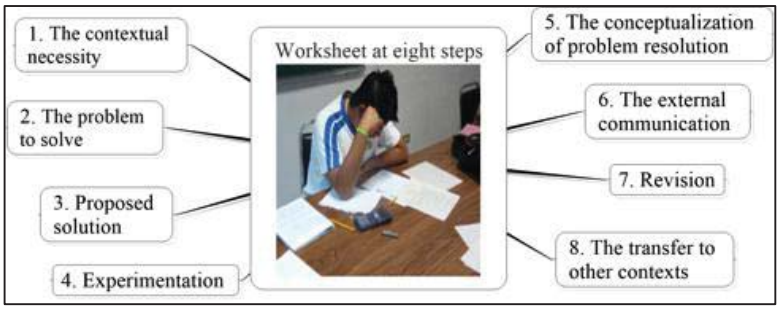

Fig. 2. Eight elements of worksheet.

The surveys features are listed below and are part of the integrated assessment through of methodology implementation. Survey I, questionnaire that provides conceptual information before methodological intervention. Survey II, questionnaire that provides information on previous experimental work on admission from course and before the methodological intervention. Survey III. Questionnaire that provides introductory information on concepts like temperature, thermal equilibrium and system, (Solbes and Tarín, 1998). Survey IV. Questionnaire that provides information on the theme of this study, which has to do with concepts the transfer of thermal energy, (conduction, convection and radiation). With this information, we have been able to document and to contrast the conceptual gain, through to the four Pre/Post Tests, before and after the methodological intervention, (Benitez, et al., 2010).

Application with an integrator project

This implies leave sideways the mechanical and memoristic learning, to focus on a job more challenging and complex; using a multicultural approach that encourages collaborative work; from the manufacture of a prototype solar energy (Rincón, 1999). By engaging of students in developing educational experiences in the classroom-laboratory, forming teams with different students and promoting research methods in order to solve real problems, (Eggen and Kauchack , 2005).

It is not the purpose to solve exercises of the final chapter, which only require a predetermined sequence and automated actions, with the possibility of obtaining a unique solution. Rather, the problem must be contextualized, open to the possibility of thinking different routes and other solution ways, (Pozo, 2002). This allows deploy collaborative dynamics between students and mediation by the teacher, with spaces for reflection and review. Thus preparing students in the constant participation: collectively, with the solar heater water, individually, with the solar stove and a team work, with the photovoltaic panel (Ramirez and Santana, 2014).

2. Objetive

To design, to implement and to evaluate the effect of integration didactic with exploration applied (IDEA), proposed methodology to develop learning on the subject of transfer of thermal energy, with college-level students, correlating conceptual and procedural aspects of physics, obtained through an integrative project on solar and with in worksheets exploration.

3. Methodology

We work with 47 students from precollege level. Students involved in the study are those who completed the four questionnaires after the intervention methodology. They have between 17 to 20 years old and 50% are women. Students are studying a year before to entrance to careers offered UACh. The specialties are around the agricultural studies, most are scholarship students and live within University or around in; are students from different Mexican states and therefore, they are of differences high schools, mostly public and many of them had not worked in the physics lab, (Barrera, 2009).

The IDEA methodology as a model of integration, It not only seeks the integration of organized bodies of knowledge, but also, the integration of educational proposals that are incorporated from the possibilities and

experience of teachers. Also it depends on the knowledge and skills developed by students at diagnosis, Figure 3.

The IDEA methodology are based on four stages; integration, teaching discipline, exploration and application. Indeed, we taken as base, the essential elements to attack of a problem situation, (Gansoso, 1999), which are: An initial state, determined by the situation in which the student is at the moment to address the problem; that is, knowledge of the problem, the attitudes on problem, motivations to find a solution, and the skills theoretical and experimental. A final state, characterized by the objective or goal that is required to achieve and that meets a need contextualized. And a problem space, consisting of all possible educational strategies to reach the final state, as active learning, problem-based learning and projects, the leaves of exploratory work, collaborative work, representational changes; and all that teachers consider, (Hillside, 2009).

The integration of different teaching methods of physics extensively tested, as well as, the contributions that the proposal adjusted IDEA to our study, are part of this alternative methodology, which aims to help students in the study of physics and you find it useful to meet problematic situations outside the classroom-laboratory.

Based on the above, we should start our study with real needs, to identify and analyze everyday problems and possible solutions (McDermott, 1996). Therefore, IDEA activities were designed to support students into cognitive construction, learning and understanding of the phenomena involved, as shown in Figure 4. All these related to the topic of study as: temperature, thermal equilibrium, heat, thermal energy transfer (conduction convection and radiation) and energy conservation.

As consequence of this were interpreted other phenomena as: the thermo syphon principle, the greenhouse, the concentration optics and the photoelectric effect. The teaching of physics helps us understand the functioning of systems that involve concepts around energy and its transformation such as solar thermal energy at a level of compression on subsystems, for instance, a solar water heater (Milena, 2013). Any photothermal prototype contains several subsystems that require physical concepts and his understanding; in order to give accurate explanations, such as solar concentration, insulating materials and heat conductors, the convective effects and interaction of electromagnetic waves, (Perrotta et al., 2013). It is clear that we need to compare studies related to alternative energies, as consequence of interest in clean energy, to help mitigate pollution and help with the family finances, considering that in Mexico every day gas prices and gasoline increase.

Learning activities IDEA

Methodology, integration didactic with exploration applied (IDEA) recovered what in recent years has been called the cognitive revolution, which are considered aspects such as: the impact of context on the thought processes of students, integration of bodies organized knowledge, the social nature of learning, the need to understand specific knowledge of the discipline (physics), problem solving developed by novice and experts; all this with the conviction that students construct their own understanding of the issues studied, (Eggen and Kauchack, 2004).

In our approach, we give opportunity to students to weave mental networks, by incorporating all types of experiential activities and information analyzed; in order to support their learning. And with this have deep understanding; and in context outside of the classroom-lab (teaching for understanding) with the integrator project, (Blythe, 1999). By working with nucleus of organized knowledge. The 47 students have already revised the mechanic topics; it corresponds to the unit previous to our study. We recover these prerequisites and prepare students so that after the methodological intervention. With this, they are getting ready to study electromagnetism, the last unit of the course.

This meant act accordingly, taking up what the student knows, and preparing them to the topic that they studied at the end of physics course, and immediately following the methodological intervention. Using a continuos knowledge spiral construction and with feedback, this is the basics for the begin of the application of the methodology. The evidences suggest that start with the students know about the issue and their misconceptions of it, (Quesada, 2005). Thus, it is about building and "genuine learning"; which involve

performing a wide and variety of activities of all kinds of experiences, not only to achieve the concept understanding, if not, at the same time, increase the understanding topic, (Perkins and Blyte, 2006). Based on information obtained in the 10 activities "IDEA", Figure 5. We implemented and applied the concepts studied in the integrator project.

In the analysis of the first survey (pretest-posttest), Showed an average rating of 3.8 out of 10, based on the exploration at entrance. Thus, we decided to choose, design and implement experiences and exteriorizations on the integrator project, as a result for the cultural differences by provenance (characteristic in Mexico). This have an effect on the goal of achieving a deeper understanding of the contents studied (declarative, procedural and attitudinal). Further, It is also of great importance to our proposal, the continuous assessment all process, (Diaz-Barriga, 2002).

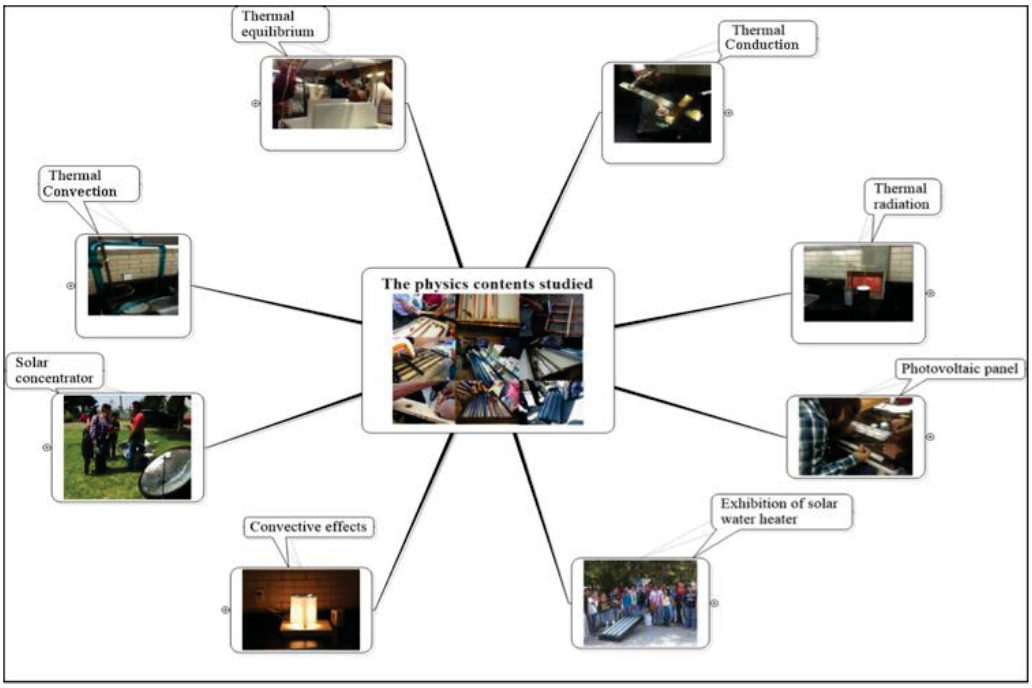

Fig. 3. Contents studied around thermal solar energy.

The entrance exploration, we reviewed general aspects of experimental work and the introductory concepts of thermodynamics at the precollege level. The experimental exploration, is central to our methodology propose, we emphasized lab job and the methodological of the sciences. In this questionnaire, students showed many shortcomings, mainly due to the few experience in a physics lab. This questionnaire has a result of 3.6 out of 10. So, emphasis on interpretation of the information obtained in learning activities. Referred to conceptual exploration (I). It gives us the opportunity on the previous ideas that the students have and the misconceptions that should be attacked with activities proposals "IDEA" .

Hence, the rate of 6.1 out of 10 that was obtained in this survey, gave us the guidelines to establish that phenomenology on temperature and thermic equilibrium, are very close to the daily life of students, and they can do inferences about the laws governing such thermodynamic phenomena to cognitive level they have in the this study, (Hierrezuelo and Molina, 1990). The conceptual exploration (II), is an accentuated exploration. It studies aspects on transfer of thermal energy; it gave us the challenge to increase the conceptual gain in this part. According, to the result obtained in the PreTest, it was 3.2 on 10. Therefore, by introducing the integrator project as a motivation means, we seek to strengthen the active participation, the collaborative job among students, and weave conceptual networks between what is known and what we are studying.

Worksheets explorative for students

For our research, the worksheets elaborated for students have been developed according to the teaching physics by inquiry. With this has been learned, how the worksheets can provide, "what ideas and what categories" were related each other, and "when and in what" context are used. Also, what alternatives and what meaning, were given during experience realized. The evidence suggests that the learning improve, when students work actively involved with worksheets guided activities in. It is clear that refers to the declarative, procedural and attitudinal content.

The IDEA learning activities are worksheets explorative for students, It enabling them to face the challenges in a flexible manner, to follow different learning issues, for instance: more directed to conceptual, formal, procedural aspects, and / or attitudinal. It is noteworthy that the worksheets explorative are own materials, these were reviewed among academic peers, and have characteristics as: phenomenological, experimental, formal and application. However, the worksheets can be combined depending on the objectives of the activity, (Michelini, et al., 2008).

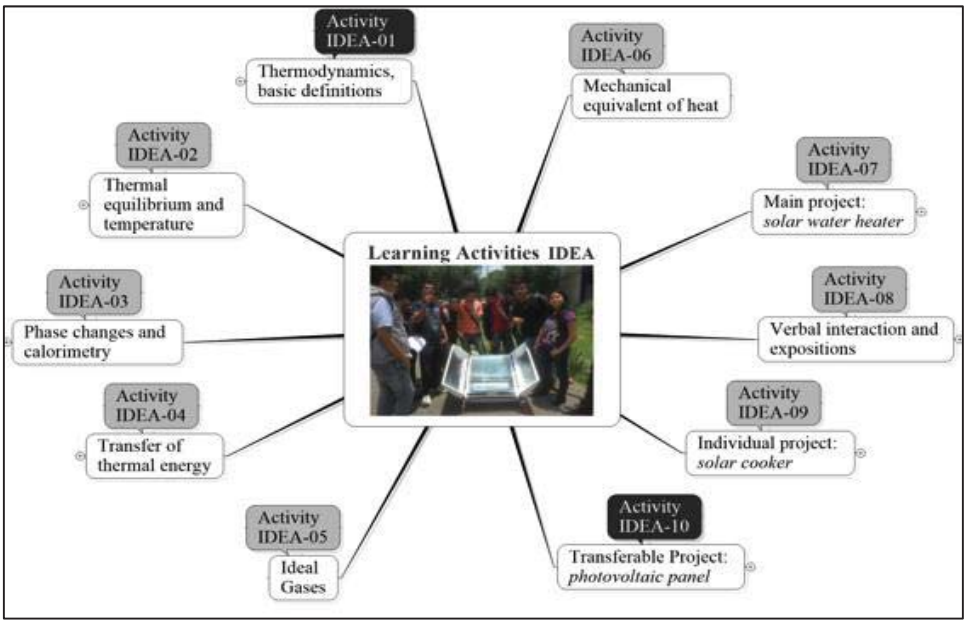

Fig. 4. Learning Activities IDEA.

Methodology implementation

After the results obtained on diagnosing, the Learning Activity IDEA-01. It has been called "Thermodynamics basic definitions" this implemented activity. It is phenomenological-experimental type. In this activity we should explain thermodynamic physical situations, ensuring that students decipher the meaning of the experience, so that the effect of the experience manages to be reflexive and with appropriation of something significant for them. Described below are the 8 steps integrated into each IDEA activity. These are listed as:

Step 1. *Contextual necessity*. With a sequence of concepts, these is presented to explore the characteristics and meaning, providing the formalism of the thermodynamic definitions.

Step 2. *Problem to solve*. In the beginning, the questions are presented based in to the concepts previously studied.

Step 3. *Proposed solution*. The students are prepared in the experimental part and they should have conceptual elements in order to start the possible solutions.

Step 4. *Experimentation*. Students carry out the experiments and make a description of each of the cases illustrated; putting attention on observation and in some specific aspects, describing the main features of processes.

Step 5. *Conceptualization of problem resolution*. The ability to solve problems successfully depends on a

number of factors related to the information processing, thus writing a solution of the problem, means to communicate and interpret the reasoning process leading to the solution.

Step 6. *External communication*. The strategy being employed is a verbal interpretation as: lab notebook, group expositions, science fairs, and another academics events.

Step 7. Revision. All the previous steps are considered again and we find a route that allowed us to study situations in the phenomenological and experimental plane in order to detect possible conceptual errors, false or unnecessary assumptions, wrong calculations, and confrontation with predicted answers.

Step 8. Transfer to other contexts. Finally, How to integrate the situations of Physics that have been learned to another context? That means, give continuity to the methodology; beginning with new questions and to transfer new goals to another project, in which concepts new can be learned, according to next unit. By way to get a virtuoso spiral of knowledge.

Integrator project

The aim of an integrator project is the application of concepts physics, through to manufacture three solar prototypes: a solar water heater, a solar oven and a solar panel. All of them are part of the integration project. The first one, a main project that involved 47 students in manufacturing solar water heater. The second one, an individual project, solar stove with readily available materials. The third one, a transferable project, a photovoltaic panel, (Chavez, 2008), which opens the possibility of transferring the methodology to another context, Figure 5. Thus, we can give continuity to the methodological, without give opportunity to traditional learning, (Harper, 2009).

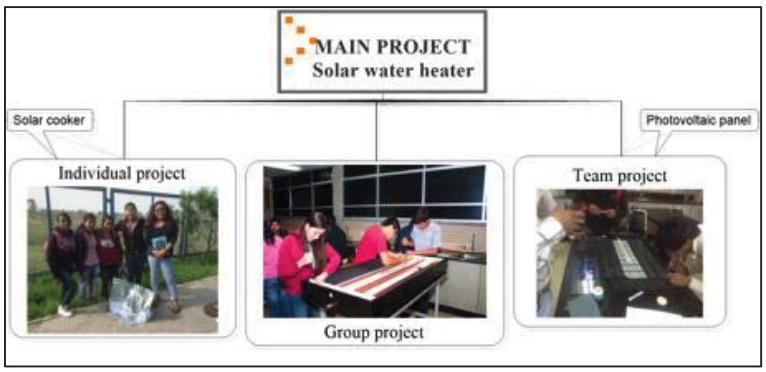

Fig. 5. Projects that are part of the proposal.

Therefore, we believe that it is necessary to provide a minimum of concepts to students not just to build their projects but also to have elements of communication in their expositions and consider physics as an important discipline for their professional development, (Parisoto, et al., 2014)

Integral evaluation

Our methodological approach does not consider the assessment as a synonym for test, exam or control; whose purpose is to qualify the student performance by a “foreground". For our proposal, evaluation is an important part of the teaching-learning process; serves as a starting point for further reflection to help us continuously improve the work of teachers, (Perez and Moreno, 1998).

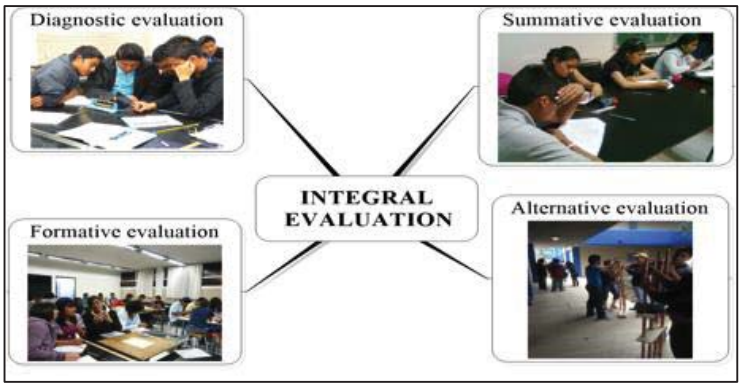

Fig. 6. Methodological assessment during intervention.

Diagnostic evaluation, the PreTest applied is compared with the PostTest, in order to know what the students have studied and act accordingly. Formative evaluation, the worksheets exploratory are analyzed with the performance rubrics, these give us guideline to attack difficulties or conceptual knots, (Michelini and Stefanel, 2012). Summative evaluation, the lab notebook, the teamwork, the PostTest result, and all kind of participation are part of this assessment. Alternative evaluation, not just the exhibitions but also the creativity in designing prototypes and application of learning in context, show us another possibility to motivate students in the physics study.

Gain Hake

It allows measuring and comparing the conceptual gain during the methodological intervention. It should be noted that students arrive at precollege level from different schools from various states of the republic, and therefore they have heterogeneous knowledge levels about physics.

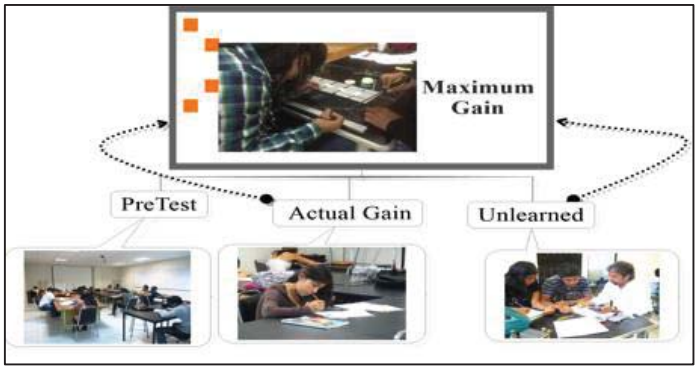

Fig. 7. Maximum gain estimation (g_max).

$$\text{PreTest effective\%} = \text{PreTest} - 20\% \quad \text{(eq. 1)}$$

$$g_{corr} = \frac{(\text{PostTest\%}) - (\text{PreTest effective\%})}{100\% - (\text{PreTest effective\%})} \quad \text{(eq. 2)}$$

where:

g_{corr} = average normalized gain

PreTest effective% = correct results in the survey

abefore methodological intervention.

PosTest % = Correct results in the survey

after methodological intervention.
Maximum gain is calculated by the follow expression:

$$g_{max} = 100 - \text{PreTest effective\%} \quad \text{(eq. 3)}$$

Average normalized gaing$_{ave}$; for group, It is calculated through determining the gain for each student and average evaluating:

$$g_{ave} = \frac{1}{n}\sum_{i=1}^{n} g_i \quad \text{(eq. 4)}$$

$$\mathbf{g}_{ave} = \frac{1}{n}\sum_{i=1}^{n} \mathbf{g_i}\left[\frac{Post_i - Pre_i}{100 - Pre_i}\right] \quad \text{(eq. 5)}$$

Where $n = 47$, are students who answered no just PretTest but also Posttest, and the sum was made with the n students of the study; obteniendo a real increase called: average normalized gain for the group, (Benitez and Mora, 2010).

Based on the above, we obtained value of ($\mathbf{g}_{corr}$); which quantifies the effectiveness of methodological intervention, shown in Table I. The Hake Gain (g), has values which cover the range [0,1]. Consequently, average differences between Pre/Post Test data give us the different ranges of the Hake Gain, and It interprets the effectiveness of methodological intervention, then: a high gain is ($g \geq 0.7$); an intermediate gain is ($0.3 \leq g < 0.7$); and a low gain is ($g < 0.3$). The results were not compared with a group traditional, considering that the results obtained by Hake for a traditional group (exhibition-conference) have an average gain of 0.2; so it was not necessary to make a comparison of student achievement between the two methods, (Seyed-Fadaei, 2014). However, we took 20% of average, according Hake traditional groups, which we was subtracted and represented the PreTest effective = PreTest-20%. Based on the above, the data allow us to project similar results for the other topics that the precollege level physics course contains, which is a general physics course. Other contents from the physics course are, mechanics and electromagnetism.

4. Results

Students involved in the study have between ages 17-20 years old, 50% are women. 47 students participated in the manufacturing of three prototypes: a solar heater (Group), a solar oven (single) and a photovoltaic panel (computer). The surveys were designed, were applied and analyzed before and after methodological intervention. During the development of the proposed 10 learning activities were implemented, and the concepts revised were: temperature, thermal effects, transfer thermal energy; we emphasized the concept of conservation and transformation of energy.

The activities called IDEA learning activities, covering three aspects: 1) the contents studied to give an overview of the subject studied; 2) The integration project, around the solar energy; and, 3) manufacturing of prototypes: a) solar water heater (collaboration skills); b) solar stoves (reflection skills); c) the photovoltaic panel (transfer skills), in order to move the proposal to other topics. Hence, there is a methodology continuing in entire course. We can see that there is no fragmentation the IDEA methodology, dismissing the possibility to apply a traditional methodology. Table 1, shows the four results of the surveys throughout the study process and the average normalized Hake gain ($\mathbf{g}_{corr}$)

By applying PreTest/Intervention/PostTest, the methodological proposals (Hake, 1998). The learning externalizations or realizations have shown from the results in the instruments applied to students before and after the proposed methodology, improves not just procedural and conceptual, but also attitudinal and application. The IDEA methodology and their tools, the worksheet, showed significantly high and positive achievement in promoting integrative theoretical learning and experimentation.

Tab. 1. Summary of survey and gain Hake.			
Type exploration	PreTest (%)	PostTest (%)	g_{corr}
Exploration income	18.00	71.65	0.6400
Experimental exploration	16.59	59.36	0.5100
Conceptual exploration (I)	41.50	83.60	0.8100
Conceptual exploration (II)	12.98	69.57	0.6600
Average	22.27	71.05	0.6550

The focus was on the different stages of development of the proposal, the consolidation of a group of teachers , which supports the development of prototypes for teaching physics. Result from the interest among teachers to give the course of precollege level with concept of energy and its conservation; and this is a reason for to use the methodology IDEA proposal. Similarly by comparing the final grade of physics course, progress is observed with respect to information of the scores at ingress/egress of intervention methodological, from 42.27% to 71.05%.

5. Conclusions

With the development of a planned and comprehensive proposal; It was possible to design, implement and analyze the methodological effect in teaching physics concepts with prototypes of solar and an evaluation along to the methodological intervention. The results were compared by analysis of the information collected, which were results the surveys and worksheets applied; in order to evaluate the proposal.

This research favor the development of a collaborative learning environment and with based on the factor of Hake, we get a conceptual Hake gain entry 0.6400. It is considered intermediate to high according to Hake rate. The evidence suggests significant progress, despite the student diversity.

For experimentation, we get a conceptual gain of 0.5100, a value low to intermediate according to Hake rate. The conceptual stage of introduction was the most effective with high gain of 0.8100, favoring the methodology in the first level of conceptual approach. The conceptual stage on accentuation; the gain is intermediate-high between 0.6600, which requires a higher abstraction level and a deep reflection on the last stage.

We can see there is an average gain of 0.6550 conceptual, which means a significant advance in understanding the concepts, involved. Also, the integration project at three levels (group, individual and team), enriches the study on organized bodies of knowledge, considering the daily needs, motivation and resolving a problematic situation.

The fundamental elements of the proposal methodological are the integration with different educational proposals interactive and the issues of transfer of thermal energy to be studied in context; achieving the effect of moving from the phenomenological (lived experience) to a thoughtful and appropriate description of the students at this university level.

It is about developing a critical thinking when transferring the information in context and a continuous assessment: diagnostic, formative, summative and alternative (exhibitions, solving everyday problems and creativity). Research supports the development of a collaborative learning environment the study of physics and with reflexive analysis and also retrieval of information is encouraged to make decisions that improve IDEA methodology and strengthen its structuration in next implementations.

Finally, the different ways to communicate information such as worksheets, all kind of information in the lab notebook, mathematical models in solving exercises, school exhibitions in scientific events, discussion between peers, the reconceptualization of problems, creativity and the use of solar energy. They are the basis of the didactic integration with applied exploration (IDEA), an alternative methodological to support students

in the study of physics.

6. References

1. Barojas, J., 2007. Problem solving and writing I: The point of view of physics. Lat. Am. J. Phys. Educ., 1 (1), pp. 4-12.
2. Barrera, S., 2009. "Guía didáctica de termodinámica clásica para el bachillerato". Maestría en docencia para la educación media superior (Física), UNAM, México.
3. Benitez, Y. y Mora, C., 2010. Enseñanza tradicional vs aprendizaje activo para alumnos de ingeniería. Rev. Cub. Fis. 27(2A), pp. 175-179.
4. Blythe, T., 1999. "La enseñanza para la comprensión, guía para el docente", Ed. Paidós, Buenos Aires.
5. Chavez J., 2008. "Introduction to Nonimaging Optics". Taylor & Francis Group, CRC Pres, U.S., pp. 3-22.
6. Díaz Barriga, F. y Hernández, G., 2004. "Estrategias docentes para un aprendizaje significativo". Mc Graw-Hill, México.
7. Eggen D. y Kauchak, D., 2005. "Estrategias docentes y desarrollo de habilidades de pensamiento". Fondo de Cultura Económica, México, pp.189-244.
8. Gros. B., 1990. La enseñanza de estrategias de resolución de problemas mal estructurados, investigaciones y experiencias, Universidad de Barcelona. Revista de Educación, 293, pp. 415-433.
9. Hake, R., 1998. Interactive-engagement versus traditional methods: A six-thousand-student survey of mechanics test data for introductory physics courses. American Journal of Physics, 64, pp. 64-74.
10. Hardin, L., 2013. Problem solving concepts and Theories. Mississippi Tate University, College of Veterinarian Medicine, JVME, 30(3), pp. 227-230.
11. Harper, E., 2009. *Tecnologías de generación de energía eléctrica*. México, Ed. Limusa, pp. 299-349.
12. Hierrezuelo M. y Gonzalez, M., 1990. Una propuesta para la introducción del concepto de energia en el bachillerato. Enseñanza de la Ciencias, 8(1), pp. 23-30.
13. Ladera, C., 2009. Evaluation in physics teaching: make it an opportunity for further learning. Latin-American Journal Physics Education, 3(3), pp. 527-534.
14. Lara, G. y Santiago, A., 2010. Detección y clasificación de los errores conceptuales en calor y temperatura. Lat. Am. J. Phys. Educ., 4(2), 399-407.
15. McDermott, L., 1996. "Physics by Inquiry". John Wiley & Sons, Inc. USA, 1, pp.163-221.
16. Méndez, D., 2014. Influencia de la inteligencia y la metodología de enseñanza en la resolución de problemas de Física. Perfiles Educativos. 34(126), pp. 30-44.
17. Michelini M. y Stefanel A., 2012. "Taller de Física Moderna". UAM-Iztapalapa, México, pp. 25-28.
18. Michelini, M., Santi, L., y Stefanel, A., 2008.Worksheets for pupils involvement in learning quantum mechanics. In Frontiers of Physics Education, Jurdana-Sepic R. et al., eds., Rijeka:Zlatni, pp. 102-111.
19. Milena, S., 2013. El equivalente mecánico del calor. Lat. Am. J. Phys. Educ., 7(4), pp. 555-559.
20. Parisoto, F., Moreira M., y Dröse B., 2014. Integrating didactical strategies to facilite meaningful learning in introductory college physics. Latin-American Journal Physics Education, 8(4), pp. 4402-1-4402-7.
21. Perkins, D. y Blyte T., 2006. "La enseñanza para la comprensión". Eduteca. Disponible en: http://www.eduteka.org/AnteTodoComprension.php.
22. Perrotta, T., Follari, B., Lambrecht, C., DIMA, G., y CAROL, E., 2013. La enseñanza de la energía en el nivel medio: una estrategia didáctica. Primera parte. Lat. Am. J. Phys. Educ., 7(3), pp. 391-398.
23. Pozo, I., 2002. La adquisición de conocimiento científico como un proceso de cambio representacional. Investigações em Ensino de Ciências, 7(3), pp. 245-270.
24. Quesada, R., 2005. "Cómo planear la enseñanza estratégica", Editorial Limusa, S.A. de C.V., Grupo Noriega Editores, México, pp. 18-69.
25. Ramírez, D. y Santana, F., 2014. El aprendizaje basado en proyecto y el aprendizaje de conceptos de calor y temperatura mediante aplicaciones en cerámica. Innovación Educativa, 14(66) pp. 65-90.
26. RINCÓN E., 1999. "Estado del Arte en investigaciones en energía solar en México". Fundación ICA, A.C. México, D.F.
27. Sampieri, R., Fernandez, C. y Baptista, P., 2006. "Metodología de la Investigación". México, D. F. McGraw Hill, pp. 285-374.
28. Sánchez, R., Mora, C., y Becerra, D., 2014. La enseñanza del equilibrio térmico a nivel Medio Superior con uso de las TIC. Latin American Journal of Science Education. 1 (1), pp. 1-14.
29. Sandino, A. y Dávalos, L., 2012. La termodinámica como origen de la revolución industrial del siglo XVIII. Lat. Am. J. Phys. Educ. 6(4), 652-654.)

30. Segura, S., 1984. Reflexiones en torno al concepto de energía, Implicaciones curriculares. Enseñanza de la Ciencias, 4(3), pp. 247-252.
31. Sokoloff D. and Thornton. R., 1997. "Using interactive lecture demonstrations to create an active learning environment", The Physics Teacher 36, 6-340.
32. Solbes, J. y Tarín, F., 2004. La conservación de la energía: un principio de toda la física. Una propuesta y unos resultados. Enseñanza de la Ciencias, 22(2), pp. 185-194.
33. TAPIA S. y DEL RIO J., 2012. Concentrador parabólico compuesto: una descripción opto-geométrica. Revista Mexicana de Física, 55 (2), pp. 141-153.
34. Torres, J., Rincón, E., Lentz, A. y Gonzalez, L., 2014. Alternative energies in Physics, a proposal for exploring the teaching of Physics concepts with the solar water heater. Energy Procedia, (57C), pp. 975-891.
35. Velásquez, S., 2012, "Propuesta metodológica para la enseñanza del concepto de energía en los grados de educación media, fundamentada en el modelo de enseñanza para la comprensión". Universidad Nacional de Colombia, Facultad de Ciencias, Escuela de Física Medellín, pp. 60-68

Teaching Renewable Energy Systems by Use of Simulation Software: Experience at Universities of Applied Sciences, in In-Service Training, and from International Know-How Transfer

Andreas Witzig[1], Markus Prandini[2], Andreas Wolf[3], Lars Kunath[3]

[1] ICP Institute of Computational Physics, and [2] Competence Center Asia Business, both at the Zurich University of Applied Sciences, Winterthur, Switzerland

[3] Vela Solaris AG, Stadthausstrasse 125, CH-8400 Winterthur, Switzerland

Abstract

Experience in using simulation software for teaching solar energy and heat pump applications are presented and discussed in this publication. The authors present suitable didactic concepts specifically developed for teaching renewable energy and energy efficiency topics.

Two main advantages of applying simulation software in solar education are identified:

1. simulation can provide an understanding of data that is otherwise not accessible (e.g. cumulated operating hours and number of starts of a heat pump depending on control strategy);
2. use of simulation software in teaching have a positive influence on the motivation and attitude of the students.

These benefits typically come with costs of some additional effort in lecture preparation.

Finally, different international teaching programs are discussed, in which simulation software currently plays a major role. It is analyzed how education programs might have to be adjusted for different cultures and industries.

Keywords: *Renewable energy education, teaching solar systems, seamless learning, simulation software*

1. Scope and Introduction

The scope of this work is professional education in renewable energy from in-service training to the technical-university level. It does not cover solar education to children or to the common public. Furthermore, this work has a special focus on the use of simulation software in teaching and is an update to previously described experiences (Witzig 2009). In all the described courses, the curriculum focusses on the renewable energy topics and the skills required by engineers, planners and consultants involved in solar energy system analysis and design. Reflections about teaching experience do not cover courses specifically on the usage of software or on software programming aspects.

It has been recognized early that computer simulation has a high potential to influence learning in science (e.g. Feurzeig 1999, Rutten 2012), many articles and books have been published about it and there was a controversial discussion about the effect of the use of simulation tools in education. Specific overview articles also summarize the use of simulation software in specialized fields of technology. Examples are health care (Cook 2011), chemical and process engineering (Edgar 2006) and unequivocal results exist for many other field.

Selection and/or peer review under responsibility of Scientific Committee
doi:10.18086/eurosun.2016.10.03 Available at http://proceedings.ises.org

2. General Observations

Three main prerequisites strongly influence learning achievements:

3. The choice of the simulation software has to closely match the interests and abilities of the students. General purpose mathematical tools like Matlab/Simulink or Mathematica are only helpful in engineering courses at university level when separate courses on how to use the tools are offered in the curriculum.

4. Simulation tools have to be user-friendly. On the one hand, the "fun" factor is not to be underestimated: if students *like* to play around with the tool, they also learn more. On the other hand, user-friendliness is required in order that students are efficient in their assignment work.

5. Personal laptops have to be available to all students. Computer laboratories have been an option at times when students have not had their own laptops. However, the advantage of bringing the exercises into the student's work environment allows a new dimension of involvement and reduces the cost of providing access to simulation tools.

These necessary conditions may vary depending on application field and teaching institution.

The authors think that temporal change of these boundary conditions are sometimes underestimated in the above cited review articles. While institutions and topics are relatively stable, simulation software improves steadily in its user-friendliness. In comparison to the first two points, the availability of laptops as a third requirement has changed dramatically in recent years. Students carry a large amount of computing power with them and have the ability to install and use standard software without any support from the teacher or the IT department.

3. Use of Simulation Software in Solar Education

Historically, the first software used in university-level solar education was TRNSYS (Kandpal 2015, Bronman 1991). The usage of TRNSYS in solar education was limited to a small group of people in the beginning due to the lack of computers. The user experience was impaired by the text based scripting interface but improved with the introduction of the TRNSYS simulation studio.

A number of software packages have been established later on in parallel to TRNSYS, most of them with a simpler user interface and somewhat reduced functionality. Some of them have successfully been applied in teaching solar energy (e.g. free: RETscren, PVGIS; commercial: T*Sol, Polysun, PVSyst, Insel).

Simulation software programs used in general physics education (e.g. Stella, Berkley Madonna, EES, Matlab) are less suitable for solar energy teaching since they are more complex and have no built-in references to renewable energy systems. It has been found that the tools have to use the specific nomenclature of the solar business and as to offer special functionality imposed by industry standards. Recent didactic concepts confirm that the "seamless" integration into the well-known environment of the student strongly increases the learning success (Milrad 2013).

The authors have been active for many years with the Polysun simulation tool and used it in the first place in solar and renewable energy teaching Swiss Universities of applied sciences, secondly in non-academic in-service training and thirdly for courses related to big companies in conjunction to commercial projects. All the above mentioned software tools have primarily been developed for professional users and not for the classroom, except some minor adaptation for educational usage is in the licensing scheme. Therefore, the graphical user interfaces are optimized to be useful for the customer target group. For Polysun these are the planners and engineers in consulting companies. Both in-service training and undergraduate courses profit from this because it makes the courses more application oriented.

In the use for undergraduate or in-service teaching courses it has been proven to be particularly useful to visualize relationships that are not accessible to measurement or analytical calculations, as discussed in the following three examples:

- While the characteristics of isolated components can be presented in lectures, it is a challenge to discuss the dynamic behavior of the hydraulic system. While governed by simple physical laws, the system performance is much more complex. Simulation software helps to let students investigate the operation of controllers and the placement of sensors. As shown in Figure 1, the Polysun simulation tool reveals the relevant details. Using trial and error or more systematic design methodology close to real planner's work, students use the software to "play around", investigate and optimize renewable energy systems.
- Yearly calculation results such as system efficiency, heat pump seasonal performance factors or cumulated operating hours and number of starts of a heat pump all strongly depend on the control strategy. With the use of a dynamic system simulation, these relationships become accessible for the teaching process and for exercises.
- Parametric studies with varying component characteristics and control strategies are another application area. Students have to learn to define an optimization target function and ask precise questions for optimization. Furthermore, the methodologies taught in renewable energy courses include the use of Excel as an analysis tool.

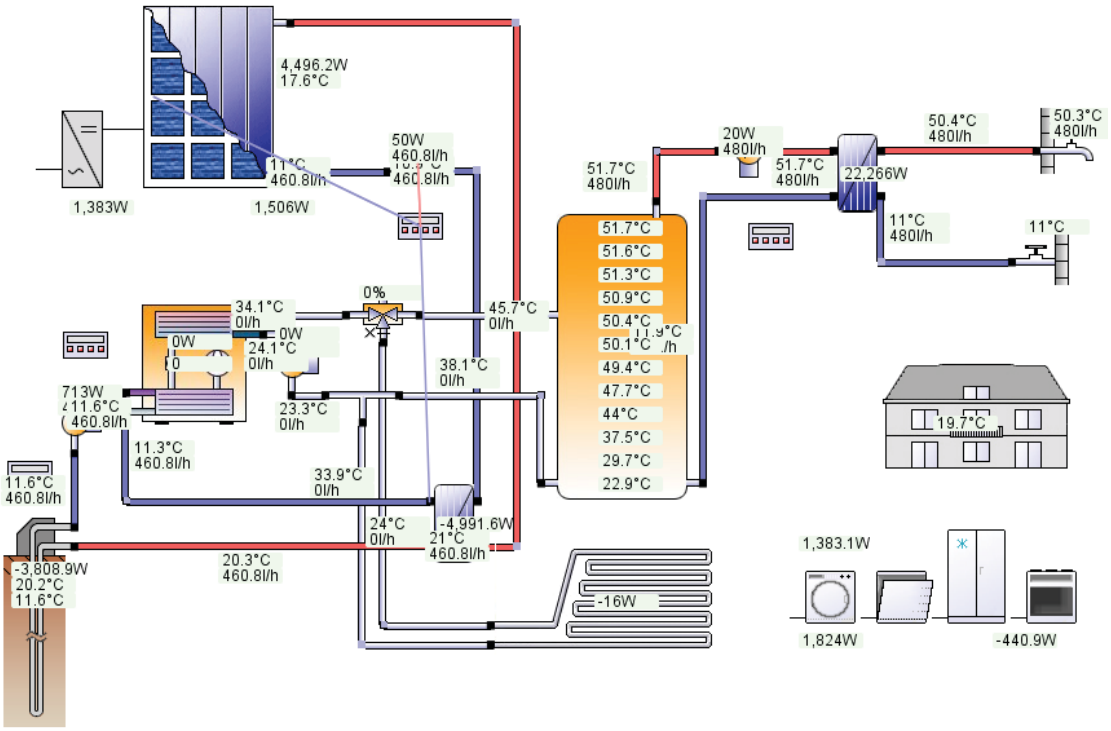

Figure 1: Polysun dynamic simulation allows to step into a certain time on a specific day of the year and follow the system behavior step by step on a short time scale. It allows students to recognize the details of the controllers, as for example in this application the controller (blue lines show connection to sensors, red lines show connection to the pump as an actuator).

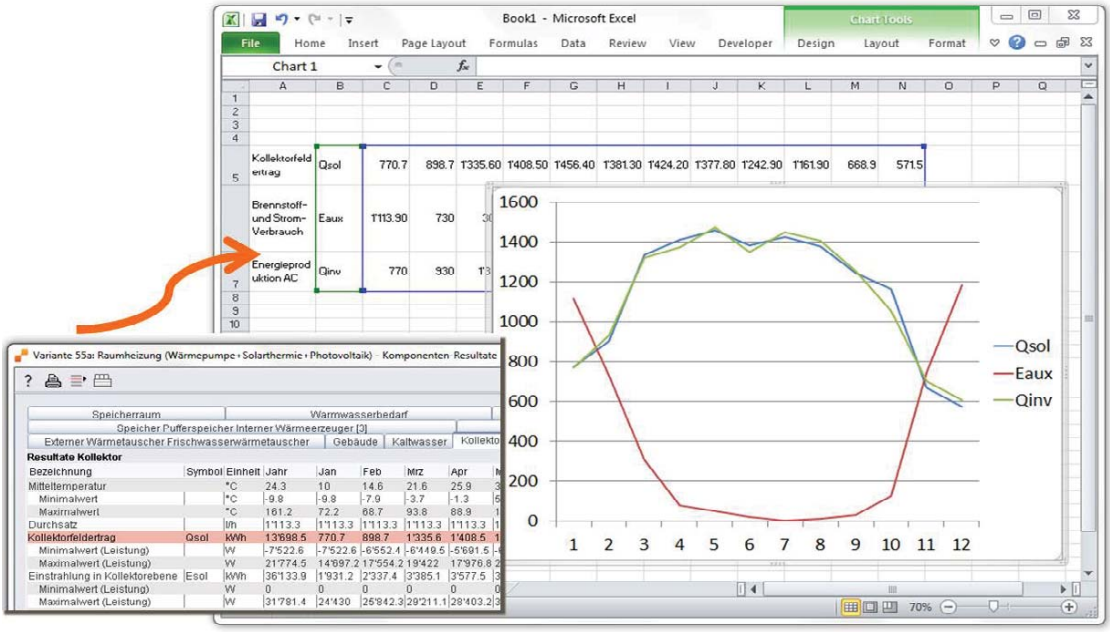

Figure 2: Simulation results can be manually or automatically transferred to other tools for advanced analysis and optimization. In this example it is shown how to transfer data to Excel.

Not least, the use of simulation software makes the renewable energy courses more attractive and increases the motivation and attitude of the students. It helps to position energy planners as high-tech consultants. Using a real-world planning tool provides a direct link to the work environment the students are likely to work in after graduation and allows showing how much impact good planning has on realistic projects and how much sense the future work will make.

While some bigger projects involve the creation of a curriculum (such as the examples reported in Section 6), the contents are typically encapsulated in smaller entities. The resulting teaching material can be used to enrich traditional solar energy or renewable energy courses in a similar manner as laboratory exercises as presented in Figure 3. It is important to convince teachers of traditional engineering topics to use examples from renewable energy systems to visualize general energy related topics. If material is provided in well-portioned entities and offered in a similar manner as experiments are in traditional engineering schools, the value of the teaching material increases and renewable energy topics have a higher chance to enter the general engineering curriculum.

Figure 3: Example for a hardware exercise from the experiment collection at Zurich University of Applied Sciences. Teachers can choose from a large collection of hardware experiments with well-prepared exercises to enrich classroom work. The authors propose to offer renewable energy topics using simulation software in a similar manner like physics experiments.

4. Recent Changes in the Solar Industry and in Solar Education

Renewable energy engineering has become more comprehensive in the last few years. In modern decentralized energy systems it is common to combine different renewable energy sources such as solar collectors and ground source loops. Some time ago, solar thermal engineering has been a self-contained topic, mostly situated in the mechanical engineering curriculum at universities of applied sciences. Now the interaction between the different disciplines (photovoltaics – energy storage – solar thermal – heat pump – ventilation and air conditioning) is addressed and in many engineering schools there are specific degree programs on energy and environment.

With the advance of the renewable energy industry, solar components have become more plug-and-play on the one hand, but renewable energy systems on the other hand have become more complex. The main expertise is therefore no longer in sizing and configuring solar components but in integrating the components into a system. Solar systems are often no longer strictly separated into solar thermal and photovoltaic systems. Hybrid systems and combination with heat pump and energy optimization controllers such as load shifting require new skills from planners and engineers. In consequence, it is required that students spend more time on understanding system dynamics and the proper functioning of controllers.

5. Learning Success and Secondary Effects of Simulation Software in Solar Education

Teaching courses using simulation software have to be supported by suitable didactic concepts, which need to cover classroom activities as well as computer homework (e.g. Rumsey 2000). In contrast to using video material in teaching, the application of simulation tools is very close to real “hands-on” activities. In so-called *seamless learning*, trainees study across boundaries such as location, time, analog/digital, and classroom/at home (Milrad 2013). Often, modern ICT technology is required to achieve a seamless learning

context (Pillay 2006). We often teach expert technicians in a 1:1 screen sharing setting, which allows immerging into the work context of the trainees and using their everyday examples. Alternatively, we use traditional classroom teaching enriched with exercises using simulation tools. During simulation sessions, the teacher acts in the role of a coach and students are actively pursuing their design projects. Interpretation of simulation results and double-checking results with simple back-of-the-envelope calculations are typically pursued with rigor and an excellent mental awareness when the example is chosen from the trainee's everyday scope of duty.

Advantages when using simulation software and modern ICT technology for teaching:

- Students are activated. They have to take responsibility, make decisions and organize their work.
- Trainees can pick the topic that is relevant for them.
- Collaboration between students: they share their findings, help each other, and discuss their results.
- Progress in the exercise is visible to the teacher during class and easily measurable after class.
- Exceptionally high motivation, in particular for in-service and screen sharing training.

Challenges and risks:

- Preparation is key for teaching with simulation software. Exercises have to be formulated in detail and test runs are indispensable.
- The teacher has to be a proficient user of the software as well as have the essential skills in the area of expertise of the course participants.

Not least, there are excellent and important practical experiments in solar education. As much as the authors believe that computer simulation has a positive learning effect, they are convinced that laboratory exercises are also a necessary requirement for solar engineers and do not consider computer simulation as a substitute for them.

Simulation makes the system aspect accessible. It has been shown in the literature that effect size of use of simulation software in teaching is especially high if it is used for phenomena that are unobservable (Trey 2008). In the case of hybrid solar system simulation there is no alternative to numerical simulation for the analysis of the dynamic system behavior. Experience shows that students get puzzled by the large number of unknowns in hybrid systems and, in particular, that rules of thumbs do only apply to limited parameter ranges. Simulation software helps to reduce the number of unknowns by the definition of adequate default values. These simplifications are necessary for good didactical best practice. The authors have experienced that it is only at the very top of University-level engineering courses, one should confront students with the large uncertainty that lies behind every system simulation. Otherwise, the learning effect regarding renewable energy topics is compromised. At any time, one has to be aware that solar simulation is only a tool used in solar education. In other courses at the MSc or postgraduate level (that go beyond the scope of this article), it is good to go into detail on computational algorithms and discuss the influence of each default parameter.

6. Teaching Experience Abroad

Solar energy is a world-wide topic and solar engineering education is in many regions of the world a limiting factor in the energy transition. The authors have been involved in renewable energy teaching in Switzerland and the neighboring countries, mostly in conjunction with the simulation software Polysun. Some specific activities also cover the Scandinavian countries (Bales 2016, Andersen 2016), the Mediterranean area and specific projects in Egypt (Khayet 2014), China (Wolf 2016, Prandini 2016) and Kuwait (Al-Yaseen 2016). In many activities, the simulation software Polysun played a major role in overcoming translation challenges and to measure and ensure the proficiency level.

Market development is very different in various regions. While in Germany, there was a strong growth in photovoltaics until 2013 with the installed photovoltaic area almost doubling several years in a row, there was a shortage of planners and installers. Teaching has been done on the job and especially the bigger institutions have been too late with offering appropriate programs and courses. On the technical side, systems have become standardized and simplified, and the required knowledge shifted from electrical engineering topics to the awareness of regulatory requirements and standards.

In many regions, certificates for students and teachers are important to award the successfully passed exams and to prove the technical and didactic skills of the local teachers. Concluding from all training activities abroad, it is essential to cope with cultural differences, to be ready to learn from one another and recognize technical discussions always as bi-directional know-how transfer.

6.1 China

The authors of this article have been involved in an exchange program funded by a Swiss platform REPIC (Renewable Energy & Efficiency Promotion in International Cooperation) and the activities included introducing software-based teaching methodology in a teach-the-teacher scheme. Close and intensive collaboration has been established prior to the project start and was a pre-requisite for a successful project.

- First, it has to be recognized that the Chinese solar market is mature and – in particular in the solar thermal field – technical solutions as well as the value chain differ significantly from European standards. The software had to be extended to cover the systems typically installed in China.

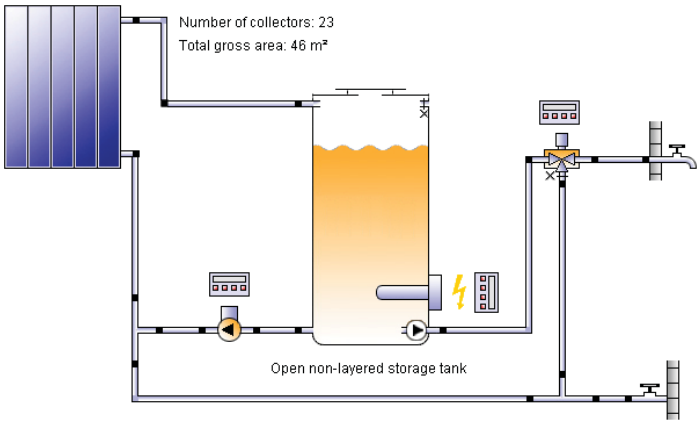

Figure 4: Typical Chinese system with open freshwater storage tank. Due to the strong circulation through the solar collector field, thermal stratification is destroyed deliberately. The tank is partially filled in times with low solar radiation, first fills up to 100% when more solar energy is available and heats up well above the required hot water temperature to increase energy storage capacity.

- Secondly, language was a major challenge since English has not been a common language between the European and the Chinese solar experts. Consecutive translation has been established for the know-how exchange and the simulation software graphical user interface has been translated into Chinese.
- Teaching methods have been adapted. As an example, the jigsaw exercise has proven to be very effective since it activated participants and trained technical expertise at the same time as teaching skills. Furthermore, it lowers language challenges when teachers and participants do not speak a common language since in jigsaw groups, Chinese-speaking participants teach their colleagues.

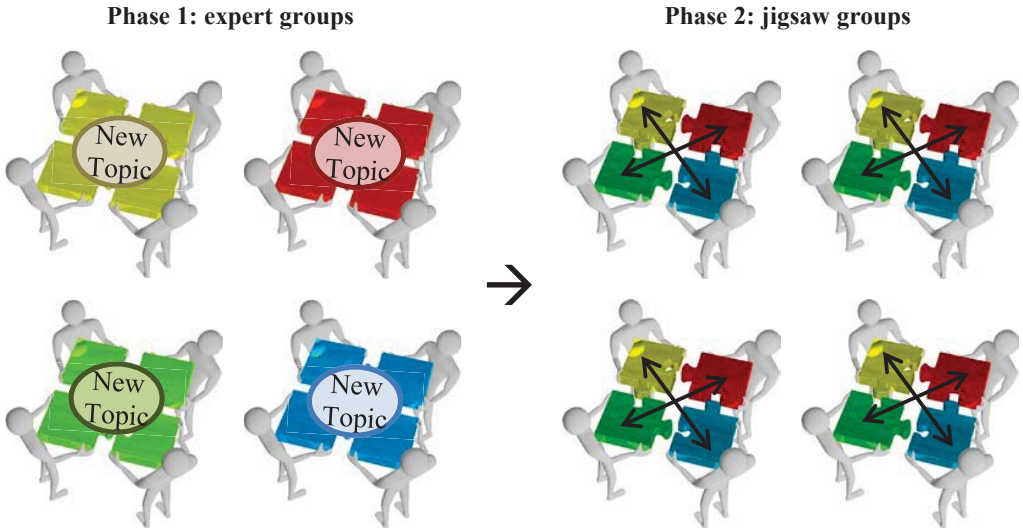

Figure 5: Jigsaw exercise. In a first round, small groups receive a new topic either by written or oral explanation. In a second round, groups are reorganized in order that participants teach each other. The jigsaw exercise proved to be a valuable didactic concept as an ice-breaker and to activate participants in teach-the-teacher courses.

6.2 Egypt

The teaching project in Egypt was supported by the EU Tempus Project SOLEDA and carried out by a large partner consortium of experts across the European Union (Khayet 2014). Simulation software only used a minor part of the budget but still played a significant role. To fulfil one of the requirements stated by the SOLEDA project plan, the Polysun graphical user interface has been translated into the Arab language, as shown in Figure 6. Furthermore, as a major contribution to the SOLEDA project, some general course content has been provided by the authors and extensive teach-the-teacher activities have been carried out at in different places in Egypt and Europe.

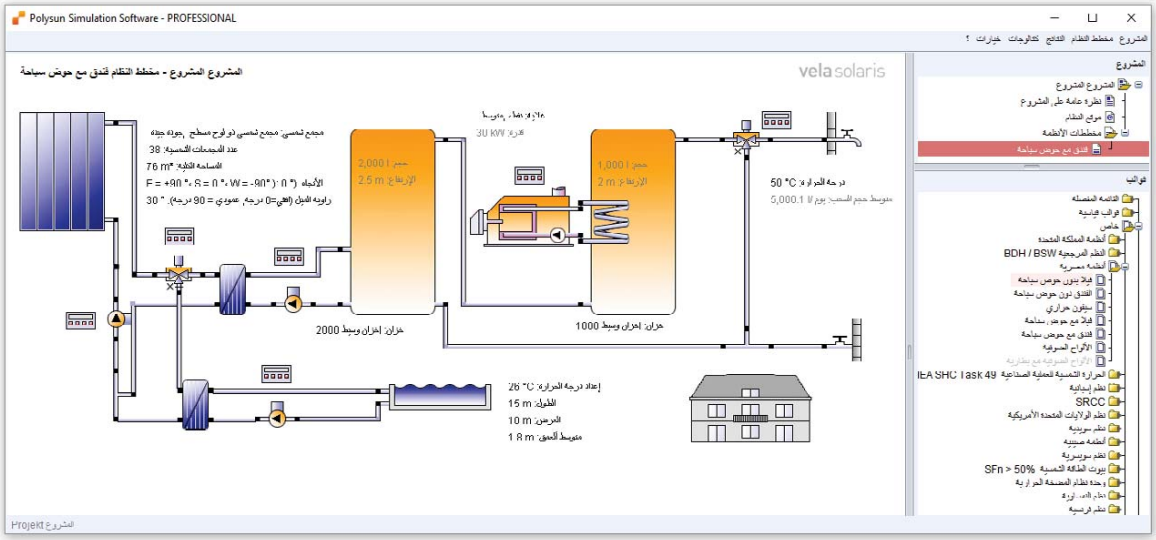

Figure 6: Polysun graphical user interface in the Arab language.

The project was running during a time of political change in Egypt. The positive attitude towards solar energy has been a constant source of motivation for all participants and also for the public (Soleda-Video 2016). Independent of political and economic boundary conditions, solar energy is a meaningful and high potential technology for Egypt and there is a shortage of skilled young professionals in this field.

6.3 Kuwait

A long collaboration with the Kuwait Solar Energy for Private Training Institute (Al-Yaseen 2016) is worth mentioning because it shows how different various regions have to be treated in regards to solar education. Even though the simulation software is available in the Arab language, it is used in English. Furthermore, high quality training material is provided by the Institute, all with animated explanations and impressively rendered. The teacher is an accredited instructor and exams for participants are carried out in Kuwait. Quality assurance is partly supported by Vela Solaris in Switzerland and the certificates are in integral part of the training courses and represent a high value for participants.

Figure 7: All teaching material is animated in high quality rendering.

7. Conclusion and Outlook

The authors have reported about experience with employing the simulation software Polysun in the educational context. The work spanned from supporting the curriculum of a new bachelor program to providing small learn objects that can be dealt with within a few lecture hours and can easily be shared between teachers. It has been found that simulation is useful to provide an understanding of data that is otherwise not accessible such as cumulated operating hours and number of starts of a heat pump depending on the control strategy. Consequently, students learn more and the solar and renewable energy topic becomes more tangible. Furthermore, the use of simulation software in teaching has a positive influence on the motivation and attitude of the students and the attractiveness of the courses. These benefits typically come with the costs of some additional effort in lecture preparation. Relieve from that additional burden could be found in building up a good system of sharing exercise material.

It is proposed to spend future work on studying the learning process when using simulation software in solar education and in measuring the effect size of these modern teaching methods. In particular, a measure should be found to estimate the attractiveness of solar education and the experience of a positive effect of using simulation software in renewable energy teaching should be quantified.

8. References

Andersen E., 2016, *Application of Polysun at DTU Denmark.* Publication in the Proceedings of SIGES, September 2016, Winterthur, Switzerland

Al-Yaseen A., *Solar Energy and Polysun Simulation Software Certificate Course in Kuwait*. Publication in the Proceedings of SIGES, September 2016, Winterthur, Switzerland

Bales C., Lorenz K., 2016, *Application of Polysun in Teaching Courses in Sweden and in the PhD Program SHINE*. Publication in the Proceedings of SIGES, September 2016, Winterthur, Switzerland

Bony J., 2016, *Application of Polysun in French speaking part of Switzerland*. Publication in the Proceedings of SIGES, September 2016, Winterthur, Switzerland

Broman L., et al, 1991, *A concentrated course in solar thermal process engineering*. Proc of the ISES Solar World Congress, Denver, Colorado, Pergamon Press. 1991: 3815-3820

Canizares, C., Faur, Z., 1997, *Advantages and Disadvantages of Using Various Computer Tools in Electrical Engineering Courses.* IEEE Transactions on Education, vol. 40, no. 3, August 1997

Cook, A., et al., 2011, *Technology-Enhanced Simulation for Health Professions Education A Systematic Review and Meta-analysis*, Journal of the American Medical Association, issue 306, pp. 978-988

Edgar. T. F., et al., 2006, *A global view of graduate process control education*. Computers & Chemical Engineering, issue 30, pp. 1763–1774

Feurzeig, W., Roberts, N, (1999), *Modeling and Simulation in Science and Mathematical Education*, Springer, New York, ISBN: 0-387-98316-3

Kandpal, T. C. & Broman, L. (2015). *Renewable energy education: a worldwide status review.* Strömstad: Strömstad Akademi., ISBN: 9789186607302

Khayet, M., Ghannam R., and A. Khalil (2014). *Solar energy system design using advanced learning aids (SOLEDA): an EU Tempus project*. In the proceedings of the 8th International Technology, Education and Development Converence INTED-2014, pp2283-2291, March 2014, Valencia, Spain.

Milrad, M., et al., 2013, *Seamless Learning: An International Perspective on Next Generation Technology Enhanced Learning*. Chapter in Z. L. Berge & L.Y. Muilenburg (eds.) *Handbook of Mobile Learning*.

Pillay, H., et al., 2006, *Some Insights into the impact of ICTs on Learning Agency and Seamless Learning*. Chapter in Cortelli, A. (ed.) *Teaching in the knowledges society: New Skills and Instruments for teachers*.

Prandini M., *Best Practice Teaching Methods in a Teach-the-Teacher Program in China*. Publication in the Proceedings of SIGES, September 2016, Winterthur, Switzerland

Rutten, N., et al., 2012, *The learning effects of computer simulation in science education*. Computers & Education, Elsevier, issue 58, pp 136-153

Rumsey, D.J., 2000, *Promoting student-centered learning in a studio classroom environment*, ASA Stat. Ed. Section Newsletter, v. 6, http://www.stat.ncsu. edu/stated/newsletter/v6n2/studio.html (6 April, 2004).

Soleda-Video 2016. *https://www.youtube.com/watch?v=B1a4RbROvuw*, Cairo, Egypt.

Trey, L., Khan, S., *How science students can learn about unobservable phenomena using computer-based analogies*. Computing in Science & Engineering, 10(5), pp 24-27.

Witzig, A., et al, 2009, *Teaching Solar Thermal System Design by Use of Simulation Software*. Publication in the Proceedings of ESTEC, May 2009, Munich, Germany.

Wolf A., Jiankun Z., et al., 2016, *Renewable Energy Training and Certificate Program in China.* Publication in the Proceedings of SIGES, September 2016, Winterthur, Switzerland

11. Renewable Energy Strategies and Policies

Conference Proceedings

EuroSun 2016

Palma (Mallorca), Spain, 11 – 14 October 2016

ENERGY CONSERVATION OPPERTUNITIES AND SOLAR ENERGY INTEGRATION PROSPECTS IN THE RESIDENTIAL SECTOR OF KSA

Hafiz M. Abd-ur-Rehman[1,*], Sahar Shakir[2]

[1]Mechanical and Manufacturing Engineering Department (SMME), National University of Sciences and Technology (NUST), H-12 Campus, Islamabad 44000, Pakistan.

[2]U.S Pakistan Center for Advanced Studies in Energy (USPCAS-E), National University of Sciences and Technology (NUST), H-12 Campus, Islamabad 44000, Pakistan.

*Corresponding author: abd-ur-rehman_@hotmail.com, Tel: +92 334 6871727.

Abstract

This study aims to explore various energy conservation opportunities in the residential sector of Saudi Arabia when available standards are employed as compared to the typical local design practices. Based on the information collected from literature, the local design practices including physical, thermal, and operational characteristics are defined and simulated as a base case scenario for a typical single family residential building in Dhahran. A proposed case study is performed according to the benchmark design considerations of International Energy Conservation Code (IECC) 2012 and the simulation results are compared with the base case scenario in order to evaluate the energy saving potential. The proposed building is integrated with solar energy to meet the part load of the building. The credibility of solar energy integrated building is justified in terms of its economic as well as eco-environmental benefits.

Keywords: *Residential buildings; Energy conservation; Solar energy integration; GHG emissions*

1. Introduction

The buildings consume about 80% of the total electricity generated in KSA, a figure well above the average electricity consumption for the buildings in all over the world. A breakdown advocates that the residential sector accounts for the major part of the consumed electricity in buildings with a very high value of 51.2 %, followed by the commercial and government buildings that stand for 13.6 % and 13.4 % consumption, respectively (Asif, 2016). Therefore, energy conservation measures in the residential buildings is an important study that needs to be examined carefully to strengthen the energy security situation in KSA. The use of computer simulations to evaluate the performance of a building is a common practice now-a-days. Several comprehensive simulation tools are available to assist designers to implement innovative ideas and evaluate the energy savings potential in their proposed designs (Hong, Chou, & Bong, 2000). In most of the published literature related to energy performance of the residential buildings in KSA, the main focus of the researches is on the design optimization of the buildings to reduce the energy consumption (Alaidroos & Krarti, 2015; Almutairi et al., 2015; Budaiwi & Abdou, 2013; Taleb & Sharples, 2011). Although generous guidelines are available to reduce the energy consumption in a typical residential building in KSA but few studies have been conducted that implemented energy conservation measures and then integrated the renewable energy sources to meet the energy requirements of these buildings. Some studies specified the prospects of integrating the renewable energy sources in residential buildings to motivate the zero energy buildings concepts in the residential sector of KSA (Alrashed & Asif, 2012; Atieh & Shariff, 2015; Banani, Vahdati, Shahrestani, & Clements-Croome, 2016; Charfi, Atieh, & Chaabene, 2015). In zero energy buildings, the complete load of a building is shifted from conventional energy sources to renewable energy sources that is currently not practical in KSA due to technical, financial, and social barriers. However, the shift of the minor load (water heating load, lighting load, etc.) of a residential building to the renewable energy sources is possible and also helpful in providing the stability during summer peak load in KSA.

This study specified the energy conservation measures and solar energy integration to meet part of the energy requirements

doi:10.18086/eurosun.2016.11.01 Available at http://proceedings.ises.org

of a residential building in KSA. A single family residential building was selected in Dhahran. A literature review was conducted on energy conservation studies related to the residential buildings in Dhahran. The architectural features were defined for a typical residential building based on the local design practices that includes physical, thermal, and operational characteristics. The building was modeled using Visual DOE 4.0 software and considered as the base case scenario. Parametric analysis was carried out for different envelope design considerations to improve the thermal performance of the building. A proposed case study was examined according to the benchmark design considerations of International Energy Conservation Code (IECC), 2012 and the simulation results were compared to the base case scenario in order to evaluate the energy saving potential. The proposed building is integrated with grid connected solar PV system to meet the lighting load. The credibility of solar energy integrated building is justified in terms of its economic as well as eco-environmental benefits.

2. Base Case for Residential Building

Significant research has been carried out to evaluate the design parameters adopted in different climates of KSA. (Al-Haddad, 1988) conducted a field survey on more than 300 houses in major cities of KSA to develop a typical villa for energy simulation studies. (A. Ahmad, 2004) stated the features of a typical residential building for single family in Dhahran. He collected the data from surveys, building plan reviews that are filled by municipal authorities, and interviews conducted with building owners. (Al-saadi & Budaiwi, 2007) also conducted a survey to summarize the characteristics of a typical residential building for a single family in Riyadh and Dhahran. Based on the data obtained from literature, the base case scenario is simulated using RETScreen software that imports authentic climatic data from its database recorded by the National Aeronautics and Space Administration (NASA). The initial base case is modelled based on the input data summarized in Table1.

The simulations were performed first for a typical residential building of Dhahran as a base case scenario. The annual energy consumption for the base case scenario is presented in Fig. 1. Fig. 1 shows that the space cooling load is the highest among all the loads and responsible for 71 % of the overall annual energy consumed in a typical residential building of Dhahran. Lighting load is the second major contributor in total annual energy consumption followed by space heating load, equipment's load, and water heating load.

Table 1. Typical architectural features of a single family residential building in Dhahran (A. Ahmad, 2004; Al-saadi & Budaiwi, 2007).

Location	Dhahran
Direction	Front elevation facing East
Shape	Rectangular
Number of floors	2
Height between floors	3.5 m
Dimensions of floor	15 x 20 m
The area of floor	300 m^2
The area of walls	490 m^2
The area of windows	20% of the total area of walls
Type of glass	Single glazed (6 mm)
The volume of house	2100 m^3
Infiltration	0.5 ACH (Airtight)
Walls construction	15 mm outside plaster (Stucco) + 200 mm CMU Hollow + 15 mm inside plaster (Stucco)
Roof construction	15 mm Cement plaster + 200 mm CMU Hourdi Slab + 100 mm Foam + 4 mm water proof membrane + 25 mm Sand Fill + 50 mm Mortar + Terrazzo
Floor construction	100 mm slab on grade
Number of occupant	6
Occupancy rate	50 % during weekdays and 75 % on weekends

Type of lights	30 % Incandescent lamps and 70 % fluorescent lamps
Lighting load	10 W/m^2 for 1st floor and 8 W/m^2 for 2nd floor
Equipment load	12 W/m^2 for 1st floor and 5 W/m^2 for 2st floor
Air conditioning system	Constant volume residential system with electric heating
Thermostat	Two position thermostat with 25ºC cooling set point and 21ºC heating set point
Coefficient of performance	2.87

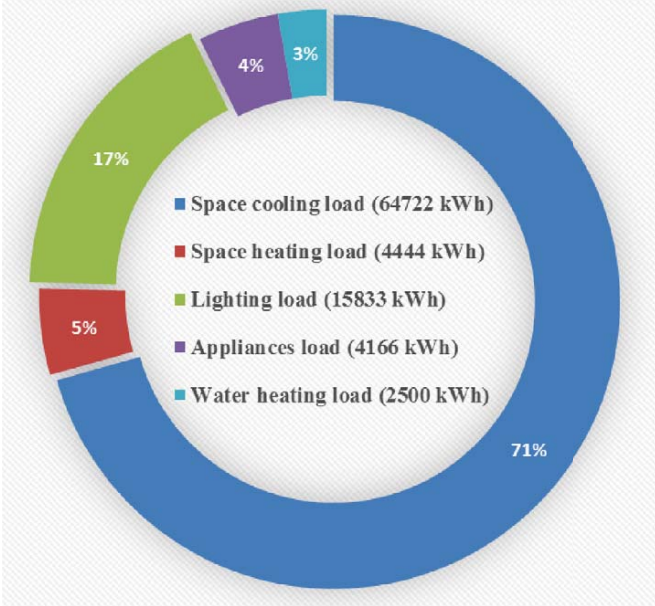

Fig.1. Annual energy consumption in a typical residential building of Dhahran (base case scenario).

2.1 Parametric analysis

Parametric analysis was performed to understand the effect of different design parameters on the energy consumption. Three different construction combinations were analyzed by varying the wall construction while keeping the roof construction same. These three combinations along with their properties are summarized in Table. 2.

Simulation results of different wall constructions were compared to the base case construction and presented in Fig. 2. Fig. 2 shows the decrease in energy consumption with the increase in thermal resistance of the walls. Construction 1 and 2 consist of a wall with higher thermal resistance and indicates a substantial decrease in the energy consumption for space cooling and heating when compared to the base construction. Although the wall in construction 3 has the highest thermal resistance, the decrease in energy consumption for Construction 3 is less as compared to construction 2.

Table 2. Different construction combinations by varying the wall construction while keeping the roof construction same.

Roof Construction	**R-value (m^2.°C/W)**	**Heat capacity (KJ/m^2.°C)**
15 mm Cement plaster + 200 mm CMU Hourdi Slab + 100 mm Foam Conc. + 4mm water proof membrane + 25 mm Sand Fill + 50mm Mortar +Terrazzo	1.69	629.8
Wall Construction	**R-value (m^2.°C/W)**	**Heat capacity (KJ/m^2.°C)**

Wall 1	15 mm cement plaster + 50 mm Precast Concrete Panel + 50 mm Polyurethane + 50 mm Precast Concrete Panel + 15 mm cement plaster	2.4	237.8
Wall 2	15 mm cement plaster + Hollow CMU Block + 50 mm Air Space + 100 mm Polyurethane + 15 mm Cement plaster	5	442.1
Wall 3	15 mm Cement plaster + 75 mm Polyurethane + 50 mm Precast Concrete + 75 mm Polyurethane + 15 mm Cement plaster	6.67	148.5

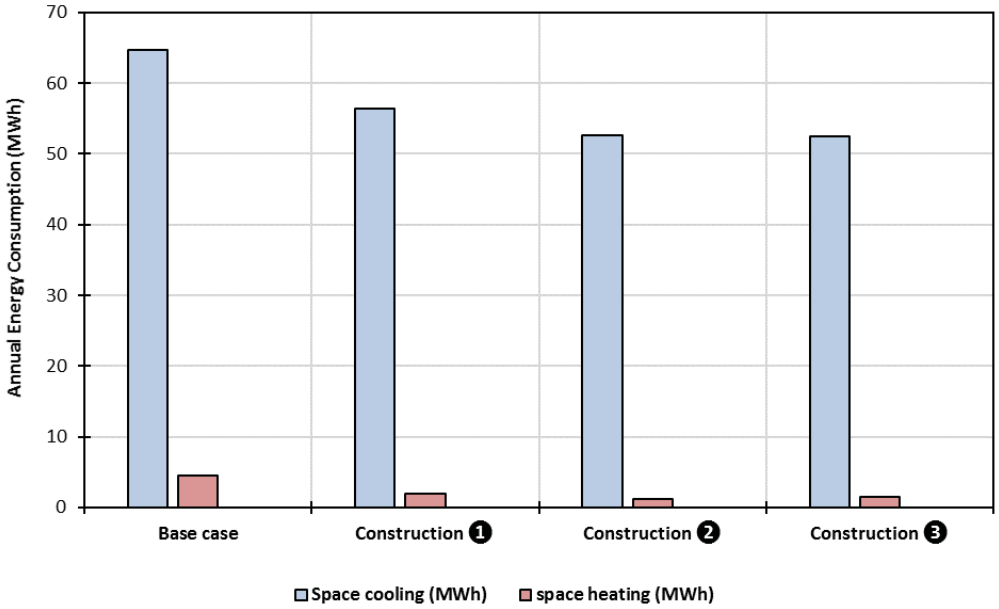

Fig.2. Annual energy consumption under different wall combinations.

The energy consumption of a typical residential building in Dhahran was also analyzed under different roof combinations. Three different construction combinations are analyzed by varying the roof construction while keeping the wall construction same. These three combinations along with their properties are given in Table. 3.

Simulation results of different roof constructions are compared to the base case and presented in Fig. 3. Fig. 3 shows the decrease in the energy consumption with the increase in thermal resistance of the roof. The impact of different roof combinations on energy consumption is not as much significant as in the case of different wall combinations. The reason of lower reduction in the energy consumption with different roof combinations is due to lower floor area as compared to gross wall area and two floors of the building. As only the second roof is directly exposed to solar radiations, the impact of different roof combinations majorly influenced the second floor energy consumption. Therefore, the impact of different roof combinations on energy reduction is not as much significant as in the case of different wall combinations.

Fig. 3 also indicates that the energy consumption for space heating is higher for construction 1 and construction 2 as compared to base case construction. These results can be justified from the heat capacity values and the location of thermal mass. For construction 1, the thermal insulation is placed on the interior side that does not allow the indoor generated heat to be stored in the construction material. In construction 2, the heat capacity value of the roof is very low as compared to the base case construction, therefore the potential to store indoor generated heat is reduced.

Table 3. Different construction combinations by varying the roof construction while keeping the wall construction same.

Wall Construction		R-value (m^2.°C/W)	Heat capacity (KJ/m^2.°C)
Single 200 mm Hollow CMU Wall + 15 mm Stucco finishes on both sides (without insulation)		0.34	380
Roof Construction		**R-value (m^2.°C/W)**	**Heat capacity (KJ/m^2.°C)**
Roof 1	15 mm Cement plaster + 50 mm Ext Polystyrene + 200 mm Clay Brick Hourdi + 100 mm Plain Concrete + 4 mm water proof membrane + 25 mm Sand + 50 mm Mortar + Tiles	2.56	567.1
Roof 2	15 mm Cement plaster + 200 mm Siporex Hourdi + 100 mm Foam Concrete + 50 mm Exp Polystyrene + 4 mm water proof membrane + 25mm Sand + 50 mm Mortar + Tiles	4.35	337
Roof 3	15 mm Cement plaster + 200 mm CMU Hourdi Slab + 100 mm Foam Concrete + 100 mm Polyurethane + 4 mm water proof membrane + 25 mm Sand + 50 mm Mortar + Tiles	5.88	638

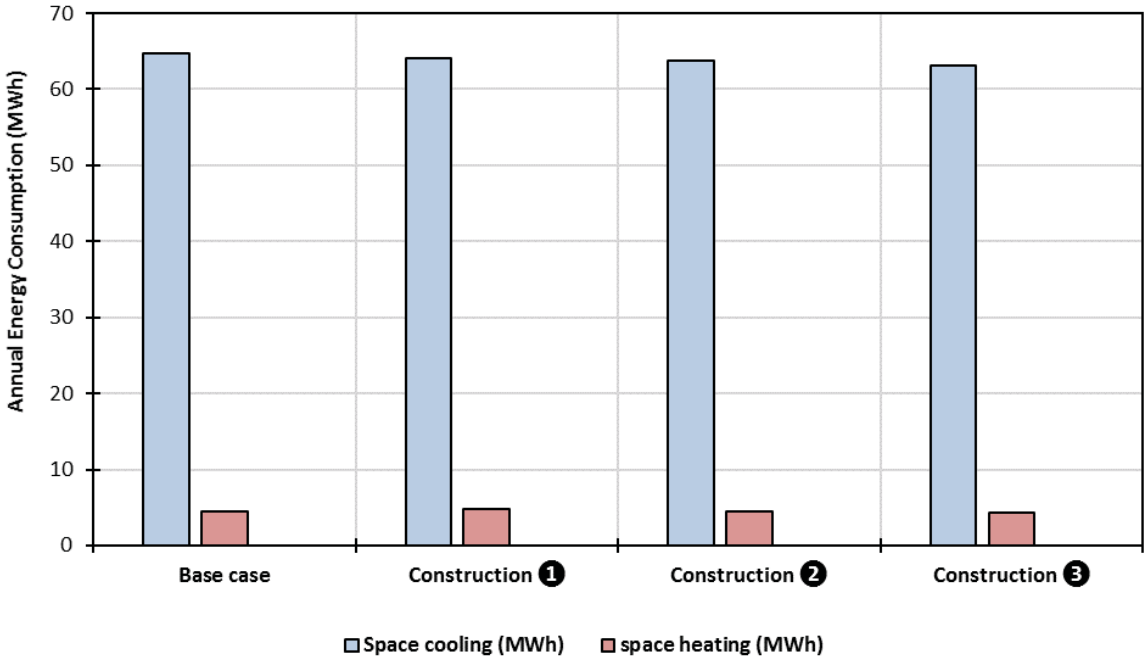

Fig.3. Annual energy Performance of Residential Building under different roof combinations.

The influence of different glazing on the energy performance of the building was also analyzed by using different glazing. Simulations were performed for double glazed, argon gas filled double glazed with low emissivity (low-e), and argon gas filled triple glazed with low-e. The characteristics of these glazing's are summarized in Table 4.

Simulation results of different glazing were compared to the base case and presented in Fig. 4 which clearly shows that the selection of glazing type plays a vital role in in the reduction of cooling and heating load. Fig. 4 shows that the energy consumption for space cooling is higher and energy consumption for space heating is lower for argon filled triple glazing when compared to argon filled double glazing. These results can be justified by the higher solar heat gain coefficient of argon filled triple glazing that allows more solar radiations to the space. Therefore, argon filled triple glazing performs

better in winter for heating purpose but it increase the cooling energy requirements in summer. The appropriate selection of the glazing U-factor (1/R-value) and the SHGC are required to balance the heating and cooling energy requirements.

Table 4. The characteristics of different types of glazing

Description	U-factor (1/R value) ($W/m^2.K$)	Solar heat gain coefficient (SHGC)
Double glazed	2.788	0.613
Double glazed, low-e, gas filled	1.317	0.278
Triple glazed,low-e, gas filled	0.772	0.471

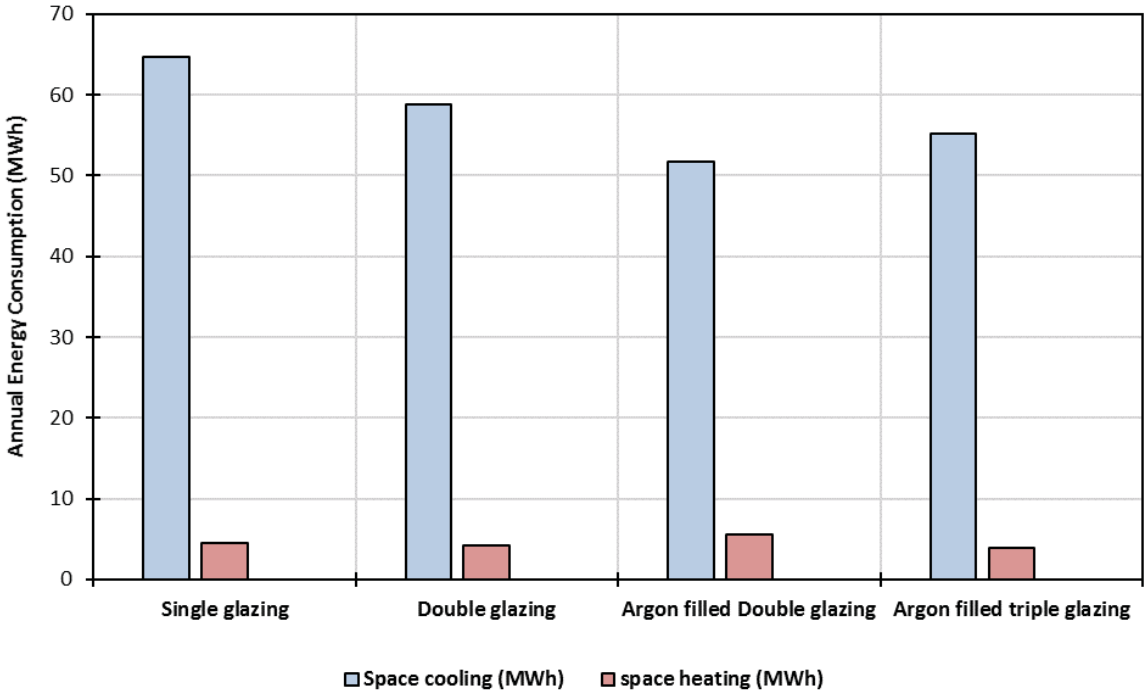

Fig.4. Annual energy Performance of Residential Building under different glazing types.

3. Proposed Case for Residential Building

A proposed case study was performed according to the benchmark design considerations of International Energy Conservation Code (IECC, 2012). IECC is intended to deliver state-of-the-art energy conservation practices for energy efficient building through model code regulations. The physical characteristics of the proposed case residential building are the same as in the base case. The minimum IECC requirements for envelope design in hot climates for residential buildings with less than or equal to 20 % windows area is as follow:

- The wall thermal resistance should be more than R-3/4.
- The roof thermal resistance (R-value) should be more than 5.28 m^2. ºC/W (R-30).
- The floor thermal resistance (R-value) should be more than 2.28 m^2. ºC/W (R-13).
- The U-value of glazing should be less than 2.27 $W/m^2.K$ with SHGC < 0.25.
- At least 75 % of the permanently installed lighting fixtures should be high efficacy lamps.
- All the appliances should be Energy Star certified.

Simulations were performed for the proposed case scenario according to the IECC standards and the results were compared

to the base case scenario to check the energy saving potential in the residential building, as shown in Table 5. It shows that there is 56 %, 37 %, 46 %, and 27 % less energy consumption for space cooling, space heating, lighting, and appliances, respectively.

Table 5. Comparison of annual energy consumption in base case and proposed case.

Type of load	Space cooling	Space heating	Lighting	Appliances
Annual energy consumption (kWh) - Base case	64722	4439	15833	4163
Annual energy consumption (kWh) - Proposed case	28611	2772	8550	3055
Annual energy savings (kWh)	36111	1667	7283	1108
Annual energy savings - %	56 %	37 %	46 %	27 %
Annual fuel consumption (GJ) - Base case	233	16	57	15
Annual fuel consumption (GJ) - Proposed case	103	10	31	11
Annual fuel savings (GJ)	130	6	26	4

4. Solar energy integration in Residential Buildings

The Kingdom of Saudi Arabia (KSA) is blessed with abundant solar radiations throughout the year. The vast open land of KSA receives high intensities of solar radiation for long periods that makes it an ideal region for solar energy conversion and its applications (Abd-Ur-Rehman & Al-Sulaiman, 2014). Irrespective of the enormous prospective of solar energy, KSA utilizes only a small portion of it and nearly all its energy requirements are met by fossil fuels. In this study an effort is being made to meet the part load of a residential building by using solar energy. Although, meeting the space cooling load by solar energy is not practical due to very high initial investment but lighting load can easily be met by using solar water heater.

Lighting load is the 2nd highest among all the loads and responsible for 17 % of the overall annual energy consumption in a typical residential building of Dhahran (as shown in figure 1). This load is satisfied by using conventional grid electric power that is generated by burning fossil fuels. The shifting of lighting load dependence from the conventional grid electric power to solar PV system could be a milestone towards improving energy savings and security in future concerns. For this purpose, grid connected PV system is simulated to fulfill the lighting load demand of a typical single family residential building in Dhahran. There are different technologies like mono-Si, poly-Si, a-Si, CIS, CdTe, and spherical-Si, that can be used for a grid connected PV system. Selection of certain PV technology type is directly related to the ambient temperature, optimum efficiency, nominal output temperature, and solar collector area (Natural Resources Canada, 1997). For the current study, year round working grid connected PV system was simulated using poly-Si technology. The implication of grid connected PV system is beneficial in two perspective: one is replacement of fossil fuels with renewable energy and second is the supply of surplus electric power to the grid system. The features of the designed grid connected poly-Si PV model are listed in Table 6.

Table 6. Characteristic features of modelled grid connected PV system (Abd-ur-Rehman & Al-Sulaiman, 2016; Natural Resources Canada, 1997).

Property/ Factor	Value
PV technology type	Poly-Si
Efficiency	16.4%
Nominal operating temperature	45 °C
Frame area / PV module	1.94 m^2
Control method	Clamped
Collector slope	Latitude of location
Solar tracking mode	Fixed
PV panel cost	2.7 $/watt
Electricity export rate	2.5 cents/KWh
Fuel cost escalation rate	4.0%
Inflation rate	2.5%
Discount rate	2.0%

Modelled grid connected PV system was analyzed in terms of its technical and main economic determinants (i.e. NPV, IRR, payback period and benefit-cost ratio). GHG emissions analysis was also carried out to visualize the environmental effects of energy transition. The economic determinants of the modelled grid connected PV system are summarized in

Table 7. The electricity export rate is assumed to be 2.5 cents/KWh that is equal to the electricity cost in the residential sector. Assuming the life time of the modelled grid connected PV system to be 25 years, the payback period is 13.3 years that is more than the half of PV system projected life. The long payback period is due to the highly subsidized cost of electricity in KSA. The high initial cost and absence of government incentive are the major restrictive factors in establishing the solar PV system. To encourage the practice of installing solar PV systems, the government should start incentive programs and should provide subsidy to substantiate the initial cost of establishing solar PV system.

Fig. 5 illustrates the effect of subsidy on the economic determinants of the modelled grid connected PV system. Results shows that the economic viability of the modelled grid connected PV system is directly influenced by the percentage of subsidy provided by the government. The incentive program that provides 50 % subsidy on the establishment of proposed grid connected PV system, the payback period could be reduced from 13.3 years to 6.6 years. Therefore, government should develop such incentives program that favors the establishment of clean energy projects to strengthen the energy security condition of KSA.

Table 7. Economic determinants of modelled grid connected PV system.

Factor	Value
Annual Electricity exported to grid	3.247 MWh
Net Present Value (NPV)	10,175 $
Internal Rate of Return (IRR)	9.8 %
Simple payback period	13.3 years
Benefit to cost ratio	2.45

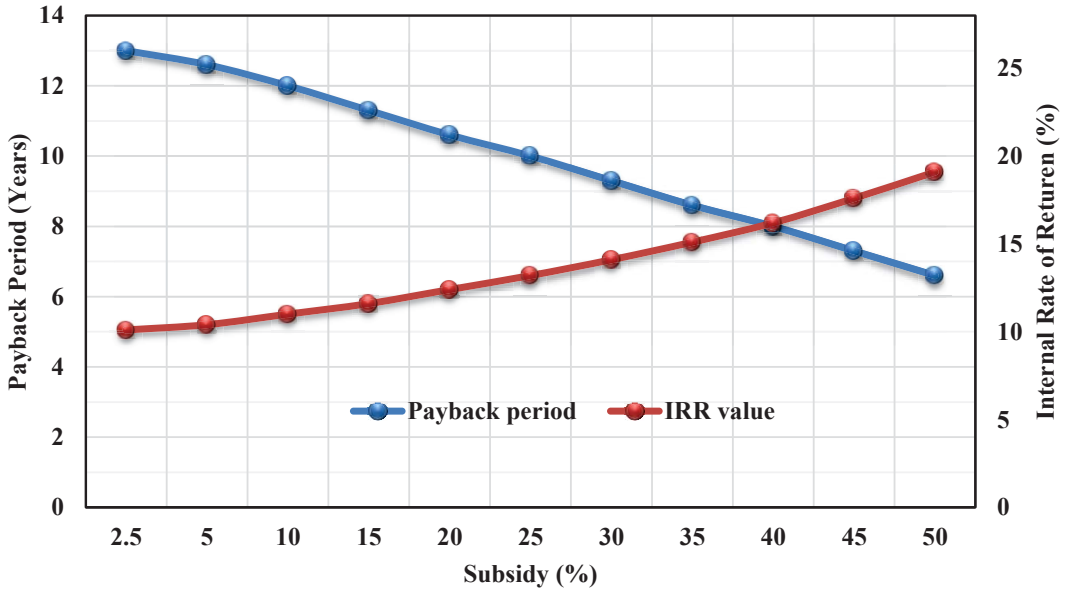

Figure 1. Effect of Subsidy on economic determinants of modelled grid connected solar PV system.

5. Conclusions

Residential buildings consume major part of the primary energy production and there is a huge energy saving potential in these buildings. Energy conservation measures in residential buildings is an important study and needs to be examined carefully to improve the energy security situation in KSA. The prevailing local design and construction practices in the residential buildings of KSA are energy inefficient. The buildings are poorly insulated, use inefficient appliances and lighting systems, and without the implementation of available standards. The implementation of IECC standards signpost the significant energy saving potential in the residential sector of KSA when compared to the typical local design practices. The simulation results for IECC standardized buildings shows 56 %, 37 %, 46 %, and 27 % less energy consumption for space cooling, space heating, lighting, and appliances, respectively.

Solar energy integration to meet the partial energy requirements in the residential buildings of KSA is technically and financially more viable as compared to zero energy building concept. The use of solar energy to meet the partial energy requirements of a residential building also provides the summer peak load energy stability in KSA. The implication of using grid connected PV system to meet the lighting load is economically justified in terms of subsidy provided by the government. Results indicate that the 50 % subsidy on the establishment of proposed grid connected PV system favors all economic determinants and results in reducing the payback period from 13.3 years to 6.6 years. Therefore, the government should start incentive programs and should provide subsidy to encourage the use of solar PV systems in residential buildings.

6. Acknowledgements

The authors acknowledge the support of National University of Sciences and Technology (NUST), H-12 Campus, Islamabad, Pakistan.

7. Abbreviations

ACH	Air change per hour
a-Si	Amorphous-silicon solar cell
CIS	copper indium gallium selenide solar cell
CdTe	Cadmium telluride solar cell
CMU	Concrete masonry unit
GHG	Greenhouse gas
IRR	Internal rate of return (%)
KSA	Kingdom of Saudi Arabia
KWh	Kilowatt hour
IECC	International energy conservation code
MWh	Megawatt hour
Poly-Si	Poly-silicon solar cell
NPV	Net present value
PV	Photovoltaic
Poly-Si	Poly-silicon solar cell
Spherical-Si	Spherical-silicon solar cell
R-value	Thermal resistance
SHGC	Solar heat gain coefficient
SWH	Solar water heating
U-factor	Rate of heat loss
tCO_2	Ton of carbon dioxide

8. References

A. Ahmad. (2004). ENERGY SIMULATION FOR A TYPICAL HOUSE BUILT WITH DIFFERENT TYPES OF MASONRY BUILDING MATERIALS. *Arabian Journal for Science and Engineering*, *29*(2), 113–126.

Abd-Ur-Rehman, H. M., & Al-Sulaiman, F. A. (2014). Techno-economic evaluation of different types of solar collectors for water heating application in domestic sector of Saudi Arabia. In *IREC 2014 - 5th International Renewable Energy Congress* (pp. 1–6). IEEE. http://doi.org/10.1109/IREC.2014.6826977

Abd-ur-Rehman, H. M., & Al-Sulaiman, F. A. (2016). Optimum selection of solar water heating (SWH) systems based on their comparative techno-economic feasibility study for the domestic sector of Saudi Arabia. *Renewable and Sustainable Energy Reviews*, *62*, 336–349. http://doi.org/10.1016/j.rser.2016.04.047

Alaidroos, A., & Krarti, M. (2015). Optimal design of residential building envelope systems in the Kingdom of Saudi Arabia. *Energy and Buildings*, *86*, 104–117. http://doi.org/10.1016/j.enbuild.2014.09.083

Al-Haddad, A. (1988). *Development of a Typical Saudi Villa for Energy Conservation Studies , Senior Thesis, College of Environmental Design, King Fahd University of Petroleum and Minerals*.

Almutairi, K., Thoma, G., Burek, J., Algarni, S., Nutter, D., & Martin, R. E. (2015). Life cycle assessment and economic analysis of residential air conditioning in Saudi Arabia. *Energy and Buildings*, *102*, 370–379. http://doi.org/10.1016/j.enbuild.2015.06.004

Alrashed, F., & Asif, M. (2012). Prospects of Renewable Energy to Promote Zero-Energy Residential Buildings in the KSA. *Energy Procedia*, *18*, 1096–1105. http://doi.org/10.1016/j.egypro.2012.05.124

Al-saadi, S. N., & Budaiwi, I. M. (2007). PERFORMANCE-BASED ENVELOPE DESIGN FOR RESIDENTIAL BUILDINGS IN HOT CLIMATES SAAD Group , Design Office , AL-Khobar 31952 , P . O . Box 3250 , Saudi Arabia Architectural Engineering Department , King Fahd University of Petroleum and Minerals , Dhahran 3126. *Building Simulation 2007*, 1726–1733.

Asif, M. (2016). Growth and sustainability trends in the buildings sector in the GCC region with particular reference to the KSA and UAE. *Renewable and Sustainable Energy Reviews*, *55*, 1267–1273. http://doi.org/10.1016/j.rser.2015.05.042

Atieh, A., & Shariff, S. Al. (2015). Case study on the return on investment (ROI) for using renewable energy to power-up typical house in Saudi Arabia. *Sustainable Cities and Society*, *17*, 56–60. http://doi.org/10.1016/j.scs.2015.03.008

Banani, R., Vahdati, M. M., Shahrestani, M., & Clements-Croome, D. (2016). The development of building assessment criteria framework for sustainable non-residential buildings in Saudi Arabia. *Sustainable Cities and Society*, *26*, 289–305. http://doi.org/10.1016/j.scs.2016.07.007

Budaiwi, I., & Abdou, A. (2013). The impact of thermal conductivity change of moist fibrous insulation on energy performance of buildings under hot-humid conditions. *Energy and Buildings*, *60*, 388–399. http://doi.org/10.1016/j.enbuild.2013.01.035

Charfi, S., Atieh, A., & Chaabene, M. (2015). Modeling and cost analysis for different PV/battery/diesel operating options driving a load in Tunisia, Jordan and KSA. *Sustainable Cities and Society*, pp. 49–56. http://doi.org/10.1016/j.scs.2016.02.006

Hong, T., Chou, S. ., & Bong, T. . (2000). Building simulation: an overview of developments and information sources. *Building and Environment*, *35*(4), 347–361. http://doi.org/10.1016/S0360-1323(99)00023-2

IECC. (2012). *The International Energy Conservation Code®*.

Natural Resources Canada. (1997). *RETScreen® Software Online User Manual*. Retrieved from http://utopia.duth.gr/~bilaisma/med/C6/wind3.pdf

Taleb, H. M., & Sharples, S. (2011). Developing sustainable residential buildings in Saudi Arabia: A case study. *Applied Energy*, *88*(1), 383–391. http://doi.org/10.1016/j.apenergy.2010.07.029

Conference Proceedings

EuroSun 2016
Palma de Mallorca (Spain), 11 - 14 October 2016

Renewable energy in Croatia: a review of present state and future development

Paolo Blecich, Marko Petrić and Bernard Franković

Faculty of Engineering, University of Rijeka (Croatia)

Abstract

Renewable energy has recently experienced a rapid expansion in Croatia. The improved feed-in tariff system attracted substantial investments and boosted the electricity generated from renewable energy systems. The installed renewable energy capacity rose rapidly from 100 MW in 2011 to more than 500 MW in 2016. In 2014 alone, 200 MW of new wind power plants were added. The total installed capacity in renewable power plants is capable of generating around 1250 GWh of renewable electricity per year. Renewable electricity represents a share of around 7% in the annual electricity consumption of Croatia. Wind energy is by far the most significant renewable energy source in Croatia, generating more than 85% of the renewable electricity. By installed capacity, the 455 MW in wind power plants is followed by 25 MW in biomass and biogas power plants, 12 MW in cogeneration and 8 MW in solar PV power plants. In order to keep up with the running expenditures within the feed-in tariff system, the incentive fee for renewable electricity support was increased fivefold by the end of 2013. At present, end consumers support renewable electricity generation with 5% of the cost of electricity. This incentive fee is expected to rise with newly added renewable power plants, aiming to double the share of renewable electricity from the present 7% up 13.6% by 2020.

Keywords: *Renewable energy, Croatia, feed-in tariff system, solar PV, solar thermal, wind energy*

1. Introduction

This paper gives an overview of the present state and future development of renewable energy in Croatia. Wind and solar PV energy are the most rapidly expanding renewable energy markets in Croatia. On the other hand, solar thermal and hydropower have slower growth rates. The substantial renewable energy growth is fueled by increasing energy demand, fossil fuel price and energy supply insecurity. Furthermore, improved policies and incentive programs as well as enhanced renewable energy components and systems have also contributed the renewable energy growth both in Croatia and worldwide [1-3]. The improved Croatian feed-in tariff system made investing in renewable energy more attractive to entrepreneurs and boosted the installed capacities of wind power in the first place. However, the feed-in tariff system collecting incentive fees presents an increasing financial burden to electricity customers since the agreed renewable electricity share targets are still far away.

2. Global renewable energy overview

The solar PV global installed capacity rose from 16 GW in 2008 to 232 GW while the wind global installed capacity rose from 121 GW in 2008 to 433 GW at the end of 2015 [1], as shown in figs. 1 and 2. The leading countries for installed solar PV capacities are China (44 GW), Germany (40 GW), Japan (36 GW), USA (27 GW) and Italy (20 GW). The country with the largest newly added solar PV capacity in 2015 was China with 15 GW, overtaking long-time leader Germany. The solar water heating collector capacity is estimated at 435 GWth (621 million m^2) in 2015, with China at the first place reaching a share of 73%, and followed by USA, Germany, Turkey and Brazil, whose combined share is 12% [4-6]. The solar water heating sector

doi:10.18086/eurosun.2016.11.02 Available at http://proceedings.ises.org

slowed down in 2014 and 2015, mainly due to shrinking markets in Europe and China. The concentrating solar thermal power (CSP) market has a global installed capacity of 4.8 GW with Spain and USA holding about 90% of the world total capacity.

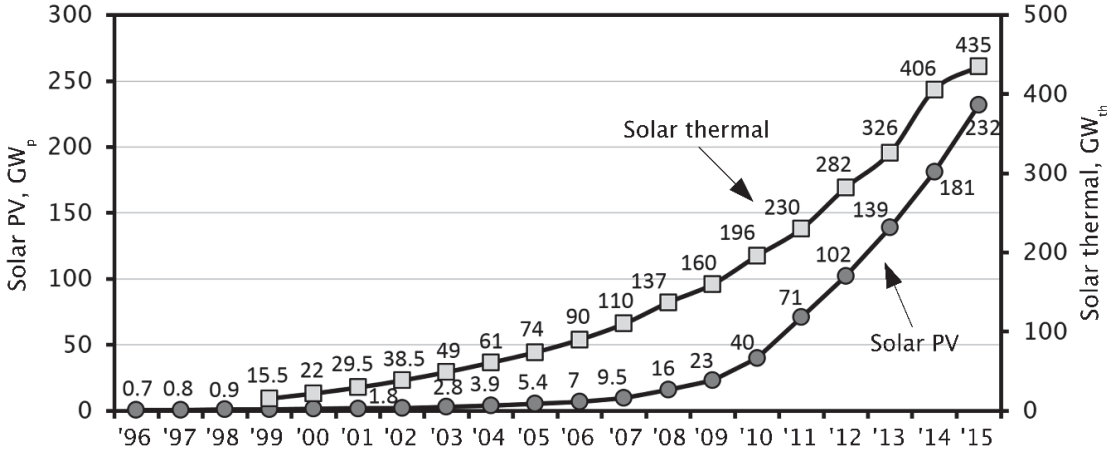

Fig. 1: Solar PV and solar thermal global installed capacity, 1996-2013, [1-6]

The leading countries for installed wind power capacities are China (145 GW), USA (74 GW), Germany (45 GW), India (25 GW) and Spain (23 GW), fig. 2. Again, China is the leading country for newly added wind power capacities with 32 GW in 2015 alone. The hydropower global capacity surpassed 1000 GW in 2013 and it was 1069 GW at the end of 2015. The leading countries for installed hydropower are China (296 GW), Brazil (92 GW), USA (80 GW), Canada (79 GW), Russia (48 GW) and India (47 GW). China added 16 GW of new hydropower plants in 2015 [1].

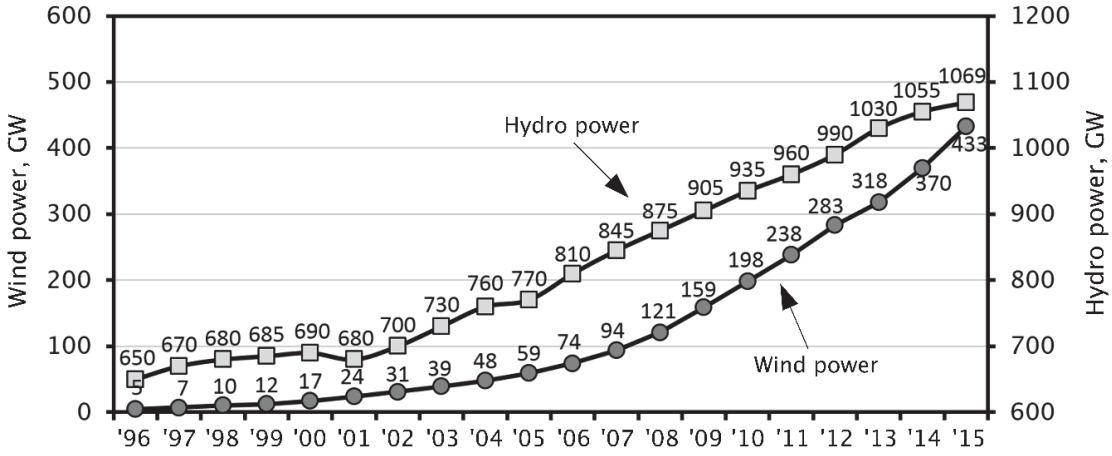

Fig. 2: Hydro and wind power global installed capacity, 1996-2013, [1-3]

Wind, hydro, biomass and geothermal energy are the most financially viable renewable energy sources on the market. The cost of electricity generation from hydro power plants is in the range of 0.02 to 0.09 €/kWh with a levelized cost (LCOE) of 0.045 €/kWh. Onshore wind power plants have costs of electricity generation in the range of 0.03 to 0.09 €/kWh with a LCOE of 0.054 €/kWh. Biomass energy, including solid, liquid and gaseous fuels, has a cost of electricity generation between 0.03 and 0.09 €/kWh with a LCOE of 0.06 €/kWh. The costs of electricity generation from geothermal sources is in the range of 0.05 to

0.11 €/kWh with a LCOE of 0.07 €/kWh. Nowadays, wind, hydro, biomass and geothermal energy provide electricity at a competitive cost, compared to the conventional fossil fuels. Electricity generation in fossil fuel power plants come at costs between 0.04 and 0.12 €/kWh and a LCOE of 0.055 €/kWh, all excluding health, environment and carbon emission costs.

Electricity generation in offshore wind power plants have significantly higher costs than those of the onshore wind power plants. The levelized cost of electricity generation (LCOE) in offshore wind power plants is almost three times the cost of electricity in onshore wind power plants: 0.15 €/kWh against 0.054 €/kWh. The cost of electricity generation from solar energy is still the highest among renewable energy sources. The cost of electricity is in the range of 0.07 to 0.20 €/kWh for utility PV power plants, 0.15 to 0.25 €/kWh for small-scale rooftop PV systems and 0.20 to 0.30 €/kWh for CSP thermal power plants. The levelized costs are 0.14 €/kWh for utility PV, 0.19 €/kWh for rooftop PV and 0.23 €/kWh for CSP. The efficiency of solar PV modules is still a major drawback, yet improvement is being made in this field as well. The efficiency of crystalline silicon PV modules is 10-20% while the efficiency of thin-film technology is only 5-12%. Nevertheless, the efficiency of concentrating PV modules (CPV) is 25% on average. The most-efficient existing PV module is a four-junction CPV which peaked a world record of 46% solar-to-grid efficiency. Hybrid photovoltaic thermal solar collectors (PVT) and concentrating PVT (CPVT) modules are capable of producing electricity and heat at efficiencies significantly higher than those of electricity-only CPV modules, with manufacturers claiming efficiencies of up to 75%. Solar thermal water heating systems reach 30-50% efficiency at an average cost between 0.05 and 0.15 €/kWh. Large-scale solar thermal systems, for multi-family houses and district heating have costs of energy generation between 0.03 and 0.10 €/kWh.

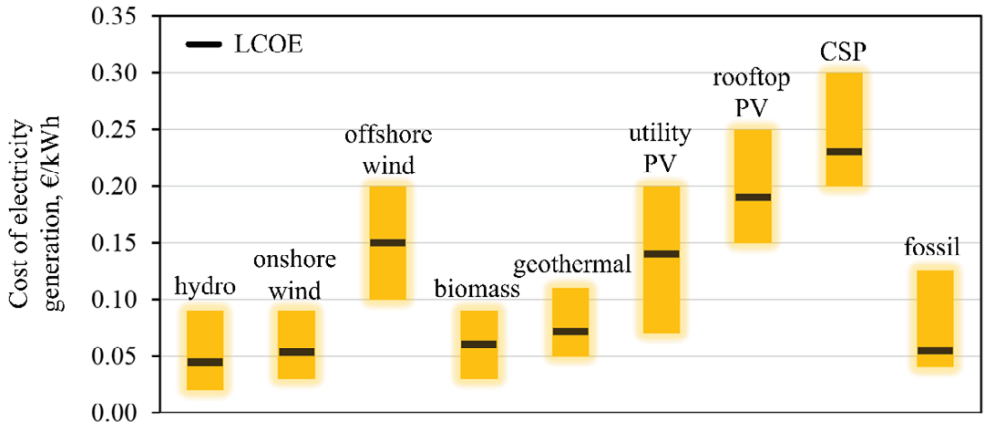

Fig. 3: Range of cost and levelized cost (LCOE) for electricity generation from renewable energy sources [1-3]

3. Renewable energy in Croatia

3.1. Present state

Under the Croatian feed-in tariff system, the currently installed renewable energy capacity of around 530 MW is capable of producing around 1250 GWh of electricity per year [7]. Ranked by installed capacity, wind energy dominates overwhelmingly with 455 MW and is followed by biomass and biogas installations, each having a total capacity of 25 MW, cogeneration with 12 MW, solar PV with 8 MW, small hydro with 3 MW and waste energy with 2 MW. Ranked by the number of operating power plants, the leading is solar PV with 155 power plants and is followed by 21 biogas installations, 17 wind power plants, 10 biomass installations, 7 small hydro power plants, 4 cogenerations and 1 waste energy power plant.

The nature of wind energy in Croatia is highly intermittent, whereas frequent and abrupt oscillations in the electricity output are expected over short periods of time, usually between morning and evening hours. In 2015, during 10% of the time the wind electricity output was negligible, usually less than 1% of the nominal capacity. On the other hand, the maximum instantaneous wind electricity output was 370 MW, which

corresponds to a maximum capacity factor of 84%. The average capacity factor for Croatian wind power plants is 25%, which corresponds to 2200 working hours at nominal capacity over a period of one year. For comparison, Danish wind power plant are able to achieve annual capacity factors between 50 and 60%.

The generated renewable electricity of 1250 GWh represents around 7% of the gross electricity generation which amounts to 17500 GWh in Croatia [7-10]. If large hydro power plants (> 10 MW) are accounted for in the renewable electricity mix of Croatia, the renewable electricity share varies significantly, depending on the quantity and distribution of rainfall throughout the year. For example, the share of renewable electricity was only 28% in 2012 but reached 58% in 2014. Likewise, the renewable energy share in the total primary energy consumption of Croatia is also variable: from 14% in 2012 up to 28% in 2014.

Under the European energy and climate plan, Croatia agreed that the share of renewable energy in the final energy consumption should reach 20% by the end of 2020. Furthermore, Croatia decided for two sub-targets: increase the renewable electricity share to 13.6% and increase the cogeneration electricity share to 4%, both with respect to the final electricity consumption. Unlike renewable electricity, the Croatian solar thermal sector is having a slower progress, because of smaller subsidies. The total installed solar thermal surface was around 200.000 m^2 by the end of 2015 in Croatia. This gives a specific solar thermal surface of only 47 m^2 per 1000 inhabitants in Croatia, whereas the EU-28 average is 85 m^2 per 1000 inhabitants [4-6].

3.2. Future development

Renewable energy has seen a fivefold increase of installed capacities in the last four years: from 100 MW in 2011 to more than 500 MW as of September 2016, as shown in Fig. 4. Wind power plants are usually installed along the coastal region of the Adriatic Sea, because of favourable wind conditions. On the contrary, solar PV systems are more frequently installed in West and North Croatia, despite lower annual solar irradiation but more attractive support schemes.

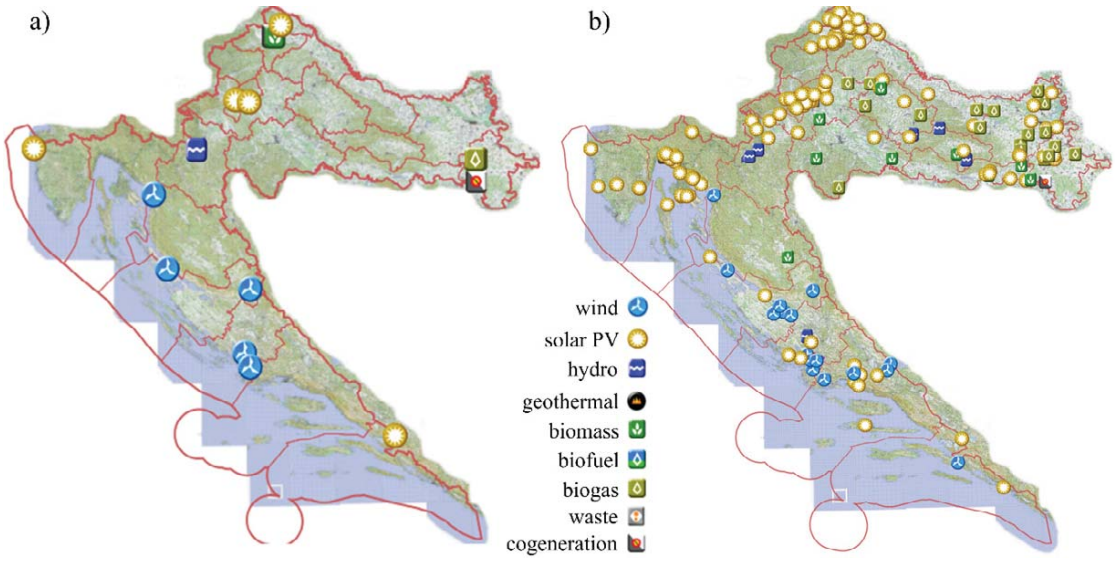

Fig. 4: Renewable energy installations in Croatia: a) 100 MW in 17 power plants in 2011; b) 530 MW in 215 power plants as of September 2016 [6]

At present, the 530 MW of installed renewable energy capacities supply around 7% of the electricity demand in Croatia. On the other hand the share of electricity from cogeneration systems is still negligible, less than 1% in the annual electricity consumption. In order to meet the agreed targets of 13.6% in renewable electricity share and 4% in cogeneration electricity share, a substantial increase in total capacity and number of installations in renewable electricity and cogeneration is necessary. It is estimated that an additional 500 MW in renewable electricity and 140 MW in cogeneration are required to meet the agreed share targets.

Wind energy will continue to dominate the renewable electricity mix in Croatia. According to the Croatian action [11] plan for renewable energy, the present wind energy capacity of 455 MW will reach 750 MW by 2020, as shown in fig. 5. Solar PV, from the present 8 MW is expected to reach 55 MW by 2020. Hydro energy (including large hydro) will be upgraded from the present 2100 MW up to 2500 MW by 2020, of which small hydro power plants will represent 100 MW. Biomass and biogas power plants have a combined total capacity of 50 MW, which is expected to increase up to 125 MW by 2020. Geothermal installations for electricity generation are at test phase at the moment and will reach 10 MW by 2020. The annual generated electricity can be estimated from the number of working hours at nominal capacity: 3000 hours for hydro, 2200 hours or wind, 1150 hours for solar PV, 6500 hours for biomass and biogas, 7200 hours for geothermal energy. Thus, the generated renewable electricity (excluding large hydro) will increase to 3200 GWh by 2020, from the present 1250 GWh. This returns a predicted renewable electricity share of around 18%, which is even more than the agreed target share of 13.6%. At present, wind power plants generate more than 85% of the renewable electricity in Croatia. However, this wind share is expected to decline to around 50% as new hydro, biomass and cogeneration capacities enter the renewable electricity mix of Croatia.

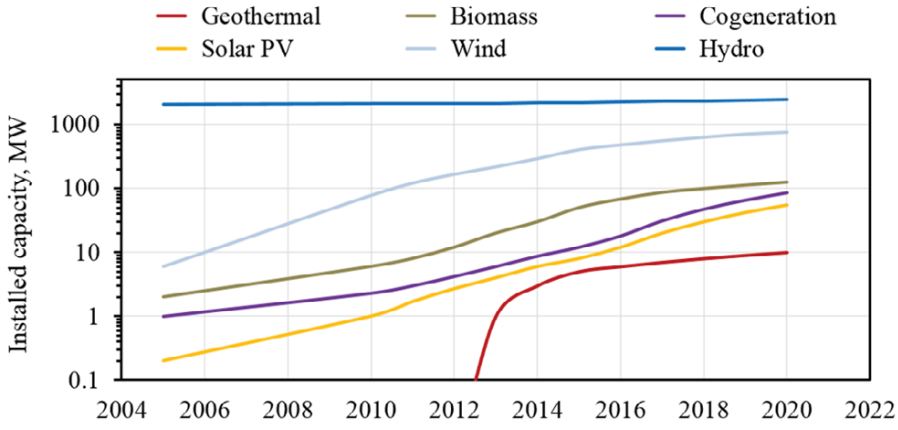

Fig. 5: Predicted renewable energy capacities in Croatia till 2020

The Croatian action plan [11] for renewable energy is a roadmap for increasing the use of renewable energy in the three major sectors of energy consumption: electricity, heating & cooling and transport, as shown in fig. 6. The overall combined share of renewable energy in the final energy consumption should be 20% or more by the end of 2020 in Croatia. The target share for renewable energy in electricity consumption of 39% by 2020, including large hydro power plants, will be achieved by upgrading hydro and wind capacities as well as installing new capacities of solar PV, biomass and cogeneration power plants.

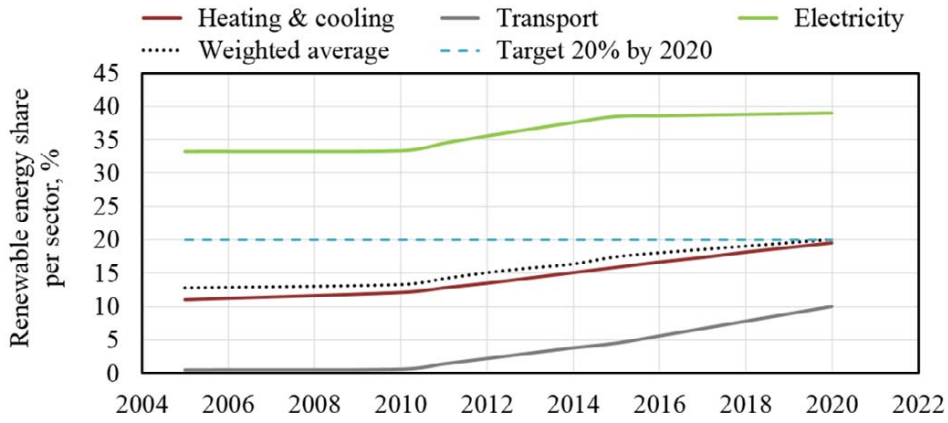

Fig. 6: Planned renewable energy share by consumption sector till 2020 in Croatia

The share of renewable energy in heating & cooling energy consumption is expected to grow from the present 15% up to 20% by 2020. This goal will be achieved with nationwide support programs for the energy retrofit of existing buildings, installation of solar collectors for space and water heating and replacement of fuel oil boilers with biomass and biogas boilers. The share of renewable energy in transport is expected to reach 10% by 2020. At the moment this goal seems hardly achievable, and attractive support programs will be necessary for the introduction of biofuel, hybrid and electric vehicles.

3.3. Economic aspects

To keep up with the running expenditures within the Croatian feed-in tariff system, domestic consumers had their taxes for renewable electricity generation increased in 2013. This increase was driven by the discrepancy between collected and distributed funds, which occurred in 2012 and 2013 [12], as shown in Fig. 7. Taking into account that the present renewable electricity tax is 5.8 €/MWh and that the price of electricity is 120 €/MWh for domestic consumers, nearly 5% of the price of electricity goes to renewable electricity support in Croatia. The renewable electricity taxes are going to rise since new renewable energy capacities are planned. The share of renewable electricity will be doubled by 2020, from the present 7% up to 13.6%. Recently, the Ministry of Economy of Croatia announced that the renewable electricity tax for domestic consumers will be raised to 20 €/MWh in 2017, and further to 23.3 €/MWh in 2018 and 25 €/MWh in 2019.

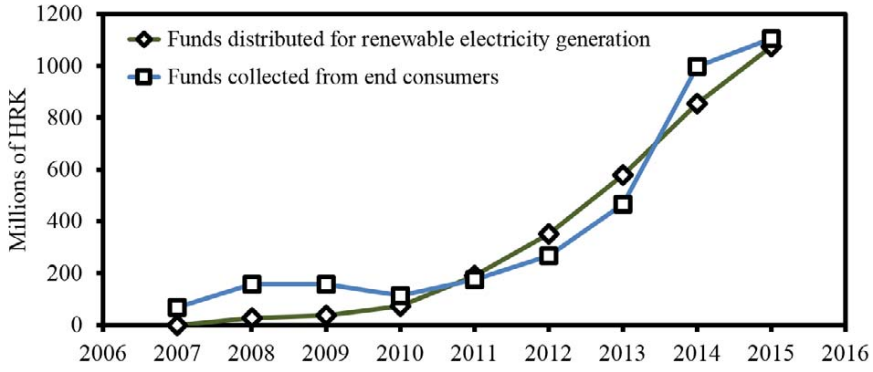

Fig. 7: Distributed and collected funds within the Croatian feed-in tariff system (1 EUR = 7.5 HRK)

The financial support for renewable electricity generation inside the Croatian feed-in tariff system was around 150€ million, or 1125 million HRK, in 2015. For a total amount of generated renewable electricity of 1250 GWh under the feed-in tariff system, the specific support for renewable electricity generation was equal to 120 €/MWh. For comparison, the European weighted average support for renewable electricity generation was 110 €/MWh in 2013 [13], as shown in figure 8.

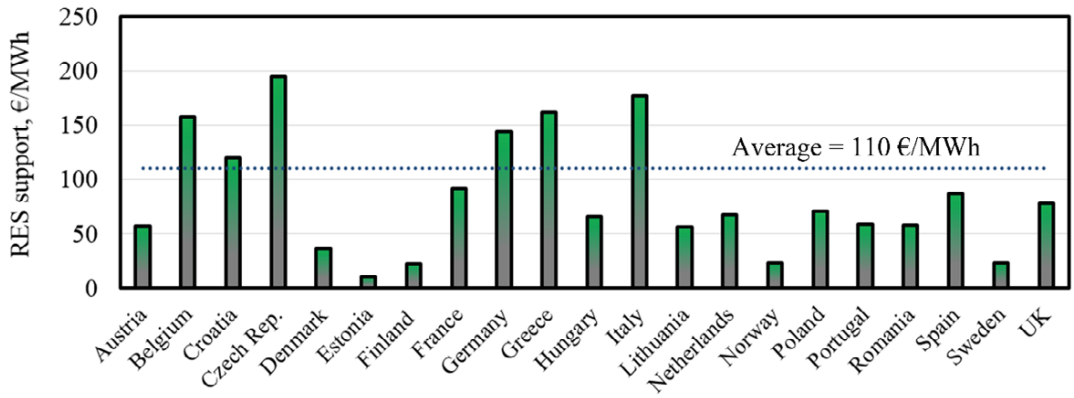

Fig. 8: Renewable energy support under the feed-in tariff system per unit of generated renewable electricity

The support for renewable electricity generation per unit of generated renewable electricity ranged between 11 €/MWh (Estonia) and 195 €/MWh (Czech Republic) in 2013. In Croatia, the specific support for renewable electricity generation was 120 €/MWh in 2015. However, this value does not take into account the penetration of renewable energy into the grid. Since the share of renewable electricity in the generated gross (renewable and conventional) electricity is 7% at the moment, the specific renewable electricity support per unit of generated gross electricity is 8.4 €/MWh in Croatia. The support for renewable electricity generation is collected from renewable electricity taxes for domestic and industrial consumers, carbon and environment taxes, grid fees, and other. At the moment, domestic consumers in Croatia have a renewable electricity tax of 5.8 €/MWh, which will be raised to 20 €/MWh in 2017 and further to 25 €/MWh in 2019. The annual electricity consumption of the average household in Croatia is 3500 kWh. Therefore, per year the average Croatian household supports renewable electricity generation with an amount of 20.3 €, which will become 87.5 € in the close future. In Europe, the specific support with respect to the gross electricity generation is up to 32 €/MWh (Italy), whereas the weighted average support is 13.7 €/MWh [13], as shown in fig. 9. Generally, countries with higher RES support in gross generated electricity have also higher shares of renewable electricity in their electricity markets.

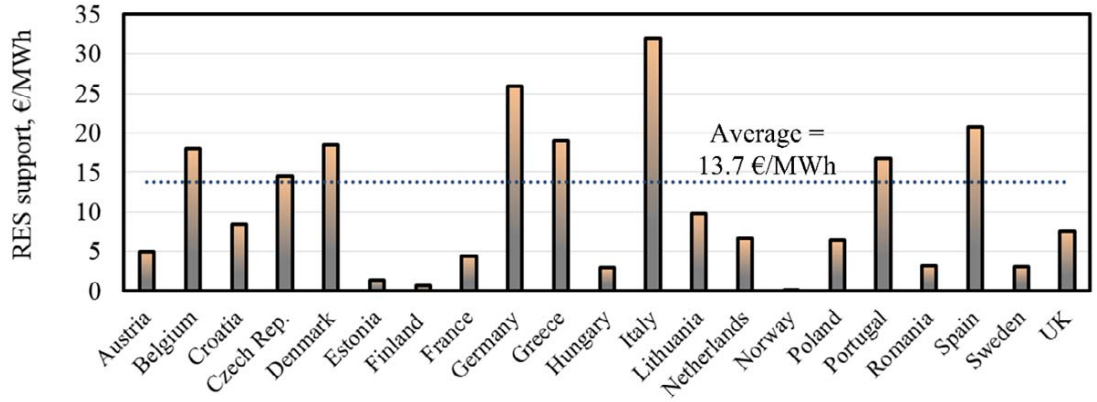

Fig. 9: Renewable energy support under the feed-in tariff system per unit of generated gross electricity

The renewable electricity support is somewhat correlated to a country's energy import dependency, as shown in fig. 10. Generally, countries with high dependency on imported energy tend to support more renewable electricity generation. For example, countries having high energy import dependency and large RES supports are: Italy with 79% and 32 €/MWh, Belgium with 77% and 18 €/MWh, Portugal with 75% and 17 €/MWh, Spain with 74% and 20 €/MWh, Greece with 66% and 19 €/MWh and Germany with 62% and 26 €/MWh. On the other hand, several countries have high energy import dependency, near or above 50%, but support renewable electricity generation to a lesser extent, such as Lithuania, Hungary, Finland, France and Croatia.

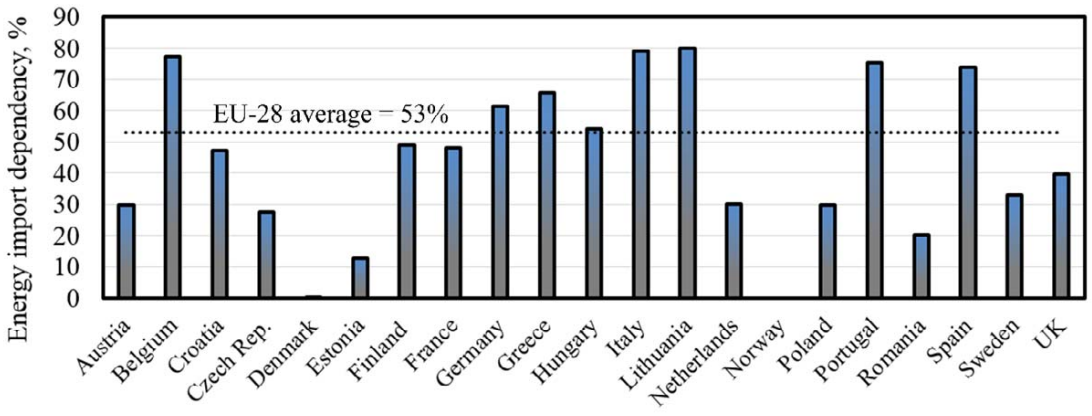

Fig. 10: Energy import dependency by country. Note: Norway is a net exporter, its energy dependency is set to 0.

4. Conclusion

Under the European energy and climate plan, Croatia agreed that the share of renewable energy in the final energy consumption should reach 20% by the end of 2020. Specific target shares have been decided for the three major energy consuming sectors: electricity, heating & cooling and transport. The target shares for renewable energy in electricity generation is 13.6% excluding large hydro or 39% including large hydro power plants. Today, excluding large hydro power plants, renewable electricity supplies 7% of the electricity consumption. If large hydro is included, the renewable electricity share is between 30 and 50%, depending on the available water resources during the year. The target shares for heating & cooling energy consumption and transport are set to 20% and 10%, respectively. At present, renewable energy represents 15% of the heating & cooling consumption and the 20% target will be most likely achieved. However, the renewable energy share in the transport sector is still negligible and the 10% target seem unreachable at the moment.

Renewable electricity is a fast growing market in Croatia. The support for renewable electricity generation will most likely continue to grow in the next 10 - 15 years. Today, the installed renewable electricity capacity is capable of supplying 7% of the electricity consumption in Croatia. The target share for renewable electricity has been set to 13.6% and the achievement of this target will require improved policy and stronger financial supports. The drawback of the fast growing renewable energy market are the increasing electricity prices in Croatia. The price of electricity is being pushed by the growing taxes for renewable electricity generation, which end consumers pay at a present rate of 5.8 €/MWh and will be paying at a rate of 20 €/MWh in 2017 and 25 €/MWh further in 2019. Inevitably, the price of electricity, which is 120 €/MWh at the moment, will grow alike. The collected funds from renewable electricity taxes are being converted into financial supports aiming to pull in new investments in the renewable sector. This renewable energy financial support, expressed in units of generated gross electricity, will grow from the present value of 8 €/MWh to around 20 or even 30 €/MWh in the next few years, whereas the EU average is 13.7 €/MWh. New renewable energy installations, especially wind farms, will need even more land to be converted to this purpose. However, the present expansion in the tourism sector opposes the expansion of renewable energy into islands and offshore areas, near seaside resorts and touristic centers.

On the other hand the solar thermal is having a slower progress. The total installed solar collector surface for water and space heating purposes was around 200.000 m^2 (140 MW_{th}) in Croatia by the end of 2015. It can be calculated that the per capita solar collector surface is 47 m^2 per 1000 inhabitants in Croatia which is only half of the EU-28 average with 85 m^2 per 1000 inhabitants. The slower progress of the solar thermal market in Croatia is mainly caused by less financial supports.

5. References

[1] REN21: Renewables 2016 Global Status Report, REN21 Secretariat, Paris, 2016
[2] REN21: Renewables 2015 Global Status Report, REN21 Secretariat, Paris, 2015
[3] REN21: Renewables 2014 Global Status Report, REN21 Secretariat, Paris, 2014
[4] Weiss, W., Mauthner, F.: Solar Heat Worldwide, Markets and Contribution to the Energy Supply 2011, IEA SHC Programme, Graz, 2013
[5] Weiss, W., Mauthner, F.: Solar Heat Worldwide, Markets and Contribution to the Energy Supply 2010, IEA SHC Programme, Graz, 2012
[6] M. Petrić: Thermodynamic analysis of a parabolic trough and spherical solar concentrators, Master thesis, Faculty of Engineering, University of Rijeka, Rijeka, 2015
[7] Ministry of Economy, Rep. of Croatia: Registry of producers of electricity from renewable energy sources and cogeneration, Zagreb, 2016
[8] Ministry of Economy, Rep. of Croatia: Energy in Croatia 2014 – Annual energy report
[9] Ministry of Economy, Rep. of Croatia: Energy in Croatia 2013 – Annual energy report
[10] Ministry of Economy, Rep. of Croatia: Energy in Croatia 2012 – Annual energy report
[11] Ministry of Economy, Rep. of Croatia: Action plan for renewable energy till 2020, Zagreb, 2013
[12] HROTE: Report on renewable electricity support fund collection and distribution, Zagreb, 2016
[13] CEER – Council of European energy regulators: Status review of renewable and energy efficiency support schemes in Europe in 2012 and 2013, Brussels, 2015

PV SITUATION IN PORTUGAL

L. Gil, G. Torres, I. Cabrita, L. Basílio, R. Costa

Direção Geral de Energia e Geologia

Summary

The situation of PV in Portugal is presented in this work, as well as statistics on the evolution of renewable energy (RE) and photovoltaic energy (PV) in Portugal in the last years. Data is also shown on the forecast of these energies for the coming years. In addition, policy measures for the use of PV are addressed, which have an impact on the larger use of PV for power generation.

Keywords: PV, Portugal, energy statistics, energy forecast, energy policy

1. Introduction

Between 2010 and 2014 the electricity consumption changed from about 24% to 25,6% of the total final energy, showing the importance of this energy resource in Portugal. So, having in mind the environmental and territorial sustainability, besides energy efficiency it is important to simultaneously increase the contribution of endogenous renewable energy sources in order to decrease Portugal's energy dependency and contribute for a competitive and low carbon economy. The NATIONAL RENEWABLE ENERGY ACTION PLAN **(**NREAP), based on the European objectives, states a target of 31% of renewable energy sources in the total energy consumption by 2020. In 2014 about 61% of the electricity generated in Portugal was based on renewable energy sources and about 27% of the gross final energy consumption was based on these resources. Solar energy is practically inexhaustible and constant, easily available in Portugal, mainly in the south, where the potential is quite considerable. Portugal is one of the European countries with better conditions for exploitation of this resource (see Fig. 1), featuring an average annual number of hours of sunshine, variable between 2200 and 3000, on the mainland (www.dgeg.pt), with an yearly global radiation from 1600 to >2100 kWh/m^2 (http://re.jrc.ec.europa.eu/pvgis/cmaps/eu_cmsaf_opt/G_opt_PT.png).

doi:10.18086/eurosun.2016.11.03 Available at http://proceedings.ises.org

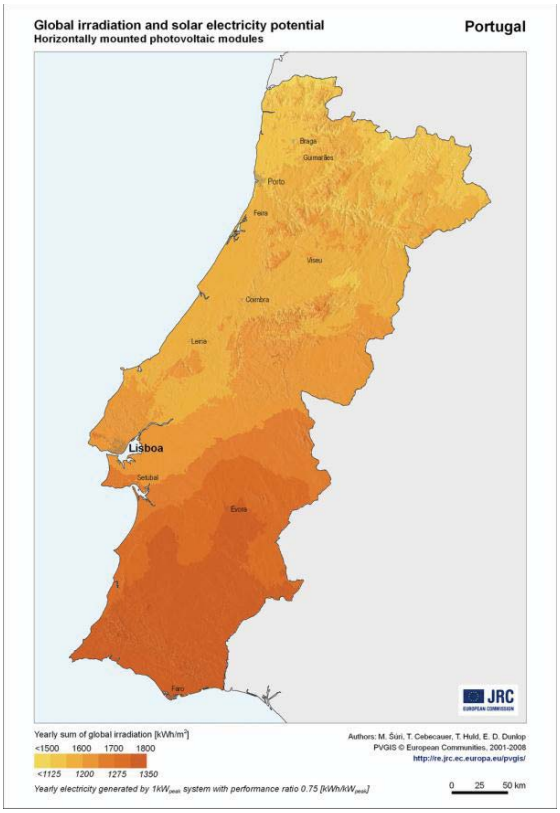

Fig. 1 – Global irradiation and solar electricity potential (re.jrc.ec.europa.eu/pvgis/cmaps/eu_cmsaf_opt/G_opt_PT.png).

2. Statistics on RE in Portugal and Europe

Data is shown (Tables 1-10, Figures 2-7) on the situation of RE in 2015 or the evolution in the last years namely: a) 2006-2015 total energy production for the different RE types; b) 2006-2015 installed capacity for the different RE types; c) distribution of installed capacity by type of RE by country region in 2014; d) 2008-2015 micro and mini-production installed capacity for the different RE types; e) 2008-2015 micro and mini-production for the different RE types; f) situation in 2005 and 2014 of total electric energy production and % of RE source in several European countries; g) situation in 2014 in several European countries of the RE production by type of RE source; h) situation in 2005 and 2014 of total electric energy production and % of RE source in several OECD countries.

Table 1 – Electricity production (GWh) in 2006-2015 (RE types).

	Electricity Production (GWh)									
	2006	2007	2008	2009	2010	2011	2012	2013	2014	2015[1]
Total Renewable production [2]	16.188	16.593	15.140	19.016	28.754	24.692	20.411	30.610	32.405	25.355
Hydro	11.467	10.449	7.298	9.009	16.547	12.114	6.660	14.868	16.412	9.761
Hydro(>30MW)	9.884	9.405	6.281	7.648	14.454	10.615	5.683	12.931	14.168	8.633
Pumped Hydro	548	422	499	724	399	578	1.038	1.138	843	1.146
Hydro (>10 e <=30 MW)	759	500	459	619	1.005	637	411	887	1.014	482
Hydro (<= 10 MW)	823	544	558	742	1.088	862	566	1.050	1.229	646
Wind	2.926	4.036	5.757	7.577	9.182	9.162	10.260	12.015	12.111	11.609
Solid Biofuels[3]	1.380	1.549	1.500	1.713	2.226	2.467	2.496	2.516	2.530	2.391
CHP	1.302	1.385	1.338	1.364	1.560	1.722	1.710	1.780	1.765	1.607
Electricity (only)	78	164	163	349	665	745	786	736	765	784
Municipal Waste	585	551	561	579	577	592	490	571	481	592
of which renewable	293	276	281	290	289	296	245	286	240	296
Biogases	33	58	71	83	100	161	210	250	278	297
Geothermal	85	201	192	184	197	210	146	197	205	204
Solar Photovoltaic	5	24	41	160	215	282	393	479	627	797

[1]provisional data

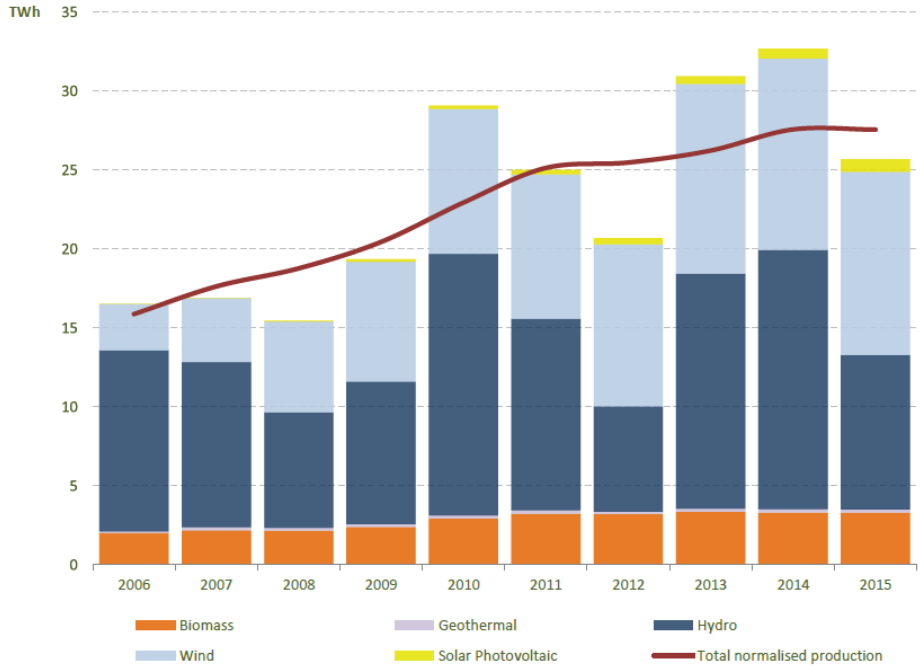

Fig. 2 - 2006-2015 total energy production for the different RE types (Portugal) (www.dgeg.pt).

The biggest changes in the several years are due to the hydro component, related with wet or dry years (rain).

Table 2 – Installed capacity (MW) by RE type for 2006-2015.

	Installed Capacity (MW)									
	2006	2007	2008	2009	2010	2011	2012	2013	2014	2015[1]
Total Renewable capacity	7.010	7.811	8.459	9.106	9.687	10.626	11.055	11.311	11.677	12.260
Hydro	4.850	4.855	4.857	4.884	4.898	5.332	5.539	5.535	5.571	6.024
Hydro (>30MW)	4.234	4.234	4.234	4.234	4.234	4.666	4.877	4.877	4.916	5.360
Hydro (>10 e ≤ 30 MW)	288	288	288	290	290	290	288	288	284	291
Hydro (≤ 10 MW)	328	333	335	361	374	377	374	370	371	372
Wind	1.699	2.464	3.058	3.564	3.914	4.378	4.531	4.731	4.953	5.013
Solid Biofuels	335	348	350	408	592	575	564	564	539	566
CHP	323	323	323	323	476	459	441	441	416	443
Electricity (only)	12	25	27	85	116	116	123	123	123	123
Municipal Waste	86	86	86	86	86	86	86	86	86	86
Biogases	8	15	16	24	34	51	62	68	81	82
Geothermal	29	29	29	29	29	29	29	29	29	29
Solar Photovoltaic	3	15	62	110	134	175	244	299	418	460

[1]provisional data

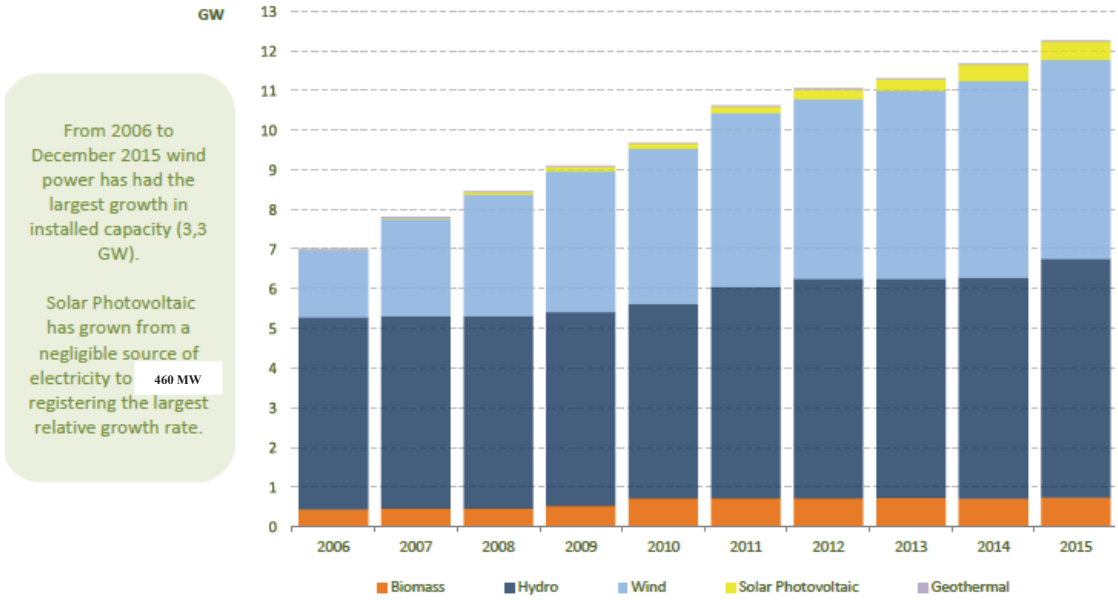

Fig. 3 - 2006-2015 installed capacity for the different RE types (Portugal) (www.dgeg.pt).

The RE installed capacity has increased constantly, namely in the solar energy case.

Table 3 – Installed capacity (MW) by country region.

	Installed Capacity by Region (MW)									
	2006	2007	2008	2009	2010	2011	2012	2013	2014	2015
Portugal	7.010	7.811	8.459	9.106	9.688	10.626	11.054	11.311	11.677	12.259
Mainland	6.886	7.687	8.330	8.954	9.521	10.429	10.863	11.109	11.467	12.038
North	3.951	4.255	4.588	4.715	4.976	5.682	5.773	5.846	5.978	6.357
Center	2.139	2.603	2.770	3.155	3.436	3.630	3.634	3.743	3.844	3.978
Lisbon	201	216	243	265	280	278	290	312	357	388
Alentejo	560	572	643	676	684	687	934	964	1.025	1.041
Algarve	35	40	86	143	145	152	232	243	264	275
Azores	46	46	50	50	50	63	62	69	69	69
Madeira	76	76	76	100	113	130	126	131	131	131
Non specified	2	2	3	2	3	4	3	3	10	22

Installed capacity distribution by technology and NUTs II in 2014

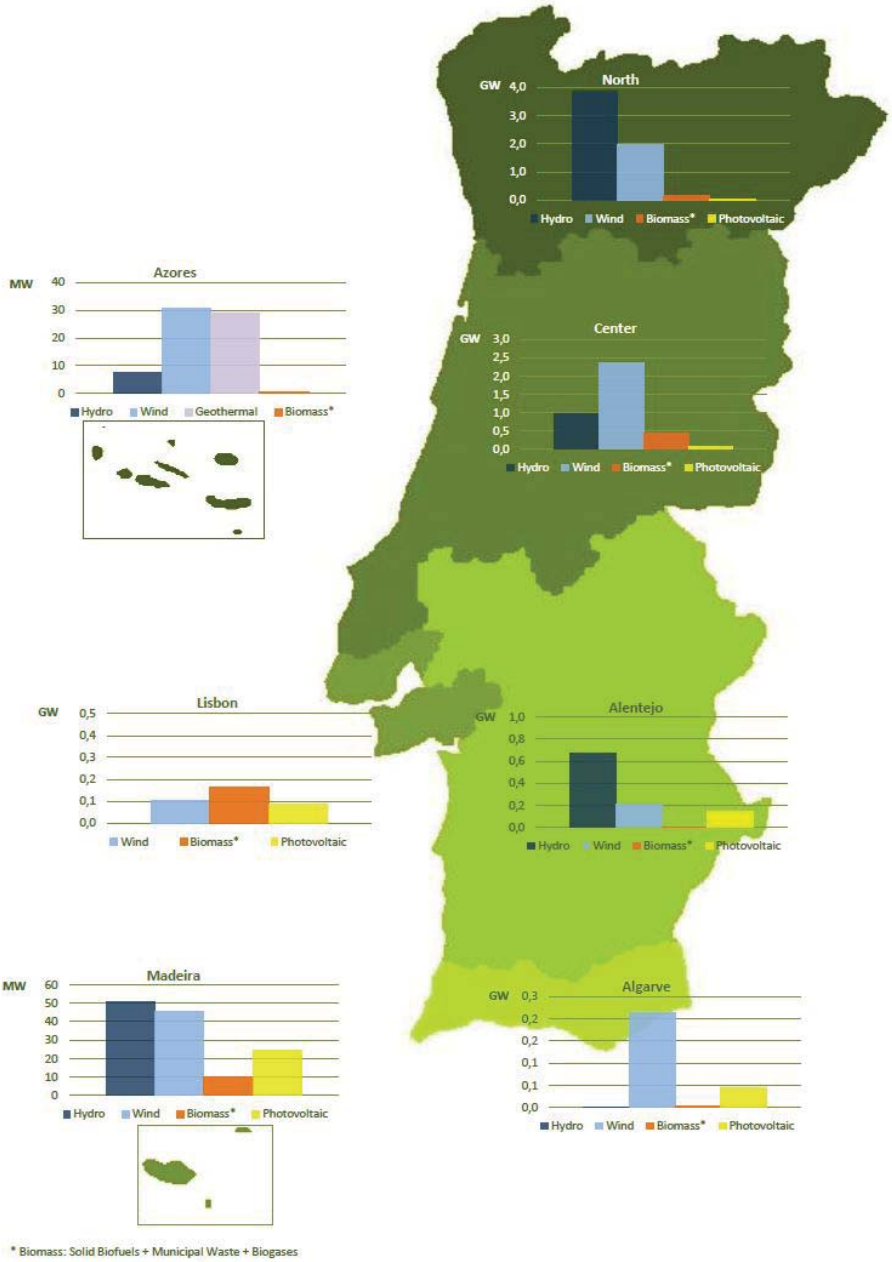

* Biomass: Solid Biofuels + Municipal Waste + Biogases

Fig. 4 - Distribution of installed capacity by type of RE by country region in 2014 (www.dgeg.pt).

Table 4 – Micro and mini-production installed capacity (kW) in 2008-2014.

	Micro/Mini Installed Capacity (kW)							
	2008	2009	2010	2011	2012	2013	2014	2015
Total Micro/Mini	10.390	27.256	35.339	65.146	105.709	138.092	163.390	174.142
Microproduction	10.390	27.256	34.692	63.536	83.338	91.899	98.156	101.533
Hydro				32	24	43	103	209
Wind				627	631	633	418	420
Solar Photovoltaic	10.390	27.256	34.692	62.877	82.683	91.223	97.635	100.904
Miniproduction			647	1.610	22.371	46.193	65.235	72.610
Hydro						20	20	20
Wind						50	60	60
Solar Photovoltaic			647	1.610	22.371	46.122	65.154	72.529
Biogases						0,7	0,7	0,7

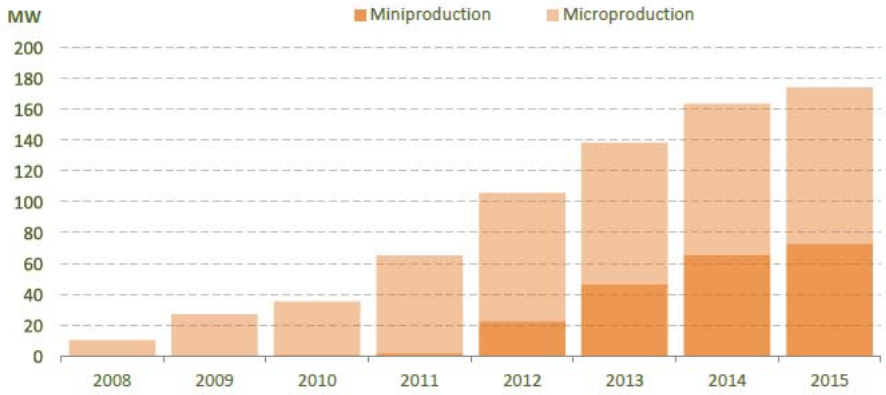

Fig. 5 - 2008-2015 micro and mini-production installed capacity (MW) for the different RE types (Portugal) (www.dgeg.pt).

Microproduction Law (Decree-Law 363/2007, of 2 November, revised by the Decree-Law 118-A/2010, of 8 October and by the Decree-Law 25/2013, of 8 March) regulates the small generation production of electricity (up to 5,75 kW) from RES. It provides for simplified licensing procedures for local grid-connected, low voltage, small/residential energy producers. The licensing of solar, wind, hydro, biomass and non-renewable CHP is conduced on-line via internet, using the System of Registration of Microgenerators (SRM). The connection capacity of a microproduction can only be up to 50% of the contracted power.

Miniproduction Law (Decree-Law 34/2011, of 8 March, revised by the Decree-Law 25/2013, of 19 February) regulates the small generation production of electricity (from 5,75 kW to 250 kW) from RES. It also provides for the same simplified licensing procedures for local grid-connected, low or medium voltage, small/commercial/industrial energy producers. The licensing of solar, wind, hydro, biomass and biomass is conduced on-line via internet, using the System of Registration of Miniproducers (SRMini). The connection capacity of a miniproduction can only be up to 50% of the contracted power and the annual consumption value of the user installation has to be at least 50% of the annual value of the generated electricity.

Table 5 - Micro and mini annual production (MWh) in 2008-2015.

	Micro/Mini Annual Production (MWh)							
	2008	2009	2010	2011	2012	2013	2014	2015[1]
Total Micro/Mini	7.120	21.215	45.047	80.176	145.088	200.103	232.271	272.355
Microproduction	7.120	21.215	44.677	78.728	131.674	148.775	148.994	164.589
Hydro				40	40	87	263	601
Wind				378	379	485	231	314
Solar Photovoltaic	7.120	21.215	44.677	78.310	131.255	148.204	148.500	163.673
Miniproduction			371	1.448	13.414	51.327	83.277	107.767
Hydro						16	61	15
Wind						5	70	94
Solar Photovoltaic			371	1.448	13.414	51.307	83.146	107.658
Biogases						1.319	2.536	2.620

[1] Provisional data.

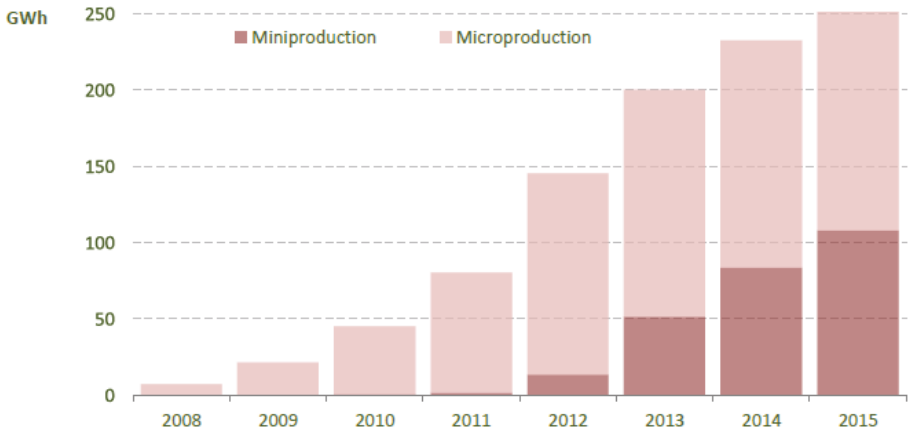

Fig. 6 - 2008-2015 micro and mini-production production for the different RE types (Portugal) (www.dgeg.pt).

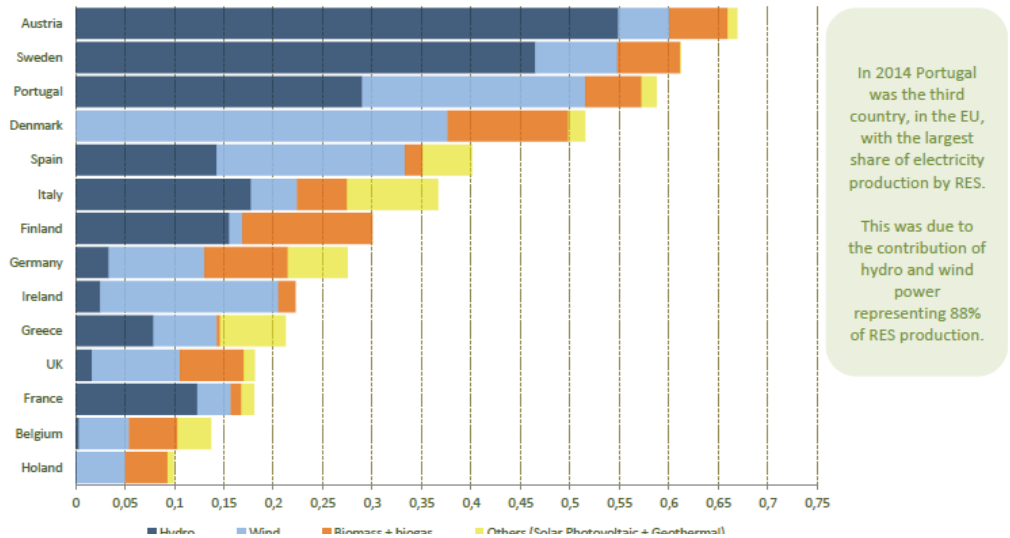

Fig. 7 - Situation in 2014 in several European countries of the RE production by type of RE source (www.dgeg.pt).

Table 6 - Situation in 2005 and 2014 of total electric energy production (TWh) and % of RE source in several European countries (www.dgeg.pt).

	Electricity production in EU countries (TWh)							
	2005			2014			Δ% 14/05	
	Total	RES	%RES	Total	RES	%RES	Total	RES
Austria	63,1	39,9	0,1%	74,7	50,0	66,9%	18,4%	25%
Sweden	159,0	80,9	0,1%	138,5	84,7	61,2%	-12,9%	5%
Portugal	53,9	15,3	0,0%	53,7	31,6	58,8%	-0,4%	106%
Denmark	36,8	9,5	0,0%	34,8	17,9	51,5%	-5,4%	89%
Spain	291,5	49,4	0,0%	274,4	109,9	40,1%	-5,9%	122%
Italy	293,6	44,1	0,0%	321,6	117,9	36,7%	9,5%	167%
Finland	70,5	22,9	0,0%	85,9	25,8	30,0%	21,8%	13%
Germany	612,1	61,8	0,0%	580,7	159,7	27,5%	-5,1%	158%
Ireland	25,7	1,9	0,0%	28,5	6,3	22,2%	10,9%	239%
Greece	59,2	5,9	0,0%	56,6	12,0	21,3%	-4,4%	103%
UK	396,6	15,0	0,0%	355,5	64,4	18,1%	-10,4%	329%
France	570,6	56,7	0,0%	495,8	89,5	18,1%	-13,1%	58%
Belgium	93,3	2,1	0,0%	90,1	12,4	13,7%	-3,4%	486%
Holand	100,2	7,5	0,0%	117,3	11,6	9,9%	17,1%	55%

Table 7 - Situation in 2005 and 2014 of total electric energy production (TWh) and % of RE source in several OECD countries (www.dgeg.pt).

	Electricity producion in other OECD countries (TWh)							
	2005			2014			Δ% 14/05	
	Total	RES	%RES	Total	RES	%RES	Total	RES
Total OECD	10.461,0	1.670,3	16,0%	10.770,3	2.354,6	21,9%	3,0%	41%
New Zealand	42,0	27,5	65,5%	43,5	34,4	79,2%	3,6%	25%
Canada	628,2	379,0	60,3%	593,0	395,8	66,7%	-5,6%	4%
Turquey	162,0	39,9	24,6%	255,5	52,0	20,4%	57,7%	30%
Mexico	233,7	37,5	16,0%	300,1	52,3	17,4%	28,4%	40%
USA	4.258,3	356,4	8,4%	4.379,1	556,6	12,7%	2,8%	56%
Japan	1.049,1	92,8	8,8%	1.025,1	148,8	14,5%	-2,3%	60%
Australia	248,2	17,3	7,0%	248,2	36,9	14,9%	0,0%	113%
Norway	126,0	136,5	108,3%	126,7	138,3	109,2%	0,6%	1%

From all this data it can be seen that in 2014 Portugal was the third European country (Sweden, Austria better) with the largest share of electricity production by RE source and that when comparing to OECD countries Portugal was only outpaced by Norway, Canada and New Zealand. In 2015, from the total electricity production in Portugal (25.355 GWh), PV (797 GWh) contributed with 3,1%.

3. Statistics on PV in Portugal

Data is shown (tables, graphics) on the situation of PV in 2015 or the evolution in the last years namely: a) number and characterization of existing PV installations; b) 2006-2015 PV total energy production by country region; c) 2006-2015 PV installed capacity by country region; d) gross PV electricity generation in several (38) European countries.

In Portugal (including Madeira and Azores), the list of photovoltaic parks account for 129, in which 63 use polycrystalline silicon technology, 19 monocrystalline silicon technology, 7 thin films, 4 amorphous silicon and 4 multi-junction (see Table 9). Besides this there exists also aggregate data in micro-production (<5.75 KW) and mini-production (5.75 kW – 250 kW). So, provisional data for 2015 are an installed capacity of about 460 MW and a produced energy of about 797 GWh, overcoming the values foreseen in NREAP which were respectively of 383 MW and 593 GWh (NREAP, Table 3, p. 2077).

Table 8 - Number and characterization of existing PV installations in Portugal in 2015.

No. installations	Polycrystaline silicon	Monocrystaline silicon	Amorphous silicon	Thin film	Multi-juntction	Unknown
129	63	19	4	7	4	32

	Production by Region (GWh)									
	2006	2007	2008	2009	2010	2011	2012	2013	2014	2015[1]
Portugal	5	24	41	160	215	282	393	479	627	797
Mainland	0	20	36	156	207	262	355	439	591	738
North	0	0	0	6	11	21	40	55	67	81
Center	0	0	0	9	16	30	51	68	97	118
Lisbon	0	0	0	5	14	19	29	43	106	159
Alentejo	0	20	36	133	162	185	206	219	247	299
Algarve	0	0	0	2	4	7	29	53	73	80
Azores	0	0	0	0	0	0	0	1	0	0
Madeira	0	0	0	0	4	19	34	37	37	43
Non specified	5	4	4	4	4	1	3	3	0	16

[1] Provisional data.

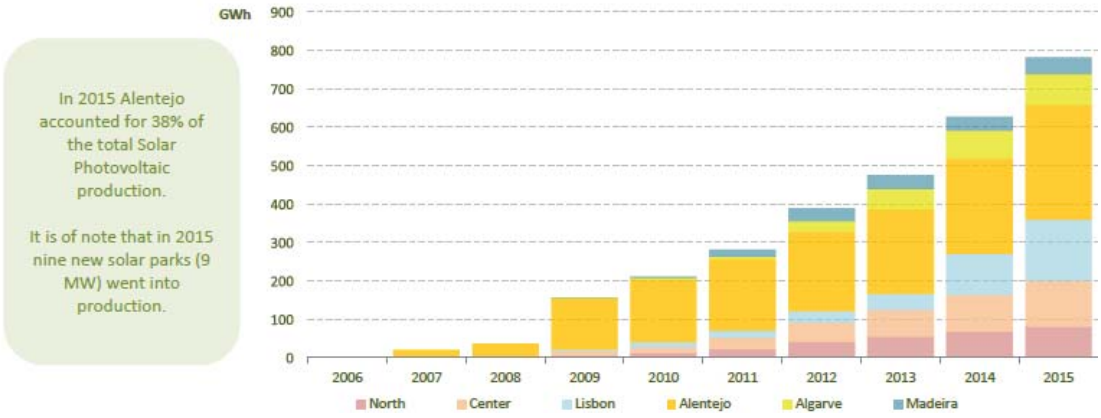

Fig. 8 – 2006-2015 PV total energy production (GWh) by country region (www.dgeg.pt).

Table 9 – 2006-2015 PV installed capacity (MW) by country region (www.dgeg.pt).

	Installed Capacity by Region (MW)									
	2006	2007	2008	2009	2010	2011	2012	2013	2014	2015
Portugal	3	15	62	110	134	175	244	299	418	460
Mainland	0	11	59	107	121	151	218	273	384	415
North	0	0	1	4	9	19	30	42	47	53
Center	0	0	1	5	12	23	36	49	65	66
Lisbon	0	0	0	8	11	16	22	44	88	91
Alentejo	0	11	57	88	86	87	103	109	140	156
Algarve	0	0	0	2	3	5	27	29	45	50
Azores	0	0	0	0	0	0	0	0	0	1
Madeira	0	0	0	1	10	21	23	24	24	24
Non specified	3	3	3	2	3	3	3	1	9	20

Table 10 – Gross PV electricity generation (GWh) in several (38) European countries (Eurostat).

COUNTRY	2005	2006	2007	2008	2009	2010	2011	2012	2013	2014
Belgium	1	2	6	42	166	560	1.169	2.148	2.644	2.883
Bulgaria	0	0	0	0	3	15	101	814	1.361	1.252
Czech Republic	0	1	2	13	89	616	2.182	2.149	2.033	2.123
Denmark	2	2	2	3	4	6	15	104	518	596
Germany	1.282	2.220	3.075	4.420	6.583	11.729	19.599	26.380	31.010	36.056
Estonia	0	0	0	0	0	0	0	0	0	0
Ireland	0	0	0	0	0	0	1	1	1	1
Greece	1	1	1	5	50	158	610	1.694	3.648	3.792
Spain	41	119	500	2.562	5.961	6.425	7.441	8.193	8.327	8.218
France	11	12	18	42	174	620	2.078	4.016	4.735	5.909
Croatia	0	0	0	0	0	0	0	2	11	35
Italy	31	35	38	193	676	1.906	10.796	18.862	21.589	22.306
Cyprus	0	1	2	3	4	7	12	22	47	84
Latvia	0	0	0	0	0	0	0	0	0	0
Lithuania	0	0	0	0	0	0	0	2	45	73
Luxembourg	18	21	21	20	20	21	26	38	74	95
Hungary	0	0	0	1	1	1	1	8	25	56
Malta	0	0	0	0	0	1	5	17	29	68
Netherlands	35	36	37	39	45	56	104	226	487	785
Austria	21	22	24	30	49	89	174	337	582	785
Poland	0	0	0	0	0	0	0	1	1	7
Portugal	3	5	24	38	160	211	280	393	479	627
Romania	0	0	0	0	0	0	1	8	420	1.616
Slovenia	0	0	0	1	4	13	65	163	215	257
Slovakia	0	0	0	0	0	17	397	424	588	597
Finland	3	3	4	4	4	5	5	6	6	8
Sweden	2	2	3	4	7	9	11	19	35	47
United Kingdom	8	11	14	17	20	41	244	1.352	1.989	4.050
Iceland	0	0	0	0	0	0	0	0	0	0
Norway	0	0	0	0	0	0	0	0	0	0
Montenegro	0	0	0	0	0	0	0	0	0	0
Macedonia	0	0	0	0	0	0	1	3	9	14
Albania	0	0	0	0	0	0	0	0	0	0
Serbia	0	0	0	0	0	0	0	0	0	6
Turkey	0	0	0	0	0	0	0	0	0	17
Kosovo	0	0	0	0	0	0	0	0	0	0
Moldova	0	0	0	0	0	0	0	0	0	1
Ukraine	0	0	0	0	0	1	30	333	570	429

From the previous data it can be seen that solar photovoltaic installed capacity has grown from very small numbers to 460 MW, registering the largest relative low rate, comparing to other renewable energy sources. In the 10 year period of 2006-2015, PV energy production grew from 5 GWh to 797 Gwh, with an average growth near to 80 GWh/year. In the period of 2008-2015 micro PV installed capacity raised from 10.390 kW to 100904 kW (about 10 times more), a value over the foreseen for 2020 (see next item) and only in 6 years (2010-2015) mini PV installed capacity raised from 647kW to 72529 kW (about 112 times more), a value representing 29% of what is foreseen for 2020 (see next item).The micro/mini production represents about 34% of the total PV production. Only in 2015 ten new solar parks went into production. In this year Alentejo (south of Portugal) accounted for 38% of the total solar photovoltaic production. Comparing with other 38 European countries Portugal is the 13th PV electricity producer.

4. RE/PV Programmes/Policies

The NREAP is defined by the Council of Ministers' Resolution nº 20/2013, published in the Republic Diary, 1st Series, Nº70 from 10th of April 2013. This official document foresees, that the contribution of PV for 2020

is 670 MW of installed capacity and 1039 GWh of produced energy, respectively. Solar energy is expected to have an important role in the increase of decentralized power production; the production cycle is adequate to the consumption peaks, and also because has great resources availability and also R&D capacity.

The Decree-Law 363/2007 of November 2nd and the Decree-Law 34/2011 of March 8th regulate the production and selling of electricity by micro and mini power plants, respectively. Another Decree-Law (nº153/2014 of October 20th) is also related with this. So, besides the micro-production program continuation, in 2011 a mini-production was set having as aim the installation of 250 MW until 2020, mainly for services and industry. The enlargement of mini-production to larger capacities in face of demand and technology evolution can be considered. Aiming also at more 80 MW of installation capacity by 2020 in micro-production the two support programs may be fused.

5. Conclusion

In the last 10 years PV power production per year grew from only 5 GWh to about 800 GWh with the installed capacity in the same period changing from 3 MW to about 460 MW. From 2010 to 2015, PV mini and micro-production raised from only 35 MW to more than 173 MW, almost five times more. PV infrastructures are mainly placed in the south of the country where the solar potential is greater. The provisional data for 2015 for PV show that the installed capacity was about 20% higher (achieving 69% of 2020 value) ant the produced energy was about 34% higher (achieving 77% of 2020 value) than what was foreseen in the NREAP, demonstrating that national policies in this field are correct.

6. References

Decree-Law 363/2007, Diário da República, 1ª série, Nº 211, 2 novembro 2007

Decree-Law 34/2011, Diário da República, 1ª série, Nº 47, 8 março 2011

Huld T., Müller R., Gambardella A., 2012. A new solar radiation database for estimating PV performance in Europe and Africa. Solar Energy, 86, 1803-1815

NATIONAL RENEWABLE ENERGY ACTION PLAN (PNAER), Diário da República, 1ª Série, Nº70, 10 abril 2013

re.jrc.ec.europa.eu/pvgis/cmaps/eu_cmsaf_opt/G_opt_PT.png

Šúri M., et al., 2007. Potential of solar electricity generation in the European Union member states and candidate countries. Solar Energy, 81, 1295–1305

www.dgeg.pt

Conference Proceedings

EuroSun 2016

Palma de Mallorca (Spain), 11 – 14 October 2016

The Forecast of the World Renewable Energy Development till 2020

Sergey M. Karabanov[1], Pavel P. Bezrukikh[2] and Pavel P. Bezrukikh (Jr.)[3]

[1] Ryazan State Radio Engineering University, Ryazan (Russia)

[2] G.M. Krzhizhanovsky Power Engineering Institute JSC, Moscow (Russia)

[3] LUCOIL JSC, Moscow (Russia)

Abstract

There are quite a lot of forecasts of renewable energy development in whole and its different kinds. The principal forecasts are developed by IEA, BP, IRENA, EWEA, WWEA, ISEA and some other institutions. Many of forecasts prefer a remote prospect – years 2030, 2035, and 2050. Probably it is assumed that the forecast for 2020 will be achievable with great probability. However, famous programs experience of "Wind Force-10" and "Wind Force-12" in which the problem of achieving a wind power share in the world overall electricity production by 2020, respectively 10% and 12%, was set, means that such forecast is too optimistic as already now it is clear that these results are unachievable. On the other hand, IEA forecasts concerning renewable energy share in 2020 in world electricity production are considered to be too pessimistic. The realization of the forecast offered by the authors seems to be the most probable.

Keywords: *forecast, program, renewable energy sources, electricity production*

1. Introduction

The main goal of the paper is to define the share of renewable energy sources in the world overall electricity production in 2020. For this purpose it is necessary to define the following by the end of 2020: the general electricity production in the world; the installed capacity of power plants on the basis of different kinds of renewable energy sources and the produced electric power; growth rates of installed capacity of various renewable energy plants. The forecasting procedure combines the analysis of the growth rates of capacity and energy for the previous period with the research of installed capacity utilization factor of power plants based on different kinds, taking into account forecasts of growth of use of different kinds of renewable energy sources.

2. Analysis of forecasts for renewable energy utilization

According to REN-21 data concerning the installed capacity of wind, PV, biomass and geothermal power plants during the period of 2004-2014 the average annual growth rate is calculated for the whole period and in 2014 in relation to 2013 [1].

According to IEA statistics on electricity production by renewable energy power plants and data of REN-21 on installed capacity the installed capacity utilization factors for the above power plants are calculated.

Ehe installed capacity utilization factors aor wind power for 24 countries for the period of 2000-2013 were determined. On the basis of the obtained data analysis the growth rates of installed capacity and electricity production for 2015-2020 according to three scenarios of overall electricity production were justified.

According to scenarios offered by the authors the share of renewable energy by 2020 will be: minimum – 9.3%; average – 11.2%; maximum – 13.4%.

doi:10.18086/eurosun.2016.11.06 Available at http://proceedings.ises.org

According to IEA (2011) the share of renewable energy will be: "New Policies Scenario" – 8.4%; "Current Policies Scenario" – 7.2%; "450 Scenario" – 10.1%.

The forecasts discrepancy is quite considerable. Below are the reasons for the optimistic forecast.

According to the optimistic forecast of wind power development made in 1997 by "Wind Force-10" program the purpose was to achieve a share of 10% of wind energy of general electricity production by 2020 (Table 1). We monitored the forecast realization within more than 10 years and the obtained result is contradictory. Until 2010 the forecast of the wind energy installed capacity was overfulfilled. But as for the energy share produced at these stations significant underrun was observed. Obviously, the installed capacity utilization factor (ICUF) was taken into account not exactly. The forecast did not indicate the data for 2011 – 2014, but the ICUF in 2015 (433 GW) shows that in 2015 the forecast indicator for the capacity (573 GW) was not fulfilled. It can be stated that the forecast of annual rate and capacity utilization factor was unnecessarily optimistic.

Tab. 1: Wind Force-10 Program (The source: «Wind Force 10» Program, *EWEA, *WWEA. Developers: EWEA, Denmark Energy and Development Forum, International Greenpeace, 1998)

Years	Annual growth, %	Annual capacity, MW	Total installed capacity by the end of the year, MW		Annual electricity production at wind power station, TWh		Annual electric energy consumption in the world, TWh		Share of wind power, %	
	Forecast	Actual	Forecast	Actual *	Forecast	Actual	Forecast	Actual	Forecast	Actual
1999	20	3120	13273	13520	29.1		14919	14764	0,19	
2000	20	3744	17017	18449	37.3	31.3	15381	15379	0,24	
2001	20	4493	21510	23794	47.1		15858	15476	0,30	
2002	20	5391	26901	30278	58.9		16350		0,36	
2003	20	6470	33371	39357	73.1		16857	16661	0,43	
2004	30	8411	41781	46880	91.5		17379	17450	0,53	
2005	30	10939	52715	59084	115.4	103.8	17918	18235	0,64	0,54
2006	30	14214	66929	74223	146.6	124.9	18474	18930	0,79	0,66
2007	30	18478	85407	94123	187.0	173.3	19046	19854	0,98	0,87
2008	30	24021	109428	121188	268.4	266	19937		1,37	
2009	30	31228	140656	157899	245.0		20245		1,70	
2010	30	40596	181252	196692	444.6	341	20873	21559	2,13	1,6
2014				370000						
2015	20	94304	537059	433000	1333.8		23894		5,58	
2020	10	150000	1209466		2966.6		27351		10,86	
2030	10	150000	2545232		6242.9		33178		18,82	
2040	10	150000	3017017		7928.7		38509		20,60	

In 2011 the International Energy Agency released the forecast for electrical energy production in the world, including renewable energy, until 2030 according to 3 scenarios. Table 2 shows the forecast data for 2020.

"New Policies Scenario" – is the central scenario combining a wide range of political obligations and plans of countries all over the world in the field of energy security, climate changes, environmental conservation, etc.

"Current Policies Scenario" – development with conservation, without changing the existing policy including obligations and plans.

"450 Scenario" provides aggressive schedule of actions necessary for limiting long-term increase of greenhouse gases concentration in the earth atmosphere up to 450 ppm of CO_2 equivalent.

Tab. 2: International Energy Agency scenarios, 2011

	Actual data				"New Policies Scenario"		"Current Policies Scenario"		"450 Scenario"	
	1990		2009		2020		2020		2020	
	bln. kWh	%	bln. kWh	%	bln. kWh	%	bln. kWh	%	bln. kWh	%
Fossil fuels	7490	63.4	13445	67.1	17593	63.1	18757	65.7	15835	59.0
Nuclear power	2013	17.0	2697	13.5	3576	12.8	3495	12.2	3741	13.9
Hydropower	2144	18.1	3252	16.2	4380	15.7	4254	14.9	4547	16.9
Renewable energy	173	1.5	650	3.2	2332	8.4	2063	7.2	2712	10.1
Renewable energy, including hydropower	2317	19.6	3902	19.5	6712	24.1	6317	22.1	7259	27.1
Whole world	11819	100.0	20043	100.0	27881	100.0	28569	100.0	26835	100.0

According to the scenarios the electric energy production in 2020 is to be 27881 – 28569 – 26835 bln. kWh, the share of renewable energy: 8.4 – 7.2 – 10.1%, accordingly.

This forecast is unduly pessimistic as it contradicts the actual status of the world energy balance. According to REN 21.2016 the share of organic fuel in the energy balance for electric energy production is 59.3%, nuclear power stations - 17% (total – 76.3%), renewables – 23.7%. The share of hydropower plants is 16.4%, "new" renewable energy power stations – 7.3%, including wind power stations - – 3.7%, biofuel power plants – 2.0%, PV power plants – 1.2%, the rest renewables – 0.4%.

The question is: what renewable energy share in the electric energy production is the most obvious?

To answer this question it is necessary to give proof of the electric energy production forecast in the world and also the forecast of growth of capacity utilization factor and electric energy production on the basis of some renewable energy sources.

3. Main results

The forecast of the word electric energy production for 2020 was made on the basis of the analysis of growth rates of electric energy production for the period of 1995 – 2014 (Table 3) taking into account a general slowdown in global economic growth. The average annual growth rate for the period of 1995 – 2014 was 3.07%; for the period of 2004-2014 – 3.0%; 2012-2014 – 2.0%, 2014 in relation to 2013 – 1.52%.

Taking into account the above data three scenarios have been accepted:

a) "Hardly probable" with the growth rate of 3.0%;

b) "Possible" with the growth rate of 2.6%;

c) "Probable" with the growth rate of 2.0%.

The comparison of the forecasts of the International Energy Agency (IEA) and Power Engineering Institute (PEI), Russia, shows high matching degree of the data for electric energy production for 2020 with the only difference that the "Probable scenario" (c) of PEI coincides with the least probable "450 Scenario" of IEA (Table 4).

To estimate the growth rate of the electric energy production on the basis of some renewable energy sources the data of REN21 (Renewable Energy Policy Network for the 21st Century) for 2016, 2015 and 2014 was used. Table 5 shows the growth rate of the installed capacity for the period 2004 – 2014, (2004 ÷ 2015) and in 2014 in relation to 2013, in 2015 in relation to 2014 for all renewable energy sources [1].

Tab. 3: World electric energy production, TWh (Source: BP Statistical Review of World Energy Workbook)

1995	1996	1997	1998	1999	2000	2001	2002	2003	2004
13258.3	13686.9	14010.6	14360.3	14776.9	15409.0	15641.1	16191.6	16787.7	17573.3
2005	**2006**	**2007**	**2008**	**2009**	**2010**	**2011**	**2012**	**2013**	**2014**
18333.8	19032.4	19926.9	20308.6	20131.7	21425.5	22100.6	22630.4	23184.0	23536.5

Tab. 4: Forecasts of the world electric energy production, TWh

IEA		PEI		Forecasts discrepancy, %
"New Policies Scenario"	27881	Possible	27866 (b)	0.05
"Current Policies Scenario"	28569	Hardly probable	28656 (a)	0.3
"450 Scenario"	26535	Probable	26764 (c)	0.8

Tab. 5: The dynamics of the world renewable energy characteristics

Characteristic	**Annual values**			**Annual average growth rate for 2004-2014/ 2004-2015, %**	**Increase in 2014 to 2013/ in 2015 to 2014, %**
	2004	**2014**	**2015**		
New annual investments, bln. USD	45	273	285.9	19.62/18.34	16.37/4.7
Renewable energy capacity (without hydropower stations), GW	85	665	785	22.7/22.39	17.32/18.04
Renewable energy capacity (with hydropower stations), GW	800	1701	1849	7.9/7.9	8.49/8.7
Hydropower capacity (hydropower stations), GW	715	1036	1064	3.7/3.7	3.63/2.7
Biomass capacity, GW	<36	101	106	9.95/10.31	5.68/4.95
Biomass electric energy production, TWh	227	429	464	6.67/6.71	9.34/8.16
Geothermal stations capacity, GW	8.9	12.9	13.2	3.7/3.5	5.78/2.32
PV stations capacity, GW	2.6	177	227	52.5/50.1	28.26/28.25
Thermodynamic PV stations capacity, GW	0.4	4.3	4.8	27.1/25.34	29.41/11.63
Wind power stations capacity, GW	48	370	433	22.65/22.13	15.99/17.03
PV heat water systems capacity, GW (heat)	86	409	435	16.79/15.88	8.85/6.36
Ethanol annual production, bln. l	28.5	94.5	98.3	12.67/11.91	7.06/4.02
Biodiesel annual production, bln. l	2,4	30.4	30.1	28.6/24.85	12.93/-1.0
Number of countries with specified goals for renewables	48	164	173	13.07/12.52	13.89/5.49

Taking into account that with the increase of installed capacity the annual average growth rate inevitably slows down and considering the growth rates slowing down in 2014, for the forecasts for 2015 and 2020 quite moderate growth rates have been accepted.

To determine the electric energy production it was necessary to define the installed capacity utilization factor (ICUF) for all renewable energy sources.

According to the analysis the most complicated thing is to determine the ICUF for wind power stations. The calculations of ICUF of wind power stations on installed capacity of first 24 countries for the period of 2000-2013 (2012) according to World Wind Energy Association (WWEA) data on installed capacity of IEA have

been made. On the basis of this data the ICUF of a wind power station was accepted to be equal to 0.25; for a PV station – 0.12-0.13; for a geothermal station – 0.75.

Table 6 shows the forecast of ICUF and electric energy produced by renewable energy sources by 2015. This forecast was made in 2013 and the degree of its matching with the reality turned out to be quite high (In brackets the actual capacity in 2015 is indicated.)

Tab. 6: Forecast for renewable energy sources development for 2015

Power station type	2010 (actual)			2015 (forecast)		
	Capacity, GW	ICUF	Electric energy production, TWh	Capacity, GW	ICUF	Electric energy production, TWh
Wind power stations	198	0.197	341	429 (433)	0.25	939
PV stations	40	0.12	42	230 (227)	0.12	242
Solar thermal power stations	1.1	0.15	1,4	5 (4.8)	0.15	6.5
Biomass power stations	64.9	0.55	313	98 (106)	0.53	456
Geothermal stations	11	0.75	72.3	13.5 (13.2)	0.75	88.5
Total	315		769.7	775.5 (785)		1728

Tab. 7: Forecast of the world renewable energy development until 2020 (without hydropower stations)

Power station type	2020			
	Annual average growth,%, 2020/2015	Capacity, GW	ICUF	Electric energy production, TWh
Wind power stations	10	690	0.25	1511
	13	790		1730
	15	863		1890
PV stations	15	462	0.13	526
	20	572		651
	25	702		799
Solar thermal power stations	10	8	0.15	10,5
	12	8,8		11,5
	15	10		13
Biomass power stations	3	113	0.53	524
	5	125		580
	10	158		733
Geothermal stations	3	16	0.75	105
	5	17		112
	10	22		144
Total		1289		2676
		1513		3084
		1755		3579

The forecast for electric energy production on the basis of renewable energy sources is shown for three values of annual average growth rate. For each renewable energy source the accepted growth rates were considerably lower than in 2014 (Table 7).

The estimation of renewable energy share with three options of development forecasts of electric energy production by all power stations and three options of electric energy production by renewable energy stations becomes a multiple-option task.

The estimation of renewable energy share according to the average values has been made. The average value of the world energy production according to three options is equal to 27768 TWh. The average value of the renewable energy production according to three options is equal to 3113 TWh. Therefore, the renewable energy share in the total electric energy production (without hydropower stations) will be 11.2 %.

Maximum renewable energy share corresponds to the largest value of renewable energy production (3579 TWh) and to the minimum value of the total electric energy production (26764 TWh) and is equal to 13.4%.

The minimum renewable energy value corresponds to the inverse ratio, 2676 TWh and 28656 TWh, respectively, and is equal to 9.3%.

The wind energy share in the total electric energy production is: 5.3 % (minimum), 6.1 % (average) and 7% (maximum). Table 8 provides the comparison with the IEA forecast.

Tab.8: Renewable energy share in the world total electric energy production in 2020 (in brackets – the wind share forecast)

	Minimum, %	Average, %	Maximum, %
PEI	9.3 (5.3)	11.2 (6.1)	13.4 (7.0)
IEA	7.2	8.4	10.1

4. Discussion

The present paper considers the renewable energy development in the near future. This process is affected by many different factors. The research confirms that in spite of obstacles the renewable energy will develop with the rates exceeding the growth rates of the world economy and traditional energy.

The significance of the performed investigation is determined by the role the renewable energy will play in the world policy and economy. This role is defined by the following factors:

- possibility to provide energy independence or considerable decrease of fuel import dependence;
- possibility (for developed countries) to win the market of high-technology equipment, to provide the diversification activity of a country industrial complex;
- inexhaustibility of renewable energy sources and impossibility of their privatization or capture by other countries (unlike oil or gas fields);
- ecological cleanness.

5. Conclusion

The average annual growth rate of installed capacity of wind, PV and other renewable energy power stations as compared with the previous year is determined. For the period of 2015-2020 the growth rates will be: for wind power stations – 13-15%, PV stations – 15-25 %, biofuel power stations – 3-10%, geothermal power stations – 3-10 %.

For all types of renewable energy power plants the installed capacity utilization factors are defined. The coefficient for the weighted average value of wind power stations will amount to 0.25, PV stations – 0.13, biofuel power stations – 0.53, geothermal power stations – 0.75.

The forecast of installed capacity and produced electricity for 2015 and 2020 for all main renewable energy power stations is made.

It is shown that overall installed capacity of renewable energy power stations in the world will be about 1500 GW, including wind, PV and biomass power stations, respectively, 800 GW, 570 GW and 125 GW.

By 2020 the electricity production at renewable energy power stations will be approximately 3000 TWh.

6. References

[1]. REN21. Renewable Energy Policy Network of the 21st Century. Renewables. Global Status Report. 2004-2016.

[2]. Pavel Bezrukikh, Pavel Bezrukikh (Jr), On Energy Indicators and the Role of Renewable Energy under Economic Crisis. Jour. "Voprosy Economiki", 2014, no. 8, pp 92-106.

[3]. Photovoltaics Report, Fraunhofer Institute for Solar Energy Systems, ISE, with support of PSE AG, Freiburg, 11 March 2016.

Conference Proceedings

EuroSun 2016
Palma de Mallorca (Spain), 11-14 October 2016

Roadmaps for Energy (R4E): How to foster the sustainable energy transition of communities

Torsten Masseck[1], Elke den Ouden[2] and Rianne Valkenburg[2]

[1] Universitat Politècnica de Catalunya (UPC), Sant Cugat del Vallès (Spain)

[2] TU/e Lighthouse, Eindhoven (Netherlands)

Abstract

The sustainable energy transition of communities is one of the main targets within the European energy policies. Consistent energy planning is needed but conditioned by difficulties of city administrations to meet the necessary skills and have the necessary knowledge in order to lead the corresponding transition processes. R4E develops roadmapping capacities of 8 European partner cities (Eindhoven, Forlì, Istanbul, Newcastle upon Tyne, Murcia, Palermo, Sant Cugat de Vallès and Tallinn) together with their local stakeholders, and provides them with the necessary knowledge about innovative energy solutions in the fields of smart buildings, smart mobility and smart urban spaces.

A specific systemic approach to these future energy solutions has been developed, based on so-called Systemic Solutions Maps and Technology Outlooks, in order to strengthen the capacities of the participating stakeholders in designing detailed roadmaps and developing together with the city authorities specific project portfolios.

Keywords: *Sustainable energy transition, Roadmapping, renewable energies, Systemic Solution Maps, participatory processes*

1. Background

Sustainable Energy Transition of society refers to long-term process which transforms radically the exiting energetic reality of a society, mobilizing diverse groups of stakeholders. (Verbong & Rotmans 2012)

Transition management has evolved during the last years offering a structured approach to the complex societal problems and difficult governance related to transition processes. (Loorbach & Rotmans 2010) These processes include generating a long term orientation where to head to as society, for instance through the use of scenarios or roadmaps, but also include leaving options open, dealing with uncertainties.

Transition processes can be organized best in so-called transition management cycles. (Loorbach & Rotmans 2010) and renewable energy communities (RECs) can be drivers of these energy transitions as communities which invest in the production of renewable energy with the aim to cover their own energy needs. (Dóci et al. 2015)

The R4E project (www.roadmapsforenergy.eu) responds to the EE-07-2014 call entitled "Enhancing the capacity of public authorities to plan and implement sustainable energy policies and measures" within the Secure, Clean and Efficient Energy Work Program of HORIZON 2020 of the European Commission. The main challenge of the partners within R4E is to develop visioning and roadmapping capacities within municipalities to initiate joint activities to spur development and implementation of innovative energy solutions in cities.

The implementation of strategies and plans on municipal level suffers from the effects of the recent global economic and financial crisis, the shifting of competences and responsibilities between government levels, difficulties within organizations to meet the necessary, and changing, skills and capacities; and a lack of

Selection and/or peer review under responsibility of Scientific Committee
doi:10.18086/eurosun.2016.11.07 Available at http://proceedings.ises.org

knowledge on the state of the art concerning technological and organizational innovation. This leads to imperfect implementation processes and loss of faith in the usefulness of strategies and action plans.

In order to overcome these barriers, R4E established the following objectives:

- Creating high quality visions and roadmaps that drive collaboration between municipalities, entrepreneurs, knowledge institutes and citizens to achieve longer term ambitious goals through short term decisions and actions
- Implementing with all partners a similar participative process for vision and roadmap development that enables continuous cross-city learning exchange of experiences, challenges and best practices.
- Building an ecosystem of relevant local parties in each city, laying the foundation for extended collaboration between partners to drive innovation for sustainability purposes, through joint projects, e.g. joint pre-commercial procurement projects.

This ambitious approach requires new processes and tools in order to foster understanding, communication and informed, shared decision-making among stakeholders.

2. Introduction

Our western societies are recently experiencing a strong shift towards participation of citizens and all type of interest groups in participatory, multi stakeholder processes, with the aim to find consensus among individual interests regarding societal changes and challenges, especially in the field of transition towards sustainability.

In the technological field so-called user-centered research has been developed in order to capture user insights or user behavior regarding innovations with the aim of shortening product-to-market periods and gaining higher security regarding user adoption and market success of a product or service. New infrastructures and processes have been developed like e.g. Living Labs and Open Innovation strategies.

Similar processes are increasingly taking place in the area of governance and decision making within municipalities, where citizens, entrepreneurs, academics and local entities as “users”, are expected to contribute to collective innovation and decision making processes.

Similar to the questionable role of users as actors in the field of innovation (lack of experts knowledge, lack of motivation for continuity, IP rights and exploitation of results) the capacity of individual stakeholders has to be questioned in overviewing the whole process e.g. of the current transformation processes of cities towards more sustainable energy models. These processes are highly complex and open ended, including technological developments and changes, legislation, governance, societal changes and social innovations, linked to individual as well as collective value discussions and behavior changes regarding our lifestyle.

The R4E project therefor takes a different approach to current energy strategies and plans, developing so-called “Energy Roadmaps”. The unique feature of the Roadmaps approach is that the process of development takes successful implementation through partnership and through an in-depth knowledge of the state of the art, now and in the near future, as a starting point. This approach is based on:

- An ongoing learning process among all stakeholders, acquiring the necessary technical and systemic knowledge of complex transition processes.
- Better communication among all participants, experts, politicians, researchers, entrepreneurs and citizens through a common language and trust building collective processes.
- More consistent and consented outcomes, which increase decisively the possibilities for a successful implementation of resulting action plans.

R4E offers a new strategy for complex transition processes of society towards a sustainable energy future, fostering within participatory processes the knowledge generation and improvement of the diverse stakeholder groups regarding renewable energy technologies, and a systemic view of energy in buildings and the urban context in general.

3. Methodology

R4E applies a specific 4-step process for the project itself, a specific 4-step structure for its desk studies as supporting documents for participatory stakeholder processes, and a specific approach for the learning and communication process of stakeholders through *Systemic Solution Maps* within the desk studies, in order to graphically represent the complexity of any energy-related transition process.

3.1 The 4-step R4E process

The R4E partner cities run through a 4-step R4E process (Figure 1), starting with the *Ambition setting* (step 1), and a *Vision development* and scenario building process (step 2) in order to discuss, define and describe a common desired future for their city with the participation of all type of local stakeholders such as citizens as well as relevant research and industry partners. In a third step partners develop *Energy Roadmaps* as the result of a cooperative process engaging, as in all previous steps, key stakeholders within the region from the business and knowledge sectors.

This results finally in the development of a specific *Project portfolio* (step 4) and well-developed implementation plans supported through a strong commitment of all participants. Figure 2 shows the general R4E approach in four steps.

Fig. 1: 4-step R4E process

The R4E process allows ideally engaging partners and stakeholder groups in a continuous process over 3 years and beyond, creating a strong collaboration based on trust and integration among all participants.

3.2 Desk Study structure

In order to support the participatory processes of the R4E project in generating consistent roadmaps for energy and solid implementation plans, desk studies about the state of the art of energy technologies and related sustainability concepts and solutions are facilitated to the participant cities.

These desk studies include the following 4-step approach in order to structure knowledge and give consistent future outlooks on technologies related to smart energy strategies of cities (Figure 2).

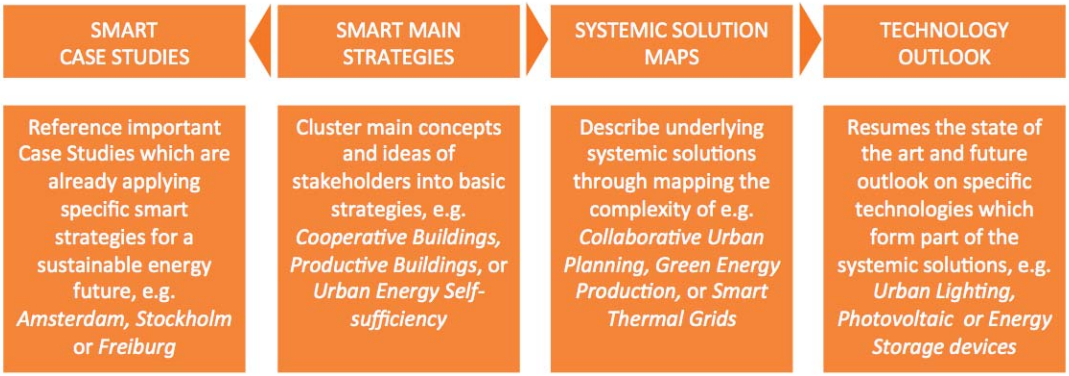

Fig. 2: R4E Desk study structure

After describing and further defining the *Smart Main Strategies* of the partner cities, based on the developed visions and scenarios for their energy future with horizon 2050, so called *Systemic Solutions Maps* are developed in order to represent graphically the complexity of each strategy and its interrelation with diverse concepts and technologies.

A third step consist in specific *Technology Outlooks* about technologies that have been mapped within the *Systemic Solutions Maps,* documenting their current state of the art, their specific challenges and their future perspectives.

In a fourth step *Case Studies* are referenced to the different Systemic Solutions in order to showcase light house projects of urban energy transition, which already apply specific smart strategies or smart technologies for a sustainable energy future.

This desk study structure allows all partners to generate and improve their knowledge in fields like e.g. the energetic refurbishment of existing buildings, or the establishment of smart energy grids with a high amount of distributed renewable energy sources, among many others, gaining a holistic and systemic vision of each strategy. The specific feature of *Systemic Solutions Maps* furthermore allows to be used as individual or collective tool for understanding complexity and interrelations among different strategies and technologies.

3.3 Systemic Solution Maps

Systemic Solution Maps are introduced as comprehensive representation of the inherent complexity of almost any strategy towards a reduced energy demand and a higher degree of sustainability on building level as well as on urban scale.

Systemic Solution Maps (Figure 3) are the connecting elements, which allow setting into the right relation the basic *Smart Main Strategies* for a sustainable energy future and the existing and developing energy technologies as well as related technological solutions described through the *Technology Outlook* section.

The systemic approach allows to map visually the interrelation of different parameters for a specific approach, e.g, in the field of material flows, water consumption or renewable energy generation, facilitating the understanding of the complexity of each specific field of action, the interrelation of technical, organizational and social aspects, as well as the corresponding developing technological solutions, which allow to transport this current representation of complexity into a vision of a possible future.

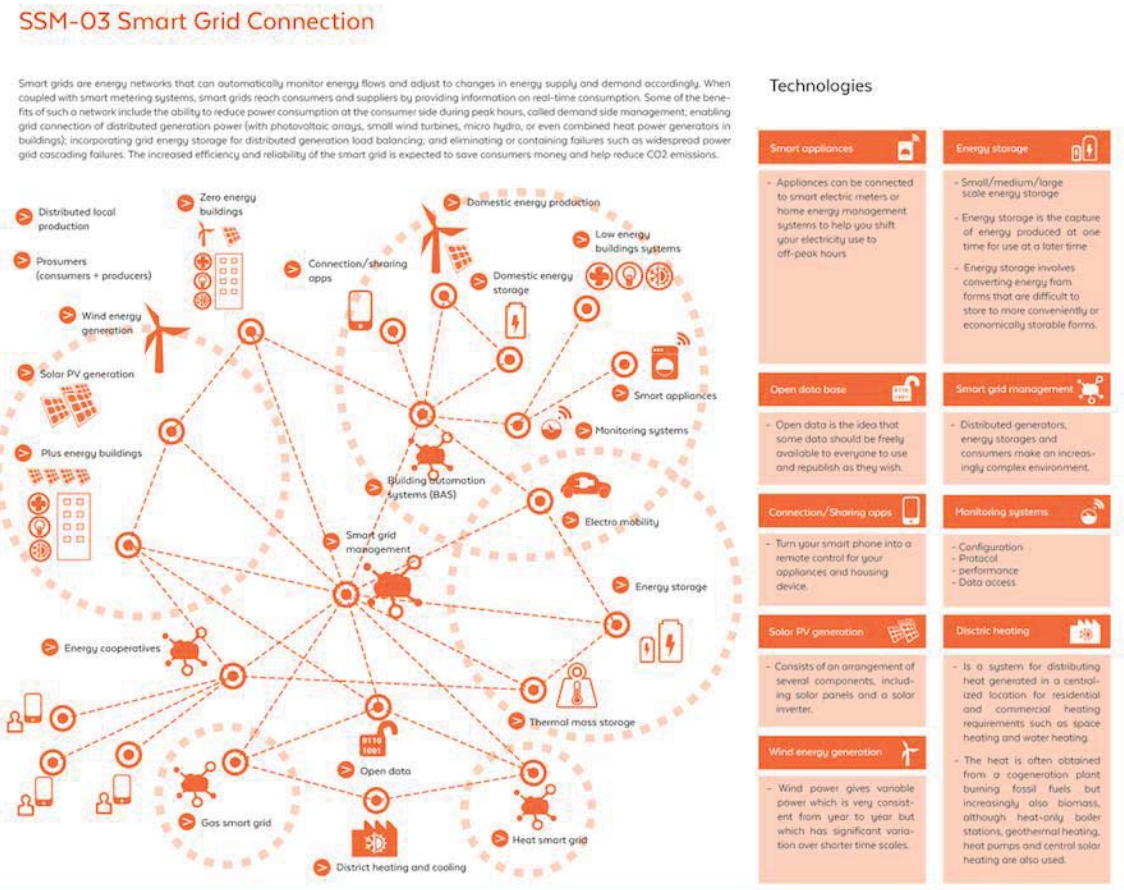

Fig. 3: General Structure of *Systemic Solution Maps*

Stakeholders may read and reflect individually on these *System Solution Maps*, may use them in their discussions and participatory processes as a tool, or even might adapt or further develop them according to their city specific social-economical, climatic, cultural and environmental background.

4. Results

The R4E project has just concluded its second step, *Vision development*, within the overall 4-step process. Desk studies have been almost terminated and will be handed out to partners during October 2016.

A total of 18 *Systemic Solutions Maps* have been developed in the fields of *Smart Buildings* and *Smart Urban Spaces* in order to map the complexity of different and diverse approaches like *Interactive Flexible Space Use, Collaborative Urban Planning*, *Communal Urban Farming, Thermal Smart Grids, Material Accounting Systems*, or *Health and Home Services* in the field or *Smart Urban Spaces*, and concepts like *Shared Use Management, Green Energy production, Smart Retrofitting Solutions, Waste Management, Building Water Management* or *Low Embodied Energy* among others in the field of *Smart Buildings*. Furthermore 50 *Technology Outlooks* have been elaborated resuming the state-of-the art and future potential of mapped technologies.

First *System Solution Maps* and *Technology Outlooks* have been presented to the city partners at the joint *Vision Building Workshop* in Istanbul in May 2016, obtaining valuable input from city representatives regarding the readability of the maps, their usefulness as tools in participatory processes, and most specially about missing or under represented issues, which should be included within the maps, e.g. stronger references to urban resilience strategies or a stronger focus on the complexity of historic buildings within the city context.

This stakeholder feedback has allowed to introduce changes and to improve the documents for their use as supporting tools in the following third step of the R4E process, the city specific *Roadmapping Workshops* from November 2016 on.

Desk studies and the applied methodology of *Systemic Solution Maps* and *Technology Outlooks* will than have to proof that they are useful tools for multi stakeholder processes, and that the applied mapping of complexities and relationships will result in a useful identification of potential synergies and even innovations.

This might contribute to the overall results to be expected of the R4E project after its successful conclusion:

- The empowerment of public authorities to develop, finance and implement ambitious sustainable energy policies and plans in order to implement efficiently recent and future European Energy Directives
- The introduction of a significant number of public officers and stakeholders in a new way of working, necessary for successful development and implementation of such plans
- The development of ambitious but effective and realistic policies and plans with an important impact on the behavior of final consumers

5. Conclusions

The sustainable energy transition of communities requires multi-stakeholder processes, which should be based on a high level of shared knowledge about related concepts, energy technologies and developments in the present and the near future in order to allow the successful collaboration of all important members of a community. The presented overall R4E process, with its desk studies as supporting documents and the specifically developed concept of *Systemic Solutions Maps* and related *Technology Outlooks* may contribute to this important knowledge generation and show their usefulness as tools for multi stakeholder processes towards a sustainable energy transition of cities.

Acknowledgements

The R4E project received funding from the European Union's Horizon 2020 research and innovation program under grant agreement Nº 649397. A special recognition must be given to Alfonso Godoy, Mariana Palumbo and Laia Nuñez Pinart for their collaboration in the project and the development of the corresponding methodologies and contents.

References

Dóci, G., Vasileiadou, E., & Petersen, A. C., 2015. Exploring the transition potential of renewable energy communities. *Futures*, *66*, 85–95. http://doi.org/10.1016/j.futures.2015.01.002

Loorbach, D., & Rotmans, J., 2010. The practice of transition management: Examples and lessons from four distinct cases. *Futures*, *42*(3), 237–246. http://doi.org/10.1016/j.futures.2009.11.009

Verbong G. & D. Loorbach, D. Introduction, *Governing the energy transition. Reality, illusion or necessity*, Routledge, New York (2012), pp. 1–23

Conference Proceedings

EuroSun 2016
Palma de Mallorca (Spain), 11 - 14 October 2016

Evolution of solar forecasting in India: The introduction of REMCs

Indradip Mitra[1], Sunil Sharma[1], Mandeep Kaur[1], Aravindakshan Ramanan[1], Markus Wypior[1], Detlev Heinemann[2]

[1]GIZ GmbH, New Delhi (India)

[2] Energy Meteorology Group, University of Oldenburg, Oldenburg (Germany)

Abstract

With increasing solar PV installed capacity in India, forecasting of its generation is gaining importance. In India forecasting for renewable energy has been recently operationalized. Two kinds of forecasting needs to be done, one for the individual plants for scheduling and accounting actions and the other for entire grid control area for grid operation. Day ahead forecasting with 15 minute resolution, 16 times intra-day revision, was made mandatory as a consequence along with several sets of rules and mechanisms introduced by the Central as well as State level authorities. One innovative development is the concept of Renewable Energy Management Centers which would be co-located with existing load dispatch centers and take care about forecasting along with a few other activities. After establishment of REMC it is assumed that environment for improved grid integration of renewables would be created.

Key Words: *Forecasting of solar power; Grid integration of solar energy; Renewable Energy Management Centre.*

1. Introduction

1.1. Need for solar power forecasting in India

As of August 2016, the total installed generation capacity is India is 304.76 GW (CEA, 2016). The RES contributes to 14 % of the total installed capacity (shown in Fig 1). The Wind energy installed capacity is 27.15 GW. The contributions of different renewable energy sources are shown in Fig 2.

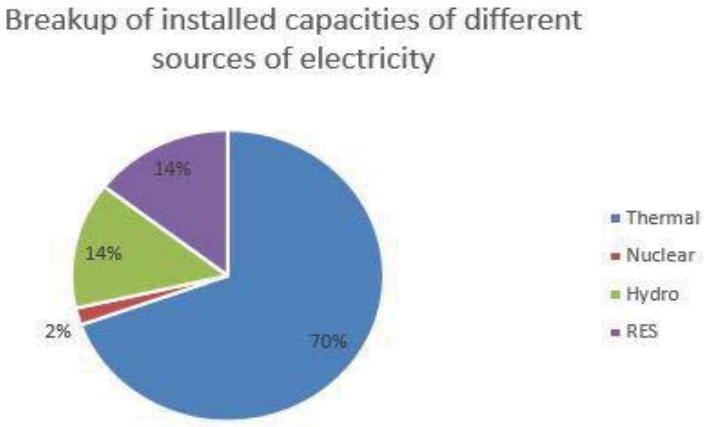

Fig. 1: The breakup of installed capacities of different electricity sources (CEA, 2016)

doi:10.18086/eurosun.2016.11.05 Available at http://proceedings.ises.org

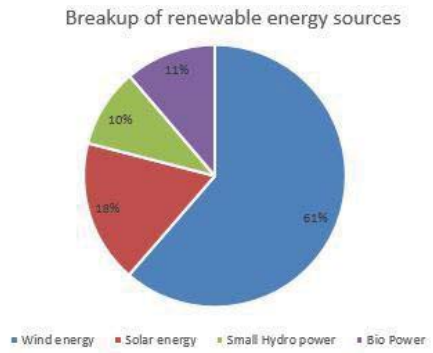

Fig.2: The breakup of installed capacities of different renewable energy sources (CEA, 2016)

In the recent years, there has been a steep increase in the solar power installations in India. Solar PV installed capacity is 8.1 GW as of August 2016. There has been an 80 % increase in the installed capacity of solar PV generations sources over the past 12 months (Economic Times, 2016). Govt. of India of also has a renewable energy installation target of 175 GW until 2022. This includes a target of installed capacity of 100 GW for solar energy, 60 GW for wind energy, 10 GW of bio energy and 5 GW for small hydro. There is a 40 GW target in roof top solar segment among the overall solar energy target (NITI Aayog, 2015). The state wise target of solar PV and wind generation installed capacities of the different states in India as per Ministry of New and Renewable Energy (MNRE) is given in Table 1 (MNRE, 2015).

The grid operators in many renewable energy rich states of India are finding it difficult to manage the grid. The absence of forecasting is hindering their operations. In year 2013, two to three billion units generated from wind were curtailed, mainly due to absence of forecasting (IWTMA, 2015). In India, primary and secondary controls are not fully operational. Therefore accurate control area wide renewable energy forecasting would go a long way for grid operators to effectively manage the grid. Accurate Forecasting by the grid operators would mitigate the actual requirement of primary, secondary and tertiary reserves.

It is also important that individual RE power plants forecasts the generation output of their power plants. This would enable them to provide accurate schedules to system operators. They can also earn better revenue by trading their electricity effectively in power exchanges.

Because of the reasons stated above, there has been a lot of developments in regulatory and institutional framework in the concept of solar power forecasting. Different important govt. institutions namely Central Electricity Regulatory Commission (CERC), State Electricity Regulatory Commission, Power System Operation Corporation (POSOCO), Load Dispatch Centres (LDC), etc. have actively worked to evolve solutions in the in the recent past. This paper has details regarding the different interesting developments in this regard.

Tab. 1: Tentative breakup of targeted installed capacity of solar PV for different states in India (MNRE, 2015)

State / UTs	Solar Power (MW)	Wind Power (MW)
Delhi	2762	
Haryana	4142	
Himachal Pradesh	776	
Jammu & Kashmir	1155	
Punjab	4772	
Rajasthan	5762	8600
Utter Pradesh	10697	
Uttrakhand	900	
Chandigarh	153	
Northern Region	**31120**	**8600**
Goa	358	
Gujarat	8020	8800
Chhattisgarh	1783	

Madhya Pradesh	5675	6200
Maharashtra	11926	7600
D. & N. Haveli	449	
Daman & Diu	199	
Western Region	**28410**	**22600**
Andhra Pradesh	9834	8100
Telangana		2000
Karnataka	5697	6200
Kerala	1870	
Tamil Nadu	8884	11900
Puducherry	246	
Southern Region	**26531**	**28200**
Bihar	2493	
Jharkhand	1995	
Orissa	2377	
West Bengal	5336	
Sikkim	36	
Eastern Region	**12237**	
Assam	663	
Manipur	105	
Meghalaya	161	
Nagaland	61	
Tripura	105	
Arunachal Pradesh	39	
Mizoram	72	
North Eastern Region	**1205**	
Andaman & Nicobar Islands	27	
Lakshadweep	4	
Other (New States)		600
All India	**99533**	**60000**

2. Discussion

2.1. Structure of Load Dispatch Centers

India's power grid is synchronously connected and the operating frequency is 50 Hz. India's electrical grid is divided into five regions, in each where there is a Regional Load Dispatch Centre (RLDC) located. Each state in India constitutes a control area, where there is a State load dispatch centre (SLDC) located. SLDC is responsible for real time operations for grid control and does optimum scheduling and dispatch of electricity within the state (CERC, 2010). The RLDC exercises supervision over SLDCs in its region and is responsible for maintaining stability of grid operations, economy and efficiency of operation in the electrical region (CERC, 2010). The National load dispatch centre (NLDC) is hierarchal above RLDC. It is responsible for monitoring operations and security of national grid. NLDC is also responsible for supervision and control over inter-regional links (CERC, 2010).

2.2. Regulatory Interventions in RE Forecasting

As indicated in section 1.1, forecasting of generation is important in the perspective of grid operators and individual RE generators. Therefore CERC, SERC and FOR have taken this into cognizance and number of regulations have been drafted. Forecasting by SLDC have been suggested to be mandatory in order to maintain the grid security (APERC, 2016; FOR, 2015; JSERC, 2016; KERC, 2015; RERC, 2016; TNERC 2016). IEGC 3rd amendment mandates RLDCs to perform forecasting (CERC, 2015b). There is a huge motivation for grid operators to perform forecasting taking into consideration its importance in grid operations. Control area wide forecasting of the cumulative RE generation would be important functionality

through the establishment of REMC's. Other kind of usages of forecasting for grid operators are congestion forecast, ramp forecast, reactive power forecast, etc.

There has been a lot of developments with respect to regulatory interventions in generation forecasting for individual wind and solar PV power plants. This has been detailed in the following section.

2.2.1 Regulatory interventions in RE forecasting for individual solar PV power plants

In India, forecasting of RE generation was conceptualised in Indian Electricity Grid Code, 2010 through the Renewable Regulatory Fund (RRF) mechanism. Forecasting was made mandatory for wind energy projects greater than 10 MW and solar energy projects greater than 5 MW (CERC, 2010). There were not any commercial implications related to accuracy of forecasting produced by solar energy projects. Owing to implementation issues, RRF mechanism was not operationalised. Central Electricity Regulator Commission (CERC) released draft regulations regarding forecasting on 31st March 2015 (CERC, 2015a) as well as corresponding draft amendments to grid code and deviation settlement mechanism. After taking public opinion into considerations, amendments to grid code and Deviation Settlement Mechanism, 2015 was finalised (CERC, 2015b, 2015c). In November 2015, Forum of Regulators (FOR) announced model regulations on RE forecasting and scheduling applicable to projects feeding power within the state boundaries (FOR, 2015). Following similar lines, states of Karnataka, Tamil Nadu, Orissa, Rajasthan, Jharkhand and Andhra Pradesh came up with their draft regulations for RE generation forecasting and scheduling applicable at intra-state level (APERC, 2016; JSERC, 2016; KERC, 2015; RERC, 2016; TNERC, 2016). After receiving public comments, Karnataka Electricity Regulatory Commission (KERC) notified the regulation on forecasting. In different regulations, 16 revisions in the schedule are allowed for RE projects on intra-day basis. The above clause encourages RE power projects to perform intra-day forecasting of generation. The regulations related to forecasting are compared in Tab 2.

Tab. 2. Detailed inter comparison of different regulations related to forecasting in India (APERC 2016; CERC, 2010, 2014, 2015b, 2015c; FOR, 2015; JSERC, 2016; KERC, 2016; RERC, 2016; TNERC, 2016)

PARAMETERS / REGULATIONS	CERC Dated 7.8.2015 DSM 2nd amendment and IEGC 3rd amendment	Forum of Regulators Dated x.x.2015	Karnataka Electricity Regulatory Commission (KERC) Dated 31.05.2016	Madhya Pradesh Electricity Regulatory Commission (MPERC) Dated 08.12.2015	Tamil Nadu Electricity Regulatory Commission (TNERC) Dated x.x.2016	Rajasthan Electricity Regulatory Commission (RERC) Dated x.02.2016	Jharkhand Electricity Regulatory Commission Dated x.x.2015	Andhra Pradesh Electricity Regulatory Commission Dated 06.09.2016
Applicability	All wind/ solar generators which are regional entities.	All wind/ solar generators connected to the state grid including those connected via pooling stations, and selling power within or outside the state.	All wind and solar generators above threshold collective capacity at the pooling station selling power within or outside the state.	All wind and solar generators connected to the state grid including those connected via pooling stations, and selling power within or outside the state	All wind and solar generators connected to the state grid, including those connected via pooling stations, and selling power within the state.	All wind and solar generators above threshold collective capacity at the pooling station selling power within or outside the state	All wind/ solar generators connected to the state grid including those connected via pooling stations, and selling power within or outside the state.	All wind/ solar generators connected to the state grid including those connected via pooling stations, and selling power within or outside the state.
Threshold Collective Capacity	50 MW and above	NA	≥ 10 MW for wind generators ≥ 5 MW for solar generators MW	NA	NA	5 MW and above	NA	NA
Data Requirement from RE Generators	Turbine availability, power output and real-time weather measurements (wind speed, temperature, pressure etc.)	Technical specifications, data relating to power system output & parameters and weather related data to the concerned SLDC in real time.	Technical specifications, data relating to power system output & parameters and weather related data to the concerned SLDC in real time.	Technical specifications, data relating to power system output & parameters and weather related data to the concerned SLDC in real time.	Technical specifications, data relating to power system output & parameters and weather related data to the concerned SLDC in real time.	Technical specifications, data relating to power system output & parameters and weather related data to the concerned SLDC in real time.	Technical specifications, data relating to power system output & parameters and weather related data to the concerned SLDC in real time.	Technical specifications, data relating to power system output & parameters and weather related data to the concerned SLDC in real time.
Who Should do forecast	RLDC as well as wind/ solar generator.	Solar/ Wind Generator or QCA on their behalf should do forecasting for the purpose of scheduling. SLDC should also do forecasting for ensuring secure grid operations.	Solar/ Wind Generators or QCA/ Aggregator on their behalf should do forecast for the purpose of scheduling. Or services from REMC could be taken. SLDC should also do forecasting for ensuring secure grid operations.	Solar/ Wind Generator or QCA on their behalf should do forecasting for the purpose of scheduling. SLDC should also do forecasting for ensuring secure grid operations.	Solar/ Wind Generator or QCA on their behalf should do forecasting for the purpose of scheduling. SLDC should also do forecasting for ensuring secure grid operations.	Solar/ Wind Generator or QCA on their behalf should do forecasting for the purpose of scheduling. SLDC should also do forecasting for ensuring secure grid operations.	Solar/ Wind Generator or QCA on their behalf should do forecasting for the purpose of scheduling. SLDC should also do forecasting for ensuring secure grid operations.	Solar/ Wind Generator or QCA on their behalf should do forecasting for the purpose of scheduling. SLDC should also do forecasting for ensuring secure grid operations.
Frequency of schedules	Day ahead	Day ahead and week ahead schedule	A week ahead, day ahead and intraday	Day ahead and week ahead schedule	Day ahead and week ahead schedule	Day ahead and week ahead schedule	Day ahead and week ahead schedule	Week ahead, day ahead and intra-day schedule.

PARAMETERS / REGULATIONS	CERC Dated 7.8.2015 DSM 2nd amendment and IEGC 3rd amendment	Forum of Regulators Dated x.x.2015	Karnataka Electricity Regulatory Commission (KERC) Dated 31.05.2016	Madhya Pradesh Electricity Regulatory Commission (MPERC) Dated 08.12.2015	Tamil Nadu Electricity Regulatory Commission (TNERC) Dated x.x.2016	Rajasthan Electricity Regulatory Commission (RERC) Dated x.02.2016	Jharkhand Electricity Regulatory Commission Dated x.x.2015	Andhra Pradesh Electricity Regulatory Commission Dated 06.09.2016
Revisions Allowed	Max 16 revisions are effective from 4th time block starting from 00:00 hours of a particular day.	Max 16 revisions are effective from 4th time block starting from 00:00 hours of a particular day.	Max 16 revisions are effective from 4th time block starting from 00:00 hours of a particular day.	Max 16 revisions are effective from 4th time block starting from 00:00 hours of a particular day.	Max 16 revisions are effective from 4th time block starting from 00:00 hours of a particular day.	Max 16 revisions are effective from 4th time block starting from 00:00 hours of a particular day.	Max 16 revisions are effective from 4th time block starting from 00:00 hours of a particular day..	Max 16 revisions are effective from 4th time block starting from 00:00 hours of a particular day..
Normalised Error Definition	$Error(\%) = \frac{(AG-SG)}{AvC}[1] x100$	$Error(\%) = \frac{(AG-SG)*100}{AvC}$	$Error(\%) = \frac{(AG-SG)*100}{AvC}$	$Error(\%) = \frac{(AG-SG)*100}{AvC}$	$Error(\%) = \frac{(AG-SG)*100}{AvC}$	$Error(\%) = \frac{(AG-SG)*100}{AvC}$	$Error(\%) = \frac{(AG-SG)*100}{AvC}$	$Error(\%) = \frac{(AG-SG)*100}{AvC}$
Tolerance band	± 15% applicable for both wind/ solar generators	Generators selling power within state can deviate upto ±15 % (prior) and ±10 % (after) this regulation Generators selling power outside state can deviate up to ±10 %	± 15 %	Generators selling power within state can deviate upto ±15 % (prior) and ±10 % (after) this regulation Generators selling power outside state can deviate up to ±10 %	10% for wind and 5% for solar generators	± 15 %	Generators selling power within state can deviate upto ±15 % (prior) and ±10 % (after) this regulation Generators selling power outside state can deviate up to ±10 %	Generators selling power within state can deviate upto ±15 % (connected prior to regulations) and ±10 % (connected after this regulation) Generators selling power outside state can deviate up to ±10 %.

2.3. Infrastructure to support the activity of solar power forecasting

2.3.1. Solar Radiation Resource Assessment (SRRA) stations

As an intermediate step in the prediction of solar PV power output, Global Horizontal Irradiance (GHI) is predicted through the run of Numerical Weather Prediction (NWP) models. Ground measured value of GHI is really important to fine tune the predicted output. This step is called post-processing. It would help in eliminating the statistical bias.

Solar Radiation Resource Assessment (SRRA) project of MNRE is an important initiative that has a huge relevance in solar PV power forecasting as explained above. MNRE initiated the SRRA project and implemented it through National Institute of Wind Energy in 2010. GIZ provided technical assistance to the project. SRRA stations were setup in 121 locations across India. It is world's largest network of solar radiation resource assessment stations setup all over the country. It measures GHI, DHI, DNI along with other environmental parameters like ambient temperature, relative humidity, atmospheric pressure, wind speed and wind direction. The different parameters are measured every second and averaged over one minute interval. Secondary standard pyrheliometers are employed for measuring DNI. First class pyranometers are employed for measuring GHI and DHI. In every station, there are two pyranometers and one pyrheliometer. The measured data is stored in the Central Receiving System (CRS) established at NIWE. Four of the measurement stations are certified by Baseline Surface Radiation Network (BSRN).

2.4 Proposed infrastructure for aggregated Solar PV power forecasting

On advice of MNRE, Forum of Regulators (FOR) and CERC, Power Grid Corporation of India Limited (PGCIL) initiated a study to identify the transmission and control infrastructure up-gradation required for integrating renewables in the 12th five year plan of government of India. The Capital expenditure requirements and strategy framework for funding the same was analysed as well. Concept of Renewable Energy Management Centres (REMC) to effectively manage the intermittency and variability of resources was proposed (PGCIL, 2012). Total cost of six billion Euros was identified as the requirement to enhance the transmission and control infrastructure. The transmission lines that is being constructed under this project would evacuate power from renewable rich states to load centres. In India, this is the first project, in which transmission lines are being built on the basis of available renewable energy resource potential. Government

[1] AvC = Available Capacity for wind or solar generators means the cumulative capacity rating of the wind turbines or solar inverters that are capable of generating power in a given time-block;
AG = Actual Generation
SG = Scheduled Generation
Time–block; means a time block of 15 minutes, for which specified electrical parameters and quantities are recorded by special energy meter, with first time block starting at 00.00 hrs

of Germany through Kreditanstalt für Wiederaufbau (KfW Bank) had sanctioned concessional loans upto 1 billion Euros. The technical assistance is provided through Deutsche Gesellschaft für Internationale Zusammenarbeit (GIZ) GmbH. GIZ did studies in the areas of forecasting of renewable energy, balancing, improved market mechanisms, ancillary services, grid code, automatic generation control, etc that would help Indian govt achieve the huge targets for renewable energy. GIZ worked with the consortium of Ernst & Young, University of Oldenburg, Fraunhofer IWES, Ficthner to perform the different studies. Detailed Project Reports (DPR) were submitted for REMCs to be established in India. By September 2016, applications for tender for the REMCs to be established at Tamil Nadu, Andhra Pradesh, Karnataka and Southern Regional Load Dispatch Centre (SRLDC) were released by PGCIL (PGCIL, 2016). Tender applications for REMCs to be established at other SLDCs and RLDCs are expected to follow soon.

Indian Meteorological Department (IMD) and National Centre for Medium Range Weather Forecasting (NCMRWF) are the govt. owned weather services of the country. They have capabilities in running numerical weather prediction models and have shown interest in supporting the initiative of renewable energy forecasting in India.

2.4.1 Renewable Energy Management Centres

The REMCs are envisaged to be co-located with the already existing load dispatch centres at seven renewable rich states. They would also be co-located with RLDCs at southern, western, northern region and NLDC. Ministry of Power will bear the cost of 11 REMC control centre development (SCADA System including maintenance, Forecasting & Scheduling Tool / Software, Wind and Solar generation forecasting services for first 4 years, Servers, other control centre equipment). The location of 11 upcoming REMCs are shown in the Fig 5.

Fig 5: The locations of envisaged REMCs.

From the tender specifications released for REMC for southern region, certain features are explained in this paper. The schematic of REMC architecture is shown in Fig 6.

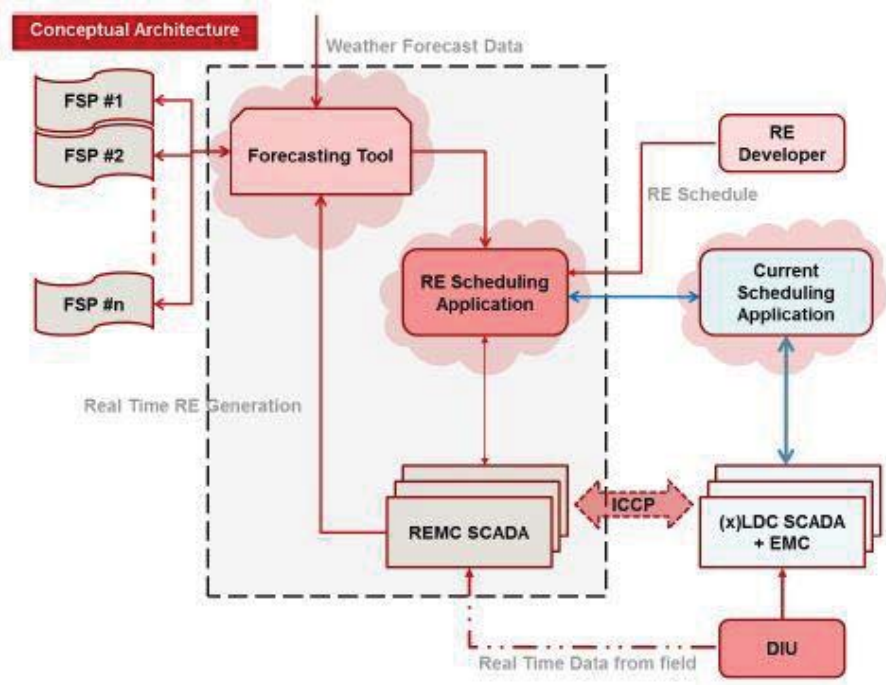

Fig.6: Schematic architecture of REMC (PGCIL, 2016)

The major functionalities of REMCs are the following:

- Real time RE generation Data Acquisition and Monitoring.
- Provide RE data to its partner xLDC, forecasting and scheduling applications.
- Forecasting of RE generation.
- Data Archiving and Retrieval.
- Providing RE information to its concerned xLDC for dispatching and balancing RE power.
- Central Repository for RE generation data that will be used by the concerned xLDC for Management Information System (MIS) and commercial settlement purposes.
- Coordination agency on behalf of xLDC for interacting with RE Developers.
- Developing future readiness for advanced functions such as Virtual Power Plants, Storage etc.

2.4.1.1. Forecasting tool

The schematic of the forecasting tool is depicted in Fig 7. The external Forecast Service Providers (FSPs) provide week ahead, day ahead and intra-day forecasts for wind and solar PV generation at pooling sub-station level as well as aggregated forecasts at state level. The forecasts are provided for intra-day, day ahead and upto week ahead time resolution. It would provide forecasts in 15 mins resolution for day ahead and intra-day forecasts and hourly resolution for week ahead forecasts. The forecast provided by the tool would assist SLDC personnel in scheduling the conventional generation, estimation of control reserves and load flow calculation. Historical SCADA data from STU pooling stations, available real time RE generation data from STU pooling station and static information about wind and solar power projects would be shared with the FSPs by the REMCs (PGCIL, 2016). It is crucial information for performing RE generation forecast.

The forecast combination and aggregation tool combines the external and internal forecasts in an optimal fashion using auto adaptive algorithms. The different FSPs and internal forecasting tool is expected to have strengths and weaknesses according to different weather situations. Therefore historical performance of the forecasts for the different weather conditions would be taken into account while arriving at combined forecasts. Through suitable upscaling technique, aggregated forecasts for the pooling stations and whole state are derived.

Internal forecasting tool produces forecasts for the different time resolutions in parallel to external FSPs. It is fully automatic and runs on an auto adaptive algorithm. It does not require operator's interaction. Static data,

historic SCADA data, real time generation data are to be provided to the internal forecasting tool. The algorithms would be tuned based on the forecasts and real time generation data. A service provider who provides weather forecast data is contracted for a period of four years to provide input to this tool.

Three external FSPs are contracted for the first two years to provide wind and solar generation forecasts. The two best performing FSPs would be retained for the subsequent two years. The contract for FSPs could be extended for further two years (beyond the serviced four years) at the same terms and conditions as per mutual agreement. The FSPs performance is continuously monitored. Normalised Root Mean Squared Error (NRMSE) is the metric according to which FSPs performance is monitored. RMSE is normalised with available generation capacity in each time block (PGCIL, 2016). The financial reward to FSPs would depend on the accuracy of the forecasts provided by them. During first year of operation, there is no financial implication as it is considered as the stabilisation period. From the second year, payment to the FSPs would be based on the following:

- Provide 100 % of payment if error (NRMSE) of the control area wide RE generation forecast is less than 7 %.
- Provide 90 % of payment if error (NRMSE) of the control area wide RE generation forecast is between 7 % and 9 %.
- Provide 80 % of payment if error (NRMSE) of the control area wide RE generation forecast is between 9 % and 11 %.
- Provide 70 % of payment if error (NRMSE) of the control area wide RE generation forecast is greater than 11 %.

If there is a slump in performance of WSP impacting the power forecast of the internal forecasting tool, then it could potentially be replaced without any additional financial implications.

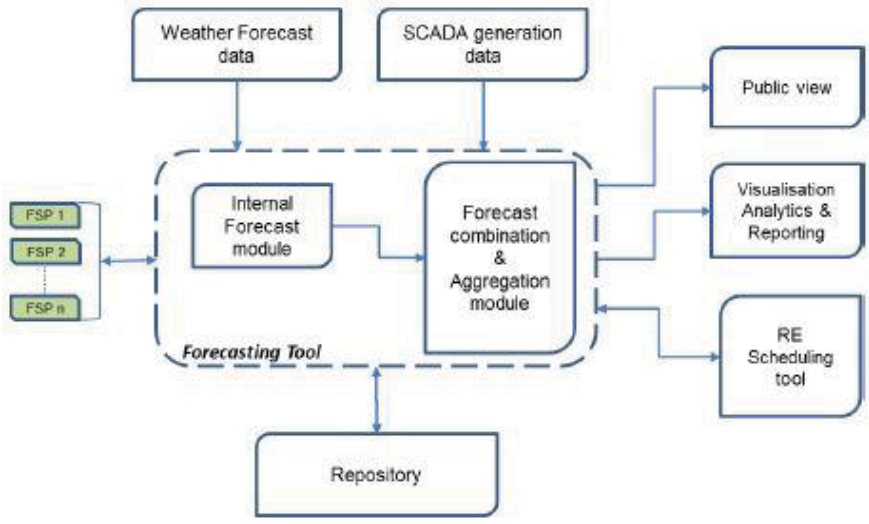

Fig.7: The schematic architecture of forecasting tool (PGCIL, 2016)

2.4.1.2. Scheduling Tool

The main functionality of the tool is collection of the proposed schedules from the RE generators. The individual RE power projects could upload the schedules into the system using web based system. The tool has the ability for bidirectional data exchange with forecasting tool and SLDC's main scheduling tool. The tool is configured for entering schedules for each time block (15 mins) on a day ahead basis. Individual RE generators must be able to provide revisions for 16 times in a day. The revised schedules are applicable from the fourth time block from which it is issued. Taking information from this tool, SLDC's main scheduling tool manages the schedule for conventional generation. Available capacity is submitted by individual

generator in every 15 min time block. This tool must have the capability to calculate the error in every time block. Therefore, real time generation through SCADA data is made available to the scheduling tool. This tool must be capable of producing alarms/ alerts for non-publishing of schedules by individual RE generators.

Due to congestion and other operational issues, there is a curtailment module that could issue instructions for reduction of power output from the RE power projects. Instructions could be given in terms of percentage reduction in generation or specifying the absolute power to be curtailed (in MW).

3. Conclusion

There has been a lot of developments in regulatory and institutional framework in the sector of wind and solar power forecasting. This is indeed very urgently required to satisfy govt. of India's huge renewable energy target. The REMCs once they are fully operational and functional, would go a long way to assuage the apprehensions of RE power projects owners. This would help in ensuring uninterrupted offtake of their generated power. REMCs could trigger more potential investments into this sector.

4. References

APERC, 2016. Forecasting, Scheduling, Deviation Settlement and Related Matters of Solar and Wind Generation Sources. <http://www.aperc.gov.in/aperc1/assets/uploads/files/d6260-public-notice.pdf> [accessed: 23.09.2016].

CEA, 2016. Installed capacity report July 2016 <http://cea.nic.in/reports/monthly/installedcapacity/2016/installed_capacity-07.pdf> [accessed: 12.09.2016].

CERC, 2010. Indian Electricity Grid Code. <http://www.cercind.gov.in/Regulations/Signed-IEGC.pdf > [accessed: 12.09.2016].

CERC, 2014. Indian Electricity Grid Code, second amendment. <http://www.cercind.gov.in/2014/regulation/noti18.pdf/> [accessed: 22.09.2016].

CERC, 2015a. Proposed Framework for Forecasting, Scheduling & Imbalance Handling for Renewable Energy (RE) Generating Stations based on wind and solar at Inter-State Level. <http://www.cercind.gov.in/2015/draft_reg/frame.pdf> [accessed: 12.09.2016].

CERC, 2015b.IEGC, third amendment. < http://www.cercind.gov.in/2015/regulation/Noti78.pdf > [accessed: 12.09.2016].

CERC, 2015c. Deviation settlement mechanism and related matters, second amendment. <http://www.cercind.gov.in/2015/regulation/Noti7.pdf> [accessed: 12.09.2016].

Economic times, 2016. <http://economictimes.indiatimes.com/industry/energy/power/india-adds-3-6-gw-to-solar-capacity/articleshow/53823001.cms> [accessed: 12.09.2016].

FOR, 2015. Model Regulations on Forecasting, Scheduling and Deviation Settlement of Wind and Solar Generating Stations at the State level. <http://www.forumofregulators.gov.in/Data/study/MR.pdf> [accessed: 12.09.2016].

IWTMA, 2015. Indian Wind power august-september 2015 issue. < http://www.indianwindpower.com/pdf/iwtma_magazine_v1_issue5_aug-sep-2015.pdf> [accessed: 12.09.2016].

JSERC, 2016. Forecasting, Scheduling, Deviation Settlement and Related Matters of Solar and Wind Generation Sources. < http://jserc.org/pdf/draft_regulations/draft_forecasting.pdf> [accessed: 12.09.2016].

KERC, 2015. Forecasting, Scheduling, Deviation settlement and related matters for Wind and Solar Generation sources. < http://www.karnataka.gov.in/kerc/Regulations/Regulations/Discussion_Note-CT-01-15.pdf> [accessed: 12.09.2016].

KERC, 2016. Notified regulation-. Forecasting, Scheduling, Deviation settlement and related matters for Wind and Solar Generation sources.

<http://www.karnataka.gov.in/kerc/Regulations/Regulations/KERC_Forecasting_Scheduling_Regulation_2015.pdf> [accessed: 23.09.2016]

MNRE, 2015. <http://mnre.gov.in/file-manager/UserFiles/Tentative-State-wise-break-up-of-Renewable-Power-by-2022.pdf> [accessed: 12.09.2016].

NITI Aayog, 2015. Report of the expert group on 175 GW RE by 2022. <http://niti.gov.in/writereaddata/files/writereaddata/files/document_publication/report-175-GW-RE.pdf> [accessed: 12.09.2016].

PGCIL, 2012. Transmission Plan for Envisaged Renewable Capacity <http://www.powergridindia.com/_layouts/PowerGrid/WriteReadData/file/ourBusiness/SmartGrid/Vol_1.pdf> [accessed: 12.09.2016].

PGCIL, 2016. Technical Specifications for REMC. < http://apps.powergridindia.com/powergrid/applications/tenders/01-0001-011.aspx> [accessed: 12.09.2016].

RERC, 2016. Forecasting, Scheduling, Deviation Settlement and Related Matters of Solar and Wind Generation Sources Regulations. < http://rerc.rajasthan.gov.in/cnpl/PDFs/F&S%20Regulations.pdf> [accessed: 12.09.2016].

TNERC, 2016. Forecasting, Scheduling, Deviation Settlement and Related Matters of Wind and Solar Generation Sources Regulations. <http://tnerc.tn.nic.in/regulation/draft%20regulations/2016/Forecast-solar%2013-1-2016-Draft.pdf> [accessed: 12.09.2016].

The potential of massive PV installation in Serbia

Dejan Doljak[1] and Djordje Samardzija[2]

[1] Faculty of Geography, University of Belgrade, Belgrade; Serbia, e-mail:, dejan.doljak@gmail.com

[2] One Degree Serbia, Belgrade, Serbia, e-mail: djordje.samardzija@1c.org.rs

Abstract

Paris climate agreement, adopted in December 2015, recognizes the need to revise voluntary submitted Intended National Determined Contribution (INDC) in order to limit global warming to 2°C.

With the objective to propose the improvement of Serbian INDC we investigate the technical potential of massive installation of residential solar PV roof top systems and utility scale solar PV power plants. Our research shows that solar may substitute around 81% of all electricity produced from coal and hydro. Thus, solar should be considered as a significant source of energy in future Serbian energy mix.

Keywords: *Serbia, low carbon economy, long term transition, solar, photovoltaic, technical potential, financial aspects*

1. Introduction

More than 180 states submitted their INDCs so far. However, estimated aggregate greenhouse gas emission levels in 2025 and 2030 resulting from existing INDCs do not fall within least-cost 2˚C scenarios but rather lead to a projected level of 55 gigatonnes in 2030. In order to hold the increase in the global average temperature to below 2˚C above pre-industrial levels States shall reduce emissions to 40 gigatonnes (UNFCCC, 2015).

Although adopted at the time of the 21st session of the Conference of the Parties (COP-21) the latest Serbian energy strategy (Republic of Serbia, 2015) suggests the continuation of usage of fossil fuels with focus on dirty lignite coal. No matter that the availability of some types of renewable energy resources (like solar) is much greater than in the Central Europe, the strategy underestimates the share of renewables in the future energy mix. Serbia and Serbian citizens already pays for their ignorance of renewables technologies. With only 6.2 $ per kilogram of oil equivalent (The World Bank, 2016a) and the high dependence on fossil fuels Serbian economy is one of the most energy and emissions intensive in the world. The increase of annual public health costs due the toxic emissions from burning lignite is estimated to 4 billion EUR (HEAL, 2016).

This paper presents new approach in the estimation of potential of solar energy in Serbia. The scope of our research includes the estimation of technical potential of massive installation of residential solar photovoltaic (PV) roof top systems and utility scale solar PV power plants. Solar thermal is out of scope. It will be addressed in the continuation of the research.

2. Solar energy potential – existing estimations for Serbia

Official data about the potential of various energy sources has been published in the national energy strategy that was adopted by the Parliament and the Government (Republic of Serbia, 2015). According to the authors of the strategy, total technically usable potential of solar power in Serbia is estimated to 0.24 million tons of oil equivalent (2.79 TWh per year). This figure includes electric and thermal potentials – 0.53 TWh and 2.26 TWh, respectively. The most important assumption in this official document that influenced entire estimation of potential of renewables was the consideration that the existing electric grid cannot handle more energy from intermittent sources than that presented in the strategy.

doi:10.18086/eurosun.2016.11.04 Available at http://proceedings.ises.org

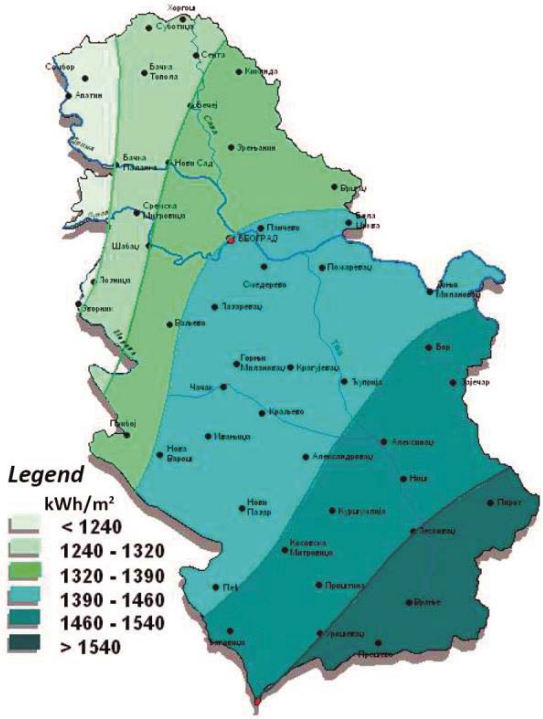

Fig. 1 Annual energy of global radiation on a horizontal surface (kWh/m^2). Source: (IMSI, 2004)

Fig. 1 shows that in Serbia, Sun energy has the tendency of increasing with decreasing latitude. The southern parts gain energy up to 1550 kWh/m^2 per year. However, solar energy is an intermittent source, which means that values vary on daily and seasonal levels. During the hot July days, square meter of horizontal surface receives an average of 5.9 to 6.6 kWh per day, but during January the radiation is reduced to only 1.1 to 1.7 kWh.

Radičević et al. (2009) claims that solar PV will represent only negligent share of energy mix in near future due to high costs of technology. Other academic and expert researchers like (IMSI, 2004) limited their exercises to the estimation of annual insolation without clear scenarios how to proceed with the installation of solar systems in Serbia.

The major obstacles of presented approaches can be summarized as:

- Existing electrical grid is considered as incapable to accept large amounts of variable power produced by renewable sources; and
- The renewables are presented and considered as very expensive.

Our opinion is that the establishment of estimations of renewables technical potential on these assumptions is entirely wrong since it is clear that the transition to renewable energy system cannot and will not happen overnight. Many publicly available researches, global policies and scenarios identify 2050 as a target year to develop sustainable and clean energy system worldwide in order to prevent catastrophic consequences of climate change. Until that time, countries should work on the improvement of electric grids and the implementation of smart grids, as well as, energy storages, in order to accommodate energy produced by intermittent sources and manage demand.

In the meantime, further researches and the economy of scale will lead to the reduction of technology costs well below current levels making renewables more efficient, more environment friendly and cheaper than today. In addition to the fact that the reduction of prices of solar PV panels is already underway it is worth to compare true costs of production of conventional energy with those produced by solar. The high air pollution and carbon costs of burning fossil fuels make conventional energy much more expensive than solar or wind.

Fortunately, other more optimistic renewables potential estimations have appeared recently. A professor from the Stanford University Mark Z. Jacobson and his team work on 100% Clean and Renewable Wind,

Water, and Sunlight (WWS) All Sector Energy Roadmaps for 139 Countries of the World. They estimate total potential capacity for solar energy in Serbia to 15.441 GW (Jacobson et al., 2016). Only 45% of this potential capacity will be enough to support country's transition to cleaner energy system entirely run on wind, water, and sunlight (WWS).

The group of independent think-tanks from South Eastern Europe has developed the SEE 2050 Carbon Calculator – regional renewable energy model and tool for the creation of individual energy transition scenarios. According to this group, the solar PV technology may provide around 24.45 TWh annually in Serbia (SEE Change Net, 2016), almost 10 times more than official estimations.

3. Massive installation of solar PV systems and power plants in Serbia

"Solar energy is the most abundant of all energy resources. Indeed, the rate at which solar energy is intercepted by the Earth is about 10,000 times greater than the rate at which humankind consumes energy. Solar technologies can deliver heat, cooling, natural lighting, electricity, and fuels. Solar technologies offer opportunities for positive social impacts, and their environmental burden is small." (Arvizu et al, 2011)

Having in mind small environmental footprint of solar, plummeting costs of solar PV technology and great natural solar resources that Serbia has (average annual insolation is around 40% higher than in Germany) our research team has developed the alternative scenario of development of Serbian energy system. The alternative scenario includes massive installation of solar PV roof-top systems and utility scale solar PV power plants.

Massive installation of solar PV roof-top systems

Solar PV technology allows residents, and public and private entities to join transition to low-carbon economy. By applying solar PV panels each of these categories can contribute to the mitigation of climate change on individual level. In addition to being energy consumers, owners of PV systems become energy producers making new class of actors in energy markets – "prosumers". Massive installation of solar power plants owned by citizens and legal entities will enable the decentralization and democratization of energy production. Such diversification of energy sources will improve energy security on individual and national level, reduce the power of monopoly of traditional state-owned fossil fuel companies, as well as, to reduce dependence on fossil fuel imports.

The researched scenario includes the installation of 6 kWp solar systems on the residential house and building roofs in Serbia. The roof area under solar panels is estimated to 40 m^2. It is assumed that commercial, utility and administration buildings with larger roofs could house larger systems – up to 15 kWp (around 100 m^2 of panels). Solar thermal collectors were out of scope of this part of the research and will be addressed in later stages.

The estimation was performed using the on-line *PVWatts* calculator (NREL, 2016). In order to validate *PVWatts* results, its estimations were compared to the output of another on-line calculator – *PV*SOL Online Calculation* (Valentin Software, 2016). No significant deviation in final results between these two on-line tools has been identified.

Having in mind that the roof orientation and tilt are uncertain categories, the estimated potential of a PV system is an average result calculated by variation of the following performance parameters:

- PV panel type (Standard, Premium);
- tilt (30° and 45°); and
- azimuth (East, South and West).

The assumed location of a solar PV system in this exercise is Belgrade, capital of the Republic of Serbia.

The exercise showed that azimuth has the greatest impact on the amount of generated electricity. The best results are obtained if solar panels are oriented to South (azimuth 180°).

Average annual amount of electricity generated by small-scale solar PV system with the capacity of 6 kWp mounted on the roof of the object in Belgrade is estimated to 6,269 kWh. The amount of generated electricity

varies during the year picking in July (Fig. 2) – 823.45 kWh, i.e. 2.5 times greater than average monthly electricity consumption of household in Serbia.

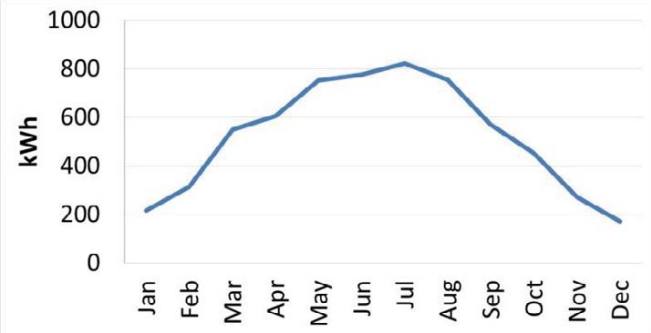

Fig. 2 Variation of production of 6kWp solar PV system located in Belgrade

The amount of electricity generated by 15 kWp solar PV system mounted on public and commercial buildings is obtained by the extrapolation of modeled small-scale solar PV system electricity production and amounts 15,671 kWh.

The total number of family houses in Serbia that can be used as locations for 6 kWp solar PV systems is estimated to 2,186,000 (Jovanović-Popović et al, 2013). The number of buildings that can house larger systems (15 kWp) is estimated to 42,389 (Statistical Office of the Republic of Serbia, 2016).

Tab. 1 Massive installation of small scale PV systems in Serbia: Estimated capacity and annual generation

Type of object	Number of objects	Capacity of installed system (kW)	Annual production of single system (kWh)	Total installed capacity (GW)	Annual generation of electricity (TWh)
Family houses	2,186,000	6	6,269	13.116	13.704
Residential buildings	9,556	15	15,671	0.143	0.150
Other buildings (commercial, admin.)	32,833	15	15,671	0.492	0.515
			Total	**13.751**	**14.369**

The amount of electricity generated by these 2.2 million solar systems mounted on rooftops is estimated to 14.369 TWh per annum (Tab. 1). The installation of these 13.751 GW of solar PV panels could cost somewhere between 30.252 and 71.505 billion USD. The costs are calculated according to the lowest and highest price of the installation of residential solar PV systems in the world published in (IRENA, 2015).

Massive installation of utility-scale PV power plants

In addition to the roof-top PV solar systems the research included the estimation of the installation of utility-scale PV power plants.

There are currently only a few major photovoltaic plants installed on the ground In Serbia. The most famous are “Solaris 1” (1 MW) and “Solaris 2” (675 kW) near Kladovo (Eastern Serbia), “Matarov” (2 MW) in Merdare (Southern Serbia) and solar power plant of capacity of 1 MW in Tancoš near Beočin (Vojvodina). According to the data provided by Serbian Ministry of Mining and Energy (MME), 17 solar PV power plants have status of privileged or temporarily privileged producers of electricity with total installed capacity of 6 MW (MME Serbia, 2016). These producers have right to receive feed-in tariffs.

Although, solar energy is considered as a clean, free and practically limitless energy source, systems for the exploitation of solar energy, such as photovoltaic plants, have certain restrictions, which depend on the type and size of projects. These restrictions primarily relate to the occupation of land which is limited and precious natural resource in today’s conditions.

In order to develop resource efficient scenario the research includes only the usage of degraded land as a location of potential big PV power plants. Degraded land is an area where the natural conditions are altered by human activity, and envisaged for rehabilitation after the exploitation. In accordance with the aim of the gradual replacement of conventional energy sources with renewable energy sources, the sites of the surface exploitation of the energy minerals (coal, lignite, bituminous rocks, oil and gas) are selected as potential

locations of solar power plant. These sites are defined and presented as a shape files. The assumption to use sites of the surface exploitation of the energy minerals as potential solar power plant locations is in line with the obligation of the Electric Power Industry of Serbia (EPS) to initiate the closure of coal power plants that do not meet requirements of the European Large Combustion Plants Directive after 2023.

In addition, the study includes areas for the exploitation of metallic and industrial raw materials, dumps of tailings and ashes, landfills, sites of conventional coal power plants, thermal power plants, brick plants etc.

For the purposes of this research, 2447 locations were identified and assessed. The total area covers 238.75 km^2 or 0.27% of the territory of Serbia.

The data on the overall installed capacity and annual production of energy have been obtained by the online software *Energy Capacity Assessment Tool* (First Solar, 2015) that uses GIS shape files as a source data about the form and size of power plant.

The total installed capacity of photovoltaic power plants on degraded land amounted to 15,531.93 MWdc for photovoltaic power plants that are built from cadmium-telluride solar cells, or to 16,178.12 MWdc power plant based on multi-crystalline solar cells. The results show, that the installation of photovoltaic power plants at all 2447 degraded locations under consideration would lead to the generation of 18.02 TWh electricity per year. This is around 33 times higher than the technically usable potential published in national energy strategy.

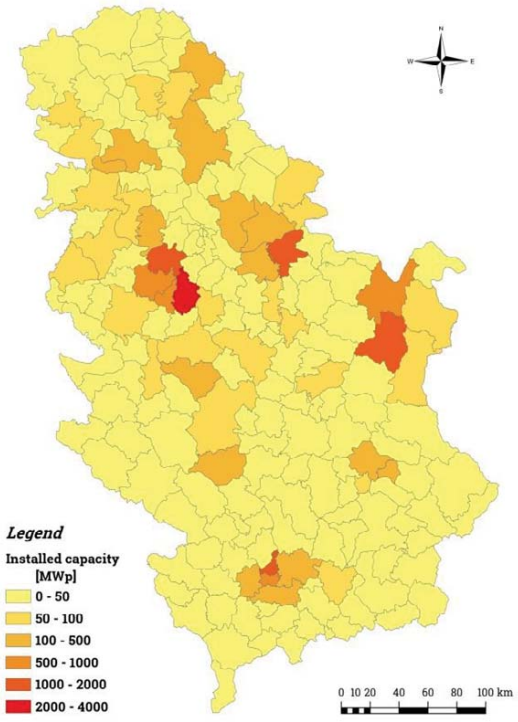

Fig. 3 Estimated total installed PV capacity per municipalities in Serbia

Fig. 3 presents the estimated capacity of installed solar PV power plants per municipality. The largest percentage of the production of solar energy (38%) would be accomplished by installing photovoltaic panels on existing mines of energy producing materials like open coal pits located in the following municipalities Obrenovac, Lazarevac and Kostolac (the darkest color on the map).

The Republic of Serbia has submitted the National Emission Reduction Plan (NERP) to the Secretariat of the Energy Community (Energy Community, 2016). Although the document is not publicly available there are indications that Serbia selected opt-out option for several operational coal power plants. This is expected to lead to the significant reduction of electricity generation capacity, by some 10% in year 2023, according to our assumptions. We recommend that Serbia prepare its energy system for this shock and make use of available renewables technology to cover the gap that will emerge after the closure of outdated coal power

plants.

The state-owned energy company EPS produced 37.433 TWh of electricity in 2013 (EPS, 2014). The implementation of utility-scale photovoltaic plants in the territory of the Republic of Serbia as presented in this article can substitute around 48% of the current production of the EPS.

Construction costs of photovoltaic systems at these locations are projected to 25 to 70 billion USD according to the lowest and highest installation costs in the world published in (IRENA, 2015).

Since the Spatial Plan of the Republic of Serbia 2010-2020 (RASP, 2010) envisions the establishment of a system of regional waste management centers, the surface of existing landfills, could be significant resource for the construction of a photovoltaic power plants, too.

4. Summary

Our research provides new outlook of solar prospective in Serbia. Unlike national energy strategy our scenario involves massive installation of solar PV systems and power plants that results in significantly greater estimations than official figures.

Tab. 2: Estimated potential for roof-top solar PV systems and utility-scale PV solar power plants in Serbia

Type of object	Number of objects/ locations	Capacity of installed system (kW)	Total installed capacity (GW)	Annual generation of electricity (TWh)
Family houses	2,186,000	6	13.116	13.704
Residential buildings	9,556	15	0.143	0.150
Other buildings (commercial, administrative)	32,833	15	0.492	0.515
Utility scale solar PV power plants	2,447	from 280 to 3,563,220	16.178	18.02
		Total	**29.929**	**32.389**

The summarized data are presented in Tab. 2 Estimated solar generated 32.389 TWh per annum can substitute around 81% of current total electric energy production in Serbia, i.e. the whole electricity produced by lignite power plants. Such huge estimated potential should make solar PV a critical element of the future country energy mix.

Initial capital installations costs have been estimated on the basis of average costs in countries across the world identified by (IRENA, 2015). The initial costs are presented in Tab. 3.

Tab. 3: Estimated total investment for the transition to solar PV-based electrical system in Serbia

Type of object	Total installed capacity (GW)	Installation costs (2014 USD/kW) (IRENA, 2015)	Initial capital installations costs (billion USD)	Estimated costs per year 2020-2050 (billion USD)
Family, residential, commercial small-scale solar PV systems (6 or 15 kW)	13.751	2,200 - 5,200	30.252-71.505	1.008-2.384
Utility scale solar PV power plants	16.178	1,570 – 4,340	25.399-70.212	0.847-2.340
Total	**29.929**		**55.651-141.717**	**1.855-4.724**

Total investment in the development of solar PV-based electrical system in Serbia by 2050 is estimated to 55 to 142 billion USD. This investment corresponds to 1.5 to 3.9 yearly gross domestic products (GDP) of Serbia (based on GDP value of 36.513 billion USD in 2015 (The World Bank, 2016b)).

Certainly these, at first glance, large figures may discourage decision makers to consider planned and persistent installation of renewable systems necessary for transition to low-carbon economy and the mitigation of climate change. Yet this total investment should not be considered as “pay at once costs” but

rather as a long-term investment up to 2050. In this case the highest amount of investment is leveled to 4.724 billion USD per annum or 13% of current GDP. In order to get clearer picture about this investment it could be compared to the economic cost of deaths from outdoor and indoor air pollution that are estimated to 33.5% of Serbian GDP (WHO, 2015).

The absence of environmental costs of solar PV energy production should be major driver to initiate and the transition to clean energy. (HEAL, 2016) claims that outdated Serbian coal power plants are responsible for 4 billion EUR (around 4.44 billion USD) of increased public health costs associated with air pollution.

The research presented in this article busts three renewable energy related myths in Serbia:

- It proves that natural resources for the transition to the low-carbon economy exist in Serbia;
- It proves that such transition can be undertaken using existing technology for the energy production; and
- Financial resources for such transition already exist in Serbian society, too. However, they are used to cover consequences of electricity generation by old technology.

The need for the transition to renewable energy sources has never been questioned from ecological and social perspectives. Our research shows that there are economic reasons for such a transition. Cost effectiveness in economic terms is added to the existing ethical reasons for the transition to renewable energy.

It is clear that the transition cannot be executed all in once and that coal will stay around for a while. The aim of this research is to stimulate national discussion and to show that alternative, clean future is possible. Our recommendation to national decision makers is to investigate possibilities of renewable energy and gradually divert capital flow from fossil fuels to renewables, particularly solar. Such strategy will ensure clean, cheap, abundant and decentralized energy available to all, while it pays for itself by reducing public health costs.

We recommend the following policy measures that can support the transition to low carbon economy:

- Incorporation of true costs of burning fossil fuels into price of energy by the implementation of carbon fee and dividend; and
- Improvement of country's capacity to effectively and efficiently perform the transition by including climate change and renewables topics/trainings in school and university education.

The presented research is the first step in the broader investigation of potential of solar energy in Serbia. Future research will include the estimation of potential of solar thermal in residential and commercial use. The presented investment includes the installation costs only. Our intention is to address operation and maintenance costs of running the electric generation system comprised of more than 2.2 million production units, as well as, to estimate the electricity costs to end-users. Envisioned transition from centralised electricity production to decentralised production based on solar technology offers new jobs. We will end research activities on this topic with the analysis of impact of transition on job market and estimate the number of lost and produced jobs.

Acknowledgments

This research was a part of project titled *Alternative INDC – Zero Carbon Serbia by 2050* executed by non-governmental organization and independent think tank One Degree Serbia (www.jedanstepen.org).

Reference list

Arvizu, D., P. Balaya, L. Cabeza, T. Hollands, A. Jäger-Waldau, M. Kondo, C. Konseibo, V. Meleshko, W. Stein, Y. Tamaura, H. Xu, R. Zilles, 2011: Direct Solar Energy. In IPCC Special Report on Renewable Energy Sources and Climate Change Mitigation (O. Edenhofer, R. Pichs-Madruga, Y. Sokona, K. Seyboth, P. Matschoss, S. Kadner, T. Zwickel, P. Eickemeier, G. Hansen, S. Schlömer, C. von Stechow (eds)), Cambridge University Press, Cambridge, United Kingdom and New York, NY, USA.

Energy Community (2016). Serbia Environment (ONLINE) Available at https://www.energy-community.org/portal/page/portal/ENC_HOME/AREAS_OF_WORK/Implementation/Serbia/Environment (Accessed: 27 Aug 2016)

EPS (2014). Annual Report 2013. The Electric Power Industry of Serbia (ONLINE) Available at: http://www.eps.rs/GodisnjiIzvestaji/Godisnji%20Izvestaj_EPS_2013_sr_CD.pdf (Accessed: 27 Aug 2016)

First Solar (2015). Energy Capacity Assessment Tool (ONLINE) Available at http://www.firstsolar.com/Home/Solutions/Utility-Scale-Generation/eCAT (Accessed: 12 July 2016)

HEAL (2016). The unpaid health bill - How coal power plants in the Western Balkans make us sick

IMSI (2004). Portal Wind and Sun Energy in Serbia - Institute for Multidisciplinary Research. Студија енергетског потенцијала Србије за коришћење енергије сунчевог зрачења и ветра (ONLINE) Available at: http://vetar-sunce.imsi.rs/tekstovi/Studija_EE704-1052A/index.php (Accessed: 12 July 2016)

IRENA (2015). Renewable power generation costs in 2014

MME Serbia (2016). Registar povlašćenih proizvođača električne energije 21.12.2015. (ONLINE) Available at: http://www.mre.gov.rs/doc/registar21.12.html. (Accessed: 29 July 2016).

NREL (2016). PVWatts Calculator. (ONLINE) Available at: http://pvwatts.nrel.gov/. (Accessed 07 April 2016).

Jacobson, M. Z. ,Delucchi, M. A., Bauer, Z. A. F., Goodman, S. C., Chapman,W. E., Cameron, M. A., et al., (2016). 100% Clean and Renewable Wind, Water, and Sunlight (WWS) All- Sector Energy Roadmaps for 139 Countries of the World. Available at: https://web.stanford.edu/group/efmh/jacobson/Articles/I/CountriesWWS.pdf (Accessed: 26 September 2016)

Jovanović-Popović M., Ignjatović D., Radivojević A., Rajčić A., Đukanović Lj., Đuković-Ignjatović N., Nedić M. (2013). Nacionalna tipologija stambenih zgrada Srbije, Arhitektonski fakultet, Univerzitet u Beogradu i GIZ

Radičević B., Mikičić D., Vukić Dj. (2009). Energetski potencijal Sunca u Srbiji i primena energije Sunca u poljoprivredi, Poljoprivredna tehnika. 4. 53-62

RASP (2010). Spatial Plan of the Republic of Serbia 2010-2020 http://www.rapp.gov.rs/en-GB/content/cid310/spatial-plan-for-the-republic-of-serbia (Accessed: 27 Aug 2016)

Republika Srbija, (2015). Strategija razvoja energetike Republike Srbije do 2025. godine sa projekcijama do 2030. godine. Službeni glasnik RS, 101/2015

SEE Change Net (2016). South East Europe 2050 Calculator | SEE Change Net. (ONLINE) Available at: https://www.see2050carboncalculator.net/2050/see/Energy.php (Accessed: 12 July 2016)

Statistical Office of the Republic of Serbia (2016). Construction | Completed buildings. (ONLINE) Available at: http://webrzs.stat.gov.rs/WebSite/Public/PageView.aspx?pKey=121 (Accessed 2 Aug 2016).

The World Bank (2016a). World Development Indicators | The World Bank. (ONLINE) Available at: http://wdi.worldbank.org/table/3.8#. (Accessed 7 April 2016).

The World Bank (2016b). GDP (current US$) | Data. (ONLINE) Available at: http://data.worldbank.org/indicator/NY.GDP.MKTP.CD?view=chart. (Accessed 27 July 2016).

United Nations Framework Convention on Climate Change (2015). Adoption of the Paris Agreement, 21st Conference of the Parties, Paris: United Nations

Valentin Software (2016). Online solar PV calculator | Valentin Software. (ONLINE) Available at: http://www.valentin-software.com/en/products/photovoltaics/0/pvsol-online-calculation. (Accessed: 12 July 2016)

WHO (2015). Economic cost of deaths from air pollution (outdoor and indoor) per country, as a percentage of GDP

A

B

C

D

E

F

G

H

I

J

K

L

M

N

O

P

R

S

T

U

V

W

Y

Z